ARO 38732.1-MS-CF

PRICM 3

The Third Pacific Rim International Conference on Advanced Materials and Processing

Volume I

Honolulu, Hawaii, USA
July 12-16, 1998

Edited by
M.A. Imam, R. DeNale,
S. Hanada, Z. Zhong
and D.N. Lee

Hosted by TMS

19990201 044

REPORT DOCUMENTATION PAGE

Form Approved
OMB NO. 0704-0188

Public reporting burden for this collection of information is estimated to average 1 hour per response, including the time for reviewing instructions, searching existing data sources, gathering and maintaining the data needed, and completing and reviewing the collection of information. Send comment regarding this burden estimates or any other aspect of this collection of information, including suggestions for reducing this burden, to Washington Headquarters Services, Directorate for information Operations and Reports, 1215 Jefferson Davis Highway, Suite 1204, Arlington, VA 22202-4302, and to the Office of Management and Budget, Paperwork Reduction Project (0704-0188), Washington, DC 20503.

1. AGENCY USE ONLY *(Leave blank)*	2. REPORT DATE	3. REPORT TYPE AND DATES COVERED
		Final Report

4. TITLE AND SUBTITLE

The Third Pacific Rim International Conference on Advanced Materials and Processing Volume I and II.

5. FUNDING NUMBERS

DAAG55-98-1-0327

6. AUTHOR(S)

Alexander Scott, principal investigator

7. PERFORMING ORGANIZATION NAMES(S) AND ADDRESS(ES)

TMS - Minerals-Metals-Materials Society
420 Commonwealth Dr.
Warrrendale, PA 15086

8. PERFORMING ORGANIZATION REPORT NUMBER

9. SPONSORING / MONITORING AGENCY NAME(S) AND ADDRESS(ES)

U.S. Army Research Office
P.O. Box 12211
Research Triangle Park, NC 27709-2211

10. SPONSORING / MONITORING AGENCY REPORT NUMBER

ARO 38732.1-MS-CF

11. SUPPLEMENTARY NOTES

The views, opinions and/or findings contained in this report are those of the author(s) and should not be construed as an official Department of the Army position, policy or decision, unless so designated by other documentation.

12a. DISTRIBUTION / AVAILABILITY STATEMENT

Approved for public release; distribution unlimited.

12 b. DISTRIBUTION CODE

13. ABSTRACT *(Maximum 200 words)*

14. SUBJECT TERMS

15. NUMBER IF PAGES
4, 767

16. PRICE CODE

17. SECURITY CLASSIFICATION OR REPORT	18. SECURITY CLASSIFICATION OF THIS PAGE	19. SECURITY CLASSIFICATION OF ABSTRACT	20. LIMITATION OF ABSTRACT

The Third Pacific Rim International Conference on

Advanced Materials and Processing (PRICM 3)

Volume I

Reproduced From
Best Available Copy

DTIC QUALITY INSPECTED 4

The Third Pacific Rim International Conference on

Advanced Materials and Processing (PRICM 3)

Volume I

Honolulu, Hawaii, USA
July 12-16, 1998

Edited by

M.A. Imam, R. DeNale, S. Hanada,
Z. Zhong and D.N. Lee

Hosted by TMS

A Publication of
TMS
Minerals • Metals • Materials

A Publication of The Minerals, Metals & Materials Society
420 Commonwealth Drive
Warrendale, Pennsylvania 15086
(412) 776-9000

The Minerals, Metals & Materials Society is not responsible for statements or opinions and is absolved of liability due to misuse of information contained in this publication.

Printed in the United States of America
Library of Congress Catalog Card Number 98-66196
ISBN Number 0-87339-408-9

Authorization to photocopy items for internal or personal use, or the internal or personal use of specific clients, is granted by The Minerals, Metals & Materials Society for users registered with the Copyright Clearance Center (CCC) Transactional Reporting Service, provided that the base fee of $3.00 per copy is paid directly to Copyright Clearance Center, 27 Congress Street, Salem, Massachusetts 01970. For those organizations that have been granted a photocopy license by Copyright Clearance Center, a separate system of payment has been arranged.

TMS
Minerals • Metals • Materials

© 1998

If you are interested in purchasing a copy of this book, or if you would like to receive the latest TMS publications catalog, please telephone 1-800-759-4867 (U.S. only) or 412-776-9000, Ext. 270.

PREFACE

Technologies emerging from the development of novel materials and innovative processing methods have grown in recent years at an unprecedented rate. The pacific-rim countries have played a significant role in this growth, embracing the evolution of many new systems and devices to meet societal needs.

In order to improve communication and exchange of ideas, a continuation of a forum for technical discussion on the development of advanced materials and processing among scientists and engineers from the pacific-rim countries as well as all around the world continues to be of utmost importance. This conference, PRICM 3, held in Honolulu, Hawaii, 12-16 July 1998 and hosted by The Minerals, Metals and Materials Society, is an attempt to build upon the solid foundation of the previous conferences by offering an opportunity for the exchange of ideas on the current status of experimental and theoretical developments in processing and characterization.

The Pacific Rim International Conference on Advanced Materials and Processing conference is held approximately every three year with each country rotating administrative responsibilities. The first conference (PRICM 1) was held in Hangzhou, China, in June 1992 and was unique in bringing together material scientists and engineers from the Chinese Society for Metals (CSM), Japan Institute of Metals (JIM), and The Korean Institute of Metals and Materials (KIM) and The Minerals, Metals and Materials Society (TMS) of the United States of America, for discussions in advanced material processing. The second conference was held in Kyonju, South Korea, in June 1995, and provided a forum for exchange of ideas on the current status of experimental and theoretical developments in processing and characterization of advanced materials.

We firmly believe and history will well record that this era is unprecedented in the explosive growth of advanced materials and processing research. Over 500 invited and contributed papers from more than thirty countries, which will be presented at PRICM 3 are indicative of the cutting edge research performed in syntheses, processing, characterization and performance in systems of electric, magnetic and optical materials as well as structural and other functional materials. We believe that the growth in this instant in time is successfully captured within these proceedings.

It is with great pleasure that we present these volumes of proceedings of current research, development and engineering in the multi-disciplinary field of materials and processing. We hope that the proceedings' timely distribution enhances discussions and potential collaborations between participants. The proceedings required significant sacrifice from many, but would not have been possible without the efforts of Mark O'Connor, Robert Makowski, Peggy Weiss, and Rich Nagy of TMS.

We would like to thank the sponsors for their generous financial support towards the success of the conference.

July 1998

M.A. Imam, Robert DeNale, S. Hanada,
Z. Zhong, and D.N. Lee

Symposium Sponsoring Societies

Chinese Society for Metals (CSM)
Japan Institute of Metals (JIM)
The Korean Institute of Metals and Materials (KIM)
The Minerals, Metals & Materials Society (TMS)

International Organizing Committee

Om P. Arora, USA
Shigeo Asai, Nagoya University, Japan
Robert DeNale, Naval Surface Warfare Center, USA
Darrel R. Frear, Sematech, USA
F.H. (Sam) Froes, University of Idaho, USA
Shuji Hanada, Tohoku University, Japan
Honglin Ge, Shanghai Huchang Steel Co., China
M. Ashraf Imam, Naval Research Laboratory, USA
Masahiro Koiwa, Kyoto University, Japan
Dong Nyung Lee, Seoul National University, Korea
Jai Young Lee, Korea Adv. Inst. of Sci. & Tech., Korea
Soo Woo Nam, Korea Adv. Inst. of Sci. & Tech., Korea
Xishan Xie, University of Science & Technology, China
Zengyong Zhong, The Chinese Society for Metals, China

International Advisory Board Members

Tara Chandra, Univ. of Wollongong, Australia
Hyung Sup Choi, Korean Fed. of Sci. & Tech., Korea
Luc Delaey, Katholieke Universeit Leuven, Belgium
Masao Doyama, Nishi-Tokyo University, Japan
E. Evangelista, Univ. of Ancona, Italy
Toru Imura, Aichi Inst. of Tech., Japan
O.M. Ivasishin, Inst. of Metal Physics, Ukraine
O. Izumi, Prof. Emeritus,Tohoku Univ., Japan
Il Koo Kang, Former President KIM, Korea
W.A. Kaysser, Aerospace Res. Est., Germany
T. Khan, ONERA, France
Sang-Joo Kim, Seoul National Univ., Korea
George Krauss, Colorado School of Mines, USA
A.G. Leatham, Osprey Metals Ltd., U.K.
Yiyi Li, Inst. of Metals Res. Academia Sinica, China
L. Martinez, Mexican Academy of Matls. Sci., Mexico
A. Mitchell, Univ. of British Columbia, Canada
K. Mukherjee, Michigan State Univ., USA
C.K. Ong, National Univ. of Singapore, Singapore
L. Ovecoglu, Istanbul Technical Univ., Turkey
S. Ranganathan, Indian Inst. of Science, India
B.B. Rath, Naval Research Laboratory, USA

International Advisory Board Members (Continued)

Changxu Shi, Chinese Academy of Engrg., China
D. Spinelli, Univ. of Sao Paulo, Brazil
P. Srichandr, King Mongkut's Inst. of Tech., Thailand
P. Vitiaz, Inst. of Powder Met., Republic of Belarus
J.C. Williams, General Electric, USA
Jing Zhu, Tsing Hua University, China

In-Country Technical Representatives

China

Professor Dr. Zengyong Zhong , Secretary General Chinese Society for Metals,
46 Dongsixi Dajie, Beijing, 100711, China
• Telephone: 861065133925 • Fax: 861065124122 • Email:csm@public.bta.net.cn

Korea

Professor Dr. Dong Nyung Lee, Seoul National University School of Matls. Sci. & Engrg.,
Res. Ctr. for Thin Film Fabrication & Crystal Growing of Advanced Matls.,
Seoul 151-742, Korea
• Telephone: 822880-7093 • Fax: 822885-9671

Japan

Professor Shuji Hanada, Tohoku University, Inst. for Matl. Res. Katahira 2-1-1, Aoba-ku,
Sendai 980-77, Japan
• Telephone: 81222152115 • Fax: 81222152116

USA & All Other Countries

Dr. M. Ashraf Imam, Naval Research Laboratory, Code 6320, Washington, DC 20375-5343, USA
• Telephone: 202-767-2185 • Fax: 202-767-2623 • Email: imam@anvil.nrl.navy.mil

Conference Secretariat and Technical Contact Points

Dr. M. Ashraf Imam, Naval Research Laboratory, Code 6320, Washington, DC 20375-5343, USA
• Telephone: 202-767-2185 • Fax: 202-767-2623 • Email: imam@anvil.nrl.navy.mil

Mr. Robert DeNale, NSWC, Carderock Division, Code 615, West Bethesda, MD 20817-5700, USA
• Telephone: 301-227-4995 • Fax: 301-227-5576 • Email: denale@oasys.dt.navy.mil

Organizations Providing Financial Support*

Naval Surface Warfare Center
U.S. Army Research Office
U.S. Department of Energy

* Known financial supporters at the time of printing.

TABLE OF CONTENTS

Preface v

Symposium Sponsoring Societies vii
International Organizing Committee vii
International Advisory Board Members vii
In-Country Technical Representatives viii
Conference Secretariat and Technical Contact Points viii

VOLUME I

Plenary Lectures

The Quiet Revolution in Material Processing 3
T.W. Eagar

The Progress of Processing Technology of Advanced Materials in China 13
S. Likai

Diffusion in Materials—History and Recent Development 23
M. Koiwa

Recent Trends in Spray Forming Process and Its Applications 29
H.Y. Ra, H.-K. Seok, K.H. Oh, J.-C. Lee and H.-I. Lee

Advanced Ferrous Alloys and Processing

Influence of Heat Treatment on the Microstructure of a C-Cr-Mo Stainless Steel 41
M. Mujahid, M.I. Qureshi and M. Ali

Metadynamic Recrystallization of AISI 304 Stainless Steel 49
S.-H. Cho, Y.-S. Kim and Y.-C. Yoo

High Temperature Mechanical Properties of Continuously Cast Austenitic Stainless Steels 59
S.K. Kim, J.J. Kim, J.W. Kim, Y.D. Lee and T. Umeda

Deformation Induced Martensitic Transformation in 304 Stainless Steel 65
H.C. Shin and Y.W. Chang

Microstructural Analysis of Vanadium Bearing High Manganese Precipitation Hardening Stainless Steel 71
Y. Haruna, A. Yamamoto and H. Tsubakino

Ti-B2 - Particle - Reinforced High Modulus Steel 77
K. Tanaka, T. Oshima, F. Nonoyama and T. Saito

Structure and Mechanical Properties of Ultra Low Carbon/Ti Added Steels 83
R. Mendoza, G. Lugo and J.A. Juarez-Islas

Interaction Between Melts and Refractory in Process of Smelting Reduction with Iron Bath 89
Q. Liu and J. Lin

The Effect of the Titanium Traces on the Mechanical Properties of an Ultra High Strength Steel 95
R.C. Tokimatsu, P.I. Ferreira and I. Ferreira

Microalloying of Steel 16Mn With Niobium 101
R. Wang, H. Zhang, G. Pang and B. Cui

Microstructure and Mechanical Properties of SUS 316L Stainless Steel Manufactured by High Strain PM Process 107
K. Ameyama, S. Senoo, J. Sudo, O. Okada and K. Nakata

The Effects of Microstructure and Prestrain on Fatigue Strength of Dual-Phase Steels 113
K. Nakajima, T. Taki and T. Miyata

Structure Control of Metastable Austenitic Stainless Steels through Deformation Induced Transformation and Aging Treatment 119
K. Tomimura, K. Miyakusu and S. Hirotsu

Local Mechanical Properties of Steel Weldments 125
D.A. LaVan, G. Shoukas and W.N. Sharpe, Jr.

On the Mechanism of Decreasing the Slab Reheating Temperature of Hi-B Steels by the Addition of Molybdenum 131
Y. Zhao and F. Gui

A New Material for the Contact Cable Part I: Feasibility Study 137
H. Wen, L. Peng, X. Mao, Z. Pan, F. Qi and K. Xu

Effect of Process Conditions on Texture and Properties of IF Steel Sheet 143
B. Kong and X. Mi

A New Development of Improving Grain Oriented Silicon Steel with the LLSA Method 149
F. Sun, X. Peng and C. Li

ND Steel—High Resistance to Sulfur Dewpoint Corrosion 155
W. Zheng and R. Wang

High Strength Nickel-Free Duplex Stainless Steels for Structural Engineering Applications 161
J. Wang, M.O. Speidel and P.J. Uggowitzer

Improving Property of 0.5% Carbon Microalloyed Steel for Hot Forging Using Intragranular Ferrite 167
J. Yin

Hydrogen Induced Cracking of HSLA Steels in Sea Water Under Potentiostatic Conditions 173
K. Banerjee and U.K. Chatterjee

Investigation on the Precipitation of Carbonitrides and Copper in a High Strength Low Alloy Steel 179
A.N. Bhagat, S.K. Pabi, O.N. Mohanty and S. Ranganathan

Prediction of Carbo-Nitride Precipitation in High Strength Low Alloy Steels (HSLA) by the Technique of Successive of Partial Equilibria 187
S. Ranganathan

Design of a New High Strength Low Alloy Steel by the Key Point Method 193
Z. Zhao, D.O. Northwood, C. Liu, Y. Liu and D. Wang

Mechanical Property and Microstructure of Structural and Fire Resistant Steels 199
W. Sha and F.S. Kelly

The Evolution of the Goss Texture in Silicon Steel 205
D.N. Lee and H.-T. Jeong

An Abnormal Effect of Phosphorous on Mechanical Properties in Nickel-Base Superalloys of Ni-Cr-Fe, Ni-Cr-Fe-Mo and Ni-Cr-Fe-Mo-Nb-Al Systems 215
X. Xie, X. Liu, J. Dong, Y. Hu, Z. Xu, M. Chen, C. Wang and R.G. Thompson

Relationship Between Texture and Magnetic Properties of Non-Oriented Si Steel ... 223
N. Chen, W. Mao and Y. Yu

Solubility Product of VN in Austenite 229
T. Gendo, K. Morita, K. Inoue, I. Onuma, H. Ohtani and K. Ishida

Cyclic Properties of a Titanium and Niobium Microalloyed Steel in Some Microstructural Conditions 235
E.J. Giordani, J.A. Martins and I. Ferreira

Austempering of Alloyed Ductile Iron 241
S. Yazdani and R. Elliott

Tensile Properties of Mo and Mo-Nb Microalloyed Fire Resistant Steels 247
W. Sha, P.J. Blair and F.S. Kelly

Preparation of Fe-C System Alloy by Mechanical Alloying 253
N.T. Rochman, K. Kawamoto, H. Sueyoshi, Y. Nakamura and T. Nishida

Improvement on Surface Cast Iron by Using Alloy Powders on the Mold 259
S. Tanabe, Y. Horikawa, K. Yoshikawa and K. Higashi

Effect of Mechanical of Grinding of Powders on the Oxidation Resistance of Stainless-Steel Compacts at High Temperatures 265
S. Tanabe, W. Takahara, H. Nishida and K. Higashi

Anti-Oxidation Coating for the Alloy Steel At High Temperature 271
X. Xu, D. Lin and X. Liao

Evaluation of the Fracture Toughness and Low and High Cycle Fatigue Properties of a Cr-Mn-N Austentitic Stainless Steel (Abstract Only) 3,047
L.V. Vareda and D. Spinelli

Microstructure and Curie Temperature of As Cast Fe-(Nd+MM)-B Alloys (MM-Brazilian Mischmetal) (Abstract Only) 3,048
C.S. Alves, S. Gama, F.A.O. Cabral, R.C. Araujo and P.R. Nei

Composite Materials

Processing of In-Situ Al-TiB2 Composites 279
H.J. Brinkman, J. Duszczyk and L. Katgerman

Microstructure and Mechanical Properties of Reaction Squeeze Cast Hybrid Al Matrix Composites 287
C. Son, I. Park, K. Cho, I. Choi and S. Lee

Development of Functionally Gradient Materials 295
H. Zhu and R. Abbaschian

In Situ Synthesis and Thermodynamic Analysis of MoSi2-SiC Composite 305
Z. Sun, L. Zhang, Y. Zhang and W. Yang

Vacuum Investment Casting of SiC Particles Reinforced Aluminum Matrix Composite 313
D. Wang, M. Gui, J. Cheng, H. Zhang and C. Li

Synthesis and Sputtering of Composite Targets and Thin Films 319
A.O. Kunrath, J.J. Moore, S. Govindarajan, J. Disam and E.A. Levashov

Development of MMC Using Liquid Metallurgy Technique: Control of Porosity and Particulates Distribution 327
M.I. Qureshi and M. Mujahid

Intelligent Methods for the Optimization of Composite Materials 333
M. Fathi and L. Hildebrand

Thermal Fatigue in Fiber Reinforced Metal Matrix Composites 341
K.K. Chawla

Preparation of Ti/TiC Microlaminates by EB-PVD and Their Mechanical Properties 349
X. Bi, X. Jin, S. Gong and H. Xu

TiAl/TiAl-SiC Gradient Coatings on Gamma Titanium Aluminides and Their Oxidation Behavior 355
S. Gong, S.R. Zohai, Q. Yu, H. Xu and C. Zhou

P/M Synthesis of Titanium Alloy-Based Particulate Composites and Their Properties 361
M. Hagiwara, S. Emura, S.J. Kim and M. Niinomi

The Initiation and Continuation of Infiltration of Al-Mg Based Alloys into Alumina Preforms 367
B.S. Rao and V. Jayaram

Sintering of Particulate Reinforced Titanium Matrix Composites 373
D.E. Alman

Comparison of In Situ Fibre and Interface Properties Between Sealed and Unsealed 3-D Woven SiC/SiC-Based Composite After Tensile Testing Up To 1380°C In Air And Vacuum 379
I.J. Davies, T. Ishikawa, N. Suzuki, M. Shibuya, T. Hirokawa and J. Gotoh

Fabrication and Modification of Mechanical Properties of Al/Al_2O_3 Composite Bodies by Reaction Between SiO_2 and Molten Al 385
N. Yoshikawa, Y. Watanabe, Z.M. Veloza, S. Taniguchi and A. Kikuchi

Combined Mechanical Alloying and Controlled Combustion Synthesis in the Production of TiB-Ti CMC's 391
S. Özbilen

The Analysis of Reclamation Mechanism of Discontinuously Reinforced Aluminum Matrix Composites 401
Z. Shi, T. Fan, M. Gu, D. Zhang and R. Wu

Laminated Metal Composites—Fracture and Ballistic Impact Behavior 407
D.R. Lesuer, C.K. Syn, O.D. Sherby and J. Wadsworth

High Temperature Interface Sliding and Deformation Behaviour of Cu-Mo Artificial Lamellar Composite 417
F. Yoshida and H. Nakashima

In Situ Observation of Cyclic Fatigue Crack Growth of SiC/SiC Composite 423
S.J. Zhu, M. Mizuno, Y. Mutoh and Y. Kagawa

Fracture Behaviour of Polymer-Hydroxyapatite Composites 429
P. Cheang and K.A. Khor

Effect Of Size of TiC Reinforcement on Abrasion and Impact-Abrasion of MMCs ... 435
Ö.N. Dogan, J.A. Hawk and R.D. Wilson

Interfacial Stress State and Failure of Scarf Joints in Metal Matrix Composites 441
D.D. Brink, J.C. Mailand, C.G. Levi and F.A. Leckie

Study on the Interfacial Reaction and Mechanical Properties of SiCP/6061Al Composites 447
R.M. Wang, Y. Cui, M.K. Surappa and C.H. Tao

Al_2O_3/AlB_{12} Composite Synthesized by SHS 453
S. Yin, Y. Liu, W. Li and H. Lai

Carbothermic Reduction of Tantalite in Iron to Produce Metal Matrix Composites 459
N.T. Mudzanapabwe, O.S. Chinyamakobvu and D.J. Simbi

Strengthening and Mechanical Stability of In-Situ Cu-Fe-Xi Composites 467
J.S. Song, M.S. Lim, S.I. Hong and K.K. Jee

Damping Capacity of Epoxy Filled Aluminum Foam 473
C. Wong

The Effect of a Functionally Graded Protective Coating on the Mechanical Behaviour of SiC Monofilament Reinforced Ti MMC's 479
S. Haque and K.L. Choy

Experimental Study of the Bond Between Concrete and Steel Reinforcement 485
W. Sha, K.W. Lau

Stresses at the Interface in Discontinuously Reinforced Composites 491
T.C. Tszeng

Processing of Al/Al3Ti Composites by Low Pressure Casting/Combustion Synthesis Process 497
K. Mizuuchi, T. Takeuchi, M. Fukusumi, M. Sugioka, Y. Ohkanda, H. Nagai and K. Inoue

Analysis of Binders and Binder Burnout in Tape Cast Ti/SiC MMCs 505
C.M. Lobley and Z.X. Guo

Interfaces in a Coated Graphite/Magnesium Composite 511
J. Zhu, F. Wu and G.D. Zhang

First-Principles Calculations of Interfaces in Materials: Grain Boundaries in SiC and SiC/Metal Interfaces 519
M. Kohyama and J. Hoekstra

Materials Characterization of Polystyrene/Tin and Polypropylene/Aluminum Mechanical Alloys 525
W.J.D. Shaw, M.A. Fraser and H.J. Danilkewich

Kinetics of Metal Organic Chemical Vapour Infiltration and Microstructures of Amorphous and Nano-Crystalline ZrO2 Incorporated into Partially Sintered MoSi2 Matrix 531
N. Yoshikawa, S. Taniguchi and A. Kikuchi

High-Temperature Strength of Microstructure-Controlled Nb3Al/Nbss In-Situ Composites in Nb-Al-Mo Ternary System 537
T. Tabaru and S. Hanada

Microstructure and Mechanical Properties of Nb-Mo-TiC In-Situ Composites 543
N. Nomura, K. Yoshimi, T. Konno and S. Hanada

Characterization of Creep Cracking in Carbon Fiber/Epoxy Composite (Abstract Only) 3,049
S.Y. Zhang

Modelling of Electrical Discharge Machining for Ceramic Composites (Abstract Only) 3,050
C. Opran

Synthesis and Characterization of Titanium Aluminide Based Alloys with Nanocrystalline and Bimodal Structures (Abstract Only) 3,050
N. Srisukhumbowornchai, O.N. Senkov and F.H. Froes

The Influence of Microstructural Damage on the Thermal Properties of CMCs (Abstract Only) 3,051
K.R. McDonald, F.W. Zok, J.R. Dryden and A. Majumdar

Role of Reinforcements on the Creep Behavior of Al-SiC Composites (Abstract Only) 3,052
K. Janghorban

High Transition Temperature Superconductors

Research and Development of Superconducting Materials in China 551
L. Zhou

Bondability and Superconductivity of YBCO Ceramics with In2O3 Additives 559
A. Suzumura and D. Zhigang

Congruent Growth of NdBa2Cu3O7-x Superconducting Oxide from the Highly Undercooled Melt by Containerless Processing 565
K. Nagashio, Y. Takamura and K. Kuribayashi

Advances in Processing of Ag-Sheathed (Bi,Pb)2Sr2Ca2Cu3Ox Superconductors 571
U. Balachandran, M. Lelovic, N.G. Eror and P. Haldar

Critical Currents Across Small Angle Grain Boundaries in High Tc Superconductors 577
C.S. Pande and R.A. Masumura

High Temperature Superconducting Magnet Applications at the Naval Research Laboratory 585
D.U. Gubser

Chemical Engineering of High - Tc Superconductors Via Chemical Doping 593
R.S. Liu, J.M. Chen and R.G. Liu

Improving the Microstructure of B12223 Tapes for High Critical Curent Densities (Abstract Only) 3,052
Q.Y Hu, S. Li, H.K. Liu and S.X. Dou

Processing of Epitaxial, Biaxially-Textured Y-Ba-Cu-O Superconducting Thick Films on Metal Substrates by Metal Organic Chemical Vapor Deposition (Abstract Only) 3,053
V. Selvamanickam, J. D'Frank, C. Trautwein, S. Alles, P. Haldar, U. Balachandran, M. Lanagan and M. Lelovic

Hydrogen Absorbing Materials

State-of-the-Art of Hydrogen Storage in Reversible Metal Hydrides 601
G. Sandrock and M.A. Imam

A Study on the Development of Over-Stoichiometric Zr-Ti-Mn-V-Ni Hydrogen Storage Alloy with High Capacity and High Rate-Capability for Ni-MH Rechargeable Battery 609
D.-M. Kim, K.-J. Jang and J.-Y. Lee

Crystal Structure and Hydrogen Absorption Properties of La(Ni, M)x (x=3~5) Melt-Spun Ribbons 619
M. Okada, T. Kuriiwa, T. Tamura, A. Kamegawa, H. Takamura and H. Nakamura

Gas Diffusion in Single Crystal Oxides 625
J.E. Shelby

The Effect of the Solidification Rate on the Hydrogen Storage Properties of Ml(NiCoMnTi)5 Alloys 631
C. Li, X. Wang, X. Li and C. Wang

Hydrogen Storage via Reversible Cycloakane Dehydrogenation Catalyzed by a Soluble Iridium Hydride Complex (Abstract Only) 3,054
C.M. Jensen, M. Gupta, R. Zidan, N. Mariels, S. Guthrie, E. Pak and C. Hagen

Catalytic Dehydrogenation of Sodium Aluminum Hydrides (Abstract Only) 3,055
R.A. Zidan, C.M. Jensen, A.G. Hee, N. Mariels and C. Hagen

Effect of Processing Parameters on the Structure, Morphology and Hydrogen Storage Properties of Mg-Based Multi-Component Alloys (Abstract Only) 3,055
K. Sapru, L. Ming, J. Evans and N.T. Stetson

Hydrogen Interaction with Quasicrystalline ZrCuNiAl Alloy (Abstract Only) 3,056
N. Eliaz, D. Eliezer, D. Zander and U. Köster

Light Metals

Calorimetric Investigation of Precipitation Kinetics in Al-Mg-Si-(Cr, Be) Alloys 639
K.D. Woo, J.S. Lee, J.H. Jeong, D.K. Kim and S.W. Kim

On Silicon Phase in Al-Mg2Si Alloy with Excess Silicon 645
A. Shan, I.G. Moon, J.E. Yoo, H.S. Ko, H.S. Kim, J.Y. Chang and J.W. Park

Refinement of Second Phase in Al-Ti Base Alloys by Repeated Working 651
G. Itoh and A. Kurihara

Effects of T4 and T6 Tempers on Post Semi-Solid Formed 319 Auminum Alloy 657
E. Cerri, S. Spigarelli, E. Evangelista and S. Paddon

Recent Developments in Light Metals 663
F.H. Froes, W. Quist and J. Liu

Techniques for Thermomechanical Property Evaluation in Titanium Based Materials 669
L. Christodoulou, R. Dashwood and H. Flower

Effect of Cr Addition on the Cycle Life of Ti-Based Alloy Electrodes for Ni/MH Rechargeable Battery 677
J.-S. Yu, H. Lee, K.-J. Jang and J.-Y. Lee

Magnesium Science, Technology and Applications 683
E. Aghion, D. Eliezer, and F.H. Froes

On the Morphology and Characteristics of Mn-Bearing Dispersoids in AlMgSi Alloys 689
I.G. Moon, A. Shan, J.E. Yoo, H.S. Ko, H.S. Kim, J.Y. Chang and J.W. Park

Effect of Quenching Rate on the Properties of a New Al-Zn-Mg-Cu Alloy 695
Y.-L. Wu, C. Li, F.H. Froes, A. Alvarez and J. Liu

Effect of HIP on the Microstructure and Mechanical Properties of the Cast A-356 Aluminum 701
C.S.C. Lei, W.E. Frazier and E.W. Lee

The Effect of 45° Rolling Mode on the Mechanical Properties of Anisotropic Metals 707
O.S. Es-Said

Microstructure and Creep Behavior of Al-Cu-Mg and Al-Cu-Mg-Ag Alloys 713
N. Wang, S.M. Kazanjian and E.A. Starke, Jr.

Process Planning for Layered Manufacturing Using Heterogeneous Solid Models 719
D. Dutta and V. Kumar

Modelling as a Basis for Microstructural Design in High Strength Al and Mg Alloys 725
J.F. Nie and B.C. Muddle

Capillary Rheometric Studies of Aluminum Alloy AlSi7Mg0.3Sr in its Semi-Solid State 731
F.C. Yee, X.P. Niu, S.W. Hao and B.H. Hu

Deformation and Fracture Behavior of Al-Mg-Si Alloys 737
S.B. Kang, L. Zhen, H.W. Kim and S.T. Lee

On the TB2 Titanium Alloy for Satellite-Rocket Link Belt 743
C. Haishan

Redistribution of Electronegative Impurities in Zirconium at Thermo Cyclization in Atomic Hydrogen 749
D. Schur and V. Pishuk

Advances in Deformation Mechanisms of Titanium Alloys 757
A. Ramesh and S. Ankem

Effects of L12 (Al,Cr)3Ti Coatings on the High Temperature Oxidation Behavior of TiAl Alloys 765
H.N. Lee, Z.M. Park, M.H. Oh, S.W. Nam and D.M. Wee

Microstructure Control of Nitrogen Doped TiAl Alloys 771
J.H. Yun, M.H. Oh, S.W. Nam, D.M. Wee, H. Inui and M. Yamaguchi

Cast TiAl Alloys as Engineering Materials 777
D.X Zou

Creep Mechanisms and Interface-Enhanced Deformation Twinning in a Two-Phase Lamellar TiAl Alloy 783
L.M. Hsiung and T.G. Nieh

Oxidation Behavior and Thermal Stability of Ti-44Al-11Nb Alloy 789
R. Mahapatra, S.K. Varma, B.A. Pregger and W.E. Frazier

Some Aspects of Creep in TiAl 795
T.S. Rong, I.P. Jones and R.E. Smallman

The Fatigue Behavior of Squeeze Cast A380.0 Alloy 801
J.R. Brevick, P.S. Cheng, H. Brucher and C.E. Mobley

An Anaylsis of the Microstructure Obtained in Atomized Al-Fe Powders 807
J.A. Juarez-Islas, C. Gonzalez-Rivera, Y. Zhou and E.J. Lavernia

Effects of RE (RE: Rare Earth Metals) Addition on Formability in Al-High Mg Alloys 815
S.-D. Park, S.-B. Kang and H.-K. Cho

Microstructure Refinement of Al-20Si-5Fe Alloy with Melt Treatment and Extrusion 821
Y.S. Choi, J.S. Lee, W.T. Kim and H.Y. Ra

Effects of Mn—Dispersoid on the Crack Initiation During Fatigue in an Al-Zn-Mg-Mn Alloy 827
Y.S. Woo and S.W. Nam

Microstructure and Mechanical Properties of Ti-48Al-2Nb-2Cr Alloy After Thermomechanical Processing 833
G.A. Salishchev, R.M. Imayev, V.M. Imayev, M.R. Shagiev, A.V. Kuznetsov, O.N. Senkov and F.H. Froes

Mechanical Properties of Partially Crystallized Amorphous Alloys 841
H.S. Kim, S.S. Cho, C.W. Won and B.S. Chun

Microstructure and Properties of Aluminum-Iron Alloys Subjected to Severe Plastic Deformation and Aging 847
O.N. Senkov, F.H. Froes, V.V. Stolyarov, R.Z. Valiev and J. Liu

Behavior of Hydrogen in a 5083 Aluminum Alloy 853
T. Ihara and G. Itoh

Texture Investigation of Deep Drawn Al Cup by ACOM and X-Ray Measurement 859
N.-J. Park and F. Springer

A Study on the Grain Refining and Age Hardening of Mg-Zn-Cu and Mg-Zn-Si Alloys 865
I.-S. Ahn, T.-H. Nam and Y.-Y. Kim

Mechanical Properties and Microstructures of Mg-Zn-(Mn) Alloys Fabricated Under an Ar Gas Atmosphere 871
J.-P. Eom, S.-G. Lim and B.-Y. Hur

A Study on Technique of Making Foam Al-Alloys 877
S. Yang, Y. Zhang, Z. Xing and H. Wang

Effect of Extrusion Temperature on the Crystallographic Texture in Al-Li-Cu Alloys (Abstract Only) 3,057
K.V. Jata

The Interface Properties of Squeeze Cast Aluminum Alloy A356 Locally Reinforced with Al_2O_3 Short Fibre (Abstract Only) 3,058
M.J. Fuller, B. Cantor, S. Gungor and M.J. Hughes

Controlled Combustion Synthesis in the TiH_2-B System (Abstract Only) 3,059
S. Özbilen

Interfacial Reactions Between CP-Ti and ZrO_2(5C) (Abstract Only) 3,060
K.-F. Lin, G.Y. Ni, C.C. Lin and J.I. Wang

MA'ed and HIP'ed TiH_2-Al Compacts Displaying Encouraging Mechanical Property Levels (Abstract Only) 3,061
S. Özbilen

Magnetics

Development of NdFeB Magnet Industry in China 885
B. Li, X. Wang and X. Yu

Development and Prospect of Rare-Earth Permanent Magnet Materials in China 891
Z.-X. Wang and B.-P. Hu

Temperature Stability of Rare Earth Permanent Magnets 899
X. Yu, J. Zhang, Z. Guo and W. Li

A Study of the Deformation Behaviour of Nano-Crystalline Nd-Fe-B Magnets 905
S.P. Narayan, K. Basu, Y.V.R.K. Prasad and V. Jayaram

Brittle Fracture in Nd2Fe14B Intermetallic Magnets 911
J.A. Horton, L. Heatherly, E.D. Specht, D. Li, J.W. Herchenroeder and P.C. Canfield

Diffusion of Interstitial Atoms in Ordered Magnetic Alloys Under Pressure 917
S. Zaginaichenko, Z. Matysina and D. Schur

Solidification Modeling in Rare Earth Permanent Magnets 921
J.E. Shield, M.J. Kramer, C.P. Li, R.W. McCallum and D.J. Branagan

Effect of Hydrogen on the Magnetic Properties of $(Er_{0.5}Pr_{0.5})_2Fe_{13}Al_4$ and its Nitride 927
K.G. Suresh, G. Markandeyulu, S.D. Mahanti and K.V.S. Rama Rao

Microstructures of GaN Films Grown by Low Pressure Metal-Organic Vapor Phase Epitaxy on Sapphire Substrates 933
Z. Zhang and L.S. Cheng

Electromagnetic Wave Absorption Properties and Microstructure of $BaFe_{12-x}(TiMn)_xO_{19}$ 941
K. Okayama, H. Ota, Y. Yoshida, T. Kagotani, H. Nakamura, S. Sugimoto and M. Homma

Synthesis and Magnetic Properties of Ferroxplana Type Co2-Y Ferrite $(Ba_{1-x}Sr_x)_2Co_2Fe_{12}O_{22}(X=0.0\text{-}1.0)$ 947
T. Kagotani, T. Suzuki, H. Nakamura, D. Book, S. Sugimoto, M. Okada and M. Homma

Microstructure and Properties of Co-C Films Prepared by a Dual Source Deposition System 953
M. Azumi, J. Shi, Y. Haga and O. Nittono

Fabrication and Characterization of Al-Co/Al-N-Co Multilayer Films 959
A.G. Roy and O. Nittono

Optical Properties of Bismuth and Gallium Substituted Thulium Iron Garnet Films Suitable for Optical Devices 965
P. Mukhopadhyay, S. Orpe and V. Chandravanshi

Carbonation of Re2Fe17 (Re=Rare Earth) Compounds By Arc Melting Technique 971
M. Venkatesan, U.V. Varadaraju and K.V.S. Rama Rao

Anisotropic Magnetic Properties of Bulk Nanocrystalline $Fe_{66}Co_{20}Nb_2Pr_7B_5$ Magnets Produced by Crystallization Under Uniaxial Pressure 975
A. Kojima, A. Makino and A. Inoue

The Novel Structure of Ultrafine Amorphous Fe-Zr-B Powders Obtained by Chemical Reduction 981
J.G. Zhang, Y.J. Lin, W.X. Xu and H.J. Jin

Effects of Surface Features of Fe-Based Amorphous Ribbons on the Two-Fold In-Plane Magnetic Anisotropy 989
H. Wang, G. Yang and K. Dong

Effect of Solid Reducing Agent on Formative Condition and Magnetic Properties of Fe_2-W Type Hexagonal Ferrite 993
H. Takamura, K. Unno, A. Kamegawa, M. Homma and M. Okada

Structural and Magnetic Characterization of Fe-N Films Prepared by Reactive Sputtering Method 999
M. Shibata, J. Shi and M. Hashimoto

Structure and Magnetic Properties of Co-Fe-Hf-O Sputtered Films with High Electrical Resistivity 1,005
Y. Sasaki, K. Ohminato, T. Hatanai and A. Makino

Magnetic Field - Induced Anisotropy of Nanocrystalline Soft Magnetic Fe-Zr-B "Nanoperm" 1,011
T. Bitoh, T. Hatanai, A. Makino, A. Inoue and T. Masumoto

Effects of Hard-Magnetic Bias on Core Loss of Mn-Zn Ferrite 1,017
K. Takadate, Y. Yamamoto and A. Makino

Effects of Additional Elements (M=Transition Metal) on the Thermal Stability and Soft Magnetic Properties in Fe-Co-Ni-Zr-M-B Amorphous Alloys with Wide Supercooled Liquid Range 1,023
H. Koshiba, A. Inoue and A. Makino

Properties of Nano Regions and Boundaries in Ferroelectrics (Abstract Only) 3,062
A.S. Bhalla

Electrical and Mechanical Properties of Perovskite O-D Ferroelectric Relaxors $Pb(InNb)O_3$ and $Pb(ScNb)O_3$:$PbTiO_3$ Systems (Abstract Only) 3,062
E. Alberta and A. Bhalla

Melt Processing and Casting

High Quality Thin Slab Casting for Hot Strip Production (Control of Initial Solidification in Thin Slab Casting) 1,031
T. Watanabe, S. Hiraki, M. Kawamoto and Y. Tozaki

Study on the Seeding Process for Producing Single Crystal Castings 1,039
Z. Giu, D. Tang, Z. Wu, Z. Zhong and X. Dai

Modeling the Deep Bed Filtration of Aluminium 1,045
R.T. Bui, D. Kocaefe and L.I. Kiss

Fundamentals of Vacuum Assisted Counter Gravity Casting 1,051
S.R. Giese

Purification of Leached Metallurgical Grade Silicon by Electron Beam Melting 1,057
A.F.B. Braga, J. Otubo and P.R. Mei

NiTi Shape Memory Alloys Produced by Electron Beam Melting: Preliminary Results 1,063
J. Otubo, P.R. Mei, S. Koshimizu and L.G. Martinez

Numerical Analysis of Effects of Electromagnetic Braking Force on Fluid Flow and Heat Transfer in Flow Control Mold 1,069
J.K. Yoon, H.S. Nam, P.R. Cha, K.H. Moon and J.E. Lee

The Application and Development of V Resource in Panzhihua 1,079
Z. Zhao, J. Ma and W. Huang

Control of Precipitating Phase Alignment by Imposition of a High Magnetic Field 1,087
H. Morikawa, K. Sassa and S. Asai

Effects of Electromagnetic Field and Cooling Rate on As-Cast and Aging Structures of Centrifugal Casting Heat-Resistant Alloy 1,093
Y. Yang, X. Wu and Z. Hu

Modeling Morphological Evolution During Dendritic Solidification Using a Cellular Automaton 1,099
R.E. Napolitano and T.H. Sanders, Jr.

Short Capillary Viscometer for Molten Metals and Alloys 1,105
Y. Shiraishi, Y. Sakurai and S. Nagasaki

Production of Fine Copper - Tin Particles with Ammonia Splashing Method 1,111
S. Yokoyama, N. Itoh, S. Nishizawa and M. Kawakami

Electron Beam Surface Melting to Study Phase Selection in 3XXX Series Al Alloys 1,117
L. Carroll, K.A.Q. O'Reilly, B. Cantor and P.V. Evans

Application of the Accelerated Crucible Rotation Technique in the Directional Solification of Metallic Alloys 1,125
W. Jie, D. Ma, Z. Guo, J. Liu, W. Xu and Y. Li

A Study of Soft Contact Electromagnetic Casting Technology 1,133
H. Kim, J.-P. Park, H. Jeong and J. Kim

Refinement of the Microstructure in Hyper-Eutectic Al-Si Alloys by Electromagnetic Vibrations 1,139
K. Miwa, A. Radjai, T. Nishio

Solidification Process of Silicon from High Undercooled Melts by Electromagnetic Levitation Method 1,145
T. Aoyama, Y. Takamura and K. Kuribayashi

Micro-Macro Modeling of Solidification Microstructures in Finite-Element Simulations 1,151
S.P. Marsh

The Effect of Cooling Rate on As-Cast Structure in Fine Grain Casting IN718 Alloy 1,159
Y. Ma, J. Sun, X. Xie, J. Zhao, Y. Hu, P. Yan and X. Shan

Surface Metallurgy of Ni-Base Alloy by Double Glow Plasma Surface Alloying ... 1,165
X. Zhang, Z. Yang, J. Dong, X. Xie, Y. Gao and Z. Xu

Formation of Surface Bleeds in Twin Roll Cast Aluminum Sheet (Abstract Only) 3,063
M. Yun, S.A. Lockyer and J.D. Hunt

A Mathematical Model for Simulating the Puddle Formation in the Single Roll Rapid Solidification Process for Producing Metallic Thin Strips (Abstract Only) 3,064
C.-W. Chen, J.-H. Kuo and W.-S. Hwang

A Numerical Simulation for the Initial Filling in Continuous Casting Tundish and Its Expermental Verification (Abstract Only) 3,065
Li-Chuan Lin, S.-M. Pan and W.-S. Hwang

New Paradigm For The Design of Safety Critical Casting (Abstract Only) 3,066
J.G. Conley and J. Huang

Phase Transformations and Their Applications

Origin of Aging Effect and Rubber-Like Behavior in Martensite 1,173
K. Otsuka and X. Ren

Time-Dependent Nature of Martensitic Transformations in Some Ferrous and Non-Ferrous Alloys 1,181
T. Kakeshita, T. Saburi and K. Shimizu

Formation of Reversed Austenite from M23C6 Type Carbide in High Chromium Martensitic Steel 1,187
T. Tsuchiyama and S. Takaki

Simulation of Martensitic Transformation in Fe-Ni Alloys 1,193
T. Suzuki and M. Shimono

Twin Interface Structures in Martensitically Transformed $\gamma 1'$Cu-Al-Ni and $\gamma 2'$Au-Cd Alloys 1,199
T. Hara, T. Ohba and K. Otsuka

Quantitative Evaluation of the Rubber Effect and Stabilization of the Martensitic Phase in Copper Alloys 1,205
K. Marukawa and K. Tsuchiya

Influence of Long Range Ordering on Martensitic Transformation in Ag-Zn-Al Alloys 1,211
K. Takezawa, H. Hoshi and K. Marukawa

Intrinsic Thermodynamic Stability and Its Implication to Characteristics of Phase Equilibria in Coherent Multilayers 1,217
J.-Y. Huh

Computational Investigations on the Microstructure Formation in Metallic Materials Based Upon the Phase Field Method 1,225
T. Miyazaki and T. Koyama

Isothermal Transformation of Au-47.5at%Cd Alloy 1,233
X. Ren, T. Ohba, S. Yamada, T. Ishii and K. Otsuka

Diffuse Phase Transition in $Pb(Fe_{0.5}Nb_{0.5})O_3$ Ferroelectric Ceramics 1,239
K. Oda

Effective Pair Interaction Energies in Random FCC Binary Alloys by Direct Configurational Averaging and Phase Diagrams 1,245
T. Hoshino, M. Asato and K. Masuda-Jindo

Growth Behavior of Ni_3Al in Ni/NiAl Diffusion Couples 1,251
K. Fujiwara, Z. Horita and M. Nemoto

Diffusion of Constituent Elements in Ni3Ge Studied by Tracer and Interdiffusion Experiments 1,257
K. Nonaka, T. Arayashiki, H. Nakajima, K. Tanaka, T. Korata, T. Ikeda, H. Numakura, M. Koiwa, and W. Sprengel

Formation of the Extraordinary Lamellar Structure due to the Decomposition of High - Temperature α Phase in γ-TiAl Based Alloys 1,263
Y. Ohmura, M. Takeyama and T. Matsuo

Preparation of Sb-Doped SnO2 Ultrafine Particles from Sol-Gel Method 1,269
Y. Hu and S.-H. Hou

High-Energy Electron Irradiation Induced Phase Transformation in Fe-Ni Binary and Ternary Alloys 1,275
Y. Murata, M. Morinaga, K. Takami and H. Mori

An Appraisal of Single Crystal Casting for Turbine Components 1,281
P. Auburtin, S.L. Cockcroft, A. Mitchell and W. Tao

Phase Transformation of Gibbsite Corundum under Hydrothermal Conditions ... 1,287
H.S. Yu, K.-I. Rhee, C.-K. Lee and D.-H. Yang

Ordering Processes in an Al-Li-Cu-Mg-Zr Alloy 1,293
Y. Ohmori, S. Ito and K. Nakai

Linear- and STE-Disclinations Consisting of Multiple Twin Boundaries in the L11-Type CuPt Ordered Alloy 1,299
Y. Kitano, K. Kitasaka and Y. Fujikawa

Modification of Electronic Structure due to Local Atomic Displacements around Carbon Interstitial in Austenite 1,305
H. Yukawa, M. Mori and M. Morinaga

Real Time Characterization of Solid/Liquid Interfaces During Directional Solidification 1,311
S. Sen, W.F. Kaukler, B.K. Dhindaw, P.A. Curreri and P. Peters

Phase Transformation Behavior and Reducing Gas Sensing Characteristics of Fe-O Thin Film Processed by Plasma-Enhanced Chemical Vapor Deposition 1,317
B.-J. Kim, E.-T. Lee and G.-E. Jang

Shape Casting Simulation: Coupling Microstructural Models into Macromodels for the Prediction of Properties 1,325
A. Giachino, P.D Lee, L. Christodoulou and S. Nishido

Crystalline-Amorphous Transformation in C15 Laves Phase TbFe2 by Hydrogen Absorption 1,331
K. Mori, K. Aoki and T. Masumoto

Anomalies of Electrical Resistivity Studied by CVM and PPM 1,337
T. Mohri and F. Nagata

Phase Transformation and Tensile Behaviour of Ti-6Al-4V and Grade 21S Titanium Alloys 1,347
W. Sha, D.P. Savage and Z. Guo

Morphological Evolution of Coherent Precipitates in Three Dimensions 1,355
J.K. Lee

Motion of Phase Boundaries by Surface Diffusion 1,363
Y. Giga and K. Ito

Effect of External Fields on Ordering of Equiatomic FePd 1,369
T. Ichitsubo, M. Nakamoto, K. Tanaka and M. Koiwa

Phenomena on the Surfaces and Along a Crack Path in a Heat Resistant Alloy During High Temperature Service 1,375
A.A. Kaya and P. Krauklis

Surface Treatment of Ni and Ni-Based Alloys for High Temperature Oxidation Performance 1,381
F. Czerwinski, S. Poplawski and J.A. Szpunar

Thermodynamics and Kinetics Aspects of the Synthesis of Titanium Nitride and Carbonitrides From TiO_2 and Carbon in Nitrogen Atmosphere 1,387
A. Jha and S.-J. Yoon

Order-Mesoscopic Transformation in Compound Semiconductor In_2Te_3 1,393
S. Abe, E. Inoue, Y. Nakamura and O. Nittono

Theoretical Investigation of the Cubic-to-Tetragonal Transition in ZrO_2-Based Alloys 1,399
J. Katamura, Y. Ikuhara and T. Sakuma

Microanalysis of Modulated Structure in Zirconia Ceramics 1,405
N. Shibata, J. Katamura, Y. Ikuhara and T. Sakuma

Short Range Order in Ni4Mo Studied by Quantitative High Resolution Transmission Electron Microscopy 1,411
S. Hata, T. Mirate, S. Matsumura, N. Kuwano, K. Oki and D. Shindo

Phase Transition in (Ndx, Sm1-x)AlO3: Structural Behavior Characterized by Ionic Radius and Temperature 1,417
H. Horiuchi, A. Saitow, A. Yoshikawa, T. Shishido, T. Fukuda, M. Tanaka, A. Inoue and T. Mizota

Role of the Interlamellar Spacing of Pearlite in the Dilatometric Characterization of Pearlite-to-Austenite Transformation in a Low Carbon Steel 1,423
C. García de Andrés, F.G. Caballero and C. Capdevila

Processing and Properties of Dual Phase Alloys in the Nb-Cr-Ti System 1,431
K.C. Chen, D.J. Thoma, P.G. Kotula, F. Chu, C.M. Cady, G.T. Gray III, P.S. Dunn, and D.R. Korzekwa

The Relations between Precipitation of Carbides and Growth of Austenite in Duplex Stainless Steel 1,437
K.-M. Lee, H.-S. Cho and D.-C. Choi

Austenite Formation and Alloy Carbide Dissolution in Fe-Cr-C Steels During Heating 1,443
D.V. Shtansky, K. Naki and Y. Ohmori

Effects of Alloying Elements on the Intragranular Precipitation in Cu-Be Alloy 1,449
M. Miki, K. Morita, S. Ishikawa and Y. Ogino

Diffuse Scattering and Huang Scattering in Al-Based Icosahedral Quasicrystals ... 1,455
M. Mori, T. Ishimasa, M. Tanaka and S. Sasaki

Local Atom Displacements around Crystal Lattice Defects Inducing Phase Transformations Studied by Molecular Dynamics Simulation 1,461
S. Muto, M. Takeuchi, Y. Masuda and T. Tanabe

TEM and Electron Diffraction on Structure and Phase Transformation of Nanometer-Sized Fe-Ni Alloy Particles 1,467
K. Asaka, T. Tadaki, Y. Sechi, B. Bo, T. Ohkubo and Y. Hirotsu

In-Situ TEM Observation of Short-Range Order State and Ordering Process of Cu3Pt 1,473
N. Chiwata, T. Sakai, A. Matsumoto, N. Kuwano and K. Oki

Phase Transformation of Bil-xCaxMnO3 Studied by TEM with Energy-Filtering 1,479
D. Shindo, Y. Murakami, H. Chiba, M. Kikuchi and Y. Syono

STM/AFM Study of Surface Relief Induced in the Phase Transformation of Fe-Ni-C, ZrO2-Y2O3 and Cu-Al-Ni Alloys 1,485
M. Yamamoto

Modifications in the Martensite Transformation of the 0.45C-13Cr Steel Caused During the Continuous Cooling Process with and without Preciptation of $M_{23}C_6$ Carbides 1,493
C. García de Andrés and L.F. Alvarez

Morphology of Martensite in Fe-Ni-Si Alloys 1,503
O. Ikeda, Y. Himuro, I. Ohnuma, R. Kainuma and K. Ishida

The Growth-Path Method for Prediction of Spurious Grain Nucleation in Single-Crystal Castings 1,509
R.E. Napolitano, A.R. Roosen and R.J. Schaefer

The Relation Between Phase Transformation and Grain Size in Y2O3-Partially Stabilized Zirconia 1,515
H. Tsubakino, T. Isobe and B. Zhang

Phase Transformation in 9mol% MgO-Partially Stabilized Zirconia During Ageing and Thermal Cycling 1,521
B. Zhang, T. Isobe and H. Tsubakino

Amorphous to Nancrystalline Transformations in Electrodeposited Ni-W Alloys 1,527
T. Yamasaki, R. Tomohira and Y. Ogino

Effects of Zr-Additions on Phase Stability and Phase Transformations in a Ti-50at.% Al Alloy 1,533
K. Nakai, O. Yamada and Y. Ohmori

Morphology and Crystallography of Triple Point Nucleated γ Phase in an (α+γ) Two Phase Stainless Steel 1,539
H. Fujiwara, T. Maeda, N. Miyano and K. Ameyama

Hardening of NiAl Alloys by Point Defects and Iron Solutes (Abstract Only) 3,067
L.M. Pike, C.T. Liu and Y.A. Chang

Equipment for On-Line Texture Measurement and Plasticity Prediction (Abstract Only) 3,068
P. Blandford and J.A. Szpunar

Alloy Design Strategies for Enhanced Solubility Ranges in Monolithic C15 Laves Phases (Abstract Only) 3,069
D.J. Thoma, F. Chu, K.C. Chen and P.G. Kotula

Rapid Prototyping

Novel Applications and Implementations of Shape Deposition Manufacturing 1,547
F.B. Prinz and L.E. Weiss

The Production of Presintered Magnetic Ferrite and Process Automation 1,555
R. Liu , C. Xu, Y. Xu, S. Wang, Q. Zhang, Y. Liao, X. Yi, B. Zhou and X. Zhang

Comparison of Experiment to Stefan Solution for Planar Flow Spin-Casting 1,561
B.L. Reed, X.-Q. Zhang and P.H. Steen

A Knowledge Based System for Rapid Prototyping of P/M Components 1,567
L. Smith and S. Midha

Calibrating Fused Deposition Modeling Rapid Prototyping Systems for Adaptive Build Layer Thicknesses 1,573
J. Tyberg and J.H. Bohn

Near Net Shape Production of Metal Components Using LENS™ 1,581
E. Schlienger, D. Dimos, M. Griffith, J. Michael, M. Oliver, T. Romero and J. Smugeresky

SLS/HIP-A Direct Freeform Fabrication Process for High Performance Metal Components 1,587
S. Das, J.J. Beaman, M. Wohlert and D.L. Bourell

Solid Freeform Fabrication (SFF) of Advanced Functional Ceramic Components 1,595
S.C. Danforth, A. Safari, N. Langrana and M. Jafari

The Metal Printing Process—Solid Freeform Fabrication of Objects in Metal and Ceramics 1,605
N.A. Ruud and R. Karlsen

Fast Freeform Fabrication of Metal Parts Using Layer Deposition Technique 1,611
A.A. Tseng, M. Lee and B. Zhao

Metal Part Processing by SLS/HIP 1,619
J. Wright and R. Knight

Development of Multi-Material Virtual Layered Manufacturing Simulation 1,625
D. Qiu, N. Langrana, S.C. Danforth, A. Safari and M. Jafari

Advance in Both Rapid Prototyping & Rapid Tooling Techniques 1,631
I. Luca, S. Luca and G. Andrea

Modeling Assisted Laser Engineered Net Shaping (LENS™) Of Functional Multi-Element Materials (Abstract Only) 3,070
D.M. Keicher, J.E. Smugeresky, J.A. Romero and M.L. Griffith

New Process and Materials Development in 3-Dimensional Printing (Abstract Only) 3,071
M. Cima, J. Moon, J. Grau, S. Uhland and E. Sachs

Layered Manufacturing of Reinforced Composites (Abstract Only) 3,072
G. Zak, M.N. Sela, C.B. Park and B. Benhabib

Direct Fabrication of Ceramic and Composites From Slurries: Robocasting Technology (Abstract Only) 3,073
J. Cesarano III, B.H. King, T.A. Baer and P. Calvert

Materials and Properties of Components Formed Using the 3DWire Process (Abstract Only) 3,074
M.L. Griffith, L.D. Harwell, D.L. Greene, J.A. Romero, T. Bucheit, T. Crenshaw and V. Tikare

VOLUME II

Spray Forming

Relationship Between Mechanical Properties and Microstructure of the Age Hardened Cu-15Ni-8Sn Alloy Prepared by Spray Forming 1,639
H.L. Ge, J.G. Zhang, D.S. Sun and H.S. Shi

Microstructure and Mechanical Properties of a Spray Formed Al-Fe-V-Si Alloy 1,645
M.F. Amateau, T.J. Eden, J.M. Galbraith, E.J. Fodran and M.J. Kaufman

Properties of Spray Formed Tool - & High Speed Steels 1,653
C. Speigelhauer

Development of High Performance High Speed Steels by Spray Casting 1,661
E.S. Lee, W.J. Park and S. Ahn

High Chromium Alloys for Shipboard Waste Incinerators 1,669
L. Kohler and R. Rebis

Progess in Clean Metal Spray Forming 1,675
W.T. Carter, Jr., M.G. Benz, B.A. Knudsen, R.J. Zabala, R.M. Forbes Jones, H.E. Lippard and R.L. Kennedy

Spraycast-X for Aerospace Applications 1,681
T. Tom, K. Bowen and G. Butzer

Spray Forming Process for Nickel-Base Superalloys 1,687
G. Zhang, G. Mi, Z. Liu, Z. Zhang, Z. Li and S. Tian

Modeling of Thermal History of the Solidification of Non-Spherical Molten Metal Droplet During Spray Forming 1,693
Y.C. Chen, C.-Y.A. Tsao and C.L. Wang

Spray Forming Commercial Products: Process Design and Optimization 1,699
A. Lawley, R.D. Doherty and R.G. Brooks

Solidification Simulation of Spray Forming Deposition 1,707
J.S. Zhang, H. Cui, X.J. Duan, Z.Q. Sun, G.L. Chen and B.Q. Xiong

Numerical Method for the Deposition Profile in Spray Forming Process 1,713
X. Fu, J. Zhang, W. Yang and Z. Sun

Microstrucuture and Yield Strength of Cu-TiB2 Alloy Produced by Spray Forming 1,719
J. Lee, E.-S. Lee, S. Ahn and N.J. Kim

Study on the Sound-Absorbing Properties of the Aluminum Foam Materials 1,725
Y. Zhang, Z.-D. Zhao and S.-Y. Yang

A Review of the Spray Forming of High Performance Aluminium Alloys (Abstract Only) 3,075
A. Leathan and A. Ogilvy

New Aluminum Cylinder Liners for Combustion Engines Manufactured from Spray Deposited (Abstract Only) 3,076
K.B. Hummert

Mechanical and Microstructural Evaluation of Spray Formed Aluminum Alloy (Abstract Only) 3,077
S.R. Horn and J.L. Rossi

Spray Formed Titanium (Abstract Only) 3,077
C. Madden, R. Rebis and L. Kohler

Tribological Behavior of Borided Coatings Produced by VPS Technique on Carbon Steels Components (Abstract Only) 3,078
G. Pradelli, E. Galvanetto, F. Borgioli, T. Bacci and B. Tesi

The Spray Forming and Evaluation Of Large Diameter Billets in Special Steels and Superalloys (Abstract Only) 3,079
L.H. Shaw and G. Oakes

Selection of Gas and Droplet Properties in the Modeling of Spray Atomization Process (Abstract Only) 3,080
B. Li and E.J. Lavernia

Modeling of Multi-Phase Transport Phenomena in a Spray Forming Process and Conditions of Porosity in the Bulk Deposits (Abstract Only) 3,080
S.J. Pien and M.G. Chu

Superplasticity and Superplastic Forming

Observations of Superplasticity in Nanocrystalline Matrix 1,733
S.X. McFadden, R.S. Mishra and A.K. Mukherjee

The Microtwinning of Martensite Variants and Linear Superelasticity in a Cold Drawn TiNi Alloy 1,739
L. Zhao, B. Huang, Y. Zheng and W. Cai

Grain Boundary Structure and Chemical Bonding State of SiO_2-Doped TZP with a Small Amount of Metal Oxide Addition 1,747
Y. Ikuhara, K. Sasaki, P. Thavorniti and T. Sakuma

The Role of Deformation Mechanisms in the Solid State Joint Formation During Superplastic Flow 1,755
O.A. Kaibyshev, V.V. Astanin and R.Y. Lutfullin

Contribution of Grain Boundary Sliding in Superplastic 7475 Alloys Processed by Powder Metallurgy and Ingot Metallurgy 1,765
T. Hirata, T. Mukai, S. Tanabe, M. Kohzu and K. Higashi

Observation of Low Temperature Superplasticity of ZK60 Magnesium Alloy 1,771
H. Watanabe, T. Mukai and K. Higashi

Model of Superplastic Deformation 1,777
O.A. Kaibyshev, V.V. Astanin and A.I. Pshenichniuk

An Examination of High Strain Rate Superplasticity in Aluminum Matrix Composites 1,785
Y. Li and T.G. Langdon

Thermomechanical Processing of a 6XXX Aluminum Alloy for Grain-Size Control and Superplasticity 1,791
L.P. Troeger, R. Crooks and E.A. Starke, Jr.

Superplastic Deformation of Al-Cu Ribbons Produced by Melt Spun Method 1,801
Y. Umakoshi and W. Fujitani

Evaluation of Grain Size Effect on Superplasticity of a Pb-Sn Eutectic Alloy Based on the Internal Variable Theory of Structural Superplasticity 1,807
T.K. Ha, K.S. Shin and Y.W. Chang

Grain Refinement and Superplasticity in Mg Alloys 1,813
M. Mabuchi, T. Mohri, N. Saito, M. Nakamura, H. Iwasaki and K. Higashi

The Effect of Yttria Content on the Superplasticity of YSZ in the C-T Phase Field 1,819
K. Sasaki, T. Kondo Y. Ikuhara and T. Sakuma

Superplasticy of Metastable Austenitic Stainless Steels with Ultra Fine Grains 1,825
T. Suzaki and S. Takaki

The Influence of Al2TiO5 Addition into Al2O3-ZrO2 Binary Ceramics on Superplastic Deformation 1,831
M. Oka and H. Yamada

Uniform Post-Formed Thickness from Mathematically Modelled Profiled Blank (Abstract Only) 3,081
A. Dutta

Internal Variable Approach to High Temperature Deformation Behavior of Superplastic Materials 1,837
T.K. Ha, Y.N. Kwon and Y.W. Chang

Temperature Dependence of Threshold Stress for Al-Based Materials Exhibiting High Strain Rate Superplasticity 1,847
D. Kum, W. Kim and G. Frommeyer

Experimental Relationships Between Maximum Gap and Depth of the Mold During Superplastic Forming 1,855
G. Torres-Villaseñor, H. Aguilar and J. Llanes

High-Strain-Rate Superplasticity of Supercooled Liguid in Zr - and La-Based Metallic Glasses 1,861
Y. Kawamura, T. Nakamura and A. Inoue

Microscopic Observation of Superplastic Deformation in a 2-Phase Ti3Al-Nb Alloy 1,867
J.-H. Kim, C.-G. Park, T.-K. Ha and Y.-W. Chang

Grain Refinement and Potential for Superplasticity in Al Alloys Containing Small Particles 1,873
H. Hasegawa, S. Komura, Z. Horita, M. Furukawa, M. Nemoto and T.G. Langdon

Superplastic Behavior and Influence of Solution Strengthening on the Ductility of Al-Mg-X Alloys 1,879
B.S. Chung, D.Y. Maeng and S.I. Hong

Experimental Analysis of Superplastic Deformation Mechanisms in a Commercial 5083 Alloy 1,885
H. Iwasaki, T. Mori, T. Tagata, and K. Higashi

Superplastic Behavior of Doubly-Extruded ZK60/SiC/17p Magnesium-Based Composite over a Wide Range of Temperature 1,891
T. Mukai, T.G. Nieh, H. Watanabe and K. Higashi

Tensile Ductility of Al-Doped β-Silicon Carbide at Elevated Temperature 1,897
T. Nagano, K. Kaneko and H. Kodama

Solid Materials Processing and Mechanisms

Micromechanical Instabilities in Materials Processing 1,905
J.C.M. Li

Strengthening and Mechanical Stability of Cu-6wt.%Ag Alloy 1,913
M.S. Lim, J.S. Song and S.I. Hong

Properties of Functionally Graded NiCrAlY-ZrO2 TBC Layers Fabricated by Plasma Spraying Technique 1,919
C.-H. Park, I.-M. Park, K.-M. Cho and M.-G. Jung

Development of P/M Nb-Base Corrosion-Resistant Material 1,925
T.W. Huang

Effects of Applied Stress and Other Factors on the Bainitic Transformation in Cu-Zn-Al Alloys 1,931
M. Tabuchi, M. Takahashi and K. Marukawa

Production of Ultrafine Fe-Cu Particles by DC Plasma Jet Method and Their Characterization 1,937
K. Tsuchiya, Y. Tokada and M. Umemoto

The Strain Path Dependence of Microstructure Developed in OFHC Cu by ECA Pressing 1,943
W.H. Huang, M.F. Li, P.W. Kao and C.P. Chang

Electrical and Opitical Properties of Oxide Films Formed on Stainless Steel 1,949
N.E. Hakiki

Advanced Materials for the Energy and Transportation Industries in the Europe of the 21st Century (Abstract Only) 3,082
M. Van De Voorde

Recent Progress in the Modeling of Materials and Processing for Optimal Properties 1,955
Y. Li, R. Yang, D. Li and Z. Hu

Ta-Si-N Barriers Against Cu Diffusion 1,963
C. Lee, Y.-H. Shin, and J.-C. Kim

Double Glow Surface Alloying Process 1,969
Z. Xu, Y. Gao, Y. Su, Z. Xu, B. Fan and J. Pang

Conductive Anodic Filament Failure: A Materials Perspective 1,977
L.J. Turbini and W.J. Ready

Rolling Texture Development in CnZn Ordered Alloy 1,983
G. Zhu, W. Mao, Y. Yu and Z. Sun

The Effect of Boron on the Mechanical Behaviors of A Ni-19Si-3Nb Based Alloy 1,989
J.S.C. Jang, S.K. Wong and C.H. Tsau

Laser-Induced Rheological-Thermal Failure in Ceramic Reinforced Metal Matrix Composites 1,995
Y.C. Zhou, S.G. Long, Z.P. Duan and Q.B. Yang

Materials and Properties of Components Formed Using the 3DWire Process 2,001
M.L. Griffith, L.D. Harwell, D.L. Greene, J.A. Romero, T.E. Buchheit, T.B. Crenshaw and V. Tikare

Simulation of High Temperature Deformation Behavior of IN 718 2,007
K.Y. Wang, R.A. Mirshams and B.Q. Li

Investigation on Critical Techniques of Iron-Powder Warm Compaction 2,013
S.-J. Gou, M.-Y.Li, T. Lin and Y.-P. Wei

Anti-Corrosivity of New-Type Nb-Base Alloy 2,019
T.-W. Huang and W.-Z. Zhong

Tribological Behaviour of P/M Self-Lubricating Porous Bronze Bearings (Abstract Only) 3,083
M.Z. Mehr, H. Alimohammadi and M. Masnavi

Smart Materials and Processing

Shape Recovery Stress of Ti-Ni and Ti-Ni-Cu Shape Memory Alloys 2,027
T.H. Nam, G.S. Ha and G.B. Cho

Effect of Thermal Cycling on Martensitic Transformation Temperatures in Ti-Ni-Cu Shape Memory Alloys 2,033
T.H. Nam, S.S. Cha and G.S. Ha

Aging Effect on the Structure and Shape Memory Property of Ti51Ni13Pd36 High Temperature Shape Memory Alloy 2,039
H. Xu, Q. Meng, C. Jiang and S. Gong

In Situ Observation of Matensitic Transformation in Shape Memory Alloys 2,045
L. Sun, S. Gong and H. Xu

Shape Memory Effects and Microstructure of RuTa High-Temperature Shape Memory (Abstract Only) 3,084
K. Inoue, K. Mizuuchi, G. Wright, J.-H. Lee and Y. Tomota

Microstructures and Mechanical Properties of Ti/TiPd Smart Composites 2,051
K. Mizuuchi, K. Inoue, K. Yamauchi, K. Enami and M. Taya

Effects of Passing Electric Current on the Crystallization Process in Amorphous Alloys 2,057
H. Mizubayashi and N. Kameyama

Local Structural Change of Amorphous Fe-Zr-B Alloy in the Course of Crystallization Studied by Modern Electron Microscope Techniques 2,063
N. Hara, Y. Hirotsu, T. Ohkubo, A. Makino, T. Oikawa and M. Matsushita

Microstructure Changes in Bilayer Films of Phase-Separation Type Alloy Systems 2,069
M. Doi, K. Kato, Y. Yamada, H. Inaba and Y. Ueda

Structural Relaxation in $Zr_{55}Al_{10}Ni_5Cu_{30}$ Bulk Metallic Glasses 2,075
T. Zhang and A. Inoue

Advanced Ceramics Research & Prospect in China 2,081
J.K. Guo

Mechanical Properties in $Al_{94}Cr_1Mn_3Cu_2$ Alloy Strengthened by Nano-Quasicrystalline Particles 2,091
H. Kanahashi, T. Mukai, K. Higashi, H. Kimura, A. Inoue and K. Kita

Self-Organized Quantum Dots: Material Growth and Device Application 2,097
Z. Wang, Q. Gong, W. Zhou, R. Xin and H. Li

Electronic Structure of Impurity-Defect Complexes with Dislocation Behavior in Metals 2,105
C. Wang and D. Zhao

Study on Novel Polyimides Alignment Materials Based on an Alicyclic Dianhydride and Long Alkyl Chain Containing Diamines 2,113
J. Yin, Z.-G. Wang, W. Zhang, Y.-F. Ye and Z.-K. Zhu

Synthesis and Characterization of xBaO-($Mg_2Al_3Si_{4.5}O_y$) Glass Ceramic from Sol-Gel Process 2,119
Y. Hu and H.-T. Tsai

Study on Novel Flourinated Copolyimides Based Second-Order Nonlinear Optical Materials 2,125
Z.-Q. Wang, J. Yin, Y. Sui, Y.-G. Liu, D.-Y. Huang and Z.-K. Zhu

The Exploration on New Approach of Strengthening and Toughening of Ceramic Materials 2,131
J.K. Guo

A New Biomaterial for Artifical Heart Valve Prepared by Ion Beam Enhanced Deposition 2,137
X. Liu, F. Zhang and X. Wang

Properties of Nanocrystalline Electrodeposited Ni-Fe Alloys 2,143
H. Kim and C.M. Gilmore

Effects of Production Methods on Treating of Ni-Ti Shape Memory Alloys (Abstract Only) 3,085
F.M.H. Zarandi and R. Sharghi

Ni-Free Ti-Based Shape Memory Alloys and Their Mechanical Properties (Abstract Only) 3,086
H. Tada, H. Hosoda, M. Takeuchi, K. Hamada, K. Mizuuchi, K. Aoki and K. Inoue

Quantitive Study of CuAlNi Shape Memory Alloy Under 4-Point-Bending By Moiré Interferometry (Abstract Only) 3,087
T.T. Xu and Q.P. Sun

Critical Issues in Nanocrystalline Materials Research for Structural Applications and Some Potential Successful Approaches (Abstract Only) 3,088
S.M.L. Sastry and V. Proverzano

Consolidation of Nanoparticles—Modeling and Experimental Validation (Abstract Only) 3,089
SM.L. Sastry and R. Suryanarayanan

Welding and Laser Processing

Solidification Behavior and Microstructural Evolution During Laser Beam-Material Interaction 2,153
P.S. Mohanty and J. Mazumder

Laser Material Processing—Recent Advances and Their Impact on the Future 2,161
J.T. Schriempf

Laser Cladding of Copper-Based Composites on 6061 Aluminum Alloy 2,169
Y.P. Hu, C.W. Chen and K. Mukherjee

XeCl Excimer Laser Annealing Effects for A-Si/A-SiNx Double Active Layer 2,177
C.-M. Park, J.-S. Yoo, C.-H. Kim, J.-H. Jeon, M.-K. Han

Nanoparticle Synthesis by a Novel Laser-Liquid-Solid Interaction Technique 2,183
D. Poondi, T. Dobbins and J. Singh

Effects of Transition Metal Alloying on Microstructural Stability and Mechanical Properties of Tin-Silver-Copper Solder Alloys 2,189
I.E. Anderson, Ö. Ünal, T.E. Bloomer and J.C. Foley

Femtosecond Lasers: A Next Generation Tool for Processing of Semiconductors and Metals 2,195
A.P. Malshe, T.A. Railkar, A.M. Ozkan, P.A. Mollian, A. Muyshondt and W.D. Brown

Effects of Inclusions and Austenite Grain Size on the Impact Behavior of a Newly Developed Low-Carbon Steel Weld Metal 2,203
J.M. Blackburn, A. Brandemarte and A.G. Fox

Residual Stress Elimination in Nickel 690 Alloy Welds 2,209
W. Wu and J.C. Chen

The Effect of the Surface Cleaning State on the Shear Strength for Steel/Epoxy/Steel 2,215
A. Damasco, M.C. Gonçalves, I. Ferreira, S. Azambuja and N.G. de Alcântara

Laser Shock Processing on CVD-Processed Alumina Coated Carbide Inserts 2,221
J.K. Park, P. Kwon and K. Mukherjee

Residual Strength of Surface Mount Lead-Free Solder Joints After Thermal Cycling 2,229
N.M. Poon, C.M.L. Wu, J.K.L. Lai and Y.C. Chan

Characterization of Welds in Gamma Titanium Aluminides 2,235
V.L. Acoff, A. Ponnusamy and D.J. Bharani

A Study on the Electron Beam Weldability of High Strength Al Alloys for the Transportation Applications 2,241
S.W. Kim and C.H. Lee

Microstructural Refinement of Aluminum Alloys during Friction Welding of Dissimilar Metals 2,247
S. Fukumoto, M. Ohashi, H. Tsubakino, K. Okita, M. Aritoshi and T. Tomita

Friction Welding of Aluminum Alloy to Copper and Evaluation of Weldability of the Joints by Ultrasonic Method 2,253
Y. Suga, A. Ikeda and D. Lian

Development of Low-Melting Active-Metal Brazing Filler for Joining Ceramics to Metals 2,259
O. Saitoh, A. Suzumura and H. Ogawa

Use of Intermetallic Alloys as Additions to Tungsten Electrodes 2,265
D.L. Olson, S. Liu and S. Caldwell

Pressurized Combustion Synthesis as a Technique to Join Advanced High Temperature Materials 2,275
W. Liu, S. Liu, F. Zhai and G. Elssner

Materials Processing with Explosives 2,283
O.T. Inal, C.A. Zimmerly and E.S. Ege

Development of an Improved MIL-100S Wire for Naval Ship Construction 2,291
J.J. Deloach, Jr., J.M. Blackburn, R.J. Wong and G.L. Franke

Development of New Weldability Test Methods for High Strength Steels 2,297
R.J. Wong

The Influence of Weld Microstructural Features on Corrosion Behavior 2,303
B. Mishra, D.L. Olson and C. Lensing

Deformation Behaviour of 7075Al/ SiCp Composite During Multi-Pass Deformation at High Temperatures (Abstract Only) 3,090
D. Yu, A. Razaghian, H. Asanuma and T. Chandra

The Effect of Welding Conditions on FCAW Hardfacing Abrasion Resistance (Abstract Only) 3,091
O.S. Hernández and N.G. Alcântara

Welding of Nickel-Base Superalloy Single Crystals (Abstract Only) 3,092
S.A. David, J.M. Vitek, S.S. Babu, L.A. Boatner and R.W. Reed

Microstructure Evolution During the Welding and Postweld Heat Treatment of Gamma Titanium Aluminide (Abstract Only) 3,093
W.A. Baeslack III, C.M. Jenson, H. Zhang and T. Kelly

Electron Beam Welding of Cast Gamma Titanium Aluminide (Ti-48Al-2Cr-2Nb) (Abstract Only) 3,093
T.J. Kelly

Enhancements in Aluminum Alloy Weld Metal Through Additions of Weld Metal Grain Refiners (Abstract Only) 3,094
K.E. Johns, R.H. Frost and D.L. Olson

Intermetallics

Small Fatigue Crack Behavior in γ–Titanium Aluminide Ti-46Al (at%) 2,311
Y. Mutoh, T. Moriya, S.J. Zhu, R. Gnanamoorthy and Y. Mizuhara

Mechanical Properties of Mo-Al Alloys with Lamellar Structure 2,317
R. Nino, S. Miura and T. Mohri

Cyclic Deformation Behavior of CoTi Single Crystals with the B2 Structure 2,323
A. Behgozin, T. Nakano and Y. Umakoshi

Effect of Microstructure on the Creep Rupture Properties of Ti-51at.%Al Alloy at High Temperatures 2,331
I. Mutoh, Y. Kawano, T. Kumagai, T. Tanabe and M. Nakamura

High-Temperature Strength Properties of Ir Doped NiAl Intermetallic Compound 2,337
A. Chiba, T. Ono, X.G. Li and S. Takahashi

Effects of Volume Fraction of Constituent Phases of Fully Lamellar TiAl Alloys on Creep Strength 2,343
R. Yamamoto, G. Wegmann and K. Maruyama

Effect of Heating Rate on the Combustion Synthesis of TiAl 2,349
S.-H. Lee, J.-H. Lee, Y.-H. Lee and Y.-S. Kim

Mechanical Properties of Co-Base Alloys Strengthened by E21-Type Intermetallic Compound Co_3AlC 2,355
K.-Y. Hwang, Y. Kimura, S. Miura and Y. Mishima

Currect Topics in Studies of TiAl-Base Alloys 2,361
M. Yamaguchi

Processing and Microstructural Control of Directionally Solidified TiAl-Mo-B Alloys 2,367
K. Chihara, D.R. Johnson, H. Inui and M. Yamaguchi

Phase Equilibria and Phase Stability Among β, α_2, α, and γ Phases in Ti-Al-M Ternary Systems at Elevated Temperatures 2,373
S. Kobayashi, M. Takeyama, T. Matsuo and M. Kikuchi

Design of Oxidation Resistant Coating Based on IrAl Alloys 2,379
H. Hosoda, T. Kingetsu and S. Hanada

Abnormal Grain Growth in $BaTiO_3$ 2,385
T. Sakuma and T. Yamamoto

Microstructure and Ductility of Multi-Phase Intermetallic Alloys in the NG-Si-Ti System 2,393
N. Sekido, S. Miura and Y. Mishima

A Study on the Chromium Modified Ni-25Al-27.5Fe Intermetallics (Abstract Only) 3,095
C.-H. Tsau, J. S.-C. Jang and J.-W. Yeh

Grain Growth Mechanism of Tungsten Carbide during Liquid Phase Sintering 2,399
H.S. Ryoo and S.K. Hwang

Phase Structure of Rapidly Solidified Al Riched Ni-Al Precursor Alloys for Catalysts 2,405
N. Shen, Y. Tang, C. Liang and X. Wang

Deformation and Fracture of Bi-PST Crystals of TiAl 2,413
D. Imamura, H. Hoshikawa, K. Kishida, H. Inui and M. Yamaguchi

Reactive Sintering of NiAl and Simultaneous Joining to Steel 2,419
K. Matsuura, K. Ohsasa, N. Sueoka and M. Kudoh

Characterization of FeAl Intermetallic Compound in the Process of Mechanical Alloying 2,425
M. Hashii and Y. Hosoi

Thermal Conductivity in Intermetallic Compounds 2,431
Y. Terada, T. Mohri and T. Suzuki

Effects of Superheat and Growth Rate on the Crystal Growth Behavior of Ni3Al 2,437
Z. Xiao and R.H. Zee

Ti45Al55-Nb45Al55 Vertical Section of Ti-Al-Nb System 2,443
X. Wang, G. Chen, K. Ni and S. Hao

Al_5Ti_3 Precipitates in Al-Rich Single-Phase TiAl 2,449
K. Chikugo, H. Inui and M. Yamaguchi

Effects of Ternary Alloying Elements on Plastic Deformation of $MoSi_2$ Single Crystals 2,455
K. Ishikawa, H. Inui and M. Yamaguchi

High Temperature Creep Deformation of Unidirectionally Solidified Ti-48at% Al Alloy 2,461
T. Nozaki, R. Izawa, S.-Y. Chang, M. Takeyama and T. Matsuo

High Temperature Strengthening Mechanism of TiAl and Nb3Al Base Intermetallics 2,467
K. Hashimoto and T. Hanamura

Superplasticity in Monolithic Intermetallics 2,473
W.-Y. Kim, S. Watanabe and S. Hanada

Creep Deformation Characteristics of the Lamellar TiAl Alloys Related with Microstructure 2,479
S.W. Nam and H.S. Cho

Microstructural Evaluation and Mechanical Behavior of a Ni3Al-Fe/B Alloy 2,489
G. Li, J.-T. Guo, H. Li, Z.-G. Wang and X.-S. Xie

AE and XPS Analysis of Air Annealed Amorphous Fe73.5Cu1Nb3Si13.5 B9 Alloy 2,495
W.Z. Chen and H.X. Wang

Analysis of Residual Stress in Damped Alternating Bending of Sheet Metal 2,499
M. Kohzu, T. Nishioka and T. Enomoto

Mechanical Alloying of Platinum Group Metal with Zr or Al 2,505
T. Tsuzuki and T. Arakawa

High Pressure Raman and X-Ray Diffraction Investigations of the High Pressure Phase of Spin-Pei Compound $CuGeO_3$ (Abstract Only) 3,095
A. Jayaraman, S.K. Sharma and L.C. Ming

Mechanical Behavior of Fe_3Al Based Intermetallic Alloys at High Temperatures (Abstract Only) 3,096
P.I. Ferreira, I. Ferreira and A.A. Couto

Materials Electronics and Electronic Packaging

Study on the Increase of Wafer Bonding Contact Area by Linear Heat Treatment 2,513
J.W. Lee and C.S. Kang

Electrical Properties of p-ZnSe/Metals Interfaces with Intermediate Semiconductor Layers 2,519
Y. Koide, T. Kagawa, H. Mori, M. Murakami, N. Teraguchi, Y. Tomomura and A. Suzuki

Electrical Properties at p-ZnSe/Metal Interfaces of Annealed Contacts 2,525
T. Kawakami, Y. Koide , M. Murakami, N. Teraguchi, Y. Tomomura and A. Suzuki

Application of In_x-Ga_{1-x} As - Based Ohmic Contacts to p-Type GaAs 2,531
M. Ogura and M. Murakami

High Temperature Growth of SiC and Group III Nitride Structures in Production Reactors 2,537
D. Schmitz, R. Beccard, E. Woelk, M. Bremser, G. Strauch and H. Juergensen

Effect of Water Chemisorption on Dielectric Underlayers on Electromigration of Al-Si-Cu/Ti/TiN/Ti Interconnects 2,543
Y. Taga, T. Ohwaki and T. Yoshida

Correlation Between Resistivity and Columnar Structure in Titanium Films Prepared By Two-Facing-Target DC Sputtering 2,551
T. Miyoshi, Y. Haga and O. Nittono

Microstructure of Porous Titanium Dioxide Films Prepared by Air-Oxidizing Pure Titanium Films 2,557
T. Kaneko and O. Nittono

Miniaturization and Reliability in the Metallurgical Elements of Microelectronic Packages 2,563
J.W. Morris, Jr. and S.-H. Kang

Prototype Circuit Boards Assembled with Non-Lead-Bearing Solders 2,571
P.T. Vianco and J.A. Rejent

Mechanical Reliability of Solder Interconnects in Multichip Modules (MCMs) 2,581
K.L. Murty, H. Yang, P. Deane and I. Turlik

Moisture Sensitivity Improvement in 28 Lead TSOP 2,589
R. Mahidhara and J. Belani

Lattice Orientation Relation of the $AuIn_2$ Phase to the Au Matrix in the Alloying Process of Gold-Indium Films on Mica and NaCl Substrates 2,597
K. Kifune, Y. Kubota, K. Yamamoto and T. Tadaki

Tantalum Powder for Solid Electrolytic Capacitors 2,603
G.J. Korinek

Mechanical Properties of Structural Polyurethane Foams 2,611
S.H. Goods, C.L. Neuschwanger, L.L. Whinnery and C.C. Henderson

Non-Electrolytic Silver Plating onto Non-Conducting Alumina Substrate 2,617
J.-H. Lee and G.P. Martins

A Novel Method for Fabrication of Hydrogenated Amorphous Silicon and High Quality Poly-Si Films on the Same Substrate by Employing Excimer Laser 2,623
K.Y. Choi, K.-C. Park, H.-B. Choi, J.-H. Jeon, M.-C. Lee, M.-K. Han and Y.-S. Kim

Interfacial Reaction Between Cobalt and Silicon 2,629
T. Irie, J. Shi and M. Hashimoto

Thermal-Mechanical Interface Crack Analysis of a TAB Assembly 2,635
N.H. Yeung, C.M.L. Wu and J.K.L. Lai

Surface Conditioning of Plastics for Metallisation with Hydrogen Peroxide (Abstract Only) 3,097
L.A. Teixeira

Chip on Board for Military Avionics Applications (Abstract Only) 3,098
D. Stark, V. Puligandla and M. Staller

Continuum Modeling of Solder Interconnects—Influence of Geometry and Loading Variations TMF Lifetime (Abstract Only) 3,098
S.N. Burchett, M.K. Neilsen, P.T. Vainco and D.R. Frear

Non-Destructive Characterization

Application of Nondestructive Materials Characterization Techniques to Advanced Materials and Processing 2,643
R.E. Green, Jr.

FIM Image Formation for Ordered Alloys 2,651
N.-X. Chen, X.-J. Ge and W.-Q. Zhang

Probabilistic Aspects of Aging of Airframe Materials: Damage versus Detection 2,657
D.G. Harlow and R.P. Wei

SEXI: A New Portable Spectrometer for X-ray Diffraction and X-Ray Fluorescence Analysis in Real Time for Non Destructive Testing of Materials (Abstract Only) 3,099
C. Abbruzzesse, F. Paglietti and P. Plescia

An Overview of Microwave Inspection of Naval Multi-Layered Composites 2,667
L.M. Brown, J.J. DeLoach, B. Bandos, N. Qaddoumi and R. Zoughi

Ultrasonic Characterisation of Anisotropic Materials 2,673
B. O'Neill and R.G. Maev

Characteristics of Local Flow Behavior and Residual Stress Effect Using Advanced Indentation Test 2,679
M.-R. Ok, J.-H. Lee, J.-H. Ahn and D. Kwon

Nondestructive Evaluation of Fracture Toughness, KIC of Turbine Rotor Steels 2,685
J.I. Suk, K.C. Kim, U.H. Sung and M.S. Kim

Real-Time Monitoring and Control of $GA_XIN_{1-X}P$ Heterostructures by P-Polarized Reflectance Spectroscopy (Abstract Only) 3,100
N. Dietz, D.E. Aspnes, K.J. Bachmann and M. Ebert

General Sessions

High-Strength Zr-Based Bulk Amorphous Alloys Containing Nanoscale Compound Particles 2,693
A. Inoue, C. Fan, T. Zhang and A. Takeuchi

Vectoral Photoinduced Effects in Amorphous (Se,S)-Based Thin Films 2,701
H.-Y. Lee, S.-H. Park, J.-Y. Chun and H.-B. Chung

Improvement of Mechanical Properties of Chromium-Nickel Sintered Compacts by Repeated Rolling and Annealing 2,707
Y. Harada, M. Ohmori, H. Ando and H. Matsui

Creep Behavior of Aluminum Thin Film at Elevated Temperature 2,713
T. Yamashita, G. Itoh and T. Nitta

Mechanical Properties of Sputter-Deposited Amorphous Ti-Ni Films 2,719
A. Gyobu, Y. Kawamura, T. Saburi and H. Horikawa

Advances in Materials Science in Central Europe from the 18th Century On 2,725
P. Tardy

The Effect of Electron Emission on the Roughness of Silicon Films in Catalytic CVD 2,733
W.S. Cheong, N.M. Hwang and D.Y. Yoon

Formation of Guinier-Preston Zones in Sputter-Deposited Ti-Ni Thin Films 2,739
Y. Nakata, T. Tadaki, H. Sakamoto, A. Tanaka and K. Shimizu

Recrystallization Textures of Silver Electrodeposits 2,745
H.-S. Nam and D.N. Lee

A Study on the Low-Temperature Crystallization of Amorphous Silicon Films by Microwave Plasma Heating 2,751
H.-Y. Kim, Y.-S. Kang, Y.-J. Yong and J.-Y. Lee

Hydrogen Induced Cracking in Amorphous Fe80B11Si9 Alloy 2,757
N. Eliaz, D. Eliezer, E. Abramov and E.J. Lavernia

Production of Alumina From Egyptian Kaolinite 2,765
A.M. Abdel-Rehim

High Temperature Creep Deformation: A Generic Analysis 2,775
S.S. Bhattacharya and K.A. Padmanabhan

Electron-Beam Skull Melting and Casting of Ti- and Ni-Based Alloys 2,783
S. Ladokhin, N. Levitsky, Y. Anikin, and V. Bolotinsky

Performance Test of Chemical Heat Pump with MH Materials for IS Hydrogen Production Chemical Process in High Temperature Gas Cooled Reactor System 2,789
S. Ishiyama

The Reactive Liquid Processing of Metal Matrix Composites 2,795
V.M. Kevorkijan

Ion Bombardment Effect upon Structure of Carbon Film on the Surface of Ni-C Alloy 2,801
S. Zaginaichenko, Z. Matysina and V. Lnyanoi

Recovery of Pure MnO2 From Medium-Grade Local Manganese Ores 2,809
M.B Morsi, S.Z. El-Tawil and K.A. Barawy

Bending Residual Strength After Impact Loading of Wet-Laminated Sandwich Construction 2,817
B.T. Sofyan, R. Suratman and D.A. Budiwati

The Morphology of High Temperature Oxidation in Inconel 625 2,825
F.A. Khalid

Fatigue of Advanced Materials 2,831
K. Sadananda and A.K. Vasudevan

Coarsening of Cr Precipitates in B2-Ordered NiAl 2,837
E. Tsutsumi, K. Oh-Ishi, Z. Horita and M. Nemoto

Strengthening Mechanism of Al Matrix Composites Reinforced by Shape Memory Alloy 2,843
G.C. Lee, Y.C. Park and D.P. Yun

Microstructure and Mechanical Properties of Al/TiNiP Shape Memory Composites Fabricated by Powder Metallurgy 2,849
C. Han, I. Choi, Y. Park, B. Kim, K. Cho and I. Park

Austempering Temperature-Mechanical Property Relationships in Unalloyed Ductile Iron Austempered in the Temperature Range 325°C-375°C 2,855
J. Zimba, D.J. Simbi, E. Navara and O.S. Chinyamakobvu

Electrical and Fatigue Failure Properties of Plastic Ball Grid Array Assemblies—Effect of Thermal Shock 2,863
Q.H. Tang, Y.C. Chan, C.M.L. Wu and J.K.L. Lai

The Study on the Cycle Lifetime of the MmNi3.45/Co0.75Mn0.7/Al0.1 Compound and Ni-MH Battery 2,869
J. Wu, W. Zhang and X. Wang

Diffusion Barrier Property of TiC Between Si and Cu 2,875
H. Mori, T. Okada and M. Murakami

Ceramic Electrostatic Chucks Made by Slip-Casting and Firing on Metal Substrates 2,881
J.N. Calata, G.-Q. Lu and A. Amith

Tantalum Silicide Sputtering Target Material for Amorphous Ta-Si-N Diffusion Barrier for Cu Metallization 2,887
E. Ivanov

LCF Behaviour of a New Type of DS Superalloy at Intermediate Temperature 2,893
J. Guo and E. Liao

A New Alloy Design Method for Nickel-Base Single Crystal Superalloys 2,899
Z.Q. Chen, Y.F. Han, Z.G. Zhong, P.Y. Wei and M.G. Yan

Role of Mn Dispersoid on the Low and High Cycle Fatigue in Weldable High Strength Al-Zn-Mg-Mn Alloy 2,905
D.H. Lee, D.S. Park and S.W. Nam

A Mossbauer Spectroscopic Study on the Mechanically Alloyed Iron-Boron Alloys 2,911
Y.Z. Yang, Q.S. Li, Y.L. Zhu, X.M. Ma and Y.D. Dong

Instabilities on Diamond Film Growth by High Power DC Arc Plasma Jet Method 2,917
F.X. Lu, G.F. Zhong, W.Z. Tang, T.B. Huang and Y.M. Tong

Low Temperature CVD Technique for Diamond 2,925
A. Hiraki

Planarization of CVD Diamond Films by Reaction with Iron Based Alloys at High Temperatures 2,933
J.D. Ayers, J.S. Lee, K.P. Cooper, H.N. Jones and J.E. Butler

Effect of Pressure on the Quality of Diamond Films Prepared by DC Arc Plasma Jet Method 2,941
G. Zhong, W. Tang, F. Shen, W. Yu, Y. Tong and F. Lu

Formation of the Diamond Thin Films for the SOD Structure 2,947
Y.-S. Lee, K.-M. Lee, J.-D. Ko, Y.-J. Baik and C.-K. Choi

Material Characterization of Dispersion Hardened Platinum 2,951
B. Fischer, D. Freund, A. Behrends, D. Lupton and J. Merker

Relation Between Optical Properties and Lithium Concentrations in Annealed Proton Exchanged Lithium Niobate Optical Waveguides 2,957
J. Spirková-Hradilová, P. Nekvindová, J. Vacík and J. Schröfel

Effects of Thermo-Mechanical Treatments on Texture and Mechanical Anisotropy of Al-Mg Alloy Sheets 2,963
Y.S. Han, S.H. Hong and S.B. Kang

Improvement in the Growth Conditions of II-VI Compound Crystals by Forced Convection 2,969
J. Liu, X. Guo and W. Jie

Solid-State Amorphization: Simulation and Experiments 2,975
B.X. Liu, W.S. Lai and Y.G. Chen

Solidification Process of Rotating Blades Melt Quenched Aluminum Alloys 3,101
Y. Tang

Recent Development of Heat Treatment of Titanium Alloys 2,983
J.M. Ma, C.X. Cao and Q.R. Wang

Particle Reinforced NiAl-Base Composites Fabricated by Reaction Compocast 2,989
R.M. Wang, Y.F. Han, Y.X. Lu and C.H. Tao

High Temperature Load Relaxation Behavior of β-Brass Alloy 2,997
K.A. Lee, Y.W. Chang and C.S. Lee

Growth Mechanism of Al2O3 in Ceramic-Lined Pipes 3,003
J. Wang, J. Li, M. Zhou, J. Zhang and T. Zuo

Oxidation and Corrosion of Overlay MCrAlX Coatings and Diffusion Aluminide 3,009
J. Sun, R. Ye, H. Wu, J. Wang, Y. Ma, R. Chen and X. Wu

NiCoCrAlSiHfY-Al Gradient Overlay Coating by Magnetron Sputtering with Double Targets 3,015
R. Ye, J. Sun, Q. Xu, H. Wu, Y. Ma, R. Chen and X. Wu

Numerical Simulation for Solid/Liquid Interface Shape Around Insoluble Particle 3,021
M. Ode, T. Suzuki and S.G. Kim

The Intrinsic Properties, Criteria and Research Prospects of Nano-Materials 3,027
R. Teng, S. Liu, J. Xu and Y. Yu

Exposure Experiment Analysis of Automotive Steel Sheet Combination Specimens Subjected to Four Kinds of Climates 3,033
X. Li, J. Hao and X. Tian

Hot Pressing of Diamond/Alumina Composites under the Thermodyamically Metastable Condition for the Diamond 3,039
S. Kume, K. Suzuki, H. Yoshida and N. Kanetake

Fractal Diffusion Simulation on Catalytic Surfaces (Abstract Only) 3,101
M.Z. Mehr and M. Majidi

Raman and Optical Investigations of Ga-Doped Zinc Oxide Films and Nano-Particles (Abstract Only) 3,102
S.K. Sharma and G.J. Exarhos

Fabrication of Al-Based Non-Equilibrium Alloy on the Route of Bulk Mechanical Alloying (Abstract Only) 3,102
T. Aizawa and Y. Katsumura

Abstracts Section ..... 3,047 - 3,102

Subject Index 3,103

Author Index 3,117

Plenary Lectures

THE QUIET REVOLUTION IN MATERIALS PROCESSING

Professor Thomas W. Eagar

POSCO Professor and
Head, Department of Materials Science and Engineering
Massachusetts Institute of Technology
Cambridge, Massachusetts 02139

The Third Pacific Rim International Conference on
Advanced Materials and Processing (PRICM 3)
Edited by M.A. Imam, R. DeNale, S. Hanada,
Z. Zhong and D.N. Lee
The Minerals, Metals & Materials Society, 1998

Introduction

In the mid-1980's, the United States, Japan and the European Economic Community declared that the three industries that would drive economic growth into the next century were advanced materials, information technology and biotechnology. Now, more than a decade later, history has proven these predictions to be halfway correct. The next decade will prove whether the remainder of these predictions will come to pass.

Clearly, the information technology industry (computers and telecommunications) can point to many tens of billions of dollars of new businesses over the past 15 years. At the other extreme, the biotechnology industry is still based on promises. Although there is still great excitement about the potential of new biotechnological advances, there simply has not been a very measurable effect on the gross domestic product, unless one wishes to include the tremendous increase in health care costs over the past decade, which represents a negative impact on the economy.

The apparent success of the materials industry lies between information technology and biotechnology. The growth of new materials businesses has been nowhere near the prognostications of ten years ago; however, the properties, durability and economy of traditional materials has improved dramatically over the past two decades. This is the quiet revolution. It is a quiet revolution because it represents a cost avoidance rather than creation of new materials companies. The average consumer does not perceive the change due to the continuous nature of the improvements, as contrasted with discontinuous changes that are claimed and advertised by the information technology industry.

The revolution is also quiet because consumers do not "purchase" the greater materials properties of a magnetic thin film storage device or the miniaturization of silicon transistors or a higher strength automobile panel. The consumer does not understand such details; they are impressed with the 200-fold increases in computer processing speed and storage capacity or the advent of cellular communications over the past ten years. These are obvious increases in functionality at no increase in overall cost. It is true that a large fraction of this improved functionality is due to improvements in materials manufacturing and processing, but these revolutions in materials performance are invisible to the consumer. The consumer is not buying the materials directly; they are purchasing functionality.

Another reason for the quietness of the materials revolution is that the industry has not been a creator of new jobs. This is because a large fraction of the materials revolution is based on tremendous increases in productivity. This, combined with the greater functionality and durability of materials over the past decade, means that the usage of materials, on a weight or volume basis, has not increased dramatically. With consumption roughly constant and productivity increasing at 3.5 to 7 percent per year, employment in the original materials industries has been decreasing by a factor of two every ten to twenty years. The new materials industries have picked up some of the slack, but the overall effect is that the materials industry, although growing dramatically by any meaningful technological measure, has not been a source of new employment.

Nonetheless, the jobs available in the materials profession are changing dramatically. Today, people are employed more for their brain than their brawn. The work is safer, more pleasant and more exciting than ever before.

The productivity and performance increases of the materials industries have probably done more to improve the strength of the United States economy than either the information technology or biotechnology industries; but materials engineers do not receive the credit from society for these advances. The negative effect to date of biotechnology on health care costs has already been noted. In comparison, a personal computer is not markedly less expensive today than ten years ago. Its functionality is greater, but this improved functionality is in large part due to the quiet revolution in the materials of construction. Thus, the predictions of 15 years ago about the future growth industries may have been most accurate with respect to jobs creation in information technology, but the materials industry has produced the most pervasive productivity

improvements. In the long run, it is improvements in productivity that have the most lasting benefit on a nation's wages as seen in Figure 1.

The Materials Revolution

Scientifically, and in the media, the growth in materials science and engineering is generally described in terms of advanced materials with dramatically improved properties. Nonetheless, the real revolution has been in continuous improvements in the properties and reductions in the processing cost of traditional materials. Over the past two decades, our consumption of all materials has not grown markedly, and the industrial growth of advanced composites, advanced ceramics, novel polymers and alternatives to silicon has not come close to the claims of a decade ago. On the other hand, as seen in Figure 2, the cost of all metals has decreased by a factor of two over the past thirty years. This is a 2.5 percent change per year; hardly dramatic on a yearly measure but truly remarkable over several decades! The cost of structural steels has decreased by two-fold in the past decade - a 7 percent per year improvement. The functionality of silicon computer chips has improved 10,000-fold; the useful life, fuel efficiency and maintenance requirements of automobiles has improved dramatically; energy conversion efficiency has accelerated and materials recyclability has improved. These advances are due to continuous improvements in the technology and processing of traditional materials. There are also notable examples of new materials industries such as optical fibers, flat panel displays, compound semiconductors, hard and soft magnetic materials, oriented high strength polymers, and the like, but none of these comes close to the economic size of the traditional steel, concrete, silicon and commodity polymer industries that existed two decades ago, and that continue to exist today. The cost reductions in these traditional materials industries is at least equal to the new businesses created by the advanced materials industries. There are a number of reasons why the new materials markets have not grown as predicted (Ref. 1) but these will not be repeated here.

The behavior of successful materials companies has changed in response to the accelerating pace of technological development in recent years. Manufacturing firms are under greater pressure than ever to bring new products and processes to market rapidly, with lower costs and higher quality than achieved in the past. In addition, the establishment of a global economy no longer dominated solely by the United States has required firms to expand their outlooks and horizons. Successful firms must take a multi-national view, understanding and serving local customer needs while maintaining the efficiency of a global enterprise. This requires greater flexibility in manufacturing and distributing new products.

As the business environment for materials processing changes, so too does our measure of materials performance. Traditionally, materials scientists and engineers have emphasized processing, structure, and properties, and the way they come together to produce performance of a product in a given application. However, as shown by Figure 3, there are several additional dimensions to performance. In particular, successful commercial performance depends not only on physical properties of the material but also on our ability to shape it into a useful object in an economical and timely manner. Without shape, the product cannot serve its intended function, and without economical production, the product's usefulness is limited to fewer, higher value applications. Achieving more rapid and more consistent commercial success from advanced materials requires emphasizing not only the process by which the material is made but the process by which the material achieves its geometry and function, while at the same time maintaining the ability to bring these materials to market rapidly at an economical price. Indeed, the time for commercializing a new material can be the key to success or failure.

A revolution which has occurred in many materials companies over the past decade, particularly the most successful ones, is development of process understanding and process control. In the old system, Figure 4, the process ran "open-loop." Product quality was "inspected into" the product by segregating the output into salable product and scrap. Yields were low. In silicon chips, 25 percent yields were not uncommon. In steel, two decades ago, 70 percent yield was typical at many producers, who had not embraced continuous casting. Today, the best producers achieve over 90 percent yield in silicon and well over 95 percent in steel. The new method, Figure 5, runs "closed-loop." Key process parameters are sensed, this information is input to a model which is used to modify and control the process. Yields are improved as production of low quality material is detected more quickly and the process is adjusted accordingly. Not only

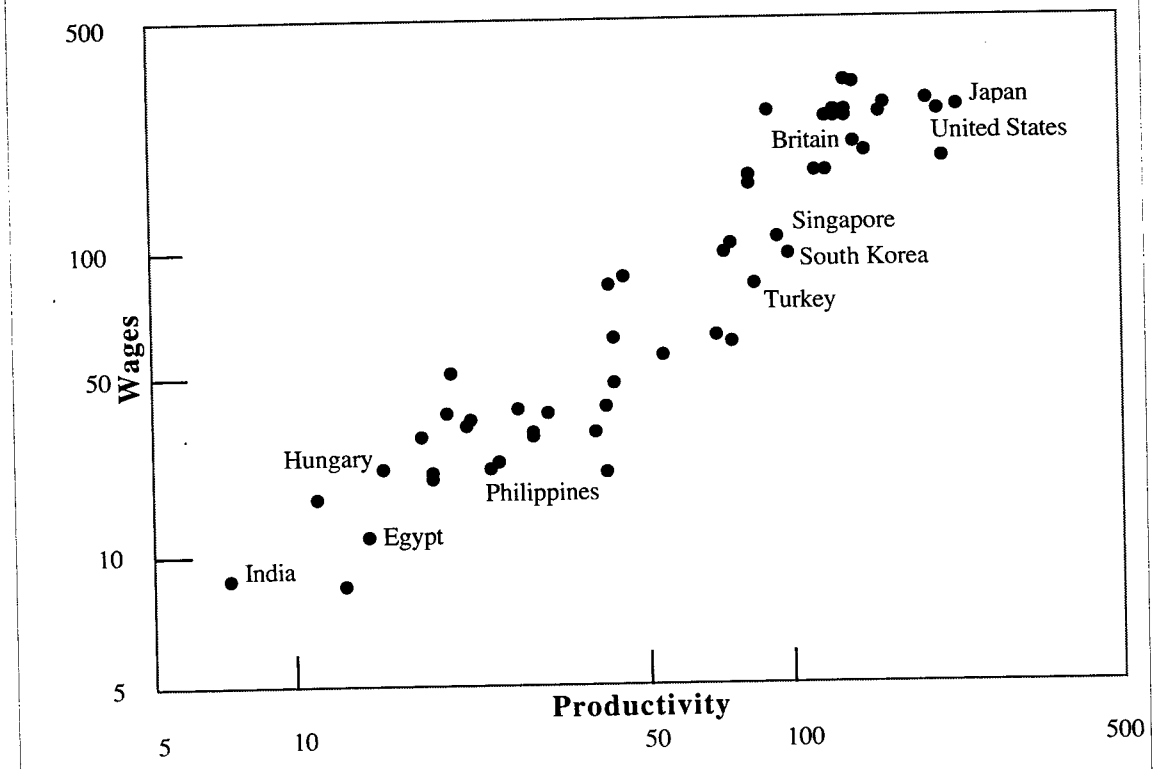


Figure 1

Wages and productivity. 1991 data as presented in The Economist, January 1998. The data are based on 1991 with South Korea normalized to 100 on both axes. The Wages are per worker per year in manufacturing and Productivity is value added per worker per year in manufacturing.

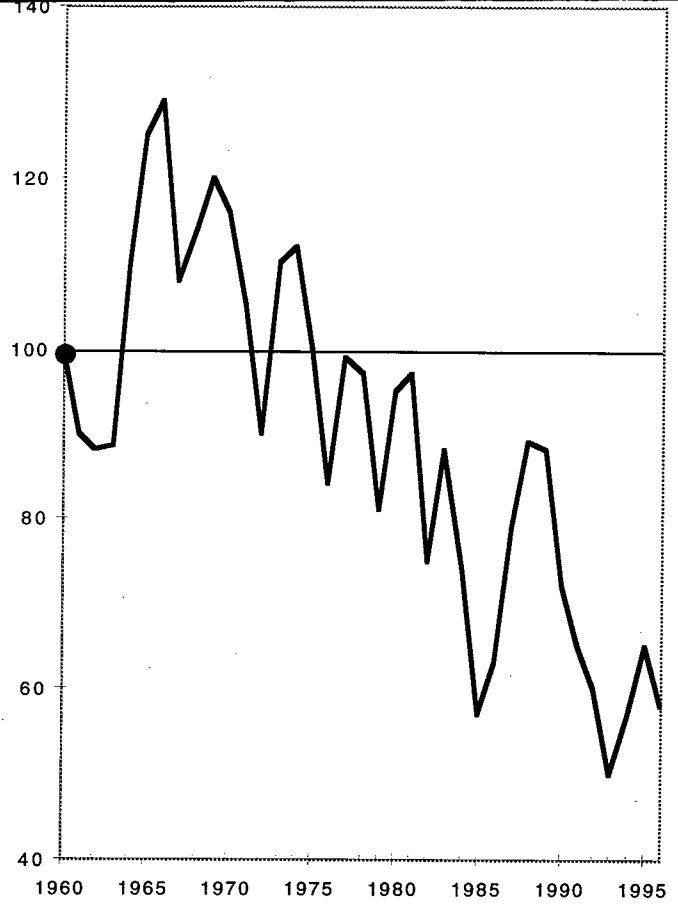


Figure 2

Metals and mineral prices as compiled by the World Bank. The value is in real terms, with 1960 = 100. The deflation factor is the dollar value index of the G5 manufacturing countries' exports.

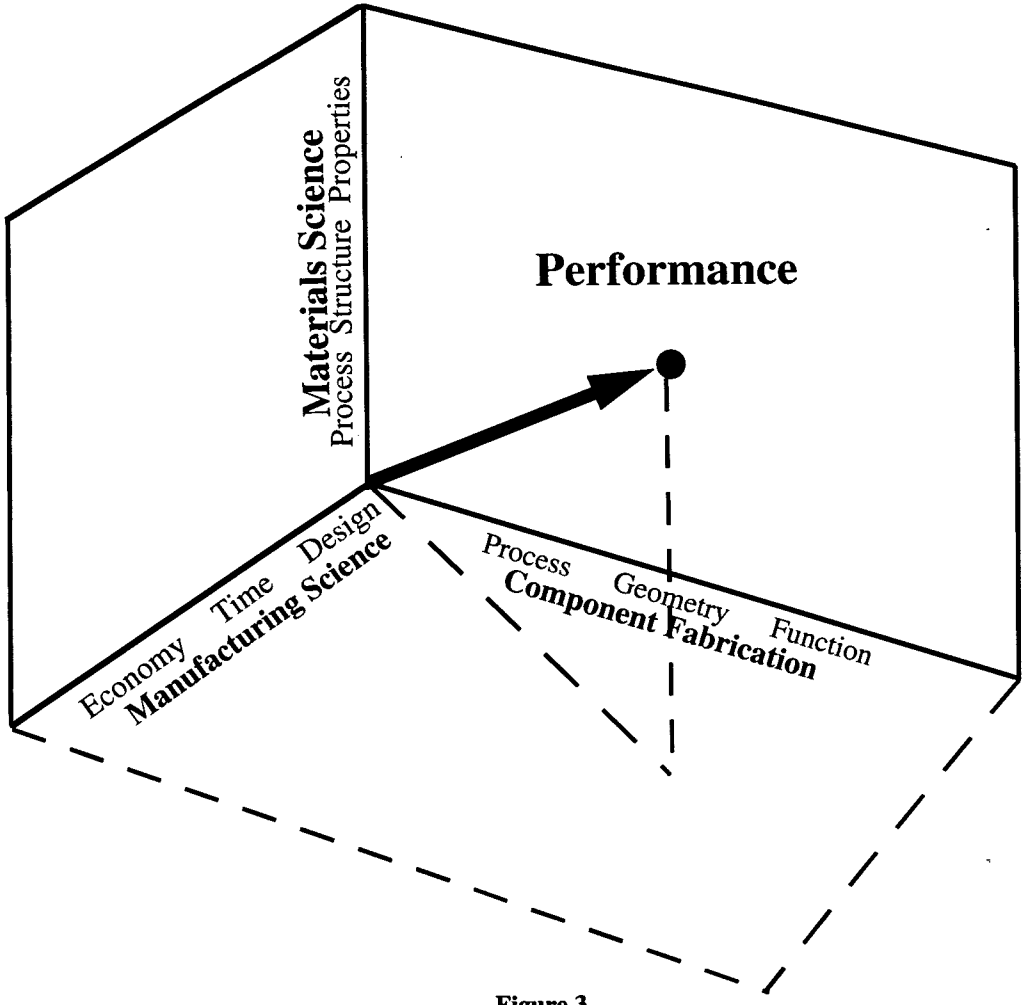
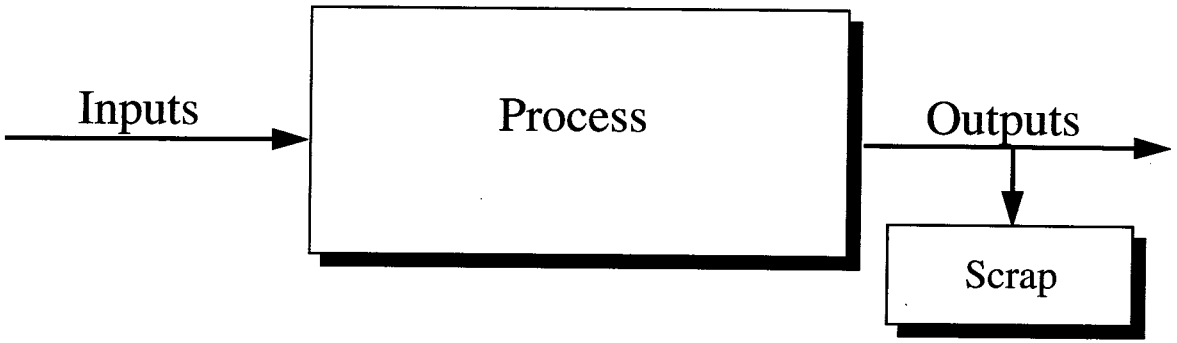


Figure 3
Diagram of how materials science, manufacturing science, and fabrication all contribute to product performance.

OLD METHOD



- Fitness for Standard

- Incoming Inspection

- Fitness for Use

- Outgoing Inspection

Figure 4

Old paradigm for materials manufacturing, in which "quality" was controlled by an outgoing inspection. The process ran open loop in the sense that information on yield and scrap rates was not received timely enough to influence the process.

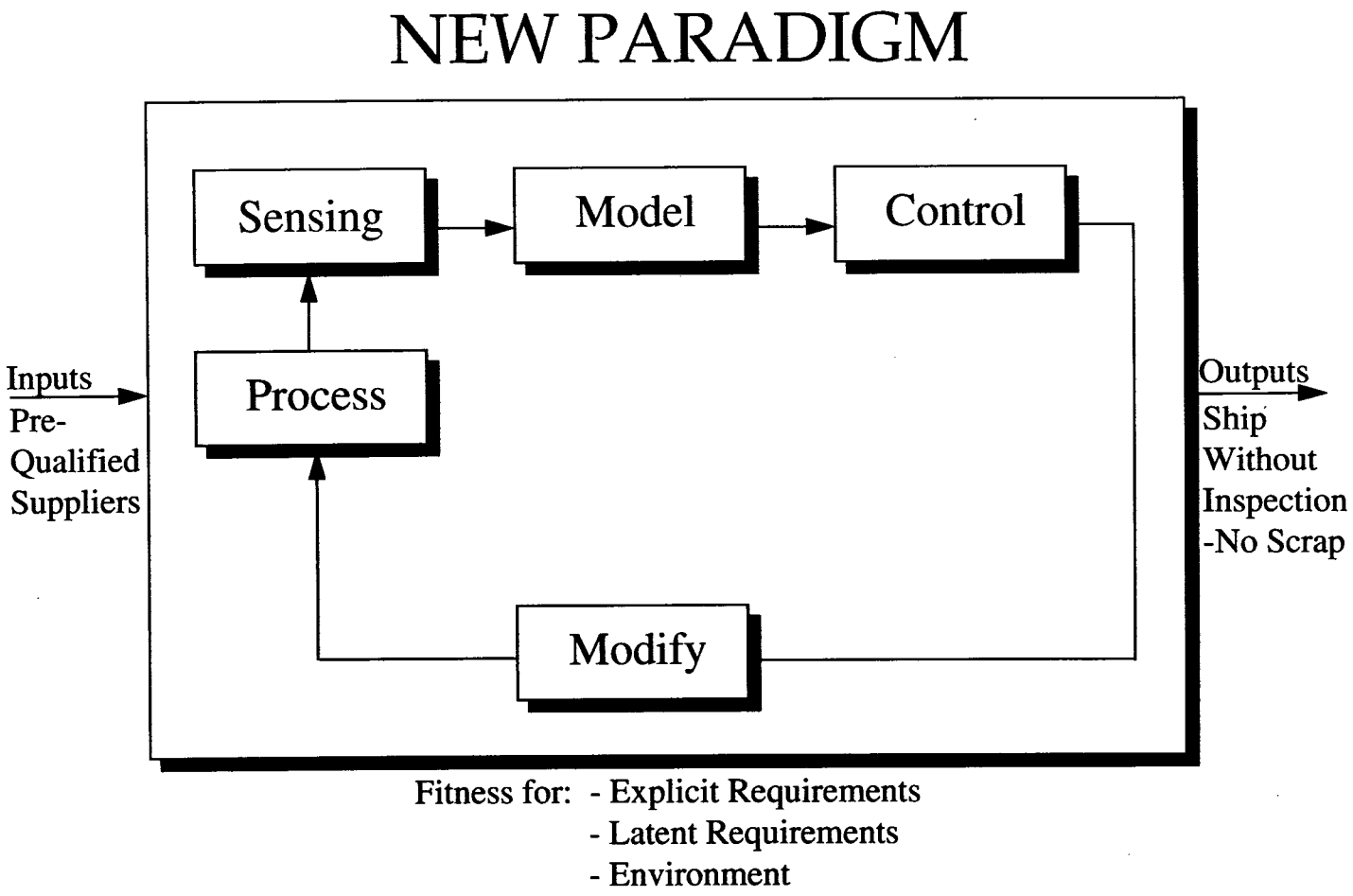


Figure 5

New paradigm used in best practice materials manufacturing companies. The process is modeled, the results are sensed in real time and the information is fed back to improve the yield and reduce the scrap.

Introduction

China always attaches importance to research and development of new materials. Since 1956, new materials has been selected as priority development field in National Science and Technology Development Outline. Since 1982 new materials research and development has been involved in National key Technology R&D Programme of China's each 5-year plan. In 1987, China started implementing of Hi-Tech Research and Development Program (so-called 863 program), advanced material was selected as one of eight priority fields. In 1998, China started implementing of Torch Program, a guideline program for developing new/ high technology industries, new material is also one of the main content. China's National Natural Science Foundation also pay great attention to basic research related to new materials. Except these, a series of engineering technology research centers and national key laboratories have been established for new materials, formatting bases for basic research and engineering research and development of new materials. Up to now, a complete new materials research, development and production system has been established. In China there are near 1000 enterprises, about 350 research institutes and 150 universities, about 100,000 scientists and engineers involved in research, development and production of new materials[1].

The high-tech advanced materials program is an integrated part of 863 program. This program is planned and managed by National Advanced Materials Committee of China, which is a 15-members experts committee appointed by State Science and Technology Commission (SSTC). The goals of this program are to develop materials science and technology, to provide key advanced materials for the related areas of 863 program, to enhance application research and engineering development of advanced materials, to increase technological innovation, to raise product competitiveness and promote the industrialization of advanced materials. The major research areas are: optoelectronic materials, advanced composite materials, high-performance metallic materials, advanced ceramics, energy-storage materials, diamond film, new material processing technology and materials design. Since execution in 1987, the remarkable progress has been made in advanced materials research and development, a series of key materials have been provided to industries and defense, more than 100 of advanced materials have been had practical applications or industrialized. In this period, a large number of excellent young or middle-aged scientists grow up, a series of research bases and engineering research centers have been established, preparing a good foundation for continuos development of advanced materials in next century.

The materials processing technology plays an important role in the development of advanced materials and occupies important position in the program. The major research topics include rapid solidification technology and spray forming, directional solidification, plasticity processing technology of hard-deformed materials such as MMC and intermetallics, superplastic forming technology for new metallic materials and ceramics, preparation of metallic and ceramic ultra-fine particles and nano-scaled particles and their consolidation technology, near-net-shape technology of metallic and ceramic materials and high temperature self-propagation synthesis (SHS) technology, thin film synthesis and thin-layer growth technology, single crystal growth technology and surface modification etc.. Most of them have had practical application and have made contributions to development of advanced materials.

THE PROGRESS OF PROCESSING TECHNOLOGY OF ADVANCED MATERIALS IN CHINA

Shi Likai

National Advanced Materials Committee of China
76, Xueyuan Nanlu, 100081, Beijing, China

Abstract

New processing technology plays an important role in the development of advanced materials. China's Hi-Tech Advanced Materials Research and Development Program always emphasizes the research and development of new processing technologies for advanced materials. Under the support of the program, in last 10 years the obvious progress has been made in spray forming, directional solidification, superplastisity forming, metallic ion implantation and surface modification, colloidal forming and in-situ solidification of ceramics, high-temperature self-propagation syntheses (SHS), high gravity synthesis of nano-scale particle etc. Some of mentioned processing technologies have made great contributions to development of advanced materials, some have had practical application in industry. This paper gives brief introduction to China's Hi-Tech Advanced Materials Research and Development Program, and summarizes some of recent progress in processing technology of the program.

The Third Pacific Rim International Conference on
Advanced Materials and Processing (PRICM 3)
Edited by M.A. Imam, R. DeNale, S. Hanada,
Z. Zhong and D.N. Lee
The Minerals, Metals & Materials Society, 1998

have yields improved but the product variations have been reduced, which has improved the overall quality. The higher yield mean higher overall productivity. The higher quality means better designs can be adopted. The consumer sees lower costs and greater functionality.

Conclusion

There has been a tremendous revolution in materials processing over the past two decades. There are very few times in history when the productivity has increased so markedly in such a brief period of time across so many industries. There are isolated examples of greater productivity increases, e.g., the Bessemer process for producing steel created much more than a doubling of productivity. This new, low cost steel did accelerate the growth of railroads, skyscrapers, shipping and the like, but the improvements in these other industries took 50 years to achieve. Over the past twenty years, we have seen a quadrupling of productivity in steel, a hundred million-fold improvement in silicon integration and magnetic storage capability, the invention and commercialization of optical storage, the commercialization of fiber optic data transmission and a host of other advances. The world is changing faster than any one person can manage. These are exciting times. New business opportunities are created everyday in both traditional and advanced materials for those astute enough to understand the technology and those savvy enough to recognize the market. This revolution is based upon a firm scientific understanding of materials processing. The benefit to society is equal in scope to the agricultural revolution and the industrial revolution of the 19th century. In the last quarter of the 20th century, we have exceeded the wealth generation of the entire 19th century. The triumphs of materials processing are benefitting more and more of the world's population. It is our challenge to extend these great improvements in materials processing productivity well into the next century.

References

1. T. W. Eagar, "Bringing New Materials to Market," Technology Review, February/March (1995), 42-49.

Rapid solidification

Rapid solidification technique (RST) offers a new way for creation of new materials and for improvement of existing materials. Rapid solidification dramatically increases solid solubility for most alloying elements, refines alloy microstructure, eliminates segregation and produces new sub-stabilizing phases in alloys. Over the last 10 years, rapid solidification technique develops very fast in China, including gas atomization, multistage rapid solidification, planar flow casting, two-roll thin strip casting, rotating blades quenching and spray forming. Some of them have been used in industry.

Atomization

Many units of inert gas atomization have been established for preparing powders of aluminum alloys, lead-tin alloys, hydrogen-storage alloys etc.. The gas atomization technique with suspension melting has been developed for preparing powders of titanium alloys and TiAl intermetallics. The large gas atomization equipment for aluminum alloys has capacity of 500 tons per year with gas sieving system and gas recycling system. The water atomization also develops fast and many facilities have been established for ferrous metals.

Rotating blades quenching

In this apparatus, a thin stream of molten metal is injected under pressure onto a high conductivity metallic blades rotating at high speed. The liquid stream is disintegrated by impact into small droplets, which are in close contact with the blades and solidified simultaneously. Its cooling rata is higher than that of gas atomization[2]. The particle can be adjusted by altering the injection hole size, injection pressure and rotating speed of the blades. Spherical powder or flake can be produced, the percentage of the flake less than 1 mm is over 80%.

Spray forming

Spray forming is an effective technology for fabrication and process of advanced materials. It can simplify consolidation process and minimize the oxygen content. It can be used to fabricate bulk materials in the shape of ingot, disk, tube (ring) and plate. It also is an effective method for fabrication of particle-reinforced MMC materials and layer/ layer composites such as clad plates, clad tubes and clad roll. The materials fabricated by spray forming process have low oxygen content, fine microstructure, low segregation and relatively high density (96-99%TD) in comparison with PM method. In China, several equipment of spray forming has been established in recent years, many materials fabricated by spray forming have had practical applications in industry. The typical samples are spray formed Al-Si alloy for video recorder drum, Al-Pb/steel strip for automobile bearing, Bi-metals for thermal sensor and clad roll for wire rolling.

Directional solidification

Directional solidification is a practical technology in fabrication of turbine blades with column crystals. Due to elimination of cross grain boundary, the longitudinal properties of the blades

are dramatically improved, thermal fatigue resistance increases by 6-10 times. The directional solidification technology is also useful to some functional materials.

Ni_3Al alloy turbine blades

The directional solidification technology has been developed for gas turbine guide blades of a Ni_3Al based IC-6 alloy. The guide blades work at the gas temperature of 1100C°. These blades passed ground testing and flight testing, and the turbine engine with these guide blades has been successfully used in airplanes.

Two-dimension radical direction solidification

It is a new technology developed for disk-shaped parts. The traditional directional solidification is one-direction technology, which is only suitable to fabrication of parts undergone only one - direction stress like blades. The developed technology can form radical directional column crystals in a disk-shaped parts by formation of a controllable strong temperature gradient from center to circular outside. This disk can be used as the parts undergone centrifugal force, if the column grain boundary are strong enough or with circular reinforcement.

Incremental melting and solidification molding

This technology[3] is combined materials preparation process with forming process, resulting to a near-net shape parts. Fig. 1 shows the principle of this technology. The metallic powder or mixture of metallic and ceramic powders is continuously fed into a mold, which has a induction coil around. The melting area in mold is limited in a very narrow layer, which moves upward from the bottom of the mold, the powder fed into mold is melted rapidly, filled in mold and solidified. By keeping proper amount of fed powder and moving speed of induction coil, a near-net shape part similar to mold can be obtained when coil reaches top of the mold. This technology can reduce or eliminate the reaction between melt and mold, and the solidification rate is fast and the crystallization is controllable. It is easy to obtain fine grain size or microstructure with fine dendrite arm spacing.

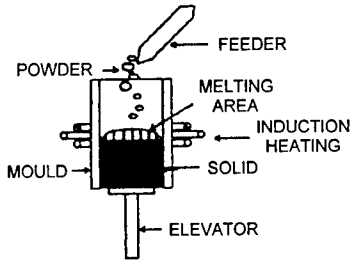


Fig.1: Principle of incremental melting and solidification molding

Superplastic forming

Superplastic forming has wide application in aeronautical industry, especially for titanium alloys. The superplastic forming of intermetallic compounds, MMC, Al-Li alloys and ceramics is the focus point in China's High-Tech Advanced Materials R&D Program.

Ordered intermetallic compounds

Intermetallics are new type of high temperature structural materials, which is listed as one of

NAMCC's priorities. The developed Ti_3Al-based alloy has excellent superplastic behavior with elongation of 1000-1240% at 960-1000°C, a complex shape pump case has been made of this alloy through superplastic forming. The superplastic behavior of Ni_3Al alloy (IC-218) pretreated by cold rolling-annealing process is also good when grain size <5μm, the maximum superplasticity reaches 646% at 1000°C and $\varepsilon=5\times10^{4}s^{-1}$. The TiAl based alloy prepared by PM or ingot method also shows good superplastic behavior and several test parts have been made. A very important development in this field is to discover large-grain superplasticity in Fe_3Al based alloy, it is reported that same phenomena also discovered in TiAl and NiAl system alloys.

SiCp MMC

SiCp particle reinforced aluminum alloy composites can be treated in simple way to get superplasticity. The LY12 aluminum alloy (similar to 7075) matrix composite with 15% SiC particle can obtain fine-grain structure through hot extrusion or other hot plastic deformation. After treatment, the material has 293-380% elongation at 520°C, from which the precision forgings of blade wheel with six blades of 2.5mm in thickness has been successfully superplastically formed[4]. Many other different parts have been made for satellite, instruments and transportation applications. By similar pretreatment process, superplastic SiCp/Al composite plate can be made and thin-walled hollow parts have been produced by plug-assisted forming or by blow forming.

Al-Li alloy Al-Li alloy is an ideal structural material for aerospace industry for its high modulus and low density. 8090 alloy has maximum elongation of 1080% at 525°C and 2091 alloy has maximum elongation of 1430% at 510°C after pretreatment, which consists of many steps: hot rolling, solid solution treatment, overaging, cold rolling or warm rolling, recrystallization and air cooling. A new pretreatment process developed consists of only hot rolling and cold rolling. The superplasticity of 2091 alloy pretreated with new process has the same level as that pretreated with traditional process. It is found that addition of more Zr is important to avoid recrystallization and grain growth during heating. Superplastic 2091 sheet has cold rolling structure before superplastic forming and the recrystallization occurs at the beginning stage of superplastic forming (at about 150-200% elongation).

Ceramics technology

The preparation technologies of ceramics with low cost and high reliability are important for industrial production of high performance ceramics. The forming technology for complex-shape parts of ceramics takes an important inter-link role between powder and sintering in ceramic processing, and is the major prerequisites for material design and composition. Development of low cost technologies for powder preparation, forming and sintering of advanced ceramics is always emphasized in the Program.

Colloidal forming

The colloid injection mouding by fast consolidation in-situ can greatly decrease production cost and remarkably improve reliability of ceramics. The developed technology is focused on the preparation and fast consolidation in-situ techniques of concentrated suspension with low

viscosity and high solids loading (50%) for dense, homogeneous and high strength green body. This method can remove agglomeration and aggregation between particles and avoid the deformation and cracking of complex-shape parts during sintering. So it can reduce machining of final parts and achieve high reliable ceramics (weibull modulus >15).

The colloid injection mouding by fast consolidation in-situ (with organic vehicle <4%) overcome intrinsic shortages for large organic contents. By fast consolidation in-situ of concentrated suspension, the structural homogeneity of green body are ensured. It is a new and advanced near-net forming technique with wide application prospects and important popularization values for ceramic industrial production.

SiC whisker orientation alignment

Several processing methods were performed to achieve whisker orientation alignment, among which extrusion was found to be a plausible way to align whisker in a uni-direction. Composites with orientation degree over 80% were prepared by optimizing the processing parameters, such as extrusion force, flow velocity, moisture content, size of extrusion nozzle. Whisker orientation alignment greatly improves not only flexure strength but also fracture toughness of SiC_w/Si_3N_4 composites in the alignment direction.

Ceramic liner steel tube by SHS

High-temperature self-propagation synthesis (SHS) is an effective method for preparation of ceramic powders and for synthesis of gradual materials. The technology of manufacturing ceramic liner steel tube by SHS has been developed and has had wide application in industries. Combined this technology with centrifugal casting, it is easy to manufacture Al_2O_3 ceramics liner steel tube. The diameter of the tube is in the range of 60 to 500 mm and the length is 3-6m. The technology of manufacturing large diameter tube up to 800mm has been developed for elbow joint. This tube has smooth inner surface and good joint strength between ceramics and steel tube. It is wear-resistant and has service live hundreds times higher than steel tube for transferring abrasive matter. It can be used as transfer tube of ore-powder, sand, coal powder or ash in metallurgical industry, power generation station and coal-mine.

Surface modification

Surface modification is an effective method to improve performance of materials and it has wide applications in industries. The research work in program focus on surface modification technology by laser, ion and electron beam, and other low-cost technologies[5].

Ion-implantation with MEVVA source[6][7]

One of the advantages of ion-implantation technology is to form desired combination of different elements beyond solid-solubility condition on the solid surface, which could be amorphous structure or be the alloy which can not be produced by conventional metallurgical technology. The ion-implantation layer improves variety of physical properties of materials surface. Metallic ion-implantation has much better effect and wider applications, than nitrogen

ion-implantation, in improvement of friction, wear, corrosion, and oxidation-proof properties of materials. For surface modification, the significant effect is usually obtained by high-dose implantation of more than $10^{17}/cm^2$, which can be satisfied by a metal vapor vacuum arc (MEVVA) ion source (Fig. 2). This new-type high-current ion source works in pulse mode and delivers an intense pulse ion current up to 1A, which elevates the temperature of the substrate obviously. The process of the diffusion of implanted atoms and correlative thermal chemical reaction lead to formation of new alloy phase in the implanted layer, which is a unique feature of MEVVA ion source relative to other conventional ion source. In recent years, 6 different types of MEVVA ion source have been developed and several type of implantation devices with MEVVA ion source established in China. Up to now, more than 30 different elements and compounds ion beam can be produced with MEVVA ion source, with pulse beam current of 0.3-0.7A, average beam current of 10 mA or more. This technology has had practical applications in surface modification of cutting tools, forging dies, extrusion dies, electric contact and machine parts. A MEVVA ion implantation device with capability of 600,000 drills per year is in operation.

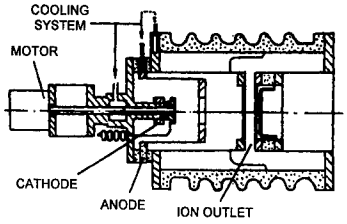


Fig.2: Principle of MEVVA ion source

PSII ion-implantation

Plasma source ion implantation is a omni-directional ion implantation technology especially suitable for surface modification of complex-shaped parts. The parts are surrounded by plasma sheath, ions come from plasma and bomb the surface of parts in all directions. This technology has been had practical application in China and several devices have been established. One device is combined with electron beam vapor source, spattering device and MEVVA ion source, it can be used for metallic ion implantation or ion enhanced deposition. The typical application of PSII is for surface modification of cutting tools, such as gear cutting hobbing, and pump parts. After treatment the hardness of parts increases by 42-88%, and the friction coefficient decreases from 0.76 to 0.07.

Micro-arc oxidation[8]

The principal of micro-arc oxidation is similar to anodizing of aluminum but applied high voltage electric field induces micro-arc (micro-plasma) in surface, which enhances electro-chemical anodizing oxidation reaction, so actually it is a plasma enhanced chemical ceramic coating. With this technology a ceramic layer of thickness of 200-300 μm can be directly formed on surface of aluminum alloys, magnesium alloys and reactive alloys such as titanium and zirconium alloys. The ceramic layer formed on surface of aluminum alloys is mainly composed of α-Al_2O_3, γ-Al_2O_3 phases in three layer structure of surface, density zone and interface zone with mico-hardness of near 30 GPa. The single micro-arc is generally in the size of several micrometers, and Al_2O_3 is melted in micro-arc area. The formed ceramic layer improves wear, corrosion, thermal impact and insulation properties of aluminum alloys. The successful application is in surface modification of textile machine parts, dramatically reducing wear and elongating their service life.

Double glow plasma surface alloying

The principle of double glow plasma surface alloying is shown in Fig.3. It consists of anode, cathode (parts), and source electrode in a vacuum chamber. The glow discharge occurs between anode / source electrode and anode / cathode, ions produced from glow discharge bomb the source electrode and spattered alloying elements deposit on the surface of parts (cathode), and diffuse into parts to form surface alloying layer. The typical application in China is for surface modification of hack saw blades, using $Mo_{80}W_{20}$ as source electrode. A production line has been put into operation with capability of 10,000,000 saw blades. After treatment, a continuos alloying layer, of 200-250μm in thickness, is formed along the contour of sawtooth of low-carbon steel saw blades. These saw blades are better than bi-metal blades or high-speed steel blades in cutting performance and much cheaper than them. This technology is expected to have applications in surface modification of valves, tubes and plates to produce high alloying layer in carbon steel.

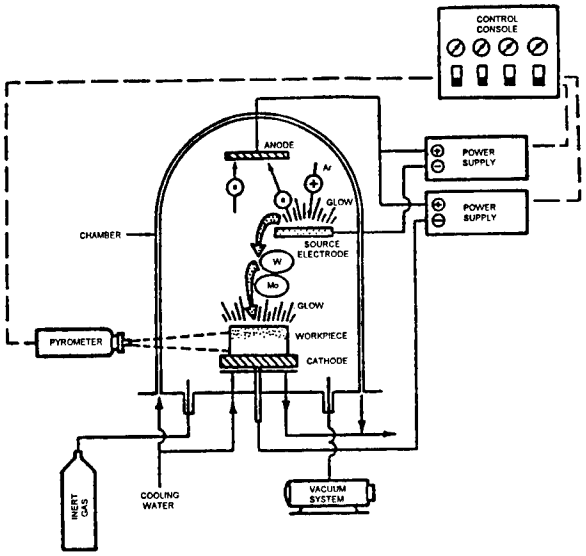


Fig. 3: Principle of double glow plasma surface alloying

Nano-particle preparation and consolidation

Laser CVD for SiC, Si_3N_4, Si particle[9]

One of the important method for synthesis of nano-scale particle is gas-phase reaction method at high temperature created by plasma or laser. Both plasma and laser synthesis technologies have been developed for Si/N/C ceramic particle. The Si/N/C particle synthesized by laser-induced gas-phase reaction is in the range of 12-40nm of mean diameter, with narrow size distribution and free of hard agglomerates. The Si3N4 content can raise to 77.77wt%. The Si/N/C particle produced is amorphous and begin to crystallize at 1500°C to form α-Si_3N_4 and β- SiC. This process has had practical application and a plant with capability of 100t/y has been in operation.

High gravity synthesis technology for fine particle[10]

Calcium carbonate has been widely used as filler in plastics, rubber, ink, pulp and coating etc..

The reinforcement property of it will be more improved when the particle size becomes smaller. The conventional technology, carbonate of lime suspension in a stirred bubbling tank or column is difficult to yield nano-particle of $CaCO_3$ with narrow size distribution, due to the low rate of mass transfer and micro-mixing. The rotating packed bed reactor (RPBR) developed can create a high gravity field by centrifugal force, resulting to significantly intensify mass transfer, micro-mixing and the multi-phase chemical reaction in it (Fig. 4). The carbonation time is shorter by 4-10 folds compared to that of conventional stirred tank reactor, and the ultra-fine particle of $CaCO_3$ with mean size of 15-30nm and very narrow size distribution can be produced. This technology has had practical application in industry and a 10000 t/y plant is under construction for $CaCO_3$ ultra-fine particle.

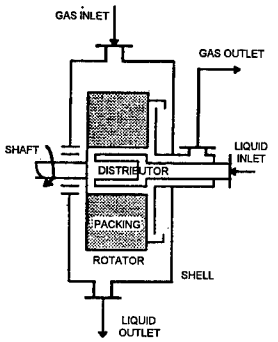


Fig. 4: Schematic diagram of RPBR

Explosive compaction

As the result of shock-wave physics in later 30 years, the high temperature and high pressure created by shock wave can be controlled and used for consolidation of new materials such as amorphous and microcrystalline powders. In explosive consolidation the compaction and sintering operation are combined together and completed at same time without heating from outside. In very short time (0.1-1 μs) the heat generated from micro-friction and micro-impaction between powders accumulates and precipitates in powder surface layer, causing its temperature to rise rapidly at the rate of 10^9-10^{10}°C/s, sometimes the temperature in powder surface reaches its melting point but the temperature inside the powder remains relatively low and get the interfaces quenched, resulting in formation of special interface structure. Explosive compaction is regarded as a possible consolidation method which can remain properties of rapid solidification products and keep the nano-scaled crystals unchanged.

In explosive compaction, the particles are enclosed in a capsule which is compacted directly by shock wave or through a driving tube. After initiation of detonation, shock wave propagates along axial direction, the capsule collapses and the particles in it are compacted and sintered. When converging tube is used, it is converged under shock wave and impacts on capsule to compact particle in it. The speed of shock wave used is in the range of 2000-3500m/s. After compaction, the compacts of rapidly solidified Al-Li alloy powder reach the density of 99%TD, without surface crack or Mach hole in the center. The density of bulk from amorphous powder of $Co_{70}Fe_2Mn_4Mo_2Si_{12}B_{10}$ reaches 99.0-99.6%TD. The XRD demonstrates that after explosive compaction, the material remains amorphous. Occasionally a small quantity of crystalline phase is found in the central area. The density of the ceramics of Si_3N_4 and SiC consolidated by explosive compaction reaches 92.3-96.5%TD and no surface macro-crack and central Mach hole.

Summary

The development of advanced materials requires new preparation and processing technologies,

and vice versa a new preparation and processing technologies will promote and accelerate the development of advanced materials. Most of advanced materials are expensive, hard-to-deform, requiring new, unusual preparation and processing technologies to keep and develop their excellent properties, or to save materials, or to reduce production cost. That is the reason why spray forming , superplastic forming, directional solidification, low-cost ceramic forming such as colloid injection molding, explosive compaction, high temperature self propagation synthesis are getting popular in development of advanced materials. Some of them have already found limited applications, but others are still under development and have long way to go to practical application. This brief introduction only covers some of main points of processing technologies in China's Hi-Tech Advanced Materials Research and Development Program, especially related to structural materials, many important areas of processing technologies are covered in other program.

References

1 Shi Likai, "Research and Development of Hi-Tech Advanced Materials in China," (NAMCC Report, National Advanced Materials Committee of China, 1996).

2 N.F. Shen et al, Chinese Patent no. 93200732.5 9 (1992).

3 Jia Chengchang, Nobuyoshi Sasaki, "Incremental Melting and Solidification Molding Process," Journal of University of Science and Technology Beijing, 18 (5) (1996), 436-439.

4 C.G.Li, L.K Shi, "Technology of Plasticity on Advanced Materials in China," Advanced Technology of Plasticity 1993, vol.1 (Beijing: International Academic Publishers,1993), 19-28.

5 Wang Yi, Liu Xianghuai, "Application and Industrialization Prospects of Surface Modification Technology in China," (NAMCC Report, National Advanced Materials Committee of China, 1995).

6 Zhang Xiaoji et al, "Development of Cathode Vacuum Arc Ion Source," Nuclear Physics Review, 14 (3) (1997), 164-166.

7 Ding Xiaoji et al, "Application of Ion Implantation by MEVVA Source in Metals Surface Modification," Nuclear Physics Review, 14 (3) (1997), 170-172.

8 Deng Zhiwei et al, "Surface Ceramics on Al and Mg Alloys with Micro-Arc Oxidation," Surface Engineering, 1996, no.4. (in Chinese)

9 Liang Yong, Li Yali, et al, "Synthesis of Nanometric Si/N/C powders by Laser Decomposition of Orgno Silazanes," Progress on Advanced Materials, (Beijing; Science Publishing House, 1995), 200-209 (in Chinese).

10 Chen Jianfeng et al, "Synthesis and Characterization of Cube-shaped $CaCO_3$ Nanometer Particles in High Gravity Field," Chinese Journal of Chemical Physics, 10 (5) (1997), 457-460. (in Chinese)

DIFFUSION IN MATERIALS HISTORY AND RECENT DEVELOPMENT

Masahiro Koiwa

Department of Materials Science and Engineering, Kyoto University
Kyoto 606–8501, Japan

Abstract

Diffusion is a process that is fundamental in the art and science of materials. The knowledge of diffusion behaviour, therefore, is essential for the production of materials or for their use in practical applications. In the first part of this paper, a brief review is given on historical development of the quantitative study of diffusion: the establishment of the diffusion law by A. Fick, the first quantitative measurement of solid state diffusion (Au in Pb) by W. Roberts-Austen and the demonstration of the self-diffusion in Pb using natural radioactive isotope by G. Hevesy. In the second part, recent investigations on the mechanism of diffusion in intermetallic compounds are reviewed.

The Third Pacific Rim International Conference on
Advanced Materials and Processing (PRICM 3)
Edited by M.A. Imam, R. DeNale, S. Hanada,
Z. Zhong and D.N. Lee
The Minerals, Metals & Materials Society, 1998

Historical development

Fick: the establishment of the diffusion law

A serious experimental study of diffusion was made by Graham on diffusion of salts in water [1]. This stimulated Fick to develop a mathematical framework to describe the phenomena of diffusion using the analogy between thermal conduction and diffusion [2]. It is interesting to quote the observation by Tyrrell [3] on the contributions by Graham and Fick:

> More than a century of experience has shown that the value of Fick's contribution to the study of diffusion in liquids, and also in its later application to gases, lies preeminently in the stimulus it gave, and is still giving, to accurate experimental work, and in the provision of a concise and easily appreciated form for the expression of experimental data. A glance at Graham's extensive, and almost unreadable, descriptions of quantitative studies on diffusion, will show how great a contribution this was.

Fick's renowned paper (2) is signed as 'Demonstrator of Anatomy, Zürich.' He entered the University of Marburg with the intention to specialise in mathematics, but switched to medicine on the advice of elder brothers. Adolph Fick became an outstanding figure in that small group of nineteenth century physiologists who applied the concepts and methods of physics to the study of living organisms, and thereby laid the foundations of modern physiology.

Roberts-Austen : the first quantitative measurement of solid-state diffusion

William Roberts-Austen studied at the Royal School of Mines graduating in 1865 when he became assistant to Thomas Graham at the Mint, where he studied salt diffusion and the absorption of hydrogen by metals and became a skilled assayer capable of measuring the most minute quantities of gold. In diffusion experiments, it is essential to keep the temperature constant for a long period of time and to measure it accurately. The difficulty in measuring temperature was overcome by adopting Le Chatelier's platinum-based thermocouples and devising an 'autographically recording pyrometer.' In his paper of 1896 entitled 'Diffusion of Solid Metals. Gold, Diffusing into Solid Lead' [4], he states:

> The following experiments constitute, so far as I am aware, the first attempt to actually measure the diffusivity of one solid metal in another.

It is surprising to observe that the value of the diffusion coefficients of Au in Pb reported by him are similar to those determined by modern techniques in the 1960's and 1970's using radioactive isotopes. The choice of the system Pb–Au was really fortunate to demonstrate the otherwise generally slow diffusion processes in solids; the diffusion of noble metals in lead is now known to be exceptionally fast, the detailed mechanism of which is still subject in dispute. It is of interest to quote the following statement of Barr in his recent review, 'The origin of quantitative diffusion measurements in solids: a centenary view' [5]:

> The most surprising omission in his diffusion paper is any discussion or analysis of the temperature dependence of the diffusion coefficient although the metallurgist R. F. Mehl [6] attributes to Roberts-Austen relating that temperature dependence to the concept of activation energy introduced by Arrhenius in 1889. It is possible that this linkage is made in the Reports of the Alloys Research Committee chaired by Roberts-Austen between 1891 and 1899. These reports are not readily accessible and the question is still not settled. Certainly, by 1922 the connection had been made by Dushman and Langmuir [7].

Hevesy : the first measurement of self-diffusion using radioactive isotopes

The idea of self-diffusion was introduced by Maxwell, when calculating the rate of diffusion of gases. No further use was made of this concept until fifty years later, when Hevesy made the experiment on self-diffusion in liquid (1920) and solid lead (1921) by using natural radioactive

isotopes, ^{210}Pb and ^{212}Pb [8,9]. He received the Nobel prize in 1943 for his work on the use of isotopes as tracers in the study of chemical processes. His name is also remembered for the discovery of the 72nd element in the periodic table, hafnium (Hf).

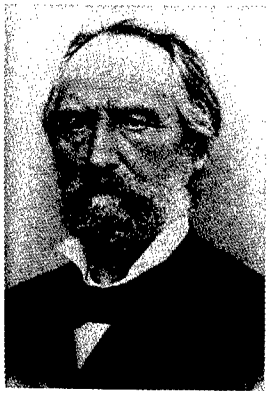


Figure 1: Adolph E. Fick (1829–1901)



Figure 2: William C. Roberts-Austen (1843–1902)



Figure 3: George Hevesy (1885–1966)

Diffusion mechanisms in intermetallic compounds

In pure metals or solid solutions, self-diffusion occurs by random motion of vacancies. In ordered alloys or compounds, however, random vacancy motion is not possible as it would disrupt the equilibrium ordered arrangement of atoms on lattice sites. Thus, the mechanism of diffusion in this type of materials is of great interest. The present author has reviewed the diffusion mechanisms in the B2 type and the $L1_2$ type compounds [10,11].

B2 compounds

The diffusion behaviour in the B2 type compounds has been more extensively studied than that in compounds of any other crystal structures. Huntington [12] first suggested the possibility of a six-jump vacancy cycle that allows diffusion to take place exclusively by means of nearest neighbour vacancy jumps. The analytical expression of the diffusion coefficient for this mechanism has been derived by Arita, Koiwa and Ishioka [13]. For this mechanism, the ratio of the diffusion coefficients of the two constituent atoms should fall in the range between 1/2 and 2.

Kao and Chang [14] have shown that the six-jump vacancy mechanism can account for the compositional dependence of the self-diffusion coefficients in the vicinity of stoichiometry using thermodynamic arguments, and proposed a new mechanism, termed anti-structure bridge mechanism, to account for the diffusion at large deviations from stoichiometry. The validity of this mechanism has been critically examined by Belova and Murch [15].

For some intermetallic compounds such as CoGa, the ratio of the two diffusion coefficients is outside the range predicted for the six-jump mechanism. Stolwijk et al. proposed a new mechanism termed as triple defect mechanism [16]; the ratio predicted for this mechanism is between 1/13.3 and 13.3 [17].

$L1_2$ compounds

Figure 4 illustrates the atomic arrangement of an A_3B compound of the $L1_2$ type structure; the arrangement is not symmetrical for A and B atoms. A atoms occupy the face-centre sites, which constitute the α sublattice, and B atoms occupy the cube-corner sites, which constitute the β sublattice. While an A atom has eight atoms of the same species at the nearest-neighbour

sites (Fig. 4b), a B atom is surrounded by twelve unlike atoms (Fig. 4c). Thus, if the diffusion occurs by vacancy jumps to nearest neighbour sites, A atoms are expected to diffuse much faster than B atoms; a jump of a B atom to the nearest-neighbour site inevitably destroys the ordered arrangement, while no disordering occurs for the jump of an A atom. The faster diffusion of the major element A in compounds of type A_mB_n where the ratio m/n is greater than 2, has been recognised and termed 'the ordered Cu_3Au rule' by d'Heurle and Gas [18].

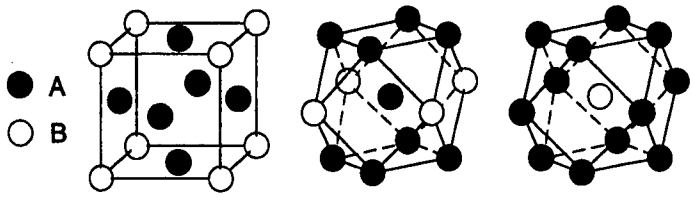


Figure 4: Atom arrangement in an A_3B alloy of the $L1_2$ type structure.

Recently, the present authors have analysed the diffusion behaviour of the Ni-based compounds of the $L1_2$ type compounds: Ni_3Al, Ni_3Ga and Ni_3Ge [19]. The following trends are observed.

(1) The diffusivity of the major element, Ni, is roughly equal for the three compounds. It is lower than the self-diffusivity in pure Ni by an order of magnitude.

(2) The diffusivity of the minor element is very different for the three compounds. The ratio of the diffusion coefficient of the minor element to that of the major element, D_B/D_A, at, for example, the temperature $T = 0.85\ T_m$ is

Ni_3Al	0.2–0.4
Ni_3Ga	0.4–0.8
Ni_3Ge	0.007

When the very low diffusivity of Ge in Ni_3Ge was discovered [20], it appeared natural and understandable from the atomic arrangement. However, in Ni_3Ga, the diffusivity of the minor element turns out to be of the same order of magnitude as that of the major element.

As a possible mechanism of diffusion in A_3B alloys of the $L1_2$ type structure, we have proposed the following model [19]. The self-diffusion of the major element A is possible through the ordinary vacancy mechanism on its own sublattice (α sublattice). When appreciable numbers of vacancies V_α and antisite atoms B_α exist, the diffusion of B atoms can also be achieved by the migration of such antisite atoms over the α sublattice. The model accounts well for

(1) the magnitudes of the diffusion coefficients of Ni in the three compounds,

and

(2) the relative magnitudes of the diffusion coefficients of Al and Ni in Ni_3Al in comparison to those in pure Ni.

The principal features observed in the self-diffusion in Ni_3Ga and Ni_3Ge can also be understood in terms of the α sublattice vacancy mechanism.

Acknowledgment

The author is grateful to Professor D. L. Beke of Kossuth University for providing the portrait of G. Hevesy.

References

1. T. Graham, "Liquid Diffusion Applied to Analysis," Phil. Trans. Roy. Soc., 151 (1861), 183–224.

2. A. Fick, "Über Diffusion," Poggendorff's Annalen, 94 (1855), 59–86; "On Liquid Diffusion," Phil. Mag, 10 (1855), 30–39.

3. H. J. V. Tyrrell, "The Origin and Present Status of Fick's Diffusion Law," J. Chem. Education, 41 (1964), 397–400.

4. W. C. Roberts-Austen, "On the Diffusion of Metals," Phil. Trans. Roy. Soc., A187 (1896), 383–414.

5. L. W. Barr, "The Origin of Quantitative Diffusion Measurements in Solids: A Centenary View," Defect Diffusion Forum, 143–147 (1997), 3–10.

6. R. F. Mehl, "The Historical Development of Physical Metallurgy," Physical Metallurgy, third, revised and enlarged edition, ed. R. W. Cahn and P. Haasen (Elsevier Science, 1983), 1–35.

7. S. Dushman and I. Langmuir, "The Diffusion Coefficient in Solids and Its Temperature Coefficient," Phys. Rev., 20 (1922), 113.

8. J. Groh and G. v. Hevesy, "Die Selbstdiffusiongeschwindigkeit des geschmolzen Bleis," Ann. Physik, 63 (1920), 85–92.

9. J. Groh and G. v. Hevesy, "Die Selbstdiffusion in festem Blei," Ann. Physik, 65 (1921), 216–222.

10. M. Koiwa, "Diffusion Mechanisms in the B2 Type Intermetallic Compounds," Ordered Intermetallics—Physical Metallurgy and Mechanical Behaviour, eds. C. T. Liu, R. W. Cahn and G. Sauthoff (Kluwer Academic Publishers, 1992), 449–464.

11. M. Koiwa, H. Numakura and S. Ishioka, "Diffusion in $L1_2$ Type Intermetallic Compounds," Defect Diffusion Forum, 143–147 (1997), 209–222.

12. H. B. Huntington, private communication to L. Slifkin.

13. M. Arita, M. Koiwa and S. Ishioka, "Diffusion Mechanisms in Ordered Alloys—A Detailed Analysis of Six-Jump Vacancy Cycle in the B2 Type Lattice," Acta metall., 37 (1989), 1363–1374.

14. C. R. Kao and Y. A. Chang, "On the Composition Dependencies of Self-Diffusion Coefficients in B2 Intermetallic Compounds," Intermetallics, 1 (1993), 237–250.

15. I. V. Belova and G. E. Murch, "The Anti-Structure Bridge Mechanism for Diffusion in Ordered Alloys of the B2 Type," Intermetallics, 6 (1998), 115–119.

16. N. A. Stolwijk, M. van Gend and H. Bakker, "Self-Diffusion in the Intermetallic Compound CoGa," Phil. Mag. A, 42, 783 (1980), 783–808.

17. H. Bakker, N. A. Stolwijk and M. A. Hoetjes-Eijkel, "Diffusion Kinetics and Isotope Effects for Atomic Migration via Divacancies and Triple Defects in the CsCl (B2) Structure," Phil. Mag. A, 43 (1981), 251–264.

18. F. M. d'Heurle and P. Gas, "Kinetics of formation of Silicides: A Review," J. Mater. Res., 1 (1986), 205–221.

19. H. Numakura, T. Ikeda, M. Koiwa and A. Almazouzi, "Self-Diffusion Mechanism in Ni-based $L1_2$ Type Intermetallic Compounds," Phil. Mag. A, 77 (1998), 887–908.

20. H. Yasuda, H. Nakajima and M. Koiwa, "Diffusion in $L1_2$-Type Intermetallic Compounds," Defect Diffusion Forum, 95–98 (1993), 823–830.

Recent Trends in Spray Forming Process and Its Applications

Hyung Yong Ra , Hyun-Kwang Seok, Kyu Hwan Oh,
Jae-Chul Lee* and Ho-In Lee*

Div. of Materials Science and Engineering, Seoul National Univ., 151-742, Seoul,
and RASOM, Korea
* Div. of Metals, Korea Institute of Science and Technology, Seoul, Korea

Abstract

In general, spray forming consists of three sequential steps: i) atomization - melt stream is broken into the small liquid droplet jet stream by a high pressure gas; ii) transfer of droplets - the force subjected on droplets by the high velocity gas accelerates droplets; and iii) deposition - droplets, which complete the flight of a certain distance, impinge the substrate in their semi-solid state.

Since the 1st international conference on Spray Forming in 1990, number of research organizations and research activities on spray forming have been continually increased. This trend stemmed from the potential of the spray forming in producing new alloys.

One of the major advantages of spray forming process is its ability in producing rapidly solidified bulk materials in the form of plate, tube or billet by deposition of semi-solidified droplets on substrate. Spray forming also offer fine and uniform microstructures, which are limited to achieve via various conventional forming processes. In addition, Spray forming is efficient for producing near-net-shape products and metal matrix composites.

However, in spite of such advantages, the commercialization of spray forming has been rather slow due to such technical difficulties as the preform shape control, low yield, secondary fabrication costs to consolidate the preform, etc. To date, some of these problems are now being solved by developing adequate mathematical modeling and efficient equipment.

This paper overviews the research activities carried out world wide, particularly on the fundamental researches, development of equipment, and commercialization of various alloys.

The Third Pacific Rim International Conference on
Advanced Materials and Processing (PRICM 3)
Edited by M.A. Imam, R. DeNale, S. Hanada,
Z. Zhong and D.N. Lee
The Minerals, Metals & Materials Society, 1998

1. Introduction

Since the 1st international conference on Spray Forming in 1990, number of research organizations and research activities on spray forming have been continually increased. This trend stemmed from the potential of the spray forming in producing new alloys. Another advantage in spray forming can be the ability to fabricate materials with fine and uniform microstructures which conventional ingot metallurgy could not achieve. As a result, as many as 28 companies world wide, as shown in Table 1, now possess the license of this technology.

However, in spite of such advantages, the commercialization of spray forming has been rather slow due to such technical difficulties as the preform shape control, low yield, secondary fabrication costs to consolidate the preform, etc. To date, some of these problems are now being solved by developing adequate mathematical modeling and efficient equipment.

Research activities on the spray forming can be categorized as the fundamental researches, development of equipment, and alloy developments which are described in following sections.

Table 1 Companies owned the osprey preform process license (April, 1996)

Field	Companies
Aluminum alloy	Peak(Germany), Sumitomo Light Metals(Japan), Pechiney(France), Aluswisse(Switzerland), Alcoa(USA)
Superalloys	Howmet(USA), General Electric(USA), Teledyne Allvac(USA)
Rolls	SHIFF(Japan), CRM(Belgium), Forged Rolls(UK), British Rollmakers(UK)
Plant Builders	Mannesmann Demag(Germany), Sumitomo Heavy Indstries(Japan)
Copper alloys	Wieland(Germany), Boillat(Switzerland), Olin(USA)
Special Steels	Sandvik(Sweden), Babcock and Wilcox(USA), Kobe Steel(Japan), Special Melted Products(UK), Danish Steel(Denmark), Rautaruukki(Filand)
Research & Development	Drexel Uinv.(USA), US Navy(USA), RIST(Korea), Penn State Univ.(USA), Ipen(Brazil)

2. Fundamental Researches on Spray Forming

In general, spray forming consists of three sequential steps[1]: i) atomization - melt stream is broken into the small liquid droplet jet stream by a high pressure gas; ii) transfer of droplets - the force subjected on droplets by the high velocity gas accelerates droplets; and iii) deposition - droplets, which complete the flight of a certain distance, impinge the substrate in their semi-solid state.

Atomization

Among various techniques used to make powders from a molten metal, the main focus in this section is the gas atomization[2]. In this technique, high pressure gas, delivered through the atomizer, brakes the stream of a molten metal into atomized droplets. Inert gases(N_2, Ar, He) are usually used as a atomizing medium to prohibit excessive oxidation. However, inert/O_2 gas mixture can also be used for controlled oxidation of alloy in reactive spray forming[3]. During the atomization, the gas/metal ratio, gas pressure, and atomizer design are the most important parameters, which influence the size and the microstructures of droplets. In general, the high gas pressure and high gas/metal ratio promote small, therefore fine microstructured droplets. In some applications, scanning atomizer, linear atomizer or twin atomizer can be used to enhance the efficiency of spray forming.

Transfer of Droplets

After atomization complete, liquid droplets are propelled away from the atomization zone by the atomizing gas. During the flight, the reaction between droplets and cooling gas results in change in the momentum and the enthalpy of droplets[4-8]. Thermal behavior of droplets in this step determines the initial microstructure of deposits and the enthalpy flow rate into preform, which affects the preform temperature during spray forming. During the flight, the normal cooling rate of droplets can be in the range of 10^2-10^6 °/sec depending on their size, leading to a very fine microstructure. In addition, the control of the droplet trajectory is of significance in order to minimize over-spray losses and maintain the preform shape.

Forming

During the forming step, the atomized droplets impinge a specially designed collector substrate[9-12]. To control the microstructure of the preform during the forming process, it is essential to have the knowledge on the shape forming mechanism. The information obtained from the forming mechanism can provide various design parameters required to build the spray forming devices and the control scheme of the process. Up to date, various numerical models[13-17] in an attempt to predict the shape of preform have been presented.

Droplets, which had undergone rapid solidification, experience a slow cooling after deposition. As soon as droplets impinge the preform surface, the ultra fine grains and the precipitates within droplets formed during the flight stage begin to grow. Although such a microstructural evolution causes relatively coarse grain(in the vicinity of 30-50 μm), the advantage of this

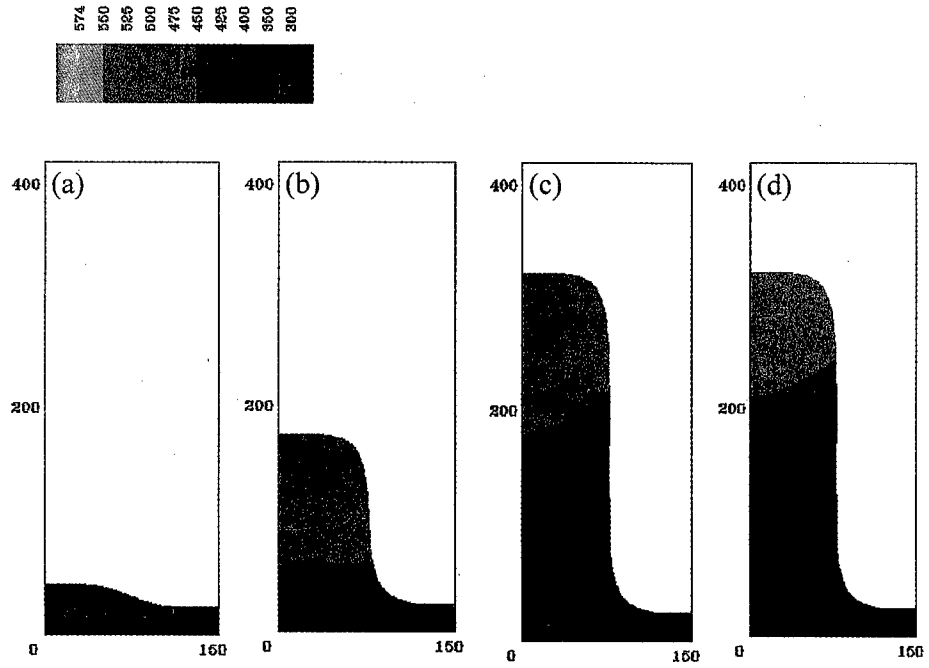


Figure 1: Temperature profile of rod during spray forming at the calculation conditions of V=0.8mm/sec, T_{in}=596 °C, T_{sub}=300°C and spray forming time 400 sec.[21]
(a) 50 sec (b) 200 sec (c) 400 sec (d) 450 sec

process lies in its ability to avoid macro-segregation of solutes, resulting in the uniform and equiaxed microstructures. Such a microstructural change of the preform can be predicted from the heat transfer analysis on the preform[17-20], which usually is performed after the thermal analysis of flying droplets and shape calculation of preform. Figure 1 shows the temperature profiles within the rod-shaped preform calculated based on the 2-Dimensioal analysis using the boundary fitted coordinate method[21]. With increasing forming time, maximum temperature, which is built up on the rod top, becomes saturated to a certain value. However, by the time when the forming stops, the very top surface of the preform cooled down rapidly, leaving the thermal island having the maximum temperature just underneath the top surface.

3. Equipment and Methodology Development for Reducing Operating Costs

Fabrication of preform with undesired dimension causes material loss during scalping, which results the high cost of the process. Therefore, accurate dimensional control is essential to minimize the material loss. Dimensional control can be possible for a 250mm diameter aluminum billets within ± 2mm range[22] by using the process control system. Cost reduction can also be achieved by using twin atomizer and design change of the forming machine. With twin atomizer, considerable cost saving can be expected due to the increased production rates, lower gas consumption, increased yield of deposited metal, and production of larger diameter billets up to 450 mm in diameter.[22] In the case of the vertical forming machine, the forming mechanism essentially consists of a disc-shaped collector, attached to a vertical drive shaft which provides collector rotational and axial movements. On the other hand, in the case of the horizontal forming machine, the collector moves along a horizontal direction rather than a vertical direction. The main advantage of the horizontal system is the possibility of producing very long or even continuous billets without being restricted by the height of the building. The horizontal concept, in conjunction with the twin atomizing system, is currently being used at Osprey Metals to fabricate special steel billets weighing up to 1 ton and 400mm in diameter in a joint project with Special Melted Products(UK), Danish Steel(Denmark) and Mannesman Demag(Germany)[23]. The reduced operating costs can be achieved by the large scale forming equipment. The equipment capable of forming up to 5 ton melt to make pipe or bimetallic billets was operated by Carderok Division Naval Surface Warfare Center(NSWC, USA) with Babcok and Wilcox Nuclear Equipment Division(B&W, USA)[24].

4. Alloy Development and Its Commercialization

Aluminum Alloy

Mazda Motor Corporation adopted the spray formed and extruded Al-17%Si-6Fe-Cu-Mg alloy to the rotor of Miller cycle engine[25]. PEAK(Germany)[26] also spray formed aluminum alloy containing 25% Si. The spray formed and extruded hyper-eutectic aluminum alloys have been tried to apply to automotive field such as cylinder liner, piston, connecting rod. Seoul National Univ., KIST and Dooray Air Metal in Korea have been studying the possibility of hyper-eutectic aluminum alloys and Al-ceramic composite on structural applications such as piston pin, valve retainer and cylinder liner, etc. The semi-solid forming of spray formed hyper-eutectic aluminum alloys and thixoformable Al-ceramic composite is also being investigated. Other new alloys, such as Al-Zn, Al-Li, and Al-Si-X have been investigated extensively by various organizations due to their high specific strength, low density, and low coefficient of thermal expansion which are suitable for structural applications.

In conventional casting, the addition of Fe in aluminum alloy introduces accicular Al-Fe inter-

metallic which causes detrimental effect on mechanical properties. On the other hand, spray forming results fine and uniform Al-Fe inter-metallic compounds such that Al-Fe alloys with improved elevated temperature properties, wear resistance and good machinability can be fabricated [27]. Such a refining effect of the second phase can also be observed in Al-20Si alloy. Figure 2 shows the size of Si particles in the Al-20Si alloy produced by the conventional DC casting (refiner Al-Cu-P was added) and the spray forming. Si particles in the cast Al-20Si alloy exhibit faceted polygonal morphology, while those in the spray formed Al-20Si alloy show irregular shape due to the agglomeration of several particles of less than 10-15μm in size. It is noted, however, that these Si agglomerates were observed to be broken into separate particles during extrusion[21].

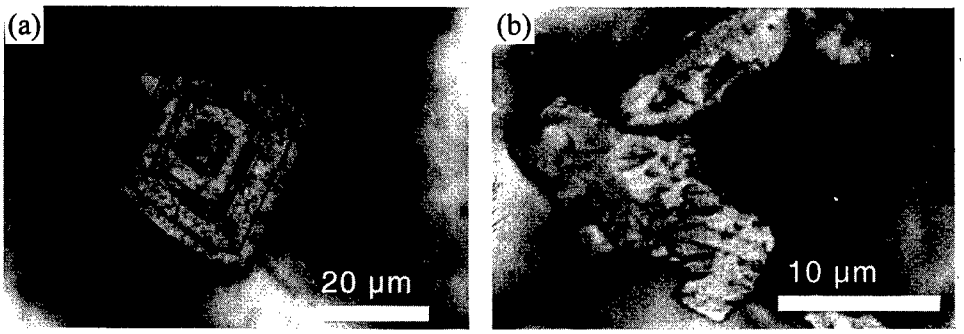


Figure 2: Magnified Si particles(etched by NaOH + H_2O) in ingot fabricated by conventional casting(a) and in the center of billet fabricated by Spray Forming(b).[21]

Super Alloy

One of the primary issues regarding the application of spray forming for superalloy is the non-metallic inclusion content in the resulting products. During spray forming, various non-metallics debris originated from crucible linings and transfer tubes can be introduced into the melt. Use of CIG(Cold-Walled-Induction Guide) was found to be efficient for avoiding the inflow of ceramic inclusions into the melt[28]. The combination of ESR(Electro-Slag-Rmelting), CIG and spray forming systems used at GE Corporate R&D(USA) results in a more efficient process for producing inclusion-free clean materials.

The new generation of large high thrust engines demands more strict requirements for rig/casing components. The spraycast-X route is considered to have potential for competing such demands. Rolls-Royce(UK) with Howmet Corp.(USA) and Ladish Corp.(USA) have produced U720 superalloy with acceptable mechanical properties and good workability by spraycasting followed by HIPing or ring rolling[29].

Table 2. The tensile results for near-net-shape processed alloy 625 pipe[31].

Piping Material	Yield Strength (ksi)	Ultimate Strength(ksi)	Elongation (%)
Conventional Ingot	72	144	40
Fully dense P/M	74	140	47
S.F/roll extruded	70	146	39
ASTM Spec. B444-84	60	120	30

Alloy 625 tube for naval submarine applications was spray formed and roll extruded by NSWC(USA) program[30]. The NSWC program indicated that near-net-shape manufacturing

by Osprey spray forming is a viable alternative for producing alloy 625 tubular preform. The tensile test results for the near-net-shape processed alloy 625 pipe are presented in Table 2.

The seamless composite tubes, outer component of Sanicro 65(Nickel base superalloy) on to a carbon steel mandrel, was spray formed by Sandvik(Sweden) to serve as evaporator and superheater material in waste incinerators. The composite tubes of Sanicro 65 on to a carbon steel mandrel meet the requirements to endure high pressure water or steam inside and a flue gas mixed with corrosive deposits on the outside[31].

Steels

The first commercialization of spray forming was succeeded in Japan by Sumitomo Heavy Industries Foundry and Forging Company[32], which has been manufacturing spray formed rings of high-chromium cast iron and high-carbon high speed steels for several years. The main advantage of such products can be found from the uniform microstructure with fine carbides, leading to improved thermal fatigue resistance and consequently longer roll lives compared to conventional cast products. Figure 3 shows the typical micrographs of high speed steel produced by the conventional casting and the spray forming.[33] In recent years, there also has been considerable interest in the direct manufacture of large clad rolls, particularly aimed for use of hot and cold strip mills. The project for manufacturing of clad rolls has been carried out by Forged Rolls Ltd.(UK), Osprey Metals Ltd.(UK), and Sheffield University(UK)[34]. Spray formed 0.8V/3-5Cr steel and 17Cr iron showed very fine and uniform microstructures. The resultant clad roll has a sound metallurgical interfacial bond between deposit and substrate even in the as-sprayed condition [34].

The European companies of Special Melted Products Ltd.(UK), Danish Steel Works Ltd.(Denmark), Mannesmann Demag Huttentechnik AG(Germany) and Osprey Metals(UK) have progressed the project to demonstrate the applicability of spray forming in the horizontal orientation as a viable process for industrial scale steel production[23]. As-sprayed preform of D2 cold work tool steel(1.5%C, 12%Cr, 1%Mo, 1%V) and Jethete M152(12%Cr) steel show uniform microstructure and superior workability.

Mechanical properties of the spray formed and forged materials were also found out to be superior to the conventional products. Spray forming and evaluation of T15 high speed steel and H13 hot work tool steel are still in hand. Spray forming of the thick walled(> 1 in) pipe with large diameters has the potential to compete with certain centrifugal cast pipe product[24].

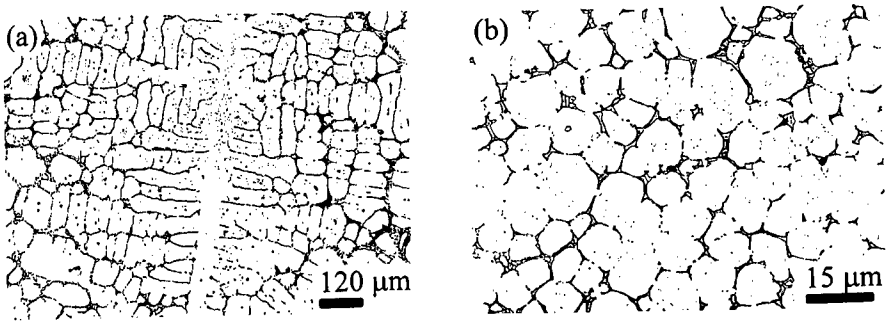


Figure 3: Micrographs showing the microstructures of Fe-1.3C-3V-4Cr-6Mo-6.5W-8Co high speed steel produced by conventional casting(a) and by spray forming (b)[33]

Spray forming of the thick walled(> 1 in) pipe with large diameters has the potential to compete with certain centrifugal cast pipe product[24]. Spray forming of various special alloys, such as bimetallic materials, corrosion resistant stainless steels, high speed steel M4, Nickel base superalloy 625, etc. on preheated carbon steel bar showed a sufficient bonding strength between the deposit and the substrate, resulting in good mechanical properties [24].

Copper Alloy

Swissmetal(Switzerland) has considered the spray forming of Cu-15Ni-8Sn(C72900) to replace machinable Beryllium-Copper alloy(C17300). Addition of special elements such as graphite particles during spray forming of Cu-15Ni-8Sn makes the alloy to acquire a very good machinability. Another research activity is to develop a new bronze with high Sn content(>8%) in an attempt to minimize the solute segaration. In the past, this alloy was produced by conventional ingot metallurgical route. However, hot or cold deformation of the cast high Sn-bronze was difficult due to the extensive macrosegregation of the solute[35].

CuCrZr has been spray formed for welding applications by Wieland(Germany). The electrode caps life of the spray formed CuCrZr were 1150 spots, which is more than doubled to caps produced by the continuous casting method. Cu alloy electrode tends to form Cu-Zn layers on the surface of hot galvanized steel. These Cu-Zn layers drastically reduce the working life of the electrode. Spray formed CuCrZr welding electrodes containing Al_2O_3 may reduce this effect and lengthen the life of electrode under certain occasion. More detailed researches to find out the types and sizes of reinforcements effective for prolonging the life of electrode are to be carried out[36].

Metal Matrix Composites

SiC_p/Al alloy composites have shown a significant improvement in their tensile strength, elastic modulus as well as wear resistance. Improved properties of SiC_p/Al composites are due to the transfer of shear load at the matrix/reinforcement interface. However, in SiC_p/Al composites, SiC reacts with Al to form Al_4C_3 and Si at elevated temperatures. The interest in Al_4C_3 stems from the fact that this phase is brittle and very sensitive to moisture contact, resulting in degradation of composite properties. As a result, fabrication of SiC/Al composite devoid of Al_4C_3 has long been one of the major concerns.

Various processing methods have been developed to fabricate metal matrix composite. Among them, such processes as compocasting, squeeze casting, powder metallurgical(PM) hot pressing, and spray forming are of commercial significance.

Melt process, such as compocasting, is known as simple and cost effective method for fabricating composites. This process, however, can only be applied to certain matrix alloys where prolonged contact time at elevated temperatures will not degrade SiC_p. For example, Al alloys have to contain high Si contents, such as 8 at. % when fabricating at 700 °C, to avoid the interfacial reactions in SiC_p/Al alloy composites. This is why melt process is usually applied for producing cast Al alloy composites, such as SiC_p/A390 Al composite. Therefore, compocasting may not be suitable for making wrought Al alloys reinforced with SiC_p, such as the SiC_p/2024 Al composite, due to the inherently low Si contents within Al matrix alloys.

By co-injection of reinforcement during spray forming, metal matrix composite devoid of the interfacial reaction products can be fabricated. This is due to the fact that fabrication

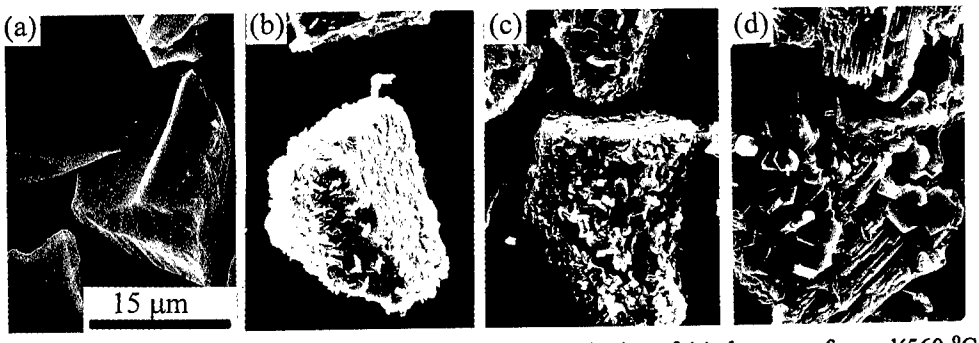


Figure 4: SEM micrographs showing the surface morphologies of (a) the spray formed(560 °C for 10 min) (b) PM hot pressed (600 °C for 10 min) (c) thixoformed (630 °C for 10 min) (d) compocast (continuously cooled from 700 °C to 640 °C during 1 hr)[37]

temperature, i.e. temperature of the billet during forming, is low enough to avoid the interfacial reaction [37]. Figure 4 are the surface morphology of SiC_p extracted from the composites fabricated by spray forming, PM hot pressing, thixoforming, and compocasting. It is evident from these figures that spray forming is the most suitable for fabricating wrought Al alloy composites reinforced with SiC.

In-Situ Composite (Reactive Spray Processing)

In-situ composites, Al_2O_3/Fe[Al] and Al_2O_3/Cu[Al], can be produced by spray forming[3]. The reactive element Al in Fe or/and Cu droplets(liquid) and N_2 in N_2/O_2(gas) mixture introduce Al_2O_3 by the reaction of oxidation. The contents of Al in Fe or/and Cu must be optimized in the limits of mechanical property or conductivity. When the particles of Fe-C were injected into a spray of Te-Ti alloy with the nitrogen gas, fine intermetallic compounds Fe_2Ti and TiC were uniformly distributed at grain boundaries and grain interiors[3]. The injection of Cr_3N_2 particles into a spray of Ti-containing stainless steel during the spray forming can make in-situ composite, too. During hot-working, the Cr_3N_2 dissociates and the dissociated free nitrogen combines with the titanium to form fine TiN(<50 nm). Some preliminary researches by Osprey and AEA Technology demonstrated that the high-temperature strength(600°/C) of a 20:25 stainless alloy could be increased to exceed that of some nickel alloys(e. g. Nimonic 80A) [22].

5. Conclusions

The spray forming research activities carried out world wide, concentrating particularly on the fundamental researches on spray forming process, development of equipment and commercialization of various alloys were reviewed. Especially some of Al-Si hyper-eutectic alloys, special steels, copper alloys and clad product by spray forming have been commercialized and others of them are at the instance of commercialization. Excellent efficiency of spray forming in super alloy, MMC and in-situ reacted composite have been exhibited, which will accelerate the commercialization of spray forming before long.

6. Acknowledgment

The authors would like to thank Dr. E. S. Lee and S. Ahn in RIST for their kindness.

7. References

1. P. S. Grant, " spray forming", Progress in Materials Science, 39(1995), 497-545
2. K. Mills et al., eds., Metals Handbook, vol. 7 (printed in USA : American Society for Metals, 1984), 25-51.
3. A. Lawley, R. Knight and A. Zavaliangos, "Reactive Spray Processing of Advanced Materials"(Paper presented at the European Conference on Advanced PM Materials, Birmingham, UK, 23-24 Oct., 1995), 158-165
4. P. S. Grant, B. Cantor and L. Katgerman, "Modeling of Droplet Dynamic and Thermal Histories During Spray Forming-1. Individual Droplet Behavior", Acta. Metall., 41(1993), 3097-3108
5. P. S. Grant, B. Cantor and L. Katgerman, "Modeling of Droplet Dynamic and Thermal Histories During Spray Forming-2. Effect of Process Parameters", Acta. Metall., 41(1993), 3109-3118
6. E-S Lee and S. Ahn, "Solidification Progress and Heat Transfer Analysis of Gas-Atomized Alloy Droplets During Spray Forming", Acta. Metall., 42 (1994), 3231-3243
7. P. S. Grant and B. Cantor, "Modeling of Droplet Dynamic and Thermal Histories During Spray Forming-3. Analysis of Spray Solid Fraction", Acta. Metall., 43 (1995), 913-921
8. H. Liu, R. H. Rangel and E. J. Lavernia,"Modeling of Droplet-Gas Interaction in Spray Atomization of Ta-2.5W Alloy", Materials Science and Engineering, A191(1995), 171-184
9. X. Liang, J. C. Earthman and E. J. Lavernia, " On the Mechanism of Grain Formation During Spray Atomization and Deposition", Acta. Metal., 40(1992), 3003-3016
10. X. Liang and E. J. Lavernia, "Evolution of Interaction Domain Microstructure During Spray Deposition", Met. Mater. Trans. A, 25A(1994), 2341-2355
11. G. Trapaga and J. Szekely, " Mathematical Medeling of the Isothermal Impingement of Liquid Droplets in Spraying Process", Met. Trans. B, 22B(1991), 901-914
12. G. Trapaga et al., " Fluid Flow, Heat Transfer and Solidification of Molten Metal Droplets Impinging on Substrate: Comparison of Numerical and Experimental Results", Met. Trans. B, 23B(1992), 701-718
13. H. K. Seok et al., "A 3-Dimensional Model of the Spray Forming Method", Met. Trans. (1998, to be published)
14. I. A. Frigaard, "The Dynamics of Spray - Formed Billets", Siam Journal Appl. Math, 55(1995), 1161-1203
15. P. Mathur et al., "Spray Casting : An Integral Model for Process Understanding and Control", Materials Science and Engineering, A142 (1991), 261-276
16. M. Muhamad, J. O. Medwell and D.T.Gethin, " Model for Predicting Buildup of Cylindrical Billets in Osprey Preform Process", Powder Metallurgy, 38 (1995), 214-220
17. S. Annavarapu, D. Apelian and A. Lawley, " Spray Casting of Steel Strip: Process Analysis", Met. Trans. A, 21A(1990), 3237-3256
18. U. Fritsching, H. Zhang and K. Bauckhage, "Numerical Simulation of Temperature Distribution and Solidification Behavior During Spray Forming", Steel Research, 65(1994), 273-278
19. U. Fritsching, H. Zhang and K. Bauckhage, "Numerical Results of Temperature Distribution and Solidification Behavior During Spray Forming", Steel Research, 65(1994), 322-325
20. E. Gutierrez-Miravete et al., "A Mathematical Model of the Spray Deposition Process", Met. Trans. A, 20A(1989), 71-85
21. H. K. Seok, "Controlling the Shape and the Microstructure of Large Preform Fabricated by Spray Forming Method"(Ph. D thesis, Seoul National University, 1998), 69-113
22. A. G. Leatham, "A Progress Review of the Osprey Process Since ICSF 1"(Paper presented at the 2nd ICSF, Swansea, UK, 13-15 Sept., 1993), 129-139
23. L. H. Shaw and C. Spiegelhauer, " Spray Forming and Evaluation of Large Diameter Billets

in Special Steels" (Paper presented at the 3rd ICSF, Cardiff, UK, 9-11, Sept., 1996), 101-113
24. P. F Chesney and J. J Mascolino, "Markets, Economics and Opportunities for Tubular and Bimetallic Spray Formed Products" (Paper presented at the 3rd ICSF, Cardiff, UK, 9-11, Sept., 1996), 115-112
25. H. Sano et al., "Spray Formed Aluminum Alloy Components for Automotive Application" (Paper presented at the 2nd ICSF, Swansea, UK, 13-15, Sept., 1993), 363-375
26. A. G. Leatham, "Commercial Spray Forming: Exploiting the Metallurgical Benefits", Materials World, (1996), 317-320
27. L. F. Mondolf, Aluminum alloys, structure and Properties (Butterworth, London, 1976), 759-774
28. W. T. Carter et al., "A Clean Metal Spray Forming System for Superalloys" (Paper presented at the 3rd ICSF, Cardiff, UK, 9-11, Sept., 1996), 53-60
29. B. David, Dalal R and Furrer D, "Spraycast-X Process for Advanced High Strength Alloys for Ring/Casting Composits" (Paper presented at the 3rd ICSF, Cardiff, UK, 9-11, Sept., 1996), 79-88
30. A. Moran, C. Madden and R. Rebis, "Industrialization and Certification of Large Diameter Spray Formed Superalloy Components for Military Applications" (Paper presented at the 2nd ICSF, Swansea, UK, 13-15, Sept., 1993), 165-170
31. U. Forsberg et al.,"Sandvik Sanicro 65 Composite Tube for Municipal Waste Incinerators" (Paper presented at the 3rd ICSF, Cardiff, UK, 9-11, Sept., 1996), 123-129
32. K. Kumagai, T. Itami and Y. Kawashima, " Latest Status of Developments and Applications of the Osprey Process" (Paper presented at the 2nd ICSF, Swansea, UK, 13-15, Sept., 1993), 207-219
33. E. S. Lee, S. Ahn, Private communication, RIST, KOREA.
34. J. Forrest, R. Price and D. Hanlon, "The Manufacture of Clad Products Using the Osprey Process" (Paper presented at the 3rd ICSF, Cardiff, UK, 9-11, Sept., 1996), 131-145
35 J. P. Tardent and P. A. Isler, " New Materials and New Combinations of Properties of Copper Alloys Made by the Spray Compacting Process"(Paper presented at the 3rd ICSF, Cardiff, UK, 9-11, Sept., 1996), 211-129
36. D. Stock and E. Lepin, "Sprayformed Copper Alloy for Welding Applications", (Paper presented at the 3rd ICSF, Cardiff, UK, 9-11, Sept., 1996), 217-223
37. J. C. Lee et al., "Effect of Various Processing Methods on the Interfacial Reactions in SiCp/2024 Al Composites", Acta. Metal. 45(1997), 5303-5315

Advanced Ferrous Alloys and Processing

INFLUENCE OF HEAT TREATMENT ON THE MICROSTRUCTURE OF A C-Cr-Mo STAINLESS STEEL

Mohammad Mujahid, M. Iqbal Qureshi and Muhammad Ali

Faculty of Metallurgy and Materials Engineering

GIK Institute of Engineering Sciences & Technology

Topi, NWFP-23460, Pakistan

ABSTRACT

Stainless steels containing enhanced chromium and carbon contents are particularly attractive for applications requiring improved wear and corrosion resistance. The as-cast microstructure of such steels is composed mainly of ferritic matrix along with a network of interdendritic primary carbides. It has been shown in the present work that heat-treatment of these steels result in microstructures, which contain more than one type of carbides. A selective dissolution technique has been employed to isolate carbides from the matrix. SEM and X-ray diffraction studies showed that the primary carbides were essentially of M_7C_3 type, whereas in heat-treated samples both M_7C_3 (primary) and $M_{23}C_6$ type carbides (secondary) have been observed. The amount of various carbides was found to depend on the heat-treatment temperatures. In addition, nucleation of austenite occurs above 900°C and around 1250°C the matrix transforms completely to austenite which is retained completely at room temperature.

The Third Pacific Rim International Conference on
Advanced Materials and Processing (PRICM 3)
Edited by M.A. Imam, R. DeNale, S. Hanada,
Z. Zhong and D.N. Lee
The Minerals, Metals & Materials Society, 1998

INTRODUCTION

Conventional stainless steels possess high corrosion resistance but low wear resistance [1]. In an effort to improve the wear properties of stainless steels while simultaneously retaining its corrosion resistance, special type of steels have been developed which contain much higher C (above 1%) and Cr (above 20%) contents as compared with the conventional stainless steels. These steels are used in the manufacturing of pumps for the transportation of media containing highly corrosive and abrasive solids [2].

Depending on the processing history, the microstructure of such steels may consist of primary carbides along the grain boundaries and/or secondary carbides precipitated within the tough matrix [3]. It improves the wear resistance by suppressing ductile as well as brittle dominated fracture mechanisms. Strength and wear resistance of these steels depend primarily on carbide formation, whereas, the corrosion resistance relies on the presence of high Cr-content in the matrix. Despite the formation of carbides, the amount of chromium in the matrix remains sufficiently high to form a continuous oxide layer on the surface. Fe-Cr phase diagram [4] shows that increase in the Cr-content causes a contraction of γ-phase field producing a so-called 'gamma-loop'. When carbon is added to this system, it expands the gamma loop towards the higher chromium content [5]. Carbon also promotes carbide formation, resulting in depletion of Cr from the matrix, and therefore, the expansion of gamma loop is limited [6]. Isothermal sections of Fe-Cr-C system suggest that with the increasing chromium content, the carbide chemistry and its crystal structure changes from M_3C - to - M_7C_3 - to - $M_{23}C_6$ [7-9]. An increase in C-content promotes the formation of carbides rich in carbon (e.g. M_3C) while higher Cr-contents favor the formation of Cr-rich ($M_{23}C_6$ type) carbides. Figure 1 shows an isopleth for Fe-Cr alloy system containing 1.5% C [10]. The contracted γ-field and the stability ranges for various chromium carbides in equilibrium with ferrite and austenite can be observed. The present work was carried out to study the effect of heat treatments on the microstructure in general and to characterize various carbides formed in particular.

EXPERIMENTAL METHODS

The material, in the as-cast form, was supplied by a local pump manufacturer with a nominal composition shown in Table 1.

Table 1. Chemical composition in weight percent.

Fe	C	Cr	Mo	Mn	Si
Bal.	1.6	26.0	2.0	1.0	1.0

The as-cast material was sectioned in order to make specimens (13x10x20 mm) for heat treatment. The specimens were heat treated to temperatures ranging from 800°C to 1300°C for two hours followed by water quenching. A Carbolite RHF1600 programmable furnace was used for this purpose.

Carbides were extracted by selective dissolution of matrix from the bulk samples using a solution of 10% HCl in methanol. The detailed microstructural examination was performed using optical microscopy and SEM for bulk samples as well as for extracted samples of carbides. X-ray diffraction studies were also carried out for the identification of carbides in the bulk samples as well as in the extracted carbides samples. Patterns were indexed in accordance with data from Joint Committee on Powder Diffraction File, JCPDS-ICDD, 1995.

RESULTS

Metallographic examination of the as-cast material showed a dendritic microstructure with large blocky type of carbides present between the ferrite dendrites (figure 2). Eutectic type structure was also observed in some areas between the dendrites. EDS analysis on SEM revealed that the

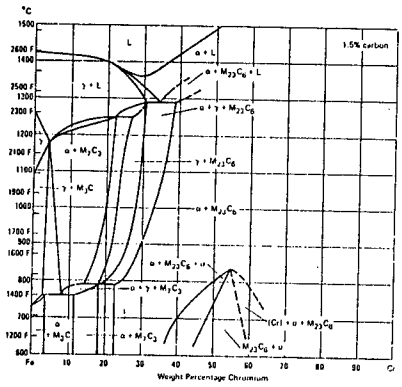


Figure 1. Fe-C isopleth for 1.5 wt.% carbon [10].

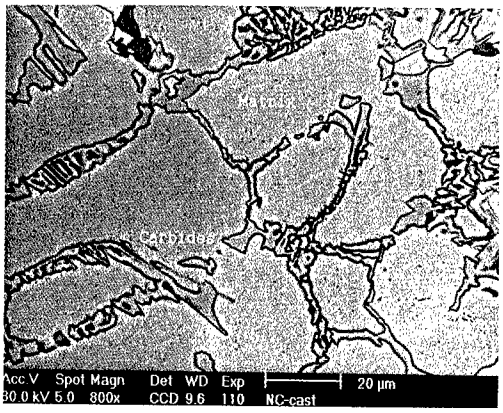


Figure 2. SEM micrograph of as-cast steel showing ferrite matrix and primary carbides.

dendrites were basically composed of Fe with approximately 20% Cr and small amount of Si and Mo. Carbides were found to be rich in Cr but a small amount of Fe and Mo was also present.

SEM examination of the carbides extracted from as-cast material showed that the large, Cr-rich carbides formed a three-dimensional continuous network of primary carbides (figure 3-a). In some isolated regions, very fine carbides of less than 3-µm size in the vicinity of large primary carbides, were also observed (figure 3-b). X-ray diffraction patterns obtained from the carbides extracted out of as-cast material contained all the strong lines of M_7C_3, present within a deviation/shift of $\pm$ 0.01Å in d-values (figure 4-a). Almost all of the peaks were accounted for.

Microstructure of specimens heat treated in the temperature range of 850-1150°C consisted of a similar network of primary carbides in the interdendritic regions. In addition, precipitation of secondary carbides occurred within the matrix (figure 5-a through figure 5-d). Primary carbide network was found to be less continuous in comparison to the as-cast samples and their volume fraction decreased gradually with increasing temperature. This suggests partial dissolution of primary carbides during heat treatment.

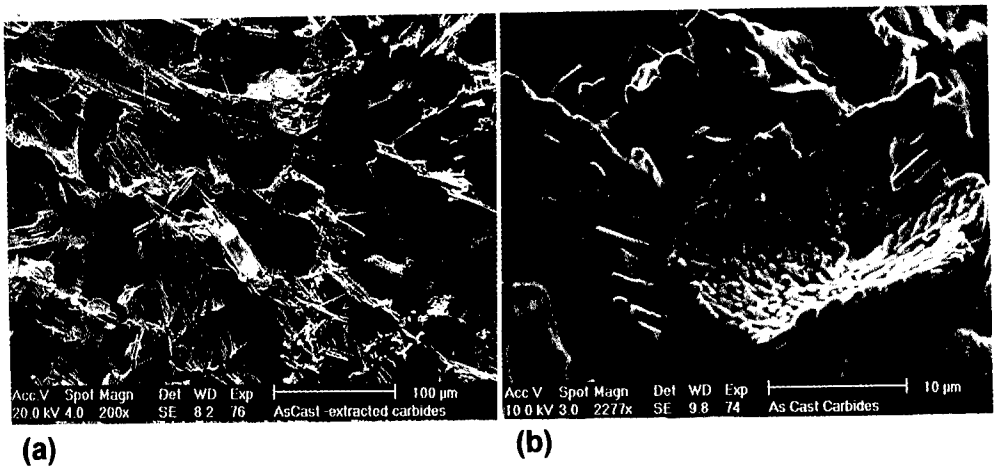


Figure 3. SEM micrograph of carbides extracted from as-cast material; (a) primary carbide network, (b) fine carbides as islands.

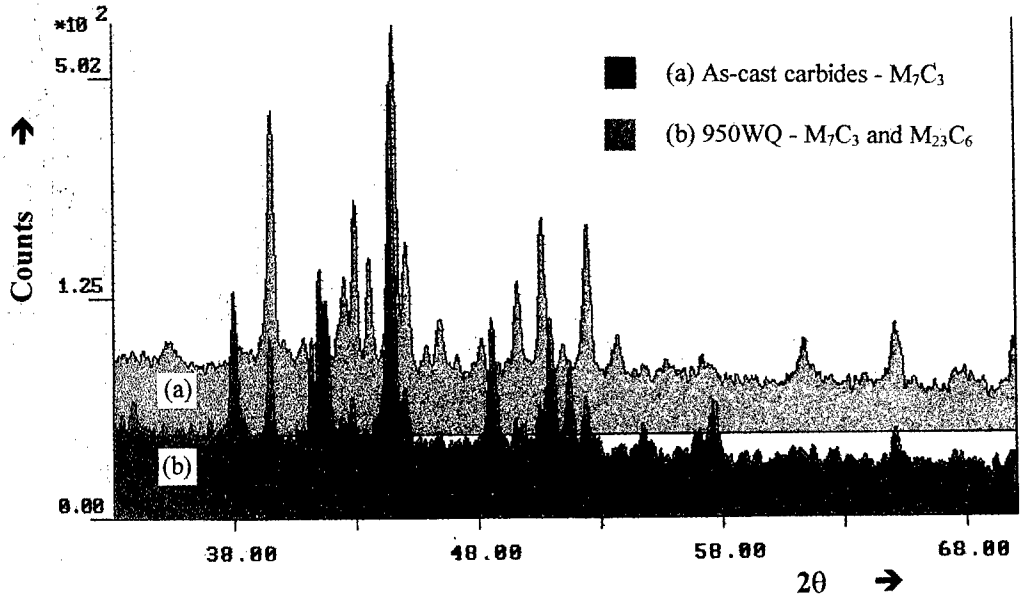


Figure 4. X-ray diffraction patterns obtained from extracted carbides; (a) as-cast, (b) 950°C/2h+WQ

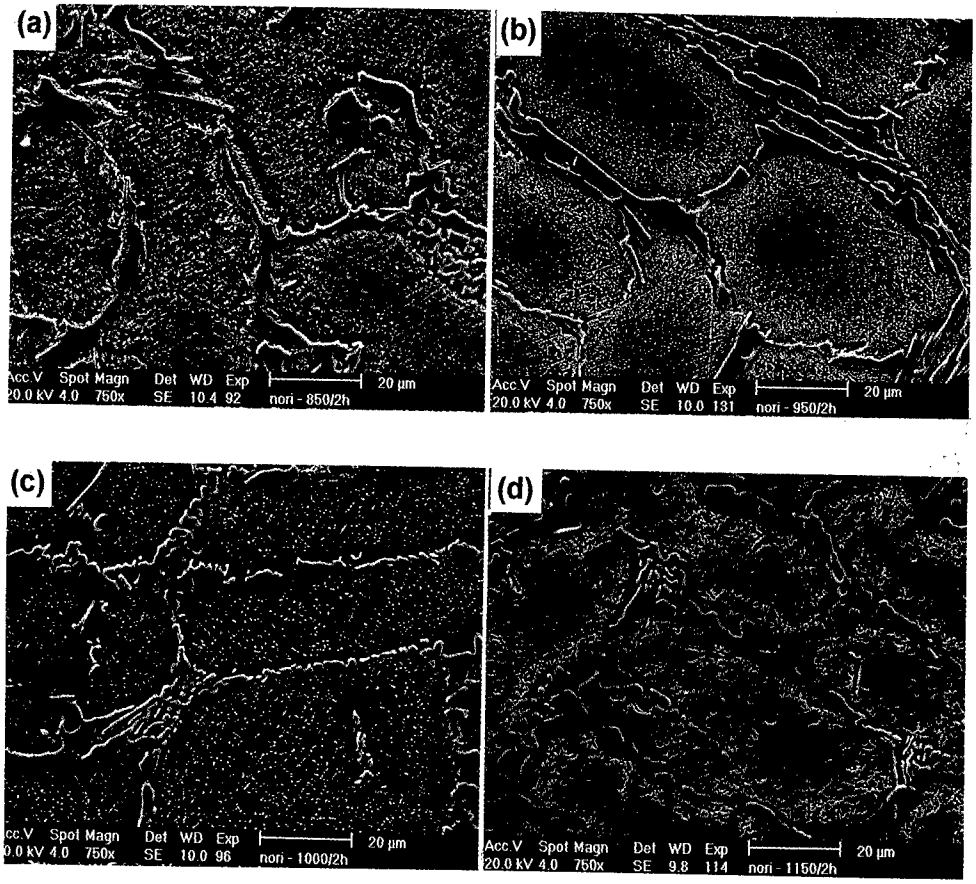


Figure 5. SEM micrograph showing general microstructure of heat treated samples; (a) 850°C/2h + WQ, (b) 950°C/2h + WQ, (c) 1000°C/2h + WQ and (d) 1150°C/2h + WQ.

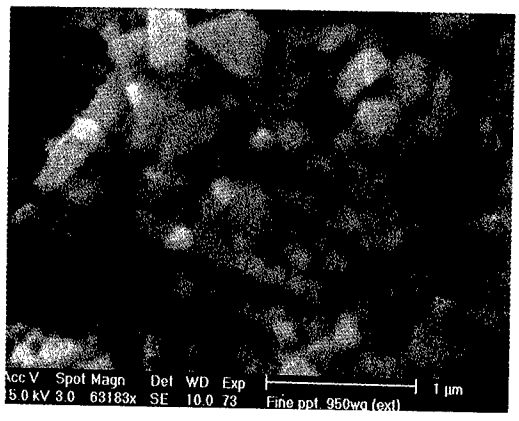


Figure 6. SEM micrograph showing fine secondary carbides extracted from sample heat treated at 950°C/2h + WQ.

Secondary carbides extracted by electrochemical dissolution of the matrix are shown in figure 6. These carbides - mostly polygonal in shape and rich in chromium - showed a gradual increase in their size with the increase in heat treatment temperature up to 1000°C (figure 7). However, heating to above 1000°C resulted in a gradual decrease in the volume fraction for such carbides. Finally, as shown in figure 7-d, the secondary carbides seemed to disappear completely at 1200°C. X-ray diffraction patterns (figure 4-b) taken from the extracted carbides (from samples heat treated at 950°C) illustrated all of the strong peaks of $M_{23}C_6$ and M_7C_3 — the former peaks being more intense. Similar results were obtained for other samples, heat-treated in the temperature range of 850-1000 °C.

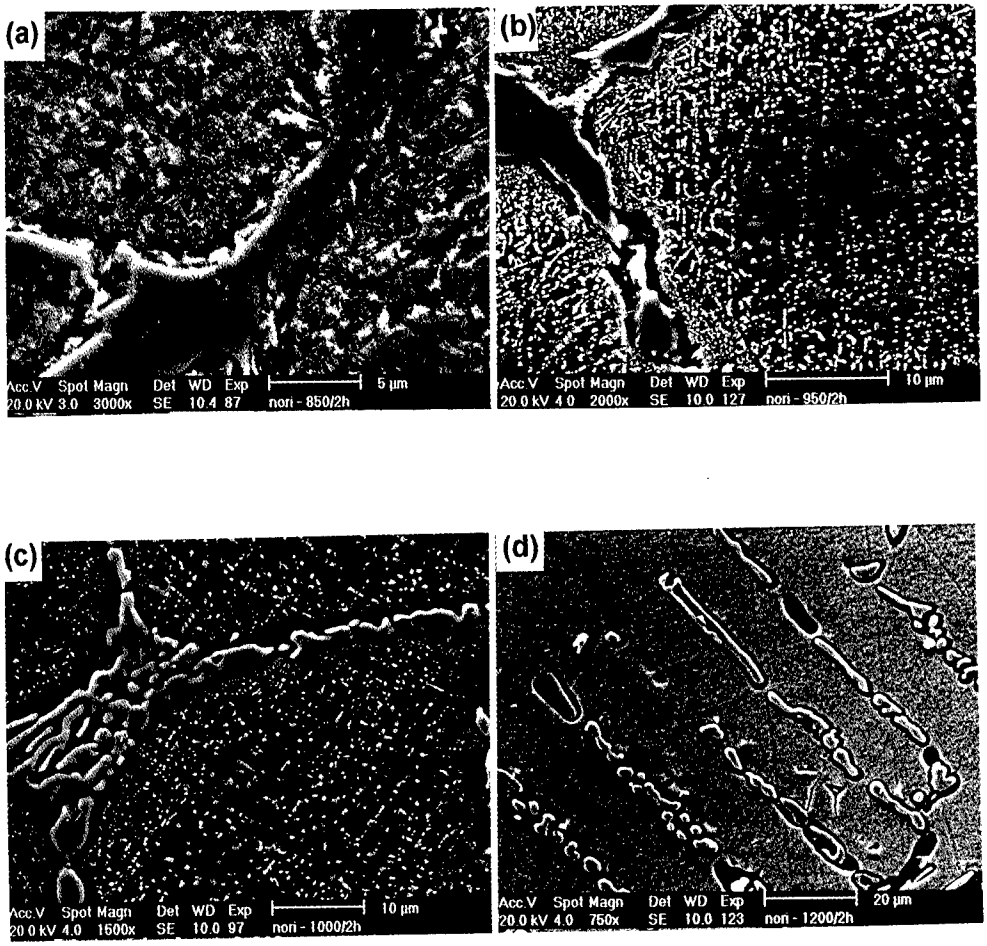


Figure 7. SEM micrographs showing variation in the secondary carbides amount and size with increasing heat treatment temperature; (a) 850°C/2h + WQ, (b) 950°C/2h + WQ, (c) 1000°C/2h + WQ, and (d) 1200°C/2h + WQ

DISCUSSION

Examination of isothermal sections of Fe-Cr-C system [8-10] shows that for 26Cr-1.6C-Fe alloy M_7C_3 type carbides are stable at higher temperature whereas $M_{23}C_6$ carbides are stable at lower temperatures. In the present work, correlation of the X-ray diffraction studies with that of microstructural examination suggests that the primary carbides present in the as-cast material are in fact of M_7C_3 type which seems to form initially during the solidification, but due to non-equilibrium cooling rates, their transformation to $M_{23}C_6$ may have been suppressed. Reheating the material to a suitable temperature and for sufficient time, the transformation from M_7C_3 to $M_{23}C_6$ may occur. Despite the partial dissolution of primary carbides during heat treatment, a major portion of these carbides persists in the structure suggesting their good stability at high temperatures.

The phase diagram in figure 1 shows that in the temperature range of 1250-1270°C, γ and $M_{23}C_6$ along with a liquid phase are present for alloy containing 26%Cr. The liquid phase may transform with a eutectic type reaction involving the formation of $\gamma + M_7C_3$. The observed islands of eutectic type microstructure in almost all the samples may be attributed to this reaction.

Figure 1 also shows that $M_{23}C_6$ carbides are stable below 1150°C, and therefore, the carbides precipitated in the temperature range of 800-1150°C are expected to be $M_{23}C_6$. The presence of both type of carbides in the heat-treated samples (as compared to mono presence of M_7C_3 in the as-cast samples) suggests that the secondary carbides precipitated within the matrix during heat treatments are of $M_{23}C_6$ type. Their precipitation can be attributed to the supersaturation of matrix with respect to Cr and C during heat treatments as the primary carbides dissolve. The increase in supersaturation with temperature (from 800°C to 1000°C) results in enhanced precipitation of $M_{23}C_6$.

Decrease in the secondary carbide volume fraction with further increase in the heat treatment temperature from 1000°C to 1150°C can be attributed to austenite formation [11] at these temperatures since most of the carbon get dissolved in austenite leaving behind less carbon for carbide precipitation. As the austenite volume fraction increases the secondary carbide volume fraction decreases and for sample treated at 1200°C, no secondary carbides precipitate within the matrix (as shown in figure 7-d).

CONCLUSIONS

Carbides in the as cast condition are primarily large and continuous, and of eutectic type. These carbides were observed to form in interdendritic regions and are composed primarily of M_7C_3. Such carbides partially dissolve and fine secondary carbides (mainly $M_{23}C_6$) precipitate within the matrix during the heat treatment in the temperature range of 800-1000°C. The observed decrease in the volume fraction of secondary carbides above 1000°C is attributed to austenite formation.

REFERENCES

1. Metals Handbook, vol. 3, 9th ed., Properties and Selection: Stainless Steels, Tool Materials and Special Purpose Metals, ASM, Metals Park, Ohio, 1980.

2. Technical Brochure, Noriloy, KSB Pumps.

3. M. Mujahid and M. I. Qureshi, On the Carbide Formation in a High Carbon Stainless Steel, Proceed. 1st Intl. Conf. on Phase Transformations, ed. A. Haq, A. Tauqir and A. Q. Khan, Islamabad, Pakistan, 1996, p119.

4. G. Krauss, Steels: Heat Treatments and Processing Principles, ASM, Metals Park, OH, 1990.

5. R. Wilson, Metallurgy and Heat Treatments of Tool Steels, McGraw-Hill, London, 1975.

6. G. A. Roberts and R. A. Cary, Tool Steels, 4th ed., ASM, Metals Park, Ohio, 1980.

7. B. Uhrenius, A Compendium of Ternary Iron-Base Phase Diagrams, in Hardenability Concepts with Applications to Steels, Eds. D. V. Doane and J. S. Kirkaldy, TMS-AIME, Warrendale, PA, 1978, p28.

8. L. R. Woodyatt and G. Krauss, Fe-Cr-C System at 870°C, Met. Trans., vol. 7A, 1976, p983.

9. J. O. Anderson, A Thermodynamic Evaluation of Fe-Cr-C System, Met. Trans., vol. 19A, 1985, p627.

10. Metals Handbook, vol. 8, 8th ed., Metallography, Structures and Phase Diagrams, ASM, Ohio, 1973.

11. M. Ali, Phase Transformation Studies of a High-C, High-Cr Stainless Steel, B. Sc. Engineering Thesis, G.I.K Institute of Engineering Sciences & Technology, Topi, NWFP, 1997.

Metadynamic Recrystallization of AISI 304 Stainless Steel

Sang-Hyun Cho, Yu-Seung Kim and Yeon-Chul Yoo

Department of Metallurgical Engineering, Inha University
253 Yonghyun-Dong, Nam-Ku, Inchon 402-751, Korea
Tel. : 82-032-860-7535 Fax. : 82-032-862-5546

Abstract

Interrupted torsion tests were performed in the temperature range of 900 ~ 1100 ℃, strain rate range of $5.0 \times 10^{-2} \sim 5.0 \times 10^{0}$/sec and interpass time range of 0.5 ~ 100 seconds to study the characteristics of metadynamic recrystallization(MDRX) for AISI 304 stainless steel. To compare the MDRX with static recrystallization(SRX), the pass strain was applied above the critical strain(ε_c) ($\varepsilon_c = 2.2 \times 10^{-3} D_o^{1/2} Z^{0.089}$, where Z is Zener-Hollomon parameter, $Z = \dot{\varepsilon} \exp((380000 \text{ J/mol}) / RT)$ and D_o is as-received grain size) to obtain the MDRX during interpass time. It was found that the kinetics of MDRX were dependent of the strain rate and deformation temperature but were nearly independent of the change in pass strain after the peak strain. The Zener-Hollomon parameter was impossible to evaluate the MDRX fraction, because the fractional softening values were different at the same Z values. The time for 50% metadynamic softening, t_{50}, was determined as follows : $t_{50} = 1.33 \times 10^{-11} \dot{\varepsilon}^{-0.41} D_o \exp((230000 \text{ J/mol}) / RT)$ and this calculated value was consistent with the measured value. The new parameter (MDRX parameter) considering deformation temperature, strain rate and interpass time was proposed to evaluate the MDRX fraction. The MDRX-parameter was determined as $3.2 \times 10^{7} \dot{\varepsilon}^{0.25} t_i^{0.6} \exp((230000 \text{ J/mol}) / RT)$

The Third Pacific Rim International Conference on
Advanced Materials and Processing (PRICM 3)
Edited by M.A. Imam, R. DeNale, S. Hanada,
Z. Zhong and D.N. Lee
The Minerals, Metals & Materials Society, 1998

1. Introduction

The grain refinement by dynamic recrystallization(DRX) is very important during hot deformation.[1~3] DRX is generally easy to occur in some early stages with a low strain rate and high deformation temperature during multipass deformation, but it is difficult to occur at the some last passes. It is also difficult for the static recrystallization(SRX) to take place between interpasses. Therefore, metadynamic recrystallization(MDRX) is nowadays interested in the hot working condition but very limited results are published until now[4,5].

Metadynamic recrystallization occurs by the continued growth of nuclei formed as a result of the occurrence of dynamic recrystallization during prestraining[4,6]. Hence the operation of MDRX does not require an incubation time and such a rapid interpass softening can increase the mechanical properties, even though not long pass strain and interpass time, especially for materials with relatively large deformation resistance such as AISI 304 stainless steel.

The aim of the present study is to investigate the contribution of the metadynamic recrystallization for the softening of AISI 304 stainless steel. The effects of strain rate, temperature, and pass strain were investigated by means of interrupted torsion testing. The mechanical data were used to derive the kinetic equation which describes the rate of softening. Finally, the new parameter, MDRX parameter, was proposed to evaluate the metadynamic fraction.

2. Experimental Procedure

The AISI 304 stainless steel of nominal composition Fe - 18.25 wt% Cr - 8.16 wt% Ni was produced by the vacuum induction melting and the torsion test specimens with a gauge section of 20mm length and 5mm radius were machined. Continuous torsion tests were carried out to calculate the critical strain at the same temperature and strain rate as the interrupted deformation. Interrupted torsion tests were conducted in the temperature range of 900 ~ 1100℃, strain rate range of 5.0×10^{-2} ~ 5.0×10^{0}/sec, interpass time range of 0.5 ~ 100 seconds, and pass strain range of 0.25 ~ 3 times of peak strain to evaluate the effects of deformation variables on metadynamic softening.

3. Results and Discussion

The stress(σ)-strain(ε) curves, obtained from continuous hot torsion tests at the condition of 900 ~ 1100℃ and 0.05 ~ 5.0/sec, were used to determine the strain hardening rate($\theta = d\sigma / d\varepsilon$) as a function of strain(ε) as shown in Fig. 1. Figure 1 consists of three stages.[7] At the first low strain stage, strain hardening rate(θ) decreases rapidly up to the strain which the subgrain formation begins. At the second stage, the strain hardening rate decreases up to the critical strain(ε_c). During this stage, subgrain formation is completed. At the third stage, strain hardening rate decreases from the critical strain, inflection point, to peak strain(ε_p), $\theta = 0$. This indicates that DRX becomes operative.

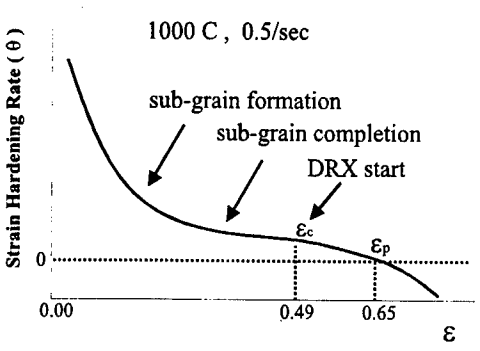


Fig. 1. $\theta - \varepsilon$ curve used to determined the critical strain of 304 stainless steel.

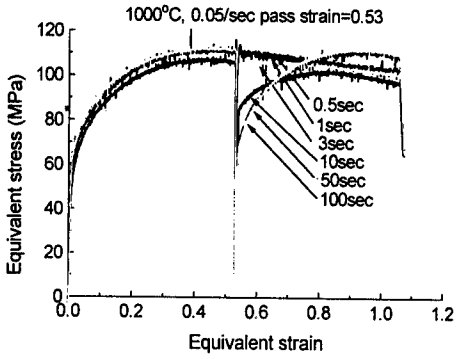


Fig. 2. Double-twist flow curves obtained from interrupted torsion tests.

From this analysis, the relationship between the ε_c and deformation variables were determined to be $\varepsilon_c = 2.2 \times 10^{-3} D_o^{1/2} Z^{0.089}$, where D_o is the as-received grain size and Z is the Zenner-Hollomon parameter. The Z calculated from the continuous deformation is equal to $Z = \dot{\varepsilon} \exp((380000 \text{ J/mol}) / RT)$, where $\dot{\varepsilon}$ is the strain rate. The pass strain can be decided by this equation. To study the metadynamic softening, the decision of critical strain for DRX is very important, because the critical strain indicates the onset of strain for DRX. If the pass strain is larger than the critical strain, it affects the shape of flow curve and fractional softening of successive passes in spite of short interpass time.

Fractional Softening, FS

The interrupted stress-strain curves obtained at the temperature of 1000℃ and strain rate of

0.05/sec, are presented in Fig. 2. The flow stress of the second curve below the interrupt time of 3 seconds rises quickly up to the level of the continuous curve. However, when interrupt times are longer than 10 seconds, much softening takes place and the second curve becomes similar to initial loading curves.

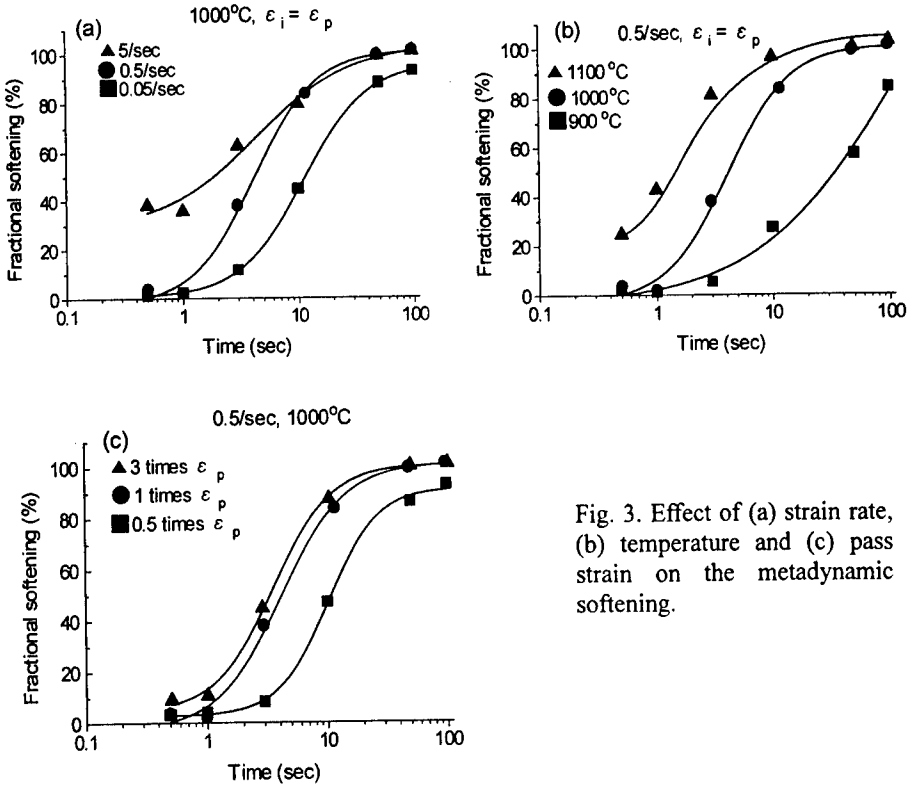


Fig. 3. Effect of (a) strain rate, (b) temperature and (c) pass strain on the metadynamic softening.

Fig. 3 is the metadynamic softening as 'a function of interrupt time, depending on deformation temperature, strain rate and pass strain. From Figs. 3 (a) and (b), as the temperature and strain rate are increased, the kinetics of metadynamic softening are increased and these results are well accepted by the classical static recrystallization. In Fig. 3 (c), a very small change in the softening kinetics was observed when the pass strain was increased from 1 to 3 times of peak strain. On the other hand, a significant increase in kinetics was observed when the pass strain was raised from 0.25 to 1 time of peak strain. These softening curves indicate that the metadynamic softening was happened during the interpass time after passing the peak strain and also that the effect of pass strain for metadynamic softening was negligible.

Kinetics of Metadynamic Recrystallization

The recrystallization process involving nucleation and growth can be expressed by the Avrami equation. Although the metadynamic softening does not involve a nucleation step, it can be described by the Avrami equation : $X= 1 - \exp[-0.693 (t / t_{50})^n]$, where X is the recrystallization fraction(%), t is the interrupt time, n is the Avrami constant and t_{50} is the time for 50% softening. The t_{50} can be expressed as $t_{50} = A \dot{\varepsilon}^{p} D \exp(Q / RT)$. Here, A and p are constants, Q is the activation energy(J/mol) and R is the universal gas constant.

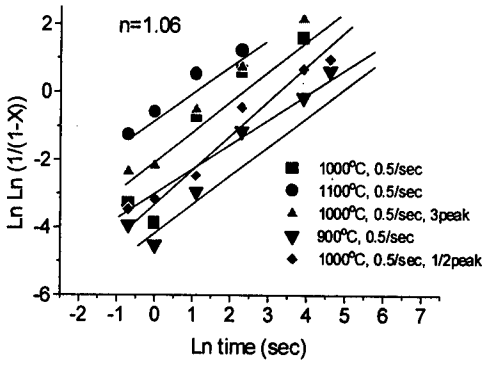


Fig. 4. Dependence of ln ln (1/(1-x)) on ln time under different pass strains, temperatures and strain rates.

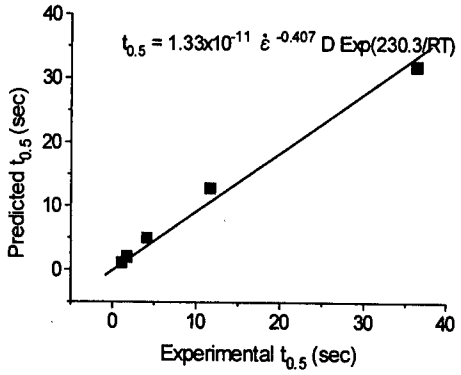


Fig. 5. Comparison of experimental and calculated t_{05} values.

Fig. 4 shows the ln ln(1/(1-X)) vs. ln time curve to determine the Avrami constant, n. The n value is determinded to be 1.06. A very few information is available regarding the n value for MDRX.[8,9] This value is closely similar to the value(1.08) for SRX on 304 stainless steel. As the pass strain does not consider in MDRX, the effects of deformation temperature and strain rate are considered to determine the t_{50}, as shown in Fig.5. The calculated t_{50} is $t_{50}=1.33 \times 10^{-11} \dot{\varepsilon}^{-0.41} D \exp((230300 \text{ J/mol}) / RT)$. This calculated value is well matched with the measured value. The relationship between the pass strain and time for softening is shown in Fig. 6. The time for 5, 20, 50 and 80% softening is presented. It was found that the MDRX is no more sensitive after peak strain and the kinetics of static recrystallization will be different from that of MDRX.

This figure shows the change in kinetics corresponding to the transition from static to metadynamic softening and this pass strain dependence on the time to FS can apply to the time for 50% softening as well as the amount of fractional softening.

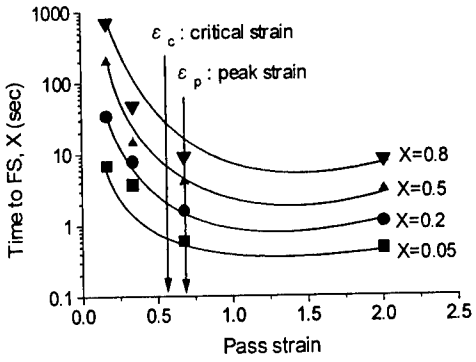


Fig. 6. Pass strain dependence of the time for 5-80% softening.

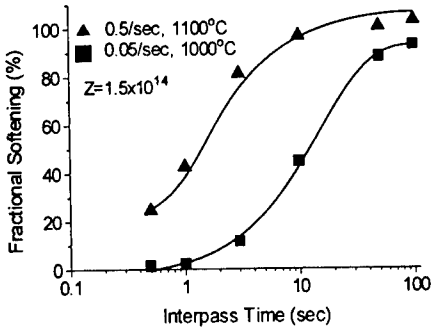


Fig. 7. Comparison of softening behaviors observed after deforming to the peak strain at the similar values of Z-parameter.

The determination of MDRX parameter

The Zener-Hollomon parameter is generally accepted as a good value to explain the dynamic restoration. This parameter can illustrate the flow stress and strain rate as a function of temperature and is associated with microstructure evolution[2]. Therefore, the Zener-Hollomon parameter can be expected to explain the MDRX behavior. Fig. 7 shows the fractional softening as a function of interpass time obtained under a constant Zener-Hollomon parameter ($\sim 1.5 \times 10^{14}$).

Although the driving force for recrystallization, i.e., the stored energy resulting from deformation, was constant, different degree of softening fraction was obtained under this Zener-Hollomon parameter. This indicates that a constant Z value did not lead to a similar softening fraction. This is because the Zener-Hollomon parameter includes the strain rate and temperature, but not interpass time. However, the MDRX fraction depends on the interpass time. Thus, the Zener-Hollomon parameter is not an adequate value to evaluate the kinetics of metadynamic softening. Therefore, it is necessary to define the new parameter considering the temperature, strain rate and interpass time.

Fig. 8 shows the dependence of MDRX fraction on interpass time. The relationship between MDRX fraction and interpass time can be expressed by the following power relation: MDRX fraction = $C\ t_i^{0.6}$, where C is constant and ti is the interpass time. Also, the dependency of the

MDRX fraction on strain rate could be obtained by the above method. Thus, the new parameter (MDRX parameter) can be determined from the analysis of dependency of MDRX fraction on temperature, strain rate and interpass time as follows :

$$\text{MDRX-parameter} = 3.2 \times 10^{7} \ \dot{\varepsilon}^{0.26} \ t_i^{0.6} \exp((230000 \text{ J/mol}) / RT)$$

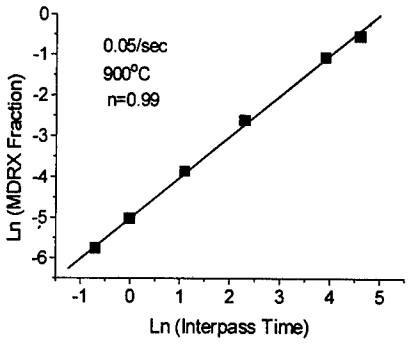


Fig. 8. Dependency of interpass time on the rate of metadynamic softening.

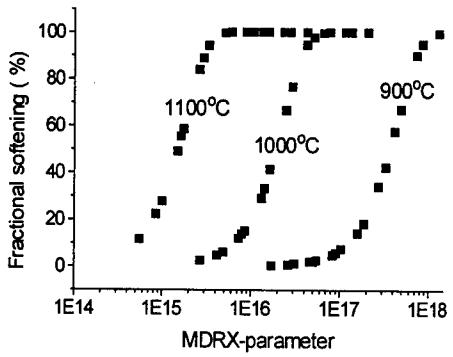


Fig. 9. MDRX fraction vs. MDRX parameter for 304 stainless steel.

Fig. 9 shows the MDRX fractional softening as a function of MDRX parameter. The MDRX fractional softening includes the effects of all the deformation variables, such as strain rate, temperature and interpass time. This figure shows the sigmoidal shape with a very small error range. Once the MDRX parameter is decided, the MDRX fraction can be determined. For example, for 50% MDRX fraction in the temperature of 1000℃, the values of MDRX parameter are closely similar ($\sim 1.0 \times 10^{16}$), even though the strain rate and interpass time are different. Thus the MDRX parameter can lead to the prediction of the metadynamic softening fraction. This new parameter can be determined easily from the relationship between the MDRX fraction and deformation variables and can also predict the MDRX fraction precisely.

4. Conclusions

The important changes in kinetics and softening occurred during the holding intervals after the initiation of dynamic recrystallization were investigated. From the analysis of high

temperature continuous and interrupted deformation behavior, the following conclusions can be drawn:

1. The critical strain(ε c) was decided by the Zenner-Hollomon parameter to obtain DRX effects during interpass time.

$\varepsilon_c = 2.2 \times 10^{-3} D_o^{1/2} Z^{0.089}$, where $Z = \dot{\varepsilon} \exp((380000 \text{ J/mol}) / RT)$

2. It was found that the softening kinetics depended on the strain rate and deformation temperature but not the pass strain.

3. The time for 50% softening(t_{50}) is determined as follow : $t_{50} = 1.33 \times 10^{-11} \dot{\varepsilon}^{-0.41} D \exp((230300 \text{ J/mol}) / RT)$. This value is well matched with the experimental value.

4. We proposed the new parameter (MDRX parameter) considering temperature, strain rate and interpass time, to evaluate the MDRX fraction. This new parameter can be determined easily from the relationship between the MDRX fraction and deformation variables and also can predict the MDRX fraction precisely.

$$\text{MDRX-parameter} = 3.2 \times 10^{7} \dot{\varepsilon}^{0.26} t_i^{0.6} \exp((230000 \text{ J/mol}) / RT)$$

References

1. L. N. Pussegoda, S. Yue, and J. J. Jonas "Effect of Alloying Elements on Metadynamic Recrystallization in HSLA Steels" Metallurgical and Materials Transactions A, 26A(1) (1995), 181

2. J. W. Bowden, F. H. Samuel and J. J. Jonas "Effect of Interpass Time on Austenite Grain Refinement by Means of Dynamic Recrystallization of Austenite"Metallurgical Transactions A, 22A (1991), 2947

3. E. A. Simielli, S. Yue and J. J. Jonas "Recrystallization KineticsMof Microalloyed Steels Deformed in the Intercritical region" Matetallurgical Transactions A, 23A (1992), 597

4. A. Laasraoui and J. J. Jonas "Recrystallization of Austenite after Deformation at High Temperature and Strain Rates" Metallurgical Transactions A 22A(1) (1991), 151

5. T. Sakai and M. Ohashi "Dislocation Substructures Developed during Dynamic Recrystallization in Polycrystalline Nickel" Materials Science and Technology 6(12) (1990), 1251

6. C. Roucoules, P. D. Hodgson, S. Yue and J. J. Jonas "Softening and Microstructural Change following the Dynamic Recrystallization of Austenite" Metallurgical Transactions A, 25A

(1994), 389

7. Y. C. Yoo, J. S. Jeon and B. C. Ko "Hot Deformation and Dynamic Recrystallization of SiCW/AA2124 Composites" Materials Science Forum Vol. 217-222 (1996), 1157

8. O. Kwon and A.J. Deardo "On the Recovery and recrystallization which Attend Static Softening in Hot-deformed Copper and Aluminum" Acta metall., 38 (1) (1990), 41

9. T. Sakai, M. Ohashi and K. Chiba and J. J. Jonas "Recovery and recrystallization of Polycrystalline Nickel after Hot Working" Acta metall., 36(7) (1988), 1781

HIGH TEMPERATURE MECHANICAL PROPERTIES OF CONTINUOUSLY CAST AUSTENITIC STAINLESS STEEL

Sun Koo Kim, Ji Joon Kim, Jong Wan Kim, Yong Deuk Lee and T. Umeda*

Technical Research Lab., POSCO, KOREA.
* Dep. of metallurgy graduate school of Engineering, Tokyo University, JAPAN.

Abstract

The tensile strength and ductility of 304 and 310S stainless steels were measured during and after solidification using a vertical tensile apparatus to investigate the high temperature mechanical properties of austenitic stainless steels in continuous casting practices. This equipment enabled the specimen to melt and solidify without a crucible at predetermined cooling rates. A specific temperature range between ZST (Zero Strength Temperature) and ZDT (Zero Ductility Temperature), meaning solidification cracking susceptibility, were greatly varied with the steel grade. Solidification cracks of 310S stainless steel were more susceptible than that of 304 stainless steel. These mechanical properties were related with solid fraction which was calculated using Thermo Calc software package. It was found that the ZSTs of 310S and 304 stainless steels were the temperatures at which their solid fraction was 0.68 and 0.95, respectively. The solidification path of stainless steel was also investigated by unidirectional solidification equipment. 304 stainless steel are found to be solidified as primary δ-ferrite phase and γ phase is formed from the interdendritic liquid around the δ-ferrite dendrite by the peritectic reaction ($L+\delta \rightarrow \gamma$). On the other hand, 310S stainless steel is solidified as primary γ phase and δ-ferrite phase are formed by the eutectic reaction ($L \rightarrow \delta + \gamma$) from the remained liquid.

The Third Pacific Rim International Conference on
Advanced Materials and Processing (PRICM 3)
Edited by M.A. Imam, R. DeNale, S. Hanada,
Z. Zhong and D.N. Lee
The Minerals, Metals & Materials Society, 1998

1. Introduction

Austenitic stainless steels have been widely used as various equipment materials in chemical plants, power stations and reactor owing to good mechanical properties as well as an excellent corrosion resistance[1], however solidification cracks have been a significant problem in the production of fully austenitic stainless steel[2].

To investigate the occurrence mechanism and prevention of solidification cracks several investigations have been made mainly by the bending tests[3-4]. In addition, mechanical properties of steel in continuous casting practice have been also measured[5-6]. Solidification cracks observed in continuously cast strand were found to originate and propagate along the interdendrites in mushy zone. Solidification cracks were caused by the ductility loss of the mushy zone, which is associated with microsegregation of solute elements at solidifying dendrite interfaces. This solute enrichment locally lowers the solidus temperature of interdendritic liquid and consequently reduces the zero ductility temperature of steel.

In the present study in order to evaluate the solidification cracking susceptibility during continuous casting practice the tensile strength and ductility of austenitic stainless steel were measured during and after solidification by using the high temperature vertical tensile apparatus. An unidirectional solidification technique was employed to investigate the solidification sequences. In addition solidification sequences and solid fraction with temperature were calculated by Thermo-Calc, thermodynamic software package and compared to investigate the relationship between tensile strength and solid fraction.

2. Experimental procedure

2.1. Unidirectional solidification apparatus

The unidirectional solidification apparatus consists of a furnace with the graphite heating element and a water quenching unit to retain high temperature structures of specimens during the process of solidification. The alumina crucible of ID 4mm × L320mm was located in the furnace in such a way that the length of 230mm was held in the hot zone and 90mm in the cold zone. Furnace was moved upward direction at a predetermined velocity which determines the growth rate dendrites. The measured temperature profile inside the alumina crucible was used to determine the temperature gradient at the solid/liquid interface. The solidification rate was set 0.1mm/s and the temperature gradient of 3 ℃/mm in order to simulate the solidification procedure in continuous casting practices.

2.2. High temperature vertical tensile apparatus

A high temperature vertical tensile apparatus was used to measure the tensile strength and ductility of austenitic stainless steel during and after solidification in continuous casting process. This apparatus consists of two characteristics. One is the high frequency induction coil which enables the specimen to melt and solidify without a crucible. The other is the load cell system which can measure the strength in the mushy zone.

A sample was heated to 30 ℃ above liquidus temperature and hold for 60 seconds and then cooled down to the desired temperature at cooling rates of 0.17K/s. A sample was pulled apart at a strain rate 0.001/s . Tensile strength and displacement were simultaneously registered by a computer. The test was conducted in Argon gas atmosphere to prevent the oxidation.

2.3. Microstructural characterization

The samples after unidirectional solidification experiment were cut along the longitudinal axis and polished and etched electrolytically in 60% HNO_3 solution. The fracture surfaces and solidification structures were investigated using optical and scanning electron microscope.

3. Results and discussion

3.1 Mechanical properties in the mushy zone

Fig.1 shows tensile strength and displacement of 304 stainless steel in the mushy zone. Tm (melting temperature), ZST (zero strength temperature) and ZDT (zero ductility temperature) of 304 are 1441 ℃, 1417 ℃ and 1407 ℃, respectively. The tensile strength of 304 stainless steel has a small value of 3MPa at the ZDT. The tensile strength increase linearly with decreasing temperature. ZDT is generally defined as the temperature at which non-equilibrium solidification completes, i.e., the interdendritic liquid film due to the micro segregation of solute elements is removed. Clyne et al. proposed the crack susceptibility region and divided the mushy zone into the mass and liquid feeding zone and the cracking zone. Cracks formed in the mass and liquid feeding zone which is the temperature range between Tm and ZST are refilled with the surrounding liquid, whereas cracks formed in the cracking zone which is the temperature range between ZST and ZDT can not refilled with the liquid because the dendrite arms compacted enough to resist feeding of the liquid[7]. Thereby solidification cracks are known to occur between ZST and ZDT in the mushy zone. Therefore in this study SCI (solidification cracking index) defined as △ T (=ZST-ZDT) was evaluated to investigate the solidification cracking susceptibility according to steel grade. As shown in Fig.1, SCI of 304 stainless steel is found to be about 10 ℃. Fig.2 shows tensile strength and displacement of 310S stainless steel in the mushy zone. Tm, ZST and ZDT of 310S stainless steel are 1391 ℃, 1365 ℃ and 1322 ℃, respectively. The tensile strength of 310S stainless steel was found to be about 13MPa at the ZDT, which values is 4.3 times higher than the tensile strength of 304. SCI of 310S is about 43 ℃. Comparing SCIs of 304 and 310S, 310S was found to be 4 times susceptible to solidification cracks than that of 304.

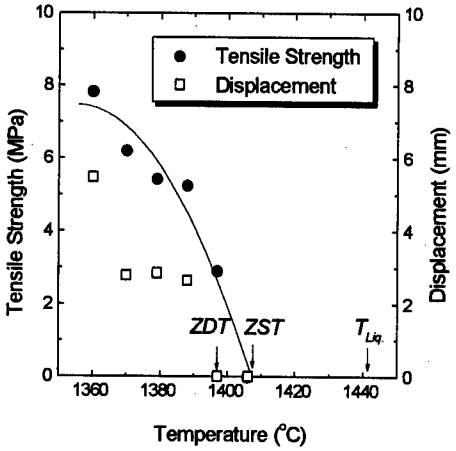


Fig. 1 Tensile strength and displacement of 304 stainless steel in the mushy zone.

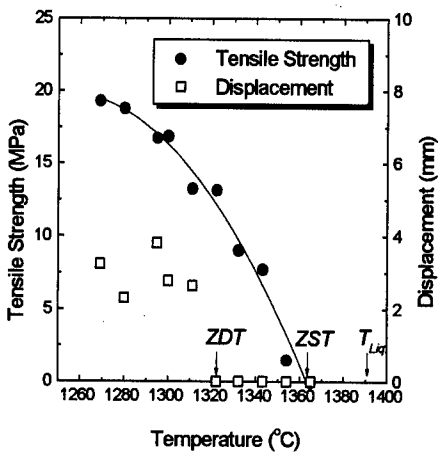


Fig. 2 Tensile strength and displacement of 310S stainless steel in the mushy zone.

3.2. Solidification sequences of 304 and 310S stainless steel

Fig.3 and 4 show a progressive solidification structure of 304 and 310S stainless steel prepared by unidirectional solidification experiment. Solidification structures of primary phase are observed on the left-hand side and the fraction of solid phase increases as going along the right-hand side. Gray area is δ-ferrite , white area is γ phase and dark area is the interdendritic liquid phase remained by quenching. As shown in Fig.3, 304 stainless steel are found to be solidified as primary δ-ferrite phase and γ phase is formed from the interdendritic liquid around δ-ferrite dendrite and continues to grow at the expense of interdendritic liquid and δ-ferrite by the peritectic reaction ($L+\delta \rightarrow \gamma$). Fig.4 shows that 310S stainless steel is solidified as primary γ phase which is coarsening and becomes larger grains as going to the right hand side. Also it is observed that γ phase and δ-ferrite phase are formed from the remained liquid by the eutectic reaction ($L \rightarrow \delta + \gamma$).

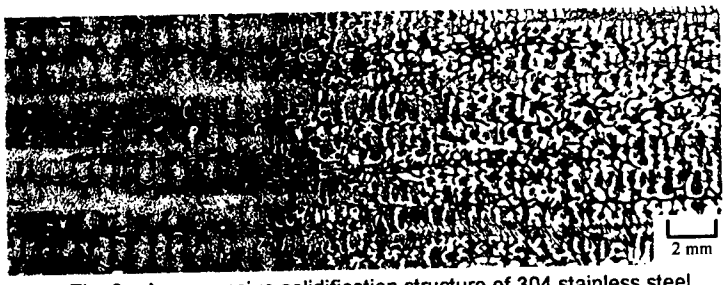


Fig. 3 A progressive solidification structure of 304 stainless steel prepared by unidirectional solidification experiment.

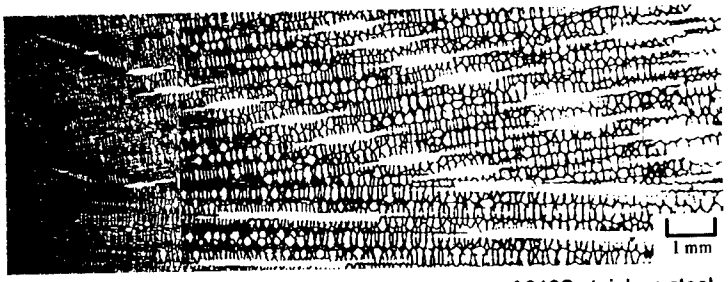


Fig. 4 A progressive solidification structure of 310S stainless steel prepared by unidirectional solidification experiment.

Solidification sequences of 304 and 310S stainless steels were calculated from Thermo-Calc, thermodynamic software package to compare the results obtained from the above unidirectional solidification experiment. Fig.5 shows the variation in the relative liquid and solid fraction as a function of temperature during equilibrium solidification of 304 stainless steel. δ-ferrite begins to solidify as a primary phase and grows to the maximum amount of about 65 vol.% , in other hand γ phase starts to form as the both of liquid and δ-ferrite decrease simultaneously. In Fig.6 showing solidification sequences of 310S stainless steel, γ phase starts to solidify and continuously grows as liquid phase decreases. The δ-ferrite appears by the eutectic reaction before completion of solidification. These calculated results fairly well agreed with the experimental results.

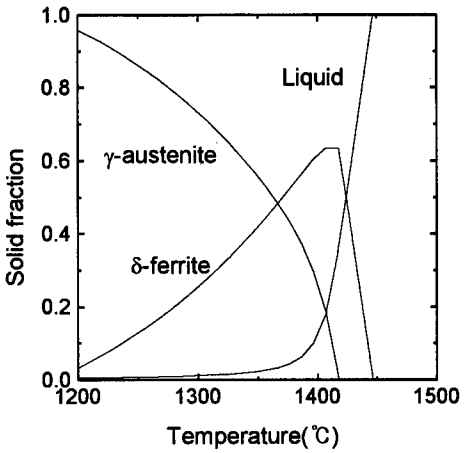


Fig. 5 Phase fraction change for 304 stainless steel during equilibrium solidification.

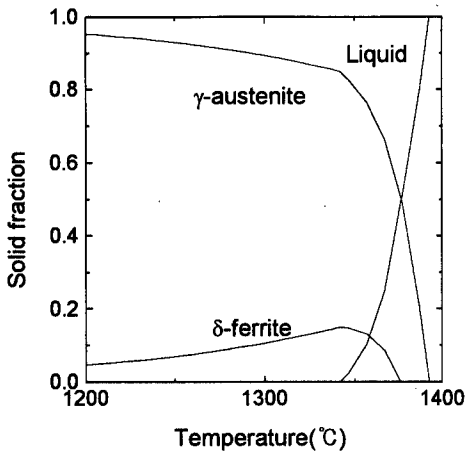


Fig. 6 Phase fraction change of 310S stainless steel during equilibrium solidification.

3.3. Relationship between tensile strength and solid fraction

Mechanical properties of austenitic stainless steel were examined in the relationship with solid fraction which was calculated from Thermo-Calc.

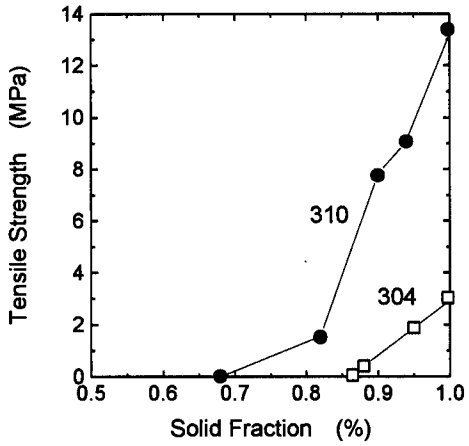


Fig. 7 Relationship between tensile strength and solid fraction for 304 and 310S stainless steel

Fig.7 shows the relationship between tensile strength and solid fraction in the mushy zone in 304 and 310S stainless steel. It was found that ZSTs of 304 and 310S stainless steel are the temperatures at which the solid fraction becomes about 0.87 and 0.68, respectively. On the other hand, in the carbon steel the solid fraction that tensile strength appears during solidification doesn't varied according to steel grade, in other words steel solid fraction of about 0.8 in the carbon correspond to ZST[3-4]. In order to find out the reason why solid fraction for ZST in stainless steel varied greatly according to steel grade, solidification sequences (Fig.3 and Fig.4) prepared from unidirectional solidification experiment and above calculated results (Fig.7) were compared. Because physical meaning of ZST is the temperature that secondary dendrite arms begin to link each other and secondary dendrite arms is coarsened. Therefore it can be thought that coarsening process of secondary dendrites of 304 stainless steel solidifying as primary δ-ferrite is very slow, which cause zero tensile strength to appear at solid fraction 0.87. On the other hand secondary dendrites of 310S stainless steel solidifying as primary γ phase grow rapidly with time into less branched and more widely spaced ones which cause zero tensile strength to appear at solid fraction 0.68.

4. Conclusion

In order to investigate the mechanical properties in the mushy zone during continuous casting practice of austenitic stainless steel, the tensile strength and ductility of 304 and 310S stainless steel were measured and their solidification sequences were observed and were predicted by Thermo-Calc, computer thermodynamic package and main results are summarized as follows.

1. The tensile strengths of 304 and 310S stainless steel at the ZDT are about 3MPa and 8MPa, respectively; the tensile strength of 310S at ZDT is 2.7 times higher than that of 304 stainless steel.

2. In evaluation of SCI (solidification cracking index)of the stainless steel grade defined as $\triangle$ T (=ZST-ZDT), SCIs of 304 and 310S stainless steel are found to be about 10 ℃ and 43 ℃, respectively.

3. ZSTs of 304 and 310S stainless steel are the temperature at which the solid fraction becomes about 0.95 and 0.77, respectively. This difference is thought to be caused that coarsening process of dendrite arms of 304 stainless steel solidified as primary δ -ferrite is slower that of 310S stainless steel solidified as primary γ phase .

References

1. H. Thielsh: Weld.J.,(1955) Jan.,22s-30s.
2. Y. Arata, F. Matsuda and S. Katayama: Transaction of JWRI, 5(1976)2, 35-51.
3. Y. Sugitani, M. Nakamura, et.al.,: Testsu-to-Hagane (J. Iron Steel Inst. Jpn), 68(1982)10, A149-152.
4. K. Wunnenberg and R. Flender: Ironmaking Steelmaking, 12(1985)1, 22-29.
5. S. Kobayashi: Testsu-to-Hagane (J. Iron Steel Inst. Jpn), 73(1987)12, S896.
6. E. Schmidtmann and F. Rakoski: Arch. Eisenhuttenwes., 54(1983)9, 357-368.
7. T.W. Clyne and G. J. Davies: Solidification and casting of metals, (London, The Metal Society), 275-278.

DEFORMATION INDUCED MARTENSITIC TRANSFORMATION IN 304 STAINLESS STEEL

HongChul Shin and YoungWon Chang

Center for Advanced Aerospace Materials(CAAM)
Pohang University of Science and Technology
Pohang 790-784, Korea

Abstract

The deformation induced martensitic transformation phenomena in 304 stainless steel have been investigated in relation to the inelastic deformation theory in this study. A new kinetics equation for a deformation induced martensitic transformation has been formulated based on the inelastic deformation theory as $f/f_s = 1 - \exp(-\beta \varepsilon^n)$ with the parameter β characterizing the stability of austenite, n denoting a deformation mode parameter, and f_s the saturation value of transformed martensite volume fraction.

The value of n was determined as n = 2.2 for this steel, while the stability parameter β was found to be inversely proportional to the test temperature. Consequently the M_d temperature, above which martensitic transformation can not occur regardless of the amount of plastic deformation, can be determined indirectly as the temperature with $\beta = 0$. The true stress vs. true strain curves at lower temperatures showed low work hardening rate region followed by rapid increase in work hardening rate, while the curves at near room temperature showed a continuously decreasing low work hardening rate. As the test temperature increased, the maximum transformation rate ($df/d\varepsilon$) decreased, but the inelastic strain corresponding to the peak transformation rate increased resulting in a substantial ductility enhancement.

The Third Pacific Rim International Conference on
Advanced Materials and Processing (PRICM 3)
Edited by M.A. Imam, R. DeNale, S. Hanada,
Z. Zhong and D.N. Lee
The Minerals, Metals & Materials Society, 1998

Introduction

Austenitic stainless steel can be strengthened via precipitation hardening, heavy working and so on, but in spite of the high strength, its application has been limited by its low ductility[1]. The low elongation during the tensile test is attributed to a local plastic instability appearing when a material is unable to work harden at a rate fast enough to compensate for the stress increase due to the reduction in cross section area. It is, therefore, necessary to increase the work-hardening rate to obtain high ductility[1,2]. This can be achieved through DIMT(Deformation Induced Martensitic Transformation) phenomenon which was first used by Zackay[3] et al. to develop a TRIP (TRansformation Induced Plasticity) steel showing a high tensile strength together with a high elongation.
In this investigation, a new kinetics equation for a DIMT has been formulated based on an inelastic deformation theory[6,7]. The DIMT is viewed here as a continuous relaxation process of an internal strain energy accumulated during plastic deformation. This, then, naturally leads into an increased elongation with an enhanced strength. In this study, it is verified experimentally that the new kinetics equation can in fact describe effectively the relationship between the inelastic strain and the transformed fraction of martensite at the various test temperatures. From the relationship between the test temperatures and the stability parameter of austenite phase(β), it was also able to determine the M_d temperature as 55℃ in the 304 stainless steel used.

Theoretical background

An internal strain energy develops naturally as a consequence of dislocation pile-ups at strong barriers such as grain boundaries during inelastic deformation according to the inelastic deformation theory proposed recently[4,5].
The internal strain energy U^I, prescribed as[5,6]

$$U^I = \frac{1}{2}\sigma^I a = \frac{1}{2}\mathbf{M}a^2 \tag{1}$$

is viewed here as the major driving force for DIMT. The internal stress σ^I and strain a in eqn. (1) are in turn related through an internal modulus **M**, as $\sigma^I = \mathbf{M}a$[7].
DIMT is thought to occur in two successive stages, viz. nucleation site formation at high internal strain energy sites such as the slip band cross points, and martensitic transformation at these sites.
The rate of nucleation site formation can be defined in terms of the internal strain variable as,

$$n = \frac{d\log N^I}{d\log a} \tag{2}$$

with N^I denoting the number of nucleation sites per unit volume. It is, however, difficult to measure the internal strain experimentally, so that the approximate relationship, $da/d\varepsilon \simeq a/\varepsilon$ at steady state is used substituting an internal strain a by an inelastic strain ε in eqn. (2). There is no accumulation of internal strain energy at $\varepsilon = 0$. The eqn. (2) can then be integrated with this initial condition to yield

$$N^I = A\varepsilon^n \tag{3}$$

with A denoting a constant. Since the deformation induced martensitic transformation is well known as a typical autocatalytic process, the increase in transformed martensite embryos can be described in terms of the number of nucleation sites N^I in an infinitesimal form as[8]

$$dN^\alpha = p(N_s^\alpha - N^\alpha)dN^I \tag{4}$$

where N^α and N_s^α are the number of martensite embryos per unit volume and its maximum value, respectively, while p denoting probability for a nucleation site to transform into martensite. Integrating the eqn. (4) with an initial condition of $N^\alpha = 0$ at $\varepsilon = 0$ together with eqn. (3) finally leads into the following kinetics equation for DIMT,

$$\frac{N^\alpha}{N_s^\alpha} = \frac{f}{f_s} = 1 - \exp(-\beta\varepsilon^n) \tag{5}$$

where f and f_s are the volume fraction of martensite and its saturation value, respectively. The parameter β defined as pA represents the stability of austenite depending on chemical composition and temperature. The stability parameter β and the deformation mode parameter n can easily be determined from experimental data from a logarithmic form of the eqn. (5),

$$\log[\ln(1 - f/f_s)^{-1}] = \log\beta + n\log\varepsilon \tag{6}$$

Experiment

The 304 stainless steel used in this experiment was produced by POSCO and its composition is given in Table I. Specimens were machined from a plate with tensile axis parallel to the rolling direction. The machined specimens, first sealed in a quartz tube to prevent oxidation, were then annealed at 1050℃ for about 7 minutes to remove the transformed phase formed possibly during a machining, followed by a water quenching. Tensile tests were performed under the strain rate of 1×10^{-3} s^{-1} at the various temperatures ranging from the liquid nitrogen temperature to 40℃. A ferritescope was used to measure the amount of transformed martensite during plastic deformation.

Table I Chemical Composition of 304 Stainless Steel Used.

C	S	Si	Mn	P	Cr	Ni	Mo	N
0.05wt%	0.004	0.56	1.05	0.025	18.07	8.50	0.18	0.0372

Results and discussion

The volume fraction of transformed martensite at the various temperatures are shown in Fig. 1 together with solid lines obtained by curve fitting the experimental data with eqn. (5). The values of transformation parameters β, n and f_s determined are listed in Table II.

Table II Transformation Parameters n, β and f_s Obtained at the Various Temperatures.

	-196℃	-67℃	-50℃	-30℃	5℃	28℃	40℃
f_s	0.625	0.592	0.538	0.503	0.487	0.415	0.324
β	32.18	18.63	16.89	13.72	6.60	1.23	0.75
n	2.2	2.2	2.2	2.2	2.2	2.2	2.2

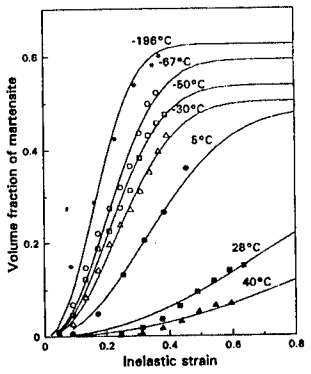


Figure 1: Volume fraction of transformed martensite as a function of inelastic strain.

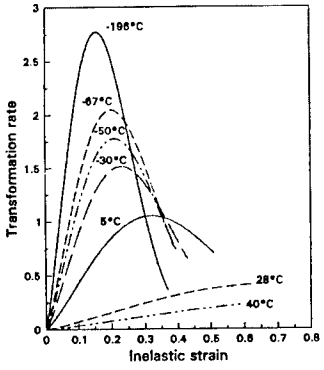


Figure 2: Transformation rate vs. ε at the various test temperatures.

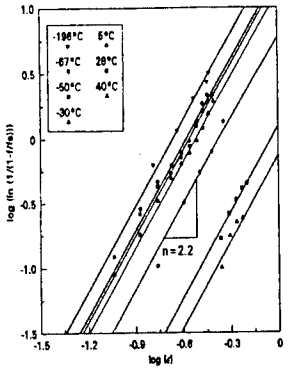


Figure 3: The plots showing n=2.2, regardless of test temperatures.

The transformation rate ($df/d\varepsilon$) vs. inelastic strain (ε) curves given in Fig. 2 show that austenite transforms into martensite more easily and faster and the maximum transformation rate is obtained at a lower strain as the stability parameter β increased. The slope of straight lines in Fig. 3, defined as the

deformation mode parameter n according to eqn. (6) can be observed to have a fixed value of n = 2.2 regardless of test temperatures for this steel, compared to the value of n=1.0 for a multi-phase cold rolled steel containing retained austenite[9]. The stability parameter β is observed inversely proportional to the test temperatures as shown in Fig. 4. Therefore the M_d temperature can be determined indirectly as the temperature where β = 0, providing M_d = 55℃ for this steel. This is, in fact, the reason why the parameter n is related to the mode of inelastic deformation.

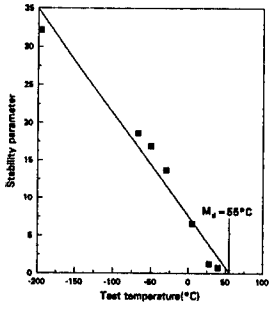


Figure 4: A plot of β vs. Temp. providing a means to determine M_d.

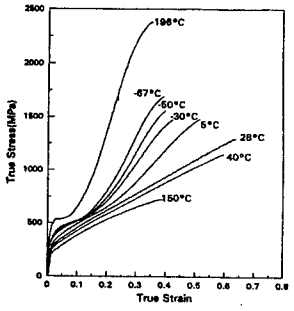


Figure 5: True stress vs. strain curves at the various test temperatures.

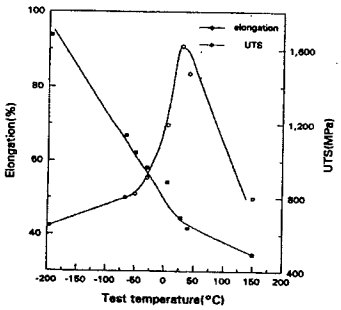


Figure 6: Effect of test temperature on tensile properties.

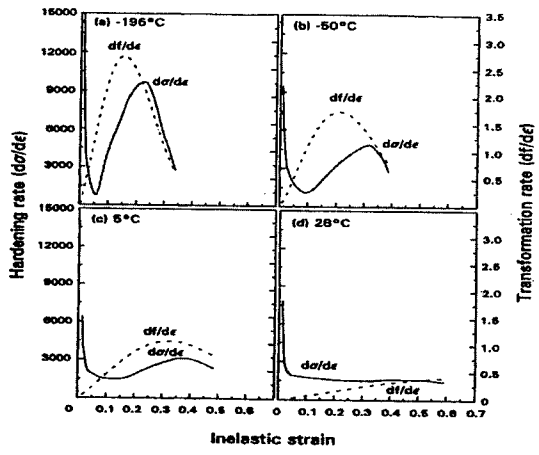


Figure 7: Variation of $df/d\varepsilon$ and $d\sigma/d\varepsilon$ as a function of ε at several temperatures.

The true stress vs. true strain curves are shown in Fig. 5 revealing serrated flow behavior, implying a continuous relaxation of internal strain energy through DIMT and hardening due to transformed martensite[10]. In the temperature range where no DIMT is observed, stress increased continuously with hardening rate decreasing rapidly with inelastic strain.

The ultimate tensile strength is observed in Fig. 6 to increase with decreasing temperature, possibly due to the increase in saturation value of transformed martensite fraction with decreasing temperature. The elongation, on the other hand, showed a maximum value at 28℃. As the stability parameter β decreased, martensitic transformation occurred

uniformly and gradually throughout plastic deformation resulting into a significant ductility enhancement. When the stability parameter β is too small, however martensitic trans -formation can not occur fast enough to prevent the rapid decrease in work-hardening rate and thus failure occurs at incipient necking.
The variation of $df/d\varepsilon$ and $d\sigma/d\varepsilon$ are shown in Fig. 7 as a function of inclastic strain at several temperatures. At low temperature, the transformation and work-hardening rates are observed to increase very rapidly in the early stage of deformation to cause early failure by necking. The transformation rate at 28℃, on the other hand, is shown to be very low and increases gradually with deformation to provide an adequate work-hardening rate up to the plastic instability point ($d\sigma/d\varepsilon = \sigma$).

Summary

In this investigation, the transformed fraction of martensite has been measured at the various temperatures and the results were then analyzed using the proposed new kinetics equation based on an inelastic deformation theory. The principal results can be summarized as follows.
1. The deformation induced martensitic transformation can be described effectively by the new kinetics equation, $f/f_s = 1 - \exp(-\beta \varepsilon^n)$.
2. M_d temperature could be determined indirectly from the relationship between the stability parameter β and test temperature. M_d temperature of 304 stainless steel used in this study was determined as 55℃.
3. DIMT can be viewed as a continuous process of successive relaxation of internal strain energy and hardening by transformed phase, providing an enhanced ductility with high strength.

References

1. G. L. Huang, D. K. Matlock and G. Krauss : Metall.Trans., **20A** (1989) 1239
2. D. Fahr : Metall. Trans., **2A** (1971) 1883
3. V. F. Zackay, E. R. Parker, D. Fahr and R. Busch : Trans. ASM, **6** (1967) 252
4. Y. W. Chang and E. C. Aifantis : Constitutive Laws for Engineering Materials; Theory and Application, C. S. Desai et al, eds., (Tuscon, 1987) 293
5. T. K. Ha, C. S. Lee and Y. W. Chang : Scripta Mater., **34** (1996) in print.
6. H. J. Sung, K. S. Kim and Y. W. Chang : J. Korean Inst. Met. Mater., **31** (1993) 48
7. E. W. Hart : J. Eng. Mater. Tech., **104** (1984) 322
8. C. J. Gunter and R. P. Reed : Trans. ASM, **55** (1962) 399
9. J.H. Chung: "A Study on the Transformation Induced Plasticity in High Strength Cold Rolled Sheet Steel Containing Retained Austenite", Ph .D Thesis, April, 1993
10. P. M. Kelly and J. Nutting : J. Iron and Steel Inst., **184** (1961) 199.

Microstructural Analysis of Vanadium Bearing High Manganese Precipitation Hardening Stainless Steel

Y. Haruna [1], A. Yamamoto [2], and H. Tsubakino [2]

[1] Technological Research Laboratory, Sanyo Special Steel Co., Ltd. Himeji 672, Japan
[2] Department of Materials Science and Engineering, Faculty of Engineering, Himeji Institute of Technology, Himeji 671-22, Japan

ABSTRACT

Aging properties of vanadium bearing high manganese precipitation hardening stainless steels have been studied by means of hardness testing and microstructural change associated with the amount and the size of secondary precipitate, i.e., chemical composition and secondary precipitate growth. Aging hardness is predominantly controlled by the change in size of VC as a secondary precipitate and the maximum hardness, which is closely related to dissolved C and V contents, is achieved at a certain aging condition determined as a function of temperature and time, $T(10+\log t) \approx 14.3$, at which VC size becomes approximately 7 nm in diameter. It is suggested that interaction mechanism between dislocations and fine carbides may change from misfit strengthening model to bowing model at the critical size of 7 nm.

The Third Pacific Rim International Conference on
Advanced Materials and Processing (PRICM 3)
Edited by M.A. Imam, R. DeNale, S. Hanada,
Z. Zhong and D.N. Lee
The Minerals, Metals & Materials Society, 1998

1. INTRODUCTION

For recent utilization of stainless steels as functional parts in electronic applications, strengthening of austenitic (γ) stainless steel combined with low permeability is of great interest as well as corrosion resistance. While cold work hardening practice of γ stainless steels is generally used to satisfy the properties, it sometimes causes deterioration of permeability because of stress-induced martensite (α') transformation. Even though γ matrix is tried to be more stable by the careful adjustment of chemical composition to avoid such a problem, an applicability of cold working practice is often limited by the shapes and dimensions of the products. Another selection for the strengthening of γ steel is precipitation hardening by carbides, nitrides, and intermetallic phases, by which both high strength and low permeability of γ steel may be satisfied. Of Mo, Ti, V, and Nb carbides, it is known [1-4] that vanadium carbide is considered to be potent contributor to hardening because it precipitates finely in the matrix and grow relatively slower. However, carbide precipitation hardening behavior of highly alloyed γ stainless steel has not been much studied. In this paper, microstructural change of the vanadium added γ stainless steel, Fe-Cr-6Ni-Mn-V-C, was investigated focusing on hardening behavior and compositional aspects.

2. EXPERIMENTAL PROCEDURE

The specimens were prepared by hot forging from 100 kg VIM ingot to ϕ25 mm bars at 1473 K followed by solution treatment at 1453 K for 3.6 ks. The temperature and time of solution treatment were chosen in order to avoid secondary grain growth. After solution treatment, aging treatment was carried out at 923 K to 1023 K and for 3.6 ks to 604.8 ks. Chemical compositions of the steels investigated are given in Table I.

Hardness was measured in Rockwell C scale on the transverse section of the specimens. Microstructural observations were carried out with an optical microscope and SEM combined with EDX, JSM-6400, by which qualitative and quantitative analysis of the carbides were also carried out. The foils for TEM observations were prepared by twin jet electropolisher and examined using HITACHI HF-2000 electron microscope at 200 kV. Contents of the solute elements in the matrix were estimated by subtracting the contents in the primary carbides analyzed by electrolytic extraction method from bulk analysis values.

Table I Chemical Compositions of the Steels (mass %)

Steel	C	Mn	Ni	Cr	V
D012	0.302	10.22	5.96	11.68	2.00
D112	0.582	10.04	5.94	11.96	2.02
D212	0.785	9.95	5.84	11.90	2.03
D312	1.001	10.08	5.95	11.91	2.08
D102	0.584	10.08	5.94	6.92	1.98
D122	0.602	10.06	5.90	15.96	2.07
D110	0.596	10.00	5.92	11.87	0.40
D111	0.596	10.00	5.97	11.90	1.03
D113	0.598	10.34	5.92	11.85	3.00
D401	0.607	2.05	6.02	11.90	1.97
D402	0.617	6.00	6.02	11.83	1.96

*Others; Si:0.20%, P:0.030%, S:0.003%, Mo:0.20

3. RESULTS AND DISCUSSION

The typical microstructure of the investigated steel after solution treatment is shown in Figure 1. Almost all steels contain relatively large primary carbides while D012 and D110 with the lowest C and V respectively exhibit a few primary carbide. Two types of primary carbides, Cr_7C_3 and VC, are identified by X-ray diffraction analysis and their chemical formulas determined by EDX analysis are listed in Table II. Both types are complex carbides, in which Cr, V, Mn and Fe are dissolved each other, and their compositions predominantly depend on Cr and V contents.

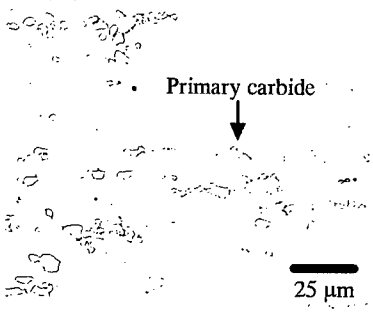


Figure 1: A typical microstructure after solution treatment of D212.

Table II Quantitative analysis result of the primary carbides.

Steel	Cr_7C_3	VC
D012	----*	$(V_{0.87}Cr_{0.10}Mn_{0.01}Fe_{0.02})C$
D112	$(Cr_{3.38}Fe_{1.88}V_{1.22}Mn_{0.52})C_3$	$(V_{0.84}Cr_{0.13}Mn_{0.01}Fe_{0.02})C$
D212	$(Cr_{3.36}Fe_{1.80}V_{1.30}Mn_{0.54})C_3$	$(V_{0.85}Cr_{0.12}Mn_{0.01}Fe_{0.02})C$
D312	$(Cr_{3.42}Fe_{1.80}V_{1.20}Mn_{0.58})C_3$	$(V_{0.85}Cr_{0.11}Mn_{0.01}Fe_{0.03})C$
D102	----*	$(V_{0.88}Cr_{0.08}Mn_{0.01}Fe_{0.03})C$
D122	$(Cr_{3.57}Fe_{2.28}V_{0.58}Mn_{0.57})C_3$	$(V_{0.18}Cr_{0.59}Mn_{0.06}Fe_{0.17})C$
D110	$(Cr_{3.62}Fe_{2.70}V_{0.02}Mn_{0.66})C_3$	----*
D111	$(Cr_{3.83}Fe_{1.60}V_{0.93}Mn_{0.64})C_3$	----*
D113	$(Cr_{3.60}Fe_{1.42}V_{1.49}Mn_{0.49})C_3$	$(V_{0.86}Cr_{0.11}Mn_{0.01}Fe_{0.02})C$
D401	$(Cr_{3.38}Fe_{2.19}V_{1.25}Mn_{0.17})C_3$	$(V_{0.85}Cr_{0.12}Mn_{0.01}Fe_{0.02})C$
D402	$(Cr_{3.38}Fe_{2.11}V_{1.20}Mn_{0.31})C_3$	$(V_{0.84}Cr_{0.13}Mn_{0.01}Fe_{0.02})C$

* Not found

Contents of C and V dissolved in the matrix are calculated in order to estimate an actual contribution of C and V to age hardening which is closely related VC type secondary carbides precipitation. Dissolved C or V content can be well estimated linearly by a regression combined mostly with nominal C, Cr, and V contents while Mn content does not affect dissolved C and V contents. The equation for dissolved C content (Cdis.%) in mass % is,

$$Cdis.\% = 0.72 + 0.27\,[C\%] - 0.02\,[Cr\%] - 0.10\,[V\%] \qquad R=0.94$$

and for dissolved V content (Vdis.%) is,

$$Vdis.\% = 1.28 - 1.14\,[C\%] - 0.03\,[Cr\%] + 0.68\,[V\%] \qquad R=0.97.$$

Hardness was measured after various aging treatments. Hardness is dependent upon aging temperature and time. A variation of hardness can be expressed in two stages, i.e., hardening and softening stages. For all the steels except D401 steel, it is found that the hardness increases with increasing aging time, and then decreases after reaching the maximum hardness. It is also clarified that the time at the maximum hardness becomes shorter with increasing temperature. In Figure 2, the hardness at various heat treatment conditions are plotted against the hardening parameter, $PH = T(10+\log t)$ as a function of absolute temperature T (K) and time t (s). As indicated in Figure 2, the hardness of aged steels can be indicated as the second order correlation with PH. Only D401 shows different hardening sequence that the hardness does not decrease even after the maximum hardness.

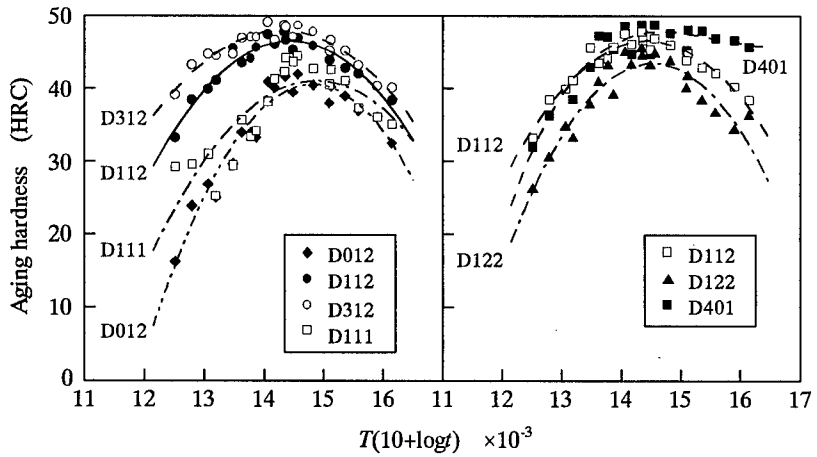


Figure 2: Relationship between aging hardness and the parameter $PH=T(10+\log t)$.

Based on the hypothesis that secondary VC carbides grow by a thermally activated process and that hardness is controlled by an interaction between the carbides and dislocations, the aging parameter *PH* can be introduced from the following equation [5]: $dg/dt = A\exp(-Q/RT)$ where dg/dt = growth rate of the carbide, Q = activation energy for the rate controlling process, R = gas constant, and A = constant. At a given time t_1, $A\exp(-Q/RT)$ becomes constant. After taking logarithm and rearranging this equation, the hardness at a given aging condition can be interpreted as a parameter $PH = T(C+\log t)$. From the results that the hardness is well expressed by *PH*, it is implied that the dominant process for precipitation strengthening and softening of the steels is a thermally diffusional process.

Typical TEM micrograph, selected area diffraction (SAD) pattern, and EDX analytical result of a fine precipitate are shown in Figure 3. In the matrix, fine precipitates observed are identified as VC type carbides. The lattice parameter of vanadium carbide is calculated as $a_0 = 0.4141$ nm compared to that of the γ matrix $a_0 \approx 0.359$ nm. It is reported [6] that VC type carbide precipitated in the steel has NaCl type of structure, which can be described as FCC VC with the interstitial octahedral sites filled with C, and that the formula varies from V_4C_3 ($VC_{0.75}$) to VC dependent on a filling ratio of C atom. Lattice parameter also varies from 0.4136 to 0.4182 nm corresponding to the change in the formula. From the lattice parameter measured, it is clarified that VC type carbides found in the steels are approximately identified to be V_4C_3 without taking an effect of the other soluble elements such as Cr and Fe into consideration. V_4C_3 is coherent to the γ matrix and crystallographic orientation relationship of V_4C_3/γ is determined as $[001]V_4C_3//[001]\gamma$; $(200)V_4C_3//(200)\gamma$; $(111)V_4C_3//(111)\gamma$. Because of relatively high lattice mismatch $\Delta a_0=0.153$ between V_4C_3 and γ matrix, the precipitation of coherent V_4C_3 causes large lattice distortion that contributes to the strengthening of these steels.

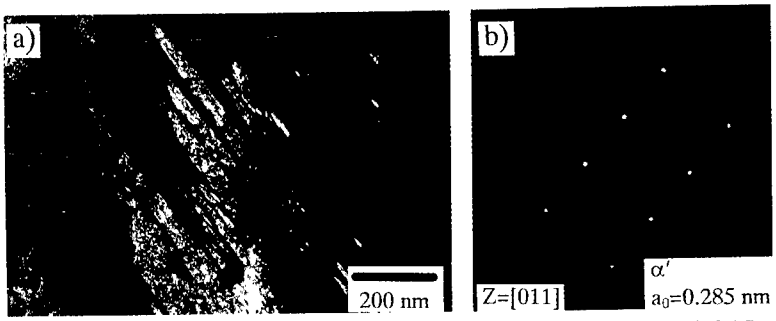


Figure 3: Martensite found after aging in D401 steel. a) Dark image and b) SAD pattern.

It was found that the matrix of D401 steel partly transformed to martensite after cooling from aging temperature as shown in Figure 4. It is implied that the γ matrix of D401 steel is not so stable because of low Mn content and that Ms temperature may rise above room temperature due to C consumption caused by VC precipitation during aging treatment.

In the case of D401 Steel, the stability of γ matrix during aging is considered to be controlled by C reduction from the matrix due to the VC precipitation and the amount of martensite at room temperature may be closely related the amount of VC precipitates even though

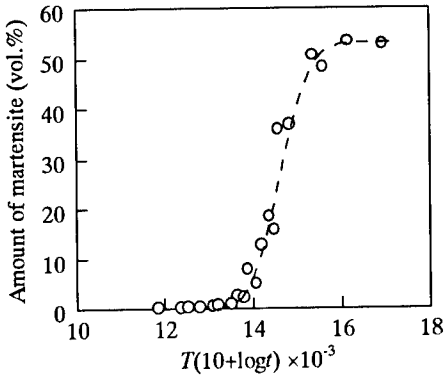


Figure 4: Relationship between amount of martensite and the parameter *PH*.

martensite transformation is athermal process. Figure 5 indicates the relationship between the amount of transformed martensite and the parameter *PH* on D401 Steel. It suggested that the amount of martensite agrees well with simply modified form of Avrami equation, $X = 1\text{-}\exp[f(T, t)]$ where X is the amount of transformed phase.

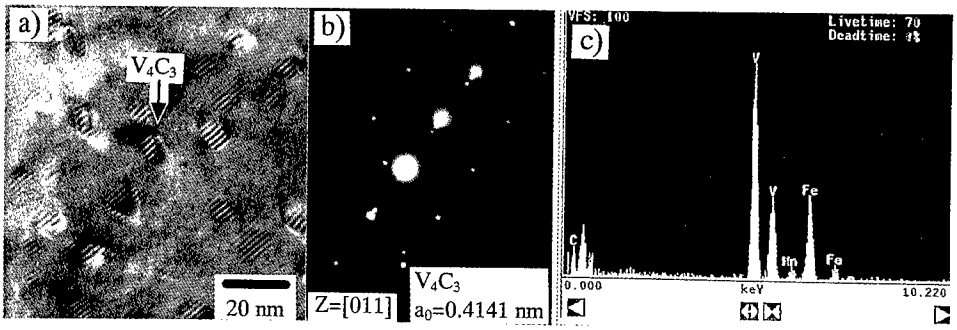


Figure 5: Typical TEM micrograph a), SAD pattern b), and analytical result by EDX c) of dispersed fine V_4C_3 carbides.

The size of V_4C_3 varies with aging conditions and controls the aging hardness. Figure 6 shows the relationship between the average size of V_4C_3 and aging hardness against the parameter *PH*. It is found that the maximum hardness can be attained at the size of around 7 nm in diameter. From the view point of the misfit strengthening by coherent precipitates, it is summarized [7, 8] that the increment of flow stress is proportional to lattice misfit ε, particle radius r_0, and the volume fraction f; $\Delta\tau \propto (\varepsilon \cdot r_0 \cdot f)^n$. Although dislocations move by cutting ordered particles in their models, the Orowan bowing model is generally considered to be applied as precipitates grow beyond a critical size. In Orowan model, bypass may occur by bowing, climb, or other processes. The overall strengthening response is represented by a combination of these mechanisms and it is suggested [9] that the maximum strength is achieved at the critical precipitate size, which can be attained at an appropriate aging condition. As indicated in Figure 6, the critical size of V_4C_3 measured for the investigated steels is 7 nm in diameter, at which the dominant strengthening mechanism may change from misfit strengthening to bowing model. In addition, it is implied from Figures 3 and 7 that the size mainly contributes to the hardening response and the volume fraction determines the magnitude of hardness.

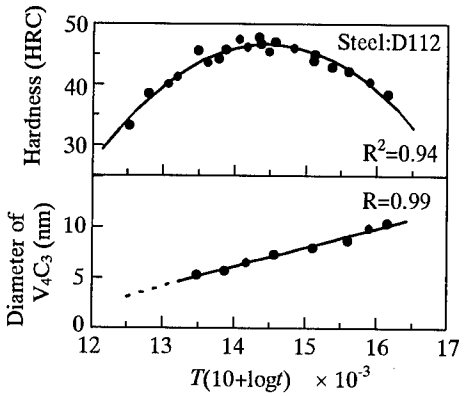


Figure 6: Relationship between average carbide size and hardening response against parameter $PH = T(10+\log t)$.

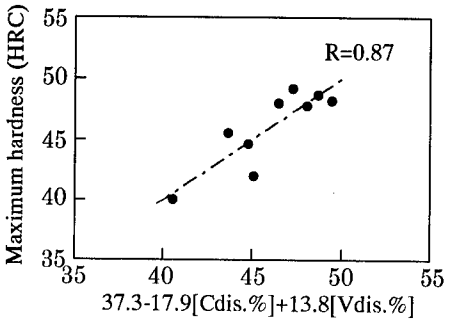


Figure 7: Relationship between the maximum hardness and C and V content dissolved based on $4\underline{V}(\gamma)+3\underline{C}(\gamma)=V_4C_3(s)$.

The maximum aging hardness can be expected from the dissolved contents of C and V. Figure 7 shows the regression calculation results of the measured and maximum hardness calculated by *PH* against the function of the dissolved C and V contents. As mentioned above, it is considered that at the critical size of 7 nm in diameter, a magnitude of the maximum hardness will be determined by the volume fraction of V_4C_3 that corresponds to the amount of dissolved element for carbide formation, i.e., C and V contents dissolved. Since V_4C_3 forms by the reaction $4\underline{V}(\gamma) + 3\underline{C}(\gamma) = V_4C_3(s)$, the ratio of dissolved C to V, C:V=3:4 in atomic %, is considered to be the most appropriate condition for the maximum hardness prediction as indicated in Figure 7.

4. CONCLUSIONS

The age hardening behavior due to VC precipitation with a corresponding microstructural change in γ phase steels are summarized.

1. During aging treatment, fine and dispersed coherent V_4C_3 precipitates in the matrix, of which lattice parameter of V_4C_3 is a_0=0.4141 nm, and crystallographic orientations are $[001]V_4C_3//[001]\gamma$, $(200)V_4C_3//(200)\gamma$, and $(111)V_4C_3//(111)\gamma$.
2. The formation of fine V_4C_3 is the main contributor for hardening due to relatively high lattice mismatch to the matrix Δa_o=0.153. The aging hardness can be predicted from two factors; 1) the amount of V_4C_3, i.e., volume fraction of precipitate, that determines the increment of the hardness, and 2) the size of V_4C_3 that controls the hardening response.
3. The maximum hardness is obtained at V_4C_3 size of approximately 7 nm in diameter and can be predicted by C and V contents dissolved in the matrix, at which a dominant strengthening mechanism is considered to change from misfit strengthening to Orowan bowing bypass mechanism.
4. It is clarified that the growth rate is proportional to the temperature-time parameter, $T(10+\log t)$, which suggests that V_4C_3 particle grows by a thermally diffusional process.

REFERENCES

1. M.Y. Wey, T. Sakuma, and T. Nishizawa, "Growth of Alloy Carbide Particles in Austenite," Trans. Japan Inst. Met., 22 (10) (1981), 733.
2. T. Sakuma, "Growth of Carbide and Nitride Particles in Steels," Bulletin of Japan Inst. Met., 20 (4) (1981), 247.
3. N.K. Bailliger and R.W.K. Honeycombe, "Coarsening of vanadium carbide, carbonitride, and nitride in low-alloy steels," Met. Sci., 14 (1980), 121 .
4. B. Miao and X. Xie, "Interfacial Structure of $M_{23}C_6/\gamma$ and VC/γ in a Carbide Strengthening Superalloy," Strength Met. Alloy, 3 (1989), 1339.
5. R.W. Hertzberg, Deformation and Fracture Mechanics of Engineering Materials 3rd Ed. (New York, NY: John Wiley and Sons, 1989), 151 and 175.
6. S. Nagakura and S. Oketani, "Structure of Transition Metal Carbides," Trans. ISIJ, 8 (1968), 265.
7. H. Gleiter, Die Erhohung der kritischen Schubspannung durch die Ausscheidung von verspannten, koharenten Teilchen, Z. Angew. Phys. 23 (2) (1967) 108
8. V. Gerold and H. Haberkorn, "On the Critical Resolved Shear Stress of Solid Solutions Containing Coherent Precipitates," Phys. Stat. Sol., 16 (1966), 675
9. C.T. Sims, N.S. Stoloff and W.C. Hagel, Superalloys II (New York, NY: John Wiley and Sons, 1987), 74.

TiB_2-PARTICLE-REINFORCED HIGH MODULUS STEEL

Kouji Tanaka, Tadashi Oshima, Fumio Nonoyama and Takashi Saito
Toyota Central Research and Development Laboratories, Inc.
41-1 Yokomichi, Nagakute, Aichi, 480-1192, JAPAN

ABSTRACT

A new TiB_2-particle-reinforced steel with an enormously high specific modulus has been developed. This article presents the high modulus steel (HMS) with respect to its benefit on high-performance machine parts, concepts for the development, cost-effective powder-metallurgical (P/M) manufacturing process, and Young's modulus / mechanical properties.
The thermodynamic assessment for Fe-X-B systems revealed the direct equilibrium between TiB_2 and ferrite, and strongly supported the most effective contribution of TiB_2 particles to improving isotropic Young's modulus in steel. Based on this phase stability, the P/M process employed *in-situ* TiB_2 synthesis reaction in sintering of compacted commercial ferrous powders blended with ferro-titanium and ferro-boron powders.
Owing to the material design in favor of the "thermodynamically-best" combination of reinforcing compound and steel matrix, the Young's modulus and specific modulus of the HMS agreed well with the theoretically predicted value. And mechanical properties including tensile and fatigue strength were also enhanced by the reinforcing TiB_2 particles.
The as-sintered HMS billet showed a sufficient hot-workability and near-net steel parts forming techniques have now being coordinated for each application.

The Third Pacific Rim International Conference on
Advanced Materials and Processing (PRICM 3)
Edited by M.A. Imam, R. DeNale, S. Hanada,
Z. Zhong and D.N. Lee
The Minerals, Metals & Materials Society, 1998

I. BACKGROUND

The Young's modulus of 190-210GPa has long been accepted as the natural value for iron and almost all kinds of steel. In fact, it is one of the physical property and hardly be improved with customary metallurgical schemes for high strength steels. For mechanical engineers, however, the elastic behavior of material used is more important in designing machine parts rather than the strength.

One reason is that those parts responsible for machine's function have to be designed with a sufficient rigidity so as to yield only a small elastic strain against applied stress. Meanwhile, in accordance with growing concerns for low energy consumption, the weight reduction has been a consistent demand imposed on every machine parts. The dimensions (thickness, diameter etc.) of automobile parts, for instance, have already been trimmed down assuring the requisite minimum rigidity.

Lightweight metals and their alloys may offer a higher specific strength. But the specific modulus (Young's modulus per density) is approximately the same as those of conventional steels, and the much smaller Young's modulus causes difficulties in providing the same rigidity within limited dimensions.

The problem of vibration characteristics also stems from the elastic behavior of material used. For high-speed moving / rotating parts, a resonance occurs when a running speed is equal to the natural frequency of components. If the specific modulus of the materials is unusually high, an increased natural frequency brings a resonance above the ordinary speed range, and promotes an improvement the maximum tolerable speed and safety margin as well as a significant noise reduction.

The Young's modulus of steel is the highest in all structural metallic material. In view of the above, however, a development of a new steel superior in both Young's modulus and specific modulus would be a breakthrough toward the high-performance machine parts with a further weight reduction or an improvement in vibration characteristics.

II. CONCEPT OF THE HIGH MODULUS STEEL

Isotropic Young's Modulus

The elastic constant of metals depends on crystallographic orientations and a higher Young's modulus was reported only in the longitudinal direction of extruded steel bar having the <111> recrystallization texture[1]. However, such an anisotropy in Young's modulus is not much useful because almost all machine parts are subject to a complex combination of non-uniaxial stresses. So the isotropic improvement in Young's modulus should be valuable, and incorporating reinforcing compound phase into steel matrix would be the only possible and promising means for that purpose.

As for steels, much of attention has been paid to the reinforcement with the aim of high strength

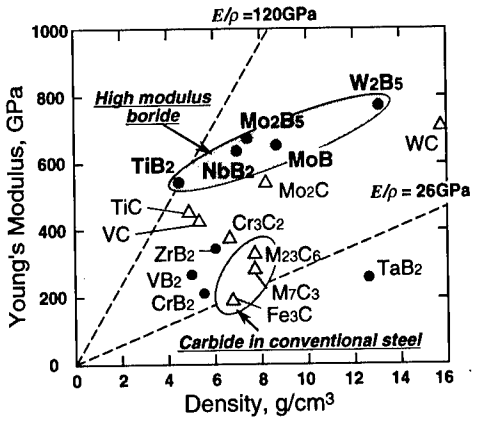


Figure 1 Property map for carbides and borides.

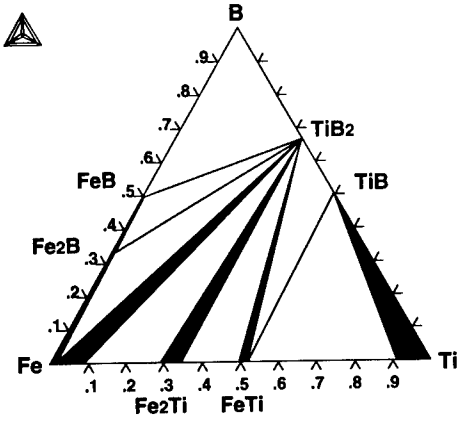


Figure 2 Calculated isothermal section of Fe-Ti-B phase diagram at 1273K.

or wear resistance rather than Young's modulus. **Figure 1** classifies carbides and borides in terms of their density and Young's modulus. Unfortunately, the Young's modulus of carbides found in conventional steels are relatively low.

Thermodynamic Aspect

Even if a compound itself has a high specific modulus, an effective contribution can not be reached when the much more important feature is disregarded. That is the phase stability in steels and the solubility of other elements. A large decline of Young's modulus occurs in steel matrix when a binary compound transforms to a ternary iron compound, or allows a high solubility of iron. Among the borides in figure 1, we have identified titanium diboride (TiB_2) to be the best reinforcement for the high modulus steel (HMS). And as the most suitable matrix of the HMS, we have selected a carbon-free steel alloyed with ferrite-former elements such as chromium or vanadium, considering that ferrite phase usually has a higher Young's modulus over austenite. The decision was supported by the reported effect of alloying elements on the Young's modulus of iron[2].

As well as the highest specific modulus of 120GPa, the decisive characteristics of TiB_2 is the direct equilibrium with steel matrix and the negligible solubility of iron which has been proved by thermodynamic calculations with CALPHAD method. The isothermal section of Fe-Ti-B phase diagram was determined as **figure 2** using *Thermo-Calc* software and the assessed database for Fe-X-B system. The details were presented elsewhere[3,4].

Other than providing isotropic high Young's modulus by the "thermodynamically-best" combination of reinforcement and matrix, the authors put emphasis on the following concept in order to extend the practical application of the HMS[5,6].

Well-balanced Mechanical Properties

As long as used for some structural parts, the HMS should provide a required balance of mechanical properties depending on each application. For the machine parts like those in automobile engines, fatigue strength and wear resistance are the important specification because they are subject to a repeated stress by the connected or opponent parts. And more seriously, the HMS parts have to carry an increased stress when redesigned to yield the same strain by reducing the dimension. In any case, any deterioration in mechanical properties are not justified even in exchange for a high Young's modulus. On the contrary, the HMS should have an enhanced mechanical strength according to the increase in Young's modulus.

Cost-effective Manufacturing Process

It is always crucial how far manufacturing cost can be lowered when trying to apply some new materials to a practical use, especially automobiles. To make the process of incorporating a large amount of TiB_2 particles cost-effective, a powder-metallurgical (P/M) process was more advantageous than casting. Stainless steel (AISI400 series) powders are widely available for Fe-Cr ferritic matrix, and less expensive iron powders can be used for other ferritic matrix by blending with ferroalloy powder containing necessary ferrite-former elements. For the raw material for TiB_2 particles, we focused on the reaction between ferro-titanium powder and ferro-boron powder which was found to synthesize TiB_2 particles *in-situ*[3,4] in the ordinary sintering condition for sintered steel product.

In addition, we were encouraged into the hot working on as-sintered products which greatly improves mechanical properties. That is also because near-net hot working processes have been established for various steel parts on an industrial basis. Therefore, the HMS should have at least a passable hot workability.

III. PROCESSING PROCEDURES AND EVALUATION

Materials Preparation

The raw powders were blended in an attritor for 0.9ks and compacted by die pressing or cold isostatic pressing (CIP) at the pressure of 392MPa. They were in a form of billet having a diameter of 20~30mm. After vacuum sintering at 1513K for 3.6ks, the billet was hot-worked by a rotary swaging machine for the following evaluation, or subjected to hot die forging and hot extrusion. All the hot workings were done immediately after reheating the as-sintered billet to 1423K, and the transverse area reduction was about 75%.

Young's Modulus Measurement

Rectangular samples of 3x4x30mm were cut out by electrically discharged machining (EDM) for the Young's modulus measurement in piezoelectric-resonance method[7]. A quartz bar with

110kHz resonance frequency was glued to the sample's edge, and the Young's modulus of the sample was calculated by examining the change in vibration characteristics using an impedance analyzer.

Mechanical Testings

The wear resistance of the HMS were evaluated in a pin-on-disk tester at the pressure of 0.4 MPa and the sliding speed of 0.4m/s, with no lubricant. Room-temperature tensile testings were carried out on smooth cylindrical specimens with 4mm in diameter by 15mm gage length. The strain rate was about $5x10^{-4}$/s. Fatigue testings were performed on cylindrical specimens with 5 mm in diameter by 10mm gage length in a rotating-bending fatigue tester at 3000rpm.

IV. MICROSTRUCTURE AND PROPERTIES

Microstructure

The results below are for the HMS prepared with Fe-17Cr (AISI430) water-atomized powder, and Fe-43Ti, Fe-21B powders pulverized from common ferro-titanium and ferro-boron block (compositions in mass% unless specified otherwise, all powders were under 45μm).

A typical micrograph is shown in **figure 3(a)** for the HMS containing 30 volume % of TiB_2 particles. (hereafter; 30vol.%TiB_2/Fe-17Cr). Fine particles are TiB_2 synthesized *in-situ* and the diameter is 0.1~0.8 μm. The matrix is a ferritic single phase.

In **figure 3 (b)**, a transmission electron image of the TiB_2 particle taken from its c-axis. It usually takes a near-hexagonal morphology with the $\{01\bar{1}0\}$ habit plane. A high-magnification in **figure 3 (c)** reveals no interlayer at the interface between the particle and the matrix. Furthermore, an energy dispersive X-ray analysis on the TiB_2 particle confirmed both solubilities of iron and chromium less than 3%. These microstructural characteristics correspond to our material design based on the direct equilibrium between TiB_2 and ferritic matrix.

Young's Modulus

Several theories have been proposed to predict the Young's modulus of particulate-reinforced composite, assuming the equal strains for particles and matrix. The Young's modulus of the HMS were determined for various TiB_2 contents and compared with the prediction by A. P. Miodownik[8].

The result is summarized in **figure 4**, showing a fair agreement between the measured Young's modulus and the predicted one. The agreement suggests that TiB_2 maintains its own properties in the steel matrix and proves our concept of incorporating the particles with the discussed thermodynamic nature.

Since the specific gravity of HMS linearly decreases with increasing TiB_2 content, the increase in specific modulus (E/ρ) is more impressive than Young's modulus itself (E). With more than 40vol%TiB_2 particles, the Young's modulus reaches over 300GPa and the specific modulus climbs to nearly as double as that of AISI430 steel.

Mechanical Properties

Figure 5 shows the change in wear loss with TiB_2 content. It clearly demonstrates the wear resistance comparative to SAE4620 hard steel at more than 20vol%TiB_2 particles.

The results for tensile test on the HMS are summarized in **table 1**, and the steady increases in both 0.2% proof strength and tensile strength are recognized with increasing TiB_2 content. Generally, hard particles in metal-matrix-composites usually enhance the static strength or hardness. In contrast, they often fail to improve the fatigue strength because such dynamic properties are highly influenced by the nature of interface between particle and matrix.

The fatigue properties of the HMS are represented by the S-N curves in **figure 6**. It can be seen that, with increasing TiB_2 content, both the low cycle and high cycle fatigue strength are remarkably improved. Fractographic examinations indicated that all fractures of the HMS originated on specimen surfaces, not related to TiB_2 particles. It has been, therefore, expected that in addition to the thermodynamic stability of TiB_2 in the ferritic matrix, the strong bond strength at the interface between the two phases are responsible for the above favorable contribution to mechanical properties.

V. APPLICATION

The applications of the HMS are highlighted in a variety of machine parts. Especially, the trial

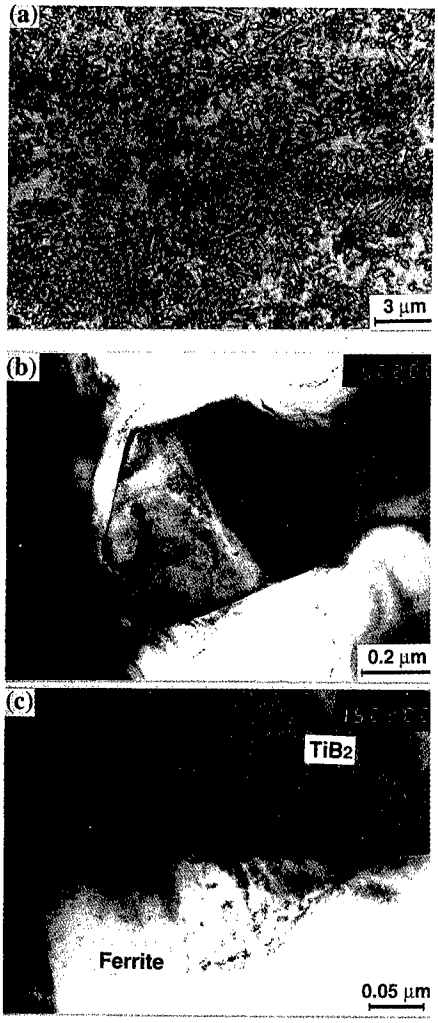


Figure 3 Microstructures of 30TiB2vol.%/ Fe-17Cr. (a) Optical micrograph, (b) TEM image of TiB_2 particle, (c) enlargement of the interface with matrix.

Table 1 Room-temperature tensile properties of 10-30vol.%TiB_2/Fe-17Cr.

TiB_2 (vol.%)	0.2% Proof Stress (MPa)	Tensile Strength (MPa)	Elongation (%)
10	565	873	10.5
20	776	1007	2.6
30	1107	1119	0.7

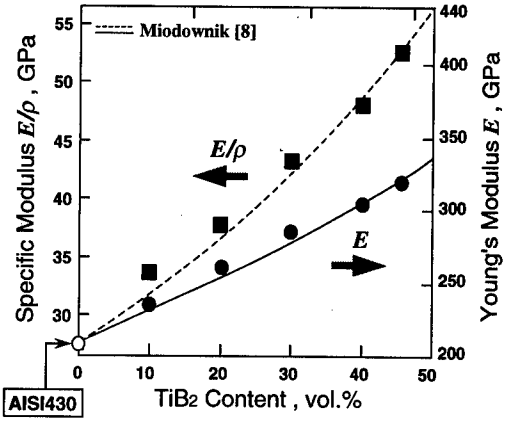


Figure 4 Change in Young's modulus and specific modulus of TiB_2/Fe-17Cr with TiB_2 content.

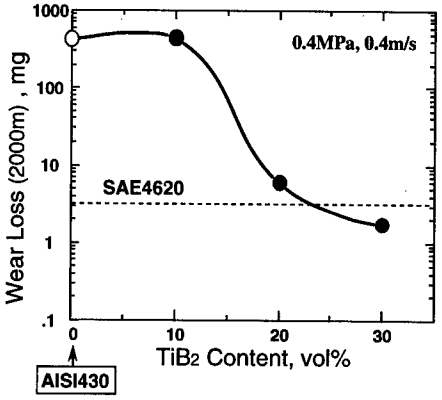


Figure 5 Change in wear resistance of TiB_2/ Fe-17Cr with TiB_2 content.

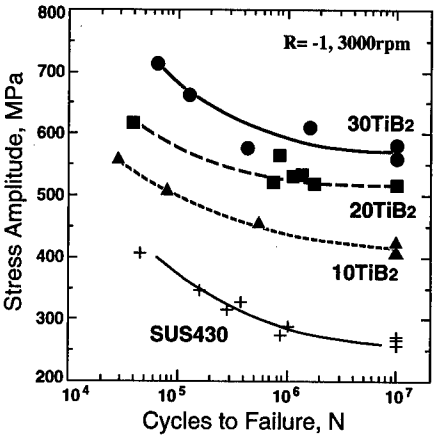


Figure 6 S-N curves for rotaing-bending fatigue test on 10-30TiB2vol.%/Fe-17Cr.

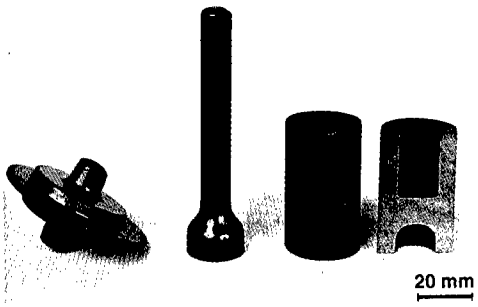


Figure 7 Hot-worked products using as-sin -tered 30vol.%TiB_2/Fe-17Cr billet.

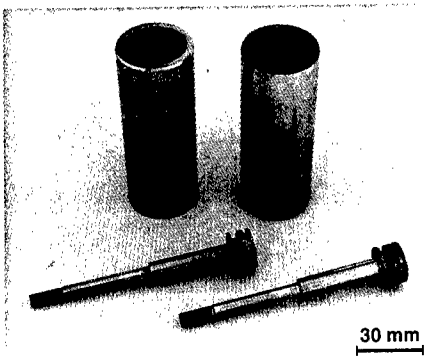


Figure 8 Engine components machined from hot-worked products.

HMS parts are being produced most enthusiastically for automobile engines. **Figure 7** shows examples of hot-worked HMS product using as-sintered 30vol.%TiB_2/Fe-17Cr cylindrical billet. No major defect are observed in their appearances. They were finished by machining into engine components like those given in **figure 8**. These were made of 30vol.TiB_2/Fe-17Cr having the specific modulus 70% higher than those of steels and other lightweight metals. The cylindrical parts were redesigned to have the same rigidity as the conventional steel one, which resulted in 25% weight reduction with the enlarged inner diameters. The shafts in the figure were intended to increase the natural frequency by 30%. Now the engine test of these HMS components are being proceeded to reveal their performance.

VI. SUMMARY

Steels or iron-based alloys have an exceptional potential in microstructural control, which enables the extensive application to structural uses. Nevertheless, a high modulus steel has scarcely been studied and it has been remained a very desirable material for users.
The high specific modulus differentiates the HMS from the competitive materials in terms of far superior benefit on the parts in need of weight reduction and/or improvement in vibration characteristics. Furthermore, the combination of well-balanced mechanical properties and highly available process would guarantee a wide application of the HMS.

References

[1] S. Yamamoto, K.Asabe, M. Nishiguchi, and Y, Maehara, "Recrystallization Texture and Young's Modulus of Ceramic Particle Dispersed Ferritic Steel Bars", *Tetsu-to-Hagane* (Journal of the Iron and Steel Insitute of Japan), **82** (1996), 771-776.

[2] G. R. Speich, A. J. Schwoeble, and W. C. Leslie, "Elastic Constants of Binary Iron-base Alloys", Metal. Trans., **3** (1972), 2031-2037.

[3] K. Tanaka, T. Oshima, and T. Saito, "Synthesis and Phase Equilibria in TiB_2-Particle-Reinforced High Modulus Steel", Synthesis of Lightweight Metallic Materials II, ed. F. H. Froes, et al. (Warrendale, PA: TMS, 1997), p.321.

[4] K. Tanaka, T. Oshima, and T. Saito, "Development of High Modulus Steel based on Thermodynamic Phase Equilibrium between TiB_2 and Ferrite", *Tetsu-to-Hagane*, **84** (1998), in print.

[5] K. Tanaka, T. Oshima, and T. Saito, "Producing Method and Mechanical Properties of TiB_2-Particle-Reinforced High Modulus Steel", in [3], p.333.

[6] K. Tanaka, T. Oshima, and T. Saito, "Mechanical Properties and Hot Workability of TiB_2-Particle-Reinforced High Modulus Steel", in [4], in print.

[7] M. Ozawa, T. Hatanaka, and H. Hasegawa, "Internal Friction of 2 and 8mol%Y_2O_3-ZrO_2 Polycrystals Measured by a Resonance-Piezoelectric Method at around 100kHz", J. Mater. Sci. Letters, **10** (1991), 774-775.

[8] Z. Fan, P. Tsakiropoulos, and A. P. Miodownik, "Prediction of Young's Modulus of Particulate Two Phase Composites", Mater. Sci. Technol., **8** (1992), 922-929.

STRUCTURE AND MECHANICAL PROPERTIES OF ULTRA LOW CARBON/Ti ADDED STEELS

R. Mendoza, G. Lugo and J. A. Juarez-Islas

Ispat Mexicana, S.A. de C.V., Fco. J. Mujica No 1B, Cd. Lazaro Cardenas, Michoacan, Mexico.

Instituto de Investigaciones en Materiales-UNAM, Circuito Exterior S/N, Cd. Universitaria, 04510, Mexico, D.F., Mexico

Abstract

A series of ultra low carbon/Ti added steels were processed in a Mexican steel company as a part of a research program which has the scope of developing ultra low carbon steels for automotive applications. Microstructural characterisation of slabs in the as-cast, re-heated and thermomechanically processed conditions are presented, giving emphasis in the resulting mechanical properties in terms of the percentage of elongation and the Lankford constant after the annealing treatment.

The Third Pacific Rim International Conference on
Advanced Materials and Processing (PRICM 3)
Edited by M.A. Imam, R. DeNale, S. Hanada,
Z. Zhong and D.N. Lee
The Minerals, Metals & Materials Society, 1998

Introduction

Vacuum degassed interstitial free (IF) sheet steels have very high formability, especially for parts requiring good deep drawability.[1] The high formability is achieved by lowering the interstitial element content to very low levels by steelmaking and by additions of stabilising elements such as titanium (Ti) or niobium (Nb) which combine with nitrogen (N) and carbon (C) not removed by the steelmaking practice.[2, 3]

On the other hand, it has been reported,[4] that the ferrite matrix of heavily cold rolled IF sheet steels recrystallizes during annealing to a polycrystalline structure with a strong (111) $<\bar{1}10>$ recrystallization texture, producing high values of the average plastic strain ratio, $\bar{r}$, which is associated with the high formability of ultra low carbon IF steels.

The deep drawing characteristics of IF sheet steels, in terms of the measured Lankford value from a tensile test, are strongly dependent upon the development of strong {111} recrystallization texture during in line annealing.[5] Furthermore, during the process of removing interstitial elements by using microalloying elements, precipitates could be left in the matrix that may adversely affect the recrystallization process.[6]

Ti left in excess,[7] in the matrix is far less effective than Nb in retarding the recristallization process, but this characteristic is considered a distinct advantage in the design and processing of Ti stabilised interstitial free steel for extra deep drawing grades.

The aim of this work is to present results in terms of the per cent of elongation and the Lankford value after hot rolling, cold rolling and annealing operations of ultra low carbon/Ti added steel of a experimental heat of 230 tons.

Experimental Procedure

Imexsa steelmaking practice to produce the experimental IF steel, whose composition is shown in Table I, has been reported elsewhere.[8] Slabs of 100X50X10 mm were reheated to a rolling start temperature of 1250°C (30 min.) and hot rolled until at 64% of total reduction was achieved (2 passes and 3 mm thick) to above 950°C.

Subsequently the rolled steel was air cooled to 730°C and kept at that temperature for 30 min., as coiling simulation. After removing scale, the 3 mm thick rolled slab was cold rolled until at 84% of total reduction in 11 passes was obtained, finishing with a 0.5 mm thick sheet.

Finally the steel sheet was annealed under an argon atmosphere at 800°C for 5 min. Specimens in all conditions were prepared by using normal metallographic procedures and etched with 2% Nital. Tensile tests were conducted on an Instron 1125 (10 tons.) test machine.

Results and Discussion

Figs. 1a shows the microstructure observed in the as-continuously cast condition, in which, it was observed in ferrite grains and grain boundaries the presence of precipitates with a rhombohedral morphology which were identified by means of scanning electron microscopic (SEM) microanalysis and electron diffraction patterns as TiN precipitates. Particles of nanometric scale were also observed and identified as carbides.

Fig. 1b shows the microstructure after the hot rolled experiments, Fig. 1c in the cold rolled condition and Fig. 1d shows the microstructure in the annealing condition.

In the as-hot rolled condition it was observed the presence of $Ti_4C_2S_2$ precipitates in hot bands. This precipitate was also identified by means of SEM microanalysis and electron diffraction patterns.

Taking into consideration the dependence of Ti and S contents and slab re-heating temperature on the precipitation of TiS and $Ti_4C_2S_2$, the last precipitate was considered the main precipitate within the present experimental conditions.

With respect to the mechanical properties achieved in ultra clean steels in the as-annealed condition at 800°C for 5 min., Table II shows the results in terms of 0.2% Yield Strength, UTS and percentage of elongation for tensile test specimens oriented at 0°, 45° and 90° with respect to the rolling direction.

From the resulting tensile test specimens, it was calculated the Lankford constant at 0°, 45° and 90° with respect to the rolling direction according with the following expression:

$r = \ln (w / w_0) / \ln (t / t_0)$

where t_0 and w_0 are the initial thickness and initial width, respectively, and after deformation are denoted by t and w.

The average Lankford constant ($\bar{r}$) was evaluated according to:

$\bar{r} = (r_o + 2r_{45} + r_{90}) / 4.$

According to the results obtained in terms of the per cent of elongation and the average Lankford values it can be mentioned that recently a grade which has been classified a IF steel grade denominated as super extra deep drawing quality grade has come to be in demand, due to the increasingly severe customer requirements and surprisingly high formability of 2.0 in $\bar{r}$ value and over 50% in elongation are required, properties that has been achieved in our experimental heats.

Conclusions

As can be observed from the data presented above, the mechanical properties of ultraclean steels processed at Imexsa, hot rolled, cold rolled and annealed showed an understanding behaviour in terms of the per cent of elongation and the Lankford constant. These steels show properties for extra deep drawing applications

References

1.- O. Kwon and K. Z. Min, International Forum for Physical Metallurgy of IF Steels-94 (The Iron and Steel Institute of Japan, May, 1994), 9-12.

2.- H. Takechi, ISIJ International, 34 (1) (1994), 1-8.

3.- H. Takechi, O. Akisue and T. Yakushiji: Tsetsu-to-Hagané, 74 (1988), 1617.

4.- D. O. Wilshynsky-Dresler, D. K. Matlock and G. Krauss, International Forum for Physical Metallurgy of IF Steels-94 (The Iron and Steel Institute of Japan, May, 1994), 13-31.

5.- W. B. Hutchinson, Int. Met. Rev., 29 (1984), 25-43.

6.- H. Takechi: Symp. On Metallurgy and Application of Modern IF Steel Grades, (VDEh, Dusseldorf, 1990).

7.- H. Inagaki: High Purity Iron, %Textures and Microstructures, Vol. 8 and 9, (Gordon and Breach Science Publishers, Inc. U. K., 1988),. 173.

8.- R. Mendoza, J. Camacho, G. Lugo, C. Lopez, L. Herrera, J. Reyes, C. Gonzalez and J. A. Juarez-Islas, ISIJ International, 37 (2) (1997), pp. 176-180.

Table I. Chemical composition in wt. % of slabs of ultra clean steels.

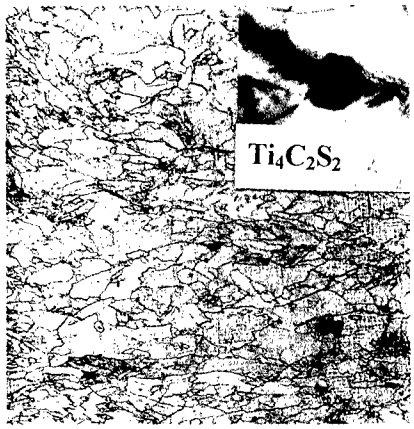
Element	U430/30119 sample 1	U430/42229 sample 2	U430/40133 sample 3	U451/36014 sample 4, ref. [8]
C	0.004	0.005	0.005	0.013
Mn	0.098	0.085	0.11	0.18
Si	0.012	0.023	0.030	0.023
P	0.004	0.004	0.004	0.010
S	0.008	0.012	0.010	0.005
Al	0.031	0.042	0.071	0.032
Nb	0.001	0.003	0.000	0.003
Cu	0.01	0.010	0.015	0.015
Ni	0.012	0.008	0.013	0.008
N_2	0.003	0.0048	0.0044	0.005
Ti	0.061	0.075	0.069	0.046

Table II. Mechanical properties and the Lankford constant for annealed sheets at 800°C per 5 minutes.

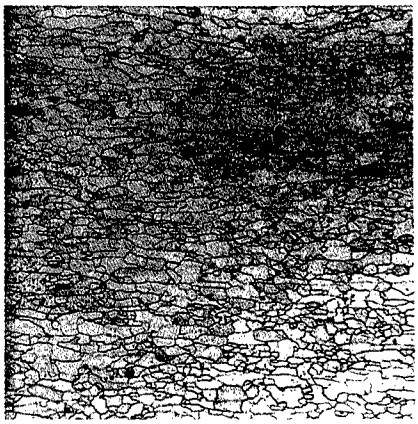
Mechanical properties	90° rolling direction				45[a] rolling direction				0° rolling direction			
Sample	(1)	(2)	(3)	(4)	(1)	(2)	(3)	(4)	(1)	(2)	(3)	(4)
0.2% Y.S (MPa)	152.6	138.5	167.1	272.0	145.3	141.8	156.5	357.0	137.0	140.5	153.5	280.0
UTS (MPa)	294.7	254.3	306.4	37.8	310.6	298.5	294.7	363.6	288.2	293.5	305.9	340.6
E (%)	45.6	61.7	56.7	52.4	75.3	71.9	62.3	70.1	61.2	64.5	68.5	66.6
r	2.07	2.19	2.03	1.91	2.01	2.05	1.99	1.86	2.34	2.28	2.07	2.01
$\bar{r}$	2.10 (1)		2.12 (2)		2.02 (3)		1.91 (4)					



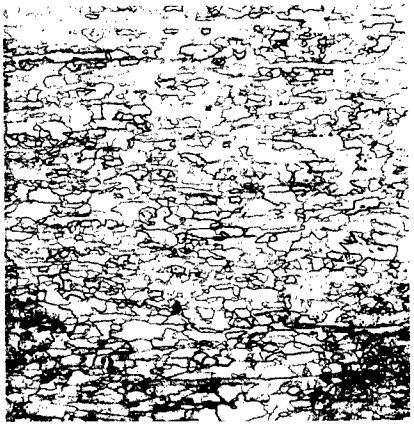
a



b



c



d

Figs. 1a Microstructure observed in the as-continuously cast condition, precipitates of rhombohedral morphology which were TiN precipitates (inset TiN precipitate) 500X. b) Microstructure after the hot rolled experiments (inset $Ti_4C_2S_2$ precipitate) 250X. c) Microstructure observed in the cold rolled condition, 250X and d) Microstructure observed annealing condition, the last precipitate was considered the main precipitate within the present experimental conditions, 250X.

INTERACTION BETWEEN MELTS AND REFRACTORY IN PROCESS OF SMELTNIG REDUCTION WITH IRON BATH

Liu Qingcai ① **Lin Jing** ②

Abstract

This investigation is focused on the interaction between refractory and melts, erosion mechanism of refractory in melts of smelting reduction with iron bath. The results show that Al_2O_3-C-TiO_2 refractory has a fine microstructure and physical character with the network of TiC. It is better to used as furnace lining materials than Al_2O_3-C-SiC and Al_2O_3-C refractory in the technology of smelting reduction with iron bath. In the process of interaction series AT refractory can form protective slag film with solid TiC and $CaO.TiO_2$ and series AS refractory can form SiO_2 and SiO protective film to hinder the interaction rate. The moving speed of slag film and diffusion ability of mass are main factors to influence the erosion rate of refractory by melts of smelting reduction with iron bath.

① Chongqing University, Chongqing 400044, P.R. of China
② Chongqing JIANZHU University, Chongqing 400045, P.R. of China

The Third Pacific Rim International Conference on
Advanced Materials and Processing (PRICM 3)
Edited by M.A. Imam, R. DeNale, S. Hanada,
Z. Zhong and D.N. Lee
The Minerals, Metals & Materials Society, 1998

Introduction

There are different kinds of smelting reduction developed in resent thirty years[1,2]. The technology of smelting reduction with iron bath is a typical technology. In this technology, the most obvious feature is the change of ferrous oxide activity and special kinetics character[3]. Because the high FeO concentration in slag and high reduction rate of ferrous oxide of melts, the erosion character and erosion mechanism of the refractory materials used as furnace lining of smelting reduction technology by melts are important factors for this technology development [4,5].

Experimental Method

Samples of Slag and Iron Bath

Samples of slag used for testing were got by mixing chemical agents and melting in electric-resistance furnace. Table I shows the composition of slag samples. Iron bath used for testing interaction was made with pig iron. It's composition (wt%) is: C 4.16, Si 0.53, Mn 0.32, P 0.10 and S 0.034.

Table I Composition of Slag (%)

slag sample	FeO	CaO	SiO2	Al2O3	MgO	CaO/SiO2
slag A	14.6	33.7	33.7	10.0	8.0	1.00
slag B	20.4	30.8	30.8	10.0	8.0	1.00
slag C	20.4	33.6	28.0	10.0	8.0	1.20

Samples of Refractory

There are two kinds of refractory used to test interaction between refractory and melts of smelting reduction with iron bath. One is series of AT (Al_2O_3-C-TiO_2), the other is series of AS (Al_2O_3-C-SiC). The composition and physical character are listed in table II.

Table II Composition and Character of Refractory

Items		*AT1*	*AT2*	*AT3*	*AT4*	*AS1*	*AS2*	*AS3*
composition:	Al_2O_3	79.4	76.2	73.5	70.8	80.7	76.2	73.4
(%)	SiO_2	5.40	4.8	4.5	4.1	5.3	5.0	4.8
	TiO_2	0	4.0	8.0	12.0	0.45	0.37	0.36
	SiC	0	0	0	0	3.0	6.0	9.0
Anti-press strength, Mpa		51.3	64.7	66.3	65.4	58.7	58.3	57.6
Resistant break strength, Mpa		10.5	14.7	13.5	11.5	12.4	14.7	11.3
Fire-resistant degree, K		2040	2075	/	2067	2073	2081	/
Pore ratio, %		9.3	7.4	6.5	7.1	7.7	8.1	7.9
Density, g/cm^3		2.8	2.91	3.01	2.94	2.96	2.89	3.03

Method of Interaction Test

The equipment used for test interaction between refractory and melts is high temperature electric-resistance furnace. Testing was done by the method of rotary immersion. Refractory sample was immersed melts under iron bath (below interface of slag and iron bath) 5-8 mm. The composition of gas in furnace was Pco 40Kpa and P_{N2} 60 Kpa. The rotary speed of refractory sample was 20 r/min, down and up times 0, 4, 8, 12, 16 and 20 time/min.

Experimental Results

Structure and Qualities of Series AT Refractory

The samples of refractory used for testing were sintered with powerful reduction atmosphere, almost all TiO_2 was reduced to form TiC. It was shown that the micro-structure of series AT refractory was a network structure[2,3] ,if the content of TiO_2 more than 8% in refractory. The more the TiC in refractory, the better and more integrated of TiC network structure. Table III is the compounds analysis of series AT refractory. Figure I shows the X-ray qualitative analysis.

TABLE III COMPOUNDS ANALYSIS OF AT REFRACTORY

sample	*Compounds*
AT1	Corundum40-50%, mullite25-30%, Al4C3 1-3%, a-Al_2O_3 10-12%
AT2	Corundum30-40%, mullite20-25%, Al_4C_3 1-2%, TiC 4-5%, a-Al_2O_3 5-10%
AT3	Corundum25-35%, mullite20%-23%, TiC 5-8%, a-Al_2O_3 5%
AT4	Corundum25-30%, mullite 8-20%, TiC 8-10%, a-Al_2O_3 2-5%

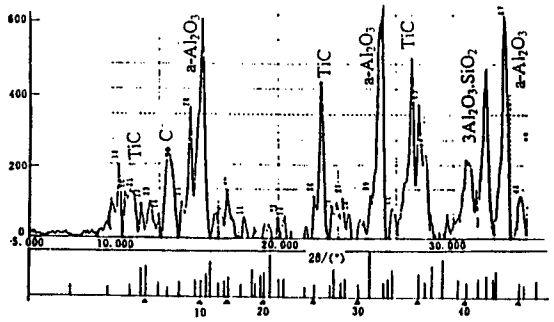


Figure 1: X-ray qualitative analysis of sample

Qualities of Series AS Refractory

SiC has a very good quality to resist erosion by the strong oxidization melts and is used in refractory industry for a long time[6]. It is not reported that refractory containing SiC resists to erosion of melts that FeO concentration up to 20% in the process of smelting reduction with iron bath. This test is to determine the resistance erosion ability of refractory containing SiC. The experiment results is given in table IV.

Table Ⅳ Erosion Rate of Series AS Refractory

$\times 10^{-3}$, $mm.min^{-1}$

Sample	*AS1*	*AS2*	*AS3*	*AT1*	*AT3*	*AT4*
slag A	15.46	11.20	5.26	22.18	4.75	3.10
slag B	27.35	14.25	8.43	34.50	8.83	4.35
slag C	28.56	15.45	9.37	32.16	8.75	4.80

Relation between TiO_2 Content and Erosion Rate of Refractory

According to testing results, the relation may be indicated as following equations:

$$Vr = 0.78 \times 10^{-4}(TiO_2\%)^2 - 9.56 \times (TiO_2\%) + 3.81 \times 10^{-2} \quad mm.min^{-1}$$

$$Vs = 6.07 \times 10^{-5}(TiO_2\%)^2 - 3.56 \times (TiO_2\%) + 4.52 \times 10^{-2} \quad mm.min^{-1}$$

$$Vi = 0.71 \times 10^{-6}(TiO_2\%)^2 - 2.25 \times (TiO_2\%) + 8.30 \times 10^{-4} \quad mm.min^{-1}$$

Vr ,Vs and Vi are the erosion rate of refractory in position of interface between slag and iron bath , the slag surface and iron bath individually. It was shown that erosion rate of series AT refractory possess character that the zone of highest erosion rate is interface of slag and iron bath, the lowest is iron bath.

Relation between Rotary Speed and Erosion Rate

The higher the moving speed of molten bath, the higher the diffusion rate of mass in the bath. The experimental results of erosion rate in different rotary speed are shown in table Ⅴ. It is shown that the erosion rate of refractory is increased with linear relation as the rotary speed increased. According to the report[7], increasing rotary speed of sample, the moving rate of slag film is also increased. It is obvious that the erosion rate of interaction between melts and refractory would be serious as the rotary speed increasing of sample in molten bath.

Table Ⅴ Relation of Erosion Rate and Rotary Speed

$\times 10^{-3}$, $mm.min^{-1}$

Sample		*AS1*	*AS2*	*AS3*	*AT1*	*AT3*	*AT4*
rotary	5	8.75	5.67	5.23	4.50	3.83	2.35
speed	10	10.56	7.45	6.37	7.16	5.75	4.80
(r/min)	15	18.35	13.23	8.35	10.60	6.78	5.18
	20	27.35	14.25	8.43	34.50	8.83	4.35
	30	35.23	21.35	18.65	56.47	14.50	10.25

Discussion

Comparison of Erosion Rate of AT with AS Refractory

As the testing results of table Ⅳ and table Ⅴ, in the same condition such as same composition of melts, rotary and testing temperature, the erosion rate of refractory is great difference. Series AT refractory has a good resisting erosion ability to melts of smelting reduction with iron bath. It's erosion rate is lower about 20-30% than that of series AS refractory . In this experimental condition, series AT refractory is the best lining materials for the technology of smelting reduction with iron bath.

Erosion Mechanism of Series AT Refractory by Melts of Smelting Reduction

Figure 2 shows the X-ray qualitative analysis results of series AT refractory in the interface of refractory surface and slag film .There were a lot of TiC(fusing point 3143K) , $CaO.TiO_2$ (fusing point2176K) and TiO_2 as well as other titanium oxides. Owing to high concentration of FeO in molten slag contacting with refractory, there must take place a series of chemical reactions in slag film and forming new products such as TiO_2, TiO, $CaO.TiO_2$, $FeO.TiO_2$, $CaO.SiO_2$ et al.. Because there are enough carbon to reduce ferrous oxide in melts, a partial of TiC can't be oxidization by melts and some TiO_2 may be reduced to TiC . TiC and $CaO.TiO_2$ existing in slag film, that must hinder the moving of slag and diffusion of mass in slag film. The final result is forming a protect layer and separating slag to refractory. The erosion rate of series AT refractory is lower than that of refractory without TiO_2.

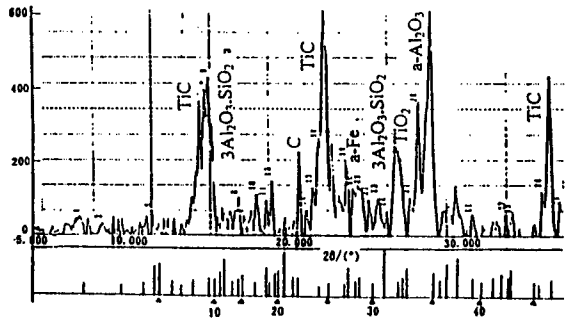


Figure 2: X-ray qualitative analysis for sample AT3

Erosion Mechanism of Series AS Refractory by Melts of Smelting Reduction

SiC used as a additional materials in refractory is very common. But SiC used as a additional materials in refractory can't form a network structure. As above testing results, erosion resistance ability of refractory contained SiC is lower than that of series AT refractory. Figure 3 is X-ray qualitative analysis for AS3.

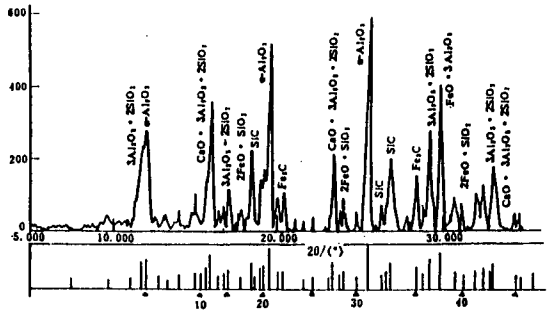


Figure 3: X-ray qualitative analysis for sample AS3

The erosion mechanism consists of three steps. First the interaction between melts and refractory takes place to form SiO_2, SiO , C and other low fusing point compounds when the melts contacting with refractory. Secondly, the reaction products diffusion or moving to slag film and melts, but there must be concentrated the reaction products in slag film, especially concentration SiO_2, SiO et al.. The third step ,owing to the concentrated of new products in slag film, the moving speed and diffusion ability is slowed and hindered. The erosion rate of refractory by melts is decreased gradually.

Summary

1 In this testing condition, series AT refractory can form a very integrated TiC network and has excellent physical characters. Owing to forming TiO_2 by oxide TiC, high fusing point product of $CaO.TiO_2$ and remain solid TiC in slag film, the moving speed of slag film and diffusion ability are hindered and the erosion rate is also decreased gradually in process of interaction .

2 AS series refractory can forming SiO_2, SiO protective layer in slag film, it has a good character to resistance erosion by melts of smelting reduction with iron bath.

3 Comparison series AT refractory with series AS refractory , AT refractory is better to used as furnace lining materials for technology of smelting reduction with iron bath.

4 The moving speed and diffusion rate of mass in slag film and melts are the main factors that influence the erosion rate of refractory. So controlling moving speed of melts , forming protective layer and decreasing diffusion ability in slag film are the efficacious ways to hindered interaction rate.

Reference

1 Zhang B. et al., Kinetics of V in the Smelting reduction slag for V-Ti-magnetite, Acta Metallurgical Sinica Serial, Vol.5 (1993) :399-403

2 Liu Q., Study of foaming of melts for smelting reduction with iron bath, J. of Iron and Steel research, Vol.2(2):5-8

3 Liu Q. et al., Study of wetting SM melts on refractory, China refractory, 4(1997): 56-60

4 Liu Q., Relation between smelting reduction rate and slag structure for V-Ti- magnetite, Acta metallurgical sinica, 10(1996): 85-89

5 Zhang B. et al., Thermodynamics of Vanadium in the SM slag for V-Ti-magnetite. Acta metallurgical sinica serial, Vol.5(1992): 287-291

6 Snsan L marr et al., Properties of tungsten core SiC monofilament , 21th Int. SAMPE Tech. Conf.,New Jersy, 989, Sep.25.

7 Huang X., Principle of Iron and steel metallurgy, (Chongqing, Chongqing Publishing Company, 1992), 347-368.

THE EFFECT OF THE TITANIUM TRACES ON THE MECHANICAL PROPERTIES OF AN ULTRA HIGH STRENGTH STEEL

Ruis Camargo Tokimatsu[(1)], Paulo Iris Ferreira[(2)], and Itamar Ferreira[(2)]

[(1)] Department of Mechanical Engineering, Faculty of Engineering of Ilha Solteira, UNESP, 15378-000 - Ilha Solteira, SP, Brazil;
[(2)] Department of Materials Engineering, College of Mechanical Engineering, UNICAMP 13083-970 - Campinas, SP, Brazil.

Abstract

The aim of this paper is to evaluate the effect of titanium traces (40 and 150 ppm) on the hardness, strength, and fracture toughness of the 300M steel. These mechanical properties have been characterized in specimens austenitized at 1,373K, quenched, and tempered at 473K and 603K. The microstructure of the heat treated specimens was characterized by optical metallography and scanning electron microscopy. The results evidenced that there was no significant differences between the mechanical properties of the 300M steels for these titanium traces, in both heat treated conditions. Typical values of mechanical parameters were: Hardness, 608 HV; Yield Strength, 1,660 MPa; Fracture Toughness K_{Ic}, 82 MPa$\sqrt{m}$. These results can be attributed probably to the size of the carbon-nitride precipitates; these titanium rich precipitates are thermal stable, and very coarse.

The Third Pacific Rim International Conference on Advanced Materials and Processing (PRICM 3)
Edited by M.A. Imam, R. DeNale, S. Hanada, Z. Zhong and D.N. Lee
The Minerals, Metals & Materials Society, 1998

Introduction

It is well known that the presence of small quantities (10 to 1,000 ppm) of Nb, Ti, V, Zr, and B in steels usually lead to significant effects on its microstructure with consequences on the mechanical properties (1-3). All these elements tend to react with interstitial elements (C, N) to form a second phase. At low temperatures these second phases can precipitate, whereas at high temperatures (austenitizing range) these precipitates can dissolve totally or partially into the matrix. However, some compounds may have low solubility even at temperatures close to the melting point.

In general, the effects of micro-additions of Ti to steels are less discussed in the literature compared to those of V and Nb, probably because the high reactivity of this element has hindered its general use for some time. More recent innovations in melting and degassing techniques have allowed good control of Ti in steels even at very low amounts (around 150 ppm). As a consequence, the beneficial effects of Ti on inclusion content and in preventing segregation of elements to grain boundaries that causes embrittlement, as well as the inhibiting effects of Ti compounds on grain growth during high temperature operations (rolling, austenitizing, welding), have been reported (1,6,7,9). It has been postulated that Ti addition to steels may reduce the embrittlement induced by nitrogen and phosphorus (10).

The main objective of this paper was to investigate the effects of small amounts of Ti on the mechanical properties of two 300M steels, steels A and B, containing 40 ppm and 150 ppm of Ti, respectively.

Experimental Procedure

Two types of air space quality 300M steels were used in this investigation. The materials were fabricated by Eletrometal S/A, a Brazilian Company, through melting and re-melting under vacuum in an electric resistance furnace and hot rolled. The material was received in the form of circular bars (ϕ = 44 mm and ϕ = 62 mm) in the as annealed condition. Table I shows the chemical composition of the alloys A and B.

Table I Chemical composition of the two variations of 300M steels.

	C	Si	Mn	P	S	Cr	Mo	Ni	V	Cu	Ti	N
Steel A	0.41	1.70	0.78	0.005	0.001	0.79	0.39	1.79	0.08	0.06	40 ppm	23 ppm
Steel B	0.42	1.68	0.74	0.009	0.001	0.84	0.37	1.82	0.09	0.04	150 ppm	156 ppm

Specimens for tensile, fracture toughness and hardness tests were fabricated from the as received bars. Tensile and fracture toughness specimens were taken with its principal axis along the rolling direction. These specimens were submitted to an austenitizing heat treatment at a temperature of 1,373 K for one hour. At the end of this heat treatment the specimens were quenched into oil. Immediately after quenching, a series of two tempering heat treatments were conducted at temperatures 473K and 603K, for one hour, both interrupted by quenching again the specimens into oil. Fracture toughness, tensile and hardness tests were conducted at room temperature according to the ASTM E 399-90, ASTM E 8M-95, and ASTM E 92-82, respectively.

Optical metallography was utilized for grain size measurements. The fracture surface was analyzed in a Cambridge Stereoscan S4-10 scanning electron microscope. Electron microprobe microanalysis was utilized for the qualitative determination of composition of particles present in the interior of the material, as well as, at certain areas of the fracture surface.

Results and Discussion

Table II illustrates the stoichiometric relation in wt. % for the compounds supposed to be formed, as well as, the weight relation in the matrix in both 300M steels investigated. Table III shows the elemental distribution in the precipitates for both steels, according to the preferential sequence of formation. As the Ti/N relation is hypostoichiometric in both 300M steels, all

titanium will probably be consumed in the formation of TiN, and the occurrence of titanium carbides or other titanium compounds will be improbable. The remaining nitrogen may be used for the formation of vanadium nitride. However, as the elemental relation in this case is hyperstoichiometric, vanadium may not be completely consumed, and the occurrence of some vanadium carbide will be expected.

Figure 1 shows the amount of TiN, VN, and VC dissolved as a function of temperature, calculated according to Henry law (10), for both steels A and B. The analysis of the results presented in this figure suggests that the formation of TiN can be initiated before the solidification of the steel, whereas the initial formation of VN and VC takes place at lower temperatures. Table IV shows the amount of precipitate dissolved after one hour stay at the austenitizing temperature, as determined from the data in Figure 1. The data in Table IV, though representing a theoretical estimation, indicates that TiN is lightly soluble at 1,373K in contrast to VC and VN which are completely dissolved.

Table II Stoichiometric Relation (SR) of the compounds and weight relations between the elements in the metallic mass (EMM) of both steels.

COMPOUND	SR	STEEL A EMM	STEEL B EMM
Titanium Nitride (TiN)	Ti/N = 3.42	Ti/N = 1.74	Ti/N = 0.96
Vanadium Nitride (VN)	V/N = 3.64	V/N = 70.80	V/N = 8.03
Vanadium Carbide (VC)	V/C = 4.24	V/C = 0.19	V/C = 0.12

Table III Estimation of the distribution of chemical elements in the precipitates (wt. ppm).

	STEEL A				STEEL B			
	Ti (ppm)	V (ppm)	N (ppm)	C (ppm)	Ti (ppm)	V (ppm)	N (ppm)	C (ppm)
Amount in the metallic mass	40	800	23	4,100	150	900	156	4,200
Amount consumed in the formation of TiN	40	-	11.7	150	150	-	43.8	-
Amount consumed in the formation of VN	-	41	11.3	-	-	408	112	-
Amount consumed in the formation of VC	-	759	-	179	-	492	-	116
Remaining amount	0	0	0	3,921	0	0	0	4,084

Table IV Amount of precipitate dissolved, during austenitization, for both steels.

	Amount dissolved - [%]	
	STEEL A	STEEL B
TiN	1.5	< 1
VN	100	100
VC	100	100

The microalloying elements tend to form precipitates whose sizes and morphologies depend on the chemical composition and type of the compound, as well as, on the temperature in which precipitation was initiated. Since in 300M steels, formation of TiN occurs at high temperatures, whereas TiC is formed at a lower temperature, it is expected that TiN particles be coarser than TiC particles. However, fine TiN particles can be obtained in steels if titanium is fed to the molten alloy just before solidification, as an example, during desoxidation (7-9).

In both 300M steels of this investigation, as the Ti/N ratio was hypostoichiometric, all titanium shall be consumed in the formation of nitrides; carbide formation will be less probable. Since Ti is originated from the scrap utilized, its presence occurred in all the stages of the alloy fabrication, making it difficult to control the size of titanium particles, which allows one to expect the occurrence of coarse titanium particles.

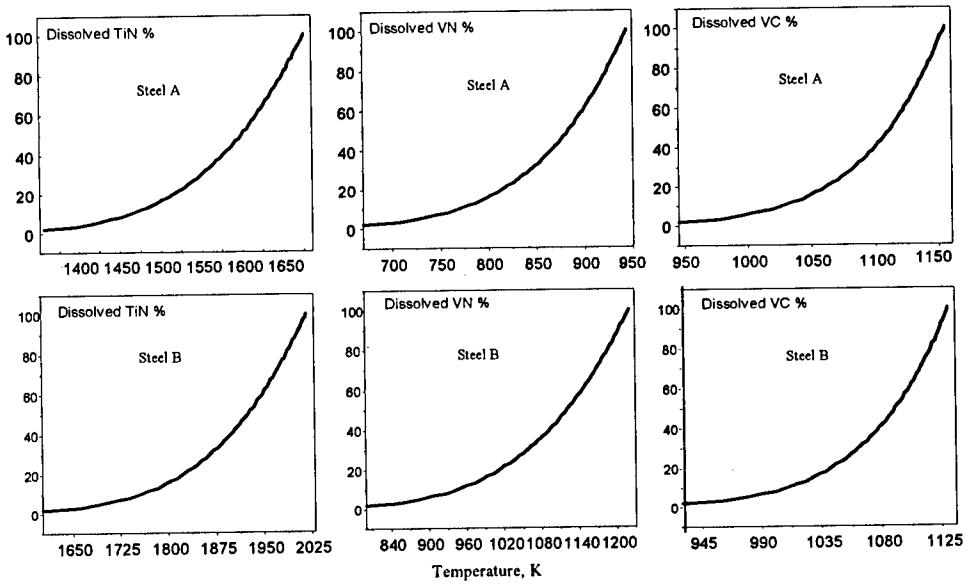


Figure 1: Estimating of precipitate solubility in steels A and B, as a function of temperature.

Optical metallography performed in both steels revealed the presence of lamellar particles, easily identifiable as titanium nitrides by its yellowish color (2). Steel B, containing a higher amount of titanium, evidenced a higher quantity of these precipitates. Figure 2 shows typical views of the precipitates rich in titanium. Microanalyses performed on these particles revealed, in general, that these particles are rich in Ti. Occasionally S and Cr were also detected in some particles. In general, when the particles contains essentially titanium its morphology tends to be more rectangular (Figure 2.a). If other elements are present besides Ti, a distortion of the rectangular shape is observed (Figure 2.b). Also, these particles were seen to be very stable during heat treatment: they were present even after the austenitizing heat treatment, in accordance with the theoretical predictions. It is interesting to note that during the fracture process, large voids were nucleated around these titanium particles.

The mechanical properties of both 300M steels are presented in Table V, in which the values of Vickers Hardness (HV), the yield strength (S_y) . 0.2% offset -, the tensile strength (S_u), the reduction of area (RA), and the plane-strain fracture toughness (K_{IC}), are discriminated for each heat treatment condition.

Table V. Mechanical properties of both 300 M steels investigated, as a function of the tempering temperature, after quenching in oil from 1,373 K for 1 h (the values between parenthesis correspond to the standard deviation).

Tempering Temperature K	Mechanical Properties				
	Hardness ($HV_{61/30}$)	S_y (MPa)	S_u (MPa)	RA (%)	K_{IC} (MPa $m^{1/2}$)
		STEEL A			
As-quenched	695 (18)	1,445 (21)	2,285 (28)	8 (1)	47 (2.5)
473	630 (2)	1,650 (25)	2,110 (6)	15 (3)	82 (3.0)
603	600 (13)	1,690 (17)	2,010 (13)	17 (2)	80 (2.5)
		STEEL B			
As-quenched	685 (14)	1,440 (13)	2,250 (28)	9 (1)	47 (3.0)
473	615 (9)	1,630 (16)	2,080 (4)	18 (3)	85 (1.0)
603	590 (4)	1,675 (24)	1,975 (20)	19 (1)	82 (1.0)

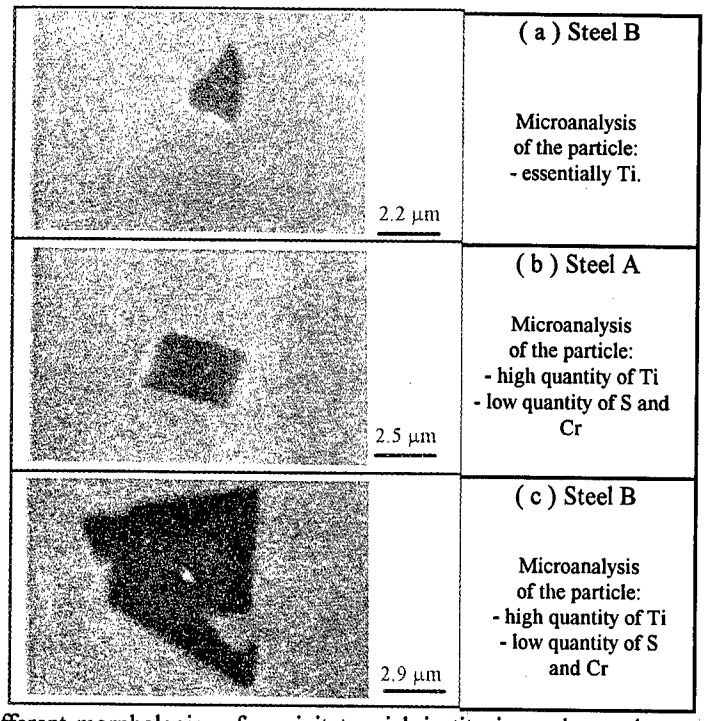


Figure 2: Different morphologies of precipitates rich in titanium, observed on as polished surfaces, for the two variation of 300M steel investigated, for tempering temperature of 603 K, after quenching in oil from 1,373 K for 1h (SEM).

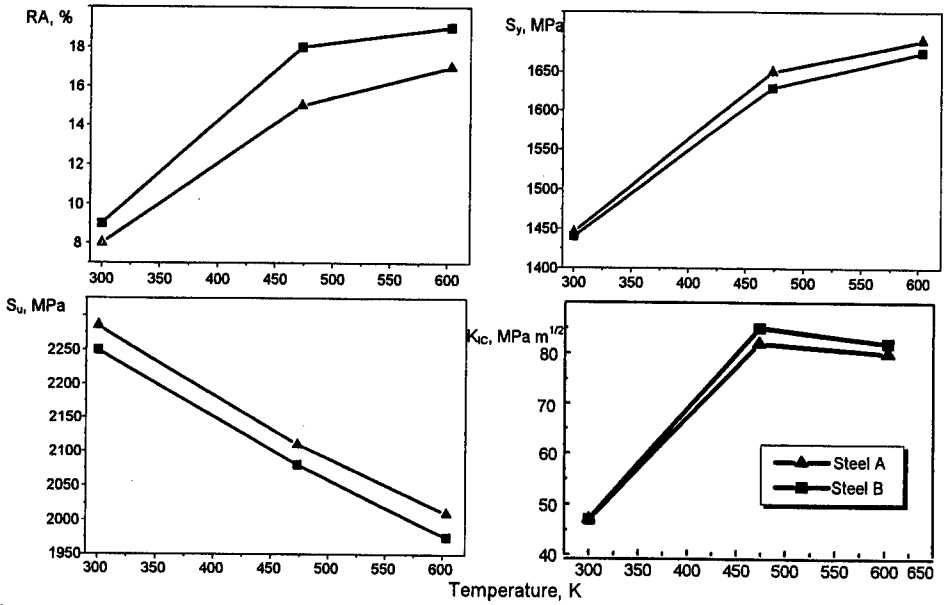


Figure 3: Mechanical properties of both 300 M steels investigated, as a function of the tempering temperature, after quenching in oil from 1,373 K for 1 h.

The results in Table V were used to obtain the plots of Figure 3 in which the room temperature

values of hardness (HV), yield strength, tensile strength, reduction of area, and plane-strain fracture toughness are presented as a function of the tempering temperature, after quenching in oil from 1,373 K. From the data shown in Figure 3 it is possible to note some slight differences in behavior of the two 300M steels investigated. Despite these differences, when standard deviations of the average values plotted are considered, steels A and B can be considered as statistically similar. Though titanium amounts differs in both steels, the titanium precipitates present in the steels are coarse and its effect on mechanical properties is only marginal, which would probably explain the observed results.

Conclusions

The investigation performed in two 300M steels containing 40 ppm and 150 ppm of titanium, evidenced that the mechanical properties of both steels, in terms of hardness Vickers, strength, and plane-strain fracture toughness, is essentially the same, for similar conditions of heat treatment. The absence of influence of titanium additions on the mechanical properties can probably be associated with the coarse character of the titanium rich particles present in the microstructure of both steels.

References

1. Shyi-Chin Wang, "The Effect of Titanium and Reheating Temperature on the Microstructure and Strength of Plain-Carbon, Vanadium - and Niobium - Microalloyed Steels," Journal of Materials Science, 25 (1990), 187-97.

2. C.O.I. Emenike and J. C. Billington, "Formation of Precipitates in Multiple Microalloyed Pipeline Steels," Materials Science and Technology, 5 (1989), 566-574.

3. L. Meyer, C. Strassburger and C. Schneider, "Effects and Present Application of the Microalloying Elements Nb, V, Ti, Zr and B IN HSLA Steels" (HSLA Steels Technology & Applications. Proceedings of International Conference, Philadelphia, American Society of Metals, 1984) 29-44.

4. H. Numakura and M. Koiwa, "Hydride Precipitation in Titanium," Acta Metallurgica, 32 (1984), 1799-807.

5. O. T. Woo et al. "The Precipitation of γ-Deuterides (Hydrides) in Titanium," Acta Metallurgica, 33 (1985),1897-1906.

6. L. J. Cuddey and J. C. Raley, "Austenite Grain Coarsening in Microalloyed Steels," Metallurgical Transaction A, 14A (1983), 1989-1995.

7. M. F. Carlson, B. V. N. Rao and G. Thomas, "The Effect of Austenitizing Temperature upon the Microstructure and Mechanical Properties of Experimental Fe/Cr/C Steels," Metallurgical Transaction A, 10A (1979), 1273-1284.

8. S. Lee, L. Majno and R. J. Asaro, "Correlation of Microstructure and Fracture Toughness in Two 4340 Steels," Metallurgical Transaction A, 16A (1985), 1633-1648.

9. S. Lee, D. Y. Lee and R. J. Asaro, "Correlation of Microstructure and Tempered Martensite Embrittlement in Two 4340 Steels," Metallurgical Transaction A, 20A (1989), 1089-1103.

10. C. L. Briant and S. K. Banerji, "Intergranular Failure in Steel: The Role of Grain-Boundary Composition," International Metals Reviews, n. 4 (1978), 164-196.

MICROALLOYING OF STEEL 16MN WITH NIOBIUM

Wang Ruizhen Zhang Hongtao Pang Ganyun Cui Baofeng

Central Iron and Steel Institute, Beijing 100081, P.R. China

Abstract

Steel 16Mn is a HSLA steel of the longest history and is widely used in China. However, there still exist some serious technical problems in its production and application. The main problems are strength insufficiency and low impact toughness. In this paper, the practicability of improving comprehensive properties of 16Mn by microalloying with Nb has been studied. Results show that when proper rolling processing is applied, steel 16MnNb possesses better comprehensive properties than those of 16Mn. Under the same rolling conditions, by microalloying of steel 16Mn with Nb, its yield strength and tensile strength can be increased by 100MPa and 85MPa respectively. Elongation can be increased by 4%. Impact toughness can be improved at the same time. Steel 16MnNb and 16Mn both show ferrite + pearlite microstructure. Comparing with steel 16Mn, there is clear grain refinement effect due to Nb-microalloying. The average grain size of steel 16MnNb is in the range of 5.4~6.7μm, while that of steel 16Mn is 12.4μm. TEM analysis indicates that adding Nb to steel 16Mn brings about changes of pearlite morphology. Pearlite colony and interlamellar spacing become smaller. Fine precipitates of Nb(C,N) occur, with sizes mainly in the range of 10~20nm.

The Third Pacific Rim International Conference on
Advanced Materials and Processing (PRICM 3)
Edited by M.A. Imam, R. DeNale, S. Hanada,
Z. Zhong and D.N. Lee
The Minerals, Metals & Materials Society, 1998

Introduction

Steel 16Mn is now the most popular HSLA steel grade in China. The steel is also of the longest history in China's development of high strength low alloy steels. Total annual production of steel 16Mn including plates, sheets, bars, tubes and sections is estimated around 2-3 million tons. However, the production of steel 16Mn, especially its flat products, still has been facing problems. Firstly, it is the strength insufficiency. Both yield and ultimate tensile strength values of final products of steel 16Mn quite often fail to meet the standard required levels. Besides insufficient strength, there are also other quality problems relating to low impact toughness, unsatisfactory fracture surface test results and high rejection rate in terms of ultrasonic testing etc. One effective way for improving mechanical properties of steel 16Mn is microalloying. Addition of small amount of Ti and sometimes also V to steel 16Mn has been applied in industrial production[1]. However, it has not been found that any steel company in China is applying Nb as a microalloying element in real production of steel 16Mn. It is anticipated that microalloying of steel 16Mn with Nb will give rise to effective grain refinement and essential improvement of mechanical properties. In this paper, we have studied the influence of Nb-microalloying on mechanical properties and microstructure of steel 16Mn.

Experimental steels and experimental procedure

Experimental steels

Two laboratory heats were melted in a vacuum high frequency induction furnace. Two ingots of 50 kg each were cast. The analyzed chemical compositions of the two heats are listed in Table I. From Table I, it is seen that both experimental steels show average alloy element contents in terms of C, Si and Mn. The C-content of steel No.2 is only 0.01% higher than that of steel No.1. Steel No.1 is without Nb, while steel No.2 contains 0.034% Nb. Both steels contain very low Al. The two ingots were then hot forged into slabs of 36×80×140mm in sizes. Ingot reheating temperature was 1150 ℃ and finish forging temperature were ≥ 850 ℃.

Table I Chemical compositions of experimental steels (in wt%)

Steel No.	C	Si	Mn	P	S	Nb	Al	N
1	0.16	0.55	1.45	<0.005	0.005	-	<0.005	0.0044
2	0.17	0.58	1.45	<0.005	0.006	0.034	<0.005	0.0054

Experimental procedure

The slabs were rolled into 5mm thick plates. The reheating temperature was 1180°C for 30 min. Start rolling temperature was around 1150°C. Table II shows the trial rolling schedule of experimental steels. According to our previous experimental results[2], steel 16MnNb is prone to form coarse bainite which is detrimental to ductility and toughness. Coarse bainite structure is formed from the original coarse austenite often present in the mixed austenite microstructure which is believed to be formed by the partial recrystallization. In order to make sure that the rolling being conducted in the nonrecrystallization temperature range, third pass rolling

temperature, 980°C, was controlled and measured for the first 4 rolling alternatives. Similarly, the second pass rolling temperature, 1020°C, was measured for the last 4 rolling alternatives. For comparison, steel 16Mn is rolled according to the rolling schedule of slab No.1.

Table II Trial rolling schedule of experimental steels

Slab No.	Thickness(mm) $\xrightarrow[\text{temperature (°C)}]{\text{reduction (\%)}}$ Change
1	$36 \xrightarrow[\sim1150]{36.1} 23 \xrightarrow[\sim1120]{32.6} 15.5 \xrightarrow[980]{32.2} 10.5 \xrightarrow[\sim950]{42.8} 6.0 \xrightarrow[900]{16.6} 5.0$
2	$36 \xrightarrow[\sim1150]{36.1} 23 \xrightarrow[\sim1120]{32.6} 15.5 \xrightarrow[980]{19.3} 12.5 \xrightarrow[\sim950]{40.0} 7.5 \xrightarrow[900]{33.3} 5.0$
3	$36 \xrightarrow[\sim1150]{36.1} 23 \xrightarrow[\sim1120]{32.6} 15.5 \xrightarrow[980]{19.3} 12.5 \xrightarrow[\sim950]{27.2} 9.1 \xrightarrow[900]{45.0} 5.0$
4	$36 \xrightarrow[\sim1150]{36.1} 23 \xrightarrow[\sim1120]{32.6} 15.5 \xrightarrow[980]{19.3} 12.5 \xrightarrow[900]{60.0} 5.0$
5	$36 \xrightarrow[\sim1150]{36.1} 23 \xrightarrow[1020]{32.6} 15.5 \xrightarrow[\sim980]{19.3} 12.5 \xrightarrow[\sim950]{27.2} 9.1 \xrightarrow[900]{45.0} 5.0$
6	$36 \xrightarrow[\sim1150]{36.1} 23 \xrightarrow[1020]{32.6} 15.5 \xrightarrow[\sim980]{19.3} 12.5 \xrightarrow[\sim950]{52.0} 6.0 \xrightarrow[900]{16.6} 5.0$
7	$36 \xrightarrow[\sim1150]{36.1} 23 \xrightarrow[1020]{32.6} 15.5 \xrightarrow[\sim980]{19.3} 12.5 \xrightarrow[\sim950]{52.0} 6.0 \xrightarrow[850]{16.6} 5.0$
8	$36 \xrightarrow[\sim1150]{36.1} 23 \xrightarrow[1020]{32.6} 15.5 \xrightarrow[\sim980]{19.3} 12.5 \xrightarrow[\sim950]{52.0} 6.0 \xrightarrow[750]{16.6} 5.0$

*Remarks: 1) ~x ℃ means estimated rolling temperature, x ℃ means measured and controlled rolling temperature.

Longitudinal tensile specimens were machined and tensile properties were tested. Longitudinal Charpy impact specimens of 10×5×55mm were machined for both steels 16Mn and 16MnNb rolled with the rolling alternative No.1. The impact energy were measured at room temperature, 0°C, -20°C, -40°C and -60°C respectively. In order to correlate the mechanical properties to microstructure, metallographic specimens were observed under optical microscope and SEM; thin foil samples of both steels 16Mn and 16MnNb and extraction replicas of steel 16MnNb were prepared and analysed under TEM.

Results and discussion

Mechanical properties of steels 16Mn and 16MnNb

Tensile properties Tensile properties of the rolled plates of steel 16Mn and steel 16MnNb with different rolling alternatives are listed in Table III. From Table III, it can be seen that all the plates of steel 16MnNb with different rolling alternatives have improved properties. Under the same rolling conditions, strength and plasticity of steel 16Mn have been increased by Nb-microalloying: yield strength increment, ΔYS, is 100MPa and tensile strength increment, ΔUTS, is 85MPa, elongation increment, ΔEl, is 4%. Though there is 0.01%C content more in the steel

No.2 than that in steel No.1, according to Pickering [3] and Leslie [4], in low carbon (< 0.30%C) steels, pearlite has little effect on the yield strength; and in the case of ultimate tensile strength, increased 0.01% carbon content bring about only a little increase of UTS as a consequence of pearlite volume fraction increase. When the yield ratio YS/UTS is regarded, the value has been increased from 0.66 to 0.73 as the consequence of Nb-microalloying.

Table III Tensile properties of steels 16Mn and 16MnNb

Steel	Rolling alternative No.	YS, MPa	UTS, MPa	YS/UTS	El., %
16Mn	1	337	510	0.66	24.5
16MnNb	1	437	595	0.73	28.5
	2	442	585	0.75	27.5
	3	495	612	0.80	31.0
	4	437	582	0.75	30.0
	5	480	602	0.79	25.0
	6	462	595	0.77	27.0
	7	460	595	0.77	30.5
	8	492	607	0.81	27.5

Impact toughness The results of Charpy impact experiment are graphically shown in Fig. 1a. It is seen clearly that the impact toughness of steel 16MnNb is much more improved than that of steel 16Mn. At room temperature the impact energy of steel 16MnNb is almost same as that of steel 16Mn. But the impact energy of steel 16Mn decreases quickly with the decrease of testing temperature. At testing temperature -60°C, the impact energy value of steel 16Mn is only 16J while steel 16MnNb maintains its good impact toughness that is still as high as 48.5J. When the FATT is concerned, it is estimated from Fig. 1b that the FATT of steel 16Mn is about -18°C, while that of steel 16MnNb is below -60°C.

From the results of tensile experiment and Charpy impact experiment, we can conclude that applying proper controlled rolling technology, comprehensive mechanical properties of steel 16Mn by microalloying with Nb have been improved.

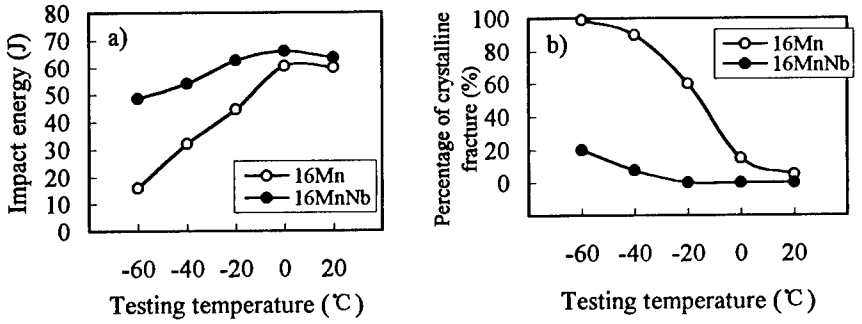
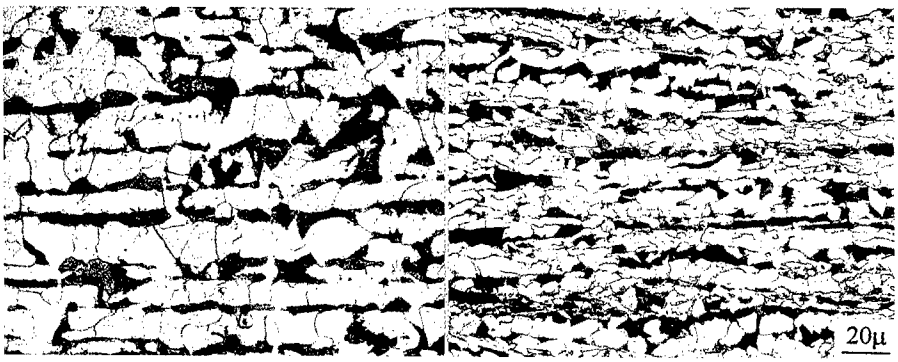


Figure 1: Dependence of impact toughness testing results on testing temperature

Microstructure

Optical Metallography Fig. 2 shows the micrograph of steel 16Mn and steel 16MnNb rolled by using alternative No. 1. Both steels are all with ferrite-pearlite microstructure. Steel 16MnNb shows the clear grain refinement by Nb-microalloying. The microstructures of rest seven alternatives are also fine grain ferrite-pearlite. The average grain size is in the range of 5.4 - 6.7μm for steel 16MnNb with designed rolling alternatives, while that for steel 16Mn is 12.4 μm with rolling alternative No.1. Grain size number of steel 16MnNb is about two numbers higher than that of steel 16Mn. Ferrite volume fraction of steel 16MnNb is in the range of 77.0-82.6 %, while that of steel 16Mn is 75%. SEM observation shows that pearlitic colony of steel 16MnNb are refined and the interlamellar spacing of pearlitic cementite is smaller when compared to that of steel 16Mn.



a) Steel 16Mn b) Steel 16MnNb

Figure 2: Micrographs of 16Mn and 16MnNb, rolling schedule alternative No. 1

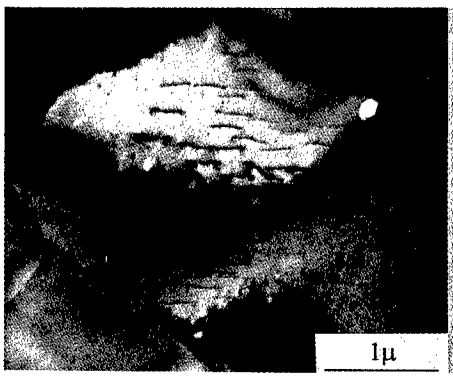


Figure 3: TEM micrograhgs of steel 16MnNb, thin foil

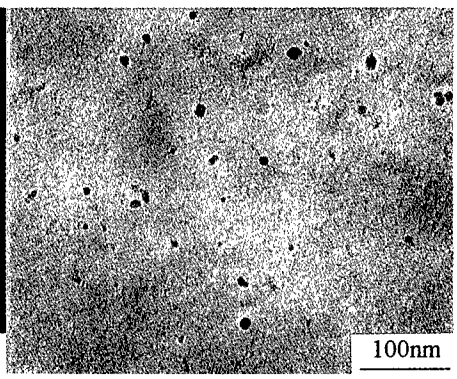


Figure 4: Finer precipitates of steel 16MnNb, extraction replica

TEM observation TEM observation shows, see Figure 3, for steel 16MnNb, grains and sub-grains are refined, dislocation density inside ferrite grain increases when compared to that of the steel 16Mn. Larger size carbides are found at the ferrite sub-grain boundaries which are alloy cementite containing Nb. There are a lot of finer precipitates inside ferrite and pearlite grains. The precipitates are dispersed homogeneously and the sizes of most of them are in the range of

10-20nm, as shown in Figure 4.

The refinement of the microstructure of 16MnNb lies in: 1) The carbonitrides and nitrides of niobium retard the growth of the austenite grains during reheating; 2) Total reduction during controlled rolling is large enough. The thickness ratio of slab to final plate is 7.2. Rolling in the partial recrystallization temperature range has to be avoided. The formation of mixed grains of austenite is then avoided. 3) Large amount of reduction is conducted in the nonrecrystallization temperature range ensuring pancaked austenite and consequent fine ferrite-pearlite. It is well known that grain-refinement contribute not only to strength, ductility but also to impact toughness. Steel 16MnNb has two numbers in grain size number higher than that of steel 16Mn, as a consequence, the contribution to YS increment by grain refinement is about 60MPa.

Since the last several rolling passes are done in the nonrecrystallization temperature range of austenite, the dislocations formed during the deformation remain after the ferrite-pearlite phase transformation. The precipitates inside and at the grain boundaries exert pinning effect on dislocations leading to the increased strength.

Conclusion

By microalloying steel 16Mn with Nb and combined with proper controlled rolling processing, the strength level, toughness level have been raised. Under the same rolling conditions, its yield strength, tensile strength can be increased by 100MPa and 85MPa respectively. Elongation can be increased by 4%. Steel 16MnNb has refined ferrite-pearlite grains and sub-grains which contribute to improvement of comprehensive mechanical properties. In the case of steel 16MnNb, large density of dislocations and fine precipitates exist inside grains and larger size carbides are found at sub-grain boundaries.

References

1. Zhang Hongtao et al., "The Improvement of Mechanical Properties of Steel 16Mn by Microalloying with Niobium—General review of the production & application of steel 16Mn in China" (Report No.1, Central Iron and Steel Research Institute, 3,1996).

2. Zhang Hongtao et al., "The Improvement of Mechanical Properties of Steel 16Mn by Microalloying with Niobium" (Report No.2, Central Iron and Steel Research Institute, 9,1996).

3. Pickering, F. B., "High Strength, Low Alloy Steel-A Decade of Progress", 《 Microalloying' 75 》 Conf. Proceeding, ed. Korchynsky, 1976, 9-30.

4. Leslie, W.C., The Physical Metallurgy of Steels(Hemisphere Publishing Corporation, 1981), 147-148.

Microstructure and Mechanical Properties of SUS316L Stainless Steel Manufactured by High Strain PM Process

K.Ameyama*, S.Senoo**, J.Sudo**, O.Okada***, K.Nakata***

* Department of Mechanical Engineering, Faculty of Science and Engineering, Ritumeikan University, Kusatsu, Shiga 525-77, Japan

** Graduate School, Ritumeikan University, Kusatsu, Shiga 525-77, Japan

*** Hitachi Research Laboratory, Hitachi Ltd., Hitachi, Ibaraki 317, Japan

Abstract

The high strain powder metallurgy (HS-PM) process is applied to an SUS 316L austenitic stainless steel. The HS-PM process is a powder metallurgy process combining mechanical milling, heat treatment and sintering processes, and enables one to produce an ultra-fine grain structure. In the case of the SUS 316L stainless steel, room temperature recrystallization and dynamic recovery of an austenite phase take place because of the existence of excess vacancies, which are stored during the milling process. Almost fully ferritic nanograin structure with an average grain size of approximately 20nm is formed after the milling. Formation of the ultra-fine grains of the ferrite phase in the HS-PM processed powder accelerates the decomposition of the ferrite to the austenite and σ phases in the sintering process. The sintered compacts with a very fine grain structure show an extremely high strength, i.e., more than three times higher than the annealed SUS 316L stainless steel, without any severe depression in the elongation.

The Third Pacific Rim International Conference on Advanced Materials and Processing (PRICM 3)
Edited by M.A. Imam, R. DeNale, S. Hanada, Z. Zhong and D.N. Lee
The Minerals, Metals & Materials Society, 1998

Introduction

The high strain powder metallurgy (HS-PM) process is a novel powder metallurgy process combining mechanical milling (MM) or mechanical alloying (MA), heat treatment and sintering processes, and enables one to produce an ultra-fine grain structure. It has three remarkable features: [1] a non-equilibrium phase, [2] a nano grain microstructure, and [3] good workability. The extremely high strain energy given by the milling process at room temperature produces a large number of defects, and this enhances the diffusion of atoms at low temperature and contributes to the formation of a non-equilibrium phase such as a supersaturated solid solution or an amorphous phase (1). A nano grain structure is obtained from the non-equilibriu m phases by controlling the heat treatment conditions, which influences the phase transformation, recovery, recrystallization, grain growth, etc (2). Grain refinement is very important to improve the mechanical properties of materials, and fine grained materials easily deform by superplasticity (3, 4). Therefore, the HS-PM process is the most efficient and useful non-equilibrium powder metallurgy process because it permits simultaneous improvement of mechanical properties and workability by the control of microstructure.

In this paper, the HS-PM process was applied to an SUS316L stainless steel, and the mechanical properties of the material at room temperature as well as the microstructural changes during the process are discussed.

Experimental Procedure

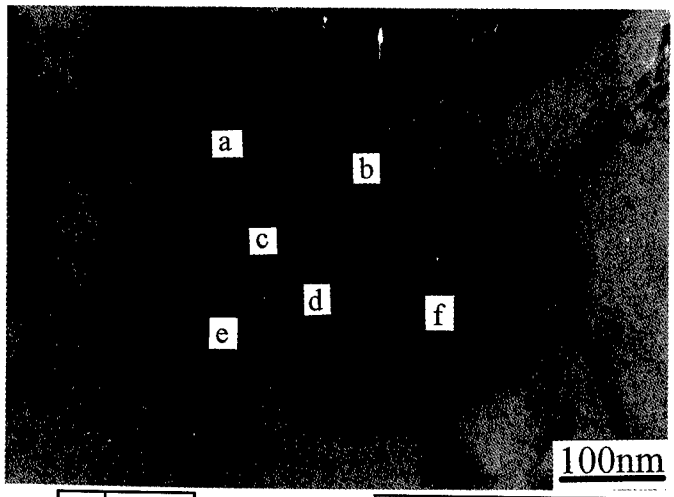
An annealed SUS 316L stainless steel bar (C: 0.008, Si: 0.51, Mn: 0.95, P: 0.018, S: 0.006, Ni: 12.56, Cr: 16.49, Mo: 2.61, Fe: bal. (mass%)) was used as a PREP (Plasma Rotating Electrode Process) electrode and PREP powder was produced. The average grain size of the electrode was 71.2 μm and the obtained powder particle size was approximately 200 μm. PREP has the advantage that the product powder is hardly contaminated by impurities such as oxygen or nitrogen gases during the process (5). A Fritsch P-5 planetary ball mill with SUS316L stainless steel vials and SUS 304 stainless steel balls was used for mechanical milling under an Ar atmosphere. The PREP powder was loaded into the vial, inside a glovebox kept under an atmosphere of purified Ar gas. Owing to cooling fins attached to the outside wall of the vials and a strong ventilating system, the temperature of the surface of the vials was kept below 323 K. A ball-to-powder weight ratio of 1.8:1 was chosen and the milling intensity was adjusted to a rotation speed of 4.2 s^{-1} (250 min^{-1}).

Consolidation of the 200 hrs-mechanically milled (MM) powder was carried out by two different conditions of Hot Isostatic Pressing (HIP). HIP-(I): at 1073 K for 10.8 ks, under a pressure of 490 MPa, and HIP-(II): at 973 K for 7.2 ks and 1073 K for 10.8 ks, under a pressure of 196 MPa. Some powders were heat treated at temperatures ranging from 333K to 1173K in an Ar atmosphere.

The MM powders and the consolidated powder compacts were characterized by means of X-ray diffraction (XRD), SEM and TEM/EDS. The misorientation angles among grains were determined by Kikuchi pattern analysis. The error associated with this technique was assessed by analysis of annealing twins in FCC crystals. This gave an average error less than 0.10 degrees.

Results and discussion

Figure 1 shows a TEM micrograph of the 400 hrs-MM powder annealed at 333K for 5 minutes. Misorientation angles among the γ grains, which are marked as a, b, c, ... in Fig.1, are indicated below. The average misorientation angle between adjoining grains was 37.0 degrees. It is obvious that recrystallization and recovery of the powder took place during milling and annealing at 333 K. Such a low temperature recovery is presumably due to the increase of excess vacancies and high angle grain boundary area (6).



b	35.9				
c	21.7	30.8			
d	-	40.3	54.3		
e	38.2	-	41.8	36.1	
f	-	55.1	-	41.8	10.6
	a	b	c	d	e

Ave.	37.0 deg.

Fig.1 TEM micrograph of a 400 hrs-MM powder annealed at 333K for 5 minutes. Misorientation angles between adjoining γ grains are also indicated.

Figure 2 shows an area of the 400 hrs-MM powder annealed at 333K for 5 minutes, which is different from that shown in Fig.1. The extremely high density of defects introduced by the milling process increased free energy of the γ phase, and thereby stabilized the BCC phase (indicated by an arrow). In the late stage of milling, an (γ+α) microduplex structure with a grain size of approximately 200 nm was formed. In case of the milling with ball-to-powder weight ratio of 12:1, higher energy milling resulted in fully ferritic structure with the grain size of approximately 20nm (7).

Figure 3 (a) and (b) shows TEM micrographs of the HS-PM processed SUS 316L powder sintered by HIP (I) and (II), respectively. Both micrographs show a very fine grained microduplex structure with an average grain size of approximately 600 - 700 nm. It is interesting to note that the microstructure is composed of γ and σ phases. Volume fractions of the σ phase in (I) and (II) are approximately 7 % and 17 %, respectively. Usually, the σ phase requires a long incubation period to precipitate in this stainless steel at these temperature range. Therefore, it is surmised that an increase in the volume fraction of the α phase as well as free energy of the γ phase accelerated the precipitation of the σ phase.

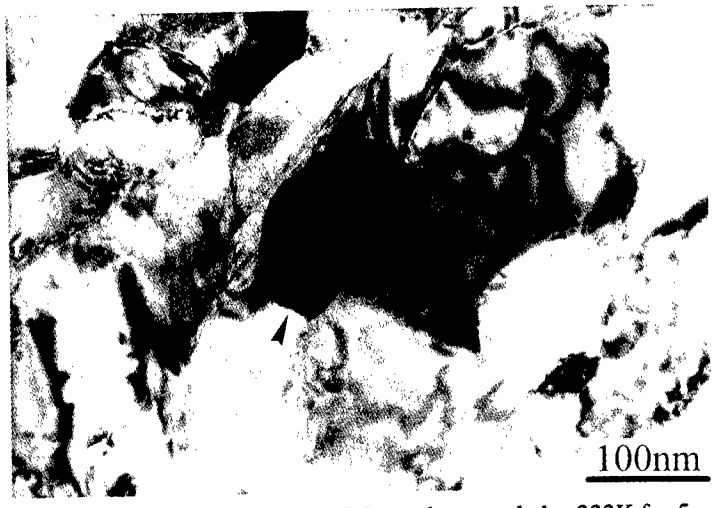


Fig. 2 TEM micrograph of the 400 hrs-MM powder annealed at 333K for 5 minutes.

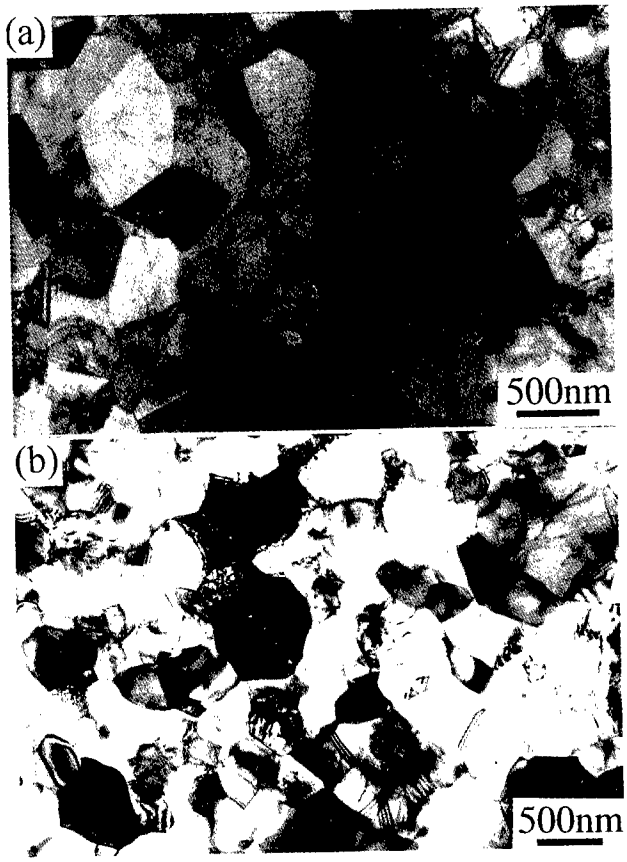


Fig.3 TEM micrographs of (a) HIP-(I) and (b) HIP-(II) compacts.

Figure 4 shows nominal stress-strain curves of the HIP materials, (I) and (II), and their parent bulk material. Both of the HS-PM processed materials offers outstanding 0.2% proof stress, tensile strength and elongation relative to the annealed bulk material.

Table 2 indicates mechanical properties of the HS-PM processed material and the parent material. The HS-PM HIP compacts had more than 3 times higher proof stress and 1.8 times higher tensile strength than the parent bulk material. It should be noted that the high strengthened HS-PM processed material had an elongation as high as 35%. An inclination of elastic region in the s-s curves shown in Fig. 4 increases with the holding period at high temperatures, since the volume fraction of harder σ phase increases. The precipitation of the σ phase has a significant influence on the hardness and grain size. By comparing holding periods at high temperatures in HIP (I) and (II), it is clear that larger volume fraction of the σ phase retards grain growth of the material.

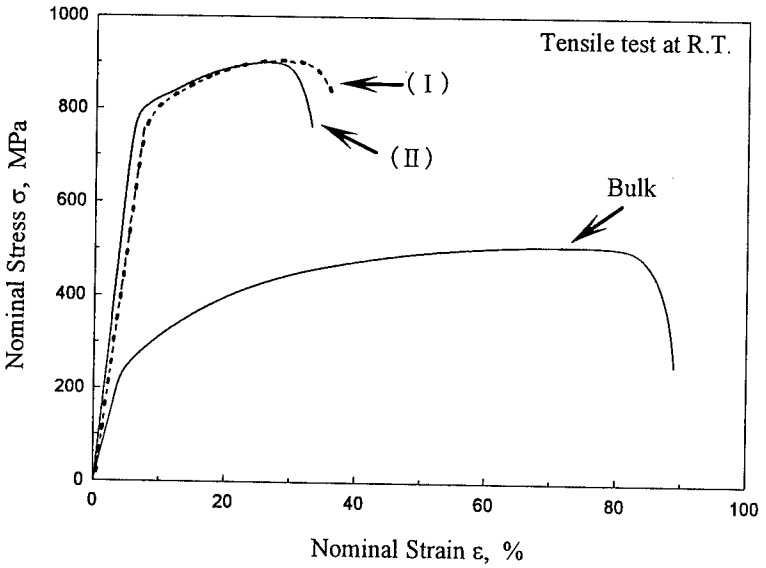


Fig.4 Nominal stress- nominal strain curves of the HIP-(I), HIP-(II), and bulk material.

Table 2 Mechanical properties of HS-PM compacts and annealed bulk SUS316L stainless steels.

	Yield Stress MPa	Tensile Stress MPa	Elongation %	Vickers Hardness (9.8N)	Average Grain Size (μm)	Volume Fraction of σ (%)
HS-PM HIP-(I)	750.7	904.2	35.8	305.9	0.62	7.3
HS-PM HIP-(II)	748.8	900.6	35.4	367.0	0.66	16.7
Annealed Bulk	227.4	508.7	88.7	140.7	71.2	0

HIP-(I): at 1073 K for 10.8 ks, under a pressure of 490 MPa.
HIP-(II): at 973 K for 7.2 ks and 1073 K for 10.8 ks, under a pressure of 196 MPa.

Conclusion

The high strain powder metallurgy (HS-PM) process was applied to an SUS316L stainless steel. The mechanical milling process of the SUS316L PREP powder resulted in a room temperature recrystallization of an austenite phase. The formation of ferrite and the large amount of defects accelerated precipitation of a σ phase during heating, and resulted in a very fine ($\gamma+\sigma$) microduplex structure. The very fine grain structure as well as the σ phase had a significant affect on the mechanical properties. The HS-PM processed materials showed outstanding mechanical properties: more than 3 times higher proof stress and 1.8 times higher tensile strength than the parent material. The HS-PM process improves the strength of the material without any severe depression in elongation.

References

1. T.Fujii, K.Ameyama, "Decomposition of massively transformed Ti-Al MA powders," Materials Science Forum, 235-238(1997), 451-456.
2. K.Ameyama, O.Okada, K.Hirai, N.Nakabo, "Microstructure of a Ti-45mol%Al MA powder and its $\alpha \rightarrow \gamma$ massive transformation during consolidation," J. Mater. Trans., JIM, 36(1995), 269 -275.
3. K.Ameyama, H.Uno, M.Tokizane, "Superplastic behavior of Ti-48at%Al two-phase titanium aluminide compacts made from mechanical alloyed powder," Intermetallics, 2(1994), 315-319.
4. K.Ameyama, T.Fujii, T.Okumura, S.Sodeoka, M.Tokizane, " Nanograin formation and superplastic deformation in TiAl mechanically alloyed compacts," Materials Science Forum, 233-234 (1997), 287-294.
5. K.Isonishi,K.Ameyama, M.Tokizane, R.Kumagaya, "Fabrication of Titanium Aluminides Powders by Plasma Rotating Electrode Process," Proc. of 1993 Powder Metallurgy World Congress, Kyoto, (1993), 31-34.
6. K.Ameyama, "Low Temperature Recrystallization and Formation of an Ultra Fine ($\gamma+\sigma$) Microduplex Structure in a SUS316L Stainless Steel," Scripta Metal.et Mater, 38(1998), 517.
7. K.Ameyama, M.Hiromitsu and N.Imai, "Room Temperature Recrystallization and Ultra Fine Grain Refinement of an SUS316L Stainless Steel by High Strain Powder Metallurgy Process," Tetsu-to-Hagane, in press.

THE EFFECTS OF MICROSTRUCTURE AND PRESTRAIN ON FATIGUE STRENGTH OF DUAL-PHASE STEELS

K. NAKAJIMA, T. TAKI and T. MIYATA

Department of Materials Science and Engineering,
Nagoya University,
Nagoya 464-01, Japan

Abstract

The effects of microstructural morphology and prestrain on various fatigue properties, particularly fatigue strength for dual-phase (DP) steels were investigated on notched specimens. It was found that the material with a continuous martensite phase around ferrite grains exhibited a higher fatigue strength than did the material with a martensite phase dispersed in a ferrite matrix. The fatigue strength of the prestrained material was larger than that of the non-prestrained material, but the gain of fatigue strength was very small, though the static strength of the prestrained material increased greatly. The observed fatigue strength among the materials is discussed in terms of metallurgical factors such as grain size, hardness, static strength and cyclic hardening or softening behavior responsible for the fatigue properties of the present materials.

The Third Pacific Rim International Conference on
Advanced Materials and Processing (PRICM 3)
Edited by M.A. Imam, R. DeNale, S. Hanada,
Z. Zhong and D.N. Lee
The Minerals, Metals & Materials Society, 1998

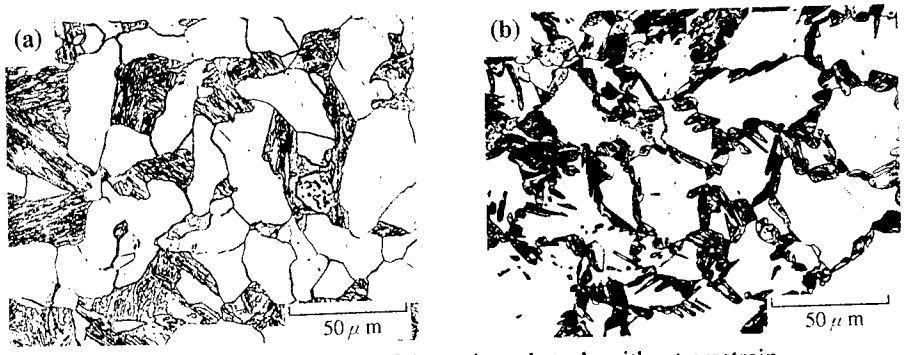


Figure 1 - Microstructure of investigated steels without prestrain.
(a) Martensite-dispersed structure (M-D steel),
(b) Martensite-continuous structure (M-C steel).

Introduction

It is well known that the ferrite-martensite DP steels offer a better combination of strength and ductility than do the other steels with equivalent static strength. The DP steels are in general use in the automobile industry where higher strengthening for fatigue in steel sheets is required. Several investigators have shown that the fatigue properties of DP steels which usually consist of a martensite phase dispersed in a ferrite matrix exhibit an improvement by controlling the heat treatment process [1, 2] . Continuity of a martensite phase seems to have an important role on fatigue properties. Additionally the effects of prestrain and notch on the fatigue strength are of great interest from a practical point of view, because DP steels are usually in use after deformed or punched or welded. It is reported that prestrain prior to fatigue testing showed a tendency to increase the fatigue strength on smooth specimens in the case of an axial tension [3] . In the present study, the relationship between the fatigue strength of notched specimens and metallurgical factors is discussed, and an improved method is proposed for estimation of an exact stress at notch root at fatigue limit, where cyclic behavior of the present materials is taken into consideration.

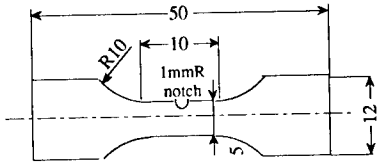


Figure 2 - 1 mmR notched specimen (in mm).

Experimental procedures

Table I Mechanical properties and martensite fraction of materials tested.

specimen	Cold Reduction (%)	0.2%P.S. (MPa)	T.S. (MPa)	El. (%)	Vol. fraction of Martensite (%)	Hv (1kg)	Hv (10g) in Ferrite	Hv (10g) in Martensite
Martensite-Dispersed structure (M-D)	—	395	690	18.8	36	239	147	427
	20.0	880	920	3.0	36	339	277	699
Martensite-Continuous structure (M-C)	—	403	688	18.9	35	228	144	400
	18.5	745	755	4.1	35	307	241	565

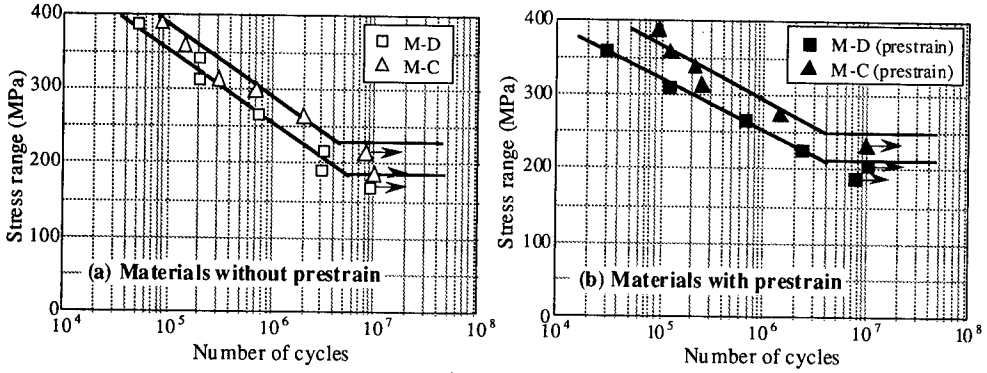


Figure 3 - S-N curves for (a)materials without prestrain and (b)materials with prestrain.

The material tested was a commercial low carbon steel with a main composition of Fe/0.2C/ 0.5Si/1.5Mn, received as 2 mm thick hot-rolled sheet. Two microstructures, one consisting of martensite dispersed in ferrite matrix (hereafter referred to as M-D) and the other continuous martensite phase (hereafter referred to as M-C), were examined, which are shown in Fig.1 . M-C material was obtained by reheating normalized steel into α - γ region, partially transforming to austenite and then quenching. Prestrain was given by a cold rolling reduction of approximately 20%. The material properties are in Table I. 1 mm thick notched specimens with 1 mm radius were machined to the geometry shown in Figure 2. Estimated notch stress concentration factor Kt is approximately 2.8 . After machining all the specimens were chemically polished to avoid possible effects of residual stresses on fatigue behavior. Fatigue experiment was carried out at a stress ratio of 0.1 with a frequency of 20 Hz with an Instron closed-loop servo-hydraulic testing machine. Strain control fatigue testing was conducted at a stress ratio of -1 with a frequency of 0.01 Hz with a smooth specimen to investigate the cyclic hardening or softening behavior of the materials. Strain was monitored with a clip gauge. Cyclic stress-strain curves were obtained from the results of several constant strains. The precise stress amplitude at notch root at fatigue limit was calculated by using an improved elastic-plastic FEM analysis.

Results and discussion

Fatigue life

Figure 3 (a) shows the S-N curves for M-D and M-C materials. The M-C material which consists of continuous martensite phase around ferrite grains shows the higher fatigue strength than the M-D material. Several investigators have shown that the martensite-continuous microstructure has superior fatigue properties [1, 2]. It is interesting to note that a difference of approximately 20% in fatigue strength exists in spite of almost the same mechanical properties, hardness and volume fraction of martensite as listed in Table I. Continuity of martensite phase seems to have an important role on fatigue properties such as fatigue strength, fatigue crack initiation, small and large crack growth. Fatigue behavior was investigated in the short life regime. It was found

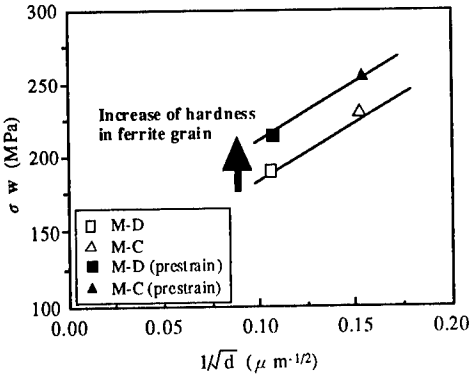


Figure 4 - Relation between fatigue limit and inverse square root of the grain size constrained by martensite.

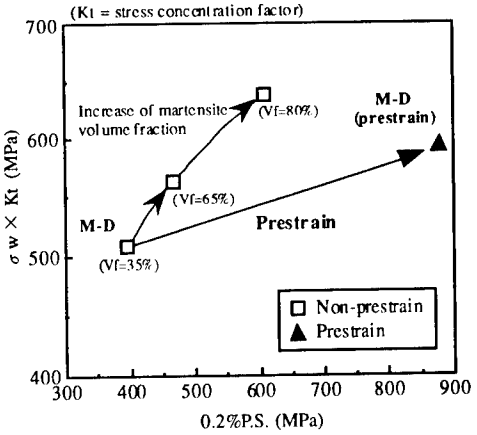
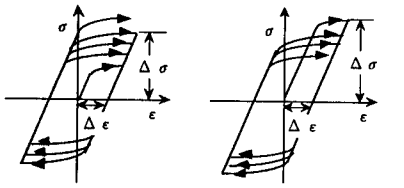


Figure 5 - Relation between static strength and fatigue limit for M-D steel.

that fatigue life was governed by particularly small crack within a range of 200~250 μ m by in-situ observation with a fatigue testing machine mounted in scanning electron microscope [4, 5] and that continuous martensite phase decreased the crack propagation rate in that small crack [5]. Prestrain of approximately 20% prior to fatigue testing increases the fatigue strength in both materials as shown in Figure 3 (b). It was found that prestrain as well as microstructural morphology had a great influence on small crack growth [5]. Fatigue strength on notched specimen is a very important factor from an industrial point of view and higher strengthening for fatigue is required without increasing static strength. For this reason, fatigue strength was examined in terms of metallurgical factors responsible for the present fatigue behaviors. Figure 4 shows the relation between fatigue strength and inverse square root of the ferrite grain size constrained by martensite. The grain size was estimated by measuring the average interval of ferrite phase crossing martensite phase to clarify the difference in continuity of martensite. The Hall-Petch type relation is seen between fatigue strength and grain size by using a ferrite grain constrained by martensite, but not a usual ferrite grain as a parameter in the case of M-D material. The increase of fatigue strength in prestrained materials is due to the increase of hardness in prestrained ferrite as shown in Table I. It is known that the fatigue strength on a smooth specimen increases according to the increase of static strength up to a certain static strength level for carbon steels [6]. Figure 5 shows the relation between static proof stress and fatigue strength modified by stress concentration factor. Other data of the materials of the same chemical composition with different volume fractions of martensite are also plotted in Figure 5. The gain of static strength due to prestraining results in a minor increase of the fatigue strength as compared with the gain of static strength achieved by the increase of volume fraction of martensite. This might be explained by cyclic hardening or softening behavior at notch root [7].

Cyclic behavior

Companion specimens method was adopted to determine a cyclic stress-strain curve and the



(a) Cyclic hardening behavior for M-D steel. (b) Cyclic softening behavior for M-D (prestrain) steel.

Figure 6 - Schematic illustration of cyclic hardening and softening behavior during strain control testing.

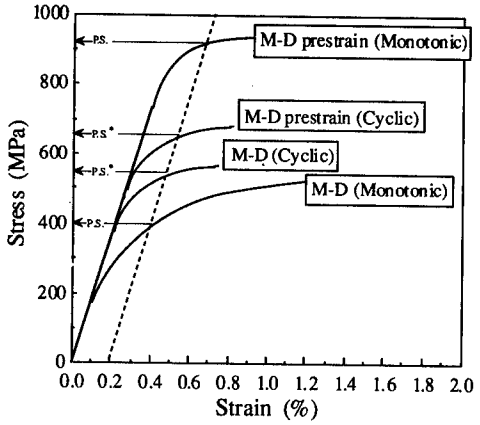


Figure 7 - Monotonic and cyclic stress-strain curves for M-D steel and M-D (prestrain) steel.

stress amplitude was measured at each cycle under a control of several constant strains. A cyclic stress-strain curve was obtained by plotting the value of saturated stress amplitude at each strain. M-D material and prestrained M-D material showed the cyclic hardening and softening behavior respectively as seen in schematic illustration of Figure 6. Figure 7 indicates the cyclic stress-strain curves for M-D and prestrained M-D materials plotted with their monotonic stress-strain curves. It was reported that cyclic stress-strain behavior was slightly affected by prestrain of up to 8% [8], but in the case of 20%, cyclic stress-strain behavior was found to be certainly affected by prestrain. Cyclic proof stress was evaluated from cyclic stress-strain curve.

Relation between fatigue strength and cyclic yield stress

So far, fatigue strength has been estimated by nominal stress. It seems to be necessary to calculate the stress at notch root at fatigue limit exactly. A precise evaluation of fatigue strength at notch root was made by using the elastic-plastic FEM analysis considering a cyclic stress-strain curve as a constitutive equation which we developed newly. Cyclic stress-strain curves obtained from the experiment described above were used. Figure 8 shows the relation between fatigue strength and cyclic yield stress. It is reported that fatigue strength has a tendency of a linear relation with cyclic yield stress, where fatigue strength is estimated as a nominal stress, as shown in Figure 8 [9]. In this study, it was found that fatigue strength almost equaled to cyclic yield stress without depending on prestraining or not,

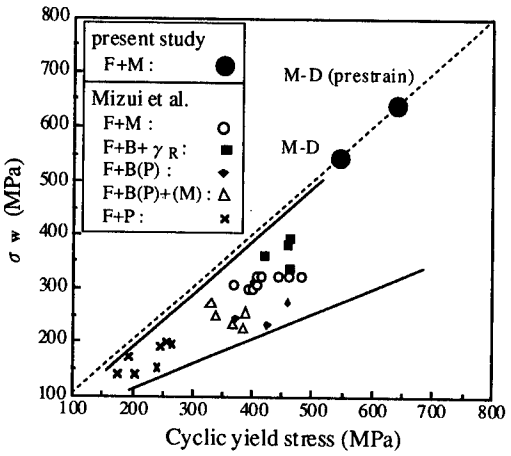


Figure 8 - Relation between cyclic yield stress and fatigue limit.

when an exact estimation of the stress was made at notch root. This might be an intrinsic factor to predict fatigue strength. Further work about the effect of microstructural morphology on cyclic behavior is needed for better understanding the fatigue strength on a notched specimen of the present materials.

Conclusions

Two ferrite-martensite dual-phase steels with different microstructures were prepared by controlling the heat treatment process and the fatigue strength on notched specimen was investigated focusing on metallurgical factors responsible for the fatigue behavior of the present materials. The following results were obtained.

1. The material with a continuous martensite phase around ferrite grains exhibited a higher fatigue strength than that of the material with martensite phase dispersed in ferrite matrix. It was found that the ferrite grain size constrained by martensite was a very important factor to determine the fatigue strength.
2. In spite of an extreme increase in static strength, the increase in fatigue strength for prestrained material is not so large because of its cyclic softening behavior. It was indicated that the stress at notch root at fatigue limit almost equaled to cyclic yield stress from minute analysis.

References

1. V. B. Dutta, S. Suresh, and R. O. Ritchie, "Fatigue crack propagation in dual-phase steels:effects of ferritic-martensitic microstructure on crack path morphology," Metall. Trans., 15A (1984), 1193-1207.
2. R. M. Ramage et al., "The effect of phase continuity on the fatigue and crack closure behavior of a dual-phase steel," Metall. Trans., 17A (1987), 1291-1298.
3. M. Nagae et al., "Fatigue properties of high strength steel sheets," Tetsu-to-Hagane, Jpn., 68 (9) (1982), 1430-1436.
4. K. Nakajima, K. Terao, and T. Miyata, "The effect of microstructure on faituge crack propagation of $\alpha + \beta$ titanium alloys," (Paper presented at international conference on thermomechanical processing of steels & other materials, Wollongong, Australia, July 1997).
5. K. Nakajima, M. Yokoe, and T. Miyata, "The effects of microstructure and prestrain on fatigue crack propagation of dual-phase steels," (Paper presented at the ninth international conference on fracture, Sydney, Australia, April 1997).
6. M. F. Garwood, "Interpretations of tests and correlation with service, correlation of laboratory tests and service performance," Amer. Soci. Mat., (1951), 1.
7. A. M. Sherman, "Fatigue properties of high strength-low alloy steels," Metall. Trans., 6A (1975), 1035-1040.
8. A. M. Sherman and R. G. Davies, "Fatigue of a dual-phase steel," Metall. Trans., 10A (1979), 929-933.
9. M. Mizui and M. Takahashi, "Fatigue properties of high strength steels for automobiles," CAMP-ISIJ, Jpn., 5 (1992), 1867-1870.

Structure Control of Metastable Austenitic Stainless Steels through Deformation Induced Transformation and Aging Treatment

Kouki Tomimura , Katsuhisa Miyakusu, Sadao Hirotsu

Stainless Steel & High Alloy Dept. Steel & Technology Development Laboratories,
Nisshin Steel Co.,Ltd.
4976 Nomuraminami-machi, Shinnanyo, Yamaguhi 746- 8666 , Japan

Abstract:

Effect of retained austenite on strength and ductility was investigated in cold rolled metastable austenitic stainless steels which have various austenite stability against deformation induced transformation. The volume fraction of martensite induced was controlled at 50 to 60vol% through the cold rolling of 50% reduction in thickness at several temperatures. Aging of 400°C-3.6ks causes marked strengthening in the cold rolled materials and 0.2% proof stress of aged materials increases with rising the austenite stability, in general. The strengthening related to the austenite stability is mainly attributed to the way of pile-up of planar dislocation within retained austenite. For the Erichsen test, the best ductility was obtained in steels with the value of 40 in the austenite stability index; Md(N) (=580-520C-2Si-16Mn-16Cr-23Ni-300N-26Cu). Such a good ductility of steels results from strain induced transformation of retained austenite to fresh martensite, so that it was concluded that the value of Md(N) should be controlled at around 40 for the steels with high tensile strength (1900 N/mm^2) in order to guarantee a moderate ductility.

The Third Pacific Rim International Conference on
Advanced Materials and Processing (PRICM 3)
Edited by M.A. Imam, R. DeNale, S. Hanada,
Z. Zhong and D.N. Lee
The Minerals, Metals & Materials Society, 1998

1. Introduction

Metastable austenitic stainless steels such as SUS301 undergo deformation induced transformation to martensite during cold rolling and this transformation is usually utilized for strengthening of these steels in connection with work hardening of austenite itself(1). With an increase of strength, ductility of steels is reduced, in general. However, deformation induced transformation is very useful for keeping good ductility at high strength level, because it produces a large work hardening during deformation. This favorable phenomenon is well known as TRIP(transformation induced plasticity)(2)(3). Ductility based on the TRIP is greatly dependent on austenite stability of steels, namely chemical composition of steels(4), so that the stability should be varied depending on the strength level applied. Author et al. have already developed a high strength steel of 1900N/mm^2 level, which is strengthened through the rout of cold working and the following aging(5). The volume fraction of retained austenite was controlled to be around 50vol% by rolling at various temperatures. In this study, several kinds of steels was chosen to investigate the effect of retained austenite on mechanical properties and an optimal austenite stability was proposed for keeping excellent ductility at the high strength level of 1900N/mm^2.

2.Materials and Experimental Procedure

Materials studied are presented in **Table I**. They contains 2.8% silicon ,2.0% copper for the purpose of strain aging and precipitation hardening. Chromium and nickel content are varied to control austenite stability to deformation induced transformation. Although there are some austenite stability indexes such as Ni equivalent (6)and Md_{30} (7), we propose experimental equation Md(N).

$$Md(N)=580-520C-2Si-16Mn-16Cr-23Ni-300N-26Cu \quad 【1】$$

Table I. Chemical compositions of steels. (mass%)

steel	C	Si	Ni	Cr	N	Cu	Md(N)
A	0.082	2.78	7.0	16.9	0.080	1.94	20
B	0.081	2.83	6.4	16.6	0.075	1.96	41
C	0.083	2.84	6.0	16.0	0.072	1.97	61
D	0.084	2.83	5.5	15.3	0.070	1.97	83
E	0.083	2.88	5.3	15.0	0.070	1.94	95

Md(N)=580-520C-2Si-16Mn-16Cr-23Ni-300N-26Cu

With lowering Md(N) index, the steels have more stable austenite to induced transformation. The steels were produced as a 12kg ingot in a vacuum of about 1Pa and forged down to a flat of 30x110x300mm. The forged flat were formed to 2mm thick plate through hot rolling, intermediate annealing and cold rolling. Solution treatment was performed at 1050℃ for 0.06ks and the plates were cold-rolled by about 5% in each pass to 50% reduction in thickness at fixed temperature in the range of 7-110℃. Aging was performed by 3.6ks isochronal treatment at a temperature of 350-550℃(mainly at 450℃).

The volume fraction of martensite was measured through sample vibration magnetic method(8)(9). Relative value of dislocation density of cold rolled austenite and deformation

induced martensite were measured from half-value width of X-ray refraction peaks. Measured peaks were {200}α' and {220}γ.

Tensile properties were measured at the strain rate of $1.7x10^{-3}$ /s. Ductility was also evaluated Erichsen value and Erichsen break stress(=load/(thickness × internal diameter of die)) by Erichsen test (JIS Z-2247 B method).

Microstructure observation was performed with 200kV transmission electron microscope(TEM). Thin foil specimens for TEM observation were prepared by the jet-polishing in a solution of 90% acetic acid 10% perchloric acid.

3. Results and Discussion

3.1 Age-hardening Behavior and Microstructure

Figure 1 shows relation between the austenite stability index Md(N) of steels and deformation induced amount of martensite in steels cold-rolled 50% at several temperatures. Volume fraction of deformation induced martensite increases with rising Md(N) index. With lowering cold rolling temperature, amount of martensite increases, so we chose the rolling temperature at which 50% cold rolling leads to formation of 50-60% martensite. For example, the rolling temperature is 7 ℃ and 110℃ in A and E steels, respectively. **Figure 2** shows changes in hardness as a function of aging temperature for A – E steels aged for 3.6ks after 50% cold rolling. Hardness of steels is markedly increased by 50% cold rolling. It is a characteristic for metastable austenitic stainless steel, and this is attributable mainly to formation of deformation induced martensite and work hardening of retained austenite. It can be seen that ,for all steels, hardness exhibits a peak at 450-500℃ and softens above 500℃. The main reason of hardness increase is precipitation hardening(5) and strain aging of containing silicon atoms(10).

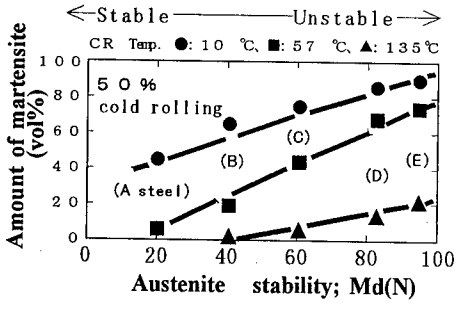


Figure 1: Relation between Md(N) and amount of martensite.

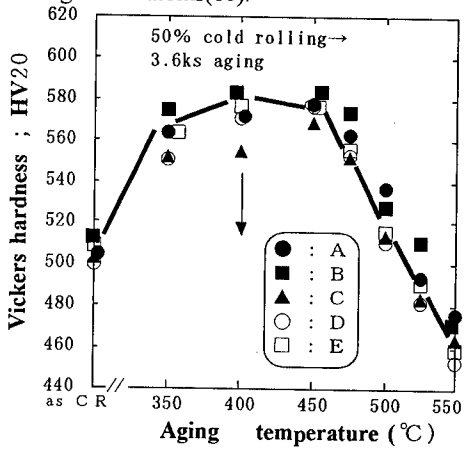
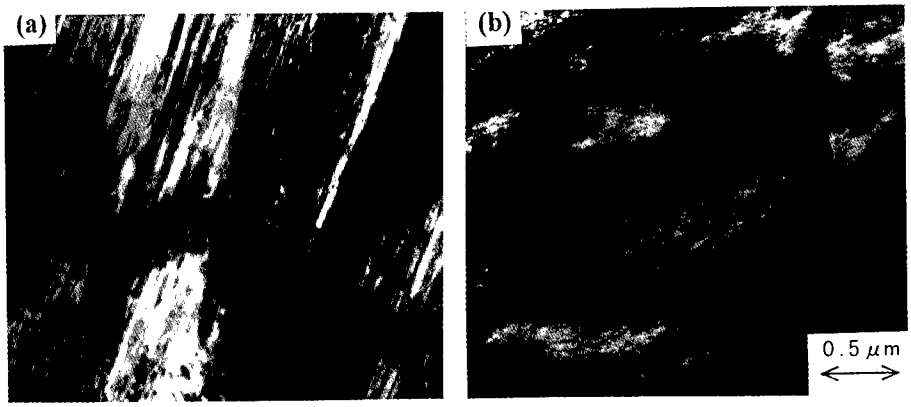


Figure 2: Changes in Vickers hardness in steels as a function of aging temperature.

The aged steels consist of deformation induced martensite and retained austenite. Deformation induced martensite is of lath type in all investigated steels. The microstructure of deformed austenite, which was aged at 400℃ for 3.6ks after 50% cold rolling in A (a) and D steels (b) are shown in **Figure 3**. The dislocation arrangement in the deformed austenite is greatly different: The morphology is characterized by planar type in A steel(a) and cell type in E steel(b). Morphology of dislocation in the steels was classified to these two type. A and B steel have

planar type austenite , while C,D and E steel have cell type austenite. Such a different is confirmed in cold-rolled steels before aging, so this means that two type dislocations are introduced into austenite during cold rolling.



(a):A steel cold rolled at 7℃ (b):D steel cold rolled at 89℃

Figure 3: TEM microstructures of deformed austenite which was aged at 400 ˚C for 3.6ks after 50% cold rolling in A and D steels.

3.2 Strength and Elongation in Aged Steels

Figure 4 shows tensile properties of aged steels with various austenite stabilities. The tensile strength and 0.2% proof stress in A and B steels is higher in comparison with those in the other steels. Amount of martensite ,which is the important factor to strengthing behavior, is almost same in all steels, so that the difference in strength shown Figure 4 is not explained with amount of martensite. The reason for this behavior is discussed later. Erichsen test results in aged steels with various austenite stabilities are shown in **Figure 5**. The best ductility is obtained in B steel with the austenite stability Md(N) =41. Above 41 in Md(N) , an increase in Md(N) generally lowered Erichsen value. **Figure 6** shows increasing behavior of deformation induced martensite during Erichsen test in A and E steels. The increasing rate of fresh martensite is large in E steel in comparison with that A steel. In metastable austenitic steels, deformation induced fresh martensite is formed at stress concentration zone to inhibit initiation of crack, and it results in improvement of ductility(11). Such a TRIP phenomenon is also caused in Erichsen

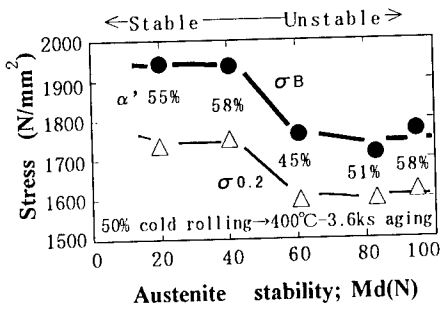


Figure 4: Tensile properties of aged steels with various austenite stabilities.

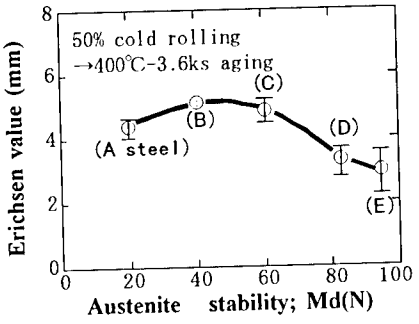


Figure 5: Effect of austenite stability on Erichsen value in steels.

test. Good ductility in A steel shown in Figure 5 is a consequence of the formation of strain induced fresh martensite during deformation. Relation between tensile strength and Erichsen value are summarized in **Figure 7**. Steel with the Md(N) of 40 have high strength and large elongation.

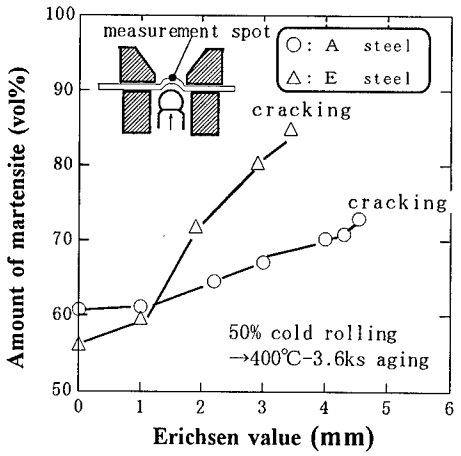


Figure 6: Increasing behavior of deformation induced martensite during Erichsen test in A and E steels.

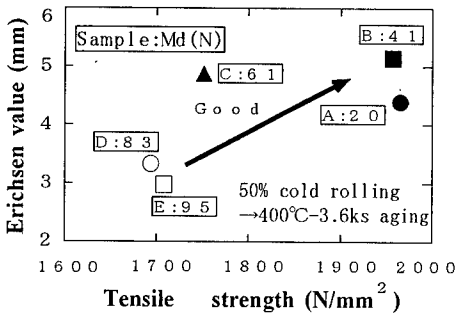


Figure 7: Relation between tensile strength and Erichsen Value in steels.

3.3 Effect of Microstructure on Strength

Strength in aged steels depends on austenite stability, as mentioned in Figure 4. Important factors which affect strength of steels are dislocation density and morphology of microstructure in addition to amount of martensite. **Figure 8** shows effect of rolling temperature on X ray half-value width of austenite and martensite phases in steels. This half-value width indirectly indicates magnitude of the dislocation density. The half-value width of austenite and martensite phases in aged steels is narrower than that in cold-rolled steels. This means that the strain introduced by cold rolling is relieved during aging. Results in Figure 8 also indicates that dislocation density of each phase is almost same in steels except for E steel. Although High dislocation density leads

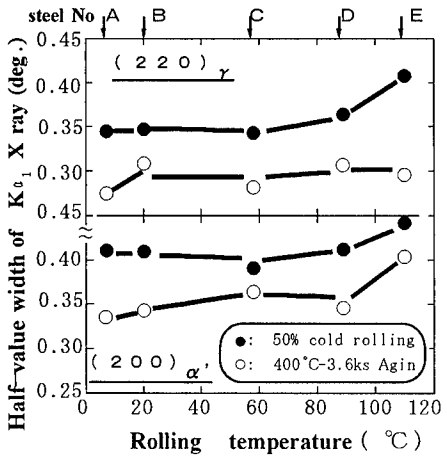


Figure 8: Effect of rolling temperature on X ray half- value width of austenite and martensite phases in steels used.

to high strength in general(12), dislocation density seems not to affect the strengthening behavior shown in Figure 6.

Dislocation arrangement of retained austenite is classified to planar type and cell type as mentioned in Figure 3. The morphology in A and B steels having higher strength is planar type. The morphology of dislocations well corresponds to the strength of steels. The 0.2% proof stress depends on dislocation mobility in microstructures In the case of planar dislocation structure in retained austenite, the width of stacking faults are larger and the stacking faults inhibit the dislocation movement and this results in increase of 0.2% proof stress. We confirmed that there is no significant difference in work hardening in steels. The change of dislocation arrangement in retained austenite results from the difference in stacking fault energy depending on cold rolling temperature. Stacking fault energy is decreased with lowering temperature(13).

A and B steels which have suitable austenite stability are cold rolled to form moderate amount of martensite and this results in favorable arrangements of dislocations, namely planar type of dislocations.

4.Conclusions

Effect of microstructure in retained austenite on strength and austenite stability on elongation have been investigated in Fe-(15~16.9)Cr-(5.3~7.0)Ni metastable austenitic stainless steels having various austenite stability against deformation induced transformation.. The results obtained are as follows:

(1) The steels achieved high strength during 50% cold rolling and following aging in the range of 400 - 450℃. They consist of almost 50vol% deformation induced martensite

(2) An Increase in austenite stability generally enhanced the 0.2% proof stress and tensile strength of steels aged at 400℃ for 3.6ks. The steel having more stable austenite is need to be cold-rolled at lower temperature to obtain fixed deformation induced martensite. The cold rolling at lower temperature makes the change of dislocation arrangement of cold-rolled austenite. It contributed to an increase in the strength and this is attributable mainly to planar dislocation of the deformed austenite.

(3) For the Erichsen test, the best ductility was obtained in steels with the value of 40 in the austenite stability index; Md(N) (=580-520C-2Si-16Mn-16Cr-23Ni-300N-26Cu). Such a good ductility of steels results from strain induced transformation of retained austenite to fresh martensite

(4) The value of Md(N) should be controlled at around 40 for the steels with high tensile strength (1900 N/mm^2) in order to guarantee a moderate ductility.

References

1. Y.Murata, S.Ohashi and Y.Uematsu, Tetsu-to-Hagane", 78(1992),346.
2. I.Tamura, Tetsu-to-Hagane,56(1970),429.
3. K.Tsuzaki and T.Maki, Journal of The Japan Society for Heat Treatment,32(1992),70.
4. T.Hirayama and M.Ogirima, J.Jpn.Inst.Met.,34(1970),507.
5. S.Hirotsu, NISSHIN STEEL Technical Report,57(1987),54.
6. T.Angel, Iron Steel Inst.,177(1954),165.
7. K.Nohara, H.Ono and N.Ohashi, Tetsu-to-Hagane, 63(1977),772.
8. K.Hoshiono, K.Ito and T.Komatsu, NISSHIN STEEL Technical Report,29(1973),26.
9. T.Tanaka and K.Hoshino, NISSHIN STEEL Technical Report,52(1985),36.
10. T.Takemoto, Y.Murata and T.Tanaka, Tetsu-to-Hagane,76(1990),894.
11. K.Tomimura,S.Ueda,S.Takaki and Y.Tokunaga, Tetsu-to-Hagane,78(1992),141.
12. J.F.Bailey,Phil.Mag.,8(1963),223.
13. R.M.Latanision and A.W.Ruff,JR., Metall.Trans.,2(1971),505.

Local Mechanical Properties of Steel Weldments

D. A. LaVan[1], G. Shoukas[2], W. N. Sharpe, Jr.[1]

[1]The Johns Hopkins University
Department of Mechanical Engineering
Baltimore, MD 21218

[2]Lehigh University
Bethlehem, PA 18015

Abstract

The application of advanced high strength steels for use in naval structures requires advanced welding processes. At this time, concerns about the cost and reliability of welds limit the maximum strength level of hull plate to 690 MPa (i.e. HY-100, HSLA-100). Undermatched welding provides an opportunity to use higher strength plate while using less expensive welding processes. Since deformation can be concentrated in the lower-strength weld metal, application of undermatched welding requires detailed study of the local behavior of this region.

Microtensile specimens were utilized to directly measure the modulus, yield and ultimate strength of selected sites within a two inch thick test weldment. The overall sample size is roughly 3 mm long with a gage length of 300 μm and a gage cross section that is 200 μm square. This test technique has been validated by recent participation in an *ASTM Cross-Comparison Exercise on Determination of Material Properties Through the Use of Miniature Mechanical Testing*. Load is measured using a small commercial load cell and strain is measured, in real time, directly on both sides of the specimen using laser interferometry.

The directional and microstrucutural dependence of the microtensile properties of a highly undermatched weld, HY-100 plate welded with MIL-70S wire, and a marginally undermatched weld, HY-100 plate welded with MIL-100S wire, were measured. Eighty tensile tests were performed at 10 locations distributed across the two welds. At each location three samples were tested in each of two or three orthogonal directions. In addition, large area microhardness maps were produced for each weld. A major finding was that the tensile properties can be anisotropic, in contrast to the microhardness measurements that did not vary with orientation.

The Third Pacific Rim International Conference on
Advanced Materials and Processing (PRICM 3)
Edited by M.A. Imam, R. DeNale, S. Hanada,
Z. Zhong and D.N. Lee
The Minerals, Metals & Materials Society, 1998

Introduction

The performance of a large naval structure is determined by the properties of individual weld beads in the hull; each weld bead is characterized by tensile properties, microhardness and microstructure. This project investigates the variations in tensile properties in relation to orientation and microhardness data. Local modulus, yield strength, ultimate strength and elongation were found in a manner consistent with ASTM definitions [1].

Microtensile Testing

Samples with gage cross section dimensions of less than 200 μm were tested using a novel microtensile test machine. Strain was measured on both sides of the sample using a two-sided measurement system, load was measured with a miniature 90 N load cell, and an air-bearing was used to support the movable grip. A classic "dog-biscuit" shaped specimen was chosen with tapered ends designed to fit into matching grips. The "dog-biscuit" shape is self-aligning and requires no clamping or gluing. Strain is measured using laser interferometry [2]. A laser is reflected from two surface markers, in this case, Vickers microhardness indents. The two reflections combine to form light and dark interference bands in a manner similar to Young's two-slit experiment. The measurement of these fringe patterns is measured using photodetectors and converted into displacement. By properly averaging the two fringe motions, the strain can be measured without any contribution from rigid body motion. This technique has been applied to other projects involving microspecimen studies of the fatigue behavior of welds [3]. Recently, it has been expanded to measure strain on two sides of the sample by applying the same technique with markers on the back surface [4].

In a related project, specimens of ASTM A533-B steel were tested as part of the *ASTM Cross-Comparison Exercise on Determination of Material Properties Through the Use of Miniature Mechanical Testing Techniques.* Each participant was supplied material from the same plate and asked to use their own techniques to measure the properties. Microtensile results were compared with macrotensile results that were produced by the Cross-Comparison administrator and were not revealed to the participants until after the exercise was completed. The microtensile results agreed almost exactly with the official results [5, 6]. By this comparison, and other tests, the force application, force measurement and strain measurements have been demonstrated to be valid when compared with traditional techniques. This microsample technique is able to sample a region of material comparable to a large microhardness indent and to directly determine the stress-strain curve.

Weld Sample Description

Two gas-metal-arc-weld (GMAW) welds were studied for this project. The first, a highly undermatched weld, labeled "HBA", was produced with ESAB L-TEC Spoolarc 86, in accordance with MIL-70S-6. It was deposited with a heat input of 65-70 kJ/in. The second, a slightly undermatched weld, labeled "HBB", was produced with Lincoln LA-100, in accordance with MIL-100S-1. The heat input was 80 kJ/in. Table 1 provides the composition of samples from the base plate and deposited filler metal. Table 2 lists the macro mechanical properties of the base plate and deposited filler metal. These composition and macro tensile properties were produced by the Naval Surface Warfare Center – Carderock Division.

Table 1. Average composition of base metal and deposited filler metals (wt. %)

	C	Mn	Ni	Si	Mo	Cr	P	S
HY-100	0.154	0.30	3.06	0.21	0.41	1.39	0.004	0.018
filler – HBA	0.087	1.18	0.30	0.74	0.044	0.15	0.007	0.005
filler – HBB	0.053	1.41	1.99	0.36	0.43	0.12	<0.002	0.006

Table 2. Macro mechanical properties of base metal and deposited filler metals (Avg ± SD)

	Yield (MPa)	Ultimate (MPa)	Elongation (%)
Base Plate	752 ± 30	856 ± 34	21 ± 4
HBA	486 ± 12	607 ± 10	31 ± 2
HBB	664 ± 38	751 ± 46	25 ± 2

Microtensile specimens were taken from five different locations within each weldment. At each location, three specimens were tested in two or three orthogonal directions. A total of 80 microspecimens were tested. The sample sites on weld HBA are labeled "A" through "E. The sample sites on weld HBB are labeled "H" through "L". The three sample orientations were along the longitudinal direction of the plate, designated "L", in the short transverse direction, designated "S", and in the transverse direction, designated "T".

Hardness

Large area microhardness scans were performed using a Clemex Technology computerized microhardness testing machine to investigate the total distribution of hardness measurements in the weld samples. These scans were performed on both weld samples HBA and HBB. The relative softness of HBA is clearly evident in the contour plots of the hardness data, while the HBB weld metal more closely matches the base plate. Contour plots of the hardness measurements are superimposed on the macro photographs of the weld cross-sections shown in Figure 1. The hardness plots mimic all the microstrucutural features seen in the macro photos. From these plots, the Vickers hardness ranged from 160 to 240 VHN for the weld metal of sample HBA, and 200 to 260 VHN for weld HBB. The base plate had a hardness of 290 VHN, and the HAZ peaked at 400 to 420 VHN.

The microhardness indents were made with a 500 gm load, and a 15 second duration. The calibration of the machine was checked immediately before beginning the scans by having the machine perform automatic measurements on a calibrated test block. This served to verify that the indenting process and automatic measurement function were performing in accordance with ASTM standard E384. The sampled area was 35 mm wide by 27.5 mm tall (70 by 55 indents). The indents were placed on a 500 micron spacing, which gave 3850 indents on each sample. The test area was selected to fall in the upper half of the weld, from the same region where the microtensile samples were; this region included mostly weld metal but also the heat affected zone and base metal.

Results and Conclusions

The technique allows the accurate measurement of the stress-strain curves of microspecimens removed from large weldments. Figure 2 shows nine actual stress-strain curves for samples tested at site "A", and Figure 3 compare the yield and ultimate strengths in the three directions with the microhardness measurements. Note the variations in strengths in contrast to the nearly constant hardness measurements. This site shows the most anisotropy seen in this investigation.

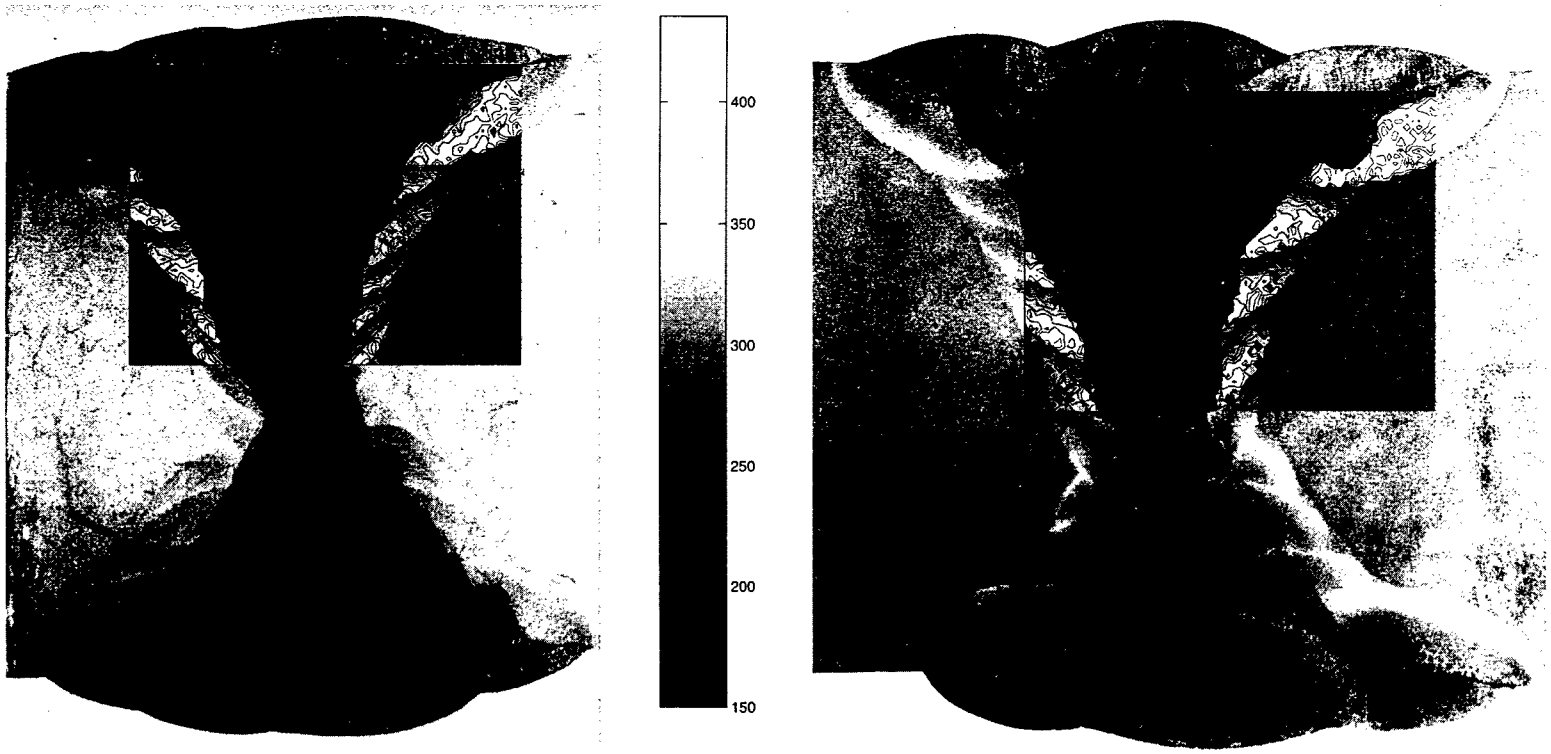


Figure 1. Macro-photographs of cross sections from weld (a) HBA and (b) HBB.
A Contour plot of Vickers microhardness is superimposed over part of each photograph.
The graybar showing the scale is in the center. Each weld is made from 2 in. plate.

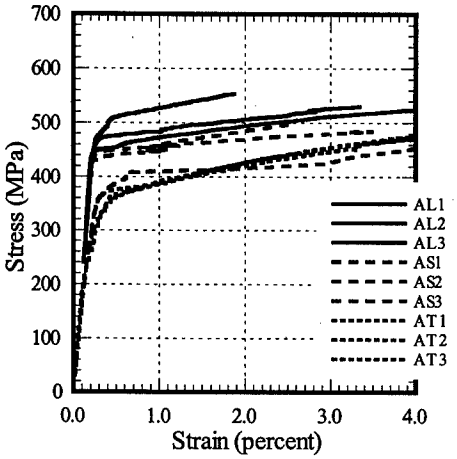


Figure 2. Nine stress-strain curves from location "A" on weld HBA. Samples were cut in three orthogonal directions L, S and T.

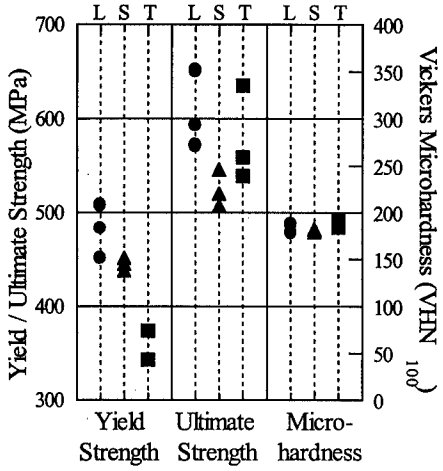


Figure 3. Summary of the mechanical properties for the samples at location "A".

Weld HBA.

The average of all the microsample yield stresses is 512 MPa with a standard deviation of 107 MPa. The coefficient of variation for these measurements is 21%. This mean value is slightly higher than the nominal yield stress shown in Table 2. Because of the constraint in cutting full size samples, the macro samples were taken from regions with generally lower yield strength (the outer region of the weld). The ultimate stress for all the samples from HBA is 638 ± 77 MPa.

Weld HBB.

The average yield for all the samples tested from weld HBB is 646 ± 75 MPa. The average ultimate strength for all the samples is 784 ± 40 MPa. This weld exhibits much less variation in the results, the average of all the microsample tests compares very closely to the macro results shown in Table 2.

Correlations.

Figure 4(a) shows a plot of strength versus hardness for all the samples from weld HBA and HBB plotted without respect to orientation. There is a general linear correlation between the strength and hardness, but the local properties show a broad scatter. The ultimate strength gives a better fit than the yield. The linear least-squares fit for these plots are:

$$\text{UTS (MPa)} = 28 + 2.84\ \text{VHN} \quad (R=0.94) \quad (1)$$

$$\text{Yield (MPa)} = -160 + 3.10\ \text{VHN} \quad (R=0.86) \quad (2)$$

Figure 4(b) shows a plot of elongation versus hardness for all the samples tested. Note that there is no simple fit for the elongation data; in fact the elongation measurements for samples from HBB were almost independent of hardness. The results reported herein are the first ever obtained to show such detail of the variation in properties with the weld metal itself.

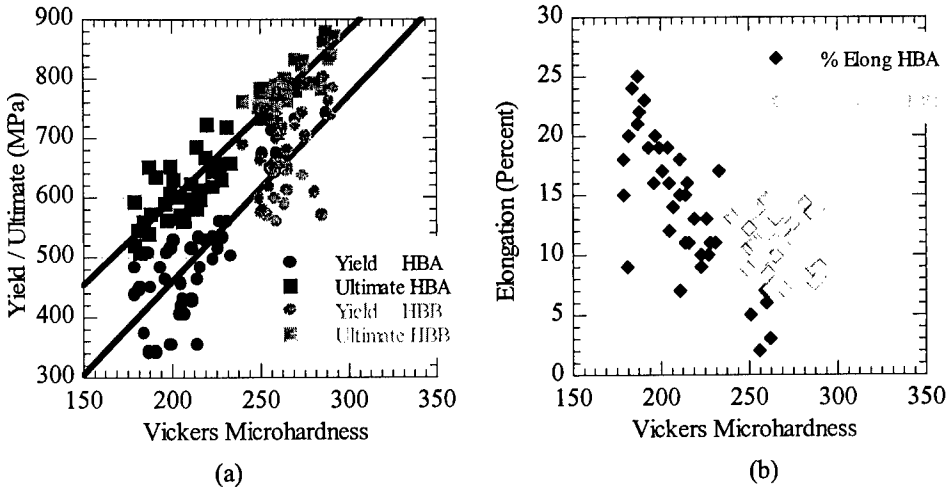


Figure 4. Correlation between Vickers Microhardness measurements and (a) Yield and ultimate strength and (b) elongation.

Acknowledgements

This work was supported by a grant from the Carderock Division of the Naval Surface Warfare Center with R. T. Tregoning as project administrator. Access to the Clemex computerized microhardness test equipment was provided by Code 615, Carderock Division of the Naval Surface Warfare Center. The authors would like to acknowledge George Coles for performing some of the microsample tests.

References

1. American Society for Testing and Materials, Standard E8-96, "Test Methods for Tension Testing of Metallic Materials", 1996.
2. Sharpe, W. N., Jr. ''An Interferometric Strain Displacement Measurement System'', NASA Technical Memorandum 101638, (1989).
3. Yuan, B. and W.N. Sharpe, Jr. "Fatigue Testing of Microspecimens", Fatigue '96, Proceedings of the Sixth International Fatigue Congress, Berlin, Germany, May 6 - 10, 1996, pp. 1943 - 1948.
4. LaVan, D. A. and W. N. Sharpe, Jr. "Strain Measurement on Miniature Tensile Samples", 1997 SEM Spring Meeting Proceedings, 1997.
5. Sharpe, W. N., Jr., Danley, D., and LaVan, D. A. "Microspecimen Tensile Tests of A533-B Steel," submitted for publication in Small Specimen Test Techniques, ASTM STP 1329, W. R. Corwin, S. T. Rosinski, and E. Van Walle, Eds., American Society for Testing and Materials, 1997.
6. Rosinski, S. T., oral presentation at *Third Symposium on Small Specimen Test Techniques,* sponsored by ASTM Committee E-10, New Orleans, January 1997.

ON THE MECHANISM OF DECREASING THE SLAB REHEATING TEMPERATURE OF Hi-B STEELS BY THE ADDITION OF MOLYBDENUM

ZHAO Yu and GUI Fusheng

New Materials Research Department
Central Iron and Steel Research Institute
Beijing100081,P.R.China

Abstract

By means of X-ray pole density and three dimensional orientation distribution function (ODF) analysis, the mechanism of the reduction of slab reheating temperatures for Hi-B grain-oriented silicon steels by Mo was studied. It was demonstrated that for both the hot rolled bands and the primary recrystallized sheets, the texture in outer layer of the Mo bearing steel slab reheated at 1310°C are very similar to that of the Mo free steel slab reheated at 1380°C but different from that of the Mo bearing steel slab reheated at 1380°C. The reason why the slab reheating temperature of Hi-B steel can be lowered to 1310°C by the addition of Mo is that when the slab of the Mo bearing steel is reheated at a relatively lower temperature 1310°C, a stronger (111) component in the outer layer of the decarburized sheet can be still retained.

The Third Pacific Rim International Conference on
Advanced Materials and Processing (PRICM 3)
Edited by M.A. Imam, R. DeNale, S. Hanada,
Z. Zhong and D.N. Lee
The Minerals, Metals & Materials Society, 1998

Introduction

In the production of Hi-B grain-oriented silicon steels, in order to achieve a perfect secondary recrystallization structure with a sharp {110}<001> texture, prior to hot rolling, the continuously casting slabs must be reheated at over 1350°C, which not only consumes a large amount of energy, but also pollutes the furnace bottom due to the melting of the slab surface oxide, and as a result, makes it necessary to clear the furnace bottom regularly. Hence, the decrease of the slab reheating temperature plays a key role in increasing the production and decreasing the production cost of Hi-B steels. Recently, it was found by researchers in Wuhan Iron and Steel Company that by adding a small amount of Mo to Hi-B steels, the slab reheating temperatures can be reduced, and at the same time, the magnetic properties become more stable. The object of this work is to study the mechanism of the reduction of slab reheating temperatures by Mo from the texture changes in each stage of processing.

Experimental Materials and Procedure

The experimental materials used in the present study were Hi-B steels taken from three heats supplied by the Wuhan Iron and Steel Company. The heat 1 and heat 2 contained about 0.04%Mo and the heat 3 was Mo free. The slab reheating temperature was 1310°C for the heat 1 and 1380°C for the heat 2 and heat 3. Apart from Mo, the chemical compositions of the three heats were approximately identical, and were roughly as follows: 3.2Si, 0.075C, 0.08Mn, 0.03S, 0.027Als, 0.008N, 0.1Cu and 0.1Sn (in wt%). With the increase of the slab reheating temperature, the hot rolling temperature increased. The starting and finishing temperatures of hot rolling after slab reheating at 1380°C (about 1180°C and 990°C respectively) were 40 to 50°C higher than those after slab reheating at 1310°C. The hot rolled bands were normalized at 1100°C, and then, cold rolled directly to the thickness of 0.3mm. Finally, the decarburization treatment was carried out at 835°C in an annealing atmosphere of wet 25%H_2+75%N_2.

In order to measure textures at different positions along the hot rolled band thickness, a layer of certain thickness was first removed from the band surface using a spark cutter. After mechanical polishing, the measured surface was pickled in the hot 50% hydrochloric acid solution to eliminate the surface stress. For the decarburized sheets, however, a corrosive of hydrofluoric acid solution was used to remove a certain thickness directly from the sheet surface.

Texture determinations were performed in an APD-10 automatic X-ray diffractometer. Both the ODF and the pole density analysis were carried out on hot rolled bands and decarburized sheets. Positions along the band (or sheet) thickness were represented by a parameter S (S=x/d, where x was the distance from the measured position to the band (or sheet) surface and d was half of the total thickness). Apparently, for the band (or sheet) surface, S=0, and for the midplane, S=1.

Experimental Results

Hot Rolled Band

Pole Density Measurements Pole density measurements show that for all the three heats used in this work, in outer layers of hot rolled bands (S=0, 0.2 and 0.5) the strongest texture component is (110). It can be clearly seen from the distribution of the pole density along the hot rolled band thickness (as shown in Figure 1) that the intensity of the (110) component reaches its highest value at S=0.2. For the Mo bearing steel slab reheated at 1310°C (heat 1), the intensity of the (110) component increases quickly as S changes from 0 to 0.2 and then falls down suddenly as S changes from 0.2 to 0.5. As a result, a very sharp peak appears at S=0.2. When the slab reheating temperature of Mo bearing steel increases to 1380°C, the intensity change of (110) component with S becomes more smooth. However, for the Mo free steel slab reheated at 1380°C, the intensity distribution of (110) component along the band thickness shows a similar character with that for the Mo bearing steel slab reheated at 1310°C.

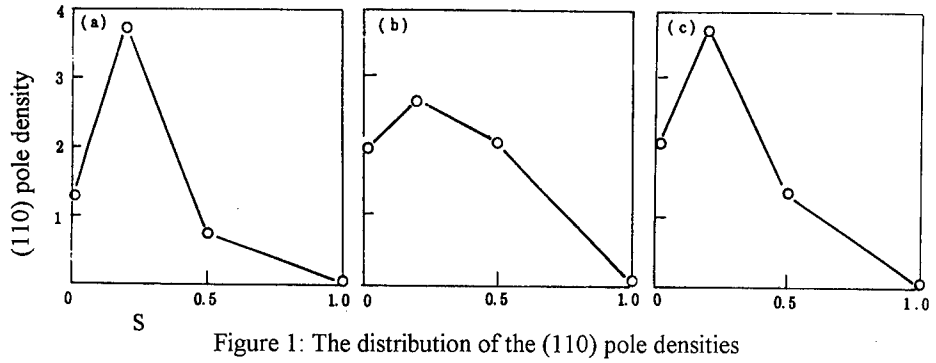
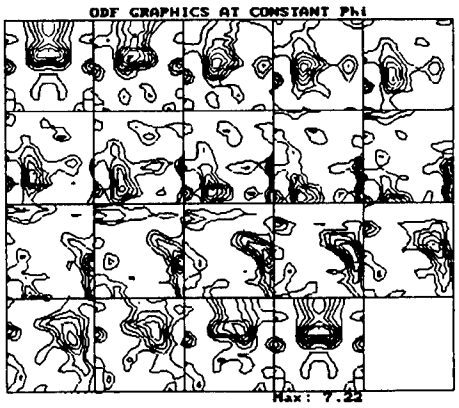


Figure 1: The distribution of the (110) pole densities
along the thickness of the hot rolled bands
(a) heat 1; (b) heat 2; (c) heat 3

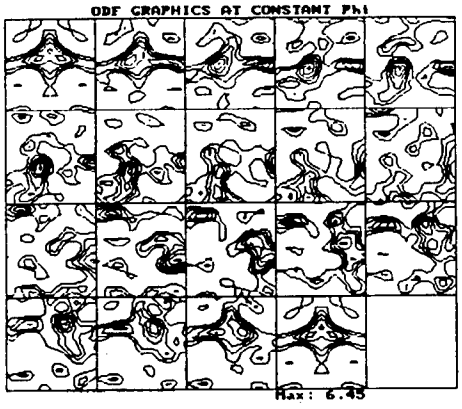
ODF Measurements At the hot band surface S=0, for the Mo bearing steel, when the slab is reheated at 1310°C (heat 1), grain orientation concentrates in a tube with a line from $(\bar{1}01)[0\bar{1}0]$ to $(\bar{1}01)[1\bar{2}1]$ along the line ξ and then from $(\bar{1}01)[1\bar{2}1]$ to $(\bar{4}411)[11\bar{1}\bar{1}8]$ along the line κ as its center, as shown in Figure 2(a). The positions of lines ξ and κ in the Euler space are shown in Figure 3. As the slab reheating temperature increases to 1380°C (heat 2), grain orientations become dispersive, and no distinct orientation concentrating line can be observed, as shown in Figure 2(b). It is worth noting from Figure 2(c) that although the slab reheating temperature of the Mo free steel (heat 3) is as high as that of heat 2 (1380°C), an orientation concentrating line, similar to that of heat 1 is still observed. This is quite different from heat 2.

At S=0.2, it is also shown that the grain orientation distribution of heat 1 is very similar to that of heat 3. The only one difference between the two measured surfaces is that at S=0.2, when the slab reheating temperature of Mo bearing steel is increased to 1380°C, a weak grain orientation concentrating line mentioned above can be still observed.

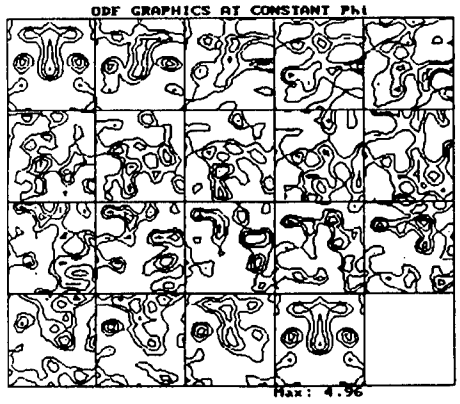
At S=0.5, however, the grain orientations have a relatively dispersive distribution.



(a)



(c)



(b)

Figure 2: ODF diagrams of (a) heat 1, (b) heat 2 and (c) heat 3 measured on the hot rolled band surfaces. ODFs are given at constant ϕ at every 5° and the increment is one grade

Decarburized Sheet

ODF Measurements ODF measurements on the outer layer of the decarburized sheet (S=0, 0.2 and 0.5) for all the three heats shows that at all measured surfaces (totally nine surfaces), grain orientations exhibit a typical primary recrystallization texture of Hi-B steel with a very strong {111}<112> (and the nearby {554}<225>) component and a weak {110}<001> component.

Pole Density Measurements Pole density measurements show that the strongest orientation component in the outer layers (S=0, 0.2 and 0.5) for all the three heats is (111). The intensity distributions of the (111)

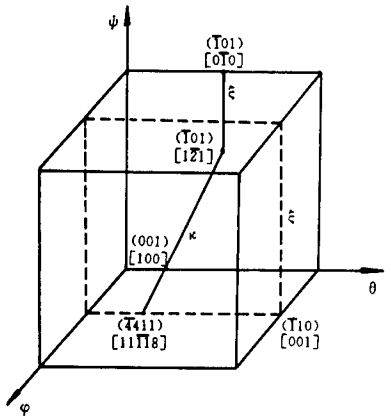


Figure 3: Positions of lines ξ and κ in Euler space.

component are given in Figure 4. It is found out once again that the intensity distribution of (111) of heat 1 is very similar to that of heat 3 but different from that of heat 2.

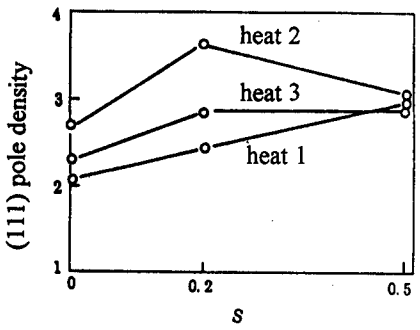


Figure 4: Distributions of the (111) pole densities along the thickness of decarburized sheets.

Discussion

From the above mentioned it can be clearly seen that for both the hot rolled bands and primary recrystallized sheets, there exists an identical phenomenon that in the outer layers the Mo bearing steel slab reheated at 1310°C has a similar texture character to the Mo free steel slab reheated at 1380°C. Since the hot rolled texture is the basis of the cold rolled and primary recrystallized textures, this phenomenon is understandable.

First of all, we think about the hot rolled texture. it has been demonstrated by experiments and theoretical calculations that the main surface deformation mode during hot rolling is shear, and all the stable end orientations of shear deformation for bcc metals will fall into the line from {110}<001> to {110}<112> along the line ξ (a rotation of the Goss orientation by 35° around <110>//ND) and then from {110}<112> to {4 4 11}<11 11 8> along the line κ (a rotation of {110}<112> by 35° around a <011> axis inclined at 60° to ND in the plane ND/RD) [1~3]. From the present results it can be seen that, at the hot rolled band surface S=0,when the slab of Mo bearing steel is reheated at a lower temperature 1310°C, the shear deformation texture remained perfectly due to the inhibition of recrystallization. However, when the slab reheating temperature increases (the hot rolling temperature increases also), the shear deformation texture is weakened and even removed by recrystallization, and as a result, the grain orientation tend to be random. Since the recrystallization develops from the surface to the interior, the shear deformation texture can survive to higher slab reheating temperatures at S=0.2. At a deeper position S=0.5, however, owing to the removal of the outer layer, grain orientation distributions are no longer those typical of shear deformation texture.

We further consider the primary recrystallization texture. In recent years, a lot of work has proved that the formation of the single {110}<001> secondary recrystallization texture during the final high temperature annealing was just for the reason that there was a great number of primary grains which had a coincident lattice orientation relationship with the {110}<001> oriented grains (secondary nuclei). In other words, among the primary recrystallized grains of the Hi-B steel, the probability of satisfying the coincidence orientation relationship with {110}<001> must be over a critical value for the success of secondary recrystallization. The main coincidence relationship with {110}<001> in grain-oriented silicon steels is Σ9 [3]. It is generally thought

that the stronger the (111) component, the higher the probability of satisfying the Σ9 coincidence relationship with {110}<001>. From the present results (as shown in Figure 4) it can be seen that the (111) component is strongest in the outer layer of the decarburized sheet of the Mo bearing steel slab reheated at 1380°C. With the decrease of the slab reheating temperature of the Mo bearing steel, the intensity of the (111) component decreases. Therefore, it can be thought that when the slab reheating temperature of the Mo free steels decrease, the intensity of the (111) component will also decreases. According to the fact that the intensity of the (111) component of the Mo free steel slab reheated at 1380°C is approximately as low as that of the Mo bearing steel slab reheated at 1310°C, it can be reasonably predicted that when the slab reheating temperature of the Mo free steel decreases to 1310°C, the intensity of the (111) component will decrease to an even lower level, which may result in the imperfection of the secondary recrystallization.

Conclusions

(1) The Mo bearing steel slab reheated at 1310°C has a similar texture to the Mo free steel slab reheated at 1380°C in outer layers of the hot rolled bands, and both of them show a typical shear deformatiom character. However, in the outer layer of the Mo bearing steel slab reheated at 1380°C, no obvious shear deformation texture is observed.

(2) In outer layers of the hot rolled bands and the decarburized sheets, the main texture components are (110) and (111), respectively. For both the hot rolled bands and the decarburized sheets, the intensity distribution of the main texture component along the thickness for the Mo bearing steel slab reheated at 1310°C is very similar to that for the Mo free steel slab reheated at 1380°C but different from that for the Mo bearing steel slab reheated at 1380°C.

(3) The mechanism of the decrease of the slab reheating temperature by Mo is that when the slab reheating temperature of the Mo bearing steel is lowered to 1310°C, the (111) component in the outer layer of the decarburized sheet will still have a higher intensity.

References

1. S. Mishra, C. Därmann and K. Lücke, "New Information on Texture Development in Regular and High-permeability Grain-oriented Silicon Steel," Metall. Trans. A, 17A(8)(1986), 1301

2. J. Harase, R. Shimizu and D. J. Dingley, "Texture Evolution in the Presence of Precipitates in Fe-3%Si Alloy," Acta Metall. Mater., 39(5)(1991), 763

3. R. Shimizu, J. Harase and D. J. Dingley, "Prediction of Secondary Recrystallization Texture in Fe-3%Si Alloy by Three-dimensional Texture Analysis," Acta Metall. Mater., 38(6)(1990), 973

A NEW MATERIAL FOR THE CONTACT CABLE PART I: FEASIBILITY STUDY

Hongquan Wen, Liming Peng, Xiemin Mao, Zhenhua Pan, Feipeng Qi, Kuangdi Xu

School of Materials Science & Engineering, Shanghai University
149 Yanchang Rd., Shanghai, 200072, P. R. China

Abstract

The Cu-Cr in-situ composites, as a new material for the contact cable, prepared by the unidirectional solidification, was proposed in the paper. The selection of alloy, solidification process, mechanical and electrical properties, and its continuous casting were discussed respectively and primarily. Experimental and analytical results showed the technical route is essentially feasible.

The Third Pacific Rim International Conference on
Advanced Materials and Processing (PRICM 3)
Edited by M.A. Imam, R. DeNale, S. Hanada,
Z. Zhong and D.N. Lee
The Minerals, Metals & Materials Society, 1998

Introduction

The rapidly developing communications and transportation demands the contact cable for a higher quality in both strength and electrical conductivity. Owing to its excellent conductivity and erosion-resistance, copper cables are employed more and more broadly, having a trend to replace the aluminum-steel composite cable. The main types of the copper contact cables include the hard copper[1], copper alloys[2], copper-steel composites[3] and the particle-reinforced copper-based composites[4], in which the high strength and high conductivity are generally difficult to obtain simultaneously since their essential strengthening mechanism. With a consideration of the special virtue of fiber reinforcing in composites, this paper will discuss the feasibility of using the unidirectional solidification technology to produce an in-situ composite cable with high strength and high conductivity.

Selection of Alloy

The selection of alloy, including the determination of alloy system and constitution, not only has an important effect on the ultimate quality of the contact cable, but also determines to a great extent the follow-up processing such as the melting and continuous casting. Several basic requirements to the alloying system should be considered: 1) high conductivity for the matrix material; 2) high strength for the second phase in the alloy; 3) low solubility of the alloying element in matrix; 4) an eutectic transformation from liquid to solid; 5) simple melting and preparing processing. Based on the above considerations, we select the Cu-Cr alloy system as the proper system, whose phase diagram at the corner of rich copper is shown in Fig.1. As one knows, copper has high conductivity, while the alloying element, Cr, is broadly employed strengthening agent. More importantly, as seen from the phase diagram, chromium has a very low solubility in the matrix, only with maximum value of 0.65%, and less than 0.03% at 400 ℃, which decreases the infliction of such a solute upon the conductivity of the matrix. Furthermore, Cu-Cr alloy is an eutectic system, whose melting temperature is lower so that the melting processing can be simplified.

After the alloying system is identified, the alloying content is a second factor to be selected, in order to harmonizing the contradiction between the strength and the conductivity. Generally speaking, the strength will increase with the increasing of Cr content, while the conductivity decreases. In the experiment, the chromium's contents were taken about 1% in the preparation of the researched alloys, adjacent to that used commonly in conductive copper alloys[2]. Within the chromium's contents, there exists a eutectic transformation which is proper to form the in-situ composites.

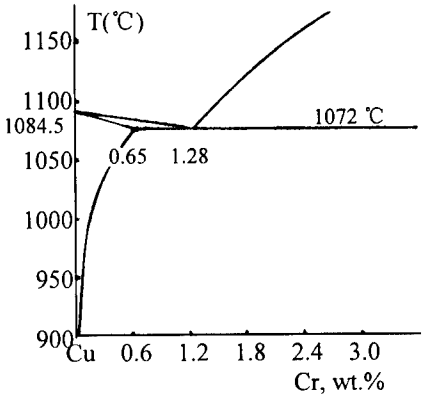


Fig.1: Phase diagram of Cu-Cr alloy

Directional Solidification

The formation of the in-situ composite cable is based on the directional solidification of the Cu-Cr alloy system. During this process, both copper matrix phase and second phase will grow forward cooperatively along the axial direction of the cable, where the former acts as the main conductor and the latter as the main reinforce. This feature seems like that of the aluminum-steel or copper-steel composite cable, so as to take into consideration of the mechanical and electrical properties of the cable. Experimental results showed that the directional solidification has a great effect on the microstructure of the Cu-Cr alloy. Fig.2(a), (b) are respectively the microstructures of the casting and the directional solidification. It can be seen that the equiaxied structure is changed into the columnar one, in which the primary α(Cu) crystals act as the main conductor and the [α(Cu)+β(Cr)] eutectics as the main reinforce. It is important to maintain a planar solid/liquid interface during the directional solidification process, to obtain more straight α(Cu) crystal in morphology, since there are no electrical discontinuities as would be the case at dendritic branches. Otherwise, the morphology will be instablized and the dendrites will appear. The planar and dendritic S/L interfaces are shown as Fig.3(a), (b).

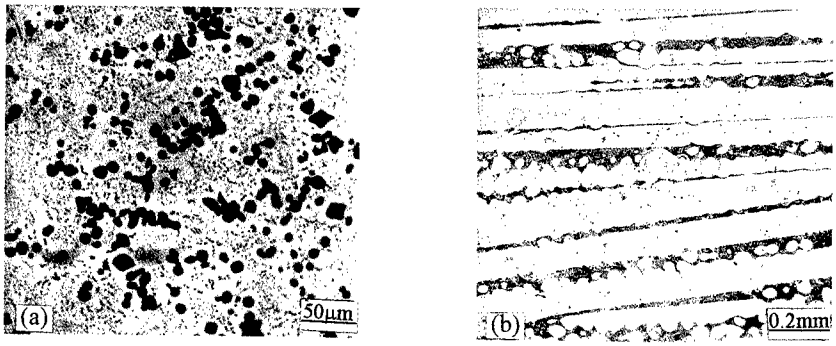


Fig.2: Microstructure of Cu-0.8wt.%Cr alloy
(a) casting (b) directional solidification

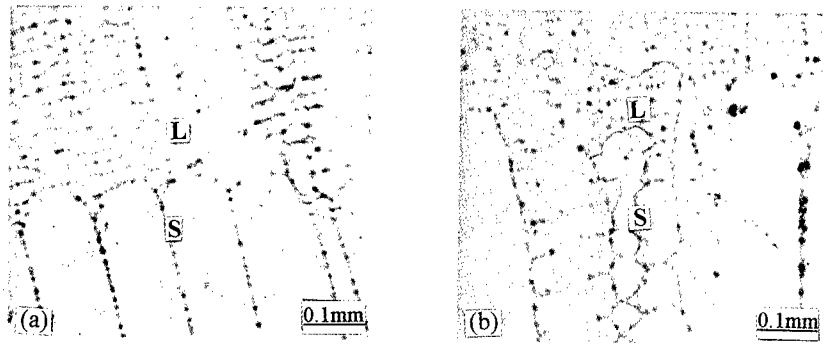


Fig.3: The S/L interface of Cu-0.8wt.%Cr alloy during directional solidification
(a) planar (b) dendritic

Properties

The mechanical property of the directionally solidified Cu-Cr alloy is shown in Table I. It can be seen that, the tensile strength, and the elongation especially, are improved to a varying content, as compared with the conventional casting ones.

Table I The Mechanical Property of the Directionally Solidified Cu-Cr Alloy

Content(Cr, wt%)	G_L(℃/cm)	V(μm/sec)	UTS, σ_b(MPa)	Elongation, δ(%)
0.69	60	22	293	29.3
1.00	60	100	363	12.0
1.42	60	53	431	9.3

The fracture morphologies also prove the reason for these results, as shown in Fig.4. From Fig.4(a), the casting alloy show a apparent crystal-interface-along fracture characteristic, while the directionally solidified one take on ductile fracture morphology as in Fig.4(b).

Restricted by the small size of the sample, the two-probe method used broadly in determination of the electrical conductivity for semiconductors, was ever employed to measure the conductivity of the researched copper samples. An anisotropy exists in the conductivity of the samples solidified directionally and the values of conductivity approximate to that of the pure copper sample. How-ever, the measured results are divergent relatively. More accurate measurement can be made on accomplishment of continuous casting.

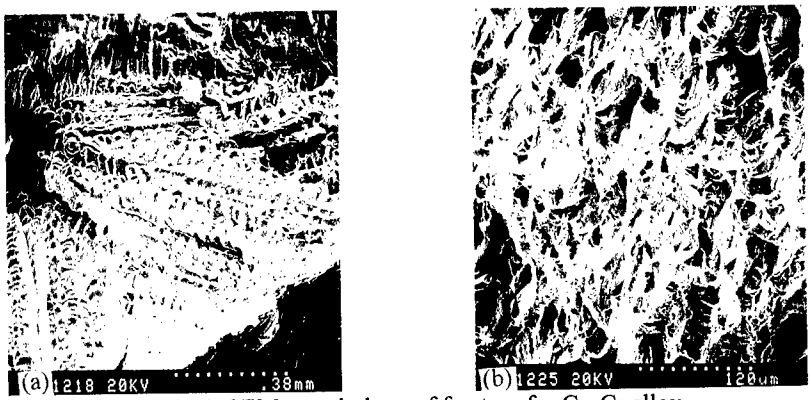


Fig.4: SEM morphology of fracture for Cu-Cr alloy
(a) casting (b) directional solidification

Continuous Casting

Continuous casting is a necessary process for production of the electric cable. For production of the in-situ composite cable, the solidification processing means simultaneously to form and to maintain the directionally and alternatively aligned microstructure in the copper wire. A special continuous casting apparatus for this destination has been set up in laboratory, as shown in Fig5, which is developed from the O.C.C. method[5]. There are two keys in the apparatus. One is how to form a proper temperature field at the heating mold, and another is how to maintain it stable during the continuous casting. Experimental results showed that there are seven effecting

factors upon the solidification process at least: 1)heating mold temperature; 2)crucible temperature; 3)piston temperature 4)flux quantity of cooling water; 5)flux quantity of nitrogen air; 6)drawing velocity; 7)melt level. Any variation in these factors will affect the shaping or internal microstructure of the contact cable. Therefore, all the parameters are managed by a microcomputer.

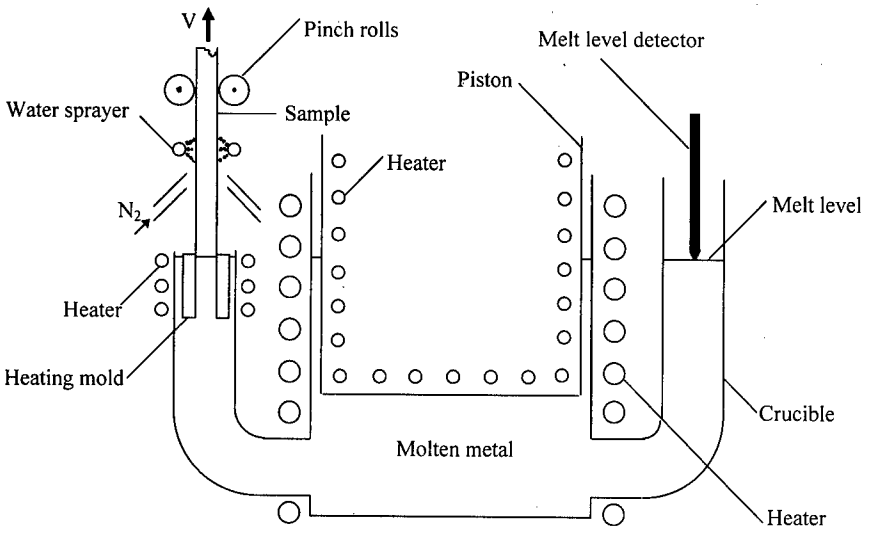


Fig.5: Schematic illustration of the continuous casting apparatus for in-situ composite cable

Conclusions

For the contact cable, a Cu-Cr in-situ composites, prepared by the unidirectional solidification, was proposed in the paper. The primary experimental and analytical results showed the technical route is essentially feasible.

References

1. Jong Wu, Guanqiu Shen, Electric Material and Its Application (Xi'an: Shaanxi Sci. Tech. Press, 1983), 38-43.

2. Chuankun Wan, "Progress of Researches on High-strength High-conductivity Copper Alloys," Materials Review, 2(1993), 23-27.

3. Weihe et al., "Development of Copper-Steel Cable," Wire and Cable, 5(1993) 13-17.

4. Mitsubishi Corporation, "Copper Alloy for Railway Transmission Cables from Mitsubishi Materials," Nonferrous Metals Alert, 8(1992), 2.

5. A. Ohno, "A Method of Continuous Casting," UK Patent Application, No. GB2132925A, 1984.

EFFECT OF PROCESS CONDITIONS ON TEXTURE AND PROPERTIES OF IF STEEL SHEET

Kong Bingyu, Mi Xiaochuan
Iron & Steel Research Institute
Baoshan Iron & Steel Corporation
Baoshan District, Shanghai, 201900, China

Abstract

The effects of cold-rolled reduction and annealing condition on the recrystallization texture and properties of IF steel sheet were studied. It was found that the cold rolled reductions obviously effected recrystallization texture of If steel sheet. The higher the cold rolled reduction is, the sharper the γ -fibre texture of IF steel sheet. It is recommended that the cold rolled reduction was taken up as high as possible for producing IF steel sheet in industrial production.

The effect of soaking temperature on the recrystallization texture and r_m value of IF steel sheet was obvious. With increasing of soaking temperature, the γ -fibre texture developed and r_m value increased. So, high recrystallization annealing temperature in continuous annealing process is obviously effective for increasing r_m value of IF steel sheet. However, it must be attended when soaking temperature was higher than Ac3, the density of γ -fibre texture decreased obviously and the unfavorable texture component <001>//ND increased, which resulted in decreasing of the r_m value of IF steel sheet immensely.

The Third Pacific Rim International Conference on
Advanced Materials and Processing (PRICM 3)
Edited by M.A. Imam, R. DeNale, S. Hanada,
Z. Zhong and D.N. Lee
The Minerals, Metals & Materials Society, 1998

Introduction

IF steel sheets bearing Ti and/or Nb are characterized by superior formability and non-aging properties. The main use of IF steel is for automotive panels. Customers have demanded super formable steel sheets which are suitable for one-body pressforming parts and oilpans with complicated shapes[1]. It's known that the drawing formability is in close relationship with recrystallization texture of IF steel sheet. The composition and production process have a decisive effect on forming and developing the textures of IF steel sheet.

Two aspects are mainly discussed in the paper, that is, the effect of cold-rolled reduction on recrystallization texture and properties, and the effect of soaking temperature of continuous annealing on recrystallization texture of IF steel sheet.

In order to work correctly out the process parameters of production, it is necessary to provide believable theoretical foundation.

Experiment

The samples of IF steel sheet were taken from Bao Steel's cold rolling strip mill, and the cold rolled reductions were 50%, 60%, 70% and 80% respectively. In order to study the effect of cold rolled reductions on the recrystallization texture and properties of IF steel sheet, a box furnace with nitrogen as shield gas was used for recrystallized annealing (830 ℃ x 60s, cooling rate was about 20 ℃/s). The cold rolled steel sheet (thickness: 0.8mm, CR.: 80%) was heated at different temperatures (640, 700, 760, 800, 840, 870 and 910 ℃) in a given soaking time (60s) to research the effect of annealing conditions on the recrystallization texture and properties of IF steel sheet.

The annealed steel sheets were machined into JIS No.5 specimens. The plastic anisotropy ratio, r-value of longitudinal (0 °), diagonal (45 °), and transverse (90 °) to the rolling direction were measured after prestraining 15% by using a mechanical testing machine, and the the mean r-value was calculated according to the formula:

$$r_m = (r_L + 2r_D + r_T) / 4 \qquad (1)$$

The texture measurement was carried out by a X-ray diffractometer. The {200}, {110}, {211} pole figures were measured at the central layer of the specimen. The orientation distribution functions (ODF) were calculated with the two-step method by using the data from three pole figures[2].

Results and Discussion

Effect of Cold Rolled Reductions on Recrystallizasion Texture and Properties of IF Steel Sheet

Figure 1 a) and b) show the recrystallization texture of IF steel sheet after annealing at different

cold-rolled reductions. All of α-fibre textures are principally the same with different cold reductions, while the {111}<110> texture is the strongest. The average orientation density of γ-fibre texture is 8.5 at 50% CR. and 12.1 at 80% CR., and the density of {111}<112> increases from 9.2 at 50% CR. to 14 at 80% CR. rapidly.

Reference [3] shows that the nucleation of recrystallization is relative to orientation density of rolled texture component and deforming stored energy of cold rolled microstructure. The nucleation probability will be the largest for grains having high deforming stored energy and

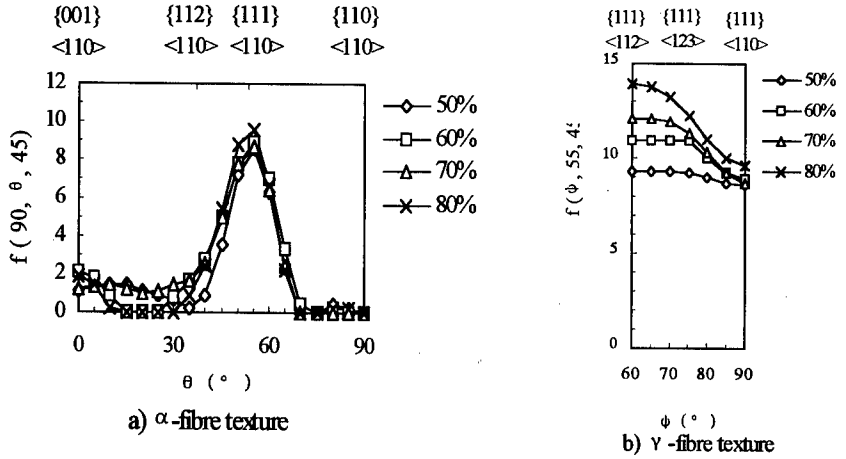


Figure 1. Effect of cold-rolled reduction on recrystallization texture of If steel

orientation densities of rolled texture components. The density of {111} orientation grains is large and the sequence of deforming stored energy is {111}>{112}>{110}>{100}. So, {111} grains prefer nucleation to others. New {111} grains nucleate and grow over and over, and form the strong {111} orientation grains finally. At the same time, the {111} grains nucleate and grow, α-fibre texture continues to rotate some angles around <110> axis [3], forming γ-fibre texture with <111>//ND, so that very strong γ-fibre texture forms after recrystallization annealing of IF steel sheet.

Table 1. The mechanical properties of IF steel at various cold-rolled reductions

CR. Reduction (%)	YS (Mpa)	TS (Mpa)	EL (%)	n	r_m
50	102	294	51	0.292	1.53
60	94	285	52	0.295	1.84
70	99	292	49	0.298	2.02
80	98	298	51	0.300	2.18

Taking large cold rolled reduction, the grains distort seriously in the deformed matrix, and the density of dislocation and deforming stored energy rise. All of these provide moving energy for

{111} grains nucleation and strong γ-fibre texture comes from α-fibre texture by grains rotation. It is of benefit to increase mean r-value of IF steel sheet. Effect of cold rolled reduction on mechanical properties of If steel sheet is shown in Table 1. YS, TS, El% and n-value change scarcely, but r-value increases remarkably with the enhancement of the reduction.

Effect of Annealing Temperatures on Recrystallization Texture and Properties of IF Steel Sheet

Figure 2 a) and b) show the change of α and γ-fibre textures in IF steel sheet with temperatures at same soaking time: (60s). The influence of temperatures on volume fraction of the grains with {111} and {001} orientation and mean r-value is shown in Figure 3. Table 2 shows the change of properties of IF steel sheet with temperatures.

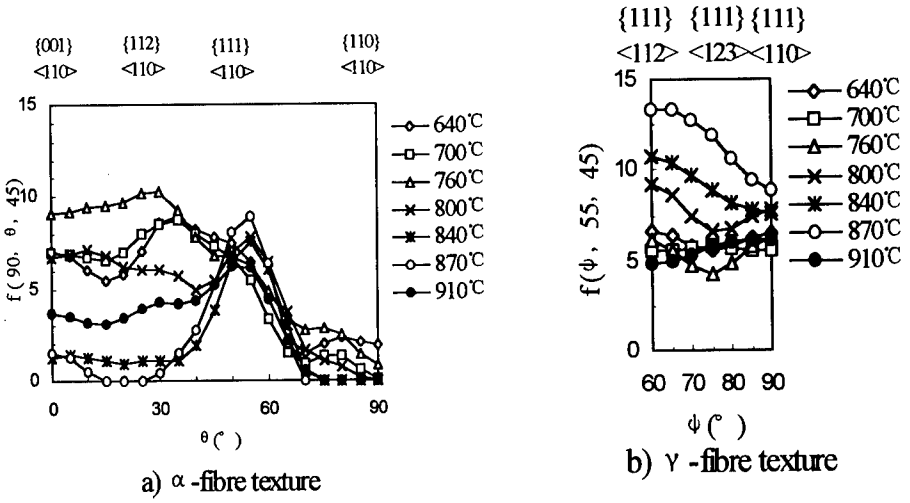
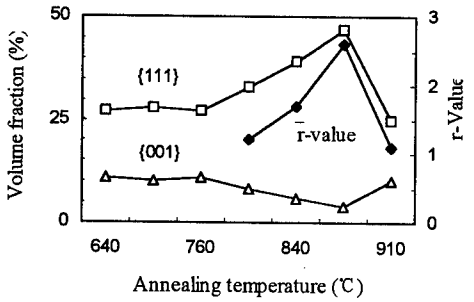


Figure 2. Textures of IF steel at various annealing temperatures (60s)

Figure 2 a) and b) show that when the temperature is lower than 800 ℃, the stronger α-fibre texture is still presented. Increasing temperature, the densities of {001}~{112}<110> orientation decrease, and the density of γ-fibre texture increases obviously. When the temperature is up to 870 ℃, the densities of {114}~{112}<110> texture decrease to a minimum. Oppositeily, the mean density of γ-fibre texture increases to a maximum, in which the main texture {111}<112> component develops to 13.2. When the temperature is up to 910 ℃, the densities of α-fibre texture increase, and the density of γ-fibre texture decreases obviously.
It's known from Figure 3, when the temperature is below 760 ℃, the volume fractions of grains with {111} and {001} orientation change slightly. When the temperature is higher than 760 ℃, the volume fractions of grains with {111} orientation increase, {001} orientation decreases with increasing temperature. When the temperature is up to 870 ℃, the volume fraction of the grains with {111} orientation increases to a maximum while the {001} decreases to a minimum. When temperature rises to 910 ℃, the volume fraction with {111} orientation

grains drops to a minimum while that of the grains with {001} rises up to a maximum. The change in mean r-value is nearly similar to the variation of volume fraction of grains with {111} orientation.

Table 2 shows that the mean r-value, El% of IF steel sheet increase, but YS, TS decrease slightly with increasing temperature. When the temperature is higher than 840 ℃, YS, TS, El% and n-value do not change basically, but mean r-value remarkably increases.



Firure 3. Effect of annealing temperatures on volume fraction of {111} and {001} grains

During annealing process, the {111} oriented grains nucleate and finally form the strong γ-fibre texture by the moving of big angle grain boundary, swallowing up the other oriented grains and rotating round <110> axis of rolling texture. The temperature directly supplies the energy for moving big angle grain boundary and rotating grain. When the temperature is above 910 ℃, the microstructure of IF steel austenizes completely, {001} and {110} oriented grains preferably nucleate and grow. Furthermore, these grains incessantly swallow up {111} oriented grains, and result in the decreasing of

Table2. Effect of annealing conditions on mechanical properties of IF steel

No.	annealing condition		mechanical properties					
	Temp.(℃)	time (s)	YS (MPa)	TS (MPa)	YS/TS	EL (%)	n	r_m
1	760	60	282	369	0.76	23	0.130	unmeasuring
2	800	60	153	312	0.49	45	0.249	1.19
3	840	69	125	285	0.44	51	0.290	1.9
4	870	60	112	270	0.41	53	0.282	2.65

{111} oriented grains obviously, {001} oriented grains possessed main proportion, and result in the decreasing of mean r-value. In annealing process, higher than Ac3 temperature must be avoided to the IF steel.

Conclusions

1. The cold rolled reductions obviously effect recrystallization texture of IF steel sheet. The higher the cold rolled reduction is, the sharper γ -fibre texture of IF steel sheet. It is generally established that deep drawability of IF steel sheet improves with increasing of cold rolled reductions. It is recommended that the cold rolled reductions are taken up as higher as possible for producing IF steel sheet in industrial production.
2. The effect of soaking temperature on the recrystallization texture and r_m value of IF steel sheet is obvious. With increasing soaking temperature, the γ -fibre texture developed and r_m value increased. So, high recrystallization soaking temperature in continuous annealing process is obviously effective for increasing r_m value of IF steel sheet.
3. It is preferable to take up continuous annealing process for producing IF steel sheet, but it is necessary to strictly control the temperature below Ac3.

References

1. Kohsaku Ushioda, "Application of Ultra Low-carbon Steels to the Development of Superformable Sheet Steels, Solution-haedened High Strength Sheet Steels and Bake-hardenable Sheet Steels" (Paper presented at the International Forum for Physical Metallurgy of IF Steels, Tokyo, Japan, 1994),227.
2. Z.D. Liang et al., Method of Orientation Distribution Function in Texture Materials (Shengyang, Northeast University Publishing Company, 1986),108-110.
3. T. Urabe, "Modeling Formation of Recrystallization Texture in Ti and Nb Bearing Ultra Low-carbon Steel," CAMP-ISIJ, 7 (1994).

A NEW DEVELOPMENT OF IMPROVING GRAIN ORIENTED SILICON STEEL WITH THE LLSA METHOD ※

Fengjiu Sun,Xingjie Peng,Chuanjun Li

Dept.of Physics,Northeastern University,Shengyang 110006,P.R.China

Abstract

For reducing the core loss of grain oriented silicon steel several refining domain techniques have developed, in which the laser scribing method [LS] is a more effective one. However the refining domain effect of the laser scribing on grain oriented silicon steel sheets has no enough temperature stability, and hence the technique is limited in uses of the temperature range lower than 200 ℃. As improvement of the LS, a new laser approach to optimizing domain distribution of grain oriented silicon steel, which is called the localized laser surface alloying method [LLSA], has been investigated in our recent work. In this paper we present the work on the LLSA experiment of using Sb as the alloying element, which is called the SLLSA method. The results show that using this laser approach can not only reduce the core loss of grain oriented silicon steel but also enhance the temperature stability of refining domain effect. The reason is stable sub-grain-boundaries formed due to the SLLSA can effectively and stably optimize domain distribution of grain oriented silicon steel.

※ Supported by The NNSF of China.

The Third Pacific Rim International Conference on
Advanced Materials and Processing (PRICM 3)
Edited by M.A. Imam, R. DeNale, S. Hanada,
Z. Zhong and D.N. Lee
The Minerals, Metals & Materials Society, 1998

Introduction

Since the needs of electric power industry development and for lack of energy source, to manufacture soft magnetic materials of quality has always been a very important task. The invention of grain oriented silicon steel brought great benefit to save energy. But there is a need for further improving its properties, especially reducing its core loss. Besides metallurgical method, many post treatment techniques for reducing the core loss of grain oriented silicon steel developed, such as the mechanic scribing method, the electric discharge method, and the laser scribing method. The reasons of reducing the core loss of grain oriented silicon steel sheets by using these methods all are due to the effect of refining main domain width. Among these the laser scribing method[LS][1,2,3] is the most convenient and effective one. However the refining domain effect of the scribing on grain oriented silicon steel sheets has no enough temperature stability, so the technique is limited in uses of the temperature range lower than about 200 ℃, i.e. while grain oriented silicon steel sheets after the LS treatment are in use at higher temperature, the aging property is getting worse. In order to solve the problem, we have suggested the LLSA method[4,5]. A new laser approach --the localized laser surface alloying method by using solid state alloying element Sb(SLLSA), as an improvement of the LS is presented in the present work. In this paper, we are going to give some explanation on reducing the core loss of grain oriented silicon steel with refining domain technique, and the basic idea of the new laser approach--SLLSA. Then we report the experiment result of using Sb as the alloying element, and give some discussions.

Basic Idea of The SLLSA

According to the domain and reverse magnetization core model[3], the formula representing the core loss of Goss texture grain oriented silicon steel was given as follows,

$$P_t = P_e + P_h = Ad + B / d^2, \quad (1)$$

or

$$P_t = P_e + P_h = A'L^{1/2} + B' / L, \quad (2)$$

here P_t is the core loss; P_e is the eddy current loss, including the classical eddy current loss P_{cc} and the extreme eddy current loss P_{ex} that is the main part of P_e in grain oriented silicon steel; P_h is hysteresis loss, A、B、A′ and B′ are constants relating to applied frequency, structure and property of silicon steel sheet material; d is the weighted average of 180^0 domain width; L is the mean grain length along the rolling direction. By use of Eq.(1) or Eq.(2) the general form of the core loss characteristic curve is quantitatively obtained as shown in Fig.1. When $L=L_0$ or $d=d_0$, P_t reaches the minimum. In general for grain oriented silicon steel sheets $L>L_0$ or $d>d_0$, if making $L\rightarrow L_0$ or $d\rightarrow d_0$, we can reach at the aim of reducing the core loss of grain oriented silicon steel. This is the reason of reducing the core loss of grain oriented silicon steel with refining domain technique.

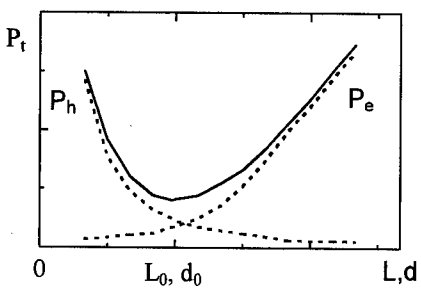


Fig.1 Scheme of core loss characteristic curve

For the LS method, refining grain and hence refining domain width is realized by those local narrow thermal stress regions, so called 'sub-grain boundaries', formed at the laser scribing regions. Fig.2 shows the statistical result of the relation between the number of grains and mean

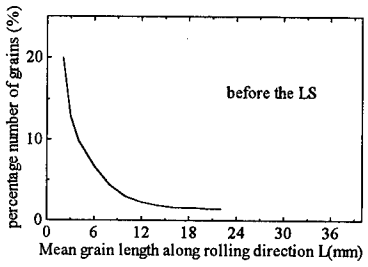


Fig.2(a) A typical distribution curve of grains

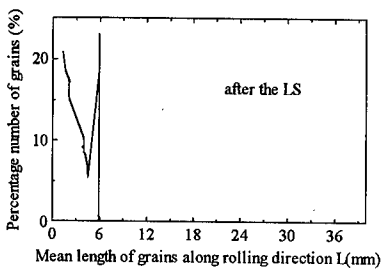


Fig.2(b) A typical distribution curve of grains

grain length for Z8 samples before and after the LS treatment. Obviously, if those sub-grain-boundaries formed by the LS were stable during and after high temperature treatment, then the aging property of grain oriented silicon steel sheets after the LS would be well. But in fact it is not so. After some high temperature annealing, the sub-grain-boundaries will disappear and annealing, the domain distribution will be restored to the original state. Hence, for realizing both reducing the core loss and improving the aging property of grain oriented silicon steel, the key point is to get stable sub-grain-boundaries on grain oriented silicon steel sheets, besides to select suitable line spacing of laser scan. To aim at this work, we use localized laser surface alloying

technique to introduce the alloying element Sb into the bulk of grain oriented silicon steel sheets and form new, stable, and narrow alloying regions instead of the thermal stress regions, i.e. sub-grain-boundaries formed by the LS. This is the basic idea of the SLLSA.

Experimental

Experimental Equipment

A set of CW-CO_2 laser, which output can be adjustable within 0—450W, wavelength is 10.6μm, and the laser beam can be focused into about 0.15mm, was prepared for the SLLSA experiment. A microcomputer was used to control the focused laser beam scanning on a working platform at which silicon steel samples were situated. The laser beam scanning path on surface of the samples was perpendicular to the rolling direction. Scanning speed and line spacing should be chosen according to characteristic of the samples and grain length distribution (the choosing method was given in our previous paper [6]), in the present study they were chosen to be 10mm/sec and 6mm respectively. A set of vacuum furnace with a temperature controller was utilized to undertake aging property experiment of the grain oriented silicon steel samples. A single sheet tester was used for the measurement of core loss of the SLLSA silicon steel samples.

Samples

Goss tixture 3% Si grain oriented silicon steel sheets, which had a [001] axis in the rolling direction and a (110) plane nearly parallel to the surface, were provided as experimental samples. After being cut off in size of 300mm×30mm×0.30mm for single sheet test and removed coating, the experiment silicon steel samples were annealed at 800 ℃ for 3 hours in the vacuum furnace and cooled for stress relief.

Alloying Element

In this SLLSA experiment Sb was chosen as the alloying element. The reason of choosing the element is as follow: (1) Sb powder is a cheap material in China; (2) It has been used as a permeation one in improving the aging property of grain oriented silicon steel after the laser scribing before; (3) Sb has a lower melting point (630.7 ℃), and a higher solid solubility with Fe, so that it may be easy to form an alloy with silicon steel bulk;(4) The Sb-Fe alloy has high temperature stability.

Procedure

The samples were evenly and thinly coated with the alloying element Sb powder, then set on the laser working platform and scanned by the focused laser beam with an equal line spacing perpendicularly to the rolling direction in order to realize the SLLSA treatment. Before and after the SLLSA, the core loss $P_{17/50}$ and induction B_{10} of the samples were measured by single sheet tester and structures of grain and domain were observed by using the ferromagnetic colloid technique. To investigate the aging property of the SLLSA samples, annealing experiments were gone at different temperatures.

Results and Discussion

The Core Loss and Aging Property

To aim at the purpose of inspecting the core loss and aging property of the samples after the LS and after the LLSA, annealing experiments for 3 hours at different temperatures were carried out .The relationship between the core loss $P_{17/50}$ and the annealing temperature, i.e. the aging property curve, is shown in Fig. 3 and Fig. 4, which indicate the results for the LS and the SLLSA with the alloying element Sb respectively.

Comparison of The LS and The SLLSA

From Fig.4, the core loss of grain oriented silicon steel sheets of the LS treatment had no obvious increase at the temperature range from the room temperature to about 200 ℃, but at higher annealing temperature it increased very fast, and finally reached its original value of before the LS treatment. This experiment result indicates the LS technique is limited in uses of the temperature range lower than 200 ℃.

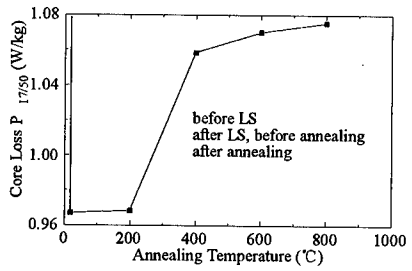


Fig.3 Aging property curve of the LS samples

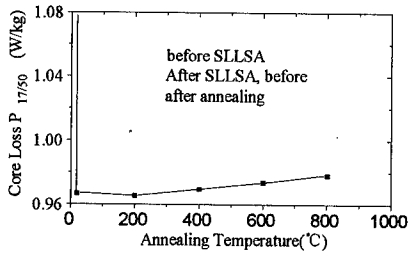


Fig.4 Aging property curve of the SLLSA samples

From Fig.5, the core loss of the SLLSA samples almost had no variation with increasing annealing temperature to 200 ℃, then slowly increased. And up to 800 ℃ the percent core loss reduction of $P_{17/50}$ was 9.3 %.Comparing Fig.5 with Fig.4, we consider the SLLSA technique does can well solve the problem of poor aging property of the LS technique.

Conclusion

1. The SLLSA technique, as a new laser approach to optimizing domain distribution of grain oriented silicon steel, is rather effective in improving properties of grain oriented silicon steel.
2. It is confirmed that under proper conditions (inducing laser parameters, scan speed, and line spacing), using the SLLSA technique, not only we can reduce the core loss of grain oriented silicon steel, but also improve its aging property. When the annealing temperature reached 800 ℃ for 3 hours, the percent core loss $P_{17/50}$ of the SLLSA samples still had 9.3% reduction relative to the original state before the SLLSA treatment. Obviously this is a very good result.
3. According to the experiment results, choosing Sb as the alloying element for the SLLSA experiment is successful to realize the SLLSA of grain oriented silicon steel.

References

1. T.Ichiet, S.Yamaguchi,and T.ichiyama, " Laser Processing for Reducing Core Loss of Grain Oriented Silicon Steel," J.Appl.Phys,53(3)(1982),2410-2412.

2. G.C.Rauch,and R.F.Krause, " Effect of Beam Dwell Time on Surface Changes during Laser Scribing," J.Appl.Phys,.57(1)(1985),4209-4211.

3. F.J.Sun et al, " Theoretical Model of Optimum Domain Control and Determination of Laser Scribing Line Spacing " (Paper presented at the 4th APPC,Seoul,13 Aug,1990),1457.

4. F.J.Sun et al, " A Study on Localized Laser Surface Alloying of Grain Oriented Silicon Steel " (Paper presented at the 2nd PRICM, Kyongju,18 June1995),613.

5. F.J.Sun et al, " The LLSA Method for Treatment of 3% Silicon Steel " (Paper presented at the 1st ISMI,Anshan,28 May 1996),55.

6. F.J.Sun et al, " The Mechanism of Using Laser Scribing to Reduce The Core Loss of Oriented Silicon Steel " (Paper presented at the 1stISMI, Anshan,28 May 1996),92.

ND Steel--High Resistance to Sulfur Dewpoint Corrosion

Zheng Wenlong Wang Rongguang
Shanghai Research Institute of Material
99 Handan Road Shanghai, 200437, P.R.China

Abstract

ND steel is a low alloy steel and has been proved to have high resistance to sulfur dewpoint corrosion compared with other steels such as mild steel, Corten, CR1A and Sten steels. The corrosion rate of ND steel (produced in batch) is lower than 10mg/cm^2.hr by submerging in 50% H_2SO_4 at 70℃ for 6 hours. Under an enclosed sulfur flue of oil refinery, the service life of economizer made of mild steel (20g) was three weeks, but that made of ND steel is over four years. ND steel not only has high corrosion resistance, but also has higher mechanical properties than mild steel. σ_s and σ_b almost keep constant from room temperature to 500℃.

ND steel also can be used in environment containing SO_4^{2-} and Cl^-, such as heat exchanger in oil field and refinery. The corrosion behavior and mechanism of ND steel were discussed.

The Third Pacific Rim International Conference on
Advanced Materials and Processing (PRICM 3)
Edited by M.A. Imam, R. DeNale, S. Hanada,
Z. Zhong and D.N. Lee
The Minerals, Metals & Materials Society, 1998

Introduction

Heavy oil and coal are universal fuels in oil refineries and power plans. Sulfur dewpoint corrosion occurs during the cooling process in an enclosed sulfur flue, such as an economizer or air-preheater, and chimney made of mild steel would suffer serious corrosion when operating under such as conditions at a temperature lower than dewpoint of sulfuric acid. The service life of the parts in energy supply system was very short, for insistence, the longest service life of economizer made of mild steel (20g) in Jinan oil refinery was only 62 days (Table I)[1] The flue gas in operating condition contains SO_2, SO_3, CO, H_2S, etc. (Table II)[1]. A air-preheater made of same carbon steel (20g) having a wall thickness of 3 mm became useless after only 30 days when the ambient temperature was lower than 10℃.

Table I: Service Life Economizer in Jinan Oil Refinery[1]

Operation period	Service life (days)	Steel
Dec. 1998 ~ Apr. 1989	21	mild steel (20g)
May 1989 ~ Apr. 1990	18	mild steel (20g)
May 1990 ~ Nov. 1990	12	mild steel (20g)
Nov. 1990 ~ Apr. 1991	62	mild steel (20g)
May 1991 ~ Apr. 1992	22	mild steel (20g)
May 1992 ~ Dec. 1997	>1600	ND steel

Table II: Flue Gas Composition of The Economizer in Jinan

O_2 /%	CO_2 /%	N / mg/l	H_2O /%	SO_2 / mg/l	H_2S / mg/l	SO_3 / mg/l
7.0	11.5	1365	9.5	300	13.5	103

The sulfur dewpoint of the flue gas varies between 140 ℃ and 240 ℃ and the concentration of liquid sulfur changes from 0 to 93% when the vapor content reaches 10%. As a general rule, the corrosion rate of mild steel observed was over 5 mm/a. There are many low copper steels, such as 09CuSn, 09CuWSn, 10CrNiCuP, CR1A, Sten steels etc., that have good resistance to sulfur dewpoint corrosion, but a new kind of low alloy steel (named ND steel) containing Cr, Cu, Sb, Ti etc. has been developed in 1990. The practice experiences get from oil refineries in Jinan, Shanghai, Dalin etc. confirm that the service life is more than 10 to 30 times longer than that of a mild steel. The typical sample is economizer in Jinan oil refinery which has been used for 4 years since 1992 under the same operating condition. The corrosion rate is lower than 1mm/a, but it was higher than 12mm/a for mild steels , and others also have been used for 2 years safely. It means that ND steel has a high resistance to sulfur dewpoint corrosion.

The Properties of ND Steel

ND steel is a low alloy steel, the chemical composition range is shown on the Table III. It should be indicated that the effective composition range is narrow for producing ND steel up to standard. The products of ND steel were annealed at 890℃ for two hours followed by cooling in air. The mechanical properties are comparable with mild steel (Table IV), but the strength of ND steel is higher than that of mild steel from room temperature to 500℃ (Figure I), and also have enough elongation (Table IV).

Table III: Chemical Composition of ND Steel (wt.%)

C	Mn	Si	S	P	Cr	Cu	Ti	Sb	Ni	Mo	B
=0.10	0.35~ 0.65	0.25~ 0.35	=0.035	=0.035	0.80~ 1.20	0.25~ 0.45	=0.10	=0.10	<0.10	<0.10	<0.10

Table IV: Mechanical Properties of ND Steel

Grade /mm	σ_s /MPa	σ_b /MPa	δ_5 /%	Bend 180° (d=0)
δ<30	≥245	395~535	≥28	no creak

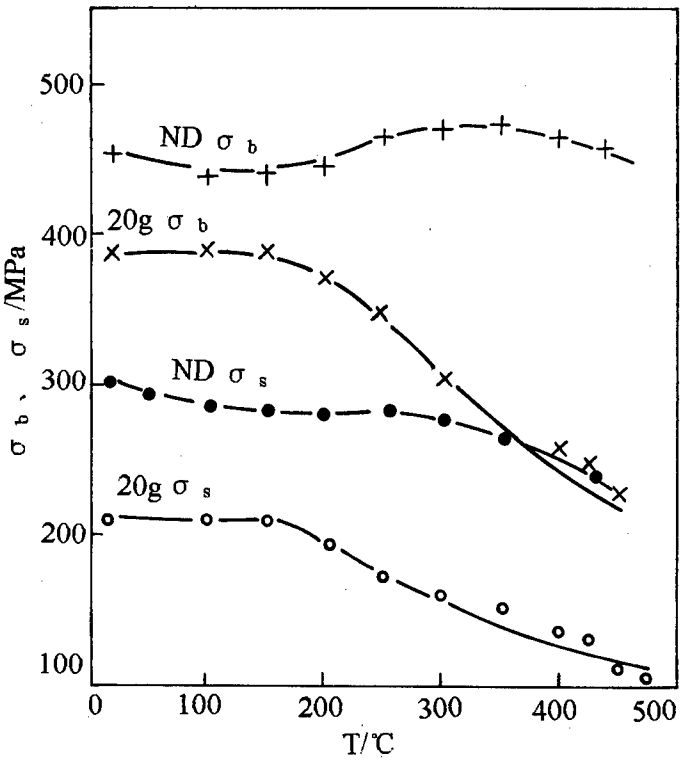


Figure I: Strength of ND Steel at Various Temperature
Comparing with Mild Steel (20g)

The most important property of ND steel is high corrosion resistance to sulfur dewpoint corrosion, which was evaluated by submerging samples in 50% H_2SO_4 at 70℃ for 6 hours , and comparing the laboratory test results with mild steel, Corten, Sten, CR1A, AISI 321 (Table V).

Table V: Corrosion Rate of Steels in 50% H_2SO_4 at 70℃ for 6 Hours

Steel	ND	A3	Corten	CR1A	AIBI 321	Sten	20g	rate
Corrosion Rate /mg.cm^{-2}.h^{-1}	7.3	103.5	63.0	13.4	21.7	27.4	56.4	average for 3 samples
normalization	1	14.1	8.63	1.84	2.97	3.75	7.73	

ND steel also had higher corrosion resistance to chromium solution or $Cl^-+SO_4^{2-}$ solutions than that of mild steel (Figure II). For insistence, a heatexchanger suffered serious corrosion under the condition inside with 85~98% H_2SO_4 at 110℃, outside with 3.5% NaCl at ambient temperature. The service life of heatexchanger made of mild steel was one or two months, but now that made of ND steel has been operated over two years. ND steel had good weldability not only welding ND steel, but also with other steels such as mild steel (20g) and low alloy steels (16MnR) etc. by arc welding or inert-gas protection welding. The weld bead had an equivalent mechanical properties and corrosion resistance to the matrix (Table VI).

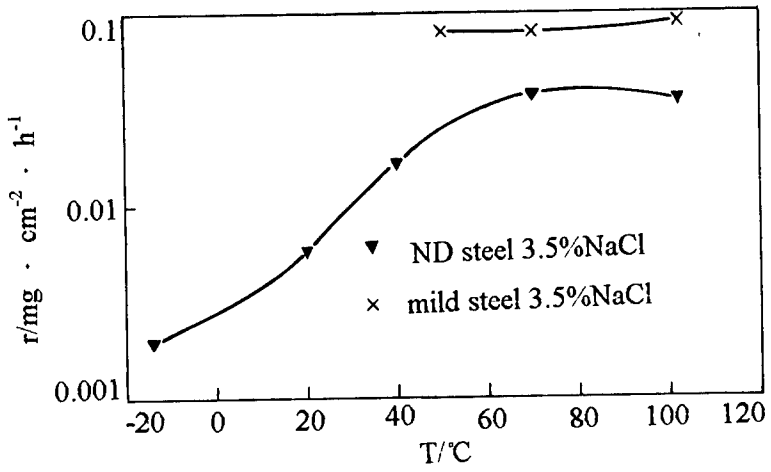


Figure II: Corrosion Rate of ND Steel in Solution with 3.5% NaCl and Comparing with Mild Steel (20g)

Table VI: Corrosion Rate of ND Weld Bead by Compared with Matrix

Test condition	30℃ 20% H_2SO_4 ×6hr		40℃ 40% H_2SO_4 ×6hr		90℃ 65% H_2SO_4 ×6hr	
Corrosion rate	bead	matrix	bead	matrix	bead	matrix
/mg.cm^{-2}.hr^{-1}	0.46	0.45	1.76	1.70	2.13	2.24

Corrosion Behavior and Mechanism of ND steel

Carbon steels, low alloy steels, even stainless steels have high corrosion rate in sulfuric acid solution, especially in low concentration and at high temperature. Sulfur dewpoint corrosion is a special form of general corrosion in which the concentration of sulfuric acid and temperature are changing. Dr. M.Kowaka[2] and Dr. H.Nagano[3] have indicated that there are three stages in the overall corrosion process: The first stage involves an actives state on the surface of mild steels, where the concentration of sulfuric acid (<30% H_2SO_4) and the temperature (<60℃) are both low, the corrosion rate is increasing sharply, but the period of corrosion is short. In the second stage, the sulfuric acid concentration and temperature are increasing, but a balanced and stable state is achieved ($H_2SO4\approx85\%$, T≈160℃). The corrosion rate is decreased, but constant and still high for mild steels, because it involves an active state. The concentration of H_2SO_4 and temperature in third stage are similar the second stage, but

corrosion product on the surface contains unburned carbon powder and Fe^{3+} ions and the corrosion rate shows no obvious change.

Figure III. shows the corrosion rate of ND steel in solutions with various concentration of H_2SO_4 and at different temperature. There is a peak of corrosion rate of ND steel in 50% H_2SO_4 solution at 70℃ which is a suitable test condition for laboratory.

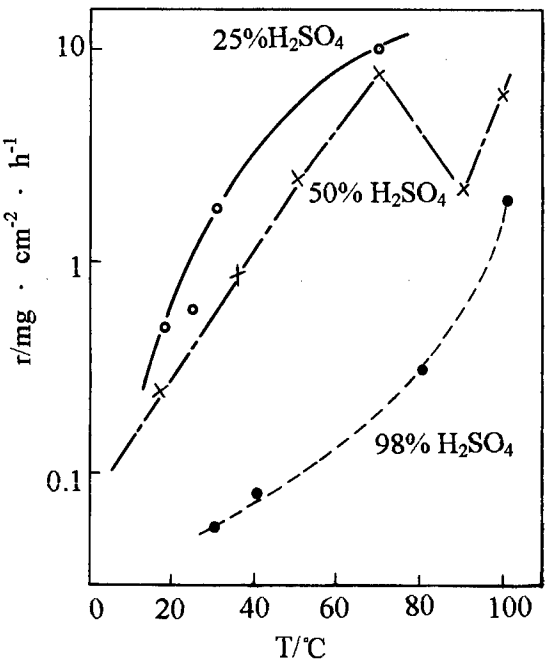


Figure III: Corrosion Rate of ND Steel in H_2SO_4 Solutions at Various Temperature

It is well known that copper and Chromium have good resistance to corrosion of sulfuric acid, It can be find that the passive film formed on the surface after immersion in sulfuric acid, and maintained low corrosion rate. Antimony , Titanium and other elements also served a useful function in enrichment of Copper and Chromium in the passive film in three stages, which causes the corrosion potential (E_c) to move into the positive region, and simultaneously produce a reduction in current density (I_c) (Figure IV). This confers on ND steel its higher resistance to sulfur dewpoint corrosion than other steels.

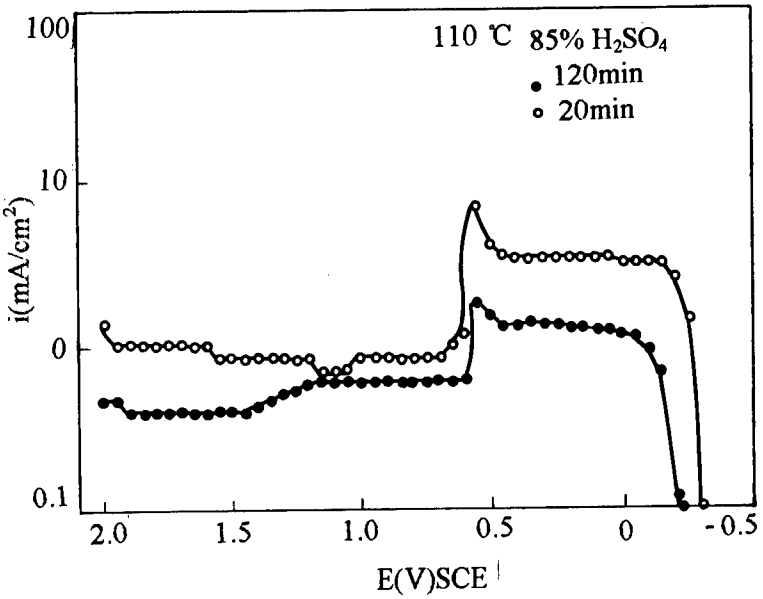


Figure IV: Polarization Cures for ND Steel in 85% H_2SO_4 at 110℃ After Submerging for Different Times

Conclusion

1. ND steel not only has a high resistance to sulfur dewpoint corrosion, but also has higher resistance to the environment with Cl^- or $Cl^-+SO_4^{2-}$ than mild steel;

2. ND steel has higher mechanical properties than mild steels from ambient temperature to 500℃;

3. A thin coherent film forms on the surface of the ND steel during rolling and early corrosion;

4. As corrosion proceeds, the corrosion potential (E_c) of the ND steel moves into the passive region and results in a decrease in I_c due to passivation.

Reference

[1]. Qu Yumin, Lian Ming,"Application of The Newly Developed ND steel in Jinan Oil Refinery to Resist Sulfur Dewpiont Corrosion",Petrochemical Corrosion and Protection, 11(4)(1994), 28-31.

[2]. Masamichi Kowaka, Hiroo Nagano, "The Mechanism of Sulfur Dewpiont Corrosion", J. of the Japan Institute of Metals, 23 (1971),273-277.

[3]. Hiroo Nagano, "Sulfur Dewpiont Corrosion", Corrosion Engineering, 26 (1977), 731-740.

HIGH STRENGTH NICKEL-FREE DUPLEX STAINLESS STEELS FOR STRUCTURAL ENGINEERING APPLICATIONS

J. Wang, M.O. Speidel, and Peter J. Uggowitzer

Institute of Metallurgy, ETH-Zentrum,
CH-8092 Zürich, Switzerland

Abstract

The cost for the maintenance and repair of concrete structures has become an important aspect of the economy of industrial countries. Corrosion of the reinforcing steel is the main cause for deterioration of structures in reinforced concrete, where chlorides are present on highways or bridges from de-icing salt or in a marine environment. Traditionally stainless steels have moderate mechanical properties and are too expensive to use in competition with standard structural steels (carbon and low alloying steels). The development and use of duplex stainless steels (DSS) with 1-2 times stronger and about half cost to austenitic stainless steels are increasingly interesting to manufacturers and users.

DSS with high content of nitrogen have several advantages. For example, higher strength and corrosion resistance, more stable austenite in high temperatures as well as lower cost due to saving the expensive alloying element nickel. With nickel-free DSS a new group of cheap duplex stainless steels was invented. In these alloys nickel is completely replaced by nitrogen.

Nickel-free DSS are not only intended to be cheap but also to have superior mechanical and corrosion properties: they could find applications where high strength and corrosion resistance are required.

The Third Pacific Rim International Conference on
Advanced Materials and Processing (PRICM 3)
Edited by M.A. Imam, R. DeNale, S. Hanada,
Z. Zhong and D.N. Lee
The Minerals, Metals & Materials Society, 1998

Introduction

Corrosion of reinforcing steel in concrete is rapidly becoming a major problem throughout the world. Parking structures, bridges, buildings, highways, marine structures, and other reinforced concrete structures are being severely damaged by corrosion of the rebars. The annual costs for maintenance and repair of concrete structures due to corrosion on the rebars is estimated at several billion US dollars. In the UK, £10 billion has been allocated for bridge repair over the next decade **(1).**

As a usual, the design life for a bridge is about 120 years, but many are reported to have failed within 25 years, and in some cases, less than 10 years. Although the corrosion of steel in portland cement concrete is a complex problem, chloride ions caused problem are believed the main sources of the corrosive damage. Millions of tonnes of salts are deposited during winter time in order to maintain traffic flow and minimise accidents, and has had a detrimental effect on the reinforcing bar in the relatively porous concrete. The chloride ions will diffuse through the concrete from de-icing salts or from seawater in marine environments. When the chloride ions contact the reinforced steel surface, the passive condition can be disrupted and corrosion will occur.

Efforts to prevent corrosion have generally focussed on keeping chlorides away from carbon steel reinforcement with a protective coating **(2)** or increasing the concrete cover. Using corrosion inhibitors in concrete **(3)** and cathodic protection **(4)** are also often reported in practice cases, but in the long run, choosing a corrosion resistant material for the rebar itself is increasingly seen as a viable solution and cost-efficient.

Traditionally austenitic stainless steels, for example, AISI 304 and AISI 316, is a group of widely-used stainless steels with good comprehensive properties and are however too expensive to be used in general structural engineering applications in competition with carbon steel. The development of duplex stainless steels (DSS) with double mechanical strength and better local corrosion resistance especially in stress corrosion resistance but low cost due to a half content of expensive alloying element nickel, however, is being seening as an economical way to use stainless steels. In regard to the thermal expension coefficient, DSS have the similar value to carbon steel and concrete.

The objective of this work is to develop a new group of nickel-free, high strength DSS as economical one for engineering applications. In these alloys nickel is completely replaced by nitrogen. The modified Schaeffler Diagram and ThermoCalc calculations were employed to balance the microstructure of new alloys. Metallography, mechanical properties and corrosion tests were carried out to evaluate the microstructure and properties of these low cost DSS.

ALLOY DESIGN

Duplex stainless steels (DSS) usually have the same amount of each phase (ferrite and austenite) which is considered to reach a desirable combination of strength, toughness and corrosion resistance. The volume ratio of two phases is a function of chemical composition and heat treatment. Table 1 gives the chemical composition of the steels investigated in this work. Cr is the

Table 1. Chemical composition of the investigated duplex stainless steels

Heat No.	Cr	Ni	Mn	Mo	C	N
D10	22.1	-	10	-	<0.01	0.35
D10-3	20.1	-	10.1	3.0	<0.01	0.45
SAF 2304	22.9	4.7	1.5	0.4	0.02	0.1
SAF 2205	21.9	5.7	1.5	3.0	0.02	0.17

basic composition to form a continuous layer of passive film. 22wt%Cr is considered as the critical content to produce duplex microstructure with nearly equal amount of ferrite and austenite without the addition of Mo (as shown in Figure 1). N, in replace of nickel is used to stabilize the austenitic content while the additions of Mn are to increase the solubility of nitrogen in steels. It is not realized to add nitrogen higher than 0.5% in DSS due to the difficulties on casting caused by nitrogen desorption as well as clevage fracture at roome temperature. The additions of Mo can improve the localized corrosion resistance but promote the precipitation of intermetallic phases. These alloying elements are well balanced to achieve a desirable microstructure according to the prediction of the modified Schaeffler Diagram (5) shown in Figure 1.

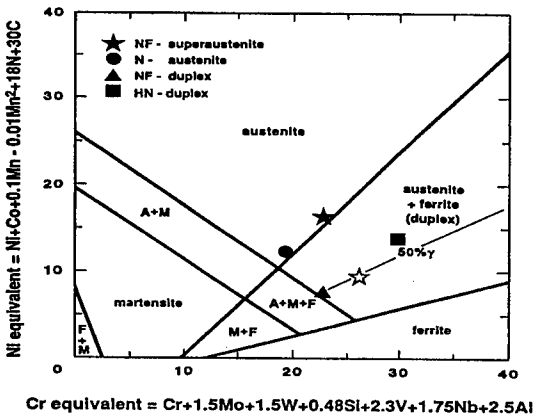


Fig.1: Microstructural control by the modified Schaeffler Diagram (4) in order to achieve the desirable phase ratio of ferrite to austenite

EXPERIMENTAL MATERIALS AND PROCEDURES

The experimental DSS were prepared in a vaccum induction melting furnace with a maximum capacity of 30 kg according to the compositions listed in Table 1. After homogenization at 1200 °C for 7 hours and cooling in the furnace, the ingots were forged into 15mm by 70mm by length billets. Solution annealing at 1050 °C for 1 hour followed by water quenching insured that all nitrogen present in the steels was dissolved interstitially and a desired duplex microstructure with nearly equal volume fraction of the two phases.

Commercial DSS 2304 and 2205 were chosen to compare with the experimental steels. Specimens were cut from rolled plates which were in solution annealed condition. Standard cylindrical specimens with a diameter of 6mm and gauge length of 30mm were used for tensile testing. The effective strain rate was 1E-4 /Sec. Impact energy was determined by testing Charpy V-notch type specimens at room temperature and the evaluated temperatures according to ASTM standard. Charpy V-notch samples with 10x10x55 mm were cut from the solution-annealed billets at 1050 °C according to the forged direction.

Microstructures were analysezed by optical microscope, scanning electron microscope (SEM) with energy dispersive X-ray analysis (EDX). For metallographic analyses, the samples were mounted to a polymer matrix and were automatically grinded from 300 grit paper to 1200 grit paper and then mechanically polished. Electrochemical polishing was performed to get a high quality, scratch-free preetching surface. Berhant solution (0.3g Na2SO4 + 30% HCl) was used to color the duplex microstructure. Ferrite was etched and showed dark color and austenite showed bright color.

Corrosion tests both crevice and pitting corrosion were investigated in this work. Crevice corrosion test was carried out in 6%FeCl3•H2O solution according to ASTM G48. The critical

pitting potentials were measured in artificial seawater at room temperature and 1 M NaCl solution at 37 °C, respectively. The detailed experimental procedures can be refered to literature **(6)**

RESULTS AND DISCUSSION

1. Microstructure

The experimental steels reveals a typical duplex microstructure with nearly equal volume fraction of each phase in the solution annealing condition (Figure 2). In comparison with commercial duplex stainless steels, such steels show stable austenitic content (nearly 40%) when exposured to above 1200 °C. Figure 3 outlines the dependence of the volume fraction of austenitic content on annealing temperatures in the investigated alloys. The changes of phase ratio of the experimental steel are also in good agreement with the results of ThermoCalc calculations.

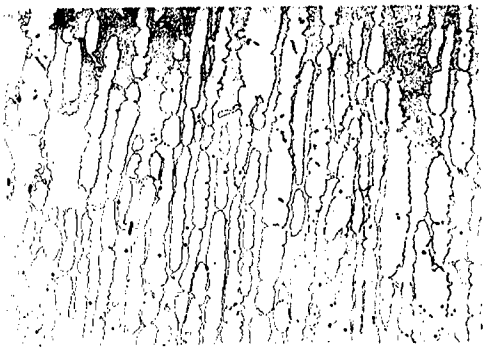


Fig. 2: Typical duplex microstructure of the experimental steels.(D10, 1050°C/1h/WQ)

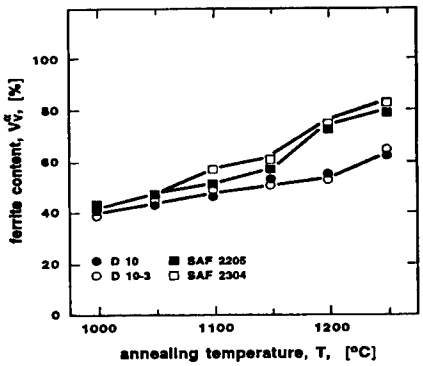


Fig.3: The dependence of the volume fraction of ferrite on annealing temperature of the investigated DSS.

Nitrogen, a potent austenitic stabilizer, has been long used as a substitute of costly nickel since World War II. Because of several times more efficient than Ni but the rapid diffusion rate in Fe-base alloys, nitrogen as alloying element has been introduced to modern DSS and SDSS in order to increase their weldability by allowing a rapid restoration of the phase balance of the ferritized region on cooling, thus improving the welding property of the earlier DSS **(7)**. However, overalloying with nitrogen could increase the difficulties of melting and welding due to the problem of nitrogen desorption.

2. Mechanical properties

The experimental steels show excellent strength and ductility upon tensile testing. Figure 4 compares the experimental steels with some selected commercial carbon and stainless steels **(8)**. Obviously, these experimental steels possess the best combination of yield strength and elongation to fracture. Both Ni-free DSS exhibit a yield strength of at least 550 MPa in combination with an elongation to fracture of at least 40%.

High strength of the experimental steels can attribute to the interstitially solid solution strengthening by nitrogen. In early DSS, the high strength could be reached by increasing the volume fraction of ferrite which was regard as the stronger phase. This is not however true in such high nitrogen containing case. Because of the basic truth that most of nitrogen is dissolved to austenite (8 to 9 times higher than that of ferrite). Austenite will become the stronger phase if the bulk content of nitrogen in steels over 0.2% **(9)**. With the difference from high carbon containing steels, high nitrogen content in steels does not decrease the ductility and toughness of but increase potently the yield strength and tensile strength **(10)**. This is also a reason to develop such nickel-free DSS by nitrogen. According to J. Charles **(9)**, the high strength of DSS is also

contributed by several factors such as composite strengthening, fine grain strengthening as well as substitutionally solid solution strengthening etc.

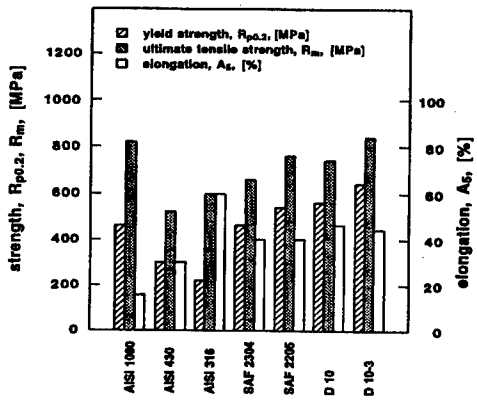


Fig.4: Mechanical properties of the experimental steels relative to selected carbon steel and stainless steels

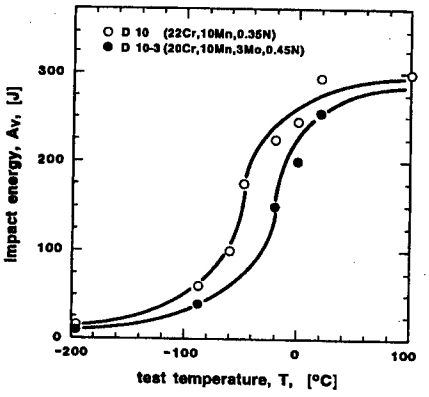


Fig.5: Ductile-to brittle transition behavior of the experimental duplex stainless steels.

Figure 5 shows the ductile-brittle transition behavior of the experimental steels. The DBTT are well below room temperature (RT) even though these steels are nickel free and high nitrogen content. At -20 °C, the charpy impact energy still remain above 150J.

3. Corrosion resistance

The results of critical crevice corrosion temperature (CCCT) measurements in 6% FeCl3•H2O are shown in Figure 6. Alloys with PREN less than 30 were impossible to pass through the start temperature -3 °C in this immersion test. Alloy D 10-3 and Duplex 2205 have similar CCCT, which is between 10 °C and 15 °C. The compared commercial alloys had the same surface condition as the experimental DSS and were immersed in the testing solution together with the experimental alloys. The correlation of the obstained CCCTs has a good agreement with their PREN.

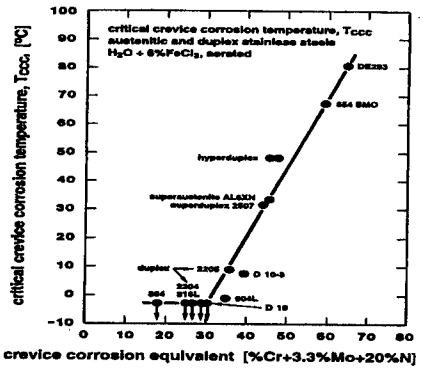


Fig.6: Critical crevice corrosion temperature (CCCT) of the selected alloys as a function of their PREN values.

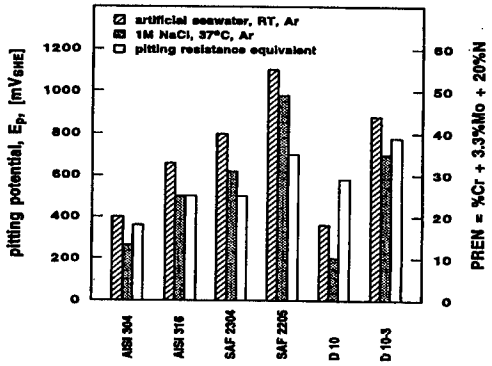


Fig. 7: Critical pitting potentials (CPP) of the investigated DSS and some selected commercial stainless steel

Figure 7 shows that critical pitting potentials of the experimental steels in comparison with commercial austenitic and duplex stainless steels. Although these experimental alloys possess high PREN values, they did not exhibit higher pitting potentials both in artificial seawater and in 1 M NaCl solution. This can be due to the high content of Mn which is detrimental to pitting resistance **(11)** as well as the unbalanced PREN values of austenitic and ferritic phases in such nickel-free DSS **(6).**

SUMMARY

A new group of nickel-free duplex stainless steels has been developed in this work in order to satisfy the potential construction industry. High mechanical strength and toughness, good microstructural stability and corrosion resistance as well as low cost because of totally replacing nickel make these alloys cost-efficient and impromising for reinforced bar and other structural engineering applications. The following conclusions can be drawn in terms of the experimental results:

1. The experimental nickel-free DSS can be characterized as excellent mechanical strength and ductility properties. Both nickel-free DSS exhibit a yield strength of at least 550 MPa in combination with an elongation to fracture of at least 40%. The DBTT are well below room temperature and the charpy impact energy remain above 150 J at -20 °C.

2. The experimental nickel-free DSS have similar CCCT in 6% $FeCl3{\bullet}H2O$ solution to and a little lower critical pitting potentials than the commercial counterparts, Duplex 2304 and Duplex 2205, respectively in both artificial seawater and 1 M NaCl solution.

3. High nitrogen contents in the experimental DSS make sure the high contents of austenite in high temperatures. Because of high diffusion rate, nitrogen is very efficient to restore the microstructural balance within HAZ in regard to weldability.

4. ThermoCalc calculations are confirmed to be very helpful to alloy design. The prediction of phase ratio and phase diagram in the experimental DSS are in good agreement with the experimental observations.

REFERENCES

1. David J. Cochrane, "Making the infrastructure work" (Paper presented at the 2nd European Congress Stainless Steels '96, Düsseldorf, Neuss, 3-5 June, 1996), 157-162.
2. W.R. Baldwin, Solving Rebar Corrosion Problems in Concrete, NACE Seminar reprints, Chicago, Illinos, Sept. 27-29, 1982, Preprint No.7.
3. J.T. Lundquist,Jr., A.M. Rosenberg and J.M. Gaidis, Materials Performance. , 11 (18), (1979), 45-48.
4. W.H. Hartt: in **(2)**, Preprint No.6
5. M.O.Speidel and P.J.Uggowitzer, Proc. Materials Week '92, Chicago, ed. by R.A. Lula, ASM Int., (1993), 135.
6. J. Wang, M.O.Speidel, P.J.Uggowitzer, to be published.
7. S.Hertzman, M.Nilsson and R.Jargelius-Pettersson, Proc. Conf. Duplex Stainless Steels '94, Glasgow, England, Vol.2, Paper No.1.
8. J.R.Davis et al, eds, Stainless Steels Handbook, ASM International, Materials Park, Ohio, (1994)
9. J. Charles, "The duplex stainless steels: materials to meet your needs" (paper presented at the Duplex Stainless Steels '91, Beaune Bourgogne,France, 28-30 October 1991) **1**, 1-48.
10. M.O.Speidel, "Properties and applications of high nitrogen steels" (paper presented at the High-Nitrogen Steels 1988,Lille, France, 18-20 May, 1988) 92-96.
11. A. Cigada et al., Proc. of 185th Meeting,Electrochem. Soc., California, 1994

IMPROVING PROPERTY OF 0.5% CARBON MICROALLOYED STEEL FOR HOT FORGING USING INTRAGRANULAR FERRITE

Jiang Yin

Shanghai No.5 Steel (Group) Co., Ltd
333 Tong Ji Road, Shanghai 200940 ,China

Abstract

In this paper ,the improvement of toughness and fatigue strength of 0.5% carbon microalloyed steel for hot forging is expressed.

Hot forging microalloyed steel usually is heated above 1523K to reduce deformation resistance to increase life of die. Its disadvantage is that the toughness is low and the fatigue initial along ferrite /pearlite boundary is obviously lengthened.

The test results presented intragranular ferrite not only can tough those steels ,but also can improve its fatigue strength as air cooling after hot forging.The toughness of the bar produced from ingot is increased 2.5 times, and the ratio of fatigue limit and tensile strength also increased from 0.47 to 0.51 under the condition of the main elements of the bars is similar.

It has been proved that it is better way to fine pearlite to improve the toughness and to fatigue strength than another way with increasing Mn or pinning grain-boundary by Ti(CN) particles.

In production, the hits of percentage of intragranular ferrite of base microalloyed steel is higher than that decreasing carbon and increasing Mn microalloyed steel. Its cost is lower.

The Third Pacific Rim International Conference on
Advanced Materials and Processing (PRICM 3)
Edited by M.A. Imam, R. DeNale, S. Hanada,
Z. Zhong and D.N. Lee
The Minerals, Metals & Materials Society, 1998

Introduction

At present several DC–LFV–CC–continuous or semicontinuous rolling line including the line of Shanghai No.5 Steel Group Co., Ltd, have already or will soon be put into production. But, up till now, most of the production line of special steel for automobile still adopt EF–LFV–ingot-conventional rolling mill in China.

Medium carbon microalloyed steel has advantage of higher yield ratio and is convenience to use.Its disadvantage is low toughness[1].The toughness can be improved by fining ferrite-pearlite structure. It is difficulty to fine ferrite-pearlite by fining austenite. On one hand, hot forging microalloyed steel usually is heated above 1523K, to reduce deformation resistance to increase the die life. on the other hand, in the case of ingot TiN or Ti(CN) size will coarsening, a function of grain-boundary pinning by TiN or Ti(CN) particles will lose in high temperature [2] .Fig.1 shows coarsening Ti(CN) particles.

It has been proved that it is better way to fine pearlite with intragranular ferrite (IGF) to improve toughness of hot forging microalloyed steel . produced from small ingot or CC [3、4].

In this report , the improvement of toughness and fatigue strength of 0.5% carbon microalloyed steel from ingot for hot forging is expressed.

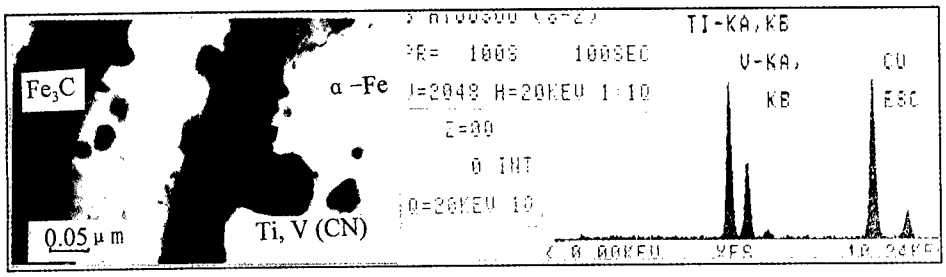


Fig.1: Coarsening Ti(CN) particles of steel (type B)

Toughening Using IGF

Author applied and studied IGF fining structure technology on the parts of hot forging microalloyed steel for car. As an example,the toughnesses of a bar and its part as air cooling after forging are increased 2.5 times under the condition of that

main composition and strength are similar (Table Ⅰ and Fig.2,3)

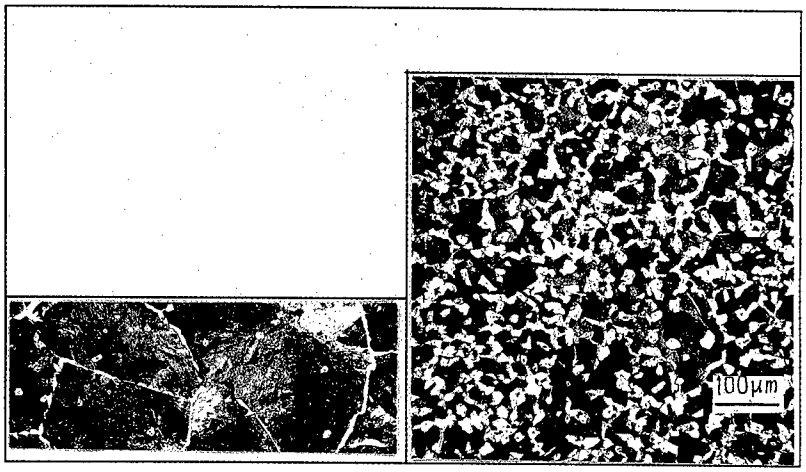
Table Ⅰ : Chemical Composition and properties of Steels

Steel type	Main chemical Composition (wt . %) C	Mn	Cr	V	S	Ti	N	Tensile Strength (N/mm^2)	Micro-structure
A	0.48	0.75	0.2	0.1	0.055		0. 011	880	P+IGF+GF
B	0.47	0.8	0.2	0.1	0.055	0.01		870	P+GF
C	0.23	1.5	0.2	0.1	0. 06		0.015		P+GF

Forging Temperature (K)： 1523 to 1373

Cooling Rate Temp. (K) from 1373K to 873K (K/s)： 0.4（type C is 0.1）

GF: Boundary Ferrite ,IGF: Intragranular Ferrite , P: Pearlite



Steel (type B) (GF) Steel (type A) (IGF)

Fig. 2: Hot forging medium carbon microalloyed steel toughed by IGF
(The diameter of the bars is 65mm and Charpy U type samples)

Improvement of Fatigue Strength

IGF not only can tough microalloyed steel, but also can improve its fatigue strength. The result of rotating bending fatigue test indicates that ratio of fatigue limit (σ w) and tensile strength (σ b) is increased from 0.47 to 0.51 under the

condition of the main composition and tensile strength is similar (Fig.4).

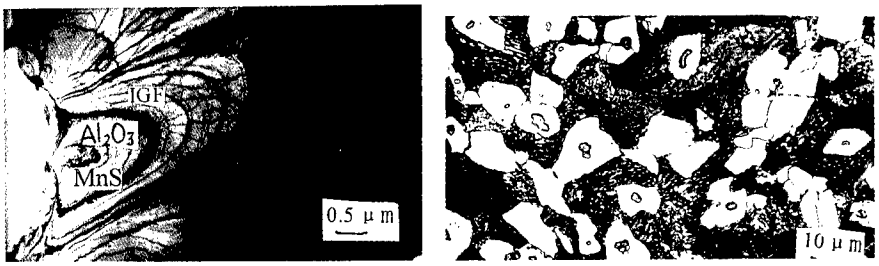


Fig. 3: IGF nucleation (steel (type A))

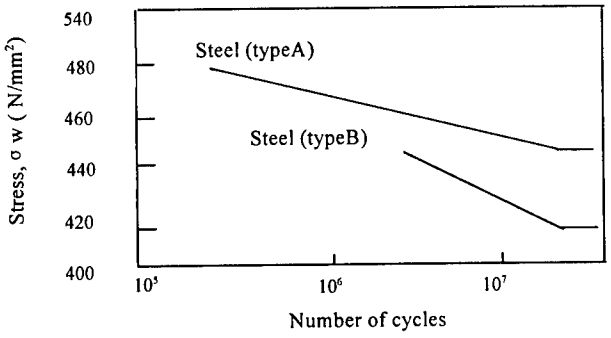


Fig.4: S-N diagrams of medium carbon microalloyed steels.
(Rotating bending fatigue test)

It's still difficulty to make fatigue limit ratio exceed 0.50 by increasing V contents to strengthen ferrite or by reducing forging temperature to fine micro-structure [5,6] .

For hot forged microalloyed steel, σw will reduce with rising of austenitizing temperature and increasing of σb, because fatigue initial crack along ferrite / pearlite boundary is obviously lengthened [7]. Due to ferrite to be precipitated along austenite boundary is on same orientation[8]. IGF formed in coarse austenite fines pearlite transformed from prior austenite and interrupts propagate of fatigue crack.

Advantage of IGF Medium Carbon Microalloyed Steel without Increasing Mn content

Decreasing C and increasing Mn are other way to improve the room temperature toughness of medium carbon microalloyed steel. Although the steel decreasing C and increasing Mn can improve the toughness level further by IGF [3.9] and decreasing C can increase α -Fe transformation drive force, increasing Mn again decreases α precipitation drive force[10]. Fig. 5 compared the temperature IGF formed between steel A and steel (type C). The temperature IGF Formed of steel A is higher 30-40K than that of steel C.

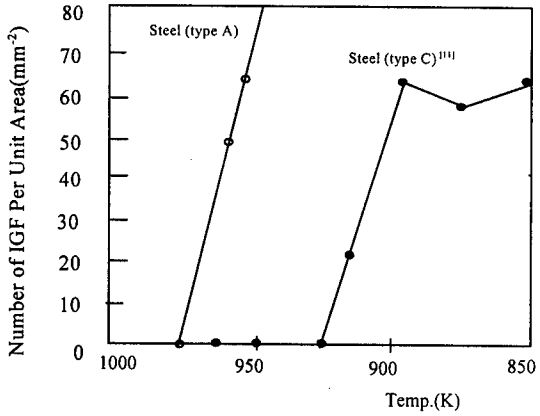


Fig. 5: Temperature IGF Formed

According to the latest investigation, steel componies think it is difficulty to get IGF in steel decreased C and increased Mn, in fact, hits of percentage of steel (type A) is over than 90% .

When the strength-toughness levels are same,to tough base medium carbon microalloyed steel by IGF is cheaper than decreasing C and increasing Mn (Fig.6).

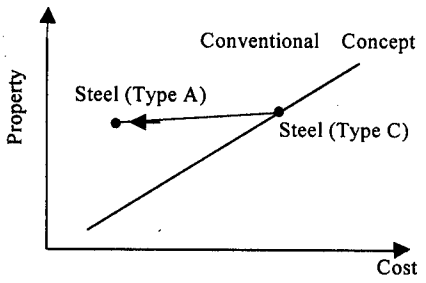


Fig.6: Relationship between property and cost [12]

Summary

0.5% C microalloyed steel heated and forged at 1523K produced from ingot can easily get IGF . The toughness of the bar is increased 2.5 time, and its fatigue limit/tensile strength increased from 0.47 to 0.51 under condition of the main elements of the bar is similar, the cost is loewer.

References

[1] G. Krauss, "Microalloyed Bar and Forging Steels," (29th Mechanical Working and Steel Processing Conference Proceedings, ISS-AIME, Toronto,Canada,1987), 67-77.

[2] H.Takada and Y. Koyasu , "The Present and the Future of Forging Steel Free of Quenching and Tempering," Shinnittetsu Giho, 354(1994) ,7.

[3] T. Ochi,T. Takahashi and H. Takada,"Improvement of the Toughness of Hot Forged Products Through Intragranular Ferrit Formation," I&SM-February (1989),21-28.

[4] H.Takada, T.Ochi and Y. Koyasu, "Study on high strength and toughness ferrite-pearlite microalloyed forging steel" CAMP-ISIJ, 5 (1992) , 777-780.

[5] I. Nomura et al, "Influence of Alloying Elements on Fatigue Strength for Microalloyed Steels" CAMP-ISIJ, 1(1988),1713.

[6] I. Nomura, "High Toughness Microalloyed Steels for Vital Automotive parts," (SAE Technical Paper Series,890511, 1989), 1-7.

[7] I. Nomura, "Influences of Microstructures of Fatigue Strengrh of Medium Carbon Microalloyed Steels" , Tetsu-to-Hagane, 83(1997),227.

[8] K. Ameyama, et al "Morphology of Proeutectoid Ferrite at Austenite Grain Boundaries in Low Carbon Steels" Tetsu-to-Hagane, 74(1988) ,1839.

[9] H. Takada,T.Ochi and F. Ishikawa, "Development of High Strength and Toughness Microalloyed Forging Steel Through Oxides Metallurgy," Bulletin of JIM,32(1993), 429-431.

[10] M. Fujioka , Use of Fine Inclusions in Microstructure Control of steels, ISIJ(1995) ,51.

[11]F.Ishikawa, T.Takahashi and T.Ochi, "Mechanism of Intragranular Ferrite Nucleation," (Solid-solid Phase Transformations, 3M Society, 1994),171.

[12] H.Takechi, Automobile Material symposium, ISIJ(1994) ,3.

HYDROGEN INDUCED CRACKING OF HSLA STEELS IN SEA WATER UNDER POTENTIOSTATIC CONDITIONS

Kumkum Banerjee & U.K.Chatterjee
Department of Metallurgical & Materials Engineering
IIT Kharagpur 721302, India

Abstract

Two HSLA steels (Code GRV and GPQ) microalloyed with Nb and precipitation hardened with Cu were tested by slow strain rate technique in synthetic seawater in the potential range of - 600mV to - 1400mV (SCE). The strain rate was maintained at 3.8×10^{-6} s^{-1} Both hardening and softening effects due to hydrogen have been observed with a minimum in YS and UTS values in the potential range of -1000mV to - 1200mV (SCE) for GRV and - 700mV to - 900mV(SCE) for GPQ. The embrittlement has been evidenced by a decrease in elongation values and the presence of quasi-cleavage features in SEM fractographs. An attempt has been made to explain the difference in properrties of the steels in the light of hydrogen-dislocation interaction, the structural difference and hydrogen trapping.

The Third Pacific Rim International Conference on
Advanced Materials and Processing (PRICM 3)
Edited by M.A. Imam, R. DeNale, S. Hanada,
Z. Zhong and D.N. Lee
The Minerals, Metals & Materials Society, 1998

Introduction

HSLA steels (YS > 500 MPa) were developed as a substitute for HY steels to meet the demand for a material with improved weldability for use in naval and other constructions. In terms of weldability, weld-crack susceptibility during welding fabrication and toughness at heat-affected zone (HAZ) during service are implied. Achievements in this regard have been reported in the literature[1-4]. However, in naval applications, since the ship hull is cathodically protected against corrosion using zinc as sacrificial anode, cathodic discharge of hydrogen atoms on the steel surface and their subsequent entry inside the material may lead to a deterioration in the mechanical properties of the steels including the occurrence of hydrogen-induced cracking (HIC). The characterization of the steels in respect of their mechanical behaviour under cathodic hydrogen charging in the corresponding range of potential is, therefore, necessary.

Experimental

Two HSLA steels (code GPQ and GRV) with chemical composition shown in Table 1 have been used in as-received condition in the present study. The dimensions and heat-treatment of the as-received steel plates are given in Table 2. GPQ corresponds to HSLA-80 steel whereas GRV corresponds to HSLA-100 steel.

Table 1 : Chemical composition of HSLA steels used

Steel	C	Mn	P	S	N	Si	Cr	Mo	Al	Nb	Cu	Ni
GPQ	0.05	1.00	0.009	0.001	0.01	0.34	0.61	0.51	0.025	0.04	1.77	1.23
GRV	0.06	0.84	0.011	0.003	0.008	0.25	0.74	0.58	0.023	0.03	3.47	1.54

Table 2 : Dimensions and heat treatments of the as-received HSLA steels

Steel	Dimensions	Heat Treatment
GPQ	460mm x 610mm x 20 mm	austenitised at 899°C for 45 mins water quenched; tempered at 671°C for 62 mins, water quenched.
GRV	460mmx610mmx25mm	austenitised at 904°C for 70mins water quenched; tempered at 638°C

A characterization of the microstructures has been made using optical microscopy and transmission electron microscopy. Tensile specimens of 4.2 mm dia and 35 mm gage length were tested in a CORTEST slow strain rate machine at a strain rate of 3.8×10^{-6} s^{-1}. Load-elongation curves were generated both in air and in synthetic seawater. In the latter medium, the studies were performed in the potential range of - 600 mv to - 1400 mv (SCE) in - 100 mV intervals using a PARC potentiostat.

The synthetic seawater was prepared from a stock solution of composition : KCl 10 gm. KBr 45 gm, $MgCl_2$ 550 gm, $CaCl_2$ 110 gm in one litre of distilled water. To 20 ml of stock solution 23 gm of NaCl and 8 gm of $Na_2 S0_4$ was added and diluted to one litre. Fractographic studies were were performed using a JEOL scanning election microscope.

Results and Discussion

The optical and TEM metallography of the as-received GPQ andGRV steels are shown in Figures 1 to 4. From the viewpoint of micro structure, HSLA-80 should exhibit polygonal ferrite in gages more than about 12 mm [5,6] and HSLA-100 should have a microstructure constituting of low-carbon martensite/bainite [7]. Optical micrograph of GPQ shows a banded structure at low magnification and polygonal ferrite plus bainitic/martensite structure at higher magnification (Fig.1a). The presence of polygonal ferrite is also evident in the optical

micrographs of GRV (Fig.1b) in the matrix of bainite/martensite. Transmission electron microscopy (Fig 2) reveals the presence of polygonal ferrite and martensite packets in GPQ with globular precipitates predominantly inside the polygonal ferrite GRV shows martensite laths and acicular ferrite containing precipitates. The precipitates in both the samples can be mixtures of niobium carbide/carbonitride and reprecipitated copper produced on ageing[8].

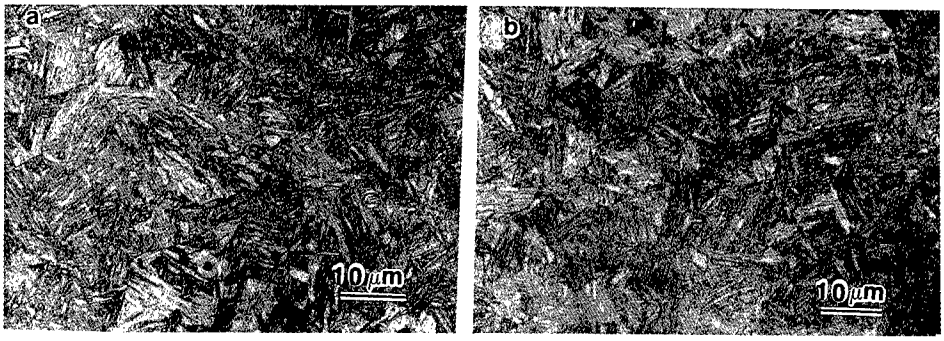


Fig. 1 Optical micrograph of (a) GPQ, (b) GRV

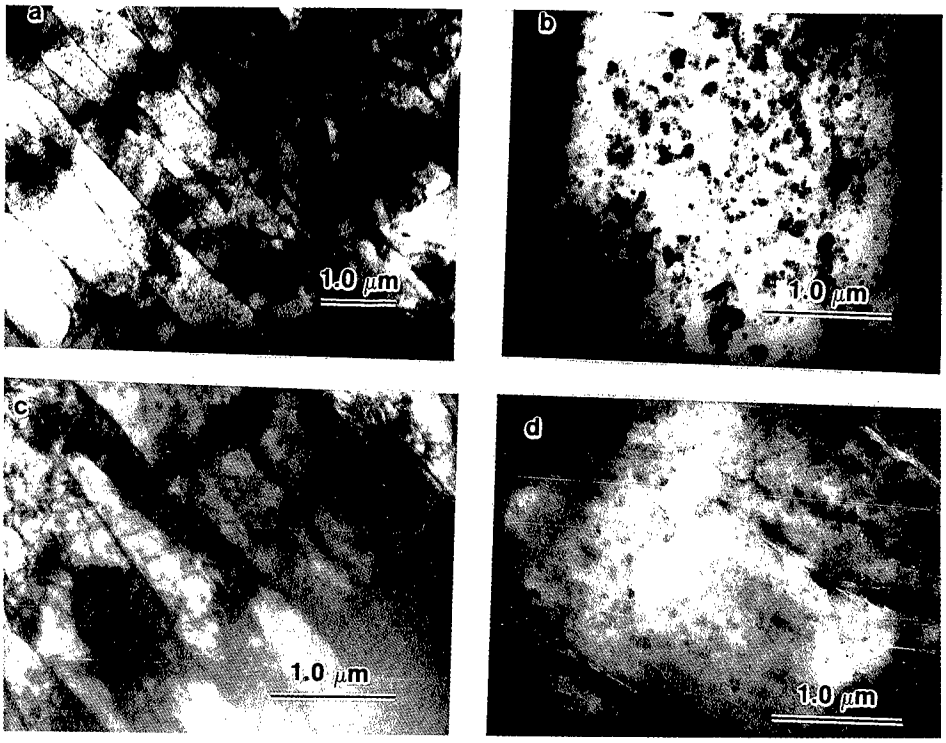


Fig. 2 TEM of (a & b) GPQ, (c&d) GRV

The curves showing the variation of YS, UTS and % elongation as a function of applied potential are shown in Figure 3. The YS, UTS and % elongation values observed for the steels in air at the slow stain rate employed are shown on Y axis. It can be seen that for both the steels, an initial increase in strength values followed by a decrease with the attainment of a minimum at some potential range has been observed. However, the minimum corresponds to the range of -700 to -800 mv (SCE) for GPQ and to the range of - 1100 to-1200 mV (SCE) for GRV.

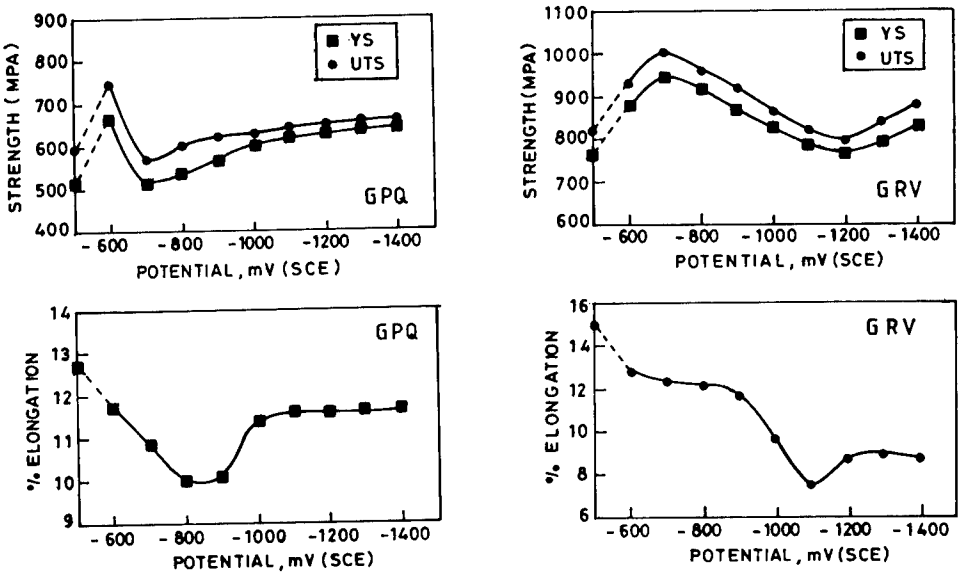


Fig. 3 Variation of mechanical properties of GPQ and GRV with applied potential

The percent elongation has varied between 12-10% for GPQ, a marginal drop from that observed in air, with a minimum in the range of - 700 to -900 mv, corresponding to the range for the minimum in strength values. For GRV, the percent elongation has dropped from 13% at - 600 mv (SCE) to a minimum of about 7% at the potential range of -1100 to -1200 mv (SCE) with some recovery of ductility at the higher cathodic potentials.

In both the steels, hydrogen hardening as well as hydrogen softening effects have been encountered. This behaviour can be explained on the basis of hydrogen dislocation interaction [9]. The initial gain in strength on hydrogen entry i.e. hydrogen hardening in both the steels can be viewed as the effect of hydrogen on edge dislocations. Hydrogen atoms may pin an edge dislocation rather than increase its mobility by reducing the Peierls stress. On the other hand, hydrogen can be assumed to enter the screw dislocation core and modify the core structure to increase the kink nucleation rate. This enhances the screw dislocation mobility and the softening effect is encountered. The softening should occur at relatively small concentrations of hydrogen atmosphere because the presence of only a few sites of easy kink nucleation facilitates the motion of a screw dislocation as a whole. At higher concentrations of hydrogen, the easily nucleated kinks are pinned before they move a considerable distance along the screw dislocations and the hardening effect is encountered.

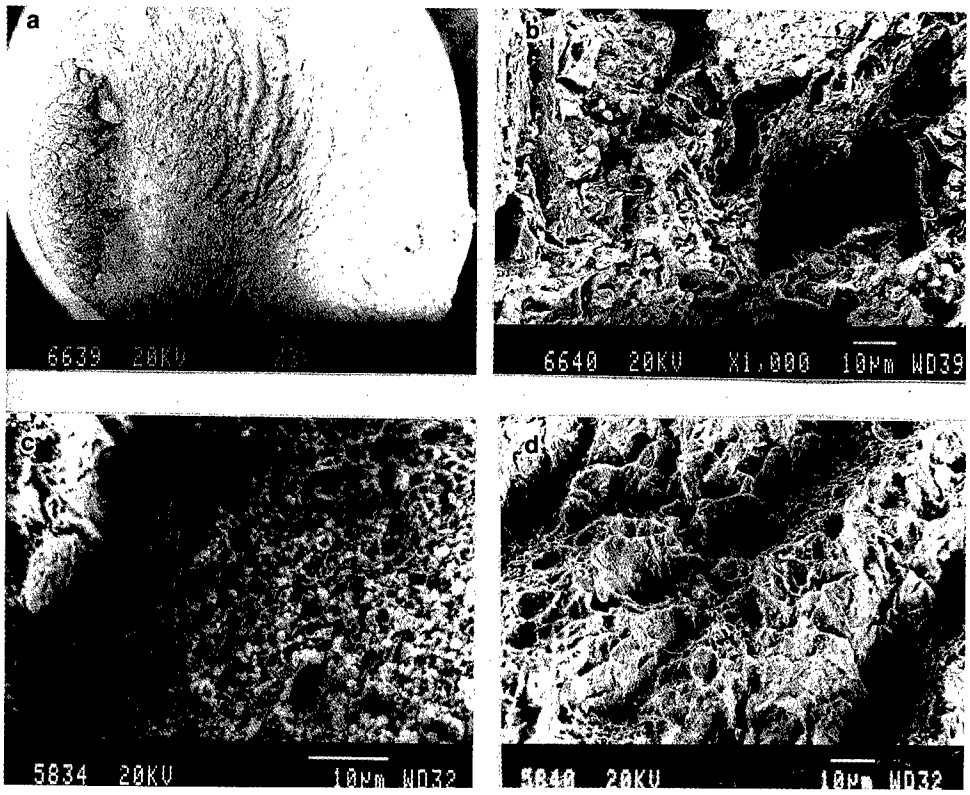


Fig. 4 SEM fractographs: (a) GRV at -1300 mV, embrittled area at periphery, (b) GRV, same area magnified showing quasi-cleavage, (c) GPQ at -700 mV, dimples:(d) GPQ at -1000 mV, quasi-cleavage.

It may be noted that the softening effect has been more in GRV than GPQ in that the strength values at the minimum dropped more in the former than in the latter compared to the values obtained in air. This can be attributed to the difference in hydrogen-impurity interaction. Hydrogen-impurity pairs also act as stress centers to facilitate kink pair nucleation [9]. Since GRV contains more copper than GPQ, copper precipitates are expected to be more in GRV and hence more softening due to their interaction with hydrogen.

The occurrence of the minimum in strength levels has been observed to be at a higher potential range in GRV compared to that in GPQ. If we assume that the concentration of hydrogen is directly proportional to the applied cathodic potential, then the post-softening hardening effect in GRV has required a higherhydrogen concentration required for hardening through an enhanced kink nucleation . Although the structural difference in the steels is not very evident, the effective traps such as voids, coherent precipitates and grain boundaries, dislocation density et cetera [10] can be very different.

Representative SEM fractographs have been shown in Figure 4. At lower magnification, the embrittled areas adjacent to the periphery are indicated, which have revealed quasi-cleavage or cleavage features at higher magnification. The central portions have shown dimples. However, the basic cause for the reduction of the strain at fracture in presence of hydrogen has been attributed to the larger number density of microvoids produced by hydrogen [11]. A comparison of SEM fractographs of GPQ at - 700 mV(SCE) and -1000 mV(SCE) corroborates this view.

Conclusions

(1) Cathodic hydrogen charging has caused both hydrogen hardening and softening in the steels and a marginal impairment of ductility.

(2) The maximum drop in ductility corresponds to the maximum softening which supports the view that the microvoids produced by hydrogen are the cause for embrittlement.

(3) The difference in the hydrogen-impurity interaction and in the number of effective hydrogen traps appear to be the cause for the difference in the softening and hardening behavior of the steels.

References

1. F Blekkenhorst, et al, British Corros. J., 21, (1986), 165-171.
2. E J Czyryca, et al, Naval Engineers J. 102(1990), 63-82.
3. A J DeArdo, HSLA Steels: Processing, Properties and Applications, eds. G Tither & Z Shouhua, (Warrandale, PA: TMS, 1992) 21-31.
4. E J Czyryca, Key Engineering Materials, 84-85(1993), 491-519.
5. A D Wilson, J. of Metals, 9(1987), 36.
6. R J Jesseman & G J Murphy, J. of Heat Treating, 3(1984), 228
7. A D Wilson et al Proceedings of Microalloying '88, World Materials Congress, (Metals Park, OH: ASM, 1988)
8. S W Thompson, D J Colvin & G. Krauss, Met. & Mat.Trans.,27A(1996), 1557.
9. H Matsui, H Kimura and S Moriya, Materials Sc. & Engg., 40(1979), 207-216.
10. G. M. Pressouyre, Met. Trans., 10A(1979), 1571-1573
11. R. A. Oriani & P. H. Josephic, Met. Trans., 11A,(1980), 1809-1820.

INVESTIGATION ON THE PRECIPITATION OF CARBONITRIDES AND COPPER IN A HIGH STRENGTH LOW ALLOY STEEL

A.N. Bhagat[*], *S.K. Pabi*[#], *O.N. Mohanty*[*] *and S. Ranganathan*[@]

[*] The Tata Iron & Steel Company, Jamshedpur 831 007, India

[#] Department of Metallurgical & Materials Engineering, Indian Institute of Technology, Kharagpur 721 302, India

[@] National Metallurgical Laboratory, Jamshedpur 831 007, India

Abstract

The precipitation behaviour of HSLA steels containing copper, niobium, carbon and nitrogen as principal precipitating elements was studied. The precipitates were studied under SEM and the morphology and size were recorded. Electrical resistivity measurements were carried out on samples equilibrated at different temperatures, from 600 to 1200°C. A maximum in resistivity occurs at about 800°C. It drops at 1000°C before increasing at 1200°C. This phenomenon has to be investigated further. The technique of successive partial equilibration was used to predict the solubility relations. The experimental observations are consistent with the predictions.

The Third Pacific Rim International Conference on Advanced Materials and Processing (PRICM 3)
Edited by M.A. Imam, R. DeNale, S. Hanada, Z. Zhong and D.N. Lee
The Minerals, Metals & Materials Society, 1998

Introduction

High strength low alloy (HSLA) steels are being developed for structural applications where strength-to-weight ratio is a critical factor. These steels contain various alloying additions such as Nb, Mo, Cr, Cu and Ni. Niobium precipitates as carbonitride and provides grain refinement. Copper strengthens the steel by age hardening. It is necessary to understand the precipitation behaviour of these steels in order to successfully design the alloy and the thermomechanical processing required for achieving the desired mechanical properties. There are some reports in literature (1-8) on the precipitation characteristics of HSLA steels. However, a tool to predict the nature of precipitation for different alloy compositions at different temperatures is yet to be evolved. This is vital for achieving the goals stated above. The precipitation characteristics of alloys containing copper along with micro-alloying elements such as niobium have not been reported in literature in any detail. Hence, studies were carried out to study the precipitation behaviour of these steels.

Experiment

The chemical analysis of the types of steels studied is given in Table 1. The GLE and GPT steels were cut into rods 10 mm diameter and 30 mm in length. Each rod was encapsulated in quartz which was flushed with high purity argon. It was then evacuated and flushed with argon again. This was repeated several times. The capsule was then sealed under vacuum. Each capsule was heated to 1200°C and maintained at this temperature for three hours. It was then quenched in water and the steel rod was recovered. Each capsule was then maintained at a specific temperature ranging from 800 to 1180°C for three hours and quenched in water. The rods were then retrieved and prepared for observations under scanning electron microscope.

TABLE 1 : CHEMICAL COMPOSITION OF THE STEELS STUDIED (wt.%)

Steel	C	Nb	Mo	Cr	Mn	Cu	Ni	Al	N	S	Si	P
GPT	0.044	0.037	0.60	0.58	0.95	1.23	1.65	0.023	0.0142	0.006	0.34	0.005
GPO	0.040	0.030	0.60	0.57	0.86	1.58	3.55	0.032	0.0145	0.004	0.27	0.002
GLE	0.020	0.032	0.57	0.54	0.87	1.98	3.39	0.038	0.0145	0.003	0.23	0.002

Rods were cut from the GPO and GPT steel samples, to measure 8 mm in diameter. These were drawn to 0.5 mm diameter in successive passes with intermediate annealing. The cold drawn wires were annealed in vacuum at 900°C for one hour. These were cooled in the furnace. The wires each measuring about 15 cm in length were encapsulated in quartz and sealed as described for the rods. Capsules were maintained at 1200°C for three hours and quenched in water. The wires were retrieved and encapsulated once again in quartz tube, under vacuum after flushing with argon. The different capsules containing the wires were maintained at different temperatures from 600°C to 1200°C. These were maintained for three hours each at the respective temperatures and quenched in water. The electrical resistivity of the wires was measured using the four point method at room temperature (20°C).

Results And Discussion

At 800°C, the GLE steel showed precipitates varying in size from less than 50 nm to 200 nm. Most of the precipitates were in the finer size-range. They were spherical. The precipitates were uniformly distributed in the cross-sections observed. At 1000°C, in the same

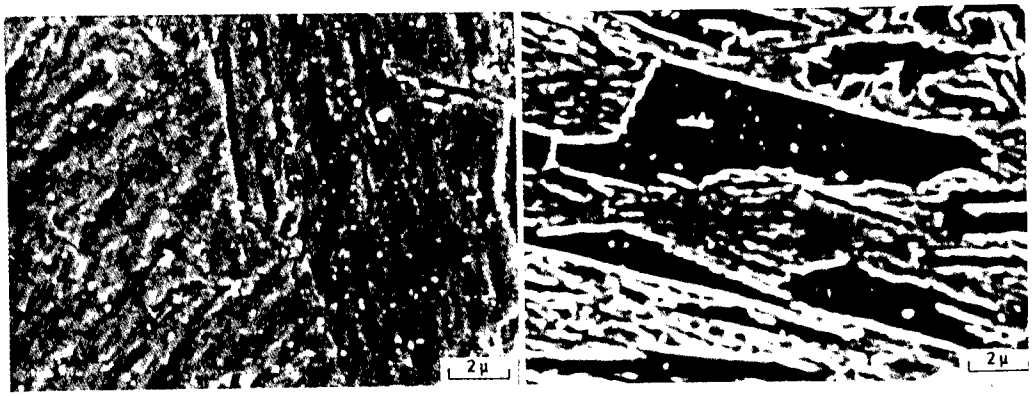
steel, precipitates showed varying morphologies such as spherical, triangular and polygonal in cross-section. The precipitates which were circular in cross-section measured about 100 nm in diameter. A few of these measured upto 200 nm. Those which had a square cross-section measured about 200 nm to 300 nm. The triangular precipitates were also about 300 nm in size. The precipitate density at this temperature was less than that at 800°C. At 1100°C, the precipitate density was much less than that at 1000°C. At this temperature also, different cross-sections such as circular, oval and triangular were noticed. Those with a triangular cross-section were observed mostly near the grain boundaries. The precipitate size varied from about 100 nm to 200 nm for those with triangular cross-section and less than 50 nm to about 100 nm for those with circular cross-section. The samples quenched from 1170°C showed practically no precipitation. Only very few precipitates, measuring less than 50 nm in cross-section were observed.

The trend was similar in the case of the GPT steel also. In this steel no precipitates were present in the sample quenched from 1180°C. Fig. 1 provides the micrographs illustrating the precipitation behaviour in these two steels at various temperatures.

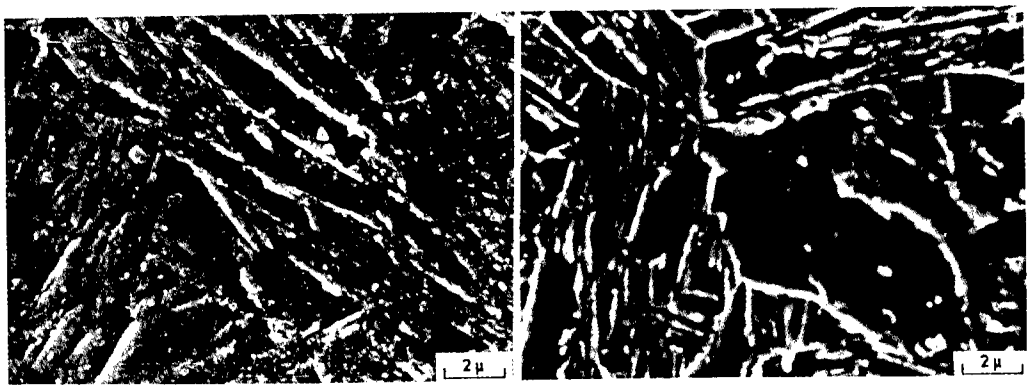
It is of interest to note that the morphological characteristics of the precipitates varied with the temperature at which the steels were equilibrated. The shapes of the precipitates observed showed a greater variety at 1000°C in both the steels. The observation of regular ploygonal shapes is also significant. Both copper and niobium carbonitride are expected to precipitates in these steels at the temperature these were equilibrated. Another precipitate that can appear is that of aluminium nitride. Because of the small size of the precipitates, energy dispersive analysis of X-ray (EDX) could not be employed here to ascertain the chemistry of the precipitates of various morphologies. Further investigations are being carried out to characterize these precipitates using transmission electron microscope (TEM) and deduce the chemistry of these. Work is also in progress (9) to chemically isolate the precipitates from the matrix and analyse the chemistry.

Many investigators have reported on the morphological characteristics of the precipitates formed in HSLA steels. Read et al (4) studies steels containing 0.165% carbon and 0.037% niobium. The samples were quenched from 850°C in water containing ice, after rolling the steel. They observed niobium carbo-nitride precipitates with polyhedral and flat (rectangular) morphologies. The polyhedral precipitates measured 200 nm. Akamatsu et al (5) studied two different types of steels containing 0.006% and 0.018% carbon and 0.142% and 0.053% niobium respectively. These samples were quenched from 975°C. They report that the particle size varied with soaking time and composition. The maximum size, as inferred from the micrographs published by these authors was 100 nm for a steel soaked for 18 ks and containing 0.006% C and 0.142% Nb. Increasing the soaking time increased the size of the precipitates. Varughese (6) has studied a steel containing 0.04% C and less than 0.05% Nb. He reports the formation of particles of size 10-15 nm in samples quenched from 905°C after holding for 75 minutes. Mujahid et al (7) note carbo-nitride precipitates of size 10-30 nm in steels quenched from 900°C, after holding for 60 minutes. This steel contained 0.04% C and 0.02% Nb. A. le Bon et al (2) obtained carbo-nitride precipitates of size 3-5 nm in steels which were deformed at 900°C and quenched. In the case of steel which was not subjected to any deformation, the particle size was 100-300 nm. Their steel contained 0.17% C and 0.04% Nb.

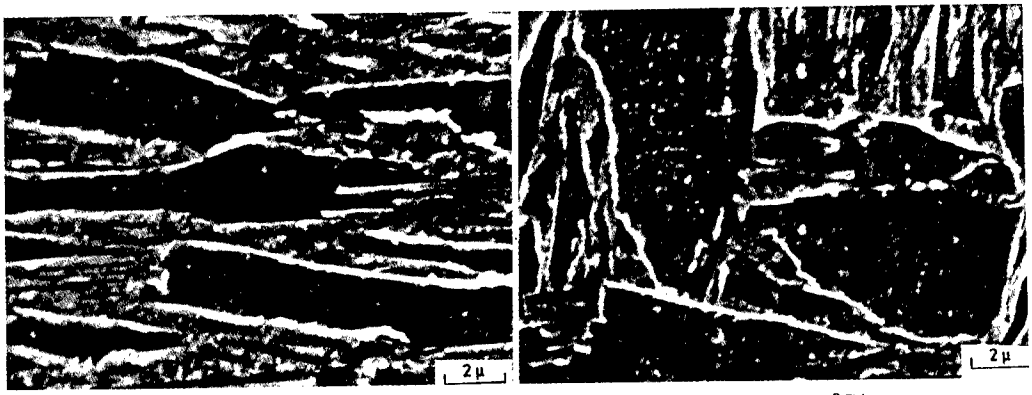
The particles size generally increases with increase in holding time. In the present study, the samples were held at the different temperatures for 3 hours. The observed particle size is consistent with those reported in the literature cited above.



GLE-800°C/q GPT-800°C/q



GLE-1000°C/q GPT-1100°C/q



GLE-1170°C/q GPT-1180°C/q

FIGURE 1 : SCANNING ELECTRON MICROGRAPHS OF GLE AND GPT STEEL EQULIBRATED AT VARIOUS TEMPERATURE FOR 3 h

The technique of successive partial equilibration was introduced recently (10) to predict the precipitation of carbides in steels. Using this technique it was predicted that all the alloying elements would go into solution at 1140°C in the case of the steel designated as GLE and 1160°C in the steel designated as GPT. The experimental observations reported here are consistent with these predictions. Further experiments are being carried out to precisely ascertain the temperature at which the precipitates completely dissolve in the matrix.

Figure 2 reports the electrical resistivity of the GPT steel quenched from different temperatures, from 600 to 1200°C. Two wire samples from the same stock were equilibrated in the quartz tube and the resistivities of the quenched wires were measured at 20°C. There was a maximum difference of 0.5 μΩ cm between the two wires at any equilibration temperature. The average of the two readings at each temperature is reported in the Fig. 2. The resistivity increases with temperature of equilibration and reaches a maximum at 800°C. It then falls at 1000°C and then increases at 1200°C. Fig. 3 depicts the change in resistivity with equilibration temperature in the case of GPO steel. In this case also, average of the two readings is reported. Similar observations were made in this steel also. A change in resistivity occurs at about 1000°C.

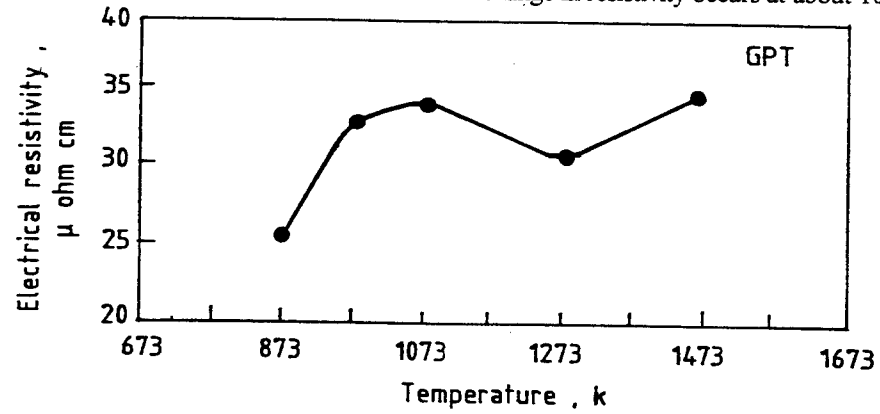


FIGURE 2 : EFFECT OF EQUILIBRATION TEMPERATURE ON THE ELECTRICAL RESISTIVITY OF GPT STEEL

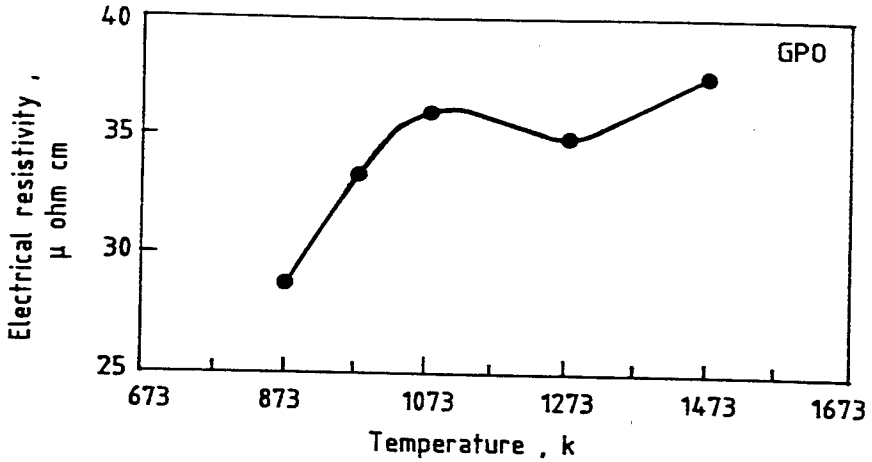


FIGURE 3 : EFFECT OF EQUILIBRATION TEMPERATURE ON THE ELECTRICAL RESISTIVITY OF GPO STEEL

It is interesting to note this phenomenon being consistently observed with two different sets of wires equilibrated independent of each other. It may also be noted that SEM observations also indicate that there is a significant change in the precipitation characteristics on increasing the temperature of equilibration from 800 to 1000°C. The electrical resistivity of the wires was calculated theoretically for the given alloy compositions using the effect of various alloying elements on the resistivity of iron reported by various authors (11, 13) as shown in the Table-2.

TABLE 2 : EFFECT OF ALLOYING ELEMENTS ON THE INCREASE OF THE RESISTIVITY OF IRON (PER 1 WT.% ADDITION OF ELEMENT)

Element	C		N	Cu	Cr	Mo	Mn	Si	Al	P	S	Nb
	≤0.002%	>0.002%										
Increase in Resistivity, μΩ cm	82.5	4.5	14.6	4.0	5.4	3.4	5.0	13.5	12.0	11.0	12.0	8.7

The calculated resistivities (34.2 and 37.0 μΩ cm for the GPT and GPO steels, respectively) are in good agreement with the measured values for the wires equilibrated at 1200°C (34.3 and 37.5 μΩ cm for GPT and GPO steels respectively) when all the precipitate is expected to dissolve in the matrix. The solubility of copper in iron has been reported in literature (12) as a function of temperature. Utilizing this, the resistivity of GPT and GPO wires was calculated for the sample quenched from 800°C. The calculated values of 33.9 and 36.0 μΩ cm are in good agreement with the measured values of 34.1 and 36.5 μΩ cm for the GPT and GPO wires respectively quenched from 800°C. This consistency between the calculated and measured values of resistivities indicates that the measurements were free from any influence of extraneous factors which were not anticipated. Due to the low levels of niobium and carbon in the alloy, these elements do not significantly influence the resistivity, compared to the influence exerted by copper. The increase in resistivity on increasing the temperature of equilibration is due to the greater level of copper in solution in the matrix at higher temperatures. At present it is not clear why there is a depression in the electrical resistivity at 1000°C. Further investigations are required for understanding this phenomenon.

Summary

The morphological characteristics of the precipitates formed in two types of HSLA steels equilibrated at different temperatures have been studied. There is significant change in the morphological characteristics on increasing the equilibration temperature from 800°C to 1000°C, in both the steels. The shapes of precipitates observed showed a greater variety at 1000°C in both the steels. Electrical resistivity measurements were carried out on thin wires of the steels after equilibration at different temperatures. A decrease in resistivity occurs at 1000°C after increasing continuously from 600°C. The resistivity again increase at 1200°C. Further investigations are required to understand this phenomenon and also to characterize the precipitates.

Acknowledgment

Financial assistance from the office of the Chief Naval Research Laboratory (OCNR)/ Naval Research Laboratory (NRL), Washington (DC), USA under grant no. N00014-95-1-00015 to carry out this work is gratefully acknowledged by the authors. Two of the authors (ANB and ONM) also acknowledge Tata Steel for permission to carry out this work and publish this paper.

References

1) Pande et al, Study of Precipitation Kinetics in High Strength Low Carbon Ferrous Alloys, Key Engineering Materials, Trans Tech Publications Switzerland, vol. 84-85, (1993).

2) A. le Bon, J. Rofes-Vernis and C. Rossard, Recrystallization and Precipitation During Hot Working of a Nb bearing HSLA Steel, Metal Science, vol. 9 (1975), pp 36-40.

3) B. Dutta and C.M. Sellars, Effect of Composition and Process Variables on Nb (CN) Precipitation in Niobium Micro-Alloyed Austenite, Material Science and Technology, vol. 3 (March 1987), pp 197-206.

4) S Read, R.K.Gibbs and B.A. Parker, Extraction and Characterisation of Precipitates Formed in Niobium HSLA Steel, Material Form, vol. 14 (1990), pp 304-307.

5) Akamatsu, T.Senuma and M. Hasebe, Generalised Nb (CN) Precipitation Model Applicable to Extra Low Carbon Steel, ISIJ International, vol. 32 (1992), No.3, pp 275-282.

6) Varughese and P.R. Howell, The Application of Metallographic Techniques to the Study of the Tempering of HSLA-100 Steel, Material Characterization, vol. 30 (1993), pp 261-267.

7) M. Mujahid et al., HSLA-100 Steels : Microstructure and properties, Key Engineering Materials, Trans Tech Publications Switzerland, vol. 84-85, (1993), pp 209-236.

8) R Simoneau, G. Begin and A.H. Marquis, Progress of NbCN Precipitation in HSLA Steels as Determined by Electrical Resistivity Measurements, Metal Science, (August 1978), pp 381-386.

9) K.K. Gupta, Dolly Ghosh, A.N. Bhagat and S. Ranganathan to be communicated.

10) S. Ranganathan, CALPHAD, vol 20 (1996), No. 4, pp 461-470.

11) A.L. Norbury, The Effect of Various Elements on the Electrical Resistivity of Iron, JISI, vol. 101, (1920), pp 627-644.

12) H.A. Wriet and L.S. Darken, The Solubility of Copper in Ferrite, Trans. Met. Soc. of AIME, vol. 218 (Feb. 1960), pp 30-36.

13) H.E. Cleaves and J.G. Thompson, The Metal Iron, Monograph Series (Mc Graw Hill Book Company, INC, 1935), pp 190-191.

PREDICTION OF CARBO-NITRIDE PRECIPITATION IN HIGH STRENGTH LOW ALLOY STEELS (HSLA) BY THE TECHNIQUE OF SUCCESSIVE OF PARTIAL EQUILIBRIA

S.Ranganathan

National Metallurgical Laboratory
Jamshedpur 831007, India

The Third Pacific Rim International Conference on
Advanced Materials and Processing (PRICM 3)
Edited by M.A. Imam, R. DeNale, S. Hanada,
Z. Zhong and D.N. Lee
The Minerals, Metals & Materials Society, 1998

Introduction

For successful design of high strength low alloy (HSLA) steels and the thermo-mechanical processing of the same, it is imperative to develop techniques that can predict the precipitation behaviour of the carbo-nitrides in these steels. Several methods have been discussed in literature to predict the solubility relations in these(1-6). These methods assume the type of precipitate formed and then predict the stoichiometry and the mass of the precipitate, by solving a set of equations for the number of unknowns present. Though this method is simple for simpler precipitate types, it becomes very complicated when analysing the precipitation behaviour of complex precipitates. The precipitates formed in these steels are complex, containing more than one element in the anionic as well as cationic sub-lattice. In these cases, the conventional methods involve the inconvenience of solving a set of non-linear equations. They require appropriate initial guesses to ensure convergence and elaborate schemes to avoid negative roots(7,8). Realistic predictions of the precipitation behaviour involves thermodynamic equilibrium at the precipitate/matrix interface combined with diffusion kinetics in the bulk of the alloy. The composition at the interface can be different from that of the bulk. Therefore, it is not possible to assume the type of precipitate formed, from a consideration of the bulk composition alone. The algorithm developed must allow predictions of the type of precipitate formed among the several that are possible. When this is considered, the conventional techniques become much more complicated.

The Technique of Successive Partial Equilibria

This communication illustrates a novel technique that can be used to predict the precipitation behaviour in HSLA steels. This technique, called the technique of successive partial equilibria was demonstrated recently to predict the precipitation in the Fe-Cr-C system and in alloy steels(9). It is simpler in application and is free from the complexities involved in the conventional methods. It is based on the following principles:

1. The thermodynamic equilibrium state of a system is independent of the path followed to reach that state.
2. At equilibrium, the chemical potential of any component is the same in all the phases.

Application

To illustrate the technique, a typical HSLA steel whose chemical composition is provided in table 1, is considered. This steel contains niobium, titanium, and manganese as the principal alloying elements apart from carbon and nitrogen. To predict the precipitation behaviour, it is assumed that all the elements are in solution in the austenitic phase. The niobium and carbon in the solution are allowed to interact to form NbC.

$$Nb + C \rightarrow NbC$$
$$K = a_{NbN}/a_{Nb}.a_C$$

K is the equilibrium constant and a_i is activity of the i^{th} species. The mass of the precipitate formed and the amounts of Nb and C in the solution in equilibrium with this are evaluated.

Table I Composition of Alloy Steel (wt%)

Steel	Ti	Nb	C	N	O	Mn
Steel 1	0.0956	0.0965	0.087	0.001	0.0007	0.0170
Steel 2	0.0370	0.0756	0.075	0.0088	0.0015	0.015
Steel 3	0.0206	0.0246	0.022	0.0027	0.0030	0.012

The niobium and carbon in solution at the end of this step are then allowed to interact to form the precipitate Nb_2C. The mass of the precipitate and the levels of Nb and C at equilibrium are evaluated as above.

The carbon in the solution at the end of the previous step is allowed to interact with the titanium in solution and form the precipitate TiC. The mass of the precipitate and the amount of Ti and C in solution are evaluated. The procedure is repeated until all the alloying elements and all the possible carbides have been considered. At each step, the chemical potentials of the different alloying elements in the solution are computed.

After all the carbides have been considered, the niobium in solution is allowed to interact with the nitrogen in solution to form the nitride, NbN. The mass of the precipitate and the amounts of Nb and N in solution are evaluated once again. The procedure is repeated for all alloying elements and all possible nitrides as in the case of the carbides. If available data indicate that any given nitride would form a solid solution with a carbide already predicted in the previous stage, these are assumed to form a solid solution. This makes the activity of the nitride less than unity. Suitable thermodynamic models are used to evaluate this activity. When all the possible nitrides have been considered, the first cycle of computation ends. Chemical potentials of all the elements in solution are computed at each stage of this cycle.

The Second Cycle of Computation

At the end of the first cycle, the chemical potential computed at different stages are compared. For equilibrium, the chemical potential of any given element computed at the different stages in equilibrium with the precipitates must be identical. This condition must be simultaneously satisfied by all the elements. If these conditions are not satisfied, equilibrium has not been reached. In this case, the next cycle of computation is initiated.

In the second cycle of computation, the niobium and carbon in solution at the end of first cycle are combined with the amounts of niobium and carbon in the precipitate 'NbC' formed in the first cycle. These quantities of Nb and C are then allowed to precipitate NbC. NbC is assumed to form a solid solution with the NbN formed in the first cycle. The mass of precipitate formed and the amounts of Nb and C in solution are evaluted again. These quantities will be different from that computed at a similar stage in the first cycle. The amounts of Nb and C in solution at the end of this stage in the second cycle are combined with those present in the carbide Nb2C formed in the first cycle. The carbide Nb2C is allowed to be precipitated from this. The mass of precipitate formed at equilibrium is computed. If a solid solution with a nitride precipitated in the first cycle is possible, this solid solution is assumed to be formed. The process is repeated for all carbides and nitrides as in the first cycle. At the end of this, the chemical potentials are compared to test for the attainment of equilibrium. If equilibrium has not been reached, the process is repeated as in the second cycle until equilibrium is reached.

The computations can be carried out choosing any order in which the various carbides and nitrides are considered. A number of paths to reach the equilibrium can thus be generated. The equilibrium predicted will be independent of the path chosen. By choosing an appropriate path, quicker convergence to equilibrium can be ensured.

The equilibrium precipitates are recorded in table 2. There is good agreement between the predictions made by the present technique and that reported in the literature(8). The differences noticed arise essentially because of the different thermodynamic models used to describe the system in the two cases.

Table II Predicted and Reported Austenite Composition
(Wt% in solution) (Steels of table 1)

Steel	Ti		Nb		C		N	
	Pre.	Rep.	Pre.	Rep.	Pre.	Rep.	Pre.	Rep.
Steel 1	0.092	0.091	0.092	0.092	0.086	0.087	0.00017	0.00057
Steel 2	0.013	0.013	0.061	0.070	0.073	0.075	0.0019	0.0016
Steel 3	0.018	0.016	0.024	0.024	0.022	0.022	0.0019	0.0014

Prediction of carbo-nitride Precipitation in HSLA Steels

The present technique has been employed to predict the precipitation behaviour in two HSLA steels being developed for structural applications. The chemical composition of these steels are provided in table 3. The precipitation of carbo-nitrides in equilibrium with the austenite phase was predicted. Wagner's interaction parameter(6,10,11) were used to describe the thermodynamics of the solution phase. The carbo-nitride was taken to be a regular solid solution of carbide and nitride. The regular solution parameter was taken from published literature(12). The free energies of formation of the carbides and nitrides were taken from Knacke et.al.(13). In these steels, the precipitates formed are very small, about a few hundred nanometres in cross-section. Hence the contribution of surface energy to the Gibb's free energy is significant. This term was incorporated in the computation of the free energy. The magnitude of interfacial energy term was taken from Hansen et.al.(14). The effect of the various parameters on the precipitation behaviour of these steels were predicted.

The general precipitation behaviour of these two steels studied is given in table 4. The carbo-nitrides dissolve in the matrix completely, at 1140 C and 1150 C, respectively, in the two steels. The ratio of site fraction occupied by nitrogen to that occupied by carbon in the anionic sublattice decreases with temperature. Whereas the fraction of nitrogen in the alloy precipiated as carbo-nitride decreases with temperature, that of carbon increases intially and then decreases. This is because, as the temperature increases the fraction of carbon in the anionic sub-lattice increases whereas the total amount of precipitate formed decreases.

Table III Steels Analysed for Precipitation Behaviour

Steel	Nb	Cr	Mo	Mn	Cu	Ni	Al	Si	C	N
GLE	0.028	0.54	0.57	0.83	1.98	3.32	0.38	0.23	0.042	0.012
GPQ	0.03	0.58	0.46	0.95	1.19	1.64	0.019	0.31	0.04	0.0145

Table IV Predicted Precipitation Behaviour of The HSLA Steels

Steel	T(C)	%C ppted	%N ppted	%Nb ppted	N/C	Ts(C)
GLE	950	2.011	23.51	93.01	75/25	1150
	1000	2.396	18.93	83.94	67/33	
	1100	1.376	6.043	33.89	53/47	
GPQ	950	1.939	23.25	94.58	79/21	1140
	1000	2.462	19.25	87.16	71/29	
	1100	1.850	7.84	44.25	57/43	

Note: ppted - Precipitated
N/C - Percent site fraction occupied in the anionic sub-lattice by N and C, respectively.
Ts - Temperature of complete dissolution of precipitate

Nitrogen level in the steel has a significant influence on the dissolution temperature of the precipitate. At 25 ppm nitrogen in the steel, the carbo-nitrides dissolve completely at 1090 C in the GLE steel. It reaches 1130 C at 100 ppm nitrogen in this steel. 4.43% of carbon is precipitated at 25 ppm level of N to 27% at 100 ppm level. The amount of niobium precipitated increases on increasing the N-content of the steel. Decreasing the amount of nitrogen in the steel decreases the amount of precipitate formed. The decreased nitrogen level in the precipitate is not compensated by any increase in the fraction of carbon going into the precipitate. A significant effect of the variation in nitrogen level is seen in the ratio of the site fraction occupied by nitrogen and carbon in the anionic sublattice. From a ratio of 35/65 at 25 ppm nitrogen, it increases to 71/29 at 100 ppm. At a size of 1 nm, the precipitates dissolve in the matrix at 1050 C. At 100 nm this temperature is 1150 C, for the GLE steel. About 90% of the Nb is precipitated when the particle has a size of 1 nm. This increases to 98% at 20 nm size of the particle, for the same steel.

Discussion

The technique of successive partial equilibria is simple in application. There is no need for eloborate numerical techniques. Usually considerable care is required in choosing the appropriate numerical technique and the choice of initial gusses to search for real positive roots to solve the mathematical equations and to ensure convergence(8). Even in the case of predicting the precipitation of sample precipitates such as niobium carbo-nitrides, the conventional methods are rather involved and require careful approach to the solution since it is required to solve a system of non-linear equations. The present technique overcomes these difficulties by considering one precipitate species at each step of computation. The problem reduces to that of predicting the quantity of one precipitate formed and the composition of the matrix at each stage. Solution of the problem by this technique is facilitated by the fact that the equilibrium state is independent of the path followed to reach that.

In the case illustrated here, the dissolution temperatures predicted for the two steels are consistent with experimental observation(15). Work is in progress to study the effects of other parameters and describe the precipitation behaviour of these steels.

Acknowledgement

The author is greatful to the Office of Naval Research,USA for financial support to carry out this work under grant No. N00014-95-1-0015.

References

1. P.R.Rios, Mater. Sci. and Technol., 4(1988),324-327.

2. Satoshi Akamatsu, Takehido Senuma and Mitsuhiro Hasebe, ISIJ International, 32(3)(1992), 275-282.

3. M. Grujicic, L.Kaufman and W.S. Owen, CALPHAD, 10(1)(1986), 37-47.

4. M. Grujicic, A.M. Sarosick, L.Kaufman and W.S.Owen,CALPHAD,9(1)(1985),117-128.
5. J.G. Speer, J.R. Michael and S.S. Hansen, Metall. Trans. A, 18A(1987), 211-222.

6. Hans-Joachim Eckstein, Mario Fennert and Joachim Osher, Steel Research, 64(3) (1993), 143-147.

7. P.R. Rios, Mater. Sci. and Engg.A, 142(1992), 87-94.

8. Heilong Zou and J.S. Kirkaldy, Metall. Treans.A, 23A,(1992),651-65.

9. S. Ranganathan, CALPHAD, 20(4)(1996), 461-470.

10. Henryk Adrian, Microalloying '95, Conf. Proceed., (Pittsburgh PA: Iron and Steel Society, June 1995), 285-305.

11. R.C. Sharma, V.K. Lakshmanan and J.S. Kirkaldy, Metall.Trans. A, 15A(1984), 545-553.

12. Heilong Zou and J.S. Kirkaldy, Metall. Trans. A, 22A(1991), 1511-1524.

13. O. Knacke, O. Kubaschewski and O. Hesselmann, Thermochemical Properties of Inorganic Substances, 2nd Edn., (Berlin: Springer-Verlag, 1991).

14. S.S. Hansen, J.B. Vander Sande and Morris Cohen, Metall. Trans.A, 11A(1980), 387-402.

15. Suman Pathak, S. Ranganathan, Samar Das and Swapan Das, In press: 'Scripta Metallurgica et Materilia'.

DESIGN OF A NEW HIGH STRENGTH LOW ALLOY STEEL BY THE KEY POINT METHOD

Zhenbo Zhao, Derek O. Northwood [+], Cheng Liu*, Yunxu Liu*, Dezun Wang*
Mechanical & Materials Engineering, University of Windsor, Windsor, ON, Canada, N9B 3P4
* Department of Materials Engineering, Jilin Institute of Technology, P R China, 130012
+ Also Faculty of Engineering & Applied Science, Ryerson Polytechnic University, Toronto, Ontario, Canada M5B 2K3

Abstract

The design principles and process are described for an 18Mn2WNbB steel (σ_y = 700MPa) which incorporates Mn, W, and Nb as major, and B as trace, alloying elements. The IT (Isothermal Transformation) and CCT (Continuous Cooling Transformation) diagrams were established for this new type high strength, low alloy steel using the key point method which is described in this paper. The mechanical and physical properties of the designed steel were in accordance with the design predictions. The key point method shows considerable promise for the construction of both IT and CCT diagrams for complex alloy steels, being much faster than standard metallographic methods and also offering other advantages over the Johnson-Mehl-Avrami or Lee and Bhadeshia methods for the prediction of IT diagrams.

The Third Pacific Rim International Conference on
Advanced Materials and Processing (PRICM 3)
Edited by M.A. Imam, R. DeNale, S. Hanada,
Z. Zhong and D.N. Lee
The Minerals, Metals & Materials Society, 1998

1. Introduction

To reliably predict steel strength on the basis of its composition and microstructure has been of worldwide interest [1,2] . However, it is hard to find the IT (Isothermal Transformation) and CCT (Continuous Cooling Transformation) diagrams which agree well with the composition of steels and the austenitizing conditions due to the complicated alloy systems used in commercial production. To establish the IT and CCT diagrams is expensive and time-consuming because of the many points needed to completely define these diagrams. The key point method of transformation is proposed here to assist in the calculation of these diagrams and the design of steels. By considering the contributions of alloying elements, phase transformations and strengthening and toughening mechanisms, a series of parameters which affect the key points of transformation are developed. Further, a new type of low carbon high strength low alloy steel(LCHSLA steel) is designed, whose σ_y(yield strength) is up to 700MPa after normalizing, when its diameter is the smaller than 20mm.

2. Composition Design Principles of Steel

Composition design of steel entails the adjustment of chemical constitution and the control of critical cooling rate within practical cooling rates, so that the steel can obtain the desired microstructures and mechanical properties, as shown in Fig.1. In order to ensure the formability and weldability, the carbon content in the high strength low alloy steel should not exceed 0.2%. However, it has been shown [3] that it is difficult for a low carbon steel containing pearlite and ferrite structures to attain this design specification(σ_y=700MPa) even though various strengthening mechanisms are applied to this steel. Hence, it is necessary to study the effects of alloying elements on phase transformations of pro-eutectoid ferrite, pearlite and bainite so that only bainite, and no pearlite or pro-eutectoid ferrite, is formed in this steel with the minimum level of alloying element content, after hot rolling or normalizing. The effects of alloying elements on solid state phase transformations in steel are very complex. In a low carbon steel,

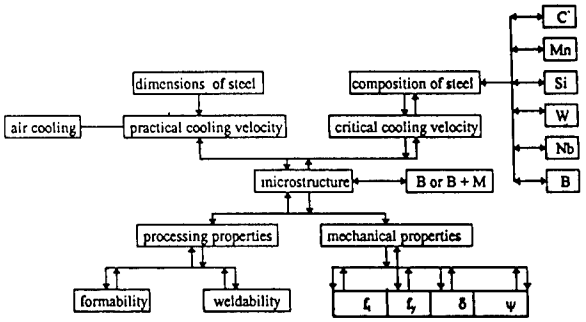


Fig. 1 Chart showing design process for steel

the relationship between alloying elements and the key points of the phase transformations is shown schematically in Fig.2. The physical meaning of the symbols in Fig.2 are as follows:

(1) A_1 : the upper temperature limit of the pearlite transformation
(2) P_f : the lower temperature limit of the pearlite transformation
(3) A_3 : the upper temperature limit of the pro-eutectoid ferrite transformation
(4) F_f : the lower temperature limit of the pro-eutectoid ferrite transformation
(5) P_m : the start point of the pearlite transformation with the maximum transition rate

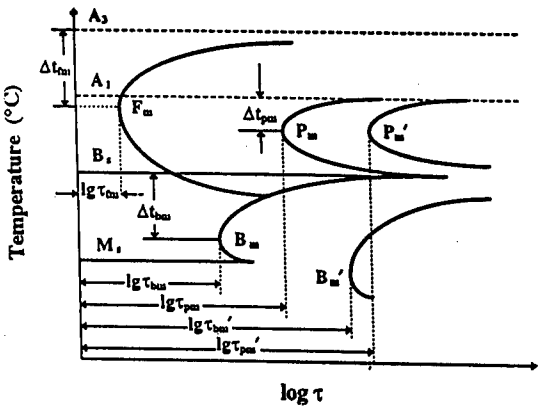


Fig.2 Effect of alloying elements on transformations

Point P_m depends on temperature t_{pm} and time τ_{pm} . (where $t_{pm}=A_1 - \Delta t_{pm}$)

(6) P_m' : the finish point of the pearlite transformation

P_m' can be defined according to $\Delta t_{pm}'(°C) = \Delta t_{pm}$ and $lg\tau_{pm}'(s) = lg(\tau_{pm} + 1)$

(7) F_m : the point of maximum transition rate of pro-eutectoid ferrite transformation

F_m is determined by temperature t_{fm} and time τ_{fm}. (where $t_{fm}=A_3 - \Delta t_{fm}$)

(8) B_s : the upper temperature limit of the bainite transformation

(9) B_f : the lower temperature limit of the bainite transformation

(10) B_m : the start point with the maximum transition rate of bainite transformation

B_m is defined by temperature t_{bm} and time τ_{bm}. (where $t_{bm} = B_s - \Delta t_{bm}$)

(11) B_m' : the finish point of the bainite transformation

B_m' can be defined according to $\Delta t_{bm}'(°C) = (t_{bm} + 50)$ and $lg\tau_{bm}'(S) = lg(\tau_{bm} + 1.5)$

(12) M_s : the upper temperature limit of the martensite transformation

Using the key points (1) to (12), a IT diagram can be obtained if the chemical composition of the steel is known. In other words, in the t - lgτ diagram, we can draw the M_s horizontal line and asymptotes respectively from P_m, P_m', F_m, B_m, B_m' points to A_1, P_f, A_3, F_f, B_s, B_f horizontal lines. The quantitative effects of alloying elements (per 1 wt% addition) used in the designed steel for the key points of the phase transformation are listed in Table 1.

Table 1 The quantitative effects of alloying elements on the key points of the phase transformations

Alloying elements	A_1	A_3	M_s	B_s	P_m		F_m		B_m	
					Δt_{pm}	$lg\tau_{pm}$	Δt_{fm}	$lg\tau_{fm}$	Δt_{bm}	$lg\tau_{bm}$
	°C	°C	°C	°C	°C	S	°C	S	°C	S
Mn	-12	-10	-45	-45	-17	+0.6	+30	+0.45	+17	+0.35
Si	+26	+18	-5	-35	-10	+0.15	-15	+0.25	-15	+0.15
W	+8	+7	-8	-12	-75	+1.5	-15	+1.0	+20	+0.16
Nb	+55	+50	-35	-40	-14	+2.0	-50	+2.5	+200	+0.2
B*	-	-	-	-	-	+1.0	-	+1.5	-	+0.2

*Effective content of B for phase transformation is 0.001~0.005%

The Mn-W-Nb-Si iron alloy used in this study had a chemical composition of 50~55%Mn, 1.1~1.3%C, 6~10%Si, 2%W, 1%Nb, balance Fe. Taking into account the reduction of carbon, Mn and Si contents in processing, the ratio of alloying elements is Mn: Si:W: Nb = 40:6:2:1, after adding this iron alloy into scrap plain carbon steel (in a ratio of about 1:100 in wt%). The Mn,W,Nb,Si alloying elements when added to steel retard the pearlite and ferrite transformations, but have a small effect on the bainite transition, particularly W and Nb. As a result, we can get bainite and martensite or bainite to arrive the design request. At the same time, B is added to the steel for good weldability and formability.

In order to further improve the strength of LCHSLA steel, as many strengthening mechanisms as possible should be utilized to increase the strength in the designed steel, as shown in Fig.3[4] . From Fig.3 it can be seen that many of the alloying elements used in this study contribute to more than one strengthening mechanism.

On the basis of our earlier work [5, 6], the following formulas can be used to calculate approximately the strength of low carbon bainite. (σ_t is tensile strength of steel)

$$\sigma_t = 12.4(16 + 125C\% + 15Mn\% + 30Si\% + 6W\% + 25Nb\%) \text{ (MPa)} \quad (1)$$

$$\sigma_y = 0.7\sim0.75\sigma_t \quad (2)$$

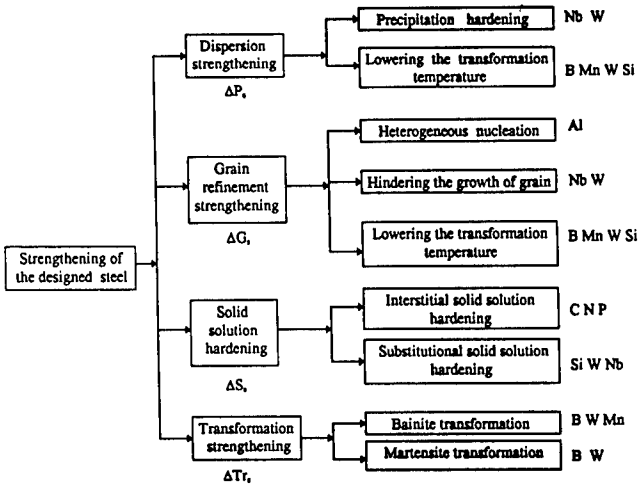


Fig.3 Strengthening mechanisms of the designed steel[4]

3. Components and Properties of the Designed Steel

3.1 Design Calculations

(1) The carbon content of steel should be within 0.15~0.2% in order to ensure weldability and formability. A value of 0.17% was used.

(2) Design the alloying element content on the basis of the requirement of steel strength.

Taking the design requirement of (σ_y=700MPa) and equation (2): $\sigma_t=\sigma_y/(0.7\sim0.75)=1000$(MPa)

Because Mn is the principal alloying element, the Si,W, and Nb contents are converted to a Mn equivalent using equation (1):

$$1000=12.4[16+125(0.17)+15Mn'\%+30(5/50Mn'\%)+6(2/50Mn'\%)+25(1/50Mn'\%)] \quad (3)$$

$$Mn'\% = 2.32$$

According to the ratio of each alloying element in the iron alloy, we can calculate the chemical composition of designed steel: $Mn\% = 2.32 \times [(50-8)/50] = 1.95$ $Si\% = 2.32 \times (5/50) = 0.23$

W% = 2.32 × (2/50) = 0.09 Nb% = 2.32 × (1/50)= 0.05 0.001~0.005%B

3.2 Construction of IT and CCT diagrams

The key points and critical points in the designed steel were calculated according to the formulas given in reference[6] , and are shown in Table 2. The IT diagram for the designed steel is then drawn using the data in Table 2. In addition, through Scheil's rule[7] , the CCT curve can be obtained as shown in Fig.4. We can then superimpose on these diagrams, actual cooling curves

Table 2 Key points and critical points of designed steel

key points and critical points	symbol	temperature (°C)	time(s)		
the critical point of the pearlite transformation	A_1	713			
the lower temperature limit of the pearlite transformation	P_f	450			
the upper temperature limit of the pro-eutectoid ferrite transformation	A_3	848			
the lower temperature limit of the pro-eutectoid ferrite transformation	F_f	450			
the upper temperature limit of the martensite transformation	M_s	382			
the upper temperature limit of the bainite transformation	B_s	523			
the lower temperature limit of the bainite transformation	B_f	150			
the key point of the pearlite transformation	P_m	Δt_{pm}	104	$lg\tau_{pm}$	2.74
	P_m'	$\Delta t'_{pm}$	104	$lg\tau'_{pm}$	3.74
the key point of bainite transformation	B_m	Δt_{bm}	41	$lg\tau$	0.48
	B_m'	$\Delta t'_{bm}$	91	$lg\tau'_{pm}$	1.98
the key point of ferrite transformation	F_m	Δt_{fm}	287	$lg\tau$	1.69

for bars of different diameters (5,10 and 20 mm). It can be seen that a bainite or bainite and martensite structure should be obtained by air cooling or normalizing at high temperature, when the diameter of designed steel does not exceed 20 mm.

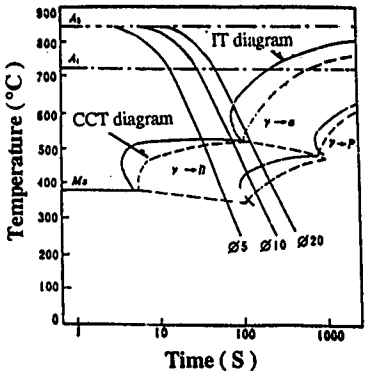


Fig.4 IT and CCT diagrams of the designed steel

3.3 Fabrication of Alloys and Determination of Properties

Two kinds of steels were melted in a 20kg medium frequency induction furnace, and their chemical compositions are shown in Table 3. It can be seen that the chemical compositions are similar to the design specification. Cast ingots of these steels were forged into steel bars(Φ=20mm), and normalized at 920°C. Tensile tests of normalized steel bar from No.1 furnace gave the following properties:

σ_t = 980MPa , σ_y = 759MPa, δ = 24%, ψ = 36.2%

Thus, it can be seen that the properties of the designed steel accord well with the design demands. These results show that the key point method may be a promising way to establish the IT and CCT diagrams for the complicated alloy steels.

Table 3 Chemical composition of the cast steel

furnace number	chemical composition, wt%								
	C	Si	Mn	W	Nb	B	S	P	Re
1	0.17	0.27	2.03	0.078	0.025	0.0014	0.033	<0.010	--
2	0.16	0.26	2.16	0.080	0.035	0.0039	0.039	<0.010	--

4. Comparison of Key Point Method With Other Methods

A Johnson-Mehl-Avrami type equation has also been used by Umemoto et al.[8] for the representation of pearlite formation kinetics in eutectoid steels. Lee and Bhadeshia [9] adopted it to estimate the increase in the volume fraction of bainite as a function of time, and developed a method for the prediction of time-temperature-transformation diagrams. However, all these models have limitations in terms of alloy chemistry or in terms of the ability to predict correctly the bay that arises between the two C-curves as the alloy concentration is increased. The key point method seems a good way to solve that problem since its application has considered the effects of a wide range of alloying elements and their concentration. (More detailed information can be found in the Ph.D. dissertation of one of authors[6] , but due to page limitations, it can not be described here.)

5. Conclusions

The key point method of transformation used to establish the IT and CCT diagrams for the complex alloy steels is described . Using this method , a new type high strength low alloy steel (18Mn2WNbB steel , σ_y = 700 MPa) is designed. The experimental results show that the designed steel accorded well with the design specifications.

6. Acknowledgments

This study was supported by the Natural Science Research Council of Jilin Province in China. Continued funding is being provided by the Natural Science and Engineering Research Council of Canada through a Research Grant (A4391) awarded to Professor Derek O. Northwood.

References

1. F.B.Pickering, Physical Metallurgy and The Design of Steels (London, Applied Science Publishers Ltd., 1978), 1-7.
2. X.T.Wang, "The Effects of Alloying Elements on the Strengthening of Steel," Ordnance Material Science and Engineering , 11(1990), 43.
3. K.J.Irvine, Steel Strengthening Mechanisms (Zurich, Climax Molybdenum Co., 1969), 55.
4. Q.H.Zhu and Y.X.Liu, "Design of A High Strength Low Carbon Low Alloy Steel," Jilin Metallurgy, 6(1993), 15-19.
5. Y.X.Liu, Principle of Heat Treatment (Beijing, China Mechanical Industry Press, 1981), 310.
6. C. Liu, "Design Study of A New Alloy Steel Used As the Steel Wire Rope of Oil Drilling,"(Ph.D. dissertation, Harbin Institute of Technology, Harbin, China, 1997), 56-87
7. J.W.Christian, Theory of Transformation in Metals and Alloys, Part I, 2nd edition (Oxford , Pergamon Press, 1975), 525.
8. M. Umemoto, N. Nishioka and I. Tamura, Trans. Iron Steel Inst. Jpn. , 22 (1982), 629-636.
9. J.L. Lee and H.K.D.H. Bhadeshia , "A Methodology For the Prediction of Time-Temperature-Transformation Diagrams," Mater. Sci. & Eng. , A171 (1993), 223-230.

MECHANICAL PROPERTY AND MICROSTRUCTURE OF STRUCTURAL AND FIRE RESISTANT STEELS

W. Sha and F.S. Kelly

Department of Civil Engineering, The Queen's University of Belfast, Belfast BT7 1NN, UK

Abstract

The mechanical properties of structural S275 steel and two fire resistant steels containing Mo and Nb-Mo, respectively, have been investigated in the room temperature to 700°C range. The study involved hardness tests, fractography, calorimetry and optical/electron microscopy. As-received and heat treated samples were studied. The results for the S275 steel are consistent with literature data. Strengthening precipitates and mode of fracture were identified in the fire resistant steels.

The Third Pacific Rim International Conference on
Advanced Materials and Processing (PRICM 3)
Edited by M.A. Imam, R. DeNale, S. Hanada,
Z. Zhong and D.N. Lee
The Minerals, Metals & Materials Society, 1998

Introduction

In the UK, fire is the biggest perceived problem of steel as a constructional product, well above other problems such as control on site, floor depth, delivery, inflexibility, cost and corrosion [1]. In the past decade, fire resistance of steel construction has received much attention, owing to its importance in terms of both economics and image [2,3,4].

Traditionally, fire resistance is achieved by applying fire protection (board, spray, or intumescent coating) to steel columns and beams [5]. Since around 1980, however, fire engineering has been rapidly developed, especially in Western Europe. The aim is to design buildings with significant built-in fire resistance but using reduced or no fire protection in traditional forms [2,3]. British Steel has extensive work in this area [2,3,6,7,8,9,10,11], the pinnacle of the work being the successful design and marketing of fabricated and asymmetric beam (ASB) slimflor [12,13] systems. In addition, over the years, stress processes developed in a building fire have been a subject of extensive investigation, with many findings leading toward a full comprehension of fire/structure interaction.

A third approach towards ensuring fire safety of steel structures is using a fire resistant type structural steel in construction. As such a steel will maintain a higher strength at elevated temperatures, it can increase the structural integrity during fire. At the same time, using such a steel will not complicate current design routines as only new strength reduction factors will need to be used in fire design calculations. These three approaches can be used in either individual or combined modes (Figure 1).

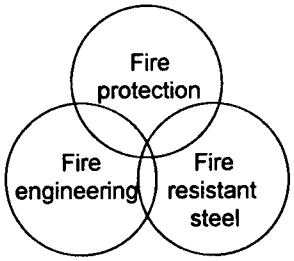


Figure 1: Three apporaches in achieving required fire resistance in steel structures.

It is the authors' belief that the development of fire resistant steels is well worthy of investigation. The drive behind the present research programme is to develop structural steels which can be used with minimal or in some cases no fire protection, so reducing overall construction costs. The aims of the overall programme are two-fold; the first responding to a challenge in scientific terms, and the second representing a technological innovation:

1. To achieve a fundamental understanding of microstructure and mechanical property development of construction steels at elevated temperatures as in a fire situation;
2. To design and make novel fire resistant steels; and to characterise their elevated temperature performance.

The methodology adopted is to investigate the metallurgical processes occurring at elevated temperatures that lead to the loss, *and gain*, of strength, and ways of controlling these processes by modifying steel chemistry and manufacturing parameters. The current work represents the first stage, characterisation and testing of existing structural and fire resistant steels.

Experimental Procedure

The fire resistant steels were received in the form of plate, 9 mm thick in the case of the Mo-containing steel and 16 mm for the Nb- and Mo-containing steel. The compositions of the steels studied and experimental details for microscopy were given in an earlier paper [14]. Samples for optical microscopy were cut from different parts of the plate and may therefore reflect some regional variations. Room temperature Rockwell hardness tests were carried out using a 16th inch diameter ball with a force of 100 kg, taking the corresponding readings from the B-scale according to ASTM E18-93 [15]. Six or more tests were carried out for each sample. The Rockwell figures were converted to Vickers hardness (HV) using conversion tables. The following equation was used to give an approximation of the ultimate tensile strength, σ_{uts}:

$$\sigma_{uts} \text{ (in N/mm}^2\text{)} = 3.4\,HV \qquad (1)$$

Results

Hardness

The results of hardness tests are shown in Table I. The average Vickers hardness numbers are displayed (HV) as well as the ultimate tensile strengths, σ_{HV}, calculated from Equation 1, and σ_{exp} obtained from the tensile experiments.

Table I Hardness and Ultimate Tensile Strength before and after Aging with Air Cooling

Steel type	Condition	HV	σ_{HV} (N/mm^2)	σ_{exp} (N/mm^2)
S275	As-received	92 ± 3	325	325
	650°C/30 mins	75 ± 4	255	-
	800°C/30 mins	50 ± 1	170	-
Mo steel	As-received	148 ± 8	503	500
	650°C/30 mins	141 ± 3	480	-
	800°C/30 mins	135 ± 1	460	-
Nb-Mo steel	As-received	166 ± 5	564	560
	650°C/30 mins	165 ± 3	561	-
	800°C/30 mins	174 ± 5	592	-

Microstructure

Optical micrographs of the fire resistant steels in as-received and heat treated conditions are shown in Figure 2. The corresponding percentages of ferrite and grain sizes are given in Table II. The somewhat abnormal grain sizes in the quenched samples could be due to regional variation within the steel plates and/or the effect of different sample orientation.

In the Mo steel, α-Mo_2C has been identified as a precipitation strengthening phase. In the Nb-Mo steel, there is a combination of different kinds of precipitates which makes the identification by electron diffraction difficult. It is not clear whether there is combined precipitation of niobium carbonitride with molybdenum carbide, or there is a mutual solution of niobium carbide with nitrides. There has been no identification of any Mo precipitates in the Nb-Mo steel, which leads credence to the former case.

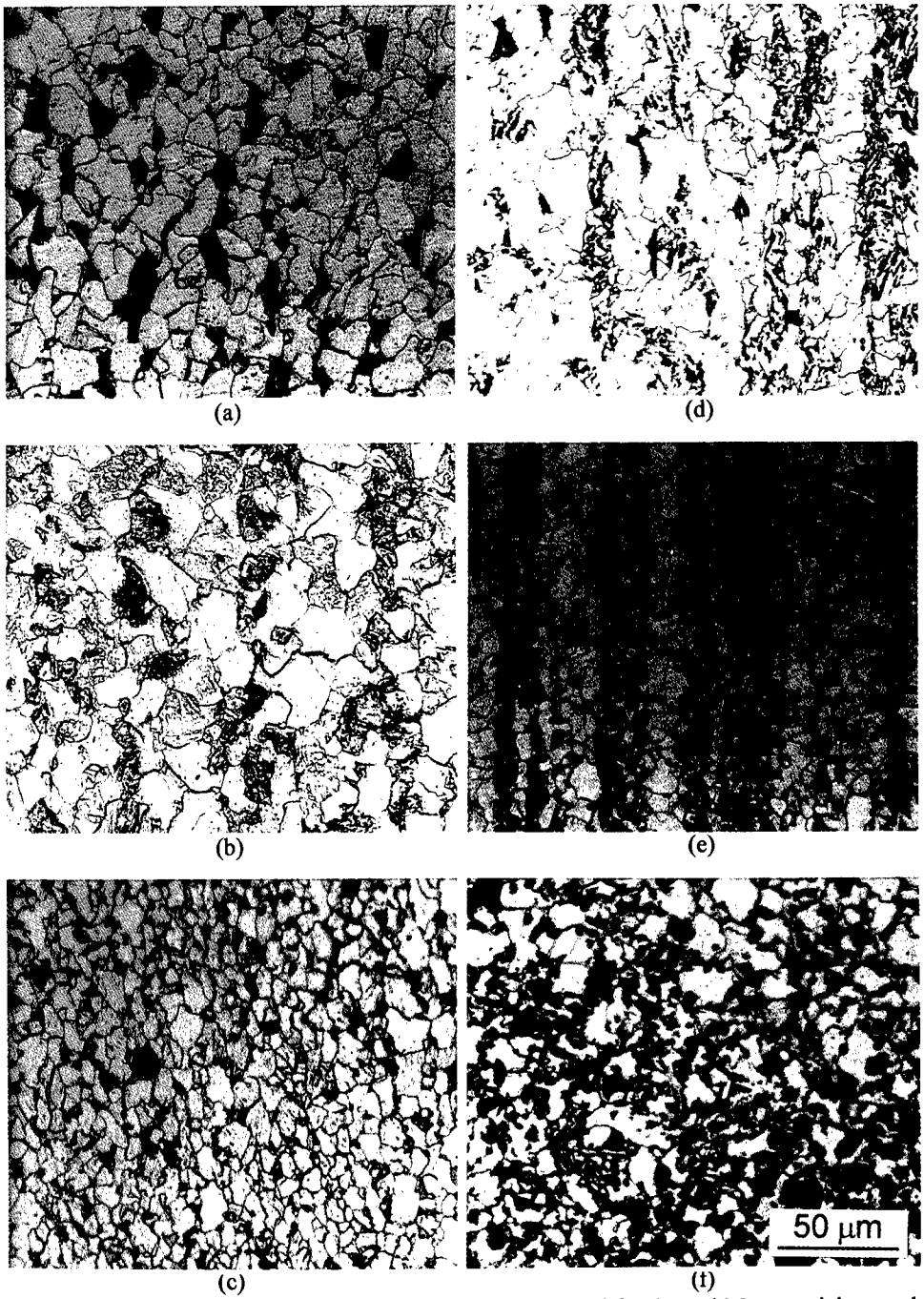


Figure 2: Optical micrographs of (a-c) Mo-containing and (d-f) Nb- and Mo-containing steels. (a,d) As-received; (b,e) heat treated at 650°C for 30 min followed by water quenching; (c,f) heat treated at 800°C for 30 min followed by air cooling. Samples for (a,b,d,e) were sectioned perpendicular to the final rolling direction, while samples for (c,f) are longitudinal sectioned.

Table II Percentage of Ferrite in the Microstructure and Grain Size before and after Aging

Steel type	Heat treatment	Cooling	Volume % of α	Grain size (μm)
Mo steel	As-received	-	83	6.1 ± 0.4
	650°C/30 mins	Water quench	87	6.6
		Air cool	88	5 ± 2
	800°C/30 min	Air cool	90	5 ± 1
Nb-Mo steel	As-received	-	77	5.7 ± 0.1
	650°C/30 mins	Water quench	79	3.7
		Air cool	87	7 ± 1
	800°C/30 min	Air cool	83	6 ± 1

The $\alpha \leftrightarrow \gamma$ transformation temperatures in the fire resistant steels have been measured using differential scanning calorimetry, and the results are given in Table III. These were measured at a heating/cooling rate of 30°C/min. The results for the conventional S275 steel are included for comparison.

Table III Transformation Temperatures of the S275 and Fire Resistant Steels

Steel	A_{c1}	A_{c3}	A_{c4}	A_{r1}	A_{r3}	A_{r4}
S275	745	919	1397	722	907	1392
Mo	745	939	1407	730	903	1374
Nb-Mo	745	971	1425	713	897	1387

Fracture Surfaces

Tensile fracture surfaces of fire resistant steel specimens tested at 700°C were studied, with the aim of identifying whether the mode of failure was intergranular due to the high temperature or transgranular, as with the specimens tested at 600°C [14]. The results showed that the fracture at 700°C was still largely transgranular. This is reasonable as the fracture mode usually changes at a homologous temperature of approximately 0.5 of the melting point. This would equate with a temperature of around 800°C for the two fire resistant steels. However, the Mo steel does seem to show an increased tendency towards well-defined cleavage planes, which was not apparent from fracture surfaces tested at lower temperatures. Although not quantified, it was found that the incidence and type of inclusions was similar to those found in samples tested at lower temperatures.

Acknowledgements

The authors are grateful to Nippon Steel for providing the fire resistant steel samples, and to Dr. J.M. Gregg, Dr. J.D. Williams and Mr. J.A. Kelso for their technical assistance. The project was partly funded by the Department of Education for Northern Ireland.

References

1. J.T. Robinson, "Commercial Scene, Slimdek/ASB" (Presentation at the Enhanced Complex Structural Steel Sections Project Concluding Meeting, Rotherham, UK, 1996).

2. Journal of Constructional Steel Research: Special Issue on Fire and Steel, 33 (1-2) (1995).

3. New Steels Construction: Special Issue Featuring Fire Engineering, 3 (1) (1995).

4. D.J. O'Connor, "Structural Engineering Design for Fire Safety in Buildings," The Structural Engineer, 73 (4) (1995), 53-58.

5. Fire Protection for Structural Steels in Buildings, 2nd edn. (Aldershot, UK: Association of Specialist Fire Protection Contractors and Manufacturers Ltd., 1992), 6.

6. J.D. Baird, A. Jamieson, R.R. Preston and R.C. Cochrane, "Strengthening Mechanisms in Ferritic Creep Resistant Steels," Proceedings of A Meeting on "Creep Strength in Steel and High Temperature Alloys" (London: The Metals Society, London, 1974), 207-216.

7. V. Jerath, K.J. Cole and C.I. Smith, "Elevated Temperature Tensile Properties of Structural Steels Manufactured by the British Steel Corporation" (Report T/RS/1189/11/80/C, British Steel, 1980).

8. R.R. Preston and T.R. Kay, "Fire Resistance of Structural Steel Beams," Metals and Materials, 2 (1986), 25-26.

9. B.R. Kirby and R.R. Preston, "High Temperature Properties of Hot-Rolled, Structural Steels for Use in Fire Engineering Design Studies," Fire Safety Journal, 13 (1988), 27-37.

10. D.J. Price, "Enhanced Complex Structural Steel Sections" (DTI–Link project, British Steel Technical, Swinden Laboratories, Rotherham, 1993-1996).

11. J. Robinson, "A Disaster Waiting to Happen?" New Steel Construction, 3 (2) (1995), 12.

12. R.M. Lawson, D.L. Mullett and J.W. Rackham, "Slimdek: Development and Testing," New Steel Construction, 5 (3) (1997), 18-22.

13. P. Wright, "Slimdek: The System," New Steel Construction, 5 (3) (1997), 12-17.

14. F.S. Kelly and W. Sha, "Mechanical Properties of Fire-Resistant Steels for Construction," Proceedings of the 5th European Conference on Advanced Materials and Processes and Applications: Materials, Functionality and Design, vol. 1, ed. L.A.J.L. Sarton and H.B. Zeedijk (Zwijndrecht: Netherlands Society for Materials Science, 1997), 1/35-1/40.

15. ASTM E18-93 (American Society of Testing and Materials, 1993).

THE EVOLUTION OF THE GOSS TEXTURE IN SILICON STEEL

Dong Nyung Lee and Hyo-Tae Jeong*

Division of Materials Science and Engineering
*Research Center for Thin Film Fabrication and Crystal Growing of Advanced Materials
Seoul National University, Seoul 151-742, Korea
dnlee@snumfc.snu.ac.kr

Abstract

The Goss orientation, {110}<001>, in about 3% silicon steel has been the subject of speculation due to its scientific and technological points of view. The grain oriented silicon steel is made by hot rolling, cold rolling, followed by annealing. The Goss texture is formed near the surface layer of steel sheet when it is rolled in the α phase region at elevated temperatures, because the friction between the sheet and rolls tends to increase with increasing temperature, which in turn increases the shear deformation. The Goss texture remains unchanged even after recrystallization of steel.

The Goss texture, which is not stable with respect to plane strain deformation, rotates toward {111}<112> orientation. The relaxed constraints(RC) model, in which shear strains parallel to the rolling direction may occur, causes the formation of the {111}<112> orientation. The {111}<112> rolling component is known to lead to the Goss orientation after annealing. The energy release maximization theory for recrystallization suggested by one of the present authors(Lee) gives rise to the recrystallization texture of {441}<118> from the {111}<112> rolling texture. The {441}<118> orientation yields the Goss orientation when the {441}<118> orientation is expressed by the Gauss type scattering calculated with L_{max}=22 and ω_0=12 deg.

The Third Pacific Rim International Conference on
Advanced Materials and Processing (PRICM 3)
Edited by M.A. Imam, R. DeNale, S. Hanada,
Z. Zhong and D.N. Lee
The Minerals, Metals & Materials Society, 1998

Introduction

The Goss orientation, {110}<001>, in about 3% silicon steel has been the subject of speculation from the scientific and technological points of view. The grain oriented silicon steel is made by hot rolling, cold rolling, followed by annealing. The Goss texture is formed near the surface layer of steel sheets when they are rolled in the α phase region at elevated temperatures. At elevated temperatures the friction between the sheet and rolls tends to increase with increasing temperature, which in turn increases the shear deformation and gives rise to the Goss texture(Appendix). The Goss orientation remains unchanged even after recrystallization of steel(1).

The Goss texture, which is not stable with respect to plane strain deformation, rotates toward the {111}<112> orientation(2). The Relaxed Constraints(RC) Taylor model, in which shear strains parallel to the rolling direction may occur, causes the formation of the {111}<112> orientation(3). The {111}<112> rolling component is known to lead to the Goss orientation after recrystallization(2). Raabe and Lücke (3) found that the orientation intensity of the Goss component in the recrystallization texture increased with increasing orientation intensity of the {111}<112> component in the rolling texture (Figure 1). The above results can explain the "structure memory" mentioned in an article by Inokuti *et al*(4). Inokuti *et al.* found that the nucleation of {110}<001> secondary grains takes place in the vicinity of the steel surface zone. The nuclei for secondary grains were found to be the large primary recrystallized grains of near {110}<001> orientation which was formed by coalescence of several subgrains (Figure 2). They called the nucleation of the Goss orientation "structure memory" because the nucleation site was thought to be the site of the original Goss orientation formed during hot rolling.

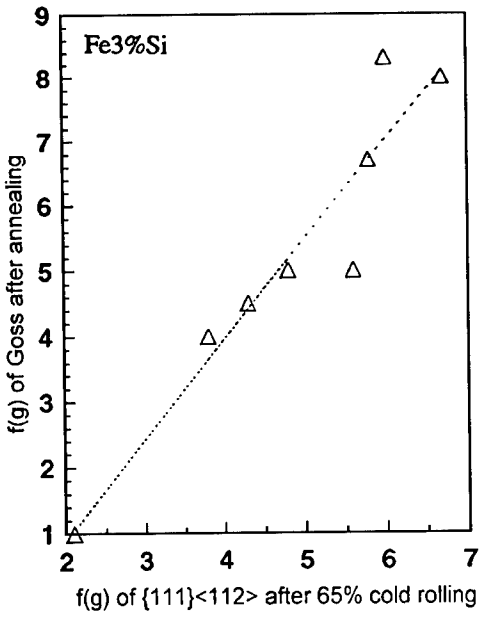


Figure 1: {111}<112> rolling component leads to Goss component {110}<001> after annealing(3).

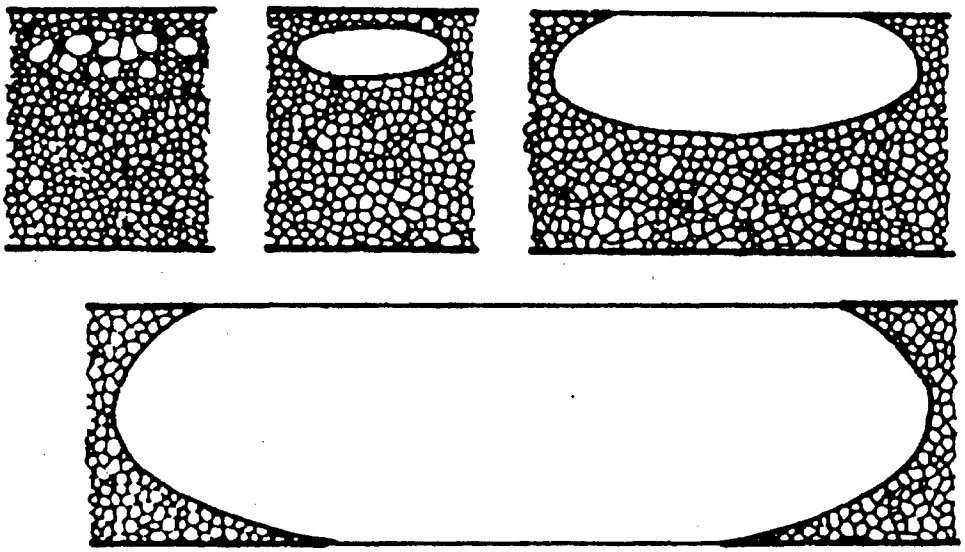


Figure 2: Sequence of nucleation and preferential growth of {110}<001> secondary grains at incipient stage during secondary recrystallization(4).

Matsuo(5) attributed this phenomenon to the nucleation of the Goss orientation in shear bands which mainly occur in {111}<112> host grains. Since the shear bands are inclined about 35 deg. about the transverse direction, the shear banding exactly rotates the {111}<112> orientation into the Goss orientation. Raabe and Lücke claimed that the Goss nuclei as parts of shear bands could grow well into the surrounding deformed {111}<112> grain during annealing since their 35 deg. <110> orientation relationship was the most favorable relationship for the growth of recrystallized nuclei(3). These explanations are based on the well known oriented nucleation and growth theories.

However, this phenomenon may be better understood by the energy release maximization theory advanced by one of the present authors(6). In the model, the absolute maximum normal stress direction of a deformed or fabricated material becomes parallel to the direction of the minimum elastic modulus of recrystallized grains, whereby the energy release during recrystallization can be maximized, because the material concerned does not change macroscopically its shape and volume during recrystallization and so the recrystallization is a displacement controlled process.

The absolute maximum stress direction may be obtained from the operating slip systems, which are related to the deformation mode and texture. If one slip system is activated, the absolute maximum normal stress direction is parallel to the slip direction. If more than one slip system are activated, the absolute maximum normal stress direction can be determined by the vector sum of related slip directions. This concept originates from the presumption that the stored energy due to dislocations is most important driving force for recrystallization. This energy release maximization theory could explain many well known recrystallization textures of fcc and bcc metals(6) such as the recrystallization textures of interstitial free steels(7), plane strain compressed aluminum single crystal(8), shear rolled copper(9), aluminum(10) and

interstitial free steel(1) sheets and the recrystallization textures of copper(11,12) and silver(13) electrodeposits.

The purpose of this work is to discuss the texture transformation from {111}<112> to {110}<001> based on the energy release maximization theory.

Recrystallization Texture

Slip systems of $(110)[1\bar{1}1]$, $(110)[\bar{1}11]$, $(101)[11\bar{1}]$ and $(011)[11\bar{1}]$ are calculated by the Relaxed Constraints Taylor model to be equally active in the $(111)[11\bar{2}]$ crystal undergoing the plane strain deformation. The $(110)[1\bar{1}1]$ and $(110)[\bar{1}11]$ systems are effectively the same as the (110)[002], and the $(101)[11\bar{1}]$ and $(011)[11\bar{1}]$ are effectively the same as the $(112)[11\bar{1}]$. Considering that the rolling direction is parallel to $[11\bar{2}]$, the (110)[002] slip system may be better expressed as the $(\bar{1}\,\bar{1}0)[00\bar{2}]$ system. The maximum stress direction is, therefore, $[11\bar{1}]+[00\bar{2}]=[11\bar{3}]$. According to the maximum energy release theory, this maximum stress direction $[11\bar{3}]$ becomes parallel to the minimum Young's modulus direction, a <100> direction in bcc iron, after recrystallization.

Another direction must be obtained to determine the recrystallization texture. The direction may be obtained by conditions of symmetry and minimum shuffling of atoms during recrystallization. Let a <100> direction be the [001] direction, then the [001] direction must be on the (100), (010) or (110) plane, taking the symmetry condition into account. One of them may be chosen by the minimum shuffling condition.

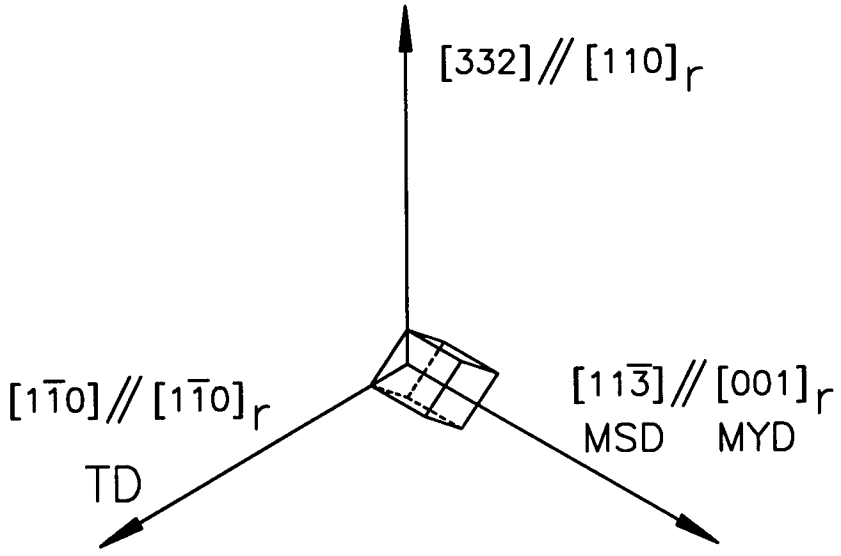


Figure 3: Relation between orientations in deformed and recrystallized states. Subscript r indicates recrystallized state. TD, MSD, MYD stand for transverse direction, absolute maximum stress direction and minimum Young's modulus direction.

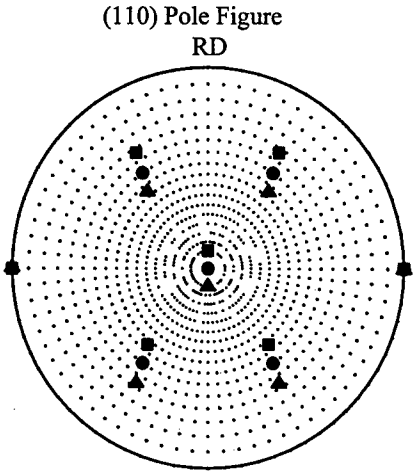


Figure 4: {110}<001> and {441}<118> orientations in (110) pole figure.

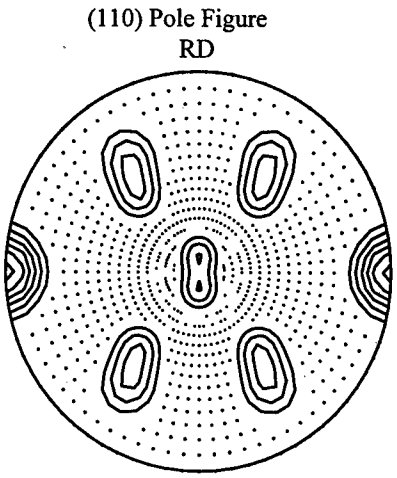


Figure 5: (110) pole figure as Gaussian function of {441}<118> orientation with a half width of 12 degree and L_{max}=22.

The transverse direction of the (111)[11$\bar{2}$] crystal is the [1$\bar{1}$0] direction, along which there is no strain due to plane strain conditions. If the [332] direction, which is normal to both [1$\bar{1}$0] and [11$\bar{3}$] directions, is parallel to the [110] direction of recrystallized grains, the [1$\bar{1}$0] direction is commonly shared by the deformed matrix and recrystallized grains, whereby the minimum shuffling condition may be achieved. In conclusion, the maximum stress direction, [11$\bar{3}$], and the [332] direction become parallel to the [001] and [110] directions in recrystallized grain, respectively (Figure 3). In other words, the [001] direction must be on the (110) plane.

It follows from the above geometrical relations that the (111)[11$\bar{2}$] orientation will become the (441)[11$\bar{8}$] orientation after recrystallization. The symmetry yields another equivalent orientation, (44$\bar{1}$)[$\bar{1}$ $\bar{1}$ 8].

The (110) pole figure of the {441}<118> orientation is shown in Figure 4 along with the Goss orientation, {110}<001>. The {441}<118> orientation is deviating from the Goss orientation by 10 deg.. If each {441}<118> orientation is represented by the Gauss type scattering with a half width angle of 12deg., the calculated result is shown in Figure 5. This is in very good agreement with the measured data in Figure 6, where the highest intensity poles are the same as those of the Goss orientation, even though it is not a real Goss orientation. It is also interesting to note that the rotation angle between (111)[11$\bar{2}$] and (441)[11$\bar{8}$] around a common pole of [110] is calculated to be 25 deg. and the rotation angle between (111)[11$\bar{2}$] and (110)[001] around a common pole of [110] is 35 deg. (Figure 7). This angular relation is often taken as an evidence for oriented growth theory for recrystallization(2,14,15), in which the relation is attributed to grain boundary mobility anisotropy. However, the angular relation is also obtained by the present method. Therefore, the angular relation may not be attributed to the grain boundary mobility anisotropy.

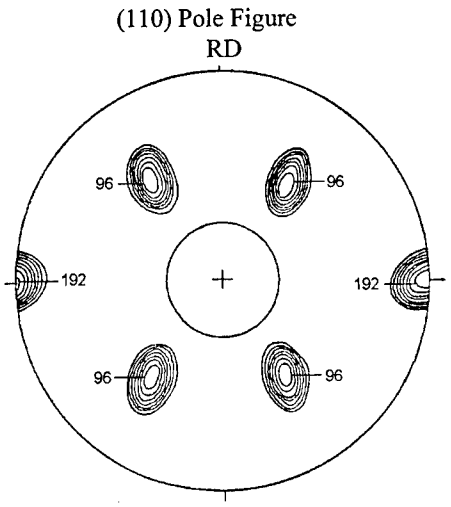


Figure 6: Pole density stereogram of (110) poles of sample of specimen 1 recrystallized 1 minute at 980°C(2).

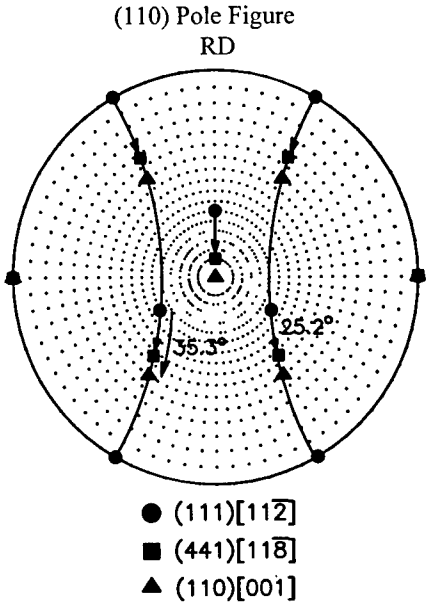


Figure 7: {111}<112> and {441}<118> orientations in (110) pole figure.

Summary

The Goss orientation, {110}<001>, formed near the surface layer of silicon steel during hot rolling rotates toward the {111}<112> orientation during cold rolling. The {111}<112> orientation is calculated by the maximum energy release model to change into the {441}<118> after recrystallization. Representing each {441}<118> orientation by the Gauss type scattering gives rise to the Goss texture in very good agreement with measured results(2).

Acknowledgment

This work has been supported by RETCAM, Seoul National University.

References

1. S. H. Lee and D. N. Lee, "Shear rolling and recrystallization textures of interstitial free steel sheet", Mater. Sci. Eng. A in press.

2. C. G. Dunn, "Cold-rolled and primary recrystallization textures in cold-rolled single crystals of silicon iron", Acta Metall., 2 (1954), 173-183.

3. D. Raabe and K. Lücke, "Rolling and Annealing Textures of BCC Metals", Materials Science Forum, 157-162 (1994), 597-610.

4. Y. Inokuti et al.,"Analysis of crystallographic orientation at an incipient stage of secondary recrystallization of grain oriented silicon steel by transmission Kossel technique", Proc. of 6th Int. Conf. On Textures Of Materials, (Tokyo : The Iron and Steel Institute of Japan, Ibaraki Printing Co. 1981), 948-957.

5. M. Matsuo,"Texture control in the production of grain oriented silicon steels", ISIJ International, 29 (1989), 809.

6. D. N. Lee, "The Evolution of Recrystallization Textures from Deformation Textures", Scripta Metall. Mater. 32 (1995), 1689-1694.

7. Y. B. Park, D. N. Lee and G. Gottstein, "Evolution of recrystallization texture from cold-rolling texture in interstitial-fee steel", Mater. Sci. Tech. 13 (1997), 289-298.

8. D. N. Lee,"Recrystallization texture of plane strain compressed aluminum single crystal", Texture and Microstructures, 26-27 (1996), 361-367.

9. S.-H. Hong et al., "Deformation and Recrystallization Textures of Surface Layer of Copper Sheet", Mater. Sci. Eng., A229 (1997), 174-181.

10. C.-H. Choi and D. N. Lee, "Evolution of Recrystallization Texture from Aluminum Sheet Cold Rolled under Unlubricated Condition", Metall. Mater. Trans., 28A (1997), 2217-2222.

11. D. N. Lee, S. Kang and J. Yang, "Relationships between initial and recrystallization textures of copper electrodeposits", Plating and Surface Finishing, 82 (1995), 76-79.

12. D. N. Lee, "Maximum energy release theory for recrystallization textures", Metals and Materials, 2 (1996), 121-131.

13. H. S. Nam and D. N. Lee "Recrystallization texture of silver electrodeposits", This proceedings.

14. G. Ibe and K. Lücke , Arch. Eisenhuyyenwes., 39 (1968), 693-703.

15. K. Lücke and M. Holscher, "Rolling and Recrystallization Textures of BCC Steels", Texture and Microstructures, 14-18 (1991), 585-596.

Appendix

In order to show the evolution of the Goss texture near the surface layer of bcc steel sheets during rolling, the rolling texture of IF steel sheet has been simulated as an example.

The deformation of IF steel sheet during rolling process was calculated by FEM using elasto-plastic material model and updated Lagrangian analysis(A1). In FEM calculations, the tensile behavior of the IF steel was described by Hollomon's relation, $\sigma = K\varepsilon^n$, with K= 500 MPa and n=0.256 which were obtained by tensile test. In this simulation, diameter of roll, initial thickness of IF steel sheet and reduction were set to be 310mm, 3.4mm and 70%, respectively.

In this case, the l/d parameter was 6.4. The Coulomb friction law between IF steel sheet and roll was assumed and the friction coefficient was assumed to be 0.3.

The rotations of crystal orientation were calculated based on the Taylor-Bishop-Hill full constraints model and the strain history calculated from FEM simulation. The {110}<111> and {112}<111> slip systems were assumed and active slip systems were calculated by linear programming method and random choice(A2). Each element was assumed to have randomly distributed 978 single crystals at the initial state. For representation of pole figures in form of continuous contour, each orientation was replaced by the Gauss-type scattering with a half-width of 7 deg.

Figure A1 shows the deformed FEM meshes in rolling process. The deformed meshes show that the distortion and rotation of elements increase to a maximum value with increasing distance from the center of sheet, which in turn increases the shear deformation. The calculated (110) pole figures are shown in figure A2. The Goss texture develops in the surface layers, while α-fiber texture develops in the center layer.

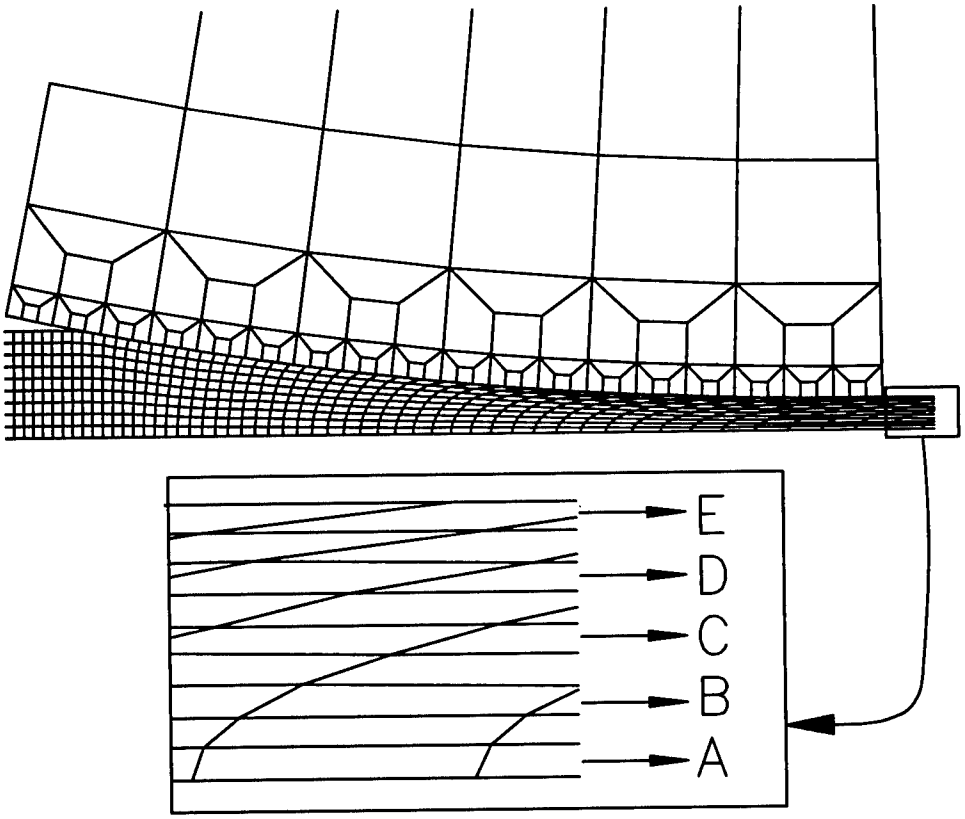


Figure A1: Deformed FEM meshes in rolling process.

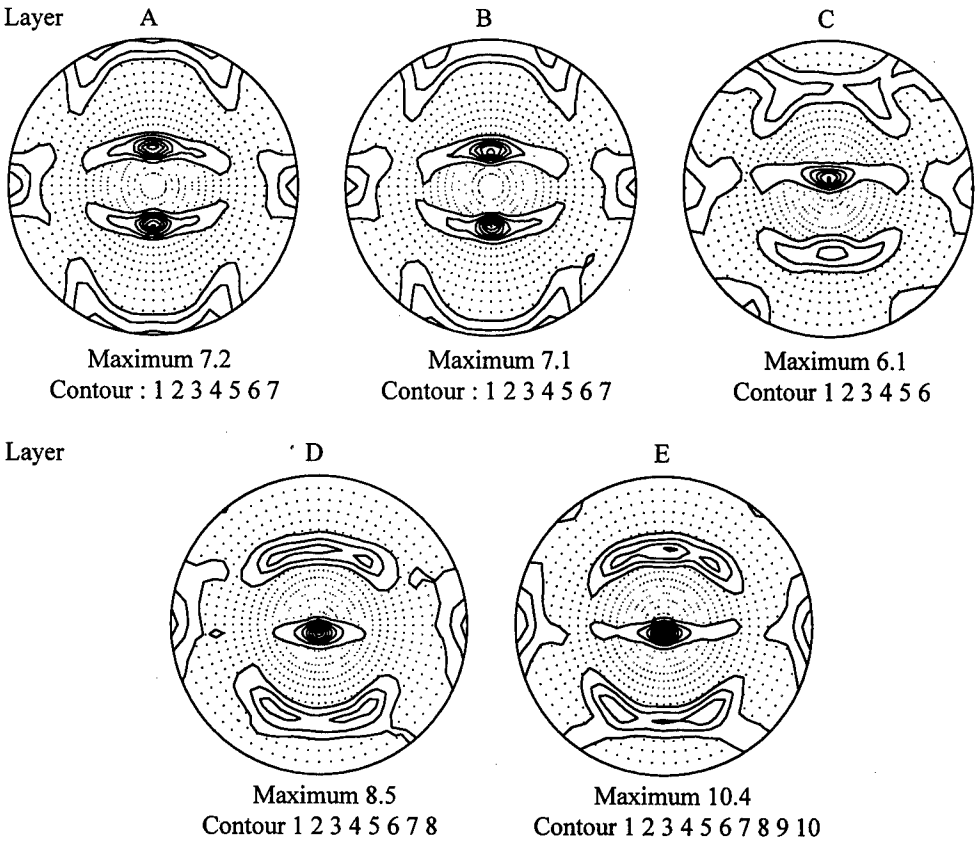


Figure A2: Calculated (110) pole figures of different layers in Figure A1.

References

A1. K. J. Bathe, Finite Element Procedures in Engineering Analysis (Prentice Hall, 1982)

A2. P. Van Houtte, "Adaptation of the Taylor theory to the typical substructure of some cold rolled fcc metals", Proc. of 6th Int. Conf. On Textures Of Materials, (Tokyo : The Iron and Steel Institute of Japan, Ibaraki Printing Co. 1981), 428-437.

AN ABNORMAL EFFECT OF PHOSPHORUS ON MECHANICAL PROPERTIES IN NICKEL-BASE SUPERALLOYS OF Ni-Cr-Fe, Ni-Cr-Fe-Mo AND Ni-Cr-Fe-Mo-Nb-Ti-Al SYSTEMS

Xishan Xie, Xingbo Liu, Jianxin Dong, Yaohe Hu, Zhichao Xu and *Mengzhe Chen*
University of Science and Technology Beijing, Beijing 100083, China
Chongyu Wang
Central Iron and Steel Research Institute, Beijing 100081, China
Raymond G. Thompson
University of Alabama at Birmingham, AL35294-4461, USA

Abstract

Phosphorus has been controlled to a low level in current specifications of advanced nickel-base superalloys, because it is considered as a most common impurity element and has detrimental effect on mechanical properties. A new way to improve cast nickel-base superalloys has been developed in China to control P to an extremely low level (less than 10 ppm) for segregation and long time high temperature structure stability improvement. However, in wrought superalloys after high temperature long time ingot homogenization treatment and hot deformation process, on the contrary, P has an abnormal effect on mechanical properties.

Four heats of each Ni-Cr-Fe and Ni-Cr-Fe-Mo alloys with 0.0005 to 0.0190%P and five heats of Ni-Cr-Fe-Mo-Nb-Ti-Al systems INCONEL 718 alloy with different contents of P in the range of 0.0010% to 0.0130%wt, were vacuum melted and poured into 15kg ingots, which were conducted with long-time high-temperature homogenization treatment for forging and hot-rolling to 18mm round test bars.Two industrial heats of INCONEL718 with different contents of P are also included in this investigation.

Phosphorus has almost no effect on tensile properties not only at room-temperature but also at 650℃ high-temperature. However, it has an abnormal effect on 650℃ stress rupture properties. Stress rupture lives are tremendously increased by P doping in alloys. Creep test results at 650℃ show the prolonging of secondary creep stage and longer creep failure lives. Experimental results indicate that P has certain strengthening effect and ductility improvement at high-temperature time-dependent mechanical properties.

SEM fractography observation, TEM and Auger analyses indicate the grain boundary segregation of P and its interaction with other elements. It has important effect on grain boundary behavior at high-temperature deformation with low strain rates.

Theoretical analysis and grain boundary model of P doping in nickel-base superalloys have been proposed to explain the abnormal effect of P in these Ni-base alloys and a new idea on development of P doping superalloys at certain conditions has been also suggested.

This research project is supported by National Natural Science Foundation and Ministry of Metallurgical Industry in China

The Third Pacific Rim International Conference on
Advanced Materials and Processing (PRICM 3)
Edited by M.A. Imam, R. DeNale, S. Hanada,
Z. Zhong and D.N. Lee
The Minerals, Metals & Materials Society, 1998

Introduction

Phosphorus, along with sulfur is considered as common impurities and detrimental elements in most structural materials such as steels and superalloys. When P segregates at ferrite grain boundary and forms the film of Fe_3P, then cause to temper embrittlement[1]. Jin-Yu and McMahon's study [2] attributed the temper embrittlement of 2.25Cr-1Mo steel to the segregation of P along grain boundary and they indicated that the beneficial effect of Mo is to suppress embrittlement by scavenging P, presumably by a Mo-P compound formation, thereby diminishing the detrimental effect of P segregation. The results of Noble et al. [3] also support the point of view that the decrease in ductility associated with the 1000h aging at 550℃ in 9Cr-1Mo Steel with high P content is caused by the segregation of P at carbide/matrix interfaces.

In the contrary, a few experimental results indicate the beneficial effect of P on various mechanical properties in alloy steels or superalloys. Wikinson's results from the study of 2.25Cr-1Mo steel [4] show that the ductility of as-tempered samples containing with higher P and Mn was found to be higher than those without P. Investigation of Nam et al. on AISI 304L stainless steel [5] show the beneficial effect of P on the fracture life under creep-fatigue test at 823K. Was et al results [6] show the intergranular cracking behavior improvement at 360℃ in argon and water environments by the addition of P into IN600 (Ni-16Cr-9Fe) alloy. Works on Monel400 (Ni-30Cu-1Fe-1Mn-0.5C)[7] alloy indicate the significant tensile elongation increasing with higher concentration of P at grain boundaries. However, any clear explanation on the beneficial effect of P has not been suggested yet.

Recently, a new way to improve cast nickel-base superalloys has been developed in China [8] to control P to an extremely low level (less than 10 ppm) for segregation and structure stability improvement. However, Cao [9] et al. and Xie [10] et al. have found that in the most world-widely used wrought superalloys INCONEL718 after long time ingot homogenization treatment and hot deformation process, P has an abnormal beneficial effect on mechanical properties, especially on stress rupture properties.

The goal of this paper is systematically to investigate the role of P in typical corrosion-resistant alloy system (Ni-Cr-Fe, Ni-Cr-Fe-Mo) and the most used superalloy INCONEL718 in the system of Ni-Cr-Fe-Mo-Nb-Ti-Al, and finds out the effect of P on mechanical properties in these alloy systems. Then we try to have some theoretical discussions for further understanding the role of P in nickel-base alloys.

Experimental Procedure

Test Materials

In consideration of the most used Ni-base alloys and the complexity of P effect on solid solution strengthening corrosion-resisting alloys and precipitation hardening (γ' and γ'') superalloys, 3 alloy systems (Ni-Cr-Fe, Ni-Cr-Fe-Mo and Ni-Cr-Fe-Mo-Nb-Ti-Al) were designed for this investigation. Experimental materials were all vacuum melted and divided into four groups. The chemical compositions are listed at Table I and II. Group I and II, each includes 4 heats of Ni-Cr-Fe and Ni-Cr-Fe-Mo with various contents of P in the range of 5ppm to 190ppm. Five heats of Group III alloys (Ni-Cr-Fe-Mo-Nb-Ti-Al system, IN718) with different contents of P in the range of 10-130ppm) were melted in 25Kg VIM furnace and poured into 15Kg ingots, which were conducted homogenization treatment, then forged and hot rolled for round test bars. In consideration with industry application, 2 commercial heats of IN718 (7ppm and 30ppm) were chosen for mechanical properties qualification including crack propagation rate testing at 650℃.

Heat Treatment Group I and II (Ni-Cr-Fe and Ni-Cr-Fe-Mo) alloys were treated as: 960℃/1hour/Air cooled. Group III and IV (IN718) alloys were subjected to standard heat treatment as: 960℃/1h/Air cooled + 720℃/8h/furnace cooling with the cooling rate of 50℃/hour to 620℃/8h/Air cooled.

Table I. Chemical Composition of Group I and II Alloys (wt%)

Group	Alloy	Ni	Cr	Fe	Mo	C	P	S
I	11	Bal.	21.59	22.02	---	0.019	0.0005	0.0015
	12	Bal.	21.58	21.59	---	0.017	0.003	0.0017
	13	Bal.	21.59	21.85	---	0.019	0.010	0.002
	14	Bal.	21.50	22.47	---	0.024	0.019	0.002
II	21	Bal.	21.90	21.75	2.80	0.015	0.0005	0.001
	22	Bal.	21.73	20.28	2.83	0.013	0.003	0.003
	23	Bal.	21.90	21.23	2.72	0.018	0.008	0.001
	24	Bal.	21.70	20.19	2.55	0.027	0.018	0.003

Table II. Chemical Composition of Group III and IV Alloys (wt%)

Group	Alloy	C	Mn	Si	S	P	Ni	Cr	Mo	Al	Ti	Nb	B	Fe
III	31	.02	.02	.05	.001	.0010	52.52	18.69	3.01	.52	1.01	5.20	.005	Bal.
	32	.03	.02	.05	.002	.0025	52.38	18.62	2.98	.47	1.01	5.15	.005	Bal.
	33	.03	.02	.06	.003	.0033	52.79	18.56	3.01	.52	1.00	5.24	.006	Bal.
	34	.02	.02	.05	.003	.0083	52.76	18.45	3.05	.52	1.01	5.17	.006	Bal.
	35	.02	.02	.05	.003	.0130	52.90	18.76	3.01	.50	1.01	5.17	.005	Bal.
IV	0H2101	.03	.02	.04	.003	.0007	51.52	18.23	2.97	.52	1.03	5.15	.004	Bal.
	1H2172	.03	.35	.35	.003	.0030	53.4	18.5	2.87	.46	1.02	5.08	.005	Bal.

Mechanical Testing and Analyses

Group I and II alloys were taken with tensile test at room temperature, stress rupture test at 650 ℃,150MPa and creep tests at 650℃,150MPa and 200MPa separately. For group III alloys, tensile tests at room temperature and 650℃, stress rupture tests at 650℃,686MPa, creep tests at 650℃,725MPa were conducted. For group IV alloys, except mechanical property tests crack propagation rate determinations were also performed at 650℃ stress controlled LCF with different dwelling times at maximum stress.

Fractography and microstructure analyses for all the alloys were conducted with optical, scanning (SEM) and transmission electronic (TEM) microscopes. Auger analysis was directly conducted at fresh surface (in situ) from the stress rupture tested specimens of Group III alloys which were hydrogen charged to produce fracture separation at grain boundaries.

Results and Discussion

Mechanical Properties

Tensile Properties Phosphorus has almost no effect on tensile properties of Ni-Cr-Fe and Ni-Cr-Fe-Mo alloys at room temperature (Fig.1,2). And similarly, P also has very few effect on tensile strength and ductility of IN718 alloy at ambient temperature and 650℃(Fig.3) both.

Stress Rupture Properties Phosphorus can remarkably increase 650℃ stress rupture life and mildly improve ductilities as shown in Fig.4,5 and 6. In all alloy systems the stress rupture lives is abnormally raised with the increasing of P content in this investigation.

Creep Properties Fig.7 shows that P tremendously prolongs secondary creep stage and results in a longer creep life in Ni-Cr-Fe-Mo-Nb-Ti-Al system alloy (IN718). IN718 alloy with high content of P(130ppm) as shown in Fig.7 characterizes with unbelievable creep properties. The similar effect of P on creep behavior can be also revealed in Ni-Cr-Fe and Ni-Cr-Fe-Mo system alloys as shown in Fig.8 and 9, but these effect

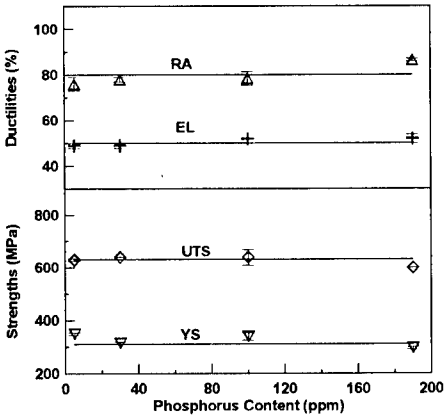


Figure 1: Effect of Phosphorus on Tensile Properties of Ni-Cr-Fe Alloys at Room Temperature.

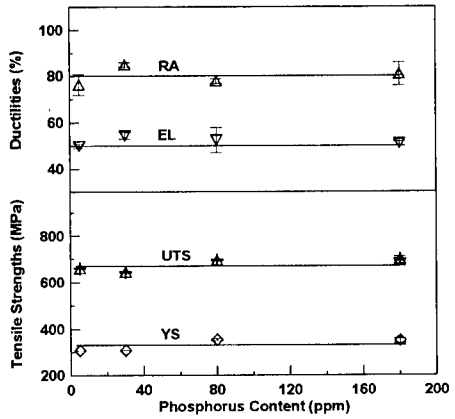


Figure 2: Effect of Phosphorus on Tensile Properties of Ni-Cr-Fe-Mo Alloys at Room Temperature.

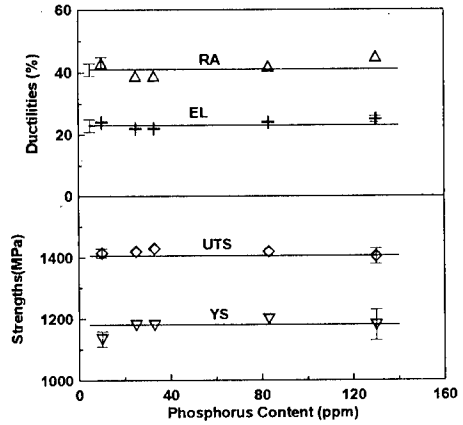


Figure 3: Effect of Phosphorus on Tensile Properties of INCONEL718 Alloys at Room Temperature.

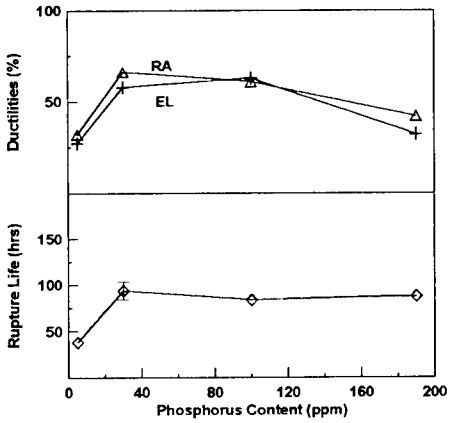


Figure 4: Effect of Phosphorus on Stress Rupture Properties of Ni-Cr-Fe Alloys at 650 C,150MPa.

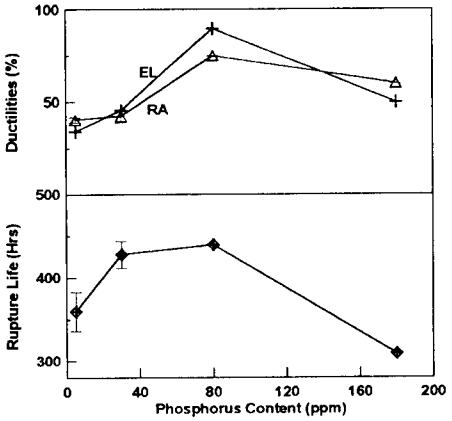


Figure 5: Effect of Phosphorus on Stress Rupture Properties of Ni-Cr-Fe-Mo Alloys at 650 C,150MPa.

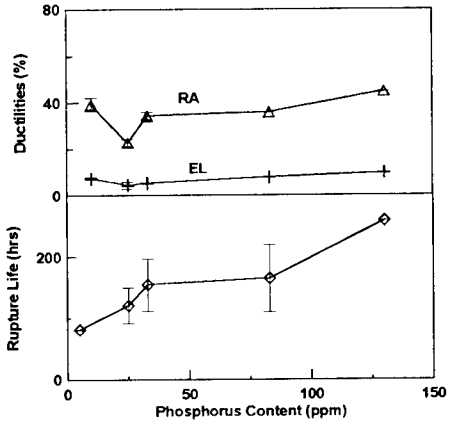


Figure 6: Effect of Phosphorus on Stress Rupture Properties of INCONEL718 at 650 C,686MPa.

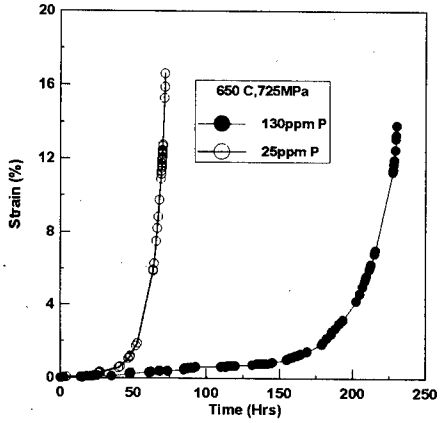


Figure 7: Effect of Phosphorus on Creep Properties of INCONEL718 Alloys at 650 C,725MPa.

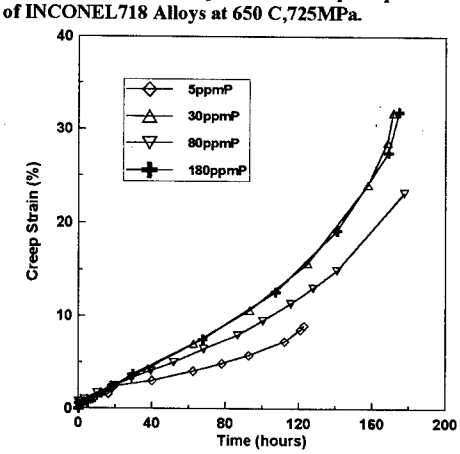


Figure 8: Effect of Phosphorus on Creep Properties of Ni-Cr-Fe Alloys at 650 C,150MPa.

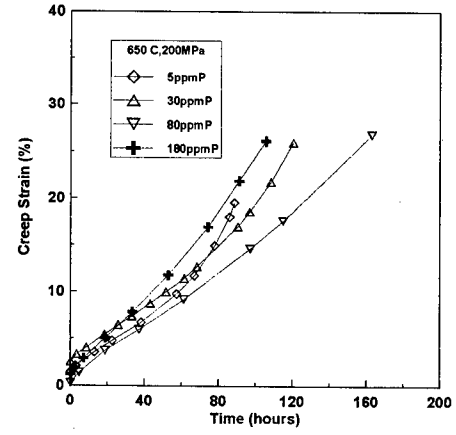


Figure 9: Effect of Phosphorus on Creep Properties of Ni-Cr-Fe-Mo Alloys at 650 C,200MPa.

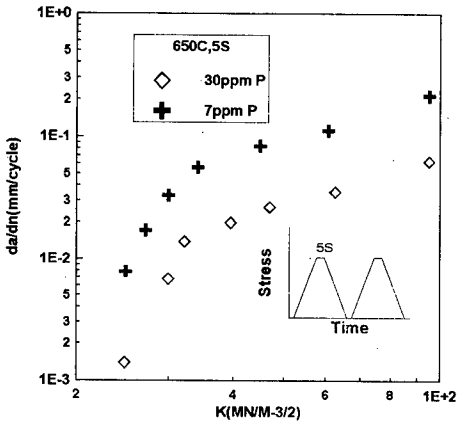


Figure 10: Effect of Phosphorus on Crack Propagation of INCONEL718 at LCF with 5S Dwelling Time.

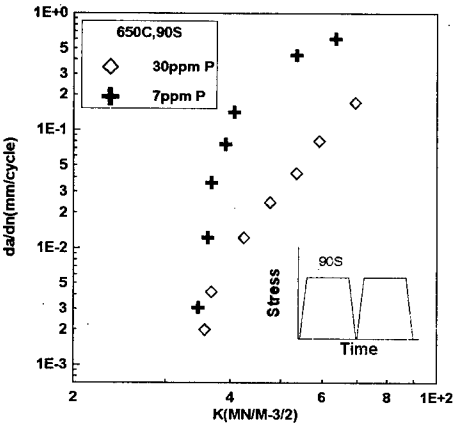


Figure 11: Effect of Phosphorus on Crack Propagation of INCONEL718 Alloys at LCF with 90S Dwelling Time.

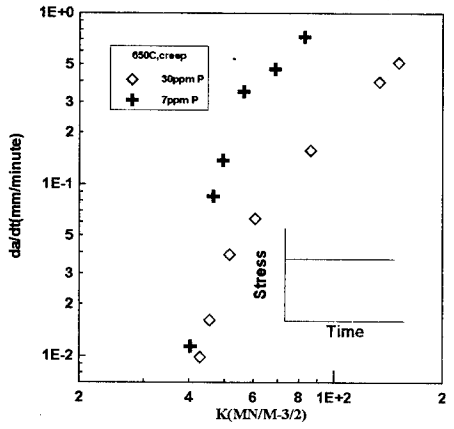


Figure 12: Effect of Phosphorus on Creep Crack Propagation Rate of INCONEL718 at 650C.

is not as typical as in Ni-Cr-Fe-Mo-Nb-Ti-Al system IN718 multi-component alloy.

Crack Propagation Rate Behavior Fig10-12 show the contrast of high temperature (650℃) crack propagation behavior of two commercial heats of IN718 alloys with different P contents. It can be clearly seen that the alloy with higher content of P has lower crack propagation rate under creep and creep/fatigue interaction condition with different dwelling times (5s, 90s) at maximum stress. It also reveals the beneficial effect of P on crack propagation resistance in Ni-Cr-Fe-Mo-Nb-Ti-Al system IN718 alloy.

Microstructure and Fractography Microstructure analysis by means of optical microscope, SEM and TEM do not reveal the effect of P on grain structure, morphology and amount of precipitates in different alloy systems. Fractography observation on the longitudinal section of stress rupture failure specimens shows the existence of typical grain boundary cracks in all specimens and it appears more grain elongation at the tip of specimens with higher creep ductilities in comparison with those with lower ductilities.

Auger Analyses Fig13 shows the typical Auger spectrum collected from the grain boundary of IN718 alloy. It shows the presence of P exception of a characteristic signature of Mo, Cr, Nb and C, N etc.. The concentration variation of impurity element P, S and metal element Mo, Nb and Ti with increasing the sputtering time is shown in Fig.14, even the concentration of sulfur was tended to zero after 60 seconds sputtering. While the concentration of metal elements such as Mo and Nb is also decreased with increasing sputtering time. It is probable that the metal elements of Mo and Nb also co-segregated to grain boundaries with P. Auger spectra of the carbide/matrix interface before and after ion sputtering is shown in Fig.15.

The extensive studies have been reported on the attractive interactions of metal-nonmetal(M-I), such as Cr-P, Ni-P, Ni-Sb, Cr-N and Mo-P couples etc.[13]. However, some results seem ambivalent because of the rather complex alloy systems. Alloy 718 is a rather complex system with many elemental species. Interactions between these elements can probably modify their segregation to interfacial surface. The higher concentrations of Mo and Nb at grain boundaries than in matrix regions may be due to element interactions. Indeed, the Auger measurements made on a large number of grain boundaries in tested samples support the contention that Mo and Nb all co-segregate to grain boundaries with phosphorous. It is shown by the plots in Fig.16, in which each point represents an individual grain boundary. These results confirm the co-segregation of some metal elements, especially Mo and Nb with P.

Discussion

Most of former experiments and electronic calculations [14] indicate that P has a segregation behavior at grain boundary(GB) and leads to an embrittlement effect in transition metals Ni and Fe. However, our results show that P has an abnormal effect on strength and ductility improvement at high temperature. Up to now have no clear understanding on nature and mechanism. We suggest that impurity-defect complex and interaction between atoms which might have different electron configuration and maybe resulting in the appearance of the abnormal bonding state at grain boundary, so the key of P behavior can result from the effect of P-GB-Mo complex or P-GB-M(metal element) complex on the binding strength and ductility behavior.

On the basis of the theoretical calculation mode for first principles interatomic potential and interatomic interaction energy developed by us[15], as well as the theoretical research for the correlation between the impurity-defect complex and the dislocation behavior presented by us[16], and some experience for the study of the electronic structure of impurity-defect complex, we are interested in and will be to deal with the problem of the mechanism of P effect in multi-component system superalloys. The corresponding calculations will be involved as follows:

a) The calculations of energies (binding energy, segregation energy and inter-atomic interaction energy) for

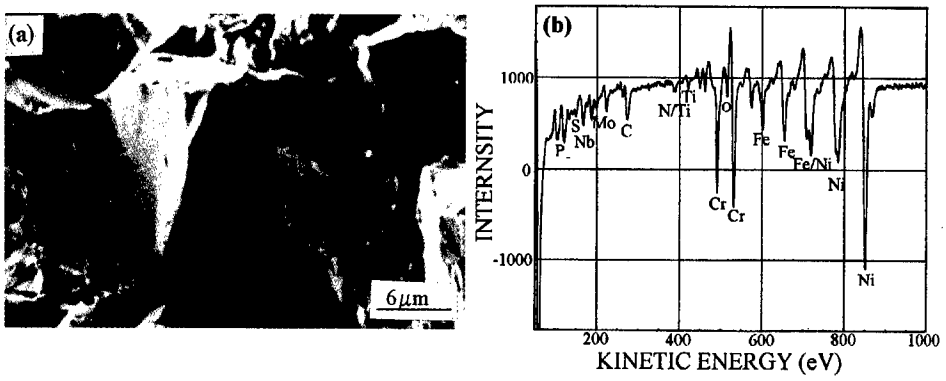


Figure 13: Fresh Fracture Grain Boundary Surface(a) and Auger Chemical Spectrum(b) of IN718

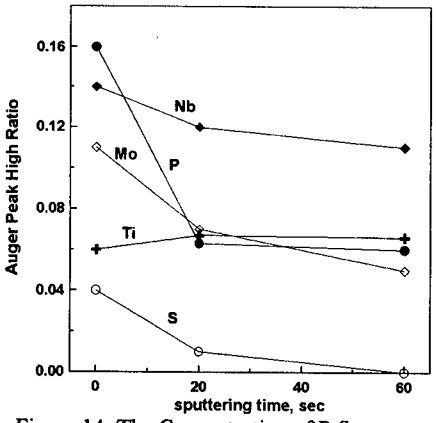


Figure 14: The Concentration of P,S etc. as a Funtion of Sputtering Time at Grain Boundary

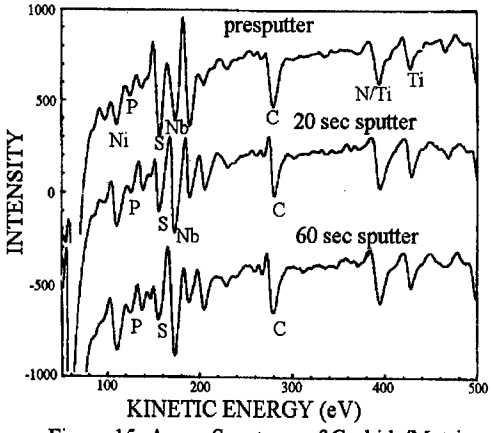
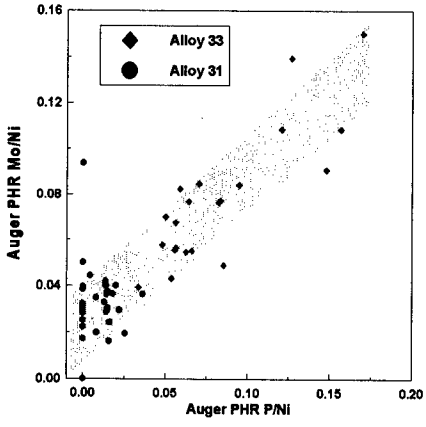


Figure 15: Auger Spectrum of Carbide/Matrix Interface of IN718



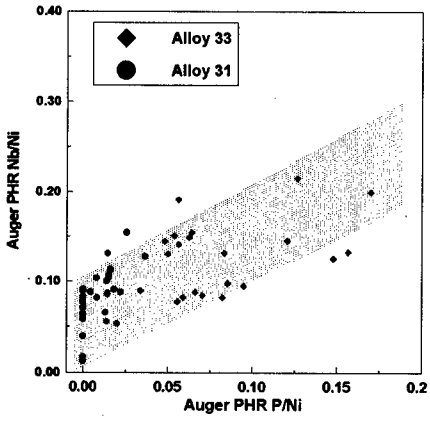


Figure 16: Relationship between the Auger Peak High Ratio of P with Mo and P with Nb

the alloys contained P.
b) The calculations of electronic structure (difference charge density, density of state and energy spectrum) for the alloys containing with P. We predict that the mechanism of action of P in alloys may be revealed if the combination among the quantum theory and classical theory as well as experiments is realized very well.

Conclusions

1. Phosphorus has almost no influence on tensile strengths and ductilities in Ni-Cr-Fe, Ni-Cr-Fe-Mo and Ni-Cr-Fe-Mo-Nb-Ti-Al (INCONEL718) system alloys.
2. Phosphorus has an abnormal effect on the improvement of stress rupture and creep properties and characterizes with strengthening effect and ductility improvement at 650℃ stress rupture and creep tests in Ni-Cr-Fe, Ni-Cr-Fe-Mo and Ni-Cr-Fe-Mo-Nb-Ti-Al (INCONEL718) alloys.
3. Phosphorus has a beneficial effect on crack propagation restitance in Ni-Cr-Fe-Mo-Nb-Ti-Al system IN718 alloy at 650℃ creep/fatigue interaction test condition.
4. Phosphorus not only severely concentrates at grain boundaries but also co-segregates with some metal elements (such as Mo and Nb) in Ni-Cr-Fe-Mo-Nb-Ti-Al (INCONEL718) alloy.
5. A new point of view on P control in industrial production of superalloys can be taken in consideration on superalloy development. The theoretical understanding on the P behavior has been suggested.

References

1. Jin Z. & Wang X, " Mechanical Properties of 1.25Cr-0.5Mo Steel Pipe Used for 1.2×10^5h at Temperature 540℃" Journal of Iron & Steel Research, 4 (1992) 79-83.
2. Jin Yu and C.J.McMahon, "The Effects of Composition and Carbide Precipitation on Temper Embrittlement of 2.25Cr-1Mo Steel: Part I. Effects of P and Sn" Met.Trans.11A (1980) 277-289.
3. F.W.Noble et al, The Effect of Phosphorus on the Ductility of 9Cr-1Mo Steels"Acta. Met. 38(1990),709-717.
4. D.S.Wikinson et al., "Compositional Effects on the Creep Ductility of a Low Alloy Steel" Met.Trans.11A (1980) ,1827-1836.
5. S.W. Nam et al., "Effect of Phosphorus on the Creep-Fatigue Interaction in AISI 304L Stainless Steel" Journal of the Korean Inst.of Met.& Mater.30 (1992),1401-1406.
6. G.S.Was, J.K.Sung and T.M.Angeliu,"Effects of Grain Bondary Chemistry on the Intergranular Cracking Behavior of Ni-16Cr-9Fe in High-Temperature Water" Met. Trans, 23A(1992),3343-3359.
7. A.W.Funkenbusch, L.A.Heldt and D.F.Stern, "The Influence of Grain Boundary P Concentration on Liquid Metal and Hydrogen Embrittlement of Monel400" Met.Trans., 13A(1982),611-618.
8. Y,Zhu et al., "A New Way to Improve Superalloys" Superalloys 1992, ed. S.D.Antolovich et al.(TMS,1992) 145-154
9. W.D.Cao, R.L.Kennedy, "The Effect of Phosphorus on Mechanical Properties of Alloy 718" Superalloys 718,625,706 and Various Derivatives, ed. E.A.Loria, (TMS,1994), 463-478.
10. X.Xie et al., "The Role of Phosphorus and Sulfur in Inconel718" Superalloys 1996 ed. R.D.Kissinger et al.(TMS,1996)599-606.
11. P.Sevc et al., "Equilibium Grain Boundary Segregation of Phosphorus in 2.6Cr-0.7Mo-0.3V Steels" Acta Metall.,43,(1995)251-258
12. Shaoping Tang, A.J.Freeman, "Phosphorus Relaxation in an Iron Grain Boundary: A Cluster-Model Study" Phys.Rev. B47(1993)2441-2445
13. Wang Chongyu et al., An Interatomic Potential on First Principles and Application to Grain Boundary in Nickel" Phys.Lett. A(1997)449-457
14. Wang Chongyu et al., "Electronic Structure of Light-Impurity(Oxygen)-Stacking Fault Complex in Nickel" Phys.Rev. B41(1990)1359-1367.

RELATIONSHIP BETWEEN TEXTURE AND MAGNETIC PROPERTIES OF NON-ORIENTED SI STEEL

N. Chen, W. Mao, Y. Yu

School of Materials Science and Engineering
University of Science and Technology Beijing
Beijing, China 100083

Abstract

The new method of predicting magnetic anisotropy in non-oriented Si steel has been investigated for the potential application in industry production. The relationship between texture and magnetic torque was analyzed. Using the phenomenological theory the pole figure of magnetocrystalline anisotropy energy (MAE) concerning magnetic torque and the corresponding magnetic anisotropy coefficients of generalized spherical harmonics of orientation distribution functions (ODFs) were calculated, which could be used to predict the magnetic torque of polycrystalline materials. According to some measured textures in non-oriented Si steel sheets the theoretical magnetic torque curve was calculated and discussed in comparison with measured torque data.

The Third Pacific Rim International Conference on
Advanced Materials and Processing (PRICM 3)
Edited by M.A. Imam, R. DeNale, S. Hanada,
Z. Zhong and D.N. Lee
The Minerals, Metals & Materials Society, 1998

Introduction

Many physical properties of a single crystal are frequently anisotropic, and the strong anisotropic properties could remain in corresponding polycrystalline if it has crystallographic texture. It is very important sometimes to predict the directional variation of a macroscopic properties of a polycrystalline, which is theoretically possible if the property anisotropy of the single crystal and the texture of the polycrystalline are known. Magnetic materials, for example, are widely used in different areas, and the corresponding property prediction is also important e.g. for quality control of the production of non-oriented Si steel.

Many efforts have been given in property prediction of magnetic materials. Hutchinson and Swift investigate the magnetic torque of some soft magnetic materials. They found a good agreement between measured torque magnetometer data and computed values based on orientation distributions derived from x-ray diffraction measurements, in which a rather simple calculation was used[1]. Based on the expansion coefficient data of pole figure Szpunar and Ojanen investigated the texture and magnetic properties in Si steels. They believed that 5 expansion coefficients of one pole figure are sufficient for calculating the torque curve of Si steels[2]. The investigations demonstrated that the magnetic torque and also the magnetization intensity should depend dominantly on the texture of the Si steels. However the calculation methods they used should be modified further, in order to reach a better accuracy and make possibility for the potential use on the industry production.

Considering the possible on-line measurement technology in the industry production[3], Bunge has introduced a method for r value calculation[4] based on the expansion coefficients of generalized spherical harmonics for the calculation of orientation distribution functions (ODFs)[5], which could be used easily in the industry production. In the present work the method proposed by Bunge was used for calculating the magnetic torque curve of non-oriented Si steel.

Calculation of Magnetocrystalline Anisotropy Energy

The magnetocrystalline anisotropy energy (MAE) of a single crystal is currently described by the phenomenological theory[6]. In the theory the anisotropy energy E is constructed in the crystal coordinate system as a function of orientation of the magnetization vector, which is shown in equation (1) for the single crystals with cubic symmetry[6],

$$\begin{aligned} E &= K_4(a_1^2a_2^2 + a_2^2a_3^2 + a_3^2a_1^2) + K_6a_1^2a_2^2a_3^2 + \cdots\cdots \\ &\approx K_4(a_1^2a_2^2 + a_2^2a_3^2 + a_3^2a_1^2) \end{aligned} \qquad (1)$$

where a_1 a_2 a_3 are the direction cosines of the magnetization vector in the crystal coordinate and K_4 and K_6 are the anisotropy constants characterizing the anisotropic properties of the material.

In polycrystalline materials the MAE is a function of texture, i.e. the function of orientation distribution of the crystallites. In addition the crystalline defects and their distribution should also influence the MAE. But texture is usually considered as the most important influence factor[1,2]. Therefore the attempts have been undertaken to give an expression for the MAE in polycrystalline materials as a function of grain orientation distribution.

For a polycrystalline material the mean value of the magnetocrystalline anisotropy energy E along a given direction in sample coordinate[4] is the integrated contribution of all grains. That is

$$E = \int M(g') f(g)\, dg \tag{2}$$

where M(g') is the contribution of a single crystal with orientation g' to the MAE, f(g) is orientation density at orientation g, and f(g)dg is the volume fraction of the grains oriented around g. The g' can be expressed as $g \cdot g_0$, where g_0 represents the observed direction of the MAE. If $g_0=\{0, 0, 0\}$ is valid, according to the orthogonality relationships of generalized spherical harmonics the equation (2) could be written as[4]

$$E = \sum_{l=0(2)}^{l_{MAX}} \sum_{\mu=1}^{M(l)} \sum_{\nu=1}^{N(l)} \frac{1}{2l+1} m_l^{\mu\nu} C_l^{\mu\nu} \tag{3}$$

where $m_l^{\mu\nu}$ and $C_l^{\mu\nu}$ are the generalized spherical harmonics expansion coefficients of M(g) and f(g) respectively. For rolling sheet materials the variation of observed directions is often limited in the sheet plane, where $g_0=\{0, 0, \omega\}$ is valid. Therefore equation (3) can be expressed as[4]

$$E(\omega) = \sum_{l=0(2)}^{l_{MAX}} \sum_{\mu=1}^{M(l)} \sum_{\nu=1}^{N(l)} \frac{1}{2l+1} m_l^{\mu\nu} C_l^{\mu\nu} \cos(\nu\omega) \tag{4}$$

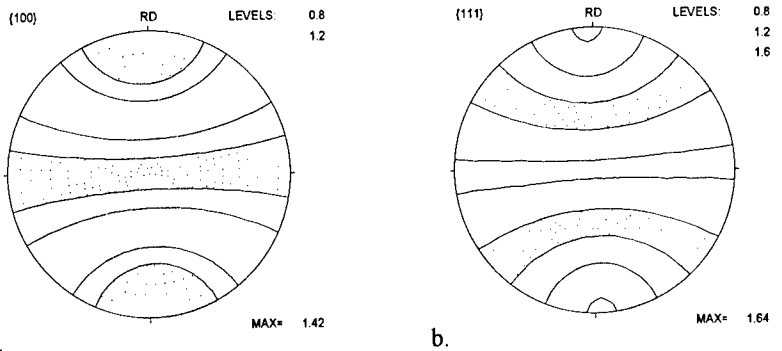
where ω is the rotation angle between the rolling direction and the observed direction[4].

Pole Figure of Magnetocrystalline Anisotropy Energy (MAE)

In order to obtain the expansion coefficients of generalized spherical harmonics M(g) four pole figures $P_{\{hkl\}}(\alpha,\beta)$ of MAE, i.e. the {100}, {110}, {111} and {112} pole figure of MAE, need to be calculated. In the case of Si rolling steel sheets the rolling directions (RD=[uvw]) of all grains can be obtained according to their orientation g. For the calculation the orientation space defined by Bunge[5] was divided homogeneously into n subspaces, and an orientation in each subspace was taken which represents the subspace. According to equation (1) the magnetocrystalline anisotropy energy E can be obtained if the RD=[uvw] is known, which can be expressed as pole figure intensity in different {hkl} pole figures at corresponding positions. At these positions the intensity distribution could be described as a very sharp Gaussian distribution, and therefore a corresponding distribution function of the pole figure $p_{\{hkl\}}(\alpha,\beta)$ can be integrated by n Gaussian distributions. So the pole figures could be calculated as

$$P_{\{hkl\}}(\alpha,\beta) = \sum_{i=1}^{n} p_{i\{hkl\}}(\alpha,\beta) = \sum_{i=1}^{n} p_{\{hkl\}}(\alpha,\beta,[uvw]_i) \tag{5}$$

where n=6912 was used. Figure 1 gives the calculated {100} and {111} pole figures of MAE.



a. b.

Fig.1 {100} and {111} pole figures of MAE for Si steel.

Magnetic torque calculation

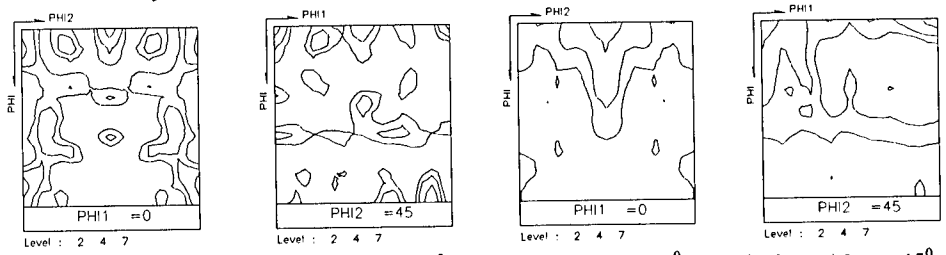
According to the pole figure of MAE the expansion coefficients $m_i^{\mu\nu}$ can be obtained using the general software calculating the orientation distribution function (ODF). Afterwards the anisotropy energy E(ω) can be obtained using equation (4). The magnetic torque T can then be obtained by equation

$$T = -\frac{dE}{d\omega} \tag{6}$$

where ω is the rotation angle in equation (4) and K_4 is 3.65×10^5 erg/cm^3 for Si steel containing 2.7-3.0%Si[2]. Therefore according to equation (4) and (6) the magnetic anisotropy energy E and torque T can be calculated as a function of ω.

Measurement of ODF and the Magnetic Anisotropy Energy

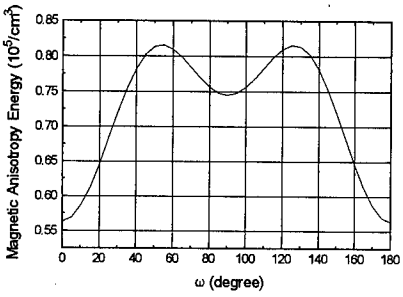
Two different Si steel sheets (A1 and A3) containing 3.0-3.2 wt.% Si were taken. The {110} {200} {112} pole figures were measured on center layer of the sheets using x ray techniques and the ODFs were calculated using the Bunge method[4]. A more emphasized {001}<100> texture with max. density value 6.6 in sheet A1 and a higher volume of {001}<110> texture with max. density value 8.8 in sheet A3 are observed in $\varphi_1=0^0$ and $\varphi_2=45^0$ ODF sections(fig. 2).



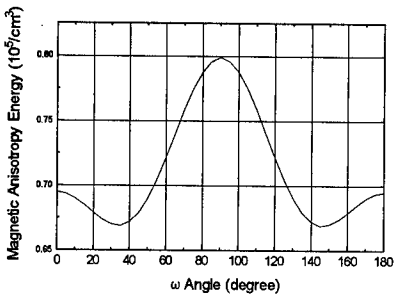
a. sheet A1 $\varphi_1=0^0$ max.=8.8 b. sheet A1 $\varphi_2=45^0$ max.=10.2 c. sheet A3 $\varphi_1=0^0$ max.=8.8 d. sheet A3 $\varphi_2=45^0$ max.=8.8

Fig.2 ODF sections of sheet A1 and A3 (density levels: 2, 4, 7)

The calculated MAE for sheet A1 and A3 is shown in figure 3, which is quite different because of the different texture in the sheets. The magnetic torque curves of sheet A1, and A3 were also measured, and are shown in figure 4 together with the calculated curves.

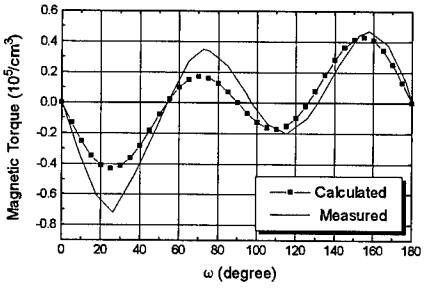


a. sheet A1

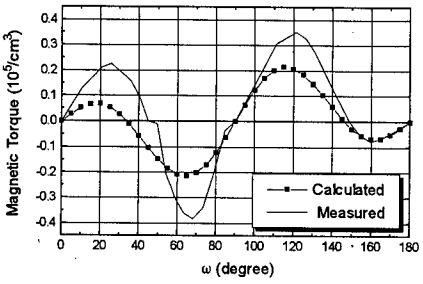


b. sheet A3

Fig.3 The Calculated MAE of sheet A1 and A3



a. sheet A1



b. sheet A3

Fig.4 calculated and measured torque curve of sheet A1 and A3

Discussion

The results in figure 4 demonstrate that good agreement is obtained between the measured torque data and the calculated torque data based on the magnetic anisotropy coefficients of generalized spherical harmonics. That indicates that there exists a very good possibility for the corresponding on line measurement techniques in the potential industry applications like that used for r value on line measurement[3]. However some deviations of the calculated value from the measured value could still be observed which should be reduced by further modification of the calculation parameters.

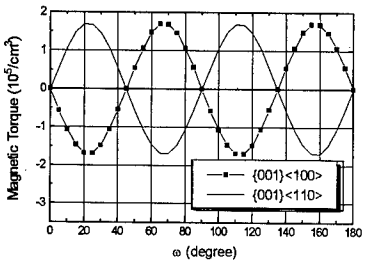


Fig 5 Torque curves of {001}<100> and {001}<110> texture

Figure 5 gives the calculated torque curves of {001}<100> and {001}<110> texture. The different curves indicate that the peak positions in the torque curves are determined mainly by the texture components in the Si steel sheets. Therefore it can be deduced that the torque curve

of sheet A1 is influenced strongly by its more emphasized {001}<100> texture(fig.2a,b), and the torque curve of sheet A3 is determined mainly by the high volume fraction of {001}<110> texture(fig.2c,d).

In both cases of sheet A1 and A3 the calculated absolute value of the torque is generally lower than that from the measurement though the curve peak positions of the measured and calculated are almost identical(fig.4). So the calculation parameters should be the main factors which will influence the accuracy of the calculations. The K_4 value for Si steel with 2.7-3.0%Si, for instance, was taken which could lead to certain deviation since the Si steels used here contain 3.0-3.2%Si. On the other hand the calculation accuracy could be better if the K_6 value in equation (1) is also used. The texture which is the dominant influence factor for the determination of magnetic torque, was measured only in the center layer of the sheet. However different texture development in different sheet layers were often observed[7]. Therefore the calculation results could be also better if texture information is obtained from different layers of the sheets.

Based on the magnetic anisotropy coefficients of generalized spherical harmonics the very important property parameter, the magnetization intensity B could also be calculated. The corresponding investigation is in progress.

Summary

Using the magnetic anisotropy coefficients of generalized spherical harmonics good agreement has been obtained between the measured and the calculated torque data of non-oriented Si steel sheets, which are mainly determined by the sheet texture. The technique could be better applied for potential industry on-line measurement. In order to reduced the calculation deviation from the measured data more accurate parameters such as K_4 and K_6 value should be used, and the texture inhomogeneity should also be considered in the calculation. Based on the method it could be attempted to calculate the magnetization intensity B.

Reference

1. W.B. Hutchinson, J.G. Swift, "Anisotropy in some Soft Magnetic Materisls" Texture, 1, (1972), 117-123.

2. J. Szpunar, M. Ojanen, "The Relationship between Texture and Magnetic Properties in Si-Fe Steel" Met Trans, 6A, (1975), 561-567.

3. H.J. Kopineck, Experimental Techniques of Texture Analysis, ed. H.J. Bunge, (GM-Informationsgesellschaft Verlag, 1986) Oberusel, 171-180.

4. H.J. Bunge, Arch. Eisenhüttenwes. 52, (1981), 407-411.

5. H.J. Bunge, Quantitative Texture Analysis, ed. H.J. Bunge and C.Esling, (GM-Informationsgesellschaft Verlag, 1982) Oberusel, 1-72.

6. F. Bitter, Introduction to ferromagnetism, Mac Graw-Hill, 1937, 213-???.

7. W. Mao, Z. Sun, Scr. "Inhomogeneity of Rolling Texture in Fe-28Al-2Cr Alloy" Met. Mat.,29, (1993), 217-220.

SOLUBILITY PRODUCT OF VN IN AUSTENITE

T. Gendo, K. Morita, K. Inoue, I. Ohnuma, H. Ohtani*, K. Ishida

Department of Materials Science, Graduate School of Engineering, Tohoku University, Sendai 980-8579, Japan

* Center for Interdisciplinary Research, Tohoku University, Sendai 980-8579, Japan

Abstract

The solubility product of VN in austenite at temperatures between 1323 and 1523 K was determined from the breakpoints of iso-activity lines for nitrogen of diffusion couples. Taking experimental results and previous data on thermodynamic properties into account, thermodynamic analysis was also carried out. The solubility products in austenite (γ) and ferrite (α) were obtained as $\log (\%V)(\%N)_{\gamma} = 2.206 - 6683 / T$ and $\log (\%V)(\%N)_{\alpha(\delta)} = 2.592 - 8790 / T$, respectively.

The Third Pacific Rim International Conference on
Advanced Materials and Processing (PRICM 3)
Edited by M.A. Imam, R. DeNale, S. Hanada,
Z. Zhong and D.N. Lee
The Minerals, Metals & Materials Society, 1998

Introduction

The solubility products of carbide and nitride in steels is of practical importance in the control of the microstructure of micro-alloyed steel. V is known as one of the most important alloying elements and forms NaCl type compounds with carbon and nitrogen. These compounds are so stable that they cause grain refinement and precipitation hardening, resulting in the significant improvement of mechanical properties of steel. Since the precise control of precipitation and dissolution behavior of these precipitates plays a key role in the development of micro-alloyed steels, the solubility products of these compounds are of fundamental importance. Even though several studies on the solubility product of VN have been reported [1-4], there are enormous differences among them because of the difficulties in measuring such small values of solubility. Furthermore, oxygen contamination makes it much more difficult to accurately determine the solubility.

The purpose of this study was to examine the solubility of VN in γ by the diffusion couple method. This method makes it possible to preclude surface contamination on each specimen and to obtain the complete iso-activity state for nitrogen throughout the diffusion couple. Then, thermodynamic analysis of the experimental data was carried out and the solubility products of VN in γ and α (or δ) were determined.

Experimental Procedures

Fe - (0.05 - 0.49) mass% V alloys were prepared from electrolytic Fe (>99.99 mass%), V (>99.7 mass%) by induction melting in a CaO crucible in a high vacuum (0.067 Pa). H_2 gas was blown onto the surface of the melt to remove oxygen. Fe - 0.05 mass% N alloy was also prepared by keeping molten Fe under a N_2 gas flow for 1 hour. Analysis showed the nitrogen content to be about 0.05 mass%. Each ingot was machined into a rod with a diameter of 15mm and sliced into 4-mm thick disks. Several disks of Fe-V alloys and one disk of Fe-N were combined at 1173 K for 1 hour under H_2 gas flow to prepare a diffusion couple. After surface contamination was removed by mechanical polishing, each diffusion couple was sealed in an evacuated quartz capsule and annealed in the range of 1323 K to 1523 K sufficiently long to obtain the iso-activity state of nitrogen throughout the diffusion couple. The diffusion couples were then sliced into each disk and cut into small pieces for analysis. Nitrogen and oxygen contents were measured by using a nitrogen and oxygen analyzer (LECO TC-436).

The affinity of V for oxygen is so strong that some V is consumed in the formation of the oxide. A great deal of attention was paid to removal of oxygen during experiments, but it was impossible to avoid oxygen contamination. Therefore, it is assumed that residual oxygen exists as V_2O_3 and the effective V concentration, $(\%V)_{eff.}$, was estimated to be $(\%V)_{eff.} = (\%V)_{total} - (\%V)_{oxide}$, where $(\%V)_{total}$ represents the measured V contents of each specimen and $(\%V)_{oxide}$ represents V concentrations consumed by V_2O_3.

Experimental Results

Figure 1(a) and (b) show the experimental results of the iso-activity lines for nitrogen at 1373 K and 1423 K, respectively. The slope of the line in the two-phase region (γ + VN), is found to be parallel with that of the atomic weight ratio, i.e., $W_N / W_V = 14.0067 / 50.942 = 0.2750$, which means that vanadium nitride has a stoichiometric composition. This fact was also confirmed by the X-ray diffraction measurement of the lattice constant of these precipitates extracted from

specimens with 0.1 N-HCl solution. The observed lattice constant is 0.414 nm, which corresponds to that of NaCl-type VN [5]. The solubility products of VN were determined from the breakpoints of the iso-activity lines in each diffusion couple. A comparison of the experimental data with the previous data [1-4] is presented in Fig. 1.

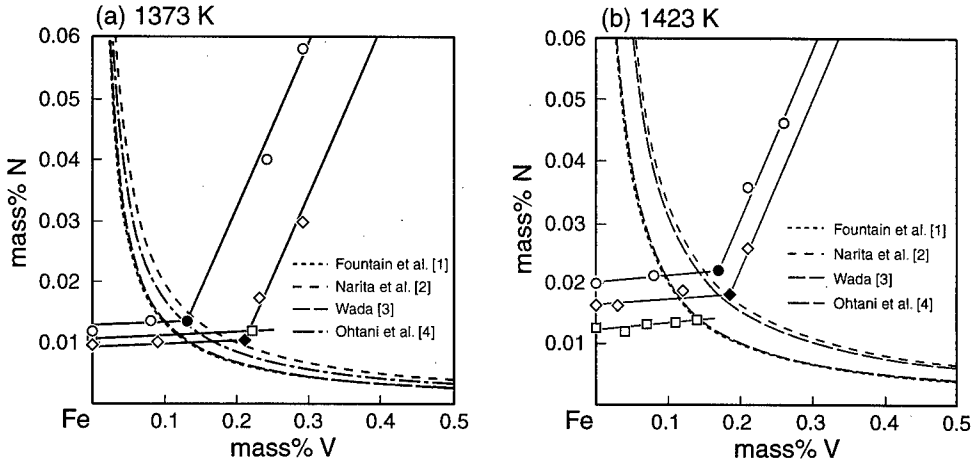


Figure 1: Iso-activity lines for nitrogen at (a)1373 K and (b)1423 K.

Thermodynamic Analysis

The Gibbs energy of the bcc (α) and fcc (γ) phases is described by the two-sublattice model [6], where it is assumed that the substitute atoms of Fe and V occupy the first sublattice (I) and the interstitial atoms of N and vacancy (denoted by Va) occupy the second one (II). The Gibbs energy is expressed as follows :

$$G = y^{I}_{Fe}y^{II}_{N}\,{}^{\circ}G_{Fe:N} + y^{I}_{Fe}y^{II}_{Va}\,{}^{\circ}G_{Fe:Va} + y^{I}_{V}y^{II}_{N}\,{}^{\circ}G_{V:N} + y^{I}_{V}y^{II}_{Va}\,{}^{\circ}G_{V:Va} + aRT(y^{I}_{Fe} \ln y^{I}_{Fe} + y^{I}_{V} \ln y^{I}_{V}) + cRT(y^{II}_{N} \ln y^{II}_{N} + y^{II}_{Va} \ln y^{II}_{Va}) + {}^{E}G_{m} + {}^{mag}G_{m} \quad (1)$$

where y^{n}_{i} represents the fraction of component i on the n-th sublattice, i.e., $y^{I}_{Fe} + y^{I}_{V} = 1$ and $y^{II}_{N} + y^{II}_{Va} = 1$, and is related to the mole fractions of component i, x_i, as follows :

$$y^{I}_{V} = x_V / (1 - x_N) \quad (2)$$

$$y^{II}_{N} = (a / c)\, x_N / (1 - x_N) \quad (3)$$

a and c represent the number of sites of each sublattice, which are given as a = 1 and c = 1 for the γ phase and a = 1 and c = 3 for the α phase. The excess Gibbs energy, ${}^{E}G_m$, is formulated as follows :

$$
\begin{aligned}
{}^{E}G_m = {} & y^{I}_{Fe} y^{II}_{N} y^{II}_{Va} L_{Fe:N,Va} + y^{I}_{V} y^{II}_{N} y^{II}_{Va} L_{V:N,Va} + y^{I}_{Fe} y^{I}_{V} y^{II}_{N} L_{Fe,V:N} + y^{I}_{Fe} y^{I}_{V} y^{II}_{Va} L_{Fe,V:Va} \\
& + y^{I}_{Fe} y^{I}_{V} y^{II}_{N} y^{II}_{Va} L_{Fe,V:N,Va}
\end{aligned} \tag{4}
$$

In the subscripts of the interaction parameters L, the components in different sublattices are separated by a colon, while those in the same sublattice are separated by a comma. ${}^{mag}G_m$ is a magnetic contribution to the Gibbs energy which is described by the model of Hillert and Jarl [7] and is taken into consideration in α phase.

The chemical potentials of V and N are approximated respectively as follows.

$$
\mu_V \approx {}^{\circ}G_{V:Va} + aRT \ln y^{I}_{V} + L_{Fe,V:Va} \tag{5}
$$

$$
\mu_N \approx {}^{\circ}G_{Fe:N} + {}^{\circ}G_{Fe:Va} + L_{Fe:N,Va} \tag{6}
$$

VN is assumed to be a stoichiometric compound and its Gibbs energy is represented by ${}^{\circ}G^{NaCl}_{V:N}$; therefore, the solubility product of VN is described based on the equilibrium condition.

$$
{}^{\circ}G^{NaCl}_{V:N} = (1/a)\,\mu_V + (1/c)\,\mu_N \tag{7}
$$

$$
\begin{aligned}
RT \ln y^{I}_{V} y^{II}_{N} = {} & \Delta G^{f}_{VN} - \frac{1}{a}\left({}^{\circ}G_{V:Va} - {}^{\circ}G^{bcc}_{V:Va} \right) - \frac{1}{c}\left[\Delta G^{f}_{nitrideFe} - \left({}^{\circ}G_{Fe:Va} - {}^{\circ}G^{bcc}_{Fe:Va} \right) \right] \\
& - \frac{1}{a} L_{Fe,V:Va} - \frac{1}{c} L_{Fe:N,Va}
\end{aligned} \tag{8}
$$

where ΔG^{f}_{VN} and $\Delta G^{f}_{nitrideFe}$ are the Gibbs energies of the formation of VN and of the hypothetical compound Fe nitride, respectively. The Gibbs energy of the liquid phase is described by the regular solution model.

$$
\begin{aligned}
G^{liq} = {} & x^{liq}_{Fe}\,{}^{\circ}G^{liq}_{Fe} + x^{liq}_{V}\,{}^{\circ}G^{liq}_{V} + x^{liq}_{N}\,{}^{\circ}G^{liq}_{N} \\
& + RT\left(x^{liq}_{Fe} \ln x^{liq}_{Fe} + x^{liq}_{V} \ln x^{liq}_{V} + x^{liq}_{N} \ln x^{liq}_{N} \right) + {}^{E}G^{liq}
\end{aligned} \tag{9}
$$

$$
{}^{E}G^{liq} = x^{liq}_{Fe} x^{liq}_{V} L^{liq}_{Fe,V} + x^{liq}_{Fe} x^{liq}_{N} L^{liq}_{Fe,N} + x^{liq}_{V} x^{liq}_{N} L^{liq}_{V,N} + x^{liq}_{Fe} x^{liq}_{V} x^{liq}_{N} L^{liq}_{Fe,V,N} \tag{10}
$$

The chemical potentials of V and N in liquid are approximated as follows :

$$
\mu^{liq}_{V} \approx {}^{\circ}G^{liq}_{V} + RT \ln x^{liq}_{V} + \left(1 - 2\,x^{liq}_{V} \right) L^{liq}_{Fe,V} + x^{liq}_{N} W^{liq}_{VN} \tag{11}
$$

$$
\mu^{liq}_{N} \approx {}^{\circ}G^{liq}_{N} + RT \ln x^{liq}_{N} + \left(1 - 2\,x^{liq}_{N} \right) L^{liq}_{Fe,N} + x^{liq}_{V} W^{liq}_{VN} \tag{12}
$$

where $W^{liq}_{VN} = L^{liq}_{V,N} - L^{liq}_{Fe,V} - L^{liq}_{Fe,N} + L^{liq}_{Fe,V,N}$ and this parameter is directly related to Wagner's interaction parameter, $\left(\varepsilon^{V}_{N} \right)_{liq} = W^{liq}_{VN} / RT$. Therefore, the solubility product of VN in liquid is obtained from the equilibrium condition ${}^{\circ}G^{NaCl}_{V:N} = \mu^{liq}_{V} + \mu^{liq}_{N}$.

$$
\begin{aligned}
RT \ln x^{liq}_{V} x^{liq}_{N} \approx {} & \Delta G^{f}_{VN} - \left({}^{\circ}G^{liq}_{V} - {}^{\circ}G^{bcc}_{V:Va} \right) - \left({}^{\circ}G^{liq}_{N} - \frac{1}{2}\,{}^{\circ}G^{gas}_{N_2} \right) \\
& - \left(1 - 2\,x^{liq}_{V} \right) L^{liq}_{Fe,V} - \left(1 - 2\,x^{liq}_{N} \right) L^{liq}_{Fe,N} - \left(x^{liq}_{V} + x^{liq}_{N} \right) W^{liq}_{VN}
\end{aligned} \tag{13}
$$

The temperature dependence of ΔG_{VN} was evaluated based on the present results and the solubility data in liquid reported by Morita et al. [8]. Using the thermodynamic parameters assessed previously [9-12] and optimized in this study, ΔG^{f}_{VN} is obtained as follows :

$$\Delta G^{f}_{VN} = -217040 + 87.34\,T \quad (J / mol) \tag{14}$$

This is compared with the value of the V-N binary system [13] in Fig. 2. Using this value, the solubility product in γ and α are obtained as follows :

$$\log (mass\%V)(mass\%N)_{\gamma} = 2.206 - \frac{6683}{T} \tag{15}$$

$$\log (mass\%V)(mass\%N)_{\alpha (or\ \delta)} = 2.592 - \frac{8790}{T} \tag{16}$$

The present assessed data on the solubility product in the γ phase are shown in Fig. 3. The solubility products of VN in α- and γ-iron are compared with those of VC [10] in Fig. 4. The solubility product of nitride is much lower than that of carbide.

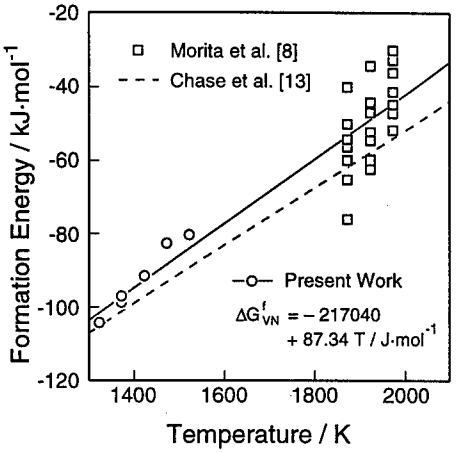


Figure 2: Temperature dependence of the formation energy of VN

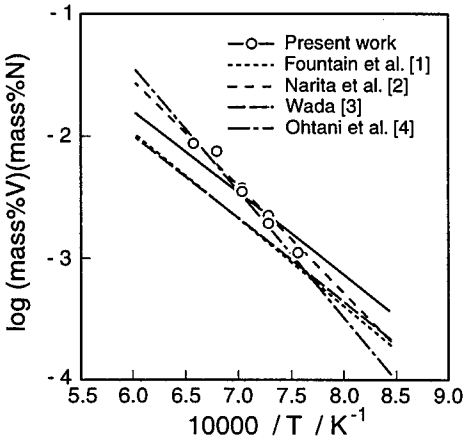


Figure 3: Comparison of solubility product of VN in austenite.

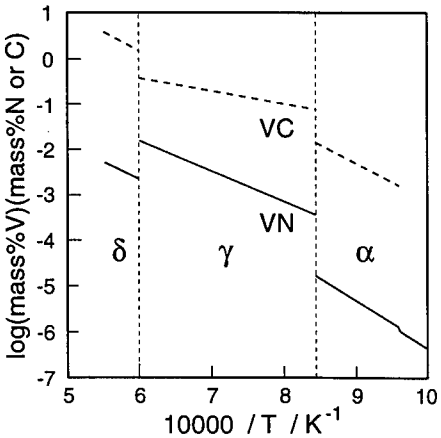


Figure 4: Comparison of solubility products of VN and VC. The value of VC in γ-iron is calculated at (mass%C)=0.1.

Conclusions

(1) The solubility of VN in γ was measured by the diffusion couple method in the range of 1323 K to 1523 K.

(2) Thermodynamic analysis was carried out to assess the solubility product of VN in γ, α as follows :

$$\log (\text{mass\%V})(\text{mass\%N})_{\gamma} = 2.206 - \frac{6683}{T}$$

$$\log (\text{mass\%V})(\text{mass\%N})_{\alpha (\text{or } \delta)} = 2.592 - \frac{8790}{T}$$

Acknowledgment - This work was supported by a Grant-in-aid for Scientific Research from the Ministry of Education, Science, Sports and Culture, Japan and also by a grant from the Proposal-Based Advanced Industrial Technology R&D Program.

References

1. R.W. Fountain and J.Chipman: "Solubility and Precipitation of Vanadium Nitride in Alpha and Gamma Iron." Trans.AIME, **212** (1958), 737-748

2. K. Narita: "Physical Chemistry on Steels Containing Vanadium, Niobium and Tantalum." Tetsu-to-Hagane, **52** (1966), 788-791

3. H. Wada: "Nitrogen Solubility and Precipitation of Nitride in Austenitic Fe-V Alloys." Trans.ISIJ, **27** (1987), 649-657

4. H. Ohtani and M. Hillert: "A Thermodynamic Assessment of the Fe-N-V System." CALPHAD, **15** (1991), 25-37

5. P. Villars and L. D. Calvert, eds., Peason's Handbook of Crystallographic Data for Intermetallic Phases vol 4 (Materials Park, OH: ASM INTERNATIONAL, 1991), 4502-4503

6. M. Hillert and L.I. Staffansson: "The Regular Solution Model for Stoichiometric Phases and Ionic Melts." Acta Chem. Scand., **24** (1970), 3618-3626

7. M.Hillert and M.Jarl: "A MODEL FOR ALLOYING EFFECTS IN FERROMAGNETIC METALS." CALPHAD, **2** (1978), 227-238.

8. Z. Morita, T. Tanaka and T. Yanai: "Equilibria of Nitride Forming Reactions in Liquid Iron Alloys." Metall.Trans.B, **18B** (1987), 195-202

9. D.B. Evans and R.D. Pehlke: "Equilibria of Nitrogen with the Refractory Metals Titanium, Zirconium, Columbium, Vanadium, and Tantalum in Liquid Iron." Trans.TMS-AIME, **233** (1965), 1620-1624

10. H. Ohtani, T. Tanaka, M. Hasebe and T. Nishizawa: "Solubility of NaCl-Type Carbides (NbC, VC and TiC) in Austenite." Proc. Japan-Canada Seminar on Secondary Steelmaking, the Canadian Steel Industry Research Association and the ISIJ, (1985), Tokyo, J-7

11. A.T. Dinsdale: "SGTE DATA FOR PURE ELEMENTS." CALPHAD, **15** (1991), 317-425

12. K. Frisk: "A Thermodynamic Evaluation of the Cr-N, Fe-N, Mo-N and Cr-Mo-N Systems." CALPHAD, **15** (1991), 79-106

13. M.W. Chase, J.L. Curnutt, H. Prophet, R.A. McDonald and A.N. Syverud: "JANAF Thermodynamical Tables Third Edition.", J. Phys. Chem. Ref. Data, **14** (1985), 1545-1546.

CYCLIC PROPERTIES OF A TITANIUM AND NIOBIUM MICROALLOYED STEEL IN SOME MICROSTRUCTURAL CONDITIONS

Enrico José Giordani, Jairo Aparecido Martins, Itamar Ferreira.
Department of Materials Engineering, College of Mechanical Engineering - UNICAMP
Campinas ,São Paulo State, Brazil.

Abstract

The purpose of this work is to analyze the monotonic and cyclic mechanical properties of the API 5L X65 steel, a titanium and niobium microalloyed low carbon steel, in some microstructural conditions from the thermal treatments: normalization (from 920 °C), quenching, and austempering from the intercritical annealing (at 770 °C). Tension and low cycle fatigue tests have been conducted in order to analyze the tension properties [yield strength (S_y), tensile strength (S_u), true fracture stress (σ_f), reduction in area (RA), and strain hardening exponent (n)] and low cycle fatigue properties [fatigue strength coefficient and exponent (σ'_f and b), fatigue ductility coefficient and exponent (ε'_f and c), and cyclic strain hardening exponent (n')] for the following microstructural conditions: as received -AR- (ferrite-perlite), normalized -N1- (ferrite-perlite), quenched from the intercritical zone -T77- (ferrite-martensite), and austempered in salt bath (at 370 °C), also from the intercritical zone -A77- (ferrite-bainite). It was observed that, in the range $0.4<\Delta\varepsilon/2<1\%$, the N1 condition showed a little better behavior for high levels of strain, when comparing to the AR condition; however, the obtained experimental value of ε'_f was 1.38 to the AR and 1.11 to the N1, what suggests that there is an inversion of the behavior for very high levels of deformation ($\Delta\varepsilon/2>6\%$). For low levels of strain, the AR condition presented better behavior when comparing to the N1 condition, in spite of the values of σ'_f for these conditions, they are practically the same and equal to 1075 MPa, due to the big difference between the fatigue strength exponent: b = -0.074 for the AR condition and b = -0.110 for the N1 condition. The AR condition presented cyclic softening for all strain range, and the N1 condition presented cyclic softening for $\Delta\varepsilon/2<0.8\%$ and cyclic hardening for $\Delta\varepsilon/2>0.8\%$. The *Incremental Step (IS)* method was very efficient for obtaining the cyclic stress-strain curve for the AR condition, when comparing to the conventional method (by using several companion specimens). However, for the N1 condition the results from *IS* method were not satisfactory. The cyclic stress-strain curves, from the *IS* method, for the T77 and A77 conditions, showed that the T77 condition presented cyclic hardening for all strain levels, and the A77 condition presented, like N1, cyclic softening for $\Delta\varepsilon/2<0.4\%$ and cyclic hardening for $\Delta\varepsilon/2>0.4\%$.

The Third Pacific Rim International Conference on
Advanced Materials and Processing (PRICM 3)
Edited by M.A. Imam, R. DeNale, S. Hanada,
Z. Zhong and D.N. Lee
The Minerals, Metals & Materials Society, 1998

Introduction

The monotonic mechanical properties are usually obtained from a tension test, that means, monotonic loading, low strain rate, and uniaxial stress state. The cyclic mechanical properties are associated with two different interpretations given to the fatigue studies: stress controlled high cycle fatigue and strain controlled low cycle fatigue (1). The cyclic mechanical properties associated with low cycle fatigue are important in applications such as materials and/or microstructure choice for use under severe conditions, that is, structural components having a need for high level nominal stress, applications where there is a wide temperature change (subjected to thermal fatigue) or even structural components having critical notching (2).

Material and Experimental Procedure

The material used in this paper was a API 5L X65 (0.098C, 1.63Mn, 0.33Si, 0.022Ti, 0.04Nb, and Fe balance), manufacture by COSIPA (Brazilian company in São Paulo State), by using a controlled rolling processes and received in the form of sheets having a thickness of 10 mm. The material in this condition will be called as-received (AR) from here on.

The steel were heat treated in three different routes: normalization from complete austenitizing at 920 °C (N1 condition); normalizing (at 920 °C) and quenching in oil from the intercritical zone at 770 °C (T77 condition); normalizing (at 920 °C) and austempering in a salt bath at 370 °C from the intercritical zone at 770 °C (A77 condition).

Low cycle fatigue (LCF) tests and tension tests have been carried out with identical specimens. Smooth cylindrical specimens of gage diameter 7.5 mm, gage length 13.0 mm, fillet radius 20 mm, grip diameter 9.5 mm, and total length 140 mm were taken along the rolling direction.

Low Cycle Fatigue Testing

Two types of LCF test have been carried out: companion specimens (CS) test to which conditions AR and N1 were submitted and *Incremental Step* (IS) test to which all the conditions have been submitted. Fully reversed LCF test were conducted at room temperature under total strain control (by using a MTS strain gage having initial length of 10 mm), on 100 kN servohydraulic MTS test machine. A triangular wave form was employed. A contant strain rate of 8.10^{-3} s^{-1} was used.

In the CS tests the nearest stress-strain hysteresi loop to the half fatigue life was considered as being stable and used to the total stain amplitude ($\Delta\varepsilon/2$), elastic strain amplitude ($\Delta\varepsilon_e/2$) and plastic strain amplitude ($\Delta\varepsilon_p/2$). The fatigue failure criteria was a 20% drop on the maximum tensile load in relation to the stabilized condition, were was also noticed the beginning of the cusp formation at the compressive portion of the hysteresi loop (3).

The IS test has been proposed by Landgraf (4) in order to determine the cyclic stress-strain curve of a given material by submitting only one specimen to strain blocks having linearly increasing and decreasing amplitudes from zero up to a maximum preset strain. Pólak and Hájek (5) have developed a full-cycle analysis for the cyclic stress-strain curve from IS which has been used herewith. Each loading block contained 10 strain level which varied from 0.1 to 1% having a increment of 0.1%.

Tension Test

Tension tests were conducted on the same MTS test machine using the same strain gage. In this case a piston displacement control was made to have the piston advance of 0.01 mm/s.

Results and Discussion

Microstructural Analysis

Figure 1 shows the microstructures of the four conditions (AR, N1, T77 and A77).

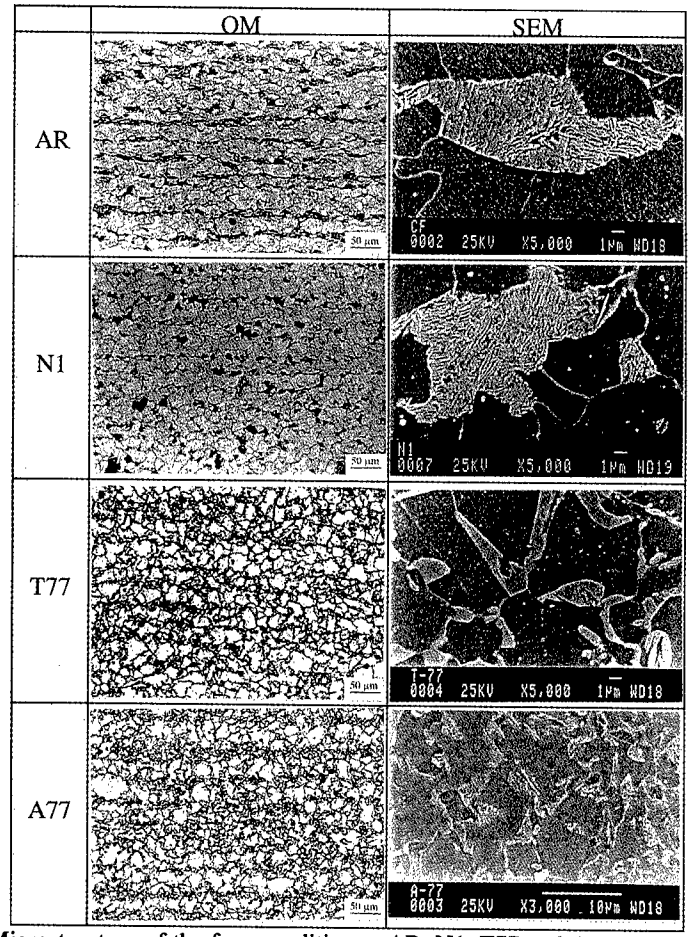


Figure 1: Microstructure of the four conditions - AR, N1, T77 and A77 - as seen under an optical microscope (OM), and a scanning electronic microscope (SEM). 2% Nital etch.

It can be noticed (figure 1) that the normalization treatment provided a significant rolling texture rupture as compared to AR condition. T77 condition shows *MA Constituent* along the ferritic grain boundary. By means of the applied cooling, by means of the austenite hardenability and by means of the mechanical properties presented by this condition, the *MA Constituent* is probably a martensite. A77 condition shows a second phase also along the ferritic grain boundary, however, due to the isothermic heat treatment at 370 °C, this phase is a bainite (6,7).

Monotonic Mechanical Properties

Table I shows the results obtained from the tension testing for four analyzed conditions.

Table I Monotonic mechanical properties obtained from tension testing.

Condition	*UYS* [MPa]	*LYS* [MPa]	S_y [MPa]	S_u [MPa]	σ_f [MPa]	*E* [GPa]	*n*	*K* [MPa]	*RA* [%]	ε_f
AR	558	530	-----	615	1415	209	0.133	948	73.0	1.31
N1	475	402	-----	520	1430	197	0.174	804	79.1	1.56
T77	-----	-----	328	700	1341	202	0.192	1079	56.5	0.83
A77	386	367	-----	575	1539	195	0.208	1035	79.9	1.60

An interesting observation may be made as to the absence of yield point elongation to T77 condition. This behavior, as well as a low yielding and a high tensile strength are characteristic of the microalloyed steels having ferritic-martensitic dual-phase microstructures. This aspect may be linked to the occurrence of the transformation of austenite to martensite in intercritical heat treatments. This transformation, from the intercritical zone, brings about a high density of dislocation within the ferritic phase which bear a high mobility that provides the occurrence of a continuous yielding (7-11).

Cyclic Mechanical Properties

Figure 2.a shows the cyclic stress-strain curves determined from the tips of stable hysteresis loops, as determined using the CS test and the monotonic obtained in the tension test for AR and N1 conditions. Figure 2.b shows strain-life curves for these conditions obtained experimentally from the total, elastic and plastic strain in function of reversals to failure. Table II shows the parameters determined from these curves.

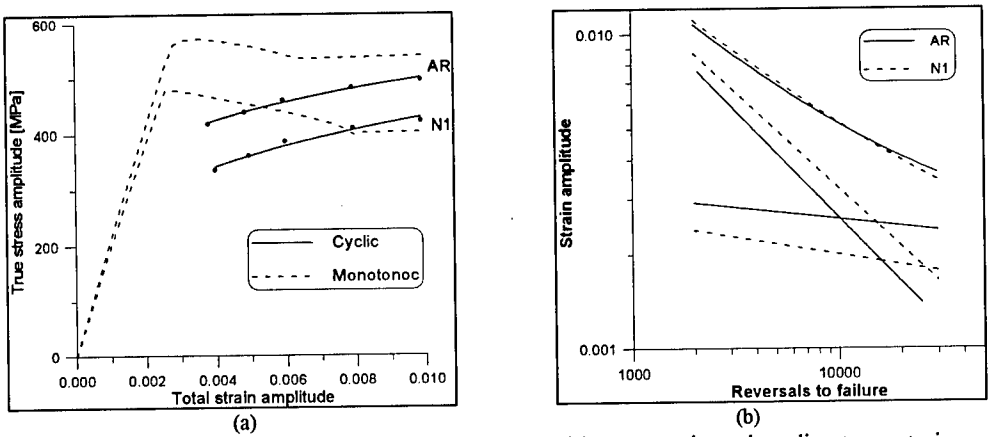


Figure 2 - Curves determined from the CS tests: (a) monotonic and cyclic stress-strain curves, (b) Strain-life curves.

Table II Cyclic mechanical properties determined from the CS test.

Condition	S'_y *[MPa]*	n'	K' *[MPa]*	σ'_f *[MPa]*	b	ε'_f	c
AR	426	0.111	865	1070	-0.074	1.38	-0.680
N1	336	0.182	1044	1084	-0.110	1.11	-0.636

On figure 2.a can be noticed that the material in AR condition bears a cyclic softening at all strain levels while N1 condition bears a cyclic softening at total strain amplitude below 0.8% and a cyclic hardening above this value. The large gain in monotonic strength properties obtained by hardening is not retained under cyclic loading because the hardened material cyclically softens (13), which may explain the cyclic softening presented by AR condition hardened by controlled rolling process that it was submitted to.

On figure 2.b can be seen that AR condition presented better fatigue properties at low strain amplitudes. At, N1 condition shows itself a little better than AR condition. At high strain amplitudes, the main factor for fatigue life of the material is the strength, and at low strain amplitudes, the predominant factor for the fatigue life control is ductility (1,12,14). However, the fatigue ductility coefficient (ε'_f) is higher for AR condition (1.38) than for N1 condition (1.11) which suggests that for very high strain levels ($\Delta\varepsilon/2 > 6\%$) a new behavior inversion will take place.

Figure 3 shows the cyclic stress-strain curves determined from the full-cycle analysis (5) together with the monotonic curves obtained in tension tests, for the four analyzed conditions. Table III shows the values of the cyclic properties obtained by means of this analysis method.

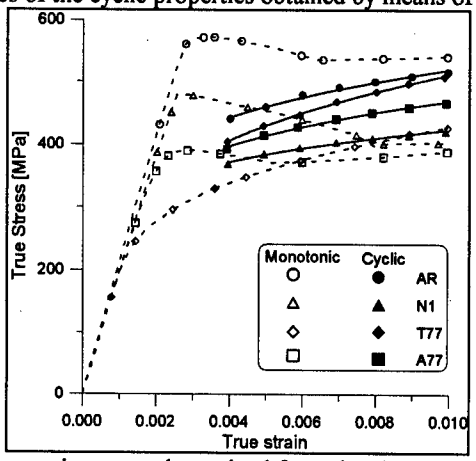


Figure 3 -Cyclic stress-strain curves determined from the IS test and monotonic (tension test) to the AR, N1, T77 and A77 conditions.

Table III Cyclic mechanical properties-determined from the IS test

Condition	S'_y *[MPa]*	n'	K' *[MPa]*
AR	444	0.109	884
N1	370	0.098	681
T77	407	0.177	1225
A77	398	0.127	871

Comparing the parameter values S'_y, n' and K' obtained by means of the IS test (table III) with the values obtained by means of the CS test (table II), it can be seen that IS test has shown itself to be extremely satisfactory in the determination of the parameters describing the cyclic behavior of the material in condition AR. On the other hand, for N1 condition, the IS test has proved to be imprecise, presenting quite different values. In figure 3 can be seen that the material in T77 condition (dual-phase) has presented a cyclic hardening at all analyzed strain level, being this a typical behavior of HSLA steels in this condition (10, 12, 14). The presented behavior by A77 condition was similar to that presented by N1 condition, that is, this condition presented a mixed behavior, where below 0.4% of strain a cyclic softening took place and above this value, a cyclic hardening.

Conclusions

At the total strain amplitude range ($\Delta\varepsilon/2$), between 0.4 and 1%, N1 condition presented a slightly better fatigue behavior, at the high strain levels, when compared to the AR condition, however, the experimentally determined parameter ε'_f has been larger for AR condition (1.38) than for N1 condition (1.11) which suggests that for the total strain amplitude above 6%, a fatigue behavior inversion takes place. At high cycle, for low strain levels, AR condition has shown a better fatigue behavior that N1 condition.

Using the companion specimens test, AR condition has presented a cyclic softening at all analyzed strain levels, while N1 condition presented a mixed behavior, that is, a cyclic softening at stain levels lower than 0.8% and a cyclic hardening at strain levels higher than this value.

The *Incremental Step* test has proved to be efficient in determining cyclic stress-strain curves of AR condition when compared to the curves determined by means of the companion specimens test. However, for N1 condition, the obtained results using this method, have not been satisfactory. The cyclic stress-strain curves, determined from the *Incremental Step* test, for T77 and A77 conditions, show that T77 condition has shown a cyclic hardening at all analyzed strain levels while A77 condition has shown a mixed behavior as noticed for N1 condition.

References

1. R. W. Hertzberg, Deformation and Fracture Mechanics of Engineering Materials. (New York: 3.ed., John Wiley & Sons, 1989), 521-590.

2. P.G. Forrest, Fatigue of Metals (Oxford: Pergamon Press, 1970).

3. K.B.S. Rao et al., "On the Failure Condition in Strain-Controlled Low Lycle Fatigue," International Jornal Fatigue, 7(3) (1985) 141-147.

4. R.W. Landgraf et al., "Determination of the Cyclic Stress-Strain Curve," Journal of Materials, JMLSA, ,4 (1) (1969),176-188.

5. J. Polák, and M. Hájek, "Cyclic Stress-Strain Curve Evaluation Using Incremental Step Test Procedure," International Jornal Fatigue, 13 (3) (1991), 216-222.

6. M.F. Mekkawy et al., "Effect of Interrupted Accelerated Cooling on Mechanical Properties and Structure of Vanadium and Titanium Microalloyed Steel Bars," Materials Science and Technology, 7 (1991), 28-36.

7. Y. Sakuma et al., "Effect of Molybdenum on Microstructure and Mechanical Properties of Intercritically Annealed and Isothermally Transformed Low Carbon Steel." Materials Science and Technology, 9 (1993), 718-724.

8. G. Krauss, Principles of Heat Treatment of Steel, (Ohio: American Society for Metals, 1980), 240-246.

9. N.J. Kim, and G. Thomas, "Effects of Morphology on the Mechanical Behavior of a Dual Phase Fe/2Si/0,1C Steel," Metallurgical Transactions A , 12 (A), (1981),483-489.

10. Y. Tomota, "Effects of Morphology and Strength of Cyclic Deformation Behaviour in Dual-Phase Steels," Materials Science and Technology, 3 (1987), 415-421.

11. G. R. Speich, "Dual-Phase Steels. ASM Handbook, vol. 1 (Ohio: American Society for Metals, 1990), 424-429.

12. S.R. Mediratta et al., "Low Cycle Fatigue of Dual Phase Steels Produced by Different Cooling Rates and a Ferrite-Pearlite Steel," Scripta Metallurgica et Materialia, 24 (1990), 793-797.

13. A.M. Sherman, "Fatigue Properties of High Strength-Low Alloy Stells," Metallurgical Transactions A, 6 (A) (1975), 1035-1040.

14. A.M. Sherman, and R.G. Davies, "Fatigue of Dual-Phase Steel," Metallurgical Transactions A, 10 (A) (1979), 929-933.

AUSTEMPERING OF ALLOYED DUCTILE IRON

S. Yazdani and R. Elliott

Manchester Materials Science Center
University of Manchester & UMIST
Grosvenor St., Manchester M1 7HS
United Kingdom

Abstract

Studies of the austempering behaviour of irons containing nominally, 3.5%C, 2.7%Si, 0.25%Cu, 0.25%Mn and Mo contents of 0.13, 0.25 and 0.45% at 400, 375, 320 and 285°C after austenitising at 870°C are described. They confirm early studies that Mo does not delay the austempering reaction significantly. Consequently, the heat treatment processing window remains open for all the irons and austempering conditions studied. This is shown to contrast with the influence of Mn which delays the reaction leading to the closure of the processing window at higher austempering temperatures and difficulty in producing the higher ductility grades of the ASTM standard. These studies show that with respect to their influence on austempering kinetics, Mo is more suitable than Mn for increasing the hardenability of the iron.

The Third Pacific Rim International Conference on
Advanced Materials and Processing (PRICM 3)
Edited by M.A. Imam, R. DeNale, S. Hanada,
Z. Zhong and D.N. Lee
The Minerals, Metals & Materials Society, 1998

Introduction

Austempered ductile iron, ADI, displays a remarkable combination of high strength and toughness compared to the standard grades of ductile iron. These properties combined with the economic and technical advantages gained from near net shape casting have led to a steady growth of the ADI market. The continuation of this growth will involve the production of higher ductility grades of the ASTM standard in thicker section components.

Figure 1 illustrates a typical austempering heat treatment cycle. It consists of heating to and holding at an austenitising temperature in the range 850-950°C (A-B) for times (B-C) to change the as-cast matrix structure into austenite. The next step is to cool rapidly to the austempering temperature (C-D) in the range 260-450°C and to hold at this temperature (D-E) to achieve the isothermal transformation of austenite to ausferrite. The iron is then cooled to room temperature (E-F). Austempering temperature and time are selected to achieve the desired grade of ADI.

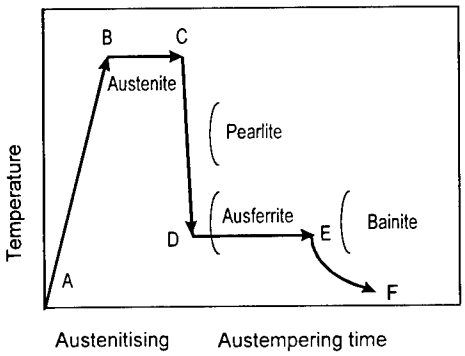


Figure 1. Schematic diagram of an austempering heat treatment cycle.

The austempering reaction in ductile irons is a two stage reaction that differs considerably from the single stage bainitic reaction in steels. In the first stage of the reaction in a ductile iron the austenite transforms into acicular ferrite (ferrite containing carbide at lower austempering temperatures) and high C austenite. In the second stage when the casting is over austempered, the high C austenite breaks down into ferrite and carbide to form a bainitic structure. The high strength associated with high ductility is not derived from the bainitic structure but from the acicular ferrite and high C austenite matrix structure, which is known as ausferrite. Insufficient holding time at austempering temperature leaves unreacted austenite in the structure at intercellular boundaries. This low C austenite is thermally unstable and transforms into martensite during cooling to room temperature. These interconnected UAV volumes reduce the ductility of the austempered iron. The time interval between the end of stage I and the beginning of stage II bainitic reaction is the heat treatment processing window within which the ausferrite structure forms and optimum mechanical properties are obtained.

Alloying elements are added to austempered ductile irons to ensure through hardening of thicker section components. Rapid cooling from the austenitising to austempering temperature is necessary to avoid ferrite or pearlite formation, which reduce the mechanical properties of ADI. Alloying elements Mo and Mn delay the formation of pearlite allowing thicker sections to be through hardened. However, these elements have important effects on the austempering reaction in addition to improving hardenability. They segregate strongly to eutectic intercellular boundaries and alter the austempering kinetics. Mn is an economical, strong hardenability promoter. However, it shrinks the processing window and moves it to longer austempering times, increasing austempering time and heat treatment expense. Segregation of Mn to the intercellular boundaries stabilises austenite in these regions increasing the possibility of these areas remaining unreacted during normal austempering treatments and transforming to martensite on cooling. As the Mn content increases the processing window eventually closes and the ADI standard is not satisfied. Mo is the most potent hardening agent. It is approximately 1.6 times stronger than Mn. It segregates more strongly than Mn to intercellular boundaries often

forming eutectic carbides with associated porosity in the as-cast structure. These are undesirable microstructural features that can reduce ADI properties.
Recently we have reported a series of studies of the influence of Mn, which confirm early studies of its delaying effect on the austempering reaction[1-4]. However, some investigators have claimed that Mo has no significant effect on the processing window[5] whilst others claim that it delays the reaction and report the presence of a large quantity of UAV in high Mo irons[6]. The present study was conducted to resolve these differences.

Experimental procedure

The analysed composition of the irons used in this study is given in table 1. After electric melting the irons were cast into standard 25mm Y-keel blocks. Kinetic samples with dimensions 15×10×10 mm were machined from the bottom section of the blocks. These samples were used to determine the high C, reacted austenite content, VRA, the austenite carbon content, C_γ, hardness and the unreacted austenite content, UAV for different combinations of austempering temperature and time. Tensile samples were machined according to the ASTM A897M: 1990 standard from the bottom section of the blocks. Unnotched Charpy impact specimens, 55×10×10 mm were machined from the same area.

Table I. Composition of ductile irons.

C	Si	Mn	Mo	Cu
3.51	2.81	0.25	0.13	0.39
3.55	2.72	0.25	0.25	0.25
3.56	2.77	0.25	0.45	0.43

Austempering heat treatment was performed by dropping the samples from the austenitising furnace directly into the austempering salt bath to promote rapid cooling to avoid pearlite formation. No pearlite was observed in any of the heat treatment samples. Austempering was performed at 400, 375, 320 and 285°C for times in the range 1-4320 minutes after austenitising at 870°C for 120 minutes. Austenitising was carried out under an argon gas atmosphere to prevent oxidation and decarburisation. The samples were air cooled after austempering.

The VRA and C_γ content were measured as a function of austempering time using X-ray diffraction with a Philips diffractometer (PW 3710) with monochromated Cu K_α radiation at 40KV and 50mA based on the ASTM E975-84 standard. Scanning was performed in the range of (39.5-97)°2θ at a rate of 0.42°2θ.min^{-1} to maintain a low standard error. The peaks from the (111), (200), (220) and (311) planes of austenite and (200) and (211) planes of ferrite were used to minimise the error from the preferred orientation of phases. Areas under the peaks were measured using the Philips APD software for curve fitting to minimise error introduced from the background radiation. The repeatability of the method was measured in the range of ±2% of the calculated VRA.

A layer of 3mm was machined from all kinetics samples to ensure freedom from any oxidation or decarburization effects. A Swift automatic point counter model E was used to measure the UAV on polished and etched samples. Point counting was performed according to the ASTM standard test method for determining volume fraction by the systematic manual point counting technique.

Tensile samples were tested after heat treatment in an Instron 6025 testing machine with a cross head speed of 1 mm.min^{-1}. The UTS, 0.2% proof strength and elongation to fracture were measured. Unnotched Charpy testing was performed in a standard Losenhausenwerk Impact testing machine at room temperature. At least four measurements were made at each

austempering time and the three highest values were used to calculate an average value according to the ASTM standard.

Experimental Results and Discussion

The change in UAV with increasing austempering time for the four austempering temperatures is shown in figure 2. All the measurements show a continuous fall in UAV during the stage I reaction. None of the curves display the pronounced arrest in the UAV fall associated with a delayed stage I reaction in the intercellular boundaries and observed in Mn rich irons. This suggests that Mo does not delay the transformation in the intercellular boundaries to the same extent as Mn.

The change in VRA with increasing austempering time is shown in figure 3. In all cases the VRA increases initially as the stage I reaction proceeds, reaches a plateau and then decreases as the stage II reaction commences. In common with previous studies, the VRA plateau level is much higher at higher austempering temperatures. There is no evidence of a peak in the curves. Peak formation indicates overlapping of the stage I and stage II reactions and closing of the processing window.

A new concept of the processing window was introduced during course of our studies on Mn alloyed irons. It defines the austempering time interval over which the mechanical properties satisfy the ASTM A897M: 1990 standard. On the basis of mechanical property-austempered microstructure observations, the beginning of the processing window (t_1) was defined as the time when UAV has decreased to 3%. The end of the processing window (t_2) was defined as the time when the VRA level has decreased to 90% of the its maximum value achieved during the stage I reaction. These criteria are used to calculate the processing window for the three Mo irons shown in figure 4. These results show that increasing the Mo level has only a small delaying effect on the austempering reaction and does not lead to closure of the processing window. Mechanical property measurements reported elswere[7] confirm that the ASTM standard is satisfied by all three Mo irons for the austempering conditions examined in the present study.

Figure 4 also shows windows determined previously for irons with a base composition of 3.5% C, 2.5% Si, 0.25% Cu, 0.25% Mo and containing 0.37 and 0.67%Mn. Increasing the Mo content with a constant Mn level (0.25%) has a small delaying effect on the completion of the stage I reaction and the beginning of the stage II reaction, whereas increasing the Mn content with a constant Mo level (0.25%) has a much greater delaying effect on the completion of the stage I reaction and delays the stage II reaction particularly at lower austempering temperatures. The overall effect is that increasing the Mo content does not change the processing window significantly whereas increasing the Mn content narrows and closes the processing window particularly at higher austempering temperatures.

The delay in the completion of the stage I reaction is a significant factor in producing higher ductility grades of the standard. The variation of UAV with austempering time, t, can be represented by equation,

$$\ln UAV = A + B \ln t$$

The slope parameter B measures the rate of fall of UAV. Figure 5 shows how B changes with increasing alloying additions for the present irons, the previous Mn series of irons[1-3] and the early measurements on a Mo and a Mn series of irons[5] for similar austempering treatments. The figure shows clearly the stronger delaying effect of Mn compared to Mo. The present measurements show good agreement with the early measurements after allowance is made for the higher alloying level in the base composition.

Conclusion

Measurements of the austempering kinetics of irons containing nominally 3.5% C, 2.7% Si, 0.25% Cu, 0.25% Mn and Mo levels of 0.13%, 0.25% and 0.45% at different austempering temperatures after austenitising at 870°C show

1- Increasing the Mo content only delays the stage I and stage II austempering reactions slightly.
2- Processing windows calculated using criteria established in previous studies show that the processing window is open for all the irons studied and all the austempering conditions used.
3- The influence of increasing Mo levels on the processing window is in direct contrast to that of Mn which moves the window to longer austempering times and closes it at a lower austempering temperature as the Mn content increases.

Acknowledgement

SY would like to thank the IDB Merit Scholarship Program for financial support. Acknowledgement is made to Prof. F.S. Sale for providing research facilities.

References

1. R. Elliott, "The Role of Research in Promoting Austempered Ductile Iron," Heat Treatment of Metals, 3 (1997), 55-59.

2. H. Bayati, R. Elliott, and G.W. Lorimer, "The Influence of Austenitising Temperature on Austempering Kinetics of High Manganese Alloyed Ductile Cast Iron," Mater. Sci. Techno., 11 (1995), 776-786.

3. A. Nazarboland and R. Elliott, "The Relationship Between Austempering Parameters, Microstructure and Mechanical Properties in a Mn-Mo-Cu Alloyed Ductile Iron," Int. J. Cast Metals Res., 9 (5) (1997), 295-308.

4. A.S. Hamid Ali and R. Elliott, "Influence of Austenitising Temperature on Austempering of a Mn-Mo-Cu Alloyed Ductile Iron," Mater. Sci. Techno., 12 (1996), 1021-1031.

5. T.N. Rouns and K.B. Rundman, "The Constitution of Austempered Ductile Iron and Kinetics of Austempering," A.F.S. Trans., 95 (1987) 851-874.

6. B.V. Kovacs, "The Effect of Alloying Elements and Their Segregation in ADI," 1991 World Conf. on Austempered Ductile Iron, (Bloomingdale, Illinois), A.F.S. Vol. I, 241-270.

7. S. Yazdani and R. Elliott, "The Influence of Molybdenum on the Austempering Behaviour of a Ductile Iron," Submitted to the Int. J. Cast Metals Res..

Figure Captions

Figure 2. The relationship between UAV and austempering time for the three irons studied.
Figure 3. The relationship between VRA and austempering time for the three irons studied.
Figure 4. The processing window calculated for the three present irons and those determined previously for a 0.37%Mn and a 0.67%Mn iron.
Figure 5. The dependence of the slope B on alloying element content for increasing Mn and Mo contents.

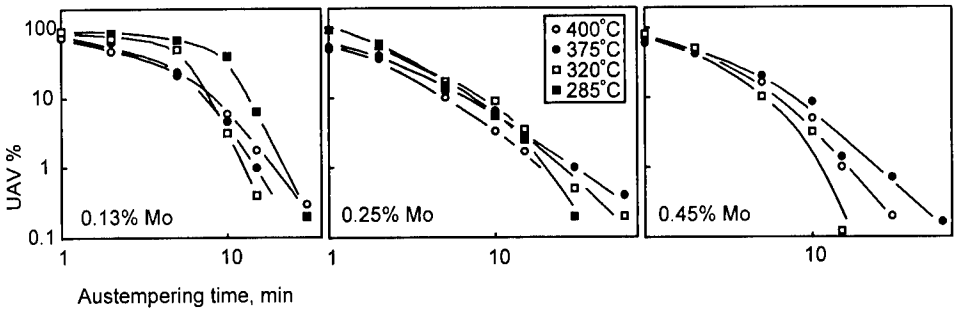


Figure 2.

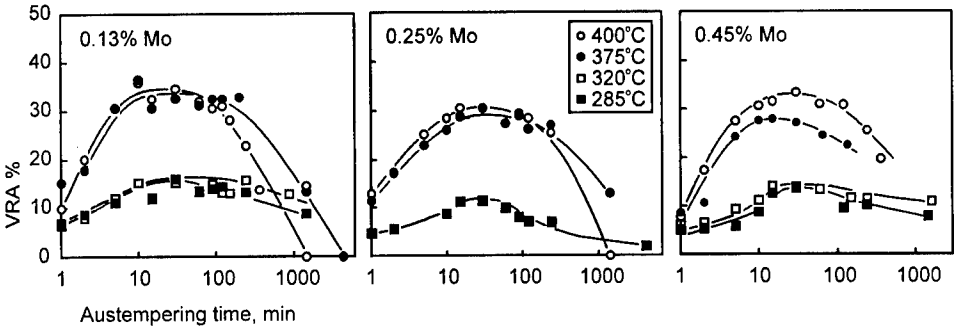


Figure 3.

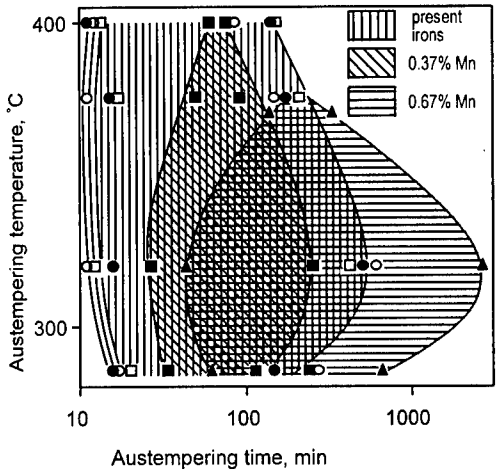


Figure 4.

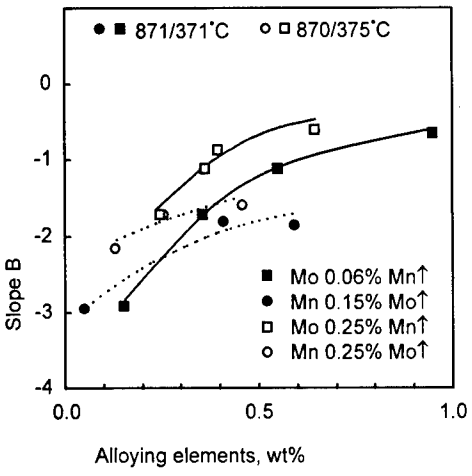


Figure 5.

TENSILE PROPERTIES OF Mo AND Mo-Nb MICROALLOYED FIRE RESISTANT STEELS

W. Sha, P.J. Blair and F.S. Kelly

Department of Civil Engineering, The Queen's University of Belfast, Belfast BT7 1NN, UK

Abstract

Tensile properties of two fire resistant microalloyed steels for building construction have been tested, as a function of temperature up to 700°C and strain rate varying from 0.1 to 1 %/min. The steel compositions are Fe-0.1%C-0.64%Mn-0.1%Si-0.51%Mo and Fe-0.11%C-1.14%Mn-0.24%Si-0.52%Mo-0.03%Nb (wt.%), respectively. Property parameters obtained from stress-strain curve measurements are yield and tensile strengths, fracture and true fracture stresses, and reduction in area. It has been found that both steels have much better elevated temperature strength than conventional structural steels. Comparing their performance shows that generally the Mo-Nb steel is stronger at all temperatures and is not affected by strain rate as much as it is for the Mo steel. At 400°C, the Mo-Nb steel has a greater yield strength than at room temperature, suggesting its ability of self-strengthening at a suitable elevated temperature. This steel exhibits a lower ductility however, likely due to its higher inclusion content.

The Third Pacific Rim International Conference on
Advanced Materials and Processing (PRICM 3)
Edited by M.A. Imam, R. DeNale, S. Hanada,
Z. Zhong and D.N. Lee
The Minerals, Metals & Materials Society, 1998

Introduction

The important properties governing the performance of a structural steel at elevated temperatures are strength, ductility (strain at a given load), thermal expansion, specific heat and thermal conductivity. The strength of conventional structural steels reduces significantly when subjected to elevated temperatures reached in a fire and it is normal practice to provide fire protection [1]. Such protection is expensive, in terms of the amount of materials and labour consumed [2].

In the past decade, fire resistance of steel structures and construction has received much attention, especially in Europe, owing to its importance in terms of both economics and image [1,2,3,4,5,6]. However, to date there has been relatively limited research on the development of fire resistant *steels*, except for a significant but isolated development work carried out by Nippon Steel. Fire resistant structural steels have resulted [7], but they are widely regarded as specifically targeted at the new Japanese building fire regulations.

In the present work, two fire resistant steels designed and manufactured by Nippon Steel have been investigated using tensile testing. The properties determined are yield and tensile strengths, fracture and true fracture stresses, and reduction of area. The work is part of a wider programme of developing fire resistant steels suitable for construction [8], especially under Western fire regulations for building safety.

Experimental Details

The compositions of the two steels studied are shown in Table I. In addition to the addition of Nb, it may be noted that there is a higher level of manganese in the Mo-Nb steel, which is commonly used for deoxidisation and desulphurisation.

Table I Compositions (wt.%) and Final Thickness of the Hot-rolled Fire-Resistant Steels

Steel type	C	Mn	Si	Mo	Nb	Plate thickness (mm)
Mo steel	0.1	0.64	0.1	0.51	-	9
Mo-Nb steel	0.11	1.14	0.24	0.52	0.03	16

Tensile specimens with a square cross-section along the gauge length were used, with original cross-section areas of 25 or 64 mm^2. The specimen gauge length is between 70 and 100 mm. The tests were carried out using a Nene machine. For testing at elevated temperatures, controlled heating was provided by a cylindrical furnace surrounding the samples. Loading started approximately 20 minutes after heating began, with the first 10 minutes for the furnace to reach the set temperature, and a further 10 minutes for the sample temperature to stabilise. Temperature fluctuation along the gauge length of the specimen was within 15°C. Strain rates varying from 0.1 to 1 %/min were used. For each condition, one to three tests were carried out, and tests showed good repeatability. This testing procedure followed the standard testing method [9].

Engineering stress, strain and tensile strength [10] were used throughout the paper, while the 0.2% proof stress was used as yield stress. Reduction in area values were measured to an accuracy of within 20%, limited by uncertainties in obtaining cross-section areas at points of fracture which usually had irregular shapes. Final cross-sectional areas were used to calculate

true fracture stresses whereas fracture stresses were calculated by using original cross-sectional areas. In diagrams that follow, estimated error values are indicated when they are available.

The experimental procedures used in the present study are similar to a previous work carried out with the same apparatus [11].

Results and Discussion

Room temperature yield strengths are 340 and 370 MPa for Mo and Mo-Nb steels, respectively, when measured at a strain rate of 1 %/min. For the Mo steel, the yield strength remains almost unchanged up to 600°C when tested at a strain rate of 1 %/min (Figure 1a). At 700°C, it only decreases by 39% of the room temperature value to 212 MPa. Under a slower strain rate, the steel showed a reduction in yield strength at 600°C (Figure 1b).

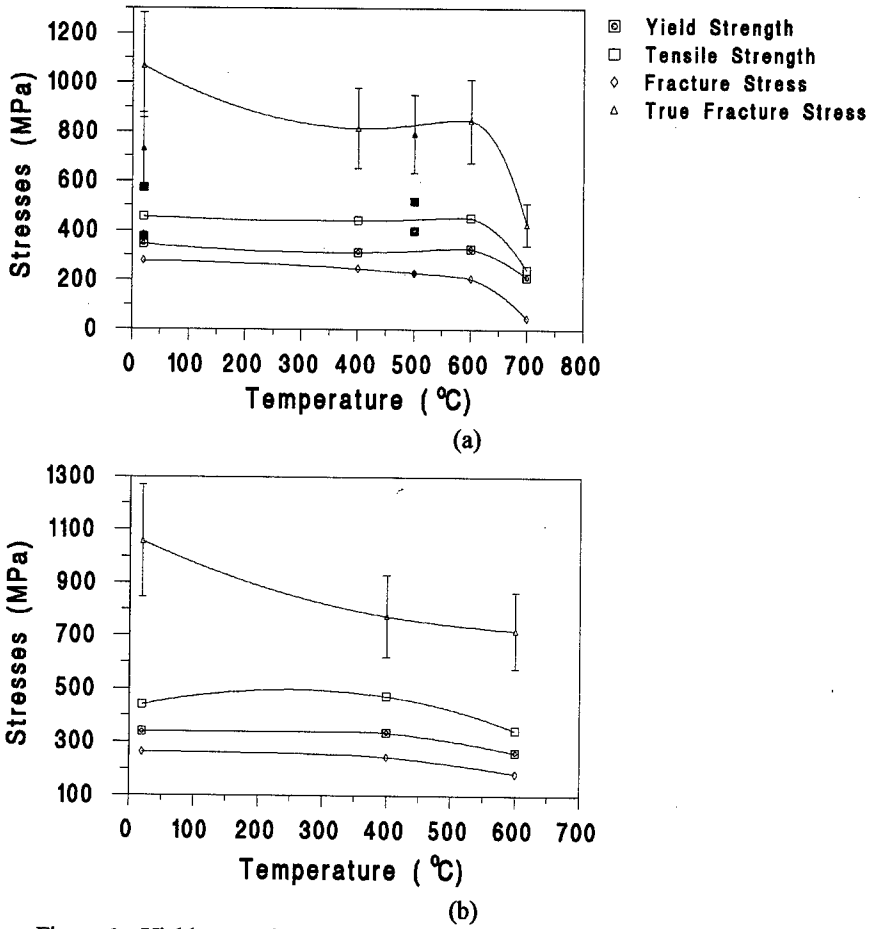


Figure 1: Yield strength, tensile strength, fracture stress and true fracture stress as a function of temperature for the Mo steel tested at strain rates of (a) 1 %/min and (b) 0.2 %/min. Results for two Mo-Nb steel samples tested with strain rate of 1 %/min at room temperature and 500°C are included in (a) for comparison (solid symbols)

The Mo-Nb steel, however, shows a different characteristics. At 400°C, the yield strength of all three samples tested was higher than the room temperature strength (Figure 2). The yield strength then drops with a further increase in temperature to 600°C. At 0.5 %/min strain rate, the 500°C yield strength was found to be 382 MPa, close to that obtained at 1 %/min (Figure 1a). This steel has a greater strength than the steel containing Mo only as the microalloying element.

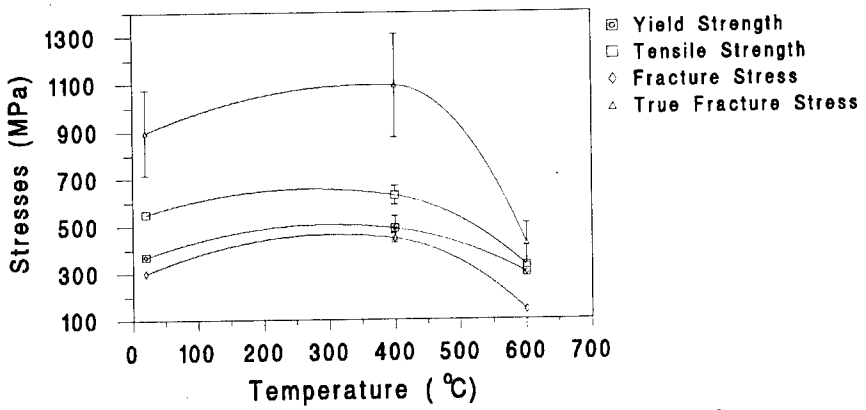


Figure 2: Yield strength, tensile strength, fracture stress and true fracture stress as a function of temperature for the Mo-Nb steel tested at a strain rate of 0.1 %/min.

Generally, the trend of tensile strength variation with temperature resembles that of the yield strength (Figures 1 and 2). For the Mo steel, as with the yield strength, the tensile strength at 700°C is still more than 50% of the room temperature value (Figure 1a). For the Mo-Nb steel the tensile strength is greatest at 400°C (Figure 2), but there is a considerable drop at 600°C. In addition to results shown in the diagrams, a sample tested at 500°C with a strain rate of 0.5 %/min gave a tensile strength of 501 MPa.

Comparing the two steels, the tensile strength is significantly higher for the Mo-Nb steel. This repeats the finding of the yield strength, which shows that the Mo-Nb steel is stronger throughout the range of temperatures for these tests.

The strain rate has the same effect on the tensile strength as it has on the yield strength, *i.e.* samples tested at a lower strain rate had a lower recorded strength value. This appears more pronounced on the Mo steel than on its Mo-Nb counterpart.

The original sample cross-sectional area was used when calculating the fracture stress, while the final cross-sectional area was used to calculate the true fracture stress. The testing results of these two parameters are included in Figures 1 and 2. In addition, a Mo-Nb steel sample tested at 500°C with a strain rate of 0.5 %/min gave a fracture stress of 232 MPa and a true fracture stress of 834 MPa.

For the Mo steel there is a large fall in elongation from room temperature to 400°C. After this temperature the decline is more gradual. This pattern is repeated for the Mo-Nb steel, although the elongation is somewhat lower. It has been found that the elongation is not significantly affected by strain rate. The reduction in area at fracture was obtained (Figure 3).

Some of the testing results demonstrated here can be explained with microstructural data obtained from the same steels [11,12]. Figure 4 shows a fractograph of the Mo-Nb steel. The inclusions have been found by electron probe to contain Al, Si, Mn and Fe.

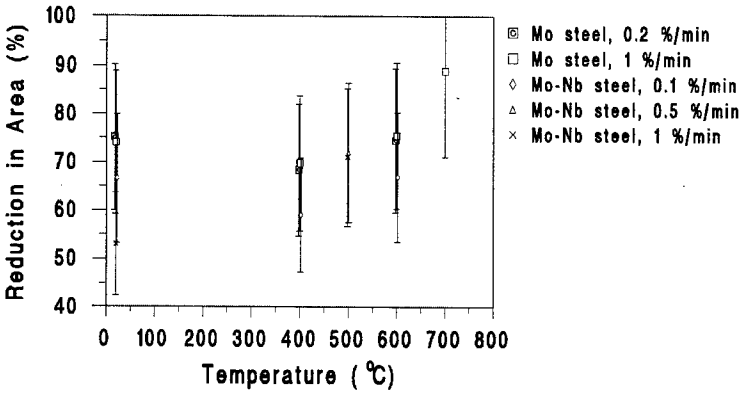


Figure 3: Reduction in area as a function of temperature and strain rate.

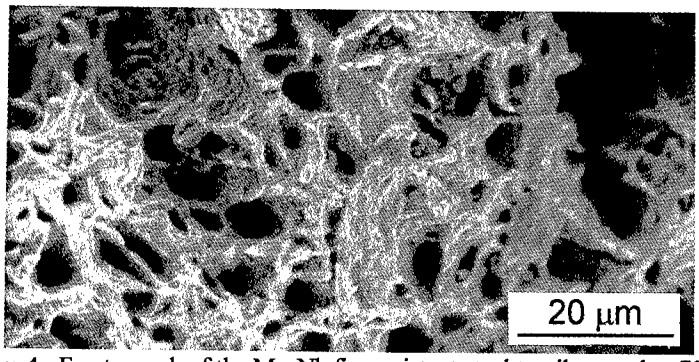


Figure 4: Fractograph of the Mo-Nb fire resistant steel tensile tested at 700°C.

Concluding Remarks

In general, a structural steel should have a yield strength greater than 250 MPa. Both fire resistant steels have yield strengths in excess of this value even at a temperature of 600°C. At 400°C, the Mo-Nb steel has a greater yield strength than at room temperature, suggesting its ability of self-strengthening at a suitable elevated temperature. Comparing with the Mo-containing steel, the Mo-Nb steel has a higher yield strength throughout the temperature range showing the effect of additional strengthening due to Nb. For temperatures up to 600°C, the yield strength increases with increasing strain rate for both steels, and this effect is more pronounced in the case of the Mo steel.

The tensile strength has a similar correlation with temperature as the yield strength. A structural steel should have a tensile strength greater than 400 MPa. The results obtained have demonstrated that both steels have tensile strengths greater than 400 MPa even at temperatures of 400°C. The results also showed that samples tested at a lower strain rate gave a lower tensile strength. The effect of strain rate was greater on the Mo than on the Mo-Nb steel.

Qualitatively, the elongation of both steels decreases with increasing temperature. The stronger Mo-Nb steel is consistently less ductile than the Mo steel, which may be explained with the fact

that the former contains a higher inclusion level. This is suggested by its significantly higher concentrations of Mn and Si, and a higher density of inclusions was indeed observed experimentally [11]. The ductility is not much affected by the strain rate during testing.

The experimental results obtained in the present work largely agree with and supplement previous studies on fire resistant steels [7,11]. Clearly, these fire resistant steels represent some major improvements over conventional strudtural steels in terms of their performance at elevated temperatures likely to be experienced in fires.

Acknowledgement

The authors are grateful to Nippon Steel for supplying the steels.

References

1. Fire Protection for Structural Steels in Buildings, 2nd edn. (Aldershot, UK: Association of Specialist Fire Protection Contractors and Manufacturers Ltd., 1992), 6.

2. H. Morris, "Rusty, eh?", Metals and Materials, 4 (1988), 345-349.

3. Journal of Constructional Steel Research: Special Issue on Fire and Steel, 33 (1-2) (1995).

4. New Steels Construction: Special Issue Featuring Fire Engineering, 3 (1) (1995).

5. D.J. O'Connor, "Structural Engineering Design for Fire Safety in Buildings," The Structural Engineer, 73 (4) (1995), 53-58.

6. J. Robinson, "A Disaster Waiting to Happen?" New Steel Construction, 3 (2) (1995), 12.

7. R. Chijiiwa, H. Tamehiro, A. Yoshie, K. Funato, Y. Yoshida, Y. Horii and R. Uemori, "Development and Practical Application of Fire-Resistant Steel for Buildings," HSLA Steels '95 Conference Proceedings, ed. G. Liu, H. Stuart, H. Zhang and C. Li (Beijing: China Science and Technology Press, 1995), 584-589.

8. "Fire-Proof Steel Being Developed," Materials World, 4 (1996), 570.

9. British Standard for Tensile Testing of Metallic Materials, BS EN 10002 (London: British Standards Institution, 1990).

10. G. Dieter, Mechanical Metallurgy, 3rd edn. (New York, NY: McGraw-Hill, 1986), 275.

11. F.S. Kelly and W. Sha, "Mechanical Properties of Fire-Resistant Steels for Construction," Proceedings of the 5th European Conference on Advanced Materials and Processes and Applications: Materials, Functionality and Design, vol. 1, ed. L.A.J.L. Sarton and H.B. Zeedijk (Zwijndrecht: Netherlands Society for Materials Science, 1997), 1/35-1/40.

12. W. Sha and F.S. Kelly, "Mechanical Property and Microstructure of Structural and Fire Resistant Steels," Advanced Materials and Processing–PRICM 3 (Warrendale, PA: TMS, 1998).

Preparation of Fe-C System Alloy by Mechanical Alloying

Nurul Taufiqu Rochman, K.Kawamoto, H.Sueyoshi,
Y.Nakamura and T.Nishida

Department of Mechanical Engineering, Faculty of Engineering,
Kagoshima University, Kagoshima 890 Japan

Abstract

Elemental iron, graphite, silicon and chromium were mechanically alloyed using a planetary ball mill. The MAed powders were characterized by X-ray diffraction, differential thermal analysis and scanning electron microscopy. The MAed powders were then HIPed, and the Vickers hardness and microstructure of the compact were examined. In the Fe-C system, increasing milling time led to the formation of super-saturated iron solid solution and iron/carbon amorphous phase, resulting in the formation of ultra-fine particles in the nano-meter order. The Vickers hardness of the HIPed compacts depended upon the number of voids and the amount of Fe_3C and graphite. The addition of silicon tended to promote graphitization, while the addition of chromium tended to retard graphitization.

The Third Pacific Rim International Conference on
Advanced Materials and Processing (PRICM 3)
Edited by M.A. Imam, R. DeNale, S. Hanada,
Z. Zhong and D.N. Lee
The Minerals, Metals & Materials Society, 1998

Introduction

Cast irons are usually produced by the melting and subsequent casting process. In this method, a coarse ledeburite structure is formed due to the eutectic reaction in which liquid metal is transformed into γ Fe and Fe_3C during solidifying. The cast irons also contain flaky or spheroidal graphite. The presence of the coarse ledeburite structure and large-sized graphite results in a decrease in both ductility and toughness of cast irons. Mechanical alloying is a unique powder production technique by which a blend of elemental powders is subjected to high energy impact forces. This technique was first employed by Kock *et al.* [1] to produce amorphous $Ni_{60}Nb_{40}$. Schwarz *et al.*[2] examined amorphization in mechanical alloying in detail. Mechanical alloying represents a new non-equilibrium process for producing metastable materials such as amorphous and ultra-fine powders. If graphite and microstructure of the matrix can be refined by mechanical alloying and subsequent sintering, new Fe-C system materials with high hardness and wear resistance may be attainable. In the present paper, we examine the application of mechanical alloying to Fe-C system alloys widely used as structural materials.

Experimental Procedure

Iron powder of 99.5 mass% and 5 μ m in particle size, graphite powder of 99.9 mass% and $<78\,\mu$ m in particle size, silicon powder of 99.9 mass% and $<85\,\mu$ m in particle size and chromium powder of 99.9 mass% and $<85\,\mu$ m in particle size were used as starting materials. Table 1 lists the mixing concentration. These powders were charged in 450 cm^3 hardened steel vials with 2 types of austenitic stainless steel balls (ϕ 12mm:ϕ 7mm= 1:1) under an Ar atmosphere in a glove box. The powder-to-ball ratio was approximately 1 : 8. Mechanical alloying runs were carried out using a planetary ball mill at various times up to100 h. The mechanical alloyed (MAed) powders were characterized by X-ray diffraction (XRD), differential thermal analysis (DTA) and scanning electron microscopy (SEM). DTA was performed under an Ar atmosphere at a heating rate of 0.33 K/s. After milling for 100 h, consolidation of the MAed powders was performed at room temperature in a uniaxial pressing system. The cold compacted pellet was charged into a copper tube, degassed and then sealed in a vacuum. The obtained copper capsule was hot isostatic pressed (HIPed) at 100 MPa for 1 h at 853 K lower than the eutectoid transformation temperature A_1 or 1053 K higher than A_1. The properties of the sintered compact were examined by XRD, Vickers hardness measurement and SEM.

Table I The concentration of mixing powders (mass%).

Mark	Fe	C	Si	Cr
Fe-4C	96	4	-	-
Fe-6C	94	6	-	-
Fe-8C	92	8	-	-
Fe-10C	90	10	-	-
Fe-6C-2Si	92	6	2	-
Fe-8C-2.5Cr	89.5	8	-	2.5

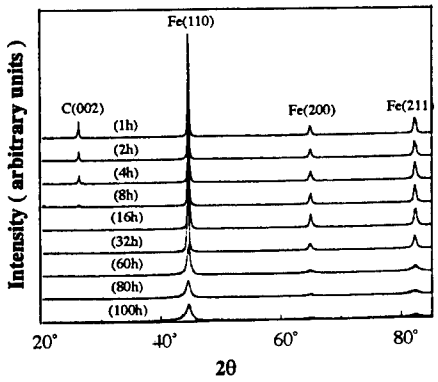


Figure 1: XRD patterns of the MAed Fe-6C powders after various milling times.

Results and Discussion

Figure 1 shows the XRD patterns of Fe-6C powders after various milling times. After 16 h of milling, the graphite diffraction peak could not be detected. The broad and low diffraction

peaks of graphite in Fig. 1 appear as a halo pattern due to the amorphous phase. Meanwhile, the iron diffraction peaks broaden when the milling time is long. This may be due to grain refinement and amorphization of the iron powders during the milling process. The diffraction peak of iron carbide was not detected in the XRD patterns of the Fe-C system powders after 100 h of milling. Figure 2 shows the change in the half-value width of the (110) plane diffraction peak of iron with milling time. The half-value width increases as the milling time exceeds 32 h. This suggests that grain refinement and amorphization of iron powders occur after amorphization of the graphite. As shown in Fig.1, the peak position of iron shifts to a lower angle when milling time is long. This suggests that carbon atoms dissolve into iron and a super-saturated iron solid solution is formed. The carbon content of the iron solid solution can be estimated by measuring the change in the lattice parameter of iron and substituting this value in the equation proposed by Fasiska *et al.*[3]. Figure 3 shows the changes in the lattice parameter and carbon content with milling time. The lattice parameter and carbon content increased remarkably when the milling time exceeded 32 h.

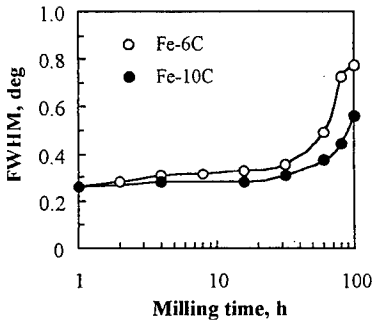


Figure 2: Changes in the half-value width (FWHM) of α Fe (110) with milling time.

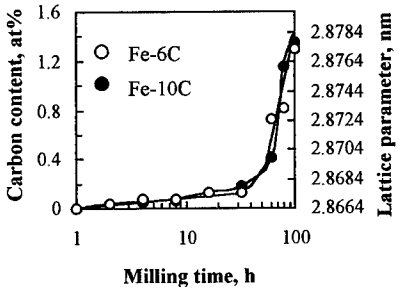


Figure 3: Changes in the lattice parameter and canbon content of iron solid solution with milling time.

Figure 4 shows the lattice parameter and carbon content of the iron solid solution after 100 h of milling as a function of the carbon concentration. The lattice parameter and carbon content showed little change regardless of the carbon concentration. From Fig.4, the limiting carbon content of the super-saturated iron solid solution was estimated to be 1.35 at% . This suggests that most of the carbon atoms exist as fine amorphous carbon and the iron/carbon amorphous phase though a small amount of carbon atoms dissolve into the iron.

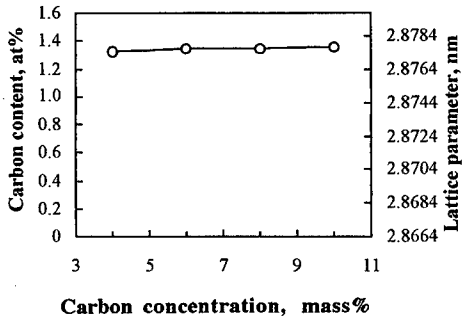


Figure 4: The lattice parameter and carbon content of iron solid solution after 100 h of milling as a function of the carbon concentration.

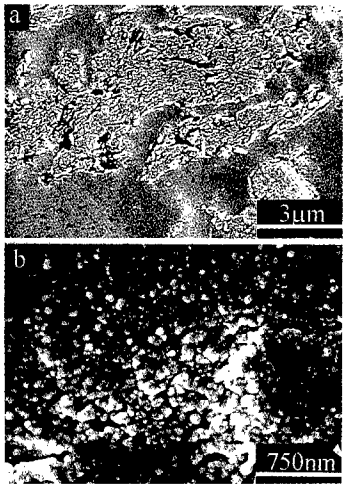


Figure 5: SEM images of the Fe-10C powders milled for (a) 1 h and (b) 60 h.

Figure 5 shows the SEM images of the MAed Fe-10C powders. Morphologically, the as-recieved iron powders were spherical. During the early stage of milling, the morphology of the ductile iron powders changed from spherical to flake-like with a high aspect ratio. Micro-cracks appeared in these powders (Fig.5(a)). During subsequent milling, the iron powders were covered by finely crushed amorphous carbon, and then solutioning of carbon atoms into the iron powders was promoted by repeated fracturing and the cold-rewelding process[4]. After 60 h of milling, the iron powders became aggregated ultra-fine particles (nano-meter order) as shown in Fig.5(b). During subsequent milling, the iron/carbon amorphous phase coexisted with the super-saturated iron solid solution as a result of the above mentioned kneading process.

Figure 6 shows the DTA curves of the MAed Fe-10C powders. The first apparent exothermic peak appears at 578 K in powders milled for longer than 60 h. Figure 7 shows the XRD pattern of the Fe-10C powders milled for 100 h, followed by heating up to 603 K. In addition to the diffraction peaks of α Fe and Fe_3O_4 due to oxidation during heating up to 603 K, the diffraction peaks of Fe_5C_2 [5], which did not appear in the XRD pattern of the as-milled powders, were detected. Figure 8 shows the changes in the lattice parameter and carbon content of the iron solid solution with heating temperature of the Fe-10C powders milled for 100 h. The carbon content of the iron solid solution decreased rapidly up to 603 K and then reached slowly to the equilibrium values of α Fe. Based on Fig.6, 7 and 8, the exothermic

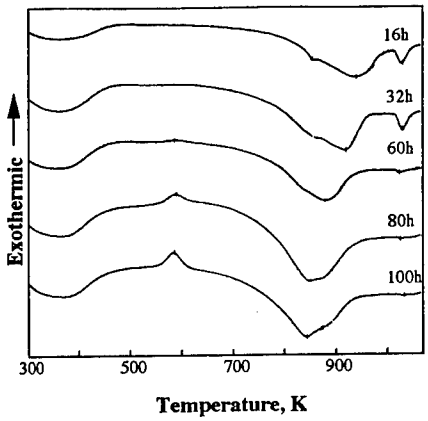


Figure 6: DTA curves of the MAed Fe-10C powders for various milling time.

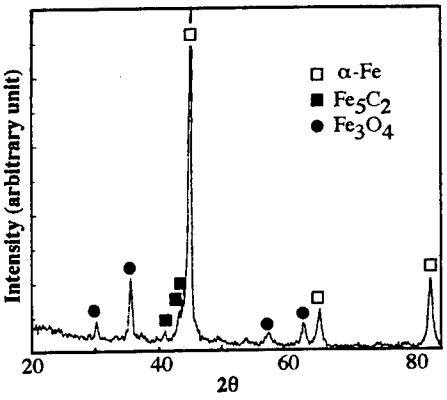


Figure 7: XRD pattern of the Fe-10C powders milled for 100 h, followed by heating up to 603 K.

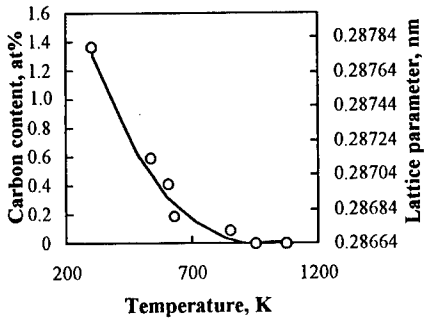


Figure 8: Changes in the lattice parameter and carbon content of the iron solid solution of Fe-10C powders with heating temperature.

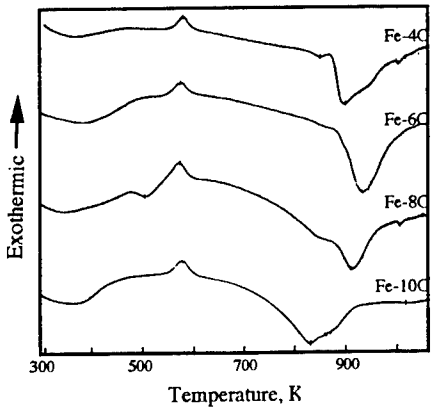


Figure 9: DTA curves of the Fe-C system powders after 100 h of milling.

peak at 578 K is caused by that the super-saturated iron solid solution and iron/carbon amorphous phase are transformed into Fe_5C_2 and α Fe. The exothermic peak intencity at 578 K increased with milling time as shown in Fig.6. This may be due to enhancement of the degree of super-saturation and amorphization. In Fig.6, a broad endothermic peak appears in the temperature range from 800 K to 930 K. According to the XRD patterns, the small endothermic reaction that occurs around 800 K is caused by the transformation of Fe_5C_2 to Fe_3C and the large endothermic reaction that occurs around 930 K is due to graphitization of Fe_3C. Thus, graphitization of MAed Fe-C system powders occurs more easily than that of plain carbon steel and cast iron. In Fig.6, the endothermic reaction at about 1023 K is due to austenitizing at A_1. Figure 9 shows the DTA curves of the Fe-C system powders after 100 h of milling. The degree of graphitization increased with increasing carbon concentration.

Figure 10 shows the changes in the relative density and Vickers hardness of the HIPed compacts with carbon concentration. In case of HIP at 853 K, a slight decrease in the relative density was evident at a carbon concentration exceeding 6 mass%. The Vickers hardness increased initially with carbon concentration up to approximately 900 at a carbon concentration of 6 mass%. However, this value decreased abruptly when the carbon concentration exceeded 6 mass%. In case of HIP at 1053 K, the relative density and Vickers hardness were maximal at a carbon concentration of about 7 mass%, followed by a decrease when carbon concentration exceeded about 7 mass%. Figure 11 shows the SEM images of the cross-sectional area of the HIPed compacts. In case of HIP at 853 K, relatively few voids were present in the HIPed Fe-4C and Fe-6C compacts. As shown in Fig.9, no graphitization occured at 853 K in the MAed Fe-4C and Fe-6C powders. Thus, the result that the Vickers hardness of the HIPed Fe-6C compact was higher than that of the HIPed Fe-4C compact is likely due to the increase in Fe_3C. Many micro-voids appeared in the HIPed Fe-10C compact (Fig.11(b)). The microstructure of the HIPed Fe-8C compact resembled a combination of the microstructures of the HIPed Fe-6C and Fe-10C compacts. As shown in Fig.9, graphitization of the MAed Fe-8C and Fe-10C powders was promoted by heating up to 853 K. The presence of graphite inhibits sintering of the iron particles, resulting in the formation of numerous micro-voids. The decreases in the relative density and Vickers hardness of the HIPed compact with increasing carbon concentration above a carbon concentration of 6 mass% may be due to both the presence of the graphite and the formation of the micro-voids. In the HIPed Fe-4C and Fe-6C compacts, a greater number of voids were observed at 1053 K than at 853 K. As shown in Fig.9, graphitization occurred to some extent during the heating process up to 1053 K in the MAed Fe-4C and Fe-6C powders. The

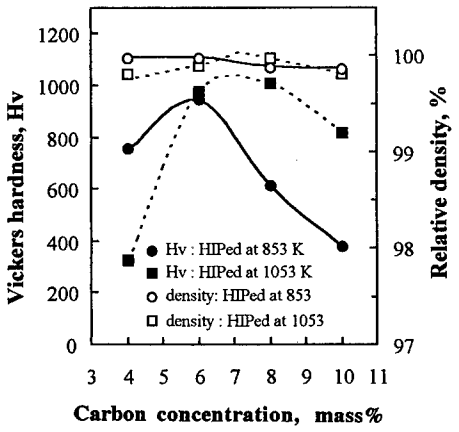


Figure 10: Changes in the relative density and Vickers hardness with carbon concentration in the HIPed compacts.

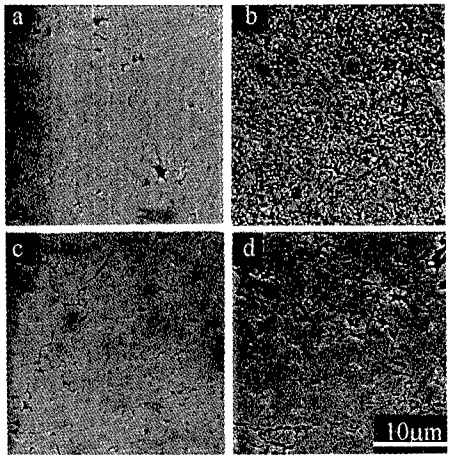


Figure 11: Micrographs of HIPed compacts of (a)Fe-6C at 853 K, (b)Fe-10C at 853 k, (c) Fe-8C at 1053K and (d)Fe-10C at 1053 K.

greater number of voids at 1053 K may be attributed to the inhibition of sintering due to graphite. The increase in the number of voids was accompanied by a decrease in the relative density and Vickers hardness. In the HIPed Fe-8C compact, few voids were observed at 1053 K than at 853 K (Fig. 11(c)). As shown in Fig. 11(d), many unredissolved graphite particles were observed in the Fe-10C compact HIPed at 1053 K. As shown in Fig. 10, Vickers hardness decreased when the carbon concentration exceeded about 7 mass%. The presence of graphite also results in the inhibition of sintering. Thus, the Vickers hardness of the HIPed compact appears to depend upon the density of voids and amount of Fe_3C and graphite.

Figure 12 shows the DTA curves of the Fe-6C, Fe-6C-2Si, Fe-8C and Fe-8C-2.5Cr powders MAed for 100 h. The first apparent exothermic peak of the MAed Fe-6C-2Si and Fe-8C-2.5Cr powders resembles that of the MAed Fe-6C and Fe-8C powders, respectively. However, endothermic reaction due to graphitization of the MAed Fe-6C-2Si powders begins at 720 K and ends at 970 K. This suggests that graphitization occurs readily in the MAed Fe-6C-2Si powders than the MAed Fe-C powders. On the other hand, the endothermic change due to graphitization of the MAed Fe-8C-2.5Cr powders was remarkably smaller than that of the MAed Fe- 8C powders. This suggests that graphitization is retarded by chromium addition.

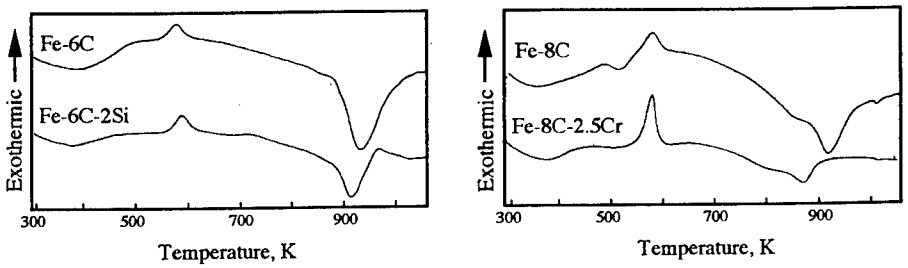


Figure 12: DTA curves of the Fe-6C, Fe-6C-2Si, Fe-8C and Fe-8C-2.5Cr powders.

Conclusions

Elemental iron, graphite, silicon and chromium were mechanically alloyed using a planetary ball mill. In the Fe-C system, amorphization of the graphite powders occurred first during the early stage of milling. During subsequent milling, the iron/carbon amorphous phase coexisted with the super-saturated iron solid solution having the limiting carbon content of 1.35 at%. Increasing milling time led to the formation of ultra-fine particles in the nano-meter order as a result of the kneading process. The super-saturated iron solid solution and iron/carbon amorphous phase were transformed into Fe_5C_2 and α Fe at 578 K. As temperature increased, Fe_5C_2 was transformed into Fe_3C. The Fe_3C was then decomposed into α Fe and graphite. The increase in carbon concentration and the addition of silicon promoted graphitization, whereas the addition of chromium tended to retard graphitization. The Vickers hardness of the HIPed compacts depended upon the number of voids and the amount of Fe_3C and graphite.

References

(1)C.C.Koch, O.B.Cavin, C.G.Mckamey and J.O.Carbrough : Appl. Phy. Lett., 43 (1983), 1017.
(2)R.B.Schwarz, R.R.Petrich and L.K.Saw : J. Non-Cryst. Solids, 76(1985), 281.
(3)E.J.Fasiska and H. Wagenblast : Trans. Metallurgical Society of AIME, 239(1967), 1818.
(4)D.Maurice and T.H.Courtney : Metallurgical and Materials Trans. A, 25A(1994),147.
(5)K.H.Jack and S.Wild: Nature, 212(1966), 248.

Improvement on Surface of Cast Iron by Using Alloy Powders on the Mold

Shigenori Tanabe, Yasuo Horikawa, Kimitsugu Yoshikawa and Kenji Higashi

Metallurgy and Materials Science, College of Engineering, Osaka Prefecture University
1-1 Gakuen-cho, Sakai, Osaka, Japan, 599-8531

Abstract

For coating functional layer on cast iron, mixed powders which consist of high performance powder and Ni-based alloy powder having low melting point are coated on the mold. By the heat of pouring, these powder layers are densified by a liquid phase sintering and then jointed with cast iron. The coated cast iron obtained by mixed Fe-Cr alloy and self-fused Ni based alloy has substantial hardness (800～1000HV1) in thickness of 2mm and good resistance to wet abrasion, and also by mixed Ni and Ni-P alloy it has soft surface layer (100～200HV1) containing 10～20%Ni and therefore good corrosion resistance to spraying of 5%NaCl solution.

The Third Pacific Rim International Conference on
Advanced Materials and Processing (PRICM 3)
Edited by M.A. Imam, R. DeNale, S. Hanada,
Z. Zhong and D.N. Lee
The Minerals, Metals & Materials Society, 1998

Introduction

This investigation is one of the surface treatments or the coating methods of functional layer on cast iron. Mixed powders contained low melting point powder previously coated on the mold, is consolidated as a layer by a liquid phase sintering and then joints with cast iron by the heat of pouring. Compared with carburization, nitriding, plating, PVD and CVD which are conventional methods of improvement of the surface, this method has prominent features below described.

1)It is possible to make an improvement layer on the surface by utilizing the heat of pouring at the same time as casting.

2)It is possible to prepare by selecting suitable powders the functional layer which has high resistance to such as abrasion, corrosion and heat.

3) This method has a few steps and is cheap and easy.

Hard coating layer formed by diffusion-cementation with Fe-Cr powder [1] and fusion of low melting point alloying powder [2] have been reported as similar methods. It is very difficult to develop layers with variously high performance on iron castings for their limited compositions.

We observed microstructure of coated layer and examine optimum conditions to form well coated layer such as combination and mass ratio of high performance powders and low melting point powders, and the thickness of coated powder and pouring temperature, etc. The hardness, resistance to wet abrasion and corrosion resistance of the coated iron castings were evaluated.

Experimental method

We examined at first forming of hard and thick coating layer on iron castings of thick section (50mm in thickness) possessing resistance to wet abrasion corrosion [3,4] and secondary Ni or Cr rich coating layer on iron castings of thin section (10mm in thickness) possessing corrosion resistance [5]. The cast irons used by casting were FC(typical compositions:Fe-3.90C-2.10Si-0.33Mn-0.080P-0.012S) in thick section castings and FCD(typical compositions:Fe-3.60C-2.50Si-0.33Mn-0.005P-0.002S-0.045Mg) in thin section castings. Composition, particle size and melting point of powders are shown in Table1,2. Powders can be classified into two groups of the principle powders having high performance and powders having low melting point. Fe-Cr powder containing carbides (M_7C_3 and a little of $M_{23}C_6$) has high hardness [6]. Powders in SUS series (SUS304L,SUS430L) have function of corrosion resistance. FP7B powder is self-fused Ni based alloy with mean hardness of 720HV1 contained very hard phases of borides and carbides, has been

Table1 Chemical composition of high performance powders

Powder	Chemical composition mass%								Particle size	Melting Point
	C	Si	Mn	P	S	Ni	Cr	Fe	μm	K
Fe-Cr	7.5	0.3	-	-	-	-	62.8	29.4	-74	1573
Ni	-	-	-	-	-	99.7	-	-	-45	1728
SUS304L	0.016	0.88	0.19	0.022	0.003	11.50	18.79	Bal.	-45	-
SUS430L	0.013	0.88	0.19	0.013	0.009	0.12	16.11	Bal.	-45	-

Table2 Chemical composition of low melting point powders

Powder	Chemical composition mass%							Particle size	Melting Point
	C	Si	P	Ni	Cr	Fe	B	μm	K
FP7B	0.8	4.7	-	69.9	17.0	4.1	3.5	-45	1333
Ni-P	-	-	11.4	88.6	-	-	-	-45	1153
Ni-Cr-P	-	-	10.6	76.8	12.6	-	-	-45	1153<

used as self-melted and spraying powder [7]. Ni-P and Ni-Cr-P powders are alloying powders of eutectic component having low melting point. PVAc(polyvinyl acetate) as a binder generating little gas at pouring was used to fix mixed powders on the mold, as a consequence of testing various inorganic and organic materials. Shapes and size of CO_2 molds are shown in Fig.1 (thick section) and Fig.2 (thin section). In Fig.1, Al_2O_3 powders were pasted in a thickness of 2mm on the mold for maintenance of pouring temperature before mixed powders were coated. Pouring temperature was 1623K and 1723K. The specimens after pouring were cut off to observe their microstructures at the position of ①～⑩(an odd number is from the ceiling and an even number is from the floor) in Fig.1 and at the position of ①～④ in Fig.2 to compare the influence of heat input from pouring on the formation of layer.

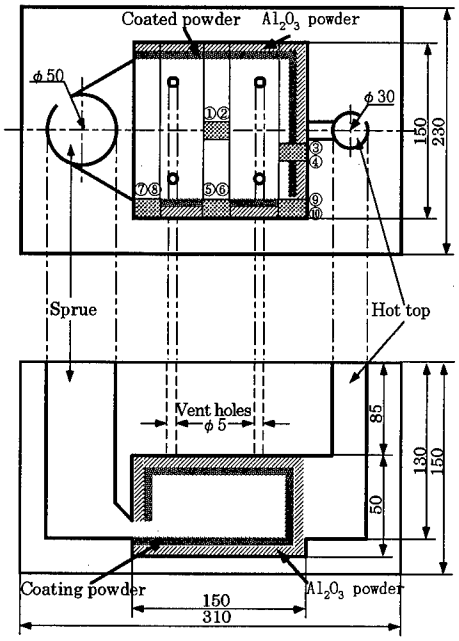


Fig.1 Shape of mold and specimen at each position

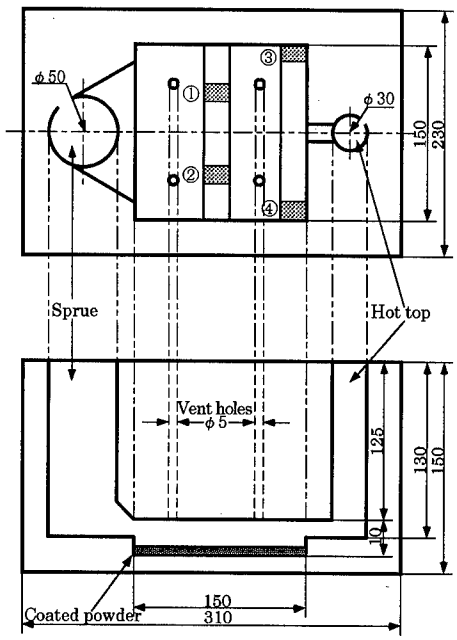


Fig.2 Shape of mold and specimen at each position

Formation of hard and thick coating layer possessing resistance to abrasion in thick castings

Fe-Cr powder as principle powder which has good resistance to wet abrasion and FP7B, Ni-P and Ni-Cr-P powders as low melting point powder were selected. Fe-Cr powders alone were hardly sintered and then not consolidated as a layer at pouring temperature of 1723K because of their high melting point. The three kinds of powders of low melting point completely melted and dissolved into cast iron and were not formed the coated layer at pouring temperature of 1623K. Mixed Fe-Cr and FP7B,Ni-P,Ni-Cr-P powders were examined with mass ratio from 90/10 to 10/90. The most closely coated layer was obtained about mass ratio of 65/35 or 50/50 and subsequent researches were then done in these ratio. The microstructures of coated layers are shown In Fig.3 at the pouring temperature of 1623K. The liquid of FP7B had nice wettability with Fe-Cr powder and their mixed powders formed densely coated layer in thickness of 1mm which had little pores.

The coated layer was strongly jointed with the parent material across carbide layer formed by diffusion of a part of powder layer. The liquids of Ni-P and Ni-Cr-P had poor wettability with Fe-Cr powder even at pouring temperature of 1723K, so the coated layer with a lot of large pores were prepared. In order to gain well coated layer at every location even if in Fe-Cr/FP7B, the mass ratio should be changed according to heat input. That is to say, it is necessary much quantity of FP7B(low melting point) where is poor heat input and cooling rate is faster. The well coated layer was obtained at the ratio of 50/50 at the place of ⑤ or ⑥. In thick and large iron casting, coated layer was obtained easily but should be kept in mind over-solution of powder because of enough quantity of heat. The microstructure of coated layer with Fe-Cr/FB7B=80/20 component is shown at center of floor in the mold size of 150×150×100(in thickness)mm in Fig.4.

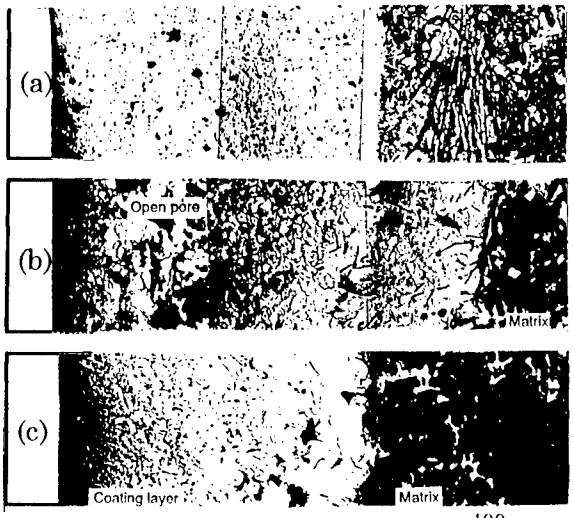


Fig.3 Microstructure of coated layer
Pouring temperature 1623K
(a)Fe-Cr/FP7B=65/35,(b)Fe-Cr/Ni-P=65/35
(c)Fe-Cr/Ni-Cr-P=65/35

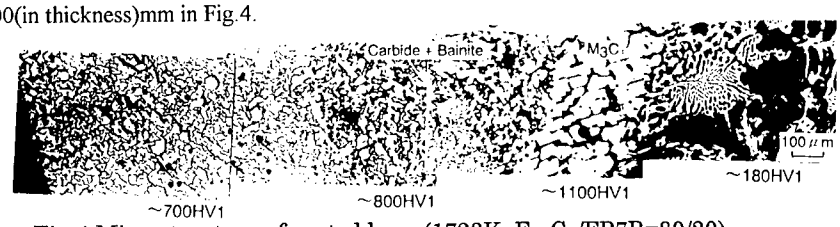


Fig.4 Microstructure of coated layer(1723K. Fe-Cr/FP7B=80/20)

According to the result of measurement of heating and then cooling temperature at position of coated layer after pouring, there was large difference of maximum temperature and cooling rate at each position(①~⑩).We could obtain coated layer with no scale off of powder layer on the ceiling as well as on the floor. Hardness of coated layer is showed in Fig.5. The most hard coating layer was as hard as 800~900HV1 in surface area and 1000~1100HV1 (M_6C phase) in the interface of parent material in Fe-Cr/FP7B. The results of wet abrasion test are shown in Fig.6. The coated cast iron showed 1/10 of FCD and 1/8 of wear resisting steel in mass loss in resistance to wet abrasion test of 3%NaCl solution for a month. Compared with pearlite or ferrite cast iron which was etched with red rust, the coated cast iron was very little in weight loss

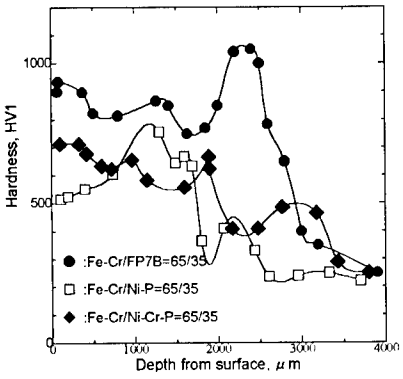


Fig.5 Hardness of coated layer

and about 1/2 of 5%Ni cast iron in the immersion test in 3%NaCl solution for 300 days.

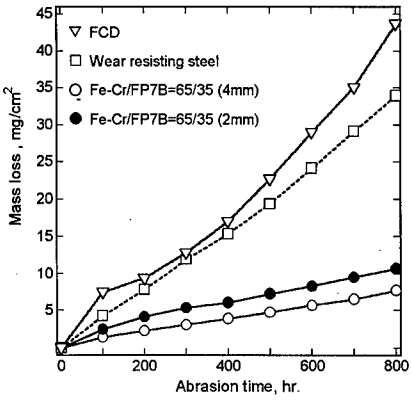


Fig.6 Wet abrasion test

Formation of coated layer possessing corrosion resistance in thin castings

Ni, SUS304L and SUS430L powders having good corrosion and Ni-P and Ni-Cr-P powders having low melting point were selected. It was found that the combination of Ni/Ni-P formed the best layer because Ni-P powder including no Cr has lower melting point than Ni-Cr-P powder and the liquid also has the best wettability with Ni powder.

Microstructures of various amount of coated powder are shown in Fig.7. The most thickness of layer was formed of 500 μ m in thickness at 180mg/cm^2. There was no layer at 70mg/cm^2 because of solution of the powder layer into cast iron. A part of coated layer was flaked from cast iron because of lack of heat in too thick powder layer at 360mg/cm^2. The hardness of coated layer on iron cast is shown in Fig.8. The coated layer was as hard as 100～200HV1 in the surface and about 400HV1 in the interface of parent material at 180mg/cm^2. We recognized the area with about 400HV1 as martenstic phase which contained about 5%Ni with composition of Nihard cast iron [8,9]. According to analysis of EPMA, there was about 20%Ni near the surface and about 5%Ni in the depth of approximately 0.5mm from the surface. Martenstic phase was formed in the surface of coated layer at thin powder layer of 70mg/cm^2. Salt-spray corrosion test in 5%NaCl solution at 308K, was done for samples of casted and then annealed with scale removed by shot blasting. The coated cast iron was about 1/8 of FCD in mass loss in corrosion test after about 80 days. The iron casting with closely coated layer generated no red rust, and but the iron castings with porous layer proceeded the corrosion, generating etch pit with red rust in large amounts.

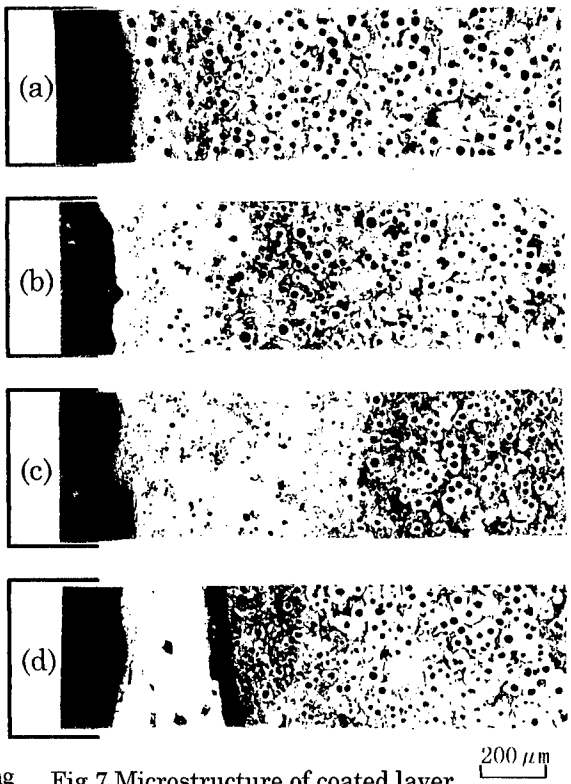


Fig.7 Microstructure of coated layer
(a) 70mg/cm^2 (b) 130mg/cm^2
(c) 180mg/cm^2 (d) 360mg/cm^2

Finally, the coated layer with Ni/Ni-P on cast iron is schematically shown in Fig.9.

Conclusion

The coating on iron castings was prepared by using a mixture of high performance powders and Ni-based alloy powders having low melting point as the coated powder on the mold. By the heat of pouring, the powders layers are consolidated by a liquid phase sintering and then jointed with cast iron. In thickness section(50mm in thickness), the coated layer obtained for Fe-Cr/FP7B=65/35 was 1～2mm in thickness and hardness of 800～1100HV1 and had good resistance to wet abrasion and corrosion. In thin section(10mm in thickness), the layer obtained for Ni/Ni-P=50/50 was 300～500 μ m in thickness and had soft surface layer (100 ～ 200HV1) containing 10～20%Ni and therefore good corrosion resistance to spraying of 5%NaCl solution.

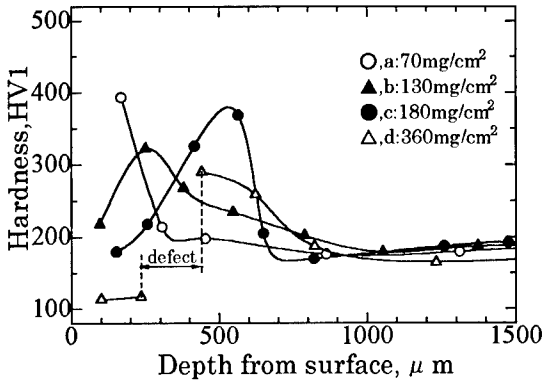


Fig.8 Hardness of coated layer

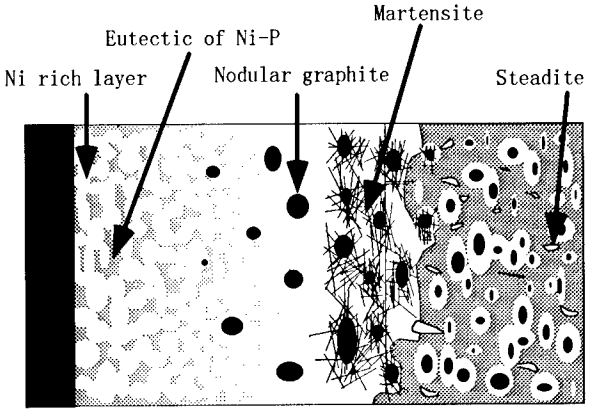


Fig.9 Schema of coated layer (Ni/Ni-P)

References

1. T. Watanabe, *The Journal of the Japan Fourdrymen's Society.*, 55 (1983) 381.
2. T. Kobayasshi and T. Saji, *The Journal of the Japan Fourdrymen's Society.*, 61 (1989) 717.
3. S. Tanabe, K.Nakamura, T. Hirotomi, H. Ichinose, Y. Michiura and M. Kitagawa, *The Journal of the Japan Foundry Engineering Society.*, 67 (1995) 77.
4. S. Tanabe, K.Nakamura, N. Terasawa, H. Ichinose, Y. Michiura and M. Kitagawa, *The Journal of the Japan Foundry Engineering Society.*, 68 (1996) 113.
5. S. Tanabe, K. Yoshikawa, N. Nii, K.Nakamura, Y. Michiura and M. Kitagawa, *The Journal of the Japan Foundry Engineering Society* ., 69 (1997) 670.
6. R. S. Jackson, *J. The Iron and Steel Institute Feb.*, (1970-2) 163.
7. H. Nagasaka, *The Japan Institute of Metals.*, 22 (1983) 1021.
8. *The Hand Book of Castings*, ed. The Japan Foundrymen's Society (1973) 1012.
9. F. B. Rote, G. A. Conger and K. A. Delonge, *AFS Trans.*,59. (1951) 509

Effect of Mechanical of Grinding of Powders on the Oxidation Resistance of Stainless-Steel Compacts at High Temperatures

Shigenori Tanabe, Wataru Takahara, Hideto Nishida and Kenji Higashi

Metallurgy and Materials Science, College of Engineering, Osaka Prefecture University
1-1 Gakuen-cho, Sakai, Osaka, Japan, 599-8531

Abstract

Oxidation resistance at high temperatures of stainless steel(SUS304L) powders treated by MG(mechanical grinding) and then consolidated by hot pressing was studied. The oxide film on the specimen without MG treatment is composed of two layers; the inner layer is spinel with the composition of $Fe(Fe,Cr)_2O_4$ and the outer layer is Fe_3O_4.and Fe_2O_3. On the other hand, the oxide film on the MG treated specimen is composed of a thin but fine layer containing a chromium oxide layer. The rapid diffusion of chromium to the surface along many grain boundaries produced by MG treatment results in the formation of the fine chromium oxide(Cr_2O_3) at early oxidation and then improved oxidation resistance.

The Third Pacific Rim International Conference on
Advanced Materials and Processing (PRICM 3)
Edited by M.A. Imam, R. DeNale, S. Hanada,
Z. Zhong and D.N. Lee
The Minerals, Metals & Materials Society, 1998

Introduction

Stainless steel has been used as heat-resisting steel for boilers or turbines because of sufficient tensile and creep strength at high temperatures. The oxidation resistance of the steel is also one of important consideration. It is important to examine what kinds of oxides are formed and how to form stable oxide films. Shot blast working on the surface has been reported to be effective for the suppression of oxidation in steam atmosphere[1]. This improvement of oxidation resistance may be due to the rapid diffusion of chromium to the surface along dislocations and defects produced by the working[1,2], or to the formation of a resultant Cr_2O_3 layer beneath an iron oxide film. Chromium makes a stable oxide film of Cr_2O_3 which has oxidation resistance. The oxidation resistance may be concerned with fine microstructure in stainless steel[3], so we used MG treatment for controlling the microstructure of stainless steel powders and obtained sintered compacts of fine grain. The powders with MG treatment were next consolidated by hot pressing. Mass gain of the compact, microstructures and compositions of the oxide film were measured and observed after oxidation test in the air. We examined the influence of MG treatment on the oxidation resistance of SUS304L powder compact at high temperatures.

Experimental method

The composition of the stainless steel powder is given in Table 1. The powder was treated by MG(by a ball mill of attritor type under conditions of the ratio powder/ball=1/15 and 350rpm for 180ks) and then consolidated in a shape of 30 ϕ x5mm in a graphite mold by hot pressing at 1373K for 3.6ks in argon atmosphere. Annealing condition to grow grain size was at 1373K for 25.2ks and at 973K for 7.2ks to eliminate twins. The consolidated specimens were polished and buffed and then oxidized at 1073,1123K and 1173K for 0～180ks in the air. After measuring the mass gain due to oxidation, the specimens plated with nickel to protect oxide films were observed under a microscopy and analyzed by X-ray diffraction and EPMA.

Table 1 Composition of SUS304L stainless steel (mass%)

C	Si	Mn	P	S	Ni	Cr	Fe
0.016	0.095	0.21	0.022	0.010	11.35	19.48	Bal.

Results and Discussion

Microstructures in cross section of powders with MG treatment are shown in Fig.1. As the treatment time becomes longer, the powder becomes more flaky by crushing and then spherical by combining. The microstructure developed into finely lamella layers with the repetition of crushing and combining.

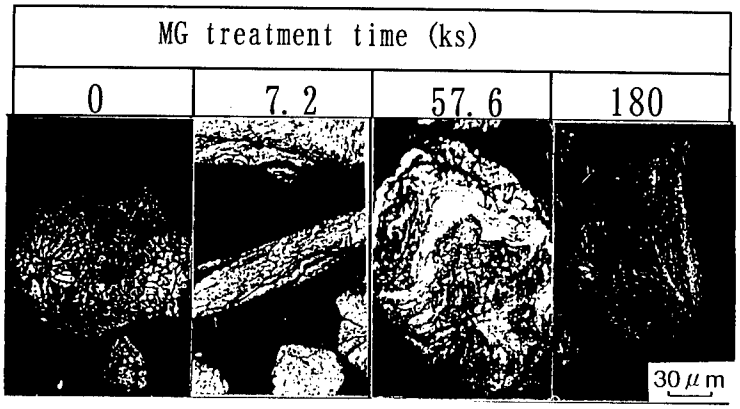
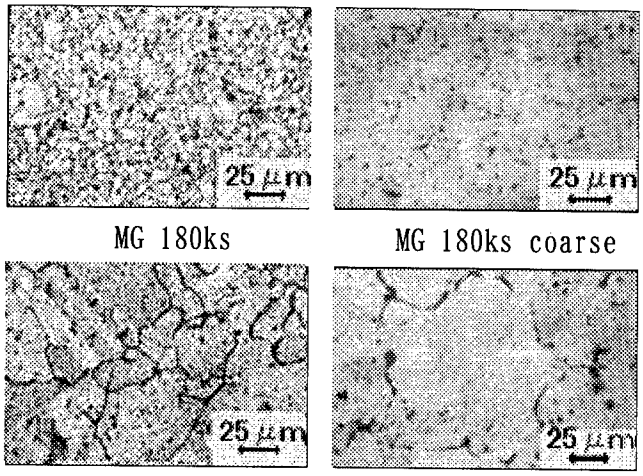


Fig. 1 Microstructures of powder with MG treatment (cross sectin)

Microstructures of the compacts by hot pressing are shown in Fig.2, and grain size of each specimen is shown in Table 2. Obviously, the grain size of the MG-treated specimen is fine even after annealing.



MG 180ks　　MG 180ks coarse

MG 0ks　　MG 0ks coarse

Fig. 2 Microstructures of powder compact

Table 2 Grain size of specimens (μ m)

	Fine grain	Coarse grain (Annealed)
MG treatment (MG 180ks)	10~15	20~30
Without MG treatment (MG 0ks)	30~40	60~70

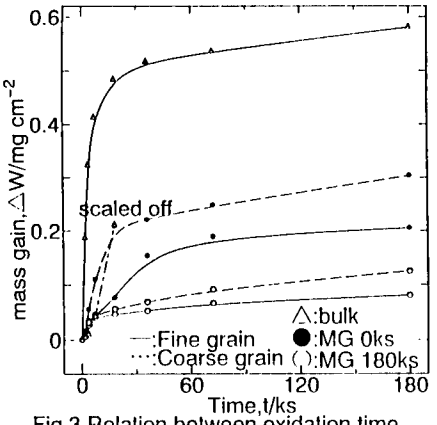


Fig.3 Relation between oxidation time and mass gain at 1073K (SUS304L)

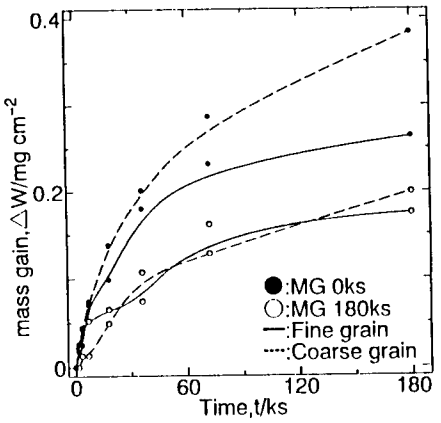


Fig.4 Relation between oxidation time and mass gain at 1123K(SUS304L)

Relations between oxidation time and mass gain at 1073,1123K and 1173K are shown in Figs.3,4,5. "Coarse grain" means annealed specimen, and that of bulk is compared in Fig.3. The mass gain of MG-treated specimens was smaller than that without MG treatment at 1023K and 1073K. It was larger in annealed specimens with course grain. In the case of fine grain without MG treatment, it was very small at early stage and linearly increases with oxidation time at 1173K. The reason why the initial oxidation is suppressed is unknown. The bulk specimen of similar composition was remarkably oxidized and the oxide film was flaked off the substrate at 1073K, so the oxidation test was discontinued over the temperatures.

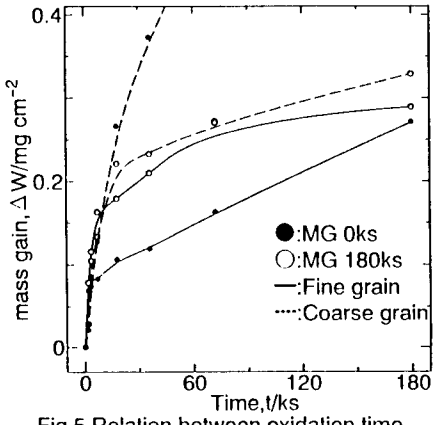


Fig.5 Relation between oxidation time and mass gain at 1173K(SUS304L)

Microstructures of specimens containing oxide films are shown in Fig.6. The specimen with MG treatment has a thin film, and that without MG treatment has a thick two layer film. According to EPMA analysis in Figs.7,8, the oxide film without MG treatment is composed of two layers;

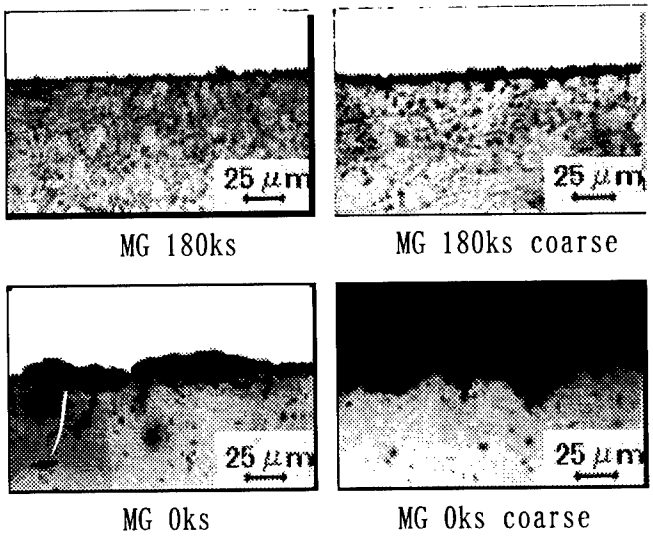


Fig. 6 Microstructures of oxide film at 1173K

Cr is rich in the inner layer and Fe is rich in the outer layer. It may be considered from the results by X-ray diffraction that the inner layer is spinel with the composition of $Fe(Fe,Cr)_2O_4$ and the outer layer is composed of both inside of Fe_3O_4 and outside of Fe_2O_3[5].

We can observe a few Cr on the surface of the oxide film and Cr-poor area along the grain boundary in the substrate. These are especially clear in the bulk by EPMA shown in Fig.9. So it was considered that Cr chiefly diffused through grain boundaries to the surface. The oxide film on the MG-treated specimen is composed of a thin layer containing much Cr which is identified chiefly the composition of Cr_2O_3 by X-ray diffraction. The thin Cr_2O_3 film is preferentially formed by diffusion of Cr to the surface along many boundaries. On the other hand, the oxide film on the specimen without MG treatment is composed of a thick layer of iron oxides, and a thin layer of spinel on the grain boundary. As it is obvious from the presence of Cr-poor area along the grain boundary in the substrate, Cr is supplied to the surface more rapidly along the grain boundary than through the grain. The oxide film on the grain boundary results to be Cr rich and a thin layer. Thus, the composition and thickness of oxide film was changed by microstructure of the parent material.

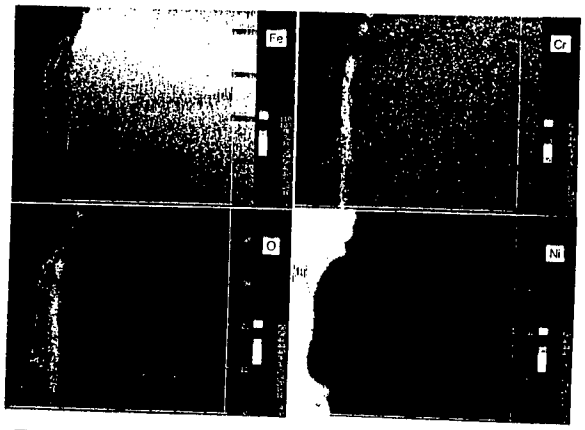


Fig.7 EPMA(MG:0ks. Oxidation:1073K,180ks)

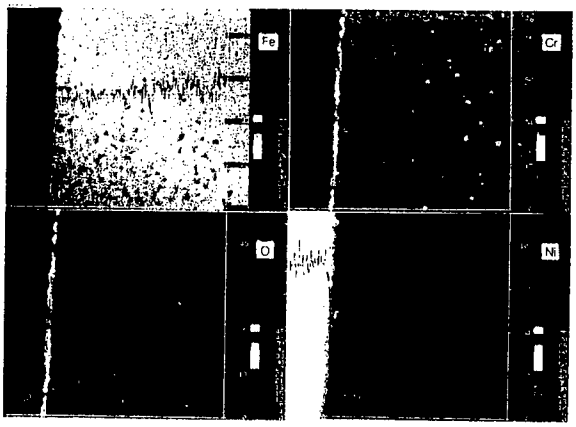
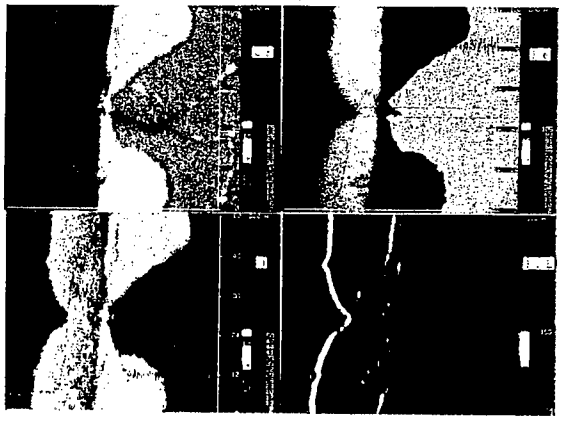


Fig.8 EPMA(MG:180ks. Oxidation:1073K,180ks)


Fig.9 EPMA(Bulk. Oxidation:1073K,180ks)

The oxide film on the MG-treated specimen which adheres to the substrate in a wedge shape, is not flaky and then suppresses the cyclic oxidation, compared with that of the bulk specimen with smooth and flat contact. Finally, the formation of oxide film is schematically shown in Fig. 10.

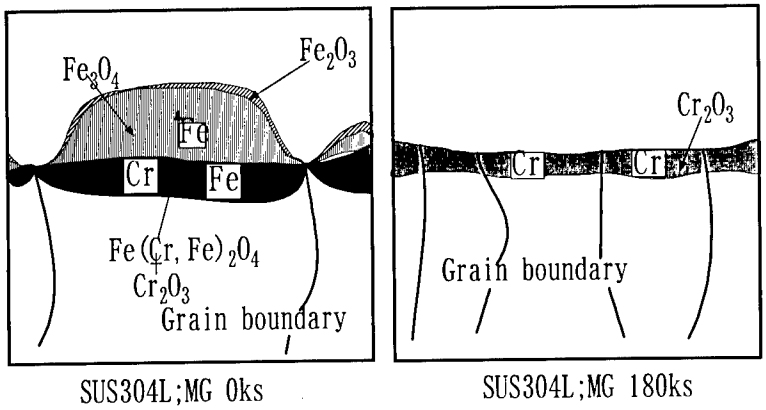


Fig. 10 Schema of oxide layer

Conclusions

1.Microstructure of the MG-treated specimen is still fine grain after hot pressing and annealing, so oxidation resistance is improved by MG treatment.
2.Oxide films on the specimen without MG treatment and on the bulk specimen are composed of two layers, the inner layer is spinel of $Fe(Fe,Cr)_2O_4$ and the outer layer is iron oxides of inside Fe_3O_4 and of outside Fe_2O_3. The shape of the oxide film is like a knob. The oxide film on the MG-treated specimen is composed of a thin layer of Cr_2O_3 .
3.Through many grain boundaries in fine microstructure produced by MG treatment, Cr preferentially diffuses to surface and forms a fine chromium oxide film which has oxidation resistance.
4. Oxidation resistance of the MG-treated specimen is improved compared with that of the bulk specimen with same composition, because of the suppression of grain growth and good adhesion to the parent material in a wedge shape of the oxide film.

Reference

1) M.Warzee, J.Hennant, M.Maurice, C.Sonnen, J.Waty and P.H.Berge, *J.Electrochem. Soc.*, **112**(1965)670.
2) S.Jansson, W.Hubner, G.Ostberg and M.de Pourbaix, *Br.Corros.J.*, **21**(1969)167.
3) S.Tanabe, Y.Hukui and H.Ichinose, *J.Japan Society of Powder and Powder Metallurgy*, **41**(1994)1019.
4) M. Kowaka and S. Nagata, *J.Japan Institute of Metals*, **36**(1972)486.
5) T.Mishima, M.Sugiyama, *The Iron and Steel Institute of Japan*, **36**(1950)263.

Anti-oxidation Coating for the Alloy Steel At High Temperature

Xu Xiaolian Liu Dong Liao Xiangwei
Technology Center, Anshan Iron & Steel Group Complex
(No.63 Wuyi Roud Anshan. 114001. China)

Abstract

Anti-oxidation coating for the alloy steel in a furnace at 800~1360℃ has been investigated. The coating is composed with refractory and non-poisonous materials. It can be easily applied to the surface of slab by spraying or brushing. The experimental results show that the coating has good adherence with slabs before coming into the furnace and that it heated from the furnace can be removed completely by the subsequent scale breaker and that the steel products after hot rolling have a surface without defects. Then using the anti-oxidation coating can increase the yield of finished products.

Key Words: anti-oxidation coating, alloy steel, high temperature

1.Introduction

During the process of hot rolling, the surface of alloy steel slab (especially containing Ni, Cr alloy steel) is oxidized. A membrane of metal-silk oxide with rich in Ni, Cr etc. is formed between a base and an oxide layer.[1] It makes adherence of the oxide layer strengthen and is removed difficulty. Therefore, it effects the surface quality of rolling-finished-product directly. The rate of qualified product is limited. No-oxidation heating on the surface of slab is attained by controlling the atmosphere for heating slab in the factories with advanced equipment. And then the question has to be solved by other way in the factories with backward equipment. It is one of effective measures for solving steel oxidized that anti-oxidation coating is applied on the surface of slab. Developed anti-oxidation coating composed of the MgO-Cr_2O_3 system, the Si-SiC system etc. is for grain oriented silicon steel slabs.[2,3,4] The anti-oxidation coating have been investigated for containing Ni, Cr alloy steel heated at 1360℃ and can removed completely itself after being put a furnace out and can be easily applied to the surface of slab in mass production.

The Third Pacific Rim International Conference on
Advanced Materials and Processing (PRICM 3)
Edited by M.A. Imam, R. DeNale, S. Hanada,
Z. Zhong and D.N. Lee
The Minerals, Metals & Materials Society, 1998

2. Experimental Methods

2.1 Specimens

Some alloy steel specimens and slabs contained Ni, Cr were taken. The size shows in Table 1.

Table 1 Size of Specimens or Slab of Ni, Cr Alloy Steel

Size / Kinds	Length (mm)	Width (mm)	Thickness (mm)	Remarks
1	50	30	6	Useful for in the laboratory.
2	100	50	6	Useful for in the laboratory.
3	500	300	7	Useful for in the product condition.
4	500	300	25	Useful for in the product condition.

The surface of first and second kinds of the specimens has been polished. The surface of third and fourth kinds of the specimens has been sprayed with pellet (same as mass production). The surface of specimens treated shows luster of metals. Smudge on the surface of specimens was removed by cleaning agent, and then anti-oxidation coating was applied on.

2.2 Applying Method

Anti-oxidation coating was applied separately on the surface by brushing and by spraying of specimens. Then the coating dried naturally or by hot wind. The pressure of the gun is 0.3 ~ 0.5 MPa when spraying.

2.3 Results Appraisal to Anti-oxidation

Weight of several specimens was weighed separately and then the coating was applied. The specimens coated and control were heated together in the furnace. The oxide on surface of the specimen during heating was removed by hammer. Then the specimens were put in 5~9 % hydrogen chloride and is electrolyzed as cathode with 1.0 A/dm^2 current density. An analysis balance weighed loss weight of all specimens after removing water by alcohol. The anti-oxidation rate was calculated.

2.4 Measuring Performance of Coating Peeling

When the specimen cooling naturally or by water after heated performance of the coating peeling is observed. The coating peeled rate (%) is calculated through measuring the area of coating and peeled.

3.Experimental Results

3.1 Development of KYH-1 Coating

Consist of coating is the base to ensure the performance of the coating. The 5 kinds of materials were determined for the special request through large amount of test on the Ni, Cr alloy steel. The coating is named KYH-1. It belongs to non-poisonous, watered coating, pH 8~9. According to the plan of Zhengjiao test the proportion of several components were ensured. The process shows in Table 2, Table 3.

Table 2 Choice of Components Amount of KYH-1 Coating

Factor \ Level	1	2	3	4
M Substrate (wt%)	15	20	25	30
G Stuff (wt%)	30	25	20	15
L Reductive (wt%)	20	25	30	35
C Additive (wt%)	2.4	2.8	3.2	3.6
J Binder (wt%)	32.6	27.2	21.8	16.4

Table 3 the Results and the Test by $L_{16}(4^5)$

Test Number		Factor (Components)					Target (Results)	
		M Substrate (wt%)	G Stuff (wt%)	L Reductive (wt%)	C Additive (wt%)	J Binder (wt%)	Anti-oxidation Rate (%)	Coating Peeling Rate (%)
1		15	30	20	2.4	32.6	88.5	98.0
2		15	25	25	2.8	27.2	99.3	100
3		15	20	30	3.2	21.8	99.5	100
4		15	15	35	3.6	16.4	88.8	100
5		20	30	25	3.2	16.4	99.8	100
6		20	25	20	3.6	21.8	97.2	100
7		20	20	35	2.4	27.2	97.5	100
8		20	15	30	2.8	32.6	99.0	99.4
9		25	30	30	3.6	27.2	98.5	100
10		25	25	35	3.2	32.6	98.9	99.5
11		25	20	20	2.8	16.4	98.3	100
12		25	15	25	2.4	21.8	98.4	100
13		30	30	35	2.8	21.8	96.5	100
14		30	25	30	2.4	16.4	98.0	100
15		30	20	25	3.6	32.6	97.8	99.8
16		30	15	20	3.2	27.2	97.6	100
Average Anti-Oxidation Rate (%)	K_1	94.0	95.8	95.4	95.6	96.1		
	K_2	98.4	98.4	98.8	98.3	98.2		
	K_3	98.5	98.3	98.8	99.0	97.9		
	K_4	97.5	96.0	95.4	95.6	96.2		
Max. Difference		4.5	2.6	3.4	3.4	2.1		

From the maximum difference in Table 3 the action order of several components in KHY-1 coating varying to anti-oxidize on surface of the specimens or the slabs is as follows:

M Substrate > L Reductive = C Additive > G Stuff > J Binder

And the binder is key to guarantee the adherence between the coating and the specimen or the slab and peeling performance of the coating after the specimen was put out from the furnace. The best components of KYH-1 coating summarized from the results tested above follows:

M Substrate	20~25 wt%
G Stuff	20~25 wt%
L Reductive	25~30 wt%
C Additive	2.8~3.2 wt%
J Binder	21.8~27.2 wt%

3.2 Applied Amount of KYH-1 Coating and Result of Anti-oxidation on the Specimen

KYH-1 coating was applied on surface of the specimen with different thickness. The specimens coated were put in the furnace after the coating dried. Temperature was raised to 1360℃. The specimens were put out from the furnace after 2 hours and then cooled naturally. According to loss weight of the specimens the relational curve between thickness of KYH-1 coating on the specimen and loss weight of the specimen was drawn (as following Figure 1). That shows that the anti-oxidation rate of the specimen is higher than 98.6% when thickness of KYH-1 coating being thicker than 0.5 mm. Figure 2 shows visual appearance of the specimen that was coated and control through treated in high temperature.

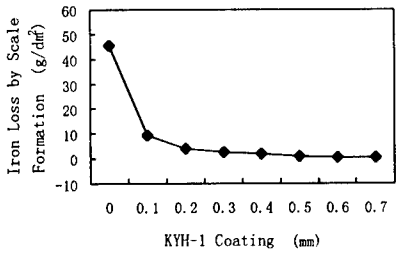


Figure 1. Relation between Thickness of KYH-1 Coating and Less Weight of the Specimen

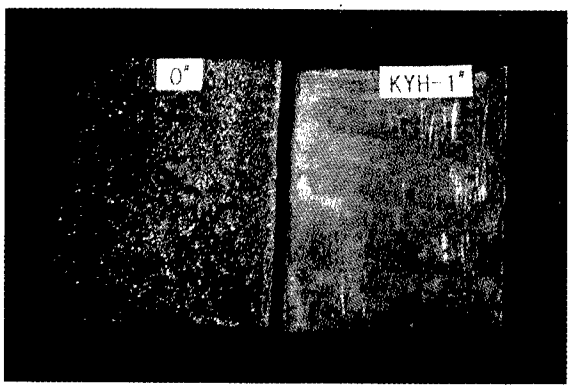


Figure 2. Visual Appearance of the Specimens Tested
0# — Control Specimen
KYH-1# —Specimen Coated

3.3 Principle of Anti-oxidation by KYH-1 Coating

With temperature of the alloy steel specimens or slabs coated by KYH-1 coating in the furnace rising the L Reductive in KYH-1 coating is oxidized gradually. And densely oxide film is formed on the surface of the specimen or the slab. At the same time crystalline shape of the other components in KYH-1 coating is changing with the temperature rising. Semi-no-crystalline shape is formed in the individual component and making KYH-1 coating being in a minute soft state. Therefore oxygen in atmosphere is prevented diffusing to surface of specimen or slab and attaining the goal to prevent oxidizing on the surface of specimen or slab.

The specimen or the slab cools when they being put out from the furnace. KYH-1 coating on the surface of specimen or slab peels with temperature lower because coefficients of line expansion between the specimen or the slab and the coating being different largely (at 20 ~ 1000℃, coefficients of line expansion of the containing Ni, Cr alloy steel and KYH-1 coating is 13.7 μ m/m.K & 4.5 μ m/m.K separately). Figure 3 shows appearance of KYH-1 coating removed.



Figure 3. Scanning electron micro-graphs showing surface of KYH-1 coating removed

4. Conclusions

4.1 KYH-1 coating is a efficient anti-oxidation coating to the containing Ni, Cr alloy steel. The anti-oxidation rate reaches more than 98.6% when the coating being over 0.5 mm at 1360℃.

4.2 KYH-1 coating is watered and no poisonous. It may be applied with spraying and brushing etc. The coating dries soon. And it is applied easily in mass production.

4.3 Taking advantage of large difference of the coefficients of line expansion between the alloy steel and the coating it makes the coating peeling during the slab cooling. It meets the requirements of technology in normal production. And then the yield of finished products is increased.

References

1. Meng Xiangwan. Forming Mechanism of Iron Oxide on 907 Steel, Restricted Publication, 1993.10.
2. Xiong Xingyun. Cui Kun. Deceleration of Scale Formation on Slab of Grain-Oriented Silicon Steel During Heating, Iron and Steel, 1996.31(9): 64~68.
3. [Japan] 特开昭 60-262919
4. H. Odsashima, M. Kitayama, K. Tanaka, Y. Saruwatari. Tetsu-to-Hagané (J. Iron Steel Inst. Jpn.), Nov. 1985, 71, (15), 1811-1817

Composite Materials

PROCESSING OF IN-SITU Al-TiB_2 COMPOSITES

H. J. Brinkman, J. Duszczyk, L. Katgerman

Laboratory of Materials Science
Delft University of Technology
Rotterdamseweg 137, 2628 AL Delft
The Netherlands

Abstract

Al matrix composites reinforced with 40 vol% in-situ synthesized TiB_2 particles are made from elemental powders via reactive processing. TiB_2 reinforcing particles are in the order of a few microns and appear to be homogeneously distributed in the matrix. Investigation of the phase formation sequence with a combination of DSC and XRD identified AlB_2 and Al_3Ti as intermediate reaction products.

Combination of reactive sintering and hot-pressing in one process, termed reactive hot-pressing (RHP), is used to produce full dense Al-TiB_2 composite products. The modifications to conventional hot-pressing set-up necessary for RHP are discussed. Also, the potential of near net shape production with RHP process is shown.

The Third Pacific Rim International Conference on
Advanced Materials and Processing (PRICM 3)
Edited by M.A. Imam, R. DeNale, S. Hanada,
Z. Zhong and D.N. Lee
The Minerals, Metals & Materials Society, 1998

Introduction

In the area of processing of particle reinforced MMCs several new technologies have been developed which allow in-situ production of the reinforcing phase [1]. Advantages of these in-situ composites are the clean particle-matrix interface and the thermal stability of the reinforcement in the matrix. Potentially, this leads to good reinforcement-matrix bonding and the high temperature properties. The XD™ process developed by Martin Marietta laboratories [2], is an in-situ processing route which has the additional advantage of capability of high volume fractions of small sized reinforcing particles. It uses exothermic reactions between elements in a powder mixture to propagate and sustain the in-situ synthesis of reinforcements in the matrix. For Aluminum based MMCs both TiB_2 and TiC have been identified as promising in earlier investigations by Kozcak [3,4], Odawara [5,6] and Munir [7,8].
The microstructure and composition of the products are quite different from the starting materials. Therefore, a good understanding of the formation mechanisms is important to optimize composition, microstructure and overall properties of the MMC. In the Al-TiB_2 system Al_3Ti is found as a reaction product which limits the ductility of the Al MMC. The phase formation sequence during the synthesis of elemental Al, Ti and B powders to Al-TiB_2 was identified with the combination of DSC and XRD [9].
A limitation of the process is the inherent high porosity of the reaction product. Additional processing steps are required to obtain structural components. The combination of synthesis and densification in one processing step is especially attractive as the heat, released by the exothermic reactions during the synthesis of the composite, leaves the material at a relative high temperature which allows easy densification. Reactive hot-pressing [10,11] has been identified as one of the most promising techniques to combine the synthesis and densification.

Experimental

Elemental powders of Al (Metalloys TypeI, average particle size 7.7 μm), Ti (Micron Metals Inc. average particle size 23 μm), and amorphous B (H.C.Starck/Poudmet., average particle size 0.9 μm) were used. Starting compositions of Al, Ti and B powders corresponding to Al-40 vol%TiB_2 after complete reaction were mixed for 4 hours and compacted to 75 % td.
A Stanton Redcroft high-temperature DSC 1500 was used for the DSC experiments. A flow of Ar gas provided an inert atmosphere. A linear heating rate of 20 °C/min was used.
Reactive Hot Pressing experiments were done on a Thermal Technology model HP 50-60120 Hot Press. BN coated graphite was used as punch and die material. A heating rate of 10 ^{0}C/min was used together with an outgassing period of 60 minutes at 500 ^{0}C.

Results and Discussion

Phase formation sequence

It is usually assumed that after melting of Al the Ti and B go into solution, and immediately react to form TiB_2 precipitates in the Al melt. However, the DSC curve for the system Al-40 vol%(Ti+2B), Figure 1, shows that there are a number of reactions before the equilibrium composition is reached. The two exothermic reactions after the endothermic melting of Al at 660 ^{0}C show that the liquid phase initiates the reactive process. The process is not completed at that stage as the 3rd exotherm at around 1000 ^{0}C indicates.

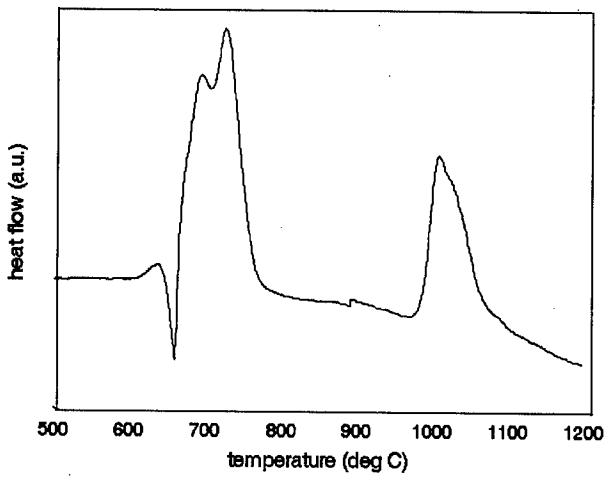


Figure 1: DSC scan of Al-40vol%(Ti+2B).

To identify the reaction path, reactions were halted at 700, 950 and 1100 °C and phases were identified with XRD. The results are shown in Figure 2.

After the melting of Al, Both B and Ti react with the Al liquid phase to form intermediate reaction products, AlB_2 and Al_3Ti respectively. After these reactions the Al is consumed, as is evidenced by the absence of the Al peaks in the XRD at 950 °C, and the reaction does not proceed until the

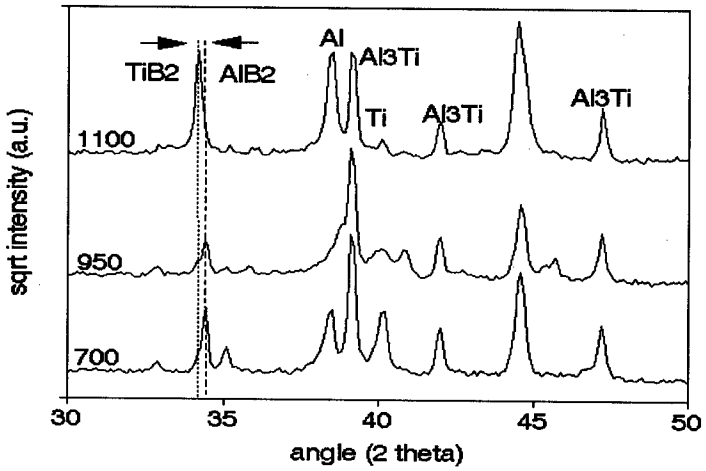


Figure 2: XRD of intermediate reaction products.

decomposition of the AlB_2 phase at 1000 °C. The decomposition of AlB_2 into the more stable AlB_{12} phase and a B rich Al liquid phase enables the reaction between Ti and B in Al to form TiB_2 which is clear from the presence of TiB_2 in the spectrum at 1100 °C and the disappearance of AlB_2 and

the diminished amount of Al_3Ti. The above findings can be summarized with the following phase formation sequence:

$Al(s) + B(s)$	$= AlB_2(s)$	at 650 °C	(1)
$Al(s)$	$= Al(l)$	at 660 °C	(2)
$Al(l) + B(s)$	$= AlB_2(s)$	at 670 °C	(3)
$3\ Al(l) + Ti(s)$	$= Al_3Ti(s)$	at 700 °C	(4)
$6\ AlB_2(s)$	$= AlB_{12}(s) + 5\ Al(l)$	at 975 °C	(5a)
$Ti + 2B$	$= TiB_2(s)$	at 975 °C	(5b)

When AlB_{12} is formed before Ti reacts with the B atoms, the strong bonding of the B atoms in the AlB_{12} structure prevents the formation of TiB_2, even if TiB_2 is thermodynamically more favorable. This explains why Al_3Ti is not completely converted into TiB_2 when the starting mixture is according to the Ti:2B stoichiometry. Optimization of the composition, i.e. complete conversion of Al_3Ti, can be achieved with an overstoichiometric amount of B. As the AlB_{12} particles are of similar size as the final TiB_2 the are not as detrimental to the composite properties. A more detailed description of the compositional optimization is published in [12].
The microstructure of the composite is shown in the SEM micrograph of Figure 3. The fine TiB_2 particles, smaller than 2-3 μm, appear to be homogeneously distributed in the Al matrix.

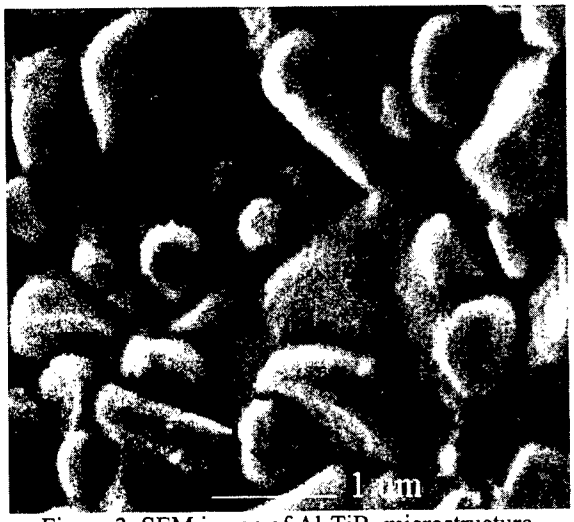


Figure 3: SEM image of Al-TiB_2 microstructure.

Reactive Hot-Pressing

The synthesis part of RHP takes place in a short time during heating whereas conventionally hot-pressing used for long time diffusion processes under pressure when the system has reached a thermal equilibrium. Thus closer temperature control is required in RHP than in other hot-pressing cycles. The incorporation of an extra thermocouple in the punch of the hot-press provides the required temperature control in the RHP process.

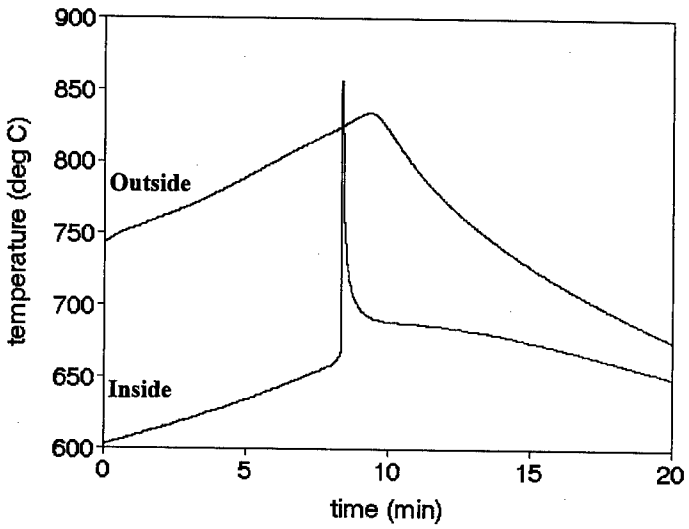


Figure 4: Time-temperature recordings of RHP process

In Figure 4 the temperature readings in and outside the die are shown. The reaction is not recorded outside the die and a difference of >100 °C exists during heating. The temperature difference during heating dependents on experimental conditions such as atmosphere, die thickness and extraction of heat by the punches. These factors are quite complicated to model theoretically. Obviously, the cooling rates in and outside the die are also different and this is illustrated in Figure 4 as well. This leads to the following improvements in RHP process control:

1. Minimization of the time the composite is in the liquid state after the reaction. This limits adverse reactions between liquid Al and graphite die parts and avoids settling of TiB_2 particles (4.5 g/cm^3) in the Al matrix (2.7 g/cm^3).
2. Optimization of the timing of the application of the load for densification.

The timing of the load is critical in this process [10] because there is only a limited temperature "window" for successful densification. If the load is applied when the matrix is still in a liquid state, the product will ooze out of the die. On the other hand, if the load is applied when the composite is already cooled below its plastic range, full densification will be difficult.
Good results, i.e. full densification without "spilling" of material, is achieved when a load of 25 MPa is applied when the material is cooled down to 575 °C. Figure 4 shows a densified part of the MMC. The homogeneity of the MMC is remained due to the limited time for settling of TiB_2 in Al. Densities of >99 % were measured with the Archimedes method.

Near Net Shaping

A first near net shape approach was attempted with the experimental setup shown in Figure 5. A negative image of a tensile test specimen with outer dimensions (60x20x4)mm was worked out in the lower punch. Full density, close dimensional tolerances and a good surface finish were achieved for Al-40 vol% TiB_2 and Al-40 vol%TiC specimens.

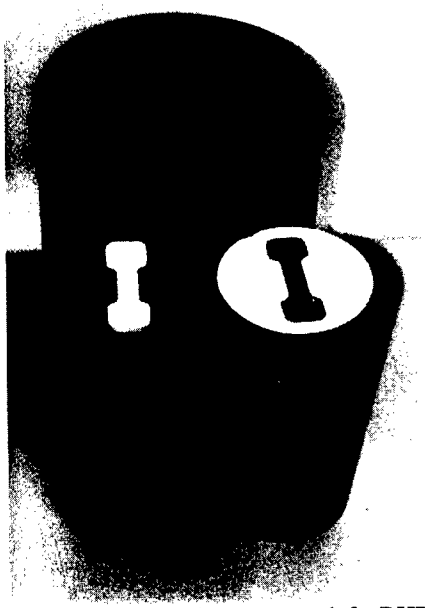


Figure 5: near net shape approach for RHP process.

Conclusions

1. With a knowledge of the reaction mechanism , phase formation sequence , the composition of in-situ reinforcement of Aluminum based MMCs can be optimized.

2. When modification to the temperature control of conventional hot-pressing cycle are made, it is possible to produce dense and homogeneous in-situ Al matrix composites from elemental powders in one process.

3. Reactive hot-pressing has capabilities of producing near net shaped part of simple, two dimensional, configurations.

References

1. M.J. Koczak and M.K. Premkumar, "Emerging technologies for the in-situ production of MMCs,"Journal of Materials, 1 (1993), 44-48

2. l. Christodoulou, D.C. Nagle, and M. Brupbacher Int. Pat. No. WO86/06366, 1986

3. I. Gotman et al., "Synthesis and processing of Al-TiB_2 composites via SHS and high-pressure consolidation from ultrafine powders," Proceedings of EPMA PM'94 conference, vol. 2 (1994), 1979-1982

4. I. Gotman, M. J. Koczak, and E. Shtessel, "Fabrication of Al matrix in-situ composites via self-propagating synthesis," Materials Science and Engineering, A187 (1994), 189-199

5. Z.Y. Fu, R.Z. Yuan, and A.Z. Munir, "Structure and structure formation of SHS Al metal matrix composites," International Journal of SHS, 2 (3) (1993), 261-268

6. Z.Y. Fu, R.Z. Yuan, A.Z. Munir, and Z.L. Yang, "Fundamental study on SHS preparation of TiB_2-Al composites," International Journal of SHS, 1 (1) (1992), 119-124

7. Y. Taneoka and O. Odawara, "Combustion synthesis of the Titanium-Aluminum-Boron system," J. Am. Ceram. Soc. , 72 (6) (1989), 1047-1049

8. Y. Taneoka, Y. Kaeida, and O. Odawara, "Influence of Al and B contents on combustion synthesis of Ti-B-Al system," (Paper presented at the 32nd Japan congress on Materials Research, Kyoto, Japan, 1989), 164-167

9. H.J. Brinkman, J. Duszczyk, and L. Katgerman, "In-Situ formation of TiB_2 in a P/M Aluminum matrix," Scripta Materiala, 39 (1997), 293-297

10. J.J. Moore, H.J. Feng, "Combustion synthesis of advanced materials part II, classification, applications, modelling" ; Prog. in Mat. Sci, 39 (1995), 275-316

11. R.Z. Yuan, "Composite materials and compositing process by SHS technology"International Journal of SHS, 6 (3) (1997), 265-276

12. H.J. Brinkman, J. Duszczyk, L. Katgerman, "Structure formation of in-situ Al-TiB_2 Composites", B.Q. Li ed., Processing of Metals and Advanced Materials, (Proc. TMS'98 annual conference San Antonio, TMS 1998), 269-277

MICROSTRUCTURE AND MECHANICAL PROPERTIES OF REACTION SQUEEZE CAST HYBRID AL MATRIX COMPOSITES

Changook Son[1], Ikmin Park[1], Kyungmox Cho[1], Ildong Choi[2] and Sunghak Lee[3]

[1]Dept. of Metallurgical Engineering, Pusan National University, Pusan 609-735, Korea
[2]Dept. of Material Engineering, Korea Maritime University, Pusan 606-791, Korea
[3]Pohang University of Science and Technology, Pohang 790-784, Korea

Abstract

Mechanical properties of ($10\%Al_2O_3 \cdot SiO_2+5\%Ni$)/Al and ($10\%Al_2O_3 \cdot SiO_2+5\%TiO_2$)/Al hybrid composites fabricated by the reaction squeeze casting were compared with those of ($15\%Al_2O_3 \cdot SiO_2$)/Al composites. Al-Ni and Al-Ti intermetallic compound formed by the reaction between molten aluminum and reinforcing powder were uniformly distributed in the Al matrix. These intermetallic compounds were identified as Al_3Ni and Al_3Ti using EDS and X-ray diffraction analysis and they enhanced room and high temperature strength and wear resistance. Microhardness of ($10\%Al_2O_3 \cdot SiO_2+5\%Ni$)/Al and ($10\%Al_2O_3 \cdot SiO_2+5\%TiO_2$)/Al hybrid composite were greater by about 100Hv and 50Hv than that of ($15\%Al_2O_3 \cdot SiO_2$)/Al composite. Wear resistance of ($10\%Al_2O_3 \cdot SiO_2+5\%Ni$)/Al and ($10\%Al_2O_3 \cdot SiO_2+5\%TiO_2$)/Al hybrid composites was superior to that of ($15\%Al_2O_3 \cdot SiO_2$)/Al composites regardless of the applied load. While tensile and yield strength of ($10\%Al_2O_3 \cdot SiO_2+5\%Ni$)/Al and ($10\%Al_2O_3 \cdot SiO_2+5\%TiO_2$)/Al hybrid composites were greater at room temperature and 300℃ than those of ($15\%Al_2O_3 \cdot SiO_2$)/Al composites, strength drop at high temperature was much smaller in hybrid composites

The Third Pacific Rim International Conference on
Advanced Materials and Processing (PRICM 3)
Edited by M.A. Imam, R. DeNale, S. Hanada,
Z. Zhong and D.N. Lee
The Minerals, Metals & Materials Society, 1998

Introduction

The application of Al alloy metal matrix composites for automotive parts has been limited due to softening of Al matrix and interfacial reaction between matrix and reinforcement at the high temperature (more than 300℃)[1-2]. Recently the new reaction squeeze casting techniques have been proposed to overcome the deterioration of Al matrix at high temperatures. Intermetallic compounds formed by the reaction between aluminum melt and the metal powder(Fe,Cu,Ni) or the metal oxide powder(TiO_2, NiO) during the squeeze casting are very effective for improving the mechanical properties such as hardness, wear resistance, and high temperature strength[3-5].

In the present study, (10%Al_2O_3 · SiO_2+5%Ni)/Al and (10%Al_2O_3 · SiO_2+5%TiO_2)/Al hybrid composites were fabricated with reaction squeeze casting. Microstructure has been analyzed and mechanical properties have been characterized for (10%Al_2O_3 · SiO_2+5%Ni)/Al and (10%Al_2O_3 · SiO_2+5%TiO_2)/Al hybrid composites. Microstructure and mechanical properties of (15%Al_2O_3 · SiO_2)/Al composites and pure Al have been also analysed for comparison.

Experimental

Pure aluminum (purity 99.9%) was chosen for matrix, Kaowool short fibers (amorphous structure with average dimensions of 2.8 ㎛ in diameter and 200 ㎛ in length, 47%Al_2O_3-53%SiO_2 : Isolite Co.), Ni powders (purity 99.9%, 2-3 ㎛ in diameter) and TiO_2 oxide powder (purity 99.9%, <1 ㎛ in diameter, anatase type) were used as reinforcements for the fabrication of reaction squeeze cast (10%Al_2O_3 · SiO_2+5%Ni)/Al and (10%Al_2O_3 · SiO_2+5%TiO_2)/Al hybrid composites. The hybrid preforms were prepared by employing the vacuum suction method. The mixture of reinforcements, silica colloidal inorganic binder and starch organic binder were dispersed in distilled water and consolidated with vacuum suction method[6-7].
The aiming volume fraction of reinforcement in the preform(20×32×84mm) was about 15% and the volume fraction of preforms was roughly controlled with vacuum suction pressure. Preforms were dried at room temperature for 3 days and at 110℃ for 7 days. (10%Al_2O_3 · SiO_2+5%Ni)/Al hybrid composites were fabricated by infiltrating the molten aluminum of 750℃, 800℃, 850℃ and 900℃ into the hybrid preform placed in the mold preheated to 400℃ and (10%Al_2O_3 · SiO_2+5%TiO_2)/Al hybrid composites were fabricated by infiltrating the molten aluminum of 800℃ into the hybrid preform placed in the mold preheated to 400℃. Preform was also heated to 400℃ to improve the wettability bewteen matrix and reinforcements. During infiltrating molten aluminum into the hybrid preform, pressure of 35MPa was applied within 7 seconds, and was held for 60 seconds. SEM-EDS and XRD analyses were carried out to investigate the microstructural characteristics of composites. Microhardness test, three-point bending test, wear test, and tensile test of the composites fabricated by infiltrating the molten aluminum of 800℃ were carried out to characterize the mechanical properties of composites.

Results and Discussion

Microstructure

Figure 1(a), 1(b) and 1(c) are SEM micrographs of Al_2O_3 · SiO_2, Al_2O_3 · SiO_2 + Ni and Al_2O_3 · SiO_2 + TiO_2 preform, respectively. Regardless of the size of reinforcement, both reinforcements of Al_2O_3 · SiO_2 short fibers and Ni powders in Figure 1(b) and reinforcements of Al_2O_3 · SiO_2 short fibers and TiO_2 powders in Figure 1(c) were uniformly distributed, thus hybrid preforms were successfully prepared by the vacuum suction method. Figure 2(a), 2(b) and 2(c) show SEM microstructures of ($15\%Al_2O_3$ · SiO_2)/Al composite, ($10\%Al_2O_3$ · SiO_2+5%Ni)/Al and ($10\%Al_2O_3$ · SiO_2+5%TiO_2)/Al hybrid composite fabricated from the preforms shown in Figure 1. Reinforcements in composites were uniformly distributed and revealed no casting defects. SEM microstructure for the hybrid composite in Figure 2(b) revealed that Al-Ni intermetallic compounds formed by the reaction between Ni powder and molten aluminum. Al-Ti intermetallic compounds formed by the reaction between TiO_2 and molten aluminum were observed in Figure 2(c). Microstructural investigation showed that ($10\%Al_2O_3$ · SiO_2+5%Ni)/Al hybrid composite in Figure 2(b) had relatively more intermetallic compounds than ($10\%Al_2O_3$ · SiO_2+5%TiO_2)/Al hybrid composite in Figure 2(c). It is considered that the difference in the quantity of reaction products is caused by the reactivity between Al matrix and reinforcement powder. That is, Ni powder is more reactive with molten aluminum than TiO_2 powder

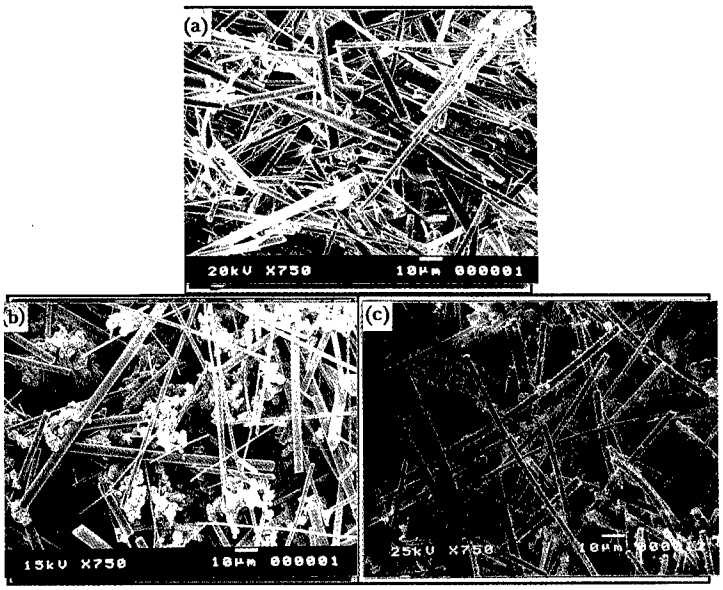


Figure 1: The preforms fabricated by the vacuum suction method with the reinforcement of (a) Al_2O_3 · SiO_2 (b) Al_2O_3 · SiO_2 + Ni (c) Al_2O_3 · SiO_2 + TiO_2

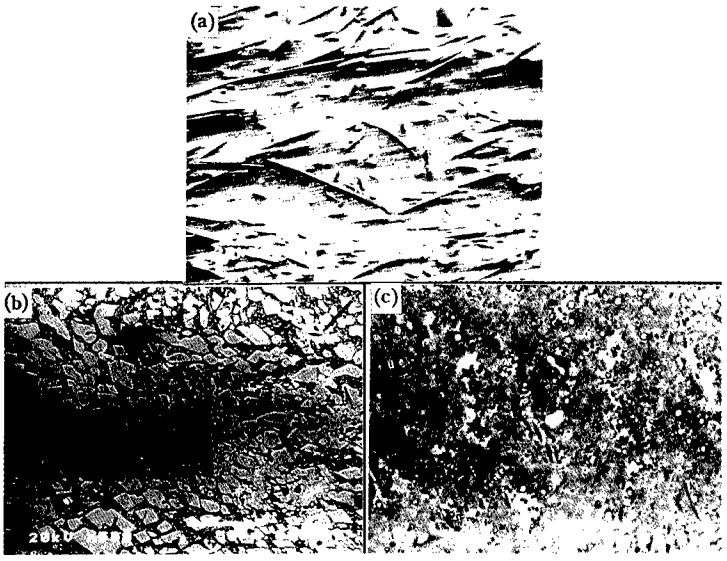


Figure 2: SEM microstructure of squeeze cast Al matrix composites.
(a) (15%Al_2O_3 · SiO_2)/Al (b) (10%Al_2O_3 · SiO_2+5%Ni)/Al
(c) (10%Al_2O_3 · SiO_2+5%TiO_2)/Al

The X-ray diffraction patterns of (10%Al_2O_3 · SiO_2+5%Ni)/Al hybrid composites in Figure 3 are shown many peaks of the Al_3Ni without any peak of other compounds regardless of the pouring temperatures of the molten aluminum and the X-ray diffraction patterns of (10%Al_2O_3 · SiO_2+5%TiO_2)/Al hybrid composites in Figure 4 are shown many peaks of Al_3Ti , Al_2O_3 and TiO_2.

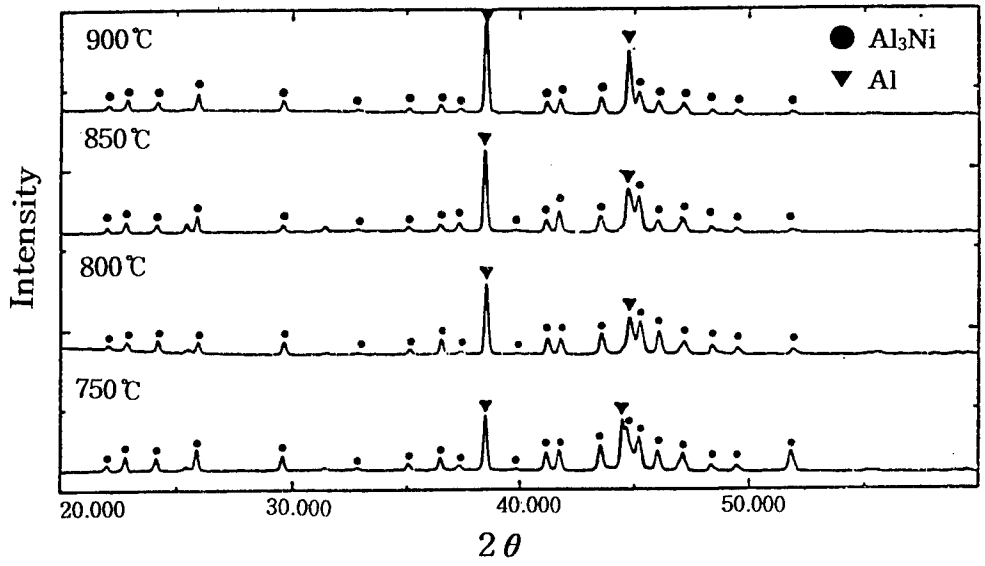


Figure 3: X-ray diffraction patterns of (10%Al_2O_3 · SiO_2+5%Ni)/Al hybrid composite according to pouring temperature of molten aluminum.

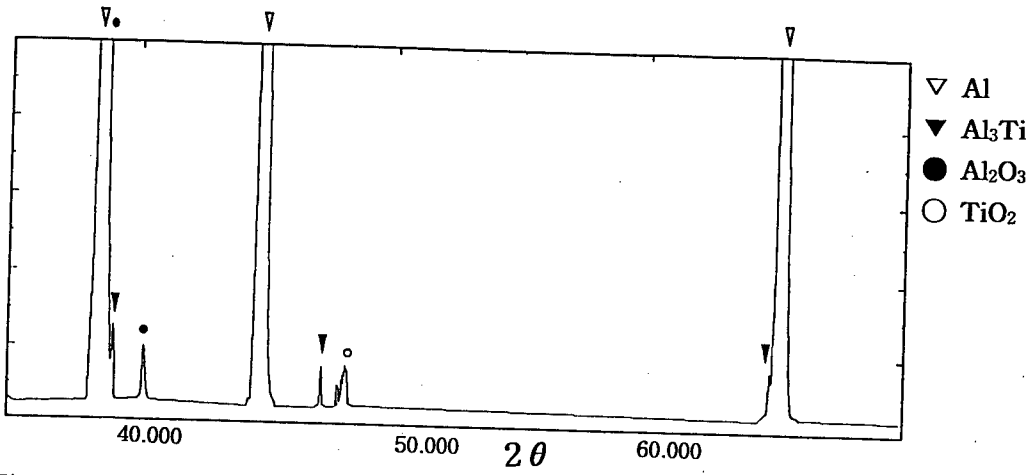


Figure 4: X-ray diffraction patterns of ($10\%Al_2O_3 \cdot SiO_2+5\%TiO_2$)/Al hybrid composites with pouring temperature of molten aluminum of 800℃

Mechanical Properties

The results of the microhardness test and three-point bending test are summarized in Figure 5 for squeeze cast Al, ($15\%Al_2O_3 \cdot SiO_2$)/Al composite, ($10\%Al_2O_3 \cdot SiO_2+5\%Ni$)/Al and ($10\%Al_2O_3 \cdot SiO_2+5\%TiO_2$)/Al hybrid composite. Microhardness of ($10\%Al_2O_3 \cdot SiO_2+5\%Ni$)/Al and ($10\%Al_2O_3 \cdot SiO_2+5\%TiO_2$)/Al hybrid composite are higher than those of ($15\%Al_2O_3 \cdot SiO_2$)/Al composite 100Hv and 50Hv, respectively. Flexural strength of ($10\%Al_2O_3 \cdot SiO_2+5\%Ni$)/Al and ($10\%Al_2O_3 \cdot SiO_2+5\%TiO_2$)/Al hybrid composite are also higher than those of ($15\%Al_2O_3 \cdot SiO_2$)/Al composite 66MPa and 37Mpa, respectively.

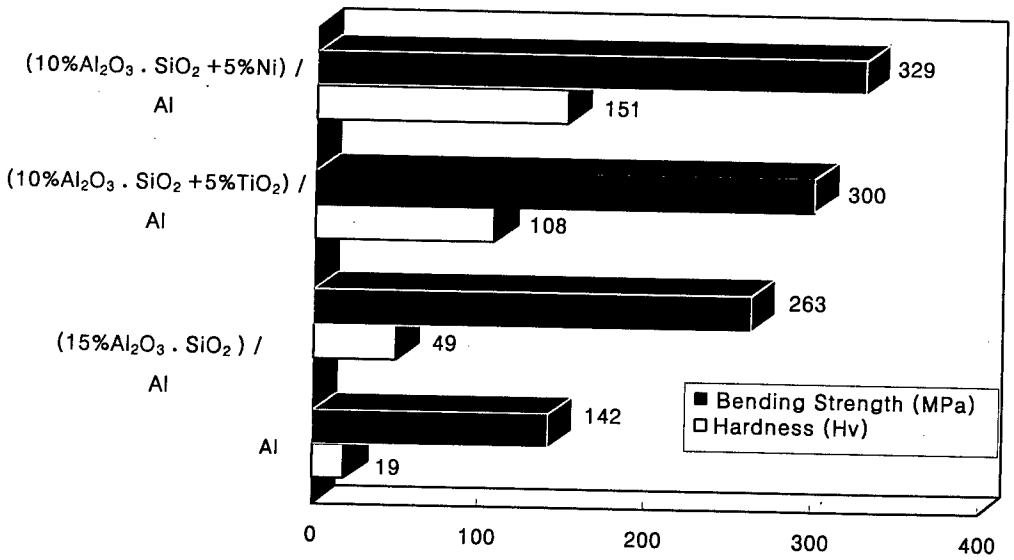


Figure 5: Hardness(Hv) and bending strength(MPa) of squeeze cast Al and Al matrix composites.

Wear loss was measured employing a total sliding contact block-on-roller type wear testing machine with variations of applied load(42N, 66.5N, 91N) at ambient temperature under dry condition. Sliding speed was 0.64m/sec and sliding distance was set to 1000m which was long enough for the onset of the steady state wear condition. Figure 6 shows the wear loss of squeeeze cast Al matrix, ($15\%Al_2O_3 \cdot SiO_2$)/Al composite, ($10\%Al_2O_3 \cdot SiO_2$+5%Ni)/Al and ($10\%Al_2O_3 \cdot SiO_2$+5%TiO_2) hybrid composite as a function of applied load at ambient temperature. As the applied load increased, the wear loss of all specimens increased. Wear resistance of ($10\%Al_2O_3 \cdot SiO_2$+5%Ni)/Al hybrid composite was highly superior to that of ($15\%Al_2O_3 \cdot SiO_2$)/Al composite regardless of the applied load. Wear resistance of (10% $Al_2O_3 \cdot SiO_2$+5%TiO_2)/Al hybrid composite was also superior to that of ($15\%Al_2O_3 \cdot SiO_2$)/Al composite regardless of the applied load. These enhancements of mechanical properties, such as microhardness, flexural strength and wear resistance, are likely to be increased due to the hard intermetallic compound particles.

Tensile tests were utilized to evaluate the composite strength at room and elevated temperature of the composites. All tensile-test data are summarized in Table 1 for the sake of quick reference. Figure 7 shows that tensile and yield strength of ($10\%Al_2O_3 \cdot SiO_2$+5%Ni)/Al and ($10\%Al_2O_3 \cdot SiO_2$+5%TiO_2)/Al hybrid composite are greater than ($15\%Al_2O_3 \cdot SiO_2$)/Al composite at both temperatures(25℃, 300℃). Strength drop at 300℃ is much smaller in hybrid composites. The improvement of the strength at elevated temperature in hybrid composites is considered that the intermetallic compound particles act as barriers to the slip behavior of the aluminum matrix

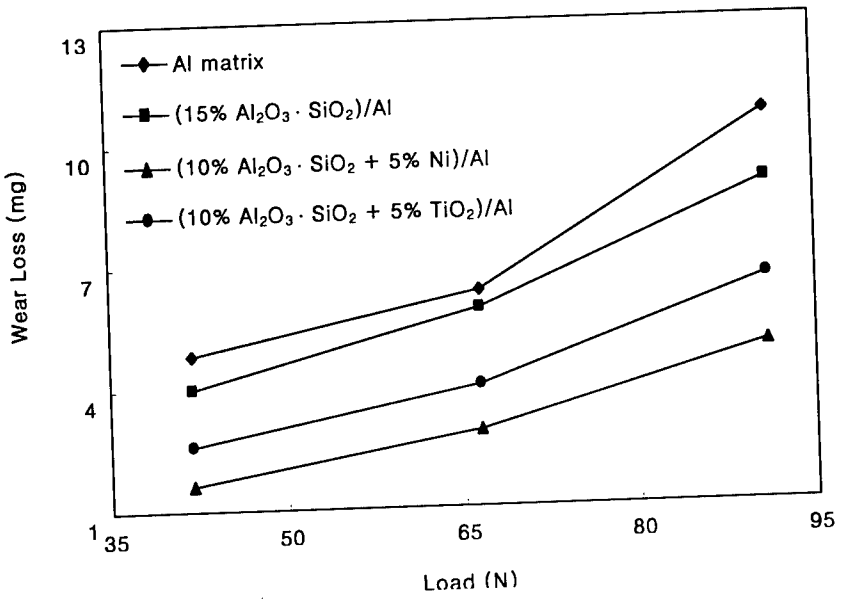


Figure 6: Wear loss of Al and Al matrix composites with variations of applied load.

Table I The results of tensile test of the Al matrix composites at the 25℃ and 300℃.

Composites	0.2%Y.S.(MPa)		U.T.S (MPa)		Elongation (%)	
	25℃	300℃	25℃	300℃	25℃	300℃
($15\%Al_2O_3 \cdot SiO_2$)/Al	83	52	118	89	5	9
($10\%Al_2O_3 \cdot SiO_2+5\%TiO_2$)/Al	121	112	129	118	2.2	4.4
($10\%Al_2O_3 \cdot SiO_2+5\%Ni$)/Al	130	123	135	130	1.2	2.3

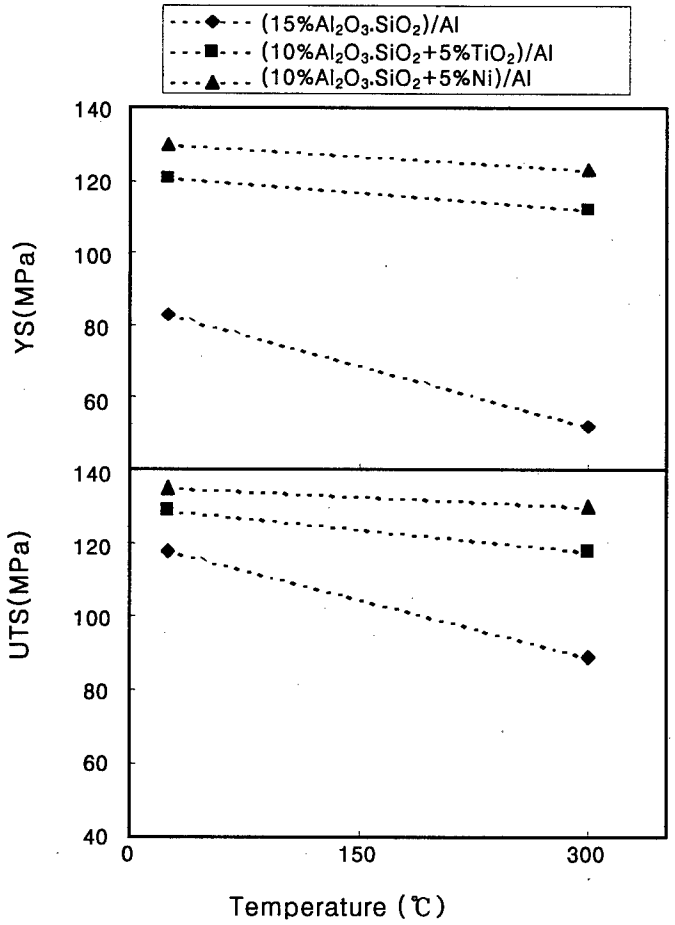


Figure 7: Tensile and yield strength of Al matrix composites at 25℃ and 300℃

Conclusions

1. ($10\%Al_2O_3 \cdot SiO_2+5\%Ni$)/Al and ($10\%Al_2O_3 \cdot SiO_2+5\%TiO_2$)/Al hybrid composites were fabricated successfully by the reaction squeeze casting.
2. Al_3Ni intermetallic compounds and Al_3Ti intermetallic compounds were formed by the reaction of molten aluminum with Ni powder and TiO_2 powder.
3. Mechanical properties such as microhardness, flexural strength and wear resistance, of ($10\%Al_2O_3 \cdot SiO_2+5\%Ni$)/Al and ($10\%Al_2O_3 \cdot SiO_2+5\%TiO_2$)/Al hybrid composite were superior to those of ($15\%Al_2O_3 \cdot SiO_2$)/Al composite. The enhancement of these mechanical properties is likely to be due to the hard intermetallic compound particles.
4. The improvement of the strength at elevated temperature is considered that the intermetallic compound particles act as barriers to the slip behavior of the aluminum matrix.
5. Mechanical properties of ($10\%Al_2O_3 \cdot SiO_2+5\%Ni$)/Al hybrid composite were superior to those of ($10\%Al_2O_3 \cdot SiO_2+5\%TiO_2$)/Al hybrid composite at room temperature and 300℃. The difference of mechanical properties is due to the amount of reaction product. Microstructural investgation showed that ($10\%Al_2O_3 \cdot SiO_2+5\%Ni$)/Al hybrid composite had more intermetallic compounds than ($10\%Al_2O_3 \cdot SiO_2+5\%TiO_2$)/Al hybrid composite.

Acknowledgment

This work was supported by RASOM(CNU) and Ministry of Education Research Fund for Advanced Materials in 1997.

References

[1] I.M.Park, B.S.Kim, Bulletin of the Korean Inst. of Met. & Mat. vol.9, No.2, (1996),112-125

[2] J.T.Blucher, "Discussion of a Liquid Metal Pressure Infiltration Process to Produce Metal Matrix Composites," J.Mat.Pross.Tech., 30 (1992), 381-390

[3] H.Fukunaga and G.K. Yeoh, J. of Jpn. Soc. of Powd. and Powd. Met., 39(6) (1992), 459-463

[4] I.Tsuchitori and H.Fukunaga, Proc. ICCM-10, Ceramic Matrix Composites and Other Systems, (2) (1993), 906-912

[5] S.S.Kim et al., Proc. ICCM-11, Metal Matrix Composites and Physical Properties, (3) (1996), 164-173

[6] K.C.Kim et al., "Fabrication Processing and Properties of AZ91D Mg/9(Al_2O_3) 2(B_2O_3) Metal Matrix Composites," Proc. of 3rd Asian Foundry Congress, (Kyongju, Korea, 1995), 328-335

[7] E.K.Jeon et al., "Microstructure of squeeze Cast Mg-Al-Zn-(Y,Nd)/Al_2O_3 Metal Matrix Composites ", PRICM-2, (Kyongju, Korea, 1995)

DEVELOPMENT OF FUNCTIONALLY GRADIENT MATERIALS

Hexiang Zhu and Reza Abbaschian
Department of Materials Science and Engineering, University of Florida, Gainesville, FL 32611

Abstract

Recent developments in the fabrication, design and optimization, and characterization of functionally gradient materials (FGMs) are reviewed. The commonly used processing techniques such as thermal spray, powder metallurgy and combustion synthesis are described. The application of the reactive hot compaction (RHC) technique to fabricate NiAl-Al_2O_3 functionally graded composites is also presented in detail. The processing involves blending Ni and Al powders in which one or both were partially preoxdized with premade NiAl powders acting as the diluent, and reactively synthesizing the powder mixture at elevated temperature under pressure. The oxidized powders led to the *in-situ* formation of alumina which formed a continuous network around the NiAl during the compaction process. Finally, the properties of the FGMs such as fracture strength, fracture toughness and microhardness are discussed.

The Third Pacific Rim International Conference on
Advanced Materials and Processing (PRICM 3)
Edited by M.A. Imam, R. DeNale, S. Hanada,
Z. Zhong and D.N. Lee
The Minerals, Metals & Materials Society, 1998

1.Introduction

It is well known that abrupt transitions in materials composition and properties within a component, for example, a thermal barrier component involving direct bonding of metals and ceramics, often result in sharp local concentrations of stress due to the CTE mismatch. The thermal stress can cause crack formation, debonding at the interface and often the spallation of the ceramic over layer. This problem may be overcome if the sharp interfaces are eliminated and there is a gradual transition from one material to the other. This approach has lead to the development of Functionally Gradient Materials (FGMs) [1-3]. These are materials with a variation of composition and microstructure along their thickness. The spatial variation in composition is introduced during the fabrication to achieve desired gradient in material properties. Thus in comparison with the monolithic materials, the FGMs offer several attractive properties, such as higher strength and toughness, improved thermal barrier characteristics, thermal shock resistance and wear resistance [1-9]. The initial attempts in the fabrication of FGMs were targeted towards the development of thermal stress relief type of material. However, because of the unique coupling of site-specific properties with the gradual transition of microstructure and properties, several other applications have emerged which include gas turbine blades, chemical reaction vessels, cutting tools, bio-implants and thermoelectric materials [10-13]. In all these applications, the satisfactory performance of the FGMs depends on the processing strategies adopted and the resulting microstructure. Functionally Gradient Composites (FGCs) are a special class of two phase FGMs, in which the gradient is introduced via a variation in the two phase mixture.

2. Design and Optimization of FGMs

The function of FGMs lies in the relaxation of residual thermal stress by the introduction of a compositional gradient and in the sharing of material functions between two sides of a single material. Watanabe [10] gave an example of the thermal stresses generated during cooling from processing temperature in the bonding of a stainless steel and a silicon nitride with and without graded layer (Fig.1). In the case of direct bonding, large thermal stresses which exceed the intrinsic strength of silicon nitride are generated, while by inserting a graded layer the thermal stress is remarkably reduced.

Williamson et al.[14, 15] studied residual stresses developed at graded metal-ceramic ($Ni-Al_2O_3$) interfaces during cooling using elastic-plastic finite element method numerical model. Strong geometrical influences on stresses were observed, particularly in constrained specimens, where the linear composition gradient was unsuccessful in reducing the axial stress near the free edge. The results showed that for both the axial and shear component, the disk graded specimen exhibited a significant reduction in residual stress. The peak stress value was reduced by approximately 70% and 30% for the shear component and axial tensile stress component, respectively. In addition, they also investigated the effects of the interlayer thickness and composition profile on strain and stress distributions established during cooling from an assumed elevated bonding temperature. Compared to a non-graded interface, significant reduction of stress and plastic strain were predicted for thicker interlayers and composition profiles that avoid large property gradient in areas exhibiting high modulus and little plasticity. According to the modeling results, an "optimized" $Ni-Al_2O_3$ FGM specimen was fabricated using HIP by Babin and Heaps[16], but the assessment of the validity and accuracy of the FEM calculation has not been reported.

Optimum fabrication design of Ni-MgO and Ni-TiC FGMs was investigated by Yuan et al.[17,18] based on the finite-element simulation of thermal stress produced in the fabrication. It was found that for the Ni-TiC FGM specimen, the optimum value of p obtained by the

elastoplastic analysis, where p is the gradient composition exponent, was smaller than that obtained by the elastic analysis. Therefore, it is believed that the consideration of material elastoplastic behavior is of critical important for optimization of the metal/ ceramic FGM. Mendelson et al.[19] analyzed NiCrAlY/(ZrO_2-8%Y_2O_3) FGM thermal barrier coatings with five gradient interlayer designs--step layer, narrow linear, wide linear, parabolic and exponential gradients, for the application to a first-stage vane in a gas turbine engine. It was found that the parabolic and exponential gradient interlayer designs had both the lowest combined stress and stress gradient across the coating.

3. Fabrication Techniques

There are several approches to obtain a compositional gradient in FGMs. Gases, liquids and solids can be used as the starting materials. For the first techniques, FGM samples are prepared by chemical vapor deposition (CVD) [4,20], physical vapor deposition (PVD) [4] and plasma spraying [21-24]. The gaseous method allows to obtain the required FGM in the form of a film or a plate directly without going through the process of melting or sintering. Electroforming [25] are utilized to prepare FGM coating via liquid phase. Bulk FGMs, on the other hand, are synthesized by various processing techniques, such as centrifugal casting [26], diffusion bonding [27], sedimentation [28-30], powder metallurgy techniques [10, 31-33], and combustion synthesis [34-36]. Among these, the most widely used processing techniques are thermal spray, powder metallurgy and combustion synthesis.

2.1.Thermal Spraying

In thermal spraying [21-24], feedstock material (in the form of powder, rod, or wire) is introduced into a combustion or plasma flame. The particles melt in transit and impinge on the substrate where they flatten, under rapid solidification, and form a deposit through successive impingement. The technique has been traditionally employed to produce a variety of protective coatings of ceramic, metals, and polymers on a range of substrates. Arc spray, combustion and plasma are the main techniques comprising thermal spray. These classifications are based on the type of heat source and the method by which feedstock is injected. Arc-spray processes use electrically conductive wire as feedstock, while combustion method uses powder or wire. Plasma spraying uses feedstock in the form of powders. Due to its high operating temperature and ability to achieve high particle velocities, plasma is most suitable for the processing of dense, high performance deposits of refractory materials. Controlled-atmosphere plasma spraying, such as low pressure plasma spraying (LPPS), has been utilized to deposit reactive metals and intermetallics. LPPS processing is usually conducted in a low-pressure inert gas-filled chamber and has proven to be a highly reliable method for depositing superalloy-type coatings on turbine blades and other aircraft engine components. NiCrAlY- PSZ, NiCr-PSZ, NiCrCoAlY-(8%Y_2O_3-ZrO_2) and Ni-Al_2O_3 FGM coatings have been successfully manufactured by means of plasma spraying.

2.2. Powder Metallurgy[10, 30-33]

Powder metallurgical (P/M) processing of FGMs provides a wide range of compositional and microstructural control, along with shape-forming capability. Powder metallurgical fabrication of FGMs involves the following sequential steps with a selected material combination of metals and ceramics: determination of the optimum composite profile for an effective thermal-stress reduction; stepwise and continuous stacking of powder premixes according to the predesigned composition profile; compaction of the stacked powder heap and sintering with or without pressuring. Compared with other techniches, the powder metallurgical method offers a wide range of material combinations with a close control over the graded composition. Further,

thicker samples can be synthesized. In particular, net shape or near net shape structural materials can be obtained, which makes the process attractive in comparison with other processing techniques. Many FGM samples such as Mo/PSZ, W/PSZ, SiC/AlN/Mo, AlN/W, Ni-alloy/Si_3N_4 and stainless steel/PSZ have been fabricated through powder metallurgical processing technique.

2.3.Combustion synthesis [34-36]

The combustion synthesis (or self-propagating high-tamperature synthesis(SHS)) process is a powder-based process in which reactants, usually elemental constituents, when ignited, spontaneously transform to products due to exothermic heat of formation. The technique is particularly useful in preparing highly refractory ceramics and high temperature intermetallics that are difficult to prepare by other synthesis methods. In addition, the process can be used to prepare ceramic-metal and ceramic-intermetallic composite materials. With some modifications, the combustion synthesis can be used to produce functionally gradient materials from these same combination of materials. Generally, sample preparation begins by the reaction of a series of mixture from the powders that will react to form the constituent materials of the FGM product. Prior to the combustion step, the samples are assembled by stacking layers of each of the mixtuers in appropriate amounts according to the desired composition gradient of the FGM. The powder mixture is then ignited, after which a combustion wave is generated that passes through the mixture--consuming the reactants and generating the product materials as it does so. FGMs such as TiC/Ni, TiC/NiAl, Cr C/Ni, TiB/Ni, ZrO_2/TiAl, (Ti-Si-O)/Ti , TiC-Al_2O_3-NiAl and Cu/TiB_2 have been prepared by combustion synthesis [34-36].

4. Reactive Hot Compaction (RHC)

Reactive hot compaction (RHC) can be thought as a subgroup of powder metallurgical processing and a variation of SHS or combustion synthesis. RHC is a volumetric combustion process as the powder mixture reactants are heated uniformly within a die under pressure to the reaction temperature. Thus, the reaction initiates at many sites throughout the powder mixture, while the application of pressure is utilized to aid densification. The reaction rate and the densification have been shown to depend on the shape and size distribution of reactants, green density of the compacts, heating rate, applied pressure and atmosphere [37, 38]. It is found that to achieve full or near full densification during RHC, it is necessary to have a fully interconnected transient liquid phase for an extended period of time. To achieve this, a diluent or inert particle may be added to the mixture of reactants to slow the combustion reaction to a controllable level. RHC has been successfully used to fabricate NiAl/Al_2O_3, NiCr/NiAl and NiCr/NiAl/Al_2O_3 FGCs [39-41] as well as other intermetallic matrix composites [42] in University of Florida. The technique has been shown to provide distinct advantages over more traditional PM techniques. The advantages include inexpensive starting materials, single-step consolidation, thermodynamically stable microstructures, lower power consumption, shorter processing time and higher product purity because of less reaction with the processing environment. Henager et al.[43,44] also fabricated NiAl-Al_2O_3 composites and NiAl-Al_2O_3 FGC consisting 7 layers of composition ranging from 0vol%Al_2O_3 to about 45vol% Al_2O_3 using solid state displacement reaction between NiAl and NiO to form in-situ Al_2O_3 by means of RHC. The technique involved a processing time of upto 5 hrs at temperature in the range of 1250 to 1350°C.

Before RHC of NiAl/Al_2O_3 FGCs, the Al powders and Ni powders are subjected to an oxidation pretreatment in moist air to form oxide shells of Al_2O_3 and NiO on the powders, respectively. It is found that the oxidation pretreatment leads to the formation of in-situ alumina reinforcement during the combustion synthesis [37]. Moreover, it is shown that the presence of the moisture during the oxidation process is necessary for improving the interconnectivity of the

in-situ alumina. Oxidation in dry oxygen or air leads to the formation of isolated alumina particles. The oxidation of aluminum has been determined to be the critical step for the development of the proper alumina morphology and interfacial properties necessary to improve the fracture toughness. It is believed that the relative humidity in the oxidizing atmosphere controls spallation from the Al powders, reduces the occurrence of isolated alumina inclusions in the matrix, especially with weak NiAl-Al_2O_3 interfaces, which were found to be less beneficial to improve the fracture toughness [37]. The preoxidized particles are then blended in the stoichiometric ratio together with 20 vol.% prealloyed NiAl diluent powder to slow the combustion reaction rate to a controllable level. The RHC technique was used by the present researchers to produce the NiAl/Al_2O_3 FGCs consisting of NiAl in one side with increasing alumina content in subsequent layers. The composition gradient was obtained through the stepwise stacking of the different powder layers. The powder mixtures were stacked together in a boron nitride coated, graphite foil lined graphite die, cold compacted at 50 Mpa, and then vacuum hot pressed at 1200°C and 50 MPa for two hours at a heating rate of 10°C/min. The typical microstructures corresponding to the individual layers in a four-layer NiAl/Al_2O_3 FGC are shown in Fig 2. The amount of alumina varied from 0vol.% in layer I to 35vol.% in layer IV. The grain size of NiAl decreased as the volume fraction of Al_2O_3 increased because of the hindrance of the NiAl grain growth by Al_2O_3 particles during the reactive hot compaction process [45].

5.Characterization of FGMs

5.1. Evaluation of Residual Stresses and Thermal Properties

M. Finot et al.[1] numerically and experimentally studied the elastoplastic deformation characteristics of a plasma-sprayed, tri-layered composite plate subjected to thermal cycling from 20 up to 800°C . By means of a scanning laser technique, the changes in the overall curvature of the unconstrained plate arising from the thermal mismatch between the constituent phases were measured. The results showed that: the introduction of a graded interlayer between the Ni and Al_2O_3 layers significantly reduces the magnitude of the thermal stresses and delays the onset of plasticity and cracking to higher temperature and that the maximum tensile stress occurs at the FGM-Al_2O_3 interface. Kesler et al.[46] has proposed an experiment method to determine processing-induced intrinsic stress, residual stress, elastic modulus and thermal expansion coefficients of thermal-sprayed homogeneous and graded Ni-Al_2O_3 coatings. The results showed that when Ni-Al_2O_3 composite coatings are plasma-sprayed onto a thick steel substrate, residual stresses as large as 200 MPa were found in the coating at room temperature. For the fully graded coatings, where the coating was sprayed in seven discrete steps, the tensile residual stresses in the coating were largest at the Ni-rich and Al_2O_3-rich ends, and decreased in the central portion of the coatings. The maximum tensile residual stress of nearly 200 MPa was found in the Al_2O_3 surface layer. The values of the in-plane Young's modulus of the graded coatings have been measured to be as low as 54 GPa.

The thermal properties of SiC/C FGM and SiC non-FGM were evaluated by Hirai et al. [4]. Some cracks were observed at the boundary between SiC films and the substrate for SiC non-FGM after 40 repeated heating cycles placing the surface at 1700-1150 K and the bottom surface at 1200-900K in the vacuum. These cracks were thought to be the result of thermal fatigue due to the repeated heating. In contrast, SiC/C FGM did not suffer such cracking under the same situation. A rapid decrease of the effective thermal conductivity with the cycle time for the SiC non-FGM was observed while no change for the SiC/C FGM. It was also found the thermal shock resistance of SiC/C FGM sample was superior to that of SiC non-FGM.

Cherradi et al. [47] investigated the thermal fatigue behavior of PSZ-(Cr-Ni alloy) functionally gradient materials with three different concentration profiles prepared by a

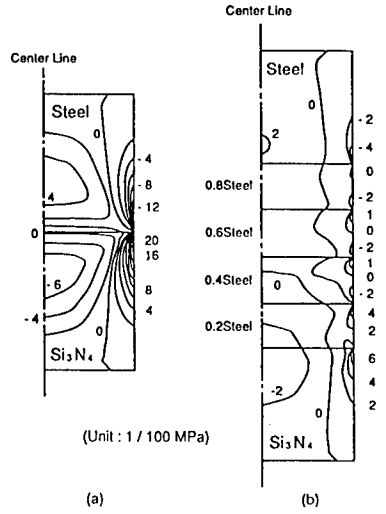
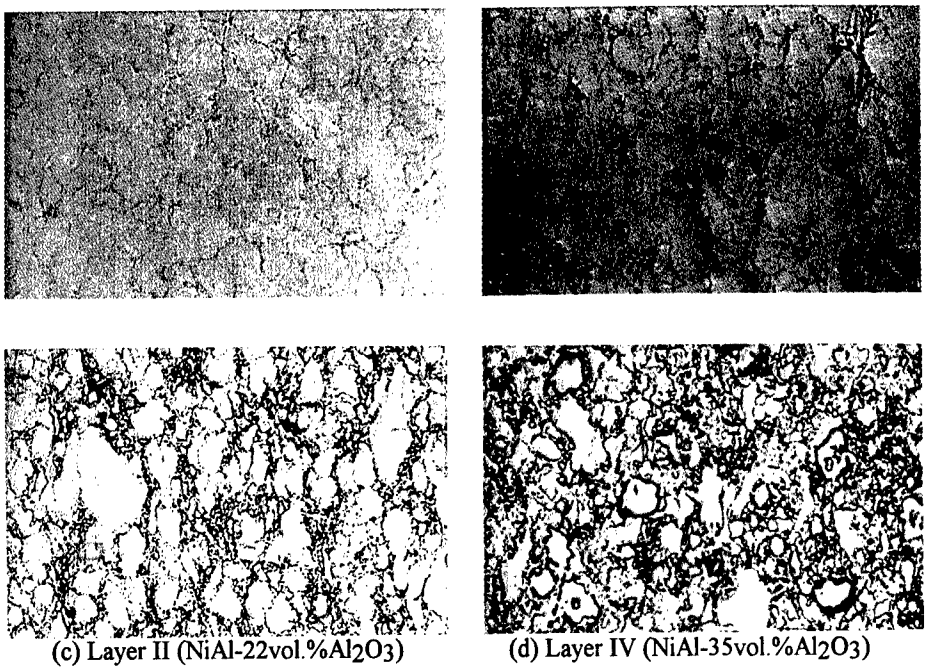


Fig.1 Contour maps of axial thermal stress in Si_3N_4/Steel bondings. (a) Butt jiont, (b) Four interlayers with linear compositional gradient [10].



(c) Layer II (NiAl-22vol.%Al_2O_3) (d) Layer IV (NiAl-35vol.%Al_2O_3)

Fig.2 Microstructures of the individual layers in a four-layer NiAl-Al_2O_3 functionally gradient composite

centrifugal P/M process The results showed that not only FGMs had better thermal fatigue resistance than classical coatings, but also different profiles retarded thermal fatigue damage differently. Jung et al. [48] studied the residual stress and thermal properties of zirconia/metal FGMs. The thermal diffusivity and the thermal conductivity of the FGMs and directly jointed materials (DJMs) were measured by the laser flash technique. The results showed that the stress concentration and the residual stress induced on cooling from the sintering temperature was relaxed for the FGMs. It was thought that the TZP/Ni FGM was excellent thermal barrier material and more stable than either TZP/SUS304 FGM or DJMs. Thermal cycling tests were conducted between room temperature and 1423K for the NiAl-Al_2O_3 FGCs by Miller and Lannutti et al. [22,23]. The results show that the FGCs are capable of withstanding extended thermal cycling and considerable high temperature strains without substantial damage to the ceramic layer.

5.2. Mechanical Properties

Miller and Lannutti et al. [22,23] studied fracture strength and fracture toughness of a four-layer NiAl-Al_2O_3 FGC consisting of NiAl, NiAl-30vol%Al_2O_3, NiAl-70Vol%Al_2O_3 and Al_2O_3 fabricated by a modified sedimentation process. It was found that the values of fracture toughness of the FGC were dependent on the location of the notch. The highest fracture toughness reached 11 MPa $m^{1/2}$ when the notch was machined in the middle of the Al_2O_3-NiAl layer, which was about twice that of the unreinforced NiAl. The bend strength of the composites were about 3-4 times of that of both the unreinforced NiAl and sapphaire-fiber reinforced NiAl (570 MPa vs approximately 150 MPa).

The microhardness profile along the NiAl-Al_2O_3 FGCs with different composition gradient were measured by the present authors [40]. Table 1 lists microhardness values in the center of each layer of NiAl-Al_2O_3 FGCs. The measured microhardness near each of the interfaces is shown in more detail in Fig.3. As can be seen, the microhardness normally increases with volume fraction of Al_2O_3, and the values near the interfaces do not differ much from those in the center of each layer. Notwithstanding, the microhardness profiles near the interface correlates well with the composition gradients across the interfaces. The steeper the composition gradient, the steeper is the microhardness gradient. Fig 3 also shows the microhardness near the interface of an identically processed NiAl-(NiAl-35%Al_2O_3) bilayer. The microhardness near the bilayer interface changes much more steeply than that near the interfaces of FGCs. From Fig.4, it can be seen that the microhardness changes gradually along the thickness of FGC III, while it changes steeply along the thickness of the bilayer material. The EPMA results along the interfaces showed that the increased microhardness was not due to the compositional changes. It is most likely due to residual stresses caused by the CTE mismatch between NiAl and NiAl-35%Al_2O_3 in the bilayer material. This correlates well with the results of finite element analysis of Williamson and Rabin *et al.*[14,15] which predicts reduced residual stresses in the FGM compared with a conventional material.

The fracture toughness values for a five-layer NiAl-Al_2O_3 FGC and the composites corresponding to the five layers are reported in Table 2 [39]. It can be seen that the composite corresponding to Layer II in FGC IV (18 vol% Al_2O_3) has the highest fracture toughness value, 16.0 MPa $m^{1/2}$; followed by the composites corresponding to Layers III and IV with 12.0 and 7.5 MPa $m^{1/2}$, respectively. Finally, Layers I and V show similar fracture toughness values with 6.5 and 6.6 MPa $m^{1/2}$, respectively. In comparison to pure NiAl, the fracture toughness values of the NiAl-Al_2O_3 composites increase substantially as the Al_2O_3 content reaches 18 vol%. The increase in toughness was found to be related to the difficulty in crack nucleation process by in-situ alumina [37]. The decrease in toughness with Al_2O_3 content (from 18vol% to 52vol%) might be associated to the increase in porosity as Al_2O_3 content increased. From Table 2, it can

be seen that the fracture toughness values of FGC IV are in the range between 13.3 to 15.2 MPa $m^{1/2}$ and are dependent on the region in which the crack nucleates. The highest fracture toughness in the FGCs was found when the tip was located in Layer II, which corresponded to the toughest composite. The crack nucleation and propagation mechanisms for FGCs are being further studied.

Table 1 Microhardness of each layer in the NiAl-Al_2O_3 FGCs

Layers	FGC I		FGC II		FGC III	
	Vol% Al_2O_3	Vickers Hardness	Vol% Al_2O_3	Vickers Hardness	Vol% Al_2O_3	Vickers Hardness
I	0	315	0	334	0	328
II	3	365	5	382	8	381
III	8	361	15	396	22	453
IV	14	373	25	421	35	561
V	20	413	35	510	-	-

Table 2 Fracture toughness values of the NiAl-Al_2O_3 composites corresponding to the five layers in FGC IV and FGC IV [39]

Composites			FGC IV	
Composite No.	Vol% Al_2O_3	Fracture Toughness (MPa $m^{1/2}$)	Fracture Toughness	
I	0	6.5	Crack Direction*	MPa $m^{1/2}$
II	18	16.0	II → I	13.3
III	26	12.0	II → V	15.2
IV	37	7.5	V → I	13.3
V	52	6.6	I → V	13.8

*The first number indicates the layer in which crack initiation occurred and the second one is the layer towards which the propagation occurred

6. Summary

A variety of processing techniques have been used to produce FGMs, but the most popular techniques are thermal spray for thin coating, and powder metallurgy and combustion synthesis for thicker or bulk FGMs. Some novel processing techniques such as reactive hot compaction (RHC) based on P/M and SHS are also developed in recent years. The development of functionally gradient materials can provide a number of distinct advantages over conventionally bonded materials, which include reduction and optimal distribution of stresses, improvement of thermal shock resistance and thermal fatigue behavior, enhanced interfacial bond strength and increase of fracture toughness.

Acknowledgments

The authors wish to thank Dr. Steven G. Fishman and gratefully acknowledge the financial support of this project by the Office of Naval Research (ONR) under contract # N000014-94-1-0285.

References

1. M. Finot, S. Suresh, C. Bull and S. Sampath, *Mat. Sci. Engg. A*, 205(1996) 59-71
2. A. Mortensen and S. Suresh, *Int. Mat. Rev.*, 40 (6)(1995) 239-264.
3. S. Suresh and A. Mortensen, *Int. Mat. Rev.*, 42 (3)(1997) 85-116.
4. M. Sasaki and T. Hirai, *J. of Ceramic Soc. of Japan*, 99(1991) 1002-1013.
5. H. Takahashi and T. Hashida, *JSME Intl. J.*, 33 (3) (1990) 281-287.

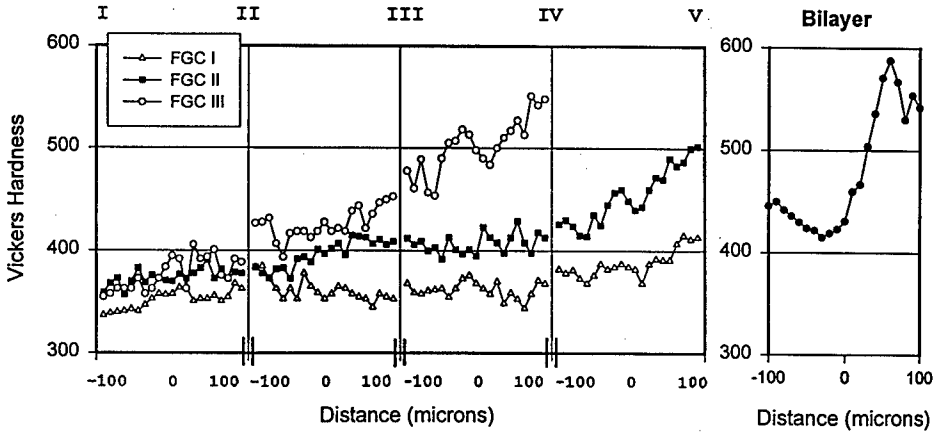


Fig 3. Microhardness near the interfaces of FGC I, FGC II, FGC III and NiAl-(NiAl-35Vol%Al_2O_3) bilayer

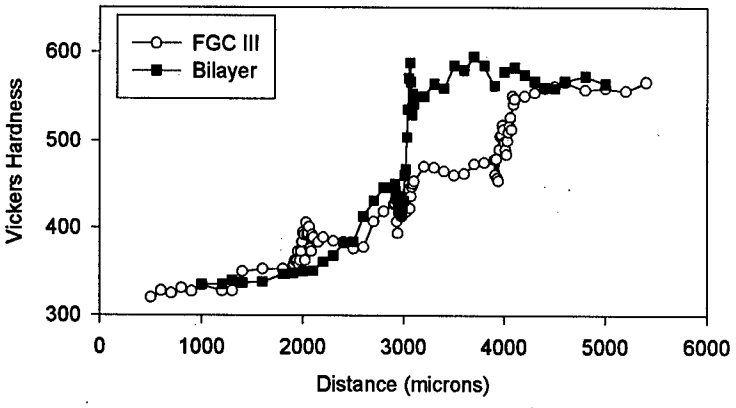


Fig.4 Microhardness profile along the thickness of FGC III and NiAl-(NiAl-35vol%Al_2O_3) bilayer

6. H. Kazumi, M. Syuji, and W. Osamu, *Trans. JSME*, Part A, 60(1994) 2350.
7. I. M. Low, R. D. Skala and D. Zhou, *J. Mat. Sci. Lett.*, 15(1996) 345-347.
8. B.H. Rabin, R.L. Williamson and S. Suresh, *MRS Bulle.*, 20(1)(1995) 37-39.
9. J. H. Abboud, D. R. F. West and R. D. Rawlings, *J. Mat. Sci.*, 29(1994) 3393-3398.
10. R. Watanabe and A. Kawasaki, in *Proc. of the Second Pacific Rim International Conference on Advanced Materials and Processing*, Ed. K. S. Shin, J. K. Yoon and S. J. Kim, The Korean Institute of Metals and Materials, 2(1995) 1705-1712.
11. M. Koizumi and M. Niino, *MRS Bulle.*, 20(1)(1995) 19-21.
12. W. Kaysser and B. Ilschner, *MRS Bulle.*, 20(1)(1995) 22-24.
13. S. Maruno, S. Ban, Y. Wang, H. Iwata and H. Itoh, *J. Ceramic Soc. Japan*, 100 (4)(1992), 362.
14. R.L.Williamson, B.H.Rabin and J.T.Drake, *J. Appl. Phys.* 74(2)(1995)1310-1320
15. J.T.Drake, R.L.Williamson and B.H.Rabin, *J. Appl. Phys.* 74(2)(1995)1321-1326
16. B.H.Rabin and R.J.Heaps, in *Functionally Gradient Materials,* Ceramic Transactions, Ame. Ceram. Soc., Westerville, OH, Ed. J. B. Holt et al. 34(1993)173-180
17. R.Z. Yuan, L.M. Zhang, Q.J. Zhang and X.F. Tang, *J. Mater. Synthesis and Processing*, 1(3)(1993) 171-179
18. C. Nan et al, *Journal of Wuhan University of Technology*, 9(2) (1994) 8-14
19. M.I. Mendelson and T.N. McKechnie, in *Functionally Gradient Materials,* Ceramic Transactions, Ame. Ceram. Soc., Westerville, OH, Ed. J. B. Holt et al. 34(1993) 417-424
20. T. Hirai, *MRS Bulle.*, 20(1)(1995) 45-47.
21. S. Sampath, H. Herman, N. Shimoda and T. Saito, *MRS Bulle.*, 20(1)(1995) 27-29
22. Z. D. Yin, X.. H. Xiang, J. C. Zhu and X. D. Li, in *Proc. of the Second Pacific Rim International Conference on Advanced Materials and Processing*, Ed. K. S. Shin, J. K. Yoon and S. J. Kim, The Korean Institute of Metals and Materials, 2(1995) 1745-1749.
23. Y. Shinohara et al, in *Functionally Gradient Materials,* Ceramic Transactions, Ame. Ceram. Soc., Westerville, OH, Ed. J. B. Holt et al., 34(1993) 255-262.
24. H. Hamatani et al, *ibid*, 385-392.
25. S. Matsumura et al, *ibid*, 331-338.
26. Z.M. Salim et al, in *Proc. of the Second Pacific Rim International Conference on Advanced Materials and Processing*, Ed. K. S. Shin, J. K. Yoon and S. J. Kim, The Korean Institute of Metals and Materials, 2(1995) 1739-1744.
27. T. Nagano and F. Wakai, *J. Mater. Sci.*, 28 (1993) 5793-5797.
28. D. P. Miller, J. J. Lannutti W. O. Soboyejo and R. D. Noebe, in *Structural Intermetallics*, Ed. R. Darolia et al, TMS, Pittsburgh, PA, (1993) 783-790.
29. D. P. Miller, J. J. Lannutti and R. D. Noebe, *J. Mater. Res.*, 8(8)(1993) 2004-2013.
30. Y. He, V. Subramanian and J. Lannutti, *MRS Symp. Proc.* 434(1996)81-92
31. R. Watanabe , *MRS Bulle.*, 20(1)(1995) 32-34
32. A. Kawasaki and R. Watanabe, in *Functionally Gradient Materials,* Ceramic Transactions, Ame. Ceram. Soc., Westerville, OH, Ed. J. B. Holt et al., 34(1993) 157-164.
33. S. Hulsmann and W. Bunk, *ibid*, 197-202.
34. S. E. Niedzialek and G. C. Stangle, *J. Mater. Res.*, 8(1993) 2026-2034.
35. G.C. Stangle and Y. Miyamoto, *MRS Bulle.*, 20(1)(1995) 52-53
36. H.J.Feng and J.J.Moore, *In-Situ Composites: Science and Technology*, Edited by M.Singh and D.Lewis (1994) 81-95.
37. H. Doty and R. Abbaschian, *Mat. Sci. Engg. A* 195(1995) 101-112
38. M. Misoilek and R. M. German, *Mat. Sci. Engg. A* 144 (1991) 1-10
39. D.Padmavardhani, A.Gomez and R.Abbaschian, to appear in *Intermetallics*
40. H. Zhu, D. Padmavardhani and R. Abbaschian, "Processing and Characterization of NiAl-Al_2O_3 Functionally Gradient Composites" (Paper presented at MRS Fall Meeting, December 1997, Boston).
41. R.Bracken, D.Padmavardhani and R.Abbaschian, submitted to *Mater. Sci. Eng.A*
42. L. Lu, A.B.Gokhale and R. Abbaschian, *Mat. Sci. Engg. A* 144(1991) 11-23
43. C. H. Henager, Jr., J. L. Brimhall and J. P. Hirth, in *Structural Intermetallics*, Ed. R. Darolia et al, TMS, Pittsburgh, PA, (1993) 799-808.
44. C. H. Henager, Jr., J. L. Brimhall and L. N. Brush, *Mat. Sci. Engg. A* 195(1995) 65-74
45. M.M.Moshksar, H.Doty and R.Abbaschian, *Intermetallics* 5 (1997) 393-399
46. O. Kesler, M. Finot, S. Suresh and S.Sampath, *Acta Mater.* 45(8)(1997)3123-3134
47. N. Cherradi, K. Dollmeier and B. Ilschner, in *Functionally Gradient Materials,* Ceramic Transactions, Ame. Ceram. Soc., Westerville, OH, Ed. J. B. Holt et al. 34(1993)229-236
48. Y.-G. Jung, S.-C. Choi and C.-S Oh, *J. Mat. Sci.* 32(1997)3841-3850

In Situ Synthesis and Thermodynamic Analysis of $MoSi_2$-SiC Composite

Zuqing Sun, Laiqi Zhang, Yue Zhang and Wangyue Yang

School of Materials Science & Engineering,
University of Science & Technology Beijing
(Beijing 100083,China)

Abstract

The $MoSi_2$-SiC composite was synthesized by reactively in situ sintering the mixtures of elementary Mo, Si and C, followed by the hot pressing. At low temperatures prior to the melting of silicon, the Mo_5Si_3, Mo_3Si and Mo_2C are predominant phase products. After the melting of silicon, the $MoSi_2$ and SiC become predominant phases. The amount of intermediate Mo_3Si and Mo_5Si_3 phases decreases and that of $MoSi_2$ and SiC phases increase as sintering temperature is increased from 1160°C to 1250°C. The formation of the intermediate phases such as Mo_5Si_3 and Mo_3Si etc was suppressed at high heating rate. The proper sintering time can eliminate the presence of intermediate phase Mo_5Si_3. The density of $MoSi_2$-SiC composite can be increased by hot pressing. The SiC particulates are uniformly distributed in the $MoSi_2$ matrix. The size of SiC particulates is about in the range of 3-5μm.

The Third Pacific Rim International Conference on
Advanced Materials and Processing (PRICM 3)
Edited by M.A. Imam, R. DeNale, S. Hanada,
Z. Zhong and D.N. Lee
The Minerals, Metals & Materials Society, 1998

Introduction

The combination of high melting point (2050℃), low density(6.24gcm^{-3}), and extremely high resistance to oxidation and corrosion makes $MoSi_2$ an attractive candidate material for high-temperature structural application[1-2]. However the use of $MoSi_2$ has been hindered because of the brittle nature of the material at ambient temperatures, inadequate elevated-temperature strength, a high creep rate at temperatures above 1200℃. Recently, an extensive amount of work has been conducted in efforts to improve the properties of $MoSi_2$[3-5], such as high-temperature strength and low-temperature ductility. Strength improvement is being achieved with additions of SiC whiskers or ceramic particulates such as SiC and partially stabilized ZrO_2[6-7]. Improvements in low-temperature toughness have been achieved by additions of ductile metallic phase such as niobium. Up to now, the $MoSi_2$-SiC composite has been synthesized by solid state displacement reaction[8], XD[9], the carbon additions to $MoSi_2$ during the compacting $MoSi_2$ [10]and the elementary powders reaction[11].

In the present study, the $MoSi_2$-SiC composite is synthesized by reactively in situ sintering the mixtures of elementary Mo, Si and C followed by the hot pressing.The phase relations and the stability of the various binary phase in the ternary system Mo-Si-C were understood by the DTA combined with XRD technique and thermodynamic analysis. The effect of processing parameters such as the heating rate, the sintering temperature and time on the synthesizing and processing of $MoSi_2$-SiC composite was investigated.

Experimental procedure

The raw materials used in the present work were >99% pure Mo powder with a size <5um, >99%pure Si powder with a size -400mesh and >99%C (graphite) powder with a size 300-mesh. The powders were thoroughly mixed with a grinding miller in the desired stoichiometry and pressed into pellets with the dimensions of 16mm diameter and 8mm depth under a certain pressure. The pellets were exhausted at 500℃.The onset and the peak temperatures of the exothermic reaction of the powder mixture were obtained from the DTA which was conducted up to 1580℃ with heating rates of 5-200℃/min in a flowing argon atmosphere using an automated high temperature DTA system of Dupont instrument (model 2100). A small piece of compact of mass 50mg were used in the DTA study.

The pellets were elevated at different heating rates and then reactively sintered at a certain temperature under flowing 99.991% pure Ar atmosphere for 0.5h or 1h respectively, followed by furnace cooling to ambient temperature.

The reactively in-situ sintered $MoSi_2$ - SiC composite was crushed into a coarse, -80mesh powders and then consolidated by hot pressing at 1700℃ and 35MPa pressure under flowing 99.991% pure Ar atmosphere for 2h in a graphite die .

SEM was employed to observe the composites morphology and to assess microstructure homogeneity, XRD analysis was performed to determine the phase constitution and the composition of the final products in the reactively sintering process.

Thermodynamics of the reactions in the Mo-Si-C system

For controlling phase constitution and morphology of the $MoSi_2$-SiC composite, it is very important to understand the phase relations and the thermodynamic stability of the various binary phases in the ternary Mo-Si-C system. It is the relative magnitude of their free energies of formation that defines which phase will be present at equilibrium. For the ternary system Mo-Si-C, all possible reactions are as follows:

$$Mo + C \rightarrow MoC \quad (1)$$

$$2Mo + C \rightarrow Mo_2C \quad (2)$$

$$Si + C \rightarrow SiC \quad (3)$$

$$3Mo + Si \rightarrow Mo_3Si \quad (4)$$

$$Mo + 2Si \rightarrow MoSi_2 \quad (5)$$

$$5Mo + 3Si \rightarrow Mo_5Si_3 \quad (6)$$

The variation of free energies of the above reactions with temperature can be calculated[12], as shown in Fig. 1, indicating that all the above reactions can take place spontaneously . As the temperature is lower than 1750K, among the carbides of Mo and Si, the magnitude of the free energy of formation of SiC was smaller than that of formation of Mo_2C and MoC, the reactions

$$Mo_2C + Si \rightarrow SiC + 2Mo \quad (7)$$

$$MoC + Si \rightarrow SiC + Mo \quad (8)$$

can take place toward the right direction and the reactions are irreversible.When temperature is higher than 1750K at which the free energy lines of Mo_2C and SiC intersect, Mo_2C phase is stabler than SiC phase, the reaction (7) can take place reversibly. Hence if we want to synthesize $MoSi_2$-SiC composite by a reactively in situ sintering technique, the onset sintering temperature of the compact bulk sample would be lower than 1750K. Among the molybdenum silicides , the magnitude of the free energy of formation of Mo_5Si_3 is the smallest. But because the free energy of reaction (9)

$$1/5Mo_5Si_3 + 7/5Si \rightarrow MoSi_2 \quad (9)$$

is less than zero and the reaction can take place spontaneously, the phase equilibrium of the binary system Mo-Si is controlled by the compositions of reactants. Therefore the thermodynamic calculations show $MoSi_2$-SiC to be a thermodynamically stable pair. In the view of thermodynamics, the $MoSi_2$-SiC composite can be synthesized by reactively in situ sintering the mixture of elementary Mo, Si and C powders.

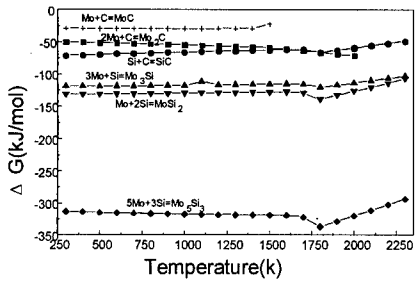


Fig. 1 Variations of free energy with temperature

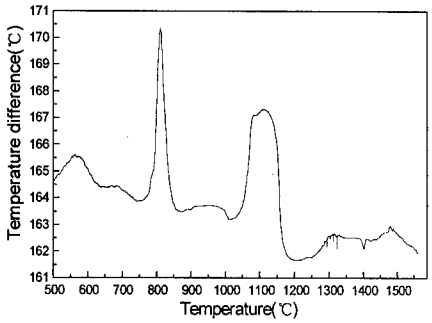


Fig. 2 DTA curve of sample $MoSi_2$/30vol.%SiC at 5℃/min heating rate

Results and discussion

DTA and phase analysis in the synthesizing process of $MoSi_2$-SiC composite

The DTA curve of sample $MoSi_2$/30vol.%SiC obtained at heating rate of 5℃/min in a flowing argon atmosphere is given in Fig. 2. Five peaks of exothermic reaction are observed and the corresponding peak temperatures of these peaks are 566℃ ,809℃,1080℃ ,1109℃ and 1476℃ respectively.The corresponding X-ray diffraction analysis demonstrates that the exothermic reaction peaks corresponding to 566℃ and 1476℃ are created by the oxidation of Mo and Si respectively. At 809℃, the phases are mainly the unreacted elements, but minute of amount of Mo_2C phase is observed, indicating that the reaction (2) takes place at this temperature. At 1080℃, a small amount of Mo_3Si and Mo_5Si_3 phases occur along with Mo_2C phase, meaning that the reaction (4) and the following reaction take place in this case: $5/3Mo_3Si + 4/3Si = Mo_5Si_3$. The X-ray pattern of samples heated to 1109℃ indicates the presence of Mo_3Si, Mo_5Si_3, Mo_2C, $MoSi_2$ and SiC. It is inferred that the reaction (3) and the following reaction take place: $1/5\ Mo_5Si_3 + 7/5Si = MoSi_2$, and $Mo_2C + 5Si = SiC + 2MoSi_2$. But these solid-solid reactions are carried out by the diffusion of solid Si and C atoms, and the rate of these solid-solid reactions is very slow since Si is the dominant diffusional atom in the Mo-Si system.

As mentioned above, the arbitrary two elementary reactants of Mo-Si-C system can react at a certain range of temperatures prior to the melting of Si (1410℃). For the binary system Mo-Si, the solid Mo and Si can form Mo_3Si phase and Mo_5Si_3 phase by the diffusional reaction of silicon. As temperature is increased, $MoSi_2$ phase forms by the reaction of the solid Si and

Mo_5Si_3. But the rate of the reaction is very slow. For the binary system Mo-C, though the free energy of formation of Mo_2C is larger than that of SiC, if the active energy of Mo_2C is smaller than that of SiC, hence Mo_2C phase can form at 800℃ which is the case for the present study . The onset temperature of formation of SiC phase is 1100℃[13], therefore Mo_2C phase forms by the diffusional reaction between solid Mo and C at 800℃ by the diffusion of carbon, and Si is substituted for Mo at the range of 1100℃-1250℃. For the binary system Si-C, SiC phase can form by the diffusional reaction between solid Si and C by the diffusion of carbon at 1109℃. But the rate of the diffusional reaction is very slow. Therefore for the ternary system Mo-Si-C, Mo_3Si, Mo_5Si_3 and Mo_2C are the predominant products under the conditions of lower temperatures and solid state.

X-ray diffraction pattern of sample $MoSi_2$/30vol.%SiC heated to 1450℃indicates that $MoSi_2$ and SiC in this case appear as the major phases and Mo_5Si_3 and unreacted elements as the minor phases without any indication of the presence of Mo_2C and Mo_3Si phases. It should be mentioned that at 1410℃ the melting of the unreacted Si has taken place already. Because of the high mobility (about 10^3-10^5 time higher than that of solid[14]) of the liquid Si and high diffusion rate, compared with the solid Si, the liquid Si can reacts with Mo_3Si to form Mo_5Si_3 and then Mo_5Si_3 reacts with liquid Si to form $MoSi_2$ again[15]. The liquid silicon also directly reacts with the unreacted Mo and C to form $MoSi_2$ phase and SiC phase. This explains why Mo_5Si_3 is the predominant phase at low temperatures, whereas $MoSi_2$ is the main phase at high temperatures at low heating rates. Fig. 3 is a X-ray diffraction pattern of a sample $MoSi_2$/30vol.%SiC sintered at 1450 ℃ for 1h at 120 ℃ /min. The diffraction peaks corresponding to t-$MoSi_2$ phase and β-SiC phase respectively occur without presence of Mo_5Si_3 and unreacted elemental phases. We conclude that $MoSi_2$-SiC composite can be synthesized by reactively in situ sintering the mixture of element Mo, Si and C powders at a certain temperature range and heating rate.

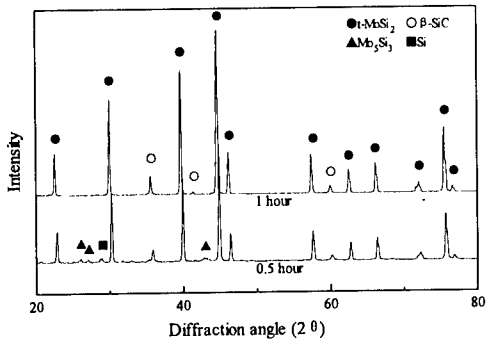


Fig. 3 XRD pattern of samples $MoSi_2$/30vol.%SiC sintered at 1450 ℃ for 0.5 h(a) and 1 h (b) at 120 ℃/min respectively

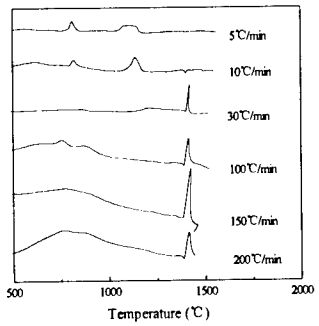


Fig. 4 DTA curves obtained at various heating rates in an argon atmosphere

The reactive sintering

The heating rate. Fig. 4 is DTA curves obtained at various heating rates in a flowing argon atmosphere.It is clear that a few different peaks are observed at low heating rates representing different exothermic reactions. As mentioned above, the peaks which occur at lower temperatures are ones cased by forming intermediate phases. Only a single peak is observed at heating rates at or above 150℃/min. The curves indicate that, at low heating rates, exothermic reactions take place over a wide temperature range. Hence the amount of intermediate phases can be suppressed by enhancing heating rates.

Fig. 5 is the diffraction pattern of sample $MoSi_2$/30vol.%SiC sintered at 1450℃ for 1h at various heating rates. The products are mainly $MoSi_2$ SiC and Mo_5Si_3. At low heating rates, minute amount of unreacted elements are also observed along with $MoSi_2$, SiC and Mo_5Si_3. An estimation of the amount of Mo_5Si_3 formed at each heating rate is carried out by integrating the areas under the reflection of Mo_5Si_3[16]. The amount of Mo_5Si_3 decreases considerably with increase in heating rate. The amount of $MoSi_2$ increases with increase in heating rate. This is in

good agreement with reference [15] which reported that with increase in heating rate the onset of exothermic reaction increased from 1256℃ at 5℃/min to 1369℃ at 150 ℃/min. Also the available diffusion reaction time of the formation of Mo_5Si_3 is relatively longer at low heating rates, the amount of the Mo_5Si_3 is relatively large and the available diffusion reaction time of the formation of Mo_5Si_3 is relatively short at high heating rates, the amount of Mo_5Si_3 is relatively small. At the heating rate of 120℃/min, there are only $MoSi_2$ and SiC phase without the presence of Mo_5Si_3 phase. This is because, at high heating rates, the melting of Si occurs first and liquid Si -solid Mo diffusional reaction takes place. Since to form $MoSi_2$ two atoms of Si are needed for every Mo atom, and Si is the dominant diffusing element in the formation of silicides, and it diffuses fast in molten state, $MoSi_2$ is formed readily[15]. Therefore, at heating rate of 120℃/min, Si(l) + Mo(s) = $MoSi_2$(s). In order to synthesize $MoSi_2$-SiC composite, the high heating rate is expected to be used to suppress the formation of the intermediate phases, such as Mo_5Si_3 and Mo_3Si etc.

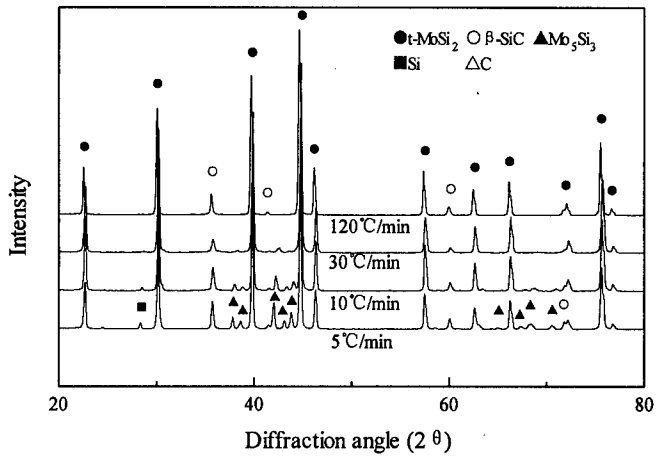


Fig. 5 XRD pattern of sample $MoSi_2$/30vol.%SiC sintered at 1450℃ for 1 hour at various heating rates

The sintering temperature. Fig. 6 is the x-ray diffraction pattern of samples $MoSi_2$/30vol.%SiC sintered for 1h at various temperatures at heating rate of 5℃/min. The results show that Mo_3Si, Mo_5Si_3 and Mo_2C are observed to be the predominant products below1250℃,and $MoSi_2$ and SiC phases increase as the sintering temperature is increased from 1160℃ to 1250℃. When the same sample was heated passing over the melting point of silicon to 1450℃, $MoSi_2$ and SiC phases are the predominant ones, while Mo_5Si_3 and unreacted elements are the minor ones. This indicates that (a) Mo_5Si_3 nucleates and grows as an initial product prior to the reaction with liquid silicon, (b) the reaction between liquid silicon and already formed Mo_5Si_3 enriches the silicon content of the lower silicide (Mo_5Si_3) to form $MoSi_2$, and also (c) the liquid silicon directly reacts with the unreacted molybdenum to form $MoSi_2$ [15]. Hence at 1450℃, the following reactions take place:

$$Si(l) + C(s) \rightarrow SiC(s),$$

$$2Si(l) + Mo(s) \rightarrow MoSi_2(s),$$

$$1/5Mo_5Si_3(s) + 7/5Si(l) \rightarrow MoSi_2(s),$$

$$5/3\ Mo_3Si(s) + 4/3Si\ (l) \rightarrow Mo_5Si_3(s).$$

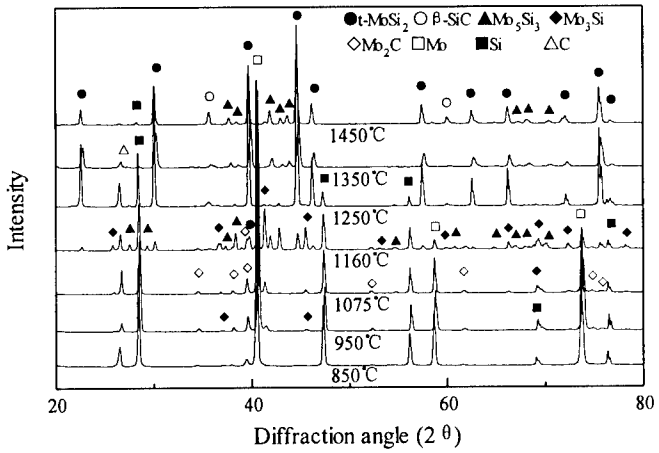


Fig. 6 XRD pattern of samples $MoSi_2$/30vol.%SiC sintered for 1 hour at various temperatures at 5℃/min

The sintering time. Fig. 3 is the x-ray diffraction pattern of samples $MoSi_2$/30vol.%SiC sintered at 1450 ℃ at heating rate of 120 ℃/min. The sintering time is 0.5h for Fig. 3 (a) and 1h for Fig.3 (b) respectively. Fig. 3 (a) shows that the intermediate phase Mo_5Si_3 and unreacted element Si are observed along with t-$MoSi_2$ and β-SiC phases when sintering time is 0.5h. The intermediate phase Mo_5Si_3 and unreacted element Si disappear and only t-$MoSi_2$ and β-SiC phases are observed when sintering time is 1h. This indicates that the reaction of sample is not complete when sintered at 1450 ℃ for 0.5h, and the reaction is complete when sintered at 1450 ℃ for 1h. It concludes that an available diffusion reaction time of liquid silicon is necessary to make the reaction be complete. Thus, the sintering time is a very important factor to eliminate the presence of intermediate phase Mo_5Si_3 .

Morphology of $MoSi_2$/30vol.%SiC. Fig.7 is SEM images of microstructure of $MoSi_2$/30vol.%SiC. The white particles are $MoSi_2$, and the small black particles are SiC particulates. There are also some pores in the $MoSi_2$ matrix. The density of $MoSi_2$/30vol.%SiC composite sintered reactively is very low, about 60% of theoretical density. Hence the density of the $MoSi_2$/30vol.%SiC composite has to be improved by the hot pressing if it is used as a high-temperature structural material.

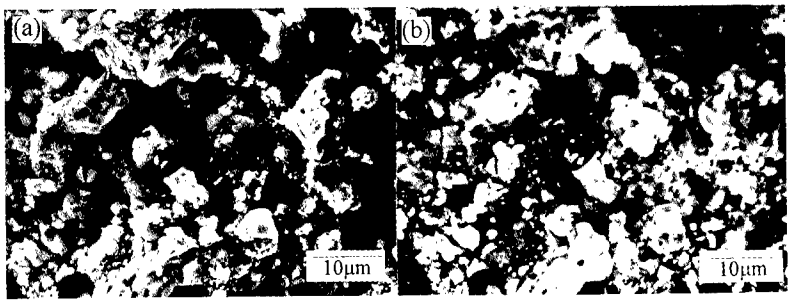


Fig. 7 Microstructure of $MoSi_2$/30vol.%SiC: (a) secondary and (b) backscattered of electron images of SEM

The hot pressing

The compositions of the crushed powders of $MoSi_2$/30vol.%SiC composite are analyzed by the EDAX. The results show that the compositions of a few piled particles are as same as those of a single particle, and are close to the compositions of the mixture of the $MoSi_2$/30vol.%SiC (21.5at.%Mo, 60.7at.%Si and 17.8at.%C). It is inferred that the crushed particles are composite particles rather than a single particle of $MoSi_2$ or SiC. The SiC particulates are incorporated in $MoSi_2$ particles matrix.

The density of $MoSi_2$/30vol.%SiC after hot-pressing is much larger than that of the $MoSi_2$/30vol.%SiC reactively in situ sintered only, and is approximately equal to 95% of the theoretical density.

The x-ray diffraction analysis of the hot-pressed $MoSi_2$/30vol.%SiC composite demonstrates that no reactions of the crushed powders of $MoSi_2$/30vol.%SiC takes place further during the hot pressing.

Fig. 8 is the SEM morphology of the hot-pressed $MoSi_2$/30vol.%SiC. We can see that the black particulates SiC with a range of 3-5μm are dispersed in the white matrix $MoSi_2$ uniformly.

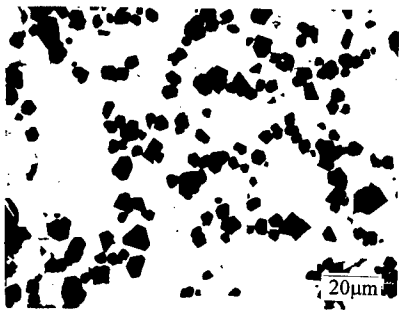


Fig. 8 SEM morphology of hot-pressed $MoSi_2$/30vol.%SiC

Conclusions

(1) The thermodynamic analysis and the experimental results show that the $MoSi_2$-SiC composite can be synthesized by the reactively in situ sintering together with the hot pressing technique successfully.

(2) The processing parameters, such as the heating rate, the sintering temperature and time are very important for the phase formation and microstructure of $MoSi_2$-SiC composite.

(3) At low temperatures prior to the melting of silicon, the Mo_5Si_3, Mo_3Si and Mo_2C are predominant phase products. The phases form by a solid-solid reaction. After the melting of silicon, the $MoSi_2$ and SiC become predominant phases.The $MoSi_2$ phase forms by liquid-solid reaction. The intermediate Mo_5Si_3 and Mo_3Si phases decrease and $MoSi_2$ and SiC phases increase as the sintering temperature is increased from 1160 ℃ to 1250 ℃. At 1450 ℃, the main phases are $MoSi_2$ and SiC.

(4) The high heating rate can be used to suppress the formation of the intermediate phases, such as Mo_5Si_3 and Mo_3Si etc. Proper sintering time can also eliminate the presence of intermediate phase Mo_5Si_3.

(5) The t-$MoSi_2$ and β-SiC can be obtained by reactively sintering at 1450 ℃ for 1 h at 120 ℃ /min heating rate. The small SiC particulates are dispersed in $MoSi_2$-matrix and some pores exist in the matrix.

(6) The phase constitutes of the hot-pressed $MoSi_2$-SiC composite consistes of $MoSi_2$ and SiC only. The density of $MoSi_2$-SiC composite can be increased by hot pressing. The particulates of SiC are dispersed in the $MoSi_2$ matrix uniformly. The size of SiC particulates is about in the

range of 3-5μm.

Acknowledgments

The authors greatefully acknowledge the support of the National Natural Science Foundation of China.

References

1. K. Sadananda,H. Jones,and J. Feng, " Creep of Monolithic and SiC Whisker-reinforced $MoSi_2$ " Ceram. Eng. Sci. Proc., 12 (9-10) (1991), 1671-1678.

2. David H. Carter, and G.H. Hurley, " Crack Deflection as a Toughening Mechanism in SiC-Whisker-Reinforced $MoSi_2$," J. Am. Ceram. Soc., 70 (4) (1987), C-79-C-81.

3. Michael J. Maloney, and Ralph J. Hecht, " Development of Continuous-Fiber-Reinforced $MoSi_2$-base Composites," Mater. Sci. Eng., A155 (1992),19-31.

4. Richard G. Castro et al., " Ductile Phase Toughening of Molybdenum Disilicide by Low Pressure Plasma Spraying," ibid. A155 (1992),101-107.

5. F.D. Gac, and J.J. Petrovic, " Feasibility of SiC Whiskers in an $MoSi_2$ Matrix, " J.Am.Ceram.Soc.,68 (1985), C-200-C-201.

6. J.J. Petrovic, and R.E. Honnel, "SiC Reinforced-$MoSi_2$/WSi_2 Alloy Matrix Composites," Ceram. Eng. Sci. Proc.,11 (1990), 734-744.

7. J.J. Petrovic and R.E. Honnel, " Partially Stabilized ZrO_2 Particle-$MoSi_2$ Matrix Composites," J.Mater.Sci., 25 (1990), 4453-4456.

8. C.H. Henager, Jr., J.L. Brimhall, L.N. Brush, " Tailoring Structure And Properties of Composites Synthesized In Situ Using Displacement Reaction, " Mater. Sci. Eng., A155 (1995),65-74.

9. R.M. Aiken, JR., "Stucture and Properties of In Situ Reinfoced $MoSi_2$," Ceram. Eng. Sci. Proc., 12 (9-10) (1991),1643-1655.

10. S. Maloy et al., " Carbon Additions to Molybdenum Disilicide :Improved High-Temperature Mechanical Properties," J. Am. Ceram.Soc.,74 (10) (1991), 2704-2706.

11. D.E. Alman and N.S. Stoloff, "Preparation of $MoSi_2$/SiC Composites from Elemental P owders by Reactive Co-synthesis," Scri. Metall.Mater., 28 (1993), 1525-1530.

12. O. Knaclee et al., Thermochemical Properties of Inorganic Substances(Springer-Verlag Berlin, Heideberg, 1991) (Second Edition).

13. S.P. Murarka, Silicides for VLSI Applications(New York, NY: Academic Press, 1983).

14. L.S. Darken and R.W. Gurry, Physical Chemistry of Metals(New York, NY: MC Graw-Hill, 1953).

15. Seetharama C. Deevi, "Diffusional Reactions in the Combustion Synthesis of $MoSi_2$," Mater. Sci. Eng., A149 (1992), 241-251.

16. H.P. Klug, and L.E. Alexander, X-ray Diffraction Procedures(New York, NY: Wiley, 1974).

VACUUM INVESTMENT CASTING OF SIC PARTICLES REINFORCED ALUMINUM MATRIX COMPOSITE

Dianbin Wang, Manchang Gui, Jianing Cheng, Hong Zhang, Chenggong Li

Institute of Aeronautical Materials, Beijing, 100095, P.R.China

Abstract

In this paper, the investment castings of SiC particles reinforced aluminum composites, including thin-wall casting, have been produced by an innovative technique, i.e., vacuum differential pressure casting process. The minimal wall thickness of castings may reach 1-2 mm. In the process, the investment mould in vacuum is filled by air pressure, to avoid the detrimental effect from air. The composite melt is solidified in air negative pressure, which is available to gain compact and sound casting. The construct of gate and riser system used in the process is quite simple. Compared with free gravity casting in atmosphere, the weight of the system decreases greatly, saving raw composite. The mechanical properties of the composite have been improved obviously. Vacuum degassing is a quite effective method for the composite melt.

The Third Pacific Rim International Conference on
Advanced Materials and Processing (PRICM 3)
Edited by M.A. Imam, R. DeNale, S. Hanada,
Z. Zhong and D.N. Lee
The Minerals, Metals & Materials Society, 1998

Introduction

Ceramic particle reinforced aluminum matrix composites possess high specific strength, specific stiffness, wear resistance, thermal stability, and a low coefficient of thermal expansion. These advantages, plus low density and relatively low cost, make them competitive with materials available now. SiCp reinforced castable aluminum matrix composites can be remelted and conventionally cast to near-net-shape, and have being attracted great attention. These composites have been produced in industrial scale by using a stir-casting process[1]. It is proved that conventional casting method that is used with unreinforced aluminum alloy has been successfully used with the composites, including sand casting, permanent mold casting (gravity and low pressure), investment casting (shell and plaster), lost foam casting, diecasting and centrifugal casting[2-4].

The remelt, degassing and casting of castable SiCp reinforced aluminum matrix composites are different from these of the unreinforced aluminum alloy due to the SiCp existence. The SiCp suspending in the melt tends to increase the viscosity of the composite melt obviously. The increase in viscosity results in some serious problem. For example, air is easily involved into the molten during the pouring, meanwhile the entrapped air escapes only slowly from the melt. If solidification takes place before this escape, air pore will be formed in the casting. For this reason, the construct of gate and riser system for the composite is different to that for the unreinforced aluminum alloy. An effective method is to use a choke and open riser in the system, so that the entrapped air bubbles and other inclusions can be collected in the riser [5]. These changes greatly increase the volume of the system, and consumption of the composite. Besides, the gates and risers are not suitable to be recycled since they contain a lot of inclusions, oxides and gas. The increase of the melt viscosity also degrades its fluidity[6]. Therefore it is rather difficult to obtain a shape-complex and thin-wall composite casting by using conventional casting processes. In addition, conventional salt and gaseous fluxes cannot be used to clean the composite melt since they would react with the SiC particles in the melt, causing them to dewet and rise to surface. In present work, an innovative technique of vacuum degassing and vacuum differential pressure casting is used for the composite, to overcome the shorts mentioned above.

Materials and Technical Equipment

The SiCp reinforced aluminum matrix composites, F3A20S and F3S20S, were purchased from Duralcan Co. Nominal SiCp content is 20vol%. The matrix alloy of F3A20S composite is A356, and the chemical composition of the matrix material of F3S20S composite is shown in Table I. The composite of low SiCp volume was obtained from diluting the 20vol%SiCp composite .
Figure 1 is the equipment designed and made especially for producing the investment casting of the particle reinforced aluminum matrix composites. Three functions, i.e., remelting, degassing and pouring can be executed in the equipment. Electrical resistance furnace is used to heat the ingot. There are two vacuum chambers, top and bottom chambers. The crucible is in the bottom, and the investment mould is in the top. In the casting process, vacuum is executed for the two chamber simultaneously, then put air into the bottom chamber, and the melt will fill the mould quickly under the pressure. After filling, air also gets into the top chamber, the casting is solidified in the condition of negative pressure .

Table I Chemical composition of the matrix alloy of F3S20S composite

Si	Mg	Fe	Cu	Ti	Al
9.5-10.5	0.75-1.25	max. 0.3	max. 0.3	max. 0.2	REM

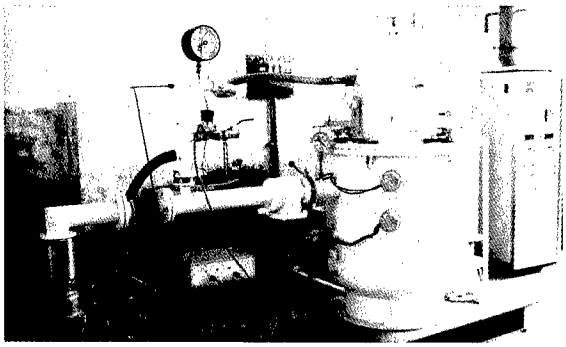


Figure 1 The equipment used for remelt, degassing and vacuum differential pressure casting of particle reinforced aluminum matrix composites.

Remelting and Degassing

The virgin composite ingot is charged to the crucible and heated. If any returns of gate and riser are recycled, they can also be added with the virgin material. Inert cover gas is not used during the melting. The molten temperature is controlled below 750 ℃. After melting, the melt is agitated for 15 min., then vacuum is executed to degas for 25min. The results of vacuum degassing are shown in Table II. The data of argon degassing are also given in Table II. The porosity is calculated from the formula: Porosity=$(\rho_{th}-\rho_m)*100/\rho_{th}$, where ρ_{th} and ρ_m are the theoretic and measuring density of the composite respectively. ρ_m is obtained from the sample poured in a sand mould. The density is measured by weight loss method. Obviously, vacuum degassing has an excellent effect for the composite melt. Meanwhile, the practice has been proven that vacuum degassing does not cause the loss of SiC particles.

Table II The results of vacuum and argon degassing of the composite melts

Composite	Porosity			
	vacuum degassing		Argon degassing	
	Before	After	Before	After
F3A15S	2.95	0.42	3.16	2.31
F3A20S	2.68	0.33	2.88	2.58
F3S15S	1.95	0.47	-	-
F3S20S	2.34	0.48	-	-

Investment Casting Process

The preparation of investment mould used for the composite investment casting is the same as conventional investment casting. In the casting process of vacuum differential pressure, since air is removed from the mould and cast system, no gas bubbles can be entrapped into the melt during the pouring. The construct of the casting system may be quite simple. A choke and large open riser in the casting system like in free gravity casting is unnecessary. Figure 2 is the schematic diagram of the typical gate and riser system of pump-housing part in investment casting in free gravity and vacuum differential pressure processes. The filter in the system is used to remove inclusions from the melt. The simplification of casting system obviously decreases the weight ratio of the gate and riser system to casting. Generally, the ratio is 5-8:1 in free gravity casting, whereas only 1-2:1 in the vacuum differential pressure casting. Table III is

the comparison of the weight ratio in different cast conditions, where free gravity casting is performed in atmosphere. The simple casting system of present process greatly reduces the consumption of the composite, hence decreasing the cost of the composite casting obviously. Table IV shows the porosity in the investment composite castings in different casting processes. The composite castings poured by vacuum differential pressure process are compact and sound. The defects such as porosity or inclusion were not found in the castings.

Comparing with conventional cast aluminum alloys, the composite melts have poorer fluidity. It is quite difficult to produce a thin-wall and complex-shape composite casting by conventional cast processes. In the case of the vacuum differential pressure process, the investment mould is filled with the aid of gas pressure, and the pressure can be controlled. By the present process, a thin-wall and complex-shape composite casting can be formed fully and readily. Several kinds of the high quality SiCp/Al composite investment castings have been produced successfully in authors' laboratory(Figure 3), including meter body, pump housing, valve housing, gulf-club head, and so on. Among the composite castings, minimal wall thickness is 1.5mm, and maximal dimension is 300mm. The composite used to cast gulf-club head is F3A15S, and the others are all F3S20S composite.

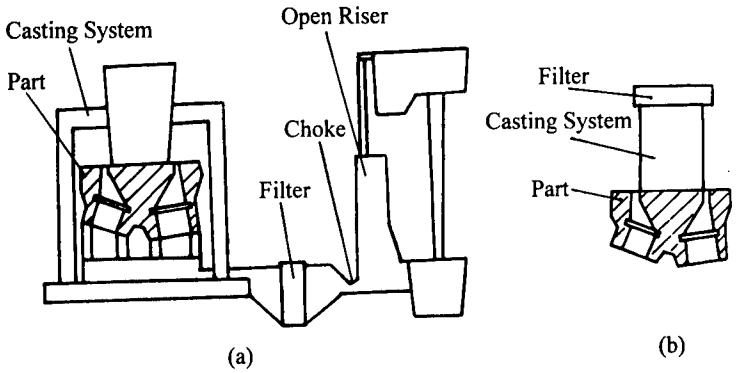


Figure 2 the schematic diagram of the typical casting system of pump-housing part investment casting (a) free gravity casting, (b) vacuum differential pressure casting.

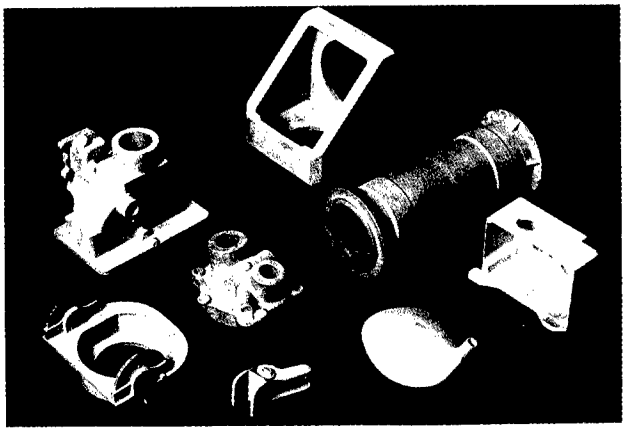


Figure 3 Investment castings of SiCp reinforced aluminum composites by the vacuum differential pressure casting, middle part is the pump-housing.

Table III The comparison of the weight ratio of casting system to casting

Process	Part	System weight(kg)	Casting weight (kg)	Weight ratio
Free gravity	Pump housing	3.4	0.65	5.2:1
	Valve housing	5.5	0.6	9.2:1
Present process	Pump housing	0.6	0.65	0.92:1
	Meter body	0.265	0.25	1.06:1

Table IV Porosity of the investment composite castings in different casting processes.

Process	Part	Porosity(%)
Free gravity casting	Pump housing	1.78-2.45
	Valve housing	1.65-3.26
Present process	Mirror housing	0.18-0.54
	Pump housing	0.43-0.51

Microstructure, Mechanical Property and Application

Figure 4 is the typical microstructure of F3S20S composite, the observed sample was cut from an investment casing. It is shown that SiC particles distribute at grain boundaries and inter-dendritic areas. The intimate contact and strong bonding between the SiC particle and aluminum matrix have been observed, and no reaction occured in the particle/matrix interface.

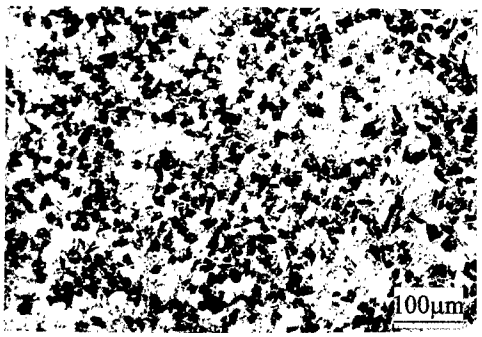


Fig. 4 Typical microstructure of the F3S20S composite in the investment casting.

Table V is typical mechanical properties of F3A and F3S composites in the investment casting. Compared with free gravity pouring process, the innovative casting process offers greater tensile strength and ductility of castings. For F3S20S, as the cooling rate in permanent mould is greater than that in investment mould, the tensile strength of the former should be higher due to finer grain structure. However it can be found that F3S20S composite in investment mould in the vacuum differential pressure process is stiffer than in permanent mould. In recent years, the application of the composites has being exploited in authers' laboratory. The composite pump housing used in an airplane engine has been on trial run. The designed material of the past is alloying steel, which is replaced by the composite now. It has been found that 60% reduction in

weight can be achieved by the replacement. The other prospective application being developed include brake of car, and component in satellite, etc.

Table V Typical properties of F3A and F3S composites in investment mould(T6)

process	Composite	Mechanical properties		
		σ_b(MPa)	δ(%)	E(GPa)
Duralcan standard*	F3A15S	303	0.4	92.4
	F3A20S	317	0.5	95.8
	F3S20S**	359	0.4	98.6
Free gravity casting	F3A20S	261	0.35	85.5
	F3A20S+HIP***	323	0.64	104
vacuum differential pressure casting	F3A15S	303	1.3	-
	F3A20S	323	1.1	106
	F3S20S	346	0.5	105

* Duralcan standard come from a data collection of mechanical properties of Duralcan™ composites. **In permanent mould, no data available in investment mould. ***Investment casting treated by heat isotropic pressure.

Conclusions

1. Vacuum pressure differential casting process is suitable to produce investment casting of SiCp reinforced aluminum matrix composite, especially in thin-wall and complex-shape composite casting.

2. Vacuum degassing has an excellent effect for the composite melt, and does not cause the loss of SiC particles.

3. The construct of gate and riser system used in the process is rather sample, greatly reducing the consumption of composite. The gates and risers can be recycled due to the absent of gas and inclusion contaminants.

4. The microstructure of the composite investment castings is compact. Their mechanical properties are improved obviously.

References

1. T. F. Kimowicz, "The Large-scale Commercialization of Aluminum-Matrix Composites," JOM, 46(11) (1994), 49-53

2. D. O. Kennedy, "SiC Particles Beef Up Investment-Cast Aluminum," Advanced Material and Processes, (June, 1991), 42-46

3. P. Rohatgi, "Cast Aluminum Matrix Composites for Automotive Applications," JOM, 43(4), (1991), 10-15

4. D. E. Hammond, "Castable Composites Target New Applications," Modern Casting, (Sept., 1990), 27-30

5. S. Ray, "Review Synthesis of Cast Metal Matrix Particulate Composites," J. Mater. Sci., 28(1993), 5397

6. D. J. Lloyd, "The Solidification Microstructure of Particulate Reinforced Aluminum/SiC Composites," Composites Sci. and Tech., 35(1989), 159-179

SYNTHESIS AND SPUTTERING OF COMPOSITE TARGETS AND THIN FILMS

A.O. Kunrath and J.J. Moore, Advanced Coatings and Surface Engineering Laboratory
Colorado School of Mines, Golden, Colorado, USA
S.Govindarajan, White Oak Semiconductor, Richmond, Virginia, USA
J. Disam, Schott Glaswerke, Mainz, Germany,
E.A. Levashov, Moscow Steel and Alloys Institute, Moscow, Russia

Abstract

Sputtering from composite targets of a specific chemical stoichiometry can effectively produce composite thin films with the same chemistry. Sputtering of these composite targets obviates the use of multiple targets, which would also need to be sputtered at different rates to produce a film of the required stoichiometry. However, the quality of the thin film depends strongly on the quality, e.g., density, microstructural homogeneity and uniformity, of the composite target. $MoSi_2$-SiC, TiC-TiB_2 and TiC-Cr_3C_2 composite targets have been produced using combustion synthesis (self-propagating, high temperature synthesis, SHS) using a combined, one-step SHS-consolidation process. The control of composite target chemistry, density, microstructure and properties with respect to the SHS process parameters, and the stoichiometry, microstructural features and phase distribution in the resulting thin film produced by rf and dc magnetron sputtering have been investigated.

The Third Pacific Rim International Conference on
Advanced Materials and Processing (PRICM 3)
Edited by M.A. Imam, R. DeNale, S. Hanada,
Z. Zhong and D.N. Lee
The Minerals, Metals & Materials Society, 1998

Introduction

There is a developing need to produce increasingly complex composite thin films for applications involving improved wear and/or oxidation resistance. The traditional, single compound, thin films and coatings that have been used successfully to date for such applications, e.g., TiN, CrN, SiC, will no longer continue to meet the increasing property demands for these applications. In this respect, coating systems need to be designed and developed for each specific application based on a total system that will, by necessity, require a combination of wear and/or oxidation resistant composite materials. In such cases, a combination of carbides, nitrides and borides have been shown to provide improved surface properties compared with single TiN, TiB_2, or CrN coatings.[1-3] However, the incorporation of a combination of such compounds into a composite thin film system would traditionally involve the use of multiple targets, e.g., Ti and Cr, together with an elaborate reactive gas system that would involve N_2, B-containing, and hydrocarbon gases in the deposition vacuum chamber. In addition, the incorporation of the higher carbides, such as Cr_3C_2, into the composite film is often only possible by incorporating this compound into the sputter target. The carbon potentials generated in physical vapor deposition (PVD) processes are generally not sufficiently high to produce Cr_3C_2 so that the lower carbides ($Cr_{23}C_6$, Cr_7C_3) only are present in the film. Hence, there is a great advantage if the higher carbide and boride compounds required in the final film system can be present in the target. The generation of the nitride compounds in the composite film can generally be readily achieved by reactive sputtering of the composite carbide-boride target in a nitrogen atmosphere.

Composite targets can be produced by a number of techniques, for example: hot pressing and sintering; hot isostatic pressing; or plasma spraying of the component materials needed to provide the composite target. However, each of these techniques can result in serious defects in the target. These defects could be porosity, non-uniform microstructure, high oxygen content and impurities. Each of the above techniques requires multi-stage processing, e.g. high purity powder production with particle size and impurity control, powder blending and mixing with binders, cold pressing, hot pressing, sintering and/or HIPing, machining, grinding and finishing. Self-propagating high temperature synthesis (SHS) provides an alternative for the production of composite targets used in the sputtering of composite thin films.

There are a number of materials, including the carbides, borides and oxides of refractory metals that offer considerable potential for both thermally and chemically stable films[1-3] for wear and oxidation resistance and microelectronic applications. This investigation explores the potential of applying self propagating high temperature synthesis (SHS)[4-6] to the production of TiC-TiB_2, $MoSi_2$-SiC, and TiC-Cr_2C_2 composite targets that could be used in sputtering composite thin films with controlled microstructures and properties.

Self Propagating High Temperature (Combustion) Synthesis (SHS) Combustion (self-propagating high temperature) synthesis (SHS) uses an exothermic reaction to provide the energy needed to synthesize ceramics, intermetallics and composites. The exothermic reactant mixture, normally in the form of powders, is pressed into a pellet of a certain green density and is subsequently ignited, either locally at one point (propagating mode) or by heating the whole pellet to the ignition temperature of the exothermic reaction (simultaneous combustion mode). A schematic representation of a typical temperature-time plot for a combustion reaction is given in Figure 1. The non-reacted ("green") reactant mixture at initial temperature, To, is heated to the ignition temperature, Tig, whereupon the reaction is initiated. Sufficient heat is released by the exothermic reaction, as indicated in Figure 1(a), in order to achieve a maximum or combustion temperature, Tc, and to sustain the reaction without the need for additional heat.

The exothermicity of the combustion synthesis reaction plays an important part in the stability of the reaction and the combustion temperature achieved which consequently affects both the microstructure and properties of the synthesized products. These parameters can best be

explained by examining the enthalpy of the reactants and products as a function of temperature as indicated in Figure 2.[5]

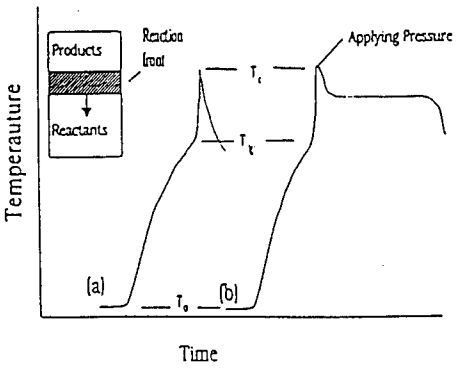


Fig. 1 Schematic representation of the temperature-time curve during (a) SHS reaction, (b) consolidating load applied to the sample prior to or immediately after the initiation of the SHS reaction and maintained at temperature for a certain time.

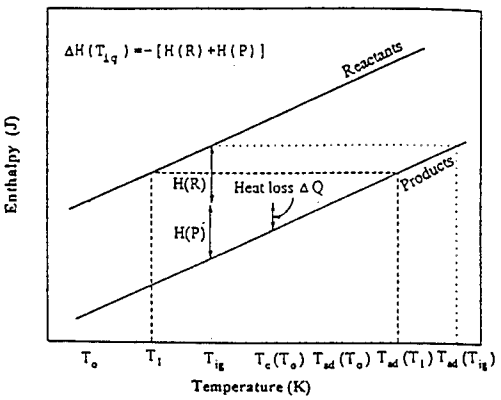


Fig. 2 Schematic representation of the enthalpy-temperature plot for reactants and products in reaction system that involves no phase changes in reactants and products.

Consider an exothermic combustion synthesis reaction, in which a "green" reactant powder mix, at an initial temperature, To, is ignited under adiabatic conditions, in the propagating mode at an ignition temperature, Tig. In order for the reaction to ignite at Tig, the reactants need to be heated from To to Tig. Therefore, the amount of heat, H(R), needed to do this is given by:

$$H(R) = \int_{To}^{Tig} \sum n_i C_P(R_i) dT + \sum_{To-Tig} n_i L(R_i) \qquad (1)$$

where n_i $C_p(R_i)$, $L(R_i)$ are the reaction stoichiometry coefficients, heat capacities and the phase transformation enthalpies (if the reactant(s) undergo a phase change, e.g., melting), of the reactant, R_i, respectively. The value of H(R) is indicated in Figure 2. Since H(R) is needed to heat the reactants from To to Tig, the amount of heat available to be absorbed by the products under adiabatic conditions is, therefore, H(P) such that H(P) raises the temperature of the products from Tig to Tad (To), and

$$\Delta H(Tig) = -[H(R) + H(P)] \qquad (2)$$

and

$$H(P) = \int_{Tig}^{Tad(To)} \sum n_j C_P(P_j) dT + \sum_{Tig-Tad(To)} n_j L(P_j) \qquad (3)$$

where n_j, $C_P(P_j)$, $L(P_j)$ are the reaction stoichiometry coefficients, heat capacities and phase transformation enthalpies [if the product(s) go through a phase change] for the products, P_j, respectively. Therefore, the maximum adiabatic temperature, Tad(To), achievable under these conditions is dependent on the value of H(P) and will be as indicated in Figure 2. Increasing the initial temperature (i.e., pre-heating) from To to T_1 will decrease H(R), increase H(P) and increase Tad(To) to Tad(Ti). This condition is also indicated in Figure 2. Increasing To to Tig will decrease H(R) to zero and all of $\Delta H(Tig)$ will be available to be absorbed by the products, resulting in an adiabatic temperature of Tad(Tig). Under these conditions, the reaction is ignited under the simultaneous combustion mode.

Since the enthalpies of reactants and products are commonly given at 298K, $\Delta H(Tig)$ can be calculated using the following relationship:

$$\Delta H(Tig) = \Delta H(298) + \int_{298}^{Tad} \left\{ \sum n_j C_P(P_j) - \sum n_j C_P(R_i) \right\} + dT \left\{ \sum_{298 \sim Tig} n_j L(P_j) - \sum_{298 - Tig} n_i L(R_i) \right\} \quad (4)$$

where $\Delta H(298)$ is the reaction enthalpy at 298K. Substituting equations (1), (3) and (4) into (2) and rearranging provides a means by which Tad can be calculated:

$$\Delta H(298) + \int_{298}^{Tad} n_j Cp(P_j) dT + \sum_{298 - Tad} n_j L(P_j) = 0 \quad (5)$$

Coupling this SHS (propagating mode) with a consolidation process, as schematically presented in Figure 1(b), provides a rapid and energetically favorable densification technique.

Experimental Procedure

Ceramic targets of TiC-TiB_2, $MoSi_2$-SiC and TiC-Cr_3C_2 were produced in selected ratios of TiC:TiB_2, $MoSi_2$:SiC, and Cr_3C_2:TiC using the SHS technology briefly described above and in more detail in references.[4-6]

Titanium, molybdenum, silicon and chromium powder, ($\leq$40μm in diameter) carbon black ($\leq$10μm in diameter), and amorphous boron ($\leq$1μm in diameter) were used as reactants for the exothermic (SHS) reactions:

$$(x + y)Ti + 2yB + xC = xTiC + yTiB_2 \quad (6)$$

$$xMo + (2x + y)Si + C = xMoSi_2 + ySiC \quad (7)$$

$$xTi + 3yCr + (x + 2yC) = xTiC + yCr_3C_2 \quad (8)$$

The reactant powders were prepared in the required stoichiometries, i.e., x and y in equations (6), (7) and (8), to provide composite targets with the mass ratios of TiC to TiB_2 of 80/20; 60/40; 40/60; $MoSi_2$ to SiC 50/50; and TiC to Cr_3C of 25/75, 50/50, 75/75. Each reactant powder system was mixed in ball mills for seven hours, dried to 120°C for one hour, and subsequently pressed into "green" discs, 64mm in diameter and approximately 6.4mm thick.

Each green disc was placed inside a graphite die under a load of 40MPa, applied by the uniaxial compression system. The SHS reaction was initiated using the simultaneous combustion mode by induction heating of the green discs in the graphie die under a uniaxial load (Figure 3). The SHS reaction was completed in a few seconds, the load on the die was released immediately, and the synthesized TiC-TiB_2, $MoSi_2$-SiC and TiC-Cr_3C_2 targets were removed from the die. The phase composition and structure of these SHS products were characterized using scanning electron microscopy (SEM), Auger electron spectroscopy (AES), energy dispersive spectroscopy (EDS) and x-ray diffraction (XRD) techniques.

The TiC-TiB_2, $MoSi_2$-SiC and TiC-Cr_3C_2 coatings were produced by both r.f. and dc magnetron sputtering of the SHS targets with a constant current in a three electrode system at a power setting of 2.5kW. The sputtering was carried out in vacuum within the pressure range of 3.5 10^{-2} to 2.66 10^{-1} Pa under a high frequency discharge of 13.56 Mhz (RF) and within the range of 6.6 10^{-2} to 2.66 10^{-1} Pa under the direct current discharge. Argon served as the working ion-producing gas. The substrate-target distance was varied within a wide range from 10 to 70 mm. The diameter of the erosion zone of the targets during the magnetron sputtering process was approximately 60 mm.

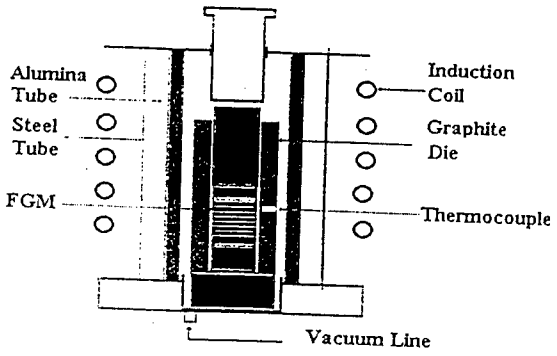


Fig. 3 Induction furnace used to produce homogeneous and layered composites in a one-step SHS consolidation technique.

Results and Discussion

X-ray diffraction (XRD) analysis of the TiC-TiB_2, $MoSi_2$-SiC and TiC-Cr_3C_2 targets using standards confirmed that the target compositions were similar to those calculated and predicted. A distinctive feature of the composite targets was their low porosity (less than 5%), and high chemical purity. Their physico-mechanical properties[7] were as expected of dense materials of these composites. Similarly, XRD analysis of the deposited thin films confirmed that these films were of the same chemical stoichiometry as the target from which they were sputtered.[7-9]

Examination of the structure of the thin films produced from the Si target using transmission electron microscopy (Figure 4) and electron diffraction analysis exhibited either an ultra fine (<4nm) (TiC-TiB_2 and TiC-Cr_3C_2) or an amorphous ($MoSi_2$-SiC) structure

Annealing of the $MoSi_2$-SiC composite film at 1000°C for 30 minutes, in a vacuum furnace, resulted in crystallization of the films (Figure 5). XRD analysis showed the presence of strong peaks of tetragonal $MoSi_2$ (which is the stable form of $MoSi_2$ above 800°C) and two polytypes of SiC – cubic and hexagonal.

The $MoSi_2$-SiC component target was also RF sputtered in a 10% N_2-Ar environment (total chamber pressure of 2.7×10^{-1}Pa). The resultant $MoSi_xC_yN_z$ nitrided layer was amorphous up to at least 1260°C as determined using differential thermal analysis.[8] This nitrated film has been found to be a successful barrier layer in preventing Si and C diffusion from a $MoSi_2$-SiC coating into the Mo substrate up to 1000°C (Figure 6).

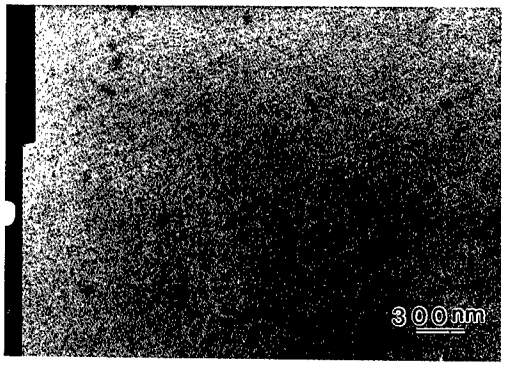


Fig 4. Transmission electron photomicrograph of the quasi amorphous TiC-TiB_2 thin film produced by sputtering target of composition 1, i.e. 80%TiC-20%TiB_2, and subsequent annealing at 40°C for 40 sec. The dark phase is TiC.

Conclusions

This work has established the conditions under which TiC-TiB_2, $MoSi_2$-SiC and TiC-Cr_3C_2 components targets can be produced by SHS - consolidation techniques and used to produce thin films with the same required stoichiometry as that of the target.

(a)

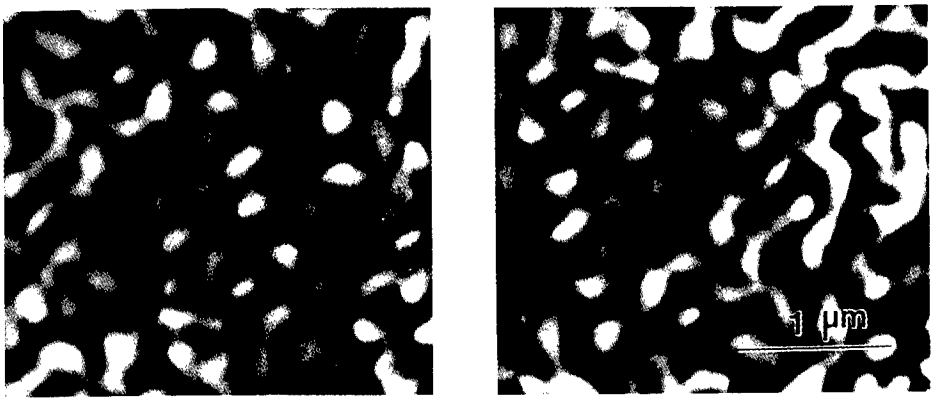


Fig. 5. (a) SEM photomicrograph of the surface of the two-layer $MoSi_2$-SiC film, after annealing at 1000°C for 30 minutes; (b) The corresponding back-scattered image showing bright areas corresponding to $MoSi_2$ and dark areas corresponding to SiC.

(a)

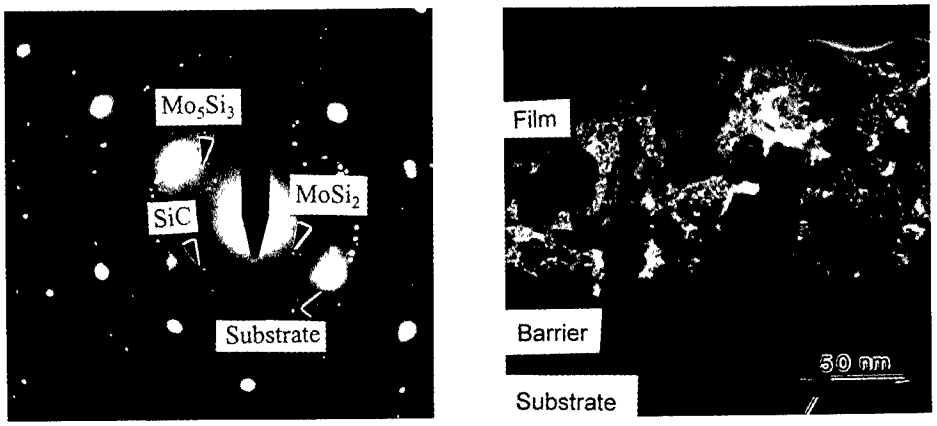


Fig. 6. (a) STEM photomicrograph of the film-substrate cross-section, after annealing at 1000°C for 30 minutes. The presence of a uniform layer of grains at the nitrided layer-composite film interface (identified as $MoSi_2$) suggests that this may be a preferential site for heterogeneous nucleation, during annealing. The nitrided layer was amorphous (evidenced by the ring diffraction pattern), while the composite film consisted of crystallites of t-$MoSi_2$, β-SiC, and t-Mo_5Si_3 as shown in the SADP and (b) from the interfacial region.

A novel $MoSi_xC_yN_z$ diffusion barrier was synthesized by reactive sputtering of the composite target in an argon + nitrogen ambient. The intended barrier layer, was amorphous after an annealing treatment at 1000°C, for thirty minutes, in vacuum. The diffusion barrier was found to be stable up to 1260°C, in an oxidizing ambient and was effective in minimizing the diffusion of silicon and carbon into the substrate.

Acknowledgments

The present work was supported jointly by NATO within the framework of Research Grant MTECH, CRG 930270, The Center of SHS, Moscow Steel and Alloys Institute, Schott Glaswerke, Germany and the Advanced Coatings and Surface Engineering Laboratory, Colorado School of Mines.

References

1. V.G. Grebenkina, *Poroshkovaya Metallurgia*, 6 (1973), p. 83-87.
2. K.A. Osipov, *Proceedings of the USSR As. Neorganicheskie Materially*, 17, 11, (1981), pp. 2032-2034.
3. Yu.P. Sipikin, *Electronic Industry*, 1988, 3, (1988), pp. 54-63.
4. A.G. Merzhanov. *Self-Propagating High Temperature Synthesis, Twenty Years of Search and Findings.* Preprint of the ISMAN, Chernogolovka, 1988, p. 93.
5. J.J. Moore, H.J. Feng. *Progress in Materials Science*, 39, 4/5, (1995), pp. 243-316.
6. Z.A. Munir, U Anselin-Tamburini, *Materials Science Reports*, 3, (1989), pp. 277-365.
7. E. Levashov, V.I. Kosazanin, L.M. Kmokova, J.J. Moore, D.L. Olson, *Surface and Coating Technology*, 92, (1997), pp. 34-41.
8. S. Govindarajan, J.J. Moore, T. Ohno, J. Disam MRS Symp. Proc., 458, (1997), pp. 489-495.
9. A.O. Kunrath, J.J. Moore, I. Reimanis, K. Upadhya, "Synthesis and Applications of Composite TiC-Cr_3C_2 Targets," Accepted for publication in *Surface and Coating Technology.*

DEVELOPMENT OF MMC USING LIQUID METALLURGY TECHNIQUE: CONTROL OF POROSITY AND PARTICULATES DISTRIBUTION

M. Iqbal Qureshi and Mohammad Mujahid

Faculty of Metallurgy and Materials Engineering,
GIK Institute of Engineering Sciences & Technology, Topi, NWFP 23460, Pakistan

ABSTRACT

Certain parameters were optimized for the production of metal matrix composites (Al/SiCp) while using cost effective liquid metallurgy technique. It was found that the maintenance of an inert environment and proper agitation are essential parameters for better retention and distribution of particulates within the matrix. It would be shown that shrinkage porosity associated with solidification is not entirely dependent upon the particulate size and elimination of mechanical stirring could result in reducing the porosity normally associated with large size particulates. The hardness of composites appear to increase significantly with particulate retention.

The Third Pacific Rim International Conference on
Advanced Materials and Processing (PRICM 3)
Edited by M.A. Imam, R. DeNale, S. Hanada,
Z. Zhong and D.N. Lee
The Minerals, Metals & Materials Society, 1998

INTRODUCTION

The development of metal matrix composites (MMCs) has come a long way since their inception in the early 1960s. A variety of processing techniques are in vogue to produce MMCs for consumer goods, automotive parts and electromechanical machinery (1-2). In general, MMCs can be classified into two major groups: those reinforced with discontinuous whiskers and particulates, and those reinforced with continuous fibers such as carbon, alumina, silicon carbide, and boron. The former type of composites have a decisive advantage in cost and versatility: though they tend to offer modest increases in properties but are more isotropic and can be processed with traditional techniques [3-4]. The property profiles of such composites fall somewhere between the dispersion strengthened and fiber strengthened extremes. They have been rapidly developed in the last two decades, with attention focused on Al-matrix composites reinforced with SiC and Al_2O_3 particulates. High specific strength, good wear resistance, high workability and enhanced performance over traditional Al-alloys have made particulates reinforced aluminum-matrix composites (AMC) particularly attractive for the automobile and aircraft industries [3, 5-8].

The high cost of equipment, fiber reinforcement and consequently of composites produced by solid state and other special techniques such as spray deposition have lead to the development of relatively inexpensive processes like the liquid metallurgy technique. By employing conventional processing, the technique enables to benefit from the improved properties while maintaining low cost [5, 8-11]. While using this technique, it was demonstrated earlier that certain parameters have to be controlled for the production of AMC's [12]. Manual addition of silicon carbide particulates and mechanical stirring of the melt showed limited particulates retention. In addition, formation a thick layer of slag melt surface inhibited particulate addition and also resulted in reduction of fluidity. The lack of particulates adherence could be attributed to poor wettability of SiC with Al-matrix as well [13]. Other studies have shown that SiC particulates are pushed into the interdendritic regions and the distribution of SiC is a function of solidification rate [14-15].

The paper presents results of a series of experiments aimed at optimization of parameters related to retention and distribution of particulates, and control of shrinkage porosity during the production of Al-based SiC_p-reinforced composites.

EXPERIMENTAL METHODS

For matrix, an Al-alloy of nominal composition Al-6.2Zn-2.8Si-0.5Fe-0.8Cr (wt. %) was used, whereas the reinforcement was affected by using silicon carbide particulates of irregular geometry having an average size of 100 μm. For the production of composites, an experimental setup, as shown in Figure 1, was utilized. A top-loading Carbolite furnace capable of achieving a maximum temperature of 1200 °C was used for melting. Particulates addition was carried out with the help of a specially designed lance whose one end was connected to nitrogen gas supply in order to maintain an inert atmosphere during the production of heats of various types, as shown in Table 1. For some heats, mechanical stirring was employed with the assistance of a rotating propeller. The composites thus produced using above heats, were characterized for microstructure and mechanical properties using optical and scanning electron microscopy (SEM) and hardness testing.

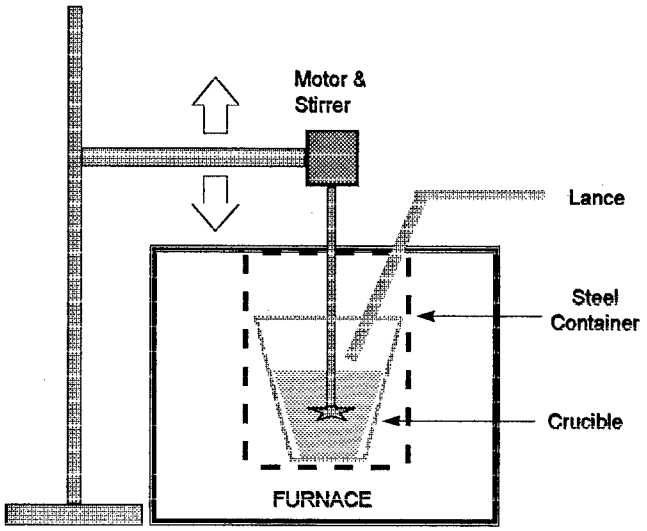


Figure 1. Composite production facility

Table 1. Process variations for different heats

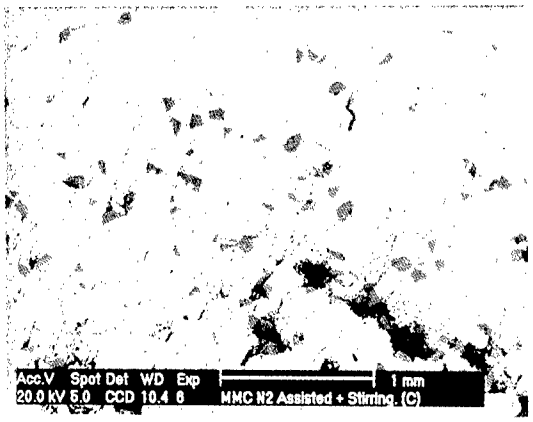
Heat	% SiC (by wt. of matrix)	Environment	Mechanical Stirring	Method for SiCp addition
H1	10 %	N2 gas	Yes	Gas aided & directed into vortex
H2	10 %	N2 gas	No	Gas bubbling
H3	10 %	N2 gas	Yes	Gas bubbling

RESULTS AND DISCUSSION

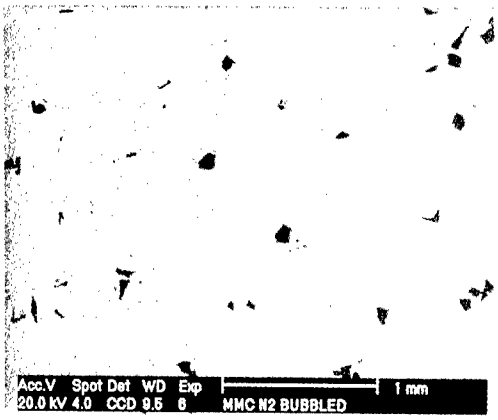
Figure 2(a) shows a micrograph of composite produced using conditions prescribed for heat, H1. Such conditions resulted in the retention of good fraction of particulates, negligible slag formation, along with adequate fluidity throughout the process. Particulates clustering, mostly associated with porosity (analogous to conventional shrinkage porosity), can also be seen in some regions of the solidified structure.

For the production of heat H2, the lance carrying particulates and nitrogen gas was made to dip inside the melt. Since sufficient agitation was available through gas bubbling, the mechanical stirring was not applied for this heat. Figure 2(b) illustrates that fairly uniform distribution and good adherence of particulates can be achieved using this procedure. The porosity was almost eliminated for this composite, as evident from comparison of figures 2 (a) & 2(b) whereas the particulates retention was somewhat reduced. The relatively low particulate retention indicates that vortex formation is important for retaining a greater percentage of particulates.

(a)



(b)



(c)

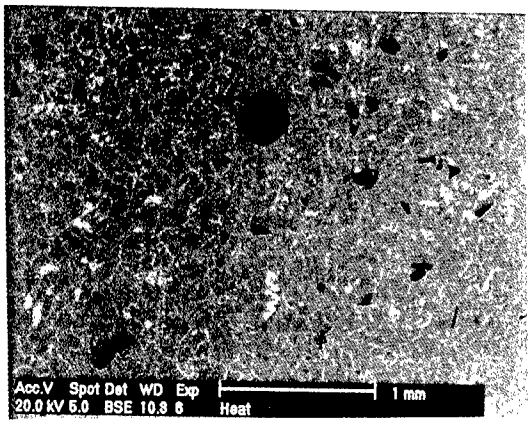


Figure 2. (a) Heat H1, porosity along with clustering of SiC particulates; (b) Heat H2, better distribution of particulates with no porosity; (c) Heat H3, porosity along larger size particulates.

The procedures used for earlier two heats were combined to produce a new heat, designated as H3, with the aim to eliminate porosity and to achieve maximum retention and uniform distribution of particulates. From figure 2(c), it may be seen that the amount of particulates retained increased slightly for this heat but a fine distribution of small pores were also observed in the vicinity of SiC particulates.

Earlier studies [16-17] have demonstrated that the cast composites, reinforced with finer (5-20 μm) and preheated particulates, produced using mechanical stirring do not exhibit any porosity. The absence of porosity was attributed to a higher detachment stress threshold at the particulates-matrix interface:

$$s = (4 (G E / 3 r)^{½} \qquad (1)$$

where 's' is the detachment stress, 'G' is the interfacial fracture energy (an intrinsic property of a given Al-alloy/SiC combination), 'E' is the elastic modulus of the matrix and 'r' is the particulates radius. Evidently, 's' is higher for smaller particulates, which may secure the particulates from possible detachment during solidification shrinkage. Although this contention seems to be true since the porosity is mainly present in the vicinity of larger particulates, or their aggregates as shown in the micrographs Fig 2(a) and Fig 2(c). However, it is evident by comparing these micrographs with figure 2(b) that the heat produced without mechanical stirring shows no porosity even for large particulate size (>20 μm) reinforcements. It implies, in reference to equation (1), that the detachment stress is not the only criterion for the control of porosity associated with shrinkage.

Preliminary evaluation of mechanical characteristics of the composites produced is indicated in figure 3 wherein the average hardness values for each heat are plotted. A significant increase in hardness was observed for all the composites in comparison to the Al-alloy used as matrix. Further the hardness achieved for composite produced via heat H3 was greater than that of heat H1 or H2. Since the hardness data was obtained in the areas devoid of any shrinkage, the observed increase in hardness may be attributed to progressive increase in particulate retention.

SUMMARY

Production of AMCs through liquid metallurgy technique can be optimized, in addition to other means, by the control of parameters such as mechanical stirring, agitation through gas bubbling and maintenance of an inert environment. It was found that the agitation through gas bubbling with out mechanical stirring results in achieving more uniform distribution of particulates as well as elimination of shrinkage porosity. Further, the particulate size appears to have no bearing on the extent of porosity.

If the hardness values are to be taken as indicator of mechanical characteristics of the composites produced during the present work then it may be speculated that the other properties are expected to improve with the uniform distribution of particulates and higher degree of their retention.

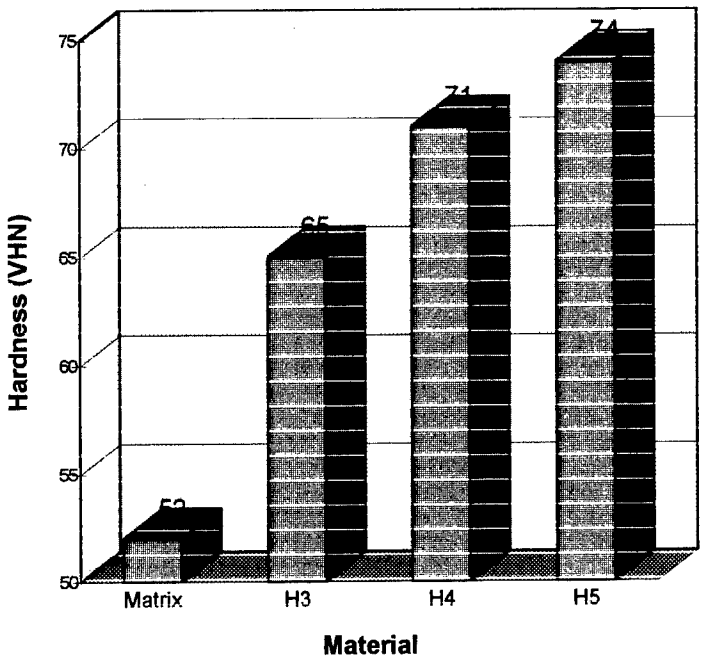


Figure 3. Variation of composite hardness with processing.

REFERENCES

1. Z. Y. Ma, Y. N. Liang, Y. Z. Zhang, Y. X. Lu and J. Bi: Mat. Sci. Tech., vol. 12, 1996, 751.
2. N. Axen and I. M. Hutchings: Mat. Sci. Tech., vol. 12, 1996, 757.
3. C. G. E. Mangin, J. A. Isaacs and J. P. Clark: JOM, Feb. 1996, 49.
4. T. G. A. Doel and P. Bowen: Mat. Sci. Tech., vol. 12, 1996, 586.
5. F. A. Girot, J. M. Quenisset and R. Naslain: Comp. Sci. Tech., 30, 1987, 155.
6. J. Q. Jiang, R. S. Tan and A. B. Ma: Mat. Sci. Tech., vol. 12, 1996, 483.
7. P. Rohatgi: JOM, Apr. 1991, 10.
8. T. W. Clyne and P. J. Withers: An Introduction to Metal Matrix Composites, CUP, 1995, 334.
9. T. F. Klimowicz: JOM, Nov. 1994, 49
10. F.L. Matthews and R.D.Rawlings Composite Materials: Engineering and Science, Chapman & Hall, London, Ist Edition.1994. P78-80
11. T.W.Clyne & P.J.Withers, An introduction to Metal Matrix Composites, Cambridge University Press, UK., 1995, P318-360
12. M. S. Salim, Senior Design Project Report, 1997, GIK Institute, Topi.
13. S. Schamm, Y. Le Petitcorps and R. Naslain: Comp. Sci. Tech., vol. 40, 1991, 193.
14. D. J. Lloyd: Comp. Sci. Tech., 35, 1989, 159.
15. G. Xie, S. Li, W. Wang and R. Wu: Proceedings 2nd Pacific Rim International Conference on Advanced Materials and Processing, Ed. K. S. Shin, J. K. Yoon and S. J. Kim, The Korean Inst. Met. Mater., 1995, 2559.
16. P. S. Robi et al, in Advances in Materials and Processes, P. Ramakrishnan, Ed., New Delhi (1993), p 291.
17. H. Sekine and R. Chen, Composites, 26 (1995), p 184.

INTELLIGENT METHODS FOR THE OPTIMIZATION OF COMPOSITE MATERIALS

Madjid Fathi* **Lars Hildebrand****

*University of Dortmund, Department of Computer Science, Chair 1, Otto-Hahn-Str. 16, 44227 Dortmund 50, Germany, e-Mail: fathi@ls1.informatik.uni-dortmund.de

**University of Dortmund, Department of Computer Science, Chair 1, Otto-Hahn-Str. 16, 44227 Dortmund 50, Germany, e-Mail: hildebra@ls1.informatik.uni-dortmund.de

SUMMARY: Fuzzy expert systems are common to many scopes of duties related to diagnose, analyse of errors and configuration. The chance to process imprecise or vague information has lead to systems which come up to the user's expectation. These systems are well accepted today. But some scopes of duties are still evading from being accessed by fuzzy expert systems. Typical for these fields is that most of the knowledge is not imprecise or vague, but exact and well structured. The construction of composite materials is used as an example to show how this kind of knowledge can be represented in a fuzzy expert system using function approximation.

Introduction

Fuzzy expert systems are able to process imprecise, vague or subjective rated information and knowledge. In medical applications they are capable of handling different extends of diseases based on a subjective diagnosis [1]. In technical applications they are well suited to take appropriate actions according to different extends of errors, different states of plants, etc.[2,3].
In this paper we introduce the application of fuzzy expert systems for the design of thermally sprayed screw compressors. According to their excellent wear behavior thermally sprayed chromia coatings provide applicability in complex machine parts, e.g. rotors in screw compressors which are used for the compression of air or other gases. Two different types of screw compressors are already on the market. One type running dry, the other is lubricated with oil thus causing environmental problems.

Due to rolling friction between the two rotors the desired properties of coated unlubricated screw compressors depend on both good coating adhesion and adequate wear behavior of the coatings. Because of the absence of any lubricant there are no problems with impurity of the compressed gas. The results concerning the investigation of adhesion and wear mechanisms of the coating system Cr_2O_3 are discussed and modeled.

The Third Pacific Rim International Conference on
Advanced Materials and Processing (PRICM 3)
Edited by M.A. Imam, R. DeNale, S. Hanada,
Z. Zhong and D.N. Lee
The Minerals, Metals & Materials Society, 1998

In this context an expert system is developed to support the work of constructing and manufacturing metallic and ceramic composites. The knowledge of the "SFB 316[1]" is used as basis. A closer view is taken on models which represent this knowledge and which give the chance to simulate technological an mechanical characteristics of this kind of materials. The model is verificated using correlation of the theoretical and experimental results. This correlation also leads to new directions for optimizing extensive experiments.

Therefore the results of these investigations should give useful ideas to create detailed models. Modern information technologies are employed to develop and optimize the models used for an expert system in a way that both functional dependencies and fuzzy knowledge can be transformed to linguistic variables. As part of the tools evolutionary algorithms are implemented to transform the different forms of knowledge and to create the fuzzy-rule base of the system. This proceeding with its segregation of knowledge acquisition and knowledge transformation enables an effective translation of human knowledge into the fuzzy-rule base of the machine and leads to a simple operation and consultation. In addition, tools have been installed to consider even interrelations which are known only as a tendency. So it is possible to built bridges between different pieces of knowledge and gaps in the model can be closed. By this approach, the design and development of composite materials can be handled as an optimization problem. The creation of fuzzy-rules and fuzzy-sets using evolutionary algorithms and evolution strategies allows that all kind of human knowledge can be depicted by an expert system.

The experimental procedure contents investigations concerning adhesion mechanisms between thermally sprayed chromia and a steel substrate. Conventional methods to improve the bonding strength - as grid blasting of the substrates combined with special bond coatings - in addition to the application of a pre-oxidation of the substrate were analyzed. Besides these investigations with standardized bond strength tests an evaluation of adhesion mechanisms using scanning electron microscopy (SEM) and transmission electron microscopy (TEM) are discussed. Both SEM and TEM concerning reactions at the interface between coating and substrate.

Further on a custom-made test facility was designed and built to simulate the rolling mechanisms between the two screw rotors adequately. Detailed calculations were carried out on the contact temperatures and stresses providing different hypotheses to wear behavior. The results of these investigations also flow into the model system.

Methodology

In many cases knowledge acquisition is more like a translation of knowledge into rules and membership functions than a process of gaining new knowledge. For this reason it differs from the classical knowledge acquisition. At first glance is seems to be an easy task to do this translation manually. But past experience has shown that experts as well as specialists of fuzzy logic are not able to determine the rules and membership functions in the required accuracy. Figure 1 shows an example relation between one input and one output variable, which is described in the terms of a fuzzy rulebase.

Modern optimization methods from the field of computational intelligence seem to be a suitable basis for the task of function approximation [4,5,6]. Its main part is an optimization loop, which assesses the current fuzzy system and tries to improve it using an evolutionstrategy until the difference between the input data and the output data of the fuzzy system is less enough.

Input is the exact knowledge in form of tables and diagrams. An initial fuzzy system is generated and evaluated over the entire range of definition. The next step adds up the differences between the input data and the output

1. SFB316: Special research area "Manufacture, treating, use and testing of metallic and metal-ceramic composites" of "Deutsche Forschungsgemeinschaft DFG"

data of this fuzzy system to calculate a single value, which describes the accuracy of the current system. The evolutionstrategy will modify this system in the next step to find an improved, which means a more accurate, one. This optimization loop will continue until a sufficient overall accuracy is obtained.

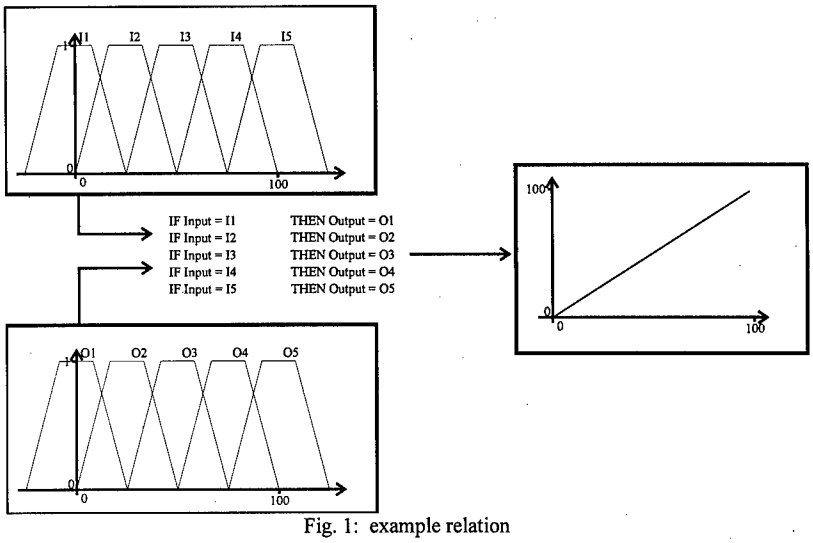


Fig. 1: example relation

Due to the fact, that evolutionstrategies are of the class of real-valued optimization methods, a fuzzy system has to be expressed in real numbers. Proceeding on the assumption that all used fuzzy sets are of trapezoid shape and normalized to a membership value between $[0, 1]$, each fuzzy set can be characterized by four real numbers. Each number stands for one of the corner-points of a single set.

Figure 2 shows the course of an evolutionstrategy. A single individual $\vec{I}_i$ of the evolutionstrategy can be defined according to the above stated convention. The entire set of all μ individuals, the generation t, is labelled as $P(t)$. λ new individuals will be created using the recombination (line 6) and mutation (line 7) operation. The best μ of them will be selected (line 10) to survive, and set up the new generation $t+1$. This loop will continue until the termination criterion is true.

```
1    t:=0;
2    initialize P(t):= {Ĩ1(t), ..,Ĩμ(t)} ;
3                    // with Ĩi ∈ o ℝ^n × ℝ^s × [−π,π]^α for all i = (1, ..., μ) //
4    evaluate Ψ(P(t)) = (Ψ(x1(t)), ..., Ψ(xμ(t)));
5    while termination_criterion T(P(t)) not true
6        ∀(k ∈ {1, ..,λ} ):Ĩ'k(t):= rec(P(t));          //recombination//
7        ∀(k ∈ {1, ..,λ} ):Ĩ"k(t):= mut(Ĩ'k(t));        //mutation//
8        P"(t):= {Ĩ"1(t), ..,Ĩ"λ(t)} ;
9        evaluate Ψ(P"(t)) = (Ψ(x"1(t)), ..., Ψ(x"λ(t)));
10       P(t+1):= sel^λ_μ (P"(t));                     //selection//
11       t:= t+1;
12   end_while
```

Fig. 2: Outline of an evolutionstrategy

Many different realizations of recombination, mutation and selection have been developed. For more details on

this see [5].

An initial fuzzy system is generated and evaluated over the entire range of definition. The next step adds up the differences between the input data and the output data of this fuzzy system to calculate a single value, which describes the accuracy of the current system. The evolutionstrategy will modify this system in the next step to find an improved, which means a more accurate, one. This optimization loop will continue until a sufficient overall accuracy is obtained. After this, the knowledge is ready for beeing processed by a traditional expert system. The next figure shows an overview of this system:

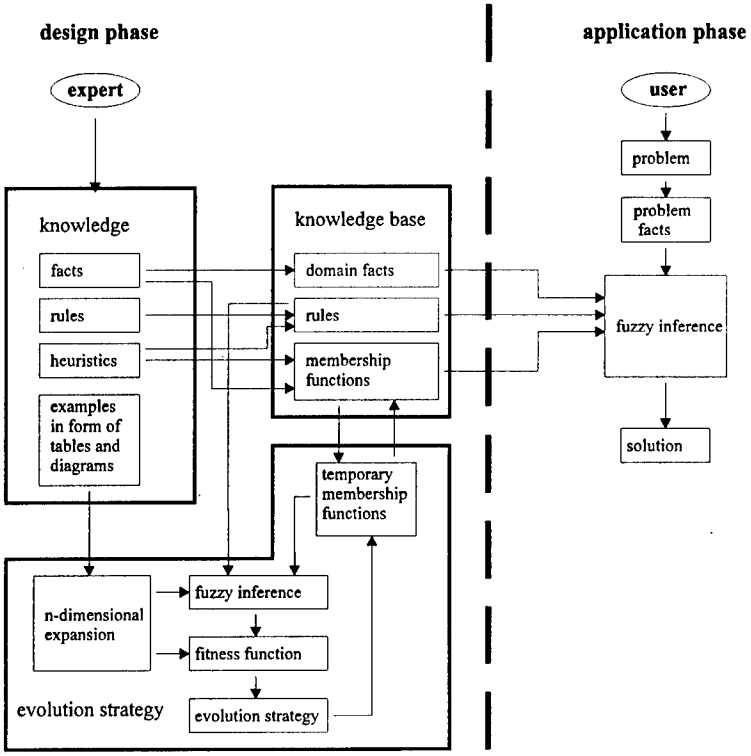


Fig. 3: Structure of the system

An example

We will describe the working of the our system with the help of an example from the field of composite material design. Our example is part of the special investigation area "Sonderforschungsbereich 316" which is financed by the german research society „Deutsche Forschungsgemeinschaft". This special investigation area is subdivided into 22 subprojects. Some projects investigate in the basics of composite material design and other develop new methods and new materials. A more detailed description of this example can be found in [8].

The raw knowledge

The most common representation of knowledge in our field of material design is a table or diagram of all results from series of tests. Due to this kind of representation we have to choose the processing of example knowledge. Figure 4 shows the diagram, which has to be translated into production rules. It shows the friction coefficients in

line contact at different contact pressures.

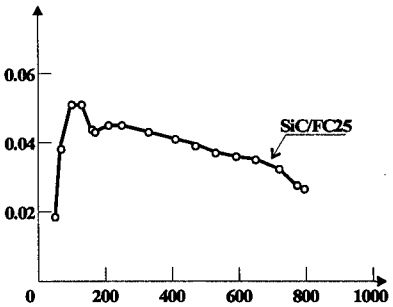


Fig. 4: Friction coefficients in line contact

The next paragraph describes, how this relation can be modelled automatically using an evolution strategy.

The translation of the knowledge

The system provides a comfortable user interface for the translation of raw knowledge into production rules. Figure 5 shows this interface. This interface consists of three main parts. The upper left table holds the examples of the function which has to be modelled. The canvas on the upper right side shows the shape of this function and is used for feedback. The lower part shows the input and output fuzzy sets and the rulebase at the current point of optimization.

As the first step of translation the system has to decide which complexity the set of production rules should have. The next step is the initialization of the fuzzy sets. Two linguistic variables are used, both with five linguistic terms. The initial shape of the variables will consist of symmetrically distributed trapezoids. This is shown in figure 6.

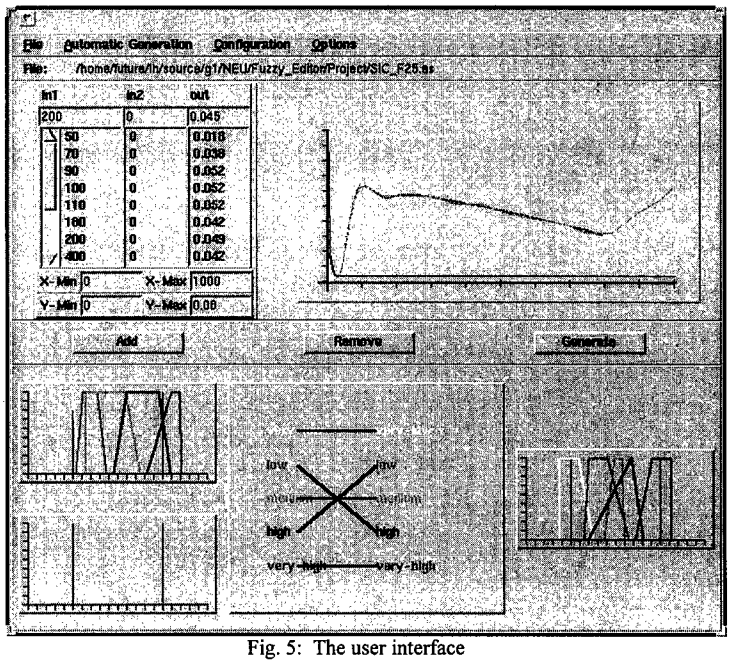


Fig. 5: The user interface

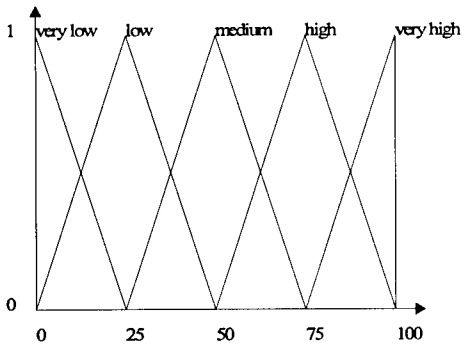


Fig. 6: The initial membership functions from Exot

After initialization the evolution strategy starts with its optimization task. The number of generations, offspring and population size can be chosen independently as well as the type of self adaptation. The system offers none, one standard deviation σ for each generation and μ different standard deviations σ_i for each individual in one generation. The next informations are related to a (15,100) evolution strategy with 1000 generations and one standard deviation for each generation.
Figures 7 shows the development of the error rate during the first 100 generations.

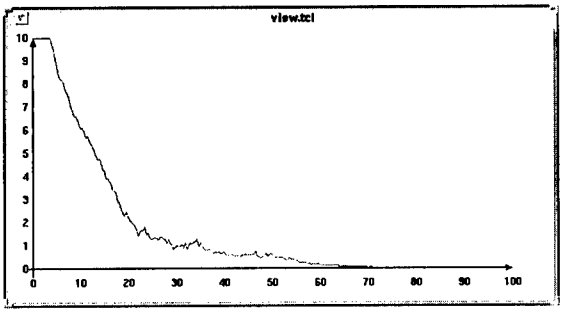


Fig. 7: The development of the error rate

After 30 generations the error rate has become smaller, the optimization task has found a minimum and the standard deviation becomes smaller to let the evolution strategy search near this minimum. After 70 generations the error rate is smaller than the resolution of the viewing tool. The error rate at the end of the optimization task is 0.00053 which yields an improvement compared to the initial error rate of 450.000 : 1 .
To show the overall results of the evolution strategy we give in the figure 8 the shape of one optimized linguistic variable and the final set of production rules.

IF IN IS very-low THEN OUT IS very-low WITH PRIORITY 100

IF IN IS low THEN OUT IS high WITH PRIORITY 100

IF IN IS medium THEN OUT IS medium WITH PRIORITY 100

IF IN IS high THEN OUT IS low WITH PRIORITY 100

IF IN IS very-high THEN OUT IS very-high WITH PRIORITY 100

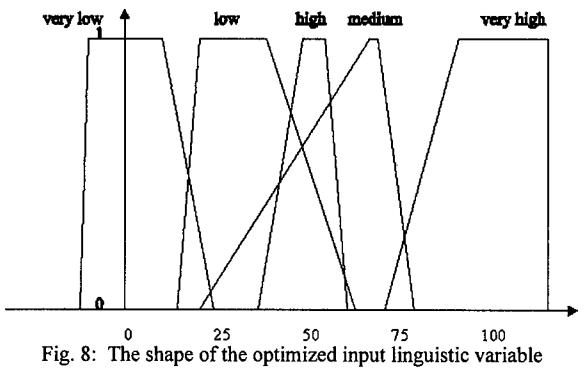


Fig. 8: The shape of the optimized input linguistic variable

The shell allows the user to chose all parameters of the evolution strategy independently. It is possible to start with a (15,100)-ES and 500 generations to yield a quick overview of the optimization results. For an accurate result the user should chose a (30,200)-ES with 2000 generations. The relation of our example has been optimized using a (15,100)-ES with 1000 generations. The whole process lasted 350 seconds on a SUN-Sparc 10 station. This time will increase linear with the number of dimensions and is nearly independent from the number of examples.

Conclusion

The process of gaining knowledge can be reduced to the entering of input data and starting an automated process. Function approximation using fuzzy logic and evolutionstrategies is able to acquire exact knowledge without the help of experts. This feature makes it possible to acquire the huge amount of knowledge which already exists in form of tables and diagrams. This kind of representation is commonly used in the field of designing screw rorors. Combined with classical acquisition methods for vague and imprecise knowledge the introduced methodology provides a good basis for the implementation of knowledge from other technical oriented fields.

References

[1] B. Reusch, "Fuzzy Logik - Theorie und Praxis", proceedings of "4. Dortmunder Fuzzy-Tage", Springer Verlag, Berlin, 1994.

[2] M. Fathi, "A fuzzy expert system for real-time monitoring in manufacturing", proceedings of "12th World congress international federation of automatic control", 1993.

[3] L. Hildebrand, et al., "Ein regelbasiertes System zur Unterstützung des Entwurfs von Verbundwerkstoffen", working report of "Sonderforschungsbereichs 316", Dortmund, 1995.

[4] I. Rechenberg, "Evolutionsstrategie: Optimierung technischer Systeme nach Prinzipien der biologischen Evolution", Frommann-Holzboog, Stuttgart, 1973.

[5] H.-P. Schwefel, "Evolution and optimum seeking", John Wiley & Sons Inc., New York, 1994.

[6] Rudolph, G., "An evolutionary algorithm for integer programming", Proceedings of "3rd International conference on evolutionary computing", Springer Verlag, Berlin, 1994.

[7] M. Fathi, L. Hildebrand, "Evolution strategies for the optimization of fuzzy rules", proceedings of "IPMU", Paris, 1994.

[8] M. Fathi, L. Hildebrand, "Model-free Optimization of Fuzzy Rulebased Systems Using Evolution Strategies", IEEE Transactions on Systems, Man, and Cybernetics - Part B, Vol. 27, No. 2, 1997.

THERMAL FATIGUE IN FIBER REINFORCED METAL MATRIX COMPOSITES

K.K. Chawla

Department of Materials and Mechanical Engineering
University of Alabama at Birmingham
1150 Tenth Ave. South, BEC 360
Birmingham, Al 35294
U.S.A.

Abstract

Thermal stresses arise in composite materials because of the difference in the thermal expansion coefficient (α) of the reinforcement and that of the matrix. In metal matrix composites (MMCs), the matrix generally has a higher α than the reinforcement (fiber or particle). The magnitude of thermal stresses in a metal matrix can easily exceed its yield stress when the composite is heated or cooled. In this paper we shall present results of thermal fatigue studies in some fiber reinforced metal matrix composites, including microstructural changes resulting from thermal cycling and techniques for evaluating thermal fatigue damage. In particular, we have shown that changes in stiffness and density can be used as damage parameters to study damage evolution as a function of thermal cycles in an alumina fiber/magnesium alloy composite.

Introduction

Metal matrix composites (MMCs) exploit the comparatively high stiffness of a ceramic component to reinforce a ductile metal matrix. In MMCs, there is generally a large mismatch between the coefficient of thermal expansion of the ceramic reinforcement and the metallic matrix. Thus, any temperature change will lead to thermal stresses, which can affect microstructural stability and alter mechanical properties. The magnitude of thermal stresses in composites is proportional to the thermal strain, $\Delta\alpha\ \Delta T$, where $\Delta\alpha$ is the difference in the expansion coefficients of the two components and ΔT is the amplitude of the thermal cycle. It should be emphasized that thermal stresses in composites will arise even if the temperature change is uniform throughout the volume of the composite. Such thermal stresses can be introduced in composites during cooling from high fabrication or annealing or curing temperatures or during any temperature excursions (inadvertent or by design) during service. Turbine blades, for example, are very much susceptible to thermal fatigue. Thermal cycling studies of MMCs have been carried out in several systems [1-12]. Thermal cycling induced damage in MMCs can take the form of plastic deformation of the matrix, damage at fiber/matrix interface, such as microvoid formation or cracking at the interface, interfacial sliding (in fiber reinforced composites), or in some cases even fiber fracture [see for example, refs.1, 2, 4, and 12].

The effects of thermal treatments on the interface microstructure and mechanical properties of Al_2O_3 fiber reinforced aluminum alloy matrix composites have been studied by various authors

The Third Pacific Rim International Conference on
Advanced Materials and Processing (PRICM 3)
Edited by M.A. Imam, R. DeNale, S. Hanada,
Z. Zhong and D.N. Lee
The Minerals, Metals & Materials Society, 1998

[13-16]. Kim et al. [13] observed a trend toward decreasing transverse tensile strength in thermally cycled specimens and attributed it to interfacial failure initiated by void formation; these voids resulted from the thermal expansion mismatch between the fiber and the matrix. Greater reductions in the transverse tensile strength occurred for thermally cycled specimens with equal total time at the maximum temperature (T_{max}) than for isothermally treated samples. Hunt [14] found the same decreasing trend with thermal cycling and attributed this drop to a reduction in interfacial shear strength caused by the thermal expansion mismatch. X-ray diffraction studies showed interfacial reaction products to be $Li_2O{\cdot}5Al_2O_3$. Hall and Barrailler [15] described similar effects in their study involving isothermally heat treated samples. Isothermal treatment can be considered to be equivalent to one cycle. Chawla [16] studied alumina fiber/Al-Li composites treated isothermally and by thermal cycling. A degradation in strength resulted from both treatments, but with a greater effect from thermal cycling. Thermal cycling also caused a preferential loss of lithium for the fiber/matrix interface regions near the surface.

An important mechanical parameter for characterizing damage in composites is elastic modulus. It would appear that this parameter is particularly important when the damage is severe, e.g., when it involves cavitation. The damage in terms of elastic modulus of composites under mechanical fatigue has been the subject of various studies. For example, it has been shown that under mechanical fatigue, a decrease in elastic modulus occurs in polymer matrix composites (PMCs) [17], in MMCs [18], and in ceramic matrix composites (CMCs) [19]. However, there have been few reported investigations on the damage in elastic modulus of composites caused by thermal cycling alone.

Plastic deformation of the metallic matrix

Thermal stresses will be generated because of a temperature change in any kind of composite because of the mismatch in expansion coefficient between the components. The special aspect of a metal matrix composite is that the metal matrix in general is soft enough to undergo plastic deformation under the action of the thermal stresses generated in the matrix. Figure 1 shows an example of plastic deformation in the polycrystalline copper matrix when a tungsten fiber/copper matrix was cycled between room temperature and 400 °C in the chamber of a scanning electron microscope. The plastic deformation is manifested by the slip lines in the copper matrix. Such plastic deformation of the matrix will tend to work harden the matrix. An example of matrix work hardening due to thermal cycling is shown in Fig. 2 where we plot the variation of matrix hardness as a function of distance from the interface outward in an alumina fiber/Al-Li matrix composite. The matrix hardness increases with number of thermal cycles, more so near the interface than far away from the interface. If the fiber volume fraction is high then the gradient in hardness will quickly attenuate with cycling. Continued thermal cycling will lead to further damage in the composite involving fiber/matrix debonding, cavitation at the interface and growth of cavities. Such damage will result in a reduction of strength of the composite, but, more importantly, it leads to a loss of stiffness. We can usefully characterize such damage by parameters defined in the next section.

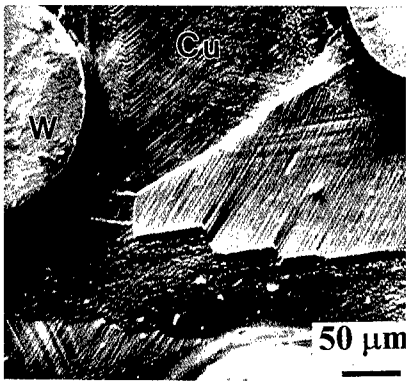


Fig. 1: Plastically deformed copper matrix in a tungsten fiber/copper matrix composite after 25 cycles between room temperature and 400 °C. The cycling was done inside the chamber of SEM. Note the slip lines produced on an initially polished copper matrix.

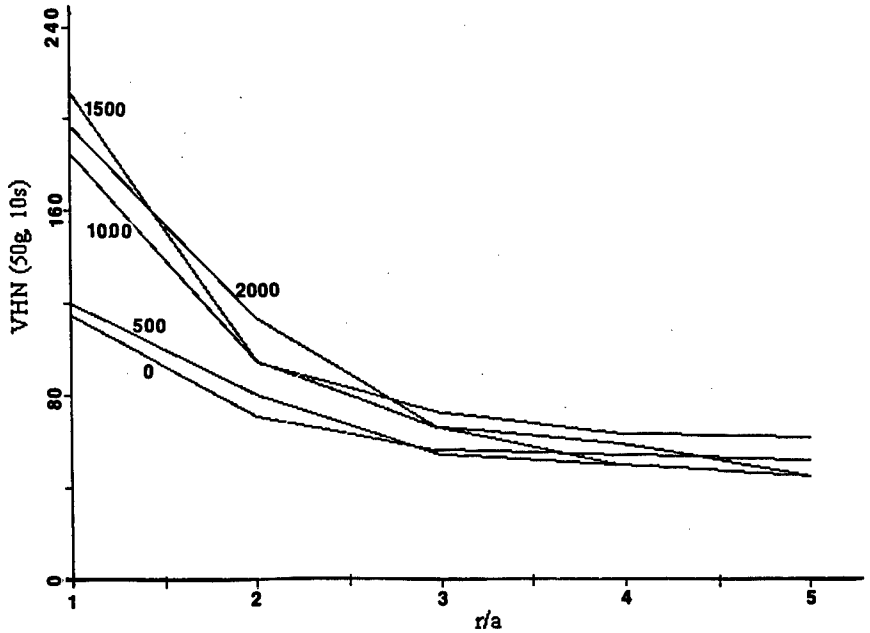


Fig. 2: Matrix hardness as a function of distance from the interface in an alumina fiber/Al-Li matrix composite after various cycles (room temperature and 300 °C). The interface is at r/a = 1, where r is the distance and a is the fiber radius.

Damage parameters

In order to evaluate the damage caused by thermal cycling, in terms of the elastic modulus, we can be express the damage in elastic modulus, D_E, as [20]

$$D_E = 1 - (E_n / E_o) \quad (1)$$

where E_n is the elastic modulus after n cycles and E_o is the initial elastic modulus before cycling. Thus, when the number of cycles is zero, i.e., $E_n = E_o$, $D_E = 0$, i.e., there is no damage. At the failure point of the material, the modulus goes to zero, i.e., $E_n = 0$, $D_E = 1$, i.e., maximum damage has occurred. Here, we have implicitly assumed that damage responsible for the stiffness loss consists of cavitation and cracking. It turns out that it is indeed so [21]. This allows to define another damage parameter in terms of density of the composite, D_ρ, as follows

$$D_\rho = 1 - (\rho_n / \rho_o) \quad (2)$$

where ρ_n is the density after n cycles and ρ_o is the initial density before cycling.

Damage evolution

In the as-received specimen, the fiber and matrix are in intimate contact with no apparent voids. The microstructures after thermal cycling showed microvoids at the fiber/matrix interface after 1000 cycles. These microvoids grew with increasing thermal cycles, indicating that the cavitation was not only a surface phenomenon, but characteristic of internal damage. Such microvoid formation was almost absent in the same composite material which had been isothermally treated at 300 °C up to 410 hours [4]. Thus, cavitation at the interface resulted from the cyclic thermal stresses. Figure 3 shows the elastic modulus of the composite after n cycles, E_n, normalized by the elastic modulus of the undamaged composite, E_o, as a function of thermal cycles. A significant damage in elastic modulus with increasing thermal cycles can be seen.

The modulus loss was accompanied by a significant damage in density with increasing thermal cycles as shown in Fig. 4. No weight loss was observed in the composites after thermal cycling, i.e., the mass was conserved. However, a measurable increase in the sample dimension after thermal cycling was observed. This corresponding dimension change was due to the microvoid formation in the sample. This indicates that the decrease in composite density was associated with microvoid formation rather than loss of matrix material due to vaporization.

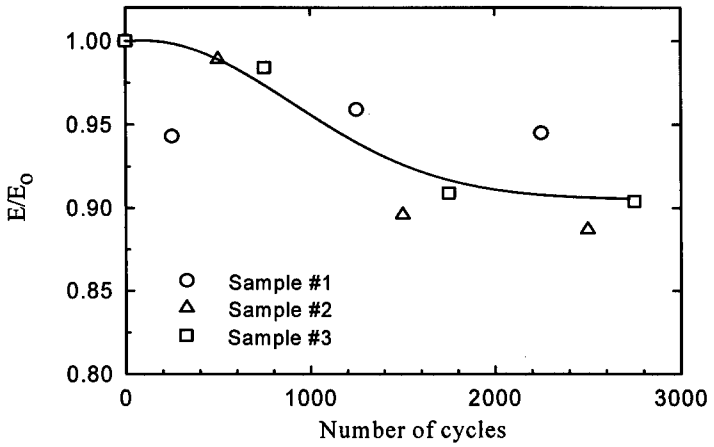


Fig. 3 Normalized elastic modulus vs. number of cycles, showing the damage in elastic modulus produced by thermal cycling.

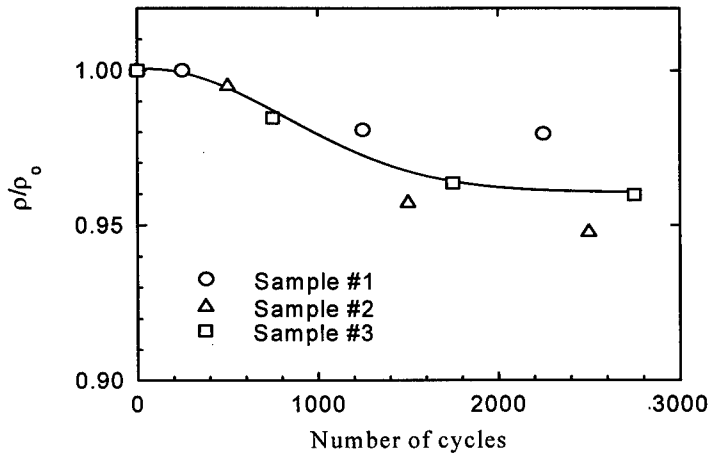


Fig.4 Normalized density vs. number of cycles, showing the damage in density produced by thermal cycling.

Correlation between D_E and D_ρ

Damage in terms of cavitation leads to a loss in modulus and density. Since the same physical phenomenon is responsible for both D_E and D_ρ, it is instructive to investigate a correlation between the two. The effect of porosity on the elastic modulus can be described by Mackenzie's equation [22]:

$$E_n = E_o (1 - bV_v - b_1 V_v^2) \quad (3)$$

where E_n is the Young's modulus, V_v is the volume fraction of voids in the composite after N cycles, E_o is the elastic modulus of the composite after zero cycles and, b and b_1 are material constants of a fully dense material. For most materials, b = 2 and $b_1 = 0.5$ [22]. Substituting Eq. (1) into Eq. (3), one can get

$$D_E = bV_v + b_1 V_v^2 \quad (4)$$

The density of composite, ρ_o and ρ_n, before and after thermal cycling, respectively, can be written in terms a rule of mixtures relationship as

$$\rho_o = \rho_m V_m + \rho_f V_f \quad (5)$$
$$\rho_n = \rho_m V'_m + \rho_f V'_f \quad (6)$$

where V_m and V'_m are the volume faction of matrix before and after thermal cycling, V_f and V'_f are the volume faction of fiber before and after thermal cycling, and ρ_m and ρ_f are density of matrix and fiber, respectively. Since the volume fraction of voids is very small and voids only exist on the matrix side of the fiber/matrix interface, $V_f = V'_f$, $V_m = V'_m + V_v$, i.e, $V_v = V_m - V'_m$. Therefore, subtracting Eq. (6) from (5), one can get

$$V_v = (\rho_o - \rho_n)/\rho_m \quad (7)$$

Accordingly, Eqs. (2), (4) and (7) can be combined as

$$D_E = b(\rho_o/\rho_m)D_\rho + b_1[(\rho_o/\rho_m)D_\rho]^2 \quad (8)$$

If we plot the experimental D_E data and the calculated D_E from Eq. (8), see Fig.5, we obtain a reasonable match between the experimental and calculated values. It should be borne in mind that any precipitation occurring in the matrix during thermal cycling would not affect the value of the elastic modulus of the composite. Microstructural characterization of interfacial reaction in the composite showed that the reaction zone thickness did not change after thermal cycling [3]. Thus, chemical influence was not a factor in the change of elastic modulus of the composite during thermal cycling. The plot of D_E vs. D_ρ via Eq. (8) and D_E vs. D_ρ from experimental data in Fig. 4 indicates that density decrease (i.e., cavitation) was responsible for the decrease in the elastic modulus.

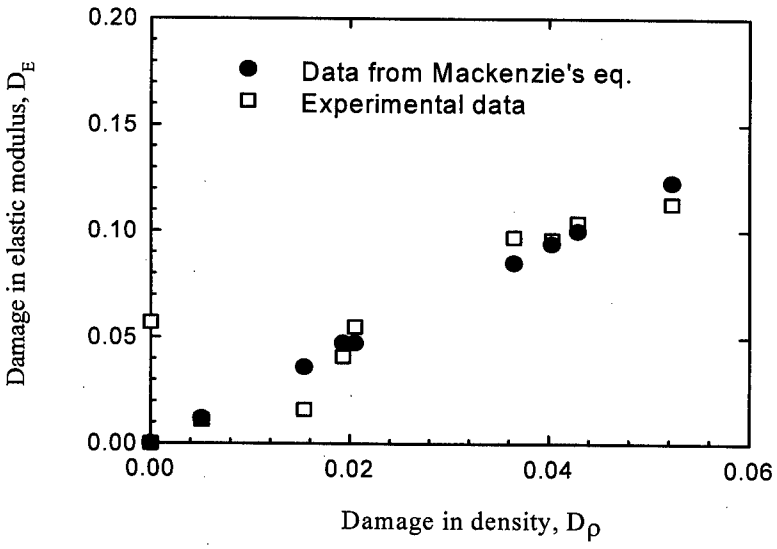


Fig. **5** Correlation between damage in elastic modulus and damage in density for alumina fiber/magnesium alloy.

Conclusions

Thermal stresses in an MMC can be relieved by one or more of the following means: plastic deformation of the matrix and cracking, debonding at the fiber/matrix interface, followed by void formation at the interface. Plastic deformation of the ductile matrix in an MMC is the first manifestation of damage under thermal fatigue. On continued cycling, damage takes the form of microvoids at the interface and/or cracking in the matrix occurred. Under these conditions, the elastic modulus and density of the composite decrease with thermal cycling. The incidence of void formation increases with number of thermal cycles. The suggested damage parameters in terms changes in the elastic modulus and density can be used to describe the evolution of damage.

References

1. K.K. Chawla, Metallography, 6 (1973) 155.
2. K.K. Chawla, Philos. Mag., 28 (1973) 401.
3. C.S. Lee and K.K. Chawla, in **Industry-University Advanced Materials Conference**, TMS, Warrendale, PA, 1987, p. 289.
4. C.S. Lee, K.K. Chawla, J.M. Rigsbee, and M. Pfeifer, in **Cast Reinforced Metal Composites**, ASM International, Metals Park, Ohio, 1988, p. 301.
5. L.K. Kwei and K.K. Chawla, J. Mater. Sci., 27 (1992) 1101.

6. R.T. Bhatt and H.H. Grimes, in **Mechanical Behavior of Metal Matrix Composites**, TMS, Warrendale, PA, 1982, p. 51.
7. S. Yoda, N. Kurihara, K. Wakashima, and S. Umekawa, Metal. Trans., 9A (1978) 1229.
8. H.H. Grimes, R.A. Lad, and J.E. Maisel, Met. Trans., 8A (1977) 1999.
9. M.A. Wright, Met. Trans., 6A (1975) 129.
10. K.K. Chawla and M. Metzger, J. Mater. Sci., 7 (1972) 34.
11. F. Rezai-Aria, T. Liechti, and G. Gagnon, Scripta Metall. et Mater., 28 (1993) 587.
12. K.K. Chawla, J. Mater. Sci. Lett. 11 (1976) 1567.
13. W.H. Kim, M.J. Koczak. and A. Lawley, in **New Developments and Applications in Composites,** TMS-AIME, Warrendale, PA, 1979, p. 40.
14. W.H. Hunt, in **Interfaces in Metal Matrix Composites,** TMS-AIME, Warrendale, PA, 1986, p. 3.
15. I.W. Hall and V. Barrailler, Metall. Trans. A, 1986, **17A**, 1075.
16. K.K. Chawla, in **Precious and Rare Metal Technologies,** Elsevier, Amsterdam, 1989, p. 639.
17. S.L. Ogin, P.A. Smith, and P.W.R. Beaumont, Composites Sci. Tech., 22 (1985) 23.
18. W.S. Johnson, in **Mechanical and Physical Behavior of Metallic and Ceramic Composites,** Risø Nat. Lab., Roskilde, Denmark, 1988.
19. P.G. Karandikar and T.-W. Chou, J. Am. Ceram. Soc., 76 (1993) 1720.
20. J. Lemaitre, **A Course on Damage Mechanics**, Springer-Verlag, Berlin 1992.
21. Z.R. Xu, K.K. Chawla, A. Wolfenden, A. Neuman, G.M. Liggett, and N. Chawla, **Mater. Sci. & Eng. A, A203** (1995) 75.
22. J.K. Mackenzie, Proc. Phys. Soc.,(London), B63 (1950) 21.

PREPARATION OF Ti/TiC MICROLAMINATES BY EB-PVD AND THEIR MECHANICAL PROPERTIES

Xiaofang BI, Xuesong JIN, Shengkai GONG and Huibin XU

Department of Material Science and Engineering
Beijing University of Aeronautics and Astronautics
Beijing 100083, China

Abstract

Ti/TiC microlaminates were prepared by Electron Beam Physical Vapor Deposition (EB-PVD) technique in order to realize one material with excellent toughness, strength and hardness. In the present work, the microstructures and mechanical properties of four kinds of Ti/TiC microlaminates with the layer thicknesses of 1.3 μm, 3 μm, 9 μm and 27 μm were analyzed. The results showed that the strength increased with the decrease of layer thickness, however, hardness had no obvious change with the layer thickness.

The Third Pacific Rim International Conference on
Advanced Materials and Processing (PRICM 3)
Edited by M.A. Imam, R. DeNale, S. Hanada,
Z. Zhong and D.N. Lee
The Minerals, Metals & Materials Society, 1998

Introduction

It is well known that Multilayer composites or laminates have wide potential applications in both structural and functional materials. However, a lot of developmental work, especially in processing, remains to be done before their properties are fully exploited. Recently, such laminates have been mainly made by rolling, co-extrusion, and electro-deposition. Although these techniques are very useful to form metallic laminates such as Cu-Fe, Al-Cu, Ni-Cu and so on, they are difficult to be applied for preparing metallic/ceramic or high melting temperature metallic laminates.

EB-PVD is known as a powerful technique for evaporating high melting temperature materials such as Mo, W and ceramics. The development of EB-PVD technology enables production of microlaminate materials due to its high deposition rate and excellent reproducibility[1]. Using four electron-guns EB-PVD equipment, in the present study, we have successfully fabricated Ti/TiC metallic/ceramic microlaminate sheets with the total thickness of about 1mm and different layer thicknesses by controlling the evaporating rate and deposition time. The mechanical properties of such microlaminates with the layer thicknesses of 1.3 μm, 3 μm, 9 μm and 27 μm were investigated. In this paper, we deal with the changes in the mechanical properties with different layer thicknesses and discuss the strengthening mechanisms.

Experimental Procedure

Four electron-guns EB-PVD equipment was used for preparing Ti/TiC metallic/ceramic laminate compositions. As shown in Figure 1, four electron beam guns are installed in the two gun-chambers and three water cooled crucibles are placed in the main chamber. Three materals,

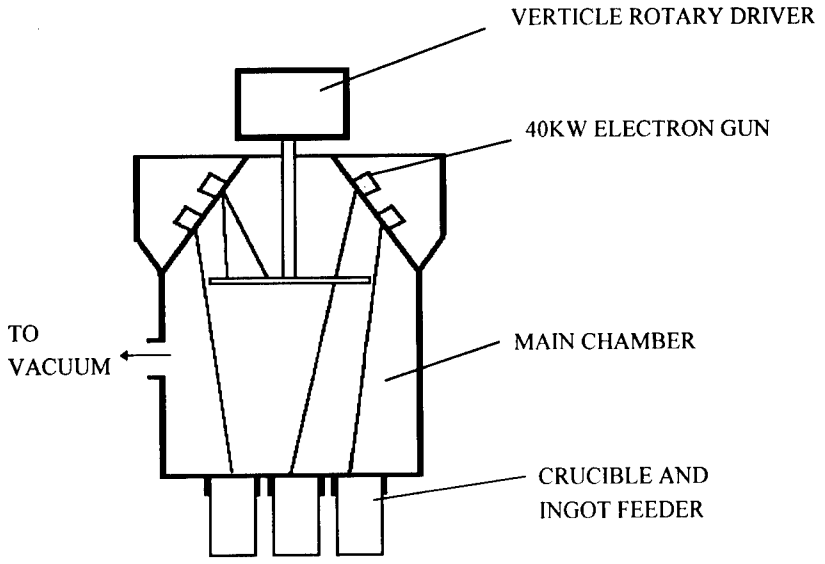


Figure 1: Schematic drawing of EB-PVD equipment

Ti, TiC and graphite ingots, with 50mm in diameter and 200mm in length were used as the evaporation sources, which are heated and evaporated by three electron beam guns respectively and deposited onto the flat horizontal disc substrate, 340mm in diameter, rotating around its vertical axis. The substrate was also heated by another electron beam gun. The main parameters were the substrate temperature, substrate rotating speed, evaporation rates of each ingot and deposition time. The thicknesses of Ti and TiC layers were controlled by the evaporation rate and deposition time. In the present study, the substrate temperature was in the range of 850 to 870 ℃. The acceleration voltage for electron-guns was 18kV. The electron beam current was set to be about 1.2A for evaporating Ti ingot, 1.0A for TiC ingot and 0.6A for graphite ingot. Under these conditions, the deposition rate was about 10 μm/min for Ti layer and about 2 μm/min for TiC. After deposition, the plate with laminate structure was annealed at 950 ℃ for 3 hours in vacuum to obtain a uniform structure of all layers.

In this study, four kinds of microlaminate with layer thicknesses of 1.3 μm, 3 μm, 9 μm and 27 μm were prepared with the same TiC layer thickness of about 0.1 μm. Microstructures of cross section were observed by means of scanning electron microscope (SEM). The layer thickness was estimated from SEM micrographs. Tensile testing was performed in a multifunction test machine at a strain rate of 2mm/min.

Results and Discussion

Figure 2 shows a set of microstructures of cross-section with different layer thicknesses. It can be seen that the layer boundary is flatter and almost independent on layer thickness in the

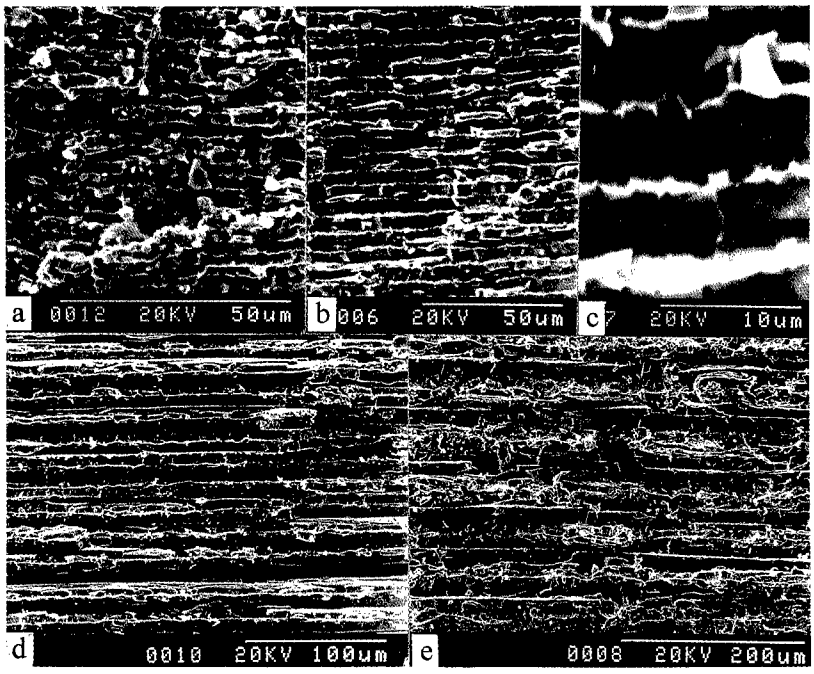


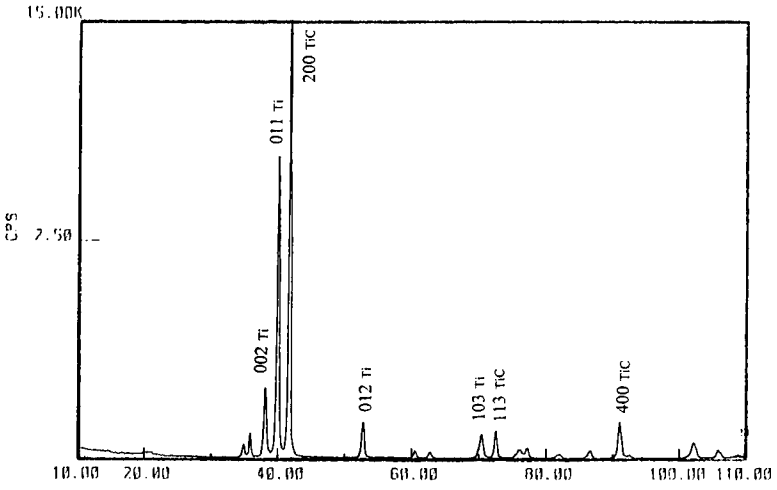
Figure 2: Microstructures of Ti/TiC laminates with different layer thicknesses

present thickness range. The microstructure is uniform in each Ti layer and the layer thickness is almost the same as shown in Figure 2c, which is the high magnification image of Figure 2b. According to the analysis of EDX, a few amounts of carbon were found in Ti layer. This indicates that diffusion of carbon occured in the layer boundary due to the high substrate temperature during the depositon. Also, the diffusion of carbon into Ti layer can be thought to contribute to the increase of the bonding force between the Ti layer and TiC layer. All of these can be considered as the characteristics of the microlaminates prepared by EB-PVD technique.

Table I The effects of layer thickness on the hardness and strength

Layer Thickness, μm	1.3	3.0	9.0	27	Pure Ti
Hardness (HR15n)	85	85	84	83	730MPa(HB)
Ultimate Tensile Strength, MPa	545	469	460	389	~ 260

The effects of layer thickness on the hardness and strength are described in Table 1. In order to compare the changes in hardness and ultimate tensile strength, data for pure Ti in the annealed state are also included[2]. No obvious change in hardness has been observed with the change of layer thickness. On the other hand, the ultimate tensile strength increases with the decrease of layer thickness. Furthermore, all the specimens showed higher ultimate tensile strength than pure Ti. This change in strength is similar to the results obtained from laminates prepared by other techniques.



Diffraction Angle (2 θ)

Figure 3: X-ray diffraction spectrum of Ti/TiC laminates with layer thickness of 1.3 μm

The mechanisms of the change in strength with layer thickness can be considered as below as summarized by K.S. Ravichandran et al[3]: (1) composite strengthening, (2) Hall-Petch type strengthening due to the formation of boundaries between dissimilar layers, (3) Koehler strengthening due to the difference in shear module, (4) dislocation strengthening and (5) texture strengthening arising from the anisotropic structure of layers formed during deposition or cold rolling process.

In addition, Figure 3 shows the result of X-ray diffraction spectrum. It is seen that although the microlaminate was prepared by EB-PVD technique, there is no preferential orientation in either Ti or TiC layers. The ratios of intensities of reflection peaks for Ti and TiC are similar to those listed in ASTM cards for all specimens. Furthermore, the peak positions are also almost the same as the values given in the cards for both Ti and TiC. This indicates that there is no obvious distortion in the microstructure.

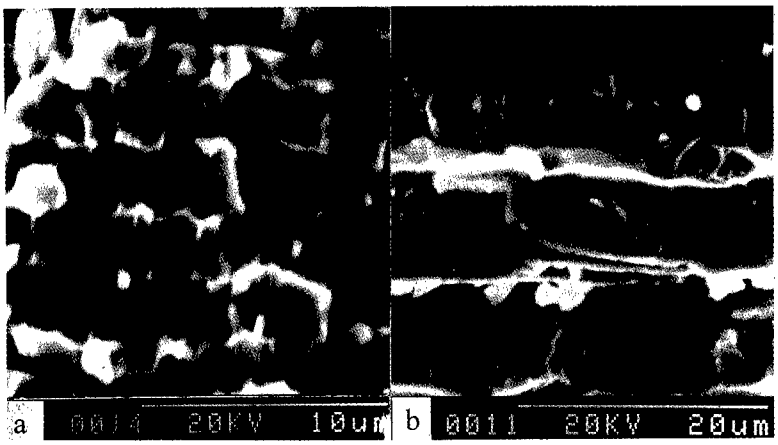


Figure 4: SEM images of the fracture section

Figure 4 shows the SEM images of the fracture section after tensile test, which are the typical feature of cleavage mode along the crystal plane. It can be observed that the grain size is in the range of the thickness of Ti layer. By considering the difference in grain size and the TiC strengthening effect, it can be assumed that the change in strength, in the present work, is mainly caused by composite strengthening and Hall-Petch type strengthening.

Conclusions

Four kinds of Ti/TiC microlaminates were prepared by EB-PVD technique and their machanical properties were investigated.

1. The microstructure of each Ti/TiC microlaminate is uniform in each Ti layer. In the present layer thickness range, the grain size of Ti layer is in the range of the layer thickness. There is no preferential orientation in either Ti or TiC layers.

2. No obvious change in hardness has been observed with the change of layer thickness.

Ultimate tensile strength increases with the decrease of layer thickness. The strengthening mechanism of microlaminates obtained in the present study can be considered as the combination of Hall-Petch effect and composite strengthening.

References

1. B.A. Movchan, "EB-PVD Technology in The Gas Turbine Industry: Present and Future," JOM, November, (1996),40-45.

2. R.J. Li, Ceramics and Metals (Beijing, Metallurgy Industry Publishing Company, 1995),13

3. K.S. Ravichandran, S.S. Sahay and J.G. Byrne, "Strength and Ductility of Microscale Brass-Steel Multilayer Composites," Scripta Materialia, 35(1996),1135-1140.

TiAl/TiAl-SiC GRADIENT COATINGS ON GAMMA TITANIUM ALUMINIDES AND THEIR OXIDATION BEHAVIOR

Shengkai GONG, Zohai. S. R., Qihui YU, Huibin XU and Chungen ZHOU

Department of Material Science and Engineering
Beijing University of Aeronautics and Astronautics
Beijing 100083, China

Abstract

Gradient TiAl/TiAl+SiC coatings on the gamma titanium aluminide were fabricated by using Electron Beam Physical Vapor Deposition(EB-PVD) technique, and the oxidation resistance behavior was investigated. The oxidation resistance depends on the ratio of the surfacial content of SiC to TiAl. In the present study, the TiAl/TiAl+SiC coating with the ratio of TiAl:SiC being about 8:3 was mainly investigated. The coating surface consisted mainly of TiAl and SiC, which were identified by X-ray diffractometer. Only 1.03mg/cm^2 mass gain was recorded after isothermal oxidation at 900 ℃ in air for 200hrs.

The Third Pacific Rim International Conference on
Advanced Materials and Processing (PRICM 3)
Edited by M.A. Imam, R. DeNale, S. Hanada,
Z. Zhong and D.N. Lee
The Minerals, Metals & Materials Society, 1998

Introduction

The gamma class of titanium aluminides is an attractive material for aerospace applications because of its excellent density-specific properties[1]. However, since gamma TiAl forms an intermixed Al_2O_3/TiO_2 scale in air instead of the desired continuous Al_2O_3 scale[2], oxidation resistance is inadequate at temperatures higher than 750-800 ℃. For the purpose of applications at these temperatures, much efforts have been made to improve the oxidation resistance, especially in the preparation of oxidation resistance coatings. However, there still exist some problems to be solved[2]. A major drawback of the current oxidation resistance coatings is known to be severe degradation in fatigue life caused by the formation of brittle coating-substrate reaction zones, the brittleness of the coating alloy, and the different thermal expansion coefficient between the coating and the substrate. It is well known that SiC ceramic forms SiO_2 at high temperatures and the SiO_2 can improve the oxidation behavior of TiAl by filling into the cracks of the oxidation scale of TiAl. D.Xu et al[3] prepared Si_3N_4 coatings on TiAl and reported that although the coatings were effective in decreasing the oxidation rate of TiAl, some problems existed mainly due to the incompatibility between substrate and coating because the thermal expansion coefficients of TiAl and SiC are very different. Therefore, the preparation of compositional gradient coating of TiAl-SiC is necessary to reduce the incompatibility caused by the different in thermal expansion coefficient. In the present study, TiAl/ TiAl+SiC gradient coatings have been fabricated by using EB-PVD equipment through controlling evaporation rates of TiAl and SiC, and the oxidation behavior of these coatings has been investigated. The coating of TiAl/ TiAl+SiC showed excellent oxidation resistance that only 1.03mg/cm^2 mass gain was recorded after isothermal oxidation at 900 ℃ in air for 200hrs.

Experimental Procedure

Four electron-guns EB-PVD equipment with three water cooled crucibles was used for preparing TiAl/TiAl+SiC coatings. TiAl and SiC ingots, with 50mm in diameter and 200mm in length were used as the evaporation sources, which were heated and evaporated by two electron beam guns respectively and deposited onto the gamma TiAl substrate rotating around the horizontal axis. The TiAl substrate was also heated by electron beam during the coating process. The gradient coatings with different surfacial composition ratios of SiC to TiAl were obtained by controlling the evaporation rate of each ingot. In the present work, the maximum evaporation rate in this work was about 2 μm/min. The substrate temperature was controlled to be about 450 ℃ in the beginning and 300 ℃ at the end of deposition process in order to improve the interfacial structure between the substrate and coating and obtain different grain sizes along the normal direction. The total thickness of the coatings was about 20 μ m. The structure of the coatings was investigated by X-ray diffractometer and the microstructure and composition were analysized by SEM/EDX. Isothermal oxidation test was carried out in air. Thermal shock test was carried out by putting the specimen into furnace and keeping for 1 hour and then taking out from the furnace and cooling it to room temperature.

Results and Discussion

Figure 1 shows the SEM image of surface and cross section of the TiAl/TiAl+SiC coatings. The distribution of composition along the direction normal to substrate surface is also added in the

figure. The coating surface consisted mainly of TiAl and SiC identified by means of X-ray diffractometer. The microstructure of the coating surface is uniform with grain size less than 2 μm. The cross section image shows that there is no clear interface between substrate TiAl and the coating. EDX results also show that both sides nearby the interface have almost the same compositions. From these results, it can be considered that the interface is in a metallic bonding state resulting from diffusion caused by the high substrate temperature during the deposition. The SiC concentration began to continuously increase with the thichness when the coating layer is thicker than 10 μm. No sharp change in composition of TiAl and SiC was detected by EDX analysis.

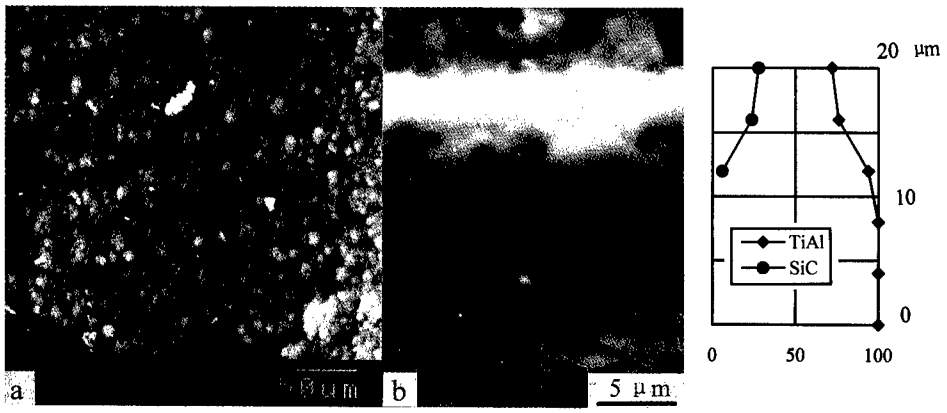


Figure 1: SEM images of surface and cross section of the TiAl/TiAl+SiC coating

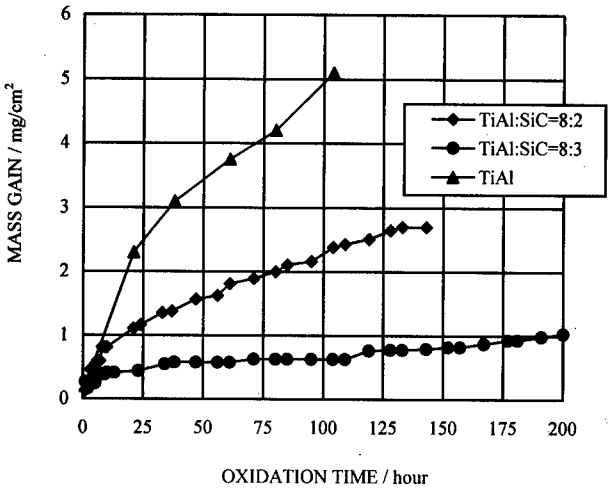


Figure 2: Isothermal oxidation kinetics of TiAl with TiAl/TiAl+SiC gradient coatings.

The isothermal oxidation kinetics of TiAl with TiAl/TiAl+SiC gradient coatings is shown in Figure 2. The coatings remarkably improve the oxidation resistance of TiAl. As shown in the

figure, the smallest mass gain was found to be only 1.03mg/cm^2 after isothermal oxidation at 900 ℃ in air for 200hrs in the present work, which is much lower than those obtained in the TiAlCr and sputtered Al_2O_3 coating systems[4]. On the other hand, the oxidation behavior of the coatings depends on the ratio of the surfacial content of TiAl to SiC. After isothermal oxidation at 900 ℃ for 140hrs, the mass gain of the coating is only about 0.8mg/cm^2 when the ratio of TiAl:SiC is about 8:3, however, when the ratio is about 8:2, the mass gain becomes about 2.7mg/cm^2, which is 3.5 times as large as the former one.

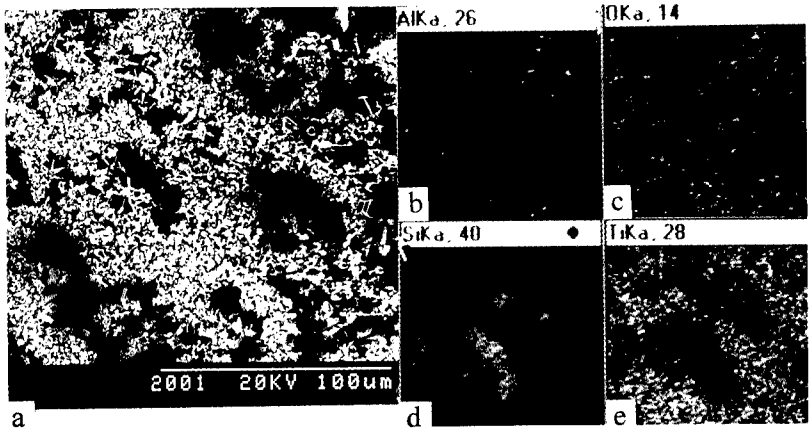


Figure 3: SEM/EDX images of the surface of TiAl/TiAl+SiC coatings after isothermal oxidation at 900 ℃ in air for 100 hours (TiAl:SiC=8:2).

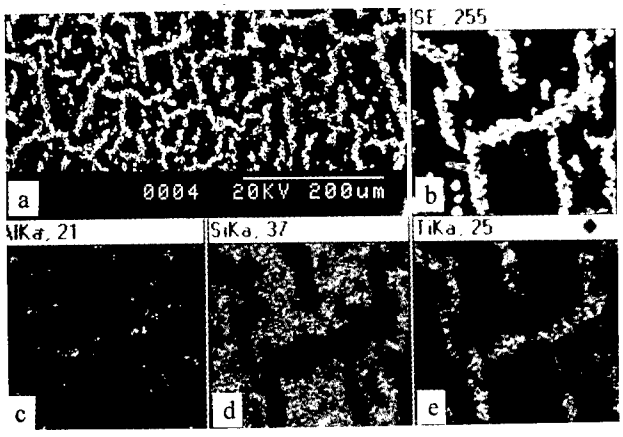


Figure 4: SEM/EDX images of the surface of TiAl/TiAl+SiC coating after isothermal oxidation at 900 ℃ in air for 200 hours (TiAl:SiC=8:3)

Figure 3 and Figure 4 show the SEM/EDX images of the surfaces of TiAl/TiAl+SiC coatings with the two different ratios of TiAl to SiC after isothermal oxidation at 900 ℃. In the both cases, the oxidation products were Al_2O_3, TiO_2 and SiO_2, which were identified by X-ray diffractometer. However, when the ratio is about 8:3, TiO_2 produces a net-like image as shown in Figure 4a. Almost no Ti element has been observed in the other place on the surface as

shown in Figure 4e. Besides the net-like TiO_2 image, Al and Si oxides appear uniform (Figure 4c and 4d). On the other hand, when the ratio is about 8:2, instead of the net-like image, Ti oxidation products cover almost the whole surface of the coating as shown in Figure 3a and 3e. Therefore, it is considerable that different ratios of TiAl to SiC could change the structure of surface oxidation products and lead to the improvement of the oxidation resistance of the coating.

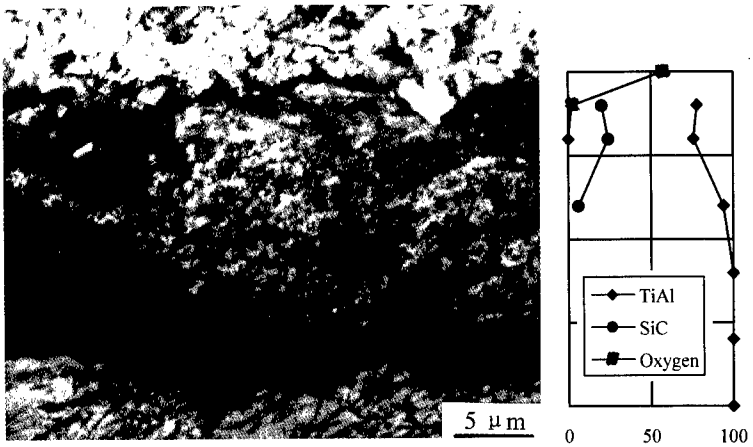


Figure 5: SEM images of the cross section of TiAl/TiAl+SiC coating after isothermal oxidation at 900 ℃ in air for 200 hours

The cross section observation by SEM/EDX shows very thin and continuous Al and Si oxide films existing just beneath the surface(Figure 5) and no crack and spallation have been observed in the cross section of coating as well as in the oxide film. No Si element has been observed in the TiAl substrate and just beneath the oxide film the distribution of the elements along the direction normal to the substrate surface keeps almost the same as that in the as-deposited state. No concentration of Ti has been observed. It can be considered that, during the oxidation process, Ti oxide formed at the grain boundaries only in the beginning caused by outward diffusion of Ti near to the surface. Thermal shock test showed that after 100 cycles from room temperature to 900 ℃, no crack or spallation were found even in the surface and the substrate/coating interface as well as in the oxide film. This means that the TiAl/TiAl+SiC gradiet coating and the oxides scale have a good compatibility to the substate. These results indicate that TiAl/TiAl+SiC gradient coatings may become one of the realistic protective coating for TiAl.

Conclusion

Gradient TiAl/TiAl+SiC coatings on the gamma titanium aluminide have been fabricated by using EB-PVD technique and their oxidation behaviors were investigated.

1. The coating layer has an excellent compatibility with TiAl substrate. The element distributions were almost the same before and after oxidation. No crack or spallation appeared in the surface and the substrate/coating interface as well as in the oxide film.

2. The oxidation resistance of TiAl has been remarkably improved by the coatings. The oxidation behavior of the coatings depends largely on the ratio of the surfacial content of TiAl to SiC. Only 1.03mg/cm^2 mass gain has been recorded after isothermal oxidation at 900 ℃ in air for 200hrs when the ratio is about 8:3.

Acknowledgement

This work is sponsered by National Natural Science Fundation of China.

References

1. Y.M. Kim, "Alloy Design of Gamma (TiAl) alloys," Acta Metall. Sinica(English Letters), 8(1995), 319-339.

2. S.Becher el al., "Mechanism of Isothermal Oxidation of the Intermetallic TiAl and TiAl alloys," Oxid.Met.,38(1992),425-464.

3. D.Xu et al., "Improvement of Oxidation Resistance of TiAl by Ion-beam-enhanced Coatings," Surf. Coat. Technol. 66(1994),486-494.

4. Z.L. Tang, F.H. Wang and W.T. Wu, "Improvement on Oxidation Resistance of Titanium Aluminide Intermetallies by Coatings," The Minerals, Metals & Materials Society,(1997),341-346.

P/M SYNTHESIS OF TITANIUM ALLOY-BASED PARTICULATE COMPOSITES AND THEIR PROPERTIES

M.Hagiwara, S.Emura, S.J.Kim* and M.Niinomi**

National Research Institute for Metals
Tsukuba 305-0047, Japan
* Korea Institute of Machinery and Materials
Changwon 641-010, Korea
** Toyohashi University of Technology
Toyohashi 441-8122, Japan

Abstract

Ti-6Al-2Sn-4Zr-2Mo/TiB particulate composites were synthesized using the blended elemental powder metallurgy processing route. The distribution of the rod-shaped TiB particulate was very homogeneous. The matrix microstructure was highly dependant on cooling rate after the sintering treatment. The composites showed excellent tensile strength, Young's modulus and high cycle fatigue strength superior to those for the unreinforced matrix alloy. However, ductility and fracture toughness decreased with increasing amount of TiB. The property data were analyzed by comparing with those predicted by the existing models.

The Third Pacific Rim International Conference on
Advanced Materials and Processing (PRICM 3)
Edited by M.A. Imam, R. DeNale, S. Hanada,
Z. Zhong and D.N. Lee
The Minerals, Metals & Materials Society, 1998

Introduction

The synthesis of titanium alloy-based particulate composites has been receiving much attention in recent years due to their potential for the improvement of various properties[1-7]. Furthermore, these composites offer the advantages of isotropic characteristics and can be processed at reasonable costs using the conventional near net shape technology. The authors have synthesized titanium-based particulate composites using the blended elemental (BE) powder metallurgy (P/M) method to improve the mechanical properties beyond the achievable limits of conventional alloys[3,4]. This paper briefly discusses the fabrication method, and summarizes the microstructures and mechanical properties such as tensile, Young's modulus, fracture toughness and high cycle fatigue obtained for the BE P/M Ti-6Al-2Sn-4Zr-2Mo/0-20TiB composites. Ti-6Al-2Sn-4Zr-2Mo is one of the most widely used α(hcp phase)-β(bcc phase) type titanium alloys. TiB can be an ideal reinforcing particulate since it has good mechanical properties such as rigidity, strength and hardness, and forms no reaction phase at the particulate/matrix interface. Therefore, Ti-6Al-2Sn-4Zr-2Mo/TiB can be regarded as one of the representative composites among the titanium alloy-based particulate composites.

Fabrication method

Processing steps for fabricating titanium alloy-based particulate composites are shown in Fig.1. The extra low chlorine (Cl<20ppm) titanium powder smaller than 45μm in diameter, 2.5Al-2Sn-1Mo-2Ti and 3.5Al-4Zr-1Mo master alloy powder smaller than 45μm and TiB_2 ceramic powder with an average diameter of 2μm were used as starting powder materials. During sintering, TiB_2 reacts with titanium to form TiB in-situ in the matrix. In order to disperse TiB_2 particulate uniformly in the blended powder, the preliminary blended powder by the V-shaped blender was subjected to the forced mixing by using an attritor, so-called as a mechanofusion machine. Vacuum sintering was done at 1573K for 14.4ks, and subsequent hot isostatic pressing (HIP) was carried out at 1203K and 200MPa for 10.8ks.

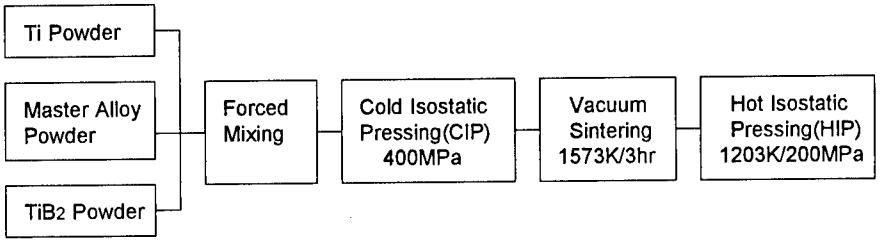


Fig.1 Processing steps for fabricating Ti-6Al-2Sn-4Zr-2Mo/TiB composites.

Microstructures

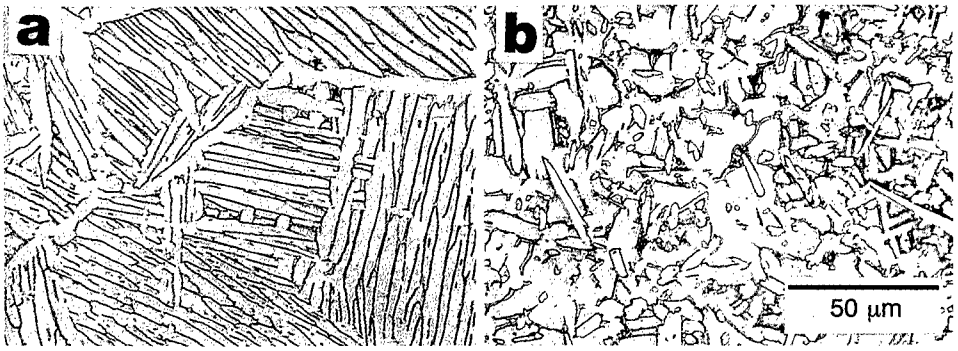
(1) Conventionally processed unreinforced matrix alloy and composites

The microstructure of the unreinforced Ti-6Al-2Sn-4Zr-2Mo matrix alloy shows a coarse colony microstructure with a massive grain boundary of α-phase, as shown in Fig.2a. This is a typical

microstructure when an α–β type titanium alloy is fabricated by the conventional BE P/M method. The rod-shaped TiB distributes uniformly in the matrix, as shown in Fig.2b. It should be noted that the matrix area of the composites looks like an equiaxed α microstructure. The length of each α-platelet is limited by the particulate spacing.

(2) Modification of matrix microstructure by the heat treatment

It was found that the matrix microstructure of the composites is highly dependent on cooling rate after sintering treatment. Subsequent HIPing in the α–β two phase region at around 1170K for 10.8ks did not cause any microstructural change except sealing pores. Since it is practically difficult to change the cooling rate arbitrarily in a sintering furnace, the microstructural dependence on cooling rate was determined by cooling the HIPed composites from above the β-transus temperature at a varying cooling rate using a laboratory electric furnace. The air cooling with average cooling rate of 10K/sec produced the well-defined colony matrix microstructure, as shown in Fig.3a. The subsequent anneal at 1170K for 10.8ks which corresponds to the HIP thermal cycle slightly coarsened this colony microstructure. The water quenching produced an α' martensitic microstructure and the subsequent anneal at 1170K for 10.8ks transformed this martensitic microstructure to a fine acicular α–β two phase microstructure, as shown in Fig.3b. The nearly equiaxed α matrix microstructure shown in Fig.2a was obtained by the cooling rate of about 0.3K/sec.



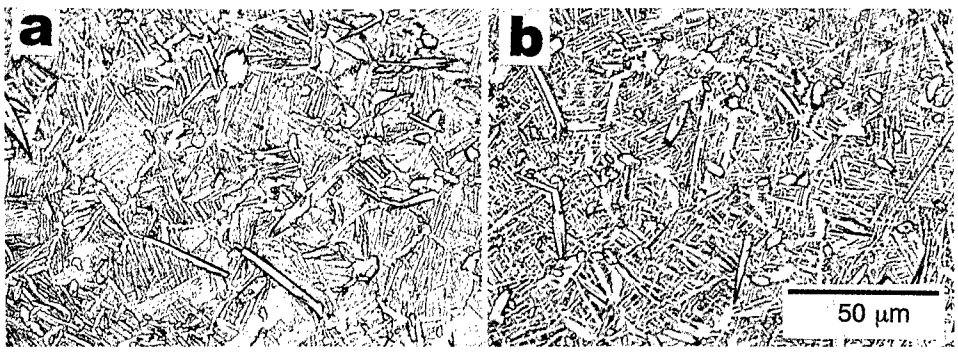


Fig.3 Microstructures of Ti-6Al-2Sn-4Zr-2Mo/10TiB composites subjected post-HIP heat treatment. (a) air cooled from above β–transus temperature, (b) quenched from above β-transus temperature and annealed at 1170K.

Mechanical properties

(a) Tensile properties and Young's modulus

Both 0.2% proof stress and tensile strength at room temperature were increased with increasing amount of TiB, as shown in Fig.4. However, elongation was only 2% for the 10%TiB composites. The proof stress was compared with the modified shear lag model proposed by Nardone and Prewo[8].

$$\sigma_{cy} = \sigma_{my}\{1/2 \cdot C_f(2+L/d) + 1-C_f\} \quad (1)$$

where σ_{cy} and σ_{my} are the proof stress of composites and matrix alloy, respectively. C_f is the volume fraction of particulate, and L/d is the aspect ratio of particulate, which is 10 for the present composites. As can be seen from Fig.4, the predicted values are far larger than the experimental values. This discrepancy is ascribed to the fact that the shear lag model was originally developed for the composites with unidirectionally-oriented short fibers and, therefore, this model is invalid for the present composites.

Young's moduli of the unreinforced matrix alloy and the composites were determined by the ultrasonic pulse echo method. As shown in Fig.5, the presence of TiB particulate leads to a substantial improvement in Young's modulus. For example, with the amount of 20%TiB, Young's modulus increased to 161GPa from 119GPa of the unreiforced matrix alloy. The comparison with the existing models revealed that the rule-of-mixture expression (Eq.2) significantly overestimates the modulus.

$$Ec = VpEp + VmEm \quad (2)$$

where Ec, Em and Ep (=550GPa) are the Young's modulus of the composites, matrix and particulate, respectively, and Vm and Vp are the volume fraction of the matrix and the particulate. According to Halpin-Tsai equation[6], the predicted Young's modulus is given by

$$Ec = Em(1 + 2sqVp)/(1-qVp) \quad (3)$$

where $q = (Ep/Em - 1)/\{(Ep/Em) + 2s\}$, s is the aspect ratio of the particulate. It is obvious that this equation also overestimates the modulus. However, the agreement with observed values is closer compared to the rule-of-mixture expression.

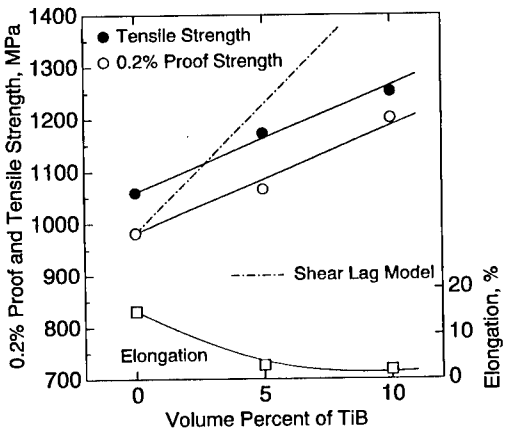


Fig.5 Changes in tensile properties of Ti-6Al-2Sn -4Zr-2Mo/TiB composites with TiB content.

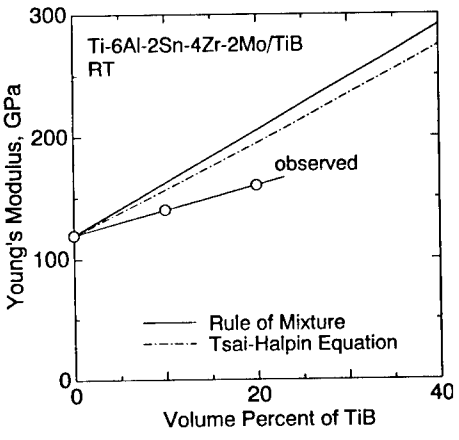


Fig.6 Changes in Young' modulus of Ti-6Al-2Sn -4Zr-2Mo /TiB composites with TiB content.

(b) High cycle fatigue strength

The smooth axial high cycle fatigue test was performed on the matrix alloy and the composites in an air at an R ratio of 0.1 in the load-controlled mode and a frequency of 80 Hz (Fig.7). The conventionally processed Ti-6Al-2Sn-4Zr-2Mo/10TiB composites (Fig.2a) exhibited a considerably higher fatigue strength in the whole cycle range than those for the unreinforced matrix alloy. The microstructural modification of the matrix area into the fine acicular α–β microstructure further increased the high cycle fatigue strength. For example, fatigue strength at 10^7 cycles was increased to 590 MPa, from 490MPa for the conventionally processed counterpart. It was found by the careful SEM examination that the fatigue crack initiated neither from the TiB/matrix interface nor from TiB particulate but rather from the matrix phase. It is well known that the high cycle fatigue strength of titanium alloy is highly dependent on its microstructure. Therefore, the fact that the fatigue damage originated from the matrix region can account for the experimental observation that the high cycle fatigue strength of the present composites is highly related to the matrix microstructure.

Besides this microstructural modification of the matrix, another factors such as the increase in tensile strength, the increase in Young's modulus, Orowan strengthening, quench hardening due to the difference in coefficient of thermal expansion between the TiB particulate and the matrix, and work hardening due to the misfit between the TiB particulate and the matrix might play a role in increasing high cycle fatigue strength. Among these factors, Orowan strengthening is not a major factor since particulate in the present composites is larger than 5μm in diameter. The coefficient of thermal expansion is almost the same between the TiB particulate and the matrix[5] and, therefore, dislocation density will be uniform in the matrix. The work hardening will not be caused because it is reported that the interface between the TiB particulate and the matrix is coherent[5]. For these reasons, Orowan strengthening, quench hardening and work hardening can be ignored from the consideration.

The three main contributions to the fatigue strengthening have been discussed in a separate paper by the present authors[4], concluding that the contribution from the increase in Young's modulus is small (15%) and the contribution from the increase in tensile strength and microstructural refinement were 35% and 49%, respectively.

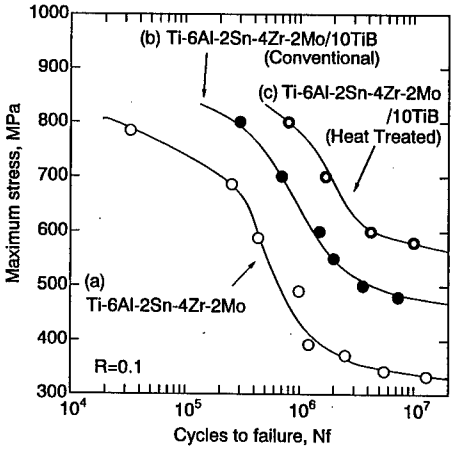


Fig.7 High cycle fatigue curves of Ti-6Al-2Sn-4Zr-2Mo matrix alloy and Ti-6Al-2Sn-4Zr-2Mo/10TiB composites.

(c) Fracture toughness

The Charpy-sized specimen (10x10x55mm) were fatigue pre-cracked so that a/w was 0.60 (a:initial

crack length, w:specimen width) according to the ASTM E813, and then static fracture toughness ($J_{in(s)}$) and dynamic fracture toughness ($J_{in(d)}$) values were evaluated by the three point bending test at a cross head speed of $5.0x10^{-6}$m/s and at an impact velocity of 1.37-3.31m/s, respectively. The crack initiation was determined by the compliance changing rate method. As shown in Fig.8 and Fig.9, static and dynamic fracture toughness values decreased drastically with increasing amount of TiB particulate. For example, the static fracture toughness value of the 10%TiB composites was about one third that of the unreinforced matrix alloy. The dynamic fracture toughness value was fairly smaller than the static fracture toughness value.

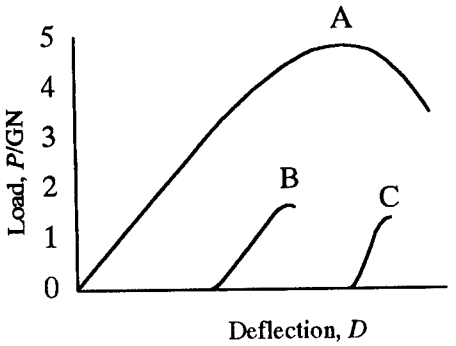


Fig.8 Load-Deflection curves of Ti-6Al-2Sn-4 Zr-2Mo/TiB composites(A:0%TiB, B:10%TiB C:20%TiB).

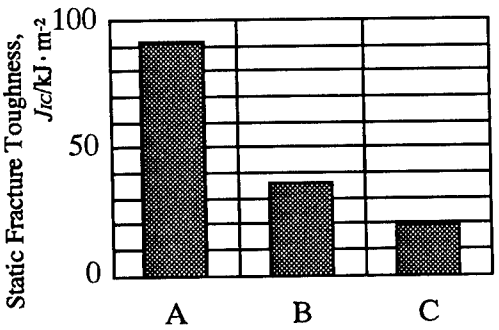


Fig.9 Changes in static fracture toughness of Ti-6Al-2Sn-4Zr-2Mo /TiB composites(A:0%TiB, B:10%TiB and C:20%TiB).

Conclusion

The titanium alloy-based particulate composites have been produced successfully using the blended elemental powder metallurgy processing route. Most of the mechanical properties such as tensile strength, Young's modulus, high cycle fatigue strength were improved by the dispersion of TiB particulate. However, ductility and fracture toughness were drastically reduced. More detailed study concerning the effect of size/shape and volume fraction of the particulate on the mechanical properties are needed.

References

1. S.Abkowitz and P.Weihrauch: Adv. Mater. Process, (1989), No 7, p.31
2. W.Takahashi, M.Okada, Y.Shida and M.Nakanishi: Tetsu to Hagane, 77(1991), p.1336
3. M.Hagiwara, S.Emura, J.Takahasi, Y.Kawabe and N.Arimoto: ISIJ Int'l, 32(1992),p.909
4. M.Hagiwara, S.Emura, Y.Kawabe and S-J.Kim: "Light Weight Alloys for Aerospace Application IV", TMS,(1997),p.219
5. T.Saito, T.Furuta and T.Yamaguchi: Proc.3rd Japan Int'l SAMPE Symp.(1993), p.1810
6. S.Ranganath: J. Mater.Sci.,32(1997),p.1
7. M.H.Loretto and D.G.Konitzer: Metall.Trans. A, 21A(1990),p.1579
8. V.C.Nardone and K.M.Prewo: Scripta Metall.,20(1986),p.43

THE INITIATION AND CONTINUATION OF INFILTRATION OF Al-Mg BASED ALLOYS INTO ALUMINA PREFORMS

B S Rao and V Jayaram
Department of Metallurgy, Indian Institute of Science
Bangalore-560 012, India

Abstract

Al-Mg alloys have been infiltrated without pressure into Al_2O_3 preforms of different particle size with interconnected porosity in the presence of a nitrogenous atmosphere above 700°C. The phenomenon of pressureless infiltration was divided, based on the experimental observations, into two regimes: (1) initiation and (2) continuation. Initiation is governed by the formation of a Mg rich porous surface oxide which allows the molten metal to come up to the oxide/preform interface to infiltrate the preform. The formation of this porous oxide is dependent on the rate at which the sample is heated from room temperature to the infiltration temperature or the combined effect of heating rate and holding at lower temperatures(<700°C). Infiltration of the preform is usually incomplete when the preform is of the same diameter as that of the alloy billet whereas full infiltration took place when the surface area exposed by the billet is larger than that of the preform. This difference has been attributed to the relative ease with which Mg vapour is able to getter oxygen at the interface between the composite and the atmosphere. When diffusion of Mg is limited, the surface passivates and terminates the growth of the composite.

The rate of infiltration is decided by the interplay of capillary, gravity and drag forces. Initially infiltration rate increases with decreasing particle size due to the increased capillary forces. Further decrease in particle size eventually contributes to increasing viscous drag which reduces the net driving force and leads to a decrease in the rate of infiltration.

The Third Pacific Rim International Conference on
Advanced Materials and Processing (PRICM 3)
Edited by M.A. Imam, R. DeNale, S. Hanada,
Z. Zhong and D.N. Lee
The Minerals, Metals & Materials Society, 1998

Introduction

Infiltration of molten metals into porous ceramic preforms is one of the most widely used methods of making metal matrix composites. Infiltration methods vary from pressure assisted[1,2] to capillarity driven[3] based on the source of driving force. Al alloys that contain magnesium infiltrate spontaneously (without the aid of the pressure) into porous ceramic preforms above 700°C in nitrogenous atmosphere. The governing process parameters are temperature, alloy composition, atmosphere, particle size and porosity. The process can be divided into two regions;(1) low temperatures(800-1000°C) where nitride formation is not significant and results in metal matrix composite[4], (2) high temperatures(1000-1200°C) where nitride formation is significant and forms ceramic matrix composite[5]. The present work focusses on low temperature range in which nitride formation is minimal. M.K.Aghajanian et al.,[6] reported the effect of various process parameters ,i.e., temperature, Mg content in the alloy, nitrogen content in the atmosphere and particle size on infiltration of Al-Mg alloys into SiC, Al_2O_3, MgO, graphite coated with SiC and TiB_2 preforms. The rate of infiltration increases with alloy Mg content and nitrogen content of the atmosphere while the latter also decreases the amount of nitride formed. Both, rate of infiltration as well as the nitride content were reported to increase with temperature. Infiltration rate increased with decreasing particle size in the range 18-216μm while no infiltration occurred into particles larger than 216μm. This process was extended to fabricate Al/AlN composites by infiltrating preforms of Si_3N_4 with Al and then converting Si_3N_4 to AlN by heat treatment at 1200°C[7].

The other pertinent background to the understanding of infiltration comes from studies of nitridation of Al-Mg based alloys[8]. These experiments have suggested that Mg aids the conversion of Al to AlN by gettering residual oxygen in the ambient. Such a conclusion is further supported by the observation that nitridation in flowing gas is slower than in a sealed chamber in which oxygen is not being continuously replenished. The studies carried out so far have given some insight into the mechanisms of the process. However, no systematic study has been undertaken so far to understand the role of various process parameters on the rate of infiltration. In particular, because of the absence of in-situ monitoring of infiltration, issues relating to the initiation and continuation of infiltration are largely unexplored. This work, examines some of the above factors in addition to the effect of particle size

Experimental procedure

Preparation of alloys, preforms and crucibles

Al-Mg alloys of nominal compositions of 2 and 8wt%Mg were prepared by melting commercial purity Al and Mg and were cast into permanent cylindrical cast iron finger moulds. The cast fingers were homogenized at 350°C for 24hrs and cut into alloy billets of 6.7mm diameter and 7mm height. The chemical composition of the alloys was analysed using inductively coupled plasma spectroscopy and shown to be 1.92 and 8.43wt%Mg. Preforms of 6.9mm diameter and a height of 6-10mm were prepared by cold pressing alumina powder of appropriate particle sizes using polyvinyl alcohol as binder and partially sintering (table I) to obtain enough strength for handling. The porosity of the preforms, which was determined by coating the preform with wax and using Archimedes principle, was kept to about 40%. Crucibles for holding preform and billet were made by sealing one side of a recrystallized tube of 7mm diameter and 15mm height with an alumina disc using alumina cement and firing at 1500°C for 2hrs.

Infiltration Experiments

The crucible containing the preform on top of the alloy billet was placed in a thermo-gravimetric analyser(CAHN TG171) and evacuated twice to 0.03mbar and back filled with N_2-

2%H_2 gas. The heating rates employed were 5-20°C/min. to a final process temperature of 800°C or 900°C. In some runs samples were held at 400°C for 30 minutes during the initial ramp. All samples were held at the final temperature for various periods and then furnace cooled. N_2-2%H_2 gas was passed at 100ml/min. through out the duration of the experiment. A few experiments were carried out with Al-6.1wt%Mg-6.5wt%Si-0.3wt%Fe alloy under the same conditions as described for Al-Mg binary alloys except that in one of the experiments, an alloy billet of cross-sectional area larger than that of the preform was used, for reasons explained in the Results section. The weight gain of the sample was continuously recorded by a computer attached to the TGA.

Characterization

Infiltrated samples were sectioned longitudinally using a high speed diamond saw and polished to 4μm diamond finish. Sectioned samples were photographed to compare infiltrated heights in different conditions. The free surface of the billet and polished samples of composite were examined under a scanning electron microscope with energy dispersive x-ray spectroscopy(EDXS) for various features of the infiltration process. X-ray diffraction(XRD) was used for phase identification.

Results and discussion

Weight gain curves of A-8wt%Mg alloy infiltrating into 53μm particulates after different heating schedules to 800°C are shown in fig.1, while the corresponding longitudinally sectioned samples are shown in fig.2.

(A) Initiation

Detailed correlations were made between the observed infiltration and different points along the weight gain curve by means of interrupted experiments. During the range 25-750°C, weight gain corresponds to the surface build up of a phase in which the Mg/(Mg+Al) weight fraction is ~40% as identified by EDXS. The formation of Mg_3N_2 can be ruled out since it decomposes at 800°C while the TGA shows no corresponding weight loss[The possibility of formation of MgO due to vapour phase oxidation is readily established by x-ray diffraction of white whiskers on the crucible walls]. This suggest that the Mg rich surface comes either from a thin layer of MgO lying on top of the billet or a mixture of MgO and $MgAl_2O_4$. The sharp rise in weight gain at ~750-800°C corresponds to the start of infiltration. The 3 curves in fig.1 along with the cross-sections in fig.2 indicate that infiltration is facilitated by slow heating and an intermediate hold at 400°C. The sample heated to 800°C at 20°C /min. did not start infiltration even after 4 hours at 800°C. However, when the runs were interrupted at 800°C, all the samples had formed Mg rich phase on the surface of the billets with no significant difference in composition to the one described above. Thus, it is inferred that the morphology of the oxide layer formed during the intermediate hold is porous enough to allow the molten metal to come up to the oxide/preform interface(fig.3) so that infiltration can begin. More extensive experiments indicate that early initiation is aided by an intermediate hold at $400<T<600$°C or heating rates<10°C/min..

(B) Continuation

Based on the above results, comparisons of infiltration as a function of alloy composition and particle size were made after a heating cycle that included a half-hour isothermal hold at 400°C. It was found that in all cases, excepting one, that the process terminated before the preform was fully infiltrated. This feature was established, once again, by interrupted experiments which revealed that when the molten metal had penetrated throughout the preform, the rate of weight gain changed to a slow increase(fig.4), corresponding to the formation of MgO as identified by XRD. In contrast, when infiltration ceased within the preform, the rate of weight gain became undetectable. This difference in weight gain suggests that Mg might be depleted at the infiltration front when termination occurs within the

preform(Gravitational effects could be ruled out when termination was observed even when infiltration took place downwards). Bulk depletion of Mg by evaporative loss was also eliminated by EDXS of Al-8.5wt%Mg billet which showed 7.7wt%Mg after 3 hours holding at 800°C. That Mg depletion at the front is the reason for termination was conclusively demonstrated by the following experiment. An Al-2wt%Mg alloy was held at 900°C till the infiltration terminated. After cooling the sample, the un-infiltrated portion of the preform was removed, 10mg of Mg powder was placed on the surface of the composite and a new preform was placed on top . When the sample was heated back to 900°C, infiltration was re-initiated and 1 mm of the preform was infiltrated before it terminated again as shown in fig.5.

This opens up the possibility that if the Mg supply to the surface could be maintained independent of the infiltrated thickness, that infiltration could be made to continue until the driving force is exhausted. The above hypothesis was confirmed by carrying out an experiment with an alloy billet larger in diameter than the preform so that Mg could evaporate from the surface of the billet without having to diffuse through the infiltrated portion of the preform(The above experiment was carried out with an Al-6.1wt%Mg-6.5wt%Si-0.3wt%Fe alloy for which the termination phenomenon is similar to that encountered in Al-8.5wt%Mg). As shown in fig.6, full 1cm infiltration of the preform takes place. This result is consistent with the reported[8] pronounced role of Mg in gettering oxygen and in thereby controlling the conversion of Al to AlN.

(C) Effect of Particle size

The above results illustrate the importance of phenomena related to initiation and continuation of infiltration while studying the role of particle size on growth kinetics. The height of infiltration displays a maximum with respect to particle size around 25μm(table I). An increase in infiltration rate with decreasing particle size was reported by earlier workers[6]. However, their studies did not extend to sub-micron particles. Transition in infiltration rate with respect to particle size is expected when we consider the various components of the drag and driving force for flow of liquid metal. Force balance leads to an equation of infiltration rate which is dependent on the total perimeter over which surface tension acts and on the channel size between the particles. As particle size decreases, the surface area per unit volume increases and consequently the capillary force increases. However, with decrease in particle size the boundary layer extends further into the channel from the surface of the particle so that at the transition particle size the rate of increase in drag force due to decreased channel size is more than the rate of increase in capillary force. The study of the dependence of these forces on pore size and volume fraction is now underway, given that it is possible to eliminate the somewhat uncontrolled retardation that is brought about by localised solute depletion at the infiltration front.

Conclusions

(1) Extended low temperature exposure($T<600°C$), either through slow heating or isothermal hold during heating facilitate the infiltration of Al-Mg based alloys into Al_2O_3 particulates at temperatures greater than 750°C.

(2) Local depletion of Mg at the surface of the composite can lead to premature termination of infiltration. This may be avoided by providing a high vapour pressure of Mg around the preform such that oxygen is continually gettered.

(3) Infiltration rate is decided by the interplay of capillary force, viscous drag and gravity. Infiltration rate increases with decreasing particle size due to increased surface area for metal to wet and decreases as it goes into very fine particles(i.e.,$<1\mu m$) where the rate of increase in viscous drag dominates the rate of increase in capillary force due to reduction in particle size.

Acknowledgements

Financial assistance for this work was provided by a grant from the Aeronautical Research & Development Board, Government of India.

References

1. T.W. Clyne, and J.F. Mason, "The Squeeze Infiltration Process for Fabrication of Metal Matrix Composites," Metall. Trans. A, 18A(1987), 1519-1530.

2. V.J. Michaud, and A. Mortenson, "Infiltration of Fiber Preforms by a Binary alloy: Part II Further theory and experiments," Metall. Trans. A, 23A(1992), 2263-2280.

3. D. Muscat, and R.A.L. Drew , "Modelling the Infiltration Kinetics of Molten Aluminum into Porous Titanium Carbide," Metall. and Mater. Trans. A, 25A(1994), 2357-2370.

4. M.K. Aghajanian, J.T. Burke, D.R. White and A.S. Nagelberg, "A New Infiltration Process for the Fabrication of Metal Matrix Composites," SAMPE Q., 20(1989), 43-46.

5. D.K. Creber, S.D. Poste, M.K. Aghajanian, and T.D. Claar, "AlN Composite Growth by Nitridation of Aluminum alloys," Ceram. Engg. Sci. Proc., 9(1988), 975-982.

6. M.K. Aghajanian, M.A. Rocazella, J.T. Burke, and S.D. Keck, "The Fabrication of Metal Matrix Composites by a Pressureless Infiltration Technique," J. Mater. Sci., 26(1991),447-454.

7. M.K. Aghajanian, J. P. Biel, and R. G. Smith, "AlN Matrix Composites Fabricated via an Infiltration and Reaction Approach," J. Am. Ceram. Soc., 77 (7) (1994), 1917-1920.

8. H. Scholz, and P. Greil, "Nitridation reactions of molten Al-(Mg-Si) alloys," J. Mater. Sci., 26(1991)669-677.

Table I Sintering schedule of preforms and height of infiltration of Al-8wt%Mg and Al-2wt%Mg alloys into 40% porosity alumina preforms at 800°C after 3 hours.

Particle size(μm)	sintering temperature(°C)	sintering time(hr)	Infiltrated height(mm) Al-8wt%Mg alloy	Al-2wt%Mg alloy
0.5*	1300	1	2.5	0.2
25-37	1500	1	7.0#	3.5
53-63	1600	1	4.5	1.0
90-120	1600	1	2.5	0.5

*Calcined alumina, mean particle size. Others are fused alumina. #Full infiltration

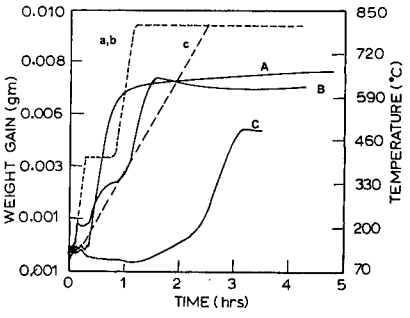


Fig.1: Weight gain data showing the initiation and termination of infiltration of Al-8wt%Mg into 53 μm alumina preform at 800°C under different heating schedules: (A) 20°C/min., (B) 20°C/min & 30min. at 400°C and (C) 5°C/min. Temperature profiles a, b and c are also shown



Fig.2: Sections of 53 μm alumina preform kept on top of Al-8wt%Mg alloy billets and heated to 800°C under different heating schedules. (**left**) 20°C/min.(No composite formed),(**middle**) 20°C/min. and 30min. at 400°C(4.5 mm infiltrated) and (**right**) 5°C/min.(4.5 mm infiltrated)

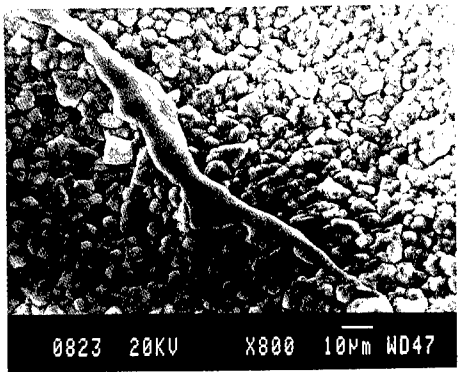


Fig.3: Al-2wt% Mg alloy coming up through the Mg-rich oxide layer to the oxide/preform interface.

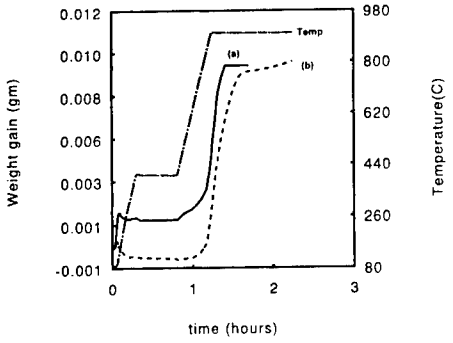


Fig.4: Weight gain data showing the termination of infiltration of Al-6.1wt%Mg-6.5wt%Si-0.3wt%Fe alloy into 53 µm alumina preform at 900°C. (a) termination inside the preform, (b) termination outside the preform (The preform in (a) was made longer to ensure termination within the preform)

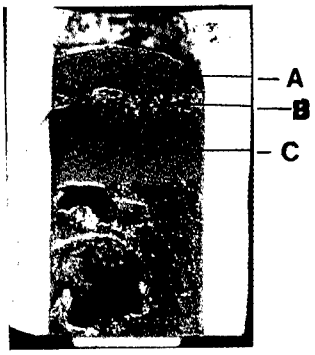


Fig.5: Re-initiation[A] of infiltration into 53 µm alumina preform with Mg powder[B]. The initial composite formed until termination is denoted by C.

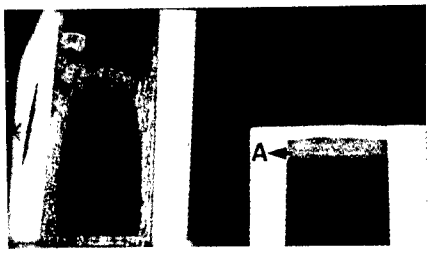


Fig.6: Eliminating the termination of infiltration due to local depletion of Mg with preform smaller in diameter than billet. ***(left)*** billet is larger in diameter than preform(full 1cm infiltrated), ***(right)*** billet and preform are of same diameter(6mm infiltrated before termination, A indicates the uninfiltrated portion of the preform).

SINTERING OF PARTICULATE REINFORCED TITANIUM MATRIX COMPOSITES

David E. Alman

U.S. Department of Energy
Albany Research Center
Albany, OR 97321

Abstract

The influence of reinforcing phase, volume fraction, and sintering temperature on the microstructure and hardness of particulate reinforced Ti-matrix composites was studied. Ti was reinforced with 0, 2.5, 5, 10, 20, and 40 volume percent (vol%) TiC, TiB_2, B_4C or Si_3N_4 particles. Composite powder blends were die pressed into cylindrical specimens and sintered at 1100, 1200, 1300, and 1400°C in vacuum for 2 hours. Ti+TiC composites could be sintered to high fractional densities, even at high volume fraction (40 vol%) TiC particles added to the Ti matrix. The Si_3N_4, B_4C and TiB_2 particles reacted with the Ti matrix during sintering. The reaction products consumed the Ti matrix and produced phases that were more dense than the starting reinforcement particles; hence, the reaction products generated porosity in the powder compact and hindered denisfication of the Ti matrix. However, at volume fractions $\leq$20 vol%, the Ti+TiB_2 composites could be densified by sintering at 1400°C and the Ti+Si_3N_4 composites by sintering at 1300°C. Extensive reactions occured during sintering of the Ti+Si_3N_4 composites at 1400°C, which produced microstructures that were detrimental to the properties of these composites. Ti+$\leq$10 vol% B_4C composites could be densified by sintering at 1400°C. All of the dense sintered composites were significantly harder than the unreinforced Ti matrix.

The Third Pacific Rim International Conference on
Advanced Materials and Processing (PRICM 3)
Edited by M.A. Imam, R. DeNale, S. Hanada,
Z. Zhong and D.N. Lee
The Minerals, Metals & Materials Society, 1998

Introduction

The high specific strength, stiffness and creep resistance, as well as excellent corrosion resistance of titanium makes it attractive for a wide variety of applications. For years titanium-based alloys and composites were primarily considered aerospace materials; however, increasingly, titanium is being considered for non-aerospace, commercial applications [1-3]. The properties of titanium-based alloys can be further augmented by composite strengthening. Unfortunately, continuous filament reinforced titanium-matrix composites are expensive, due to high fiber costs and limited formability, and their properties are highly anisotropic. Hence, these materials have been restricted to very specialized applications. By contrast, discontinuous (or particulate) reinforced composites are less expensive to fabricate and their properties are nearly isotropic. Particulate-reinforced titanium-matrix composites are being considered for wear resistant (gears, bearings, shafts), erosion and corrosion resistant (tubing) and creep resistant (engine) applications [4].

The present study is part of an effort to develop low cost fabrication methods for advanced materials. This paper details the processing and microstructure of Ti-matrix composites reinforced with either TiC, B_4C, TiB_2 or Si_3N_4 particles produced by traditional press-and-sinter powder metallurgy (p/m). P/M has been utilized for years as a low cost fabrication method for producing near-net-shape components (primarily for ferrous alloys). Based on results of a previous study on the wear resistance of hot-pressed Ti matrix composites, the reinforcing phases that imparted the greatest enhancement in wear resistance to the matrix were selected for this study [5]. The influence of reinforcing phase, volume fraction, and sintering temperature on the resultant composite microstructure was investigated.

Experimental Procedure

Titanium powder was dry blended with 0, 2.5, 5, 10, 20 and 40 volume percent (vol%) TiC,TiB_2, B_4C or Si_3N_4 powder. All powders were commercially available and were -325 mesh (44 μm) in size. A turbula-type mixer was utilized for dry blending. The powders were mixed in glass jars for 1 hour. Nominally, 15 grams of the composite powder mixtures were cold pressed in a steel die (walls lubricated with a zinc sterite-alcohol slurry) to form cylindrical specimens (approximately, 19 mm in diameter and 18 mm in height). The green density of the compacts ranged from 68 to 72 percent of theoretical density for the appropriate composite blend. Samples were vacuum sintered ($x10^{-4}$ Torr) at 1100, 1200, 1300, and 1400°C for 2 hours. The heating rate was 10°C/min, and after 2 hours at the sintering temperature, specimens were furnace cooled.

The densities of the resultant composites were measured by the Archimedes (water immersion) method. The microstructures were evaluated by optical and scanning electron microscopy (SEM) in both secondary and backscattering imaging modes. The phases present after sintering were determined by standard X-ray diffraction (XRD) techniques and SEM with energy dispersive X-ray (SEM-EDX) analysis. Also, Vickers hardness of the composites was measured (diamond indenter, 5 kg load).

Results

The density and hardness of all composites as a function of reinforcement phase and sintering temperature are listed in Table I. Inspection of the results reveals that increasing the sintering temperature increases the density of sintered monolithic Ti. Sintering at 1400°C produced 98 percent dense Ti, while sintering at 1100°C produced a specimen only 92 percent dense. Sintering

Table I: Sintered Density and Hardness of Particulate Reinforced Ti- Matrix Composites as a Function of Sintering Temperature

Composite\Sintering Temperature	Density (% Theoretical)				Vickers Hardness Number			
	1100°C	1200°C	1300°C	1400°C	1100°C	1200°C	1300°C	1400°C
Monolithic Ti	91.9	93.7	96.1	97.9	181	206	224	253
Ti + 2.5 vol% TiC	93.4	96.0	98.1	99.8	222	245	263	277
Ti + 5 vol% TiC	95.9	94.4	99.1	100	243	253	282	296
Ti + 10 vol% TiC	93.6	97.4	99.5	100	225	279	296	304
Ti + 20 vol% TiC	96.7	98.3	98.9	99.4	328	356	371	354
Ti + 40 vol% TiC	93.7	95.4	95.8	96.9	553	655	666	671
Ti + 2.5 vol% TiB_2	92.1	94.1	98.7	100	146	233	268	331
Ti + 5 vol% TiB_2	90.3	85.2	97.7	100	125	218	299	357
Ti + 10 vol% TiB_2	71.5	75.7	95.8	100	161	165	327	413
Ti + 20 vol% TiB_2	68.7	68.9	93.7	100	180	164	217	585
Ti + 40 vol% TiB_2	60.9	61.6	62.2	74.4	204	221	213	341
Ti + 2.5 vol% B_4C	93.0	93.9	97.7	100	183	211	255	346
Ti + 5 vol% B_4C	84.2	88.7	96.9	100	169	201	272	346
Ti + 10 vol% B_4C	79.1	82.4	90.4	100	177	184	298	470
Ti + 20 vol% B_4C	71.4	73.1	77.0	92.8	167	126	196	389
Ti + 40 vol% B_4C	63.0	63.5	62.8	54.0	124	141	146	94
Ti + 2.5 vol% Si_3N_4	93.2	95.6	98.3	100	316	362	411	331
Ti + 5 vol% Si_3N_4	89.5	96.4	99.6	76.7	372	494	533	357
Ti + 10 vol% Si_3N_4	86.9	94.8	99.5	71.5	412	544	634	413
Ti + 20 vol% Si_3N_4	87.3	91.3	98.5	100	478	674	748	585
Ti + 40 vol% Si_3N_4	76.7	76.5	75.1	71.9	281	280	240	341

at 1200 and 1300°C produced specimens that were roughly 94 and 96 percent dense, respectively. Concomitant with the increase in density was an increase in hardness with higher sintering temperatures. Sintering at 1400°C produced a sample that was 28 percent harder than sintering at 1100°C (253 versus 181 HVN). This is expected, as sintering at higher temperatures resulted in less porous materials. The results for each composite system are discussed in detail below:

All of the TiC containing composites were sintered to greater than 98 percent density at 1300°C and 1400°C, with the exception of the 40 vol% composite, which approximately 96 and 97 percent dense. At the lower temperatures the composites contained more porosity; however, all specimens were sintered to greater than 93 percent of the theoretical density. Interestingly, there appears to be no identifiable trend between porosity and volume fraction of TiC phase (below 20 vol%). At 1100 and 1200°C, the 20 vol% TiC composite contained slightly less porosity than several composites with lower volume fractions of TiC. Porosity should increase with increasing volume fraction, as the addition of high melting TiC particles should hinder densification. Figure 1a shows the microstructure of the Ti+10vol% TiC sintered at 1400°C. The TiC particles reside within the Ti matrix, and there is no visible reaction zone between the phases. XRD and SEM-EDX confirmed that only Ti and TiC were present in the sintered microstructures. (However, this only indicates that within the resolution limits of optical microscopy, SEM, and XRD no reaction products, such as Ti_2C, formed.)

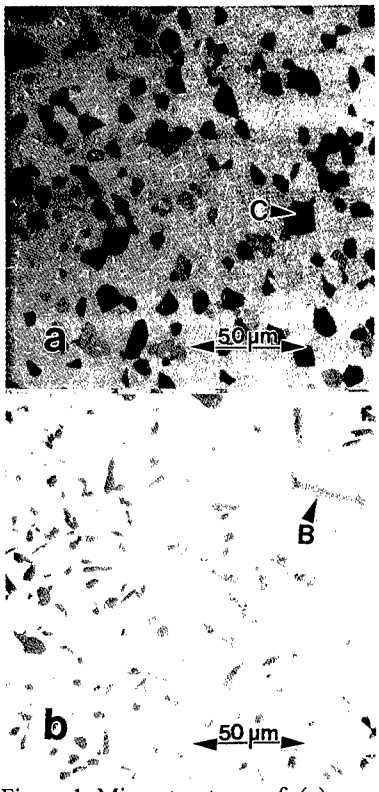


Figure 1. Microstructures of: (a) Ti+10vol%TiC; and (b) Ti+10vol% TiB_2 composites sintered at 1400°C. (B) = boride and (C) = TiC.

Unlike the Ti+TiC composites, there was a direct relation between density, volume fraction and sintering temperature for the Ti+TiB_2 composites. At all sintering temperatures below 1400°C, the sintered density decreases with increasing TiB_2 content; and at all TiB_2 volume fractions, the sintered density increases with increasing sintering temperature. This indicates that the addition of TiB_2 particles impedes the densification of Ti. However, sintering at 1400°C produced essentially fully dense composites, with TiB_2 additions of 20vol% or less. Figure 1b shows the microstructures of Ti-10vol%TiB_2 composites sintered 1400°C. XRD detected Ti, TiB, and TiB_2 in all of the composites, revealing that the Ti reacts with the TiB_2 particles.

The addition of B_4C particles, like TiB_2 particles, impedes the densification of Ti matrix during sintering. The sintered densities of the Ti+B_4C composites generally increase with increasing sintering temperature and decreasing B_4C content. None of the Ti+40 vol% B_4C composites could be densified, and the maximum density achieved by sintering the Ti+20vol% B_4C composites was only 92.8 percent. However, essentially fully dense composites containing 10 vol% or less B_4C particles were obtained by sintering at 1400°C. The B_4C particles reacted with the Ti matrix to form titanium-borides and titanium-carbides. XRD revealed that at volume fractions less than 20 percent, the B_4C particles were consumed during sintering. These composites contained Ti, TiC,

TiB and TiB_2. At 40 vol%, the titanium matrix was consumed and the composites consisted of TiB, TiC, B_4C and TiB_2.

The Ti+Si_3N_4 composites behaved in a very interesting manner. The porosity, of the composites sintered at 1300°C and below, increased with increasing Si_3N_4 volume fraction; expected behavior. However, at 1400°C, the composites that contained 5 and 10 vol% Si_3N_4 were porous, while the composites containing 2.5, and 20 vol% Si_3N_4 were dense. The 5 and 10 vol% Si_3N_4 composites sintered at 1400°C were the only specimens that did not maintain shape retention (i.e., slumped) during processing. Also, the pore structure of these two samples was radically different from all the other composites. These composites contained very large pores that were surrounded by dense regions (Figure 2), while all the other samples contained very small, uniformly dispersed pores. During sintering the Si_3N_4 reacted with the Ti to primarily form a variety of titanium-silicide phases, as shown on Table II. Also, sintering at 1200 and 1300°C produced composites that were harder than those sintered at 1400°C (see, Table I).

Table II: Influence of Sintering Temperature on the Phases Formed During Processing of Ti+Si_3N_4 Composites

Ti +	1100°C	1300°C	1400°C
2.5 vol% Si_3N_4	α-Ti(N), Ti_5Si_3, Ti_3Si	same as 1100°C	same as 1100°C
5 vol% Si_3N_4	α-Ti(N) Ti, Ti_5Si_3, Ti_3Si	α-Ti(N), TiSi, Ti_3Si,Ti_5Si_3	α-Ti(N), Ti_3Si, TiSi
10 vol% Si_3N_4	α-Ti(N), Ti_5Si_3, Si_3N_4, Ti_3Si, Ti_2N	α-Ti(N), Ti_5Si_3, Ti_3Si	α-Ti(N), Ti_5Si_3, Ti_3Si
20 vol% Si_3N_4	α-Ti(N), Ti_5Si_3, Ti_2N, Si_3N_4,Ti_3Si	α-Ti(N), Ti_2N,Ti_5Si_3	α-Ti(N), Ti_2N,Ti_5Si_3, Si

* Phases determined by XRD analysis. α-Ti(N) is a solid solution of Ti containing 0.3%N and was index using powder diffraction file card no: 41-1352.

Discussion

Significant interactions occur between the Ti matrix and the B_4C and Si_3N_4 particles. The phases that form between the Ti and B_4C (ρ=2.5 g/cm^3) are TiB (ρ=4.5 g/cm^3) and TiC (ρ=5.0 g/cm^3) and the phases that formed between Ti and Si_3N_4 (ρ=3.4 g/cm^3) are TiSi (ρ=4.3 g/cm^3), Ti_5Si_3 (ρ=4.4 g/cm^3), Ti_3Si (ρ=4.3 g/cm^3) and Ti_2N (ρ=4.8 g/cm^3). All these phases are denser than the starting reinforcement phase. During sintering of systems with interacting components, the formation of reaction products can impede densification if the new phase is significantly more dense than the starting constituent phases [6]. Porosity will be generated in the powder compact, if the shrinkage during sintering does not equal (or is greater than) the concomitant decrease in volume associated with phase formation [6].

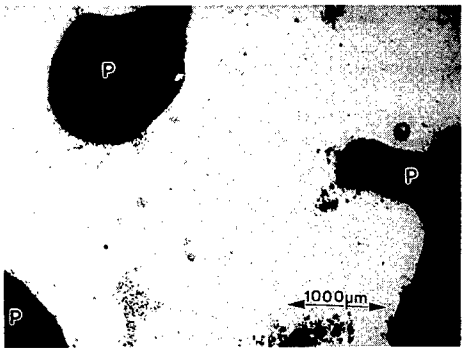


Figure 2. Microstructure of Ti+10vol% Si_3N_4 sintered at 1400°C. (P) = large pore.

The reaction product (TiB) that forms during sintering of the Ti+TiB_2 composite, has has a similar density to the starting matrix and reinforcing phase (4.5 g/cm^3). Thus the formation of TiB does not generate porosity during sintering

of this composite system. However, the reaction does consume some of the Ti matrix, hence, the composites contain more than the intended volume fraction of high melting boride reinforcement (e.g., the sintered Ti+40 vol % TiB_2 composite contains more than 40 vol% borides). Thus, the addition of the boride particles hinders densification during sintering due to the consumption of Ti to form TiB.

On a "macroscopic" scale, the Ti and TiC are thermodynamically compatible. Hence, the addition of TiC particles does not impede densification of the Ti matrix, due to the phase formation effects, and composites with high volume fractions of TiC particles can be sintered to high fractional densities.

Densification of the Ti+Si_3N_4 system, at elevated temperatures, is also complicated by the formation of a eutectic liquid between Ti and Si (at 1335°C). This results in the distortion and slumping that occurs during sintering at 1400°C at intermediate volume fractions (5-20vol%).

All of the dense composites are harder than the monolithic Ti-matrix, indicating they should possess improved the wear resistance. The Ti +≤20 Si_3N_4 vol% sintered at 1300°C produced the hardest composites at the respective volume fractions. In fact, the Ti+20v% Si_3N_4 composite was the hardest of all the composites produced for this study. At the 40 vol% level, the hardest material produced was the TiC containing composite, as it was the only near fully dense composite.

Summary

Particulate reinforced Ti-matrix composites were produced by pressureless sintering. Ti+TiC composites could be sintered to high fractional densities, even with high levels (40 vol%) of TiC particles. No observable reaction product was dectected at the Ti-TiC interface. During sintering, the Si_3N_4, B_4C and TiB_2 particles react with the Ti matrix. The reaction products consumed the Ti matrix and produced reaction phases that were more dense than the starting reinforcement particles; hence, reaction phases generated porosity in the powder compacts. As a consequence, these composites are difficult to sinter to high fractional densities with the addition of large volume fractions of reinforcing particles. However, at volume fractions ≤20 vol%, the Ti+TiB_2 composites could be densified by sintering at 1400°C and the Ti+Si_3N_4 composites by sintering at 1300°C. Extensive reactions occured during sintering of the Ti+Si_3N_4 composites at 1400°C, which produced microstructures that were detrimental to the properties. Ti+≤10 B_4C composites could be densified by sintering at 1400°C.

Acknowledgments

The assistance of Mr. B. Luo and Mr. D. Davis in performing the sintering experiments, Ms. H. White for sample preparation, and Mr. R.D. Govier for microstructural analysis is gratefully acknowledged.

References

1. S.R. Seagle, *Mater. Sci. Engr.*, **A213**, 1996, 1.
2. M. Yamada, *Mater. Sci. Engr.*, **A213**, 1996, 8.
3. R. Vandermark, *JOM*, **49 (6)**, 1997, 24
4. S. Ranganath, *J. Mater. Sci.*, **32**, 1997, 1.
5. D.E. Alman, J.A. Hawk and J.S. Simmons, in Advances in Powder Metallurgy and Particulate Materials- 1997, Part-7 , MPIF/AMPI, Princeton, NJ, 1997, pp 3.
6. R.W. Rice and W.J. McDounough, *J. Amer. Ceram. Soc.*, **68**, 1985, C122.

COMPARISON OF *IN SITU* FIBRE AND INTERFACE PROPERTIES BETWEEN SEALED AND UNSEALED 3-D WOVEN SiC/SiC-BASED COMPOSITE AFTER TENSILE TESTING UP TO 1380 °C IN AIR AND VACUUM.

Ian J. Davies[1], Takashi Ishikawa[1], Naoto Suzuki[2], Masaki Shibuya[3], Tetsuro Hirokawa[4], and Jun Gotoh[5]

1 Airframe Division, National Aerospace Laboratory, Mitaka Shi, Tokyo 181, Japan
2 Kogakuin University, Shinjuku ku, Tokyo 163, Japan
3 Corporate Research and Development, Ube Industries Ltd., Ube Shi, Yamaguchi 755, Japan
4 Industrial Textile Division, Shikibo Ltd., Yokaichi Shi, Shiga 527, Japan
5 Kawasaki Heavy Industries, Kakamigahara Shi, Gifu 504, Japan

Abstract

The *in situ* fibre strength Weibull parameters, S_o and m, and fibre/matrix interface shear strength, τ, were compared for 3-D woven SiC/SiC-based composite with and without a glass-based sealant after tensile testing up to 1380 °C in vacuum and air. Unsealed specimens tested in vacuum up to 1380 °C showed high S_o (>3 GPa) and low τ (<10 MPa) in agreement with the superior mechanical properties observed. Conversely, unsealed specimens tested in air at 1100 °C and 1200 °C possessed low S_o (<1.5 GPa) together with an order of magnitude increase in τ and accompanied by significantly reduced mechanical properties - attributed to oxidation of the fibre/matrix interface. However, sealed specimens tested in air at 1000-1200 °C showed S_o, m, and τ values similar to those of the unsealed specimens tested in vacuum, as was also the case for mechanical properties. It was concluded that the glass-based oxidation protection system utilised was extremely effective for the test conditions employed, i.e., short-term up to 1200 °C in air.

The Third Pacific Rim International Conference on
Advanced Materials and Processing (PRICM 3)
Edited by M.A. Imam, R. DeNale, S. Hanada,
Z. Zhong and D.N. Lee
The Minerals, Metals & Materials Society, 1998

Introduction

The superior structural properties above 1100 °C of ceramic matrix composites (CMCs) has resulted in numerous applications including afterburner flaps, rocket combustion chambers, turbine disks, and airframe structures for re-entry vehicles. An important class of CMCs is that based on continuous fibre reinforcement which includes silicon carbide (SiC/SiC). Although recent advances have increased the operating temperature of fibres and matrix to in excess of 1200 °C, a major weakness of CMCs is oxidation of the fibre/matrix interface at elevated temperature (e.g., >800 °C) in oxidising environments [1]. The fibre/matrix interface in CMCs is often based on pyrolytic carbon or boron nitride which are chosen due to their low coefficient of friction and hence fibre/matrix interface shear stress, τ. Oxidation of this region has been shown to increase τ by an order of magnitude and change the failure mode from multiple to single matrix cracking, i.e., notch insensitive to notch sensitive [1]. The final result is often a significant decrease in mechanical properties for the composite.

One method to increase the oxidation resistance of CMCs is through impregnating or sealing the composite with a material that acts as a barrier to oxygen diffusion and keeps τ at a desired level (typically <10 MPa) during mechanical testing. The present work investigates the effect of a glass-based oxidation protection system on the *in situ* fibre strength properties of a 3-D woven SiC/SiC-based composite.

Experimental procedure

The composite studied in this report was based on the SiC/SiC system and utilised Tyranno® LoxM Si-Ti-C-O fibres which had undergone a proprietary surface treatment in order to produce a 40 nm carbon-rich layer beneath a 10 nm SiO_x outer layer at the fibre surface [2]. It was believed that such a carbon-rich layer should then act as the fibre/matrix interface during subsequent mechanical testing [2]. Prior to matrix consolidation the fibres were woven into an orthogonal 3-D configuration with fibre volume fractions of approximately 0.19, 0.19, and 0.02 in the x, y, and z directions, respectively. The matrix precursor was a polymer similar to polytitanocarbosilane with repeated impregnation and pyrolysis cycles until a satisfactory density was achieved. Following machining to a geometry suitable for mechanical testing, several specimens were impregnated (i.e., sealed) with a proprietary glass-based compound with the aim of increasing the oxidation resistance of the composite. Mechanical testing was carried out in tension with the loading direction parallel to the specimen y axis - details given elsewhere [3]. Unsealed specimens were tested up to 1380 °C in vacuum and air whilst sealed specimens were tested in air between 1000-1200 °C.

Following mechanical testing, the specimen fracture surfaces were examined using optical microscopy (OM) and scanning electron microscopy (SEM). The fracture surface of individual fibres was investigated for evidence of a "fracture mirror" from which the *in situ* fibre strength, S, could be determined using [4]:

$$S = \frac{A_m K_F}{\sqrt{r_m}} \tag{1}$$

where A_m is a constant (values of 3.5 and 2.51 have been reported [5,6]) and taken to be 2.51 in the present case [7], K_F is the fibre fracture toughness (taken to be 1 MPa.m^{½} in this case [1,8]) and r_m is the fracture mirror radius. A typical fibre exhibiting evidence of a fracture mirror is shown in Figure 1(a). More than one hundred fibres were investigated for each test condition

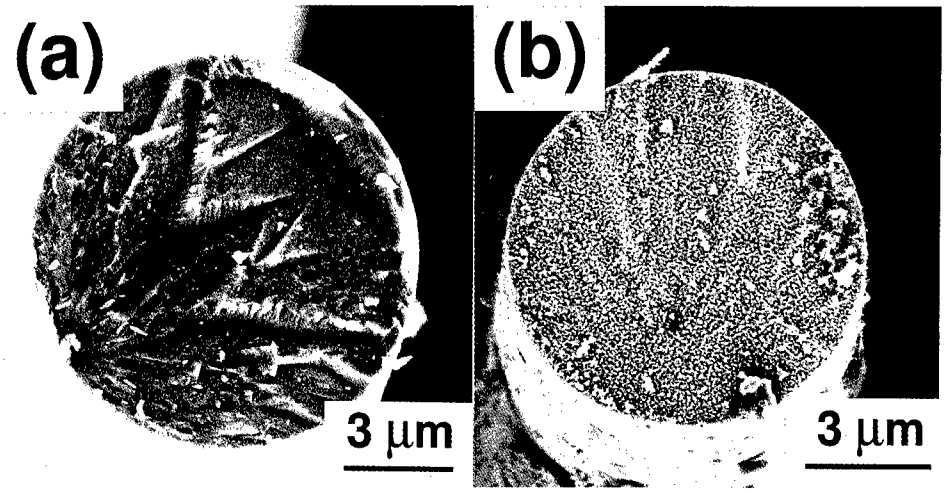


Figure 1: Scanning electron micrographs of fibre fracture surfaces in unsealed 3-D woven SiC/SiC-based composite after tensile testing in vacuum: (a) 1200 °C, and (b) 1380 °C.

from which the (uncorrected) *in situ* fibre strength Weibull parameters, S_o* and m*, could be obtained [4]. Following application of a correction factor and normalising to a standard gauge length of 10^{-3} m, the *in situ* fibre strength Weibull parameters, S_o and m, were derived [4]. Using fibre pullout length data for the specimens [9] it was further possible to obtain τ for each test condition using [4]:

$$\tau = \frac{r\lambda(m)S_o}{4<h>} \tag{2}$$

$$\lambda(m) \approx 0.716 + \frac{1.36}{m^{0.6}} \qquad \text{for } m \geq 1 \tag{3}$$

where r is the fibre radius (taken to be 4.03 μm [7]) and <h> is the mean fibre pullout length. Thus, data for S_o, m, and τ could be compared for unsealed and sealed specimens at each test condition.

Results and discussion

In situ fibre strength vs. cumulative failure for each test condition has been presented in Figure 2 whilst resultant S_o, m, and τ values have been included in Table I - normalised to a gauge length of 10^{-3} m in all cases. It should be noted that fracture mirror radii could only be measured for test temperatures up to 1300 °C [8] due to significant fibre decomposition beyond that point (Figure 1(b)). The first point of note from Table I is that S_o showed a slight decrease with increasing test temperature for unsealed specimens tested in vacuum whilst m increased under the same conditions. These trends were attributed to the interaction of fibres failing at surface and internal defects, as follows [8]:

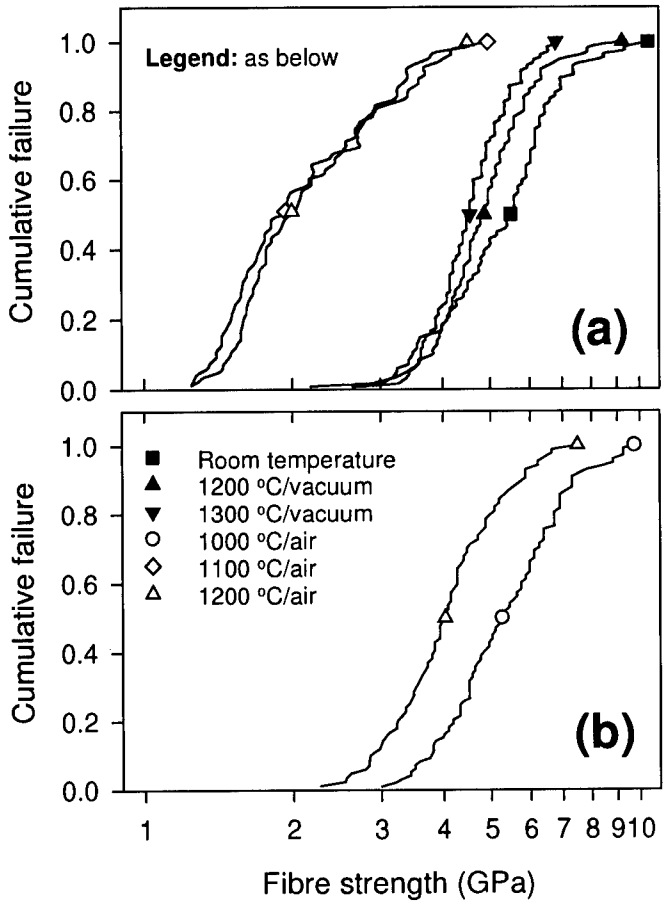


Figure 2: *In situ* fibre strength distributions for Tyranno Si-Ti-C-O fibres in 3-D woven SiC/SiC-based composite: (a) unsealed, and (b) sealed.

Table I: *In situ* strength parameters for Tyranno Si-Ti-C-O fibres in 3-D woven SiC/SiC-based composite after testing in vacuum and air up to 1380 °C.

	Test condition	S_o GPa	m	<h> 10^{-3} m	τ MPa
Unsealed	Room temperature	3.86 (+/- 0.13)	4.19 (+/- 0.05)	0.81 (+/- 0.02)	4.94 (+/- 0.16)
	1200 °C/vacuum	3.45 (+/- 0.20)	5.72 (+/- 0.10)	0.59 (+/- 0.03)	6.27 (+/- 0.35)
	1300 °C/vacuum	3.18 (+/- 0.34)	6.56 (+/- 0.11)	0.39 (+/- 0.04)	9.13 (+/- 0.96)
	1100 °C/air	1.37 (+/- 0.15)	2.91 (+/- 0.13)	0.07 (+/- 0.01)	54.75 (+/- 5.40)
	1200 °C/air	1.26 (+/- 0.18)	2.68 (+/- 0.11)	0.06 (+/- 0.01)	60.50 (+/- 8.43)
Sealed	1000 °C/air	4.22 (+/- 0.29)	4.00 (+/- 0.07)	1.06 (+/- 0.07)	3.92 (+/- 0.26)
	1200 °C/air	3.12 (+/- 0.31)	4.64 (+/- 0.10)	0.57 (+/- 0.06)	6.06 (+/- 0.61)

Fibres that failed at room temperature usually showed fracture origins at the fibre surface due to surface flaws presumably introduced during fibre and/or composite manufacture. However, it is known that Si-Ti-C-O fibres start to decompose above 1000 °C in vacuum which gives rise to a large number of internal voids with narrow size distribution (concluded from Figure 1(b)). As the test temperature is increased, the average internal void size will increase and a larger proportion of fibres fail due to internal voids compared to surface flaws, i.e., S_o will decrease. In addition, the internal voids (with narrow size distribution) will increasingly dominate the broader size distributed surface flaws, i.e., m will increase. The slight increase in τ with increasing test temperature was attributed, at least partially, to differences in the coefficients of thermal expansion between matrix and fibre components.

Values of τ for unsealed specimens were calculated to be <10 MPa in all cases and presumably due to the carbon-rich layer near the fibre surface acting as the fibre/matrix interface [2]. Such low values of τ have previously been associated with extensive fibre pullout and good mechanical properties [1] as was also the case for the current specimens [10]. This result was in contrast to unsealed specimens tested in air where most fibres (>80%) possessed a flat fracture surface and negligible fibre pullout, which suggested no crack deflection mechanism having taken place at the fibre/matrix interface. Such a phenomena has also been described in terms of the critical strain energy release rates for the interface, G_i, and fibre, G_f, i.e.,

$$\frac{G_i}{G_f} \geq \frac{1}{4} \tag{4}$$

so that a crack propagating perpendicular to the fibre/matrix interface will not deflect when this inequality is true [11].

The remaining fibres that did show fracture mirrors had a significantly decreased S_o compared to unsealed specimens tested in vacuum, together with an order of magnitude increase in τ. As in previous cases, this significant increase in τ was attributed tq oxidation of the fibre/matrix interface and replacement of the carbon-rich layer by SiO_2 which has a higher coefficient of friction [1].

It can be seen from Figure 2 and Table I that S_o, m, and τ for sealed specimens tested in air were similar to those of unsealed specimens tested in vacuum. It is known that τ in particular is extremely sensitive to oxidation [1] so that these results strongly imply negligible oxidation to have occurred during mechanical testing. Thus, it may be concluded that the glass-based oxidation protection system utilised was extremely effective for the test conditions employed.

Summary

The *in situ* fibre strength Weibull parameters, S_o and m, and fibre/matrix interface shear strength, τ, were compared for 3-D woven SiC/SiC-based composite with and without a glass-based sealant after tensile testing up to 1380 °C in vacuum and air. Unsealed specimens tested in vacuum up to 1380 °C showed high S_o (>3 GPa) and low τ (<10 MPa) in agreement with the good mechanical properties observed. Conversely, unsealed specimens tested in air at 1100 °C and 1200 °C possessed low S_o (<1.5 GPa) together with an order of magnitude increase in τ and accompanied by significantly reduced mechanical properties - attributed to oxidation of the fibre/matrix interface. However, sealed specimens tested in air at 1000-1200 °C showed S_o, m, and τ values similar to those of the unsealed specimens tested in vacuum, as was also the case

for mechanical properties. It was concluded that the glass-based oxidation protection system utilised was extremely effective for the test conditions employed, i.e., short-term up to 1200 °C in air.

Acknowledgements

This work was supported by the Science and Technology Agency of Japan whilst one of the authors (IJD) was supported as a Science and Technology Agency Fellow. The authors also gratefully acknowledge Y. Nomura for help with mechanical testing.

References

1. M. D. Thouless et al., "Effect of interface mechanical properties on pullout in a SiC-fiber-reinforced lithium aluminum silicate glass-ceramic", J. Am. Ceram. Soc., 74 (4) (1989) 525-532

2. S. Masaki et al., "Development of Si-Ti-C-O fiber reinforced SiC composites by chemical vapor infiltration and polymer impregnation and pyrolysis", in High-Temperature Ceramic-Matrix Composites II, eds. A. G. Evans and R. Naslain, (Ceramic Transaction volume 58, The American Ceramic Society, Westerville, 1995), 187-192

3. T. Ishikawa et al., "Experimental stress-strain behavior of Si-Ti-C-O fiber/SiC matrix composites and estimation of matrix elastic modulus", accepted for publication in Comp. Sci. Technol., 1996

4. Curtin, W. A., Theory of mechanical properties of ceramic-matrix composites, J. Am. Ceram. Soc., 74 (11) (1991) 2837-2845

5. Rice, R. W., Treatise on Materials Science and Technology, volume 11, (Academic Press, New York, 1978), 199

6. Eckel, A. J. and Bradt, R. C., Strength distribution of reinforcing fibers in a Nicalon fiber/chemically vapor infiltrated silicon carbide matrix composite, J. Am. Ceram. Soc., 72 (3) (1989) 455-458

7. I. J. Davies et al., "Fibre and interfacial properties measured in situ for a 3-D woven SiC/SiC-based composite with glass sealant", accepted for publicated in Composites Part A, 1997

8. I. J. Davies et al., "In situ fibre strength parameters for ceramic matrix composites tested at elevated temperature in vacuum and air", submitted to Comp. Sci. Technol., 1997

9. I . J. Davies et al., Optical microscopy of 3-D woven SiC/SiC-based composites, submitted to Comp. Sci. Technol. (1997)

10. I. J. Davies et al., "Stress/strain behaviour of 3-D woven SiC/SiC-based composites", submitted to J. Am. Ceram. Soc., 1997

11. M. He and J. W. Hutchinson, "Kinking of a crack out of an interface", J. Appl. Mech., 56 (1989) 270-278

Fabrication and Modification of Mechanical Properties of Al/Al_2O_3 Composite bodies by Reaction between SiO_2 and Molten Al

Noboru Yoshikawa*, Yoshiyuki Watanabe**, Zully Matamoros Veloza***,
Shoji Taniguchi* and Atsushi Kikuchi*
*School of Metallurgy, Graduate Schools, Tohoku University, Aza-Aoba, Aramaki, Aoba-ku, Sendai, Miyagi, Japan 980-77, ** Ingeominas, Diagonal 53, Santafe de Bogota, D.C., Colombia, ***Graduate Student at Tohoku University, Present at Dowa Mining Co., Ltd.

Abstract

Fused silica(SiO_2) rods having 5~15mm in diameter were dipped into molten Al, and the rods were converted into Al/Al_2O_3 composite bodies by substitutional reaction between Si and Al. Microstructures and mechanical properties of the specimens fabricated at different reaction temperature were investigated.

It was found that the composite bodies fabricated at lower temperature(less than 1273K)had higher hardness and brittle nature, on the other hand, the composite bodies fabricated at higher temperature had less scattering data of the compressive fracture strength and a little increase of the ductility was obtained.

Gradation of hardness in the composite bodies was accomplished by varying the reaction temperature during the fabrication process. Hardness of the composites were modified by means of reaction with Al-Cu alloy melt followed by aging treatment.

The Third Pacific Rim International Conference on
Advanced Materials and Processing (PRICM 3)
Edited by M.A. Imam, R. DeNale, S. Hanada,
Z. Zhong and D.N. Lee
The Minerals, Metals & Materials Society, 1998

Introduction

"In-situ Composites" have been recently[1] remarked as their potentiality for reducing fabrication cost of composite materials. In-situ Al/Al_2O_3 composites are known to be obtained by means of direct oxidation of molten aluminum, the method has been known as DIMOX process[2]. Al/Al_2O_3 composites having similar microstructures are reported[3,4] to be obtained by means of substitutional reaction between SiO_2 and molten aluminum. By means of the latter method, it is possible to fabricate the arbitrary shaped composite bodies, having the same shape and scale as the starting SiO_2 bodies. Application of this material for machine components has been taken into consideration[3].

However, there are remaining fundamental problems[5,6] to be clarified on the reaction kinetics, microstructures and their relationship with mechanical properties, which are essential information for their fabrication and for designing the composites in the practical use. Moreover, it is possible to take advantage of these knowledge for modifying the composite properties.

The purpose of the present study is to investigate the reaction kinetics, microstructures, mechanical properties of the composite bodies fabricated at different reaction temperature between SiO_2 and molten Al. In addition, studies are conducted in order to survey the possibilities to modify the composites' mechanical properties(hardness). The first is to fabricate the functionally graded materials and the second is to increase the hardness by means of reaction with Al-Cu alloy melt followed by age hardening[7].

Experimental

The aluminum ingots having four nines in purity was cut into pieces and they were etched with 0.1N-NaOH aqueous solution for 1.8ks, then cleansed with purified water for 3.6ks. They were melted with electric furnace in Air. Commercial fused silica rods(Toshiba Ceramic Inc.)having diameters of 5mm were dipped into molten Al or Al-8at%Cu. Before the reaction, the rods were cleansed with alcohol for 10min with application of ultrasonic agitation.

The microstructures of the reaction layers were observed by means of Optical Microscope, Scanning Electron Microscope(SEM), Transmission Electron Microscope(TEM), and X-ray Diffraction(XRD). Vickers hardness and compression fracture strength were measured at room temperature. The applied load for the hardness measurements was 5kg. Dimensions for the cylindrical specimens used for the compression test were 5mm in diameter and 7mm in length.

Results

Growth rate of the reacted layer

Thickness of the reacted layer for the reaction time of 3.6ks obtained at different reaction temperature is shown in Fig. 1. It is seen that the growth rate increased as the reaction temperature between 973K and 1073K, however, the reaction rate decreased between 1073K to 1273K. The rate increased with reaction temperature again above 1373K.

According to X-ray diffraction, the produced alumina changed from low temperature phase (γ - Al_2O_3 etc.) to high temperature phase(α - Al_2O_3) between 1073K and 1273K. This phase transition is considered to be related with the change in the growth rate.

The relationships between the reacted layer thickness and the reaction time above 1373K are shown in Fig. 2. The thickness of the reacted layer increased parabolically and the rate constant increased as the increase of the reaction temperature. The apparent activation energy of the temperature dependence was about 78.4kJ/mol.

Microstructues of the reacted layer at different reaction temperature

The microstructures of the reacted layer(composite bodies) fabricated at different temperature are shown in Fig. 3. Specimens reacted at 1073K had very fine microstructures and they were observed with TEM(Fig. 3a), As indicated in Figs. 3(b),(c), microstructures above 1373K had similar duplex structure of Al(bright area) and Al_2O_3(dark area). The ratio of volume fraction of Al and Al_2O_3 was about 1:3, regardless of the fabrication temperature. Coarsening of the microstructutre occurred as the reaction temperature increased, especially above 1373K.

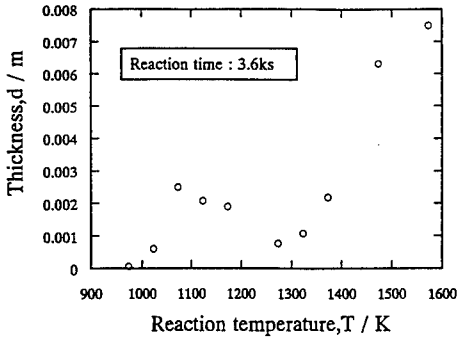


Fig. 1: Thickness of the reacted layer at different reaction temperature for 1hr.

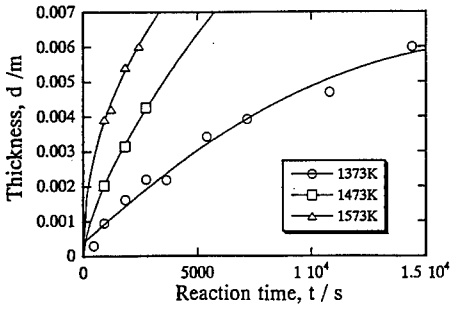


Fig. 2 : Relationship between the reaction time and thickness of the reacted layer.

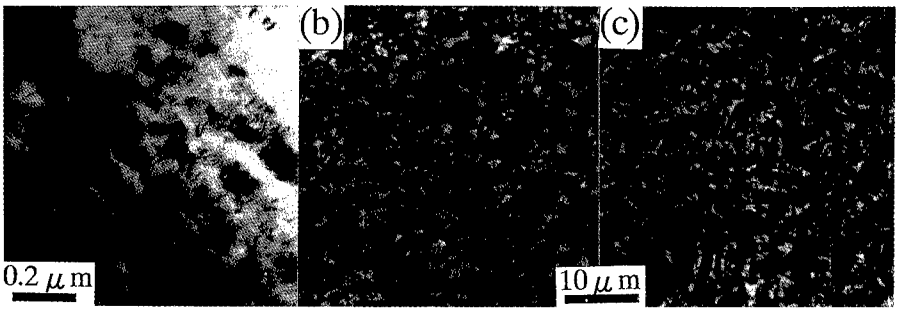


Fig. 3 : (a)TEM photograph of the composite reacted at 1073K, optical micrographs of the composite bodies, (b) reacted at 1373K and (c) reacted at 1473K.

It was observed that Si content in the composite was less than 5% and there was no gradient of Si concentration. The increase of the rate constants(shown in Fig. 2) above 1373K was considered to be caused by the microstructural change(shown in Fig. 3), where the width of the Al layer increased and resulted in the less resistance of the molten Al to flow through the reacted layer. The apparent activation energy(78.7kJ/mol) of the rate constant is higher than the activation energy of viscous flow of Al(about 13.1kJ/mol), therefore the coarsening of microstructures influenced the temperature dependence of growth rates.

Mechanical properties of the composite bodies

Vickers hardness was measured for the specimens fabricated at different reaction temperature, and they are plotted in Fig. 4. It was found that the hardness of specimens fabricated at higher temperature was lower. Cracks were generated at the corner of the indent[7] in the case of specimen fabricated at 1073K. On the other hand, bulging took place at the rim of the indent in the specimens fabricated at higher temperature above 1273K.

Compression test was conducted and the fracture stress of the specimens obtained at different temperature was measured and plotted in Fig. 5. Specimens fabricated at 1173K had the maximum strength. Large scattering in strength data was obtained from the specimens fabricated at lower temperature, however, the average strength did not vary with the fabrication temperature, comparing with the hardness. The fracture surface of the specimens was observed with SEM. Specimens fabricated at 1073K had typical brittle fracture surface(Fig. 6(a)). On the other hand, in a view of the fracture surface of specimen fabricated at 1473K(Fig. 6(b)), the metal parts were elongated and extruded, which look like forming domains. Transition of the fracture surface appearance was considered to be caused not only by the change of produced Al_2O_3 phases but also by coarsening of the microstructures, namely plastic deformation within the widened Al layer became possible.

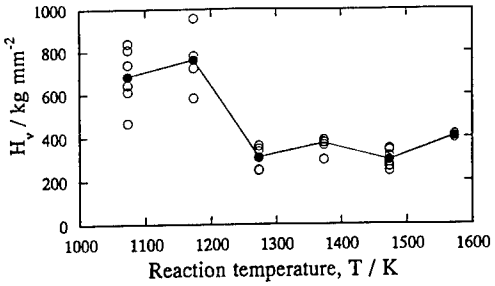


Fig. 4: Vickers hardness(H_v) of composite bodies fabricated at different reaction temperature.

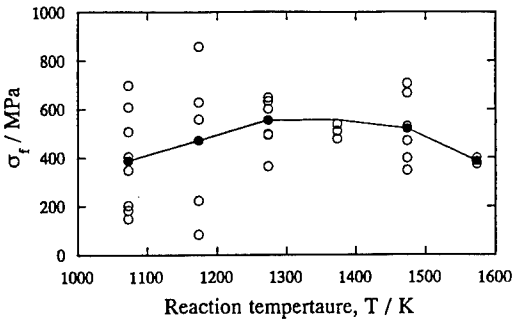


Fig. 5 : Compressive fracture strength of of composite bodies fabricated at different reaction temperature.

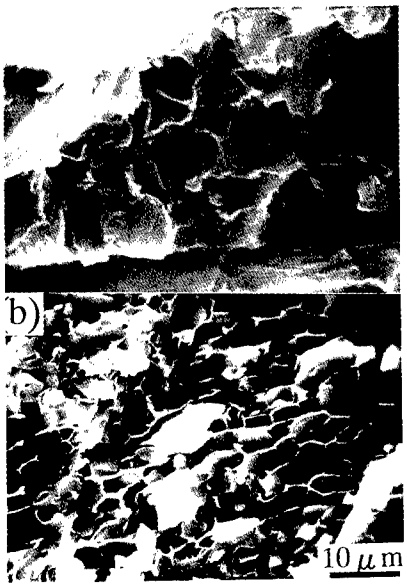


Fig. 6: SEM photographs of fracture surface of the composite bodies fabricated at (a) 1073K and (b) 1473K.

Modification of hardness

The composite bodies fabricated at higher temperature range had less scattering of strength data and a little increase in ductility, however, they lack the hardness. It was intended to investigate the possibilities for modifying the hardness of composite bodies, either obtaining local hardness variation or increase of hardness. The following experiments were conducted:

1) Gradation of hardness by controlling the reaction temperature

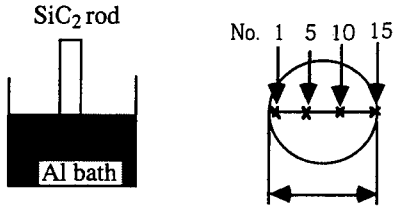
Relationship between reaction temperature and hardness of the composites(Fig.4) indicates the possibility of fabricating the hardness graded materials by controlling the reaction temperature. Two kinds of experiments were conducted. First method was to dip SiO_2 rods into Al melt and the reaction temperature was varied in the range between 1073K and 1373K either by cooling or heating during 3hrs. The second method was to plunge rods into the melts with simultaneous cooling, as schematically illustrated in Fig. 7.

The radial distributions of the hardness in the specimen cross section by the first method were measured and plotted in Fig. 8(a),(b). It was found that the hardness gradation was possible by means of cooling the specimens(Fig. 8(a)), however, the degree of hardness change was smaller than expected form the relationship in Fig. 4. Gradation was not possible by heating(Fig. 8(b)), because the heating caused coarsening of the microstructures initially formed and theAl_2O_3 phase transformed to high temperature phase.

Larger degree of hardness gradation along the longitudinal direction was accomplished by the second method. In this cases, low tempertaure(γ -)Al_2O_3 phase having fine microstructure was formed discontinuously at the certain position and grown. It was of interest that this hard microstructure was not possible to obtain by means of the first method(simple cooling). Further study on the detailed conditions for formation of the low temperature Al_2O_3 phase and the effects of composite structures are required.

(a) Heating(1073K - 1373K)

(b) Cooling(1373K - 1073K)



(c) Cooling and plunging(1373K - 1073K)

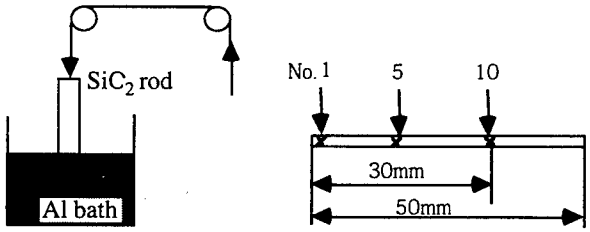


Fig. 7 : Schematic illustration of the experimental methods for hardness gradation. (a,b)Dipping and temperature variation, (c) temperature variation with plunging. Positions for hardness measurement in the rod cross section(a,b) and along the longitudinal direction(c) are also illustrated in the right hand sides.

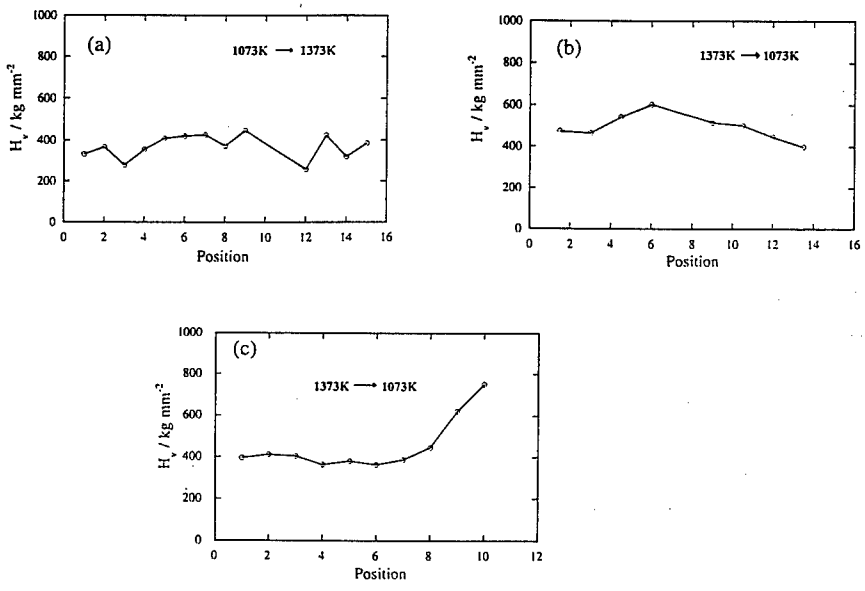


Fig. 8 : Distribution of hardness along the radial direction in the (a) heated specimen, (b) cooled specimen and the along the longitudinal direction in the (c) plunged and cooled.

2) Modification of hardness(Fabrication by reaction between SiO_2 and molten Al-Cu)

As shown in Fig. 4, hardness of the specimens fabricated at higher temperature was lower. The plastic deformation in the widened metal channels was considered to be one of the causes for this phenomena. In order to modify the hardness of specimens fabricated at higher temperature, the following procedures were taken for fabrication: SiO_2 rods were dipped into the molten Al-8at%Cu at 1373K. After completion of the reaction, specimens were heated at 673K for 1hr (solution treatment) and quenched in water. Lastly they were aged at different temperature for 4hrs. The relationship between the aging temperature and the hardness was shown in Fig. 9.

The hardness increased as the aging temperate increased to 473K. The increase in hardness was caused by formation of fine precipitates in Al layer in the composites, as TEM photograph in Fig. 10 indicates. Cu was more noble than Al, and it does not cause the substitutional reaction with Si, so Cu existed in the Al part, selectively, and precipitated by aging. The increase in hardness was considered to be related with hindrance of plastic deformation by the precipitates in the metal layer.

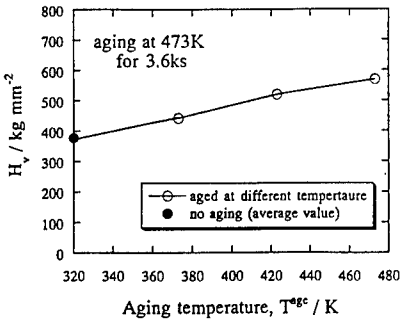


Fig. 9 : Relationship between the aging temperature and hardness.

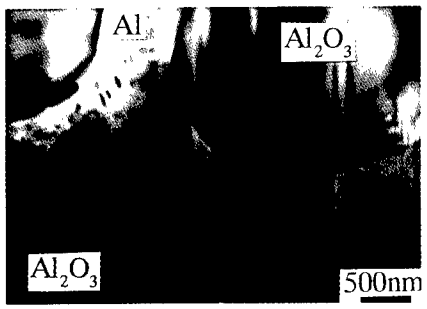


Fig. 10 : TEM photograph of the microstructure of aged specimen.

Summary

Al/Al_2O_3 composite bodies were obtained by means of substitutional reaction between SiO_2 and molten Al. The composite microstructures and the properties were dependent on the reaction temperature. Hard and brittle composites were obtained at lower fabrication temperature. On the other hand, the composites fabricated at higher temperature decreased in hardness. Elongation in the metal part was observed in the fracture surface. The ductility was considered to be caused by the plastic deformation in Al layer due to coarsening of microstructure during reaction process at higher temperature, which also influenced the growth rate of the reaction layer .

The hardness gradation in the composites was attempted by controlling the reaction temperature. The large degree of hardness gradation was obtained along the longitudinal direction by plunging the rods into Al melt with simultaneous cooling. The low hardness of the specimens fabricated at higher temperature was modified by incorporating Cu atoms into Al layer in the composites and followed by occurrence of precipitation hardening.

References

1. "In-situ Composites", ed. M.Singh and D.Lewis (The minerals, Metals and Materials Society, 1994)
2. M.S.Newkirk, A.W.Urquhart, H.R.Zwicker and E.Breval, "Formation of Lanxide Ceramic Composite Materials," J. Mater. Res., 1 (1986), 81-89
3. M.C. Breslin et al., "Processing, microstructure and properties of co-continuous alumina-aluminum composites," Mater. Sci. Eng., A195 (1995) 113-119.
4. S.Matsuo and T.Inaba, Ceramics 26 (1991), 222-223
5. S.Matsuo, private communication.
6. M.C.Breslin, private communivation.
7. N.Yoshikawa et al., " Mechanical properties of Al/Al_2O_3 composites fabricated by reaction between SiO_2 and molten Al.Al-Cu, " J. mater. Sci. Letters, 16 (1997) 1547-1550.

COMBINED MECHANICAL ALLOYING AND CONTROLLED COMBUSTION SYNTHESIS IN THE PRODUCTION OF TiB-Ti CMC`s

Sedat ÖZBILEN

Gazi University,
Faculty of Technical Education,
Metallurgical Education Department,
Teknikokullar, Ankara, Turkey.

Abstract

A nanocrystalline compact fabrication route by Mechanical alloying (MA) synthesizing technology and controlled combustion synthesis (CCS) during hot pressing were utilized to produce dense and tough TiB-Ti CMC`s by using Ti-B powder mixtures. In the first step mixtures of Ti and B powders (78, 80, 82, 84 and 86 wt%Ti and the rest is boron) are converted into nanocrystalline form without compound formation. For this purpose, powders MA´ed up to 8 hours and were examined by X-ray diffraction and SEM study. On subsequent hot pressing, the compound formation (TiB and TiB_2 depending on the composition) develops via SPS. An appropriate hot pressing cycle prevents significant grain coarsening of the microstructure, but with attendant consolidation to near full density. Detailed XRD and DTA study of the compacted samples were carried out to determine feasibility of the production of TiB-Ti CMC`s from TiB-off-stoichiometric compositions (<18wt%B) by MA+controlled CS during hot press.

The Third Pacific Rim International Conference on
Advanced Materials and Processing (PRICM 3)
Edited by M.A. Imam, R. DeNale, S. Hanada,
Z. Zhong and D.N. Lee
The Minerals, Metals & Materials Society, 1998

Introduction

Nanocrytalline structures have been proposed recently as a means to improve poor ambient temperature ductility and fracture toughness of certain materials such as ceramic matrix composites [1-3]. In nanocrystalline materials up to 50 v\o of the solid consists of incoherent interfaces between small differently oriented crystals. Single grain boundaries occupy a large volume fraction of the structure, they result in anomalously high diffusivity, alloying and capability for plastic deformation [4, 5]. The high grain boundary diffusivity rates (D_{gb}) and small grain size (dg) suggest that considerable creep deformation can occur even at room temperature since the creep rate is proportional to D_{gb}/d^3g [4]. Thus, creep is the prevalent deformation mechanism in nanocrystalline materials and it can occur irrespective of the existance of the slip system constraints [5]. Mechanical alloying is a powder processing technique involving repeated welding, fracturing and rewelding of powder particles in a dry high energy ball charge. Refinement of grain size to nano scale, second phase particles, or segregation patterns, extension of solid solubility limits, formation of non-equilibrium crystalline or quasicrystalline intermediate phases are attributes of this technique [6-9]. Application of MA technique to Ti alloys and compounds is of recent origin [10-12] and only limited studies have been reported on nanocrytalline compact fabrication. By choosing appropriate processing parameters attempts have been made to retain this structure in the fabricated compact. Combustion synthesis, also known as Self-propagating high temperature synthesis (SHS), is a novel and a potentially useful technique for production of high temperature ceramics, structural intermetallic compounds, and metal and ceramic matrix composites [13]. SHS was developed by A. G. Merzhanov and his co-workers in the former Soviet Union in the early 1970`s [14]. The subject has been reviewed by Anselmi-Tamburini and Munir [15] and Merzhanov [16]. The mechanisms of reaction synthesis are given by Munir [17] and Yi and Moore [18]. Extensive reseach efforts in Russia by Merzhanov [14, 16] have led to the industrialization of this method and to the synthesis of hundreds of materials. In the U.S., the early efforts in SHS are by Munir and co-workers [15, 17]. The SHS process has lately been receiving considerable attention as an alternative to the conventional processing technology in ceramics and powder metallurgy. Reaction between any of the metals in groups IV, V and VI of the periodic table with non-metals such as carbon, boron, silicon etc are examples of SHS reactions. SHS is the description of a process in which a mixture of compacted reactant powders e. g., Ti+B is heated rapidly to a temperature (T_{ig}) at which a reaction is initiated. If this reaction is sufficiently exothermic, the large enthalpy released when the reactants (solid, liquid or gaseous) react results in the formation of a combustion front propagating through the material and the process can become self-sustaining and propagate through the entire reactant mixture [19]. Many reactions between metals and certain non-metals and gases are highly exothermic and are thus suitable for SHS.

In the present study an alternate route is assessed for fabricating nano-crysralline CMC`s based on TiB-Ti system. This route starts with a mixture of elemental Ti and non-metallic B powder which was transformed to an unreacted nanocrystalline powder mixture by MA. The TiB matrix compound and TiB_2 are formed via self propagating synthesis (SPS) during elevated temperature compaction with free Ti in its pores and cracks, thus causing an increase in fracture toughness. In a continuation of this research program, detailed TEM study of MA+CCS`ed samples is currently underway and the results pertaining to this work will be presented in a subsequent publication.

Experimental Procedure

Charge materials used in the present study for mechanical alloying were powders of titanium and amorphous boron mix. Compositions of these powder mixes was

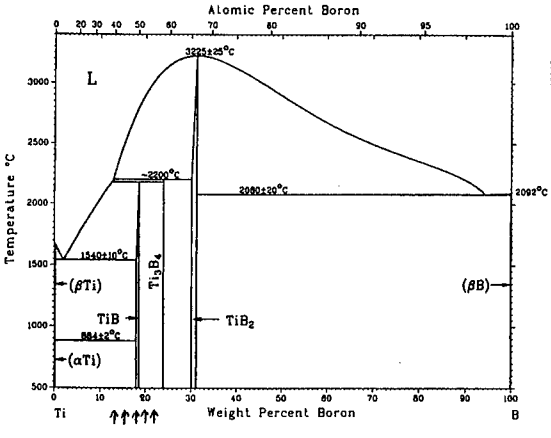


Figure. 1. Ti-B phase diagram

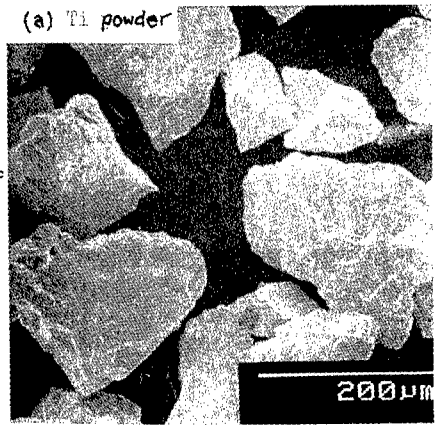


Figure. 2. SEM images of Ti (a)

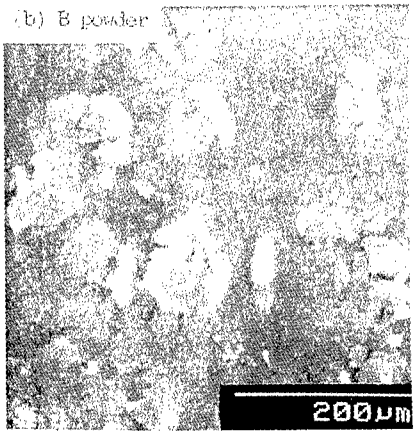


Figure. 2 (cont'd) and B (b) powders

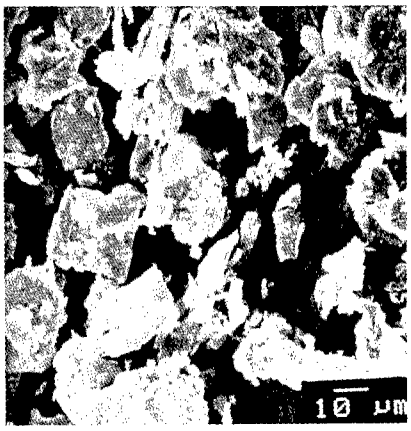


Figure. 3. SEM image of 86wt Ti-14wt%B sample after 8 hrs of MA

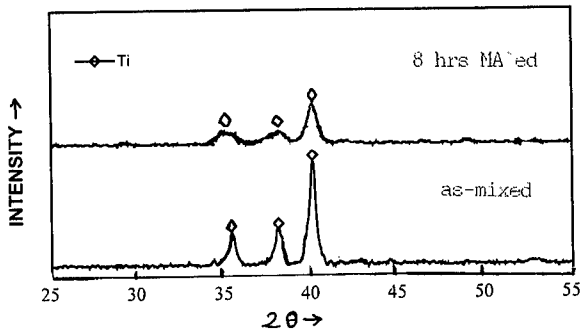


Figure. 4. XRD patterns of 82wt%Ti-18wt%B sample before and after 8 hrs of MA

chosen in such a way that they were conforming to TiB-stoichiometric and off-stoichiometric compositions in Ti-B binary phase diagram [20] (Figure 1). These powders were mixed in the proportions necessary to produce five mixtures of 78, 80, 82, 84 and 86wt%Ti with the rest being boron. Ti powder with 99.6% purity had a mean particle size of around 100μm determined with laser particle sizer and B powder with 99.2% purity had around 10μm particle size as shown in Figure 2. Mechanical alloying up to 8 hrs was carried out with a high energy ball mill using an argon filled stainless steel vessel and hardened chromium steel balls. The temperature of the mill vial was kept near room temperature with forced air cooling from the outside of the mill. Ball-to-powder weight ratio was 10:1. Morphology and crystal structure change of the powders during mechanical alloying was investigated by extracting small amounts of powder samples from the vial after 8 hrs of MA time. These samples were examined by Siemens d500 XRD and Cambridge ST44 Steroscan SEM equipment. MA`ed powders were afterwards hot pressed to obtain near full density nanocrystalline compacts with SHS. Characterisation of these samples were carried out with XRD and conventional DTA study performed in a Stanton Redcroft DTA 1200 under Ar.

Experimental Results and Discussion

Figure 3 shows the change in powder size and morphology in 86wt%Ti-14wt%B sample after 8 hrs of mechanical alloying. Ma`ed powder was in flake shapes of around 20μm size. The as-mixed 82wt%Ti-18wt%B powder sample shows all the peaks of Ti at the expected Bragg positions (Figure 4) while it is not possible to detect boron with XRD due to its low weight. Figure 4 also shows XRD pattern of the same powder sample after 8 hrs of MA time. With increasing mechanical alloying time, the peaks corresponding to Ti becomes broader indicating that there was an accumulation of strain and a decrease in the crystal size down to around 20μm [21-23] as indicated in Figures 2.a and 3. Similar observations were also seen in the other samples regardless of compositional differences. It is well known that compound formation during MA occurs by a reaction between the components, similar to thermally ignited self-propagating high-temperature synthesis (SHS) [24]. It proceeds spontaneously when the powder temperature in the mill jar (which rises due to heat dissipated by collision events) reaches the ignition temperature of the reaction, T_{ig}. This temperature decreases with increasing milling time until it becomes equal to the powder temperature in the mill jar [25]. If the milling conditions are chosen correctly, it is possible to avoid significant powder temperature rise and consequently to avoid compound formation during milling as is done in the present work. This does not effect the basic phenomena occuring in mechanical alloying, namely repeated fracture and cold welding of the powder particles (Figure 3). Microstructural refinement occurs during MA [26, 27], and in the limit the interphase spacing is reduced to several atomic distances. A long MA time is necessary to achieve this condition but an intimate mixture of the components can be achieved within each powder particle in a reasonable time. For this microstructure diffusion rates and the interface area are large and diffusion path lengths are minimized. This drives the reaction into a `critical` thermodynamic state [1, 25]. If MA is stopped at this stage which is the case for the present study, the powder possesses a nanocrystalline structure [21, 22, 26] exhibiting high reactivity. A small activation energy is required for reaction ignition. This energy can be supplied to the powder during compaction by hot pressing at a relatively low temperature as is done in this work. Therefore SPS will occur under pressure concurrent with consolidation. Since each powder particle has the structure described, the reaction will go to completion. Also, since compounds form during MA by reactions at temperatures substantial lower than T_{ad} in thermal induced systems [1, 25], it is likely that the heat release in SPS will not give rise to a large temperature increase and, consequently, to significant grain coarsening [28]. Since diffusivity and creep capability in the MA powders are high, near full density is expected in the nanocrystalline compact after sintering. Figure 5

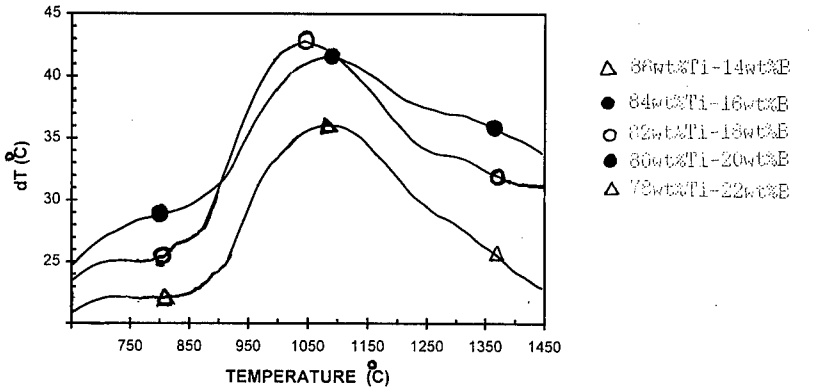


Figure. 5. Section of DTA curve for all five samples after combined MA and CCS

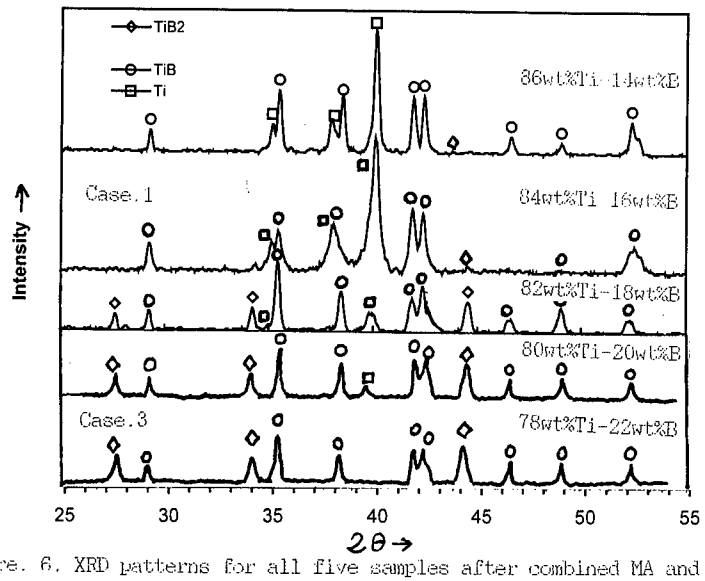


Figure. 6. XRD patterns for all five samples after combined MA and CCS

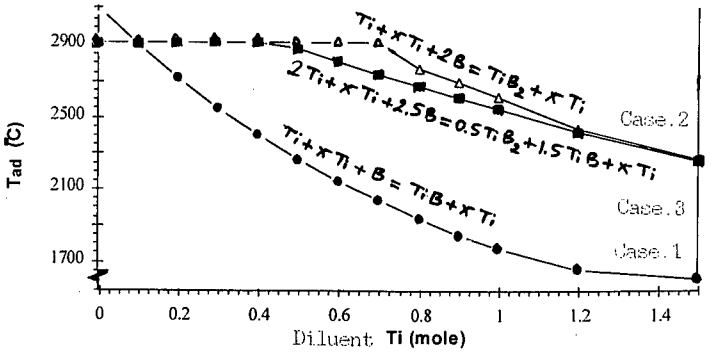


Figure. 7. The effect of diluent Ti amount on the theoretical adiabatic temperature of CS

shows DTA results of the five mixtures of Ti-B studied in the present work after combined ma and CCS. The major peaks of around 1000-1100°C are due to TiB compound formation. The powder mix of 82wt%Ti-18wt%B is the TiB stoichiometric composition. The others are at off-stoichiometric compositions from that of TiB. When the composition of the powder mix shifts away from the stoichiometric composition, TiB peak area gets reduced as shown in Figure 5 indicating the decrease in the amount of TiB forming at off-stoichiometric compositions. Figure 6 shows XRD patterns of the all five compositions after elevated temperature consolidation. In 86 wt%Ti-14 wt%B and 84 wt%Ti-16 wt%B compositions intense Ti, TiB and intense-not TiB_2 peaks; in 82wt%Ti-18wt%B composition less intense Ti and TiB_2 peaks and mainly intense TiB peaks; in 80 wt%Ti-20 wt%B and 78 wt%Ti-22 wt%B compositions less intense Ti peaks and mainly intense TiB and TiB_2 peaks were observed. In TiB stoichiometric composition (18wt%B) free Ti retained seems to be less compared to mixtures with <18wt%B whereas in mixtures with >18wt%B, there are very few free Ti retained. The amount of TiB_2 formed decreases as wt%B decreases from 22 to 14 wt%B indicating that SHS reactions can be easily controlled in mixtures with B contents less than 18 wt%. Controlled CS reactions occuring during hot pressing after MA in powder compositions of Ti-B mixtures do cause TiB and TiB_2 formation [29-31] as shown by DTA (Figure 5) and XRD (Figure 6) results. In Ti-B powder mix compositions with <18wt%B, the presence of diluent, liquid Ti (during CCS reactions concurrent with hot pressing) causes an increase not only at theoretical density by decreasing the amount of porosity since it fills the pores and cracks during processing cycle after MA, but also fracture toughness. Thermodynamic analysis of the reactions occuring during CCS can be given as follows: All the heat required for the synthesis of Ti-borides are from the enthalpies of the products or the exothermic combustion reaction. The exothermicity of the reaction between the reactants Ti and B under the TiB_2 stoichiometric composition, in particular, is too high to control the reaction synthesis. This allows a successful choice of more Ti as diluent, which absorbs the reaction energy and therefore plays a role of reducing the reaction temperature. The maximum temperature to which both the product(s) and unreactant Ti can be raised as a result of the exothermic reaction is the adiabatic temperature, T_{ad}. Thus, it is important to know how T_{ad} may be controlled by investigating the following three hypothetical reactions:

$$(1+x)Ti+B \rightarrow TiB+xTi-38.3\ Kcal/mole \qquad (1)\quad (case.1)$$

$$(1+x)Ti+2B \rightarrow TiB_2+xTi-77.39\ Kcal/mole \qquad (2)\quad (case.2)$$

$$(2+x)Ti+2.5B \rightarrow 0.5TiB_2+1.5TiB+xTi \qquad (3)\quad (case.3)$$

Assuming the adiabatic conditions are hold for SHS-process, the heat, ΔH, needed for heating Ti-borides and the unreacted Ti to the temperature T_{ad} can be, respectively, represented in the following equations:

$$\Delta H^{TiB}_{T_{ad}} = \int_{298}^{2500} C^{cs}_{TiB}\,dT + f_1\Delta H^{TiB}_{m} + m_1\int_{298}^{T_{ad}} 8\,dT \qquad (4)$$

$$\Delta H^{TiB_2}_{T_{ad}} = \int_{298}^{3193} C^{cs}_{TiB_2}\,dT + f_2\Delta H^{TiB_2}_{m} + m_2\int_{3193}^{T_{ad}} C^{l}_{TiB_2}\,dT \qquad (5)$$

$$\Delta H^{Ti}_{T_{ad}} = \int_{298}^{1160} C^{\alpha}_{Ti}\,dT + \int_{1160}^{1939} C^{\beta}_{Ti}\,dT + f_3\Delta H^{Ti}_{m} + m_3\int_{1939}^{T_{ad}} C^{l}_{Ti}\,dT \qquad (6)$$

Where C and T are, respectively, the heat capacities and temperatures with sub and superscripts indicating solids (s, α or β-phase)/liquid (l) states and temperatures; ΔH_m and f are the melting enthalpies and molten fractions of the phases indicated by the superscripts. The dimensionless coefficients m_1, m_2 and m_3 are either 1 (if the corresponding f is 100%) or 0 (f<100%) [32].

The sum of the heat supplied by the exothermic reaction is the only heat source of SHS-process. An energy balance equation, therefore can be given as below:

$$n_1\Delta H^{TiB}_{298} + n_2\Delta H^{TiB_2}_{298} = n_1\Delta H^{TiB}_{T_{ad}} + n_2\Delta H^{TiB_2}_{T_{ad}} + x\Delta H^{Ti}_{T_{ad}} \quad (7)$$

where n_1, n_2 and x are the molar fraction or stoichiometric coefficients of TiB, TiB_2 and the unreacted or free Ti in the final product. The left part of eqn.(7) is the sum of the enthalpies of Ti-borides at 298 K while the right part is the total heat needed for heating the product to T_{ad}. Based on eqns. (4)~(7), T_{ad} can be solved for each of the reactions (1)~(3) with the relevant thermodynamic data from [33, 34]. Thermodynamic analysis of CCS reactions in Ti-B system studied in the present work indicates (figure. 7) the change in T_{ad} with respect to diluent Ti amount. In case. 2, T_{ad} is equal to T^{TiB2} up to 0.7 mole of free Ti, after which it drops and this case corresponds to TiB_2 stoichiometric composition (i. e., 30wt%B). In case.1, T_{ad} decreases very fast with an increase in the amount of free Ti, corresponding to powder mixtures with B contents less than 18wt% as shown in Figure 6. In case.1 of Figure 7 it is shown that the formation of TiB can be easily controlled than that of TiB_2. In this case in addition to TiB formation, diluent Ti in liquid form is also observed (Figure 6) and this is confirmed by above theoretical calculations (Figure 7) in Ti-B powder mixes with <18Wt%B contents. Case.3 corresponds to an in-between position between case.1 and 2 limiting conditions (Figure 6) for 18 to 22 wt%B mixtures having TiB and TiB_2 compound formations with the amounts depending on the level of B in the powder mixes. Data in Figure 7 shows that it is important to select compositions having less than 18wt%B to control CS reactions which opens up new processing routes for the fabrication of TiB-Ti CMC`s from TiB-off-stoichiometric compositions by combined MA and CCS concurrent with hot pressing. It can finally be said that when controlled, self-propagating high temperature synthesis (SHS) after MA has been used to produce compounds, which subsequently, are further processed (hot pressing, hot isostatic pressing) after MA to yield CMC`s, the potential of using SHS in conjunction with densification and plastic deformation of the reaction products is considerable [19]. A one-step synthesis (i. e., combined MA and CCS) and densification process (e. g., hot press as is done in the present work) might have significant benefits because advantage could be taken of the high temperature generated by the reactions, that render CMC`s and may be ceramics in the future workable, as shown in this work.

Conclusions

Flake powders of Ti-B mix with nanograins were produced by MA. These nanocrstalline and unreacted powders are highly reactive and therefore ignition temperatures are lowered. This makes compact fabrication by SPS at low temperatures possible to prevent grain size coarsening. And in compositions with <18wt%B, liquid Ti causes an increase in theoretical density and fracture toughness by filling pores and cracks that form during CCS reactions occuring concurrent with hot press consolidation. With this route, it is possible to fabricate compacts of TiB-Ti CMC`s from TiB-off-stoichiometric compositions (i. e., B contents less than 18wt%) by MA and controlled CS during hot pressing.

Acknowledgments

The present work was carried out with a financial support from TUBITAK through its NATO scholarships program which is greatfully acknowledged by the author.

References

1. A. Lawley, M. J. Kocjak, R. L. Orban, "Fabrication of nanocrystalline NiAl compacts via combined mechanical alloying and self-propagating synthesis", Proc. of the European Conf. on `Advanced PM materials`, Birmingham,UK, 23-25 Oct., 1995, 88.

2. W. D. Kingery, H. K. Bowen, D. R. Uhlmann, Introduction to ceramics, New

York, John Wiley and Sons, 1976.

3. R. Y. Lin, S. G. Fishman, eds., Control of interfaces in metal and ceramic composites, TMS Annual Meeting, San Fransisco, CA, USA, 27 March 1994.

4. C. Suryanarayana, F. H. Froes, The structure and mechanical properties of metallic nano-crystals, Met. Trans. A., 23, 1992, 1071.

5. S. Bose, Application of nanocrystalline materials as matrices of composites:processing and performance advantages, Mat. Sci. and Eng. A., 196, 1995, 105.

6. J. J. de Barbadillo, "Rebirth of mechanical alloying", Key Engineering Materials, 77 (1993) 187.

7. M. Bodart, D. Brenet, F. Moret, "Kinematics of the mechanical alloying process", Key Engineering Materials, 77 (1993) 197.

8. A. Calka, J. I. Nikolov, "The dynamics of magneto-ball milling and its effect on phase transformations during MA", Mat. Sci. Forum, 179-181 (1995) 333.

9. A. A. Popovich, V. P.Reva, V. N. Vasilenko, O. A. Belous, "Mechanochemical technology of synthesis of refractory compounds and alloys based upon them", Mat. Sci. Forum, 88 (1992) 737.

10. "Synthesis, processing, and modelling of advanced materials", 2nd ASM Paris Conf., F. H. Froes and T. Khan, eds., Trans Tech Publications, Paris, France, 11-13 Sept., 1991.

11. F. H. Froes, C. Suryanarayana, W. Quist, E. Lavernia, B. I. Bondarev, N. F. Anoshkin, I. S. Polkin, O. K. Fatkullin, V. Samarov, A. B. Notkin, Advanced aerospace metals requirements and characteristics-an overview", Key Engineering Materials, 77 (1993) 1.

12. W. T. Nachtrab, P. R. Roberts, H. A. Newborn, "Powder metallurgy of advanced Ti-alloys", Key Engineering Materials, 77 (1993) 115.

13. J. V. Wood, A. Saidi, M. J. Capaldi, J. L. F. Callie, P. Davies, "Production of TiC containing powders and particulates by self propagating high temperature synthesis reactions", Proc. of the European Conf. on `Advanced PM materials`, Birmingham,UK, 23-25 Oct., 1995, 73.

14. A.G.Merzhanov, and I.P.Borovinskaya, Dokl. Akad. Nauk. SSSR, 204, 1972, 429.

15. Z. A. Munir, U. Anselmi-Tamburini, Self-propagating exothermic reactions: The synthesis of high-temperature materials by combustion, Mat. Sci. Reports, (1989) 277.

16. A. G. Merzhanov,"Combustion and plasma synthesis of high temperature materials", VCH, Z. A. Munir, J. B. Holt, eds., (1990) 1.

17. Z. A. Munir, "Synthesis of high temperature materials by self-propagating combustion methods", Amer. Cer. Soc. Bullt., (1988) 342.

18. H. C. Yi, J. J. Moore, "Self-propagating high-temperature (combustion) synthesis (SHS) of powder compacted materials", J. of Mat. Sci., 25 (1990) 1159.

19. M. A. Meyers, J. C. LaSalvia, D. Hoke, J-M. Jarnet, D. K. Kim, "Combustion synthesis-densification of ceramics and ceramic composites", Proc. of the Int.

Conf. on Advanced Synthesis of Engineered Structural Materials, ASM International, San Fransisco, CA, USA, 31 August-2 September 1992, 43.

20. T. B. Massalski, Binary alloy phase diagrams, ASM, 1 (1986) 392.

21. B. D. Cullity, "Elements of X-ray Diffraction", 2nd. ed., Addison Wesley Pub. Co., Reading (1978) 99.

22. R. W. Siegel, "Nanophase ultrafine-grained materials", Mat. Sci. Forum, 37 (1989) 299.

23. Weissmuller, R. Birringer, H. Gleiter, "Nanostructured crystalline and amorphous solids", Key Engineering Materials, 77 (1993) 161.

24. G. B. Schaffer, "On the kinetics of mechanical alloying", Met. Trans. A., 23 (1992) 1285.

25. G. B. Schaffer, P. G. McCormick, "Anomalous combustion effects during mechanical alloying", Met. Trans. A., 22 (1991) 3019.

26. K. A. Padmanabhan, H. Hahn, "Microstructures, mechanical properties and possible applications of nanostructured materials", Synthesis and processing of nanocrystalline powders, D. L.Baurell, ed., TMS, Anaheim, CA, USA (1996) 21.

27. J. Weissmuller, "Nanocrystalline materials", Synthesis and processing of nanocrystalline powders, D. L.Baurell, ed., TMS, Anaheim, CA, USA (1996) 3.

28. T. R. Malow, C. C. Koch, "Grain growth of nanocrystalline materials-a review", Synthesis and processing of nanocrystalline powders, D. L. Baurell, ed., TMS Anaheim, CA, USA (1996) 33.

29. B. Aronson, T. Lundstrom, S. Rundquist, Borides, Silicides and Phosphides, John Wiley and Sons, New York, NY (1965) 47.

30. A. Calka, "Formation of TiB_2 by mechanical alloying", J. of Less Common Met., L25, (1991).

31. D. D. Radev, D. Klisurski, "Properties of TiB_2 powders obtained in a mechanochemical way", J. of Alloys and Comp., 206 (1994) 39.

32. Z. X. Peng, M.Sc Thesis, Univ. of Idaho, Moscow, Idaho, USA,1997

33. B. Rupp, J. B. Holt, J. Wang, The calculation and analysis of the adiabatic temperature of solid combustion reactions, CALPHAD, 16, 1992, 377.

34. I. Barin, O. Knacke and O. Kubaschewski, Thermal properties of inorganic substances, Springer Verlag, Berlin 1977.

THE ANALYSIS OF RECLAMATION MECHANISM OF DISCONTINUOUSLY REINFORCED ALUMINUM MATRIX COMPOSITES

Zhongliang SHI, Tongxiang FAN, Mingyuan GU, Di ZHANG and Renjie WU

State Key Laboratory of Metal Matrix Composites,
Shanghai Jiao Tong University, Shanghai 200030, China

Abstract

The study of their reclamation of discontinuously reinforced aluminum matrix composites is directly related on the application in industry. According to the tests, it is shown that SiC or Al_2O_3 particulate reinforced as-cast aluminum alloys A356 matrix composites can remelt and reuse and their remelting have not effect on their properties and they are insensitive for remelting overheating temperature and holding time, Al_2O_3 particulate reinforced deformation aluminum alloys matrix composites can also remelt and reuse but SiC particulate reinforced deformation aluminum alloys matrix composites are not like above materials, their processing parameters must be strictly controlled because of seriously interfacial reactions during their remelting, therefore, holding time at high temperature and overheating temperature of the composite should be reduced as lowly as possible.

The Third Pacific Rim International Conference on
Advanced Materials and Processing (PRICM 3)
Edited by M.A. Imam, R. DeNale, S. Hanada,
Z. Zhong and D.N. Lee
The Minerals, Metals & Materials Society, 1998

Introduction

The discontinuously reinforced metal matrix composites (abbreviated DRMMCs) is one of the most prospect for industry application of metal matrix composite materials. In addition to the good attractive attention of their mechanical and physical properties, they have dominant position in the fabrication, forming and machining. i.e., they can use these conventional methods such as casting, forging and heat treatment [1-4]. Therefore, both their fabrications and their properties have competitive in commercial use. Especially, a lot of investigations on the composites processing and properties of DRMMCs have been done in recent 20 years and their properties and the processing get to stable. They will be widely used in the vehicles of communications and transportation and aviation and spaceflight industries sooner or later. With their wider use in industry, the waste recovery and reclamation of the composites will be sure to be paid attention to. It is reclaimable in theory for the composites because the interfacial reactions and their reaction products can be effectively controlled through relative reaction kinetics and thermodynamics. The interfacial conbined state between reinforcements and the matrix of composites have directly effect on their mechanical properties. Few are studied on the interfacial reactions and their reaction products and the effect of alloying elements on these products after multiple remelting of composites. Therefore, the reclamation mechanisms and the microstructures and interfacial reactions characteristics between SiC and Al_2O_3 particulate reinforced as-cast and deformation aluminum matrix composites have been analyzed in this paper .

Experimental Procedure

The matrix of discontinuously reinforced aluminum matrix composites are often adopted two kinds of aluminum alloys, e.g. as-cast aluminum alloys and deformation aluminum alloys. Because of poor deformation ability of as-cast aluminum alloys, the squeeze casting processing are often used to achieve the effect of near net shape and it can avoid secondary deformation metalworking. But because of good secondary metalworking of deformation aluminum alloys as the matrix of composites, besides squeeze casting, the fabrication processing often uses stirring casting method to make the composite ingots, then to form by secondary working in spite of their poor casting properties. These composites can also strengthen through heating treatment. The composites in this work were fabricated by stirring casting technique and the composition of their matrix wee shown on Table I. The number of reinforcements , either SiC or Al_2O_3 particulate is 10 vol% respectively. Then to remelt above the composites at the furnace and to analyze the effect of the parameters such as remelting and holding temperature and holding time on the change of silicon increment and other reaction products and mechanical properties.

Table I The chemical compositions and their properties of aluminum alloys as composites matrix

kind of alloy	Si	Mg	Cu	Mn	Al	σ (MPa)	E	impurity elements
ZL101(A356)	6.0-8.0	0.2-0.4	0.2	-	rest	140-230	69	Fe ≤ 0.6
ZL109(4032)	11.-13.	0.8-1.5	0.5-1.5	-	rest	150-210	72	Fe≤ 0.6
LY12(2024)	≤ 0.5	1.2-1.8	3.8-4.9	0.3-0.9	rest	≥400	72.4	Fe+Ni≤ 0.5
LD30(6061)	0.4-0.8	0.8-1.2	0.15-0.4	≤ 0.15	rest	150-300	68.3	Cr 0.04-0.35, Fe ≤ 0.7

Results and Discussions

Microstructure Characteristics of Discontinuously Reinforced Aluminum Matrix Composites The Compositions and Their Microstructures of Aluminum Alloys as the Matrix of Composites The common as-cast aluminum alloys are mainly aluminum-silicon alloys, for example A356, 4032, shown on Table I. The chief characteristic of this kind of alloys is up to silicon content and good fluidity. The microstructures of the kind of alloys are composed of α phase riched-aluminum and silicon phases. The morphologies of silicon phases are usually needle-like, short bar and blocky, the tensile strengths of these alloys are down to 300MPa and their ductilities are poor.

The composition of common deformation aluminum alloys are shown on the Table I, such as 2024, 6061. The kind of deformation aluminum alloys has various alloying elements and its strengthening mainly consists of solution strengthening and aging precipitation dispersion strengthening. The tensile strength of these matrix are up to 350 MPa. The deformation aluminum alloys are often chosen to take as these composite matrix for improving their mechanical properties.

The Microstructures and Interfacial Characteristics of Aluminum Matrix Composites The microstructures and their interfacial reaction phenomena of aluminum matrix composites which are made by as-cast aluminum-silicon alloys and deformation aluminum alloys as their matrix and particulates SiC and Al_2O_3 as reinforcements, are analyzed as following.

SiC particulate reinforced Al-Si alloys matrix composites SiC particulates as reinforcement, like eutectic silicon phases, mainly distributes along the boundaries of α phases due to being pushed by solidified interfacial front and segregation. The morphology of eutectic silicon phases is fine needle-like, they have greatly effects on the strength and plasticity of the composites. The boundary distribution and segregation of SiC particulates are also harmful to their properties although SiC particulates are good to improving and fining eutectic silicons because of the affect of liquid-solid interfacial front, thus fine needle-like eutectic silicons are crushed because of pushing of SiC particulates. Further more, the interfacial reaction can take place:

$$4Al + 3SiC \rightarrow Al_4C_3 + 3Si \quad (1)$$

theoretically at high temperature. Actually, the above interfacial reaction is controlled to some extent because of up concentration of [Si] in the alloys solution as composites matrix. Only are the number of silicon phases increasing even if the above interfacial reaction is intensive and forms some free silicons. The relationship among temperature, holding time and silicon increment of SiC particulates reinforced as-cast Al-Si alloy matrix composite is shown on the Fig.1, which the composites are fabricated by stirring cast. These silicon phases formed by interfacial reaction have not greatly effect on their properties. The interfacial reaction product Al_4C_3 has also not greatly effect on their properties. Therefore, the interfacial reactions are little effect on the properties of SiC particulates reinforced Al-Si alloys matrix composites.

Al_2O_3 particulates Reinforced Al-Si Alloys Matrix Composites The morphology and the distribution of Al_2O_3 particulate reinforced aluminum matrix composites are the same as that of above mentioned SiC particulate reinforce aluminum matrix composite. Only is the difference in the reinforcements. Although Al_2O_3 particulate can not react with Al and Si , there is a small amount magnesium in the matrix alloys, the interface reaction between magnesium and Al_2O_3 can take place and form spinel ($MgO.Al_2O_3$). i.e.

$$3\,Mg + 4\,Al_2O_3 \rightarrow 3\,MgAl_2O_4 + 2\,Al \quad (2)$$

The formation of spinel is harmful to the mechanical properties of the composites. But the amount interfacial reaction product spinel is small and its effect on cutting apart to

matrix can not compare with that of silicon phases. So the interfacial reaction is not greatly influence on the mechanical properties of the composites.

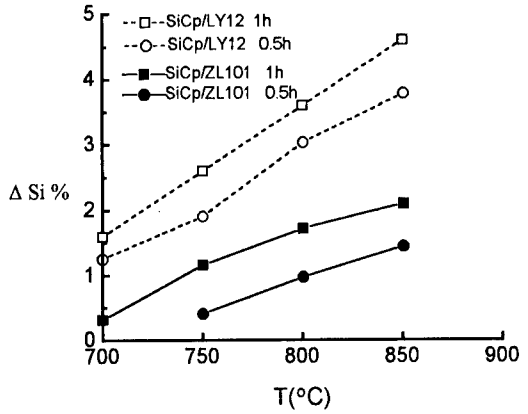


Figure1 The relationship between temperature, holding time and silicon increment of composites

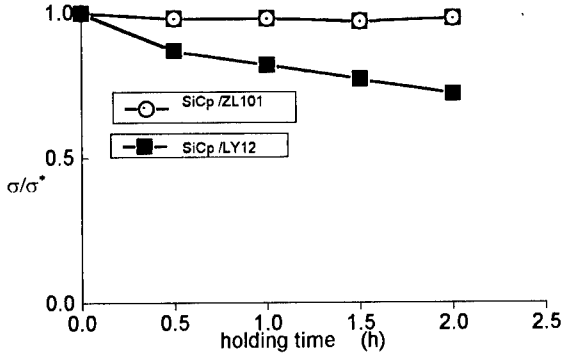


Figure 2 The influence of holding time on their tensile strength between SiCp/ZL101 and SiCp/LY12 at remelting temperature 750°C

SiC Particulate Reinforced Deformation Aluminum Alloys Matrix Composites The interfacial reaction between SiC particulate and Al is great due to the small silicon content in the matrix of deformation aluminum alloys. The more the interfacial reaction products Al_4C_3 and free silicon are, the greater affection the mechanical properties of the composites are because the above reaction products are harmful to the properties of the composites such as tensile strength, plasticity. The relationship between temperature, holding time and silicon increment of 2024(LY12) aluminum matrix composites is shown on Fig.1. With the extension of high temperature and holding time, the silicon increment rises. According to the reaction (1), the reaction product Al_4C_3 is also like the change of silicon. Therefore, the composite processing parameters especially over heat temperature and time at high temperature must be controlled strictly under fabrication of the composites.

Al_2O_3 Particulate Reinforced Deformation Aluminum Alloys Matrix Composites: Although between magnesium and Al_2O_3 can take place the interfacial reaction, the reaction product $MgAl_2O_4$ will not greatly effect on the properties of the composites because its amount is small and the element magnesium is trace element, at the meantime, silicon phases are exist and the influence is much greater than the interfacial reaction products.. Compared with the above composites, the influence of interfacial reaction product $MgAl_2O_4$ can not neglect in the deformation aluminum alloys matrix composites. The processing parameters should be controlled strictly and the amount of reaction product $MgAl_2O_4$ should be also lower as soon as possible.

Microstructures Characteristics of DRMMC at Remelting

The Mcrostructures Characteristics of Matrix Alloys at Remelting As shown on Table I, both as-cast aluminum alloys and deformation aluminum aluminum alloys as composites matrix usually consist of active alloying elements like magnesium, which will be heating loss and segregated after remelting and multiple remelting. This will be harmful to morphologies of silicon phases and properties of aluminum alloys as matrix. The phenomenon show the reason that as-cast aluminum silicon alloys must add some modifying agent when they are remelting and also show that the effect of modification occur modifying decline after remelting modification.

Above mentioned, the alloying elements will also be heating loss and segregated at remelting that will be directly effect on aging precipitation and the properties.

Microstructures characteristics of DRMMC at remelting With the increasing of remelting temperature and the elongation of holding time, the silicon increments are increasing gradually, actually the number of silicon increments also shows the increasing of the other interfacial reaction product Al_4C_3 according to reaction equation (1), but the properties of SiC paticulates reinforced A356 matrix composites will be a small change at remelting even though the interfacial reaction products either Al_4C_3 or $MgAl_2O_4$ have formed, because a lot of eutectic silicon phases exist and they conceal the harmful effect of its interfacial reaction products. Fig.2 shows the influence of holding time on its tensile strength of SiC particulate reinforced ZL101(hypoeutectic Al-Si alloy) composite at the remelting temperature750°C.

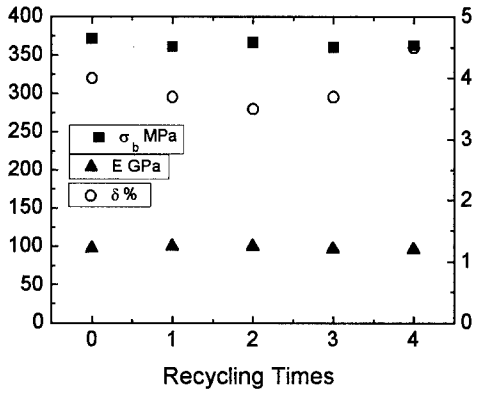


Figure 3 The changes of strength, elongation and elastic modulus of Al_2O_3p /6061Al after multiple remelting recycling times

The properties of tensile strength, elongation and elastic modulus of Al_2O_3 particulate reinforced 6061 aluminum matrix composite are not change basically after multiple

remelting as shown on Fig.3, because the distribution of interfacial reaction product $MgAl_2O_4$ shows discontinuously blacky microstructure, observed by TEM. Although the number of interfacial reaction product $MgAl_2O_4$ is increasing with the remelting times, as shown on Fig.4.

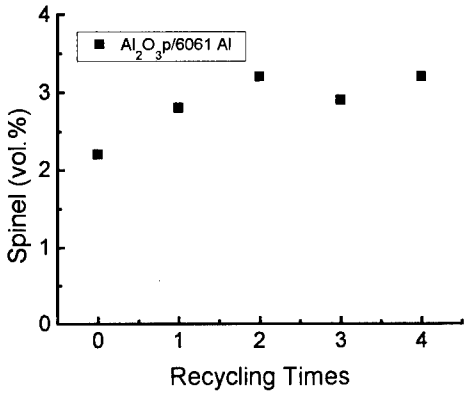


Figure 4 The relationship between interfacial reaction product $MgAl_2O_4$ of Al_2O_3p/6061Al and recycling times

Conclusions

1. It has been shown that the remelting process parameters such as overheating temperature and holding time are insensitive because they have not greatly effect on the properties of either SiC or Al_2O_3 particulates reinforced as-cast Al-Si alloys matrix composites.
2. It has been shown that Al_2O_3 particulate reinforced deformation aluminum alloys matrix composites can also remelt and reclaim but SiC particulate reinforced deformation aluminum alloys matrix composites are not like above materials, their processing parameters must be strictly controlled because of seriously interfacial reactions during their remelting, therefore, holding time at high temperature and overheating temperature of the composite should be reduced as lowly as possible.

Acknowledgment : The authors are grateful for the financial support of the National Natural Science Foundation of China under grant No. 59631080.

References

1 Thomas F. Klimowicz, "The large-scale commercialization of aluminum-matrix composites," JOM , 1994, No.11 : 49-53.
2 K. A Moore, " Progress report - Investment casting of light alloy metal matrix composite materials," (Report BNF Metals Technology Centre1991).
3 J. Lin , P. Li , R. Wu, "A review of study on the deformation and damage in particle reinforced metal matrix composite," (Proceeding of the ASM 1993 Materials Congress, Pittsburgh, Pennsylvania, 17-21 Oct.,1993: 9-15)
4 Hideki Sekine, Rong Chen, " A combined microstructure strengthening analysis of SiCp/Al metal matrix composites," Composites 26(1995)183-188

LAMINATED METAL COMPOSITES - FRACTURE AND BALLISTIC IMPACT BEHAVIOR

D.R. Lesuer, C.K. Syn, O.D. Sherby, and J. Wadsworth

Lawrence Livermore National Laboratory
Livermore, CA 94551

Abstract

Recent advances in the fracture and ballistic impact response of laminated metal composites (LMCs) are reviewed. The laminate structure can provide significant improvements to these properties relative to the component materials. Typical fracture and ballistic impact properties in LMCs are illustrated for systems containing Al alloys and Al matrix composites. The unique mechanisms operating in a layered structure that contribute to fracture or ballistic impact resistance are discussed. The influence of laminate architecture, component material properties, and interface strength on mechanisms and properties are briefly reviewed for these Al-based LMCs.

The Third Pacific Rim International Conference on
Advanced Materials and Processing (PRICM 3)
Edited by M.A. Imam, R. DeNale, S. Hanada,
Z. Zhong and D.N. Lee
The Minerals, Metals & Materials Society, 1998

Introduction

Recent studies have shown that laminated metal composites (LMCs) can dramatically improve many properties including fracture toughness, fatigue behavior, impact behavior, wear, corrosion, and damping capacity or provide enhanced formability or ductility for otherwise brittle materials [1]. In addition, in many cases through the choice of laminate architecture (such as volume percent of the component materials and layer thickness), component materials and processing history, LMCs can be engineered to produce a material with prescribed properties. Despite these attractive characteristics, virtually no LMCs have become commercially available that use these materials for their unique structural properties. Some LMCs have been commercialized as clad materials, because of their unique surface markings or for their performance in less-demanding structural applications. Three examples of commercially available laminated products are shown in Figs 1, 2(a) and 2(b). Figure 1 shows typical laminated Swedish knives used in wood working. The blade of each knife is made from a three layer laminate consisting of a layer of high carbon steel contained within layers of soft iron. The layers are joined by solid state brazing. The laminated structure is designed to provide a hard cutting tool with high durability. These characteristics are achieved by the high carbon steel center layer (hardened to Rc 62) with the tough outside layers improving durability by resisting surface cracking. In Japan, laminated knives and scissors are available with unique surface markings resulting from the layered structure. Typical examples are shown in Figs 2(a) and 2(b). In these examples, the layered structure is used for aesthetic reasons rather than for improvements in properties and in-service performance. The inset photographs in Figs. 2(a) and 2(b) show additional detail of this layered structure.

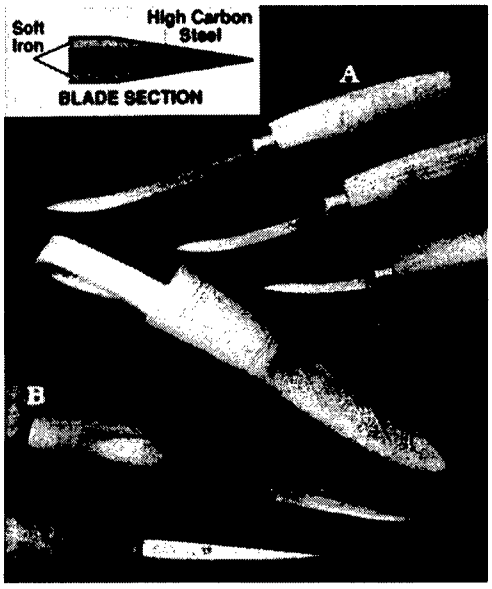


Fig. 1. Typical laminated Swedish knife. The laminate structure is shown in the inset drawing.

This paper addresses the fracture and ballistic impact behavior of LMCs - two properties with near-term commercial potential. Generally speaking, the improvement in these properties with a layered structure results from the ability of this material form to introduce additional energy absorbing mechanisms during damage development or to change failure modes from low energy modes to high energy modes. Laminate architecture (including component material volume fraction and layer thickness), component material properties, and interface strength can strongly influence the active mechanism(s) and resulting properties. In the following sections we will discuss these mechanisms, their influence on properties, and how these mechanisms are influenced by the laminate characteristics described above. Examples are provided for LMCs containing Al alloys and Al matrix composites.

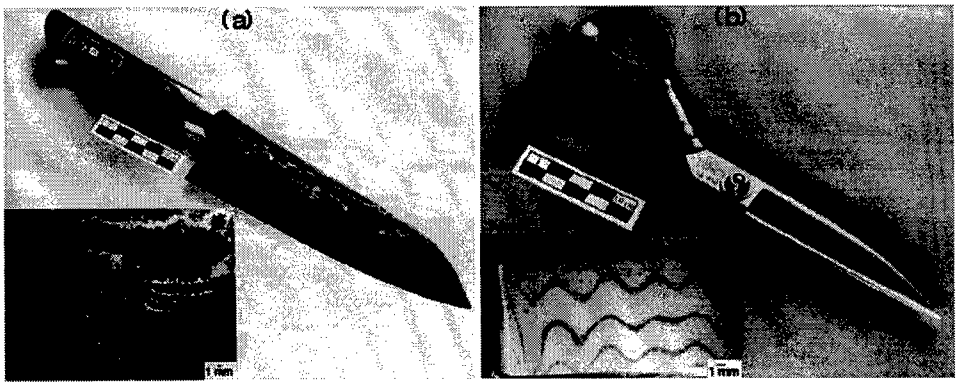


Fig. 2. Laminated knife (a) and scissors (b) commercially available from Japan. Lamination is used to develop unique surface markings shown in detail in the inset photograph.

Fracture Toughness

Enhancements in toughness

The improvements in fracture toughness that are possible with LMCs are illustrated in Fig. 3, which shows toughness versus global volume percent SiC for two laminates containing alternate layers of a metal matrix composite (6090/SiC/25p-T6) and a ductile Al alloy (6013-T6 or 5182) [2]. The materials were all press-bonded, multiple-layer laminates containing 13 to 31 layers. The laminates were tested in the crack divider orientation using compact tension samples and toughness values for crack initiation are shown in the figure. The toughnesses of the individual components are also indicated. For both systems shown in Fig. 3, data is given for combinations containing 50% and 95% of the stronger metal matrix composite (MMC) component. The figure shows that the LMC can increase the fracture toughness by 70% to over 100% (depending on volume fraction of the MMC component) relative to values expected from a rule of averages calculation.

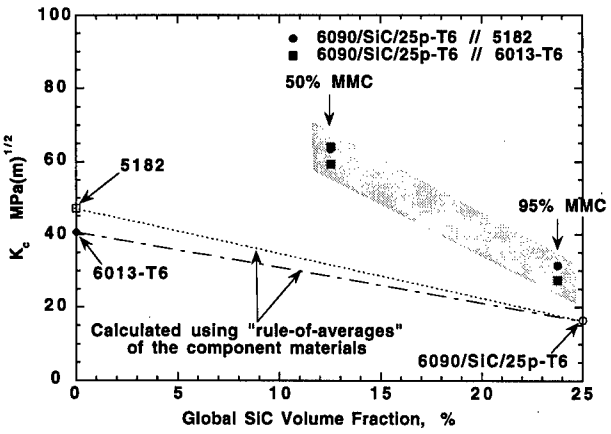


Fig. 3. Fracture toughness versus SiC content for two laminates containing alternating layers of a metal matrix composite (6090/SiC/25p-T6) and a ductile aluminum alloy (5182 or 6013-T6). Toughness is also shown for the component materials.

A number of other laminate systems have also shown significant improvements in fracture toughness. Examples include self laminates (such as 7075-T6 [3,4] and 2024-T3 [5]), laminates consisting of alternating layers of different metals (such as UHCS // Brass [6] and 2024-T3 // 7075-T6 [5]) or laminates consisting of alternating layers of a MMC and a ductile metal (such as 6090/SiC/25p // 5182 [6, 7], 7093/SiC/20p // 7093 [2, 8], and 2080/SiC/20p // 2080 [8]).

Mechanisms

Toughening in LMCs can arise from many different sources. Recent work has shown that toughening in materials can result from two different types of mechanisms - intrinsic and extrinsic [9, 10]. Intrinsic toughening results from the inherent resistance of the microstructure to crack growth and thus is influenced by such microstructural characteristics as grain size, particle spacing, particle size etc. Extrinsic toughening, on the other hand, results from mechanisms that reduce the local stress intensity at the crack tip and thus the local "driving force" for crack growth. The distinct layers present in LMCs toughen these materials by various extrinsic mechanisms, which are shown schematically in Fig. 4. The laminate orientation that will be influenced by the mechanism is indicated in the figure. These mechanisms have been recently reviewed in detail [1]. All the mechanisms shown in Fig. 4 are strongly influenced by local delaminations at or near the crack tip. For a crack intersecting an interface, local delaminations can result in crack deflection (as shown schematically in Fig. 4(a)), which can significantly reduce the mode I component of the local stress intensity because of the large deviations in crack path (up to 90° in the crack arrester orientation) that are possible. For example, work by Lesuer et al. [1] has shown that in the crack arrester orientation, a crack deflection length equal to the layer thickness (commonly observed in fractured laminates) results in a local stress intensity that is approximately 75% of the applied stress intensity. Delamination can also provide extrinsic toughening by reducing the stresses in layers ahead of the advancing crack. This mechanism referred to as stress redistribution in Fig. 4(b), has been studied most extensively in metal/ceramic laminates [11].

Component material properties can also influence the active extrinsic toughening mechanism. A good example is the competition that exists between the crack blunting and crack bridging mechanisms. For a LMC in which toughening in a brittle material is achieved by lamination with a ductile interlayer, then the ductility of the interlayer can influence the active mechanism [12]. As shown in Fig. 4(c), if the ductile interlayer ruptures before the crack advances to the layer, then crack blunting will occur. If, on the other hand, the ductile interlayer possesses sufficient ductility to avoid rupture before the crack advances into the next layer, then crack bridging (Fig. 4(d)) results. In this mechanism, unbroken individual layers span the wake of the crack. This mechanism can be a dramatic source of toughening, since growth of the crack requires stretching these bridging ligaments. The last two mechanisms shown in Fig. 4 (crack front convolution and local plane stress deformation) apply to laminates tested in the crack divider orientation. In the crack front convolution mechanism (Fig. 4(e)), the crack front in the less ductile component leads the crack front in the more ductile component. The shape of the crack front is highly convoluted with the depth of the convolutions related to the extent of delamination at the interfaces. Overall crack front growth is retarded by the plastic tearing required for crack growth in the more ductile layer. In the local plane stress deformation mechanism (Fig 4(f)), substantial delamination at the crack tip causes individual layers to deform and fracture in the more energy intensive plane stress fracture mode rather than plane strain mode. This mechanism has been observed in relatively thick layer self-laminates of 7075-T6 and 2024-T3.

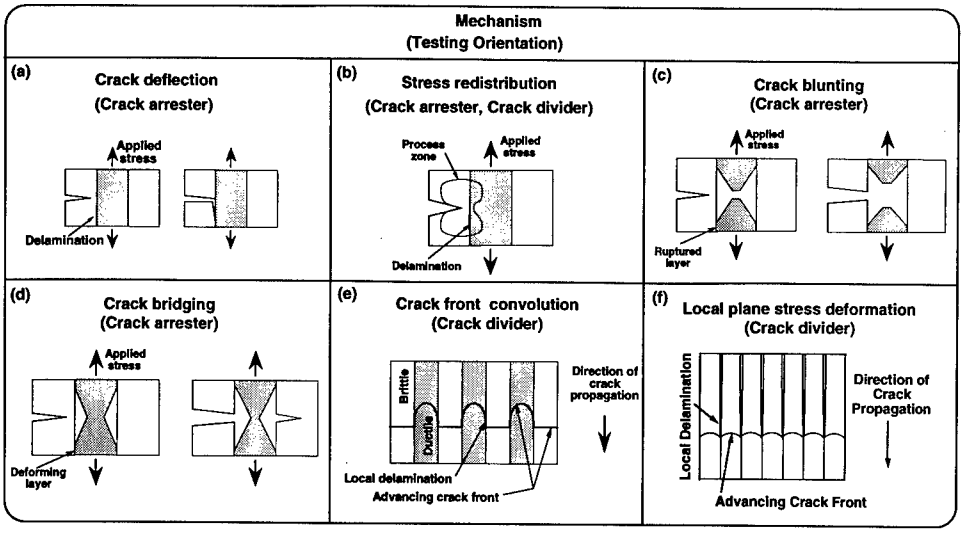


Fig. 4. Extrinsic toughening mechanisms for laminated metal composites.

Laminates as structural materials

The fracture toughness data shown in Fig. 3 illustrates that LMCs can dramatically improve the fracture resistance of materials. For weight critical applications, these improvements can be particularly dramatic. In Figs. 5(a) and 5(b) the density-normalized strength, stiffness and toughness properties are compared for a number of structural materials including two ceramics and two laminates. One laminate consists of 50% 6090/SiC/25p-T6 and 50% 5182 while the other consists of 95% 6090/SiC/25p-T6 and 5% 5182. The laminate strength data was obtained from reference [2]. The data for the quench and tempered 4340 steel in Figs 5(a) and 5(b) were derived from a UTS of 1465 MPa and a fracture toughness of 85 MPa $m^{.5}$ [13]. The figures show that the laminates have very attractive properties for weight critical structures. The laminate containing 50% MMC is particularly impressive since it has a specific toughness significantly greater than any of the other materials in the figures. Figure 5 shows that the laminates reported here can be particularly effective for applications requiring lightweight materials with high stiffness, strength, and fracture toughness.

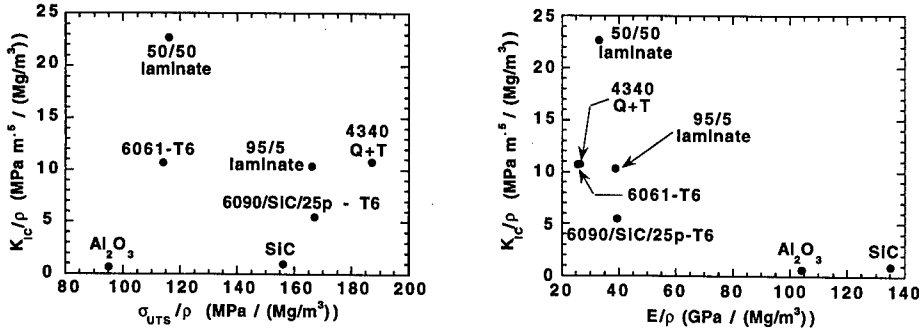


Fig. 5. Specific toughness versus specific strength (a) and specific toughness versus specific stiffness (b) for a number of structural materials including two laminates.

Ballistic Impact Resistance

Enhancements in ballistic impact properties

The response of metallic laminates to ballistic impact has been studied by several investigators (see, for example, references [14-18]) and, in general, the results have shown that laminate plates can be designed to increase the amount of energy absorbed during impact and thus improve the materials resistance to penetration, perforation, and spall relative to non-laminated targets. A good example is the terminal ballistic data for adhesively bonded 7075 laminates impacted by a rigid, blunt projectile [15, 16]. The results are shown in Fig. 6 and compared with data for a homogeneous 7075 plate. The laminates contained six layers and three different bonding conditions were studied - thin adhesive layer (approximately 60 μm thick), thick adhesive layer (approximately 400 μm thick) and thick adhesive layer reinforced by Kevlar 49 fiber (approximately 400 μm thick). In all cases the six aluminum layers were approximately 1 mm thick. The results, which are for projectile velocities between 200 and 300 m/s, are presented as perforation energy (the minimum incident projectile energy required for target perforation) as a function of areal density (the product of target density and thickness). The results show that the homogeneous target required less incident projectile energy for perforation than any of the laminate targets. The laminate with the thick adhesive layer required significantly more energy for perforation than the homogeneous target (approximately 74% more energy at a target areal density of 15 kg/mm^2). The laminate targets with thin layer adhesive and thick layer adhesive plus Kevlar exhibited perforation energies between those for the homogeneous and the thick adhesive laminate targets. The results shown in Fig. 6 can be understood relative to the amount of bending and in-plane stretching introduced into the back layers of the target before perforation occurred. In-plane stretching represents a high energy deformation mode and the adhesive layer in the thick adhesive laminate permitted large amounts of bulging in the aluminum layers. Relative to the thick adhesive laminate, both the thin adhesive laminate and the thick adhesive laminate with Kevlar experienced significantly less bulging of the aluminum layers; in the case of the thin adhesive laminate, the reduced bulging resulted from the smaller thickness of the adhesive layer, while in the case of the thick adhesive laminate with Kevlar the reduced bulging resulted from the constraining effects of the Kevlar 49 fiber.

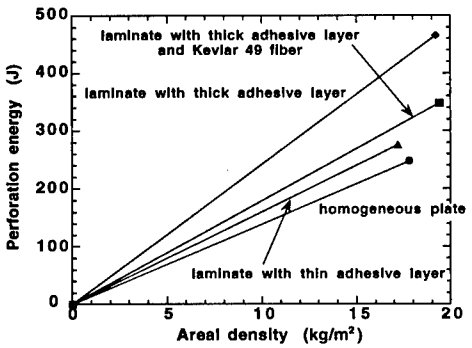


Fig. 6. Perforation energy versus target areal density for adhesively bonded 7075 self-laminates and a homogeneous 7075 plate. Targets were impacted by blunt steel projectiles. Curves were calculated from the data of Woodward, Tracy and Crouch [15] *and Woodward and Crouch* [16].

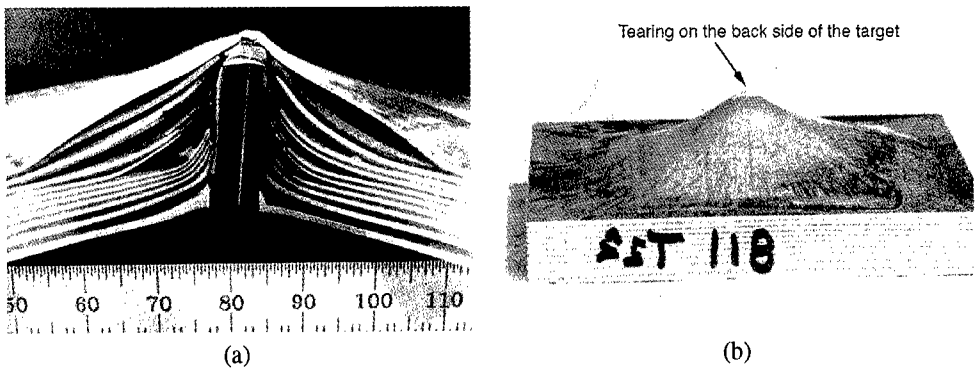
Mechanisms

The extrinsic mechanisms described in the Fracture Toughness section increase the amount of energy required for crack growth and thus can be significant sources of improved ballistic impact properties. However, lamination can also change the mechanism of failure during ballistic impact, which can dramatically increase the amount of energy absorbed. Typically during ballistic impact by blunt projectiles, monolithic aluminum alloys and aluminum matrix composites fail by low energy failure mechanisms involving

shear localization and the acceleration and compression of a shear plug [17]. The result is a shear plug of material being ejected from the target with relatively low energy. However, in laminate form, materials, which fail by shear localization during ballistic impact, can undergo local delaminations at component interfaces during impact. These local delaminations reduce the stiffness of individual layers, which allows them to bend and increases the volume of material absorbing energy during impact. The result is significantly more energy is required for penetration and perforation.

An example of the ballistic performance of a LMC target is shown in Figs. 7(a) and (b). The LMC, which consists of alternating layers of 6090/SiC/25p-T6 (dark layers in Fig. 7) and 5182 (light layers), has been impacted by a rigid, hardened steel projectile traveling at 400 m/s. Homogeneous plates of either component material would be perforated by the rigid projectile at this velocity with intense shear and little energy dissipated by the target. The sectioned LMC target is shown in Fig. 7(a). For this LMC target, the outer layers on the impact side show a shear-intensive failure representative of perforation modes typically encountered in homogeneous targets. Layers deeper into the target, however, show increasing amounts of delamination and layer flexure with the bottom layers undergoing significant biaxial stretching. These flexure and stretching deformation modes dramatically increase the volume of material deformed during the penetration process and the amount of energy required for perforation of the target. Figure 7(b) shows the back side of the LMC target and the failure of the back layer by the high energy failure modes of stretching and ductile tearing.

The change in deformation and failure mode resulting from lamination has also been studied using finite element simulations of the ballistic impact event [17]. Figures 8(a) and (b) show the deformation produced during impact of a monolithic 6061 aluminum plate and a three layer self-laminate of the 6061 alloy by a hardened steel projectile traveling at approximately 300 m/s. The overall thickness of both targets is the same. The simulations, which were done using the finite element code DYNA2D, clearly show the deformation of the monolithic target by highly localized shear (Fig. 8(a)). The three layer laminate (Fig. 8(b)), on the other hand, shows a distinct change in deformation mode from the inside layer (which deforms by shear localization) to the two outside layers (which deform largely by bending and stretching).



(a) (b)

Fig. 7. Laminated metal composite target impacted by a hardened steel projectile traveling at 400 m/s. Dark layers are 6090/SiC/25p-T6 and light layers are 5182. A cross-section of the target is shown in (a) and the back side of the target is shown in (b).

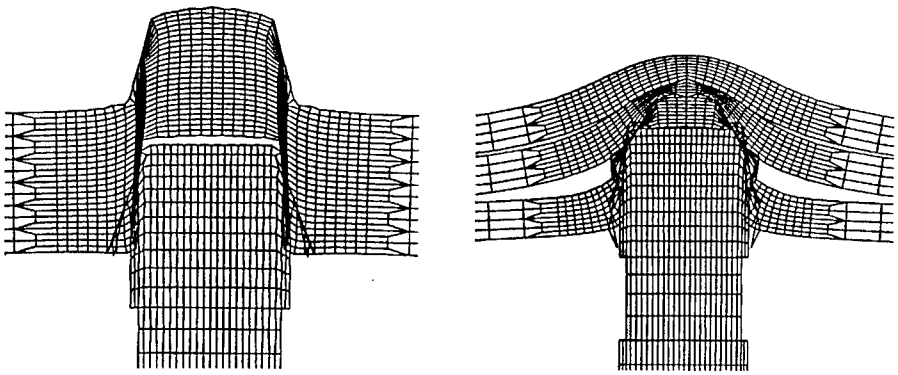


Fig. 8. Finite element simulation of the ballistic impact of a homogeneous 6061 target (a) and a three layer self-laminate of the 6061 alloy (b). Projectile is hardened steel traveling at approximately 300 m/s.

Influence of interfaces and component materials

The above analysis suggests that laminate target performance during ballistic impact is a strong function of interfacial strength. This concept is supported by the results shown in Fig. 9 in which the relative kinetic energy loss resulting from target perforation is plotted against target areal density. The projectiles were blunt-end Ti-6Al-4V cylinders traveling at about 300 m/s. In these experiments, a projectile was deliberately fired through a target and the velocities before and after target perforation were measured. The projectile kinetic energy loss resulting from target perforation was then calculated and normalized to the incident projectile kinetic energy. Data is presented for an 6090/SiC/25p // 5182 laminate (containing 50% of each component) with and without T6 heat treatment, as well as the component materials. As expected, the LMC absorbed more energy than either of the component materials. Especially noteworthy, however, is that the heat treated LMC absorbed more energy than the as-pressed (non-heat treated) LMC. As previously reported [19], the heat treated LMC studied here has significantly weaker interfaces than the non-heat treated LMC. Thus, during ballistic impact testing, greater delamination would occur in the heat treated targets and more material would be subjected to biaxial stretching during target penetration. The result is more energy would be required for perforation. Post-test analysis of the targets in these experiments confirmed that, during ballistic testing, greater delaminations were obtained in the heat treated targets than the non-heat treated targets.

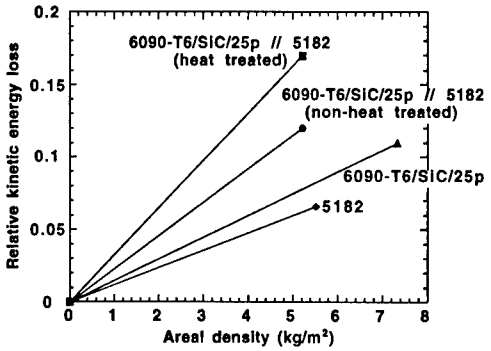


Fig. 9. Relative kinetic loss versus target areal density for a 6090/SiC/25p // 5182 laminate with and without T6 heat treatment, as well as the component materials. Targets were impacted by blunt Ti-6Al-4V projectiles traveling at 300 m/s.

The influence of component materials on ballistic penetration resistance has also been studied for the 6090/SiC/25 // 5182 laminate. Results are shown in Fig. 10 for three different volume percentages of 6090/SiC/25p and 5182 - 32%/68%, 50%/50% and 68%/32%. The amount of energy dissipated during target perforation increases with increasing volume percentage of the stronger component (6090/SiC/25p). This observation is consistent with the overall trend reported above - namely penetration resistance increases if low energy failure modes are avoided. For these targets the low energy failure mode is shear localization, which becomes more difficult as target strength increases with the higher volume fraction of the strong material.

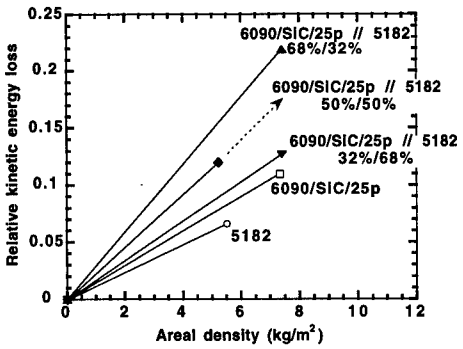


Fig. 10. Relative kinetic loss versus target areal density for a 6090/SiC/25p // 5182 laminate containing different volume percent of the component layers, as well as the component materials. Targets were impacted by blunt Ti-6Al-4V projectiles traveling at 300 m/s.

Summary and Conclusions

The fracture resistance and impact behavior of LMCs has been reviewed with examples for systems containing Al alloys and Al matrix composites. These properties have been found to be sensitive to laminate architecture (including component material volume fraction and layer thickness), component material properties and interface strength. The resulting properties and mechanisms can be summarized as follows.

1. Lamination can significantly improve the fracture and ballistic impact resistance of materials.
2. Improvements in fracture resistance result from the activation of extrinsic toughening mechanisms. These include crack deflection, crack blunting, crack front convolution, stress redistribution, and local plane stress deformation.
3. Laminates can have very attractive properties relative to other structural materials for lightweight critical applications requiring high stiffness, strength, and fracture toughness.
4. In ballistic impact tests, lamination has been found to change the failure mode from shear localization to ones involving significant energy absorption by bending and stretching.
5. The activation of extrinsic toughening mechanisms as well as high energy failure modes during ballistic impact is very sensitive to local delaminations.

Acknowledgments

The authors are indebted to Bob Riddle for finite element modeling of the ballistic impact problem and to Ray Gogolewski and Bruce Cunningham for experimental assistance with the ballistic impact tests. They also thank John Lewandowski, Warren Hunt, and Todd Osman for many valuable discussions. This work was performed under the auspices of the U.S. Department of Energy by Lawrence Livermore National Laboratory under contract No. W-7405-Eng-48.

References

1. D. R. Lesuer, C. K. Syn, O. D. Sherby, J. Wadsworth, J. J. Lewandowski, and W.H. Hunt, Jr., "Mechanical Behavior of Laminated Metal Composites", International Materials Reviews, 41 (5) (1996), 169-197.

2. R. W. Bush, "Extrinsic Toughening of Discontinuously Reinforced Aluminum: An Experimental Study of DRA Laminates," (Report 57-95-08, Alcoa Technical Center, 1995).

3. J. G. Kaufman, "Fracture Toughness of 7075-T6 and -T651 Sheet, Plate and Multilayered Adhesive-Bonded Panels", Transactions of the ASME - Journal of Basic Engineering, Sept., (1967), 503-507.

4. J. A. Alic, "Fractue Resistance of Adhesively-Bonded 7075-T6 Aluminum Alloy Laminates", Advances in Research on the Strength and Fracture of Materials, ed. D.M.R. Taplin, (New York: Pergamon Press, 1977), 1031-1037.

5. J. A. Alic and A. Danesh, "Fracture of Laminates Combining 2024-T3 and 7075-T6 Aluminum Alloys", Engineering Fracture Mechanics, 10 (1978), 177-186.

6. D. Lesuer, C. Syn, R. Riddle, and O. Sherby, "Extrinsic Toughening Mechanisms in Two Laminated Metal Composites". Intrinsic and Extrinsic Fracture Mechanisms in Organic Composite Systems, eds. J.J. Lewandowski and W.H. Hunt, Jr., (Warrendale, PA: The Minerals, Metals & Materials Society, 1995), 93-102.

7. D. R. Lesuer and C. K. Syn, "Metallic Laminates for Engine Applications", High Performance Materials in Engine Technology, Advances in Science and Technology 9, ed. P. Vincenzini, (Florence, Italy: Techna, 1995), 27-38.

8. J. J. Lewandowski and P. M. Singh, "Toughness of DRA and Extrinsically Toughened DRA/Aluminum Alloy Laminates". Intrinsic and Extrinsic Fracture Mechanisms in Organic Composite Systems, eds. J.J. Lewandowski and W.H. Hunt, Jr., (Warrendale, PA: The Minerals, Metals & Materials Society, 1995), 129-146.

9. R. O. Ritchie and W. Yu, "Short Crack Effects in Fatigue: A Consequence of Crack Tip Shielding," Small Fatigue Cracks, eds. R.O. Ritchie and J. Langford, (Warrendale, PA: The Minerals, Metals & Materials Society, 1986), 167-189.

10. R. O. Ritchie, "Mechanisms of Fatigue Crack Propagation in Metals, Ceramics and Composites: Role of Crack Tip Shielding", Materials Science and Engineering, A103 (1988), 15-28.

11. M. C. Shaw, D. B. Marshall, B. J. Dalgleish, M. S. Dadkhah, M. Y. He, and A. G. Evans, "Fatigue Crack Growth and Stress Redistribution at Interfaces", Acta Metallurgica et Materialia, 42 (12), (1994), 4091-4099.

12. D. R. Lesuer, J. Wadsworth, R. A. Riddle, C. K. Syn, J. J. Lewandowski, and W. H. Hunt, Jr., "Toughening Mechanisms in Al/Al-SiC Laminated Metal Composites", Layered Materials for Structural Applications, eds. J.J. Lewandowski, W.H. Hunt, Jr., C.H. Ward, and M.R. Jackson, (Pittsburgh, PA: Materials Research Society, 1996), 205-211.

13. R. W. Hertzberg, Deformation and Fracture Mechanics of Engineering Materials, (New York: John Wiley and Sons, 1983), 356-358.

14. N. R. Chitkara and M. K. Wong, "Deformation in Thin Composite Laminated Plates in Ballistic Impact", International Symposium on Intense Dynamic Loading and its Effects, Beijing, China, (Beijing, China: Science Press, 1986), 352-356.

15. R. L. Woodward, S. R. Tracey, and I. G. Crouch, "The Response of Homogenous and Laminated Metallic Sheet Material to Ballistic Impact", Journal de Physique IV, 1 (C3) (1991), 277-282.

16. R. L. Woodward and I. G. Crouch, "Analysis of the Perforation of Monolithic and Simple Laminate Aluminum Targets as a Test of Analytical Deformation Models", (Report MRL-R-1111, Defence Science and Technology Organisation, 1988).

17. R. A. Riddle, D. R. Lesuer, C. K. Syn, R. Gogolewski, and B. Cunningham, "Application of Metal Laminates to Aircraft Structures: Prediction of Penetration Performance", Finite Elements in Analysis and Design, 23 (1996), 173-192.

18. R. P. Gogolewski, B. J. Cunningham, R. O. Riddle, D. R. Lesuer, and C. K. Syn, "On the Importance of Target Materials Interfaces During Low Speed Impact," presented at 16th International Symposium on Ballistics, San Francisco, 1996.

19. C. K. Syn, S. Stoner, D. R. Lesuer, and O. D. Sherby, "Influence of Volume Fraction of Component Materials and Interlayer Bond Strength on Fracture Toughness of Multi-Layer Al 6090-25 vol.% SiC and Al 5182 Laminates" High Performance Metal and Ceramic Matrix Composites, ed. K. Upadhya, (Warrendale, PA: The Minerals, Metals & Materials Society, 1994), 125-136.

High Temperature Interface Sliding and Deformation Behaviour of Cu-Mo Artificial Lamellar Composite

F. Yoshida and H. Nakashima

Department of Materials Science and Technology
Graduate School of Engineering Sciences, Kyushu University
Kasuga-shi, Fukuoka 816-8580, Japan

Abstract

In order to clarify the interface sliding mechanism in a lamellar composite material at high-temperatures, Cu-Mo artificial lamellar composites were produced by an infiltration method and deformed by compression at temperatures from 893K to 993K and interface sliding rates from $1.3x10^{-2}$ to $8.4x10^{-2}$ μm/s. In addition, the interface sliding was observed in-situ by a gap of scratched lines at the interface. It was found that the interface sliding strongly depends on the interface structure. The stress exponent of interface sliding rate agrees with the theoretical value predicted by a dislocation model of sliding in which the absorption of lattice dislocations into the interface is considered to be an important elementally process.

The Third Pacific Rim International Conference on
Advanced Materials and Processing (PRICM 3)
Edited by M.A. Imam, R. DeNale, S. Hanada,
Z. Zhong and D.N. Lee
The Minerals, Metals & Materials Society, 1998

Introduction

It is well known that the interface sliding strongly affects mechanical properties of composite materials at high temperatures. However, the mechanism has not yet been clarified. On the other hand, the grain boundary sliding mechanism has been studied and clarified fairly in detail by many investigations[1] conducted so far. One of the grain boundary sliding model is based on the movement of crystal lattice dislocations or grain boundary structural dislocations[2-6]. Recently, such a model representative of McLean's model[2] for grain boundary sliding has been generally accepted. However, the applicability of McLean's model to the interface sliding has not yet been examined.

In this paper, the interface sliding behaviour of the Cu-Mo artificial lamellar composite is observed in-situ using scratched lines on the surface. Based on the experimental results, the governing factor of the interface sliding behaviour and the applicability of McLean's model to the interface sliding are discussed. The reason for selecting the Cu-Mo artificial lamellar composite as a model material is that copper and molybdenum are not soluble to each other. The intermetallic compounds are not formed. A single crystal can be easily grown. Copper has a good wettability to molybdenum, making it easy to obtain ideal interfaces[7, 8].

Experimental Procedure

Preparation of Cu-Mo artificial lamellar composite

Oriented molybdenum single crystals were grown using an r.f. floating zone technique. The starting molybdenum contained less than 10 mass ppm C and 2 mass ppm O. Single crystal plates as shown in Fig.1 (a) were cut out with a low speed diamond cutter from oriented molybdenum single crystals. The surfaces to be joined were polished with water-proof emery paper and finally buff-finished to a mirror plane with diamond paste of 1μm in particle size. The laminated block of Mo plates with a crystallographic orientation shown in Fig.1 (a) was made of the plates and molybdenum wire.

The laminated block was placed on the bottom of a alumina crucible and packed with 99.99% oxygen-free copper. After the copper was infiltrated into the laminated block by r. f. heating in a He atmosphere of approximately $5x10^{-5}$Pa, the infiltrated copper phase was made single crystal by r. f. heating and growing directionally.

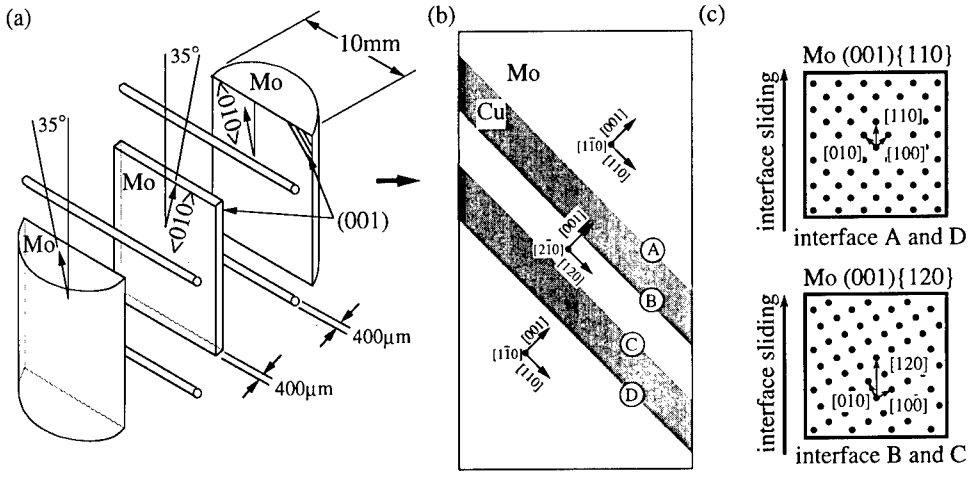


Figure 1: Schematic illustration of laminated block (a) and compression test specimen (b). The arrows indicate the crystallographic orientation of Mo components.

Compression test and in-situ observation of interface sliding

The specimens were cut from the lamellar composite with a low-speed diamond cutter. They

were fixed with an instant glue on a special polishing jig and then polished with a water-proof emery paper and finally buffed with diamond paste. The interface was made inclined at 45° to the compression axis. The final size of specimens was approximately 2mm x 2mm x 5mm. The crystallographic orientation of molybdenum components of specimen is shown in Fig.1 (b). As shown in Fig.1(c), for the interfaces indicated by A and D, the [110] direction is parallel to the interface sliding direction. For the interfaces B and C, the [120] direction is parallel to the interface sliding direction. In addition, the copper components are single crystal and the crystallographic orientation of each layer is same. Therefore, the structures of the interfaces A and D, and B and C are the same respectively, but the structure of A and D differs from that of B and C.

The compression test was conducted in a vacuum of 70 mPa at temperatures of 893 to 993K at applied interface sliding rates, V_{cbs}, from $1.3x10^{-2}$ to $8.4x10^{-2}$ μm/s using an electrically controlled hydraulic machine based on Shimazu Servo Pulsar EHF-2 type. Here, the applied interface sliding rate, V_{cbs} , was defined from the cross head speed, assuming all the deformation to be carried by interface sliding. The details of the experimental procedure were the same as those described in a previous paper[9]. In the present study, however, a hard metal was used as compression rods. At the tip of the rod, sintered SiC, which has a low thermal conductivity, was joined. As a result the temperature of the specimen was kept within ±5K during the test. The interface sliding was directly observed by measuring the gap of a scratched line. The details of the experimental procedure were the same as those described in a previous paper[10].

Experimental Results and Discussion

Deformation behaviour and interface sliding

Figure 2 shows stress-strain curves obtained under several different deformation conditions. The interface sliding rates were indicated in the figure. In this figure, the real interface sliding contribution to the total deformation, ζ_{is}, is shown.

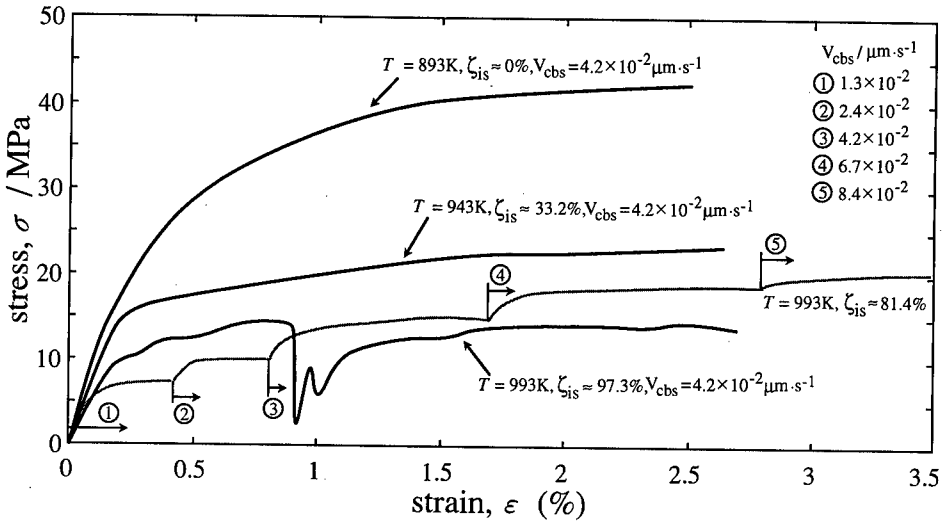


Figure 2: Stress-strain curves of Cu-Mo artificial lamellar composites compressed at various temperatures and various V_{cbs}s.

At 893K, the interface sliding contribution was 0% to the total deformation, the interface sliding could not be observed. However, the interface sliding contribution increased with temperature, at 993K the interface sliding contribution was 97.3% and a clear interface sliding was observed. On the other hand, the flow stress rapidly decreases with increasing temperature.

In the stress-strain curve at 993K and at $V_{cbs} = 4.2x10^{-2}$μm/s, the flow stress oscillated at a strain about 0.9%. The oscillation may have come from the dynamic recrystallization of copper component during deformation. But, new grains could not be observed in the copper component. Therefore

this type of stress oscillation seems to be caused by the interface sliding, and the real cause of the stress oscillation is not known.

Figure 3 shows an optical micrograph of interface sliding observed during deformation to a strain of 2.7% at 993K, V_{cbs}=4.2x10^{-2}μm/s. The gap of scratched lines at the A and D interfaces is not observed. On the other hand, the gap of scratched lines at the B and C interfaces is clearly observed. Since the interface sliding contribution to the total deformation is 97.3%, the deformation mainly occurred at the B and C interfaces. As mentioned earlier, the structure of the interfaces A and D, and the interfaces B and C are the same respectively , but the structure of the interfaces A and D, differs from that of the interfaces B and C. Hence, taking into account the difference of the interface structure it is concluded that the interface sliding behaviour of the Cu-Mo composite strongly depends on the interface structure.

In-situ observation of the interface sliding behaviour

Figure 4 shows in-situ observations of the interface sliding during deformation at 993K and V_{cbs}=4.2x10^{-2}μm/s. The gap of scratched lines at the interface increases with increasing strain.

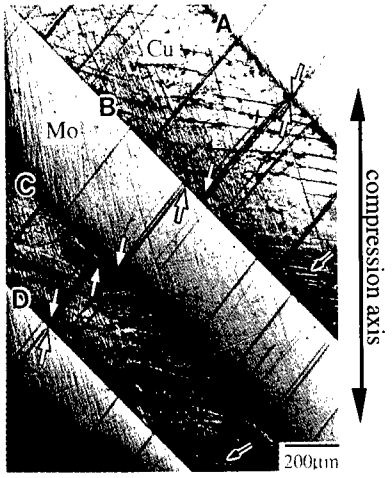


Figure 3: Optical micrograph of Cu-Mo artificial lamellar composite compressed by 2.7% at 993K under V_{cbs} = 4.2x10^{-2} μm/s.

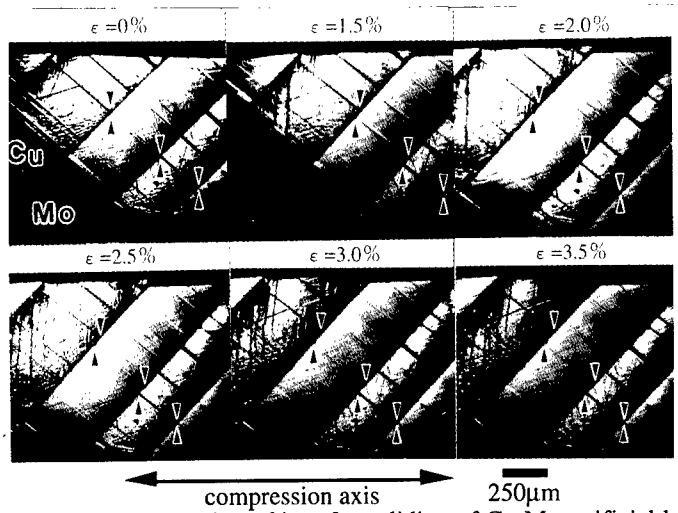


Figure 4: In-situ observation of interface sliding of Cu-Mo artificial lamellar composite during compression at 993K under V_{cbs} = 4.2x10^{-2} μm/s.

The relation between the amount of interface sliding obtained by in-situ observation and the applied strain at 993K under V_{cbs}=4.2x10^{-2}μm/s is shown in Fig.5. The total amount of interface sliding (□) is equal to the ideal values(solid line) which are estimated from the transfer length of the cross head, assuming all the deformation occurred by the interface sliding. The datum points for the interfaces B and C linearly increase with strain. On the other hand, the datum points for A and D do not increase at all with increasing strain. From these results, it is found that the interface sliding behaviour of the Cu-Mo artificial lamellar composites strongly depends on the interface structure.

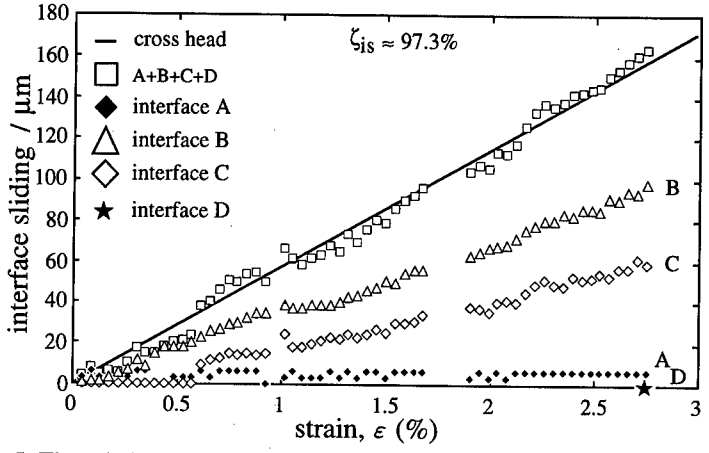


Figure 5: The relation between the amount of interface sliding obtained by in-situ observation and the compression strain at 993K under Vcbs = 4.2x10^{-2} μm/s.

Figure 6 shows that the relation between the total amount of interface sliding(○) obtained by in-situ observation and testing time at 993K for various V_{cbs}s. In this figure, the ideal interface sliding (solid line) is also shown. Under applied interface sliding rates of less than 6.7x10^{-2}μm/s, the datum points in the figure lie nearly on the solid line. But under applied interface sliding rates of faster than 6.7x10^{-2}μm/s, the datum points do not lie on the solid line.

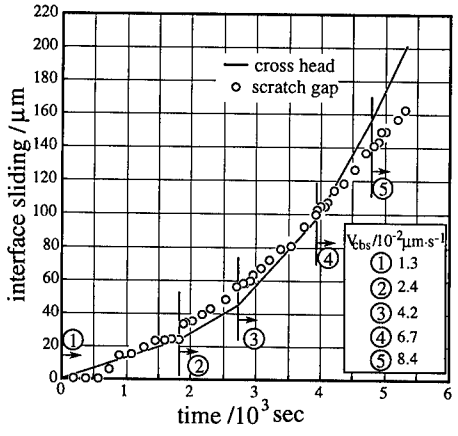


Figure 6: The relation between the amount of interface sliding obtained by in-situ observation and time at 993K under various V_{cbs}s.

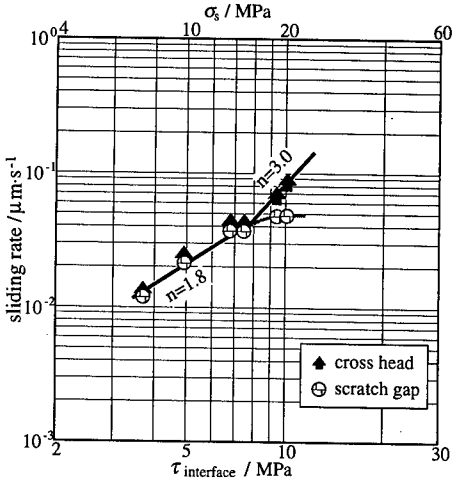


Figure 7: The relation between interface sliding rate and resolved stress.

The applied interface sliding rate and true interface sliding rate obtained from the slope of the datum points(○) in Fig.6 are double-logarithmically plotted against the resolved shear stress on the interface (assuming that the slide direction is parallel to the gap direction) in Fig. 7. In the slower interface sliding rate region below 6.7x10^{-2}μm/s, the true interface sliding rate approximately

agrees with the applied interface sliding rate. In this region, the stress exponent, n, which is given by the slope of the straight line in Fig.7 is 1.8 and agrees with the theoretical value (2) predicted by the McLean's model[4]. In addition, as shown in Fig.3, the slip lines are observed in the copper component caused by the movement of crystal lattice dislocations. From these results, it may be concluded that the interface sliding was induced by the McLean's mechanism which was originally proposed for grain boundary sliding. On the other hand, in the region of interface sliding rate over $6.7x10^{-2}\mu m/s$, the true interface sliding rate is lower than the applied interface sliding rate, and the stress exponent, n, of the applied interface sliding rate increases from 1.8 to 3.

Based on the McLean's model for grain boundary sliding, the reason for the change of the stress exponent from 1.8 to 3 may be considered as follows.

According to the McLean's model, the grain boundary sliding is brought about by climb-glide motion of lattice dislocations along the grain boundary. Therefore, it is considered that the grain boundary sliding is controlled by the climb motion of grain boundary dislocations. With increasing the applied sliding rate, the diffusion required for the climb motion of grain boundary dislocations becomes more difficult to catch up the applied sliding rate, and the deformation in the copper components more and more contributes to the total deformation. As a result, it is concluded that stress exponent, n, changes from 1.8 to 3.

Conclusions

In order to clarify the interface sliding mechanism in a lamellar composite material at high-temperatures, Cu-Mo artificial lamellar composites were produced by infiltration method and deformed by compression at temperatures between 893K to 993K and interface sliding rates of $1.3x10^{-2}$ to $8.4x10^{-2}\mu m/s$. The interface sliding was measured by in-situ observations of scratched lines on the surface. The results obtained are as follows.

(1) At 993K, the interface sliding contribution to the total defamation is about 100% for the sliding rate less than about $6.7x10^{-2}\mu m/s$. (2) The interface sliding behaviour strongly depends on the interface structure. (3) The stress exponents of interface sliding rate agree with the theoretical value predicted by the McLean's model. (4) The stress exponent for the total strain rate, n, increases from 1.8 to 3 with increasing the applied strain rate. This result shows that the deformation mechanism changes from interface sliding to the deformation in the copper component .

References

[1] *For example*, D. McLean, and M. H. Farmer, "The Relation during Creep between Grain-Boundary Sliding, Sub-Crystal Size and Extension," J. Inst. Metals, 85(1956/57), 41-50.

[2] D. McLean, "Grain Boundary Dislocations : their Effect on Vacancies and Sliding," Phil. Mag., 23(1971), 467-472.

[3] T. Watanabe, M. Yamada, S. Shima, and S. Karashima, "Misorientation Dependence of Grain Boundary Sliding in ⟨1010⟩ tilt Zinc Bicrystals," Phil. Mag., 40 (5) (1979),667-683.

[4] H. Fukutomi, H. Takatori, and R. Horiuchi, "Behavior of Grain Boundary Sliding in Cadmium Bicrystals," J. Japan Inst. Metals, 46 (8) (1982), 755-759.

[5] T. Takahashi, and R. Horiuchi, "Relationship between Grain Boundary Sliding and Crystal Slip in Zn Bicrystal," J. Japan Inst. Metals, 48 (5) (1984), 461-467.

[6] T. Takahashi, and R. Horiuchi, "Coupling of Grain Boundary Migration and Sliding in Coincidence Boundary of Zn Bicrystal as an Evidence of DSC Dislocation Model," J. Japan Inst. Metals, 45 (11) (1984), 1035-1040.

[7] T. Massalski, ed., Binary Alloy Phase Diagrams, (Metals Park, OH: American Society for Metals, 1986), vol.1, 993.

[8] Y. Muramatsu, K. Halada, T. Dan, and Y. Isoda, "Solid-Liquid Interfacial Tension of the W-Cu System," J. Japan Inst. Metals, 54 (6) (1990), 679-684.

[9] H. Kurishita, J. Shiraishi, R. Matsubara, and H. Yoshinaga, "Measurement and Analysis of the Strength of Mo-TiC Composites in Temperature Range 285K - 2270K," Trans. Japan Inst. Metal, 28 (1986) 22-31.

[10] T. Morikawa, T. Ohtsuyama, H. Murakami, H. Nakashima, S. Goto, and H. Yoshinaga, "Thermal Fatigue and High-Temperature Deformation Behavior Cu-W Artificial Lamellar Composite," Engineering Sciences Report, Kyushu University, 14 (3) (1992), 305-316.

IN SITU OBSERVATION OF CYCLIC FATIGUE CRACK GROWTH OF SiC/SiC COMPOSITE

S.J. Zhu[#], M. Mizuno*, Y. Mutoh[#], Y. Kagawa[@]

[#]Nagaoka University of Technology, Nagaoka 940-21, Japan
*Japan Fine Ceramics Center, Atsuta-ku, Nagoya 456, Japan
[@]University of Tokyo, Minato-ku, Tokyo 106, Japan

Abstract

In situ observation of cyclic fatigue crack propagation of SiC-fiber reinforced SiC composite at room temperature has been carried out by laser microscopy. Both smooth (unnotched) and notched specimens are used for tension-tension cyclic fatigue tests. Cracks initiate at the corners of large pores during loading in smooth specimens. In notched specimens cracks are formed at the interfaces between fibers and matrix that connect with the notch. The balance between the fiber bridging in the wake of propagating crack tip and the breakage of bridged fibers by the degradation of interfaces maintains a steady state cyclic crack propagation. Crack propagation rate gradually decreases with time after the maximum load being applied.

The Third Pacific Rim International Conference on
Advanced Materials and Processing (PRICM 3)
Edited by M.A. Imam, R. DeNale, S. Hanada,
Z. Zhong and D.N. Lee
The Minerals, Metals & Materials Society, 1998

Introduction

Continuous fiber reinforced ceramic matrix composites (CMCs) are promising candidates for high temperature structures because they have good fracture toughness and other performances. As cyclic fatigue properties are important considerations for applications, there are increasingly papers on them published [1-6]. SiC/SiC composites exhibited a definite fatigue limit in a classical S-N curve, hysteresis loops and the reduction of Young's modulus with number of loading cycles [5,6]. Although possible fatigue mechanisms have been proposed [1-6], little in situ observation of fatigue crack initiation and propagation in SiC/SiC composite has been reported. While, this approach will give direct image of crack initiation and propagation as well as frictional sliding of fiber-matrix interfaces. In situ observation of cyclic fatigue in a plain woven graphite-fiber/SiC composite showed that fatigue was confined to crack wake where attrition reduced the efficacy of bridging fibers [2]. It is inferred that the crack tip advances at some critical value of the crack tip stress intensity factor, as in monotonic growth, rather than by any intrinsic fatigue mechanism in the matrix.

In SiC/SiC, substantial toughening and marked R-curve behavior have been attributed to crack bridging in the wake of the crack tip; this occurs via unbroken fibers that span the crack faces and inhibit crack opening. For such a mechanism to operate, the shear strength of the fiber-matrix interface is tailored to be sufficiently low to permit fiber pull-out with passage of the main crack. However, the microstructural parameters that are required for high fracture toughness under monotonic loading, such as low interfacial shear strength, matrix microcracking, and crack bridging by fibers, typically have a negative impact on fatigue and creep resistance.

In this paper, in situ surface observation method was used to observe cyclic fatigue crack initiation and propagation in SiC-fiber/SiC at room temperature. Crack propagation behavior in longitudinal bundles was compared with that in transverse bundles. The effects of pores and interfaces on crack initiation and propagation were examined to understand the fatigue damage mechanism.

Materials and Experimental Procedure

The composites used in the investigation were processed by chemical vapor infiltration (CVI) of SiC into plane woven 0°/90° SiC-fiber bundle preforms (made by Du Pont Lanxide Composites Inc., DE, U.S.A.). Before the infiltration the preforms were coated with carbon by CVD to decrease interface bonding between fibers and the matrix. The composites, processed as 200 x 200 mm panels with a thickness of 3.2 mm, contained 40 vol% SiC fibers and 9.7 % porosity. The diameter of a fiber was about 12 μm and each bundle consisted of 500 fibers.

The testing specimens were machined from the panels using diamond cutting tools. The notched specimens are with a gage dimension of 5 x 1 x 20 mm. The depth of V-shaped notch is 1 mm and the root radius of notch tip is 15 μm. One surface of the specimens was carefully polished to allow in situ observation of microstructures and the others were machined by an 800 grit grinding wheel before testing.

The tension-tension cyclic fatigue tests were performed with a floor-type Shimadzu hydraulic-servo fatigue testing system (Shimadzu Corp. Kyoto, Japan) under load control with a sinusoidal loading frequency of 2-10 Hz in air at room temperature. The stress ratio (R), which was defined as the ratio of minimum stress to maximum stress, was 0.1. Laser microscopy and or scanning electron microscopy were attached to the fatigue machine for in situ observation . The light resource of the laser microscopy is He-Ne (632.7 nm in wave length). The magnifications of the laser microscope are from 10 to 1000. The movement of the specimen is so easy to be operated that finding crack initiation sites and tracing a propagating crack are not difficult. The fractured specimens were observed by scanning electron microscopy to see crack propagation characteristics in 2 or 3 dimensional space at higher magnification.

Results and Discussion

Crack Initiation

Plane woven microstructures of SiC-fiber/SiC composite have large pores between 0° and 90° fiber bundles as shown in Fig. 1(a). Cracks usually initiate at sharp corners of large pores (Fig. 1(b)) after loading in smooth specimens. It can be seen that the two cracks formed propagate into 0° bundle and 90° bundle, respectively.

The crack initiation is randomly distributed in the whole smooth specimens. However, in notched specimens cracks are formed only at the interfaces between fibers and matrix that connect with the notch. The mechanical machining of the notch causes microcracking at the fiber-matrix interfaces connected with the notch (Fig. 2). The microcracks induced by machining may propagate during subsequent loading.

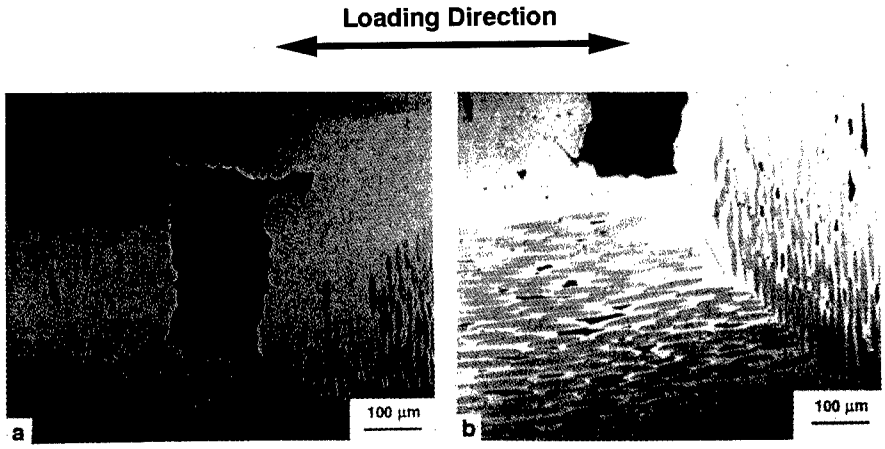


Fig. 1 Pores among fiber bundles in a smooth specimen. (a) in original state; (b) crack initiation after loading to 100 MPa.

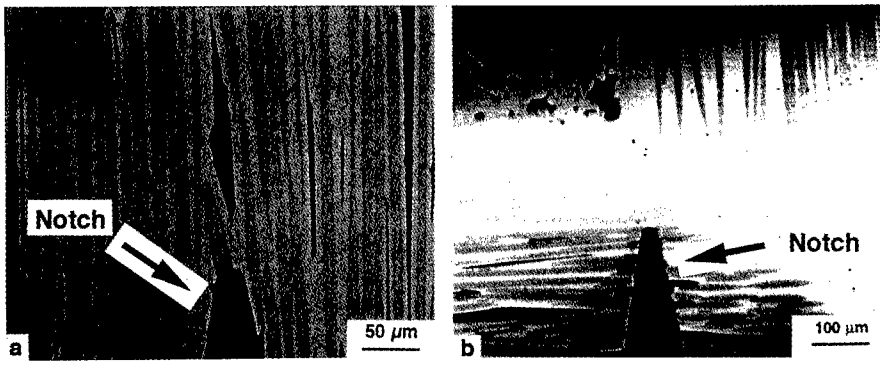


Fig. 2 Microcracks formed by mechanical machining of notches. (a) notch in 90° bundle; (b) notch in 0° bundle.

Crack Propagation

Whether cracks initiated at corners of large pores in smooth specimens or formed by machining in notched specimens, cracks always prefer to propagate in 90 ° bundles in a higher velocity. Then, the cracks extend laterally into 0° bundles. 0° fibers bridge cracks and therefore cause crack propagation rate to decrease.

Figure 3 shows a typical example of crack propagation processes in 0° bundle during cyclic fatigue. It can be seen that first 0° fibers in the wake of crack are intact and bridge the crack. Then, the bridged fiber-matrix interfaces are debonded on one side. This side is close to crossover points of bundles weaving. This is different from the double sides debonding of fiber-matrix interfaces in unidirectional CMCs. The interface sliding and degradation (wear of carbon layer) lead to the breakage of the bridged fibers and therefore the fibers lose effect to inhibit crack propagation. Crack propagation can normally last several thousands cycles after cyclic loading. Then crack propagation rate becomes very low, even can not be detected within 10^4-10^5 cycles. At this stage, we increase the maximum stress to make crack propagation. Crack propagation rate again gradually decreases. This seems to be a characteristic of cyclic crack propagation of SiC-fiber/SiC composite.

A crack propagation process in a notched specimen is shown in Fig. 4. Since the notch is located in a 0° bundle, microcracks formed during machining are in the same direction with the tensile axis. During loading to 150 N, the crack propagates in 45° direction until the crack tip contacts with a 90° fiber. Then the load is kept constant for two hours, no crack propagation occurred. Subsequently, the load is increased to 250 N, leading to crack propagation (Fig. 4 (a)). However, at constant load of 250 N, still there is no crack propagation within two hours. Then, cyclic loading is applied with a maximum load of 250 N. The fiber-matrix interface is gradually debonded and the crack propagates along the interface during cyclic loading and unloading (Fig. 4 (b)). After 1000 cycles, the crack does not further propagate up to 30000 cycles. Then, the maximum stress is increased to 280 N, the crack propagates again (Fig. 4 (c)). The crack turns to 45° direction and stops at another 90° fiber. The fibers-matrix interfaces in the wake of the crack frictionally slide up to 1.4 x 10^5 cycles, but the crack tip never advances. Increasing stress to 300 N does not induce visible crack propagation within 6000 cycles, but after 6000 cycles new cracks are gradually produced near notch tip region. One of the new cracks propagates in both directions instead of the old crack. Cyclic fatigue at 350 N causes the crack tip to reach the notch root in one direction and the crack propagates along 90° fibers-matrix interfaces in another (Fig. 4(d)).

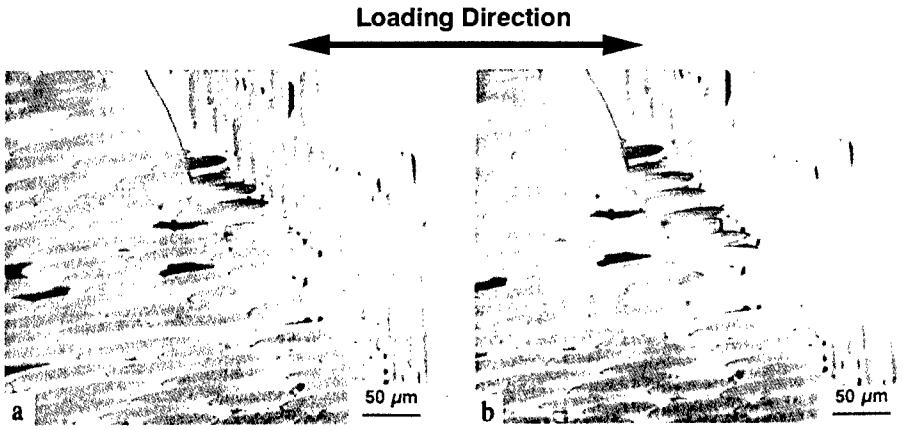


Fig. 3 Cyclic fatigue crack propagation process during cyclic fatigue in above specimen. (a) cyclic fatigue at the maximum stress of 100 MPa for 3500 cycles; (b) cyclic fatigue at the maximum stress of 100 MPa for 6300 cycles.

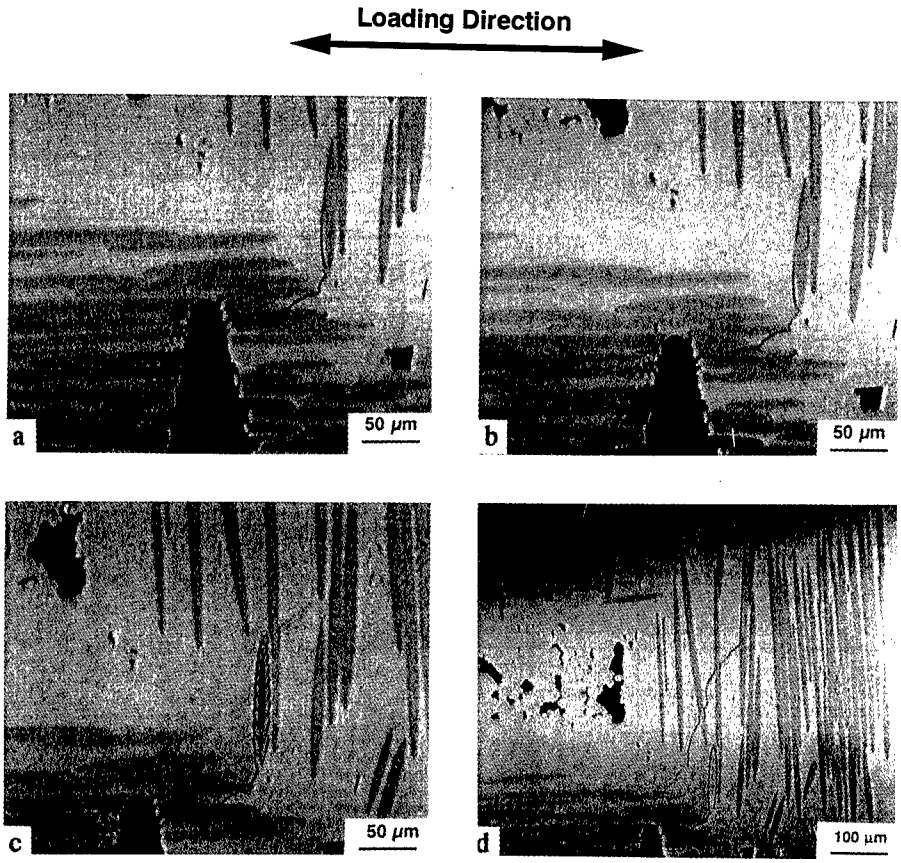


Fig. 4 Cyclic fatigue crack propagation process in a notched specimen. (a) after loading to 250 N; (b) cyclic fatigue for 1000 cycles at 250 N; (c) cyclic fatigue for 1.4 x 10^5 cycles at 280 N; (d) cyclic fatigue for 1000 cycles at 350 N.

When a notch tip is in 90° bundle, a crack can easily propagate following microcrack s formed by machining in 90° direction. Crack propagation in 90° bundles was expected to be an instant process due to the same direction as fibers, but it is a process of gradual advance. Moreover, cracks stopped in matrix can also be seen. This reflects that cyclic fatigue crack propagation is indeed governed by the bridged fibers in the wake of crack.

Recently, Evans et al [1] reviewed fatigue of ceramic matrix composites at room temperature. Two possible mechanisms for CMCs were proposed: one is the changes in the interface sliding resistance during cycling [5,6]; another is the degradation of the strength of the fibers by cyclic sliding along the interface by means of an abrasion mechanism [2-4], which introduces flaws in the fibers. When ceramic fibers are used (rather than carbon fiber), interface degradation is the dominant fatigue mechanism [5,6].

It was found that the interface sliding resistance was decreased by cyclic fatigue in SiC/SiC [6]. The decrease of sliding resistance of interfaces can cause the debonding length of interfaces to increase. Both interface debonding and sliding occur under cyclic loading and

unloading. The interface debonding is important for fiber bridging since it can retard fibers failure by dissipating energy (decreasing stress concentration). However, the increase in the debonding length during fatigue implies the increase in the effective fiber gauge length in the composite. This leads to fiber failure due to decreased strength of fibers. The balance between the fiber bridging in the wake of propagating crack and the breakage of the bridged fibers by interfacial degradation maintains a steady state cyclic crack propagation. Multiplied cracks are observed just before the final fracture of the specimens.

The present observation showed that the debonding and sliding of interfaces between 0° fibers and the matrix were only on the side near the crossover points of fibers weaving architecture. This reflects that the stress concentration at crossover points is important to crack propagation. With increasing debonding length during fatigue, the effective fiber gauge length increases, leading to decreased ultimate tensile strength (UTS) of fibers [1]. As a result, the fracture of bridging fibers promotes crack propagation. This is the mechanism of fatigue crack propagation in SiC/SiC.

Conclusion

Cracks initiate at the corners of large pores in smooth specimens. The crack initiation is uniformly distributed in the whole smooth specimens. While in notched specimens cracks are formed at the interfaces between fibers and the matrix which connect with the notch.

Cyclic fatigue crack propagation is governed by the bridged fibers in the wake of crack. The interface debonding and sliding occur under cyclic loading and unloading. The balance between the fiber bridging in the wake of propagating crack and the breakage of bridged fibers by interface degradation maintains a steady state cyclic crack propagation.

Acknowledgments

The authors are grateful for the assistance of Dr. S. Guo and Mr. Y. Nagano during the experiments. This work is a part of basic research and development programs operated by Petroleum Energy Center, Japan. S.J. Zhu is grateful for the Grant-in-Aid for Encouragement of Young Scientists (No. 09750105) by the Ministry of Education, Science, Sports and Culture, Japan.

References

1. A. G. Evans, F. W. Zok and R. M. McMeeking, "Fatigue of Ceramic Matrix Composites," Acta Metall. Mater., 43 (1995), 859-875.
2. W. L. Morris, B. N. Cox, D. B. Marshall, R. V. Inman and M. R. James, "Fatigue Mechanisms in Graphite/SiC Composites at Room and High Temperature," J. Am. Ceram. Soc., 77 (1994), 792-800.
3. S. F. Shuler, J. W. Holmes and X. Wu, "Influence of Loading Frequency on the Room-Temperature Fatigue of a Carbon-Fiber/SiC-Matrix Composite," J. Am. Ceram. Soc., 76 (1993), 2327-2336.
4. Z. G. Wang, C. Laird, Z. Hashin, W. Rosen, C. F. Yen, "Mechanical Behaviour of a Cross-Weave Ceramic Matrix Composite, Part II Repeated Loading," J. Mater. Sci., 26 (1991), 5335-5341.
5. P. Reynaud, "Cyclic Fatigue of Ceramic-Matrix Composites at Ambient and Elevated Temperatures," Comp. Sci. Tech., 56 (1996), 809-814.
6. M. Mizuno, S. Zhu, Y. Nagano, Y. Sakaida, Y. Kagawa, M. Watanabe, "Cyclic Fatigue Behavior of SiC/SiC Composite at Room and High Temperatures," J. Am. Ceram. Soc., 79 (1996), 3065-3077.

FRACTURE BEHAVIOUR OF POLYMER-HYDROXYAPATITE COMPOSITES

P. Cheang and K.A. Khor

Advanced Materials Research Center
Nanyang Technological University
Nanyang Avenue, Singapore 639798

Abstract

Biomaterial composites have a greater advantage over monolithic systems because of their ability to satisfy far wider biological and mechanical requirements. However, composites made from a combination of HA and polymer, particularly polyethylene, have evidently limited properties such as moderate tensile modulus and low tensile strength. These limitations are mainly associated with interfacial and structural factors which are not well understood. Our studies on the fracture behaviour of polymer-HA composites suggest that the surface morphology and structural integrity of the HA powder have considerable influence on the mechanical property of the composite. The tensile modulus of the composite was particularly sensitive to the surface characteristics of the HA particles. Rough particles tend to promote higher tensile modulus because of enhanced interfacial bonding arising from mechanical interlocking. The tensile strength of the composite was governed by the intrinsic weakness of the composite which were either interfacial or structural in nature. Lower tensile strength was evident with porous agglomerated HA particles that fractured easily in a brittle manner. Strong and spherical HA particles that prevented the initiation and propagation of sharp cracks attained higher tensile strength, provided good interfacial bonding was assured. Finally, a combination of both high strength and modulus was achieved by applying appropriate post-treatment to microwave sensitive materials.

The Third Pacific Rim International Conference on
Advanced Materials and Processing (PRICM 3)
Edited by M.A. Imam, R. DeNale, S. Hanada,
Z. Zhong and D.N. Lee
The Minerals, Metals & Materials Society, 1998

Introduction

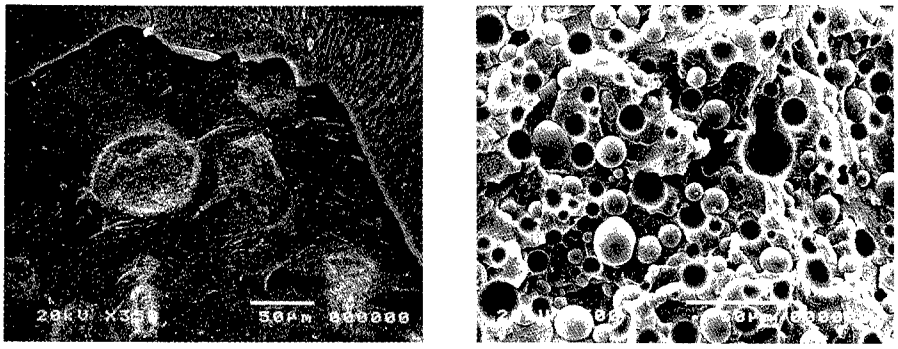
The development of biomaterial composites for orthopeadic applications has often modeled their design concept closely resembling natural bone. This generally involves a harder reinforcement phase within a softer matrix. The blending of specific amounts of various types of reinforcement is often introduced to achieve certain desirable properties. Bioceramics such as bioglass and hydroxyapatite (HA) are preferred reinforcements because of their stiffness, density and bioactivity. Matrix materials often comprise polymers which include high density polyethylene (HDPE), polyurathane, poly(L-lactide)(PLLA), polyetheretherketone(PEEK), polymethylmethacrylate (PMMA), and collagen. Typical polymer-HA systems that have been investigated are HDPE-HA [1-3], PLLA-HA [4], PMMA-HA [5-7] and Collagen-HA [8]. The major problem faced is the interfacial adhesion between the reinforcement and the matrix. Unless effective stress transfer takes place across interfaces, the mechanical properties are not expected to reach useful values. Interfacial adhesion may be increased by mechanical and chemical means. In this study the effect of powder loading and powder morphology on the fracture behaviour, hence mechanical properties of the polymer-HA composites will be examined. Post treatment using microwave energy will be applied to enhance the properties of as-moulded composites

Experimental Technique

Hydroxyapatite ($Ca_{10}(PO_4)_6(OH)_2$) was prepared by reacting 0.5M of calcium hydroxide with 0.3M of orthophosphoric acid in a controlled temperature bath (40°C+5°C). The HA suspension was subsequently used to produce spray dried and spheroidised powders. Spray drying was performed on a Model LT-8 rotary spray atomizer from Ohkawara Kakohki Co., LTD. Spheroidised HA powders were prepared by oxy-acetylene flame spraying spray dried powders. HDPE and PMMA pellets were obtained from Exxon Chemicals. The polymer-HA composite was compounded using a Haake Rheocord 90 torque rheometer fitted with an internal RheoMix-600 mixer and a cam rotor. Mixing was done between 150-220°C and 40 rpm. HDPE-HA test pieces were injection moulded using a Battenfeld BA 300/050 CD injection moulding machine. PMMA-HA compounded samples were hot pressed at 220 °C under 20 metric tons to form square sheets. Tensile test samples were cut according to ASTM standard E 8 requirements. Post heat-treatment of the tensile test specimens were carried out using a microwave oven operating at 600W power output and a frequency of 2450 MHz. Tensile tests were carried out using Instron IX series materials testing system.

Results and Discussion

The mechanical behaviour of a composite system is often dependent on the physical nature and concentration of the reinforcing phase. Fig. 1 and 2 show the effect of powder loading on the tensile modulus and tensile strength of injection moulded HDPE-HA and hot-pressed PMMA-HA composites containing spray dried HA (SDHA) and spheroidised HA (SHA) powders. The tensile modulus of these composites generally increased with increasing powder loading. This suggests sufficient stress transfer across the polymer-HA interface. The HA powder in the matrix restrains movement of the matrix phase in the vicinity of each particle which contributes to an overall increase in the elastic modulus. The effect of powder morphology on the elastic modulus of the polymer-HA composites is evident in these plots. The polymer-HA composites containing spray dried powders have higher tensile modulus than those with spheroidised HA. The surface characteristics of the particles have significant influence on the tensile modulus of the composite. Clearly,



(a) (b)

Fig. 4 Fracture surface of a) SDHA/PMMA composite b) SHA/PMMA composite.

Microwave treatment was applied to as-moulded polymer-HA composites. Significant improvement was evident in the tensile moduli for the PMMA-HA composites (Fig.5). Composite strengthening only occurred in the PMMA-HA systems containing spheroidised HA powders. Here, the tensile modulus for SHA/PMMA composite increased by over two folds, and reached a value comparable to microwave treated spray dried sample while maintaining high tensile strength. The degree of improvement in the SHA/PMMA composites (2.5 times at 20 vol%) was higher compared to SDHA/PMMA composites (1.9 times at 20 vol%).

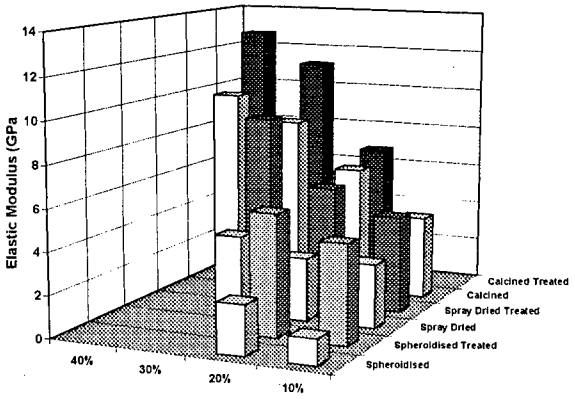
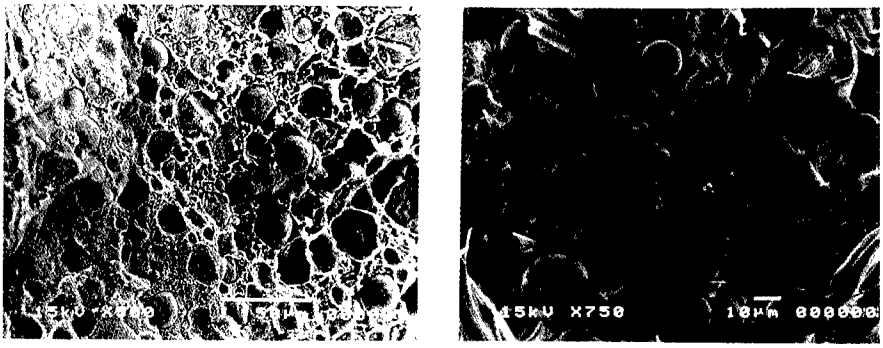


Fig.5 Elastic modulus of microwave treated PMMA-HA composite

With agglomerated spray dried powders, good interfacial adhesion is achieved via mechanical interlocking. Further enhancement of an already strong interface using microwave treatment appears marginal. With spheroidised HA powders, mechanical adhesion is limited because of surface smoothness. This permits greater enhancement of this weak interface using microwave treatment. No improvement in mechanical properties was observed with pure PMMA and HDPE-HA composites. The apparent improvement in the tensile modulus after microwave treatment suggests limited interfacial bonding arising from this moulding process. This emphasizes the value of post-treatment in enhancing the performance of microwave sensitive composite implants.

stretching of the polymeric matrix. Failure of the SDHA particles is evident from the fractured particles embedded in the polymer. For the SHA/HDPE composite (Fig.3b), a distinctly different fracture morphology appears. It is ductile-like with considerable deformation or stretching of the HDPE material. The dense spherical SHA particles are trapped between the fibrous polymer network. The SHA particles remain intact and are detached from the polymer matrix. The brittle-like fracture surface of SDHA/HDPE suggests that there is sufficient stress transfer resulting from mechanical interlocking of the rough surface to cause restrain and stiffening of the composite. Progressive loading of the composite at high modulus is sustainable until fracturing of the weakly agglomerated SDHA occurs which leads to stress-overload of the remaining polymer matrix resulting in catastrophic failure of the composite. The limiting factor in this system is the fracture strength of the SDHA particle. With the SHA/HDPE composite, weak interfacial bonding between the polymer and the smooth SHA particle lowers the tensile modulus of the composite. During loading, composite stiffening is effective until particle debonding occurs, thereafter load bearing is completely sustained by the remaining polymer matrix. Since debonding takes place below the fracture stress of the HDPE, further deformation is possible as shown by the stretching of the fibrous polymeric strands. The fracture strength is lower because of the reduced cross-section created by the detached particles dispersed within the polymer matrix. The limiting factor in this SDHA/HDPE composite is therefore the interfacial bond strength.



(a) (b)

Fig. 3 Fracture surface of a) SDHA/HDPE composite b) SHA/HDPE composite.

The fracture surfaces of SDHA/PMMA composites (Fig.4a) have a characteristic brittle appearance with planar cracks traversing both matrix and particulate. Fracturing of the spray dried HA particle is clearly evident. With the spheroidised HA composite (Fig.4b), greater surface area is generated from the propagation of torturous crack paths around particulates instead of fracturing through the particles in the previous case. In Fig.4a, the crack propagated from within the weakly agglomerated spray dried HA powders as opposed to circumventing the stronger spheroidised HA which remained intact. With this polymer-HA system, failure takes place in the particle for spray dried HA powder and at the PMMA-HA interface for spheroidised HA powder. For the composite containing spray dried HA, the tensile strength is governed by the cohesive strength of the weakly agglomerated particles. With spheroidised HA, the tensile strength is dependent on the interfacial bonding which in this case is lower than the cohesive strength of the strong SHA particle. The higher tensile strength of SHA/PMMA composite compared to SDHA/PMMA is attributed to higher bond strength of the SHA/PMMA interface than the cohesive bond strength of the agglomerated SDHA particle.

SDHA particles with rougher surfaces attained higher modulus which is attributed to better mechanical interlocking. The modulus was lower with spheroidised HA particles because of smoother surfaces.

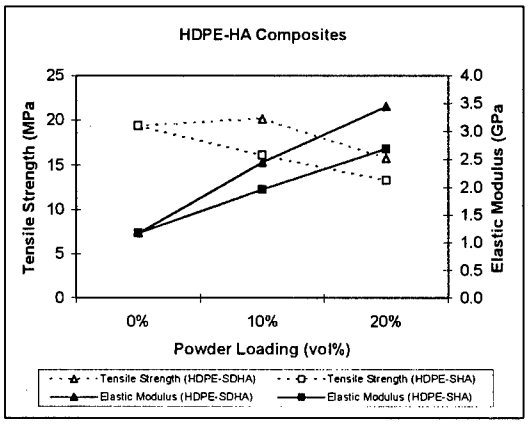


Fig. 1 Effect of powder loading and morphology on the tensile modulus and tensile strength of injection moulded HDPE-HA composites

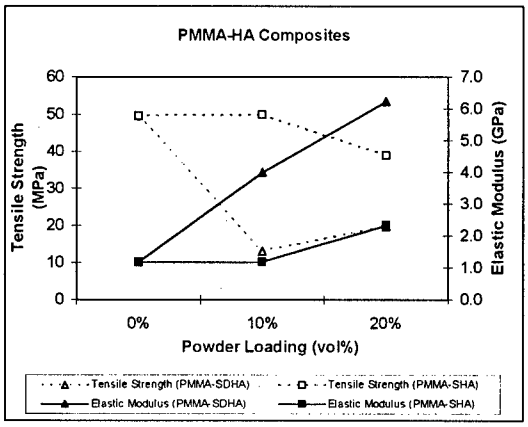


Fig. 2 Effect of powder loading and morphology on the tensile modulus and tensile strength of hot-pressed PMMA-HA composites.

As shown in Fig. 1 and 2, the tensile strength of the composite mainly decreases with increasing powder loading. With the HDPE-HA system, the tensile strength of the composite containing spray dried HA powder is higher than those with spheroidised HA. This trend is reversed with the PMMA-HA system which shows higher tensile strength in composites containing spheroidised HA than those containing spray dried HA. The differences in the tensile strengths can best be explained by examining the fracture surfaces (Fig. 3-4).

The fracture surface of HDPE-HA composite containing spray dried HA powder is shown in Fig.3a. The fracture morphology is relatively flat resembling brittle failure with little

Conclusion

This investigation has shown that the elastic modulus of the composite is strongly dependent on interfacial bonding whereas the tensile strength is governed by either particle integrity or interfacial bonding. The highest tensile modulus was observed in polymer-HA composites comprising spray dried HA powders because of enhanced mechanical interlocking arising from the porous surface. The tensile strength of composites containing SHA powder was higher in PMMA matrix but lower in HDPE matrix. This behaviour is characteristic of the powder integrity and the interface bonding between the two materials. For the SHA/PMMA system, the cohesive strength of the SHA particle is higher than the interfacial bond strength, hence failure occurred at the SHA-PMMA interface. This interfacial bond strength is higher than the cohesive strength of the porous SDHA powder which accounts for the higher tensile strength of SHA/PMMA composite. In SDHA/HDPE system, fracturing of the SDHA particles occurred because of the lower cohesive strength of the porous SDHA powder compared to the interfacial bond strength at the SDHA-HDPE interface. Microwave treatment enhances the elastic modulus of the PMMA-HA composites by promoting interfacial bonding. Its effect on tensile strength is more apparent if strengthening is governed by interfacial interaction (e.g. SHA/PMMA system). The best mechanical properties were achieved by using spheroidised HA powder followed by microwave treatment of the composite to obtain a combination of both high elastic modulus and tensile strength.

Acknowledgement

The facilities of Advanced Materials Research Center (AMRC). The technical assistance provided by Mr Tan Yao Hong, Mr Goh Hua Kooi and Ms Ho Chiew Nyuk is gratefully acknowledged.

References

1. Tanner K.E., W. Bonfield and R.N. Downes, 7th International Conference on Biomedical Engineering, Singapore, 400-401, (1992).
2. Wang. M, D. Porter and W. Bonfield, "Processing, characterisation, and evaluation of hydroxyapatite reinforced polyethylene composites" British Ceramic Transactions, Vol 93, No.3, 91-93, (1994).
3. Deb S., M. Wang, K.E. Tanner and W. Bonfield, "Hydroxyapatite-polyethylene composites: Effect of grafting and surface treatment of hydroxyapatite", Journal of Material Science: Materials in Medicine, Vol 7, 191-193, (1996).
4. Verheyen C.C.C.P., J.R. de Wijn, Van Blitterswijk, K. de Groot, "Evaluation of hydroxylapatite/poly(L-lactide) composites: physico-chemical properties", Journal of Biomedical Material Research, Vol 26, 1277-1296, (1992).
5. Ravaglioli A., A. Krajewski, Biochemics-materials, properties and applications, Chapman and Hall. (1992)
6. Driessens F.C.M., M.G. Boltong, O.Bermudez, J.A. Planell, M.P. Ginebra, and E. Fernandez, "Effective formulations for the preparation of calcium phosphate bone cements", Journal of Biomedical Material Research, Vol 5, 164-170, (1994).
7. Kazuhiko Ishihara, Hiroki Arai, Nobuo Nakabayashi, Sadao Morita and Kotaro Furuya, "Adhesive bone cement containing hydroxyapatite particle as bone compatible filler", Journal of Biomedical Material Research, Vol 26, 937-945, (1992).
8. Hirota K, K. Nishihara and H. Tanaka, Bio-medical Materials and Engineering, Vol 3, 147-151, (1993).

Effect of Size of TiC Reinforcement on Abrasion and Impact-Abrasion of MMCs

Ö.N. Doğan, J.A. Hawk, and R. D. Wilson

U.S. Department of Energy
Albany Research Center
Albany, Oregon 97321

Abstract

Wear resistance of eight titanium carbide reinforced metal matrix composites was investigated under different wear conditions. Volume fraction of TiC particles in these composites varies between 0.35 and 0.45 as well as the size of the TiC particles. A high-stress abrasion test (pin abrasion test), a low-stress abrasion test (dry sand rubber wheel test) and an abrasion-impact test (impeller-in-drum test) were utilized to understand the wear behavior of these materials under different conditions. While in the low-stress abrasion environment, finer TiC particles (smaller interparticle spacing) provide better wear resistance, the coarse TiC particles are more effective in protecting the softer matrix from abrasion in the high-stress environment.

The Third Pacific Rim International Conference on
Advanced Materials and Processing (PRICM 3)
Edited by M.A. Imam, R. DeNale, S. Hanada,
Z. Zhong and D.N. Lee
The Minerals, Metals & Materials Society, 1998

Introduction

Titanium carbide is one of the hardest carbides in nature with hardness values between 2000 and 3200 HV (19.6-31.4 GPa) [1]. However, its use as a monolithic material is limited due to its low impact resistance. Powder metallurgy (PM) techniques [2,3] allow TiC particles to be dispersed in metallic matrices, and as a result, TiC particles are effectively used as the primary reinforcing phase in metal matrix composites (MMC) to increase their hardness, wear resistance, and thermal shock resistance.

The present work investigates the wear resistance of particulate TiC reinforced MMCs in three different abrasive wear environments.

Experimental Procedure

Eight commercially available TiC reinforced MMC PM alloys [4,5] were used in this study. The matrices of all of the composites were hardened prior to testing. Table 1 lists the TiC volume fraction, metal matrix type, and hardness of the materials.

In order to better understand the wear behavior of these materials, three wear tests were performed.

The dry-sand, rubber-wheel (DSRW) abrasion test follows an ASTM Standard Practice, G65 Procedure B [6]. The wear environment is considered as three-body and low-stress. In this study, three tests for each specimen were run and the results averaged. The DSRW specimens were sectioned from the castings and machined to size (15- by 25- by 75-mm). The two largest opposing surfaces were then ground flat and parallel for testing.

The pin abrasion wear test [7,8] involves the wear of the flat end of a cylindrical pin (6.35 mm diameter by 25 mm length) of a sample material and a reference material in contact with an abrasive cloth (garnet, alumina, and SiC in this case) on a large slowly rotating cylindrical drum. The test condition is considered as two-body and high-stress. A dead weight loading system applies a 66.7 N load to the specimen. All the abrasive particles used in these tests are 150 grit, possessing a nominal size of 100 μm.

After a specimen break-in cycle of four revolutions, wear data were collected after 10 revolutions, equivalent in magnitude to a sliding distance of 16 m. Four sets of tests were performed for the specified number of drum revolutions for each material. The weight loss of the sample and the standard pin was measured after each test. The results were averaged with standard deviations calculated. Abrasion data were calculated as volume loss.

The impeller wear test [9] involves the impact of 20-25 mm diameter chunks of high silica quartzite against a rapidly rotating set of metal paddles. The result of the quartzite hitting the metal paddles is a wear environment that has elements of both impact and abrasion. In this test, three sample paddles, 15- by 25- by 75-mm, are securely placed in the impeller hub assembly which sits inside an enclosed drum. Approximately 37.5 mm of the length of the sample protrudes from the outer periphery of the impeller hub and is susceptible to impacts from the quartzite abrasive. Six hundred grams of quartzite is placed within the drum. The impeller-in-drum wear test machine is then started. During the test the hub assembly rotates at approximately 620 revolutions per minute

Table 1. TiC reinforced MMCs used in this investigation.

Material	TiC vol. fraction	Matrix Type	HR_c
HT-6A	0.40	Nickel base	54.1
CHW-45	0.45	Hot work tool steel	61.0
SK	0.35	Impact resistant tool steel	61.8
MS-5A	0.41	Martensitic stainless steel	63.1
CS-40	0.45	Martensitic stainless steel	67.4
CM	0.45	High chrome tool steel	66.5
PK	0.42	Maraging steel	66.6
C	0.45	Medium alloy tool steel	70.9

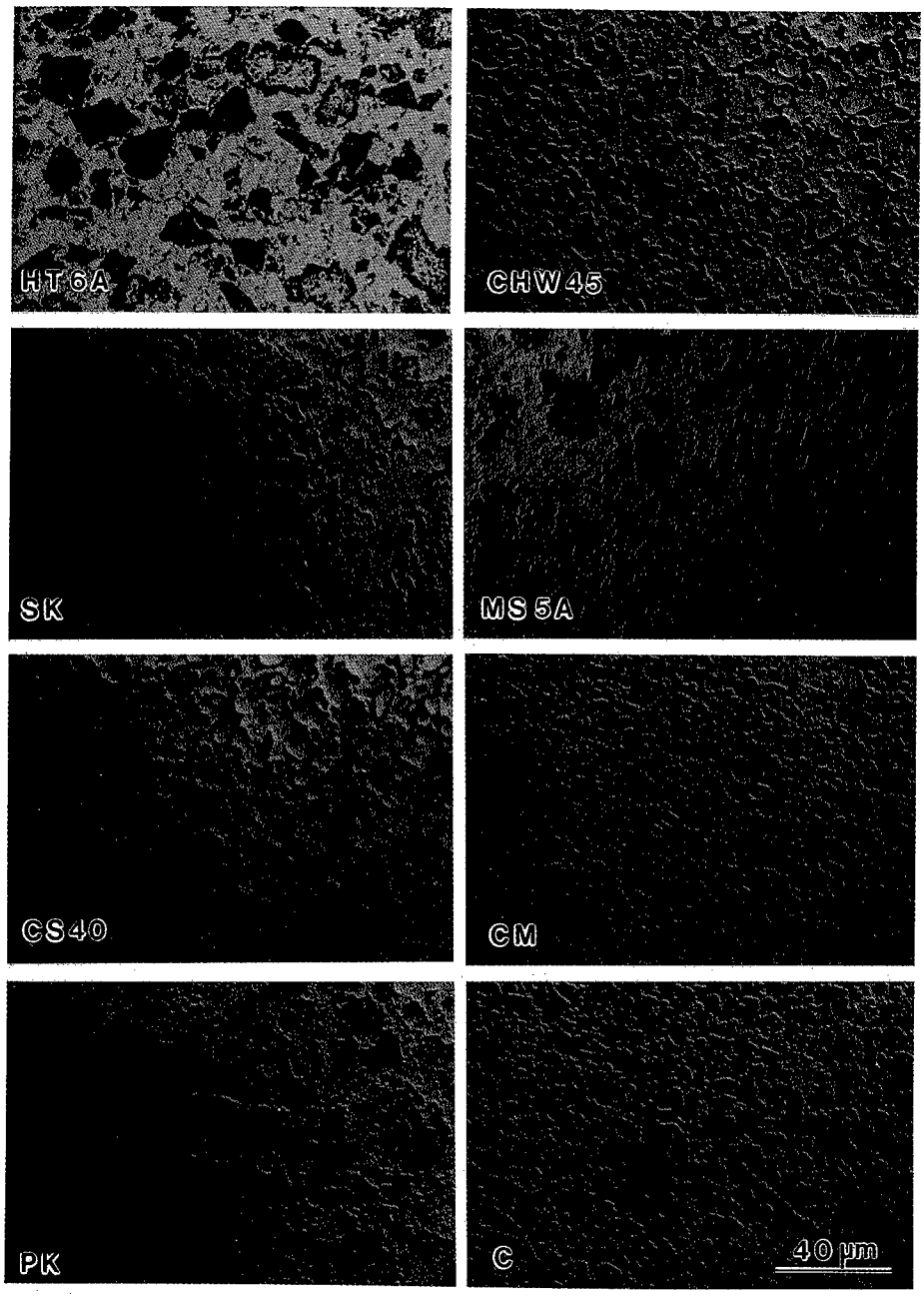


Figure 1. Optical micrographs of TiC reinforced MMCs. Unetched.

(velocity of the specimens is about 6 m/s) while the drum rotates at 45 revolutions per minute. Both impeller and drum rotate in the same direction. The test is run for 15 minutes with the quartzite comminuted into smaller size fractions. After 15 minutes the test is stopped, the comminuted quartzite is removed, and a new charge (600 g) of quartzite is placed within the drum. The test is restarted and run for another 15 minutes. This process is repeated another two times, so the metal paddles see a total of one hour of impact wear. At this point the paddles are removed, cleaned and weighed. The mass loss is determined and a wear rate calculated in terms of volume of material lost per hour of operation. The samples are then reversed and a second one hour test is run.

Results and Discussion

Morphology and spatial distribution of TiC particles in the composite materials are shown in the optical micrographs in Fig. 1. While composites PK, MS-5A, and HT-6A contain large angular TiC particles, other composites are reinforced with smaller rounder TiC particles. Some dissolution of TiC particles during processing is apparent in all composites. Frequently, the large angular carbides and the small rounded carbides dissolve in such a way that concave interfaces between the TiC particles and the matrix form. This interesting phenomenon is attributed to coherency strain between certain faces of TiC and the matrix [10].

Hardness values of the composites are listed in Table 1. They range from 54 HRC for a Ni base matrix with TiC volume fraction of 0.40 to 71 HRC for a medium alloy tool steel matrix with TiC volume fraction of 0.45. From these values, it is clear that the hardness is not only a function of volume fraction of TiC particles but also that of matrix type.

All of the composite materials tested showed high wear resistance in all three conditions. Fig. 2 shows the volume loss of the composite materials as measured on the garnet, alumina, and silicon carbide abrasive clothes in the pin abrasion test. In general, the wear rates of the composites decrease with increasing hardness under the high stress abrasion conditions on all three abrasive clothes. These relationships are fairly linear except for the data points for the composites HT-6A and MS-5A. In these softer composites, the coarse carbide structure protects the matrix better than the smaller TiC particles of composites SK and CHW-45. This behavior has also been observed previously with austenitic high Cr white cast irons in the same high stress abrasive environment [11,12]. This is due to their higher resistance to fracture against the tangential forces exerted by the abrasive particles under the conditions of high stress abrasion [13]. It has also been shown that the coarse reinforcing particles can also lower the wear volume loss by dislodging the abrasive

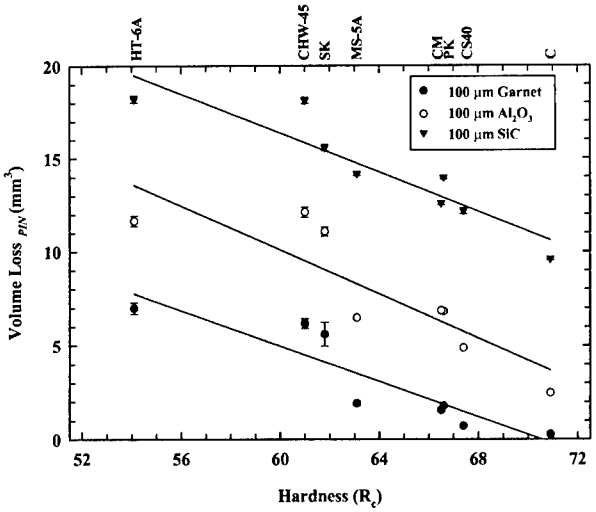


Figure 2. Wear loss in pin abrasion test as a function of composite hardness.

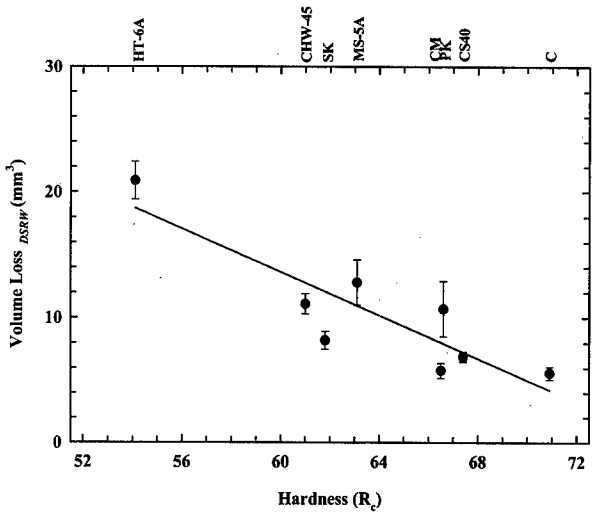


Figure 3. Wear loss in DSRW test as a function of composite hardness.

particles from the cloth. However, these effects of carbide size were not observed on the harder composite, PK, with the coarse carbide structure.

Fig. 3 illustrates the variation in volume loss of the composite materials with hardness in the DSRW test. Again the general trend is a decrease in wear loss with increasing hardness of the materials. In addition, under the conditions of low stress abrasion, two trends emerge with respect to TiC particle size in the composite materials. First is the larger error bars in the materials with the coarser TiC particles (HT-6A, MS-5A, and PK). These bars indicate the standard deviation from the average of three tests. The second is, irrespective of hardness, the composites with coarse

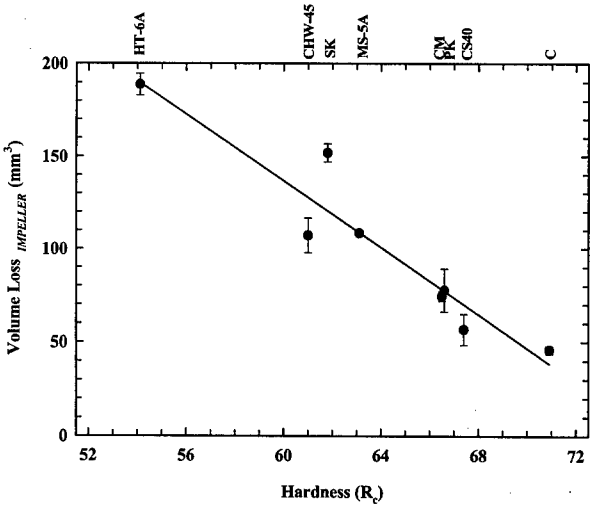


Figure 4. Wear loss in the impeller test as a function of composite hardness.

TiC particles show higher wear losses compared to the composites with finer TiC particles. As a matter of fact, one may draw two separate lines through the data points in Figure 3: One for the composites with the coarse TiC structure, and a lower line for the composites with the finer TiC structure. These results suggest that interparticle spacing in these materials plays an important role in the DSRW test. Large interparticle spacing in the composites with the coarse TiC particles gives rise to an easier removal of matrix between the TiC particles by the abrasive. When the interparticle spacing is small as in the composites with finer TiC particles, the matrix is protected by the TiC particles more effectively. This type of wear was studied previously in white irons and similar results with respect to the interparticle spacing were found by the present authors [12].

The results of the impeller-in-drum test are shown in Fig. 4. In this test, too, the general trend is decreasing volume loss with increasing hardness of the materials. Unlike the other two tests, this test does not distinguish between the coarse and fine TiC structure of the composites. This result was unexpected because the previous studies [12,14] done on white irons found that the finer particle distribution provided better wear resistance in this type of test. The finer hard particles dispersed in a ductile matrix are more resistant to fracturing under impacting erosive particles than the coarse particles [14].

Conclusions

In all three wear environments employed in this study, the wear volume loss of TiC reinforced MMCs decreases with increasing hardness.

In a low-stress abrasion environment such as the dry sand rubber wheel test, removal of matrix material between the TiC particles by the abrasive appears to be the primary mechanism of material removal in the TiC reinforced MMCs. Therefore, it is critical to minimize the interparticle spacing in these materials for applications in a low-stress abrasion environment.

In a high-stress abrasion environment such as the pin abrasion test, larger TiC particles provide better protection for the softer matrices. With the harder matrices, no TiC size effect is observed.

In an impact-abrasion environment such as the impeller-in-drum test, the variation in the size of the TiC particles in the composites does not change the linearity of the wear volume loss versus hardness data.

Acknowledgments

The authors would like to thank Mr. John F. Marconi, Alloy Technology International, Inc., for providing the materials used in this study.

References

1. E.K. Storms; The Refractory Carbides, Academic Press, New York, p.11, (1967).
2. B.K. Lograsso and R.M. German; *Progress in Powder Metallurgy*, vol. 43, MPIF, Princeton, NJ, p.415 (1987).
3. Ö.N. Doğan, D.E. Alman, and J.A. Hawk; *Advances in Powder Metallurgy and Particulate Materials*, MPIF, Princeton, NJ, p.83 (1996).
4. Alloy Technology International, Inc., West Nyack, NY.
5. S.E. Tarkan and M.K. Mal, Technical Paper MR 73, Society of Manufacturing Engineers, 1973.
6. ASTM, "Measuring Abrasion Using the Dry Sand/Rubber Wheel Apparatus", G65-94, vol.03-02, American Society of Testing and Materials, Philadelphia, PA, (1996).
7. R. Blickensderfer and G. Laird II, *J. Test. Eval.*, vol. 16, pp. 516-526, (1988).
8. R. Blickensderfer, J.H. Tylczak and B.W. Madsen, Bureau of Mines Information Circular IC 9001 (1985).
9. J.A. Hawk, R.D. Wilson, J.H. Tylczak, and Ö.N. Doğan, submitted for publication in *AFS Transactions*, (1998).
10. K.-W. Chae, D.-I. Chun, D.-Y. Kim, Y.-J. Baik, and K.-Y. Eun; *J. Am. Ceram. Soc.*, vol.73 (7), p.1979 (1990).
11. Ö.N. Doğan, J.A. Hawk, and G. Laird II, *Metall. Mater. Trans. A.*, vol. 28A, p.1315 (1997).
12. Ö.N. Doğan, and J.A. Hawk; submitted for publication in *AFS Transactions*, (1998).
13. Ö.N. Doğan and J.A. Hawk, *Wear*, vol. 189, p.136, (1995).
14. Ö.N. Doğan and T.A. Adler, in Wear of Engineering Materials, Conference Proceedings from Materials Solutions' 97, Ed. J.A. Hawk, ASM International, (1997).

INTERFACIAL STRESS STATE AND FAILURE OF SCARF JOINTS IN METAL MATRIX COMPOSITES

D.D. Brink[1], J.C. Mailand[2], C.G. Levi[1,2], and F.A. Leckie[2]

The University of California at Santa Barbara
[1] Materials Department
[2] Department of Mechanical and Environmental Engineering
Santa Barbara, CA 93106

Abstract

The stress state in the interlayers of scarf joints between metal matrix composites was investigated using finite element methods and compared to the fracture behavior of model joint specimens. The geometry of the model joints consisted of thin metal interlayers sandwiched between two Al-matrix composite sub-elements reinforced with continuous polycrystalline alumina fibers. The finite element work reveals the existence of stress and strain concentrations at the edges and corners of the composite/interlayer interfaces as well as the dependence of these concentrations on scarf angle. The stress and strain distributions predicted by the FEM analysis are consistent with observations of initiation and propagation of fracture in the model scarf joints. The results suggest that joint failure, which occurs by local debonding of the fiber/interlayer interfaces followed by ductile tearing of the metal ligaments between the fiber tips, is determined by a critical combination of stresses and plastic strains. Criteria for this type of failure are under development.

The Third Pacific Rim International Conference on
Advanced Materials and Processing (PRICM 3)
Edited by M.A. Imam, R. DeNale, S. Hanada,
Z. Zhong and D.N. Lee
The Minerals, Metals & Materials Society, 1998

Introduction

The superior specific strength and stiffness of continuous fiber reinforced metal-matrix composites (MMCs) make them attractive for many applications, but joining these materials into useful structures has proven difficult. Material anisotropy and uncertainties in interface properties have fostered a design philosophy based primarily in load transfer through shear, often resulting in bulky joints which offset the weight saving benefits of the MMC. A better understanding of the behavior of composite/composite and composite/monolithic interfaces under different loading conditions should enable the development of more efficient joint designs. The present work is part of a broader project aimed at studying the load carrying ability of interfaces involving fiber terminations at the joint, with different orientations of the joint plane relative to the direction of reinforcement.

Efforts to elucidate the relevant issues have hinged on the manufacture and testing of model scarf joints, shown schematically in Figure 1(a), complemented by simplified close-form models as well as full 3-D finite element analysis of the specimens. The joints are fabricated by pressurized infiltration of molten Al alloys into preforms of continuous Al_2O_3 fibers containing prescribed discontinuities, as described elsewhere [1]. This process achieves continuity between the matrix and interlayer, which are formed simultaneously, minimizing the interfacial defects common to conventional joining methods [2]. The mechanical performance of these samples should thus define a baseline against which other joints can be compared.

The general features of the mechanical behavior of these model scarf joints are discussed in [3]. Briefly, the joint failure occurs consistently along the composite/interlayer interface via a mechanism involving debonding of the fiber tips, followed by linkage of the ensuing "cracks" by ductile tearing of the metal ligaments between them. Debonding, in turn, appears to involve microvoid nucleation and coalescence at the fiber tip/metal interface. The failure strain increases consistently with scarf angle, θ, for $\theta \leq 60°$, while the UTS appears to first decrease slightly with θ and then increase markedly for $\theta > 45°$. Research into the specifics of the failure process has lead to the development of both analytical and finite element models describing the interlayer stress state and the possible conditions for interface failure by the experimentally observed mechanisms. The analytical models in [1,3] describe the stress state in the interlayer mid- plane, Figure 1(b), and reveal the development of large hydrostatic stresses in the core of the interlayer due to the constraint imparted by the composite subelements. Comparison with experimental results suggests that joint failure occurs when the tensile stress normal to the composite/interlayer interface within the core region reaches a critical value. This model, however, does not readily explain other experimental observations. For example, it has been shown that the interface can tolerate much higher tensile stresses than those found in [3] if the interlayer is reinforced with particulates. This paper explores further the issues of interface failure in scarf joints using finite element analysis.

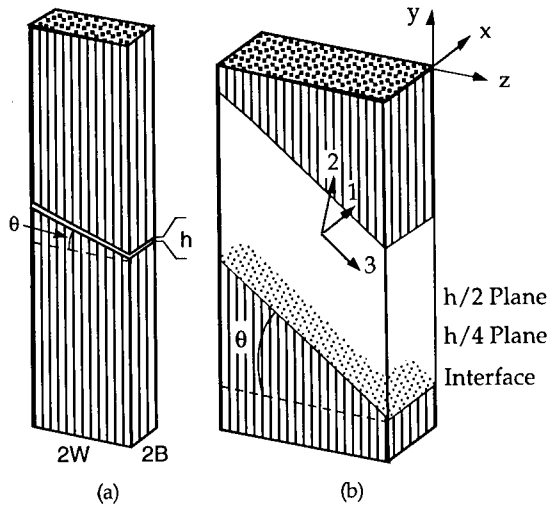


Fig. 1: Model joint geometry (a) and blowup of the interlayer region (b) depicting the different planes of interest. The interlayer is typically 100-300 μm.

Experimental Observations of Failure Initiation

While there are many similarities in the failure mode of the butt (θ=0°) and scarf (θ>0°) joints, there are also important differences. Notably, failure in butt joints often exhibits multiple initiation points, consistent with the idea of a critical "debond" stress reached simultaneously across the "core" region of the interface. As the angle increases, however, there are indications that failure actually starts at the edges, and not within the core. This is particularly evident in the fracture surfaces of the 30° and 60° joints shown in Figure 2, where failure appears to initiate at the narrower edges and in opposite sides of the interlayer, with the interlayer failing by ductile tearing where the two interfacial cracks meet. More significantly, the initiation sites appear to flip from one interface to the opposite one (at the same edge) when the angle increases from 30° to 60° (see sketch in Figure 2c). These issues cannot be explained on the basis of the simpler models proposed previously [3]. This paper presents results from FEM analyses illustrating the development of stress concentrations near the interlayer boundaries, and discusses the potential importance of these edge effects in the failure mechanism.

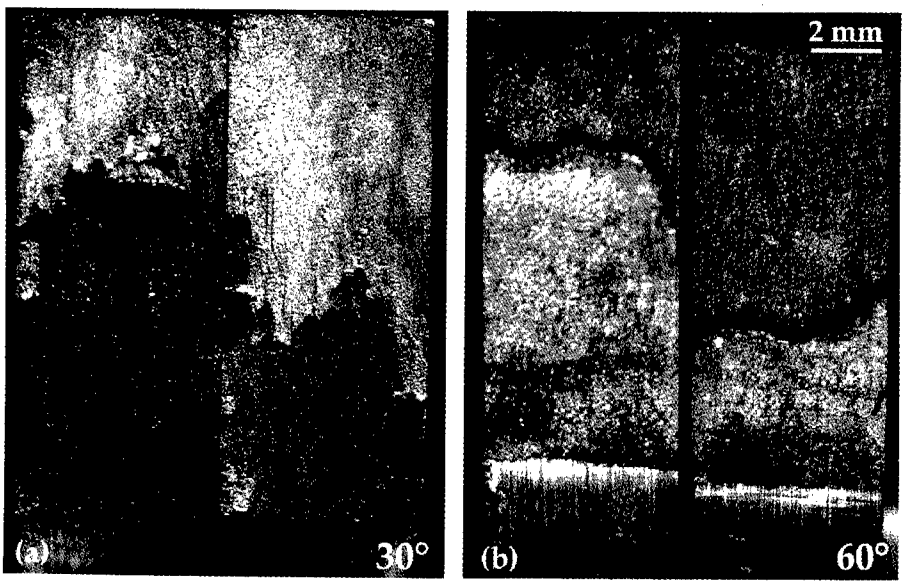
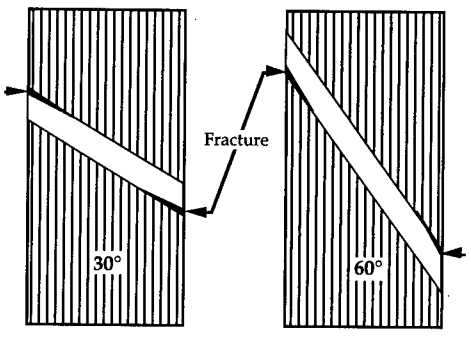


Figure 2: Fracture surfaces of the 30 and 60° joints. Note the evolution of debonding from opposite ends of the interlayer: the top left hand corner of the 30° specimen is covered with metal whereas the corresponding region in the 60° joint shows the debonded fiber ends (cf. sketch in c). The specimen halves are rotated by 180° relative to each other so that the matching surface for the top end on the left side corresponds to the bottom end on the right side. Also note the final failure by ductile tearing of the metal between the two opposite interfaces undergoing debonding, particularly evident in the 30° specimen.



(c)

Finite Element Model

The geometry of the model joint specimens analyzed by FEM is shown in Figure 1. In all cases the fibers are aligned along the length of the specimen and coincide with the tensile axis. The composite subelements are joined by a thin layer of unreinforced matrix with thickness h, tilted by an angle θ between its normal (2-axis) and the fiber direction (y-axis).

The mesh consisted of 2,816, 20-noded quadratic brick elements (C3D20) arranged in an 8 by 8 grid within the composite ends and refined to an 8 by 32 grid in the metal interlayer. Uniform displacements were applied in the y-direction along the top plane of nodes, while the node set which defined the specimen bottom was constrained against both transverse and axial motion. The calculations were performed on a Convex computer using the ABAQUS™ FEM code.

The constitutive behavior of both composite and interlayer were incorporated into the calculations as measured independently from experiments [1], so that the results would facilitate direct comparison with the model joints. However, the large level of constraint may allow more work hardening to occur in the interlayer than in a monolithic specimen, and may cause stresses to be underestimated while plastic strains may be somewhat elevated [4]. Although this effect will be significant only for plastic equivalent strains greater than 10%, the results should be evaluated with this in mind. The FEM output was transformed to a set of coordinates suitable to assess the normal and shear stresses and strains for three parallel planes within the interlayer, as depicted in Figure 1(b). These planes are at the composite/interlayer interface, as well as at one-quarter (h/4) and one-half (h/2) of the interlayer thickness. The reference coordinate system is one in which the 2-direction is normal to the interlayer, as indicated in Figure 1(b).

Interlayer Stress State

The approximate analysis in [3] indicated that the magnitude of the hydrostatic stress, which is expected to be largely responsible for void nucleation and growth [5], decreases with increasing θ for a given level of applied stress. Substantial insight was added by the FEM analysis, which showed significant concentrations of the hydrostatic stress at the interface, near the edges of the interlayer—Figure 3(a). It is also noted that these are markedly different from the distributions through the middle of the interlayer for the 30° and 60° joints, but not for the one at 45°—see Figure 3(e). Similar trends are observed in the ratio of the hydrostatic to the effective stress (not shown), which is sometimes cited as the relevant parameter in determining ductile failure in metals [6].

Figure 3(b) reveals significant concentrations of plastic strain at the end regions of the interlayer width (2W) which reach values in excess of 30%.[1] In addition, the strain distributions for the interfaces are asymmetric, with the maximum strain occurring at opposite edges in the 30° and 60° specimens. These large strains can promote the growth and linkage of voids, and cause failure to initiate preferentially in these regions [4]. Their occurrence at opposite edges (for the same interlayer side) in the 30° and 60° joints would then be consistent with the experimental observations in Figure 2. However, it is noted that the 30° joint shows a favorable combination of high plastic strains with high tensile hydrostatic stress in the purported site of failure initiation, whereas the 60° joint shows the plastic strain concentration combined with a compressive hydrostatic stress. In principle, compressive hydrostatic stresses would result in unfavorable conditions for void nucleation, which the experimental observations suggest is the likely initiation step in the mechanism of fiber tip debonding and eventual failure of the composite/interlayer interface.

[1] These values may overestimate actual strains. See previous section.

In an attempt to clarify the apparent inconsistency between the stress/strain conditions in the interlayer and the observed failure initiation site, a 2D (plane strain) FEM analysis of the stress distribution around fiber tips was undertaken. Because the composite/interlayer interface is not planar in the microscopic scale, as assumed in the 3D FEM calculations, one may envision a situation in which plastic shear parallel to the "macroscopic" interface defined by the

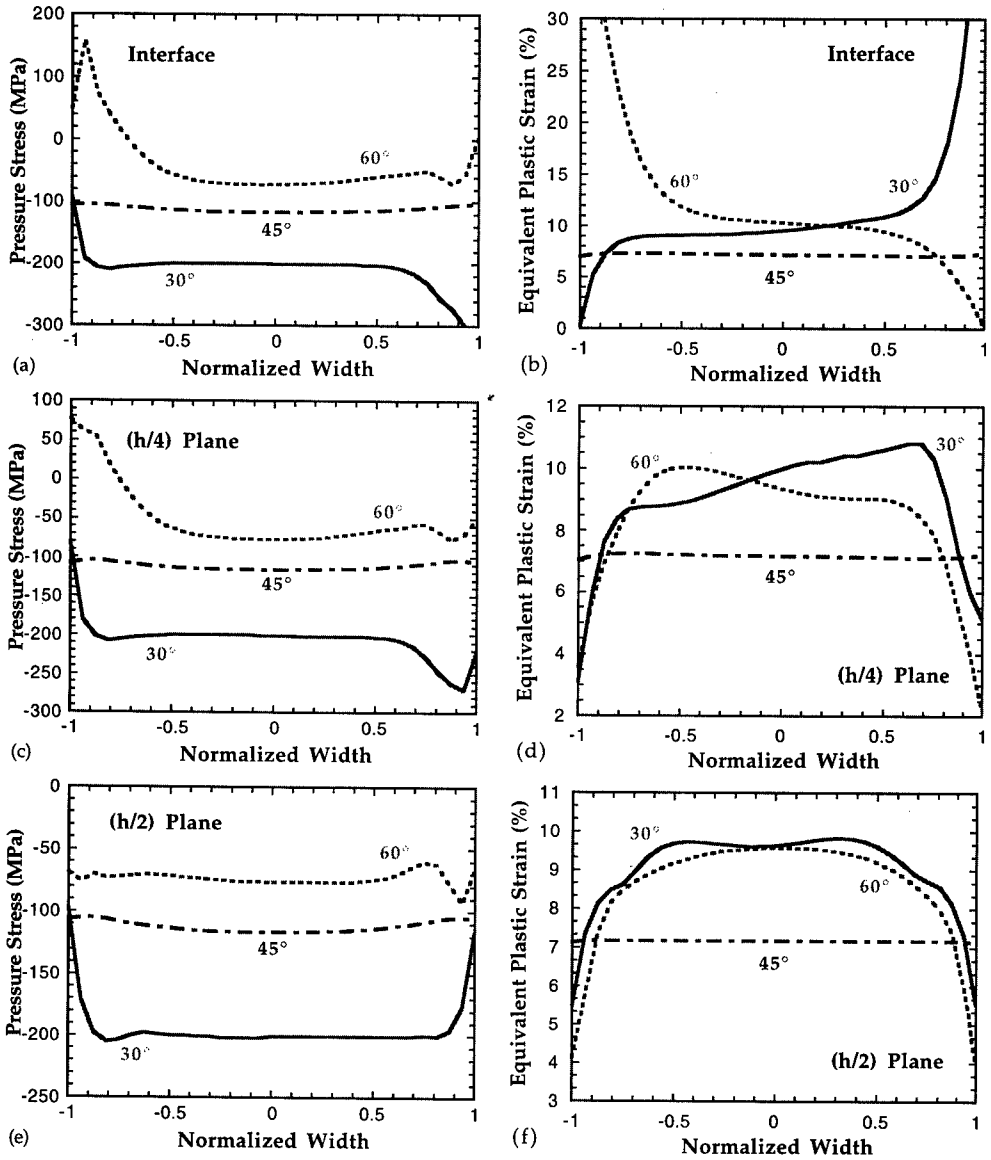


Figure 3: Distributions of the pressure stresses (a,c,e) and plastic equivalent strain (b,d,f) within the interlayer for 3 different scarf angles. The applied loads are slightly different: 255, 212 and 251 for the 30°, 45° and 60° angles, respectively. The curves correspond to the plane parallel to the broader face of the specimen (23), for x1 = 0. (cf. Fig. 1b). The curves for the (3h/4) plane along the width are mirror images of those in 2(c) and (d), with the mirror plane passing through the origin. The same applies to the opposite interface (x2 = h), where the stress distributions are mirror images of those in 6(a) and (b). Curves representing the pressure stress and plastic equivalent strain in the orthogonal direction (12 plane - not shown) are symmetric about the interlayer center.

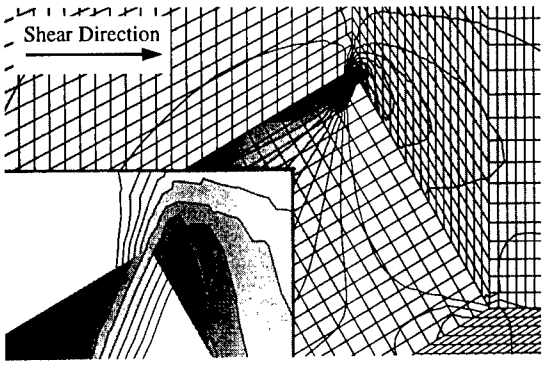


Figure 4: Pressure stress contours around a fiber tip on the interface of a 60° joint obtained from a 2D finite element model. The model was subjected to remote compressive stresses and large shear strains which mirror the conditions at the edge of the 60° interface as obtained from the 3D FEM model. The darker regions are tensile in nature (350 MPa near the fiber corner) while light regions are indicative of compressive pressure stresses. The inset is an enlarged view of the fiber corner region.

fiber tips can actually give rise to local tensile stresses in the "downstream" side of the fiber tip, even when the remote hydrostatic stress is compressive. This is indeed the case, as suggested by the FEM calculation of the local plastic flow around the fiber tips created by large shear strains parallel to the interlayer.[2] The results for the 60° joint, where the controversy is most evident, are given in Figure 4. These calculations suggest that the large plastic strains are then primarily responsible for the failure initiation.. Conversely, the role of the hydrostatic stress cannot be neglected, as indicated by the fact that the 60° joint fails at much higher applied stresses (and concomitantly higher interfacial plastic strains) than the 30° joint, where the superposed hydrostatic stress is always tensile [3].

Conclusions

Finite element analysis of scarf joints showed the development of significant plastic equivalent strains and hydrostatic stresses at the interface edges of 30° and 60° scarf joints. The stress and strain concentrations were asymmetric for a given interface, suggesting regions of preferential debond initiation. Moreover, the maximum plastic equivalent strain concentration occurred at opposite edges of the interlayer for the 30° and 60° joints. These observations correlated well with failure in model joint specimens which fractured along interfaces harboring the largest plastic equivalent strains. The analysis supports the view that the plastic strain plays a significant role in the debond failure process, originally thought to be controlled primarily by the stress normal to the interface in the core region of the joint.

References

1. A. Burr, J.Y. Yang, C.G. Levi, and F.A. Leckie, "The Strength of Metal-Matrix Composite Joints," Acta Metall. Mater. 43 (5) (1995), 3361-3373.
2. R.W. Messler, Jr., Joining of Advanced Materials (MA: Butterworths-Heinemann, Stoneman, 1993), 270-274, 492-496.
3. D.D. Brink, C.G. Levi, A.C.F. Cocks, and F.A. Leckie, "The Role of Scarf Angle in the Performance of Aluminum Matrix Composite Joints," Acta Materialia, 45 (7) (1997), 2765-2275.
4. Frank A. McClintock and Ali S. Argon, Mechanical Behavior of Materials (Reading, MA: Addison-Wesley, 1966), 226-330, 524-527.
5. V. Tvergaard, "Failure by Ductile Cavity Growth at a Metal Ceramic Interface," Acta Metall. Mater. 39 (3) (1991), 419-426.
6. J.R. Rice and D.M. Tracey, "On the Ductile Enlargement of Voids in Triaxial Stress Fields," Journal of the Mechanics and Physics of Solids, 17 (3) (1969), 201-17.

[2] The details of this mechanism, which is specific to the system studied, exceed the scope of this paper and will be presented in a latter publication.

STUDY ON THE INTERFACIAL REACTION AND MECHANICAL PROPERTIES OF SiCp/6061Al COMPOSITES

R. M. Wang [1,2], Y. Cui [1], M. K. Surappa [3], C. H. Tao [1]

[1] Beijing Institute of Aeronautical Materials, Beijing 100095, China

[2] Laboratory of Atomic Imaging of Solids, Institute of Metal Research, Chinese Academy of Sciences, Shenyang 110015, China

[3] Department of Metallurgy, India Institute of Science, Bangalore 560 012, India

Abstract

The interfacial reactions in SiC_p/6061Al composites produced by vortex and squeeze-cast techniques have been studied. The effect of the acid-leaching treatment of the SiC particles on the interfacial reaction and mechanical properties has also been investigated. The SiC reinforcements are well bonded with the matrix in the SiC_p/6061Al composite fabricated by vortex method. The interface between the SiC particles and the matrix is clean and no reaction product was observed in most cases. However, discrete $MgAl_2O_4$ reaction products have been found at the interface in the squeeze-cast composite. With slight acid-leaching of the SiC particles, the interface becomes smooth and clean. The mechanism of the reaction has also been investigated. The results of flexure tests show that the slight interfacial reaction can increase the elastic properties significantly, but is not beneficial to the fracture strength and ductility of the composites.

The Third Pacific Rim International Conference on
Advanced Materials and Processing (PRICM 3)
Edited by M.A. Imam, R. DeNale, S. Hanada,
Z. Zhong and D.N. Lee
The Minerals, Metals & Materials Society, 1998

Introduction

The aluminum matrix composites containing particles of silicon carbide have been extensively studied in recent years because of their unique combination of such good advantages as excellent mechanical properties, light weight and low cost, which make them attractive as candidate materials in aerospace applications [1,2]. The nature of the interface between matrix and reinforcement plays a significant role in determining the properties and strengthening mechanism of metal matrix composites (MMCs) [3]. It is important to characterize the interface microstructure in order to understand the interaction between reinforcement and matrix during processing and to establish the relationship between process, microstructure and mechanical behavior.

Previous investigations have shown that the formation of a significant amount of brittle compounds of Al_4C_3 or $MgAl_2O_4$ at the SiC_p/Al interface is detrimental to the stiffness and strength of the composites [4,5]. However, only few studies have been carried out on a slight interfacial reaction in SiCp/Al composites [6,7] and the effect of such reaction has never been reported. In this paper the microstructures and mechanical properties of the SiC particles reinforced 6061 aluminum matrix composites have been studied, with particular emphasis on the relationship between the process, interfacial reactions and mechanical behavior.

Experimental Procedure

Commercial 6061aluminium alloy was used as the matrix. α-SiC particles with the size ranging from -250mesh to +350mesh were used to fabricate 25vol.%SiC_p/6061Al composite using vortex method [8]. Composite billets of 50mm diameter were homogenized at 540°C for 3 hours and extruded into 8mm diameter rods at 500°C. The extrusion ratio works out to be 20. The angular-shaped SiC particles about 3.5μm in size were used to fabricate 45vol.%SiC_p/6061Al composites using squeeze casting method. Some of the SiC particles have been treated in hydrofluoric acid before the fabrication of the composites [9].

Interface characterization was carried out using TEM, HREM and EDX. Conventional transmission electron microscopy (TEM) was performed using an H-800 electron microscope operated at 200kV. High resolution electron microscopy was performed using JEOL 2000EX-II electron microscope operated at 200kV. Energy dispersive X-ray spectroscopy was performed by means of an Oxford Link ISIS 6498 spectroscope attached to JEOL 2010 electron microscope. The software for the chemical composition calculation was ISIS ver. 2.0. Flexure tests were performed on an Instron 1186 universal testing machine at a cross head speed of 0.5mm/min. The specimens were 3.0×4.0×36.0mm according to JIS specifications.

Results and Discussions

Microstructures

Figure 1 shows the microstructure of the 25vol.%SiC_p/6061Al composite produced by vortex method. The SiC particles are angular in shape with a size varying from 20μm to 80μm. The particle distribution is reasonably homogeneous. The results of the TEM and HREM analysis show that both allotropes, hexagonal α-SiC and cubic β-SiC are present in the composites. Investigations also indicate that the particles in the squeeze cast composites distribute rather homogeneously with a size varying from 1μm to 5μm.

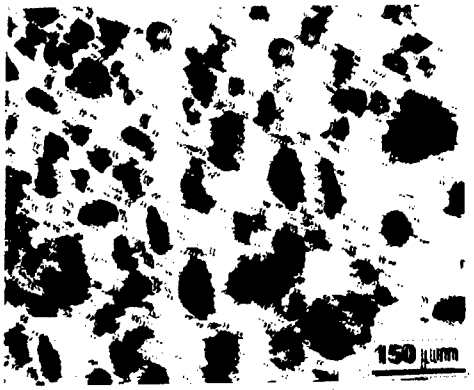


Figure 1 Microstructure of the SiC_p/Al composite produced by vortex method.

Figure 2 gives a typical bright field image of the interface in the as-cast 6061Al matrix composites, showing the presence of the isolated reaction product particles with a size of about 50-100nm at the interface. The nanocrystallines grow from the SiC surface into the Al matrix and most of them have angular shapes. The results of selected area diffraction (SAD) analysis of the nanocrystallines at the interface indicate that they have an FCC crystal structure with lattice parameter about a=0.8nm. The energy dispersive X-ray (EDX) spectrum analysis show that the Mg:O atomic ratio of the nanocrystallines is nearly 1:4. By considering the various phases that would possibly appear in the composite, the nanocrystalline particle at the interface is determined as $MgAl_2O_4$ (Space group Fd3m, lattice parameter a=0.81nm). EDX analysis, chemical analysis and TEM images also indicate that 10~20% surface of SiC particles was covered by $MgAl_2O_4$ nanocrystallines, which confirms that the extent of interfacial reaction taken place during the fabrication of the squeeze cast composites is slight. The formation mechanism may be as follows. During the squeeze casting, the first reaction between the SiC particles and the molten Al alloy (containing 1.03% Mg) would be reactions among SiO_2, Al_2O_3, molten Al and Mg described as equations (1)-(3), as the SiC particles and the matrix are always slightly oxidized before the fabrication of the composites.

$$2SiO_2+2Al+Mg=MgAl_2O_4+2Si \quad (1)$$
$$3Mg+4Al_2O_3=3MgAl_2O_4+2Al \quad (2)$$
$$3Mg+Al_2O_3=3MgO+2Al \quad (3)$$

However, the Gibes energy of equation (3) is higher than those of equation (1) and equation (2). Then MgO is not stable and $MgAl_2O_4$ is the only type of interfacial reaction products.

If such interpretation is correct, the extent of the $MgAl_2O_4$ nanocrystallines at the interface will be much lower if the SiO_2 has been removed prior to the fabrication of the composites. Figure 3 shows a typical high resolution image of the SiC/Al interface in the composite with deoxidization acid-leaching treated SiC particles. It can be seen that the interface is clean and

smooth without any reaction products or amorphous transition layer, which indicate that the reaction described as equation (1) is the predominant one in the process.

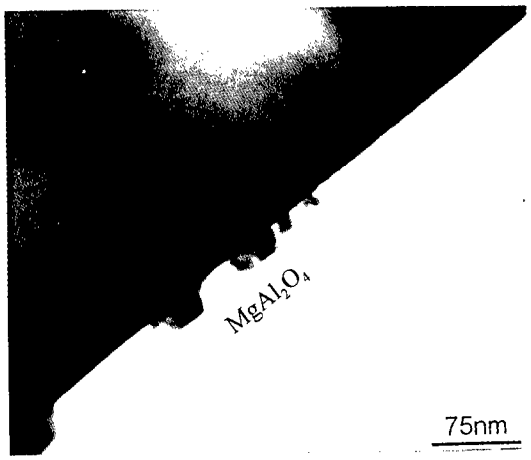


Figure 2 Bright field image of the interface in the squeeze cast composite showing discrete interfacial reaction products.

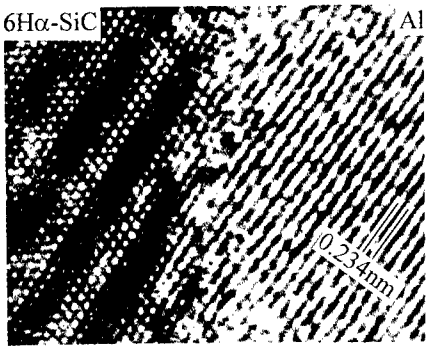


Figure 3 Typical HR image of the SiC/Al interface in the composite with treated SiC particles.

On the other hand, the lower magnesium composition, the less amount of $MgAl_2O_4$ nanocrystallines at the interface. For the 25vol.%SiC_p/6061Al composite prepared by vortex method, the results of the EDX analysis show that the Mg composition at the interface is only 0.7%, which makes the reactions described as equations (1)-(3) difficult to occur. In the meantime, the purity of large SiC particles is higher than the small ones. The purity of the large SiC particles (average size 54μm) is 98.5% while that of small ones (average size 3.5μm) is about 94%. Then the amount of SiO_2 in the large SiC particles is much lower, which also makes the interfacial reaction negligible. The well-bonded interface between SiC particles and the matrix in the 25vol.%SiC_p/6061Al composites confirms the conclusion [8]. Figure 4 gives a typical high resolution (HR) image of the interface between the reinforcement particle and the matrix. The incident beam is parallel with $[001]_{Al}$ and $[011]_{\alpha\text{-}SiC}$ and the interface is parallel

with $(020)_{Al}$. The interface, as indicated by double arrows in Figure 4, is very clean, smooth and straight. No reaction product has been found at the interface. The atomic spacing of the α-SiC and the matrix along the interface are 0.242nm and 0.203nm, respectively, which gives a semicoherent interface where every six $(200)_{Al}$ atoms correspond to five $(01\bar{1})_{\alpha\text{-SiC}}$ atom with a mismatch of less than one percent.

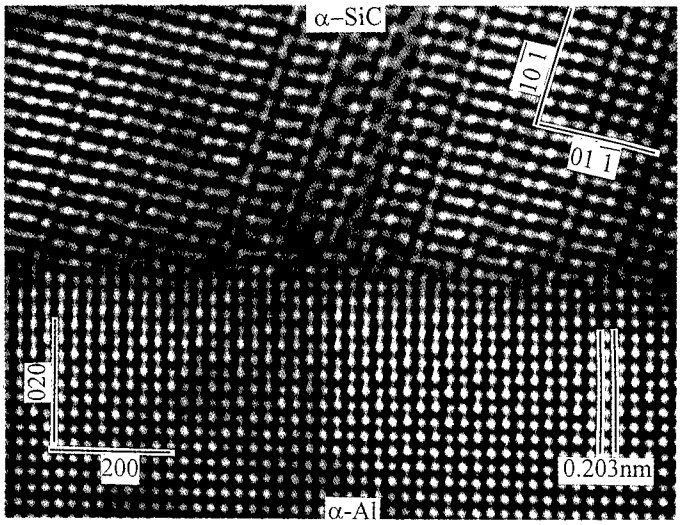


Figure 4 Typical HR image of the SiC/Al interface of the composite using vortex method.

Mechanical Properties

Table I shows the flexural properties of squeeze cast SiC_p/Al composites with and without acid-leaching treatment. The numbers in the brackets are experimental errors. The results indicate that the interfacial reaction has a significant effect on the flexural properties of the composites. Compared with composites with clean interface, the presence of $MgAl_2O_4$ nanocrystallines at the interface increases the elastic modulus by 11.4% and the elastic limit (0.01 offset) by 7.3%. These improvements may be contributed to the higher bind energy and better load transfer efficiency for the discrete $MgAl_2O_4$ nanocrystallines embedded in both phases. However, the nanocrystallines at the interface decrease the ultimate flexural strength about 12% and fracture strain about 30%. It is because that the fracture toughness of $MgAl_2O_4$ nanocrystallines is only one-third of that of SiC and the surplus oxides, i.e. SiO_2, at the interface are harmful to the flexural strength and fracture strain of the composites.

Table I Flexural properties of squeeze cast SiC_p/Al composites with different interfacial conditions.

Materials	E (GPa)	$\sigma_{0.01}$ (MPa)	σ_{fs} (MPa)	ε_f (%)
Reacted interface	164.9 (2.1)	156.7 (6.6)	497.8 (7.2)	0.73 (0.03)
Clean interface	148.0 (2.0)	146.0 (4.5)	564.4 (13.7)	1.05 (0.03)

Conclusions

1) SiC_p/6061Al metal matrix composites have been successfully fabricated by the squeeze cast and vortex method. The SiC particles are homogeneously distributed within the matrix.

2) The reaction at the interface occurs mainly among SiO_2, Al_2O_3, molten Al and Mg, and the reaction equations are also proposed. $MgAl_2O_4$ nanocrystallines have been found at the interface in 45vol.%SiC_p/6061Al composites using squeeze casting method. However, the interfaces are clean and smooth for both the acid-leaching pretreated composite using squeeze casting method and large SiC particles reinforced composite using vortex method as the reaction conditions at the interface are not met.

3) The presence of $MgAl_2O_4$ nanocrystallines at the interface increases the elastic modulus of the composites, but decrease the flexural strength and fracture strain of the composites. The acid-leaching pretreatment process is proved to be a good way to tailor the flexural properties of the composites.

Reference

1. S. V. Nair, J. K. Tien, R. C. Bates, "SiC-Reinforced Aluminum Metal Matrix Composites", Int. Mater. Rev., 30(6), (1985) 275-290.

2. D. J. Lloyd, "Particle Reinforced Aluminum and Magnesium Matrix Composites", Int. Mater. Rev., 39(1), (1994) 1-23.

3. V. Radmilovic, G. Thomas, S. K. Das, "Microstructure of α-Al Base Matrix and SiC particulate Composites", Mater. Sci. Eng., A132 (1991) 171-179.

4. M. Vedani *et al*, "Influence of Interface Properties on Mechanical Behavior of Particle Reinforced Metal Matrix Composites ", Mater. Sci. Tech., 10(2) (1994) 132-140.

5. S. D. Peteves *et al*, "Microstructure and Microchemistry of the Al/SiC Interface", J. Mater. Sci., 25 (1990) 3765-3772.

6. N. Wang, Z. R. Wang, G. C. Weatherly, "Formation of Magnesium Aluminum (Spinel) in Cast SiC Particulate-Reinforced Al (A356) Metal Matrix Composites". Metall. Trans. 23A (1992) 1423-1430.

7. L. Salvo *et al*, "Interfacial Reactions and Age Harding in Al-Mg-Si Metal Matrix Composites Reinforced with SiC Particles", Mater. Sci. Eng., (1994), A177, 173-183.

8. R. M. Wang *et al*, "Microstructure and Interface Structure Studies of SiCp Reinforced Al(6061) Metal-Matrix Composites", Proceedings of the International Conference on "Recent Advances in Metallurgical Processes", Eds. D. .H. Sastry *et al*, (New Age International Publishers, New Delhl, 1997), 567-572.

9. Y. Cui *et al*, "Effect of a Slight Interfacial Reaction on Mechanical Properties of SiC_p/Al Composites", High Technology Letters, 3(1), (1997) 96-100.

Al_2O_3/AlB_{12} COMPOSITE SYNTHESIZED BY SHS

Yin Sheng, Liu Yonghe, Li Wenxia, Lai Hoyi

P/M Laboratory, University of Science and Technology Beigjing,
Beijing 100083, P.R.China

Abstract

Al_2O_3/AlB_{12} composites are of interest in the development of neutron absorber and lightweight armor materials. This paper describes the thermochemical evaluation and the synthesis of the material by SHS. By optimizing the process parameters Al_2O_3/AlB_{12} powder of high purity was obtained.

The Third Pacific Rim International Conference on
Advanced Materials and Processing (PRICM 3)
Edited by M.A. Imam, R. DeNale, S. Hanada,
Z. Zhong and D.N. Lee
The Minerals, Metals & Materials Society, 1998

Introduction

As a potential neutron absorber and light armor material, AlB_{12} has drawn much attention recently. Meschel [1] evaluated its standard enthalpy of formation by high temperature direct synthesis calorimetry. Chuzhko [2] prepared AlB_{12} powder by reaction of aluminum and boron oxide. The oxidization behavior [3], mechanical and electrical properties [4~5] and the densification process [6] of the materials have also been investigated. Gosset [7] suggested that AlB_{12} should be reinforced when it was used as neutron absorber based on the study of the thermal properties of the material. The armor materials require a balance between elastic impedance, compressive yield strength and ability to withstand tensile stresses before fracture [8]. Al_2O_3/AlB_{12} is of interest in the development of both neutron absorber and armor materials.

Self-propagating High-temperature Synthesis (SHS), also known as combustion synthesis is a promising technology in preparing ceramics composite because of low cost and efficiency of the process. Preparation of TiB_2-Al-AlB_{12} by SHS has been reported by Odawara [9].

This paper describes the thermochemical evaluation and preparation of Al_2O_3/AlB_{12} composite by the following SHS reaction:

$$13Al+6B_2O_3=6Al_2O_3+AlB_{12} \quad (1)$$

Thermochemical Evaluation

According to the reaction mechanism [10], the SHS reaction (1) involves first the reduction of B_2O_3 by Al to form element B followed by the interaction of elemental B with Al to form AlB_{12}. The two-step sequence can be represented as thermite reaction (2) and synthesis reaction (3):

$$2Al+B_2O_3=Al_2O_3+2B \quad (2)$$

$$12B+Al=AlB_{12} \quad (3)$$

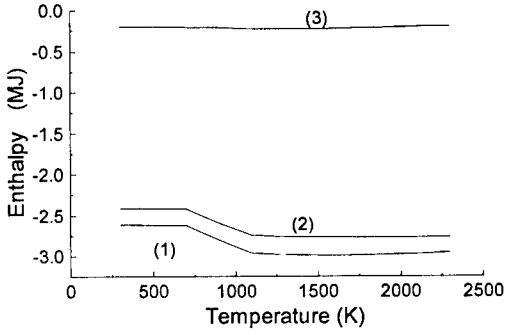


Figure 1. Enthalpy-temperature plot for the reactions

The enthalpy of the reactions based on thermodynamic data from reference [11] is given in figure 1. The heat released by thermite reaction (2) is significantly higher than AlB_{12} synthesis

reaction (3). The dominant reaction in the SHS process is thermite reaction (2).

The exothermicity of the SHS reactions can be represented by the adiabatic combustion temperature $T_{ad,}$ which is calculated from the enthalpy of reaction ΔH^{o}_{T0}:

$$\Delta H^{o}_{T0} = \int_{T0}^{Tad} CpdT \qquad (4)$$

where T_0 is the initial temperature , T_{ad} is the adiabatic temperature, and C_p is the heat capacity of the products. Figure 2 is the adiabatic temperature of the reactions for different initial temperatures. The adiabatic temperatures of both reaction (1) and (2) are 2327K (equal to the melting point of Al_2O_3) for an initial temperature of 298K while for reaction (3) it is 1063K. That means the synthesis of AlB_{12} by SHS from elements is impossible when it is initiated at room temperature independently according to the self sustaining criterion of T_{ad}>1800K [12]. By coupling with thermite reaction (2) the adiabatic temperature of the system is raised to 2327K, so the SHS of Al_2O_3/AlB_{12} can be self-sustained without preheating.

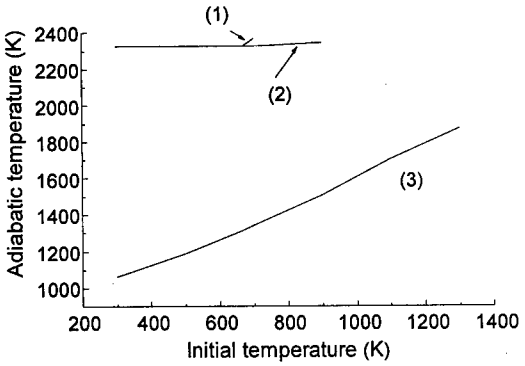


Figure 2. The effect of initial temperature on adiabatic temperature

Experimental Procedure

The reactant powders of -300 mesh aluminum and -120 mesh boron oxide B_2O_3 were vacuum dehydrated at 100℃ for 2 hours and mixed in a polyethylene vessel followed by cold pressing to pellets with diameter 25mm and relative density of ~50%. The pellets were ignited by passing electrical current through the tungsten coil in a SHS reaction chamber filled with argon gas with pressure range from 500Pa to 0.1MPa. The temperature was measured by W-Re thermal couple and recorded by a data acquisition system (DAS). Phases in the products were identified by the X-ray diffraction. The morphology were examined by optical microscope and scanning electron microscope (SEM) equipped with energy-dispersive spectrometer (EDS).

Results and Discussion

The typical combustion temperature profile of SHS reaction measured in $13Al+6B_2O_3$ system was shown in figure 3 . The maximum combustion temperature was 1873℃ which was lower than the calculated adiabatic temperature due to the heat loss.

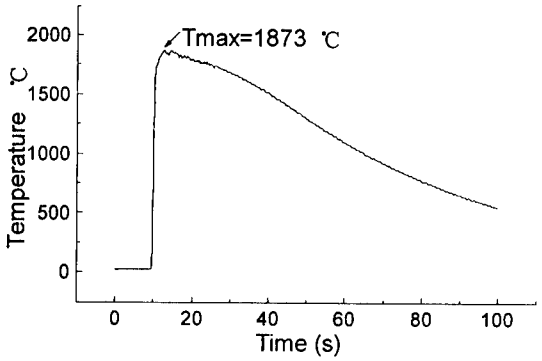


Figure 3. Temperature profile during the SHS of $13Al+6B_2O_3$ system at 0.1MPa

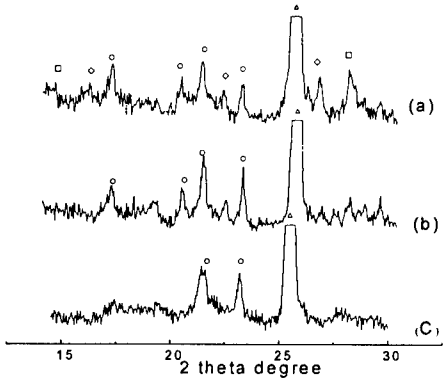


Figure 4. X-ray diffraction pattern of (a) the outer ring , (b) the center region of the synthesized sample ignited at 0.1MPa and (c) ignited at 500 Pa,
(○ AlB_{12}, △ Al_2O_3, ◇ $9Al_2O_3.2B_2O_3$, □ B_2O_3)

The X-ray diffraction patterns in the outer ring and the center region of the reacted sample are shown in figure 4 (a) and figure 4 (b) respectively. Both of the patterns show that the major phases presented are alumina and AlB_{12}. By products B_2O_3 and $9Al_2O_3.B_2O_3$ can be found in the outer ring.

The SEM morphology of the synthesized products and Al line profile are shown in figure 5. The aluminum distribution line shows few aluminum near the surface (left) , however, in the center region (right) the aluminum is evenly distributed. It was found that after combustion the gas deposits on the cold wall of the reactor contained B_2O_3 [13]. The green combustion flame was observed in the combustion which indicated the presence of elemental boron [14] . we assume that B_2O_3 and other boron suboxide in the gas react with Al_2O_3 to form $9Al_2O_3.B_2O_3$ in the outer ring of the sample. The gas deposits also obstruct the detection of aluminum.

In order to eliminate the gaseous deposits on the reacted product, a sample of the stoichiometric system was ignited at 500Pa . Figure 4(c) is the X-ray diffraction pattern of this system , it can be seen that the by-products in the reacted sample are obviously low.

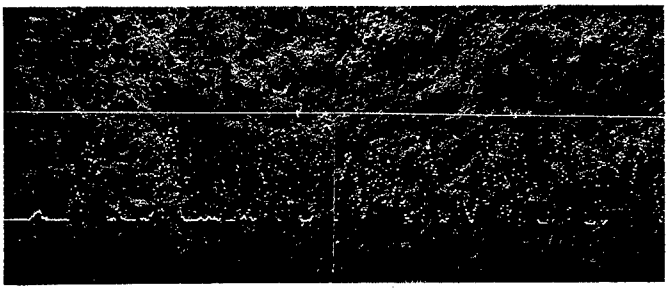
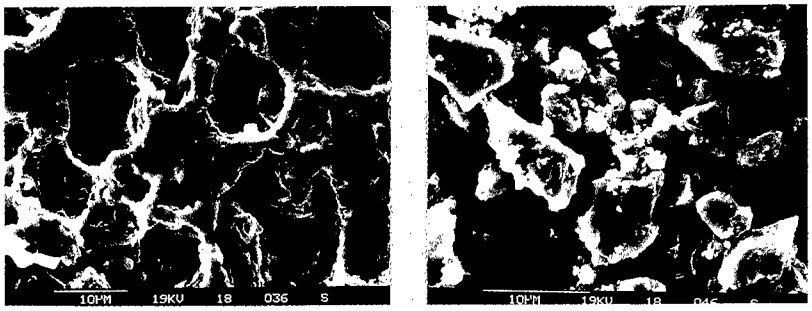


Figure 5. SEM morphology of the products under 0.1MPa with Al distribution line

Figure 6 (a) shows the morphology of the as-synthesized products (a) and the milled powder (b). The sintering or partial fusion of the products was observed due to the high combustion temperature as shown in figure 3.



(a) (b)

Figure 6. SEM morphology of (a) as-synthesized product and (b) the milled powder

The composite powder was pressureless sintered at 1700 ℃ for 0.5 hour and resulted in 85% of theoretical density. The density of hot pressed (HP) composite (1600 ℃, 20MPa) was 92% of the theoretical value.

Conclusions

Al_2O_3/AlB_{12} composite was prepared by SHS. The AlB_{12} synthesis with weakly exothermic reaction could be self-sustained by coupling with the thermite reaction in which large amount of heat was released. The measured combustion temperature of this system was 1873 ℃ that was lower than the calculated adiabatic temperature. Gases released in the reaction affected the microstructure and purity of the products Al_2O_3/AlB_{12}. The composite of high purity could be synthesized in vacuum conditions.

References

1. S.V. Meschel, O.J. Kleppa, "Standard enthalpies of formation of AlB_{12} and Al_4C_3 by high temperature direct synthesis calorimetry", Journal of Alloys and CoMPands, 227(1995), 93-96

2. R.K. Chuzhako et al, "Synthesis and Properties of Aluminum Borides" Inorg. Mater.,31(8) (1995)961-964

3. A.I.Kharlamov, T.I.Duda, and V.V.Fomenko "Preparation and Properties of High-dispersive Powders of Aluminum Dodecaboride and Carboborides", AIP Conference Proceedings 231, Boron rich Solids, ed. D.Emin, and T.L.Aselage (Albuquerque, NM 1990) 512-515

4. A.I.Kharlamov, S.V. Loichenko, "Electronic Transport Properties of Hot-pressed Boron-rich Compounds of The Al-B-C System" AIP Conference Proceedings 231, Boron rich Solids, ed. D.Emin, and T.L.Aselage (Albuquerque, NM 1990),94-104

5. T.A.Prikhna, P.S.Kisly, "Aluminium Borides and Carboborides" AIP Conference Proceedings 231, Boron rich Solids, ed. D.Emin, and T.L.Aselage (Albuquerque, NM 1990), 590-593

6. A.I.Kharlamov, S.V. Loichenko in D.Emin, "Investigation: The Process of Densification of Boron-rich Compounds of the Al-B-C System" AIP Conference Proceedings 231, Boron rich Solids, ed. D.Emin, and T.L.Aselage (Albuquerque, NM 1990),473-481

7. D.Gosset, M.Guery and B.Kryger, " Thermal Properties of Some Boron-rich Compounds ("B_nC and AlB_{12})", AIP Conference Proceedings 231, Boron rich Solids, ed. D.Emin, and T.L.Aselage (Albuquerque, NM 1990), 380-383

8. M.L.Wilkins, "Use of Boron Conpounds in Lightweight Armor", Boron and Refractory Borides, ed. V.I.Matkovich (Springer-Verlag Press, 1977), 633-648

9. O. Odawara, K. Mori, Combustion "Synthesis of High-temperature Composite Materials Under Short-time Microgravity Enviroments", Tran.Mater.Res.Soc.Jpn. 16A(1994),659-62

10. V.Subramanian, M.G.Lakshmikantha, and J.A.Sekhar,"Modeling of sequential Reactions during Micropyretic Synthesis" , J.Mater.Res.,10(5)(1995),961-972

11 O.Knacke,O.Kubaschewski, and K.Hesselmann, Thermochemical Properties of Inorganic Substance, Second edition,I.Springer-verlag Press

12. M. Eslamloo-Grami and Z. A. Munir, "Self-propagating Exothermic Reactions: The Synthesis of High-temperature Materials by Combustion",Mater. Sci. Report 3(1989), 227-365

13. Zhang Haibo, "$Al2O_3$-B_4C-TiB_2 Composite Synthesized by SHS",(Ph.D. Thesis , Univ. Sci.&Tech. Beijing, 1995),25-32

14. D. R. Lide, CRC Hand Book of Chemistry and Physics,(71th Edition, 1990-1991),4-6

Carbothermic Reduction of Tantalite in Iron to Produce Metal Matrix Composites.

N.T. Mudzanapabwe, O. S. Chinyamakobvu, and D. J. Simbi
Department of Metallurgical Engineering, University of Zimbabwe, Harare, Zimbabwe.

ABSTRACT

A tantalite/columbite ore was identified by XRD to be the complex phase ferrocolumbite ($(Fe,Mn)(Nb,Ta)_2O_6$) containing 42.77 wt% and 33.33 wt% Nb_2O_5 and Ta_2O_5 respectively. The ore was mixed with 99.9 % pure electrolytic iron powder and collie coal in stoichiometric proportions designed to yield iron based metal matrix composites containing 20 wt% Nb/TaC after reaction under argon in a tube furnace at temperatures between 1200°C and 1300°C. Two size fractions of the ferrocolumbite were used, 106 - 150um and 1 - 18um, and greater reduction kinetics were observed with the finer powder. A maximum of 60% reduction was achieved after 2 hours with the fine powder but some ferrocolumbite remained unreacted. The carbide particles were formed in-situ in iron as a reaction product layer around the original oxide particles. The composite was porous due to the release of CO gas. The matrix alloy was observed to be a grey cast iron after etching. It is suggested that both the extent of reaction and carbide particle dispersion can be improved by raising the temperature sufficiently to obtain melting of the matrix.

1. Introduction

Particulate reinforced metal matrix composites comprising a tough metallic alloy matrix with a hard but light ceramic reinforcing phase are usually made by powder metallurgy or by casting. A typical example of the former is in the fabrication of cobalt based cutting tool inserts with tungsten carbide (WC) particles as the hardwearing phase[1]. Aluminium-silicon carbide (Al-SiC) are the commonest example of cast MMCs where careful control of the solidification process results in an even dispersion of hard particles (SiC) in a relatively tough and ductile matrix (Al) [2]. It is now generally accepted that such materials exhibit superior mechanical properties than comparable monolithic alloys and perform particularly well in dynamic loading abrasive wear resistance applications [3]. One drawback with these materials is the need to manufacture the matrix and particulate phases separately before combining them in an additional step.

The possibility of forming particulate reinforced metal matrix composites in a one step operation has been demonstrated using iron and rutile [4]. In this case titanium oxide was reduced *in-situ* in iron with carbon to give an "Fe-TiC_p" composite. The distribution of titanium carbide particles in the iron were found to be comparable to that observed when "Fe-TiC_p" is made by the more conventional Powder Metallurgy route[5].

The Third Pacific Rim International Conference on
Advanced Materials and Processing (PRICM 3)
Edited by M.A. Imam, R. DeNale, S. Hanada,
Z. Zhong and D.N. Lee
The Minerals, Metals & Materials Society, 1998

The work reported in this paper are results of the preliminary trials carried out to form particulate MMC's in a single step operation by the *in-situ* reduction with carbon of ferrocolumbite in iron. The tantalite contained large volume fractions of Ta_2O_5 and Nb_2O_5 and it was expected that an "Fe-TaC/NbC" composite would be formed.

2. Experimental

2.1 Raw materials

The raw materials used in this investigation were:

(i) a tantalite/columbite ore rich in Ta_2O_5 and Nb_2O_5 ;
XRD identified this ore as ferrocolumbite with the nominal formula $(Fe,Mn)(Nb,Ta)_2O_6$. The chemical composition is given in **Table 1**. The particle size of the ferrocolumbite was 106-150μm but some of it was pulverised to smaller size of 1-18 μm.

Table 1. Chemical composition of tantalite ore used in the reduction experiments

Element	Nb	Ta	Fe	Mn	W	Ti	Al	Ni	Zn
Weight %	29.9	27.3	9.11	2.95	0.41	0.16	0.17	0.13	0.13

(ii) a Polish coal, collie coal with low sulphur and ash levels. The constituent analysis of the coal is given in **Table 2.**

Table 2. Constituent analysis of collie coal used as the reductant, given as wt %

Total Carbon	59.5
Fixed carbon	48.4
Hydrogen	3.60
Sulphur	0.34
Ash	2.65
LOI($105^{o}C$)	23.3

(iii) electrolytic iron powder of 99.9 % purity.

2.2 Reaction mixture preparation

Based on the quantitative proportions of the Ta_2O_5 , Nb_2O_5 and FeO constituents of the ferrocolumbite and the available carbon content of the coal, mixtures of iron, coal and ferrocolumbite powders were prepared so that on the basis of the stoichiometric balance of equations 1, 2 and 3 below, a composite of Fe and 20 wt% TaC/NbC would be formed. This was on the assumption that total conversion of Ta_2O_5 and Nb_2O_5 to TaC and NbC respectively would be take place.

Nb_2O_5	+	7C	→	2NbC	+	5CO	Equation 1
Ta_2O_5	+	7C	→	2TaC	+	5CO	Equation 2
FeO	+	C	→	Fe	+	CO	Equation 3

The iron formed in equation 3 would just become part of the matrix alloy. A stock mixture of the above powders with a total weight of approximately 1 kg was prepared with the ferrocolumbite: collie coal: iron powder ratio being 0.26: 0.12: 0.63. This was done for both the coarse ore (106 - 150um) and the pulverised ore (1 - 18 um).

2.3 Furnace experiments:

A total sample weight of 50 g was compacted into pellets in a die and each pellet heated in a tube furnace under flowing argon at temperatures 1200 - 1300°C. The furnace configuration is shown in Figure 1.

2.4 Metallography and XRD

The reacted pellets were sectioned, mounted and prepared for metallographic examination by Optical Microscopy and Scanning Electron Microscopy. The phases in the reacted samples were identified by XRD

3. Results

3.1 Kinetics

The reaction kinetics were monitored by calculating the fraction reacted, F, of ferrocolumbite through measuring the weight loss as a function of time and temperature. F is defined as

$$F = \frac{(W_o - W)}{(W_o - W_T)} \qquad \text{Equation 4}$$

W_o - original wt of pellet
W - weight of pellet at time t
W_T - pellet weight after complete conversion to TaC/NbC and Fe.

Figure 2 shows kinetic graphs for the above reaction at 1200°C for the coarse ferrocolumbite (106 - 150 μm) and the fine ferrocolumbite (1-18μm).

3.2 *Metallography and Phase Identification*

Figures 3 and **4** are micrographs of the samples reacted at 1200°C for 0.5 hrs and 1300°C for 0.5 hrs respectively. The reacted samples were also analysed by X-ray diffraction and the phases identified under different conditions were TaC, NbC, Carbon, Fe and ferrocolumbite $(Fe,Mn)(Nb,Ta)_2O_6$. The presence of $(Fe,Mn)(Nb,Ta)_2O_6$ shows that the reaction did not go to completion in all cases considered.

4. Discussion

The rate results for the carbothermic reduction of both size fractions are shown in Figure 2. Nearly 40% of reduction is achieved within the first 15 minutes in both cases. After this initial period, however, the rate of reaction reduces considerably as indicated by the reduced slope of the rate curves. The fine powder registers a higher total reduction after two hours than the coarse powder. This is due to the greater contact area provided between oxide and reductant by the smaller particles of the fine powder.

The SEM micrograph in **Figure 4** shows how a product layer forms on the periphery of each oxide particle. Reduction of the FeO component of the ferrocolumbite also takes place and globules of iron are normally observed within the product layer. The product layer consists mainly of Fe and Ta/NbC phases and as the reaction progresses it thickens and acts as a diffusion barrier for carbon, carbon monoxide and carbon dioxide. The accessibility of the remaining oxide by carbon, and the ease with which gaseous products can escape from the reaction interface determine how quickly the reduction continues to take place. The effect of the barrier/product layer is therefore more pronounced in slowing down reaction on the coarse size fraction powder where the diameter of the remaining unreacted oxide is always large compared to the thickness of the product layer.

The maximum percentage reduction observed was 60% with the fine powder. This indicates that either conversion of oxide to carbide did not take place in some instances, or that the reaction product was some intermediate compound between oxide and carbide. In similar trials carried out using less reactive carbon black as a reductant, it was observed that an intermediate phase, ixiolite, was formed before conversion to carbide [7]. In the experiments reported here, however, XRD analysis showed that unreacted original material (ferrocolumbite) was present after reaction as well as iron and TaC/NbC. TaC and NbC have very similar crystallographic structures and are probably in solid solution. The matrix microstructure was observed to be flake grey cast iron after etching. The composite was highly porous due to the gases released. It is suggested that full densification could be obtained by allowing the composite to melt and resolidify. The temperature required would be quite low since the matrix is cast iron with a relatively low melting point.

In **Figure 3**, completely reacted carbide particle clusters can be seen (grey). Their position is probably related to the position of the original oxide particle. Such clustering

would not be the best morphology from a mechanical propeties point of view. It would be better for the broken up particles to be more evenly dispersed within the matrix. This could be achieved if melting of the iron with some agitation (induction) is effected. There was no separating of the carbide particles from the iron indicating that good wetting is present.

5. Conclusions

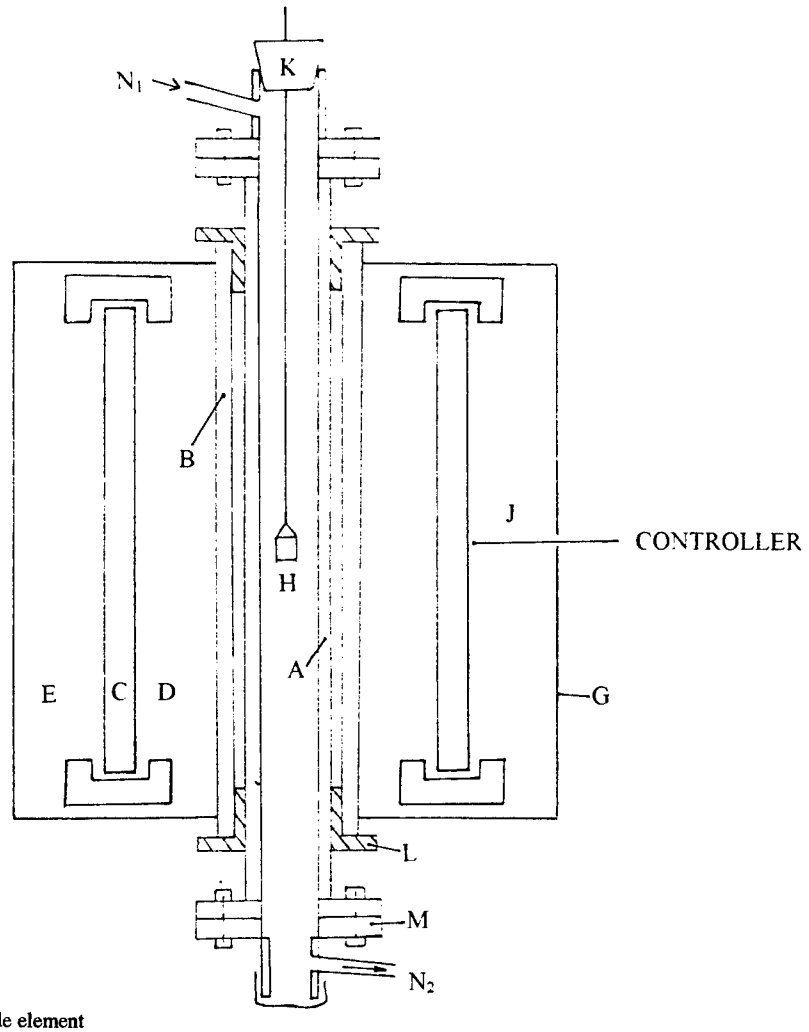
(i) It has been shown that the *in-situ* reduction of ferrocolumbite with carbon in iron to form "Fe - Ta/NbC" metal matrix composites is feasible.

(ii) Faster reaction kinetics are achieved when the ferrocolumbite powder particles are fine (1 - 18um) rather than coarse.

(iii) At high temperature (>1200°C) the TaC/NbC particles form in clusters around the position of the original oxide particles. The composite formed is porous due to the release of gases during the reduction reaction.

References

1. Superhard Tool Materials, Metals Handbook, 9th Edition, Volume 3, p448 Published by ASM
2. Warren R. and Anderson C.H *"Silicon carbide Fibres and their Potential for use in composite materials"* Composites (1984) pp 101.
3. Feest A. *"Exploitation of the Metal Matrix Composite Concept"* Metals and Materials, Vol. 4, No. 5, p273, May 1988
4. Chinyamakobvu O.S and Terry B.S. *"Carbothermic Reduction of Ilmenite and Rutile as means of Production of Iron based Ti(O,C) Metal Matrix Composites"* Materials Science and Technology, Vol. 7, p842, September 1991.
5. Wood .J.V, Dinsdale . K, Davies . P and Kellie J.L.F *"Production and properties of Steel-TiC compounds for wear applications"* Materials Science and Technology, Vol. 1, December 1995.
6. Premkumar R. and Chu M.G. *"Synthesis of TiC Particulates and their Segregation during Solidification in in-situ Processed Al - TiC Composites"* Metallurgical Transactions A, Vol. 24A, pp2358 - 2362, October 1993.
7. Chrysanthou A., McFarlane D. and Chinyamakobvu O.S. *"Carbothermic Reduction of Columbite concentrate to produce Cemented Carbides and Metal Matrix Composites"* Journal of Alloys and Compounds, Vol. 206, p77, (1994)



Key

A- Worktube
B- Silicon carbide element
C- Alumina tube
D- Air space
E- Mineral wool "Kao wool"
F- Ring of sandanue (refractory bricks)
G- Stainless steel shell
H- Thermocouple/Sample
J- Thermocouple controller
K- Rubber stopper
L- Spacer of sandanue
M- water cooled jacket
N_1-Argon inlet
N_2-Argon outlet

Figure1. Tube furnace design

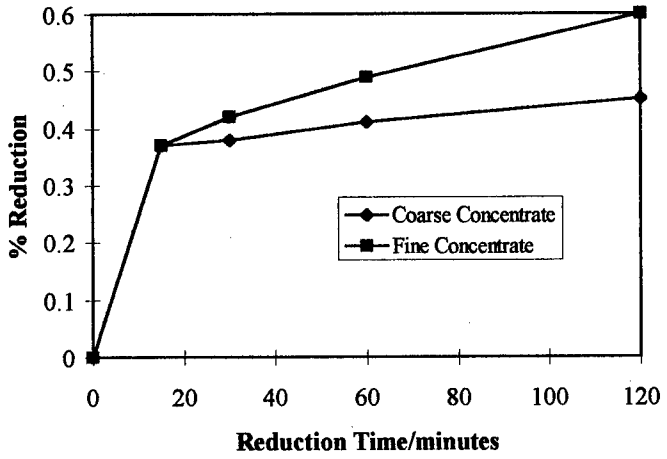


Figure 2. Graphs showing kinetics of reduction of *pulverised* and coarse ferrocolumbite concentrate with *collie coal* at 1200°C.

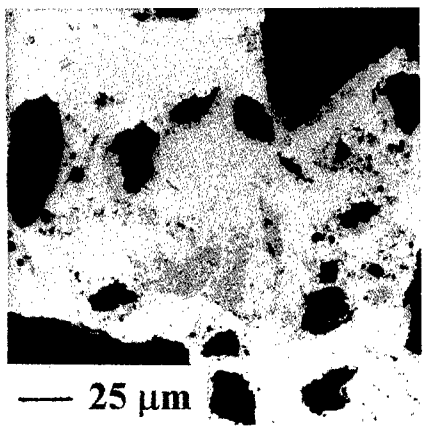


Figure 3. Micrograph after 30 minutes of reaction at 1200°C showing carbides (grey)in iron matrix (light grey). The black phase are oxide particles.

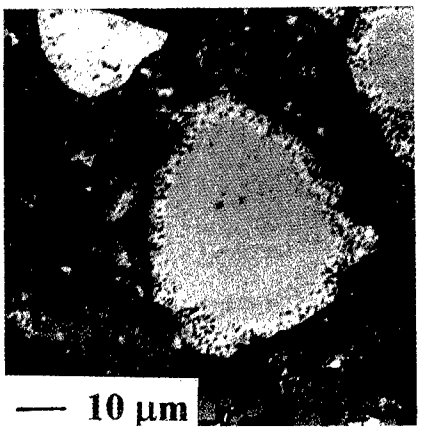


Figure 4. Back Scattered Electron Image of a partially reduced oxide particle in iron (dark grey) matrix showing a "shrinking core model" type of reaction; 1300°C, 30 mins.

Strengthening and Mechanical Stability of In-Situ Cu-Fe-Xi Composites

Jae Sook Song, Moon Su Lim, Sun Ig Hong and Kwang Koo Jee*
Department of Metallurgical Engineering and RASOM, Chungnam National University,
Taedok Science Town, Taejon 305-764, Korea.
* Korea Institute of Science and Technology, Cheongryang, Seoul 130-650, Korea.

Abstract

In this study, microstructure and mechanical properties of in situ Cu-Fe-Xi (Xi=Ag, Cr or Co) alloy wires and plates obtained by cold drawing or cold rolling combined with intermediate heat treatments have been investigated. During cold working the primary and secondary dendrite arms are aligned along the rolling direction and elongated into filaments after thermo-mechanical deformation processing. The addition of Ag or Co was found to reduce the filament spacings at the given draw ratio throughout the drawing or rolling processing. The ultimate tensile strength and the conductivity of the Cu-Fe based composites containing Ag were higher than those of Cu-Fe composites containing Co or Cr. The good mechanical and electrical properties of wires may be associated with the more uniform distribution of the finer filaments in the wires containing silver. The strength of Cu-Fe-Xi composites is dependent on the spacing of the Fe filaments in accord with a Hall-Petch relationship. The fracture surfaces of all the specimens showed ductile-type fracture and iron filaments occasionally observed on the fracture surfaces. The change of mechanical and electrical properties of these composites were correlated to the microstructural evolution examined by EDS and SEM.

The Third Pacific Rim International Conference on
Advanced Materials and Processing (PRICM 3)
Edited by M.A. Imam, R. DeNale, S. Hanada,
Z. Zhong and D.N. Lee
The Minerals, Metals & Materials Society, 1998

Introduction

Composites formed by the thermo-mechanical working of ductile two phase mixtures prepared by various techniques have been the subject of considerable research.[1~3] Tensile strengths greater than those predicted by a rule of mixtures are observed in heavily cold worked in situ composites. However, the tensile strengths resulting from cold working are dependent on the crystal structures of the two phase, being greater for f.c.c.-b.c.c. combinations than for f.c.c.-f.c.c. combinations.[5~6] The greater strengthening which results in the former composites has been attributed to the b.c.c. filaments developing a ribbon like cross section. These ribbons are a result of the [110] fiber texture that develops during cold working of b.c.c. metals. In the latter composites the f.c.c. filaments undergo axisymmetric deformation during cold working and their cross sectional shapes do not significantly change during cold working.[5~7]

Recently, the tensile strengths of deformation processed composites have been shown to correlate with filament spacings, leading to a Hall-Petch type relationship.[1,3] Spitzig et al.[1,4] showed that the strength of heavily cold-worked Cu-Nb composite wires increased as the spacing between filaments decreased. In situ composites are the combination of high strength plus high electrical and thermal conductivity. The Cu-Fe system is of particular interest because of the relatively low cost of iron compared to the other possible insoluble b.c.c. phase.[7] The present study examines the influence of the thermo-mechanical deformation processing and alloy elements on improving the strength without reducing the electrical conductivity of Cu-Fe-X composites.

Experimental procedure

Billets of Cu -9Fe-1.2X(all in w.t.%) with X being Ag, Cr or Co were prepared by induction melting. Cylinder billets were about 60mm in diameter and about 112mm in length. Extrusion of cylinder billets was carried out at about 500°C, reducing the billets from 60mm diameter to bar of 24mm diameter. The extruded rods were rod rolled to 6mm in a series of steps and subsequently drawn into wires with intermediate heat treatments, using successively smaller dies, to a minimum diameter of 1mm. Square billets were cold rolled to 0.5mm thickness with intermediate heat treatments.

The evaluation of mechanical properties of plates and wires was carried out by tensile testing using a United machine equipped with an extensometer for accurate strain measurements. All tensile tests were performed at room temperature using a strain rate of $5.5\times10^{-4}s^{-1}$. The evolution of the microstructure was examined by optical and scanning electron microscope. Fracture surfaces of the tensile specimens were examined in a scanning electron microscope to characterize fracture behavior. Electrical resistivity measurements were made using a standard four-probe technique.

Results

Fig.1 shows optical micrographs of the as cast microstructure of Cu-Fe-X composites. As shown in this figure, the size of dendrites was found to be influenced by the addition of the third element. Cu-Fe-Ag composite showed the finest dendrite whereas the Cu-Fe-Cr showed relatively coarse dendrites. Fig.2 shows the transverse sections of drawn Cu-Fe-X wires, showing the ribbon-like morphology of the filaments. The second phase filaments in the drawn wires were found to be the finest in Cu-Fe-Ag, consistent with the observation of the as-cast structure. Fig.3 shows the microstructure of longitudinal sections of the Cu-Fe-X sheet/ or wires

after cold-working. During cold working the primary and secondary dendrite arms are aligned along the rolling direction and elongated into filaments after thermo-mechanical deformation processing. Filaments were found to be much more well-developed in the wires than in the plates, which shows the relatively thick filaments. Cu-Fe-Ag composite was observed to have the finest filaments and Cu-Fe-Cr composite was shown to have the coarse filaments.

Fig.4(a). shows the ultimate tensile stresses of Cu-Fe-X plates and wires at the final deformation ratio. The strength of Cu-9Fe-1.2Ag composites were found to be greater than those of Cu-9Fe-1.2Cr or Cu-9Fe-1.2Co composites. The strengthening in these composites results from the presence of the aligned filaments and the higher strength of Cu-Fe-Ag composites correlates with the fineness of the filament spacing. The strengths of the wires were found to be greater than those of the plates, which also can be associated with the presence of finer filaments in the wires. The electrical conductivities of Cu-9Fe-X plates and wires are shown in Fig. 4(b). The electrical conductivity of Cu-9Fe-1.2Ag composites was found to be better than those of Cu-9Fe-1.2Cr and Cu-9Fe-1.2Co composites. The conductivities of Cu -9Fe-1.2Ag and Cu-9Fe-1.2Co wires were found to be approximately 55%IACS whereas Cu-9Fe-1.2Cr wires showed relatively low conductivity(46%IACS). It is interesting to note that the electrical conductivities of wires are generally higher than those of plates despite the higher strength of wires. The good mechanical and electrical properties of wires may be associated with the more uniform distribution of the finer filaments in the wires.

The fracture characteristics of Cu-9Fe-1.2X composite plates are shown in Figs. 5. Cu-9Fe-1.2X Composite plates exhibited highly ductile fractures. The surfaces of the Cu-9Fe-1.2X Composites show many fine dimples and relatively coarse dimples. Examination of the coarse dimples on the fracture surfaces revealed the fractured Fe filaments in the center. The fracture surfaces of the Cu-9Fe-1.2Ag composites showed generally finer fracture surfaces than those of Cu-9Fe-1.2Cr and Cu-9Fe-1.2Co composites, consistent with the finer microstructure in Cu-9Fe-1.2Ag composite. The size of the filaments in Cu-9Fe-1.2Cr was much larger because the filaments were strengthened by the addition of Cr. The observation that the strengthes of Cu-9Fe-1.2Ag and Cu-9Fe-1.2Co composites were greater than that of Cu-9Fe-1.2Cr suggests that the refinement of the filaments is more effective than the strengthening of the filaments in strengthening the microcomposites.

Conclusions

1. During thermo-mechanical deformation processing, the Fe dendrites develop a filamentary morphology. Cu-Fe-Ag composite was observed to have the finest filaments whereas Cu-Fe-Cr composite showed relatively coarse filaments.
2. The Cu-9Fe-1.2Ag composites were found to have the good combination of the strength and electrical properties, which may be associated with the more uniform distribution of the finer filaments.
3. The fracture mode of the Cu-9Fe-1.2X composites was found to be ductile. The fracture surfaces of the composites exhibited fine dimples along with relatively coarse dimples in which the fractured filaments were observed.
4. The refinement of the filaments were found to be more effective than the strengthening of the filaments in strengthening the composites.

Acknowledgments

The authors acknowledge the support from Kumwon Co. and Korea Science and Engineering Foundation (971-0803-034-2).

References

1. W.A. Spitzig, A.R. Pelton and F.C. Laabs, Acta Metall. Vol.35, No.10, P.2427, 1987.
2. C. Biselli and D.G. Morris, Acta Mater. Vol.44, No.2, P.493, 1996.
3. Y.S. Go and W.A. Spitzig, J. of Materials Science 26, P.163, 1991.
4. P.D. Krotz, W.A. Spitzig and F.C. Laabs, Mater. Sci. and Eng., A110, P.27, 1989.
5. P.D. Funkenbusch and T.H. Courtney, Acta Metall. Vol.33, No.5, P.913, 1985.
6. P.D. Funkenbusch, T.H. Courtney and D.G Kubisch, Scripta metall. 18, P.1099, 1984.
7. J.D. Verhoeven, S.C. Chueh and E.D. Gibson, J. of Materials Science 24, P.1748, 1989.

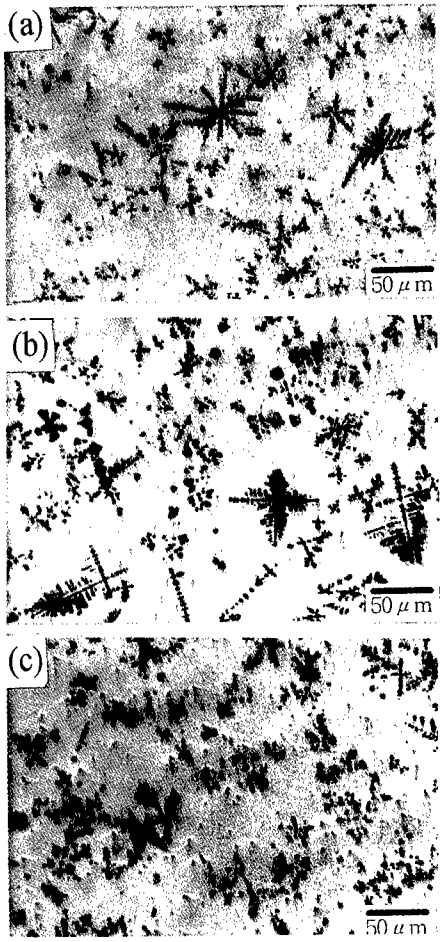


Fig. 1. Optical micrographs of as-cast Cu-Fe-Xi composites
a) Cu-9Fe-1.2Ag, b) Cu-9Fe-1.2Cr,
c) Cu-9Fe-1.2Co

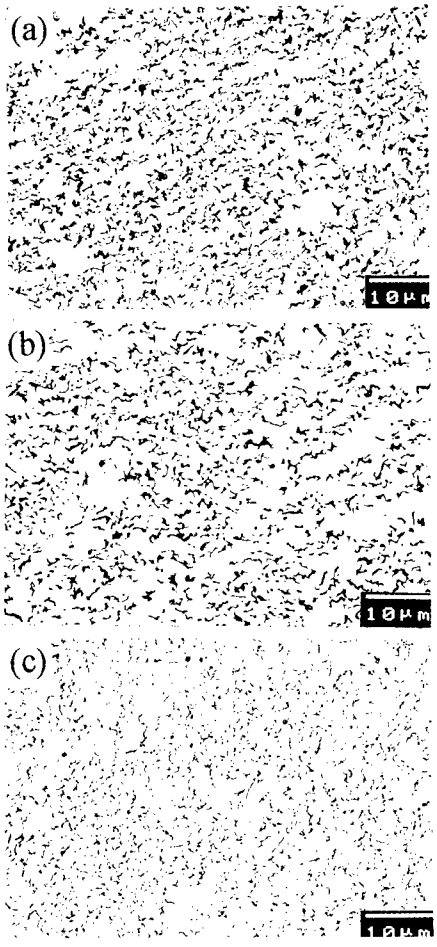


Fig. 2. Optical micrographs of the transverse sections of drawn Cu-Fe-Xi composite wires
a) Cu-9Fe-1.2Ag, b) Cu-9Fe-1.2Cr,
c) Cu-9Fe-1.2Co

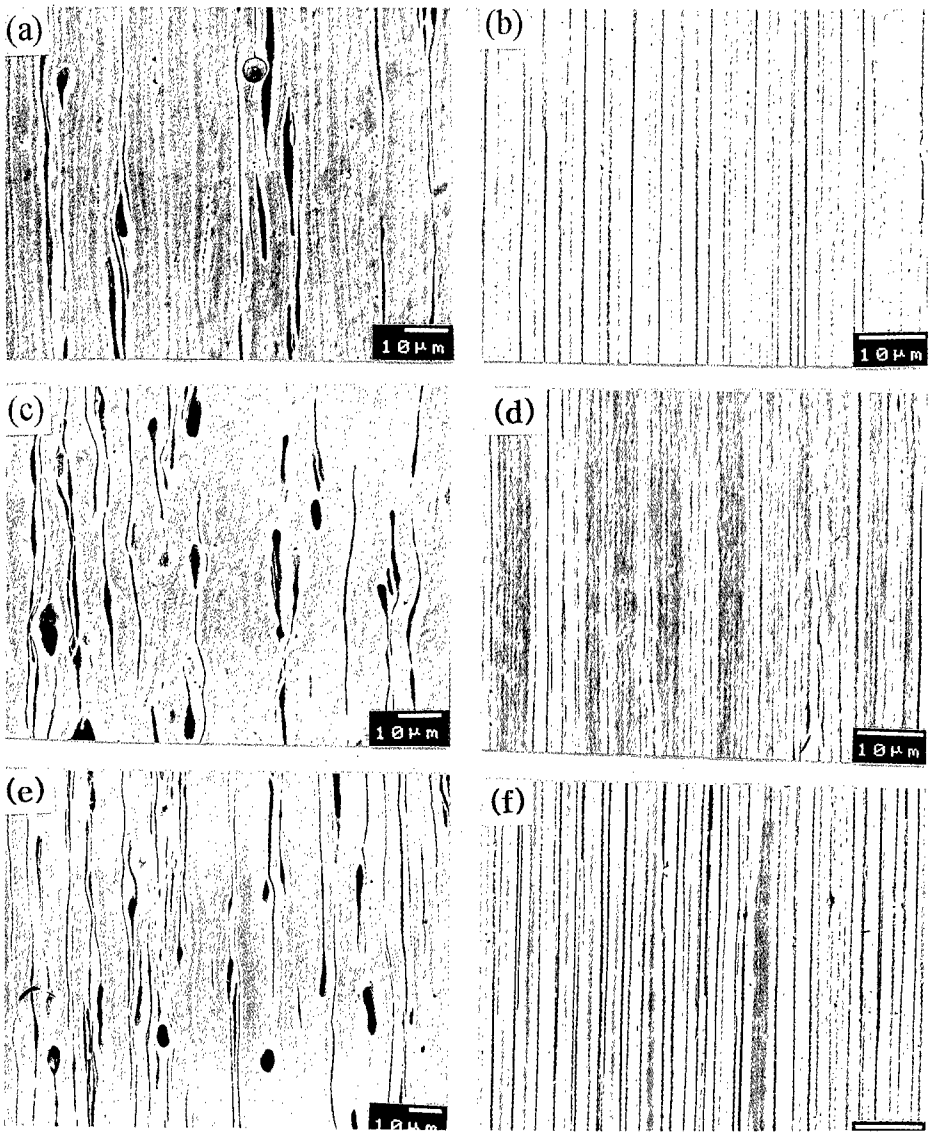


Fig.3. Microstructures of longitudinal sections of the Cu-Fe-Xi composite plates(a, b, c) and wires(e, f, g).
a, b) Cu-9Fe-1.2Ag ; c, d) Cu-9Fe-1.2Cr ; e, f) Cu-9Fe-1.2Co

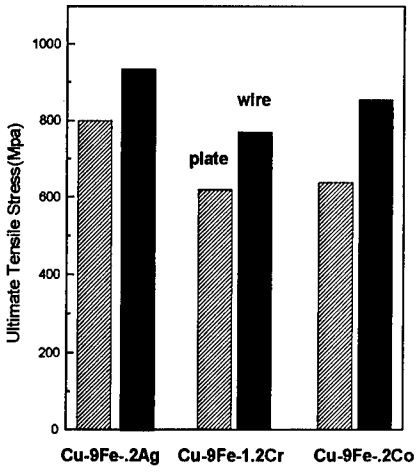


Fig.4. Ultimate tensile stress of heavily deformed Cu-Fe-Xi composites

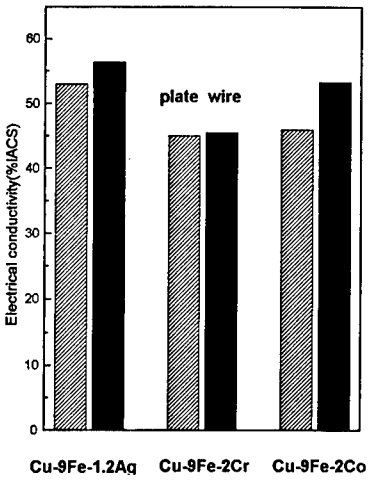


Fig.5. Electrical conductivity of heavily deformed Cu-Fe-Xi composites

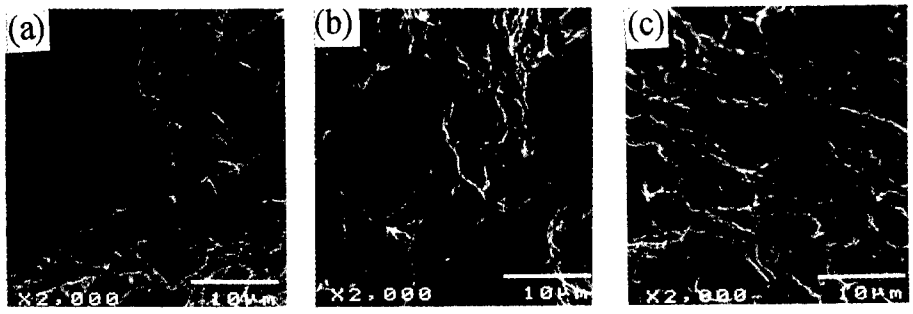


Fig.6. Fracture surfaces of the Cu-Fe-Xi composite plates.
a) Cu-9Fe-1.2Ag, b) Cu-9Fe-1.2Cr, c) Cu-9Fe-1.2Co

DAMPING CAPACITY OF EPOXY FILLED ALUMINUM FOAM

Catherine Wong
Naval Surface Warfare Center, Carderock Division, Code 612, 9500 MacArthur Blvd, West Bethesda MD 208717-5700.
301 227 4972
301 227 5548 FAX
CWONG@METALS.DT.NAVY.MIL

Abstract

Generally speaking, polymers have excellent intrinsic damping capacity but little structural strength while the opposite can be said for metals. In order to design composites that take advantage of the strength of metal and the damping of viscoelastic plastics, the role of morphology must be understood. When reticulated metallic foams are filled with a viscoelastic material a composite with two continuous phases is made. The damping capacity and elastic modulus are some combination of the properties of the two materials. Although many models have been put forth to predict the modulus of composites, only a few cases have analytical solutions. For linear viscoelastic or anelastic material, when an analytical linear elastic solution exists the complex modulus can be substituted for the elastic modulus and the damping determined. The constant stress and constant strain limits are examples of morphologies which have analytical solutions. Where a composite of differing morphology falls between the constant stress and constant strain limits cannot be analytically predicted, but some composites have been modeled using finite element analysis (FEA).

This paper discusses the damping measurements made on epoxy filled aluminum foam samples and compared to these FEA results. The samples were tested at two temperatures, one above and one below the glass transition temperature at the test frequency. The epoxy exhibited markedly different moduli at these two temperatures so the effect of the difference between the modulus of the two phases could be evaluated.

The damping capacity of the composite was found to be proportionally closer to that of the stiffer materials when the difference in elastic modulus of the two materials was larger. The damping capacity measurements confirmed previous finite element analysis which showed that a smaller phase size leads to lower damping. The larger the difference in elastic modulus the larger this effect was.

The Third Pacific Rim International Conference on
Advanced Materials and Processing (PRICM 3)
Edited by M.A. Imam, R. DeNale, S. Hanada,
Z. Zhong and D.N. Lee
The Minerals, Metals & Materials Society, 1998

Introduction

For linear viscoelastic or anelastic material, when an analytical linear elastic solution exists the complex modulus can be substituted for the elastic modulus in the form [1]

$$k = k_1 + ik_2 \tag{1}$$

where k is the complex modulus and k_1 is the elastic modulus and k_2 is the loss modulus. The loss factor, η

$$\eta = \frac{k_1}{k_2} \tag{2}$$

can then be analytically found. Two specific cases which have analytic solutions are taken to be the upper and lower bounds. They are the Voigt or constant strain condition and the Reuss or constant stress condition. In both of these cases the composite consists of parallel phases of both materials. In the Voigt conditions the load is applied parallel to the phases so that all of the phases undergo the same strain. In the Reuss condition the load is applied perpendicular to the phases so that all of the phases are subject to the same stress. The modulus, k, for the constant strain condition is

$$k_1 = k_1^{Al} V^{Al} + k_1^e V^e \tag{3}$$

where k_1^{Al} and k_1^e are the elastic modulus of the Al and epoxy phases and V^{Al} and V^e are the volume fractions of the Al and epoxy phases. Since this is an analytical solution the complex modulus can be substituted for the elastic modulus and using equation 1 equation 3 becomes

$$k = \left(k_1^{Al} + ik_2^{Al}\right)V^{Al} + \left(k_1^e + ik_2^e\right)V^e \tag{4}$$

Substituting equation 2 into equation 4, separating into real and imaginary parts, and equating the imaginary sections of the equation yields

$$\eta = \frac{k_1^{Al}\eta^{Al}V^{Al} + k_1^e\eta^e V^e}{k_1^{Al}V^{Al} + k_1^e V^e} \tag{5}$$

Similarly for the constant stress condition the elastic modulus is

$$\frac{1}{k_1} = \frac{V^{Al}}{k_1^{Al}} + \frac{V^e}{k_1^e} \tag{6}$$

and again substituting the complex modulus for the elastic modulus, using equations 1 and 2 and solving for the loss factor by equating the imaginary parts we get

$$\eta = \frac{\eta^{Al}k_1^{Al}V^{Al}\left(1+\left(\eta^e\right)^2\right) + \eta^e k_1^e V^e\left(1+\left(\eta^{Al}\right)^2\right)}{k_1^{Al}V^e\left(1+\left(\eta^{Al}\right)^2\right) + k_1^e V^{Al}\left(1+\left(\eta^e\right)^2\right)} \tag{7}$$

Where a composite falls between the constant stress and constant strain limits cannot be analytically predicted but composites have been modeled using finite element analysis (FEA) [2]. It was found that for the same volume fraction of Al the damping was higher when the epoxy was the matrix than when the Al was the matrix. Here matrix refers to the continuous phase. When the epoxy is the matrix, it can deform relatively freely which gives rise to high damping. When the epoxy is a discrete phase it can only deform to the extent that the stiffer Al allows, which results in lower damping. Additionally for a given volume fraction of Al the loss factor increased with increasing particle size.

Experimental Procedure

Preparation of Samples

The samples were fabricated from 12% dense 10, 20 and 40 pore per inch aluminum foam produced by Energy Research and Generation Inc. from 6001 aluminum using a patented process. Organic reticulated foam was invested with an inorganic material that is inert to aluminum, such as plaster. When the plaster hardened the foam was dissolved leaving a mold of the foam. Molten metal was poured into this mold under vacuum and directionally solidified in order to insure complete infiltration of the mold. The plaster mold was then dissolved away leaving open celled foam with nearly the same density and pore size as the original organic foam. The foam was given a T6 heat treatment. The foam was cut to the lengths shown in Table 1 and slowly compressed to 15 mm. The resulting densities are in Table 1. The compressed foam was put in a mold and liquid metallographic epoxy was poured in. The molds were set in a small vacuum chamber and a vacuum was drawn, the air pressure reapplied and the sample left to harden.

Table 1. Densities and Deformation History of Aluminum Foams

Pores per inch before compression	Initial length (mm)	Final density %	Time to compress(min.)	Max. load (lb.)
10	15	12	31	340
20	15	12	34	280
40	15	12	33	470
10	20	16	60	690
20	20	16	30	690
40	20	16	61	510
10	31.25	25	53	810
20	31.25	25	80	1150
40	31.25	25	61	1150
10	62.3	50	207	4280
20	62.3	50	159	6020
40	62.3	50	226	5430

Damping Capacity Measurements

The samples were ground to 10 x 4 x 40 mm on a grinding wheel with 60 grit grinding paper. The epoxy was further cured at 80 °C for 4 hours. The damping capacity was measured using a Dynamic Mechanical Thermal Analysis unit (DMTA). The DMTA uses a fixed-guided cantilevered test configuration shown in Figure 1. In this configuration, the clamp on the left holds the sample to a stationary frame while the clamp on the right attaches the sample to the controlled drive shaft. In order to minimize errors resulting from the sample slipping in the

clamps, two pronged clamps were tightened to a torque of 60 cN-m. A small sinusoidal time-varying mechanical force is applied to the drive shaft and the displacement of the sample is measured. The phase angle, ϕ, of the lag between the applied load and the measured displacement is calculated. The tangent of ϕ is a measure of the damping capacity commonly called the loss factor and it is equivalent to η in equation 2. The DMTA initially applies a high load which is then reduced until the specified displacement is achieved. The damping measurements were performed at 3 Hz and 11 microns displacement, and a maximum strain of $2x10^{-4}$. Preliminary testing (Figure 2) showed that the epoxy exhibited a dramatic decrease in modulus by 80°C. The samples were tested at 30°C for one hour and then at 80°C for one hour. A minimum of 70 data points was taken at each temperature.

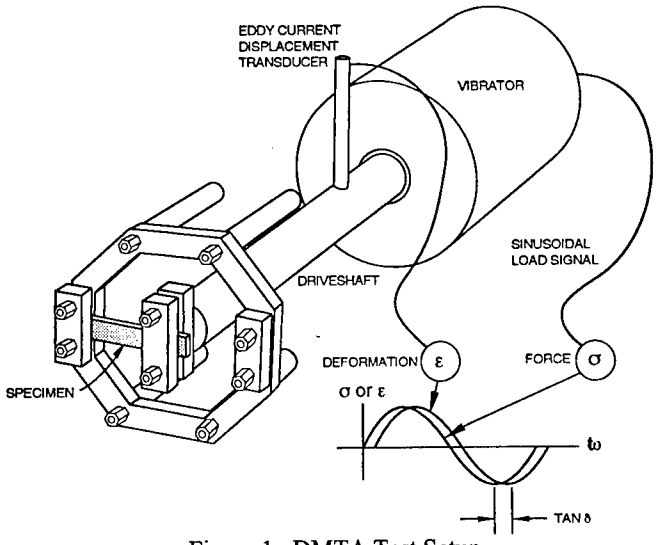


Figure 1. DMTA Test Setup

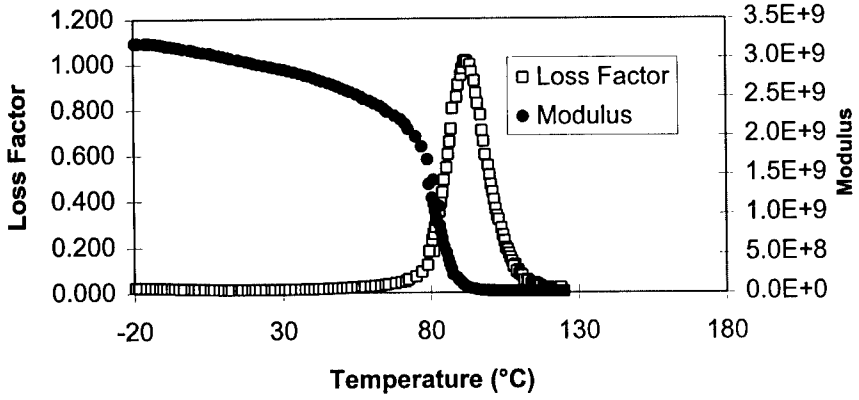


Figure 2. Loss Factor and Modulus of Epoxy at 1 Hz

Results and Discussion

The damping capacity and moduli of the monolithic materials are shown in Table 2. These values were used along with equations 5 and 7 to generate the curves in Figure 3 and 4. The damping capacities of the composites, listed in Table 3, generally fall between the upper and lower bounds. It is evident that crushing the foam may have added a source of damping in the 10 and 20 PPI samples measured at 30°C. In general, however the smaller the microstructure the lower the damping at both temperatures. It also appears that at 30°C, where the damping capacity and modulus of each phase differed by an order of magnitude, the resulting composite was near the constant stress curve. At 80°C where the damping capacity and modulus of each phase differed by two orders of magnitude, the resulting composite was closer to the constant strain curve. The FEA [2] indicated that the stresses are higher in the stiffer Al phase whether Al is in the form of particles or matrix and the extent of the stress gradients depends on the volume fraction and particle size. The higher the gradient between the two phases, the less the more compliant epoxy is stressed. In a linear material, the stress is proportional to the loss factor. Therefore, since the stress is higher in the lower damping Al than the high damping epoxy, the loss factor of the resulting composite is lower.

Table 2. Loss Factors and Moduli of Monolithic Materials

Aluminum		Epoxy measured at 30°C		Epoxy measured at 80°C	
loss factor	modulus (Pa)	loss factor	modulus (Pa)	loss factor	modulus (Pa)
0.0045	6.70E+10	0.013	2.36E+09	0.647698	1.32E+08

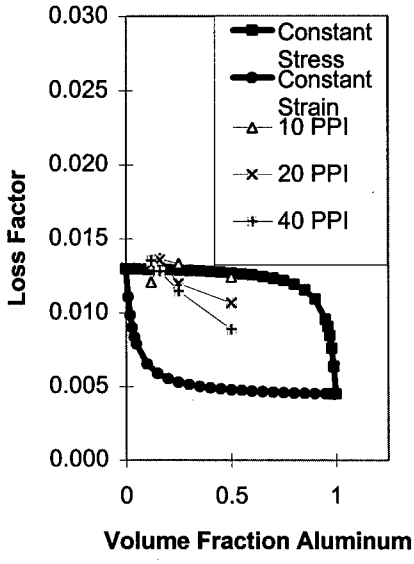


Figure 3. Damping Capacity of Aluminum Epoxy Composites Measured at 30°C

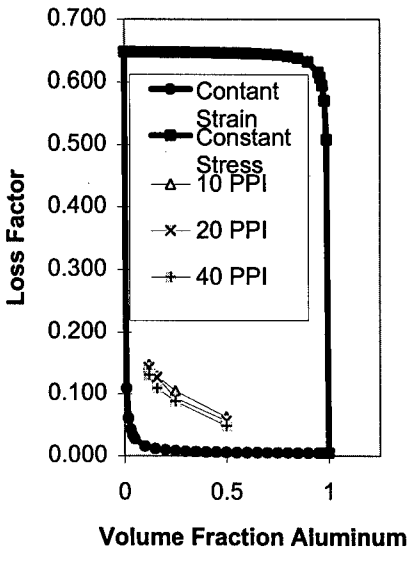


Figure 4. Damping Capacity of Aluminum Epoxy Composites Measured at 80°C.

Table 3. Loss Factors for Aluminum-Epoxy composites

Volume fraction of aluminum	Initial PPI	Measurements at 30°C		Measurements at 80°C	
		loss factor	standard deviation	loss factor	standard deviation
0.12	10	0.0121	0.000153	0.14673	0.006765
0.16	10	0.013691	0.000104	0.128816	0.00778
0.25	10	0.013333	0.000128	0.105011	0.00684
0.5	10	0.012437	0.000267	0.062749	0.003588
0.12	20	0.0133	0.000234	0.142678	0.008771
0.16	20	0.013594	0.000136	0.126991	0.007747
0.25	20	0.012014	0.000146	0.093572	0.005475
0.50	20	0.010689	0.000139	0.056678	0.003109
0.12	40	0.013553	0.000181	0.131143	0.00782
0.16	40	0.012833	0.000110	0.109505	0.00646
0.25	40	0.011496	0.00012	0.088068	0.005295
0.5	40	0.008905	0.000172	0.048373	0.002232

Although the FEA was two dimensional and thus not able to model a composite such as this with two continuous phases, it is clear that the unequal partitioning of the stress is still occurring. This effect is especially obvious in the case where the elastic modulus of the epoxy is low. In that case, less of the stress can be taken up by the compliant epoxy and the damping capacity of the composite is closer to that of the monolithic Al. It is also evident that the scale of the microstructure changed the stress gradient, and therefore the damping, in a manner consistent with the FEA and this effect was amplified by increasing the difference in elastic modulus between the two phases.

Conclusions

The damping capacity of the composite was found to be proportionally closer to that of the stiffer materials when the difference in elastic modulus of the two materials was larger. This is likely due to the increased partitioning of the stress to the stiffer phase.

It was found that the damping capacity measurements on Al foam filled with epoxy confirmed previous finite element analysis that showed that a smaller phase size leads to lower damping. The larger the difference in elastic modulus the larger this effect was. This could have been due to an increasing stress gradient between the two phases of the composite.

References

1. Biot, M.A., U.S. Nat. Cong. of App. Mech., 1, (1958).

2. Rao, J.G. and S Ankem, "The Effect of Volume Percent and Morphology of Phases on the Damping Behavior of Epoxy/Aluminum Composites", Metallurgical and Materials Transactions A V 27a, 2366, (1996).

The effect of a functionally graded protective coating on the mechanical behaviour of SiC monofilament reinforced Ti MMC's

S Haque & K L Choy

Department of Materials, Imperial College of Science Technology and Medicine, London, SW7 2BP

Metal matrix composites consisting of SiC monofilaments in Ti based matrices show great promise for aerospace applications. This work is a continuation of previous work on a novel graded coating system for SiC monofilaments used to reinforce Ti matrices. SiC Sigma monofilaments were coated with a functionally graded (FG) TiC based coating (SiC_f/C/(Ti,C)/Ti) and the fibres incorporated into Ti matrices. The tensile properties of the bulk composites were then evaluated, in order to asses the effect of the graded coating. The fracture surfaces were analysed using scanning electron microscopy (SEM). The test results indicate that the FG coating offers an improvement on composite mechanical properties, and in particular a 3% improvement in the peak load was observed with the use of the FG coating over the as-received fibres.

The Third Pacific Rim International Conference on Advanced Materials and Processing (PRICM 3)
Edited by M.A. Imam, R. DeNale, S. Hanada, Z. Zhong and D.N. Lee
The Minerals, Metals & Materials Society, 1998

Introduction

Composites based on Ti with SiC reinforcements are known to suffer from deleterious interfacial reactions at elevated temperatures (>800°C). The composite experiences these temperatures during composite manufacture (hot consolidation), or in service, and this results in the formation of titanium carbides and titanium silicides at the fibre/matrix interface[1]. The formation of a reaction product is thermodynamically favourable at elevated temperatures. Compounds that may form are non-stoichiometric TiC as well as ternary compounds such as Ti_3SiC_2. The low failure strain and brittle nature of these interfacial reaction products leads to a degradation in composite mechanical properties. Thus SiC_f/Ti must be considered as a non-equilibrium system at high temperatures. The most favoured approach to overcome these problems is to coat the fibre prior to incorporation into the matrix.

When cooling from the consolidation temperature, residual stresses are set up due to the difference in thermal expansion coefficient (CTE mismatch) between the matrix and reinforcement. If a coating has a CTE in between that of the matrix and the reinforcement then accomodation of these residual stresses is observed, although some stresses will still be present. Coating materials which result in the coating surface being in compression due to CTE mismatch are desirable as the fibre is then less susceptible to surface damage.

A number of criteria have been formulated which a suitable coating must meet [4]. The coating must be physically and chemically compatible with the fibre and the matrix, it must adhere well to the fibre and matrix thus producing efficient load transfer, it must adequately impair the diffusion of matrix and reinforcement atoms across the interface, it must act as a compliant layer to help accommodate residual thermal stresses, and lastly it should adjust interfacial shear strength to control crack propagation and failure mode. Many coatings have been investigated in an attempt to fulfil the above criteria [5,6,7,8]. However, a suitable coating that fulfils all the requirements has not been found. This has prompted the development of functionally graded (FG) coatings which have been used on carbon fibres [9], and SiC monofilaments [1]. FG materials posses a gradual change in composition and microstructure, and thus properties, across the material. The FG coating applied to the fibres in this work was a graded Ti/C coating (C/(Ti,C)/Ti), previously investigated by Choy[1]. The FG coating itself is not novel, however the application of the coating to SiC monofilaments is novel. The coating based on a graded TiC system has demonstrated the capability to be able to solve the interfacial problems (formation of a brittle reaction layer, residual stresses set up due to thermal expansion mismatch) encountered in SiC/Ti, conserve the strength of the as-received SiC fibres, and provide effective protection for SiC fibres in Ti-matrices at elevated temperatures (1100°C). The objective of this study was to investigate the effect of the FG coating on bulk composite properties.

Experimental

Mechanical testing of the bulk composites was carried out in order to evaluate the effect of the FG coating on bulk behaviour by testing of titanium containing axially aligned SiC monofilaments with and without a functionally graded TiC coating. The fibres were first FG coated using closed field unbalanced magnetron sputtering [1],

and the composites were then manufactured by first depositing a thick Ti matrix coating on top of the FG coating and then hot isostatic pressing (HIPing) to consolidate the composites fully [10]. Tensile test pieces were then machined. The spacing between fibre centres was between 250μm and 300μm, with between 50 and 60 fibres per specimen. The tests carried out are shown in table 1.

Table 1 Tensile tests carried out with sample description

Sample	Description
1	Ti
2	$SiC_f/C/Ti_{matrix}$
3	$SiC_f/C/(Ti,C)/Ti_{matrix}$

Tensile specimens used were conventional round tensile test pieces, with the fibres mounted axially within the a 3 mm diameter central portion of the specimen. The overall length of the specimens was 26.8 mm, and the two diameters being 4.5 mm and 7.11 mm. The sample was too small to allow the use of strain gauges, thus load/extension plots were produced. All tests were carried out at room temperature using a computer controlled Nene 30kN tensile testing machine. After testing the fracture surfaces were examined using scanning electron mircroscopy (SEM).

Results and Discussion

Tensile test results

Table 2 shows the data obtained from the tensile testing of samples 1 to 3. In addition to the values presented the shape of the load/extension plots shown in figure 1 are also significant as an indicator of relative stiffness.

Table 2 Tensile test data.

Sample	1	2	3
Load at peak (kN)	7.29	7.84	8.08
Load at break (kN)	5.28	6.06	5.22
Yield point (kN)	7.28	7.61	8.07

The volume fraction of reinforcement within the reinforced area was found to be approximately 12%. However the reinforced samples were not found to be significantly stiffer than the pure Ti samples, this may be due to the large unreinforced area surrounding the central core containing the fibres. In terms of area only half the cros-section was reinforced.

All the tensile samples exhibited similar behaviour (figure 1), upon loading a period of elastic behaviour was observed until the fibres and the immediately surrounding area failed, accompanied by a sharp drop in load, the remaining unreinforced area of the sample then plastically deformed under the applied load until complete failure of the sample. In the case of the sample containing the FG coated fibres, some fibre pullout was observed accounting for the change in apparent stiffness prior to the sharp drop in load. The sample containing the as-received fibres exhibited a characteristic brittle fracture surface with no fibre pullout. In addition, the FG sample reached a greater peak load (a 3% improvement) than the as received sample shown in figure 2(a) and (b). Clearly the FG coating affected the fracture behaviour of the system. The FG coating favours crack propagation around the fibre allowing fibres to retain their

load bearing capability after the crack has passed them, and allowing energy absorption mechansims such as fibre-pullout and crack bridging to occur. This results in the gradual failure of the composite.

Conclusions

The application of the FG coating to SiC monofilaments was seen to improve the bulk mechanical behaviour of the Ti composite by conserving the strength of the as-received fibres. In addition the absorption of residual stresses generated due to CTE mismatch by the FG coating tailors fracture behaviour across the interface allowing processes such as fibre-pullout to occur. Finite element modelling has shown that use of a graded TiC layer over a monolithic TiC layer is beneficial to this system [11]. Toughening mechanisms such as fibre pullout was only observed in the FG sample.

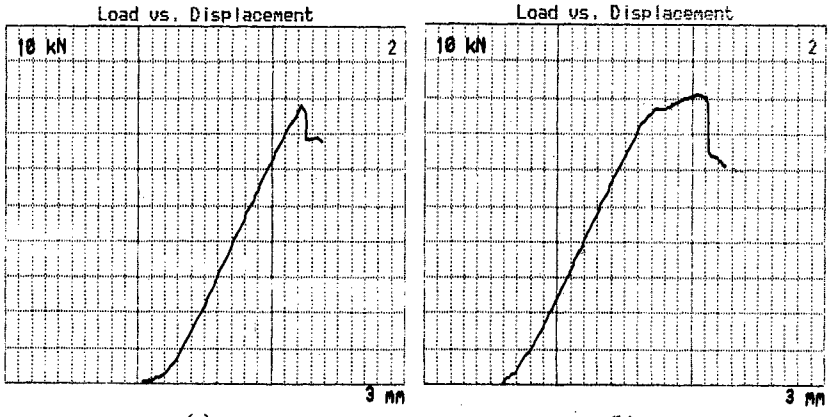
Thermomechanical analysis of the system in bending and tension is at present underway. Overall a higher volume fraction of reinforcement and a smaller unreinforced volume would allow better analysis of the effect of different coating systems.

Acknowledgements

The author wishes to thank DERA Sigma for the provision of SiC monofilament fibres, D.G.Teer and J.Hampshire for technical assistance in applying the coatings, M.Ward-Close and M.Wood for producing the composite samples, and the EPSRC and DERA for financial support.

References

1. K L Choy, Scripta Mat, 34, 11, 1753, (1996)
2. D B Grundel, F E Wawner, Scripta Mat, 25, 437, (1991)
3. R L Crane, V J Krukonis, Strength and Properties of SiC filaments, 74th Annual Meeting of the American Ceramic Society, (1972)
4. S M Jeng, J M Yang, J Mater Res, 8, 4, (1993)
5. R R Kiesche, T W Clyne, Mat Sci and Eng A135, 145, (1991)
6. R R Kiesche, R E Somekh, T W Clyne, Acta Mat 4(39), 427, (1991)
7. K L Choy, J F Durodola, B Derby, C Ruiz, Composites 26, 531, (1995)
8. K L Choy, B Derby, JOM 29, 3774, (1994)
9. J K Yu, H L Li, B L Shang, JOMS 29, 2641, (1994)
10. C.M.Ward-Close,P.G.Partridge,JOM 25 (1990) 4315-4323
11. K L Choy, S Haque, to be published in Scripta Mat



(a) (b)

Figure 1 Load/extension plots (a) Sample 2 (b) Sample 3.

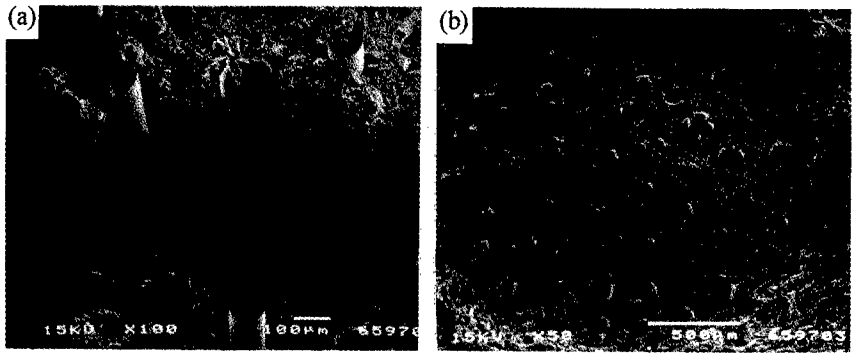


Figure 2 Fracture surfaces from tensile tests, (a) FG sample, (b) As-received sample

EXPERIMENTAL STUDY OF THE BOND BETWEEN CONCRETE AND STEEL REINFORCEMENT

W. Sha and K.W. Lau

Department of Civil Engineering, The Queen's University of Belfast, Belfast BT7 1NN, UK

Abstract

This paper describes experimental work on the evaluation of bonding between concrete and reinforcing steel, using pull-out tests. The effects of surface anti-corrosive coating on the reinforcement and the varying concrete water/cement ratio have been examined. It has been found that the concrete strength affected the bond strength for uncoated plain bars. In the case of coated bars, the pull-out failure can be between coating and concrete, or between coating and reinforcement. The bond strength between coating and reinforcement is similar to that between concrete and bare reinforcement.

The Third Pacific Rim International Conference on
Advanced Materials and Processing (PRICM 3)
Edited by M.A. Imam, R. DeNale, S. Hanada,
Z. Zhong and D.N. Lee
The Minerals, Metals & Materials Society, 1998

Introduction

The bond strength between reinforcement and concrete is not a major concern in the criteria of reinforced concrete design [1], because the limit states of deflection and cracking as far as bonding is concerned are not so critical as the ultimate limit states. In other words, the load required for small slippage at the interface of the composite is far from the load required (ultimate load) to fail the structural member. Therefore, even when the serviceability is reached, the member remains satisfactory from the structural point of view. However, deflection and cracking usually appear first before a reinforced concrete member fails. Small amount of deflection and cracking is a good indication of what the member is experiencing. This always occurs as slippage at the interface of the composite. Cracking will lead to oxidation of steel. Therefore, adequate calculations and necessary prevention are required. Improvement on the bonding strength may give a structural member or a building as a whole a longer service life.

When plain bars are used, the bonding depends primarily on chemical adhesion and friction. Chemical adhesion usually depends on the constituents and their proportion in the concrete mix. With a wide variety of materials available for the mixing of concrete, certain combinations and proportion of materials can achieve better result in bonding strength. Such variations include water/cement ratio, use of admixtures in the mix and types of cement and aggregates used.

Some of the concrete structures have to be exposed to severe environmental conditions, but steel can easily be corroded in the presence of oxide ions. To prevent corrosion, coating on reinforcing bars can be applied. However, coating changes the surface condition of the reinforcement and may therefore alter the structural interaction, or bond, between concrete and reinforcement. It is also necessary to consider the adhesion properties of the coating.

The present study has investigated two areas related to bonding; water/cement ratio of concrete and the effect of coating.

Experimental

All of the constituent materials used in the concrete mixes for this study were oven-dried. The proportions are shown in Table I. The procedure for mixing conformed to BS1881 [2]. To show the strength variation of different mixes, 100 mm cubes were cast for 7, 28 and 42 day cube tests, for each mix. Three to six cubes were tested to get an average strength value. The results are included in Table I. For the purpose of bond test, also conducted at 28 days after casting, 150 mm cube moulds were used with reinforcing bar inserted in the centre of the sample vertically.

Table I Concrete Mixes (kg/m^3)

w/c ratio		0.35	0.45	0.55
10 mm aggregate		400	400	400
20 mm aggregate		950	950	950
Sand		390	470	510
Water		185	180	193
Cement		529	400	350
strength (N/mm^2)	7 day	61±1	45±1	28±2
	28 day	67±3	53±3	37±3
	42 day	-	-	40.7±0.9

All bond and tensile tests of reinforcement were conducted in a pull-out testing machine. For bonding tests, 12 mm plain reinforcing bar (BS4449 [3]) was made to 750 mm long. The reinforcing bar extended through the bearing block assembly and the bottom plate of the tensile testing machine, and was gripped by the top jaws. A small metal plate was placed towards the edge of each of the two opposing sides of the concrete specimen. The bottom plate was then adjusted to a position such that it just touched the two metal plates. During tests, force was transferred from the bottom plate to the specimen. The extension was measured by clamping two dial gauges onto the reinforcing bar, with the average of the two gauge readings used as the mean displacement. The load was increased manually.

Larcem RP coating was applied to some bars. This is a two component polymer modified cement based protective and anti-corrosive slurry coating specially for application to steel reinforcement. It can be applied prior to or during concrete repair work to protect against corrosion due to carbonation and reactions of calcium chloride and de-icing salts. The total coating thickness, applied in two coats, was approximately 2 mm. Some degree of roughness was apparent.

The yield and tensile strengths of the reinforcement were tested to be 364 and 469 N/mm^2, respectively, which agree very well with the nominal strengths. None of the bars in pull-out tests yielded before de-bonding.

Results and Discussion

Bond Strength and Failure Modes

Bond shear stress-strain curves were obtained from pull-out tests. They show a largely linear relationship, with the stress usually levelling off nearer to failure. The test results are best presented in terms of bond strength, defined as the pull-out load at failure divided by the surface area of the bar embedded in the concrete. The test results are summarised in Table II. The extensions at failure are also included.

Table II Bond Strength under Different Conditions

Bar surface	w/c ratio	Bond strength (N/mm^2)	Extension at failure (mm)
Plain	0.35	3.5±0.3	1.1±0.4
	0.45	3.8±0.1	1.3±0.6
	0.55	2.7±0.1	0.82±0.07
Coated	0.35	3.03	1.1*
		3.60	0.9**
	0.45	3.22±0.05	0.9±0.4*
		3.66	1.0**
	0.55	3.17±0.02	0.91±0.05*
		3.70	1.53**

*Coating remained on bar;
**Coating lost.

The result for uncoated plain bar reinforcement shows that variation of the water/cement ratio affects bonding. When the ratio is increased to 0.55, the bond strength shows a significant drop. This can be explained with the fact that with higher water/cement ratio, there are more pores in

the concrete and the actual contact area between solid part of cement and the steel bar is reduced.

When coated bar was used, while the effect of water/cement ratio was not obvious, there were two modes of failure. The failure could be between coating and concrete, or between coating and steel. The adhesion strength of coating on the plain bar can be taken as the stress at which the coating is lost. From the data in Table II, this is 3.65±0.05 N/mm^2 (the average of 3.60, 3.66 and 3.70), which is the same as the average bond strength between concrete and uncoated bars when the water/cement ratio is not higher than 0.45. This proves that the coating is very similar in nature to ordinary cement with sensible water/cement ratios as far as bonding characteristics is concerned.

While it is satisfactory to know that the bond strength between the coating and steel bars is the same as the bond strength between normal concrete and steel, in more occasions during tests, the bond between the coating and concrete failed, at lower stress levels. It is not known presently why some coatings preserved a better bonding with the surrounding concrete while others did not. In the case of water/cement ratio being 0.55, the failure load was significantly increased when coating was used, for either failure modes. The coating effectively acts as a "buffer" here, between steel and the "wet" concrete. The wetter concrete might have a better mixing effect with the coating.

In BS5400, bond stress of 1.7~2.7 N/mm^2 for plain bars is given, the exact value being determined by the concrete strength. However the bond test in this standard does not measure a quantity that is directly related to a pull-out situation. The stresses are the local bond failure caused by large changes in tension over short lengths of reinforcement. The value of the local bond stress, f_{bs}, which is given in the following equation (applicable when the bar is parallel to the compression face), should not exceed the value stated above:

$$f_{bs} = \frac{V}{u_s \, d} \tag{1}$$

where V is the shear force due to ultimate loads, u_s is the sum of the effective perimeters of the tension reinforcement, and d is the effective depth of the tension reinforcement. This equation is the same as used for the calculation of the bond strength in pull-out tests. The measured bond strengths for similar concrete strength given in the British Standard are always satisfactory, i.e. higher than those specified.

Stress at 0.25 mm Extension

The average bond stresses at 0.25 mm extension were measured from the stress-strain curves obtained during pull-out tests (Table III). It can be seen that different material and testing conditions do not have any significant effect on this parameter, although there are relatively large errors.

Table III Bond Stress (N/mm^2) at 0.25 mm Extension

w/c ratio	Uncoated bar	Coated bar
0.35	0.7±0.2	0.86±0.05
0.45	1.0±0.4	0.8±0.2
0.55	1.1±0.3	0.9±0.2

The above measured bond stress values at the specific extension are low when compared with previous studies by other authors. In the present work, the contribution to measured extension from the elastic deformation within the concrete block is not considered. The bulk concrete would deform during a pull-out test, very likely to a significant extent. This would contribute to the relatively large extension recorded in the experiments.

Summary

The bond strength between plain bar and concrete depends on the water/cement ratio of the concrete. It decreases when the water/cement ratio is increased to 0.55. In the case of coated bars, such a change becomes insignificant. However, the bond between coating and concrete is likely to fail before the bond strength between the coating and the steel bar is reached. The latter value is essentially the same as the bond strength between bare steel and concrete with water/cement ratio below 0.55.

References

1. Structural Use of Concrete, BS8110 (London: British Standards Institution, 1985).

2. Testing Concrete, BS1881 (London: British Standards Institution, 1983).

3. Specification for Carbon Steel Bars for the Reinforcement of Concrete, BS4449 (London: British Standards Institution, 1988).

Stresses at the Interface In Discontinuously Reinforced Composites

T. Calvin Tszeng
Department of Mechanical Engineering
University of Nebraska-Lincoln
Lincoln, NE 68588, USA

Abstract

This paper presents the theoretical study of the stress state at the inclusion-matrix interface in discontinuously reinforced metal matrix composites. The generalized inclusion method is modified to consider the elastoplastic deformation in the metal matrix. A SiC/2124 aluminum alloy composite is used as the model material which is subjected to an axisymmetric macroscopic stress. The present study found that the peak tensile normal stress always appears at the pole, and increases with the deformation. The plastic zone at the interface first appears at an angle of 45° from the pole, and spreads in both directions along the interface; the pole and the equator essentially remain elastic throughout the deformation.

The Third Pacific Rim International Conference on
Advanced Materials and Processing (PRICM 3)
Edited by M.A. Imam, R. DeNale, S. Hanada,
Z. Zhong and D.N. Lee
The Minerals, Metals & Materials Society, 1998

Introduction

Stress state at the inclusion/matrix interface relative to the bonding strength plays a very important role in determining the mechanical strength of discontinuously (e.g., whisker, short fiber, or particulate) reinforced metal matrix composites. As far as ductile fracture is concerned, a number of studies have been focused on the mechanism of void nucleation in particle-strengthened alloys [1-6]. The previous studies have led to the conclusion that void nucleation at the interface between the inclusion and the matrix is one of the controlling phenomena in ductile fracture in particle-strengthened alloys, especially in cases where the volume fraction of the second phase particles is high. Stress criterion is the prevailing criterion of void nucleation for typical SiC_p-reinforced composites containing SiC_p particles of a size in the oder of 10 μm. This criterion states that voids will nucleate at the interface if the tensile normal stress σ_n at the inclusion-matrix interface exceeded the bonding strength σ_I of the interface. Among the theoretical studies of inclusion-matrix interfacial stress surrounding the particle, both a continuum mechanics based finite element method [2,7] and the theory of dislocations [5,8] have been employed. The approach based on FEM certainly gives the detailed stress state in the vicinity of interface, but, the choice of unit cell for computation and the associated boundary conditions become more difficult with reinforcement of higher volume fraction and of non-spherical shapes.

This study is to provide a theoretical view of the stress state at the interface between inclusion and matrix, and relate these theoretical predictions to the occurrence of void nucleation. A SiC/2124 aluminum alloy composite will be used as the model material.

Theoretical Treatment

The present study assumes that all the fibers have the same aspect ratio. The analysis method is an extension of the Eshelby inclusion method [9,10] combined with the Mori-Tanaka mean field theory [11]. The full formulation can be found in [9,12]. In the following, we provide a brief account as related to the calculations of interfacial stress by the generalized inclusion method.

According to the generalized inclusion method, the stress in the considered reinforcement, σ^F, is calculated by (bold-faced variables denote tensors):

$$\sigma^F = \mathbf{L}^F(\mathbf{e}^A + \mathbf{e}^C + \mathbf{e}') \quad \text{Inhomogeneous composite} \quad (1)$$

$$= \mathbf{L}^M(\mathbf{e}^A + \mathbf{e}^C + \mathbf{e}' - \mathbf{e}^T) \quad \text{Reference homogeneous composite} \quad (2)$$

where $\mathbf{e}^A$ is the strain in homogeneous, unreinforced matrix metal, $\mathbf{e}^C$ is the constrained strain, $\mathbf{e}'$ is the additional term due to the interaction between inclusions, $\mathbf{e}^T$ is the incompatible transformation strain, and $\mathbf{L}^F$ and $\mathbf{L}^M$ are the stiffness tensors of the reinforcement and matrix material, respectively. In fact, $\mathbf{L}^M$ is the secant stiffness tensor of the matrix material at σ^M and $\mathbf{e}^M$ when it goes into plastic deformation, i.e., $\sigma^M = \mathbf{L}^M \mathbf{e}^M$. The secant Young's modulus and the corresponding Poisson's ratio for plastic incompressibility are given in [9,12].

The reinforcement stress in equations (1) or (2) is the stress in a single fiber of particular orientation in the matrix. A volume average procedure given by Tszeng [12] shows the average transformation strain $\langle \mathbf{e}^T \rangle$ is obtained by solving the following equation:

$$[(1-f)L^M(\langle S \rangle - I) - L^F((1-f)\langle S \rangle + fI)]\langle e^T \rangle = (L^F - L^M)(I + \bar{L})e^A \quad (3)$$

where $\mathbf{S}$ is the forth-order Eshelby tensor which depends only on the inclusion geometry (aspect ratio) and the Poisson's ratio of the matrix, $\mathbf{I}$ is the fourth-order identity tensor, $\bar{\mathbf{L}} = (\mathbf{L}^M)^{-1}(L^R - L^M)$, and $\mathbf{L}^R$ is the secant stiffness tensor of the matrix material at σ^A and $\mathbf{e}^A$, i.e., $\sigma^A = \mathbf{L}^R \mathbf{e}^A$. After the average

transformation strain <eT> is obtained, the transformation strain, eT, in equation (2), associated with the considered inclusion can be obtained [9,12].

The stress state at a point immediately outside the inclusion surface is obtained by modifying the original formulation of Eshelby [10]. The strain at the interface is:

$$\mathbf{e}^{(Int)} = \mathbf{e}^{C(Int)} + \mathbf{e}^{M}, \tag{4}$$

where $\mathbf{e}^{M} = \langle \mathbf{e}^{T} \rangle + \mathbf{e}'$, is the average matrix strain. The hydrostatic and deviatoric part of the interfacial constrained strain $\mathbf{e}^{C(Int)}$ are respectively given by, in indicial form [10]:

$$e_o^{C(Int)} = e_o^{C} - \frac{1}{3}\frac{1+\nu^S}{1-\nu^S}\, e_o^{T} - \frac{1-2\nu^S}{1-\nu^S}\, {}'e_{ij}^{T} n_i n_j, \tag{5}$$

and

$$\begin{aligned} {}'e_{il}^{C(Int)} = {}'e_{il}^{C} &+ \frac{1}{1-\nu^S}\, {}'e_{jk}^{T} n_j n_k n_i n_l - {}'e_{ik}^{T} n_k n_l - {}'e_{lk}^{T} n_k n_i \\ &+ \frac{1-2\nu^S}{3(1-\nu^S)}\, {}'e_{jk}^{T} n_j n_k \delta_{il} - \frac{1}{3}\frac{1+\nu^S}{1-\nu^S}\, e_o^{T} (n_i n_l - \tfrac{1}{3}\delta_{il}). \end{aligned} \tag{6}$$

where $\mathbf{e}^{T}$ is the stress free transformation strain associated with the considered inclusion. In these expressions, a variable primed at the left top represents the deviatoric part, and a subscript "o" represents the hydrostatic part. Note that ν^S in the equations above is the secant Poisson's ratio of the matrix material. The corresponding interfacial stress $\sigma^{(Int)}$ is obtained through simple calculation, i.e., $\sigma^{(Int)} = \mathbf{L}^{(Int)}\mathbf{e}^{(Int)}$, where $\mathbf{L}^{(Int)}$ is the secant modulus at $\mathbf{e}^{(Int)}$. For convenience, the interfacial stress is transformed to the local coordinate which has the 3-axis coincident with the surface outer normal **n**.

Results and Discussion

In the following, the mechanical properties are based on SiC reinforced 2124 aluminum alloys which were recently studied by several investigaters [9,12-14]. This composite system is chosen simply as a model material, the general observations to be derived from the theoretical calculations are rather generic and therefore should be applicable to other composite systems as well. The Young's modulus and Poisson's ratio are $E^M = 60$ GPa and $\nu^M = 0.3$ for the matrix and $E^F = 342.6$ GPa and $\nu^F = 0.21$ for the inclusion. The flow stress, σ_Y, of the matrix material is given by the modified Ludwick relation: $\sigma_Y = \sigma_o + h(\bar{e}^p)^n$, with $\sigma_o = 300$ MPa, $h = 442.1$ MPa, and $n = 0.478$.

To elucidate the calculations, we first consider a simple composite comprising ellipsoidal reinforcement of an aspect ratio $a = 1$ (i.e., spherical particulate), volume fraction $f = 0.1$, and loaded by a uniaxial stress $\sigma_{33}^A = 1$MPa in the fiber direction (i.e., the 3-axis). The distribution of interfacial stress is plotted as a function of the angle θ measured from the pole in Figure 1. The normal stress shows a maximum tension, $\sigma_{n\,max}$, at the pole ($\theta = 0$). In contrast, the von Mises stress has the peak at about $\theta = 45^o$ from the pole.

In the present analysis, there is no separate yield criterion for the interface, yielding is allowed to occur only in the matrix which, by definition, includes the interface. Nonetheless, it will be of interest to examine the possibility of interfacial yielding. We apply the von Mises yield criterion on the data presented in Figure 1. According to Figure 1, yielding at the interface first occurs at a macroscopic stress of about 200 MPa in the region around $\theta = 45^o$, and spreads along the interface as the macroscopic stress becomes higher. The macroscopic stress is $\sigma_{33}^A = 324$ MPa when initial yielding occurs globally in the matrix as based on the average matrix stress σ^M. At that moment, the interfacial

von Mises stress at $\theta \sim 0^o$ actually just exceeds the flow stress, whereas the interface away from the pole (e.g., $\theta > 70^o$) remains elastic. Figure 2 illustrates the stress distributions at different levels of deformation. Several interesting phenomena can be seen in Figure 2. First, the peak tensile normal stress always appears at the pole, and increases with the deformation. In this respect, Argon, et al. [2] determined that the normal stress in the polar region seemed to have a flat distribution in the case of a cylindrical inclusion. This observation is different from Orr and Brown [15] (on cylindrical inclusion) or Thomson and Hancock [7] (on spherical inclusion) who indicated that the maximum normal stress moves away from the pole as the deformation becomes larger. Although the materials studied by these works had a very low volume fraction (< 1%), we have found essentially the same pattern of distribution as that in Figures 1 and 2, regardless of particle volume fraction.

According to Figure 2, the overall von Mises stress at the interface is increasing with strain. However, distinctly different phenomenon occurs at the pole and the equator. As discussed earlier, the von Mises stress at the interface between angles 0^o and 70^o from the pole already exceeds the flow stress of the matrix material when the composite initially yielded. In the transition from elastic to plastic deformation, the von Mises stress at the pole decreases and becomes lower than the matrix's yield stress. To further illustrate the stress state in the polar region, the von Mises stress at the pole is plotted as a function of the macroscopic effective stress, as shown in Figure 3. The von Mises stress at the pole does exceed the yielding stress in the transition from elastic to plastic deformation, followed by an asymptotic decrease. The interface in the polar region therefore experiences unloading after the early, minimum plastic deformation. To facilitate discussion, let us use two angles θ_1 and θ_2 such that the plastic zone at the interface is defined by $\theta_1 \le \theta \le \theta_2$. That is, the regions in $0^o \le \theta \le \theta_1$ and $\theta_2 \le \theta \le 90^o$ are elastic. These angles are plotted as functions of the effective plastic strain in Figure 3. The angle θ_1 is equal to 0^o at the elastic limit and increases very rapidly immediately after the composite plastically deformed, followed by monotonic decrease as the deformation becomes even larger. Thus, the material at the pole remains mostly in the elastic range, although the location of the elastic limit, θ_1, is approaching the pole when the deformation becomes larger. The FEM calculations [7] also indicated the similar tendency of a very low level of plastic deformation at the pole (see Figures 9 and 14 of [7]).

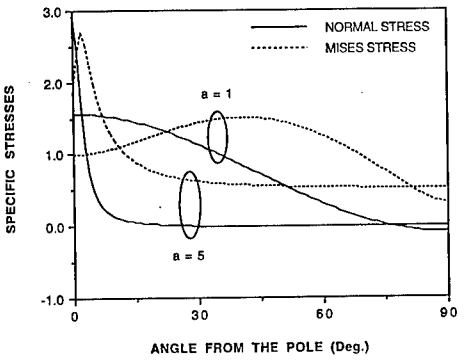


Figure 1. The distribution of interfacial specific stresses (interfacial stress divided by σ_{33}^A) as a function of the angle from the pole in a composite deformed elastically during uniaxial loading. The aspect ratio of the inclusion a = 1 and 5, volume fraction f = 0.1.

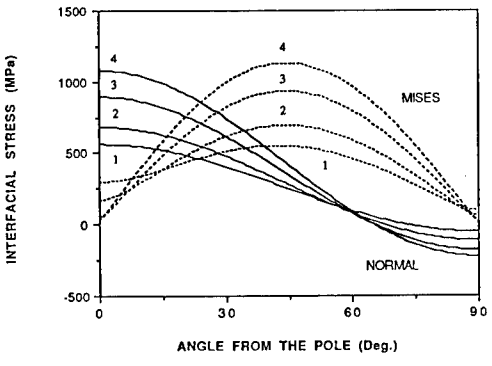


Figure 2. The distribution of normal stress and von Mises stress at the particle-matrix interface in a composite deformed plastically during uniaxial loading. The aspect ratio of the inclusion a = 1, volume fraction f = 0.1. σ_{33}^A = (1) 350 MPa; (2) 400 MPa; (3) 500 MPa; (4) 600 MPa.

According to [7], the observed yielding at the polar element in their study may be a consequence of the finite dimensions of the finite element mesh, and therefore may not represent the actual phenomenon. Similar phenomena also happen at the equator, where the von Mises stress reaches its peak of 101 MPa ($< \sigma_o = 300$ MPa) at the macroscopic elastic limit, and decreases monotonically after the composite yielding globally (see Figure 3). The plastic zone at the interface spreads toward the equator at larger deformation, as indicated by the increasing θ_2 in Figure 4. However, the material in the region of the equator would not go into plastic deformation, regardless the level of macroscopic deformation.

Based on the above observations, one can configure that the plastic zone first appears at an $\theta \sim 45^o$ and spreads in both directions along the interface; the pole ($\theta = 0^o$) and the equator ($\theta = 90^o$) essentially remain elastic throughout the deformation. This conclusion is generally in accord with the FEM calculations of Thomson and Hancock [7] (see Figure 7 of that paper).

The curves of specific interfacial stress for a composite comprising ellipsoidal inclusions (fibers) of an aspect ratio of 5 are also shown in Figure 1. Obviously, at the same macroscopic stress, inclusions of a higher aspect ratio experience a high peak stress at the inclusion-matrix interface. Thus, particulate-reinforced composites is expected to possess a better ductility compared with the whisker-reinforced composites, which is actually what generally observed [16].

According to the curve corresponding to an aspect ratio of 5 in Figure 1, initial yielding at the interface may have started at the location of peak Mises stress at a σ_{33}^A as low as 110 MPa, which is about one-third of the initial yield stress of the matrix aluminum alloy. To ensure the composite is free from localized plastic deformation, the macroscopic stress has to be below the elastic limit which is about 110 MPa in the considered case. As mentioned earlier, the corresponding limit stress in composites comprising spherical particulates is 200 MPa. It is generally accepted that local concentrations of plastic deformation should be avoided for a better fatigue resistance [17]. Hence, a higher elastic limit corresponds to better fatigue resistance, especially in the cases involved a high level of stress. Since it has been shown that the elastic limit is lower for composites comprising fibers of a larger aspect ratio, one may expect composites comprising fibers of a higher aspect ratio should possess a lower fatigue resistance. This remark is actually contradictory to what generally observed [16]. This is a topic subjected to further study.

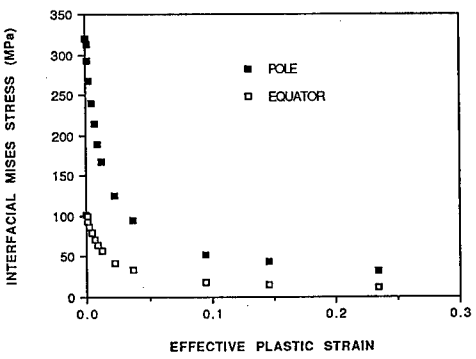


Figure 3. The changing of interfacial von Mises at the pole and at the equator as functions of the effective plastic strain.

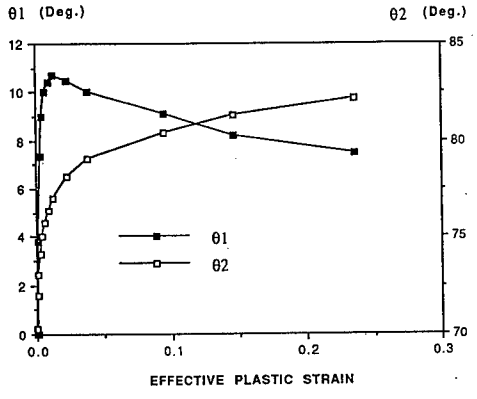


Figure 4. The angles (θ_1, θ_2) defining the plastic zone at the interface are changing as the deformation proceeds.

Conclusion

This paper presents the theoretical prediction of the stress state at the inclusion-matrix interface in discontinuously metal matrix composites when subjected to axisymmetric macroscopic stress state. Several remarks are made in the following.

1. The present study found that the peak tensile normal stress always appears at the pole, and increases with the deformation. This finding is different from previous study on cylindrical inclusion (flat distribution) and on spherical inclusion (the maximum normal stress moves away from the pole as the deformation becomes larger).
2. The matrix at the vicinity of pole essentially remains elastic regardless the level of deformation, although the size of the elastic region keeps decreasing as deformation becomes larger.
3. The plastic zone first appears at an $\theta \sim 45^{o}$ and spreads in both directions along the interface; the pole ($\theta = 0^{o}$) and the equator ($\theta = 90^{o}$) essentially remain elastic throughout the deformation.

References

1. Fisher, J. R. and Gurland, J., 1981, "Void Nucleation in Spheroidized Carbon Steels Part 2: Model," Metal Science, pp.193-202.
2. Argon, A. S., Im, J., and Safoglu, R., 1975, "Cavity Formation from Inclusions in Ductile Fracture," Metallurgical Transactions, Vol. 6A, pp. 825-837.
3. Hunt Jr., W. H., Richmond, O., and Young, R. D., 1989, "Fracture Initiation in Particle Hardened Materials with High Volume Fraction," ICCM/VI, Vol. 2, pp. 2.209-223.
4. Embury, J. D., 1985, "Plastic Flow in Dispersion Hardened Materials," Metallurgical Transactions, Vol. 16A, pp. 2191.
5. LeRoy, G., Embury, J. D., Edward, G., and Ashby, M. F., "A Model of Ductile Fracture Based on the Nucleation and Growth of Voids," Acta Metallurgica, Vol. 29, pp. 1509-1522.
6. Tszeng, T. C., 1993, "A Model of Void Nucleation from Ellipsoidal Inclusions," Scripta Metallurgica et Materialia, Vol. 28, pp. 1065-1070.
7. Thomson, R. D. and Hancock, J. W., 1984, "Local Stress and Strain Fields near a Spherical Elastic Inclusion in a Plastically Deforming Matrix," International Journal of Fracture, Vol. 24, pp. 209-228.
8. Goods, S. H. and Brown, L. M., 1979, "The Nucleation of Cavities by Plastic Deformation," Acta Metallurgica, Vol. 27, pp. 1-15.
9. Tszeng, T. C., 1994, "Micromechanics Characterization of Unidirectional Composites during Multiaxial Plastic Deformation," J. Composite Materials, Vol. 28, pp. 800-820.
10. Eshelby, J. D., 1957, "The Determination of the Elastic Field of an Ellipsoidal Inclusion, and Related Problems," Proc. Royal Soc. London, Vol. A241, pp. 376-396.
11. Mori, T. and Tanaka, K., 1973, "Average Stress in Matrix and Average Elastic Energy of Materials with Misfitting Inclusion," Acta Metallurgica, Vol. 21, pp. 571.
12. Tszeng, T. C., 1994, "Micromechanics of Partially Aligned Short Fiber Composites with Reference to Deformation Processing," Composites Science and Technology, Vol. 51, pp. 75-84.
13. Christman, T., Needleman, A., and Suresh, S. 1989, "An Experimental and Numerical Study of Deformation in Metal-Ceramic Composites," Acta Metallurgica. Vol. 37, pp. 3029-3050.
14. Tvergaard, V., 1990, "Analysis of Tensile Properties for a Whisker-Reinforced Metal-Matrix Composite," Acta Metallurgica et Materialia,. Vol. 38, pp. 185-194.
15. Orr, J. and Brown, D. K., 1974, Engineering Fracture Mechanics, Vol. 6, pp. 261-274.
16. Rack, H. J. and Ratnaparkhi, P., 1988, "Damage Tolerance in Discontinuously Reinforced Metal-Matrix Composites," Journal of Metals, November, pp. 55-57.
17. Dieter, G. E., 1976, Mechanical Metallurgy, 2nd edition, McGraw-Hill Book Company, New York.

Processing of Al/Al_3Ti Composites by Low Pressure Casting/Combustion Synthesis Process

K.Mizuuchi*, T. Takeuchi*, M. Fukusumi*, M. Sugioka*, Y. Ohkanda*, H. Nagai**
and
K. Inoue***

*Osaka Municipal Technical Research Institute, Osaka 536-8551, Japan
**Materials Science and Processing, Graduate School of Osaka University, Suita 565, Japan
***Materials Science and Engineering, University of Washington, Seattle, WA 98195-2120, USA.

Abstract

The low-pressure casting/combustion synthesis (LCCS) process has been proposed to fabricate near-net-shape metal-matrix composites (MMCs), where combined effects occurring during these two processes are utilized. Near-net-shape Al_3Ti-reinforced Ti-matrix composite has been produced without cavities by LCCS, and the microstructure and mechanical properties have been investigated. It is found that molten Al substantially can infiltrate into a mixture of Al and Ti powders when the mixture ratio of Al to Ti is high, or a mixture of Al and Ti powders contains more than 50at. % Al. In the case when the mixture ratio is low, or a mixture of Al and Ti powders contains less than 50 at. % Al, infiltration by molten Al becomes negligible. A critical mixture ratio of Ti powder to Al powder can be estimated by using a simple formula expressed by the relative density of Al and Ti powder mixtures to produce MMCs. When the powder ratio of Ti to Al is larger than the critical value, the volume fraction of Al_3Ti decreases with increasing content of Ti powder.

Introduction

Metal matrix composites (MMCs) can possess a desirable combination of mechanical and physical properties, such as high melting points and low density. Such a unique combination makes MMCs attractive for use in various applications including compressor vanes of automobiles, where high strength is required at elevated temperatures. In addition to such applications in automobile industries, applications in aircraft industries are also potential. In any cases, however, the cost of materials is one important factor in determining whether they can be used in specific applications [1,2]. Thus, it is significant to develop new fabrication methods for making similar MMCs in economic ways. Combustion synthesis is believed to be an environmentally benign technique and can be used to form MMCs in-situ via reactions occurring between elemental constituents [3-5]. This technique may also have another advantage being is a relatively inexpensive process. This is because starting materials are powders, which can be available in a wide variety of form and purity, compared with specially pre-alloyed intermetallic powders. Out of intermetallic compounds that can be used in combustion synthesis, trialuminide Al_3Ti is considered to be attractive as reinforcement for a MMC. This is because it has a high melting point (1620K) and low density (3.36g/cm^3). Al_3Ti has, however, some disadvantages, including a tetragonal DO_{22} structure, brittleness at room temperature and a tendency of having a high density of cavities when produced by combustion synthesis without application of pressure. From the above-mentioned viewpoints, we propose a new processing technique to produce a near-net-shaped MMC containing Al_3Ti. The process is involved in both low pressure casting [6-8] and combustion synthesis, and called a low-pressure casting/combustion synthesis (LCCS) process. Through this process, Al matrix composites with Al_3Ti can directly be fabricated from powders of Al and Ti and molten Al. Micro- and crystal-structural observations of Al/Al_3Ti composites fabricated by the process have been performed by means of scanning electron microscopy and X-ray diffraction.

Tensile properties of the composites have also been investigated.

Experimental

Fabrication process of composites is shown in Figure 1. In order to make rod-shaped composites, 304 stainless steel pipe was used as a metallic mold. The outside and internal diameters and the length of the mold were 8mm, 6mm and 220mm, respectively. Mitsuwa 99.98% purity Al powder and 99% purity Ti powder, whose average diameters are respectively 86.2 and 43.7 μ m, were used as law materials. Their particle size distribution is shown in Table 1. As shown in Figure 1, first, the 10mm-long central part of a pipe is compressed to 2.5mm thick so as to have a clearance of about 0.5 mm. Then, a small amount of Al_2O_3-SiO_2 ceramic fiber is inserted into this pipe from its one end and softly packed in order to close the narrow channel. Then, the mixture of Al and Ti powders is tapped after insertion in a stainless steel pipe from the same end of the pipe where the ceramic fiber is already packed. The relative packing density achieved by tapping is around 50% regardless mixture ratios of Al and Ti powders, as shown in Figure 2. This result may be due to a wide particle size distribution of powders used. The open end of the pipe containing the powder mixture is capped with

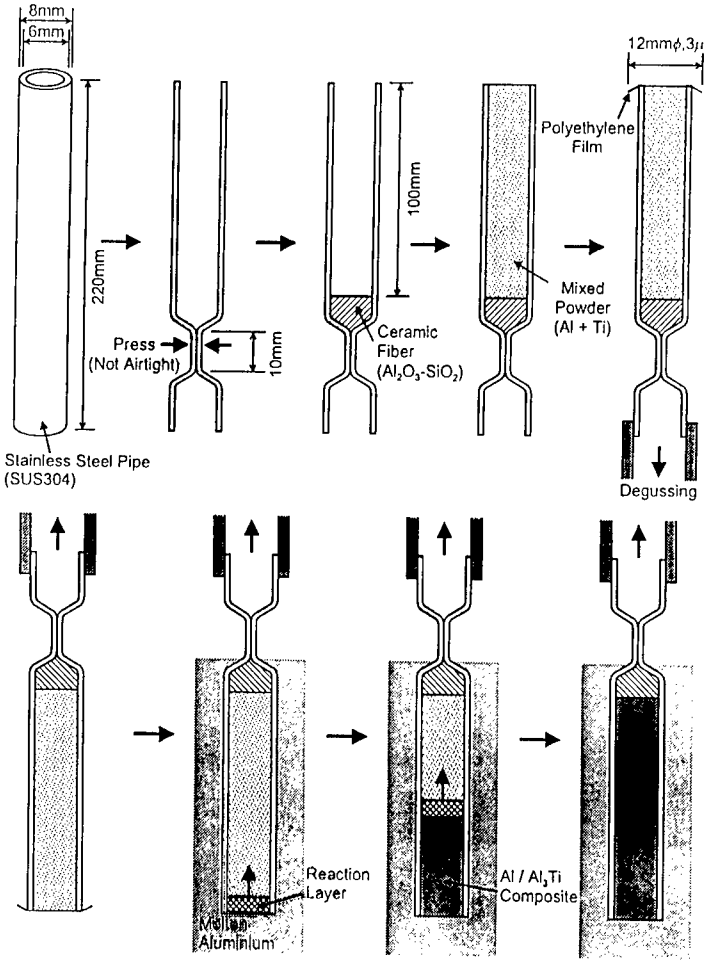


Figure 1 Low-pressure casting/combustion synthesis (LCCS) process.

Table 1 Particle size distribution of as-received Al and Ti powders.

Particle diameter (μm)	150-125	125-106	106-90	90-75	75-63	63-53	53-45	45-25	25-
Al (%)	0.8	7.3	23.8	38.3	24.3	4.5	0.8	0.2	-
Ti (%)	-	-	-	0.08	0.12	5.3	59.3	31.4	3.8

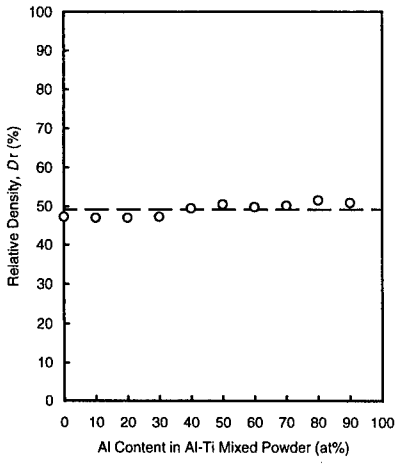


Figure 2 Relative packing density of as-tapped Al and Ti powder mixtures

plastic film 3μm thick and 12 mm in diameter and the other end is connected to a mechanical vacuum pump with a vacuum rubber hose. The pipe is then pumped for degassing, through which the powder mixture is more densely packed. After reaching a vacuum of 0.1Pa, the pipe is inserted in air into molten Al from the pipe end covered with plastic film, which is burnt out immediately by the molten metal. Combustion synthesis reaction is then initiated by the direct contact of Ti powder and molten Al, resulting in the formation of Al_3Ti occurring near the pipe end. Al_3Ti formed in this stage is porous and thus molten Al infiltrates into the pipe through cavities in skeletons of Al_3Ti. Molten Al thus contacts non- or in part-reacted Ti powder around Al_3Ti. Through this continuous process, the porous Al_3Ti skeleton is formed from the end to the pressed, center portion of pipe. Simultaneously, molten Al moves from the pipe end to the pipe center filling cavities in Al_3Ti skeleton. After reaction is terminated, the pipe is cooled in air and molten Al in the pipe solidifies, resulting in formation of Al/Al_3Ti metal matrix composites. In the present study, the temperature of molten Al has been kept at 1193K. Composites produced at various processing conditions were examined by SEM, X-ray diffraction and EPMA techniques. A JOEL 5800LVC scanning electron microscope and Mac Science MXP-18 X-ray diffraction apparatus were used. Mechanical properties were examined at room temperature using a Vickers micro hardness tester at a load of 2.94N (300g) and an Instron testing machine.

Results and Discussion

Molten Al can infiltrate the mixture of Al and Ti powders during the process described in a previous section. Infiltration height was measured as a function of Al content (at.%) in the mixture of Al and Ti powders and the result obtained is shown in Figure 3. As seen in the figure, the infiltration of molten Al into elemental powder mixtures was found to be substantial

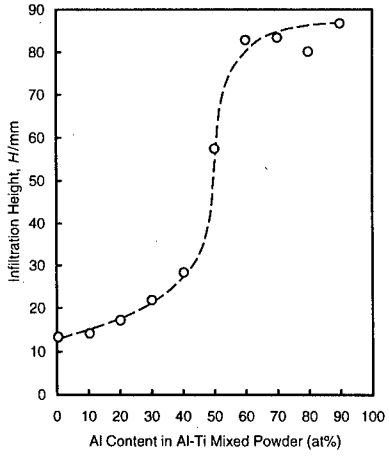


Figure 3 Changes in infiltration height as a function of Al content in the mixture of Al and Ti powders.

in the case of high Al content, or when Al and Ti powders are mixed with Al content of more than 50at%Al. In the case of low Al content, or when Al and Ti powders are mixed with Al content less than 50at% Al, on the other hand, the infiltration of molten Al becomes insubstantial. This result indicates that there is a critical value in powder mixture ratios, above which the infiltration of molten Al into powder mixtures becomes considerably large. At that value or above, metal matrix composites can be produced with low cavities by the process employed in the present work. The critical ratio of the mixture of Al and Ti powders can be calculated as follows. Al_3Ti is composed of three Al atoms and one Ti atom. The volume fraction of Al and Ti in Al_3Ti is 73.8 vol.% and 26.2 vol.%, respectively. As will be mentioned later, the volume fraction of Al_3Ti formed in composite increases and that of matrix Al in composite decreases with increasing volume fraction of Ti powder when elemental powder mixture is used. When all Al powders in a powder mixture and molten Al infiltrated into powder mixture are consumed for forming Al_3Ti, the volume fraction of matrix Al in the composite become 0 vol.%. Assuming no residual Ti elemental powder in a composite, the critical powder mixture ratio is expressed in the following equation,

$$V_{Ti}*D_r/\{V_{Ti}*D_r+V_{Al}*D_r+(1-D_r)\}=0.262 \qquad (1)$$

where V_{Al} is the critical volume fraction of Al powder in a powder mixture, V_{Ti} the critical volume fraction of Ti powder in the powder mixture, and D_r the relative density of the powder mixture in a pipe. Because $V_{Al}+V_{Ti}=1$, the equation (1) can be described in the form,

$$V_{Ti}*D_r=0.262 \qquad (2)$$

Using this simple formula, V_{Ti} can be calculated easily as a function of D_r. For example, when D_r is 50 vol.% as shown in Fig. 2, V_{Ti} (the critical mixing ratio of Ti powder in a powder mixture) can be calculated to be 50.9vol%, using the equation (2) indicating reasonably good agreement with the results shown in Fig.3.

X-ray diffraction analysis and Microstructure

Composites fabricated in the present study with various mixture ratios were examined by X-ray diffraction for identification of phases. For example, X-ray diffraction patterns taken from composites a, b, c, d and e are shown in Fig. 4. All the phases present in these composites can be identified as Ti, Al and Al_3Ti compound. As seen, the diffraction intensity ratio of Al_3Ti to Al matrix seems to decrease with increasing Al content in an element powder mixture. This tendency is also seen from scanning electron micrographs taken from composites a, b, c, d and e, as shown in Figure 5. As seen, all composites consist of three phases: gray, white and black regions. Quantitative chemical analyses have indicated that Ti appears as gray (region 1), Al_3Ti as white (region 2) and Al as black (region 3). The volume fraction of Al_3Ti in the composites is seen to increase with increasing Ti content.

Mechanical properties

Vickers microhardness measurements were performed for composites produced by the present LCCS process. It was found that the hardness of the composites increased as a function of Ti powder content, as shown in figure 6. That is, the hardness increased with increasing Al_3Ti content in the composites. Composites were machined to make tensile specimens with gauge dimensions of approximately ϕ5 mm x 10 mm and tests were carried out at room temperature at a strain rate of $1x10^{-4}$ s^{-1}. Results obtained are shown in Fig. 7. As seen, the tensile strength becomes higher with increasing Ti content in powder mixtures. When Ti

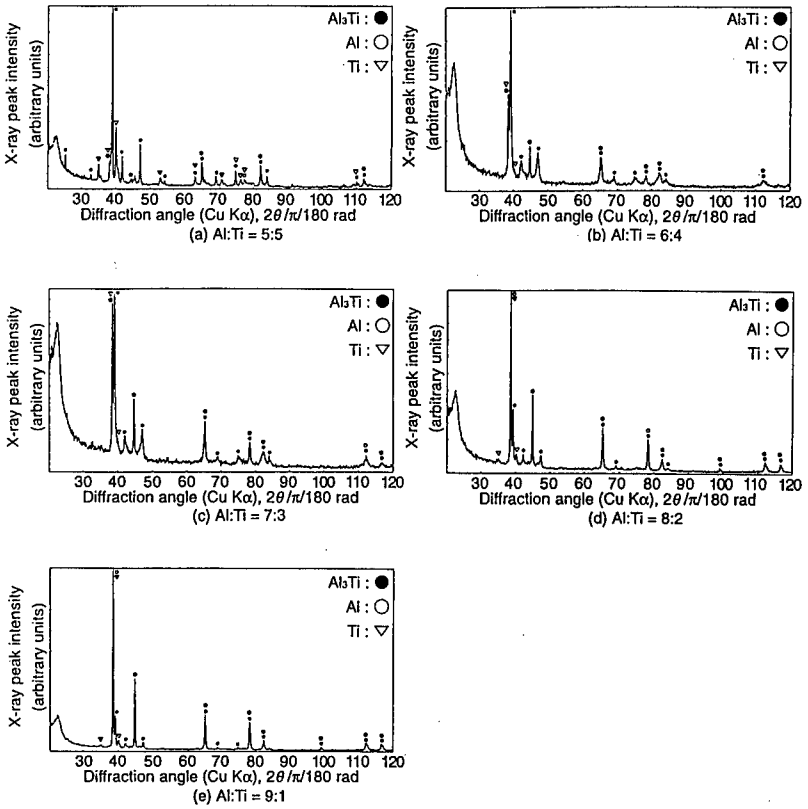


Figure 4 X-ray diffraction profiles taken from Al matrix composites containing Al_3Ti fabricated by the LCCS process.

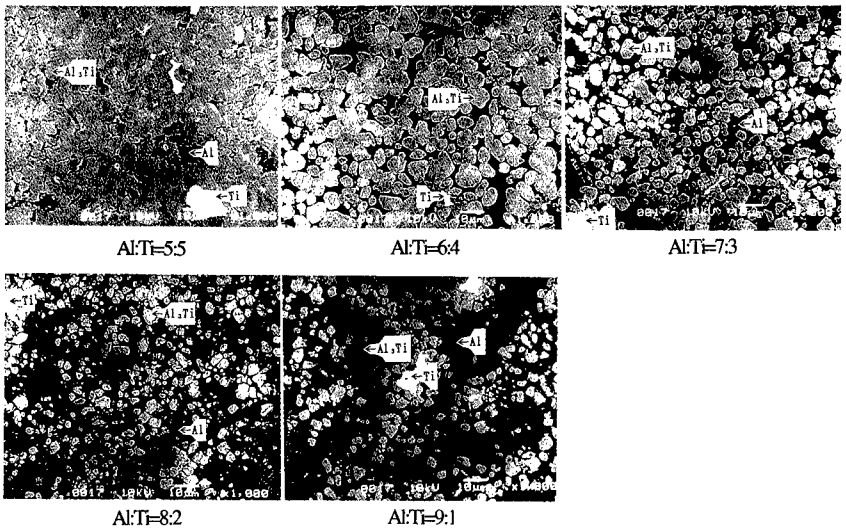


Figure 5 Scanning electron micrographs taken Al matrix composites containing Al_3Ti with various ratios of Al to Ti, fabricated by the LCCS process. Ti as gray regions; Al_3Ti white regions; and Al black regions.

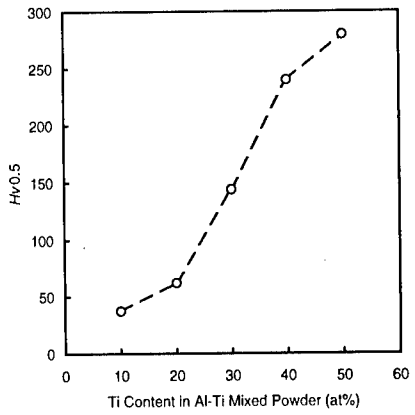


Figure 6 Changes in Vickers microhardness (a load of 300 g) as a function of Ti content in Al matrix composites containing Al_3Ti.

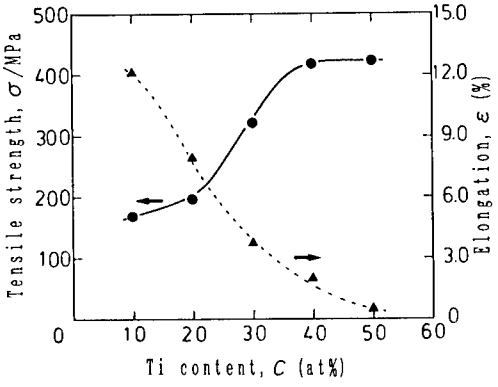


Figure 7 Tensile strength and elongation as a function of Ti content in Al matrix composites containing Al_3Ti.

content is 40 or 50 vol.%, the tensile strength of the composites reaches slightly higher than 400MPa. On the other hand, the elongation of the composites decreases with increasing Ti content. These results and microstructural observations indicate that the increase of the volume fraction of Al_3Ti in a composite improves its tensile strength at the expense of the ductility of composites. It should be pointed out that as seen in Figure 7, Al-matrix composites containing Al_3Ti show reasonably high tensile strength and relatively high ductility when Ti content is around 25%. Because some ductility improvement is obtained by modification of the crystal structure of Al_3Ti from $D0_{22}$ to $L1_2$ by ternary additions [9-11], such elemental additions also could improve ductility and strength in this case.

Summary

The low-pressure casting/combustion synthesis (LCCS) process was proposed to fabricate near-net-shape metal-matrix composites (MMCs), where combined effects occurring during these two processes were utilized. Near-net-shape Al_3Ti-reinforced Ti-matrix composite was produced without cavities by the LCCS process. It is found that molten Al substantially infiltrated into a mixture of Al and Ti powders when the mixture ratio of Al to Ti was high, or a mixture of Al and Ti powders contained more than 50 at. % Al. In the case when the mixture ratio was low, or a mixture of Al and Ti powders contained less than 50 at. % Al, infiltration by molten Al became unsubstantial. A critical mixture ratio of Ti powder to Al powder was estimated by using a simple formula expressed by the relative density of Al and Ti powder mixtures to produce MMCs. When the powder ratio of Ti to Al was higher than the critical value, the volume fraction of Al_3Ti decreased with increasing content of Ti powder. With increasing Al_3Ti in MMC, the tensile strength of composites was improved at the expense of their ductility.

References

[1] Y. Nishizawa, t. Miyashita, S. Isobe and T. Noda; High temperature Aluminides and Intermetallics, eds.S. H. Wang, C. T. Liu, D. P. Pope and J. O. Stiegler,(Warrendale, PA: The Metallurgical Society, (1990),557-584.

[2] M. C. Flemings; Advanced materials and Processes, 145 (1) (1994), 22-24

[3] D. E. Alman and N. S. Stoloff;Intl. J. Powder Metallurgy, 27(1991), 29-41.
[4] D. E. Alman and N. S. Stoloff; Scripta Metallugia et Materialia, 28(1993), 1525-1530.
[5] D. E. Alman, J. A. Hawk, A. V. Petty, Jr., and J. C. Rawers; Journal of Metals, 46(1994), 31-35.
[6] K. Kubo, I. Ohnaka, T. Fukusako and K. Mizuuchi;Imono, 53(1981), 627-634.
[7] K. Kubo, I. Ohnaka, T. Fukusako and K. Mizuuchi;Imono, 55(1983), 362-368.
[8] K. Kubo, K.Mizuuchi, I. Ohnaka and T. Fukusako;Proc. 50th Intl. Foundry Congress, 6(1983),1-12.
[9] H. R. P. Inoue, C. V. Cooper, L. H. Favrow, Y. Hamada and C. M. Wayman;Mat. Rec. Soc. Symp. Proc.,213(1991), 493.
[10] H. R. P. Inoue, M. Kitamura, C. M. Wayman and H. Chen;Philos. Mag. letters,63(1991), 345.
[11] K. Mizuuchi, Y. Okanda, M. Kitamura, C. V. Cooper, A. F. Giamei and H. R. P. Inoue;Mat. Res. Soc. Symp. Proc. vol.288(1993)1191-1196.

ANALYSIS OF BINDERS AND BINDER BURNOUT IN TAPE CAST Ti/SiC MMCs

C. M. Lobley and Z. X. Guo,

Department of Materials, Queen Mary and Westfield College, University of London,
Mile End Road, London, E1 4NS, UK

Abstract

In addition to various technical obstacles, current manufacturing processes for SiC fibre-reinforced titanium are largely hindered by high cost. Tape casting is a cost-effective processing route involving the manufacture of powder tapes held together by a polymeric binder. The roles of the binder are discussed here. The additional requirement is that it should be efficiently removed prior to full consolidation of the composite, in a stage known as burnout. Study of various potential binders using mass spectrometry yields ideal dwell temperatures for the burnout, and reveals the complexity of the burnout process for all the binders investigated.

The Third Pacific Rim International Conference on
Advanced Materials and Processing (PRICM 3)
Edited by M.A. Imam, R. DeNale, S. Hanada,
Z. Zhong and D.N. Lee
The Minerals, Metals & Materials Society, 1998

1. Introduction

Titanium-based continuous SiC fibre composites possess high specific strength and modulus at temperatures up to 800°C, making them ideal for a variety of applications, notably in the aerospace industry.

Foil-Fibre-Foil (FFF), Vacuum Plasma Spraying (VPS) and Physical Vapour Deposition (PVD) are current manufacturing routes used to produce the material[1]. Control of the fibre distribution and the complexity in the manufacture of useful component shapes are difficulties associated with the FFF route[2]. The PVD process coats each fibre precisely and ensures fibre distribution, but is relatively slow, requiring long processing times. The VPS process deposits molten matrix material on the fibres, which can cause thermal shock and fibre damage[3] ultimately leading to degraded mechanical properties. In addition to various technical disadvantages, these techniques are also expensive.

Tape casting (TC) has been used mainly in the ceramics industry for the production of thin, flat sheets[4]. The composite manufacture procedure developed is shown in *Fig. 1*, and has been described in detail elsewhere[5]. Basically, titanium powder is mixed with various organic components in a solvent; binders hold the powder together, and plasticisers allow manipulation of the dried tape. The resulting slurry is then cast to form a uniform tape. After drying, the tapes are shaped and laid-up with filament-wound SiC fibre mats held together with binder. Finally the lay-up is consolidated into a fully dense composite using a vacuum hot press. During consolidation, a hold at moderate temperature under vacuum is employed to remove the remaining organics; this is known as the burnout stage.

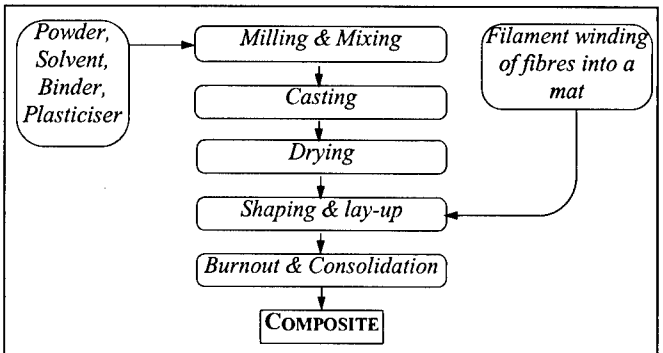


Figure 1: The Tape Casting route to Ti/SiC_f MMC manufacture

In addition to much reduced costs, the casting operation is relatively simple and easy to control and is carried out at room temperature. Fibre management during consolidation is achieved by powder particles occupying inter-fibre spaces.

The technique has been successfully applied to SiC-reinforced glass matrix[6], but with the exception of a patent[7], little has been published on the experimental study of titanium-based composites. Hence the objective of this work is to investigate whether tape casting can be developed as a cost-effective method of producing high quality Ti-based continuous fibre composites. The binder is one of the crucial elements of the procedure and carries out a number of roles, therefore finding the best binder to fit all the requirements is of great importance.

2. The Slurry

The binder system must be able to form a thixotropic slurry with the solvent and powder components. This allows the slurry to flow evenly under the blade when cast, but causes it to remain static on the substrate during the removal of the solvent. The binder must be strong enough to hold the powder particles together during the removal of the tape from the substrate. It must also be added in minimum quantity to ensure a practical volume fraction of powder in the tape. Most importantly it should readily decompose into gaseous species at intermediate temperatures and be removed completely under vacuum.

Commercial ceramic tape casting utilises an additional slurry component to disperse the powders and stabilise the slurry. Some binders possess a stabilising quality[8] which is advantageous in limiting the number of slurry components. To simplify the slurry system is beneficial, as it is necessary that all the organic components be removed in the burnout stage, and if there are fewer components to remove then the process is more efficient. Furthermore, there is some evidence to suggest that dispersants leave contamination upon burnout[9], it is logical therefore to use a binder which also exhibits stabilising properties, to allow a separate dispersant component to be omitted.

The polymeric binder system has to lead to the formation of a strong, flexible tape. The latter characteristic is related to the polymer crystalinity after casting. A plasticiser may be used to reduce cross-linking in the binder, lowering the T_g and therefore increasing flexibility, but although this practice is common, it does introduce another separate component to the slurry which needs removal prior to full consolidation. By choosing a binder polymer which is amorphous at room temperature, the need for a separate plasticiser is removed, thus the slurry and the burnout are simpler.

The solvents used in the slurry often call for special precautions in terms of health and safety. The use of a binder which is soluble in water would reduce both the cost and the safety requirements. Aqueous ceramic tape casting slurries have been studied and found to be very sensitive to processing changes[10], but whether this is the case for metallic powder is not known.

It is clear that the binder system can be responsible for many features of the casting process. However, its presence is only temporary, and its removal has to be as clean and efficient as possible, to prevent contamination by residuals. In the case of titanium composites, any carbon left behind will probably react with the matrix to form brittle TiC, which may severely degrade the mechanical properties.

3. Binder Burnout

To examine the thermal degradation of organics within a powder tape, pyrolysis mass spectrometry was carried in a Kratos MS-50RF analyser. Slurry was mixed for 1 hour in a planetary ball mill, and then tapes of 150μm thickness were cast with a speed of 25cm/s. Four different slurries, shown in *Table I*, were mixed using 20g titanium powder, where PVB is poly(vinyl butyral), PMMA is poly(methyl methacrylate), PIB is poly(isobutylene), MC is methyl cellulose, BBP is benzyl butyl phthalate and MEK is methyl ethyl ketone. Pieces of dried tape were loaded into the analyser and subjected to a thermal gradient from room temperature to 700° under a vacuum of 10^{-7} Torr.

Table I: Slurry compositions

Binder	Plasticiser	Solvent
1.2g PVB	0.6g BBP	13.2g MEK, 6.8g ethanol
1.2g PMMA	1.0g BBP	19.8g MEK, 10.2g ethanol
1.2g PIB	-	40g cyclohexane
1.0g MC	-	60g water

Reports showing ion count against temperature have revealed the temperatures at which the binders degraded, and the profile of the peaks suggest the complexity of the degradation, see *Fig. 2*. Mass spectra taken at the maximum point of ion detection, show the species detected (in terms of mass:charge ratio m/z) and their relative abundances (given as a percentage of the most abundant), see *Fig. 3*.

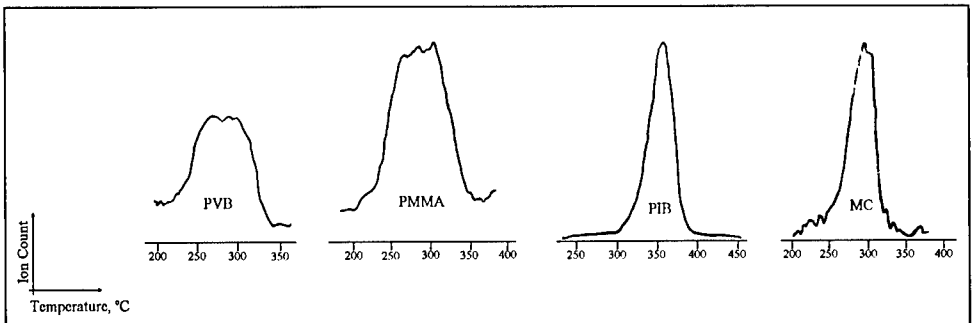


Figure 2: Binder ion count profiles from the mass spectrometry on titanium powder tape

Comparison of the profiles on the ion count reports, suggest the complexity of the degradation process, with a sharp well-defined peak suggesting a quick, simple degradation and a more flattened peak suggesting a more complicated process. The mass spectra give the total number of species detected and also the number of major species for each powder tape. The results are shown on *Table II* with the ideal hold temperature for a typical composite consolidation cycle.

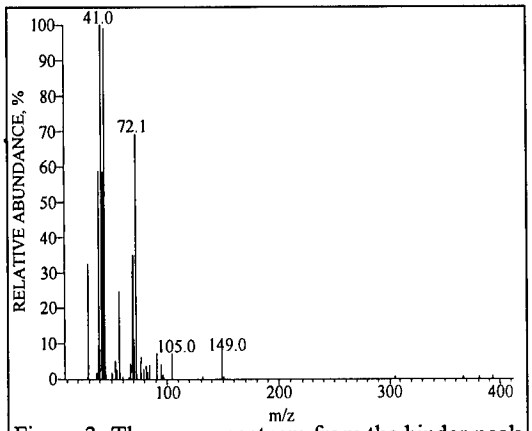


Figure 3: The mass spectrum from the binder peak of the PVB tape

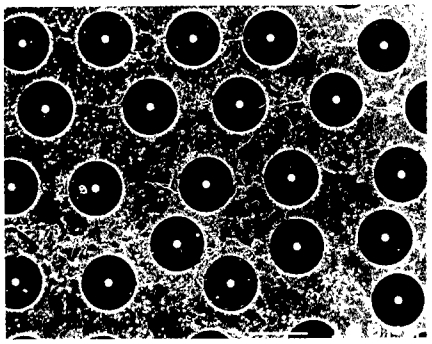


Figure 4: Ti/SiC composite produced by tape casting, consolidated at 900°C, 45MPa for 1 hour

The PVB system is a copolymer, which may be one reason for the complicated ion count profile, but PMMA is well-known for its relatively simple thermal degradation characteristics, yielding 100% monomer. Evidence here suggests that the degradation is altered by the presence of other components, with 12 separate species produced, and monomer yield only 50%. There may be residual solvent trapped in the tape, but this is thought to be low in quantity. Although the BBP plasticiser was removed at 135°C, its removal may not be complete and it is possible that interactions with the degrading binder may cause complications[11]. One other explanation may be that the titanium, in the high-surface-area powder form, is influencing the degradation and causing it to be altered, by reacting with the gaseous products before they can escape from the porous body.

Table II: Results from burnout analysis by pyrolysis mass spectrometry

Binder	Ideal dwell temp	Number of species >50%RA	Total number of species	Ion count profile
Poly(vinyl butyral)	256°C	5	24	complex
Poly(methyl methacrylate)	255°C	3	12	complex
Poly(isobutylene)	346°C	4	24	simple
Methyl Cellulose	280°C	1	32	simple

The other two - unplasticised - binders, PIB and MC, both seemed much simpler according to the ion count profiles. Although large numbers of species were detected, their evolution was carried out quickly and, for MC, at lower temperatures with only one major species.

By comparison with tests performed for pure binder, and with literature detailing the thermal degradation of these polymers, it seems clear that the process is complicated by the presence of other components. Minimising the total number of slurry components reduces the number of potential interactions, and also the raw materials cost. Ideal dwell temperatures have been determined to maximise organics removal and therefore optimise the burnout stage, with the dwell time dependent presumably upon the size of the component, the powder size and morphology and the fibre volume fraction. It is desired for the dwell to be carried out at a temperature high enough for degraded binder species to evolve, but low enough to avoid reactions between evolved species and the titanium powder. The presence of continuous reinforcement is thought to provide extra channels for the gaseous species to escape.

Specimens produced so far have shown fairly regular fibre spacing with no apparent fibre damage, and no visual signs of contamination, see *Fig. 4*.

4. Conclusions

It has been explained that the binder is a critical component in the slurry formulation and can undertake a number of roles, yet it must be efficiently removed prior to full consolidation, leaving no contamination.

Binder burnout investigation has been conducted on four viable systems. It has been identified that the PVB and PMMA tapes, both containing plasticiser, exhibit a complex burnout, probably due to interactions with other slurry components. More simple burnout behaviour was observed for PIB and MC tapes, where no plasticiser and only one solvent was used.

Further study will analyse the amount of carbon remaining subsequent to burnout, using combustion analysis and high resolution TEM. Quantification of the stabilising properties for the various binder systems will also be undertaken. Finally, mechanical tests of the resulting composite and comparison with results from material by other routes, are hoped to validate the tape casting route as a low-cost fabrication technique for high-quality composites.

Acknowledgements

The authors gratefully acknowledge the support of the EPSRC and the Structural Materials Centre at DERA Farnborough, UK.

References

[1] Z.X. Guo and B. Derby, "Solid-State Fabrication and Interfaces of Fibre-reinforced Metal Matrix Composites," Progress in Materials Science, 39 (4/5) (1995), 411-455.

[2]C.M. Ward-Close and J.G. Robertson, "Advances in the Fabrication of Titanium Based Composites," Advanced Performance Materials, 1996, no. 3:251-262.

[3] A.M. Baker et al., "Characterisation of Sigma SiC Fibre/Titanium Alloy MMCs Fabricated by Plasma Spraying and Foil/Fibre Methods," Synthesis/Processing of Lightweight Metallic Materials II, ed. C.M. Ward-Close et al., (Warrendale, PA: TMS, 1997), 207-218.

[4] R.E. Mistler, D.J. Shanefield, and R.B. Runk, "Tape Casting of Ceramics," Ceramic Processing Before Firing, ed. G.Y. Onoda Jr and L.L. Hench (New York, NY: J. Wiley and Sons, 1978), 411-448.

[5] C.M. Lobley and Z.X. Guo, submitted to Materials Science and Technology.

[6] C.M. Gustafson, R.E. Dutton, and R. Kerans, "Fabrication of Glass Matrix Composites by Tape Casting," Journal of the American Ceramic Society, 78 (5) (1995), 1423-24.

[7]W.G. Truckner and J.F. Edd, "Tape Casting Fiber Reinforced Composite Structures," US Patent, no. 5 405 571, 11 April 1995.

[8] M.D. Sacks and G.W. Scheiffele, "Polymer Adsorption and Particulate Dispersion in Nonaqueous Al_2O_3 Suspensions Containing Poly(vinyl butyral) Resins," Advances in Ceramics, 19 (1986), 175-184.

[9] S. Bhattacharjee, M.K. Paria, and H.S. Maiti, "PVB as a Dispersant for $BaTiO_3$ in a Non-Aqueous Suspension," Journal of Materials Science, 28 (1993), 6490-6495.

[10] P. Nahass et al., "A Comparison of Aqueous and Non-Aqueous Slurries for Tape-casting, and Dimensional Stability in Green Tapes," Ceramic Transactions, 15 (1990), 355-364.

[11] H. Yan, W.R. Cannon, and D.J. Shanefield, "Poly(vinyl butyral) Pyrolysis: Interactions with Plasticiser and AlN Ceramic Powder," Materials Research Society Symposium Proceedings, 249 (1992), 377-382.

INTERFACES IN A COATED GRAPHITE / MAGNESIUM COMPOSITE

Jing Zhu[1,2,3], Feng Wu[2] and G.D.Zhang[3]

[1] School of Mat. Sci. & Eng., Tsinghua University, Beijing 100084, P.R.China
[2] Central Iron and Steel Research Institute, Beijing 100081, P.R.China
[3] State Key Lab. of MMCs, Shanghai Jiao Tong Univ., Shanghai 200030, P.R.China

Abstract

The coated graphite fibers are incorporated into magnesium alloy matrix to form a graphite-magnesium composite by pressure infiltration casting. The composite exhibits good bonding between the fibers and matrix. The interfaces between the coated graphite and magnesium show a multiple layer microstructure. An amorphous SiC coating was detected on the surfaces of the graphite fibers. The MgO grains were found, they are of two kinds of shapes, some of them are fine MgO grains that exist in the area between the coating and matrix, and other MgO platelets insert into the matrix. The oxygen at the interface comes from the oxidation of the coating, and MgO is the outcome of the chemical reaction between the molten magnesium and Si_2O on the surface of the coating. There is a γ-$Mg_{17}Al_{12}$ phase close to MgO in some area of the interface, no obvious boundary can be seen between the two phases. MgO is beneficial to the bonding of the interface in the composite due to good compatibility between the coating, MgO and Matrix. The observation and examination are carried out by using an analytical field emission gun electron microscope JEM 2010F with nanometer scale.

The Third Pacific Rim International Conference on
Advanced Materials and Processing (PRICM 3)
Edited by M.A. Imam, R. DeNale, S. Hanada,
Z. Zhong and D.N. Lee
The Minerals, Metals & Materials Society, 1998

Introduction

Graphite-magnesium metal matrix composites (MMCs) are of great technological interests for application in space structures because of their special strength, stiffness and the possibility of tailoring them in order to have a zero coefficient of expansion. The primary difficulty of fabricating these materials is that the molten metal does not wet or bond to graphite fibers[1], and then it is impossible to achieve a load transfer from the matrix to the graphite fibers. To overcome this problem, the fibers are usually coated with a material that can be wetted by molten metal[2-4]. A good coating material should be good compatible with the reinforcement and matrix in physical and mechanical properties.

In this work, coated graphite fibers are incorporated into magnesium alloy matrix to form a graphite-magnesium composite by pressure infiltration casting. The composite exhibits good bonding between the fibers and matrix. It is thought the coating had played an important role. The changes in chemical composition and structure at the interfaces of the composite have been studied in order to understand the effect of the coating on the composite.

Material and Experimental Conditions

Magnesium alloy reinforced with graphite fiber that had coated in liquid silicon was produced using vacuum pressure infiltration casting. The preheating temperature of the fiber (perform) is 660°C and the temperature of the melt is 730°C.

The interface in the composite was observed in a JEOL 2000FX electron microscope and a JEM 2010F field emission gun electron microscope, the micro-analysis and micro-diffraction were carried out by using a probe with 0.8 nm in diameter.

Results and Analysis

The composite exhibits a good bonding between fiber and matrix. Observed in the lower magnification mode, the interface is clear and smooth as shown in Fig.1. Only a few particles are distributed nearby the interface. The particles were analyzed to be $Mg_{17}Al_{12}$[5-7] in previous work. Some needle-like phases were found growing from the coated fiber to the matrix.

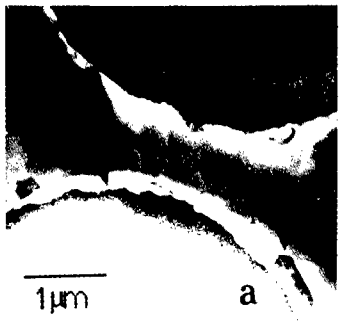


Fig.1 A morphology of the coated graphite / magnesium composite.

Figs.2-4 show a high resolution image of the interface, the diffraction patterns and the EDS spectrums corresponding to the different areas of the interface. The upper right insert of Fig.2 indicates the location of the Fig.2 under low magnification image. On the surface of the graphite fiber there is a coating layer, it distributes homogeneously with about 20 nm thick. By micro-diffraction and chemical micro-analysis, the coating layer was identified as an amorphous SiC layer.

Some small grains are observed closely distributing on the surface of the coating. From the EDS, the oxygen was found only at the interface between the coating and matrix, that is the area where the small grains exits. The micro-diffraction pattern from one of the grains was analyzed and shown that these grains are MgO. It suggests that the segregated oxygen exists at the interface in a chemical bonding way.

In Fig.2, the plate-like image including about 10 fringes marked $(111)_{MgO}$ is the magnified needle-like phase in Fig.1. From the fringe image and its diffraction pattern as well as EDS results, the phase was identified as MgO also. Those oxides are platelets and the parallel arraying crystal planes are the close packed planes (111) of MgO. Growing of the oxide is fast in the direction parallel to the close packed planes, and slow in the direction vertical to the close packed planes. Obviously, the growing mechanism is step growth. Many screw dislocations were observed in the platelet, and some of them were marked with arrows in Fig.2. The screw dislocations as growing steps enhance the growing speed in the direction vertical to the close packed planes. It can be seen that the platelets array perfectly near the matrix and become disordered toward to the coating. The ends of the platelets penetrating into the coating change gradually in direction and connect discontinuously with small oxide magnesium grains.

The matrix is outside the MgO and consisted of only magnesium grains. There is no any small crystalline magnesium grain observed in the matrix nearby the interface between MgO and coating layer. It implies that there is no any magnesium grain or other than MgO magnesium oxide nucleated on the surface of the coated fiber. It is interesting that one could not find matrix joining the coating directly, they are separated by MgO.

There is a $Mg_{17}Al_{12}$ phase at the interface as marked in Fig.2. The fringe spacing is about 0.73 nm, that is equal to the spacing of (011), the close packed plane of $Mg_{17}Al_{12}$. Then the lattice parameter of $Mg_{17}Al_{12}$ is calculated to be a_0 = 1.03 nm. Some MgO platelets were found growing along the close packed plane of $Mg_{17}Al_{12}$. The close packed planes of MgO(111) and $Mg_{17}Al_{12}$(011) are parallel to each other, their planar spacing ratio is about 1:3. There is no obvious interface between the two phases. The relevant mismatch is about 0.03%.

From the results obtained above, between the amorphous coating layer and matrix, there exist some oxygen. It was thought that the coating absorbed oxygen after it was coated onto the fiber. However, if it true, when the fiber is preheated to about 600°C for composite fabrication, the oxygen should escape from the coating surface. It is possible that the oxygen is then strongly adhered on the coating surface. Henriken and Johnsen [8] reported that they found MgO and Al_2O_3 at the interfaces of SiC whiskers and the aluminum matrix, as a result

of the chemical reactions between the matrix and the thin layer of SiO_2, formed by oxidation, which covered the whiskers. In this work, it is more possible that there exists SiO_2 on the surface of SiC amorphous coating layer. The reason that SiO_2 was not found, could be explained as that the SiO_2 turns into MgO during composite fabrication at 660°C to 730°C. The reaction formula is as following:

$$SiO_2 + 2Mg = 2MgO + Si$$

The outcome silicon did not find. This may be due to the quantity of silicon is not enough for detection. If this reaction occurs between the molten magnesium and the SiO_2, wetting should be achieved. This conclusion was also seen in the magnesium matrix composite reinforced with SiO_2 coated graphite fibers[9]. Another opportunity to introduce oxygen in is probably during fabrication of composite.

The MgO is FCC structure and its lattice parameter is 0.421 nm. The rings in the diffraction pattern from the amorphous coating layer show that the spacings in the real space are very close to the spacings of the planar (111) and (200) of the FCC structure of SiC. The lattice parameter of FCC SiC is 0.439 nm. The difference of atomic size and spacing between the MgO and the SiC is small. From the geometry point of view, MgO is easy to grow on the surface of SiC and there should be less mismatch between the oxide and coating layer.

MgO improves the bonding of the composite not only by the chemical reaction, but also by increasing the mechanical bonding when the platelet's quantity is small and they insert into the matrix. Moreover, when there exists $Mg_{17}Al_{12}$ at an interface, the MgO inserts into the matrix more strongly due to the good bonding between MgO and $Mg_{17}Al_{12}$. However if the quantity of MgO is larger, then the MgO platelets become thicker and shorter, it would be harmful to the composite.

Forming platelet MgO requires more magnesium and oxygen. At the area with less oxygen the formed magnesium oxide is the small grain type. Only when the oxygen concentration increases to a certain number, the magnesium oxide turns into the platelet type. It implies that the concentration of oxygen does not only affect the quantity of MgO but also affects the morphology of the MgO, and that existing of oxygen in a certain quantity is benefit to the interface bonding.

Summary

1. There is a SiC amorphous layer on the surface of the graphite fiber. The amorphous layer has a good bonding with the graphite fiber.

2. MgO was found at the interface between the coating layer and matrix. The MgO may come from the chemical reaction between the molten magnesium and SiO_2 on the surface of the coating layer, or come from the reaction between the molten magnesium and oxygen in environment during fabrication. The MgO are of two types of shapes, one is of small crystalline grain and the another one is of platelet. Both of them play a role to improve the

interface in the composite.

3. One of facet in $Mg_{17}Al_{12}$ is (011) when it exists at an interface. Then the MgO platelet easily grows along the facet.

4. There is a good bonding between the SiC amorphous layer and MgO due to the similar geometry of atomic configuration and spacing.

Acknowledgments

This work was supported by the National Nature Science Foundation of China, the National Advanced Materials Committee of China and the National MMCs Key Lab. of China.

References

1. R.J.Diefendorf, Proceedings-Critical Issues in Materials Technology Workshop on Transverse Strength in Carbon Fiber/Aluminum Composites, ed. R.N.Lee (Naval Surface Weapon Center), 2-43.

2. S. Abraham, B.C. Pai, K.G. Satyanarayana, V.K. Viadyan, "Copper coating on carbon fibres and their composites with aluminium matrix," J. Mater. Sci., 27(1992), 3479-3486.

3. A.P. Diwanji, I.W. Hall, "Fibre and Fibre-surface treatment effects in carbon/aluminium metal matrix composites," J. Mater. Sci., 27(1992), 2093-2100.

4. I.W. Hall, "The interface in carbon-magnesium composites: fibre and matrix effects," J. Mater. Sci., 26(1991), 776-781.

5. Feng Wu, Jing Zhu, Yu Chen and G.D.Zhang, "Microstructure of Interface in C/Mg Metal Matrix Composite", J. of Chinese Electron Microscopy Society, 14(1995), 10-14. (Chinese edition)

6. A.Kleine, H.J.Dudck, and G.Ziegler, Proc. of 4th Eur. Conf. on Composite Materials, vol.2, (London and New York: Elserier Applied Science, 1991), 267-272.

7. S.P.Rawal, and M.Misra, Interface in Polymer, Ceramic and Metal Matrix Composites, ed. H.Ishida, (London and New York: Elserier Science Publishing Co., Inc., 1988), 179-184.

8. B.R. Henriken and T.E. Johnsen, "Influence of microstructure of fibre/matrix interface on mechanical properties of Al/SiC composites," Mater. Sci. Technol., 6(1990), 857-861.

9. H.A. Katzman, "Fibre coating for the fabrication of graphite-reinforced magnesium composites," J. Mater. Sci., 22(1987), 144-148.

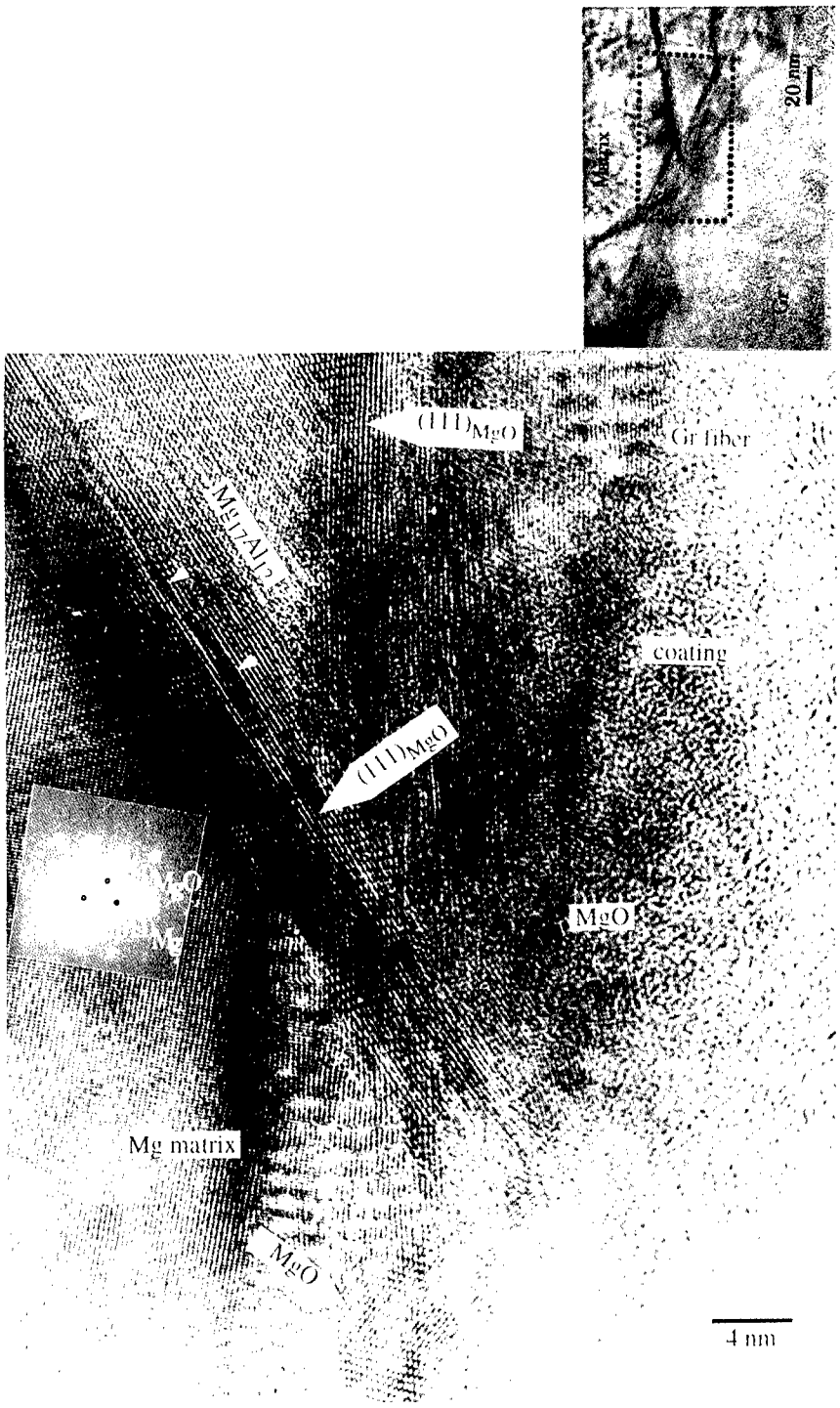


Fig.2 A high resolution image of the coated graphite / magnesium composite.

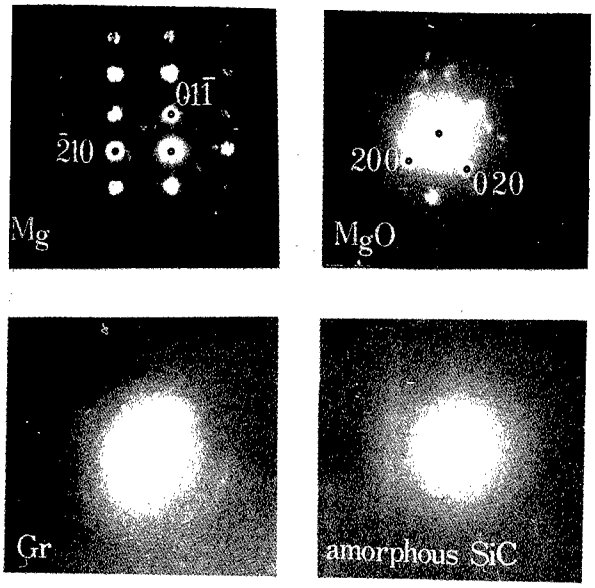


Fig.3 The microdiffraction patterns from each corresponding region in Fig.2.

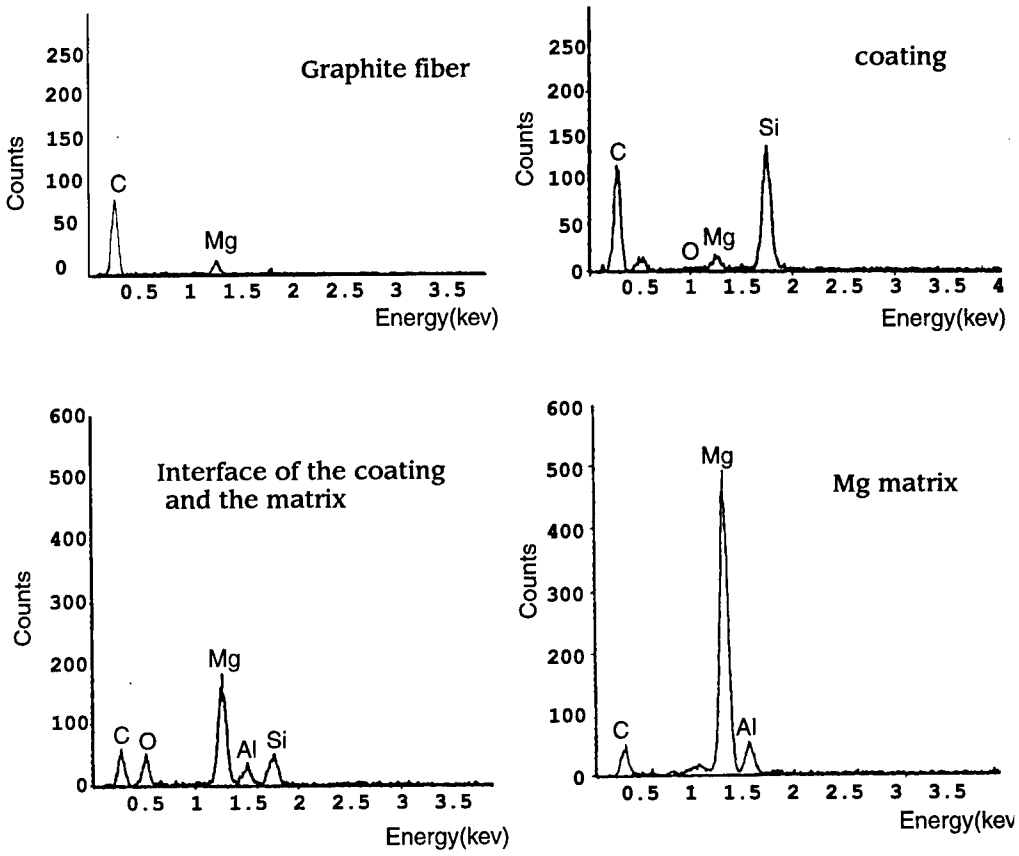


Fig.4 The EDS spectrums from each corresponding region in Fig.2.

FIRST-PRINCIPLES CALCULATIONS OF INTERFACES IN MATERIALS: GRAIN BOUNDARIES IN SiC AND SiC/METAL INTERFACES

Masanori Kohyama and John Hoekstra

Department of Material Physics, Osaka National Research Institute, AIST, 1-8-31, Midorigaoka, Ikeda, Osaka 563, Japan

Abstract

First-principles calculations of materials interfaces such as SiC grain boundaries and SiC/Al interfaces have been performed by using the first-principles molecular dynamics method based on the density-functional theory. For the $\{122\}\Sigma=9$ boundary in SiC, stable configurations of polar and non-polar interfaces contain C-C or Si-Si wrong bonds, which have bond lengths and bond charges rather similar to those in bulk diamond and Si, and generate peculiar localized states. By performing "*ab initio* tensile tests", the intrinsic strength of each interface and the behavior of interfacial fracture have been examined for the first time. Significant effects of wrong bonds have been found. For the SiC(001)/Al interface, the C-terminated and Si-terminated interfaces have been examined in order to clarify the C-Al and Si-Al interactions. Both interfaces have quite different features, such as atomic configurations, bonding nature, bond adhesion and Schottky-barrier height (SBH). However, both interfaces have much larger adhesive energies than non-reactive ceramic/metal interfaces such as the MgO(001)/Al interface. The present dependence of the SBH on the interfacial structure is contrary to previous models for the SBH, although this can be reasonably explained by the large interfacial dipole at the C-terminated interface.

The Third Pacific Rim International Conference on
Advanced Materials and Processing (PRICM 3)
Edited by M.A. Imam, R. DeNale, S. Hanada,
Z. Zhong and D.N. Lee
The Minerals, Metals & Materials Society, 1998

Introduction

Important subjects in the science and technology of materials are often associated with interfaces. Intergranular or interphase boundaries dominate various properties of materials. Interfaces are often associated with novel functions of materials. In electronic devices, it is crucial to control interfaces atomistically. Currently, it is possible to obtain information of interfaces at the atomic and electronic scales by recent techniques of electron microscopy. On the theoretical side, by virtue of the development of the first-principles molecular dynamics (FPMD) method [1], it is possible to perform *ab initio* calculations of interfaces based on the density-functional theory [2]. Such quantitative calculations should contribute greatly to the understanding and design of interfaces.

In this paper, we report our recent *ab initio* calculations of interfaces. First, we deal with a grain boundary in SiC [3,4]. SiC is a very important material for high-performance ceramics and high-temperature devices. There exist complexities such as interface stoichiometry, polar and non-polar interfaces and interfacial C-C or Si-Si wrong bonds in grain boundaries in SiC [5], in contrast to those in Si. We investigate stable configurations. Then we perform "*ab initio* tensile tests", which can reveal basic mechanical properties of interfaces, such as the intrinsic strength and the behavior of interfacial fracture.

Second, we deal with SiC-Al interfaces [4,6]. Ceramic-metal interfaces are very important for structural or electronic applications of ceramics. This is the first *ab initio* calculations of *reactive* ceramic-metal interfaces between covalent solids and metals, in contrast to previous *ab initio* calculations of *non-reactive* interfaces between ionic solids and metals [7]. We examine stable configurations, adhesive energies and electronic properties such as Schottky-barrier height (SBH). SBH is especially important for the electronic applications.

Theoretical Method

Ab initio calculations based on the density-functional theory can predict the energies, structures and basic properties of solids in the ground state within the error less than few percent. Such calculations can be applied to large complex systems by using the FPMD method in the framework of the plane-wave pseudopotential method. We have constructed the computer programs of the FPMD method specialized for interfaces [8]. We use the conjugate-gradient techniques for efficient electronic minimization [9,10] and optimized pseudopotentials [11] to reduce the number of plane-wave basis functions.

Grain Boundaries in SiC

Stable Configurations

We deal with the $\{122\}\Sigma = 9$ boundary in SiC as a typical coincidence tilt boundary. This boundary is considered to be constructed by five- and seven-membered rings without any dangling bonds as the same boundary in Si [5]. Two kinds of polar and one kind of non-polar interfaces are constructed by inverting the polarity of grains. We use 64-atom supercells. Two special $\mathbf{k}$ points and the plane-wave cutoff energy E_{cut} of $60Ry$ are used.

Figs. 1 and 2 show stable configurations. The non-polar interface contains both C-C and Si-Si bonds, and the polar interfaces contain either C-C or Si-Si bonds. C-C and Si-Si bonds have bond lengths and charges similar to those in diamond and Si. In the non-polar

interface, the C-C bond is 3.6% longer than that in diamond. The Si-Si bond is 4.4% shorter than that in Si. The distortions of the other bonds range from -2.9% to +2.9% and from -22.4° to +27.9°. In the N-type interface, the C-C bond is 4.5% longer than that in diamond, and the other distortions range from -2.7% to +2.0% and from -20.1° to +22.5°. In the P-type interface, the Si-Si bond is 1.1% shorter than that in Si, and the other distortions range from -2.7% to +2.5% and from -13.0° to +24.0°.

The boundary energy of the non-polar interface is $1.27J/m^2$. The total energy of a pair of the polar interfaces is slightly lower than that of the non-polar interfaces by about 0.1eV per supercell.

These interfaces have clear band gaps. This feature as well as the bond distortions indicates that all the bonds are well reconstructed. However, C-C bonds generate localized states at the top and bottom of the valence band. The C-C bond states at the valence-band top exist at $0.3eV$ (non-polar) and $0.5eV$ (N-type polar) above the bulk valence-band top. The origin of these states can be explained by the analogy to a diamond cluster embedded in SiC. The width of the valence band of diamond is very much larger, which should cause electronic states above and/or below the bulk valence-band edges of SiC.

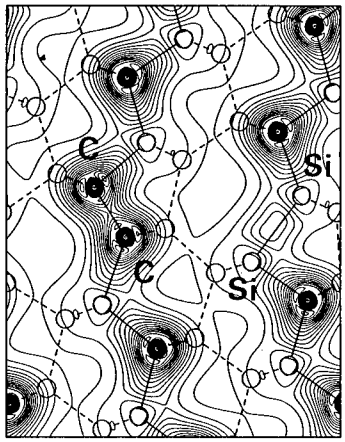
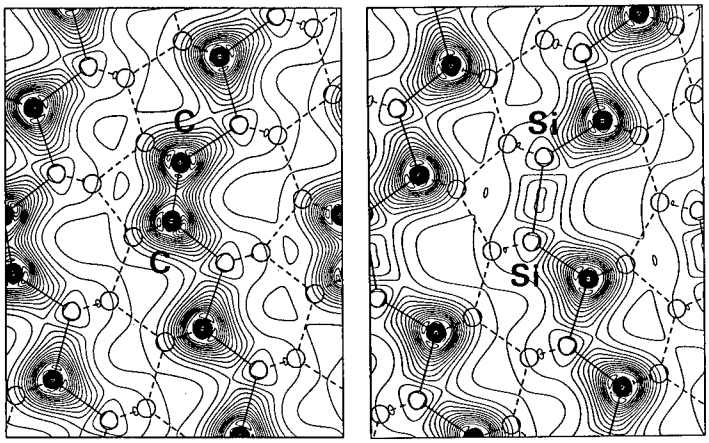


Figure 1. Relaxed configuration of the non-polar interface of the $\Sigma = 9$ boundary in SiC. Contours of the valence electron density are plotted from $0.015a.u.^{-3}$ to $0.295a.u.^{-3}$ in spacing of $0.020a.u.^{-3}$.

Figure 2. Relaxed configurations of the N-type polar (left) and P-type polar (right) interfaces. Circles indicate atomic positions. Solid lines indicate bonds on the (011) plane on which the charge density is plotted.



Ab Initio Tensile Tests

In the *ab initio* tensile tests, uniaxial tensile strain normal to the interface is introduced into the above stable configurations. First, the cell is stretched in a small increment, and the atomic positions are changed by uniform scaling. Second, all the atoms are relaxed, and the total energy and stress tensor are calculated. This cycle is iterated until the interfaces are broken. This procedure corresponds to real tensile tests at T=0K [12].

Fig. 3 shows the results of the non-polar interface. The interface starts to break at the strain of 12%, where the averaged tensile stress is 41.5GPa. This interface is rather strong because of reconstruction. Note that the present system contains no defects other than the interface. This situation is quite different from real materials, although this makes it possible to examine the intrinsic strength of the interface.

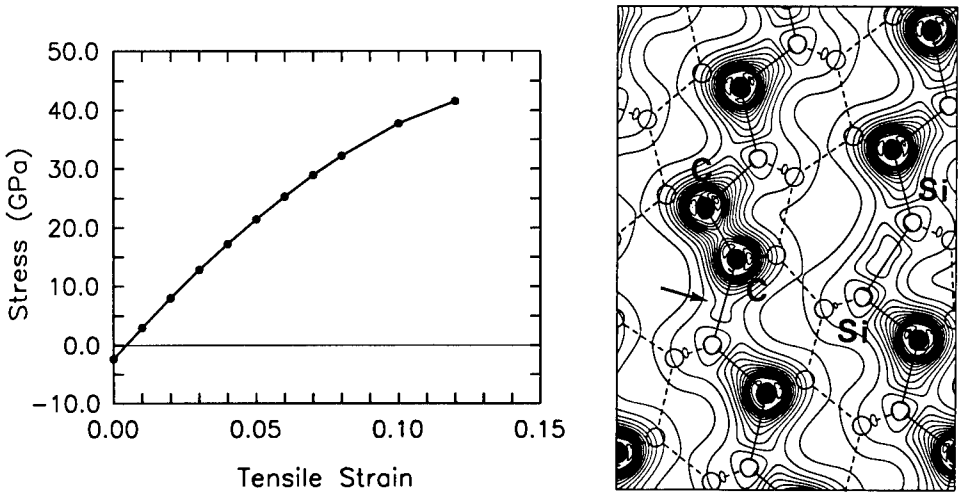


Figure 3. Left: Stress-strain curve of the non-polar interface of the $\Sigma = 9$ boundary in SiC by the *ab initio* tensile test. Right: Relaxed configuration at a tensile strain of 12%. The back bond of the C-C bond indicated by an arrow is almost broken.

The back bonds of the C-C bonds are broken first at the strain of 12%. This can be seen from the bond charge in Fig. 3. This is because the C-C bond has short bond length and large strength. At the strain of 10%, the bond-length distortions of the C-C bond and the back bond are +7.0% and +19.4% against the bond lengths of bulk diamond and SiC, respectively. At the strain of 12%, the back bond is stretched into +27.8%, while the C-C bond shrinks into +6.4%. After this point, other interfacial bonds start to be broken.

SiC-Metal Interfaces

Stable Configurations

We deal with the SiC(001)/Al (1x1) interface. In preliminary calculations of the SiC(110)/Al interface [8], we found the strong C-Al interaction. For the SiC(001)/Al interface, the C-Al and Si-Al interactions can be clarified by examining both C-terminated and Si-terminated interfaces. The supercell contains a slab of 9 SiC(001) layers with 5 Al(001) layers stacked on both surfaces. Two free Al surfaces separated by a vacuum region ensure stable interlayer distances without any constraint. We use E_{cut} of $45Ry$ and 10 special $\mathbf{k}$ points.

Fig. 4 shows the stable configurations. In the C-terminated interface, the interfacial C atoms are three-fold coordinated. The C-Al bond length is similar to the back C-Si bond length. The charge density is pulled from the Al atom toward the C atom. This charge transfer is also clear in Fig. 5(a), where a charge depletion region exists near the interfacial Al atom. In the Si-terminated interface, the interfacial Si atoms are four-fold coordinated. The Si-Al bond length is much larger than the C-Al bond length. The charge density is rather broadly distributed. In Fig. 5(b), only a shallow depletion region is present.

Fig. 6 shows the local densities of states (LDOS). For the C-terminated interface, the LDOS curves at the interface and at the back Si-C bonds are substantially different from the bulk regions. This indicates that the back Si-C bonds and the interface have peculiar electronic structure caused by the three-fold coordination. For the Si-terminated interface, the LDOS at the interface region has an appearance similar to that of the metallic Al region. This suggests a more metallic nature of the Si-Al bond, as well as the broad charge distribution.

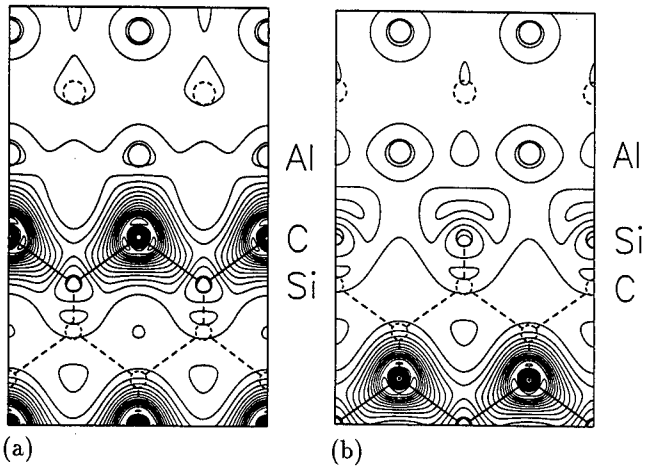


Figure 4. Stable configurations of the SiC(001)/Al interface. (a) $(1\bar{1}0)$ cross section of the C-terminated interface, and (b) (110) cross section of the Si-terminated interface. Contours of the valence electron density are plotted from $0.01 a.u.^{-3}$ to $0.29 a.u.^{-3}$ in spacing of $0.02 a.u.^{-3}$.

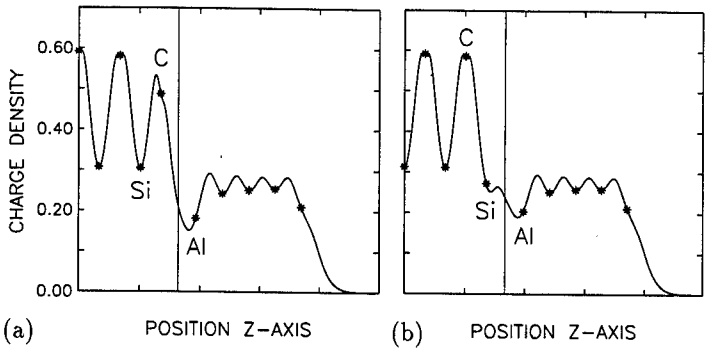


Figure 5. Charge density averaged on each (001) plane in the supercell plotted along the ⟨001⟩ axis. Asterisks indicate atomic positions. (a) The C-terminated interface and (b) the Si-terminated interface.

The adhesive energy is $6.42 J/m^2$ for the C-terminated interface, and $3.74 J/m^2$ for the Si-terminated one. The C-Al bond with covalent and ionic characters is twice as strong as the Si-Al bond with more metallic characters. However, both values are much larger than the values for *non-reactive* ceramic/metal interfaces, for example, $1.10 J/m^2$ for the MgO(001)/Al interface [7]. This confirms the hypothesis that *reactive* interfaces should have much larger adhesive energies than *non-reactive* ones. The present values are also larger than the adhesive energy of two Al(001) surfaces, $2.04 J/m^2$ [7].

Schottky-Barrier Height

The SBH can be calculated as the difference between the Fermi level of the supercell and the valence-band top in the bulk SiC region of the supercell, which corresponds to the SBH for p-type samples. For the C-terminated interface, the SBH is $0.08 eV$, and for the Si-terminated one, $0.85 eV$. The latter is in good agreement with the experimental value, $0.9 eV$, for the Si-terminated interface [13]. The dramatically smaller SBH of the C-terminated interface

can be explained by the interface dipole caused by the charge transfer from the Al layer to the C layer as shown in Fig. 5(a). The present dependence of the SBH on the interfacial structure is contrary to previous models for the SBH. However, this is consistent with recent experiments and *ab initio* calculations of other semiconductor-metal interfaces.

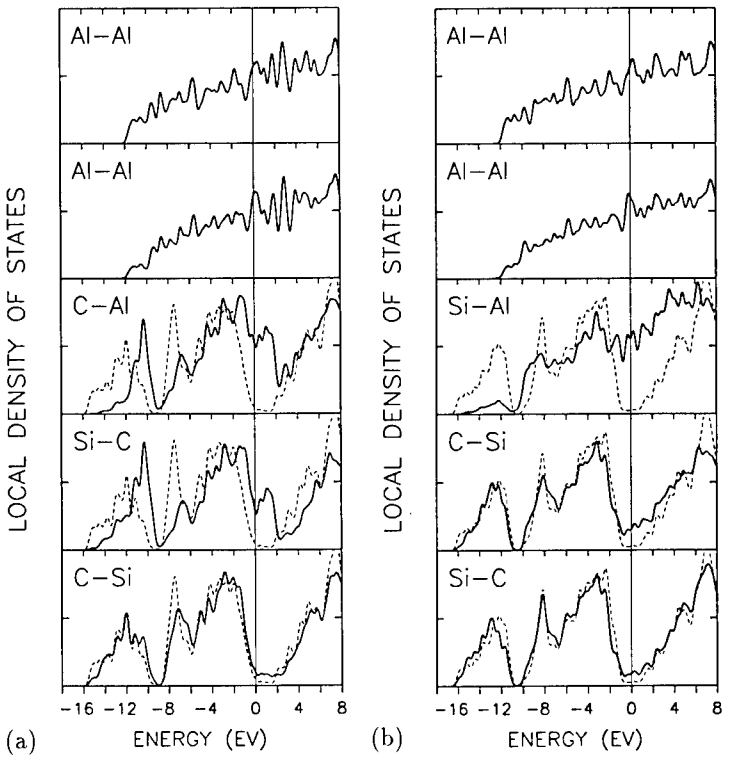


Figure 6. Local densities of states of the SiC(001)/Al interface. (a) The C-terminated interface and (b) the Si-terminated interface. LDOS curves are calculated for each region between successive (001) atomic layers in each supercell. Broken lines indicate the LDOS of the bulk SiC region in each supercell. Vertical lines indicate the Fermi level of each supercell.

In conclusion, the present kind of theoretical calculatons are promising tools for the understanding and design of materials interfaces.

References

[1] R. Car and M. Parrinello, *Phys. Rev. Lett.*, **55**(1985), 2471-2474.

[2] P. Hohenberg and W. Kohn, *Phys. Rev.*, **136**(1964), B864-B871; W. Kohn and J.L. Sham, *Phys. Rev.*, **140**(1965), A1133-A1138.

[3] M. Kohyama, submitted to *Phys. Rev. B.*

[4] M. Kohyama and J. Hoekstra, to appear in *Computer-Aided Design of High-Temperature Materials*, ed. A. Pechenik, R.K. Kalia and P. Vashishta (Oxford, 1998).

[5] M. Kohyama, S. Kose and R. Yamamoto, *J. Phys. Condens. Matter*, **3**(1991), 7555-7573.

[6] J.Hoekstra and M. Kohyama, *Phys. Rev. B.* (in press).

[7] J.R. Smith, T. Hong and D.J. Srolovitz, *Phys. Rev. Lett.*, **72**(1994), 4021-4024.

[8] M. Kohyama, *Modelling Simul. Mater. Sci. Eng.*, **4**(1996), 397-408.

[9] M.C. Payne *et al.*, *Rev. Mod. Phys.*, **64**(1992), 1045-1097.

[10] D.M. Bylander, L. Kleinman, and S. Lee, *Phys. Rev. B*, **42**(1990), 1394-1403.

[11] N. Troullier and J.L. Martins, *Phys. Rev. B*, **43**(1991), 1993-2006.

[12] V.B. Deyirmenjian *et al.*, *Phys. Rev. B*, **52**(1995), 15191-15207.

[13] V.M. Bermudez, *J. Appl. Phys.*, **63**(1988), 4951-4959.

MATERIALS CHARACTERIZATION OF POLYSTYRENE/TIN AND POLYPROPYLENE /ALUMINUM MECHANICAL ALLOYS

W.J.D. Shaw, M.A. Fraser and H.J. Danilkewich

Department of Mechanical Engineering
The University of Calgary
Calgary, Alberta, Canada T2N 1N4

Abstract

Mechanical Alloying has successfully been applied to polymer/polymer alloys as well as polymer/ceramic and more recently to polymer/metallic materials. In this work two polymer/metal alloys were synthesized, these being polystyrene/tin and polypropylene/ aluminum. This study was conducted in order to gain further understanding of interactions between polymers and metals when mechanical alloys are formed. Some mechanical properties were measured and related to the structures formed for these particular materials. Material characterization takes a form of Scanning Electron Microscopy, SEM, and more quantitative analytical techniques such as Fourier Transformation Infrared, FTIR, as well as X-ray Diffraction, XRD. These techniques help to identify the preferential bonding sites of the metals as they attach themselves onto the polymer structures. In addition to the alloy combination, individual batches of the base polymer materials are also compared. This work is one step in helping to lay down a more fundamental understanding of the mechanical alloying technique as applied to polymer materials and in particular to the interaction of metals with polymers in the formation of a new class of alloys.

The Third Pacific Rim International Conference on
Advanced Materials and Processing (PRICM 3)
Edited by M.A. Imam, R. DeNale, S. Hanada,
Z. Zhong and D.N. Lee
The Minerals, Metals & Materials Society, 1998

Introduction

Application of the mechanical alloying technique to polymers is a relatively new phenomena. Reporting of the first work in this area was made using single polymer materials [1,2], which was shortly followed by polymer/polymer alloys [3,4]. Considerable ground work has been laid down in a start towards gaining an understanding of polymer/polymer mechanical alloys [5-8]. A program was also extended to examining in a preliminary way the formation of a polymer/ceramic mechanical alloy [9]. Our initial studies in the polymer/metal area have to date resulted in a thesis [10] and one other publication [11]. The work contained herein is an extension of these initial studies. Currently other researchers are also starting to investigate polymer/metal interactions [12,13] using the mechanical alloying technique.

The use of the mechanical alloying technique as extended to polymers results in a number of unexpected reactions. First the material does not degradate even though the chains are broken during the grinding process, this is because the energy present allows re-bonding of the chains during consolidation. In fact some combinations have been found to give increases in molecular weight after consolidation. Second the material stores a large amount of internal energy and is highly reactive, which results in low temperature consolidation and in bond formation with other constituents. Third the ease of bond formation between normally incompatible polymers allows alloying without the use of compatibilizers or any presently known restrictions. Fourth incompatible polymers when formed into alloys do not separate or breakdown when heated above their melting point temperatures as would be expected based upon the behaviour of mechanically alloyed metals. Fifth when ceramics are added, organo-ceramics are formed and when metals are added, organo-metallic form. These interactions open up tremendous possibilities of alloy synthesis based upon utilization of polymers as the base material. Thus nearly unlimited permutations of polymer/polymer, polymer/ceramic, polymer/metal and polymer/ceramic/metal alloys can be developed. Towards achievement of these truly engineered materials of the future a small step in the foundations is laid down in the polymer/metal alloy area within the work of this paper.

Experimental

The materials used in this study were polystyrene, PS, of reactor grade pellets being 2 mm in diameter, polypropylene, PP, being 3.5 mm in diameter, the tin being 20 μm in diameter and the aluminum being 3 μm in diameter. The materials were mixed on a weight basis such that both PS/Sn and PP/Al were combined as 70% polymer to 30% metal.

Processing of the material was carried out using a shaker ball mill capable of producing 12 g's of acceleration. The amount of material processed was approximately 300 g for one batch. Processing was carried out under either air or argon environment. The material being processed was cooled using an external heat exchanger with a controlled flow of liquid nitrogen as the cooling media. The temperature was set below the glass transition temperature of the PS or PP. The PS/Sn was processed at -50 °C while the PP/Al was processed at -160 °C. Mechanical milling was conducted for a period of 24 hours for PS/Sn and 16 hours for PP/Al, at the end of this time the powder was collected and transferred to a hydraulic press with a split furnace. The confined area in the press containing the powder material was evacuated under rough vacuum and slowly heated allowing degassing to occur. The material under a pressure of 69 MPa was set at a temperature of 100 °C for the PS/Sn and 140 °C for the PP/Al material. The material was held at this condition for 20 hours after which it was removed as a solid billet of material, ready for analysis and testing

The processing method is designated as either mechanical alloyed, MA or thermal melted

TP. Thermal melting was achieved by placing the reactor pellets in the consolidation press, degassing and applying the same amount of pressure as for the MA materials, but heating to approximately 20 °C above the melting point temperature of the material. The material was then held for 2 hours prior to cooling back down to room temperature.

Mechanical Properties

Microhardness values were measured using a Knoop indentor with a 50 gm load, giving Vickers Hardness Numbers, HV. These tests were also carried out on material processed by thermal melting as a comparative base to the mechanically alloying materials. The results are shown in Table I and are for a total of ten indentations for each condition with a mean value and the corresponding standard deviation.

Table I Microhardness Results of Various Processed Materials

Material	HV, mean & std. dev
MA PS/Sn (air)	19.48 ± 1.02
MA PS/Sn (argon)	18.80 ± 1.03
MA PP/Al (air)	10.12 ± 0.58
TM PS	18.13 ± 0.45
TM PP	12.48 ± 0.98

It can be seen from Table I that the microhardness of MA PS/Sn has increased slightly over that of thermal melt PS. However MA PP/Al has responded in an opposite manner, showing a reduction in hardness as compared to the thermal melt PP. Thus complexities occur depending upon the alloy formed and no general rule can be made in terms of hardness behaviour.

Compressive stress/strain tests were conducted on round cylinder type specimens being approximately 10 mm in diameter by 24 mm in length. The results from these tests are found in Table II. The machine stiffness was separated out in order to establish the modulus of elasticity of the different materials. The results are analysed using engineering stress and strain. A mean value of two separate tests is given in this table.

Table II Compressive Mechanical Properties

Material	Elastic Modulus, MPa	Ultimate Stress, MPa	Fracture Strain %
MA PS/Sn (air)	1660	47.2	2.8
MA PS/Sn (argon)	1530	52.4	3.4
MA PP/Al (air)	1628	23.8	3.0
TM PS	1200	53.2	8.2
TM PP	648	46.9	36.0

The results show that the stiffness of the mechanically alloyed material is considerably larger than the thermal melt material as a result of the addition of metal which is in keeping with what would normally be expected. Based upon composite theory of rule of mixtures the stiffness in the mechanical alloyed conditions is predicted to be 1428 MPa for the MA PS/Sn material and 9248 MPa for the MA PP/Al material. Comparing these values to those found in Table II shows that the measured stiffness resulting from mechanical alloying is greater for MA PS/Sn and much less for MA PP/Al than what is predicted based solely on micro-mechanical additive property concepts governing composite materials. This indicates that chemical reactions, organo-metallic, have taken place as a result of mechanical alloying.

The strengths of these MA materials are not as good as the base TM materials. This is likely a result of the location of bonding of the metal onto the polymer chains. In polymer/polymer alloys the strength obtained from MA processing was always found to be better that the base materials [8]. Different combinations of polymer/metal alloying will no doubt give various strengthening or weakening behaviour depending upon bonding conditions. The ductility loss as a result of mechanical alloying is in keeping with what has been found in polymer/polymer alloys [8].

Materials Powder Morphology

The powder morphology of the MA materials is in keeping with what has been found in the past for polymer/polymer alloys. A typical scanning electron microscope, SEM, picture is shown for the PS/Sn material as seen after 24 hrs of processing in argon, Figure 1. The powder particles show a fine interaction or conglomeration of small particles making up the main particle sizes. This is an indication of the fracture/cold weld mechanism at work.

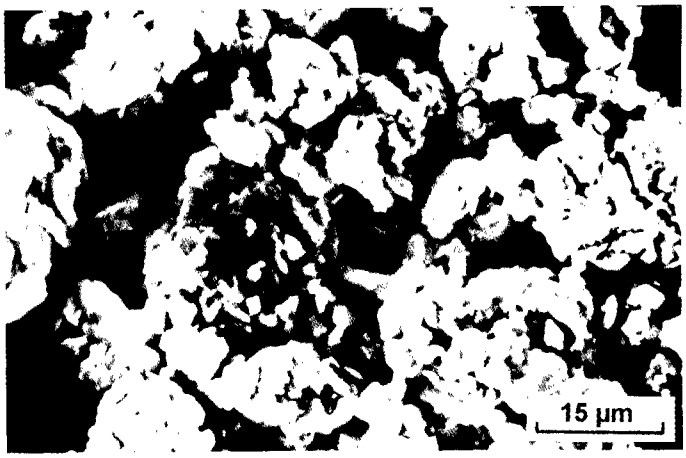


Figure 1. Power Morphology of MA PS/Sn Processed in Argon

The rate of particle size reduction of PS/Sn in argon is shown in Figure 2. The time of processing is a function of the efficiency of the equipment and the operating conditions. It can be seen that the material reduces to an overall particle size of 2 µm after 24 hours of processing. Recent work on using computer simulation of a shaker ball mill [14,15] has resulted in an improvement of the equipment and operating conditions such that now the same fine particle size can be obtained in 2.5 hours. Thus as equipment is improved the mechanical alloying process

becomes shorter and shorter in terms of time and hence more efficient and cost effective.

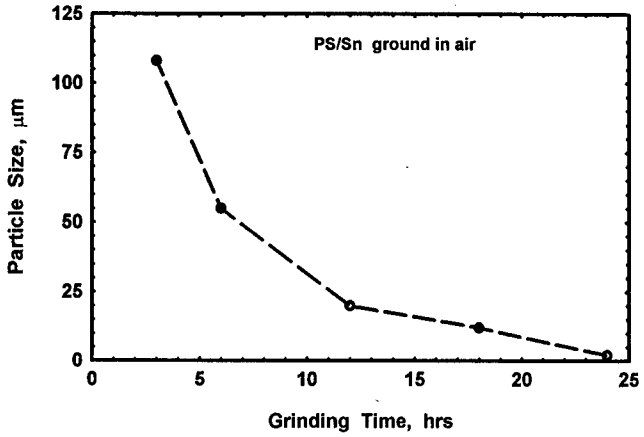


Figure 2. Particle Size verses Grinding Time for PS/Sn Processed in Argon

Analytical Characterization

X-ray diffraction, XRD, is a very effective technique in sorting out changes occurring as a result of mechanical alloying. Extensive alterations in d-spacing and intensity occur between thermal melted polymers and mechanically processed. The addition of metal also results in a reduction and disappearance of many of the Sn peaks in the MA PS/Sn material and disappearance of all the Al peaks in the MA PP/Al material. In addition new peaks form in the metal alloys, one at a d-space of 1.5985 for the MA PS/Sn and two for the MA PP/Al, these being at d= 4.779 and d= 2.3415. These alterations indicate that the metals have formed bonds with the polymers.

Fourier transform infra-red, FTIR, analysis in a transmittance mode also show changes. In both MA PS/Sn and MA PP/Al a number of wavelength vibrations are missing. In particular the benzene-H ring in PS and the CH_3 attachment in PP. These missing wave numbers occur between 2800 to 3000. Thus it would appear that the metals have attached themselves to the external branched portions of the polymers. These alterations strongly suggest an organo-metallic bond formation.

Discussion

The importance of mechanical alloying polymer/metal combinations as found from this work is that useful mechanical properties result, chemical interactions occur and the possibility of creating unique alloys exists. The metals used in this study appear to have a preference of attachment to the branched portions of the polymer and not to the main backbone itself. The combined results of both XRD and FTIR point towards a conclusion that organo-metallic bonding has occurred.

Conclusions

Synthesis of polymer/metal mechanical alloys has been shown to be a viable method. The possibilities exist whereby wide and varied combinations of new alloys can be made. The resulting alloys form organo-metallic bonds resulting in true alloying and not just blending or composite

material formation. As more work is conducted, it is likely that eventually it will be possible to predict how a particular metal will interact with a specific polymer. This work is an initial start in this new material alloy development.

Acknowledgements

This work was supported by a grant from the University of Calgary and by the Natural Science and Engineering Research Council of Canada. Technical support in keeping the mechanical alloying equipment operational was made by Rob Scory and the Engineering Faculty Shops personnel.

References

1. J. Pan and W.J.D. Shaw, Microstructural Science, V19 (1992), pp. 659-669.
2. J. Pan and W.J.D. Shaw, in Conference Proceedings on Advanced Materials: Meeting the Economics Challenge, SAMPE, ed's. T.S. Reinhart, M. Rosenow, R.A. Cull and E. Struckholt, V24 (1992), pp.. T762-T775.
3. J. Pan and W.J.D. Shaw, Microstructural Science, V20 (1993), pp.. 351-365.
4. J. Pan and W.J.D. Shaw, Microstructural Science, V21 (1994), pp.. 95-106.
5. J. Pan and W.J.D. Shaw, J. Of Applied Polymer Science, V52 (1994), pp.. 507-514.
6. J. Pan and W.J.D. Shaw, J. Of Applied Polymer Science, V56 (1995), pp.. 557-566.
7. W.J.D. Shaw, J. Pan and M.A. Gowler, in Conference Proceedings on Mechanical Alloying for Structural Applications, ASM, (1993), pp.. 431-437.
8. W.J.D. Shaw, in International Symposium on Metastable, Mechanically Alloyed and Nanocrystalline Materials, Sitges, Spain, Aug 31-Sept 5, 1997.
9. W.J.D. Shaw and M.A. Gowler, in Conference Proceedings on Processing Materials for Properties, TMS, (1993), pp.. 687-690.
10. H.J. Danilkewich, M.Sc. Thesis, University of Calgary (1994).
11. W.J.D. Shaw and H.J. Danilkewich, Microstructural Science, ASM, V25 (1998), in press.
12. M. Karttunen and P. Ruuskanen, "The Microstructure and electrical Properties of Mechanically -Alloyed Copper-Polymer Composites", Poster, ISMANAM, Sitges, Spain, Aug 31-Sept 5, 1997.
13. T. Ishida and S. Tamaru, J of Mat. Sci. Letters, V12 (1993), pp. 1851-1853..
14. Gavrilov, D., Vinogradov, O. and Shaw, W.J.D., in Proceedings Composite Processing and Microstructure, Queensland, Australia, Ed. M.L. Scott, July 1997, PP. 370-378.
15. Gavrilov, D., Vinogradov, O. and Shaw, W.J.D., in Proceedings of the Tenth International Conference on Composite Materials, ICCM-10, Whistler, B.C. Canada, Aug 1995, pp. III.11-III.17.

Kinetics of Metal Organic Chemical Vapour Infiltration and Microstructures of Amorphous and Nano-Crystalline ZrO_2 incorporated into Partially Sintered $MoSi_2$ Matrix.

Noboru Yoshikawa, Shoji Taniguchi and Atsushi Kikuchi

School of Metallurgy, Division of Engineering, Graduate Schools, Tohoku University, Aza-Aoba, Aramaki, Aoba-ku, Sendai, Miyagi, Japan 980-77

Abstract

ZrO_2 was incorporated into partially sintered $MoSi_2$ by means of Chemical Vapour Infiltration(CVI). The infiltration distance of about two hundred micrometers was obtained at 2.6kPa for 1hr, however, smaller infiltration distance resulted at 1.3kPa. Considering ZrO_2 film growth rate by CVD, larger deposition rate at 1.3kPa led to earlier pore closure and formation of the deposition layer on the surface of the sintered body. The infiltrated ZrO_2 was possible to cover $MoSi_2$ grains well and to form the coating layer on them, however, the entire pore closure was difficult to be accomplished.

The as-infiltrated or deposited ZrO_2 appeared to be amorphous under all the deposition conditions studied(lower than 773K). From the XRD profiles, ZrO_2 found to be crystallized by post annealing. The nano-crystals consisting of tetragonal ZrO_2 was obtained by annealing at 873K for 1hr and the monoclinic ZrO_2 appeared with little amount when annealed at 1073K for 1 hr. TEM observation, showed that the crystallized ZrO_2 grains had diameters of less than 100nm. The optimal fabrication conditions for the composite macro/micro structures were discussed, considering the macroscopic infiltration kinetics and formation of ZrO_2 microstructures.

The Third Pacific Rim International Conference on
Advanced Materials and Processing (PRICM 3)
Edited by M.A. Imam, R. DeNale, S. Hanada,
Z. Zhong and D.N. Lee
The Minerals, Metals & Materials Society, 1998

Introduction

$MoSi_2$ intermetallic compounds have excellent properties of resistance against creep and oxidation at high temperature[1]. It is expected to apply them for the high temperature structural materials. However, this material is reported to lack the toughness and strength at room temperature.

Addition of ZrO_2(or Partially Stabilized Zirconia(PSZ)) to the $MoSi_2$ sintered bodies has been attempted, in order to strengthen them, as ZrO_2 ceramics are known to possess high toughness and strength due to transformation toughening. General method for its incorporation is by sintering the blended powder of $MoSi_2$ and ZrO_2(or PSZ) with application of pressure, however, it requires the process temperature above 1800K[2].

In the present study, ZrO_2 was incorporated into the partially sintered porous $MoSi_2$ bodies by CVI method, which made it possible to add ZrO_2 at much lower temperature, especially by using the metal-organic precursors. In fabrication of the electronic devices by means of MOCVD, using these precursors enabled not only lower deposition temperature but also excellent step coverage[3], which is demanded for filling out the narrow trenches in the multi-layered device structures. In this study, it is attempted to take advantage of the latter features to fill out the fine pore networks in the sintered bodies.

The first purpose of the present study is to investigate the CVI kinetics to infiltrate ZrO_2 into the porous bodies. Measurement of film growth rate by CVD was conducted in order to obtain the basic knowledge on the reaction rates. On the other hand, low infiltration(deposition) temperature usually results in lower crystallinity of the deposited ZrO_2. In order to make use of the transformation toughening, metastable tetragonal ZrO_2phase is required to be formed by post annealing.

The second purpose is to observe the microstructure of ZrO_2 deposited inside of the porous $MoSi_2$ bodies and their phase changes due to post annealing. The reaction kinetics for CVI of ZrO_2 and microstructural change caused by the post annealing are discussed in relation with formation of the composite microstructures.

Experimental

Zirconium normal propoxide($Zr(OC_3H_7)_4$) was utilized as the precursor, it was vaporized and fed into the reactor with He carrier. The ZrO_2 film was deposited on Si wafer to measure the CVD rates and the deposition kinetics was investigated. The overall reaction of depositing ZrO_2 is as follows:

$$Zr(OC_3H_7)_4(g) = ZrO_2(s) + 4C_3H_6(g) + 2H_2O(g)$$

$MoSi_2$ powder particles(Wako Chem. Inc.) had diameter between 6-12 micrometers. $MoSi_2$ was partially sintered at 1373K in Ar atmosphere, having porosity of less than 15.4%.

ZrO_2 was chemical-vapour-infiltrated into the sintered $MoSi_2$. CVD and CVI were conducted in the temperature range between 573K to 773K under the reduced pressure between 1.3kPa to 26.7kPa. The experimental conditions are listed in Table 1.

The experimental apparatus is schematically illustrated in Fig. 1. The apparatus consists of gas feeding system, a vaporizer, a reactor and a vacuum pump. Gas chromatograph was attached to the apparatus and the outlet gas from the reactor was analyzed with the chromatograph. Gas of He was selected for the carrier so as to guarantee the higher sensitivity of the analysis. The reactor was made of stainless steel tube, having diameter of 10mm and length of 300mm. Si wafer was set in the reactor and ZrO_2 film was deposited on it. Partially sintered $MoSi_2$ rods having diameter of about 5mm and length of 8mm were also placed in the reactor for CVI. The post annealing was conducted at different temperature in air. The microstructural observation was conducted with SEM-EDX, TEM and XRD. The film thickness was measured with an optical microscope with interferometry.

Results

MOCVD kinetics for deposition of ZrO_2 films

In order to investigate the reaction kinetics and to obtain the optimum conditions for CVI, CVD-ZrO_2 film growth rates were measured under different deposition conditions. The results

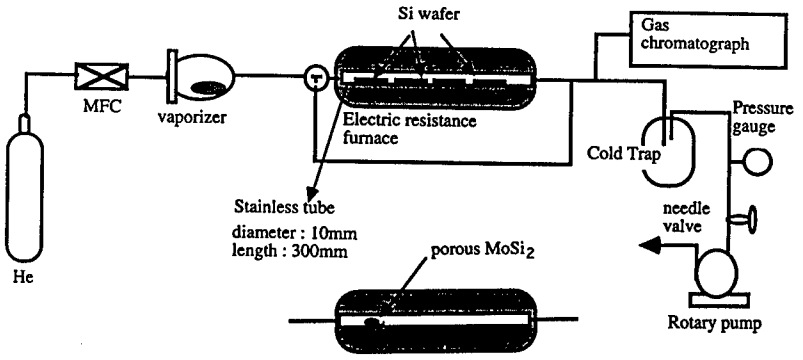


Fig. 1 : Schematic illustration of apparatus.

Table 1 : Experimental conditions.

Gas flow rate, Q_T	$1.7\times10^{-6}\sim5.0\times10^{-6}m^3s^{-1}$
Vaporization temperature	481K
Deposition temperature(T)	573~773K
Process Pressure(P_T)	1.3~26.7kPa

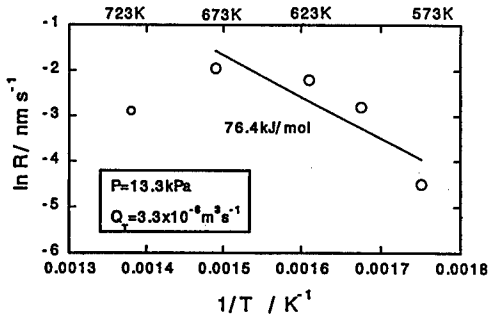


Fig. 2: Relationship between deposition temperature and film growth rate.

are shown in Figs. 2-4. The film growth rate had distribution along the axial direction of the reactor, such that the maximum occurred at the inlet region.

Temperature dependence of the maximum growth rate is plotted in Fig. 2. The growth rate increased in the temperature range between 573K and 673K.The reaction rate decreased above 673K, which was considered to be due to occurrence of the gas phase reaction to form particles. The apparent activation energy for the film growth rate was estimated to be 76.4kJ/mol between 573K and 673K. The experiments in the present study was mostly done under the condition of 673K and for 3.6ks. The film growth rates were obtained under different process pressure at constant gas flow rate. The relationship between the process pressure and the maximum growth rate is shown in Fig. 3. It was found that the film growth rate increased as the decrease of the process pressure. Analyzed result of the gas out of the reactor is shown in Fig. 4. It was shown that the concentration of C_3H_6 was larger as the lower process pressure.

Considering the fact that the vapour pressure of zirconium normal propoxide(13Pa at 481K, the vaporization temperature) is lower than the process pressure, the more amount of precursor was supplied into the reactor under the lower process pressure, the higher growth rate resulted. So the value of the activation energy was obtained under the influence of gas transport.

Infiltration distance and the effects of process pressure.

The microstructures of the infiltrated $MoSi_2$ porous body were observed with SEM. The infiltration distance was measured from the concentration profiles obtained by EDX. Contrary to expectation of the increase in diffusivity, it was found that the infiltration distance decreased when the process pressure was lowered to 1.3kPa. The observed microstructure and the compositional distributions at two different process pressure are shown in Fig. 5. Deposition rate was larger in the case of lower process pressure(1.3kPa), as shown in Fig. 3 , so the earlier pore closure in the sintered body occurred. Then, ZrO_2 infiltration was attained only within the surface layer of several tens of micrometers. Deposited ZrO_2 layer was observed on the specimen surface in Fig. 5(a), which must be formed after pore closure. On the other hand at 2.6kPa, the larger infiltration distance of several hundred micrometers was obtained, without forming the

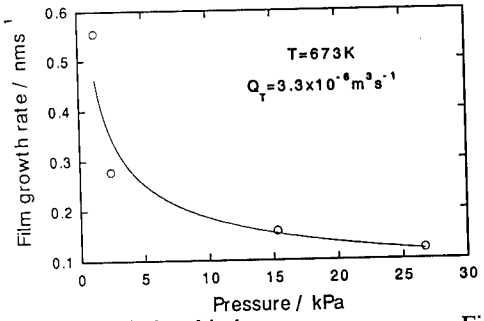


Fig. 3 : Relationship between process pressure and film growth rate.

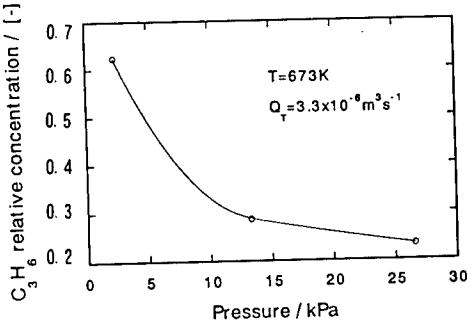


Fig. 4: Relationship between process pressure and C_3H_6 concentration in the output gas

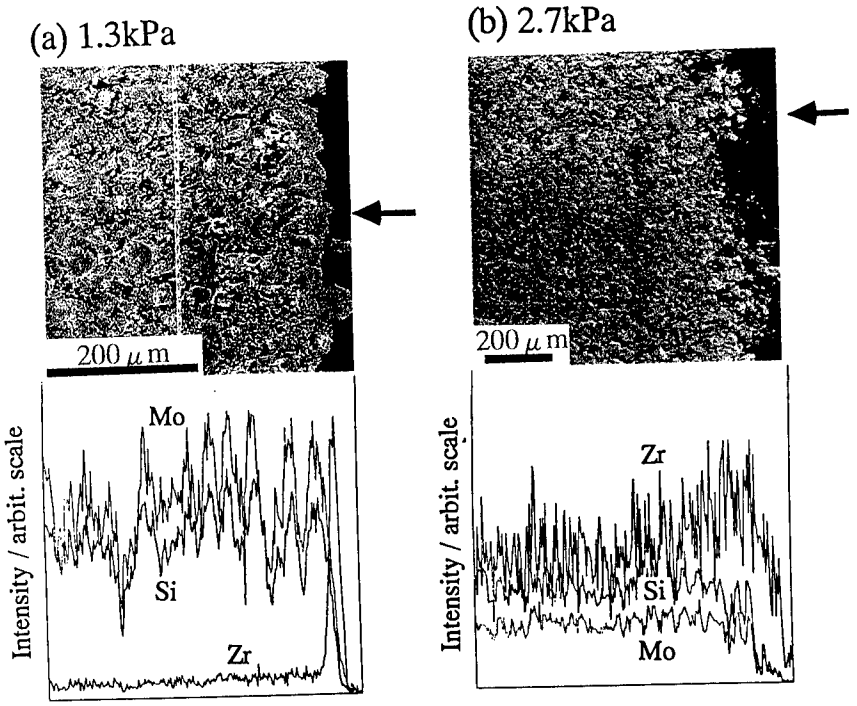


Fig. 5: SEM photographs of the ZrO_2 infiltrated $MoSi_2$ sintered bodies at two different process pressures and the compositional distribution analyzed with EDX.

deposited ZrO_2 layer on the surface. The difference in infiltration distance was considered to be caused by the difference in reaction rate due to the process pressure, as shown in the CVD deposition rate measurements(Fig. 3). It is considered that further infiltration is possible to be accomplished using lower deposition rate and spend much longer infiltration time for densification of the entire sintered body. However, it is not appropriate to increase process pressure too much, because of decrease in the diffusivity, so lowering the vaporization temperature decreasing the precursor concentration must be the taken into account.

Microstructures of the infiltrated specimens and their change by post annealing

In the TEM photographs shown in Fig. 6(a),(b) and (c), it is seen that the surface of $MoSi_2$ grains were coated well with ZrO_2 thin films. It was confirmed that the excellent surface coverage was obtained, as had been expected, using the metal organic precursors. However,

pores were observed between the $MoSi_2$ grains and it was difficult to fill out the entire pore space. The XRD profiles obtained from the infiltrated specimens are shown in Fig. 7. It was observed that the as-deposited ZrO_2(a) was amorphous under all the deposition conditions studied, and it was shown that the ZrO_2 crystallized by post annealing(b)(c).

Selected area electron diffraction patterns were obtained from the ZrO_2 portions in the specimens of as-infiltrated, annealed at 873K and annealed at 1073K, they are shown in Fig. 6(d),(e) and (f), respectively. These are consistent with the XRD results. Tetragonal ZrO_2 was obtained by annealing at 873K for 1hr. In the case of a specimen annealed at 1073K for 1 hr, major consisting phase was tetragonal ZrO_2, however, monoclinic ZrO_2 appeared with less amount.

The crystal size of both specimens was less than 100nm. It was observed that the largest grain size of the crystals in 873K annealed specimens had several tens of nano meters, which are at the same order as the crystals annealed at 1273K. The crystals in the former specimens, however, had less population in the coated films on $MoSi_2$ grains. Most of them are considered to be tetragonal(Fig. 7(b)).

In order to make use of transformation toughening, formation of tetragonal ZrO_2 in the composites is important. Conditions for obtaining tetragonal phase are discussed with regard to the present case. A tendency has been reported that the ZrO_2 crystals with larger grain size possess monoclinic phase. The critical size for retention of meta-stable ZrO_2 varies with the conditions, such that 30nm in ZrO_2 powder[5], 200~600nm in the case of ZrO_2 in Al_2O_3 matrix[6]. It was observed in the present case, monoclinic phase was formed by annealing at 1073K, and the critical size must be lying between 10nm and 100nm, which is rather similar to the former example. The monoclinic fraction reported for the sol-gel derived ZrO_2 films (from Zr normal propoxide) annealed at 1273K had similar value to the present case[7].

Taking account of the fact that the largest grain size of ZrO_2 crystals were similar by annealing at 873K and 1073K(Fig. 6(b),(c)) and the fact that there were difference in the degree of crystallization, ZrO_2 phase changes are not only determined by the crystal size, but another fundamental processes of crystallization and grain growth has to be investigated in the further study.

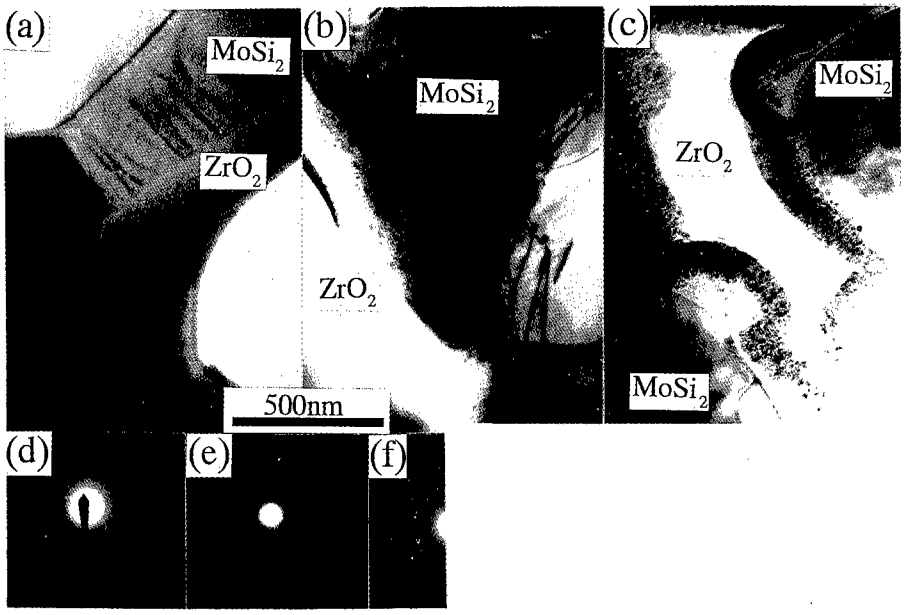


Fig. 6 : Bright field TEM images of the (a) as-infiltrated specimen, (b) annealed at 873K and (c) annealed at 1073K specimens. Electron diffraction patterns(d),(e) and (f), which were obtained from ZrO_2 thin films on $MoSi_2$ grains in the photographs of (a),(b) and (c), respectively.

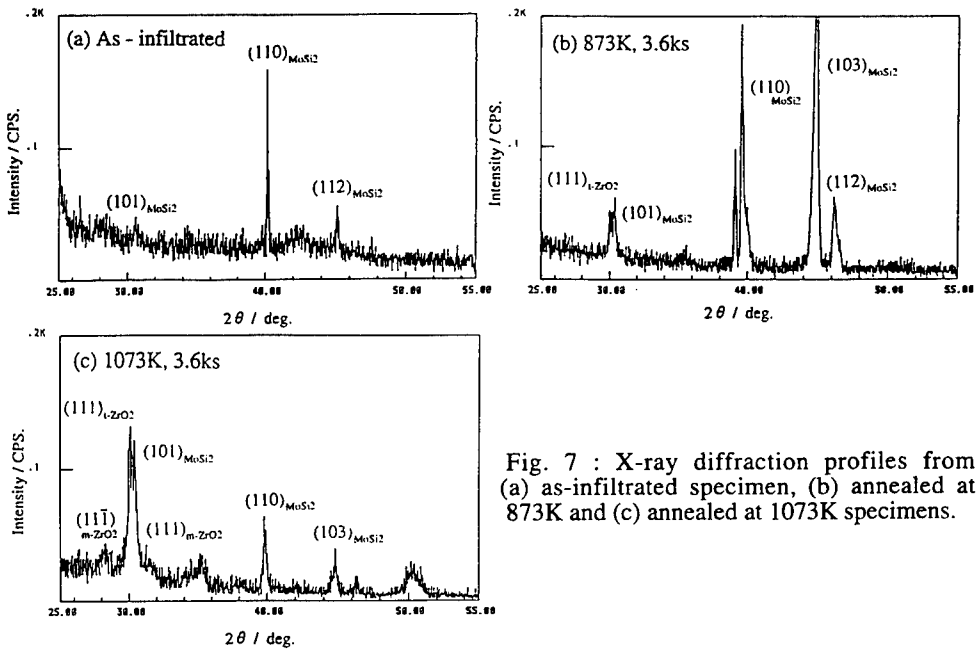


Fig. 7 : X-ray diffraction profiles from (a) as-infiltrated specimen, (b) annealed at 873K and (c) annealed at 1073K specimens.

Discussion and Summery on fabrication of the optimal composite microstructure

ZrO_2 was incorporated into $MoSi_2$ partially sintered body by means of CVI, which is expected to contribute to the transformation toughening, if tetragonal ZrO_2 phase is formed. Addition of stabilizer, such as Y_2O_3 and MgO would be effective, however, the present study was conducted in order to investigate simpler infiltration kinetics and the microstructural changes.

For obtaining low deposition temperature and large infiltration into the pore networks, metal organic precursor was utilized. It was possible to deposit ZrO_2 film on the fine $MoSi_2$ grain surface and cover them well in the sintered body. The longer deposition time is required for the complete fill out of the sintered bodies, with lower deposition rate by selecting the deposition conditions either by reducing the deposition temperature or by reducing precursor concentration.

Low deposition temperature by metal organic precursor resulted in formation of amorphous ZrO_2 and post annealing was conducted to obtain crystallized ZrO_2. The equi-axed ZrO_2 grains having several tens of nano meters are obtained by post annealing at 1073K and the deposits were completely crystallized, however, formation of monoclinic phase was observed. From a view point of nano-sized t-ZrO_2 retention, annealing temperature below 1073K was recommended.

References

1. A. C. Silva, S. Jayashankar, P.Krishnan and M.J.Kaufman, " Processing and Fabrication of Advanced Materials for High Temperature Applications II", ed. V.A.Ravi and T.S.Srivatsan (TMS-AIME, Warrendale, PA)
2. K.Hayashi, M.Yoneyama and Y.Okamoto, "Mechanical Properties of $MoSi_2$/ZrO_2 Composites at Room Temperature," J.Cream. Soc. Jpn.,104 [6] (1996) 550-555. (in Japanese)
3. M.de Keijser and G.J.M. Dormans, "Chemical Vapour Deposition of Electroceramic Thin Films," MRS Bulletin, 21 [6] (1996) 37-43.
4. F.F. Lange, "Transformation toughening, Part I,II,III,IV and V," J.Mater.Sci.,17(1982)225-263.
5. R. Garvie, "The occurrence of Metastable Tetragonal Zirconia as a Crystallite Size Effect, " J. Phys. Chem. 69 (1965) 1238-1243.
6. A.H.Heuer, N.Claussen, W.M.Kriven and M.Ruhle, " Stability of Tetragonal Zirconia Particles in Ceramic Materials," J.Am.Ceram. Soc., 65 (1982) 642-650.
7. H.Yamamura, Y.Iwata and C.Matsuno," Synthesis of Highly Oriented Zirconia Film by Sol-Gel Method," J.Cream. Soc. Jpn.,105 [10] (1997) 918-921. (in Japanese)

HIGH-TEMPERATURE STRENGTH OF MICROSTRUCTURE-CONTROLLED Nb_3Al/Nb_{SS} *IN-SITU* COMPOSITES IN Nb-Al-Mo TERNARY SYSTEM

T. Tabaru and S. Hanada

Institute for Materials Research, Tohoku University
Sendai 980-8577, Japan

Abstract

Mo alloyed Nb_3Al(A15)/Nb_{SS}(A2) *in-situ* composites were fabricated via ingot metallurgy, and their microstructure was controlled by heat-treatment or thermo-mechanical processing. Using these *in-situ* composites, mechanical properties were investigated at elevated temperature. Isothermally forged A15 phase-rich alloys consist of equiaxed grains of A15 and A2 phases. Heat treated A15 phase-rich alloys without isothermal forging are composed of unidirectionally arranged A2 filaments in the A15 matrix. Mo alloying of 30-60 mol% improves high-temperature strength of the equiaxed *in-situ* composites with a constant volume content of the A15 phase. Nb-18Al-31Mo alloy containing the filament-like A2 phase possesses excellent creep strength at 1573 K compared with other refractory intermetallic compounds. Stress exponent of Nb-18Al-31Mo alloy with the equiaxed microstructure alters from 1 to 5 at about 250 MPa of applied stress. The decrease in the stress exponent at lower stresses is ascribed to grain boundary diffusion creep. Strengthening of Nb_3Al/Nb_{SS} *in-situ* composites is discussed in terms of Mo alloying and microstructure controlling.

The Third Pacific Rim International Conference on
Advanced Materials and Processing (PRICM 3)
Edited by M.A. Imam, R. DeNale, S. Hanada,
Z. Zhong and D.N. Lee
The Minerals, Metals & Materials Society, 1998

Introduction

The Nb_3Al/Nb_{SS} *in-situ* composites, which consist of Nb_3Al with excellent high-temperature strength and Nb_{SS} with acceptable room-temperature fracture toughness, are attractive candidates for structural use at high-temperature. It has been found, however, that increased content of Nb_{SS} improves room-temperature fracture toughness of the composites, while it simultaneously decreases high-temperature strength [1-3]. To increase high-temperature strength it will be effective to alloy with ternary elements such as Ta, Mo or W having higher melting temperature than Nb. Among these ternary elements, Mo is considered to be the most efficient additive for strengthening, since solution hardening usually depends on atomic size mismatch between solvent and solute atoms, and atomic radii of Nb, Ta, Mo and W are 143, 143, 136 and 137 pm, respectively. Moreover, Mo has no solubility limit to both Nb_{SS}(A2) and Nb_3Al(A15) phases, and A15/A2 two-phase region extends continuously from Nb_3Al(A15)/Nb_{SS}(A2) to Mo_3Al(A15)/Mo_{SS}(A2) [4]. The investigation of high-temperature strength of the A15/A2 *in-situ* composites as a function of Mo content will suggest alloy composition to further strengthen the *in-situ* composites.

Present study aims at examining high-temperature strength of several A15/A2 *in-situ* composites in the Nb-Al-Mo ternary system and at evaluating creep strength of a representative Mo-alloyed Nb_3Al/Nb_{SS} *in-situ* composite, Nb-18mol%Al-31mol%Mo. These mechanical properties are evaluated by using the microstructure-controlled composites, since they depends sensitively on microstructures such as grain size, grain shape and volume content of a second phase. In order to examine the effect of composition on high-temperature strength, we have prepared Nb_3Al/Nb_{SS} *in-situ* composites with equiaxed microstructures by solution-treatment followed by isothermal forging. Moreover, alloy compositions are selected so that the volume content of a second phase is kept constant. In creep tests we have prepared the *in-situ* composites with microstructure consisting of unidirectionally arranged A2 filaments in the A15 matrix as well as with the equiaxed microstructure.

Experimental Procedure

The chemical compositions of the alloys including about 75 vol% A15 phase were selected as (Nb, Mo)-(17~21)mol%Al at substitutional ratios of Mo to Nb of 0 to 1. Arc melting using a non-consumable tungsten electrode and water-cooled copper hearth was performed in an Ar atmosphere. Arc-melted ingots were isothermally forged at 1873 K and then solutioned at 2173 K for 3 h. The isothermal forging was performed to about 75 % reduction of original height at a nominal strain rate of approximately 3×10^{-5} s^{-1} and in a vacuum of 1×10^{-3} Pa. Final annealing was carried out at 1773 K for 100 h in a vacuum of 2×10^{-4} Pa. The fabrication process described above is called process A. Alloy compositions fabricated by process A were determined to be Nb-18.4Al, Nb-18.1Al-31.4Mo, Nb-20.3Al-40.4Mo, Nb-18.1Al-51.5Mo, Nb-19.0Al-60.8Mo and Mo-20.6Al by inductively coupled plasma emission spectrochemical analysis. Only Nb-18.1Al-31.4Mo alloy was prepared by another process called process B: after annealing at 1773 K in process A, a part of ingot was solution-treated again and then heat-treated at 1773 K for 100 h.

Table I Properties of A15/A2 *in-situ* composites fabricated by process A: all alloys have an equiaxed two-phase microstructure

Alloys	Composition							Lattice constant / pm		Average grain size / μm		Volume percent / %
	Alloy / mol%			A15 / mol%		A2 / mol%						
	Nb	Al	Mo	Al	Mo	Al	Mo	A15	A2	A15	A2	A15
Nb-18Al	81.6	18.4	-	19.6	-	9.3	-	519.8	329.1	20	8	92
Nb-18Al-31Mo	50.5	18.1	31.4	21.9	28.6	9.2	36.8	510.4	322.6	16	12	72
Nb-20Al-40Mo	39.3	20.3	40.4	22.5	38.4	8.5	47.3	-	-	18	4	88
Nb-18Al-52Mo	30.4	18.1	51.5	22.8	47.6	7.6	57.3	-	-	7	5	72
Nb-19Al-61Mo	20.2	19.0	60.8	23.6	57.6	7.3	68.5	500.7	317.7	7	4	77
Mo-21Al	-	20.6	79.4	24.1	75.9	7.8	92.2	495.1	314.1	10	6	69

High-temperature strength was examined by "compression tests" under a constant crosshead speed and by "compressive creep tests" under a constant load. Compression tests for all alloys prepared by process A were carried out in a vacuum of 2 x 10^{-3} Pa at 1273, 1473, 1573, 1673 and 1773 K. Compressive creep tests for Nb-18Al-31Mo alloy prepared by process A and B were carried out in an Ar atmosphere at 1573 K. For microstructural observations an optical microscope (OM), a scanning electron microscope (SEM) and a transmission electron microscope (TEM) were used. HITACHI S-3100H for SEM observations and HITACHI H-8100D for TEM observations were operated at 25 and 200 kV, respectively. To identify constituent phases X-ray diffraction (XRD) measurements were carried out at 40 kV and 20 mA using Cu-Kα. An electron prove micro analyzer (EPMA), JEOL JXA-8621MX, was also used for quantitative measurement of Nb, Al and Mo in constituent phases. An image analysis for microstructural quantification was carried out. These results are listed in Table I.

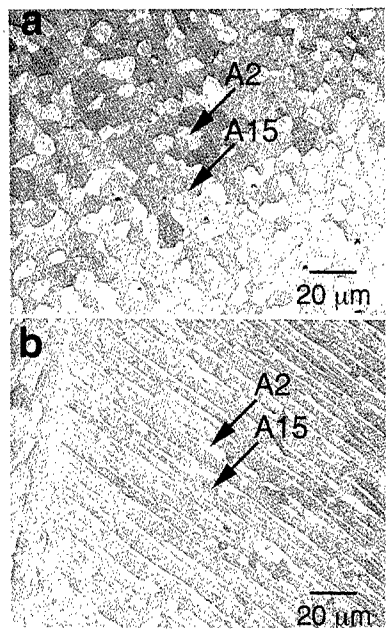


Figure 1: Typical microstructures of A15-rich A15/A2 *in-situ* composites: (a) Nb-18Al-31Mo fabricated by process A and (b) Nb-18Al-31Mo fabricated by process B.

Results and Discussion

Microstructure

From microstructural observations and XRD analysis, all alloys fabricated by process A were found that they had fine and uniform two-phase microstructure consisting of A15 and A2 phases. The volume fraction of the A15 phase was dependent on alloy composition and it ranged from 0.69 to 0.92. Nb-18Al-31Mo alloy fabricated by process B has a characteristic microstructure composed of the A15 and the A2 phases. Figure 1 shows typical microstructures of Nb-18Al-31Mo alloys fabricated by process A and B. An equiaxed microstructure is produced by process A, as can be seen in Figure 1 (a), where A2 particles are dispersed in A15 matrix. Similar microstructures were obtained in other alloys fabricated by process A. In process B, as shown in Figure 1 (b), A2 filaments are arranged unidirectionally in A15 matrix. Since this microstructure was formed on the heat-treatment at 1773 K after solution-treatment, the A15 phase of a single variant appears to precipitate with preferential growth directions from the supersaturated A2 phase. As listed in Table I the volume percentage of the A15 phase of Nb-18Al-31Mo, Nb-18Al-52Mo, Nb-19Al-61Mo and Mo-21Al alloys is within 73±4 %.

Figure 2 shows XRD patterns taken from four alloys fabricated by process A. It is evident that

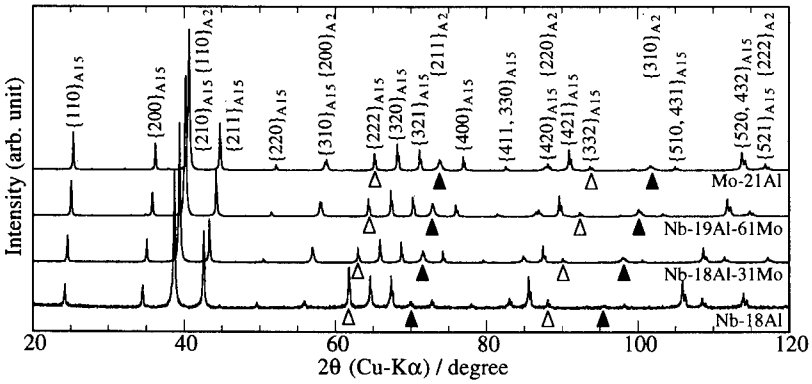


Figure 2: X-ray diffraction patterns taken from A15/A2 *in-situ* composites.

lattice constants of both A15 and A2 phases decrease with increasing Mo content, because Bragg peaks shift to higher angles with increasing Mo. The lattice parameters of both phases in the four alloys are included in Table I. Although Al content of each alloy is slightly different from others, both lattice parameters of A15 and A2 phases indicate a linear dependence on Mo content, suggesting that Vegard's law is satisfied.

Table II Calculated densities of A15/A2 *in-situ* composites and constituents

Alloys	Density		
	Alloy / Mgm^{-3}	A15 phase / Mgm^{-3}	A2 phase / Mgm^{-3}
Nb-18Al	7.35	7.28	8.11
Nb-18Al-31Mo	7.94	7.63	8.73
Nb-19Al-61Mo	7.92	7.61	8.94
Mo-21Al	8.05	7.63	8.98

Densities of the four alloys and of the constituents were calculated using the lattice parameters, the chemical compositions of both phases and the volume fraction of the A15 phase. The calculated results are listed in Table II. Since the density of conventional Ni-based superalloys is about 8~9 Mgm^{-3}, the Nb-Al-Mo ternary A15/A2 *in-situ* composites investigated are found to have densities comparable to or rather lower than conventional Ni-based superalloys.

Strengthening by Mo alloying at high temperature

Figure 3 shows temperature dependence of compressive stress-strain curves of Nb-18Al-31Mo alloy at an initial strain rate of 1.7×10^{-4} s^{-1}. Flow behavior at various temperatures is quite similar to each other: flow stress reaches a maximum stress just after yielding and then it decreases gradually. With increasing temperature, flow stress as well as the peak stress decreases. The cause of decrease in flow stress will be discussed elsewhere.

Figure 4 shows temperature dependence of the peak stress. High peak stresses are obtained at each temperature in Nb-20Al-40Mo, Nb-18Al-52Mo and Nb-19Al-61Mo, as compared to Nb-18Al, Nb-18Al-31Mo and Mo-21Al. As shown in Table I, however, Nb-20Al-40Mo and Nb-18Al include higher content of the A15 phase than others. The effect of Mo content on the peak stress should be compared in Nb-18Al-31Mo, Nb-19Al-52Mo, Nb-19Al-61Mo and Mo-21Al, because these alloys contain 73±4 vol% A15 phase. It is clearly seen from Figure 4 that the *in-situ* composite is strengthened most effectively by Mo addition ranging from 50 to 60 mol%. According to Jackson et al., high temperature strength in binary Nb-Mo alloys seems to exhibit a maximum in the compositional region of Nb-(60~80)mol%Mo, because minimum creep rate at 1573 K and at 90 MPa was found to be the lowest in this region [5]. Recently, Hanada et al. have demonstrated that monolithic A15 phase alloy in the Nb-Al-Mo system displays maximum strength at high temperatures below 1773 K when Mo is substituted for Nb by a half content of Nb [6]. These results indicate that both of the A15 and the A2 phases in Nb-Al and Mo-Al binary systems are strengthened by ternary alloying with Mo and Nb, respectively. If a slight difference of Al content is assumed to have no effect on high-temperature strength in the A15/A2 *in-situ*

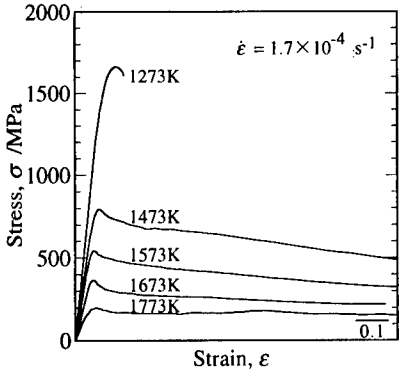


Figure 3: Temperature dependence of stress-strain curve of Nb-18Al-31Mo alloy (A).

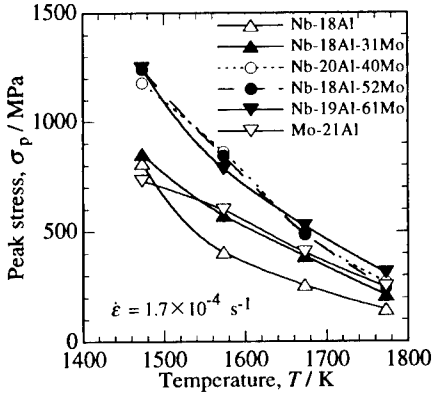


Figure 4: High temperature strength of ternary A15/A2 *in-situ* composites.

composites, maximum strength of those composites with the constant volume fraction and the similar microstructure will be attained in the region of substitutional ratio of Mo to Nb from 0.5 to 0.8. Considering that the investigated composites are composed of the A15 and A2 phases, the A2 phase rather than the A15 phase may affect strongly the strength of the *in-situ* composites containing about 73 vol% A15 phase. TEM observations of Nb-18Al-31Mo alloy compressed to the peak stress revealed uniform distributions of many dislocations in the A2 phase in contrast to a very low dislocation density in the A15 phase.

Figure 5 shows specific strength normalized by calculated density. Data of Nb_3Al monolithic alloy of Nb-22Al are referred to a paper by Saito et al. [7]. Except for the Nb-22Al alloy, all alloys are A15/A2 *in-situ* composites including about 73 vol% A15 phase. Specific strength of the Nb-19Al-61Mo alloy is much higher than that of others. The strength of A15-based *in-situ* composites incorporating A2 phase usually decreases with increasing content of A2 phase. However, 31 mol% Mo bearing *in-situ* composite has specific strength comparable to monolithic Nb-22Al alloy and its specific strength at higher temperature is superior to Nb-22Al alloy. And also Nb-18Al-31Mo alloy exhibited appreciable plasticity at 1273 K, although the monolithic Nb_3Al alloy failed before plastic yielding below 1400 K.

Creep strength of Nb-18Al-31Mo alloy

Creep strength of the Nb-18Al-31Mo alloy fabricated by process A and B was examined as a typical alloy of the A15/A2 *in-situ* composites including about 73 vol% A15 phase, because the alloy was found to have strength superior to a monolithic Nb_3Al alloy at high temperature. Creep rate of two-phase alloys is usually affected by microstructural morphology, grain size and creep rate of the phase with lower creep rate. Figure 6 shows secondary creep rate of the Nb-18Al-31Mo alloy fabricated by process A and B together with a Nb-8Al-37Mo alloy, which consists of an A2 single phase with the chemical composition close to that of an A2 phase in Nb-18Al-31Mo alloy, Nb-9Al-37Mo. As shown in Figure 1, Nb-18Al-31Mo (A) has the equiaxed two-phase microstructure with average grain sizes of 16 and 12 μm in the A15 and A2 phases, respectively, whereas Nb-18Al-31Mo (B) has the microstructure consisting of A2 filaments in A15 matrix. The Nb-8Al-37Mo alloy had a large grain size over 800 μm. For comparison with these alloys, minimum creep rates of binary Nb_3Al/Nb_{SS} *in-situ* composites, a $MoSi_2$ alloy and a $(Cr, Mo)_5Si_3/(Cr, Mo)_3Si$ composite [8-10] are also included in Figure 6. Nb-18Al-31Mo (B) and the Nb-8Al-37Mo alloy display 1 % creep strain in 100 h at 110 and 40 MPa, respectively, indicating superior creep resistance compared to the other intermetallic-based alloys. Creep behavior of Nb-18Al-31Mo (A) is, however, quite different from other alloys. The stress exponent n of Nb-18Al-31Mo (A) alters from 1 to 5 at about 250 MPa with an increase in applied stress, although that of Nb-18Al-31Mo (B) or of Nb-8Al-37Mo alloy does not alter through the whole range of applied stress examined in present work. In general, n≈1 implies that the deformation is controlled by diffusion creep. Microstructure observation of Nb-18Al-31Mo (A) crept to about 20 % at 1573 K and at 80 MPa corresponding to the region n≈1 indicated that dislocations are introduced dominantly in the A2 phase and little dislocations exist in the A15 phase. Also, no

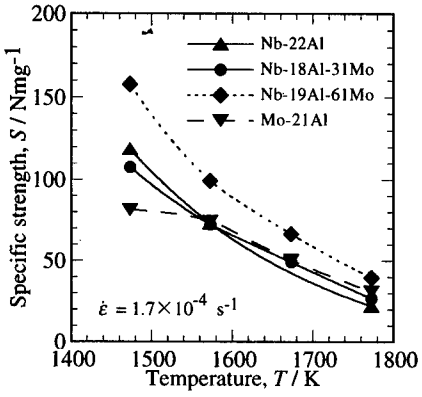


Figure 5: Specific strength of 75 vol% A15 phase containing A15/A2 *in-situ* composites.

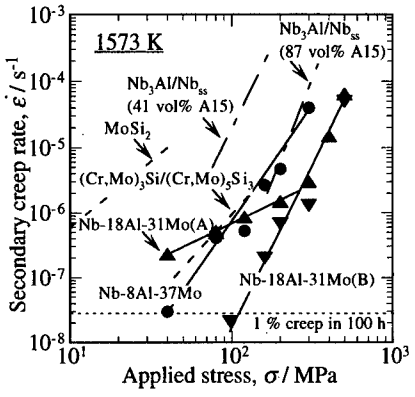


Figure 6: Secondary creep rate of Nb-18Al-31Mo and Nb-8Al-37Mo alloys

apparent difference was observed in the two-phase SEM microstructures before and after creep testing. These observations suggest that creep in Nb-18Al-31Mo (A) is associated with grain boundary diffusion. By contrast, the formation of anisotropic microstructure in Nb-18Al-31Mo (B) seems to make grain boundary diffusion difficult, thereby decreasing creep rate.

Summary

High-temperature strength of Nb_3Al/Nb_{SS} *in-situ* composites in the Nb-Al-Mo system has been investigated. The Nb_3Al/Nb_{SS} *in-situ* composites are solution strengthened by ternary alloying with Mo. The maximum strength appears in the compositional region with substitutional ratio of Mo to Nb of 0.6~0.8 when *in-situ* composites containing about 73 vol% A15 phase are compared. The strength obtained in the *in-situ* composites is comparable to that in a monolithic binary Nb_3Al alloy. Creep resistance has been investigated using Nb-18Al-31Mo alloy with two kinds of microstructures prepared by heat-treatment or by thermo-mechanical processing. One has an equiaxed two-phase microstructure and the other has a microstructure with unidirectionally arranged A2 filaments in A15 matrix. Stress exponent of secondary creep rate in the former alters from 1 to 5 at about 250 MPa with increasing applied stress, whereas that in the latter is about 5 above 98 MPa. The remarkable decrease of the stress exponent at lower stress is attributable to the equiaxed grain microstructure. The Nb-18Al-31Mo alloy with the filament-like microstructure possesses excellent creep resistance at 1573 K among intermetallic-based alloys.

References

1. Y. Murayama, T. Kumagai and S. Hanada, "Processing and High Temperature Deformation of Nb_3Al," High-Temperature Ordered Intermetallic Alloy V, I. Baker et al. eds., Mat. Res. Soc. Symp. Proc., 288(1993), 95-105

2. R. Gnanamoorthy and S. Hanada, "Ductile-Phase-Toughening and Fatigue Crack Growth in Nb_3al Base Alloys," Scripta Materialia, 34 (1996) 999-1003.

3. L. Murugesh, K. T. V. Rao and R. O. Ritchie, "Crack Growth in a Ductile-Phase-Toughened Nb/Nb_3Al in situ Intermetallic Composite under Monotonic and Cyclic Loading," Scripta Metall., 29 (1993) 1107-1112.

4. C. R. Hunt jr. and A. Raman, "Alloy chemistry of σ (β-U)-related phases I. Extension μ- and occurrence of μ'-phases in the ternary systems Nb(Ta)-X-Al (X= Fe, Co, Ni, Cu, Cr, Mo)," Z. Metallkd., 59 (1968) 701-707

5. R. Jackson, H. J. Carvalhinhos and B. B. Argent, "The Creep of Niobium-Molybdenum Alloys," J. Inst. Metals, 96 (1968), 210-220

6. S. Hanada et al., "High Temperature Strength and Ambient Temperature Fracture Toughness of Nb_3Al/Nb_{SS} *in-situ* Composites," Thermec-97 International Symposium on Intermetallics and Their Composites, in press

7. S. Saito et al., "Fabrication of single phase Nb_3Al bulk material by clad-chip extrusion method," J. Japan Inst. Materials, 58 (1994), 1080-1085

8. K. Sadananda, C. R. Feng, H. N. Jones and J. J. Petrovic, "Creep of Intermetallic Composites: Effect of Grain Size Versus Reinforcements," Structural Intermetallics, R. Darolia et al. eds., TMS, (1993), 809-818

9. M. Nazamy, C. Noseda, G. Sauthoff, B. Zeumer and D. Anton, "Mechanical Behavior and Oxidation Properties of Molybdenum-Modified Cr_3Si/Cr_5Si_3 Intermetallics," High-Temperature Ordered Intermetallic Alloy VI Part 2, J. A. Horton et al. eds., Mat. Res. Soc. Symp. Proc., 364 (1995), 1333-1338

10. N. Nomura, K. Yoshimi and S. Hanada, "Microstructure and Creep Resistance of Nb_3Al/Nb *in-situ* Composites," Structural Intermetallics 1997, M. V. Nathal et al. eds., TMS, (1997), 923-928

MICROSTRUCTURE AND MECHANICAL PROPERTIES OF Nb-Mo-TiC *IN-SITU* COMPOSITES

N. Nomura[1], K. Yoshimi[2†], T. Konno[2] and S. Hanada[2]
[1]Graduate Student, Department of Materials Processing, Tohoku University, Sendai 980-8577, Japan
[2]Institute for Materials Research, Tohoku University, Sendai 980-8577, Japan
[†]Present address : Metals and Ceramics Division, Oak Ridge National Laboratory, P.O.Box 2008, Oak Ridge, TN 37831-6115, USA

Abstract

In-situ Nb-Mo-TiC composites were produced by arc-melting, and their microstructure and mechanical properties were investigated in this study. Four samples having nominal compositions of Nb-40mol%TiC, Nb-20mol%Mo-40mol%TiC, Nb-40mol%Mo-40mol%TiC and Mo-40mol%TiC were prepared. For as-arc-melted samples, no precipitate is discerned in primarily-solidified TiC except for Nb-40mol%TiC. After annealing at 1873 K for 24 h, fine precipitates are observed in the primary TiC for all samples. The precipitates are found to have bcc structure (A2) by XRD. The precipitated particle size increases with increasing Nb concentration. TEM-EDX analysis for annealed Nb-40mol%Mo-40mol%TiC shows that the relative concentration of Mo is higher than that of Nb in precipitates, while the relative concentration of Nb is higher than that of Mo in TiC.

In as-arc-melted samples, cracks introduced by an indenter are propagated straight to a long distance. On the other hand, in annealed samples, introduced cracks are deflected by precipitates and the length of cracks is shortened, indicating that the composites are "ductile phase toughened" by the bcc phase. Furthermore, above 1473 K compressive yield strength of Nb-40mol%Mo-40mol%TiC and Mo-40mol%TiC is found to be higher than that of single phase TiC. It is concluded from these observeations that room temperature fracture toughness is improved by incorporating a bcc phase and high temperature strength of TiC is increased by alloying with Mo.

The Third Pacific Rim International Conference on Advanced Materials and Processing (PRICM 3)
Edited by M.A. Imam, R. DeNale, S. Hanada, Z. Zhong and D.N. Lee
The Minerals, Metals & Materials Society, 1998

Introduction

Recently, studies on high temperature structural materials, which can be used above 1500 K, have been carried out extensively. Refractory ceramic TiC, which has a high melting point (3340 K) and a relatively low density (4.9 Mg/m^3) is one of the candidates and very attractive material for high temperature structural applications. TiC has been used, however, only as one of the elements for hard materials or cutting tools because of its low fracture toughness. It is desired that the TiC application is developed by improving the toughness. On the other hand, refractory metals such as Nb or Mo are also expected as high temperature structural materials because of its relatively low density and high fracture toughness. It is of great interest that the ternary phase diagrams of Nb-Ti-C and Mo-Ti-C systems[2] show that Nb or Mo solid solution and TiC phases coexist within a relatively wide range. In the phase diagram of the quasi-binary system of Mo-TiC[3] (Fig. 1), it is shown that Mo dissolves in TiC up to 23 mol% at eutectic temperature, but that the solubility limit of Mo in TiC decreases down to only 14 mol% at 2073 K. This suggests that if Mo-TiC composites can be fabricated by a melting process with a relatively high cooling rate, solute Mo in TiC at eutectic temperature would be precipitated during annealing at lower temperatures. Mo (or Nb) introduced in such a way should behave as a second phase making a hard TiC phase toughen. Furthermore, it was reported that solid solution hardening occurs when Nb or Mo is dissolved in TiC[4,5]. Therefore, it is expected that the combination of Nb-Mo-TiC significantly improves high temperature strength and low temperature toughness of TiC as a composite material.

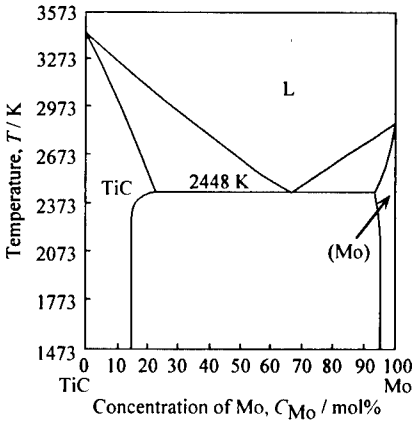


Fig. 1 The phase diagram of quasi-binary system Mo-40TiC[3].

The purposes of this study are to produce Nb-Mo-TiC *in-situ* composites, to investigate the microstructure depending on heat treatments and to evaluate their mechanical properties. Compressive properties at high temperatures and crack propagation behavior at room temperature by indentation tests were examined.

Experimental procedure

Nominal compositions of the materials used in this study were Nb-40mol%TiC, Nb-20mol%Mo-40mol%TiC, Nb-40mol%Mo-40mol%TiC and Mo-40mol%TiC. These alloys will be hereafter abbreviated as Nb-40TiC, Nb-20Mo-40TiC, Nb-40Mo-40TiC and Mo-40TiC. The samples were prepared from 99.6 mass%Nb, 99.98 mass%Mo and 99.4 mass%TiC powders. They were mixed by a cross rotary type machine for 5 hours and were arc-melted in an Ar atmosphere. The results of chemical analysis are shown in Table 1. Single phase TiC was also arc-melted for comparison.

The microstructural stability was studied by comparing the samples annealed at 1873 K for 24 hours with the as-cast samples. Microstructure was observed in an optical microscope (OM) and a scanning electron microscope (SEM). Phase identification was performed by a X-ray diffractometer (XRD), an electron probe micro analyzer (EPMA) and a transmission electron microscope equipped with energy dispersive X-ray spectroscopy (TEM-EDX).

The resistivity of the ductile phase to cracking introduced by indentation was investigated at 2.9 N as

a relative measurement of toughness. All indentation tests were conducted at room temperature.

Compression tests were carried out at temperatures from 1473 K to 1873 K in an Ar atmosphere at a strain rate of 1.6×10^{-4} s^{-1} on an Instron 8562-type machine. The test samples were cut into 2 mm x 2 mm x 5 mm by EDM and then polished with SiC paper.

Table 1 Chemical compositions of the samples (mol %)

Samples	Nb	Mo	Ti	W	Cu	C	O	N	H
Nb-40TiC	42.5	---	26.4	0.02	<0.01	30.8	0.03	0.17	0.07
Nb-20Mo-40TiC	29.1	16.7	25.4	0.07	<0.01	28.5	0.07	0.14	0.06
Nb-40Mo-40TiC	13.2	34.9	30.2	<0.01	<0.01	21.3	0.06	0.24	0.13
Mo-40TiC	---	40.9	29.7	0.04	0.06	29.1	0.02	0.07	0.06

Results and Discussion

Microstructure of Nb-Mo-TiC in-situ composites

Figure 2 shows microstructures of as-cast composites. Primary particles and lamellar eutectic microstructure are observed in Mo-40TiC. As Mo content decreases, the volume fraction of the eutectic reaction phase decreases, and it disappears in Nb-40TiC. The primary phase was identified as TiC by EPMA analysis. No discernible precipitate was observed in TiC phase except for Nb-40TiC.

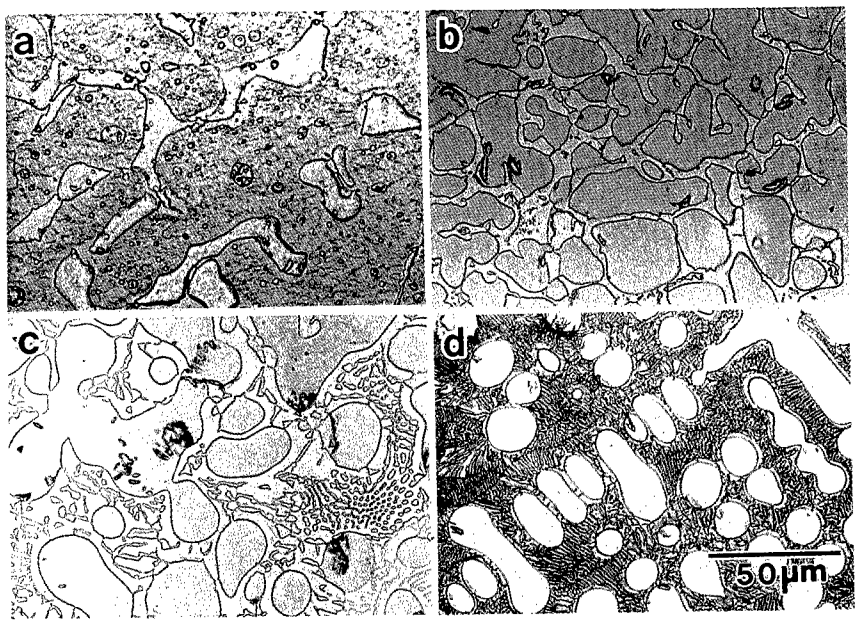


Fig. 2 Optical micrographs of as-cast Nb-Mo-40TiC composites.
(a) Nb-40TiC, (b) Nb-20Mo-40TiC, (c) Nb-40Mo-40TiC, (d) Mo-40TiC

After annealing at 1873 K for 24 h, fine precipitates were observed in the TiC primary phase for all samples. The size of these precipitates increased with increasing Nb concentration. Since no phase was detected by XRD except A2 and B1 phases, the precipitates in TiC were identified as an A2 (bcc) phase.

To examine the composition of precipitates in TiC, TEM-EDX analysis was performed for Nb-40Mo-40TiC, and the results are shown in Figure 3 and Table 2. Since carbon content was not analysed, compositions are indicated by the relative content of Nb, Mo and Ti. The relative content of Mo is higher than that of Nb in precipitates, while the relative content of Nb is higher than that of Mo in matrix TiC. TiC and NbC; both of them have B1 structure, form a complete solid solution at 1773 K. In Mo-C binary system, αMoC has B1 structure, but it is stable only above 2233 K. In Mo-Ti-C ternary system, TiC and MoC do not form a solid solution below 2273 K[2]. Accordingly, it is considered that the substitution of Nb for Ti in TiC at 1873 K is more preferable than that of Mo.

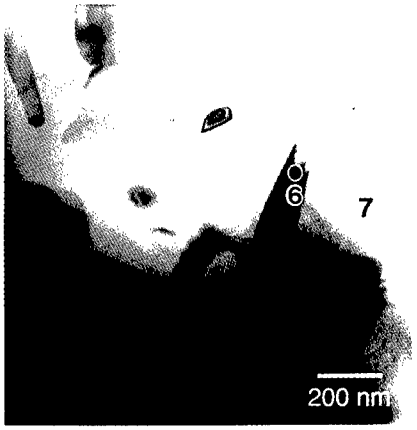


Fig. 3 TEM micrograph of Nb-40Mo-40TiC annealed at 1873 K for 70 hours.

Table 2 The relative content of metallic elements in Nb-40Mo-40TiC.

Location	Nb	Mo	Ti	Phase
6	29.4	59.1	11.5	β
7	25.4	11.8	62.8	δ

Mechanical properties

Indentation tests were carried out, and crack propagation was observed. Figure 4 shows indented traces introduced at 2.9 N for Nb-20Mo-40TiC. While cracks propagate almost straight to a long distance in the TiC single phase of as-cast sample as shown in Fig. 4(a), the length of cracks is distinctly reduced in annealed sample as shown in Fig. 4(b). Highly-magnified observation at a crack tip (Fig. 4(c)) demonstrates the bridging of bcc ligaments, although the plastic deformability of ligaments per se was not dealt with in this study. This tendency was observed in other samples. Results of indentation tests at 2.9 N are tabulated in Table 3. Crack length was measured from the corner of an indenter trace to the tip of a crack. The hardness in the TiC single phase shows the highest value, which would be measured as the apparent value due to extensive cracking around the indented trace. In Mo-containing samples, the hardness of annealed ones decreases in comparison with as-cast ones because of the precipitation of bcc solid solution. The average crack length in each annealed sample is less than half of that in the TiC single phase and as-cast samples. This indicates that the crack propagation is restrained by bcc precipitates in TiC. Furthermore, the average crack length also increases as Mo concentration increases. This change of the average crack length with Mo content is attributed to the particle size of bcc precipitates, because the volume fraction of them is almost the same in each composite. It has been reported that ductile phase toughening is effective when the particle size of a ductile phase is larger than the process zone at a

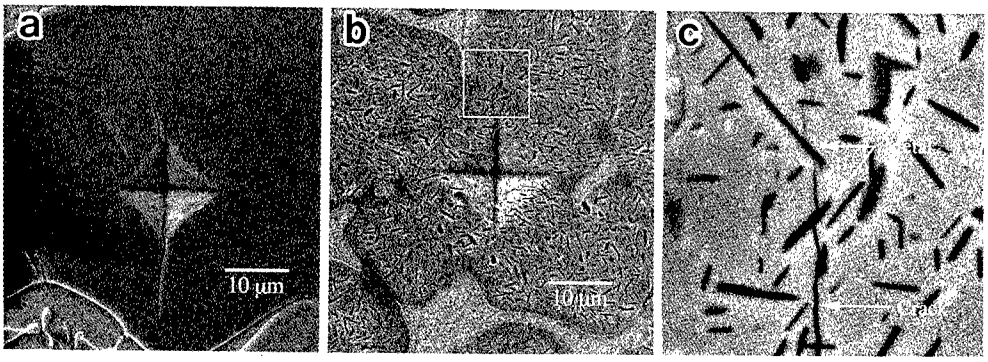


Fig. 4 Microstructure of Nb-20Mo-40TiC after indentation test in the (a) as-cast, (b) annealed and (c) crack tip of annealed composites.

crack tip[6]. In the present composites, however, the effective size of bcc precipitates is less than 1 μm as shown in Fig. 4(c). This particle size might be too small to act as a ductile phase. If the size of ductile phases is optimized by heat treatments, ductile phase toughening would appear more clearly.

Table 3 Results of indentation test.

Sample	VHN (2.9 N)	Average crack length / μm
TiC single phase	2470	11.0
Nb-40TiC as-cast	971	4.6
Nb-40TiC annealed	1116	1.5
Nb-20Mo-40TiC as-cast	1823	7.5
Nb-20Mo-40TiC annealed	1213	2.4
Nb-40Mo-40TiC as-cast	1730	9.7
Nb-40Mo-40TiC annealed	1368	4.1
Mo-40TiC as-cast	1777*	Fracture
Mo-40TiC annealed	1636	7.8

* Note that applied force was used at 0.98 N.

Results on compression tests performed in the range of temperatures from 1473 K to 1873 K are shown in Fig. 7. By alloying with Mo, yield stress increases, and Nb-40Mo-40TiC alloy shows the highest yield stress above 1673 K. It should be noted that yield stresses of Nb-40Mo-40TiC and Mo-40TiC are higher than that of single phase TiC[7] in compression tests above 1473 K. Evidently, the TiC phase is solid solution strengthened by alloying with Mo. In order to discuss the

strengthening of *in-situ* composite quantitatively, solid solution strengthening of the constituen phase, bcc or TiC, should be investigated as a function of temperature.

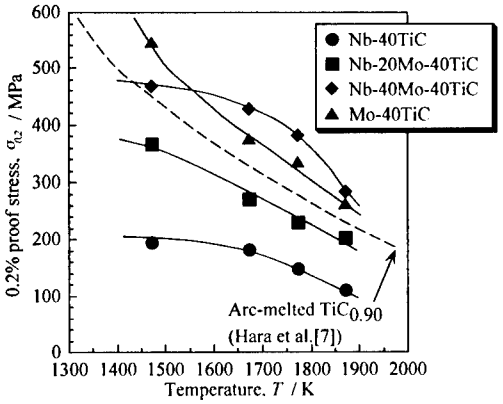


Fig. 5 Temperature dependence of 0.2% proof stress of Nb-Mo-40TiC composites.

Conclusions

A great potential of Nb-Mo-TiC *in-situ* composites for high temperature applications is demonstrated through this work. The Nb-Mo-TiC *in-situ* composites are produced by arc-melting, and fine bcc precipitates can be dispersed in a primarily-solidified TiC phase by the following isothermal heat treatment. Indentation tests reveal that the average crack length in annealed samples is less than half of that in as-cast samples. In addition, crack bridging by precipitates is observed to occur. These results indicate that the primary TiC phase is toughened by the bcc phase ("ductile phase toughening"). Also, the composites have excellent high temperature strength performance. In particular, Nb-40Mo-40TiC and Mo-40TiC show higher yield stresses than that of monolithic TiC above 1473 K.

Acknowledgements

The authors would like to thank Mr. Y. Murakami for his experimental support of EPMA. This research was supported by Research Fellowships of Japan Society for the Promotion of Science for Young Scientist and Postdoctoral Fellowships for Research Abroad from Japan Society for the Promotion of Science.

Reference

1. S. Mazdiyashi and D. B. Miracle, Intermetallic Matrix Composites, D. L. Anton, P. L. Martin, D. B. Miracle and R. McMeeking, eds., Mat.Res.Soc.Symp.Proc.,194 (1990), 155-162.
2. P. Villars et al., Handbook of Ternary Alloy Phase Diagrams, vol.6 (Materials Park, OH:American Society for Metals, 1995), 7199-7203 and 7082-7097.
3. V. N. Eremenko and T. Ya. Velikanova, Poroshkovaya Met., 5 (1963), 3-9.
4. Tsurekawa et al., J. Japan Inst. Metals, 55 (1991), 390-397.
5. Kurishita et al., J. Japan Inst. Metals, 49 (1985), 1064-1073.
6. D. L. Anton and D. M. Shah, Intermetallic Matrix Composites, D. L. Anton, P. L. Martin, D. B. Miracle and R. McMeeking, eds., Mat.Res.Soc.Symp.Proc.,194 (1990), 45-52.
7. Keiji Hara, Hideo Yoshinaga and Shotaro Morozumi, J. Japan Inst. Metals, 42 (1978), 1039-1047.

High Transition Temperature Superconductors

RESEARCH AND DEVELOPMENT OF SUPERCONDUCTING MATERIALS IN CHINA

Lian Zhou
Northwest Institute for Nonferrous Metal Research
P.O.Box 51, Xi'an, Shaanxi 710016, P.R.China

Abstract

In recent years, a great of achievements in research and development of superconducting materials including both high-T_c and low-T_c conventional superconductors have been made in China. For high-T_c materials, a new method - 'Powder Melting Process' (PMP) has been invented to fabricate high quality YBCO bulks with J_c values more than $10^5 A/cm^2$ (77,1T). The effective flux pinning centers such as dispersively distributed fine Y_2BaCuO_5 inclusions, stacking faults and dislocations can be introduced into the Y-system superconductors by PMP method. The melt-textured YBCO big bulks has been used to construct the demonstrators of maglev application. The mechanisms of formation and texturization of Bi-2223 phase in Ag-clad tapes have been studied in details. The results indicated that the texture of 2223 phase has a strong correlation with the texture of precursor 2212 phase. The texturization of 2223 phase during phase formation could be described as preferential grain growth mechanism. TEM observation pointed out that the 2223 phases are formed through the insertion of additional Ca and CuO layer into the 2212 structure. The silver layer was found take an important role in 2223 phase formation by supplying fast facilitating liquid formation. Based on understanding of the 2223 phase formation mechanism, high J_c mono- and multi-filamentary Bi-2223/Ag tapes have been fabricated by modified PIT method. For conventional low-T_c materials, the main research and development works were done in Northwest Institute for Nonferrous Metal Research (NIN). The J_c values of NbTi/Cu multifilamentary wires with Nb barriers have been reached $3.5x10^5 A/cm^2$ (4.2K, 5T). Long (>10^4meters) ultra-fine filamentary (less than 0.5μm) NbTi/Cu-CuNi wires for AC uses were successfully fabricated. Furthermore, techniques for introducing artificial pinning centers in NbTi superconductors have been developed and J_c value of multifilamentary wires with island–shaped Nb flux pinning centers reached $3.2 \times 10^5 A/cm^2$(4.2K,5T).

The Third Pacific Rim International Conference on
Advanced Materials and Processing (PRICM 3)
Edited by M.A. Imam, R. DeNale, S. Hanada,
Z. Zhong and D.N. Lee
The Minerals, Metals & Materials Society, 1998

Introduction

The discovery of high temperature superconductivity (HTSC) has not only opened many possibilities for potential technical applications, but also has provided a unique, challenging research subject for condensed matter physics and materials sciences. In the past years, research and development has been steadily carrying out and rapid progress has been made in all aspects of HTSC science and technology, from materials through physics to applications. For example, more than 75 cuprate high-T_c superconductors were discovered with transition temperatures up to 133K in $HgBa_2Ca_2Cu_3O_{8+y}$ under ambient pressure and to 164K under high pressure(1). Many techniques have been proposed to prepare good quality high-T_c superconductors with usable forms, e.g. bulk, wire and film (2-4). Among them, melt processed YBCO bulk materials can be fabricated in small scale production with high superconducting properties for applications. Many HTSC prototype devices using melt textured YBCO , such as flywheel energy storage system, electric motor and magnetic levitation train model, have been constructed and tested successfully. Moreover, long wires of (Bi,Pb) -Sr-Ca-Cu-O superconductors with high-J_c have been produced and small magnets (up to 7T at 4.2K) using these materials have been fabricated (5). Also, the weak link problem in Y-based superconducting thick films has been eliminated by choosing suitable materials for a buffer layer on the substrate and J_c value in these films is exceeding $10^6 A/cm^2$ (77K, 0T).

In the mean time, high-T_c superconductivity research in China has made a great progress. Northwest Institute for Nonferrous Metal Research (NIN) has invented a new technique-powder melting process (PMP) to fabricate high quality YBCO bulks with J_c values higher than $10^5 A/cm^2$ (77K,1T) (6,7). As compared to other melt processes including melt textured growth (MTG) and melt powder melt growth (MPMG), the effective flux pinning centers such as dispersively distributed fine Y_2BaCuO_5 (211) inclusions, stacking faults and dislocations can be easily introduced into YBCO by PMP method. As for Bi-based supercon ductors, achievements has been made on the mechanism of formation and texturization of Bi2223 phase, the processing control, the microstructure, J_c properties and flux pinning in Ag-clad Bi2223 tapes. Long mono- and multi-filamentary tapes with high J_c can be produced using the modified powder-in-tube (PIT) method. The best J_c value of the short Bi2223/Ag tapes is $5.2x10^4 A/cm^2$ (77K,self-field) . These exiting new development show prosperous application and market potential for HTSC in the near future.

In this paper, a brief review is given in the view of material aspect on the recent progress in Y-system and Bi-system superconductors as well as low-T_c superconductors.

Progress in melt-processed YBCO materials

Characteristics of PMP-processed YBCO

In PMP method, 211 and Ba-Cu-O powders rather than $YBa_2Cu_3O_y$ (Y123) are used as precursor materials for the melt process, which can avoid the segregation of the 211 phase created by the decomposition of the Y123 phase in the high temperature region. Thus, we can obtain better microstructure in PMP YBCO than in YBCO samples prepared by other melt processes. Figure 1 shows the SEM photograph of fracture surface of PMP YBCO specimens, indicating that the Y123 crystals are well oriented with their ab basal planes parallel to the length direction of the specimens. The 211 inclusions (elliptical particles in the figure) with average size less than 1μm are dispersively distributed within the 123 matrix, as shown in Fig.1. The small holes in the graph are not pores, they are the cavities left by the 211 particles

removed when we fractured the sample for the SEM observation, so the sample shows almost 100% dense no any voids or microcracks. Detail investigation on samples by TEM



Figure 1: SEM image of fracture surface.

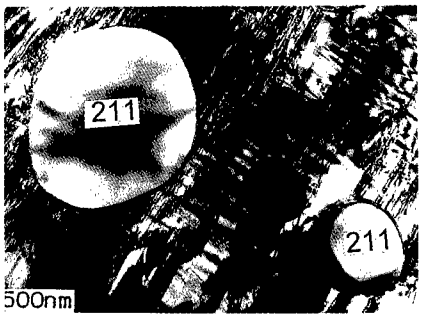


Figure 2: TEM image showing dense stacking faults

indicated that the 123 grain boundaries are clean, narrow, low angle boundaries, which resulted in the elimination of 'weak links' in PMP-processed YBCO bulks . A high density (~$2x10^6 cm^{-1}$) of stacking faults with their habit plane perpendicular to c-axis (as shown in Fig.2) and dislocations, which is much higher than those of MTG and MPMG samples, were observed in PMP samples. Further study shows that almost all the stacking faults form a series of collective "stair-like" ones, being quite different from those in other melt processed YBCO (8). These crystal defects have been considered as effective pinning centers.

Flux pinning centers in YBCO

The transport critical current densities exceeding $7x10^4$ A/cm^2 (1T, HIIc), $2.4x10^4$ (12T, HIIab), and $1.2x10^4$ (20T, HIIab) at 77K have been obtained in PMP samples (9,10). Recently, we have found that the stacking faults and dislocations can be eliminated considerably by re-annealing the PMP samples at 830 to 900 °C for about 30 hours (11), while other microstructural characteristics were unchanged. .The density of stacking faults decreases from $10^6 cm^{-1}$ to $10^3 cm^{-1}$ after the re-annealing. Figure 3. shows the J_c dependence on magnetic

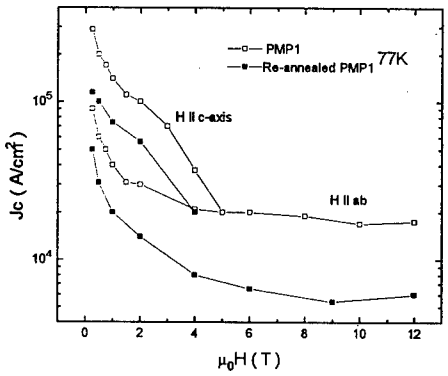


Figure 3: J_c values versus magnetic field of sample before and after re-annealing.

fields of one sample before and after re-annealing at 880 °C. It can be seen that the J_c values at 77K (both for Hllc and Hllab) drop significantly after re-annealing. J_c decreases from $1.4X10^5A/cm^2$ in the original YBCO to $7x10^4A/cm^2$ in the re-annealed one at 77K in 1T. Furthermore, the irreversibility lines were found to move to lower temperature and fields. Because the main effect of the re-annealing process is related to an elimination of stacking faults and dislocations, we can assume that the observed decrease of flux pinning is due to the disappearance of these defects. In other words, the dense stacking faults and dislocations are effective pinning centers in PMP YBCO bulks . Moreover, the effectiveness of 211 particles as flux pinning centers has been confirmed by the same way (12).

Effect of element additions on superconducting properties

Because the weak link has been overcome in PMP YBCO specimens, it is of significance to investigate the influence of substitutes on the properties. Recently, we have prepared element-doped YBCO samples by the PMP method and found that J_c and flux pinning can be largely improved by Ho, Gd or Er substitutions for Y in Y-system superconductors. Also, the Sn-added YBCO sample exhibits much higher J_c value and lower flux creep rate than pure YBCO (13). These results provide a new, convenient and effective way to increase J_c. J_c value is enhanced about 5 times larger by Ho addition, achieving $3.9x10^5A/cm^2$ (0T) and $1.6x10^5A/cm^2$(1T) at 70K. Our investigations suggest that the reduction of the size of 211 particles, stress-field pinning and magnetic pinning created by rare earth element substitutions can be responsible for the improvement of J_c.

Large single-domain YBCO

For practical applications such as magnetic levitation energy storage and conversion system, large bulk YBCO materials are required. By using PMP and modified MTG methods with $NdBa_2Cu_3O_y$ seeds or MgO seeds, the large single-domain YBCO (Diameter:ϕ18mm-ϕ40mm) with high magnetic levitation force ($12N/cm^2$ at 77k as shown in Figure 4) can be prepared in NIN. The trapping field measured above the center of the YBCO sample is about 700mT at 77K. The X-ray Φ-scan pattern for (103) plane of YBCO was given in Figure 5. It can be seen that there are four symmetric and very sharp diffraction peaks, one in every 90°. This result shows that the YBCO sample has a single-domain structure. In addition, NIN has the ability to fabricate the large single-domain YBCO materials in a small scale production with high quality for applications.

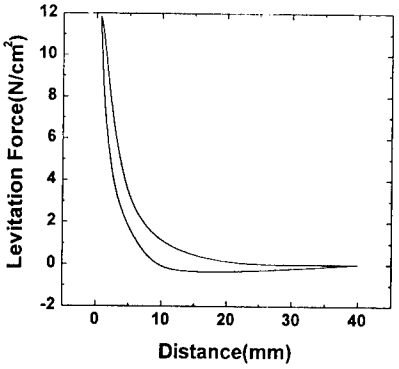


Figure 4: Magnetic levitation force density of large YBCO bulk.

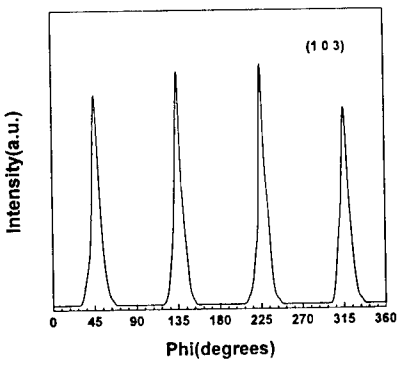


Figure 5: Typical X-ray Φ sacn of the YBCO sample.

Progress In Bi-system Tapes

The Ag-sheathed Bi-system tape is one of the most important superconductors used at liquid nitrogen temperature and has been planed to applied for practical application. In addition to its higher T_c, the layered structure of Bi-2223 can help in texturing the grains by mechanical deformation, and presence of liquid phase during the sintering process for 2223 phase formation can improve densification and seals the damage of due to mechanical processing. These properties enable the powder-in-tube (PIT) method to be successfully used for fabricating high quality Ag-sheathed Bi-2223 tapes.

Mechanism of Bi-2223 phase formation

In the typical PIT process, the Bi-2223 phase is formed during sintering by the reaction between Bi-2212 and Ca-Cu-O phases. Understanding the mechanism of the 2223 phase formation in the tape will be helpful to control the phase purity and grain alignment, and thereby improve the critical current density. The diffusion couples composed of 2212 and Ca-Cu-O phases have been carefully designed to study the mechanism of the 2223 phase formation (14). The results indicated that the 2212 (Pb-poor) and Ca_2PbO_4 firstly interact to form Pb-rich 2212, Bi_2O_3, CaO, PbO and O_2, resulting in the formation of Ca_2CuO and Bi/Pb rich liquid due to the presence of CuO, then the (Bi,Pb)-2212, Ca_2CuO and CuO react to form 2223 phase, which is accelerated by the presence of Bi/Pb rich liquid. In addition, we found that the important role of silver sheath is a combination of preventing the Pb loss, supplying a fast out-diffusion path, introducing liquid phase, and acting as a quasi-two-dimensional space (15). During 2212 to 2223 phase transformation, oxygen will be released from the BiO planes of 2212 to compensate the valence reduction of Pb after Pb^{4+} enters the BiO plane of 2212 as Pb^{2+} to make 2223 nucleate. The silver layer just supplies a favorable out-diffusion path for the produced oxygen to escape in time and thereby promotes 2223 phase formation. The silver sheath, especially the broad layer, effectively prevents Pb loss to maintain an adequate Pb concentration of 2223 formation.

PIT-processed multifilamentary tapes

Multifilamentary tapes with filaments of 19, 37, 61 and 85 have been successfully fabricated by PIT process. Typically, the precursor powders which mainly composed of (Bi,Pb)-2212, calcium cuprate and other secondary phases were packed into silver tube. Subsequent deformation included cold swaging and drawing the monofilamentary rod to a diameter of several mm, after which the wire was drawn to a hexagonal shape. These hexagonal wires were bundled and stacked into a Ag or Ag-alloy tube, which was deformed again into a diameter of 1.5 - 2.5 mm. Then, a two- times rolling and heat treatment process was used to fabricated the multifilamentary tapes with thickness of 0.2 - 0.3mm, the width varying between 2.5 - 4 mm. In order to have sufficient unreacted phases to heal the cracks induced during rolling process, the first heat treatment time was chosen less than 50 hours. But a longer sintering time (more than 150 hours) is needed for the final heat treatment to obtain higher J_c values. This two-times rolling and heat treatment technique is more suitable for fabricating long Bi-2223/Ag tapes. By carefully controlling the processing parameters, the gas induced "bubbling phenomenon" and the unhomogeneous deformation induced "sausaging" of filaments

have been considerably suppressed. As a result, a high J_c value of 2.1x 10^4A/cm^2 (77K, 0T) have been obtained in these multifilamentary tapes with diffrent filaments. In order to increase mechanical strength of the tapes, the Ag-Mg and Ag-Mn alloy have been used as the outer tube for fabricating the multifilamentary tapes. The same J_c value were achieved, while the tensile stress increase from 80 MPa to 150 MPa.

Introduction of flux pinning centers

The research group in NIN have successfully developed a special technique to introduce Ag foils with thickness of several nanometers into their multifilamentary tapes as flux pinning centers. Because silver has been considered no side-effect when it exist within the superconducting core, the transport J_c value was not degraded in the tapes with Ag foils, while the dependence of J_c on applied magnetic field are obvious improved, as shown in Fig.6. As the Ag foils are configured parallel to the tape plane, the flux lines are effectively pinned only when the applied field perpendicular to the c-axis, that is why the J_c-B dependence was not improve when the magnetic field parallel to the c-axis.

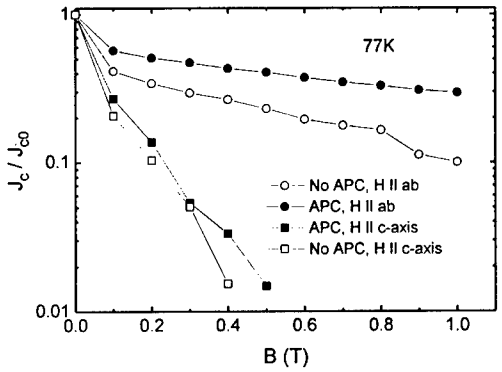


Figure 6: Normalized critical current density of both multifilamentary tapes with and without Ag foils as artificial pinning centers.

Progress in NbTi Superconductors

High quality ingot

Recently, low impurity content and high homogeneous NbTi ingots with size up to ϕ220x1000mm^2 were successfully manufactured by a new process in NIN as show in Table I, in which the vacuum arc skull furnace was combined with the vacuum arc furnace during the melting process. There is no any freckle and niobium-rich inclusions in this kind of NbTi ingots.

Table I. Specification of Nb46.5wt%Ti ingot(% by weight)

Element	Ti	H	O	C	N	Fe	Si	HB
Content	46.5 ± 1.5wt%	0.002	0.02	0.01	0.008	0.0065	0.01	126-136

High J_c NbTi wires

By utilizing high quality Nb46.5wt%Ti ingot, the high J_c multifilamentary wires have been fabricated by a new pre–heat treatment process in NIN. The initial heat treatment was performed at low temperature for a few hours, and the final heat treatment was carried out at higher temperature for a longer time. Figure 7 shows the J_c-B curve for the NbTi wires (with a strand diameter of 0.3mm, a filament diameter of 3.5mm and filament number of 3025).

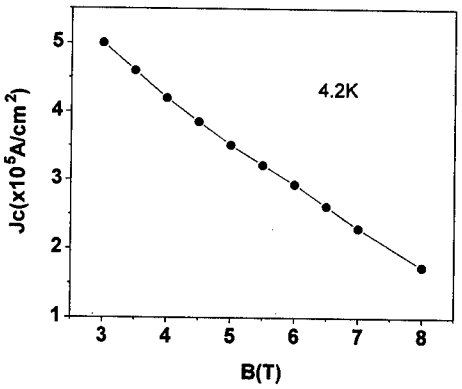


Figure 7: J_c-B curve for Nb46.5wt%Ti composites.

The NbTi wires have a higher J_c values of $3.5 \times 10^5 A/cm^2$ especially in higher fields For example, at 8T, 4.2K, J_c reaches $1.74 \times 10^5 A/cm^2$ (16).

NbTi wires for A.C uses

A large quantities of high J_c and low A.C.loss superconductors for A.C. use have been produced in NIN. The conductors were composed of ultrafine filaments with Nb barriers(17).Table II shows the specification of the A.C. use strand.

Table II. Specification of the strand for A.C. use.

Wire diameter:	Φ 0.146mm
Filament diameter:	0.48mm
Number of filament:	24462
Twist:	2.0mm
Matrix:	CuNi+Cu
Nominal	Copper to NbTi ratio: 2.57
J_c(D.C.):	$4.8 \times 10^5 A/cm^2$(2T,4.2K, 0.1μv/cm)

Introduction of artificial pinning centers

In order to improve the J_c values of NbTi superconductor, the effect of the shape, content and material of flux pinning center on J_c has been investigated, and the J_c value of multifilamentary

NbTi wire with island–shaped Nb flux pinning centers reached 3.2 × 10^5A/cm^2(4.2K,5T). In addition, a new process has been developed to prepare NbTi superconductors by diffusion between pure Nb and Ti layers at high temperature in NIN. The J_c value of 2.6x10^5A/cm^2(4.2K,5T) was achieved (18).

Reference

1. G.B.Peacock et al., "Fluorination of mercury-based high-temperature superconductors," Physica C 289 (1997), 153-160.
2. K.Salama and D.F.Lee, " Progress in melting texturing of YBa2Cu3Oy superconductor, " Supercond. Sci. Technol., 7 (1994), 177-193,
3. M.Murakami, " Processing of bulk YBaCuO," Supercond. Sci. Technol., 5 (1992), 185-203,
4. R.Flukiger et al., " Phase formation and critical current density in Bi,Pb(2223) tapes," Supercond. Sci. Technol., 10 (1997), A68-92.
5.K.Sato et al., "HTS wires and application progress" (Paper presented at the MT-15 Conference, Beijing China, 20 October 1997)
6. L. Zhou et al, " The properties of YBCO superconductors prepared a new approach: the "powder melting process," Supercond. Sci. Technol. **3** 1990). 490-492.
7. P. X. Zhang , H.W.Weber and L.Zhou, " Irreversibility lines and critical current densities of PMP-processed YBCO,: Supercond. Sci. Technol. **8** (1995). 701-704.
8.Y.Feng et al, " Flux pinning by collective stair-like stacking faults in $Y_{0.6}Ho_{0.4}Ba_2Cu_3O_y$ prepared by powder melting process," Appl.Phys.Lett. 70 (1997), 28942896
9. L.Zhou, "High-T_c Research in The People's Republic of China" Superconductor Industry/ Winter 1997, 18-23.
10. P. X. Zhang et al., " Identification of Stacking Faults with Flux Pinning in Powder Melting Processed $YBa_2Cu_3O_y$," Phys. Stat. Sol.(a) 149 (1995)., 669-676.
11. P.X.Zhang et al., "The effect of annealing on stacking faults and J_c values of PMP processed YBCO," Supercond. Sci. Technol. 8 (1995),15-19.
12. P.X.Zhang etal., "Idenyification of Y_2BaCuO_5 inclusions with Flux Pinning in Powder Melting Processed $YBa_2Cu_3O_y$," Phys. Stat. Sol.(a) 154 (1996), 727-733.
13. Y.Feng et al., "Critical current density and flux pinning mechanism in Ho-doped Powder melting processed YBCO," J.Appl.Phys. 80 (1996), 993-998.
14. L. Zhou et al., "Formation Mechanism of Textured Bi-2223 Phase in Ag-clad Tapes" (Paper presented at the SPA'97, Xi'an, China, 6 March 1997),6.
15. C.B.Mao et al., "New Understanding of Silver-induced Texture in Powder-in-tube Processed Ag/Bi(2223) Tape," Physica C, 281(1997), 159-175.
16.X.Z.Wu et al., " Effect of Heat Treatment of The J_c Values in Industrial Scale Multifilamentary Nb46.5wt%Ti Superconductors," (Proceedings of 8th IWCC, Kitakyushu, Japan 27 May 1996), p499.
17. S.J.Du et al., " Study of Ultrafine Multifilamentory NbTi Wires for A.C. Use,"(Paper presented at the SPA'97, Xi'an China, 6 March 1997),4.
18.Y.Yun et al., "Study of Superconductor Forming by Niobiu and Titanium Diffusion,"(Paper presented at the SPA'97, Xi'an China, 6 March 1997),4.

BONDABILITY AND SUPERCONDUCTIVITY OF YBCO CERAMICS WITH In_2O_3 ADDITIVES

Akio Suzumura, Dai Zhigang

Department of Mechanical and Intelligent Systems Engineering
Faculty of Engineering, Tokyo Institute of Technology
2-12-1, O-okayama, Meguro-ku, Tokyo, 152 Japan

Abstract

Influence of the addition of indium oxide on the bondability and superconductivity of YBCO($YBa_2Cu_3O_{7-X}$) superconductors was studied. The YBCO sintered bulk specimens were bonded at 1223K for 1 hr under a bonding pressure of 2.4kPa in air without an interlayer. Bondability of the joints was examined by both the X-ray diffraction and shear tests as well as the thermal analysis. The critical temperature(Tc) and the critical current density(Jc) were measured by the standard D.C. 4-probe resistive method. The strength of joints of the specimens increased, and on the contrary, their mass density and the Jc values decreased with the addition of indium oxide. Tc's of the specimens before bonding slightly decreased with In_2O_3 content up to 7mass%, showing the same tendency at the joints. It was observed that during the sintering process the added In_2O_3 was reacted with YBCO matrix to form the $Ba_2In_2O_5$ particle shaped crystals, and that the thermal cycle subjected in bonding process would not affect the crystal structure of the YBCO matrix.

The Third Pacific Rim International Conference on
Advanced Materials and Processing (PRICM 3)
Edited by M.A. Imam, R. DeNale, S. Hanada,
Z. Zhong and D.N. Lee
The Minerals, Metals & Materials Society, 1998

Introduction

It is considered that the YBCO oxide superconductor is one of the most promising superconductors which can be used in practical applications. In order to realize the applications, various processing and manufacturing technologies have been studied. Usually, the oxides are extremely brittle and hard to form into mechanical and electric parts. At present, the development of bonding technology for the oxide superconductors is required from the application points of view. But only a few papers on the bonding technology have been reported[1-5]. In this study, therefore, the bonding technology of YBCO superconductor with the addition of indium oxide has been investigated.

After the discovery of oxide superconductors, the additions of the other oxide elements have been carried out to examine the various properties of the superconductors. Fagan et al. reported the improvement of the microstructure of YBCO superconductors by various oxide additions: in bulk specimens the interaction of a number of oxides, including SnO_2, In_2O_3 etc. with YBCO matrix, resulted in exaggerated grain growth and domain formation through the liquid-phase wetting mechanism[6]. Other papers[7-11] reported the influence of SnO_2 addition into YBCO superconductors, to enhance the critical current density Jc due to the decrease of grain size as well as the increase of flux pinning force because of the formation of fine $BaSnO_3$ precipitates. We reported the bondability of BSCCO(Bi-Sr-Ca-Cu-O) superconductors, inserted the layer screen-printed on the bonding surfaces using the mixed In-Ag oxide powders. Furthermore, we discussed the influence of SnO_2 on the bondability and superconductivity of YBCO superconductors. As to the In_2O_3, addition, however, there is no report on the bondability, although the indium oxide has the similar chemical properties to the SnO_2. Therefore, in this paper, the In_2O_3 is selected as one of the additives and the effect on the bondability and superconductivity of YBCO was studied.

Experimental Procedures

The YBCO powder was synthesized by the conventional solid state reaction: high purity Y_2O_3, $BaCO_3$ and CuO powders in a molar ratio of 1:4:6 were mixed in ethanol and calcined in an alumina crucible at 1173K for 12 hr. The crystal structure of calcined powder was examined by using X-ray diffraction technique, and then the YBCO powder was thoroughly mixed with various amounts of In_2O_3 powder. The powder was compacted under a pressure of 200MPa into pellets of 10mm and 12mm in diameter, 2mm in thickness. These pellets were sintered at 1203K for 12 hr and then cooled at a cooling rate of about 1.7K/min down to room temperature.

The critical temperature Tc and the critical current density Jc of YBCO specimens were measured using samples of 12×2×2mm cut from the pellets by the DC standard 4-probe resistive technique in a magnetic field of 0T. The Jc measurements were carried out at temperatures between 50K and 90K with an interval of 10K. The Meissner effect of sintered specimens was checked at the liquid nitrogen temperature. Then, the surfaces of the sintered specimens with 10 and 12mm in diameter were mechanically polished with sand papers up to the #1500 grit and buff, followed by cleaning with ultrasonic wave. The cleaned surfaces of the specimens were diffusion-bonded to each other by heating in air at 1223K for 1 hr under a pressure of 2.4kPa.

The shear test of the specimens was carried out to investigate the strengths of the bonded joints, and differential thermal analysis(DTA) and X-ray diffraction measurements to study thermal properties and crystal structure of the specimens during the sintering and bonding processes were also used.

Results and Discussion

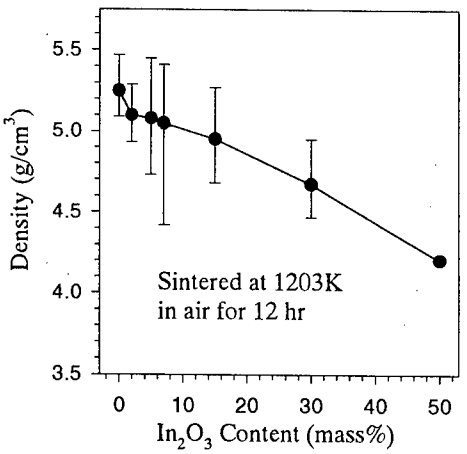


Fig.1 Relationship between density and In_2O_3content of sintered specimens

Effects of In_2O_3 Content on the Density of Sintered Specimens

In general, when the specimen is sintered at higher temperature, the density becomes higher. As shown in Fig.1, the density is 5.25g/cm^3 for the pure YBCO samples. By a small amount of 2mass% In_2O_3 addition, the density decreases to 5.1g/cm^3. By the further addition, the density of specimens continues to decrease with the increase of In_2O_3 content down to 4.2 g/cm^3 at 50mass%. Comparing the results with our previous results on the Ag_2O and SnO_2 additions, it is obvious that the effect of In_2O_3 on the density is different from those of Ag_2O and SnO_2, in both cases the densities increase with the additions.

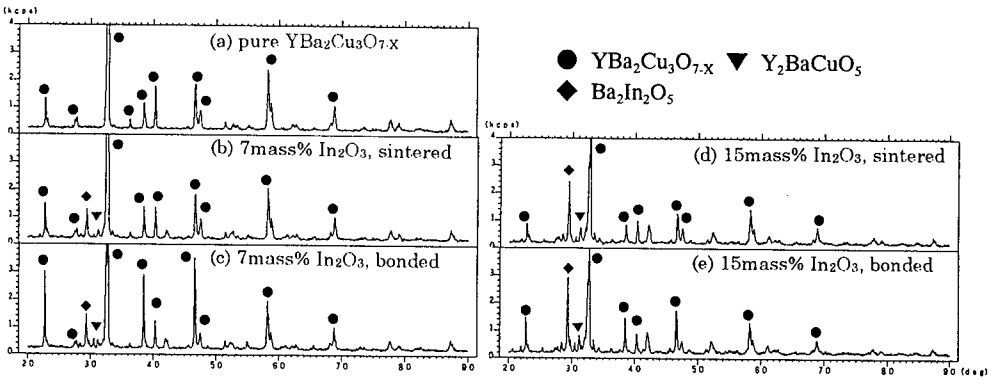


Fig.2 X-ray diffraction patterns for (a) pure YBCO sintered in 1173K
(b) YBCO+7mass%In_2O_3 sintered in 1203K (c) YBCO+7mass%In_2O_3 bonded in 1223K
(d) YBCO+15mass%In_2O_3 sintered in 1203K (e)YBCO+15mass%In_2O_3 bonded in 1223K

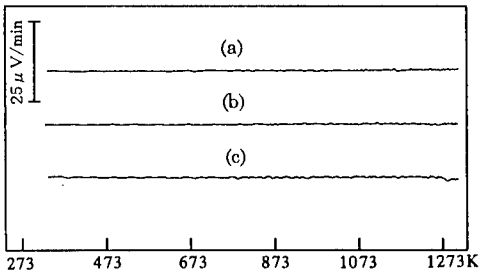


Fig.3 DTA curves for various specimens
(a) pure In_2O_3 (b) pure $YBa_2Cu_3O_{7-x}$
(c) YBCO+15mass% In_2O_3

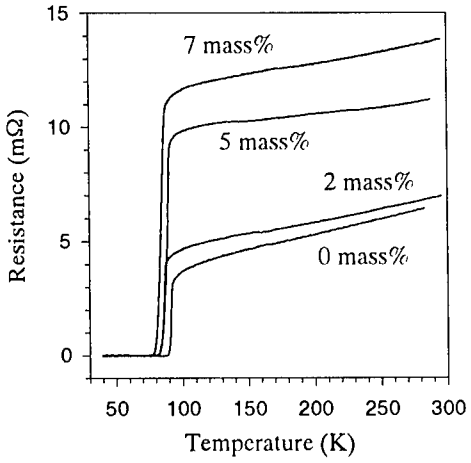


Fig.4 Relationship between resistance and temperature of the specimens with different In_2O_3 contents

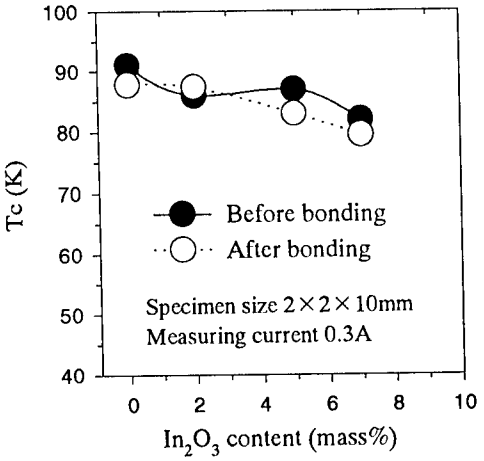


Fig.5 Relationship between critical temperature and In_2O_3 contents before and after bonding

Effects of Additives and Bonding Thermal Cycle on the YBCO Structure

Figure 2 shows the X-ray diffraction patterns of the specimens with 7mass% and 15mass% In_2O_3, where (a) is for the pure YBCO sintered in 1173K, (b) for the YBCO+7mass% In_2O_3 sintered in 1203K, (c) for the YBCO+7mass% In_2O_3 bonded in 1223K, (d) for the YBCO+15mass% In_2O_3 sintered in 1203K, and (e) for the YBCO+15mass% In_2O_3 bonded in 1223K, respectively. From the patterns, it is revealed that the YBCO matrix reacts with the added In_2O_3 to form the $Ba_2In_2O_5$ crystal during the sintering process. The peak intensity of $Ba_2In_2O_5$ patterns becomes stronger with increasing the In_2O_3 content. Comparing (b) with (c), it is observed that the same crystal structure before and after bonding is appeared, which means that the bonding thermal cycle does not affect the crystal structure of YBCO.

Figure 3 shows the effect of temperature on the interaction of In_2O_3 with YBCO powders obtained by DTA measurements. Pure In_2O_3 powder (a) and YBCO powder (b) show no transformation during the sintering process up to 1273K. The X-ray diffraction patterns in Fig.2 show that YBCO has the chemical reaction with In_2O_3 to form $Ba_2In_2O_5$, however, in DTA measurement any change due to such reaction is not appeared at lower temperatures. In fact, in the previous papers[1,6], no change in the DTA curves due to the reaction between the YBCO and added oxides including SnO_2 is not observed. It is considered that the thermal effects of these kinds of reactions are too small so that the DTA failed to reveal the reactions, although the behavior of added In_2O_3 is much different from that of Ag_2O which thermally decomposes during the sintering process[2].

Effects of In_2O_3 Content on Tc and Jc

Figure 4 shows the relationship between the temperature and electric resistance for the specimens with different In_2O_3 content. The resistances of the specimens in the normal conductive state increase with the increase of In_2O_3 content. It is considered that the insulating $Ba_2In_2O_5$ particles precipitated in the specimens make for the worse in the electrical conductivity of YBCO. All of the specimens show the sharp transition from the normal to superconductor.

Figure 5 shows the effect of In_2O_3 additions on the critical temperature Tc for specimens before and after bonding. The Tc values are 91K for the pure YBCO, and 82K for the specimen added 7mass% In_2O_3, with a tendency to slightly decrease with increasing the content of In_2O_3, and after bonding, these Tc values become down to 87.8K and 79.5K, respectively. For the specimen added 15mass% In_2O_3, there appears no superconductivity above 40K.

Figure 6 shows the relationship between the In_2O_3 content and the critical current density Jc measured at different temperatures in a magnetic field of 0T. The Jc values decrease with increasing the addition of In_2O_3, showing the same tendency as the density (Fig.1). From Figs.5 and 6, it is obvious that the addition of In_2O_3 decreases both Tc and Jc values. The Jc's of YBCO obtained are considerably lower compared with those of thin films or HIP-treated bulks. Because the specimens used are bulk pellet samples with not so high density prepared by the conventional pressing process. In fact, the Jc values are coincident with those obtained in bulk pellet samples[4,12].

Effect of In_2O_3 Content on the Shear Strength of the Joint

The influence of the In_2O_3 addition on the bonding strength is illustrated in Fig.7. These data indicate that addition of 2mass% In_2O_3 improves the average shear strength from 4.9MPa to

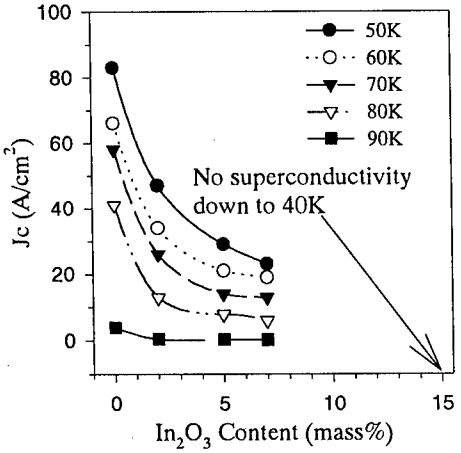


Fig.6 Relationship between Jc and In_2O_3 contents at different temperatures

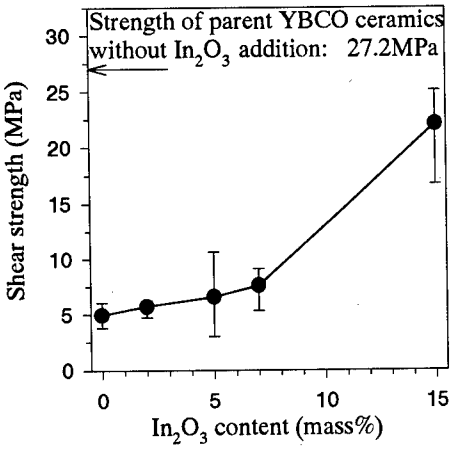


Fig.7 Relationship between In_2O_3 content and shear strength of joints bonded at a temperature of 1223K in air for 1 hr under the pressure of 2.4kPa.

5.7MPa. Further improvement to 6.6MPa results from the addition of 5mass%. It is considered that the precipitated $Ba_2In_2O_5$ induced by chemical reaction between the added In_2O_3 and the YBCO may relax residual thermal stresses, resulting from the expansion anisotropy of grains, and provide the increased resistance to crack propagation, and thus the strength increases. The strength of sintered YBCO bulks made by solid reaction is still low[4,12]. Further efforts have been directed toward improving the microstructure of YBCO to obtain both high Jc and improved mechanical properties[13,14].

Conclusions

The effect of In_2O_3 additions up to 15mass% has been investigated in YBCO superconductors. The results obtained are summarized as follows:

(1) The In_2O_3 added into YBCO bulks reacts to form the $Ba_2In_2O_5$ precipitate during sintering process.
(2) Shear strength of the specimens increases with the increase of In_2O_3 content.
(3) The bonding thermal cycle does not affect the crystal structure of YBCO matrix, although the added In_2O_3 reacts with a part of YBCO.
(4) Up to 7mass% In_2O_3 addition, the Tc's of bulks and joints decrease slightly with increasing the In_2O_3 content, and the Jc's greatly decrease, resulting from the decrease of the mass density by In_2O_3 addition.

References

1. Akio Suzumura, Dai Zhigang, and Hirotaka Ogawa, "Effects of SnO_2 additives on the bondability and superconductivity of YBCO superconductors," Materials Transactions, Japan Institute of Metals(JIM), Vol. 37, No.5 (1996.5) 1116-1121.
2. Akio Suzumura et al., "Effects of Insert Materials on the Bondability and Superconductivity of YBCO Superconductors," Proceedings of the 6th International Symposium of Japan Welding Society, Vol. 1 (1996.11.) 71-76.
3. Akio Suzumura et al., New Advances in Allied Processes (International Academic Publishers, 1991) Vol. 1, pp. 426-431.
4. H.Nakao, Welding Technology, Sept.1989, 66-70.(in Japanese).
5. H.Ogawa et al., New Advances in Allied Processes (International Academic Publishers, 1991) Vol. 1, pp. 396-399.
6. James G. Fagan, VasanthaR.W.Amarakkoon, and James Richmond Hope, Physica C 225 (1994) 240.
7. I.Monot et al., Physica C 233 (1994) 155.
8. K.V.Paulose, J.Koshy and A.D. Damodaran, Solid State Communications , Vol.79,No.10 (1991) 815.
9. K.V.Paulose et al., Jpn. J. Appl. Phys. 31 (1992) 1323.
10. Myoung-Youp Song et al., Supercond. Sci. Technol.8 (1995) 20.
11. C.Varanasi, M.A. Black and P.J. McGinn, Supercond. Sci. Technol. 7 (1994) 10.
12. J.P.Singh et al., J.Appl.Phys. 66(7),1 Oct.1989,3154-3159.
13. F.Yeh and K.W.White, J.Appl.Phys. 70(9), 1 Nov.1991, 4989-4994.
14. Whang-Jin Kang et al., Jpn.J.Appl.Phys.Vol.31(1992) pp.3311-3316.

CONGRUENT GROWTH OF $NdBa_2Cu_3O_{7-x}$ SUPERCONDUCTING OXIDE FROM THE HIGHLY UNDERCOOLED MELT BY CONTAINERLESS PROCESSING

K. Nagashio*, Y. Takamura, and K. Kuribayashi

The Institute of Space and Astronautical Science
3-1-1 Yoshinodai, Sagamihara, Kanagawa 229, JAPAN
*Graduate Student, The University of Tokyo

Abstract

Nonequilibrium solidification from highly undercooled melt by containerless processing is an attractive route to achieve direct growth of peritectic phase. Containerless processing of $NdBa_2Cu_3O_{7-x}$ (Nd123) superconducting oxide was achieved by combining an aero-acoustic levitation with CO_2 laser heating. Melt of pre-sintered specimen with Nd:Ba:Cu=1:2:3 atomic concentration was undercooled to 1207K below peritectic temperature (Tp=1359K) of Nd123 and spontaneously solidified. XRD peaks of the specimen well corresponded with standard ones of tetragonal Nd123. Subsequent to solidification processing, these specimens were annealed to orthorhombic Nd123 at 573K in pure oxygen gas flow. SQUID magnetometer measurements indicated high Tc value of 94.7K.

The Third Pacific Rim International Conference on
Advanced Materials and Processing (PRICM 3)
Edited by M.A. Imam, R. DeNale, S. Hanada,
Z. Zhong and D.N. Lee
The Minerals, Metals & Materials Society, 1998

Introduction

Solidification process of the superconducting oxides is usually dominated by peritectic reaction. The bulk materials are obtained by melt growth methods such as MTG (Melt Textured Growth)[1], QMG (Quench and Melt Growth)[2], and MPMG (Melting and Powdering Melting Growth)[3]. The all processes take a very long time because the peritectic reaction is controlled by the solid phase diffusion. To realize the high speed crystal growth of the RE123 (RE=Y, Nd, Sm, etc.), the process which makes solid RE123 directly from liquid RE123 avoiding peritectic reaction may be needed. If the major source of heterogeneous nucleation, such as a container wall, is removed by the containerless solidification process, the melt of RE123 composition will be deeply undercooled. Two different containerless processing techniques have been developed to provide the undercooling. One is electromagnetic levitation method which is mainly used for metallic materials[4-6]. Another is aero-acoustic levitation (AAL) method which combines aerodynamic and acoustic forces to achieve stable levitation and positioning of specimens (Figure 1)[7,8]. AAL and CO_2 laser system is mainly used for nonelectrical conductive high melting-point ceramics such as $YBa_2Cu_3O_{7-x}$[9-12] and aluminum oxide[13]. If the melt of RE123 composition undercools below its congruent melting point by the containerless solidification processing, it may be possible that solid RE123 phase grows at high speed congruently from the melt without the primary crystallization of the RE211 phase. The objective of this study is direct crystallization of peritectic phase $NdBa_2Cu_3O_{7-x}$ from nonequiliblium undercooled liquid using AAL with CO_2 laser.

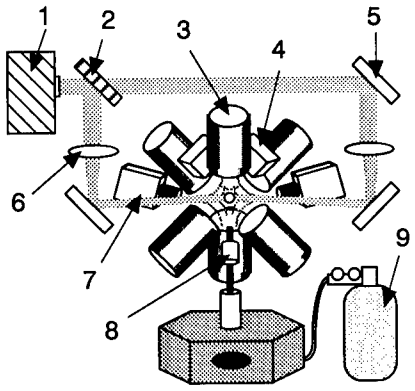


Fig. 1:
Schematic diagram of the aero-acoustic levitation apparatus. 1: CO_2 laser, 2: beam splitter; 3: acoustic transducer (three-axis), 4: specimen position detecter (three-axis), 5: mirror, 6: lens, 7: video camera, 8: diode laser, 9: air gas.

Experimental

Figure 2 shows the quasi binary phase diagram of the $Nd_4Ba_2Cu_2O_{10}$-$Ba_3Cu_5O_8$ system in air[14]. The peritectic temperature (Tp) for Nd422+L→Nd123 reaction is 1359K. Spherical specimens about 3mm diameter of Nd123 composition were prepared from powders to be positioned stably in air. They were levitated in dry air by AAL and heated to 1900K for 10s to melt completely by CO_2 laser. Molten specimens were cooled down by blocking the heating laser beam to be nucleated spontaneously and solidified. Specimen temperature was monitored by high-speed two-color pyrometer whose wavelengths are 0.90μm and 1.55μm. In addition, the

molten specimens were dropped on a copper chill plate to trigger the nucleation of solidification at given temperatures of 1273, 1373 and 1473K. The processed specimens were weighed immediately after recovery and evaporation loss of mass were less than 0.5%. The processed samples were characterized by optical microscopy (OMS), scanning electron microscopy (SEM), powder X-ray diffraction (XRD) and energy dispersion spectroscopy (EDS). The specimen with pronounced recalescence was annealed at 573K in pure oxygen gas flow for 3 weeks. Then, superconducting transision temperature (Tc) measurements were performed by a superconducting quantum interference device (SQUID) magnetometer.

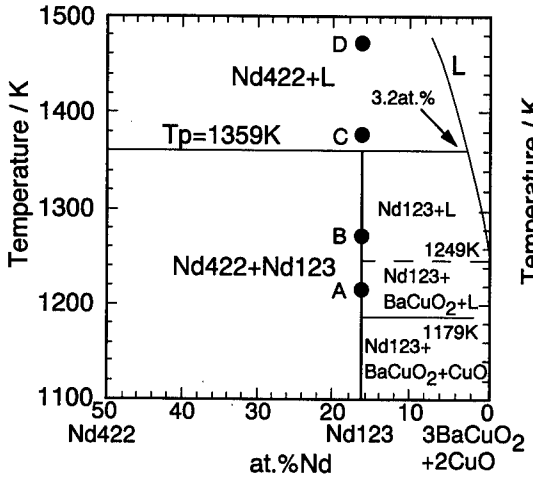


Fig. 2: Quasi-binary phase diagram of the $Nd_4Ba_2Cu_2O_{10}$-$Ba_3Cu_5O_8$ system (A: 1207K, B: 1273K, C: 1373K, D: 1473K).

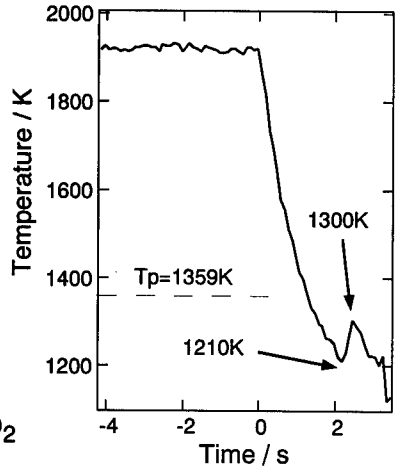


Fig. 3: Cooling curves showing undercooling and recalescence.

Results and Discussion

Figure 3 presents a typical cooling curve of the spontaneously nucleated specimen. The specimen was undercooled to 1210K below Tp=1359K, and solidified with pronounced recalescence. Maximum temperature after recalescence was 1300K. Cooling rate was 400K/s.

Figure 4 shows powder X-ray diffraction patterns for specimens which was forced-nucleated at different temperatures [A: 1207K(spontaneously), B: 1273K, C: 1373K, D: 1473K], together with that for sintered Nd123 powder as a standard of tetragonal Nd123 phase. As is evident from Figure 4, intensity of the peaks for Nd123 phase increase with the depth of undercooling. The XRD pattern of the largest undercooled specimen A well corresponds to that of standard Nd123 phase. These results clearly reveal that the formation of Nd123 phase is closely related to the depth of undercooling. Contrarily peaks of $Nd_4Ba_2Cu_2$, $BaCuO_2$, and CuO phases increased.

Figure 5 shows a cross-sectional optical micrograph of the specimen with pronounced recalescence at 1218K. Many dendrite structures were observed. The phases consisting of dendrite structures were identified as Nd123 phases by EDS and XRD. This indicates that Nd123 phase grew not by peritectic reaction but congruently from the undercooled melt, because the dendrites of Nd123 phase should not grow by peritectic reaction controlled by a solid

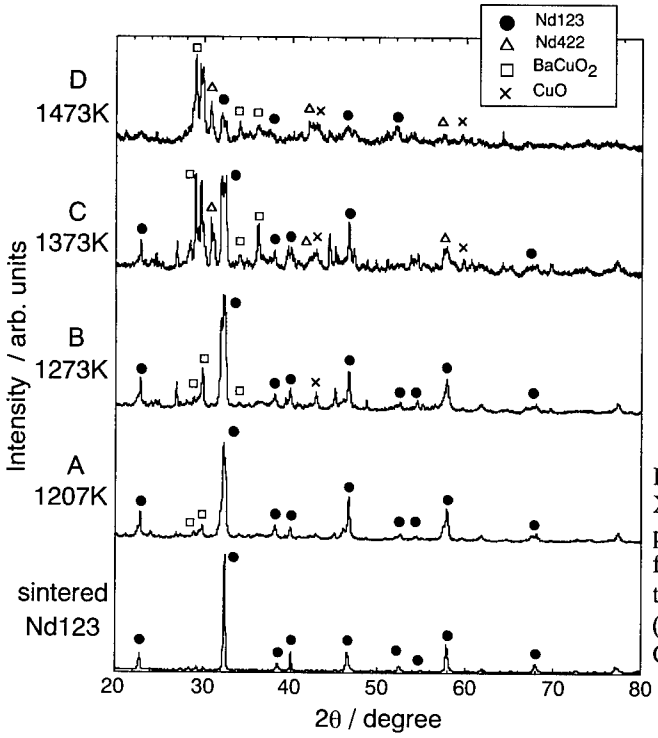


Fig. 4:
X-ray powder diffraction patterns for specimens forced-nucleated at different temperatures,:A:1207K (spontaneously), B: 1273K, C: 1373K, D: 1473K.

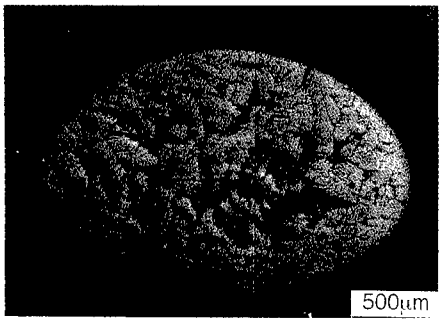


Fig. 5: Optical micrograph of the cross section for a spontaneously nucleated specimen at 1218K.

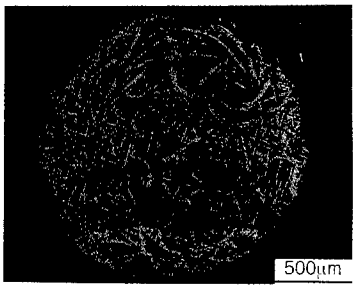


Fig. 6: Optical micrograph of the cross section for a specimen solidified in container.

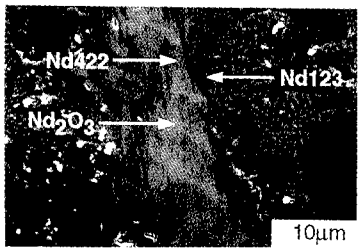


Fig. 7: Close up of the bright region of the specimen in Fig. 6.

phase diffusion. Figure 6 shows the cross section of the specimen solidified with the nearly same cooling rate "in container". This solidification structure was clearly different from dendrite morphology. Figure 7 shows a magnified image of the bright region in Figure 6. Nd_2O_3 was identified in the center, Nd422 adjacent to Nd_2O_3, Nd123 is located around outside of Nd422. This means Nd123 in Figure 7 grew by peritectic reaction. The solidification behavior in the container process is evidently different from that in the containerless process.

It is well known that tetragonal Nd123 phase transforms to orthorhombic Nd123 phase at low temperature. Ortho-Nd123 is superconducting phase. The spontaneously nucleated specimen was annealed at 573K for 3 weeks. XRD measurements were performed on as-grown specimen (a) and annealed specimen (b)(Figure 8). It is observed that (200) Nd123 reflection in (a) split into (200) and (020) Nd123 reflections in (b). Transformation from tetra-Nd123 to ortho-Nd123 phase was indicated. Then, superconducting critical temperature Tc measurements were performed by a SQUID magnetometer. Figure 9 shows the temperature dependence of magnetization for bulk specimen, as-grown and annealed for 1 and 3 weeks. The specimen annealed for 1 week displays a superconducting transition at 94.7K. This value is close to the value Tc=96K of Nd123 single crystal. The important point is that this containerless process was performed in air. It has been reported that in the normal case of Nd123 made in air, solid solution of $Nd_{1+y}Ba_{2-y}Cu_3O_{7-x}$ formed and Tc decreased with increasing the value of y[15]. The high Tc value for specimen processed in air means that Nd123 phase of low substitutions was made by this containerless processing. Moreover the fact that the specimen annealed only at 573K ,without any other high temperature treatment such as ref. 9,11, showed high Tc value reveals that the tetra-Nd123 phase had grown in as-grown specimen.

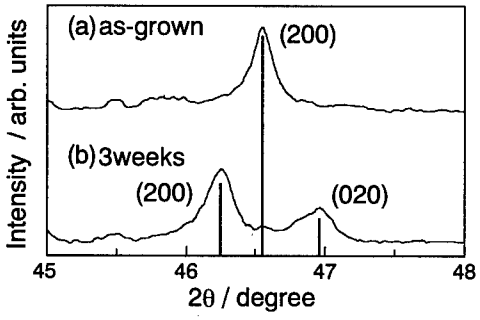


Fig. 8:
X-ray diffraction pattern change from before annealing (a) to after annealing (b), for the specimen spontaneously nucleated at 1207K.

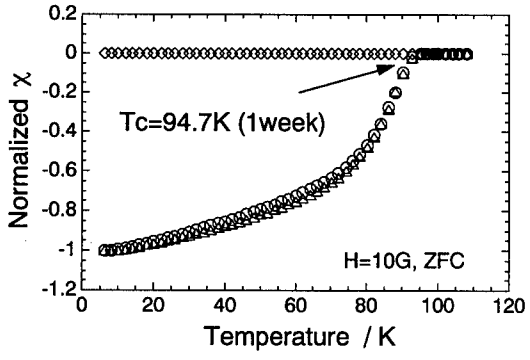


Fig. 9:
Magnetization vs temperature curves measured using SQUID for the specimens before and after annealing at 573K for 1 and 3 weeks. The symbols ◇, ○ and △ corespond to as-grown, 1 and 3 weeks annealed specimen, respectively.

Conclusions

$NdBa_2Cu_3O_{7-x}$ melt was undercooled to 1207K using aero-acoustic levitation and tetragonal $NdBa_2Cu_3O_{7-x}$ phase was solidified congruently from the undercooled melt. The specimen annealed at 573K for 1 week showed Tc value of 94.7K.

References

[1] S. Jin et al., "High Critical Currents in Y-Ba-Cu-O Superconductors," Appl. Phys. Lett., **52** (1988), 2047-2076.

[2] M. Murakami, M. Morita, and N. Koyama, "Magnetization of a $YBa_2Cu_3O_7$ Crystal Prepared by the Quench and Melt Growth Process," Jpn. J. Appl. Phys., **28** (1989), L1125-1127.

[3] H. Fujimoto et al., Advances in Superconductivity-2, Proc. 2nd. Int. Symp. on Superconductivity (1989), 285.

[4] D. M. Herlach et al., International Materials Reviews, **38** (1993), 273.

[5] T. Volkmann, W. Loser, and D. M. Herlach, "Nucleation and Phase Selection in Undercooled Fe-Cr-Ni Melts: Part I.Theoretical Analysis of Nucleation Behavior," Metall. Mater. Trans., 28A (1997), 453-460.

[6] T. Volkmann, W. Loser, and D. M. Herlach, "Nucleation and Phase Selection in Undercooled Fe-Cr-Ni Melts: Part II. Containerless Solidification Experiments."Metall. Mater. Trans., 28A (1997), 461-469.

[7] J. K. R. Weber et al., "Aero-acoustic Levitation: A Method for Containerless Liquid-Phase Processing at High Temperatures," Rev. Sci. Instrum., **65** (1994), 456-465.

[8] P. C. Nordine, and R. M. Atkins, "Aerodynamic Levitation of Laser-Heated Solids in Gas Jets," Rev. Sci. Instrum., **53** (1982), 1456-1464.

[9] J. R. Olive et al, "Formation of Tetragonal $YBa_2Cu_3O_{7-\delta}$ form an Undercooled Melt," J. Mater. Res., **9** (1994), 1-3.

[10] J. K. R. Weber et al., "Effects of Oxygen Pressure on the Structure of Y-Ba-Cu-O Materials Formed by Containerless Melting and Solidification," J. Mater. Res., **9** (1994), 1657-1660.

[11] J. R. Olive et al., "Containerless Processing of $YBa_2Cu_3O_{7-\delta}$ Superconductors," in Containerless Processing Techniques and Applications, ed. W. Hofmeister (The Minerals, Metals & Materials Society, 1993), 111-121.

[12] J. K. R. Weber et al., "Containerless Processing of Ceramic Superconductors,"in Containerless Processing Techniques and Applications, ed. W. Hofmeister (The Minerals, Metals & Materials Society, 1993), 123-128.

[13] J. K. R. Weber et al., "Solidification Behavior of Undercooled Liquid Aluminum Oxide," J. Am. Ceram. Soc., **78** (1995), 577-582.

[14] M. Kambara et al., "Quasi-Binary Phase Diagram of $Nd_4Ba_2Cu_2O_{10}$-$Ba_3Cu_5O_8$ System," Physica C, **275** (1997), 127-134.

[15] S. I. Yoo et al., "Melt Processing for Obtaining $NdBa_2Cu_3O_y$ Superconductors with High Tc," Appl. Phys. Lett., **65** (1994), 633-635.

ADVANCES IN PROCESSING OF Ag-SHEATHED $(Bi,Pb)_2Sr_2Ca_2Cu_3O_x$ SUPERCONDUCTORS

U. Balachandran
Energy Technology Division
Argonne National Laboratory, Argonne, IL 60439

M. Lelovic and N. G. Eror
Department of Materials Science and Engineering
University of Pittsburgh, Pittsburgh, PA 15261

P. Haldar
Intermagnetics General Corporation, Latham, NY 12110

Abstract

Advances in the processing and fabrication of Ag-sheathed $(Bi,Pb)_2Sr_2Ca_2Cu_3O_x$ (Bi-2223) high-T_c superconductors by the powder-in-tube technique continue to bring this material closer to commercial applications. Enhancement of the transport critical current density (J_c) of Ag-sheathed Bi-2223 tapes was achieved by increasing the packing density of the precursor powder, improving mechanical deformation, and adjusting the cooling rate. Long lengths (>150 m) of multifilamentary Bi-2223 tapes have been fabricated and carry critical currents (I_c) of >50 A ($J_c \approx 25$ kA/cm^2) at 77 K in self-field. A 1260-m-long tape carried an I_c of 18 A ($J_c \approx 12$ kA/cm^2) from end-to-end. Several prototype coils have been assembled from these long-length tapes. Recent progress in the fabrication of Bi-2223 tapes is presented in this paper.

The Third Pacific Rim International Conference on
Advanced Materials and Processing (PRICM 3)
Edited by M.A. Imam, R. DeNale, S. Hanada,
Z. Zhong and D.N. Lee
The Minerals, Metals & Materials Society, 1998

Introduction

The powder-in-tube (PIT) process continues to be the most promising approach to fabricate long-length superconductors. Critical current density (J_c) remains the most important property for practical application of high-temperature (high-T_c) superconductor tapes. Ag-sheathed Bi-2223 tapes have been incorporated into prototype high-T_c superconductor motors, transmission cables, and fault current limiters; performance has generally been acceptable. However, because high J_c in magnetic fields is generally necessary, the applicability of such tapes in large electrical equipment has been limited to temperatures <30 K (1). Substantial effort is now focused on addressing this limitation.

Within the past four years, several research groups have reported that, in Ag-sheathed Bi-2223 tapes, the supercurrent is transported through a thin region at the Ag/superconductor interface (2-8). The high-current superconducting layers are generally ≈2-3 μm thick and have been shown to support a transport current with $J_c > 10^5$ A/cm^2 at 77 K and zero applied field (4,5). Transport J_c values of tapes with identical superconductor cross-sectional areas but with differing Ag/Bi-2223 interfacial lengths confirm the importance of the interfacial region (8). The critical current was shown to be proportional to the Ag/Bi-2223 interface perimeter length (IPL); hence, J_c values can be increased through microstructural design by optimizing the IPL.

Efforts to enhance J_c by increasing the Ag/Bi-2223 interfacial area continue. Fabrication of multifilamentary tapes achieves this goal, but, in general, the areal fraction of Ag increases in such tapes. An alternative approach is to incorporate Ag wires into a Bi-2223 core. Initial work focused on the use of a single Ag wire [4,9]. In addition to offering the possibility of an improved transport J_c, significant enhancement of bend-strain tolerance by a wire-in-tube approach has been reported (10). The duplex-core work reported in Refs. 4 and 9 has recently been extended to a two-step process in which many fine Ag wires are coated with Bi-2223 precursor powder and then loaded into a Ag tube. Conventional PIT processing then produces a tape with a very high Ag/Bi-2223 interfacial area (11,12). To date, up to 600 Ag wires coated with Bi-2223 precursor have been loaded into a single Ag tube and processed into tapes. Despite the smaller cross-sectional area of the superconducting core, transport J_c values are now greater than those of corresponding monofilament tapes (11).

Significant effort is being expended to improve the J_c of Bi-2223 conductors by tailoring powder stoichiometry, phase assemblage, morphology, mechanical processing, and heat treatment (13,14). Recently, we varied the packing density of the precursor powder, improved the mechanical processing, and modified the heat treatment schedule; the results are described in this paper.

Experimental Procedure and Results

Multifilament (37-filament) Ag-sheathed Bi-2223 tapes were made by the PIT technique, with precursor powders that exhibit the overall stoichiometry of Bi-2223. Packing density in the Ag tubes was varied by inserting powdered precursor, as well as precursor powder that was prepressed into billets, into the Ag tubes. The precursor powder was packed into the Ag tubes at a density of ≈2.3 g/cm^3, whereas the prepressed precursor billets were of two densities: ≈3.5 g/cm^3 (low packing density) and ≈4.5 g/cm^3 (high packing density). The powder and prepressed billet Ag tubes were swaged, drawn through a series of dies, and then rolled to a final thickness of ≈200 μm. Standard mechanical processing that consisted of >10% reduction per pass was used to fabricate these tapes. Samples that measured ≈1.2 m in length

were cut from these three tapes and heat treated in an 8% oxygen atmosphere at 810-825°C. The transport critical currents, I_c (77 K, self-field, 1 μV/cm criterion) that were measured in these tapes are shown in Fig. 1. The tapes with the higher packing density achieved higher I_c values when they were heat treated at 820°C. These higher I_c values were maintained uniformly over a length of ≈1.2 m. The ratio of Ag to superconductor core cross-sectional area in the tape depends on precursor packing density. Higher initial packing density might lead to an increase in superconductor cross-sectional area and thereby to an increase in I_c.

In another set of experiments, we varied the mechanical deformation schedule. The Ag tubes packed with the precursor powder and prepressed billets were drawn and rolled according to various reduction ratios per pass. Load cells were mounted on the dies, and the pressure that was exerted on the wires that were being drawn was monitored. Onset of mechanical instability during wire drawing was recorded by monitoring the pressure exerted on the wires. The die pressure measurements formed the basis for optimizing reduction ratios per pass. The cross-sectional area of each sample was observed by scanning electron microscopy (SEM). Figure 2 is a composite of low-magnification SEM images that show the effect of mechanical deformation on the cross sections of two multifilament tapes. Improved mechanical processing of the Ag tube that contained the high-density precursor billet significantly affected the uniformity of the Ag/superconductor interface. The standard mechanical processing included a reduction of >10% per pass, whereas the improved mechanical processing reduced the rate of mechanical deformation to <10% reduction per pass. Tapes that were processed under improved mechanical deformation conditions exhibited uniform I_c values of ≈36 A.

In a parallel experiment, we studied the effect of cooling rate on the I_c of tapes. Approximately 1-m-long tapes were heated in an 8% oxygen atmosphere to ≈820°C at a rate of ≈2°C/min, held for 50 h, and then cooled. The standard cooling rate was 1-2°C/min, but slower rates were also used. Figure 3 shows the effect of cooling rate on the I_c values of a

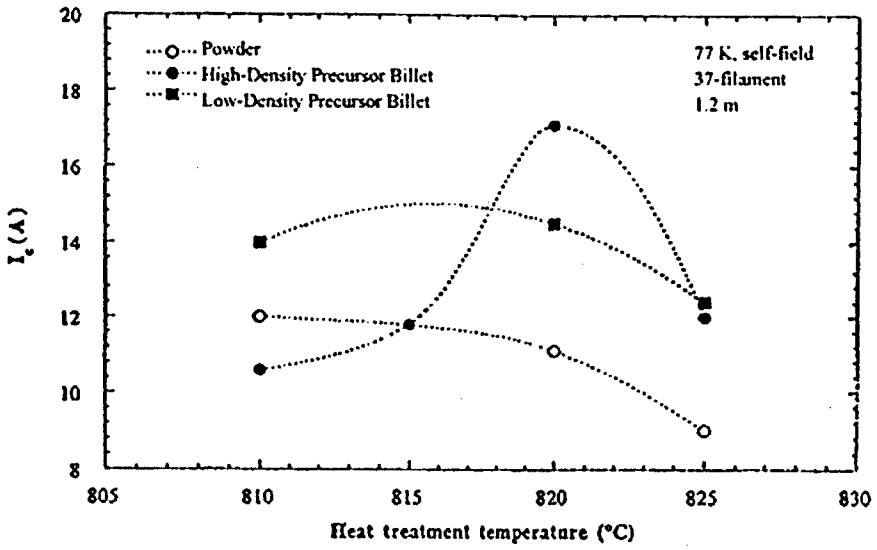


Fig. 1. Transport critical current (I_c) as a function of heat treatment temperature for tapes with various precursor powder packing densities.

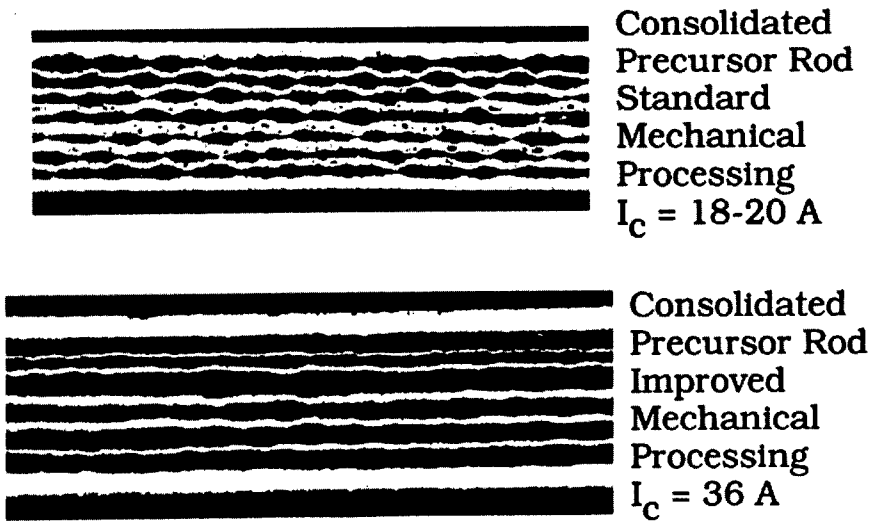


Fig. 2. SEM photomicrograph of multifilament tapes showing effect of improved mechanical processing. Tapes processed by standard mechanical processing are shown for comparison.

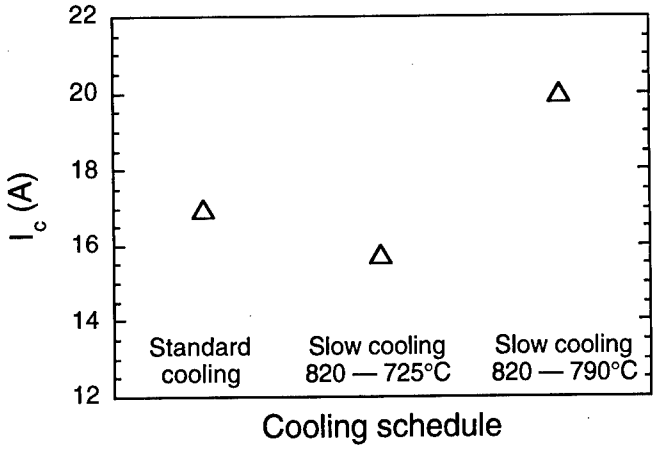


Fig. 3. Transport I_c of a 1.2-m-long tape vs. cooling conditions.

1.2-m-long tape made from a Ag tube that contained prepressed billets (high packing density). Slow cooling at ≈10°C/h from 820 to 790°C improved I_c to a level over that achieved with the standard cooling rate. Slow cooling at ≈10°C/h from 820 to 725°C resulted in I_c values that are similar to those obtained in samples that were cooled at the standard rate. Because of the difference in the thermal conductivity of Ag and the superconducting core, a thermal gradient exists between the core and the Ag in fast-cooled samples. The thermal gradient exerts a stress on the thin layer of Bi-2223 adjacent to the Ag; this stress affects grain alignment and connectivity and thereby influences the I_c. In extreme cases, the stresses caused by a strong

thermal gradient have induced microcracking in the superconducting layer close to the Ag/Bi-2223 interface (15). Parrel et al. (16) observed that the cooling rate from the sintering temperature had a significant effect on J_c and attributed the effect to partial decomposition of Bi-2223 during slow cooling. However, other changes in the Bi-2223 also arise from slow cooling, e.g., increase in oxygen content (17). Singh and Vasanthamohan (18) studied the cooling rate effect on Bi-2223 samples sintered at 815 and 825°C in an 8% O_2 atmosphere and noticed that, when the cooling rate was decreased from 100 to 10°C/h, tapes sintered at 815°C showed very little change in J_c, whereas tapes sintered at 825°C showed an increased J_c. This difference was attributed to how the Bi-2223 phase is formed at the two temperatures. For the tapes sintered at 825°C, the authors of Ref. 18 noticed an increase in Bi-2223 phase with a decrease in cooling rate; hence, J_c increases with a decrease in cooling rate. Incorporation of the improvements in packing density of powders, mechanical deformation, and cooling rate has now resulted in I_c values of ≈55 A for long lengths (>100 m) of superconductor tapes. We have also fabricated an ≈1260-m-long multifilamentary tape that carried an I_c of 18 A (J_c ≈12 kA/cm^2) from end to end at 77 K and self-field.

Poor mechanical properties have seriously hampered the commercial application of high-T_c superconductors. During fabrication and service, the conductors are subjected to axial and bending stresses. During operation, the material is subjected to additional stresses by temperature gradients and magnetic fields. In the presence of large and/or high-field magnets, electromagnetic hoop stresses could even reach the ultimate strength of the material. These stresses can cause microstructural damage in the conductors and thereby degrade current transport properties. Although Ag is widely used as a sheath material, its mechanical properties are not adequate to withstand the stresses developed during fabrication and service. Therefore, techniques, such as adding Ag to the superconductor powder, using alloy sheath material as an alternative to Ag, and fabricating multifilament conductors, have been developed to improve the strain tolerance characteristics of the superconductors.

Conclusions

Powder-in-tube-fabricated Ag-sheathed Bi-2223 tapes exhibit good transport J_c values, but transport at 77 K, especially in large applied magnetic fields, must be improved. Good transport of supercurrent seems to be confined to core regions adjacent to the Ag sheath. The packing density of precursor powder, improved mechanical deformation, and cooling rate all exerted a pronounced effect on the critical current of the superconducting tapes.

Acknowledgments

The work is supported by the U.S. Department of Energy (DOE), Energy Efficiency and Renewable Energy, as part of a DOE program to develop electric power technology, under Contract W-31-109-Eng-38.

References

1. A. N. Iyer, R. Jammy, U. Balachandran, M. Suenaga, and P. Haldar, J. Electron. Mater., 24 1873 (1995).

2. S. P. Ashworth and B. A. Glowacki, Physica C, 226 159 (1994).

3. Y. Feng and D. C. Larbalestier, Interface Sci., 1 401 (1994).

4. M. Lelovic, P. Krishnaraj, N. G. Eror, and U. Balachandran, Supercond. Sci. Technol., 8 334 (1995).

5. M. Lelovic, P. Krishnaraj, N. G. Eror, A. N. Iyer, and U. Balachandran, Supercond. Sci. Technol., 9 201 (1996).

6. D. C. Larbalestier, X. Y. Cai, Y. Feng, H. Edelman, A. Umezawa, G. N. Riley, Jr., and W. L. Carter, Physica C, 221 299 (1994).

7. U. Welp, D. O. Gunter, G. W. Crabtree, W. Zhong, U. Balachandran, P. Haldar, R. S. Sokolowski, V. K. Vlasko-Blasov, and V. I. Nikitenko, Nature, 367 44 (1995).

8. B. C. Prorok, M. Lelovic, T. A. Deis, P. Krishnaraj, N. G. Eror, A. N. Iyer, and U. Balachandran, Adv. Cryo. Eng., 42 739 (1997).

9. J. Schwartz, H. Sekine, T. Asano, T. Kuroda, K. Inoue, and H. Maeda, IEEE Trans. Magn., 27 1247 (1991).

10. N. Vasanthamohan and J. P. Singh, Supercond. Sci. Technol., 10 113 (1997).

11. S. E. Dorris, N. Ashcom, T. Truchan, N. Vasanthamohan, D. A. Burlone, and L. D. Woolf, to be published in Proc. Supercond. Symp., 99th Ann. Mtg. Am. Ceram. Soc., Cincinnati, May 4-7, 1997.

12. S. E. Dorris, in Practical Superconductor Development for Electrical Power Systems, Argonne National laboratory Report ANL-95/42, 13 (1995).

13. U. Balachandran, A. N. Iyer, R. Jammy, P. Haldar, J. G. Hoehn, Jr., and M. Suenga, Adv. Cryo. Eng., 42 753 (1997).

14. Z. Han and T. Freltoft, Appl. Supercond., 2 201 (1994).

15. M. Lelovic, T. Deis, N. G. Eror, U. Balachandran, and P. Haldar, Supercond. Sci. Technol., 9 965 (1996).

16. J. A. Parrel, D. C. Larbalestier, and S. E. Dorris, IEEE Trans. Appl. Supercond., 5 1275 (1995).

17. M. Tetenbaum and V. A. Maroni, Physica C, 260 71 (1996).

18. J. P. Singh and N. Vasanthamohan, J. Mater. Res. (1998, in press).

CRITICAL CURRENTS ACROSS SMALL ANGLE GRAIN BOUNDARIES IN HIGH T_C SUPERCONDUCTORS

C.S. Pande and R.A. Masumura
Materials Science and Technology Division
Naval Research Laboratory
Washington DC 29375-5343

Abstract

It is well established that the critical current of even carefully prepared polycrytalline high T_c material is extremely low (In the range of 100-1000 A/cm^2 at 77K). This value drops further in the presence of even a small magnetic field of a small fraction of a Tesla. On the other hand, the J_c value for single crystals, in bulk as well as in thin film form, is as at least three orders of magnitude higher. Two papers by Dimos and co-workers have firmly established that J_c is a very sensitive function of the grain boundary orientation at least in thin films. They measured the critical current across the grain boundary (J_{cgb}) and also through the crystal (J_{cs}) and showed that the ratio of J_{cgb}/J_{cs} decreasing on increasing misorientation. We discuss possible sources of the increasing depression in critical current across a low angle tilt grain boundary with increasing misorientation. The roles of the dislocation cores and dislocation strains from the dislocation wall comprising the boundary are compared. It is shown that the dislocation strains around dislocation cores are more likely to be responsible for such a depression in the critical current.

The Third Pacific Rim International Conference on
Advanced Materials and Processing (PRICM 3)
Edited by M.A. Imam, R. DeNale, S. Hanada,
Z. Zhong and D.N. Lee
The Minerals, Metals & Materials Society, 1998

Introduction

Two papers by Dimos and co-workers [1,2] have firmly established that J_c is a very sensitive function of the grain boundary orientation. They measured the critical current across the grain boundary (J_{cgb}) and also through the crystal (J_{cs}) and showed that the ratio of J_{cgb}/J_{cs} depends upon the misorientation. Although recent experimental results indicate this may not be true for all boundaries [3] the result is considered valid in most cases. It is important to understand what limits J_c in polycrystals so that suitable processing conditions can be developed to optimize J_c.

The aim of this paper is to analyze briefly the source of drop in critical current across tilt boundaries with misorientation up to 15 degrees where the boundary geometry is similar to those used in bicrystal experiments [3]. (See also references [4-13] for other pertinent papers.). Analysis of the small angle tilt boundaries is facilitated by the fact that these boundaries, can be considered as a wall of equally spaced edge dislocations as shown in Fig. (1). The tilt angle θ is related to the dislocation spacing h by the well known relation

$$\frac{b}{h} = 2 \sin(\theta/2) \simeq \theta \text{ for small } \theta \qquad (1)$$

where b is the Burgers' vector of the dislocation.

An important conclusion from Dimos et al. [1,2] is that the critical current across the grain boundary when normalized by the critical current parallel to the grain boundary, appears to be a function of the tilt misorientation alone irrespective of the quality of the material. This suggest that the source of J_c reduction is something fundamental such as the structure of the boundary itself. In it simplest aspect one can assume the role of dislocations forming the boundary as nothing more than providing a reduction in cross section as has been proposed by Pande and others [14-16]. Such a reduction is provided by the dislocation cores or dislocation strains.

The possibility that the drop may be caused by dislocation cores looks appealing since it is found that the drop saturates at $\theta \approx 15$ degrees. At this misorientation, the dislocation cores should begin to overlap. However, Nabarro [6] correctly points out that the model cannot account for a large decrease observed at $\theta \approx$ 3-5 degrees where the cores are far apart and core size is expected to be of the same order as the Burgers' vector b, which according to Dimos et al. [1,2] was 3.8 Å. Nabarro [6] mentions a way out of this dilemma, viz., the core sizes are large (of the order of the coherence length $\approx$ 20 Å). This would explain the result at small θ, but then the saturation would occur not at 15 but at less than 9 degrees in tilt misorientation. Obviously, if the dislocation cores are responsible for the decrease in J_{cgb}/J_{cs} with θ, the core size should be large for small θ and should gradually decrease with increasing θ. It appears, therfore, worthwhile to reexamine the effect of core size or some other measure of its influence on critical current.

Analysis

Dislocation Core Effects

The dislocation in its mathematical construct has a singularity at center that has plagued those trying utilize this concept. Several attempts have been made to obviate this singularity by considering a cut-off radius based upon some criterion or by considering the core to be hollow. Some grain boundary models have been proposed to include an infinite array of edge dislocations with hollow cores.

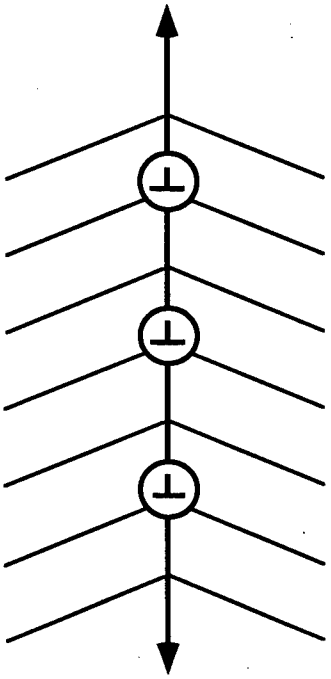


Figure 1 - Tilt boundary composed of equally spaced dislocations. The distance between dislocations is h and each has a core radius of r_0.

In particular two such grain boundary models were proposed by Li [17] and by Masumura and Glicksman [18] . Li's model consisted of an infinite array of hollow core dislocations that are characterized as being stress free at the core. He then summed the stress fields to determine the effect of the infinite wall. However, this method does not maintain a traction free core at each and every dislocation. But in order to find a core dependence with tilt misorientation, Li [17] used cleverly crafted arguments as first approximation to determine the traction free core condition. At small tilt misorientation, the core can reasonably be assumed to be circular. As θ increases, the core size becomes larger based upon the following two criteria: The first requires that the shear stress be greater than zero in the slip plane and hence on can determine the extent of the core in that direction. The second criteria deals with the requirement that the tensile stress at the core interface along the grain boundary be zero. In both cases, the values determined become larger as

θ increases, and reaches a point where the interface along the boundary impinge and merge into a slab.

The model used by Masumura and Glicksman [18] also used a hollow core traction free dislocation core. But in their analysis the interaction between the cores was included by mapping a single strip, i.e., one periodic dislocation and slip plane into an infinite plane and solving the problem using elastic potentials resulting in a integral equation. Their analysis showed that the core radius *shrank* as θ increased .This is what we require to explain Dimos et al. [1,2] results. But the reduction in core size may be due to the stringent requirement that the cores remain circular for any misorientation.

To remove this limitation, the correct model is to solve a free boundary value problem, e.g., find the shape of the core subject to its traction conditions at the interface. This has as yet not been attempted. But the larger question is whether a traction free, hollow core dislocation is the correct model.

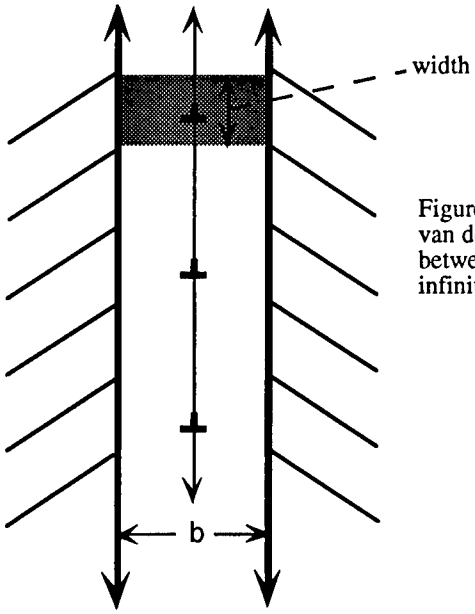


Figure 2- Tilt boundary model of van der Merwe where the spacing between the two elastic semi-infinite media is b.

Another measure of the core effect is to determine its width (usually defined as the region where the greatest mismatch) using the model by van der Merwe [19] who considers two elastic slabs whose interaction is determined by atoms in each interface under the influence of a sinusoidal potential. We are interested in the width along the tilt boundary (in contrast to that along a slip plane of a dislocation) as shown in Fig. (2). As is well known the slip plane width is given by a Peierls-Nabarro type of analysis, whereas for the width along the boundary one has to use a van der Merwe type of analysis. Bullough and Tewary [20] have noted that the displacement as given by van der Merwe can be used to obtain the width and thus a measure of variation of the tensile relation across the boundary as a function of angle of tilt.

Pande and Masumura [14] have used this model to derive an explicit relation between core size W and misorientation as:

$$W = \frac{h}{\pi} \tan^{-1}\left[\frac{\pi \mu (1-2\nu)}{\mu_o (1-\nu)} \tan(\theta/2) \sec(\theta/2)\right]. \qquad (2)$$

It is seen that the width depends on the value of ν chosen, but is almost independent of θ. As expected for $\theta = 0$, the result for a single dislocation is regained. Thus according to this model the width of the dislocations comprising the tilt boundary has almost the same width as single dislocations. Thus these width calculations for a distributed dislocation cannot explain the drastic decrease in critical current with increasing tilt misorientation.

Thus out of the three methods of calculation, only the model of Masumura and Glicksman [18] shows the correct trend. However because of the drastic assumption of maintaining the circularity of the cores, it is doubtful that it can be used for our purpose. In general, we find that core size calculations do not predict the right trend.

Dislocation Stress Extent around the Cores

If, we can identify r_o, the "cut-off" radius with a region of high dislocation stresses instead of the core size, the trend appears to be correct since it will well known that the extent of dislocation stress scale with h, the inter-dislocation spacing. To us this appears to be the correct size to take for the calculations of critical current. This has been emphasized by Pande [14,15] in several previous publications. A detailed model based on this idea was presented by Agassi, Pande and Masumura [21].We believe that this is the correct explanation for the reduction in J_c in polycrystals. However what is the extent of this distorted region around the core and how exactly J_c reduction takes place is still not fully understood and is discussed in the rest of this paper.

Model

To include the effect of stresses around the core, we assume that each dislocation core is surrounded by a "bad" region where the superconducting properties are degraded. Such a region of stress should extend from the core of one dislocation to the core of the surrounding dislocations. We have arbitrarily selected a critical value for this stress to determine the extent of the bad region when the integrated average of shear stress at a fixed radial distance from the core equals this critical value superconductivity is assumed to be totally degraded. The goal is to calculate the radius r_o of a circular region around each of the dislocations' center, Fig. (2) such that the averaged value of the absolute shear stress $|\sigma_{xy}|$, over the circle equals a prescribed value σ_c:

$$\sigma_c = \int_0^{2\pi} \frac{\left|\sigma_{xy}(\alpha; r_o)\right|}{2\pi} d\alpha \qquad (3)$$

In Eq. (3), $x = r_o \cos(\alpha)$, $y = r_o \sin(\alpha)$ and the dislocation wall or array is along the y axis. The expression for the shear stress of an infinite array of edge dislocations is

$$\sigma_{xy} = \frac{\pi \sigma_o X \mu b \left[\cosh(2\pi X)\cos(2\pi Y) - 1\right]}{h(1-\nu)\left[\cosh(2\pi X) - \cos(2\pi Y)\right]^2} \tag{4}$$

X= x/h, y = Y/h, ν is the Poisson ratio, μ is the elastic shear modulus, b is the Burgers vector and r_o, h are defined in Fig. (2). For small misalignment angles, the Read-Schockley relation gives h=b/θ. This equation is derived from superposition of the stress field of the entire dislocation array, disregarding core-core interaction.

The numerical method for evaluating Eq. (3) utilizes a simple adaptive scheme. Using a least squares fit and assuming $\nu \approx 1/3$, Eq.(3) is obtained, where $C \approx 2\sigma_c/\mu$. Employing the other stress components σ_{xx} and σ_{yy} in Eq.(3) yield a similar dependence. In an actual situation this transition from good to bad would not, of course, occur so suddenly. Based upon the numerical integration of the shear stress and fitting a power dependence to our result, we obtain the following result between the radius of '"bad" region R_b and misorientation θ as

$$R_b/h = 0.16(\theta/C)^{1/2}\,;\ \theta \neq 0 \tag{5}$$

and $R_b/h \propto \theta as\ \theta \to 0$, where h is the distance between dislocations, θ is the tilt misorientation and C is a material constant involving the flow criterion and Poisson's ratio. The preliminary calculations given above used shear stresses and simple summations of the stresses due to the individual dislocations in the wall.

The calculations used previously for calculating the extent of disordered region using shear stress can be extended to other stresses. However one can also obtain this result by a physical argument It is well known that from St.Venant's principle all the stresses must scale with a characteristic length in the system. In this case the length has to be the separation of the dislocations h forming the grain boundary. We have already shown that the strained region R_b scales with h. Therefore we surmise that a similar results for other stresses. Then R_b, the strained region for the other stress components must be of the form

$$R_b/h = k\sqrt{\theta} \tag{6}$$

or

$$R_b/b = \frac{k}{\sqrt{\theta}} \tag{7}$$

The constant as before must involve a numerical constant and C which depends on the critical stress. An estimate for k can be made as follows. It almost certain that by the time θ reaches 15 degrees, these regions must be within b of each other so that

$$R/h \to b/b = \frac{k}{\sqrt{\pi/12}} \tag{8}$$

leading to k ≈ 0.5 which provides a good estimate of R_b needed to fit the data. This should be considered an upper limit. If R_b were equal to b at 10 degrees in lieu of 15 degrees, k would have a value of approximately 0.4.

To determine the effect of this "bad region" precisely [21], the grain boundary configuration was modeled by a superconductor superlattice , where the disordered regions near the dislocation cores and host superconductor material between the disordered regions represented by "bad" and "good" superconducting slabs. The model was based on two key assumptions. The first is that the observed disordered, stressed material or near the core constitutes a degraded phase of the host-superconductor. Consequently, the observed linear equidistant array of dislocations constitutes a periodic configuration of "bad" superconducting regions, embedded in the "good" host-superconductor material. It was also assumed that this simplified superlattice geometry captures the essential physics of the original configuration. specifically, the superlattice configuration retains the feature of periodic alternate of good and bad domains and implies the flux pinning relevant to the measured J_c. The tilt misorientation θ enters the model via superlattice periodicity and thickness of the layers, d_B and d_G. In the London limit (penetration length >> coherence length) and low field limit and temperature domain, the free energy can be evaluated from the solution of the London equation.

This calculation predicts that

$$\frac{J_c(\theta)}{J_c(\theta_0)} = \left| \frac{K_0\left(\frac{\xi}{\lambda_G}\right) - K_0\left(\frac{d_G(\theta)}{\lambda_G}\right)}{K_0\left(\frac{\xi}{\lambda_G}\right) - K_0\left(\frac{d_G(\theta_0)}{\lambda_G}\right)} \right| \qquad (9)$$

where K_O is the zeroth order modified Bessel function of the second kind, λ_G is the penetration length of the good material, ξ is the coherence length and θ_O is a fixed reference orientation. The results obtained are in rough agreement with the very approximate results given earlier and with experiments . When misorientation is more than 10 degrees, the size of the good region is less than the coherence length and the validity of the conclusion becomes questionable. The results are thus are limited to small angle grain boundaries.

In order to extend these results to tilt boundary of any misorientation the following model is suggested. We propose that each disordered region around the dislocation cores act likes a Josephson junction, since disordered region can be considered normal and it is surrounded by superconducting material resulting in the S-N-S junctions. The tilt boundary itself thus can be considered as a grating of equally spaced Josephson junctions, the separations between the dislocations as before is related to tilt misorientation. The advantage of this model over the previous model is that the calculation for small theta can be extended to larger and larger angles till all the disorder regions coincide so that at some θ probably around 15 degrees, the grain boundary can be considered as a slab of disordered material acting like a single Josephson junction. It is well known that large angle boundaries do act like a single Josephson junction[1,2].

Conclusions

In summary, we have discussed the source of depression of J_C, the critical current capacity as a function increasing misorientation, viz., dislocation strains around dislocation forming the grain boundary. The extent of strain regions could be relatively large leading to substantially large drop in J_C even for very small misorientations. Though for $\theta > 15°$, the dislocation cores will probably overlap, leading to a Josephson like behavior for those boundaries. We have already provided a procedure to calculate the drop in J_C as a function of misorientation using London equation as discussed in the text. An improvement to the calculation will be to treat the grain boundary as a grating of equally spaced grating of Josephson junctions, the extent of each junction given by the method discussed here.

Acknowledgments

We wish to thank Dr. B.B. Rath, Professor F.R.N. Nabarro and Dr. D.U. Gubser for many stimulating discussions.

References

1. D. Dimos, P. Chaudhari, J. Mannhart and F. K. LeGoues, Phys. Rev. Letters, 61 (1988) 219.
2. D. Dimos, P. Chaudhari and J. Mannhart, Phys. Rev. B, 41 (1990) 4038.
3. S. E. Babcock, X. Y. Cai, D. L. Kaiser and D. C. Larbalestier, Nature, 347 (1990) 167.
4. J. R. Clem, Phys. Rev. B, 43 (1991) 7837.
5. K. Jagannadham and J. Narayan, Phil. Mag. B, 61 (1990) 129.117.
6. F. R. N. Nabarro , Solid State Communications, 71 (1989) 281
7. Y. Zhu, Z. L. Wang and M. Suenaga, Phil. Mag., A67 (1993) 11.
8. Y. Zhu, Y. L. Corcoran and M. Suenaga, Interface Science, 1 (1994) 359.
9. S. E. Babcock, T. F. Kelly, P. J. Lee, J. M. Seuntjens, L. A. Lavanier and D. C. Larbalestier, Physica C, 152 (1988) 25.
10. S. E. Babcock and D. C. Larbalestier, App. Physics Letters, 55 (1989) 393.
11. D. M. Kroeger, A. Choudhury, J. Brynestad, R. K. Williams, R. A. Padgett and W. A. Coghlan, J. App. Phys., 64 (1988) 331.
12. K. B. Alexander, D. M. Kroeger, J. Bentley and J. Brynestad, Physica C, 180 (1991) 337.
13. P. Chaudhari as quoted by F. R. N. Nabarro in Ref. 6.
14.C. S. Pande and R. A. Masumura, High-Temperature Supeconductors: Synthesis, Processing, and Applications II, eds. U. Balachandran and P. G. McGinn, (TMS. 1997), 81.
15. C. S. Pande, H. A. Hoff, A. K. Singh, M. S. Osofsky, M. A. Imam, K. Sadanada and L. E. Richards, IEEE Trans. Magn., 25 (1989) 2004.
16. M. F. Chisholm and S. J. Pennycook, Nature, 351 (1991) 47.
17. J.C. M. Li, J. Appl. Physics, 32 (1961) 525.
18. R. A. Masumura and M. E. Glicksman, J. Appl. Mechanics, 44 (1977) 595.
19. J.H. van der Merwe, Proc. Phys. Soc., London, A63 (1950) 616.
20. R. Bullough and V. K. Tewary, Dislocations in Solids,Volume 2, ed. F. R. N. Nabarro 1 D.
21. D. Agassi, C. S. Pande and R. A. Masumura, Phys. Rev. B, 52 (1995) 16237.

HIGH TEMPERATURE SUPERCONDUCTING MAGNET APPLICATIONS AT THE NAVAL RESEARCH LABORATORY

D. U. Gubser
Naval Research Laboratory
Code 6300
Washington DC 20375-5343

Abstract

The Naval Research Laboratory has three major development projects involving high temperature superconducting magnet systems. These systems include motor development for ship propulsion, high field laboratory magnet to support solid state research programs, and a magnet for a gyroklystron amplifier in a high-frequency, high-power radar system. These development projects are described in this article.

Introduction

The Navy is interested in superconductivity in order to improve power efficiency and performance capability while at the same time to reduce the overall costs (acquisition and life-cycle) of military systems. High temperature superconductivity (HTS) offers an advantage over conventional superconductivity systems in that HTS systems will operate at higher temperatures, thereby reducing the costs, complexity, and power consumption of the cryogenic system.

Power applications of HTS superconductivity at the Naval Research Laboratory have focused on three major development projects involving superconducting magnet systems: magnets of ship propulsion motors, magnets for solid state research, and magnets for a gyroklystron. All these systems will have major demonstration milestones in 1998.

Ship Propulsion Motors

Superconducting motors for ship propulsion offer significant performance improvements in areas of overall ship system efficiency and power density.[1] These factors translate into military advantages such as extended range capability, reduced fuel consumption, or increased payload. It has been estimated that superconducting motors can increase the range of a combatant ship by factors of 2 to 3 depending on the particular design.[1]

The Navy has focused motor development on the homopolar type due to its unique attributes of acoustically quiet propulsion, high torque at low speeds [typical propulsion speeds are 50-150 revolutions per minute (rpm)], and easy speed control. The homopolar motor has been described in a number of recent articles,[1,2] hence will only be discussed briefly here. In the homopolar motor, torque is developed by the interaction of a dc current in the rotor with a perpendicular dc magnetic field. The homopolar motor is the only truly dc motor. Since no ac electromagnetic fields are generated, the motor is acoustically quiet, and the superconducting magnets, which generate the field, experience no ac losses, common in other motor designs. In addition, the homopolar motor design uses a stationary solenoid type magnet system which experiences no shaft torque; hence, the magnet design and cryogenic support systems are relatively easy to design compared to other types of superconducting motors which involve a rotating, saddle-type magnet system which must support motor torque.

High temperature superconductivity brings to the motor the ability to operate at higher temperatures. Low temperature systems operate in the 4K-7K temperature range, whereas the HTS motors will operate in the 30K-70K range – an order of magnitude higher in temperature. This higher operating temperature eases the complexity of the cryogenic system design, and reduces

the overall refrigeration power consumption. Furthermore, thermal conductivities and heat capacities of materials are higher in this elevated temperature range providing more system stability against temperature fluctuations and hence, increasing the reliability and safety margin of the propulsion motor.

Figure 1 shows the homopolar motor presently being demonstrated with an HTS magnet system. The intent of the present program was to provide assistance to develop industrial capability for the manufacture of superconducting magnets of sufficient size and strength for motor applications, and to demonstrate that capability by operation of the homopolar motor shown in Figure 1 with an HTS magnet system. The magnet system as originally designed required immersion in a cryogenic fluid. For the HTS motor, the liquid cryogens used were helium (4.2K), neon (27K), and nitrogen (77K). In 1997 the motor was operated at levels of 320 hp (helium), 220 hp (neon), and 100 hp (nitrogen). In 1998, the motor was modified to permit conduction cooling of the magnets, and the motor was operated at temperatures intermediate to those reports for liquid immersion testing.

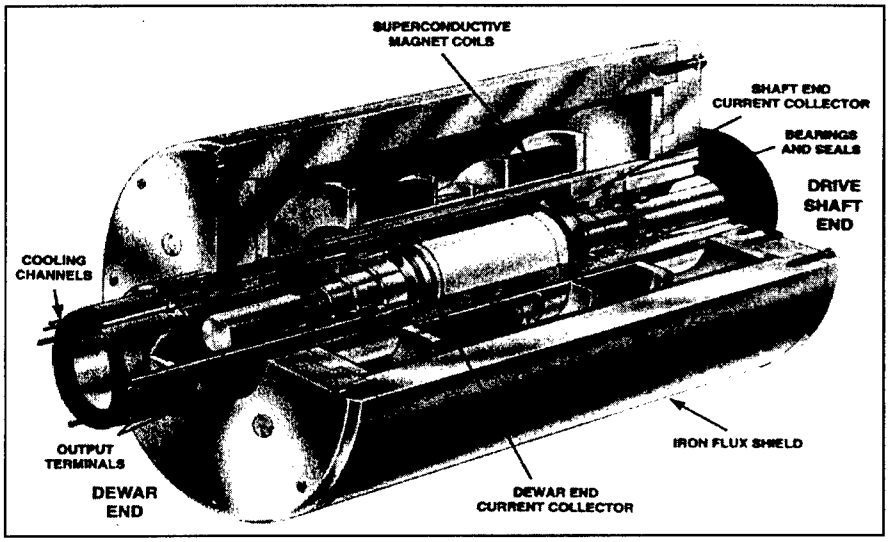


Figure 1: Demonstration Homopolar Motor

In the motor tests, the HTS conductor used was a silver-clad, multi-filament $Bi_2Sr_2Ca_2Cu_3O_{10}$ (BSSCO-2223) conductor. This conductor had a superconducting transition temperature of 110K and at 4.2K had an overall critical current value (J_c) of 10,000 amperes/cm^2. The magnet system was composed of two magnets arranged in opposite polarity in order to produce a radial field in the central region. This radial field penetrated the copper rotor producing the motor torque. Current to the rotor was injected at each end of the cylinder by annular current collectors. The operating magnet current was about 110 amperes and was limited by a criteria set on the maximum allowable overall power consumption of 2 watts to the HTS magnet. (In magnetic fields near the J_c limit, the power loss in HTS conductors is not zero!) Almost 2/3 of this power was consumed in the inner quarter of the magnet system where the radial field is maximum; hence, improved magnet design to limit the radial field component on these innermost windings would greatly increase the performance of the motor.

Figure 2 shows the increased performance level, J_c, of HTS conductors during the course of our program. At the time the motor coils were fabricated the conductor performance had improved by a factor of 10 from the inception of the program. Today the HTS conductor performance levels have increased by another factor of 2; hence, motor performance double that presently achieved could be expected with minimal design changes.

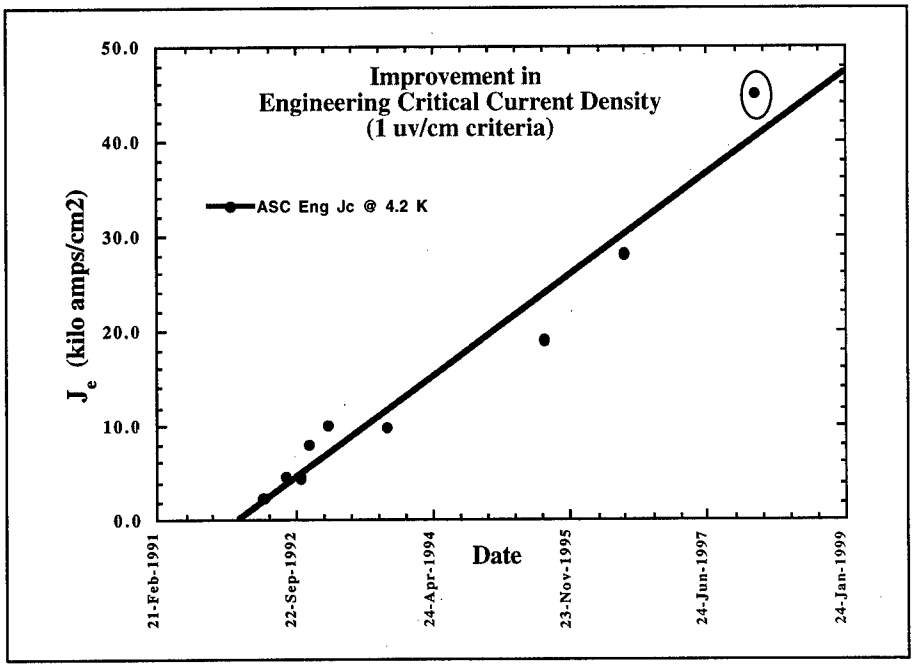


Figure 2: Performance improvement of HTS conductor. Circled point is estimated value from higher temperature measurements.

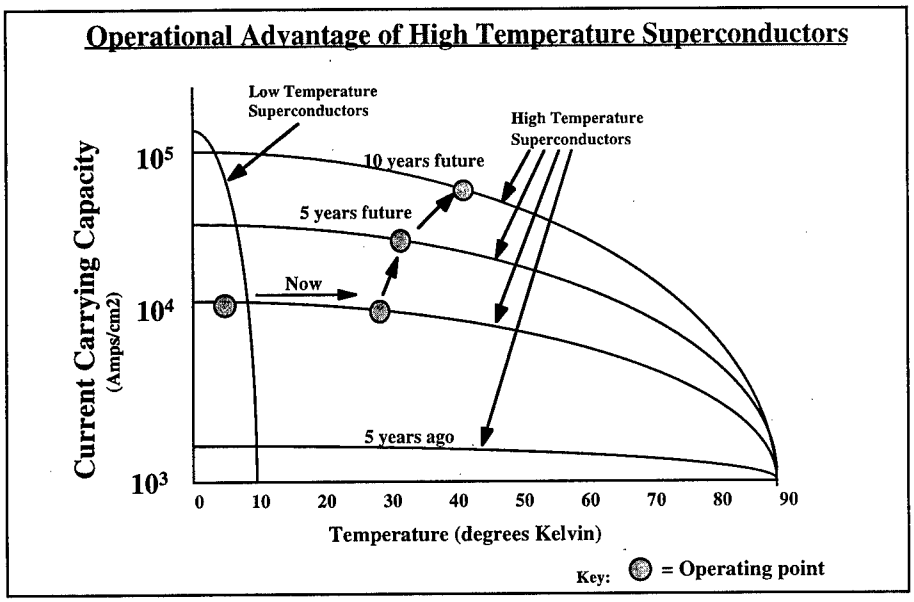


Figure 3: Operational temperature for a 200 hp motor (now); a 5000 hp motor (5 years); and a 20,000 hp motor (10 years). Curves indicate expected performance improvements for HTS conductors.

Figure 3 shows conceptually, how HTS homopolar motor performance is envisioned to improve in the future. We have demonstrated in this program the ability to produce motor performance of greater that 200 hp at 27K. With expected HTS conductor performance improvements and with improved motor magnet designs, it is envisioned that motor performance between 1000 hp and 5000 hp at operating temperatures near 30K will be possible within the next 5 years. If progress continues, HTS homopolar motors in the 20,000 hp to 30,000 hp operating at temperatures near 40K should be available within 10 years.

Laboratory Magnet System

A second major demonstration project of HTS magnet technology was to design and construct a high field magnet test facility for solid state research. The magnet system has a central field maximum of between 7T and 8T at an operating temperature near 20K. The magnet system has a warm bore with a field homogeneity of about 1 percent over a 2-inch diameter volume at the center of the magnet.

The refrigeration power of 6 watts maintains the magnet at operating temperatures under steady state operation, and the field can be energized at a maximum rate of 2T/minute.



Figure 4: High Field Laboratory Magnet

Figure 4 shows a photograph of the magnet system. The magnet itself is composed of 34 pancake type coils operating at 100 amperes (at 6T). These coils are stacked and connected to a copper bus cooling system which in turn is attached to the cold head of a closed cycle refrigerator. The first stage of the cooler cools a thermal shield while the second stage cools the copper bus system which is thermally connected to each pancake of the HTS coil. The total system inductance is 11 Henry, giving a total stored energy at full field of about 100 kjoules. A total of 15 km of HTS conductor was used in this magnet.

The magnet system requires about two days to cool to operating temperatures. After two days, the magnet system reached a temperature of 22K, and the radiation shield reached a temperature of 55K.

Figure 5 shows the central magnetic field and magnet temperature of a 6T demonstration run. It is seen that at a field of 6T the magnet reached a steady state temperature of just over 22K. Higher fields have also been achieved for periods of time well over 30 minutes. This magnet system will be maintained at operating temperatures indefinitely and used for solid state research on superconducting and magnetic materials.

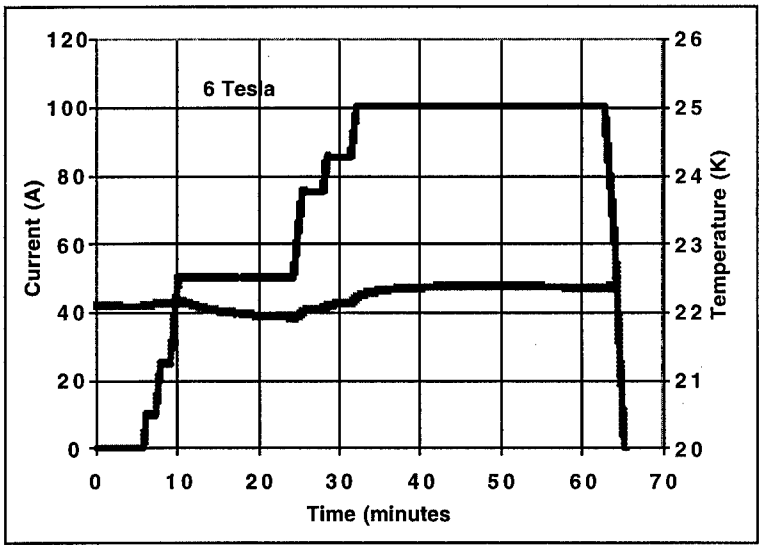


Figure 5: First test run of high field laboratory magnet

Gyroklystron Magnet

There is current interest within the Navy to develop high average power gyroklystron amplifiers to generate millimeter wave electromagnetic radiation for enhanced performance W-band (94 Ghz) radar applications.[3] Gyroklystron amplifiers operating at the fundamental of the cyclotron frequency require a magnetic field of 3.4T to generate a frequency of 94 Ghz. The most efficient means for generating this magnetic field level is through superconducting magnets.

Present radar demonstration programs use a liquid helium-cooled niobium-titanium (NbTi) magnet operating at 4.2K. While suitable for laboratory tests, difficulty with liquid helium logistics precludes fleet deployment of such a system. Although these NbTi magnets can be conduction-cooled to eliminate the liquid helium, the small heat capacity of the low temperature superconducting magnets and the very limited temperature operating range make the risk of this technology extremely high in a military environment.

HTS magnet systems ease many of the problems encountered in a NbTi magnet system. Both the heat capacities and the range of operational temperatures will increase by an order of magnitude making the system much more portable and reliable.

The complications of providing an HTS magnet is that very stringent field homogeneity is required (±1% over 4.45 cm in the cavity region) and the limited axial space (retrofitting an existing system). Nevertheless, an all HTS design has been developed, and construction is underway.

To meet the design requirements, a Helmholtz split coil pair is utilized with a small trim coil. The small trim coil is placed within the Helmholtz pair and is run in opposition to the main windings in order to shape the central field to meet the uniformity requirements. In addition, a secondary bucking coil is provided in order to minimize the fringing field at the location of the electron beam injection. For this magnet, a $Bi_2Sr_2Ca_1Cu_2O_8$ (BSSCO-2212) conductor was used as it was the most cost effective means of obtaining the field. A BSSCO-2221 conductor cannot operate as high in temperature as BSSCO-2223; however, for this application an operating temperature of between 10K and 20K was deemed adequate and, both types of BSSCO perform similarly in this temperature range.

The conductor was a surface coating tape conductor; 6.5 kilometers were required to construct the magnet. The current density of the wire was 12,000 amperes/cm^2 at 10K. Figure 6 shows a schematic of the magnet system used in the gyroklystron magnet. The gyroklystron amplifier unit is positioned along the central axis of the coil. Cooling the HTS magnet is accomplished using a 2-stage Gifford-McMahon (GM) cryocooler. The first stage of the cooler cools the thermal shield to 60K; the second stage cools the magnet system to about 14K. Copper heat transfer plates are used to interface the magnets to the cold head of the cryo-cooler. The total heat load to the cryocooler is on the order of 7 watts.

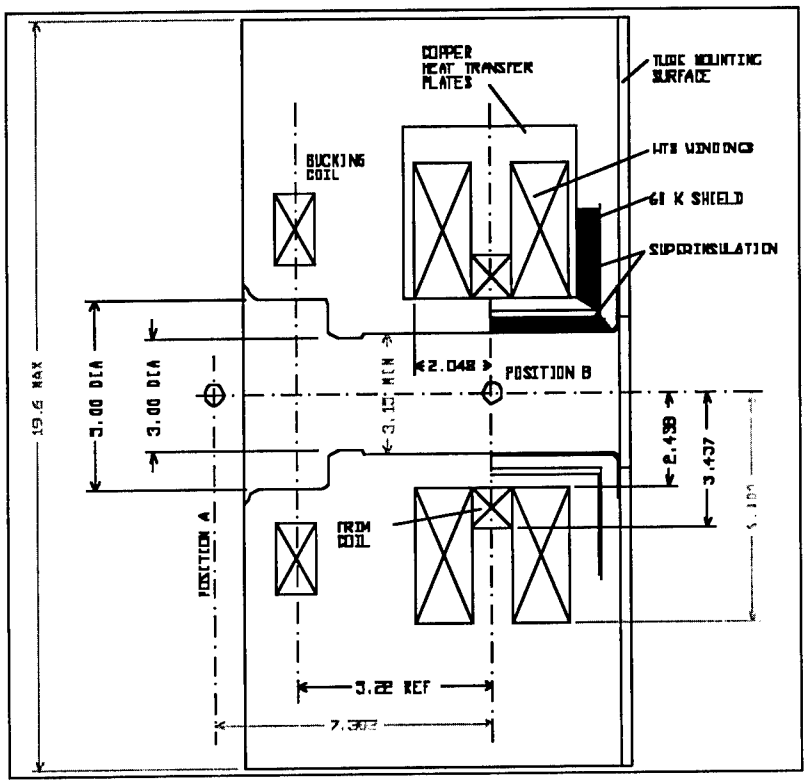


Figure 6: Diagram of the magnet system for the gyroklystron amplifier for 94 Ghz radar.

Conclusion

Three demonstration projections have shown the performance capabilities of HTS magnets system. Military applications in ship propulsion and radar as well as other areas will benefit from HTS technology. The motor and the radar systems have been retrofit demonstrations; hence, full

system benefits are difficult to evaluate. Further demonstrations designed with an HTS magnet system as an integral part are required to fully analyze the cost performance benefits of this new technology.

References

1. J.D. Walters, N.A. Sondergaard, J. Levedahl, D.J. Waltman, E.M. Golda, and T.H. Fikse, "Reexamination of Superconductive Homopolar Motors for Propulsion," Proceedings of the ASNE 1998 Conference.

2. D.U. Gubser, "Superconducting Homopolar Motor and Conductor Development," Journal of Materials, 48, (30) 1996.

3. D.W. Hazelton, B.G. Danly and D.U. Gubser "Cryogen-Free High Temperature Superconducting Magnets for 94 Ghz Gyroklystron-Powered Radar Applications," Proceedings of the ASNE 1998 Conference.

CHEMICAL ENGINEERING OF HIGH-T_c SUPERCONDUCTORS VIA CHEMICAL DOPING

R. S. Liu[1], J. M. Chen[2] and R. G. Liu[2]
[1] Department of Chemistry, National Taiwan University, Taipei, Taiwan, R.O.C.
[2] Synchrotron Radiation Research Center (SRRC), Hsinchu, Taiwan, R.O.C.

Abstract

The chemical engineering of high-T_c superconductors via appropriate chemical substitution leading to the materials in underdoped, optimum-doped and overdoped states in three series of $(Y_{1-x}Ca_x)Ba_2Cu_3O_{7-\delta}$, $(Tl_{0.5}Pb_{0.5})Sr_2(Ca_{1-x}Y_x)Cu_2O_{7-\delta}$ and $(Hg_{0.5}Pb_{0.5})Sr_2(Ca_{1-x}Y_x)Cu_2O_{7-\delta}$ compounds has been investigated by high-resolution O K-edge X-ray absorption near-edge-structure spectra. Near the O *1s* edge, a well pronounced pre-edge peak with maxima at ~ 528 eV is observed, which is ascribed to the excitations of O *1s* electrons to O *2p* holes located in the CuO_2 planes of $(Y_{1-x}Ca_x)Ba_2Cu_3O_{7-\delta}$ $(Tl_{0.5}Pb_{0.5})Sr_2(Ca_{1-x}Y_x)Cu_2O_{7-\delta}$, and $(Hg_{0.5}Pb_{0.5})Sr_2(Ca_{1-x}Y_x)Cu_2O_{7-\delta}$. The intensity of this pre-edge peak increases linearly with increasing the Ca content for these three series of materials. This indicates that the effect of chemical substitution of Ca^{2+} for Y^{3+} is to induce hole states near the Fermi level, which are important to control the T_c for these three series of compounds.

The Third Pacific Rim International Conference on
Advanced Materials and Processing (PRICM 3)
Edited by M.A. Imam, R. DeNale, S. Hanada,
Z. Zhong and D.N. Lee
The Minerals, Metals & Materials Society, 1998

Introduction

The most similarity of the cuprate high temperature superconductors is the existence in all types of the CuO_2 sheets, which are believed to be essential structural componenet for high-T_c behavior [1]. The copper-oxygen component (CuO_2 plane), together with associated cations such as Ca^{2+} and Y^{3+}, forms only one part of the structure. The second structural component interleaves the copper-oxygen components and has been referred as the "charge reservoir". This component has various forms, ranging from simple double layers of metals of (La,Sr) in the $(La,Sr)CuO_4$ phase to either a system of copper-oxygen chains in $YBa_2Cu_3O_7$ or a much more complex double or single layer of two metals and oxygens as the case with the Tl-Ba-O component in $Tl_2Ba_2Ca_2Cu_3O_{10}$ and $TlBa_2Ca_2Cu_3O_9$. One way of visualizing this family is to consider a general structural formula of the type: (charge reservoir)$[M_2Cu_{n+1}(Ca, Y)_nO_{2n+2}$ (M = Ba or Sr). The "tuning" of superconductivity can be generally achieved by manipulating the chemical species and composition of the hole reservoir together with the Ca/Y ratio in cuprates. In order to demonstrate such kind of concept, the $(Y_{1-x}Ca_x)Ba_2Cu_3O_{7-\delta}$, $(Tl_{0.5}Pb_{0.5})Sr_2(Ca_{1-x}Y_x)Cu_2O_{7-\delta}$, and $(Hg_{0.5}Pb_{0.5})Sr_2(Ca_{1-x}Y_x)Cu_2O_{7-\delta}$ systems were chosen for this study.

It is well known that hole states play a pivotal role in the p-type cuprate high-T_c superconductors. Therefore, a knowledge of the electronic structure near the Fermi level of these compounds is an important step toward unveiling the mechanism of superconductivity. The X-ray absorption spectra are determined by electronic transitions from a selected atomic core level to the unoccupied electronic states near the Fermi level. X-ray absorption near-edge structure (XANES) is therefore a direct probe of the character and local density of hole states responsible for high-T_c superconductivity. To improve the understanding on the variation of T_c as a function of the effect of the chemical substituion between Ca^{2+} and Y^{3+}, a detailed study on $(Y_{1-x}Ca_x)Ba_2Cu_3O_{7-\delta}$, $(Tl_{0.5}Pb_{0.5})Sr_2(Ca_{1-x}Y_x)Cu_2O_{7-\delta}$, and $(Hg_{0.5}Pb_{0.5})Sr_2(Ca_{1-x}Y_x)Cu_2O_{7-\delta}$ systems by using the X-ray absorption spectroscopy will be carried out.

Experimental

The samples of $(Y_{1-x}Ca_x)Ba_2Cu_3O_{7-\delta}$ (x = 0 ~ 0.25) were prepared by mixing powders of Y_2O_3, $CaCO_3$, $BaCO_3$ and CuO. The mixtures were calcined at 950 °C for 20 h in air. The resulting mixtures were ground and pressed into pellets. The pellets were sintered at 950 °C for 20 h in air. The fully oxygenated samples were obtained when the sintered pellets were annealed at 400 °C for 20 h in O_2.

The samples of $(Tl_{0.5}Pb_{0.5})Sr_2(Ca_{1-x}Y_x)Cu_2O_{7-\delta}$ (x = 0 ~ 1) were prepared by mixing powders of $SrCO_3$, $CaCO_3$, Y_2O_3 and CuO. The mixture were calcined at 970 °C for 12 h in air to form the precursor Sr-Ca-Y-Cu-O powders. The powders were then mixed with PbO and Tl_2O_3 to form the compositions of $(Tl_{0.5}Pb_{0.5})Sr_2(Ca_{1-x}Y_x)Cu_2O_{7-\delta}$. The resulting mixtures were ground and pressed into pellets. The pellets were sealed in gold foil (to prevent of the loss of lead and thallium at elevated temperatures) and then sintered at 970 °C for 3 h in flowing oxygen. Subsequently, the samples were cooled down to room temperature by a cooling rate of 5 °C /min.

Samples traversing the compositional range $(Hg_{0.5}Pb_{0.5})Sr_2(Ca_{1-x}Y_x)Cu_2O_{7-\delta}$ (x = 0.3 ~ 1) were prepared by mixing high purity powders of HgO, PbO, SrO_2, CaO, Y_2O_3 and CuO. The mixtures were then pressed into pellets. The pellets were wrapped in gold foil to prevent the loss of lead and mercury and also a possible reaction with quartz at alevated temperatures, and encapsulated in an evacuated quartz tube. Subsequently, the pellets were sintered at 970 °C for

24 h then cooled down to room temperature by a cooling rate of 2 °C /min.

The X-ray powder diffraction measurements were carried out with a SCINTAG (X1) diffractometer (CuKα radiation). All the samples are in single phase across the compositional parameter of x in the three systems.

The T_c's of the samples were measured by both a four-point probe and a superconducting quantum interference design (SQUID). The chemical substituion of the Ca^{2+} ions for the Y^{3+} ions in $(Y_{1-x}Ca_x)Ba_2Cu_3O_{7-\delta}$ leads to a decrease in the T_c's from 92 K for x = 0 to 82 K for x = 0.25. This indicates that the x = 0 ($YBa_2Cu_3O_{7-\delta}$) sample is in the optimun hole concentration within the CuO_2 planes. The $(Tl_{0.5}Pb_{0.5})Sr_2(Ca_{1-x}Y_x)Cu_2O_{7-\delta}$ system exhibits superconductivity over the homogeneity range x = 0 ~ 0.5, showing a maximum T_c's of 108 K at x = 0.2.[2] Across the homogeniety range x = 0.6 ~ 1.0, the material also undergoes a metal-insulator transition at temperature above T_c. The chemical substitution of Ca^{2+} for Y^{3+} in the $(Hg_{0.5}Pb_{0.5})Sr_2(Ca_{1-x}Y_x)Cu_2O_{7-\delta}$ system increases the superconducting temperature from T_c = 15 K for x = 0.6 to T_c = 90 K for x = 0.3.[3] For x < 0.3, the T_c's are decreased due to the multiphasic samples.

Using the 6-m high-energy spherical grating monochromator (HSGM) beamline, the x-ray absorption measurements were performed at the Synchrotron Radiation Research Center (SRRC) with an electron beam energy of 1.5 GeV and a maximum stored current of 240 mA. X-ray absorption spectra recorded by X-ray fluorescence yield were measured by a microchannel plate (MCP) detector.[4]

Results and Discussion

In Fig. 1, the O K-edge X-ray absorption spectra for a series of fully-oxygenated $(Y_{1-x}Ca_x)Ba_2Cu_3O_{7-\delta}$ samples with x = 0 ~ 0.25 are shown in the energy range of 525 - 550 eV obtained using a bulk-sensitive total X-ray fluorescence yield method.

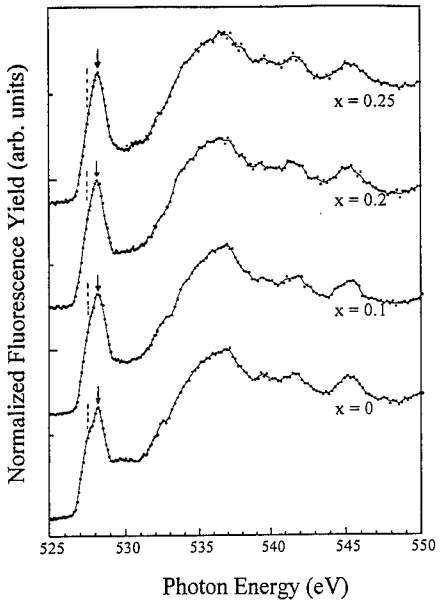


Figure 1: The O K-edge X-ray absorption spectra for a series of fully-oxygenated $(Y_{1-x}Ca_x)Ba_2Cu_3O_{7-\delta}$ samples with x = 0 ~ 0.25.

The low-energy prepeaks at ~ 527.7 eV in Fig. 1 (marked by dash lines) are due to the superposition of O 2p hole states in the apical oxygen sites and the CuO chains. The high-energy prepeak at ~ 528.3 eV as shown in Fig. 1 (denoted by arrows) is attributed to the excitation of O 1s electrons to O 2p holes in the CuO_2 planes.[5] Based on the analyses by curve fitting of the data, an increase in the intensity of the pre-edge peaks at 527.7 eV and 528.3 eV with increasing the Ca-doping was found. Moreover, the increasing rate is higher in the CuO_2 planes (528.3 eV) as compared to that of in the apical oxygen and CuO chain sites(527.7 eV). This indicates that the effect of chemical substituion of Ca^{2+} for Y^{3+} in $(Y_{1-x}Ca_x)Ba_2Cu_3O_{7-\delta}$ is to induce hole states with the O 2p character near the Fermi level and leads the system to ungergoing the over-doping state. This may be the reason for the Tc's decreasing with increasing the Ca-doping in $(Y_{1-x}Ca_x)Ba_2Cu_3O_{7-\delta}$.

In Fig. 2 high-resolution O K-edge X-ray-absorption near-edge structure (XANES) spectra for the series of $(Tl_{0.5}Pb_{0.5})Sr_2(Ca_{1-x}Y_x)Cu_2O_{7-\delta}$ samples in the energy range of 526 - 550 eV were shown by measuring the total X-ray-fluorescence yield. As the Ca doping increases, this gives rise to a new pre-edge feature at ~ 528.3 eV (as indicated by arrows in Fig. 2) for $x \leq 0.5$. This indicates that the effect of chemical substitution of Ca^{2+} for Y^{3+} is to induce hole states with the O 2p character near the Fermi level. The first pre-edge peak at ~ 528.3 eV in Fig. 2 (as indicated by arrows) for the series of $(Tl_{0.5}Pb_{0.5})Sr_2(Ca_{1-x}Y_x)Cu_2O_{7-\delta}$ samples can be ascribed to the excitations of O 1s electrons to O 2p holes located in the CuO_2 planes. The intensity of this pre-edge peak increases linearly with increasing the Ca doping for $0 \leq x \leq 0.5$. This indicates that the effect of chemical substitution of Ca^{2+} for Y^{3+} is to induce hole states in the CuO_2 planes near the Fermi level. Moreover, the increase in the intensities of the second pre-edge peak (~529.4 eV; as indicated by straight line) and the decrease in the intensities of the third pre-edge peak (~529.9 eV) with increasing the Ca content were observed, corresponding to the increase in the hole concentration within the apical oxygen sites and the decrease in the hole concentration within the hole reservoir Tl-O layers, respectively. The intensity of the pre-edge peak at 528.3 eV closely correlates with the compositional variation of superconducting transition temperature, showing that holes generated in the O 2p orbitals within the CuO_2 planes play an important role to control the T_c's of the title system. This may give the evidence to demonstrate that the hole transformation is from the hole reservoir layers of Tl-O through apical oxygen into the CuO_2 planes.

In Fig. 3 we show O K-edge X-ray-absorption spectra for the series of $(Hg_{0.5}Pb_{0.5})Sr_2(Ca_{1-x}Y_x)Cu_2O_{7-\delta}$ samples with x = 0.3, 0.5, 0.6, and 0.7 in the energy range of 526 - 550 eV obtained by the total X-ray-fluorescence yield technique. At high level of Ca doping for $x \leq 0.6$, this gives rise to a new pre-edge feature at ~ 528.3 eV. The pre-edge peak at ~ 528.3 eV in Fig. 3 (as indicated by arrows) for the series of $(Hg_{0.5}Pb_{0.5})Sr_2(Ca_{1-x}Y_x)Cu_2O_{7-\delta}$ samples can be ascribed to the excitations of O 1s electrons to O 2p holes located in the CuO_2 planes. As seen from Fig. 3, the intensity of this pre-edge peak increases with increasing doping level of Ca^{2+} into the Y^{3+} sites. This indicates that chemical substitution of the low valent Ca^{2+} ions for the high valent Y^{3+} ions gives rise to O 2p hole states within the CuO_2 planes near the Fermi level which cause the Tc's increase with incrasing Ca-doping.

Conclusion

In this study, we report high-resolution O K-edge X-ray absorption near-edge structure spectra for the three systems, $(Y_{1-x}Ca_x)Ba_2Cu_3O_{7-\delta}$, $(Tl_{0.5}Pb_{0.5})Sr_2(Ca_{1-x}Y_x)Cu_2O_{7-\delta}$ and $(Hg_{0.5}Pb_{0.5})Sr_2(Ca_{1-x}Y_x)Cu_2O_{7-\delta}$ systems using a bulk-sensitive X-ray fluorescence-yield technique. The results demonstrate that the effect of chemical substitution of Ca^{2+} for Y^{3+} is predominately to induce hole states in the CuO_2 planes near the Fermi level. The intensity of this pre-edge peak closely correlates with the compositional variation of superconducting

transition temperature, showing that holes generated in the O 2p orbitals within the CuO_2 planes play an important role to control the T_c of the title systems.

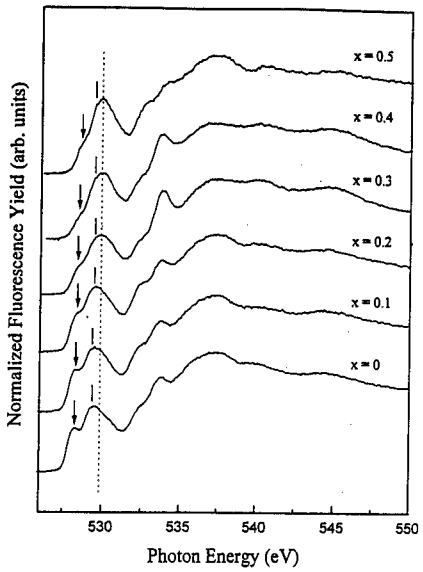


Figure 2: The O K-edge X-ray absorption spectra for a series of $(Tl_{0.5}Pb_{0.5})Sr_2(Ca_{1-x}Y_x)Cu_2O_{7-\delta}$ samples with $x = 0 \sim 0.5$.

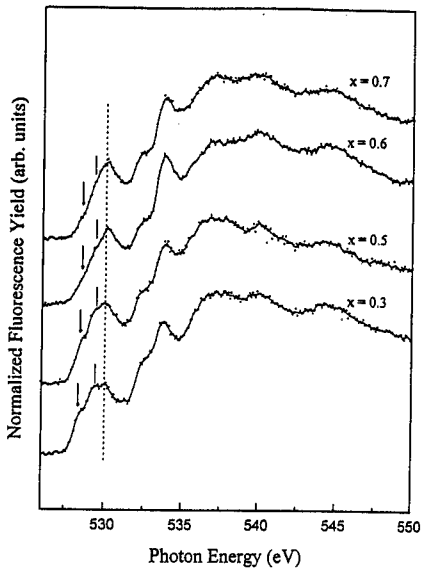


Figure 3: The O K-edge X-ray absorption spectra for a series of $(Hg_{0.5}Pb_{0.5})Sr_2(Ca_{1-x}Y_x)Cu_2O_{7-\delta}$ samples with $x = 0.3$, 0.5, 0.6, and 0.7.

Acknowledgments

This research is financially supported by National Science Council of the Republic of China under the Grant NSC 87-2113-M-002-005.

References

[1] B. Raveau et al., Crystal Chemistry of High-Tc Superconducting Copper Oxides (New York, NY: Springer-Verlag, 1991), 1-150.

[2] R. S. Liu and P. P. Edwards,"The Metal-Superconductor-Insulator Transition in $(Tl_{1-y}Pb_y)Sr_2(Ca_{1-x}Y_x)Cu_2O_7$," Mater. Sci. Forum, 130 (1993), 435-464.

[3] S. F. Hu et al.,"Superconductivity up to 90 K in a New Family of the $(Pb,Hg)Sr_2(Ca,Y)Cu_2O_7$ system," J. Solid State Chem,103 (1993), 280-286.

[4] J. M. Chen, S. C. Chung, and R. S. Liu,"High-Resolution X-ray Absorption Near Edge Structures Studies of Monophasic $Tl_2Ba_2Ca_2Cu_3O_{10-\delta}$ (Tl-1223) Superconductor," Solid State Commu., 99(1996), 493-498.

[5] J. M. Chen et al.,"The Origin of the Superconductivity Suppression in $Dy_{1-x}Pr_xBa_2Cu_3O_7$ Studied by Soft X-ray Absorption Spectroscopy," Phys. Rev. B, 55(1997), 14586-14591.

Hydrogen Absorbing Materials

STATE-OF-THE-ART OF HYDROGEN STORAGE IN REVERSIBLE METAL HYDRIDES

G. Sandrock and M.A. Imam*

Suna Tech, Inc., 113 Kraft Place, Ringwood, NJ 07456
*Naval Research Laboratory, Code 6320, Washington, DC 20375

Abstract

The concept of storing hydrogen in reversible metal hydrides is more than a century old. However practical R&D on reversible metal hydrides really started about 30 years ago with the discovery of room temperature hydrides of certain intermetallic compounds. This paper reviews the present state-of-the art of reversible metal hydrides for possible use as hydrogen storage and supply media. Emphasis is placed on hydrides that can use near-ambient-temperature heat (say 0-100°C) to release H_2 in the 1-10 atmosphere pressure range, although other hydrides are also briefly mentioned. The main part of the review summarizes the hydriding properties and use potential of the elements, solid-solution alloys and five classes of intermetallic compounds: AB_5, AB_2, AB, A_2B and miscellaneous others. Although there are many available alloys with useful properties, shortcomings remain in the areas of H-capacity, cost and resistance to impurity gases in the H_2 used. These conventional hydrides are approaching practical thermodynamic limits, so there is a modern tendency to look toward the complex hydrides and unconventional alloys such as nanocrystalline and amorphous as the principal hopes for the future.

Introduction

Of the four methods of hydrogen storage, compressed gas, cryogenic liquid, metal hydrides, and gas-solid adsorption, the metal hydride storage method is more attractive from the point of view of high volumetric density and safety. Compressed gas storage has disadvantages of extreme pressure, weight, and volume requirements, whereas storage of hydrogen as cryogenic liquid is unattractive due to the requirements of extremely low temperatures and high consumption of primary energy. Moreover, the number hydrogen atoms present per cm^3 (n_H) in liquid hydrogen state (~ 20K) is $4.2X10^{22}$ whereas number of hydrogen (in units of 10^{22} per cm^3) of various hydrides are as follows: LiH--5.9, MgH_2--6.7, TiH_2--9.2, ZrH_2--9.2, VH_2--11.4. High hydrogen concentration is usually associated with a large H/Metal atomic ratio but is also a function of structure. Although some hydrides like LiH and MgH_2 might seem to offer respectable H weight percents (12.7 and 7.6, respectively), in fact such capacities are available only at impracticably high temperatures.

The fuel cell offers a silent and efficient source of electrical power derived from the electrochemical reaction of hydrogen and oxygen. The storage of hydrogen is, therefore, important to the concept and this paper reviews the use of metal hydrides (MH) as H_2 storage media for coupling with fuel cell.

State-of-the-Art Reviews

The primary objective of this study is to review the current state of hydride art. It is presented on a class by class basis relative to the type of hydriding metals or alloys. The review will focus on materials that exhibit hydride dissociation pressures of 1-10 atmospheres (absolute) in the 0-100°C temperature range, typical of operating conditions for Proton Exchange Membrane (PEM) fuel cells. Materials with dissociation temperatures and pressures outside these ranges are also briefly considered (e.g., Mg alloys). A much more thorough listing of available alloys, properties and references can be found on the Internet (1).

Elemental Hydrides

Most of the elements will form hydrides under the appropriate chemical conditions (2). Many (but certainly not all) will react directly and reversibly with H_2 gas at favorable temperatures and H_2 pressures. Except for vanadium, unfortunately, none will release H_2 near ambient temperature.

Vanadium: In the practical H-storage limit of VH_2 the metal structure transforms to face-centered cubic structure to provide enough tetrahedral sites. V exhibits a number of hydride phases (3). For room-temperature H-storage, the usable range of stoichiometry is about $VH_{0.95}$ <----> VH_2, representing about 1.9 wt.% reversible hydrogen storage. Although a volumetric H-density of $11.4X10^{22}$ atoms/cm^3 for VH_2, only slightly more than half of these atoms are really available in a reversible isothermal sense (i.e., about $6.0X10^{22}$ atoms/cm^3). V has been extensively studied as a possible hydride for a thermal hydrogen compressor for an aerospace Joule-Thompson cooler (4). Because of high cost, large-scale use of unalloyed V for fuel cells is not practical but it can play an important role in H-storage solid solution alloys and intermetallic compounds.

Hydrides of Intermetallic Compounds

Intermetallic compounds are highly ordered alloys that take on many structures (5). By combining strong hydride-forming elements A with weak hydride formers B, a large variety of useful intermetallic hydrides can be created. The ability to vary the interstitial environments by varying the composition has led to the modern world of rechargeable metal hydrides.

AB_5 Intermetallic Hydrides: The hydrides based on AB_5 intermetallic compounds, where A are lanthanide elements and B is mainly Ni, are used for the anodes of most of the nickel metal hydride batteries manufactured today. AB_5 intermetallic compounds are actually a structural derivative to the C14 Laves phase AB_2 (5), an important family of hydriding intermetallics. The AB_5 structure contains a variety of tetrahedral and octahedral interstices and the H-atom occupancy depends on the composition (6).

The AB_5 family of intermetallic hydrides is large and properties are ideal for PEM fuel cell applications. Volumetric H-contents are good but gravimetric H-densities are limited to the order of 1-1.25 wt.% on a reversible (plateau width) basis. In general, gaseous impurity resistance is good and resistance to disproportionation is good if stabilized with Al or Sn additions. Alloys based on partially substituted $MmNi_5$ are made commercially in large quantities for NiMH battery uses (Mm=mischmetal). Except for Co (used only in battery applications) no critical strategic elements are really needed. The AB_5s are borderline expensive. They are safe to use, but are mildly pyrophoric when suddenly exposed to air in the activated state.

AB_2 Intermetallic Hydrides: The AB_2 family of intermetallic compounds, like the AB_5s, represents a large and versatile group of hydriding materials with properties of value for the ambient temperature realm of PEM fuel cells. The A-elements are usually from the IVA group (Ti, Zr, Hf). The B-elements can be a variety of transition or nontransition metals with something of a preference for atomic numbers 23-26 (V, Cr, Mn, Fe). A very wide variety of substitutions are possible for both A- and B-elements, thus providing a high degree of fine tuning of PCT properties. Almost all of the practical AB_2 hydriding intermetallic compounds come from the Laves phases. There are three Laves phase structures: C14, C15 and C36 (5). Unlike the AB_5 line compounds, the AB_2 intermetallics often have some homogeneity range (i.e., A:B need not be exactly 1:2). Volumetric H-contents are not quite as good as the AB_5s, but gravimetric H-densities are up to 1.3 wt.% on a reversible basis and potentially better than the AB_5s given an appropriate thermal and pressure cycle. In general, impurity resistance of the AB_2s appears to be not quite as good as the AB_5s, although there is scant data. Resistance to disproportionation seems to be fairly good for practical alloys based $(Ti,Zr)(Mn,Cr,X)_2$.

AB Intermetallic Hydrides: There are a number of AB structures, but most of the practical hydriding compounds are of the relatively simple B2 structure. It is essentially a body-centered-cubic cell with one formula unit per unit cell. Each cell contains 12 tetrahedral and 6 octahedral interstices. Only the octahedral sites become occupied with H-atoms with strong preference to those that have [Ti_4Fe_2] co-ordination (6,7). Among the AB intermetallic compounds, only those based on TiFe have PCT properties that are useful to PEM fuel cell applications (7). They can be easily modified for selected PCT properties by the partial substitutions of Mn or Ni. Other advantages include low cost, safety, and good initial H-capacity (both gravimetric and volumetric). Unfortunately the TiFe-subfamily of AB compounds is hindered by the following problems of high sensitivity to gaseous impurities in the H_2 used, especially O_2 and H_2O vapor; cyclic instability associated with the upper plateau and slow activation.

A_2B Intermetallic Hydrides: The A_2B family of compounds represent the fourth group of intermetallic in terms of activity. Unfortunately, the A_2Bs offer little in the 0-100°C, 1-10 atm range useful for PEM fuel cells, at least with the present state of the art. A_2B intermetallics form very stable hydrides compared to the AB_5, AB_2 and AB compounds. Most practical interest in the A_2B hydrides centers around Mg_2NiH_4, which represents about 3.6 wt.% H. Unfortunately, nearly 300°C is needed to release the H_2 (8).

Miscellaneous Other Intermetallic Hydrides: In addition to the AB_5, AB_2, AB and A_2B intermetallic compounds discussed above, several other families of intermetallics have been shown capable of reversible hydriding/dehydriding reactions (1). Examples include AB_3, A_2B_7, A_6B_{23}, A_2B_{17}, A_3B and others. Although none of these have attained commercial levels of interest, at least the AB_3 and A_2B_7 phases are deserve brief inclusion in this review because PCT properties are in the range of interest for PEM fuel cell applications. In addition, there has been some controversy centered around the La_2Mg_{17} phase.

AB_3 Compounds: The structures of the AB_3 compounds are closely related to the AB_5 and AB_2 structures in that they are simply stacking of equal numbers of AB_5 and AB_2 units. A quick review indicates most AB_3 hydrides are on the stable side, but clearly some have at least 1 atm dissociation pressure within the 100°C limit we have chosen for fuel cell applications (1). There is an undesirable tendency for the AB_3s to either show multiple plateaux (e.g., $NdCo_3$) or a short plateau with a sloping upper leg and a low-pressure offset (e.g., $GdFe_3$). On the positive side, they tend to have low absorption/desorption hysteresis (9).

A_2B_7 Compounds: Similar to the AB_3 phases, A_2B_7 phases consist of sequenced stacking of 2 AB_5 and 1 AB_2 layers, again giving essentially the same interstitial environments. There is a general tendency for the A_2B_7 phases to show multiple plateaux, e.g. two plateaux for Pr_2Ni_7. Plateau pressures are generally in the useful range for PEM fuel cells; however, the capacities are not particularly good because often only one plateau is usable in a multiple plateau alloy. Although the PCT properties of the A_2B_7 hydrides are more appropriate to PEM fuel cell applications than are those for AB_3s, the A_2B_7s also suffer from lack of data on properties other than PCT, such as cyclic stability and impurity effects.

La_2Mg_{17}: The structure of La_2Mg_{17} is related to the AB_5 structure. The first data on the hydriding properties of La_2Mg_{17} was reported by Brookhaven in 1972 and said to have an H-capacity of 5.3 wt.% with a desorption pressure about 10% higher than MgH_2, i.e., unremarkable over Mg (10). Then, in 1977, a short paper suggested significant potential for the reversible storage of H in La_2Mg_{17} at temperatures well below the 300°C needed for Mg (11). Later work in France and Bulgaria reported that a two-step series of disproportionation reactions was involved in the absorption and desorption of H_2 in La_2Mg_{17}, at least at temperatures well above ambient (12,13). Capacities reported were up to 5.5wt.% with implications of desorption pressures similar to MgH_2 (≈3.5 atm at 325°C), thus confirming the earlier work (10).

A dramatically different picture was presented for the hydriding properties of La_2Mg_{17} having "ambient temperature" H-capacity of more than 6 wt.% (14). If La_2Mg_{17} behaved as reported by Dutta and Srivastava (14), a major theoretical anomaly would be born and the practical culmination of decades-long Mg-alloy hydride quests would be at hand. La_2Mg_{17} would represent the best hydride for PEM fuel cells. Unfortunately, ambient temperature La_2Mg_{17} hydride has not been independently confirmed. One directed published work (15) failed to confirm the hydriding and dehydriding results of Dutta and Srivastava. In particular, temperatures of 275+°C were needed for significant H_2 release from La_2Mg_{17}-hydride.

Solid Solution Alloy Hydrides

Unlike the intermetallic compound, the solute need not be present at an integer or near-integer stoichiometric relationship to the solvent and can be in a random (non-ordered) substitutional or interstitial distribution within the basic crystal structure. Several solid solution alloys form reversible hydrides, in particular those based on the solvents Pd, Ti, Zr, Nb and V.

Pd, Ti and Zr Solid Solutions: Perhaps the largest family of solid solution hydrides consists of the face-centered-cubic (A1) Pd-based alloys(1). Although the PCT properties of many of the Pd solid solution alloys are compatible with our PEM fuel cell range of 1-10 atm at 0-100°C, they are of generally low gravimetric and volumetric H-capacity, e.g., seldom exceeding 1.0 wt.%H. In addition they are prohibitively expensive and using them for H-storage would add further to the cost burden of the precious metals already required in the PEM fuel cell for electrocatalysis. Ti- and Zr-base solid solution alloys form hydrides that are too stable for PEM fuel cell application, even when highly alloyed.

Nb and V Solid Solutions: Although there are many possibilities, the only practical V-based solid solution alloys must contain the solute element Fe because this allows the alloys to be made with relatively inexpensive ferrovanadium. Because of its strong ability to control PCT properties, Ti is also useful as a solute element. Thus, the most practical solid solution alloy families for PEM fuel cell H-storage are V-Ti-Fe (16) or V-Ti-Mn (17). Although gaseous impurity effects have not been well quantified for for the V alloys, they are apparently much easier to activate than elemental V (16).

Other Approaches

Thus far we have reviewed predominantly single phase alloys and intermetallic compounds made by more or less conventional metallurgy. Other approaches have been considered, especially in recent years. Because these approaches are experimentally and conceptually incomplete relative to practical H-storage, it is important to identify potential for future progress.

Multiphase Alloys and Composites: For the purpose of electrochemical applications (e.g., NiMH batteries), multiphase hydriding alloys are said to offer advantages as to capacity, charge/discharge rate capability or cyclic capacity retention, the second phases apparently acting as beneficial electrocatalysts or preferred paths for hydrogen penetration (19-21).

There are more interesting possibilities in the area of composite hydrides. Composites are made by powder plating or mechanical mixing that may or may not be followed by sintering or partial melting. For example, the simple blending of two hydriding alloys to produce custom PCT properties such as stepped plateaux has been known for nearly two decades (22). Another composite class is the "microencapsulated" hydrides. Here hydriding alloy powder particles are plated with Cu or Ni. (23). A similar approach, especially useful in making MH electrodes, is to dry-blend the hydriding alloy (usually AB_5 or AB_2) with Ni or Cu flake (24). Non-metallic coatings have been applied to AB_5 and A_2B compounds to impart corrosion resistance and improved activation properties (25).

Amorphous and Nanocrystalline Alloys: Certain amorphous and glassy metals can be made in thin film or ribbon form by sputtering or rapid quenching from the melt, respectively. The subject of amorphous or glassy hydrides has been an active research area for many years,

perhaps more for academic than practical reasons. Compared to identical crystalline compositions, amorphous or glassy metals always exhibit P-C isotherms that have no plateaux, a consequence of the broad range of interstitial environments. The complete absence of a plateau is usually undesirable for gas-based practical hydride devices like H-storage where limited charging and discharging pressure ranges are imposed, i.e. they generally have lower effective H-capacitiy than their crystalline counterpart. The absence of a plateau is not necessarily a barrier to the use of amorphous or glassy alloys in a battery (26,27). Recent work on nanocrystalline alloys has demonstrated dramatically increased hydriding and dehydriding kinetics (28,29).

Quasicrystalline Alloys: Quasicrystals, offering icosahedral symmetry, offer the possibility of interstitial environments somewhat different from the classic crystal structures. Recently, some Ti-based quasicrystals have been shown to hydride (30). Compositions such as $Ti_{45}Zr_{38}Ni_{17}$ and $Ti_{53}Zr_{27}Ni_{20}$ have been hydrided up to 1.6 H/M. As might be expected from the high Ti+Zr contents, temperatures for the desorption of the H_2 are impracticably high (>650°C) and disproportionation is sometimes apparent at such temperatures.

Polyhydrides: In recent years Jensen and coworkers have identified the potential of certain nonclassical metal complex hydrides for H_2 storage (31). They have concentrated on Group VIIIA based materials such as $IrH_aX_b(H_2)(PR_3)_2$, where X = Cl, Br or I; R = C_6H_{11}, $C(CH_3)_3$ or $CH(CH_3)_2$; a = 1-2; and b= 1-2. In this general formula (H_2) represents a dihydrogen species (a sort of H_2 molecule) that can bound to the Ir metal atom to form a weak ligand. This ligand can be easily broken and reformed during the reversible H_2 desorption / absorption storage reactions. A new concept has surfaced for using the polyhydrides not as storage media, but as catalysts for the reversible hydrogenation/dehydrogenation of unsaturated hydrocarbons (32). In this case reversible H-contents of 7 wt.% are at least theoretically possible using only limited amount of the expensive PM-containing polyhydride catalysts.

Complex Hydrides: There are families of hydrides with more complex bonding than metallic that offer the potential of higher H-capacities. They are almost always poorly reversible and used mainly for H_2 generation by nonreversible reaction with water, e.g., $LiBH_4$. Some have R&D potential for future storage applications if they can be made more reversible, as in the Na-Al example below.

Ti-doped Na-Al Hydrides: $NaAlH_4$ and Ni_3AlH_6 are related examples of non-transition-metal complex hydrides that are not considered very reversible at all. Recently, Bogdanovic´ has discovered that the two-step H/D reactions can be made reversible by the addition of Ti-catalysts, e.g. ß-$TiCl_3$ (33). Although the required temperatures are higher that we have available from a PEM fuel cell, Bogdanovic´ has made significant progress in converting what has been considered a classic non-reversible hydride system into one that shows clear potential for practical H-storage at very attractive weight percents.

Summary

Although hydride comparisons were made during this review, it is perhaps worthwhile to stand back and make a comparative summary in relation to other storage methods such as compressed gas, LH_2, Fe-H_2O reaction and carbon physisorption. This is done Figure 1, which is a published map of volumetric vs. gravimetric H-densities for these options (34). Each data point

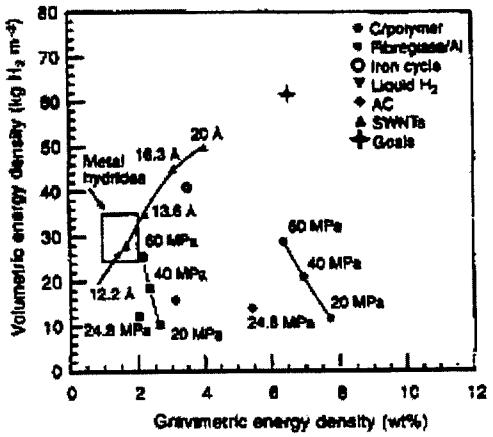


Figure 1

Volumetric and Gravimetric H-Densities for H-Storage Systems
Storage Methods: C/polymer = C-wrapped polymer gas cylinders;
Fiberglass/Al = fiberglass-wrapped Al gas cylinders;
Iron cycle = steam-Fe reaction;
AC = activated C; SWNTs = single-walled C nanotubes
Dillon et al (34)

represents an estimate of the system - H-storage medium and container. Metal hydrides are included as a box representing a range of storage systems containing both ambient and high dissociation temperature materials . Such a comparison as Fig.1 is dependent on many assumptions as to the systems design and pressure-code safety factors, but for our purposes gives a good reference frame. The goal shown is that of the US DoE for fuel cell powered land vehicles. The metal hydride options offer good volumetric H-densities but poor gravimetric densities, as we have long known. Although far from perfected at this moment, the authors of Fig.1 feel that single-walled carbon nanotubes (not discussed here) have the potential to exceed hydrides in both volumetric and gravimetric H-densities. If one does not care about volumetric density and very high required pressures (200-600 atm), then C-wrapped polymer gas tanks offer the best gravimetric densities other than LH_2, namely several wt.%.

Acknowledgements

The authors wish to acknowledge the support and encouragement of Dr. J. Sedriks, Office of Naval Research, and Dr. B.B. Rath, Naval Research Laboratory. This work was done, in part, under ONR Contract N00014-97-M-0001

References

1. Sandrock, G; Thomas, G., Internet URL **http://hydpark.ca.sandia.gov** (see also "Compilation of IEA/DOE/SNL Hydride Databases", Report IEA/H2/TR-97, International Energy Agency, Paris, 1997)

2. Mueller, W. M.; Blackledge, J. P.; Libowitz, G. G., Eds., Metal Hydrides, Academic, New York, 1968

3. Schober, T.; Wenzl, H; "The Systems NbH(D), TaH(D), VH(D): Structure, Phase Diagrams, Morphologies, Methods of Preparation", Hydrogen in Metals II, G. Alefeld and J. Völkl, Eds., Topics in Appl. Phys., 29 (1978), 11-71

4. Bowman, R. C.; Freeman, B. D., and Philips, J. R., "Evaluation of metal hydride compressors for appl. in Joule-Thompson cryocoolers", Cryogenics, 32 (1992), 127-137

5. Barrett, C. S.; Massalski, T.B., Structure of Metals, 3rd Ed., (Pergamon, Oxford, 1980)

6. Yvon, K.; Fischer, P., "Crystal and Magnetic Structures of Ternary Metal Hydrides", Hydrogen in Intermetallic Compounds, L. Schlapbach, Ed., Topics in Appl. Phys., (Springer, Berlin, 63, 1988), 87-138

7. Reilly, J. J.; Sandrock, G. D., "Hydrogen Storage in Metal Hydrides", Scientific American, 242 (No.2), Feb. 1980, 118-129

8. Reilly, J. J.; Wiswall Jr., R. H., "The Reaction of Hydrogen with Alloys of Magnesium and Nickel and the Formation of Mg_2NiH_4", Inorgan. Chem., 7 (1968), 2254-2256

9. Goudy, A. J., "Hydrogen Solubility in Rare Earth Intermetallic Compounds", Thesis, University of Pittsburgh (1976)

10. Reilly, J. J.; Wiswall, R. H., "Hydrogen Storage and Purification Systems", (BNL Report 17136, Brookhaven National Laboratory, 1972)

11. Yajima, S.; Kayano, H.; and Toma, H., "Hydrogen Sorption in La_2Mg_{17}", J. of Less-Common Metals, 55 (1977), 139-141

12. Darriet, B.; Pezat, M.; Hbika, A.; and Hagenmuller, P., "Application of Magnesium Rich Rare-Earth Alloys to Hydrogen Storage", Int. J. Hydrogen Energy, 5 (1980), 173-178

13. Khrussanova, M.; Terzieva, M.; Peshev, P.; Petrov, K.; Pezat, M.; Manaud, J. P.; and Darriet, B., "Calcium-Substituted Lanthanum-Magnesium Alloys for Hydrogen Storage", Int. J. Hydrogen Energy, 9 (1985), 591-594

14. Dutta, K.; N. Srivastava, O., "Investigation on Synthesis, Characterization and Hydrogenation Behavior of La_2Mg_{17} and Related Intermetallics", Hydrogen Energy progress VIII, T. N. Veziroglu and P. K. Takahashi, Eds., (Pergamon, 2, 1990), 1027-1034

15. Slattery, D. K., "The Hydriding-Dehydriding Characteristics of La_2Mg_{17}", Int. J. Hydrogen Energy, 20 (1995), 971-973

16. Libowitz, G. G.; Maeland, A. J., "Hydride Formation by B.C.C. Solid Solution Alloys", Materials Science Forum, 31 (1988), 177-196

17. Iba H.; Akiba, E., "Hydrogen absorption and modulated structure in Ti-V-Mn alloys" J. Alloys and Compounds, 253-254 (1997), 21-24

18. Gutjahr, M. A.; Bucher, H.; and Beccu, K. D., "A New Type of Rev. Neg. Electrode for Alkaline Storage Batteries Based on Metal Alloy Hydrides", Power Sources, 4 (1973), 79

19. Notten, P. H. L.; Hokkeling, P., "Double-Phase hydride Forming Compounds: A New Class of Highly Electrocatalytic Materials", J. Electrochemical Soc., 138 (1991), 1877-1885

20. Fetcenko, M. A.; Venkatesan, S.; and Ovshinsky, S. R., "Selection of Metal Hydride Alloys for Electrochemical Applications", Hydrogen Storage Materials, Batteries, and Electrochemistry, D. A. Corrigan and S. Srinivasan, Eds., (The Electrochemical Soc., 92-5 1992), 141-167

21. Joubert, J.-M.; Latroche, M.; Percheron-Guegan, A.; and Bouet, J.: "Improvement of the electrochemical activity of Zr-Ni-Cr Laves phase hydride electrodes by secondary phase precipitation", J. Alloys and Compounds, 240 (1996), 219-228

22. Suda, S.; Uchida, M., "Mixing Effects of Two Different Types of Hydrides", Hydrides for Energy Storage, A. F. Andresen and A. J. Maeland, Eds., (Pergamon Press, Oxford, 1978), 515-525

23. Ishikawa, H.; Oguro, K.; Kato, A.; Suzuki, H.; and Ishii, E., "Preparation and Properties of Hydrogen Storage Alloys Microencapsulated by Copper", J. of Less-Common Metals, 120 (1986), 123-133

24. Yoshinaga, H.; Wada, M.; Sakai, T.; Miyamura, H.; Kuriyama, N.; and Uehara, I., "Metal Hydride Electrodes Made by Dry Powder Process Using Flake Copper and Flake Nickel Powders", Denki Kagaku, 63 (1995), 847-852

25. Liu, F.J.; Suda, S., "Properties and characteristics of fluorinated hydriding alloys", J. Alloys and Compounds, 231 (1995), 742-750

26. Sapru, K.; Reichman, A. R.; and Ovshinsky, S. R.; , "Rechargeable Battery and Electrode used Therein", US Pat. 4 623 597, Nov. 18, 1986

27. Ryan, D. H.; Dumias, F.; Patel, B.; Kycia, J.; and Ström-Olsen, J. O., "A rechargeable cell based on amorphous Ni-Zr", J. of Less-Common. Met., 172-174 (1991), 1246-1251

28. Zaluski, L.; Zaluska, A.; Ström-Olsen, "Nanocrystalline metal hydrides", J. Alloys and Compounds, 253-254 (1997), 70-79

29. Fujii, H.; Orimo, S.; Ikeda, K., "Cooperative hydriding properties in nanostructured Mg_2Ni-H system", J. Alloys and Compounds, 253-254 (1997), 80-83

30. Vivano, A. M.; Stroud, R. M.; Gibbons, P. C.; McDowell, A. F.; Conradi, M. S.; and Kelton, K. F., "Hydrogenation of titanium-based quasicrystals", Phys. Rev. B, 51 (1995), 12026-12029

31. Mediati, M.; Tachibana, G. N.; and Jensen, C. M., "Solid-State and Solution Dynamics of the Reversible Loss of Hydrogen from the Iridium Nonclassical Polyhydride Complexes $IrClH_2(PR_3)_2$ (R = Pr^i, Cy, Bu^t)", Inorg. Chem., 31 (1992), 1827-1832

32. Jensen, C. M., "Hydrogen Storage via Polyhydride Complexes ", Proc. 1996 U.S. DOE Program Review(Rept. NREL/CP-430-21968, II, Nat. Renew. Energy Lab, 1996), 787-793

33. Bogdanovic´, B.; Schwickardi, M.; "Ti-doped alkali metal aluminum hydrides as potential novel reversible hydrogen storage materials", J. Alloys and Compds, 253-254 (1997), 1-9

34. Dillon, A. C.; Jones, K. M.; Bekkedahl, T. A.; Kiang, C. H.; Bethune,D. S.; and Heben, M. J., "Storage of hydrogen in single-walled nanotubes", Nature, 386 (1997), 377-379

A STUDY ON THE DEVELOPMENT OF OVER-STOICHIOMETRIC Zr-Ti-Mn-V-Ni HYDROGEN STORAGE ALLOY WITH HIGH CAPACITY AND HIGH RATE-CAPABILITY FOR Ni-MH RECHARGEABLE BATTERY

Dong-Myung Kim, Kuk-Jin Jang and Jai-Young Lee

Dept. of Materials Sci. and Eng., Korea Advanced Institute of Science and Technology,
373-1 Kusong-dong , Yusong-gu, Taejon, South Korea

Abstract

Extensive work has been carried out on developing the Zr-based Laves phase alloy with high capacity and especially with high rate-capability for electrochemical application. After careful alloy design of $ZrMn_2$-based Laves phase alloys through varying their stoichiometry by substituting or adding some alloying elements, $Zr_{0.9}Ti_{0.1}(Mn_{0.7}V_{0.5}Ni_{1.4})_{0.92}$ alloy with high capacity and high rate-capability was developed consequently. This alloy has the discharge capacity of 392 mAh/g, i.e. 35% higher capacity than that of commercialized AB_5 type alloys, at the discharge rate of 0.25C and shows a high rate-capability.

The Third Pacific Rim International Conference on
Advanced Materials and Processing (PRICM 3)
Edited by M.A. Imam, R. DeNale, S. Hanada,
Z. Zhong and D.N. Lee
The Minerals, Metals & Materials Society, 1998

Introduction

Zr-based Laves phase metal hydrides have been attracting much attention because of their larger hydrogen storage capacity than that of commercialized AB_5 type alloy and relatively long electrochemical charge-discharge cycle life[1]. In general, however, most of them were disappointing as to the rate-capability compared with that of the commercialized AB_5 type alloys. Therefore, many researches have been focused on developing Zr-based alloy with high capacity and especially with high rate-capability for electrochemical application. It has been reported that the rate-capability is mainly controlled by surface reaction kinetics which depends on the metallic Ni or some Ni-rich phase on the alloy surface[2]. From this point of view, in order to improve the rate-capability of Zr-based alloys, it seems to be necessary to increase the Ni content in these alloys. On the other hand, it has been reported recently that some over-stoichiometric Zr-based Laves phase alloys showed excellent hydriding and electrochemical characteristics compared with stoichiometric alloys[3]. In this work, extensive research has been carried out on developing the over-stoichiometric Zr-based Laves phase alloy with high capacity and especially with high rate-capability for practical application. Also the relationship between the discharge performance and the alloy characteristics is discussed.

Experimental

Alloys were prepared by arc-melting under argon atmosphere and remelted several times to obtain a homogeneous phase. Then the alloys were mechanically crushed into a powder of less than 37μm. The crystal structures of the alloys were determined by XRD analysis. In order to investigate the hydrogen storage performance of the alloys, pressure-composition-temperature(PCT) curves were measured using an automatic Sieverts-type apparatus made by ourselves. The metal hydride electrode was made by mixing alloy powder with Cu powder (about 1 μm) at a weight ratio of 1:0.25. The mixture was cold pressed to a pellet with diameter of 10 mm and a thickness of about 1 mm at a compacting pressure of 10 ton/cm^2. The charge-discharge test of MH electrode was carried out in the three compartment half cell by an automatic galvanostatic charge-discharge apparatus. The electrode was charged with a current density of 100mA/g for 6 hours and discharged with the same current density to -0.75 V vs. Hg/HgO. In order to determine surface reaction kinetics of the electrode, exchange current was measured using the linear polarization method. The SEM, BET(Braunauer-Emmett-Teller) analysis was performed and the micro-hardness was also measured.

Results and discussion

Compositional optimization of Zr-Mn-V-Ni alloy

The $ZrMn_2$ compound has a large hydrogen storage capacity of about 1.5wt.%, but it cannot be discharged in KOH solution itself. After careful design of the $ZrMn_2$-based alloy to have suitable hydrogen equilibrium pressure and to achieve higher discharging capacity in KOH solution, $ZrMn_{0.5}V_{0.5}Ni_{1.4}$ alloy reveals rather good properties in view of hydrogen storage capacity of about 1.5wt% at hydrogen equilibrium pressure ranges of application and electrochemical discharge capacity of about 315mAh/g(Fig. 1). In order to optimize the composition of these quaternary alloy with high capacity and high rate-capability, the major factor affecting the discharge capacity and the rate-capability of this alloy system should be determined. Therefore, in our previous work[4], the hydrogen storage performance, i.e. PCT curve, and discharge characteristics, i.e. discharge capacity and rate-capability, of

$ZrMn_{0.5}V_{0.5}Ni_{1.4+y}$ (y = 0.0, 0.2, 0.4 and 0.6) alloys were observed for variable Ni content. The Ni is believed to be of influence on the rate-capability because of its high catalytic activity. As the amount of Ni increases in above alloys, the hydrogen equilibrium pressure increases and the hydrogen storage capacity decreases. From the XRD results, it seemes that the increase of the hydrogen equilibrium pressure and the decrease of the amount of stored hydrogen can be attributed to the lattice shrinkage and the change of chemical affinity between hydrogen and the Ni(Ni is not a hydride forming element[5]) As shown in Fig. 2, as the amount of Ni increases in $ZrMn_{0.5}V_{0.5}Ni_{1.4+y}$ (y = 0.0, 0.2, 0.4 and 0.6) alloys, the discharge capacity decreases. However, it is unexpectedly found that the rate-capability decreases with increasing Ni content in the alloys. After separating the factors affecting the rate-capability into the factors related to specific reaction surface area(S) and specific surface catalytic activity, i.e. the exchange current density(i_o), it is identified that the major factor affecting the rate-capability of this alloy system is the specific reaction surface area, not the specific surface catalytic activity(Fig. 3). The reaction surface area of the alloy can be changed according to its own pulverization rate related to internal stress in the alloy during charge/discharge cycles and to brittleness of the alloy itself. On the other hand, it was reported that Mn-containing alloys were brittle so that they were easily pulverized during charge/discharge cycles[6]. Therefore, in order to identify the role of Mn in this Zr-based alloy system, the volume expansion ratio and mechanical strength of $ZrMn_{0.5}V_{0.5}Ni_{1.4+y}$ (= the Mn-rich alloy) and $ZrMn_{0.3}V_{0.7}Ni_{1.4+y}$ (= the less Mn-rich alloy) (y = 0.0, 0.2, 0.4 and 0.6) were measured. From the above study, it is found that the Mn-rich system, i.e. the $ZrMn_{0.5}V_{0.5}Ni_{1.4}$ alloys, show a higher rate-capability(Fig. 4) because of a larger reaction surface area as shown in Fig. 5 due to the higher brittleness associated with the larger amount of Mn. Based on the above results, Mn is identified to be more effective in improving the rate-capability than Ni and is also known to lead to a more stable hydride than Ni[5]. Therefore, the substitution of Mn for Ni may improve both the rate-capability and the discharge capacity. After determining the hydrogen storage performance and discharge characteristics of $ZrMn_{0.5+x}V_{0.5}Ni_{1.4-x}$ (x = 0.0, 0.2 and 0.4) alloys for variable amount of substituted Mn, it was found that the charge transfer reaction resistance increased drastically as the amount of Mn increased(Fig. 6). So the alloy composition was optimized for $ZrMn_{0.7}V_{0.5}Ni_{1.2}$. This alloy shows a discharge capacity of about 330mAh/g and somewhat good rate-capability(Fig. 7).

Compositional optimization of Zr-Ti-Mn-V-Ni alloy

In order to improve the discharge capacity much more, Zr was partially substituted by Ti in the $ZrMn_{0.7}V_{0.5}Ni_{1.2}$ alloy. Zr in the $ZrMn_{0.7}V_{0.5}Ni_{1.2}$ alloy has larger atomic weight than Ti. Therefore, if Zr is substituted by Ti, it may be possible to increase unit weight discharge capacity. After observation of discharge capacity, it is found in Fig. 8 that the electrochemical discharge capacity passes through a maximum with respect to Ti content in the alloy. In order to analyze the above phenomenon, the PCT curve measurement was performed on $Zr_{1-x}Ti_xMn_{0.7}V_{0.5}Ni_{1.2}$ (x = 0.0, 0.1, 0.15 and 0.2) alloys. From PCT curves in Fig. 9, it is observed that the hydrogen storage capacity decreases continuously and hydrogen equilibrium pressure increases with increasing Ti content in the alloys. From their XRD results shown in Fig. 10, all of these alloys are identified to be in single phase range with C14-type hexagonal structure and their lattice parameters decrease with the increasing amount of substituted Ti. These mean that both the lattice volume and the size of hydrogen occupation sites(i.e. tetrahedral interstices) decrease. Therefore it seems that an increase of the hydrogen equilibrium pressure and a decrease of the amount of stored hydrogen can be attributed to the lattice shrinkage and the change of chemical affinity for hydrogen of the metals(Zr has the stronger chemical affinity for hydrogen than Ti[5]). In spite of continuous decrese of the hydrogen storage capacity with

respect to Ti content, the electrochemical discharge capacity passed through a maximum with respect to the substituted Ti content in the alloy. Therefore it is thought that there exists another factor affecting the electrochemical discharge capacity. And this factor is supposed to be discharge kinetics, i.e. rate-capability. After observation of the rate-capabilities of $Zr_{1-x}Ti_xMn_{0.7}V_{0.5}Ni_{1.2}$ (x = 0.0, 0.1, 0.15 and 0.2) alloys with respect to Ti content at 30°C, it is found that as the amount of substituted Ti increases, the rate-capability increases. The maxima trends of the electrochemical discharge capacity of the alloys for the variable substituted Ti content is attributed to the cooperation between decrease of hydrogen storage capacity and increase of rate-capability. On the other hand, the increase of the rate-capability of this alloy system with respect to increasing substituted Ti content may be due to the formation of Ti-oxide film on the MH surface, which is believed to be more porous than Zr-oxide and the hydrogen penetrate easily through this porous surface of Ti-oxide[7]. This alloy system reveals the best electrochemical properties at the composition of $Zr_{0.9}Ti_{0.1}Mn_{0.7}V_{0.5}Ni_{1.2}$ which shows about 360mAh/g of discharge capacity at the current density of 100mA/g.

The optimization of the stoichiometry of (Zr-Ti)(Mn-V-Ni)$_x$ alloy

In this work, the discharge efficiency of a hydrogen storage alloy is defined as the ratio of discharge capacity at the current density of 25mA/g, i.e. at the low discharge current density, to theoretical capacity calculated from PCT curves. The discharge efficiency of $Zr_{0.9}Ti_{0.1}Mn_{0.7}V_{0.5}Ni_{1.2}$ alloy is identified to be as high as about 92%. Considering the discharge efficiency of $Zr_{0.9}Ti_{0.1}Mn_{0.7}V_{0.5}Ni_{1.2}$ alloy, to increase the discharge capacity of this alloy, it is necessary to increase theoretical capacity rather than to increase discharge efficiency. On the other hand, it is generally known that the amount of hydrogen stored reversibly in the hydrogen storage alloy only with the pressure range between about 0.01 and 5 atm attributes to the theoretical capacity. Also, the hydrogen equilibrium pressure can be changed by substitution of some elements because of their different chemical affinity for hydrogen or by varying the stoichiometric ratio of hydride forming element part(i.e. Zr, Ti) to transition element part(i.e. Mn, V, Ni). However because the alloy has been optimized until now by the substitution work, then it is necessary to vary hydrogen equilibrium pressure by changing the stoichiometric ratio of hydride forming element part to transition element part. To adjust the hydrogen equilibrium pressure of $Zr_{0.9}Ti_{0.1}Mn_{0.7}V_{0.5}Ni_{1.2}$ alloy in above mentioned pressure range, the PCT curves were measured for the $(Zr_{0.9}Ti_{0.1})(Mn_{0.7}V_{0.5}Ni_{1.2})_x$ alloys with the various stoichiometric ratios, i.e. x = 1.0, 0.95, 0.92, 0.88 and 0.84. As the x value, i.e. the amount of $(Mn_{0.7}V_{0.5}Ni_{1.2})$ part, decreases, the hydrogen equilibrium pressure also decreases, as expected(Fig. 11). However, the theoretical capacity passes again through a maximum with respect to x value. On the other hand, it is shown in Fig. 12 that the rate-capability is rarely changed corresponding to the x value. Accordingly, as shown in Fig. 13, the discharge capacity passes through a maximum with respect to x value and the highest discharge capacity is obtained at the composition of $Zr_{0.9}Ti_{0.1}(Mn_{0.7}V_{0.5}Ni_{1.2})_{0.92}$.

Evaluation of $Zr_{0.9}Ti_{0.1}(Mn_{0.7}V_{0.5}Ni_{1.2})_{0.92}$ alloy developed in this work

The $Zr_{0.9}Ti_{0.1}(Mn_{0.7}V_{0.5}Ni_{1.2})_{0.92}$ alloy developed finally in this work has the discharge capacity of 392 mAh/g at the discharge rate of 0.25C, whichi is higher about 35% than that of commercialized AB_5 type alloy(Fig. 14), and shows high rate-capability equaling to that of commercialized AB_5 type alloy(Fig. 15).

Conclusions

After careful modification of composition of $ZrMn_{0.5}V_{0.5}Ni_{1.4}$ alloy system through varying their stoichiometry, $Zr_{0.9}Ti_{0.1}(Mn_{0.7}V_{0.5}Ni_{1.4})_{0.92}$ alloys with high capacity and high rate-capability was developed. This alloy has the discharge capacity of 392 mAh/g at the discharge current density of 0.25C and shows high rate-capability equaling to that of commercialized AB_5 type alloys.

Acknowledgements

This work was conducted under the Research and Development programs on "a development of metal hydride anode for high performance secondary battery" in the projects sponsored by Ministry of Science and Technology(MOST) and Dukeun Industrial Co., Ltd. Authors also wish to express their thanks to the Hydrogen Energy Research Center at KAIST for financial support for a part of this work.

References

1. S. R. Kim and J. Y. Lee, "Electrode characteristics of C14-type Zr-based Laves phase alloys", J. Alloys and Compounds, 210 (1994) 109-113

2. D. M. Kim, K. Y. Lee and J. Y. Lee, "The electrode characteristics and modified surface properties of $V_{0.9}Ti_{0.1}$ alloy sintered with Ni powder", J. Alloys and Compounds, 231 (1995) 650-654

3. S. Wakao, H. Sawa and J. Furukawa, "Effects of partial substitution and anodic oxidation treatment of Zr-V-Ni alloys on electrochemical properties", J. Less-Common Metals, 172-174 (1991) 1219

4. D. M. Kim J. H. Jung, K. J. Jang and J. Y. Lee, "Electrochemical properties of over-stoichiometric $ZrMn_{1-x}V_xNi_{1.4+y}$ (x = 0.5, 0.7; y = 0.0, 0.2, 0.4 and 0.6) alloys with C15 Laves phase", J. Electrochem. Soc., (1997) in press

5. L. Schlapbach, Hydrogen in Intermetallic Compounds I (Springer-Verlag Berlin Heidelberg New York, 1988), 266-273

6. T. Sakai, H. Miyamura, N. Kuriyama, H. Ishikawa and I. Uchida, "Hydrogen storage alloys for Nickel-Metal Hydride battery", Zeitschrift für Physikalische Chemie, Bd. 183, S. 333-346 (1994)

7. A. Züttel, F. Meli, L. Schlapbach, "Surface and bulk properties of the TiyZr1-y(VxNi1-x)2 alloy system as active electrode material in alkaline electrolyte", J. Alloys and Compounds, 231 (1995) 645-649

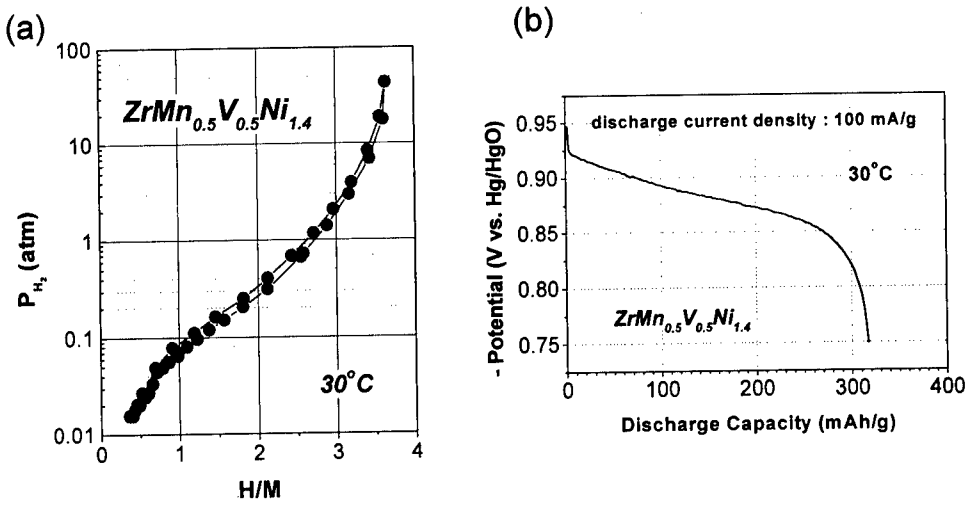


Fig. 1 (a) The PCT curves of $ZrMn_{0.5}V_{0.5}Ni_{1.4}$ alloys at 30°C; (b) The discharge curves of $ZrMn_{0.5}V_{0.5}Ni_{1.4}$ alloys at the discharge current density of 100mA/g

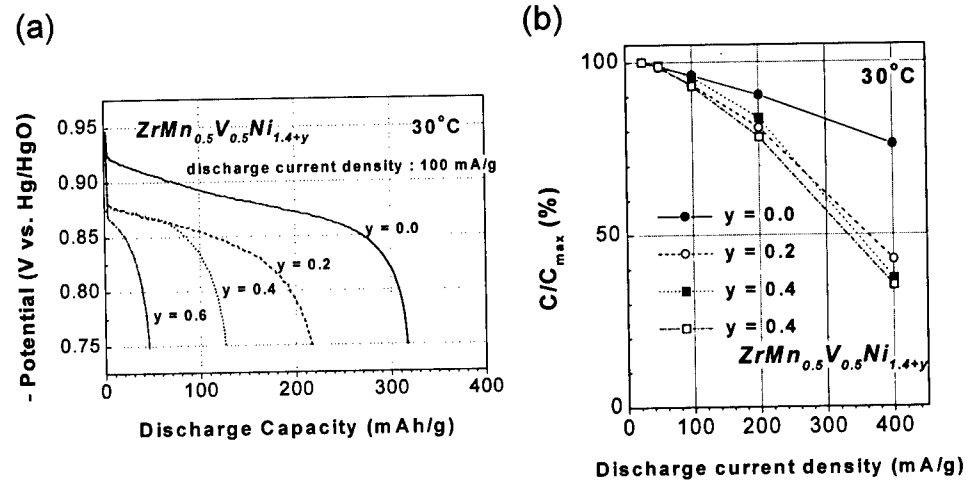


Fig. 2 (a) The discharge curves of $ZrMn_{0.5}V_{0.5}Ni_{1.4+y}$ (y=0.0, 0.2, 0.4 and 0.6) alloys at the discharge current density of 100mA/g; (b) The rate-capabilities of $ZrMn_{0.5}V_{0.5}Ni_{1.4+y}$ (y=0.0, 0.2, 0.4 and 0.6) alloys

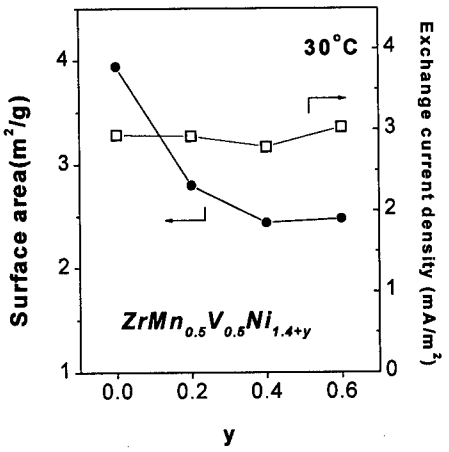


Fig. 3 Comparison of reaction surface area and exchange current density of $ZrMn_{0.5}V_{0.5}Ni_{1.4+y}$ (y=0.0, 0.2, 0.4 and 0.6) alloys at 30°C

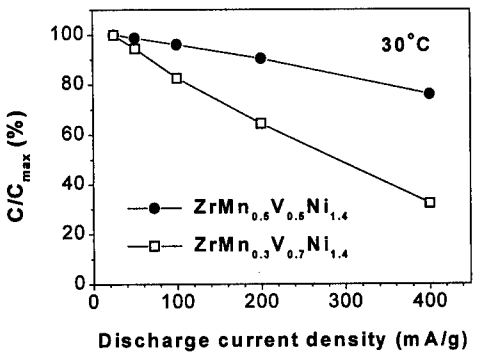


Fig. 4 Comparison of rate-capability of $ZrMn_{0.5}V_{0.5}Ni_{1.4+y}$ and $ZrMn_{0.3}V_{0.7}Ni_{1.4+y}$ (y=0.0, 0.2, 0.4 and 0.6) alloys at 30°C

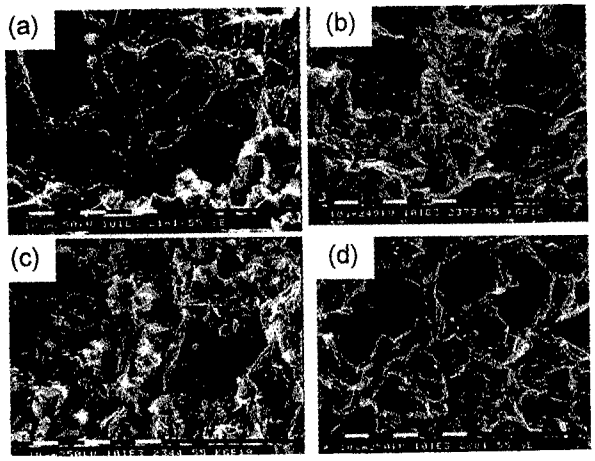


Fig. 5 (a) (b) the surface morpholorgy of $ZrMn_{0.5}V_{0.5}Ni_{1.4+y}$ (y=0.0 and 0.6); (c) (d) the surface morpholorgy of $ZrMn_{0.3}V_{0.7}Ni_{1.4+y}$ (y=0.0 and 0.6)

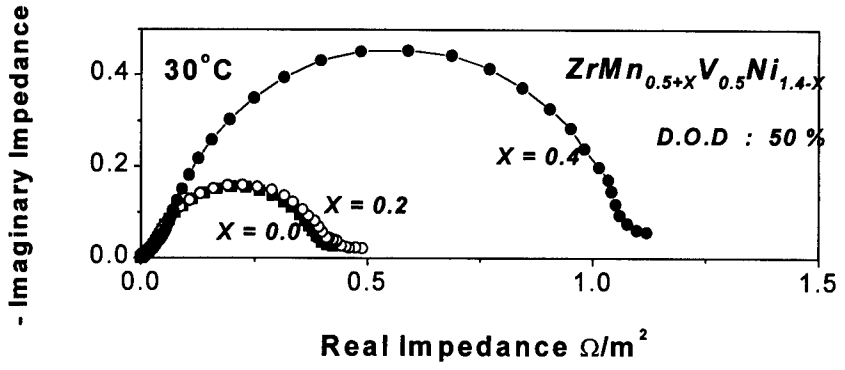


Fig. 6 The electrochemical impedance spectroscopy of $ZrMn_{0.5+x}V_{0.5}Ni_{1.4-x}$ (x=0.0, 0.2 and 0.4) alloys with respect to substituted Mn content in the alloy

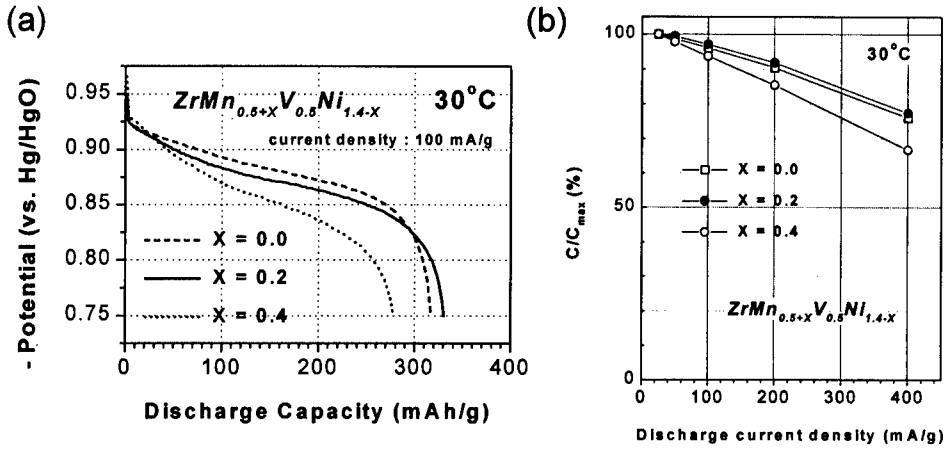


Fig. 7 (a) The discharge curves of $ZrMn_{0.5+x}V_{0.5}Ni_{1.4-x}$ (x=0.0, 0.2 and 0.4) alloys at the discharge current density of 100mA/g; (b) The rate-capabilities of $ZrMn_{0.5+x}V_{0.5}Ni_{1.4-x}$ (x=0.0, 0.2 and 0.4) alloys

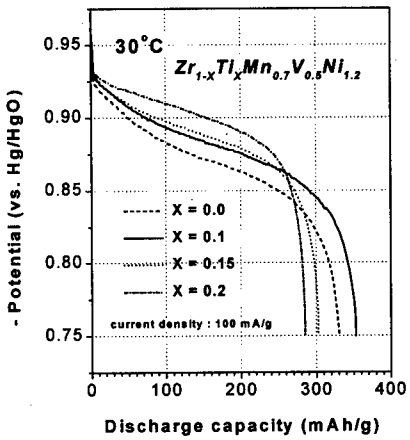


Fig. 8 Discharge curves of $Zr_{1-x}Ti_xMn_{0.5}V_{0.5}Ni_{1.4+y}$ (y=0.0, 0.1, 0.15 and 0.2) alloys at the current density of 100mA/g

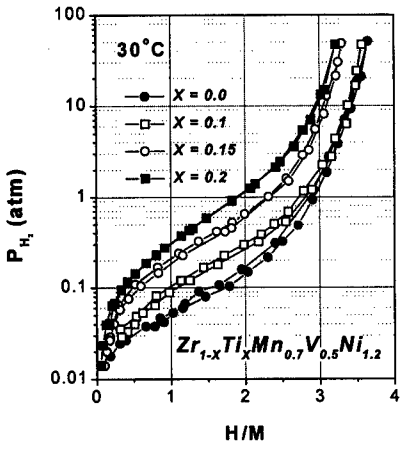


Fig. 9 PCT curves of $Zr_{1-x}Ti_xMn_{0.5}V_{0.5}Ni_{1.4+y}$ (y=0.0, 0.1, 0.15 and 0.2) alloys for variable Ti content at 30°C

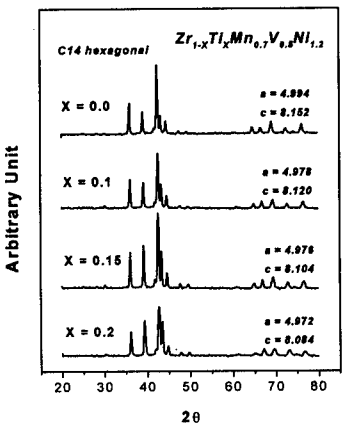


Fig. 10 XRD patterns and lattice parameters of $Zr_{1-x}Ti_xMn_{0.5}V_{0.5}Ni_{1.4+y}$ (y=0.0, 0.1, 0.15 and 0.2) alloys for variable Ti content

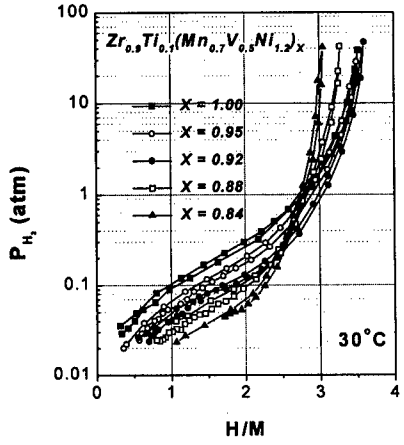


Fig. 11 PCT curves of $Zr_{0.9}Ti_{0.1}(Mn_{0.7}V_{0.5}Ni_{1.2})_x$ (x=1.0, 0.95, 0.92, 0.88 and 0.84) alloys for variable stoichiometric ratio at 30°C

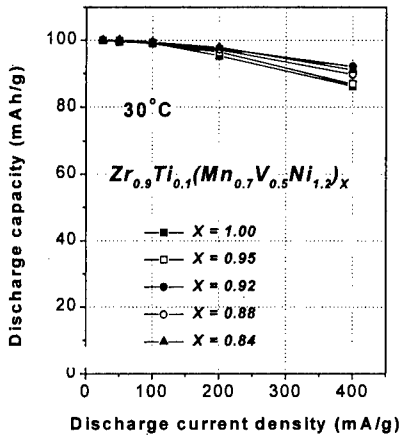


Fig. 12 Rate-capability of $Zr_{0.9}Ti_{0.1}(Mn_{0.7}V_{0.5}Ni_{1.2})_x$ (x=1.0, 0.95, 0.92, 0.88 and 0.84) alloys for variable stoichiometric ratio at 30°C

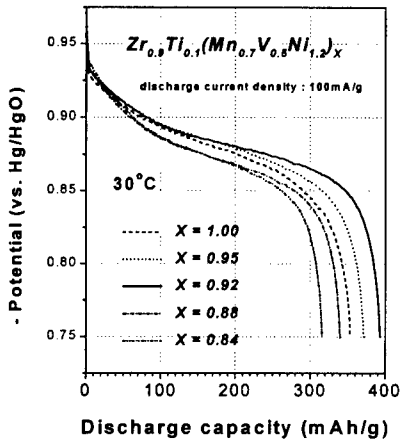


Fig. 13 Discharge curves of $Zr_{0.9}Ti_{0.1}(Mn_{0.7}V_{0.5}Ni_{1.2})_x$ (x=1.0, 0.95, 0.92, 0.88 and 0.84) alloys for variable stoichiometric ratio at 30°C

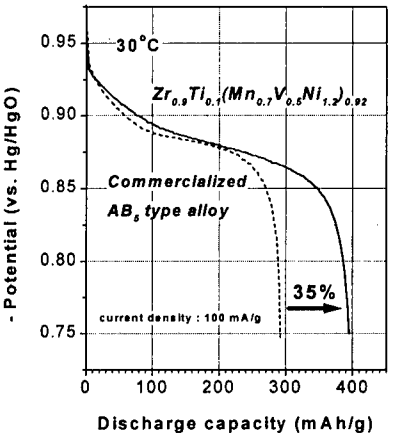


Fig. 14 The discharge curves of commercialized AB_5 type alloy and $Zr_{0.9}Ti_{0.1}(Mn_{0.7}V_{0.5}Ni_{1.2})_{0.92}$ at 30°C

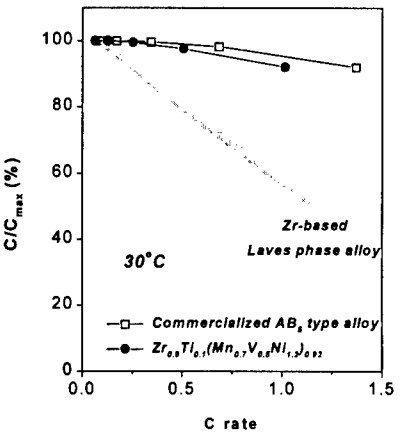


Fig. 15 The rate-capabilities of commercialized AB_5 type alloy and $Zr_{0.9}Ti_{0.1}(Mn_{0.7}V_{0.5}Ni_{1.2})_{0.92}$ at 30°C

CRYSTAL STRUCTURE AND HYDROGEN ABSORPTION PROPERTIES OF La(Ni, M)$_x$ (x=3~ 5) MELT-SPUN RIBBONS

M. Okada, T. Kuriiwa, T. Tamura, A. Kamegawa, H. Takamura and H. Nakamura

Department of Materials Science, Graduate School of Engineering,
Tohoku University, Sendai JAPAN 980-77

Abstract

The present study describes the rapid quenching effects on the solid-solution range of La(Ni, M)$_x$ (x=3~ 5) alloys prepared by melt-spinning in discussing their hydrogen absorption properties. It is found that the single phase with $CaCu_5$ crystal structure extends to $LaNi_{4.65}$ compositional alloys. A variation of lattice constants of these ribbons is different from that of homogenized samples reported before.When the compositional x in $LaNi_{5-x}$ becomes smaller, the alloys show better hydrogen absorption properties such as quite easy activation, flat plateau pressure and good hydrogen storage capacity comparable to that of $LaNi_5$ homogenized sample. Adopting a melt-spun technique is able to form a single $CaCu_5$ type-structure phase with wide non-stoichiometric compositions in La-Ni-M alloy systems.

The Third Pacific Rim International Conference on
Advanced Materials and Processing (PRICM 3)
Edited by M.A. Imam, R. DeNale, S. Hanada,
Z. Zhong and D.N. Lee
The Minerals, Metals & Materials Society, 1998

Introduction

The $LaNi_5$ intermetallic compound exhibits excellent hydrogen storage properties such as easy activation, low plateau pressure and high hydrogen storage capacity. Therefore, $LaNi_5$ compound has been extensively studied for the negative electrode of Ni-MH batteries. In today's use for the negative electrode of Ni-MH batteries, alloys must be a single phase. But it is well-known that it is difficult to make non-stoichiometric $LaNi_5$ alloys as a single phase because of its limited solid-solution range[1]. Therefore, only a few studies on non-stoichiometric $LaNi_5$ alloys have been reported[2][3][4].

Since the rapid quenching from molten metals has the effect on excluding the segregation of alloys, and sometime on expanding the sold-solution range of intermetallic alloys, and will possibly form a metastable phase. It is reported that the new metastable phase with $TbCu_7$-type structure was observed in $LaNi_x$(x>5) melt -spun ribbons[5], and that Mn or Si addition stabilizes the $CaCu_5$ structure in wide compositional range of $LaNi_{x-1}Mn$(x=5~6.6), or $LaNi_{x-1}Si$(x=5~8) melt-spun ribbons.

The purpose of the present study is to investigate rapid quenching effects on the solid-solution range of $LaNi_5$ phase with $CaCu_5$-type structure for the $La(Ni,M)_x$ (x=3~5) alloys prepared by melt-spinning with a single roller, in discussing their hydrogen absorption properties and the effects of partial substitutional elements such as Al, Co, Mn and Si on the solid-solution range of $LaNi_5$ compound with $CaCu_5$-type structure.

Experimental Procedures

All the $La(Ni,M)_x$ (x=3~5) alloys used in this study were prepared by arc-melting under purified argon atmosphere from starting metal with a purity of better than 99 mass%. The alloy was melted into a button form. The buttons were remelted several times in order to be homogeneous. Then, the ribbons were prepared by melt-spinning at the surface velocity of 60m/s with a single roller under purified argon atmosphere. Appeared phases in melt-spun ribbons were determined by X-ray diffractometer (XRD) with Cu-Kα radiation. The pressure-composition isotherms(PCT) of the specimen were measured at 313K by the Siverts-type apparatus.

Results and Discussions

$LaNi_x$ (x=4.5~5.5) Melt-spun Ribbons

The $LaNi_x$ (x=4.5~5.5) alloys were prepared by the melt-spun techniques, since it is important to know how the solid-solution range of $LaNi_5$ phase with $CaCu_5$-type structure will be expanded by the technique. Figure 1 shows X-ray diffraction patterns of $LaNi_x$ (x=4.5~5.5) melt-spun ribbons. The $LaNi_{5.5}$ melt -spun ribbons contain Ni phase besides $LaNi_5$ phase, and $LaNi_x$(x=4.5 or 4.6) ribbons consist of $LaNi_3$ and $LaNi_5$ phase, which are expected from La-Ni binary phase diagram[1]. But the $LaNi_x$ (x=4.65~5) ribbons show $CaCu_5$-type structure, which indicates that the solid-solution range of the $LaNi_5$ phase is larger than reported one(x=4.9) for the as-cast or homogenized alloys[1]. This result consistents with the works by Itagaki[6]. It is found that the melt-spun technique has an

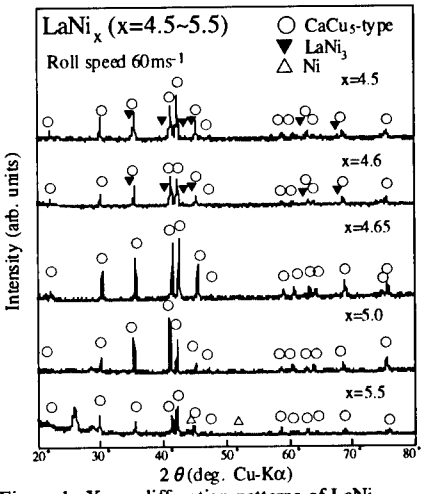


Figure 1 : X-ray diffraction patterns of $LaNi_x$ (x=4.5~5.5) melt-spun ribbons

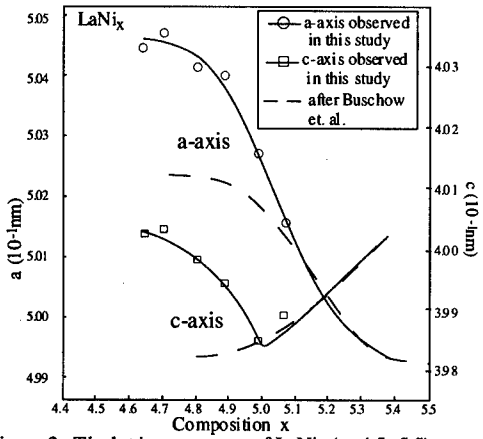


Figure 2 : The lattice constants of $LaNi_x$ (x=4.5~5.5) melt-spun ribbons as a function of composition x.

effect for expanding the solid-solution range of $CaCu_5$-type crystal structure in La-Ni system. Figure 2 shows the lattice constants of $LaNi_x$ (x=4.5~5.5) melt-spun ribbons as a function of composition x. The lattice constants monotonously increase with increasing the La content. It was reported that the a-axes shrink, and c-axes expand with increasing the Ni content for the $LaNi_x$ (x>5)[7]. For the La-rich $LaNi_x$ (x<5) alloys, it has been said that excess La atoms will randomly occupy the Ni sites in $CaCu_5$-type crystal structure, which expects that both of a-axes and c-axes will expand with increasing the number of substituted Ni atoms with excess La atoms. But it was regarded that c-axes would shrink with increasing the La content. The present study clarifies that the a-axes and c-axes expand for the La-rich $LaNi_x$ ($4.65 \leqq x \leqq 5$) alloys, since the relatively large solid-solution range of $CaCu_5$-type crystal structure was obtained by melt-spinning in this study. This variation of lattice constants would be considered to be reasonable in assuming that larger size of La atoms will be substituted for Ni atoms with increasing the La content.

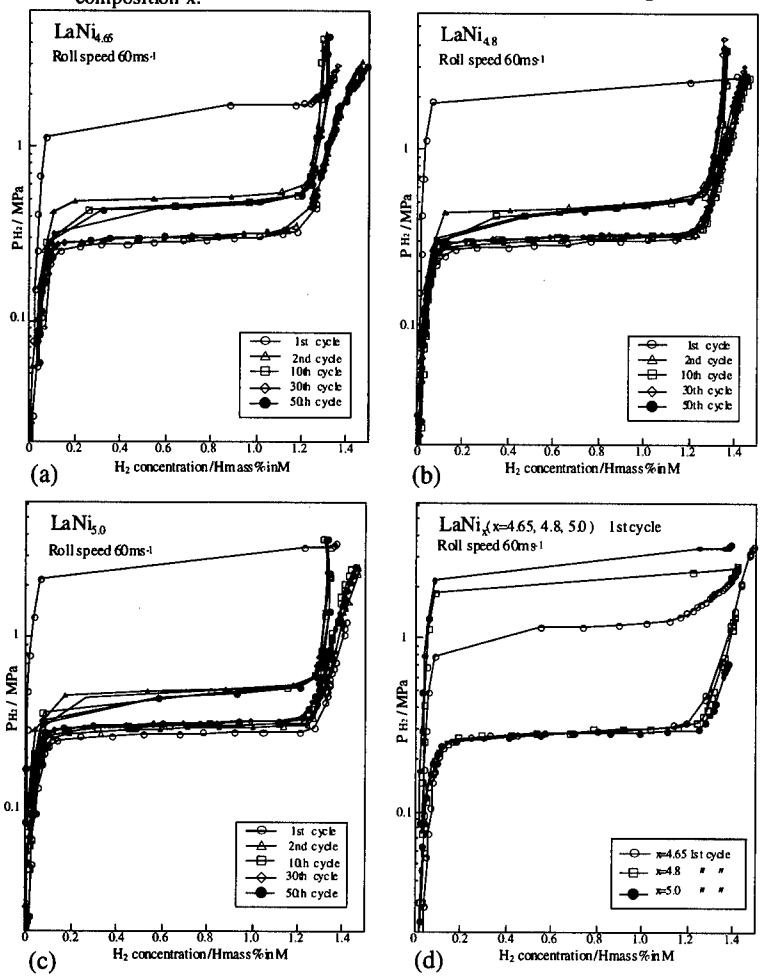


Figure 3 : PCT curves of (a)$LaNi_{4.65}$, (b)$LaNi_{4.8}$, (c)$LaNi_5$ melt-spun ribbons without activation treatment after measuring 1st-50th cycles and (d)their first cycle curves.

Figure 3 shows the PCT curves of (a)$LaNi_{4.65}$, (b)$LaNi_{4.8}$, (c)$LaNi_5$ melt-spun ribbons without activation treatment after measuring 1st-50th cycles and (d)their first cycle

curves. The 1st cycle of the curve in the Figure corresponds to the activation treatments, and the pressure of the 1st cycle for absorbing hydrogen turn out to be high. But the total amount of absorbing hydrogen nearly remains same after the cycling over 2nd times. This means that the 1st cycle of the measurement can be regarded as enough activation treatments. Figure 3(d) summarizes the 1st cycle of the curve and show that pressure of the 1st cycle for absorbing hydrogen turns out to be lower for La-rich $LaNi_{4.65}$ ribbons. This result suggests that the alloys with higher content of La will undergo easier activation treatments.

Figure 4(a) shows the PCT curves of 30th cycle for the $LaNi_5$ melt-spun ribbons in comparing with that of homogenized ingots. The ribbons show the higher content of hydrogen, and better plateau region than those of homogenized ingots even after 30th cycle. Figure 4(b) shows the PCT curves of 50th cycle for the $LaNi_x$ (x=4.65, 4.8, 5.0) melt-spun ribbons and indicates that hydrogen content remains almost unchanged after 50th cycle for the ribbons. No hydrogen induced amorphasization has been observed in La-rich ribbons. It can be said that melt-spinning is the effective sample preparation technique in yielding the higher amount of hydrogen content, better plateau region, easier activation and better stabilities than the conventional cast-anneal-pulverizing technique.

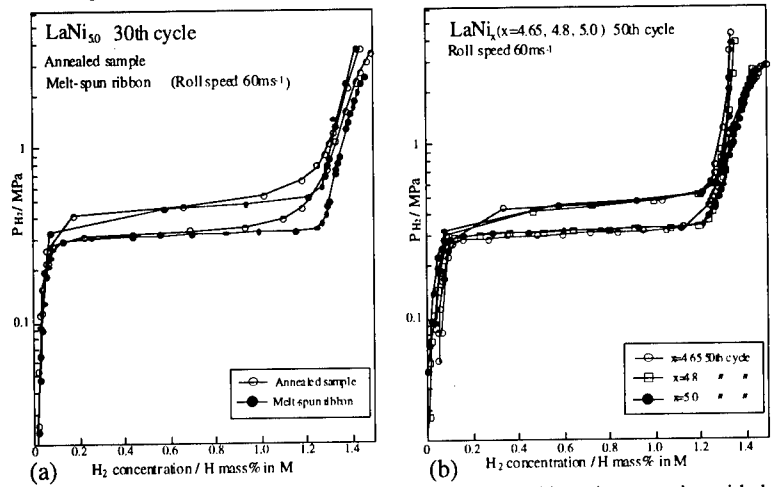


Figure 4 : (a)PCT curves of 30th cycle for the $LaNi_5$ melt-spun ribbons in comparing with that of homogenized ingots and (b) PCT curves of 50th cycle for the $LaNi_x$ (x=4.65, 4.8, 5.0) melt-spun ribbons.

$LaNi_{x-1}M$(M=Al, Co, Mn, Si)(x=3~5) Melt-spun Ribbons

$LaNi_{x-1}M$(M=Al, Co, Mn, Si)(x=3~5) melt-spun ribbons were prepared in order to pursuit the possibility of obtaining the La-rich $CaCu_5$-typecrystal structure by substitutional elements.

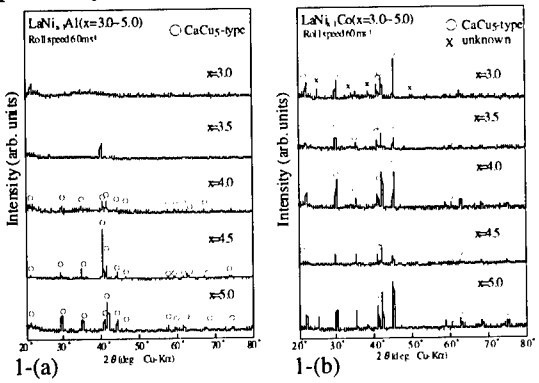


Figure 5-1 : XRD patterns of 1-(a)$LaNi_{x-1}Al$ and 1-(b)$LaNi_{x-1}Co$ (x=3~5) melt-spun ribbons.

Figure 5 shows the XRD patterns of 1-(a)$LaNi_{x-1}Al$, 1-(b)$LaNi_{x-1}Co$, 2-(a)$LaNi_{x-1}Mn$ and 2-(b)$LaNi_{x-1}Si$ (x=3~5) melt-spun ribbons. The Si substitution tends to form the wide compositional range of amorphous phase and the Co one forms the wide compositional range ($LaNi_{2.5}Co$~$LaNi_4Co$) of $CaCu_5$-typecrystal structure. Besides Si substitution, Co, Al and Mn are effective for forming larger compositional range of $CaCu_5$-type crystal structure than that without

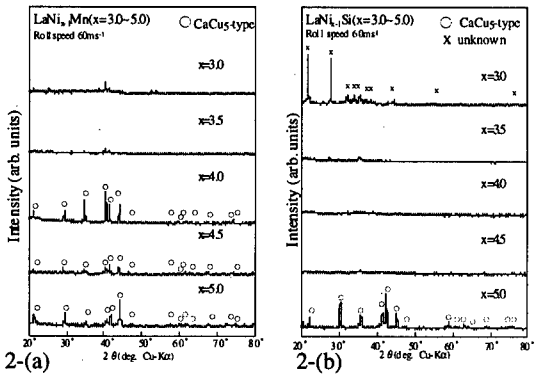
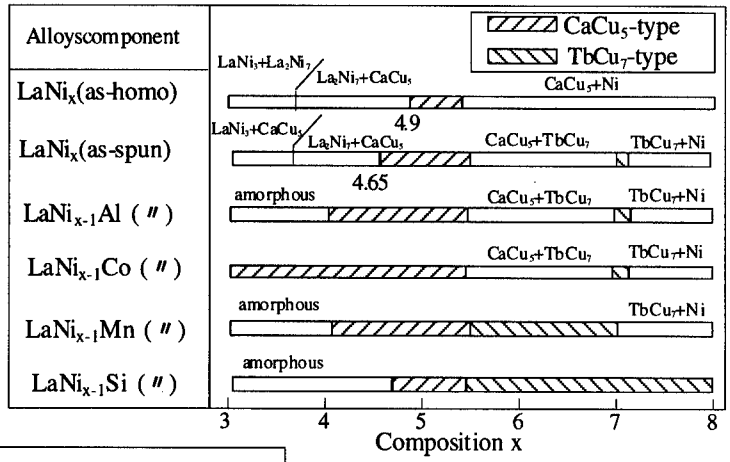


Figure 5-2 : XRD patterns of 2-(a)LaNi$_{x-1}$Mn and 2-(b)LaNi$_{x-1}$Si (x=3~5) melt-spun ribbons.

substitutional elements. Table I summarizes the appeared phases in the LaNi$_{x-1}$ M(M=Al, Co, Mn, Si) (x=3~7) and LaNi$_x$(x=3~ 7) melt-spun ribbons in comparing with those of LaNi$_x$(x=3~7) homogenized alloys. It is found that the Si substitution is most effective on forming the amorphous phase among other elements. Judging from the required amount of elements to form the amorphous phase, the formational ability of amorphous phase in La-Ni-M system will be in orders of Si>Al≧Mn>Co. From the hydrogen absorbing point of view, the Si substitution is not desirable.

Table I The appeared phases in the LaNi$_{x-1}$M(M=Al, Co, Mn, Si)(x=3~7) and LaNi$_x$(x=3~7) melt-spun ribbons in comparing with those of LaNi$_x$(x=3~7) homogenized alloys.



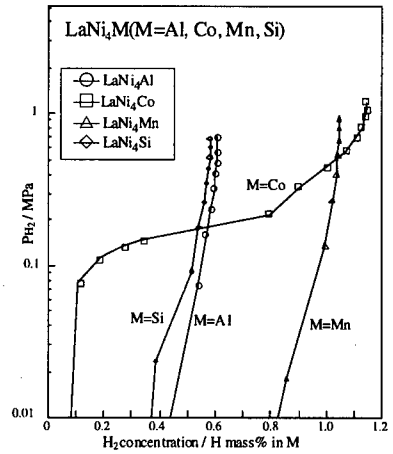


Figure 6 : PCT curves (absorbing process) of LaNi$_4$M(M=Al, Co, Mn, Si) melt-spun ribbons after 30th cycle.

Figure 6 shows the PCT curves (absorbing process) of LaNi$_4$M(M=Al, Co, Mn, Si) melt-spun ribbons after 30th cycle, where the ribbons consist of single phase with CaCu$_5$-type crystal structure. The plateau pressure reduces remarkably for the Al, Mn and Si substituted ribbons, which was also reported in LaNi$_{4.55}$Al$_{0.55}$ melt-spun ribbons[8]. The Co substitution forms the two plateau region, which was also repoted[9]. Although the substitutional elements are effective on forming wide range of CaCu$_5$-type crystal structure, the hydrogen absorbing properties turn out to be not better than that of the binary alloys. The presently adopted amount (x=1)of substitutional elements may be too large, so that effects of smaller amount (x=0.2 or 0.3) of additional elements on the forming of CaCu$_5$-type crystal structure should be tried in future.

Conclusion

The rapid quenching effects on the solid-solution range of $LaNi_x$ (x=3~5) alloys prepared by melt-spinning. It is found that the single phase with $CaCu_5$ crystal structure appeared in $LaNi_{4.65}$ alloys. The lattice constants of these ribbons are expanding with increasing La content, which is different rom that of annealed samples reported before. When the compositional x in $LaNi_{5-x}$ became smaller, it becomes better hydrogen absorption properties such as quite easier activation, flat plateau pressure and better hydrogen storage capacity than those of $LaNi_5$ homogenized samples. $LaNi_{x-1}M$(M=Al, Co, Mn, Si)(x=3~5) melt-spun ribbons were also prepared in order to pursuit the possibility to obtain the La-rich $CaCu_5$-typecrystal structure by substitutional elements. Besides Si substitution, Co, Al and Mn are effective on forming larger compositional range of $CaCu_5$-type crystal structure than that without substitutional elements. Judging from the required amount of elements to form the amorphous phase, the formational ability of amorphous phase in La-Ni-M system will be in orders of Si>Al≧Mn>Co. But, the hydrogen absorbing properties of $LaNi_4M$(M=Al, Co, Mn, Si) melt-spun ribbons turn out to be not better than that of the binary alloys.

References

(1) Y.Y.Pan and P.Nash:Phase Diagrams of Binary Nickel Alloys (edited by P.Nash), ASM International (1991), 183

(2) D.Chandra, S.Bagchi, S.W.Lambert and W.N.Cathey:J.Less-Common Metals, (1993), 93

(3) P.H.L.Notten, R.E.F.Einerhand and J.L.C.Damms:J.Less-Common Metals, **210** (1994), 221

(4) R.Mishima, H.Miyamura, T.Sakai, N.Nakamura, H.Ishikawa, and I.Ueda:J.Less-Common Metals, **192** (1993), 176

(5) T.Kuriiwa, Y.Ohno, H.Nakamura, H.Takamura, T.Tanaka, M.Homma and M,Okada, Material Trans:JIM, **37**(1996),839

(6)D.Y.Kim, M.Ohtsuka and K,Itagaki:Shigen-to-Sozai, **108**(No.12) (1992), 873

(7)K.H.J.Buschow and H.H.Vanmal:.Less-Common Metals, **29** (1972), 203

(8)Y.Nakamura, H.Nakamura, S.Fujita and I.Yonezu:J. Less-Common Metals, **210** (1994), 299

(9)J.J.Reilly, K.C.Hoffman, G.Strickland, R.H.Wiswall:26th Annual Proceedings Power Sources Conference, May(1974).

GAS DIFFUSION IN SINGLE CRYSTAL OXIDES

James E. Shelby

McMahon Professor of Ceramic Engineering
New York State College of Ceramics at Alfred University
Alfred, NY 14802

Abstract

The existing literature on diffusion and solubility of inert gases and hydrogen and oxygen isotopes in single crystal oxides is summarized. Very little information exists regarding inert gas diffusion in non-network structure crystals. Hydrogen diffusion studies are based on either molecular hydrogen or water, with very different results depending on the source of the hydrogen. Oxygen diffusion measurements are highly sensitive to point defects in the structure. Possible mechanisms for gas diffusion include direct molecular diffusion, as found in oxide glasses, proton hopping, and isotope exchange.

The Third Pacific Rim International Conference on
Advanced Materials and Processing (PRICM 3)
Edited by M.A. Imam, R. DeNale, S. Hanada,
Z. Zhong and D.N. Lee
The Minerals, Metals & Materials Society, 1998

Introduction

Diffusion of gases in polycrystalline oxides usually occurs by migration along grain boundaries or through an amorphous phase.(1) Diffusion of gases through single crystals of oxides, however, must occur through the lattice. As a result, point and line defects are much important in diffusion through single crystals. Reactions involving hydrogen, oxygen, and their isotopes often control the rate of migration of these gases through a lattice, so that measurements actually yield information about the reaction process and not about the diffusivity of the gas itself.

Three categories of gas diffusion must be considered(1) for single crystal oxides. Inert gases (helium or neon) can diffuse through large open channels such as those found in polymorphs of silica or through structures which contain a large concentration of defects. Hydrogen isotopes can diffuse into, and react with, oxides to form bound hydrogen species, e.g. hydroxyl or hydrides. The diffusion process can be monitored by determining the concentration of these bound species instead of directly following the migration of the diffusing entity. Finally, diffusion of oxygen, which is a major constituent of oxides, is usually studied by means of isotope exchange measurements, which often yield only effective diffusivities since the rate of exchange may be controlled by reaction kinetics and not by the mobility of the oxygen molecules in the structure.

The following paper will address each of these types of diffusion processes. A summary of the existing data for a variety of oxides will be provided. Mechanisms for diffusion of hydrogen isotopes will be presented.

Inert Gas Diffusion and Solubility

Most studies of inert gas diffusion and solubility in single crystal oxides deal with polymorphs of silica. Barrer and Vaughan,(2) reported helium and neon solubilities and diffusivities in α and β-cristobalite and in α, β_1, and β_2-tridymite. The solubility of helium and neon varies linearly with the partial pressure of the gas in both cristobalites and tridymites. Solubilities of both gases are about one order of magnitude greater in the tridymites than in the cristobalites. Gas solubility in all three forms of tridymite was independent of the particular polymorph studied. A similar effect was noted for the two forms of cristobalite. Solubilities of helium and neon are almost identical within each group of polymorphs. The solubilities of these gases decrease very slightly with increasing temperature, but the enthalpy of solution is quite small.

Helium diffusivities are considerably greater than neon diffusivities in silica polymorphs. Helium diffusivities for the alpha forms of cristobalite and tridymite lie on the same line. The activation energy for helium diffusion lies in the range of 50 to 60 kJ/mol, while that for neon is closer to 100 kJ/mol.

Barrer and Vaughan(2) suggested that the Langmuir adsorption isotherm model can be used to explain inert gas solubility in open network structures. This model not only satisfactorily explained their results, but has been extended with great success to modeling of gas solubility in many inorganic glasses.(1)

Studies(3,4) of helium solubility and diffusion in UO_2 suggest that helium migration occurs via oxygen vacancies and that the high solubility is due to occupancy of these vacancies by the helium atoms.

Hydrogen Isotope Diffusion and Solubility

Diffusion of hydrogen isotopes has been measured for many single crystal oxides, including BeO, CaO, MgO, SrO, ZnO, Al_2O_3, Y_2O_3, SiO_2, TiO_2, ZrO_2, UO_2, several perovskites, and spinel. The results of a number of these studies are summarized in reference 1 and are shown in Figure 1. Little solubility data exists for hydrogen isotopes in these or other single crystal oxides.

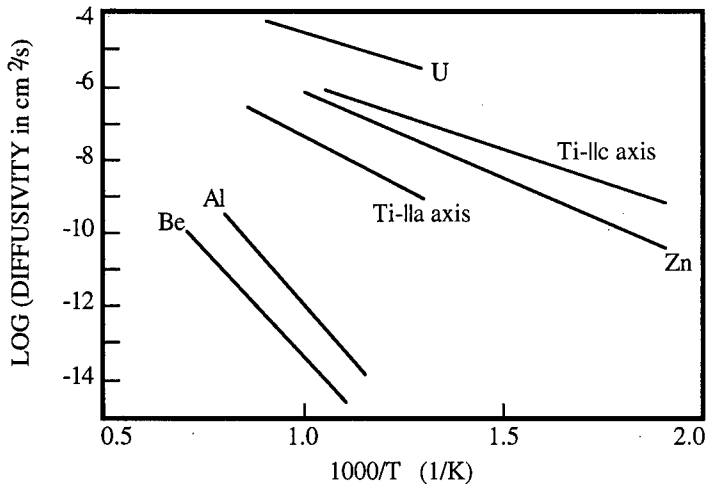


Figure 1: Temperature dependence of hydrogen isotope diffusivity in the oxides of the metals indicated on the figure.

Hydrogen isotope diffusion measurements have been made by a wide variety of techniques, including tritium recoil(5) and other implantation methods, isotope exchange,(6) and saturation/outgassing methods similar to those used for inert gases.(7) Many of these studies actually used X_2O (X = H, D, or T) instead of the equivalent X_2 species. In those cases, the results should be considered to be for isotopic forms of water rather than for diatomic gas molecules. Results are usually explained by either movement of molecular X_2 species or by X^+ hopping from one OX^- site to another. Results of the few studies which can be interpreted to yield solubilities usually yield a square root of pressure dependence for the solubility. The results of many of these studies clearly indicate the major role of initial concentrations of bound species of hydrogen isotopes such as hydroxyl or the concentration of defects due to non-stoichiometry, impurities, or dopants.

A number of possible mechanisms have been proposed(1) for hydrogen isotope migration in oxide crystals (Figure 2). It is well established that hydrogen isotopes diffuse through oxide glasses in the molecular form. A similar mechanism, indicated by path 1 in Figure 2, could occur in single crystal oxides. Indeed, such a mechanism has been proposed for a small portion of the hydrogen migration through rutile. In general, however, this mechanism is unlikely for crystalline materials due to the small channel diameters in most crystalline oxides (exceptions are found for the network structures found for

silica polymorphs). It seems unlikely that hydrogen molecules can diffuse through any material at a rate greater than that of the smaller helium atom. If helium diffusivities are vanishingly small, molecular hydrogen diffusivities should also be extremely small.

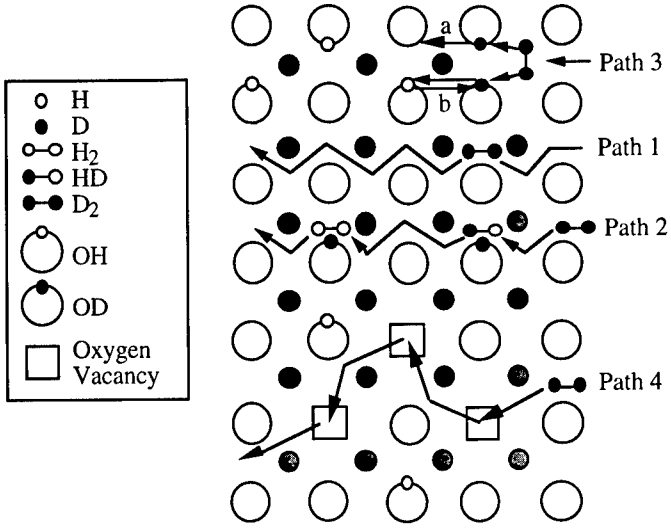


Figure 2. Possible mechanisms for hydrogen isotope diffusion in single crystal oxides. Reprinted from Handbook of Gas Diffusion in Solids and Melts, by James E. Shelby (1996), ASM International, Materials Park, OH 44073-0002, p 90 fig 4.16.

A second phenomena can occur when molecular diffusion occurs. If the isotope in the surrounding gas is different from that originally in the sample, isotope exchange can occur (path 2). In this case, exposure to D_2, for example, will result in conversion of bound H^+ in the form of hydroxyl to a mobile species, with trapping of the D^+ which exchanges at that site. It is possible that exposure to D_2, therefore, will reduce the OH content of a sample by replacing OH by OD and releasing HD and H_2 molecules.

Proton hopping from one bound site to another can occur via path 3a and 3b. In case 3a, the molecule enters the sample and dissociates at an oxygen to form an hydroxyl, which then "hops" to a neighboring oxygen, advancing through the sample. In the second case (3b), hopping occurs by exchange with a pre-existing proton on a neighboring oxygen. In either case, diffusion can be more rapid because the moving species is a proton and not a molecule.

A final path (4) can exist through a series of oxygen vacancies. In this case, molecular migration is allowed by utilization of the openings in the structure arising from vacancy formation. This mechanism is most likely in non-stoichiometric or doped samples, where vacancy concentrations are large.

Similar mechanisms can be proposed for diffusion of protons originating from water molecules.(1) Simple diffusion of water as a molecular species could possibly occur. The large size of the molecule, however, makes this mechanism

unlikely. It is also possible that the water molecules dissociate, the resulting oxygen ion is trapped at a vacancy, and the protons diffuse via a hopping mechanism identical to paths 3a and 3b in Figure 2. Diffusion of hydroxyl ions must also be considered, but is believed to be less likely due to the relatively large size of the ion.

Oxygen Isotope Diffusion

Most studies of oxygen diffusion in single crystal oxides involve isotope exchange between ^{16}O and ^{18}O. Other studies involve the measurement of weight gain during the oxidation of reduced oxides in an oxygen atmosphere or hydrothermal methods, where oxygen is supplied from water.

Oxygen diffusion data for a number of oxides(8-12) are shown in Figure 3. In addition to the results shown here, data(1) exist for oxygen diffusion in a number of other oxides, including Sc_2O_3, $SrTiO_3$, ZnO, nickel ferrous ferrite, and several rare earth (Dy, Er, Ho, Lu, Tm) oxides.

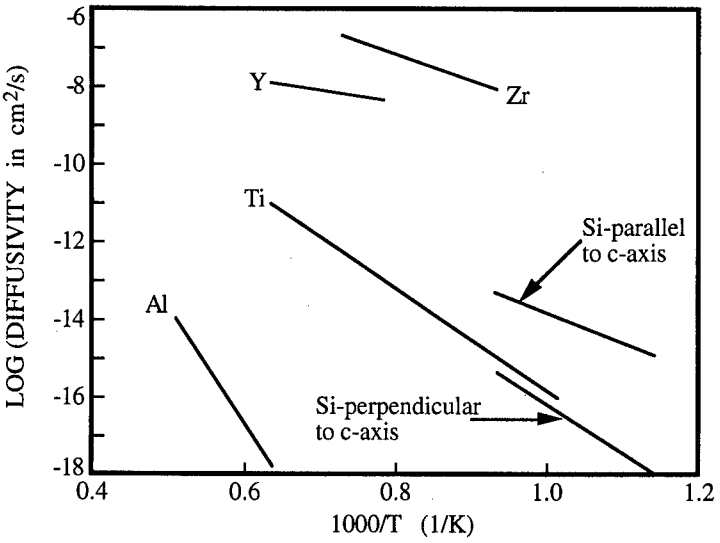


Figure 3. Temperature dependence of oxygen diffusivity in the oxides of the metals indicated on the figure.

Although results of oxygen diffusion studies in alumina differ by more than 50% in the activation energy for diffusion,(8,9) the diffusivities reported in the literature all lie within about 1 order of magnitude. While some controversy exists concerning the role of impurities in altering oxygen diffusion coefficients, it appears that magnesium doping of alumina does increase oxygen diffusivities, while titanium doping decreases oxygen diffusivities.(9)

Oxygen diffusion in quartz varies dramatically with crystallographic direction.(10) Diffusion parallel to the c-axis is much faster than diffusion normal to the c-axis. A large increase in the enthalpy for diffusion occurs when α-quartz transforms to β-quartz. In either case, oxygen diffusion in the crystalline silica is much slower than in vitreous silica.(11)

Crystallographic orientation effects have been noted for oxygen diffusion in rutile.(11) In this case, however, the diffusivity of oxygen is greater in the direction perpendicular to the c-axis than in the direction parallel to that axis.

References

1. James E. Shelby, Handbook of Gas Diffusion in Solids and Melts, (Materials Park, OH: ASM International, 1996), Chapter 4.

2. R.M. Barrer and D.E.W. Vaughan, "Solution and Diffusion of Helium and Neon in Tridymite and Cristobalite," Trans. Faraday Soc., 63 (1967), 2275-2290.

3. D.R. Olander, "Theory of Helium Dissolution in Uranium Oxide. II. Helium Solubility," J. Chem. Phys., 43 (1965), 785-788.

4. V.J. Wheeler, "The Diffusion and Solubility of Hydrogen in Uranium Dioxide Single Crystals," J. Nucl. Mater., 40 (1971), 189-194.

5. J.D. Fowler et al., "Tritium Diffusion in Al_2O_3 and BeO," J. Am. Ceram. Soc., 60 (1977), 155-161.

6. R. Gonzalez, Y. Chen, and K.L. Tsang, "Diffusion of Deuterium and Hydrogen in Doped and Undoped MgO Crystals," Phys. Rev. B, 26 (1982), 4637-4645.

7. K. Park and D.R. Olander, "Hydrogen Dissolution in and Release from Nonmetals. III. Tetragonal Zirconia," J. Am. Ceram. Soc., 74 (1991), 72-77.

8. J.D. Cawley, J.W. Halloran, and A.R. Cooper, "Oxygen Tracer Diffusion in Single-Crystal Alumina," J. Am. Ceram. Soc., 74 (1991), 2086-2092.

9. H. Haneda and C. Monty, "Oxygen Self-Diffusion in Magnesium- or Titanium-Doped Alumina Single Crystals," J. Am. Ceram. Soc., 72 (1989), 1153-1157.

10. B.J. Giletti and R.A. Yund, "Oxygen Diffusion in Quartz," J. Geophys. Res., 89 (1984), 4039-4046.

11. V.R. Haul and G. Dumbgen, "Untersuchung der Sauerstoffbeweglichkeit in Titandioxyd, Quarz, und Quarzglas mit Hilfe des heterogenen Isotopenaustausches," Z. Elektrochem., 66 (1962), 636-641.

12. L.A. Simpson and R.E. Carter, "Oxygen Exchange and Diffusion in Calcia-Stabilized Zirconia," J. Am. Ceram. Soc., 49 (1966), 139-144.

THE EFFECT OF THE SOLIDIFICATION RATE ON THE HYDROGEN STORAGE PROPERTIES OF ML(NICOMNTI)$_5$ ALLOYS

Chuanjian Li, Xinlin Wang, Xiumei Li, and Chongyu Wang

Institute of Advanced Materials,
Central Iron & Steel Research Institute of MMI,
Beijing 100081, P. R. China

Abstract

The effect of the solidification rate on the hydrogen storage properties of Ml(NiCoMnTi)$_5$ alloy has been investigated in detail. The stability of the rapidly quenched materials was generally much better than that of the conventionally prepared materials with the same composition and, high solidification rate could flatten the discharge plateau region and increase the discharge voltage at a high discharge rate (e.g. 300mA/g). However, the high solidification rate led to a remarkable decrease in capacity and slowed down the initial activation of the alloy electrode. The X-ray diffraction measurements showed that the cast alloy and the quenched alloy were different from each other in phase structure. It is the difference in phase structure and microstructure of the alloy that made the difference in electrochemical property.

The Third Pacific Rim International Conference on
Advanced Materials and Processing (PRICM 3)
Edited by M.A. Imam, R. DeNale, S. Hanada,
Z. Zhong and D.N. Lee
The Minerals, Metals & Materials Society, 1998

Introduction

Hydrogen storage alloys have been widely studied for their application as energy storage media and battery electrodes since the discovery of $LaNi_5$. The hydriding alloys (metal hydrides: MH) are used as the negative electrode of a rechargeable battery, essentially replacing the cadmium electrode in the widely used Ni-Cd battery. The main driving force for replacing the cadmium is environmental for Cd being a relatively toxic material. And as a by-product in the production of zinc, there is a shortage of cadmium on the world market.[1]. There are other advantages of the Ni-MH battery over the Ni-Cd battery, including higher energy density, higher charge/discharge rates, low temperature capability and an absence of a memory effect [2]. However, the storage capacity of $LaNi_5$ electrodes declines drastically during repeated charge/discharge cycling. The cycle stability of $LaNi_5$ alloy can be improved by cobalt substitution for part of nickel [2-3]. Unfortunately, cobalt can also decrease the capacity of the high discharge current density and, moreover, it is also an expensive metal. It has been found that rapid quenching could greatly influence the electrode performance [6-10]. In this paper, the relationship between the electrochemical properties and the solidification rate of the melted $LaNi_5$-type alloy is of our interest.

Experimental

The master alloy with composition $Ml(NiCoMnTi)_5$ (Ml denotes La-rich misch metal) was prepared with an induction-melting furnace in an atmosphere of purified argon under a pressure of 1 atm. Part of the cast alloy was re-melted and quenched with single roll method. The solidification rates of the quenched alloys were presented with corresponding linear velocities of the surface of the copper wheel.

The alloy samples were pulverized mechanically to particle sizes below 200 mesh.

X-ray diffraction studies were performed on the powder samples with a Rigaku X-ray diffractometer using Co $K_{\alpha 1}$ radiation.

Electrochemical measurements were performed in a similar manner to that reported previously [8]. Electrode pellets (11mm in diameter) were prepared by mixing 1g of alloy powder with fine nickel powder in a weight ratio of 1:1, together with a small amount of polyvinyl alcohol (PVA) solution as a binder, and then pressing at 3500 $Kgfcm^{-2}$ after vacuum drying at 80 ℃ for 1hr. Before the electrochemical measurements the sample electrodes were immersed in the electrolyte (6M KOH) for at least 1 day to wet fully the electrode. A sintered nickel hydroxide ($Ni(OH)_2$/NiOOH) plate served as the counter electrode. Every cycle was performed by charging fully and discharging to -0.500V with respect to a Hg/HgO 6M KOH reference electrode, at a fixed temperature of 25 ℃.

Results and discussion

Electrochemical properties

The discharge capacity It was found that the initial activation of the alloy is very sensitive to the solidification rate. The higher the solidification rate, the slower the initial activation. For example, the complete activation of the cast alloy needs only 2~3 cycles when using a charge/discharge current of 60mA/g, while it needs more than 20 cycles for the quenched alloy with a quenching rate of 27m/s when using the same current.

After the complete activation of the alloys, the capacities at different discharge current were measured. The results are listed in Table Ⅰ.

As shown in Table Ⅰ, the capacity of the alloy decreases with the increasing solidification

rate of the melted alloy.

Table I The Maximum Capacities of the Sample Alloys

sample	the maximum discharge capacities at different discharge currents		
	60mA/g	150mA/g	300mA/g
cast	316	295	280
10m/s	305	290	264
15m/s	299	281	251
18m/s	294	270	242
20m/s	290	264	238
22m/s	281	255	230
23m/s	280	257	226
25m/s	274	248	215
27m/s	270	243	210
30m/s	262	234	195

The decrease in discharge capacity is ascribed to the existence of the amorphous phase. Previous studies have shown that the capacity of the amorphous AB_5 alloy was only half of the corresponding crystalline alloy which had the same composition [9-10]. So, when the solidification rate is high enough (in our experiment, it is about 15m/s in linear velocity of the surface of the copper roll) to introduce the amorphous phase, the discharge capacity decreases with the increasing solidification rate because of the increasing amount of amorphous phase.

The charge/discharge cycling durability The cycle durability is defined as the following here:

$$\text{durability} = C_{550}/C_{max} \times 100\% \quad (1)$$

Where C_{550} denotes the discharge capacity of the alloy having cycled for about 550 cylces and C_{max}, the maximum discharge capacity of the alloy.

However, as shown in Table II, high solidification rate can improve the charge/discharge cycling durability of the AB_5-type alloy though it leads to the decrease in the discharge capacity.

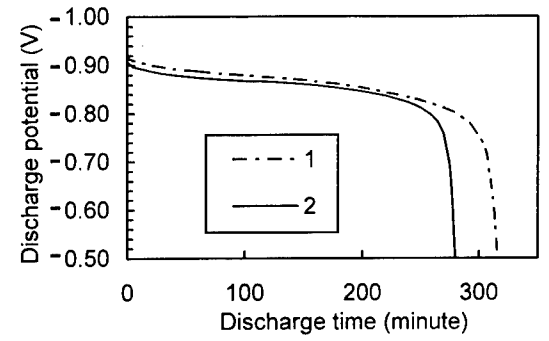
Table II The Charge/Discharges Cycle Durability of the Sample Alloys

sample	as-cast	10m/s	15m/s	18m/s	20m/s	22m/s	23m/s	25m/s	27m/s	30m/s
durability	35.2	43	51.7	60	65	70.3	74.5	82.2	86.3	89.2

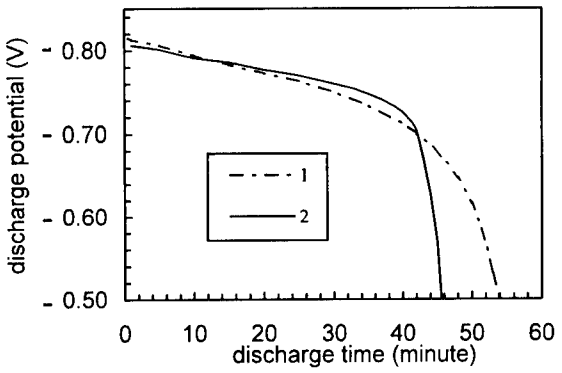
There are two possible reasons for the increasing cycle durability. One is that segregations can be suppressed when the solidification rate is high enough, and another is the well-known excellent corrosion resistance of the amorphous alloy. The latter reason plays an more important role in improving the cycle durability when the solidification rate is at a higher level because of segregations can be well suppressed in case the solidification rate be high enough which is around 10m/s. With SEM and TEM observations, no seregation can be found in

samples with a solidification rate of more than 10m/s. Moreover, the cycle durability may reach nearly 100% when the solidification rate is so high that the alloy is wholly in amorphous state because it has been reported that the discharge capacity of the electrodeposited amorphous $LaNi_5$-type alloy did not decrease after 1000 cycles [10].

Discharge voltage characteristics The discharge characteristics of all the sample alloys were measured at different discharge currents. It is found that high solidification rate can flatten the discharge plateau area evidently at both high (e.g. 300mA/g) and low (e.g. 60mA/g) discharge currents (Figure 1).
However, the high solidification leads to a slight decrease in discharge voltage at a lower discharge current (Figure 1(a)). This can be ascribed to their actually different discharge rates because their capacities are not the same though at the same discharge current and, as we know, the discharge voltage decreases with the increasing discharge rate for the same alloy electrode.



(a)



(b)

Figure 1: Discharge voltage characteristics of electrodes made of (1) as-cast alloy and as-quenched alloy with solidification rate of 23m/s at discharge rates of (a) 60mA/g (b) 300mA/g (vs. Hg/HgO)

Phase comparison

As shown in Figure 2, segregation phase is found in the master alloy which is indexed to TiNi phase, while there is no visible diffraction peak other than $LaNi_5$-type phase. This means that quenching can prevent composition segregations effectively.

Microstructure observations

With TEM and SEM observations and EDAX measurements, at least five types of segregations are found in as-cast alloy, which is mainly TiNi phase. No segregation is found in all the as-quenched alloys. Selected area diffraction studies showed that a small amount of amorphous phase existed in the wheel-side of the melt-spun flakes of the alloy with a solidification rate of more than 15m/s.

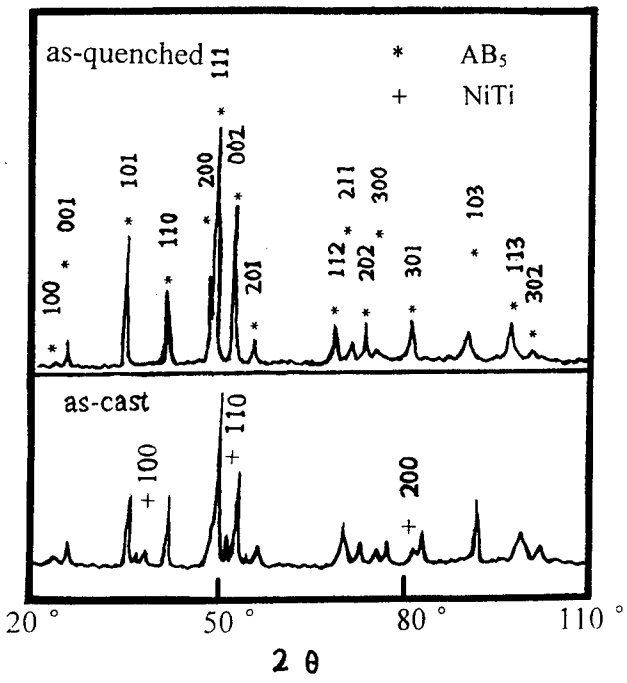


Figure 2: The X-ray diffraction patterns of the master and the quenched alloys

Conclusions

The hydrogen-storage Ml(NiCoMnTi)$_5$ alloys with different solidification rates have been investigated in details. High-rate solidification such as melt-spinning have made alloys with much different electrochemical properties compared with the alloy made with a lower solidification rate using water-cooled copper mold.

The advantages were that the long-term stability of the rapidly quenched materials were generally much better than that of the conventionally prepared materials with the same composition, and, high solidification rate could flatten the discharge plateau region and increase the discharge voltage with a high discharge rate(e.g. 300mA/g).

However, high solidification rate led to a remarkable decrease in capacity as well as in discharge voltage at the low discharge rate(e.g. 60mA/g) and slowed down the activation of the

electrode. The cycle durability increased with the solidification rate, but the capacity decreased with it. So a proper quenching rate should be chosen to keep balance between capacity and cycle durability.
The X-ray diffraction measurements showed that the cast alloy and the quenched alloy were different from each other in phase structure, which was account for the difference in electrochemical property.

References

1. M. Geng, D. O. Northwood, "The Characteristics of the Negative Electrode of a Nickel-Metal Hydride Battery," Int. J. Hydrogen Engergy, 21(1996), 887-896.

2. J. J. G. Willems, "Metal Hydrogen Electrodes Stability of $LaNi_5$-Related Compound," Philips J. Res., 39(suppl.1)(1984), 1-94.

3. J. J. G. Willems and K. H. J. Buschow, "From Permanent Magnets to Rechargeable Hydride Electrodes," J. Less-common Met., 129(1987), 13-30.

4. T. Sakai et al., "Rechargeable Hydrogen Batteries Using Rare-Earth-Based Hydrogen Storage Alloys," J. Alloys Comp., 180(1992), 37-54.

5. W. Tang and G. Sun, "Electrode Stability of La-Ni-Mn Hydride-Forming Materials Prepared by Conventional and Rapid Quenching Techniques," J. Alloys Comp., 203(1994), 195-198.

6. R. Mishima, H. Ishikawa and I. Uehara, "Hydrogen Storage Alloys Rapidly Solidified by the Melt-Spinning Methods and Their Characteristics as Metal Hydride Electrodes," J. Alloys Comp., 192(1993), 176-178.

7. Y. Nakamura et al., "Homogenizing Behavior in a Hydrogen-Absorbing $LaNi_{4.55}Al_{0.45}$ Alloy Through Annealing and Rapid Quenching," J. Alloys Comp., 210(1994), 299-303.

8. C. -J. Li et al., "The Effect of Technological Designs on the Electrochemical Property of $Ml(NiCoMnTi)_5$ Hydrogen Storage Alloys," Battery Bimonthly, 27(1997), 209-213. (in Chinese)

9. H. Sakaguchi et al., "The Local Structure Around Hydrogen Atoms in a Hydrogenated Amorphous $LaNi_{5.0}$ Film Studied by Neutron Diffraction," J. Alloys Comp., 221(1995), 212-217.

10. Y. Li, Y. -T. Cheng, "Amorphous La-Ni Thin Film Electrodes," J. Alloys Comp., 223(1995), 6-12.

Light Metals

CALORIMETRIC INVESTIGATION OF PRECIPITATION KINETICS IN Al-Mg-Si-(Cr, Be) ALLOYS

K.D. Woo*, J.S. Lee, J.H. Jeong, D.K. Kim* and S.W. Kim*

* Faculty of Advanced Materials Science and Engineering,
*Research Institute of Advanced Materials Development. Chonbuk National University
Dept. of Metallurgical Engineering, Chonbuk National University, Chonbuk, Korea561-756.

Abstract

Al-Mg-Si system alloys are capable of providing a good combination of formability and paint bake response. For this reason, they have been proved suitable for automotive panel applications. This study has been examined by means of measurement of hardness, differential scanning calorimetry and transmission electron microscope. Differential scanning calorimetry(DSC) was used to study the kinetics of precipitation and the dissolution of metastable and stable phase in aluminum alloys. The effect of heat on characteristics of the precipitation process in the as-quenched specimen were calculated from DSC thermograms obtained from various heating rate of 5, 10, 15 and 20℃/min. Two exothermic peaks may be attributed to the formation of G.P.zones and the β' phases, and two endothermic peaks may be attributed to the dissolution of G. P. zones and the β' phases, respectively. The kinetic equation $(dY/dt)=f(Y)k_o\exp(-Q^*/RT)$ can be used to study the precipitation kinetics of Ai-Mg-Si-(Cr,Be) alloys. Where Q^*, k_o, and $f(Y)$ are the activation energy, frequency factors and the function of the Y, respectively. The kinetic parameters measured from DSC curves can be used to expect the transformations kinetics. The rate of β' formation in the Al-Mg-Si alloy was accelerated by the small addition of Be. This is because Be increases the nucleation rate of the β' phase due to the decrease of the matrix/β' interface energy. By the addition of Be or Be and Cr in Al-Mg-Si alloy, G.P.zone was easily decomposed during retrogression treatment at 225℃ for 3 min. Therefore, high hardness due to high density of β' precipitates can be obtained by RRA(retrogression and reaging) treatment (150℃/20min→225℃/3min→180℃/30min) in Al-Mg-Si-Be and Al-Mg-Si-Be-Cr alloys.

The Third Pacific Rim International Conference on
Advanced Materials and Processing (PRICM 3)
Edited by M.A. Imam, R. DeNale, S. Hanada,
Z. Zhong and D.N. Lee
The Minerals, Metals & Materials Society, 1998

Introduction

The precipitation process of Al-Mg-Si alloy has been reported as follow[1]. Super-saturated solid solution→Cluster→Acicular G.P.zone→Metastable phase of bar type(β':Mg_2Si)→Stable phase of plate type(β). DSC is used to clarify the precipitation and dissolution kinetics of metastable and stable phases in aluminum alloys.[2-4] Jena et al[2] calculated the kinetic parameters for precipitation in an Al-Cu-Mg alloy from DSC thermograms. Luo[3] developed a new analytical method for calorimetric studies of precipitation kinetics in aluminum alloy. In this study the kinetics of precipitation in the Al-Mg-Si-X(Be, Cr) alloys have been investigated by Luo's method[3]. Also, the effects of Be and Cr addition in Al-Mg-Si alloy on bake hardening and RRA treatment has been investigated.

Experimental procedure

The Al-Mg-Si-X(Be, Cr) alloys were melted and casted in a high frequency melting furnace under Ar atmosphere, using 99.99% aluminum, high purity master alloys of Al-10%Mg, Al-20%Si, Al-2.5%Be and Al-75%Cr. The alloy designs and chemical compositions of the alloys are shown in Table I.

Table I Alloy designs and chemical compositions of Al-Mg-Si-X(Be, Cr) alloys(wt.%)

No	Alloy designs	Mg	Si	Ti	Be	Cr	Al
A	Al-0.8%Mg-1.0%Si	0.85	1.02	-	-	-	bal
B	Al-0.8%Mg-1.0%Si-0.05%Be	0.86	1.09	0.01	0.054	-	bal
C	Al-0.8%Mg-1.0%Si-0.05%Be-0.1%Cr	0.98	0.95	0.01	0.057	0.1	bal

After all the as-cast ingots were scalped and were homogenized at 560℃ for 24 hrs, all ingots were forged in 35 mm thickness, and then were hot and cold rolled to 1.2 mm strips. The specimens for DSC were solution treated at 550℃ for 0.5 hrs in salt bath and quenched into iced water. All the pre-aging treatments were carried out at 150℃ for 5 min to 24 hrs in silicon oil bath, respectively. Each pre-aged specimens were then aged at 180℃ for 0.5 hrs to simulate paint baking. This treatment is called the bake hardening treatment. For the observation of the effect of retrogression of G.P.zone on the β' precipitation, RRA treatment was carried out. Table II shows the processes of heat treatments used in this study.

Table II Aging processes used in this study

	Processes
Pre-aging treatment	150℃
Bake hardening treatment	Pre-aging(150℃) → Bake hardening(180℃/30min)
RRA(Retrogression and Re-aging treatment)	Pre-aging(150℃) → Retrogression(225℃/3min) → Re-aging(180℃/30min)

The hardness of specimens were tested with Rockwell hardness tester. DSC analyses were performed with Dupont 910 calorimeter. The discs of specimen were analysed by DSC from room temperature to 600℃ with heating rates of 5, 10, 15, and 20℃/min. The output data unit was in W/g, and the net heat flow to the reference relative to the sample was recorded as a function of temperature, with the baseline subtracted from the data. Base line were obtained by scanning couple of pure aluminum discs for each heating rate.

Result and Discussion

Figure 1~3 show the hardness changes of pre-aged, bake treated and RRA treated Al-Mg-Si-(Be, Cr) alloys aged at 150℃ with aging time, respectively. In figure 1, the hardness increased and accelerated with the addition of Be, Be and Cr in Al-Mg-Si alloy aged at 150℃. This phenomenon shows the formation of G. P. zone accelerated by the addition of Be in Al-Mg-Si alloy. But formation rate of G. P. zone was diminished by the simultaneous addition of Be and Cr in Al-Mg-Si rather than that of Al-Mg-Si-Be alloy. Bake hardening ability was increased by the addition of Cr and Mn[5], but by the results of Baba et al.[6] age hardening rate in Al-Mg-Si alloy decreased by the addition of Mn and Cr. Figure 2 shows the hardness change of bake hardening treated Al-Mg-Si-(Be, Cr) alloys with pre-aging time at 150℃. By the addition of Be in Al-Mg-Si alloy, the hardness of these alloys increased rapidly with short pre-aging time at 150℃ compare with base Al-Mg-Si alloy. The β' phase is considered main precipitate to affect on hardness in this aging temperature. The amount of β' phases was decreased by the existence of G. P. zone[7]. Therefore if a lot of G. P. zone are formed during natural aging, it is difficult to obtain high strength in Al-Mg-Si system alloy due to the decrease of amount of β' phase. Figure 3 shows the hardness changes of RRA treated Al-Mg-Si-(Be,Cr) alloy with the pre-aging time when the alloy was pre-aged at 150℃. By the retrogression of G. P. zone during aging at 22 5℃ for 3 min, the hardness of Al-Mg-Si alloy was sharply increased by the precipitation of β' phases during aging at 180℃ for 30 min in the addition of Be or Be and Cr in Al-Mg-Si alloy. But the effect of RRA is not shown in Al-Mg-Si alloy. By this result, G. P. zones in Al-Mg-Si alloy might be unstable by the addition of Be. Therefore, the G. P. zones in Al-Mg-Si-Be or Al-Mg-Si-Be-Cr alloys are easy to dissolve into matrix during aging at 225℃ rather than that in Al-Mg-Si alloy. But Cr might not be affect of stability of G. P. zones. Figure 4 shows the DSC thermograms of as quenched Al-Mg-Si-(Cr,Be) alloys at the heating rates of 5, 10, 15 and 20℃/min. Two exothermic peaks A and C and two endothermic peaks B and D are shown. The exothermic peak A and C may be attributed to the formation of G. P. zone and precipitation of β' phase, respectively. The endothermic peaks B and D are due to the dissolution of G. P. zone and β' phase, respectively. By the addition of Be or Be and Cr in Al-Mg-Si alloy, the temperature of β' precipitation shifts to the lower temperature. This results show that β'

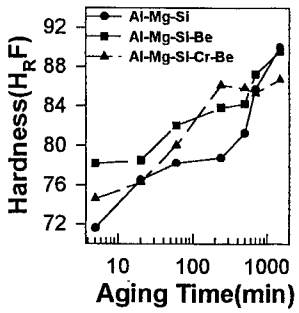


Figure 1:Variation of the hardness of Al-Mg-Si-(Cr, Be) alloy aged at 150℃.

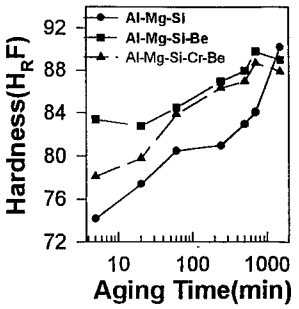


Figure 2: Variation of the hardness with bake treatment Al-Mg-Si-(Cr,Be) alloy pre-aged at 150℃.

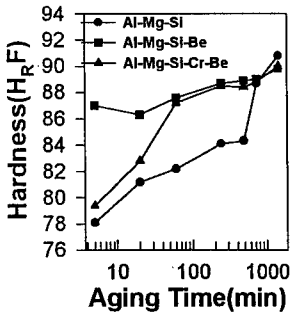


Figure 3:Variation of the hardness with RRA treatment Al-Mg-Si-(Cr,Be) alloy pre-aged at 150℃.

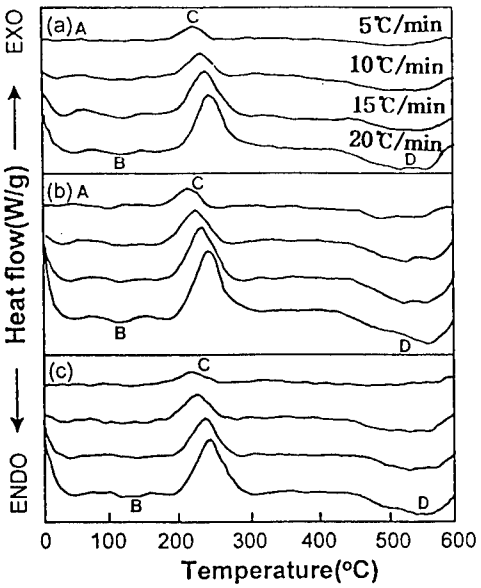


Figure 4 : DSC thermogram for the as quenched Al-Mg-Si-X(Cr, Be) alloys for various heating rate. (a) Al-Mg-Si (b) Al-Mg-Si-Be (c) Al-Mg-Si-Cr-Be

phase in Al-Mg-Si-(Be, Cr) alloy precipitates at lower temperature than that in Al-Mg-Si alloy. Figure 5 shows the precipitate amount (mole fraction, Y) and precipitation rate (dY/dt), calculated from the DSC peak C of Al-Mg-Si alloy using equations described by Luo et al.[3] The fraction of transformed phases, i.e. the amount of a particular phase precipitated or dissolved at a given temperature, Y(T), is here defined by the peak at temperature(T) to the total area of peak, A_f

$$Y(T) = A(T)/ A_f \qquad (1)$$

The transformation rate (dY/dT) is related to the heating rate (Φ) for DSC scan by

$$dY/dt=(dY/dT)(dT/dt) = \Phi(dY/dT) \qquad (2)$$

The Y-T curves (figure 5(a)) have the expected sigmoidal shape and shift to higher temperatures with the increase of heating rate. There are also considerable shifts in the maximum of the rate of transformation curves (figure 5(b)) to higher temperatures with the increase of heating rate. It implies that transformation is kinetically controlled. The data showing in figure 6 are plotted by equation (1) in figure 5 for three values of Y'(0.25, 0.5 and 0.75). The activation energy of the process can be determined by using the following equation.[3]

$$\ln [(dY / dT)_{Y'} \Phi_j] = \ln [f(Y') k_{10}] - (Q / R)(1 / T_j) \qquad (3)$$

where Φ is the j-th heating rate, $(dY/dT)_{Y'}$ is the rate at a given mole fraction(Y'), and T_j is the temperature at which the mole fraction is Y' at heating rate Φ_j. Therefore, a plot from equation (3) will give a straight line

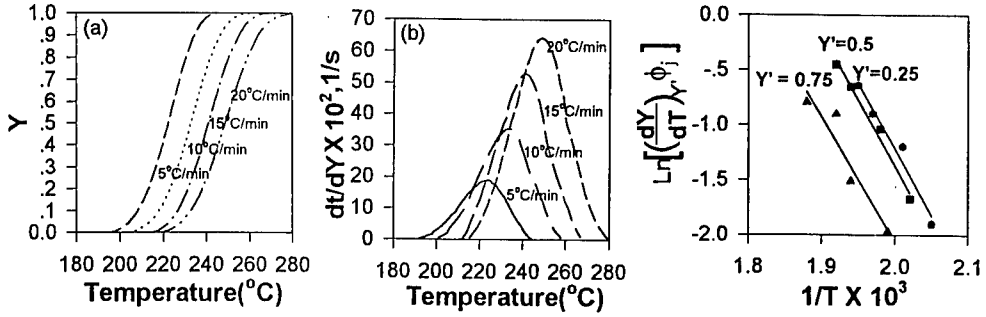


Figure 5 : Y vs T and (dY/dt) vs T plot for β' precipitation at different heating rate of as quenched Al-Mg-Si alloy.

Figure 6 : Plots for the determination of the activation energy for β' precipitation of as quenched Al-Mg-Si alloy.

whose slope gives the activation energy Q. The least square slopes of the three straight lines obtained by equation (3) give the 97.7 kJ/mole for the precipitating activation energy(Q) of of β' phase in Al-Mg-Si alloy. The activation energy of β' phase in Al-Mg-Si-Be and Al-Mg-Si-Cr-Be alloys are 102 KJ/mol and 109.0KJ/mol, respectively. The activation data are obtained by the same method as Al-Mg-Si alloy. These activation energies are lower than those of activation energy 115.9 KJ/mol and 135 KJ/mol for diffusion of Mg and Si solute atoms in aluminum[8], respectively. The change in the activation energy between Al-Mg-Si and Al-Mg-Si-Be alloy are explained by assuming that the activation energy is affected by the concentration of quenched vacancies contained in Mg and Si. Also, binding energy of solute atoms and vacancies in aluminum is in order Be, Si and Mg.[9] The activation energy of Al-Mg-Si-Cr-Be alloy is higher than that (102 KJ/mol) of Al-Mg-Si-Be alloy. From this results, Cr decreases the affect of Be on the precipitation of β' phase in Al-Mg-Si-Be alloy. The above results show that all of three alloy indicate alike activation energy for β' precipitation. The effects of Be and Cr addition on the growth and dissolution of β' precipitation are not remarkable. The shifts of DSC peak B to lower temperature by Be addition as shown in DSC curves would suggest that nucleation of β' phase was accelerated by the addition of Be in Al-Mg-Si alloy also suggest an earlier transition from G. P. zone to β' phase during the aging process. Figure 7 shows the DSC curves of Al-Mg-Si-(Cr, Be) alloy aged at 150℃ for 5 min, 4 hrs and 12 hrs. All the three alloys, one exothermic peak C and two endothermic peaks B and D are evident in the scans. In all of the three alloys, the peak C due to the precipitation of β' decreased with increasing of aging time. The peak C decreased remarkable with increasing of aging time by the addition of Be in Al-Mg-Si alloy. And the peak of β' precipitation was shifted to lower temperature by the Be addition.These results show that the precipitation of β' phase was accelerated by addition of Be in Al-Mg-Si alloy. Figure 8 shows that the DSC curves of the alloy pre-aged at 150℃ for 5 min, 4 hrs, and 12 hrs, respectively and then baked at 180℃ for 30 min. G. P. zone and β' phase co-precipitated by the aging treated at 150℃, the precipitation content of β' increased with increasing pre-aging time. In this results, Be or Be and Cr addition in Al-Mg-Si alloys accelerate the precipitation reaction of β' phase. Figure 9 shows that the DSC curves of the alloy RRA treated (225℃ for 3 min after pre-aging at 150℃ for 5 min, 4 hrs, and 12 hrs and then aging at 180℃ for 30 min). G.P. zones formed during the pre-aging at 150℃ was decomposed during the retrogression treatment at 225℃ for 3 min. The β' phase

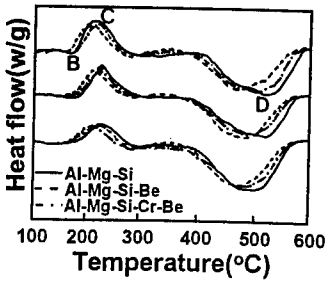


Figure 7 : DSC curves of Al-Mg-Si-(Cr, Be) alloy aged at 150℃.

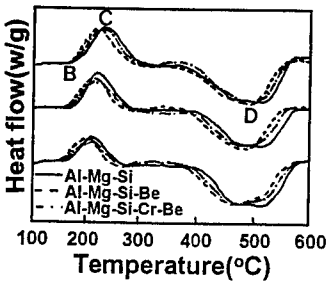


Figure 8 : DSC curves of bake treated Al-Mg-Si-(Cr, Be) alloy

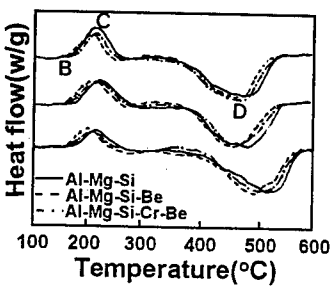


Figure 9 : DSC curves of RRA treated Al-Mg-Si-(Cr, Be) alloy

precipitates during aging at 180℃ for 30 min. This result identified by the hardness measurement. The hardness of Be or Be and Cr addition Al-Mg-Si alloys increased by the RRA treatment. But the hardness of Al-Mg-Si alloy is not remarkably increased by the RRA treatment. From these results, the existence of G. P. zones causes to reduce the amount of β' precipitated during bake hardening treatment in Al-Mg-Si alloy. This is because G. P. zone precipitated in Al-Mg-Si alloy is more stable than that in Al-Mg-Si-Be or Al-Mg-Si-Be-Cr alloys. Therefore the hardness of Al-Mg-Si alloy after baking treatment is lower than that of Al-Mg-Si alloys with Be or, Be and Cr. If G. P. zone was decomposed by retrogression process at the 225℃ for 3 min, the amount of β' precipitation increased by bake hardening treatment at 180℃ for 30 min, so the hardness due to high density of β' precipitates increased. By the addition of Be or Be and Cr, G. P. zone easily decomposes during retrogression treatment at 225℃ for 3 min. Therefore high hardness can be obtained by RRA treatment in Al-Mg-Si-Be and Al-Mg-Si-Be-Cr alloy.

Conclusion

1. The precipitation of β' phase was accelerated by the addition of Be or complex of Be and Cr in Al-Mg-Si alloy.
2. Baking hardness at 180℃ was prominently increased by the addition of Be or Be and Cr in Al-Mg-Si alloy pre-aging treated at 150℃.
3. By the addition of Be or Be and Cr in Al-Mg-Si alloy, G.P.zone was easily decomposed by retrogression treatment at 225℃ for 3 min.

Acknowledgements

This work has been carried out with the financial supports of the Korean Foundrymen's Society and Research Institute of Advanced Materials Development in Chonbuk National University.

References

1. G.Thomas : J. Inst. Metals, 90 (1961-62) 57
2. A.K.jena, A.K.Gupta and M.C.Chaturved : Acta Metal., 37 (1989) 885
3. A.Luo, D.J.Lloyd, A.Gupta and W.V.Youdelis : Acta Met., 41 (1993) 769
4. H.K.Cho, K.D.Woo and I.S.Eun : 2nd Inter. Conf. on Al Alloys(ed., C.Q.Chen and E.A.Starke.Jr) (1990) 83-87
5. M.Yanagawa, M.Abe and S.Ohie : J.Japan Institute of Light Metal, 46 (1969) 90
6. Y.Baba and A.Takashima : Trans. JIM, (1969) 169
7. S.B.Kang and C.Y.Lim : Bull. of the Korean Insti. of Met. & Mater., 7(1994) 19
8. K.Hirano : J.Japan Institute of Light Metal, 29 (1979) 249
9. S.Fujikawa and K.Hirano : J.Nucl.Mater., 69,70(1978) 564

ON SILICON PHASE IN Al-Mg_2Si ALLOY WITH EXCESS SILICON

A. Shan[1,2], I. G. Moon[1], J. E. Yoo,[1] H. S. Ko,[1] H. S. Kim[1], J. Y. Chang[1] and J. W. Park[1]

[1] Division of Metals, Korea Institute of Science and Technology, Cheongryang P.O.Box 131, Seoul, Korea

[2] Department of Materials Science, Shanghai Jiao Tong University, 200030, Shanghai, P. R. China

Abstract

This paper reports a study on silicon phase in Al-Mg2Si alloy with excess silicon. It was found that silicon phase could be formed during isothermal heating in a temperature range from 300°C to 450°C. These silicon phases are formed through decomposition of metastable Mg-Si phases. They are in amorphous form under employed experimental conditions.

The Third Pacific Rim International Conference on Advanced Materials and Processing (PRICM 3)
Edited by M.A. Imam, R. DeNale, S. Hanada, Z. Zhong and D.N. Lee
The Minerals, Metals & Materials Society, 1998

Introduction

In Al-Mg-Si alloy system, Al-Mg2Si alloys with excess silicon are known for their better mechanical properties. But the detail mechanism by which the excess silicon increases the strength is not clear. Many efforts have been made to understand the hardening mechanism in these alloys [e.g. 1]. These efforts revealed that the precipitates in excess silicon alloy were different from that in balanced alloys. At least four types of metastable phases were found in these alloys. Among them three types are newly found phases which have not been found in balanced alloys.[1-4]. While most researches are put on precipitates and their effects on properties, few attention has been paid on the silicon phase and its effect. It is claimed that fine silicon crystal particles can be formed in Al-Mg-Si alloys and these fine silicon particles help to increase the formability of these alloys [5]. However, controversial results were also reported [6]which say fine silicon particles can not be formed at studied temperature. So further research is necessary for understanding the formation and effect of silicon phase in the Al-Mg2Si alloy system with excess silicon. In this paper we will report our study on the silicon phase formed during isothermal heating in an Al-Mg2Si alloy with excess silicon.

Experimental procedure

An alloy with a composition of Al-0.50Mg-0.65Si-0.20Mn-0.12Fe-0.034Cu was made by air melting and direct chill (DC) casting method using commercial facilities. After homogenizing at 560°C for 8 hours, the alloy was extruded at 470°C to 1.5mm thick hollows. Specimens for research were cut from these hollows. Isothermal heat treatment was conducted at 300°C, 350°C, 400°C and 450°C for 30 minutes using as extruded specimens. After isothermal heating the specimens were quenched into cold water. The composition and crystal structure analysis were performed on a transmission electron microscope(TEM) (Philips CM-30) equipped with an energy-dispersive x-ray spectrometer (EDS). Thin foils for TEM observation were made by standard chemical polishing method. This was performed at -25°C in a solution with 25% nitric acid in methanol. Polishing voltage is 16V and polishing current is 30-50mA.

Results and discussion

After heat treatment at 300°C. Figure 1. (a) Shows the morphology of precipitates after heat treatment at 300°C for 30 minutes. In this figure, all precipitates are in rod shape and arranged in a parallel pattern. By analyzing the SAD patterns taken from these precipitates, it is found that these precipitates are TYPE-B precipitates with an orthorhombic crystal structure. Figure 1. (b) Shows the SAD pattern taken from a precipitate. It is indexed as TYPE-B precipitate with the beam direction parallel to $[3\text{-}10]_P$. Table I shows the calculated data from TYPE-B phase and that measured from Figure 1. (b), A good agreement can be seen from this table. The

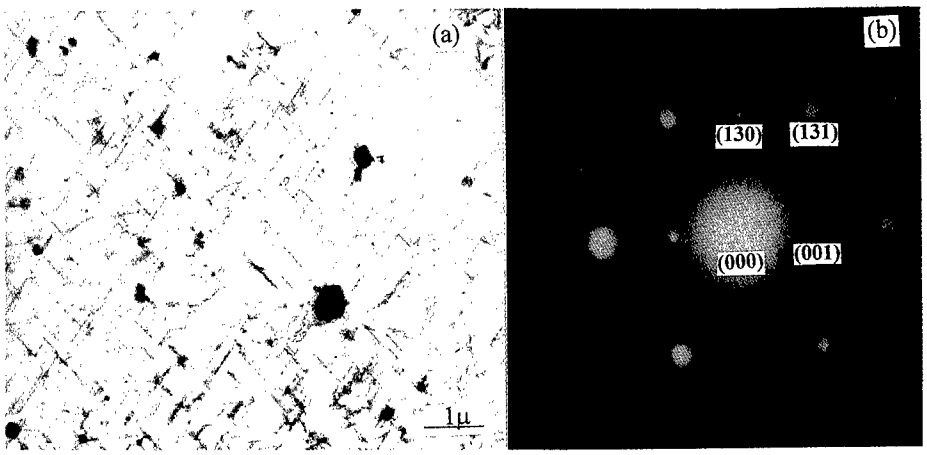


Figure 1. (a) Morphology of precipitates at 300°C/30minutes, water quenched, and (b) SAD pattern from precipitates.

Table I Crystallographic data from TYPE-B phase and that measured from Fig. 1.(b)

Parameter	Interplanar spacing (angstrom)			Angle between planes (degree)	
	(001)	(130)	(131)	(001) ^ (130)	(001) ^ (131)
Theoretical	2.03	2.13	2.13	57.46	67.07
Measured	2.04	2.16	2.16	57	66

terminology "TYPE-B" was suggested by Mastuda et al [1-4]. In their study, the alloy, which is a ternary alloy with excess silicon, was solutionized and heat treated at 250°C for 12 or 60ks. Three types of new metastable intermetallic phases were found which are different from traditional β' phase. The three types of metastable phases were called TYPE-A, TYPE-B and TYPE-C phases. They suggested that the TYPE-B precipitate has an orthorhombic lattice with a=6.83Å, b=7.94Å, c=4.05Å. they also found that TYPE-B precipitate occupy the majority of all precipitates. Their Si/Mg (in atomic ratio) ratio is about 1.2. In our case all SADs taken from these precipitates can be readily indexed as TYPE-B precipitates. So it is evident that at this temperature all precipitates are TYPE-B precipitates with an orthorhombic crystal structure. And the EDS data shows that they contain more silicon than magnesium. This study strongly supports the suggestion of Matsuda et al. More over, the TYPE-B precipitate was found stable at higher temperature compared with Matsuda et al.'s results.

After heat treatment at 350°C. Compared to the microstructure of the specimens treated at 300°C, precipitate density decreases and size increases after heat treatment at 350°C for 30 minutes. Detailed examination of these precipitates reveals that all these precipitates consist of

two phases. This was shown in Figure 2. (a) and (b). This is a rather new phenomenon which has not been reported. By EDS and SAD pattern analysis, it is found that the two phase are silicon phase and TYPE-B precipitates. But for the silicon phase we can not get its SAD pattern.

After heat treatment at 400°C. As shown in Figure 3. at 400°C, only silicon phase was found. These silicon phases have a plate shape and they are different in size. The morphology of these silicon phases is almost identical to the Mg_2Si reported in balanced alloys. But EDS analysis show that they contain only silicon, and SAD give diffused ring patterns. The SAD pattern was

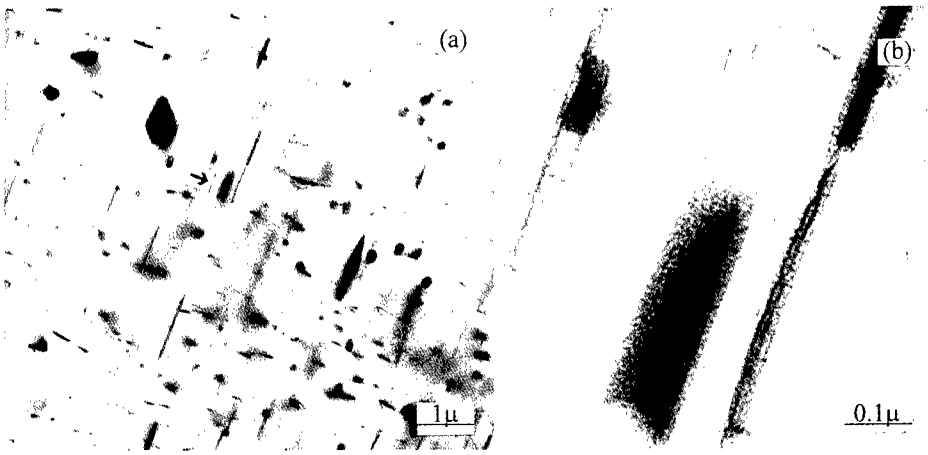


Figure 2. (a) Morphology of precipitates in specimen isothermal treated at 350°C for 30 minutes followed by water quenching, and (b) higher magnification of the arrowed phase in (a).

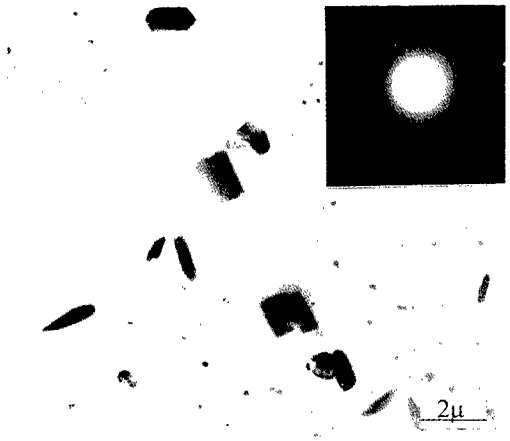


Figure 3. Silicon phase and its SAD pattern in specimen isothermal treated at 400°C for 30 minutes followed by water quenching.

shown in the upper right part of Figure 3. It is well known that this kind of SAD pattern is a indication of amorphous phase. Amorphous silicon was also found in the same alloy during continuous cooling from 560°C[7]. In that case amorphous silicon was found to appear together with TYPE-B precipitate. From this result, it is reasonable to suggest that the silicon phase formed near TYPE-B precipitates at 350°C is also amorphous silicon.

After heat treatment at 450°C. Figure 4. Shows the morphology of amorphous silicon phase in alloy heat treated at 450°C for 30 minutes. From this figure it can be seen that heat treatment at 450°C does not change the morphology of amorphous silicon phase compared to that at 400°C. Only the size of these phases have grown bigger. But they are still amorphous. No Mg_2Si or silicon crystals are found in this state.

This results shows that above 400°C silicon phase are in big size. Literature[6] showed that at 490°C for 30minutes, silicon phase has a size around 1 micron. However, in this study, it seems heat treatment at above 400°C results in even coarser silicon phases. And fine silicon particles can not be obtained in the studied states.

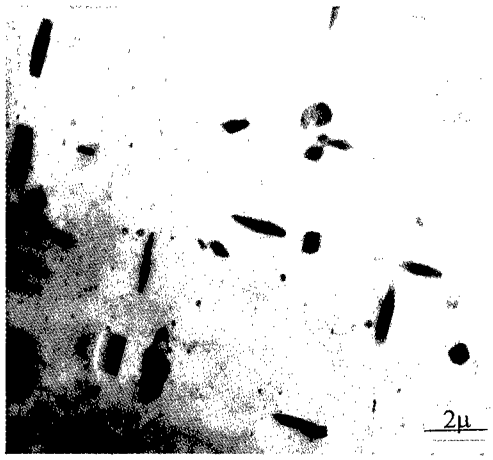


Figure 4. Morphology of silicon phase in specimen isothermal treated at 450°C for 30 minutes followed by water quenching.

Conclusions

From this study it is evident that silicon phase can be formed during isothermal heat treatment in the Al-Mg2Si alloy with excess silicon. These silicon phases are formed from the decomposition of TYPE-B precipitates rather than directly precipitating from matrix. They are in amorphous form in the studied states.

Acknowledgment

A. Shan thanks to the KOSEF and KOFST for financial support under Brain Pool Program.

References

1. K. Matsuda et al., "HRTEM observation of precipitates in Al-Mg-Si alloys"(paper presented at *the third international conference on aluminum alloys*, Trondheim, Norway, 22-26, June, 1992), 272.
2. K. Matsuda et al., "Classification of metastable phases in Al-Mg_2Si alloys by HRTEM" Mater. Sci. Forum, Vol:217-222 (1996), 707-712.
3. K. Matsuda et al., "Crystal system of rod-shaped precipitate in an Al-1.0massMg2Si-0.4mass%Si alloy" , Scripa Mater., 32 (1995), 1175-1180.
4. K. Matsuda et al., A metastable phas ehaving the orthorhombic crystal lattice in an Al-1.0mass%Mg2Si-0.4mass%Si alloy, Scripa Mater., 34 (1996), 1797-1802.
5. Aluminum Suisse, European Patent Nr.661992, Dec. 1977.
6. T. Moons et al., "A comparative study of two Al-Mg-Si alloys for automotive application" Sripta Mater. 35 (1996), 939-945.
7. A. Shan et al. "Discovery of amorphous silicon phase in Al-Mg_2Si alloy with excess silicon", submitted to Scripta Mater. 1997.

REFINEMENT OF SECOND PHASE IN Al-Ti BASE ALLOYS BY REPEATED WORKING

Goroh ITOH and Atsuki KURIHARA*

Nagaoka University of Technology (*Graduate Student)
Kami-Tomioka, Nagaoka,
Niigata-pref., 940-2188 Japan

Abstract

Research program of applying repeated working process to aluminum alloys is underway to obtain a fine dispersion of second phase particles with high volume fraction. As a first step, in this study, uniaxial compression by reduction up to 88% has been applied to ingots of Al-10mol%Ti-3.2mol%Cr and Al-10mol%Ti-3.6mol%Mn alloys at room temperature, and the distribution of second phase has been examined in relation to the reduction. As a result, the dispersion of second phase became finer as the reduction was increased. It was found from X-ray diffraction analysis that two intermetallic phases, $Al_{13}Cr_2$ (or Al_6Mn) and $Al_3Ti(DO_{22})$, were present together with aluminum matrix in the ingots, and that they slightly increased in amount when compressed by 88% and then annealed at 650℃ for 24h. A repeated working process similar to ECAP (Equal Channel Angular Pressing) was also applied to the Al-Ti-Mn alloy ingot at 600℃. Although the bolts clamping the dies were seriously deformed at the first pass and further working became impossible, significant refinement of the second phase particles was observed.

The Third Pacific Rim International Conference on
Advanced Materials and Processing (PRICM 3)
Edited by M.A. Imam, R. DeNale, S. Hanada,
Z. Zhong and D.N. Lee
The Minerals, Metals & Materials Society, 1998

Introduction

Fine dispersion of second phase particles with high volume fraction by means of heat treatment is limited in aluminum alloys, since there is no allotropic transformation and there are few alloying elements that have large solid solubility. Although to break through this drawback rapid solidification and mechanical alloying processes have been attempted, none of them has yet been commercialized, because both processes are involved with powder metallurgy route, resulting in serious disadvantage such as impurity pick-up and high cost. However, mechanical alloying is based on repeated working of a great number of cycles[1], and thus seems possible to be applied to the bulk material. A kind of repeated working process, Equal Channel Angular Pressing (ECAP) illustrated in Figure 1, has been already applied to bulk aluminum base materials consisting of single phase (pure aluminum and Al-3mol%Mg alloy), resulting in the increase in dislocation density and the reduction in the grain size[2]-[4].
Research project has been started by the authors in which a repeated working process similar to ECAP is applied to Al-Ti base alloys that contain coarse second phase particles with high volume fraction in the as-cast state, in order to refine the dispersion of the particles. The reason for selecting titanium as a primary alloying element is that it does not seriously harm the light weight, an advantage of aluminum, and that coarsening of the second phase particle was expected to be inhibited even in hot working because of extremely small diffusivity of titanium in aluminum[5]. It is thus expected that a new lightweight material with high heat resistance can be obtained.
In Al-Ti binary alloy, the second phase that exists with aluminum matrix in equilibrium, is Al_3Ti, having poor deformability caused by its tetragonal DO_{22} structure. When the second phase particle is hard with lower deformability, a marked refining effect of repeated working can not be expected since the deformation will be restricted in the matrix after the morphology of the particle becomes equiaxed. In contrast, when deformed to some extent together with the matrix, the particle will be elongated and then cracked, leading to a more marked refinement. Addition of Cr or Mn to Al_3Ti monolithic intermetallic compound was reported to induce replacement of Al with the additive, forming $(Al,Cr)_3Ti$ or $(Al,Mn)_3Ti$ (aproximate composition : $Al_{67}Ti_{25}Cr_8$, $Al_{66}Ti_{25}Mn_9$) and changing the structure into a cubic $L1_2$[6]-[8] which is frequently associated with higher deformability.
In this study, Al-10mol%Ti-3.2mol%Cr and Al-10mol%Ti-3.6mol%Mn alloys, having the same Ti/Cr and Ti/Mn ratios as the momolithic $L1_2$ compounds, have been used as specimens. It is reported that a metastable $L1_2$ Al_3Ti phase forms during rapid solidification in Al-Ti binary alloys[9]. Hence, the alloys might contain the $L1_2$ $(Al,Cr)_3Ti$ and $(Al,Mn)_3Ti$ compounds as second phases, respectively, possibly having greater deformability, although the

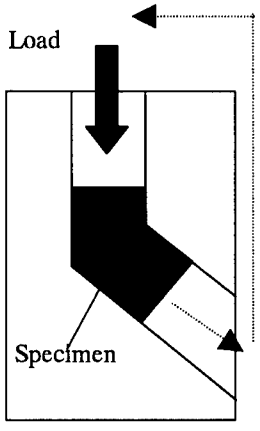


Figure 1: Schematic illustration for ECAP process.

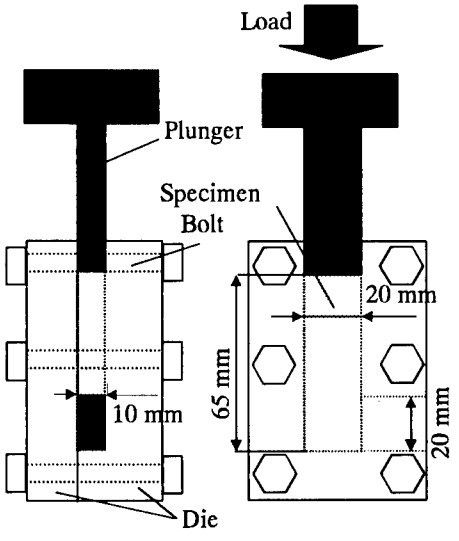


Figure 2: Dies and related components used in this study.

Al-Ti-Cr and Al-Ti-Mn ternary phase diagrams near the aluminum corner do not seem to have been well established yet. As a first step, this paper deals mainly with the change in microstructure in these alloy ingots caused by heavy uniaxial compressive working.

Experimental Procedures

From raw materials (99.99%Al, 99.9%Ti, 99.9%Cr, 99.9%Mn), the two alloys of the above nominal composition were induction melted under argon atmosphere and then cast in an iron mold. Pieces of 10×20×65mm were cut from the ingots. To reduce the amount of defects caused by solidification, the pieces were inserted in a set of closed dies, soaked at 600℃ for 1h together with the dies, hot-pressed at a load of 100kN in longitudinal direction at room temperature immediately after the soaking without any artificial cooling. Specimens of 8×8 ×8mm were cut from the pressed pieces for uniaxial compression. Uniaxial compression was conducted on a hydrolytic compression-testing machine with a load capacity of 2MN by different reductions up to 88%. The compressed samples were subjected to microstructural characterization by means of optical microscopy and X-ray diffraction after filing. Thermal stability of the compressed samples was accessed by means of the same microstructural characterization after annealing at 650℃ for 24h.
One of the hot-pressed pieces of the Al-Ti-Mn alloy of 10×20×65mm was inserted in a set of dies illustrated in Figure 2, soaked at 600℃ for 1h, and immediately subjected to a process schematically shown in Figure 2 at room temperature without any artificial cooling. This process, a kind of repeated working process similar to ECAP, will be referred to as side extrusion from now on. Although during the first pass the bolts fixing the two dies were seriously deformed and damaged because of lack of high-temperature strength, resulting in insufficient processing, optical microscopic observation was carried out on a part of the specimen which was plastically deformed.

Experimental Results and Discussion

Figure 3 shows optical micrographs of the two alloy specimens uniaxially compressed at room temperature by different reductions, along with those of the as-cast ingots. Both as-cast ingots contain coarse second phase particles (light area) of about 200μm in width. It is evident that these particles are markedly refined as the reduction is increased. However,

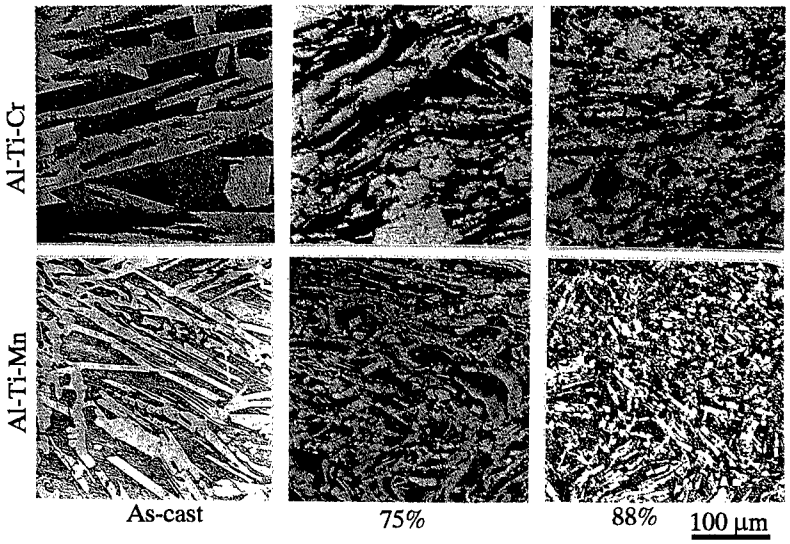
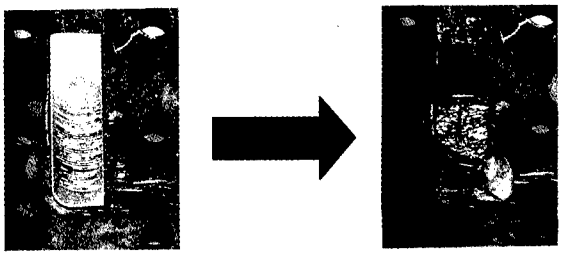


Figure 3: Optical micrographs of the as-cast ingots and the specimens unaxially compressed by the indicated reduction.



(a) (b)

Figure 4: Photographs showing the change in shape of the Al-Ti-Mn alloy specimen by incomplete side extrusion. (a) and (b): before and after the extrusion, respectivity.

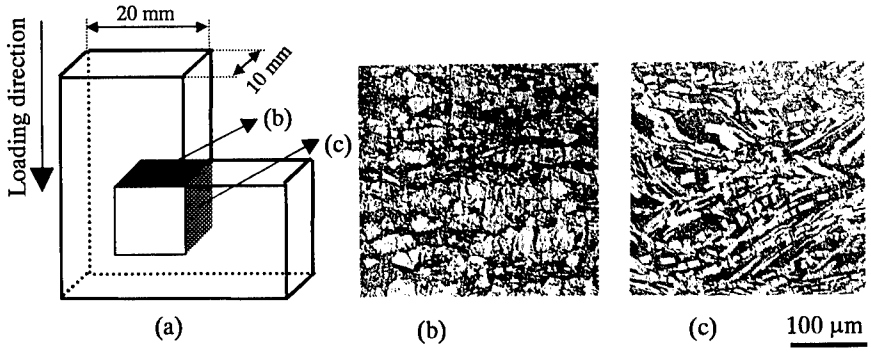


Figure 5: Microstructures of the specimen shown in Figure 5 (b). (a): schematic illustration of the sample subjected to observation. (b,c):optical micrographs taken from the area indicated in (a).

further reduction was not attainable in the uniaxial compression arising from the limit both in the load capacity of the machine and in the deformability of the specimen; many side cracks were observed in the specimen deformed by 88%. From a practical point of view, this process has a disadvantage that only thin sheet, not bulk material, can be obtained.

Then an attempt to apply repeated working by the side extrusion shown in Fig 2 to the Al-Ti-Mn alloy ingot was made at 600℃. As mentioned earlier, however, the bolts fixing the two dies in Figure 2 were seriously deformed and damaged during the first pass from lack of the high-temperature strength, and thus even single (non-repeated) extrusion was not completed. Figure 4 shows the change in specimen shape caused by this incomplete extrusion. New set of dies is being designed by modifying the shape and the way of fixing.

The microstructures of the specimen shown in Figure 4(b) were observed from two directions, as illustrated in Figure 5(a), and are shown in Figure 5(b) and (c). In comparison to the microstructure prior to the extrusion, i.e., as-cast structure shown in Figure 4, second phase particles are confirmed to be slightly but significantly refined by the incomplete extrusion. Therefore, by increasing the reduction through this repeated working process using deformation-free dies and bolts, sufficient refinement of the second phase particles will be achieved.

To identify the second phase in the two alloys X-ray diffraction was carried out on the as-cast ingots. The results obtained are shown in Figure 6, indicating that $Al_{13}Cr_2$ or Al_6Mn and Al_3Ti (DO_{22}) phases are present together with aluminum matrix. In other words, both alloys contain two intermetallic phases but no $L1_2$ phase out of accord with the expectation mentioned earlier. Since the equilibrium is not always attained in as-cast conditions, frequently with unstable phases, $L1_2$ phase might be present in the equilibrium state. To examine this possibility, the specimens uniaxially compressed by 88% were annealed at 650℃ for 24h and then subjected to X-ray diffraction.

The resultant patterns are presented in Figure 7, showing that $Al_{13}Cr_2$ or Al_6Mn and Al_3Ti (DO_{22}) phases exist in addition to aluminum, which is qualitatively the same as those for the as-cast ingots shown in Figure 6. Comparing the peak height ratio of the intermetallic compound phases to the matrix phase in Figure 7 with that in Figure 6, relative amount of the intermetallic phases, especially of Al_3Ti (DO_{22}) phase, is found to be increased by the annealing. To produce $(Al,Cr)_3Ti$ or $(Al,Mn)_3Ti$ phase, the amount of $Al_{13}Cr_2$ or Al_6Mn and Al_3Ti (DO_{22}) phases must decrease. Therefore, formation of the $L1_2$ phase can not be expected by further annealing. Hence, in spite of the initial expectation, it is concluded that addition of Cr or Mn to Al-10mol%Ti alloy does not bring about the occurrence of $L1_2$ phase. Figure 8 shows optical micrographs of the two alloy specimens annealed at 650℃ for 24h corresponding to Figure 7. It is noted that virtually no coarsening of the second phase particles is observed in comparison to the as-compressed structure shown in Figure 3. Therefore, as mentioned earlier, it is expected that the second phase particles do not coarsen significantly during hot working in the Al-Ti base alloys, and that the alloys have excellent heat resistance, in relation to the small diffusivity of Ti and the other alloying elements in aluminum[5].

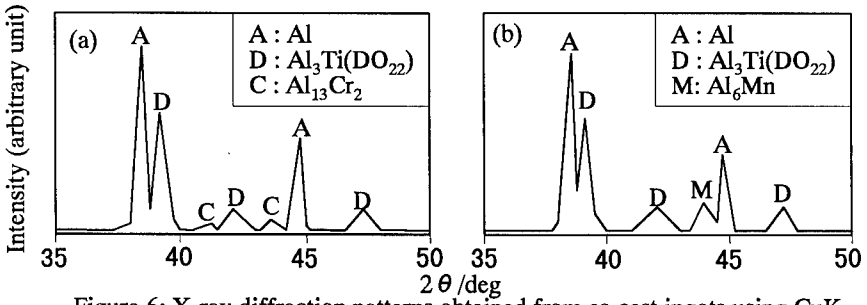


Figure 6: X-ray diffraction patterns obtained from as-cast ingots using CuK_α. (a): Al-Ti-Cr , (b): Al-Ti-Mn

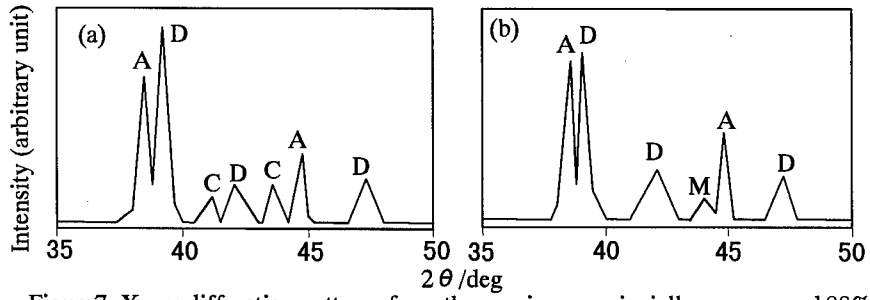
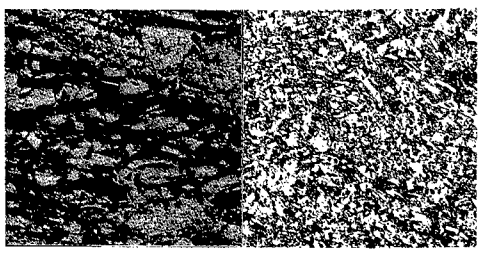


Figure7: X-ray diffraction patterns from the specimens uniaxially compressed 88% and then annealed at 650℃ for 24h. (a): Al-Ti-Cr , (b): Al-Ti-Mn



(a) Al-Ti-Cr (b) Al-Ti-Mn 100 μm

Figure 8: Optical micrographs corresponding to Figure 7.

Summary

To refine second phase particles in Al-10mol%Ti-3.2mol%Cr and Al-10mol%Ti-3.6mol%Mn alloys, ingots were subjected to uniaxial compression at room temperature by reduction up to 88% and to side extrusion at 600℃, and then microstructurally characterized.
The results obtained have been summarized as follows:

(1) In unaxial compression, the second phase particles were refined more markedly as the reduction amount increased.
(2) Although slight refinement was attained in the side extrusion at 600℃, repeated working became impossible since the bolts which fixed the dies were seriously deformed because of lack in high-temperature strength.
(3) It was shown by means of X-ray diffraction that there is no $L1_2$ phase in the ingot of either alloy, and $Al_{13}Cr_2$ or Al_6Mn and Al_3Ti (DO_{22}) phases are present in addition to the matrix phase.
(4) The intermetallic phases mentioned above existed stably with little coarsening after the specimens uniaxially compressed by 88% were annealed at 650℃ for 24h.

Acknowledgments

This work has been conducted with a financial support from the Amada Foundation for Metal Work Technology, which is highly acknowledged.

References

1. H. Shingu, "Mechanical Alloying," J. Japan Inst. Light Metals., 40 (1990), 850-855.

2. J. Wang, et al., "Structural Evolution and Deformation in an Aluminum-Based Solid Solution Alloy with Submicron Grain Size," Mater. Res. Soc. Symp. Proc., 319 (1994), 293-298.

3. J. Wang et al., "An Investigation of Microstructural Stability in an Al-Mg Alloy with Submicrometer Grain Size," Acta Mater., 44 (1996), 2973.

4. Y. Iwahashi, et al., "An Investigation of Microstructural Evolution During Equal-Channel Angular Pressing," Acta Mater., 45 (1997), 4733.

5. K. Hirano, "Diffusion in Aluminum," J. Japan Inst. Light Metals., 29 (1979), 249-262.

6. S. Zhang, J. P. Nic and D. E.Mikkola, "New Cubic Phases Formed by Alloying Al_3Ti with Mn and Cr," Scripta Metall. Mater, 24 (1990), 57.

7. E. P. George, et al., "Brittle Cleavage of $L1_2$ Trialuminides," Mater. Res., 5 (1990), 1639.

8. H. Mabuchi, et al., "Microstructure and Mechanical Properties of Ternary $L1_2$ Intermetallic Compound in Al-Ti-Cr System," Mater. Trans. JIM., 6 (1997), 560-565.

9. J. Kaneko, T. Murakami and N. Furushiro, "Aluminum-Transition Metal Alloys," J. Japan Inst. Light Metals., 39 (1989), 147-166.

EFFECTS OF T4 AND T6 TEMPERS ON POST SEMI-SOLID FORMED 319 ALUMINUM ALLOY

Emanuela Cerri°, Stefano Spigarelli°, Enrico Evangelista°, Stephen Paddon°*

°Dipartimento di Meccanica-INFM, Università di Ancona, 60131-Ancona, Italy
* now at Department of Mechanical Engineering, O.S.U., Corvallis-OR, USA

Abstract

An investigation was performed in the interest of realizing the optimum T4 and T6-type tempers for post semi-solid formed 319 aluminum alloy (Al-6%Si-3%Cu). The investigation was limited to heat treatment times reasonable for an industrial process. Changes in hardness, electrical conductivity and microstructure were examined against thermal history for different combinations of solution treatment and natural or artificial aging times and temperatures. Microstructural changes were observed using optical and scanning electron microscopy.

The Third Pacific Rim International Conference on
Advanced Materials and Processing (PRICM 3)
Edited by M.A. Imam, R. DeNale, S. Hanada,
Z. Zhong and D.N. Lee
The Minerals, Metals & Materials Society, 1998

Introduction

The A319 alloy is considered an all-purpose casting alloy for its combination of good casting characteristics and mechanical properties. Semi-solid forming (SSF) offers a new method for economical production of near-shape parts. This is due to its lower process temperatures, increased dye life and reduced geometrical variations in post-cast parts relative to sand cast and permanent mold methods [1,2]. However, few aluminum alloys have been extensively studied for their viability in SSF processes. The demand for SSF parts over a range of mechanical properties has driven semi-solid research towards an increasing number of cast and even wrought aluminum alloys [1].

Silicon (6%), copper (3%) and magnesium (0.3%) give the 319 alloy relatively moderate tensile properties, a lower specific gravity and superior casting characteristics [3,4]. In addition, copper and magnesium allow heat treatment of this alloy [3-5]. Literature concerning the T4 and T6-type heat treatments along with subsequent tensile properties are readily available in the sand cast or permanent mold state [3-5]. However, information subsequent to semi-solid forming processes is lacking. Chiarmetta [1] has compiled data that show large differences in mechanical properties between semi-solid formed, wrought, permanent mold and closed die forging processes for various aluminum alloys with the same heat treatments. This suggests that the optimum heat treatment conditions will also vary from sand cast or permanent mold to semi-solid formed parts. In this study, 319 was investigated to determine T4 and T6 tempers specific to the semi-solid formed structure within a time frame reasonable for an industrial process.

Experimental Procedure

Material used in this study was provided by Pechiney (France) in the form of slightly conical semisolid bars. These bars had radii of 25 and 30 mm at each end and a length of 196 mm. The bars were formed using an electromagnetic stirring process by Pechiney. The composition of the 319 alloy is shown in TableI.

Table I. Chemical Composition of the 319 thixocast alloy (wt%)

Si	Cu	Mg	Ti	Fe	Mn	Ni	Zn	Al
5.8	2.9	0.3	0.02	0.13	0.02	<0.01	0.02	rem

To determine the optimum solution treatment time for the 319 alloy, samples were solution treated at 500°C for 0.5-16 hours, quenched in water at room temperature and then aged at 170°C for times ranging from 0.5-24 hours. The solution treatment temperature was recommended by Pechiney, and is consistent with other work for this alloy [3-5]. Samples were hardness tested using a Rockwell F scale after the surfaces were ground with 1200 grit silicon carbide paper. Samples with the same solution treatment times as above were aged also at room temperature for 5, 20, and 160 hours. After these results were analyzed, an optimum solution time (4 h) was determined and used for subsequent tests that included aging at 170, 200 and 220°C. Samples were water quenched immediately following aging. Conductivity measurements were performed using a Foster probe on sample surfaces ground with 1200 grit silicon carbide paper.

For optical and scanning electron microscopy observations, specimens were ground with 4000 grit silicon carbide paper and polished with one micron diamond paste. An etch of one

part 40% hydrofluoric acid to 20 parts water was found to contrast the constituents of the 319 alloy well, and was used for microscopic observations.

Results and Discussion

Increased solution treatment resulted an initial softening and then hardening of the post SSF 319 alloy. Figure 1 shows that after one hour of solution treatment, the hardness reached a minimum and increased with further solution treatment. Additional solution treatment resulted in a maximum hardness that is approximately the same as the as cast. The conductivity response to solution treatment nearly mirrors the hardness, and reaches a maximum after 30-60 minutes.

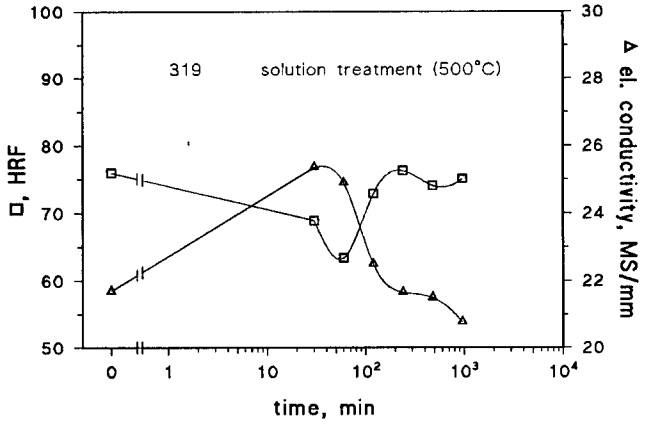


Figure 1: Solution treatment effects on hardness and electrical conductivity of 319.

The initial softening in the first 60 minutes is believed to be primarily the result of coarsening of the dendritic silicon-rich phase. The subsequent increase in hardness and accompanying decrease in conductivity are attributed to solid solution hardening that occurs because of the higher solubility of copper, magnesium and silicon at elevated temperatures. After 4 hours of solution treatment, the hardness leveled off. This suggests that the aluminum matrix was saturated, since the solution hardening mechanism slowed.

There are three readily observable physical changes occurring during solution treatment at 500°C: the coarsening and spheroidizing of silicon rich precipitates in the eutectic phase, coarsening/formation of small precipitates inside the solid phase (not visible in the as cast state), and the shrinking and eventual disappearance of a copper rich phase inside the eutectic region. The initial structure (figure 2a) is of semi-solid type that has approximately 70 percent solid phase based on surface area. The solid phase contains eutectic 'islands' that vary in composition (percentage of copper and silicon are not consistent). The eutectic phase contains primarily interdendritic copper-rich and silicon-rich particles. After 0.5 h solution treatment (figure 2b), the silicon precipitates begin to spheroidize and coalesce, while the copper rich phase begins to dissolve into the matrix. Also, a small intermetallic phase inside the solid globules becomes visible, believed to be the precipitation reaction of Al_2Cu. For the

319 alloy, Al_2Cu precipitates form below 506°C, which is 6°C above the solution temperature used in this experiment [6].

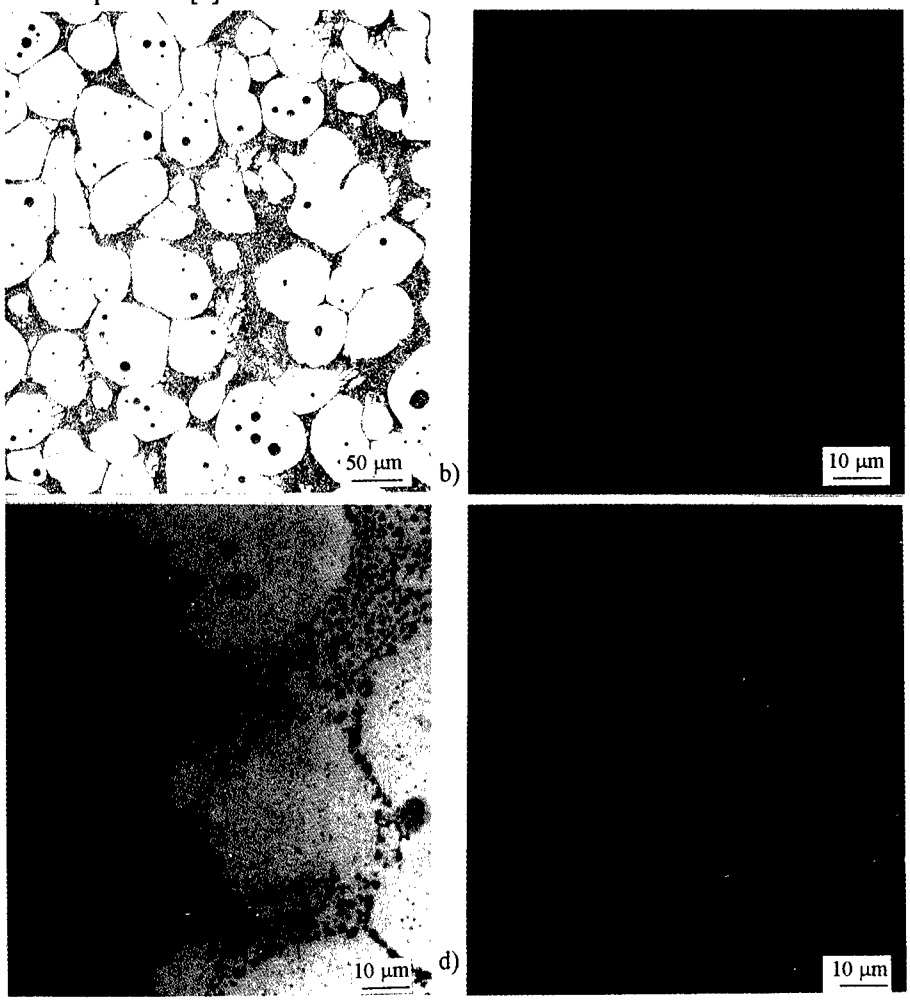


Figure 2. Optical micrographs of 319 aluminum alloy after different solution times: a) as thixocast, b) 0.5h, c) 2h and d)16h.

In figure 2c, the silicon-rich phase has become primarily globular, and the copper-rich particles are no longer visible. The Al_2Cu precipitates in the solid phase continue to grow and coarsen. This microstructural evolution continues with the solution treatment as can be seen in fig. 2d after 16 hours.

The first stage of this investigation was to determine a solution time sufficiently long such that a longer solution time would result in minimal or no changes in the aging curves. The changes in hardness when aged at 170°C after various solution treatment times at 500°C are shown in Figure 3a. From this graph, solution times less than 4 hours resulted in substantially lower hardness values, while solution times of four hours and longer revealed no clear increase in the hardness. For the one-half and one hour solution treatments little or no strengthening was imparted to the alloy after artificial aging.

A similar behavior is reported for the alloy in figure 3b when subjected to natural aging for the same solution treatment time intervals. However, the maximum hardness achieved at room temperature was significantly lower. This solution time (four hours) was again realized as minimum in the room temperature aging curves. That is, additional solution treatment beyond four hours resulted in no substantial increase in hardness. As a result, four hours at 500°C was chosen as the solution treatment for all subsequent aging experiments.

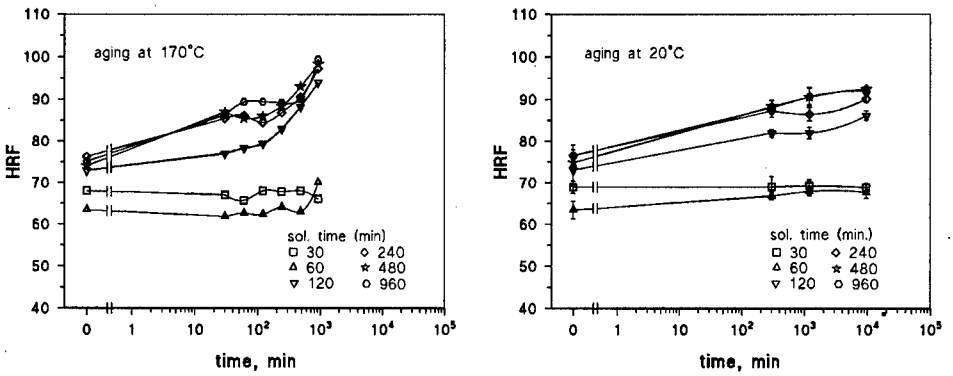


Figure 3. Hardness response of 319 when aged a) at 170°C and b) at 20°C after various solution treatment times.

Once the solution time was determined, samples were aged at three artificial aging temperatures, 170, 200 and 220°C, shown in Figure 4. At 220°C, overaging occurs after 1 hour. At 200°C, hardness peaked at about 4 hours and overaging occurred for longer aging times. The 170°C aging curve continued to increase in hardness within the range of this study.

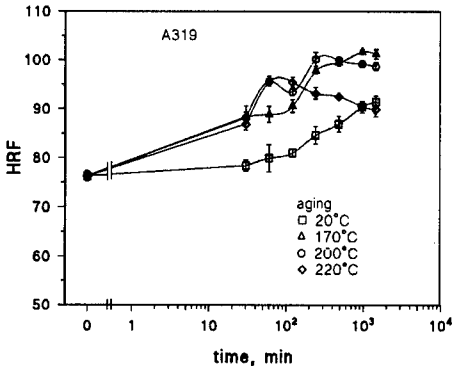


Figure 4. Aging at different temperatures.

The substantial hardening occurring during room temperature aging is believed to be the formation of coherent or semi-coherent clusters, such as the initial stages of Al_2Cu and Mg_2Si precipitates [7]. Since these clusters remain dissolved in the aluminum matrix, their impedance to conductivity is minimal.

Conclusion

The effects of T4 and T6 tempers on post semi-solid formed 319-aluminum alloy were investigated in a range of time reasonable for an industrial process. Four hours was realized as the minimum solution treatment time at 500°C for imparting maximum strengthening for T4 and T6-type tempers. The T4 treatment resulted in substantially lower hardness values than for T6-type tempers. These effects were explained in terms of the microstructural evolution.

Acknowledgements

The authors would like to thank Pechiney (France) for providing the material. The work has been performed in the framework of the Brite-Euram Program BRPR-CT95-0095.

References

1. Chiarmetta, G., Thixoforming of automobile components. Proc. 4th Inter. Conf. on Semi-Solid Proc. of Alloys and Comp., Sheffield, 204, (1996).
2. Sigworth, G., Defect formation during semi-solid casting, Int. J. Cast Metals Res., 1996, 9, 113-123.
3. Brooks, C. R., Heat Treatment, Structure and Properties of Nonferrous Alloys. American Society for Metals, Metals Park, Ohio, 1982.
4. Davis, J. R., ASM Specialty Handbook: Aluminum and Aluminum Alloys. ASM International, Materials Park, Ohio, 1993.
5. Northwood, D., Sun, X., Byczynski, G., Sokolowski, J. Oswald, J., Penrod, D., Thomas, R., and Esselting, W., A metallurgical study of the heat treatment of aluminum alloy 319 (Al - 6Si - 3.5 Cu) castings. Proc. of the Int'l Symposium on Recent Metallurgical Advances in Light Metals Industries, Canadian Institute of Mining, Metallurgy and Petroleum, Montreal, 1995.
6. Samuel, A. and Samuel, F., Effect of melt treatment, solidification conditions and porosity level on the tensile properties of 319.2 endchill aluminum castings. Journal of Material Science, Vol. 30, 1995.
7. Hatch, J. E., Aluminum: Properties and Physical Metallurgy, American Society of Metals, Metals Park, Ohio, 1984.

RECENT DEVELOPMENTS IN LIGHT METALS

F.H. (Sam) Froes[1], W. Quist[2], and J. Liu[3]

1. Director, Institute for Materials and Advanced Processes (IMAP), University of Idaho, Moscow, ID 83844-3026, USA
2. Deceased, Formerly with Boeing Commercial Airplane Group, Seattle, WA 98124, USA
3. Aluminum Company of America (ALCOA), Alcoa Center, PA 15069-0001, USA

Abstract

Recent developments in the light metals aluminum, magnesium, and titanium are discussed. Consideration is given to both conventional ingot metallurgy approaches and to advanced "far from equilibrium" techniques, including rapid solidification, spray forming, mechanical alloying, plasma processing and vapor deposition. These materials are seeing potential and actual use in various industries including aerospace, automobile, rolling stock (trains), ships, sporting equipment and body implants.

The Third Pacific Rim International Conference on
Advanced Materials and Processing (PRICM 3)
Edited by M.A. Imam, R. DeNale, S. Hanada,
Z. Zhong and D.N. Lee
The Minerals, Metals & Materials Society, 1998

Introduction

As performance demands increase, so do the demands for enhanced mechanical property combinations at reduced overall weight; and reduced weight can most efficiently be realized by the use of light (low density) metals such as aluminum, magnesium, and titanium (Fig. 1) [1]. Improvements are being made via ingot metallurgy processing but more substantial developments require "far from equilibrium" synthesis [2-5].

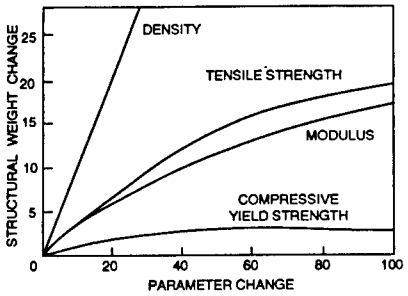


Fig. 1. Effect of Property Improvement on Structural Weight.

Synthesis/Processing

Ingot Metallurgy

Development of aluminum alloys for aerospace applications has changed from an emphasis on high strength to concern over other characteristics including cost and durability [2]. For example Alcoa developed the T77 temper for alloy 7150 (Al-Zn-Mg-Cu) which combined good corrosion resistance with no sacrifice in strength. Currently a major concern is the need for lower cost because of the gap between airplane cost per seat and yield per passenger. Castings, Al-Li alloys, composite concepts (including lamellar ARALL and GLARE), superplastic forming and Al-Mg-Sc alloys are all contributing to the material mix available. The major concern in the automobile industry is cost.

Emphasis in the titanium arena has been on reduced cost alloys using lower cost Al-Fe master alloys rather than the traditional Al-V (i.e. for the work-horse Ti-6Al-4V alloy) master alloys.

Rapid Solidification

The rapid solidification (RS) technique allows extension of solubility limits, production of novel phases, and much more refined microstructures than is possible using the ingot metallurgy (IM) technique. The greatly increased chemistry/microstructure "window" can lead to enhanced mechanical and physical properties.

The five families of aluminum alloys being explored using the RS approach are the high strength corrosion resistant alloys based on traditional 7000-series alloys, low density Al-Li alloys with increased lithium levels over those possible using the IM approach, dispersoid strengthened elevated temperature alloys based on low solubility/low diffusion rate additions such as the transition metals (Fe, Mo, Ni) (Table I) and rare earth elements (Ce), wear resistant

high Si alloys, and recycling of normally impossible to recycle alloys (i.e. avoidance of detrimental segregation).

Cast magnesium alloys exhibit lower than desirable strength, ductility, and creep behavior, and the non-protective oxide skin can lead to severe corrosion problems. Using RS high strength/corrosion-resistant magnesium alloys containing rare earth additions (Y, Nd, Ce) have been developed.

The major concentration on RS terminal titanium alloys to date has been to enhance elevated temperature capability beyond IM alloy levels (i.e. >700°C) through dispersion hardening. The additions of Er and other rare earth elements produces dispersoids which resist coarsening at least up to 800°C; however, much further optimization is required particularly in increasing the volume fraction of second phase particles.

In combination with the near net shape advantages offered by the PM approach, RS may offer some advantages for the processing of gamma alloys over the IM approach; presently, the same cannot be said for RS processing of alpha-2 alloys.

Spray Deposition

In spray deposition finely divided molten metal droplets, produced by disintegration of a stream of molten metal using high energy inert gases, impinge on a substrate before they completely solidify. This allows some of the characteristics of RS to be achieved in combination with a near net shape capability.

Mechanical behavior can be enhanced in conventional aluminum alloys, a result of the refinement in constituent particle size.

The spray deposition of titanium based alloys has been investigated only recently with some early successes.

Mechanical Alloying

Mechanical alloying (MA) is a process in which heavy working of powder particles results in intimate alloying by repeated welding and fracturing. This process has the same attributes as RS - extension of solubility limits, production of novel structures and refinement of the microstructure (down to the nanostructure range); and additionally allows production of a dispersion of second phase particles.

High temperature aluminum alloys with Ti additions, low density alloys with Mg additions, and extra low density alloys with Li additions have been developed through MA. The mechanical property combination which can be obtained in an MA Al-base alloy is shown in Table I. The MA Al-Li alloys exhibit minimal degradation of properties when stressed in the transverse direction and are characterized by excellent general corrosion resistance which is 100x better than that exhibited by the IM alloy.

MA has been employed in the development of "supercorroding" magnesium alloys for submarine applications, such as a heat source in diver suits, and as a hydrogen gas generator.

MA of titanium alloys has resulted in supersaturated solid solutions, metastable crystalline and glassy phases as well as nanometer-sized grain structures.

Table I. Room Temperature Mechanical Properties of MA Aluminum Alloys (Longitudinal)

Process	Alloy	UTS (MPa)	YS (MPa)	El. (%)	K_{IC} MPaÖm	Density (g/cm^3)
MA	Al-Li-Mg-O-C	510	450	10	45	2.55
IM	7075-T73	505	435	13	32	2.81

Work on MA of the titanium aluminides indicates that this is an interesting fabrication method for both the alpha-2 and gamma families of alloys, resulting in the formation of surprisingly stable nanosized grains, which are stable even after compaction by hot isostatic pressing (HIP'ing).

Plasma Processing

In plasma processing, solid feed-stock is converted to the vapor phase at elevated temperatures due to the highly concentrated enthalpy. Chemical reactions occur and a solid product nucleates and grows at a lower temperature. A number of studies have led to the formation of nanometer sized metallic powders.

Vapor Deposition

Production of alloys directly from the vapor phase allows even greater flexibility in constitutional and microstructural development than RS and MA. Either monolithic material or alternate layers of two or more metals can be produced.

The strength of a vapor deposited Al-7.5Cr-1.5Fe alloy is significantly higher than the strength of RS alloys up to at least 250°C, a result of the fine microstructure produced by the vapor deposition technique. It is also possible to produce nanostructured layered structures which exhibit novel strength and modulus combinations.

The electron beam vapor quenching technique has been used to produce titanium alloys which are not possible by IM or even RS. One example is the production of low density Ti-Mg alloys. Mg boils below the melting point of titanium making production of a liquid alloy impossible by conventional methods.

Applications

Applications for advanced materials can occur in various segments of the economy. However since the processes used to synthesize these materials are generally more expensive than conventional ingot processes use must be justified by increased system performance. A major success story is the use of advanced materials on the Boeing 777 which has a greater number of advanced materials than any other Boeing Commercial Airplane (Fig. 2). These materials earned their way in the vehicle became of their contribution to weight reduction, cost and

maintainability/durability (Fig. 3). For an automobile an important aspect of increased system performance is reduced weight and hence improved fuel economy (Figs. 4 and 5).

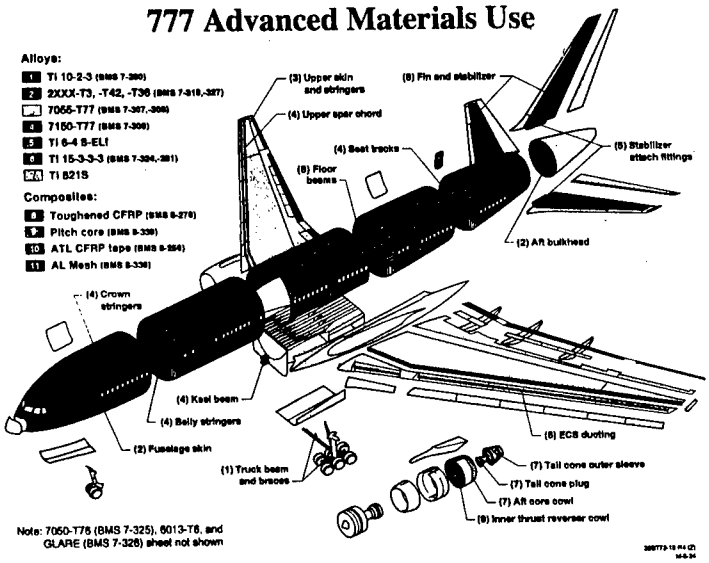


Fig. 2. Boeing 777 Advanced Materials Use.

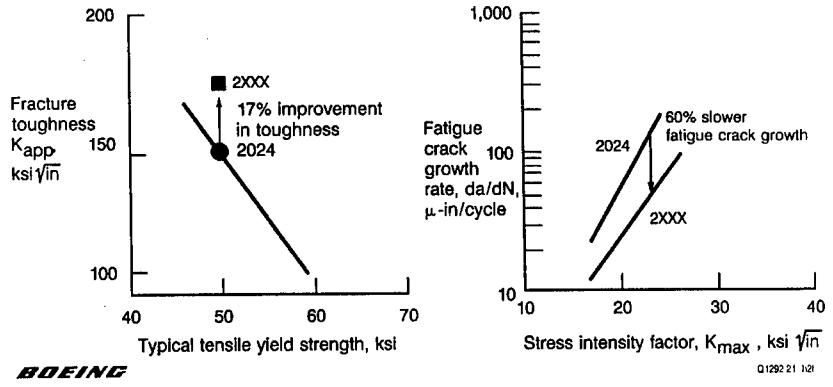


Fig. 3. An Example of Reduced Operating Cost (Fuel and Maintenance) on the Boeing 777 by Use of Advanced Materials.

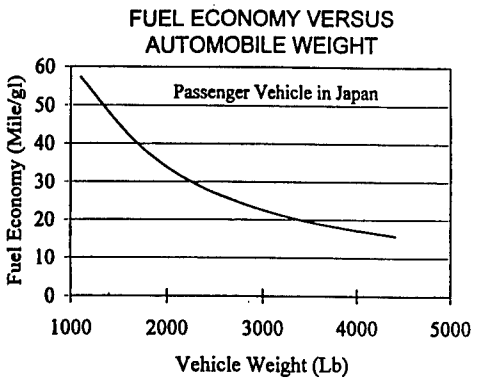


Fig. 4. Effect of Weight Reduction on Fuel Consumption for an Automobile.

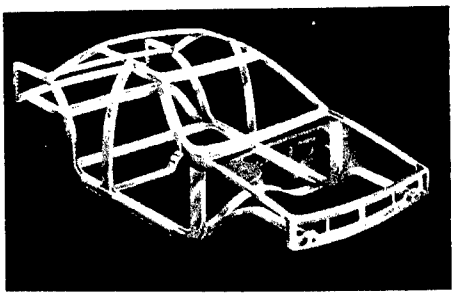


Fig. 5. Alcoa Extruded Aluminum Space Frame [1].

Conclusions

This paper has discussed a number of innovative materials/synthesis techniques as applied to the light metals aluminum, magnesium and titanium; and the intermetallic titanium aluminides. Some potential applications have been presented.

Acknowledgments

This paper is dedicated to the memory of Dr. W. ("Bill") Quist, a giant in aluminum science and technology and a "man" to match. We'll miss him. The author appreciates useful discussions with E.G. Baburaj, G.B. Erazamuth, E.B. Ghothehellareu, J. Hebeisen, L. Öveçoglu and O.N. Senkov. In addition the author would like to acknowledge the assistance of Ms. B. Olsen in manuscript preparation.

References

1. I.J. Polmear, Light Alloys—Metallurgy of the Light Metals, 3rd Edition, 1995, Halstead Press, John Wiley and Sons, New York, USA.

2. John Liu, J.T. Staley and W.H. Hunt, Jr., Third ASM Paris Conf., Eds. F.H. Froes, T. Khan and C.M. Ward-Close, ASM Int., Materials Park, OH, 1997, 91.

3. F.H. Froes and C. Suryanarayana: "Powder Processing of Titanium Alloys", Book Series on Reviews in Particulate Materials, eds. A. Bose, R. German, and A. Lawley, (1993) MPIF, Princeton, NJ.

4. F.H. Froes, P Tsakiropoulos, C. Suryanarayana, and W. Baeslack: Light Materials for Transportation Systems, ed. N. Kim, Center for Advanced Aerospace Materials, Pohang Univ. of Sci. and Tech., Pohang, Korea, 1993, 27.

5. L. Öveçoglu, F.H. Froes, N. Srisukhumbowornchai and D. K. Mukhopadhyay "Grain Growth Behavior of Nanograined Gamma TiAl Compacted by Hot Isostatic Pressing," ASM Int. Conf. HIP '96, eds. F.H. Froes, R. Widmer and J. Hebeisen, ASM Int. Materials Park, OH, 227.

TECHNIQUES FOR THERMOMECHANICAL PROPERTY EVALUATION IN TITANIUM BASED MATERIALS

Leo Christodoulou, Richard Dashwood, and Harvey Flower

The Department of Materials
Imperial College of Science Technology & Medicine
Prince Consort Road
London SW7 2BP
UK

Abstract

This paper is concerned with the exploitation of a specimen design and testing strategy which can be used to readily assess the effect of thermomechanical processing on microstructural development during the hot working of Ti-based materials. A novel test geometry is presented which can be used to obtain controlled strain distributions within a single specimen. The application of FEM based software in interpreting the results of this test is discussed and the results of a parametric study investigating the effect of process (friction) and material (strain rate sensitivity) parameters on the strain distributions obtained during this test are given. The importance of accurate friction information in interpreting the results of this test is highlighted. Inherent weaknesses in the ring compression test for friction evaluation are presented, and it is shown that accurate analysis of this test can be obtained by applying FEM techniques. Particular attention is paid to the importance of strain rate sensitivity and the errors that can be obtained if this parameter is ignored when evaluating the ring compression test. The paper concludes by presenting some initial results of this testing strategy as applied to the forging of Ti-10-2-3. Flow stress – temperature - strain rate information for this alloy is presented, and the effect of strain on the as-forged microstructure is discussed.

The Third Pacific Rim International Conference on
Advanced Materials and Processing (PRICM 3)
Edited by M.A. Imam, R. DeNale, S. Hanada,
Z. Zhong and D.N. Lee
The Minerals, Metals & Materials Society, 1998

Introduction

It has long been recognised[1] that thermomechanical processing of conventional α/β and near β, Ti alloys can be difficult due to the narrow $\alpha + \beta$ temperature range and the extreme sensitivity of the microstructural development to small variations in temperature during processing close to the β transus. Super-transus processing can lead to rapid grain growth and is generally avoided other than during the initial ingot breakdown operation. Most commercial operations involve a through-transus or sub-transus forging[2]. The kinetics of α nucleation close to the β transus are quite slow and heterogeneous nucleation as opposed to homogeneous intragranular nucleation can lead to formation of near continuous grain boundary layers of α phase. This leads to reduced fracture toughness[3] in particular and is generally to be avoided. Given the above characteristics and low thermal conductivity, Ti alloys can develop significant through-thickness microstructural differences due to adiabatic heating during forging. Increasingly process-modelling techniques are being employed[4,5,6] to capture the important parameters of the process and to aid in tooling design and processes optimisation. In order to implement any FEM based forging simulation programme for the prediction of final as forged microstructure a database of information relating final microstructure to thermomechanical condition has to be established. This can represent a significant work effort due to the fact that the key property - determining microstructural features are strongly effected by the strain rate, temperature and strain pertaining to the deformation process. Even during a relatively simple hot die forging significant through section variations in these variables are encountered. Using classical uniaxial compression testing of cylinders, the test matrix required to evaluate the individual and combined effect of these variables, would be extremely complex. The authors propose to overcome this problem by using a novel test specimen design that permits the effect of a range of strains to be studied in one test; the technique is presented in this communication.

Thermomechanical Simulation

The double truncated cone sample (see figures 1 & 2) enables controlled strain distributions within a single specimen and can readily identify the specific strain required to achieve a specific microstructural event (for example recrystallisation) by matching the metallographic data with the strain profiles calculated from finite element software. The sample is isothermally forged at a constant strain rate from an initial height of 15.8mm to a final height of 4mm to yield a continuous strain variation from ~ 0.4 to 2. The exact strain variation within the sample is determined by mathematical simulation of the compression test using finite element software.

The isothermal forging is performed on a servo-hydraulic 100 kN MAYES testing machine (Model No. ESH 100D). The servo hydraulic machine is interfaced to 386 50 MHz PC via a 16 bit intelligent multi-function I/O card (CIL PC Super Card), which both controls the test and acquires the data, using in-house software developed by one of the authors (RD). The program performs a minimum of 10 output/input functions per second, and will run constant strain rate tests in the range $5x10^{-5}$ to 10 s^{-1}. Data is only recorded when there is a variation in load greater than 0.5% of the pre-set load range. Sample heating is provided by a Severn Furnaces 1000°C Radiant Furnace (Model No. RHS1259) controlled by a EUROTHERM Model 902P programmable controller. The control (k type) thermocouple is located 2mm into the bottom ram; 5mm below the platen. Under standard conditions the sample is loaded 'cold', and then heated to the test temperature at a rate of 25°C a minute. During heating the control software moves the rams, to compensate for thermal expansion of the entire loading system, and maintains a clamping load of 0.1 kN. A thermocouple is attached to the sample to permit monitoring of the specimen temperature during heating testing and cooling. A schematic of the test set-up including dimensions is given in figure 3. The rams are manufactured from a nickel based super alloy MAR-M 246. The forging process is simulated using a commercial finite

element based package Forge2 developed by Ecole des Mines and Transvalor (France)[7]. Input data required includes geometric definition of the tooling and starting material, rheology data for the material, thermal data pertaining to the material, tooling, and tooling/material interface, as well as friction behaviour at the tooling/material interface. The package allows automatic remeshing of the workpiece to be conducted during the computation, and includes a subroutine for user defined calculations. The software will model either viscoplastic or elasto-viscoplastic behaviour using either 4 node linear elements or 6 node quadratic elements. Output from the package includes strain, strain rate and temperature distributions within deforming material.

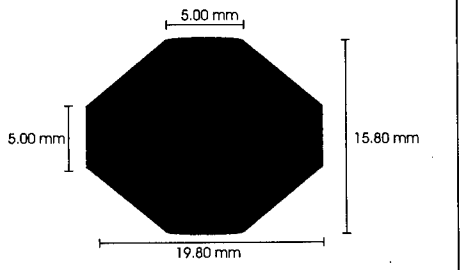


Figure 1: Specimen dimensions used for microstructural evaluation

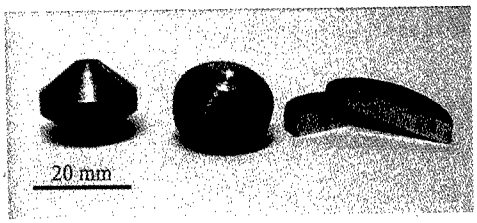


Figure 2: Specimen configuration before and after compression

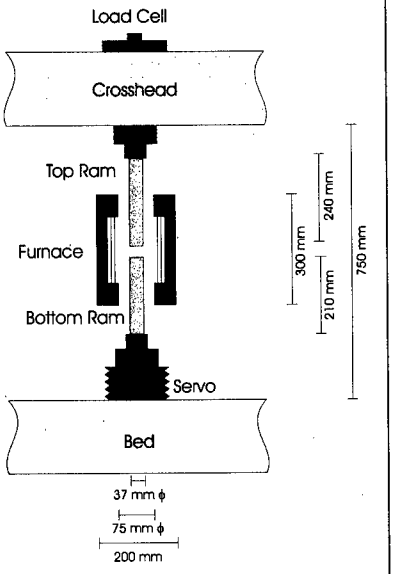
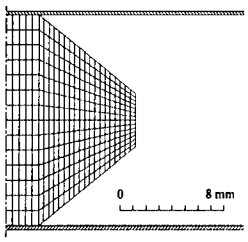


Figure 3: Schematic of the thermomechanical simulation rig

Figure 4 shows a typical mesh used for the mathematical simulation along with the strain and strain rate evolution during the test. The specimen geometry given in figure 1 was designed to give final strains compatible with hot die forging operations, and to produce a final deformed sample size that can be prepared metallographically and examined in its entirety. This provides continuous strain microstructure information, allowing the use of automated SEM and image analysis techniques. Another benefit of the small size of this specimen is that deformation heating and thermal variations are minimised giving truly isothermal test conditions even at relatively high strain rates. Whilst the current specimen geometry provides continuous strain variations for ~0.4 to 2, changes can be made to the geometry to provide any strain gradients of interest.

As with all forging processes the shape change, and hence the final strain distribution, is affected by the local friction conditions and the strain rate sensitivity of the material being tested. A parametric study has been conducted to examine the effect of these two variables on the predicted centre line strain profiles and results are presented in figures 5 and 6. The effect of strain rate sensitivity on the strain profile is relatively small, with a significant effect only being observed at the mid section of the sample, where the strains are highest. As would be expected, increasing the strain rate sensitivity has the effect of 'homogenising' the deformation leading to lower mid section strain.



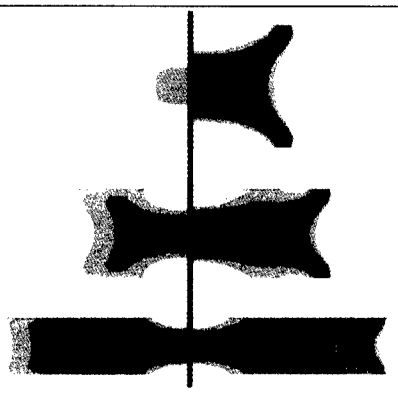


Figure 4: Typical Mesh used for simulation of the isothermal forging (above) and predicted strain and strain rate evolution (right) during the test. (simulation conducted with a friction factor of 0.5 and a strain rate sensitivity of 0.3 – both figures to same scale)

Changes in the friction factor also only give rise to major variations in the strain profile at the mid section region. However even small changes in the friction conditions significantly effect the strain distribution in this region. Increasing the friction coefficient increases the centre line mid section strain due to the fact that deformation becomes localised at the centre line due to the resistance to deformation at the die - workpiece interface. Variations in both strain rate sensitivity and friction coefficient lead to significant variations in the predicted strain distribution, and hence the strain rate sensitivity and friction coefficient should be established and used for the strain distribution predictions. This is particularly important when relating microstructural development in the high strain regime.

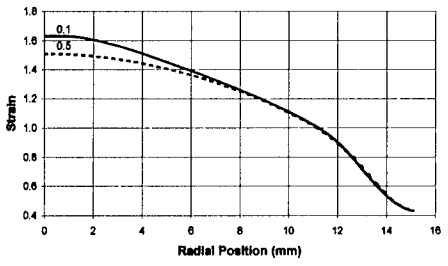


Figure 5: The effect of strain rate sensitivity on the predicted strain profile (Strain profiles for a strain rate sensitivity of 0.1 & 0.5)

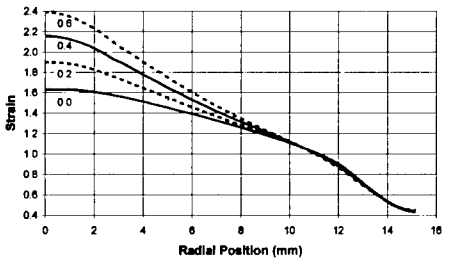


Figure 6: The effect of friction factor on the predicted strain profile (Strain profiles for a friction factor of 0.0, 0.2, 0.4, & 0.6)

Whilst every effort is made to reduce the friction during compression testing, it is extremely difficult to achieve frictionless conditions due to the lack of suitable lubricants. In order to evaluate friction conditions the authors have applied the conventional ring friction test[8] to assess the friction conditions pertaining to the compression test. The major problem with this approach is that when friction is present barrelling of the inner surface occurs and an average diameter has to be measured before the standard calibration curves are used. Obtaining an average diameter is subjective and can lead to significant errors. The approach taken by the authors is to utilise Forge2 to simulate the ring test and to obtain calibration curves that take barrelling into account.

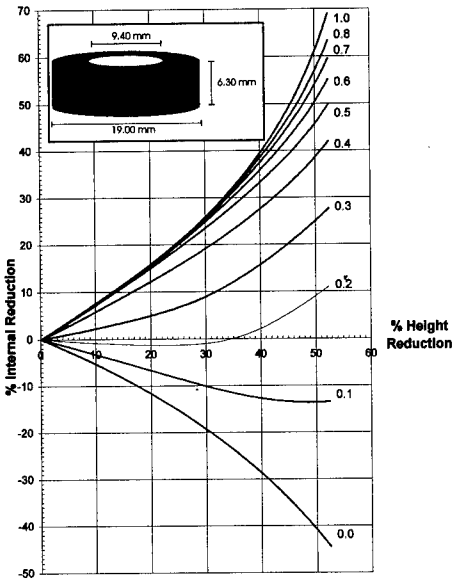


Figure 7: Calibration curves for the ring compression friction test as determined using Forge2 (curves plotted for friction factors of 0 to 1.0 and a zero strain rate sensitivity)

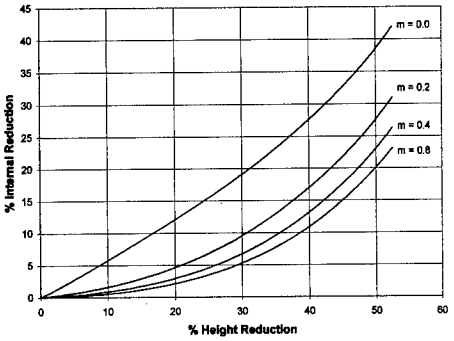


Figure 8: Effect of strain rate sensitivity (m) on the ring test calibration curves. Friction factor of 0.4)

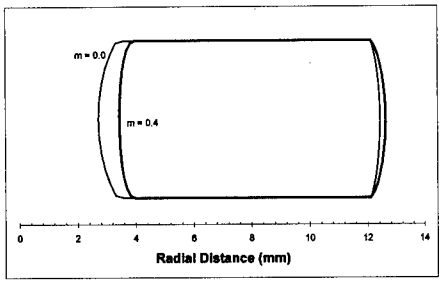


Figure 9: Effect of strain rate sensitivity on predicted final specimen geometry (friction factor of 0.4)

By so doing a measurement of the internal diameter including barrelling only needs to be taken. The calibration curves obtained using Forge2 are presented in figure 7. Another important consideration with respect to the ring compression test is the effect that the strain rate sensitivity has on the shape change of the ring. Increasing the strain rate sensitivity has the effect of reducing the level of barrelling for a set friction condition, and therefore this has to be taken into account when evaluating the ring compression test. The importance of this can be seen from figure 8 where calibration curves are plotted for varying values of strain rate sensitivity, and figure 9 where the effect of strain rate sensitivity on the final sample shape is shown. For correct analysis of the friction factor the strain rate sensitivity of the material being investigated must be known; this being particularly important considering the high strain rate sensitivities that can be encountered in Ti based materials.

For rheological analysis samples 10mm high 8 mm diameter are employed which are compressed to a final height of 4mm ($\varepsilon_{max} = 0.9$), using the same procedure as described for the double truncated cone sample. After testing the data is corrected to take into account the machine stiffness and friction between the ram and the sample.

Results & Discussion

At present this specimen geometry and test strategy is being applied to several classes of materials including titanium alloys, steels, aluminium alloys and titanium aluminides. To demonstrate the effectiveness of this technique some preliminary results obtained from the near β alloy Ti-10-2-3 are presented. Ti-10-2-3 has attracted much interest in recent years as a result of its forgeability, high fracture toughness in relatively high strength conditions, with

comparable fatigue properties to other titanium forging alloys. Although the relationship between microstructure and properties in Ti-10-2-3 is reasonably well understood the means of reproducibly attaining these desirable microstructures in complex sections are not presently well established. This is in part due to the sensitivity of the alloy to the exact strain, strain rate and cooling rate through the β transus. For example limited data is available to indicate the precise strain/temperature conditions which promote β recrystallisation and precipitation (and break up of layers) of the α phase. Currently there is very little data available in the literature on the elevated temperature characteristics of β alloys, nor has there been significant microstructural modelling to date. In order to address these issues a series of isothermal forgings have been conducted on this alloy around the β transus temperature (~800°C).

In order to assess the flow stress temperature strain rate behaviour of this material a series of simple cylindrical compression tests have been conducted in the temperature range 760 – 835°C within a strain rate regime of 10^{-4} to 10^{-1} s^{-1}. The results of these tests are summarised in figures 10 & 11. The rate of change of flow stress with increasing temperature significantly reduces on moving from the two phase α + β regime into the single phase β regime, as a result of the reduction in the thermal activation energy of the restoration processes in the single phase microstructure. The strain rate sensitivity (m) is affected by both temperature and strain rate, with m increasing with decreasing strain rate over the whole temperature range and reaching a maximum value near to the β transus temperature.

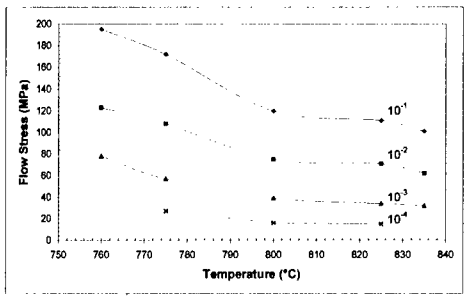


Figure 10: Effect of temperature and strain rate on the flow stress of Ti-10-2-3

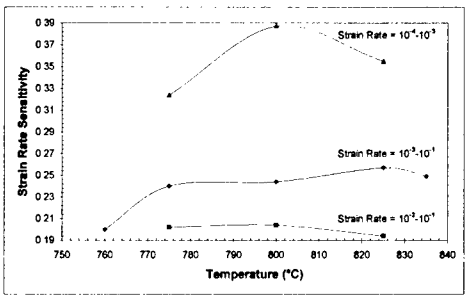


Figure 11: Effect of temperature and strain rate on the strain rate sensitivity of Ti-10-2-3

The effect of strain on microstructure has been investigated by applying the double truncated cone specimen methodology at both sub and super β transus temperatures and at low and high strain rates. The most dramatic effects are observed in the sub β transus forgings and the results of this are presented in figure 12. The backscattered electron micrographs were taken from an electro-polished sample of a 760°C forging conducted at a strain rate of 10^{-2} s^{-1}. The strain profile was simulated for a strain rate sensitivity of 0.2 (characteristic of Ti-10-2-3 under these conditions) and a friction factor of 0.51 (this being evaluated using the method referred to earlier). The initial microstructure consists of large grain β (~300μm) with Widmanstatten α plates of high aspect ratio within the grains and a near continuous distribution of α particles on the β grain boundaries. At low levels of strain the β deforms with little visible effect on the α (ε = 0 – 0.8). As strain increases the Widmanstatten α plates start to deform and in the backscattered electron images regions of local misorientation are seen to develop within the β grains indicating dynamic recovery is taking place (ε = 0.8 – 1.5). This continues with increasing strain until the α plates break up into spheroidal particles and the misorientation within the β grains become very large and the microstructure becomes increasingly a recrystallised equiaxed fine grain (~3μm) β structure with a relatively uniform dispersion of sub micron α particles (ε > 1.5). Additionally the near continuous network of grain boundary α is completely broken up in the high strain regime.

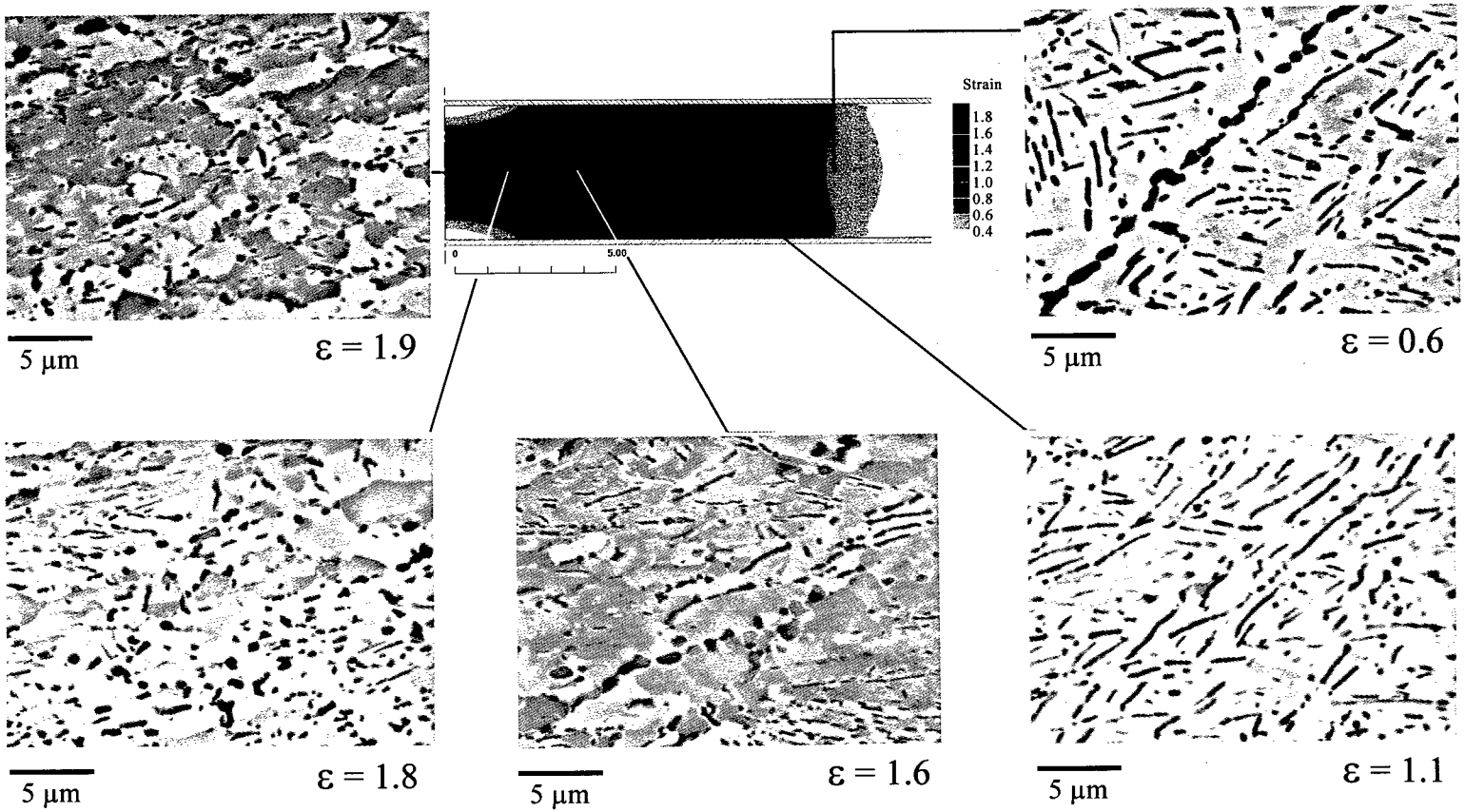


Figure 12: Effect of strain on microstructure during isothermal forging of Ti-10-2-3 at 760°C (strain rate of 10^{-2} s^{-1})

Summary

- A novel specimen geometry and test strategy has been exploited which can be used to readily assess the effect of thermomechanical processing on microstructural development during the hot working Ti based materials
- FEM software has been applied to aid in the interpretation of the results obtained from this test methodology
- The effect friction and strain rate sensitivity on the results obtained from this test has been studied, and the need for accurate information with respect to these variables has been highlighted.
- The application of the ring compression test for assessing friction has been re-evaluated utilising FEM techniques, and a modified methodology has been developed that eliminates errors that can be encountered where conditions of high friction and strain rate sensitivity pertain.
- The application of this novel test geometry with respect to microstructure/strain relationships in Ti-10-2-3 has been presented.
- It has been demonstrated that this approach can be employed to establish the critical strain for recrystallisation under set conditions of strain - strain rate – temperature utilising a single test piece.

Acknowledgements

The authors would like to acknowledge Ms S. Yong for her assistance with the experimental work; Drs S. L. Kampe, Virginia Polytechnic Institute, Blacksburg, Virginia and T.H. Howson, Wyman Gordon, Worcester, Massachusetts for discussions relating to the development of the specimen design; and Dr. A. Wisbey and Professor M. Ward-Close, Structural Materials Centre, Defence Evaluation and Research Agency, Farnborough, England for provision of materials and partial support of one of the authors (LC) under the DERA Fellowship Programme.

References

1. J. V. Scanlon and G. J. Chambers , The Science, Technology and Application of Titanium,ed. R.I Jaffe and N.E. Promisel, (New York NY Pergamon Press, 1970), 82-95
2. H. M. Flower, "Microstructural Development in Relation to Hot working of Titanium Alloys" Materials Science and Technology, 6, (1990),1082-1092.
3. J. C. Williams, "Titanium Alloys: production, behaviour and application", High Performance Materials in Aerospace, ed. H.M. Flower (London, England: Chapman Hall, 1995), 85-134
4. S. P. Fox and D. F. Neal, "The role of computer modelling in the Development of large Scale primary forging of Ti alloys", Titanium'95, ed. P.A. Blenkinsop, W.J. Evans and H.M. Flower (London, England: The Institute of Materials, 1995), 628-635
5. T. E. Howson and R.G. Broadwell, " The design production and metallurgy of very large Aerospace Forgings", Titanium'95, ed. P.A. Blenkinsop, W.J. Evans and H.M. Flower (London, England: The Institute of Materials, 1995), 636-643.
6. G. Dumas et.al., "Control of Large Diameter Ti-6-4 billet microstructures through modeling of the forging process", Titanium'95, ed. P.A. Blenkinsop, W.J. Evans and H.M. Flower (London, England: The Institute of Materials, 1995), 651-658
7. Forge2®, version2.7, Transvalor S.A., Sophia Antipolis, France (1997)
8. A.T. Male and M.G. Cockcroft, "A Method for the Determination of the Coefficient of Friction of Metals under Conditions of Bulk Plastic Deformation," Journal of the Institute of Materials, 93 (1964-65), 38-46.

EFFECT OF Cr ADDITION ON THE CYCLE LIFE OF Ti-BASED ALLOY ELECTRODES FOR Ni/MH RECHARGEABLE BATTERY

Ji-Sang Yu, Ho Lee, Kuk-Jin Jang and Jai-Young Lee

Department of Materials Science and Engineering, Korea Advanced Institute of Science and Technology, 373-1 Kusong-dong Yusung-gu, Taejon 305-701, South Korea

Abstract

Ti-Zr-Mn-V-Ni alloys demonstrate high discharge capacities in KOH electrolyte. However, the rapid degradation of their capacities makes them impossible to be used as the negative electrode material in the Ni-Metal hydride battery. In this work , Mn was partially substituted by Cr in Ti-Zr-Mn-V-Ni alloys to improve their cycle life. The effects of Cr substitution on microstructure, hydrogenation properties, electrochemical characteristics of alloys were investigated. It has been found that Cr substitution is very effective to improve the cyclic durability of alloys although the discharge capacity is decreased with the increase of Cr. Based on the results of EIS, SEM, ICP, hardness test and AES analyses, the effects of Cr on their cycle life of alloy have been discussed.

The Third Pacific Rim International Conference on
Advanced Materials and Processing (PRICM 3)
Edited by M.A. Imam, R. DeNale, S. Hanada,
Z. Zhong and D.N. Lee
The Minerals, Metals & Materials Society, 1998

1. Introduction

Although the Ni-MH battery has gained wide recognition for its higher capacity and less envirionmental pollutants than the Ni-Cd battery, many researchers are still striving to search for new alloys with higher hydrogen capacity and lower cost as its negative electrode material. $Ti_{0.8}Zr_{0.2}V_{0.5}Mn_{0.5}Ni_{0.8}$ alloy has the highest electrochemical capacity of the AB_2 Laves phase alloy reported previously, low cost and are easy to be activated[1]. However, their capacities deteriorate within tens of charging-discharging cycles, making them unsuitable as the negative electrode material in the Ni-MH battery. Fast degradation is caused by the deterioration of the surface properties followed by growth of Ti-oxide on the surface[1]. It has been reported that Cr is very effective to improve the cycle life of AB_2 alloy electrodes[2]. In this work, Mn is partially substituted by Cr in $Ti_{0.8}Zr_{0.2}V_{0.5}Mn_{0.5}Ni_{0.8}$ alloy in order to improve their cyclic durability. The microstructure, gaseous hydrogenation properties, electrochemical performance especially cycle life of these Cr-substituted alloys is investigated and we also discuss the role of Cr on the cycle life.

2. Experimental details

All alloys were prepared by arc melting starting pure metals under an argon atmosphere. The ingots were mechanically crashed and the powder less than 325 mesh. P-C isotherms were measured on an automatic Sievert's apparatus. And alloy electrodes were prepared as follows: an alloy powder(0.1g) was mixed with Ni powder(0.3g, ~2μm) and PTFE (0.02g). The mixture was pressed with a fine nickel mesh into a pellet of 12mm in diameter. The electrodes were charged with a current density of 100mA/g for 6h and discharged under a current density of 50mA/g to -0.V (vs. Hg/HgO). The microstructures of alloys were characterized by X-Ray Diffraction (XRD), Scanning Electron Microscopy(SEM) and Energy Dispersive X-Ray Spectroscopy(EDS). Auger Electron Spectroscopy (AES) analysis was conducted to examine surface conditions. I.C.P(Inductively coupled plasma) analysis was examined to investigate the dissolution of each element of the alloy. To investigate the change of mechanical strength of the alloy with Cr content, the microhardness was measured by Vickers hardness test. Electrochemical impedance spectroscopy (EIS) analysis was performed to examine the change of internal resistance during cycling, which the scanning frequencies were from 100kHz to 10mHz and the ac amplitude was 5mV at –0.875V vs Hg/HgO electrode.

3. Results and Discussion

The P-C-T characteristics and structure of the $Ti_{0.8}Zr_{0.2}V_{0.5}Mn_{0.5-x}Cr_xNi_{0.8}$ (x=0~0.5) alloy are shown in Table.1. As the substituted amount of Cr increase, the reversible hydrogen storage capacity decreases and the structure is chanegd from C14 to TiNi+ BCC (2nd phase). Fig.1 shows the SEM characterization of $Ti_{0.8}Zr_{0.2}V_{0.5}Mn_{0.5-x}Cr_xNi_{0.8}$ (x=0, 0.2, 0.5) alloy system. From the SEM and XRD results, it is apparent that $Ti_{0.8}Zr_{0.2}V_{0.5}Mn_{0.5}Ni_{0.8}$ alloy is a single phase with a C14 Laves phase structure. After Cr substitution, the alloys gradually change to multiphase structures. In the case of $Ti_{0.8}Zr_{0.2}V_{0.5}Mn_{0.2}Cr_{0.3}Ni_{0.8}$, it still maintains a C14 Laves phase structure, but a small amount of a secondary phase has already appeared . EDS examination demonstrated that the secondary phase was a vanadium solid solution containing $V_{53}Cr_{19}Ti_{10}Mn_{14}Ni_4$. When the Cr content was further increased to more than Mn, the alloys form a multiphase structure which contains a C14 Laves phase, a BCC phase, a TiNi-type phase. From the SEM and EDS results, it is concluded that the reversible storage capacity of the alloy is decreased as the structure of alloy divide into TiNi and V-Cr solid solution having

small reversible storage capacity. The electrochemical charging-discharging cycles are shown in Fig.2. All the electrodes appeared to be easily activated, but the alloy $Ti_{0.8}Zr_{0.2}V_{0.5}Mn_{0.5}Ni_{0.8}$ demonstrated a very poor stability in the electrolyte. The initial electrochemical discharge capacities of the alloys decreased with the increase of Cr. To identify the effect of Cr on the cycle life of the electrode, electrochemical and surface properties of the electrode with Cr content were investigated. Fig.3 shows the change of mechanical strength of the alloy with Cr content. It is known that the cyclic stability of the electrode is largely dependent on the pulverization rate [3] and the pulverization rate of alloy particles is closely related to the mechanical strength of the alloy[3]. As the Cr amount increases, the strength of the alloy decreases. The charging-discharging curves of the $Ti_{0.8}Zr_{0.2}V_{0.5}Mn_{0.5-x}Cr_xNi_{0.8}$ electrode(x=0,0.5) is shown in Fig.4. The charging/discharging overpotential of $Ti_{0.8}Zr_{0.2}V_{0.5}Mn_{0.5}Ni_{0.8}$ electrode gradually increased but that of $Ti_{0.8}Zr_{0.2}V_{0.5}Cr_{0.5}Ni_{0.8}$ electrode changed little during the cycling. The overpotential of the charging/discharging is closely related to the catalytic activity of the surface of electrode. The changes of exchange current density of the electrodes during cycling are shown in Fig.5. The exchange current density is a measure of the catalytic activity of the electrode. The exchange current density of $Ti_{0.8}Zr_{0.2}V_{0.5}Mn_{0.5}Ni_{0.8}$ electrode decrease rapidly during cycling, but that of $Ti_{0.8}Zr_{0.2}V_{0.5}Cr_{0.5}Ni_{0.8}$ electrode doesn't decrease during cycling. As the Cr content increase, the electrode can keep catalytic activity. The EIS analysis results of the electrode are shown in Fig.6. The impedance spectra in Fig.6 disclose that the $Ti_{0.8}Zr_{0.2}V_{0.5}Mn_{0.5}Ni_{0.8}$ electrode had an increased contact resistance and charge transfer resistance compared with those at the second cycle, while the $Ti_{0.8}Zr_{0.2}V_{0.5}Cr_{0.5}Ni_{0.8}$ electrode had little change of contact resistance and charge transfer resistance. From the results, the surface oxidation should be restrained as the Cr content increase. The I.C.P results of the $Ti_{0.8}Zr_{0.2}V_{0.5}Mn_{0.5-x}Cr_xNi_{0.8}$ electrode shown in Table.2 demonstrates that the dissolution of V and Zr decrease with Cr content. And Mn, Ti, Cr, Ni element are not detected The AES depth profile of the $Ti_{0.8}Zr_{0.2}V_{0.5}Mn_{0.5}Ni_{0.8}$ electrode shown in Fig.7(a) demonstrates that the surface of the degraded electrode was covered by a very thick layer of TiO_2 , ZrO_2 and MnO_2. V nearly disappeared from the surface due to its easy dissolution into KOH solution. The Ni content on the surface was very small. The AES depth profile in Fig.7(b) of the in $Ti_{0.8}Zr_{0.2}V_{0.5}Cr_{0.5}Ni_{0.8}$ electrode after 87 cycles shows that the oxygen content on the surface was still low and Ni content was high. From the results, the surface condition of $Ti_{0.8}Zr_{0.2}V_{0.5}Mn_{0.5}Ni_{0.8}$ alloy is expected to be inferior in electric conductivity as well as catalytic activity on the charge transfer reaction because TiO_2 film is passive and semi-conductive. Moreover, charge transfer through such a thick oxide layer is also expected to be difficult because metallic Ni is depleted on the surface due to the dense Ti-oxide film. Comparing with that of $Ti_{0.8}Zr_{0.2}V_{0.5}Mn_{0.5}Ni_{0.8}$ alloy, we found that the oxidation of the surface in $Ti_{0.8}Zr_{0.2}V_{0.5}Cr_{0.5}Ni_{0.8}$ electrode was largely inhibited and metallic Ni is enriched in the surface, suggesting it was still an active surface. The surface of the $Ti_{0.8}Zr_{0.2}V_{0.5}Cr_{0.5}Ni_{0.8}$ electrode is very stable because Cr element is more stable in the electrolyte and has an effect on restraining the dissolution of vanadium. Although the alloys with high Cr content demonstrate good durability, their discharge capacities were decreased too much. Further work is necessary to improve the discharge capacity and cycle life together by optimizing the ratio of alloying element.

4. Conclusions

(1) Ti-Mn-Ni based alloys show poor cyclic durability in the electrolyte because of the poor corrosion resistance of their surfaces caused by the fast growth of TiO_2 film and quick dissolution of Mn and V.

(2) The cycle life can be improved by Cr substitution for Mn, because of increased corrosion resistance of the surface and decreased pulverization rate of alloy particles. However the discharge capacity decreases with the increase of Cr amount. Further work is necessary to improve the discharge capacity and cycle life together by optimizing the ratio of alloying element.

Acknowledgements

The author gratefully acknowledges the partial financial support of the Hydrogen Energy Research Center at KAIST, Korea.

References

1. [1] Han-Ho Lee, Ki-Young Lee and Jai-Young Lee, " Degradation mechanism of Ti-Zr-V-Mn-Ni metal hydride electrodes ", J. of Alloys and Compounds, 260 (1997) 201-207

[2] H.Miyamura, T. Sakai, N. Kuriyama, K. Oguro, I. Uehara and H. Ishikawa, " Hydrogen absorption and electrode characteristics of (Ti,Zr)-(Ni,V,X)$_{2+a}$ alloys " , Z. Phys. Chem. 183(1994) 347

[3] T.Sakai, K.Oguro, H.Miyamura, N.Kuriyama, and H.Isikawa, " Some factors affecting the cycle life of electordes of hydrogen batteries", J.Less-Common Metals 161(1990)193

Table 1. The hydrogenation characteristics and structure of the $Ti_{0.8}Zr_{0.2}V_{0.5}Mn_{0.5-x}Cr_xNi_{0.8}$ (x=0~0.5) alloy

Cr Content	Storage capacity (wt.%)	Structure	2nd phase
0	1.667	C14 (a= 4.930 Å, C=8.024 Å)	-
0.1	1.5897	C14 (a= 4.938 Å, C=8.036 Å)	-
0.2	1.502	C14(a= 4.954 Å, C=8.068 Å)	-
0.3	1.483	TiNi + C14(a= 4.960 Å, C=8.068 Å)	BCC (a= 3.033 Å)
0.4	1.426	TiNi + C14 (a= 2.968 Å)	BCC (a= 3.045 Å)
0.5	1.351	TiNi (a= 2.969 Å)	BCC(a= 3.058 Å)

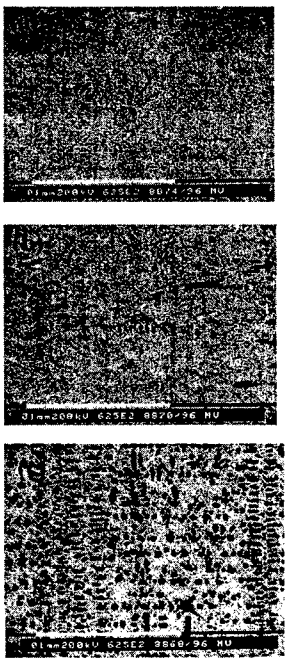
Table.2 The dissolution amount of the each element of the $Ti_{0.8}Zr_{0.2}V_{0.5}Mn_{0.5-x}Cr_xNi_{0.8}$ (x=0~0.5) alloy

(μ g/ml)

	X=0	X=0.1	X=0.2	X=0.3	X=0.5
Vanadium	35.5	16.9	0	5.6	8.4
Zirconium	7	6.2	2.2	2.2	2.6

** Ti,Mn,Cr, Ni are not detected.*

Fig.1 The SEM images of the $Ti_{0.8}Zr_{0.2}V_{0.5}Mn_{0.5-x}Cr_xNi_{0.8}$ (x=0~0.5) alloy (a) x=0, (b) x=0.3, (c) x=0.5



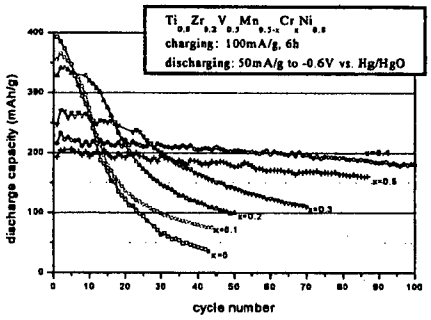


Fig.2 The discharge capacity vs cycle of $Ti_{0.8}Zr_{0.2}V_{0.5}Mn_{0.5-x}Cr_xNi_{0.8}$ (x=0~0.5) alloy

Fig.3 The mechanical strength of the $Ti_{0.8}Zr_{0.2}V_{0.5}Mn_{0.5-x}Cr_xNi_{0.8}$ (x=0~0.5) alloy

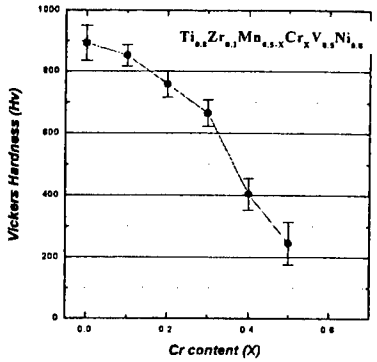


Fig.4 The charge-discharge curves of the $Ti_{0.8}Zr_{0.2}V_{0.5}Mn_{0.5-x}Cr_xNi_{0.8}$ (x=0~0.5) alloy (a) x=0, (b)x=0.5

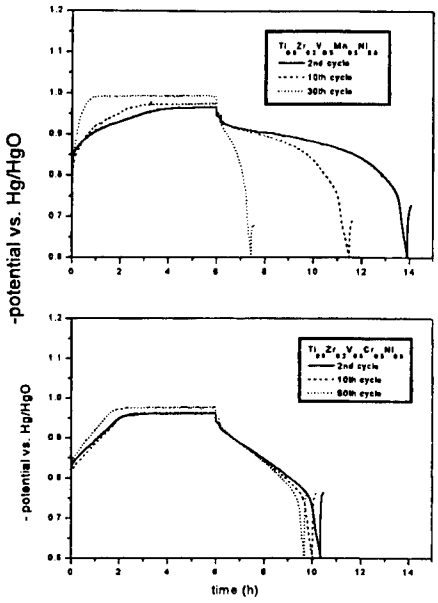


Fig.5 The exchange current density vs cycle of the $Ti_{0.8}Zr_{0.2}V_{0.5}Mn_{0.5-x}Cr_xNi_{0.8}$ (x=0~0.5) alloy

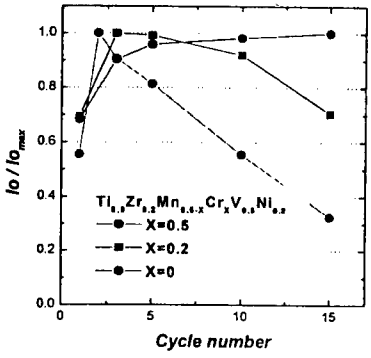


Fig.6 The impedance spectra of the $Ti_{0.8}Zr_{0.2}V_{0.5}Mn_{0.5-x}Cr_xNi_{0.8}$ (x=0~0.5) alloy (a) x=0, (b)x=0.5

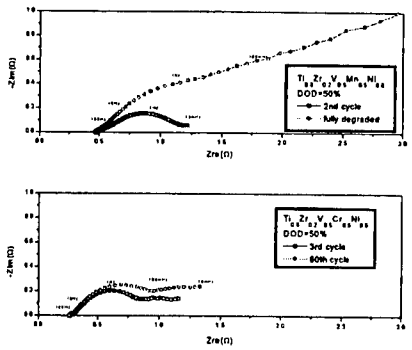
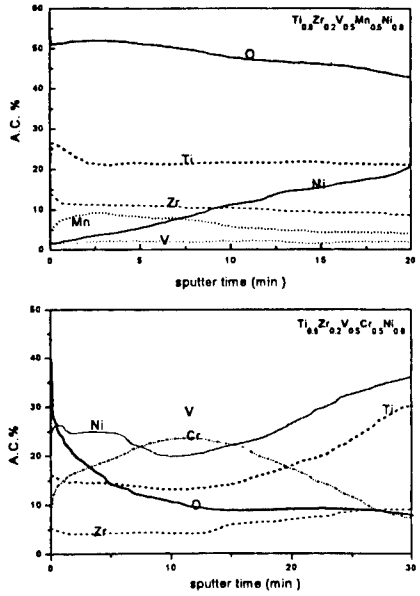


Fig.7 The AES depth profiles of the $Ti_{0.8}Zr_{0.2}V_{0.5}Mn_{0.5-x}Cr_xNi_{0.8}$ (x=0~0.5) alloy (a) x=0, (b)x=0.5



MAGNESIUM SCIENCE, TECHNOLOGY AND APPLICATIONS

E. Aghion[1], D.Eliezer[2], and F.H. (Sam) Froes[3]

[1]Dead Sea Works, Ltd., Potash House, PO Box 75, Beer-Sheva 84100, Israel.
[2]Ben-Gurion University of the Negev, PO Box 653, Beer-Sheva 84105, Israel.
[3]Institute for Materials and Advanced Processes, University of Idaho, Moscow, ID 83844-3026.

Abstract

The science , technology and applications of magnesium alloys are reviewed. The very low density of magnesium in combination with excellent castability is leading to increased use, despite poor galvanic corrosion resistance and a higher cost than aluminum, especially in automotive applications. Even further expansion of the magnesium market should come from an expanded design base, a better understanding of the scientific "under-pinning" of magnesium alloys, and development of cost-affordable cast and wrought products.

The Third Pacific Rim International Conference on
Advanced Materials and Processing (PRICM 3)
Edited by M.A. Imam, R. DeNale, S. Hanada,
Z. Zhong and D.N. Lee
The Minerals, Metals & Materials Society, 1998

Introduction

Magnesium is the lightest of all the commonly used metals and is thus very attractive for applications in transportation (1-4). It also has a number of other desirable features including good ductility, better damping characteristics than aluminum and excellent castability. However there are some negative features including high reactivity in the molten state, inferior fatigue and creep compared to aluminum and galvanic corrosion resistance which has been described as "awful" (2), a limited supply base, a lack of fundamental knowledge of the behavior of magnesium alloys, and a cost which is about twice that of aluminum (3). However with the dramatically increased emphasis on weight reduction magnesium is receiving a lot of attention as a material for use on next generation automobiles (2) especially using a casting approach. Magnesium is produced from sea water, brines and magnesium-bearing minerals which gives it a virtually unlimited supply of ore reserves, for example it has been estimated that at current world use levels there is enough magnesium in the Dead Sea for at least 22,000 years.

Magnesium metal for structural applications is processed into casting (die, sand, permanent mold and investment), extrusions, forgings, impact extrusions and flat rolled products. Castings far exceed cast and wrought products for reasons which will be discussed later and die castings account for 70% of the castings shipped; with demand for automobile parts produced by this technique (about 85% of the die castings total) projected to reach greater than 100,000 metric tons world-wide by the turn of the century. Magnesium can be joined by riveting or welding and can be machined faster, and has the best strength-to-density ratio of any of the commonly used structural metals.

Total magnesium shipments, by category, are shown for the first half of 1996 and 1997 in Table I with internal Chinese and Former Soviet Union consumption (≈ 20,000 tons each) not included. To put magnesium into perspective 1997 estimated shipments of the light metals (Al, Mg, and Ti) and steel are shown in Table II.

Table I. MAGNESIUM SHIPMENTS (METRIC TONS)*

Category	1st Half '96	1st Half '97
Al Alloying	72.3	72.3
Nodular Fe/ Desulphurization	27.4	29.7
Die Casting	33.1	44.6
Wrought Products	2.2	1.7
Others	Bal.	Bal.
Total	**150.6**	**161.9**

*Primary Mg, World Totals, x 10^3, Courtesy IMA.

Table II. METAL SHIPMENTS (METRIC TONS)* 1997 ESTIMATES

Metal	Estimate x10^3
Titanium	50
Magnesium	320
Aluminum	25,000
Steel	700,000

* World Totals, x 10^3, Courtesy B. Clow, IMA.

In this paper we will review the science, technology and applications of magnesium based materials with emphasis on new developments, and make some projections for the future.

Science

General Behavior

Magnesium has a hexagonal crystal structure, and its alloying behavior because of a favorable size factor (atomic diameter 0.320nm), is characterized by an ability to form a solid solution with a variety of elements particularly those which are of commercial importance including Al, Zn, Li, Ce, Ag, Zr, and Th.

Cast alloys predominate over wrought products, in part because of difficulties in fabricating mill product forms (Mg alloys are hot worked above 250° C to allow additional slip systems to operate). The hexagonal close packed structure and a large and variable grain size have led to less than optimum mechanical properties. Development of alloys to compete more effectively with wrought aluminum alloys has suffered from a lack of detailed knowledge of the physical metallurgy of magnesium alloys.

The corrosion behavior of magnesium alloys is dictated by the electrode potential which is high in the electrochemical series. The $Mg(OH)_2$ film which forms, while offering protection in rural environments, is non-adhering. Galvanic corrosion necessitates protection when there is contact with other metals (1-4).

Technology

Extraction

The two principal extraction processes in use today (1) are (a) electrolysis of molten magnesium chloride and (b) thermal reduction of magnesium oxide. Both processes are used to produce significant quantities of magnesium, although currently the majority of production on a worldwide scale is by the electrolytic method.

Production

Casting Most magnesium alloy components are produced via high pressure die casting. Cold chamber machines are used for the largest castings and molten shot weights of >10 Kg can now be injected in less than 100 ms at pressures that may be as high as 150 MPa (1-4). Hot chamber machines are used for most applications and are more competitive for smaller sizes owing to the shorter cycle times that are obtainable. Magnesium alloys offer particular advantages for both these processes (1-4): (a) most alloys show high fluidity which allows casting of intricate and thin walled parts (b) magnesium has a low specific heat per unit volume compared with other metals, thereby allowing faster cycle times and reduce die wear (c) high gate pressures can be achieved at moderate pressures because of the low density of magnesium (d) iron from the dies has very low solubility in magnesium alloys which is beneficial because it reduces any tendency to sticking.

Wrought Alloys Production of wrought magnesium alloys products is usually carried out by hot working, mainly by extrusion, rolling and press forging at temperatures in the range 300-500°C (1).

Applications

The four principal uses of magnesium are shown in Table I, and can be summarized as alloying with aluminum, iron and steel processing, as a structural metal, and electrochemical and other uses. In the following text we will only consider structural uses.

Aerospace

Magnesium is employed extensively in aircraft engines, airframes, including helicopter components, and landing wheels (2-4). The main factors dictating the use of magnesium have been strength/density ratio in casting and stiffness/density ratio in the wrought forms, combined, as required, with factors such as good elevated temperature, fatigue and impact properties, always with good machinability.

Strength and rigidity at minimum weight, coupled with ease of fabrication are important for missile and space applications. However the designer of missiles and space probes needs other properties in his materials of constructions. Conditions in space flight are rigorous, involving extremes of temperature from aerodynamic heating, sudden immersion in shadows, and proximity of some components to liquefied fuels: ozone and free radicals in the upper atmosphere: bombardment by short wave electromagnetic radiation, high energy particles and micrometeorites: vacuum down to 10^{-11} mmHg.

Cars and light trucks

Use of magnesium in automobiles despite its high cost compared to competing metals (conventional steel and aluminum) is justified on the basis of component integration and the near-net shape castability. The most promising applications for magnesium are those where aluminum or plastic are not desirable substitutes for heavier materials such as steel; i.e. substitution for either of these light-weight materials in existing applications is unlikely (2). This is borne out by the 1997 model cars in North America in which increased use of magnesium has occurred largely at the expense of steel. The use of magnesium in the new models ranges from about 1.4-9kg per vehicle giving an average of 2.9 kg per family car, about 16% more than for 1966 models.

The dramatic benefit that reduced automobile weight can give in terms of improved fuel consumption is shown in Fig. 1 (1-4). Hence the great interest in magnesium on Partnership for a New Generation of Vehicles (PNGV) automobiles such as the Ford stretched Mondeo/Contour P2000 which is expected to achieve nearly 80mpg (3.4L/100km) (2). In addition to new power train requirements, this aggressive fuel efficiency goal requires that the vehicles body weight and chassis must be reduced by nearly 50% and the total mass be reduced some 30% or 450kg (from 1450kg down to 950kg) (2). This has led to extensive evaluation of the potential use of magnesium components to levels in excess of 103kg (10% magnesium) from a present 2.6kg; a magnesium intensive vehicle (2).

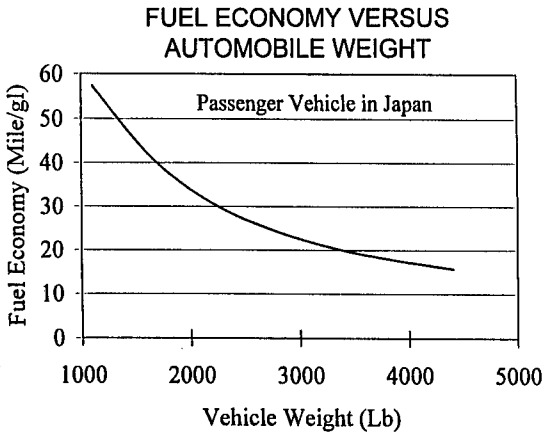


Fig. 1. Fuel Economy versus Vehicle Weight (1).

The magnesium industry has made great efforts to educate the automotive industry on the benefits of utilizing magnesium to reduce vehicle weight, cost, and/or complexity. Applications for magnesium in automobiles, using the die casting approach, has been in components such as instrument panels, steering wheels, steering columns and seat risers which take advantage of magnesium's high strength-to-density ratio, excellent ductility combined with attractive energy absorbing characteristics. Typical applications for magnesium in automobiles are shown in Figs. 2 and 3.



Fig. 2. Diecast Magnesium alloy seat frame (4).

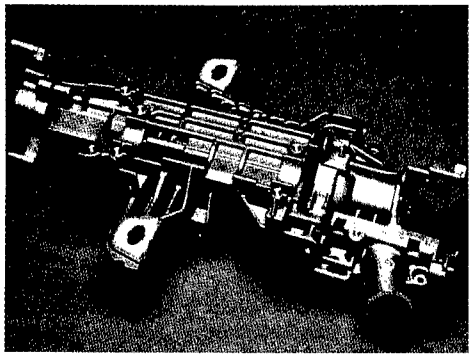


Fig.3. Steering column assembly composed of three magnesium diecastings (4).

Nuclear Energy Industry

Magnesium sees use in nuclear energy industry applications because of its low tendency to absorb neutrons, resistance to alloying with uranium, adequate resistance to carbon dioxide, and good thermal conductivity.

Appliances and sporting goods

The trend has been for an increase in the use of magnesium die castings and examples are computer housings and mobile telephone cases where lightness, suitability for thin wall casting and the characteristic of electromagnetic shielding are particular advantages.

Conclusions and Future Trends

The science, technology and applications of magnesium and its alloys has been reviewed. The very low density of magnesium, in combination with other attractive features such as castability is leading to an expanded market especially for automobiles. The pressure, particularly in the USA to decrease the weight of automobiles in programs such as PNGV could see up to 103kg of magnesium in vehicles such as the Ford P2000. Increased use can come from an expanded design base, better understanding of the fundamentals of magnesium behavior, and development of cost-affordable cast and wrought alloys.

References

1. D. Eliezer, E. Aghion, and F.H. Froes, Dead Sea Magnesium Conference, Nov. '97 and to appear in the Proceedings.

2. Gerald Cole, "Magnesium Applications in Ford's PNGV" Mondeo, 24.

3. Milton Nurse, MBM Feb. 1997, 52.

4. I.J. Polmear, Materials Science and Technology, Vol. 10, (1994), pp. 1-14.

5. F.H. Froes, Light Metal Age, Feb. 1998, 54.

ON THE MORPHOLOGY AND CHARACTERISTICS OF Mn-BEARING DISPERSOIDS IN AlMgSi ALLOYS

I. G. Moon[1], A. Shan[1,2], J. E. Yoo,[1] H. S. Ko,[1] H. S. Kim[1], J. Y. Chang[1] and J. W. Park[1]

[1] Division of Metals, Korea Institute of Science and Technology, Cheongryang P.O.Box 131, Seoul, Korea

[2] Department of Materials Science, Shanghai Jiao Tong University, 200030, Shanghai, P. R. China

Abstract

Mn bearing dispersoids play a very important role in recrystallization and solution-aging process in AlMgSi alloys. Plenty of researches have been made on the effect of the dispersoids on recrystallization and quenching sensitivity in these alloys But study on the nature of these dispersoids is very limited. With an idea to understand the nature of these dispersoids and hence to control their size and distribution, this study was performed. It was found that in the as homogenized state, the morphology of the dispersoids changes with nominal Mn content while their crystal structures are same. However in the extruded and solutionized alloys, the size and crystal structure of the dispersoids are dependent on their practical Mn/Fe ratio.

The Third Pacific Rim International Conference on Advanced Materials and Processing (PRICM 3)
Edited by M.A. Imam, R. DeNale, S. Hanada, Z. Zhong and D.N. Lee
The Minerals, Metals & Materials Society, 1998

Introduction

Mn bearing dispersoids in AlMgSi alloys are introduced for grain refinement during recrystallization for their pinning effect on grain boundaries. While many studies have been performed on the effect of these dispersoids on microstructures, research on the morphology, composition and crystal structure of these dispersoids are quite limited. In high purity AlMgSi alloys it is said that these dispersoids are ternary phase which can be described as $Al_{12}Mn_3Si$[1]. Recently, in 6013 alloys, Donnadieu et al [2] reported that these dispersoids may contain some iron with a Mn/Fe (in atomic ratio) ratio more than 3. Since iron virtually exists in all commercial alloys, it is clear that the dispersoids in practical AlMgSi alloys are quaternary phase which contain Al, Mn, Fe and Si.

For the crystal structure of this quaternary phase, it is suggested as isomorphous to α-AlMnSi with a Pm3 space group [3] and α-AlFeSi with an Im3 space group[4]. The formula can be written as α-Al(Mn,Fe)Si [5]. The crystal structure could be determined from the ratio of Mn and Fe. But the critical ratio has not been decided yet [5,6]. However, in an effort to find the effect of Mn induced ordering in this phase Donnadieu et al [5] imply that this ratio may fall between 1 and 3.

In this paper we will report our study on the effect of Mn content on the morphology composition and crystal structure of dispersoids.

Experimental procedure

Alloys for research, with compositions of Al-0.50Mg-0.65Si-0.12Fe and 0.1, 0.2, 0.5Mn respectively, were made by air melting and chill cast method using commercial facilities. (here after call 0.1Mn, 0.2Mn and 0.5Mn alloys). One group of specimens were cut from these chill cast billets and homogenized at 560C for 8 hours and water quenched. Another group of specimens were taken from 0.2Mn extruded plates. These plates were solutionized at 470°C for 30 minutes and then water quenched. The composition and crystal structure analysis of the dispersoids were performed on a transmission electron microscope(TEM) (Philips CM-30) equipped with an energy-dispersive x-ray spectrometer (EDS) (EDAX9900). Thin foils for TEM observation were made by standard chemical method.

The atomic ratio of Mn/Fe (where Mn and Fe contents are in at.%) was estimated through a standardless quantification of spectra. When the dispersoids have a very small size, the spectra may contain contribution from surrounding matrix. But considering the very low contents of Mn and Fe in matrix, the Mn/Fe ratio will not be affected significantly by those contribution from matrix. This was also suggested by literature [2].

For crystal structure analysis, we use SAD(selected area diffraction) pattern together with CBED pattern for quick analyzing. By CBED(convergent beam electron diffraction) pattern, primitive cell volume can be calculated. This volume data can be used for pre-identification of crystal structure without indexing the SAD patterns[7].

Results and Discussion

Mn effect in as homogenized specimens. Dispersoids can be revealed clearly under optical microscope. But corrosion effect makes them look bigger. Figure 1. (a) (b) (c) shows the effect of Mn nominal content on the morphology of the dispersoid. From these photos it can be seen that at lower Mn content, dispersoids density is some lower compared to the higher Mn content alloy. In all three alloys, dispersoids are mostly in round shape. However, with increasing Mn content , some rod shaped dispersoids appeared. In the 0.5Mn alloy, some rod dispersoids have very big size compared to the round dispersoids.

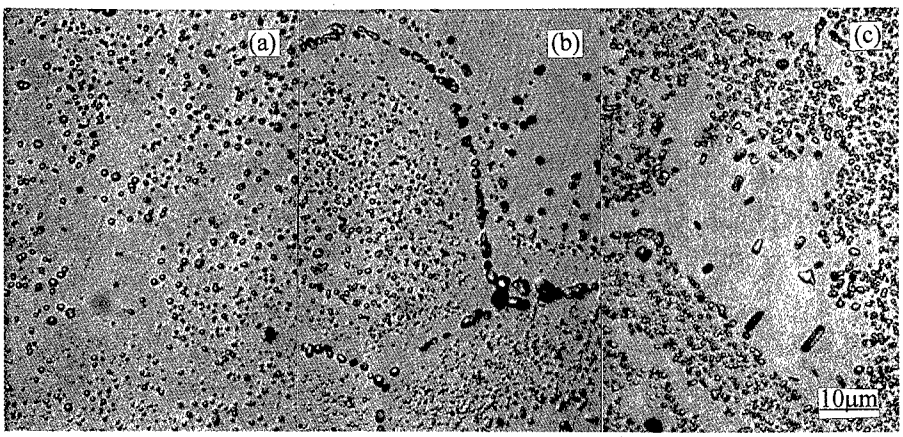


Fig.1 Dispersoid morphology under optical microscope, (a) 0.1Mn, (b) 0.2Mn, (c) 0.5Mn, homogenized and water quenched

By TEM, it is very clear that the dispersoids have much smaller size than that shown under optical microscope. They are not uniform in size. This was shown in figure 2. EDS analysis

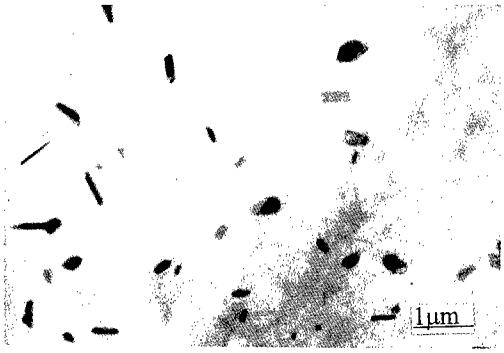


Figure.2. Dispersoids in 0.5Mn alloy, homogenized and water quenched

show that they contain Al, Mn, Fe, Si, with a variable Mn/Fe ratio (in atomic ratio) but all are above 2. No difference was found in the three alloys. These results are then in agreement with Donnadieu et al.'s result, with the critical Mn/Fe ratio slightly lower (They reported that all

dispersoids have a Mn/Fe ratio above three). This might be caused by alloy composition difference or by the EDS analyzer.

SAD and CBED analysis revealed that all these dispersoids have a simple cubic crystal structure with a=12.54 angstrom despite of their different morphology and composition. Figure 3. (a) (b) shows a rod shaped dispersoids and its CBED pattern. This dispersoid was found in 0.5Mn alloy. It also has a simple cubic crystal structure with a=12.54 angstrom.

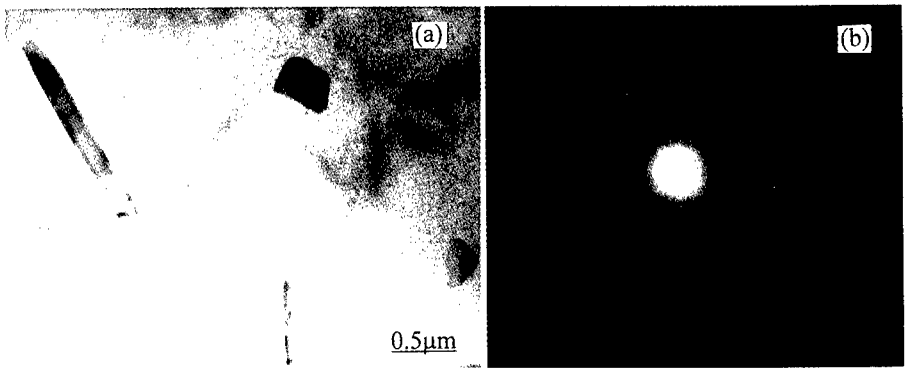


Fig. 3. (a) Rod shaped dispersoids and (b) its CBED pattern, in 0.5Mn alloy. Homogenized and water quenched

In 0.2Mn alloy after extrusion and solution treatment. Fig.4. shows the typical morphology of dispersoids in 0.2Mn alloy. This alloy was extruded and solutionized at 470°C for 30 minutes followed by water quenching. From this figure it can be seen that most dispersoids are round, but there are also rod shaped dispersoids. The morphology of the round shaped dispersoids are identical to that reported by Donnadiu et al in 6013 alloy. But they did not mention the rod shaped dispersoids. For comparison with earlier work, here we concern the round shaped dispersoids which occupy the majority of all dispersoids. The size of these dispersoids covers a range from 0.03 to 0.5 μm. The EDS data shows that all dispersoids contain Al, Mn, Fe, and Si

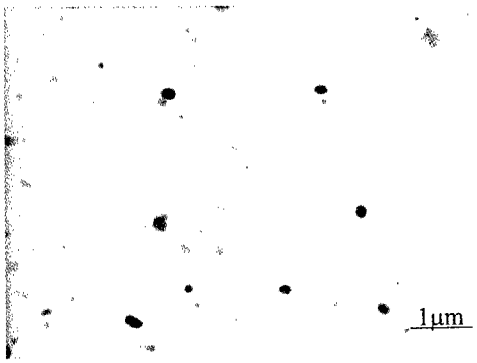


Fig. 4. Dispersoids in 0.2Mn alloy after extrusion and solution treatment

elements. Mn/Fe ratio was calculated from EDS data, but for dispersoids with size below 0.08 micrometer contribution from dispersoids is too weak to be analyzed. Figure 5. shows the distribution of Mn/Fe ratio *versus* size of dispersoids. From this figure a trend that the size

increases with the decrease of Mn/Fe ratio is quite apparent. It was reported[2, 8] that in 6013 alloys, all dispersoids (with size between 0.1 and 0.3μm) have a Mn/Fe ratio of more than 3 regardless of the nominal composition of the alloys. And for constituent particles (their size generally bigger than 1μm), they have a Mn/Fe ratio of a range from 0.2 to 1 depending on the nominal Mn/Fe ratio of the alloys. In our case, considering the small size of the particles studied here they should be dispersoids which were formed during homogenization. In Figure 5. the Mn/Fe ratio is in a range from about 0.7 to about 7 and the size of dispersoids is in a range of 0.08 to 0.5 micrometer. So it covers a more wider range than that of the dispersoids studied by Donnadieu et al[2]. The reason why dispersoid size increases with the decrease of Mn/Fe ratio is not clear now but it may be suggested that when these dispersoids were formed under different local surroundings, e.g. different local iron and manganese content, they may grow to different sizes.

SAD pattern analysis shows that the dispersoids have two kinds of crystal structures, one is B.C.C, the other is simple cubic. However, the unit cell parameters of the two crystals are the same. By SAD pattern it can be calculated to be about 12.54 angstrom.

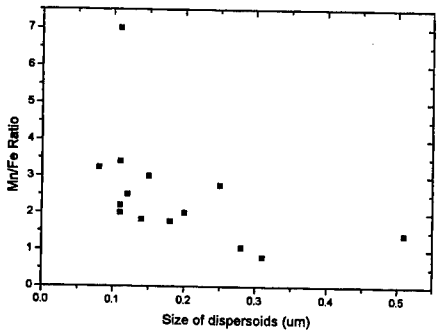


Fig. 5. Mn/Fe ratio versus size of dispersoids in 0.2Mn alloy after extrusion and solution treatment

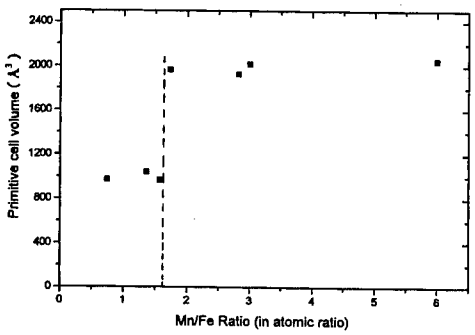


Fig. 6. Primitive cell volume versus Mn/Fe ratio of dispersoids in 0.2Mn alloy after extrusion and solution treatment

Using the method developed by Kim et al[7], with CBED pattern, the primitive cell volume of dispersoids with different Mn/Fe ratio was calculated. Calculated results were shown in Figure 6. From this figure it can be seen that the dispersoids with high Mn/Fe ratio have a primitive cell volume of around 2000Å^3, and that have lower Mn/Fe ratio have a primitive cell volume of around 1000 Å^3. A critical Mn/Fe ratio of about 1.6 can be decided by the figure. Although

there are no report on the primitive cell volume of these dispersoids, according to space group and reported data [2, 6] on the unit cell parameter (from 1.25 to 1.27nm) the primitive cell volume of Im3 and Pm3 crystal structure can be calculated to be 977-1024Å^3 and 1953-2048Å^3 respectively. These results are then in good agreement with present study.

Conclusions

1. Nominal Mn content can affect the morphology of the dispersoids. With high Mn content, the number of rod shaped dispersoids increase while some rod dispersoids can be very large.
2. In the extruded and solutionized 0.2Mn alloy, the size and crystal structure of the dispersoids depend on their real Mn/Fe ratio. The higher the Mn/Fe ratio, the smaller the size of the dispersoids. And with high Mn/Fe ratio, the crystal structure is a simple cubic structure and with lower Mn/Fe ratio it is a BCC structure. A critical Mn/Fe ratio of about 1.6 was found in the studied heat treatment state.

Acknowledgment

A. Shan thanks to the KOSEF and KOFST for financial support under Brain Pool Program.

References

1. J.M. Dowling and J.W. Martin, "The influence of Mn additions on the deformation behaviour of an Al-Mg-Si Alloy" *Acta Metall.* 24 (1976) 1147-1153
2. P Donnadieu, et al., "Alpha-phase particles in 6XXX aluminum alloys"(Paper presented at *the 4th International Conference on Aluminum Alloys,* Atlanta, U.S.A. 11-14, September, 1994), 668.
3. M. Cooper and K. Robinson, "The crystal structure of the ternary alloy α(AlMnSi)" *Acta Cryst.*, 20 (1966), 614-616.
4. M. Cooper, "The crystal structure of the ternary alloy α(AlFeSi)" *Acta Cryst.*, *Acta Cryst.*, 23 (1967), 1106-1108.
5. P. Donnadieu, G. Lapasset, T. H. Sanders Jr, "Manganese induced ordering in the α-(Al-Mn-Fe-Si) approximant phase" *Philos. Mag. Lett.* 70 (1994), 319-326.
6. Z. H. Lai, and C.H. Li, "The order-disorder transformation of C-Al(Mn,Fe)Si phase" *Scripta Metall. Mater.* 29 (1993), 895-900.
7. G.H. Kim, H.S. Kim and D.W. Kum, "Simple procedure of phase identification using convergent beam electron diffraction," *Microscopy Research and Technique*, 33(1996), 510-515.
8. Jr, R. A. Jeniski , B. Thanaboonsombut, and T. H. Sanders Jr "The effect of iron and manganese on the recrystallization behavior of hot-rolled and solution-heat-treated aluminum alloy 6013" *Metall. and Mater.Trans.* 27A,(1996) 19-27.

EFFECT OF QUENCHING RATE ON THE PROPERTIES OF A NEW Al-Zn-Mg-Cu ALLOY

Yi-Lei Wu[1], Chenggong Li[1], F.H.Froes[2], Alex Alvarez[2], John Liu[3]

Institute of Aeronautical Materials, Beijing (BIAM), P.R.C.[1]
Institute for Materials and Advanced Processes (IMAP),
University of Idaho, Moscow, ID83844-3026, USA [2]
Alcoa Technical Center (ATC), Alcoa, PA15069, USA [3]

Abstract

Using Transmission Electron Microscopy (TEM), the effects of quenching rate on the microstructures of a new super high strength Al-Zn-Mg-Cu alloy class (C912B, C912C, C912N and C912S) have been correlated with their tensile properties and stress corrosion cracking (SCC) behavior. The changes in SCC resistance of the C912 alloys studied in this paper correlate very well with the grain boundary precipitate shape and size, and the loss in strength is the result of the heterogeneously nucleated precipitates in the matrix at lower quenching rate. In general, the C912 alloy class in the peak aged condition have less sensitivity to quench rate than other 7000 series alloys, especially the alloys C912N and C912C. The C912 alloys are suitable for thicker gauge plate and forging exhibiting super high strength and good corrosion resistance.

The Third Pacific Rim International Conference on
Advanced Materials and Processing (PRICM 3)
Edited by M.A. Imam, R. DeNale, S. Hanada,
Z. Zhong and D.N. Lee
The Minerals, Metals & Materials Society, 1998

Introduction

For aluminum alloys, the highest strengths attainable and the best combinations of strength and toughness are those associated with the most rapid quenching rates. Resistance to corrosion and to SCC are generally improved by rapid quenching. However, both the degree of part warpage or distortion that occurs during quenching and the magnitude of residual stresses that develop in the product tend to increase with the rate of cooling. In addition, the maximum attainable quench rate decreases as the thickness of the product increases.

The new super high strength IM/Al-Zn-Mg-Cu alloy C912 is developed by the Beijing Institute of Aeronautical Materials (BIAM). Its tensile and compressive strengths are higher than the traditional 7000 aluminum alloys, such as the 7178 and 7075 alloys, and are similar to the new Alcoa aluminum 7055 and the Russian alloy B96, which have the highest strengths of the commercial IM/Al-Zn-Mg-Cu alloys. With proper microalloying and heat treatment, the C912 alloy can exhibit very high strength and good SCC resistance. In this paper, for the use of the C912 alloys in thick parts which have widely use in aircraft, a definition of the relationships between quenching rate, strength and SCC resistance was studied.

Experimental Procedure

The alloys investigated belong to the 7000 series of aluminum alloys, and include four alloys — baseline C912 alloy (C912B), C912 alloy with Ce addition (C912C), C912 alloy with Ni addition (C912N), and C912 alloy with Sc addition (C912S). The C912 alloys have the norminal composition in wt pct of 8.6Zn, 2.6Mg, 2.4Cu, ≤0.05Fe, ≤0.05Si, and balance aluminum. The Ce, Ni, Sc levels are set at 0.1wt.%, 0.1wt.% and 0.2wt.%, respectively. The C912B,C,N and S alloys were melted in an electrical resistance furnace using a 5Kg crucible, and cast in a water cooled mold. Ø10mm extruded bars were obtained by using a 400t extrusion press. Homogenization of cast ingots was carried out at 450°C for 24 hours in a air furnace, followed by furnace cooling to 200°C, and then air cooling. Solution heat treatment temperature was set at 455°C to avoid nonequilibrium eutectic melting, and the solution time was set at 85 minutes. Cold water and liquid nitrogen were chosen as the quenching media in the studies to get the required quench rate. The average cooling rate in cold water was greater than 150°C/s and less than 15°C/s for liquid nitrogen. The artificial aging treatment (CS1) was carried out at 121°C for 24 hours.

In accordance with the Chinese GB228-87 specification (equivalent to ASTM B557-79), 5mm round tension test specimens with a 25mm gage length taken from the Ø10mm extruded bars were used to measure the UTS, YS and El of the alloys. According to the Chinese HB5254-83 specification (equivalent to ASTM G49-76), tension test specimens were used to investigate the susceptibility to stress-corrosion cracking. As smaller cross-section specimens have a greater sensitivity to the initiation of stress-corrosion cracking, and can give results more rapidly, this type of test is more suitable than C-ring test to contrast the SCC susceptibility of different alloys or one alloy with different tempers. Specimens were tested by immersing in 3% NaCl + 0.5%H_2O_2 solution at 35°C. According to the HB5254-83 specification, tension tests of replicate specimens exposed with no applied stress, in conjunction with stressed specimens (exposed for the same times), were used to provide the (1-α) parameter for stress-corrosion susceptibility evaluation:

$$1-\alpha = (\sigma_{b1} - \times\times\%\sigma_{0.2}) / (\sigma_b - \times\times\%\sigma_{0.2})$$

where:

σ_{b1} = ultimate tensile strength of the exposed specimens with no applied stress (MPa)

$\times\times\%\sigma_{0.2}$ = applied stress on the specimens (MPa)

σ_b = ultimate tensile strength of the unexposed specimens (MPa)

$\sigma_{0.2}$ = yield tensile strength of the unexposed specimens (MPa)

If σ_{b1} is greater than the applied stress $\times\times\%\sigma_{0.2}$, the sample has a SCC tendency. The parameter (1-α) means the percentage of SCC fracture in the whole fracture:

1-α = 0 means that the specimen is not susceptible to SCC

1-α = 1 means that the specimen is very susceptible to SCC

The study of grain boundary precipitates, matrix precipitates after different heat treatments was performed with H-800 transmission electron microscope (TEM) at 200KV. Samples for TEM analysis were cut in the form of thin slices, 0.25mm thick, using an electric spark erosion machine. After mechanical polishing, the final thinning was achieved by means of a twin-jet electropolishing unit, to further reduce the thickness as well as to remove the damage due to spark machining. For this operation, a solution of 30% HNO_3 + 70% CH_3OH was used, and the electrical conditions were -23°C and 40V/0.4A.

Results and Discussion

In the present study, two quenching media were used, cold water (CW), and liquid nitrogen (LN). The cooling rate in the LN is very low (<15°C/s) because a stable vapor film forms around the part during quenching.

Table I lists the tensile properties of the C912 alloys quenched in CW and LN. The strength losses of the C912C-CS1 and C912N-CS1 alloys are smaller than that of the C912B-CS1 and C912S-CS1 alloys.

Table I Effect of Quench Medium on the Tensile Properties of the C912 Alloys

Alloy/Temper	UTS, (MPa) LN/CW*	Δ** %	YS, (MPa) LN/CW	Δ %	El, (%) LN/CW	Δ %
C912B-CS1	634/672	5.6	588/649	9.4	8.7/12.4	29.8
C912C-CS1	632/644	1.9	583/618	5.7	11.3/14.0	19.3
C912N-CS1	664/679	2.2	627/660	5.0	8.4/12.2	31.1
C912S-CS1	676/715	5.4	620/689	10.0	8.5/11.8	28.8

* Property loss percentage after quenching into nitrogen compared to that obtained after quenching into cold water

** LN — liquid nitrogen, CW — cold water

Although there is no obvious microstructure differences between the C912B and C912C,N,S alloys in their normal CS1 temper condition (quenched into cold water), it is easy to distinguish these four alloys after they were quenched into liquid nitrogen. Figure 1a,d,e and f show the microstructures of the C912B,C,N and S alloys quenched into liquid nitrogen and then natural aged (NA) for two months, and Figures 1b and 1c show their microstructures quenched into LN and CN and then artificially aged (CS1) at 121°C/24h for contrast.

For the C912B alloy, there are many needle-like phases in the grain boundaries (Fig.1a), and a lot of coarse precipitates exist in the grain (Fig.1b). The same situation also exists in the C912S alloy (Fig.1f). For the C912C and N alloys, the situation is quite different. Only some coarse precipitates exist in the grain (Fig.1d,1e), and less needle-like phases form in the grain boundaries, only coarsened η precipitates.

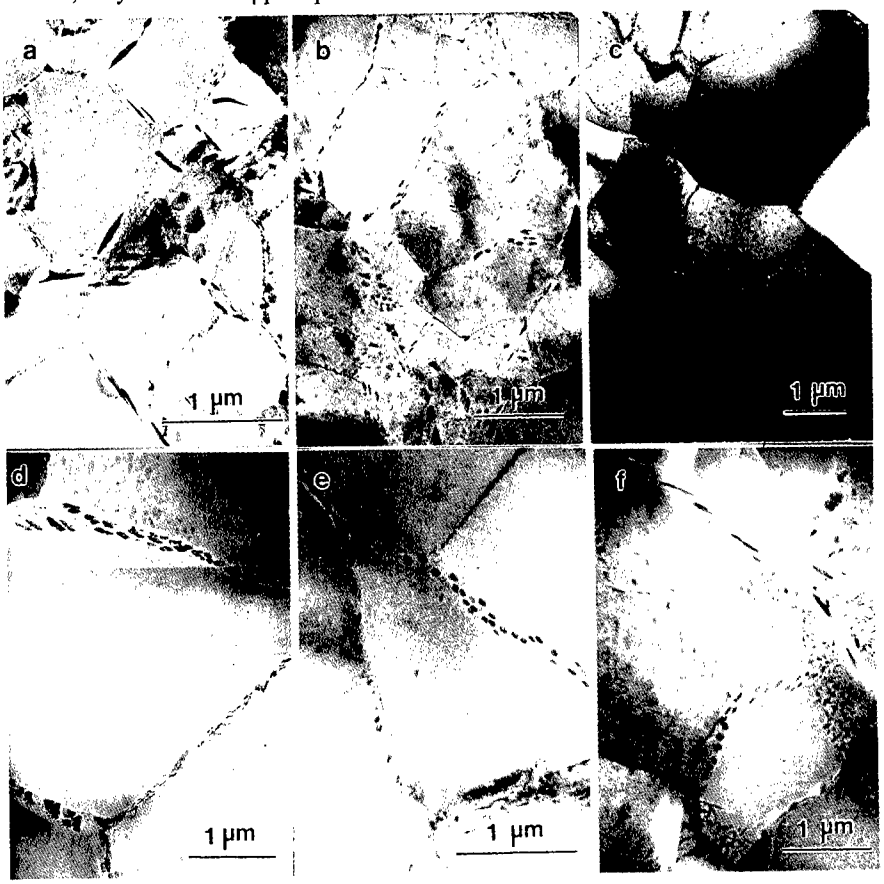


Figure 1: TEM micrographs of the C912 alloys with different heat treatment
a. C912B-NA (LN); b. C912B-CS1 (LN); c. C912B-CS1 (CW)
d. C912C-NA (LN); e. C912N-NA (LN); f. C912S-NA (LN)

Strength depends in part on whether the precipitates are homogeneously or heterogeneously nucleated [1], and it is known that slow cooling rates promote the precipitation of grain boundary phases and incoherent phases in the matrix [2], degrading the properties of the alloys.

The grain boundary/matrix precipitates in the C912-CS1 alloys quenched into cold water (Fig. 1c) are finer than those in the C912B,C,N and S alloys quenched into liquid nitrogen (Fig.1). However, the volume fractions of large precipitates in the matrix of the C912B and S alloys are greater than that in the C912C and N alloys, and additionally many needle-like phases precipitate in the grain boundaries and the matrix of the former two alloys. Since the alloys were aged at room temperature, all the coarse particles showed in Fig.1a,d,e,and f precipitated during the quench leading to a decrease in the solute in supersaturated solid solution, then the effect of solid solution strengthening is degraded. In addition, the homogeneous nucleation temperature

for GP zones decreases with decreasing quench rate because of the decreasing supersaturation [1], this in turn leads to a coarser precipitate distribution because of heterogeneous nucleation of the GP zones. As a result, the C912B, C, N and S alloys quenched at very low rates develop low strength after aged at 121°C.

The strength losses in the C912C, N alloys are less than that in the C912B,S alloys (Table I), this may be explained based upon two reasons. First, provided that Ni and Ce can bond with vacancies easily, it can be inferred that these two elements will increase the stability of the vacancies in the solution, even during a slow quench, leading to less strength loss. Secondly, the diffusion coefficients of Ni and Ce in aluminum are both very low, giving the same effect.

In general, low quenching rate will degrade the SCC resistance of the aluminum alloys, but for the C912 alloys, only the C912B and S alloys obey the rule, the SCC sensitivities of the C912C and N alloys decrease using lower quenching rate (Table II). This can be explained by the mechanisms of active path dissolution and hydrogen assisted cracking.

Table II Effect of Quench Medium on the SCC Sensitivity of the C912 Alloys

Alloy/Temper	Applied Stress MPa	Failure Time h LN/CW	Blank Sample's Surplus UTS* MPa	1-α LN/CW
C912B-CS1	470	8.5/96.2	595/579	1.06/0.61
C912C-CS1	470	14.5/34.8	500/581	0.27/0.75
C912N-CS1	470	50.5/115.3	537/585	0.43/0.61
C912S-CS1	470	118/313.4	570/545	0.48/0.34

* Ultimate tensile strength of the SCC specimens exposed with no applied stress

In the active path dissolution mechanism, the propagation rate of cracking depends mainly on the anodic dissolution rate, i.e., the dissolution rate of grain boundary precipitates [3]. Thus if grain boundary particles (GBP) are large with a large interparticle spacing, they will decrease the propagation rate of cracking, thereby decreasing the anodic dissolution rate also[3]. Compared Figure 1d,e and 1c, it can be found that the GBP in the C912C and N alloys (LN) have a larger size than that of the C912B (CW). Therefore, the lower dissolution rate of particles and the slow propagation rate of crack in the C912C and C912N could be expected.

In the theory of hydrogen assisted cracking, many studies have shown that incoherent precipitates larger than a critical size (~20nm) can act as hydrogen atom irreversible traps, and it has been ovserved that these traps serve as nucleation sites for molecular hydrogen[3,4]. In the C912B,C,N and S alloys, the sizes of η phases in the grain boundary are all larger than 20nm, this means that in the SCC process, these particles can all act as nucleation sites for molecular hydrogen. As the shapes of the GBP in the C912B and C912S are more sharp than that in the C912C and C912N alloys, the effect of crack blunting of hydrogen bubbles in the grain boundary of the C912B and C912S alloys would be smaller than that in the C912C and C912N alloys. Thus, the stress concentration at the tip of crack along the grain boundary in the C912B and S alloys would be greater, leading to a increasing propagation rate of the crack, resulting the decrease of SCC resistance. In other hand, although the sizes of the GBP in the C912B and S alloys (LN) are larger than those in the CW condition, the GBP shape is still the key factor that controling the SCC resistance.

Figure 2 shows the tensile strengths of the C912B,C,N and S alloys and other eight alloys

which are a function of average cooling rate during quench. It is clear that the C912 alloys have higher strengths than those of the other eight alloys. In addition, in the critical temperature range (400 to 290°C), the loss in strength characteristic of the C912B,C,N and S alloys in the CS1 temper are all smaller than that of the 7075-T6, -T73 and 7178-T6 alloys (they have losses in tensile strength of about 13%,13% and 20%, respectively). The 7050-T73 alloy is not sensitive to quench rate and can be quenched into hot water (its tensile strength loss is about 2.6%). The C912C, N alloys in CS1 (T6) temper exhibit a similar behavior while their losses in strength are about 2.2% and 1.9%, respectively.

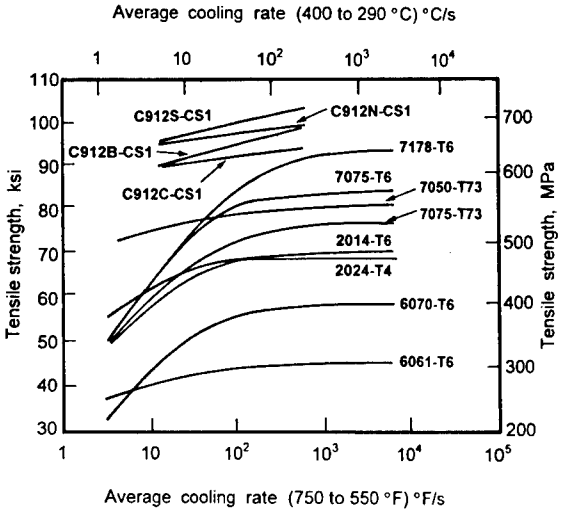


Figure 2: Tensile strengths of twelve alloys as a function of average cooling rate during quenching

Conclusions

1. The C912 alloy class in the CS1 temper have less sensitivity to quench rate than other 7000 series alloys, especially the alloys contain Ni and Ce. The C912 alloys are suitable for super high strength and thicker gauge forging and plate which have widely use in aircraft.

2. The strength loss using lower quench rate in the C912 alloys can be contributed to the heterogeneous nucleation of the GP zones which leads to a decreasing effect of solid solution strengthening, the larger volume fractions of large precipitates in the matrix, and the needle-like phases precipitate in the grain boundary and the matrix.

3. At the lower quench rate, needle-like phases form in the grain boundary degrade the SCC resistance of the C912B and S alloys.

References

1. J.T. Staley, "Quench Factor Analysis of Aluminium Alloys," Materials Science and Technology, 3 (11) (1987), 923-935.

2. R.C. Dorward and D.J. Beerntsen, "Grain Structure and Quench-Rate Effects on Strength and Toughness of AA7050 Plate," Metall. and Material Trans. A., 26A (1995), 2481-2484.

3. T.D. Burleigh, "The Postulated Mechanisms for Stress Corrosion Cracking of Aluminium Alloys," Corrosion, 47 (2) (1991), 89-98.

4. K. Rajan, W. Wallace and J.C. Beddoes, "Microstructural Study of a High-Strength Stress-Corrosion Resistant 7075 Al Alloy," Journal of Materials Science, 17 (1982), 2817-2824.

EFFECT OF HIP ON THE MICROSRTUCTURE AND MECHANICAL PROPERTIES OF THE CAST A-356 ALUMINUM

Charles S. C. Lei, William E. Frazier and E. W. Lee

NAWCAD
48066 Shaw Road, Bldg. 2188
Patuxent River, MD

Abstract

While the cast aluminums are extensively manufactured, there exists a problem where voids are formed during the casting process. Hot Isostatic Pressing has been commonly used to densify porous materials. However, the effect of HIP-healing of porosity on the mechanical properties of aluminum alloys is not well understood, especially on their fatigue behavior. This paper presents the influence of HIP on the porosity content and in term the fatigue properties of the peak-aged cast aluminum, A356. The porosity contents of the cast aluminum under HIPing and the low cost Densal HIP cycles were analyzed. The effect of HIPing on the tensile and fatigue properties of the cast aluminums is examined as well. The results show that the porosity content of HIPed specimens is much less than that of as-cast specimens. HIPing does not improve the yield stress and ultimate tensile strength significantly although the void content in the material is greatly reduced. From the S-N curves, HIPing improves the fatigue properties, such as cycles-to-failure and fatigue limit, by healing the voids in the material.

The Third Pacific Rim International Conference on
Advanced Materials and Processing (PRICM 3)
Edited by M.A. Imam, R. DeNale, S. Hanada,
Z. Zhong and D.N. Lee
The Minerals, Metals & Materials Society, 1998

Introduction

Casting aluminum alloys are widely used in the aircraft industry because they offer near net-shape manufacturing of aerospace structural components of high complexity, which reduces the manufacturing cost. Affordability or cost reduction strategy is, currently, the primary concern for the airframe manufacturers. Airframe manufaturers have traditionally hesitated to use castings because of inconsistent mechanical properties and quality. One of the factors which governs the quality of the cast aluminum is the volume fraction, morphology, and distribution of porosity. Micro-porosity is formed during the casting process as a result of alloy shrinkage and gas evolution during solidification. Although today's premium quality castings are manufactured and inspected using much more refined and tightly controlled process, complete avoidance of porosity formation is still impossible. The porosity degrades properties like fracture toughness, fatigue resistance, and tensile strength. Therefore, fatigue-critical cast parts are required to be densified in order to heal voids in the material.

Previous work has shown that some micro-porosities can be eliminated by working and heat treatment, however, even after extensive working and heat treatment, small amounts of micro-porosity still exist.(1) Hot isostatic press (HIP) is the only process that has so far provided effectiveness in healing from a wide range of materials. It offers some flexibility in manufacturing procedures because components which were previously unacceptable due to porosity, can show significant properties improved by the HIP process. HIP is a process which uses high temperatures in combination with high isostatic pressures to heal porosity. During HIP, densification occurs because of the elimination of some porosities. In literature, phenomenological theories and models of HIP are mostly based on investigations conducted on powder compacts. Four models have been attempted to explain the closure mechanism of porosities, namely, plastic flow, power law creep, lattice diffusion, and grain boundary diffusion. During a HIP cycle, all of the closure mechanisms may be contributing. According to Chama(1), only one mechanism will be dominant in the elimination of porosity. Although work on HIP has been performed mostly on powder compacts, very little study has been done on castings. Specifically, it has not been fully established if all forms of porosity present in castings can be eliminated by HIP and consequently improve mechanical properties, especially on their fatigue properties.

Aluminum alloy A356 is among the premium-quality sand and permanent mold casting alloys specified for military and aircraft applications. Alloy A356 is in the group of aluminum-silicon alloys which have excellent casting characteristics, weldability, pressure tightness, and corrosion resistance. These alloys are heat treatable to provide various combinations of tensile and physical properties. The effects of these microstructural parameters on tensile properties have been extensively studied.(2,3,4) However, the fracture, fatigue, and impact properties have not been the subject of investigation. Only recently, the role of fracture, fatigue, and impact property data in optimizing design parameters has become important to the designers of A356 castings, and several studies have been initiated.(5,6) In this paper, the tensile and fatigue properties of unHIPed, HIPed and Densal HIPed cast A356 specimens are presented. The effect of HIPing on the porosity healing and fracture is discussed as well.

Experimental Procedure

Aluminum alloy A356 specimens were produced and tested in (i) the as-cast, (ii) the HIPed, and (iii) the Densal conditions in order to achieve an understanding on the effect of HIPing on microstructure and mechanical properties. Half of the specimens were cast in premium

condition (cast condition I), and the rest were cast in higher temperature (cast condition II), which results in higher porosity content. HIPed specimens were processed at a pressure of 103MPa (15 Ksi) and a temperature of 516 °C (960°F) for two hours. Densal is a company proprietary HIP process which employs reduced temperature, pressure and hold time as compared to the conventional HIP process for cast aluminum.

The microstructure and volume fraction porosity for each type of processing condition was assessed. The main objective was to determine whether HIP closes the voids in the material and to assess whether low cost Densal HIP can achieve the same results as premium HIP. For each group of specimens, static tensile and high cycle fatigue tests were conducted to relate the tensile properties, such as yield stress and strength, and fatigue S-N curves with the casting conditions and HIPing.

Results and discussions

The effect of HIP on porosity

The porosity content was quantified for A356 aluminum specimens in the as-cast, HIPed, and the HIPed + T6 conditions. Each type of specimen was cut in order to provide two internal sections for polishing and examination under optical microscope. Sectioning is necessary because HIP only heals internal rather than surface porosity. Twenty-five different fields from each section were interrogated using an image analyzer. The size distribution and measurement of volume fraction of porosity for each field were documented. The representative structures of the as-cast, HIPed+T6, and Densal HIPed+T6 specimens, respectively were presented in (7). The results show that the size of the porosities is greatly reduced after HIPing. According to Chama's study,(1) significant densification of cast aluminum occurs in the early stage of a HIPing cycle. He also proved that the most probable dominant mechanism responsible for the elimination of porosity from aluminum castings during HIPing was plastic flow.

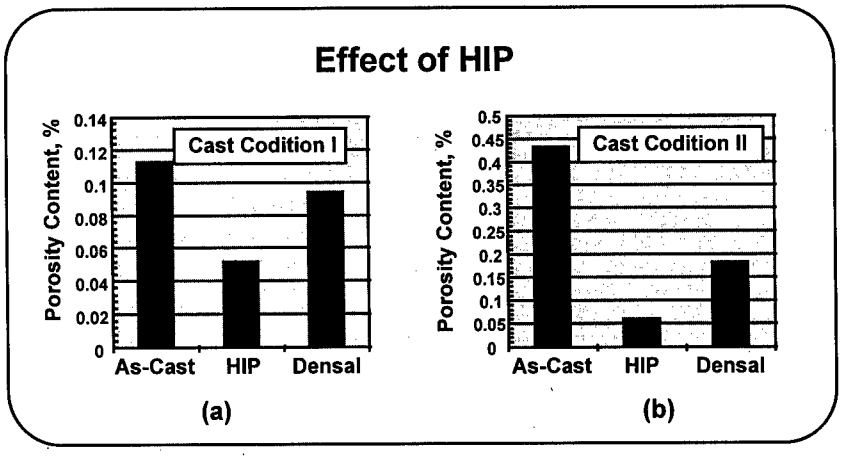


Figure 1: Effect of HIPing on volume fraction of porosity

Figure 1 shows the HIPing effect on the porosity content of the specimens without heat treatment. In premium casting condition, the porosity content is reduced about 50% for HIPed and 20% for Densal HIPed specimens, respectively, compared with as-cast specimens. While in casting condition II, the porosity content is reduced over 85% after HIPing and 60% after

Densal HIPing, respectively. The premium HIP closes more porosities than the low cost Densal HIP does because higher temperature and pressure in the premium process allow larger plastic deformation, which is the main mechanism of pore closure.

Because most A356 castings are used in the T6 condition, it is important to know the effect of T6 on the HIPed castings. From observation on Figure 2, the solution treatment and aging did not open the closed porosities, and instead, T6 helps further eliminate the pores. For specimens whether in premium casting condition or in higher temperature casting condition, the porosity content is confined to less than 0.015% after premium HIP and T6.

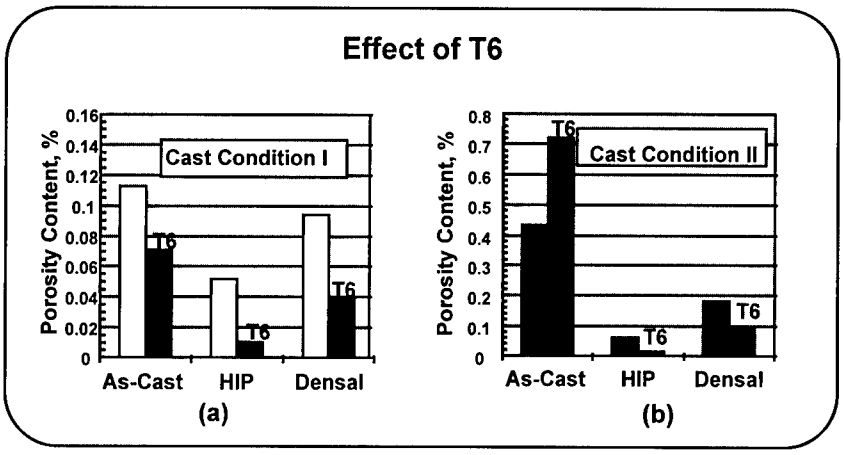
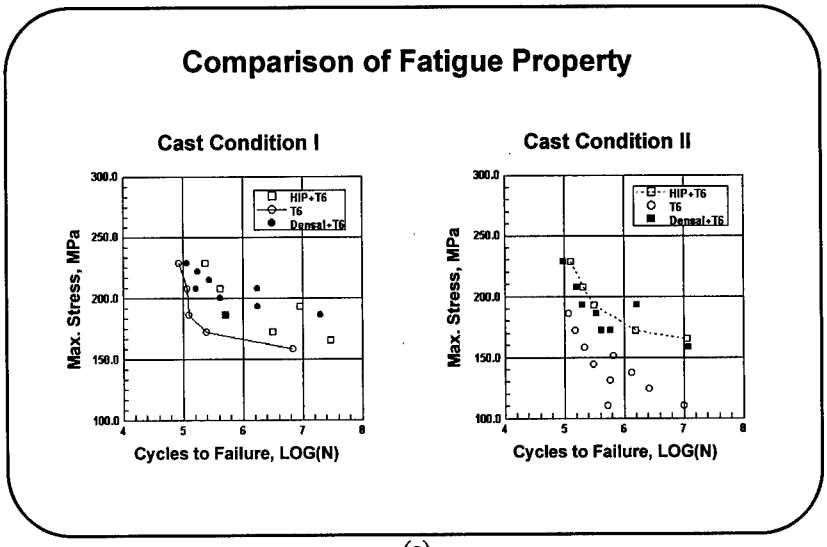


Figure 2: Effect of T6 on volume fraction of porosity

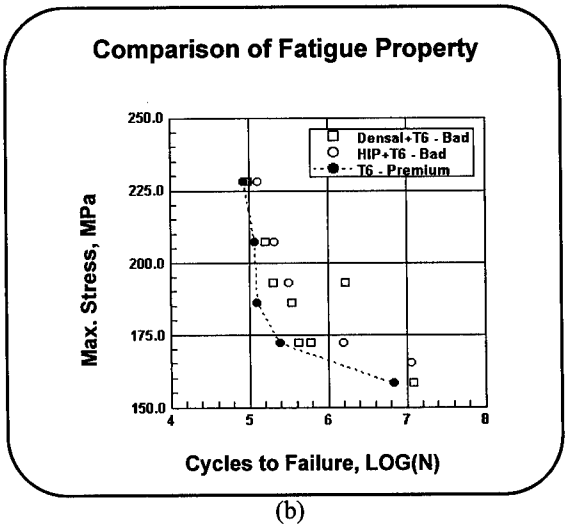
Fatigue Properties

The averaged values of static tension tests were presented in (7), where the results show that HIPing does not improve the yield stress and ultimate tensile strength significantly although the void content in the material is greatly reduced. As illustrated in Figure 2, the greatest void content is less than 1%, which is very small compared with the whole structure. Fatigue crack initiation is very sensitive to the void content of a material. HIPing helps to close the voids present in the cast material, and in this way enhances their fatigue properties. Figure 3(a) shows the preliminary S-N results for the specimens in their peak aged condition. Evidently, both the premium HIP and the lower cost Densal HIP improves the S-N fatigue life of cast A356 regardless of casting conditions. Most specimens exhibit similar fatigue limit, 165 MPa (24 Ksi), while specimens in higher temperature cast condition have only 110 MPa (16 Ksi). Comparing the fatigue life of material premium cast condition, the HIPed specimens show about 14 MPa higher than the specimens without HIP. Regarding the cycles-to-failure, the premium cast specimens have 3 to 4 times longer life than the higher temperature cast specimens at lower fatigue stress (172 MPa). The HIPed premium cast specimens exhibit more than a decade longer life than the unHIPed premium cast specimens at 172 MPa (25 Ksi) fatigue stress, while about seven times longer life at 206 MPa (30 Ksi) fatigue stress. Another observation from Figure 3(b) shows that even in higher temperature casting condition, the specimens after either premium HIP (HIP+T6-Bad) or Densal HIP (Densal+T6-Bad) exhibit better fatigue life than unHIPed specimens in premium casting condition. In general, the premium HIPed specimens have better fatigue life, and premium casting specimens show better

fatigue life. The SEM fractograph study of a HIPed+T6 and T6 only specimens has been conducted and presented in (7). In summary, for the HIPed specimens, the fatigue crack initiated at the specimen surface because the HIPing suppressed the voids in the interior of the material. While the fatigue crack initiated at the void nearby the specimen surface in T6-only specimens.



(a)



(b)

Figure 3: Experimental S-N curves of HIPed and unHIPed specimens

Concluding Remarks

Experimental results indicate that HIPing helps to close voids in cast aluminum. Although HIPing does not improve the material's yield and ultimate tensile strength significantly, it does

enhance fatigue resistance. In general, the HIPed specimens have better fatigue life. Even in higher temperature casting condition, the specimens after either premium HIP or Densal HIP exhibit better fatigue life than the unHIPed specimens in premium casting condition. The future work will be conducted on the porosity content and fatigue properties of the thick cast aluminums due to HIP, and also on the optimum conditions of HIP to obtain the desired fatigue property with acceptable degree of porosity content.

References

1. C. C. Chama, "Elimination of Porosity from Aluminum-Silicon Castings by Hot Isostatic Pressing", Journal of Materials Engineering and Performance, 1 (Oct.) (1992), 773-780.
2. S. Shivkumar, S. Ricci, Jr, and D. Apelian, "Influence of Solution Parameters and Simplified Supersaturation Treatments on Tensile Properties of A356 Alloy", AFS Transactions, 97(1990) , 913-922.
3. S. Shivkumar, et al, "An Experimental Study to Optimize the Heat Treatment of A356 Alloy", AFS Transactions, 97(1989), 791-810.
4. C. C. Chama, "Mechanical Properties of Hot Isostatically Pressed Aluminum-Silicon Castings", Scripta Metallurgica et Materialia, 26(1992), 1153-1156.
5. C. M. Sonino and J. Ziese, "Fatigue Strength and Applications of Cast Aluminum Alloys with Different Degrees of Porosity", International Journal of Fatigue, 15 (2) (1993), 75-84.
6. M. J. Couper and J. R. Griffiths, "Effects of Crack, Closure and Mean Stress on the Threshold Stress Intensity Factor for Fatigue of An Aluminum Casting Alloy", Fatigue Fracture Engineering Material structure, 13 (6) (1990), 615-624.
7. C. S. C. Lei, W. Frazier, and E. Lee, "Effect of HIP on the Cast Aluminum", Journal of Metals, 49 (11) (1997), 38-39.

THE EFFECT OF 45° ROLLING MODE ON THE MECHANICAL PROPERTIES OF ANISOTROPIC METALS

O. S. Es-Said

Mechanical Engineering Department,
Loyola Marymount University
Los Angeles, CA 90045

Abstract

The 45° rolling mode was performed on several mechanically anisotropic systems: 2090, 2095, and 8090 Al-Li, and rhenium metal. The three different systems displayed improved mechanical properties and ease of fabrication. The correlation between mechanical properties and the microstructure is discussed. Crystallographic texture analysis and planar anisotropy modeling still needs to be carried out to clarify the experimental results presented in this paper.

The Third Pacific Rim International Conference on
Advanced Materials and Processing (PRICM 3)
Edited by M.A. Imam, R. DeNale, S. Hanada,
Z. Zhong and D.N. Lee
The Minerals, Metals & Materials Society, 1998

Introduction

The 2090, 2095, and 8090 Al-Li alloys and rhenium metal are materials which exhibit mechanical anisotropic behavior. Each of these systems has different aerospace applications. Aluminum lithium alloys are used in structural aerospace applications; and rhenium, in the design of parts having thin sections. Problem areas in the aluminum lithium alloys include poor ductility and tensile strength anisotropy, and in rhenium, the cost effectiveness of fabrication. The objective of this paper is to review the thermomechanical processes proposed by Es-Said and coworkers, [3,9,10,13], where the 45° rolling mode appears to have improved the fabrication process and mechanical properties of the aluminum lithium and rhenium systems.

The 2090 Al-Li Alloy Plate

Aluminum-Lithium alloys are attractive candidates for aerospace and aircraft applications because of their high specific stiffnesses and low densities. However, several problem areas have delayed the substitution of Al-Li alloys for conventional aluminum alloys in aerospace applications. Among those are poor ductility. The poor ductility of Al-Li alloys has been attributed to the intense coplanar slip during deformation associated with the shearable δ' (Al_3Li) second phase particles and the soft precipitate free zone (PFZs) resulting from the heterogenous intergranular precipitation of δ (Al Li) particles, [1,2]. Cracks initiating at grain boundary precipitates and triple junctions propage at the PFZ mediums.

Es-Said and co-workers [3] studied the effect of varying the rolling mode on the ductility of 2090 AL-Li alloy after recrystallization. The as-received 2090 Al-Li hot rolled plate was cut into 9.5 mm thick samples, homogenized at 482°C for 10 hours and then cold rolled to 95% reduction in thickness in four directions. The first was along the longitudinal direction of the initial hot rolling, L, the second was along the transverse direction, T, (long transverse, TD), the third along a 45° angle to the rolling direction and the last was rolled along the 45°, longitudinal and transverse directions in equal increments. The four groups were subsequently annealed at 456°C up to 24 hours.

The deformation of all the samples rolled in the four modes showed similar patterns where the longitudinal views revealed a wavy pattern with triple points and grain boundary intersections. These together with the large intermetallic particles provide nucleation sites for the newly recrystallized grains. The transverse views, on the other hand, revealed parallel microbands with a less intense deformation, Figure 1. After annealing, the four groups recrystallized in less than one hour with a coarse elongated structure. The grain sizes were finer in the longitudinal view which accords with the earlier observation that the rate of nucleation of recrystallization would be expected to be high in the wavy heavily deformed region. The recrystallized grain sizes are summarized in Table 1. The width of the grains was about 25-50 μm. The length of the recrystallized grains in the transverse view to that in the longitudinal view will be defined as R. The values of R for samples rolled in the longitudinal mode is 2.5, for samples rolled in the transverse mode is 3, for samples rolled in the 45° mode is 2, and for samples rolled in the 45°-L-T mode is 1.5. The difference in the length of the recrystallized grain sizes along the longitudinal and transverse views becomes less pronounced as the 45° rolling is employed.

The mechanical strength (yield and ultimate stresses) of the different groups after 1, 10 and 24 hours of annealing at 456°C were similar, however, the ductility behavior was very different,

Figure 2. The ductility improved with the onset of 45° rolling and was best with a combined rolling mode of 45°, longitudinal and transverse respectively. The poor ductility of Al-Li alloys are attributed to slip localization through the δ' (Al_3Li) precipitates. Deformation proceeds by dislocations shearing the δ' precipitates and their reduction in area encourages planar inhomogeneous slip leading to loss of ductility [4]. Thus, although the δ' is a strengthening phase, it embrittles the alloy through concentrating the deformation in intense slip bands leading to premature failure. The onset of the 45° rolling mode and preferentially the combined rolling mode of 45°, L and T appears to diffuse the localized slip bands and promotes the homogeneity of plastic flow. The reduction in elongation with aging in the L and T conditions might be associated with the coarse elongated grains in the L and T directions together with the inhomogeneity of the grain sizes in the L view and T view of each rolling mode, the R value previously defined. It is well established that coarse elongated grains are associated with low ductility.

The 2090 T8E41, 8090 T851, and 2095 HT72 Aluminum-Lithium Alloys

In sheet form, aluminum lithium alloys exhibit tensile strength anisotropy when compared to conventional 2xxx and 7xxx type aerospace alloys. The anisotropy is manifested when moving away from the rolling direction in the plane of the sheet, and is attributed to both crystallographic texture [5,6] and the role of oriented precipitates [7,8].

The 2090 T8E41, 8090 T852, and 2095 HT72 were provided in the form of sheets of 1.52 mm (0.06 in) thickness. The sheets were solution treated: 550°C for the 2090 T8E41, 525°C for the 8090T851, and 510°C for the 2095 HT72. The duration of the solution treatment was thirty minutes followed by water quenching. All samples were subsequently rolled along the 45° direction. Aging was performed at 170°C/24 hours for the 2090 T8E41, 175°C/20 hours for the 8090 T851, and 180°C/24 hours for the 2095 HT72. Tensile specimens were machined from each set at 0, 30, 45, 60, and 90° angles to the original rolling direction. The yield strength anisotropy is 8% in the 2090 T8E41, 11.1% in the 8090 T851, and 13.1% in the 2095 HT72. These results show significant improvement over conventionally stretched aluminum lithium alloys, [9,10], and are in accord with recent studies reported by Cho, [11,12], who indicated that cross rolling at 45° reduced the mechanical anisotropy of the Al 2095 alloy.

Rolling in the 45° mode, in the 2095 HT72 alloy prior to aging reduced the Brass component {011}<211> and the P component {011}<122> while it increased the R component {123}<634>, however, the tensile strength anisotropy cannot be explained by texture effects only, [10].

The Rhenium Metal

Rhenium metal products are typically used in wear resistant electrical contacts, mass-spectrometer cathodes, and rocket thruster nozzles. Its scarcity, poor oxidation resistance, and difficulty of fabrication prevents its use for large structural components. Rhenium is universally fabricated by cold working, however, even a small degree of strain will increase its hardness, tensile strength and its ability for further deformation, [13]. Frequent intermediate annealing in a controlled atmosphere is a major part of the fabrication process.

In a recent work by Es-Said, et. al, [14], rhenium samples of dimensions 17.8 mm in length and 5.2 mms in width and in thickness were successfully rolled in three different modes without intermittent annealing, once along the length of the samples (nominally termed longitudinal), the

second time along the width (transversely) and at a 45° angle in between both directions. Over 25% reduction in thickness was obtained in the transverse direction and over 39% reduction was possible in the longitudinal and 45° directions. In the longitudinal rolling mode, edge cracks initiated after a 10% reduction in thickness, while in the 45° mode, edge cracks did not initiate until after a 20% reduction in thickness. In a second experiment the rhenium bars were annealed at 1500°C for 30 minutes in H_2 atmosphere and subsequently rolled in the 45° rolling direction. The material was reduced to 51.5% of its original thickness before failure. From the previous results, an optimum processing method of light rolling along the 45° direction followed by intermittent annealing was carried out. Rhenium bars of 7.8 mm thickness were pre-sintered to 2200°C for 30 minutes in hydrogen, cold rolled in a 45° direction to about 10% reduction and annealed at 1650°C for 30 minutes in a hydrogen atmosphere. The partial reduction and intermittent annealing were repeated until 82.9% reduction. The microstructural and mechanical properties of the as sintered, 55% reduced (3.51 mm thickness) and 82.9% reduced (1.33 mm thickness) samples were evaluated, Table 2. It can be noted from the results that a combination of 2388 MPa (346.6 Ksi) and 3.3% elongation had not been achieved in the literature of rhenium processing.

The fracture surfaces of the non cold-rolled and the 50%-reduced specimens show a considerable shearing (or fibrous appearance), which is an indication of plastic deformation. The fracture surface of the 80% reduced specimen, however, shows a considerable granular appearance with limited shearing mechanism, which would explain its low ductility, [14]. Despite the 80% reduction, grain boundaries are still well defined. This implies that the 80% reduced specimen is not fully deformed, and that further cold rolling can be performed to increase the ultimate tensile strength of the specimens.

Summary

It was proposed that the introduction of the 45° rolling mode or preferably the combined rolling mode of 45°, L and T to the 2090 Al-Li alloy plate had the effect of diffusing localized slip bands and increasing the homogeneity of plastic flow. In the 2090 T8E41, 8090 T851, and 2095 HT72 alloys, the introduction of a 45° rolling mode reduced the tensile strength anisotropy. In rhenium, the light rolling along the 45° direction followed by intermittent annealing, improved the mechanical properties and ease of processing.

References

1. F.S. Lin, S.B. Chakrabortty and E.A. Starke, Jr., Met. Trans., 13A (1982) 401.
2. E.A. Starke, Jr., and F.S. Lin, Met. Trans., 13A (1982) 2259.
3. O.S. Es-Said et. al., J. Mat. Eng. & Perf., 3(2) (1994) 292.
4. W. Wang and M. Wells - E. Lee and N. Kim (eds.), Light-Weight Alloys for Aerospace Applications, II, TMS, Louisiana, (1991) 189.
5. P.J. Gregson and H.M. Flower, Acta Metall., 33 (1985) 527.
6. S. Fox, H.M. Flower, and D.S. McDarmaid - E.A. Starke, Jr., and T.H. Sanders, Jr. (Eds.), Aluminum Alloys - Their Physical and Mechanical Properties, EMAS, U.K. (1986) 939.
7. A.K. Vasudevan, et. al, Met. Trans., 19A (1988) 731.
8. N.J. Kim and E.W. Lee, Acta Metall., 41 (1993) 941.
9. O.S. Es-Said and E.W. Lee - E.W. Lee, N. Kim, W. Frazier, and K. Jata (eds.), Light Weight Alloys for Aerospace Applications, III, TMS, Las Vegas, (1995) 57.
10. E.W. Lee, P. Kalu, L. Brando, H. Garmestani, and O.S. Es-Said to be submitted to J. Mat. Science & Engineering.

11. Cho, Alex, United States Patent, 5, 393, 357, (1995).
12. Cho, Alex, United States Patent, 5, 439, 536, (1995).
13. B. Bryskin, Adv. Mat. & Proc., 142-3 (1992) 22.
14. O.S. Es-Said, J. Foyos, and V. Heng, J. Mat. and Manuf. Processes, in press.

Table 1: Grain Sizes (Linear Intercepts) of the Recrystallized Grain Structures

	Isothermal anneal at 454°C for:				
Mode of rolling	**0.5 h**	**1 h**	**5 h**	**10 h**	**24 h**
Longitudinal direction					
Longitudinal view					100-175 μm in length, 30-40 μm in width
Transverse view			300-400 μm in length, 25-30 μm in width	300-400 μm in length, 25-30 μm in width	300-400 μm in length 30-40 μm in width
Transverse direction					
Longitudinal view		125-175μm in length, 20-40 μm in width			
Transverse view	400-500 μm in length, 30-40 μm in width				400-500 μm in length, 30-40 μm in width
45° direction					
Longitudinal view		100-200 μm in length, 30-40 μm in width		100-200 μm in length, 30-40 μm in width	
Transverse view	150-300 μm in length, 20-40 μm in width		200-400μm in length, 20-30 μm in width	250-400 μm in length, 30-40 μm in width	300-400 μm in length, 40-50 μm in width
45° L-T direction					
Longitudinal view		100-200 μm in length, 20-30 μm in width		100-200 μm in length, 30-40 μm in width	100-250 μm in length, 30-40 μm in width
Transverse view		150-200 μm in length, 20-30 μm in width		150-300 μm in length, 30-40 μm in width	

Table 2: Property Comparison of Non-Cold Worked and Cold Worked Rhenium

PROPERTY	NON COLD ROLLED	50% REDUCED	81.50% REDUCED
% Theoretical Dentisy	96.00%	97.50%	98.40%
Porosity Diameter (micrometers)	3.0 - 5.0	0.5 - 1.5	<< 0.5
Vicker Hardness (VHN)	220 - 240	480 - 500	700 - 800
Tensile Strengh (MPa)	827.6	1091	2388
Yield Strength at 0.2% Offset (MPa)	206.9	351.4	734.5
Elongation (%) in 12.7 mm gage length	30%	14.30%	3.30%

Figure 1: The Grain Structure of 2090 Al-Li Alloy Homogenized and Rolled to .051mm in the Transverse Direction, Transverse View in (A), Longitudinal View in (B)

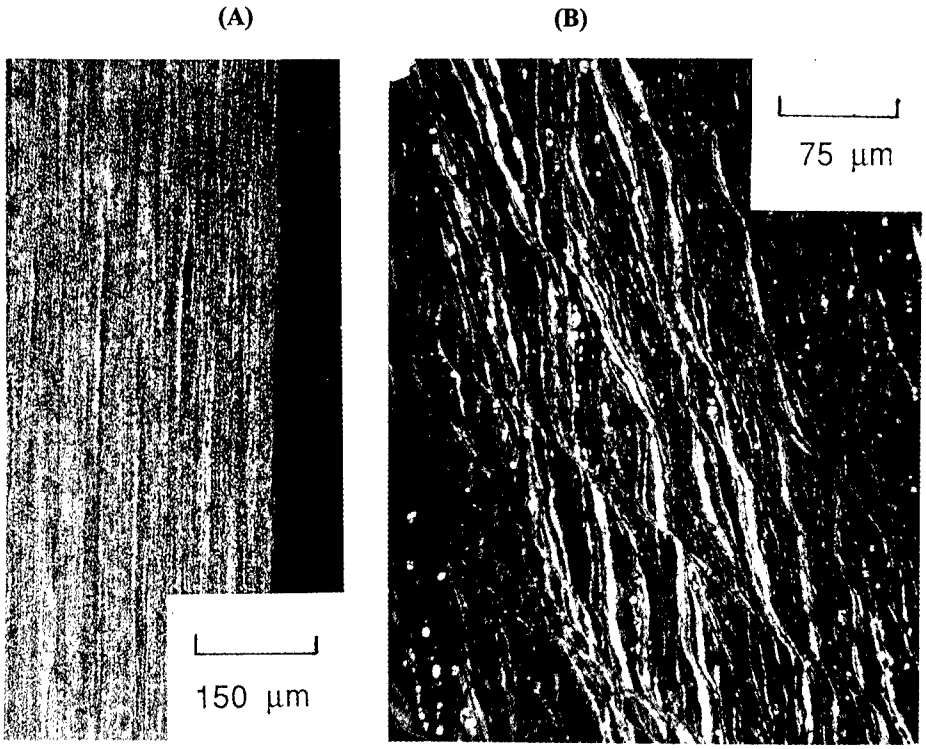
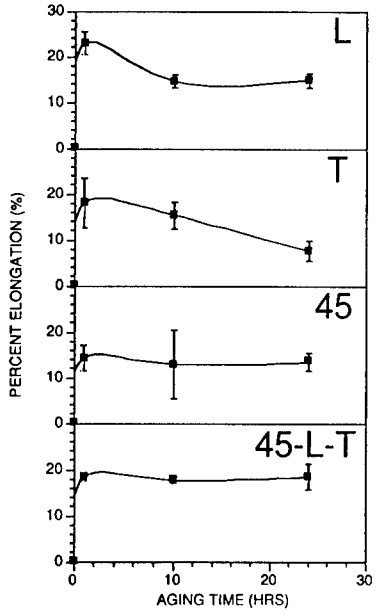


Figure 2: Percent Elongation Changes at 454° C for 24 Hours



MICROSTRUCTURE AND CREEP BEHAVIOR OF Al-Cu-Mg and Al-Cu-Mg-Ag ALLOYS

Ning Wang, Susan M. Kazanjian, and Edgar A. Starke Jr.
Dept. of Materials Science and Engineering
University of Virginia
Charlottesville, VA 22903

Abstract

Aluminum alloys could be viable structural materials for a Mach 2.0-2.2 aircraft providing they can meet the long-term creep resistance required. This paper will describe the creep behavior of two Al-Cu-Mg-Ag candidate alloys in comparison with the Concorde alloy 2618 (Al-Cu-Mg). The alloys were crept under stresses and temperatures predicted to be experienced when cruising at Mach 2.0-2.2. The microstructures of the alloys have been characterized before and after creep by transmission and analytical electron microscopy in order to develop an understanding of their evolution during creep.

Introduction

A supersonic transport (SST) designed to fly 60,000 hours at Mach 2.0-2.4 is predicted to have the best potential to meet the long-range international market needs. Light-weight structural materials with long-term resistance to thermomechanical fatigue, creep and environmental degradation are required to attain the speed, payload and range necessary for an economically successful aircraft [1]. Aluminum alloys are competitive candidates for structural applications of a SST with ultimate cruising speeds of Mach 2.0-2.2. at which the skin temperature of the aircraft would reach a maximum of 120°C.

The technical success of the Concorde has demonstrated that aluminum alloys can be viable at Mach 2.05. The Concorde was constructed from the creep resistant aluminum alloy 2618 (an Al-Cu-Mg alloy) and endured general structural temperatures of 90°-100°C. The flight cycle for a new Mach 2 SST will be similar to the Concorde, except that the expected greater range and payload will result in longer times at cruise conditions and will require materials with improved mechanical properties (strength, creep resistance, etc.). For a new SST, the required cruising life may be four times that of the Concorde (15,000h) and the overall level of stress may be 20% higher than that imposed on the Concorde. No existing commercial aluminum alloys can meet these requirements and the development of advanced aluminum alloys with higher strength and excellent long-term creep resistance and damage tolerance is required.

The Third Pacific Rim International Conference on
Advanced Materials and Processing (PRICM 3)
Edited by M.A. Imam, R. DeNale, S. Hanada,
Z. Zhong and D.N. Lee
The Minerals, Metals & Materials Society, 1998

Initial investigation indicated that alloys based on the Al-Cu-Mg-Ag system possess attractive mechanical properties and thermal stability. Small additions of Ag to Al-Cu-Mg alloys with high Cu:Mg ratios significantly enhance strength and thermal stability. The improvement has been attributed to the replacement of the θ' phase, which precipitates on {100} planes, with Ω, which precipitates on {111} planes in the matrix. Results show that a small amount of Mg is essential for the precipitation of the Ω phase and Ag acts to promote this precipitation. Segregation of Ag and Mg has been detected at the α matrix/Ω interface [2,3]. The plate-shaped Ω precipitates exhibit higher resistance to thermal coarsening and provide a more effective barrier to moving dislocations relative to other strengthening phases (i.e. θ' and S') found in this class of alloys [4,5,6]. Recent work at Alcoa showed that small additions of Ag and Mg to 2519 can increase the peak aged tensile yield strength by 10%. Alloys C415 and C416 are modifications of alloy 2519 with variations in Cu, Mg, and Mn and with 0.5%Ag and 0.13%Zr. The alloys contain less Cu than 2519 and sufficient Ag and Mg to promote the formation of the Ω phase. Both also contain Mn in the form of submicron $Al_{20}Cu_2Mn_3$ particles and Zr in an unidentified dispersoid for grain structure control.

The objective of the present paper is to evaluate the creep properties and structural evolution of C415 and C416, in comparison with 2618 (CM.001), under stresses and temperatures predicted to be experienced when cruising at Mach 2.0-2.2. The resulting creep curves are well described by polynomial expressions and are analyzed and extrapolated to a 60,000 hours lifetime. The responses of microstructures during creep are characterized using transmission and analytical electron microscopy to develop an understanding of possible degradation mechanisms associated with the operation of a SST.

Experimental procedures

Table I gives the room temperature yield strengths, chemical compositions and average grain sizes of the alloys used in the present study. Flat tensile specimens were prepared for creep tests in accordance with ASTM Specification No. E139. Strain over time was recorded from the output of two strain gages per specimen, then averaged to display curves. Isothermal constant-load creep tests were conducted at temperatures of 107°C and 135°C and at stresses ranging from 138MPa to 207MPa. The creep times lasted from 1300 hours to more than 10,000 hours. Specimen foils for transmission electron microscopy (TEM) were prepared by twin-jet electropolishing in a solution of one part nitric acid to three parts methanol at -30°C.

Results and discussion

Figure 1 and Figure 2 show the creep curves for C415, C416 and CM.001 tested at 135°C and 107°C, respectively. These curves do not include the initial instantaneous strain on loading. All three alloys started in stage I and remained in stage I or II of creep over the range of test conditions. The candidate alloys exhibited much lower creep strain than the Concorde alloy under equivalent test conditions, while C416 demonstrated the most superior creep resistance. Based on Andrade's equation ($\varepsilon_c \approx At^{1/3}+kt$) which gives fairly good fit to the primary creep regimes of alloys[7], we found that the creep curves could be more accurately represented by adding a $t^{1/2}$ to the equation. Table II gives the equations, in form of $\varepsilon_c=At^{1/3}+Bt^{1/2}+kt$, that described the creep curves over the temperatures and stresses tested. Assuming that the creep mechanism did not change at each test condition, extrapolations of creep data could be performed in terms of these equations. The predicated creep strains for 60,000 hours and times for reaching creep strain of 0.1% are listed in Table II for all three alloys under our test conditions. The results can be used to help to identify the temperature and stress level for each

alloy below which the requirement of less than 0.1% creep strain over 60,000 hours cruising time of the aircraft can be met. None of the three alloys met the creep requirement at 135°C even at the lowest stress level tested (138MPa). However, at 107°C and 207MPa, conditions of particular interest for a MACH 2 SST, C415 and C416 could almost meet this requirement, reaching 0.1% creep strain over 50,601h and 58,190h, respectively. The Concorde alloy crept 0.1% ε_c over only 6228h at the above condition and could not meet the requirement even at 107°C and 138MPa.

The superior creep resistance of C415 and C416 compared to the Concorde alloy is attributed to their strength advantages and the presence of the Ω phase as the primary strengthening phase. TEM micrographs of precipitates present in C415 and C416 after the T8 temper are shown in Figure 3. A finely dispersed Ω phase together with a small amount of θ' can be observed. C416 contains more θ' but less Ω because of its higher Cu and lower Mg content. This explains why C415 possesses higher strength than C416. However, surprisingly, C416 exhibited higher creep resistance than C415. This appears in conflict with studies that suggest that Ω plates on {111} provides a more effective barrier to gliding dislocations than θ' on {100} planes [6] and that creep resistance can be improved by increasing the grain size in precipitation-strengthened alloys (see Table I). TEM examination of microstructures of C415 and C416 before and after creep revealed that creep induced microstructural changes determined these creep behaviors. Figure 4 shows typical microstructures of C415 and C416 prior to and after creep and Figure 5 gives the corresponding selected area electron diffraction patterns. It is evident that under the given creep condition, severe microstructural changes occurred in C415 associated with an increased amount of heterogeneously precipitated S' phase. Less severe microstructural changes took place in C416 with additional θ' phase precipitated on dislocations. The creep induced or promoted S' and θ' precipitates were confirmed by the energy dispersive X-ray analysis on TEM.

It has been recognized that time-dependent flow should be governed by two kinds of laws, kinetic laws and structure-evolution laws. Kinetic laws refer to the kinetics of flow at a fixed structure, whereas structure-evolution laws describe the way in which the structure changes during the course of deformation [7,8]. Following the general principles of thermally activated processes, the creep strain rate can be expressed as:

$$\dot{\epsilon} = \dot{\epsilon}_o \exp(-\Delta G / kT)$$

where ΔG is the free energy for activation which depends on the strength and precipitates of the alloy, and the applied stress. For regularly distributed 'rectangular' precipitates, Kocks et al. obtained the free energy expression as $\Delta G = \Delta F(1-\sigma/\tau)$, where ΔF is the enthalpy of activation in the absence of applied stress σ, and τ is the maximum attainable stress state related to the dislocation structure ($\tau = 3\mu b\rho^{1/2}$, where ρ is the dislocation density, μ the shear modulus and b the Burgers vector) [9]. During creep, the dislocation structure is changed by the competition between strain hardening processes and recovery-type processes. In general, strain hardening occurs as a result of the statistical storage of dislocations, while recovery occurs by annihilation of dislocations. In the present study, large amounts of heterogeneously precipitated S' on dislocations in C415 during creep could annihilate these dislocations, thus reducing the dislocation density, ρ, and resulting in a higher creep rate. We can assume that when a stress is applied at high temperatures, dislocations quickly move and multiply until the strength of the dislocation structure is balanced by the applied stress. If the number of dislocations is reduced at a given stress state, new dislocations must be created to maintain the dislocation strength. As a result, the plastic strain increases. Figure 6 shows the microstructure

of CM.001 prior to and after creep. An increased density of apparent dislocation lines decorated by S' precipitates (as arrows indicate) is observed in the crept sample after a small amount of creep strain. Moreover, the S' is the least effective in strengthening among Ω, θ' and S' precipitates. Since Mg segregation has been detected at the interfaces of Ω and the aluminum matrix, heterogeneous precipitation of S' (Al_2CuMg) at these interfaces might occur at the expense of the Ω phase during creep, leading to a reduction in strength and acceleration of the creep rate. Additional quantitative microstructural analysis is required to determine the exact mechanism involved.

Conclusions

The candidate alloys of the Al-Cu-Mg-Ag system have superior creep resistance compared to the Concorde alloy (Al-Cu-Mg) for long-term high temperature applications. Less than 0.1 percent creep strain over 50,000 hours can be obtained for the candidate alloys at Mach 2 if the temperature-stress state subjected to the aircraft during flight is below 107°C-207MPa. The marked microstructural changes that occur in the candidate alloys during the creep conditions of this study are heterogeneous precipitation of S' and θ', mainly on dislocations. The reduction of creep resistance for C415 is attributed to the excessive precipitates of S' which possibly annihilate dislocations and/or consume the Ω phase. The differences in creep resistance, strength and thermal stability of the investigated alloys provide valuable information for further improvement of the microstructure and composition of these alloys.

Acknowledgments

The authors wish to acknowledge the support of Lockheed-Martin and NASA-Langley Research Center under Grant No. NAG 1-745, Dennis Dicus program monitor.

References

1. E.A. Starke, Jr. and J.T. Staley, "Application of Modern Aluminum Alloys to Aircraft", Prog. Aerospace Sci., Vol. 32 (1995), 131-172.
2. K. Hono et al., "Atom Probe Study of the Precipitation Process in Al-Cu-Mg-Ag Alloys", Acta metall. mater., Vol. 41, No.3, (1993), 829-838.
3. W.A. Cassada and M.F. Bartholomeusz, "The Effect of Cu and Mg Content on Mechanical Properties of Al-Cu-Mg Alloys with and without Ag Additions", Materials Science Forum, Vols. 217-222 (1996), 1765-1770.
4. S.P. Ringer et al., "Precipitate Stability in Al-Cu-Mg-Ag Alloys Aged at High Temperatures", Acta metall. mater., Vol. 42, No. 5, (1994), 1715-1725.
5. I.J. Polmear and R.J. Chester, "Abnormal Age Hardening in an Al-Cu-Mg Alloy Containing Silver and Lithium", Scripta Metallurgica, Vol. 23 (1989), 1213-1218.
6. J.F. Nie, B.C. Muddle, and I.J. Polmear, "The Effect of Precipitate Shape and Orientation on Dispersion Strengthening in High Strength Aluminum Alloys", Materials Science Forum, Vols. 217-222 (1996), 1257-1262.
7. Jean-Paul Poirier, Creep of Crystals (Cambridge Earth Science Series, 1985), 25-33.
8. Rishi Raj, ed., Flow and Fracture at Elevated Temperatures (ASM Seminar, Philadelphia,1983), 23-58.
9. A.D. Freed, S.V. Raj, and K.P. Walker, "Stress Versus Temperature Dependence of Activation Energies for Creep", Transactions of the ASME, Vol. 114 (1992), 46-50.

Table I Alloys Used in This Study

Alloy	Yield Strength at RT (MPa)	Grain Size (μm)	Chemical Composition (wt.%) Al	Cu	Mg	Mn	Ag	Zr	Fe	Si	Ni
C415	490-517	80	Bal	5.0	0.8	0.6	0.5	0.13	0.06	0.04	-
C416	483-496	30	Bal	5.4	0.5	0.3	0.5	0.13	0.06	0.04	-
CM.001	386	40	Bal	2.5	1.5	-	-	-	1.1	0.22	1.1

Table II The Equations of Creep Curve Fits and Extrapolation of Creep Data

Alloy	Creep Condition T (°C)	σ (MPa)	Equations: $\varepsilon_c=At^{1/3}+Bt^{1/2}+kt$ A x10^{-6}	B x10^{-6}	k x10^{-8}	Extrapolated Creep Data t (h) /ε_c=0.1%	ε_c/60,000h	Creep Rate at 1200 h (x10^{-7}/h) Experimental	Calculated
C415	135	207	3.1	16.0	26.3	1,396	1.98%	4.9	5.0
	135	172.5	2.9	8.8	21.3	2,466	1.50%	3.3	3.5
	135	138	8.2	5.1	12.6	4,242	0.91%	2.7	2.3
	107	207	15.8	-1.4	1.45	50,601	0.11%	0.42	0.41
C416	135	207	4.4	14.6	8.05	2,531	0.86%	3.0	3.0
	107	207	12.6	-1.2	1.38	58,190	0.10%	0.29	0.33
	107	138	8.3	-0.92	0.54	168,413	0.04%	0.17	0.17
CM.001	135	207	146	-12.3	11.6	591	0.98%	3.4	3.7
	107	207	64	-5.0	3.46	6,228	0.33%	1.5	1.5
	107	138	24	-2.3	1.45	44,536	0.12%	0.46	0.51

Figure 1 Creep Curves of Alloys Tested at 135°C. Figure 2 Creep Curves of Alloys Tested at 107°C.

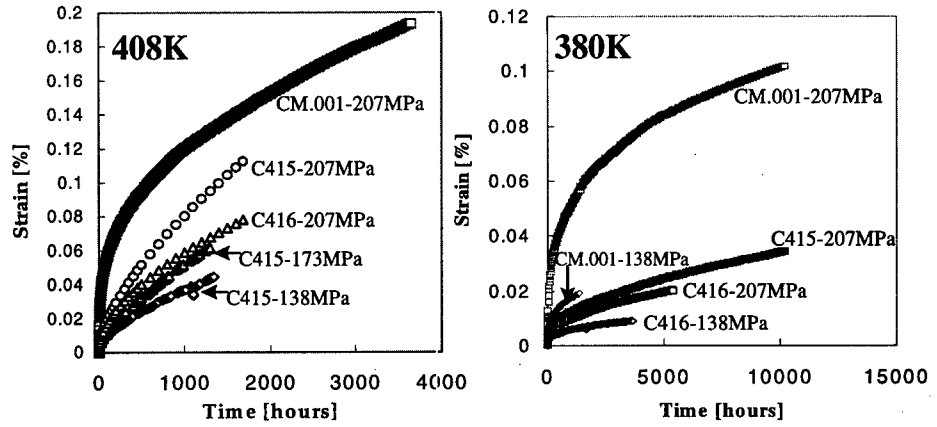


Figure 3 Bright-field Electron Micrographs of Alloy C415 (a) and C416 (b) in the T8 Condition. The electron beam is approximately parallel to a <011>α direction.

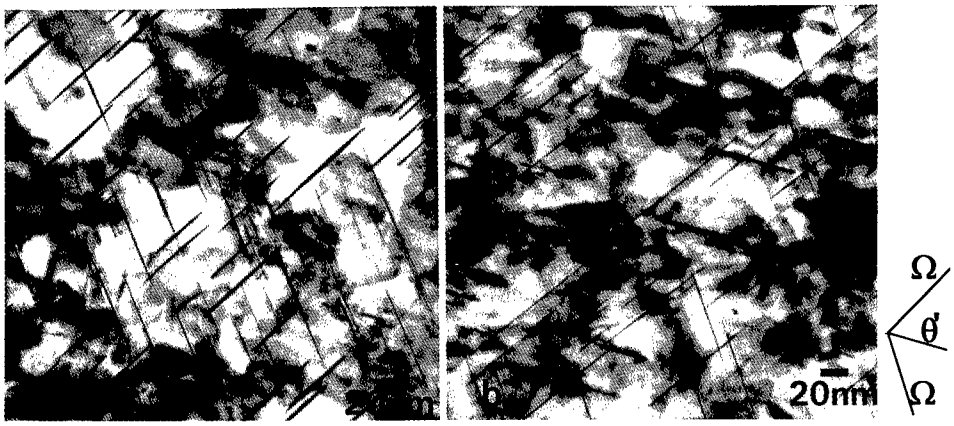


Figure 4 Bright-field Electron Micrographs of Alloy C415 (a, c) and C416 (b, d) Prior to Creep (a, b) and Subject to Creep for 1681h at 135°C-207MPa (c, d).
The electron beam is approximately parallel to a <001>α zone axis.

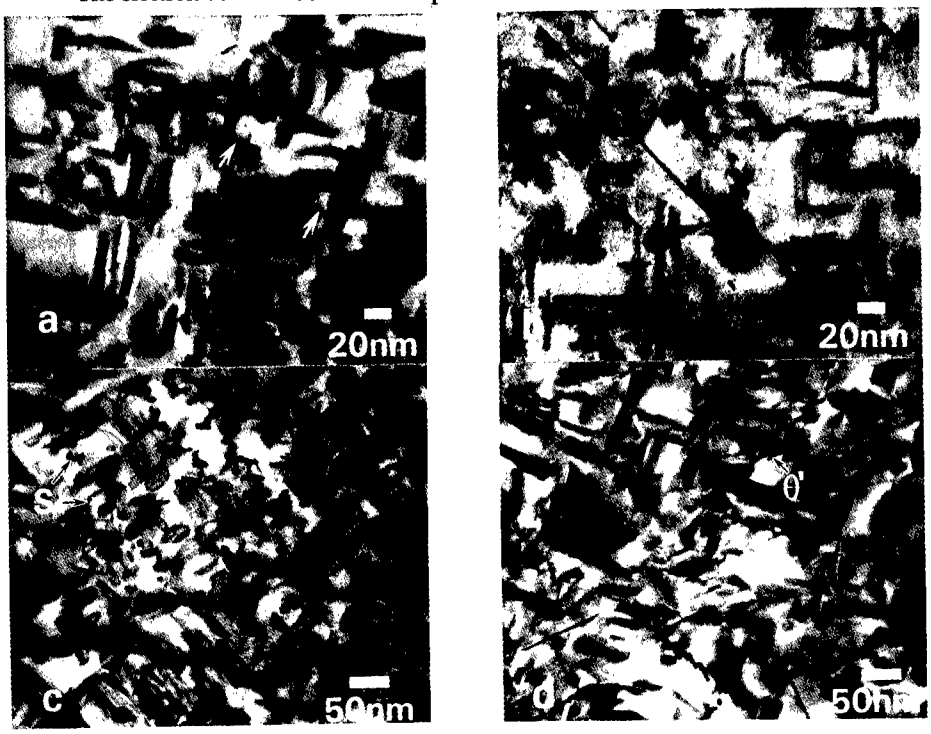


Figure 5 Selected Area Electron Diffraction Patterns Showing the <001>α from Samples of:
C415 and C416 in the T8 condition (a and c, respectively);
C415 and C416 in the crept condition of 135°C-207MPa-1681h (b and d, respectively).

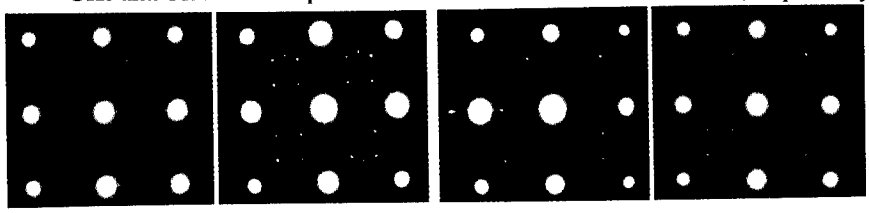
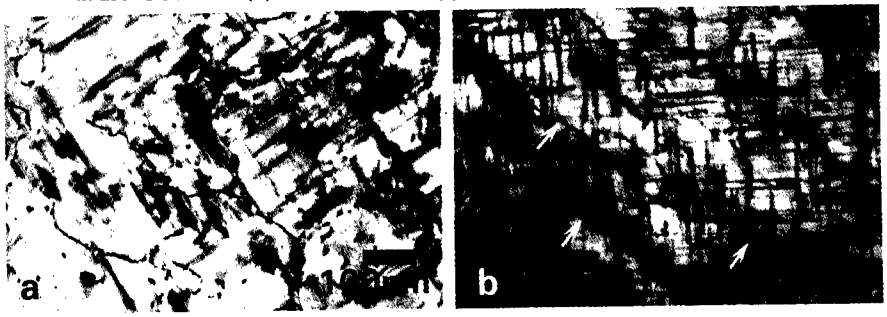


Figure 6 Bright-field Electron Micrographs of Alloy CM.001 before creep (a) and Crept 3647h at 135°C-207MPa (b). Electron beam approximately parallel to <001>α zone axis.



PROCESS PLANNING FOR LAYERED MANUFACTURING USING HETEROGENEOUS SOLID MODELS

Deba Dutta
dutta@engin.umich.edu

Vinod Kumar
vinodk@engin.umich.edu

Department of Mechanical Engineering
University of Michigan, Ann Arbor, MI 48109-2125

Abstract

By layered manufacturing (LM), we refer to the host of manufacturing technologies in which physical parts are "built" by depositing material layer by layer under computer control. The outer (nominal) geometry of the part and interior material distribution is simultaneously realized in LM. All LM technologies are computer-based and require the CAD model of the part that is to be manufactured. LM is now emerging as a new fabrication technology rather than being a prototyping technology. This is largely attributed to the improvements in existing processes, capability to deposit new materials and development of new processes. These have brought about better products (accuracy and finish), functional products (molds, metal parts) and significantly, new products (multiple material or heterogeneous objects).

Heterogeneous objects are objects composed of different constituent materials and could exhibit continuously varying composition and/or microstructure. Already, there are LM technologies such as DMD, SDM, LENS, DLF etc. that can selectively deposit materials and fabricate these heterogeneous objects. Also, recent advances in structural and material design can yield optimal product shapes having non-homogenous material distribution. However, the missing link in this product design and layered manufacturing environment is the capability to create a 3D CAD solid model that can represent the "solid interior". Current commercial CAD systems are not capable of representing these objects. Hence, there is a lack of CAD tools to perform process planning tasks for the manufacture of these objects in LM.

Our ongoing work is focussed on developing CAD tools which would facilitate the modeling and automated processing of heterogeneous objects. In this paper, we present our efforts in this direction to perform process planning tasks (issues in orientation, slicing and toolpath generation) for the manufacture of heterogeneous objects by LM. We identify issues in orientation and toolpath generation. We also explain the adaptive slicing algorithm for heterogeneous objects in greater detail.

The Third Pacific Rim International Conference on
Advanced Materials and Processing (PRICM 3)
Edited by M.A. Imam, R. DeNale, S. Hanada,
Z. Zhong and D.N. Lee
The Minerals, Metals & Materials Society, 1998

CAD Representation for Heterogeneous Objects

Traditional geometric/solid modeling has focussed on modeling objects based on their geometry and topology. The geometry of the object is modeled by considering the mathematical space $\mathbf{T} = \mathbf{R}^3$. Certain subsets of this space called r-sets and manifold solids are widely accepted as valid mathematical models of physical objects. The most commonly used representation schemes for this model are the Constructive Solid Geometry (CSG), Boundary Representation (B-Rep) or a hybrid. There is no material information present in the solid model.

An heterogeneous solid model is developed as a collection of material domains with each domain being discrete or mixed (graded). A discrete material domain is made of only one material or it could be an embedded component. In a mixed material domain, each point in the object is made up of many materials and could possibly contain voids. Now, the mathematical space $\mathbf{T}$ has to include a material space ($\mathbf{M}$) along with the geometry space $\mathbf{R}^3$. The choice of material space $\mathbf{M}$ is dictated by the kind of material information that needs to be included. For heterogeneous objects, the space $\mathbf{M}$ is chosen to be $\mathbf{R}^n$ where n is the number of materials. The material at each point of the object is characterized by a point in $\mathbf{R}^n$ where each coordinate indicates the volume fraction of a particular material. Thus, the product space $\mathbf{T} = \mathbf{R}^3 \times \mathbf{M}$ with the product topology formed the new modeling space for representing these objects. Subsets of this space $\mathbf{T}$ called r_m-objects were proposed to model these objects. In these models, the geometry was still modeled by the traditional r-sets and the additional attributes identifies the material of the domain. Boolean operations were also defined to create and manipulate these models.

Computer representation to implement this model was developed by including additional data structure on the B-Rep scheme. The main advantage of this approach is that the geometry is still modeled using traditional solid modeling methods and hence, the internal structure of the representation is unaffected. Details on this work can be found in [2][3]. A sample heterogeneous object modeled in our scheme is shown below in Figure 1.

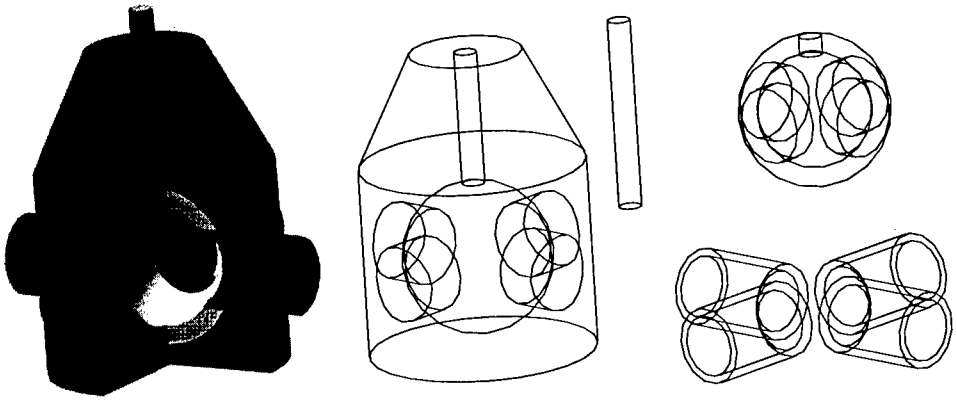


FIGURE 1. Heterogeneous object. The inner spherical shell region is modeled as a graded material.

Process planning tools for LM

While fabrication of homogeneous objects by LM typically require orientation, slicing, and support structure determination, fabricating heterogeneous objects require additional processing in each of the process planning tasks. We discuss these issues below.

Orientation

The orientation or the build direction of an object determines the direction in which the object is to be fabricated. There are several issues in selecting this build direction. These include:

- Minimization of support volume to reduce build time.
- Minimize support contact area to reduce surface roughness and finish cost.
- Minimize surface finish/roughness by orienting critical surfaces appropriately.
- Reduce build time by minimizing the height of the model in the build direction. This reduces the number of layers to be built.
- Minimization of trapped volume (especially for liquid resin based processes like SLA).

Most of these issues have been addressed to a great extent in the literature. However, the orientation problem for heterogeneous objects poses two additional issues:

- Process related constraints in orienting different material regions. A particular process might have some constraints regarding deposition of one material on top of the other.
- Minimizing the variation of material in a layer. Some process might limit the rate of change in material in each layer due to process constraints. In these case, the material variation in each layer must be kept as low as possible.

These two material based issues form a part of our ongoing work in process planning.

Adaptive Slicing

The oriented model is sliced perpendicular to the build direction to yield the slices. The procedure we use adaptively slices the model to minimize the error (cusp height) due to the stairstep effect in the final manufactured part. This procedure yields variable thickness layers where the thickness of the layers varies according to the curvature of the surface. Adaptive slicing algorithm for a homogeneous object is discussed in [4]. However, this algorithm is not directly applicable to heterogeneous objects. This procedure has to be modified to take into account the material information present [5]. The modified slicing procedure is summarized below:

Input: Heterogeneous CAD model, required cusp height, surface selection (all surfaces or external surfaces only), minimum and maximum permissible slice thickness, deposition requirement (excess or deficient).

Output: Sliced model of the heterogeneous object (set of heterogeneous layers)

Preprocessing: *Subdivide the heterogeneous model into blocks*:

The heterogeneous object is divided into blocks along the build direction. The vertices are sorted in the build direction and the portion of the object between two successive vertices is defined as a block. The blocks are created by slicing the object at each vertex. All the vertices including the internal ones (from the internal material boundaries) are considered. It must be noted that each block would still contain more than one material region.

Algorithm: For each block generated above, perform adaptive slicing.

Calculate layer thickness:

The slicing procedure is used to calculate the layer thickness for each slice. Depending on the input for surface selection, either all surfaces or only the external surfaces of the block are considered for calculating the layer thickness. For surface finish, only the exterior surfaces are considered as internal material boundaries do not contribute to the finish. If the

internal surfaces are equally important, then all surfaces are used for calculating the layer thickness. The layer thickness calculations is based on the curvature of these surfaces. For more details on curvature based calculations, refer [4]. If the layer thickness is less (greater) than the minimum (maximum) permissible thickness, the minimum (maximum) permissible thickness value is used.

Obtain the slice:

Each material domain in the heterogeneous object is individually sliced with the calculated layer thickness to generate the slice at that z-height. Here, all the surfaces (from each material domain) of the heterogeneous model are sliced to obtain the different material regions in each slice.

Calculate material distribution for the slice:

Each slice will now comprise of several material regions obtained by slicing the material domains. Within each region, the material can be a constant or vary continuously. Hence, the material distribution for each region of the slice is evaluated from the material distribution function of that corresponding domain of the object. This is achieved by slicing the material distribution of the domain at that particular z-height.

Calculate the layer based on deposition strategy:

The adaptive slicing procedure generates the slices for either positive or negative deposition i.e., the fabricated object will completely enclose the CAD model or vice-versa. A sliced model which does not satisfy either of the deposition strategy is not desired as it distorts the shape of the final fabricated part.

In order to ensure the positive or negative deposition, each layer must be fabricated either by the top-down approach (the upper slice defines the layer below it) or the bottom-up approach (the lower slice defines the layer on top of it). The appropriate approach for a layer is determined by the deposition strategy chosen (positive or negative) and by the z-component of the surface normal of all surfaces along the external contour of the defining slice. It is assumed that the z-component will either be positive or negative for the entire external contour (called as the normal sign assumption in [4]). The normal sign condition implies that the upper or lower slice of a layer is completely contained in the other. This can be easily verified by checking if the standard boolean intersection on the two external contours (by projecting one slice onto the other) is empty. Note that, only the external contours (contributed by the external surfaces) of the two slices have to be considered and hence, the standard intersection operation can be used.

If the normal sign condition is violated, the external curves of the upper and lower slices intersect. For the negative deposition, the two slices are intersected and the intersecting region is used as the defining slice. Here, the intersection involves two slices unlike the situation mentioned above where only the external contours were intersected. As each slice contains several material regions, the intersection operation defined for heterogeneous models (i.e., intersection on r_m-classes / r_m-objects [3]) have to be used instead of the standard boolean intersection which would not be applicable. Likewise, for the positive deposition, the two slices are united using the union operation defined for the heterogeneous models.

Represent the layer information as a heterogeneous model

Each of the slices and layers generated contains several material regions and hence, they can be represented only using the heterogeneous solid modeling scheme. They can be trivially represented as a two-dimensional heterogeneous model without any additional work or modification in the modeler. The existing solid modeling scheme are not capable of representing these material regions in a slice.

The algorithm ends when all the blocks are sliced. A sample sliced model is shown below in Figure 2.

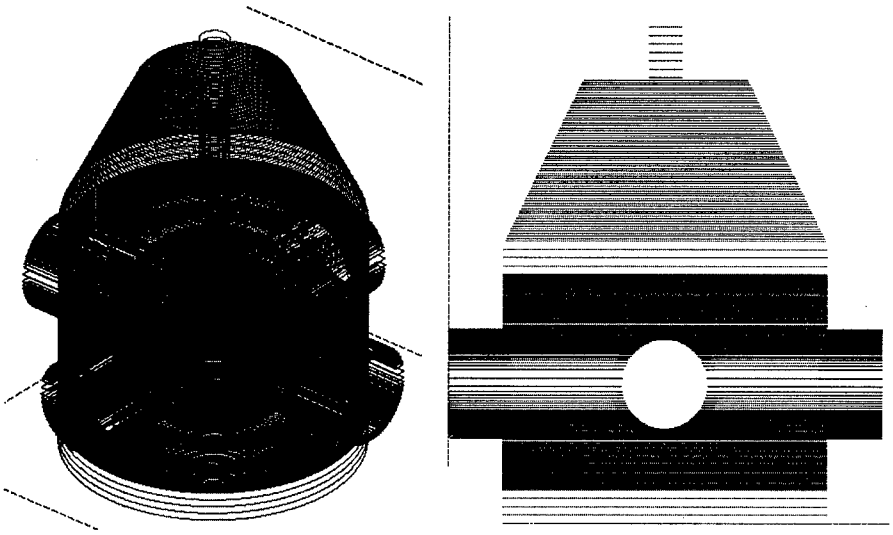


FIGURE 2. Adaptively sliced model - isometric and front view

Toolpath generation

The term "toolpath" refers to the path which the head (nozzle, laser etc.) would follow. The toolpath generation for each heterogeneous layer involves the following:

- Both material resolution and geometry resolution of the process must be taken into account for toolpath generation. An example of a one dimensional material distribution $F_z(x)$ at a particular slice (z) and its approximation based on resolution is shown below in Figure 3.

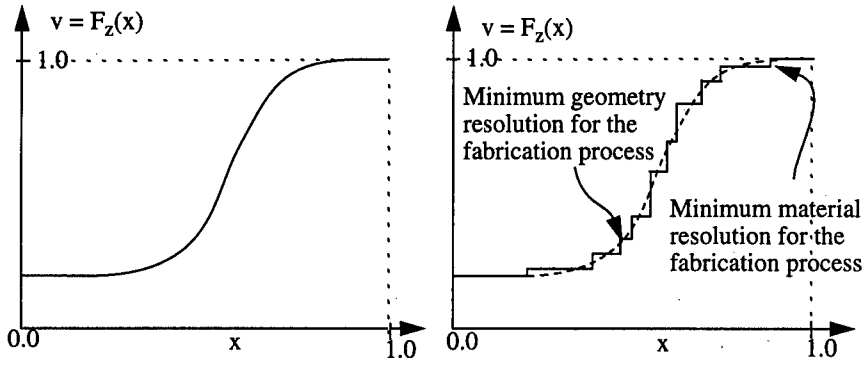


FIGURE 3. Approximation of a distribution function by series of step functions

- The variation of material along the path must be minimized.

Each of these issues can be handled separately and either one of them can be performed first followed by the other. Sample toolpath for a single layer is shown below in Figure 4.

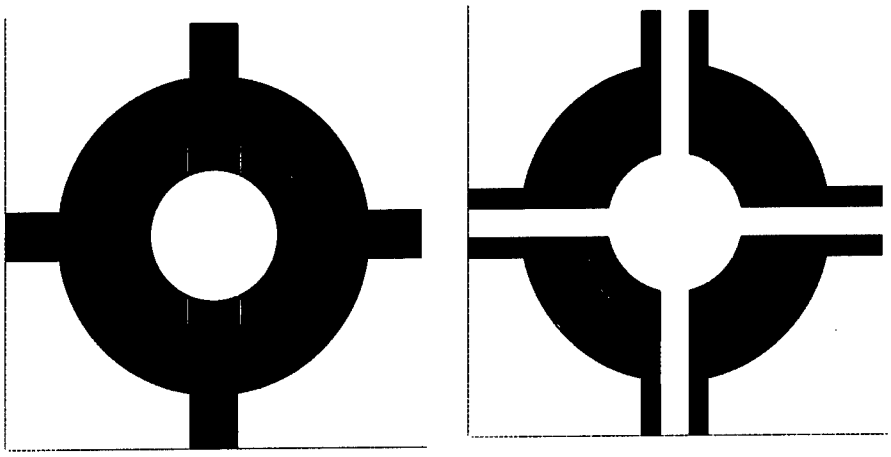


FIGURE 4. Toolpath for two different layers

Summary

With the rapid developments in design techniques and fabrication methods to design and manufacture heterogeneous objects, CAD modeling and CAD based process planning have become crucial. In our continuing work, we are developing CAD solid models which are capable of representing heterogeneous objects. Process planning of these heterogeneous models is a challenging task which poses several additional problems during process planning stages of orientation, slicing and toolpath generation. In this paper, we summarized all the issues that are faced during these stages. In particular, we focussed on the adaptive slicing algorithm. Future work will be dedicated to developing material based orientation strategy and generating toolpath for each layer minimizing the material variation.

Acknowledgments

Financial support for this work was received from Office of Naval Research grants N00014-95-1-0767 and N00014-97-1-0245 and is gratefully acknowledged. We would like to acknowledge Prashant Kulkarni for his help in processing of sample heterogeneous objects.

References

1. V. Kumar and D. Dutta, "An Assessment of Data Formats for Layered Manufacturing", Advances in Engineering Software, 28 (3) (1997), 151-164.
2. V. Kumar and D. Dutta, "An Approach to Modeling Multiple Material Objects", Proceedings of 4th ACM Solid Modeling Symposium, Atlanta, (1997), 336-345.
3. V. Kumar and D. Dutta, "An Approach to Modeling & Representation of Heterogeneous Objects", (Technical Report UM-MEAM-97-05, Department of Mechanical Engineering, University of Michigan, Ann Arbor, 1997).
4. P. Kulkarni and D. Dutta, "An Accurate Slicing Procedure for Layered Manufacturing", Computer Aided Design, 28 (9) (1996), 683-697.
5. V. Kumar, P. Kulkarni and D. Dutta, "Adaptive Slicing of Heterogeneous Solid Models for Layered Manufacturing", (Technical Report UM-MEAM-98-02, Department of Mechanical Engineering, University of Michigan, Ann Arbor, 1998).

MODELLING AS A BASIS FOR MICROSTRUCTURAL DESIGN IN HIGH STRENGTH Al AND Mg ALLOYS

J.F. Nie and B.C. Muddle

Department of Materials Engineering, Monash University
Clayton, Victoria, Australia 3168

Abstract

The quantitative effects of precipitate shape, orientation and distribution on yield strength have been examined using models of particle strengthening developed for aluminium and magnesium alloys containing rationally-oriented precipitate plates or rods. It has been found that, for precipitates which are either shearable or shear-resistant, the models of particle strengthening predict that high tensile yield strength is associated with microstructures containing a high density of intrinsically strong, plate-shaped precipitates of large aspect ratio. The results of modelling suggest that further improvement in the strength might be achieved by increasing the number density and/or aspect ratio of $\{111\}_\alpha$ and $\{100\}_\alpha$ precipitate plates for precipitation-hardened aluminium alloys, and by increasing the number density and/or aspect ratio of prismatic and pyramidal precipitate plates for precipitation-hardened magnesium alloys.

The Third Pacific Rim International Conference on
Advanced Materials and Processing (PRICM 3)
Edited by M.A. Imam, R. DeNale, S. Hanada,
Z. Zhong and D.N. Lee
The Minerals, Metals & Materials Society, 1998

Introduction

The effects of the shape, orientation and distribution of precipitate particles on yield strength of precipitation-hardened aluminium and magnesium alloys have received little attention, although they have long been recognised as potentially important factors in determining the mechanical properties of such alloys [1]. A common microstructural feature associated with maximum strength of high strength aluminium and magnesium alloys is the presence of rationally-oriented precipitate plates and/or rods [2-3], Fig. 1. An understanding of the quantitative relationship between yield strength and precipitate microstructures is limited by a lack of appropriate versions of the Orowan equation and equations defining precipitation-strengthening for such structures. The development of high strength aluminium and magnesium alloys remains largely empirical, and there is a need for an improved theoretical basis for alloy design [4].

It is the purpose of the present paper to review results of the modelling of the effects of precipitate shape, orientation and distribution on the yield strength of aluminium and magnesium alloys, using models of particle strengthening developed for rationally-oriented precipitate plates and rods. The work seeks to identify those microstructural parameters which are important in optimising precipitation hardening or dispersion strengthening.

Theoretical Modelling

Shearable precipitates can impede the movement of gliding dislocations through a variety of dislocation/particle interaction mechanisms, including those described as interfacial (chemical) strengthening, coherency strengthening, stacking-fault strengthening, modulus strengthening and order strengthening [5]. For each such proposed mechanism of strengthening, the contribution of the precipitates to the critical resolved shear stress (CRSS) of an alloy can be represented generally by an equation of the form:

$$\Delta\tau = \left(\frac{2}{b\sqrt{\Gamma}}\right)\left(\frac{1}{L_P}\right)\left(\frac{F}{2}\right)^{3/2}, \qquad (1)$$

where $\Delta\tau$ is the increment in CRSS, **b** is the magnitude of the Burgers vector of the slip dislocations, Γ is the dislocation line tension in the matrix phase, L_P is the mean planar centre-to-centre precipitate spacing, and force F is a measure of the resistance of the precipitates to dislocation shearing.

If it is assumed that a dispersion of precipitate particles is distributed uniformly over the slip plane of the matrix phase, then the Orowan increment in CRSS produced by the need for dislocations to by-pass these particles is given as [5]:

$$\Delta\tau = \left(\frac{Gb}{2\pi\sqrt{1-\nu}}\right)\left(\frac{1}{\lambda}\right)\left(\ln\frac{d_p}{r_0}\right), \qquad (2)$$

where G is the shear modulus of the matrix phase, υ is Poisson's ratio, r_0 is the core radius of

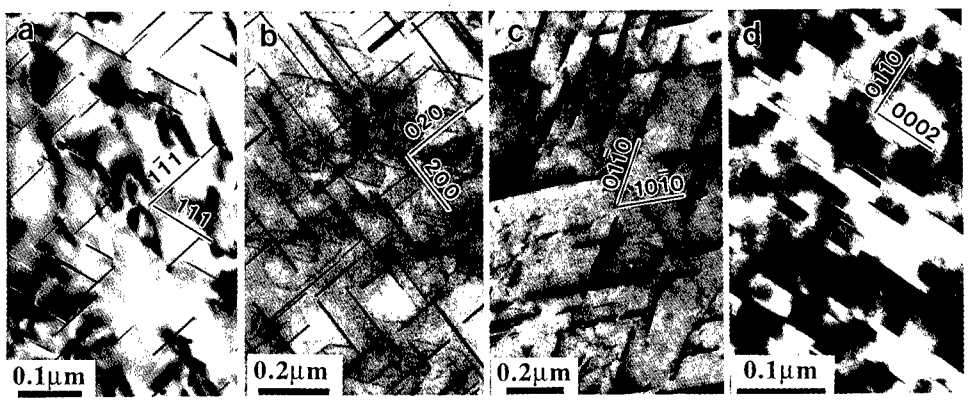


Figure 1: Transmission electron micrographs showing (a) $\{111\}_\alpha$ plates in Al-2.9Cu-2.1Li (wt%) alloy, (b) $\{100\}_\alpha$ plates in Al-4Cu (wt%) alloy, (c) $\{10\bar{1}0\}_\alpha$ plates in Mg-5Y-4RE (wt%) alloy (RE represents rare earth elements), and (d) $\{0001\}_\alpha$ plates in Mg-1Ca-1Zn (wt%) alloy.

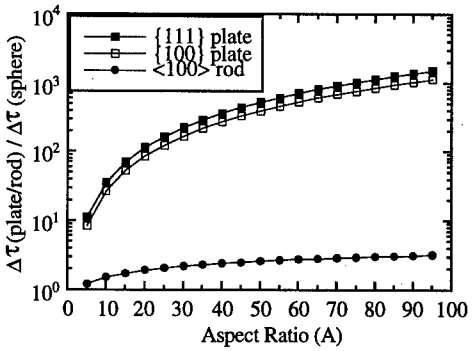


Figure 2: Variation of ratio $\Delta\tau$(plate/rod)/$\Delta\tau$ (sphere) with aspect ratio for $\{111\}_\alpha$ and $\{100\}_\alpha$ precipitate plates and $<100>_\alpha$ precipitate rods, calculated assuming interfacial strengthening of sheared particles.

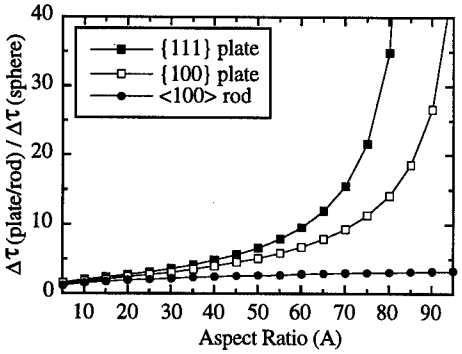


Figure 3: Variation of ratio $\Delta\tau$(plate/rod)/$\Delta\tau$ (sphere) with aspect ratio for Orowan strengthening attributable to $\{111\}_\alpha$ and $\{100\}_\alpha$ precipitate plates and $<100>_\alpha$ precipitate rods (f = 0.05).

dislocations, d_p is the planar diameter of the precipitate particles, and λ is the effective planar inter-precipitate spacing. Within equations (1) and (2), it is L_P, λ and F that vary with the shape, orientation and distribution of the particles. The development of appropriate versions of the Orowan and precipitation-hardening equations for alloys containing rationally-oriented precipitate plates or rods thus requires the calculation of these parameters for appropriate particle arrays. Details of the models are presented elsewhere [6].

Precipitation-Hardened Aluminium Alloys

Models of particle strengthening have been developed [6] to account for the contributions of both interfacial strengthening and Orowan strengthening to CRSS for aluminium alloys containing rationally-oriented precipitate plates or rods. For shearable precipitates, the variations in the ratio $\Delta\tau$(plate/rod)/$\Delta\tau$(sphere) with plate/rod aspect ratio for various forms of particle are shown in Fig. 2. Unlike the results for spherical particles, it is evident that the contribution due to interfacial strengthening may become significant when particles take, in particular, a plate-shaped form. For identical volume fractions and number densities of precipitates per unit volume, the yield stress increments produced by $\{111\}_\alpha$ and $\{100\}_\alpha$ precipitate plates are orders of magnitude larger than those produced by $<100>_\alpha$ precipitate rods and by spherical particles. The increments in CRSS produced by $\{111\}_\alpha$ and $\{100\}_\alpha$ plates increase substantially with an increase in plate

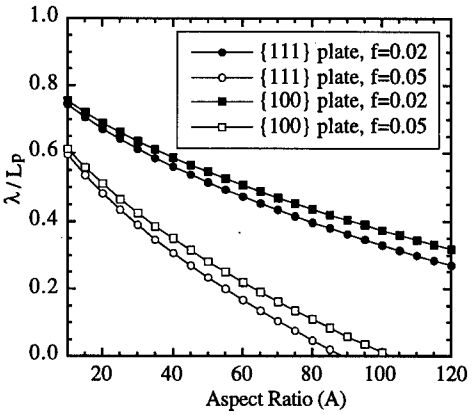


Figure 4: Variation of ratio λ/L_p with aspect ratio for $\{111\}_\alpha$ and $\{100\}_\alpha$ precipitate plates at volume fractions of 0.02 and 0.05.

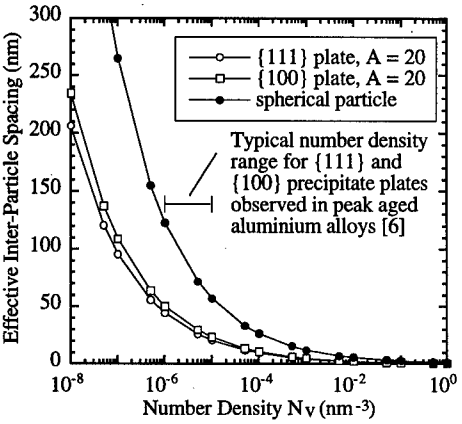


Figure 5: Variation of effective inter-particle spacing with number density of particles per unit volume, at a volume fraction of 0.05.

aspect ratio, and are up to three orders of magnitude larger than that produced by spheres, when the plate aspect ratio is in the range of 5:1 to 105:1. Interfacial strengthening can thus potentially be a major strengthening mechanism in aluminium alloys containing rationally-oriented, shearable precipitate plates of large aspect ratio.

For shear-resistant precipitates, comparison of similar precipitate volume fractions and number densities of precipitates per unit volume indicates that the Orowan increments in CRSS produced by $\{111\}_\alpha$ and $\{100\}_\alpha$ precipitate plates are invariably larger than those produced by $<100>_\alpha$ precipitate rods and spherical particles, Fig. 3. The yield stress increment produced by $\{111\}_\alpha$ plates is larger than that arising from $\{100\}_\alpha$ plates and, for both precipitate orientations, the yield stress increment increases substantially with an increase in plate aspect ratio.

When the aspect ratio exceeds a critical value, the precipitate plates form an essentially continuous three-dimensional network. For f = 0.05, the effective inter-particle spacing, λ/L_P, approaches zero when the aspect ratios for $\{111\}_\alpha$ and $\{100\}_\alpha$ plates reach values of approximately 90 and 100 respectively, Fig. 4. This implies that the $\{111\}_\alpha$ or $\{100\}_\alpha$ plates form closed tetrahedral or cubic volumes and, provided that the plates resist dislocation shearing, those dislocations generated within these volumes will be constrained. In practice, accumulation of dislocations may lead to local stress concentrations exceeding the yield strength of precipitates and thus to precipitate shearing.

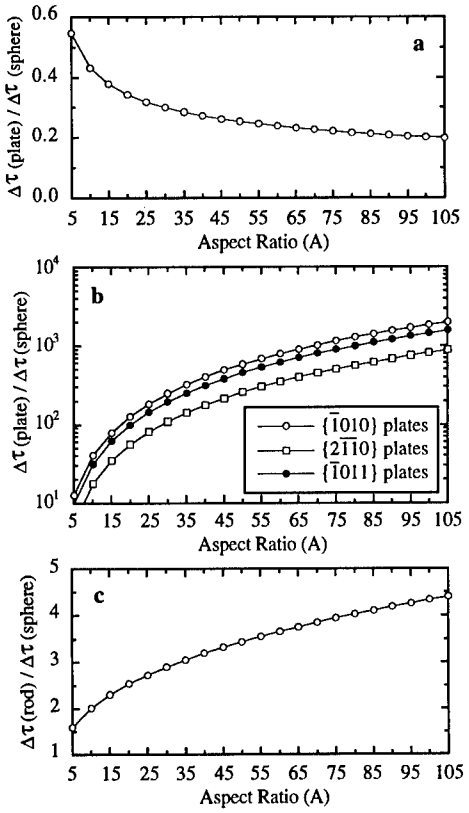


Figure 6: Variation of $\Delta\tau$(plate/rod)/$\Delta\tau$(sphere) as a function of aspect ratio for (a) $\{0001\}_\alpha$ plates, (b) prismatic and pyramidal plates, and (c) $<0001>_\alpha$ rods, calculated assuming interfacial strengthening of sheared particles.

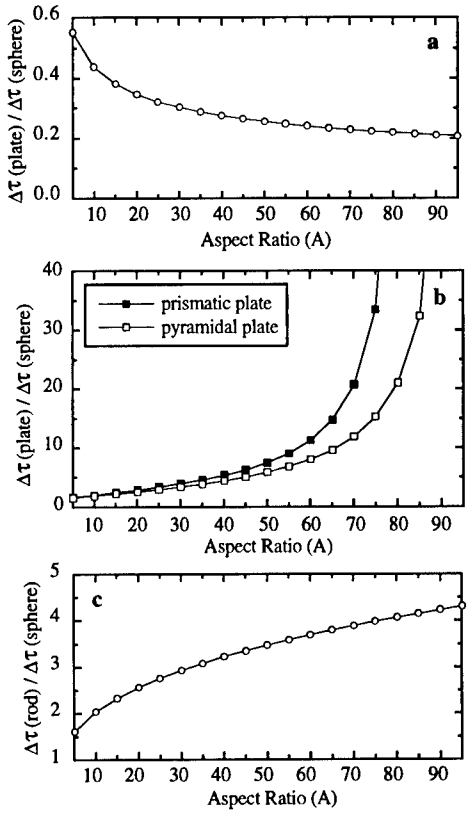


Figure 7: Variation of $\Delta\tau$(plate/rod)/$\Delta\tau$(sphere) with aspect ratio for Orowan strengthening attributable to (a) $\{0001\}_\alpha$ plates, (b) prismatic and pyramidal plates, and (c) $<0001>_\alpha$ rods, at a volume fraction of 0.05.

The variation of effective inter-particle spacing with precipitate number density is shown in Fig.5 for $\{111\}_\alpha$ and $\{100\}_\alpha$ plates. For identical volume fractions and number densities of precipitates, the $\{111\}_\alpha$ and $\{100\}_\alpha$ plates are much more effective in achieving a reduction in inter-particle spacing when N_V is less than 10^{-3} nm^{-3}. Typical values of N_V in high strength alloys of interest are in the range 10^{-6} - 10^{-5} nm^{-3}.

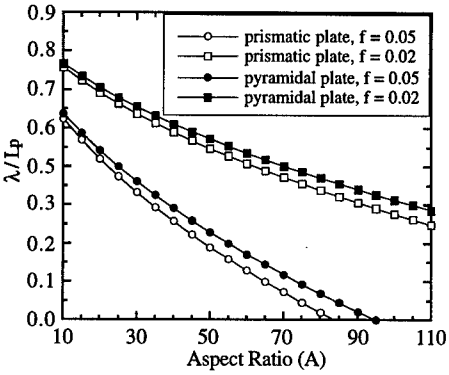


Figure 8: Variation of ratio λ/L_P with aspect ratio for prismatic and $\{10\bar{1}1\}_\alpha$ pyramidal precipitate plates at volume fractions of 0.02 and 0.05.

Precipitation-Hardened Magnesium Alloys

The contribution of interfacial strengthening to CRSS has also been calculated for hexagonal magnesium alloy matrices containing rationally-oriented precipitate plates or rods. The variations in the ratio $\Delta\tau$(plate/rod)/$\Delta\tau$(sphere) with plate/rod aspect ratio for various forms and orientations of particle are shown in Fig. 6. The contribution due to interfacial strengthening may again become significant when particles take, in particular, a plate-shaped form on the prismatic or pyramidal planes of the magnesium matrix phase. The yield stress increments produced by prismatic and pyramidal precipitate plates are orders of magnitude larger than those produced by basal precipitate plates, by $<0001>_\alpha$ precipitate rods and by spherical particles, for a given volume fraction and number density of precipitates per unit volume. Interfacial strengthening can again potentially be a major strengthening mechanism in magnesium alloys containing shearable precipitate plates of large aspect ratio formed on prismatic or pyramidal planes of the matrix phase.

For magnesium alloys containing shear-resistant precipitates, the variations of the ratio $\Delta\tau$(plate/rod)/$\Delta\tau$(sphere) with plate/rod aspect ratio, for a precipitate volume fraction of 0.05, is shown in Fig. 7 for identical precipitate volume fractions and number densities of precipitates per unit volume. The Orowan increments in CRSS produced by prismatic and pyramidal precipitate plates are invariably larger than those produced by basal precipitate plates, $<0001>_\alpha$ precipitate rods and spherical particles. The yield stress increment produced by prismatic plates is larger than that arising from pyramidal plates and, for both precipitate orientations, the yield stress increment increases substantially with an increase in plate aspect ratio. There is a critical value of aspect ratio for each for which the effective inter-particle spacing becomes zero and the plates form a continuous three-dimensional network, Fig. 8. If the plates are assumed to remain shear-resistant, then the Orowan increment becomes infinitely large as λ/L_P approaches zero.

Microstructural Design

For precipitation-hardened aluminium alloys containing precipitates which are either shearable or shear-resistant, modelling of the effects of precipitate shape, orientation and distribution on yield strength predicts that high tensile yield strength is associated with microstructures containing a high density of intrinsically strong, plate-shaped precipitates with $\{111\}_\alpha$ or $\{100\}_\alpha$ habit planes and large aspect ratios. The ultra-high tensile yield strength ($\geq$ 700 MPa) observed in Al-Cu-Li-Mg-Ag (X2095) alloy [2] and the high yield strength (550 MPa) of Al-Cu-Li (AA2090) alloys [7] may, for example, be attributable to a uniform distribution of T_1 precipitate plates of large aspect ratio (in the range 40:1 to 100:1) formed on $\{111\}_\alpha$ planes. It has also been shown that Al-Cu-Mg-Ag alloy, strengthened by the presence of thin plates (typical aspect ratio 30:1) of the metastable orthorhombic phase (Ω) on the $\{111\}_\alpha$ planes, may develop a tensile yield strength exceeding 500 MPa [8]. Furthermore, the well known high strength of Al-Zn-Mg-Cu alloys (e.g. 7075) is associated with the combined effects of the number density and aspect ratio of precipitate platelets of the phase η', which also form on the $\{111\}_\alpha$ planes [2]. A remarkably high value of hardness (180 HV) has also been obtained [9] in Al-Cu-Mg-Si alloys by refining the distribution of θ' precipitate plates formed on the $\{100\}_\alpha$ planes, and complementing this by a fine-scale distribution of $<100>_\alpha$ rods of a quaternary Q phase.

The strengthening phases in precipitation-hardened aluminium alloys are almost invariably metastable intermediate precipitates that are partially coherent or semi-coherent with the matrix phase and, in many cases, the metastable phase equilibria that determine the formation of key strengthening phases have not been examined critically. For many such alloys, it has been established empirically that selected microalloying additions lead to significant changes in precipitation behaviour, often with improvements in mechanical properties. The combined addition of Mg and Ag (levels of typically < 0.5 wt%) to the classical Al-4wt%Cu alloy leads, for example, to the replacement of the metastable tetragonal $\{100\}_\alpha$ precipitate θ' by the phase Ω of similar composition, formed as thin plates on $\{111\}_\alpha$ planes [2]. The resulting microstructure exhibits substantial improvements in strength and thermal stability. Systematic additions of Li to Al-Cu-Mg-Ag alloys lead to an increase in aspect ratio of $\{111\}_\alpha$ precipitate plates and replacement of Ω by T_1 phase [2].

For precipitation-hardened magnesium alloys, whether particles are sheared or shear-resistant, the particle strengthening models predict that high strength is associated with microstructures containing a high density of intrinsically strong, plate-shaped precipitates with prismatic or pyramidal habit planes and large aspect ratios, and that precipitate plates formed on the basal plane of the matrix phase provide the least effective barrier to gliding dislocations. Although a critical examination of the validity of the models is limited by a lack of reliable quantitative experimental data on the size and distribution of appropriate precipitate arrays, examination of existing precipitation-hardened magnesium alloys indicates that the predictions are in broad qualitative agreement with experimental observations. The relatively high strength developed in Mg-Y-RE (WE54 and WE43) alloys, where RE represents rare earth elements, can be attributable to the formation of precipitate plates on the prismatic planes of the matrix phase [3], and the relatively low strength of Mg-Al-Zn (AZ91) alloys is associated with the formation of precipitate plates on the basal plane of the matrix phase [3]. Compared to those precipitate plates formed in precipitation-hardened aluminium alloys, the prismatic precipitate plates formed in Mg-Y-RE alloys have a relatively low number density and small aspect ratio.

Further improvements in the design of aluminium and magnesium alloys for high strength will require an improved understanding of the metastable phase equilibria leading to those intermediate phases forming as plate-shaped products on low index habit planes. In particular, there needs to be a concerted systematic effort to better understand the role of microalloying additions in determining metastable phase equilibria. For existing alloys strengthened by plate-shaped precipitates, the models outlined here suggest that further improvements in strength might be achieved by increasing the number density and/or aspect ratios of the plates. One approach to achieving an increase in plate aspect ratio may lie in the use of microalloying additions, which partition to either matrix or precipitate phase to improve coherency of the precipitate phase in the habit plane.

Acknowledgments

This work was supported by the Australian Research Council. JFN acknowledges gratefully the support of a Logan Research Fellowship, Monash University.

References

1. P.M. Kelly, Int. Metall. Review, 18 (1973), 31-36.
2. B.C. Muddle, S.P. Ringer and I.J. Polmear, Advanced Materials '93, VI / Frontiers in Materials Science and Engineering, Trans. Mat. Res. Soc. Jpn., ed. S. Somiya, M. Doyama and R. Roy (Elsevier Science B.V. 1994), 19B, 999-1023.
3. G.W. Lorimer, Magnesium Technology, ed. C. Baker, G.W. Lorimer and W. Unsworth (The Institute of Metals, London 1987), 47-53.
4. E. Hornbogen and E.A. Starke, Acta Metall. Mater., 41 (1993), 1-16.
5. A.J. Ardell, Metall. Trans. A, 16A (1985), 2131-2165.
6. J.F. Nie and B.C. Muddle, to be published, 1998.
7. W.A. Cassada, G.J. Shiflet and E.A. Starke, Metall. Trans. A, 22A (1991), 299-306.
8. I.J. Polmear and M.J. Couper, Metall. Trans. A, 19A (1988), 1027-1035.
9. X. Gao, J.F. Nie and B.C. Muddle, Proc. Materials Research 96, Institute of Metals and Materials Australasia, Melbourne, Australia, Vol. 1 (1996), 33-36.

Capillary Rheometric Studies of Aluminium Alloy AlSi7Mg0.3Sr in its Semi-Solid State

F.C. Yee, X.P. Niu, S.W. Hao and B.H. Hu

Gintic Institute of Manufacturing Technology
71 Nanyang Drive, Singapore 638075
Republic of Singapore

Abstract

One of the more popular methods of forming semi-solid material is through injection moulding on a pressure die casting machine. However, not much is understood of the process owing to the lack of experimental data on the rheology of semi-solid materials under such flow conditions. This paper documents the results of experimental work which serves to close this gap.

A high temperature capillary rheometer was designed and fabricated for the extrusion of aluminium alloy AlSi7Mg0.3Sr under varying material temperatures and shear rates. The shear rates of 10^1 to 10^4 s^{-1} were designed to match that experienced by semi-solid materials during moulding on a pressure die casting machine. The viscosity and shear stress data obtained are thus more representative than those obtained at lower shear rates and those obtained using Coutte or Searle type viscometers. In addition, the extrudate were also examined to determine the onset of flow instability which will affect the flow front and consequently the quality of the casting. The results point to an optimal processing window for this alloy.

The Third Pacific Rim International Conference on
Advanced Materials and Processing (PRICM 3)
Edited by M.A. Imam, R. DeNale, S. Hanada,
Z. Zhong and D.N. Lee
The Minerals, Metals & Materials Society, 1998

Introduction

In the 20 years since Spencer's [1] discovery that shearing alloys during solidification results in a material with fine spherical grains and unusual flow properties in the semi-solid state, a good deal of experimental work [2,3] has been undertaken to better understand and characterize the properties of such semi-solid materials. However, many of such studies [4,5] have been conducted under conditions different from those found in commercial metal forming processes. In experiments using Couette or Searle type viscometer, the alloy never completely solidifies. The alloy was cooled from a point above the liquidus to a point in the semi-solid region. In commercial forming of aluminium alloys, however, rheocast billets were allowed to solidify completely. The billets were later reheated from room temperature to the semi-solid state. Further, as the capillary rheometer closely resembles the injection moulding machine during the injection phase of the production cycle, it would yield viscosity data that are more relevant to commercial production.

Experiment

In order to examine the rheological properties of aluminium alloy AlSi7Mg0.3Sr (Table I) at shear rates comparable to that experienced during moulding, an experiment was designed to collect viscosity data at varying material temperatures. The absence of commercial high temperature capillary rheometers necessitated the development of an experimental rheometer. The experiment thus involved the design and fabrication of an extrusion die (functioning as a capillary rheometer), design of the pressure driven flow process, collection and analysis of the data collected. The various components of the rheometer are shown in Figures 1 and 2.



Figure 1. Extrusion die (functioning as a capillary rheometer), disassembled.

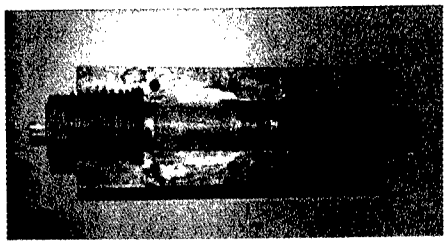


Figure 2. Extrusion die, opened to show internal set-up.

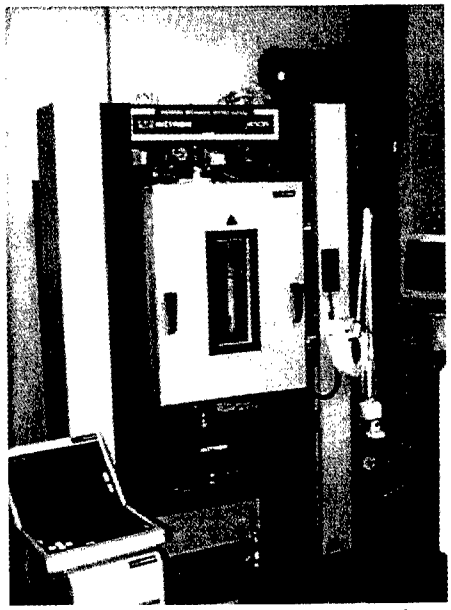


Figure 3. Instron Model 4500 Testing System fitted with the Instron 3119-008 Temperature Chamber

The capillary rheometric experiment was conducted in a furnace (INSTRON 3119-008 Temperature Chamber) to ensure uniform heating and to minimize temperature variation. The pressure was applied via an INSTRON Model 4500 Testing System (Figure 3). The experiment was an uni-axial compression test under varying conditions of temperature, loading speed, capillary length and capillary diameter. At any particular temperature, the experiment was conducted under isothermal conditions. The load versus displacement curves were obtained for each experimental condition. The steady state load value was then extracted and used in the derivation of the shear stress and viscosity values. The experiment was designed to achieve a "gate speed" or material velocity in the capillary of between 0.01 and 1.67 ms^{-1}, and a shear rate of between 10^0 and 10^4 s^{-1} . This is comparable to actual die casting conditions although the gate speed can be slightly higher. The stress vs. shear rate curves for the experimental matrix of parameters were plotted and the true and apparent viscosity behaviour derived.

Table I. Chemical Composition of Aluminium Alloy AlSi7Mg0.3Sr

Material	Si	Fe	Cu	Mn	Mg	Ni	Zn	Pb+Sn	Ti	Sr	Others
AlSi7Mg0.3Sr	6.5				0.30					0.01	
(A356)	7.5	0.15	0.03	0.03	0.40	0.03	0.05	0.03	0.2	0.05	0.10

Results and Discussion

Test data revealed, as expected, a steady state load level during the extrusion (Figure 4).

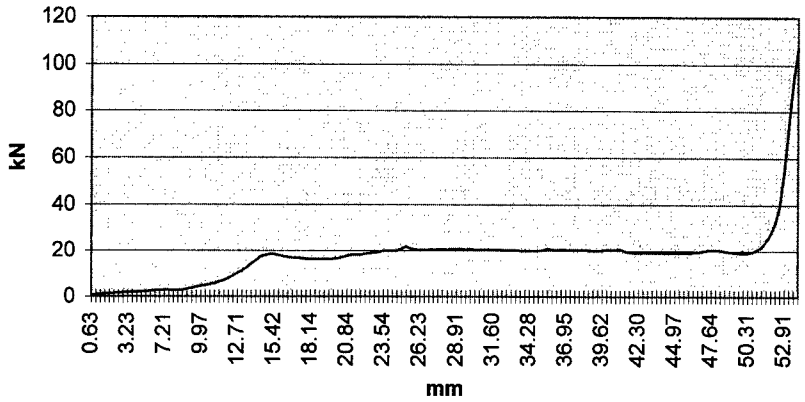


Figure 4. A typical load vs. displacement plot showing a steady state load.

The viscosity was found to be inversely proportional, on a logarithmic scale, to the shear rate (Figure 5). This shear thinning can be explained as follows. In the semi-solid state, the solid grains tend to stick together because of surface tension effects. The breaking of solid-solid bonds under shear contributes significantly to the overall energy dissipation, giving a higher effective viscosity, especially at low shear rates. The relative contribution of particle bonds to the viscosity decreases as the shear rate increases, however, because particle flocs or clusters are broken down at higher shear rates. Consequently, the material exhibits shear thinning over several decades of shear rate.

The models proposed to describe the effect of shear rate, $\dot{\gamma}$, on viscosity, μ, have been numerous [6]. A detailed analysis of the various methods will be presented in a later report. It is sufficient here to describe the shear thinning behaviour using the power law:

$$\mu = k\,\dot{\gamma}^{-n} \qquad (1)$$

where k and n are empirically determined constants. The relationships derived from the experimental data are:

At 570 °C $\quad \mu = 4\text{x}10^{6}\,\dot{\gamma}^{-0.9385}$ (2)

At 580 °C $\quad \mu = 3\text{x}10^{6}\,\dot{\gamma}^{-0.9855}$ (3)

At 590 °C $\quad \mu = 339.85\,\dot{\gamma}^{-0.6212}$ (4)

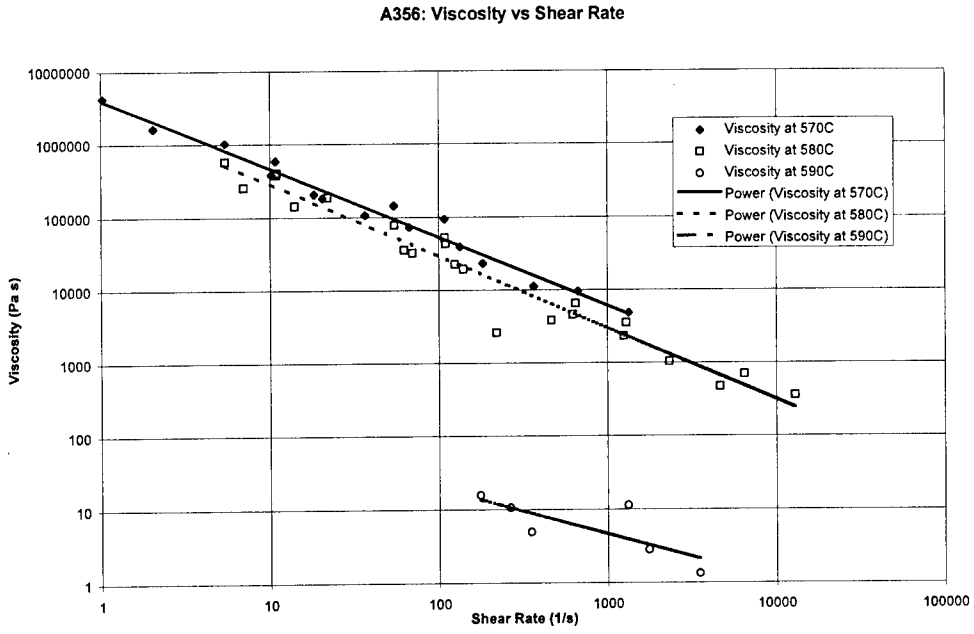


Figure 5. Graph of viscosity vs. shear rate for Alloy AlSi7Mg at 570 °C, 580 °C and 590°C.

The surfaces of the extrudate (Figure 6) were also examined to establish the flow conditions. Preliminary observations revealed instances of wall slip, melt fracture and extrudate swell (Figure 8). Owing to the impenetrability of the die wall, the layer of grains next to the wall is typically more dilute than in the bulk [7]. During flow, the shear rate gradient causes grains to migrate away from the wall. This shear induced migration is greater for smaller capillaries and higher shear rates. The thin, dilute layer near the wall will have a much lower viscosity and will act as if the bulk fluid is slipping along the wall.

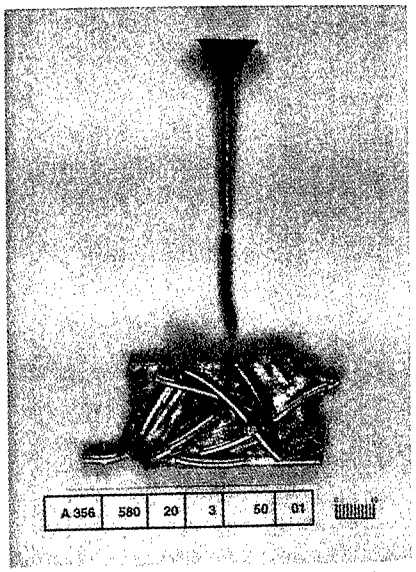


Figure 6. A typical example of an extrudate from the extrusion die.

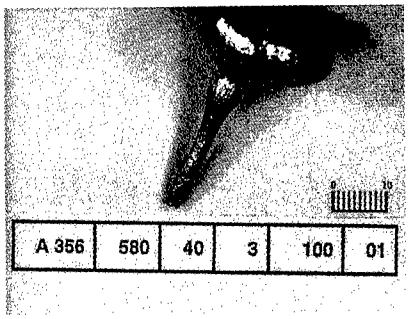
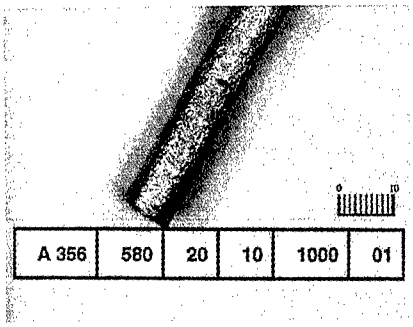
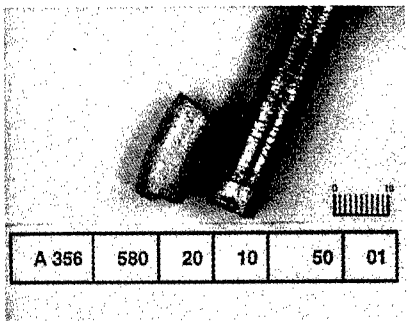


Figure 7. An example of a die swell at the exit from the capillary.

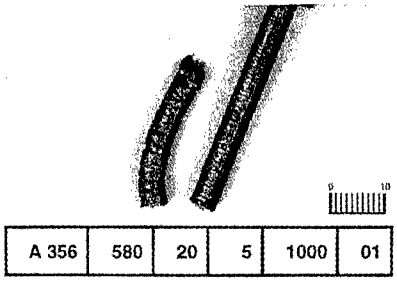
(a)



(b)



(c)



(d)

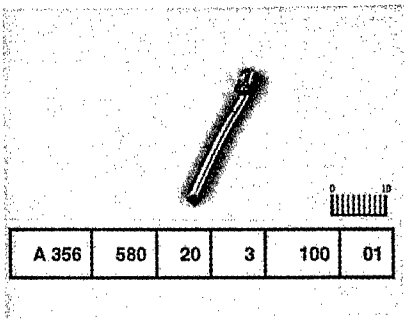


Figure 8. Some typical surface conditions observed on the extrudate. (a) Normal surface. (b) Mixed, showing transition from stable to unstable flow. (c) Regularly distorted, resulting from melt fracture.(d) Shiny, resulting from wall slip.

The extrudate surface appears distorted, usually in a regular pattern at first and then very rough at higher flow rates. This is similar to the phenomenon of "melt fracture" in polymers. This melt distortion phenomenon is not well understood. Clearly it involves a loss of adhesion at the

die wall and slip or stick-slip flow [8]. It can also arise from unstable flow in the die entry region or from rapid acceleration of the surface layer as it exits the die [9].

In some instances the extrudate also behaves like an elastic liquid. There is an expansion (extrudate swell) as it leaves the capillary die (Figure 7). This expansion probably results from tension along the streamlines [7]. This is analogous to recoverable strain after steady shearing where the confining walls are removed at the onset of recovery.

Conclusion

A study the rheological properties of alloy AlSi7Mg indicates that the alloy exhibits both thixotropic and pseudo-plastic properties at the temperatures of 570 °C, 580 °C and 590 °C. It also displays shear thinning behaviour at these temperatures. Under certain flow conditions, the flow becomes unstable and this is manifested as wall slip, melt fracture and extrudate swell. Experimental results seem to indicate that the shear thinning behaviour can be described by the power law model.

Acknowledgements

This work was fully funded by the National Science and Technology Board, Singapore. The authors are grateful to Mr Ingo Söller, an undergraduate from Fachhochschule Aachen Fachbereich Maschinenbau, Germany for his assistance in data collection and in preparing the digital images.

References

1. Spencer, D.B., Mehrebian, R. and Flemings, M.C., Met. Trans., 3 (1972), 1925.
2. Flemings, M.C., "Behaviour of Metal Alloys in the Semisolid State," Met. Trans. A, 22A (1991), 957-981.
3. Kenny, M.P. et al., Metals Handbook, vol. 15 - Casting (Metals Park, Ohio: ASM, 1988), 327-338.
4. Joly, P.A. and Mehrabian, R., J. Mater. Sci., 11, (1976), 1393.
5. Kattamis, T.Z. and Piconne, Mater. Sci. Engng., A131, (1991), 265.
6. Kamal, M.R. and Mutel, A., J. Polym. Engng., 5, (1985), 293.
7. Macosko, C.W., Rheology: Principles, Measurements and Applications. (VCH Publishers, New York, 1994), 237-256.
8. Lim, F.J., and Schowalter, W.R., J. Rheol. 33, (1989), 1359.
9. White, J.L., J. Appl. Polym. Sci. Symp., 20, (1973), 155.

DEFORMATION AND FRACTURE BEHAVIOR OF AL-MG-SI ALLOYS

S.B.Kang[1], L.Zhen[2], H.W.Kim[1] and S.T.Lee[3]

1) Korea Institute of Machinery and Materials, Changwon 641-010, Korea
2) Harbin Institute of Technology, Harbin 150001, People's Republic of China
3) Aluminum of Korea Ltd., Ulsan 680-090, Korea

Abstract

Deformation and fracture behavior of two Al-Mg-Si alloys in different aging conditions has been studied by tensile testing, TEM and SEM observation. Tensile test results show that the strain hardening exponents (n values) of the two alloys decrease sharply at the early stage of artificial aging. In fully aged conditions, dislocations are concentrated in narrow bands during plastic deformation of these alloys, which is responsible for the very low n values of the Al-Mg-Si alloys in peak aged and overaged conditions. The TEM results show that large precipitates and precipitate free zones (PFZs) along grain boundaries are formed in peak aged and overaged conditions, and SEM observations demonstrate that the tensile fracture modes of the two alloys in these aging conditions are completely intergranular with many small cusps decorated on facets of the fractured grain boundaries. Thus, the fracture process of both alloys is suggested to be that in which the high local stresses, built up where the slip band impinges on the grain boundaries, nucleate voids at the grain boundary precipitates by decohesion of the particle/PFZ interface, and then coalescence of these voids within the PFZ leads to the final fracture of these alloys.

The Third Pacific Rim International Conference on
Advanced Materials and Processing (PRICM 3)
Edited by M.A. Imam, R. DeNale, S. Hanada,
Z. Zhong and D.N. Lee
The Minerals, Metals & Materials Society, 1998

Introduction

The demand for more lightweight, fuel efficient and enhanced performance automobiles stimulates the research and development of high-strength and high formability aluminum alloys. Recent research has focused on the 6xxx series aluminum alloys[1-5]. These alloys have the properties of medium to high strength, excellent formability and good corrosion resistance. Because of the short time during the paint baking process, high strength is usually difficult to achieve for commercial Al-Mg-Si alloys. Through composition design and special heat treatment techniques, the strength of new Al-Mg-Si alloys in the paint baked conditions can be improved significantly[6]. Therefore, the prospects for practical use of these Al-Mg-Si alloys as automotive body sheet are good. In order to make full use of the potential of these alloys, detailed investigation of the deformation and fracture behavior in different aging conditions is of great importance.

Experimental

Compositions of the Al-Mg-Si alloys studied here are listed in Table I.

Table I Compositions of Al-Mg-Si alloys (wt%)

Identification	Mg	Si	Mn	Zr	Fe	Al	Remarks
alloy A	0.95	0.85	0.3	0.1	0.06	bal.	Al-1.5Mg_2Si-0.3Si
alloy B	0.95	1.55	0.3	0.1	0.07	bal.	Al-1.5Mg_2Si-1.0Si

The homogenizing treatment of the ingots was carried out by the following process: 430°C, 4h → 530°C, 20h then air cooled to room temperature. After hot rolling (rolling reduction is about 87%) and annealing (400°C/1h), the materials were cold rolled to 1 mm with the cold rolling reduction of 67%.

After cold rolling, the specimens were solution treated at 550°C for 30min, and then quenched into water at room temperature. Thereafter, some specimens were held at room temperature for different times before tensile tests, and the other specimens were firstly naturally aged for 3 months and then artificially aged at 180°C for different times. Tensile tests were performed on an Instron testing machine with a cross head speed of 2.5 mm/min. Observations of dislocation distributions and fractured surface were carried out at 160 kV using JEOL-2000EX type transmission electron microscope(TEM) and a JEOL JSM-35CF scanning electron microscope (SEM), respectively.

Results and Discussion

Tensile properties

Figure 1 shows the change of tensile properties of alloy A and alloy B during natural aging. It is seen that both the tensile and yield strengths increase continuously with the increase of natural aging time due to the direct result of a clustering process. The clustering process of solute atoms usually takes place with the help of vacancies during natural aging of Al-Mg-Si alloys. The clusters formed during natural aging consume both vacancies and solute atoms and are difficult to dissolve during artificial aging. Therefore, long time natural aging leads to a decrease in the concentration of both solute atoms and vacancies in the solid solution, which will appreciably affect the precipitation process of strengthening phases during subsequent artificial aging. However, the increase of elongation with natural aging time is somewhat difficult to understand and needs further detailed study.

After natural aging for 3 months specimens were artificially aged at 180°C for different times. The change of tensile properties of alloy A and alloy B with artificial aging time is shown in Fig.2. Peak strength of alloy A is reached when specimens were aged for 180 minutes. The peak strength of alloy B is reached later than that of alloy A,

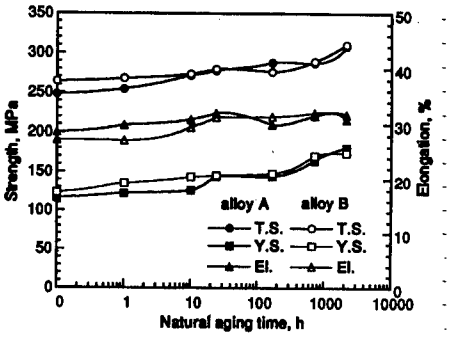


Figure 1 : Change of tensile properties of alloy A and alloy B during natural aging.

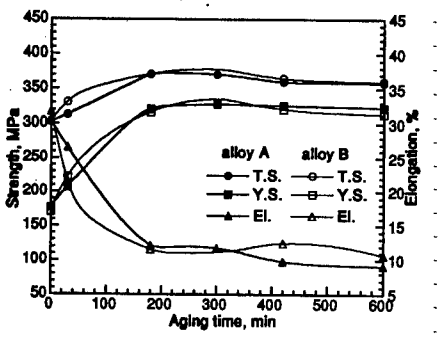


Figure 2 : Change of tensile properties of alloy A and alloy B during artificial aging at 180°C

and TEM results show that the size of β" phase in alloy A is larger than that in alloy B in the same aging condition.(described later in Fig.5) This means that the precipitation rate of β" phase in alloy A is faster than that in alloy B. This phenomenon could be explained by assuming that when the excess Si reaches a certain amount, Si atoms tend to form Si particles preferentially, which reduces both the Si content and the vacancies and affects the precipitation of β" phase.

Further aging leads to a decrease of strength gradually. The elongation decreases sharply when specimens were aged at 180°C with increasing aging time up to 180 minutes; then the decrease is very slow on further aging. The elongation of alloy B specimens aged at 180°C for more than 300 minutes is higher than that of alloy A.

Tensile stress-strain curves and dislocation distributions in fractured specimens

The tensile stress-strain curves for alloy A in different aging conditions are shown in Fig.3. Those for alloy B in different aging condition show nearly the same deformation tendency as those of alloy A. The strain hardening exponents (n values) of the two alloys naturally aged for different times decreases gradually with increasing natural aging time, from 0.25 in as-quenched condition to 0.22 in 3 months natural aging condition. Changes of n values and uniform elongations of the two alloys during the artificial aging are shown in Fig.4. The values for alloy A and alloy B are only 0.06 and 0.08 in the peak aged condition, and 0.045 and 0.06 in overaged condition, respectively. The values of uniform elongation for alloy A and alloy B also decrease from 26.0% and 24.4% at the zero artificial aging time to 6.4% and 8.0% at the 5

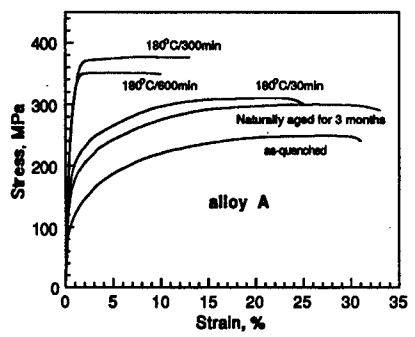


Figure 3 : Tensile stress-strain curves of alloy A in different aging conditions

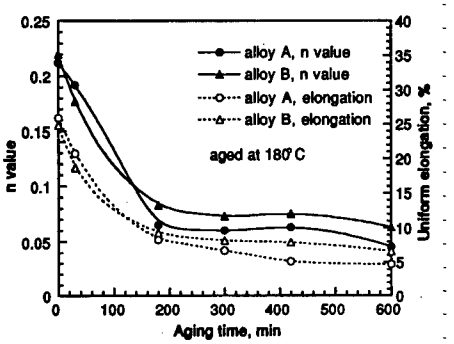


Figure 4 : Change of n value and uniform elongation during artificial aging at 180°C for alloys A and B

hour artificial aging time, respectively. It is seen that the trends in behavior of the uniform elongation and the n value during artificial aging are very similar.

In order to study the plastic deformation behavior, TEM specimens were prepared from the uniformly deformed region of tensile fractured specimens. Dislocation configurations for alloy A and alloy B specimens in different aging conditions are shown in Fig.5. In the alloy A specimen naturally aged for 3 months the dislocation density is very high and in some foil orientations regions with varying contrast could be seen to delineate very ragged and elongated cell structures, as shown in Fig.5(a). In the alloy A specimen artificially aged at 180°C for 30 minutes, dislocations show some tendency to form a banded structure (Fig.5(b)). While, in alloy A specimens artificially aged at 180°C for 600 minutes the banded structures are very distinct, showing that the dislocations were concentrated in rather well-defined bands, see Fig.5(c). Diffraction patterns demonstrate that these bands are parallel to {111} planes. It is easy for dislocations to cut through β'' phase due to its coherency with the matrix and its small size. This produces local softening of the slip plane so that subsequent dislocations will glide preferentially along this path and, thus, be concentrated in narrow bands. Such a deformation mode will lead to low work hardening rate, because the local softening of the slip plane induces the formation of banded structure. Therefore, the n value for specimens aged at 180°C for more than 180 minutes is very low. The dislocation configurations in fractured specimens of alloy B in naturally aged and underaged conditions are essentially the same as those of alloy A. However, the banded dislocation structures of alloy B in the peak aged and overaged conditions are not so distinct as those of alloy A, as shown in Fig.5(d). Many Si particles are formed within grains of alloy B. Unlike the β'' precipitates, the Si particles can not be sheared by matrix dislocations, so that dislocations will accumulate at each Si particle during plastic deformation. This will harden each active slip plane and cause slip to be transferred to adjacent planes. Therefore, the banded dislocation structure in alloy B is not so distinct as that in alloy A, which is supposed to be the reason that n values of alloy B specimens artificially aged for longer times are higher than that of alloy A.

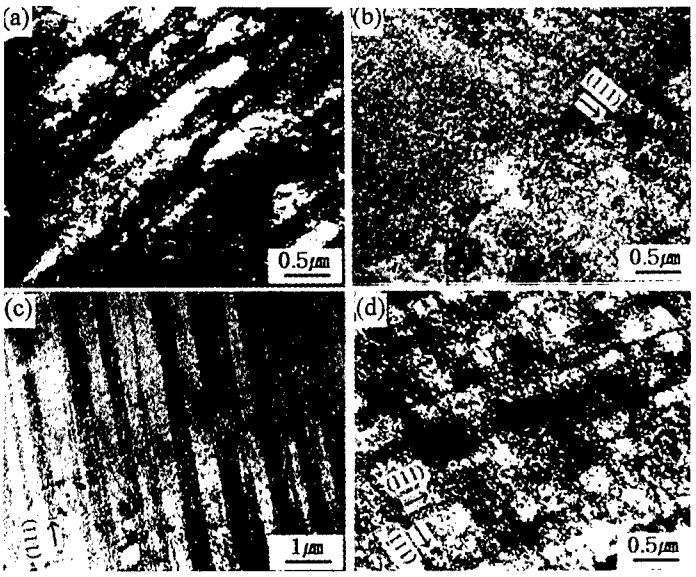


Figure 5 : TEM micrographs showing dislocation distributions in tensile fractured specimens of alloy A and alloy B in different aging conditions.
(a) alloy A naturally aged for 3 months; (b) alloy A aged at 180°C/30min;
(c) alloy A aged at 180°C/600min; (d) alloy B aged at 180°C/600min

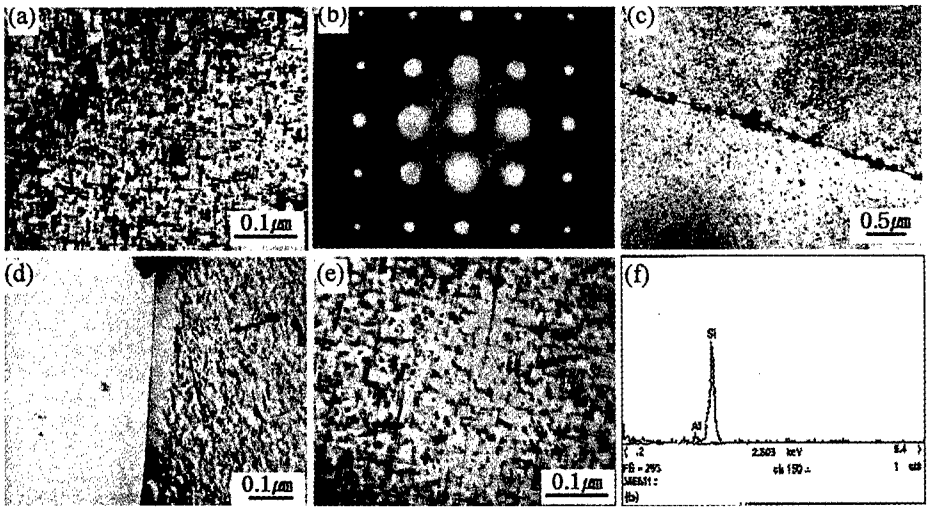


Figure 6 : TEM micrographs showing microstructures, SADP and EDS spectra in alloy A and alloy B specimens aged at 180°C for 300 minutes.
(a) bright field image taken with B=$[001]_{Al}$ in alloy B; (b) corresponding diffraction patterns of (a); (c) Si particles within grain and along grain boundary in alloy B; (d) PFZs in alloy B; (e) bright field image taken with B=$[001]_{Al}$ in alloy A; (f) identification of Si particles by EDS spectra in alloy A and alloy B

Microstructures

Although the strength of the alloys is obviously increased by natural aging, no precipitates can be observed in the specimen naturally aged for 3 months. Specimens aged at 180°C for 300 minutes contain needle-shaped precipitates that are clearly delineated by strain-field contrast as shown in Fig.6(a). Selected area diffraction patterns (SADPs) taken with B=$[001]_{Al}$ show streaks along $[010]_{Al}$ and $[100]_{Al}$ (Fig.6(b)). The appearance of the precipitates, and the SADPs are in agreement with previous observations for the β'' phase[7,8]. Small particles are seen within grains, and larger precipitates along grain boundaries are also observed (Fig.6(c)). The size of grain boundary precipitates is about 100nm. Narrow precipitate free zones (PFZs) are observed near grain boundaries with a half width of about 45nm (Fig.6(d)). It is seen that the size of the β'' phase in alloy A specimen is larger than that in alloy B at the same aging condition, and very few Si particles are observed within grains of alloy A specimens (Fig.6(e)). The particles have been confirmed to be Si precipitates by SADPs and EDS spectra (Fig.6(f)). When specimens were aged at 180°C for 600 minutes, both β'' precipitates and Si particles become coarser and the half width of PFZ becomes to about 60nm.

Fracture surface observation

The fracture surface of alloy B specimens naturally aged for 3 months consists of two parts, that is, ductile dimple fracture in the center region (Fig.7(a)) and sheared band fracture near the edge of the specimen (Fig.7(b)). A ductile transgranular fracture surface is observed in the specimen aged at 180°C for 30 minutes (Fig.7(c)). However, specimens aged at 180°C for more than 180 minutes show completely intergranular fracture (see Fig.7(d) and (e)). At high magnification, the fracture surface is shown to be covered with fine cusps whose measurements correspond closely to the average spacing of the grain boundary precipitates (Fig.7(f)).

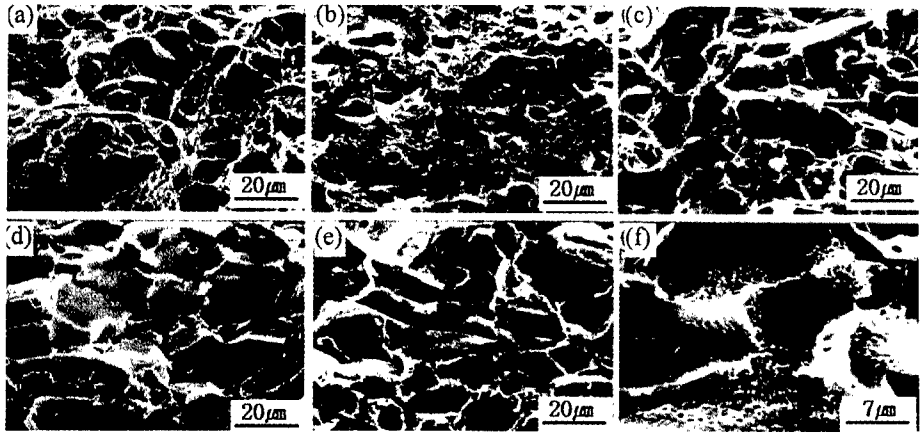


Figure 7 : SEM fractographs of alloy B specimens in different aging conditions.
(a) naturally aged for 3 months, center region of the specimen; (b) naturally aged for 3 months, near edge of the specimen; (c) aged at 180°C for 30minutes; (d) aged at 180°C for 180minutes; (e) aged at 180°C for 300minutes; (f) high magnification of (e)

The PFZ will deform more easily than the interior of grains. The strain within the PFZ contributes little to the whole strain due to its small volume fraction. However, the highly accumulated strain within the PFZ acts as the origin of fracturing for preferential formation of voids[9]. It is known that the interface of grain boundary precipitate and PFZ is relatively weak. Therefore, the high stress concentrations at the head of the slip bands nucleate voids at the grain boundary precipitates by decohesion of the particle/PFZ interface. Fracture then propagates by coalescence of these voids within the PFZ, leading to intergranular failure.

Conclusions

1. The influence of the inhomogeneous deformation mode on the mechanical properties has two effects. Firstly, very low n values in peak aged and overaged conditions result from the inhomogeneous deformation. Secondly, high local stresses are built up where the slip band impinges on the grain boundaries leading to intergranular fracture after peak aging.
2. The Si particles can be formed rather uniformly, which is beneficial to alleviate the inhomogeneous deformation behavior of the Al-Mg-Si alloy, leading to higher n value and elongation.
3. The formation of PFZs and large Si particles along grain boundaries is another major factor that results in the intergranular fracture of Al-Mg-Si alloys in fully aged conditions.

References

1. S. A. Arnold, JOM, .45 (1993) 12-15.
2. S. J. Andersen, Metall. Mater. Trans., 26A (1995) 1931-1937.
3. I. Dutta and S. M. Allen, J. Mater. Sci. Letters, 10 (1991) 323-326.
4. W. D. Fei, S. B. Kang, J. Mater. Sci. Letters, 14 (1995) 1795-1797.
5. A. K. Gupta et al., Proc. of the 4th Int. Conf. on Aluminium Alloys, T. H. Sanders, Jr., E. A. Starke, Jr. eds., Atlanta, Georgia USA,vol.III, (1994) 177-186.
6. L. Zhen and S. B. Kang, Scripta Metall. Mater, 36 (1997) 1089-1094
7. G. Thomas, J. Inst. Metals, 90 (1961-62) 57-63.
8. L. Zhen et al., J. Mater. Sci., 32 (1997) 1895-1902
9. T. Kawabata and O. Izumi, Acta, Metall., 24 (1976) 817-825.

On the TB2 Titanium Alloy for Satellite-Rocket Link Belt

Chen Haishan
General Research Institute for Non-ferrous Metals, Beijing 100088, China

Abstract

As one of the successful applications of TB2 Titanium alloy, the Satellite-Rocket Link Belt bears great significance to the successful launch of satellites since it guarantees the joining of satellite and rocket in the launching and flying process and also ensures their infallible separation once the satellite goes into orbit. This study specifies the working, heat-treatment and heated calibration of the TB2 alloy link belt which turns out to satisfy all the design requirements. To date there have been 16 successful launches using the TB2 Titanium alloy for the link belts of satellites and rockets.

The Third Pacific Rim International Conference on
Advanced Materials and Processing (PRICM 3)
Edited by M.A. Imam, R. DeNale, S. Hanada,
Z. Zhong and D.N. Lee
The Minerals, Metals & Materials Society, 1998

Introduction

China succeeded in its first launch of pilot communications satellite in 1984, which employed for the first time the satellite-rocket unlocking and separation unit in the form of V-shaped compassive Satellite-Rocket Link Belt(SRLB) made of self-developed high strength Titanium alloy TB2. This marked a new leap-forward in the fields of structural material research for rockets and satellites as well as the progress of astronautic technology.

The SRLB is a key part for the launch of communications satellite in ensuring absolute safety and reliability of satellite-rocket linkage during the launching and flying period and vouchsafing its infallible unlocking and separation from the rocket once the satellite goes into orbit. For these reasons the SRLB bears great significance on the success of satellite launches.

In China's traditional astronautic manipulations the separations between different stages and between rocket and satellite all took form of axial installaiton and unlocking characteristic of explosion bolt connection which presented the disadvantages of high load shock to the assembly, large interference at separation and low reliability. This disadvantagous connection gave way to SRLB by TB2 alloy at the successful launch of the communications satellite in 1984.

Material requirements

The design of SRLB for connection of the satellite with the rocket demands that the material have excellent workability and formability. The communications satellite revolves at high altitude. It is firstly launched by the rocket into its stay orbit 200～300 kms high and then to an elliptical orbit with an apogee of 36,000 kms high where the satellite separates from the rocket. Since high load is applied to the link belt in the flying process, the material must also have high strength. Early link belts were made of Ti-5Al-2.5Sn, which was subject to fractures from time to time due to the inadequate formbility of the alloy. Upon this the users put up the request that suitable Titanium alloy be developed and manufactured for the SRLB.

The following properties were specified:

1. Room temperature tensile properties: $\sigma_b \geqslant 1100$ MPa, $\delta \geqslant 10\%$.
2. No fracture within 100 hours of loading of 800 MPa at room temperature.
3. Elastic modulus, linear expansion coefficient to be tested and also tensile properties at +100 ℃ and −60 ℃.
4. Good cold-bending behavior.

Development of TB2 Alloy for SRLB

Working Process

The link belt supplied to the customer was produced from 24 mm thick TB2 hot-rolled plates with compositions as follows:
Mo 4.98, V 5.00, Cr 7.92, Al 2.80, Fe 0.11, Si 0.036, C 0.018, N 0.016, O 0.13, H 0.0054 and Ti balance.

Traditionally β alloy were often manufactured through the following processes: hot-rolling → solution treatment → sand-blasting → pickling → cold-rolling → solution treatment → sand-blasting → pickling → finished sheets, where upon great difficulties arose from twice sand-blasting and twice pickling which discouraged almost all the Titanium material suppliers. Washing was once proposed as an alternative to sand-blasting and pickling, but with this process the often high soda temperature resulted in aging of the solution-treated sheets so as to render further cold-rolling or cold-forming impossible.

In this study the sheet manufacturing process has been changed so that hot-rolling directly precedes pickling which is in turn followed by vacuum annealing and then cold-rolling. This process is made possible by the fact that the oxide scale is relatively loose at the hot-rolled state for direct pickling since the hot-rolling process is featured by gradually decreasing temperatures. This eliminates the necessity of sand-blasting and also stems out worries about hydrogen intake at pickling.

Question arises as to whether the small amount of α-phase in the morphology after vacuum annealing impairs the cold-forming behavior. To this end, however, experiments show that this small quantity of α-phase does not adversely affect the cold-rolling performance of TB2 alloy. In summary, this change in the process facilitates the manufacture of β-Ti alloy sheets.

Heat Treatemt amd Alloy Properties

Final heat-treatment in the single β-phase field followed by water-quenching(WQ) or air cooling(AC) without annealing by furnace cooling(FC) has long been employed for the cold-rolled sheets of β-phase alloy to retain good cold-formability. This practice introduces sheet oxidization as a result of water quenching or air cooling. In this study the vacuum annealing is used as the final heat-treatment to the 2 m long TB2 strip to eliminate the necessity of sand-blasting and pickling.

The alloy displays slightly lower strength but higher elongation in the as-annealed state than

those after solution-treating and water quenching with similar cold-bending behavior of the sheets. As shown in Tab. 1, the effect of both heat-treatment schedules on the properties of TB2 alloy, furnace cooling gives rise to slightly lower strength in the "soft" state and rather high strength is associated with solution treating plus water quenching after one-stage aging (500 ℃, 8 h) since the wholely β-phase state resulting from water-quenching readily lends itself to age-strengthening while both treating strategies lead to similar properties after two-stage aging(500 ℃, 8 h; 620 ℃, 30 ′). The relatively lower strength following the annealing treatment is desirable since this brings down the resistance to cold-bending in the manufacturing of SRLB.

Tab. 1 Effect of Solution-treatment + water quenching and annealing treatment on the properties of TB2 alloy

Solution Treating	"Soft" State			500 ℃, 8 h Aging		500℃、8h + 620℃30′	
	σ_bMPa	δ%	α	σ_bMPa	δ%	σ_bMPa	δ%
800 ℃ WQ	900	28.5	180°	1370	10.0	1180	16.0
800 ℃ FC	860	30~32.5	180°	1240	10.0	1180	16.0

Tensile Properties of TB2 Strip

(1) At Room Temperature

	σ_b MPa	$\alpha_{0.2}$ MPa	δ%	E GPa
800 ℃, FC	850		32.5	
	860		30.0	
FC + Two-Stage Aging	1220	1170	15.6	110
	1210	1160	14.4	110
	1240	1190	15.2	110

(2) At + 100 ℃

	σ_b MPa	δ%
	1140	16.0
FC + Two-Stage Aging	1140	13.0
	1150	15.0

(3) At − 60 ℃

	σ_b MPa	δ%
	1440	4.5
FC + Two-Stage Aging	1470	5.5
	1460	4.5

Conclusions

The TB2 alloy strip for making SRLB used in launching of communications satellite has been developed to meet the design-specified property requirements. Batches of products have been turned out which have batch-independent strength of not less than 1100 MPa and elongation not less than 10%. Vacuum annealing is employed for treatment of β-Ti alloy which facilitates industrial production of β-Ti alloy sheets. The good properties of the alloy and its successful applicatin in the communications satellite-rocket link belt prove that TB2 is comparable with same series of advanced alloys in the world which is practically available as a structural material of high strength Titanium alloy.

REDISTRIBUTION OF ELECTRONEGATIVE IMPURITIES IN ZIRCONIUM AT THERMO CYCLIZATION IN ATOMIC HYDROGEN

Dmitriy Schur, and Vasiliy Pishuk

Institute of Hydrogen and Solar Energy, Kiev, 252150, Ukraine

Abstract

The effect of dehydrogenation process temperature on the peculiarities of electronegative impurities redistribution in the volume and on the surface of zirconium have been studied by kinetic method and Auger electron spectroscopy. The influence of hydrogenation and dehydrogenation processes on the density of electronic charge on ^{57}Fe nucleus in Zr_2Fe compound have been examined by method of nuclear γ-resonant spectroscopy.

The obtained scientific results by γ-resonant spectroscopy method have shown that cubic structure of Zr_2Fe alloy forms only as a result of carrying out of hydrogenation process at temperature of 873 K. It can be explained that at this temperature the allotropic transformation ($\alpha \rightarrow \beta$) of zirconium matrix occurs at hydrogen concentration of ~7 at.% (solid phase transition from hexagonal close-packed lattice into body-centered cubic lattice). In this case in bcc lattice the volume diffusion of oxygen predominates. The prolonged hydrogenation of zirconium at this temperature promotes the intensive dissolution of oxygen in specimens.

The Third Pacific Rim International Conference on
Advanced Materials and Processing (PRICM 3)
Edited by M.A. Imam, R. DeNale, S. Hanada,
Z. Zhong and D.N. Lee
The Minerals, Metals & Materials Society, 1998

Introduction

The main impurities accompanying to hydrogen in plasma are oxygen, nitrogen and carbon. They concern to electronegative impurities because of their high electronegativity at formation of chemical bonds. As previously shown in [1], in the beginning of plasma hydrogenation process these impurities form protective film on zirconium surface and under certain conditions they are dissolved partially in matrix volume essentially influencing on the rate of subsequent cycles of hydrogenation.

The special features of redistribution process of electronegative impurities (acquired in the course of plasma hydrogenation) at dehydrogenation of zirconium specimens have been considered in the present work.

The results of kinetic researches by kinetic method [1], study of elements redistribution on surface by Auger electron spectroscopy and investigation of structural transformations in specimen volume by nuclear γ-resonant spectroscopy have been used with aim of elucidation the dehydrogenation temperature influence on the rate of solid phase changes in matrix at ensuing hydrogenation.

Experimental conditions

Results of kinetic measurements have been received by kinetic method which provide the study of process of interaction between zirconium foil and hydrogen plasma of electrodeless discharge. This method has been detailed in [1]. An investigation of chemical composition of specimen surface have been carried out by method of Auger electron spectroscopy on Auger-microprobe JAMP-10 at accelerating voltage of 10 kV in vacuum ($P=5\cdot10^{-6}$ Pa) in the energy range between 50 and 1000 eV. The specimens have been exposed to argon etching. The energy of argon ions beam makes up 3 eV, the emission current amount to 30 mA. For a time of 5 or 10 minutes the thickness of spraying layer run to 350 A or 700 A correspondingly.

For investigation of structural transformations in zirconium the method of nuclear gamma-resonance spectroscopy have been used with utilization of ^{57}Fe isotope. For all this it has been used the values of isomeric shift (δE) and quadrupole splitting (ΔE_Q) which are different for known stable and metastable compounds in Zr-Fe system. This method is sensitive to the change of local short-range order and electron structure of ^{57}Fe atoms at interaction between alloy and interstitial impurities. The Mössbauer absorption spectrums have been received at the room temperature with the use of ^{57}Co isotope in chromium matrix. The specimens have been prepared by two ways allowed the production of the same Zr_2Fe phase in the form of thin layer on sample surface and in matrix volume. The $ZrFe_x$ alloys at $x<0,33$ in the matrix volume consist of mixture of two paramagnetic phases: α-solid solution of Fe in Zr and Zr_2Fe metallic compound. The Zr_2Fe compound can be find in the volume in two modifications differing in crystalline structure: with tetragonal lattice of $CuAl_2$ type and with cubic lattice of diamond ($NiTi_2$) type, which is usually stabilized by oxygen [3].

The results discussion

Kinetic measurements

It has been presented in paper [2] that cyclicity of zirconium hydrogenation at temperature of 723 K practically has no effect on the rate of subsequent hydrogenation. At the same time at cyclic recurrence of zirconium temperature at 873 K with following hydrogenation the rate of

hydride phase formation slightly decreases and induction periods preceded the nucleation of new phase are extended.

This can be explained by the fact that rate constant of interaction between α-zirconium and oxygen at 723 K is defined mainly by oxygen diffusion along grain boundaries. The interaction nature is somewhat changed at temperature of 873 K, the constant of reaction rate is increased on the order and is still determined by diffusion along grain boundaries. But in temperature interval of 1073-1173 K which is used in the present experiments for dehydrogenation processes the rate constant of zirconium interaction with oxygen is increased already in two orders in comparison with the rate of oxidation at 723 K. The volume diffusion plays the dominant role in interaction process because of allotropic transition of zirconium matrix to body-centred cubic structure of β-phase.

The presence of electronegative impurities which stabilize the α-phase in volume of zirconium matrix results in change of yield point of zirconium and increase of potential energy of elastic deformation. These factors exert the essential influence on the nucleation rate and the growth of new phase grains at isothermal interaction of hydrogen with zirconium.

This effect gives positive results at study of processes of hydride formation in metal by kinetic method [1], as kinetic curves received during the first cycle of hydrogenation not always have curve breaks in the region of phase transitions. After dissolution of interstitial impurities in the volume the rate of solid phase transformations is slowed down and the moments of phase changes become clearly seen on the kinetic curves of interaction.

At zirconium hydrogenation at 723 K impurities accompanying to hydrogen in plasma accumulate on specimen surface and on grain boundaries and do not exert the essential effect neither on the absorption of atomic hydrogen nor on the solid phase transitions in metal volume.

Study of phase transformations

After specimens annealing in vacuum the received Mössbauer spectra have ΔE_Q and δE parameters identical to parameters of standard spectra of Zr_2Fe compound (tetrag.) (Fig. 1 a).

The successive reduction of δE value and lines broadening (Fig. 1 b, c) are observed on spectra with increasing time of specimen heat treatment in hydrogen at temperatures of 873 K (1 hour) and 673 K (1 hour). After four cycles of heat treatment the ΔE_Q is increased from 0.70 up to 1.01 mm/sec and the δE value determined in relation to ^{57}Fe is decreased from -0.35 up to -0.40 mm/sec With increase in time of heat treatment of Zr_2Fe (tetrag.) compound the ΔE_Q value grows, that testifies about anisotropic expansion of lattice. As is shown in [4], in metals with hexagonal close-packed lattice the ΔE_Q value is proportional to ratio c/a, which usually grows with a rise in concentration of interstitial impurities. A reduction in δE value during the process of heat treatment points to the fact of increase of s-electrons density on ^{57}Fe nucleus in Zr_2Fe compound (tetrag.) located in Zr-matrix. The appearing single spectral line with enlarged width testifies about the partial transformation of Zr_2Fe compound from tetragonal lattice into cubic of diamond type. The phase transition is accomplished completely after dehydrogenation process at 1073 K (above the temperature of allotropic transition of zirconium matrix to β-phase).

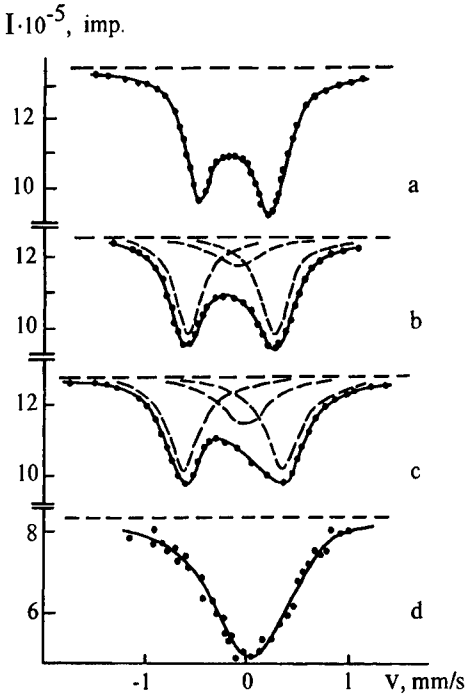


Figure 1: Mössbauer spectrums of Zr_2Fe compound (tetragonal) presented in Zr - 1 at% Fe alloy:
a) after annealing during an hour at 873 K in vacuum ($P=1.3\cdot10^{-4}$ Pa);
b) after 3 cycles of hydrogenation during an hour at 673 K and hydrogen pressure of 26.6 Pa;
c) after 4 cycles of hydrogenation during an hour at 673 K and hydrogen pressure of 26.6 Pa;
d) after hydrogenation during an hour at 873 K and hydrogen pressure of 26.6 Pa.

Stresses arising in the course of phase transitions in zirconium matrix

Hydrogenation of Zr_2Fe compound (tetrag.) located on the Zr surface results in the ΔE_Q increase from 0.66 to 1.05 mm/sec and the δE change from -0.35 to -0.32 mm/sec, when there are no obstacles to lattice expansion. The spectrum shift in direction of positive rates (Fig. 2) at the hydrogenation is typical for metals with dissolved Mössbauer isotope [5]. This fact is explained by the lattice expansion in the presence of interstitial atoms and by the partial transition of their 1s-electrons to local 3d-states of Fe. This transition raises the shielding influence of 3d-electrons as a result of which the electron density ($|\Psi(0)|^2$) decreases.

Experimental evidence of Fig. 1 and 2 points up the potent effect of interstitial impurities on crystalline and electronic structure of Zr_2Fe compound (tetrag.). The spectrum shift of specimen comprised of two phases (Zr_2Fe and Zr) in direction of negative rates indicates the increase of $|\Psi(0)|^2$. This is anormal and can be explained by the rise of internal stresses in Zr_2Fe (tetrag.) in consequence of presence of electronegative impurities stabilized the phase

Zr_2Fe (cubic). These impurities stabilize α-phase in Zr. This is because of the change of yield point and the rise of potential energy of elastic deformation. The similar change of $|\Psi(0)|^2$, as a rule, is observed in metals under pressure.

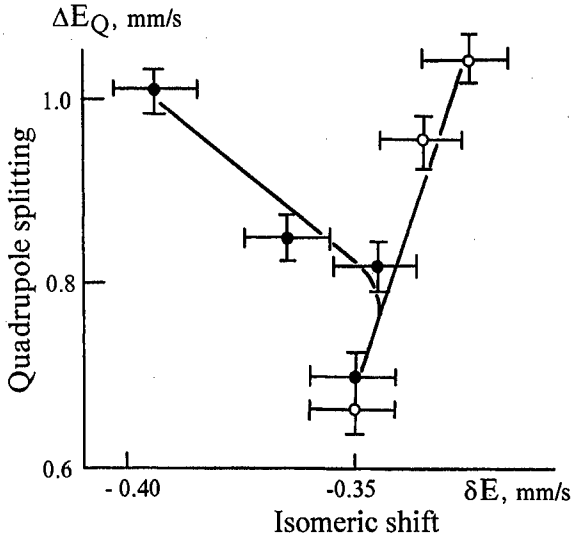


Figure 2: Isomeric shift change in dependence on quantity of hydrogenation cycles for Zr_2Fe compound (tetragonal) placed on the surface of Zr- substrate (○) and in the volume of Zr- matrix (●).

The influence of hydrostatic compression at pressure up to $3 \cdot 10^{10}$ Pa on the isomeric shift of ^{57}Fe in transition metals have been studied in work [6]. For all metals the δE value tends to decrease with increasing pressure. Therefore the δE diminution can be interpreted as origination of great stresses resulted in the process of hydride formation and presence of electronegative impurities which hinder the flow of given process. In order to evaluate the value of internal pressure in Zr_2Fe particles (tetrag.) located inside of zirconium matrix the difference of isomeric shifts ($\Delta = \delta E_1 - \delta E_2$) of two test specimens is determined. In one specimen ^{57}Fe isotope is at the zirconium surface, in another it is in the volume. δE_1 and δE_2 are isomeric shifts of hydride phase Zr_2FeH_x dissolved at the surface and in the volume correspondingly. The values $d\delta E/dp$ for various iron-containing alloys are not too different and take a value $\sim 10^{-10}$ mm/sec Pa [6]. If this value adopt for Zr_2Fe compound (tetrag.), the local internal pressure at hydrogenation according to assessment ranges up to 10^9 Pa.

We have considered some features of the changes of material electronic structure at hydrogenation which are responsible for the observed changes of Mössbauer spectra. The density of electronic charge $|\Psi(0)|^2$ on ^{57}Fe nucleus is determined principally by s-electrons of different shells. 3d-electrons do not create the appreciable density on nucleus, however the change of their state affects the degree of shielding of s-electronic cloud. The broadening of s- and d-zone is caused by pressure increase with more strong dependence for d-zone

$$d\ln\Delta_d/d\ln V = -5/3, \qquad d\ln\Delta_s/d\ln V = -2/3,$$

where V is volume, Δ_d and Δ_s are widths of d- and s-zone [7].

As noted in [8], the 3d-states are more sensitive to changes in pressure, their energy is built up steeply at compression. In this case the observed broadening is attended with electrons redistribution between s- and d-zone owing to their relative shift [7]. It follows that under pressure in consequence of 3d-4s transitions at displacement of 3d-band about the 4s-states there is a decrease in the number of 3d-electrons shielding s-electronic cloud. As a result the electron density $|\Psi(0)|^2$ increases. It manifests itself in a decrease of δE_2 at the hydrogenation of Zr_2Fe compound (tetrag.) (Fig.2). The broadening of 3d-band points also to the spreading of wave function of 3d-electrons, reducing the shielding of s-electron density and can attests the amplification of covalent component bonds between components of Zr_2Fe compound (tetrag.). From this follows the conclusion that compression of Zr_2Fe particles (tetrag.) during the process of hydrogenation has an effect on electronic structure and manifests itself as observed isomeric shift.

The value of local stresses realized in present research is not true value for hydride forming process in zirconium because it define the specified content of electronegative impurities and hydrogen in matrix volume. The value of local stresses have undergone a change under the change of the number of hydrogenation cycles (the variations in amounts of soluble impurities) and hydrogen content, as the yield point of zirconium matrix vary.

The analysis of chemical composition of zirconium surface (Fig. 3) by the method of Auger electron spectroscopy have demonstrated that hydrogenation at temperature of 673 K brings about the elements redistribution on surface. This shows itself as nitrogen appearance and carbon removal from surface. Carbon presented on the surface in the form of graphite.

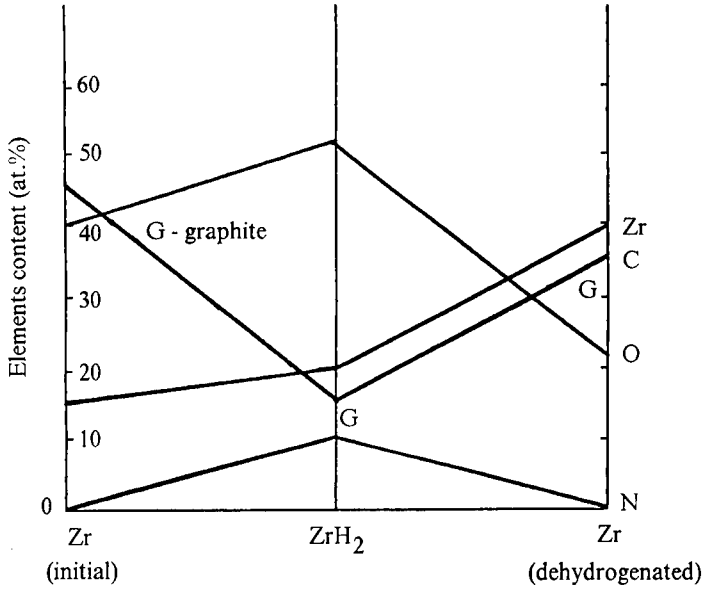


Figure 3: The chemical composition of Zr-surface after the process of hydrogenation (673 K) and dehydrogenation (1073 K).

At dehydrogenation at temperature of 1073 K the percentage of nitrogen and oxygen on zirconium surface is substantially reduced. The subsequent processes of Zr hydrogenation in atomic hydrogen are particularly sensitive to the availability of these impurities in volume [3]. But as experiment suggests, their influence is not observed in this case. Thus, we have concluded from this that dehydrogenation process of short duration and stream of desorbed hydrogen which is in the active form (atomic state) promote the desorption of oxygen and nitrogen from surface and inhibit their dissolution in volume.

As Fig. 1 suggests, the compound cubic structure of diamond type ($NiTi_2$), which is commonly stabilized by oxygen, is formed only from the process carried out at temperature of 873 K and dehydrogenation process conducted at 1073 K. As mentioned in [2], the process realization at this temperature could result in allotropic conversion of zirconium matrix even at hydrogen concentration of 7 at.% (solid phase transformation from hexagonal close-packed α-phase to cubic body centered β-phase). As this takes place, the volume diffusion of electronegative impurities increases sharply in body centered cubic lattice. The experiment data points to the fact that these impurities stabilize the cubic structure of Zr_2Fe alloy of diamond type ($NiTi_2$). This is reflected on Fig. 1 in transition from Mössbauer double-spectrum to one-main line.

Conclusion

The presence of electronegative impurities in zirconium matrix volume brings about the change of yield point of zirconium owing to an increase of potential energy of elastic deformation. This have a pronounced effect on the rate of solid phase transformations at the ever-growing hydrogen concentration in zirconium and is expressed by appreciable increase of energy of elastic deformation in zirconium-hydrogen system. According to Fig. 2 this makes itself evident in displacement of isomeric shift to more negative range of values and conform to local pressure in matrix equal to $\sim 10^9$ Pa in magnitude order.

Thus, this paper as [2] confirm to the fact that at cyclic heating of specimen up to 673 K in hydrogen plasma of electrodeless discharge the electronegative impurities are dissolved only slightly in specimen volume. The performance of the experiment at 873 K is useful in their volume dissolution in zirconium matrix and $\alpha \rightarrow \beta$ phase transition takes place at hydrogen content of 7 at.%. The mechanism of impurity diffusion in specimen changes and diffusion coefficient increases on two orders.

References

1. D.V. Schur, A.P. Zavalishin, «Investigation of the Hydride-Formation Mechanism in Metals by Plasmochemical Thermogravimetry Method», Hydrogen Energy Progress X, Proc. of the 10th World Hydrogen Energy Conference, vol.2 (Cocoa Beach, Florida: Int. Association for Hydrogen Energy, 1994), 1183-1188.

2. D.V. Schur et. al., «Thin Film Formation on Ti and Zr Surface in Hydrogen Plasma», Hydrogen Energy Progress X, Proc. of the 10th World Hydrogen Energy Conference, vol.2 (Cocoa Beach, Florida: Int. Association for Hydrogen Energy, 1994), 1279-1290.

3. J. Vincze, F. van der Woude, and M.G. Scott, «Local Structure of Amorphous Zr_3Fe», Solid State Communications, 37 (1981), 567-570.

4. G.K. Wertheim, A. Hausmann, and W. Sander, The Electronic Structure of Point Defects (Amsterdam: North-Holland Publishing Company, 1971), 204.

5. Friedrich E. Wagner, and Gerhard Wortmann, «Mössbauer Investigation of Metal-Hydrogen System», Hydrogen in Metals, ed. G. Alefeld and J. Völkl, vol.1 (New York, NY: Springer-Verlag, 1978), 161-204.

6. I.Ya. Dehtyar, and V.V. Nemoshkalenko, Electron Structure and Electron Properties of Transition Metals and Alloys (Kiev, Ukraine: Naukova Dumka, 1971), 301.

7. M.M. Nischenko, V.L. Tikush, and D.V. Schur, «Investigation of Homogeneous Hydrogenated Alloys Zr - 1 at.% ^{57}Fe by Method of Mössbauer Spectroscopy», Metallofizika, 10(5) (1988), 21-24.

8. Edwin B. Royce, «Stability of Electron Configurations in Metals under High Dynamic Pressure», Physics of High Energy Density, ed. P. Caldirola and H. Knoepfel (New York, NY: Academic Press, 1971), 109-120.

ADVANCES IN DEFORMATION MECHANISMS OF TITANIUM ALLOYS

Anand Ramesh, Sreeramamurthy Ankem
Department of Materials and Nuclear Engineering
University of Maryland, College Park, MD 20742-2115
U.S.A

Abstract

Within the past few years, significant progress has been made in understanding deformation mechanisms of Titanium alloys and their relation to mechanical properties. These include multiplication of mobile dislocation density in Beta Titanium Alloys at high temperatures and strain rates resulting in flow stress drops, interface sliding in Alpha-Beta Titanium alloys contributing to creep, and time dependent twinning in Alpha alloys resulting in higher creep strain. The aim of this paper is to review these developments and try to correlate between alloying elements, microstructure, deformation mechanisms and mechanical properties.

The Third Pacific Rim International Conference on
Advanced Materials and Processing (PRICM 3)
Edited by M.A. Imam, R. DeNale, S. Hanada,
Z. Zhong and D.N. Lee
The Minerals, Metals & Materials Society, 1998

Introduction

In the past few years, extensive work has been carried out in understanding the deformation behavior of α, β and α–β Titanium alloys. Needless to say, the deformation modes and their dependencies differ vastly in all three systems. This paper seeks to address dependencies of deformation modes on factors such as microstructure, alloying elements etc. in the three systems in the temperature regime under consideration.

Ambient temperature deformation modes in α-Ti alloys include fine slip and twinning[1], those in β-Ti alloys include coarse slip and stress induced plate formation[2] and while those in α–β Ti alloys include slip, twinning and interface sliding[3].

Elevated temperature deformation in α-Ti alloys seems to be controlled by diffusion controlled climb[4]. β-Ti alloys exhibit glide controlled deformation dominated by lattice diffusion at elevated temperatures[4,5]. α–β alloys deform in a more interesting way, the deformation being controlled by the strain rate and the volume percent of the β phase. Interface sliding seems to be a major mode of deformation mode at β volume percents of ~50, deformation switches to a lattice diffusion controlled type as β volume fraction tends toward both extremes[4,6].

Low Temperature Deformation

α-Ti alloys

These alloys deform by prismatic slip[8], basal slip[9], slip of c+a dislocations on prismatic planes[10,11,12,13] and twinning[1,14]. However, the extent of twinning depends on the grain size. As expected, twinning becomes more difficult with decreasing grain size[14]. Studies on 500μm and 40μm grain size samples confirm this. It therefore follows that creep strain is larger for materials with larger grain size.

Creep is initiated by means of methods which require the lowest activation energy[15,16,17,18]. In the case of ambient temperatures, this happens to be slip. Though the slip is often not visible in optical microscopy, it has been proven conclusively that it indeed does occur[1]. This was done with the help of fiducial lines of Au deposited on the sample surface. This method has been described elsewhere[1,7]. Line spacing was measured before and after deformation in the same areas. Elongation was found to have occurred in the direction of loading[1]. Slip continues with further deformation. Slip is known to occur in α-Ti on the basal and prismatic planes in the 'a' direction, the systems being the $<11\bar{2}0>(0002)$ basal system or the $<11\bar{2}0>(1\bar{1}00)$ prismatic system. It has been postulated that in order to explain the ductility of some HCP metals, another deformation mode was prevalent, namely the $<\bar{1}\bar{1}23>$ or 'c + a' slip. The planes that these dislocations glide on are $\{10\bar{1}1\}$ for Ti-Al and Ti-6 wt. % Al-4 wt. % V alloys[19].

Twinning is of importance in Ti alloys with larger grain sizes. Work has not been done to establish threshold grain size for twinning, it will suffice to say that increased grain size facilitates twinning. Deformation twins have been found to be of $\{10\bar{1}2\}$, $\{11\bar{2}1\}$, $\{11\bar{2}2\}$, $\{10\bar{1}1\}$ types in CP Titanium[9,20,21]. In addition to the above, $\{11\bar{2}2\}$ and $\{11\bar{2}4\}$ twins have also been observed[13,22]. Another issue is whether slip is a prerequisite for twinning. As mentioned earlier, it seems favorable from an energy point of view, and twinned regions have been observed to form where slip has occurred. The data at this point seem to support this assertion.

One of the most interesting features about twinning observed in these alloys is their time dependency. Interrupt tests were carried out in a Ti-0.4 wt. % Mn alloy of 500μm grain size,

and it was found that twins not only nucleated at different stages in the deformation, but also grew with time. It was also observed that some areas where twins formed after a time delay had been deformed by slip. Figure 1 is an illustration of the above phenomenon[1]. It is speculated that this occurs due to high local stresses in these regions caused by dislocation pile ups at obstacles[23]. It has also been found that the presence of interstitial and substitutional atoms raises the stress required for twinning[13,24,25]. The time delay could also be due to the diffusion of these atoms[1].

Another effect observed in the creep deformation of these alloys is saturation, i.e., the strain rate drops off to negligible values as the test proceeds. This has been attributed to a lack of recovery at ambient temperatures.

The above results have been proved for tensile loading. Recently, studies done on compressive loading of Ti-0.4 wt. % Mn alloy of 500μm grain size material by Hultgren and Ankem[26] revealed the same deformation modes, namely fine slip and twinning. In addition, the time dependency of twinning was borne out in compression too.

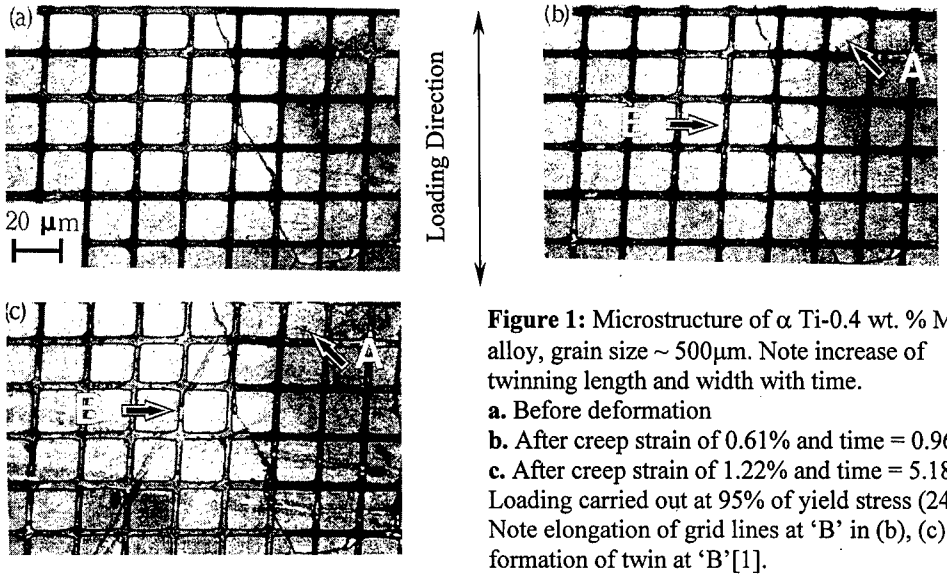


Figure 1: Microstructure of α Ti-0.4 wt. % Mn alloy, grain size ~ 500μm. Note increase of twinning length and width with time.
a. Before deformation
b. After creep strain of 0.61% and time = 0.96 hr
c. After creep strain of 1.22% and time = 5.18 hr
Loading carried out at 95% of yield stress (249 MPa)
Note elongation of grid lines at 'B' in (b), (c) shows formation of twin at 'B'[1].

β-Ti Alloys

β-Ti alloys play a major role in aerospace and other industrial applications. Reliability is a key issue here, and understanding deformation modes is extremely important in order to design alloys with requisite properties. Tensile testing at ambient temperatures has been widely reported, but data on ambient temperature creep behavior is scarce.

All β alloys have been reported to deform at ambient temperatures by slip only or by slip and formation of stress induced plates (SIP). The exact nature of these plates is a controversial topic, as conclusive evidence is still lacking. They have been reported to be:

a. Twins: Work done Ti-V, Ti-Mo and Ti-Mo-Zr alloys with Vanadium contents ranging from 20 to 40 wt. % has shown the SIP are {112}<111> twins[34], {332}<113> twins [34,35,36,37]. Some authors have reported that twinning occurs where the stability of the β phase is lower[36,38]. However, it was noted that twinning activity increased as Vanadium content approached 40 wt. %.

b. α' HCP martensite: Results from deformation carried out on Ti-Mo and Ti-V systems with Molybdenum content in the range of 8-20 wt. % and Vanadium contents in the range of 20-40 wt. % indicate formation of HCP martensite[39,40,41,42]. Wood has reported that the ω phase is formed when the deformation exceeds 5%[41]. Hida et al have reported that the SIP nature changes from a twin like mode with $(111)_\beta$ // $(00\bar{1})_T$ and $[110]_\beta$ //$[110]_T$, to α' martensite as the Molybdenum content is increased from 14 to 20 wt. %.
c. Tetragonal/Orthorhombic/BCC martensite: Results from Ti-Mo alloys with Molybdenum contents ranging from 7 to 13.5 wt. % and a Ti-20 wt. % V alloy indicate that the stress induced product is orthorhombic/tetragonal[43] and BCC/BCT[44].
d. Variant of the omega phase: This intermediate ω phase seems to be a transition phase formed in the $\beta-\alpha'$ transformation.

Greene, Sil and Ankem[2] showed that a Ti-13 wt. % Mn alloy deformed solely by coarse planar and wavy slip. This was observed by Ling et al for Ti-V alloys, but their results indicated twinning as well[38].

Ambient temperature tensile creep studies carried out by Ramesh and Ankem[46] on Ti-14.8 wt. % V alloys of different grain sizes show the existence of SIP and slip. Further, it has been observed from interrupt testing that these SIP grow with time. The grain size does not seem to determine whether the SIP form or not. Wood observed stress induced HCP martensite formed in tensile deformation of a Ti-15 wt. % Mo alloy of varying grain size which confirms the above results.

From the above information, it appears that the stability of the β phase determines the deformation behavior of these alloys. The effect of the athermal ω phase in relation to the deformation mode needs to be examined, and the effect of interstitials such as oxygen in the alloy needs to be taken into account. A clearer picture of the deformation mode will hopefully then begin to emerge.

$\alpha-\beta$ Ti Alloys

Considerable work has been done on this family of alloys due to their commercial significance. Ti-6Al-4V is still the major alloy used in aerospace applications which accounts for a significant chunk of the Titanium market. Work has been done on equiaxed as well as Widmanstatten microstructures. Results have shown that slip occurs across both phases due to orientation relationships, twinning in the α phase, interface sliding and individual slip in α and β phases.

Fine slip occurring in the α phase was monitored using the same technique outlined under the previous heading, and was reported earlier by Ankem and Margolin[3,27] and Greene[14]. Work done on Ti-8.1 wt. % V and Ti-6.0 wt. % Mn $\alpha-\beta$ systems show differences in deformation behavior, indicating the importance of the nature and content of alloying element, which in turn determines the stability of the β phase. Another difference was the presence of coarse slip in the Ti-Mn system, which penetrated but did not pass through the α phase. This is in direct contrast to the Ti-V system, where coarse slip penetrated the $\alpha-\beta$ interfaces and proceeded across the α phase. This appears to be as a result of the stability of the β phase[14]. The observation that slip did indeed penetrate the $\alpha-\beta$ interfaces has been widely reported[28,31]. Burgers orientation relationships between the α and β phases have been derived[29,30]. The above results are for Widmanstatten microstructures in both cases. Slip between phases in the same colony occurs due to the Burgers relationships that are shared by α and β phases, the $(0001)[11\bar{2}0]_\alpha$ system is coplanar with the $(110)[111]_\beta$ system.

Deformation by sliding has been documented to be of three types, namely, interphase sliding, grain boundary sliding and colony boundary sliding. For low strains, almost all sliding

was observed to have occurred at colony boundaries, by increasing the strain however, grain boundary sliding became evident

Effect of microstructure on the deformation behavior has also been widely documented. Heat treatment above the β transus has shown early crack nucleation and strain localization in the α phase along β grain boundaries for a Ti-6Al-2Nb-1Ta alloy. In addition, it was shown that deformation was localized to colonies within grains[31].

The Ti-V alloy strained more than the Ti-Mn alloy under creep when tested at a stress level of 95% of the 0.2% proof stress. Work done on a Ti-4.5Al-5Mo-1.5Cr by Martin et al[32] supports this observation that increasing the stability of the β phase increases the strength of the alloy.

The extent of deformation under creep for a given composition seems to be controlled by the slip length, which in turn is determined by the spacing between obstacles for slip. It is therefore the heat treatment temperature which plays a major role in controlling the creep deformation behavior for a given composition.

Imam and Gilmore[16] reported the existence of dual deformation mechanisms in ambient temperature dynamic load creep testing of Ti-6Al-4V. They postulate a deformation mode that comes into play once a threshold strain has been achieved. It was found that the effect of prestrain revolved around the stress applied during creep testing and the extent of prestrain. In general, it was observed that as the creep testing stress was increased, larger amounts of prestrain were required to inhibit creep. It has been postulated that this is the case because of "exhaustion" of dislocation sources. Saturation of creep curves at stress levels below the yield stress has been reported by many authors[17,31]. This has been attributed to a lack of recovery at temperatures under test.

ELEVATED TEMPERATURE DEFORMATION

α–Ti Alloys

High temperature flow stresses for an α-Ti-0.4 wt. % Mn alloy increase with strain rate and decrease with temperature with mild strain hardening behavior[4]. However, the steady state stress for a given strain rate and temperature for CP Ti increased with increasing grain size till about 800μm grain size, beyond which a plateau was reached[47].

Stress exponents obtained by different investigators show good correlation. The activation energy for deformation was calculated to be in the range of 210-250 kJ/mol in the temperature range 650^0C-750^0C by Vijayshankar and Ankem and around 210 kJ/mol in the temperature range 570^0C-827^0C by Oikawa and Cui[4,47]. This corresponds closely to the value for self-diffusion in α-Ti, thereby indicating that the process is controlled by lattice diffusion.

The range of stress exponents (<5) obtained further indicate that the deformation is predominantly climb controlled. Such a value for the stress exponent points to the fact that a greater number of slip systems exist than those for ordinary HCP metals. An analysis of activation energies for climb should confirm the above. Further evidence for this comes from TEM observations of deformed samples which showed the existence of subgrains[48].

β-Ti Alloys

One of the most significant features in the deformation behavior of β-Ti alloys at elevated temperatures is the occurrence of flow stress drops. The magnitude of these drops increases with strain rate and decreases with temperature. Also, work done on Ti-13 wt. % Mn and Ti-9.4 wt. % Mn has shown that flow stress and extent of flow stress drop increase with an increase in solute content. Testing for the above alloys was carried out at 750^0C and 700^0C.

Testing carried out on a Ti-14.8 wt. % V alloy at 700^0C showed the same behavior. Also, examination of microstructures after deformation showed the formation of subgrains[49].

That the flow stress drops are due to dislocation solute interaction is evident from the fact that this effect was not observed in pure β-Ti[5]. Work done by Johnston and Gilman attributes the flow stress drop to the low initial mobile dislocation density and subsequent rapid multiplication of dislocations[50]. Work done on materials with low initial dislocation densities show similar flow stress drops.

Samples loaded to 0.03% strain and annealed at the testing temperature for 12h showed a drop in flow stress. This shows that the drop in flow stress is not merely due to unlocking of sources, as the peak stress would have been attained after the anneal in this case, but the presence of additional dislocations as would happen with multiplication of dislocations[49].

Effect of the nature of solute on the drop in flow stress has also been studied[49]. Experiments were done on Ti-11.8 wt. % Mn and Ti-14.8 wt. % V alloys, which have similar stability of the β phase. It was found that the magnitude of the flow stress drop was higher for the Ti-Mn system. This is explained by the fact that the relative atomic size difference between Ti and Mn is higher, resulting in higher dislocation solute interactions. Stronger interactions result in higher peak stresses and hence larger flow stress drops. Steady state behavior was attained after the flow stress drop. This has been explained with respect to the presence of subgrain formation[51].

Study of the β phase in a T-6Al-4V alloy under torsion at 800^0C showed activation energies to be the order of 170 kJ/mol, about the value required for self diffusion. The mode of recovery in the β field here is speculated to be that of dynamic recovery type. This corresponds to the steady state region after the flow stress drop[52].

α–β Ti Alloys

Stress strain curves from studies performed on α–β alloys with β contents ranging from 20-90% on Ti-Mn alloys at 700^0C lie between those of α and β phases. Flow stress drops similar to those observed in β alloys were also observed here. The extent of drop increased with increasing β volume percent, and decreased with increasing temperature. Flow stresses did not vary linearly with β volume percent, but were found to depend on the strain rate also. Flow stress for an alloy with 50% β tested at a strain rate of 0.00011/s was actually found to be lower than that for an alloy with 20 %β[4]. The strength of such an alloy at the testing temperature was found to be much lower than expected, suggesting a hitherto overlooked deformation mechanism. Interface sliding has been found to occur in these alloys[48].

An increase in activation energy with strain rates was observed. This corresponds to increase in flow stress with increasing strain rates. It is suggested that interface sliding may therefore not be the primary mechanism for deformation at high strain rates. Lattice diffusion seems to dominate at these strain rates.

Work done on Ti-6Al-4V alloy suggests the deformation mode to be that of dynamic recrystallization in the α + β phase field[52]. Activation energies determined for deformation in the α + β phase field were found to correlate well with the work of Sastry et al[53].

Creep testing of Ti-6Al-2Nb-1Ta-0.8Mo was carried out at 600^0C until fracture. Rupture occurred by microvoid nucleation and growth. Fracture occurred along colony boundaries. Interface sliding was observed to be the major mode of deformation in a range of Widmanstatten structures. A plot of log of strain rate vs. inverse of absolute temperature yielded a very interesting result. The graph comprised two distinct straight line regions, or two regimes. Activation energy for higher temperatures(>500^0C) was found to correlate well with that of self diffusion in Ti. The conclusion is that deformation is controlled by diffusion at higher temperatures. Activation energy in the low temperature regime (less than 500^0C) was found to be near that of diffusion of oxygen in α–Ti[32].

Testing on IMI834 (Ti-5.8Al-3.5Zr-0.7Ni-0.5Mo-0.35Si-0.06Si) was carried out at 575^{0}C over a wide range of stresses[54]. The deformation observed was found to be similar in all cases. Rupture was found to have occurred due to nucleation and growth of cavities on $\alpha-\beta$ as well as $\beta-\beta$ interfaces. Testing carried out on the same alloy at 600^{0}C showed a strong dependence of aging temperature on creep properties. The best properties were obtained by aging at 700^{0}C for 2 hours prior to oil quenching. It is suspected that precipitation of prismatic dislocations of type c<0001> at lamellar boundaries prevents dislocation motion[55].

SUMMARY

Significant progress has been made in the understanding of deformation behavior of Titanium alloys. It has been established that at ambient temperatures, α-Ti alloys deform by fine slip and twinning, $\alpha-\beta$ Ti alloys by slip, twinning and interface sliding and β-Ti alloys by slip and stress induced plate formation.

At elevated temperatures, α-Ti alloys deform by a climb controlled lattice diffusion process. There is a strong interaction between dislocations and solute atoms in β-Ti alloys which explains flow stress drops at elevated temperatures. Flow stress drops were observed in $\alpha-\beta$ alloys also particularly at high strain rates, with interface sliding contributing in a large part to the total deformation at low strain rates.

With respect to future studies, testing under compressive loads at ambient as well as elevated temperatures needs to be carried out for β and $\alpha-\beta$ systems with regard to understanding deformation modes and their dependencies on factors such as microstructure, composition and strain rates. The exact nature of SIP formed in deformation β-Ti alloys is to be resolved.

ACKNOWLEDGEMENTS

The authors would like to express their appreciation to Dr. George Yoder of The Office of Naval Research for his stimulating discussions and constant encouragement. RMI Company, Niles, OH, supplied the material used in the investigation. This research is being funded by The Office of Naval Research under grant number N0001496101819.

REFERENCES

1. S. Ankem, C. A. Greene, S. Singh, *Scripta. Metall. et Mater.*, **30**, 803 (1994)
2. D.Sil, C. A. Greene, S. Ankem: *Beta Titanium Alloys*, ed. by A. Vassel, D. Eylon, Y. Combres, 173 (1994)
3. S. Ankem, H. Margolin, *Metall. Trans.*, **14A**, 500 (1983)
4. M. N. Vijayshankar, S. Ankem: *Titanium '92, Science and Technology*, ed. by F. H. Froes, A. Caplan, TMS(1993)
5. H. Oikawa, K. Nishimura, M. X. Cui, *Scr. Metall.*, **19**, 826 (1985)
6. S. Ankem, *Proceedings of the 2nd Pacific Rim International Conference on Advanced Materials and Processes*, Ed. By K. S. Shin, J. K. Yoon, S. J. Kim, The Korean Inst. Of Metals, 2275 (1995)
7. D. G. Attwood, R. M. Hazzeldine, Metallography, **9**, 483 (1976)
8. A. Akhtar, E. Teghtsoonian, *Metall. Trans.*, **6A**, 2201 (1975)
9. A. Akhtar, *Metall. Trans.*, **6A**, 1105 (1975)
10. F. D. Rossi, *J. Metal. Trans. AIME*, Feb., 257 (1953)
11. W. J. McG. Tegart, *Phil. Mag.*, **9**, 339 (1964)
12. H. Numakura, Y. Minonishi, M. Koiwa, *Scripta Metall.*, **20**, 1581 (1986)
13. H. Conrad, *Progress in Materials Science*,**26**, pp123-403 (1981)

14. C. A. Greene, *Ph.D Thesis*, University of Maryland at College Park (1994)
15. H. P. Chu, *J. of Mater.*, **5**, 633 (1970)
16. M. A. Imam, C. M. Gilmore, *Metall. Trans.*, **10A**, 419 (1979)
17. B. C. Odegard, A. W. Thompson, *Metall. Trans.*, **5**, 1207 (1974)
18. R. Zeyfund, R. Martin, H. Conrad, *Mat. Sci. & Engg.*, **8**, 134 (1971)
19. T. R. Cass: *The Science, Technology and Application of Titanium*, ed. by R. I. Jaffee, N. E. Promisel, Pergamon Press, 459 (1970)
20. M. H. Yoo, *Trans. Metall. Soc. AIME*, **245**, 2051 (1969)
21. D. J. Bacon, A. Serra, *Mat. Res. Soc. Symp. Proc.*, **238**, 73 (1992)
22. Y. Lii, V. Ramachandran, R. E. Reed-Hill, *Metall. Trans.*, **1**, 447 (1970)
23. G. F. Bolling, R. H. Richman, *Acta Met.*, **13**, 745, (1965)
24. S. Mahajan, D. F. Williams, *Int. Metall. Rev.*, **18**, 43 (1973)
25. C. J. Beevers, J. L. Robinson, *J. Less-Common Metals*, **17**, 345 (1969)
26. C. A. Hultgren, S. Ankem, *Unpublished Research*, University of Maryland, College Park (1997)
27. S. Ankem, H. Margolin, Metall. Trans., **17A**, 2209(1986)
28. S. Ankem, H. Margolin, *Metall. Trans.*, **11A**, 963 (1980)
29. P. A. Albert, *J. of Metals*, **197**, 1449 (1953)
30. C. G. Rhodes, J. C. Williams, *Metall. Trans.*, **6A**, 2103 (1975)
31. W. H. Miller Jr., R. T. Chen, E. A. Starke Jr., *Metall. Trans.*, **18A**, 1451 (1987)
32. P. L. Martin: *Titanium '95, Science and Technology*, ed. by P. A. Blenkinsop, W. J. Evans, H. M. Flower, The Institute of Materials, **Vol. II**, 940 (1995)
33. H. G. Paris, B. G. LeFevre, E. A. Starke Jr., *Metall. Trans.*, **7A**, 273 (1976)
34. S. Hanada, T. Yoshio, O. Izumi, *Trans. Japan Inst. Metals*, **27**, 496 (1986)
35. G. Carter, H. M. Flower, G. M. Pennock, D. R. F. West, *J. Mat. Sci.*, **12**, 2149 (1977)
36. S. Hanada, O. Izumi, *Metall. Trans.*, **18A**, 265 (1987)
37. M. Oka, Y. Taniguchi, *Metall. Trans.*, **10A**, 651, 1979
38. Fu-Wen Ling, E. A. Starke Jr., B. G. LeFevre, *Metall. Trans.*, **5**, 179 (1974)
39. M. Hida, E. Sukedai, C. Henmi, K. Sakaue, H. Terauchi, *Acta Metall.*, **30**, 1471 (1982)
40. M. K. Koul, J. F. Breedis, *Acta Metall.*, **18**, 579 (1970)
41. R. M. Wood, *Acta Metall.*, **11**, 907 (1963)
42. F. C. Holden, H. R. Ogden, R. I. Jaffee, *J. of Metals*, 1388 (1956)
43. D. N. Williams, R. A. Wood, E. S. Bartlett, *Metall. Trans.*, **3**, 1529 (1972)
44. M. J. Blackburn, J. C. Williams, *Trans Metall. Soc. AIME*, **242**, 2461 (1968)
45. T. S. Kuan, R. R. Ahrens, S. L. Sass, *Metall. Trans.*, **6A**, 1767 (1975)
46. A. Ramesh, S. Ankem, *Unpublished Research*, University of Maryland, College Park, 1997
47. H. Oikawa, M. X. Cui, Strength of Materials and Alloys, Proc. of ICSMA 7, Ed. By H. J. McQueen, J. P. Bailon, J. I. Dickson, J. J. Jonas, M. G. Akben, Pergamon Press, 601 (1985)
48. M. N. Vijayshankar, S. Ankem, *Unpublished Research*, University of Maryland at College Park (1992)
49. M. N. Vijayshankar, S. Ankem, *Mat. Sci. & Engg.*, **A129**, 229 (1990)
50. W. G. Johnston, J. J. Gilman, *J. Appl. Physics*, **30**, 129 (1959)
51. P. Griffith, C. Hammond, *Acta Metall.*, **20**, 935, (1972)
52. T. Sheppard, J. Norley, Mater. Sci. Technol., 903 (1988)
53. S. M. L. Sastry et. al: *Proc. of 4th Intl. Conf. on Titanium*, Japan Inst. of Metals, **1**, 873 (1980)
54. R. W. Evans, R. J. Hull: *Titanium '95: Science and Technology*, ed. by P. A. Blenkinsop, W.J. Evans, H. M. Flower, The Institute of Materials, **Vol. II**, 1058 (1995)
55. H. Kestler, H. Mughrabi, H. Renner: *Science and Technology*, ed. by P. A. Blenkinsop, W. J. Evans, H. M. Flower, The Institute of Materials, **Vol. II**, 1171 (1995)

EFFECTS OF $L1_2$ $(Al,Cr)_3Ti$ COATINGS ON THE HIGH TEMPERATURE OXIDATION BEHAVIOR OF TiAl ALLOYS

H. N. Lee, Z. M. Park, M. H. Oh*, S. W. Nam and D. M. Wee
Dept. of Matls. Sci. & Eng., KAIST, Taejon 305-701, Korea
Jointly Appointed at the Center for Advanced Aerospace Materials, POSTECH, Korea
*Dept. of Matls. Sci. & Eng., KNUT, Kumi 730-701, Korea

Abstract

The oxidation behavior and the mechanical property of gamma TiAl alloys coated with the Al-21Ti-23Cr and the Al-21Ti-23Cr-0.1Y films were investigated. The increase in the thickness of the Al-21Ti-23Cr film was effective in decreasing the oxidation rate of Ti-48Al. However, a small addition of yttrium to the coating material was more effective in the improvement of the oxidation resistance of Ti-48Al. From the scratch test, it was found that the specimen coated with the Al-21Ti-23Cr-0.1Y film had better adhesion between the Al_2O_3 scale and the coating layer than one coated with Al-21Ti-23Cr film. Thus, it is suggested that this excellent oxidation resistance is attributable to the excellent adhesion between the Al_2O_3 scale and the Al-21Ti-23Cr-0.1Y film. Moreover, the specimen coated with the Al-21Ti-23Cr-0.1Y film showed lower creep rate and longer time to rupture than the specimen without coating, under the constant stress of 200 MPa at 1123 K in air. Therefore, it could be assumed that the Al-21Ti-23Cr-0.1Y alloy was prospective as an oxidation-resistant coating material for gamma titanium aluminides.

The Third Pacific Rim International Conference on
Advanced Materials and Processing (PRICM 3)
Edited by M.A. Imam, R. DeNale, S. Hanada,
Z. Zhong and D.N. Lee
The Minerals, Metals & Materials Society, 1998

Introduction

The gamma-based TiAl has great potential for applications in aircraft engines, due to their low density, high specific strength and excellent high-temperature properties compared to currently used nickel-base superalloys [1]. However, the poor oxidation resistance limits the use of TiAl above 800°C because the external layer formed on these compounds is not a protective Al_2O_3 scale, but rather TiO_2, or mixture of Al_2O_3 and TiO_2 [2]. One of the ways to improve the oxidation resistance of TiAl is the surface coating, which is expected to be effective in improving oxidation resistance while maintaining good mechanical properties. Though three general coating alloy approaches (MCrAlY, aluminizing, and silicides/ceramics) have been taken for protecting titanium aluminides, successful results have not yet been reported [3-5].

Recently, however, some promising results were found in the Ti-Al-Cr system. Meier et al. found that Ti-Al-Cr alloys containing a minimum of 8-10 % chromium are continuous Al_2O_3 scale formers up to 1573 K in air [6]. Furthermore, it is suggested that the alloy composed of γ-phase and Laves phase in the Ti-Al-Cr system is prospective as a coating material for TiAl by Brady et al. [7]. Also, in the previous works [8-10], we had reported that Al-21Ti-23Cr coating was very effective in decreasing the oxidation rate of Ti-48Al compared to the CoCrAl and the CoCrAlY coatings, as shown in Figure 1 [3, 9]. The aim of this study is to investigate the possibility of applying $L1_2$ $(Al,Cr)_3Ti$-based two-phase alloys as a coating material for TiAl. Some gamma-based TiAl specimens were coated with the Al-21Ti-23Cr and the Al-21Ti-23Cr-0.1Y film using the RF magnetron sputtering method. The oxidation behavior of the coated specimen was examined through a cyclic oxidation test, and the creep property of the coated specimens was also investigated.

Experimental Procedures

The alloys used in this study were Ti-48Al, Ti-48.5Al-1.5Mo-1N, Al-21Ti-23Cr and Al-21Ti-23Cr-0.1Y (at.%). Ingots of the alloys were prepared by arc melting in an argon atmosphere and remelted at least five times to promote homogeneity of the as-cast structure. The substrates for coating, 20×10×1 mm^3 in size, were cut by a diamond wheel cutter from a Ti-48Al ingot homogenized at 1473 K for 6 h, and then polished with up to 0.25 μm diamond paste. The creep specimens were machined out of a Ti-48.5Al-1.5Mo-1N ingot. The Ti-48.5Al-1.5Mo-1N ingot was homogenized at 1473 K for 24 h and then the aging treatment at 1173 K for 12 h was added after a heat treatment at 1663 K for 2 h. The targets for the coating, 76 mm in diameter and 8 mm thick, were machined out of the Al-21Ti-23Cr and the Al-21Ti-23Cr-0.1Y ingots. Then, the coating was performed using the RF magnetron sputtering apparatus. The conditions for the coating in this study were similar to those of the previous studies [8-9].

The cyclic oxidation tests were also performed at 1273 K for 200 cycles. One cycle consisted of heating to 1273 K, holding for 2 h, and then cooling to room temperature. In order to evaluate the adhesion between the Al_2O_3 scale and the coating layers, the scratch tests were performed at least ten times for the specimens coated with the Al-21Ti-23Cr and the Al-21Ti-23Cr-0.1Y films after an isothermal oxidation at 1273 K for 100 h. An AFM study was also carried out at least five times in air at room temperature with the PSI-Autoprobe under the scan size of 5 μm and the scan rate of 1 μm/min. Creep tests were performed for the uncoated and the coated Ti-48.5Al-1.5Mo-1N specimens under the constant stress of 200 MPa at 1123 K in air. Phase identification of the coated specimen was done with an XRD using a Cu-K_α characteristic X-ray. Microstructural and chemical features of the coated specimens were examined by an SEM equipped with EDS.

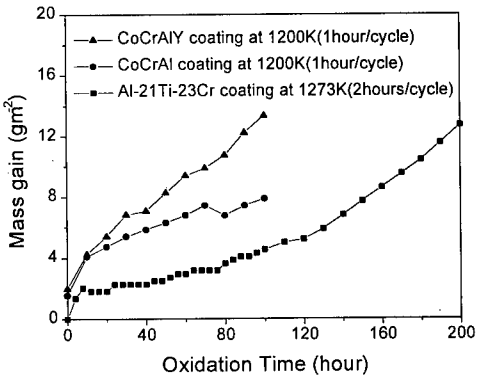


Figure I: Comparison of cyclic oxidation curves coated with the Al-21Ti-23Cr, CoCrAl and CoCrAlY films for given conditions [3, 9].

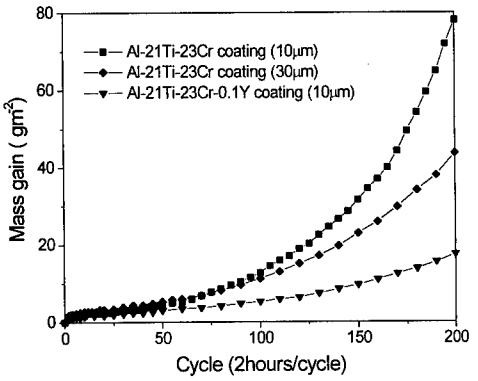


Figure II: Cyclic oxidation curves of Ti-48Al coated with the Al-21Ti-23Cr (10, 30 μm) and the Al-21Ti-23Cr-0.1Y films (10 μm) at 1273 K for 200 cycles.

Results & Discussion

The cyclic oxidation tests of Ti-48Al specimens coated with the Al-21Ti-23Cr (10, 30 μm) and Al-21Ti-23Cr-0.1Y film (10 μm), were performed to investigate the high temperature oxidation behavior of coated specimens. The mass gain due to the oxidation is plotted against the number of cycle with the change of the thickness and the composition in Figure II. The mass gain of Ti-48Al specimens coated with the Al-21Ti-23Cr film decreases as the film thickness is increased to 30 μm, which is found out especially after 100 cycles. The reason for the above result is that the Al-21Ti-23Cr coating with the thickness of 30 μm had more sufficient aluminum content needed to form a continuous Al_2O_3 scale during oxidation compared to that of the 10 μm coating. Also, this result indicates that Ti-48Al specimens coated with the Al-21Ti-23Cr film up to 30 μm, maintains its oxidation resistance and bears the thermal stresses. Moreover, a small addition of yttrium to the film is more effective in the improvement of the oxidation resistance than the change in the thickness of the film.

It is suggested that this excellent oxidation resistance is attributable to the better adhesion between the Al_2O_3 scale and Al-21Ti-23Cr-0.1Y film than between the Al_2O_3 scale and Al-21Ti-23Cr film. In order to prove this fact, the scratch tests were performed for the specimens coated with the Al-21Ti-23Cr and the Al-21Ti-23Cr-0.1Y film after isothermal oxidation at 1273 K for 100 hours. The results of a typical scratch test are shown in Figure III. Figure III (a), (b) are SEM (scanning electron microscopy) images of the surfaces and (c), (d) are the acoustic emission results of the Al-21Ti-23Cr and the Al-21Ti-23Cr-0.1Y films after oxidation. The average critical loads were 17 N and 29 N for the Al_2O_3 scale on the Al-21Ti-23Cr and the Al-21Ti-23Cr-0.1Y films which considered SEM images and acoustic emission results. This agrees with the adhesion improvement owing to the yttrium addition in the literature [10, 11]. Therefore, the yttrium addition to the Al-21Ti-23Cr film was very effective in decreasing the oxidation rate of the Ti-48Al because it increases the adhesion of the Al_2O_3 scale on the coating layer.

An AFM study was carried out to examine the relationship between the surface morphology and the adhesion. The surface morphology of the specimens coated with the Al-21Ti-23Cr

and the Al-21Ti-23Cr-0.1Y film obtained from the AFM study was shown in Figure IV after an isothermal oxidation at 1273 K for 3 h, 10 h and 100 h, respectively. Regardless of the yttrium addition, the average roughness increased to the peak point during the early stage of the oxidation behavior. With increasing time, however, the roughness decreases as the oxidation progressed. On the contrary, the difference between the two specimens is that the surface of the Al-21Ti-23Cr-0.1Y film is smoother than that of the Al-21Ti-23Cr film after the early stage of oxidation. The average roughness of the surfaces coated with Al-21Ti-23Cr-xY (x = 0, 0.1) film were summarized for each specimen in Table I. Since the roughness of the

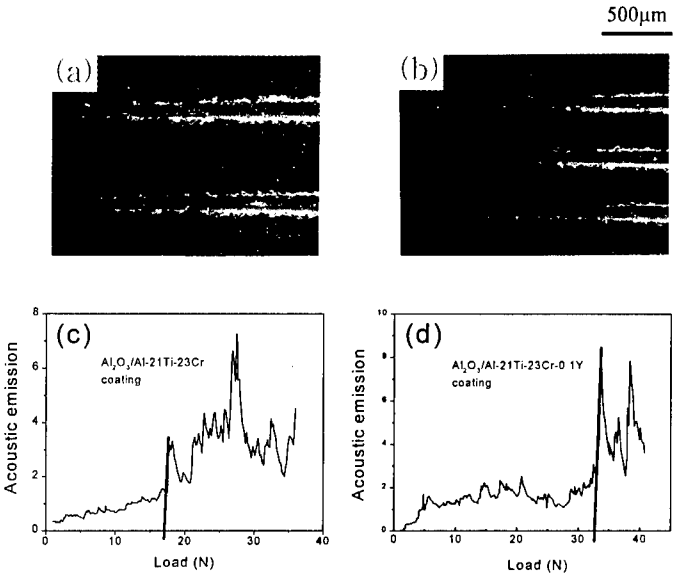


Figure III: SEM images (a, b) and acoustic emission results (c, d) of specimens coated with the Al-21Ti-23Cr (a, c) and the Al-21Ti-23Cr-0.1Y (b, d) films after isothermal oxidation at 1273 K for 100 h.

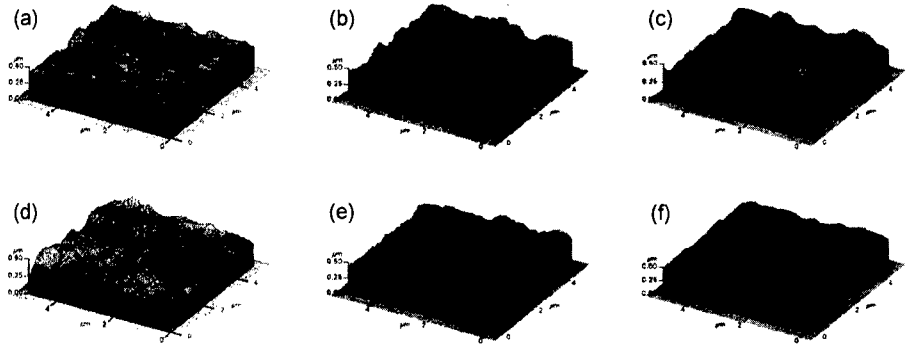


Figure IV: AFM images of the surface microstructure for the Al-21Ti-23Cr (a, b, c) and the Al-21Ti-23Cr-0.1Y (d, e, f) films oxidized at 1273 K for 3 h (a, d), 10 h (b, e) and 100 h (c, f), respectively.

Table I Average roughness of specimens coated with the Al-21Ti-23Cr and the Al-21Ti-23Cr-0.1Y film oxidized at 1273 K for 0 h, 3 h, 10 h, 100 h, respectively.

Oxidation Time (h)	Average Roughness (Al-21Ti-23Cr)	Average Roughness (Al-21Ti-23Cr-0.1Y)
0	50	53
3	276.7	419
10	432	357.5
100	326.7	268

surface is related with the stress that originated from the formation of the oxide at the oxide grain boundary [10], the specimen which has a rougher surface on the Al_2O_3 scale may retain higher stress than the flatter one. Therefore, the resistance to the failure of the Al_2O_3 scale is increased by the yttrium addition because a small addition of yttrium to the coating results in flat Al_2O_3 scales [3]. Thus, it is suggested that the excellent oxidation behavior of the Al-21Ti-23Cr-0.1Y film is mainly due to the improvement of adhesion between the Al_2O_3 scale and the Al-21Ti-23Cr-0.1Y film, which is generally accepted as a reactive element effect including yttrium [10].

To evaluate the probability of the Al-21Ti-23Cr-xY (x = 0, 0.1) in practical usage, creep tests were performed for the Ti-48.5Al-1.5Mo-1N specimens coated with the Al-21Ti-23Cr and the Al-21Ti-23Cr-0.1Y film and without coating under the constant stress of 200 MPa at 1123 K in air (Figure V). The coated specimens had a lower creep rate than the uncoated one. Moreover, the specimen coated with Al-21Ti-23Cr-0.1Y showed excellent creep properties. In this case, the creep rate and the time to rupture were much lower and longer than in other cases. Despite of creep deformation being a bulk deformation phenomenon, one of the reasons for the above results may be that creep fracture of this alloy is somewhat sensitive to oxidation, which has been reported in other system [11, 12]. Thus, it is suggested that Al-21Ti-23Cr-0.1Y film prevents the Ti-48.5Al-1.5Mo-1N from degrading its creep properties in an oxidizing environment because the Al_2O_3 scale on the film acts as a diffusion barrier, which reduces the environmental attack. Therefore, it could be assumed that the Al-21Ti-23Cr-0.1Y alloy was a good prospect as an oxidation-resistant coating material for gamma titanium aluminides.

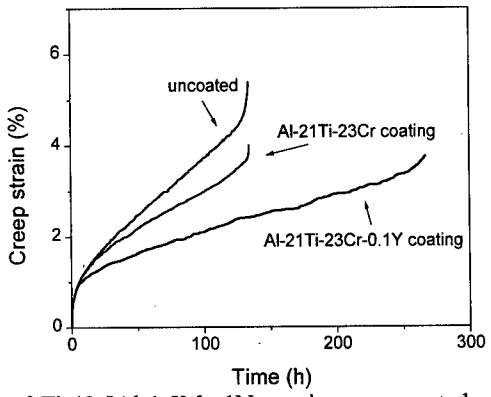


Figure V: Creep curves of Ti-48.5Al-1.5Mo-1N specimens uncoated and coated with the Al-21Ti-23Cr and the Al-21Ti-23Cr-0.1Y films.

Summary

(1) The increase in the thickness of the Al-21Ti-23Cr film improved the oxidation resistance of the coated specimen. However, the yttrium addition to the Al-21Ti-23Cr film was more effective in decreasing the oxidation rate of the Ti-48Al

(2) From the scratch test, it was found that the specimen coated with the Al-21Ti-23Cr-0.1Y film had better adhesion between the Al_2O_3 scale and the coating layer than the one coated with the Al-21Ti-23Cr film. Thus, the excellent oxidation resistance is attributable to the excellent adhesion between the Al_2O_3 scale and the Al-21Ti-23Cr-0.1Y film.

(3) The specimen coated with Al-21Ti-23Cr-0.1Y film showed a lower creep rate and a longer time to rupture than the specimen without the coating. Therefore, it could be assumed that Al-21Ti-23Cr-0.1Y alloy has a good potential as an oxidation-resistant coating material for gamma titanium aluminides.

Acknowledgement

The authors would like to thank Professor M. Yamaguchi at Kyoto University for his useful advice and helpful discussions. The authors also thank Mr. H. S. Cho for his assistance in the creep tests. The financial support of KOSEF (Contract No. 95-0300-10-01-3) is gratefully acknowledged.

References

1. M. Yamaguchi and H. Inui, "TiAl Compounds for Structural Applications," Structural Intermetallics, (Champion, PA: TMS, 1993), 127-142.
2. S. Becker et al., "Mechanism of isothermal oxidation of the intermetallic TiAl and of TiAl Alloys," Oxid. Met., 38 (1992), 425-464.
3. S. Taniguchi et al., "Oxidation Resistance of TiAl Improved by CoCrAl and CoCrAlY Coating," J. Japan Inst. Metals, 57 (1993), 781-789.
4. H. Mabuchi, T. Asai and T. Nakayama, "Aluminide Coatings on TiAl Compound," Scripta Metall., 23 (1989), 685-689.
5. S. Taniguchi et al., "High-Temperature Oxidation Resistance of TiAl Improved by IBED Si_3N_4 Coating," ISIJ International, 33 (1993), 869-876.
6. G. H. Meier et al., Structural Intermetallics (Champion, PA: TMS, 1993), 861-877.
7. M. P. Brady et al., "The Oxidation and Protection of Gamma Titanium Aluminides," JOM, 48 (1996), 46-50.
8. J. Y. Park et al., "$L1_2$ $(Al,Cr)_3Ti$-Based Two-Phase Intermetallic Compounds-II. Application to Coating Material on TiAl," Scr. Mater., 36 (1997), 801-806.
9. J. Y. Park et al., High Temperature Ordered Intermetallic Alloys VII (Pittsburgh, PA: MRS, 1997), 655-660.
10. F. H. Stott and G. C. Wood, "Growth and Adhesion of Oxide Scales on Al_2O_3-Forming Alloys and Coatings," Mat. Sci. & Eng., 87 (1987), 267-274.
11. J. S. Huang and Y. W. Kim, "Creep Deformation and Fracture of a Two-Phase TiAl Alloy," Scripta Metall., 25 (1991), 1901-1906.
12. M. Yoshihara, K. Miura and Y-W. Kim, Gamma Titanium Aluminides (Warendale, PA: TMS, 1995), 93-100.

MICROSTRUCTURE CONTROL OF NITROGEN DOPED TiAl ALLOYS

J. H. Yun, M. H. Oh*, S. W. Nam, D. M. Wee, H. Inui** and M. Yamaguchi**

Dept. of Matls. Sci. & Eng., KAIST, Taejon 305-701, Korea
Jointly Appointed at the Center for Advanced Aerospace Materials, POSTECH, Korea
*Dept. of Matls. Sci. & Eng., KNUT, Kumi 730-701, Korea
** Dept. of Matls. Sci. & Eng., Kyoto Univ., Kyoto 606-01, Japan

Abstract

Effects of nitrogen addition on the microstructure control of two-phase TiAl intermetallic compounds were investigated. Ti-48.5Al-1.5Mo(at.%) and its nitrogen doped alloys were prepared by vacuum arc melting and then annealed at 1390°C for the lamellar microstructure, and at 1300°C for the duplex microstructure. Ti-48.5Al-1.5Mo-1.0N alloys required much longer heat treatment time than Ti-48.5Al-1.5Mo in order to obtain both the fully lamellar microstructure and the duplex microstructure. Therefore, it could be supposed that the nitrogen has acted as the lamellar stabilizing element by slowing down the kinetics of the formation of equiaxed gamma grains in the lamellar grain boundaries. In addition, the nitrogen doped alloy had much better high-temperature creep properties than the nitrogen-free alloy. This may be caused by a nitrogen solid solution hardening effect and a Ti_3AlN precipitate hardening effect.

The Third Pacific Rim International Conference on
Advanced Materials and Processing (PRICM 3)
Edited by M.A. Imam, R. DeNale, S. Hanada,
Z. Zhong and D.N. Lee
The Minerals, Metals & Materials Society, 1998

Introduction

The gamma-based TiAl alloy has been known to be one of the most promising candidates for high-temperature structural applications[1,2]. However, two typical microstructures of the TiAl alloy, such as the duplex microstructure and the fully lamellar microstructure, have shown a so-called inverse relationship between room-temperature ductility and fracture toughness /creep resistance. Therefore, it is necessary to develop the TiAl alloy system with balanced mechanical properties.

In the previous study[3], we reported that the 1.0N doped TiAl+Mo alloy with the fully lamellar structure had sustained room-temperature ductility due to grain refinement and enhanced high-temperature tensile strength and creep resistance due to the formation of precipitates. The aim of the present paper is to report on an application of enhancement of high-temperature mechanical properties to the duplex microstructure. We studied the effect of nitrogen addition on the microstructure control and the phase transformation of the TiAl+Mo alloys with the duplex microstructure. The paper also reported the results of a preliminary creep test of the TiAl+Mo and its nitrogen doped alloys with the duplex microstructure at 800°C, and compared them with those of the fully lamellar microstructure.

Experimental Procedures

The alloys used in this study were prepared from starting materials of 99.99wt% Ti and Al, 99.9wt% Mo, and 99.9wt% TiN powder by vacuum arc melting under an argon atmosphere. The alloys were named by the content of nitrogen, such as 1.5Mo (Ti-48.5Al-1.5Mo(at.%)) and 1.0N (Ti-48.5Al-1.5Mo-1.0) alloys. In the present study, two types of heat treatment schemes were performed. One is for only microstructure control: (1200-1390)°C/(2-48)hr/FC. The other is added the aging treatment for 12hours at 900°C after the above-mentioned schemes to enhance the precipitate formation. Microstructure observations were performed using an optical microscope and a transmission electron microscope. The samples for TEM observations were prepared by electropolishing in a 60% methyl alcohol+35% n-butyl alcohol+5% percloric acid solution using a twin-jet polishing method. Constant stress creep tests were performed under a tensile stress of 200MPa at 800°C using a creep machine equipped with a constant stress Andrade-Chalmers cam. Round-shaped creep specimens, approximately 3.2mm in diameter and 15mm in gauge length, were machined and then polished mechanically.

Results and Discussion

Effects of nitrogen on microstructure control

Figure 1(a) is the optical micrograph of the 1.5Mo alloy heat-treated for 2 hours at 1390°C and Figure 1(b) is that of the 1.0N alloy heat-treated for 24 hours at 1390°C in order to obtain the fully lamellar microstructure. As seen in the figure, the addition of 1.0at.% nitrogen led to a remarkable grain refinement. The grain sizes of the 1.5Mo alloy with over 1700μm decreased to about 100μm by the addition of 1.0at.% nitrogen. Although the fully lamellar microstructure in the 1.0N alloy was also obtained by a short heat treatment such as 2 hours, it was similar to an as-cast lamellar microstructure, which has uncertain grain boundaries and undefined gamma layer existed along them. However, after a longer heat treatment such as 24 hours, the fully lamellar microstructure with obvious grain boundary was obtained, as shown in the Figure 1 (b).

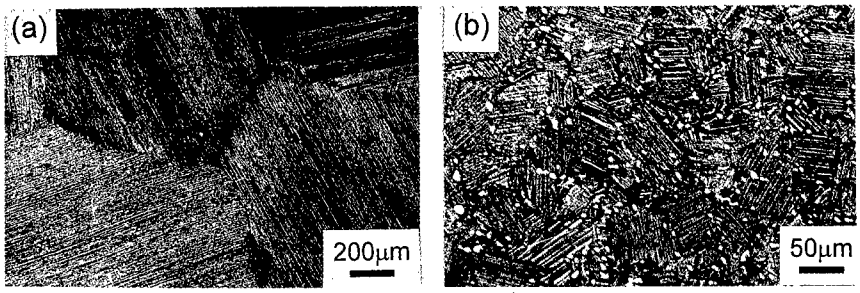


Figure 1: Optical micrographs of (a) Ti-48.5Al-1.5Mo alloys and (b) Ti-48.5Al-1.5Mo-1.0N alloys with the fully lamellar microstructure.

On the other hand, in a general case of the TiAl alloy, the heat treatment time for the duplex microstructure was approximately 6 hours at 1300°C[1,4]. In the present work, the duplex microstructure of the 1.5Mo alloy was also obtained in the same condition. However, as far as the 1.0N alloy was concerned, it was not the case. Figure 2 shows the microstructural change of the 1.0N alloy after performing the various heat treatments to obtain the duplex microstructure. As can be seen in Figure 2 (a)-(d), the duplex microstructure of the 1.0N alloy could be obtained after a much longer heat treatment time than 24 hours at 1300°C. This suggests that the growth of the gamma phase delayed by the addition of 1.0at.% nitrogen. Figure 2 (c), (e) and (f) show the duplex microstructure control at 1300, 1250 and 1200°C for 24 hours, respectively. According to the binary phase diagram of Ti-Al system, the volume fraction of gamma phase should increase with decreasing heat treatment temperature. However, as seen in the figures 2(c), (e) and (f), it seems to increase with increasing the heat treatment temperature. Therefore, from these results, it was supposed that the duplex microstructure control of 1.0N alloy required a longer heat treatment time than 24 hours when the heat treatment was performed at lower temperature.

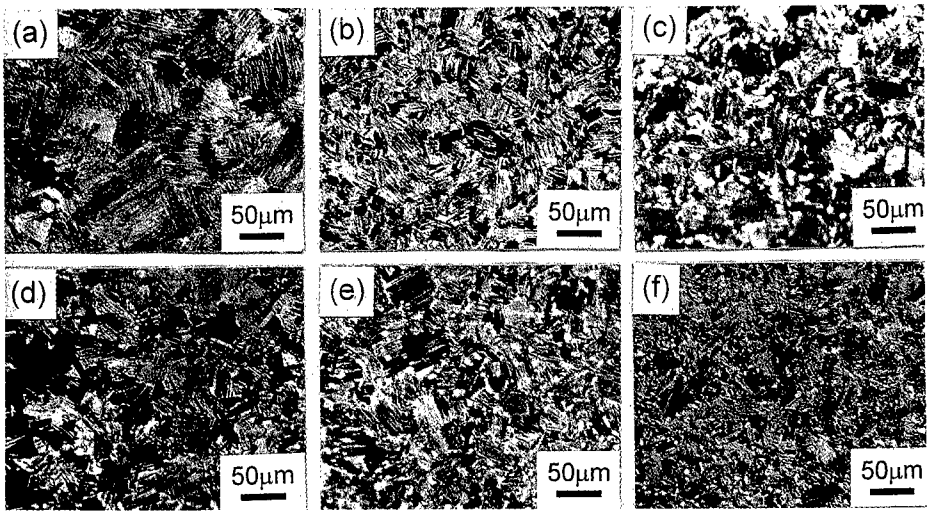


Figure 2: Optical micrographs of Ti-48.5Al-1.5Mo-1.0N alloy after the various heat treatments: (a) 2 hours, (b) 12 hours, (c) 24 hours and (d) 48 hours at 1300°C and 24hours at (e) 1250°C and (f) 1200°C, respectively.

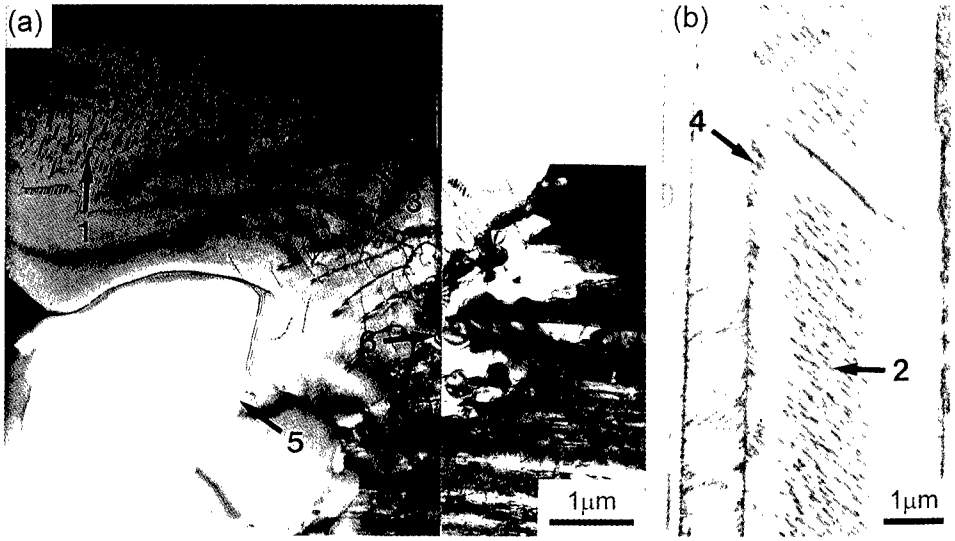


Figure 3: TEM image of (a) the gamma grain and (b) the gamma lamellae of the lamellar grain observed in Ti-48.5Al-1.5Mo-1.0N with the duplex microstructure.

Figure 3 shows the precipitate morphology through TEM observations in the 1.0N alloy, which received the heat treatment for 24 hours at 1300°C and then aging treatment for 12 hours at 900°C. As Tian *et al.* reported[5], it was found that two types of precipitate were formed after aging treatment. One is the Ti_3AlN precipitate of submicrometer size and the other is the Ti_2AlN precipitate with a few micrometers in size. As can be seen in Figure 3, the Ti_3AlN precipitates had needle shape and formed mainly inside gamma grains (marked 1 in Figure 3 (a)) and gamma lamellae of the lamellar grain (marked 2 in Figure 3 (b)) through the aging treatment. In addition, from the precise observations on them, it was found that the Ti_3AlN precipitates also formed on dislocations (marked 3 in Figure 3(a)) and lamellar/lamellar interfaces (marked 4 in Figure 3(b)), and they were larger than the Ti_3AlN precipitates marked 1 and 2. Moreover, precipitate-free zones (PFZ) were formed around Ti_3AlN precipitates of the mark 3 and 4. This suggests that the interstitial nitrogen atoms diffuse toward dislocations and lamellar/lamellar interfaces, which results in formation of larger Ti_3AlN precipitates through the aging treatment. On the other hand, the Ti_2AlN precipitates tended to form among the equiaxed gamma grain boundaries (marked 5 in Figure 3(a)) and the lamellar grain boundaries (marked 6 in Figure 3(a)). In this case, a wide precipitation-free zone (PFZ) was also observed around the Ti_2AlN precipitate, as indicated by the mark 5 of Figure 3(a). This means that the nitrogen atoms were depleted around the Ti_2AlN precipitate due to the diffusion of nitrogen atom to Ti_2AlN precipitate.

The 1.0N alloy required much longer heat treatment time than the 1.5Mo alloy. This fact can be explained by the diffusivity of the matrix atoms such as Ti and Al. It could be supposed that the nitrogen addition decreased the diffusion rate of Ti and Al atoms. In other words, the interstitial nitrogen atoms may cause "the locking effect" on Ti and Al atoms. "The locking effect" means that interstitial nitrogen atom lead to distort the lattice and the movement of Ti and Al may be disturbed. Therefore, if the heat treatment time is sufficient to form the nitride precipitates, the growth rate of gamma grains accelerates subsequently because the nitrogen

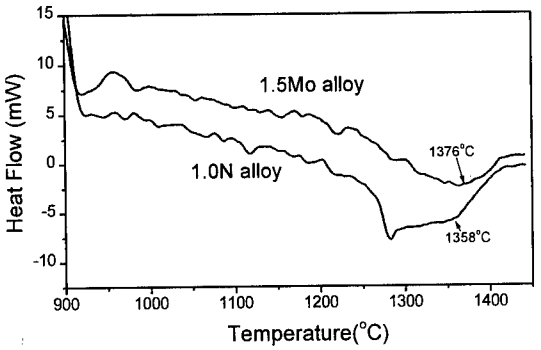


Figure 4: DTA curves of the Ti-48.5Al-1.5Mo and the Ti-48.5Al-1.5Mo-1.0N alloy.

content in matrix decreased. In consequence, the long-term heat treatment is needed for the sound duplex microstructure because the diffusion of Ti and Al atoms is retarded by the locking effect.

Figure 4 shows the DTA curves of the1.5Mo and the 1.0N alloys. The peaks indicate the phase transformation from the gamma + alpha phase region to the alpha single phase region. On the basis of the endpoint of the peak, the α transus line decreased about 20°C by the addition of nitrogen. Therefore, the 1.0N alloy should contain less volume fraction of gamma phase than the 1.5Mo alloy at the same heat treatment temperature. Thus, the nitrogen-doped alloy required a lower temperature and a much longer time than the nitrogen-free alloy for duplex microstructure control.

Effect of nitrogen on creep properties

Figure 5 shows the creep curves of 1.5Mo and 1.0N alloys with the duplex and the fully lamellar microstructure at 800°C under a constant tensile stress of 200MPa, respectively[6]. When the specimen had the same microstructure, the minimum creep rate decreased by the nitrogen addition. The time to 0.3% creep strain rose from 0.02 hours in 1.5Mo alloy to 9.8 hours in 1.0N alloy with the duplex microstructure. In particular, the 1.0N alloy with the duplex microstructure shows most beneficial resistance to the primary creep deformation.

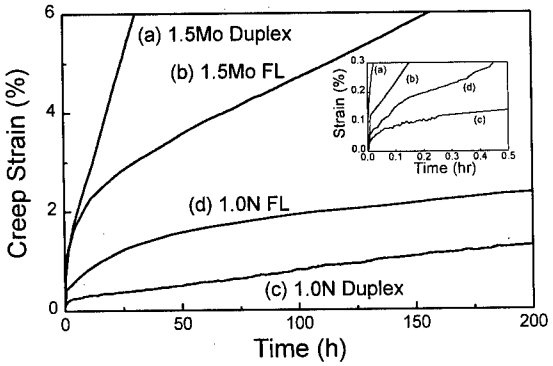


Figure 5: Creep curves obtained for the 1.5Mo alloy, the 0.3N alloy and the 1.0N alloys with the duplex and the fully lamellar microstructure under the constant tensile stress of 200MPa at 800°C.

Since no precipitate is formed in the 1.5Mo alloy, the creep curves followed the typical tendency of TiAl alloys, the lamellar microstructure having better creep resistance than the duplex microstructure, as shown in curves (a) and (b). However, the nitrogen-doped alloys had a similar minimum creep rate regardless of the microstructure. Moreover, from the standpoint of the resistance to primary creep deformation, the 1.0N alloy with the duplex microstructure shows longest time to 0.3% creep strain among the alloys tested. Thus, it could be suggested that nitrogen addition enhance the creep resistance not only for the fully lamellar microstructure but also for the duplex microstructure. Although the improvement in creep properties is supposed to occur due to the solid solution hardening and the precipitation hardening of fine Ti_3AlN precipitates, more detailed investigation is needed to interpret this mechanism. Relevant creep investigations are now in progress.

Summary

(1) 1.0at.% nitrogen addition leads to remarkable grain refinement in the fully lamellar microstructure but had little effect in the duplex microstructure.
(2) Since the formation of the gamma phase is retarded by nitrogen addition, long-term heat treatment is needed for the duplex microstructure in the 1.0N alloy.
(3) Nitrogen addition enhanced the creep resistance of the alloys with the duplex microstructure as well as the fully lamellar microstructure.

Acknowledgment

This work was supported by the Korea Science and Engineering Foundation through the Center for Advanced Aerospace Materials, POSTECH.

References

1. Y. W. Kim, "Ordered Intermetaillc Alloys. Part III: Gamma Titanium Aluminides," JOM, 46 (1994), 30-39.

2. M. Yamaguchi and H. Inui, "TiAl compounds for Structural Applications," R. Daloria et al., eds., Structural Intermetallics, (Warrendale, PA: TMS, 1993), 127-142.

3. J. H. Yun et al., "Microalloying Effects in TiAl+Mo Alloys," Mater. Sci. Eng. A, A239-240 (1997), 702-708.

4. R. S. Mishra et al., "Mechanism of Superplasticity in TiAl Alloys," Y. W. Kim et al., eds., Gamma Titanium Aluminides, (Warrendale, PA: TMS, 1995), 571-578.

5. W. H. Tian and M. Nemoto, "Effect of Carbon Addition on the Microstructures and Mechanical Properties of γ-TiAl Alloys," Intermetallics, 5 (1997) 237-244.

6. H. S. Cho et al., "Effect of 1at.% Nitrogen Addition on the Creep Resistance of Two Phase TiAl Alloys," Mater. Sci. Eng. A, *submitted* (1998).

CAST TiAl ALLOYS AS ENGINEERING MATERIALS

D.X.Zou

Central Iron and Steel Research Institute
Beijing 100081, China

Abstract

The advances of the new melting technique, investment cast mould and heat treatment for the candidate engineering TiAl alloys have been reviewed. The cold crucible vacuum induction levitation melting system has been successfully introduced as a satisfactory method to make the TiAl alloy being homogeneous and no contamination. Secondly, a new type Al_2O_3-Y_2O_3 ceramic investment cast mould for fabricating TiAl alloy components has been experimentally evaluated. Furthermore, the multi-step heat treatment for adjusting the microstructures of the cast Ti-46.5Al-2.5V-1.0Cr (at%) has been developed.

The Third Pacific Rim International Conference on
Advanced Materials and Processing (PRICM 3)
Edited by M.A. Imam, R. DeNale, S. Hanada,
Z. Zhong and D.N. Lee
The Minerals, Metals & Materials Society, 1998

Introduction

γ-based TiAl alloys have generated a great deal of interest as candidate high-temperature materials [1]. Besides the material studies on improving the mechanical properties, especially the room-temperature ductility, the technology development in manufacturing TiAl components has recently attracted much intention and the heat treatment for modifying the microstructures turn to be applied to the practical alloy cases [2]. This paper reviews the advances on the melting and casting technologies of TiAl alloys and the heat treatment for refining the as-cast microstructure.

Melting Technologies

The melting TiAl alloys are chemically active somehow like Titanium alloys [3]. Besides, the properties of TiAl alloys are sensitive to the Ti/Al atomic ratio and the amount of the alloying elements [4]. So, the new melting equipment and technologies are needed.

The cold crucible vacuum induction levitation melting (CCVILM) technique has been established in CISRI in the recent years [5]. It is experimentally proved that this new technique has many advantages in making TiAl alloys.

In this equipment as shown schematically in Figure 1, the raw materials of the TiAl alloys are put in the copper crucible which has the water cooling system inside the splits. When imposed on the high-frequency alternating electric current, the raw materials are melted and stirred by the magnetic induction and then the melting alloy is lifted by the electromagnetic interactions between the molten substance and the splits. The melting and levitation effects of this type equipment are mainly determined by the number of the slits in crucible and the frequency of the imposed electric current [6]. It has been found that the TiAl alloys weighing from 1.0 to 3.0 kg have been satisfactorily made using the crucible with 20~28 slits in the crucible wall and the 6~10 kHz induction current.

The chemical analyses performed on a ∅20×150 mm^2 cast ingot indicated that there were nearly no composition loss and the copper contamination occurred (see Table I) in the Ti-46.5Al-2.5V-1.0Cr (at%) alloy melted by the CCVILM technique, and that the composition undulations of the Al and (V, Cr) along the axial direction of the ingot were less than 0.5 and 0.3 (at%) respectively (listed in Table II).

Table I. The composition comparison between the designed and remelted alloys

	Al (at%)	V (at%)	Cr (at%)	C (wt%)	O (wt%)	Cu (wt%)	Ti
Design composition	46.50	2.50	1.00	-	-	-	balanced
Remelted alloy	46.36	2.42	1.03	0.03	0.61	<0.001	balanced

Table II. The composition (at%) distribution along the axial direction of the Ti-46.5Al-2.5V-1.0Cr alloy ingot

	1*	2	3	4	5
Al	46.41	46.65	46.32	46.25	46.17
V	2.54	2.36	2.31	2.48	2.41
Cr	1.08	0.96	1.10	0.98	1.02

*The distance between the analysis positions was about 30 mm

Mould for Investment Cast

Many experimental and real TiAl components have been successfully fabricated using conventional investment cast technologies [7]. However, the retardation of the reactions between the melting alloy and the mould surface still remained to be a challenge since the reactions impede the flow of the melting alloys and induce the occurrence of gas holes in the components.

A new type of the investment moulds has been developed through adding 1~5 (wt%) Y_2O_3 powder and 1~5 (wt%) bubbly substance into a conventional Al_2O_3-type ceramic mould. The surface morphologies and the composition features of the cast TiAl components were examined with SEM and EDX, indicating that reaction layer in the casting with conventional mould is about 0.58 mm thick containing 0.90 (wt%) Si and that in the casting with newly developed mould is around 0.33 μm thick contain only 0.35 (wt%) Si (Figure 2 (a) (b)). It has been proved that the reaction between the melting and the Al_2O_3-type mould was mainly caused by the SiO_2 which came from the paste in the mould [8]. So the obvious reduction of the Si contamination means the abatement of the reactions between the melting and the mould. Besides, the sooth finish of the cast TiAl alloy component has been obviously improved by using the new mould as well. Recently the automobile turbochargers and turbine blades of the TiAl alloys have been successfully fabricated by centrifugal investment casting (Figure 3 (a) (b)).

Heat Treatment of the Cast TiAl Alloys

The as-cast microstructure of the TiAl alloys (Figure 4 (a)) are usually composed of the coarse, inhomogeneous fully lamellar colonies [2]. Although the well-studied heat treatments for the wrought TiAl alloys can be principally adopted to the cast alloys, the high thermal stability of the lamellar microstructures [9] turns out a big problem when employing only heat treatments to modify the microstructures.

First, the as-cast microstructure can only be homogenized by the heat treatment at the temperature up to the single α phase (usually higher than 1320 ℃) [10]. Since there is no potent pinning mechanism to retard the growth of the α grains at that high temperature, the homogenized microstructures are generally fully lamellar microstructure with still coarse colonies (Figure 4 (b)) [10].

Then, a cyclic heat treatment (CHT) between 900 and 1150 ℃ plus a thermal treatment at 1150 ℃ were applied to decompose the fully lamellar microstructure as a breakthrough in modifying the microstructures of the cast Ti-46.5Al-2.5V-1.0Cr (at%) alloy [11]. After 6 periods of CHT, there were a number of inner edges emerged in the lamellar structure (Figure 4 (c)). The breakdown of the lamellar was believed to be due to the increase of the energy undulation generated in the heating and cooling processes of CHT and naturally existed shape perturbation of the lamellar. The fully lamellar microstructure with previously produced inner edges has been decomposed to a comparatively fine equiaxed near gamma (NG) microstructure (Figure 4 (d)). The spheriodation of the lamellae was generated by the segmental continuous coarsening in the process of thermal treatment at 1150 ℃.

Finally, the fine fully lamellar microstructure and duplex microstructure (Figure 5 (a) and (b)) were successfully obtained through reheating the NG microstructure up to 1370 ℃ or 1290 ℃. Since there are 4 {111} habit planes for the precipitating of the α in the γ matrix, the transformed fine fully lamellar and duplex microstructures can get further refined [12].

The obtained fine fully lamellar and duplex microstructures of the cast Ti-46.5Al-2.5V-1.0Cr (at%) alloy have shown quite good ambient tensile properties and fracture toughness (listed in Table III).

Table III. The ambient mechanical properties of the fully lamellar (FFL) and duplex microstructure (DM) of the cast Ti-46.5Al-2.5V-1.0Cr (at%) alloy

	σ_s, MPa	σ_b, MPa	δ, %	K_{1c}, Mpa$\sqrt{m}$
FFL	388	471	3.1	20.1
DM	418	496	3.3	-

Summary

The TiAl alloys can be homogeneously made by the cold crucible vacuum induction levitation melting technique without obvious composition loss and the contamination from the crucible material. Several TiAl alloy components have been successfully fabricated by the investment-cast using the modified Al_2O_3-type ceramic moulds bearing Y_2O_3 and bubbly substance. Furthermore, the as-cast microstructure of the cast Ti-46.5Al-2.5V-1.0Cr (at%) alloy can be transformed to the homogeneous fine fully lamellar and duplex microstructures.

References

1. M.Yamaguchi and H.Inui, Structural Intermetallics, ed. R.Daralia, J.J.Lewandowski, C.T.Liu, P.L.Martin, D.B.Miracle and M.W.Nathal (Warrendale, PA: TMS, 1993), 127-136.
2. Y-M. Kim, JOM, 46 (1994), 30-42.
3. Z-Y. Zhong and Y.F.Han, J. of Iron and Steel Research, 9 (1997), 1-8.
4. Y-M. Kim and D.M.Dimiduk, JOM, 43 (1991), 40-49.
5. D.Feng, H.Luo, D.X.Zou, C.Zhang, J. of Iron and Steel Research, 6 (1994), 24-30.

6. A.Gagnoud, Trans. ISIJ, 28 (1988), 36-40.
7. Y-M. Kim, JOM, 47 (1995), 30-39.
8. L.Ning, Rare Metals Letters, 10 (1997), 7-8.
9. E. Werner, Z. Metallkde, 81 (1990), 790-796.
10. S.L.Semiatin and P.A.McQuay, Metall. Trans., 23A (1992), 149-154.
11. J.Zhang, W.Ma, D.X.Zou et al., Trans. of Metal Heat Treatment, 17 (3) (1996), 16-21.
12. J.Zhang, J.W.Zhang, D.X.Zou et al., Trans. of Metal Heat Treatment, 17 (4) (1996), 12-16.

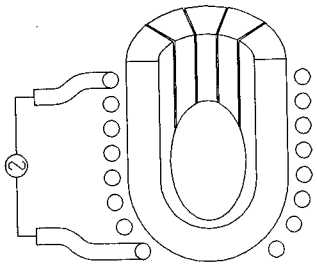


Figure 1: Schemetic of the cold crucible induction levitation melting system.

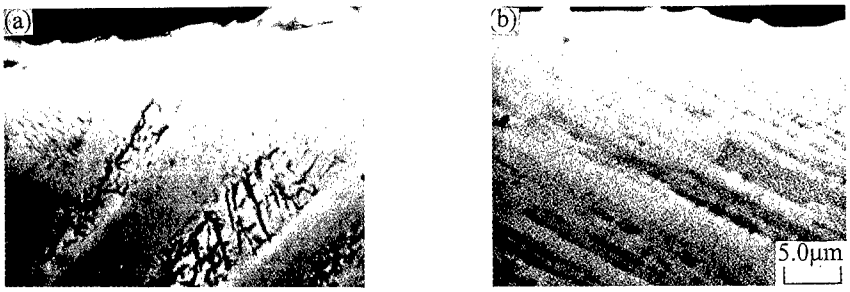


Figure 2: SEM micrographs showing morphologies of the surface areas in the cast Ti-46.5Al-2.5V-1.0Cr (at%) alloy components using (a) the conventional Al_2O_3 mould and (b) modified Al_2O_3 mould containing Y_2O_3 and bubbly substance respectively.

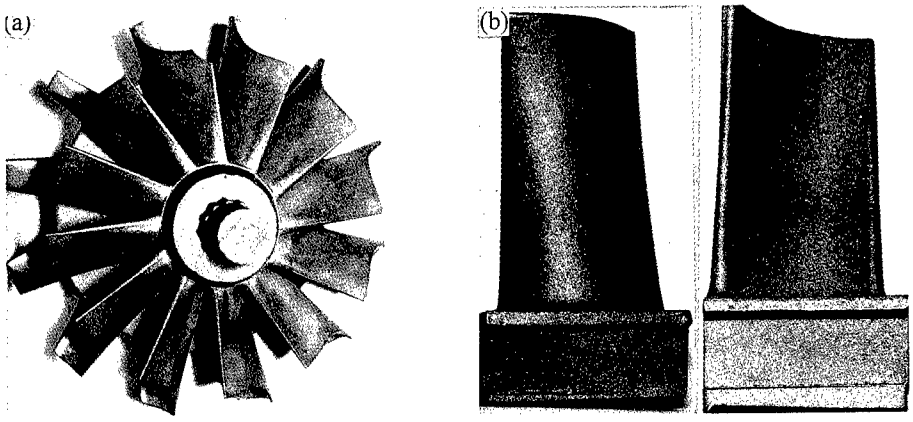


Figure 3: The (a) automobile turbochargers and (b) turbine blades of the TiAl alloy fabricated by centrifugal investment casting.

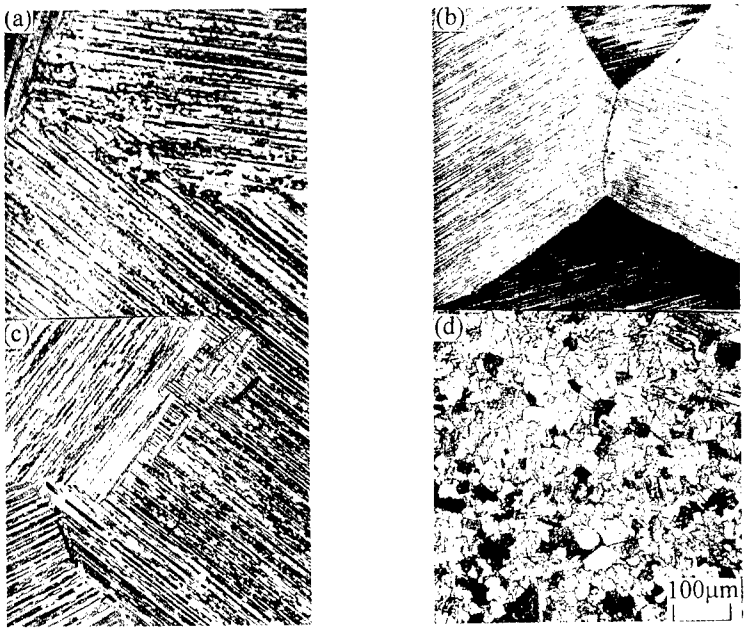


Figure 4: Optical metallographs indicating the (a) as-cast, (b) homogenized, (c) CHTed and (d) refined NG microstructures of the cast Ti-46.5Al-2.5V-1.0Cr (at%) alloy.

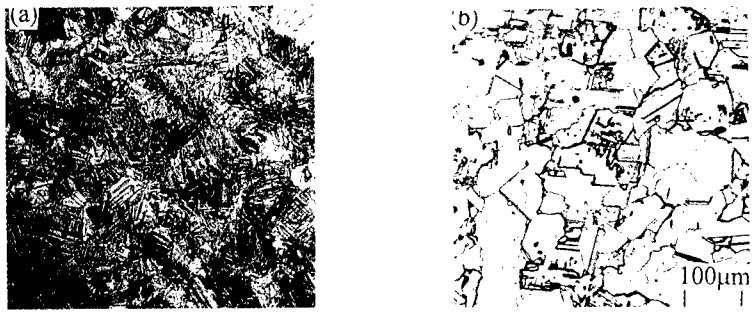


Figure 5: The transformed (a) fine fully lamellar and (b) duplex microstructures of the cast Ti-46.5Al-2.5V-1.0Cr (at%) alloy.

CREEP MECHANISMS AND INTERFACE-ENHANCED DEFORMATION TWINNING IN A TWO-PHASE LAMELLAR TiAl ALLOY

L. M. Hsiung and T. G. Nieh

Materials Science and Technology Division
Lawrence Livermore National Laboratory
P.O. Box 808, L-370
Livermore, CA 94551-9900

Abstract

Deformation mechanisms and the role of interfaces in deformation twinning of a two-phase [TiAl (γ)/Ti_3Al (α_2)] lamellar alloy creep deformed at elevated temperatures have been investigated. Since the multiplication of lattice dislocations within both γ and α_2 lamellae is very limited at a low stress level due to a refined lamellar microstructure, the glide of interfacial dislocations on both γ/α_2 and γ/γ interfaces (i.e. interface sliding) becomes an important deformation mode. Obstacles such as impinged lattice dislocations can impede the movement of interfacial dislocations, which glide in a cooperative fashion along the lamellar interfaces. The impediment of dislocation motion subsequently causes a dislocation pile-up in front of obstacles as creep strain accumulates. When the crystals deform at high stress level, deformation twinning becomes a predominant deformation mode. Deformation twins are found to nucleate from the interfaces as a result of a local stress concentration generated from dislocation pile-ups. It is suggested that the deformation twinning in lamellar TiAl/Ti_3Al crystals can be viewed as a stress relaxation process for the concentration of stress at the head of each dislocation pile-up. An interface-assisted twinning mechanism is accordingly proposed and discussed.

The Third Pacific Rim International Conference on
Advanced Materials and Processing (PRICM 3)
Edited by M.A. Imam, R. DeNale, S. Hanada,
Z. Zhong and D.N. Lee
The Minerals, Metals & Materials Society, 1998

Introduction

Two-phase TiAl alloys with a lamellar microstructure where TiAl (γ) and Ti_3Al (α_2) phases are present as alternating sheets are appealing for applications in advanced turbine engine components due to their high specific strength, stiffness, creep resistance and environmental resistance at elevated temperatures. However, a major draw back of the alloys for the structural applications is their inadequate fracture resistance (ductility and toughness) at low temperatures. In order to overcome this obstacle, a recent development of the alloys has focused on refining the γ/α_2 lamellar microstructure through advanced processing routes such as a powder metallurgy (P/M) process. The mechanical properties of P/M lamellar alloys with a refined microstructure have been demonstrated to be superior to those of the lamellar alloys fabricated by conventional ingot metallurgy (I/M) [1]. Deformation twinning provides not only an additional deformation mechanism to facilitate the room temperature ductility [2] but also effective dislocation obstacles for enhancing creep resistance of the lamellar alloys. It has been demonstrated that the alloys become more creep-resistant at a low stress level (138 MPa) after mechanically twinned at a high stress level (518 MPa) [3,4]. Since the lamellar interfaces can provide additional nucleation sites for deformation twins (DT hereafter), the interfaces essentially promote twinning processes in the alloys. Although the formation of DT can be attributed to the homogeneous glide of $1/6<11\bar{2}>$ twinning dislocations on every {111} plane [5], the underlying twinning mechanism still remains unclear. To better design the lamellar alloys for high temperature applications, it is of importance to understand and gain insights for the role of lamellar interfaces in the twinning process as well as the mechanical behavior of the alloys. Accordingly, this investigation has been conducted in order to elucidate the mechanisms of deformation twinning in two-phase lamellar TiAl alloys.

Experimental

A two-phase lamellar TiAl alloy [a nominal composition of Ti-47Al-2Cr-2Nb (at. %)] was fabricated at Oak Ridge National Laboratory by a powder metallurgy process involving a hot-extrusion of gas-atomized titanium aluminide powder at 1400 °C. After extrusion, the alloy was stress-relieved at 900 °C in a vacuum (~10^{-4} Pa) for 2 h. Creep tests were conducted at 760 °C in a dead-load creep machine with a lever arm ratio of 16:1. Detailed information regarding creep experiment and the experimental data were reported elsewhere [1]. For current study, the deformation substructures of two tested specimens [one crept at a stress of 138 MPa (creep strain: ~0.25%) and the other crept at a stress 518 MPa (creep strain: ~3.6%)] were investigated. TEM foils were prepared by twin-jet electropolishing in a solution of 60 vol. % methanol, 35 vol. % butyl alcohol and 5 vol. % perchloric acid at ~15 V and -30 °C. The microstructures of the crept alloys were examined using a JEOL-200CX transmission electron microscope equipped with a double-tilt goniometer stage. Images of dislocations were recorded using a weak-beam dark field (WBDF) imaging technique under ***g (3g)*** two-beam diffraction conditions.

Results and Discussion

Microstructure

Figure 1 shows a typical edge-on lamellar microstructure of the two-phase TiAl alloy. In general, there exist two types of lamellar interfaces within the alloy [6]: (1) The γ/α_2 interphase interface which has a usual orientation relationship $(0001)_{\alpha 2} \parallel (111)_\gamma$ and $<11\bar{2}0>_{\alpha 2} \parallel <1\bar{1}0>_\gamma$. (2) The γ/γ twin-related interfaces which includes true-twin (180° rotational) and pseudo-twin (60 and/or 120° rotational) interfaces. The width of α_2 lamella ranges from 10 to 50 nm, and that of γ lamella ranges from 150 to 300 nm. Figure 2 shows a typical dislocation substructure within a lamellar grain. Both lattice dislocations (LD hereafter) within γ lamellae and a high density of interfacial dislocations (ID hereafter) on inclined lamellar interfaces can be clearly seen. The density of ID is much greater than that of LD, and the LD are mainly threading dislocation lines which terminate their two ends at lamellar interfaces. While those ID on semi-coherent γ/α_2 and γ/γ pseudo-twin interfaces are $1/6<112>$ or $1/3<112>$ type [] misfit dislocations,

those on γ/γ true-twin interface are 1/6<112> type geometry necessary dislocations for accommodating the departure of the twin interface from the exact twin plane.



Fig. 1 A bright-field TEM image showing a typical edge-on lamellar substructure.

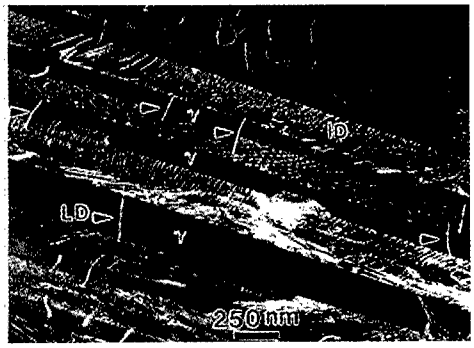


Fig. 2 A WBDF image showing a typical dislocation structure within a lamellar grain.

Glide of interfacial dislocations

Since the volume fraction of the α_2 lamella is small (~10%), the deformation strain is mainly carried by γ lamellae through the multiplication of LD (mainly threading dislocations). The critical shear stress ($\tau_b \approx \mu b/l$, where l is the distance between two pinning points) required to bow the threading dislocations however is considerably high because of thin γ lamellae. Taking $\mu \sim 59$ GPa (at 760 ° C), $b \sim 0.56$ nm, $l \sim 100 - 300$ nm (interface spacing), and $\tau_b \sim 165$ -330 MPa, the critical stresses ($\sigma_c \approx 2\tau_b$) are estimated to be 330 – 660 MPa, which are greater than the applied stress of 138 MPa.

Since the multiplication of lattice dislocations within γ lamellae is very limited due to a refined lamellar microstructure, the glide of interfacial dislocations (i.e. interface sliding) becomes a predominant deformation mode. This has been demonstrated in the result of a room temperature *in situ* straining study reported elsewhere [7]. Figures 4 and 5 show the deformation substructures of a soft lamellar grain (oriented nearly ~45 ° with respect to the stress axis) within a specimen tested at a low stress level (138 MPa). The *ID* on both the γ/γ and γ/α_2 interfaces become mobile at elevated temperatures even with a low shear stress (~69 MPa) resolved on the interfaces. As a result, interface sliding occurs due to the movement of *ID* and resulting in the formation of grain boundary steps (Fig. 4). The wavy appearance of interfacial dislocation lines (site A in Fig. 4) suggests that solute or impurity atoms may have dragged the movement of *ID*. The mobility of *ID* can also be impeded by dislocation obstacles formed by the impingement of *LD* on the lamellar interface as shown in Fig. 5. Here in Fig. 5(a), several *ID* are piled up as a result of the impingement of *LD* on a γ/γ interface. Furthermore, a more effective obstacle can be formed if a number of impinged *LD* react with *ID* to form dislocation nodes as shown in Fig. 5(b). Consequently, the nodded *ID* becomes less mobile and resulting in a dislocation pile-up.

Deformation twinning

When the alloy is creep deformed at a high stress level, deformation twinning starts to engage as a predominant deformation mode. Figure 6 shows the formation of $(\bar{1}\,11)$ [211]-type deformation twins (*DT* hereafter) within a specimen tested at 518 MPa. Notice that one of the

($\bar{1}$ 11) twin lamellae (marked by an arrow) was emitted from the upper interface, and eventually will be blocked by the lower interface if it continues to grow. This observation suggests that the DT is originally nucleated from the lamellar interfaces as a result of a local stress concentration caused by the pile-up of interfacial dislocations. Accordingly, it is proposed that deformation twinning in lamellar TiAl/Ti_3Al can be viewed as a stress relaxation process to relief the local stress concentration caused by the pile-up of interfacial dislocations during deformation. The effective stress (τ_e) at the tip of the pile-up of n dislocations is $\tau_e = n\tau_i$ [9], where τ_i is the resolved shear stress acting on the interface. To relieve the stress concentration, DT in γ lamellae is therefore formed by a dislocation reaction based upon a stair-rod cross-slip mechanism [10]. As for an example of the ($\bar{1}$ 11)-type DT formed in an alloy deformed at a high stress level, the corresponding dislocation reaction (dissociation) is proposed to be $1/6[\bar{1}\,2\,\bar{1}]_{(111)} \rightarrow 1/6[011]_{(100)}$ + $1/6[\bar{1}\,1\,\bar{2}]_{(\bar{1}\,11)}$. The ($\bar{1}$ 11) type DT is accordingly formed by a successive cross-slip of the twinning dislocations $1/6[1\,\bar{1}\,2]$ on the ($\bar{1}$ 11) plane and leaving the stair-rod dislocations 1/6 [011] on the (100) plane. Twin (stacking) faults are subsequently formed on the interfaces between the γ lamellae and DT. This is schematically illustrated in Fig. 5 (b).

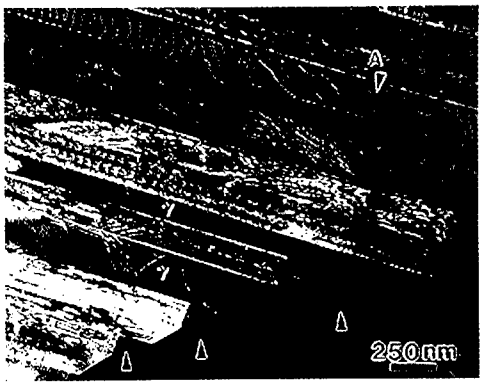


Fig. 3 A WBDF image showing a typical microstructure of a nearly 45° -oriented lamellar grain within a sample creep deformed at 138 MPa. Grain boundary ledges (indicated by arrows) were formed due to interface sliding. The wavy appearance of interfacial dislocation lines is noted at site A.

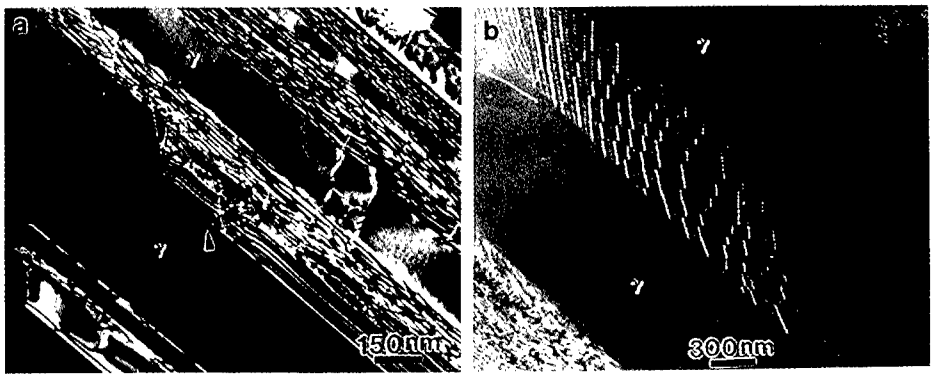


Fig. 4 (a) A WBDF image showing the pile-up of several ID (indicated by an arrow) on a γ/γ related interface. (b) A WBDF image showing that the motion of interfacial dislocations is impeded as a result of the formation of dislocation nodes due to the reaction between impinged LD (stronger contrast) and intrinsic ID (weaker contrast).

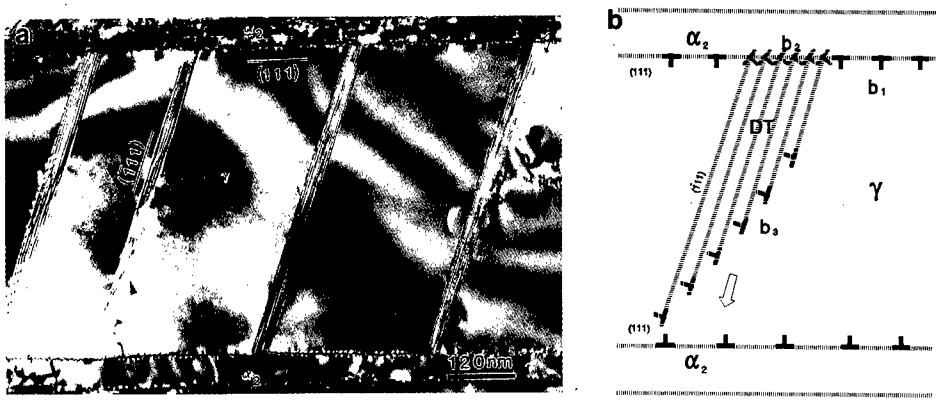


Fig. 5 (a) A bright-field TEM image showing several ($\bar{1}$ 11) type deformation twins formed growing process toward another lamellar interface. (b) Schematic illustration of the nucleation of a ($\bar{1}$ 11) type DT from a γ/α_2 interface, where b_1, b_2, and b_3 denote the interfacial, stair-rod, and twinning dislocations, respectively.

The formation of stair-rod dislocations at the intersections between DT and a α_2 lamella is evidenced in Fig. 6, where the array of 1/6[011] stair-rod dislocations become invisible [Fig. 6(a)] or visible [Fig. 6(b)] when a reflection vector (*g*) *200* or *021* is used for imaging. It is noted that the individual stair-rod dislocation is not resolvable because of a narrow distance (0.25 nm) between two stair-rod dislocations. The existence of the stair-rod dislocations can also be indirectly evidenced in Figs. 7 (a) and (b). Here, a pair of approximately aligned DT is originally formed on the opposite side of a α_2 lamella. These two aligned DT eventually coalesce at the joints adhered to the α_2 lamella. This coalescence is considered to be resulted from the annihilation of stair-rod dislocations (with opposite Burgers vectors) through a thermally activated process. A schematic representation of a pair of approximately aligned DT on the opposite side of a α_2 lamella and the formation of stair-rod dislocations with opposite Burgers vectors is shown in Fig. 8. The significance of the proposed mechanism is to reveal that there are several barriers to be overcome in order to activate the twinning reaction. These barriers include (1) the repulsive force between the interfacial (Shockley) and stair-rod dislocations, (2) the increase of line energy due to the dislocation dissociation, and (3) the increase of interfacial energy due to the formation of twin (stacking) faults. The resolved shear stresses on both the interfacial and cross-slip planes and a local stress concentration due to the pile-up of interfacial dislocations are considered to be important factors for the formation of deformation twins in lamellar TiAl/Ti_3Al.

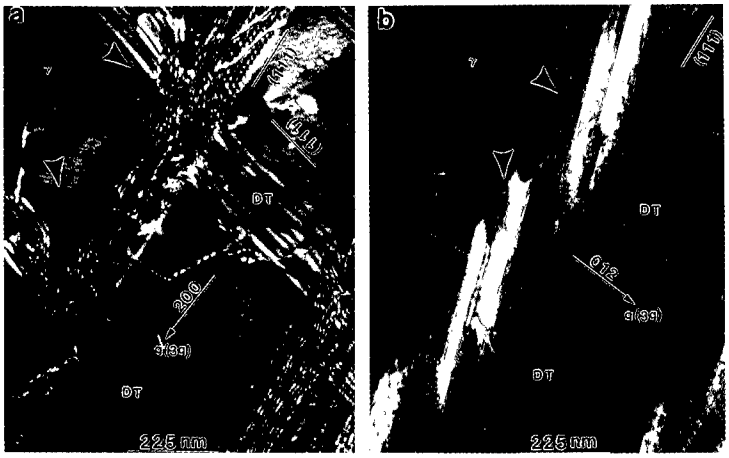


Fig. 6 Paired WBDF images demonstrating the existence of the array of 1/6[011] stair-rod dislocations at the intersections (indicated by arrows) between the ($\bar{1}$ 11) type DT and a α_2 lamella. (a) Invisible at g = *200* ($g \cdot b$ = *0*), (b) visible at g = *021*, **Z** (zone axis) ≈ [0 $\bar{1}$ 2].

Fig. 7 WBDF images showing the faulting of α_2 lamellae [indicated by an arrow in (a)] resulted from the coalescence of two approximately aligned DT at the joints adhered to a α_2 lamella [indicated by an arrow in (b)]. Images generated from the same region using γ and DT reflections, respectively.

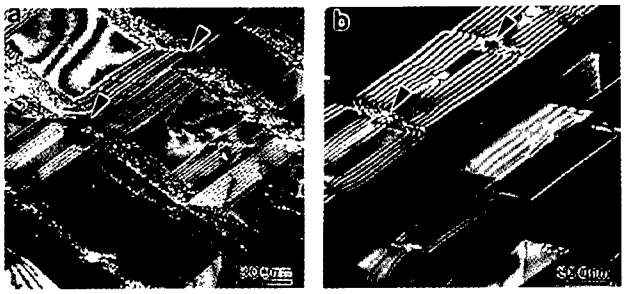
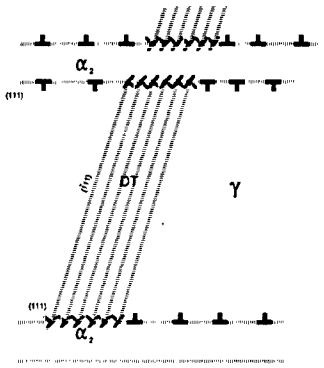


Fig. 8 A schematic representation of a pair of approximately aligned DT formed on the opposite side of a α_2 lamella and the existence of stair-rod dislocations (with opposite Burgers vectors) at the interceptions between DT and a α_2 lamella.



Summary

Creep mechanisms and the role of interfaces in deformation twinning of a two-phase lamellar TiAl alloy have been investigated. Since the multiplication of lattice dislocations within both γ and α_2 lamellae becomes very limited at a low stress level, the gliding of interfacial dislocations (i.e. interface sliding) becomes an important deformation mode. Impinged lattice dislocations are observed to impede the movement of interfacial dislocations, which glide in a cooperative fashion along the lamellar interfaces. The impediment of dislocation motion subsequently causes a dislocation pile-up in front of the obstacle as creep strain accumulates. When the alloy deform at high stress level, deformation twinning becomes a predominant deformation mode. The deformation twinning in the lamellar TiAl/Ti_3Al crystals is suggested to be a stress relaxation process for the concentration of stress at the head of each dislocation pile-up. An interface-assisted twinning mechanism based upon a stair-rod cross-slip dislocation reaction is proposed.

Acknowledgment

This work was partly performed under the auspices of the U.S. Department of Energy through contract # W-7405-Eng-48 with Lawrence Livermore National Laboratory.

References

1. J. N. Wang, A. J. Schwartz, T. G. Nieh, C. T. Liu, V. K. Sikka and D. R. Clemens, in *Gamma Titanium Aluminides*, ed. Y-W. Kim et al., TMS, Warrendale, PA, p. 949 (1995).
2. Y-W. Kim, *JOM*, **40**, p. 30 (1994).
3. T.G. Nieh and J.N. Wang, *Scripta Metall.*, **33**, p. 1101 (1995).
4. L. M. Hsiung and T. G. Nieh, *Scripta Mater.*, **36**, p. 323 (1997).
5. Z. Jin and T. R. Bieler, *Phil. Mag. A*, **71**, p. 925 (1995).
6. M. Yamaguchi and Y. Umakoshi, *Progress in Materials Science*, **34**, p. 1 (1990).
7. L. M. Hsiung, A. J. Schwartz and T. G. Nieh, *Scripta Mater.* **36**, p. 1017 (1997).
8. J.D. Eshelby, F.C. Frank and F.R.N. Nabarro, *Phil. Mag.*, **42**, p. 351 (1951).
9. H. Fujita and T. Mori, *Scripta Metall.*, **9**, p. 631 (1975).
10. T. Mori and H. Fujita, *Acta Metall.*, **28**, p. 771 (1980).

OXIDATION BEHAVIOR AND THERMAL STABILITY OF Ti-44Al-11Nb ALLOY

R. Mahapatra[1], S. K. Varma[2], B. A. Pregger[1], and W. E. Frazier[1]

[1]Naval Air Warfare Center, Aircraft Division, Patuxent River, MD 20670, USA

[2]Department of Metallurgical and Materials Engineering, The University of Texas at El Paso
El Paso, Texas 79968-0520, USA

Abstract

The oxidation behavior and thermal stability of Ti-44Al-11Nb alloy in air has been investigated. The specimens of directionally solidified alloy were exposed to air at 900 and 1000°C for 168 to 200 hours. The oxide characteristics have been determined by weight gain measurements as a function of exposure time. The oxide-metal interface has been studied in terms of microstructural features as well as the compositions of the oxide products using SEM/EDS. The evolution of microstructures and oxide products have been correlated. Thermal stability of the alloy has been examined by exposing the alloy for 168 to 200 thermal cycles (a cycle consists of a heating period of 55 minutes at the maximum temperature in the furnace followed by the cool down for 5 minutes outside the furnace) at 900 and 1000°C to determine the changes in the microstructures of the alloy. The microstructural development due to thermal cycling has been correlated to the oxidation behavior of the alloy.

The Third Pacific Rim International Conference on
Advanced Materials and Processing (PRICM 3)
Edited by M.A. Imam, R. DeNale, S. Hanada,
Z. Zhong and D.N. Lee
The Minerals, Metals & Materials Society, 1998

Introduction

The intermetallic compounds are being considered as materials for many high temperature applications. The compounds involving the combinations of elements such as Ni and Al, Ti and Al in various proportions have been developed for the defense and industry in the past couple of decades. Ti and Al metals have been basically selected because of their low densities and of the two Ti is particularly an attractive candidate since it has much higher strength than aluminum. One of the disadvantages of the use of intermetallics is their lack of ductility and thus restricting formability for processing.

The two significant intermetallic compounds in Ti-Al system in the γ rich side consists of Ti_3Al (α_2, ordered hexagonal) and TiAl (γ, ordered fct). The important microconstituent in these systems consist of alternate lamellae of α_2 and γ [1-3]. Mitao and Bendersky [1] have studied the coarsening of such structures and report three types of morphology. The three types of morphologies differ in the orientation of the α_2 plates with respect to the original lamellae and the orientation relationships between the plates at the interface.

High strength to weight ratio characteristics of Ti-Al intermetallics is one of the reasons why Ti-Al-X (where X is another metal such as Nb, Mo, W, Cr, Ta, Mn and V etc.) ternary systems have been extensively studied for its potential applications in aerospace industry [4-10]. The effect of thermal processing on the microstructures of Ti-44Al-11Nb alloy has been examined by Mahapatra et al. [4]. These authors reported the formation of directionally aligned lamellar structure and the extent of alignment depends on the processing variables. Some of the interesting features of the Ti-Al-Nb ternary system have been summarized by Kattner and Boettinger [7]: there is abundance of binary intermetallic compounds involving Nb-Al and Ti-Al systems, solid solutions of $NbAl_3$ and $TiAl_3$ exist, two ternary compounds exist (Ti_2AlNb and Ti_4Al_3Nb), the bcc β-Ti,Nb phase orders to β_o-Ti,Nb phase with CsCl type of structure and a miscibility gap exists in the ordered β_o-Ti,Nb phase.

Kandra and Lee [8] have performed the compression testing of Ti-44Al-11Nb alloy, annealed in the temperature range from 1000 to 1500°C, in the range of temperature from 1000 to 1300°C. An increase in grain size from 138 to 1017 μm could be produced by annealing. A systematic decrease in yield strength values were observed as a function of increasing temperature of testing for a given microstructure. However, a quaternary compound Ti-49.5Al-2.5Nb-1.1Mn shows necking, strain localization and even dynamic recrystallization in the as cast and wrought form when tested in tension in a range of temperature from 850 to 1377°C [5]. The growth of cavities and wedge cracks were controlled by dynamic recrystallization.

The purpose of this research is to investigate the oxidation behavior and thermal stability of Ti-44Al-11Nb alloy in air at temperatures of 900 and 1000°C. The thermal cycles of an hour, approximately, have been used for cyclic oxidation for more than 190 cycles while the oxidation behavior has been studied for 162 to 190 hours.

Experimental Details

The Ti-44Al-11Nb (compositions are in atomic percents) alloy used for this study was prepared by non-consumable electrode arc melting of Ti , Al and Nb with a 99.998, 99.999, and 99.988% purity, respectively, with respect to metallic elements under a purified argon gas atmosphere. The actual composition of the alloy as determined by the analytical scanning microprobe technique are shown in the Table I.

Table 1. Chemical Analysis of Directionally Solidified Ti-44Al-11Nb Alloy

	Ti	Al	Nb	C	O	H	N
Atomic Percent	44.97	43.96	10.98	0.084	560 ppm	14 ppm	88 ppm

The melting procedure was repeated several times in the arc melter to obtain a homogeneous starting material in the form of 5 mm buttons weighing approximately 10 grams each. The buttons were used to produce rods of 10 mm diameter and 80 mm length using the same arc melter. The melting was carried out in a pure gettered argon gas atmosphere in order to minimize the interstitial oxygen and nitrogen contamination in the alloy.

An ASGAL Optical Imaging Floating Zone (OIFZ) crystal growth furnace was used to grow directionally aligned crystal of this composition. The polycrystalline rods, prepared in arc melter, were used to grow directionally aligned crystal rods through directional solidification in

OIFZ at a growth rate of 5 mm/h. The oxidation behavior and thermal stability studies were conducted using samples of 8 mm diameter and 2 mm thickness obtained by cutting directionally solidified aligned crystals by electro discharge machining (EDM). The cyclic oxidation tests were performed in air at 900 and 1000°C using a high temperature furnace and automatic withdrawal apparatus to cycle the samples from the hot zone to a position outside the furnace. A typical thermal cycle consists of 55 minutes at the maximum temperature inside the furnace and followed by cool down period for 5 minutes outside the furnace. The tests were run for 168 or 196 hours with mass gain being measured to within 0.0001 gram at increasing intervals of time or cycles. The optical and scanning electron microscopic analysis were performed to determine the thermal shock resistance of the aligned composite structure and their protective oxide coating under cyclic oxidation conditions.

Results and Discussion

A typical microstructure of the as grown directionally solidified aligned crystal rod is shown in Figure 1. The direction of the growth is indicated by an arrow. The lamellar microstructure consists of alternate plates of α_2 (dark phase) and γ (light phase) almost perpendicular to the direction of growth. There is another microconstituent which is a complex Ti-Al-Nb intermetallic phase in a specific orientation and is being analyzed in detail at this time.

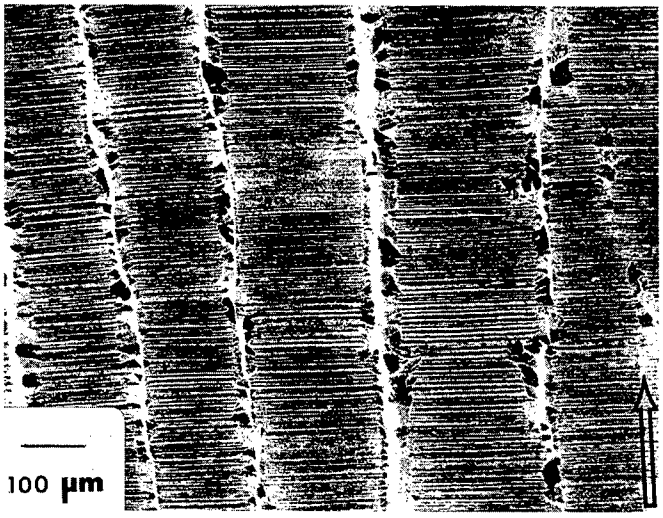


Figure 1 The microstructure of as grown directionally solidified crystal of Ti-44Al-11Nb alloy. The arrow indicates the direction of growth.

Thermal stability of the alloy in terms of number of heating cycles has been evaluated through weight gain measurements. Figure 2 shows the graph between weight gain as a function of number of cycles at 900 and 1000°C. It can be easily seen that the oxidation rate at higher temperature is rather high. However, a typical power law behavior has been observed at only lower temperature. A linear fit between the weight gain and number of heating cycles has been shown in this figure for the data at higher temperature. It is anticipated that the typical decrease in oxidation rates, almost reaching to a constant value, associated with large number of cycles has not been achieved for the 240 cycles of this study. Perhaps, the almost steady state oxidation rate exists at higher number of cycles.

It is interesting to compare the oxidation behavior of this alloy under cyclic and static conditions. The static oxidation rate was determined by the weight gain method after the samples have been heated for 168 hours without interruption at 900, 950 and 1000°C in air. It can be seen that the comparison is being made at almost similar experimental conditions. Table 2 shows data of static oxidation experiments of this study. This table compares data for static oxidation of

polycrystalline alloy (as cast condition) with the directionally solidified single crystal at three temperatures. It shows that even though the differences in the oxidation rates appear to be quite small at 900 and 950°C yet the rates are consistently lower in polycrystalline alloy. However, the data at 1000°C not only shows a larger increase in the rate for the polycrystalline alloy but the directionally solidified alloy has a lower rate. It could be attributed to the significant changes in microstructures that are taking place at 1000°C.

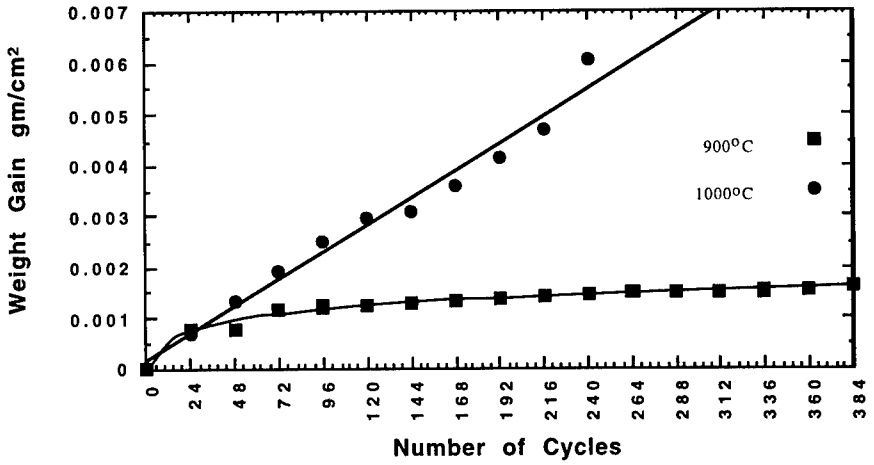


Figure 2 The oxidation behavior of Ti-44Al-11Nb alloy at 900 and 1000°C under cyclic heating conditions.

Table 2. Static Oxidation Rate Comparison Between the Polycrystalline and Directionally Solidified Crystals

Test Temperature (°C)	Oxidation Rate (gm/cm^2) Directionally Solidified Alloy	Oxidation Rate (gm/cm^2) Polycrystalline Alloy
900	0.0018	0.00173
950	0.0028	0.00245
1000	0.0048	0.00581

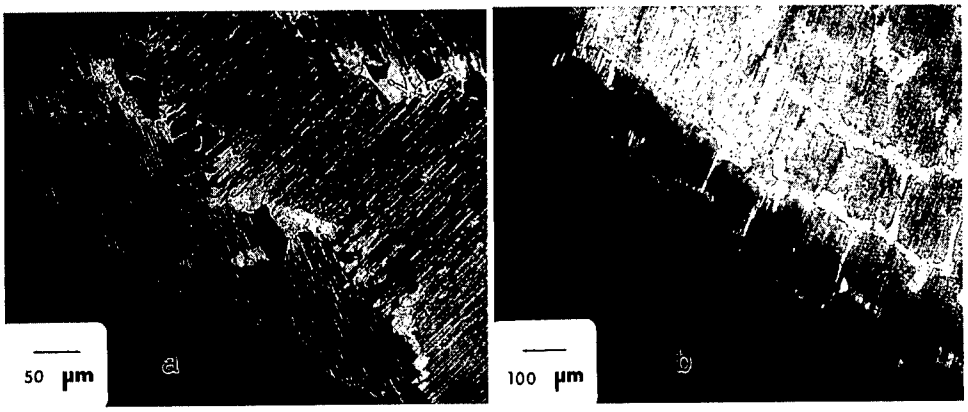


Figure 3 The optical micrographs of the Ti-44Al-11Nb alloy after they have been subjected to 168 hours of static thermal treatment at (a) 900 and (b) 1000°C.

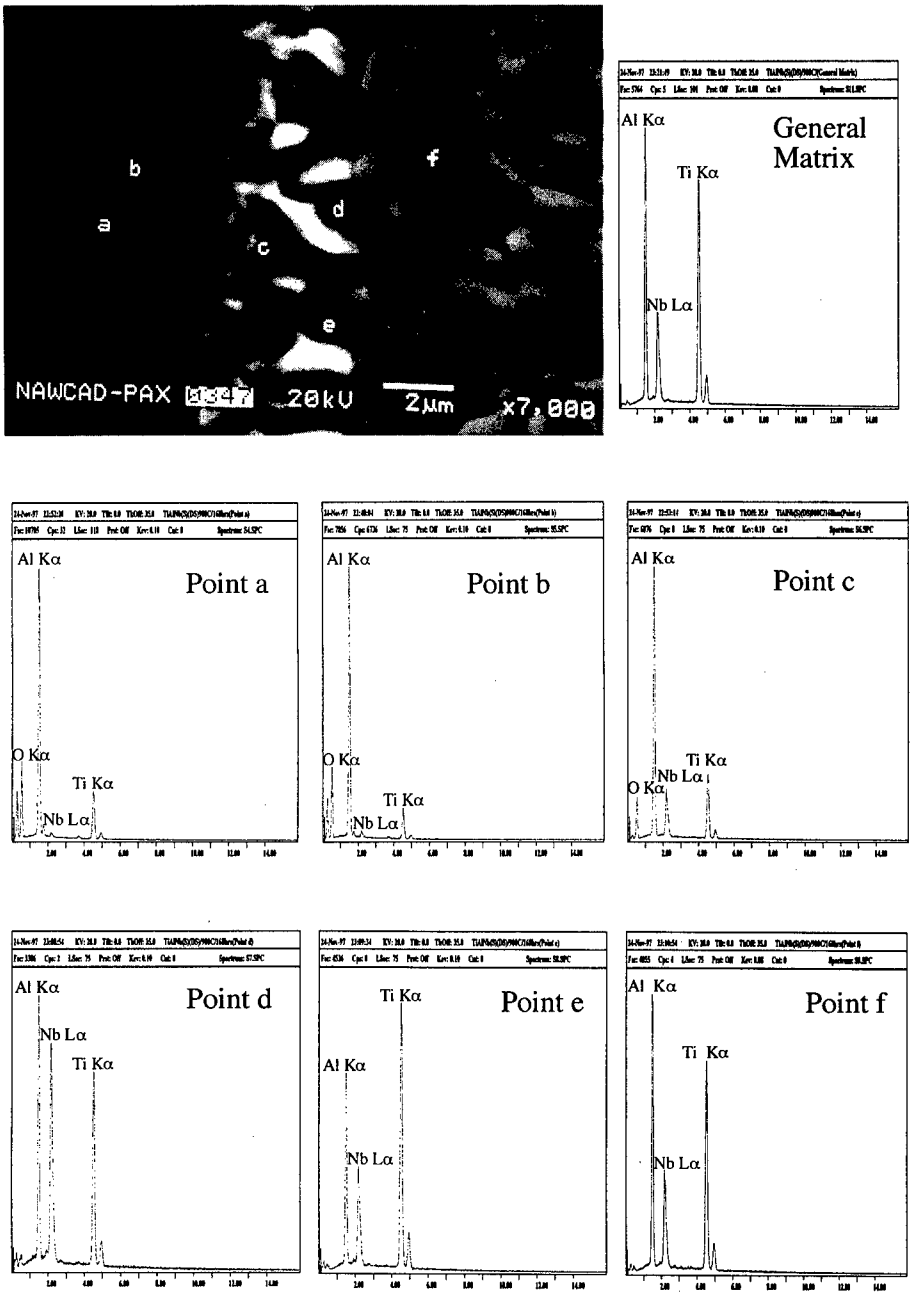


Figure 4 Characterization of the oxides formed at the surface of the alloy after cyclic oxidation for 168 cycles at 900°C through SEM/EDS.

The microstructures observed in the alloy after a static exposure of 168 hours at 900 and 1000°C is shown in Figure 3. The coarsening of the microstructures at 1000°C appears to be the main difference in the microstructures. The bridging between the dendrite arms appears to be taking place only at 1000°C and the third, as yet, unidentified phase, as mentioned above in this paper, still seems to be present at 900°C.

The nature of the oxides formed at the surface of the directionally solidified crystals after exposing it to 168 cycles of thermal stability study may be recognized by SEM/EDS analysis as shown in Figure 4 at 900°C. This analysis indicates that the entire oxidized layer may be divided in three different zones, which may not be exclusive of one another, and, in fact they may be overlapping, which have been devised for discussion purposes only. The EDS spectrum for the matrix (a region far away from the oxide zones) clearly shows the approximate composition of the alloy in the correct proportion as evidenced by the peak heights for Al, Ti and Nb. The zone at the top surface of the alloy appears to be rich in aluminum and oxygen according to the EDS analysis shown in Figure 4. The concentration of Nb increases with increase in distance from the top surface of the oxide layer. However, the aluminum also seems to be present in large quantities in this zone. Thus it maybe concluded that the middle zone may consists of some complex oxides of both Nb and Al or a mixture of the oxides of these two metals. The deepest zone of this oxide layer is rich in Ti. The exact nature of the oxide layer is being investigated and results will be presented later elsewhere.

Conclusions

1. The directionally solidified Ti-44Al-11Nb alloy can be grown in single crystal form containing a lamellar structure of α_2 (ordered hexagonal phase) and γ (ordered fct).
2. The static oxidation results at 900 and 950°C indicate that the oxidation rates are higher in directionally solidified crystal compared to polycrystals. However, at higher temperature, 1000°C, opposite trend has been observed.
3. The cyclic oxidation results at 900 and 1000°C show that oxidation rates are significantly higher at higher temperatures and the oxide layer consists of three separate zones, perhaps overlapping, rich in the three primary metals of the alloy.

Acknowledgment

The authors appreciate financial support of the Office of Naval Research (ONR). One of the authors (SKV) acknowledges the support of Defense Logistics Agency (DLA) through the grant number DN-009. Mr John Dennison of NAWCAD was very helpful in the sample preparation for optical microscopy.

References

1. S. Mitao and L. A. Bendersky, Acta Materialia, 45(1997)4475-4489.
2. J. H. Perepezko, Y. A. Chang, L. E. Seitzman, J. C. Lin, N. R. Bonda, T. J. Jewett and J. C. Mishurda, High Temperature Aluminides and Intermetallics, edited by S. H. Wang, C. T. Liu, D. P. Pope and J. O. Siegler, The Minerals, Metals & Materials Society, Warrendale, PA, (1990)19-46.
3. C. McCullough, J. J. Valencia, C. G. Levi and R. Mehrabian, Acta Metallurgica, 37(1989)1321-1336.
4. R. Mahapatra, E. W. Lee and J. Waldman, and J. H. Perepezko, Low Density, High Temperature Powder Metallurgy Alloys, edited by W. E, Frazier, M. J. Koczak and P. W. Lee, The Minerals, Metals & Materials Society, Warrendale, PA, (1991)71-80.
5. V. Seetharaman and S. L. Semiatin, Metallurgical and Materials Transactions A, 28A(1997)2309-2321.
6. Y-Won Kim, Journal of Metals, July(19989)24-30.
7 U. R. Kattner and W. J. Boettinger, Materials Science and Engineering, A152(1992)9-17.
8. J. T. Kandra and E. W. Lee, Metallurgical and Materials Transactions A, 25A(1994)1667-1679.
9. H. E. Deve, A. G. Evans, G. R. Odette, R. Mehrabian, M. L. Emiliani and R. J. Hecht, Acta Metallurgica et Materialia, 38(1990)1491-1502.
10. W. O. Soboyejo, D. S. Schwartz and S. M. L. Sastry, Metallurgical Transactions A, 23A(1992)2039-2059.

SOME ASPECTS OF CREEP IN TiAl

T.S. Rong*, I.P. Jones* ** and R.E. Smallman*
*School of Metallurgy & Materials,
**IRC in Materials for High Performance Applications
The University of Birmingham, Birmingham B15 2TT, U.K.

Abstract

Duplex tests including constant strain rate deformation and creep have been performed on polycrystalline single-phase titanium aluminide of nominal atomic composition Ti-52Al. It is found that predeformation (2%) at either room temperature or 800°C speeds up the subsequent primary creep rate and increases the critical strain corresponding to the transition from the creep rate decreasing to that where it is increasing, but has little influence on the corresponding *time*, i.e. there is no obvious change in the time duration of primary creep for the virgin and prestrained specimens. Double creep tests, consisting of creep, annealing and creep, indicate that if the first creep test is interrupted for annealing in the primary creep region, the creep rate decreases with time in the subsequent creep. However, if the first creep is interrupted in the region of increasing creep strain rate, the creep rate increases with time almost immediately after re-loading. Microstructures after various duplex deformations were examined by optical and transmission electron microscopy. No evidence of recrystallization has been observed after creep at 800°C and 120 MPa with or without prestrain, except in the one case where the specimen was pre-crept for about 2% and annealed for 30 h at 800°C, and then re-crept for 13%, with a total strain about 15%.

The Third Pacific Rim International Conference on
Advanced Materials and Processing (PRICM 3)
Edited by M.A. Imam, R. DeNale, S. Hanada,
Z. Zhong and D.N. Lee
The Minerals, Metals & Materials Society, 1998

Introduction

Previous publications on the creep of polycrystralline single-phase γ-TiAl[1-4] suggest that high temperature creep of γ-TiAl does not display the classical three stages of primary, steady state and tertiary creep. Rather, there is a minimum creep rate marking a transition between a decelerating stage and an accelerating stage. Usually, the accelerating stage occupies more than 90% of the rupture life and can start at a very small creep strain, e.g. less than $\varepsilon = 0.4\%$ at low stress. It is worth pointing out that at certain stress levels a steady-state regime can however appear following the accelerating stage [1]. Therefore, the accelerating stage is not the usual tertiary creep, in which creep damage normally occurs. Another term: inverse creep - that is creep rate increasing with strain (or time) [5, 6] - is probably more suitable for describing this phenomenon.

The increase of creep rate with strain, which occurs at a later stage, has been ascribed to recrystallisation [2]. It is, however, unlike the usual situation where recrystallisation occurs during creep. In Ni-based alloys, for example, the critical strain for commencing the accelerating creep drops with increasing stress in the low stress regime, which is presumably because the necessary critical dislocation density for recrystallisation can be reached with a smaller strain at a high strain rate than at a low strain rate [7]. In contrast, for γ-TiAl the critical strain for inverse creep increases rather than decreases with increasing stress, although the time duration of the primary creep decreases [1, 4]. It is still unclear why the critical strain for commencing inverse creep is proportional to creep stress for γ-TiAl.

Microstructural observations indicate that both ordinary dislocations and super- dislocations are operative during high-temperature creep (800°C or above), but that ordinary dislocations predominate [4]. As well as dislocations, mechanical twins are reported. Although Koo et al. [8] stated that only a few twins were observed after creep into the tertiary stage, Martin and Hayes [9] have reported a gradually increasing propensity for mechanical twinning from the minimum strain rate stage to the early tertiary stage.

In the present investigation, in an attempt to understand the mechanism of high-temperature inverse creep of single phase γ-TiAl, several duplex tests involving constant strain rate deformation and creep have been performed and deformation structures examined by both optical and electron microscopy.

Experimental

An ingot with nominal atomic composition Ti-52Al was prepared by a plasma melter. Specimens for compression tests were cut to dimensions 4.5x4.5x9.0 mm and then homogenised at 1300°C for a week in vacuum (~10^{-4} Pa). The conditions for mechanical testing are listed in the following table:

Specimen No	Pre-strain	Anneal	Creep
1	None	None	800°C and 120 MPa
2	None	None	800°C and 180 MPa
3	None	None	800°C and 240 MPa
4	RT 2% (~10^{-4}/s)	None	800°C and 120 MPa
5	800°C 2% (~10^{-4}/s)	None	800°C and 120 MPa
6	800°C 2% (~10^{-4}/s)	800°C 30 h	800°C and 120 MPa
7	Crept at 800°C and 120 MPa for 8 h	800°C 30 h	800°C and 120 MPa
8	Crept at 800°C and 120 MPa for 68 h	800°C 30 h	800°C and 120 MPa

To look for recrystallisation, some deformed specimens were examined by optical microscopy. Microstructure after mechanical tests was also examined by TEM.

Results

i) Mechanical testing

a) Single creep tests

A typical compressive creep for γ-TiAl at 800°C and 120 MPa exhibits a normal primary regime where creep rate decreases with increase of strain. Subsequent to this, creep rate increases with strain, i.e. inverse creep, which is in agreement with previous reports [1- 4].

With increasing stress, inverse creep became less and less obvious. Also, it is noted that although the time duration of primary creep is reduced, the critical strain corresponding to the minimum creep rate increases with stress.

b) Duplex tests involving constant strain-rate deformation and creep

The creep curves for the specimens prestrained 2% at either 800°C or room temperature at constant strain-rate (~10^{-4}/s) both have the same shape as those for the virgin specimen, i.e. a decelerating stage followed by an accelerating stage (Fig. 1). However, it is noted that in the primary regime, the creep rates of the specimens prestrained 2% are obviously higher than that in the virgin specimen. Although the critical strains corresponding to the commencing inverse transient vary (about 1.35%, 1.03% and 0.4% respectively for the specimens prestrained 2% at 800°C, 2% at RT and for the virgin specimen), there is little influence of prestrain on the corresponding critical time.

For the specimen prestrained at 800°C for 2% and then annealed at 800°C for 30 h, the subsequent creep rate in the primary stage is again higher than that in the virgin specimen. Again the critical time is about 15 hours, but the inverse creep is less obvious as compared with that in the virgin specimen or in the specimens prestrained without annealing (Fig. 2).

c) Creep, annealing and creep

The results of the double creep tests are shown in Fig. 3. After the specimen had been crept for 8 h (before the inverse transient started) and then annealed at 800°C for 30 h, the creep rate, in the subsequent creep test, initially decreased and then increased. It is worth noting that in the subsequent creep test the primary creep regime was much shorter than that in the virgin specimen. Interestingly, the critical time (t_c) is roughly the same for the single and double creep tests, i.e. annealing between the two creep tests did not affect the duration of primary creep. However, if the creep test was interrupted well into the inverse creep regime, i.e. 68 h, and annealed at 800°C for 30 h, the creep rate increased almost immediately after reloading, that is inverse creep started straightaway and the creep rate became very high.

ii) Microstructure

a) Virgin specimens after creep

After examination of several TEM foils, it was found that the number of dislocation networks (or subgrain boundaries) increased with time and more twins were observed in the specimen crept for 68 h than for 4 h.

c) Prestrained specimens after creep

No evidence for recrystallization was found in specimens crept for a long period, well into the inverse creep regime, after 2% predeformation at room temperature and 800°C, respectively.

Compared with the microstructure in the virgin specimen crept at the same conditions, there is obviously more twinning; presumably these twins were introduced by predeformation at a much higher strain rate than that in creep.

Although it would be expected that more superdislocations would be introduced by RT prestrain than by high temperature prestrain [10], it was found that after creeping for 4 h most of the dislocations were ordinary in the specimens prestrained at both temperatures. The microstructures were very similar.

d) Prestrained and annealed specimens after creep

No recrystallization was observed after the specimen had been prestrained by 2% and annealed for 30 h at 800°C and then crept for 68 h.

e) Creep, annealing and creep
For the specimen pre-crept for 8 h, the microstructure after re-creep is very similar to that in the virgin specimen. Again, no obvious recrystallization was found. However, for the specimen that was pre-crept for a longer time (into the inverse transient region) and annealed, after re-creeping for about 70 h to a total plastic strain ~15%, recrystallization can be seen.

Discussion

Two kinds of reasons can usually lead to the creep rate increasing with creep strain. One is a reduction of load-bearing cross-section. The other involves an intrinsic instability of the microstructure, for example dynamic recrystallization during creep, or an instability of the dislocation substructure such as that found in Ni_3Al in which, for certain temperatures and stresses, the slip system changes [6, 11]. In the present investigation, since the creep tests were conducted at constant load in compression, the applied stress decreased during creep. This completely rules out inverse transients caused by the reduction of stress as is possible in tension. Also, cavities are unlikely to be the cause of inverse creep. If they were, inverse creep should occur much earlier in the prestrained specimen than in the virgin specimen because the predeformation (2%) is much larger than the critical strain for the inverse creep, which is not in agreement with the experimental observation. Intrinsic instabilities are therefore likely to be responsible for the inverse creep during high-temperature creep of γ-TiAl.

Although it has been suggested that it is recrystallisation which leads to the increase of creep strain rate, there is no evidence for recrystallization at the low stress level where inverse creep also happens. Two things need to be explained in the creep of TiAl: why the critical strain for the inverse creep increases with stress and why there is little influence of pre-creep deformation on the time of commencement (t_c) of inverse creep.

Large amounts of dislocation network (or low angle boundary) were generated during creep, which implies a recovery process. At low stress, because of the interaction of dislocations, i.e. work hardening, the creep rate reduces initially. Low angle boundaries form gradually, due to climb of dislocations. The distribution of dislocations during creep is not uniform. At subgrain boundaries there is a much higher dislocation concentration than inside subgrains. Ishikawa et al. [12] measured the density of dislocations as a function of creep strain at low stress levels, where recrystallization was not observed. Their results suggest that the total dislocation density inside grains (or subgrains) is nearly constant during inverse creep, which implies that the acceleration of creep rate is unlikely to be caused by the movement of those dislocations. However, the mobility of subgrain boundaries is a function of misorientation. Generally, low angle boundaries consisting of more than one family of dislocations have low mobility, because the natural directions of glide for the different kinds of dislocations are different from one another. Lattice diffusion is necessary to allow climb to provide the requisite kinematic freedom. This process depends on the concentration of vacant atomic sites at boundaries. With an increase of subgrain boundary misorientation, the concentration of vacancies at boundaries increases [13]. Thus, the mobility of subgrain boundaries increases naturally with increasing misorientation as well. If this effect dominates that of work hardening, the creep rate will increase, i.e. inverse creep will occur.

As creep stress increases, more dislocations accumulate at subgrain boundaries at higher than lower strain rate for the same time interval. This leads to the reduction of the primary creep as time is concerned. However, more and more twins are introduced at the same time. These twins contribute to the plastic strain. As a consequence, with increase of stress, the critical strain for the commencement of inverse creep increases. Similarly, in the case of predeformed specimens, high strain-rate prestrain stimulates twinning which contributes to the plastic strain, but does not give enough time for dislocation climb to form low angle boundaries. In the subsequent creep, the primary creep rate is higher than for the virgin specimen, presumably because more mobile single dislocations are introduced by predeformation. The creep rate still decreases gradually due to work hardening. Similar to the situation in the virgin specimen, low angle boundaries form gradually and the mobility of grain boundaries rises with increasing

misorientation. If this recovery process compensates for the effect of work-hardening, inverse creep occurs.

As recrystallization occurred after inverse creep at high stress [1, 2], presumably in this case recrystallization does lead to inverse creep. A critical strain to create suitable sites, usually at grain boundaries, is needed for the nucleation of recrystallization. If dislocations are the only operative mechanism, recrystallization should occur, with increase of stress, at a smaller strain due to more dislocations accumulating at grain boundaries at a higher strain rate. However, if both dislocation and twinning mechanisms are operative, although twinning contributes to plastic deformation and creates twin boundaries, due to relatively lower interface energy these twin boundaries are unlikely to be the sites for nucleation of recrystallization as compared with grain boundaries. It is therefore expected that, with increase of stress, the critical strain for recrystallization increases rather than decreases. As a result, inverse creep occurs at a larger strain at a higher stress.

Summary

Creep of γ-TiAl at 800°C shows that the critical strain corresponding to the transition of creep rate from decreasing to increasing (ε_c) varies with creep stress. Pre-deformation of 2% at either room temperature or high temperature increases the primary creep rate and ε_c, but has little effect on t_c.

Double creep tests, consisting of creep, annealing and creep, suggest that if creep is interrupted in the primary creep regime and the specimen is then annealed, the subsequent creep rate decreases initially and later increases with strain. If, however, creep is interrupted in the inverse creep regime and the specimen is then annealed, the subsequent initial creep rate increases rather than decreases.

After creep of γ-TiAl at 800°C and 120 MPa 1/2<110> ordinary dislocations are the most abundant, but superdislocations are not unusual. As time increases, more and more low angle boundaries are created, presumably due to there being more chance for dislocation climb. In addition, the density of twins increases slowly with time, but more rapidly at higher strain rates. Twin boundaries act as barriers, which leads to obvious differences of dislocation densities between matrix and twins.

References

1. N. Hamada and H. Oikawa, Mat. Trans., JIM, 37 (1996) 1447.
2. N. Hamada, Y. Ishikawa, K. Maruyama and H. Oikawa, Mat. Sci & Eng. A, 192/193 (1995) 716.
3. R.W. Hayes and P.L. Martin, Acta metall. 43 (1995) 2761.
4. Y. Ishikawa and H. Oikawa, Mat. Trans., JIM, 35 (1994) 336.
5. J.H. Schneibel and J.A. Horton, J. Mater. Res. 3 (1988) 651.
6. K.J. Hemker, M.J. Mills and W.D. Nix, Acta metall., 39 (1991) 1901.
7. A.K. Koul and J-P. A. Immarigeon, Metall. Trans. A, 16 (1985) 51.
8. M. Koo, T. Matsuo and M. Kikuchi, Proc. Int. Sym. Intermetallic Compounds- Structure and Mechanical Properties, JIMIS-6 (1991) 519.
9. P.L. Martin and R.W. Hayes, 5th Int. Conf. Creep and Fracture of Engineering Materials and Structures, Edited by B. Wilshire and R.W. Evans, The Institute of Materials, London, (1993) 285.
10. Q. Xu, PhD thesis, Beijing University of Aeronautics & Astronautics (1993).
11. K.J. Hemker, PhD thesis, Stanford University (1990).
12. Y. Ishikawa, T. Kiyokawa and H. Oikawa, Mat. Trans. JIM, 36 (1995) 1041.
13. A.H. Cottrell, Dislocations and Plastic Flow in Crystals, Oxford University Press (1953)

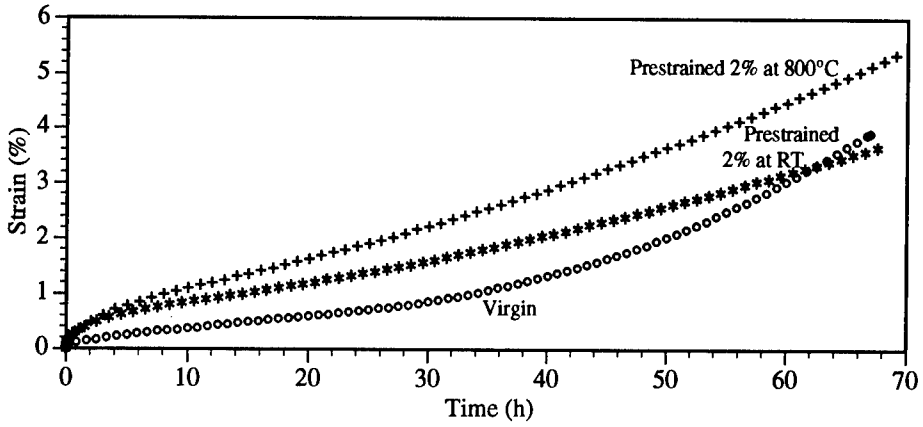


Fig. 1 Creep curves at 800°C and 120 MPa after prestrain of 2% at RT and 800°C, respectively.

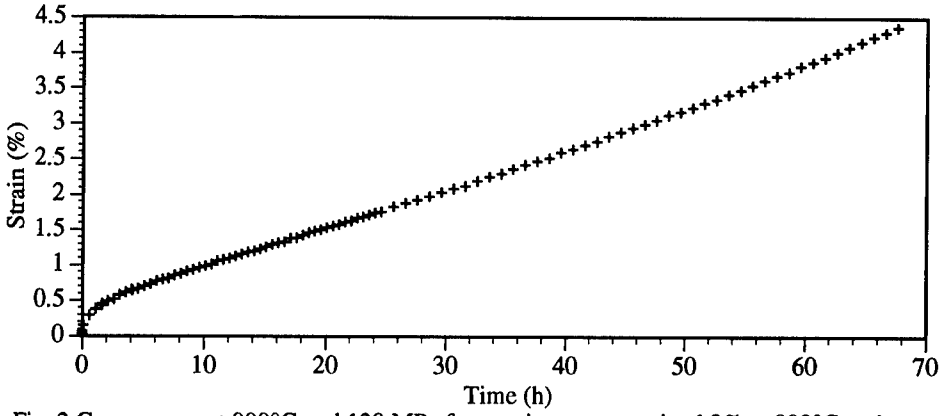


Fig. 2 Creep curve at 800°C and 120 MPa for specimens prestrained 2% at 800°C and annealed.

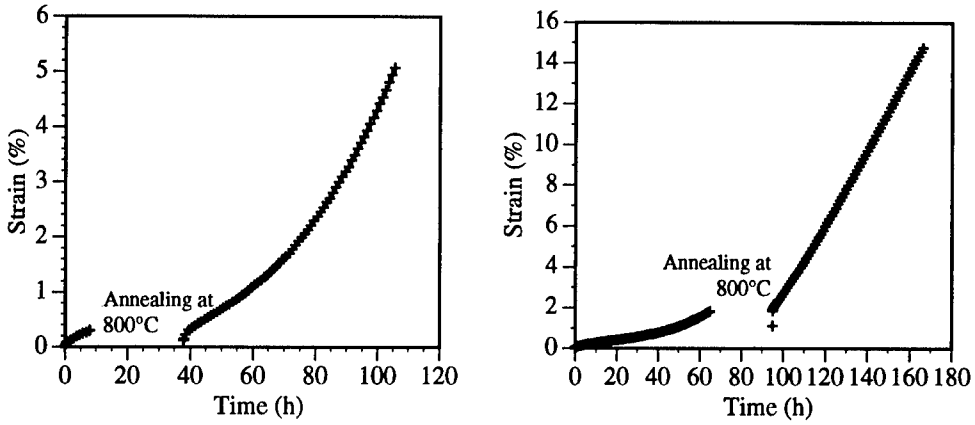


Fig. 3 Creep curves after creep, annealing and creep (double creep) at 800°C and 120 MPa.

The Fatigue Behavior of Squeeze Cast A380.0 Alloy

Jerald R. Brevick, Patrick S. Cheng, Herb Brucher, and Carroll E. Mobley

The Ohio State University
210 Baker Systems Building
1971 Neil Avenue
Columbus, OH 43210

Abstract

By conducting rotating beam fatigue tests, the S-N fatigue curve of squeeze cast aluminum-base alloy A380.0 was developed. Results showed that the fatigue strength of squeeze cast A380.0 alloy is in the range of 138 ~ 152 MPa (20 ~ 22 ksi) at 1.0 x 10^8 cycles. SEM fractography and metallography performed on selected failed fatigue specimens revealed that cold shuts, entrapped lubricant particles, and the mixture of both casting defects in the specimen surface layers were the leading failure causes of the test specimens. Cold shuts were found to have greater effect on the fatigue life of castings than the entrapped lubricants. No evidence was found in this investigation that internal porosity, such as gas porosity or shrinkage porosity, induced fatigue crack initiation. The dominant factor which controls the fatigue life of the cast alloy was found to be the initiation process of the fatigue crack on the surface of the test specimens. Regardless of the number of cycles required to initiate a fatigue crack, the number of cycles required to propagate the crack to specimen failure was nearly constant (about 1.0 x 10^6 cycles).

The Third Pacific Rim International Conference on
Advanced Materials and Processing (PRICM 3)
Edited by M.A. Imam, R. DeNale, S. Hanada,
Z. Zhong and D.N. Lee
The Minerals, Metals & Materials Society, 1998

Introduction

Squeeze casting, as a relatively new casting technique, is being utilized with greater frequency in the past few years to manufacture high performance aluminum components. In the United States, aluminum-based A380.0 alloy is a widely used die casting alloy. The mechanical properties of A380.0 alloy cast by the conventional die casting process, including fatigue properties, have been well-established [1] [2]. Squeeze casting is a process designed toward the production of high integrity castings. However, a systematic study of the mechanical properties obtained from squeeze cast alloys, especially fatigue properties, has not been conducted.

The objectives of this work were: 1) to evaluate the fatigue behavior of A380.0 alloy, using standard test bars made by the squeeze casting process, 2) to generate the S-N curve, and 3) to document various causes which resulted in the fatigue failure of test bars, based on SEM fractography of fracture surfaces and metallographic examination of the fracture specimens.

Experimental Procedure

Material and Specimens

The chemical composition of the test bars was determined using spectro-chemical analysis per ASTM Standard E607-90, and is listed in Table I. The composition of the fatigue test bars used in this investigation was found to be in the expected range of the nominal chemical composition of A380.0 aluminum casting alloy [3].

Table I. The Chemical Composition (wt. %) of A380.0 Test Bars

Element	Si	Cu	Mg	Mn	Fe	Ti	Cr	Ni	Zn	Sn	Pb	Others (Each)	Others (Total)	Al
Composition (wt.%)	9.23	3.39	0.09	0.19	0.94	0.05	0.09	0.07	2.47	<0.05	0.12	<0.05	<0.50	Rem

The mechanical properties of A380.0 alloy used in this investigation are shown in Table II. The tensile test bars used were cast under the same casting conditions and in the same die as the fatigue bars used in this investigation.

Table II. Mechanical Properties of the Test A380.0 Alloy

Tensile strength (MPa)	Yield strength (MPa)	Elongation (%)	Hardness (HRB)
43.2	20.4	3.5	55

The specimens tested in this investigation, shown in Fig. 1, were produced on an UBE HVSC 800 Casting Machine. The pouring temperature of the molten alloy was 732 °C. In this investigation, 53 specimens cast from the same batch were tested at random. The nominal minimum diameter of test bars were 6.35 mm (0.25 in). The specimens were partially machined (grip ends only) to match the size of the grips of the test machines. The curved surface in the neck region of specimens were kept in the as-cast condition during testing,

except that any parting line flash was removed by grinding along the longitudinal direction of the specimens with No. 1000 grit metallographic abrasive paper. To investigate the effect of parting line flash on the fatigue life, 3 specimens were fatigue tested without removing existing parting line flash. In addition, to investigate the detrimental effects of casting defects, 13 specimens with visually obvious casting defects on the surface were tested.

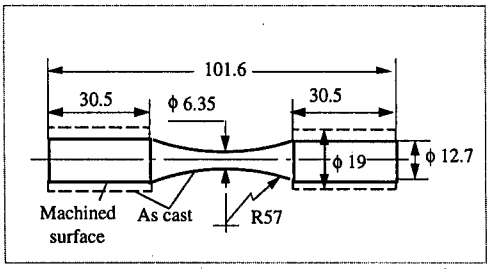


Figure 1: Geometry of fatigue test specimens (mm).

Fatigue Testing

The fatigue test machines used in this research were R.R.Moore type rotating beam fatigue test machines. The fatigue tests were run at 10,000 rpm until specimen failure occurred. The bending moment was calculated by the following formula:

$$M = 0.0111\ SD^3 \qquad (1)$$

where M = bending moment (setting of the poise weight), N-m
S = desired stress level in the specimen, MPa
D = diameter of specimen at minimum cross section, mm.

SEM Fractography and Metallography

After fatigue testing of all specimens was complete, a S-N curve was constructed. To obtain a preliminary determination of the possible causes of fatigue failure, the fracture surfaces for each broken specimen were visually, and then further macro-examined using a Nikon SMZ-10. During the examination, special attention was paid to the fatigue initiation sites of the specimens. Of the 53 specimens tested, 13 specimens were examined using a Scanning Electron Microscope (SEM). After the SEM fractography examination, the specimens were sectioned through the fatigue origin, mounted using transparent mounting material, ground, polished and etched (0.5% HF) for microstructural analysis. The microscope used in this investigation was a REICHENT-JUNG MeF3. Based on the visual, macroscopic, SEM, and microscopic analysis, the fatigue failure causes for these selected specimens were evaluated.

Results

S-N Curve and Fatigue Strength

Based on the fatigue lives and the corresponding applied stresses of the 53 specimens, an S-N curve (band) of squeeze cast A380.0 alloy was established (Fig. 2). Considering that the

results from the fatigue bars with severe surface casting defects and parting line flash were not representative of the fatigue properties of the test alloy, the data from 3 specimens with parting line flash, and 13 specimens with severe casting defects, were removed from the S-N curve in Fig. 2. A modified S-N curve (band) is shown in Fig. 3. Analysis of the curve indicated that the fatigue strength of squeeze cast A380.0 alloy is in the range of 138 ~ 152 MPa (20.0 ~ 22.0 ksi), at 1.0 x 10^8 cycles.

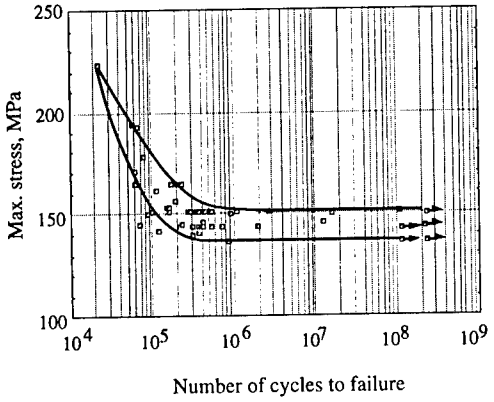


Figure 2: S-N curve of squeeze cast A380.0 alloy including data from all 53 specimens tested.

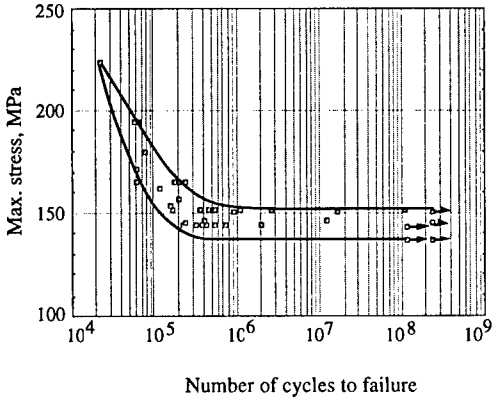


Figure 3: Modified S-N curve of squeeze cast A380.0 alloy based on data from 37 tested specimens not having parting line flash or externally visible casting defects.

Fatigue Origins

To determine the fatigue mechanisms of squeeze cast A380.0 alloy, in particular for identifying the casting defects which induced initiation of fatigue cracks, visual, macroscopic, microscopic and SEM examinations on fatigue fracture specimens were conducted. Preliminary observations by visual and macroscopic examination indicated:

- 3 specimens with the parting line flash not removed failed prematurely at low a stress level, as expected.
- 13 specimens failed due to visually-severe surface defects such as cold shuts.
- 12 specimens failed due to obvious casting defects (under a macroscope).
- 13 specimens failed due to possible casting defects (under an SEM)
- 12 specimens failed without showing obvious casting defects.

Discussion

Effect of Casting Defects on Fatigue Life

This investigation revealed cold shuts, existing in surface and sub-surface layers, were the leading cause which resulted in fatigue fracture of the specimens. Entrapped lubricants on the surface of specimens also induce fatigue crack initiation, but its negative effect on fatigue lives of the specimens was less than that of cold shuts. It was found that all specimens with cold shuts inducing fatigue cracks had low fatigue lives, most of them being less than 1.0×10^6 cycles, while the specimens with entrapped lubricant as fatigue origins had much higher fatigue lives, more than 1.0×10^8 cycles. This indicated cold shuts reduce fatigue life more severely than entrapped lubricant. Table III is a comparison of the fatigue lives of specimens with different fatigue origins.

Table III. Fatigue Origins and Fatigue Life of Examined Specimens

Cold shuts		Entrapped lubricant	
Specimen No.	Fatigue life	Specimen No.	Fatigue Life
83	67,100	115	2,539,500
86	359,500	131	> 205,591,700
89	1,066,900	104	> 130,386,000
90	94,300	95	> 206,523,000
98	366,200	102	> 133,580,100
101	281,200	99	105, 990,000

Dominant Factor of Fatigue Life

In this investigation, it was found that all specimens tested displayed almost the same length of fatigue zones on the fracture surface, regardless of whether the total fatigue life of a specimen was high or low. This implied that the fatigue life subsequent to fatigue crack initiation (a function of fatigue zone length) of all specimens was almost same.

The overall fatigue life of the test specimens consists of two phases: crack initiation (phase I) and crack propagation (phase II) [4]. From SEM observation and measurement of the striations on the fracture surfaces of a typical specimen, the fatigue cracks propagated at a growth rate of 0.3 μm per cycle during phase II. This suggests that the phase II component of fatigue life in these samples less than 1/1000 of the total fatigue life. Therefore, the crack initiation phase is the dominant factor controlling the fatigue life of these specimens. As soon as a fatigue crack forms on the surface of a specimen, the remaining fatigue life is rather short.

Conclusions

1. A S-N fatigue curve (band) for squeeze cast A380.0 alloy was developed, based on test results of 53 as-cast specimens on rotating beam fatigue test machines. Analysis of the S-N curve shows that the fatigue strength of squeeze cast A380.0 alloy is in the range of 138 ~ 152 MPa (20 ~ 22 ksi) at 1.0×10^8 cycles. The published fatigue life of die cast A380.0 alloy is 140 MPa (20 ksi) [5].

2. The casting defects which induced fatigue cracks and resulted in the final failure of cast specimens were identified. SEM and metallographic examination revealed that cold shuts, entrapped lubricants, and combinations of both in the specimen surface layers, were the leading failure causes of test specimens. Cold shuts were found to have greater effect on the fatigue life of castings than the entrapped lubricants. No evidence was found in this investigation that internal porosity, such as gas porosity or shrinkage porosity, induced fatigue crack initiation.

3. The dominant factor which controls the fatigue life of the specimens was found to be the initiation process of the fatigue crack on the surface of the test specimens. Regardless of the number of cycles required to initiate fatigue crack, the number of cycles required to propagate the crack to specimen failure was nearly constant (about 1.0×10^6 cycles).

References

[1] A.L. Kearney, Properties of Cast Aluminum Alloys, Properties and Selection: Nonferrous Alloys and Special-Purpose Materials, ASM Handbook, 10th Ed., Vol.2, (ASM International, 1990).

[2] G.W. Powell, S.H. Cheng, and C.E. Mobley, A Fractography Atlas of Casting Alloys, (Battelle Press, 1992).

[3] Registration Record of Aluminum Association Alloy Designations and Chemical Composition Limits for Aluminum Alloys in The Form of Castings and Ingot, (The Aluminum Association, Inc., Washington, D.C., 1989).

[4] J. Fong, ed., Fatigue Mechanisms, (ASTM, Philadelphia, PA., 1979).

[5] Product Specification Standards for Die Castings, (Die Casting Development Council of the North American Die Casting Association, LaGrange, IL, 1994).

AN ANALYSIS OF THE MICROSTRUCTURE OBTAINED IN ATOMIZED Al-Fe POWDERS

J. A. Juarez-Islas[1], C. Gonzalez-Rivera[1], Y. Zhou[2] and E. J. Lavernia[2]
[1]Instituto de Investigaciones en Materiales, UNAM, Mexico, D.F., 04510, Mexico.
[2]Department of Chemical Engineering and Materials Science, University of California, Irvine, CA 92717-2575, USA.

Abstract

The model of Lipton, Glicksman and Trivedi[1] for rapid dendrite growth in undercooled alloys and extended by Lipton, Kurz and Trivedi[2] to the case of dendrite growth with large undercoolings was applied to nitrogen atomized Al-2.56 wt. % Fe powders. Results of the model in terms of plots of dimensionless bath undercooling, $\overline{\Delta T}$, vs dimensionless growth rate, $\overline{V}$, and dimensionless bath undercooling, $\overline{\Delta T}$, vs dimensionless dendrite tip radius, $\overline{R}$, were similar to those reported by the above authors and its interpretation, in special the plot of dimensionless bath undercooling, $\overline{\Delta T}$, vs dimensionless dendrite tip, $\overline{R}$, was carried out from the microstructural characterization of powders, identifying two types of microstructures in the atomized powders. The first one corresponded to a dendrite growth mode as that observed in highly undercooled alloys and the second one corresponded to a featureless + dendrite growth mode.

The Third Pacific Rim International Conference on
Advanced Materials and Processing (PRICM 3)
Edited by M.A. Imam, R. DeNale, S. Hanada,
Z. Zhong and D.N. Lee
The Minerals, Metals & Materials Society, 1998

Introduction

The extent of undercooling during solidification of metals plays a critical role in microstructural evolution by dictating phase selection. There are two general approaches that may be effectively utilized to enhance undercooling, i.e. reducing the potency of heterogeneous nucleants or extracting thermal energy at a rate that is sufficiently high to delay crystallization of the undercooled liquid.

The first approach involves the progressive elimination or isolation of potential catalysts.[3-5] The second approach is generally associated with achieving high cooling rate through rapid extraction of thermal energy.[6-7] Among the available techniques that may be effectively used to enhanced the degree of undercooling during solidification, atomization remains a popular choice as a result of its versatility and potential for tonnage production.[8]

Control of the amount of undercooling prior to solidification may be effectively used to promote the formation of non-equilibrium phases as highly refined microstructures with concomitant benefits to mechanical behavior. Increasing the extent undercooling may expand the range of available phases by allowing competitive nucleation and growth[3-7, 9] Accordingly, an understanding of the factors that control the extent of undercooling may be helpful to tailor the microstructure.

The objective of the present investigation was to enhance the understanding of the effect of solidification condition on the resultant microstructure and phase stability of an Al-2.56 wt. % Fe alloy.

Experimental Procedure

An alloy with nominal composition of Al-2.56 wt. % Fe was selected for this study. The alloy was prepared by using pure Al (99.99%) and Fe (99.98%). In the atomization experiment, the alloy was first superheated to a temperature of 200K above the equilibrium liquidus and atomized into a distribution of droplets by using nitrogen gas. The resultant powders were then mounted for microstructural analysis using standard metallographic techniques and etched with Keller's reagent in order to reveal microstructural features. Characterization of powders and Fe content in specific phases were conducted by using a scanning electron microscope (SEM) which has microanalysis facilities.

Results and Discussion

Results obtained from metallographic studies in the as-atomized Al-2.56 wt. % Fe powders revealed the following kind of microstructures: Droplets with sizes in the range between 10

μm and 40 μm in diameter showed dendritic domains (Fig. 1a) and some of them exhibited a predendritic feature (Fig. 1b).

The dendritic domains present the development of regular dendritic growth from an initially predendritic mode. The distribution of solute (Fe) in the predendritic region as shown by scanning electron microscopic analyses is given in Table I. The wt. % Fe in single phase (**a**) was within experimental limits, the same as the parent melt. In region (**b**) the Fe content showed a minimum and in region (**c**), before cells or dendrites start to form, the average composition was again that of the liquid.

This predendritic formation was identified by Biloni and Chalmers,[10] in chill casted Al-Cu alloys and also reported in Al-Mn alloys,[11] and were identified on the side of the ingot which was in direct contact with a chill-copper wall.

These morphologies show the extreme condition of solid solubility extension which occurs when solidification occurs effectively without solute partitioning to give single-phase solid of uniform composition, C_o, the same as the parent melt. SEM observations of pre-dendritic zones, suggest that regions such as region **a** and region **c** of high solute content were the first regions where nucleation occurred and from which growth occurred initially with a smooth spherical front without net segregation.

In order to explain the formation of the observed predendritic, cellular and/or dendritic structures, predictions of rapid dendrite growth in undercooled alloys were calculated according to the theory of dendrite growth into undercooled alloy melts for the case of large undercoolings, reported by Lipton, Kurz, Trivedi,[2] where a complete stability analysis of a plane interface to the tip of a Ivantsov dendrite was considered.

The dendrite growth model assumed a simplified isolated dendrite tip of the form described by a paraboloid of revolution,[12] growing with a constant dimensionless growth rate, $\overline{V}$, and dimensionless tip radius, $\overline{R}$, into the bath with a given dimensionless undercooling, $\overline{\Delta T}$, defined by equations (1) to (3):

$$\overline{\Delta T} = \mathrm{Iv}\ (P_t) + \overline{Co}\ (A\text{-}1)^{-1} + 2\,\sigma^*\,P_t F(A), \qquad (1)$$

$$\overline{R} = [\sigma^*\,P_t\,F(A)]^{-1}, \qquad (2)$$

$$\overline{V} = \sigma^*\,P_t^2\,F(A), \qquad (3)$$

The parameters fed into the mathematical model are shown in Table II, for the Al-Fe system under study. Results of equations (1 to 3) are plotted in Fig. 2 showing the behavior of $\overline{V}$ and

$\overline{R}$ as a function of $\overline{\Delta T}$ for $\overline{Co}$ = 0.02, k_o = 0.038 and η = 1.41 x 10^{-4}. According to that figure, the behavior of $\overline{V}$ as a function of $\overline{\Delta T}$ and $\overline{R}$ as a function of $\overline{\Delta T}$ were similar to those reported by Lipton et. al.[2] In particular, it can be observed that at high undercoolings, the dimensionless tip radius shows a minimum ($\overline{R} \approx 10$, $\overline{\Delta T} \approx 0.58$) followed by a maximum ($\overline{R} \approx 153$, $\overline{\Delta T} \approx 0.85$) before going to infinity, and $\overline{V}$ approaches to a maximum value close to 0.5.

The complex behavior of $\overline{R}$ as a function of $\overline{\Delta T}$, was explained as a change from an almost purely solute diffusion controlled dendrite growth (minimum in Fig. 2b) to a thermal plus solutal control (maximum in Fig. 2b).[2]

With regards to the microstructure observed in nitrogen atomized Al-Fe powders and in particular those presented in Figs. 1a and 1b, represent the main morphologies observed in the powders.

Fig. 1a shows a powder particle in which, it can be observed a dendrite solidification growth mode and its dendrite tip (inset) adopting a form closely described by a paraboloid of revolution. Assuming that this dendrite tip grew with a constant $\overline{V}$ and $\overline{R}$ into the bath with a given undercooling, then the observed dendrites in the powder particle grew at some point positioned to the left of the coordinate point ($\overline{\Delta T}_3$, $\overline{R}_3$) shown in Fig 2b.

Observing the behavior of Fig. 2b and analyzing it from low to high values of $\overline{\Delta T}$, with respect to the microstructural features of Fig. 1b, it can be pointed out that the dendrite tip radius, R, of dendrites observed close to the grain boundary ($R \approx 0.2$ μm) will decrease in dimension as $\overline{\Delta T}$ and $\overline{V}$ increase until those parameters forc that $\overline{R}$ reaches a minimum value in the plot of $\overline{\Delta T}$ vs $\overline{R}$ ($\overline{\Delta T} \approx 0.58$, $\overline{R} \approx 10$ and $R \approx 0.01\mu m$, with d_o = 3.33 x 10^{-10} m).

This minimum in $\overline{R}$ of Fig. 2b will correspond to the interface dendrite/concentric ring (marked with c), in Fig. 1b. In that interface, $R \approx 0.05$ μm, which is close to the value of R determined from the plot of $\overline{\Delta T}$ vs $\overline{R}$ ($R \approx 0.01\mu m$). The maximum in $\overline{R}$ from that plot and located as a coordinate point ($\overline{\Delta T}_2$, $\overline{R}_2$) will correspond to the interface concentric ring/circle of Fig. 1b. And finally, the circle of Fig. 1b correspond to the portion of the plot of $\overline{\Delta T}$ vs $\overline{R}$ when the value of $\overline{R}$ goes to infinity.

Conclusions

1 - In the present study, two types of microstructures in the atomized Al-Fe powders were identified; dendrites of α-Al and predendrite structures.

2.- The model of Lipton-Kurz-Trivedi,[2] for rapid dendrite growth in undercooled alloys was applied to explain the resulting microstructures of rapid solidification of nitrogen atomized Al-2.56 wt. % Fe alloy powders. The outcome of the model in terms of $\overline{\Delta T}$ vs $\overline{V}$ and $\overline{\Delta T}$ vs $\overline{R}$ showed a similar behavior as those reported by the above authors. The plot of $\overline{\Delta T}$ vs $\overline{R}$ was explained in terms of the microstructure observed in the atomized powders, as: i) a region which shows an interface concentric ring/dendrites, corresponding to the minimum in the plot of $\overline{\Delta T}$ vs $\overline{R}$, from this minimum (interface), dendrites start to growth and stop at grain boundary, ii) a region which shows an interface circle/concentric ring, and correspond to the maximum in the plot of $\overline{\Delta T}$ vs $\overline{R}$, dendrites are not longer observed and the solute content is the same as the parent melt, and iii) a region of a circle which correspond to the portion of the plot of $\overline{\Delta T}$ vs $\overline{R}$, when $\overline{R}$ goes to infinity, which correspond to regions where a segregation-free solid is formed due to the trapping of solute in the solid.

References

1.- J. Lipton, M. E. Glicksman and W. Kurz, Mat. Sci. Engng., 64 (1984), 957-964.

2.- J. Lipton, W. Kurz and R. Trivedi, Acta Metall., 35 (1987), 57-63.

3.- D. Turnbull, in Undercooled Alloy Phases, eds. E. W. Collings and C. C. Koch (AIME-TMS, Warrandale, PA, 1987), 3-22.

4.- J. H. Perepezco, B. A. Mueller and K. Ohsaka, in Undercooled Alloy Phases, eds E. W. Collings and C. C. Koch (AIME-TMS, Warrandale, PA, 1987),. 298-320.

5.- M. C. Flemings, Y. Shiohara, Y. Wu and T. J. Piccone, in Undercooled Alloy Phases, eds. E. W. Collings and C. C. Koch (AIME-TMS, Warrandale, PA, 1987), 321-343.

6.- A. J. Drehman and D. Turnbull, Scripta Metallurgica 15 (1981), 543

7.- Y. E. Anderson and M. P. Kemppainen, in Undercooled Alloy Phases, eds. E. W. Collings and C. C. Koch (AIME-TMS, Warrandale, PA, 1987), 269-285.

8.- A. Lawley, in Processing of structural Metals by Rapid solidification, eds. F. H. Froes and J. S. Savage (ASM International, 1987), pp. 31-40.

9.- W. J. Boettinger, in Rapid Solidified Amorphous and Crystalline Alloys, eds. B. H. Kear, B. C. Giessen and M. Cohen (Proceedings of Materials Research Society Symposium, Vol. 8, 1982), pp. 15-31.

10.- H. Biloni and B. Chalmers, Transactions of the Metallurgical Society of AIME, 233(1965), 373

11.- J. A. Juarez-Islas, Ph. D. Thesis, University of Sheffield, England, 1987, pp. 35 .

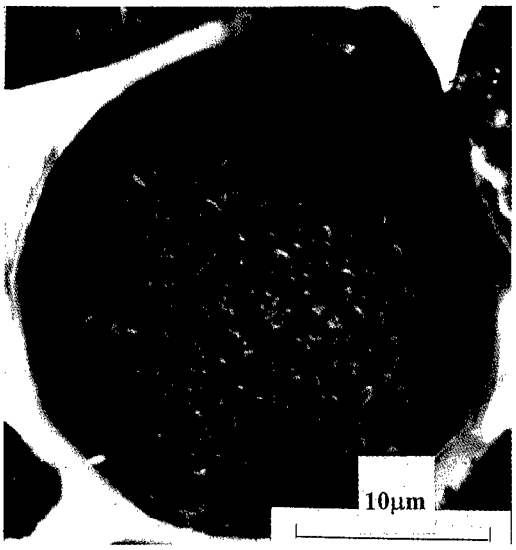
12.- G. P. Ivantsov, Dokl. Akad. Nauk SSSR, 58 (1947), 567

Table I. SEM microanalyses (in wt. % Fe) carried out in powders of Fig. 1b.

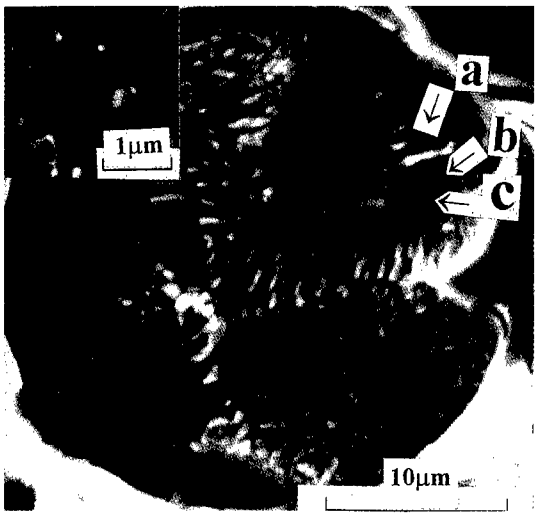
Microanalyses	Region a	Region b	Region c	Dendrites
Center	2.56		2.56	
1 μm from center	2.56			
Region b		2.52		
Near region c				2.54
5 μm far from Region c				2.49
Close to grain boundary				2.45

Table II. Parameters fed into the mathematical model.

Unit undercooling	$\theta = H / c_p$	368.7 (K)
capillarity length	$d_o = \Gamma / \theta$	2.71×10^{-10} (m)
ratio thermal/solutal diffusivity	$\eta = \alpha / D$	1.41×10^{-4} (--)
alloy concentration	$C_o = \overline{Co}\,\theta / \lvert m \rvert$	99.6 $\overline{Co}$ (wt%)
bath undercooling	$\Delta T = \theta\ \overline{\Delta T}$	$368.7\,\overline{\Delta T}$ (K)
growth rate	$V = 2a\overline{V} / d_o$	$2.51 \times 10^{5}\ \overline{V}$ (m/s)
dendrite tip radius	$R = \overline{R}\, d_o$	$2.71 \times 10^{-10}\ \overline{R}$ (m)
liquidus slope	m	-3.7 (k/wt%)
equilibrium partition coefficient	k_o	0.038 (--)

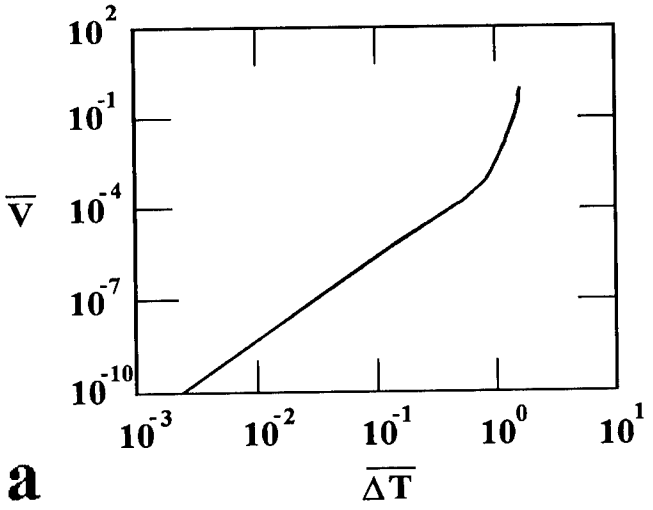


a



b

Figure 1. a) Dendritic α-Al solid solution (inset a dendritic tip morphology), b) predendritic morphology showing regions of solute concentrations (a and c) equal to the parent melt, position (b) shows a minimum in composition.



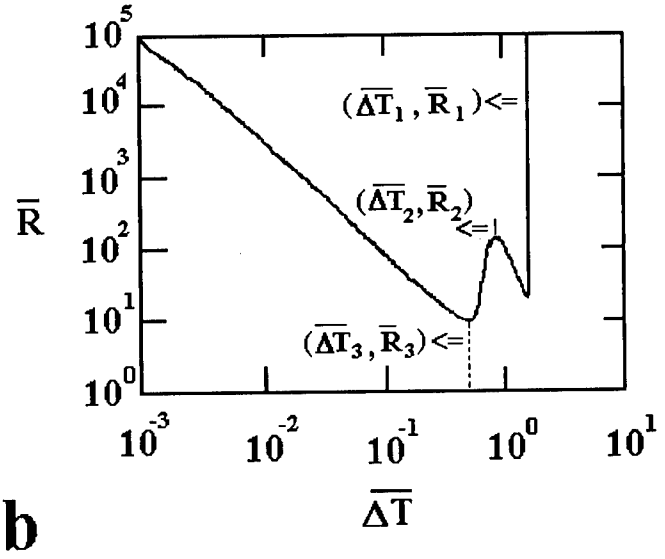


Figure 2. a) Behavior of $\overline{V}$ and b) $\overline{R}$ as a function of $\overline{\Delta T}$ for $\overline{Co}$ = 0.02, k_o = 0.038 and η = 1.41 x 10^{-4}. The coordinate points ($\overline{\Delta T}_3, \overline{R}_3$), ($\overline{\Delta T}_2, \overline{R}_2$) and ($\overline{\Delta T}_1, \overline{R}_1$) show the position of $\overline{R}$ in the curve which correspond to a minimum, maximum and infinity, respectively.

EFFECTS OF RE(RE: Rare Earth Metals) ADDITION ON FORMABILITY IN Al-HIGH Mg ALLOYS

Su-Dong PARK*, Suk-Bong KANG**, Hyun-Kee CHO*

* Departments of Metallurgical Engineering, Kyungpook National University, Teagu, Korea, 702-701

** Korea Institute of Machinery and Metals, Changwon, Korea, 641-010

Abstract

The Changes of formability by RE addition in Al-High Mg Alloys whose most serious problem to their applications were well known as poor heat-stability, were investigated by ODF(Orientation Distribution Funtion) analysis and measurements of formability index, as like work hardenability index, n, average R value and planar anisotropy, ΔR, at T4 heat treated condition.

By RE(RE:Rare Earth Metals) addition, work hardenability and anisotropy was improved and it may reasons of why changes of deformation texture as like that, in the case of free RE alloys, {011}<211> B component, {112}<111> C component and {123}<364> S component were developed at 85% deformation after T4 treatment, typical {100}<011>texture was developed in Al-high Mg-RE alloys. Process of texture development with deformation ratio in Al-10Mg-0.1MM alloy were that random component at 10% deformation and {011}<100> G component and {011}<211> B component were observed as a major one until 50% deformation and just intensity of G component increase considerably with deformation. But, At more 80% deformation, G, B components nearly disappeared, and {001}<110> texture was developed as a major one.

The Third Pacific Rim International Conference on
Advanced Materials and Processing (PRICM 3)
Edited by M.A. Imam, R. DeNale, S. Hanada,
Z. Zhong and D.N. Lee
The Minerals, Metals & Materials Society, 1998

Introduction

Recently, Al-Mg 5000 series alloys, which was known as typical non heat-treatable Al alloys, have been spotlighted due to applications for automobile body in spite of their poor thermal workability. The major strengthening factors in these alloys are solid solution strengthening and work hardening so that to maximize there potential properties, increasing of Mg content should be first under consideration, whereas it also causes serious problems, which are thermal-instability of properties due to the precipitation of β phase. But, according to Park et al.[1], precipitation of β could restrained by RE(RE : Rare Earth Metals) addition in even Al-high Mg($\geq$7wt%) alloys and it may give some possibility to maximizing of potential properties by increasing Mg contents. So, it is worth while to evaluate the formability in Al-high Mg-(RE) alloys. In present works, therefore, the formability of Al-high Mg alloys would be estimated with various formability factors and investigated the change of deformation texture through RE addition by ODF(Orientation Distribution Function) analysis.

Experimental Procedure

The Al-Mg alloys were melted and cast in a high frequency melting furnace under Ar atmosphere using 99.99%Al, 99.9%Mg, Al-La mother alloys, and Misch Metal. The alloy designs and the chemical compositions of these alloys are shown in Table 1.

Table I Chemical composition of Al-Mg-RE alloys (wt%)

Alloy	Mg	Fe	Si	La	Al	Remark
Al-5Mg	5.23	0.05	0.08	-	bal.	
Al-7Mg	7.12	0.08	0.09	-	bal.	MM : Misch Metal (Ce:50.9% La:23.0% Nd:15.1% Pr:6.2% etc)
Al-10Mg	10.56	0.07	0.07	-	bal.	
Al-11Mg	11.01	0.07	0.09	-	bal.	
Al-7Mg-0.1La	7.8	0.002	0.03	0.115	bal.	
Al-8Mg-0.3La	8.45	0.03	0.03	0.29	bal.	
Al-10Mg-0.1La	10.9	0.09	0.04	0.36	bal.	
Al-10Mg-0.1MM	10.51	0.09	0.03	Remark	bal.	

After all as-cast ingots were homogenized at 753K for 48hr, they were hot and cold rolled to plates with given thickness. All the specimens were T_4 heat-treated as like solution treatment for 2hr at 723K followed by ice water quenching. The heat exposure treatment were carried out at 423K in silicon bath, and room temperature tensile test were performed with ASTM E8 subsize specimens by Instron type tensile tester to evaluate formability factors as like UTS(MPa), elongation(%), work hardening index, n, , average R value and planar anisotropy, ΔR. The change of grain behavior was observed using a optical microscope after T4 treated. Interplenar spacing of (111), (200), (220) and (311) with heat exposure, pole figures at each plane was measured by fully automatic X-ray diffractometer after surface polishing. The procedure of ODF analysis is as follows; that is, T4 treated sheet specimens were cold rolled reduction ratio $\sim$18% at each pass at room temperature, producing the specimens with 10$\sim$90% rolling ratio. ODF was determinated by Bunge method on the base of the measurements of three pole figures (111), (200) and (220) plans.

Results

Evaluation of formability in Al-high Mg-(RE) alloys

In Al-Mg alloys, the poor hot workability was due to β precipitation. Increasing of β precipitation arising from high Mg contents bring about big changes on properties in Al-high Mg alloys. So, in present work, just T4 heat treatments was considered as heat treatment T4 treatment can be expected to eliminate β precipitate. Table 2 shows the change of mechanical properties as like UTS(MPa), elongation(%), work hardening index, n, and cold-workability as like anisotropy ratio, average R value, and planar anisotropy, ΔR, on 85% cold-rolled specimen T4 treated with various Mg contents.

Table II Cold workability in Al-Mg-(RE) alloys T4 treated

Heat Treatment		Al-5Mg	Al-7Mg	Al-10Mg	Al-7Mg-0.1La	Al-10Mg-0.1MM
As T4 Treated	UTS(MPa)	310	350	365	372	402
	e (%)	30	33.5	42	42	49
As Cold Rolled	n	0.33	0.37	0.40	0.39	0.42
	Average R	0.72	0.88	0.87	0.83	0.88
	ΔR	0.22	-0.1	-0.3	-0.11	-0.08

It reveals the increase of elongation and work hardening index with Mg addition and especially, in case of RE addition, these values were higher than those of RE free alloys. Whereas average R value which was connected with deep drawabilty almost had no change between alloys whether RE added or not, the alloys with RE addition were showed more predominant tendency of isotropy than RE free alloys as ΔR values approaching near zero.

It has been known that increase of UTS, elongation, and work hardening index with Mg contents were due to decrease of stacking fault energy with Mg which give rise to interference of cross slip and increase of UTS, elongation, and work hardening exponent with RE addition could be explained as to maximize of solid solution strengthening by restarted β precipitation[1]. Nevertheless, it has not been reported about improvement of anisotropy by RE addition as like present result, so, present work attempt to extend the analysis of texture development in rolling process after T4 treatment.

Changes of deformation texture with cold rolling

Figure 1. shows (111) pole figures in Al-2.46wt%Mg, Al-7.19wt%Mg, Al-11.07wt%Mg and β fiber alloy which was 85% cold rolled after T4 treated during 12hr at 673K (which were worked by Kang el at.[2]. Regardless of Mg contents, it reveals major component was {110}<112> B component and mixed texture with both {213}<364> S component and {112}<111> C component together that would be typical β fiber components [3] in FCC crystal.. From Kang et al.[2], typical cold rolled texture should be β fiber which was composed of B, S, C texture in Al-Mg alloys, and intensity of B components increased gradually with Mg Content and Lücke et al.[4] described that stable B texture developed with Mg in Al-Mg alloys due to much lower stacking fault energy, making cross slip difficult. In spite of these results by advanced workers, big difference in texture developments was observed in RE addition alloys.

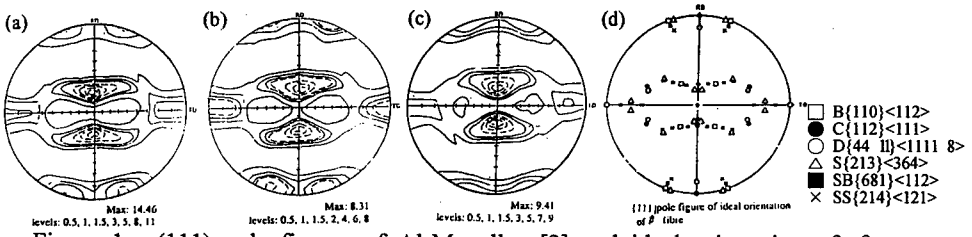


Figure 1 : (111) pole figures of Al-Mg alloys[2] and ideal orientation of β fiber.[3] a) Al-2.46wt%Mg b)Al-7.19wt%Mg c) Al-11.07wt%Mg

Figure 2 shows the result of (111) pole figures and ODF analysis in Al-7Mg-0.1La and Al-10Mg-0.1MM alloys. In RE addition alloys, distinct {100}<011> texture was observed as predominant component, and it is quite different from the case of RE free alloys, showing typical β fiber texture as Figure 1. It is enough to make interesting because that there was any report about {001}<110> texture in Al-Mg alloys until now. To observe the formation process of {100}<011>texture by cold rolling, the ODF of Al-10Mg-0.1MM was shown with increased deformation in Figure3. In case of less 80% deformation, random component at 10% deformation, and {011}<100> G component and {011}<211> B component were observed as a major until 50%

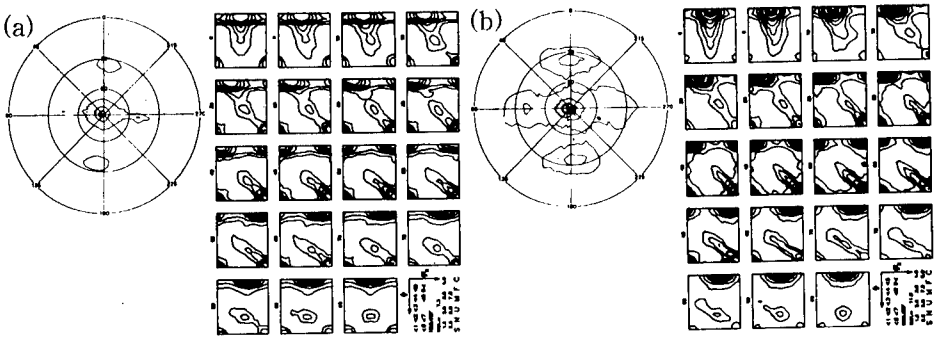


Figure 2 :(111) pole figures and ODFs(φ_1 section) of rolling texture after T4 treatment. a) Al-7Mg-0.1La b) Al-10Mg-0.1MM

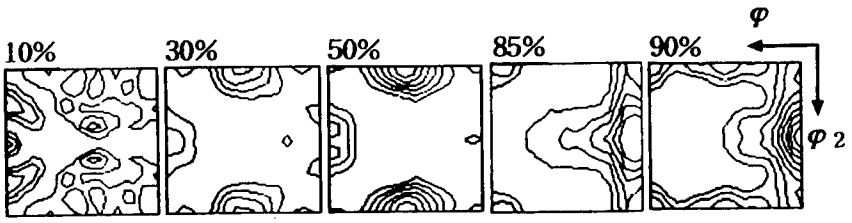


Figure 3 :The change of ODF(φ_1=0 section) with deformation ratio after T4 treatment.

deformation and just intensity of G component increased considerably with deformation. But, at more 80% deformation, G, B components nearly disappeared, and {001}<110> Texture was observed as a major one. From the present result, strong development of G component in condition of low deformation was not general phenomena in Al or Al alloys. Therefore, it may be considered that some different deformation mechanism was operated in RE addition alloys.

Discussion

Bunsch et al.[5] regarded {001}<110> texture as typical shear texture, observed in case of Pure Al serious deformed, and Truszkowski et al.[6] suggested that this texture is surface component which appears only on surface, not a major, due to geometrical factor, as like rolling friction and rolling gab in more 90% deformed Al. In present work, however, some surface could be eliminated by mechanical polishing, and typical β fiber was turned up as a result of the same condition in case of RE free alloys. Therefore, it is doubtful to look on this texture as just surface component. In spite that fuller discussion about {001}<110> component developed by RE addition will be presented in the next paper because of work on yet to detail researching, it is valid think to estimate some possibilities for development of {001}<110> texture through follow consideration

It has been known that texture development during deformation was affected by stacking fault possibilities, grain size, solute atom and precipitate and stacking fault possibilities depend on solute atom behavior as like a kind of atom, state of solid solution etc. Figure 4 showed behaviors of Debye diffraction peak with heat exposure at 423K. As T4 treated condition, diffraction peak was shift to low angle with Mg contents and it means that more Mg atoms exist as solid solution. With exposure time, they revealed typical behaviors which each diffraction peak moving to high angle by β precipitation in free RE alloy. On the contrary, diffraction peaks were still located on lower angle in RE addition alloys. It is in good agreement with the result reported by Park el at.[1] what is restrain of β phase by RE addition. But, in this study, it must be noted that intensity of diffraction peaks was reverse at heat exposure for 24hr, marked marked, in case of a small amount of RE addition (Al-7Mg-0.1La, Al-10Mg-0.1MM), namely, peak intensity on (111) and (200) was reversed. This must be

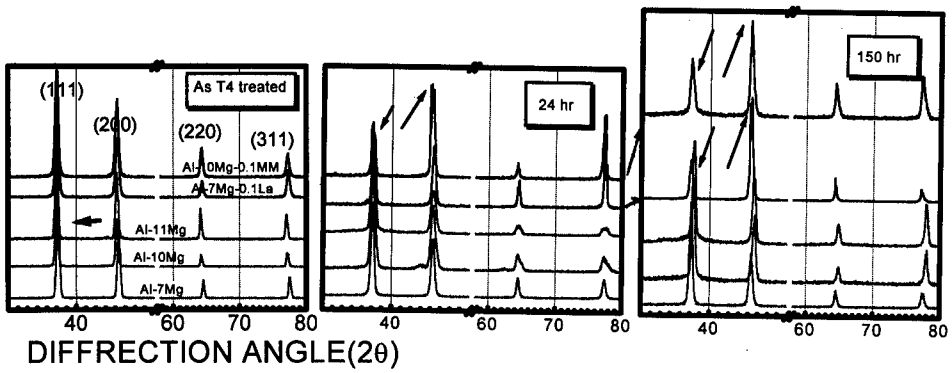


Figure 4 :Diffraction peak behaviors during heat exposure(423K) in Al-Mg-(RE)alloys

particular appearance, almost not shown in Al and Al alloys as FCC structured.. This result gives some information about the situation of solid solution of solute Mg solute atoms by RE addition during heat exposure. In other words, it may estimate that by RE addition, (200) crystal perfection increased, but (111) crystal perfection decreased. Figure 5. shows the change of Interplanar spacing of (111) plane and (200) plane which is calculated from diffraction peak. With heat exposure, Interplanar spacing was reduced by β precipitate in free RE alloy in both (111) and (200) planes, but Interplanar spacing of (200) not change in RE addition, rather interplanar spacing of (111) plane increase. Therefore, it is possible to think that to addition of RE in Al-high Mg alloy make to increase moving tendency of Mg atoms to (111) plane which make decrease crystal perfection in (111) planes and cross slip on (111) plane may restrained.

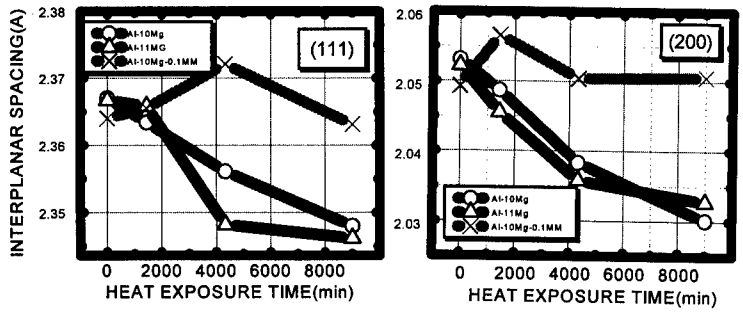


Figure 5 :Changes of (111),(200) interplanar spacing with heat exposure in Al-Mg-(RE)alloys

Of coarse, situation of heat exposure are different from cold deformation's and above consideration, as heat exposure condition, cannot apply to explanation of (001) <110>texture development during cold deformation directly. But, it can be considered that some effects of above mentioned may act on development of (001)<110>texture because condition of just before deformation, T4 treated condition is similar to long term heat exposure condition and thermal redistribution may similar with dynamic redistribution by hard deformation.

Also, Bunsch et al.[7] etc. proposed that {001}<110>texture was developed at coarse grains condition before deformation in commercial Aluminum. Photo 1. shows optical micrographs as T_4 treated condition. In RE free alloys, grain size decreased with Mg contents, but coarse grain was observed, compared with free RE alloys, in RE addition alloys. Especially Al-10Mg-0,1MM alloy had the coarse grain, so grain coarsening by RE addition would be considered to affect on {001}<110>texture formation. On reports of Bunsch et al.[6], however, {001}<110>texture was observed at coarse grain (about 400μm), whereas average grain size was not over 100μm even in case of Al-10Mg-0.1MM alloys in present work, also, there was no big difference between RE

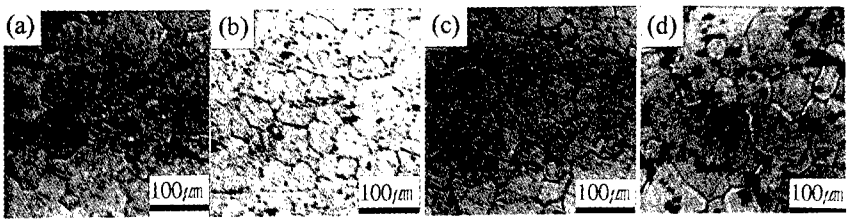


Photo 1 : Optical Micrographs as T4(423K) treated in Al-Mg-(RE) alloy.
a) Al-7Mg b) Al-10Mg c) Al-7Mg-0.1La d) Al-10Mg-0.1MM

add or not as T4 treated condition. Therefore, the formation of {001}<110>texture could not be explained perfectly by grain coarsening in RE addition alloys, though some effect are expected.(Actually, there is strong effect on grain growth in heat exposure by RE addition). Also, though T4 treated, There was a lot of grain precipitate was observed. Especially, in Al-high Mg Alloys, formation of grain is strong affected by precipitation. So, restraint effect of β precipitation by RE addition also affect on grain size and that is reason of why coarse grain in RE addition. Therefore, it is better consideration also that precipitate effect is considered as one of factors on texture development.

In spite of some consideration about development of {001}<110>texture as above mentioned, we shall accept that we have only limited information till this time. So, the exact reasons of why development of {001}<110> texture will be reported in next paper more detail.

Conclusion

1. In Al-high Mg alloys, work hardening index, n, increased with Mg content and by RE addition, much higher value ratio of work hardening index, n, was showed. These results could be considered to be due to maximize of Mg contents as solid solution state by restraint of β precipitation. In addition, improvement of planar anisotropy, ΔR, was observed by RE addition.

2. It may estimated that improvement of planar anisotropy, ΔR, was due to development of {001}<110>Texture by RE addition. With deformation ratio, random component at 10% deformation, and {011}<100> G component and {011}<211> B component were observed as a major from 30% deformation to 50% deformation and just intensity of G component increased considerably with deformation. but, At more 85% deformation, G, B components nearly disappeared, and {001}<110>texture was observed as a major one.

Reference

1. S. D. Park, Light Weight Alloys for Aerospace ApplicationsⅣ (Pennsylvania : Publication of TMS, 1997),85-89

2. S. B. Kang, "A Study on the Development of High-Strength Aluminum Alloys" (Report, Korea Institute of Machinery and Metals, 1995).

3. I. L. Dillamore and W. T. Roberts, Acta Met.,12,(1964), 281

4. O. Engler, J. Hirsch and K. Lücke, Acta metall, 37(1989),2743-2753

5. W.Truszkowski, J. Krol, and B. Major, Metall. Trans. A, 13A, 1982, 665

6. S. H. Yu, International J. Modern Physics B, 1(2), 1987, 599

7. A.Bunsch, J. Karp, The 3rd International Conference on ALUMINUM ALLOYS Vol.1(Trondheim,Norway:N.T.H.,1992),396-401

Microstructure Refinement of Al-20Si-5Fe Alloy with Melt Treatment and Extrusion

Yi Sik Choi, Jae Sang Lee, Won Tae Kim* and Hyung Yong Ra

Division of Materials Science and Engineering, Seoul National University, Seoul 151-741, Korea
& RASOM
* : Department of Physics, Chongju University, 36 Naedokdong, Chongju 360-764, Korea

Abstract

Melt treatment of Al-20Si-5Fe alloy with addition of P via AlCuP alloy and subsequent hot extrusion have been adopted to get fine and uniform distribution of primary phases in the alloy. Solidification behavior of melt treated Al-20Si-5Fe alloy has been studied by using differential thermal analysis and by quenching experiment during cooling from fully liquid state. Al-20Si-5Fe alloy refined by the addition of AlCuP alloy shows finer distribution of both primary Si and intermetallic compound(δ-phase) than the alloy casted without melt treatment. Needle shaped δ-phase was broken into fine particles during hot extrusion and became finer with increasing extrusion ratio. Nucleation temperature of the δ-phase was independent of the addition of AlCuP. Nucleation temperature of primary Si was raised by 19K by addition of AlCuP, which resulting in refinements of Si and δ-phase.

The Third Pacific Rim International Conference on
Advanced Materials and Processing (PRICM 3)
Edited by M.A. Imam, R. DeNale, S. Hanada,
Z. Zhong and D.N. Lee
The Minerals, Metals & Materials Society, 1998

Introduction

Hypereutectic Al-Si alloy fabricated by conventional casting technology showed low toughness and poor machinability due to the formation of coarse primary Si during slow cooling. Several techniques have been applied to refine the primary Si such as addition of phosphorus (P) [1] or rapid solidification of the alloy[2-3]. In order to use hypereutectic Al-Si alloy for automative parts, the alloy should maintain its required mechanical properties at service temperature. The Al-Si-X alloys containing transient elements like Fe and Ni, which can form a compound stable at high temperature, have been developed by using a rapid solidification process and applied successfully to car air-conditioner parts and cylinder liner, etc [4-7]. However, in casting processes other than rapid solidification process, the content of transient elements, especially, Fe in Al-Si alloy has been limited because they form large intermetallic compound due to their low solubility, resulting in deteriorating effect on ductility.

The present work was aimed at refinement of primary phases in the hypereutectic Al-Si alloy containing large content of Fe by combining conventional casting with melt treatment and extrusion process. In permanent mold casting of Al-20Si-5Fe alloy, melt treatment was carried out by using AlCuP alloy and then the alloy cast was extruded with increasing extrusion ratio. Microstructures of melt treated and extruded alloy was characterized, and thermal analysis and quenching experiment were performed to study the change in solidification behavior of Al-20Si-5Fe alloy by the addition of P.

Experimental Procedure

Master alloy of Al-20wt%Si-5wt%Fe was manufactured by induction melting of commercially pure metals in graphite crucible. The master alloy was re-melted in a resistance furnace, AlCuP alloy was added to the melt, held for 10 minutes at 1123K and then poured into steel mold with outer diameter of 45mm, inner diameter of 25mm and height of 120mm. The mold was preheated to be 673K and nominal concentration of P in the refined alloy was fixed to be 300ppm, which was determined after several experiments. Unrefined alloy was also prepared under the same casting condition for comparison. Both refined and unrefined Al-20Si-5Fe alloy casts were extruded at 573K with reduction ratios of 6.25:1, 13:1 and 25:1. The microstructures of the casts and the extruded bars were observed by an optical microscope.

The effect of P addition on solidification behavior Al-20Si-5Fe alloys was investigated by thermal analysis and quenching experiments. Samples of about 50mg, obtained from the extruded Al-20Si-5Fe alloy bars to ensure alloy composition, were heated to 1173K with a heating rate 20K/min, held for 10 minutes and then cooled to 673K with a cooling rate 20K/min in a differential thermal analyzer. Master alloys were quenched into water after cooling from fully liquid state to predetermined temperatures with a cooling rate about 20K/min in a resistance furnace. The quenching temperatures were, determined after differential thermal analysis experiment, 953, 893 and 833K.

Results

Fig. 1(a) and (b) show typical Al-20Si-5Fe microstructure of unrefined and refined with P respectively. The unrefined alloy shows microstructure consisting of coarse faceted primary Si

and needle shaped intermetallic compound in ternary eutectic matrix. However the refined alloy shows microstructure consisting of coarse intermetallic compound and fine primary Si particles in ternary eutectic matrix. By addition of P, the size of primary Si reduced significantly from about 150μm to 30μm and the length of needle shaped intermetallic compound reduced too.

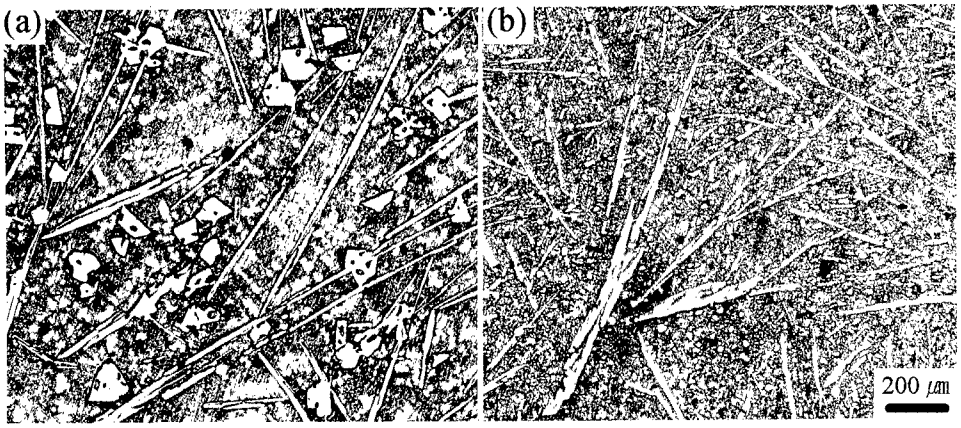


Fig. 1. Typical optical micrographs of Al-20Si-5Fe alloys, (a) unrefined and (b) refined by addition of 300ppm P.

Figs. 2(a)-(c) show typical microstructures of unrefined Al-20Si-5Fe alloy bars, extruded with reduction ratios of 6.25:1, 13:1 and 25:1 respectively. The size and morphology of primary Si were kept unchanged irrespective of extrusion ratio, but the needle shaped intermetallic compound was broken into fine particles and became finer with increasing reduction ratio. Similar results were observed in the alloy refined with P as shown in Figs. 3(a)-(c) and were reported during hot extrusion of rapidly solidified Al-Si-Fe powders[11]. It can be explained that primary Si has polyhedral shape with a small aspect ratio, which is difficult to be broken in extrusion, but the intermetallic compound showing needle shape with very large aspect ratio can be broken easily during hot extrusion due to severe plastic deformation. Also it should be mentioned that the scale of final microstructure of extruded Al-Si-Fe bars depends on initial alloy microstructure before extrusion. For a given extrusion ratio, Al-20Si-5Fe alloy refined with P show finer distribution of intermeltallic compound than unrefined alloy, which is resulting from the difference in initial microstructural scale between refined and unrefined alloys. By melt treatment with P addition via AlCuP alloy and hot extursion process, Al-20Si-5Fe alloy showing fine distributions of intermetallic compound and primary Si in ternary eutectic structure can be manufactured. The alloy bar extruded with reduction ratio of 15:1 shows distribution of primary Si with Size under 20μm and intermetallic compound with size under 10μm in fine ternary eutectic structure.

Fig. 4(a) shows typical DTA trace obtained during cooling unrefined Al-20Si-5Fe alloy bar. Three exothermic peaks appeared during cooling, indicating the presence of three different solidification procedures. Two small exotherms with onset temperature of 971K and 928K correspond to crystallization of two types of primary phases and a sharp exotherm with onset temperature of 843K corresponds to ternary eutectic solidification.

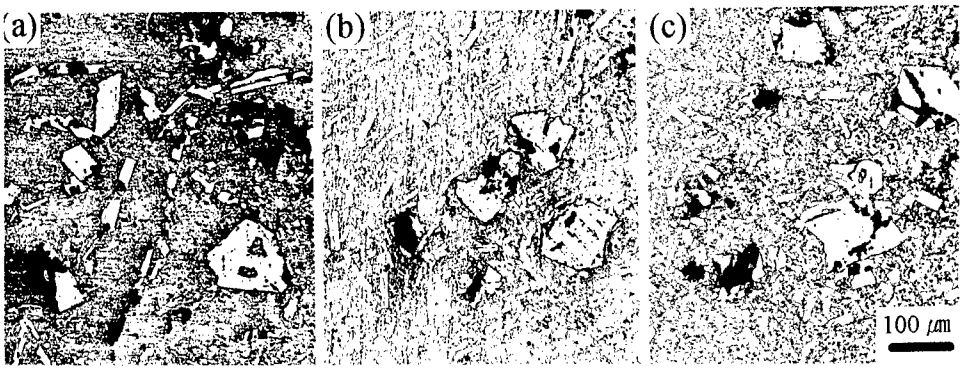


Figure 2. Optical micrographs of unrefined Al-20Si-5Fe alloy bars, extruded with three different reduction ratios: (a) 6.25:1 (b) 13:1 (c) 25:1

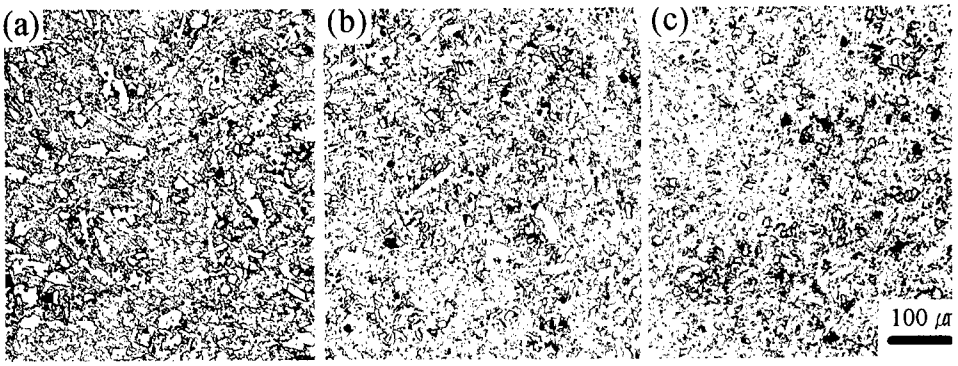


Figure 3. Optical micrographs of refined Al-20Si-5Fe alloy bars, extruded with three different reduction ratios: (a) 6.25:1 (b) 13:1 (c) 25:1

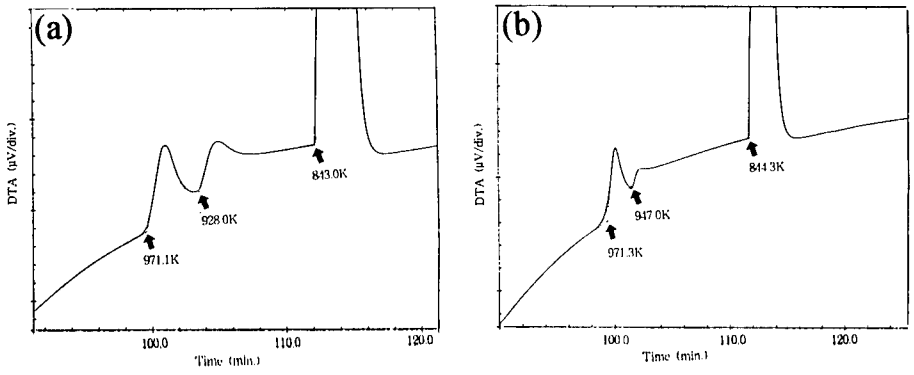


Fig. 4. Typical DTA traces obtained during cooling Al-20Si-5Fe alloys (a) unrefined and (b) refined with 300ppm P via AlCuP alloy, with cooling rate of 20K/min.

The quenching experiment was performed to study the solidification procedures in unrefined and refined Al-20Si-5Fe alloys. The quenching temperatures were chosen to be temperatures between each exotherms and below the last exotherm to find which phase formed in each solidification steps. Figs. 5(a)-(c) show typical micrographs of unrefined Al-20Si-5Fe alloy, quenched into water during cooling at 958, 893 and 833K, respectively. It is known from the figures that Al-20Si-5Fe alloy solidifies with following sequence: In the beginning of solidification, primary intermetallic compound is crystallized and then primary Si forms. Finally, remaining liquid solidifies into irregular ternary eutectic of α-Al, Si and intermetallic compound.

Fig. 4(b) shows typical DTA trace of the Al-20Si-5Fe alloy refined with P. There is no change in the onset temperature of the first exotherm, indicating that the first exotherm corresponds to the crystallization of intermetallic compound. However, the onset temperature of the second peak, corresponding to primary Si crystallization, is different from that in Fig. 4(a). The crystallization of primary Si started at 947K in refined alloy, which is 19K higher than that of unrefined alloy.

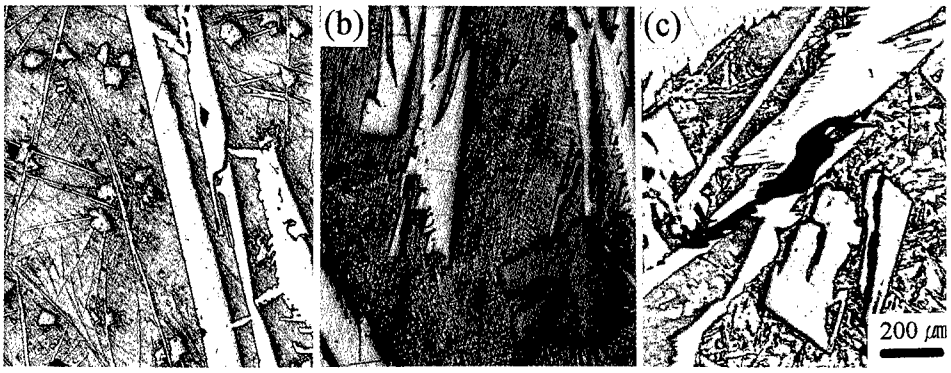


Fig. 5. Typical optical micrographs of Al-20Si-5Fe alloy, quenched into water during cooling with cooling rate of about 20K/min. at (a) 958K (b) 893K (c) 833K.

Discussion

By addition of AlCuP into Al-20Si-5Fe alloy, refinement of both primary Si and intermetallic compound were achieved as shown in Fig.1. The result of DTA experiments shown in Fig.4 indicates that the crystallization temperature of intermetallic compound was independent of P addition, but the onset temperature of primary Si crystallization rose by 19K by adding P via AlCuP alloy, showing that addition of AlCuP alloy in the Al-20Si-5Fe melt promotes heterogeneous nucleation of primary Si phase. This result is in agreement with the result obtained in binary Al-Si alloy[9]. It is generally recognized that heterogeneous nucleation of primary Si on Aluminum Phosphide (AlP) is very effective[8-10] because AlP (zinc blende structure, 5.45-5.47Å) has a similar crystal structure and a lattice parameter with Si (diamond cubic structure, 5.42Å). Refinement of primary Si can be achieved effectively with lower P content and at lower holding temperature by adding AlCuP alloy than by direct addition of P into melt. Because in the AlCuP alloy P exists in the form of AlP[9] and reaction time to form AlP is not required. However, the intermetallic compound in Al-20Si-5Fe alloy is δ-Al_4FeSi_2 phase with tetragonal structure and lattice parameter of a=6.12-6.16Å and c=9.48-9.49Å [12-14], which are

quite different from that of AlP. Therefore, AlP is not expected to act as an effective nucleation site for δ-Al_4FeSi_2 phase. Promotion of heterogeneous nucleation of primary Si phase can affect the growth kinetics of δ-phase(Al_4FeSi_2). Once Si nucleates and starts to grow, compositional distribution in liquid melt changes and the growth kinetics of δ-phase may be reduced. During solidification of unrefined Al-20Si-5Fe alloy, δ-phase nucleates at 971K and then continue to grow until primary Si phase nucleates at 927K. However the temperature range for δ-phase growth during refined alloy solidification becomes narrower due to the higher primary Si nucleation temperature. After Si nucleation, competition between δ-phase growth and primary Si phase growth may take place until ternary eutectic solidification starts to occur. By the addition of AlCuP alloy into Al-20Si-5Fe melt, refinements of primary Si and δ-phase were achieved by promoted heterogeneous nucleation and reduced growth kinetics respectively.

Conclusion

1. Refinement of both primary Si and δ-phase were achieved by the addition of AlCuP alloy into Al-20Si-5Fe melt and further refinement of the δ-phase was achieved by hot extrusion of the alloy casts.
2. Al-20Si-5Fe alloy solidified with following sequence : In the beginning of solidification, primary δ-phase is crystallized and then primary Si is formed. Finally, remaining liquid solidifies into an irregular ternary eutectic of α-Al, Si, and δ-phase.
3. Nucleation temperature of primary δ-phase was independent of the addition of P, but the heterogeneous nucleation of primary Si is promoted by the addition of P.
4. By the addition of AlCuP alloy into Al-20Si-5Fe melt, refinements of primary Si and δ-phase were achieved by increased heterogeneous nucleation and reduced growth kinetics respectively.

Reference

1. P. B. Crosely and L. F. Mondolfo, AFS Trans. 74(1966), 53
2. I. Yamauchi, I. Ohnaka, S. Kawamoto, T. Fukusako, Rapidly Quenched Metals, vol. 1, edited by S. Steeb and H. Warimont (North Holland, 1978) p. 1729
3. Y. Ohata, K. Fukui, I. Iwai and I. Murase, Bull. Japan Inst. Metals 24(1985), 307
4. J. L. Estrada and J. Duszczyk, J. Mater. Sci. 25(1990) 886
5. T. Hirano and T. Fujita, J. Japan Inst. Light Metals 37(1987), 670
6. T. Hayashi, Y. Takeda, and T. Fujiwara, SAE Technical Paper Series 900407(1990)
7. E. Koya, Y. Hagiwara, S.Miura, T. Hayashi, T. Fujiwara and M. Onoda, SAE Technical Paper Series 940847(1994)
8. L. F. Mondolfo, Aluminium Alloys, Structure and Properties (Butterworth, London, 1976), p. 672
9. J. S. Lee, Ph. D Thesis, Seoul National University (1998)
10. S. J. Paik, Ms. Thesis, Seoul National University (1994)
11. J. Zhou, J. Duszczyk and B. M. Korevaar, J. Mater. Sci. 25(1991) 824
12. Y. S. Choi and H. Y. Ra, J. Korean Inst. Met. & Mater. 34(1996) 230
13. Y. S. Choi, J. S. Lee, W. T. Kim and H. Y. Ra, J. Mater. Sci submitted
14. L. F. Mondolfo, Aluminium Alloys, Structure and Properties (Butterworth, London, 1976), p. 534

EFFECTS OF Mn-DISPERSOID ON THE CRACK INITIATION DURING FATIGUE IN AN Al-Zn-Mg-Mn ALLOY

Y. S. Woo and S. W. Nam*

Department of Materials Science and Engineering,
Korea Advanced Institute of Science and Technology
373-1 Kusong-dong Yusong-gu, Teajon, 305-701, Korea
* Jointly Appointed at the Center for Advanced Aerospace Materials

Abstract

Using the tensile stage installed in the scanning electron microscope (JSM 840A), surface slip trace was observed in-situ during fatigue. From the result of in-situ fatigue test, it is seen that Mn containing alloy (Al-4.6Zn-2.0Mg-0.75Mn-0.15Zr) exhibits a homogeneously distributed deformation, whereas commercial Al alloy having no Mn (Al-4.0Zn-2.6Mg-0.15Zr) displays localized coarse slip steps. Also differently from commercial Al alloy, surface extrusions which provide the crack initiation site are not observed in the Mn containing alloy. The TEM analysis of the dislocation that interacts with Mn-dispersoid shows that Mn-dispersoid induces the dislocation to cross-slip and results in the homogeneous deformation in Mn containing alloy. From these observations, it is concluded that homogeneously dispersed deformation due to the dislocation cross-slip at Mn-dispersoid retards the crack initiation and increases the fatigue life in Mn containing alloy.

The Third Pacific Rim International Conference on
Advanced Materials and Processing (PRICM 3)
Edited by M.A. Imam, R. DeNale, S. Hanada,
Z. Zhong and D.N. Lee
The Minerals, Metals & Materials Society, 1998

Introduction

It is well known that small amounts of Mn added to aluminum alloys play an interesting role in fracture toughness, recrystallization, and grain refinement. According to Nam et al[1-3], it is reported that the Mn-bearing Al-Zn-Mg alloy has a superior properties in fracture toughness, corrosion resistance, and low cycle fatigue, compared with commercial Al-Zn-Mg alloy. In particular, ductility does not decrease, though strength increase substantially. These improved mechanical properties in the Mn-bearing Al-Zn-Mg alloy are thought to be the result of homogeneous deformation due to the interaction between dislocation and Mn-dispersoid.

In low cycle fatigue, crack initiation is the important factor in determining the LCF properties. Generally, crack initiation occurs on the places where the deformation is concentrated, such as persistent slip bands and grain boundaries. Therefore, to increase the low cycle fatigue life, it is needed to hinder the deformation concentration which causes crack initiation.

From this point of view, the main purpose of the present study is to understand the role of Mn-dispersoid in crack initiation in low cycle fatigue and the mechanism of LCF life increase in Al-Zn-Mg-Mn alloys.

Experimental Procedure

For these experiments, two different alloys were used. The chemical composition of the experimental alloys are given in table 1.

For the in-situ observation of the deforming surface morphology continuously, in-situ low cycle fatigue test was performed in a JEOL SM TS40 tensile stage with a tensile-compression auto-toggling system attached to SEM (JEOL JSM 840A). Test specimens were made with a gauge length 5.5mm and a diameter of 2.5mm. In-situ low cycle fatigue test was conducted with a strain rate of 1mm min^{-1} and a total strain range of $\pm 2\%$.

Specimens for TEM investigations were sampled from conventional low cycle fatigue test. These tests were undertaken using subsize specimens with a 7mm gauge length and 8mm in diameter in a Instron 1380 testing machine interfaced to a personal computer for data acquisition. Fatigue test specimens were solution treated at 460℃ for 1.5h, water quenched, and tested.

In order to analyze the dislocation character before and after interaction with the Mn-dispersoids during fatigue test, trace analysis[4] was applied. After trace analysis, using the Burgers vector[5] and dislocation line direction[4,6], it was possible to obtain each slip plane for a particular dislocation. From such analysis, it was possible to see whether the dislocation can cross-slip or not at the Mn-dispersoid.

Table I Chemical Compositions of The Tested Aluminum Alloys (wt.%)

Alloy	Al	Mg	Mn	Zr	Zn
MN00	Balance	2.6	—	0.15	4.0
MN75	Balance	2.0	0.75	0.15	4.6

Results and Discussion

In-situ SEM observation

The experimental results of in-situ fatigue test of MN00 alloy show the typical coarse slip bands formed along 45° angle to the stress axis (see Fig. 1). As fatigue deformation proceeds,

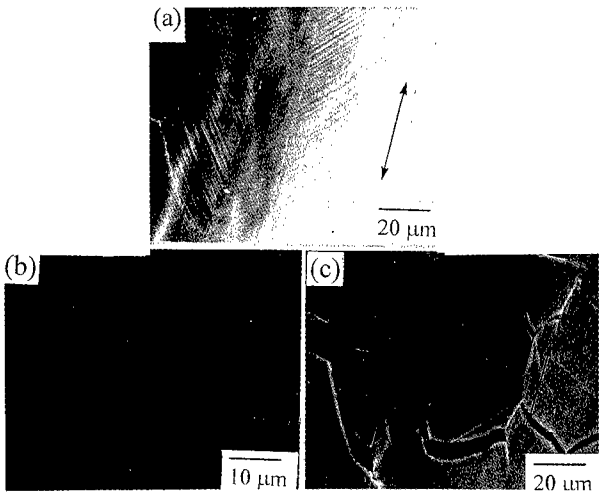


Fig 1. SEM micrographs from in-situ fatigue tests of MN00 alloy at $\Delta \varepsilon_t = \pm$ 2%. (Arrows indicate fatigue stress axis.) (a) after 120 cycles (b) after 790 cycles (c) after 1100 cycles

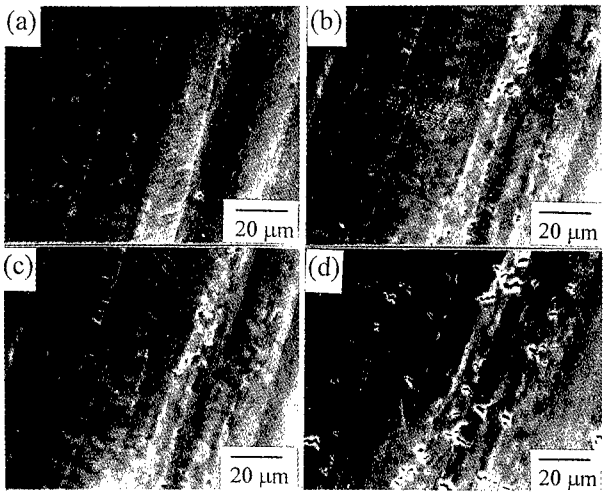


Fig 2. SEM micrographs from in-situ fatigue tests of MN75 alloy at $\Delta \varepsilon_t = \pm$ 2%. (Arrows indicate fatigue stress axis.) (a) after 170 cycles (b) after 250 cycles (c) after 800 cycles (d) after 1200 cycles

the slip band traces may build up local stresses that can cause fatigue crack initiation at grain boundary (Fig. 1 (b)). These cracks are enlarged and coalesced together during further fatigue (Fig. 1 (c)). The localized slip bands in this alloy seem to be caused by localized planar dislocation movements and this is verified by TEM observations later.

The corresponding results of in-situ fatigue test of MN75 alloy was shown in Fig. 2. The MN75 alloy does not show a well-developed slip band traces and crack initiation at grain boundary. Alternatively, small cracks are seen all over the specimen surface throughout the fatigue life. This indicates that they were neither caused nor affected by the concentrated slip bands close to the grain boundaries. From these SEM observations, it can be said that the homogeneous deformation of MN75 alloy retards the crack initiation and extends the low cycle fatigue life.

TEM observations

To understand the role of Mn-dispersoid in retarding the crack initiation, it is needed to observe the interaction between Mn-dispersoid and dislocation by TEM.

To analyze the dislocation character in deformed alloys, such as Burger vector and line directions, trace analysis[4] was applied. Also, to avoid the difficulty in analysis due to the dislocation complication of multiplication and tangling, observations were made after only one cycle. Mn-dispersoids shown in MN75 alloy are about 0.05-0.5 μm in size and known to be Al_6Mn with the orthorhombic crystal structure[7].

Fig. 3 shows a TEM micrograph of MN00 alloy after one cycle. The dislocation character was determined by trace analysis. The result are listed in Table. 2. As can be seen in Table. 2, all dislocations which have same Burgers vector are lying on the same slip plane. From this fact, it can be said that these dislocations in MN00 alloy are slipping in planar mode. These results give a support in explaining the in-situ SEM observation in the following way. As the deformation proceeds, the localized planar slip prevails and grain boundary cracks are initiated by dislocations concentrated at the grain boundary.

In Fig. 4, a TEM micrograph and schematic diagram of the characteristic feature of dislocations and the interaction between dislocations and Mn-dispersoid of MN75 alloy after one cycle. Burgers vector and line directions of analyzed dislocations are listed in Table. 3. According to

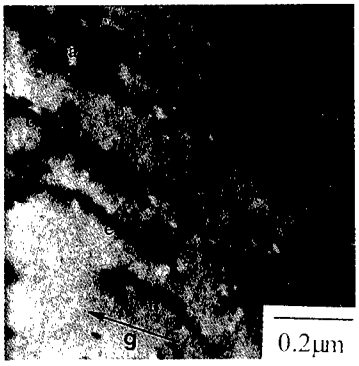


Fig 3. TEM micrographs showing the dislocations structure of MN00 alloy after 1 cycle at $\Delta\varepsilon_t = \pm$ 1.5%. Dislocations are labeled from a to f. The corresponding dislocation parameters are shown in Talble 2 (B=[0 1 1], g=[1 1 $\bar{1}$]).

Table II. Dislocations characters. Burgers vector $\vec{b}$ and dislocation line direction $\vec{\xi}$ and slip planes shown in Fig. 3 (MN00 alloy after one cycle).

Dislocations	Parameters			
	$\vec{b}$	$\vec{\xi}$	slip plane	slip system
A	1/2[1 0 $\bar{1}$]	[21 4 $\bar{24}$]	(1 1 1)	primary
B	1/2[1 0 $\bar{1}$]	[3 $\bar{1}$ $\bar{2}$]	(1 1 1)	primary
C	1/2[1 0 $\bar{1}$]	[21 4 $\bar{24}$]	(1 1 1)	primary
D	1/2[1 0 $\bar{1}$]	[15 2 $\bar{19}$]	(1 1 1)	primary
E	1/2[1 0 $\bar{1}$]	[22 $\bar{1}$ 23]	(1 1 1)	primary
f	1/2[1 0 $\bar{1}$]	[12 $\bar{2}$ $\bar{9}$]	(1 1 1)	primary

the trace analysis, dislocations are founded to be moving on the (1 1 1) slip plane having larger value of Schmid factor (0.308) until they are blocked by Mn-dispersoid. Because of non-shearable Mn-dispersoid, the dislocations tend to cross-slip to the intersecting (1 $\bar{1}$ 1) plane having smaller value of Schmid factor(0.207). As shown in Fig. 5 and schematic diagram, dislocations labeled a and b are lying on the primary slip plane (1 1 1). In addition, dislocations labeled c and d are thought to be cross-slipped to secondary slip plane (1 $\bar{1}$ 1)

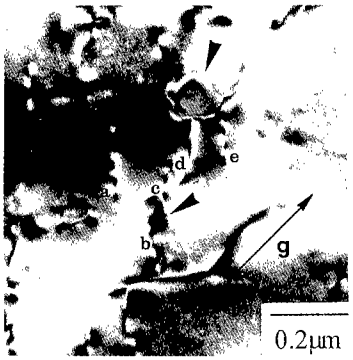


Fig 4. TEM micrographs showing the dislocation structure of the MN75 alloy after 1 cycle at $\Delta\varepsilon$ = 0 ~ 1.5% (upper). Two types of identified dislocations are labeled a, b, e and c, d respectively. The schematic 3D drawings show dislocations lying on the different slip planes, respectively (below). The corresponding dislocation parameters are shown in Table 3 (B=[0 3 1], g=[2 0 0]).

Table Ⅲ. Dislocations characters. Burgers vector $\vec{b}$ and dislocation line direction $\vec{\xi}$ and slip planes shown in Fig. 4 (MN75 alloy after one cycle).

Dislocations	Parameters				
	$\vec{b}$	$\vec{\xi}$	slip plane	slip system	Schmid factor
a	1/2[1 0 $\bar{1}$]	[41 6 $\overline{47}$]	(1 1 1)	primary	0.308
b	1/2[1 0 $\bar{1}$]	[23 8 $\overline{27}$]	(1 1 1)	primary	0.308
c	1/2[1 0 $\bar{1}$]	[11 15 2]	(1 $\bar{1}$ 1)	secondary	0.207
d	1/2[1 0 $\bar{1}$]	[29 12 21]	(1 $\bar{1}$ 1)	secondary	0.207
e	1/2[1 0 $\bar{1}$]	[59 9 $\overline{67}$]	(1 1 1)	primary	0.308

due to the interaction with Mn-dispersoid. But these once cross-slipped dislocations came back to primary slip plane by cross-slip. Such phenomenon of blocking and cross-slip of dislocations corresponds with the SEM in-situ test result in that slip steps are very fine and evenly distributed. This suggests that dispersed slip and homogeneous deformation through cross-slip is caused by non-shearable Mn-dispersoid in MN75 alloy.

Considering the foregoing discussion, one may easily understand the role of Mn-dispersoid in retarding the crack initiation at grain boundary in the Al-Zn-Mg-Mn alloy. In other words, dislocations are blocked and cross-slipped due to the interaction with Mn-dispersoid. And the deformation is homogenized and not concentrated at grain boundary in Mn-bearing alloy. Therefore, the low cycle fatigue life of Al-Zn-Mg-Mn alloy can be extended due to delayed crack initiation.

Conclusions

From the present investigations, it can be concluded that the Mn-dispersoid in Al-Zn-Mg-Mn alloy acts as a barrier to the dislocation motions and promote cross-slip. Hence the fatigue deformation is homogenized and not concentrated at grain boundary. Consequently, fatigue cracks initiation is retarded, thus extending the fatigue life in Al-Zn-Mg-Mn alloy.

References

1. B. O. Kong, D. S. Park, and S. W. Nam, "Effect of Mn-Dispersoid on the Low Cycle fatigue in Al-Zn-Mg Alloy", Metall. Trans. A, 25(1994), 1547-1550.

2. B. L. Jo, D. S. Park and S. W. Nam, "Effect of Mn-Dispersoid on the Fatigue Crack Propagation of Al-Zn-Mg Alloys", Metall. Mater. Trans. A, 27 (A) (1996), 490-493

3. H. S. Cho and S. W. Nam, "The Low Cycle Fatigue Properties of Weldable Al-Zn-Mg-Mn Alloy and Al 7039 in Various Environments", J. Kor. Inst. Met. Mater.,32 (7) (1994), 765-770.

4. F. Rong Chen and A. H. King, "Determination of the Crystallographic Directions and Planes of Features and of the Misorientations of Crystals With High Accuracy and Internal Estimate of Errors", J. Elec. Micro. Tech, 6 (1987), 55-61.

5. J. W. Edington, Practical Electron Microscopy in Materials Science, monograph. 3 (Macmilian: Philips Technical Library, 1975), 10-20.

6. J. W. Edington, Practical Electron Microscopy in Materials Science, monograph. 2 (Macmilian: Philips Technical Library, 1975), 57-58.

7. B. O. Kong and S. W. Nam, "Investigation of Growth Mechanism and Orientation Relationship of Mn-dispersoid in an Al-Zn-Mg-Mn alloy", Mater. Lett, 28(1996), 385-391.

MICROSTRUCTURE AND MECHANICAL PROPERTIES OF Ti-48Al-2Nb-2Cr ALLOY AFTER THERMOMECHANICAL PROCESSING

G.A. Salishchev[1], R.M. Imayev[1], V.M. Imayev[1], M.R. Shagiev[1], A.V.Kuznetsov[1], O.N. Senkov[2], F.H. Froes[2]

[1] Institute for Metals Superplasticity Problems, 39 Khalturina, Ufa, 450001, Russia
[2] Institute for Materials and Advanced Processes, University of Idaho Moscow, ID 83844-3026, USA

Abstract

Specimens of a Ti-48Al-2Nb-2Cr alloy with equiaxed near-gamma and lamellar structures, with different grain, colony and lamellar sizes, were produced by thermomechanical processing and annealing. Compression mechanical properties were studied at room temperature and strain rate of 8.3×10^{-4} s^{-1}. Total compressive strain increased when the grain size was increased in specimens with the equiaxed grain structure, while it decreased when the colony size was increased in specimens with a lamellar structure. The yield stress versus grain/colony size was described by the Hall-Petch (HP) relation. The HP parameter k_y had a value of 0.5 MPa·$m^{1/2}$ for the specimens with the equiaxed structure and much higher values, 2.5 to 7.7 MPa·$m^{1/2}$, for the specimens with the lamellar structure, increasing when the lamellar spacing was decreased. It was suggested that the effective slip length, not colony size, should be used in the HP equation. The effective slip length was estimated to be much lower than the colony size and higher than the lamellar spacing. It was suggested that the α_2/γ interfaces should be considered as effective barriers to the deformation slip, instead of the γ/γ interfaces.

Introduction

Gamma titanium aluminides possess excellent specific strength and creep resistance at temperatures up to 800°C, however they are brittle at room temperature. To obtain a balance of both room and high-temperature properties, an understanding of strengthening and ductility features of these alloys is necessary. Investigations of the two-phase alloys based on the γ-phase (TiAl) and the α_2-phase (Ti_3Al) have shown that the yield strength of these materials with equiaxed and lamellar microstructures follows the HP relationship [1]. However the values of the HP constant k_y differ considerably for these microstructural forms [1-5]. In the intermetallics with equiaxed microstructures this parameter varies in the range from 0.4 to 1.4 MPa$\sqrt{m}$ [2-5]. For the materials with a lamellar microstructure, much higher values of k_y were obtained (~5 MPa$\sqrt{m}$) [1,6,7]; in this case the colony size was used in the HP relationship. The reason for this difference is not yet clear. Unfortunately, these studies were carried out on specimens from different producers, with different chemical compositions, which made them difficult to compare. In the present work mechanical properties of specimens with equiaxed and lamellar structures prepared from one Ti-48Al-2Nb-2Cr alloy casting were studied and the results were compared with literature data. Possible reasons of high values of the HP constant in the material with the lamellar structure are discussed

The Third Pacific Rim International Conference on Advanced Materials and Processing (PRICM 3)
Edited by M.A. Imam, R. DeNale, S. Hanada, Z. Zhong and D.N. Lee
The Minerals, Metals & Materials Society, 1998

Experimental Procedure

The cast and hot isostatically pressed (HIP'd) alloy Ti-48Al-2Nb-2Cr (at. %, hereafter Ti-48-2-2) used as a starting material was produced in OREMET Titanium, Albany, OR. Specimens with an equiaxed near gamma microstructure and average grain size varying from 0.4 μm to 12 μm were prepared with the use of a thermomechanical processing, which included primary annealing at 1200°C for 4 hours and subsequent multistep forging at 1030°C to 750°C, with annealing at 1050°C to 700°C between the steps. To produce the average grain size of d=0.4 μm, for example, the cast and HIP'd alloy was consequently annealed at 1200°C for 4 hours, 12-step forged at 1030°C (ε=55-60%, $\dot{\varepsilon}\sim10^{-3}$ s^{-1}), annealed at 900°C for 8 hours, 2-step forged at 850°C, annealed at 770°C for 2hours, 2-step forged at 800°C, annealed at 750°C for 2 hours, 2-step forged at 750°C, and annealed at 700°C for 2 hours. Fully lamellar microstructures with various colony sizes, d_c, were produced by annealing the alloy at 1400°C for different annealing time, followed by air cooling (AC) or furnace cooling (FC).

Room temperature compression tests of specimens of 8×8×12 mm^3 in size were performed in air and at an initial strain rate of 8.3×10^{-4} s^{-1}. Optical microscopes Neophot-32 and Epiquant were used for metallographic studies. An average grain (or colony) size was measured using a linear intercept method. The measuring error was estimated with a confidence coefficient of 0.5. A lamellar spacing, λ, was estimated with the use of a transmission electron microscope JEM-2000EX working at an accelerating voltage of 200 kV.

Results

Microstructure Preparation

A typical non-homogeneous microstructure of the as-cast and HIP'd alloy is shown in Figure 1a consisting of equiaxed gamma-grains of 30 to 70 mm in size and lamellar colonies of 100 to 400 mm in size. Around 10 vol.% of the α_2 phase was present in the colonies. After the thermomechanical processing (which was performed at temperatures below the eutectoid temperature) a very fine near gamma equiaxed structure was formed with an average grain size

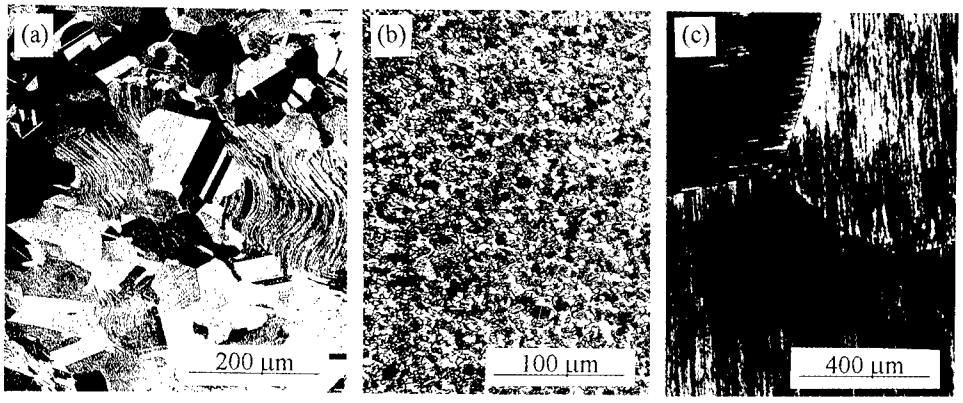


Figure 1 – Microstructure of the Ti-48Al-2Nb-2Cr alloy: (a) as-cast and HIP'd, (b) as-cast, HIP'd, and thermomechanically processed, (c) as-cast, HIP'd, annealed at 1400°C for 45 min. and air-cooled.

varying from 0.4 μm to 12 μm, depending on regimes of the processing. An example of this kind of the microstructure, with an average grain size of 7 μm is shown in Figure 1b. When the as-cast and HIP'd alloy was annealed at 1400°C and cooled, a fully lamellar microstructure was produced, Figure 1c. The colony size and lamellar spacing increased with the annealing time and the lamellar spacing also increased when the cooling rate was decreased, Table I.

Table I – Dependence of the Colony Size, d_c, Lamellar Spacing, λ, Effective Slip Length, l_{eff}, and yield stress, $\sigma_{0.2}$, on the Annealing Time, t, and Cooling Conditions.

	Lamellar microstructure (air cooling)					Lamellar microstructure (furnace cooling)		
t, min	5	15	45	75	120	5	45	60
D_c, μm	330	375	780	1500	2000	450	825	1400
l_{eff}, μm	0.71	1.16	1.58	5.71	11.56	10.88	23.89	32.25
λ, μm	-	-	0.1	-	0.25	0.6	-	0.9
$\sigma_{0.2}$, MPa	840	745	690	550	500	420	380	370

Compression Tests

Stress-strain compression curves for the specimens with equiaxed and lamellar structures are shown in Figure 2. The flow stress increased when strain increased and the grain/colony size were decreased. The compression ductility (the total compression strain before fracture) depended on the grain/colony size, Figure 3. In specimens with the equiaxed grain structure, the ductility increased when the grain size was increased, Figure 3a, while in specimens with the lamellar structure the ductility tended to decrease when the colony size was increased, Figure 3b.

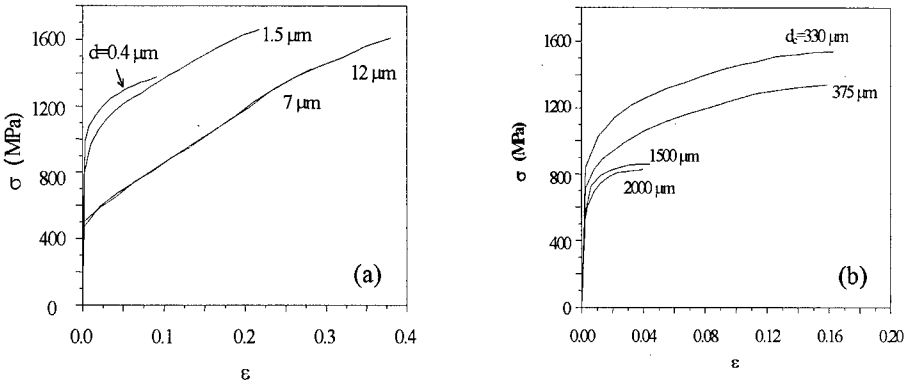


Figure 2 – Stress-strain compression curves of specimens with (a) equiaxed grain and (b) lamellar (AC) structures at different grain/colony sizes.

The yield stress, $\sigma_{0.2}$, increased when the grain/colony size was increased, Figure 4, following THE HP relation:

$$\sigma_{0.2} = \sigma_o + k_y D^{-1/2} \qquad (1)$$

In (1), σ_o is the yield stress of the material with infinitely large grains, k_y is the HP constant, and D is the grain size, d, in the case of an equiaxed grain structure, and the colony size, d_c, in the case of a lamellar structure. The values of σ_o and k_y for the material with different structural conditions are shown in Figure 4. It can be seen that the specimens with a lamellar structure had much higher values of k_y than the specimens with an equiaxed structure. The HP constant was higher for the AC specimens than for the FC specimens.

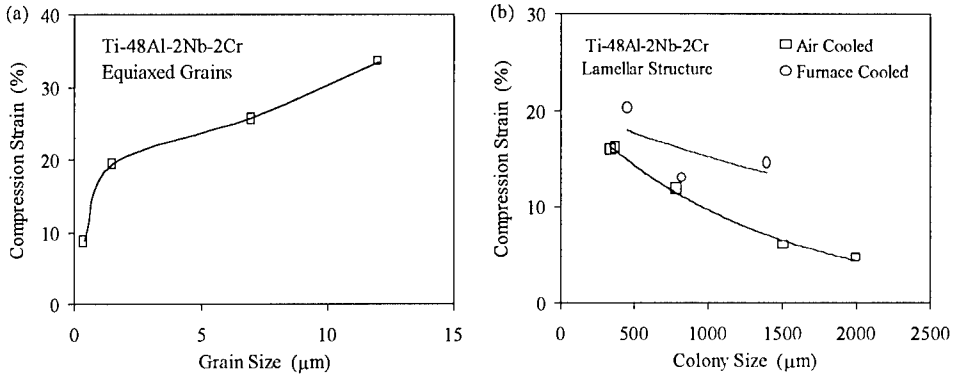


Figure 3 – Dependence of the compression strain to fracture on grain/colony size in specimens with (a) equiaxed grains and (b) lamellar structures.

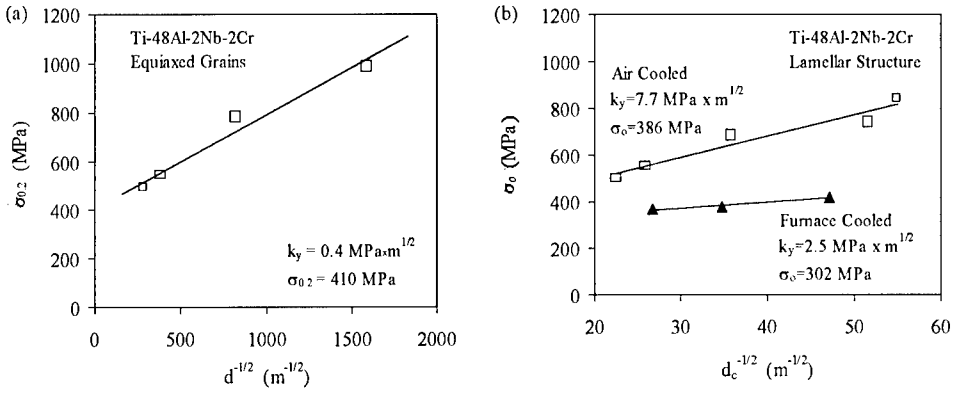


Figure 4 – Dependence of the yield stress on reciprocal square root of the grain/colony size in specimens with (a) equiaxed grains and (b) lamellar structures.

Discussion

Microstructure Preparation

The non-homogeneous microstructure of the as-cast and HIP'd alloy was probably caused by an alloy segregation during casting, which led to regions with larger and smaller concentrations of aluminum, as compared to the average value of 48%, and correspondingly smaller and larger volume fractions of the α_2 phase. Annealing at 1200°C for 4 hours and subsequent multi-step forging homogenized the alloy and led to a decomposition of the metastable α_2 phase and formation of a very fine near-gamma grain structure. It was found in earlier work [2] that the

homogeneous fine-grain structure resulted from the dynamic recrystallization and superplastic flow of the material during the multi-step forging; both of these processes involve extensive diffusion.

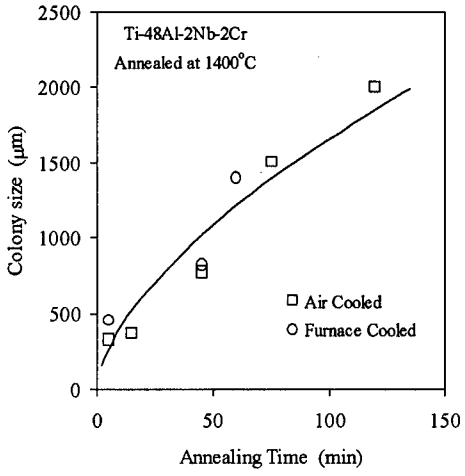


Figure 5 – Dependence of the colony size on annealing time

The fully lamellar structure was produced by annealing at 1400°C and subsequent air- or furnace- cooling. The temperature of 1400°C corresponds to the single-phase α field, where the alloy homogenization occurs relatively fast [3], leading to a homogeneous distribution of the α_2 phase after cooling. Growth of the α grains occurred during the annealing, which can be described with the following equation:

$$d_c = A \cdot t^{0.6} \qquad (2)$$

where t is the annealing time and $A = 9 \cdot 10^{-6}$ m/s$^{0.6}$ is the kinetic parameter. Figure 5, where the experimental data are plotted together with a solid curve described by the equation (2), shows a good fit the equation to the data. The time exponent n=0.6 is close to a theoretically predicted value of n=0.5 for the normal grain growth, when the driving force is the decrease in interfacial free energy [8].

It can be seen from the Table 1 that the lamellar spacing, λ, increases with the annealing time, and its values are lower in the AC specimens than in the FC specimens. The increase of the lamellar spacing when the cooling rate is decreased is a general tendency, and this is due to an increasing time of being the material in the α+γ field during cooling [1,9]. The observed increase of the lamellar spacing with the annealing time could be explained by improving the concentration homogeneity during annealing, which, consequently, leads to a decrease of the number of nucleation sites for the γ lamellae, since these may be the areas with local concentration inhomogeneity.

Compression Tests

Specimens with equiaxed and lamellar structures showed different dependence of ductility (the compression strain to failure in the present case) on the grain/colony size. In specimens with an equiaxed structure, the ductility increased when the grain size was increased. This behavior was observed previously in a Ti-50.7Al alloy and was explained by an increase in the twinning contribution in the deformation [2,10]. When the grain size was very small, only dislocation slip was developed. When the grain size increased, twinning as an additional deformation mode was introduced, leading to a ductility increase when only one twin system was developed. However if the grain size was sufficiently large for multi-system twinning, the ductility decreased [2]. One can suggest that the same mechanism, i.e. development of a single-system twinning, was responsible for the increase of ductility in the specimens with a fine equiaxed structure in the present work.

The decrease in ductility when the colony size is increased in specimens with the lamellar structure, could be explained by an increased constrains at the colony boundaries. When the lamelae are perpendicular to the loading axis, they are extremely brittle and the crack

propagation work in this case is small [11]. The larger the colony size, the greater deformation must accommodate the neighboring colonies, leading to earlier fracture.

The yield stress of the material increased when the grain/colony size decreased, following to the HP relation with the HP parameter k_y much depended on microstructure. The HP constant k_y obtained for the material with equiaxed near gamma structure had a value of 0.4 MPa$\sqrt{m}$. Close values of k_y were determined recently for the near stoichiometric Ti-50.7Al alloy with an equiaxed grain structure (k_y=0.5 MPa$\sqrt{m}$) [2]. The grain size range (0.4-10μm) in [2] was very close to that in the present study (0.4-12 μm). However, higher values of the HP constant k_y (0.9 to 1.2 MPa$\sqrt{m}$) were obtained when grains were larger in size [3-5], Figure 6. To define possible reasons for these differences in k_y let consider an equation derived earlier for the yield stress of a material with an equiaxial grain structure [12]:

$$\sigma_y = M\{\tau_o + [(2-\nu)\pi\tau^*\mu b/(2(1-\nu)d)]^{1/2}\} \qquad (3)$$

where M is a Taylor factor, τ_o is the shear stress to move a dislocation through a single crystal material, ν is the Poisson's ratio, μ is the shear modulus, b is the Burgers vector and τ^* is the barrier strength of grain boundaries. It can be seen from Equation (3) that

$$k_y = M[(2-\nu)\pi\tau^*\mu b/(2(1-\nu))]^{1/2} \qquad (4)$$

Taking M=3.1, b=0.282 nm, μ=70 GPa, and ν=0.23 [13], the grain-boundary barrier strength τ^* was estimated from (4) to fit experimentally determined values of k_y by supposing that only the grain boundaries were the effective barriers for the dislocations at yielding. In the case of a fine-grained structure (k_y = 0.4 to 0.5 MPa$\sqrt{m}$, Figure 6) τ^* was determined to be 0.004μ to 0.006μ, while in the case of a coarse-grained structure ($k_y \cong$ 1.0 MPa$\sqrt{m}$), $\tau^* \cong$ 0.021μ. It is apparent from these estimations that the different barrier strength for grain boundaries in fine-grained and coarse-grained materials could be a reason in different values of k_y for these materials. The relatively small values of τ^* for the fine-grain structure could indicate also that additional soft modes of deformation such as grain-boundary sliding were facilitated when the grain size decreased. Another reason of a high value of k_y for the coarse-grained materials could be a presence of sub-grain boundaries inside large grains as additional barriers to dislocation glide. In this case, the sub-grain size should be used in the HP equation, leading to a decrease in k_y. More experiments are required to determine a real mechanism of yielding.

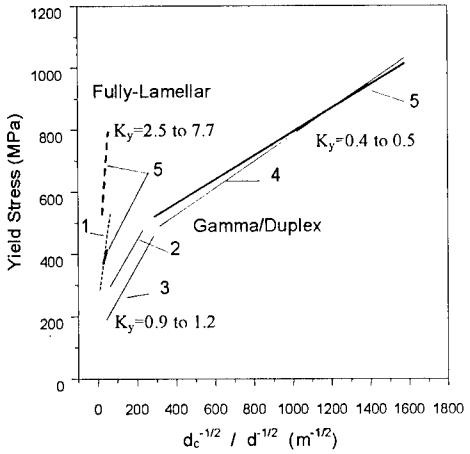


Figure 6 – Hall-Petch relations for the TiAl-based alloys: Comparison of present results with results of others.

1 – Y.-W. Kim [1], k_y = 5 MPa$\sqrt{m}$ (lamellar), 2 – S.-C. Huang and D.S. Shin [4], k_y = 1.2 MPa$\sqrt{m}$ (equiaxed), 3 – C. Koeppe et al. [3], k_y = 0.91 MPa$\sqrt{m}$ (equiaxed), 4 – R. Imaev et al. [2], k_y = 0.5 MPa$\sqrt{m}$ (equiaxed), and 5 – present study, k_y = 0.4 MPa$\sqrt{m}$ (equiaxed), 2.5 MPa$\sqrt{m}$ (lamellar, FC) and 7.7 MPa$\sqrt{m}$ (lamellar, AC).

The situation becomes a more complicated for understanding in the case of the material with a fully lamellar structure. The HP parameter k_y was determined for these structures to be much higher than for equiaxed grain structures, i.e. 2.5 MPa$\sqrt{m}$ for the FC and 7.7 MPa$\sqrt{m}$ for the AC materials, Figure 6. Similar values of k_y were reported in other investigations [1,6,7,14]. Recently this value was corrected to k_y = 2.5 MPa$\sqrt{m}$ for $\lambda \cong 1$ μm and assumed to increase with λ decreasing [10]. The latter is confirmed by the present study: an increase in the cooling rate (from FC to AC) resulted in a considerable decrease in the lamellar spacing λ, see Table I, and, consequently, to an increase of the k_y parameter. It should be noted that in all these experiments the colony size d_c was used as the Hall-Petch variable, and this might be a reason of the high values of k_y. Indead, at least four barriers to dislocation glide are present in the lamellar structure, i.e. two kinds of lamellar boundaries (γ/γ and α_2/γ interfaces), domain boundaries, and colony boundaries, and all of these could affect the yield stress. For example, in the PST crystals, where no colony boundaries were present, k_y was determined from a dependence of the θ-dependent flow stress (θ is the angle between the lamellar planes and the loading axis) on the lamellar spacing λ (hard orientations) or domain size d_d (soft orientation) [11,15]. For the soft orientation (θ=45°), k_y was evaluated to be 0.27 MPa$\sqrt{m}$, while for the hard orientations k_y = 0.41 MPa$\sqrt{m}$ (θ=0°) and k_y = 0.5 MPa$\sqrt{m}$ (θ=90°). One can see, that the k_y values for the PST crystals are close to that obtained for the fine-grained material in the present work and in [2]. The spacing between the barriers were from parts of a micrometer to several dozens micrometers, i.e. similar to the grain size range of the fine-grained materials. Evidently, that the effective slip length l_{eff} producing yielding is considerably lower than the colony size d_c, and the l_{eff}, not the colony size, should be used in the HP relation (1) as a D variable. Assuming that the real value of k_y for the lamellar structure is almost the same as for the fine-grained structure, i.e. k_y = 0.4 MPa$\sqrt{m}$, the effective slip length can be estimated. The results are given in Table I. One can see that l_{eff} increased considerably when the cooling rate was decreased and the colony size increased. The l_{eff} values are considerably lower than the colony size and higher than the lamellar spacing. Probably not all the lamellar boundaries are effective barriers to dislocation glide, and the α_2/γ interfaces provide higher barrier strength when compared with the γ/γ interfaces.

The results obtained in the present and previous work allow a conclusion to be drawn regarding relationships between strength and ductile properties in the gamma titanium aluminides with lamellar and equiaxed gamma microstructures. The highest strength is exhibited by alloys with the least effective slip length, i.e. alloys with the smallest grain size and lamellar spacing. At the same time, as it was established recently [10], in order to obtain acceptable ductility, the effective slip length should be sufficient for activation of deformation twinning. In this regard further investigations are needed to determine the balance between strength and ductility in these materials.

Summary and Conclusions

1. Room temperature mechanical properties of Ti-48Al-2Nb-2Cr alloy with equiaxed and lamellar structures were studied using compression tests.
2. In specimens with an equiaxed fine-grained structure the total compression strain increased when the grain size was increased. In specimens with a lamellar structure the total compression strain decreased when the colony size was increased.
3. The yield stress versus grain/colony size followed the Hall-Petch relation. The Hall-Petch parameter k_y was 0.4 MPa$\sqrt{m}$ in the material with an equiaxed fine-grained structure, and it was 2.5 to 7.7 MPa$\sqrt{m}$ in the material with a lamellar structure, increasing when the lamellar spacing was decreased.

4. It was suggested that the high values of the HP parameter k_y for the lamellar structures were due to the fact that the effective slip length, not the colony size, should be used as the D-variable in the HP equation (1). The effective slip length was estimated to be much lower than the colony size, however, higher than the lamellar spacing.
5. Further investigations are needed to determine relationships between strength and ductile properties of the titanium aluminides.

Acknowledgment

This work was supported by the NATO Linkage Grant No. HTECH.LG 961178. The authors would like to thank Mr. S. Reichman of OREMET Titanium for supplying the material studied.

References

1. Y.-W. Kim, JOM, 46 (1994), 30.
2. R. Imayev, V. Imayev, and G.Salishchev, Scripta Metall., 29 (1993), 719.
3. C. Koeppe, A. Bartles, J. Seeger, and H. Mecking, Metall. Trans., 24A (1993), 1795-1806.
4. S.-C. Huang and D.S. Shin, Titanium Aluminides and Alloys, Y.-W. Kim and R.R. Boyer, eds., (Warrendale, PA: The Metallurgical Society, 1990), 105.
5. V.K. Vasudevan, S.A. Court, P. Kurath and H.L. Fraser, Scripta Metall., 23 (1989), 467.
6. Y.-W. Kim and D.M. Dimiduk, JOM, 43 (1991), 40.
7. K. Wurzwallner, H. Clemens, P. Schretter, A. Bartels, and C. Koeppe, High Temperature Ordered Intermetallic Alloys V, I. Baker, R. Darolia, J.D. Whittenberger, and M.H. Yoo, eds., (Pittsburgh, PA: Materials Research Society 1993), 867.
8. H.V. Atkinson, Acta Metall., 1988, 36 (1988), 469-491.
9. Y.-W. Kim and D.M. Dimiduk, Structural Intermetallics 1997, M.V. Nathal, R. Darolia, C.T. Liu, P.L. Martin, D.B. Miracle, R. Wagner, and M. Yamaguchi, eds., (Warrendale, PA: The Metallurgical Society, 1997), 531.
10. V.M. Imayev, R.M. Imayev, G.A. Salishchev, K.B. Povarova, M.R. Shagiev, and A.V. Kuznetsov, Scripta Metall., 36, (1997), 891.
11. Y. Umakoshi, T. Nakano, and T. Yamane, Mater. Sci. Eng., A152 (1992), 81.
12. J.D. Eshelby, Physica Status Solidi, 3 (1963), 2057-2060.
13. R.E. Schafrik, Metall. Trans. A, 8A (1977), 1003-1006.
14. C.T. Liu, P.J. Maziasz, D.R. Clemens, J.H. Scheibel, V.K. Sikka, T.G. Nieh, J. Wright, and L.R. Walker, Gamma Titanium Aluminides, Y.-W. Kim, R.Wagner, and M. Yamaguchi, eds., (Warrendale, PA: The Metallurgical Society, 1995), 679-688.
15. Y. Umakoshi, T. Nakano, Acta Metall. Mater., 41 (1993), 1155.

MECHANICAL PROPERTIES OF PARTIALLY CRYSTALLIZED AMORPHOUS ALLOYS

H.S. Kim, S,S. Cho, C.W. Won, and B.S. Chun

Department of Metallurgical Engineering & RASOM ERC,
Chungnam National University,
Taejeon 305-764, KOREA

Abstract

Melt spun and heat treated Al-Ni-Y alloy ribbons have fine structures consisting of nanocrystalline Al particles or intermetallic phases embedded in an amorphous matrix. The strength (and hardness) changes according to the composition and microstructure from approximately 1000 MPa for the as melt spun amorphous ribbon to 1500 MPa after heat treatment. In order to describe this high strength and strength change after heat treatment, a mixture model based on the volume fraction of amorphous matrix and Al particles is proposed. The nano-sized particles are treated as perfect materials and the matrix is treated as amorphous material, in which the solute concentration increases as the volume fraction of Al particles increases. The calculated results for various compositions and heat treated specimens are compared with experimental data in literature. This model not only explains the experimental results but can also be used to select alloy compositions and heat treatment schedules for the desired properties.

The Third Pacific Rim International Conference on
Advanced Materials and Processing (PRICM 3)
Edited by M.A. Imam, R. DeNale, S. Hanada,
Z. Zhong and D.N. Lee
The Minerals, Metals & Materials Society, 1998

Introduction

Since the discovery of amorphous alloys with good ductility in the Al-Ni-Si system [1], numerous Al-based amorphous alloys have been reported in the Al-Ln [2], Al-M1-M2 [3], and Al-Ln-M1 [4,5] (Ln=lanthanide metal, Ml and M2=transition metal) systems. Furthermore, it has been reported that these Al-based amorphous alloys exhibit high tensile strength above 1000 MPa even at Al-rich compositions of 84 to 86 at% [6] and the highest strength reaches as high as 1150 MPa in the as-melt spun ribbons [7]. It has subsequently been found [8,9] that a homogeneous dispersion of nanoscale fcc-Al particles within the amorphous matrix can significantly increase the tensile strength upto 1560 MPa. Kim *et al.* [9] suggested that the increase of strength is due to an enhancement of the resistance to shear deformation caused by the nanoscale fcc particles. Recently, Zhong *et al.* [10] attributed the hardening of Al-Ni-Y alloys to the solute enrichment of the remaining amorphous phase, but they appear not to have taken into consideration the presence of nanoscale Al particles and the decrease of the volume fraction of the remaining amorphous phase.
In this paper, we present a quantitative description of the change of mechanical properties in Al-Ni-Y alloys consisting of amorphous matrix and nanoscale precipitates using a composite model.

Mixture Model

The alloy was modeled as a nanocomposite consisting of particles embedded in a matrix as shown in figure 1. In this case the rule of mixtures agrees well with the results of finite element analysis [11]. The rule of mixtures for the tensile strength σ of the alloy is represented by equation 1,

$$\sigma = f_{am} \cdot \sigma_{am} + f_{Al} \cdot \sigma_{Al} \qquad (1)$$

where f is the volume fraction of each phase, and subscript am and Al represent the amorphous matrix and the nanocrystalline Al particles, respectively. The volume fraction f's can be measured indirectly from DSC curves [12] or directly from image analysis of TEM images [13].

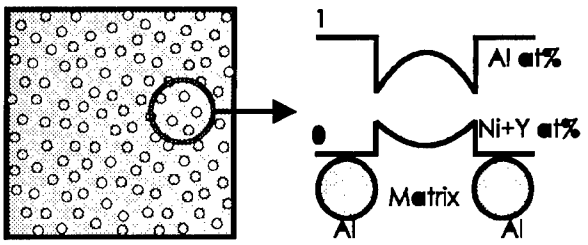


Figure 1: Schematic model of fcc Al particles embedded in amorphous matrix and schematic concentration profile of Al and solute (Ni+Y).

It is assumed that the particle grain size is so small that two dislocations can not co-exist on the same slip plane within one grain and that the deformation behavior of the amorphous phase is flow-like, therefore dislocations do not contribute to the deformation behavior of this material. The main factor determining the mechanical properties of the amorphous matrix is the chemical composition. The particles can be assumed to have the theoretical maximum strength, since they contain no dislocations or other imperfections [9] and appear to be essentially devoid of solute as shown by atom-probe field-ion microscopy [14], they can be treated as a perfect material and have a

theoretical strength. Considering the slip systems of fcc structure, Wang *et al.* [15] calculated the shear modulus $G_{\{111\}<110>}$ of Al to be approximately 24.5 GPa. Therefore, the theoretical shear strength τ_{th} of Al, which is G/16 from the force balance between of atoms [16], is 1.54 GPa. Using the following relationships between shear stress τ and tensile/compressive stress at yield σ (equation 2) and between tensile/compressive stress and hardness H (equation 3) [17] gives a theoretical hardness value H_{Al} 816 Kgf/mm^2.

$$\sigma=\sqrt{3}\tau \tag{2}$$

$$H=3\sigma \tag{3}$$

During microstructural evolution the composition of the amorphous matrix will change as the volume fraction of the particles increases. The composition change of the alloy matrix can be solved using the following reaction (equation 4) assuming that there is no volume change during the reaction. This assumption is reasonable since the length change during the reaction is about 0.1 %, so the volume change is order of 10^{-9}, which is negligible [18].

$$Al_{1-x-y}Ni_xY_y \rightarrow f_{Al}Al + (1-f_{Al})Al_{\frac{1-f_{Al}-x-y}{1-f_{Al}}}Ni_{\frac{x}{1-f_{Al}}}Y_{\frac{y}{1-f_{Al}}} \tag{4}$$

where x and y are the compositions of Ni and Y, respectively. In reality, atom probe data [18] has shown that there is enrichment of rejected solute near the particle/matrix interface as shown in schematic figure 1. The concentration is assumed to be constant as an average value calculated by mass conservation. This assumption is reasonable if the concentration dependency of the hardness of matrix is linear.

Results and Discussions

Using the mixture model, the hardness behavior of Al-Ni-Y alloys with various compositions has been investigated. According to Inoue *et al*'s results, the glass formation for Al-Ni-Y system is in the range of 3 to 22 %Y and 4 to 33 %Ni , that is about 10 to 50 % of solute. Above 20 % of solute the amorphous phase becomes brittle [4]. In the model as the volume fraction of fcc-Al particles f_{Al} increases, the average concentration of solute in the amorphous matrix $\left(\frac{x+y}{1-f_{Al}}\right)$ increases slowly at first and faster during the later stages according to the equation 4, as shown in figure 2. $Al_{50}(Ni+Y)_{50}$ represents the maximum amorphous solute concentration, $Al_{90}(Ni+Y)_{10}$ represents the minimum initial amorphous solute concentration, and $Al_{80}(Ni+Y)_{20}$ represents the initial maximum solute concentration for ductile behavior. The dotted 20 % solute concentration line divides the solute range into two parts. The phase compositions above the dotted line are brittle. Therefore, even if the initial ribbon, for example $Al_{85}(Ni+Y)_{15}$, is ductile, the solute content of the amorphous matrix increases during heat treatment as the volume fraction of fcc-Al increases. And the amorphous phase becomes brittle. Alloys with greater than 20 % solute are always brittle. This will be explained more below in relation to hardness drop.

In figure 3, the composition dependency of the hardness of fully amorphous alloys measured by others [4,10] is shown. As the solute concentration of the amorphous matrix increases, the hardness increases. However, above 20 % solute, which is the brittle amorphous range, there is no hardness data available in the literature. The concentration dependence of the hardness fits a linear relation, H_{am}=-90+2950(x+y), within the amorphous formation range shown (solute concentration between

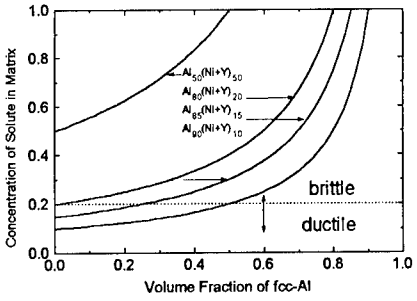


Figure 2: The average concentration of solute (Ni+Y) in the amorphous matrix as a function of the volume fraction of fcc-Al particles in Al-Ni-Y alloys showing the maximum concentration of solute (50 %) for amorphous formation, the minimum concentration

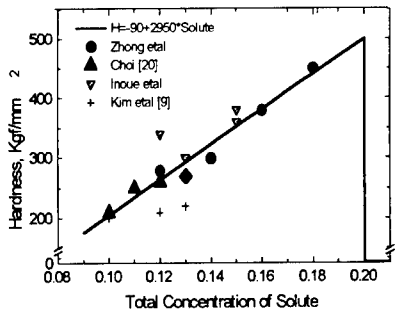


Figure 3. The microvickers hardness of melt-spun fully amorphous Al-Ni-Y alloys as a function of the solute composition.

0.1 and 0.2). In order to model the effect of solute enrichment of the amorphous phase during precipitation of the fcc-Al particles, hardness data is needed for higher solute ranges. Instead of extrapolation for concentration greater than 20 %, we set the hardness of the amorphous phase to zero, because it is brittle and cannot sustain its shape during loading.

The comparison in figure 4 shows the calculated contributions of the hardening of the residual amorphous matrix due to solute enrichment and the hardening due to the precipitation of fcc-Al to the total hardening of $Al_{85}Ni_{15}Y_5$ alloys. Since the defect-free fcc-Al has higher hardness, 816 Kgf/mm^2, than the amorphous matrix, between 300 and 500 Kgf/mm^2, the fcc-Al contributes more to the total hardening caused by heat treatment. Although the hardness increase DH_{am} of the amorphous matrix alone by solute enrichment is high, its volume fraction decreases and the overall contribution by solute enrichment $f_{am}H_{am}$ becomes less. Therefore, solute enrichment of the remaining amorphous phase alone, as suggested by Jhong *et al* (10), cannot explain the total hardness increase observed. After the solute concentration of matrix reaches the brittle range (20 % solute) as the volume fraction of fcc-Al increases, the hardness of amorphous matrix becomes negligible and the total hardness drops.

Figure 5 compares our calculated hardness values and experimental hardness values from the literature [4,10] as a function of the volume fraction of fcc-Al particles for various alloy compositions. Considering the inaccuracy of the experimental measurements of the volume fraction and the hardness and the inhomogeneity of solute in the matrix, the agreement between the experimental and calculated results is satisfactory. In the experimental data, as the volume fraction of fcc-Al increases during the heat treatment, the hardness of the specimen increases linearly with the similar gradients. In the calculations the hardness also increases linearly with the same gradient regardless of the composition and drops when the solute contents of the amorphous matrix reaches the brittle composition region (20 %). The dropping point appears at lower volume fraction of fcc-Al in higher solute concentration alloy and appears at higher f_{Al} in lower solute concentration alloy, since the solute contents of amorphous matrix reaches the brittle region earlier in the higher solute fully amorphous alloy during heat treatment as we can see in figure 2. In addition, even though there can be large difference between the initial hardness of different alloys, the difference between the maximum hardnesses is small, which fits well with the experimental results. This is also the reason why the maximum tensile strength of various alloy systems with nanoscale fcc-Al particles embedded in the amorphous matrix show similar values.

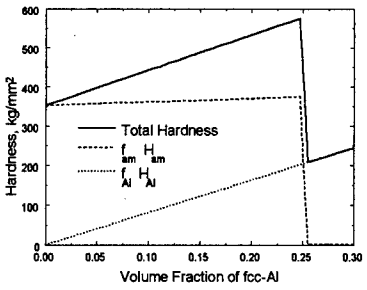


Figure 4. The microvickers hardness of the $Al_{85}Ni_{10}Y_5$ as a function of the volume fraction of fcc-Al particles. The total hardness H is the summation of an amorphous matrix's contribution $f_{am}H_{am}$ and the fcc-Al's contribution $f_{Al}H_{Al}$.

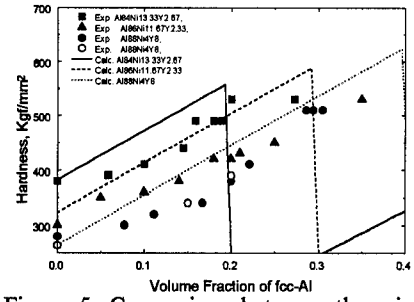


Figure 5. Comparison between the mixture model calculations and published experimental hardness values (9, 19) as a function of the volume fraction of fcc-Al particles for various alloy compositions

Conclusions

The mechanical properties of melt spun and heat treated Al-Ni-Y alloys with fine nanoscale particles embedded in the amorphous matrix have been analyzed using a composite model which uses the rule of mixtures. The nanoscale fcc-Al particles are treated as a perfect material with a theoretical shear strength. The strength of the amorphous matrix is used from the fully amorphous ribbon's experimental results assuming that the solute composition is constant as an average value throughout the matrix. Comparison between the calculated results and the experimental results in the literature shows good agreement. The proposed model explains the experimental phenomena very well, such as similar hardness dependence as a function of the volume fraction of fcc-Al and the similar maximum hardness values regardless of the initial hardness. This model not only explains the experimental results but can also be used to select alloy compositions and heat treatment schedules for the desired properties.

References

1. A. Inoue, M. Yamamoto, H. M. Kimura, and T. Matsumoto, "Ductile Aluminium-base Amorphous Alloys with Two Separate Phases ", J. Mater. Sci. Lett., (1987) 194-200.

2. A. Inoue, K. Ohtera, and T. Matsumoto, "New Amorphous Al-Y, Al-La and Al-Ce Alloys Prepared by Melt Spinning", J. Appl. Phys., 27 (1988) L736.

3. A.P. Tsai, A. Inoue, and T. Matsumoto, "Ductile Al-Ni-Zr Amorphous Alloys with High Mechanical Strength", J. Mat. Sci. Let., 7 (1988) 805-807.

4. A. Inoue et al., "New Amorphous Alloys with Good Ductility in Al-Y-M and Al-La-M (M=Fe, Co, Ni or Cu) Systems, Jpn. J. Appl. Phys., 27 (1988) L280-L282.

5. A. Inoue, K. Ohtera, and T. Matsumoto, "New Amorphous-Alloys With Good Ductility in Al-Ce-Nb, Al-Ce-Fe, Al-Ce-Co, Al-Ce-Ni, Al-Ce-Cu Systems", Jpn. J. Appl. Phys., 27 (1988) L1796.

6. A. Inoue, K. Ohtera, and T. Matsumoto, "Aluminum-based Amorphous Alloys with Tensile Strength above 980 MPa", Jpn. J. Appl. Phys., 27 (1988) L479-L482.

7. A. Inoue, N. Matsumoto, and T. Matsumoto, "Al-Ni-Y-Co Amorphous Alloys with High Mechanical Strengths, Wide Supercooled Liquid Region and Large Glass-Forming Capacity", Mater. Trans. JIM, 31 (1990) 493-500.

8. Y.H. Kim, A. Inoue, and T. Matsumoto, "Ultrahigh Tensile Strengths of $Al_{88}Y_2Ni_9M1$ (M=Mn or Fe) Amorphous Alloys Containing Finely Dispersed fcc-Al Particles", Mater. Trans. JIM, 31 (1990) 747-749.

9. Y.H. Kim, A. Inoue, and T. Matsumoto, "Increase in Mechanical Strength of Al-Y-Ni Amorphous Alloys by Dispersion of Nanoscale fcc-Al Particles", Mater. Trans. JIM, 32 (1991) 331-338.

10. Z.C. Zhong, X.Y. Jiang, and A.L. Greer, "Microstructure and Hardening of Al-Based Nanophase Composites", Mater. Sci. Eng., A226-228 (1997) 531-535.

11. H.S. Kim, C. Suryanarayana, S-J. Kim and B.S. Chun, "A Finite Element Analysis of Mechanical Behavior of Nanocrystalline Copper", Powder Metall., (1997) in press.

12. A. Inoue, H. Tomika, and T. Matsumoto, "Mechanical properties of Ductile Fe-Ni-Zr and Fe-Ni-Zr (Na or Ta) Amorphous Alloys Containing Fine Crystalline Particles", J. Mater. Sci., 18 (1983) 153-158.

13. A. Inoue et al., "Structure and Mechanical Strength of Al-V-Fe Melt-Spun Ribbons containing High Volume Fraction of Nanoscale Amorphous Particles", NanoStructured Mater., 7 (1996) 363-382.

14. K. Hono, Y. Zhang, A. P. Tsai, A. Inoue, and T. Sakurai, "Solute Partitioning in Partially Crystallized Al-Ni-Ce(-Cu) Metallic Glasses", Scripta Metall., 32 (1995) 191-194.

15. N. Wang, Z. Wang, K. T. Aust, and U. Erb, "Effect of Grain Size on Mechanical Properties of Nanaocrystalline Materials", Acta Metall. Mater., 43 (1995) 519-525.

16. W. R. Tyson, "Theoretical Strength of Perfect Crystals", Phil. Mag., 14 (1966) 925-930.

17. D. Tabor : The Hardness of Metals, (London : Oxford University Press, 1951) 107.

18. P. J. Warren : Unpublished data, University of Oxford, 1996.

19. Z.C. Zhong, X.Y. Jiang, and A.L. Greer, "Nanocrystallization in Al-based Amorphous Alloys" Phil. Mag. B, in press.

20. Y.T. Choi, "The Current Manufacturing Technology of Aluminum Amorphous Materials" Machine and Materials, 7 (1995) 81-90, in Korean.

MICROSTRUCTURE AND PROPERTIES OF ALUMINUM-IRON ALLOYS SUBJECTED TO SEVERE PLASTIC DEFORMATION AND AGING

O.N. Senkov[1], F.H. Froes[1] , V.V. Stolyarov[2], R.Z. Valiev[2], and J. Liu[3]

[1]University of Idaho, Moscow, Idaho 83844-3026
[2]Ufa State Aviation Technical University, Ufa, Russia 450000
[3]ALCOA Technical Center, Alcoa Center, PA 15069

Abstract

A novel technique of severe plastic deformation (SPD) of ingots by torsion under high imposed pressure, which results in a large departure from equilibrium, was applied to a number of aluminum-iron alloys. The microstructure of the alloys was studied with the use of TEM and EDS analyses. The SPD led to solid solubility extension of iron in the aluminum matrix, dispersion and dissolution of second phase particles, grain size reduction into nanometer range, and partial amorphization. Microhardness of the alloys increased substantially after the severe plastic deformation due to the grain refinement and the solid solubility extension. Aging of the severe plastically deformed samples led to further increase of the microhardness because of decomposition of the supersaturated solid solution and fine precipitation on dislocations and grain boundaries.

Introduction

Severe plastic deformation performed at low temperatures (usually less than 0.4 T_m) can refine the microstructure of metals and alloys to the nanometer-sized range [1-3]. Recent work has also demonstrated possible changes in phase compositions, formation of metastable phases, and extension of solid-solubility limits during processing by severe plastic deformation [4-6]. These novel constitutional and microstructural effects can lead to enhanced physical and mechanical properties. For example, an enhancement of aging processes in a hardened commercial Al-Cu-Zn-Mg-Zr alloy due to severe torsional straining has been demonstrated [7].

Aluminum-iron alloys are attractive for engine applications. Alloying of aluminum with iron can increase the high temperature strength due to a dispersion of second-phase particles [8]. Unfortunately, the equilibrium solubility of iron in the aluminum lattice is very low and even at high temperatures it does not exceed 0.03 at.% [9], and these alloys cannot be dispersion-strengthened with the use of conventional thermal treatments. The solid-solubility extension of iron in the aluminum matrix can be achieved by "far-from-equilibrium" techniques such as rapid solidification [10,11], mechanical alloying [12-16] or even a laser treatment [17]. In the present work, the severe plastic deformation approach has been used to extend the iron solubility in aluminum and to produce after aging a nano-grained dispersion-strengthened structure in the Al-Fe alloys.

The Third Pacific Rim International Conference on
Advanced Materials and Processing (PRICM 3)
Edited by M.A. Imam, R. DeNale, S. Hanada,
Z. Zhong and D.N. Lee
The Minerals, Metals & Materials Society, 1998

Experimental Procedure

Cast rods of three aluminum-iron alloys, i.e. Al-7.5Fe, Al-11Fe, and Al-16Fe (in wt. %) were produced by ALCOA. Disk-shape samples were cut from these rods, with a diameter of 12 mm and a thickness of 0.3 mm. The samples were strained in torsion on a Bridgman anvil at room temperature to a true logarithmic strain $\varepsilon = 7$ under a quasi-hydrostatic pressure of 6 GPa. The deformed samples were aged at the temperature of 100°C in boiled water for the period of time of 0.25 hours to 12 hours.

Transmission (JEM 2010) and scanning (Hitachi 2000) electron microscopes and a X-ray diffractometer (Siemens 5000, Cu K_α irradiation, $\lambda = 1.54056$ E) were used for microstructure and phase composition studies. The transmission electron microscope (TEM) was equipped with an energy dispersive X-ray spectrometer (EDS) Link ISIS, which allowed chemical microanalysis of the phases.

Microhardness measurements were carried out on the samples with flat polished surfaces, with the use of a Vickers device under an applied load of 0.98 N for 10-15 seconds. Ten measurements at different points of the sample were used to calculate an average value of the microhardness.

Results and Discussion

Microstructural Evolution

The alloys in the initial cast state had a typical dendritic type microstructure and contained fcc Al (matrix), and monoclinic $Al_{13}Fe_4$ phases, Figure 1. The dendrites became coarser and their volume fraction increased when the concentration of the iron was increased. The average grain size in the aluminum matrix was ~ 15 μm. An analysis of the XRD patterns taken from the alloys showed that virtually no iron was in solution in the aluminum matrix, in agreement with the equilibrium Al-Fe phase diagram [9].

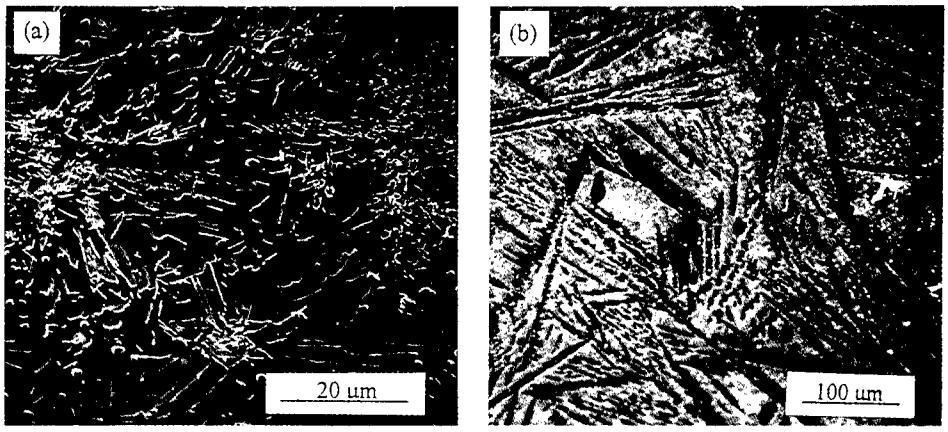


Figure 1. Microstructure of the as-cast alloys (a) Al-7.5%Fe and (b) Al-16%Fe.

A very fine microstructure was produced in the alloy samples by the severe plastic deformation, which could be detectable only with the use of TEM. Two phases were present in

the deformed alloy: fcc Al-rich and monoclinic $Al_{13}Fe_4$. Figure 2 shows typical microstructure of the Al-rich phase in bright and dark field images, together with a selected area diffraction pattern (SADP) obtained from a region 0.5 μm in diameter. The aluminum-rich phase had a homogeneous grain structure with a mean grain size of about 100 nm. According to the selected electron diffraction pattern, Figure 2c, the grains have high angle grain boundaries and random crystallographic orientations. Figure 2a shows that some grain boundaries are poorly defined and the contrast within the grains is not uniform but often changes in a complex fashion that indicates a high level of internal stresses and elastic distortions in the crystal lattice. The EDS analysis of the aluminum-rich matrix showed that it contained from 1.34 to 2.24 wt.% Fe in solid solution. Figure 3 shows a grain and the EDS spectrum taken from the region in this grain, marked with an arrow. No second phase particles were observed in the grain, although 1.96 wt.% Fe was detected.

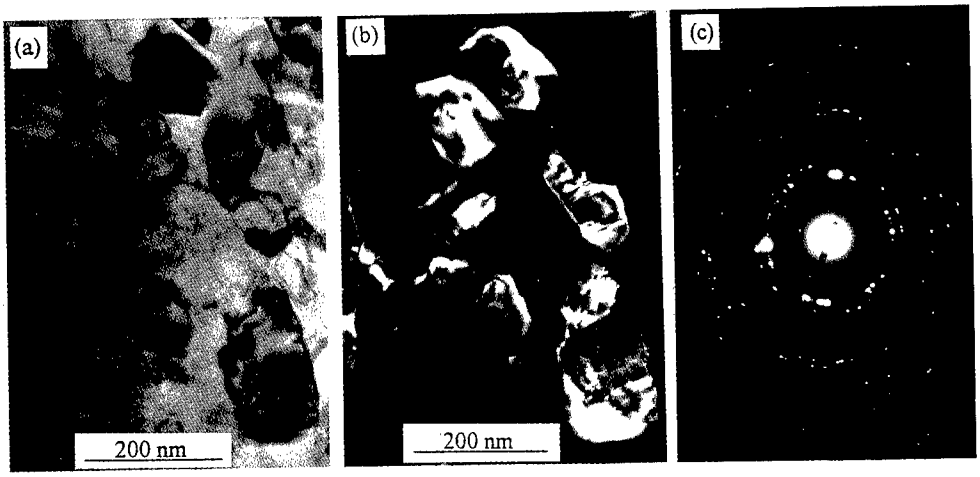


Figure 2. Microstructure of the as-deformed alloy: aluminum-based matrix phase: (a) bright field image, (b) dark field image, and (c) microdiffraction.

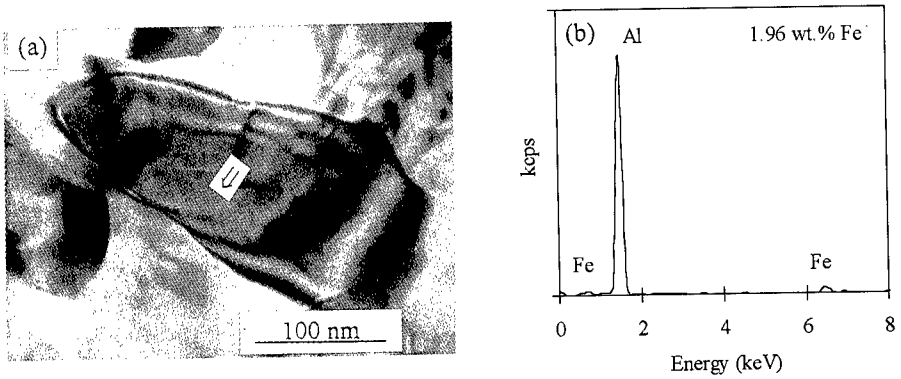


Figure 3. (a) A selected grain of the aluminum-based matrix in the alloy after severe torsional straining and (b) EDS spectrum from the grain interior.

The $Al_{13}Fe_4$-phase was homogeneously distributed in the deformed alloys as particles of less than 1 μm in size, Figure 4. Very often these particles have diffuse boundaries with the aluminum-rich matrix. The EDS analysis of the compound particles showed that they contain of 35.0 to 38.0 wt.% Fe, which is between the Al_3Fe and Al_4Fe compositions.

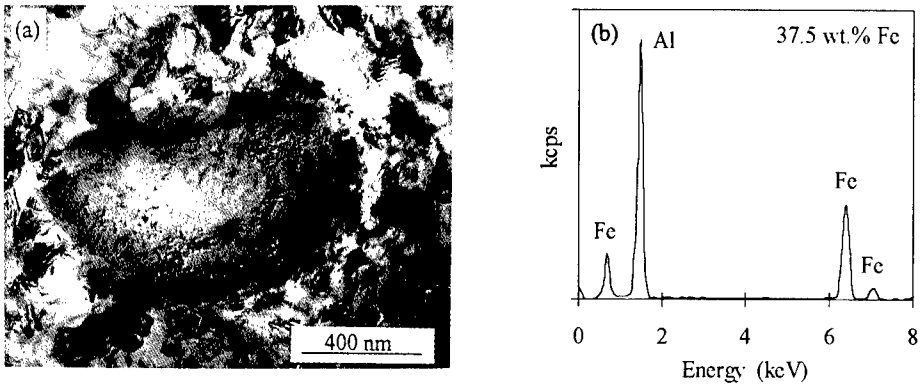


Figure 4. (a) Microstructure of the as-deformed alloy: an $Al_{13}Fe_4$ particle in the aluminum-based matrix; (b) EDS spectrum from the compound particle.

An increase of grain sizes in the aluminum-based matrix and the simultaneous appearance of common banded contrasts at the grain boundaries were observed during aging at 100°C, Figure 5. A well developed dislocation sub-grain structure and extinction contours resulted from elastic stresses inside the grains are other features of the aged microstructures. The dark field image analysis showed a specific dotted contrast on the dislocations and grain boundaries, Figure 5b, which was probably due to very fine precipitation of the second phase. The use of different-diameter electron beam at the EDS analysis showed that the concentration of iron in the solid solution gradually decreased, although the average iron concentration in the aluminum-based grains remained almost unchanged, indicating the iron precipitation from the solid solution during the aging.

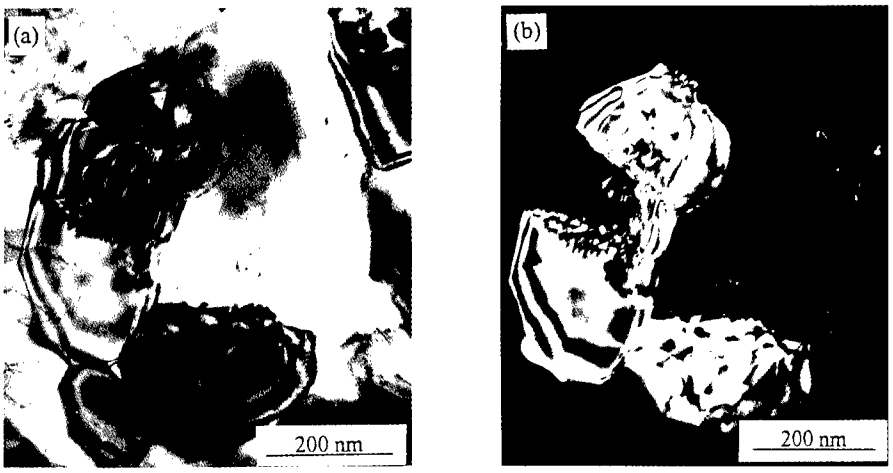


Figure 5. Microstructure of the severe plastically deformed alloy after aging at 100°C for 4 hours: (a) bright field and (b) dark field images.

Microhardness

The as-cast Al-11%Fe alloy had the Vicker's microhardness of 750 MPa. After the severe torsional straining the microhardness increased to 1750 MPa, being higher by a factor of 2.3 as compared to the cast state. Such a considerable increase in the microhardness may be caused by several reasons, including grain refinement, increasing the defect density and internal stresses, fragmentation of the second-phase particles, and formation of the supersaturated solid solution of iron in the aluminum matrix.

Aging of the as-deformed alloy at 100°C led to a further increase of the microhardness, and the maximum value of 3020 MPa was reached after 5 hours of aging, Figure 6. This large increase in the microhardness during aging was apparently caused by a precipitation of the second phase particles on dislocations and grain boundaries, although some relaxation processes also occurred. Further increase of the aging time, up to 12 hours, led to a continuous decrease of the microhardness, however the values were still higher than that in the as-deformed state.

The changes of the microhardness during aging of the as-deformed alloy represent the typical behavior of hardened aluminum alloys on aging. Obviously, the first stage of aging, when the microhardness increases, is due to a redistribution of the iron in the supersaturated solid solution and precipitation of the iron on dislocations and grain boundaries. The second stage of the aging, when the microhardness decreases, is obviously caused by a coarsening of the second-phase particles, grain coarsening in the matrix phase and relaxation of the internal stresses.

A very important result of the present work is the possibility of aging of the conventionally non-hardenable alloy by employing severe plastic deformation to produce a supersaturated solid solution, with a considerable strengthening effect after aging.

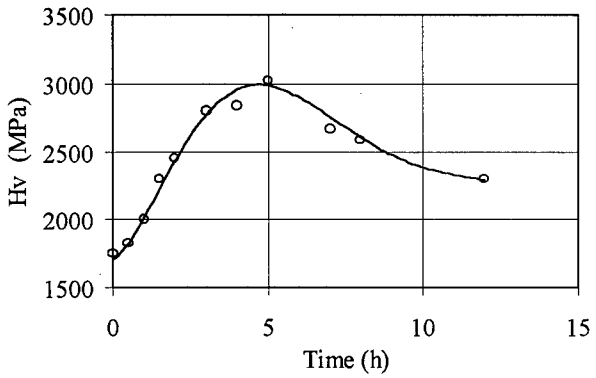


Figure 6. Dependence of the microhardness on aging time at 100°C

Conclusions

1. Severe plastic deformation of cast aluminum-iron alloys led to microstructural refinement and formation of a nanocrystalline structure in the aluminum-based matrix with a homogeneously distribution of small (<1 μm) second phase particles of $Al_{13}Fe_4$.
2. The solubility of iron in the aluminum matrix was extended up to 2.2 wt.% by the severe plastic deformation, which allowed aging (hardening) of the conventionally non-hardenable alloy to occur.
3. The microhardness of the as-cast Al-11%Fe alloy of 750 MPa was increased up to 1750 MPa after the severe plastic deformation. The subsequent artificial aging at 100°C led to a

further increase in the microhardness up to 3020 MPa due to decomposition of the supersaturated solid solution and precipitation strengthening.

References

1. R.Z. Valiev, A.V. Korznikov and R.R. Mulykov, "Structure and Properties of Ultrafine-Grained Materials Produced by Severe Plastic Deformation," Mat. Sci. Eng. A, A168 (2) (1993), 141-148.
2. R.Z. Valiev, ed., "Ultrafine-Grained Materials Prepared by Severe Plastic Deformation. Special Issue," Annales de Chimie-Mater. Science, Fr. 5-6, (1996).
3. V.A. Pavlov, "Amorphization at Intense Rolling ", Phys. Metal. Metallogr., 67 (1989), 924-932.
4. H. Shen, Z. Li, B. Gunther, A.V. Korznikov, and R.Z. Valiev, "Influence of Powder Consolidation Methods on the Structural and Thermal Treatment of a Nanophase Cu-50 wt.%Ag Alloy," NanoStructr. Mater., 6 (1-4) (1995), 385-388.
5. Yu.V. Ivanisenko, A.V. Korznikov, I.M. Safarov, R.Z. Valiev, "Formation of Submicrocrystalline Structure in Iron and Allows After Severe Plastic Deformation," NanoStruct. Mater., 6 (1-4) (1995), 433-436.
6. O.N. Senkov, F.H. Froes, V.V. Stolyarov, R.Z. Valiev, and J. Liu, "Non-Equilibrium Structures in Al-Fe Alloys Subjected to Severe Plastic Deformation," Advanced Particulate Materials and Processes 1997, F.H. Froes and J.C. Hebeisen, eds., (Princeton, NJ: Metal Powder Industries Federation, 1997), 95-102.
7. V.V. Stolyarov, V.V. Latysh, V.A. Salimonenko, R.K. Islamgaliev, R.Z. Valiev "Influence of Severe Plastic Deformation on Aging Effect of Al-Zn-Mg-Cu-Zr Alloy," Mat. Sci. & Eng., A234-236 (1997), 339-342.
8. Y.-W. Kim and W.M. Griffith, eds., Dispersion Strengthened Aluminum Alloys, (Warrendale, PA: The Metallurgical Society, 1988).
9. U.R. Kattner, "Al-Fe (Aluminum-Iron)," Binary Alloy Phase Diagrams, T.B. Massalski, ed., Vol. 1, (Metals Park, OH: ASM International, 1986), 147-149.
10. A. Tonejc and A. Bonefacic, "Enhanced Solubility of Iron in Aluminum Obtained by Rapid Quenching Technique," J.Appl. Phys., 40 (1) (1968), 419-420.
11. R.M.K. Young and T.W. Clyne, "An Al-Fe Intermetallic Phase Formed During Controlled Solidification," Scripta Metall., 15 (11) (1981), 1211-1216.
12. D.K. Mukhopadhyay, C. Suryanarayana, and F.H. Froes, "Structural Evolution in Mechanically Alloyed Al-Fe Powders," Metall. Mater. Trans. A, 26A (1995), 1939-1946.
13. V.I. Fadeeva and A.V. Leonov, "Formation of Al-Fe Supersaturated Solid Solution by Mechanical Alloying," Mater. Sci. Forum, 88-90 (1992), 481-488.
14. B. Huang, N. Tokizane, K.N. Ishihara, P.H. Shingu, and S. Nasu, "Amorphization of Al-Fe Alloys Formed by Ball Milling and Repeated Rolling," J. Non-Cryst. Solids, 117/118 (1990), 688-691.
15. D.K. Mukhopadhyay, C. Suryanarayana, and F.H. Froes, "Synthesis of Nanocrystalline Al_5Fe_2 by Mechanical Alloying," Scripta Metall. Mater., 31 (3) (1994), 333-338.
16. M.L. Öveçoglu, C. Suryanarayana, and W.D. Nix, "Identification of Precipitate Phases in a Mechanically Alloyed Rapidly Solidified Al-Fe-Ce Alloy," Metall. Mater. Trans. A, 27A (1996), 1033-1041.
17. A.A. Uglov, M.B. Ignatev, V.I. Titov, "Anomalous Solubility of Iron in Aluminum Produced as a Result of Laser Alloying," Soviet Physics Doclady, 35 (11) (1990), 977-979.

BEHAVIOR OF HYDROGEN IN A 5083 ALUMINUM ALLOY

Tomoaki IHARA* and Goroh ITOH

Nagaoka University of Technology (*Graduate Student)
Kami-Tomioka, Nagaoka,
Niigata-pref., 940-2188 Japan

Abstract

Hydrogen microprint (HMP) technique was applied to a 5083 aluminum alloy sheet to investigate the behavior of internal or impurity hydrogen. In the present technique, the microscopic location in the specimen surface where an internal hydrogen atom is evolved by tensile deformation is detected as a silver grain through a pseudo-photographic action of hydrogen. The examination was also made on an Al-4.5%Mg binary alloy consisting of single matrix phase to investigate the effect of second phase particles contained in 5083 alloy.
In the 5083 alloy, hydrogen atoms were seen to surround a non-metallic inclusion and second phase particle, while in the Al-Mg binary alloy, they were observed along slip lines and grain boundary. The latter result was in qualitative accordance with that of pure aluminum reported before, indicating that internal or impurity hydrogen atoms move with gliding dislocations in single phase materials irrespective of the presence of solute Mg atoms. The result obtained in the 5083 alloy was understood by considering that hydrogen atoms moving with gliding dislocations are trapped and accumulated in the particle/matrix interface when dislocations interact with particles, as was expected by Tien et al.

The Third Pacific Rim International Conference on
Advanced Materials and Processing (PRICM 3)
Edited by M.A. Imam, R. DeNale, S. Hanada,
Z. Zhong and D.N. Lee
The Minerals, Metals & Materials Society, 1998

Introduction

Taking the protection of the global environment into account, the importance of hydrogen as a clean energy has been increasing rapidly particularly from the viewpoint that exhaust of carbon dioxide must be reduced from now on. A project of producing molecular hydrogen from water and transporting it to the consuming area, which is now proceeding, involves marine transportation of liquid hydrogen. Tank material is required to resist possible hydrogen invasion, as well as to have sufficient strength, toughness and corrosion resistance at room and cryogenic temperatures.

Generally, hydrogen related to a structural material can be classified into internal (or impurity) hydrogen and environmental hydrogen. Hydrogen atoms of the former type have been contained from the starting material or picked up during processing, while those of the latter type penetrate from the atmosphere into the material under tensile stress during the service. Although serious environmental embrittlement of metallic materials by molecular hydrogen has not been reported so far at ambient temperature or below, internal hydrogen atoms have been proved to move with gliding dislocations in pure aluminum[1-4], as illustrated in Figure 1. In the liquid hydrogen tank shown Figure 2, one side of the sheet material is exposed to high pressure of hydrogen gas, while no hydrogen partial pressure will be applied onto the other side. The permeation of hydrogen and embrittlement by environmental hydrogen have not been examined in this condition in detail.

In this study, to approach the final goal of elucidating the permeation and migration behavior of hydrogen atoms during loading in the above condition, a preliminary examination on the migration behavior of internal hydrogen atoms has been made by means of hydrogen microprint (HMP) technique on a 5083 aluminum alloy sheet, candidate material for the tank in marine transportation, as well as an Al-Mg binary alloy as a reference material.

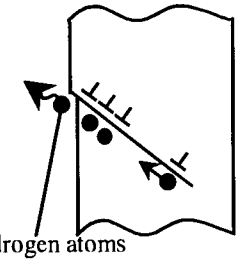


Figure 1: Schematic figure showing the behavior of hydrogen atoms in pure aluminum.

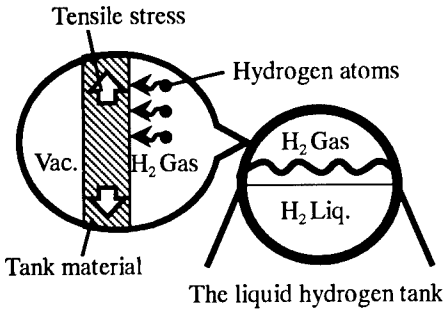


Figure 2: Schematic drawing showing possible penetration of hydrogen atoms into the liquid hydrogen tank material subjected to tensile stress.

Experimental Procedure

Specimens

Hot-rolled plate of a commercial 5083 aluminum alloy of 10mm thickness was further hot-rolled at 400℃ using laboratory mill to 2mm in thickness, annealed at 400℃ for 1h and finally cold-rolled to a 1mm thick sheet. Tensile specimens with gage length of 50mm and gage width of 12.5mm were machined from the above sheet in the longitudinal direction, annealed at 400℃ for 1h and then electro-polished. Constituent particles arising from impurity Fe and Si and dispersoid particles containing Mn, existing in 5083 alloy, are thought to have some effects on the behavior of internal hydrogen atoms as Tien et al. suggested[5]. To see such effects, an Al-4.5mass%Mg binary alloy with virtually no second phase particles was prepared from raw materials of a purity over 99.99%. The alloy was melted in air, cast in an iron mold, homogenized at 430℃ for 1h, warm-rolled from 10mm to 2mm in thickness at 200℃, and then processed into tensile specimens in the same way as in the 5083 alloy. Analyzed composition of the specimens is indicated in Table 1.

Table I Composition of the Alloy Specimens in Mass %.

Alloy	Si	Fe	Cu	Mn	Mg	Cr	Ti	Al
A5083	0.08	0.19	0.02	0.59	4.56	0.05	0.02	Bal
Al-Mg	0.007	0.004	0.002	-	4.37	-	-	Bal

Hydrogen Microprint Technique

Behavior of hydrogen has been investigated by mean of HMP technique, which can visualize microscopic location in the surface where a hydrogen atom has been evolved utilizing a reductive (pseudo-photographic) reaction of hydrogen atom in metals. In this paper the evolution of hydrogen will arise from hydrogen atom motion with gliding dislocation and the principle of HMP technique used in present study is schematically illustrated in Figure 3. The polished specimens were covered with a collodion layer to get a closer adherence of the emulsion layer to the specimen and to prevent the following reaction between photographic emulsion and metallic aluminum atom[6,7].

$$3AgBr + Al \rightarrow 3Ag + AlBr_3 \quad (1)$$

The specimens were next covered with photographic emulsion Konica NR-H2 (silver bromide grain size 0.08μm) diluted by four times, by wire loop method in a darkroom as previously reported[7]. Then they were covered with a shading film, and deformed in tension to fracture at room temperature at a constant speed of 2.0 mm/min (initial strain rate, $5.6 \times 10^{-4} s^{-1}$) on an Instron 1185 testing machine.

If a hydrogen atom moves by some mechanism and arrives at a surface from the inside, it induce, the reaction

$$AgBr + H \rightarrow Ag + HBr, \quad (2)$$

forming a silver atom which will act as a nucleus of silver grain when developed. In the present experiment both deformed and undeformed specimens were developed in Fuji SPD and fixed in Super Fuji Fix. The average time from the coverage of emulsion layer to the development was about 24 h.

The resultant silver grains were observed together with the microstructure on the specimen surface using an SEM (Jeol 7330) equipped with an EDXS device.

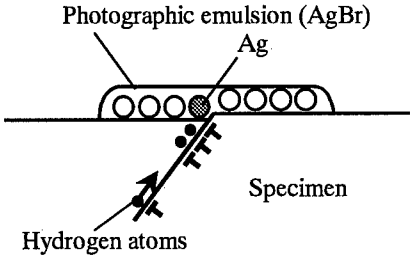


Figure 3: Principle of hydrogen microprint technique.

Experimental Results and Discussion

Prior to HMP technique, usual tensile tests were performed on the two alloy specimens. Table 2 shows the resultant tensile properties together with grain size measured in longitudinal direction. Since Al-Mg binary alloy doses not include dispersoid, it has coarser grains and lower strength. Because of the lower strength and the absence of constituent particles, the binary alloy has higher ductility.

Micrographs of the two alloy specimens HMP-treated without deformation are shown in Figure 4. A few white particles are seen in both specimens, which were found to be rich in silicon or sodium without silver using EDXS. These particles were regarded as a kind of contaminant, and no silver particle was observed in other regions. This means that hydrogen atoms are not emitted from the specimen surface unless the specimen is deformed.

Table II Properties of Specimens

Specimens	Yield Stress (MPa)	Ultimate Tensile Strength (MPa)	Elongation (%)	Grain Size (μm)
A5083	133	302	22	18
Al-Mg	80	227	28	120

Silver particles that were regarded as the product of HMP technique were observed in only a limited number of areas in the 5083 alloy specimen even though deformed. These rather exceptional examples of HMP image are shown in Figure 5 (a, b). In Fig. 5 (a), a number of fine white particles (about 1 μm) are observed in contact with a coarse particle (5 μm) in the middle of the micrograph. Figure 5 (c) shows an EDXS spectrum obtained from one of the fine particles in Fig. 5 (a). A strong silver peak implies hydrogen evolution caused by the deformation, while weaker peaks of aluminum, magnesium and silicon are also seen, which are considered to arise from the background coarse particle. An EDXS spectrum from the matrix is shown in Figure 5 (d), consisting of main aluminum and minor magnesium peaks, corresponding to the alloy composition. The peak height rations of magnesium and silicon to aluminum in Figure 5 (c) are far greater than those in Figure 5 (d). Taking this fact and the particle size into account, the coarse particle was thought to be a constituent Mg_2Si particle. In another area shown in Figure 5 (b), silver particles ("S") are also seen in contact with a coarse particle ("A"). Since no other element than aluminum was detected from the latter particle, this was regarded as non-metallic inclusion of alumina.

An example of HMP image in the Al-Mg binary alloy specimen stretched to failure is shown in Figure 6 (a). An array of white particles is revealed on the grain boundary, while a few particles are visible on slip lines. An EDXS spectrum as shown in Figure 6 (b) was obtained from any of both types of particles, meaning that all of them are silver particles. This result is in accord with that reported in pure aluminum[1-4]. The silver particles on slip lines indicate that hydrogen atoms move with gliding dislocations in the binary alloy, as well as in pure aluminum. The silver particles on grain boundary have not been discussed so for in detail. They are well understood by assuming that hydrogen atoms, which have reached the grain boundary inside the specimen with gliding dislocations, move toward the surface by grain boundary diffusion, leading to the hydrogen evolution.

Hydrogen evolution on slip lines or grain boundary was not observed in the 5083 alloy. This can be attributed to the shorter glide path caused by the smaller grain size (see Table 2), and to the trap of hydrogen at the interface between second phase particles and the matrix on an occasion of the interaction of moving dislocations with the particles. The latter mechanism was proposed by Tien et al.[5], and seemed to interpret the silver particles that were observed in touch with constituent or inclusion particle in Figure 5 as well. Hydrogen atoms moving with dislocations are thought to be trapped and accumulated at the particle/matrix interface when the dislocations interact with the particle, and then to move toward the surface by interface diffusion.

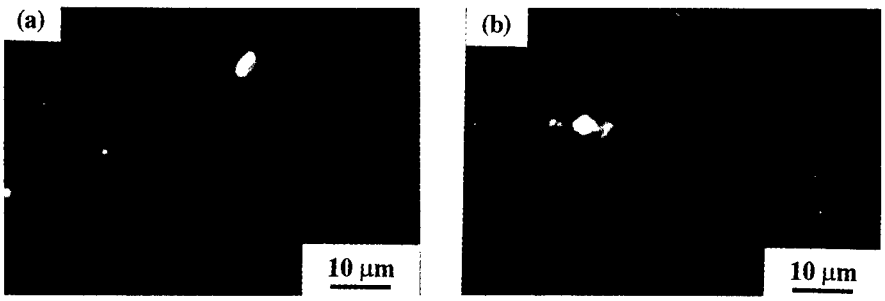


Figure 4: SEM/HMP images of undeformed specimens.(a): 5083 alloy, (b): binary alloy.

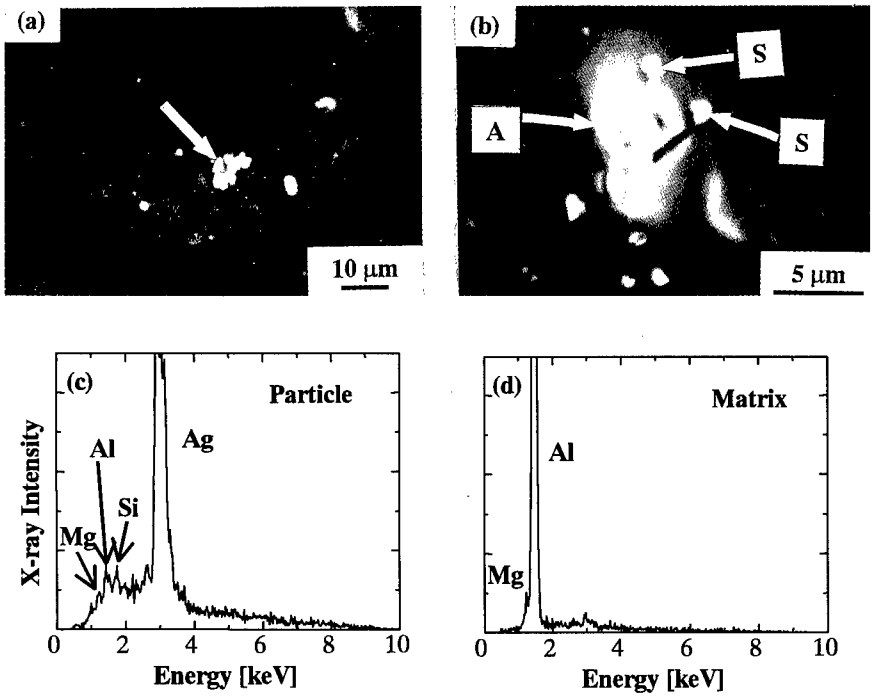


Figure 5: HMP images (a, b) and EDXS spectra (c, d) of 5083 alloy specimen stretched to fracture. (c): taken from the white particle indicated by an arrow in (a), (d): taken from the matrix in (a).

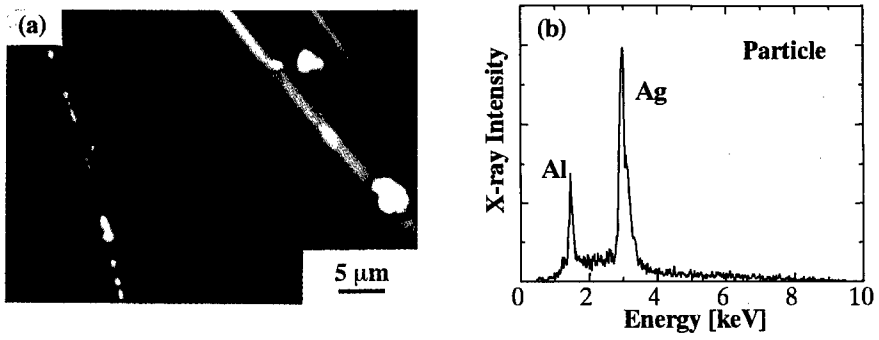


Figure 6: (a) HMP image of binary alloy specimen stretched to fracture. (b): EDXS spectrum taken from a white particle shown in (a).

Summary

The behavior of internal or impurity hydrogen was investigated by means of hydrogen microprint technique on 5083 aluminum and Al-4.5mass%Mg binary alloys. It was confirmed that internal hydrogen atoms moved with gliding dislocations, and were evolved at slip lines in the surface in the binary alloy. This is in accord with the result previously reported in pure aluminum, and hence is regarded as a common feature in single phase material. Hydrogen evolution was also detected at a grain boundary in the binary alloy and at the interface between second phase or inclusion particle and the matrix in the 5083 alloy. This can be understood by assuming that hydrogen atoms moving with gliding dislocations were trapped at the grain boundary or the particle/matrix interface and that they diffused out along the boundary.

Acknowledgment

This work was financially supported by the Iwatani Naoji Foundation's Research Grant, which is highly acknowledged. The authors would like to thank Mr. K. Nagamine, a bachelor course student, for his experimental assistance, and to the Furukawa Electric Co., Ltd. for the offer and composition analysis of the specimens.

References

1. K. Koyama, G. Itoh and M. Kanno, "Visualizing Technique of Impurity Hydrogen Evolved from Aluminum during Deformation," J. Japan Inst. Metals, 61 (1997), 366-367.

2. G. Itoh, K. Koyama and M. Kanno, "Evidence for the Transport of Impurity Hydrogen with Gliding Dislocations in Aluminum," Scripta Mater., 35 (1996), 695-698.

3. K. Koyama, G. Itoh and M. Kanno, "Visualization of Hydrogen by means of Hydrogen Microprint Technique," J. Japan Soc. for Heat Treatment, 37 (1997), 253-254.

4. G. Itoh and M. Kanno, "Hydrogen in Aluminum," KINZOKU (Metals & Technology), 66 (1996), 599-610.

5. J. K. Tien, A.W. Thompson I. M. Bernstein and R. J. Richards, "Hydrogen Transport by Dislocations." Metall. Trans. A, 7A (1976), 821-829.

6. H. Saito, K. Miyazawa and Y. Ishida, "Tritium Transmission Electron Microscopic Autoradiography of Hydrogen Trapping Sites at Interfaces in an Austenitic Stainless Steel SUS316L," J. Japan Inst. Metals, 55 (1991), 366-375.

7. H. Okada, G. Itoh and M. Kanno, "Microscopic Analysis of hydrogen by tritium autoradiograhy," J. Japan Inst. Light Metals, 42 (1992), 112-120.

Texture Investigation of Deep Drawn Al Cup by ACOM and X-ray Measurement

No-Jin Park and Frank Springer*

Dept. Mat. Sci. & Eng., Kumoh Nat. Uni. of Tech., Kumi 730-701 Rep. of Korea
* Dept. Physical Metallurgy, TU Clausthal 38678 Clausthal-Zellerfeld, Germany

Abstract

The texture development during deep drawing is important for the understanding of anisotropy of plastic deformation. In this study the texture development of deep drawn aluminum cup has been investigated by ACOM (**A**utomated **C**rystal **O**rientation **M**apping) and compared with results from the X-ray pole figure measurement and ODF-analysis including the inverse pole figures. An aluminum sheet with 1 mm thickness was deep drawn from 60 mm diameter with a drawing ratio of 1.8. The samples for the texture analysis were taken at 45° and 90° to the initial rolling direction from the outer wall of deep drawn cup. Same samples were used for the ACOM and X-ray measurement. Initial texture after heat-treatment can be described by very strong cube texture with a weak β-fiber. After deep drawing the earings were found at 0° and 90° to the initial rolling direction. After deep drawing the intensities of orientations are strongly reduced. After deformation the sharp components of initial texture remained but the weak β-fiber disappeared. The texture by 90° to the rolling direction: after drawing the new {011}<100> orientation ({011}-plane is parallel to the cup-wall and <100>-direction is parallel to the drawing direction) was formed. This can also be shown also clearly by ACOM analysis. The orientations were spread to the perpendicular to the drawing direction. The texture by 45° to the rolling direction: after drawing the orientations were spread to the direction of deep drawing. The estimated textures from the ACOM and X-ray measurement were in this case nearly same.

The Third Pacific Rim International Conference on
Advanced Materials and Processing (PRICM 3)
Edited by M.A. Imam, R. DeNale, S. Hanada,
Z. Zhong and D.N. Lee
The Minerals, Metals & Materials Society, 1998

Introduction

The texture can be inhomogeneously formed according to the process of manufacture. In the case of the cup drawing the texture was differently developed by the various cup wall [1]. Texture development during deep drawing is important for the understanding of the anisotropy of plastic deformation and followed anisotropy of the properties, e.g. the earing behavior [2,3]. In this study the texture development has been investigated by X-ray and SEM measurement. The pole figures are measured by X-ray and the ODF-analysis are carried out with triclin sample symmetry. The ACOM is able to determine the crystallographic orientation of single grains with a high spatial resolution by the automatic interpolation of backscatter Kikuchi patterns in the SEM [4,5]. Using the computer-controlled beam scan the orientation with lies in a selected area of the specimen-surface can be measured unattendedly. From these data the texture information can be derived and displayed in pole figures or orientation distribution functions can be calculated [2].

Experimental

An aluminum sheet was heat-treated at 500°C for 20 minutes and deep drawn from 60 mm diameter with a drawing ratio of 1.8. After deep drawing the earings were found at 0° and 90° to the initial rolling direction. The gap between peak and valley was 2 mm (Fig.1). The samples for texture analysis were taken from the initial heat-treated sheet and from the deep drawn sheet at 45° and 90° to the initial rolling direction. The same samples were used for ACOM and X-ray measurement. The pole figure measurements were carried out with Co K α radiation in steps 5° (tilting) and 3.6° (rotation) up to 70° in tilt-angle. The measured range of the sample was ca. 8 mm in diameter. Three incomplete measured (111), (200) and (220) pole figures were used for the ODF-analysis with cubic crystal and triclin sample symmetry. The maximum series expansion degree was 32 [2,3].
In the right picture of figure 2 a SEM-image shows the scanned area of the sample which is taken from the outer wall of the deep drawn cup at 90° to the initial rolling direction. The crystal orientation map(COM) is displayed by two maps on the left. Each of the maps displays the measured crystallographic orientation with respect to the reference direction (RD, hereby the deep drawing direction) and the normal direction (ND, hereby the normal direction to the cup wall) as shown in figure 3. Each data point in the map is presented in a gray scale corresponding to its orientation. Crystallographic direction near <001> are presented in black, direction between <111> and <011> are colored in white. The scanned area is 0.26 mm wide with 100 scan steps and 0.86 mm high with 200 scan steps. In figure 2 the y-axis is foreshortened because of the steep tilt angle of the sample during the measurement (fig.3). The grain shape becomes more visible in the COM than in the microscope image, but the agreement is obvious. From the set of single orientation data belonging to the map texture information can be calculated [2]. Before calculation a filter routine removes less reliable data set [5].

Results and Discussion

The measured (111) pole figure, two cuts (φ_2 = 0° and 60°) of the ODF and two inverse pole figures for the normal (ND) and rolling direction (RD) of the initial sheet are given in figure 4. The initial texture after heat treatment can be described by a very strong {001}<100> cube texture with the maximum intensity of 88.86 x random and a weak β-fiber which runs from {112}<111> to {123}<634> and {011}<211>.

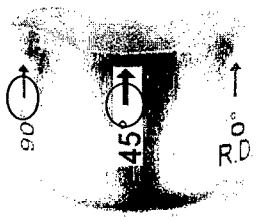


Figure 1: Deep drawn Al cup marked the measured range

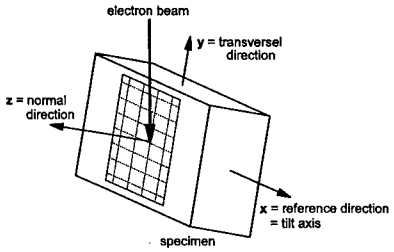


Figure 3: The steeply tilted specimen with reference system in the SEM

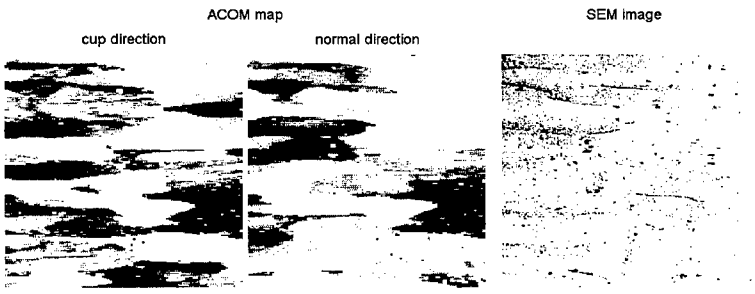


Figure 2: Orientation Map and SEM image before correction of the tilt-angle by the sample at 90° to the initial rolling direction

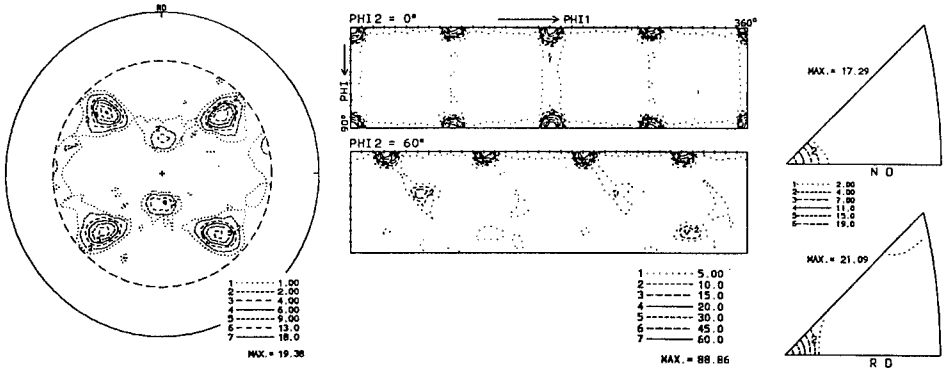


Figure 4: With X-ray measured (111) pole figure, $\varphi_2 = 0^\circ$ and 60° cuts of the ODF and inverse pole figures for the normal (ND) and rolling direction (RD) of initial sheet

After deep drawing the intensities of orientations are drastically reduced to a maximum intensity of only ca. 15% of the initial one, and the spread range of the orientation components are expanded. After deformation the sharp components of initial texture were remained but the weak β-fiber has disappeared.

Texture by 90° to the initial rolling direction

The measured (111) pole figure, two ODF-cuts and inverse pole figures for the normal direction (ND) to the cup wall and for the deep drawing direction (RD) are given in figure 5. The orientations which is shown in the (111) pole figure were spread to the perpendicular to the deep drawing direction. After deep drawing together with the strong {001}<100> orientation the new orientation near by {023}<100> orientation (at {0°, 35°, 0°} in Euler-space) was formed. This means here the {023} plane is parallel to the cup-wall and <100> direction is parallel to the deep drawing direction, which is shown also in both inverse pole figures. Another weak new component is also found at near the {011}<111> orientation (at {120°, 50°, 0°} in Euler-space). This is shown clearly by ACOM analysis (fig.6). The COMs are corrected with respect to the tilt angle of the sample. The with ACOM measured single orientations calculated ODF is given in figure 6. The orientations of the near {023}<100> and {012}<100> component are more sharper. This is slightly different from the ODF with X-ray measurement. This can be described with the different measured range. By the single orientation measurement the measured range is 0.26 mm x 0.86 mm which is much smaller than by X-ray measurement. This represents a more local texture. The white spots in the maps correspond to pores in the specimen surface which are shown by SEM image in figure 2. At such preparation artifacts show no Kukuchi pattern can take place and therefore the orientation can't be determined.

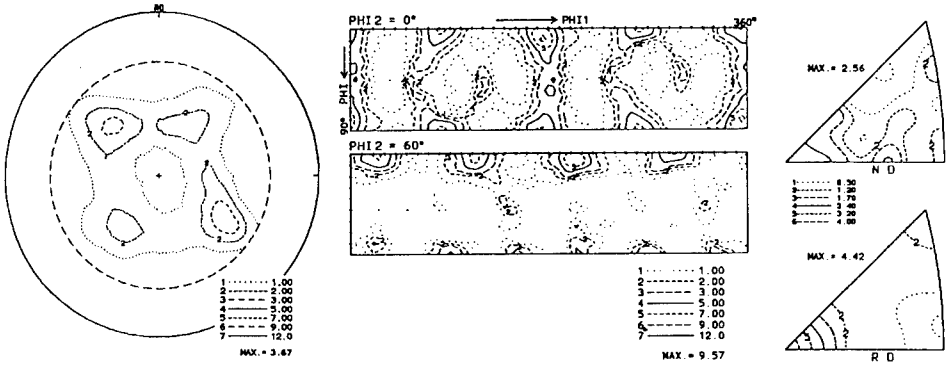


Figure 5: After deep drawing with X-ray measured (111) pole figure, $\varphi_2 = 0°$ and 60° cuts of the ODF and inverse pole figures for the normal direction (ND) to the cup wall and for the deep drawing direction (RD) by the sample at 90° to the initial rolling direction

Texture by 45° to the initial rolling direction

The (111) pole figure and two cuts of the ODF are given in figure 7. After deep drawing the orientations were spread to the direction of deep drawing. The maximum intensity is higher than that by 90° to the rolling direction measured one. This is caused by the low deformation degrees during the deep drawing. (It can be recognized that the peaks of earing were found at 90° and 0° to the initial rolling direction and valley at 45°, fig.1). By the 45° to the rolling

direction the {001}<110> orientation was found as the predominant component which originated from the main {001}<100> orientation of the initial sheet. In this case the estimated texture from ACOM and X-ray measurement are very similar (fig.7, 8). A new orientation near by {011}<100> orientation (at {0°, 45°, 0°} in Euler-space) was found with low intensity. This component is formed during the deep drawing processes.

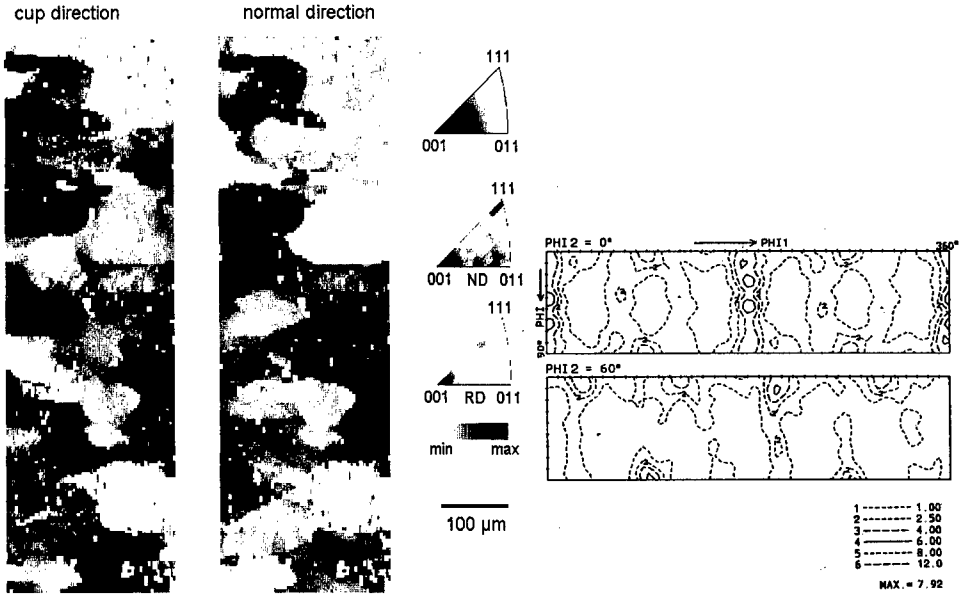


Figure 6: Orientation map and with single orientations calculated ODF by the sample at 90° to the initial rolling direction (SEM measurement)

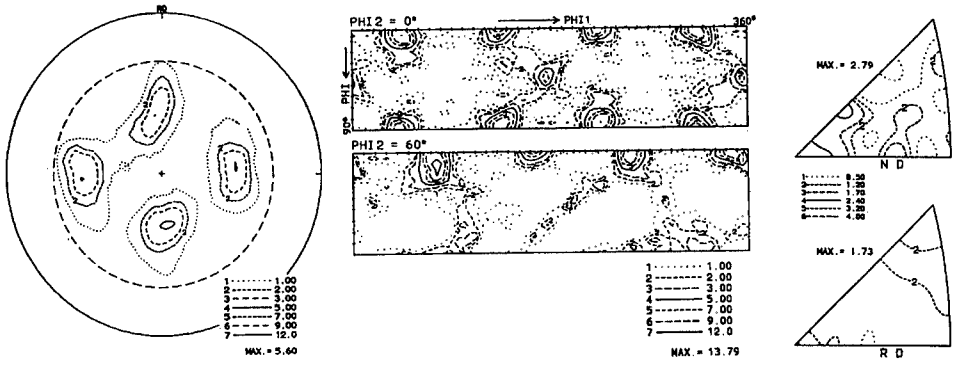


Figure 7: After deep drawing with X-ray measured (111) pole figure, $\varphi_2 = 0°$ and 60° cuts of the ODF and inverse pole figures for the normal direction (ND) to the cup wall and for the deep drawing direction (RD) by the sample at 45° to the initial rolling direction

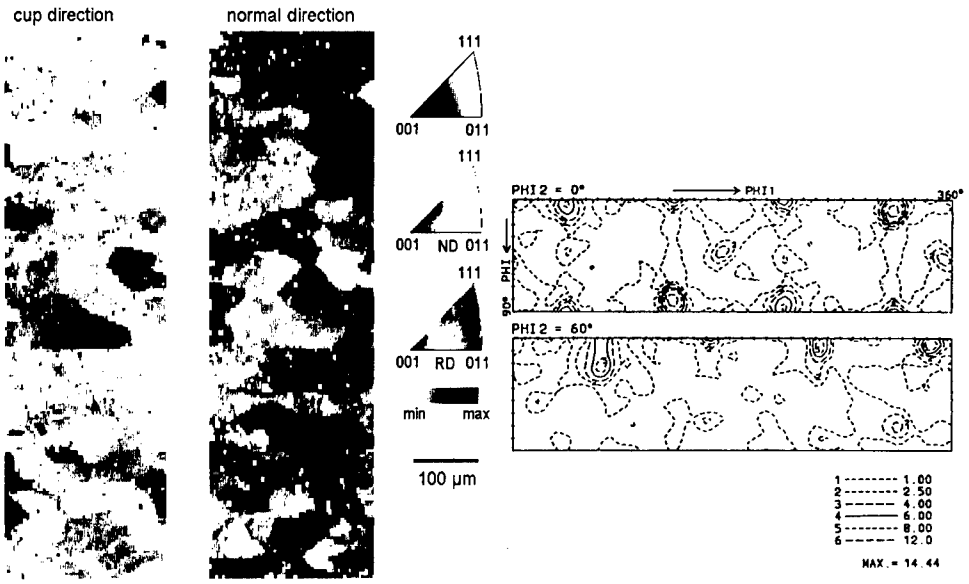


Figure 8: Orientation map and with single orientations calculated ODF by the sample at 45° to the rolling direction (SEM measurement)

Conclusion

After deep drawing the sharp cube component of the initial texture still remained with much reduced intensity. New orientations are formed near {023}<100> at 90° to the rolling direction, which is represented with the cup-symmetry (cup-wall and deep drawing direction) and by {011}<100> at 45° to the rolling direction. The results measured by ACOM are qualitatively very similar to the results which are acquired with the X-ray technique which yields an integrated texture information of a large region of the specimen. With ACOM it is possible to measure local textures with a high spatial resolution, therefore the small-angle grain boundaries in the same grain which causes by the deformation can be measured..

References

[1] J.R. Hirsch, T.J. Rickert, "Texture Evolution During deep drawing in Aluminium Sheet", Materials Science Forum, 157-162 (1994), 1979-1984

[2] H.J. Bunge, "Texture Analysis in Materials Science", Butterworths Pub., London (1982)

[3] N.J. Park, H. Klein, E. Dahlem-Klein, "Program System Physical Properties of Textured Materials", Cuvillier Verlag, Goettingen (1994)

[4] R.A. Schwarzer, "The Study of Crystal Texture by Electron Diffraction on a Grain-Specific Scale" Microscopy and Analysis, 45 (1997), 35-37

[5] F. Springer, "Recent Development in Automated Crystal Orientation Mapping (ACOM) - Quantitative Evolution and Graphical Representation of Individual Grain Orientation Data", Materials Science Forum, 273-275 (1998), 191-200

A STUDY ON THE GRAIN REFINING AND AGE HARDENING OF Mg-Zn-Cu AND Mg-Zn-Si ALLOYS

In-Shup Ahn, Tae-Hyun Nam, Yoo-Young Kim

Deptartment of Metallurgical & Materials Engineering and Research Center for Aircraft Parts Techanology, Gyeongsang National University, Chinju, Gyeongnam 660-701, Korea

Abstract

The microstructure and aging behavior of Mg-6wt%Zn-2wt%Cu and Mg-6wt%Zn-1.5wt%Si alloys were investigated. Alloy ingot was made under the vacuum atmosphere of 4 x 10^{-4} torr in the quartz tube coated by BN. Grain size and hardness were measured after solution treatment for 8 hours at 435°C. Addition of 2wt%Cu to Mg-6wt%Zn alloy results in the formation of spherical type $MgZn_2$ and Mg_2Cu of 1.5 ㎛ mean particle size at the grain boundary. Addition of 1.5wt%Si to Mg-6wt%Zn alloy result in the formation of 15㎛ mean particle size chinese script type Mg_2Si at the grain boundary and in the matrix. The hardness increment due to fine grain size was higher at the Mg-Zn-Cu alloy system, but the hardness increment due to age hardening was higher at the Mg-Zn-Si alloy system. Second phase particles of several micron size were present at the grain boundary of these alloy systems after age hardening treatment at 180℃. Precipitated second phases were confirmed as Mg_2Zn_3 in Mg-Zn-Cu alloy and Mg_2Zn_{11} in Mg-Zn-Si alloy by transmission electron microscope analysis.

The Third Pacific Rim International Conference on
Advanced Materials and Processing (PRICM 3)
Edited by M.A. Imam, R. DeNale, S. Hanada,
Z. Zhong and D.N. Lee
The Minerals, Metals & Materials Society, 1998

Introduction

Magnesium alloys are used extensively in the aircraft industry and for space applications on account of the favourable strength : weight ratio. In order to enhancing the strength of magnesium alloy, third element addition to magnesium alloy was used for grain size refining and solution hardening.[1] To produce optimum tensile properties and adequate toughness it is imperative to obtain effective grain refinement during casting. In most Mg casting alloys, grain refinement is accomplished by the addition of Zr to the melt.[2] The exact mechanism by which the Zr produces the grain refinement is not clear. Certainly Zr is concentrated at the center grain in cast micro structure. If the Zr particles precipitated first from the liquid they could act as effective nucleating agents.[3,4] Recently grain refinement is accomplished by the addition of Cu, Si or Al to the melt instead of Zr.[5,6]

The addition of small amounts of Cu or Si to Mg-Zn alloys eliminates the tendency of the binary alloy to tear the crack and reduces the susceptibility of the alloy to micro porosity. The third element addition was to change the morphology of the eutectic phase from divorced eutectic of Mg-6Zn to a lamellar inter growth of Mg and inter metallics. This change in morphology increase in ductility of the cast Mg-Zn alloy. The addition of Si or Cu to the binary Mg-6Zn effects the grain size refining and age hardening by second phase precipitation. Optimal condition for grain size refining effect was obtained at the minimum composition of 2wt.%Cu or 1.5wt.%Si addition to Mg-6wt.%Zn alloy as known in the previous paper.[7] However, the exact grain refinement mechanism by the addition of Cu or Si and precipitation phenomena is not clear. In this study, precipitation phenomena of second phase was analysed by the addition of Cu or Si to Mg-6%Zn alloy after solution and aging treatment.

Experimental procedure

Alloy ingot was melted at the 760℃ for 10 minutes under the vacuum atmosphere of 4 x 10^{-4} torr in the quartz tube coated by BN. Grain size and hardness were measured after solution treatment for 8 hours at 435°C under the vacuum atmosphere of 4 x 10^{-4} torr in the quartz tube. Age hardening was treated at the temperature between 180 and 200℃. Microstructures of solution treated and age hardened alloys were observed with optical microscopy and scanning electron microscopy(SEM). The precipitated phase was analyzed with X-ray diffractometer(XRD) and transmission electron microschopy (TEM). Rockwell hardness of solution treated and age hardened ingots was measured.

Results and discussion

Figure 1(a) and (b) show the microstructure of Mg-6Zn-2Cu and Mg-6Zn-1.5Si alloys after solution treatment for 8 hours at 435℃. Figure 1(a) shows the grains of 20μm mean size and homogeneous distribution of spherical type second phase particles at the grain boundary. Figure 1(b) shows the mean grain size of 40μm and homogeneously distributed chinese script type second phase at the grain boundary and in the grains. This difference of precipitated region and particle shape will effect on the grain growth and on the mechanical properties. Figure 2(a) shows the bright field TEM image of Mg-6Zn-2Cu matrix and (b) shows the dark field image of (a) after solution treatment. Matrix phase is well coincided with $[0\bar{1}1\bar{1}]_{Mg}$ zone of h.c.p crystal structure of Mg. Figure 2 (c) is the bright field TEM image of Mg-6Zn-1.5Si matrix and (d) is the dark field TEM morphologies of (c) after solution treatment. Fig. 2(d) pattern is well coincided with $[7\,1\,\bar{8}\,2]_{Mg}$ zone of h.c.p Mg crystal structure. Mg matrix phase was confirmed in both alloy systems from Figure 2 (b) and (d), because other phase was not obtained in both alloys.

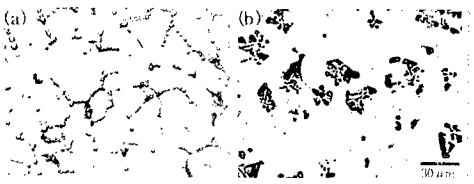


Fig.1 Optical micrographs of Mg-6Zn-2Cu and (b) Mg-6Zn-1.5Si alloys after solution treatment for 8hours at 435℃.

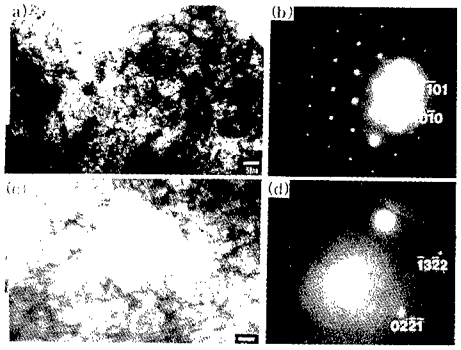
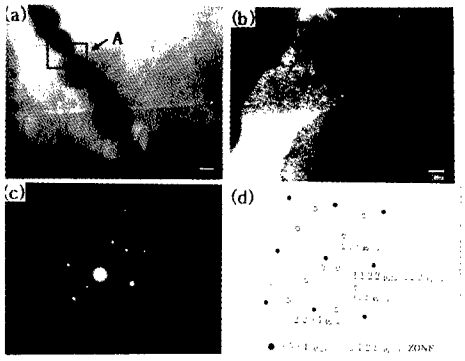


Fig.2 Bright-field TEM micrographs of (a) Mg-6Zn-2Cu and (c) Mg-6Zn-1.5Si alloys in matrix after solution treatment and selected area electron diffraction patterns of (b) showing an $[0\bar{1}1\bar{1}]_{Mg}$ zone in (a) and (d) $[71\bar{8}2]_{Mg}$ zone in (c).

Figure 3(a) and (b) show bright field TEM image of precipitated phase of Mg-6Zn-2Cu. after solution treatment. (c) is dark field TEM images of figure 3 (b) and (d) is schematic diffraction patterns for analysis of the diffraction in (c). Figure 3 (a) shows the spherical particles of $1\,\mu m \sim 2\,\mu m$ size precipitated on the grain boundary. Figure 3(b) is enlarged picture of the region A in figure 3 (a). Superimposed patterns were appeared from the schematic diffraction patterns of figure 3(d), one is h.c.p crystal structure of $MgZn_2$ $[\bar{3}\bar{5}84]$ zone, the other is orthorthombic crystal structure of Mg_2Cu $[12\bar{1}]$ zone.[8] Diffraction pattern of Figure 3(d) shows $(\bar{2}22)_{Mg_2Cu}$// $(\bar{1}3\bar{2}3)_{MgZn_2}$, $[12\bar{1}]_{Mg_2Cu}$// $[\bar{3}\bar{5}84]_{MgZn_2}$.



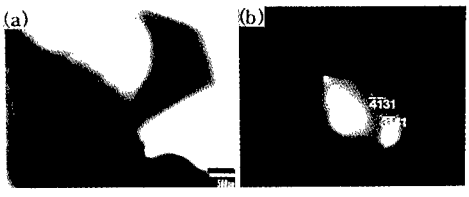


Fig.3 Bright-field TEM micrographs of Mg-6Zn-2Cu alloy in precipitated phases (a),(b) after solution treatment, and (c)diffraction patterns in (b) and (d)schematic diffraction patterns of (c).

Fig.4 (a) Bright-field TEM micrographs of Mg-6Zn-1.5Si alloy in precipitated phase after solution treatment and (b) selected area electron diffraction patterns showing $[0\bar{1}1\bar{1}]_{Mg_2Si}$ zone in (a).

Figure 4(a) and (b) are the bright field TEM image and diffraction pattern of precipitated phase of Mg-6Zn-1.5Si alloy after solution treatment. Figure 4(a) shows the faceted precipitate particles of $10\sim20\,\mu m$ size and (b) is selected area electron diffraction pattern showing h.c.p crystal structure Mg_2Si $[0\,\bar{1}\,1\,\bar{1}]$ zone in (a). [9]

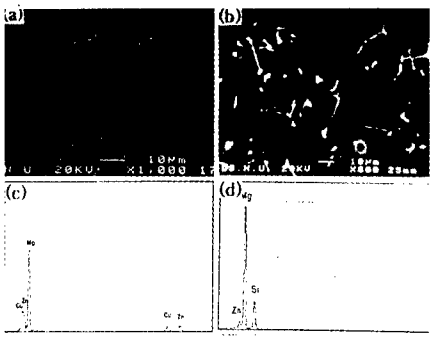


Fig.5 SEM micrographs of (a) Mg-6Zn-2Cu and (b) Mg-6Zn-1.5Si alloys after solution treatment and EDS analysis of precipitated phases of (c) Mg-6Zn-2Cu and (d)Mg-6Zn-1.5Si alloys

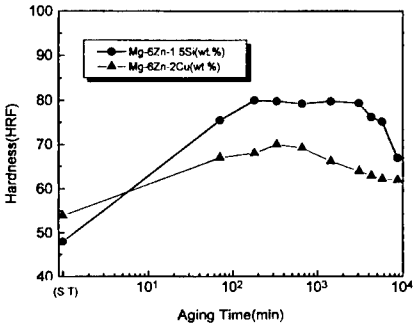


Fig.6 The relationship between aging time and hardness of Mg-6Zn-2Cu and Mg-6Zn-1.5Si alloys after solution treatment for 8hours at 435℃.

Figure 5 (a) and (b) show SEM morphologies of Mg-6Zn-2Cu and Mg-6Zn-1.5Si alloys after solution treatment for 8 hours at 435℃, and (c) and (d) are the EDS analysis of precipitated phases of (a) and (b) alloys. Fig. 5(a) shows the spherical particles of 1 $\mu m\sim2\,\mu m$ size precipitated on the grain boundary, which is coincided with the results of figure 3(a). This particles are the Mg, Zn and Cu compounds shown in figure 5(c). Figure 5(b) shows the chinese script type precipitate particles of Mg-6Zn-6Si alloys. This particles precipitated both at the grain boundary and matrix which is the compounds of Mg and Si shown in Figure 5(d). This is well coincided with the results of Figure 4. It is considered that the detected Zn came from the matrix.

Figure 6 shows the relationship between aging time and hardness of Mg-6Zn-2Cu and Mg-6Zn-1.5Si alloys after aging treatment at 180℃.

Both alloys show the age hardening behaviour, maximum hardness was obtained at 320 minutes aging times of Mg-6Zn-2Cu and at 180 minutes aging times of Mg-6Zn-1.5Si. Initial hardness was higher value at the Mg-6Zn-2Cu alloy, which was due to grain size refining. Maximum hardness, however, was higher at the Mg-6Zn-1.5Si alloy systems and age hardening rate of Mg-6Zn-1.5Si alloys was higher than that of the Mg-6Zn-2Cu alloys. Age hardening of Mg-Zn alloy system is due to the precipitate phase of Mg and Zn compounds, and in the case of Mg-Zn-Cu alloy, precipitate phase contains Zn as shown in figure 5, which is reduce the residual Zn amounts in matrix, it is considered that this effects results in the low slope of hardness increase. Precipitated phase at the time which maximum hardness could be obtained was analyzed by XRD as shown in figure 7. Figure 7 shows the XRD patterns of (a) Mg-6Zn-2Cu after aging treatment for 320 minutes at 180℃ and (b) Mg-6Zn-1.5Si alloy after aging treatment for 180 minutes at 180℃. Mg_2Cu and $MgZn_2$ were obtained from solution treatment at 450℃, Mg_2Zn_3 were obtained from the aging treatment as shown in figure 7(a). Figure 7(b) shows two kinds of precipitated phases of Mg_2Si and Mg_2Zn_{11}. Precipitated phase Mg_2Zn_{11} appeared newly after age hardening treatment.

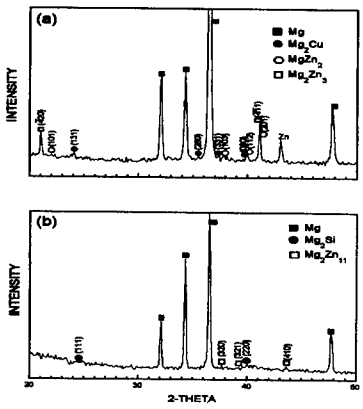


Fig.7 XRD patterns of (a) Mg-6Zn-2Cu alloy after aging treatment for 320min. and (b) Mg-6Zn-1.5Si alloy after aging treatment for 180min. at 180℃.

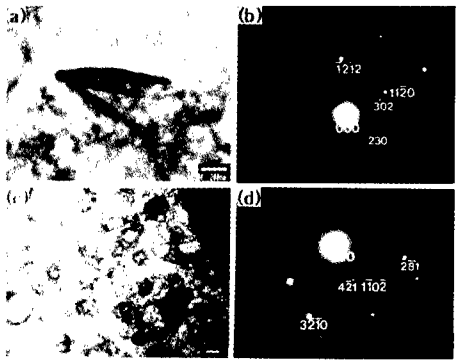


Fig.8 Bright-field TEM images of (a) Mg-6Zn-2Cu and (c) Mg-6Zn-1.5Si alloy in after aging treatment for 180min. at 180℃, and (b)(d) selected area electron diffraction patterns of (a) and (c).

Figure 8 shows (a) bright field TEM image of precipitate phase in Mg-6Zn-2Cu alloy after aging treatment for 320 minutes at 180℃ and (c) bright field TEM image of precipitate phase in Mg-6Zn-1.5Si alloy after aging treatment for 320 minutes at 180℃, and (b) and (d) is individually dark field image of (a) and (c). Figure 8(a) shows the needle shape phase of 0.7~1㎛ length and 50~100㎚ width precipitated in Mg-6Zn-2Cu alloy. Figure 8(b) shows h.c.p. crystal structure of Mg $[2\,\bar{2}\,0\,3]_{Mg}$ zone, and superimposed triclinic crystal structure Mg_2Zn_3 $[6\ \bar{4}\ \bar{9}]_{Mg_2Zn_3}$ zone. Rounded shape particles of 150~200㎚ size was distributed homogeneously as shown in figure 8(c), which is superimposed patterns of h.c.p Mg $[4\,6\,\bar{10}\,\bar{1}]_{Mg}$ zone and b.c.c. Mg_2Zn_{11} well coincided with $[3\,\bar{1}\,\bar{19}]_{Mg_2Zn_{11}}$ zone.

Conclusions

1. The precipitate phase by adding 2%Cu to Mg-6wt.%Zn alloy were $MgZn_2$ and Mg_2Cu, and Mg_2Si was formed by adding 1.5wt.%Si.
2. In the case of Mg-6Zn-2Cu alloy, precipitate phase contains the Zn which reduce the residual Zn amount in matrix, results in the low slope of hardness increase.
3. After aging treatment the precipitated phase formed by adding 2%Cu or Si were Mg_2Zn_3 or Mg_2Zn_{11} at the Mg-6Zn alloy system.

Acknowledgements

The authors would like to thank for financial support of the Korean Science and Engineering Foundation through the project 93-0300-07-01-3.

References

1. B. Kittilsen, Magnesium Technology(The Inst. of Met., 1987), 36.
2. Robert S. Busk, Magnesium Products Design(Marcel Dekker INC, 1987), 149.
3. Japanese Casting Association, Casting Handbook (Dae Kwang Co, 1979), 1422.
4. D.H.Kim, H.I.Lee, E.P.Yoon, "Development of Aluminium and Magnesium alloys by rapid solidification techniques", J. of Korean Institute of Metals and Materials, 4 (1991), 340.
5. E. Ivanov, B. Bokhonov, I. Konstanchuk, "Synthesis and process characterization of mechanically alloyed icosahedral phase Mg-Zn-Al", J. of Mater. Sci., (1991), 1409.
6. Toshiyuki Sato, Junichi Kaneko and Makoto Sugamata, "Structures and mechanical properties of rapidly solidified Mg-6wt%Zn alloys with addition of Zr,Mn,Ni,Si and Ce", Light Metals, 42 (12) (1992), 720.
7. J.H.Whang et al., "Grain refining and age hardening of Mg-Zn alloys by addition of Cu and Si", Korean J. of Materials Research, 5, (1995), 682.
8. A. A. Nayeb-Hashemi and J. B. Clark, Binary alloy phase diagrams, 2th ed., 2 (1988), 1433.
9. J. A. Juarez-Islas, "Rapid solidification of Mg-Al-Zn-Si alloys", Material Science and Engineering, Al34 (1991), 1193.

MECHANICAL PROPERTIES AND MICROSTRUCTURE OF Mg-Zn-(Mn) ALLOYS FABRICATED UNDER AN Ar GAS ATMOSPHERE

Jeong-Pil Eom, Su-Geun Lim and Bo-Young Hur

Dept. of Metallurgical & Materials Eng., Gyeongsang National Univ.
Research Center for Aircraft Parts Technology,
Chinju, Gyeongnam, 667-701, KOREA

Abstract

Mg-Zn and Mg-Zn-Mn alloys were fabricated under an Ar gas atmosphere. The liquid Mg alloys were casted into the metallic mold, and cooling part was located at the bottom of mold. The microstructure of Mg-Zn cast alloys revealed that MgZn compounds were around the secondary dendrite arms. The addition of Mn in Mg-Zn alloys refined the grain size in as-casted alloys. The yield strength and ultimate tensile strength of the Mg-1~6wt%Zn alloys increased with increasing Zn content, the ductility did not change with increasing Zn content. The maximum yield strength, tensile strength and ductility obtained in the Mg-6wt%Zn alloy were $\sigma_{0.2}$ = 104 MPa, σ_u = 235 MPa, and e = 9.2%. The addition of Mn improves the yield strength and ultimate tensile strength of the alloys, but the ductility did not change. Tensile fracture of the alloys revealed brittle failure. The variation of stress with strain obeyed the relationship of the $\sigma = K\varepsilon^n$.

The Third Pacific Rim International Conference on
Advanced Materials and Processing (PRICM 3)
Edited by M.A. Imam, R. DeNale, S. Hanada,
Z. Zhong and D.N. Lee
The Minerals, Metals & Materials Society, 1998

Introduction

The binary Mg-Zn system was the maximum solid solubility of zinc is 6.2% at 613K decreasing to about 1.7% at room temperature. Zinc addition to magnesium was of outstanding interest in promoting strength in castings, due to the solid solution strengthening and precipitation strengthening[1~4].

Effects of manganese addition to Mg-Zn alloy is increase of strength, due to fine compoud formation, and impurities(present in the magnesuim, iron, copper, nickel) acts as microscopic cathodes which destroyed the protective oxide film on the metal surface. Manganese addition to molten magnesuim precipitate iron, copper, nickel and harmful impurities from solution, thus greatly improving the corrosion resistance[5].

Therefore, in the present study the microstructure of Mg-Zn alloys with and without manganese will be compared. The influence of manganese addition on mechanical properties will also be investigated.

Experimental procedure

Magnesium or its alloys of total amount 150g was melted in the low carbon steel crucible(coated with boron nitride) by cylindrical electric furnace under an argon atmosphere. The melting and casting apparatus is specially designed for magnesium alloys. The liquid Mg alloys were casted into the metallic mold at 993K, and cooling part was located at the bottom of mold.

For optical metallography, samples were mechanically polished and etched with a dilute solution of nitric acid in ethyl alcohol.

The tensile specimens, conformed to sub-size. The gauge length of the specimens was 12.6mm with 2mm thickness, 5mm width. To minimize the effects of surface irregularities and finish, the gauge sections were ground using 1000 grit silicon carbide paper in order to remove any and all circumferential scratches and surface machine marks. Tensile tests were performed on the Instron No. 4306 machine in a room temperature(25℃), laboratory air environment. Specimens of each magnesium alloy were deformed at a constant cross head speed of 1mm/min.

Fracture surfaces of the deformed tensile specimens were examined in a scanning electron microscope in order to characterize the predominant fracture mode and the fine scale features on the tensile fracture surface.

Results and discussion

Optical micrographs of the Mg cast alloys are shown in Figure 1. All alloys had typical dendritic solidification microstructures with significant amounts of interdendritic phases. The microstructure of the Mg-Zn alloy was significantly coarser than the Mg-Zn-Mn alloy. The grain size and the volume fraction of the intergranular phases in the Mg-Zn-Mn alloy was less than for the Mg-Zn alloy. The mean grain size of Mg-Zn binary alloys were about 130 ㎛ But the mean grain size of Mg-Zn-Mn alloys were about 65㎛ The grain size in the cast alloys was measured by the linear intersect method.

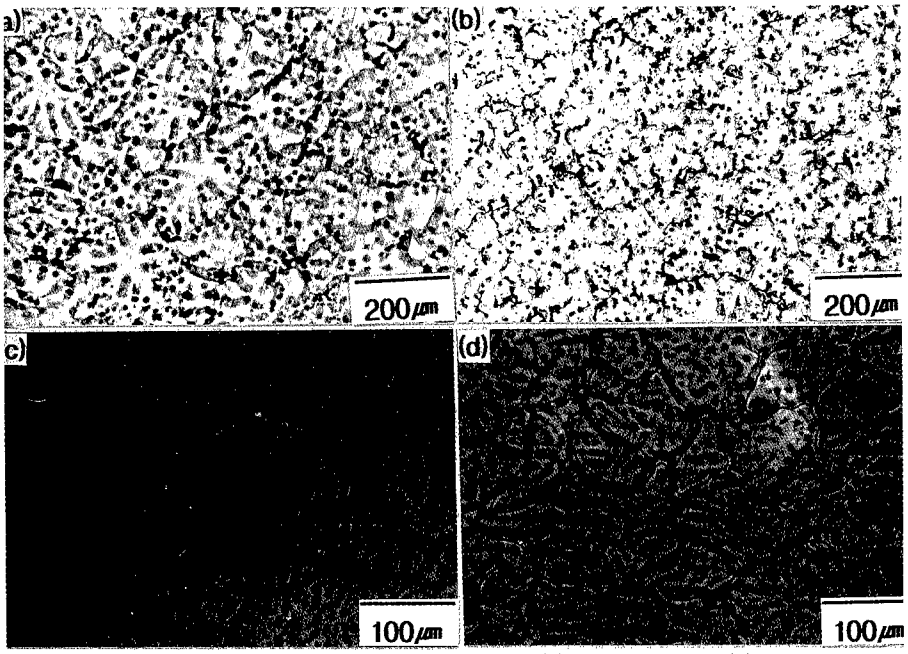


Figure 1: Optical micrographs of Mg alloy castings. (a) Mg-3wt%Zn, (b) Mg-6wt%Zn, (c) Mg-3wt%Zn-1wt%Mn, (d) Mg-6wt%Zn-1wt%Mn.

Figure 2 shows SEM and EDS of interdendritic regions from the as-cast specimen of the Mg-6wt%Zn alloy. The microstructure of Mg-Zn cast alloys revealed that MgZn compounds were around the secondary dendrite arms. Scanning electron microscope and energy dispersive spectroscopy showed that the composition of MgZn compound was Mg-77wt%Zn±2%, which corresponds with the value of Mg-74.5wt%Zn given by Clark and Rhines[6] for virtually stoichiometric MgZn. This phase maybe decomposed to α + MgZn eutectoid during slower cooling.

Figure 3 shows SEM and EDS of the Mg-6wt%Zn-1wt%Mn alloy. The microstructure of Mg-Zn-Mn alloy revealed that MgZn compounds of interdendritic(A of Figure 3) and Mn-rich compounds of the intradendritic(B of Figure 3).

The room temperature tensile properties of the magnesium alloys are summarized Table I. Duplicate samples were tested for each condition and no significant variation between the pairs of samples was observed.

The yield strength, $\sigma_{0.2}$, defined as the stress required at a plastic strain of 0.2% and ultimate tensile strength of the Mg-1~6wt%Zn alloys increased with increasing Zn content, the ductility measured by elongation over a 12.6 mm guage length of the specimen, did not change with increasing Zn content. The ultimate tensile strength, of all magnesuim alloys, is significantly higher than the yield strength, indicating that the work hardening rate past yielding is high. Whereas, the yield strength and ultimate tensile strength of the Mg-Zn-Mn alloy was significantly higher than that of Mg-Zn binary alloy. But the ductility of alloy was decreased. The high strengthing of the Mg-Zn-Mn alloys can be ascribed to the conjoint action of :

1. fine grain size,
2. dispersion strengthing from the presence of Mn-rich compound.

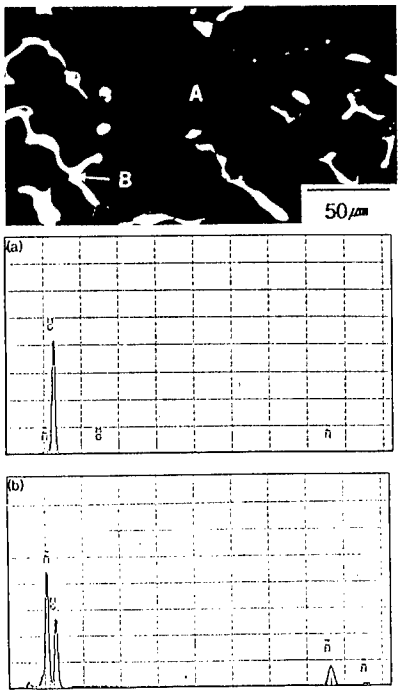


Figure 2: SEM-EDS analysis of Mg-6wt%Zn alloy castings. (a)EDS of A, (b) EDS of B.

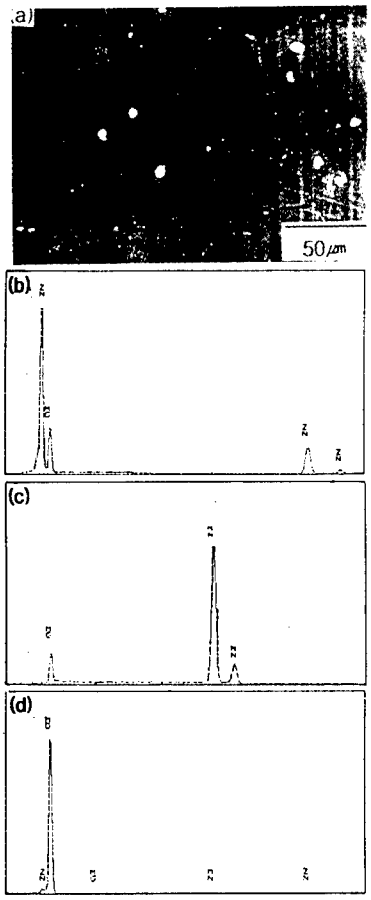


Figure 3: SEM-EDS analysis of Mg-6wt%Zn -1wt%Mn alloy castings. (a)SEM of alloy castings. (b) EDS of A, (c) EDS of B, (d) EDS of C

Table I Mechanical properties of Mg-Zn and Mg-Zn-Mn magnesium alloys

Specimens	U T S, σ_u MPa	0.2% yield strength, $\sigma_{0.2}$ MPa	Elongation, e (%)
Mg-1wt%Zn-F	143	62	9.2
Mg-2wt%Zn-F	162	65	8.5
Mg-3wt%Zn-F	184	74	10.4
Mg-4wt%Zn-T6	211	91	10.5
Mg-5wt%Zn-T6	225	102	9.9
Mg-6wt%Zn-T6	235	104	9.2
Mg-3wt%Zn-1wt%Mn-F	212	107	6.7
Mg-6wt%Zn-1wt%Mn-F	237	118	6.8

Table II showed strain hardening exponent, n and strength coefficient K for magnesium alloys at room temperature. n and K of the alloys was evaluated from examining the variation of stress with strain plotted on a bilogarithmic scale for true stress-strain curve. The variation of stress with strain obeyed the relationship of the $\sigma = K\varepsilon^n$. The strain hardening exponent of the all alloys did not change with zinc content. In the present work, strain-hardening exponent of the Mg-Zn binary, Mg-Zn-Mn ternary alloys was n = 0.19, 0.24, respectively.

Table II Values for n and K for Mg-Zn and Mg-Zn-Mn alloys at room temperature.

Alloy	Strain-hardening exponent, n	Strength coefficient, K, MPa
Mg-1wt%Zn-F	0.19	215
Mg-2wt%Zn-F	0.20	250
Mg-3wt%Zn-F	0.19	322
Mg-4wt%Zn-T6	0.18	310
Mg-5wt%Zn-T6	0.18	340
Mg-6wt%Zn-T6	0.20	567
Mg-3wt%Zn-1wt%Mn-F	0.25	344
Mg-6wt%Zn-1wt%Mn-F	0.23	395

Figure 4 shows tensile fracture surfaces of Mg-Zn and Mg-Zn-Mn alloys. Tensile fracture of the all alloys revealed brittle fracture, and fractography of the tensile samples revealed near similar features, for the all magnesium alloys.

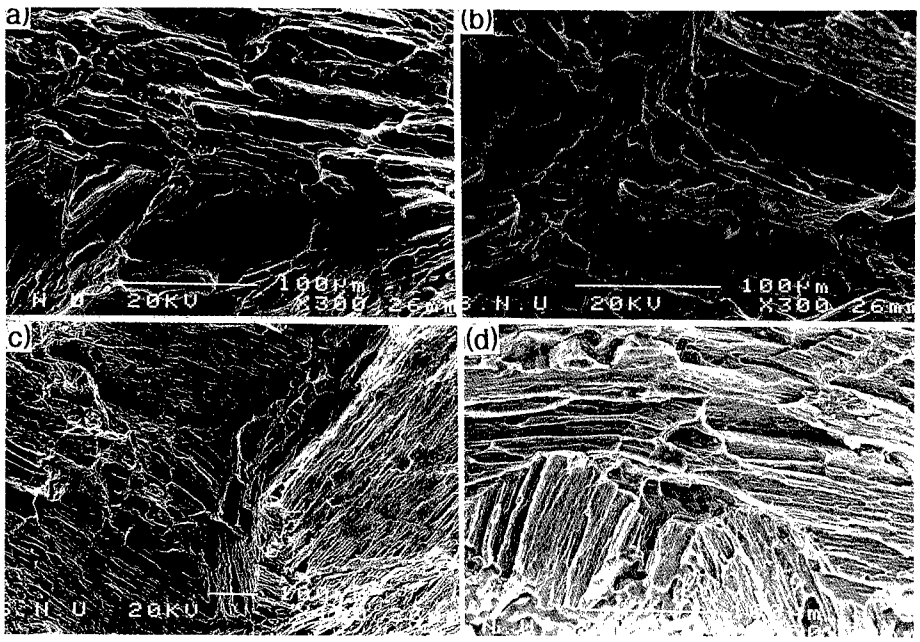


Figure 4: Scanning electron micrographs of the tensile fracture surface of Mg alloys. (a) Mg-3wt%Zn, (b) Mg-6wt%Zn, (c) Mg-3wt%Zn-1wt%Mn, (d) Mg-6wt%Zn-1wt%Mn.

Conclusions

Based on a study of the microstructures and mechanical properties of the Mg-Zn-(Mn) alloys, the following are key observations:

1. The main interdendritic phase which formed during slow cooling of the Mg-Zn binary alloys was the MgZn compound.

2. The microstructure of Mg-Zn-Mn alloy revealed that MgZn compounds of interdendritic, and Mn-rich compounds of the intradendritic.

3. The strength of the Mg-Zn-(Mn) magnesuim alloys increased with an increase in zinc content. The strain hardening capability of the alloys was high.

4. The strength of the Mg-Zn-Mn alloys was significantly higher than that of Mg-Zn binary alloys. But the ductility of alloy is decreased.

5. The variation of stress with strain obeyed the relationship of the $\sigma = K\varepsilon^n$, did not change with zinc content.

6. Tensile fracture of the alloys revealed features reminiscent of brittle failure.

Acknowledgements

The authors are grateful to the Korea Science and Engineering Foundation for their kind support of this project under Grant No. 93-0300-07-01-3.

References

1. W. Unsworth, Light Metal Age, 45 (1987) 10.

2. E. F. Emely, "Principles of Magnesium Technology", Pergamon Press, (1966) 272.

3. L. B. Duffy, Foundary Trade J., 3 (1991) 319.

4. I. J. Polmear, "Light Alloys", 2nd (1989) 169.

5. B. Kittilsen, "Magnesium Technology", (1987) 36.

6. J. B. Clark and F. N. Rhines, J. Met., 209 (1957) 423.

A STUDY ON TECHNIQUE OF MAKING FOAM Al-ALLOYS

Siyi Yang, Yong Zhang, Zicong Xing, Haochen Wang

Department of Mechanical Engineering
Shandong Institute of Technology
Zibo, China 255012

Abstract

The effects of preheating temperature of granules, pouring temperature of melt and forming pressure on the forming process of penetrating casting of foam Al-alloys around granules were systematically studied using orthogonal experiment method and choosing three kinds of the granules size. The experimental results were theoretically analyzed. It is considered that the reasonable selection of granules preheating temperature is prerequisite to produce the foam metal castings, proper increase of pouring temperature is a key to achieve the homogeneous foam structure and the moderate forming pressure can increase the product porosity and technological stability.

The Third Pacific Rim International Conference on
Advanced Materials and Processing (PRICM 3)
Edited by M.A. Imam, R. DeNale, S. Hanada,
Z. Zhong and D.N. Lee
The Minerals, Metals & Materials Society, 1998

Introduction

There are many methods available to produce metallic foams. Casting metal around granules is one of the more simple methods[1,2]. The technique has been used to produce foam Al-alloys which possesses porosity ranging from 60 to 80vol% and the size of pore from 0.1 to 10mm.The greatest size of foam Al-alloys production reaches to Φ80×300mm and it has an interconnected cellular structure. There are many factors of influencing casting metal around granules. It was found through the experiment that the main factors are preheating temperature of granules, pouring temperature and forming pressure. In order to probe the law of those factors we made the experiment.

Experimental method

Take alloy of Al and Si as example. Take the granules of ordinary table salt as the filling. The diameters of granules are 1～2mm,2～3mm and 3～4mm. The experimental unit of casting metal around granules by exerting an external pressure on the melt is shown in Figure 1.

After having been sieved the granules are heated in the furnace. Al-alloy is melted in the crucible and is processed by inpoisonous purified agent. Within the workable processing parameters it was arranged orthogonal experiments with three factors (A is preheating temperature of granules, B is pouring temperature and C is forming pressure) and four levels. Orthogonal form $L_{16}(4^5)$ was chosen. The experimental result is the effective length of experimental rod of foam Al. The effective length is the section of porosity above 60% after experimental rod of foam Al is processed.

Experimental result

The sequence of three factors is A→B→C. The excellent program is $A_3B_3C_4$

The correlation between factorial levels and experimental indexes is shown in Figure 2. With the same method set up the level designs of granules of which diameters are 2～3mm and 3～4mm. The correlations of factorial levels and experimental indexes are shown in Figure 3 and Figure 4 respectively.

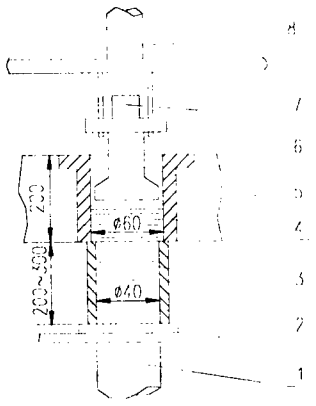


Figure 1: The experimental unit of casting metal around granules
by exerting an external pressure on the melt
1.support 2.mould 3.granules 4.pressure cavity 5.pressure head
6.fixed platform 7.regulating weight lump 8.upper pressure head support

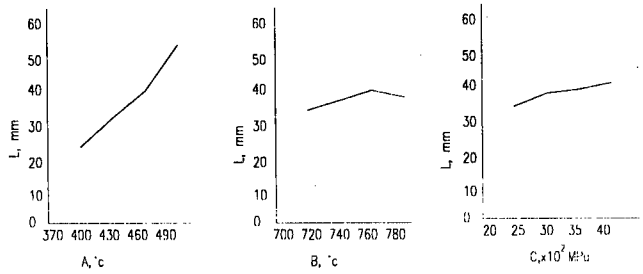


Figure 2: Correlation between the factorial levels and the experimental indexes at granules size 1～2mm

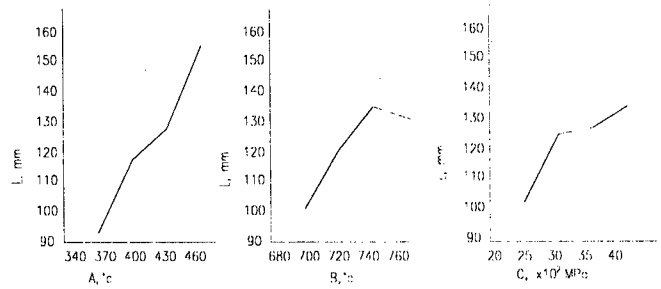


Figure 3: Correlation between the factorial levels and the experimental indexes at granules size 2～3mm

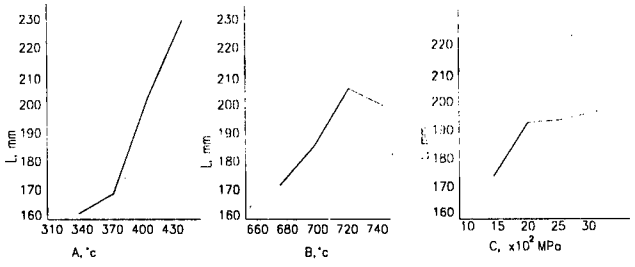


Figure 4: Correlation between the factorial levels and the experimental indexes at granules size 3～4mm

The analysis of the experimental result

The analysis of the preheating temperature of granules

The experiment showed that the preheating temperature of granules plays a decisive role in casting metal around granules. It is shown in Figure 2,Figure 3 and Figure 4 that within the workable processing parameters the effective length of experimental rod of foam Al increases as the preheating temperature of granules increases however great the diameter of granules is. The lower the preheating temperature of granules, the greater the difference in temperature of the melt and granules is. The heat exchange between the melt and granules becomes strong. Melt that surrounds granules condenses and

forms a shell when its temperature drops. As the shell becomes thick the melt in space between granules is divided into many melted baths so that the passage of the melt is blocked up. It is quite evident that every kind of granules has a suitable interval of the preheating temperature. Generally satisfied foam structure can be gained in the interval. If the preheating temperature of granules lie at the low limit of the interval pouring temperature and forming pressure must be increased in order to ensure quality. Otherwise the effective length of experimental rod of foam Al will become short. If the preheating temperature of granules is lower than the low limit of the interval technological quality can not be ensured even though pouring temperature and forming pressure are increased. Metal part that does not contain granules and granules part that does not contain metal can be found in the experimental rod. The low limit of suitable interval of the preheating temperature of granules has much to do with pouring temperature, forming pressure, the condition of dissipating heat of permanent or sand mold, the size and the shape of granules, the compression degree of granules and the intensity of heat exchange. All technological parameters must be harmoniously arranged through experiment.

The effect of casting metal around granules differs from each other when the size of granules differs from each other. The smaller the size of granules, the greater the resistance of flow and heat exchange area between melt and granules are. In the process of flow the melt is liable to condense and to block up the passage of flow so that the effective length of experimental rod of foam Al will becomes short.

As the size of granules increases the space between granules increases, the resistance of flow becomes small and the intensity of heat exchange lessens. This is conducive to casting metal around granules. Preheating temperature of granules, pouring temperature of melt and forming pressure can be reduced appropriately. Otherwise leaking and splashing of the melt happens easily.

The analysis of forming pressure

Having the melt get into the space between granules we must exert moderate pressure on it. Though the experimental result showed that the change of pressure had little influence on the effective length of experimental rod of foam Al choosing the moderate forming pressure was quite necessary. Static pressure of the melt and little external pressure can not make the melt get into the space between granules. The overgreat external pressure may compress granules into pieces or into solid so that the mixture of broken granules and metal emerges in the castings. Porosity drops.

The state of granule stresses in the layer of filling metal around granules is shown in Figure 5[3].

Cut a little column. The analysis of force is:

$$\frac{\pi}{4}D^2\sigma + \frac{\pi}{4}D^2\theta dl = \frac{\pi}{4}D^2(\sigma + d\sigma) + \pi D\,\mu_w\, k\sigma dl$$

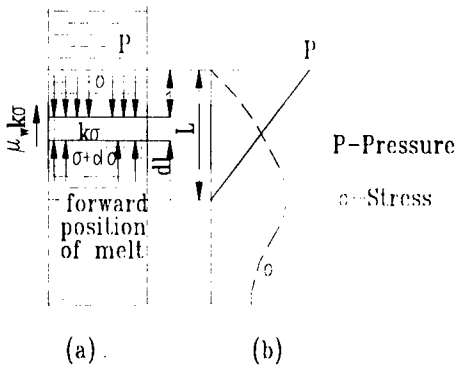


Figure 5: Distribution of stress in the filling layer
(a) stress analysis (b) stress distribution

where

kσ=the stress that is perpendicular to the axis of sample (Pa)
μ_w=the frictional coefficient between granules and wall of permanent mold
θ=P/L =pressure drop of the melt per unit length (N/mm)
L=length of the melt flowing around granules (mm)
D=inner diameter of permanent mold (mm)

Former equation is rearranged. There is

$$\frac{d\sigma}{dl}+\frac{4\mu_w k\sigma}{D}-\theta=0$$

Solve the equation. Where 0≤l≤L there is

$$\sigma = \frac{D\theta}{4\mu_w k}\left[1-\exp\left(-\frac{4\mu_w k}{D}l\right)\right]$$

where l≥L

$$\sigma = \frac{D\theta}{4\mu_w k}\left[1-\exp\left(-\frac{4\mu_w k}{D}L\right)\right]\exp\left[-\frac{4\mu_w k}{D}(l-L)\right]$$

According to the solution the stress distribution in the layer of filling metal around granules in the vertical direction is shown in Figure 5 (b) . It is quite evident that there is greatest axial compressive stress acting on granules at l=L where the forward position of the melt lies. The greatest axial compressive stress is

$$\sigma_{max} = \frac{D\theta}{4\mu_w k}\left[1-\exp\left(-\frac{4\mu_w k}{D}L\right)\right]$$

It increases as forming pressure does. θ =P/L and axial compressive force acting on granules increase as forming pressure does. When the axial compressive force acting on granules reaches to a certain extent it is possible to compress granules into pieces or into solid. Hence forming pressure must have a certain limit. The value of the limit has something to do with size, strength and shape of granules, the outline of castings and the nature of the melt. It is found through experiment that suitable forming pressure must be less than 1MPa generally when we make foam Al with salt granules.

The analysis of pouring temperature

Generally high pouring temperature is beneficial to casting metal around granules. In the process of heat exchange of the melt and granules the melt has been penetrating the layer of granules before its overheated degree disappears. According to theory of heat transfer the length of experimental rod of casting metal around granules consists of two parts. A part is the length of the melt flowing before overheated degree vanishes. The other is the length of the melt flowing at the condition of crystallizing heat after overheated degree vanishes. Of course the boundary of two parts can not be seen from experimental rod and the correlation of overheated degree and total length of experimental rod is only considered.
The model of casing metal around granules and the temperature distribution are shown in Figure 6[4]. It is conducive to form that pouring temperature and preheating temperature of

granules are increased appropriately. But it was shown by experimental result that overhigh pouring temperature can shorten the effective length of experimental rod. Overhigh pouring temperature can make granules melt and the size of granules becomes small. The melt

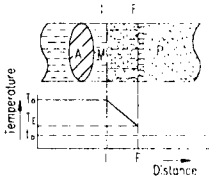


Figure 6: Penetrating model and temperature distribution of metallic liquor

surrounds granules so that they are isolated separately. Foam structure becomes uncontinuous. Granules or the melt may accumulate in some parts. Although experimental rod looks very long the effective length of experimental rod structure of which is good becomes short.

Conclusion

1. The main measure of casting metal around granules to produce foam Al-alloys is choosing and arranging of three parameters: preheating temperature of granules, pouring temperature of the melt and forming pressure. The preheating temperature of granules of them is most important.
2. The basis of determining preheating temperature of granules is material, size, shape, compression degree of granules and the intensity of heat exchange between the metal mold and the melt. As long as there is not leakage and spatter of the melt and inhomogeneous structure of foam metal we must increase the preheating temperature of granules.
3. When preheating temperature of granules is higher than some critical point forming pressure is adjusted within the greater limit. Overgreat forming pressure can make the axial compressive force acting on granules increase so that granules are compressed into pieces or into solid and foam structure becomes inhomogeneous and incomplete.
4. Pouring temperature has great influence on the effective length of experimental rod. When the size of granules is small pouring temperature must be increased. Overhigh pouring temperature can make mold leak.

References

1. G. J. Davies and Z. Shu, "Review Metallic Foam: Their Production ,Properties and Applications," Journal of Materials Science,18 (1983) ,1899-1911.
2. S. Y. Yang, B. Y. Wu and H. Q. Su, "Casting Foam Metal and Present Situation of the Study on Foam Aluminum," Jiang Su Metallurgy, (6) (1989) ,8-11.
3. 长田纯夫,松田公扶,铸物,54 (1982) 657-663.
4. 秋山茂,轻金属,26 (5) (1972) 219-224.

Magnetics

Development of NdFeB Magnet Industry in China

Li Bo, Wang Xinling and Yu Xiaojun

Advanced Materials Institute
Central Iron and Steel Research Institute, Beijing 100081, P.R. China

Abstract

It is well known that China is the major rare earth (RE) supplier and one of the largest producers of rare earth permanent magnets in the world because of the advantages of its abundant rare earth resources, high qualified researchers and technicians involved in the field, and low cost of labor. The Nd-Fe-B magnet industry in China has been developed with a good pace in recent years. From 1988 to 1996, the average annual increasing rate of the total global output for Nd-Fe-B permanent magnet was 29%. During the same period, it was about 50% in China. The extremely high increasing rate of the total output reflects a fast development of Nd-Fe-B permanent industry in China. Development of Nd-Fe-B magnet industry in China has been mainly focused on sintered magnets. In 1984, the total output of the sintered Nd-Fe-B magnet in China was only 2 tons, but it was about 2602 tons in 1996. The total output was increased about 1000 times within the 12 years.

In recent years, the global bonded Nd-Fe-B magnet industry has been rapidly developed with an annual increasing rate of 30%. However, the development of the bonded Nd-Fe-B magnets in China does not keep the same pace with the global development. Nowadays, it is only at an initial stage. The total output of the Nd-Fe-B magnetic powder was 56.65 tons in 1996, only 81% of the output from 1995, showing a negative increasing. The total output of the bonded Nd-Fe-B magnets was 70.22 tons in 1996, almost as same as that in 1995.

The maximum energy product, (BH)max, of commercially sintered Nd-Fe-B magnets produced in China, ranges from 33 to 38 MGOe. Some manufacturers (such as Central Iron and Steel Research Institute, CISRI) are able to produce high grade sintered Nd-Fe-B magnets with the magnetic properties of (BH)max=40-45 MGOe, as well as (BH)max=28-30 MGOe with jHc$\geqslant$ 2.6 kOe.

The number of Nd-Fe-B manufacturers in China is about 110 at present. Among them, only 7 manufacturers have the annual production capacity over 100 tons, 15 have the annual production capacity of 30-90 tons. The output of the Nd-Fe-B magnets produced by these 22 manufacturers (about 20% of the total) is almost 65% of the total output of the sintered Nd-Fe-B magnets in China.

The Third Pacific Rim International Conference on
Advanced Materials and Processing (PRICM 3)
Edited by M.A. Imam, R. DeNale, S. Hanada,
Z. Zhong and D.N. Lee
The Minerals, Metals & Materials Society, 1998

Abundant Rare Earth Resource

There is the most abundant RE resource in China. Currently, the proved RE reserve has been more than 48 million tons, and it is predicted that the total RE resources is over 100 million tons [1]. These RE minerals are mainly distributed in Baotou area, Jiangxi, Sichuan and Shandong provinces. The outputs of REO and various RE products in 1996 were 55,373 tons and 45,338 tons respectively (as shown in Table I and II) with the increase of 15.3% and 13.3% from 1995. The RE export volume in 1996 was 30,800 tons, up 14.1% from 1995. The output of RE minerals in 1996 and 1995 reached 80% of the worldwide total output.

Table I Structure of Chinese Rare Earth Mineral in 1996 (REO in ton)

Baotou Concentrates	RE Ion Compound Oxides	Fluorocarbon Ce Mineral		Monazite	Total
		Sichuan Provence	Shandong provence		
34359 (70728)	7473	12500 (25000)	951 (2612)	90 (180)	55373

Table II Structure of Chinese Rare Earth Products in 1996 (REO in ton)

RE Chloride	RE-Si-Fe Alloy	Mischmetal	Flint Stone	Polishing Powder	Carbonate RE	Permanent Magnet	Fluor Powder	Sm-Eu-Gd Rich Ore	Others
15,711	6,870	2,860	390	632	6,200	1,200	283	397	998

Single Oxides and Metals								
Yttrium Oxide	Lanthanum Oxide	Cerium Oxide	Praseodymium Oxide	Neodymium Oxide	Samarium Oxide	Europium Oxide	Gadolinium Oxide	Total
2,033	1,548	3,503	400	3,090	252	40	102	**45,338**
Terbium Oxide	Dysprosium Oxide	Erbium Oxide	La Metal	Nd Metal	Sm Matal	Dy Metal	Others	
29	255	28	170	368	6	24	2	
11,280								

Development of Chinese RE permanent magnetic materials

The research on RE magnets (RE-Co type magnets) in China was started from 70's. Nowadays, The RE-Co type magnets with excellent permanent magnetic properties are commercially available. There are many RE-Co magnet manufacturers in China. Among them Shanghai Yelong Chemical factory has the largest annual production capacity of 30 tons. Table III lists the main RE-Co type magnet manufacturers and the magnetic properties of their Sm-Co (2:17) products.

Since the discovery of Nd-Fe-B based permanent magnets with theoretical maximum energy product of 64 MGOe in 1983, numbers of physics and materials science research institutes and universities in China were involved in the study on Nd-Fe-B magnets. Central Iron and Steel Research Institute (CISRI) is the representative among these research institutes which were firstly starts R/D work on Nd-Fe-B magnets in 1983. Chinese R/D work on the Nd-Fe-B based magnets has been keeping a good pace with the international development. In 1989 Nd-Fe-B magnets with the maximum energy product of 390 kJ/m^3 was produced at CISRI. In 1990 the

Nd-Fe-B magnets with $(BH)_{max}$=417.6 kJ/m^3 were produced through carefully controlling oxygen method at Baotou Rare Earth Material Research Institute.

Table III Typical Magnetic Properties of Sm-Co (2:17) Magnets Made in China

Manufacturer	Grade	Br (T)	H_{cb} (kA/m)	(BH)m (kJ/m^3)
Southwest Institute of Magnetism and Applications	YXG27	1.05-1.15	540-1,000	200-224
Shanghai Yelong Chemical Factory	YLSZ-200H	1	680	192-216
Shanghai Magnetic Steel Factory	XGS191/96	1	680	192-224
Jilin 8272 Factory	XGS-200	1.1-1.12	540-720	192-208
Yibin 899 Factory	XG208/120H	⩾1	⩾680	192-224
CISRI	GYRM-28B	1.06-1.1	720-800	208-240
Shengzheng Jindong Magnetic Materials Co.	JDS26	1.06	752	208

Due to the advantages of abundant RE resources, high-qualified researchers and technicians involved in the field, and low cost of labor, the Nd-Fe-B magnet industry in China has been developed at full speed over the past 14 years. The output of the Nd-Fe-B magnets in China was only 2 tons in 1984, 10 tons in 1985, 120 tons in 1989. The output in 1992 was up to 490 tons, surpassed USA. In 1996 China became the world's largest RE magnets producers with the output of 2400 tons. From 1988 to 1996, the average annual increasing rate of the total global output of the Nd-Fe-B magnets was 29%. During the same period it was about 50% in China. The extremely fast increasing rate is attributed to the advantages of abundant row materials, technical experts, cheap labor and the big domestic market. The outputs and increasing rates of the Nd-Fe-B magnets in Japan, USA, Europe and China since 1989 are summarized in Table IV.

The shares of the global output in 1986 in Japan, USA, Europe and China were 53.6%, 26%, 9.4% and 11% respectively, while in 1996 the percentages were changed to 42.2%, 7.3%, 6.4% and 44.1%[(2)].

In recent years, the global bonded Nd-Fe-B magnet industry has been rapidly developed with an annual increasing rate of 30%. However the development of bonded Nd-Fe-B magnets in China does not keep the same pace with the global development. To date, it is only at an initial stage. The total output and sales volume of Nd-Fe-B magnetic powder in 1996 were 56.65 tons and 53.4 tons respectively, only 81% and 86% from 1995, both showing negative increasing. The total annual output of the bonded Nd-Fe-B magnets in 1996 was 70.22 tons, almost as same as that in 1995. The annual outputs and sales volume of the bonded magnets in China from 1993 to 1996 were summarized in Table V.

Current Situation of Nd-Fe-B Magnet Industry in China

Over the past 14 years, the production technologies and techniques of sintered Nd-Fe-B magnets have been greatly developed. Nowadays, the sintered Nd-Fe-B magnets of N48, 44H, 39SH and 33UH are commercially produced in China. But there still exist a gap in the sintered Nd-Fe-B magnet production technologies and techniques in comparison to other developed countries, such as Japan who is able to commercially produce N50 sintered Nd-Fe-B magnet.

Table IV Outputs and Increasing Rates of Nd-Fe-B Magnets in Japan, USA, Europe and China since 1989 [2]

	1989	1990	1991	1992	1993	1994	1995	1996
Japan	470t (53.40%) +24%	800t (56.30%) +70%	1,160t (58%) +45	1,200t (54%) +3%	1,435t (52%) +20%	1,555t (45.30%) +8%	1,900t (42.40%) +22%	2,300t (42.20%) +21%
USA	220t (25%) +10%	320t (22.50%) +45%	360t (18%) +13%	380t (17.10%) +6%	400t (14.50%) +5%	420t (12.20%) +5%	480t (10.70%) +14%	400t (7.3%) -20%
Europe	70t (8%) +40%	120t (8.50%) +73%	140t (7%) +17%	150t (6.80%) +7%	185t (6.70%) +23%	230t (6.70%) +24%	280t (6.30%) +22%	350t (6.40%) +25%
China	120t (13.6%) +60%	180t (12.70%) +50%	340t (17%) +89%	490t (22.10%) +44%	740t (26.80%) +51%	1.230t (35.80%) +66%	1,820t (40.60%) +48%	2,400t (44.10%) +32%
Total	880t +25%	1,420t +61%	2,000t +41%	2,220t +11%	2,760t +24%	3,435t +24%	4,480t +30%	5,450t +22%

Table V Annual Outputs and Sales Volume of Bonded Magnets in China

Year	Output (ton)	Sales Volume (ton)
1993	23	22
1994	30	27
1995	70	62
1996	56.65	53.4

The number of Nd-Fe-B manufacturers in China is around 110 at present. Among them only 7 manufacturers have the annual production capacity over 100 tons, 15 have the annual production capacity of 30-90 tons. The annual output of the Nd-Fe-B magnet from these 22 manufacturers (about 20% of the total) is almost 65% of the total annual output of the sintered Nd-Fe-B magnets in China.

The sintered Nd-Fe-B products made from the manufacturers with the production capacity less than 30 tons are only N28, N30 and N32. High grade sintered Nd-Fe-B magnets, such as N40, N42 38H, 35SH as well as the magnets with the coercivity over 2000kA/m, are produced by a few manufacturers (such as CISRI). Table VI and VII list the typical properties of sintered Nd-Fe-B magnets and rapidly quenched Nd-Fe-B magnetic powders both made from CISRI.

Closing Remarks

China is the country who owns abundant rare earth resource and has the advantages of high-qualified researchers and technicians involved in the field as well as cheap labor. Over the past 14 years the magnetic properties of Nd-Fe-B magnets made in China have been steadily improved, and the output has been sharply increased. To date, the development trend of Chinese Nd-Fe-B magnet industry is grouped and internationalized. The inexpensive magnets with acceptable magnetic properties are being developed in order to meet the requirement of market. (The references are omitted).

Table Ⅵ. Properties of Sintered Nd-Fe-B Magnets Made from CISRI

Properties \ Grade		GYRON 30	GYRON 33	GYRON 35	GYRON 37	GYRON 40	GYRON 42	GYRON 30H	GYRON 33H	GYRON 35H	GYRON 38H	GYRON 27SH	GYRON 30SH	GYRON 33SH	GYRON 35SH	GYRON 30HT	GYRON 26UH	GYRON 28UH
Br Residual Induction	KGS	11.2-11.5	11.3-11.7	11.7-12.4	12.1-12.9	12.5-13.0	13.0-13.4	11.2-11.5	11.0-11.7	11.6-12.3	12.4-12.7	10.4-11.0	10.8-11.2	11.3-11.7	11.6-1.23	11.3-11.6	9.8-10.2	10.4-10.8
	T	1.12-1.15	1.13-1.17	1.17-1.24	1.21-1.29	1.25-1.30	1.30-1.34	1.12-1.15	1.10-1.17	1.16-1.23	1.24-1.27	1.04-1.10	1.08-1.12	1.13-1.17	1.16-1.23	1.13-1.16	0.98-1.02	1.04-1.08
bHc Coercive Force	KOe	≥9.0	≥10.5	≥11.0	≥11.0	≥11.0	≥11.0	≥10.5	≥10.8	≥10.8	≥11.7	≥10.0	≥10.3	≥10.5	≥11.0	≥9.0	≥8.9	≥8.9
	KA/m	≥716	≥835	≥875	≥875	≥875	≥875	≥835	≥859	≥859	≥859	≥795	≥819	≥835	≥859	≥716	≥708	≥708
jHc Instrinsic Coercivity	KOe	≥11.0	≥12.0	≥12.0	≥12.0	≥12.0	≥12.0	≥17.0	≥17.0	≥17.0	≥16.0	≥20	≥20	≥20	≥20	≥15	≥25	≥25
	KA/m	≥875	≥955	≥955	≥955	≥955	≥955	≥1352	≥1352	≥1352	≥1273	≥1591	≥1591	≥1591	≥1591	≥1193	≥1989	≥1989
(BH)max	MGOe	28-32	31-33	33-36	35-38	37-40	41-43	28-32	31-33	33-36	37-39	25-28	28-32	31-33	33-36	28-32	24-26	27-29
Max.Energy Product	KJ/m³	224-256	248-264	264-288	279-318	295-318	328-344	224-256	248-264	264-288	296-312	200-224	224-256	248-264	264-288	224-256	192-208	216-232
α Br (20℃-100℃) Temperature Coefficient of Br	%/℃	-0.12	-0.12	-0.12	-0.12	-0.12	-0.12	-0.11	-0.11	-0.11	-0.11	-0.11	-0.11	-0.11	-0.11	-0.08	-0.10	-0.10
α Hc (20℃-100℃) Temperature Coefficient of Hc	%/℃	-0.6	-0.6	-0.6	-0.6	-0.6	-0.6	-0.6	-0.6	-0.6	-0.6	-0.6	-0.6	-0.6	-0.6	-0.55	-0.6	-0.6
Tc Curie Temperature	℃	312	312	312	312	312	312	320	320	320	320	340	340	340	340	450	350	350

Table Ⅶ. Properties of Rapidly Quenched Nd-Fe-B Magnetic Powder Made from CISRI

Properties \ Grade		GKF-11	GKF-9	GKF-7	GKF-10
Br Residual Induction	KGs	7.4~8.0	6.5~7.4	6.0~6.5	8.0~9.0
	(T)	(0.74~0.80)	(0.65~0.74)	(0.60~0.65)	(0.80~0.90)
$_{b}$Hc Coercive Force	KOe	5.5~6.5	5.0~5.5	3.5~5.0	2.5~3.0
	(KA/m)	(440~520)	(400~440)	(280~400)	(200~240)
$_{j}$Hc Intrinsic Coercivity	KOe	9.0~17.0	9.0~17.0	9.0~17.0	3.0~3.5
	(KA/m)	(720~1360)	(720~1360)	(720~1360)	(240~280)
$(BH)_{max}$ Max. Energy Product	MGOe	10~12	8~10	6~8	10~12
	(KJ/m^3)	(80~96)	(64~80)	(48~64)	(80~96)
μ_r Recoil Permeability		1.15	1.15	1.15	1.67
α_{Br} (25~100℃) Temperature Coefficient of Br	%/℃	-0.09~ -0.13	-0.09~ -0.13	-0.09~ -0.13	-0.13
α_{Hc} (25~100℃) Temperature Coefficient of Hc	%/℃	-0.40~ -0.45	-0.40~ -0.45	-0.40~ -0.45	-0.45
Tc Curie Temperature	℃	310~470	310~470	310~470	310

DEVELOPMENT AND PROSPECT OF RARE-EARTH PERMANENT MAGNET MATERIALS IN CHINA

Zhen-Xi Wang and Bo-Ping Hu
San Huan Inc., Chinese Academy of Sciences, P. O. Box 603,
Beijing 100080, China

Abstract

This is a brief review on rare-earth permanent magnet materials in China, including the rich rare-earth resources of China, the development of rare-earth permanent magnets, the applications of rare-earth permanent magnets, the rare-earth permanent magnet industry in China, the recent progress on research of rare-earth permanent magnet materials and prospect of rare-earth permanent magnets.

China has very rich rare-earth resources. The capacity is about 80% of the total in the world. The proven reserves is about 48 million tons and the prospective reserves is over 100 million tons. Distribution areas are Baotou in North China (light rare earth), Jiangxi in South China (middle-heavy rare earth), Sichuan Mianning in South-West China and Shandong Weisanhu in East China. In 1995, total output of Rare Earth (REO) is 40,000 tons and pure oxides and Metals are 8500 tons. The market share is 70-80% of the world. The average increase rate of output is 25%/year.

The rare-earth permanent magnet materials, especially Nd-Fe-B magnets, have been developing remarkably in recent years in China and as well in the world. The global Nd-Fe-B product output was about 285 tons in 1987 and 6710 tons in 1996, with a average increase rate of 42%. In 1996, the product output of Nd-Fe-B magnets of China was 2460 tons, which is about 37% of the total in the world.

The main application fields of rare-earth permanent magnets are energy, transportation, machinery, chemical engineering, medical treatment, electricity industry, information and daily life. Computers, MRI and motors are the biggest application areas for Nd-Fe-B magnets.

The research work on permanent magnet materials in recent years are focused on $ThMn_{12}$-structure intermetallic compounds, novel $Nd_3(Fe,Ti)_{29}$ -structure phases, interstitial intermetallic nitrides and carbides, nanostructure composite magnets (exchange spring materials).

The Third Pacific Rim International Conference on
Advanced Materials and Processing (PRICM 3)
Edited by M.A. Imam, R. DeNale, S. Hanada,
Z. Zhong and D.N. Lee
The Minerals, Metals & Materials Society, 1998

Introduction

Magnetic materials and their applications have known for millennia. The early history of magnetism involves the natural substance loadstone which exhibits strong magnetic forces. For example, more than 2000 years ago, the ancient Chinese used loadstone (mainly composed of magnetite, Fe_3O_4) to make compasses [1]. The first artificial permanent magnets were made in China in the Song period (960-1279), and were magnetized needles made of steel. Until the turn of the nineteenth century, magnets were week, unstable and made of carbon steel. Alnicos, aluminium-nickel-cobalt alloys discovered in Japan by Mishima in 1931, were the first truly permanent magnets. The next step forward came in the early 1950s, with the development of synthetic hard ferrites at Philips in The Netherlands.

The first generation of rare-earth permanent magnets was developed from the rare-earth cobalt alloys with $CaCu_5$ crystalline structure discovered by Stranat in USA. The first successful Sm-Co magnet was produced in 1967 at Philips, by Velge and Buschow, who bonded oriented $SmCo_5$ powder in resin to yield an energy product of 65 kJm^{-3}. Subsequent development of sintered magnets based on $SmCo_5$ led to energy product up to 190 kJm^{-3} which already doubles that of the best Alnicos. The second generation of rare-earth permanent magnets is based on Sm_2Co_{17} alloys, appeared in 1970's, has energy product up to 240 kJm^{-3}. In order to reduce the cost, the magnets based on iron was expected since then. The discovery of novel rare-earth permanent magnet Nd-Fe-B in 1983 by Sagawa in Japan [2] and the significant jump in the energy product $(BH)_{max}$ record not only sparked off a spate of research worldwide on the new $Nd_2Fe_{14}B$-type materials and gave new impetus to the research for other iron-rich rare-earth intermetallic compounds, but also expanded permanent magnet applications extensively. As the third generation of rare-earth permanent magnets, the Nd-Fe-B has advantages of high performance and low cost. The quality of the permanent magnets has increased exponentially in the 20th-century (Figure 1).

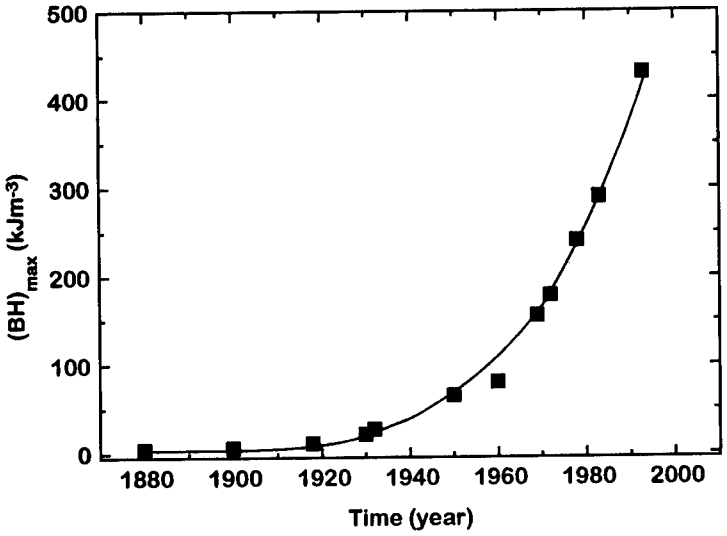


Figure 1: The exponential progress of permanent magnets, characterized by the energy product record, $(BH)_{max}$, since the turn of the century.

Rich Rare-earth Resources in China

China has very rich rare-earth resources. The capacity is about 80% of the total in the world. The proven reserves is about 48 million tons and the prospective reserves is over 100 million tons. Distribution areas are Baotou in North China (light rare earth), Jiangxi in South China (middle-heavy rare earth), Sichuan Mianning in South-West China and Shandong Weisanhu in East China. In 1995, the total output of Rare Earth (REO) is 40,000 tons and pure oxides and metals are 8500 tons. The market share for the Chinese product is 70-80% of the world. The average increase rate of output is 25%/year. Figure 2 shows the increase tendency of product output of rare earth in China in recent years.

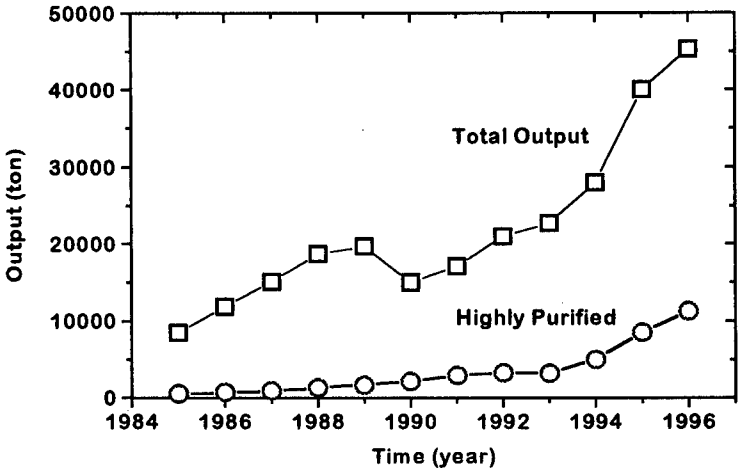


Figure 2: Product output of rare earth in China in recent years.

Rare-earth Permanent Magnet Industry in China

As one of the main application field of rare earth, the rare-earth permanent magnet materials, especially Nd-Fe-B magnets, have been developing remarkably in recent years in China and as well in the world. During 1969 and 1983, as a starting period, Sm-Co permanent magnets were studied and manufactured in small quantity in China. Around 1984 the wave of the third generation of rare-earth permanent magnets Nd-Fe-B impacted China and laboratory results were achieved with energy product of 320 kJm^{-3}. In 1985, San Huan Inc. of Chinese Academy of Sciences was established and the industry of Chinese rare-earth permanent magnet industry started to fly.

In 1989, the output of sintered Nd-Fe-B magnets was 120 tons and the capacity was 810 tons per year. 1996, the output of sintered Nd-Fe-B magnets in China 2460 tons which is about 37% of the total in the world. The average increase rate is about 60% per year. For the bonded rare-earth permanent magnets, the scale is very small in China. In 1995, the output of Nd-Fe-B powder and bonded magnets was 120 tons. At present, there are about 120 manufactures of sintered Nd-Fe-B permanent magnets. Only one third of them has capacities over 30 tons per year. San Huan Inc., having 4 joint-venture companies in Nd-Fe-B magnet manufacturing, is the

leading group in China (~1/3 of China's total output) and one of the biggest producers of Nd-Fe-B magnets in the world. Figure 3 shows the output increase of Nd-Fe-B sintered magnets in China and in the world as well.

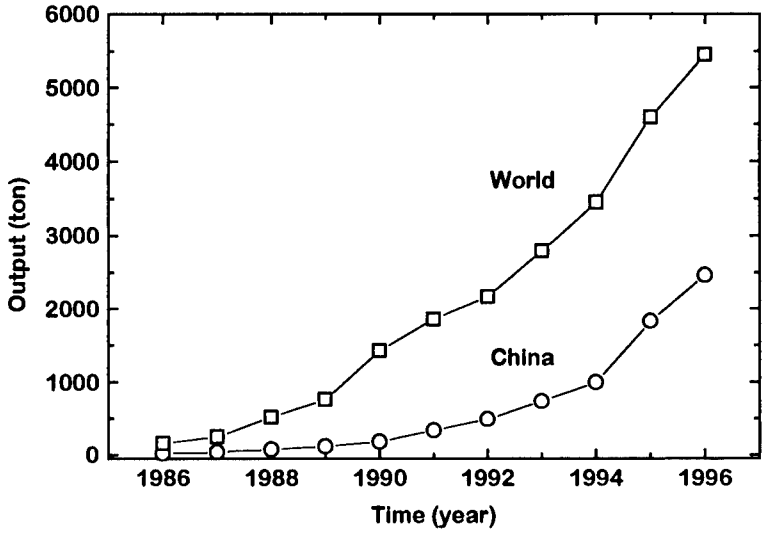


Figure 3: Product output of sintered Nd-Fe-B in China and in the world.

Applications of Rare-earth Permanent Magnets

The main application fields of rare-earth permanent magnets are energy, transportation, machinery, chemical engineering, medical treatment, electricity industry, information and daily life. Computers, magnetic resonance image (MRI) and motors are the biggest application areas for Nd-Fe-B magnets. Figure 4 and Figure 5 gives the global applications of bonded Nd-Fe-B magnets and sintered Nd-Fe-B magnets respectively [3].

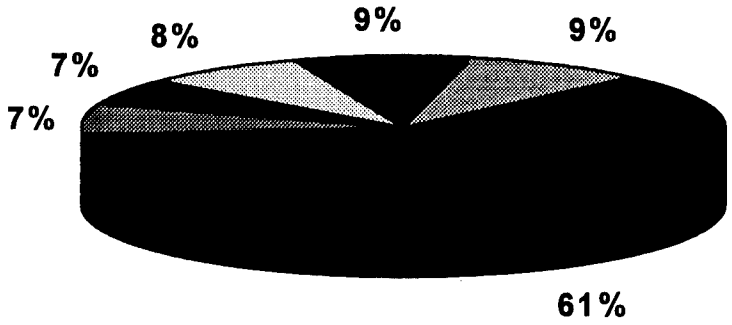


Figure 4: Application of bonded Nd-Fe-B magnets. Hard disc drive and CD-ROM for Computer are major applications (61%). Automotive 7%; Appliance 6%; Office Auto. 8%: Electronic 9% and Other 9%.[3]

The biggest application field for Chinese Nd-Fe-B magnets is loudspeakers and more than 50% of the used Nd-Fe-B magnets for loudspeakers of the world is produced in China. The other applications for Chinese sintered Nd-Fe-B magnets are the dewaxers used extensively in the oil fields to reduce the condensation of oil on the pipe wall, the magnetizers used to magnetize the water for the central heating station and apartments for protecting the scale formation of heavy water and the separators used in food industry and in mineral industry. The Nd-Fe-B magnets with low temperature coefficients are used in electric meters, replacing Alnico magnets. San Huan Inc. of Chinese Academy of Sciences has developed a series of brushless electric motors employed in electric vehicles using sintered Nd-Fe-B permanent magnets [4].

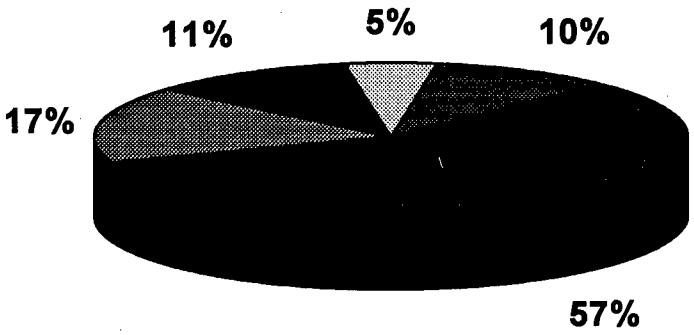


Figure 5: Application of sintered Nd-Fe-B magnets. Voice Coil Motor for Computer is the dominant application (57%). Motors 17%; MRI 11%; Acoustics 5% and Others 10%.[3]

Recent Progress on Research of Rare-earth Permanent Magnet materials in China

The research work on permanent magnet materials in China are carried out in many laboratories of the institutes and universities.

Since the discovery of $Sm_2Fe_{17}N_y$ nitride using gas-solid reaction, which has excellent intrinsic magnetic properties, by Coey and Hong Sun in 1990 [5], much work has been done both on its intrinsic magnetic properties and its hard magnetic properties. Due to the decomposition of $Sm_2Fe_{17}N_y$ nitride at high temperature (>650 ^{0}C), the conventional powder metallurgy technique cannot be used for making the sintered $Sm_2Fe_{17}N_y$ permanent magnet. In order to overcome this difficulty, the explosion technique was specially applied on making the nitride magnets [6] (San Huan Research Laboratory, Chinese Academy of Sciences (CAS)). The explosion sintered $Sm_2Fe_{17}N_y$ magnets retained both the crystalline structure and the magnetic properties during the process. The sintered magnets had a density 6.0-7.4 gcm^{-1}, a remanence B_r=0.83 T, intrinsic coercivity $\mu_{0i}H_c$=0.57 T and energy product $(BH)_{max}$=88 kJm^{-3}. The temperature dependence of coercivity and remanence were -0.076%/^{0}C and -0.51%/^{0}C respectively, which are better than those corresponding values of Nd-Fe-B magnets.

The novel interstitial compounds with $ThMn_{12}$-structure was discovered by Ying-Chang Yang in 1990 [7] (Magnetism Laboratory, Peking University), followed the discovery of $R_2Fe_{17}N_y$ nitrides [5]. Recently, magnetic properties of remanence B_r=1.06 T, intrinsic coercivity $\mu_{0i}H_c$=0.42 T and energy product $(BH)_{max}$=135 kJm^{-3} were achieved on $NdFe_{10.5}V_{1.5}N_x$ fine powders with better temperature stability than Nd-Fe-B magnet, which indicated that the $NdFe_{10.5}V_{1.5}N_x$ is a promising candidate for permanent magnet [8].

In recent years, researchers in the field of permanent magnetic materials paid much attention to the new type rare-earth iron intermetallic compounds $R_3(Fe,M)_{29}$ (M=Ti, V, Cr, Mn) and their nitrides and carbides. Among them, the $Sm_3(Fe,M)_{29}N_y$ nitrides and $Sm_3(Fe,M)_{29}C_y$ carbides (M=Ti,Cr) have excellent magnetic properties with high room temperature saturation magnetization and large anisotropy field and are potential candidates for permanent magnet application. At room temperature, remanence B_r=1.04 T, intrinsic coercivity $\mu_{0i}H_c$=0.83 T and energy product $(BH)_{max}$= 105 kJm^{-3} on $Sm_3(Fe,Ti)_{29}N_y$ were achieved [9]; a coercivity of $\mu_{0i}H_c$=0.3 T on $Sm_3(Fe,Ti)_{29}C_y$ carbides was developed [10]; B_r=0.87 T, $\mu_{0i}H_c$=0.79 T and $(BH)_{max}$= 105 kJm^{-3} on $Sm_3(Fe,Cr)_{29}N_y$ were achieved [11] and a coercivity of $\mu_{0i}H_c$=0.8 T on $Sm_3(Fe,Cr)_{29}C_y$ carbides was also developed [12] (Magnetism Laboratory, Institute of Physics and San Huan Research Laboratory, CAS).

It was found that the substitution of Ga or Si for Fe in $Sm_2Fe_{17}C_x$ helps the formation of high-carbon rare-earth iron compounds with 2:17-type structure [13] (Magnetism Laboratory, Institute of Physics, CAS). It was succeeded to synthesize $Sm_2Fe_{15}M_2C_x$ (M=Ga, x=0, 1.0, 2.0 and 3.0; M=Si, x=0, 0.5, 1.0 and 1.5) compounds with Th_2Zn_{17}-type structure by arc melting. The carbides are single phase except for $Sm_2Fe_{15}Ga_2C_{3.0}$, which contains a few percent of α-Fe. The Curie temperature T_C of $Sm_2Fe_{15}Si_2C_x$ compounds is found to increase from 550 K to 590 K, as x increases from 0 to 1.5. For $Sm_2Fe_{15}Ga_2C_x$, T_C increases with x from 565 K for x=0 to 635 K for x=2.0, and then decreases with x. Room-temperature saturation magnetization μ_0M_r of these carbides is in excess of 1 T and has a small dependence on carbon content. The carbides exhibit an easy c-axis anisotropy at room temperature and show anisotropy field $\mu_{0i}H_A$ of higher than 9 T for x≥1.0. This work suggested the possibility of producing high performance sintering permanent magnets on 2:17 interstitial compounds. The magnetic hardening of the $Sm_2Fe_{14}Ga_3C_x$ was investigated by melting spinning. The intrinsic coercivity $\mu_{0i}H_c$ of 1.26-1.50 T were obtained with carbon content x from 1.0 to 2.5 [14].

Prospect of Rare-earth Permanent Magnets

The key points on study of novel rare-earth permanent magnet materials are to search the rare-earth transition-metal intermetallic compounds with excellent intrinsic magnetic properties for high performance permanent magnets.

Nanostructure composite magnets (exchange spring materials) is a hot point for study of high performance permanent magnets in recent years. The remanence may be improved by exchange coupling of hard and soft regions on a nanometer scale [15]. The prospects of finding a rare-earth intermetallic with a magnetization significantly larger than that of $Nd_2Fe_{14}B$ (μ_0M_r = 1.6 T) are poor, so the greatest achievable energy product may be about 500 kJm^{-3}. However, some soft materials such as α-Fe and Fe-Co alloys have polarization in the range 2.1-2.3 T. An as-yet hypothetical nanostructure of an oriented hard phase with very high anisotropy and a soft phase

with high magnetization(e.g. $Sm_2Fe_{17}N_3/Fe_{65}Co_{35}$) could prove to be the ultimate rare-earth iron permanent magnet, with an energy product in excess of 1 M Jm^{-3} [16].

There are many laboratories in China doing research work on permanent magnet materials, such as State Key Laboratory of Magnetism, Institute of Physics, Chinese Academy of Sciences; San Huan Research Laboratory, Chinese Academy of Sciences; Magnetism Laboratory, Institute of Metals, Chinese Academy of Sciences; Magnetism Laboratory, Physics Department, Peking University; Magnetism Laboratory, Physics Department, Lanzhou University; Magnetism Laboratory, Physics Department, Nanjing University; Magnetism Laboratory, Physics Department, Shandong University; Department of Materials Science, Beijing University of Science and Technology; National Engineering Research Center for magnetic Materials. Many scientists working on study of permanent magnets studied and worked abroad and have very close contact with international communication.

After the discovery of Nd-Fe-B magnet, China's rare-earth permanent magnet industry has been developing rapidly due to the abundance of raw materials, low labour cost and technical experts resource. Although the grades of the magnets are lower than those of developed countries, the progress has been made year by year. In 1996, the output of sintered Nd-Fe-B magnets reached 2460 tons in China and exceeded the output of 2300 tons in Japan. Now China takes the first place in producing sintered Nd-Fe-B magnets globally.

In October 1995, San Huan Inc., Chinese Academy of Sciences and China National Nonferrous Metals Industry Corporation (CNNC) completed the acquisition of General Motor's Magnequench factory (now it is Magnequench International Inc.), cooperating with Sextant Group Inc., USA. This indicated that the Chinese rare-earth industry entered international permanent magnet industry.

The Chinese domestic market is a crucial factor for the development of Nd-Fe-B magnet industry of China. With the improvement of the quality of magnets, the applications will further expands in China.

By the year of 2000, Chinese rare-earth permanent magnet industry will stand on a new stage. The reconstruction is undergoing and many big factories with capacity more than 200 ton/year will be formed. China will be the largest producer of the rare-earth permanent magnets in the world. For developing rare-earth permanent magnets industry, China has its unique advantages of rich rare-earth resource and low labour cost and the developed countries have advanced technologies and abundant funds. The combination of these two aspects will give great energy to the development of rare-earth permanent magnets industry. In the last 20 years, Chinese rare-earth permanent magnets industry has made great achievements, growing from small to large. We are very pleased to cooperate with friends worldwide to bring brighter future for the rare-earth permanent magnets industry in the world.

References

1. Joseph Needham, Science and Civilazation in China (London: Cambridge University Press, 1962), Vol. 4, 269.

2. M. Sagawa et al., "A New Material for Permanent Magnets on a Base of Nd and Fe", J. Appl. Phys., 55 (1984), 2083-2089.

3. J-M. Tourre, "Supplying the Magnetic Market: Achallenge for Rare-earth Producers", Gorham/Intertech Conference in April 1997, Chicago, USA.

4. Bo-Ping Hu, "Applications of Nd-Fe-B Magnets on Electric Vehicles with Brushless Motors, Water Magnetizers and Gas Magnetizers", Gorham/Intertech China Conference in October 1996, Guilin, China.

5. J. M. D. Coey and Hong Sun, "Improved Magnetic Properties by Treatment of Iron-based Rare-earth Intermetallic Compounds in Ammonia", J. Magn. Magn. Mater., 87 (1990), L251-L254.

6. Bo-Ping Hu et al., "Magnetic Properties of Sintered $Sm_2Fe_{17}N_y$ Magnets", J. Appl. Phys., 74 (1993), 489-494.

7. Y. C. Yang et al., "Magnetic Properties of Nitrides of the Rare-earth Iron Intermetallic Compounds", Proceedings of the 6th Int. Symp. on Magnetic Anasotropy and Coercivity in Rare-earth Transition-metal Alloys, Pittsburgh, USA, October 1990, pp. 190-194

8. J. B. Yang et al., "Preparation of $NdFe_{10.5}V_{1.5}N_x$ Powders with Potential as High-performance Permanent Magnets", J. Phys. D: Appl. Phys., 30 (1997), 1-5.

9. Bo-Ping Hu et al., "A Hard Magnetic Property Study of a Novel $Sm_3(Fe,M)_{29}N_y$ Nitride" J. Phys. D: Appl. Phys., 6 (1994), L197-L200.

10. Bo-Ping Hu et al., "Magnetic Propertyies of $R_3(Fe,M)_{29}C_y$ Carbides (R=Nd,Sm)" J. Phys. D: Appl. Phys., 6 (1994), L595-L599.

11. Yi-Zhong Wang et al., "Hard Magnetic Properties of the Novel Compound $Sm_3(Fe,M)_{29}N_y$" J. Phys. D: Appl. Phys., 9 (1997), 2787-2791.

12. Yi-Zhong Wang et al., "Hard Magnetic Propertyies of the Novel Compound $R_3(Fe,M)_{29}C_y$" J. Phys. D: Appl. Phys., 9 (1997), 2793-2798.

13. Bao-Gen Shen et al., "A Novel Hard Magnetic Material for Sintering Permanent Magnets", J. Appl. Phys., 75 (1994), 6253-6255.

14. Lin-Shu Kong et al., "High-coercivity Sm-Fe-Ga-C Compounds with Th_2Zn_{17}-structure by Melt Spinning", J. Appl. Phys., 75 (1994), 6250-6252.

15. E. F. Kneller and R. Hawig, "The Exchange-spring Magnets: A New Materials Principle for Permanent Magnets", IEEE Trans. Magn., 27 (1991), 3588-3600.

16. R. Skomski and J. M. D Coey, "Nucleation Field and Energy Product of Aligned Two-phase Magnets - Progress Towards the '1 M Jm^{-3}' Magnet", IEEE Trans. Magn., 29 (1993), 2860-2862.

Temperature Stability of Rare Earth Permanent Magnets

Xiaojun Yu, Jikai Zhang, Zhaohui Guo, and Wei Li

Central Iron & Steel Research Institute, Beijing 100081, P.R.China

Abstract

According to the relationship between the saturation magnetization of rare earth compound $(Sm_{1-x}HRE_x)_2TM_{17}$ and operating temperature, the computer program has been used to predict the temperature coefficient of saturation magnetization for $(Sm,Gd,Dy)_2TM_{17}$ and $(Sm,Gd,Er)_2TM_{17}$ magnets. The good comprehensive properties were obtained for some 2:17 type RE permanent magnet which are lower temperature coefficient of magnetization, $-(6 — 9) \times 10^{-6}$ and higher (BH)m, more than 18MGOe at room temperature, and more than 17MGOe in the range of 20 — 200 ℃.

The Third Pacific Rim International Conference on
Advanced Materials and Processing (PRICM 3)
Edited by M.A. Imam, R. DeNale, S. Hanada,
Z. Zhong and D.N. Lee
The Minerals, Metals & Materials Society, 1998

Introduction

The temperature compensated permanent magnets with high energy products and low temperature coefficients over a wide range of operating temperature are required for designs of some modern device such as microwave tube, gyros and accelerometer. Permanent magnets based on the light rare earth (LRE) and transition metal (TM) compounds $SmCo_5$, $Sm_2(Co,Fe,Cu,Zr)_{17}$, and $Nd_2Fe_{14}B$ are all the candidates for this application. However, the relatively low $4\pi Ms$ of $SmCo_5$ compound and the low Curie temperature and large temperature coefficient of saturation magnetization of $Nd_2Fe_{14}B$ compound limit their usefulness at these area. On the other hand, the high magnetization and high Curie temperature of $Sm_2(Co_{1-x}Fe_x)_{17}$ compound make 2:17 type permanent magnet attractive for the application at higher and more stable magnetic flux over a wide temperature, especially at elevated temperature.

As we know, in RE-TM compounds, the magnetic moment of the light rare earth atom is parallel to that of Co, and decreases with the increasing of the temperature, so the temperature coefficient of the magnetic moment of these LRE-Co compounds is negative value. Nevertheless, the magnetic moment of heavy rare earth is antiparallel to that of Co, and increases with the increasing of the temperature, so the temperature coefficient of magnetic moment of these HRE-Co compounds is positive valve. Li[1] et al. studied the HRE-substituted 2:17 type magnet and concluded that the Gd-substituted magnet has the better temperature compensated properties. However, the effect of one kind of HER compensation isn't good for application in the wide temperature range of -60—200 ℃.

The present study is directed to develope a high energy product in temperature compensated magnet by partially substituting Gd, Dy and Er for Sm in these 2:17 type magnets. The preparing of the large numbers of magnets with varying compositions and the measuring of the temperature coefficients and magnetic properties over wide temperature ranges are laborious and time consuming. Especially true when more than one kind of HRE element is employed. In order to solve this problem, the compute programs were developed to predict the temperature coefficients of saturation magnetization based on the experimental data obtained from LRE_2TM_{17} and HRE_2TM_{17}. The similar attempts were reported earlier[2], but the algorithm employed was not mentioned.

Experimental and Calculation Procedures

Magnet alloys of nominal compositions $Sm_{1-x}(HRE1_{1-y}HRE2_y)_x(Co_{0.69}Fe_{0.22}Cu_{0.08}Zr_{0.02})_{7.22}$ with x=0—0.5, y=0—0.5 were studied. Magnets were prepared from conventionally cast ingots using classical powder metallurgy techniques. All the alloys were cast by vacuum induction melting via controlled directional solidification. The cast ingots were milled in toluene to an average particle size of 3.0 ~ 5.0 μm by attrition. Vacuum evaporation was applied to remove the toluene from the powder slurry. The dry powder were pressed in perpendicular magnetic field of 15KOe, and then pressed isostatically with a pressure of $4t/cm^2$. All the green compacts were sintered under vacuum at 1180 ~ 1210 ℃ for 2 ~ 3hr. Post sintering treatment at a temperature of 830 ~ 400 ℃ for 25 ~ 35hr was applied to obtain the optimum intrinsic coercivity of each magnets. Magnetic properties at room temperature were measured with a hysteresigraph meter. Magnetic

properties at higher or lower temperature were measured with a vibrating sample magnetometer or the pull coil method. Temperature coefficient (α) at a given temperature is defined as α = dQ/dT $\times$ 100/Q(%/℃), where T is temperature, Q is one of the magnetic properties, such as 4πMs, Br, open circuit residual magnetization(OCRM), open circuit remnant flux (OCPF), (BH)m, $_m$Hc, or $_b$Hc.

In order to predict the temperature coefficient of saturation magnetization of $Sm_{1-x}(HRE1_{1-y}HRE2_y)_x(Co_{0.69}Fe_{0.22}Cu_{0.08}Zr_{0.02})_{7.22}$, the variations of magnetization versus temperature of Sm_2TM_{17}, Gd_2TM_{17}, Dy_2TM_{17} and Er_2TM_{17} have been measured respectively[1]. The experimental data were represented by polynomials obtained by the method of least squares.

$$(4\pi Ms)_{Sm2TM17} = a_0 + a_1T + a_2T^2 + \cdots + a_nT^n = \sum_{i=0}^{n} a_iT^i = f_1(T) \quad (1)$$

$$(4\pi Ms)_{Gd2TM17} = b_0 + b_1T + b_2T^2 + \cdots + b_nT^n = \sum_{i=0}^{n} b_iT^i = f_2(T) \quad (2)$$

$$(4\pi Ms)_{Dy2TM17} = c_0 + c_1T + c_2T^2 + \cdots + c_nT^n = \sum_{i=0}^{n} c_iT^i = f_3(T) \quad (3)$$

Adequate fits were obtained with n = 3--5. We assumed that the magnetization is an additive quantity in $Sm_{1-x}(HRE1_{1-y}HRE2_y)_x(Co_{0.69}Fe_{0.22}Cu_{0.08}Zr_{0.02})_{7.22}$ magnet alloys within the temperature range of the experiments. Thus, the variation of the magnetization versus temperature for $Sm_{1-x}(Gd_{1-y}Dy_y)_xTM_{7.22}$ is

$$(4\pi Ms)_{Sm1-x(Gd1-yDyy)xTM7.22} = (1-x)f_1(T) + x(1-y)f_2(T) + xyf_3(T) = f_4(T) \quad (4)$$

The relationship between the temperature coefficient of the magnetization of $Sm_{1-x}(Gd_{1-y}Dy_y)_xTM_{7.22}$ and the temperature T within the experimental range can be obtained by differentiating Eq.(3) with respect to T .

$$\alpha = \frac{d(4\pi Ms)}{dT} \cdot \frac{100}{4\pi Ms} = \frac{df_3(T)}{dT} \cdot \frac{100}{4\pi Ms} = f_5(T) \quad (5)$$

By Eqs. (3) and (4), the relational curves of the magnetization and the temperature coefficient versus temperature for various Gd and Dy contents can be drawn.

Results and Discussion

Figure 1 shows the temperature dependence of magnetization at 15KOe for $Sm_{1-x}(Gd_{1-y}Dy_y)_x(Co_{0.69}Fe_{0.22}Cu_{0.08}Zr_{0.02})_{7.22}$. In this figure, the solid lines represent the calculated results while the various symbols are the data obtained by experiment. A good agreement between the calculated and experimental data is obtained. Figure 1 shows that the magnetization curves are essentially flat over a wide temperature when the Gd+Dy content is between 40 and 50 at.%.

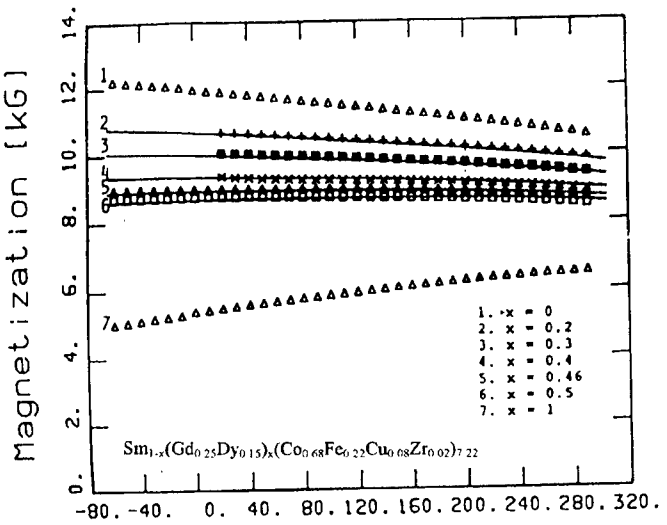


Figure 1. Dependence of magnetization as a function of temperature for $Sm_{1-x}(Gd_{0.25}Dy_{0.15})_x(Co_{0.68}Fe_{0.22}Cu_{0.08}Zr_{0.02})_{7.22}$ magnet

The temperature coefficients of magnetization of the magnet with various Gd+Dy content versus temperature are given in Fig.2. Again, the solid lines are the calculated results. The temperature coefficient of the magnet with x = 0.4 is zero at about -50 ℃. For magnets with x = 0.46, 0.5, and 0.6, the temperature coefficients approach zero at 50, 100, and 200 ℃. For x =0.46, the temperature coefficients is very close to zero over a wide temperature from -50 to 200 ℃. A small discrepancy between measured and calculated values is obtained. The deviation of the measured values is slight positive at lower temperature and negative at higher temperature.

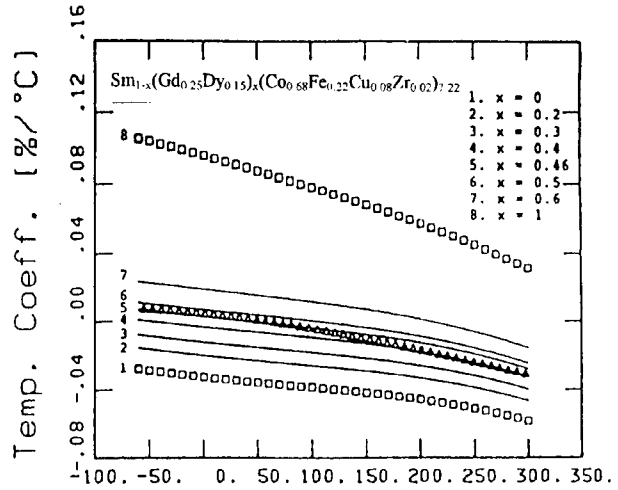


Figure 2. Variation of temperature coefficient of magnetization vs. temperature for $Sm_{1-x}(Gd_{0.25}Dy_{0.15})_x(Co_{0.68}Fe_{0.22}Cu_{0.08}Zr_{0.02})_{7.22}$ magnet

Table I Magnetic properties and temperature coefficient of magnetization of $Sm_{1-x}(Gd_{0.25}Dy_{0.15})_x(Co_{0.68}Fe_{0.22}Cu_{0.08}Zr_{0.02})_{7.22}$ magnet

Composition	Mgnetic Properties				α(%/℃)	(-50--200 ℃)
x	Br kGs(T)	$_mHc$ kOe(kA/m)	$_bHc$ kOe(kA/m)	(BH)m MGOe(kJ/m^3)	Measured	Predicted
0	11.0 (1.10)	>20.0 (>1592)	10.1 (804)	28.0 (223)	-0.034	
0.2	9.40 (0.94)	>20.0 (>1592)	9.10 (724)	21.6 (172)	-0.026	-0.030
0.4	9.10 (0.905)	25.7 (2045)	8.39 (668)	19.6 (156)	-0.012	0.0095
0.45	9.00 (0.90)	23.1 (1838)	8.26 (657)	19.1 (151.7)	-0.0099	-0.0082
0.6	8.10 (0.81)	13.2 (1050)	7.15 (569)	14.8 (117.8)	-0.0017	-0.0020
0.8	7.40 (0.74)	7.4 (589)	5.70 (454)	10.4 (82.7)	+0.0044	+0.0045

Table I shows the magnetic properties and temperature coefficient of magnetization of $Sm_{1-x}(Gd_{0.25}Dy_{0.15})_x(Co_{0.68}Fe_{0.22}Cu_{0.08}Zr_{0.02})_{7.22}$ magnet. Br, $_bHc$ and (BH)m decrease monotonically with increasing Gd+Dy content. $_mHc$ increases slightly and begin to decrease when $x \geq 0.4$. Compared with these date, the best comprehensive properties are obtained when $x = 0.45$.

Table II Magnetic properties and temperature coefficient of magnetization of $Sm_{0.55}(HRE)_{0.45}(Co_{0.68}Fe_{0.22}Cu_{0.08}Zr_{0.02})_{7.22}$ magnet

Composition	Mag netic Properties			α(%/℃)	(-50--200 ℃)
HRE	Br kGs(T)	$_bHc$ kOe(kA/m)	(BH)m MGOe(kJ/m^3)	Measured	Predicted
$Gd_{0.25}Dy_{0.15}$	9.0 (0.90)	8.26 (657)	19.1 (151.7)	-0.0099	-0.0082
$Gd_{0.3}Er_{0.1}$	9.15 (0.915)	8.20 (653)	19.0 (151)	-0.0084	-0.0072
$Gd_{0.2}Er_{0.2}$	9.00 (0.90)	8.05 (641)	18.4 (146.5)	-0.0085	-0.0082
$Gd_{0.1}Er_{0.3}$	9.10 (0.91)	8.20 (18.90)	18.9 (150.4)	-0.0080	-0.0068
$Dy_{0.15}Er_{0.25}$	9.30 (0.93)	8.00 (637)	20.0 (159.2)	-0.0057	-0.0062

Table II summarizes the effect of two kind of HRE elements substitution for Sm on the magnetic properties and temperature coefficient of magnetization in 2:17 type RE magnets. If the proper substitution of HRE for Sm is attained, (BH)m up to 20MGOe and $|\alpha|$ up to 0.0057 (-50 — 200 ℃) can be obtained in $Sm_{0.55}(Dy_{0.15}Er_{0.25})_{0.45}(Co_{0.68}Fe_{0.22}Cu_{0.08}Zr_{0.02})_{7.22}$ magnet.

Figure 3 is the variation of magnetic properties vs temerature for $Sm_{1-x}(Gd_{0.25}Dy_{0.15})_x$

$(Co_{0.68}Fe_{0.22}Cu_{0.08}Zr_{0.02})_{7.22}$ magnet. It can be known that Br is almost constant over the temperature range of 20 — 200 ℃. Although $_mHc$ drops sharply with increasing temperature, $_bHc$ decreases slightly until to 150 ℃.

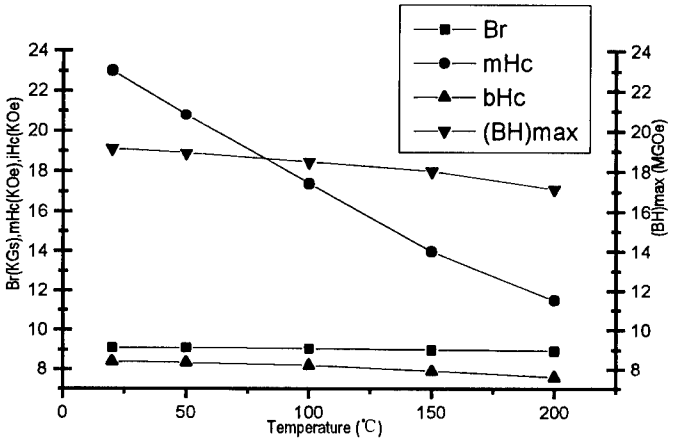


Figure 3. Variation of magnetic properties vs. temperature for $Sm_{1-x}(Gd_{0.25}Dy_{0.15})_x(Co_{0.68}Fe_{0.22}Cu_{0.08}Zr_{0.02})_{7.22}$ magnet

Conclusion

For 2:17 type RE permanent magnets, the Magnetic properties of the compound which Sm is substituted by two kinds of heavy rare element are better than that of one. For example, $Sm_{0.55}(Gd_{0.25}Dy_{0.15})_{0.45}TM_{7.22}$, $Sm_{0.55}(Gd_{0.3}Er_{0.1})_{0.45}TM_{7.22}$, and $Sm_{0.55}(Dy_{0.15}Er_{0.25})_{0.45}TM_{7.22}$ magnets have better comprehensive properties: (BH)m ≥ 18.0 MGOe, $\alpha_{-60-200℃} = -(6 — 9)\times 10^{-6}$, which was not obtained before.

Computer calculation is a good method to study temperature compensated 2:17 type permanent magnet, which also can be used for other RE magnets such as NdFeB magnet. But some work should be improved to reduce the discrepancy between the results measured and predicted.

References

1. D.Li et al., Proceedings of the 7th International Workshop on Rare-Earth Permanent Magnets, (X.Pan, W.Ho and C.Yu, Beijing, 1983), 495-502.

2. B.M.Ma, K.S.V.L. Narasimhan, and J.C.Hurt, " NdFeB Magnet with Zero Temperature Coefficient of Magnetization " , IEEE. Trans. Magn., **MAG**-22 (1986), 1081-1084.

A STUDY OF THE DEFORMATION BEHAVIOUR OF NANO-CRYSTALLINE Nd-Fe-B MAGNETS

S. Prakash Narayan and Kunal Basu
Regional Research Laboratory, Bhopal (INDIA)
and
Y.V.R.K. Prasad and V. Jayaram
Indian Institute of Science, Bangalore (INDIA)

Abstract

It is well established that magnetic alignment in melt-spun consolidated Nd-Fe-B alloy is induced by the process of hot deformation which causes preferential growth of favorably oriented grains and develops a crystallographic texture (i.e, preferential orientation of grains) along the C-axis of the unit cell of the alloy which is the easy direction of magnetization. It has also been reported that grain growth and grain boundary sliding are responsible for the texture and that the kinetics of texture development is a function of strain, strain rate and temperature, out of which strain rate i.e. the rate of deformation, highly influences texturing. To understand the effect of strain rate on texturing, hot deformation studies were carried out between 973 K to 1173 K at constant true strain rates. The study reveals magnetic alignment through the enhancement of energy product to 34 MGOe and the best magnetic properties were obtained between the strain rate of $1x10^{-2}$ to $1x10^{-1}$ sec^{-1} at 1073 K. X-ray diffraction on deformed samples exhibited enhanced peak intensity on basal planes [001] of the crystallographic unit cell of the alloy confirming existence of texture along the C-axis in the direction of applied compressive stress.

The Third Pacific Rim International Conference on
Advanced Materials and Processing (PRICM 3)
Edited by M.A. Imam, R. DeNale, S. Hanada,
Z. Zhong and D.N. Lee
The Minerals, Metals & Materials Society, 1998

Introduction

The advent of high energy Nd-Fe-B magnets has created a new era in magnet manufacturing technology [1]. In case of melt spun ribbons, the optimum magnetic properties can be achieved by hot consolidation and subsequent hot deformation only. The optimal parameters of the hot deformation process leading to preferred orientation is the most crucial part of the total processing cycle which generally remains confined as trade secret. A number of attempts have however been made to understand the mechanism which leads to the development of the texture during hot deformation. Croat has mentioned that the maximum magnetic properties develops at 50-60% deformation [2]. Through theoretical modeling, Li et. al. [3] have also shown that the degree of texture saturates at 67% compressive deformation. So, an acceptance of the relationship between deformation and anisotropy already exists. However the effect of strain rate has not been suitably addressed. Possibility exists that at different strain rates, the amount of strain required to obtain maximum anisotropy may vary. Since the process is dynamic, the rate of deformation becomes a dominant factor in developing the texture and subsequent enhancement of the magnetic properties. In this investigation, an attempt has been made to establish and optimize the effect of strain rate on magnetic anisotropy.

Experimental

Melt spun hot compacted samples of cylindrical shape of 14.0 mm diameter and 15.0 mm height were procured from M/s Magnequench International, Anderson, Indiana (USA). These samples (MQ2-E 14) were isotropic in nature. The samples have magnetic properties of remanence (B_r): 7 to 8 kG; intrinsic coercive force (H_{ci}): 18 to 20 kOe and energy product $(BH)_{max}$: 11 to 13 MGOe. The samples were first coated with boron nitride to prevent oxidation and were encased in a stainless steel tube to reduce the hoof-stress which generates during deformation. The equipment used for test was equipped with an exponential decay of the speed of an actuator so that constant true strain rates in the range of $3x10^{-4}$ to $1x10^{2}$ sec^{-1} could be imposed on the specimen. In order to obtain constant true strain rate, the speed of the ram was instantaneously corrected at each strain value by taking into account the change in strain at very small intervals of strain. Isothermal tests were conducted by surrounding the specimens, platens and push rod (connected to the ram) by a three zone furnace. The temperature was controlled within $\pm$ 2 K.

The following experimental techniques were adopted for hot deformation using a machine of identical capabilities :

(a) The samples encased in the stainless steel tube were vacuum sealed in a stainless steel pouch and then subjected to hot deformation in open atmosphere.

(b) The samples encased in steel tubes were directly subjected to hot deformation in an open-air furnace.

In each case, the specimens were finally compressed to about half of their height, i.e. to 0.5 of engineering strain and the load-stroke data were converted into true stress-true strain curves using the standard equations [4].

The deformed samples were examined by X-ray diffraction in the diffraction angular range of 10° to 90° with Cu Kα radiation using a Phillips APD 1700 X-ray Diffraction equipment. To evaluate the magnetic properties, 2 mm cubes were carefully cut and were tested using a Vibrating Sample Magnetometer (VSM) fabricated by Naval Research Laboratory, Washington D.C. (U.S.A).

Results And Discussion

A typical true stress and true strain curve for isothermal deformation at 1073 K at different constant true strain rates is shown in Figure 1. The stress-strain curves show a peak after 0.1 true strain and then almost steady state of flow stress up to the end of deformation. This steady state portion of flow stress is attributed to dynamic recrystallization [5]. It is already established that dynamic recrystallization gives rise to preferred nucleation sites and re-orientation of misaligned grains such that all are normal to the directions in which plastic deformation occurs [6]. It is known that the typical grain size of MQ-2E 14 isotropic samples is in the range of 20-50 nm which on deformation changes to platelet shapes of 200-400 nm [7] by alignment which occurs by a combination of rotation and rapid growth of certain grains [8]. The intrinsic coercive force (H_{ci}) of samples deformed at 1073 K shows a gradual decrease with decreasing strain rate. (Figure 2), whereas the remanence (B_r) increased substantially upto $1x10^{-2}$ $sec.^{-1}$ strain rate but at higher strain rates Br shows a reverse trend (Figure 3). This appears to indicate that at strain rates lower than $1x10^{-2}$ sec^{-1}, the grains probably get an opportunity to grow in size but only randomly as the drop in magnetic properties can only be attributed to the lack of texture.

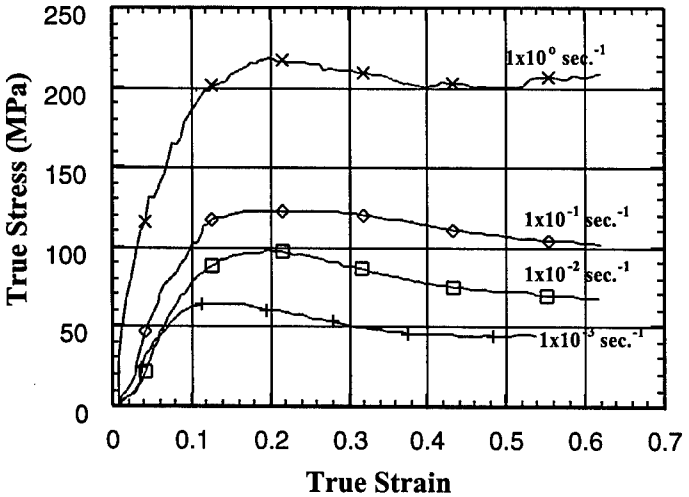


Fig. 1: Flow Stress curves of nanocrystalline Nd-Fe-B magnets deformed at 1073 K at different strain rates.

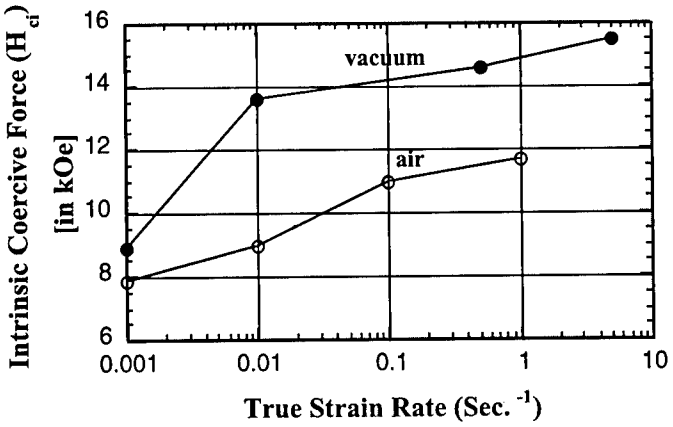


Fig. 2: Effect of strain rate on the intrinsic coercive force of Nd-Fe-B magnet, deformed at 1073 K in air and in vacuum.

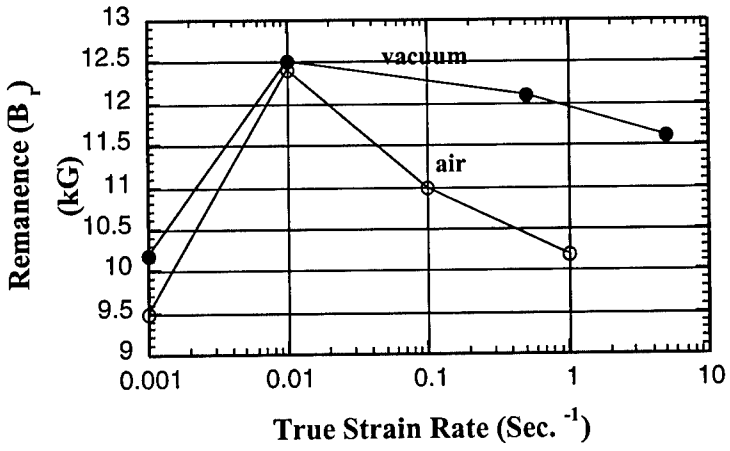


Fig. 3: Effect of strain rate on the remanence of Nd-Fe-B magnet, deformed at 1073 K in air and in vacuum.

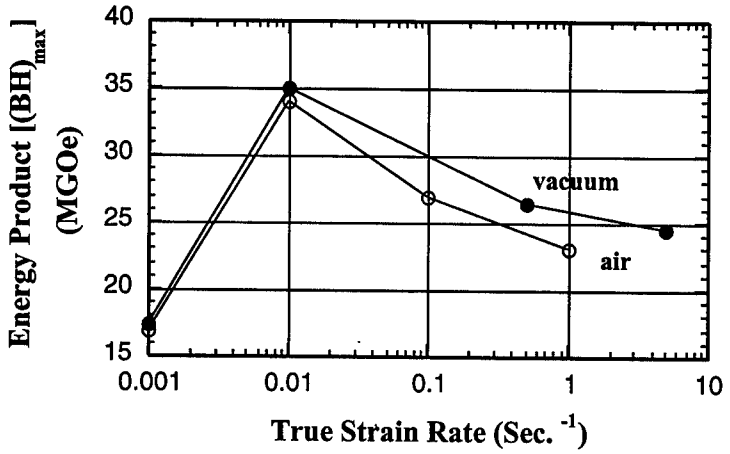


Fig. 4: Effect of strain rate on the energy product of Nd-Fe-B magnet, deformed at 1073 K in air and in vacuum.

The Energy product shows also the similar trend (Figure 4) as that of remanence. The intrinsic coercive force and remanence of samples deformed in a vacuum sealed pouch are better than those deformed in air. This indicates that the boron nitride coating may not be even effecting in controlling the oxidation. For this purpose the envelope of argon is maintained during deformation [7].

At lower strain rate, due to a long period of working time, the grains get sufficient time to grow and hence coercive force is low due to reduced domain wall pinning effect. Again at the strain rate of $1x10^{-1}$ sec^{-1} both the values show a decrease. Hence the strain rate between $1x10^{-2}$ to $1x10^{-1}$ sec^{-1} is the most suitable strain rate for obtaining the best alignment. This is further supported by X-ray diffraction of samples deformed up to $1x10^{-2}$ sec^{-1} which shows high intensity reflection peaks from (006) plane, confirming the orientation of grains along C-axis parallel to the direction of applied compression [9].

To understand the effect of higher strain rates establishment of deformation maps at various temperatures within the temperature range of 973 K to 1173 K are being conducted to identify parameters for efficient deformation. These initial studies indicates a zone of super plasticity in these alloys. Detailed investigation is necessary to establish its existence.

Conclusions

Our studies have established that the magnetic properties of deformed magnets have great dependence on strain rate. Strain rate can be used as an important tool to optimize the magnetic properties. This also shows that tailor-made magnetic properties can be obtained to suit various applications through judicious use of strain, strain-rate and temperature from Nd-Fe-B alloys of same composition.

Acknowledgment

One of the authors (SPN) wishes to acknowledge the kind support of Dr. B.B. Rath for the permission given to work for nine months at Naval Research laboratory, Washington D.C. USA, under the Indo-US Science & Technology Fellowship program. The authors also wishes to thank Office of Naval Research for financial support (under Grant No. N 00014-93-1-1353) and Dr.V.Panchanathan, Magnequench International, Anderson, Indiana, USA for providing the test samples and Director, Regional Research Laboratory, Bhopal (India) for the permission of publication of this paper.

REFERENCES

[1]. N.C.Koon and B.N.Das, "Crystallization of FeB alloys with rare earths to produce hard magnetic materials (invited)" J. Appl. Phy. 55 (6), (1984), 2063-2068,.

[2]. J. J. Croat, " Current Status of rapidly solidified Nd-Fe-B Permanent Magnet" - IEEE Transaction on Magnetics 25 (5) (1989), 3550-3354,

[3]. Lin Li and C.D. Graham Jr., " The origin of crystallographic texture produced during hot deformation in rapidly solidified Nd-Fe-B permanent magnets", IEEE Transactions on Magnetics, 28 (5) (1992), 2130-2132.

[4]. Y.V.R.K. Prasad and S.Sasidhara ed., "Hot Working Guide- A Compendium of Processing Maps" (ASM, Metal Park, Ohio-1997), 20-23.

[5]. Harold J. Frost, Michael F. Ashby ed., Deformation Mechanism Maps - (Pergamon Press Oxford, U.K., 1982.) 1-5

[6]. J.J. Croat, " Current status of rapidly solidified Nd-Fe-B permanent Magnets" C.A.F. Manwaring et al. ed. Proc. of 13th Int. Workshop on Rare Earth Magnets and their Applications, Birmingham (U.K.), Sept. 1994, 65-78.

[7]. V. Panchanathan, "Magnequench Magnets Status Overview" Published by Magnequench, AC Delco Systems- for internal circulation, 1994.

[8]. M. Lenowicz and H.A. Davies , " Induced magnetic anisotropy in hot deformed Fe-RE-B alloys ," C.A.F. Manwaring et al. ed. Proc. of 13th Int. Workshop on Rare Earth Magnets and their Applications, Birmingham (U.K.), Sept. 1994, 623-634.

[9]. Tsung -Shume Chin, S.H. Huang and J.M. Yao , " Preferred Crystalline Orientation of melt-spun Nd-Fe-B falkes (M=Ti/Zr/Hf/V/Nb/Ta)" IEEE Transactions on Magnetics 28 (5) (1992), 2136-2138,

BRITTLE FRACTURE IN $Nd_2Fe_{14}B$ INTERMETALLIC MAGNETS

J. A. Horton, L. Heatherly, E. D. Specht, D. Li†, J. W. Herchenroeder†,and P. C. Canfield*

Metals and Ceramics Division,
Oak Ridge National Laboratory
Oak Ridge, TN 37830

†Magnequench International, Inc.
Anderson, Indiana 46013

*Ames Laboratory and
Department of Physics and Astronomy,
Iowa State University,
Ames, Iowa 50011

Abstract

Efforts to understand and improve the fracture toughness of $Nd_2Fe_{14}B$ permanent magnets require an understanding of the fracture process itself. Cleavage plane orientations in $Nd_2Fe_{14}B$ were identified by X-ray diffraction and found to be rather random. Cleavage fracture surfaces often exhibited smooth curvatures with no evidence for cleavage steps. The small grain sizes of less than 100 nm in Magnequench MQ material preclude an easy assessment of the fracture mode by scanning electron microscopy. Auger electron spectroscopy showed that much of the surface is covered with a 1 nm thick layer of a neodymium-rich phase, presumably the 70Nd-30Fe eutectic phase, suggesting that the hard $Nd_2Fe_{14}B$ grains do not cleave but instead failure is at or in the grain boundary phase.

Introduction

Efforts to understand and improve the fracture toughness of $Nd_2Fe_{14}B$ permanent magnets require an understanding of the fracture process itself. It has been known that $Nd_2Fe_{14}B$ has no deformation modes and therefore is completely brittle. Earlier studies have measured toughness and strength but have not addressed the fracture process [1-3]. Generally, low symmetry, large-unit-cell intermetallics fail by cleavage. Even at hot pressing temperatures of 750°C, when the low melting point eutectic phase forms and serves as a sintering aid, no slip deformation is thought to occur. Cleavage during this step in processing may aid development of anisotropy much as slip does in texture development in many metal alloys. Because of the small grain sizes (less than 100 nm) in the melt spun Magnequench MQ magnets, it is difficult to conclude much about the fracture process based on images from a scanning electron microscope (SEM) of the fracture surface.

In this paper, orientations of cleavage faces formed from fracture of single crystals of $Nd_2Fe_{14}B$ were identified by x-ray diffraction (XRD). Auger electron spectroscopy (AES) analysis was used to measure the composition of the fracture surface as a function of depth in order to confirm the presence of the expected grain boundary phases.

The Third Pacific Rim International Conference on
Advanced Materials and Processing (PRICM 3)
Edited by M.A. Imam, R. DeNale, S. Hanada,
Z. Zhong and D.N. Lee
The Minerals, Metals & Materials Society, 1998

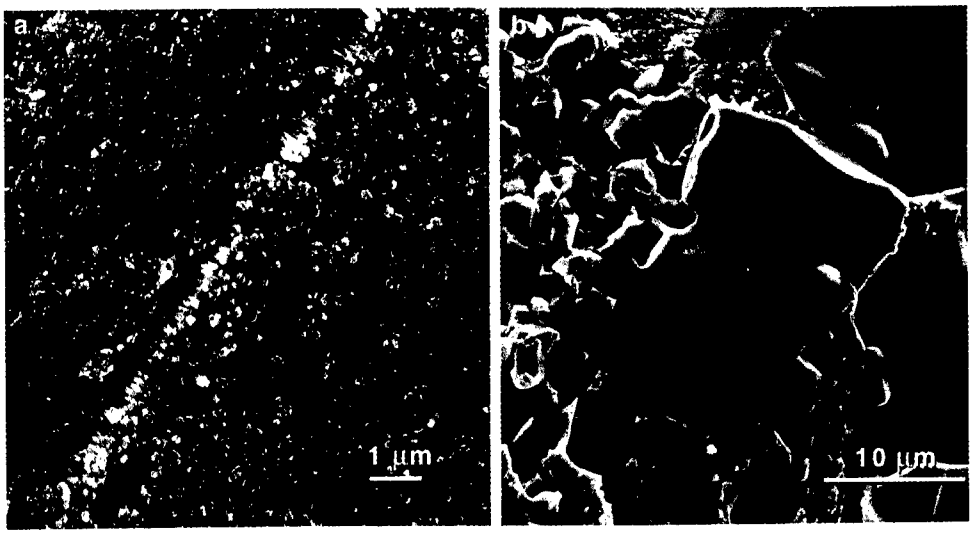


Figure 1: SEM micrographs of fracture surfaces in a MQII magnet showing (a) the small grain size and difficulty in assessing the fracture mode and (b) a similar sample after a 4 hr anneal at 800°C.

Experimental Procedure

Single crystals of $Nd_2Fe_{14}B$ were grown at Ames Laboratory by the slow cooling of a Nd-rich ternary melt. Crystals as large as $10 \times 10 \times 2$ mm^3 can be grown using this technique. These crystals were crushed to obtain cleavage faces. XRD orientations of crystals with fairly flat cleavage faces were made using a 4-circle x-ray diffractometer. After orientation in the goniometer, reflected laser light was used to measure the angular curvature of the face. Stereo images were made of these cleavage faces in a field emission SEM. Surface imaging was also performed in the contact mode in a Park Scientific AutoProbe XL atomic force microscope (AFM). To measure grain boundary compositions, a series of alloys, all processed by the normal MQII route, were analyzed by AES. After specimen insertion and bake out, the specimens were fractured under UHV conditions inside the spectrometer immediately before analysis. The AES data were collected using a PHI Model 590 Scanning Auger Microprobe with a beam energy of 5 keV and a current of ~140 nA. The data were collected in a voltage to frequency conversion mode.

Results and Discussion

Figure 1a shows a fracture surface of a Magnequench MQII magnet. The grain size is generally less than 100 nm and much too small to determine orientations. Figure 1b shows a similar specimen after an anneal for 4 h at 800°C. Attempts were made to orient the larger faces using electron backscattered patterns (EBSP) also called backscattered Kikuchi patterns (BKP) in a SEM. However, due to the low symmetry, large unit cell and the low incidence angle (the specimen was tilted nearly parallel to the incident electron beam) and the roughness of the fracture surface, images could not be obtained that were analyzable.

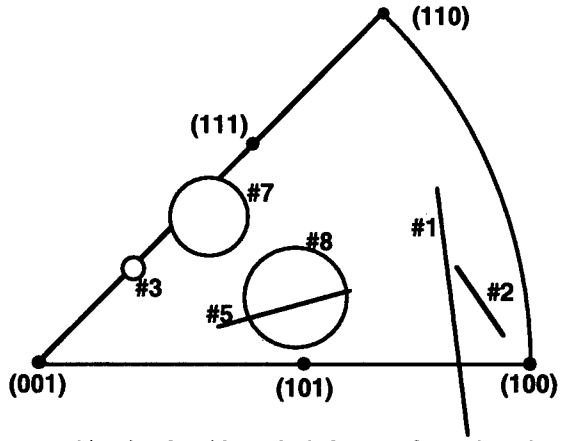


Figure 2: Stereographic triangle with marked cleavage face orientations as measured by XRD. Faces labelled 1, 2, and 5 are drawn as lines since they were curved in one direction. The length of the line represents the angular range. The areas labelled 3, 7, and 8 were hemispherical and the circle covers the angular range of the cleavage faces.

The orientations of cleavage plane normals measured on single crystals are listed in Table I and shown graphically on a stereographic triangle in Fig. 2. The circles in Fig. 2 represent the approximate angular range of the hemispherical faces oriented by XRD. The lines in Fig. 2 represent the approximate cylindrical angular range of the other faces analyzed. Note that $Nd_2Fe_{14}B$ has a tetragonal unit cell and so the stereographic triangle shown consists of what looks like two regular cubic stereographic triangles. Even though these orientations appear in a band, they cover such a large fraction of the stereographic projection that they therefore are quite random.

Table I: XRD Determined Cleavage Plane Normals

Area #	Cleavage Plane Normals		
	h	k	l
1	4.0	0.4	0.7
2	4.0	0.6	0.5
3	1.5	1.4	4.8
5	3.2	0.7	3.4
7	2.4	1.9	3.7
8	2.8	0.7	2.6

Often, curved cleavage fracture surfaces in intermetallic alloys are actually stepped. Stereo SEM micrographs of specimens in this study showed curved faces with no evidence of stepping. Figure 3 shows two SEM micrographs of two flat areas that were oriented and had adjacent chipped areas with highly curved surfaces. AFM scans, Fig. 4, also indicated that curved surfaces were present. Cleavage in intermetallic alloys is often planar with particularly "weak" planes favored. In tetragonal structures, the c-face is often the cleavage plane. The unit cell of $Nd_2Fe_{14}B$ is a layered structure with a mixed layer on the c plane followed by two iron-only layers. Because of this structure, cleavage on (001) was expected. However, no calculations of weak bonding directions have been performed on this structure as has been done on several other intermetallic alloys. The lack of preferred cleavage planes and the curved nature observed here suggest a fracture similar to that expected in amorphous or glassy materials.

The $Nd_2Fe_{14}B$ magnets consist of a mechanically-hard, nondeforming boride phase sintered together with a metallic Nd-rich phase at the grain boundaries. Transmission electron microscopy (TEM) images of the MQII material show very little grain boundary phase mainly due to the near stoichiometric composition used. Detailed TEM analyses of these materials have described the presence of several grain boundary phases from 1 to 10 nm thick [4-5]. The thinner areas were

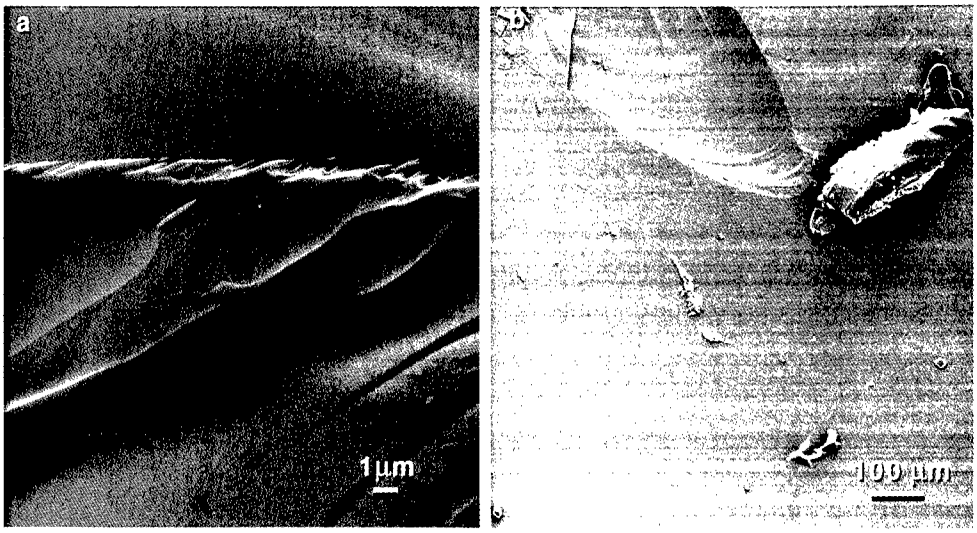


Figure 3: SEM micrographs of cleavage fracture surfaces in $Nd_2Fe_{14}B$ single crystals. Flat fracture surfaces were oriented by XRD. The top of figure 3a is looking obliquely at an almost flat region analyzed as area 1, while the lower half of the figure is a chipped edge showing the smoothly curved fracture surfaces. Figure 3b is looking down on a relatively flat region analyzed as area 2.

found to have a composition of $NdFe_3$, the thicker areas were neodymium rich and 70Nd-30Fe was present at grain boundary junctions. However, these results covered a limited number of boundaries and areas analyzed. AES was used first to help confirm that the fracture surface was intergranular and secondly to gain an estimate of the area fraction covered by grain boundary phase and a confirmation to the composition. So far, similar analysis by atom probe has failed on bulk MQII material due to the difficulty in specimen preparation.

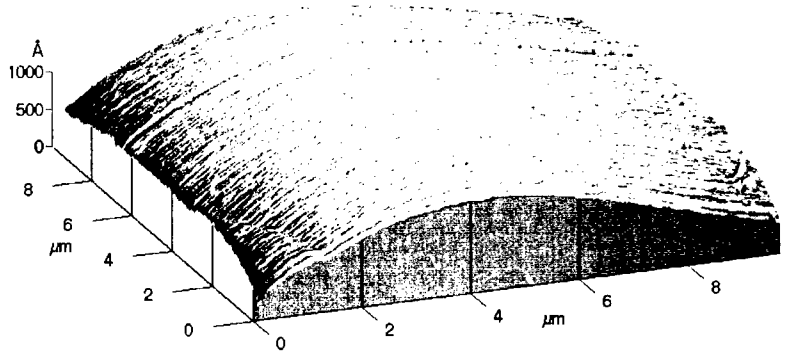


Figure 4: AFM image of surface of cleavage face of area #3. No small steps were imaged.

Figure 5 shows AES data for 5 alloys analyzed, all processed similarly. The data plotted are averages of more than 5 scans on each alloy. The curve labelled 10 is a normal E grade MQII magnet. Base compositions are given in Table II. Note, the boron compositions after 30 mins (~30 nm removed) of argon sputtering from the lowest data point on the graph to the highest are in the correct order, 0.81, 0.87, 0.89, 0.97, and 1.01 wt.%, suggesting that the measurement technique is relatively accurate. The neodymium concentration after 30 m of sputtering are almost in order. From the lowest to highest curve on the graph, the data points are from alloys with 29.4, 29.9, 30.9, 32.2 and 31.9 wt.% total rare earth. However, the absolute bulk composition from the AES analysis is high. The surface concentration of neodymium is more than twice the bulk concentration. The iron concentration curves, not shown, are opposite that of the neodymium. The neodymium

Table II Compositions of alloys analyzed by AES.

Alloy #	RE level		B level	
	wt.%	at.%	wt.%	at.%
75	29.4	13.3	0.87	5.3
74	29.9	13.5	0.97	5.9
10	30.9	14.1	0.89	5.4
73	31.9	14.7	0.81	5.0
71	32.2	14.8	1.01	6.2

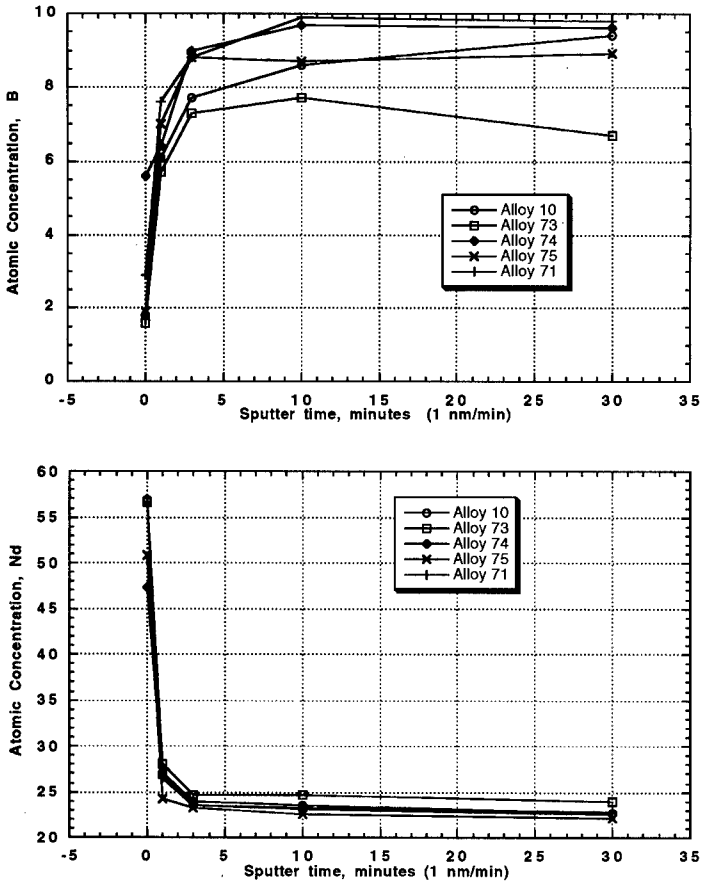


Figure 5: Averaged AES scans for neodymium and boron levels as a function of depth for the 5 alloys listed in Table II. The surface composition was close to that of the low melting point eutectic 70Nd-30Fe phase suggesting that a substantial fraction of the fracture surface was covered with a 1 nm thick layer of the eutectic phase.

enrichment levels observed suggest that up to 3/4 of the surface is coated with a 1 nm thick layer of the 70Nd-30Fe phase. After 3 min of sputtering (3 nm removed) bulk compositions are reached.

Summary and Conclusions

Fracture in the small-grained $Nd_2Fe_{14}B$ MQII magnets is intergranular with a 1 nm thick layer of the eutectic 70Nd-30Fe phase over possibly 3/4 of the fracture surface. While brittle intermetallics usually cleave on preferred planes, $Nd_2Fe_{14}B$ appears to be non-directional when cleaving.

Acknowledgments

This research was sponsored by the U.S. Department of Energy, Office of Energy Research by the Laboratory Technology Research Program and by the Division of Materials Sciences, through the Center of Excellence for Synthesis and Processing of Advanced Materials under contract DE-AC05-96OR22464 with Oak Ridge National Laboratory managed by Lockheed Martin Energy Research Corp. Ames Laboratory is operated for the U.S. Department of Energy by Iowa State University under Contract No. W-7405-Eng-82.

References

1. J. A. Horton, J. L. Wright, and J. W. Herchenroeder, "Fracture Toughness of Commercial Magnets," *IEEE Trans. on Magn.* **32**, (5), (1996), 4374-4376.

2. Yu. M. Rabinovich, V. V. Sergeev, A. D. Maystrenko, V. Kulakovsky, S. Szymura, and H. Bala, "Physical and Mechanical Properties of Sintered Nd-Fe-B type Permanent Magnets," *Intermetallics* **4** (1996), 641-645.

3. P. A. Withey, H. M. Kennett, P. Bowen and I. R. Harris, "The Magnetic and Mechanical Properties of NdFeB Type Permanent Magnets and the Effect of Quenching," *IEEE Trans. on Magn.* **26** (5) (1990), 2619-2621.

4. T. D. Nguyen, K. M. Krishnan, L. H. Lewis, Y. Zhu, and D. O. Welch, "Microstructure and Composition in Rapidly Quenched NdFeB-Based Hard Magnet Alloys," *J. Appl. Phys.* **79** (8) (1996), 4848-4850.

5. L. H. Lewis, Y. Zhu, and D. O. Welch, "Ferromagnetic Grain Boundary Signature in Die-Upset RE-Fe-B Magnets," *Scripta Met.* **33** (10/11) (1995), 1775-1780.

DIFFUSION OF INTERSTITIAL ATOMS IN ORDERED MAGNETIC ALLOYS UNDER PRESSURE

Svetlana Zaginaichenko, Zinaida Matysina*, and Dmitriy Schur

Institute for Problems of Materials Science of NAS, Kiev, 252680, Ukraine,
* Dnepropetrovsk State University, 320000, Ukraine

Abstract

Theoretical investigation of interstitial atom diffusion in a binary alloy A-B with crystal lattice of CsCl type with atomic and magnetic (ferromagnetic or antiferromagnetic) order has been performed. The influence of external pressure on diffusion of hydrogen atoms has been defined. Calculations has been carried out by methods of statistical physics with application of thermodynamic functions. Two mechanisms of magnetism influence on diffusion have been taken into account: a) by atomic ordering, b) by volumetric effects. The simplifying assumption has been accepted. It is supposed that magnetic moments of A and B atoms are collinear and every atom has single magnetic moment. Correlation in substitution of lattice sites by atoms and in orientation of atoms magnetic moments are not taken into consideration. It is assumed that crystal lattice is geometrically ideal. Hydrogen atoms are disposed in octahedral interstitial sites. Interaction of atoms and their magnetic moments is taken into account only for the first coordinational sphere.

The dependence of diffusion factor on temperature, pressure, alloy composition, parameters of atomic and magnetic orders and energy constants has been defined. The particular cases have been analysed: a) absence of external pressure, b)absence of volumetric effects and c) nonmagnetic alloy. The plots of temperature and concentration dependences of diffusion factor have been constructed, they shows breaks which corresponds to Kurnakov, Curie and Neel temperatures.

The obtained formulae can permit to predetermine the functional dependences of diffusion factors of interstitial atoms in alloys, the influence nature of phase transformations on them if energetic constants of electrochemical and exchange interactions of atoms are known from independent experiments.

The Third Pacific Rim International Conference on
Advanced Materials and Processing (PRICM 3)
Edited by M.A. Imam, R. DeNale, S. Hanada,
Z. Zhong and D.N. Lee
The Minerals, Metals & Materials Society, 1998

Introduction

Diffusion of interstitial atoms C in ordered substitution alloys AB with different crystal lattices has been investigated by experiments and theory [1-3]. In magnetic alloys the interrelationship of the cooperative phenomena between atomic and spontaneous magnetization takes place [4]. Therefore magnetism must have an effect on the diffusion of interstitial atoms. It must also effect the magneto-striction mechanism on atomic ordering, on solubility of interstitial impurity and also on diffusion of interstitial atoms.

Calculation of Diffusion Coefficient, Equations of Equilibrium

The influence of atomic ordering and spontaneous magnetization on diffusion of interstitial hydrogen atoms in binary A-B alloys of body-centred cubic structure from transition metals has been studied in the presence of external hydrostate pressure. Magnetization has been examined in quasi-classical Geizenberg approximation and alloy ordering investigated in the Gorsky-Bragg-Wiliams model. The method of average energies has been used for study of interstitial atom diffusion with the assumptions of availability of C impurity gradient in the direction of one of cube edges of alloy lattice and of C atoms arranged in octahedral interstitial sites.

The calculation of diffusion coefficient up to the constant multiplier D_0 gives the following equation

$$D = D_0 \exp\frac{-\left[(U_0)' + (U_1)' x_2 + (U_2)'(x_2)^2\right]}{kT} \Big/ \operatorname{ch}\frac{\left[(U_0)'' + (U_1)'' x_2 + (U_2)''(x_2)^2\right]x_1}{kT} \qquad (1)$$

where k is Boltzmann's constant, T is absolute temperature, x_1 , x_2 are the atomic order parameters on sites and interstitial sites, which are dependent on parameters x_3 , x_4 of magnetization of crystal sublattices (the alloy is ferromagnetic material at $x_3 = x_4$ and is antiferromagnetic material at $x_3 = -x_4$). The values of (1) are energetic parameters which are dependent on alloy composition and independent of order parameters.

The thermodynamic potential of the system has been calculated to determine the equilibrium values of x_i (i = 1,2,3,4). The system of equilibrium equations have been found by minimization of thermodynamic potential

$$\ln\frac{(c_A + x_1)(c_B + x_1)}{(c_A - x_1)(c_B - x_1)} - \frac{z}{kT}\left\{2\left[W_0 + W_1 x_2 + W_2(x_2)^2\right]x_1 + \right.$$
$$\left. + \left[\mu_0 + \mu_1 x_2 + \mu_2(x_2)^2\right]x_2 \pm \left[J_0 + J_1 x_2 + J_2(x_2)^2\right]x_1(x_3)^2\right\} = 0 , \qquad (2)$$

$$\ln\frac{(c + x_2)(3 - c + x_2)}{(c - x_2)(3 - c - x_2)} - \frac{z}{kT}\left\{\frac{2(\omega_1 - \omega_2)}{z}P + \omega_1 + 2\omega_2 x_2 + \right.$$
$$+ c(\alpha + 2\alpha x_2) + 2\left[\mu_0 + \mu_1 x_2 + 3\mu_2(x_2)^2\right]x_1 + 2(W_1 + 2W_2 x_2)(x_1)^2 \pm$$
$$\left. \pm \left[R_1 + 2R_2 x_2 + (J_1 + 2J_2 x_2)(x_1)^2\right](x_3)^2\right\} = 0 , \qquad (3)$$

$$\ln\frac{(1+x_3)}{(1-x_3)} \mp \frac{z}{kT}\left[R_0 + R_1x_2 + R_2(x_2)^2 + \left(J_0 + J_1x_2 + J_2(x_2)^2\right)(x_1)^2\right]x_3 = 0\,, \qquad (4)$$

where N is the lattice sites number (A,B atoms), c_A , c_B , c are concentrations of A,B,C atoms, ω_1 , ω_2 are the changes of crystal volume with appearance of each C atom in interstitial sites of first and second type, z is coordination number, the remaining terms are energetic parameters which are dependent on alloy composition. Equation (2)-(4) takes account of $x_3 = \pm x_4$ and the double signs $(\pm)$ or $(\mp)$ have been used so that the upper sign corresponds to ferromagnetism and the lower sign to antiferromagnetism. It is clear from this system of equations that order parameters x_1 , x_2 in formula (1) for diffusion coefficient depends on temperature T, pressure P, degree of alloy magnetization and alloy composition.

For illustration we shall elucidate the character of diffusion coefficient dependence on temperature and alloy composition in the range of Kurnakov and Curie phase transformations for particular case. We shall study the magnetic alloy with atomic order on sites and disorder on interstitial sites $(x_2 = 0)$. For that case formulae (1)-(4) are considerably simplified. The dependence $x_1(x_3, T)$ is determined from equations of equilibrium and then by formula (1) we calculate the diffusion coefficient in dependence on temperature and alloy composition. For definiteness, assume that temperature T_A of atomic ordering is above the temperature T_M of magnetic ordering.

The $\ln\frac{D}{D_0}$ dependence on inverse temperature $\frac{1}{kT}$ for alloys of stoichiometric composition and energetic parameters (5) is shown in the Fig.1a,

$$(U_0)' = 0.1575 \text{ eV}, \ (U_0)'' = -0.195 \text{ eV}, \ W_0 = 0.035 \text{ eV},$$
$$J_0 = 0.035 \text{ eV}, \ R_0 = 0.014 \text{ eV (curve 3)},$$
$$J_0 = -0.035 \text{ eV}, \ R_0 = 0.014 \text{ eV (curve 4)}. \qquad (5)$$

The concentration dependence of diffusion coefficient for some temperature T ($T < T_A$, T_M near stoichiometric alloy composition and $T > T_A$, T_M for small values c_A , c_B) have been presented at the Fig.1b. Fig.1 shows that plots of temperature and concentration dependences of diffusion coefficient in phase transformations points undergo the curve breaks.

Conclusions

Atomic order suppress the diffusion, magnetic order can both suppress and promote the diffusion of interstitial hydrogen atoms in dependence on contribute or prevent the spontaneous magnetization to atomic ordering.

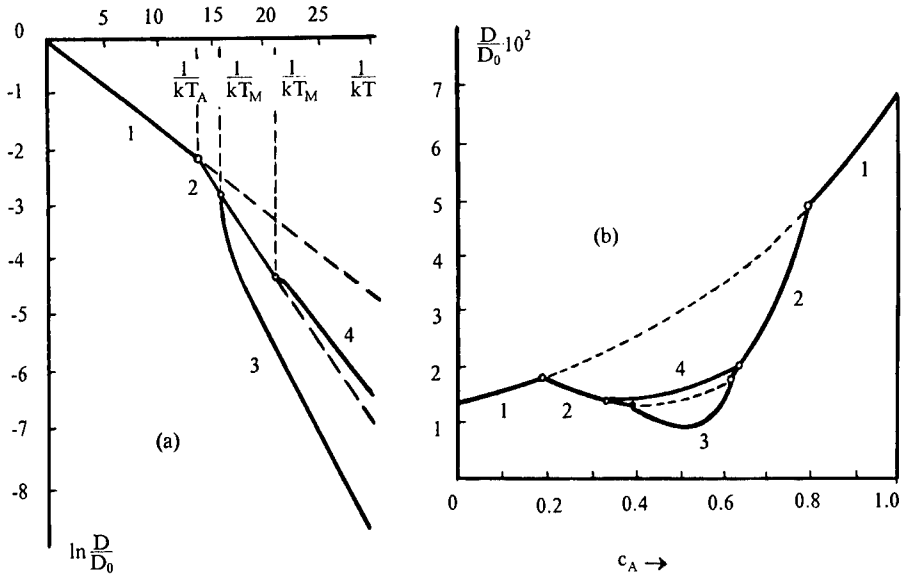


Figure 1: Temperature (a) and concentration (b) dependences of interstitial atoms diffusion factor in ordered magnetic alloys. Parameters of atomic x_1 and magnetic x_3 orders for different section of plots are:

1) $x_1 = 0$, $x_3 = 0$;
2) $x_1 \neq 0$, $x_3 = 0$;
3) $x_1 \neq 0$, $x_3 \neq 0$, x_3 increase x_1;
4) $x_1 \neq 0$, $x_3 \neq 0$, x_3 decrease x_1.

The experimental construction of plots of temperature and concentration dependences of interstitial atoms diffusion coefficient can permit to estimate the Kurnakov, Curie , Neel temperatures of phase transformations and also the kind of such transitions. The phase transition can be of first-kind at the expense of mutual influence of atomic and magnetic order and the dependence curve can undergo an abrupt changes instead of the breaks.

References

1. V.B.Vykhodets, V.A.Goltsov, and P.V.Geld, "For Theory of Hydrogen Diffusion in Ordering Alloys of Cu_3Au," Fizika Tverdogo Tela, 12(9) (1970), 2692-2697.

2. M.A.Krivoglaz, A.A.Smirnov, "Theory of Interstitial Atoms Diffusion in Ordering Alloys," Zhurnal Experimentalnoy Teoreticheskoy Fiziki, I 24(4) (1953), 409-418, II 24(6) (1953), 673-680.

3. Adrian A.Smirnov, Teoriya Splavov Vnedreniya, (Moscow: Nauka, 1979), 365.

4. S.Yu.Zaginaichenko, Z.A.Matysina, and V.I.Ryzhkov, "Magnetic order in ordered phases $B8_1$", Metallofizika, 5(2) (1983), 43-47.

SOLIDIFICATION MODELING IN RARE EARTH PERMANENT MAGNETS

J.E. Shield*, M.J. Kramer#, C.P. Li#, R.W. McCallum# and D.J. Branagan**

*Department of Materials Science and Engineering, University of Utah, Salt Lake City, UT 84112
#Ames Laboratory, USDOE, Ames, IA 50011
**Idaho National Engineering and Environmental Laboratory, Idaho Falls, ID 83415

Abstract

The solidification of $Nd_2Fe_{14}B$ under appropriate conditions of high undercooling results in abrupt transitions in microstructural scale. Considering a dendritic breakup model, an analysis of pertinent solidification parameters including undercooling, recalescence, and the temperature profile of the melt reveals that the model can account for the observed microstructure, including transitions in microstructural scale, the equiaxed $Nd_2Fe_{14}B$ grain structure and the presence of Fe inclusions and dendrites.

The Third Pacific Rim International Conference on
Advanced Materials and Processing (PRICM 3)
Edited by M.A. Imam, R. DeNale, S. Hanada,
Z. Zhong and D.N. Lee
The Minerals, Metals & Materials Society, 1998

Introduction

Unexpected microstructures have been observed at high undercoolings in a number of soli solution systems [1,2]. These unexpected microstructures consist of a transition from a columnz microstructure to a grain-refined equiaxed microstructure with a concomitant drastic reduction i microstructural scale over a very small range of undercoolings [3]. Unusual microstructures have als been observed in alloys based on Nd-Fe-B produced by melt spinning and inert gas atomization [4] In both cases, nanometer-sized equiaxed grains were observed in the first stages of solidificatio This nanoscale microstructure extended only briefly through the ribbon or powder cross section an changed abruptly to coarser grains. Conventional solidification theory does not adequately account fc these transitions in microstructures. There is a strong desire to account for the microstructure observed in both solid solution alloys such as Ni-Cu and peritectic systems such as Nd-Fe-B on physical basis in order to optimize properties of materials, which necessitates uniform, predictabl microstructures.

The transition to a grain refined equiaxed microstructure over a small range of undercooling has been explained in a number of ways. The sharp transition as a function of undercooling has bee explained as a result of copious nucleation due to cavitation effects [5]. Locally collapsing cavitie result in pressure increases, enhancing the undercooling to the limit for homogeneous nucleation. I addition, the reduction in grain size has been explained by a nucleation/denucleation process, whe smaller nuclei clusters and heterogeneous nucleation sites become important at higher undercooling [4]. The change in microstructure has also been attributed to dendrite remelting and/or coarsening. I this case, the heat for remelting and coarsening is provided by the latent heat of fusion durin recalescence [4].

Recently, two theories have been proposed that describe the transition from a coarse dendrit microstructure to a grain refined equiaxed microstructure [6,7]. Both models predict sharp transitio in the microstructure as a function of undercooling. In the first model, hereafter called the SKE model, surface energy minimization leads to dendritic breakup (and an equiaxed microstructure) if t time for breakup is less than a "plateau time" for the solidification of interdendritic liquid. The platea time is related to recalescence and the heat extraction rate. This model appears to describe t microstructural evolution as a function of undercooling in a number of solid solution alloys. In t second model, dendritic fragmentation occurs if a small velocity perturbation is unstable. The stabili of the velocity perturbation is dependent on undercooling, resulting in transitions in stability as function of undercooling. Comparisons with experimental results from pure Ni agree reasonably wel

In this paper, we will consider the unusual microstructures observed in Nd-Fe-B alloys relation to the SKEH solidification model. From the microstructure, the total undercooling and t recalescence will be estimated in order to determine the validity of the SKEH model to solidification this system.

Experimental Procedures

Ingots of $Nd_2Fe_{14}B$ were prepared by arc melting in an Ar atmosphere. Charges approximately 10 g were loaded in quartz tubes and inductively melted to about 1650 K, whic corresponds to a super heat of approximately 200 K. The molten metal was ejected through an orifi of 0.8 mm in diameter with 150 T over-pressure onto a rotating copper wheel. Wheel velociti ranged from 5 to 40 m/s. Preparation of cross-sections for transmission electron microscopy w accomplished by inserting several ribbons into a 3 mm quartz tubes. The tubes were then filled wi epoxy, cured, and sliced into thin wafers. Thin sections were produced by mechanical thinning a ion milling at 5 kV on a cold stage. A Philips CM30 operating at 300 kV was utilized for t microscopic evaluation.

Results

Microstructures

The cross-sectional microstructures of melt spun ribbon were characterized by abrupt transitions in microstructural scale. Near the wheel, 30 to 60 nm equiaxed $Nd_2Fe_{14}B$ grains were present. This fine-grained region extended for approximately 0.4 μm and ended abruptly. The next region consisted of coarser equiaxed grains with diameters of 100 to 300 nm. In this region, α-Fe was observed in the triple junctions of the $Nd_2Fe_{14}B$ grains. Another sharp transition occurs further from the wheel, this time to a region of extremely coarse 1 μm grains with a thin intragranular phase. Finally, the wheel side consists of >10 μm $Nd_2Fe_{14}B$ grains with aligned α-Fe inclusions. The microstructure is described in more detail elsewhere [8].

Modeling

The numerous transition regions observed in the melt spun ribbon cross sections is indicative of several discrete stages of solidification. The development of regions solidified under distinct conditions can be explained qualitatively by the SKEH model, where intermediate recalescence, fragmentation, and solidification at lower and lower undercoolings would lead to transitions to coarser and coarser grain structures.

Qualitatively, the SKEH model explains solidification in the Nd-Fe-B system as follows: initial solidification occurs via a classic dendritic solidification front. The high undercooling at the wheel-melt interface results in a small dendrite tip radius and dendrite spacing. The heat of fusion evolved during solidification is transferred to the liquid melt, raising its temperature above the peritectic temperature and halting the solidification front. This transfer of heat to the liquid necessitates a low heat transfer through the $Nd_2Fe_{14}B$ to the wheel. While the melt temperature is above the peritectic temperature, the initial dendrites develop longitudinal instabilities and break up into equiaxed grains on the order of the initial dendrite trunk radius. While the melt is above the peritectic temperature, γ-Fe dendrites form. This is followed by the solidification of the $Nd_2Fe_{14}B$ phase as the remaining liquid again cools below the peritectic temperature. This explains both the coarser $Nd_2Fe_{14}B$ grains, which are due to a reduced undercooling, and the α-Fe inclusions. In the melt spun ribbon, this sequence occurs several times, leading to the multiple transitions observed experimentally. A schematic temperature profile is shown in Figure 1.

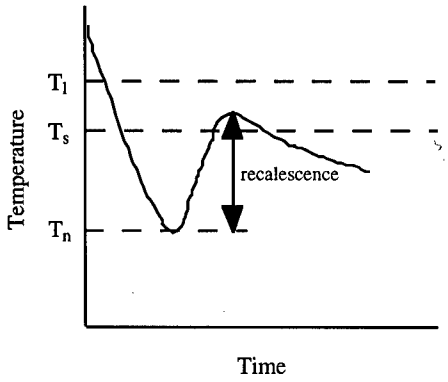


Figure 1: Schematic time-temperature profile illustrating the solidification profile for melt spun $Nd_2Fe_{14}B$.

Table I: Definitions and values of symbols.

Symbol	Definition	Value
k	distribution coefficient	0.01
ΔT_o	liquidus-solidus range (K)	100
$Iv(P)$	Ivantsov function of P	
P	solute Peclet number	$V R_t/2D$
V	interface velocity (m/s)	
R_t	dendrite tip radius (m)	10^{-8}
D	diffusion coefficient in liquid (m^2/s)	10^{-10}
Γ	Gibbs-Thomson coefficient	$\gamma V_m T_m/\Delta H_f$
γ	solid-liquid interfacial energy (J/m^2)	0.2
V_m	molar volume (m^3/mol)	8.5(10)-6
T_m	melting temperature (K)	1428 K
ΔH_f	latent heat of fusion (kJ/mol)	11.9
m	equilibrium liquidus slope (K/at.%)	
m_v	non-equilibrium liquidus slope (K/at.%)	
C_l	heat capacity of liquid (J/K·mol)	40

The modified SKEH model described above qualitatively explains the microstructure observed in melt spun Nd-Fe-B alloys. In order to quantifiably establish the validity of the mode several parameters must be determined. These include the amount of undercooling achieved in th melt, the recalescence affect, and the temperature profile in the liquid.

Undercooling. The undercooling, which is defined in this case as the difference between the dendri tip temperature and the liquidus temperature, is dependent on a number of factors. In direction solidification, which describes the solidification conditions during melt spinning, factors contributin to the total undercooling ΔT include solutal, non-equilibrium, capillarity and kinetic effects, resultin in the equation [5]

$$\Delta T = \left[\frac{k_v \Delta T_o \, Iv(P)}{1 - (1 - k_v)\, Iv(P)}\right] + (m_l - m_v)C_o + \left[\frac{2\Gamma}{R_t}\right] + \left[\frac{V}{\mu_k}\right] \qquad (1$$

The various parameters are listed in Table I along with values used in the calculations, whe appropriate. The Ivantsov number was calculated according to reference [2]. The pseudo-binary F $Nd_2Fe_{14}B$ phase diagram [9] was utilized in the analysis, and non-equilibrium effects on the diagra were considered in the determination of values for k and ΔT_o. The dendrite tip radius was estimate from the experimental grain size. The non-equilibrium term was neglected because of the inhere non-equilibrium nature of the first term, the minimal influence of $m\text{-}m_v$, and the fact we are nominal stoichiometric. The latent heat of fusion for the liquid$\rightarrow Nd_2Fe_{14}B$ transformation was approximate from the relationship $\Delta H_f/T_m \approx R$ [10], where R is the gas constant, resulting in $\Delta H_f \approx 11.9$ kJ/mol.

Figure 2 shows the undercooling calculated from eqn. (2) as a function of velocity. This is t undercooling below the peritectic temperature. As the interface velocity increased from 1 to 50 m/s t undercooling ranged from 150 to 200 K. This provides an estimate of the undercooling at the whe side upon initial dendrite formation.

Recalescence. The recalescence can be determined by considering the volume fraction of solid form and the volume fraction of liquid that is affected by the latent heat of fusion. Consider first t situation that all of the heat of fusion is transferred to the remaining liquid. Implicit to this is po thermal conduction in the $Nd_2Fe_{14}B$ solid and to the melt spinning wheel. This simplified picture

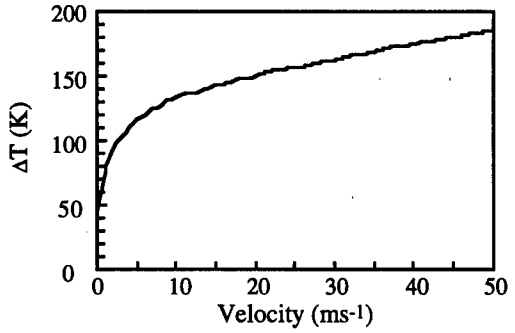


Figure 2: Calculated relationship between the undercooling ΔT and solidification velocity.

provides the maximum affect of recalescence. The change in temperature ΔT_R associated with the recalescence is

$$\Delta T_R = \Delta H_f \cdot f_s / C_l \cdot f_l \qquad (2)$$

where C_l is the heat capacity of the liquid and f_s and f_l are the fraction of solid and liquid, respectively. For the melt spun ribbon, f_s/f_l is simply the ratio of the linear expanses of different regions (e.g., 0.4/19.6 considering a 20 μm thick region). Considering that heat is dissipated to the entire remaining liquid, ΔT_R is approximately 6 K. This is obviously much less than the undercooling and the melt temperature would not approach the peritectic temperature. However, if we consider relatively poor mixing in the liquid and the fact that latent heat transfer occurs more quickly than the heat conduction in the melt, a "heat affected zone," or HAZ, is developed. The recalescence will only affect melt temperature in the HAZ. The ΔT_R is plotted as a function of the size of the HAZ in Figure 3. The recalescence increases significantly as the HAZ decreases in size. With a HAZ of $3f_s$, the associated ΔT_R is approximately 100 K.

Discussion

Considering the calculated undercooling, recalescence and the temperature profile in the liquid, we can more quantitatively determine the validity of the SKEH dendritic breakup model in describing the solidification behavior in the melt spun Nd-Fe-B alloys. First, consider an intermediate value of solidification velocity of 20 m/s. At this velocity, the corresponding undercooling was calculated to be 133 K from eqn. 1. In addition, consider a HAZ of $3f_s \approx 1.2$ μm. The corresponding increase in temperature in the HAZ is 100 K. From this analysis, it is apparent that the melt temperature can rise above the peritectic temperature, halting the initial solidification front.

While this analysis appears to support the SKEH dendritic breakup model, further work is necessary to fully explain the solidification microstructure. For example, a more accurate undercooling could be obtained by estimating the solidification velocity from the microstructure. Finally, the breakup and plateau times, the temperature profile in the melt, and the critical undercoolings must be evaluated to fully verify the solidification model. These aspects are currently being investigated.

Conclusions

The dendritic breakup model developed to explain spontaneous formation of an equiaxed grain structure at high undercoolings appears to explain the observed microstructures in rapidly solidified Nd-Fe-B alloys. Calculations of the undercooling and recalescence considering a heat affected zone

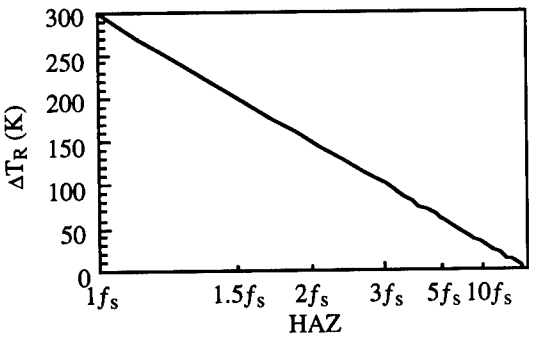


Figure 3: The change in melt temperature due to recalescence shown as a function of the HAZ.

showed that the temperature increase due to dissipation of the latent heat of fusion could result in an increase of melt temperature above the peritectic temperature, thereby halting the advancing solidification front. Dendritic break-up, resulting in an equiaxed grain structure, then occurs. The remaining liquid solidifies at a lower rate, resulting in coarser microstructures.

Acknowledgments

Work at Ames Laboratory was supported by USDOE through Iowa State University under contract No. W-7405-Eng-82. Work at INEEL was supported by the office of Basic Energy Sciences and the USDOE under DOE Idaho Operations Office contract no. DE-AC07-76IDO1570. Discussions with J. Lighty and G. Silcox were also greatly appreciated.

References

1. A. Munitz and G.J. Abbaschian, Undercooled Alloy Phases, ed. E.W. Collings and C.C. Koch (AIME, Warrendale, PA, 1986), p. 23, and references therein.

2. W. Kurz and R. Trivedi, Acta metall. mater. **38**, 1 (1990).

3. R. Willnecker, D.M. Herlach and B. Feuerbacher, Appl. Phys. Lett. **56**, 324 (1990).

4. M.J. Kramer, C.P. Li, K.W. Dennis, R.W. McCallum, C.H. Sellers, D.J. Branagan and J.E. Shield, J. Appl. Phys. **81**, 4459 (1997).

5. J.L. Walker, The Physical Chemistry of Process Metallurgy, Part 2, ed. G.R. St. Pierre (Interscience, New York, 1959), p. 845.

6. M. Schwarz, A. Karma, K. Eckler and D.M. Herlach, Phys. Rev. Lett. 73, 1380 (1994).

7. A.M. Mullis and R.F. Cochrane, J. Appl. Phys. **82**, 3783 (1997).

8. M.J. Kramer, et al., Solidification 1998, ed. S.P. Marxh, et al. (TMS, Warrendale, PA, 1998).

9. M. Sagawa, S. Hirowawa, H. Yamamoto, S. Fujimura and T. Matsuura, Jap. J. Appl. Phys. **26**, 785 (1987).

10. D.A. Porter and K.E. Easterling, Phase Transformations in Metals and Alloys (Van Nostrand Reinhold Co., New York,1981), p. 171.

EFFECT OF HYDROGEN ON THE MAGNETIC PROPERTIES OF $(Er_{0.5}Pr_{0.5})_2Fe_{13}Al_4$ AND ITS NITRIDE

K. G. Suresh[a], G. Markandeyulu[a], S. D. Mahanti[b] and K. V. S. Rama Rao[a]
[a]Magnetism and Magnetic Materials Laboratory, Department of Physics,
Indian Institute of Technology, Madras - 600 036, India
and
[b]Department of Physics and Astronomy, Michigan State University,
East Lansing, MI 48824, U.S.A.

Abstract

Effect of hydrogen on the magnetic properties of $(Er_{0.5}Pr_{0.5})_2Fe_{13}Al_4$ and its nitride has been investigated. It was found that there is no change in the crystal structure on hydrogenation both for the parent compound and its nitride. Hydrogen is found to decrease the magnetization, which has been explained on the basis of magnetovolume effect and chemical effect. Curie temperature does not vary appreciably with hydrogen. Anisotropy is found to decrease both for the parent compound and the nitride on hydrogenation.

The Third Pacific Rim International Conference on
Advanced Materials and Processing (PRICM 3)
Edited by M.A. Imam, R. DeNale, S. Hanada,
Z. Zhong and D.N. Lee
The Minerals, Metals & Materials Society, 1998

Introduction

Iron-rich rare earth intermetallic compounds of the type RE_2Fe_{17} [RE-rare earth] and their nitrides have been drawing considerable attention in recent years owing to their applications in the field of permanent magnets [1,2]. A permanent magnetic material should possess high values of saturation magnetization, Curie temperature and uniaxial anisotropy. Eventhough RE_2Fe_{17} compounds possess high saturation magnetization, the Curie temperature and anisotropy are rather small. Interstitial modification with nitrogen has been reported to increase the Curie temperature and anisotropy considerably [3,4]. Similarly the effect of hydrogen on the magnetic properties has also been studied. It is also reported that substitution of non-magnetic elements such as Al, Ga increase the Curie temperature and the anisotropy[5].

As part of the studies on these compounds, we have earlier reported the structural, magnetic and electrical properties of $(Er,Pr)_2$ $(Fe,Al)_{17}$ compounds and their nitrides [6-10]. The rare earths Er and Pr have been chosen with the view of increasing the rare earth sublattice anisotropy. It was found that there is an increase in the magnetization, Curie temperature and anisotropy of these compounds on nitrogenation. Also, Al was found to increase the Curie temperature for small Al concentrations. Considerable increase in the anisotropy has been observed for compounds with high Al concentrations.

It is known from neutron diffraction studies that there are two types of interstitial sites in these compounds[11]. They are octahedral and tetrahedral sites. The size of the former is larger and can accommodate elements like nitogen (N) and carbon (C). On the other hand, the tetrahedral sites are smaller in size and can be occupied only by hydrogen (H). The maximum amount of nitrogen atoms that can be absorbed per formula unit is 3, whereas that of hydrogen is 5. Therefore, it is of interest to study the effect of hydrogen and nitrogen as well as their combined effect on the magnetic properties of these compounds. With this in view, the magnetic properties of $(Er_{0.5}Pr_{0.5})_2Fe_{13}Al_4$ and its nitride with hydrogen have been investigated and the results are presented in this paper.

Experimental Details

The parent alloy $[(Er_{0.5}Pr_{0.5})_2Fe_{13}Al_4]$ was prepared by arc melting the constituent elements (Er and Pr of 99.9% purity and Fe and Al of 99.99 % purity) and subsequently annealing the ingot in vacuum at 900 oC for seven days. Nitrogenation and hydrogenation were carried out using the high pressure facility developed for this purpose, the details of which are reported elsewhere [6]. The exact amount of nitrogen/hydrogen absorbed by the sample was determined by the pressure reduction method. The samples were characterized using the Powder X-ray diffraction with Cr Kα radiation. Magnetization measurements were carried out using a vibrating sample magnetometer in the temperature range 28-500K. The easy magnetization directions were found out by taking the powder X-ray diffractograms of the magnetically aligned samples. Aligning was done in a magnetic field of 10 kOe.

Results and Discussion

Powder X-ray diffractogram showed that the parent compound $[(Er_{0.5}Pr_{0.5})_2Fe_{13}Al_4]$ crystallizes in the rhombohedral Th_2Zn_{17} structure. There was no change in the crystal structure on nitrogenation and hydrogenation. Table 1 shows the lattice parameters for the parent compound, its nitride and the hydrides.

Table I Lattice parameters, saturation magnetization (at 28K) and the Curie temperatures of $(Er_{0.5}Pr_{0.5})_2Fe_{13}Al_4NH$ system.

Compound	a (Å)	c (Å)	M* (emu/g)	T_C (K)
$(Er_{0.5}Pr_{0.5})_2Fe_{13}Al_4$	8.64	12.61	75	420
$(Er_{0.5}Pr_{0.5})_2Fe_{13}Al_4N_{0.9}$	8.69	12.67	93	425
$(Er_{0.5}Pr_{0.5})_2Fe_{13}Al_4H_{1.2}$	8.65	12.62	75	435
$(Er_{0.5}Pr_{0.5})_2Fe_{13}Al_4N_{0.9}H_{0.4}$	8.68	12.66	80	435

* magnetization at 28 K.

It can be seen from the table that there is an increase in the magnetization on nitrogenation, which can be explained on the basis of the magnetovolume effect [7,8]. Nitrogenation causes a unit cell expansion and consequently the Fe 3d band gets narrowed. This leads to an increase in the Fe magnetic moment. Chemical effect involving the transfer of electrons between N and Fe 3d band causes a reduction in the Fe magnetic moment. However, this effect is smaller compared with the band narrowing effect and therefore, there is a net increase in the magnetization. On the other hand, hydrogenation causes only a nominal lattice expansion and therefore, the band narrowing effect may be comparable with the chemical effect. Therefore, the magnetization remains unchanged on hydrogenation, as can be seen from the table. Hydrogenation of $(Er_{0.5}Pr_{0.5})_2Fe_{13}Al_4N_{0.9}$ causes a reduction in the magnetization, which is followed by a reduction in the lattice parameters, which brings about the 3d band broadening. This effect in conjunction with the chemical effect brought about by N and H causes a reduction in the magnetization. It can also be seen from the table that the Curie temperatures do not vary much on hydrogenation of $(Er_{0.5}Pr_{0.5})_2Fe_{13}Al_4$ and its nitride.

The easy magnetization direction (EMD) can be found out by taking the powder X-ray diffractograms of the magnetically aligned samples and comparing with that of nonaligned samples [7,9]. Using this approach, it has been found that the EMD of $(Er_{0.5}Pr_{0.5})_2Fe_{13}Al_4$ and its nitride lies along a cone about the c-axis [9]. The fact that there is an increase in the anisotropy is indicated by the drastic increase in the intensity of the (006) reflection. Fig. 1 shows the powder X-ray diffractograms of the aligned sample of $(Er_{0.5}Pr_{0.5})_2Fe_{13}Al_4N_{0.9}H_{0.4}$ along with that of the nonaligned sample. It can be seen that there is no increase in the relative intensity of the (006) reflection after aligning, which implies that the EMD lies in the basal plane. Similar diffractograms were obtained for $(Er_{0.5}Pr_{0.5})_2Fe_{13}Al_4H_{1.2}$ as well. This suggests that the anisotropy has decreased on hydrogenation both for the parent compound and its nitride. The first order magnetocrystalline anisotropy constant (K_1) for the rare earth sublattice can be expressed as [12]

$$K_1(RE) = (-3/2)\,\alpha_J\langle r_{4f}^2\rangle \langle 3J_Z^2 - J(J+1)\rangle A_2^0 \qquad (1)$$

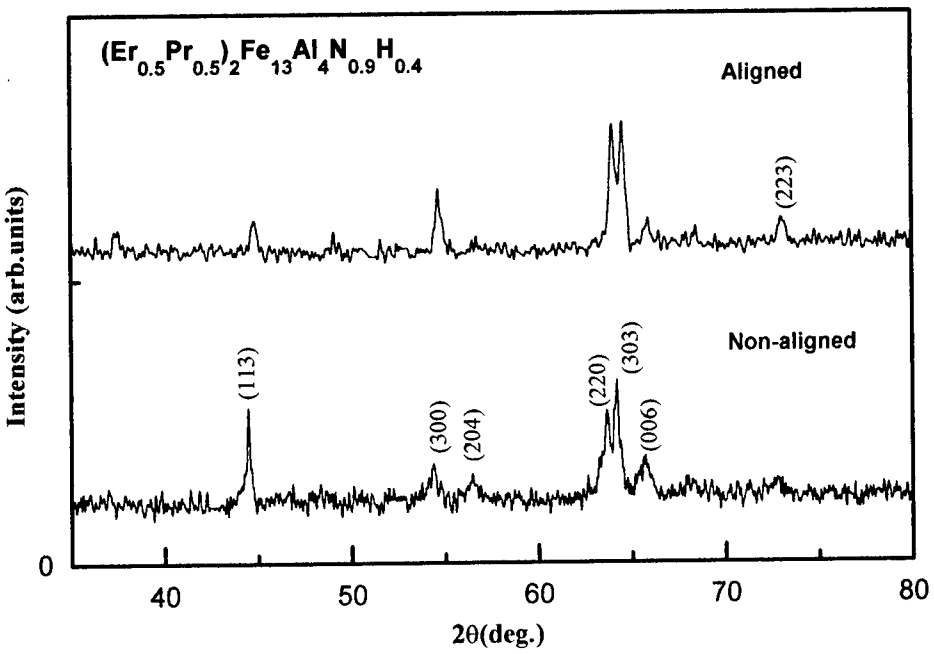


Fig. 1 Powder X-ray diffractograms of the magnetically aligned and nonaligned samples of $(Er_{0.5}Pr_{0.5})_2Fe_{13}Al_4N_{0.9}H_{0.4}$

Where α_J is the second order Stevens factor, r_{4f} is the radius of the 4f orbital, J and J_Z are the total and Z component of the total angular momentum and A_2^0 is the second order crystal field parameter. Hydrogenation may result in a reduction in the magnitude of A_2^0 owing to the alteration in the basal plane charge density and hence reduces K_1.

References

1. K.H.J.Buschow, "New Developments in Hard Magnetic Materials," Rep. Prog. Phys., 54 (1991), 1123-1213.

2. F.J.Cadieu, "Recent Advances in Pseudo-binary Iron Based Permanent Magntes," International Materials Reviews, 40 (1995), 137-148.

3. J.M.D.Coey and H.Sun, "Improved Magnetic Properties by Treatment of Fe-based Rare-earth Intermetallic Compounds in Ammonia," J. Magn. Magn. Mater., 87 (1990), L254-L254.

4. M.Katter, J.Wecker, C.Kuhrt, L.Schultz and R.Grossinger, "Magnetic Properties and Thermal Stability of $Sm_2Fe_{17}N_x$ with Intermediate Nitrogen Concentration," J. Magn. Magn. Mater., 117 (1992), 419-427.

5. Z.Wang and R.A.Dunlap, "Effect of Al Substitution on the Magnetic Anisotropy of Sm_2Fe_{17} Compound," J. Phys. Condensed Matter., 5 (1993), 2407-2414.

6. K.G.Suresh and K.V.S.Rama Rao, "Magnetic and Electrical Properties of $(Er_{1-x}Pr_x)_2Fe_{17}N_y$ IEEE Trans. Magn., 31 (1995), 3722-3724.

7. K.G.Suresh and K.V.S.Rama Rao, "Structural, Magnetic and Electrical Properties of $(Pr_{0.5}Er_{0.5})_2Fe_{17-x}Al_x$," J. Appl. Phys., 79 (1996), 345-350.

8. K.G.Suresh and K.V.S.Rama Rao, "Electrical Resistivity Studies on $(Er_{1-x}Pr_x)_2Fe_{17}$," J. Alloys and Compounds, 238 (1996), 90-94.

9. K.G.Suresh and K.V.S.Rama Rao, "Effect of Nitrogen on the Magnetic Properties of $(Pr_{0.5}Er_{0.5})_2Fe_{17-x}Al_x$," Proceedings of the ninth International Conference on Mgnetic Anisotropy and Coercivity in Rare earth - Transition Metal Alloys, [Eds. F.P.Missel, V.Villas-Boas, H.R.Rechenberg and F.J.G.Landgraf] Worl Scientific, Singapore, 2 (1996), 391-398.

10. K.G.Suresh and K.V.S.Rama Rao, "^{57}Fe Mossbauer Investigations on $(Er,Pr)_2$ $(Fe,Al)_{17}$ Compounds and Their Nitrides," Phys. Rev. B, 55 (1997), 15060-15066.

11. Y.C.Yang, X.D.Zhang, L.S.Kong, Q.Pan, J.L.Yang, Y.F.Ding, B.S.Zhang, C.T.Ye and L.Jin, "Neutron Diffraction Study of Ternary Nitrides of the Type $R_2Fe_{17}N_x$," J. Appl. Phys., 70 (1991), 6018-6020.

12. Z.Hu, W.B.Yelon, S.Mishra, G.J.Long, O.A.Pringle, D.P.Middleton, K.H.J.Buschow and F.Grandjean, "A Magnetic, Neutron Diffraction and Mossbauer Spectral Study of $Nd_2Fe_{15}Ga_2$ and $Tb_2Fe_{17-x}Ga_x$ Solid Solutions, " J. Appl. Phys., 76 (1994) 443-450.

MICROSTRUCTURES OF GaN FILMS GROWN BY LOW PRESSURE METAL-ORGANIC VAPOR PHASE EPITAXY ON SAPPHIRE SUBSTRATES

Z. Zhang and L. S. Cheng

Beijing Laboratory of Electron Microscopy, Center for Condensed Matter Physics, Chinese Academy of Sciences, P. O. Box 2724, 100080, Beijing, China

G. Y. Zhang and Z. J. Yang
Laboratory of Mesoscopic Physics, Department of Physics, Peking University, 100871, Beijing, China

Abstract

Microstructures of both GaN buffer layer and epitaxial layer grown by low pressure metal-organic vapor phase epitaxy were investigated systematically. Either the hexagonal or cubic phase with Wurtzite and Zincblende structure, respectively, has been found being the predominate phase in the GaN buffer layer. The GaN buffer layer is grown with a three dimensional growth mechanism and in a polycrystalline form. High density of grain boundaries, stacking faults, and microtwins were observed in the as-grown GaN buffer layer with predominantly cubic structure. Evolution of GaN buffer layer surface during thermal annealing process was proposed upon a possible GaN decomposition. Formation mechanism of inversion domain boundaries in GaN epitaxial layer was also studied systematically.

The Third Pacific Rim International Conference on
Advanced Materials and Processing (PRICM 3)
Edited by M.A. Imam, R. DeNale, S. Hanada,
Z. Zhong and D.N. Lee
The Minerals, Metals & Materials Society, 1998

Introduction

GaN and other III/V nitride thin films have received much attention recently because of their wide band gaps (from 2.0 to 6.3 ev) and thermal stability at high temperatures. These characteristics of GaN make it suitable for fabrication of light emitting diodes (LEDs) and laser diodes (LDs) operated in the light wavelength region from yellow to ultraviolet. LEDs fabricated from GaN and its alloys with other III/V nitrides are commercially available at present and the life time of GaN based LDs has exceeded 10,000 hours under the continuous operation conditions. These great achievements are attribute to the acquirement of both high quality thin films of GaN and related ternary III/V nitride alloys and p-type doping in GaN. Owing to the fact that transmission electron microscopy (TEM) can provide a direct observation of microstructures of such quasi-two-dimensional thin films at atomic scale, a systematic TEM investigation of the GaN thin films grown under different growth conditions is carried out to get guidelines to both the film growth and understanding of physical properties of the films.

Crystal Growth of GaN Thin Films

GaN thin films are usually grown by metal-organic vapor phase epitaxy(MOVPE) or molecular beam epitaxy (MBE)[1-3]. At the early stage of GaN film growth, there were always cracks in the grown films. The quality of the GaN films are so poor that it is very difficult to fabricate GaN-based opto-electronic devices. Since the introduction of a AlN or GaN buffer layer grown at low temperatures into the film growth process, great progress has been achieved in obtaining high quality GaN films. This growth technique is the so-called two-step growth technique.

Since the buffer layer has a dramatic influence on the film quality, it is necessary to investigate the microstructures of the as-grown GaN buffer layers. For convenience, both pure GaN buffer layer and GaN films (including the buffer layer and epitaxial layer) were grown by low pressure MOVPE in this investigation. During the growth process, trimethyl gallium and ammonia were used as the precursors of Ga and N, respectively, and H_2 was utilized as the carrier gas. The pressure of the growth system was controlled to 76 torr. Pure GaN buffer layers was grown at 550 °C with the thickness from 20 to about 1000 nm. In the growth process of GaN thin films, the two-step growth technique is used. That is a 25 nm thick GaN buffer layer was first grown over the sapphire substrates at 550 °C, and then, the temperature was heated to 1030 °C for 2-minute annealing, finally GaN epitaxial layer with the thickness of about 1 μm was deposited at 1030 °C. All the samples were deposited over the (0001) surface of sapphire.

Microstructures of GaN Buffer Layers

Thin foils of cross section specimens used for TEM observations were prepared by mechanical grinding and subsequent ion milling. Diffraction contrast analysis was performed on Phillips CM-12 transmission electron microscope with the accelerating voltage of 120 KV. High resolution electron microscopy (HREM) investigation is carried out on a JEM-2010 high resolution electron microscope with the accelerating voltage of 200 KV and a point to point resolution of 0.19 nm.

The crystallographic structure of the as-grown GaN buffer layer is some times predominantly hexagonal with the Wurtzite structure, and some times predominantly cubic with Zincblende structure, which will be shown in the following.

Microstructures of GaN Buffer Layers with Predominantly Wurtzite Structure

Figure 1(a) shows a low magnification of cross section image of a thicker GaN buffer layer recorded with the electron beam parallel to the $[1\bar{1}00]$ zone axis of GaN. The thickness of the as-grown buffer layer is measured to be 1.1 μm. Pyramid-shaped growth front and columnar-

shaped crystallites, from several tens to over two hundred nanometer in width, are apparently seen, which implies that the buffer layer is grown with a three dimensional growth mechanism and in polycrystalline form.

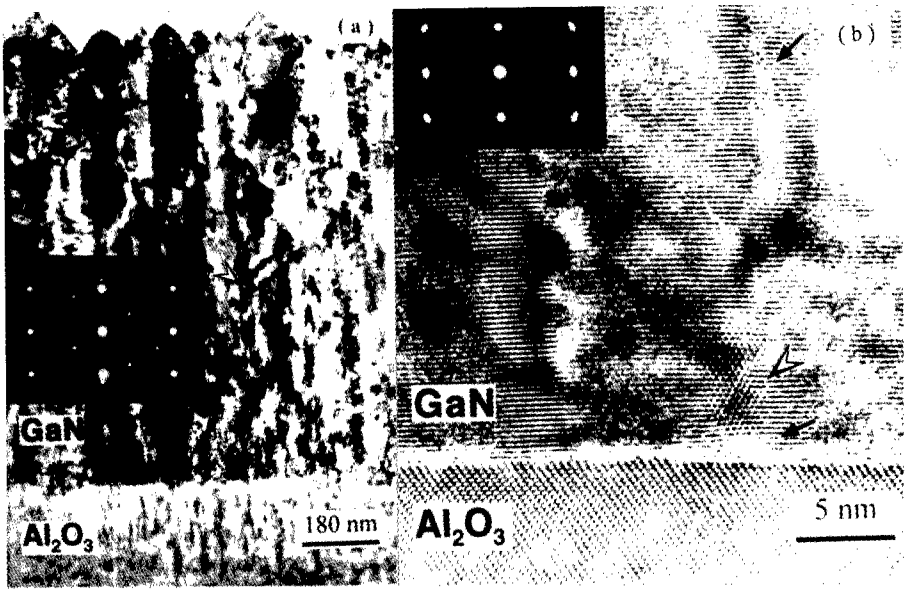


Figure 1: A micro-graph of predominantly hexagonal GaN buffer layer with a SAD pattern recorded at the interface between GaN and sapphire substrate as the inset (a) . (b) HREM image of the interface between GaN and sapphire with the corresponding $[1\bar{1}00]$ SAD pattern recorded at the top part of the GaN buffer layer as the inset.

A composite selected area electron diffraction (SAD) pattern taken at the interface between GaN buffer layer and sapphire substrate is presented in figure 1(a) as the inset. This pattern is indexed as the $[11\bar{2}0]$ of sapphire superimposed by $[1\bar{1}00]$ of GaN. The orientation relationship between GaN buffer layer and sapphire substrate can be obtained as follows:

$$(0001)_{GaN} // (0001)_{sapphire}, [11\bar{2}0]_{GaN} // [1\bar{1}00]_{sapphire}$$

It should be pointed out that no diffraction spots of cubic GaN are visible in SAD patterns such as the inset in figure 1 (a), which indicates that the crystallographic structure of as-grown GaN buffer layer is predominantly hexagonal.

From the SAD analysis, the change in strains introduced by the lattice mismatch and thermal expansion coefficient difference between GaN and sapphire substrate can also be observed as the existence of 0 to 7° tilts among columnar GaN crystallites, evidenced by the diffraction spot elongation in the inset in figure 1 (b) taken from the top part of the as-grown GaN buffer layer. It is easy to understand that the small angle relative tilt is beneficial to the relief of strains. It should also be noted that GaN buffer layers grow epitaxially over the (0001) surface of sapphire as shown in a HREM image of figure 1 (b), a close inspection indicate that a very small portion of cubic GaN (Zincblende structure) is also formed in the as-grown buffer layer (as indicated by the open arrow head) though they could not be identified from SAD patterns as the inset in figure 1 (a). Further detailed HREM studies demonstrated that most of the cubic phase GaN crystallites distribute selectively in grain boundaries. This phenomenon may be related to the

rather large supersaturation and the three dimensional growth mechanism, which may be, again, beneficial for the strain relaxation.

Microstructures of GaN Buffer Layers with Predominantly Zincblende Structure

Different with the literature, our extensive TEM investigations clearly shows that there is a predominately cubic phase in the as-grown GaN buffer layers, under a certain condition, as shown in figure 2 (a). Stacking faults and micro-twins are also clearly observed in the GaN. A composite SAD pattern superimposed by [1 $\bar{1}$ 00] sapphire and a [$\bar{1}$ 10] GaN With Zincblende

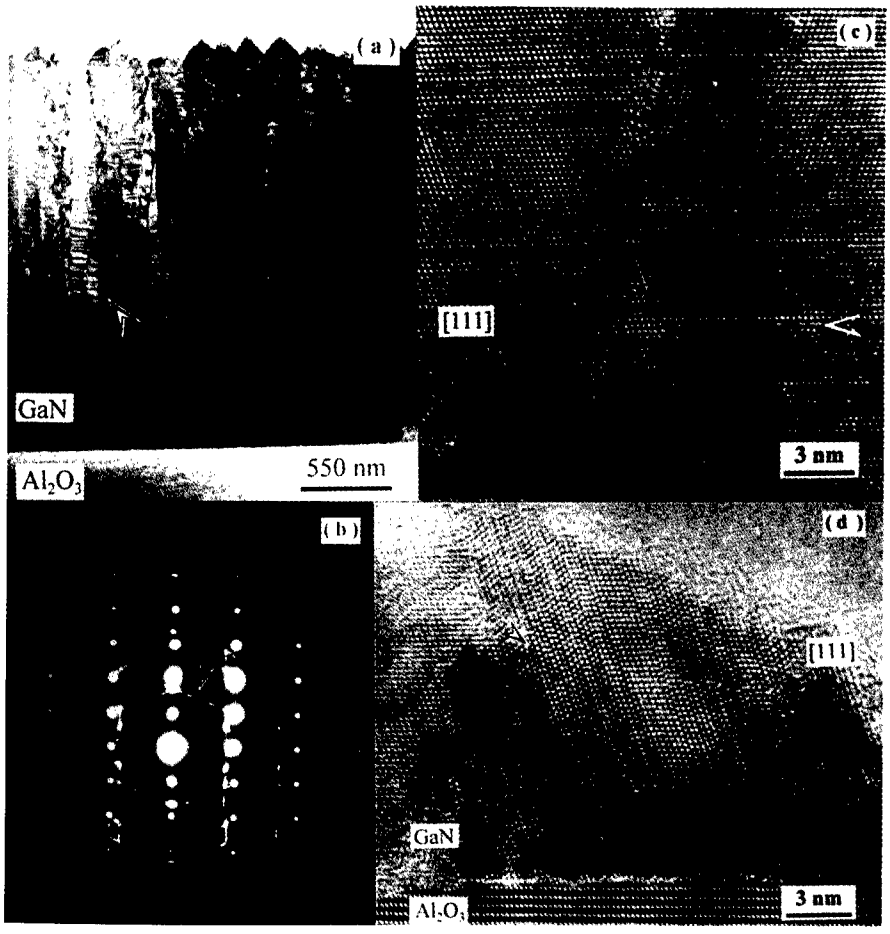


Figure 2: (a) Low magnification image of GaN buffer layer with predominantly cubic structure. (b) Composite SAD pattern recorded at the interface between GaN and sapphire substrate with the electron beam parallel to the [1 $\bar{1}$ 00] zone axis of sapphire. (c) HREM image recorded in the middle part of predominantly cubic GaN buffer layer. (d) HREM image of a thin layer of GaN buffer near the interface between GaN and sapphire.

structure at the interface between GaN and sapphire substrate is presented in figure 2(b). Contrary to the previous case, no diffraction spots of the hexagonal GaN presented in this pattern. Accordingly, the crystallographic structure of the as-grown GaN buffer layer is predominantly cubic and the orientation relationships between cubic GaN and sapphire

substrate can be obtained as :

$$(0001)_{sapphire} // (111)_{GaN}, [1\bar{1}00]_{sapphire} // [1\bar{1}0]_{GaN} \text{ or } // [\bar{1}10]_{GaN}$$

It is apparent that there are also diffraction streaks along both [111] and $[11\bar{1}]$ direction of GaN in the superimposed SAD pattern, implying the existence of planar defects as stacking faults and/or micro-twins. This has been confirmed by HREM investigation. Both twinning configuration of two adjacent crystallites and micro-twins have been observed in the as grown GaN buffer layer as shown in Figure 2 (c) and (d) respectively. In Figure 2 (c), not only showing the twinning domains or grains, but also micro-twins parallel to the growth planes. The micro-twins shown in (d) are local periodically arranged which result in the diffraction maximum on the streaks in figure 2(b). We believe that the high density of micro-twins and/or stacking faults will be beneficial to relies the interface strain introduced by the large lattice mismatch and thermal expansion coefficient difference between GaN and sapphire substrate. It is interesting to note that when SAD patterns taken far away from the interface, streaks in the $[11\bar{1}]$ direction will disappear, only those parallel to the [111] direction are remained . This implies that the density of stacking faults and micro-twins in the $[11\bar{1}]$ direction, which is not parallel to the growth direction, of GaN buffer layer will decrease and eventually disappear as the buffer layer thickness increases. This is reasonable because the strains caused by the lattice mismatch and the thermal expansion coefficient difference between the buffer layer and the substrate will be reduced as the buffer layer thickness increases. Nevertheless, stacking faults and micro-twins in the [111] direction of GaN can not be reduced by the extension of the buffer layer thickness, as shown in figure 2 (c).

Morphology Evolution of GaN Buffer Layers During The Two-step Growth Process

As we have mentioned previously, during the two-step growth process, a short time annealing process is applied to the GaN buffer layer prior to the growth of GaN epitaxial layer. It has been demonstrated by atomic force microscopy (AFM) that the surface morphologies of GaN buffer layers vary with the duration of annealing process[4]. Surface roughness of the GaN buffer layer can be reduced by the increase of annealing time. However, prolonged annealing treatment (over 20 minutes) will lead to roughening again of the buffer layer surface. This is why 2-minute annealing of the GaN buffer layer is usually employed during the two-step growth process. The variation of surface roughness with the duration of annealing process was once regarded as the results of a recrystallization process which takes place during the thermal annealing of GaN buffer layer at high temperatures[4]. It has been demonstrated in this investigation that the reality is different from that.

Samples of GaN films (including GaN buffer layer and epitaxial layer) grown by using the two-step growth technique were examined by HREM in this investigation. One typical HREM image recorded near the interface between GaN and sapphire substrate with the electron beam parallel to the $[11\bar{2}0]$ zone axis of GaN is given in figure 3 (a). It was found that the crystallographic structure of GaN epitaxial layer grown at high temperatures is uniquely hexagonal. Atomically abrupt interfaces both between GaN buffer layer and epitaxial layer and between the GaN buffer and sapphire substrate are apparently seen. It is obvious that the crystallographic structure of the buffer layer shown in this image is cubic. This cubic structure of GaN buffer layer is also demonstrated by the micro electron diffraction pattern shown as the inset in the same image. For comparison, a characteristic $[1\bar{1}0]$ HREM image of a pure GaN buffer layer grown under the same growth conditions as those for growing the buffer layer shown in figure 3 (a) is also presented in figure 3 (b) showing typical growth front of the buffer layer — a pyramid-shaped growth tip which is similar with those observed in both figure 1 (a) and 2 (a). Small portion of hexagonal GaN is observed in this image and indicated by

the arrow head. The buffer layer shown in figure 3 (b) should reflect the morphology of the GaN buffer layer before exposure to high temperature. The difference between morphologies of GaN buffer layers shown in figure 3 (a) and (b), respectively, should results from the short time annealing of the buffer layer shown in figure 3 (a). By comparison of figure 3 (a) with (b), we can find out that the pyramid-shaped growth front shown in figure 3 (b) becomes flat after 2-minute annealing as that shown in figure 3 (a), which is coincident with the AFM results [4]. Moreover, one can see remarkable difference of thickness between the buffer layers shown in figure 3 (a) and (b). Average thickness of the buffer layer as shown, for example, in

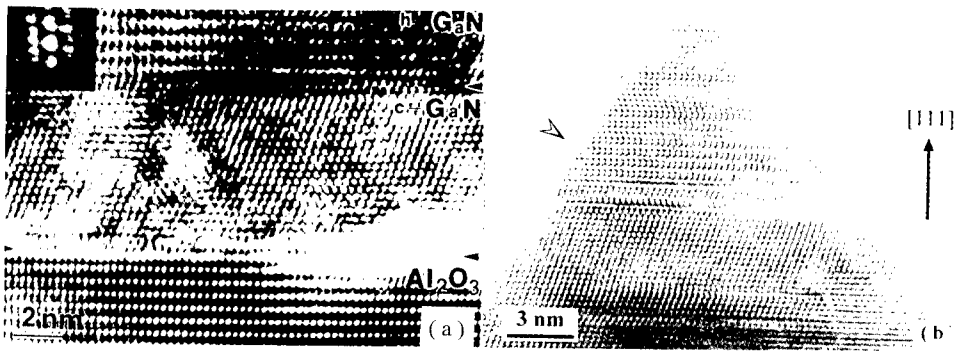


Figure 3: HREM images of a GaN thin film grown by the two-step growth technique(a) and a thin GaN buffer layer showing the growth front (b).

figure 3 (b) is about 25 nm which is in good agreement with the expected value designed during the two-step growth process. However, the buffer layer shown in figure 3 (a) is only 6 nm in thickness. A reasonable explanation to the thickness discrepancy between the two buffer layers is the decomposition of GaN happened during the exposure of GaN buffer layer to high temperature. Taking into account of that a direction in which a crystal grows fastest is also the direction the crystal decomposes fastest. Therefore, decomposition of GaN should preferentially take place on the pyramid-shaped growth tips when the temperature reaches to 1030 °C. Consequently, these tips of GaN buffer layer should be lapped first during the early stage of decomposition process, and the roughness of the buffer layer surface will be reduced until the surface becomes flat. If further high temperature annealing is applied to the flat surface, decomposition will preferentially occur in the gain boundary areas, and the flat surface will become rough again. Thus, the relatively flat surface of the buffer layer shown in figure 3 (a) is not a result of recrystallization but decomposition occurred during the annealing process of GaN buffer layer at high temperature.

Formation of Domain Boundaries in The Epitaxial Layers of GaN

It has been demonstrated that inversion domain boundaries exist in the GaN epitaxial layer[5]. They have remarkable influence on the electrical properties of GaN films grown by MOVPE. therefore, it is important to investigate the formation mechanism of the inversion domain boundaries in the GaN epitaxial layer. Owing to the use of two-step growth technique, direct connection of GaN epitaxial layers (grown at high temperatures) with the sapphire substrates is isolated by GaN buffer layer grown at low temperatures. Thereafter, there should exist certain relationships between domain boundaries in GaN epitaxial layer and microstructures of GaN buffer layer. Systematic observations along the interface indicated that most of the defects in

GaN buffer layer are limited in this layer. Only portion of them can penetrate through the buffer layer into the epitaxial layer. The most interesting result obtained in this investigation is that most of the domain boundaries in GaN epitaxial layer arise from the grain or domain boundaries in the buffer layer, as shown in figure 4 (a) and (b). Figure 4 (a) shows a domain boundary (indicated by the arrow head) in the epitaxial layer resulted from a twin boundary of

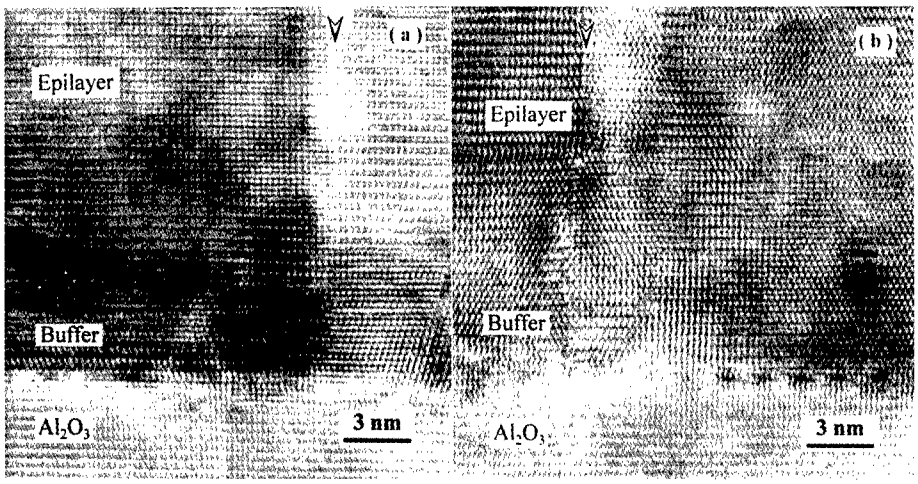


Figure 4: HREM images of GaN thin films recorded near the interface between GaN and sapphire and with the electron beam parallel to the $[1\bar{1}00]$ zone axis of sapphire showing domain boundaries in the GaN epitaxial layers resulted from a cubic twin boundary (a) and a grain boundary between hexagonal crystallites (b) in GaN buffer layer.

cubic GaN in the buffer layer, and (b) shows another one (see where indicated by the arrow head) resulted from a grain boundary between hexagonal crystallites in the buffer layer. The symmetry relationship between the twin and matrix in the buffer layer shown in figure 4 (a) is 180° rotation, and the two fold rotational axis is located parallel to the [111] of GaN in the twin boundary. Because of the growth inertia of GaN, the two fold rotational symmetry between the twin and matrix in the buffer layer will be kept on during the respective growth of domain and matrix in the epitaxial layer. As the space group of GaN with Wurtzite structure is p 6_3mc, there is a 2_1 axis parallel to [0001] of the crystal structure. The 2_1 axis in the domain is also parallel to the domain wall in the epitaxial layer. When a combination of symmetry operations with the sequence of first, two fold rotation with respect to the two fold axis located in and parallel to the domain wall, and then followed by two 2_1 operations relative to any 2_1 axis in the domain are performed to a general lattice point located in the matrix in the epitaxial layer, an equivalent lattice point at the position located on the domain side from the domain wall will be produced. The symmetry between the general lattice point and the as-produced equivalent lattice point is just an inversion. Therefore, the as-formed domain boundaries as that shown in figure 4 (a) are inversion domain boundaries. This has also been confirmed by a central dark field diffraction contrast image analysis as shown in figure 5, where (a) was obtained with the operative vector of $\boldsymbol{g} = 0002$ and $\boldsymbol{g} = 000\bar{2}$ for (b). It can be easily identified that the contrast between some of the two adjacent crystallites (indicated by the arrow head) becomes reversed when the operative $\boldsymbol{g}$ with opposite sign are employed, which is the characteristic displayed by the inversion domain and matrix.

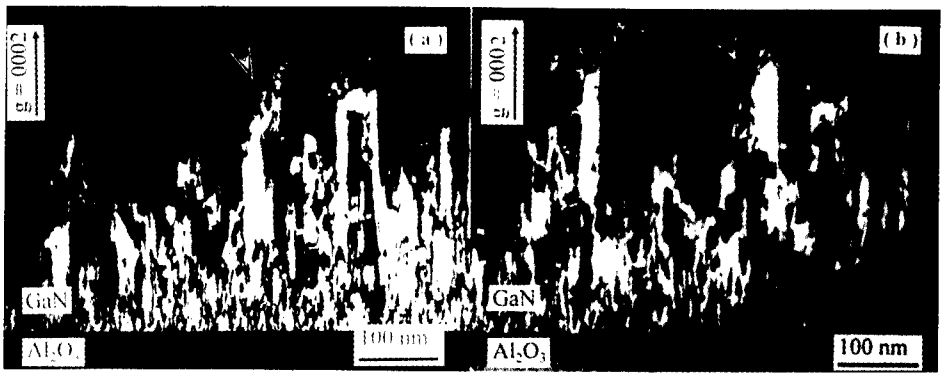


Figure 5: Central dark field images of the GaN buffer layer shown in figure 1 (a) recorded with the operative $\boldsymbol{g} = 0002$(a) and $\boldsymbol{g} = 000\bar{2}$ (b), respectively.

Conclusions

1. The predominate crystallographic structures of the as-grown GaN buffer layers can be either hexagonal (Wurtzite) or cubic with Zincblende structure, upon experimental condition.
2.GaN buffer layers with predominantly Zincblende structure should be preferentially formed during the two-step growth process.
3. During the thermal annealing process of GaN buffer layer at high temperature, decomposition of GaN takes place. Time-controlled thermal treatment to the GaN buffer layer prior to the growth of GaN epitaxial layer can improve the flatness of the buffer layer surface.
4. Inversion domain boundaries in GaN epitaxial layers are extensions of inversion domain boundaries or cubic GaN twin boundaries in GaN buffer layer grown at low temperature.

References

1. I. Akasaki et al., " Effects of AlN Buffer Layer on Crystallographic Structure and on Electrical and Optical Properties of GaN and $Ga_{1-x}Al_xN$ Films Grown on Sapphire Substrate by MOVPE," J. Cryst. Growth, 98 (1989) 209-219.

2. T. D. Moustakas, T. Lei, and R. J. Molnar, " Growth of GaN by ECR-assisted MBE," Physica B, 185 (1993) 36-49.

3. W. A. Melton and J. I. Pankove, "GaN Growth on Sapphire," J. Cryst. Growth, 178 (1997)168-173.

4. A. E. Wickenden, D. K. Wickenden, and T. J. Kistenmacher, "The Effect of Thermal Annealing on GaN Nucleation Layers Deposited on (0001) Sapphire by Metalorganic Chemical Vapor Deposition," J. Appl. Phys.,75 (1994) 5367-5371

5. B.Daudin, J. L. Rouviere, and M. Arlery, "Polarity Determination of GaN Films by Ion Channeling and Convergent Beam Electron Diffraction," Appl. Phys. Lett., 69 (1996) 2480-2482.

Electromagnetic Wave Absorption Properties and Microstructure of $BaFe_{12-x}(TiMn)_xO_{19}$

K. Okayama, *H. Ota, *Y. Yoshida, T. Kagotani, H. Nakamura, S. Sugimoto and M. Homma

Department of Materials Science, Graduate School of Engineering,
Tohoku University, Sendai 980-77, Japan
*Electromagnetic Compatibility Research Laboratories Co., Ltd., Sendai 989-32, Japan

Abstract

This paper describes the relationship between the electromagnetic wave absorption properties and the microstructures of M-type hexagonal ferrites, in which $(TiMn)^{3+}$ is partially substituted for Fe^{3+}. The electromagnetic wave absorption properties were changed by altering the sample preparation processes, in particularly the sintering conditions. The natural resonance frequency (f_r) decreases and the imaginary part of permeability (μ_r'') increases with increasing sintering temperature or time. These results are closely related to the progress of the sintering process. The shift of f_r to lower frequencies is attributed to the change of demagnetizing fields within the samples caused by a decrease in porosity, and the increment of μ_r'' is due to the increased homogeneity of the microstructure. However, all the samples had reflection losses less than -20dB, and the matching frequency (F_m) and matching thickness (D_m) were calculated to be 13-20 GHz and 0.66-1.16mm, respectively.

The Third Pacific Rim International Conference on
Advanced Materials and Processing (PRICM 3)
Edited by M.A. Imam, R. DeNale, S. Hanada,
Z. Zhong and D.N. Lee
The Minerals, Metals & Materials Society, 1998

Introduction

Recently, wireless communication tools such as the personal handy-phone system (PHS) and local area networks (LAN), which use electromagnetic waves in the 1-20 GHz range, have become very popular. The electromagnetic compatibility (EMC) problems[1] have become serious with the increasing use of electromagnetic waves in this frequency range, and so much attention has been paid to finding suitable electromagnetic wave absorption materials.

The spinel type ferrites, such as NiZn/MnZn, have been used as electromagnetic wave absorbers in the MHz range[2]. However, these spinel type ferrites do not work well in the GHz range because of a decrease in magnetic loss (μ_r") [3-4] M-type Ba ferrites with an hexagonal magnetoplumbite structure ($BaFe_{12}O_{19}$) exhibit a uniaxial magnetic anisotropy and have been used for permanent magnets. The anisotropy field (H_A) of M-type Ba ferrite is 1.36 MA/m (17kOe), which corresponds to a natural resonance frequency (f_r) of 48 GHz. Therefore, we investigated the possibility of using this type of ferrite as an electromagnetic wave absorber in the GHz range.

In our previous work[5], M-type hexagonal ferrites $BaFe_{12-x}(TiM)_xO_{19}$ (M=Co, Ni, Zn, Mn, Cu, Mg), in which $(TiM)^{3+}$ was substituted for Fe^{3+} , were prepared. These materials exhibited the natural resonance with fairly high μ_r" values in the 1-20 GHz range. In the case of M=Mn, with the chemical composition of $BaFe_9(TiMn)_3O_{19}$, a μ_r" value of over 4.0 was obtained. From these results it was shown that M-type ferrites candidates for electromagnetic wave absorbers in the GHz range.

It is well known that the electromagnetic wave absorption properties of metal-backed, single-layer absorbers depend upon the frequency dependencies of ε_r and μ_r[6], which are sensitive to the microstructure of the ferrites. However, the relationship between the electromagnetic wave absorption properties and microstructure is not clear in M-type ferrites[7]. In this study, M-type $BaFe_9(TiMn)_3O_{19}$ ferrites were prepared by conventional powder metallurgy using various sintering conditions, and the relationships between preparation processes, microstructure and the electromagnetic wave absorption properties, were investigated.

Experimental Procedure

$BaFe_9(TiMn)_3O_{19}$ M-type ferrites were prepared by a conventional powder metallurgy method. Starting materials of $BaCO_3$, TiO_2, $MnCO_3$ and α-Fe_2O_3 powders (purity > 99%) were mixed in a planetary ball-mill and compacted into a cylindrical shape. These compacts were crushed into powders of size less than 300μm after calcination at 1200°C for 4h, and then pulverized into fine powders of size less than 1μm using a planetary ball mill. These powders were compacted into of 20×10×10 mm^3 blocks and sintered at 1150-1350°C for 6min-100h in air.

Magnetic properties such as the saturation magnetization (M_s) and the anisotropy field (H_A) were measured using a VSM. To measure the relative complex permittibity (ε_r) and the permeability (μ_r), the sintered blocks were cut into a toroidal shapes of ϕ_{out}7.00×ϕ_{in}3.04×1.00 mm^3. Measurements of ε_r and μ_r were carried out using a HP8510C network analyzer, in the frequency range 0.05 to 20.05 GHz, and their values were calculated from the measured reflected and transmitted scattering parameters, S_{11} and S_{21}. The electromagnetic wave absorption properties were determined from the frequency dependence of reflection losses (RL), which were calculated from the following formulae:

$$z = \sqrt{\frac{\mu_r}{\varepsilon_r}} \tanh\left\{ j \cdot \frac{2\pi}{\lambda} \sqrt{\mu_r \cdot \varepsilon_r} \cdot d \right\} \quad (1)$$

$$RL\ [dB] = 20 \log\left(\frac{z-1}{z+1}\right) \quad (2)$$

These formulae are adapted to the metal-backed, single-layer absorber, in which z, d and λ represent, the normalized input impedance at the absorber surface, the thickness of an absorber, and the wavelength of electromagnetic wave in free space, respectively.

The density of the samples was determined from the sintered block cut into the size of $8\times8\times5$ mm^3. The phases present were determined by X-ray diffraction using Fe-Kα radiation. Microstructural analysis of the samples was carried out by SEM.

Results and Discussion

Figure 1 shows the X-ray diffraction patterns of $BaFe_9(TiMn)_3O_{19}$ M-type ferrite after calcination at 1200°C for 4h in air. All the peaks were indexed using JCPDS cards, and determined to be those of M-type hexagonal ferrite. The X-ray diffraction pattern reveals that the lattice parameters and the X-ray density of this sample were a=0.591nm, c=2.324nm and 5.19Mg/m^3, respectively. The following experiments were performed using these calcined powders.

Figure 2 shows the frequency dependence of the imaginary part of permeability (μ_r" curve) of $BaFe_9(TiMn)_3O_{19}$ after sintering at 1200°C for 6min-100h. The natural resonance frequencies (f_r), which corresponds to a peak in μ_r", were not the same, even though from Figure 1, all the samples could be considered to be single phase $BaFe_9(TiMn)_3O_{19}$. The f_r exhibits a tendency to shift to lower frequencies with increasing sintering time. From the anisotropy field (H_A) values, which were measured using a VSM, the f_r of this sample is estimated to be 12.5 GHz. It can be said that the f_r approaches the theoretical value with increasing sintering time. μ_r" shows higher values in the samples sintered for longer times, varying from 1.0 to 3.3.

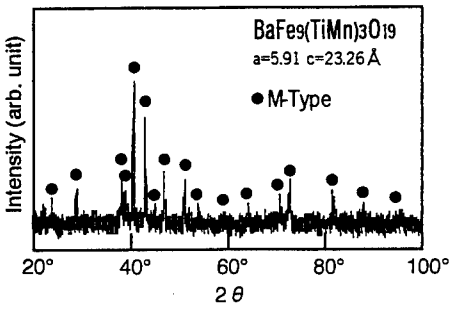


Figure: 1 X-ray diffraction pattern of $BaFe_9(TiMn)_3O_{19}$ powder after calcination at 1200°C for 4h.

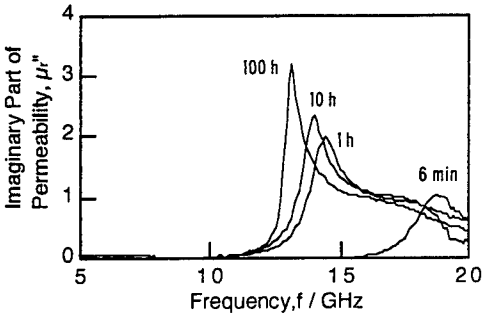


Figure 2: Frequency dependence of imaginary part of permeability of $BaFe_9(TiMn)_3O_{19}$ sintered at 1200°C

The sintering time dependence of the resonance frequency (f_r) and density are shown in Figure 3. The f_r shifts to lower frequencies with increasing sintering time; f_r drops from 18 to 14GHz between 6min and 1h. Density increases with increasing sintering time, and approaches full density after 1h. As shown in Figure 3, the change of f_r can be related to that of density. Figure 4 shows SEM micrographs of $BaFe_9(TiMn)_3O_{19}$ sintered at 1200°C for (a) 6min, (b) 1h and (c) 100h. When the sintering time is 6min (Figure 4 (a)), the grain size is less than 1μm, and grains are isolated from one another. It can be said that sintering has not reached completion in this sample, resulting in the low density of 83% (Figure 3). In the sample sintered for 1h (Figure 4 (b)), necking among the separated particles starts and pores starts to disappear, which leads to a high density of 95%. Grain growth occurs after sintering for 100h (Figure 4(c)), with the grain size exceeding 50μm.

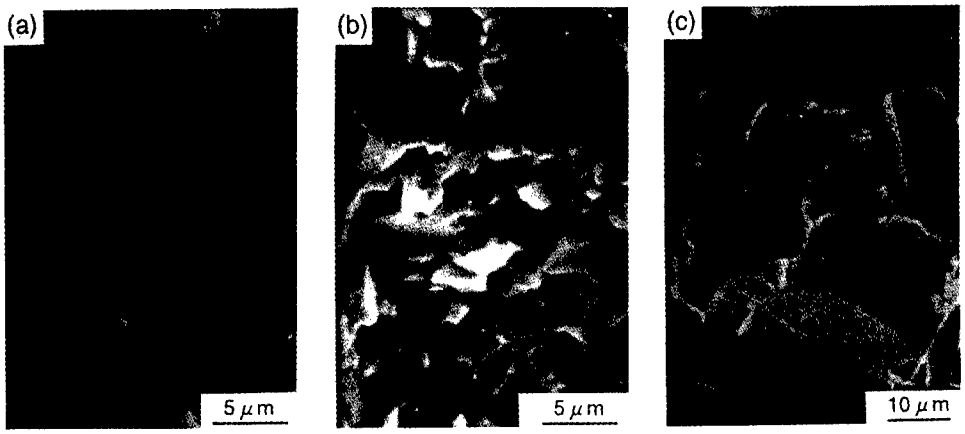


Figure 4: Microstructures of the $BaFe_9(TiMn)_3O_{19}$ sintered at 1200°C for (a) 6 min (b) 1 h and (c) 100 h.

Figure 5 summarizes the frequency dependencies of μ_r" of all the samples sintered between 1150-1350°C for 6min-100h. There is a tendency for the samples sintered at a higher temperature or for a longer time to have lower f_r and higher μ_r" values at f_r. Therefore, from the results shown in Figures 2-5, it can be concluded that these f_r and μ_r" values change as sintering process progresses.

The shift in f_r is explained by Nakamura et al.[8-9] using a simple model that considers the demagnetizing field. When the toroidal sample is used for measuring the electromagnetic wave absorption properties, the f_r can be described by:

$$\omega = 2\pi f_r = \gamma\left[H_A + (N_x - N_z)M_0\right] \tag{3}$$

in which M_0 is the magnetization of the sample, and N_x and N_z represent the demagnetizing coefficient along the circumference and longitudinal directions of the toroidal sample, respectively. The pores observed in the samples sintered at lower temperatures or for shorter times, work as "gaps" in the magnetic circuits of the sample. N_x increases and N_z decreases with the introduction of these gaps, which leads to the increase of f_r. Alternatively, the increase of the maximum μ_r" value after sintering at higher temperatures or for longer times, may be due to the more homogeneous microstructure that accompanies grain growth.

Figure 6 shows the frequency dependence of the calculated reflection losses. All the samples exhibit reflection losses of less than -20dB in the 10-20 GHz range. The optimum thickness and frequency were defined as the matching thickness (D_m) and matching frequency (F_m), respectively. The F_m values are mostly close to those of f_r and D_m values vary from 0.66-1.16mm. Figures 7 and 8 show the frequency dependence of F_m and D_m, respectively, obtained

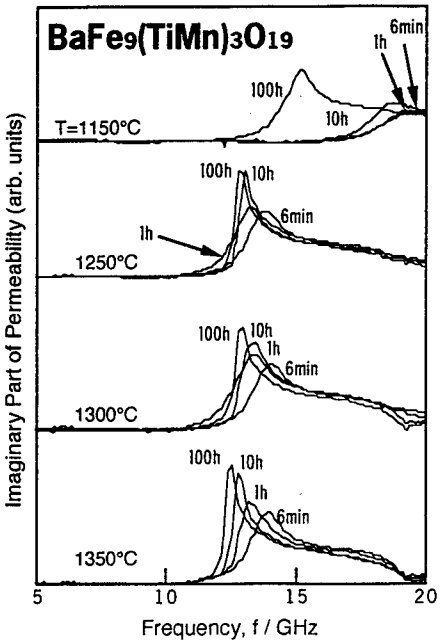


Figure 5: Frequency dependencies of μ_r" of all $BaFe_9(TiMn)_3O_{19}$ samples sintered at 1150-1350°C for 6min-100h.

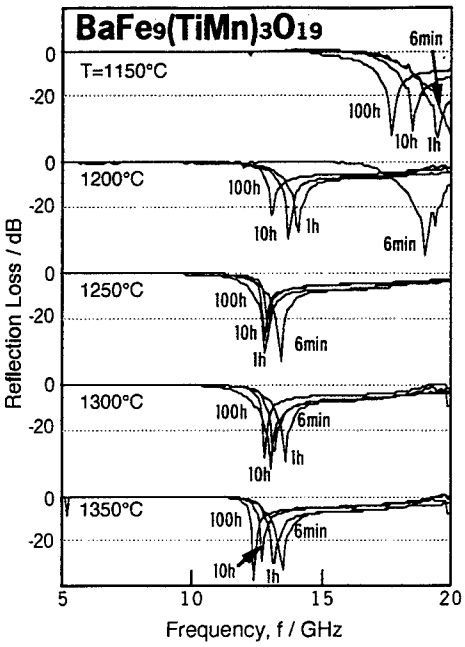


Figure 6: Frequency dependencies of RL of $BaFe_9(TiMn)_3O_{19}$ samples sintered at 1150-1350°C for 6min-100h.

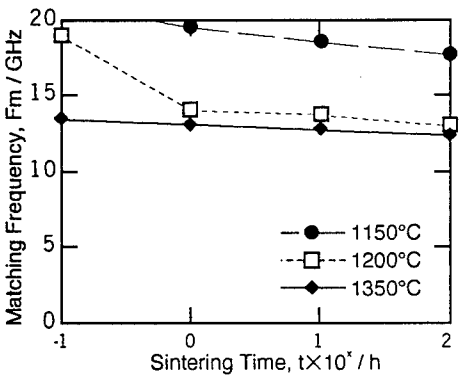


Figure 7: Matching frequency, F_m of $BaFe_9(TiMn)_3O_{19}$ samples sintered at 1150-1350°C for 6min-100h.

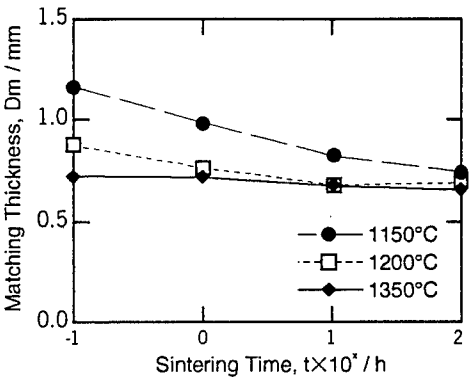


Figure 8: Matching thickness, D_m of $BaFe_9(TiMn)_3O_{19}$ samples sintered at 1150-1350°C for 6min-100h.

with samples sintered between 1150-1350°C. These results revealed that F_m and D_m decrease with increasing sintering temperature or time. D_m is expressed by the following formula[2]

$$D_m = \frac{c}{2\pi f \cdot \mu_r''} \tag{4}$$

in which c represents the velocity of light. According to formula (4), D_m decreases with increasing frequency or μ_r''. Samples sintered for longer times exhibit a higher μ_r'' value, resulting in a smaller value of D_m. The minimum value of D_m (0.66mm) was obtained for the sample sintered at 1350°C for 100h, which is much smaller than that of electromagnetic wave absorbers used with ship radar (5 to 10mm).

For the practical use of electromagnetic wave absorbers, the bandwidth in which the reflection loss shows less than -20 dB, is an important property. The sintering time dependence of the bandwidth calculated from the samples sintered at 1150-1350°C, is shown in Figure 9. The bandwidth decreases with increasing sintering temperature or time, and a maximum value of 7.6% was obtained for a sample sintered at 1150°C for 6min. It is concluded that the bandwidth becomes wider in samples with smaller grains and porous microstructures.

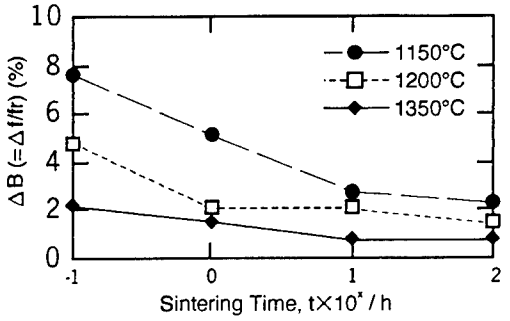


Figure 9: Sintering time dependencies of bandwidth, $\triangle B$ (=f/f_r), of $BaFe_9(TiMn)_3O_{19}$ samples sintered at 1150-1350°C.

Acknowledgement

This work was partly supported by Grants-in Aid for Scientific Research, from the Ministry of Education, Science, Sports and Culture of Japan.

References

1. Y. Kami, J. IEE Japan, 113 (1993), 377-380.
2. Y. Naito and K. Suetake, IEEE Trans. Microwave Theory Tech., 19 (1971), 65-72.
3. J. L. Snoek, Physica, 8 (1948), 207.
4. J. Smit and H. P. J. Wijin, Ferrites (Eindhoven, Philips Technical Library, 1959), 208.
5. K. Okayama, H. Ota, Y. Yoshida, H. Nakamura, T. Kagotani, S. Sugimoto, M. Homma, J. Magn. Soc. Jpn., submitted.
6. H. M. Musal, Jr. and H. T. Hahn, IEEE Trans. Magn., 25 (1989), 3851-3853.
7. W. Grunberger, B. Springmann, M. Schmidt and R. Jahnke, J. Magn. Magn. Mater., 101 (1991), 173-174.
8. T. Nakamura, S. Yamamoto, T. Tsutaoka, S. Shimizu, E. Hankui and K. Hatakeyama Proceedings of The Sixth International Conference on Ferrites (1992), 1298-1301.
9. T. Nakamura and Y. Okano, J. Appl. Phys., 79(1996), 7129-7133.

SYNTHESIS AND MAGNETIC PROPERTIES OF FERROXPLANA TYPE CO_2-Y FERRITE $(Ba_{1-X}\ Sr_X)_2\ CO_2\ FE_{12}\ O_{22}$ (X=0.0-1.0)

Toshio Kagotani,Takaaki Suzuki, Hajime Nakamura, David Book,
Satoshi Sugimoto, Masuo Okada and Motofumi Homma
Department of Materials Science,Graduate School of Engineering,
Tohoku University, Sendai 980-77,Japan

Abstract.

The hexagonal ferrites called ferroxplana exhibit a preferred plane of magnetization. These materials have the advantage that their ferromagnetic resonance frequency is higher than that of spinel ferrites, thus they can be used for magnetic cores at very high frequencies. Examples of such materials are the ferrites with Y-type and Z-type structure containing Co^{2+},Mn^{2+},Zn^{2-},or a mixture of them as divalent ions.

The purpose of the present study is to investigate the sintering conditions necessary to obtain the single phase Y-type ferrite $(Ba_{1-x}\ Sr_x)_2Co_2Fe_{12}O_{22}$ (x=0.0-1.0)which contains Sr to enhance the resonance frequency. Mixtures of $BaCO_3$, $SrCO_3$, CoO and α-Fe_2O_3 powders were calcined in air at 1423K, sintered at 1373-1523K in a flow of O_2 for 6 hours and then furnace-cooled. The phase present in the sintered samples were identified, and the following properties were determinded : lattice constants, density, saturation magnetization, magnetic permeability and electrical resistivity. The single phase Y-type ferrite $[(Ba_{1-x}\ Sr_x)_2Co_2Fe_{12}O_{22}$ x=0.0-0.75] wereobserved in the samples sintered at 1373-1523K. The sample with x=0.75, sintered at 1423K, exhibited a higher resonance frequency over 1.8GHz, due to its high electrical resistivity of $1.8x10^7\ \Omega \cdot m$.

The Third Pacific Rim International Conference on
Advanced Materials and Processing (PRICM 3)
Edited by M.A. Imam, R. DeNale, S. Hanada,
Z. Zhong and D.N. Lee
The Minerals, Metals & Materials Society, 1998

Introduction

A group of ferromagnetic oxides with hexagonal structures has been developed over the past four decades, and it can now be said that the fundamental stage of the investigation into the properties of these hexagonal ferrites is now largely complete. Smit and Wijn[1] have collected comprehensive data on these compounds, as have many other researchers, such as Kojima[2] and Sugimoto[3].

The hexagonal ferrites represent a large family of ferrimagnetic oxides which have complex crystallographic structures and very interesting magnetic properties. Some of these oxides exhibit a preferred direction or plane of magnetization and are used for the production of magnets and magnetic cores. In particular, the hexagonal ferrites called ferroxplana exhibit a preferred plane of magnetization, i.e. the direction of magnetization can easily change within that plane but it requires much more energy to orientate in a direction out of that plane. The initial permeability of these ferroxplana materials is as that of cubic ferrites with spinel structures, but ferroxplana have the advantage in that they exhibit a higher ferromagnetic resonance frequency. Therefore they can be used for magnetic cores at very high frequencies. Examples of such materials are the ferrites containing cobalt as a divalent ion, such as those with a Z-type structure, a W-type structure, ($BaCo_2Fe_{16}O_{27}$), and some cobalt substituted M-type ferrites ($BaCo_xTi_xFe_{12-2x}O_{19}$).

Different methods can be used to produce these ferrites, however for various applications in high frequency technology it is necessary to consider various factors : composition, additive, size and shape of particle, sintering conditions and so on.

In this work, we have investigated Co_2-Y type ferrite, which is usually represented by the chemical formula $Ba_2Co_2Fe_{12}O_{22}$.

Sr ferrites with M-type or W-type structures have a larger anisotropic magnetic field H_A and higher electrical resistivity than Ba ferrites with similar structures.

Furthermore, A.Deria et al reported that Sr-substituted Zn_2-Y type ferrites have higher saturation magnetizations(79 $\mu Wbmkg^{-1}$) and initial permeabilities, than Ba ferrites[4]. This lead us to consider whether similar phenomena may occur with Y-type ferrites.

Therefore, in the present study we adopted Co^{2+} as the divalent ion and substituted Sr for Ba in a Y-type ferrite with of the compositions $(Ba_{1-x}Sr_x)_2Co_2Fe_{12}O_{22}$ (x=0.0-1.0), and examined the magnetic, electrical and high frequency properties of synthesized samples.

Experimental Procedure

Powders of α-Fe_2O_3 with 99.9% purity, and $BaCO_3$, $SrCO_3$ and CoO with spectroscopic grade purity, were adopted as the starting materials. Y-type ferrite samples were synthesized by firing pellets of the mixture of α-Fe_2O_3, $BaCO_3$, $SrCO_3$ and CoO powders, weighed in accordance with x in the chemical composition of $(Ba_{1-x}Sr_x)_2Co_2Fe_{12}O_{22}$. The pellets were compacted at a pressure of 14.7 MPa. Calcination of the mixtures was carried out at 1150K for 2 hours in air and then furnaced-cooled to room temperature. The calcined bulks were fine-ground to a particle size less than 1 μm by ball milling. Y-type compound of about 5g was pressed at 24.5 MPa and formed to a size of 10x10x20 mm^3. The pressed pelltets were then heated at 1150K-1573K for 2 hours in a flow of O_2. The reason that O_2 flow was used as the atmospheric gas, was to enhance the electrical resistivity which is closely related to the magnetic loss of ferrite.

Results and Considerations

Figure 1 shows x-ray diffraction patterns of Y-type ferrites of $(Ba_{1-x}Sr_x)_2Co_2Fe_{12}O_{22}$ with x=0.0,0.25,0.5,0.75 and 1.0, in descending order. The XRD pattern of the sample with composition x=0, i.e. $Ba_2Co_2Fe_{12}O_{22}$, exhibits reflections for the Y-type ferrite phase. For the x=0.25 and

x=0.5 samples the intensities of the Y-type ferrite reflections increase with increaseing x, and in the case of 0.5 a few reflections of Co-spinel phase can be seen. The x=0.75 sample XRD pattern includes reflections for Y-type, Co-spinel and Co_2-Z type ferrite phases. Finally, for the x=1.0 sample, i.e. $Sr_2Co_2Fe_{12}O_{22}$, only the reflections for the Co-spinel and Co_2-Z phases are present. That is to say, in this study, it was not possible to form Y-type ferrite with the composition of $Sr_2Co_2Fe_{12}O_{22}$. As a result of the XRD analysis, it was found that Y-type phase was present in sample in the range x=0.0-0.75, and that the x=0.25 sample contained only the Y-type phase. Therefore it is reasonable to conclude that the composition x= 0.25 is suitable for the purpose of obtaining single phase Y-type ferrite in the mixed system of Ba- and Sr-ferrites. Also it was found that Y-type ferrite with the chemical composition of $Sr_2Co_2Fe_{12}O_{22}$ could not be produced.

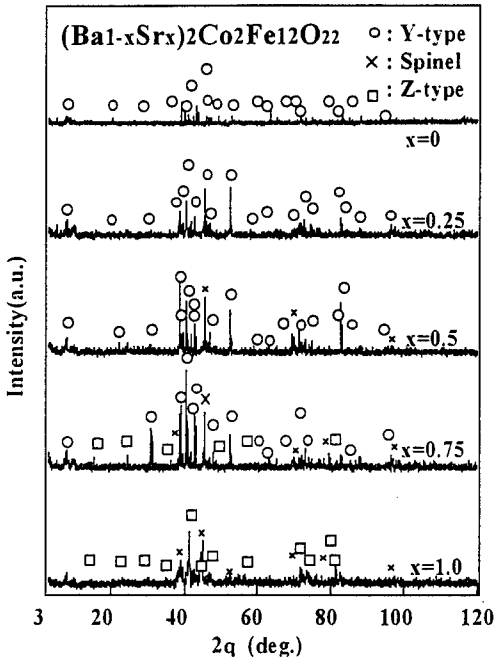


Figure 1 : XRD patterns of ferrite sample with the compositions $(Ba_{1-x}Sr_x)_2Co_2Fe_{12}O_{22}$, where Sr mol fraction x=0.0-1.0

Figure 2 shows the dependence of the saturation magnetization Ms of ferrite compounds with the compositions $(Ba_{1-x}Sr_x)_2Co_2Fe_{12}O_{22}$, on the Sr mol fraction, x. Ms increases gradually in the range x=0.0-0.75 and acutely in the range x>0.75. This behaviour means that the x=0.0-0.75 samples mainly consist of Y-type ferrite, which supports the XRD analysis(Figure 1).

The gradual increase in Ms observed between compositions x=0 to x=0.75 may be explained by the formation of Co-spinel and Co_2-Z phases, which contribute to the magnetization of the samples. So it can be said that Sr substitution is effective in enhancing the magnetization.

As shown by XRD (Figure 1), Y-type ferrite was not formed at the composition x=1.0, therefore it is apparent that the sharp increase in Ms must be owed the combined magnetization of the Co-spinel and Co_2-Z phases is larger than the magnetization of the Co_2-Y phase.

Figure 3 shows the dependence of the specific electrical resistivity ρ of the samples shown in Figure 2 on the Sr mol fraction, x. The specific resistivity ρ of the $(Ba_{1-x}Sr_x)_2Co_2Fe_{12}O_{22}$

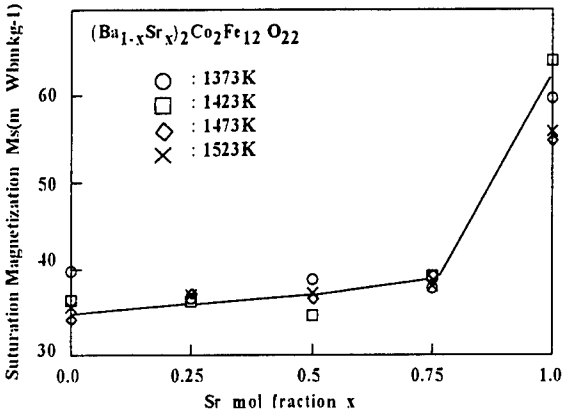


Figure 2 : Dependence of saturation magnetization of Sr substituted (Ba1-xSrx)2Co2Fe12O22,sintered for 6 hours in O2 flow, on Sr mol fration x

compounds was, more than 10^7 Ω•m in the sintering temperature range of 1373-1473K, but was of the order of 10^2 at 1523K. This large difference in the value of ρ is because the Fe^{2+} ion can exist comparatively stabley above 1473K. At temperatures greater than 1473K, Fe^{2+} ions are much favoured over Fe^{3+} in accordance with the reaction :$Fe^{3+} + e^- \Leftrightarrow Fe^{2+}$. On the other hand, the Fe^{3+} ion is more stable below 1423K and has a larger specific resistivity ρ than the Fe^{2+} ion. Therefore, it can be said that the sample sintered at 1523K contains many more Fe^{2+} ions and consequently exhibits a much lower resistivity than the sample sintered below 1523K. In practice, the samples sintered in the range of 1373-1473K in an O_2 flow showed high electrical resistivity over 10^6 Ω•m. The specific resistivity of the x=0.75 sample is sintered at 1423K reached a maximum of 1.8 x 10^7Ω•m in this work.

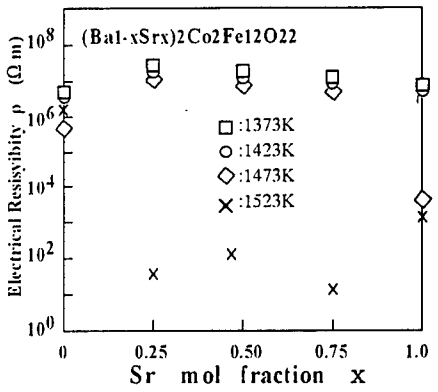


Figure 3 : Dependence of electrical resistivity ρ of Y-type Ferrite with the compositions of $(Ba_{1-x}Sr_x)_2Co_2Fe_{12}O_{22}$, on Sr mol fraction x

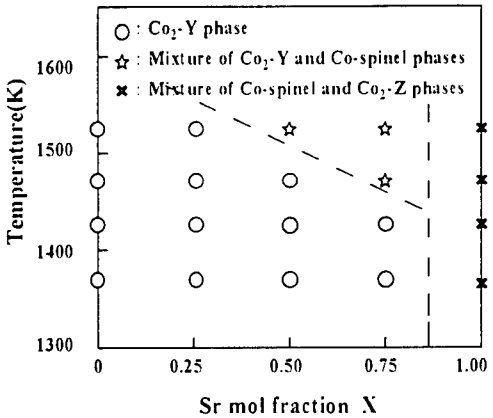


Figure 4 : A pseudo-phase diagram of Sr-substituted Co2-Y ferrite, a mixture of Co2-Y ferrite and Co-spinel phases, and a mixture of Co-spinel and Co2-Z phases

Figure 4 summarizes the results of Figure 1, Figure 2 and Figure 3, and showed the region where the Y-type ferrite phase exists, in the phase diagram of the pseudo binary system $Ba_2Co_2Fe_{12}O_{22}$-$Sr_2Co_2Fe_{12}O_{22}$. In Figure 4, the open circle represents the Y-type ferrite phase, and the star and the saltire cross represent, mixtures of Y-type and Co-spinel, and Co-spinel and Co_2-Z phases, respectively. The broken lines represent the boundaries between these three regions. From this diagram, it can be seen that Co_2-Y ferrite exists in the range x=0.0-0.75 below 1523K, and cannot be present when x is greater than 0.75.

Figure 5 shows the frequency dispersion of the magnetic permeability μ' of $(Ba_{1-x}Sr_x)_2Co_2Fe_{12}O_{22}$ Y-type ferrite, with Sr mol fraction x=0.0-0.75. It can be seen that the vaues of the magnetic permeability μ' of all the samples remain relatively constant in the frequency range 1 MHz to 1GHz, and that abobe 1 GHz there is a tendency for μ' to slightly decrease. It has been reported [5] that the permeability μ' of the Co_2-Z type ferrite called feroxplana (which was developed by Philips Co.), decreases sharply at frequencies above 4MHz.

Also the Z-type ferrite $Ba_3Co_2Fe_{24}O_{41}$, which we prepared using the same sintering conditions

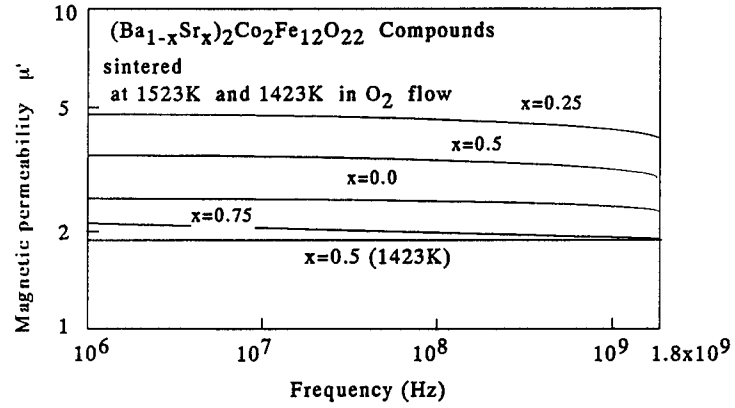


Figure 5 : Frequency dispersion of the magnetic permeability μ' of $(Ba_{1-x}Sr_x)_2Co_2Fe_{12}O_{22}$ compounds sintered at 1523K and 1423K

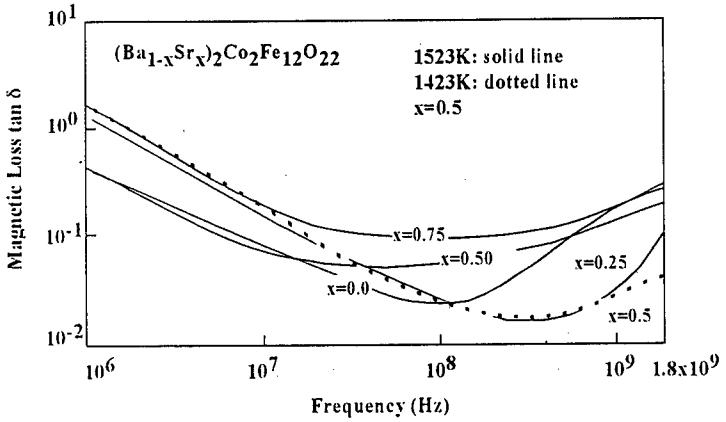


Figure 6 : Frequency Dspersion of Magnetic Loss tan δ of (Ba1-xSrx)2Co2Fe12O22 sitered at 1523K and 1423K

as the present work, exhibited a constant μ' of 18 up to 800 MHz[6]. The constant μ' range of the Y-type ferrite in this investgation exceeds the Snoek limit[7], and is greater than the ranges for the two Z-type ferrites mensioned above. The x=0.25 sample sintered at 1523K had a value of μ'=4.8 which was the highest in this work. The x=0.5 sample sintered at 1423K had a constant μ'-value over the extire measurement range of 1MHz-1.8GHz. Both the samples x=0.25 and x=0.5 had higher values of μ' than the $Ba_2Co_2Fe_{12}O_{22}$ compound. Therefore it can be said that Sr substitution for Ba in the Y-type ferrite $Ba_2Co_2Fe_{12}O_{22}$, enhances the high frequency characteristics of the magnetic permeability μ'.

Figure 6 showed the frequency dispersion of the magnetic loss tan δ of the samples indicated in Figure.5. Generally, the loss of tan δ gradually decreases as the frequency increases from 1 MHz to 30 MHz, remains fairly constant at about 10^{-2} in the intermediate range of 30MHz-300MHz, and then tends to increase above 300 MHz. The loss of tan δ increases gradually above 300 MHz and reachs about 10^{-1} at 1GHz. The fact that the loss tan δ can maintain a low value of 10^{-1}-10^{-2}, means that entering the samples in a flow of O_2 is an effective means of enhancing the electrical resistivity.

Conclusion

The following may be concluded from this study on the Sr substituted Y-type ferrite compound $(Ba_{1-x}Sr_x)_2Co_2Fe_{12}O_{22}$:

1. Single phase Y-type ferrite was obtained for the composition $Ba_2Co_2Fe_{12}O_{22}$ in which Sr was substituted for Ba, by sintering at tmperatures of 1373-1523K in an O_2 flow.
2. It was shown that Sr subsitution for Ba in Y-type ferrite, $Ba_2Co_2Fe_{12}O_{22}$, was effective in enhancing the high frequency characteristics of the magnetic permeability μ', in the frequency range 1 MHz-1.8 GHz.
3. Sintering in an O_2 flow resulted in a high electrical resistivity for the Y-type ferrite, following the reduction of its magnetic loss.

Refernces

1. J.Smit and H.P.J.Wijn, Ferrites(Eindhoven,The Netherlands:Philips Tecnical Library, 1959),177-228
2. H.Kojima , Ferromagnetism, .vol.3(Eindhoven, The Netherlands: No0rth-Holland Publishing Companny, 1982):305-391
3. M.Sugimoto, "Properties of Ferroxplana-type hexagonal Ferrites", Ferromagnetism, vol 3 (Eindhoven, The Netherlands :North-Holland Publishing Compaany, 1982)393-440
4. A.Deriu et al.,"Y-type Hexagonal Ferrite Containing Zinc, Copper and Cadmium : Magnetic Properties and Cation Distibution" Journal of Magnetism and Magnetic Materials, 22(1981)257-262
5. H.P.J.Wijn and P.B.Braun, "Ferroxplana Hexagnal Ferromagnetic iron-Oxide Compounds for very high Frequencies" Philips Tech. Rev., 18(1956),145-154
6. O.Sakaguchi and T.Kagotani et al.,"Synthesis and Magnetic Properties of Ferroxplana type Ferrite"Materials Transaction, JIM,37(1996), 878-882.
7.J.L.Snoek,"Dispersion and Absorbtion in Magnetic Ferrites at Frequencies above one Mc/ s ", Physica, 16(1948)207-217

MICROSTRUCTURE AND PROPERTIES OF Co-C FILMS PREPARED BY A DUAL SOURCE DEPOSITION SYSTEM

M.Azumi, J.Shi*, Y.Haga and O.Nittono

Department of Metallurgical Engineering, Tokyo Institute of Technology
2-12-1 Oh-okayama, Meguro-ku, Tokyo 152-0011, Japan
*Present address: The University of Electro-Communications

Abstract

Co-C composite films were prepared by a codeposition method which combines ion beam sputtering deposition (for the deposition of Co) and microwave plasma chemical vapor deposition (for C). The microstructure of such films was characterized by X-ray diffraction and transmission electron microscopy. As-deposited Co-C composite films were found to be amorphous Co-C alloys. The magnetic properties of such films were investigated by VSM. The Co-C films show ferromagnetic characteristics in as-deposited state. These films were annealed at different temperatures, and thermal stability and crystallization process of these films were studied. When the film was annealed at 573K, crystallization process began. Both α-Co and δ-Co_2C phases appeared, and when annealed at 673K, the δ-Co2C carbide decomposed into α-Co and graphite. When annealing temperature increased, more cobalt segregated out of the matrix phase as α-Co (low temperature phase) and β-Co (high temperature phase); the former was more than the latter which was stabilized at room temperature. To change the coercivity with Co layer thicknesses Co/C multilayered films were prepared and their structure and magnetic properties were studied. The Co layers consisted of fine grains of Co-C alloy and the carbon layers were of amorphous carbon. The Co/C multilayered films with large periods showed soft magnetic properties in as-deposited state.

The Third Pacific Rim International Conference on
Advanced Materials and Processing (PRICM 3)
Edited by M.A. Imam, R. DeNale, S. Hanada,
Z. Zhong and D.N. Lee
The Minerals, Metals & Materials Society, 1998

Introduction

Transition metal-carbon alloy systems have attracted research interests so far because of their scientific and technological importance. Among transition metals, cobalt, one of the ferromagnetic triad (Fe, Co and Ni), is known to form a simple eutectic binary phase diagram with carbon (graphite), and there is no thermodynamically stable carbide between them[1]. Early in 1940's through 1960's, the formation behavior and crystal structures of nonequilibrium cobalt carbides were investigated mainly through the cementation of cobalt powder and cobalt thin films, then two kinds of carbides have been formed: Co_2C and Co_3C[2~4]. Both carbides were orthorhombic in crystal structure, and the latter was considered to be isomorphous with the cementite (Fe_3C)[4]. However, the microstructure and magnetic properties of these carbides have not been studied yet, because of the difficulty in synthesizing samples of these carbides suitable for analysis. On the other hand, amorphous metal-carbon alloys had been very difficult to fabricate through thermal processes such as splat-cooling because of high melting point of carbon (4300K). It is known that amorphous phase can not be obtained by splat-cooling of Co-C melt, and that the addition of third element such as B and Si is needed to stabilize the amorphous structure[5,6]. However, in recent years, amorphous Co-C alloys have been prepared by co-sputtering methods[7~9]. And a recent approach in studying the Co-C alloy system is aimed at exploiting the application potentials. Cobalt carbide films synthesized by radio-frequency magnetron sputtering were expected to develop new magnetic recording materials. Recently, for the same purpose, Co-C films which contain cobalt nanocrystallites encapsulated in graphite-like carbon were prepared by ion beam sputtering and successive annealing[10]. It was reported that the saturation magnetization of the films was at the same level as those of cobalt-based alloy media, whose coercivity was too small to meet the requirements for ultra-high-density recording media.

In our previous work, we have designed a dual source deposition system (CVD+IBS) and applied it to the Ni-C alloy system. As a result, nonequilibrium Ni_3C nanocrystallites have been formed in the Ni-C films, and amorphous and granular Ni-C films have also been prepared by the same method[11,12]. It has been proved that this codeposition method is a powerful tool to study the structure and properties of transition metal-carbon alloy films, since various film structures such as carbides, amorphous and granular M-C films with different carbon concentrations can be obtained by controlling deposition conditions. In this study, we tried to form Co-C films by the same deposition method, and studied their misrostructure and the magnetic properties.

Experimentals

The schematic diagram of the deposition system used is shown in Fig.1. It consists of a Kaufman-type ion source for sputtering deposition of metals (Co), and a compact ECR microwave plasma source for CVD deposition of carbon. The chamber is evacuated with a turbo molecular pump backed with a rotary mechanical pump, and can achieve a base pressure of less than $1x10^{-7}$Torr. For sputtering deposition of Co, a target was pure Co disc (99.98%, 70mm in diameter), and sputtering gas was Ar gas, which was

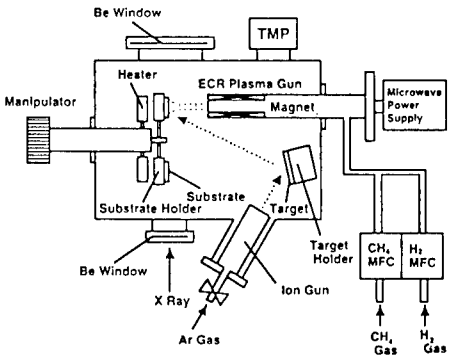


Fig.1 Schematic diagram of the dual-source depositiion system

introduced into the ion source through a precision valve. For the deposition of carbon, the reaction gas was a pre-mixed gas of methane (CH_4) and hydrogen (H_2), and the flow rates of both gases were controlled respectively by mass flow controllers. Corning 7059 glass slides were used as substrates. Substrate temperature is variable from room temperature to 873K. Moreover, it is also equipped with an energy-dispresive X-ray diffractometer (EDXRD) which can be used for in-situ analysis of films under deposition.

The crystal structures of deposited films were determined by X-ray diffraction (XRD) using the CuKα radiation, and the film microstructure was observed by a transmission electron microscope (TEM) operated at 200keV. Some of cross-sectional microstructure were also observed. The magnetic properties of the films were measured by a vibrating sample magnetometer (VSM).

Results and Discussion

Microstructure and magnetic properties of Co-C composite films

In our previous work for the Ni-C alloy system, nonequilibrium Ni carbides were found to form when deposition was conducted with low flow rates of CH_4 (<0.1sccm), and amorphous Ni-C alloy films were found to form with higher CH_4 flow rates.Therefore we also prepared Co-C films with several flow rates of CH_4, and investigated their microstructures and properties[11,12]. X-ray diffraction profiles of the Co-C films deposited at various substrate temperatures with a CH_4 flow rate of 0.02 sccm are given in Fig.2. Fig.2 (a) shows the result of a Co-C film deposited at ambient temperature (about 300K). The result reveals that a Co_3C(hcp) phase formed in the film with a strong preferred (10·1) orientation. And it can be seen from Fig.2 (a) that there is a broad shoulder to the right side of the 10·0 peak of Co_3C(hcp) carbide, and this may be attributed to either α-Co or β-Co according to its angular position. For films deposited at substrate temperatures between 473K and 673K, the X-ray diffraction results demonstrate the formation of a different phase which is identified as another kind of cobalt carbide, orthorhombic Co_2C, according to the previous results[4]. It should be noted that, when deposited at 673K, the α-Co phase also appeared together with Co_2C, because this carbide phase becomes unstable at this temperature.

Fig.3 shows magnetic hysteresis loops of the Co-C films deposited at 300K (a) and 573K (b). These films are composed of the Co_3C(hcp) and Co_2C(orth.) carbides respectively. Pure Co may slightly exist, but it is considered that Co_3C(hcp) and Co_2C(orth.) mainly take part in magnetism of these films. It seems that both Co_3C(hcp) and Co_2C(orth.) show ferromagnetic characteristics, and the saturation magnetization of Co_3C(hcp) is much higher than that of

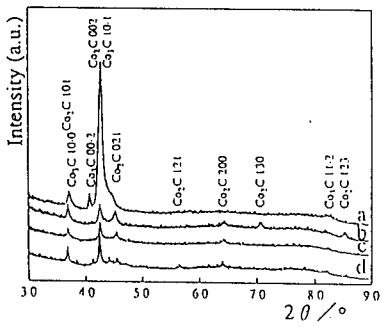


Fig.2 X-ray diffraction profiles of Co-C films deposited at (a)300K, (b)473K, (c)573K and (d)673K with a CH_4 flow rate of 0.02 sccm

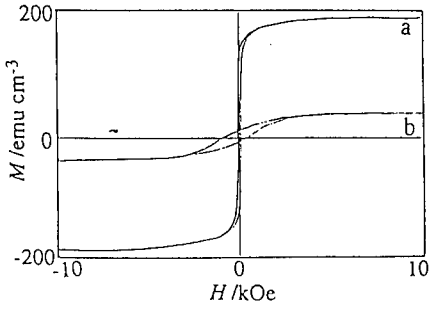


Fig.3 Magnetic hysteresis loops of Co-C films deposited at (a)300K and (b)573K with a CH_4 flow rate of 0.02 sccm

Co_2C(orth.).

When the CH_4 flow rate was increased to 0.3 sccm, Co-C films deposited at ambient temperature were amorphous-like, or rather composed of fine particles, and those deposited at 523K were granular. This is clearly seen from the X-ray diffraction results shown in Fig.4. The X-ray diffraction profile in Fig.4 (a) shows only a broad peak around the angle where several diffraction peaks from the α-Co phase and cobalt carbides are expected to appear, indicating that the as-deposited films are in amorphous-like state. Fig.4 (b) shows 00·2 peak from the α-Co phase. This indicates that a crystalline phase, α-Co phase with a strong (00·1) orientation, is formed within the film. Furthermore, a relatively broad peak suggests that cobalt crystals have very fine grain size. Fig.5 shows TEM bright field images and electron diffraction patterns of these two kinds of films. For the film deposited at ambient temperature, Fig.5 (a), the halo diffraction pattern also shows the amorphous-like nature of the film. The film deposited at 523K, Fig.5 (b), reveals a kind of granular structure containing very fine cobalt crystallites. The average size of these crystallites is about 8nm in diameter as estimated from the bright field image. And individual Co crystallites are isolated

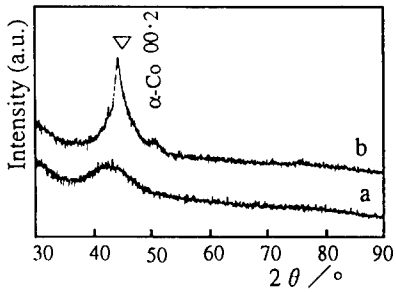


Fig.4 X-ray diffraction profile of Co-C films deposited at (a)300K and (b)523K with a CH_4 flow rate 0.3 sccm

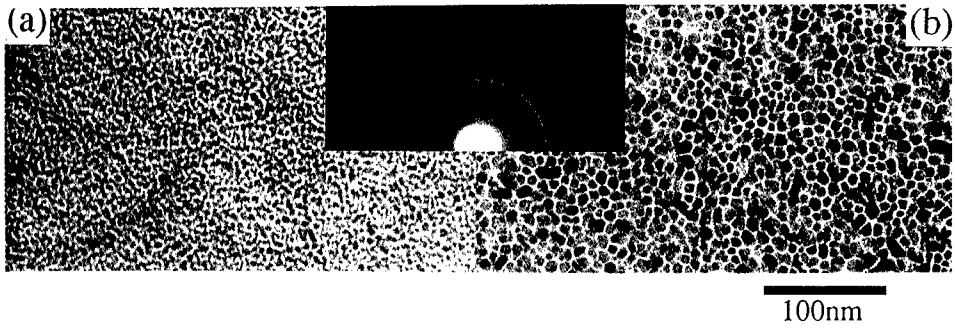


Fig.5 TEM images and diffraction patterns of (a)amorphous-like and (b)granular Co-C films

by amorphous carbon.

Hysteresis loops for amorphous-like and granular Co-C films are shown in Fig.6. Both films show ferromagnetic characteristics. The saturation magnetization of the amorphous-like Co-C film is found to be much lower than that of bulk cobalt. On the other hand, for the granular Co-C film, although the carbon content is almost the same, the saturation magnetization is twice as large as that of the amorphous-like Co-C film. This is due to the structural change of cobalt from amorphous-like to crystalline. Taking into account of the volume fraction of cobalt crystallites in the film, the effective saturation magnetization of these cobalt crystallites in granular Co-C film should be more higher than the measured value.

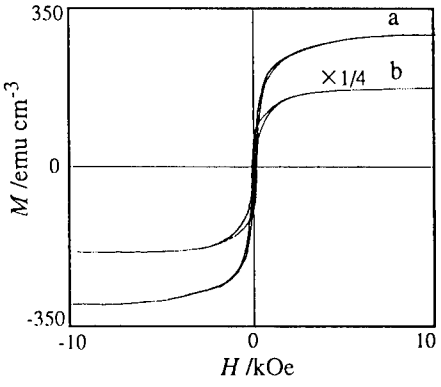


Fig.6 Hysteresis loops of (a)amorphous-like and (b)granular Co-C films

Microstructure and magnetic properties of Co/C multilayered films

Amorphous-like and granular films of 700nm thick showed respectively 12.0Oe and 63.5Oe of coercivity as shown in Fig.6 . The reason why the granular films show a relatively large coercivity is considered as follows: one is that Co grain size is very small in the lateral direction but relatively large in the direction normal to the film surface, the other is that the ferromagnetic coupling among the grains is not so strong. In order to decrease the coercivity of granular films, we tried to insert an amorphous carbon layer between neighboring Co layers. Such Co/C multilayered films were prepared by operating CVD and IBS alternately. The CH_4 flow rate is 0.3 sccm, and substrate temperature is ambient temperature. Fig.7 shows a TEM image of the cross-sectional microstructure of a $(Co400Å/C300Å)_8$ film. This result clearly shows very sharp and very flat interfaces between Co and amorphous carbon layers. In addition, the diffraction pattern showed a streak in the direction perpendicular to the film surface. Fig.8 shows the magnetic hysteresis loops of a $(Co400Å/C300Å)_8$ film. This film shows soft magnetic characteristics and develops strongly in plane anisotropy. The coecivity of the Co/C multilayered films is expected to decrease with decreasing layer period, thus we investigated the relationship between the period and the coercivity of the Co/C multilayered films. Table. I shows the coecivity of the Co/C multilayered films with various periods. This result shows that the coesivity depends on the period, but it does not show just a systematic dependence. With regard to this result, we considered the reason as follows. Fig.9 shows that

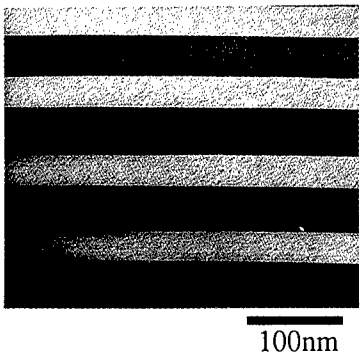


Fig.7 Cross-section TEM image of $(Co400Å/C300Å)_8$

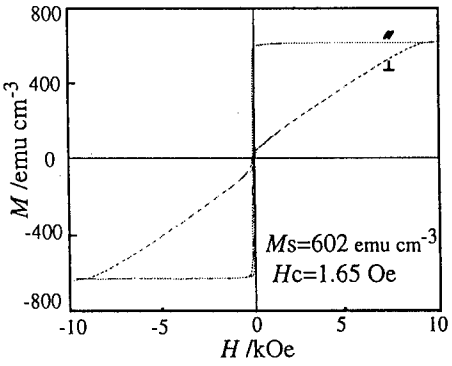


Fig.8 Magnetic hysteresis loops of $(Co400Å/C300Å)_8$

Table. I Coecivity of the Co/C multilayered films with various periods

period	coercivity
$(Co400Å/C300Å)_8$	1.65 Oe
$(Co100Å/C200Å)_{24}$	1.25 Oe
$(Co40Å/C120Å)_{24}$	38.5 Oe
$(Co10Å/C10Å)_{150}$	48.5 Oe
$(Co4Å/C20Å)_{135}$	61.8 Oe

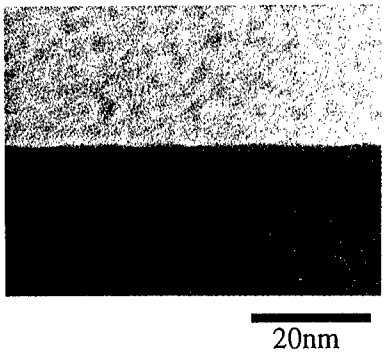


Fig.9 Enlarged cross-section image of $(Co400Å/C300Å)_8$

no grain-like structure is seen in the Co layer. The low angle X-ray diffraction result of such a film is shown in Fig.10. A broad peak appeared around 3.5 degree in 2θ, therefore it is considered that the grain size of cobalt layer is about 2.5nm. Those results indicate that the Co layers deposited in the present chamber are already in amorphous-like phase containing fine Co particles. This is thought to be related to the preparation process: in this chamber, when the Co/C multilayered films are formed by operating IBS and CVD alternately, and gas atmosphere from the ECR source can effect the deposition of Co films resulting in amorphous-like films, because of lack of gas shielding. The observed low coesivity in the large period multilayer is probably due to fine Co particles distributed in the constituent layers whose magnetic coupling becomes relatively strong among magnetic particles.

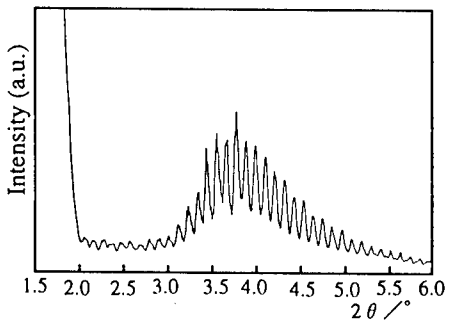


Fig.10 Low angle X-ray diffraction profile of $(Co400Å/C300Å)_8$

Concluding Remarks

In this study, it has been established that a dual source deposition system which combines ECR microwave plasma CVD and ion beam sputtering is a powerful method to synthesize a variety of Co-C composite films. The microstructure and properties of such films depend on the deposition conditions. With low CH_4 flow rates, two cobalt carbides have been synthesized. Co_3C formed at ambient temperature, and Co_2C formed at higher temperatures, and both carbides show ferromagnetic characteristics. With high CH_4 flow rates, the films deposited at ambient temperature are in amorphous state, and those deposited at 523K show granular structure. Both films show ferromagnetic characteristics, and the saturation magnetization of granular Co-C films is higher than those of amorphous-like Co-C films. The Co/C multilayered films deposited at ambient temperature show very good periodicity and flat Co-C interfaces, and such films show soft magnetic characteristics in the large period multilayers. However, the coercivity of the Co/C films does not always depend on the period. In this point, further work is needed to get sufficient soft magnetic properties.

References

[1] T.B.Massalski, J.L.Murray, L.H.Bennet and H.Baker eds. Binary Alloy Phase Diagrams (American Society for Metals), (1986), p.556.
[2] L.J.E.Hofer and W.C.Peebles, J. American Chem. Soc. **69**, (1947), 893
[3] J.Clark and K.H.Jack, Chem. and Ind. **46**, (1951), 1004
[4] S.Nagakura, J. Phys. Soc. Japan **16**, (1961), 15
[5] M.Pont, K.V.Rao, A.Inoue and T.Masumoto, J. Appl. Phys. **63**, (1988), 3397
[6] A.Inoue S.Fukukawa and T.Masumoto, J. Mater. Sci. **22**, (1987), 1670
[7] K.Oda and T.Yoshio, J. Mater. Sci. Lett. **9**, (1990), 1319
[8] T.J.Konno and R.Sinclair, Acta Metall. Mater. **42**, (1994), 1231
[9] T.J.Konno and R.Sinclair, Mater. Sci. and Eng. **A179/180**, (1994), 297
[10] T.Hayashi, S.Hirano, M.Tomota and S.Umemura, Nature **381**, 772 (1996)
[11] J.Shi and O.Nittono, J. Mater. Sci. Lett. **11**, (1992), 22
[12] J.Shi, Y.Hashiba, Y.Haga and O.Nittono, Proc. of International Conference on Microstructures and Functions of Materials Sept. 9-11 1996,Tokyo,Japan

FABRICATION AND CHARACTERIZATION OF Al-Co/Al-N-Co MULTILAYER FILMS

A.G. Roy and O. Nittono

Department of Metallurgical Engineering, Tokyo Institute of Technology
2-12-1 Oh-okayama, Meguro-ku, Tokyo 152, Japan

Abstract

A new approach is described for preparing Al-Co/Al-N-Co multilayer films having different layer thicknesses by using a two-facing target type dc sputtering (TFTS) system. The deposited films were annealed isothermally at different temperatures and their microstructure, magnetic properties and resistivity were investigated. The magnetization of as-deposited films is very small irrespective of layer thickness. It was found that annealing conditions and layer thickness ratio of Al-Co to Al-N-Co (LTR) can control the microstructure as well as the physical properties of the prepared films. The resistivity and magnetization increase and the coercivity decreases with decreasing LTR. A High resistivity of 2500$\mu\Omega$-cm, a magnetization of 360 emu/cm^3 and a coercivity of 5Oe were obtained for the films with LTR = 0.35.

The Third Pacific Rim International Conference on
Advanced Materials and Processing (PRICM 3)
Edited by M.A. Imam, R. DeNale, S. Hanada,
Z. Zhong and D.N. Lee
The Minerals, Metals & Materials Society, 1998

Introduction

Recent high technology developments of electronic devices have led to a demand for miniaturization of magnetic devices, operating at frequencies higher than 50 MHz. Such devices require that magnetic materials have a sufficiently large electric resistivity ρ and are in the form of thin films, in order to suppress eddy current losses. In order to solve those problems, high resistive metal films possessing a very fine two-phase hetero-amorphous structure have been studied, and magnetic granular system, where magnetic particles are embedded in an insulator matrix, has also been studied(1,2). The authors reported the microstructure and magnetic and electrical properties of Al-N-Co thin films in the previous study (3). These films showed high resistivity and sufficient saturation magnetization, and the coercivity of the films was 22~94 Oe at a magnetic field of 1kOe. Moreover, it was found that multilayer films show better soft magnetic properties than monolayer films (4). An ideal high-density recording magnetic material must have high permeability, high electric resistivity, large saturation magnetization coupled with low energy loss and also a high corrosion resistance. This is why we used AlN as a high resistive and high corrosion resistance insulator matrix and Co as a magnetic particle embedded or dispersed in that matrix. And Al-Co inter layer in the multilayers was used to control grain growth which will result in smaller coercivity. In this paper, a new approach for preparing Al-Co/Al-N-Co multilayer films by a TFTS is described. We investigate the formation of Al-Co/Al-N-Co films and compare their microstructure, magnetic and electrical properties with those of the Al-N-Co films.

Experimental Procedure

Predetermined conditions were applied to prepare Al-Co/Al-N-Co thin films(3). In this work, an Al(99.95% pure) target of 100mm diameter and 5mm thickness was used as an upper target while a composite target of Al(99.95%) and Co(99.98%) with an area fraction of Co(Co/(Al+Co)) = 0.087(referred as to TAF) was used as a lower target (Fig.1). Corning glass(7059) was mostly used as a substrate. Substrate temperature was lower than 310K. Target voltage was between -300V and -500V(DC). Sputtering currents were 400mA and 200mA for the deposition of Al-N-Co and Al-Co layers, respectively. N_2 partial gas pressures of 0.052 and 0 were used for the deposition of Al-N-Co and Al-Co layers , but the total gas pressure was fixed at 0.4Pa for both layers. The initial pressure of the chamber was lower than $2X10^{-4}$Pa. The total thickness of the films varied from 880nm to 550 nm. Films having a wide range of layer thickness(30~10nm for Al-N-Co layer and 80~3.5nm for Al-Co inter layer) were prepared and studied. As-deposited films were annealed isothermally in a vacuum of $2.6X10^{-4}$Pa at different temperatures. The micro-structure of thus prepared films was examined by X-ray diffraction (XRD), and electron microscopy observations (TEM, HRTEM, X-TEM, NBD). Atomic percentage of the contents of the films was checked by electron dispersive spectroscopy (EDS), as listed in Table I. Magnetic and electrical properties were measured by a vibrational sample magnetometer (VSM) and the four probe method respectively. All the measurements were performed at room temperature(RT).

Results and Discussion

As-deposited films

Microstructure. The microstructure of Al-Co/Al-N-Co films strongly depends on the ratio of layer thickness of Al-Co layer. Fig.2 shows X-ray profiles for films deposited with a Co target area fraction of 0.087 with different LTR's. The profile for LTR=2.7 ($(Al\text{-}Co)_{80nm}/(Al\text{-}N\text{-}Co)_{30nm}$) shows two broad peaks: first one around the angular position of 2Θ~36°, which is for 0002 peak of AlN and the other one around the angular position of 2Θ~44°, which is for the peaks of β–Co 111 and also peaks ascribed to the compounds of AlCo. With decreasing LTR (0.7 in Fig.2 (b) and 0.35 in Fig.2(c)), the second peak becomes broader, while the first peak is still intact. Fig.3 shows cross-sectional TEM images for as-deposited films with a LTR=2.7 ($(Al\text{-}Co)_{80nm}/(Al\text{-}N\text{-}Co)_{30nm}$). Alternative stacking of Al-N-Co/Al-Co layers appears clearly. The existence of the growth of a vivid interfacial ultrathin layer is also seen. Fig.3(b) shows the aging effect on such

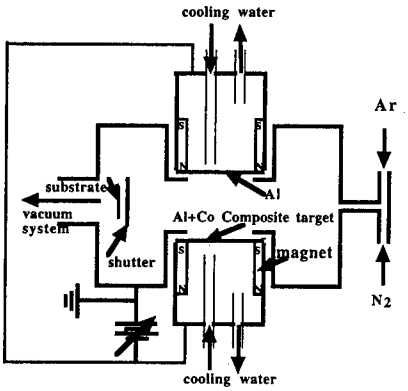


Figure 1: Schematic diagram of a TFTS system.

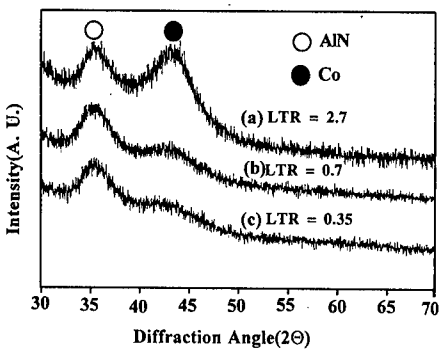


Figure 2: Typical XRD profiles of as-deposited films with different LTR's.

a thin film which was aged for 15 days after thinning. Drastic changes of microstructure including changes in layer thickness were observed clearly. Both the layers expand and particles of AlCo compound grow during aging in the Al-Co layer. The layer expansion is probably due to the release of film stress enhanced by aging at RT because of the film being ultra-thin.

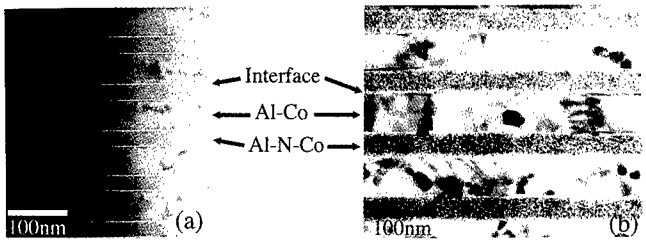


Figure 3: Cross-sectional TEM images of as-deposited film with LTR=2.7; (a) just after ion thinning, (b) aged for 15 days.

Magnetic and Electrical properties. For all the as-deposited films, the magnetization is too small irrespective of LTR of the films. This may be due to the fact that in as-deposited films Co is not in crystalline state, and/or its Curie temperature decreases below room temperature. This is not clear yet. The resistivity increases with decreasing LTR on account of decreasing in volume fraction of the conducting elements in the films. Numerical results for magnetization and resistivity for different films are summarized and listed in Table I.

Table I Properties of As-deposited Films

Kind of film	TAF of Co(Co at%(approx.))	Magnetization emu/cm^3	Resistivity μΩ-cm
Al-N-Co	0.047 (20 at%)	3.5 ~ 5.0	2500 ~ 2900
Al-N-Co	0.087 (25 at%)	1.5 ~ 6.0	990 ~ 1360
(Al-Co)80nm/ (Al-N-Co)30nm	0.087	1.7 ~ 2.9	~ 600
(Al-Co)12nm/ (Al-N-Co)15nm	0.087	~ 260	~ 800
(Al-Co)7nm/ (Al-N-Co)10nm	0.087	~ 270	~ 830
(Al-Co)3.5nm/ (Al-N-Co)10nm	0.087	~ 360	~ 970

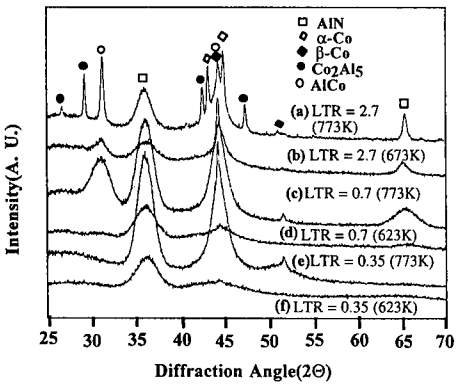


Figure 4: Typical XRD profiles of films with different LTR's, annealed at different temperatures for 120ks.

Effect of Heat Treatment

Microstructure and Phase Separation. Microstructural change and phase separation depend on annealing conditions. When a film with LTR=2.7 was annealed at 673K for 120ks, three phases of AlN, AlCo and β- Co are detected (Fig.4(b)), but when annealed at 773K for the same period, they crystallize into five distinct phases of AlN, AlCo, Co_2Al_5, α-Co and β-Co(Fig.4(a)). Among these phases, a related AlCo phase is temporarily identified to be an ordered AlCo phase, although it was not confirmed clearly. Three phases of AlN, AlCo and β-Co were detected for a film with LTR=0.7 ($(Al\text{-}Co)_{7nm}/(Al\text{-}N\text{-}Co)_{10nm}$), annealed at 773K for 120ks (Fig.4(c)), where the peaks for individual phases are broad for lower annealing temperatures (Fig.4(d)). On the other hand, for a film with lower LTR=0.35 ($(Al\text{-}Co)_{3.5nm}/(Al\text{-}N\text{-}Co)_{10nm}$), only two phases of AlN and β-Co are detected and no phase ascribed to the compounds of AlCo is seen under the same annealing conditions (Fig.4(e)) and the peaks are broader at 623K (Fig.4(f)).

Fig.5 shows TEM micrographs and electron diffraction pattern for an annealed film with LTR=2.7. Fig.5(a) reveals that the layer and the interfacial growths are still intact just after annealing. But we can observe large precipitates in Al-Co layers and fine particles in Al-N-Co layers. Fig.5(b) shows the microstructure of the same ion-thinned film observed after aging for 15 days. Such particles coarsened to grow larger in both the layers. Another finding is that the layer thickness increases, probably due to the further release of film stress during aging. Fig.5(c) is a high resolution image taken from the indicated particle of the aged film and Fig.5(d) is the corresponding nano beam diffraction (NBD) from such a particle.

Magnetic Properties. Magnetic properties of annealed films change in accordance with the changes in microstructure. Fig.6 shows the saturation magnetization as a function of annealing time at different annealing temperatures for the films with different LTR's. The magnetization is mainly dependent on annealing temperatures: it is larger at higher annealing temperatures for the films with the same LTR. However, it increases with decreasing LTR. A drastic change in magnetization occurs before 10.8ks of annealing, and then the increment is moderate. For the films with LTR =2.7, the magnetization is almost steady after 10.8ks when annealed at 673K.

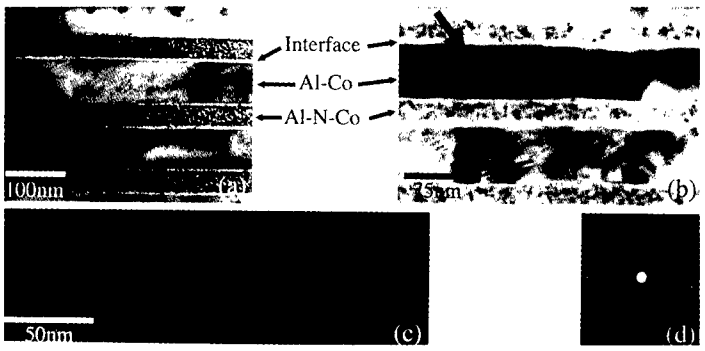


Figure 5: Cross-sectional TEM images of a film with LTR =2.7 annealed at 773K for 120ks; (a) just after ion thinning, (b) aged for 15 days (c) high resolution image taken from the indicated portion and (d) nano-beam diffraction patterns taken from such an indicated portion.

But when the film is annealed at 773K, its magnetization slightly decreases with annealing time after the same period (Fig.6(a). This can be explained by the microstructural changes of the films as follows: the phase separation is dominant at higher temperatures than at lower temperatures, and it progresses with annealing time(Fig.4(a),(b)). The progress of the formation of AlCo and Co_2Al_5 compounds, whose magnetic moments are considered to be lower than those of the pure Co phases, decreases the magnetization with increasing annealing time. The highest

magnetization of about 360 emu/cm^3 was obtained for a film with LTR=0.35 (Fig.6(b)), annealed at 773K for 120ks. This phenomenon can be also explained in terms of the changes in microstructure caused by annealing. This film have the thinnest Al-Co inter layer among the films examined and its corresponding XRD profile (Fig.4(e)) shows that the film separates into the phases of AlN and Co, but no trace for AlCo and Co_2Al_5 compound formation is detected. As annealing time and temperature increase the separation of Co phases from Al-N-Co layer becomes more dominant, and the crystallinity of Co phases becomes more and more improved (3). Thus, the Co phases dispersed in the AlN matrix of the Al-N-Co layers leads to an increase of the magnetization in such films. The coercivity decreases with decreasing layer thickness and LTR. It was observed that the coercivity decreases for low annealing temperatures for the same LTR films. The numerical values of coercivity are summarized and listed in Table.II.

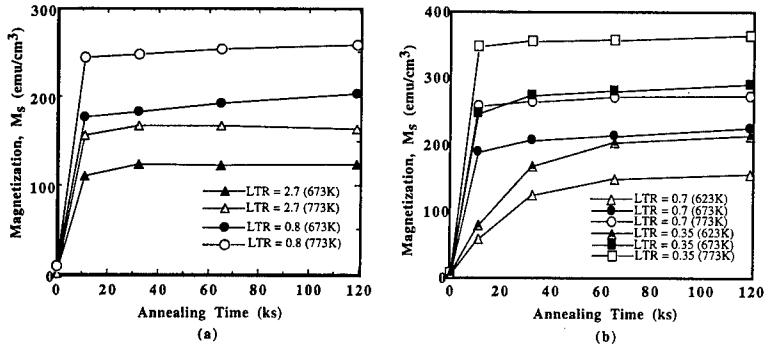


Figure 6: Magnetization as a function of annealing time at different annealing temperatures for different LTR's films

Resistivity.The resistivity of Al-Co/Al-N-Co multilayer films having different LTR's was examined for different isothermal annealings. It was found that the resistivity is strongly dependent on LTR and also on the change of microstructure. Fig.7 shows the resistivity as a function of annealing time at different temperatures for different LTR films. It is clear from the figure that a dominant change in resistivity occurs before 10.8ks annealing and then the change is moderate for all the films. For the films higher than LTR=2.7, the resistivity decreases with increasing annealing time and temperature, and the decrement is sharp at higher temperatures (Fig.7(a)). This is probably due to the fact that at higher temperatures the phase separation is dominant and rapid formation of AlCo and Co_2Al_5 compounds (Fig.4(a)), which make connecting networks with Co particles, decreases the resistivity. For the films with LTR=0.8, the resistivity decreases throughout the annealing period at 773K, but when annealed at 673K the resistivity first decreases up to 10.8ks and then slowly increases with annealing time(Fig.7(a)).

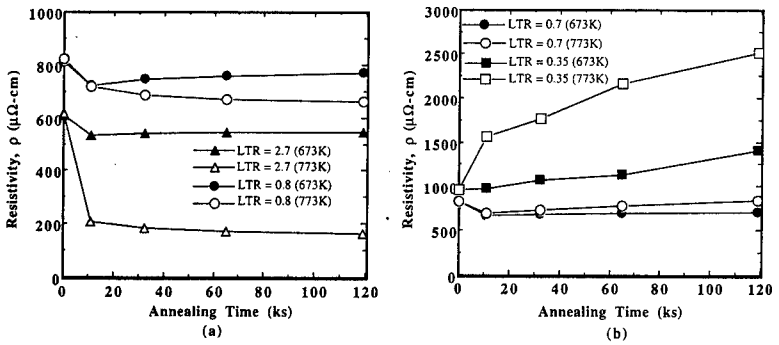


Figure 7: Resistivity as a function of annealing time at different annealing temperatures for different LTR's films.

As shown in the Fig.7(b), for the films with LTR=0.7 the resistivity first decreases and then increases with annealing time and temperature. On the contrary, for the films with LTR=0.35, the resistivity increases throughout the annealing period with increasing annealing time and temperatures, and the increment is large at higher temperatures. This is mainly due to structural changes in Al-N-Co layers caused by annealing: nano-crystallites of Co phase may be dispersed homogeneously in Al-N-Co layers, resulting in low coercivity and in high magnetization with large resistivities, as shown in Table II. The highest resistivity of 2500μΩ-cm was obtained for a film with LTR=0.35, annealed at 773K for 120ks. In this connection, the XRD profile (fig.4(e)) of the film with LTR=0.35 (the thinnest Al-Co inter layer) reveals that the film separates into the phases of AlN and Co, no appreciable trace for AlCo and Co_2Al_5 compound formation is detected. As explained in the previous section, the dispersed Co phases in the AlN insulator matrix of the Al-N-Co layers leads to the increase of the resistivity in the film. The properties of annealed films examined are summarized and tabulated in Table II.

Table II Properties for Annealed Films

Kind of film	TAF of Co(Co at% (approx.))	Magnetization emu/cm^3	Coercivity Oe	Resistivity μΩ-cm
Al-N-Co	0.047 (20 at%)	~ 260	90 ~ 95	~ 11X 10^5
Al-N-Co	0.087 (25 at%)	~ 360	20 ~ 90	~ 2200
(Al-Co)80nm/ (Al-N-Co)30nm	0.087	~ 162	22 ~ 73	~ 170
(Al-Co)12nm/ (Al-N-Co)15nm	0.087	~ 260	15 ~ 50	~ 770
(Al-Co)7nm/ (Al-N-Co)10nm	0.087	~ 270	15 ~ 59	~ 850
(Al-Co)3.5nm/ (Al-N-Co)10nm	0.087	~ 360	5 ~ 46	~ 2520

Concluding Remarks

A new approach was introduced for preparing Al-Co/Al-N-Co multilayer films prepared by a TFTS system. The deposited films were annealed isothermally at different temperatures and their microstructure, magnetic properties and resistivity were investigated. The main results are summarized as follows: a) This TFTS method is suitable for preparing Al-Co/Al-N-Co multilayer films with different LTR's. b) Annealing conditions, layer thickness and LTR can adjust the microstructure as well as the physical properties of the prepared films. c) High resistivity and sufficient magnetization were obtained for the films with LTR=0.35. Films having such considerable magnetization and resistivity will be a potential candidate to be used for a high density recording material. Further detailed studies must be done for such a purpose.

References

1. H. Karamon, "A New Type of High-resistive Soft Magnetic Amorphous Films Utilized for a Very High-frequency range," J. Appl. Phys. 63 (8) (1988), 4306-4308.

2. H. Fujimori et al., "High Electrical Resistivity and Permeability of Soft Magnetic Granular Alloys," IEEE Trans. Magn., 30 (6) (1994), 4779-4781.

3. " Microstructure and Magnetic Properties of AlN Thin Films Containing Cobalt (Co) Particles Prepared by Reactive Sputtering," Microstructures and Functions of materials, ed. N. Igata et al. (Tokyo, Japan: Proceedings of International Conference on Microstructures and Functions of Materials, 1996), 189-192.

4. S. Yaegashi, T. Kurihara, and K. Satoh, "Preparation and Soft Magnetic Properties of Epitaxial Fe-Si(111) Monolayer Films and Fe-Si(111)/Cr(111) Multilayer Films," J. Appl. Phys. 81 (9) (1997), 6303-6309.

OPTICAL PROPERTIES OF BISMUTH AND GALLIUM SUBSTITUTED THULIUM IRON GARNET FILMS SUITABLE FOR OPTICAL DEVICES

P. Mukhopadhyay, S. Orpe and V. Chandravanshi

Advanced Centre For Research in Electronics,
Indian Institute of Technology, Bombay-400076

Abstract

Magnetic garnet films are potential materials for optical waveguide and devices. Considerable work has been done in the last three decades to study the Magneto-optic (MO) effects in rare earth iron garnets (RE:IG). Bi-ion and light rare earth ions (Ce, Pr, Lu, Tb etc) are known to enhance MO activity in the garnet system at wavelength range λ= 0.5 - 2.0 μm . Substitution of Bi increases drastically the Faraday effect whereas the lighter rare earth ions balance the mismatch caused by Bi ions. Bismuth substituted thulium garnet films are another promising materials for optical isolators and sensors. we report here the preparation and comparision of optical properties of bismuth and bismuth/gallium-substituted thulium iron garnet films (Bi:TmIG, Bi,Ga:TmIG) incorporating high bismuth content by Liquid Phase Epitaxy (LPE) on paramagnetic substrates of Gadolinium Gallium Garnet (GGG).

The Third Pacific Rim International Conference on
Advanced Materials and Processing (PRICM 3)
Edited by M.A. Imam, R. DeNale, S. Hanada,
Z. Zhong and D.N. Lee
The Minerals, Metals & Materials Society, 1998

Introduction

Single crystal magneto-optic thulium iron garnet films substituted with bismuth and gallium (Bi: TmIG and Bi,Ga: IG) are promising materials for magneto-optic devices like optical isolators, sensors etc . The forward loss L(dB) is directly related to the optical absorption coefficient $\alpha(cm^{-1})$ and the Specific Faraday rotation F(deg/cm) as given by

$$L = 195\ \alpha/F \qquad (1)$$

To have low loss devices, it is important to increase F and reduce α . Magnetic garnet films have been used in optical isolators and waveguides in the near infrared region between 1.3 and 1.5 μm, a wavelength region in which optical absorption of the magnetic garnet is very small (1). Near 0.8μm wavelength band , magnetic garnets have an optical absorption due to : (i) transition caused by Fe^{2+} or Fe^{4+} ions for charge uncompensated films , (ii) due to intrinsic crystal field transition of Fe^{3+} ions and (iii) Pb^{2+} - Pb^{4+}pair transitions from excess Pb when PbO flux is used (2).

It was the purpose of this paper to make films of Bi:TmIG and Bi,Ga:IG and optimize their properties to reduce the optical absorptions in the range of 0.7-0.8μm. Films were grown from a lead containing (PbO - Bi_2O_3) and a lead-free (Bi_2O_3) flux. Films grown from Pb-containing flux could be grown at lower growth temperatures T_g (770 - 800C) compared to films from Pb-free flux which could be grown at 850C and above only.

Both bismuth and lead content increase in the films grown at lower temperatures. The Ga- content increses with deposition time while Bi and Pb-contents decrese . An optimized growth temperature and growth time was selected to grow films and the optical measurements in the range of 400 to 900 nm. were compared for films grown from different melts. The magneto-optic properties of the Bi,Ga: TmIG films grown under optimized conditions show the material to be suited for use in a magneto-optic device.

Experiment

Growth. Films of composition of the type $(Tm,Bi,Pb)_3Fe_5O_{12}$, $(Tm,Bi)_3Fe_5O_{12}$ and $(Tm,Bi)_3(Fe,Ga)_5O_{12}$ were grown on [111] oriented Gadolinium Gallium Garnet (GGG) substrates by LPE technique from a supersaturated solution of rare earth oxides and a lead based (PbO - Bi_2O_3) , lead free (Bi_2O_3) flux and lead free (Bi_2O_3) flux with Ga .

The growth procedure was similar to the bismuth, lutetium substituted iron garnet LPE films made and reported by us (3). The films were grown in our LPE furnace (4) with a 8cm vertical isothermal zone with a temperature stability of ± 1°C. The films were dipped in the vertical plane and no rotation during the growth period. The growth time was 30 minutes, 10 minutes and 5 minutes respectively for the three films reported here. After the film growth and prior to analysis the films were cleaned in 20% acetic acid solution at 85C for 15 - 20 min to wash off any traces of flux etc. Details of the three melts composition from which films were grown , are given in Table I .

TABLE I. Flux-Melt composition (wt%)

Constituent	I- Melt (gms)	II - Melt (gms)	III - Melt (gms)
PbO	66.11	-	-
Bi_2O_3	27.50	92.33	92.64
Tm_2O_3	0.36	1.88	1.40
Fe_2O_3	5.93	5.79	4.37
Ga_2O_3	-	-	1.59
T_s(C)	800	850	950
T_g(C)	785	800	850
Bi (x)	0.86	0.97	0.87
Pb(z)	0.03-0.06	-	-
Ga (y)	-	-	0.8

* Ts(C)- Saturation Temperature of the melt, Tg(C)-Growth Temperature of films Bi(x)- bismuth content , Pb(z) -lead content and Ga(y) -Galium content in the film

Characterization. The film thickness was calculated from the difference between the weight of the substrate before and after the film growth and using a density of 7.1 g/cm^3 for the film. The chemical analysis was done by electron micro-probe analysis (EPMA). The film lattice constant in [111] direction were obtained by observing (888) reflections and measuring lattice constants with Cu$K\alpha_1$ radiation. The optical absorption was measured using IR-UV spectrometer in the optical range of 400- 900 nm and the Faraday rotation F(deg/cm) was measured with a polarizing microscope .

Result and discussions

For the Pb-containing melt , 780-789C was favourable temperature range for optimum growth. At lower T_g, incorporation of larger Bi and Pb-contents give rise to compression in the film i.e., with $a_s < a_f$,where a_s and a_f are the substarte and film lattice constants. Lattice mismatch , $\Delta a = a_s - a_f$, is negative in such films with magnetization lying in the plane of the film and showing weak magnetic linear birefringent pattern instead of the normal serpentine patterns. For the films #1, #2, and #3, Δa was positive and ranged between 0.005 - 0.009. 785C was found to be optimum T_g for this melt to incorporate high Bi-content with Pb-content between 0.03-0.06 to maintain high F and low α values. For lead free melt and with Ga added melt, the optimum T_g was 800C and 850C respectively. The maximum Bi-content for the films grown from the three different melts was 0.86, 0.97 and 0.87 giving specific Faraday rotation values of 2700-3000(deg/cm).

For the optical measurements, the transmission of light on two samples with different thickness was measured and the absorption coefficient $\alpha(cm^{-1})$ was calculated using the relation ,

$$\alpha(cm^{-1}) = \ln (I_2-I_1)/ (t_1-t_2) \qquad (2)$$

where I_1 and I_2 are the intensities of transmitted light through the substrate (thickness t_1) and film (thickness t_2) respectively. Table II compares the absorption coefficient α for the three films grown from lead containing (Melt-I), lead-free (Melt-II) and Ga-added ,lead-free (Melt-III) melts respectively 3-5 μm thick.

TABLE II. Variation of Absorption Coefficient (α /cm)

λ (μm)	α/cm Melt-I Sample #1	Melt-II Sample#2	Melt-III Sample# 3
0.40	136.6	309.0	121.7
0.45	146.0	326.0	125.0
0.50	147.0	345.0	115.5
0.55	147.0	220.0	26.7
0.60	22.2	176.1	27.0
0.65	5.8	148.3	14.5
0.70	5.8	118.4	1.4
0.75	11.3	93.0	10.1
0.80	16.4	83.0	12.4
0.85	16.4	80.4	9.0

* Melt-1: (with Pb), Melt-II : (Pb-free) and Melt-3 : (Pb-free with Ga).

The minimmum absorption coefficient was observed at 0.7 μm for all three samples. α was much higher in the lead free films as compared to the films containing Pb. This is due to the fact that the impurity Pt^{4+} ions , present in the melt from the platinum cruicible, are charge compensated by Pb^{2+} ions in the lead containing films whereas in the films grown from the Pb-free melt Fe^{2+} ions are formed for charge compensation of the Pt^{4+} ions and cause absorption. Further in the Pb-free flux , Bi_2O_3 attacks platinum cruicible more at higher temperatures giving rise to higher Pt^{4+} impurity ions . This was rectified for the melt-III by adding small amount of CaO for charge compensation of Pt^{4+} ions by Ca^{2+} ions without producing Fe^{2+} ions. The absorption in the Bi,Ga :TmIG films grown from this melt was reduced by a factor of 4 compared to films grown from Pb containing melt. The absorption coefficient at 800nm was reduced about by a factor two in the Bi,Ga: TmIG films compared to Bi,Pb: TmIG films. This may be due to partial substitution of Ga for Fe or lower Pb-content.

The minimum value of $\alpha = 9.0\ cm^{-1}$ at 800nm with specific Faraday rotation F gives forward optical loss L in the range of 0.65-0.7 dB. Our value of α at 800nm are reduced by a factor of 6 than that reported in reference(2). The optical measurements show that we have a optimized value of Bi-content for a practical low loss optical device. Further substitution may lead to lower value of F/α due increase of optical absorption by the high Bi substitution.

References

1. R. Gerhardt, S. Sure, H. Dötsch, T. Linkewitz and W. Tolksdorf, "Optical properties of bismuth and gallium substituted thulium iron garnet films ", Optics Communications 102 (1993), 31-35.

2. M.Kaneko, T.Okamoto, H. Tamada and T. Yamada, " Reduction of Optical Absorption at a wavelength of around 0.8 μm in LPE Garnet $(TmBiCa)_3(FeGaPt)_5O_{12}$" Appl Phys A 38 (1985), 281-284.

3. P. Mukhopadhyay and S. Orpe," Magneto-Optic $(Bi,Lu)_3Fe_5O_{12}$ garnet films", Proc .Solid State Phys (India) 37C (1994), 158.

4. P. Mukhopadhyay and B.U.M. Rao, " Preparation of single crystal films of magnetic bubble materials-Rare earth Yttrium iron garnets by liquid phase epitaxy and their physical properties ", Bull Mater. Sci.(India) 6(1) (1984), 47-52.

CARBONATION OF RE_2Fe_{17} (RE=RARE EARTH) COMPOUNDS BY ARC MELTING TECHNIQUE

M. Venkatesan[a], U.V. Varadaraju[a] and K.V.S. Rama Rao[b]
[a]Materials Science Research Centre
[b]Magnetism and Magnetic Materials Laboratory, Department of Physics
Indian Institute of Technology, MADRAS 600 036, INDIA.

Abstract

The compounds $HoErFe_{15}Ga_2C_y$ (y=0,0.5,1.0,1.5,2.0) were synthesized by arc melting technique. The hexagonal Th_2Ni_{17} type structure persisted in all compounds. The unit cell volume increase of Ga substituted carbide $HoErFe_{15}Ga_2C_{2.0}$ is around 6.1% compared to $HoErFe_{17}$. The Curie temperature increases with increasing carbon content which is due to the strengthening of exchange interaction

The Third Pacific Rim International Conference on
Advanced Materials and Processing (PRICM 3)
Edited by M.A. Imam, R. DeNale, S. Hanada,
Z. Zhong and D.N. Lee
The Minerals, Metals & Materials Society, 1998

Introduction

The rare earth iron intermetallic compounds of type R_2Fe_{17} have attracted much attention in recent years as possible candidates for permanent magnetic materials after suitable substitution and interstitial modification [1,2]. Extensive studies on the substitution of non magnetic elements such as Al,Ga at Fe site and further insertion of interstitial atoms (N, C) show dramatic enhancement in Curie temperature (T_C) [3,4]. Although the iron magnetic moments may be diluted by this replacement, the possibility of producing useful hard permanent magnets is, nevertheless, worth pursuing. On the otherhand, the nitrides and carbides synthesized by gas-phase interstitial modification process (GIM) have poor thermal stability and degrade on heating to temperatures above 500°C, thereby limiting their widespread applications. But the carbides $R_2Fe_{17}C_x$ can be stabilized by arc melting technique after non mangetic substitution at Fe site [5]. In the present study, we report the synthesis of intermetallic carbides $HoErFe_{15}Ga_2C_x$ ($x = 0 - 2$) by arc melting technique and the effect of carbon on the Curie temperature, Magnetization and Magnetocrystalline Anistotropy.

Experimental

The compounds with composition $HoErFe_{15}Ga_2C_x$ ($x = 0 - 2$) were synthesized by arc melting method from the high purity starting elements (Ho, Er ,Ga, C : 99.9% ; Fe:99.99%). Due to the high melting point of carbon, Fe and C were melted together first to form Fe_3C alloy which have a lower melting temperature. Then, it is mixed with corresponding constitutent elements and melted by arc melting in an argon atmosphere of high purity. The ingots were remelted several times to ensure homogeneity. The samples were then wrapped in tantalum foil and annealed at 1100 °C for 3 days. In order to avoid the formation of $R_2Fe_{14}C$ phase during cooling, the ingots have to be quenched from the annealing temperature in cold water. Powder X-ray diffraction measurements were carried out on the compounds using $CrK\alpha$ radiation ($\lambda = 2.289$ Å) to identify the phase purity and the crystallographic structure. The Curie temperatures were determined from the temperature dependence of the magnetization measured by a Vibrating Sample Magnetometer in a magnetic field of 500 Oe. The aligned samples for determining easy magnetization direction (EMD) were prepared by mixing the powder with epoxy resin and then aligning in a magnetic field of 12 kOe.

Results and discussion

The X-ray diffractograms of Ga substituted carbides reveal that the compounds crystallize in hexagonal Th_2Ni_{17} type structure. Fig.1 shows the XRD patterns of $HoErFe_{15}Ga_2C_x$ ($x = 0 - 2$) compounds. The lattice constants a,c and the unit cell volume V of all compounds are summarized in Table I. It is noteworthy that the substitution of both larger Ga for Fe and the interstitial carbon atom merely produces an expansion of the lattice. An approximately linear dependence of the unit cell volume on carbon content is observed. The expansion of the unit cell results from the combined effect of Ga and C additions. The $HoErFe_{15}Ga_2C_2$ compound have a unit cell volume of about 6.1 % larger than that of $HoErFe_{17}$ [5].

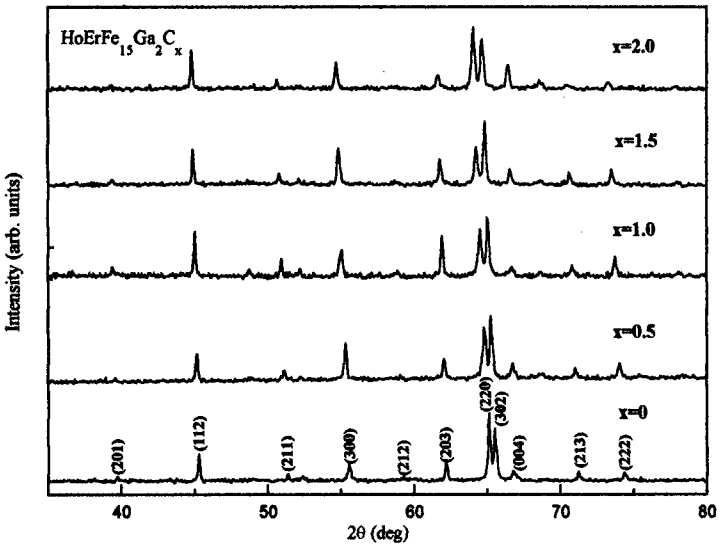


Fig.1 X-ray diffraction patterns of $HoErFe_{15}Ga_2C_x$ (x = 0 - 2) compounds

Table I Lattice parameters, unit cell volume, Curie temperature of $HoErFe_{15}Ga_2C_x$ compounds

Compound	a (Å)	c (Å)	V ($Å^3$)	ΔV/V %	T_C (K)
$HoErFe_{17}$	8.409	8.285	507.4	-	328
$HoErFe_{15}Ga_2$	8.511	8.328	522.4	2.9	480
$HoErFe_{15}Ga_2C_{0.5}$	8.551	8.329	527.4	3.8	525
$HoErFe_{15}Ga_2C_{1.0}$	8.585	8.334	532.0	4.6	538
$HoErFe_{15}Ga_2C_{1.5}$	8.612	8.349	536.3	5.4	584
$HoErFe_{15}Ga_2C_{2.0}$	8.637	8.367	540.6	6.1	587

The carbon concentration dependence of the Curie temperature of $HoErFe_{15}Ga_2C_x$ compounds is shown in Table I. For the carbides, T_C is found to increase with increasing carbon content. The Curie temperature increases from 480 K for x=0 to 587 K for x=2. But the T_C of $HoErFe_{15}Ga_2C_2$ compound is 260 K higher than that of $HoErFe_{17}$ [4]. It is commonly assumed that the magnetic ordering temperature in rare earth compounds is determined by the Fe-Fe exchange interactions. The low values of T_C in R_2Fe_{17} compounds result from the relatively small Fe-Fe distances in these materials. The increase in T_C corresponds to an increase in the positive Fe-Fe exchange coupling as a result of increased interatomic distance [6]. Both carbon and Ga atoms will influence the Curie temperature.

In order to study the effect of Ga and Carbon on the magnetocrystalline anisotropy, powder x-ray diffraction measurements have been carried out on the magnetic field aligned samples which can provide information concerning the magnetocrystalline anisotropy on the basis of diffraction peaks. Fig.2 shows the X-ray diffraction patterns of $HoErFe_{15}Ga_2C_2$ compound before and after alignment.

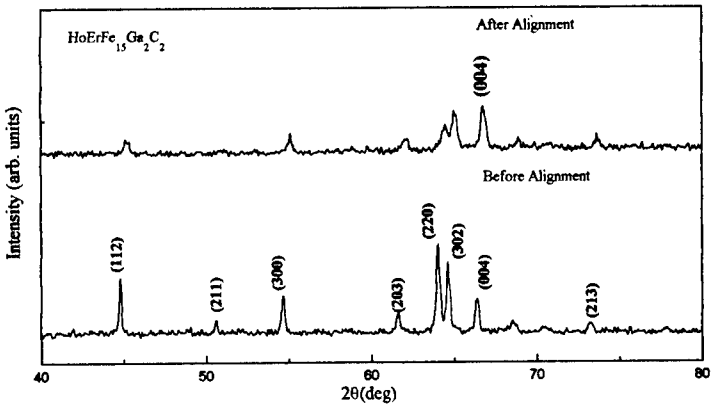


Fig.2 X-ray diffractograms of $HoErFe_{15}Ga_2C_2$ before and after magnetic alignment

The enhancement in the intensity of (004) reflection suggests that the easy magnetization direction (EMD) changes from the basal plane to a cone about c axis on Ga substitution as observed in the case of Al substituted $ErPrFe_{17}$ [3]. The change in the EMD suggests that there is an increase in the uniaxial anisotropy.

References

1. B.G. Shen, L.S. Kong, F.W. Wang and L. Cao, " Structure and magnetic properties of $Sm_2Fe_{14}Ga_3C_x$ (x=0-2.5) compounds", Appl. Phys. Lett. 63 (1993) 2288-2290.

2. B.G. Shen, F.W. Wang, L.S. Kong, L. Cao, B. Zhang and J.G. Zhao, "Structure and magnetic properties of $Gd_2Fe_{17-x}Ga_xC_2$ compounds", J. Appl. Phys. 75 (1994) 6259-6261.

3. K.G. Suresh and K.V.S. Rama Rao, "Structural, magnetic and electrical properties of $(Pr_{0.5}Er_{0.5})_2Fe_{17-x}Al_x$ compounds", J. Appl. Phys. 79 (1996) 345-350.

4. M. Venkatesan, U.V. Varadaraju and K.V.S. Rama Rao, "Structural and magnetic properties of $HoErFe_{17-x}Ga_x$ compounds", J. Magn. Magn. Mater. (in press)

5. B.G. Shen , F.W. Wang, L.S. Kong, L. Cao and H.Q. Guo, "Formation and magnetic properties of $R_2Fe_{17-x}Ga_xC_2$ compounds" , J. Magn. Magn. Mater. 127 (1993) L267- L272.

6. T.H. Jacobs, K.H.J. Buschow, G.F. Zhou, X. Li and F.R. de Boer, "Magnetic interactions in $R_2Fe_{17-x}Al_x$ compounds", J. Magn. Magn. Mater. 116 (1992) 220-230.

ANISOTROPIC MAGNETIC PROPERTIES OF BULK NANOCRYSTALLINE $Fe_{66}Co_{20}Nb_2Pr_7B_5$ MAGNETS PRODUCED BY CRYSTALLIZATION UNDER UNIAXIAL PRESSURE

Akinori Kojima [1], Akihiro Makino [2] and Akihisa Inoue [3]

[1] Graduate School of Engineering, Tohoku Univ., Aoba, Aramaki, Aoba-ku, Sendai 980, Japan
[2] Central Research Lab. (Nagaoka), Alps Electric Co., Ltd., 1-3-5 Higashi-Takami, Nagaoka 940-8572, Japan
[3] Institute for Materials Research, Tohoku Univ., 2-1-1 Katahira, Aoba-ku, Sendai 980-8577, Japan

Abstract

Bulk nanocrystalline $Fe_{66}Co_{20}Nb_2Pr_7B_5$ alloys were produced by consolidation and crystallization of amorphous powders under uniaxial pressure and their magnetic properties were investigated. Bulk alloy produced by consolidating amorphous powder at a temperature (T_s) of 870 K under a uniaxial pressure (P_s) of 640 MPa had a relative density (D_r) of 97.4 % and consisted of a nanocrystalline composite structure of bcc-(Fe,Co), $(Fe,Co)_3B$ and $Pr_2(Fe,Co)_{14}B$ phases in the as-consolidated and annealed (970K) states. Bulk nanocrystalline $Fe_{66}Co_{20}Nb_2Pr_7B_5$ alloys showed remanence enhancement, which was associated with an exchange-spring magnet, and anisotropic magnetic properties presumably due to the slight alignment of $Pr_2(Fe,Co)_{14}B$ phase caused by crystallization under uniaxial pressure. The maximum energy product ($(BH)_{max}$) was 94 kJ/m^3 for the bulk alloy consolidated at T_s of 870 K under P_s of 640 MPa.

I. Introduction

A magnet with a high maximum energy product ($(BH)_{max}$) becomes significant with the miniaturization of magnetic devices, and a number of studies have been done for such a high $(BH)_{max}$ magnet. Recently, Kneller et al. have reported [1] that a nanocomposite alloy consisting of soft and hard magnetic phases behaves as a magnet consisting of a single hard magnetic phase, and Skomski et al. have reported [2] that the nanocomposite magnets have a potentiality showing higher $(BH)_{max}$ as compared with the $Nd_2Fe_{14}B$ magnet. Thereafter, a number of studies on nanocomposite $Fe_3B/Nd_2Fe_{14}B$ [3, 4] and bcc-Fe/$Nd_2Fe_{14}B$ [5-8] magnets have been made. However, the nanocomposite magnets obtained in experiments hitherto, which are usually produced by crystallization of amorphous alloy or rapid-quenching directly, have isotropic microstructure and magnetic properties and their $(BH)_{max}$ are much inferior to the value expected in theoretical simulations. The optimization of exchange-interaction between soft and hard magnetic phases by controlling microstructure and the alignment of hard magnetic phase are necessary for improving their hard magnetic properties. We have already reported [8, 9] that melt spun Fe-rich Fe-(Nb,Zr)-(Nd,Pr)-B amorphous ribbons change to a nanocomposite structure of bcc-Fe and $(Nd,Pr)_2Fe_{14}B$ phases with remaining amorphous phase in their boundary and show $(BH)_{max}$ of 60 - 110 kJ/m^3 after annealing at 970 - 1020 K. Furthermore, the amorphous powder can be consolidated into a fully dense nanocomposite bulk magnet by utilizing the deformability of the amorphous alloy [10]. This paper aims to report the magnetic properties and structure of the bulk nanocomposite $Fe_{66}Co_{20}Nb_2Pr_7B_5$ alloy produced by consolidation and crystallization of amorphous powder under uniaxial pressure.

II. Experiments

An alloy ingot with composition of $Fe_{66}Co_{10}Nb_2Pr_7B_5$ (at%) was prepared by an arc-melting method. Amorphous ribbon was obtained by a melt spinning method and crushed into powders with particle sizes of 37 - 105 μm with a rotor milling machine. The powders were stuffed into a die made of WC with an inner diameter of 10 mm and consolidated into a bulk form using an electric-pulse current sintering machine. The consolidation was performed by heating the powder up to temperatures (T_s) between 670 and 870 K with a rate of 1.7 K/s and keeping for 480 s under uniaxial pressures (P_s) between 370 and 640 MPa in an evacuated state of 4 x 10^{-3} Pa. The compact was annealed at a temperature (T_a) of 970 K for 180 s with a heating rate of 3 K/s in a highly evacuated furnace. Structure was investigated by X-ray diffractometry using Co-$K\alpha$ radiation. Density was measured by the Archmedian method. Magnetic properties were measured at room temperature with a pulse-*BH* tracer under an applied field of 4 MAm^{-1}, and corrected with the demagnetization factor (N) = 0.33 and 0.072 for the cubic (5 x 5 x 5 mm^3) and strip (2.3 x 0.5 x 5 mm^3) shape samples, respectively.

III. Results and discussion

The relative density (D_r) as a function of T_s and P_s for the consolidated bulk $Fe_{66}Co_{20}Nb_2Pr_7B_5$ alloys are shown in Fig. 1 (a) and (b), respectively, along with the data on the consolidated sample of previously crystallized powder. The D_r value increases with increasing T_s and P_s, and reaches 97.6 % at T_s = 870 K, which is the endurance limit temperature of a WC die, under P_s = 640 MPa in consolidating amorphous powder, though this is a lower value of 94.1 % in consolidating crystalline powder. We have already reported [10] that the consolidated bulk of amorphous powders has a higher density as compared with the consolidated bulk of crystalline powders because an amorphous alloy deforms intensely during crystallization. It is supposed that

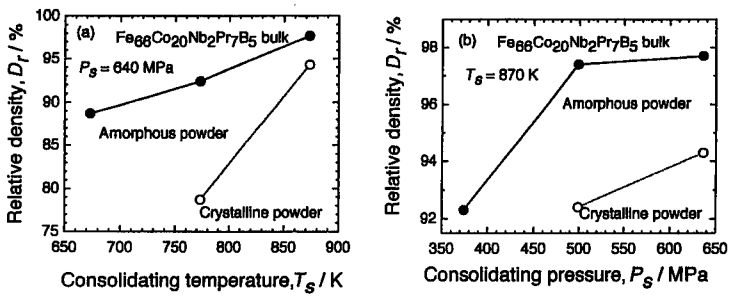


Figure 1 : Relative density (D_r) as a function of T_s (a) and P_s, (b) for bulk $Fe_{66}Co_{20}Nb_2Pr_7B_5$ alloys produced by consolidation of amorphous and previously crystallized powder.

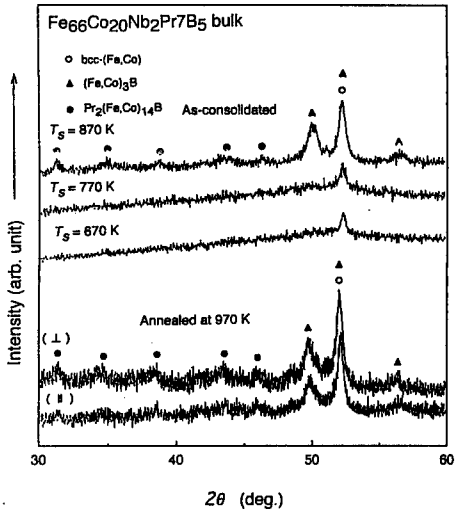


Figure 2 : X-ray diffraction patterns of bulk $Fe_{66}Co_{20}Nb_2Pr_7B_5$ alloy produced by consolidating amorphous powders at temperatures (T_s) between 670 and 870 K in the as-consolidated state, and after annealing at 970 K in the case of T_s = 870 K. The measurement was made along the directions parallel (∥) and perpendicular (⊥) to the press direction.

Figure 2 shows the X-ray diffraction patterns for the bulk $Fe_{66}Co_{20}Nb_2Pr_7B_5$ alloys prepared by consolidation of amorphous powders at T_s between 670 and 870 K under P_s = 640 MPa. The diffraction peaks corresponding to bcc-(Fe, Co) and $(Fe, Co)_3B$ phases are seen for the bulk alloys at T_s = 670 and 770 K, and the peaks corresponding to bcc-(Fe, Co), $(Fe, Co)_3B$ and $Pr_2(Fe, Co)_{14}B$ phases are seen for the bulk alloy at T_s = 870 K, indicating that the amorphous powder crystallized during the consolidation process and the precipitation and grain growth progressed because of the increase of T_s.

The consolidated bulk alloy was cut into a cubic form with z direction parallel to the direction of press stress, and x and y directions perpendicular to the press direction, and annealed at an optimum temperature of 970 K. Figure 3 shows the demagnetization curves measured in the x, y and z directions for the bulk $Fe_{66}Co_{20}Nb_2Pr_7B_5$ alloy consolidated at T_s = 870 K under P_s = 640 MPa after annealing. The demagnetization curve measured in the z direction swells as compared

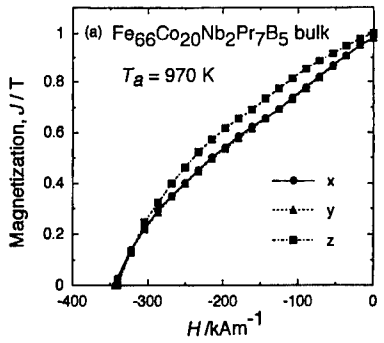


Figure 3 : Demagnetization curves of bulk $Fe_{66}Co_{20}Nb_2Pr_7B_5$ alloys after annealing measured parallel (z) and perpendicular (x and y) to the press direction.

with those in the x and y directions, resulting in the higher $(BH)_{max}$ for the z direction. The high $(BH)_{max}$ value obtained in the z direction is presumably due to the slight alignment of $Pr_2(Fe,Co)_{14}B$ phase caused by crystallization under uniaxial pressure. The X-ray diffraction patterns obtained from the planes parallel (∥) and perpendicular (⊥) to the press direction are also shown in Fig. 1 for the bulk alloy annealed at 970 K. We can see the peaks corresponding to bcc-(Fe,Co), $(Fe,Co)_3B$ and $Pr_2(Fe,Co)_{14}B$ phases, and the average grain size evaluated from the half-width of bcc (110) peak using Sccherrer's equation is 24 nm. These results suggest that the bulk alloy forms a nanocomposite structure of soft and hard magnetic phases in the annealed state. There is no distinct difference in the X-ray diffraction patterns between the (∥) and (⊥) planes, presumably because that the volume fraction of aligned $Pr_2(Fe,Co)_{14}B$ phase is small.

$(BH)_{max\text{-}par.}$ and $(BH)_{max\text{-}per.}$ denote the maximum energy product measured at the directions parallel and perpendicular to the press direction, respectively. Figure 4 shows the values of $(BH)_{max\text{-}par.}/(BH)_{max\text{-}per.}$ as a function of T_s. The value of $(BH)_{max\text{-}par.}/(BH)_{max\text{-}per.}$ increases with increasing T_s and P_s and reaches 1.17 for T_s = 870 K and P_s = 640 MPa. It is supposed that the volume fraction of aligned $Pr_2(Fe,Co)_{14}B$ phase precipitated under uniaxial pressure increases with increasing T_s and the $Pr_2(Fe,Co)_{14}B$ phase becomes more aligned with increasing P_s. As a result, the magnetic anisotropy becomes greater as T_s and P_s increase.

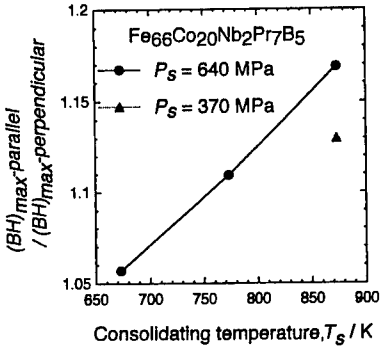


Figure 4 : $(BH)_{max\text{-}par.}/(BH)_{max\text{-}per.}$ values as a function of consolidation temperature (T_s) for bulk $Fe_{66}Co_{20}Nb_2Pr_7B_5$ alloys produced by consolidating amorphous powders under uniaxial pressures (P_s) of 370 and 640 MPa.

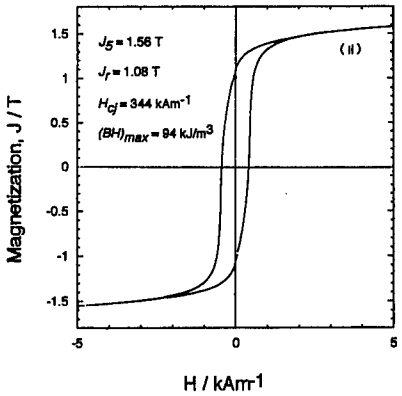


Figure 5 : *J-H* curve of the strip-shape $Fe_{66}Co_{20}Nb_2Pr_7B_5$ alloy prepared by consolidation of amorphous powder at T_s = 870 K under P_s = 640 MPa and then annealing at 970 K.

Lee et al. have already reported [11] that anisotropic magnets are obtained by uniaxial-pressing $Nd_{0.13}(Fe_{0.95}B_{0.05})$ powders which are heated to 970 - 1020 K previously (Hot-press). In this study, the amorphous powders were pressed at room temperature and heated to T_s under pressing (Cold press and heating). It is suggested that the crystallization and grain growth of $Pr_2(Fe,Co)_{14}B$ phase under uniaxial pressure cause the alignment of $Pr_2(Fe,Co)_{14}B$ phase. Generally, a thin film magnet consisting of soft and aligned hard magnetic layers is proposed as an anisotropic nanocomposite magnet, but it needs a complicated procedure. It is said that the procedure of crystallization under uniaxial pressure is simple and a good candidate to obtain anisotropic nanocomposite bulk magnets.

Figure 5 shows the *J-H* curve for the strip-shape $Fe_{66}Co_{20}Nb_2Pr_7B_5$ alloy prepared by consolidation of amorphous powder at T_s = 870 K under P_s = 640 MPa after annealing at 970 K. The *J-H* curve is smooth without any steps and shows a high reduced remanence (J_r / J_s) value of 0.69, which are associated with an exchange-spring magnet. The magnetic properties of the bulk $Fe_{66}Co_{20}Nb_2Pr_7B_5$ alloy along the press direction are J_r = 1.08 T, H_{cJ} = 344 kA/m and $(BH)_{max}$ = 94 kJ/m^3.

IV. Conclusions

Bulk nanocrystalline $Fe_{66}Co_{20}Nb_2Pr_7B_5$ alloys were produced by consolidation and crystallization of amorphous powders under uniaxial pressure using an electric pulse-current sintering machine, and their magnetic properties and microstructure were investigated. The results obtained are summarized as follows.

1. The bulk $Fe_{66}Co_{20}Nb_2Pr_7B_5$ alloy prepared at a temperature (T_s) of 870 K under a pressure (P_s) of 640 MPa has a relative density (D_r) of 97.6 % though the bulk alloy prepared by consolidation of crystalline powder shows a lower D_r of 94.1 %. The high densification in consolidating amorphous powder is due to the high deformability of an amorphous phase during crystallization. 2. The bulk $Fe_{66}Co_{20}Nb_2Pr_7B_5$ alloy annealed at 970 K shows higher $(BH)_{max}$ in the case of the press direction and the magnetic anisotropy increases with increasing T_s and P_s. It is supposed that the crystallization and grain growth of $Pr_2(Fe,Co)_{14}B$ phase under uniaxial pressure cause the slight alignment of $Pr_2(Fe,Co)_{14}B$ phase. 3. The bulk $Fe_{66}Co_{20}Nb_2Pr_7B_5$ alloy forms a nanocomposite structure of bcc-(Fe,Co), $(Fe,Co)_3B$ and $Pr_2(Fe,Co)_{14}B$ phases in the as-

consolidated and annealed (970 K) states, and exhibits a smooth *J-H* curve without any steps and remanence enhancement, indicating that the bulk alloy is an exchange-spring magnet. The magnetic properties of the bulk nanocomposite $Fe_{66}Co_{20}Nb_2Pr_7B_5$ alloy prepared by consolidating amorphous powders at T_s = 870 K under P_s = 640 MPa are J_r = 1.08 T, H_{cJ} = 344 kA/m and $(BH)_{max}$ = 94 kJ/m^3 after annealing at 970 K.

References

1. E. F. Kneller and R. Hawing, " The Exchange-Spring Magnet : A New Material Principle for Permanent Magnets," IEEE Transactions on Magnetics, 27 (4) (1991), 3588 - 3600.

2. R. Skomski and J. M. D. Coey, "Giant energy product in nanostructrued two-phase magnets," Physical Review B, 48 (21) (1993), 15812 - 15816.

3. R. Coehoorm, D. B. de Mooiji, J. P. W. B Duchateau, and K.H.J.Buschow, "Novel Permanent Magnetic Materials Made by Rapid Quenching," Journal de Physique, C8 (1988), 669 - 670.

4. S. Hirosawa, H. Kanekiyo and M. Uehara, " High-coercivity iron-rich rare-earth permanent magnet material based on $(Fe, Co)_3$-B-Nd-M (M = Al, Si, Cu, Ga, Ag, Au)," Journal of Applied Physics, 73 (10) (1993), 6488 - 6490.

5. A. Manaf, R. A. Buckly and H. A. Davis, "New nanocrystalline high-remanence Nd-Fe-B alloys by rapid solidification," Journal of Magnetism and Magnetic Materials," 128 (1993), 302 - 306.

6. A. Inoue, A. Takeuchi, A. Makino and T. Masumoto, "Hard Magnetic Properties of Fe-Nd-B Alloys Containing Intergranular Amorphous Phase," IEEE Transactions on Magnetics, 31 (6) (1995), 3626 - 3628.

7. G. C. Hadijipanayis, L. Withanawasam and R. F. Krause, "Nanocomposite $R_2Fe_{14}B/\alpha$-Fe Permanent Magnets," IEEE Transactions on Magnetics, 31(6) (1995), 3596 - 3600.

8. A. Kojima, F. Ogiwara, A. Makino, A. Inoue and T. Masumoto, "Magnetic Properties of Nanocrystalline Fe-Nb-R-B and Fe-Zr-R-B (R = Pr, Nd) Alloys," Journal of the Magnetic society of Japan, 20 (1996), 233 - 236.

9. A. Kojima, F. Ogiwara, A. Makino, A. Inoue and T. Masumoto, "Micro structure of nanocrystalline Fe-Nb-Pr-B alloys produced by crystallization of amorphous phase," Mater. Sci. Eng., A226 - 228 (1997), 520 - 525.

10. A.Kojima, A.Makino, A.Inoue, "STRUCTURAL AND MAGNETIC PROPERTIES OF NANOCRYSTALLINE Fe-RICH Fe-Nb-Nd-B SINTERED MAGNETS PRODUCED BY CONSOLIDATING AMORPHOUS POWDERS," IEEE Transactions on Magnetics, 33 (5) (1997), 3817 - 3819.

11. R. W. Lee, E. G. Brewer and N. A. Schaffel, "Processing of Neodymium-iron-boron Melt-spun Ribbons to Fully Dense Magnets," IEEE Transactions on Magnetics, 21 (5) (1985), 1958 - 1963.

THE NOVEL STRUCTURE OF ULTRAFINE AMORPHOUS Fe-Zr-B POWDERS OBTAINED BY CHEMICAL REDUCTION

Jing Guo Zhang, Yi Jian Lin, Wei Xin Xu, and Hui Juan Jin
Shanghai Iron & Steel Research Institute
1001Tai He Road, Shanghai 200940, P. R. CHINA

Abstract

Ultrafine amorphous Fe-Zr-B powders were first obtained by chemical reduction using a borohydride. The X-ray diffraction traces of the Fe-Zr-B powders demonstrate two halos. The Mössbauer spectra, DSC curves, coercivity, and TEM micrograph of the Fe-Zr-B powders obtained in the present paper were investigated.

The Third Pacific Rim International Conference on
Advanced Materials and Processing (PRICM 3)
Edited by M.A. Imam, R. DeNale, S. Hanada,
Z. Zhong and D.N. Lee
The Minerals, Metals & Materials Society, 1998

Introduction

Ultrafine amorphous powders prepared by chemical reduction techniques have been extensively investigated because of their interesting applications in ferrofluids, magnetic recording media, and catalysis. These powders of Fe-B[1], Fe-Co-B[2], and Fe-Ni-B[3] can be produced by chemical reduction of metal salts in aqueous solutions by use of an alkali metal borohydride. Recently Saida et al. [4] have successfully obtained Ni-Mo-B amorphous ultrafine powders by a chemical reduction method using KBH_4 as a reducing agent and Na_2MoO_4 instead of the salt of Mo. It is worthy to note that even though amorphous ultrafine powders of different alloys have been obtained by chemical reduction, an investigation of Fe-Zr-B powders produced by the use of an alkali metal borohydride has not been reported until now, probably due to the difficulties in experimental procedure for preparing Fe-Zr-B powders. On the other hand, amorphous Fe-Zr-B alloys obtained by different methods, such as mechanical alloying, melt spinning, solid state reaction, and sputtering, have been investigated extensively. Therefore, it is interesting to compare the amorphous Fe-Zr-B alloys prepared by chemical reduction with those produced by other methods, if it is possible to obtain amorphous Fe-Zr-B powders by borohydride reduction. The present paper reported preliminary results of investigations on ultrafine amorphous Fe-Zr-B powders first obtained by borohydride reduction.

Experimental Procedure

Fe-Zr-B powders were prepared by the reduction of aqueous solutions of $FeSO_4$ and $Zr(SO_4)_2$ using aqueous of $NaBH_4$ or KBH_4. The 0.1mol/L metallic salt solutions of Fe+Zr with different ratios of $FeSO_4$ to $Zr(SO_4)_2$ were prepared. Then a $NaBH_4$ or KBH_4 aqueous solution of 0.5 mol/L was added to the above metallic salt solutions with vigorous stirring. After the reaction finished, the

formed powders were treated by a chromating procedure in a potassium dichromate solution. The chromated powders were immediately collected on a filter, washed, dried, and preserved in a desiccator.

The chemical composition of the powder was determined by wet-chemical method. Thermal analysis was carried out by DSC using Al_2O_3 as the reference materiel at a heating rate of 20K/min. X-ray diffraction analysis was preformed on a Siemens D-500 diffractometer using Cu K_α radiation with 25mA at 35KV. The morphology of powder was observed with a Hitachi H-700 TEM at 200KV. Mössbauer spectra were obtained by a constant-acceleration spectrometer with a 10 mCi(milliCuries) source of ^{57}Co in rhodium.

Results and Discussion

The chemical compositions of the Fe-Zr-B powders shown in table I indicate that the atomic ratio between iron and zirconium is close to that in the original aqueous solutions, particularly for the case of Fe/Zr=9/1. This fact is similar to that in amorphous Fe-Ni-B powders obtained by chemical reduction [3]. Therefore, it is easy to control the ratio of iron to zirconium in powders precisely. Table I also shows that the boron content of the powders slightly increases with an increase of Fe/Zr from 7/3 to 9/1.

Table I Chemical Compositions of the Fe-Zr-B powders (at.%)

Sample No.	Fe	Zr	B	Fe/Zr^1	Fe/Zr^2	Fe/Zr^1 :Fe/Zr^2
1	45.33	21.54	33.13	7/3	2.10	1.11
2	50.00	12.38	37.64	7/1.5	4.04	1.16
3	55.59	6.41	38.00	9/1	8.67	1.04

$Fe:Ze^1$ and $Fe:Zr^2$ are the atomic ratio between Fe and Zr in aqueous solutions and powders respectively.

Fig.1 demonstrates the X-ray diffractograph of the Fe-Zr-B powders, showing the amorphous state of the powders. Fig.1(a) reveals two halos in the XRD trace of the sample 1, which means that there are two different amorphous phases in the powder. A comparison of the intensities of the halos shown in Fig.1(a)(b)(c) indicates an interesting fact that the intensity of the first halo decreases with an increase of Fe/Zr from 7/3 to 9/1. For the lowest Zr content of sample 3 in the three samples, the first halo is hardly seen, as shown in Fig.1 (c). The new findings imply that first halo in Fig.1 is due to a Zr-rich amorphous phase, but the second halo is due to a Fe-rich amorphous phase. Regarding the second halo in the XRD trace of the Fe-Zr-B powders, it is not a surprising result, because halos at similar positions are often observed in amorphous Fe-M-B (M: transition metal) alloys. For examples, the d value at peak position of the halo of 0.213 nm and 0.203 nm, for $Fe_{76.1}Zr_{11.7}B_{12.2}$[5] and $Fe_{48}Ni_{21}B_{31}$[3], by comparison with that of 0.206 nm for $Fe_{45.3}Zr_{21.5}B_{33.1}$ of the sample 1 in the present study. Since the d value corresponding to peak of the halo in XRD of amorphous alloys is lacking in exact physical meaning, further work, such as EXAFS (Extended X-ray Absorption Fine Structure) and HRTEM, is planned to clarify the origin of two halos illustrated in Fig.1.

Fig.2 presents of Mössbauer spectra of the samples 1, 2, and 3 respectively, showing further evidence for the amorphous state of the samples. Fig.2 also demonstrates a paramagnetic doublet, which is probably due to paramagnetic phases, e.g. oxides and products formed by chromating procedure on surfaces of powders. The other possible origin for the paramagnetic doublet is superparamagnetism resulting from ultrafine powder size.

Table II gives results obtained from DSC measurement, showing the height and area of the exothermic peak due to crystallization, and onset temperature Tx and the peak temperature Tp for the sample 1, 2 and 3. It can be seen from Table II that the height and area of the crystallization peak increase with an increase

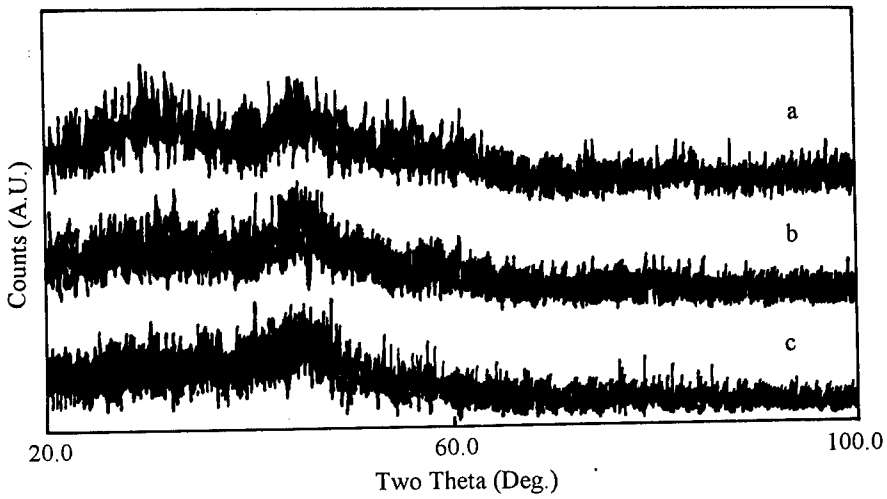


Figure 1: X-ray diffractograph of the Fe-Zr-B powders
(a) Sample 1, (b) Sample 2, (c) Sample 3

of Fe/Zr from 7/3 to 9/1, whereas Tx and Tp only slight vary according to Fe/Zr. The value of coercivity Hc of the powder samples are also given in Table II. The high value of coercivity of the Fe-Zr-B powders, which can be comparable with the data of Hc for Fe-Ni-B powders [3], is due to the ultrafine powder morphology and the thin oxide film on the surfaces of the powders.

In addition to amorphous structure, the ultrafine powder size is the most important characteristic of the powders obtained by chemical reduction. We infer from the high values of coercivity Hc and superparamagnetism of the powders that the size of powders is of the order of magnitude of $10 \sim 10^2$ nm. To prove the above inference directly, the morphology of the Fe-Zr-B powders was observed by TEM (Fig.3). As shown in Fig.3, the average size of the powders is about 80nm. In contrast to the chain shape of the Fe-Ni-B powder cluster, the Fe-Zr-B powder cluster is in a nodular shape.

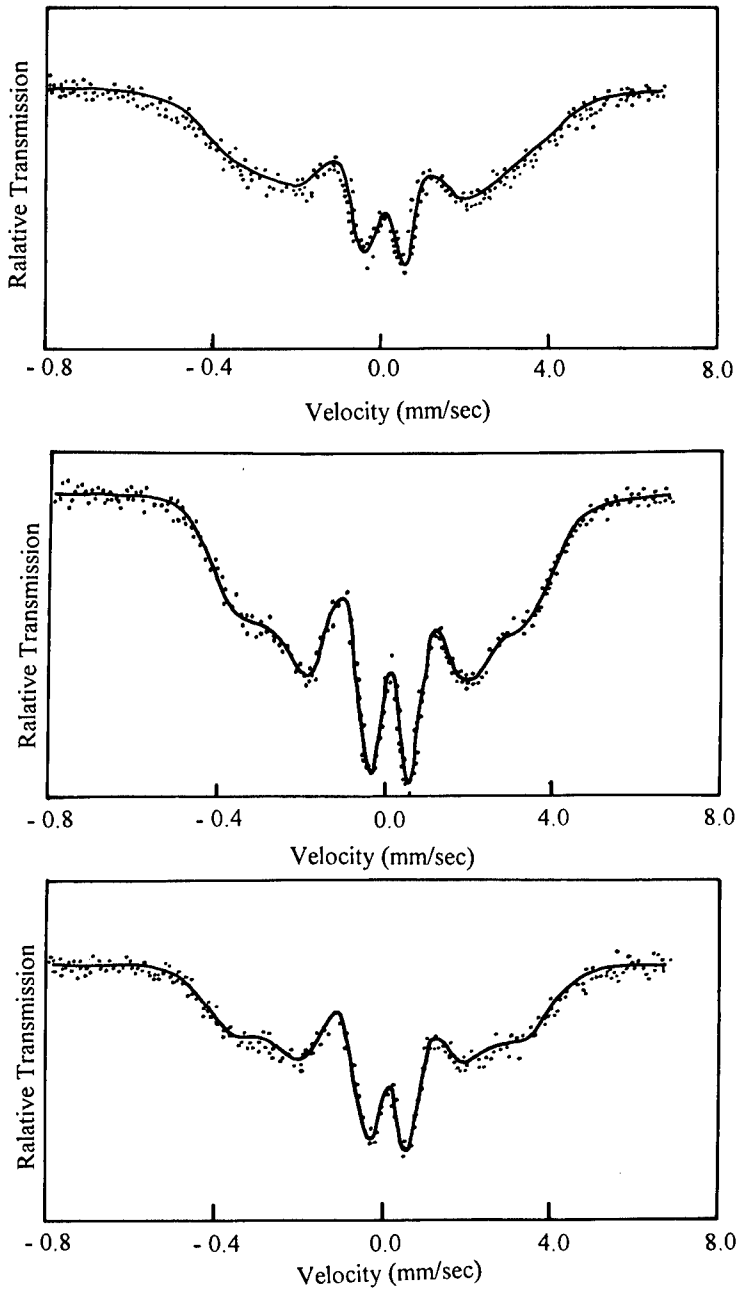


Figure 2: Mössbaure spectra of the Fe-Zr-B powders

(a) Sample 1, (b) Sample 2, (c) Sample 3

Table II Characteristic of Crystallization and Magnetic Properties of the Fe-Zr-B Powders

Sample No.	H*	A*	Tx(℃)	Tp(℃)	Hc(KA/m)
1	28	400	425	475	11.94
2	33	475	425	475	10.98
3	35	600	430	480	11.22

H* and A* are the height and area of the crystallization peak respectively, in arbitrary units.

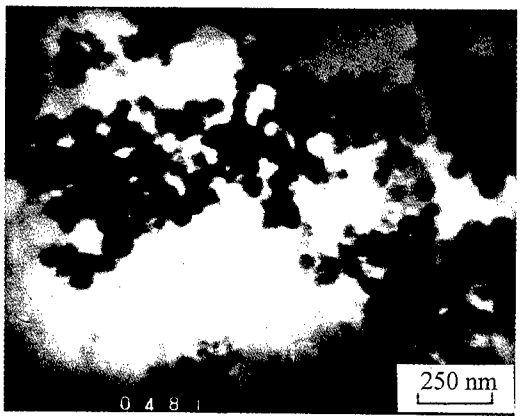


Fig.3: TEM micrograph of the Fe-Zr-B powders (Sample 2)

Conclusions

1. Ultrafine amorphous Fe-Zr-B powders were first obtained by chemical reduction of metal salts in aqueous solutions using an alkali metal borohydride.

2. The X-ray diffraction traces of the Fe-Zr-B powders demonstrate two halos. The intensity of the first halo decreases with an increase of Fe/Zr from 7/3 to 9/1. The first halo is hardly seen in the X-ray diffraction pattern for the sample with Fe/Zr of 9/1. The Mössbauer spectrum of the Fe-Zr-B powder presents a paramagnetic doublet.

3. The Fe-Zr-B powder obtained in the present paper has a high value of coercivity of ~ 11 KA/m and has an average size of 80 nm. The Fe-Zr-B powder cluster is in a nodular shape.

4. The atomic ratio of Fe/Zr in the Fe-Zr-B powder is close to that in the original aqueous solution.

Acknowledgements

This research was funded in part by National Natural Science Foundation of China and Shanghai Research Centre For Advanced Materials.

References

1. S. Linderoth and S. Morup, "Amorphous $TM_{1-x}B_x$ Alloy Particles Prepared by Chemical Reduction," J. Appl. Phys., 69(8)(1991), 5256-5261.

2. J. V. Wonterghem et. al., "Formation of Ultra-Fine Amorphous Alloy Particles by Reduction in Aqueous Solution," Nature, 322(6080)(1986), 622-623.

3. J. G. Zhang, "Properties and Structure of Ultrafine Amorphous Fe-Ni-B Powder Obtained by Borohydride Reduction," J. Mater. Eng. Perform., 4(4)(1995), 453-459.

4. J. Saida et al., "XPS Study of Ni-Mo-B Amorphous Ultra-fine Particles Prepared by Chemical Reduction," (in Japanese) J. Japan Inst. Metals, 60(1)(1996), 79-83.

5. A. Makino et al., "Soft Magnetic Properties of bcc Fe-Zr-B Sputtered Films with Nanoscale Grain Size,' Mater. Trans. JIM, 33(1)(1992), 80-86.

Effects of Surface Features of Fe-based Amorphous Ribbons on the Two-fold In-plane Magnetic Anisotropy

Hongxia Wang, Guobin Yang and Kezhu Dong

National Amorphous & Nanocrystalline Alloy Engineering Research Centre,
Central Iron and steel Research Institute, 100081 Beijing, China

Abstract

In order to understand the origins of the two-fold in-plane anisotropy, the relations between the surface topograhies, thickness, mechanical thinning and the two-fold in-plane magnetic anisotropy of Fe-based amorphous ribbons made by normal casting and controlling air flow condition methods have been investigated by torque curve measurment, Scanning Electron Microscope, surface roughness measurement and so on. It has been found that the geometry of the surface features which formed in casting process have very important influence on the two-fold in-plane anisotropy Ku. It was concluded that the origins of the two-fold in-plane anisotropy of amoprphous ribbons are mainly on the geometry effects of air pockets in the roll-side surface.

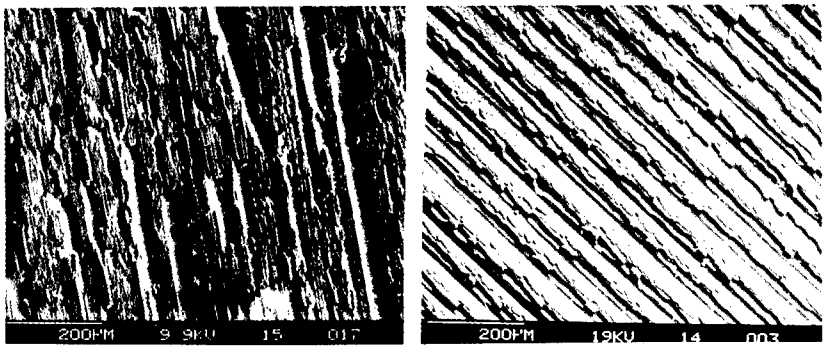
The Third Pacific Rim International Conference on
Advanced Materials and Processing (PRICM 3)
Edited by M.A. Imam, R. DeNale, S. Hanada,
Z. Zhong and D.N. Lee
The Minerals, Metals & Materials Society, 1998

Introduction

It was well known that amorphous ribbons made by rapidly quenched methods always show two-fold in-plane magnetic anisotropy of about $10^3 \sim 10^5$ erg/cm^3 values, that is the ribbons are easy magnetized along the longitudinal direction and hard along the transverse direction. It was said that the origins of the in-plane anisotropy are relationed to: stress-magnetostriction coupling effect, atom-pairs order effect and microcrystalline effect and so on. Morita et al. have found that neither magnetostriction-stress coupling nor internal shape effect can explain the in-plane anisotropy. In addition, the anisotropy also has been found not to be much altered by heat treatment, even at high temperatures where the internal stress relief was completed. And almost the same anisotropy remained after the crystallization by a higher temperature or prolonged annealing. In this paper, in order to understand the origins of the two-fold in-plane anisotropy, the relations between the surface topograhies, thickness, mechanical thinning and the two-fold in-plane magnetic anisotropy of Fe-based amorphous ribbons made by normal casting and controlling air flow methods have been investigated by torque curve measurment, Scanning Electron Microscope, surface roughness measuring and so on.

Experimental Results and Discussion

Fig.1 shows the SEM's surface features of Fe-based amorphous ribbons's roll-side casted by normal method and controlling air flow condition method. It can be seen that ther are many air pockets align uniformly along the longitudinal direction of the ribbons. When the ribbons were casted by the controlling air flow method, the air pockets on the roll-side surface are smaller and align uniformer than the normal casting method's. The surface roughness decrease, and the Ku values also decrease largely from about 50 $\times$ 10^3 erg/cm^3 for normal casting condition to about 10 $\times$ 10^3 erg/cm^3. It can be said that the geometry of the surface features which formed in casting process have very important influence on the uniaxial anisotropy Ku.



(a) normal casting condition (b) controlling air flow condition

Figure 1: The SEM's surface features of Fe-based amorphous ribbons's roll-side casted by (a) normal casting method, (b) controlling air flow condition method

In order to understand the origins of the in-plane anisotropy, the surface models were assumed and the theory of the demagnetization energy of surface geometry effects was derived. Fig.2 shows the surface models of amorphous ribbons. The x and y are the longitudinal and transverse directions of the ribbon, and the z is the thickness' direction of the ribbon. Assuming the air pockets in the roll-side align uniformly and regularly, they have the hightness of Rz and the wideness of b, and the numbers of the air pockets in one unit (1 cm) along the transverse direction's are N_r. The demagnetization energy for one air pocket is: $E_i = 1/2\ NM^2\ V_i$. The air pocket's volume V_i is $R_z b \times 10^{-8}$ cm^3. N is demagnetization factor and M is magnetization of the air pocket. The demagnetization energy for one unit is:

$$E = E_i = 1/2\ NM^2\ R_z\ bN_r \times 10^{-8}$$

The density of the demagnetization energy for one unit is:

$$E_d = E/V = 1/2\ NM^2\ R_z\ b/d\ N_r \times 10^{-8} = 1/2\ NM^2\ F$$

F is factor of surface geometry effect. V is the volume of the unit. N is demagnetization factor and M is magnetization of the unit. $E_d = 1/2\ NM^2F$ are called the surface geometry effects formula of the two-fold in-plane anisotropy (SGE). Besides relating to the saturation magnetization Ms^2, this SGE formula also include the factors of the thickness and the para-meters of surface features of the ribbons.

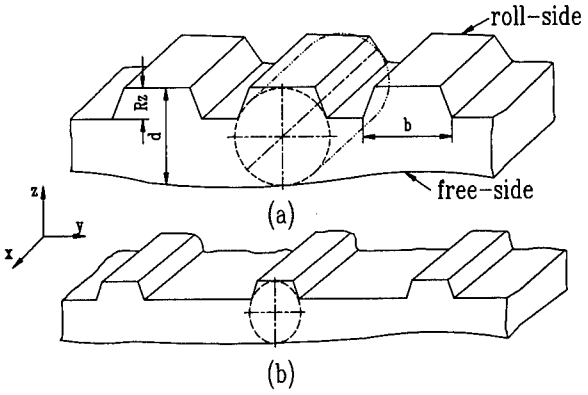


Figure: 2 The surface model of amorphous ribbons

Table 1 shows the results of the calculated magnetic anisotropies Kuj from the SGE formula and the measured Ku from torque curves measurment. The calculated values of magnetic anisotropies from the SGE formula are close to the values of Ku which were measured from the torque curves. It can be confirmed that the origins of the two-fold in-plane anisotropy of amoprphous ribbons are mainly on the geometry effects of air pockets in the roll-side surface.

The relations between the Ku and the thickness during thinning are also investigated. The Ku values increase with thinning from the free-side surface and decrease with thinning from the roll-side surface of the amorphous ribbons. The changes in Ku are caused by the variation of the surface features effects during thinning process, the

calculated values of Kuj of the magnetic anisotropies from the SGE formula are close to the values of Ku which were measured from the torque curves (see Tab. I). The SGE formula also can be used to explain the variation of the in-plane anisotropy with the thinning process.

Table I . The relations of the calculated magnetic anisotropies Kuj from the SGE formula and the measured Ku from torque curves measurment

Composition	Ms(Gs)	d(μ m)	Rz(μ m)	Nr(No./cm)	Kuj(10^3erg/cm^3)	Ku(10^3erg/cm^3)	
$Fe_{74}Mo_3Si_{15}B_{18}$	1022	27	12.4	272	67.8	53.4	normal casting
$Fe_{74}Mo_3Si_{15}B_{18}$	1022	29	6.1	184	16.7	14.5	contrilling air flow
$Fe_{80}C_2Si_2B_{16}$	1317	30	4.5	232	22.6	28.0	contrilling air flow
$Fe_{74}Mo_3Si_8B_{15}$	998	30	4.5	192	10.7	8.2	contrilling air flow
$Fe_{74}Mo_3Si_{11}B_{12}$	991	37	3.9	160	6.4	6.5	contrilling air flow
$Fe_{74}Mo_3Si_6B_{17}$	976	40	5.1	192	10.7	9.0	contrilling air flow
$Fe_{74}Mo_3Si_7B_{16}$	989	31	3.6	248	9.9	8.6	contrilling air flow
$Fe_{74}Mo_3Si_7B_{16}$		29	2.21	248	4.7	6.3	thinning from roll side
$Fe_{74}Mo_3Si_7B_{16}$		29	3.6	248	10.2	11.7	thinning from roll side
$Fe_{74}Mo_3Si_7B_{16}$		26	3.6	248	10.7	11.9	thinning from roll side

Conclusions

The geometry of the surface features of amorphous ribbon's formed in casting process have very important influence on the two-fold in-plane uniaxial anisotropy Ku. The demagnetization energy of the air pockets in the roll-side of the ribbon's play the main function to the anisotropy. The origins the ansotropy of Fe-based amorphous ribbons are mainly on the surface geometry effects of the air pockets of the ribbons.

References

1. H. Fujimori, "Magnetic Anisotropy", Amorphous Metallic Alloys, Chap.16, 1983
2. Hongxia Wang, etal. "The Relations between the Surface Scraching and the two-fold in-plane anisotropy of Fe-based Amorphous Ribbons", Research in Metallic Material, No.4, Vol.15 (1989), P5
3. Hongxia Wang, etal. "The Variation of the Anisotropy with the Width Direction of the $Fe_{75}Mo_3Si_7B_{15}$ Amorphous Ribbon", Research in Metallic Material, No.5, Vol.15 (1989), P1
4. Hongxia Wang, etal. "The Effect of the Add-plate Quenching Method to the Anisotropy of Amorphous Ribbons", Research in Metallic Material, No.6, Vol.15 (1989), P39
5. Hongxia Wang, etal. "The Surface Geometry Effect Model and Calculation of Demagnetization Energy of the Two-fold In-plane Anisotropy of Fe-based Amorphous Ribbons", Amorphous Alloys and Applications, Science and Tecnology, Ministry of Metallurgical Industry Press, 1990, P175.

Effect of Solid Reducing Agent on Formative Condition and Magnetic Properties of Fe_2-W Type Hexagonal Ferrite

H. Takamura, K. Unno, A. Kamegawa, M. Homma, and M. Okada

Department of Materials Science, Graduate School of Engineering, Tohoku University,
Aoba, Aramaki, Aoba-ku, Sendai 980-8579, JAPAN

Abstract

Present works describe the formative condition of Fe_2-W type ferrite utilizing a solid reducing agent such as carbon and the possibility of adopting new solid reducing agent. The drying treatment at 473K and following by firing at 1473K in less than $P_{O2}=2.5x10^2$ Pa are the suitable formative conditions for carbon addition to achieve high volume fraction of Fe_2-W phase. It is difficult to utilize the iron powder as a solid reducing agent because of the unavoidable formation of considerable amount of Fe_3O_4 and α-Fe_2O_3. It is, however, clarified that the silicon powder acts as a new solid reducing agent in various partial oxygen pressure.

The Third Pacific Rim International Conference on
Advanced Materials and Processing (PRICM 3)
Edited by M.A. Imam, R. DeNale, S. Hanada,
Z. Zhong and D.N. Lee
The Minerals, Metals & Materials Society, 1998

Introduction

Hexagonal ferrites have widely studied because of their potential applications as permanent magnets, microwave devices and magnetic recording media[1]. Among them, the W-type hexagonal ferrite, which chemical composition is expressed as $Sr(Ba)Fe^{2+}{}_2Fe^{3+}{}_{16}O_{27}$, is the most attractive compound for the permanent magnet because of its 10% higher saturation magnetization of 98 $\mu Wb \cdot m \cdot kg^{-1}$ in comparing with that of M-type ferrite[2].

The W-type ferrite is, however, unstable phase without divalent cation or combination of monovalent and trivalent cations Me^{2+} such as Zn^{2+}, Co^{2+}, Mg^{2+}, Mn^{2+}, $1/2(Li^{+}Fe^{3+})$, $1/2(Cu^{+}Fe^{3+})$[3]-[6]. Then chemical formula of W-type ferrite is usually expressed as $Sr(Ba)Me_2Fe_{16}O_{27}$ (Me_2-W). These substitutions were widely explored to improve the thermal stability, the saturation magnetization, or the other intrinsic magnetic properties. They, however, usually comprise characteristically rather low coercivity H_c and as a result the energy product $(BH)_{max}$ is still low.

Recently, Toyoda reported a novel method using a carbon powder as a solid reducing agent in a nitrogen atmosphere to produce a high performance Fe_2-W type ferrite without Me^{2+}. The energy product $(BH)_{max}$ of this Fe_2-W exceeded $40 kJ \cdot m^{-3}$[7]. In this investigation, it was mentioned that the phases appeared after firing and their magnetic properties strongly depend on the drying temperature of green compacts. But the effect of the solid reducing agent on formative conditions of Fe_2-W type ferrite and a relation of the phases that appeared after firing and drying temperature of green compacts have not been clarified.

The purpose of this study is to clarify the formative conditions of Fe_2-W type ferrite utilizing the solid reducing agent in a various partial oxygen pressure, and to examine the possibility of adopting new solid reducing agent such as iron and silicon.

Experimental Procedures

The samples were prepared by conventional ceramics processing techniques. The sample had a composition of $SrO \cdot nFe_2O_3$, where n=8.5 for carbon and silicon addition as solid reducing agent and n=8 for iron addition. Mixture of the weighed raw material in the form of $SrCO_3$ and Fe_2O_3 were pressed into pellets, and then each pellet was introduced into a platinum crucible and calcined at 1623K for 10hs in $P_{O2} = 5.0 \times 10^2$ Pa. After coarse grinding, they were milled for 20hs with solid reducing agent of carbon, silicon or iron powders in C_2H_5OH. Each amount of additive was 0.2 mass% of carbon, 0.47 mass% of silicon and 3.89 mass% of iron, respectively. Then, they were pressed into green compacts with dimensions of approximately $10 \times 10 \times 20$ mm^3 in applying magnetic field of 960 $kA \cdot m^{-1}$, and dried at various temperature (T_d) ranging from 373 to 573K for 3 hs in air. Subsequently, each green compact was fired at 1473K for 10hs in various partial oxygen pressure (P_{O2}) ranging from 5.1×10^1 to 5.0×10^2 Pa controlled by utilizing Ar-O_2 mixed gas. After firing, the pellets were quenched into cold water.

The phases that appeared after each heat treatment were identified by X-ray powder diffraction using Fe-Kα radiation. Microstructural observation and determination of chemical composition were performed by scanning electron microscopy (SEM) and energy dispersive X-ray (EDX) spectroscopy. The distribution of solid reducing agent was observed by EPMA using element mapping techniques. Magnetic properties were measured by a vibrating sample magnetometer (VSM) with a maximum applied field of 1.2 $MA \cdot m^{-1}$.

Results and Discussion

Figure 1 shows the firing temperature and partial oxygen pressure adopted in this study with stable region of Fe_2-W type ferrite determined by Tsuchiya *et al.*[8]. The samples were calcined at 1623K in $P_{O2}=5.0 \times 10^2$ to obtain Fe_2-W type ferrite as a single phase. In order to clarify the formative condition of Fe_2-W type ferrite with solid reducing agent, the partial oxygen pressure was changed into (1) 5.1×10^1, (2) 2.5×10^2 and (3) 5.0×10^2 Pa at 1473K as shown in the figure.

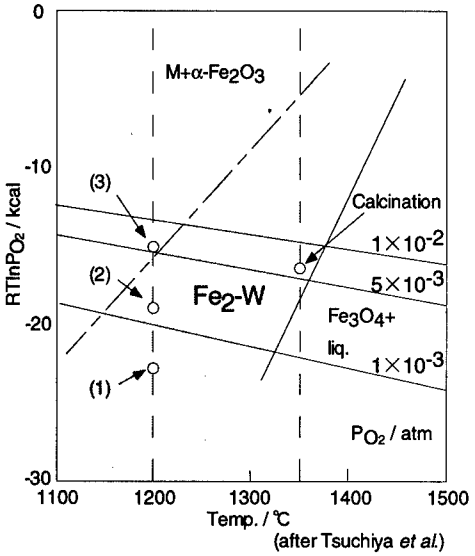


Figure 1: The firing temperature and partial oxygen pressure adopted in this study and stable region of Fe_2-W type ferrite determined by Tsuchiya *et al.*.

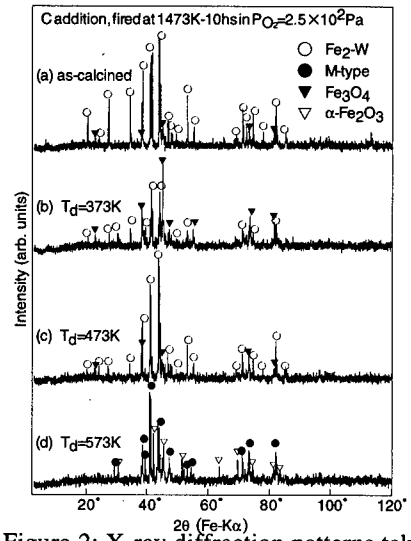


Figure 2: X-ray diffraction patterns taken from (a) $SrO{\bullet}8.5Fe_2O_3$ calcined at 1623K, and the pellets fired with carbon at 1473K for 10hs in $P_{O2} = 2.5x10^2$ Pa after drying the green compacts at (b) 373K, (c) 473K, and (d) 573K.

Carbon addition

Figure 2 shows X-ray diffraction patterns taken from (a) $SrO{\bullet}8.5Fe_2O_3$ calcined at 1623K, and the pellets fired with carbon at 1473K for 10hs in $P_{O2} = 2.5x10^2$ Pa after drying the green compacts at (b) 373K, (c) 473K, and (d) 573K. The $SrO{\bullet}8.5Fe_2O_3$ after calcination consists of two phases such as Fe_2-W main phase and Fe_3O_4 minor phase. The sample after drying treatment at 373K and following by firing consists of Fe_3O_4 major phase and Fe_2-W minor phase, while the Fe_2-W phase was formed as main phase when the green compact was dried at 473K. The firing after drying treatment at 573K formed M-type ferrite with considerable amount of α-Fe_2O_3, instead of vanished the Fe_2-W and Fe_3O_4 phases. Thus, it is obvious that the phases appeared after firing strongly depend on the drying treatment.

The phases that appeared after firing in various P_{O2} are summarized in Table 1. The Fe_2-W phase was obtained at lower P_{O2} ($P_{O2} \leqq 2.5x10^2$ Pa). With increasing P_{O2} and drying temperature T_d, oxidation reaction of Fe_2-W phase was progressing, and as a results M-type and α-Fe_2O_3 phases were formed. It is interesting to note that the final state of Fe_2-W with carbon powder is not only dominated by P_{O2}, but also by drying temperature T_d. Subsequently, magnetic measurement was performed in order to confirm these phase changes.

Figure 3 shows the magnetization intensity of the powders as a function of T_d. $\sigma_{1.2}$ is defined as the magnetization intensity at the applying field of 1.2 $MA{\bullet}m^{-1}$. The dashed line means the magnetizing intensity of 84 $\mu Wb{\bullet}m{\bullet}kg^{-1}$ obtained in the calcined powder. $\sigma_{1.2}$ of powders after firing decreased with increasing of T_d. This behavior is consistent with phase changes shown in Table 1. $\sigma_{1.2}$ of as-dried powder without firing, which is identified as the Fe_2-W by X-ray diffraction, is lower than that of the calcined powder because of remaining the strain induced during ball-milling process. But it also slightly decreased with increasing of drying temperature. This behavior suggests that a partial decomposition or oxidation reaction of the Fe_2-W were occurred during drying treatment. It can be considered that this partial decomposition strongly affects the final state of powders after firing. Judging from X-ray diffraction patterns and magnetic measurement, drying treatment at 473K and following by firing in less than $P_{O2}=2.5x10^2$ Pa are the suitable conditions for carbon addition to achieve high volume fraction of the Fe_2-W phase.

Table 1: The phases that appeared after drying treatment of T_d and following by firing at 1473K in P_{O2} (Carbon addition).

P_{O_2} (Pa)	Drying Temp., T_d (K)		
	373	473	573
(1)5.1×10^1	Mag. + W	W + Mag.	W + Mag.
(2)2.5×10^2	Mag. + W	W + Mag.	M + α
(3)5.0×10^2	M + α	M + α	M + α

W : Fe_2-W, M : M-type, Mag. : Fe_3O_4, α : α-Fe_2O_3

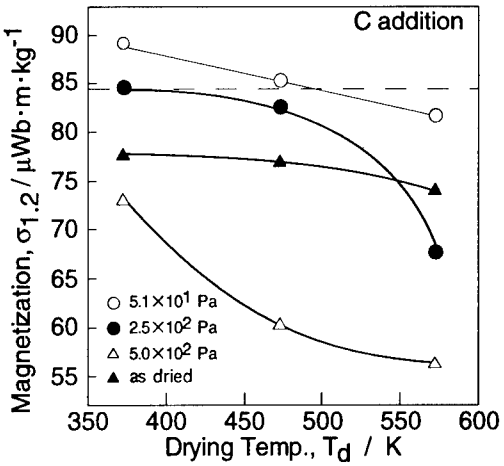


Figure 3: The variation of magnetization intensity $\sigma_{1.2}$ of carbon addition powders versus drying temperature T_d.

Iron addition

Table 2 summarized the phases that were observed in the samples containing metallic iron powder as a solid reducing agent after drying and following by firing treatment. The experimental conditions are almost same as those of carbon addition mentioned above except for amount of additives and composition of the calcined powder. The amount of iron powder (3.8mass%) and the nominal composition of calcined powder ($SrO{\bullet}8Fe_2O_3$) were decided to compose $SrO{\bullet}8.5Fe_2O_3$ after firing. In this iron addition, Fe_2-W phase was obtained as main phase when dried at 573K and following by firing in $P_{O2}=5.1x10^r$ Pa. But it is difficult to achieve the high volume fraction of Fe_2-W phase in comparing with that of carbon addition, because the formation of considerable amount of Fe_3O_4 or α-Fe_2O_3 phase was unavoidable under this experimental conditions.

Silicon addition

In order to select a solid reducing agent, the calculation of standard free energy (ΔG^0) for formation of oxides is useful. The ΔG^0 for formation of SiO_2 and CO_2 examined above are given as follows.

$Si(s)+O_2(g)=SiO_2(s)$ $\quad \Delta G^0=-902{,}000+174T$ (J) $\quad \cdots(1)$

$C(s)+O_2(g)=CO_2(g)$ $\quad \Delta G^0=-394{,}100-0.84T$ (J) $\quad \cdots(2)$

Then, the ΔG^0 at 1473K is given as -645.70 kJ for SiO_2, and -395.34kJ for CO_2. Thus, it is expected that metallic silicon powder work as a solid reducing agent, as well as carbon powder.

Table 3 summarized the phases that appeared after drying and following by firing at 1473K. The

Table 2: The phases that appeared after drying treatment of T_d and following by firing at 1473K in P_{O2} (Iron addition).

P_{O_2} (Pa)	Drying Temp., T_d (K)		
	373	473	573
(1)5.1×10^1	Mag.	Mag. + W	W + Mag.
(2)2.5×10^2	Mag. + M	Mag. + $\frac{M}{W}$	$\frac{M}{W}$ + α
(3)5.0×10^2	Mag. + M	Mag. + M + W + α	α + M

W : Fe_2-W, M : M-type, Mag. : Fe_3O_4, α : α-Fe_2O_3

Table 3: The phases that appeared after drying treatment of T_d and following by firing at 1473K in P_{O2} (Silicon addition).

P_{O_2} (Pa)	Drying Temp., T_d (K)		
	373	473	573
(1)5.1×10^1	W + Mag.	W + Mag.	M + α
(2)2.5×10^2	W + Mag.	M + α	M + α
(3)5.0×10^2	M + α	M + α	M + α

W : Fe_2-W, M : M-type, Mag. : Fe_3O_4, α : α-Fe_2O_3

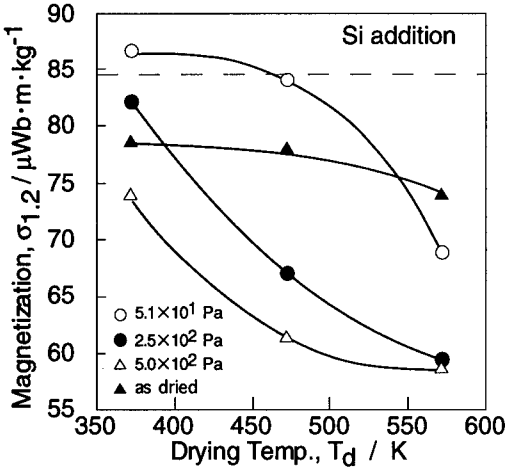


Figure 4: The variation of magnetization intensity $\sigma_{1.2}$ of silicon addition powders versus drying temperature T_d.

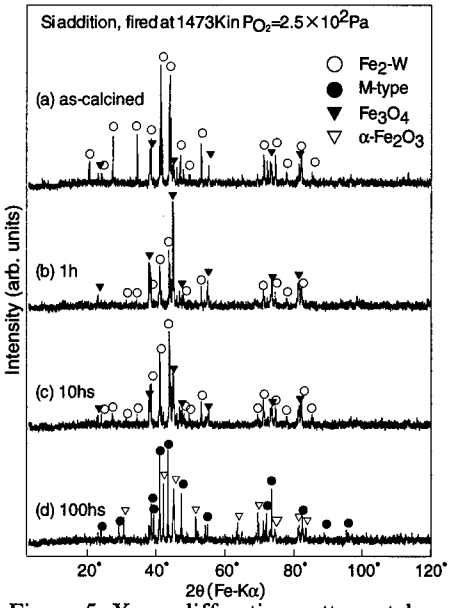


Figure 5: X-ray diffraction patterns taken from silicon addition powders fired at 1473K in P_{O2}=2.5x10^2 Pa for (b) 1h, (c) 10hs, and (d) 100hs.

Fe_2-W phase was obtained as a main phase at drying temperature T_d of 373 and 473K for P_{O2}=5.1x10^1 Pa, and at T_d of 373K for P_{O2}=2.5x10^2 Pa. It is important that the silicon powder acts as a solid reducing agent as well as carbon.

Figure 4 shows variation of magnetization intensity $\sigma_{1.2}$ of silicon addition powders versus drying temperature T_d. The powders, which consists of main Fe_2-W phase and minor Fe_3O_4 phase, exhibit the magnetization of around 85 μWb•m•kg^{-1} as large as that of calcined powder. With increasing of T_d and P_{O2}, namely increasing of volume fraction of M-type and nonmagnetic α-Fe_2O_3 phase, $\sigma_{1.2}$ drastically decreased.

The phases that appeared after firing in P_{O2} = 2.5x10^2 Pa were different depending on the T_d as well as carbon addition. In order to verify which is equilibrium phases, the samples fired at 1473K for different times were prepared. Figure 5 shows X-ray diffraction patterns taken from powders fired at 1473K in P_{O2}=2.5x10^2 Pa for (b) 1h, (c) 10hs, and (d) 100hs. The powder after firing for 1h consists of major Fe_3O_4 phase and minor Fe_2-W phase, while the X-ray intensities of Fe_2-W phase increased with increasing of firing time. After firing for 100hs, which is enough time to monitor the equilibrium phases, M-type and α-Fe_2O_3 phases appeared as the equilibrium phases. This phase change depending on firing times can be interpreted as follows. In the first stage of firing, reducing reaction of Fe_2-W phase into Fe_3O_4 and Sr-rich phase will be occured due to the solid reducing agent within the powder rather than the partial oxygen pressure P_{O2}, then, the effect of solid reducing agent is gradually weaken by oxidizing itself, and equilibrium phases dominated by P_{O2} will appear after firing for 100hs.

In order to reveal the role of solid reducing agent, the microstructural observation was performed by EPMA. Figure 6 shows back-scattering electron image of silicon addition sample fired at 1473K in P_{O2}=2.5x10^2 Pa for 10hs. By using element mapping method, it is clarified that the matrix is Fe_2-W phase, the dark contrasts indicate the Fe_3O_4 phase, and the white dots consist of (Si, Sr)-concentrated phase. This morphology suggests that silicon powders work as a solid reducing agent, because the Fe_3O_4 phase and (Si, Sr)-concentrated phase tend to exist adjacent to each other.

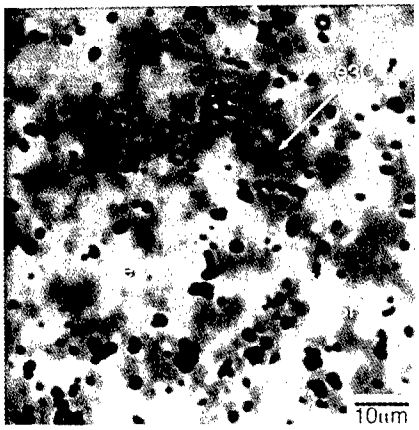


Figure 6: The back-scattering electron image of silicon addition sample fired at 1473K in P_{O2}=2.5x10^2 Pa for 10hs.

Conclusions

The formative conditions of Fe_2-W type ferrite utilizing the solid reducing agent such as carbon, iron, silicon in a various partial oxygen pressure were studied.

In the solid reducing agent addition, the phases that appeared after firing strongly depend on the drying temperature of green compacts. The drying treatment at 473K and following by firing at 1473K in less than P_{O2}=2.5x10^2 Pa are the suitable formative conditions for carbon addition to achieve high volume fraction of Fe_2-W phase. It is clarified that the silicon powder acts as a new solid reducing agent in various partial oxygen pressure.

References

1. H. Kojima and M. Sugimmoto, Ferromagnetic Materials vol. 3, ed. E. P. Wohlfarth (North-Holland, Amsterdam, 1982), 305-393.
2. F. K. Lotgering *et al.*, "Permanent-magnet material obtained by sintering the hexagonal ferrite W=$BaFe_{18}O_{27}$" J. Appl. Phys., **51** (1980), 5913-5918.
3. A. Collomb *et al.*, "Crystal Structure and Magnesium Location in the W-Type Hexagonal Ferrite: [Ba]Mg_2-W," J. Magn. Magn. Mater., **58** (1986), 247-253.
4. A. Collomb and J. P. Mignot, "The Ba(Sr)$Mn_2Fe_{16}O_{27}$ W-Type Hexagonal Ferrites as Permanent Magnets," J. Magn. Magn. Mater., **69** (1987), 330-336.
5. J. P. Mignot, "A New Series of Materials for Permanent Magnets: The W Ferrites $BaZn_{2(1-x)}(LiFe)_xFe_{16}O_{27}$," J. Magn. Magn. Mater., **51** (1985), 337-341.
6. A. Collomb *et al.*, "Stability of Monovalent Copper in the W-Type Hexagonal Ferrite:$Ba(Cu^+Fe^{3+})Fe_{16}O_{27}$," J. Magn. Magn. Mater., **61** (1986), 4-12.
7. S. Toyoda, "Synthesis and Magnetic Properties of SrO•2FeO•8Fe_2O_3 W-type Hexagonal Ferrite," Journal of the Japan Society of Powder and Powder Metallurgy, **44** (1997), 17-21.
8. N. Tsuchiya et al., "Thermal Stabilities of SrO•2FeO•8Fe_2O_3 (SrW) and SrO•FeO•7Fe_2O_3 Hexa-Ferrites," Journal of the Japan Society of Powder and Powder Metallurgy, **39** (1992), 922-928.

STRUCTURAL AND MAGNETIC CHARACTERIZATION OF Fe-N FILMS PREPARED BY REACTIVE SPUTTERING METHOD

M. Shibata, J. Shi, and M. Hashimoto
Department of Applied Physics and Chemistry, University of Electro-Communications,
1-5-1, Chofugaoka, Chofu, 182, Japan

Abstract

In this work, Fe-N film were grown on Si (001) and Cornning 7059 glass substrates at 250°C, using a dc reactive sputtering method. The effects of N_2 partial pressure, substrate bias and thermal annealing on the microstructure and magnetic properties of the Fe-N films have been studied. It has been found that for the as-deposited films, up to the nitrogen content of 13 atm.%, the films are composed of α-Fe(N) single phase. And the nitrogen exists in the films in the form of solid solution. When increasing the nitrogen content to about 20 atm.%, the films are composed mainly of γ'-Fe_4N. Also the magnetic properties of the Fe-N films depend strongly on the nitrogen content in this composition region. A substrate bias of DC -140 V did not change the crystal structure of the films, however the grain size of the film increased obviously compared with that of the as-deposited films. Furthermore, thermal annealing of the γ'-Fe_4N film causes the phase transformation from γ'-Fe_4N to α-Fe(N) and another type of iron nitride, but without substantial change in the saturation magnetization.

The Third Pacific Rim International Conference on
Advanced Materials and Processing (PRICM 3)
Edited by M.A. Imam, R. DeNale, S. Hanada,
Z. Zhong and D.N. Lee
The Minerals, Metals & Materials Society, 1998

Introduction

It has been known that there exist several nitrides in the Fe-N system, such as α''-$Fe_{16}N_4$, γ'-Fe_4N, ε-$Fe_{2-3}N$ and ζ-Fe_2N[1-2]. Among them, α''-$Fe_{16}N_2$ has been proved to show higher saturation magnetization than pure α-Fe[3]. This has stimulated more and more research interests for the Fe-N system for the past years. Especially, extensive work has been done on the Fe-N films deposition aiming at developing magnetic recording materials[4-6]. However we noted that the phase formation and transformation behaviors in Fe-N films are very complicated and depend strongly on experimental conditions. Therefore it is our purpose of this work to study the microstructure and magnetic properties of Fe-N films prepared by a dc reactive sputtering method, and we focus our work on the phase formation and transformation during deposition and thermal annealing processes.

Experimental

The Fe-N films were deposited in a dc sputtering device, with argon as the sputtering gas and nitrogen (N_2) as the reaction gas. Prior to depositions, the chamber was evacuated to a base pressure lower than 7×10^{-5} Pa. The working pressure and substrate temperature were kept at 6.7×10^{-1} Pa and 250°C respectively during depositions. The N_2 partial pressure was varied from $1.2 - 8 \times 10^{-4}$ Pa. Samples were prepared both without substrate bias and with a substrate bias of dc -140 V. Annealing treatments of the Fe-N samples were conducted in a vacuum of lower than 7×10^{-5} Pa.

Two kinds of substrate materials were used for different purposes, Corning 7059 glass substrates for X-ray diffraction and magnetic property measurements, and silicon wafer (100) for X-ray photo spectroscopy (XPS) analysis and cross-sectional transmission electron microscopy (XTEM) observation. Glass substrates were ultrasonically cleaned in acetone before mounting into the vacuum chamber, while silicon substrates were used directly without any surface processing.

The crystal structure of the Fe-N films were determined by X-ray diffraction using Cu Kα radiation. The compositions of the films were estimated by XPS using Mg Kα radiation, no standard sample was used for the quantitative calculation. Furthermore, the film microstructure was observed by TEM operating at 200 kV and cross-section samples were thinned by ion milling after mechanical grinding. The magnetic measurements of the Fe-N films were performed on a vibrating sample magnetometer (VSM).

Results and Discussion

Microstructure of Fe-N films

The relation between N_2 partial pressure and nitrogen content in the Fe-N films estimated by XPS is shown in Table 1. As can be seen, nitrogen content in the Fe-N films increases abruptly with the N_2 partial pressure. However, no substantial chemical shift of Fe spectra (2p1/2, 2p 3/2) could be observed for all these three samples.

Table 1 Nitrogen content in the Fe-N Films

N_2 partial pressure ($\times 10^{-4}$ Pa)	Nitrogen content (atm%)
1.2	5
2.7	13
8	21

Figure 1 shows the X-ray diffraction profiles of Fe-N films deposited at different N_2 partial

conditions. According to the XRD diffraction result (not shown here), there was almost no change in the crystal structure of the films deposited with a dc substrate bias of -140 V, however, some change in microstructure occurred compared with that of the film deposited without substrate bias. The microstructure of such film is featured with large grains and some mixing at the film-substrate interface. The above results indicate that the substrate bias could promote the surface diffusion of adatoms thus improve the crystallinity of the film, but the phase formation in the film depends mainly on the nitrogen content in the film.

The effect of vacuum thermal annealing on the structure of the Fe-N films are shown in Figure 3. For the γ'-Fe_4N film, after annealing at 400°C for 3 hours, no phase transformation could be observed from the XRD profile (Figure 3 b). The 200 diffraction peak becomes slightly stronger compared with that of the as-deposited film (Figure 3 a), which indicates some improvement of the crystallinity of the γ'-Fe_4N phase. However, when the sample was annealed at 500°C for 3 hours, the diffraction peaks of γ'-Fe_4N disappeared completely, instead two stronger peaks appeared around 45 and 31 degree (Figure 3 c). The former is identified as the 011 reflection of α-Fe(N) phase. As to the latter, it possibly be the 200 reflection of α''-$Fe_{16}N_2$ according to the angular position. Gao and coworkers[8] also reported the formation of α''-$Fe_{16}N_2$ in Fe-N films after annealed at 500°C, which is originally composed of α-Fe(N). But in the present work, the formation of α''-$Fe_{16}N_2$ can not be confirmed positively at this stage. The above result illustrates that the γ'-Fe_4N transformed into α-Fe(N) and another iron nitride under such condition.

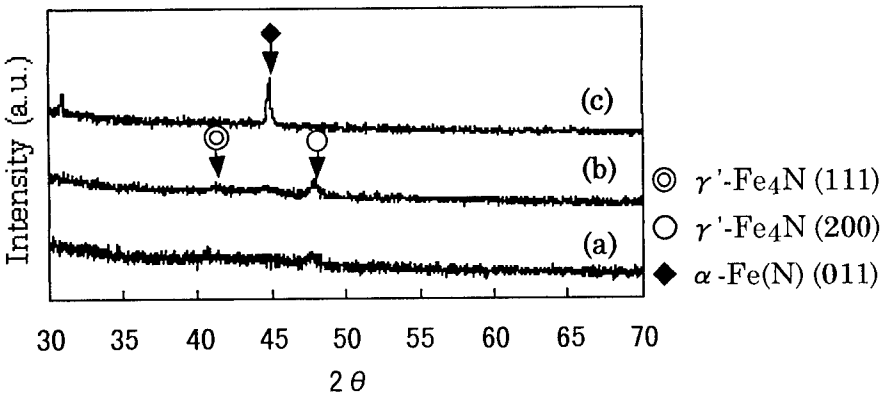


Figure 3: X-ray diffraction profiles of Fe-N films annealed at different temperatures. a) as-deposited, b) 400°C for 3 h, and c) 500°C for 3h.

Magnetic properties of Fe-N films

The typical M-H loops of Fe-N films prepared in the present work are shown in Figure 4. And the saturation magnetization and coercivity of the films determined from these hysteresis loops are listed in Table 2.

It can be seen from these results that for the two α'-Fe-N films, the coercivity increases with the nitrogen content in the film. And the saturation magnetization are much lower than the value of pure α-Fe. These may be ascribed to the solution of nitrogen atoms in the lattice of α-Fe. With the formation of γ'-Fe_4N, the coercivity decreases abruptly, while the saturation magnetization is in agreement with the reported value (17 kG)[6]. For the film annealed at 500°C, the coercivity increased abruptly compared with the as-deposited samples, however, there was no substantial change in the saturation magnetization although phase transformation occurred during the annealing process.

pressure. These results have shown that, up to the N_2 partial pressure to 2.7 x 10^{-4} Pa, only the a diffraction peak near the angular position of 110 reflection of α-Fe can be observed on the diffraction profile. Considering the nitrogen content in the films, we consider that the films are composed of single α'-Fe-N phase, and nitrogen is considered exists in the film in the form of solid solution. This can be seen from the obvious shift of 011 diffraction peak towards the lower angle with increasing N_2 partial pressure (Figure 1 a-b). The above results are in good agreement with those of Morisako and coworkers[7], who have demonstrated that the lattice

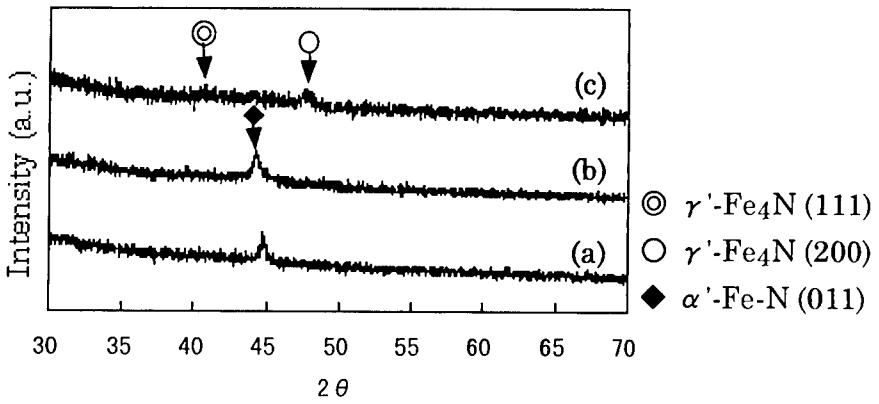


Figure 1: X-ray diffraction profiles of Fe-N films deposited at a N_2 partial pressure of: a) 1.2x10^{-4} Pa, b) 2.7x10^{-4} Pa, and c) 8x10^{-4} Pa.

constant of α-Fe increases monotonically with the N_2 partial pressure. With further increasing the N_2 partial pressure, the crystal structure of the film changed. The weak peak observed on the X-ray diffraction profile can be attributed to the 200 reflection of γ'-Fe_4N. Therefore we consider that the film is composed mainly of γ'-Fe_4N phase with a 100 orientation under this condition. This result is in good accordance with the XPS composition analysis, which give an Fe/N ratio of approximately 4 : 1.

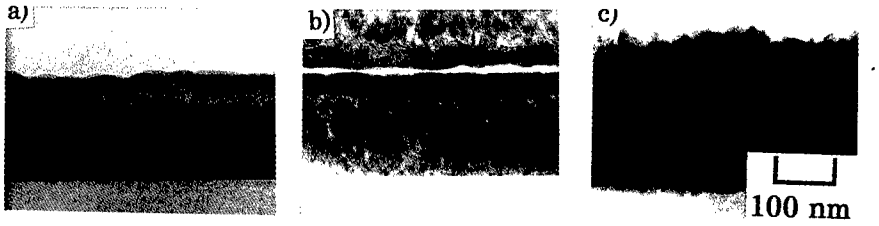


Figure 2: Cross-sectional electron micrographs of Fe-N films deposited under different conditions . a) N_2 partial pressure 2.7x10^{-4} Pa, b) N_2 partial pressure 8x10^{-4} Pa, c) N_2 partial pressure 8x10^{-4} Pa,with a -140 V substrate bias.

Figure 2 shows some typical microstructures of Fe-N films prepared at different experimental conditions. Figure 2 a) and b) compares the microstructure of Fe-N films deposited at the N_2 partial pressure of 2.7 and 8x10^{-4} Pa respectively. Although the component phases are different from each other as illustrated by the XRD results shown above, the microstructure of these two films are quite similar, both of them are featured with very fine microstructure and very sharp interfaces with the substrates. On the other hand, Figure 2 b) and c) compares the microstructure of Fe-N films deposited at the same N_2 partial pressure but under different substrate bias

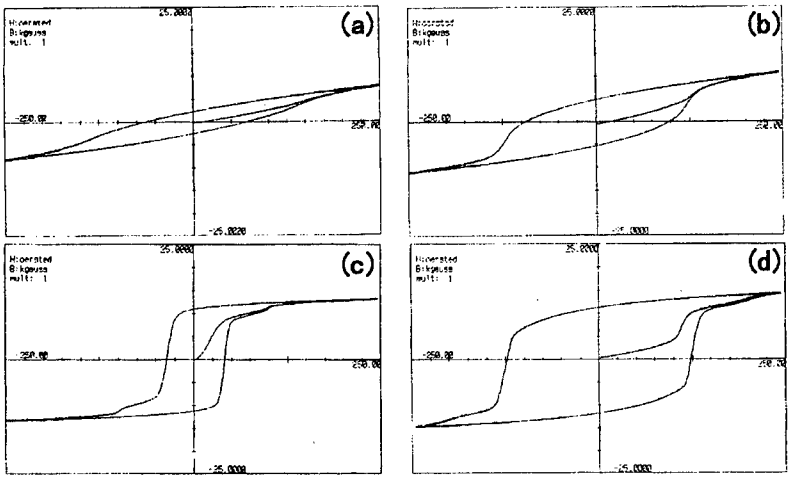


Figure 4 M-H loops of Fe-N films prepared under different conditions.a) N_2 partial pressure 1.2x10-4 Pa, b) N_2 partial pressure 2.7x10-4 Pa, c) N_2 partial pressure 8x10-4 Pa, and d) N_2 partial pressure 8x10-4 Pa, annealed at 500°C for 3 h.

Table 2 Magnetic properties of Fe-N films

N_2 partial pressure (x10-4Pa)	Annealing T (°C) x t (hours)	4πMs (kG)	Hc (A/m)
1.2	-	13.0	5800
2.7	-	17.8	7600
8	-	16.7	2288
8	500 x 3	17.9	11800

Summary

In summary, the structure and magnetic properties of Fe-N films depend strongly on the nitrogen content in the film. Two kinds of microstructure revealed for the as-deposited films prepared in the present work. They are single phase α'-Fe-N with nitrogen contents less than 13 atm% and γ'-Fe_4N with nitrogen content of about 21 atm% respectively. The coercivity of the films increases with the nitrogen content in the α-Fe phase region and drops abruptly upon the formation of γ'-Fe_4N phase in the films. The γ'-Fe_4N phase transforms into α-Fe and another type of iron nitride when the film was subjected to thermal annealing at 500°C in vacuum, but it did not cause substantial change in the saturation magnetization.

References

1. R.M. Metzger et al, " Magnetism of α''-$Fe_{16}N_2$," J. Appl. Phys. 76 (10) (1994) 6626-6631.

2. M. Hansen, Constitution of Binary Alloys (McGRAW-HILL BOOK COMPANY, INC. 1958) 670-675.

3. T.K. Kim and M. Takahashi, "New Material Having Ultrahigh Magnetic Moment" App.Phys. Lett. 20 (12) (1972) 492-494.

4. M. Takahashi et al, "Magnetic Moment of α''-$Fe_{16}N_2$ Films" J. Appl. Phys. 76 (10) (1994) 6642-6647.

5. K. Sin et al, "Effects of Lamination on Soft Magnetic Properties of FeN Films on Sloping Surfaces" J. Appl. Phys. 81 (8) (1997) 4507-4509.

6. S. Gong and H. Xu, High Resolution Electron Microscopy Observations of Structural Changes in Iron Nitride Films Annealed in Vacuum" J. Mater. Sci. Technol. 13 (1997) 123-126.

7. A. Morisako et al, "Iron Nitride Films Prepared by Facing Targets Sputtering" J. Appl. Phys. 63 (8) (1988) 3230-3232.

8. C. Gao and W.D. Doyle, Quantitative Correlation of Phase Structure with the Magnetic Moment in RF Sputtered Fe-N Films" J. Appl. Phys. 73 (10) (1993) 6579-6581.

Structure and magnetic properties of Co-Fe-Hf-O sputtered films with high electrical resistivity

Yoshito Sasaki, Kumiko Ohminato, Takashi Hatanai, Akihiro Makino

Central Research Laboratory, Alps Electric Co., Ltd
1-3-5 Higashi-Takami, Nagaoka 940, Japan.

Abstract

We have reported nanocrystalline Fe-M-O films with good soft magnetic properties and high electrical resistivity, resulting from a mixed structure consisting of nanocrystalline bcc-Fe particles and amorphous phase. In order to improve these properties, an additional effect of Co to the Fe-Hf-O films was investigated. Nanocrystalline Co-Fe-Hf-O films consisting of bcc particles and amorphous phase exhibit the soft magnetism. The nanocrystalline $Co_{44}Fe_{19}Hf_{15}O_{22}$ film with reduced bcc grain size of 3-4 nm show good soft magnetic properties at high frequencies and exhibits high permeability (μ') of 180 and high quality factor ($Q=\mu'/\mu''$) of 3 up to 1GHz. Therefore, the nanocrystalline bcc Co-Fe-Hf-O film was concluded to be more suitable for the high frequency application above 100MHz than the Fe-Hf-Ofilm.

The Third Pacific Rim International Conference on
Advanced Materials and Processing (PRICM 3)
Edited by M.A. Imam, R. DeNale, S. Hanada,
Z. Zhong and D.N. Lee
The Minerals, Metals & Materials Society, 1998

1. INTRODUCTION

As the magnetic devices are getting more and more miniaturized, magnetic films for higher frequency are increasingly required. We have already reported the nanocrystalline Fe-M-O films as a soft magnetic film for high frequency.[1][2][3][4] The nanocrystalline Fe-M-O films with a composite structure consisting of nanocrystalline bcc-Fe particles and amorphous phases exhibit better soft magnetic properties in a high frequency range than the Co based amorphous films. Although the nanocrystalline Fe-M-O films exhibit high permeability of 1000 at 100MHz, the addition of Co to the nanocrystalline Fe-M-O films improves high frequency characteristics mainly due to the increase in the magnetic anisotropy field. However, if all Fe are substituted by Co with a hcp structure, soft magnetic property is deteriorated by crystalline magnetic anisotropy. Then it is expected that the Co-Fe-Hf-O films which partially substituted Co for Fe improve the high frequency characteristics. In this paper we describe the microstructure, magnetic properties and electrical resistivity in the Co-Fe-Hf-O films.

2. EXPERIMENTAL PROCEDURE

The Co-Fe-Hf-O films were made onto glass substrates by a RF reactive sputtering technique in a mixed gas atmosphere of pure Ar and O_2. The composition of the films was controlled by changing the number of pellets of Fe and Hf elements placed onto an Co target and by changing the oxygen flow ratio. The films were sputtered in the non-magnetic field and in the uniaxial magnetic field of 4kA/m. After sputtering in the non-magnetic field, the films were subjected to annealing for 10.8 ks under a uniaxial magnetic field (uniaxial field annealing, UFA) of 160 kA/m at 773K in an evacuated atmosphere below 10^{-3} Pa. The film composition was determined by electron probe microanalysis for Co, Fe and Hf, by inert-gas fusion-IR technique for O. The film structure was investigated by x-ray diffractmetry (XRD) using Co K α radiation, by field-emission-type 200 kV transmission electron microscopy (FE-TEM) combined with nanobeam electron diffraction and energy dispersive x-ray spectroscopy (EDX) using a beam diameter of 1 nm. Saturation magnetization (Is) at room temperature to 973K was measured by a vibrating sample magnetometer (VSM) under a magnetic field of 800 kA/m. Coercive force (Hc) was determined by a dc B-H loop tracer. Permeability (μ ', μ ") was measured by a parallel line technique under an applied field of 160 mA/m.[5]. Electrical resistivity (ρ) was measured by a four-probe method.

3. RESULTS AND DISCUSSION

Microstructure

Fig. 1 shows the crystalline structure of the as-deposited Co-Fe-Hf-O films which was sputtered in non-magnetic field. The addition of Co to the Fe-Hf-O films changes the part of nanocrystalline structure. As a result, various composite structures of bcc+amorphous, hcp+ amorphous, fcc+amorphous and fcc+CoO+amorphous was obtained. A part of the nanocrystalline structure is different from that of a CoFe alloy in a thermal equilibrium state. It is thought that the crystalline structure is complicated, because Hf and O prevent the spread of Co and Fe, and the flicker in composition is generated in a micro region. When Co ratio in the CoFe is 70-85 at% at 1.5 vol% of O_2 flow ratio and 75-77 at% at 2.0 vol% of O_2 flow ratio as sputtering, the composite structure of bcc and amorphous phases was obtained as is the case for the Fe-Hf-O films.

Fig. 2 show high-resolution TEM micrograph, nanobeam electron difraction patterns and EDX

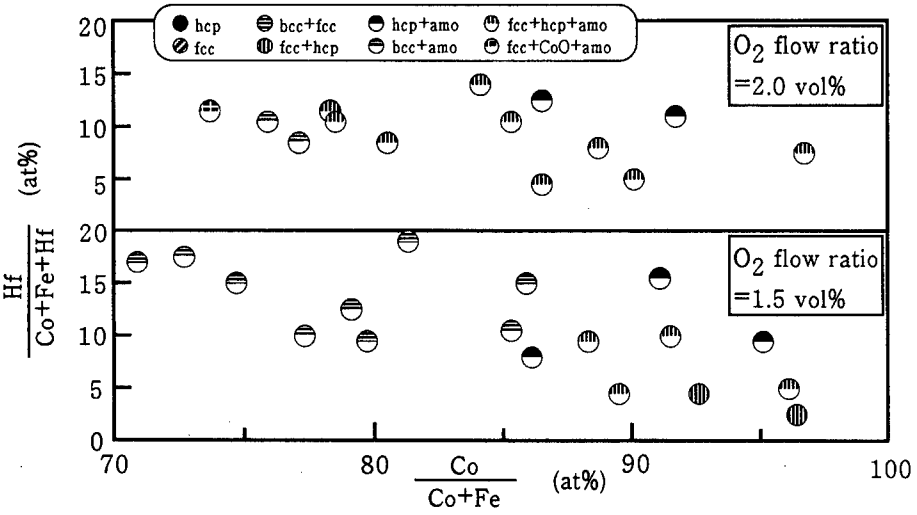


Fig. 1 Crystalline structure of the as-deposited Co-Fe-Hf-O films which were sputtered in no magnetic field.

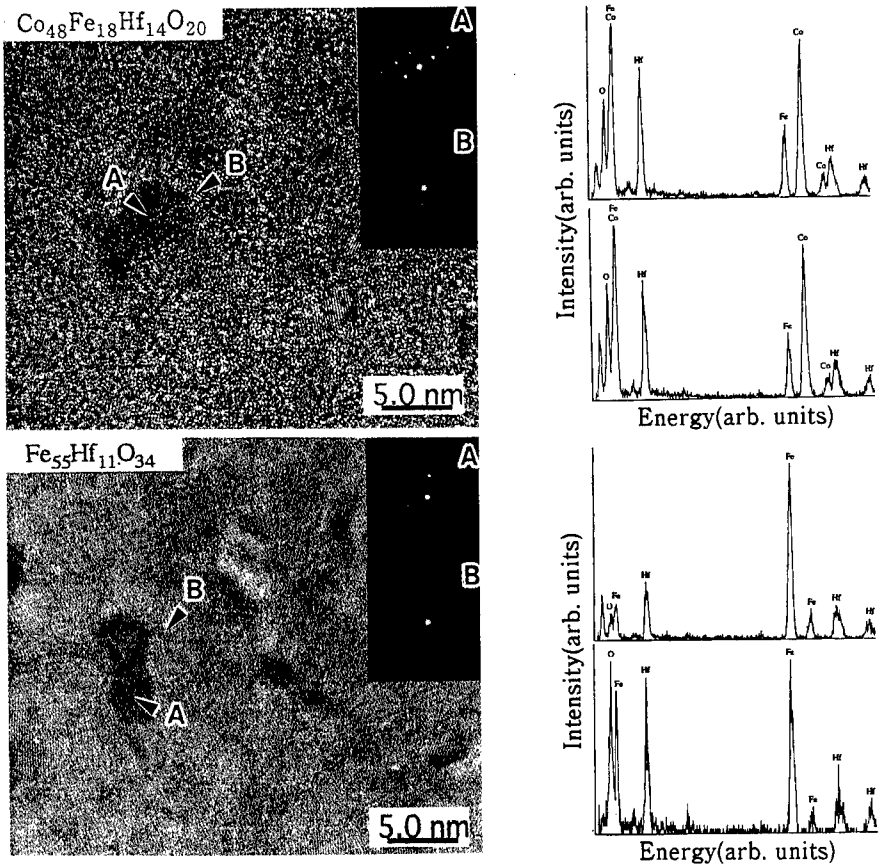


Fig. 2 High-resolution TEM micrograph, electron diffraction patterns and EDX spectra taken from each microregion for as-deposited $Co_{48}Fe_{18}Hf_{14}O_{20}$ and $Fe_{55}Hf_{11}O_{34}$ films.

spectra taken from each microregion for the as-deposited $Co_{48}Fe_{18}Hf_{14}O_{20}$ and $Fe_{55}Hf_{11}O_{34}$ films,which show the bcc and amorphous phases by the XRD, respectively. The EDX spectra and the electron difraction patterns were taken from the points indicated in the figure. The $Co_{48}Fe_{18}Hf_{14}O_{20}$ film indicates the same microstructure as that of the $Fe_{55}Hf_{11}O_{34}$ film, which was identified to the nanocrystalline grains and amorphous phases by the high-resolution TEM micrograph and the electron difraction patterns. The nanocrystalline grains have very small size of 3-4 nm in the $Co_{48}Fe_{18}Hf_{14}O_{20}$ film which is equal to that in the $Fe_{55}Hf_{11}O_{34}$ film. The composition of nanocrystalline grains in the $Co_{48}Fe_{18}Hf_{14}O_{20}$ film have much Hf and O which is similar to the composition of amorphous phases even if those in the $Fe_{55}Hf_{11}O_{34}$ film have a little Hf and O by the EDX spectra.

Magnetic Properties and Electrical Resistivity

Fig. 3 shows the relation between the crystalline structure and the coercive force in the Co-Fe-Hf-O films which were sputtered in non-magnetic field and annealed for 10.8 ks under UFA of 160 kA/m at 773K. The composite structure of nanocrystalline bcc and amorphous phases exhibits soft magnetism and another structure containing hcp phase deteriorates soft magnetism.

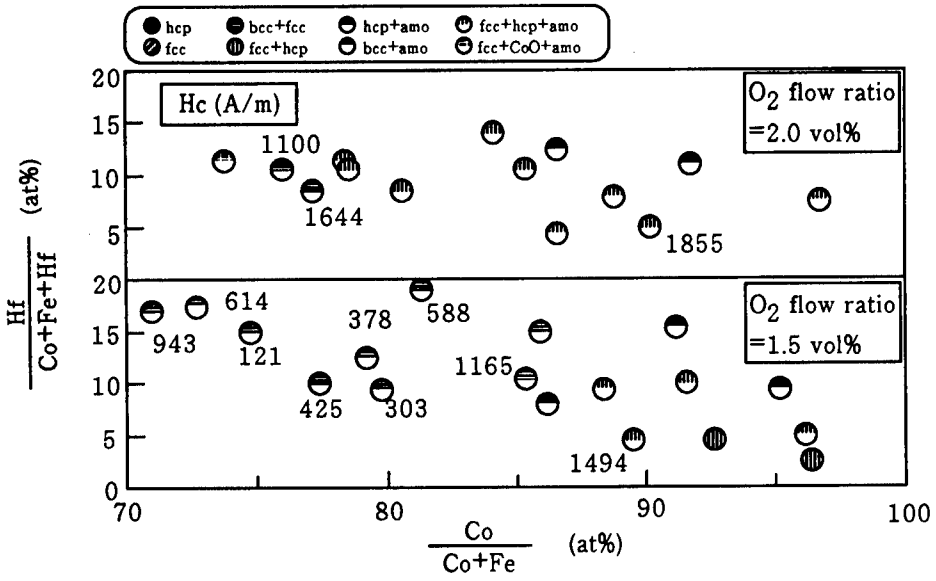


Fig. 3 Relation between the crystalline structure and the coercive force in the Co-Fe-Hf-O films which were sputtered in non magnetic field and annealed for 10.8 ks under UFA of 160 kA/m at 773 K.

Table I shows the magnetic properties and electrical resistivity in the $Co_{48}Fe_{18}Hf_{14}O_{20}$ film which was sputtered in non-magnetic field and annealed in UFA at 500 K. By the inductive magnetic anisotropy in Co, the $Co_{48}Fe_{18}Hf_{14}O_{20}$ film exhibits large Hk of 4 kA/m which is about 10 times larger than that of the $Fe_{55}Hf_{11}O_{34}$ film.

Furthermore, Table II shows the magnetic properties and electrical resistivity, and Fig. 4 shows the frequency dependence of the permeability (μ ', μ ") in the as-deposited

Table I Magnetic properties and electrical resistivity in the $Co_{48}Fe_{18}Hf_{14}O_{20}$ film sputtered in non-magnetic field.

Is	1.24 (T)
Hc	199 (A/m)
Hk	4181 (A/m)
ρ	4.6 ($\mu\Omega$m)

Table II Magnetic properties and electrical resistivity in the $Co_{44}Fe_{19}Hf_{15}O_{22}$ film in a uniaxial magnetic field.

Is	1.11 (T)
Hc	443 (A/m)
Hk	4787 (A/m)
μ'_{1GHz}	180
$Q(=\mu'/\mu'')_{1GHz}$	3
ρ	15.1 ($\mu\Omega$m)

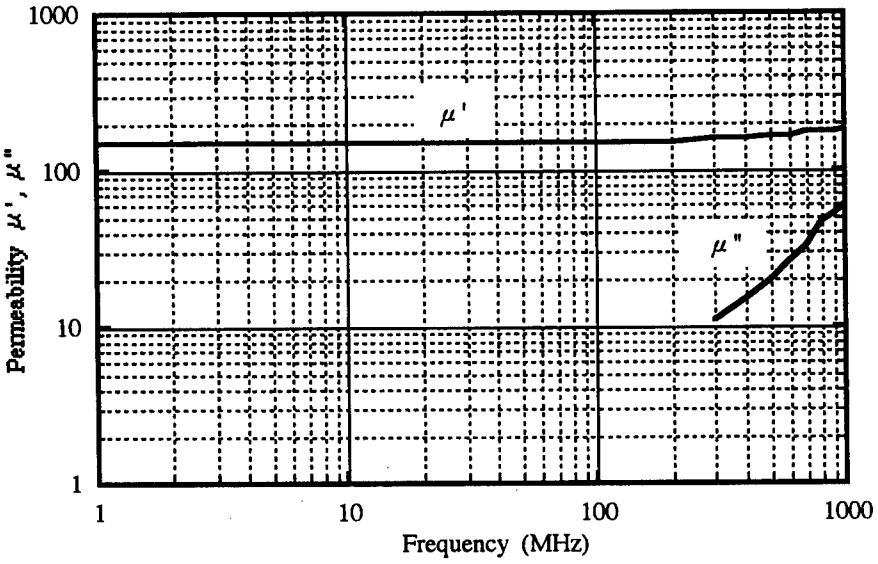


Fig. 4 Frequency dependence of the permeability (μ', μ'') in the as-deposited $Co_{44}Fe_{19}Hf_{15}O_{22}$ film.

$Co_{44}Fe_{19}Hf_{15}O_{22}$ film which was sputtered in the uniaxial magnetic field of 4 kA/m. The $Co_{44}Fe_{19}Hf_{15}O_{22}$ film exhibits also large Hk of 4 kA/m, and very high electrical resistivity (ρ) of 15 $\mu\Omega$m because of no annealing. As a result, the $Co_{44}Fe_{19}Hf_{15}O_{22}$ film maintains high permeability (μ') of 180 and also exhibits high quality factor ($Q=\mu'/\mu''$) of 3 up to 1GHz, which are more superior to the $Fe_{55}Hf_{11}O_{34}$ film in high frequency property.

Fig. 5 shows the temperature dependence of saturation magnetization (Is) for the as-deposited $Co_{44}Fe_{19}Hf_{15}O_{22}$ and $Fe_{55}Hf_{11}O_{34}$ films. The $Co_{44}Fe_{19}Hf_{15}O_{22}$ film exhibits a better thermal stability as compared to the $Fe_{55}Hf_{11}O_{34}$ film. This is because the Curie point in Co is higher than that in Fe and also because the thermal stability in amorphous phases which are nearly equal composition to the bcc nanocrystalline grains containing large amount of Co and Fe in the

$Co_{44}Fe_{19}Hf_{15}O_{22}$ film is higher than that in the $Fe_{55}Hf_{11}O_{34}$ film.

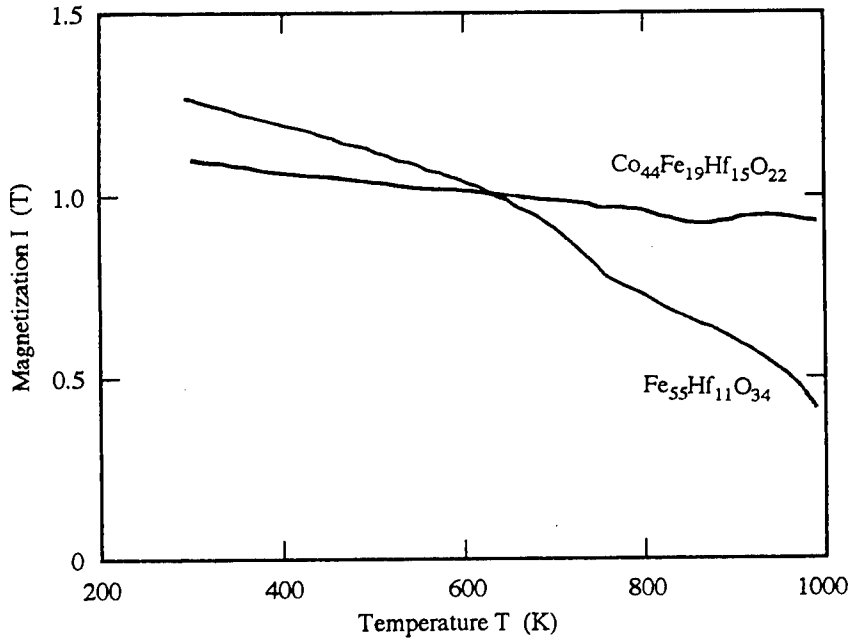


Fig.5 Temperature dependence of the magnetization Is for as-deposited $Co_{44}Fe_{19}Hf_{15}O_{22}$ film and the $Fe_{55}Hf_{11}O_{34}$ film.

4. CONCLUSIONS

When Co is added to the Fe-Hf-O films, various composite structures of bcc+amorphous, hcp+ amorphous, fcc+amorphous and fcc+CoO+amorphous were obtained. The size of the nanocrystalline grains was 3-4 nm in the Co-Fe-Hf-O films. The compositions of the nanocrystalline grains and amorphous phases in the Co-Fe-Hf-O films are very similar with each other.

The Co-Fe-Hf-O films exhibit soft magnetism in the composite structure of nanocrystalline bcc and amorphous phases. The $Co_{44}Fe_{19}Hf_{15}O_{22}$ film sputtered in the uniaxial magnetic field exhibits large Hk of 4 kA/m and high electrical resistivity of 15 $\mu\ \Omega$ m. The $Co_{44}Fe_{19}Hf_{15}O_{22}$ film maintains high permeability (μ') of 180 and exhibits high quality factor ($Q=\mu'/\mu''$) of 3 up to 1GHz. The Co-Fe-Hf-O films exhibit higher thermal stability than the Fe-Hf-O films.

References

1. Y.Hayakawa, A. Makino, H. Fujimori and A. Inoue, J. Appl. Phys.81,3747 (1997)
2. A. Makino and Y. Hayakawa, J. Jpn. Inst. Met. 57, 1301 (1993)
3. A. Makino and Y. Hayakawa, Mat. Sci. Eng. A182, 1020 (1994)
4. Y.Hayakawa, A. Makino, Nano. structured. Mat, 6, 989 (1995)
5. T. Kimura, M. Mitera, S. Terasaka, M. Nose, F. Matsumoto, H. Matsuki, H. Fujimori and T. Masumoto, J. Magn. Soc. Jpn. 17, 497 (1993)

MAGNETIC FIELD-INDUCED ANISOTROPY OF NANOCRYSTALLINE SOFT MAGNETIC Fe-Zr-B ALLOY "NANOPERM"

Teruo Bitoh,[1] Takashi Hatanai,[1] Akihiro Makino,[1] Akihisa Inoue[2] and Tsuyoshi Masumoto[3]

[1] Central Research Laboratory, Alps Electric Co., Ltd., Nagaoka 940-8572, Japan
[2] Institute for Materials Research, Tohoku University, Sendai 980-8577, Japan
[3] The Research Institute of Electrical and Magnetic Materials, Sendai 982-0807, Japan

Abstract

The magnetic field-induced anisotropy of a nanocrystalline soft magnetic $Fe_{90}Zr_7B_3$ alloy has been studied. The magnetic-field annealing treatment of the alloy induces a uniaxial magnetic anisotropy with an easy axis parallel to the direction of the magnetic field applied during the heat treatment. The changes of an induced anisotropy constant, K_u, on annealing conditions and the relationship between K_u and the microstructure of the alloy have been examined. The experimental results indicate that the anisotropy is mainly induced in the precipitated α-Fe grains during crystallization. The anisotropy constant is strongly related to the grain size; the K_u increases as the grain size becomes larger.

The Third Pacific Rim International Conference on
Advanced Materials and Processing (PRICM 3)
Edited by M.A. Imam, R. DeNale, S. Hanada,
Z. Zhong and D.N. Lee
The Minerals, Metals & Materials Society, 1998

Introduction

Since the observation of the nanocrystalline Fe-Si-B-Nb-Cu alloys with good soft magnetic properties,[1] the microstructure and the magnetic properties of the nanocrystalline soft magnetic alloys have been a subject of extensive investigations. The nanocrystalline soft magnetic alloys are produced by crystallization of the amorphous alloys obtained by rapid quenching. Annealing treatment at temperatures above its crystallization temperature produces a homogeneous ultrafine grain structure of bcc phase with grain size of typically 10 to 20 nm and random orientation, embedded in a residual amorphous minority matrix. The simultaneous addition of Nb and Cu to Fe-Si-B amorphous alloys enables the controlled crystallization. Owing to the strong ferromagnetic exchange interaction between the grains, the net magnetocrystalline anisotropy is canceled.[2,3] This is a reason why the nanocrystalline alloys exhibit good soft magnetic properties.

In 1990, we have reported that the small addition of B to Fe-Zr amorphous alloys enables the formation of the nanocrystalline structure consisting of α-Fe crystallites with grain size of 10 to 20 nm after crystallization even if the alloys do not contain Cu.[4] The Fe concentration of the Fe-Zr-B alloys is very high (up to 91 at.%) because of high glass-forming ability of Zr. We have further reported that the similar nanocrystalline structure is obtained for Fe-Hf-B and Fe-Nb-B alloys.[5,6] The nanocrystalline Fe-M-B (M = Zr, Hf, Nb) alloys, which are called "NANOPERM," exhibit good soft magnetic properties as well as high saturation magnetic flux density, B_s, of 1.5 to 1.7 T. This B_s is higher than that of the nanocrystalline Fe-Si-B-Nb-Cu alloys and is comparable to that of Fe-based amorphous alloys. Because of their high B_s and good soft magnetic properties, NANOPERM is expected to be used as the core material in many kinds of magnetic components.

It is very useful for applications of magnetic materials that the shape of the hysteresis curve of the core material can be controlled according to the demands of applications. As well known, the technique of magnetic-field annealing has been widely used to control the shape of the hysteresis loop. It has been reported that the magnetic field annealing for the nanocrystalline Fe-Si-B-Nb-Cu alloys induces a uniaxial magnetic anisotropy with an easy axis parallel to the direction of the magnetic field applied during the annealing.[7] The anisotropy is primary induced in the crystalline Fe-Si phase, and the anisotropy constant is strongly related to the Si content in the Fe-Si crystallites.[8,9] For the nanocrystalline Fe-M-B alloys (NANOPERM), it has been reported that the hysteresis curve can be controlled by the magnetic field annealing; the direction of the easy axis is parallel to that of the magnetic field applied during the annealing.[10,11] However, detailed studies have not been preformed.

In this paper, we report the results of the systematic study of the magnetic field annealing for the nanocrystalline soft magnetic $Fe_{90}Zr_7B_3$ alloy. The $Fe_{90}Zr_7B_3$ alloy is a typical example of the nanocrystalline Fe-M-B alloys (NANOPERM) and exhibits high B_s of about 1.7 T and high permeability about 30,000 at 1 kHz, simultaneously.[5,6]

Experimental Procedure

The $Fe_{90}Zr_7B_3$ alloy ingot was prepared by arc melting mixtures of pure Fe (99.9 %), Zr (99.7 %) and B (99.5 %) in an Ar atmosphere. A rapidly solidified ribbon with 15 mm in width and 20 μm in thickness was produced by a single-roller melt spinning method in an Ar atmosphere. The as-quenched ribbon was slit and wound into toroidal cores with 19 mm in outer diameter, 14 mm in inner diameter and 5.5 mm in height. The toroidal cores were annealed in vacuum to prevent oxidation. The annealing treatment was carried out by holding the cores at 833 to 913 K for 0 to 18 ks. A transverse magnetic field of 160 kA/m was applied during the heat treatment to induce a magnetic anisotropy.

The DC hysteresis loop was measured with a DC *B-H* loop tracer under the maximum field of 800 A/m. The induced anisotropy constant, K_u, was determined from the anisotropy field, H_K, of the DC hysteresis loop as the following relationship: $K_u = B_s H_K / 2$. In this paper, the magnetic flux density under the applied magnetic field of 800 A/m (B_{800}) was used instead of B_s because B_{800} is almost the same as B_s. The structure of the annealed samples was examined by X-ray diffractometry using Co Kα radiation. The lattice parameter, a, of the α-Fe crystallites was evaluated from the bcc (110) refraction peak. The diffraction angle was calibrated on the basis of the reflection angle of the internal standard material (pure Si powder). The mean grain size, D, was evaluated by using Scherrer's equation[12] from the half-width of the bcc (110) reflection peak. The broadening of diffraction line due to the width of X-ray source was removed by Warren's method.[12] All the measurements were carried out at room temperature.

Results and Discussion

Dependence of Anisotropy Constant on Annealing Condition

Figure 1 shows the changes of K_u on annealing conditions, (a) annealing temperature, T_a, (b) annealing time, t_a, (c) heating rate, α, and (d) cooling rate, β. Here, $t_a = 0$ means that the sample was heated up to T_a first, and it was cooled as soon as the temperature reached T_a. The saturation magnetic flux density (1.7 T) is almost independent of the annealing conditions. With increasing T_a or t_a, then K_u increases monotonously. On the other hand, K_u decreases with increasing α or β. Especially, K_u strongly depends on α in the low α region loss than 0.2 K/s.

The nanocrystalline Fe-Zr-B alloy consists of fine α-Fe grains, which contain a small amount of B (about 2 at.%[13]), with 10 to 20 nm in size embedded in a residual amorphous matrix enriched by Zr and B.[5,13] Next, we examine that the magnetic anisotropy is induced in either the crystalline grains or the residual amorphous matrix. The annealing treatment can be divided into three processes, the heating process, the holding process and the cooling process. In order to make clear when the magnetic anisotropy is induced, the transverse magnetic field was applied only to one process during the

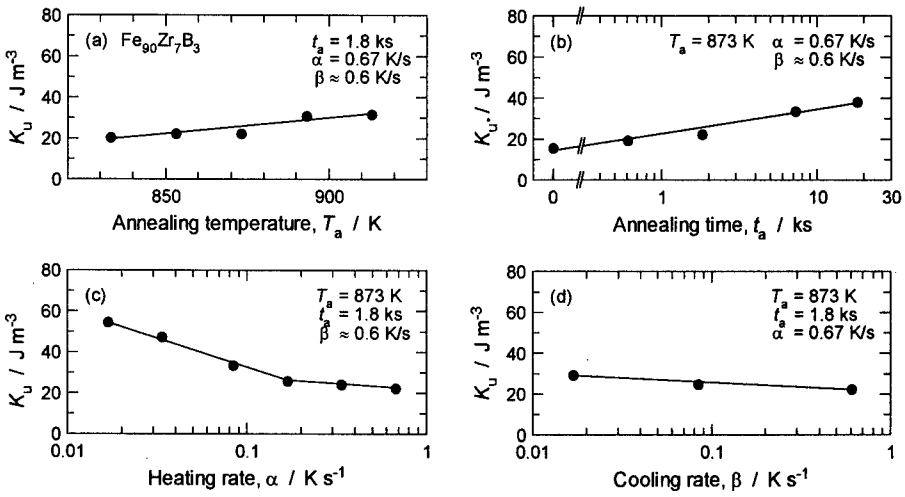


Figure 1: Changes of induced anisotropy constant (K_u) of $Fe_{90}Zr_7B_3$ alloy toroidal cores on annealing conditions. All annealing processes were performed under transverse magnetic field of 160 kA/m.

Table 1: Comparison of induced anisotropy constant (K_u) of toroidal cores of $Fe_{90}Zr_7B_3$ alloy. (#1) All annealing processes were preformed under transverse magnetic field. (#2) Transverse magnetic field was applied only to heating process, (#3) holding process and (#4) cooling process.

	Applied transverse magnetic field, $H_\perp$ / kAm^{-1}			Anisotropy constant
	Heating	Holding	Cooling	K_u / Jm^{-3}
#1	160	160	160	23
#2	160	0	0	12
#3	0	160	0	10
#4	0	0	160	3

Table 2: Curie temperature (T_c) and crystallization temperature (T_x) of $Fe_{90}Zr_7B_3$ alloy.[5,14]

Curie temperature, T_c / K			Crystallization temperature
As-quenched (amorphous)	After crystallization		T_x / K
	Crystalline grains	Amorphous matrix	
267	~ 1000	393	797

heat treatment. The other two processes were done under zero magnetic field. Table 1 shows the results of the experiment. When the magnetic field was applied only to the heating process (#2), obtained K_u is 12 J/m^3. This value is 52 % that obtained when all the annealing processes were done under the magnetic field (#1). Next, K_u is 10 J/m^3 when the magnetic field was applied only to the holding process (#3). This is nearly the same as that of #2. On the other hand, when the magnetic field was applied only to the cooling process (#4), we obtain a small K_u value of 3 J/m^3. Therefore, it can be said that the magnetic anisotropy is mainly induced during the heating process and the holding process. The Curie temperature, T_c, and the crystallization temperature, T_x, of the alloy are summarized in Table 2. The Curie temperature of the as-quenched amorphous sample is about room temperature.[14] It is clear that the magnetic anisotropy is induced during and after crystallization because the samples before crystallization are nonmagnetic. After crystallization, T_c of the crystalline grain is about 1,000 K and that of the residual amorphous matrix is about 390 K.[5] The crystallization temperature[5] (about 800 K) and the annealing temperature (873 K) is below T_c of the crystalline grains, but clearly above that of the residual amorphous matrix. This indicates that the magnetic anisotropy is primary induced in the crystalline grains.

Relationship between Anisotropy and Microstructure

Next, we have studied the relationship between K_u and the microstructure of the alloy. Figure 2 shows the changes in the mean grain size, D, and the lattice parameter, a, of the α-Fe crystallites on annealing conditions. The lattice parameter is slightly larger than that of pure α-Fe because the α-Fe grains contain a small amount of solute elements. With increasing annealing temperature or annealing time, D increases slightly and a decreases gradually. The change of a indicates that the dissolution amount of the solute elements in the grains is decreased with increasing annealing temperature or annealing time. On the other hand, D decreases with increasing heating rate but a is almost constant. The heating rate independence of a indicates that K_u is not related to a. Thus K_u is not related to the amount of solute elements in the α-Fe crystallites. On the other hand, K_u is strongly related to D. The relationship between K_u and D is shown in Fig. 3. The result clearly shows that the K_u increases as the grain size becomes larger.

The origin of the magnetic anisotropy is still unclear. However, the present results imply that atomic pair ordering of both Fe and the solute elements (Zr and/or B) may not be dominant because K_u is

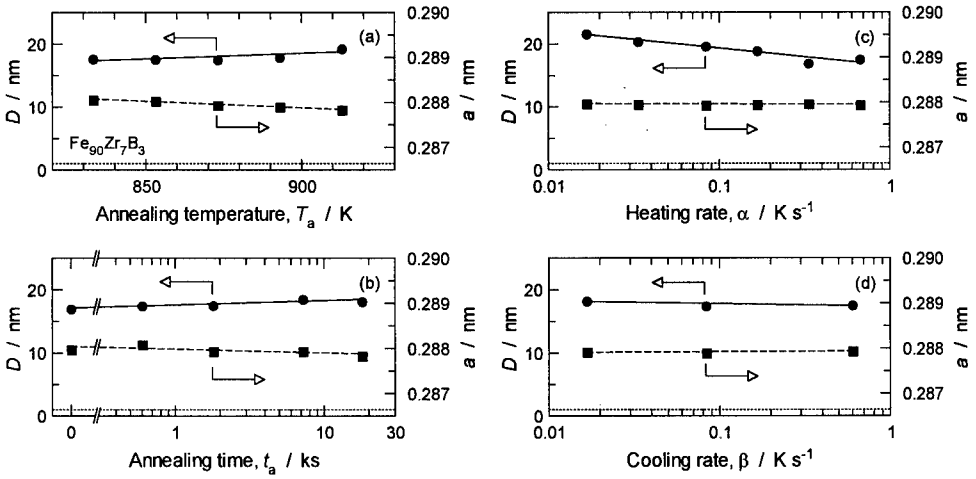


Figure 2: Changes of mean grain size (D) and lattice parameter (a) of α-Fe crystallites in $Fe_{90}Zr_7B_3$ alloy on annealing conditions. All annealing processes were performed under transverse magnetic field of 160 kA/m. The dotted lines show the lattice parameter of pure α-Fe.

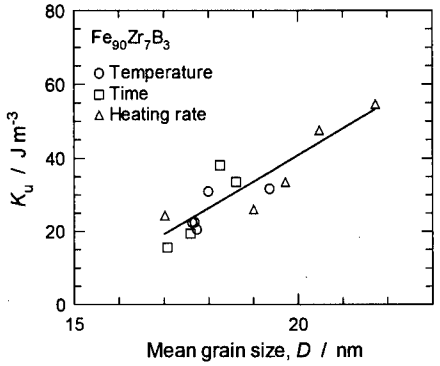


Figure 3: Relationship between induced anisotropy constant (K_u) and mean grain size (D) of α-Fe crystallites of $Fe_{90}Zr_7B_3$ alloy.

not related to the amount of the solute elements in the α-Fe grains. It seems to us that other origins such as shape anisotropy of the grains or crystalline orientation are important. Especially, the dependence of K_u on D implies that the shape anisotropy is dominant; i.e., the α-Fe grains are grown into a uniaxial shape. The dependence of K_u on D can be explained qualitatively by considering the boundary energy. The smaller grains hardly change their shape from sphere because it brings the significant increase of the boundary energy due to the increase of the grain surface area. Unfortunately, we could not obtain the evidence of the microstructural change of the alloy by transmission electron microscopy and X-ray diffractometry. Further investigations are required to clarify the origin of the magnetic field-induced anisotropy of the nanocrystalline Fe-Zr-B alloys.

Conclusion

The magnetic-field annealing treatment of the nanocrystalline soft magnetic $Fe_{90}Zr_7B_3$ alloy induces the uniaxial magnetic anisotropy with the easy axis parallel to the direction of the magnetic field applied during the heat treatment. The induced anisotropy constant strongly depends on the annealing conditions, especially heating rate. Analysis of the experimental results suggests that the anisotropy is mainly induced in the precipitated α-Fe grains and K_u is strongly related to the grain size; K_u increases with increasing grain size.

References

1. Y. Yoshizawa, S. Oguma, and K. Yamauchi, "New Fe-based Soft Magnetic Alloys Composed of Ultrafine Grain Structure," Journal of Applied Physics, 64 (1988), 6044-6046.

2. G. Herzer, "Grain Structure and Magnetism of Nanocrystalline Ferromagnets," IEEE Transactions on Magnetics, 25 (1989), 3327-3329.

3. G. Herzer, "Grain Size Dependence of Coercivity and Permeability in Nanocrystalline Ferromagnets," IEEE Transactions on Magnetics, 26 (1990), 1397-1402.

4. K. Suzuki, N. Kataoka, A. Inoue, A. Makino, and T. Masumoto, "High Saturation Magnetization and Soft Magnetic Properties of bcc Fe-Zr-B Alloys with Ultrafine Grain Structure," Materials Transactions, JIM, 31 (1990), 743-746.

5. A. Makino, A. Inoue, and T. Masumoto, "Nanocrystalline Soft Magnetic Fe-M-B (M = Zr, Hf, Nb) Alloys Produced by Crystallization of Amorphous Phase," Materials Transactions, JIM, 36 (1995), 924-938.

6. A. Makino, A. Inoue, and T. Masumoto, "Soft Magnetic Properties of Nanocrystalline Fe-M-B (M = Zr, Hf, Nb) Alloys with High Magnetization," Nanostructured Materials, 6 (1995), 985-988.

7. Y. Yoshizawa, and K. Yamauchi, "Effects of Magnetic Field Annealing on Magnetic Properties in Ultrafine Crystalline Fe-Cu-Nb-Si-B Alloys," IEEE Transactions on Magnetics, 25 (1989), 3324-3326.

8. G. Herzer, "Magnetic Field Induced Anisotropy in Nanocrystalline Fe-Cu-Nb-Si-B Alloys," Materials Science and Engineering, A181/A182 (1994), 876-879.

9. G. Herzer, "Magnetostriction and Induced Anisotropies in Nanocrystalline Fe-Cu-Nb-Si-B Alloys," Nanostructured and Non-Crystalline Materials, eds. by M. Vázquez and A. Hernando (Madrid, World Scientific, 1994), 449-460.

10. A. Makino, T. Hatanai, Y. Naitoh, T. Bitoh, A. Inoue, and T. Masumoto, "Applications of Nanocrystalline Soft Magnetic Fe-M-B (M = Zr, Nb) Alloys NANOPERM," IEEE Transactions on Magnetics, 33 (1997), 3793-3798.

11. Y. Park, S. J. Suh, K. Y. Kim, and T. H. Noh, "The Effect of Magnetic Field Annealing on Magnetic properties in Ultrafine Fe-based Nanocrystalline Alloys," IEEE Transactions on Magnetics, 33 (1997), 3799-3801.

12. D. Cullity, Elements of X-ray Diffraction 2nd ed. (Addison-Wesley, 1959), 262.

13. Y. Zhang, K. Hono, A. Inoue, A. Makino, and T. Masumoto, "Nanocrystalline Structure Evolution in $Fe_{90}Zr_7B_3$ Soft Magnetic Material," Acta Materialia, 44 (1996), 1497-1510.

14. K. Suzuki, A. Makino, A. Inoue, and T. Masumoto, "Soft Magnetic Properties of Nanocrystalline Fe-Co-Zr-B Alloys," Journal of the Magnetic Society of Japan, 18 (1994) 800-804.

EFFECTS OF HARD-MAGNET BIAS ON CORE LOSS IN Mn-Zn FERRITE

Kinshiro Takadate, Yutaka Yamamoto, Akihiro Makino

Central laboratory, Alps Electric Co. Ltd.,
1-3-5 Higashitakami, Nagaoka, Niigata 940, Japan.

Abstract

The effects of superposing a DC magnetic field on core loss of Mn-Zn ferrites were investigated. The core losses at 3MHz are reduced to 56% by superposing a magnetic field of 2kOe perpendicularly to the magnetic path. The reduction of the core losses is mainly resulting from the decrease of the residual loss, which occupies a large part of the core loss at 3MHz. The magnetization of the samples becomes about 80% of the saturation magnetization by applying a magnetic field of 2kOe perpendicularly to the magnetic path. The decrease of the residual losses can be explained by the change of magnetization process from the domain wall displacement to the rotation magnetization with increasing the superposed DC magnetic field.

The Third Pacific Rim International Conference on
Advanced Materials and Processing (PRICM 3)
Edited by M.A. Imam, R. DeNale, S. Hanada,
Z. Zhong and D.N. Lee
The Minerals, Metals & Materials Society, 1998

1. Introduction

Mn-Zn ferrites have been extensively used for many kinds of magnetic devices such as transformers, inductors and magnetic heads because of their low core losses at high frequency. However, if a high frequency driving up to MHz range is needed, an increase of the core loss of Mn-Zn ferrites will be a serious problem. Therefore the reduction of the core loss in MHz range is desired.

We have reported that Mn-Zn ferrites with fine grain sizes under 3μm show the low core loss compared with a conventional Mn-Zn ferrite with grain size of 10 μm at a frequency from 0.5 to 2MHz[1, 2]. And it has been reported that the dominant component of the core losses of Mn-Zn ferrites in MHz range is the residual loss and the residual loss is reduced with decreasing the grain size [3-6]. However, other means to reduce the core loss in MHz range have been hardly reported.

The magnetization process of bulk ferrites is considered to be the domain wall displacement and the residual loss is supposed to be an energy loss for damping of the domain wall motion [5]. Therefore changing the magnetization process from the domain wall displacement to the rotation magnetization is expected to be effective in the reduction of the residual loss or the core loss. In this paper, the effect of hard-magnet bias on core loss of Mn-Zn ferrites is investigated as a new means to reduce the core loss in MHz range.

2. Experiments

Two kinds of Mn-Zn ferrites with the properties as shown in Table 1 were used for measurements of core losses and magnetization curves. The samples have toroidal shape and dimensions of the samples are outer diameter of 8mm, inner diameter of 4mm and thickness of 2mm. The core losses of the samples were measured with an ac B-H loop tracer at a frequency (f) from 100kHz to 5MHz and a maximum flux density (B_m) of 20mT and 40mT superposing a DC magnetic field by 2.5kOe perpendicularly to the magnetic path of the toroidal cores with hard magnets. The magnetization curves in the direction that the DC magnetic field was superposed were measured with a VSM. All measurements were carried out at room temperature.

Table 1. Properties of the samples.

	Sample A	Sample B
Composition	$Mn_{0.72}Zn_{0.16}Fe_{2.12}O_4$	
Grain size (μm)	2.2	4.3
Resistivity (Ωcm)	6.3	12.7
Saturation flux density (T)	>0.55	
Relative permeability (100kHz)	1800	2200

3. Results and Discussion

A. Core loss of the samples

Figure 1 shows the frequency dependence of the core losses per cycle (Pcv/f) for each sample. Pcv/f increase with increasing f and an inclination of the increase steepens at more than 1MHz in both samples. The increase of Pcv/f in MHz range is associated with the increase of the residual loss (Pr) because Pr occupies the largest part of the core loss (Pcv) of Mn-Zn ferrite in MHz range[3-6]. The analysis of Pcv was carried out to specify the main loss

component of *P*cv in MHz range for the samples. In the analysis of *P*cv, the hysteresis loss (*P*h) was determined by *P*cv at 5kHz because *P*cv/*f* is almost constant under 10kHz. And from the frequency dependence of *P*cv, *P*cv was computatively separated into three loss components, which were the magnetic loss (*P*m), the eddy current loss (*P*e) and the equivalent dielectric loss (*P*d) due to displacement current [5]. Moreover, *P*r was calculated as *P*r =*P*m−*P*h assuming that *P*h is proportional to frequency. Table 2 shows the separated loss components of *P*cv at 3MHz. *P*r occupies more than 80% of *P*cv at 3MHz in each sample. Therefore the reduction of *P*r is necessary for reduction of *P*cv in MHz range.

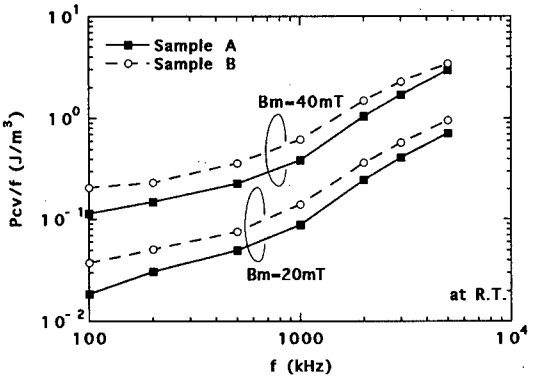


Fig.1 Frequency dependence of the core losses for each sample.

Table 2 Separated loss components at 3MHz.

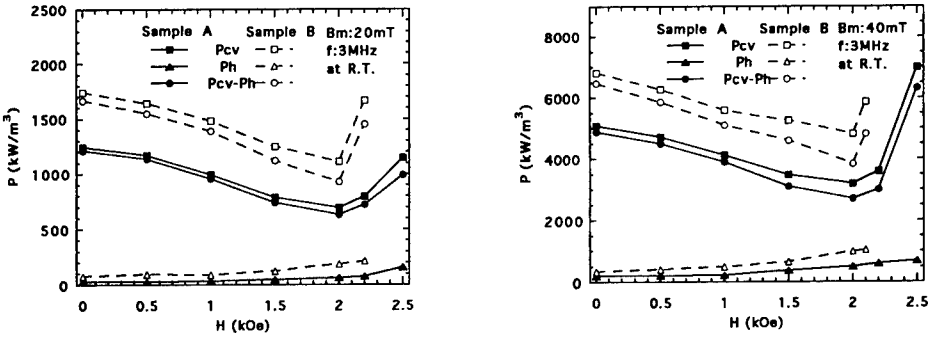
	*B*m(mT)	*P*cv	*P*h	*P*r	*P*e	*P*d
Sample A	20	1243	30	1015	178	20
	40	5091	213	4182	704	82
Sample B	20	1743	77	1557	92	17
	40	6811	340	6042	361	68

(unit : kW/m³)

B. Effect of superposing a DC magnetic field on core loss

Figure 2 shows *P*cv , *P*h and *P*cv-*P*h at 3MHz as a function of the superposed DC magnetic field (*H*). *P*cv exhibits a minimum value at *H* of 2kOe irrespective of B_m in each sample and the minimum values are about 56 to 71% of the values of *P*cv for which *H* = 0. *P*h increases monotonously with increasing *H* and occupies less than 20% of *P*cv. On the other hand, *P*cv-*P*h occupies more than 80% of *P*cv and exhibits a minimum value at *H* of 2kOe as well as *P*cv. *P*cv-*P*h, which is caused by dynamic magnetization process and consists of *P*e, *P*d and *P*r, is occupied by mainly *P*r at 3MHz as shown in Table 2. Therefore, the reduction of *P*cv by superposing a DC field up to 2kOe corresponds to that of *P*r. It seems reasonable to suppose that the increases of *P*cv-*P*h by superposing a DC field of more than 2kOe arise from the pinning of spin near the core surface by the strong field. Supposing that the area spin is pinned enlarge with increasing *H*, the induction level of the inductive area around the core center will become lager than B_m and core loss will increase.

Figure 3 shows the changes of the frequency dependence of *P*cv/*f* with the superposing a DC field of 2kOe for sample A. *P*cv/*f* is decreased by superposing a DC field over 1MHz, although increased under 1MHz because *P*h increases with increasing *H*. Consequently the superposing a DC-magnetic field is effective in reducing the core loss in MHz range.



(a) B_m =20mT (b) B_m =40mT

Fig.2 Pcv, Ph, Pcv-Ph at 3MHz as a function of the superposed DC magnetic field.

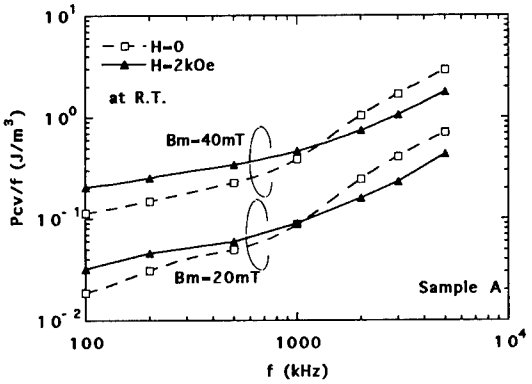


Fig.3 Changes of the frequency dependence of the core losses with the applied DC magnetic field of 2kOe.

C. Mechanism for the effect of superposing a DC magnetic field

Figure 4 shows the magnetization curves of the samples. The two curves are much the same. At a field of 2kOe, in which the minimum values of the core losses are obtained, the magnetization is about 80% of the saturation magnetization. Hence the magnetic domain of the samples would almost become extinct and the rotation magnetization would be a main magnetization process at H of 2kOe. Therefore, the reduction of core losses are associated with the change of the magnetization process from the domain wall displacement to the rotation magnetization. *Pcv-Ph*, which is mainly occupied by *Pr* at 3MHz, is considered as a damping energy loss for domain wall motion (P) in the case of the domain wall displacement and P is expressed by following equation [5].

$$P = \pi^2 \frac{\beta}{B_s} B_m^2 f^2 = \frac{2\pi^2}{\lambda_f} B_m^2 f^2 \quad \left[W/m^3\right] \tag{1}$$

Where B_s is the saturation flux density, β and λ_f are the damping constant and the dynamic

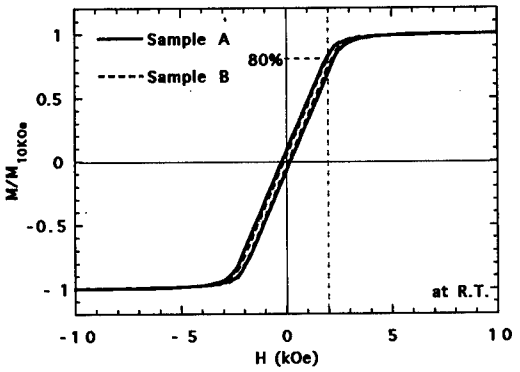


Fig.4 Magntization curves of each sample in the direction of the superposed DC magnetic field.

magnetic loss parameter[5] and depend on the domain structure and the microstructure of the material. Although the substance of β or λ_f has been not so clear in ferrites, it has been reported that λ_f increases with decreasing the grain size of Mn-Zn ferrites [4]. This tendency is perhaps associated with the fact that the domain size decreases with decreasing the grain size of ferrites [7]. Hence the relationship between β or λ_f and the domain size(L) is supposed to be following equation.

$$\beta = \frac{2B_s}{\lambda_f} = \left(\frac{L}{\delta}\right)^x \beta' \quad [As/m] \tag{2}$$

Where β' is the damping constant depending only on the microstructure of the materials, x is positive unknown value. And L is normalized by the domain wall thickness δ in the equation and $L/\delta > 1$. The decrease of *P*cv-*P*h by the change of magnetization process is caused by the decrease of β as follows. The rotation magnetization is considered as the state $L/\delta = 1$ and P is minimized by the change of magnetization process into the rotation magnetization because β becomes the minimum value β'. Therefore if the fraction of the rotation magnetization with low loss increases with increasing the superposing DC field, *P*cv-*P*h will be reduced.

As the another cause of the loss reduction by the change of the magnetization process, a change of switching frequency of spin (f_s) could be expected. There is a difference of f_s between the domain wall displacement and the rotation magnetization in alternating magnetization process. In the rotation magnetization, f_s coincides with the driving frequency (f). However in the domain wall displacement, f_s of the spin inside the domain wall changes depending on the domain structure and the induction level (B_m). f_s inside the domain wall is expressed by following equation that is calculated from the cubic domain model [8].

$$f_s = 1.67\frac{B_m L}{B_s \delta} f \quad [Hz] \tag{3}$$

f_s of sample A and B is 7.3MHz and 8.7MHz at f of 3MHz, B_m of 20mT respectively. Here B_s and δ are supposed to be 0.55T and 50nm respectively. L of sample A and B are estimated

to be 2.0μm and 2.4μm basing on the reference [7]. Although rough estimates, it can be seen that f_s is larger than f at the level of B_m in the measurements of the core loss. Hence it is supposed that f_s reaches the magnetic resonance frequency and the core loss increases at relatively low f in the domain wall displacement [9]. The reduction of core losses by the change of the magnetization process is presumably associated with the decrease in the influence of the magnetic resonance caused by the change of f_s into f.

4. Conclusion

The effect of superposing a DC magnetic field on core loss of the Mn-Zn ferrites was investigated. The core losses in MHz range were reduced by superposing a proper DC magnetic field perpendicularly to the magnetic path. The reduction of the core losses is mainly caused from the decrease of the residual loss. The decrease of the residual losses are associated with the change of magnetization process from the domain wall displacement to the rotation magnetization. It is concluded that the hard magnet bias is effective in reduction of the core loss of Mn-Zn ferrite in MHz range.

References

1. Y. Yamamoto, A. Makino, "Core losses and magnetic properties of Mn-Zn ferrites with fine grain sizes," J. Magn. Magn. Mater., **133** (1994), 500.

2. Akihiro Makino, Yutaka Yamamoto, "Magnetic properties of Mn-Zn ferrites with fine grain sizes for high frequency transformer," New Horizons for Materials, Techna Srl (1995), 361.

3. T. Nakano, N. Sato, T. Nomura, "Core loss characteristics of MnZn ferrite at high frequencies," Journal of the Magnetics Society of Japan, **20** (1996), 501.

4. H. Kobiki, A. Fujita, S. Gotoh, "Relationship between residual loss and microstructure of Mn-Zn ferrite," Proceedings of the 7th International Conference on Ferrites, C1-103 (1996).

5. H. Saotome, Y. Sakaki, "Iron loss analysis of Mn-Zn ferrite cores," IEEE Trans. Magn., **33** (1) (1997), 728.

6. K. Takadate, Y. Yamamoto, A. Makino, "Effect of grain size on residual loss of Mn-Zn ferrite," Proceedings of International Symposium on Ferrites in Asia '97, to be published.

7. P. J. van der Zaag et al., "Domain structures in polycrystalline MnZn-ferrites," Proceedings of the 6th International Conference on Ferrites (1992), 819.

8. K. Takadate, Y. Yamamoto, A. Makino, "Effect of applied DC magnetic field on core loss of Mn-Zn ferrite" (Paper presented at *Magnetics Kenkyukai*, the branch of Institute of Electrical Engineers of Japan, Osaka, Japan, 18 November 1997), Mag-97-158.

9. S. Yamada, E. Otsuki, "Analysis of eddy current loss in Mn-Zn ferrite for power supplies," J. Appl. Phys., **81 (8)** (1997), 4791.

EFFECTS OF ADDITIONAL ELEMENTS (M=TRANSITION METAL) ON THE THERMAL STABILITY AND SOFT MAGNETIC PROPERTIES IN Fe-Co-Ni-Zr-M-B AMORPHOUS ALLOYS WITH WIDE SUPERCOOLED LIQUID RANGE

H. Koshiba and A. Inoue, Institute for Materials Research, Tohoku University, Sendai, 980-77, Japan.
A. Makino, Central Research Laboratory, Alps Electric Co., Ltd., Nagaoka, 940, Japan.

Abstract

Amorphous alloys with a wide supercooled liquid region (ΔT_x) before crystallization were found to be formed in the $Fe_{56}Co_7Ni_7Zr_8M_2B_{20}$(M=IV a-VI a group transition metals) alloys by melt spinning. The ΔT_x which is considered as a criterion of glass-forming ability increases to large values exceeding 80K by the addition of 2at%M (M=Ti,Hf,Nb,Ta,Mo or W), being larger by about 10K than the largest value for newly developed $(Fe,Co,Ni)_{70}Zr_{10}B_{20}$ alloys. By the addition of the M metals, magnetic properties also changed. The good soft magnetic properties were obtained for the alloys containing 2at%Ti,Hf,Nb,Ta and Cr subjected to annealing for 300s at 800K. The saturation magnetization (I_s), coercive force (H_c) and effective permeability (μ_e) at 1kHz are 0.75-0.82T, 1-6A/m and 10000-25000, respectively. The finding of the Fe-based amorphous alloys exhibiting simultaneously the wide supercooled liquid region before crystallization and the good soft magnetic properties seems to enable future development of a new ferromagnetic bulk amorphous alloy.

The Third Pacific Rim International Conference on
Advanced Materials and Processing (PRICM 3)
Edited by M.A. Imam, R. DeNale, S. Hanada,
Z. Zhong and D.N. Lee
The Minerals, Metals & Materials Society, 1998

Introduction

Recently, Fe-based bulk amorphous alloys with thicknesses up to about 2 mm have been reported to be formed by conventional casting processes[1]. These alloys consist of multicomponents as is evidenced for Fe-Al-Ga-P-C-B-Si system, and exhibit a glass transition, followed by a wide supercooled liquid region which is defined by the difference between the glass transition temperature (T_g) and crystallization temperature (T_x), $\Delta T_x(=T_x-T_g)$. There is a clear tendency for glass-forming ability to increase with increasing ΔT_x[1-6]. The above-described bulk amorphous alloys always satisfy the following three empirical rules[7-9] for achievement of large glass-forming ability; i.e., (1) multicomponent alloy systems consisting of more than three elements, (2) significantly different atomic size ratios above about 12 % among the main constituent elements, and (3) negative heats of mixing among their elements. Based on the three empirical rules, Inoue et al. has succeeded in finding new Fe-based amorphous alloys in $(Fe,Co,Ni)_{70}Zr_{10}B_{20}$ system with a wide supercooled liquid region reaching about 70K before crystallization[10]. Subsequently, we have examined the effect of partial replacement of Zr by the M elements and noticed that the replacement by 2at%Nb causes a significant increase in ΔT_x[11]. This paper aims to present the influence of additional M elements (M=Ⅳ a to Ⅵ a group transition metals) on the thermal stability and magnetic properties for $Fe_{56}Co_7Ni_7Zr_8M_2B_{20}$ amorphous alloys and to investigate the reason of the increase in the thermal stability of these alloys by the addition of M elements.

Experimental

Master ingots of $Fe_{56}Co_7Ni_7Zr_8M_2B_{20}$ (M=Ti,Zr,Hf,V,Nb,Ta,Cr,Mo or W) alloys were prepared by arc melting the mixture of pure Fe, Co, Ni, Zr and M metals and pure B crystal in an argon atmosphere. The alloy compositions represent the nominal atomic percentage of the mixtures. Rapidly solidified ribbons with a cross section of 0.02 x 1.0 mm^2 were prepared by melt spinning. The crystallized structure was examined by X-ray diffractometry (XRD). Thermal stability associated with glass transition, supercooled liquid region and crystallization was examined at a heating rate of 0.67 K/s by differential scanning calorimetry (DSC). Magnetization at room temperature was measured in a maximum applied field of 1260 kA/m with a vibrating sample magnetometer (VSM). Coercive force was measured with a I-H curve tracer. Permeability was evaluated at 1 kHz with an impedance analyzer. Curie temperature (T_c) was determined by extrapolating the magnetization-temperature (I-T) curve in the constant coupling approximation manner.

Results and Discussion

Figure 1 shows X-ray diffraction patterns of the melt-spun $Fe_{56}Co_7Ni_7Zr_8M_2B_{20}$ (M=Ti,Hf,V,Nb,Ta,Cr,Mo or W) alloys. Only a broad peak is seen at a waver vector ($K_p=4\pi\sin\theta/\lambda$) of about 30.2 nm^{-1} for all alloy systems and no diffraction peak corresponding to a crystalline phase is seen. The X-ray diffraction data indicate clearly that these melt-spun alloys are

composed of an amorphous phase without crystallinity. Figure 2 shows DSC curves of the melt-spun $Fe_{56}Co_7Ni_7Zr_8M_2B_{20}$ (M=Ti,Hf,V,Nb,Ta,Cr,Mo or W) amorphous alloys. It is to be noticed that a distinct glass transition, followed by a wide supercooled liquid region is observed in the temperature range before crystallization for all the alloys. It seems that these results are due to the satisfaction of the above-mentioned three empirical rules. The glass transition temperature (T_g) remains constant at about 830K for all the alloys. However, the crystallization temperature (T_x) increases in the order of V < Cr << Hf < Ti << Mo < Nb < W < Ta and are significantly dependent on the kind of the M elements. The ΔT_x is 66K for V, 73K for Cr, about 80K for Hf and Ti and about 85K for Mo, Nb, W and Ta by the addition of 2at%M. As a result, the addition of 2at% Nb, Ta, Mo or W for the $Fe_{56}Co_7Ni_7Zr_8M_2B_{20}$ amorphous alloys was found to be effective for the increase of ΔT_x. These results indicate that there is a close relation between the M elements and the glass forming ability.

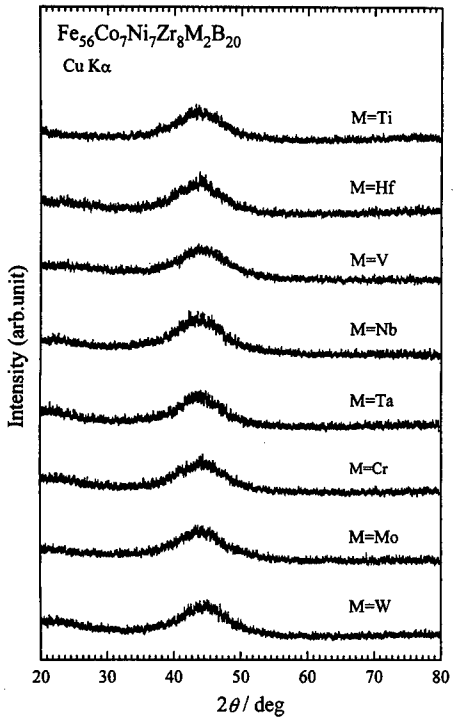


Figure 1 : X-ray diffraction patterns of melt-spun $Fe_{56}Co_7Ni_7Zr_8M_2B_{20}$ (M=Ti,Hf,V,Nb,Ta,Cr,Mo or W) alloys.

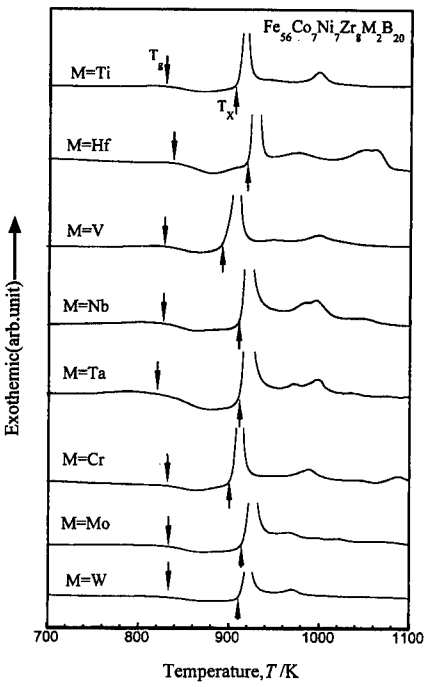


Figure 2 : Differential scanning calorimetric curves of the amorphous $Fe_{56}Co_7Ni_7Zr_8M_2B_{20}$ (M=Ti,Hf,V,Nb,Ta,Cr,Mo or W) alloys.

Subsequently, we consider the reason for the difference of the supercooled liquid region by the kind of the M elements in the framework of the three empirical rules. The present alloys consist of six components, being the same for all alloy systems. However, the atomic size ratios among their a

constituent elements change significantly depending on the M elements. The atomic radii of the M elements are in the range of 0.125 to 0.157nm and arranged in the order of Cr<V<Mo<W<Nb<Ta<Ti<Hf[12]. Figure 3 shows the change in ΔT_x with atomic radius of the M elements for the $Fe_{56}Co_7Ni_7Zr_8M_2B_{20}$ alloys. The atomic radii of Fe, Zr and B elements are also shown for composition. The ΔT_x significantly increases by the addition of Nb, Ta, Mo or W which has atomic radii between Zr and Fe. The ΔT_x remains almost constant in the case of the addition of V or Cr which has the nearly the same atomic radii as that of Fe and of Ti or Hf which is similar to that of Zr. The atomic radii of the M elements are thought to have great influence on ΔT_x. In addition, the negative heats of mixing(ΔHmix) among the constituent elements also change with M elements. The ΔHmix is 0 to 37kJ/mol for Fe-M pairs and 45 to 102 kJ/mol for M-B pairs and changes in the order of Cr<V<Mo<W<Nb<Ta<Ti<Hf for Fe-M pairs[13]. The same tendency is also recognized for M-B pairs. Thus, these pairs have the large negative heats of mixing. Figure 4 shows the relation between ΔT_x value and negative heats of mixing of Fe-M and M-B pairs for the $Fe_{56}Co_7Ni_7Zr_8M_2B_{20}$ alloys. No distinct relation is recognized and hence the significant change in ΔT_x with M elements seems to be attributed to the atomic size ratios rather than the negative heats of mixing.

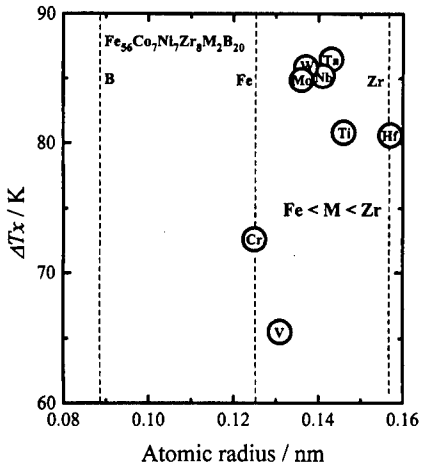


Figure 3 : Relation between ΔT_x and atomic radii of M elements for the $Fe_{56}Co_7Ni_7Zr_8M_2B_{20}$ alloys.

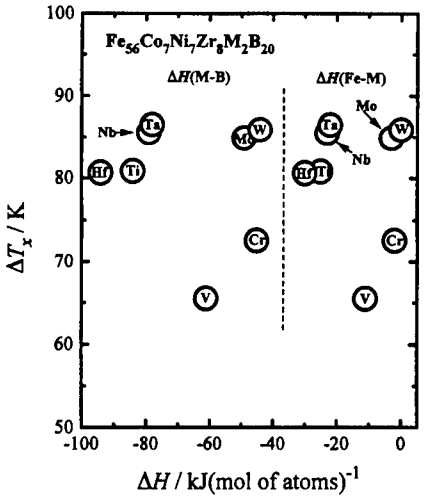


Figure 4 : Relation between ΔT_x and negative heats of mixing of Fe-M and M-B pairs for the $Fe_{56}Co_7Ni_7Zr_8M_2B_{20}$ alloys.

Table 1 summarizes I_s, H_c, and μ_e at 1 kHz for the $Fe_{56}Co_7Ni_7Zr_8M_2B_{20}$ amorphous alloys subjected to annealing for 300s at 800K just below T_x. It is seen that the replacement of Zr by M elements cause a decrease of I_s from 0.96 T at 0 %M. Although the total content of Fe and Co elements remains constant, the I_s decreases by 0.13 to 0.26T only by the addition of 2 %M. Since the same tendency is observed in T_c, the change in I_s by the addition of the M elements seems to reflect the change in T_c. The μ_e values are in the range of 5000 to 25000 A/m and have appreciable compositional dependence.

The maximum μ_e value reaches 25000 at 2 %Nb. The composition showing the maximum μ_e value roughly corresponds to that with the lowest H_c. Thus, there is a close relation between μ_e and H_c, as is the case for I_s and T_c. From the compositional dependence of the thermal stability of the supercooled liquid and the magnetic properties, it is concluded that the $Fe_{56}Co_7Ni_7Zr_8M_2B_{20}$ (M=Nb or Ta) amorphous alloys have the useful characteristics of high glass-forming ability and good soft magnetic properties.

Table I Saturation magnetization (I_s), coercive force (H_c) and effective permeability at 1 kHz (μ_e) for the $Fe_{56}Co_7Ni_7Zr_8M_2B_{20}$ (M=Ti,Hf,V,Nb,Ta,Cr,Mo or W) amorphous alloys annealed for 300 s at 800 K.

composition	I_s / T	H_c / Am^{-1}	μ_e(1kHz)	T_c / K
M=Ti	0.82	1.9	12470	528
M=Hf	0.80	2.2	9270	509
M=V	0.83	4.4	5210	530
M=Nb	0.75	1.1	25000	531
M=Ta	0.74	2.7	11970	503
M=Cr	0.75	1.9	10040	508
M=Mo	0.73	4.9	6490	490
M=W	0.70	5.7	8320	476

Conclusions

The glass transition and subsequent supercooled liquid region were observed in the temperature range before crystallization for all the $Fe_{56}Co_7Ni_7Zr_8M_2B_{20}$ alloys. The ΔT_x increases by the addition of 2 %M, leading to the maximum ΔT_x of about 85 K for the 2 %Nb, Ta, Mo, W alloys. The ΔT_x is the largest among Fe-based amorphous alloys reported hitherto and affected significantly by the atomic radii of the M elements. The good soft magnetic properties were obtained for the alloys containing Ti,Hf,Nb,Ta or Cr of 2at% subjected to annealing for 300s at 800K. The I_s, H_c and μ_e at 1kHz are 0.75-0.82T, 1-6A/m, and 10000-25000, respectively. The alloys containing 2 %Nb or Ta exhibit the good combination of the wide supercooled liquid region and good soft magnetic properties. The finding of the new amorphous alloys with the two characteristics is important for future development of bulk amorphous alloys in the application of soft magnetic materials.

References

1 A. Inoue et al., "Soft Magnetic Properties of Bulk Amorphous Alloys Prepared by Copper Mold Casting ," IEEE Trans. Mag., **32** (1996), 4866-4871.

2 A. Inoue et al., "An Amorphous $La_{55}Al_{25}Ni_{20}$ Alloy Prepared by Water Quenching," Mater. Trans., JIM, **30**, (1989), 722-725.

3 A. Inoue et al., "Bulky La-Al-TM(TM=Transition Metal) Amorphous Alloys with High Tensile Strength Produced by High Pressure Die Casting Method," Mater. Trans., JIM, **34**, 351-358 (1993).

4 A. Inoue et al., "Mg-Cu-Y Bulk amorphous Alloys with High Tensile strength Produced by a High-Pressure Die Casting Method," Mater. Trans., JIM, **33**, 937-945 (1992).

5 A. Peker and W.L. Johnson, Appl. Phys. Lett., **63**, 2342 (1993).

6 A. Inoue, N. Nishiyama, and T. Matsuda, "Preparation Of Bulk Glassy $Pd_{40}Ni_{10}Cu_{30}P_{20}$ Alloy of 40 mm in Diameter by Water Quenching," Mater. Trans., JIM, **37**, 181-184 (1996).

7 A. Inoue, T. Zhang, and T. Masumoto, "Glass-Forming Ability of Alloys," J. Non-Crsyt. Solids, 156-158, 473-480 (1993).

8 A. Inoue, "High Strength Bulk Amorphous Alloys with Low Critical Cooling Rates," Mater. Trans., JIM, **36**, 866-875 (1995).

9 A. Inoue, "Slowly-Cooled Bulk Amorphous Alloys." Mater. Sci. Forum, **179-181**, 691-700 (1995).

10 A. Inoue et al., "New Fe-Co-Ni-Zr-B amorphous alloys with wide supercooled liquid regions and good soft Magnetic properties," Mater. Trans., JIM, **38** (1997), 359-362.

11 A. Inoue et al., "Thermal and Magnetic Properties of $Fe_{56}Co_7Ni_7Zr_{10-x}M_xB_{20}$ Amorphous Alloys with Supercooled Liquid Range," Mater. Trans., JIM, **38** (1997), 577-582.

12 Kakihana, Yoshino and Hukutomi, Inorganic Chemistry, (Tokyo, Hirokawa Publishing Co., 1986), 417.

13 F.R. de Boer et al., Cohesion in Metals (Elsevier Science Publishers B.V., Amsterdam 1988).

Melt Processing and Casting

High Quality Thin Slab Casting for Hot Strip Production.

(Control of Initial Solidification in Thin Slab Casting.)

Tadao Watanabe, Sei Hiraki, Masayuki Kawamoto and Yasuyuki Tozaki

Sumitomo Metal Industries, Ltd.
16-1, Hasaki-machi Kashima-gun Ibaraki Prefecture

Abstract

In the TSC-compact HSM process, there are three trends. High Productivity, high quality and manufacturing of thinner gauge hot coils. Especially the trend towards high quality will be accelerated by the driving force of the expanding flat products market with the near net shape process. TSC-compact HSM processes are classified into five types in the world. One of them is Quality Strip Production(QSP) process developed by Sumitomo. QSP process is advantageous for the high quality hot strip production, because it has a prominent control technology for the initial solidification in a continuous casting mold.

The Third Pacific Rim International Conference on
Advanced Materials and Processing (PRICM 3)
Edited by M.A. Imam, R. DeNale, S. Hanada,
Z. Zhong and D.N. Lee
The Minerals, Metals & Materials Society, 1998

1. Introduction

For the purpose of minimizing the cost of construction and production, two technical developments have been proceeding forward for about 10 years in the iron- and steel making process of the steelmakers in the world. One is the technology of applying various iron resources for steel products and the other is that of producing hot strips with the near net shape process. In this report the second trend, that is, the technologies of the near net shape process are presented. The processes of thin slab continuous casting and compact hot rolling are discussed from the viewpoint of the technology for the thin slab casting.

2. General trends of thin slab casting technology for common grade hot strip steel.

2. 1 Diversification of manufacturing process for hot-rolled strip steel.

Hot coils have been produced conventionally in integrated steelworks with the process using a blast furnace, converter, continuous caster and a hot strip mill. Recently the mini-mill maker has easily joined the hot coil market with electric arc furnaces after the TSC-compact HSM process called Compact Strip Production process (CSP) was first developed by Schloemann-Siemag Aktiengesellschaft (SMS) in Germany as shown in Fig. 1. [1) 2)] In the TSC-compact HSM process, in addition to the mini-mill steelmaker utilizing steel supplied by EAF as shown the route B in Fig. 1, integrated steelworks with TSC-compact HSM process has appeared recently. They supply steel from the converter as shown the route B' in Fig. 1. The diversification of the process for manufacturing hot coils is proceeding rapidly.

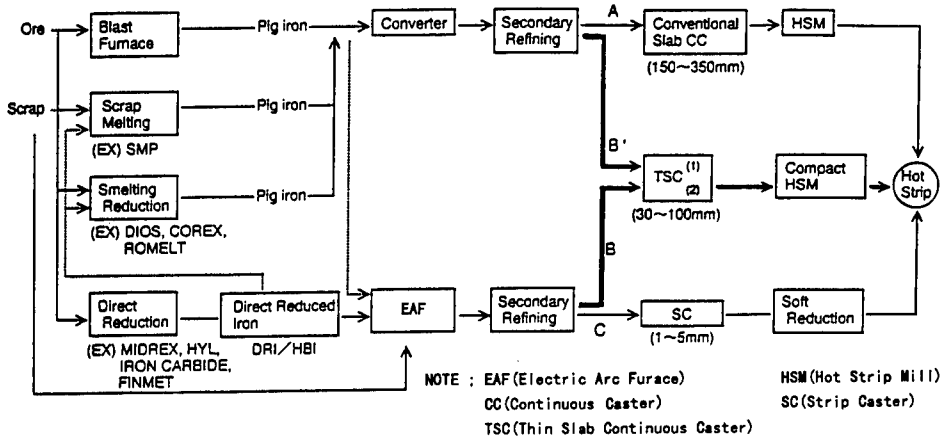


Fig. 1 Various manufacturing process for hot strip.

2. 2 Trends of thin slab casting technology for hot strip production.

The biggest advantage of TSC process compared with the conventional process is low in construction cost. For example the construction cost for TSC process is about one third of that for integrated steelworks. The running cost of the TSC process is also lower because

the caster is directly connected to the hot strip mill. Concerning the decision for the introduction of TSC-compact HSM process, there are three important items,

(1)Productivity

(2)Quality

(3)Feasibility of manufacturing thinner gauge hot coils.

Key points of productivity are due to exact time schedule of individual process and the casting performance. Productivity for several casting processes is compared in Fig. 2. Assuming that the availability and average slab width are constant, casting performance is decided by the slab thickness and casting speed. The productivity of TSC(1) type for slab 50mm thick at 5.0m/min is 50% of that of conventional caster and that of TSC(2) type for slab 90 mm thick at 5.0m/min is 85%.

Classification of the flat products market in USA is shown in Fig. 3. Concerning the quality of coils, the TSC(1) process is located in class-B and a part of class-A. The TSC(2) process is in class-A but does not reach class-AA which is the rank of conventional process. The improvement of the quality to class-AA is the near future aim. In the case of molten steel supplied by EAF, it will be necessary to increase the added amount of high grade scrap or direct reduced iron because the residual elements in molten steel should be heavily controlled in class-AA. From this viewpoint molten steel supplied by the converter process has a great advantage.

The TSC process easily produces ultra-thin gauge coils less than 1.2 mm because the thickness of slabs is thinner than the one by a conventional process. It suggests that the flat products market of ultra-thin gauge hot coils, which cannot be participated in by the conventional process, would expand much more. Consequently there are three items which contribute to the future trend of TSC-compact HSM process: high productivity, high quality and the feasibility of ultra-thin gauge coils. Especially if higher quality such as class-AA could be achieved, the flat products market with the near net shape process would be expected to expand much more.

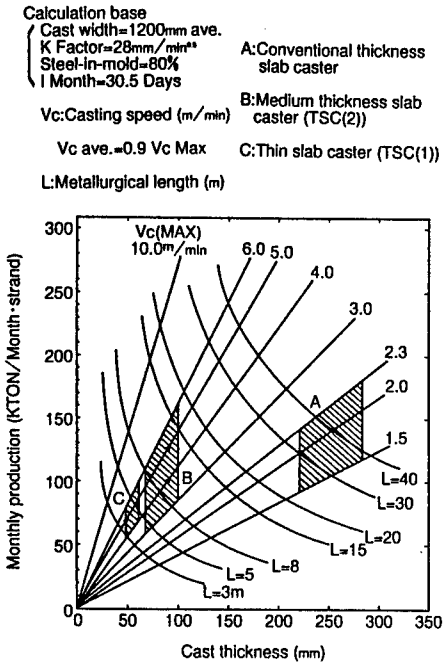


Fig. 2 Effect of casting speed and slab thickness on productivity and metallugical length.

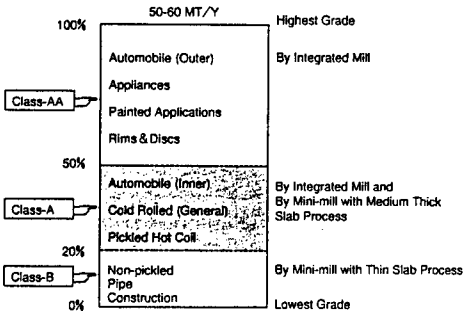


Fig. 3 Classification of flat products market in the USA.

2. 3 Problems of thin slab casting process compared with conventional slab casting process.

The basic problems in TSC-compact HSM process compared with conventional CC-HSM process are as follows:

1)Casting instability : decrease of breakout

2)Quality instability in slabs and coils.

: Prevention of longitudinal cracks, powder defects and scale defects.

3)Time schedule confusion of individual process.

: Prevention of troubles in each process through EAF-Ladle Furnace-TSC-compact HSM.

For the above basic problems, it is the most effective to control appropriately the initial solidification phenomena in the mold. TSC-compact HSM processes industrialized in the world at present are classified into five different processes based on the difference of mold shape and liquid core reduction technique as shown in Table Ⅰ. Mold shape divides five processes into two types: funnel-shaped with the form of bulge and plane parallel. The selection of mold type unequivocally decides the specification, such as pouring technique in the mold, mold thickness and so on. These points all concern the initial solidification phenomena. In the above five processes great efforts have been made individually to study the solidification phenomena in the mold which influences productivity, casting stability and the quality in slabs and coils.

Table Ⅰ Main specification of typical TSC processes in the world.

Process name		CSP	ISP	FTSC	QSP	CONROLL
Process owner (Nation)		SMS (Germany)	MDH (Germany)	DANIELI (Italy)	SUMITOMO (Japan)	VAI (Austlia)
Caster type from mold to crater end		V	V-Curved	VB	VB	VB
Mold	Type	Funnel Vertical	CROWN Vertical-bow	LENS-SHAPED Vertical	Parallel Vertical	Parallel Vertical
Mold	Thickness (mm) Top (Center/Edge)	170/50	70/60 *	160/80 *	90/90	75/75 *
Mold	Thickness (mm) Bottom (Center/Edge)	50/50	60/60	110/80	90/90	75/75
Mold	Narrow face	—	—	—	Multi-tapered	—
Mold	Length (mm)	1100	1000	1200	950	1200
Top zone segment		—	—	Lens-Shaped ends inside top zone segment	—	—
LCR (Reduction mm)		with (10~15)	with (15~20)	with (15~20)	with (20~40)	without (0)
Reduction immediately after solidification		without	with	without	without	without
Remarks			* The other case Parallel vertical mold. thickness80mm	* Operation 90/90 mm		* Operation 100/100mm

3. Quality Strip Production (QSP) Process.

3. 1 Characteristics of QSP process.

QSP process has been developed by SUMITOMO. The basic concept is to produce high quality coils while maintaining high productivity. In realizing the above concept, SUMITOMO decided the thickness of slab to be 90mm. It corresponds to adopt the TSC (2) process in Fig. 2. Furthermore, a lot of techniques described later have been developed based on the following aims.

1)Sound formation of initially solidified shell in the mold.

2)Decrease of tensile strain occurring at the solid-liquid interface in the solidifed shell during secondary cooling zone.

3)Descaling on the slab surface before hot rolling.

In addition to the above techniques concerning the high productivity and high quality, the technique of a flexible liquid core reduction was developed. Maximum amount of reduction is 40mm. So that it is possible to reduce 50 mm thick slab at the discharged exit of the caster from the mold 90 mm thick. Fig. 4 shows the process of TRICO STEEL in USA as a materialized example of the QSP process. At the present, casting steel grades are ; Low carbon aluminum killed, Medium carbon including hipo-peritectic, High carbon and High Strength Low Alloy (HSLA) steel. In addition North Star BHP Steel in USA is also using QSP process. Furthermore, startup of the Siam Strip Mill in Thailand is slated for early 1999.

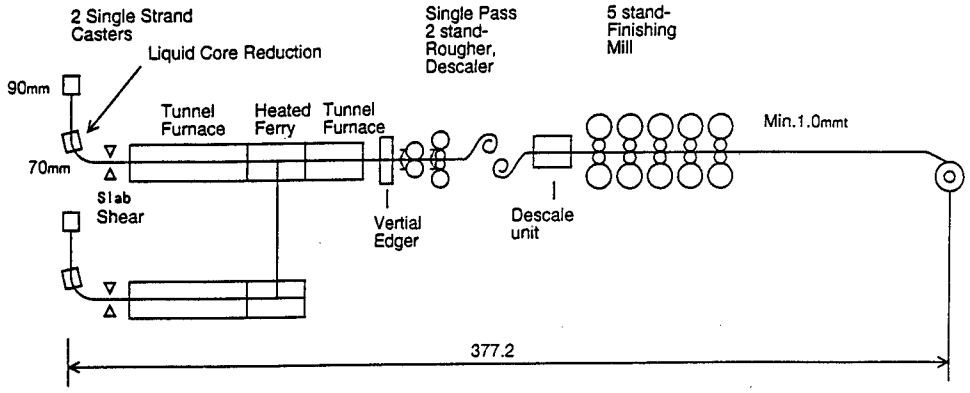


Fig. 4 An example of QSP process (process configuration of TSC(2) and compact hot strip mill).

3. 2 Highly advanced technologies developed for the Sumitomo medium thick slab caster.

3. 2. 1 Control of initial solidification.

(1) Plane parallel mold with multi-tapered narrow face.

A funnel shaped mold developed by SMS was based on an epoch-making idea to improve the pouring technique to the mold. By contrast, SUMITOMO adopted a plane parallel straight design from the viewpoint of the surface cracks prevention as shown in

Table I. The reason was to decrease the tensile strain caused in the initially solidified shell in the mold whenever the casting speed and width of slab changed in a wide range. The multi-tapered narrow face as shown in Fig. 5 was developed for the purpose of preventing tensile strain in the slab by fitting the narrow face taper to the shrinkage of solidified shell in the mold. [3] As a result, the prevention of longitudinal corner cracks was achieved during high speed casting as shown in Fig. 6. [3]

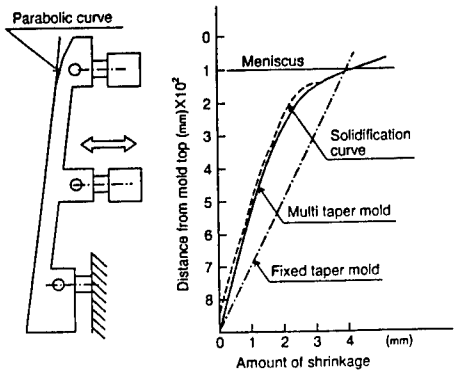


Fig. 5 Comparison between multi-taper curve and solidification curve.

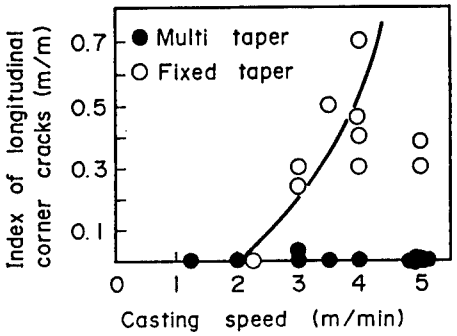


Fig. 6 Decrease of longitudinal corner cracks by the multi-tapered narrow face.

(2) Mold level control system

The mold is equipped with an electro-magnetic brake (EMBr) for the purpose of minimizing disturbance of the molten steel level in the mold. The wave height near the narrow face at the meniscus was decreased by EMBr. As a result, the meniscus was approximately maintained to a flat shape. Actual molten steel level control within ±5 mm was achieved at 5.0m/min as shown in Fig. 7. [4] It was established by the highly accurate molten steel level control system using an eddy current type sensor. [4] This system also enables the automatic start and finish of the casting. Flow control in the mold contributed to the stabilization of casting and the soundness of slab surface.

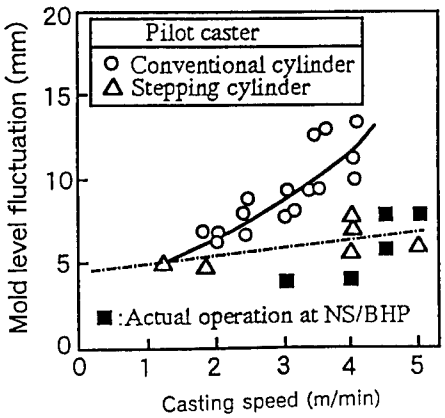


Fig. 7 Comparison of molten steel level fluctuation beween stepping and and conventional cylinder.

(3) Mold powder

Mold powder developed by SUMITOMO provides high lubrication and high thermal resistance between solidified shell and mold. These characteristics lead to sound skin formation and result in the prevention of shell-sticking, breakouts and longitudinal surface cracks. SUMITOMO mold powder has the following features, [5]

1)High basicity (CaO /SiO $_2$) ratio.
2)ZrO $_2$ addition.
3)High solidification temperature.

Controlled cooling at the meniscus was established by decreasing heat fluxes in the mold. [6] As a result, for example, the originally developed powder A enables the prevention of the occurrence of longitudinal surface cracks compared with other type of powders D, E as shown in Fig. 8 at casting speed of 5.0 m/min. SUMITOMO has succeeded to decrease cooling in the vicinity at the meniscus by newly developed mold powders as shown in Fig. 9. [7) 8)] Consequently the hipoperitectic steel which has high sensitivity of longitudinal surface cracks has been free from these cracks under the high speed casting condition.

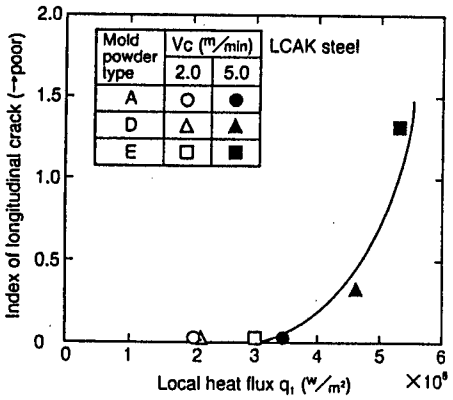


Fig. 8 Influence of the local heat fluxes at the vicinity of meniscus in the mold on longitudinal cracks.

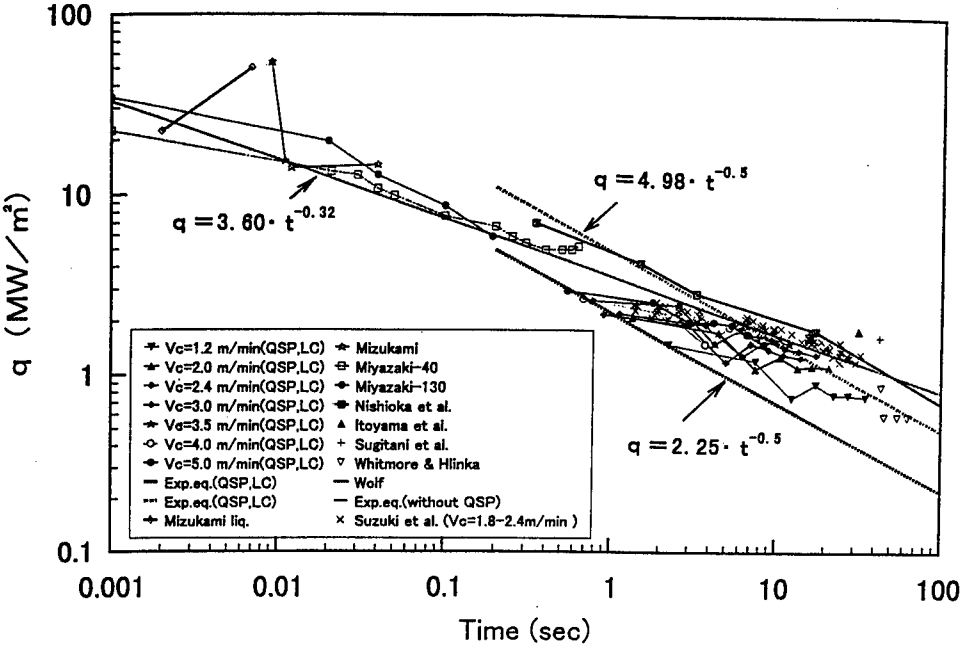


Fig. 9 Local heat flux in QSP process compared with the relation between local heat flux and dwell time in heat extraction device reported by Umeda et al. [8)]

3. 2. 2 Strain accumulation model and liquid core reduction.

It has been found that internal cracks would occur at the area within the fraction solid from 0.8 to 0.99 when tensile force over a certain limit amount was worked on the liquid-

solid interface in front of solidified shell.[9] Also, it has been found that strain which generated in the musy zone in front of the solidified shell would accumulate when the slab was deformed intermittently.[9] Thus the accumulation strain model was studied as an evaluation method for predicting the occurrence of internal cracks. Based on this model the optimum reduction pattern without internal cracks was found in the thin slab casting. A flexible liquid core reduction process has been established and has enabled one to select the suitable amount of reduction to maximum 40 mm according to casting conditions as shown in Fig. 10.

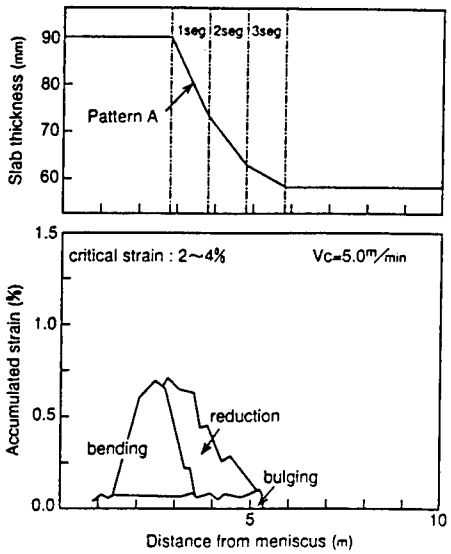


Fig. 10 Calculated value of tensile strain in liquid core reduction for low carbon steel.

4. Conclusion

1)In the TSC-compact HSM process, there are three trends. High Productivity, high quality and manufacturing of thinner gauge hot coils.

2)Especially the trend towards high quality will remarkably accelerate in the near future. And the initial solidification control technology will become more important.

3)Quality Strip Production (QSP) process developed by SUMITOMO is the flexible process available for high productivity, high quality and the manufacture of ultra-thin hot gauge coils.

REFERENCES

1)F. K Iverson, K. Busse, "A review of first year CSP operations at Nucor Steel's new thin slab casting facility", Metallugical Plant Technology International, 1/1991, 40-51

2)SHOUN T Kerbaugh, "The continuing expansion and utilization of CSP process", 36TH NWSP CONF. PROC., SS-AIME, Vol. XXXⅡ, 1995, 87-97

3)T. Murakami et al., "Improvement of Longitudinal Corner Cracks at High Speed Casting", CAMP-ISIJ, 8(1995), 145

4)K. Hanazaki et al., "Development of Level Control System for High Speed Casting", CAMP-ISIJ, 5(1992), 353

5)M. Kawamoto et al., "Design Principles of Mold Powder for High Speed Continuous Casting", Tetsu-to-Hagane, 80(1994), 219-224

6)S. Hiraki et al., "Influence of Heat Flux in Mold on Surface Quality of Slab in High Speed Casitng", CAMP-ISIJ, 4(1991), 1284

7)T. Kanazawa et al., "Behavior of Lubrication and Heat Transfer in mold at High Speed Continuous Casting", Tetsu-to-Hagane, 83(1997), 701-706

8)T. Umeda et al., "Heat Transfer and Solidification under Fluid Flow", CAMP-ISIJ, 9 (1996), 588-589

9)A. Yamanaka et al., "Mechanism of International Cracking in Continuous Casting", Tetsu-to-Hagane, 82(1996), 999-1004

STUDY ON THE SEEDING PROCESS FOR PRODUCING SINGLE CRYSTAL CASTINGS

Gui Zhonglou, Tang Dingzhong, Wu Zhongtang, Zhong Zhengang, Dai Xiuyan

Beijing Institute of Aeronautical Materials (BIAM) Beijing 100095, P. R. China

Abstract

Two kinds of seeding processes were designed in the present investigation to produce single crystal (SC) castings. It was shown that crystallographic orientation was well controlled by both processes. The second seeding process results in higher SC yield than the first one. Several kinds of airfoils were manufactured by the second seeding process with more than 60% yield. In the case of producing a small solid blade, 78.6% blades manufactured by the second seeding process had a less than 5° mis-orientation (MO) from [001], while only 30% blades manufactured by the spiral selector process had such orientation.

The Third Pacific Rim International Conference on
Advanced Materials and Processing (PRICM 3)
Edited by M.A. Imam, R. DeNale, S. Hanada,
Z. Zhong and D.N. Lee
The Minerals, Metals & Materials Society, 1998

Introduction

Since SC superalloy has excellent combination of creep rupture strength, transverse mechanical properties, thin-wall properties, good fatigue, corrosion resistance, and oxidation resistance, it has been developing rapidly from the first generation with temperature capability of 1040°C to the second generation with temperature capability 1070°C and the third generation with temperature capability 1100°C [1]. Today the first and second generation SC superalloys are widely used for advanced military and commercial turbine airfoils[1-6].

There are two processes for production of SC superalloy articles, i.e., the selector process and the seeding process. Selector process is based on the principle of competitive growth of grains to produce SC article with [001] orientation. However, in this case, transverse crystallographic orientation can't be controlled, and the crystallographic mis-orientation (MO) from [001] orientation is greater than that by the seeding process. In seeding process, SC growth originates from SC seed. Crystallographic orientation of castings depends on the crystallographic orientation of seed, therefore crystallographic orientation of casting can be controlled very well.

For the engineering application of SC airfoil, property data of different orientations, such as [001], [011], [012] and [111], are often required for strength calculation and life prediction. In this case, seeding process is necessary to be used for manufacturing specimens with desired orientation. Usually, creep rupture strength of [111] orientation is better than that of [001]. Therefore, if the intrinsic anisotropy of SC is going to be brought full play, i.e., to manufacture SC blade with [111] orientation, the seeding process will be the only way. It has been found that seeding process is suit to produce complicated SC parts. The turbine vane doublet with a sophisticated, cored configuration is difficult to be manufactured, however, seeding processes results in 90% yield for this turbine vane doublet [2]. For the manufacture of multi-piece, cast and bonded SC airfoil with very complicated internal cooling channel and with high cooling effect, it's required that the crystallographic MO must not exceed 3°. In order to meet this requirement, seeding process has to be used [2]. In a word, whether for the application of SC superalloy or for the manufacture of airfoil with very complicated internal cooling channel, the seeding process has to be used. In this investigation, two kinds of seeding processes had been designed to study the process of SC castings comparatively , and the second seeding process had been compared with spiral selector process in the production of a small solid blade.

Design of Seeding Processes

There are several factors to affect the yield of SC, such as, the shape and size of seed, the surface-roughness of seed, the gap between the seed and the internal surface of shell-mold, and the parameters of directional solidification. In order to get excellent combination of the above factors, and to force seed play only one nuclear role in directional solidification, two seeding processes are designed.

The first seeding process

Fig.1-A is a schematic illustration of the first process. In this process, the surface roughness and the size of the seed must be strictly controlled to provide a smaller gap between the seed and the shell-mold, which results a less opportunity of a nuclear in the space between the seed and the mold, and makes seed to be easily placed into mold. If the gap between seed and shell-mold, or other factors are not well controlled, several grains will appear in the zone under the thin

channel (see Fig.1-A). when these grains pass through the thin channel, the thin channel can play competitive selector role, which may increase SC yield. Cylindrical SC seeds with desired orientations, such as [011], [012] and [111], are obtained by rough cutting, lathing and grinding from SC bars with orientation [001]. The wax-patterns of seed and bar are assembled together, then shell-mold are manufactured by ordinary manufacturing shell-mold process in author's laboratory.

The experimental work on this seeding process has been carried out in HRS-type directional solidification furnace ZGD-1. Before positioned into the directional solidification furnace, shell-mold is cleaned, and the seed is fixed into shell-mold. To ensure that the upper part of seed is melted, a thermocouple is fitted to the middle of the seed to record and control the temperature of the seed by a computer(see Fig.1-A). Temperature of seed is controlled at the temperature range of mushy-zone. Experiment in furnace ZGD-1 is carried out in usual directional solidification parameters for SC castings in author's laboratory.

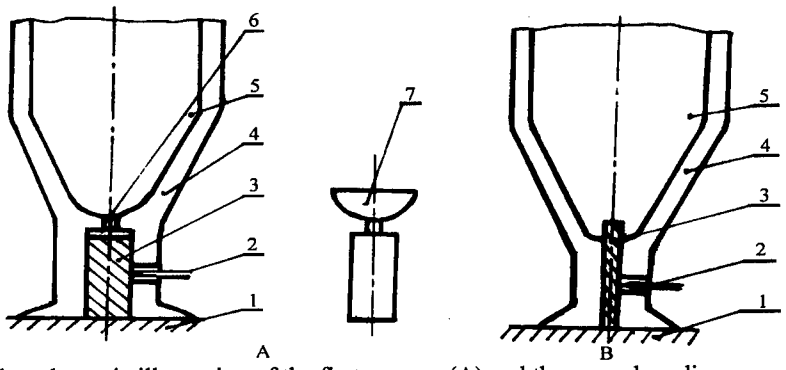


Figure 1: The schematic illustration of the first process (A) and the second seeding process(B)
1. Cu-chill, 2. thermocouple, 3. seed, 4. mold, 5. cavity, 6. thin channel, 7. wax-pattern for seed fit

The second seeding process

The second seeding process is illustrated in Fig.1-B. The SC seed and the wax-pattern of bar or blade are assembled together with the help of a special wax and a special device. Then shell-mold is produced by ordinary manufacturing shell-mold process in this laboratory . After dewaxing and special firing procedures, shell-mold with SC seed is obtained. The problems related to the gap between the seed and the shell-mold can be avoided by this process. The seed is easily prepared by electric sparking machining, and the surface roughness and the size of the seed are not strictly required. Before being positioned shell-mold into furnace, shell-mold must be cleared carefully by a special method.

The experimental work on this seeding process has been carried out in both HRS-type directional solidification furnace ZGD-1 and LMC type directional solidification furnace YBHK-8 П. Directional solidification parameters for this process in the furnace ZGD-1 are the same as these for the first process. The parameters in the furnace YBHK-8 П are the same as usual directional solidification parameters for SC castings in the furnace YBHK-8 П in this laboratory. In the directional solidification process, in order to only melt the upper part of seed, thermocouple is fitted to the middle of seed (see Fig.1-B) to record and control the temperature of the seed by a computer. The material of seed and SC superalloy for articles in this

experiment are SC superalloy DD3.

Experimental Results and Discussion

The first seeding process

Forty bars have been cast by the first process, of which 17 bars were qualified with different orientation. The crystallographic orientations of the bars are listed in table I. The left of the bars were not SC, but the lower parts of almost all the bars were SC.

Table I: The crystallographic orientations of bars manufactured by the first process

[011]			[012]			[111]		
bar No	MO of bars	MO of bars from the orientation of seed*	bar No.	MO of bars	MO of bars from the orientation of seed**	bar No.	MO of bars	MO of bars from the orientation of seed***
1	9.5°	4.5°	1	12.0°	4.0°	1	3.0°	3.0°
2	11.0°	6.0°	2	13.0°	5.0°	2	2.0°	2.0°
3	10.5°	5.5°	3	12.0°	4.0°	3	2.0°	2.0°
4	9.0°	4.0°	4	14.0°	6.0°	4	6.0°	6.0°
5	9.0°	4.0°	5	9.0°	1.0°	5	5.0°	5.0°
6	9.5°	4.5°				6	4.°0	4.0°

*The MO of seed from orientation [011] is 5°; ** the MO of seed from orientation [012] is 8°; *** the MO of seed from orientation [111] is less than 1°.

The fact that the lower part of almost all the bars is SC shows that all directional solidification of the bars is successfully started from seed, and that this process is acceptable in seeding process design. However, the SC yield is only 42.5%, which indicates that it's necessary to regulate directional solidification parameters and find reasonable directional solidification parameters for this seeding process to increase SC yield; This process can control MO from the orientation of the seed under 6° for the above orientations, but the orientations of the seed and the casting are not same. The reason may be that in the process of assembling the wax-pattern of seed and bar, the orientations of the wax-pattern of seed and bar are not well controlled. It has been found that the MO of bar depends on that of seed, i.e.,the less of MO of seed, the less of the MO of bar. For examples, if the MO of seed far from orientation [111] is less than 1°, the MO of bar from the orientation [111] is less than 6°, and if the MO of seed far from orientation [012] is 8°, the MOs of bars from the orientation [012] varies from 9 ° to 14°. The great miss-orientation of seed is the results of many procedures during the seed machining.

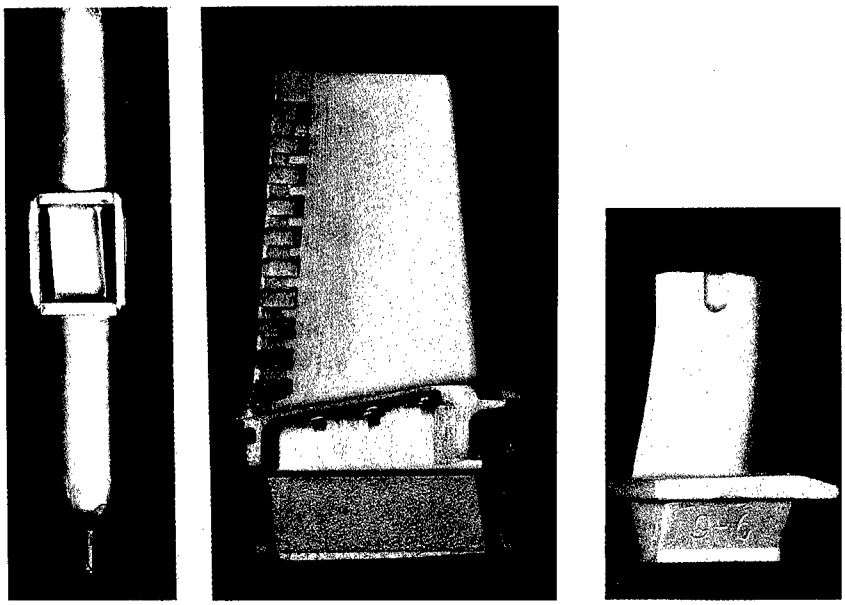
The second seeding process

As the seed for second seeding process is very easily manufactured, several kinds of blades as shown in Fig.2 are produced by the second seeding process, and the results are listed in Table II. The results in Table II shows that the SC yield is in the range of 60 ~ 75% which is quite acceptable for engineering application. These rejects were mainly attributed to the formation of spurious grains in the transition region of the seed and the casting. The formation of spurious grains in the transition region of the seed and the casting may be attributed to that when the

wax-pattern of blade and seed are assembled together, the transition region is not smooth enough.

Table II. The SC yields of several blades manufactured by the second seeding process

blade	furnace	yield %
simulated blade (Fig.2-A)	ZGD-1	75
solid blade (Fig.2-B)	YBHK-8 П	60
hollow blade (Fig.2-B)	ZGD-1	67
solid blade (Fig.2-C)	ZGD-1	>75



A B C

Figure 2: The blades manufactured by the second seeding process
A. Single crystal simulated blade, B. Single crystal blade, C. Small single crystal blade

Table III: The results of the MOs of blades manufactured by different processes

Process	Percentage of blades with MO far from [001], %				
	<5°	5° ~ 6°	7°	8° ~ 10°	>10°
second seeding	78.6	14.3	7.1	0	0
spiral selector	31.0	11.9	11.9	28.5	16.7

The measured results of the orientations of small SC solid blades as shown in Fig.2-C, manufactured by the second seeding process and spiral selector process in the HRS-type directional furnace are listed in Table III. It can be seen that the MO of 78.6% blades manufactured by this process far from [001] is less than 5°, and the MO of 100% blades far

from [001] is less than 8°. These results indicate that this process can control the MO of all castings within 8°, which is a satisfactary value for crystallographic orientation of SC process control. The success of this process may be due to the fact that the problem related to the gap between seed and shell-mold is eliminated, seed machining procedures are decreased by comparison with the first process, and the orientation of seed is easily controlled.

From the above experimental results, it can be seen that both seeding processes are able to well control crystallographic orientation. In the first process, as seed structure has a combination of the seed process and the competitive selector process, and the surface-roughness of seed, the shape and the size of the seed, and the gap between the seed and the internal surface of shell-mold are well controlled, therefore the lower part of almost all the bars is SC. However the yield of the first process is comparatively lower, the main reason is that there is a thin channel which decreases the velocity of dissipating heat from the Cu-chill and makes the temperature gradient lower. In the case of the second seeding process, machining seed is easier, the orientations of the seed are easily controlled in the machining seed process, the surface roughness and the size of the seed are not strictly required, and there is not thin channel shown in the first process, so this process has a higher SC yield. In a word, the second seeding process is better than the first one.

Conclusion

The both developed seeding processes can well control crystallographic orientation. The second seeding process results in higher SC yield than the first one. Several kinds of airfoils have been cast by the second seeding process with more than 60% yield. For the production of SC castings the second seeding process is better than the first one.

Reference

1. K. Harris, G. L. Erickson, and R. E. Schwer, " Directionally Solidified and Single Crystal Superalloys, Specially Steel and Heat-Resistant Alloys " Metals Handbook 1 (1990), 995-1006.

2. D. J. Frasier et al., " Process and Alloy Optimization for CMSX-4 Superalloy, " High Temperature Superalloy for Power Engineering, (1990), 1281-1300.

3. A. D. Cetel and D. N. Duhl, " Second-Generation Nickel-Base Single Crystal Superalloys, " in Sixth International Symposium on Superalloys, The Metallurgical Society, (1988), 235-244.

4. G. L. Erickson *et al.* " The Development of CMSX-10, a Third Generation SC Superalloy, " Paper Presented at The Second Pacific RIM International Conference on Advanced Materials and Processing, (1995).

5. W. R. Walston, *et al.*, USP 5270123, (1993) 12

6. P. S. Burkholda, M. C. Thomas and D. J. Frasier, " Allison Engine Testing CMSX-4 Single Crystal Turbine Blades and Vanes, " The Institute of Materials 3rd International Charles Parsons Turbine Conference " Material Engineering in Turbines and Compressors " , 4(1995), 25-27.

MODELLING THE DEEP BED FILTRATION OF ALUMINIUM

Rung T. Bui, Duygu Kocaefe, Laszlo I. Kiss
Université du Québec à Chicoutimi
Chicoutimi, Québec, Canada, G7H 2B1

Abstract

Inclusions of micrometric dimensions in liquid aluminium must be removed to allow the fabrication of high quality alloys. The presence of inclusions may cause costly defects in small-size high-precision products. Industry uses deep bed filters made of granular collectors to capture the inclusions. The mechanism is complicated by an interplay of fluid flow, turbulence, surface forces, body forces resulting in not only capture but also re-entrainment of the inclusions by the flow, and release of inclusions back into the flow, under some conditions. Bed filters constitute a modern technlology that is still capable of worthwhile improvements.

A computer modelling is proposed to help study the behavior and performance of bed filters. A physical modelling is also proposed to complement the study by analyzing, on an enlarged scale, the effects on filtration efficiency of flow instabilities, fluctuations, and of different geometries and arrangements of collectors .

The Third Pacific Rim International Conference on
Advanced Materials and Processing (PRICM 3)
Edited by M.A. Imam, R. DeNale, S. Hanada,
Z. Zhong and D.N. Lee
The Minerals, Metals & Materials Society, 1998

Introduction

Inclusions of micrometric dimensions present in liquid aluminium must be removed to allow the fabrication of high-quality alloys. The presence of inclusions may lead to costly defects in high-precision products.

Deep bed filtration uses collectors made of granular media to capture the inclusions in liquid metal flowing through the bed. Capture is brought about by a number of mechanisms, some of which are of hydrodynamic origin, others are of physico-chemical origin. Some of those mechanisms are well understood whereas others are still at an early stage of investigation. Filtration is a complex process involving an interplay of fluid flow, turbulence, surface forces, body forces, boundary layer effects, resulting in not only the deposition of inclusions on the collector elements'surfaces, but also their agglomeration, re-entrainment by the flow of liquid metal, and even massive release of deposited inclusions back into the metal, under some conditions.

Deep bed filtration is a modern technology that, though operational for a number of years, is still in need of more understanding, both qualitatively and quantitatively. There is still room for improvements, and improvements promise high economic payback.

The granular media can be made of various materials, with alumina particles being the most commonly used in the aluminium industry. Different particle sizes are used, each is referred to as a filter media grade.

The removal of inclusions occurs when the latter are deposited on the surface or inside the pores of the granular media. The media will not succeed in retaining the totality of the deposition, as part of it will be re-entrained by the metal's fluid motion, whereas another part can be released back into the metal as a result of mechanical effects such as shocks, vibrations, or hydrodynamic effects such as sudden changes or instabilities in the flow regime. Those mechanisms result in a decrease in the deposition rate.

There is a strong motivation to find ways to improve the design and operation of the bed with a view to maximizing the deposition rate, minimizing the re-entrainment and release rates and consequently optimizing the overall removal of inclusions. For commercial reasons, it is important not only to reach a high quality of filtration but also to maintain reliability over time, which means predictability of the inclusion removal rate. This stresses the importance of properly managing the process.

Previous work

Past work laid emphasis mostly on mathematical modelling, in a few cases physical modelling, the latter aiming at clarifying some of the mechanisms, through experimental means such as scale modelling using water as the working fluid.

Most mathematical models can be classified as microscopic models and macroscopic models. Microscopic models aim at analyzing the behavior of individual inclusions during their journey through the filtering media. They are based on trajectory analysis, the trajectory equations account for the forces acting on the inclusions. Trajectory analysis together with a proper representation of the porous medium is used to evaluate the filtration rate. The porous medium is represented either as a single collector or as a collection of connected elements. Each element contains an assembly of collectors with a specific geometry. Depending on the porous medium representation, microscopic models are reported in the literature as capillary models [1], constricted tube models [2], single sphere models [3], sphere-in-cell models [4] or network models [5].

Whereas microscopic models cannot simulate the long-term dynamic behavior of the filter, macroscopic models involve the solution of the mass conservation equation together with a rate law describing the inclusion deposition, and they can simulate the overall dynamic behavior of the bed. They use different parameters such as permeability, filter coefficient or filtration

efficiency to describe bed behavior. Results obtained from microscopic models can also be used to represent some of the parameters. A variety of macroscopic modelling work is reported in the literature [6] [7] [8]. An in-depth review can be seen in Tien's work [9].

Physical modelling is rather infrequently found in the literature, in part because work of this kind often involves proprietary information. An example can be found in Frisvold [10] using spherical and cylindrical collectors, and water as working fluid, to study the collection efficiency, whereas in a study of the sand-water system Kau and Lawler [11] analyzed the dynamics of particle capture and pressure loss in laboratory filters.

Scope of this work

In this paper a two-fold modelling work is reported. In the first part, a transient macroscopic mathematical model is developed using a rate expression to describe the inclusion deposition together with its negative component, the re-entrainment. As it is a macroscopic representation, it gives the bed's overall dynamic behavior but says nothing about the microscopic behavior of the collector elements in terms of flow pattern, fluctuations, turbulence, attachment mechanisms, which affect the inclusion removal rate. The study of these microscopic mechanisms constitutes the purpose of physical modelling in the second part of the work, using plexiglas models with water as the working fluid.

Mathematical modelling

The model is one-dimensional, the dimension being the dominant flow direction through the bed, namely the vertical downward direction. The macroscopic mass balance for inclusions is written as function of superficial velocity, inclusion concentration in the fluid, and specific deposit.

The rate equation for deposition, written as function of the filter coefficient, accounts for inclusion deposition with a positive accumulation term, and for re-entrainment with a negative accumulation term. The constants are determined by fitting of model prediction with experimental data.

The pressure gradient in the bed is calculated as function of viscosity, velocity and density of the fluid, porosity and granular size of the bed, using the Ergun equation. The model is solved using the finite-difference technique.

Simulation results

Whereas all rate equations have the same general form, to each media grade must correspond specific values for constants. In order to test the mathematical model, experimental data is taken from a pilot-scale column filter using water as fluid, PVC particles as inclusions and granular alumina as filter media. The inclusions are mixed with water prior to entering the column. Inclusion counts are carried out by Coulter-type counter probes, positioned upstream and dowstream from the filter.

Four different media grades numbered 1 to 4 are used. Grade 1 corresponds to the smallest particle size and Grade 4 to the largest. For each grade, the constants are determined through data fitting. Fitting can be carried out in a straightforward manner, which shows that the assumed form of the rate expression was reasonable.

As an example, Figure 1 gives a comparison of model prediction with experimental data for Grade 1. Comparisons carried out for Grades 2 to 4 yield similarly coherent results.

The model was next used to predict the performance of three multi-grade bed configurations, which for proprietary reason will only be identified as Configurations A, B and C. For illustrative purpose, Figure 2 shows a comparison of model prediction with experimental data for Configuration A. Predictions carried out for the other two configurations also yield good comparison without requiring any additional adjustment.

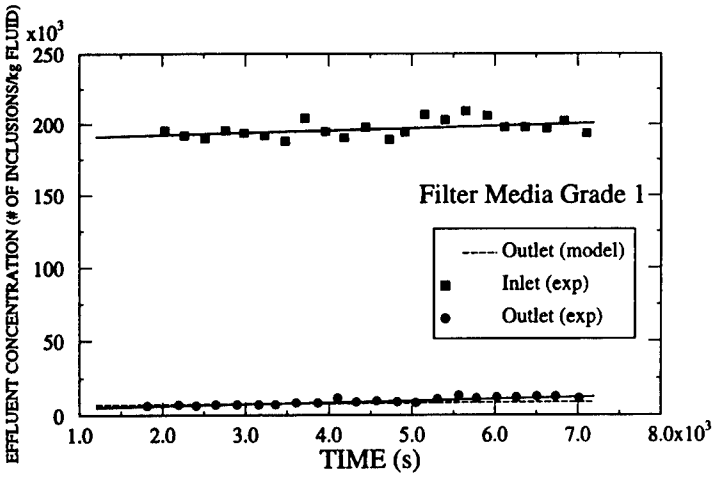


Fig. 1 - Comparing prediction with data, for Grade 1

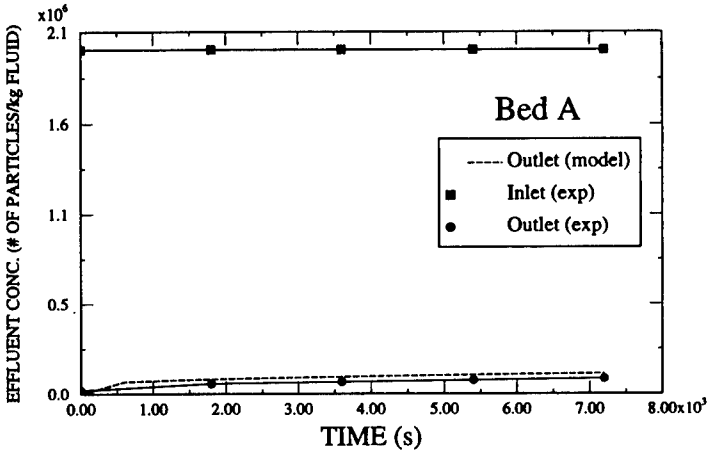


Fig. 2 - Comparing prediction with data, for bed configuration A

Figure 3 presents the inclusion concentration in the fluid for Bed Configuration A. It decreases along the bed depth at a given time. At a given position it increases with time as inclusions are deposited. The inclusion concentration in the effluent increases 1.5 times between 1200 and 7200 seconds. This loss of filtration efficiency is known as filter aging. Further scrutiny of simulation results show that the deposition increases with time, whereas the deposition rate decreases with time, which concurs with observations.

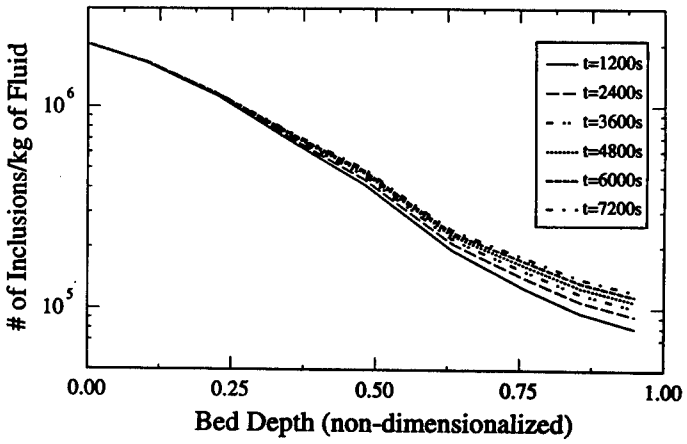


Fig. 3 - Predicted inclusion concentration in the fluid, for bed configuration A

Physical modelling

Physical modelling also helps to analyze the deposition pattern on the surface of the collector, as well as the possible formation of preferential flow channels through the bed. Special attention is also paid to the study of the mechanisms causing the re-entrainment and release of inclusions, especially the effects of shocks, vibrations, flow instabilities and changing flow rates.

Visualization of flow structure is carried out using tracers including milk, fluorescein and solid powders under laser sheet illumination. Velocity distribution is measured along selected sections by laser doppler velocimetry. The deposition of inclusions is studied by introducing solid particles into the water.

Experiments are carried out on single, three by three, seven by seven collector arrangements, either in-line or staggered. Circular, square and semicircular collectors are used. Steady-state flow patterns are determined at different velocities, the effects of increasing and decreasing flow velocities are recorded and analysed. In operating the model, the conditions of hydrodynamic similarity between the model and the real filter element are respected by observing the similarity of the flow pattern including geometric similarity, and the similarity of the movement of the inclusions. The first is met by matching the Reynolds numbers and the second by matching the Stokes numbers. Combining the two conditions yields a criterion that helps select the right particles to represent the inclusions among commercially available powders such as alumina, teflon and nylon.

An important part of the analysis concerns the transient effects such as fluctuations and oscillations, as well as those accompanying flow velocity increases or decreases. Figure 4 gives an example of flow pattern observed in a staggered arrangement of square collectors, using fluorescein tracer under laser sheet illumination.

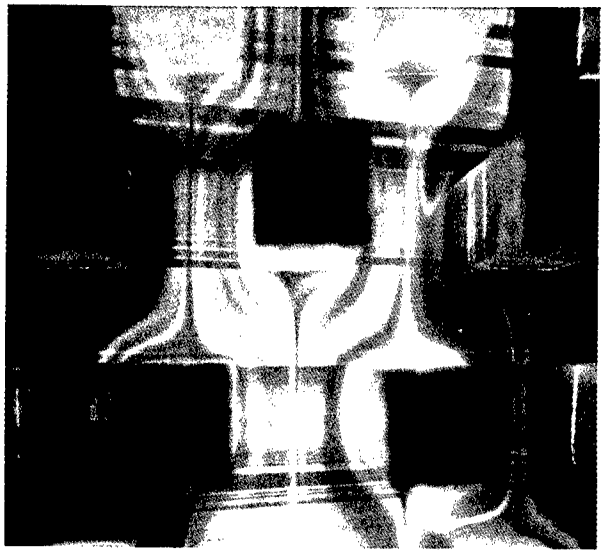


Fig. 4 - Physical modelling: flow pattern in a staggered arrangement of square collectors

Conclusions

A mathematical model has been proposed that provides a good prediction for the behavior of the deep bed filter. The predicted concentration profiles of inclusions along the bed depth as well as the time evolution of concentration at the effluent display the same trends as those observed experimentally. This macroscopic study of the bed filter is complemented by a microscopic analysis using a physical model that allows the investigation of the effects of collectors'size and shape, bed arrangements, flow instabilities and fluctuations, on the behavior and performance of the bed.

Acknowledgements

This study was carried out within the work program of the Industrial Research Chair funded by the Natural Science and Engineering Research Council (NSERC) of Canada, the Arvida Research and Development Center (ARDC) of Alcan International Ltd and La Fondation de l'UQAC. The authors acknowledge the many contributions from T. Bourgeois, A. Chapdelaine, G. Dubé and other scientists of ARDC, together with F. Frischkorn and P. Paquette of UQAC. They thank Alcan for the clearance to publish this text.

Reference

[1] A.C. Payatakes, R. Rajagopalan, C. Tien, *Can J. Chem. Eng.*, 1974, 722-731.
[2] P. Netter, C. Conti, *Light Metals*, 1986, 2, 847-860.
[3] R. Rajagopalan, C. Tien, *Can. J. Chem. Eng.*, 1977, 55, 246-255.
[4] R. Rjagopalan, C. Tien, *AIChE Journal*, 1976, 22, 3, 523-533.
[5] V.N. Burganos, C.A. Paraskeva, *Colloid and Interface Sc.* 1992, 148, 1, 167-181.
[6] C. Tien, R. M. Turian, H. Pendse, *AIchE*, 1979, 25, 3, 385-395.
[7] S. Sembi, K. J. Ives, *Filtration and Separation*, 1983, 398-402.
[8] C. Tien, C. Choo, *Water Sc. and Technology*, 1993, 27, 10, 101-116.
[9] C. Tien, *Granular Filt. of Aerosols Hydrosols*, Butterworth, Ed. H. Brenner, 1989.
[10] F. Frisvold, *Ph.D. Thesis*, Univ. of Trondheim, 1990.
[11] S. Kau, D. Lawler, *J. of Envir. Eng.*, 1995, 850-859.

Fundamentals of Vacuum Assisted Counter Gravity Casting

Dr. Scott R. Giese, University of Northern Iowa

The Minerals, Metals & Materials Society
420 Commonwealth Drive
Warrendale, Pennsylvania 15086

Abstract

Recently, there is a growing trend in the aluminum foundry industry to develop improved melting and casting processes to produce clean, thin walled castings. One casting method that has demonstrated industrial potential for producing clean, thin wall castings is counter gravity casting. Because of its infancy, most of the published work on these processes has been focused on technological advantages of counter gravity casting without any emphasis on the physical characteristics of the process. Because of the lack of information regarding the fundamental process attributes of counter gravity casting methods, industry has not fully adopted these resourceful casting techniques in the production of high quality castings. In this paper, the vacuum assisted counter gravity casting method was utilized to establish rudimentary, but yet fundamental, processing parameters to understand the filling behavior of counter gravity methods. From the research work, it was established that the final pressure and casting temperature determines the potential height of liquid metal filling for vacuum assisted counter gravity casting.

The Third Pacific Rim International Conference on
Advanced Materials and Processing (PRICM 3)
Edited by M.A. Imam, R. DeNale, S. Hanada,
Z. Zhong and D.N. Lee
The Minerals, Metals & Materials Society, 1998

Introduction

Counter gravity casting processes have emerged to the technological forefront as an innovative casting technique for improving the quality of castings. In counter gravity casting, the mold is slightly positioned below the slag line of the melt and an applied pressure, either as a positive pressure on the liquid bath or a negative pressure in the mold, is utilized to siphon the liquid metal from the furnace into the casting cavity. In principle, the liquid metal level never rises until the lower region in the casting cavity is filled, permitting the mold to fill at a controlled, quiescent rate. After the gates are completely solidified, the applied pressure is released and the residual liquid metal in the gating system flows back into the furnace.

Counter gravity casting methods can be divided into two different categories. The first process is low pressure assisted filling where a positive pressure is applied to the liquid metal in the furnace, forcing the metal into the mold[1-6]. The second counter gravity technique is vacuum assisted filling[7,8]. In this technique, a vacuum pressure is applied to the mold cavity and the metal is siphoned from the furnace. Each of these techniques has reported improved mechanical properties and the ability to successfully fill thin sections.

There are numerous advantages of using counter gravity casting methods. Since the mold is lowered below the slag line, mixing of slag and dross is avoided during metal transport from the furnace to the pouring ladle. In addition to avoiding of turbulent agitation during liquid metal transfer, further reoxidation of metal droplets during gravity casting is evaded by the unperturbed, level filling rate of counter gravity casting. Filling rates can be controlled to provide quiescent introduction of liquid metal into thin sections. After the gates have solidified, the applied can be released and any residual metal in the gating system flows back to the furnace. High casting yields are then obtained since the casting gates are not attached to the runner or sprue.

Technical Discussion

Regardless of the pressure method employed for counter gravity casting, designing castings for these resourceful casting techniques requires a sound fundamental understanding of the physical behavior of fluid filling coupled with solidification behavior of the casting alloy. In this research work, vacuum assisted counter gravity method was employed to qualitatively investigate the processing characteristics of this casting technique. By qualitatively establishing the basic understanding of the processing variables, the foundation for future development of theoretical research can be conceived.

Figure 1 illustrates the physical characteristics of counter gravity filling. At the liquid metal interface, fluid motion is controlled by the pressure balance between the applied pressure (positive or negative), $P_{applied}$, the weight of the liquid metal as it rises in the casting cavity, P_{weight}, and the frictional losses of the moving liquid metal, $P_{friction}$. The rate of filling is therefore determined by rate of applied pressure to lift the liquid metal from the furnace. Process controls can be optimized by understanding the physical characteristics of counter gravity casting leading to a better comprehension on how to design castings for these processes.

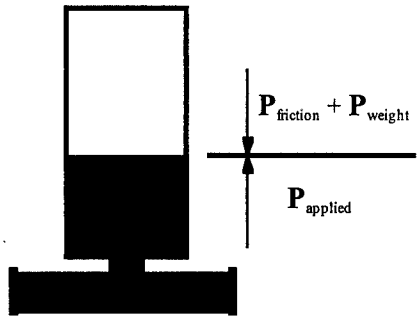


Figure 1. Schematic illustration of liquid metal filling for counter gravity casting.

Metallostatic Height Pressure

During counter gravity filling, as the height of the metal increases, the applied pressure must be continuously adjusted for the increase in metal weight. Ignoring other factors affecting counter gravity casting, the filling rate is a function determined by the required pressure to lift the liquid metal to a prescribed height. To determine the necessary applied pressure to lift the liquid metal to a height to completely fill the casting cavity, one can roughly approximate the necessary pressure for a given commercial alloy by using

$$P_w = \rho g h \qquad (1)$$

where ρ is the density of the liquid metal, g is the gravitational constant, and h is the height of the liquid metal. From the equation, the applied pressure for counter gravity filling is dependent on the density of the liquid metal. It can be easily demonstrated that liquid aluminum can be raised two and half times higher than liquid iron at a constant pressure.

Experimental Approach

An A356 aluminum rectangular plate was incorporated to study the filling and solidification characteristics of vacuum assisted casting. The dimensions of the casting arrangement are schematically illustrated in figure 2. Phenolic urethane bonded silica sand (AFS GFN 58) molds were made using a continuous mixer. For the inlet sprue, an insulating fiber tube was inserted into the bottom on the phenolic urethane mold package and sealed with an epoxy adhesive. During the preparation of the molds, 30 kg of A356 alloy was melted in a ceramic coated, gas fired steel pot furnace. When the experimental temperature stabilized, the melt bath was degassed using 5% sulfur hexaflouride (SF_6) and 95% nitrogen injected through a graphite lance at a rate of 80cm^3/sec for five minutes prior to each casting session. Since the research work was directed towards the filling behavior of vacuum assisted casting, no grain refinement or modifier was added to the melt.

For vacuum assisted counter gravity casting method, the phenolic urethane mold package was lowered into the vacuum chamber with an insulating tube extending 12.7 cm from the bottom of the canister. The canister was filled with coarse, dry silica sand (AFS GFN 28) and then sealed. The vacuum canister was transferred to the gas fired holding furnace and lowered to a programmed height where the insulating filling tube was immersed to approximately 10 cm below the aluminum melt surface. A programmed vacuum cycle initiated the filling process, starting at ambient pressure and ending at the experimental vacuum pressure. The total vacuum cycle time was determined to account for filling and solidification of the aluminum plate casting.

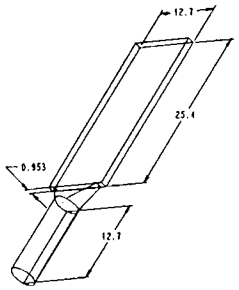


Figure 2. Schematic drawing the experimental casting arrangement. All shown dimensions are given in centimeters. The diameter for the inlet sprue that is inserted into the furnace is 3.175 cm. The depth of the flange connecting the sprue and casting is 3.175 cm.

Discussion of Results

Influence of Pressure

For vacuum assisted filling, the applied vacuum cycle controls the filling rate and is dependent on the volumetric removal of the mold gases from the mold chamber. Factors influencing the filling rate is the permeability of the backing sand, permeability of the core wash, generation of mold gases from the decomposition of the molding material, and the vacuum pump efficiency. For the production of castings using the vacuum assisted counter gravity method, the required vacuum pressure is determined by the height of the casting and the density of casting alloy as determined by Eq 1. In this investigation, the objective was to raise the liquid aluminum partially in the plate casting and hold the vacuum pressure for a programmed period of time. As the metal is suspended in the plate cavity, solidification proceeds from the mold wall, capturing the raised height of the liquid aluminum at a steady state pressure.

A series of experiments was conducted at different target vacuum pressures of 6.77 kPa, 10.16 kPa, and 11.85 kPa at 648°C to verify this hypothesis. A single stage vacuum profile was used with a vacuum cycle time of 30 secs. A typical vacuum profile is shown in figure 3. 95% of the target vacuum profile was reached in approximately 18 secs. For all vacuum pressures tested, none of the plate castings completely filled. Table I shows the calculated height using Eq. 1 and the measured height for the given pressure. For all vacuum pressures investigated, the measured filling height showed good correlation with the calculated height, confirming that Eq. 1 can be used to determine the target vacuum pressure for vacuum assisted counter gravity casting.

Table I. The Influence of Vacuum Pressure on the Casting Height for A356

Target Vacuum Pressure (kPa)	Actual Vacuum Pressure After 30 secs. (kPa)	Calculated Height using Target Vacuum Pressure (cm)	Calculated Height using Actual Vacuum Pressure (cm)	Measured Height (cm)
6.77	6.57	24.9	24.2	24.1
10.16	9.55	37.4	35.1	36.2
11.85	11.48	43.6	42.3	39.4

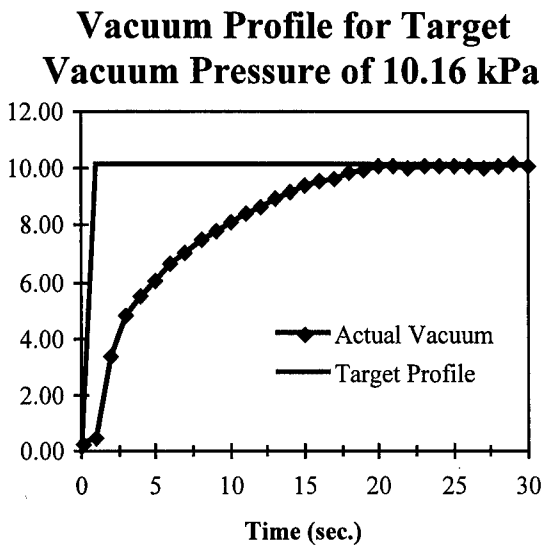


Figure 3. Single cycle vacuum profile used to investigate the influence of vacuum pressure on casting height for A356 alloy.

Effect of Superheat

Another critical factor to consider during vacuum assisted casting is the effect of superheat temperature. For traditional gravity casting, superheat is required to improve the fluidity of the liquid metal into thin sections, insuring complete filling of the section. If the superheat temperature is insufficient, incomplete filling of the casting occurs. In counter gravity casting, as the liquid rises in the casting cavity, fluidity is decreased by the lost of superheat to the contact surface area of the mold and solidification can further prohibit filling. The investigation was directed towards determining the influence of superheat temperature on filling height using a constant vacuum pressure.

In determining the superheat temperature, it was assumed that Newtonian flow stops when the first solid begins to form in the liquid, or at the liquidus temperature. For A356 aluminum, the liquidus temperature is 582°C. The following superheat temperatures were investigated: 10°C, 48°C, 86°C, and 124°C. The vacuum profile selected was 10.16 kPa with a 30 sec. vacuum cycle time. The measured height and casting observations are presented in Table II. The results of the experiments clearly show that insufficient superheat temperature inhibits complete filling of the casting cavity.

Complete filling of the casting cavity was achieved with a superheat temperature above 86°C. However, for both castings that completely filled the casting cavity, the castings were hollow. Based on solidification time calculations, it was expected that the casting would be solid with only solidification shrinkage cavities. During the processing of the castings, furnace bath fluctuations were observed for both castings approximately 20 seconds into the vacuum profile cycle. Because of the large voids observed in the castings, it was concluded that the source of the voids was directly attributed to the porous fiber inlet tube. Since the fibrous insulating tube is permeable, air can be siphoned into the inflow stream during casting. It is recommended that a nonporous inlet tube be used to insure a vacuum seal is maintained between the melt bath and the casting canister and will be incorporated in future studies.

Table II. The Influence of Superheat Temperature on the Casting Height for A356

Superheat Temperature (°C)	Measured Height (cm)	Comments
10°C	23.6	Solid, Partially Filled
48°C	27.4	Solid, Partially Filled, Cold Shut Defects
86°C	39.8	Partially Hollow, Completely Filled
124°C	39.8	Partially Hollow, Completely Filled

Summary

The processing variables of vacuum assisted counter gravity casting were qualitatively investigated. The research work demonstrated that the height of filling is dependent on the final vacuum pressure determined by the potential metallostatic height and superheat temperature. The vacuum assisted counter gravity process offers a novel technique for the production of high quality aluminum castings. Though its ability to fill thin section castings is well documented, large sectioned areas still need further investigation to develop gating and risers design guidelines to maximize casting yield. Future research work in vacuum assisted counter gravity casting is investigating how the shape of vacuum profile controls the rate of filling to insure complete filling of the casting cavity.

References

1. Wilkens, P.S.A., "GKN + Cosworth - A New Concept in Aluminum Casting." *Foundry Trade Journal*, Vol. 151, No. 3223, Oct. 8, 1981, pp. 592-598.
2. Tomlin, D.J. and Wilkins, P.S.A., "The GKN - Cosworth Process for the Precision Casting of Aluminum." *Foundry Trade Journal*, Vol. 154, No. 3254, Jan. 13, 1983, pp. 46-47.
3. Webster, P.D. and Mufti, N.A., "Pressure Sand Casting." *Foundry Trade Journal*, Vol. 169, No. 3505, April 3, 1995, pp. 157-160.
4. Cowdrey, M., "Differential Pressure Sand Casting System." *Foundry Trade Journal*, Vol. 166, No 3458, July 24, 1992, pp. 458.
5. Edwards, D.S. and Hunter, T., "The Cosworth Process.", *Foundry Trade Journal*, Vol. 166, No. 3458, July 24, 1992, pp. 446-453.
6. Grant, M., Guy, S., and Thomas, J., "The Castyral Process Improvement to Lost Foam Process." *Foundryman*, January 1991, pp. 29.
7. Chandley, G.D., "Making Castings Without Ladles or Sprues." AFS Transactions, Vol. 84, 1976.
8. Chandley, G.D., "Automatic Counter Gravity Casting of Shell Molds." AFS Transactions, Vol. 91, 1983, pp. 199-204.

PURIFICATION OF LEACHED METALLURGICAL GRADE SILICON BY ELECTRON BEAM MELTING

A. F. B. Braga[(1)], J. Otubo[(1,2)] and P. R. Mei[(1)]
[(1)] State University of Campinas, Dept. of Materials Engineering,
13083-970, Campinas, S P, Brazil, e-mail: jotubo@fem.unicamp.br
[(2)] IPEN/CNEN, Dept. of Materials Engineering, 05508-900, S. Paulo, SP, Brazil

Abstract

Silicon is commonly used to convert solar energy into electrical energy. To make this source of energy economically viable we should decrease the cost of silicon and solar cells devices. One of the possibility for the cost reduction is by the use of polycrystalline silicon. In this work we present the results of leached metallurgical grade silicon (MG-Si) purified by electron beam melting (EBM). The advantages of this process are to work in high vacuum (10^{-3}Pa) inside the chamber and the non existence of reaction between molten silicon and copper crucible. The parameters varied to prepare the samples were the electron beam power and beam incidence time on the molten pool. It was concluded that the process can reduce the impurity concentration of the Fe, Al, P, Cr, Ni, Cu and the C. The preliminary results look promising and the best result was 99.999% pure silicon.

The Third Pacific Rim International Conference on
Advanced Materials and Processing (PRICM 3)
Edited by M.A. Imam, R. DeNale, S. Hanada,
Z. Zhong and D.N. Lee
The Minerals, Metals & Materials Society, 1998

Introduction

The use of silicon to convert solar energy into electric energy is very common. However for the photovoltaic energy to compete in terms of cost with other sources of energy, the price, in module, of the solar cell device should be substantially reduced (1). That reduction can be made with the use of the polycrystalline silicon. In that sense several groups have been working with different processes to produce polycrystalline solar grade silicon (SG-Si) directly from the metallurgical grade silicon (MG-Si). One of the proposed processes to purify MG-Si is by electron beam melting (EBM). The advantages of this process are the high vacuum to eliminate impurity elements with vapor pressure higher than the one of the silicon and the elimination of the reaction between the melt and water cooled copper crucible.

The objective of this work is to study the purification of the MG-Si by EBM where the related literature is rare (2, 3, 4, 5, 6). Another motivation for this work is that the Brazil possesses one of the world largest quartz reserve, the raw materials for silicon production and it is also the one of the world largest producer of MG-Si (7). Besides that, the Brazilian MG-Si is one of the best in quality with 99.5 to 99.7% purity. Researchers from another countries have worked with 98-99% purity MG-Si (8, 9).

Experimental procedures

In this work it was used leached 150 to 250 μm MG-Si powder with 99.97wt% purity. The material was ultrasonically cleaned with acetone, rinsed in water and finally it was dried. The starting charge for each sample was 280g. The material was supplied by the RIMA Industrial SA.

The melting was done in an 80kW EB furnace, model EMO 80-LEW. The figure 1 shows the melting chamber and the water cooled copper crucible with the charge. Once charged, the chamber was closed and evacuated to initiate the heating. The heating was made by increasing the EB power in steps up to the point where all silicon had melted. On the molten material, the beam power was maintained for a certain time. After that time, the EB power was gradually decreased until its extinction. The varied parameters were the EB power and the time of beam maintenance on the liquid bath as can be seen in the Table I. The initial chamber internal pressure was the order of 10^{-3}Pa.

The carbon was determined by infrared spectroscopy (FTIR) in the 300μm thick samples, mechanically polished in diamond paste up to 0.25μm measured in the 605cm^{-1} wave number that characterizes the presence of the substitutional carbon. The same samples were used for resistivity measurement by the four points probe method using Keithley Instruments equipment, model 503. Al, Fe, P and B were analyzed by Glow Discharge Mass Spectrometry, VG Instruments, models VG 9000.



Figure 1. Melting chamber with charged water cooled copper crucible

Table I - Samples processing conditions

beam maintenance time (minute)	0; 10; 20
EB power (kW)	12; 16; 18,7
Initial chamber pressure (Pa)	10^{-3}

Results and discussions

In terms of processing, it was observed that minimum necessary EB power for melting 280g of silicon is 12kW. The upper limit for the same amount of material is 18.7kW for a 10 minutes of beam maintenance time. Longer time at this power promotes unstable process and the melt starts to stir. The process showed viable in the intermediate combinations of EB power and time. It was observed that the chamber internal pressure increases during the heating period due to degassing reaching values of the order of 10^{-1}Pa. Once the charge starts to melt, the chamber internal pressure remains high due to the evaporation of elements with vapor pressure higher than that of the silicon. For a longer time of EB incidence the chamber internal pressure start to decrease reaching 10^{-2}Pa. The best condition for the impurity removal was 16kW EB power with 20 minutes of beam maintenance whose sample is shown in the figure 2, top view. It was observed that the last part to solidify is the center of the sample because this is the most distant part in relation to the bottom of the water cooled copper crucible. Beside that, the EB power is decreased gradually and its extinction happens in the center of sample. A close look of figure 2 shows a series of loops on the sample surface indicating the solidification front. These loops, in fact, are isothermal loops indicating the existence of a temperature gradient toward the center like in a directional solidification. This fact was proved by chemical analysis. The top area, or center part, presents higher impurity content compared to the edge as can be seen in the Table II. For comparison it is also shown in Table II, the results obtained by Ikeda and Maeda (5). In the same manner, they used MG-Si purified by EBM using 50g samples. It can be seen that they did not succeed in removing boron, iron and the titanium. In our work it was seen that the removal of the boron is really difficult and the best result was a decrease of

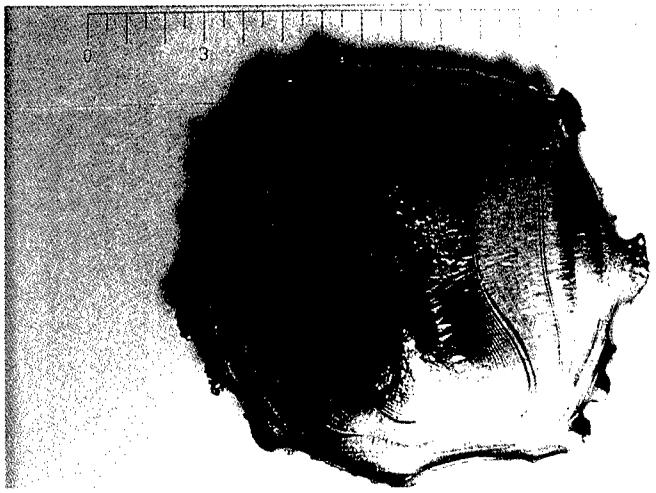


Figure 2. Top view of silicon sample

Table II Chemical composition of the sample before and after EBM (ppmwt).

	Ikeda (5)		(This work)		
Element	Raw material	After EBM	raw material	After EBM (edge)	after EBM (center)
B	15-20	15-20	13	7.9	11
Al	1800-2000	470	65	0.11	2.4
P	38-45	15	25	1	2.6
Ca	1300-1400	150	110	0.024	4.7
Ti	250-270	>270	2.8	0.001	0.31
V			0.2	<0.001	0.015
Cr			3.1	0.005	0.023
Mn			1.5	0.005	0.097
Fe	3200-3800	>3800	50	0.025	9.3
Ni			0.72	0.01	0.48
Cu			0.82	0.016	0.085
Zn			0.63	<0.1	<0.1
Sr			1	<0.05	0.079
Zr			0.37	<0.01	<0.1
C	150-180	15	540	0.5	
Remainder			23.83	0.624	0.851
Total metallic impurity (ppmwt in mass)	>7715	>4740	298	10	32
Removal efficiency (%)		39		97	89

in boron content near the sample edge. However, the removal of the iron and of the titanium was good and they were respectively of 99.95 and 99.96% with residual content of 0.001 and 0.025 ppmwt in mass. The removal efficiency of the other elements such as phosphorous, calcium and aluminum were respectively of 96.01, 99.8 and 99.98%, also determined near the sample edge. The carbon was reduced from 540ppmwt to 0.5ppmwt showing that the process is efficient to remove this element. In other processes like unidirectional solidification the carbon contamination is one of the problems because of the use of graphite crucible. Taking into account all the elements, the removal efficiency was 96.7% in the edge and of 89.2% in the top area. This tendency of the impurity concentration toward the center area of the sample could also be detected by electric resistivity measurement as can be seen in the Table III. For various processing combinations (beam power and beam maintenance time), the central part always presented smaller resistivity compared to the sample edge (~10 times smaller). Corroborating the data of chemical analysis, the best result with highest electrical resistivity was the combination of 16kW EB power and 20 minutes of beam maintenance on the melt. The result of 89% of impurity removal in the center part means that most of them are eliminated by evaporation process. Beside that, the removal of elements like boron and the titanium that have lower vapor pressure than the one of the silicon could indicate the compound formation with higher vapor pressure than that of the silicon.

Table III Electrical resistivity measurement

EB power (kW)	EB time maintenance (minute)	Sample region	Electrical Resistivity (Ω.cm)
16	10	center	0.03
16	10	edge	0.40
16	20	center	0.05
16	20	edge	0.60
18.7	10	center	0.08
18.7	10	edge	0.50

Starting with 99.97% pure MG-Si it was possible to obtain 99.999% pure silicon, near the edge of the sample, which could be considered solar grade silicon proving that the purification by EBM is a viable and promising process.

Conclusions

This work showed that the EBM is a viable process for MG-Si purification removing impurities such as: Fe, Al, Ti, Cr, Zr, Cu, Ni, P and C.

In terms of EB power and EB incidence time on molten silicon, it was concluded that the 12kW is the minimum necessary to melt 280g MG-Si and that the 18.7kW beam power with 10 minutes beam maintenance is the upper limit. Longer time or higher EB power make the process unstable. The 16kW EB power and 20 minutes beam maintenance on the molten silicon was the best condition for the impurities removal for 280g of starting charge.

Due to the temperature gradient, the center portion of the samples always presented higher impurity content. However, the efficiency of the removal in that part was 89% indicating that most of the impurities were eliminated by evaporation.

Starting with 99.97% pure MG-Si it was possible to purify to 99.999% pure silicon proving that the purification by EBM is viable and promising process.

Acknowledgments

To CNPq for the financial support for two of the authors: A. F. B. Braga and J. Otubo
To Prof. Dr. Luís Carlos Kretly for the resistivity measurement and discussions;
To Emílcio Cardoso, Claudia Aoki and Rita Jacon for the samples preparations and
To the Rima Industrial for the material donation and chemical analyses and
To Eltese GmbH and RayTec for the support in the EB maintenance.

References

1. R. H. Hopkins and A. Roahatgi, "Impurity effects in silicon for high efficiency solar cells", Journal of Crystal Growth, 75, (1986), 67-79.

2. D. Casenave, R. Gauthier and P. Pinard, "A study of the purification process during the elaboration by electron bombardment of polysilicon ribbons designed for photovoltaic conversion", Solar Energy Materials, 5, (1981), 417-423.

3. D. Casenave, R. Gauthier, L. Vandekerkove and P. Pinard, "Silicon ribbon growth using electron bombardment", Applied Physics Letters, 40, (1982), 698-700.

4. C. E. Noman, E. M. Absi and R. E. Thomas, "Solar-grade silicon substrates by a powder-to-ribbon process", Canadian Journal of Physics, 63, (1985), 859-862.

5. T. Ikeda and M. Maeda, "Purification of metallurgical silicon for solar-grade silicon by electron beam button melting", ISIJ International, 32, (1992), 635-642.

6. T. Ikeda and M. Maeda, "Refining of silicon for solar cells", First International Conference on Processing Materials for Properties, Honolulu, Hawaii (USA), 7-10 Nov., 1993.

8. Y. Sakagushi, M. Ishizaki, T. Kawahara, M. Fukai, M. Yoshikawa and F. Aratani, "Production of high purity silicon by carbothermic reduction of silica using AC-arc furnace with heated shaft", ISIJ International, 32, (1992), 643-649.

7. U.S. Geological Survey, United States Department of the Interior - Bureau of Mines, October 1997 .

9. B. R. Bathey and M. C. Cretella, "Review: solar-grade silicon", Journal of Materials Science, 17, (1982), 3077-3096.

NiTi SHAPE MEMORY ALLOYS PRODUCED BY ELECTRON BEAM MELTING: PRELIMINARY RESULTS

J. Otubo[1,2] and P. R. Mei[1], S. Koshimizu[2] and L. G. Martinez[2],

[1] State University of Campinas, Dept. of Materials Engineering,
13083-970, Campinas, SP, Brazil, e-mail: jotubo@fem.unicamp.br
[2] IPEN/CNEN, Dept. of Materials Engineering, 05508-900, S. Paulo, SP, Brazil

Abstract

The NiTi alloys known since the early 70's present one of the best performance in terms of shape memory effect with shape recovery up to 7%. The transformation temperature of these alloys can be varied from -50°C to +100°C depending upon the chemical composition and the thermomechanical treatment. However, the fabrication process for these alloys is not an easy task due to the contamination by carbon and oxygen in the usual vacuum induction melting (VIM) process. This work will present the preliminary results of the production of these alloys by electron beam melting (EBM). If on one side this process has the advantage of avoiding the contamination by oxygen and carbon, on the other hand it presents difficulty in the control of the chemical composition due to operation in high vacuum. The work will present three nominal composition: Ni44Ti, Ni45Ti and Ni46Ti. The preliminary results of EBM melting look promising with total mass loss smaller than 0.5wt% and final carbon content ranging from 0.012 to 0.016wt% compared to the usually observed values of 0.03 to 0.08wt% of VIM processed materials.

The Third Pacific Rim International Conference on
Advanced Materials and Processing (PRICM 3)
Edited by M.A. Imam, R. DeNale, S. Hanada,
Z. Zhong and D.N. Lee
The Minerals, Metals & Materials Society, 1998

Introduction

The NiTi alloys, known since the decade of 70, developed initially by the NASA (1), possess one of the best performance among the shape memory alloys presenting shape recovery up to 7% with a wide range of technological and medical applications. The alloys are fatigue and corrosion resistant and highly biocompatible (2,3). The temperature of shape recovery can be varied from -50°C up to +100°C, depending upon the chemical composition of the alloys. However its production is very difficult due to the ease of contamination by carbon and oxygen. It also presents difficulties in the mechanical processing needing special procedures.

The usual method of obtaining the alloys is by vacuum induction melting (VIM) using special graphite crucible. The carbon contamination comes from the graphite that reacts with the nickel and titanium. The carbon is highly soluble in the liquid nickel and it possesses a great affinity for titanium. To minimize the contamination, the special graphite of high density and low porosity is used. The use of another type of crucibles such as the MgO crucible or the alumina crucible can provoke oxygen contamination (1). The oxygen contamination could also come from residual oxygen inside the melting chamber, whose internal pressure is of the order of 10Pa.

An alternative process for obtaining the NiTi alloys would be by electron beam melting (EBM). In this process, the carbon contamination is completely eliminated because the alloy is melted in a water cooled copper crucible and the oxygen contamination would be minimized due to operation in a vacuum better than 10^{-2}Pa. It should be noted that one of the most difficult parameter to control in the melting and remelting in a electron beam furnace is the alloy chemical composition due to the operation in high vacuum that promote evaporation of the components. The homogeneity of the chemical composition is fundamental for these alloys because small composition change can result in a large variation in the transformation temperatures. In this work, the preliminary results of obtaining the NiTi alloys by electron beam melting on a laboratory scale will be presented. The samples were produced in button shape with varying the chemical composition of the starting charge. The objective was to analyze the mass loss and consequently the final chemical composition of the EB melted samples. The next step will be the production of small ingots to study process parameters such as: melting rate, ingot surface quality and, mainly, control of the chemical composition along the ingot.

Experimental procedures

For the experiment, three samples were prepared in a button shape: the first with excess of nickel content, Ni43.9%Ti, (named Ni44Ti), the second almost stoichiometric, Ni45.1%Ti, (named Ni45Ti) and the last with excess of titanium content, Ni46%Ti, (named Ni46Ti). The percentages are in weight. The starting raw materials were 99.95% purity electrolytic nickel and 99.56% purity titanium. The two materials were cold rolled to 1mm thick foils, cut in small pieces, pickled in a solution of HNO3 + HF + H_2O and rinsed in water before weighting. The initial charge was of the order of 30g. The samples were melted in an 80 kW electron beam furnace (LEW, model EMO80) in a water cooled copper crucible. The EB power varied from 2 to 4kW and the pressure inside the furnace chamber was kept between $4x10^{-2}$ and $7x10^{-2}$Pa during the melting. For better homogenization the samples were remelted and in each stage they were weighted to check the mass loss. The chamber was opened after ten minutes of cooling time. The characterization of the samples were done by chemicals analysis, X-ray diffraction and differential scanning calorimetry (DSC) (STA409C, Netzsch) with cooling and heating rate of 5°C/minute.

Results and discussions

The visual aspect of the samples after second melting can be seen in Figure 1. The surfaces were shiny and clean without any oxidation.

Table I presents the absolute chemical composition of the elements after the second melting. It can be observed that the carbon content was relatively low (0.012, 0.015 and 0.016% respectively for the samples Ni445Ti, Ni45Ti and Ni46Ti) compared to the materials produced in vacuum induction furnace with graphite crucible which presents carbon content in the range of 0.04 to 0.08% (1). The final iron content was almost the same for the three samples indicating no removal of this element (the initial iron content was around 0.2%). The reduction in the oxygen content was small and after second melting it was around 0.15% compared to 0.19% of starting material. The usual values are between 0.10 and 0.19% (4)

From the Table II, by analyzing the nickel and titanium content and also the ratio Ni/Ti, we can observe that there was a relative loss of the nickel content compared to titanium content mainly in samples Ni44Ti and Ni46Ti while for the Ni45Ti sample, the initial composition was unchanged. Thermodynamically the larger loss of the nickel content in relation to titanium is predicted due to the higher vapor pressure of the former (5). The maximum total loss (Ni + Ti) after second melting was 0.45% for the sample Ni44Ti which is considered perfectly controllable (6).

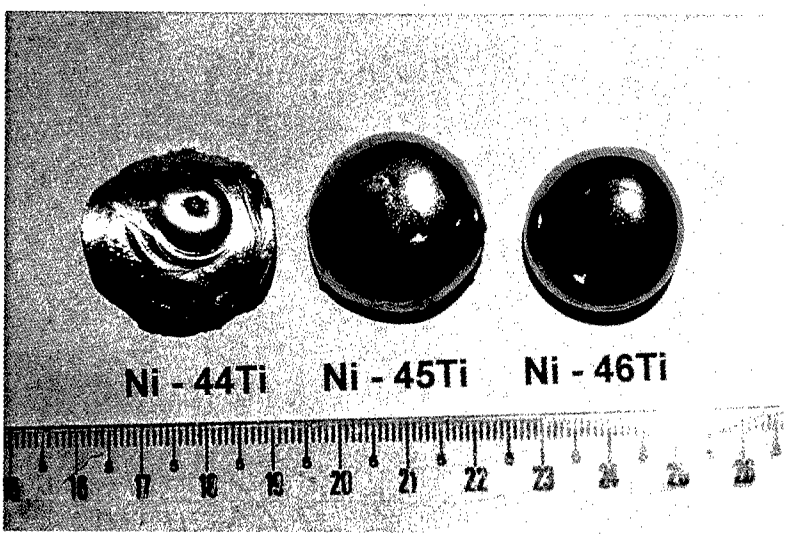


Figure 1. Samples of the NiTi alloys in form of buttons

Table I Samples final chemical composition after second melting in (wt%)

Elements	Ni44Ti	Ni45Ti	Ni46Ti
C	0.012	0.015	0.016
Fe	0.20	0.19	0.21
O	0.1466	0.1482	0.1536

Table II Relative samples composition before and after second melting in (wt%)

Samples	Initial composition		Ni/Ti	composition after 2nd melting		Ni/Ti	Ni + Ti loss
	Ni	Ti		Ni	Ti		
Ni44Ti	56.1	43.9	1.28	55.6	44.4	1.25	0.45
Ni45Ti	54.9	45.1	1.22	54.8	45.2	1.21	0.37
Ni46Ti	54.0	46.0	1.17	53.2	46.8	1.14	0.26

The X-ray diffraction analysis revealed the presence of the following phases in all the samples: stoichiometric NiTi phase, $NiTi_2$ titanium rich phase and Ni_3Ti nickel rich phase. However, by semi-quantitative analysis, the ratios between the relative intensity of $[I/I_o(Ni_3Ti)]/[I/I_o(NiTi_2)]$ were as follow: 18.7 for Ni44Ti; 4.2 for Ni45Ti and 0.16 for Ni46Ti, that is, the sample with high nickel content presented higher content of Ni_3Ti while the one with higher titanium content presented higher content of $NiTi_2$ and coherently the sample Ni45Ti which presents nickel content little bit higher than the stoychiometric composition, presented more Ni_3Ti than $NiTi_2$ but the ratio was only 4.2. According to equilibrium phase diagram (7), $NiTi_2$ phase should not appear in the samples Ni44Ti and Ni45Ti and Ni_3Ti phase should not appear in the Ni46Ti sample. This discrepancies could be attributed to the fluctuations in the samples composition as far as they were in a as-cast condition.

Table III Phase transformation temperatures measured by DSC (°C)

Sample	M_S	M_F	A_S	A_F	M_P	A_P
Ni44Ti	-	-	10.5	21.3	-	14.9
Ni45Ti	24.3	10.1	39.8	52.9	22.8	50.7
Ni46Ti	69.3	45.0	84.4	108.4	54.1	98.4
Ni44.9Ti [12]	58.5	30.1	66.9	97.2	44.3	86.8

Table III shows the transformation temperatures for the three samples extrapolated from DSC curves. The M_S and M_F are respectively the starting and finishing temperatures for martensitic transformation and A_S and A_F are respectively the starting and finishing temperatures for reverse transformation. The M_P and the A_P are respectively the temperatures where the energy involved reaches its maximum or minimum values, that is, the pick temperatures of martensitic transformation or reverse transformation. The martensitic transformation temperatures M_S and M_F for Ni44Ti were not measured (due to disturbance during cooling by liquid nitrogen) but certainly M_S is below 10°C because the A_S for this sample was 10.6°C and A_F was 21.3°C and its A_P was 14.9°C. The Ni45Ti sample had its martensitic transformation completed at 10.1°C (M_F) starting around the room temperature, 24.3°C (M_S), while the A_P was 50.7°C. Therefore comparing the two samples it means that the change in A_P temperature due to increase of 0.8% in titanium content was 35.8°C, or 48.5°C/1wt%Ti. In spite of having twice increase in titanium content (1.6%) when comparing Ni45Ti sample to Ni46Ti sample, the increase in A_P was not so high. It changed from 50.7°C (Ni45Ti) to 98.4°C (Ni46Ti), an increase of 47.7°C, or ~30°C/1wt%Ti. As shown by (8), the above results also indicate that when the composition goes to titanium rich side, mainly above stoichiometric value, the influence of composition change on

the transformation temperatures is small. Now for nickel rich side, the influence of composition on the transformation temperature is much more pronounced and a small change in composition could cause drastic change in transformation temperature. For reference, the Table III also present data of transformation temperatures of a Ni44,9%Ti alloy (9) which are between those presented by the Ni45Ti and Ni46Ti samples. Actually, these values should be located between those presented by the Ni44Ti and Ni45Ti samples. However it should be observed that the transformation temperatures depend upon the composition and also upon the thermomechanical history of the sample (10), what would justify those discrepancies.

These preliminary results showed the importance of controlling the chemical composition that control the transformation temperatures. Beside that, factors such as thermomechanical treatment also should be taken into account because they can alter those temperatures and also the properties of shape memory effect and pseudo-elasticity.

The goals for the future are the scale up of EBM, producing small ingots taking into account parameters such as EB power, melting rate, initial charge as a function of mass loss, composition control along the ingot, surface quality, etc. Also are the goals for the future the domain of mechanical working of the ingots seeking mainly practical applications.

Conclusions

The carbon content after EBM could be kept around the 0.015wt% compared to the usual values of 0.03 to 0.08wt% for VIM;

The total mass loss after double melting was relatively small for all the samples and the maximum loss was 0.45% for Ni44Ti sample and a double melting provoked a relative loss of nickel mainly for the Ni44Ti and for the Ni46Ti samples;

All samples presented stoychiometric NiTi phase and precipitation of the $NiTi_2$ and Ni_3Ti phases;

The transformation temperature is very sensitive to the variation in the chemical composition being more pronounced in the nickel rich side;

These preliminaries results show that the EBM is a viable technique for producing NiTi alloys. The next step will be the scale up of EBM process producing small ingots in the sense to get control of EB power, continuous melting and ingot pulling rate, etc.

Acknowledgment

To CNPq for the support to one of the researchers (J. Otubo);

To IPEN where this project is being developed;

To FEM/DEMA/UNICAMP for the support in the EBM and laboratory test;

To Villares Metals S.A. (Eng. Celso Barbosa and Dr. Elisa Akemi Okasaki) for the support to this project;

To Eltese GmbH and RayTec for the support in the EB maintenance and

To Mr. Odair Rigo (COPESP) and to Emílcio Cardoso, Rita Jacon, José Luís and Cláudia Aoki (FEM/DEMA/UNICAMP) for the support in the laboratory test.

References

1. C. M. Jackson, H. J. Wagner and R. J. Waslewski, NASA Report - SP 5110, (1972.)

2. Y. Oshida and S. Miyazaki, , "Corrosion and biocompatibility of shape memory alloys", Corrosion Engineering, 40 (1991), 1009-1025.

3. R. S. Dutta, K. Madangopal, H.S. Gadiyar and S. Banerjee, "Biocompatibility of NiTi shape memory alloy", British Corrosion Journal, 28 (1993), 217-221.

4. D. C. Brennen, C. M. Jackson and H. J.Wagner,, "Development of melting and casting procedure for Nitinol nickel base alloy", Battelle Memorial Institute, Columbus, Ohio, Report SC-CR-69-3070, (1968)

5. R. E. Honig and D. A. Kramer, "Vapor pressure data for the solid and liquid elements", RCA Review, 30, (1969), 285.

6. H. Matsumoto, "Addition of an elements to NiTi alloy by electron-beam melting method", Journal of Materials Science Letters, 10, (1991), 417-419.

7. P. Bellen, K. C. Hari Kumar and P. Wollants, " Thermodynamic assessment of the NiTi phase diagram ", Z. Metallkd., 87, 1996, 972-978.

8. W. Tang, "Thermodynamic study of the low temperature phase B19' and martensitic transformation in near-equiatomic Ti-Ni shape memory alloys", Metallurgical and Materials Transactions A, 28A, (1997), 537- 544.

9. E. Hornbogen and E. Kobus, "A metallographic study of plastic deformation of martensiticNiTi", Z. Metallkd., 87, (1996), 442-447.

10 S. Koshimizu and C. S. Yamamoto, "Martensitic transformation of NiTi shape memoryalloy", Annals of 10th Brazilian Congress of Engineering and Science of Materials (CBECIMAT), Águas de Lindóia, SP, (1992), 449-451.

NUMERICAL ANALYSIS OF EFFECTS OF ELECTROMAGNETIC BRAKING FORCE ON FLUID FLOW AND HEAT TRANSFER IN FLOW CONTROL MOLD

J.K. Yoon, H.S. Nam, P.R. Cha, K.H. Moon* and J.E. Lee*

School of Materials Science & Engineering, Seoul National University
Seoul 151-742, Korea
*Kwangyang Technical Research Laboratories, POSCO
Kwangyang 544-090, Korea

Abstract

FC-mold(flow control mold) is an equipment to control the molten steel flow in a mold of continuous casting process using electromagnetic braking force. This new generation of the EMBR is characterized by two-level static magnetic field imposed across the entire width of the mold by upper and lower pairs of poles, with the aims of suppressing surface turbulent flow at the meniscus as well as reducing the local downward flow velocity.

A mathematical model has been developed for the coupled analysis of fluid flow, heat transfer and induced current in FC-mold. In order to evaluate the electromagnetic braking force, magnetic field was analyzed with finite element method using A-φ formulation and the result was verified by comparing with experimental data and other calculated data. Fluid flow, heat transfer, induced current and argon gas concentration were analyzed with 3-dimensional finite volume method based on body fitted coordinate.

In FC-mold, it was found that the flow velocity at meniscus was reduced and inclusion behavior pattern was improved in comparison with no magnetic field, and that the flow pattern was less sensitive to different casting conditions in comparison with the conventional EMBR. The influences of some operating parameters such as magnetic flux density, casting width, casting speed, and argon gas bubbling on fluid flow were investigated. Heat transfer and distribution of solidifying shell were also simulated and the result show that the EMBR effects give rise of meniscus temperature and uniform distribution of solidifying shell.

The Third Pacific Rim International Conference on
Advanced Materials and Processing (PRICM 3)
Edited by M.A. Imam, R. DeNale, S. Hanada,
Z. Zhong and D.N. Lee
The Minerals, Metals & Materials Society, 1998

1. Introduction

The surface and internal defects in continuously cast slab are closely related to the fluid flow condition of the liquid steel in the continuous casting mold. Therefore, control of the steel flow by application of electromagnetic force on continuous casting process has become an important technology for quality and productivity improvements. The EMBR creates transverse static magnetic field in the mold and the interaction of this field with the liquid steel flow creates a braking force. This braking force is expected to brake and redistribute the velocity of the steel jets from the nozzle and suppress vorticity and turbulence, finally result in various beneficial effects. The effects of the EMBR on the fluid flow phenomena in the mold can be summarized as the substantial reduction of two major circulations of molten steel flow in the mold. The important advantages obtained by the suppression of such circulations are as follows: reduction of inner or subsurface inclusions, elimination of mold flux entrapment, reduction of the longitudinal and transverse cracks, reduction of static and dynamic waves at the meniscus, and so on.

The EMBR technology has been rapidly advanced from the localized imposition of the field to today's design covering the entire width of the strand[1]. FC-mold is an equipment to control the molten steel flow in a mold of continuous casting process using a two-level static magnetic field. This new type of electromagnetic braking equipment is designed to maximize the beneficial effects of conventional level magnetic field, based on the operation experiences of the EMBR for many years.

In this study, a 3-dimensional mathematical model has been developed for the coupled analysis of the fluid flow, heat transfer and induced current in FC-mold. Fluid flow, heat transfer, induced current and argon gas concentration were analyzed with finite volume method based on body fitted coordinate which is capable of calculating three dimensional fluid flow considering complex geometry of the SEN. For systematic analysis of the influence of the EMBR on the fluid flow, velocity profile beneath the meniscus and inclusion behavior were investigated. A series of parametric studies were conducted to understand the influence of the EMBR on the fluid flow of the slab caster. Additionally, heat transfer and distribution of solidifying shell were also simulated.

2. Calculation of Electromagnetic Field

2.1 Electromagnetic System of FC-mold

The EMBR system related with this study is shown in Figure 1.

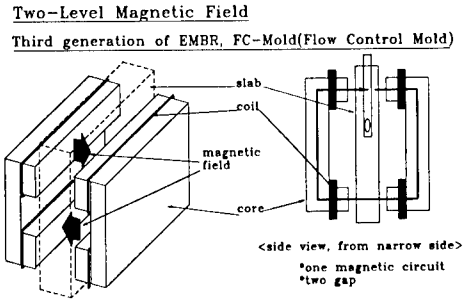


Figure 1. Schematic diagram of FC-mold

In FC-mold, two pairs of magnetic cores exist. One of the magnetic fields is imposed on the molten steel flow at the meniscus level in order to suppress the surface turbulent flow. The other is imposed on the flow below the outlet ports of the SEN in order to acquire a uniform downward stream in the lower half of the mold. This EMBR system has been installed in the slab casters of POSCO, Kwangyang works since last year.

2.2 Governing Equations for Electromagnetic Phenomena

The governing equation of electromagnetic phenomena is represented by Maxwell Equation. In the case of magnetic field calculation, the Ampere's law is applied.

$$\nabla \times \vec{B} = \vec{J} \tag{1}$$

The current can be regarded as the sum of source current J_s imposed in coil and eddy current J_E induced by the fluid flow motion in the steel melt.

Since we can neglect the effect of induced current in melt steel on magnetic field generation, the current can be made up by imposing current $\vec{J}_s$ and the equation can be simplified as following.

$$\nabla \times [\frac{1}{\mu} (\nabla \times \vec{A})] = \vec{J}_s \tag{2}$$

In order to evaluate the electromagnetic braking force, magnetic field was analyzed with finite element method using A-φ formulation[2].

2.3 Magnetic Field Distribution in FC-mold

Magnetic field distribution obtained by three dimensional FEM calculations using A-φ formulation is shown in Figure 2. This figure represents the variation of magnetic flux density along the casting direction at mold center. The distribution of magnetic flux density is compared with experimental data from POSCO and that obtained by three dimensional FEM calculations by ABB Metallurgy. This figure shows good agreements among our calculated data and other data.

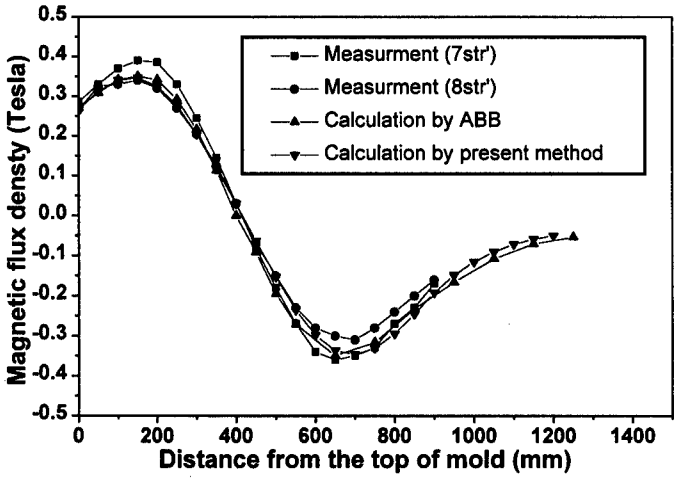


Figure 2. Magnetic field created by the the EMBR system in FC-mold

3. Numerical Analysis Method

The overall calculation process is composed of several mutually coupled elementary calculation processes: calculations of magnetic field, fluid flow field, argon gas distribution and heat transfer.

3.1 Calculation of Velocity Field and Heat Transfer

The 3-dimensional governing equation for turbulent velocity and temperature fields with tensor form in the Cartesian coordinate system is as follows.

$$\frac{\partial}{\partial x_j}(\rho u_j \phi) = \frac{\partial}{\partial x_j}\left[\Gamma_\phi\left(\frac{\partial \phi}{\partial x_j}\right)\right] + S_\phi \tag{3}$$

where ρ is the density and u_i is the velocity component in the x_i-direction and ϕ can be the dependent variables such as 1 for continuity equation, velocity u_i, temperature T, turbulent kinetic energy k and rate of energy dissipation ε. Γ_ϕ is the effective diffusion coefficient of ϕ and S_ϕ is the source term of ϕ.

When the coordinate system is transformed from the Cartesian coordinate system(x, y, z) to the general curvilinear coordinate system(ξ, η, ζ), the mapping leads to a one-to-one correspondence between the points on the real domain and those on the transformed space and the governing equation in Eq. (3) can be transformed as follows.

$$\frac{1}{J}\left\{\frac{\partial}{\partial \xi_i}(\rho G^i u_i)\right\} = \frac{1}{J}\left\{\frac{\partial}{\partial \xi_i}\Gamma_\phi J\left(g^{ij}\frac{\partial u_i}{\partial \xi_j}\right)\right\} + S_{u_i} \tag{4}$$

where $G^i = J\frac{\partial \xi_i}{\partial x_j}u_j$, $g^{ij} = \frac{\partial \xi_i}{\partial x_k}\frac{\partial \xi_j}{\partial x_k}$. and J is the Jacobian of the coordinate system transformation. $S_{u_i} = -\frac{\partial p}{\partial x_i} + \frac{\partial}{\partial x_j}\left(\mu_t \frac{\partial u_j}{\partial x_i}\right) + F_{mag,i} + F_{Ar,i}$

In this study, covariant velocity components are used as dependent variables.

For the simulation of turbulence, k-ε turbulent model is used. Viscosity and diffusion coefficients appeared in Eq. (4) mean the effective quantity by turbulent eddy motion described as

$$\mu_{eff} = \mu_l + \mu_t, \tag{5}$$

where, effective viscosity μ_{eff} is the sum of laminar viscosity μ_l and turbulent viscosity μ_t. $\mu_t = \rho l^2 \left|\frac{du}{dy}\right| = \rho C_\mu \frac{k^2}{\varepsilon}$ from k-ε model, where l, k, ε and C_μ are mixing length, turbulent kinetic energy, turbulent dissipation energy and constant(=0.09), respectively.

3.2 Calculation of Induced Electric Field

The electric current density induced in the moving conducting fluid under magnetic field is given by the following Ohm's equation.

$$\vec{J} = \sigma(-\nabla\phi + \vec{V}\times\vec{B}) \tag{6}$$

The induced current should satisfy the continuity equation and this become as follows.

$$\nabla^2\phi = \nabla\cdot(\vec{V}\times\vec{B}) \tag{7}$$

To solve this governing equation in BFC grid system, it is converted as

$$\frac{1}{J}\left[\frac{\partial}{\partial\xi_k}\left\{\sigma J\left(g^{ij}\frac{\partial\phi}{\partial\xi_j}\right)\right\}\right] = S_\phi, \tag{8}$$

where, source term $S_\phi = \frac{\partial}{\partial x_i}(u_jB_k - u_kB_j)$.

The electromagnetic force F_m is obtained by the following equation.

$$\vec{F}_m = \vec{J}\times\vec{B} \tag{9}$$

It is used as the source term in the calculation of Navier-Stokes equation.

3.3 Calculation of Argon Gas Distribution

Argon gas bubbles blown into the molten steel for protecting clogging give rise to a vertical buoyant force corresponding to the density difference between the gas and molten steel. Such a buoyant force acts as a body force on the liquid steel. Therefore, the effect of argon gas on the fluid flow of molten steel can be obtained by calculating the distribution of argon gas. The following is a governing equation known as low concentration model, which describes the volume fraction of argon gas to the molten steel in the mold[3].

$$v_x'\frac{\partial\alpha}{\partial x} + v_y'\frac{\partial\alpha}{\partial y} + v_z'\frac{\partial\alpha}{\partial z} = \frac{\partial}{\partial x}(D_{ea}\frac{\partial\alpha}{\partial x}) + \frac{\partial}{\partial y}(D_{ea}\frac{\partial\alpha}{\partial y}) + \frac{\partial}{\partial z}(D_{ea}\frac{\partial\alpha}{\partial z}) \tag{10}$$

where, α, D_{ea}, $\vec{v}'$ are the volume fraction of argon, effective diffusivity of argon gas in molten steel, and the velocity of argon bubble, respectively. ($\vec{v}' = \vec{v} + \vec{v}_{t,a}$, $\vec{v}$: the velocity of fluid and $\vec{v}_{t,a}$: the terminal velocity of the bubble)[3].

The body force acting on the molten steel can be obtained by treating the change of density created by the existence of argon gas in the similar manner as the natural convection problem. This treatment is expressed as following.

$$\vec{F}_{Ag} = \rho\vec{g}\alpha \tag{11}$$

3.4 Simulation of Inclusion Tracking

Considering the forces such as drag force by the fluid flow motion and buoyant force by gravity, the motion of nonmetallic inclusion particle can be determined by the following equation.

$$\frac{\pi}{6}d^3\rho_P\frac{d\vec{U^P}}{dt} = -g\frac{\pi d^3}{6}(\rho-\rho_P) + \frac{\rho C_D'\pi d^2}{8}\,|\vec{U}-\vec{U^P}|\,(\vec{U}-\vec{U^P}) \tag{12}$$

The trajectory of particles in the flow field can be obtained by integrating the velocity solved by Eq. (12)

4. Results and Discussion

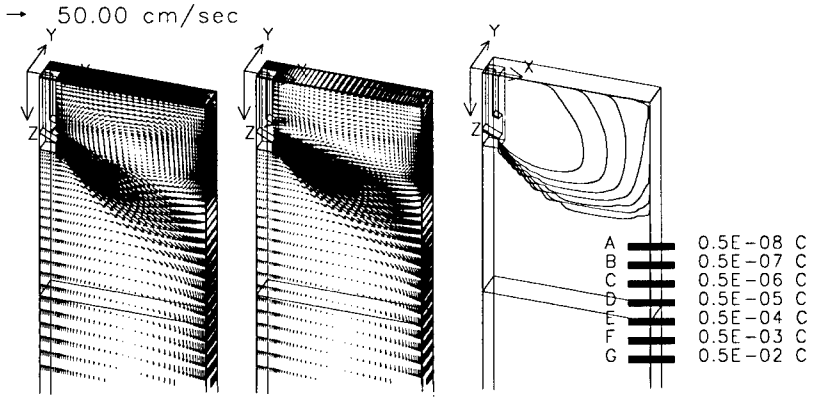
The casting conditions considered in the analysis are shown in Table 1. The flow pattern in FC-mold was investigated compared with that of no magnetic field or one-level field EMBR. Several operating parameters such as magnetic flux density, type of magnetic field, slab width, and inlet velocity was tested and the influence of magnetic flux density were discussed.

Table 1. Values of operating parameters used in this study

maximun magnetic flux density	0.1, 0.2, 0.3 Tesla (EMBR ON)
slab width	1270 mm
slab thickmess	250 mm
casting speed	1.6 m/min
argon inflow rate	5.0 l/min
outlet angle of SEN	25°
magnetic core	one-level or two-level field

4.1 General Influence of Argon Gas bubbling on the Fluid Flow

Figure 3 shows the flow pattern in mold without the EMBR. Both the flows with and without argon gas bubbling were compared in figure 3, and the corresponding argon void fraction contour was plotted. When no magnetic field is imposed, the strong flow from the outlet port of the SEN strikes the narrow face and penetrates down along the narrow faces. But, the buoyant force by argon gas bubble is relatively considerable and affect on the flow pattern remarkably. With the argon gas bubbling, the upper circulation flow is disturbed and upward flow is created near the SEN due to the rapidly floating argon bubbles. As a result, the flow pattern is somewhat changed differently in upper part of mold and the local opposite flow directed from the SEN towards the narrow face is expected near the SEN wall. This phenomena is still more effective when the EMBR is applied.



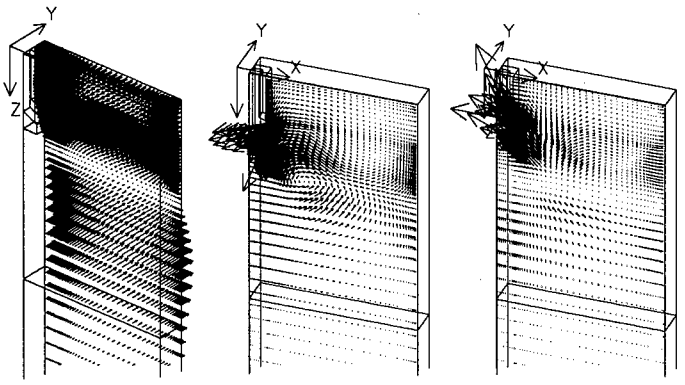
(a) No Ar-gas (b) 5.0 l/m Ar inflow (c) Argon concentration

Figure 3. Fluid flow in common slab caster

4.2 Fluid Flow Characteristics in the FC-Mold

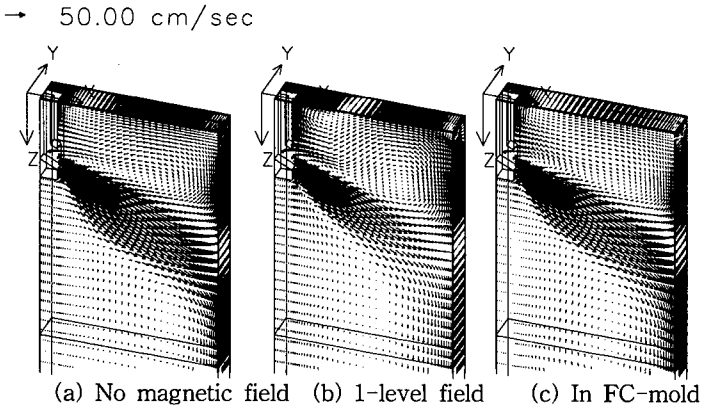
Figure 4 shows the generation of electromagnetic braking force in FC-mold. When the molten steel moves in the magnetic field, eddy currents are induced in the melt, as shown in figure 4(b), interacting with the magnetic field and thus creating a braking force in the opposite direction to the flow of the melt as shown in figure 4(c).

Figure 5 shows the fluid flow without the EMBR force(a), fluid flow with 0.1T of one-level magnetic field(b) and fluid flow with same strength of two-level magnetic field in FC-mold.



(a) Magnetic field (b) Induced current (c) Magnetic force

Figure 4. Generation of electromagnetic filed



(a) No magnetic field (b) 1-level field (c) In FC-mold

Figure 5. Fluid flow with the EMBR force (0.1T)

The strong downward stream in Figure 5(a) could carry nonmetallic inclusions, preventing the floating of such impurities and cause remelting of solidified shell at impinging point at narrow side. Also the eddy flow under the meniscus with high velocity has been known as main cause of the meniscus instability and mold flux entrapment. By the way, as one of important roles of the EMBR is to decelerate the velocity of this eddy flow and stabilize the meniscus, the dispersion and suppression of input stream can be noticed in both cases of one-level and two-level magnetic field.

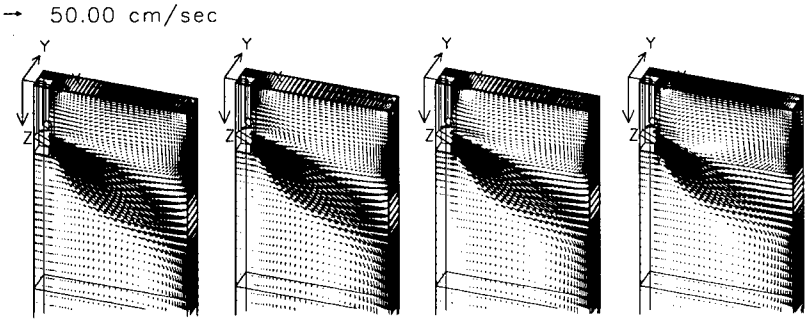
When the one-level magnetic field is imposed, the strong flow that is spouted from SEN is decelerated and the velocity of the flow striking the narrow faces is greatly reduced. However, the velocity at meniscus is still high and near the SEN, a strong reverse flow directed from the SEN towards the narrow wall is created forming another small circulation. This also can provide the possibility of meniscus instability and mold flux entrapment.

In FC-mold, the flow is also dispersed and decelerated but this effect is relatively

small compared with same magnitude of one-level field. However, the velocity at meniscus is remarkably reduced. This can be explained as followings. One-level magnetic field is positioned directly below the SEN and this can increase the strength of upward circulation as well as it decelerates the flow. But in FC-mold, as shown in figure 4(a), the strong flow from SEN passed through upper magnetic field region reaches the region of no magnetic field and then flows down along this region to the narrow side. However, the magnetic field applied on meniscus cannot affect the flow at meniscus directly. As shown in figure 4(b) and (c), induced electric current flows not perpendicular to but along the meniscus or walls because the wall of the mold has a role of insulator due to the flux. Therefore, the fluids that once have reached meniscus or narrow wall, cannot feel the magnetic force as shown in figure 4(c). In other words, the directions of molten steel stream and electric current are parallel and there exists almost no braking force. So, it may be wrong to think that the upper magnetic field can suppress the meniscus velocity of the flow and stabilize the fluid flow at meniscus directly.

4.3 Influence of Magnetic flux density on the Effects of the EMBR

In order to investigate the influence of magnetic field intensity, calculations were carried out with several magnetic flux density. Figure 6 shows the flow fields calculated with different magnitudes of magnetic field. The flow patterns with different intensity of magnetic field are similar. In some cases of one-level magnetic field such as wide slab casting or too strong magnetic field, it can be seen that a stream pushed out to meniscus moves toward narrow wall and goes down along the narrow wall. In this case, molten steel jet may make a detour around magnetic field region to reach the narrow wall[4]. This disadvantageous phenomenon has a tendency to grow under some conditions. However, in FC-mold, there is little possibility of making the negative detour flow because there exists flow-guide region of no magnetic field in the middle of the mold and strong magnetic field is also imposed in upper part of the mold.



(a) no field (b) 0.1T FC-mold (c) 0.2T FC-mold (d) 0.3T in FC-mold

Figure 6. Flow pattern with various magnetic flux density

In order to analyze the effects of magnetic field more quantitatively, the velocity at the meniscus and the ratio of inclusions penetrated or captured by solidified shell were compared in figure 7 & 8. Figure 9 shows inclusion behavior of each case.

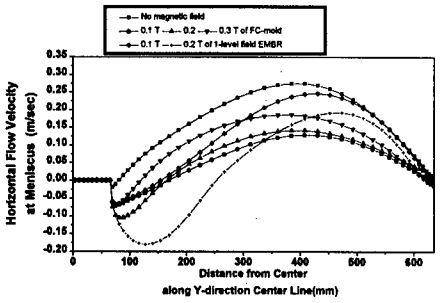


Figure 7. Velocity at meniscus

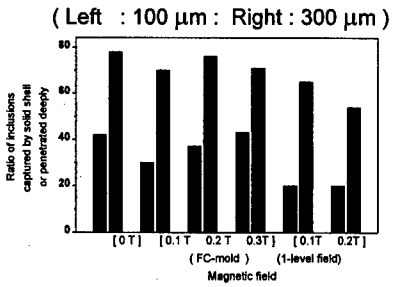


Figure 8. Inclusion behavior

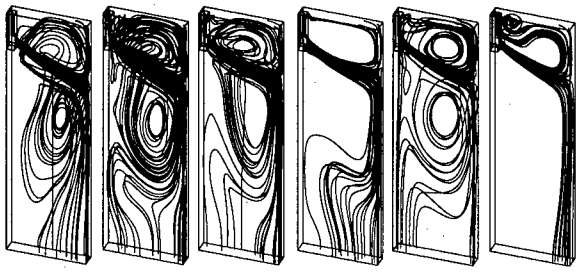


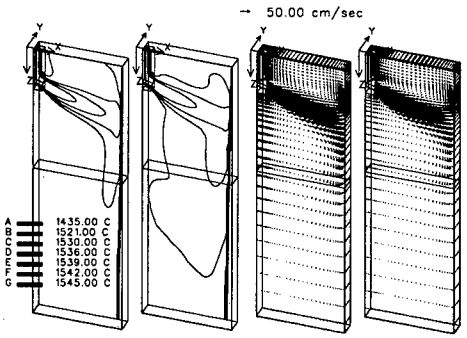
Figure 9. Inclusion trajectory

As mentioned before, the meniscus velocity was decreased in FC-mold as shown in figure7. But two-level magnetic field is less effective in suppressing of inclusion than one-level magnetic field with same magnitude of magnetic field. Another important fact is that although the FC-mold is less sensitive to strength of field, there still exists an optimum value of magnetic field and too strong magnetic field increase the meniscus velocity and may bring about detrimental results.

4.4 Fluid Flow Characteristics and Heat Transfer in the FC-Mold

Fluid flow coupled with heat transfer in FC-mold was analyzed. We assumed that mold wall has constant temperature and heat transfer coefficient was evaluated on the assumption of no air gap between mold and solidified shell[5].

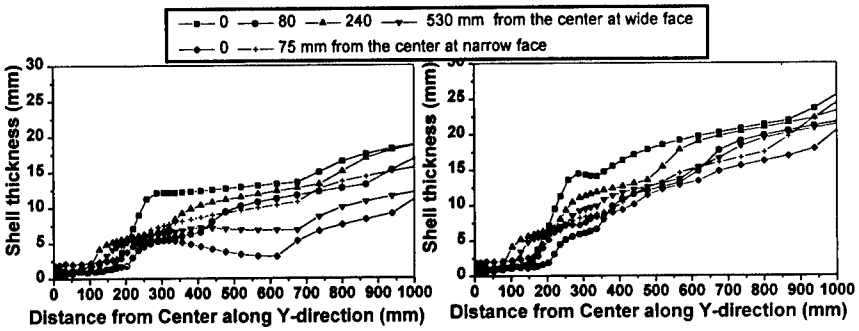
In Figure 10, the temperature profiles and the flow patterns with no magnetic field and with 0.1T magnetic field in FC-mold are shown.



(a) Temperature profile (b) flow pattern

Figure 10 Comparison of Temperature profiles and flow patterns

Figure 11 shows solidified shell distribution in those cases. As the effect of natural convection and the formation of solidified shell was considered, the flow pattern is a little different. Nevertheless, the qualitative flow pattern is similar to that of no heat transfer. When no magnetic field was applied, the strong steel flow impinges on mold wall and remelting of shell occurred. But in FC-mold, uniform distribution of solidified shell was obtained and surface temperature was increased about 8-12 °C. This predicts good effects of FC-mold.



(a) no magnetic field (b) In FC-mold

Figure 11. Shell thickness distribution

5. Conclusion

A mathematical model which could calculate magnetic field, fluid flow, induced electric current as well as heat transfer was developed. The evaluation of the effect of FC-mold was conducted and the following results were obtained.

In FC-mold, the flow velocity at meniscus was somewhat reduced and inclusion behavior pattern was improved in comparison with no magnetic field. Besides, the flow pattern was less sensitive to different casting condition in comparison with conventional one-level field EMBR. This is not because the upper magnetic field acts the braking force to the meniscus flow directly but because it creates a flow-guide region of no magnetic field in the middle of mold and magnetic field imposed on upper part of mold suppress the flow to the meniscus.

Heat transfer and distribution of solidifying shell were also simulated and this shows that the EMBR effects result in the rise of the meniscus temperature and uniform distribution of solidifying shell.

Acknowledgement

The authors would like to thank POSCO for the financial supports during the period of this work.

REFERENCES

[1] Anders F. et al., Int. Symp. on Electromagnetic Processing Materials, ed. by S. Asai et al., ISIJ, Tokyo, Japan, (1994), 372.

[2] S. P. Hong, Ph. D thesis, Seoul National University, 1989

[3] Pascal Grdin et al., Int. Symp. on Electromagnetic Processing Materials, ed. by S. Asai et al., ISIJ, Tokyo, Japan, (1994), 390.

[4] Y. S. Hwang et al., ISIJ Int., 37 (1997), 659

[5] J. E. Lee, Ph. D thesis, Seoul National University, 1993

THE APPLICATION AND DEVELOPMENT OF V RESOURCE IN PANZHIHUA

ZHAO Zhongyu
President, V Inter. Tech. Comm.; Chairman, Pan - Steel Co.
MA Jiayuan
Vice President and General Engineer, Pan - Steel Co.,
HUANG Wudi
Professor, University of Science and Technology Beijing

Abstract

More than 10 billion tons of vanadous titanomagnitite ores with valuable elements such as Fe,Ti,Co,Ni,Ga and Sc are reserved in the Pan-Xi region, Sichuan,China. The reserves of Vanadium resources in such doposits are up to 15.788 million tons, 11.6% of world reserves. The processes of Vanadium extract, application and development in Pan-Steel (Group) Co. are introduced and discussed. Such as atomizing process and converter for V-bearing slag, V_2O_5 production, ferrovanadium technology as well as Vanadium HSLA Steel development and application in construction, automobile industry, petroleum equipments and high pressure containers are involved. The specialty of the steelamking process based on semi-steel instead of hot metal is discussed and direct alloying process with V-bearing slag is also introduced. The main aspects of vanadium extraction involved in the process of iron and steel making are as follows:

*mineral processing, about 90% of V distributed into iron concentrates;
*blast furnace, about 60% of V reduced into hot metal;
*converter for V extracting, about 75% of V into V-bearing slag;
*hydrometallurgy for V_2O_5 manufacturing;
*ferrovanadium manufacturing.

At the present time, the annual capacity of 110,000 tons of V-bearing slag, 2000 tons of V_2O_5 and 2000 tons of Ferro-vanadium has been established with steel capacity of 2.5 million tons per year in Pan-Steel.

The Third Pacific Rim International Conference on
Advanced Materials and Processing (PRICM 3)
Edited by M.A. Imam, R. DeNale, S. Hanada,
Z. Zhong and D.N. Lee
The Minerals, Metals & Materials Society, 1998

Introduction

The deposits with more than 10 billion tons of vanadous titanomagnetite ores, which are usable not only as iron ore, but also as Ti,V,Co, Ni,Ga,Sc and some other valuable resources, are reserved in the Pan-Xi region,Sichuan Province,China and belong to Panzhihua Iron and Steel (Group) Co. abbreviated to Pan-Steel. The reserves of vanadium resource in the despots are up to 15.788 million tons, 62% of domestic and 11.6% of world reserves respectively[1].

Because of the multiplex components in the ores, the extractive processes for various metals must be very comprehensive, dealing with mineral processing, pyrometallurgy, hydrometallurgy and elctrometallurgy. From the various existing mineral processing practice and/or tests, the following results could be obtained:

(a)titanomagnetite could be collected by magnetic separation in the iron-vanadium concentrates, from which Fe,V and Cr can be extracted further;

(b)the granular ilmenite, at the same time,is separated into titanium concentrates, from which Ti can be extracted further;

(c) Co,Ni and S can be recovered from sulfides in S-Co concentrates;

(d) the other valuable elements, such as Ga,Sc,Pt,Cu,etc would possibly be recovered by different processes in the future.

In addition of vanadous titanomagnetite iron ores, the Pan-Xi region is also rich in coal, limestone,refractory materials, especially abundant cooking coal resourrce,which become the solid basis of the current Pan-Steel. Passing through the last 20 years, the company becomes not only one of the largest iron and steel producers, but also the production center of vanadium and titanium products in China.

In respect to the utilization of vanadium resource, a lot of research and development have been done that made China become one of the biggest V.-producers in the world, from a net importing to exporting country of V-products. Now, the annual capacity of 110,000 tons of V-bearing slag, 2000 tons of V_2O_5 and 2000 tons of qualified ferro-vanadium has been established in Pan - Steel with steel capacity of 2.5 million tons per year.

Processes

Vanadium Extraction and Production[2]

Extraction Procedures. The vanadium extraction technology consists of the following steps:

In the mineral processing, about 90% of vanadium in the R.O.M.(Run of Mine) is distributed in the iron concentrates and 10% or so in the titanium concentrates, the average V_2O_5 contents of which are 0.53% and 0.068% respectively (Table I).

In the blast furnace, about 60~70% of vanadium in the iron concentrates is reduced and soluted in hot metal, the average V content of hot metal is around 0.32%.

Table I. Basic Chemical Composition of R.O.M. and Products

Items	Tfe	TiO_2	V_2O_5	Cr_2O_3	Co	Ni	Ga	Sc	Ga	Sc	Cu	S
R.O.M.	31.5	11.0	.311	.29	.018	.013	.0027	.0028	.0027	.0028	.022	.60
A*	51.56	12.88	.56	.032	.02	.016	.0044	.0013	.0044	.0044	.0044	--
B**	32.65	47.50	.068	--	.019	--	--	--	--	--	--	--
C***	53.67	.28	.30	--	--	--	--	--	--	--	--	34.28

* Fe-Concentrates
**Ti-Concentrates
*** S-Co Concentrates

For extraction of V from hot metal in Pan-Steel, there are tow ways, atomizing process and/or converter process, to oxidize V in hot metal into V_2O_5 in slag, so called V-bearing slag. It's average content of V_2O_5 is 17-21% and the recovery rate of V is 75-85%. The total recovery rate from ROM to V-bearing slag is 35-38%. The V-bearing slag is used for various purposes, such as manufacture of V_2O_5, ferrovanadium and other vanadium products, also for direct alloying and even for sale.

The V-bearing slag is further treated by hydrochemical process to produce V_2O_5 with capacity of 2000 tons. At the same time, high quality ferrovanadium has been produced with capacity of 1000 tons per year.

In addition, the experiment and pilot test for V_2O_3 making had been conducted and a plant is under construction. The V_2O_3 would be used for high V containing ferrovanadium making with capacity of 4000 tons and 2000tons respectively. To make high V ferrovanadium with V_2O_3 would be more effective than with V_2O_5. A few new products are going to be developed, under consideration, such as V-Al alloy, metallic vanadium and high purified V_2O_5.

The soda salt was used to treat hot metal in the pilot plant of Pan-Steel with the assistance of some research institutes, The test results show that process is essential not only for devanadization with high V recovery rate(85.1%) but also for desulphurization and dephosphorization of hot metal, so that the process would be possible to simplify the V extracting process and benefit steelmaking with low sulphur and phosphorous semi-steel after soda treatment. But, at the same time, the soda treated V-bearing slag with high contents of S and P, which makes V_2O_5 extraction difficult, hence the conventional hydro metallurgical process could not help. In addition, the environment pollution and corrosion problems from soda salt are hard to be resolved. That is why this process could not be accepted for production.

Comparison Between Atomizing and Converter Processes for V Extracting

The Atomizing Process. The atomizing process for V recovering consists of atomizer and atomizing furnace. The hot metal from blast furnace is poured firstly and then sprayed by compressed air into the atomizing furnace through a atomizer, where the hot metal is dispersed into fine drops, like mist, and falls to the bottom of the atomizing furnace. The oxidation of V in hot metal occurs originally at atomizer by 60% and then continues the another 40% in the

atomizing furnace to form the V-bearing slag and semi-steel, which flow together into the ladle and then to be separated each other.

The advantages of atomizing process are:

(1)Excellent kinetic conditions for oxidation of V from hot metal sprayed by compressed air.

(2) Air is not only a cheaper oxygen supplier but also used for coolant because of the N_2 content. So, any additional coolant is unnecessary for the oxidizing process. A little bit of oxygen would be enriched in the air, if necessary, to regulate the temperature enough for higher V oxidizing rate, but not too high for carbon retaining.

(3) The intermediate ladle, established before atomizer, as a depot of hot metal, makes the atomizing process continuous to increase the productivity of V-bearing slag.

(4) The process technology and equipments are simple, so the investment and operation expenses are less than converter process of V recovery.

But there are three principle disadvantages:

(1) The atomizing process is very hard to run steadily, so that would influence the productivity, quality of products and recovery rate of vanadium.

(2) The iron content in V-bearing slag is too high. The total iron content usually reaches 40% with 22% metallic iron involved.

(3) The temperature of Semi-Steel would not be quite enough for continuous casting.

The Converter Process for V Extracting from Hot Metal Because the atomizing process could not meet the requirement of Pan-Steel development further, the two atomizing furnaces with 120 tons each, which used to play important role in the past years, were no longer used recently. Instead, two 120 ton converters had been established since 1995 and the effectiveness, productivity and quality of products are better than atomizing process ones [3].

Table II. Chemical Composition of V-bearing Slag, %

Item	V_2O_5	TFe*	MFe**	SiO_2	CaO
Converter	17-21	30-33	7-10	15-17	0.4-0.7
Atomizing	18-20	38-42	20-22	11-13	1.4-1.7

*Total iron

**Metallic iron

Comparing the chemical composition of the two kind of slag (Table II), it is obvious that the V_2O_5 content of converter slag is higher and Fe content is lower.

For the sake of promotion for V extracting in the converter, some aspects should be emphasized:

(a) The reaction temperature must be controlled at reasonable level, which would facilitate the V oxidizing as well as C retaining. So the coolant must be necessary during oxygen blowing. The solid pig iron, scrap and roll scale are used not only as coolants but also as additional iron source. According to proper order, the cooling effect of pig iron is weaker than scrap and roll scale with the equivalent coefficients 1:1.5:4.7 respectively. So, pig iron would be the best one because of the bigger amount of consumption i.e. more yield rate of semi-steel. Different choice of coolant consumption was recommended for Pan-Steel in Table III.

Table III. Recommended Consumption of Coolants kg/THM

Choices	pig iron	scrap	roll scale
1	117	--	--
2	70	31	--
3	44	31	5.6

(b)The consumption, blow rate and pressure of oxygen as well as the position of oxygen lance are the principle factors for bath reaction controlling and oxidation rate of vanadium. The parameters in Pan-Steel are shown in Table IV.

Table IV. Oxygen Blowing Paramenters

Number of Lance holes	4
Oxygen Pressure	0.7Mpa
Oxygen Consumption	16.38 M^3
Oxygen intensity	2.11 m3/min·ton
Blowing time	7.41 min
Lance position	2.2-1.0 m
Oxidation rate	>80%

(c)The flowability of slag must be enough for separation of metallic iron from slag, but the Si content in hot metal is too low (about 0.1%) in Pan-Steel that makes the SiO_2 too low in slag and too viscous. So, some siliceous sands have to be added into converter to make slag with good flowability, but decreasing the V_2O_5 content. To schedule the slag tap once every 2-3 taps of semi-steel that would extend the duration of slag in converter to separate the involved metallic iron off. It is so called " remaining slag practice".
It would be more effective, if the top and bottom combined blowing technology would be used for V extraction. Pan-Steel is going to realize it before long.

Specialty of Semi-Steel Process in Pan-Steel [4][5].

Semi-Steel Composition. Because of the multiple mineral resource, the semi-steel has to be used for steelmaking. After treatment, the carbon content of semi-steel is lower than hot metal (Table V).

Table V. Typical Composition of Hot Metal and Semi-Steel

Items %	hot metal	semi-steel
C	4.32	3.80
Si	0.069	<0.05
Mn	0.162	<0.05
P	0.0467	0.046
S	0.0783	0.078
V	0.295	0.049
Ti	0.12	<0.01

The lower Si content would be beneficial for steelmaking with less slag operation, but the higher S content is harmful. The pretreatment shop with capacity of 2.5 million tons of hot metal desulphurizing has been established to desulphurize to less than 0.01% in hot metal.

The Main Technical Aspects of Semi-steel Practice for Steelmaking. The steelmaking technology at the base of semi-steel would be different from general steelmaking. Therefore some technical aspects should be emphasized, such as:

*slag forming with addition of siliceous sands, manganese ores, dolomites etc. to control the melting process;

*special designed oxygen lance and proper operating height;

*to guarantee the tapping temperature of steel for continuous casting, using the pre-heated ladle with refractory fiber line;

*the low sulfur content in semi-steel, less than 0.018%;

*hybrid blown at the three steelmaking converters.

These are also the experience of steelmaking as well as quality and grades improvement at Pan-Steel in the past years.

Application

Taking Advantage of Vanadium Resource to Make HSLA Steel [2].

Heavy Rail Production. During the early stage of steelmaking without extraction of vanadium, the residual V in steel used to be around 0.05%, which makes the heavy rail steel of better mechanical properties than normal one. However, since the vanadium was recovered from hot metal and semi-steel was supplied for steelmaking , the residual V in steel decreased to less than 0.014%, and the mechanical properties became worse. Then research program had been conducted and new steel rail with more than0.03% V by allowing was developed successfully. The high strength and toughness of heavy rails (PD3) have been obtained by heat-treatment. The 60 and 75 kg/m rails are manufactured by full-length quenching to compare favorably with other counterparts in the would. The high C and low V rail after heat-treatment could be provided for special services with better fatigue resistance and wearable properties. More and more quality heavy rails would be expected to supply the consumers either domestic or abroad.

Vanadium in Structural and Other Steel. In addition of rail steel (PD3), a lot of V-bearing structural, forging and other steels have been developed, such as:

*09V, which contains 0.06-0.12% C and 0.07-0.14V, to be used for heavy I - section steels and 310 Z-shape steels with smaller grain size and higher mechanical properties;

*20MnSiV,20-25 MnV for bars; 20MnVBH, 40MnV for gears;

*27 MnMoVB (0.22-0.32%C, 0.08-0.15%V and others) and 35 MnMoVTi (0.32-0.40%C, 0.04-0.10%V and others), which are used for geological drilling pipe with good hot plasticity, suitable for medium and deep well drilling, 27 MnMoVB also with S corrosion resistance;

*30 Mn2VB 0.30-0.37%C, 0.07-0.12%V; 40Mn2V and 37MnV used for anchor chain with Ocear environmental corrosion resistance;

*34Mn2V 0.30-0.37%C, 0.07-0.12%V; 40Mn2V and 37 MnV used for oxygen bottle and/or other high pressure containers satisfying the safety regulations;

*55 SiMnVB and 50CrV for auto spring; 12 Mn2VB for auto shafts; 09 SiVL,P510L,P440L, P420L for auto frame; 35 MnVN for crank shaft and connecting rod;
*X42, X52, X60 for oil (gas) transportation; J55 for casing;29MnV, 30MnV and45 CrMnVH for petroleum well drill rod.

The V-bearing Foundry Pig Iron and Steel Casts

A less part of hot metal is used for casting and various grades of cast iron with V content such as V-Ti gray cast iron, V-Ti nodular cast iron, V Ti wear resisting cast iron, V-Ti malleable cast iron are developed. The superior mechanical properties and cheaper costs make the V-bearing casts competent in the market.
The V-bearing cast steel is of the same situation with cast iron. A small amount of V and Ti in cast steel makes it's properties much better, such as 45# carbon steel used for gypsywheel, heat-resisting cast steel for grates of sinter machine, wear-resisting cast steel for crusher's lining, dipper's teeth and caterpillar's tread, etc. The economic benefit of such casts is obvious and expectable.

Direct Alloying with V-bearing Slag[6]

The direct alloying process is completed by adding briquettes or bagged powders of blended vanadium bearing slag with reducing agent instead of ferrovanadium. Since the ferrovanadium making process is omitted, the alloying cost of low vanadium alloyed steel is reduced about 40% in Pan-Steel. No considerable differences are found in comparison with mechanical properties, inclusions and other defects between conventional and direct alloying steels. It is successful that a lot of steels such as constructional steel, rail steel and other HSLA -V containing steel are manufactured by direct alloying. The vanadium recovery rate is equal to or even higher than the total recovery rate of conventional alloying with ferrovanadium.

Summary

The principal aspects could be summarized as follows:
On the basis of the development as indicated, the V resource in Pan-Xi region has been applied in many objects with good progress. Self-reliance has been realized for blast furnace practice on the complex vanadous titanomagnitite, V extraction from hot metal and semi-steel making practice.
A series of V containing HSLA steels has been developed successfully to produce not only constructional steel, but also heavy rail and other HSLA steel, as well as vanadium containing iron and steel casts.
The direct alloying with V-bearing slag and/or V_2O_5,insteadd of conventional alloying with ferrovanadium, has been developed and applied in the manufacture of HSLA steel successfully and ecconomically.
With the development of more than 20 years, Pan-Steel becomes the largest steel producer in west China and , at the same time, to be the vanadium producing base, which makes China

from a vanadium products importer to exporter.

Even the big progress has been made on the development of vanadium resource in Pan-Steel, there is still a long way to go, because the resources in Pan-Xi region are so complex and abundant that more effective and comprehensive technical processes should be conducted to improve steel grates and quality, as well as to recovery more valuable metals such as V, Ti, Co, Ni, Ga, Sc etc. which are very potential and the bright further would be expected.

References

1. Zhao Zhongyu, "To Make Best Use of Advantages and Disadvantages To Achieve Enterprise Development", **Proc. Of Inter. Sym on Steel Industry Development and Management**, held in Shanghai, CSM (1997),41-44.
2. **Proc. of Inter. Sym. on Exploitation and Utilization of V-bearing Titanomagnetite**, held in Panzhihua, China,CSM (1989).
3. Pan Shufan "Domestic and International Technologies of V recovery in BOF and Discussion on The Problems with V recovery in Converters at Panzhiihua Iron and Steel Co.," **Iron Steel Vanadium Titanium** 16-1 (1995),. 6-16.
4. Ji Kebin et al. "Practice of steelmaking Technology with V-bearing Hot Metal at panzhihua Iron & Steel (Group) Co." **Iron and Steel** 32 (1997), 583-585.
5. Pan Shufan "Study on Temperature Control During Semi-Steel Steelmaking in LD Converters", **Iron Steel Vanadium Titanium** 17-1 (1996), 37-45.
6. **Proc. of Inter. Conf. on HSLA Steels, Metallurgy and Application**, held in Beijing, TMS,CSM, (1985), 423-430.

CONTROL OF PRECIPITATING PHASE ALIGNMENT BY IMPOSITION OF A HIGH MAGNETIC FIELD

Hiroshi MORIKAWA, Kensuke SASSA and Shigeo ASAI

Department of Materials Processing Engineering
Nagoya University, Nagoya 464-8603 Japan

Abstract

In general, materials have different magnetic susceptibilities depending on the crystal orientation and the magnetic field appearing inside a material is influenced by the susceptibility and the shape of materials. The utilization of this property will enable us not only to control the crystal orientation but also to make reinforced fibers in a composite materials align. In this paper, the theoretical expressions which determine the alignment of a precipitating phase under the imposition of a magnetic field are derived. In experiments it was found that the application of a magnetic field makes the primary dendrite arms of MnBi in Bi-4mass%Mn alloy align along the magnetic field and planers of Al-7mass%Si-5mass%Fe intermetallic compound in Al-11mass%Si-2mass%Fe alloy align in perpendicular to the magnetic field. The theoretical predictions agree well with the experimental results.

The Third Pacific Rim International Conference on
Advanced Materials and Processing (PRICM 3)
Edited by M.A. Imam, R. DeNale, S. Hanada,
Z. Zhong and D.N. Lee
The Minerals, Metals & Materials Society, 1998

Introduction

These days, by the development and the advance of a super conducting magnet, a high magnetic field is going to be applied in various academic fields such as biology, chemistry and physics. In this trend various interesting phenomena relating with the high magnetic field have been found. That is, the science relating with the high magnetic field is going to open the gate as a new academic field. Particularly for the materials science and engineering, the phenomena observed under the high magnetic field are so interesting and useful that a new engineering branch making use of the high magnetic field is going to be founded.

So far, the utilization of a magnetic field has been limited to ferromagnetic materials such as iron, nickel, cobalt and some of rare earth metals. The reason is that a magnetic moment M_f in ferromagnetic materials and that M_n in nonmagnetic materials such as paramagnetic and diamagnetic ones are very different and the ratio of M_n to M_f is as low as 10^{-6}. That is, the effect of magnetic field appearing in the nonmagnetic materials has been neglected hitherto. But recently the applicable intensity of a magnetic field has increased as much as 10^3 times (say 10T if the base magnetic field is taken at 0.01T). The magnetization energy of the nonmagnetic materials is in proportion to the product of the square of the intensity of a magnetic field and the specific magnetic susceptibility so that the ratio of $M_n/M_f = 10^{-6}$ could be compensated by the increase of magnetic intensity $[(10^3)^2 \fallingdotseq 10^6]$. That is, under such a high intensity of a magnetic field the magnetic influence acting on nonmagnetic materials is not negligible any more[1)-8)].

In general, materials have different magnetic susceptibilities depending on the orientation of an unit crystal and moreover the magnetic field appearing inside a material is influenced by the susceptibility and the shape of the material. The utilization of these physical properties will enable us not only to control the crystal orientation but also to make reinforced fibers in a composite material align.

In this paper, the relations between the directions of the alignment of the precipitating phase and an applied magnetic field have been investigated and the experimental results have been interpreted by taking account of shape magnetic anisotropy due to the shape of a precipitating phase. That is, the theoretical expressions which determine the alignment of the precipitating phase under the imposition of a magnetic field are derived .

Experimental Method

A supper conducting magnet (a bore diameter 90mm, the maximum magnetic flux 5.5T at the center of the bore and the maximum product of the magnetic flux and its gradient $173T^2/m$) was installed to get a high magnetic field. A water cooling jacket made by glass was inserted into the bore so as to keep the room temperature on the bore wall during melting and solidifying of alloys in a furnace set in the jacket.

Regarding the study on alignment of the precipitating phase, the two specimens 1)Bi-4wt%Mn and 2)Al-11wt%Si-2wt%Fe were prepared. Those were set in an inert gas atmosphere in the furnace and kept in the temperature range precipitating a primary phase for a given period of time in the presence and the absence of the magnetic field and then were cooled to the room temperature. The structures of the treated specimens were examined by use of a microscope.

Experimental Result

Figure 1 shows the microstructure of the specimen in a Mn-Bi alloy which precipitates

ferromagnetic intermetallic compound MnBi as a primary phase from a nonmagnetic melt. Photo1 (a) is with a magnetic field of 4.5T and (b) is without any. It was found that the application of a magnetic field makes the primary dendrite arms of MnBi align along the magnetic field direction. Figure 2 shows the microstructures of a specimen of Al-11wt%Si-2wt%Fe. In Photo2 (a) with a magnetic field of 5T, the intermetallic compound Al-9wt%Si-15wt%Fe which looks to precipitate in a planar shape aligns perpendicular to the magnetic field direction and in (b) without any magnetic field the intermetallic compound distributes at random.

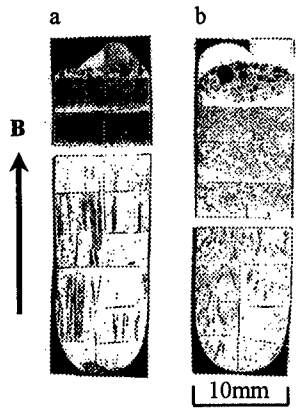


Figure 1: Macrostructures of Bi-4mass%Mn alloy
a: with magnetic field (4.5T)
b: without magnetic field

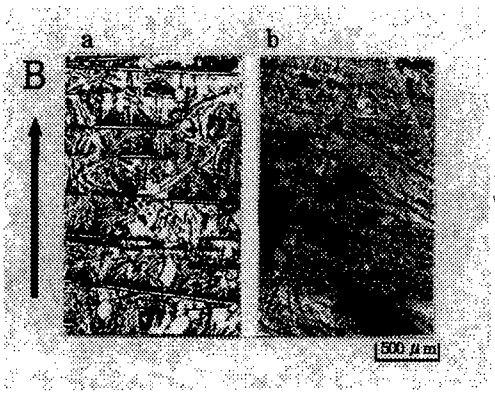


Figure 2: Microstructures of Al-11mass%Si -2mass%Fe alloy
a: with magnetic field (5T)
b: without magnetic field

Theoretical Consideration

The experimental results mentioned above have been interpreted in the consideration of magnetization energy as followings:

Derivation of Magnetization Energy

The basic principle of the alignment of a precipitating phase is that the imposition of a magnetic field makes the precipitating phase rotate so as to take a lower magnetization energy position which basically depends on the shape and the susceptibility of the precipitating phase. The magnetization energy U is defined as Eq.(1) by the use of magnetic moment M and the magnetic field appearing inside a material H_{eff}, which is different from the imposed magnetic field H_{ex}[9],

$$U = -\int_0^{H_{eff}} \mu_0 M dH_{eff} \qquad (1)$$

In the case of nonmagnetic materials ($|\chi|<<1$) such as diamagnetic ($\chi<0$) and paramagnetic ($\chi>0$) ones, Eq.(2) is obtained from the relations of $M=\chi H_{eff}$ and $H_{eff}=H_{ex}-NM$.

$$\therefore H_{ex} = (1 + N\chi)H_{eff} \qquad (2)$$

where N is a demagnetizing coefficient.

U is evaluated from the Eqs.(1) and (2) as Eq.(3)

$$U_n = -\frac{\mu_0 \chi}{2(1 + N\chi)^2} H_{ex}^2 \qquad (3)$$

In the case of ferromagnetic materials ($|\chi_f|>>1$) the approximate expression of U can be obtained from the assumption that M is saturated at a certain magnetic intensity H_s.

$$\begin{aligned} U_f &= -\int_0^{H_s} \mu_0 \chi H_{eff} dH_{eff} - \int_{H_s}^{H_{ex}} \mu_0 M_s dH_{eff} \\ &= -\mu_0 M_s H_{ex} + \left\{1 - \frac{1}{2(1 + N\chi)^2}\right\} \mu_0 M_s H_s \end{aligned} \qquad (4)$$

Shape Magnetic Anisotropy Energy

When evaluating the magnetization energy of the system consisting of the precipitating and the medium phases, we should take account of not only the positive contribution from the energy of the precipitating phase but also the negative contribution from the energy of the medium phase which has been removed by the precipitating phase. By considering the case in Mn-Bi alloy in the experiment, the precipitating phase MnBi is a ferromagnetic material and the medium a nonmagnetic one. In such a case, the energies in each case where the precipitating phase aligns perpendicular to or parallel to the magnetic field direction are given in Eqs.(5) and (6).

$$U_\perp = -\mu_0 M_s H_{ex} + \left\{1 - \frac{1}{2(1 + N_\perp \chi_p)^2}\right\} \mu_0 M_s H_s + \frac{\mu_0 \chi_m}{2(1 + N_\perp \chi_m)^2} H_{ex}^2 \qquad (5)$$

$$U_{//} = -\mu_0 M_s H_{ex} + \left\{1 - \frac{1}{2(1+N_{//}\chi_p)^2}\right\}\mu_0 M_s H_s + \frac{\mu_0 \chi_m}{2(1+N_{//}\chi_m)^2} H_{ex}^{\ 2} \qquad (6)$$

where χ_p and χ_m are the specific magnetic susceptibilities of the precipitating and the medium phases, respectively.

When the precipitating phase has a needle like shape such as a primary dendrite arm, the demagnetizing coefficient parallel to the needle axis $N_{//}$ may be smaller than that perpendicular to the axis $N_{\perp}$. That is, $N_{\perp} >> N_{//}$. As the saturated magnetic moment of a ferromagnetic material M_s is independent of the crystalline direction, Eq.(7) is obtained under the assumption of $\frac{\mu_0 M_s H_s}{2(1+N\chi_p)^2} \rangle\rangle \left|\frac{\mu_0 \chi_m H_{ex}^{\ 2}}{2(1+N\chi_m)^2}\right|$.

$$U_{\perp} - U_{//} \approx \frac{(N_{\perp} - N_{//})\{2\chi_p + \chi_p^{\ 2}(N_{\perp} + N_{//})\}}{2(1+N_{\perp}\chi_p)^2(1+N_{//}\chi_p)^2}\mu_0 M_s H_s \qquad (7)$$

Since $N_{\perp} > N_{//}$ is, the relation $U_{\perp} > U_{//}$ holds. It indicates that the primary dendrite arm of a ferromagnetic materials should align parallel to the imposed magnetic field so as to take a lower energy state. This theoretical consideration coincides with the observed morphology in the specimen of Mn-Bi alloy in the experiment.

When both the precipitating and the medium phases are nonmagnetic materials, Eqs(8) and (9) are obtained depending on the direction of the precipitating phase with respect to the imposed magnetic field.

$$U_{\perp} = -\frac{\mu_0 \chi_p}{2(1+N_{\perp}\chi_p)^2} H_{ex}^{\ 2} + \frac{\mu_0 \chi_m}{2(1+N_{\perp}\chi_m)^2} H_{ex}^{\ 2} \qquad (8)$$

$$U_{//} = -\frac{\mu_0 \chi_p}{2(1+N_{//}\chi_p)^2} H_{ex}^{\ 2} + \frac{\mu_0 \chi_m}{2(1+N_{//}\chi_m)^2} H_{ex}^{\ 2} \qquad (9)$$

As the precipitating phase is a polycrystal in the case of the experiment, the relation of $\chi_{\perp} \approx \chi_{//}\left(\chi = \chi_p \text{ and } \chi_m\right)$ in the precipitating and the medium phases holds in Eqs.(8) and (9). Then, Eq.(10) is obtained under the condition of $|\chi_p| \langle\langle 1$ and $|\chi_m| \langle\langle 1$.

$$\Delta U = U_{\perp} - U_{//} \propto \frac{\mu_0 H_{ex}^{\ 2}}{2}\left(\chi_p^{\ 2} - \chi_m^{\ 2}\right)(N_{\perp} - N_{//}) \qquad (10)$$

From Eq(10), $\Delta U \rangle 0$ when $|\chi_p| \rangle |\chi_m|$, where the precipitating phase should be parallel to the imposed magnetic field direction. And $\Delta U \langle 0$ when $|\chi_p| \langle |\chi_m|$, where the precipitating phase should align perpendicular to the magnetic direction. Based on the theoretical consideration developed here, $|\chi_p| \langle |\chi_m|$ is expected in the case of Al-Si-Fe alloy from the fact that the precipitating phase aligned perpendicular to the magnetic field direction.

Conclusion

The theoretical expressions which determine the alignment of a precipitating phase under the imposition of a high magnetic field have been derived and confirmed in the experiments.

Regarding to the shape magnetic anisotropy, a primary dendrite arm of a ferromagnetic phase precipitating from a nonmagnetic medium phase aligns parallel to the magnetic field direction. When both precipitating and medium phases are nonmagnetic, the precipitating phase aligns parallel to the magnetic field direction when $|\chi_p| > |\chi_m|$ and perpendicular to it when $|\chi_p| < |\chi_m|$.

Acknowledgments

We would like to express the deep thanks to Profs. Masaaki Matsui and Masaaki Doi in Dept. of Materials Science and Engineering, Nagoya University, for their helpful discussions in the derivation of the theoretical expressions.

Reference

1) D.E.Farrell, B.S.Chandrasekher, M.R.Deguire, M.M.Fang, V.G.Kogen, J.R.Clen and D.K.Finnemore, Phys.Rev.B36(1987)4025.
2) A.Lusnikov, L.L.Miller, R.W.McCaullum, S.Mitra, W.C.Lee and D.C.Johnson, "Mechanical and High-temperature (920 ℃) Magnetic Field Grain Alignment of Polycrystalline (Ho,Y)$Ba_2Cu_3O_{7-\delta}$," J.Appl.phys., 65(1989)3136-3141.
3) J.E.Tkazyk and K.W.Lay, J.Mater.Res.5(1990)1368.
4) P.de Rango, M.Lee, P.Lejay, A.Sulpice, R.Tournier, M.Ingold, P.Gerni and M.Pernet, "Texturing of Magnetic Materials at High Temperature by Solidification in a Magnetic Field," NATURE, 349(1991)770-772.
5) R.H.Arendt, M.F.Garbauskas, K.W.Lay and J.E.Tkaczyk, "An Alternate Preparation for Grain Aligned Structures of $(Bi,Pd)_2Ca_2Ae_2Cu_3O_z$," Physica C 176(1991)131-136.
6) A.Holloway, R.W.McCallun and S.R.Arrasmith, J.Mater.Res8(1993)727.
7) S.Stassenn, R.Cloots, A.Rulmont, F.Gillet, H.Bougrine, P.A.Godelaine, A.Dang and M.Ausloos, "Magnetic Alignment in Rare-earth Substituted Bi-based 2212 Superconducting Materials," Physica C 235-240(1994)515-516.
8) S.Stassenn, R.Cloots, Rh.Vanderbemden, P.A.Godelaine, H.Bougrine, A.Rulmont, M.Ausloos, J.Mater.Res.11(1996)1082.
9) K.Ota : Jikikogaku-no-kiso, (Tokyo: Kyouritsu Publishing Company, 1973),42

EFFECTS OF ELECTROMAGNETIC FIELD AND COOLING RATE ON AS-CAST AND AGING STRUCTURES OF CENTRIFUGAL CASTING HEAT-RESISTANT ALLOY

Yuansheng YANG, Xinqiang WU, and Zhuangqi HU
State Key Laboratory of Rapidly Solidified Nonequilibrium Alloy, Institute of Metal Research, Chinese Academy of Sciences, 72 Wenhua Road, Shenyang, 110015, P.R. China

Abstract

The influences of exerted electromagnetic field and cooling rate on as-cast and aging structures of heat-resistant HK40 alloy are investigated in the present work. The results indicate that both electromagnetic field and cooling rate have significant effects on carbides in as-cast structure as well as in subsequent aging structure. The amount of eutectic carbides in both the equiaxed zone and the columnar zone decreases with increase of the cooling rate, but the exerted electromagnetic field during solidification can increase the volume fraction of eutectic carbides, especially for grain boundary eutectic carbides. Moreover, the higher cooling rate or exerted electromagnetic field can give rise to more homogeneous distribution of eutectic carbides as well as subsequent aging carbides between the equiaxed zone and the columnar zone. The difference of as-cast structures and subsequent aging structures of HK40 alloy cast under different casting conditions should be attributed to the difference of solidification processes of cast tubes. The application of electromagnetic field during solidification is very beneficial to the improvement of creep resistance of tubes. The reasonable association between cooling rate and electromagnetic field can give rise to better creep property of cracking tubes. In view of long-term application, it is the eutectic carbides formed initially that are the lasting consolidation factor of cracking tubes serving at elevated temperature.

The Third Pacific Rim International Conference on
Advanced Materials and Processing (PRICM 3)
Edited by M.A. Imam, R. DeNale, S. Hanada,
Z. Zhong and D.N. Lee
The Minerals, Metals & Materials Society, 1998

Introduction

Cracking tube is one of the most common and important components in petrochemical plants. In service, the tubes are welded parallel with each other and subjected to the long-term operating conditions of elevated temperature (the outer surface temperature of tubes can often exceed 1373K) [1]. So the elevated temperature properties of tube materials constitute the critical factor for service life design and prospective application of tubes. In order to improve the elevated temperature property of cracking tubes and meet the quick development of petrochemical industries, two ways have been adopted primarily in the past three decades. One is the composition improvement of tube materials and the other is the optimization of fabricating processes[2-5]. In recent years, a casting process which connects electromagnetic and centrifugal force fields has been developed and it is possible to be applied in industry production[6]. Although a considerable amount of information is now available on structures and properties of tube materials, it is still necessary to clarify their relation to the casting processes of tubes. In this paper, standard tube material HK40 is taken as an example to investigate the effects of applied electromagnetic field and cooling conditions on its as-cast and aging structures, on the basis of which the possible influences of different casting processes on the elevated temperature properties of tube materials are discussed.

Experimental Procedure

The chemical composition (wt%) of the HK40 heat-resistant alloy used for present study is Cr 24.81, Ni 20.05, C 0.37, Si 1.27, Mn 1.32, Mo<0.03, P<0.005, S<0.007, and balanced by Fe. The process parameters of electromagnetic centrifugal casting are listed in table I.

Table I Casting Process Parameters

Tubes Code	Exciting Current I (A)	Casting Mold Material	Pouring Temperature T (K)	Rotation Speed ω (rpm)
A	0	Graphite	1923	1700
B	0	Cast Iron	1923	1700
C	10	Cast Iron	1923	1700

Both as-cast and aging samples are cut from cast tubes and prepared *via* standard metallurgical technique. The volume fraction of eutectic carbides is measured by means of the lineal analyzing method.

Results and Discussion

As-cast Structures

The predominant variation in as-cast structure due to the effects of electromagnetic field and different cooling rate is focused on the volume fraction of eutectic carbides, which is shown in Figure 1. It is obvious that the amount of eutectic carbides in both the equiaxed zone and the columnar zone decreases with the increase of cooling rate, but the application of electromagnetic field during solidification can markedly increase the volume fraction of eutectic carbides, especially for grain boundary eutectic carbides. Moreover, the higher cooling rate or exerted magnetic field can give rise to the more homogeneous distribution of eutectic carbides between the columnar zone and the equiaxed zone (*i.e.* along the radial direction of tubes).

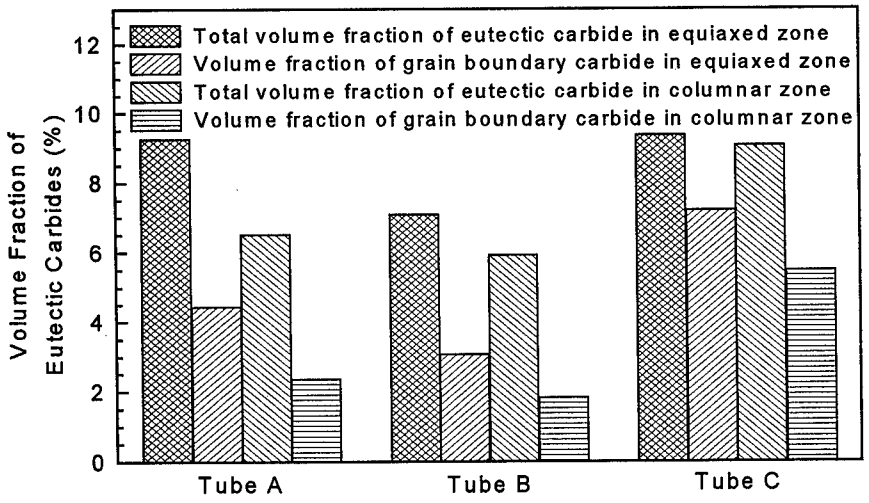


Figure 1: Volume fraction of eutectic carbides

Aging Structures

Both exerted electromagnetic field and different cooling rate during solidification have remarkable effects on distribution of subsequent aging structure of cast tubes. It is clear from Figure 2 that the distribution of secondary carbides between the columnar zone and the equiaxed

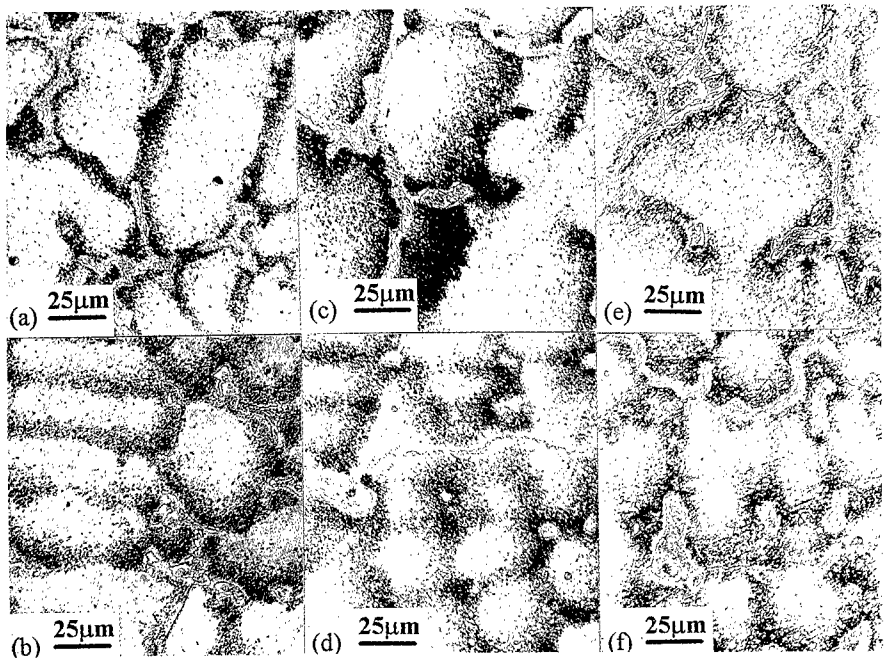


Figure 2: Microstructures after 1100℃/1hr aging of (a), (c), (e): equiaxed zone of tube A, B and C; (b), (d), (f): columnar zone of tube A, B and C.

zone in tube B and tube C is more homogeneous than that in tube A. Moreover, the width of the precipitation zone along grain boundaries and dendritic boundaries in tube B and tube C appears much larger than that in tube A. This indicates that the inhomogeneous precipitation can be limited to a certain extent by using a higher cooling rate or electromagnetic field. During long-term exposure, eutectic carbides show higher stability than secondary precipitated ones. The experimental result of decarburization illustrated in Figure 3 also reveals that initial eutectic carbides are much more stable than secondary carbides.

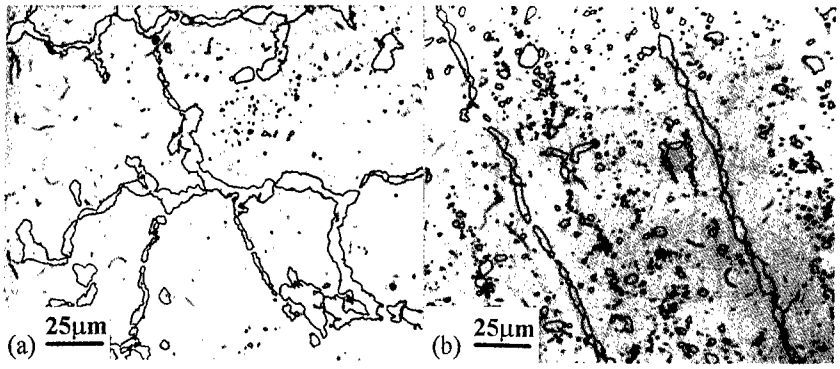


Figure 3: Microstructures after 200hr decarburization of (a) equiaxed zone; (b) columnar zone.

Analysis of Solidification Process

During the solidification of HK40, the solute atoms are released into bulk liquid continuously from the solid/liquid interface. With the moving of interface and the dropping of temperature, the solutes gradually concentrate in residual liquid, finally the liquid reaches the eutectic composition of HK40 alloy and the eutectic transformation takes place. Under the condition of cooling in a graphite mold, the solidification rate is slower and more solute atoms are released into residual liquid, therefore, more residual liquid having reached the eutectic composition is aggravated in the inner zone of cast tube during the later stage of solidification and finally transformed into eutectic structures. Consequently, the tube A exhibits larger amount of eutectic carbides distributed heterogeneously in austenitic matrix along the radial direction. However, with enhance of cooling ability of cast mold and solidification rate, most of solute atoms can not be released into bulk liquid during solidification, but remain in austenitic matrix in the form of solution state, which gives rise to smaller volume fraction and more homogeneous distribution of eutectic carbides in tube B. Then, as mentioned previously[7-8], the exerted electromagnetic field during solidification can promote fluid flow, which can accelerate the solute transfer process in liquid ahead the solidification interface and make it easier for solute atoms to be released into bulk liquid. So the fluid flow can cause larger amount of residual liquid in which the solutes distribute homogeneously. Moreover, the fluid flow is able to accelerate the formation and transportation of nuclei from the solid/liquid interface to the center of melt, homogenize the temperature distribution and quicken the thermal dissipation in residual liquid phase, all of which can strongly promote the simultaneous nucleation in most region of residual liquid and result in much finer structures. For the reason above, after complete solidification, the tube C exhibits the largest amount of homogeneous eutectic carbides primarily distributed on grain boundaries.

The difference in aging structure is also attributed to the different solidification processes.

According to the solidification sequence, grain boundaries and dendritic boundaries are the final solidification zones in cast tubes, so the solution of solute carbon in these zones is higher as compared with center of grains and dendritic cells and thereafter the precipitation is much heavier in these zones. For tube B solidified with a cast iron mold, higher cooling rate retards solute transfer and causes larger amount of solute atoms to remain in most of matrix. Thus, it is easy for those solutes fixed in matrix to precipitate in the form of secondary carbides during aging and give rise to wider precipitation band along the grain boundaries either in the equiaxed grain zone or in the columnar grain zone. The graphite mold capable of lower cooling ability results in heterogeneous distribution of solutes between the columnar zone and the equiaxed zone as well as in different regions within a grain, which in turn induces some precipitation difference between the two zones and within a grain. The introduction of electromagnetic field during solidification further homogenize the solutes distribution in the cast tube, so the precipitated secondary carbides appear more uniformly distributed along the radial direction as well as within grains.

Possible Influences on Elevated Temperature Properties

In accordance with general argument[9], the creep resistance of heat-resistant alloys appears to depend on carbides to prevent grain boundary sliding and to restrict dislocation motion. It is clear that the eutectic carbides are critical for the former and the secondary carbides are critical for the latter. Therefore the creep resistance of heat-resistant alloys must be improved by increasing both amount of eutectic carbides and distribution of secondary carbides. As indicated in Figure 1 (tube C), under the condition of electromagnetic centrifugal solidification, the eutectic volume fraction is increased markedly. In particular, the volume fraction of grain boundary eutectic carbides increases quickly with the effect of electromagnetic field. Moreover, it is shown by aging analysis that precipitation of secondary carbides is more homogeneous along the radial direction of tube C. So, the application of electromagnetic field during solidification will be very beneficial to the improvement of creep resistance of tube. In spite of higher total volume fraction of eutectic carbides in tube A, more than half amount of eutectic carbides keeps within grains, which has little contribution to the improvement of creep resistance at elevated temperature. Furthermore, both the distribution of eutectic and aging carbides along the radial direction in tube A is not as homogeneous as that in tube C, on account of which, the heterogeneous creep property along the tube radius should be induced. Then for tube B, although its lower volume fraction of total eutectic carbides is a loss for the creep property, such a loss is made up to some extent by the more homogeneous and heavy secondary carbides that precipitate rapidly along the radial direction during aging. From above analysis, it is also indicated that the reasonable association between cooling rate and electromagnetic field can result in better creep property of cracking tubes. In addition, in view of stability of carbides, it is the eutectic carbides formed initially that are the lasting consolidation factor of cracking tubes serving at elevated temperature for a long-term view.

Conclusions

The predominant variation in microstructure due to the effects of electromagnetic field and cooling rate is focused on the volume fraction of eutectic carbides and subsequent aging carbides distribution of cast tubes. The amount of eutectic carbides in both the equiaxed zone and the columnar zone decreases with increase of the cooling rate, but the exerted electromagnetic field during solidification can increase the volume fraction of eutectic carbides, especially for grain boundary eutectic carbides. Moreover, the higher cooling rate or stronger exerted electromagnetic field can give rise to more homogeneous distribution of eutectic

carbides as well as subsequent secondary carbides between equiaxed zone and columnar zone.The difference of as-cast structures and subsequent aging structures of HK40 alloy cast with different casting conditions should be attributed to the difference of solidification processes of cast tubes.

The application of electromagnetic field during solidification is very beneficial to the improvement of creep resistance of tube. The reasonable association between cooling rate and electromagnetic field can result in better creep property of cracking tubes. In view of long-term application, it is the eutectic carbides formed initially that are the lasting consolidation factor of cracking tubes serving at elevated temperature.

Acknowledgments

The work is supported by the National Natural Science Foundation of China (No. 59431013) and Science Foundation of Liaoning (No. 963002).

References

1. M.W. Mucek, Laboratory Detection of Degree of Carburization in Ethylene Pyrolysis Furnace Tubing, Mater Perform, 9 (1983), 25-28.

2. G. D. de Almeida Soares et al., Niobium Additions in HP Heat-Resistant Cast Stainless Steels, Mater Cahr, 29 (4) (1992), 387-396.

3. R.A.P. Ibanez et al., Effects of Si Content on the Microstructure of Modified-HP Austenitic Steels, Mater Char, 30 (4) (1993), 243-249.

4. J. Kelly, New High Strength High Temperature Microalloy Particularly Suited for Service in Carburizing and Oxidizing Atmospheres, Indust Heat, 10 (1995), 42-46.

5. T. Shinohara et al, Development of Nondestructive Technique for Measuring Carburization Thickness and of a New Carburization-resistant Alloy, Werkst Korros, 37 (1986), 410-418.

6. Y.S. Yang et al., Application of Steady Magnetic Field for Refining Solidification Structure and Enhancing Mechanical Properties of 25Cr-20Ni-Fe-C Alloy in Centrifugal Casting, ISIJ Inter, 35 (1995), 389-391.

7. W.D. Griffiths, D.G. McCartney, "the Effect of Electromagnetic Stirring during Solification on the Structure of Al-Si Alloys," Mater Sci Eng, A216 (1996), 47-60.

8. A. Prodhan, D. Sanyal, "Cooling Curves Analysis of Aluminium Solified Without and With Magnetic or Electric Field," J Mater Sci Lett, 16 (1997), 958-961.

9. E.A.A.G. Ribeiro et al., Microstructure and Creep Behavior of a Niobium Alloyed Cast Heat-Resistant 26 Pct Cr Steel, Metall Trans, 17A (1986), 691-696.

MODELING MORPHOLOGICAL EVOLUTION DURING DENDRITIC SOLIDIFICATION USING A CELLULAR AUTOMATON

R. E. Napolitano[1] and T. H. Sanders, Jr.[2]

[1]National Institute of Standards and Technology
Metallurgy Division, Materials Science and Engineering Laboratory
Gaithersburg, Maryland, USA

[2]Georgia Institute of Technology
School of Materials Science and Engineering
Atlanta, Georgia, USA

Abstract

Morphological evolution of a dendritic growth front in a binary alloy is simulated using a cellular automaton approach to establish the feasibility of modeling such growth with a local rule-based scheme. The motivation for this work is derived from the need to predict the development of solidification structures within real components of complex geometry, where significant constraint of the thermal and solutal fields may exist. Such cases present complex boundaries and large domain sizes, which may preclude the effective use of more conventional methods. In this work, a model is presented which couples a two-dimensional alternate-direction-implicit finite-difference diffusion solution with a cellular automaton growth algorithm to simulate morphological evolution in alloys solidifying under directional growth conditions. Temperature, composition, and interface configuration are formulated into a local growth potential which is incorporated into a cellular automaton. Alloy solidification is simulated over a range of experimental conditions, producing various structures. The effects of anisotropic configurational contributions are examined.

The Third Pacific Rim International Conference on
Advanced Materials and Processing (PRICM 3)
Edited by M.A. Imam, R. DeNale, S. Hanada,
Z. Zhong and D.N. Lee
The Minerals, Metals & Materials Society, 1998

Introduction

Virtually every microstructural feature in a cast alloy component is related to the interface morphology present during solidification. Conventional solidification theory, describing dendrite tip kinetics and mushy zone phenomena, provides a means for estimating overall microstructural parameters for an alloy solidified under steady-state conditions. Microstructural prediction for actual components, which are finite in size and complex in geometry, requires a description of the evolution of the interface morphology under transient conditions and geometrical constraint and an understanding of how the structure propagates through the mold. Any useful simulation tool must be equipped to handle these circumstances within the limits of computational feasibility. In recent years, various phase-field[1-6] and cellular automaton (CA)[7-14] models have been used to simulate many features of dendritic solidification. Previous CA models use steady-state dendrite kinetic relationships to simulate cast grain structures, without simulating the morphology of the interface.[9-14] Phase field techniques utilize a diffuse interface to simulate morphological evolution, however the requirement of a very thin yet well resolved interface may limit the application of these models.

The objective of this modeling effort is to develop a local rule-based modeling scheme which can be used to simulate the evolution of an advancing dendritic interface in a casting of realistic size and geometry. The value of such a model is clear, since it would lay the framework upon which the effect of any physical influence could be included in a tool that could be applied to industrial and laboratory applications virtually without restriction.

Description of the Model

The simulation domain is a square mesh where each cell is assigned a value for temperature, composition, and phase. Temperature and composition are continuous field variables while the phase is a discrete binary variable. The overall operation of the model involves coupling the evolution of the temperature and solute field with the motion of the phase boundary. The solute field is updated using an alternate-direction-implicit finite-difference (ADI-FD) method with periodic lateral boundaries. Conditions for directional solidification are implemented by employing a uniform temperature gradient and a constant isotherm velocity. The simulation frame is permitted to move in order to follow the front over distances much greater than the domain itself.

The morphology of the solid is evolved using a CA technique which is intended to simulate the morphological evolution of an advancing solidification front by including the relevant physical factors such as temperature, composition, and interface curvature. The contribution from each is incorporated into a growth function which can be applied to every cell within the domain. Each cell is, thus, free to grow as the local conditions allow, and no explicit distinction is made for dendrite tips or other features. The morphology is updated by comparing random numbers to a growth probability $p(\phi)$, where ϕ is a growth potential based on the local conditions of temperature, composition, and morphology. This method automatically imparts a random noise component to the structure, which is necessary for morphological changes. The function p must be bounded by zero and one and should vary monotonically with the growth potential, ϕ. The following function is chosen:

$$p = 1 - \exp\left[-\left(\frac{\phi}{\kappa}\right)^{\eta\kappa}\right] \qquad (1)$$

where κ and η can be used to control the shape of the function over the potential domain. The task at hand, which is the essential characteristic of the model, is the formulation of the potential ϕ and the description of the constants η and κ, in terms of the physical properties of the alloy.

For a site at position *(i,j)*, the growth potential at time t is defined as the kinetic undercooling:

$$\phi_{ij}^{k} = \Delta T - (\Delta T_C + \Delta T_R) \qquad (2)$$

where ΔT is the total undercooling, and the subscripts C and R indicate compositional and curvature related contributions, respectively. With knowledge of the phase diagram, ΔT_C at any cell can be calculated based on the local temperature and composition. With a configurational term for ΔT_R, (2) becomes:

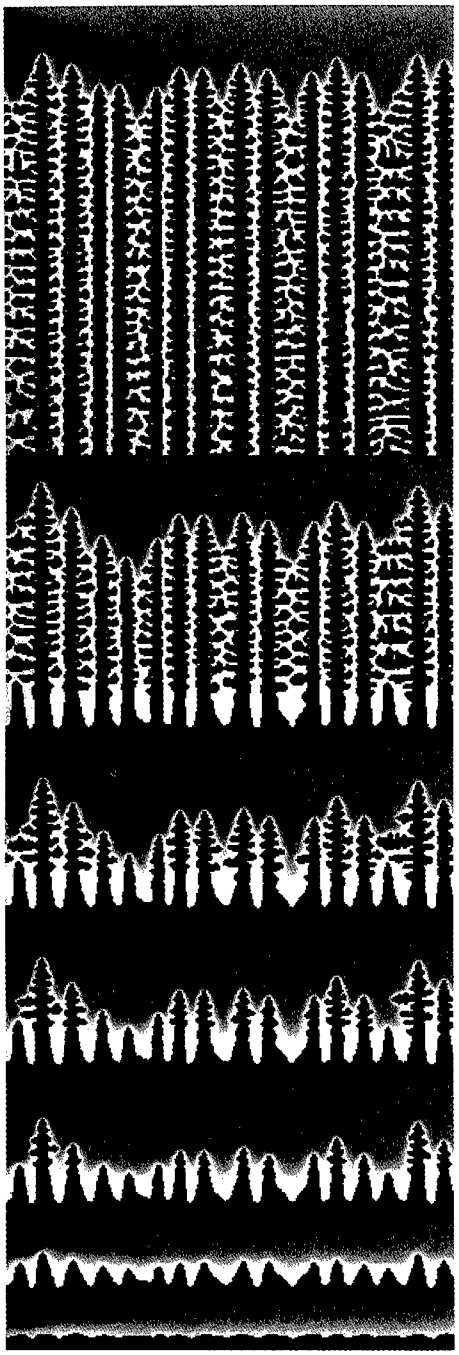


Figure 1. A sequence of composition plots showing simulated structures for G=5 K/mm and V=0.5 mm/s. Black to white indicates 0 to 5wt% Cu. The lateral dimension is 2mm. Time progresses from bottom to top.

$$\phi_{ij}^{k} = T_m - mC_{ij}^{k} - f(S_{ij}^{k}) - T_{ij}^{k} \qquad (3)$$

where T_m is the melting temperature, m is the liquidus slope, C is the solute concentration, and S_{ij}^{k} is the configuration of the neighborhood about cell *(i,j)* at time k. The configurational contribution to undercooling is computed as:

$$f(S_{ij}^{k}) = \Gamma \frac{(\alpha_r H_r + \alpha_a H_a)^{\xi}}{\Delta z} \qquad (4)$$

where Γ is the Gibbs-Thompson coefficient, and Δz is the grid resolution. The H values are contributions due to interfacial curvature (r) and anisotropy (a), weighted by the coefficients α_r and α_a, respectively. The exponent ξ is a modeling parameter.

At this point, we have a method for moving the interface based on the local value of ϕ, which can be computed from the field variables and solid morphology. To determine the kinetic resistance imparted by (1), we evaluate $dp/d\phi$ at a characteristic undercooling of κ.

$$\frac{dp}{d\phi}\Big|_{\kappa} = \frac{\eta}{\exp(1)} \equiv \eta' \qquad (5)$$

Generally, the velocity of an interface is related to the kinetic undercooling through a proportionality constant:

$$V = M\Delta T \qquad (6)$$

where, neglecting kinetic anisotropy,

$$M = J_o \nu \frac{\Delta s_f}{RT} \exp\left(\frac{-Q}{RT}\right)$$

J_0 is vibrational frequency, ν is atomic volume, Q is activation energy for diffusion, R is the gas constant, and Δs_f is the entropy associated with solidification.[15] In the model, the velocity is given by the product of the growth probability, the time step frequency, and the cell size of the grid:

$$V = p \frac{\Delta z}{\Delta t} = pV_{max} \qquad (7)$$

where V_{max} is the limiting velocity. Combining (6) and (7):

$$p = \frac{M\Delta T}{V_{max}} \qquad (8)$$

Considering (1) and (8), η' can be computed by relating the relating the differentials:

$$\frac{M}{V_{max}} = \frac{dp}{d\phi} = \frac{dp}{d(\Delta T)} = \eta' \qquad (9)$$

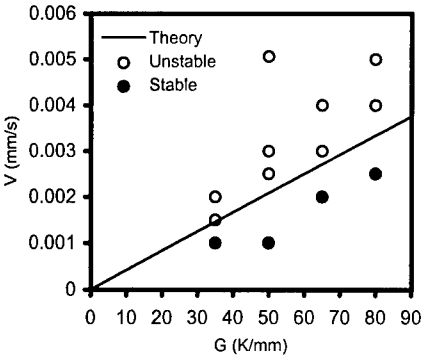


Figure 2. The stability of the simulated front for a range of gradients (G) and velocities (V).

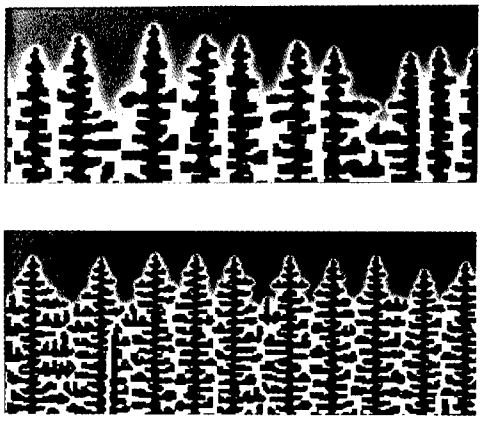


Figure 3. Simulation results showing the difference in primary spacing selected for V=0.2 mm/s (upper) and V=0.5 mm/s (lower). For both: G=5 K/mm. Black to white indicates 0 to 5 wt % Cu.

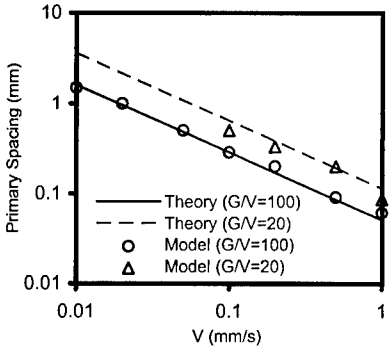


Figure 4. Primary spacing results plotted with the model of Kurz and Fisher.[17]

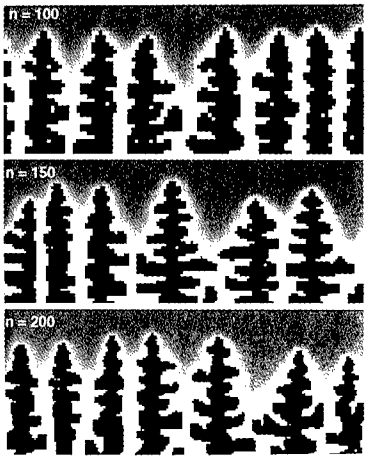


Figure 5. Simulated structure for three different (nxn) grid sizes.

We now have a technique for calculating the value of p at each cell, based on the relevant physical parameters. To update the solid morphology, a random number ($0 \le r \le 1$) is generated for each cell at each time step for comparison with p. If $p_{ij}^{k} > r_{ij}^{k}$, the cell is set to solid. The composition is then set to kC_{ij}^{k}, and the excess solute $(1-k)C_{ij}^{k}$ is distributed among the available neighboring cells.

Modeling Results

All results presented in the following sections were obtained using input parameters associated with Al-4.5 wt% Cu. Unless otherwise noted, all simulations were performed using a 300x300 mesh over a 2mm square domain, which is permitted to move in space to follow the growth front.

As a method of verifying the solute redistribution techniques, planar growth was forced to occur by specifying p=1 for any undercooled interfacial site and p=0 for all other sites. This forces the growth front to follow the liquidus isotherm at a prescribed velocity. The solute profiles for the initial transient, steady-state growth, and growth under Scheil conditions compared favorably with analytical solutions, indicating that the solute handling technique within the CA is appropriate.[16] Removing the restriction which forced planar growth in the examples given above, we define $p(\phi)$ with (1). The stochastic component of the CA provides the necessary perturbations for morphological

instability. If conditions permit, these random perturbations will trigger the breakdown of the growth front. Such a situation is shown in Figure 1. The simulation begins with a planar front sitting at the liquidus temperature. The system cools directionally, according to a specified gradient and isotherm velocity. As positive undercooling develops, the solid begins to grow at random locations. The stability of the planar front with respect to these local perturbations is dictated by diffusivity and interface velocity in a realistic fashion, since the solute rejected at a growing location decreases the probability for growth at neighboring sites. The structure which develops depends on the $f(S_{ij}^{k})$ term in (3), which suppresses the growth of sharply curved features. The coupling between capillarity and diffusion is evident as the growing structure begins to evolve from random perturbations into a well organized waveform. A cellular structure emerges as solute is channeled away from the fastest growing regions. As the cells deepen, the tips begin to grow at a rate determined by their individual shape, indicating the onset of dendritic growth. Side-branches develop gradually due to secondary instability and a dendritic structure evolves. Later in the simulation, a steady-state is reached where the structure consists of an array of uniformly spaced primary dendrites aligned along an isotherm.

To show that the model is correctly simulating morphological instability, a series of 13 simulations were performed, using a range of conditions near the stability limit. The results are summarized in Figure 2 which shows that the model correctly simulates planar stability or instability, as predicted by constitutional supercooling.

Figure 3 illustrates the simulated effect of velocity on the primary spacing. As expected, higher velocities promote finer spacings. To quantify the relationship between this simulated steady-state primary spacing and the parameters G and V, two sets of tests were run for various values of V. For each set, G/V was held constant. The results of these tests, shown in Figure 4, are compared with the analytical prediction of Kurz and Fisher.[17] This figure clearly indicates that the model accurately simulates the evolution of the proper primary spacing. It is particularly noteworthy that the model not only exhibits agreement with the $V^{-1/4}G^{-1/2}$ dependence, but also that it provides excellent agreement with the values themselves. Additionally, due to the inclusion of $(\Gamma/\Delta z)$ in the expression for ΔT_R, the spacing is not dependent on the mesh resolution, as demonstrated in Figure 5.

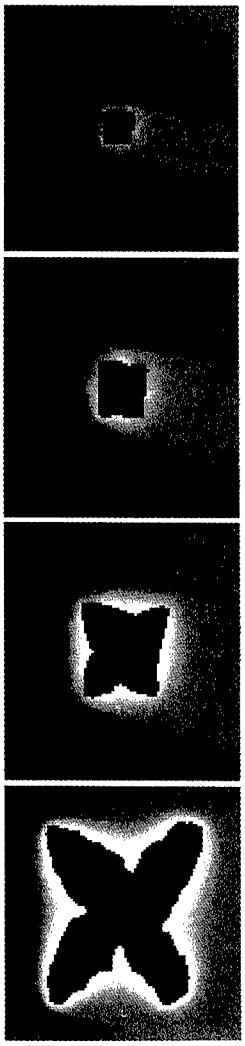


Figure 6. A simulation progression of the growth shape for α_a=0. The physical size of the shown frame increases from top to bottom.

Figures 6 and 7 show that the weighting parameters in the configurational undercooling, particularly the α_a term, can be used to affect the anisotropy of the growing solid. Figure 6 shows the evolution of a single dendrite in a uniform temperature field, under constant cooling conditions, with α_a=0. The anisotropy of the growth is solely due to the square grid. This grid effect promotes {01} interfaces in favor of {11} interfaces. Figure 7 shows the same progression of simulation results for α_a=0.5. In this case, the grid anisotropy is overcome and the {11} interfaces are favored over the {01} interfaces. The resulting <01> growth direction is necessary to achieve steady-state dendritic growth conditions in the directional solidification simulations. The grid anisotropy can also result in unnatural rectangular features at the interface during the development of a dendritic front. As shown in a previous paper, this is most evident in the cellular regime where cells maintain flat fronts with corners near the cell divisions.[16] The dramatic effect on the cellular to dendritic transition is shown in Figure 3 of reference 16. Due to the suppression of {11} interfaces, the transition is delayed. The cells begin to develop instabilities on their flat fronts until dendritic growth emerges from these. In contrast, the cellular to dendritic transition in Figure 1 consists of a gradual increase in cell curvature, followed by secondary instability and side-branch generation.

Conclusions

A cellular automaton was applied to the growth of dendritic structures in an alloy under conditions for directional solidification. With the incorporation of growth anisotropy, the method reproduces many features of dendritic solidification and can operate with realistic values of G and V. This technique can predict solidification structures at a large enough scale to make it practical for simulating real casting processes, and because the growth algorithm used here depends only on local conditions, this model may be well suited for application to systems with complex geometry, where other methods may be difficult to implement. These features indicate the potential usefulness of the CA as a tool for the simulation of dendritic growth in actual castings.

References

1. R. Kobayashi; *Physica D*, **63** (1993) 410-423.
2. A.A. Wheeler, B.T. Murray, and R.J. Schaefer; *Physica D*, **66** (1993) 243-262.
3. S.L. Wang, R.F. Sekerka, A.A. Wheeler, B.T. Murray, S.R. Coriell, R.J. Braun, and G.B. McFadden; *Physica D*, **69** (1993) 189-200.
4. A.A.Wheeler, W.J. Boettinger, and G.B. McFadden; *Physical Review E*, **47 3** (1993) 1893.
5. J.A. Warren and W.J. Boettinger; *Acta Metallurgica et Materialia*, **43** (1995) 689-703.
6. W.J. Boettinger and J.A. Warren; *Metallurgical and Materials Transactions*, **27A** (1996) 657-669.
7. N.H. Packard; *Proceedings of the First Int. Symposium for Science on Form*, (Y. Katoh, R. Takaki, J. Toriwaki, and S. Ishizaka, Eds.), KTK Scientific Publishers (1986).
8. S.G.R. Brown and J.A. Spittle; *Scripta Metallurgica*, **27** (1992) 1599-1603.
9. M. Rappaz and Ch.-A. Gandin; *Acta Metallurgica et Materialia*, **41** (1993) 345-360.
10. Ch.A. Gandin, M. Rappaz, and R. Tintillier; *Metallurgical Transactions*, **24A** (1993) 467-479.
11 Ch.A. Gandin, M. Rappaz, and R. Tintillier; *Metallurgical Transactions*, **25A** (1994) 629-635.
12. M. Rappaz, Ch.A. Gandin, and R. Sasikumar; *Acta Metallurgica et Materialia*, **42** (1994) 2365-2374.
13. Ch.-A. Gandin and M. Rappaz; *Acta Metallurgica et Materialia*, **42** (1994) 2233-2246.
14. Ch.-A. Gandin, Ch. Charbon, and M. Rappaz, *ISIJ International*, **35** (1995) 651-657.
15. K.A. Jackson, *Journal of Crystal Growth*, 3/4 (1968) 507-517.
16. R.E. Napolitano and T.H. Sanders, Jr., *Proc. Int. Symp. on Processing of Metal and Advanced Materials: Modeling, Design, and Properties*; B.Q. Li, Ed., TMS (1998) 63-74.
17. W. Kurz and D.J. Fisher, Fundamentals of Solidification, 3ed, Trans Tech Publications, Switzerland (1989) 80-84.

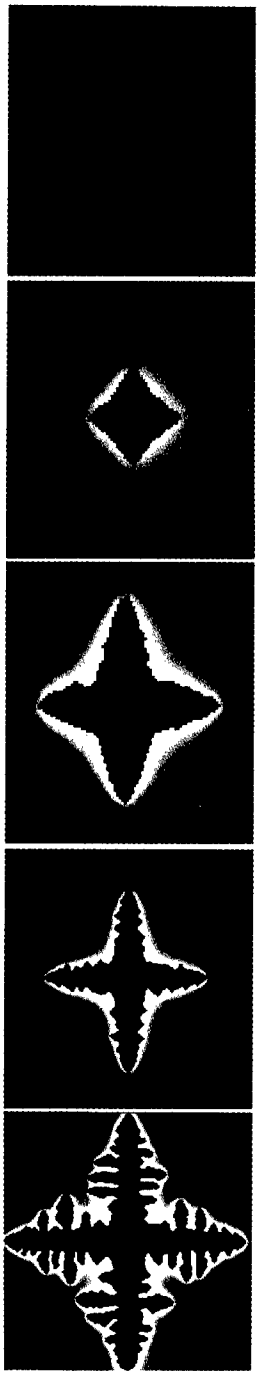


Figure 7. A simulation progression of the growth shape for α_a=0.5. The physical size of the shown frame increases from top to bottom.

Short Capillary Viscometer for Molten Metals and Alloys.

Y.Shiraishi, Y.Sakurai and S.Nagasaki
AGNE Gijutsu Center Ltd., Minami-aoyama 5-1-25, Kitamura Bldg.,
Minato-ku, Tokyo, 107-0062, Japan.

Abstract

In order to investigate the applicability of short capillary viscometer to molten metals which is characterized by low kinematic viscosity, preliminary tests were carried out using a quartz vessel with a capillary of 0.1 mm inner diameter and 20 mm long in the bottom. Suitable volume of water, mercury, molten tin and molten lead was effused from the vessel through the capillary and the efflux was measured continuously using a load cell. On the other hand, effusion curve was simulated by the calculation based on the capillary flow equation in which the viscosity of the sample was regarded as a parameter. The simulated effusion curves were reproduced well the observed curves except for mercury in which high Reynolds number of mercury the flow probably affects.

New apparatus was developed to operate the short capillary viscometer in a vacuum or an inert atmosphere at elevated temperatures. Viscosity of gallium was measured to demonstrate the applicability of the apparatus.

The Third Pacific Rim International Conference on
Advanced Materials and Processing (PRICM 3)
Edited by M.A. Imam, R. DeNale, S. Hanada,
Z. Zhong and D.N. Lee
The Minerals, Metals & Materials Society, 1998

Introduction

Since viscosity is a fundamental property which characterizes the nature of fluid, the knowledge of viscosity is very important for the better understanding of metallurgical processes in which molten metals are treated. Since molten metals are characterized by low viscosity and high density beside their high temperatures, the method of viscosity measurement is limited and an oscillation method is known as the only method which is applicable for the molten metals. A capillary method which is based on the established principle has not been applied to molten metals due to the difficulty of manufacturing of a viscometer having a fine and long capillary, except the work reported by Iida et al. (1).

As described elsewhere (1,2), very severe condition is imposed on the shape and size of the capillary to fulfill the necessary condition of the Hagen–Poiseuille equation. On the other hand, a short capillary viscometer having relatively thick and short capillary is frequently used in industrial purpose, e.g. Seybolt viscometer and so on. It has a fine tube at the bottom and the effusion time of a definite volume of the sample through this tube is measured as an index of the viscosity. The lower limit of these viscometers can be cited as $2 \times 10^{-6} m^2/s$ from the conversion table of Seybolt second, for example. This value encourages us to apply this type of viscometer to molten metals, since molten metals have a kinematic viscosity of same order of magnitude. If the short capillary viscometer can be applied to molten metal, viscosity measurement of molten metals will be greatly simplified as compared with an oscillation method. Thus we challenge the development of the apparatus for the viscosity measurement of molten metals using short capillary viscometer.

Experimental

Method of measurement

The fundamental equation of the capillary flow can be expressed as;

$$\eta = \pi r^4 P / 8 l q - m \rho q / 8 \pi l \qquad (1)$$

where η is viscosity, r and l are the radius and length of the capillary, P is a head of the capillary flow ($= \rho g h$), q is an efflux (V / t), m is called the coefficient of the correction of motion having a value between 0 to 1.5, and ρ is a density of the fluid. This equation can be applied to non–compressible Newtonian fluid flowing at steady and laminar condition without slip on the capillary wall. Capillary method is based on this equation and viscosity is determined from the measured efflux q combining with the pressure head P and the capillary geometry. An relative measurement using the reference standard materials is frequently adopted for many purpose, since the enough condition for ensuring the eq.(1) is not easy to realize. At the relative measurement, the

equation can be transformed as;

$$\eta = C_1 P t - C_2 \rho / t \qquad (2)$$

where C_1 and C_2 are constants depending on the capillary geometry and measuring condiction. Thus, the viscosity can be determined from the effused time for the certain volume of the sample, if the capillary constants are known. On the contrary, the equation for the short capillary viscometer consists of the first term of eq.(2), namely, the correction of motion is omitted. This omission may be allowed only for the highly viscous samples. In this experiment using short capillary, the effusion rate was measured through out the whole effusion process and is compared with the calculated effusion curve based on eq.(1). The procedure of the calculation is as follows: When the equation 1 is solved for q, then next expression is derived,

$$q=(V/t)=[-\eta \pm (\eta^2 + 4k_1 k_2 mH)^{1/2}] / 2 k_2 m \qquad (3)$$

where $k_1 = \pi r^4 \rho g/8 l$, *and* $k_2 = \rho /8 \pi l$. H is the head of fluid in a viscometer. Negative sign before root term is not taken because it has no physical meaning.

Assuming the constant value of H during a small time interval Δt, we calculate the volume of effusion, ΔV from eq.(3) and then obtain the change of head corresponded to ΔV. Iteration of these calculations from the beginning gives a effusion curve for whole effusion process. Actual observation of the effusion process was carried out by the apparatus shown in Fig.2. The geometry of short capillary is shown in Fig.1. Water and mercury at room temperature and molten tin and lead at moderate temperatures were selected for the sample fluids because their handling is relatively easy.

Results and discussion

Effusion curves for water and molten tin (at 527 K) are shown in Figs.3,4 for examples. Dots in the figure show the fitted values by the calculation using m as an adjustable parameter. As can be seen in the figures, calculation reproduced well the observed effusion curves through the whole range of effusion for both cases. Fitting in mercury and molten lead also agreed well with those observed curves. However, the coefficients of the correction of motion, m did not stay at constant but varied with sample materials. Figure 5 shows the relation between m and the Reynolds number of the sample flow, Rd referring the diameter of the capillary. There is no information about the relation between m and Rd because the capillary method is used only in the range of small Reynolds number. However, the behaviour that m increases with increasing Reynolds number, seems to be reasonable though the theoretical dependency is not known. The reason for the deviation of mercury from the smooth relation as depicted in Fig.5, may be interpreted by its large value of the Reynolds number.

New apparatus

From the results obtained here, we considered that the short capillary viscometer can be applied to the viscosity measurement of molten metals and alloys. For the viscosity measurement of molten metals and alloys, the apparatus should be operated under such conditions as; (1) an inert or a vacuum atmosphere to protect the sample from the oxidation, (2) successive measurements without breaking atmosphere and (3) operation without stopper to avoid the disturbance at the beginning of flowing. New apparatus illustrated in Fig.6 is constructed to realize these conditions described above.

The apparatus consists of two parts; the viscometer which is almost the same as Fig.1 and a crucible containing sample melt which is supported by alumina tube from a load cell. Both parts can be evacuated separately and placed in a Kanthal wound furnace. A system of data processing is the same as Fig.2. Procedure of the measurement is illustrated by Fig.7. Up and down mechanism of a load cell makes the operation to be possible. This viscometer does not require the exact volume of the sample at the initial stage of flow, since the effusion curve is calculated based on the effused volume of the sample. This simplifies the measuring procedure so much.

Viscosity of molten gallium

Obtained result for molten gallium is shown in Fig.8 for example. Effusion curve measured at 423 K was fitted by the calculated values using eq.(3) in which the viscosity of gallium was taken as a variable parameter against the fixed value of m determined by the relation shown in Fig.5. Iteration was necessary to get the compatible values of viscosity and m. Determined value of viscosity from Fig.8 was 1.7 mPa.s and is compared with 1.4 mPa.s which is measured by Iida et al. (3) using a capillary viscometer. Agreement is not so bad since gallium wets a quartz vessel and capillary tremendously and such tendency makes a poor reproducibility of the measurements.

Conclusion

New apparatus for viscosity measurement of molten metals and alloys was developed using a short capillary. Observed effusion curve was well reproduced by the calculation based on the capillary flow equation with the viscosity as a variable parameter. Thus, the viscometer developed here can be applied well to the molten metals and alloys.

References

1. T.Iida, Z.Morita, and S.Takeuchi, "Viscosity Measurements of Pure Liquid Metals by Capillary Method (Jap.)," Nippon Kinzoku Gakkai-shi, 39(1975),1169-1179.
2. T.Iida, "Viscosity Measurement of Molten Metals (Jap.)," Kinzoku, 67(1997),901-911.
3. Y.Kawai and Y.Shiraishi, ed., Handbook of Physico-chemical Properties at High Temperatures, (Tokyo, Japan: The Iron and steel Inst. Japan, 1988), p.94.

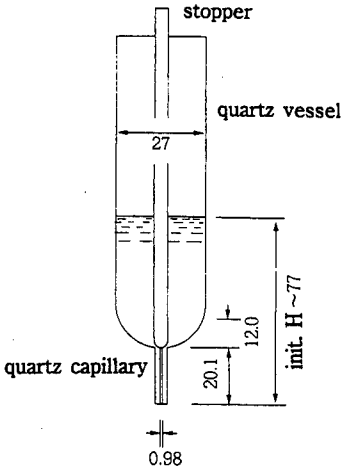


Fig.1 Shape of the short capillary viscometer. (unit; mm).

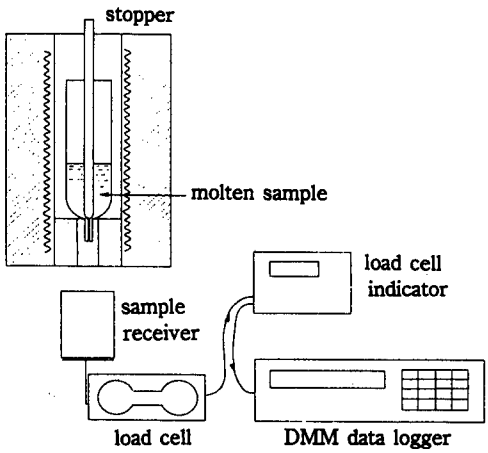


Fig.2 Apparatus of the efflux measurement.

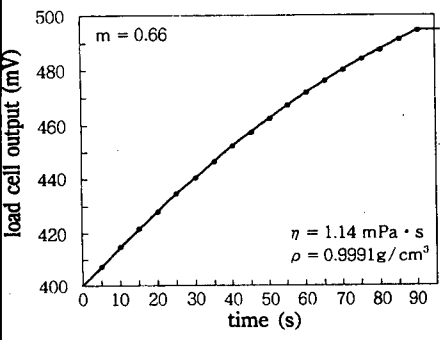


Fig.3 Effusion curve of water.

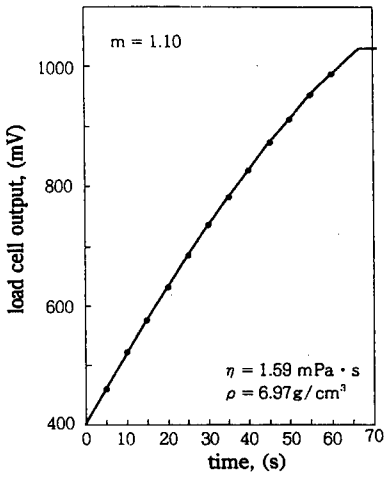


Fig.4 Effusion curve of molten tin at 573 K.

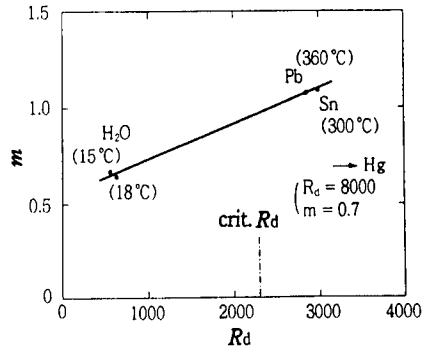


Fig.5 Correlation between the correction factor for energy of motion, m and the Reynolds number of the flow, Rd.

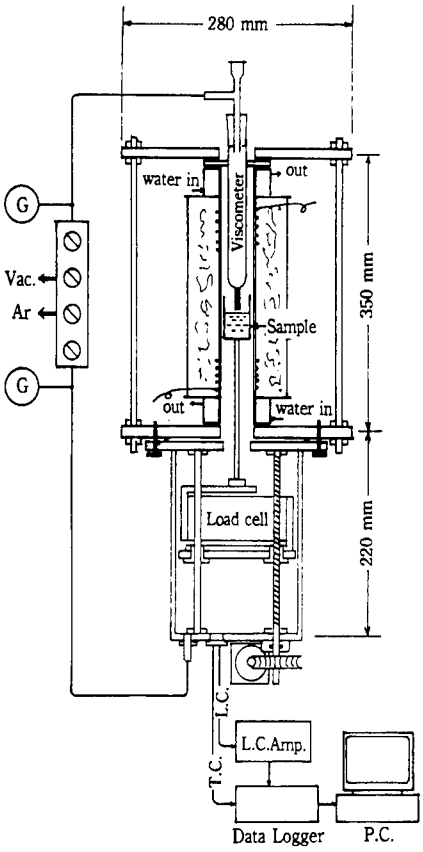


Fig.6 Schematic diagram of the apparatus for viscosity measurement.

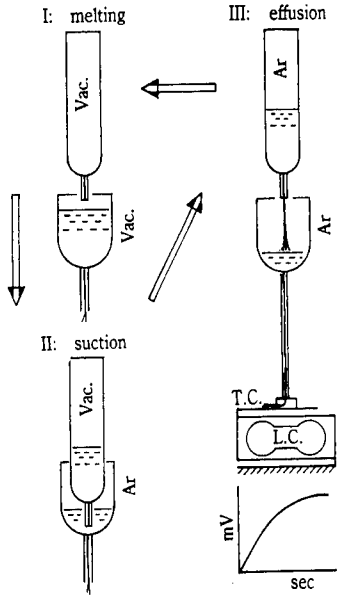


Fig.7 Procedure of the measurements.

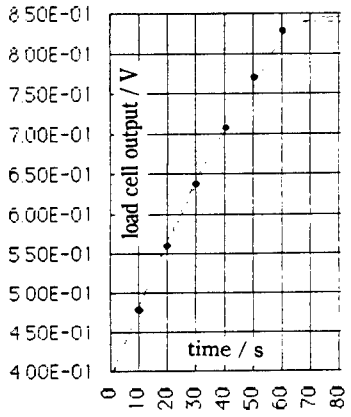


Fig.8 Effusion curve of molten Ga fitted with a viscosity of 1.7 mPa.s and m=0.96 at 423 K.

PRODUCTION OF FINE COPPER - TIN PARTICLES WITH AMMONIA SPLASHING METHOD

Seiji Yokoyama*, Naoto Itoh**, Sugahito Nishizawa*** and Masahiro Kawakami*

*:Department of Production Systems Engineering, Toyohashi University of Technology
Hibarigaoka 1-1, Tempaku-cho, Toyohashi 441, Japan
**:Graduate School, Toyohashi University of Technology
(Now, KYOWA INDUSTRIAL Co. Ltd.)
**:Graduate School, Toyohashi University of Technology

Abstract

In previous studies on evaporation of molten metals in reactive gas flows, it was found that molten copper held in an ammonia gas flow was splashed. The splashing phenomenon gave us a new idea for producing fine metallic particles. Then we named the new method "ammonia splashing method". In this work, as a fundamental study on the production of fine metallic particles with the ammonia splashing method, copper-tin alloy in the graphite crucible were induction-melted in ammonia gas stream in order to investigate the production rate of particles and the characteristics of particles. The rate of splash, i.e. the production rate of the particles, increased with increasing temperature. While, below approximately 40 mass% tin, the rate of splash decreases rapidly with increasing the content of tin, it increases with increasing the content of tin above approximately 80 mass%. The rate of splash in case that the distance between the tip of the silica tube which is gas lance and the melt surface is 5 mm is somewhat larger than that in case that the distance is 10 mm. The obtained particles were spheric and metallic copper-tin alloy. Above approximately 40 mass%Sn, segregation of composition in a particle was observed. Both the range of the particle size distribution and the mean diameter of the particles increase with increasing the tin content in Cu-Sn alloy. The mean diameter decreases with decreasing the distance between the tip of the silica tube and the melt surface.

The Third Pacific Rim International Conference on
Advanced Materials and Processing (PRICM 3)
Edited by M.A. Imam, R. DeNale, S. Hanada,
Z. Zhong and D.N. Lee
The Minerals, Metals & Materials Society, 1998

Introduction

In previous studies[1-5] on evaporation of molten metals(Al, Cu, Fe) in reactive gas(Ar+N_2, Ar+O_2, Ar+NH_3) flows, it was found that molten copper held in an ammonia gas flow was splashed[5]. Accordingly, the particles obtained in an ammonia gas flow were classified into two groups. One group was the particles which were formed by condensation of copper vapor and the size of the particles ranged from 10 to 300 nm. The other group was the particles which were formed by the splash and the size of the particles ranged from 1 to 100 μm.

Recently, fine particles whose diameter are below about 10 μm have been required for metal injection molding, soldering of large-scale integrated circuit and so on. Such fine particles might be produced by application of the splashing phenomena of metal due to ammonia. This production method of particles utilizing the splashing phenomena was named "ammonia splashing method". In previous work[6], pure copper particles were produced with the ammonia splashing method. In this work, as a fundamental study on the ammonia splashing method, production of copper-tin particles was attempted in order to investigate the characteristics of the particles and the rate of splash, i.e. the production rate of the particles.

Experimental

The experimental apparatus is schematically shown in figure 1. Cu-Sn alloy weighing about 0.4 kg was charged into a graphite crucible which was 38 mm in inner diameter. It was heated and melted in 50 mol% Ar + 50 mol%CO mixed gas flow by high frequency induction furnace. After the temperature of the molten alloy reached predetermined temperature, ammonia gas was introduced onto the melt surface through the silica tube which was 13 mm in inner diameter. After the melt was kept in the experimental conditions as shown in table I, the melt was cooled under argon gas flow. Temperature of the molten alloy was measured by two color eye pyrometer and thermocouple, and controlled manually within ±10 K. Gas flow rate was controlled by the mass flow controller within ±2 %. Experiments were mainly carried out at 1673 K.

The mass of splashed copper was determined by weighing the alloy in the graphite crucible before and after experiment. The splashed alloy particles mainly adhered to the silica reaction tube, the upper cap and the top end of crucibles, they were collected by a brush. The characteristics of the obtained particles were measured by SEM, EPMA and XRD.

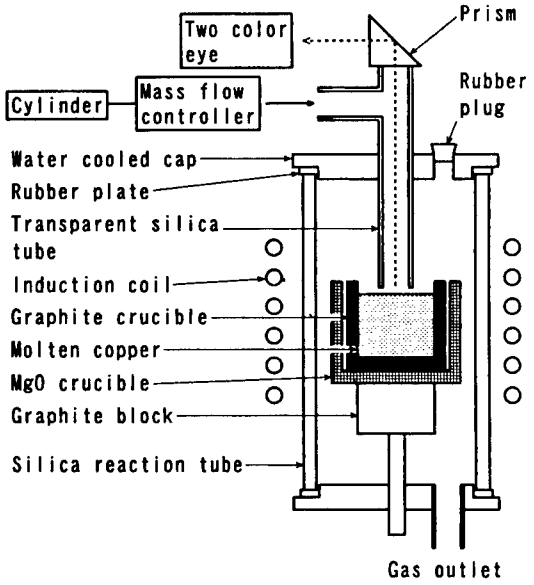


Figure 1 : Schematic diagram of the experimental apparatus.

Table I Experimental conditions.

Tin content in Cu-Sn alloy C_{Sn} /mass%	0 ~100
Temperature, T /K	873 ~1873
Gas	NH_3, Ar
Gas flow rate, Q /$10^{-5}m^3 \cdot s^{-1}$ (NTP)	6.64
Distance between tip of silica tube and melt surface, L /mm	5, 10

Results and discussions

Rate of splash

Since the mass of copper-tin alloy splashed increases linearly with time, the rate of splash is obtained from dividing the gradient of the straight line by cross-sectional area of the graphite crucible. Figure 2 shows the relation between the rate of splash and the tin content in alloy. While, below approximately 40 mass% tin, the rate of splash decreases rapidly with increasing the content of tin, it increases with increasing the content of tin above approximately 80 mass%. The rate of splash in case that the distance between the tip of the silica tube and melt surface is 5 mm is somewhat larger than that in case that the distance is 10 mm. The tin content dependency of the rate of splash cannot be explained by the properties, such as density, surface tension, and viscosity, because the properties decrease monotonously with an increase in the tin content.

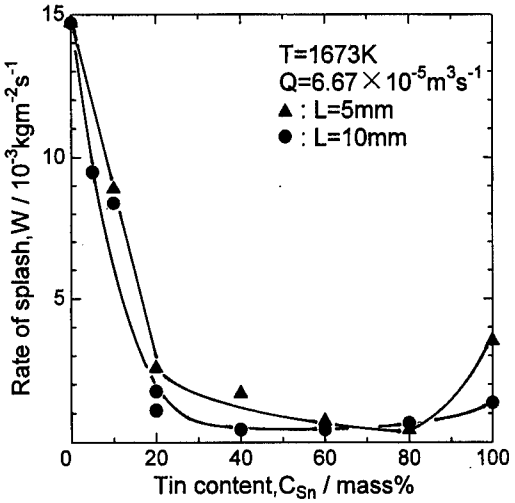


Figure 2 : Relation between the rate of splash and tin content in Cu-Sn alloy.

Figure 3 shows Arrhenius plot of the rate of splash. The Arrhenius plots of the rate of splash for copper and tin reveal good linear relationship. The gradients of the straight lines give the apparent activation energies. The obtained apparent activation energies of the rate of splash are 110 kJ • mol^{-1} for copper and 86 kJ • mol^{-1} for tin respectively.

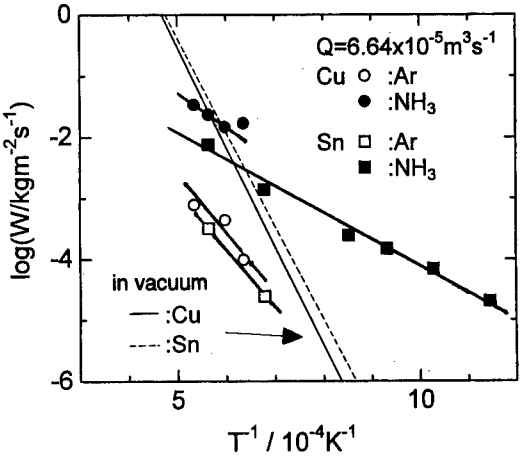


Figure 3 : Arrhenius plot of the rate of splash. (L = 5 mm)

The mechanism of the splash may be considered as follows; An ammonia gas diffuses onto the melt surface. An ammonia gas dissociates on the surface and dissolves into the melt. The overall reaction of dissolution of ammonia into the molten alloy is expressed by

$$NH_3 \rightarrow \underline{N} + 3\underline{H} \qquad (1)$$

Since the synthetic reaction of ammonia cannot proceed in this experimental conditions, the dissolved nitrogen and hydrogen form nitrogen gas and hydrogen gas as given by

$$2\underline{N} \rightarrow N_2 \qquad (2)$$

$$2\underline{H} \rightarrow H_2 \qquad (3)$$

It has been reported that ammonia dissolve in liquid copper more than nitrogen gas with respect to solubility of nitrogen in liquid copper[7]. Then, micro-bubble of nitrogen gas and hydrogen gas

may form at inside of molten copper by the difference of solubilities. The molten alloy is splashed by explosion of the micro-bubbles at a surface of the molten alloy. Since the mechanism of splash is very complicated and ammonia is easy to dissociate at higher temperature (thermodynamically, an ammonia decomposes at about 460 K), the rate controlling step cannot be determined from those activation energies. But the rate controlling step seems to be the chemical reaction rate for the reactions expressed by eqs. (1)-(3) because of the relatively high values of the apparent activation energies and the tin content dependency of the rate of splash.

For the purpose of comparison, the evaporation rates obtained experimentally of copper and tin in argon gas stream are shown in figure 3. The rate of splash is about 10 to 100 times larger than the evaporation rate in argon gas flow. While the rate of splash obtained in this work can be expressed by the sum of the evaporation rate and the rate of splash in itself, the rate of splash obtained can be regarded as the rate of splash in itself. The obtained apparent activation energies of the evaporation rate in argon gas flow are 172 kJ • mol^{-1} for copper and 133 kJ • mol^{-1} for tin respectively and the values are larger than those of the rate of splash. It originates in that a temperature dependency of the evaporation rate contains that of vapor pressure.

The calculated evaporation rates[8] of copper and tin in vacuum are also included in figure 3. It can be said that a productivity of the ammonia splashing method is superior to that of a process utilizing vacuum below certain temperature.

Characteristics of particles

Morphology of the particles are exemplified in figure 4. Usually, the spherical particles as shown in figure 4 (a) are obtained. When the temperature of the melt rises, the particles coag-

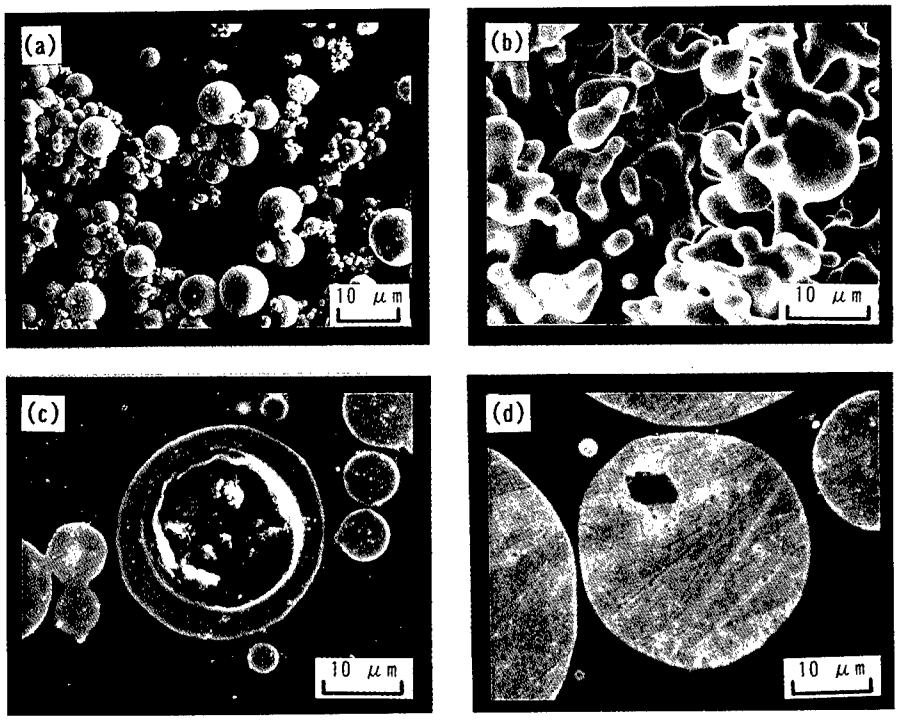


Figure 4 : SEM image of the obtained particles in ammonia gas stream.
(a) Cu-5mass%Sn at 1673 K ; (b) Cu at 1773 K ; (c) Cu-5mass%Sn at 1673 K ; (d) Sn at 1773 K.

ulate each other as shown in figure 4 (b) and the size of the primary particles of which secondary agglomerate particles are composed decrease. When pure copper is melted in ammonia gas below 1673 K, a few of particles which are about 2 to 5 mm in size are observed. XRD studies reveal that no nitride forms.

The observation of the cross-section of the particles reveals that a few of the particles which are more than 10 μm in diameter have large voids as shown in figures 4 (c) and 4 (d). With an increase in tin content in Cu-Sn alloy, the size of the void becomes small and the particles which contain the void decrease. Accordingly, it may be considered that the voids in the particle is formed by being wrapped in liquid film of the micro-bubble and/or by the formation of bubble in a particle due to decrement of the solubility of nitrogen and hydrogen with an decrease in temperature of a splashed particle under cooling.

EPMA studies reveal that segregation of composition in a particle is observed when the tin content is more than approximately 40 mass%. The segregation of composition originates in the large temperature difference between liquidus and solidus lines.

The particle size distribution are exemplified in figure 5. The value of ordinate in this figure is obtained from dividing frequency (total frequency is unity) by the width of classification of the particles and it corresponds to probability density. With increasing temperature, the particle size distribution can hardly be measured, because the coagulation of the particles, as shown in figure 4 (b), highly proceeds. The particle size distributions are approximately the exponential distribution. The range of the particle size distribution increases with increasing the tin content in Cu-Sn alloy.

Figure 6 shows the relation between the mean diameter of the obtained particles and the tin content. The mean diameter increases with increasing the tin content in Cu-Sn alloy. It results from that which the splashed particle grows by the collision of them, because the melting point of the alloy decreases with increas-

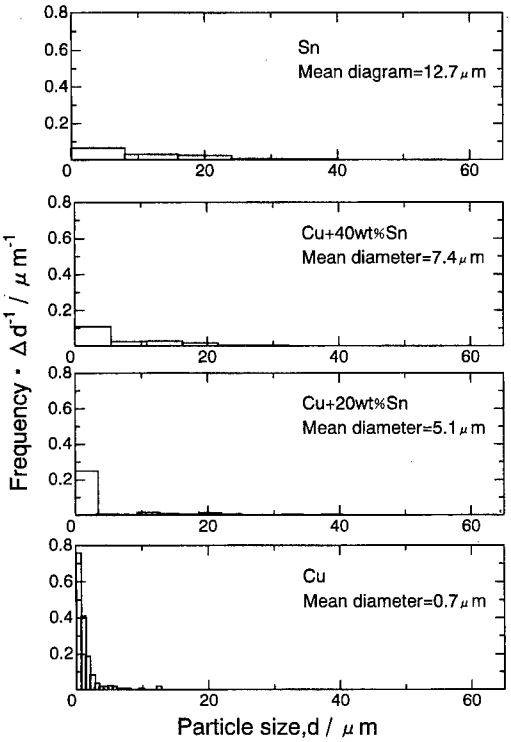


Figure 5 : Example of particle size distribution. (T =1673 K, L = 10 mm)

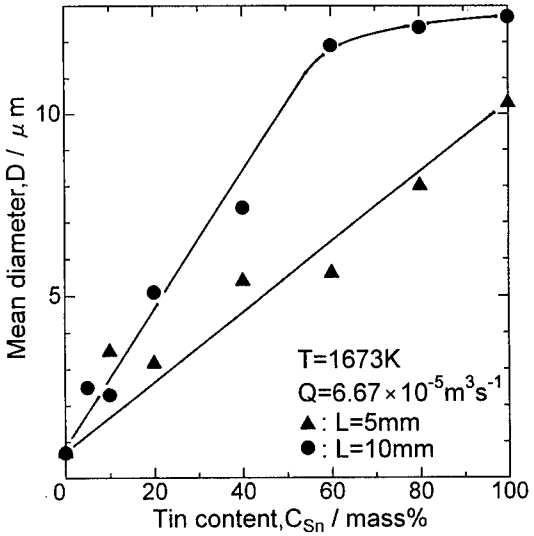


Figure 6 : Relation between mean particle size and tin content in Cu-Sn alloy.

ing the tin content. The mean diameter is affected by the distance between the tip of silica tube and the melt surface, L, and the mean diameter for the distance of 10mm is larger than that for the distance of 5 mm. That which the distance is short means that the temperature gradient, which extends from the melt surface in to the gas phase, is steepened. In addition, because an ammonia gas diffuses on to the melt surface easily, the temperature gradient is more steepened by endothermic reaction of ammonia dissociation. The splashed particles are cooled rapidly by the steepening of the temperature gradient. Therefore, the mean diameter of the obtained particles decreases with decreasing the distance , because the particle growth by the collision doesn't proceed.

Conclusions

For developing the new production method of fine particles utilizing the phenomena of splash occurred under an ammonia gas flow, i.e. the ammonia splashing method, copper-tin alloys were melted in ammonia gas stream in order to investigate the rate of splash and the characteristics of particles.

The rate of splash increased with increasing temperature. While, below approximately 40 mass% tin, the rate of splash decreases rapidly with increasing the content of tin, it increases with increasing the content of tin above approximately 80 mass%. The rate of splash in case that the distance between the tip of the silica tube and the melt surface is 5 mm is somewhat larger than that in case that the distance is 10 mm.

The obtained particles were metallic copper-tin alloy and, above approximately 40 mass%Sn, segregation of composition in a particle is observed. Both the range of the particle size distribution and the mean diameter of the particles increases with increasing the tin content in Cu-Sn alloy. The mean diameter decreases with decreasing the distance between the tip of the silica tube and the melt surface.

Reference

1.S.Yokoyama et al.,"Evaporation Rate of Molten Al in Inert Gas Flows and Characteristics of Condensed Paricles,":J.Japan Inst. Metals, 57(1993), 54-62.

2.S.Yokoyama et al.,"Evaporation Rate of Molten Aluminum in Ar+O_2 Gas Flow and Characteristics of Condensed Paricles,":J.Japan Inst. Metals, 57(1993), 282-62.

3.S.Yokoyama et al.,"Evaporation Rate of Molten Iron in Argon Gas Stream and Characteristics of Condensed Paricles,":J.Japan Inst. Metals, 57(1995), 814-820.

4.S.Yokoyama et al.,"Evaporation Rate of Molten Iron in Ar+O_2 Gas Stream and Characteristics of Formed Ultrafine Paricles,":J.Japan Inst. Metals, 57(1995), 1030-1035.

5..S.Yokoyama et al.,"Evaporation Rate of Molten Copper in Argon+Ammonia Gas Mixture," ABSTRACTS International Symposium on Advanced Materials and Technology for 21st Century, JIM, (1995), 418.

6.S. Yokoyama, N. Itoh and M. Kawakami,"Production of Fine Copper Particles with Ammonia Splashing Method,"Proceedings of ISAEM-97, (in printing)

7.K.Ono,"Vaporization of Copper by Ammonia Gas,"CAMP-ISIJ, 7(1994), 1142

8.F.D.Richardson, Physical Chemistry of Melts in Metallurgy (Academic Press, London, New York, 1974), 483-487

Electron Beam Surface Melting to Study Phase Selection in 3XXX Series Al Alloys

L. Carroll[1], K. A. Q. O'Reilly[1], B. Cantor[1], P. V. Evans[2]

[1]Oxford Centre for Advanced Materials and Composites, Department of Materials, University of Oxford, Parks Road, Oxford OX1 3PH, U.K., Fax +44 1865 283333
[2]Alcan International Limited, Banbury Laboratory, Southam Road, Banbury, Oxon. OX16 7SP, U.K., Fax +44 1295 452800

Abstract

Electron beam surface melting is an experimental method capable of achieving the growth velocities seen in strip casting. The intermetallic phase selection behaviour of model 3xxx series Al alloys has been investigated over a range of growth velocities produced by a range of beam velocities (10-100mms^{-1}) and Fe/Mn ratios. Accurate phase identification has been accomplished through a combination of phase extraction, x-ray diffraction, transmission electron microscopy (TEM) and energy dispersive x-ray microanalysis (EDX). The resulting phase selection map has been compared to results obtained at slower growth velocities typical of those seen in direct chill (D. C.) casting for similar alloys. In the electron beam surface melting studies $Al_6(Fe,Mn)$ is found to be replaced by cubic α-$Al_{12}(Fe,Mn)_3Si$ as the predominant 'as-cast' phase produced in all of the 3xxx-based alloys in the range of compositions and solidification conditions investigated.

The Third Pacific Rim International Conference on Advanced Materials and Processing (PRICM 3)
Edited by M.A. Imam, R. DeNale, S. Hanada, Z. Zhong and D.N. Lee
The Minerals, Metals & Materials Society, 1998

Introduction

The conventional manufacturing route for Al can body sheet is essentially a two-stage cast and roll process. Ingots are initially direct chill (D. C.) cast to ~0.3m x 1.0m x 3.0m and undergo thermal and thermomechanical treatments during the downstream processing to help to control the microstructure as the material is reduced to final gauge. Strip casting, where the melt is cast directly to near final gauge dimensions, results in a more refined microstructure produced at higher solidification rates or growth velocities. Growth velocity is an important factor in determining intermetallic phase selection during solidification which can in turn affect both the subsequent processing and final gauge properties of the cast material. It is necessary therefore to investigate the effect of growth velocity on intermetallic phase selection for can body stock alloys in the strip casting regime. This will enable the alloy composition to be optimised in order to take full advantage of this more cost and energy efficient method of producing can body sheet.

Electron beam surface melting is an experimental method capable of simulating strip casting conditions by producing growth velocities in the appropriate range 1-100mms^{-1}. An energetic electron beam is focused on the surface of a sample to generate a molten pool and is then traversed over the surface at a constant velocity. The unmelted bulk alloy acts as an epitaxial substrate to renucleate the primary Al and is an efficient heat sink which facilitates the rapid resolidification.

This paper describes an investigation of electron beam surface melting of model 3xxx series Al alloys to study phase selection. Current can body-stock is taken from the 3xxx series which are Al-Mn alloys with additions of Fe, Mg, Si and Cu. In the standard production route $Al_6(Fe,Mn)$ and Mg_2Si with traces of cubic α-$Al_{12}(Fe,Mn)_3Si$ occur in the as-cast microstructure. Some of the $Al_6(Fe,Mn)$ is transformed to cubic α-$Al_{12}(Fe,Mn)_3Si$ during subsequent homogenisation treatments [1]. The α phase is preferred due to its greater hardness which results in improved product surface quality by cleaning the die and preventing galling [2]. In this paper the effect of Fe/Mn ratio on the formation and composition of intermetallic phases is examined over a range of solidification rates and presented as a phase selection map. The phase selection map shows fields of occurrence of different phases as a function of composition and beam velocity and will be useful in alloy and process design for the strip casting of can body stock.

Experimental

A series of four model 3xxx series Al alloys of 99.999% base Al purity were prepared with a constant level of Fe+Mn=1.5wt.% and with Fe/Mn ratios varying from 0.21-5.77. The compositions were measured by spectrographic analysis and are given in table I.

Table I Alloy compositions in wt.% (balance is Al)

Alloy	Fe	Mn	Si	Mg	Cu	Fe/Mn ratio
A	1.27	0.22	0.21	1.16	0.21	5.77
B	0.90	0.55	0.21	1.17	0.20	1.64
C	0.51	0.94	0.20	1.20	0.20	0.54
D	0.24	1.17	0.20	1.17	0.20	0.21

Alloys were cast into 100 x 200 x 30mm steel moulds and subsequently machined into 100 x 30 x 25mm blocks. The as-cast surfaces were removed by milling and grinding with 1200 grit SiC to produce parallel surfaces to be electron beam surface melted. Sample blocks were surface

melted with an initial temperature of 25°C using a 120kV focused electron beam. This was rastered laterally using electromagnetic deflection coils at a frequency of 640Hz to produce a melted zone 8mm in width. The beam was traversed in a direction at right angles to the rastering at rates of 10, 50 and 100mms^{-1} with beam powers of 1320, 2100 and 3120W respectively to produce melted depths of ~500μm in each case.

Longitudinal sections from the centres of each of the surface melted zones were ground and polished using 6μm diamond and colloidal silica. The samples were then electrolytically etched at 20V in Barker's solution (2% fluoboric acid) and examined optically under polarised light to reveal grain structures from which the growth velocity through the surface melted zone could be estimated. From fig. 1 [3], the growth velocity v_g is given by $v_g = v_b \cos\theta$ where v_b is the beam traverse rate and θ is determined by measuring the orientation of interdendritic phases and grain boundaries with respect to the beam traverse direction.

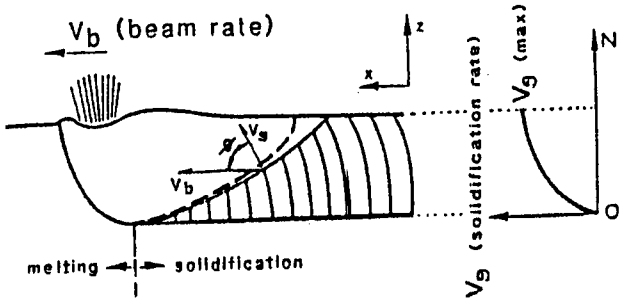


Fig.1: Longitudinal section through surface melted zone during treatment and vector analysis of growth velocity.

Additional samples were electrolytically etched at 20V in a mixture of 30gl^{-1} potassium iodide in methanol. The Al matrix was then dissolved to leave intermetallic particles standing proud, and examination using a JEOL 6300 scanning electron microscope (SEM) allowed the growth behaviour of the intermetallic particles to be observed.

Intermetallic particles were identified from both the surface melted zone and the as-cast substrate. The fine scale of the intermetallic particles in the surface melted material made them difficult to identify by in-situ EDX measurements and necessitated the use of extensive TEM and selected area diffraction for complete phase analysis. Accurate phase identification was therefore facilitated by the extraction of intermetallic particles from the Al matrix and their subsequent analysis by x-ray diffraction (XRD). The matrix was dissolved in butanol without affecting the intermetallic particles using a method based on that described by Simensen et al. [4]. Alloy samples were etched to remove the oxide film, placed in a pressure vessel containing pre-dried butanol and an inert atmosphere, and then heated up to 408K until the matrix dissolution was complete. The undissolved intermetallic particles were collected on a PTFE filter of 0.45μm pore diameter through which the butanol containing the dissolved Al solution was forced under pressure. Extracted intermetallic particles were mounted onto an amorphous Si disc and investigated by x-ray diffraction (XRD) using a Philips 1700 series x-ray diffractometer with a Cu-Kα radiation source and a wavelength of 1.54Å. Readings were taken at 35kV and 50mA with a scan rate of 0.002°s^{-1}. The XRD patterns were analysed with reference to the Si standard and XRD patterns from samples of known phase content prepared by Bridgman growth. The detection limit of a given phase in the extracted mixture was determined to be 5 wt.% [5]. Extracted intermetallic particles were also ultrasonically dispersed in methanol and then pipetted onto gold carbon-coated TEM grids, for TEM/EDX analysis.

Results

All electron beam surface melted specimens demonstrated a greatly refined sub-grain microstructure with respect to the as-cast substrate. The grain structure within the surface melted zone was predominantly columnar and epitaxial with the as-cast substrate, as shown in fig.2 for alloy C surface melted at $100mms^{-1}$[6]. The variations in orientation of grain boundaries through the surface melted zone were shown by vector analysis to indicate increasing growth velocity from the substrate towards the surface. A complete analysis of the effect of beam velocity on growth velocity variations through the surface melted zone will be published elsewhere.

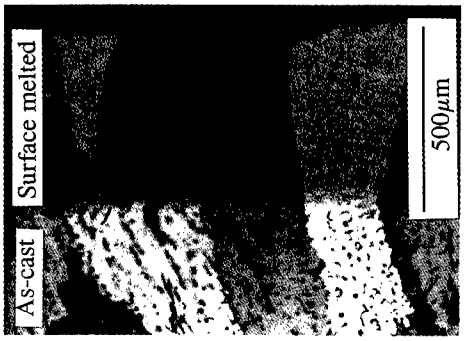


Fig.2: Epitaxial growth from as-cast substrate into surface melted zone.

A deep etched sample of alloy C processed at $10mms^{-1}$ in fig.3 shows as-cast intermetallic particles connected to intermetallic particles in the surface melted zone. The connected intermetallic particles are of different morphology, but another region of the sample showed intermetallic particles connected between the as-cast substrate and the surface melted zone of similar morphology. No phase identification of these connected intermetallic particles has yet been performed.

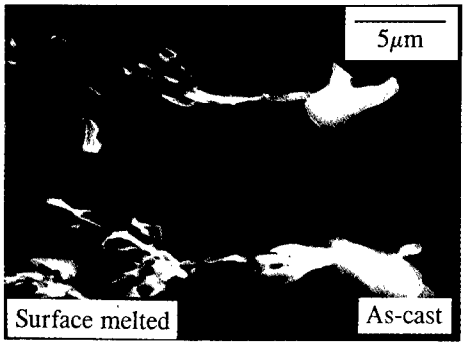


Fig.3: Deep etch sample of alloy C surface melted at $10mms^{-1}$ showing intermetallics connected across as-cast/surface melted zone interface.

The growth path of the intermetallic particles, as investigated by deep etching is shown for alloy C processed at $10mms^{-1}$ in fig.4. Intermetallic particles up to $60\mu m$ in length were seen to have grown in the channels between the Al dendrites.

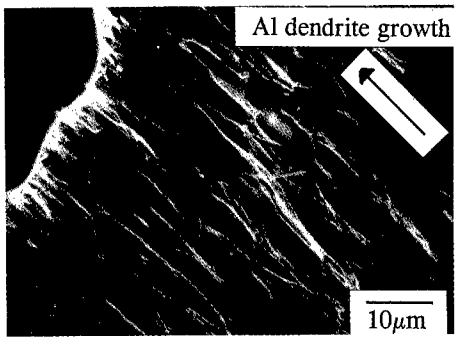


Fig.4: Deep etch sample of alloy C surface melted at 10mms^{-1} showing lengths of connected intermetallic.

The phase selection results are presented in fig.5 as a map of surface melting rate, or beam velocity, versus alloy composition and showing qualitativevalues for the different phases present for each condition.

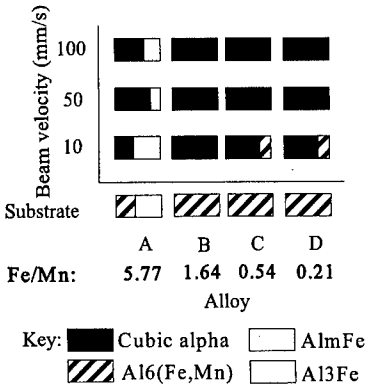


Fig.5: Summary of phase analysis results.

The secondary phases present in the surface melted material did not fully correspond with the secondary phases present in the as-cast substrate for all alloys. In addition cubic α was promoted in the surface melted material over $Al_6(Fe,Mn)$ in the as-cast substrate as a result of the more rapid solidification.

In the relatively Fe-rich alloy A (Fe/Mn=5.77) a mixture of cubic α and Al_mFe was formed at all surface melting speeds. Alloy B (Fe/Mn=1.64) formed only cubic α under all surface melting conditions. In the more Mn-rich alloys C and D (Fe/Mn = 0.54 and 0.21 respectively) $Al_6(Fe,Mn)$ and cubic α formed at 10mms^{-1} but cubic α dominated at the higher surface melting speeds.

The variation in the composition of cubic α with bulk Fe/Mn ratio is shown in fig.6 as an EDX map of Fe versus Mn for alloys A and D processed at 10mms^{-1}. In the Fe-rich alloy A the average Fe/Mn ratio in the intermetallic α particles was ~24 whereas in the Mn-rich alloy D the Fe/Mn ratio of the intermetallic α particles was ~3.

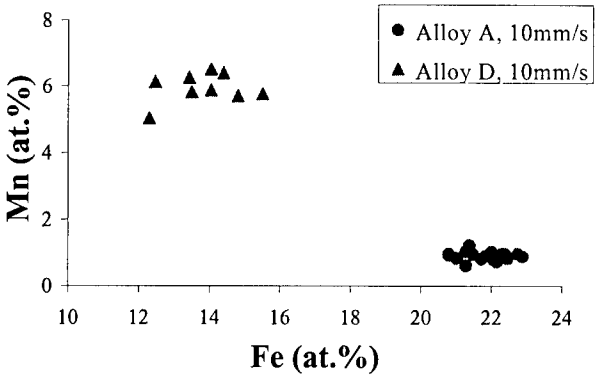


Fig.6: EDX map showing Fe and Mn contents for extracted cubic alpha particles.

Discussion

Electron beam surface melting is successful in producing rapid epitaxial solidification in the Al alloys tested. The epitaxial growth encouraged by the surface melting supports the assumption that nucleation effects for the resolidifying Al are minimised. The apparent nucleation of intermetallic particles after surface melting on as-cast particles does not govern the subsequent phase selection as demonstrated by the differences between as-cast phases and those formed in the surface melted zone. New phases formed on resolidification are nucleated in the surface melted zone but the mechanism by which this takes place is not yet known. However, the extent of the interconnection of the intermetallic particles in the surface melted zone shows that their solidification does not take place by repeated nucleation, and is growth dominated.

The phase selection results for alloy B demonstrate the general trend for the promotion of cubic α over $Al_6(Fe,Mn)$ with increasing growth velocity. A similar effect has been observed previously as the promotion of Si-rich phases at higher cooling rates in Al-Fe-Si alloys [7]. With increasing growth velocity, the liquid becomes increasingly enriched in solute such as Si, encouraging the formation of the Si-containing cubic α over the Si-intolerant phase $Al_6(Fe,Mn)$ [7].

The high Fe content of alloy A shifts the alloy to a different equilibrium phase field at a temperature just below the liquidus from alloy B as predicted by the thermodynamics calculation software package MTDATA [8] using the phase equilibrium database provided by Thermotech Ltd. [9]. The formation of Al_mFe in conjunction with cubic α can accommodate the excess Fe. $Al_6(Fe,Mn)$ forms in the Mn-rich alloys C and D at $10mms^{-1}$, and has the lowest formation energy at $Al_6(Fe_{0.5},Mn_{0.5})$ [10]. Fe has a lower partition coefficient than Mn [11] resulting in the intermetallic particles having a higher Fe/Mn ratio then in the bulk alloy. There may be insufficient Mn available in the liquid of the solidifying alloy A to form detectable amounts of $Al_6(Fe_{0.5},Mn_{0.5})$ and Al_mFe is formed instead. At higher growth velocities, up to $100mms^{-1}$, Al_mFe still forms due to its tolerance of Si (up to 3wt.%).

The variation of the composition of the α phase with the bulk alloy composition demonstrates that cubic α intermetallic particles take up Fe more efficiently than Mn. At high bulk Fe/Mn ratios, the cubic α particles have a high Fe/Mn content, but at high Mn/Fe ratios the particles still contain more Fe than Mn.

The potential for controlling the formation of the $Al_6(Fe,Mn)$ and cubic α phases in 3xxx series Al alloys under strip casting solidification rates can be seen to depend on the composition and processing. The rapid solidification conditions given by electron beam surface melting promote the direct formation of the α phase. However, the α composition depends on the bulk alloy composition and this may affect the hardness of the α particles and their ability to prevent galling. The finer scale on which the α phase is produced at these faster solidification rates, relative to if it had been produced by conventional D.C. casting and homogenisation, may also affect its efficiency to prevent galling in the final sheet material.

Conclusion

Electron beam surface melting is a successful method of producing rapid epitaxial solidification. Experimental evidence suggests that the intermetallic solidification and phase selection is also growth dominated for this process. The technique has been used to investigate phase selection in model 3xxx series Al alloys over a range of growth velocities in the strip casting regime and Fe/Mn ratios. The phase selection map produced shows that cubic α-$Al_{12}Fe_3Si$ predominates in the range of alloy compositions and solidification conditions investigated. However, the actual composition of cubic α was found to depend on the bulk Fe/Mn ratio.

References

[1] G. J. Marshall, Mat. Sci. Forum, 1996, **19**, 217-222

[2] H. Watanabe, K. Ohori and Y. Takeuchi, Aluminium, 1984, **60**, E310

[3] M. Gremaud, M. Carrard and W. Kurz, Acta Met., 1990, **38**, 2587

[4] C. J. Siemensen, P. Fartrum and A. Andersen, Z. Anal. Chem., 1984, **319**, 286

[5] P. V. Evans, J. Worth, A. Bosland and S. C. Flood, Proc. of 4th Dec. Int. Conf. on Solidification Processing, 1997, 531-535

[6] L. Carroll, K. A. Q. O'Reilly, B. Cantor and P. V. Evans, Proc. of 4th Dec. Int. Conf. on Solidification Processing, 1997, 546-549

[7] Y. Langsrud, Eng. Mat., 1990, **44** & **45**, 95-116

[8] R.H.Davies, A.T.Dinsdale, J.A.Gisby, S.M.Hodson and T.I.Barry, 1994, "MTDATA Handbook", National Physical Laboratory, Teddington, Middlesex, TW11 0LW, U.K, Crown Copyright.

[9] N.Saunders, "Al data information", Thermotech Ltd., Surrey Technology Centre, 40 Occam Rd., The Surrey Research Park, Guildford, Surrey GU2 5YG, U.K.

[10] L. Backerud, Jernkont. Ann., 1968, **152**

[11] L. F. Mondolfo, 'Al Alloys - Structure and Properties', Butterworth and Co. Ltd., 1976

Acknowledgements

The authors would like to acknowledge the help of John Worth at Alcan International Ltd. for preparing the alloys, Bruce Dance at TWI for carrying out the electron beam surface processing, and John Hunt at Oxford University for use of his intermetallic extraction apparatus. L. Carroll is grateful to Alcan International Ltd. and the EPSRC for financial support.

APPLICATION OF THE ACCELERATED CRUCIBLE ROTATION TECHNIQUE IN THE DIRECTIONAL SOLIDIFICATION OF METALLIC ALLOYS

JIE Wanqi, Ma Dong*, Guo Xiping, Liu Juncheng**, Xu Wei, and Li Yong

State Key Laboratory of Solidification Processing, Northwestern Polytechnical University, Xi'an 710072, China

Abstract

Accelerated Crucible Rotation Technique (ACRT) was developed to introduce regular forced convection in the directional solidification process to control microstructures. The technique has been widely used in single crystal growth of semiconductor compounds. In the present experimental researches, the technique is applied to Al-Cu hypoeutectic and eutectic alloys. The rotation rate varies in the trapezoidal way during the process. For Al-4.5%Cu hypoeutectic alloys, the maximum rotation rate up to 400 rpm is adopted. It is concluded that the forced convection during the process exerts strong influences on the growth interface. The development of the dendrite branches is confined and the dendrite spacing is reduced. For the Al-$CuAl_2$ eutectic alloy, the maximum rate of 100, 200, 300 and 400 rpm respectively and the growth rate varying in the region of 5~60μm/s are adopted. The results show that: (1) the effects of ACRT on the growth structure depend on the Renald's number *Re*, where the lamella faults are aroused when $Re<270$, and the periodic structure related to the crucible rotation periods is caused when $Re>500$; (2) the average eutectic spacing decreases with the increase of *Re*; (3) the lamella spacing is no longer uniform along the radial direction of the samples when ACRT is applied, the maximum spacing is obtained near the crucible wall while the minimum at the center of the samples.

* Present Address: Department of Materials Science, National University of Singapore, Lower Kent Road, Singapore 119260

** Present Address: Department of Mechanical Engineering, Hong Kong University of Science and Technology, Clear Water Bay, Koonlong, Hong Kong

◆ The research is funded by the Natural Science Foundation of China

The Third Pacific Rim International Conference on Advanced Materials and Processing (PRICM 3)
Edited by M.A. Imam, R. DeNale, S. Hanada, Z. Zhong and D.N. Lee
The Minerals, Metals & Materials Society, 1998

Introduction

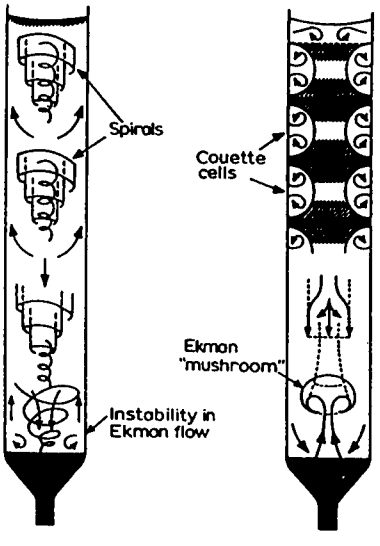
In conventional Bridgman process, unidirectional growth of liquid/solid interface is controlled by heat transfer. More and more researches show that convection has strong effect on the growth morphology and the microstructures[1-3]. Magnetic field[4-7] and super gravity[8,9] have been used to introduce convection in front of interface. However, accelerated crucible rotation technique (ACRT) is a simple way to arouse regular convection in the Bridgman process and was used first for the single crystal growth of II-VI compounds[10-12]. Horowitz et al[13] managed to use the technique for the directional solidification of eutectic alloy. One of the present authors applied the technique for the microstructure control of Al-Si eutectic and got some interesting results[14]. In the present paper, the influences of the forced convection by ACRT method on the directional solidification microstructure of both Al-4.5%Cu hypoeutectic and Al-Cu eutectic will be studied.

Forced convection during ACRT process

The semi-quantity analysis of the forced convection during ACRT process with the step changes of the crucible rotation was described by Brice etal[15] and sketched in Figure 1. It is shown that the flowing method of the liquid in the crucible depends on the Renald's number *Re*, which is defined to be as follows,

$$Re = \frac{r_0^2 \Delta\Omega}{\gamma} \tag{1}$$

where r_0 is the inner radius of the crucible, $\Delta\Omega$ is the change of the crucible rotation angle velocity, and γ is the viscosity.



(a) (b)

Figure 1: forced flow in ACRT Process
(a)Speed up process (b) slow down process

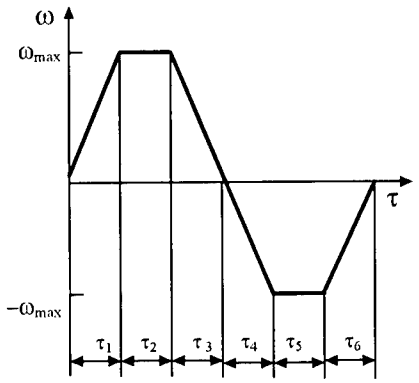


Figure 2: Rotation waves of the crucible.

When *Re* is less than 40, spiral shearing flow happens. When *Re* is over 40 but less than 270 for slow down process or 500 for speed up process, regular Ekman flow as well as spiral shearing flow will be introduced. If *Re* is over 500, Couette flow near the crucible wall during slow down process will be aroused except for the Ekman flow near the growth interface.

In the process of continuous change of crucible rotation rate, convection becomes complicated and thus numerical method has to be used to analyze it. In our recent researches, SOLA-VOF method is used for the calculation. The accuracy of the calculation method was confirmed by comparing the calculated free surface shape with that evaluated with the well confirmed theory for the liquid in a rotating crucible at constant speed. The calculation results are shown by the stream lines and the marking particles.

One example corresponding to the rotation method shown in Figure 2, with crucible inner diameter of 16 mm, is calculated. The stream lines calculated are shown in Figure 3. *F* and *S* in

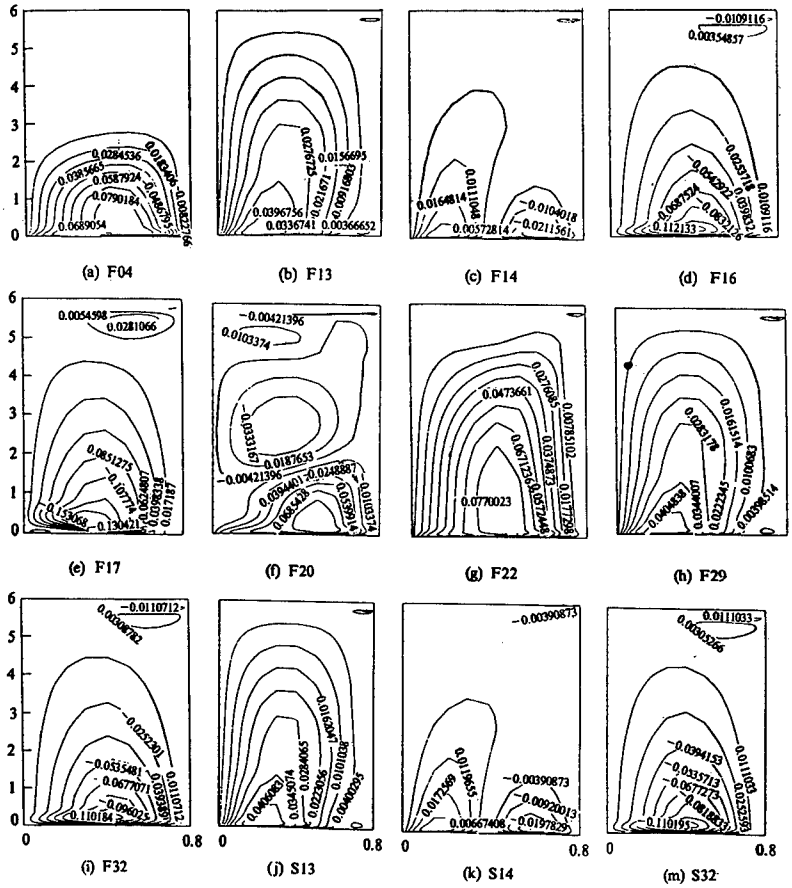


Figure 3: Evolution of the stream lines during the ACRT process. The abscissa is the distance from the crucible center in cm and the ordinate is that from the growth interface in cm. The flow flux is in cm^2/s, a the positive value is for counterclockwise flow and a negative value is for clockwise flow. *F* and *S* refer to the first and second period of ACRT process, and the values after are the time lasted from the starting point. ω_{max}=60rpm, $\tau_1=\tau_3=\tau_4=\tau_6=$ 4s, $\tau_2=\tau_5$=8s, viscosity of the liquid, ν=0.01cm^2/s

the caption mean the first period and the second period respectively, and the values after are the time from the beginning of ACRT process in second. During speed up process, counterclockwise flow appears and develops in the ways shown in Figure 3a. At the time of 4s from the beginning, the flow flux near L/S interface reaches a maximum value of 0.079 cm^2/s. After that the flow area gradually expands, but the flow flux declines. When the crucible starts to decelerate, a weak clockwise flow appears in the corner confined by the crucible wall and the bottom as shown in Figure 3b, and becomes strong until the 17th second. The counterclockwise flow declines from 4th to 5th second continuously, and finally vanishes (see Figures 3a to 3d). From the 17th second, the crucible is accelerated in another direction, the counterclockwise flow appears again near the center of the bottom (see Fig. 3e) and develops (Figures 3e to 3g). The flowing rates changes in the aforementioned method periodically.

The marking particle is also used to show the forced convection during ACRT process. The particle has no mass itself, and therefore has no effect on all the variables. The movement of the marking particles traces the flowing direction and rate of the fluid near the crucible bottom approximately. The liquid moves up along the crucible wall during the speed up process but moves up in the center during the slow down process. The height of the particle trace, h_e, reveals the tendency of Ekman flow. The stronger the Ekman flow is, the larger the h_e will be. Figure 4 shows the effect of the Renald's Number *Re* on dimensionless height of Ekman zone, h_e/r_0. The calculated results show that h_e/r_0 increases with the increase of *Re*.

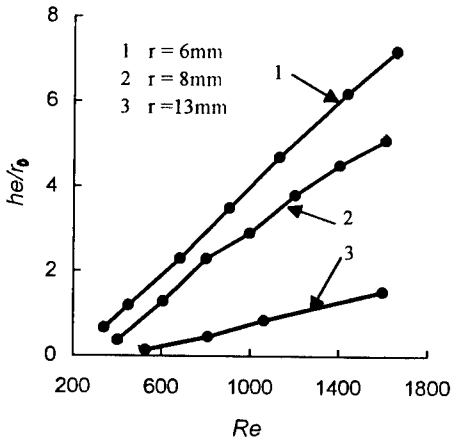


Figure 4: The relationship between Renald's Number *Re* and the dimensionless height of the Ekman region h_e/r_0 , where $\tau_1 = \tau_3 = \tau_5 = \tau_6 = 4s$; $\tau_2 = \tau_5 = 8s$

Effect of the forced convection in ACRT process on the thermal field

In directional solidification process, the crystal grows against heat flux. When convection exists, the heat transfer will be strengthened outside of the adherent boundary. The finite difference method is used for the calculation and the results reveal the following two important factors:

(1) If the forced convection is introduced by ACRT method in Bridgman process for materials with low thermal conductivity, the depth of the concave interface will be reduced significantly.

(2) Temperature in bulk liquid will tend to be uniform and the local temperature gradient near L/S interface will be increased with the application of ACRT. This is also confirmed by the experiments. The experiment was done with Al-4.5%Cu sample in the diameter of 10mm. Temperature distribution is measured with thermal couple. The steady temperature gradient (non-ACRT) is 199.3K/cm for all the samples. The rotation rate varies in trapezoidal way as

shown in Figure 5. The measured temperature distribution is shown in Figure 6, from which the local temperature gradients near L/S interface are calculated to be 248.5, 301.5 and 370.2K/cm when the maximum rotation rates of 200, 300 and 400rpm are adopted respectively.

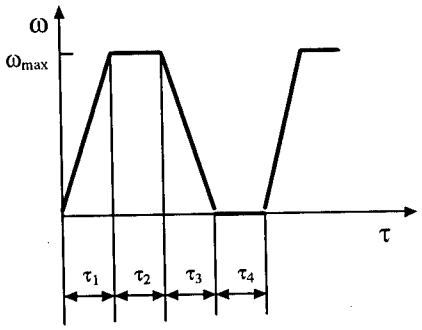


Figure 5: The rotation method for the temperature measurement of the ACRT process.

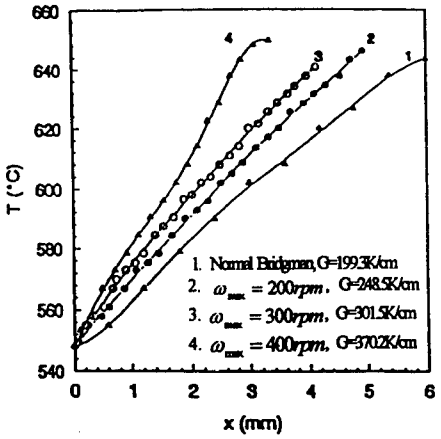
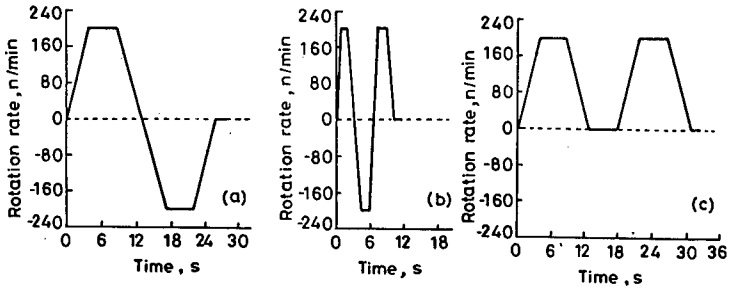


Figure 6: The influences of ACRT parameters on the temperature distribution in front of interface, where $\tau_1 = \tau_3 = 1s$; $\tau_2 = \tau_4 = 4s$

Experimental researches on directional solidification of Al-4.5%Cu by ACRT-B method

In the first set of experiments, Al-4.5%Cu samples in diameter of 8mm were directional solidified under the steady temperature gradient of 177K/cm and the withdrawal rate of 2.50μm/s. The rotation method is shown in Figure 7. The typical L/S interface morphologies at different ACRT parameters are shown in Figure 8. It is seen that the application of ACRT prevents the formation of dendrites, reduces the width of solidification region, and therefore decreases the cell spacing.



(a) (b) (c)

Figure 7: The rotation method of the ACRT growth of Al-4.5%Cu alloy.

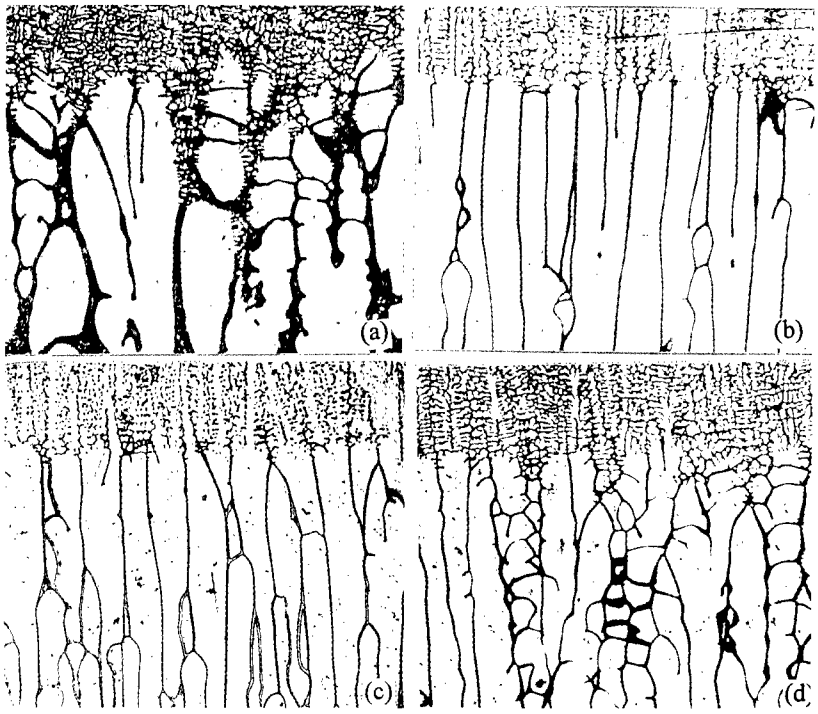


Figure 8: The influences of the ACRT on the growth morphologies of Al-4.5%Cu alloy. a) no crucible rotation, (b) rotation in the way of Figure 7(a), (c) rotation in the way of Figure 7(b), (d) rotation in the way of Figure 7(c).

More experiments has been done to study the effect of ACRT parameters at different growth rates. The results are presented in Figure 9. The corresponding crucible rotation method is also in the trapezoidal way as shown in Figure 5. The steady temperature gradient is 120K/cm. It shows that the cell spacing is reduced in the growth rate region from 3μm/s to 100μm/s when proper ACRT is applied. The regression equations for the curves a, b and c in Figure 9 are $\lambda = 434.8R^{-0.375}$, $\lambda = 348.1R^{-0.342}$ and $\lambda = 281.9R^{-0.314}$ respectively.

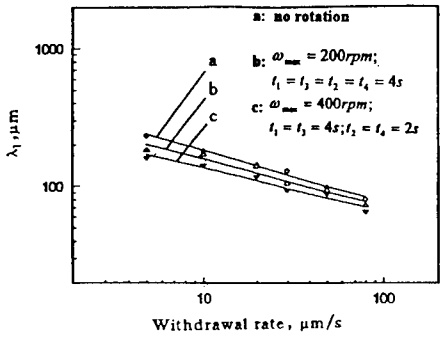


Figure 9: The influences of the ACRT on cell spacing of Al-4.5%Cu alloy.

Experimental researches on ACRT-B growth of Al-Cu eutectic

For ACRT growth of eutectic alloys, Popov and Wilcox[16] studied Pb-Sn system, Eisa and Wilcox studied Bi-MnBi system[17] and JIE[14] studied Al-Si system. The results in different

system have quite different characteristics. In the present researches, ACRT growth of Al-$CuAl_2$ eutectic is studied. This is a typical non-faceted/non-faceted eutectic. The eutectic alloy is melted with 99.99 pct Al and 99.99 pct Cu. The graphite crucible with the inner diameter of 8mm is used. The steady temperature gradient is 199.6 K/cm for all the samples. Five growth rates of 5, 10, 20, 30 and 60μm/s and four rotation methods as shown in figure 5 are adopted. The experimental results reveal the followings:

(1) The lamella spacing in around the center of the samples is smaller, but it is larger that near the crucible wall. The structure distributes symmetrically around the centerline.

(2) Eutectic spacing changes periodically according to the periodic of the crucible rotation rates as shown in Figure 10. During the acceleration process, the interface is warmed up by the hotter liquid coming down along the center line and thus the growth rate is slowed. The eutectic spacing is therefore increased. During the deceleration process, the cooler liquid coming down along the crucible wall causes the speed up growth. The eutectic spacing is decreased.

(3) The average eutectic spacing is reduced with application of crucible rotation as shown in Figure 11. The influences becomes strong when the growth rate is low.

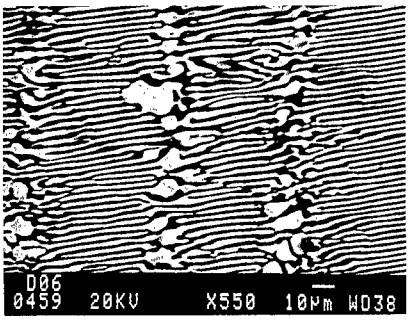


Figure 10: Periodic structure of Al-Cu eutectic in ACRT grown sample.

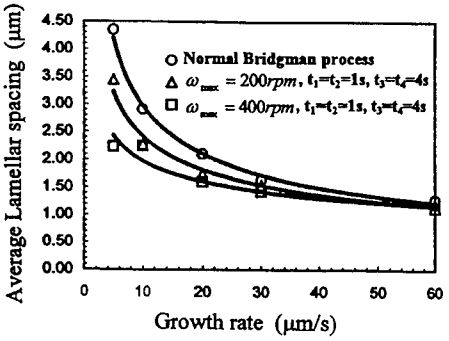


Figure 11: Effect of ACRT on interlamellar spacing of Al-Cu eutectic. where $\tau_1 = \tau_3 = 1s$; $\tau_2 = \tau_4 = 4s$

Conclusions

(1) The numerical calculation reveals the details of the forced convection during ACRT process. The convection can be shown by streamlines and the marking particles. The strength of the Ekman flow described by the height of the Ekman area depends on the Renald's number.

(2) The Ekman flow promotes the mixture in liquid zone and confines the temperature difference in the local region near L/S interface, and therefore, increases the local temperature gradient.

(3) Application of the ACRT in directional solidification process of Al-4.5%Cu alloy increases the stability of the cell structure and reduces the cell spacing significantly.

(4) In Al-Cu eutectic alloy, ACRT causes the periodic change of the eutectic spacing and the decrease of the eutectic lamella spacing. Meanwhile, the eutectic spacing in the intersection becomes non-uniform. The spacing is small in the center and large in the edge area.

References

[1] M. D. Dupouy, D. Camel and J. J. Favier, Natural convective effects in directional dendritic solidification of binary metallic alloys: Dendritic array primary spacing, Acta Metallurgica Materials, 1992, 40:1791-1801

[2] D. T. J. Hurle, Convective transport in melt growth system, Journal of Crystal Growth, 1983, 65:124-132

[3] Liu Shan, Lu Deyang, Huang Tao and Zhou Yaohe, Effect of melt flow on growth direction during constrained columnar crystal growth, Journal of Northwestern Polytechnical University, 1991, 9(1):13-18

[4] Do Hyum KIM, P. M. Adornato and R. A. Brown, Effect of vertical magnetic field on convection and segregation in vertical Bridgman crystal growth, Journal of Crystal Growth, 1988, 89:334-356

[5] Ch. Vives, Solidification of TIN in the presence of electric and magnetic field, Journal of Crystal Growth, 1986, 76:170-184

[6] Ren Zhongming and Jin Junze, Formation of a separated eutectic in Al-Si eutectic alloy, Journal of Materials Science, 1992, 27:4663-4666

[7] Yuning Jiao, Qingmin Liu, Yuansheng Yang, Zhuangqi Hu, Yunyan Gao, Guanglin Jia, Guozhi Zhang, Yuanjun Qiao. Analysis of fluid field in electromagnetic centrifugal casting, Acta Metallurgica Sinica (English Ed.). 1994, 7:145~148

[8] M. H. Johnston, P. A. Curreri, R. A. Parr, W. S. Alter. Superalloy microstructural variations induced by gravity level during directional solidification, Metallurgical Transactions. 1985, 16A: 1683~1687

[9] P. Capper, W. G. Coates, C. L. Jones, J. J. Gosney, C. K. Ard and I. Kenworthy, Quenching studies in Cadmium mercury telluride crystals grown using ACRT, Journal of Crystal Growth, 1987, 83(1):69-76

[10] P. Capper, J. C. Birce, C. L. Jones, W. G. Coates, J. J. G. Gosney, C. Ard and I. Kenwothy, Interfaces and flow regimes in ACRT grown $Cd_xHg_{1-x}Te$ crystals, Journal of Crystal Growth. 1988, 89:171-176

[11] P. Capper, J. J. G. Gosney, C. L. Jones and I Kenworthy, Fluid flow induced in tall containers by ACRT, Journal of Electronic Materials, 1986, 15(6):361-170

[12] A. Horowitz, D. Gazit, J. Makosky and L. Ben-Dor, Bridgman growth of rubidium manganese chloride (Rb2MnC14) via accelerated crucible rotation technique, Journal of Crystal Growth, 1983, 61:323-328

[13] JIE Wanqi, Unidirectional solidification of Al-Si eutectic with the accelerated crucible rotation technique, Metallurgical Transactions, 1992, 23A:1363-1370

[14] J. C. Brice, P. Capper, C. L. jones, J. J. G. Gosney and E. J. Pearce, Bridgman growth of cadmium mercury telluride using ACRT, Journal of Electronic Materials, 1986, 15:371-376

[15] D. Popov and W. R. Wilcox, Influence of convection on the spiral structures in Lead-Tin eutectic, Journal of Crystal Growth, 1986, 78(1)175-176

[16] G. Eisa and W. R. Wilcox, Effect of convection on the microstructure of MnBi/Bi eutectic, Journal of Crystal Growth, 1986, 78:159-174

A Study of Soft Contact Electromagnetic Casting Technology

Hoyoung Kim, Joon-Pyo Park, Heetae Jeong, and Jongkeun Kim

Research Institute of Industrial Science and Technology
P.O.Box 135 Pohang, Korea 790-600

Abstract

Electromagnetic casting technology of a soft contact type with high frequency electricity has been examined for steel application. A special copper mold of cold crucible type was fabricated and usage of cold insert was established to predict and analyze the effect of the operating parameters. The continuous casting experiments with tin and steel were conducted to quantify the effect of the electromagnetic field on the surface quality of the cast. The result shows that the surface quality of the cast was improved for the optimal electric power. The optimum value of the electric power was heavily dependent on the relative position of the meniscus and the coil top. It was also observed that the electromagnetic casting made the solidified shell thinner near the meniscus and made it thicker just below the mold than the conventional casting.

The Third Pacific Rim International Conference on
Advanced Materials and Processing (PRICM 3)
Edited by M.A. Imam, R. DeNale, S. Hanada,
Z. Zhong and D.N. Lee
The Minerals, Metals & Materials Society, 1998

1. Introduction

Electromagnetic processing of materials draws lots of attention due to its performance on enhancing product quality and productivity, and its potential application for cost reduction through energy saving and process minimization[1]. Particularly, electromagnetic casting technology is considered as a good candidate to dramatically upgrade the surface quality of the cast [2,3], whereas couple of approaches, such as a control of mold oscillation pattern [4] and variation of mold powder properties [5], have made a partial achievement. Electromagnetic casting technology has been well established and commercialized for aluminum [6]. However, its application to steel stays in laboratory owing to its low electric conductivity, heavy specific weight, and high temperature of the melting point.
In this study, the soft contact type with high frequency electricity has been examined. Usage of cold insert was introduced to measure the effect of the magnetic flux density. Experimental works of continuous casting of tin and steel were conducted, and the result was discussed.

2. Experimental Apparatus

The experimental apparatus for continuous casting is shown in Fig.1. The experimental caster is a vertical type with a mechanical oscillator of the variable range 40-120[cpm] and 8-20[mm] stroke. Its casting length is up to 2[m], and the casting speed is up to 1[m/min].
For high frequency electromagnetic casting, a special billet mold of size 100x100x400(l) [mm] was fabricated. By taking the concept of cold crucible, it is composed of 20 pieces of copper block and each block is electrically isolated with 0.3[mm] thick mica sheets. The blocks have separate cooling channels, and the temperature of the cooling water is monitored and recorded during whole casting to watch mold and casting conditions. The electric power is supplied to 5 turn coil of 85[mm] height by a generator of the capacity 200[kW], and of the frequency range 10-30[kHz].

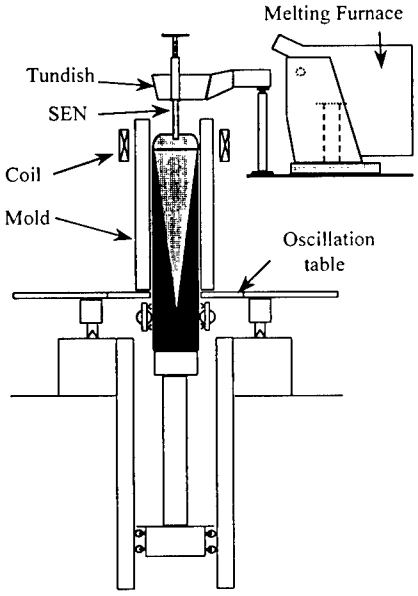


Fig.1. Experimental apparatus

3. Magnetic Flux Density in the Mold

The magnetic flux density along the casting direction was measured in the mold for the empty state and for the partially filled state with cold inserts of tin. The cold inserts were used to simulate the state of casting, and their sizes are 60x60x400(l), 80x80x400(l) [mm^3]. Fig.2 shows the magnetic flux density at mold corner and at mold face center for the coil current of 670 [A], where the coil was located at 50[mm] below the mold top, and the top of cold inserts were positioned at the coil top. For the empty mold, the maximum value was obtained at about 30[mm] below the coil top and the strength at the corner was higher than that at the mold face. However, with the cold inserts the maximum value was seen around top of the inserts, and the strength at the corner was not higher than that at the mold face any more. These facts

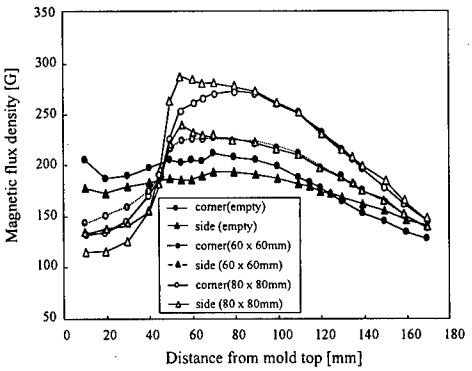


Fig.2. Magnetic flux density along casting direction at coil current of 670[A].

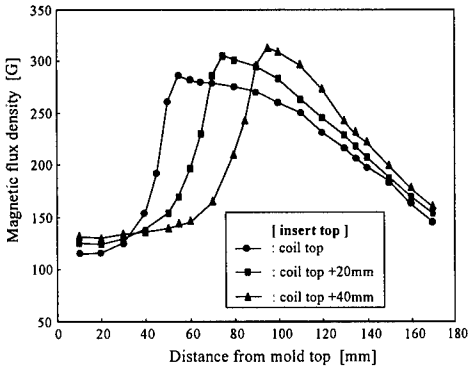


Fig.3. Magnetic flux density along casting direction at coil current of 670[A].

well agree to the results of the numerical simulation [7].

Fig.3 shows the effect of the insert locations. As the insert top moves to the center of the coil height, the maximum value increases and the distributions get stiffer. This suggests that the fluctuation of meniscus level on casting changes the amount of Joule heating and magnetic pressure, and eventually affects the quality of the cast surface. In this way, a magnetic flux density with cold inserts reveals information on its strength and distribution on casting.

4. Casting Experiment of Tin

The experimental conditions are listed in Table I. When the electric power was optimal, the

Table I. Experimental Conditions of Electromagnetic Casting of Tin

Material	Tin
Casting Speed	0.3-0.8 [m/min]
Oscillation	60 [cpm], 8[mm] stroke
Lubricant	Silicon Oil
Electric Power	0-50 [kW], 22[kHz]

surface roughness of the cast reduced to 1/10 of that of zero power. As the power increased from the optimum, wave-like marks appeared at the surface and finally longitudinal gutters formed at the locations in between each copper block, where the spacing of gutters was almost identical to the width of the copper block.

Fig.4 shows a typical result of the surface roughness of tin cast at various casting speeds and meniscus levels for electric power 20[kW]. The surface roughness of the casts was evaluated as a sum of

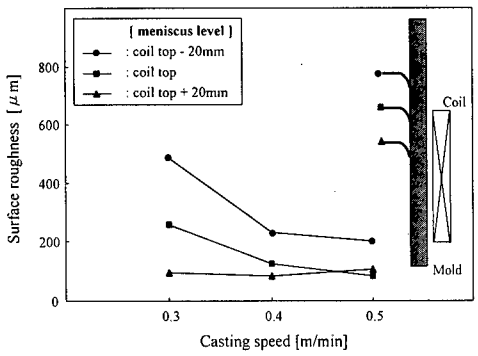


Fig.4. Surface roughness at 20[kW].

oscillation mark depths within 40[mm] long region. The surface roughness got improved as the casting speed increased and as the meniscus level got lowered. For meniscus level of coil top+20[mm], even 20[kW] power seemed in between optimum and excessive level, and thus wave marks was nearly seen. It reveals that the surface quality of the cast is determined by the combination of casting speed, meniscus level, and electric power.

On the surface quality of tin cast, the relation of meniscus level and casting speed is shown in Fig.5, and that of electric power and casting speed is in Fig.6. The symbol (-) denotes a reduced oscillation mark, (~) is wave-like mark without oscillation mark, and (O) means the optimal surface quality. For a given electric power, for instance 20[kW], an optimal surface

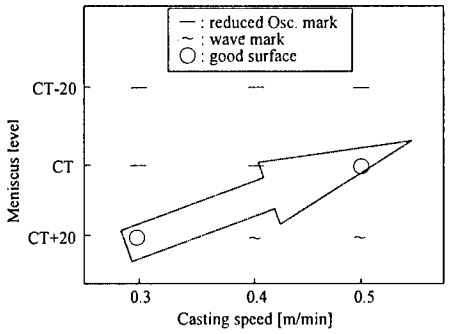


Fig.5. Surface quality of tin cast vs. casting speed and meniscus level at 20[kW].

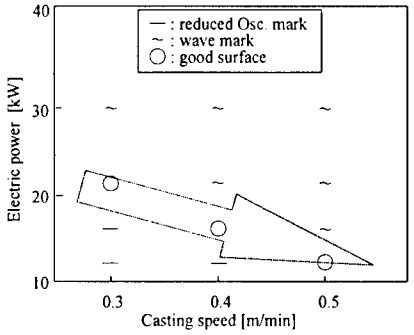


Fig.6. Surface quality of tin cast vs. casting speed and electric power at the same level of meniscus and coil top.

was obtained at the conditions of meniscus equal to the coil top+20[mm] and 0.3[m/min] casting speed, and of meniscus equal to the coil top and 0.5[m/min] casting speed. It shows a qualitative agreement to the magnetic flux density variation with the meniscus level given in Fig.3. For a fixed meniscus level at the coil top, a proper electric power decreased as the casting speed increased. It seemed related to a solidified shell thickness in the coil region; the shell thickness in the coil region is thinner for a fast casting speed.

Fig.7 shows the solidified shell thickness at just below the mold. For the measurement, molten Sn-46wt%Pb was poured into the mold at the final stage of casting. The shell of the optimal power is thicker, in solid area 6.5% wider, than that of no electric power. It seemed that the reduced surface roughness of the shell enhanced heat transfer between the shell and the mold, and eventually the amount of heat extraction from the melt was increased. The amount of energy evaluated from the cooling water of the mold confirmed this fact. For a casting speed of 0.5[m/min], 39[kW] was measured for an optimal power condition, whereas 27[kW] was for 0 power with the identical flow rate of water. The difference, 12[kW], was almost identical to the electric energy input to the mold and the cast plus the extra latent heat of the solidified shell.[8)]

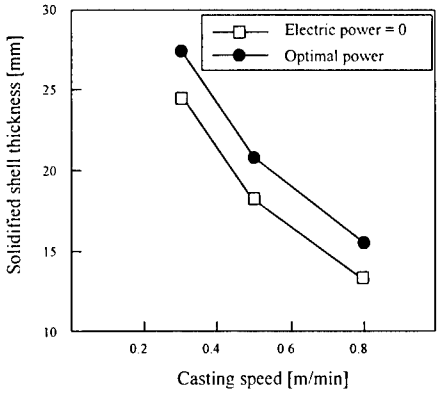


Fig.7. Solidified shell thickness of the cast.

5. Casting Experiment of Steel

The casting conditions of steel are shown in Table II. Differently from tin casting, mold powder was employed as a lubricant and FeS compound was added to capture the shape of the early solidified shell near the meniscus.

Table II. Experimental Conditions of Electromagnetic Casting of Steel

Material	0.08% C steel
Casting Speed	0.3-0.5 [m/min]
Oscillation	60 [cpm], 8[mm] stroke
Lubricant	commercial mold powder
Electric Power	0-100 [kW], 22[kHz]

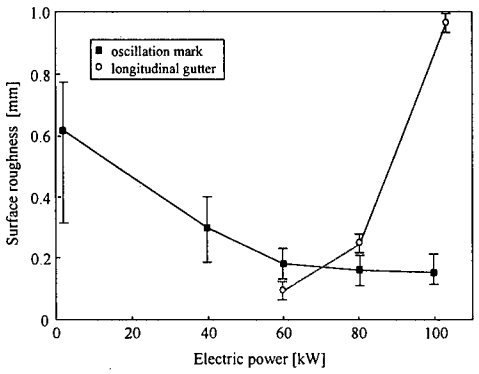


Fig.8. Surface roughness vs. electric power for steel.

The surface roughness variation for the electric power is shown in Fig.8. The casting speed was 0.5[m/min], and the meniscus was located at the coil top. At 0 power, a nominal value of the oscillation mark depth was 0.6[mm]. As the power increased to 60[kW], the depth reduced to 0.2[mm]. When the power got greater than 60[kW], the oscillation mark depth did not reduce any more and the wave-like mark and the longitudinal gutter appeared. The phenomena were almost identical to tin casting. When the shape of the early solidified shell was examined by adding FeS compound, the specimen of proper power showed a thin and uniform shell compared to that of 0 power, as shown in Fig.9. This confirms the conjecture that the early solidified shell is cooled slowly in electromagnetic casting.



(a) power, 0[kW] (b) power, 60[kW]

Fig.9. The shapes of early solidified shell.

6. Conclusion

In conclusion, experimental works were done for the high frequency electromagnetic casting of tin and steel. Usage of tin inserts proved quite useful in predicting and analyzing the experimental results. It was seen that the surface roughness of the cast was improved a lot for the optimal electric power. The optimal electric power was heavily dependent on the relative position of the meniscus and the coil top. It was also observed that the electromagnetic casting made the solidified shell thinner near meniscus and made it thicker just below the mold than the conventional casting.

References

1. S. Asai, "Theoretical Base of Application of Electromagnetic Force," Nishiyama Memorial Seminar, ISIJ, (1994), 89-102.

2. H. Nakata et al., "Improvement of Surface Quality of Continuously Cast Steel by Electromagnetic Mold," Tetsu-to-Hagane 80(1994), 711-716.

3. T. Toh et al., "Electromagnetic Control of Initial Solidification in Continuous Casting of Steel by Low Frequency Alternating Magnetic Field," ISIJ International, 37(1997), 1112-1119.

4. M.M. Wolf, "Mold Oscillation Guidelines," Steelmaking Conference Proceedings, (1991), 51-71.

5. H. Nakato et al., "Optimizing Mold Lublication for High-Speed Continuous Casting of Slabs," Journal of Metals. March, (1984), 44-50.

6. C.Vives, "Electromagnetic Refining of Aluminum Alloys by the CREM Process," Metallugical Transactions B, 20B(1989), 623-629.

7. H. Jeong et al., "Development of Electromagnetic Casting for Steel", (Paper presented at 1997 Annual Meeting of Korean Institute of Metals and Materials, Seoul, Korea, 24-25 October 1997), 145.

8. H. Jeong, H. Kim, and P.J. Park, "Estimation of Joule Heat in High Frequency Electromagnetic Casting" (Paper will be presented at the Spring Annual Meeting of the Korean Society of Mechanical Engineers, Jinju, Korea, 23-24 April 1998).

REFINEMENT OF THE MICROSTRUCTURE IN HYPER-EUTECTIC AL-SI ALLOYS BY ELECTROMAGNETIC VIBRATIONS

Kenji Miwa, Alireza Radjai* and Toshiyuki Nishio

National Industrial Research Institute of Nagoya, AIST, MITI
1-1 Hirate-cho, Kita-ku, Nagoya 462, Japan
*School of Engineerings, Shiraz University
Zand Ave., Shiraz, Iran

Abstract

In order to study the effects of electromagnetic vibrations induced by alternating electric and stationary magnetic fields on the solidified structure of Al-Si alloys, an experimental apparatus which enables the simultaneous application of electric and magnetic fields under different cooling conditions, ranging from rapid to furnace cooling, was developed. Vibrations were induced in a hyper-eutectic Al-Si alloy containing suspended silicon particles and the effects were studied. The mechanism by which vibrations bring about microstructural changes was investigated by interrupting the process at different temperatures before and after the start of solidification through water quenching. The conditions for obtaining identical cooling rates in experiments with different experimental conditions were established which permit the exclusion of the effects caused by differences in cooling rates and recognition of the ones merely caused by electromagnetic vibrations. It was found that the application of any of the two fields alone had no significant effect on the microstructure of the alloys, while profound effects were observed when the two fields were applied simultaneously. Suspended silicon particles multiplied in number with a reduction in size by vibrations at temperatures higher than the liquidus and agglomerated and repelled to the outer surface after the start of solidification. Metallographic observations showed that the cavitation phenomenon was a main responsible for the crushing of the suspended silicon particles.

The Third Pacific Rim International Conference on
Advanced Materials and Processing (PRICM 3)
Edited by M.A. Imam, R. DeNale, S. Hanada,
Z. Zhong and D.N. Lee
The Minerals, Metals & Materials Society, 1998

Introduction

Application of electric and/or magnetic fields to the processing or treatment of materials has been of particular interest for almost two decades. Different combinations of these fields, stationary and/or alternating, have been used for a wide range of purposes including stirring, shaping, etc (1). However, in most of these applications electromagnetic forces are used to control the molten metal flow on a macroscopic scale and not as powerful waves which can affect the solidification structure in a microscopic level. On the other hand, the effects of electromagnetic vibrations are not fully investigated. In two recent works Vives studied the effects of electromagnetic vibrations induced by the interaction of collinear variable and stationary magnetic fields, and alternating electric and stationary magnetic fields during the solidification of aluminum alloys and reported considerable structural refinements (2, 3). In the latter extensive refinement was reported to be observed after a threshold electromagnetic pressure where cavitation phenomenon was likely to occur. Cavitation phenomenon which is widely studied in the field of ultrasonic technology (4-6) and not well practiced in metallurgy due to the difficulties arising from the implementation of ultrasonic devices at high temperatures, can be generated by electromagnetic vibrations.

This research is intended to study the effects of electromagnetic vibrations induced by the simultaneous application of alternating electric and stationary magnetic fields and investigate the mechanism by which they are brought about. For this purpose, an experimental apparatus which enables the freezing of the ongoing process at any desired temperature and acquiring an exact knowledge of its progress is designed and assembled. A hyper-eutectic Al-Si alloy melt containing suspended silicon particles is used as the starting material and the effects of vibrations are investigated before and after the start of solidification. Variations of cooling rate under different experimental conditions are studied for the experimental apparatus and conditions for obtaining identical cooling rates are established.

Experimental Procedure

Commercial Al-25wt%Si ingots were used to prepare hyper-eutectic (17wt%) Al-Si alloy ingots by melting in an induction furnace and diluting with commercially pure aluminum ingots. The produced ingots were then remelted in an electric furnace and cast into a preheated steel mold to produce 6 mm Al-Si rods in diameter.The rods were cut into 2 cm long pieces and filed to the appropriate shape to fit the quartz tube with the thermocouple installed.

Samples were fixed between the graphite electrodes in the quartz tube as shown in Fig. 1 placed between the poles of the electromagnet and electrodes were connected to an alternating electric current source. When graphite electrodes were used samples could be melted without using the furnace, taking advantage of the joule heat generated in the electrodes and the sample when an appropriate amount of electric current was passed through them. In this case, an alternating electric current of about 80 A with a frequency of 50 Hz was passed through the electrodes to melt and heat up the

sample to 710°C. After keeping the temperature fixed at 710°C for 2 minutes, the current was reduced to 0 or 70 A, and the DC magnetic field was also switched on and set at 1.4 T or not used depending on the experimental condition. The heating furnace was used when external heating was needed to balance the cooling rate between different experiments. Water was sprayed from the nozzles fixed on both sides of the sample for quenching at temperatures. The average cooling rate of the samples was 90°C/s when quenched. For naturally cooled samples the cooling rate varied under different experimental conditions.

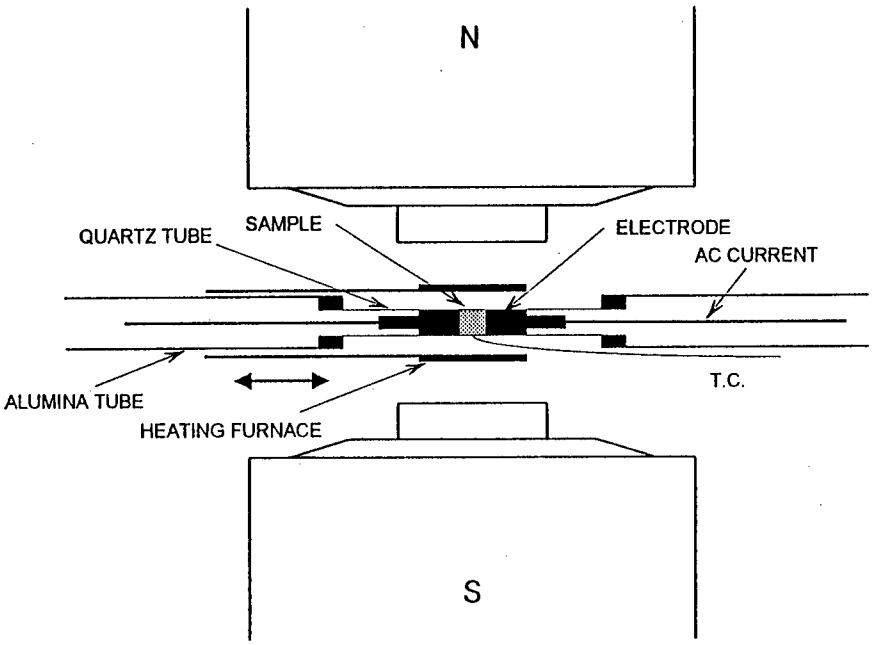


Fig. 1 Schematic view of the experimental apparatus.

The electromagnetic body force (**J** x **B**) induced in the liquid in the horizontal direction when a magnetic field of 1.4 T was applied in the vertical direction reached the value of 4.2 x $10^6 N/m^3$, imposing a magnetic pressure of about 2.0 x 10^4 Pa at the center and higher values at increasing radial distances from the center.

Results and discussion

In these experiments samples were melted, heated up to the temperature of 710°C and kept for a time period of 2 minutes which are not enough conditions for primary silicon particles to be completely dissolved in the molten metal. This can be confirmed from Fig. 2a which shows the microstructure of

a sample melted and kept at 710°C for 2 minutes and then rapidly quenched to room temperature at a rate of about 90°C/s.

Comparing Figure 2a and 2b it can be seen that the application of electromagnetic vibration has resulted in a decrease in size and increase in number of the suspended silicon particles.This effect continues as cooling proceeds, but stops as a certain particle size is reached, so that the size and number of the particles do not change with further application of the vibrations. However, continuation of the process to the temperatures below the liquidus (642~3°C) results in another effect which tends to agglomerate the particles and repel the agglomerates from the central regions toward the outer surface of the sample. This trend continues as the cooling proceeds with the difference that some new primary silicon particles start to appear in the matrix. These newly nucleated particles are also agglomerated and repelled to the outer surface or trapped in the solidifying matrix and remained.

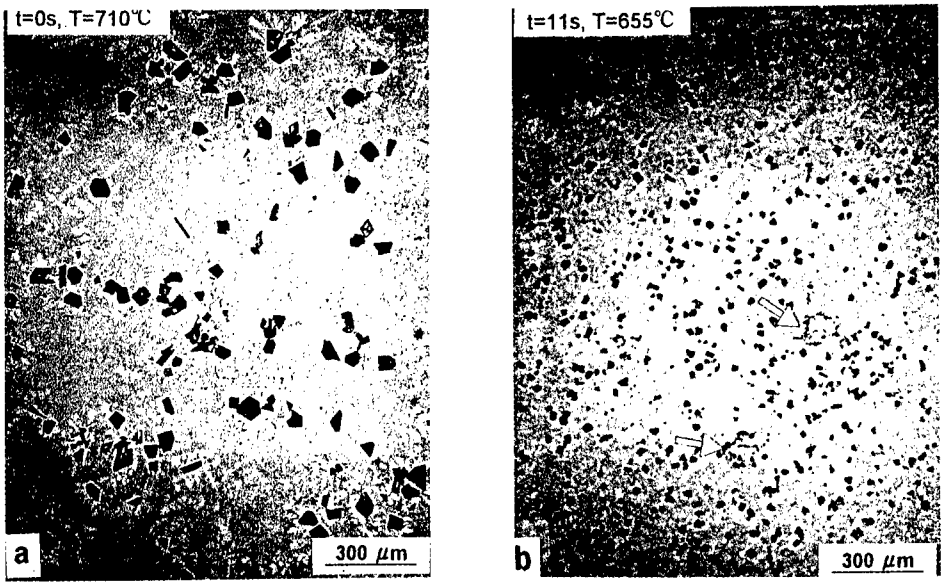


Fig. 2 Microstructures of Al-17%Si samples solidified under different conditions. a:quenched at 710°C under 0 T and 0 A/m^2, b:quenched at 655°C under 1.4 T and 3 x 10^6 A/m^2.

Effects of electromagnetic vibrations described above can be divided into those observed before the start of solidification and the ones appearing after that. Before the liquidus temperature is reached, vibrations seem to have crashed the silicon particles increasing their number and decreasing their average size. This is supposed to be mainly due to the occurrence of cavitation phenomenon.

When electromagnetic vibrations are imposed upon the molten metal containing suspended silicon particles cyclic forces are induced which behave as periodic forces of compression and tension and put the liquid into an oscillatory motion. The suspended particles which are not directly affected by the simultaneous application of the two fields due to their low electrical conductivity when subjected to the sinusoidal motion imposed by the vibrating liquid develop a shear force resisting the motion depending on their shape and size. Therefore, forces of tension are developed on one side of the particles and forces of compression on the other side in a half cycle of the sinusoidal motion and the reverse takes place in the other half. In such a situation cavities can form on the surface of particles under tension and build up high pressure in some successive cycles and collapse under compression forces when it can no longer resist the compressive forces. Cavities, shown to be capable of building pressures of more than a thousand atmospheres in ultrasonic experiments (7), can generate powerful shock waves in the liquid when they collapse and are able to crush suspended particles and smash them into each other for further refinement on their propagation before loosing their energy.

Micrograph presented in Fig.3, which belongs to the samples quenched at 670°C demonstrates a clear evidence of the cavitation phenomenon frozen by quenching process. Examining the situation depicted in Fig.3, the fact that in the area covered by the shock waves before they were frozen by quenching not only the silicon particles but also the flakes of silicon in the eutectic matrix are crashed into small pieces implies that the cavities shown here collapsed at the final stages of solidification during quenching.

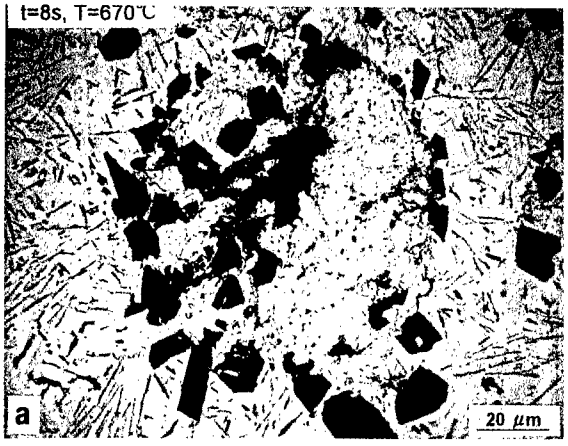


Fig.3 Silicon particles crushed into pieces by cavitation phenomenon.

After the temperature is decreased to values lower than the liquidus temperature primary silicon starts to nucleate from the surrounding walls and the suspended silicon particles start to grow in size by absorbing silicon from the melt. Oscillatory motion of these particles caused by vibrations of the melt

and the fact that they have an active surface going under solidification results in sticking of the particles to their neighboring ones and their local agglomeration. These agglomerates having an electrical conductivity much lower than the melt and therefore not being directly affected by the pinch or the vibrational forces move toward the surrounding surface against the direction of the pinch force confining the melt as a reaction.

Conclusions

It was found that the application of any of the two fields alone had almost no effect on the solidified structure of the alloy. However, simultaneous application of the two fields resulted in an increase in number and decrease in size of the suspended silicon particles at temperatures higher than the liquidus. At temperatures lower than the liquidus particles started to agglomerate locally and were expelled toward the outer surface of the sample as the temperature got closer to that of the eutectic. The final structure was therefore composed of an almost completely eutectic matrix with agglomerates of silicon particles at the outer surface. Microscopic observation of the quenched samples revealed that the cavitation phenomenon was a main responsible for the crushing of silicon particles. A combination of the vibrations and pinch force are supposed to be behind the agglomeration and driving of the agglomerates toward the outer surfaces.

References

1. S.Asai, ISIJ International, 29(12)(1989), 981-992.
2. C.Vives, Metall. Trans. B, 27B(1996), 457-464.
3. C.Vives, Materials Science and Engineering, A173(1993), 169-172.
4. O.Abramov, Ultrasound in Liquid and Solid Metals, (Boca Raton, FL:CRC Press, 1994)
5. T. Leighton, The Acoustic Bubble, (London:Academic Press Ltd., 1994)
6. K. S. Suslick, Science, 247(1990), 1068.
7. K. S. Suslick, Application of Ultrasound to Materials Chemistry, (MRS Bulletin, April 1995), 29.

SOLIDIFICATION PROCESS OF SILICON FROM HIGH UNDERCOOLED MELTS BY ELECTROMAGNETIC LEVITATION METHOD

Tomotsugu Aoyama*, Yuzuru Takamura and Kazuhiko Kuribayashi

The Institute of Space and Astronautical Science,
3-1-1 Yoshinodai, Sagamihara, Kanagawa 229, Japan
**Graduate Student, The University of Tokyo*

Abstract

The crystal growth behavior of semiconductor from very high undercooled melts is expected to be different from that of metallic melts. In the present experiment, highly pure undoped Si was undercooled by electromagnetic levitation method, and the crystal growth velocity, V for pure Si was measured as a function of undercooling, ΔT. V increased with ΔT, and V = 26 ms^{-1} was observed at ΔT = 260 K. This result corresponded well with the predicted value according to the dendrite growth theory by J. Lipton et al. in 1987. Since the critical interface undercooling reported by D. Li et al. in Ge-based alloy was not observed in the present study, the growth of Si was thermally controlled in the measured range of undercooling. The microstructures of silicon samples solidified from undercooled liquid were also investigated. The amount of dendrites immediately after recalescence increased with undercooling.

The Third Pacific Rim International Conference on
Advanced Materials and Processing (PRICM 3)
Edited by M.A. Imam, R. DeNale, S. Hanada,
Z. Zhong and D.N. Lee
The Minerals, Metals & Materials Society, 1998

Introduction

The crystal growth behavior from highly undercooled melt has been attracting a great deal of attention because microstructure, growth velocity and crystal structure are expected to depend heavily on the bulk undercooling. Highly undercooled melts can be obtained with a good reproducibility and directly analyzed in the solidification processes by using various containerless methods such as electromagnetic (EM) [1], electrostatic [2] or aero-acoustic levitation [3]. Some investigations about these undercooling experiments have been carried out, especially for metals [4, 5]. Studies on the solidification of undercooled semiconductors are, however, at an early stage. Several interesting results were reported about the growth velocities for pure Ge and Ge-based alloys by Li et al., in which the crystal growth behavior was classified into three categories of lateral growth at low, continuous growth at moderate, and rapid growth at high undercoolings [6]. It is impossible to give a sufficient explanation of the phenomenon only by the current dendrite growth theories for metallic systems.

In this work, the growth behavior of highly undercooled Si was investigated by means of measuring the growth velocities and observing the microstructures in a wide range of undercoolings. It was compared with studies on Ge and growth theories for metals.

Experiments

Figure 1 shows a schematic illustration of the apparatus. The chamber was evacuated to 10^{-5} Torr by a turbo molecular pump and filled with argon gas of 99.999 % purity. Undoped Si of 99.999 % purity was used as a source material. That was put on the sintered BN holder located in the EM levitation coil. The coil was connected to a 10 kW , 200 kHz radio frequency (RF) generator. The specimen was preheated by a 200 W continuous wave CO_2 laser to a temperature at which it achieved sufficient electrical conductivity, and then was levitated by the EM force. The specimen temperature was measured with a monocolor pyrometer (operating wavelength : 900 nm and spot size : 1 mm) and was controlled by laser irradiation, RF power, and helium gas blowing. By this procedure the specimen could be successfully levitated and became a droplet of about 4 mm diameter.

Crystal growth velocities were measured by means of two photodiodes, which are shown in figure 2 (a). The levitated droplet image was projected on a screen, in which two high speed optical sensors were attached. The movement of growth front at each spot was detected by changes in sample brightness owing to the abrupt temperature rise. The time lag of the recalescence between two photodiodes is shown in figure 2 (b). From this time lag, the growth velocity can be estimated. In order to initiate the solidification from the bottom of the droplet at any given temperatures, the sample was seeded externally by a trigger needle made of alumina.

Moreover, the final solidification microstructures of pure Si nucleated by dropping the undercooled melt on a copper plate at various temperatures were also observed by optical microscope.

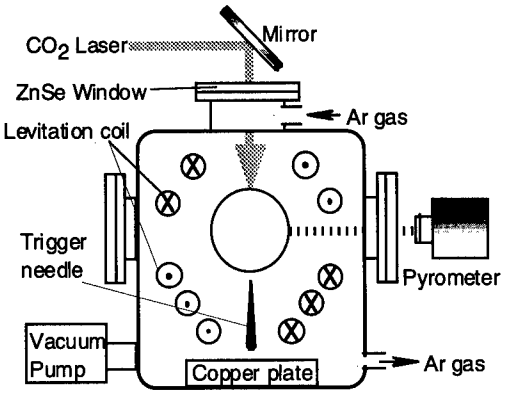


Fig. 1. Schematic drawing of electromagnetic levitation apparatus and laser heating units. The alumina needle is movable perpendicularly and horizontally. The copper plate is set just below the levitating sample.

Results and Discussion

Growth Velocities

Growth velocities of pure Si were measured as a function of undercooling. They are plotted in figure 3, where full circles show the velocities measured by above-mentioned method. Full triangles show the velocities estimated statistically from spontaneously nucleated samples instead of triggered one. Growth velocities measured with same sequence on spontaneously nucleated samples tend to be overestimated because solidification front proceeding from spontaneous nucleated point, which is randomly located in the droplet, is likely to pass through the two measuring spots at the shorter distance than the triggered one. Therefore a minimum value in the distribution of these measured values at certain undercooling should be close to a real growth velocity. The solid line shows the growth velocity calculated from the model of Lipton, Kurz and Trivedi (LKT) [7]. The material parameters used in this calculation are shown in Table I. All parameter for this calculation is known and no fitting parameter is used. Since the growth process of only pure material is discussed in this paper, it is assumed that the total undercooling (ΔT) is expressed as the sum of the thermal (ΔT_t), curvature (ΔT_r) and kinetic (ΔT_k) undercooling while neglecting the constitutional undercooling. According to this calculation for pure Si, ΔT_r and ΔT_k were smaller than 10 K even when ΔT = 300 K, and so their contributions to the total ΔT were negligible. Because of good agreement between the observed and calculated data, dendrite growth for Si was revealed to be controlled by thermal diffusion to the extent of measured undercooling.

Microstructures and Solidification Mechanism of Rapidly Solidified Si

The structural morphologies are presented in figure 4 (a), (b), (c), which show the cross-section of pure Si solidified rapidly at undercoolings of 50 K, 180 K and 260 K, respectively. In Fig. 4 (b), (c), secondary or higher order arms of dendrite can be observed obviously and the number of

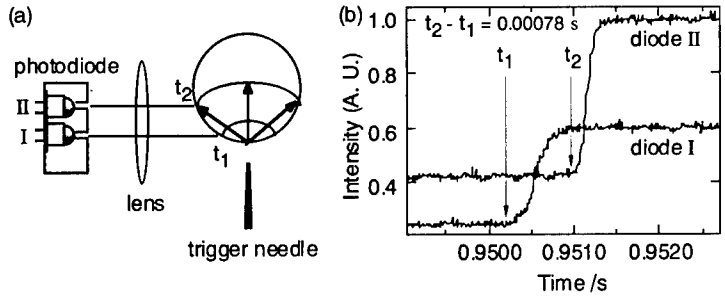


Fig. 2. Principles of the measurement of crystal-growth velocities by means of photodiode method. (a) Solidification is initiated externally at the bottom of the sample. (b) Time lag of the recalescence between two photodiodes.

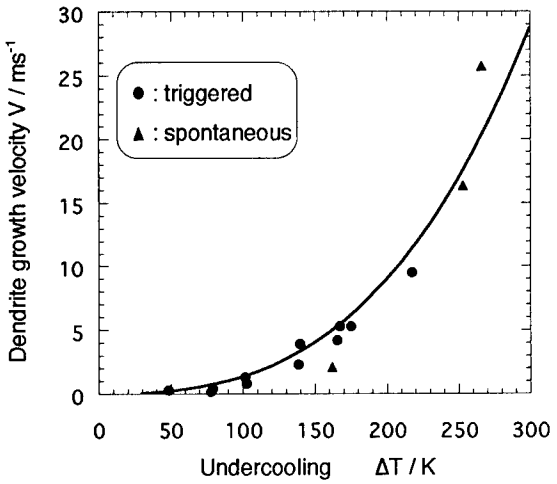


Fig. 3. Growth velocities as a function of undercooling. The solid line shows the theoretically predicted curve. The circles show velocities when the solidification is initiated by the trigger needle. Each triangle shows a minimum value of velocities measured for the spontaneously solidified sample at certain undercooling.

arms per unit area increase with undercooling. There seems to be direct relation to the volume fraction of dendrite, f, immediately after recalescence, which increase with undercooling. This estimate is supported by a fact that the hypercooling limit of Si, ΔT_{hyp}, is larger than 1900 K, which is derived from $(\Delta H_f / C_p)$, where C_p is the specific heat of the liquid and ΔH_f is the heat of fusion (Table I). The factor $f = 0.13$ at $\Delta T = 260$ K and $f = 0.025$ at $\Delta T = 50$ K, which are derived from $(\Delta T / \Delta T_{hyp})$. No dendrite structure is observed in Fig. 4(a) owing to the small f at $\Delta T = 50$ K. Consequently, irrespective of undercooling, the rapid solidification behavior from undercooled melt of Si may be dendrite growth, which can be predicted by LKT model.

The drastic changes in the velocity and the transition of the solidification mechanism with the change of the microstructure, which is reported for Ge, was not observed.

Table I. Material parameters of pure Si as used in the calculations

Melting point	T_M	1687	K
Heat of fusion	ΔHf	5.06×10^4	J/mol
Specific heat of the liquid	C_p	25.6	J/mol K
Thermal diffusivity of the liquid	α	1.3×10^{-5}	m^2/s
Solid-liquid interface energy	σ	0.438 *	J/m^2
Sound speed in the liquid	V_s	3400	m/s

* From ref. 8.

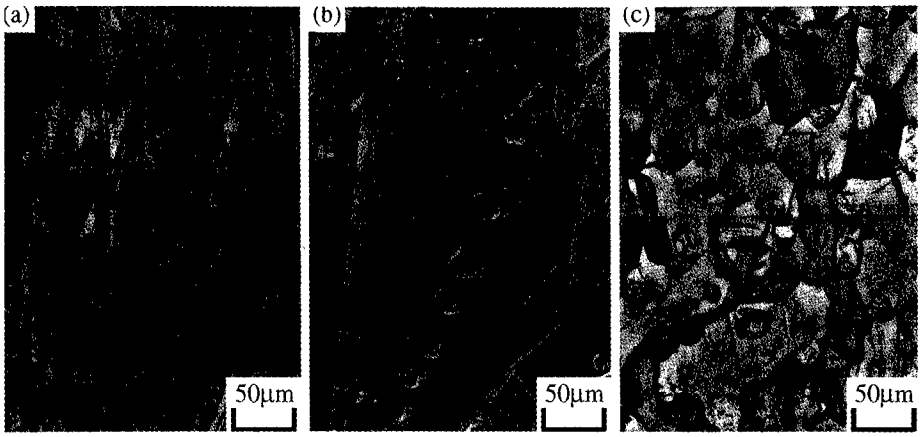


Fig. 4. Microstructures of Si solidified at various undercooling, ΔT. (a) ΔT = 50 K, (b) ΔT = 180 K, (c) ΔT = 260 K.

Conclusions

By electromagnetic levitation of Si, a maximum undercooling of 280 K was achieved with a corresponding dendrite growth velocity of 26 ms^{-1}. Since the measured V-ΔT function is sufficiently described by the current theory of dendrite growth, the solidification process from highly undercooled Si melt was predicted to be metallic. That prediction was supported by the microstructural observation of dendrite arms.

Acknowledgements

The authors express sincere thanks to a Grant-in-Aid for Scientific Research from the Ministry of Education, Science, Sports and Culture of Japan. They also appreciate the financial supports from the Mitsubishi Foundation, and the Iketani Science and Technology Foundation.

References

1. D. M. Herlach, "Containerless solidification of undercooled metallic melts," Trans. Mat. Res. Soc. Jpn., 16A (1994), 585-592.

2. W. K. Rhim, S. K. Chung, A. J. Rulison, and R. E. Spjut, "Measurements of Thermophysical Properties of Molten Silicon by a High-Temperature Electrostatic Levitator," Int. J. Thermophys., 18 (2) (1997), 459-469.

3. J. K. R. Weber, D. S. Hampton, D. R. Merkley, C. A. Rey, M. M. Zatarski and P. C. Nordine, "Aero-acoustic levitation: A method for containerless liquid-phase processing at high temperatures," Rev. Sci. Instrum., 65 (2) (1994), 456-465.

4. K. Eckler, R. F. Cochrane, D. M. Herlach, B. Feuerbacher and M. Jurisch, "Evidence for a transition from diffusion-controlled to thermally controlled solidification in metallic alloys," Phys. Rev., 45B (1992), 5019-5022.

5. K. Eckler, A. F. Norman, F. Gärtner, A. L. Greer, D. M. Herlach, "Microstructures of dilute Ni-C alloys obtained from undercooled droplets," J. Cryst. Growth, 173 (1997), 528-540.

6. D. Li, K. Eckler and D. M. Herlach, "Undercooling, crystal growth and grain structure of levitation melted pure Ge and Ge-Sn alloy," Acta mater., 44 (1996), 2437-2443.

7. J. Lipton, W. Kurz and R. Trivedi, "Rapid dendrite growth in undercooled alloys," Acta metall., 35 (4) (1987), 957-964.

8. D. Li and D. M. Herlach, "High undercooling of bulk molten silicon by containerless processing," Europhys. Lett., 34 (6) (1996), 423-428.

MICRO-MACRO MODELING OF SOLIDIFICATION MICROSTRUCTURES IN FINITE-ELEMENT SIMULATIONS

S.P. Marsh

U.S. Naval Research Laboratory
Washington, DC 20375-5343

Abstract

Solidification processes involve phenomena that operate over a broad range of length scales. A stereology-based modeling and simulation approach is presented that simplifies incorporation of micromodels into macroscale finite-element calculations. A set of stereological parameters is used to track the geometric properties of the evolving microstructures at the same spatial and temporal resolution as the other field variables. The thermophysical parameter values at each finite-element node serve as global constraints on the local unit volume of microstructure over the subsequent time-step, which permits direct coupling within and between the micro and macro regimes. Application of this stereological approach to such phenomena as equiaxed dendritic growth and directional (cellular) growth are presented.

This work is being supported by NASA under Grant NAG8–1272, and by the Office of Naval Research. Early funding for this research by DARPA through the Investment Casting Cooperative Agreement (ICCA) is also gratefully acknowledged.

The Third Pacific Rim International Conference on
Advanced Materials and Processing (PRICM 3)
Edited by M.A. Imam, R. DeNale, S. Hanada,
Z. Zhong and D.N. Lee
The Minerals, Metals & Materials Society, 1998

Introduction

In recent years, the development of numerical simulations of materials processes has led to an improved understanding of the effect of process conditions on resulting material structure and properties. This computational approach has already been applied to industrial processes such as casting operations [1]. One outstanding computational challenge in this field stems from the range of size scales that must be addressed in many material operations. Solidification processes involve physical mechanisms that occur over a wide range of lengthscales, ranging from the macroscopic conditions down to the microstructural and atomic regimes. Overviews of the various thermophysical phenomena and computational considerations relevant to micro/macro modeling of solidification processes are provided by Rappaz [2] and Tseng *et al.* [3].

This paper presents a formalism and simulation approach that addresses micro/macro coupling through the use of a consistent stereological parameter set that allows various micromodels to be expressed in a computationally efficient form. This approach is able to incorporate multiple mechanisms, based on either physical or empirical models, directly into existing finite-element calculations. Coupling and transitioning between the various mechanisms may be based on a wide variety of physical criteria.

Stereology-Based Micromodeling

Material process simulations generally employ finite-element or finite-difference methods to solve field equations governing such phenomena as heat and mass flow. The spatial resolution of these calculations, determined by the mesh spacings used to discretized the continuum field equations, are typically on the order of 10^{-3} to 10^{-2} meters. It is at this level that state variables such as temperature and composition are tracked directly, and their temporal evolution calculated using discretized field equations.

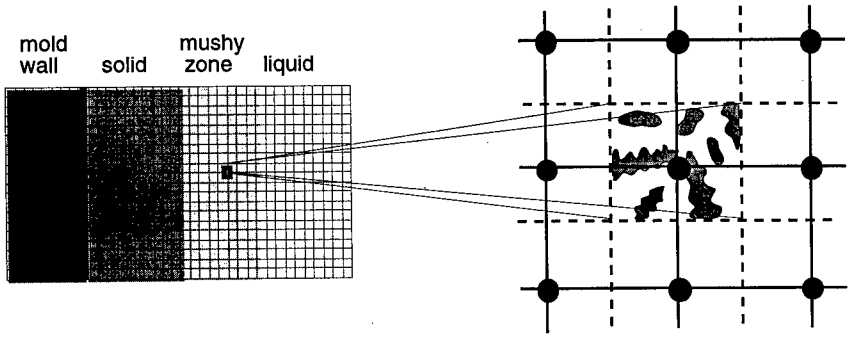
The formation and evolution of microstructural features are determined by thermophysical mechanisms operating at much smaller size scales, and include such phenomena as capillary effects, solute rejection, and geometric evolution of interfaces. It is not feasible to simulate the geometry of these microscopic processes directly at the macroscopic level throughout the casting. In the present approach, parameters describing locally averaged microstructural characteristics are tracked at the same finite-element resolution as the field variables that govern their evolution.

The present stereology-based approach for bridging the microscopic and macroscopic regimes is based on the observation that the macroscopic field variables represent the average conditions in the local volume of material associated with each computational node. This approach is illustrated in Figure 1. The left side of this figure, Figure 1(a), represents a computational finite-element mesh used to simulate a solidification operation. Figure 1(b) illustrates the local volume of material associated with a mesh point. This unit volume is defined as the locus of points that lie closer to the mesh point of interest than to any neighboring point. The microstructure within this unit volume is assumed to be uniform at this scale and characterized by a single set of parameters defined at the central node point. For example, the temperature at a given node point represents the average temperature of the associated unit volume over the current timestep.

The mesh, together with the chosen numerical time-step, determine the spatial and temporal resolution of the field parameters that govern the formation of local microstructure. In the present approach, the same resolution is applied to micromodels within each unit volume. The finer structural features are quantified through global stereological properties, which represent the local "density" of geometric features. (An overview of stereological concepts and measurement techniques has been written by Underwood [4].) The volume associated with each mesh point (proportional to the node spacing) is used as a weighting factor for the global properties to determine the total amount of the geometric quantities associated with a given mesh point.

The three primary stereological parameters used to describe typical microstructures are the number density, N_V, the volume fraction, V_V, and the specific surface area, S_V. N_V is the number of a given feature present per unit volume of microstructure. V_V represents the total volume of a particular phase per unit volume of material, and is a dimensionless quantity having a value between zero and unity. S_V is the total interfacial area present, S, per unit volume of the structure, v. S_V has units of reciprocal length, and provides a single size scale of the microstructure that is well-defined for any morphology.

The stereological formalism allows for direct combination of various micromodels in a straightforward manner. Combining micromodels based on different geometries is greatly simplified by first converting them to a common stereological parameter basis, which is consistent with the smooth variation in volumes and surface areas that occur during shape changes. The effect of simultaneously operating mechanisms are addressed by summing the various contributions to changes in these parameters over each timestep. Cross-terms among mechanisms may be formulated and incorporated into simulations as necessary.



(a) (b)

Figure 1 – Schematic showing the coupling concept employed between the microscopic and macroscopic regimes. (a) A typical finite-element mesh is used to calculate discretized field equations at the macroscopic level. (b) A local "unit volume" (enclosed by dashed lines) having a statistically uniform microstructure is associated with each node point in the mesh (black dots).

Model Coupling in Equiaxed Dendritic Growth

Many alloys solidify from undercooled melts by forming equiaxed dendritic grains. This process begins with nucleation of the solid phase in the melt, followed by growth of dendritic equiaxed grains that is limited initially by diffusion of rejected solute to the surrounding liquid matrix [5]. These grains continue to grow until the dendrite tips encounter those of neighboring grains, when the relatively unconstrained dendrite growth slows and subsequent solidification is governed by the local temperature and concentration. Coarsening of the dendritic structure, driven by the free energy in the solid–liquid interfaces, becomes significant during the late-stage solidification. (See [6] for a more detailed description of this process.)

A model of equiaxed dendritic solidification has been developed to address all of the above mechanisms [7]. The follwing outline of this model illustrates the types of coupling that can been formulated to address the interactions of multiple operating mechanisms during solidification.

The density of nuclei, N_v, is calculated using an empirical instantaneous nucleation model at each mesh point. The instantaneous nucleation model [8] assumes that all nuclei form locally at a single time. This model is applied to each mesh point in the liquid phase at the appropriate nucleation time as determined by the local temperature and cooling rate. Spatial variations in the resulting nucleus density are thus resolved at the same level as the parameters that govern them.

The equiaxed model adapts the analytical model developed by Rappaz and Thévoz [5], which describes the diffusion-limited growth rate of dendritic grains. To add lengthscale information to this model, a geometric construction [7] is used to relate the surface area of the newly-formed dendrite branches to the volume of solid formed. The absolute size scale for this ratio is set by the tip radius, R_{tip}, which is determined from material parameters and local growth conditions [6]. The parameters describing the size and kinetics of a single grain at each mesh point are representative of the average grain state within each local unit volume. Enthalpy generated during equiaxed growth is coupled directly to the macroscopic heat flow equations as a local source term.

When the outer boundaries of equiaxed grains approach those of neighboring grains, solute diffusion from the grain envelope no longer limits the growth rate. At this point, the dendritic structure essentially fills the available volume and further solidification is determined by the local temperature and composition. The local average grain radius at each node point, R_{tot}, is calculated (in the absence of convection effects) from the nucleus density N_v as $R_{tot}=[3/4\pi N_v]^{1/3}$, where N_v^{-1} represents the average volume per grain. When the current equiaxed grain radius is within a few percent of R_{tot}, the equiaxed model is turned off at that node point and a temperature-dependent growth model is initiated.

During late-stage solidification, two mechanisms govern further lengthscale evolution in the microstructure. The dendritic branches tend to thicken as further solidification occurs epitaxially on the existing structure during further cooling. Simultaneously, capillary-driven coarsening reduces the surface area while maintaining a constant volume of the solid phase. The effects of these mechanisms on S_v are calculated separately and added over each timestep.

The increase in surface area due to epitaxial solidification on the predominantly cylindrical structure is treated as being equivalent to that of a single growing cylinder having the same overall area/volume ratio. This leads to a simple expression for the increase in surface area over a timestep for the epitaxial growth as $\Delta S_V=(S_V/2V_V)\Delta V_V$. To address the coarsening behavior, the statistical coarsening theory of Marsh and Glicksman [9] is used to formulate the volume-fraction dependence of the coarsening rate. The kinetic equation for the decay of S_V with time can be written as $\Delta(S_V^{-3})=K(V_V)\Delta t$. This equation expresses the well-known scaling law for diffusion-limited coarsening that the cube of any characteristic lengthscale in the structure (such as average radius) grows linearly with time [10]. $K(V_V)$ is a dimensionless rate constant that is updated based on the local volume fraction of solid and then applied over each timestep.

Once the eutectic temperature is reached at a particular node point, the remaining melt solidifies uniformly as a finely-divided structure. In the present model, details of the finer eutectic structure are ignored. The coupling criteria described above permit various micromodels to be applied throughout the casting, each based on the governing local conditions. The models in stereological form tend to be mathematically simple, which permits a useful compromise between physical accuracy and computational efficiency.

The equiaxed growth model outlined here has been applied in a casting simulation of an Al-7% Si alloy brake drum, using the ProCAST™ software package. Computed values of S_V obtained via simulation agree to within 15% with the values measured directly from cross sections of the casting [11]. The good agreement between simulation and experiment suggests that the stereology-based modeling approach, which combines specific physical mechanisms and geometric models to describe the evolution of lengthscales, is a robust technique that may be used under a variety of casting and processing conditions.

Modeling of Directional Growth

The stereological micromodeling approach was developed initially to address structural features that are much finer than the resolution of the macroscopic calculations. This approach is now being extended to describe the formation of cellular and directional dendritic structures, where the lengthscales present may be comparable to or larger than the computational grid spacings. The conceptual approach is the same, in that stereological parameters are still used to describe the average local geometrical properties.

Cellular growth is commonly observed in multicomponent systems where a planar solidification front is often unstable [6]. This leads to the formation of an array of rod-like "cells" of the primary solid phase, growing roughly parallel to the heat flow direction. The size and spacing of these cells depend on local growth conditions, including melt supersaturation and temperature gradient. Extension of the model to describe directional dendritic growth can be handled, with some modifications, by treating the cells as envelopes containing the primary dendrites [12].

One particular challenge in modeling cellular growth is the fact that the cell sizes can be of the same order as typical mesh spacings, and individual cells may span many such spacings. Consistent with the stereological approach described earlier, we define the cellular region as a

uniform "phase" containing the primary cells and intercellular liquid. Further back from the tips, the volume fraction of cells is the equilibrium fraction, defined such that $V_{v,c}=1.0$. The volume fraction of cells will be between zero to unity in the unit volumes containing the developing tip region of the cells. Using this approach, the extent of the cell arrays can be expressed by a simple phase parameter. The direction of the primary cell axes is also tracked as a local vector at each node point. This direction will not vary significantly within a single array, and serves to identify separate arrays that may originate in different regions of a casting.

The critical growth mechanisms occur in the tip region, where $0<V_{v,c}<1$. Mass and heat transport in this region, together with interfacial considerations, determine the primary axis spacings [13]. In contrast, the region further behind the cell tips ($V_{v,c}\approx 1$) is in a near-equilibrium state, with solidification rates governed by the local temperature. Convection effects tend to be small in this region, and the solute fluxes are predominantly lateral (perpendicular to the primary cell axes).

To describe the size scales of the cellular array, the cells are represented locally as a uniform cluster of parallel cylinders. The radius of these cylinders is constant within a single unit volume, but is allowed to vary between mesh points. The cell structure within a unit volume is thus represented by a set of parallel cylinders, uniformly dispersed, having unit length. This local cellular arrangement is shown in Figure 2 as a set of hexagonally-arranged circles in a plane, with the cylinders having unit depth into the page.

In the cell geometry of Figure 2, the specific surface area, S_V, is equal to the total perimeter of circular cells per unit cross-sectional area perpendicular to the primary cell axis direction. An additional parameter that describes the spatial density of cells is N_A, which represents the number of distinct cells per unit cross-sectional area perpendicular to the primary axes.

To describe the cell geometry quantitatively, we begin by using the local cell diameter, d, and the cell spacing, l, defined as the distance between the primary axis of adjacent cells. These quantities are labeled in the basic repeating unit of the uniform cellular array in Figure 2(b). This repeat unit is an equilateral triangle (representing the uniform hexagonal array of cells) having edge length l.

From this diagram, it can be shown that S_V is equal to the total perimeter of the cells divided by the area of the repeat unit, or

$$S_v = \frac{perimeter}{area} = \frac{0.5\,\pi d}{A} = \frac{2\pi}{\sqrt{3}}\frac{d}{\lambda^2} = 3.63\,\frac{d}{\lambda^2}. \qquad (1)$$

The number density of cells, N_A, is calculated as

$$N_A = \frac{\#\ of\ cells}{area} = \frac{0.5}{A} = \frac{2}{\sqrt{3}\lambda^2} = 1.15\,\lambda^{-2}. \qquad (2)$$

The local volume fraction of primary solid cells, $V_{v,S}$, is equal to the area fraction of cells in the cross section, A_A. This can be expressed as

$$V_{v,s} = A_A = 0.907 \left(\frac{d}{\lambda}\right)^2 . \qquad (3)$$

By combining the above equations, we obtain the following relations in terms of S_V and $V_{v,s}$:

$$d = 0.25 \frac{V_{v,s}}{S_v} \quad ; \quad \lambda = 3.81 \frac{V_{v,s}^{1/2}}{S_v} \quad ; \quad \text{and} \quad N_A = 0.079 \frac{S_v^2}{V_{v,s}} . \qquad (4a\text{-}c)$$

Thus, the conventional modeling parameters often used to describe cellular arrays can each be expressed in terms of the local solid volume fraction and specific surface area.

The mass balance equations for cellular growth are expressed concisely in terms of the phase fractions and average concentration, c_i^n of each species within each phase. The fluxes entering the mass balance equations can be decoupled into two primary categories within each control volume. Lateral fluxes between the cells reject solute from the cell walls into the intercellular liquid. Longitudinal fluxes in the direction of the cell axes tend to be fairly small back from the tip, and are driven mainly by solubility gradients associated with longitudinal temperature gradients.

Solidification in the tip region is a key mechanism that affects the characteristics of cellular and dendritic arrays by determining the spacing of the primary branches. A number of physical and empirical models exist in the literature to describe this phenomenon [13]. The cellular model described in this section, together with conventional macroscopic calculations, will be used to test a number of such models, and utilize or refine the ones that yield the best results as compared with experimental measurements. Because there is no single accepted model for branch spacing that works in all materials under all conditions, this optimization approach is best for developing a predictive model that describes the system(s) of interest.

Discussion and Summary

A general formalism is described that permits a physically consistent coupling between microstructural models and macroscopic field equations in material process simulations. In this approach, a unit volume of microstructure is associated with each node point in the macroscopic numerical mesh. The state variables at each point represent the average local conditions within the local unit volume over the current timestep. The grid spacing employed in the finite-element calculations determines the spatial resolution of both the macroscopic field variables and the local microstructural characteristics. One key advantage of the stereological modeling approach is that it adapts easily to existing numerical codes and requires minimal additional computational resources because of the compact form of the micromodel equations.

This technique is being extended to describe features that are comparable in size to the finite-element mesh spacings. A combination of microscopic mechanisms and macroscopic correlations are being developed to quantify the characteristics of directional cellular growth. This model will be used, in conjunction with experimental observations, to determine and refine the optimal tip spacing criterion based on local solidification conditions.

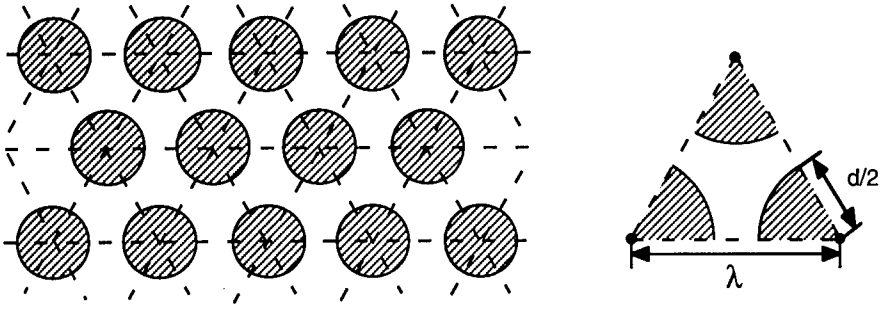


Figure 2 – (a) Cross-sectional view of a regular array of cells. (b) Basic repeating unit of a regular array of cells showing the primary cell spacing, λ, and cell diameter, d.

References

1. J.S. Tu, R.K. Foran, A.M. Hines, and P.R. Aimone, "An Integrated Procedure for Modeling Investment Castings," JOM, 47 (10) (1995), 64–68.
2. M. Rappaz, "Modelling of Microstructure Formation in Solidification Processes," International Materials Reviews, 34 (1989), 93–123.
3. A.A. Tseng, J. Zou, H.P. Wang, and S.R.H. Hoole, "Numerical Modeling of Macro and Micro Behaviors of Materials in Processing: A Review," Journal of Computational Physics, 102 (1992), 1–17.
4. E.E. Underwood, Quantitative Stereology (Reading, Mass.: Addison-Wesley Publishing Company, Inc., 1970).
5. M. Rappaz and P. Thévoz, "Solute Diffusion Model for Equiaxed Dendritic Growth: Analytical Solution," Acta Metallurgica, 35 (12) (1987), 2929-2933.
6 W. Kurz and D.J. Fisher, Fundamentals of Solidification (Aedermannsdorf, Switzerland; TransTech Publications, 1985).
7. S.P. Marsh and D. Banerjee, "Micro-Macro Coupling in Casting Simulations," in Materials Processing in the Computer Age II, ed. V.R. Voller, S.P. Marsh and N. El-Kaddah (The Minerals, Metals and Materials Society, Warrendale, PA, 1994), 105–116.
8. P. Thévoz, J.L. Desboilles, and M. Rappaz, "Modeling of Equiaxed Microstructure Formation in Casting," Metallurgical Transactions A, 20A (1989), 311-322.
9. S.P. Marsh and M.E. Glicksman, "Kinetics of Phase Coarsening in Dense Systems," Acta Materialia, 44 (1996), 3761–3771.
10. W.W. Mullins, "The Statistical Self-Similarity Hypothesis in Grain Growth and Particle Coarsening," Journal of Applied Physics, 59 (4) (1986), 1341–1349.
11. S.P. Marsh, D. Banerjee, and L.E. Richards, "Stereology–Based Modeling and Analysis of Equiaxed Solidification in Casting Simulations," in Modeling of Casting, Welding and Advanced Solidification Processes VII, ed. M. Cross and J. Campbell (The Metallurgical Society, Warrendale, PA, 1995), 713–720.
12. M. Rappaz and P. Thévoz, "Solute Diffusion Model for Equiaxed Dendritic Growth," Acta Metallurgica, 35 (7) (1987), 1487–1497.
13. R. Trivedi and W. Kurz, "Solidification Microstructures: A Conceptual Approach," Acta Metallurgica et Materialia, 42 (1) (1994), 15–23.

The Effect of Cooling Rate on As-Cast Structure of Fine Grain Casting IN718 Alloy

Yue Ma*, Jiahua Sun**, Xishan Xie*,
Jingchen Zhao**, Yaohe Hu*, Ping Yan** and Xi Shan**

* University of Science & Technology Beijing, Beijing 100083, China
** Central Iron & Steel Research Institute, Beijing 100081, China

Abstract

Fine grain cast processes (FGCP) have been investigated since 1980. However , the investigation on detail dendritic structure existing in fine-grain cast superalloy is scarce. The extra-fine grain size(ASTM 3.5~5) in cast structure of IN718 can be achieved by means of fine-grain casting technology with a wide range of cooling rates ranging from 0.13~9.48 ℃/s in this investigation. Typical dendritic and granular structure can be formed in fine grain cast IN718. The granular structure can be formed by the dendritic coarsening during solidification. This mechanism is confirmed by a special designed isothermal holding test at 1300 ℃ in solid and liquid two phase region of IN718 superalloy.

The Third Pacific Rim International Conference on
Advanced Materials and Processing (PRICM 3)
Edited by M.A. Imam, R. DeNale, S. Hanada,
Z. Zhong and D.N. Lee
The Minerals, Metals & Materials Society, 1998

Introduction

Fine grain cast processes(FGCP)have been investigated since 1980. Recently , this technology, such as Grainex and Microcast-X processes, has been developed by Howmet Co. in USA[1,2]. Most of the research works were conducted on mechanical properties of alloys and their applications. It is necessary to know the microstructures relevant to mechanical properties in grain-refined cast superalloys. However, up to date, the investigation on dendritic structure existing in as-cast superalloys is scarce.

In early papers[3-5], as-cast dendritic structure of low melting point alloys , such as Sn-Pb, Zn-Al ,were analyzed , but less reports on that of superalloys. The purpose of this paper is to study the different kinds of dendritic structures obtained during solidification and the dendritic coarsening mechanism in formation of granular structure in grain-refined cast IN718 superalloy.

Experimental Procedure

The alloy IN718 (see Tab.I) was melted in a 10 kg vacuum induction furnace and poured into mold heated up to different temperatures according to fine grain casting technology required. Two kinds of mold condition, which is without back-sand around shell and fill back-sand around shell, were taken in our experiments. The cooling rates were controlled by pouring temperature and mold temperature. The cooling rates of investigated heats as indicated in Tab.II were calculated by equation (1) through measuring the secondary dendritic spacing.

$$d = \beta (GV)^{-1/3} \quad (1)$$

Where d is secondary dendritic spacing (mm),
β is material coefficient, for IN718 $\beta = 0.147$
and Gv is cooling rate (℃/sec)

Time needed for solidfication in Tab.II was calculated from following equation

$$t = \Delta T / GV \quad (2)$$

Where t is solidification time (sec)
Δ T is the temperature range between liquidus and solidus (℃)

Table I. Chemical composition of investigated IN718 Alloy (wt %)

C	Cr	Ni	Fe	Mo	Nb	Ti	Al
0.042	18.46	53.12	19.1	2.87	5.14	0.96	0.15

Table II. Calculated solidification parameters at different conditions

Sample No.	Cooling Rate , ℃/s	Solidification Time (sec)
1	9.48	18.54
2	2.00	87.87
3	0.87	202.00
4	0.50	351.00
5	0.13	1351.00

Structure analysis samples were polished and chemical etched with 1g $KMnO_4$ + 10ml H_2SO_4

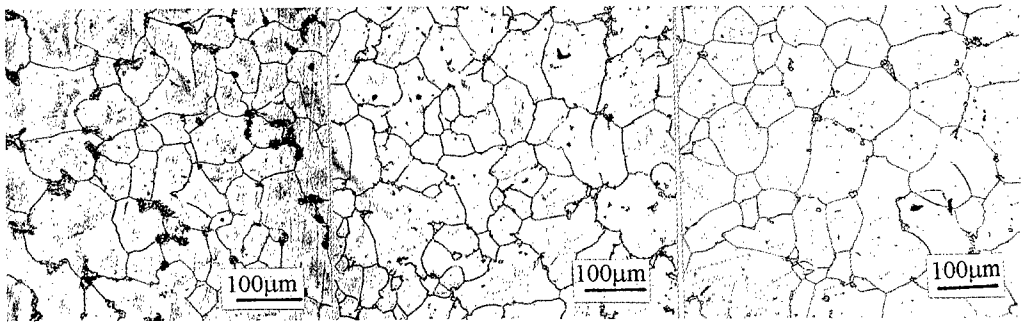
+ 90ml H_2O for grain size evaluation and electrolytic etched with 16g CrO_3 + 10ml H_2SO_4 + 170ml H_3PO_4 for dendritic structure observation.

In order to reveal the formation of granular structure from dendrites during solidification , a special isothermal treatment was designed as follows. Specimens with original state of dendritic structure of IN718 were heated up to 1300 ℃ at two- phase (liquid-solid) region containing with approximate 50 % solid phase in the melt, and held at this temperature for 25 sec, 75 sec, 150sec by means of Gleeble 1500 Thermal Stress-Strain Simulator, then quickly water quenched. Microstructure analyses were conducted with optical and scanning electron-microscopy(SEM).

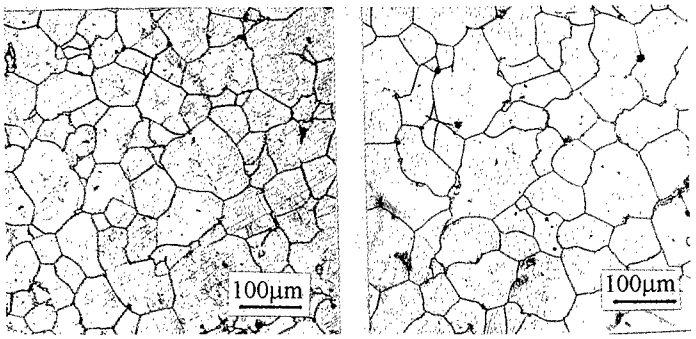
Results & Discussion

Solidification Structure at Different Cooling Rates

Fine grain size structure ranged from 50~100um(ASTM3.5~5.0) as shown in Fig.1 can be obtained by means of our fine-grain casting technology with different cooling rates.



(a) (b) (c)

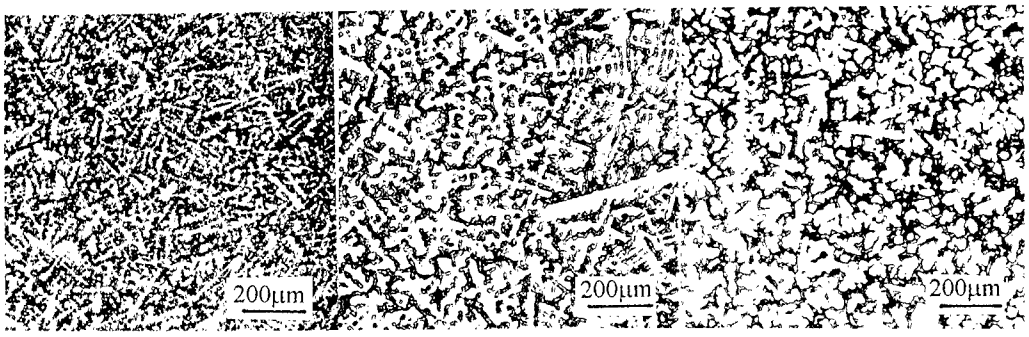


(d) (e)

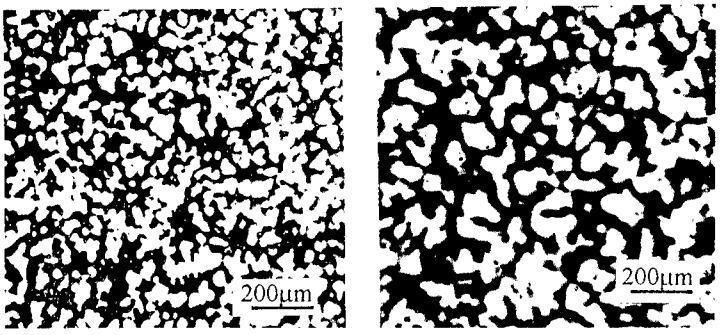
Figure 1: Grain size structure of IN718 by fine-grain casting technology with 5 cooling rates during solidification (chemical etching)
(a) 9.48 ℃/s , (b) 2.00 ℃/s , (c) 0.87 ℃/s , (d) 0.50 ℃/s , (e) 0.13 ℃/s

The detail dendritic structure can be revealed by electrolytic etching as shown in figure 2. At "fast" cooling rates (>2 ℃/s) or " short" solidification time (< 87 sec)typical dendritic structure can appear in our fine-grain casting IN718 samples 1and 2 (see Fig.2 (a) and (b)). However, at "slow" cooling rates (< 0.5 ℃/s) or "long" solidification time (>202 sec) the typical dendritic structure disappears and granular structure forms as indicated in Fig.2 (d) and (e).

The character of dendritic structure can be expressed by primary dendrite width (W), secondary dendritic space (S) and dendrite length (L). Figure 3 shows the primary dendritic width (W) and secondary dendritic arm spacing (S) are growing with the solidification time and the secondary dendritic length (L) is decreased with the increasing of solidification time. These experimental results remind us that the granular cast structure can be formed by the dendritic coarsening mechanism duing "long" time solidification of IN718 alloy by means of fine-grain casting technology.



(a) (b) (c)



(d) (e)

Figure 2: The morphology of dendritic structure of fine-grain cast IN718 with 5 different cooling rates during solidification (electrolytic etching)
(a) 9.48 ℃/s (b) 2.00 ℃/s (c) 0.87 ℃/s (d) 0.50 ℃/s (e) 0.13 ℃/s

Structure Change at 1300 ℃ Isothermal Holding

The effect of 1300 ℃ isothermal holding time on dendritic structure is clearly shown in Figure4. Fig.4(a) shows typical dendritic structure of sample 2 at as cast condition. At 1300 ℃ isothermal

holding the dendritic coarsening mechanism happens and the granular structure forms during 150

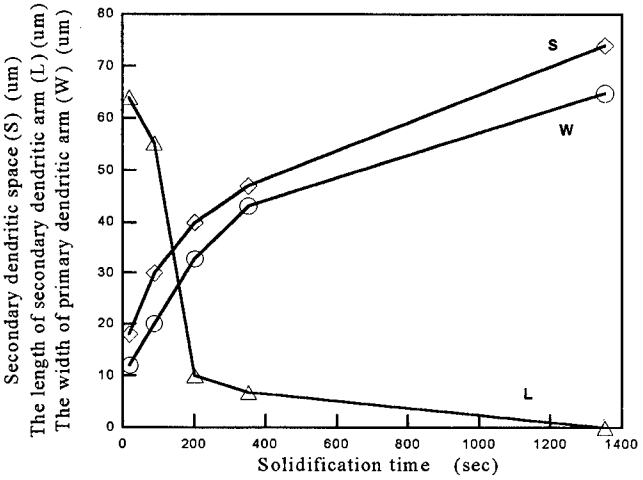


Figure 3: The effect of solidfication time on secondary space (S) and Length (L), and primary dendritic width (W)

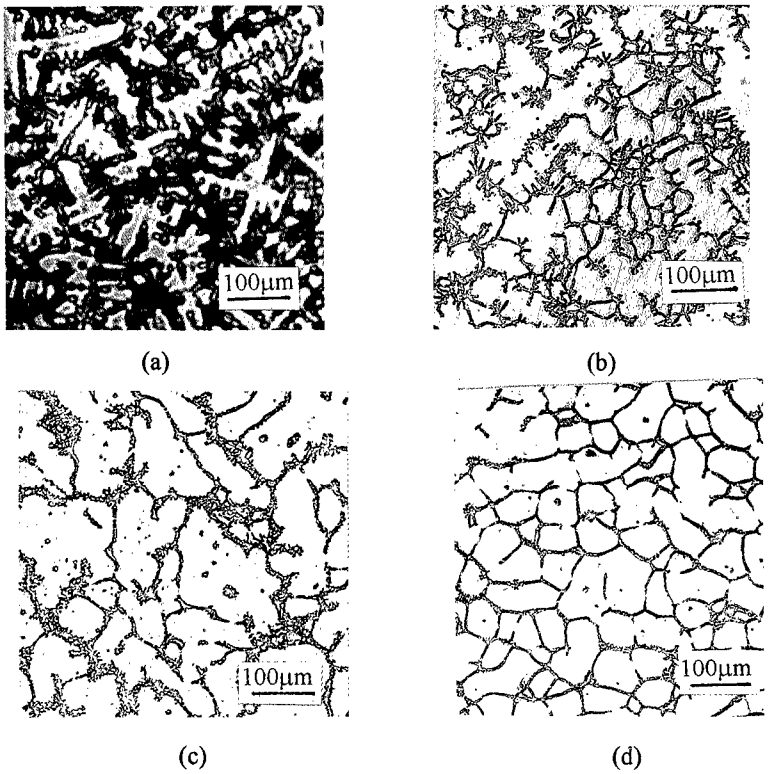


Figure 4: Structure change at 1300 ℃ isothermal holding in fine-grain cast IN718 alloy
(a) as-cast, (b) 25 sec holding, (c) 75 sec holding, (d) 150 sec holding

sec holding time as shown in Fig4. The granular structure as indicated in fig.4(d) is very similar to the samples 4 and 5 as indicated in fig.2(d) and (e) at very slow solidification rates(0.13- 0.50 ℃ /s) or very long solidification time (351- 1351sec).

Fig. 5 shows the effect of isothermal treatment at 1300 ℃ on secondary dendrite length (L), primary dendrite width (W) and secondary dendritic spacing (S). In comparison with Fig.3 and Fig.5, which have samilar tendency of these curves (L, W and S). It is valuable to indicate that the granular structure can be formed as following steps. Firstly, small dendritic cores form at the begining of solidification and then the dendritic coarsening mechanism happens along the long time solidification to form granular structure in fine-grain cast IN718 superalloy.

Conclusions

1. Fine grain cast IN718 superalloy can be achieved in the grain size range of 50~100um(ASTM 3.5~5)with a wide range of cooling rates (0.13 ℃/s~9.48 ℃/s) in this investigation.
2. Typical dendritic and granular structure can be formed in fine grain cast IN718 superalloy.
3. The granular structure forms by dendritic coarsening mechanism in fine grain cast IN718 superalloy.

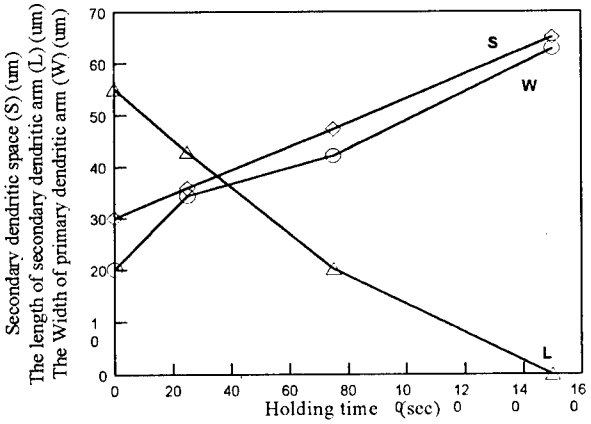


Figure 5: The efffect of isothermal treatment at 1300C on secondary dendritic space (S) and length (L), and primary dendritic width (W)

References

1. G. K. Bouse, and M. R. Behrendt "Mechanical Properties Of Microcast-X Alloy 718 Fine Grain Investment Castings" Superalloy 718-Metallurgy and Applications, TMS,(1989), 319-328
2. J.R.Brinegar, et al "Microcast-X Fine Grain Casting-A Progress Report" Superalloys 1984 , ed. Maurice Gell et al (1984) 23-32
3. K.H.Chien, and T.Z.Kattamis, "Role of Dendritic Coarsening and Coalescence in the Establishment of Cast Microstructure" Z. Metallkde 61 (1970), 475-479
4. T.Z..Kattamis and R.B.Williamson, "Chemical and Mechanical Grain Refinement of Alminium-Copper Alloy" J. Inst. Metals 96 (1968), 251-252
5. T.Z..Kattamis, J.C.Coughlin, and M.C.Flemings, "Influence of Coarsening on Dendritic Arm Spacing of Alminum-Copper Alloys" Transactions of the Metallurgical Soliety of AIME 239 (1967), 1504-1511

SURFACE METALLURGY OF Ni–BASE ALLOY BY DOUBLE GLOW PLASMA SURFACE ALLOYING

Zhang Xu, Yang Zhongmin, Dong Jianxin, Xie Xishan
University of Science & Technology Beijing, Beijing, 100083, P.R. China
Gao Yuan , Xu Zhong
Taiyuan University of Technology, Taiyuan, 030024, P.R. China

Abstract

The Double Glow Plasma Surface Alloying Technique, the Xu-Tec Process, is an updated technology in the field of surface alloying. In this paper the surface alloying layer similar to superalloy Inconel 625 is obtained on the surface of three kind of steels (low carbon steel, pure iron, stainless steel 304) by using Double Glow Plasma Surface Alloying Technique. The effects of technological parameters such as temperature, source electrode and cathode voltage etc. on the composition, microstructures and properties of alloying layer of different steels are also studied. The composition and microstructure are analyzed by SEM and XRD, and show that the alloying layer consists of γ matrix and several precipitates (laves intermetallic phase etc.). The results of the experiment indicate that it is an effective way to obtain the different composition of alloying layer even on the surfaces of different steels by using Double Glow Plasma Surface Alloying Technique.

The Third Pacific Rim International Conference on
Advanced Materials and Processing (PRICM 3)
Edited by M.A. Imam, R. DeNale, S. Hanada,
Z. Zhong and D.N. Lee
The Minerals, Metals & Materials Society, 1998

Introduction

The Double Glow Plasma Surface Alloying Technique,[1] which is also called XU-TEC is an updated technology in the field of surface alloying. By using this technology, the alloy layer with special physical, chemical and mechanical properties can be obtained on the surface of metallic materials. The alloying element content of this surface layer varies from 0 to 95%, and the thickness of the surface layer varies from 0 to 500 μm. Now researches have been done on the Double Glow Plasma Surface Alloying Technique, such as mono-element alloying of alloying element of Ni, Cr, Mo, W, Ta, Al, Ti etc.[2] and multi-element alloying of alloying element of Ni-Cr, W-Mo, Ni-Cr-Mo, W-Mo-Cr-V etc.[3] The Double Glow Plasma Surface Alloying with Mo-W is a method of surface alloying which can increase the wear resistance and red hardness of the alloyed layer ,and it is successful for hack saw blade.[4] To increase the corrosion resistance, the highly alloyed Ni-Cr surface layer can be formed on plain steels.[5]

The supper alloy Inconel 625 is a highly alloyed solid solution strengthening nickel base alloy that can provide high strength, corrosion resistance in a variety of environments, and good weldability. Because of this attractive combination of properties, Inconel 625 has wide-spread applications in chemistry, pulp and paper, off shore and marine industries and geothermal power systems.

At present, little research has been done on the Xu-Tec nickel base alloy. In this paper a nickel base alloy similar to Inconel 625 is formed on the surface of pure iron, low carbon steel 1020 and AISI304 stainless steel by using Double Glow Plasma Surface Alloying Technique. The effects of technological parameters and the microstructures and properties of the surface alloy layer have also been studied.

Experimental method

The nickel base alloying layer is formed by using Double Glow Plasma Surface Alloying Devise. The principle sketch is shown in figure 1. The super alloy Inconel 625 (the composition is shown in table I) plate is used as the source cathode(150 × 50 × 4 mm). Low carbon steel 1020, pure

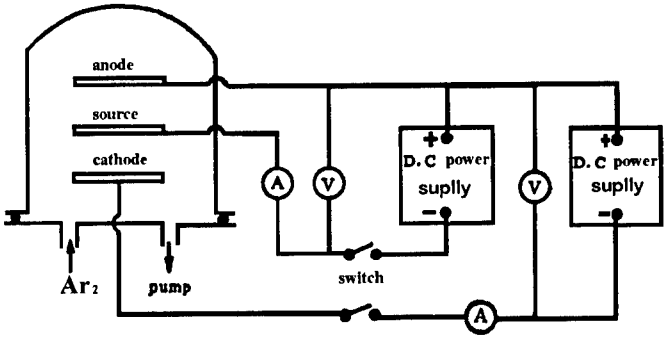


Figure 1 Sketch of Glow Plasma Surface Alloying Devise

iron, AISI 304 stainless steel are used as workpiece(50 × 25 × 3 mm). The technological parameters are : working pressure : 30 Pa, processing temperature : 850-1000 ℃, source cathode voltage : 700-1400 V, workpiece voltage : 250-600V, distance between two cathode : 15 -

20mm.

The chemical compositions in the surface layer and microstructure are analyzed by SEM and X-EDS. The phase structure is determined by XRD.

The corrosion test is performed on Model 351 corrosion measurement system. The test medium is 3.5% NaCl solution. The electrochemical parameters are following: 600 sec. hold time at corrosion potential. scan rate is 0.33 mV/s.

Table I Composition of Inconel625

Ni	Cr	Mo	Nb	Fe	C	Mn	Al	Ti	Si	Co
>58	20.0-23.0	8.0-10.0	3.15-4.15	<5.0	<0.01	<0.5	<0.4	<0.4	<0.015	<1.0

Result and discussion

1. Selection of technological parameters and its effect on the alloy layer

The Double Glow Plasma Surface Alloying is energy (include electric energy and thermal energy etc.) transference and equilibrium process. As a result , different composition, thickness and microstructure of the alloyed layer can be obtained by changing output power of source cathode and workpiece in specified working pressure and distance between source cathode and workpiece. The changing of current is related to the changing of voltage. Following experiments (as shown in table II) are designed.

Table II Technological parameters of experiment

specimen No.	temperature ℃	working pressure Pa	workpiece power kW	source cathode power kW	distance mm	time h
6	850	30	0.67	1.0	15	4.5
5	900	30	0.9	1.3	15	4.5
4	1000	30	1.79	1.92	15	3
8	1050	30	1.88	1.82	15	3
2	1000	30	1.29	1.9	15	3
9	1000	30	2.54	1.31	15	3
11	1000	30	0.87	2.04	15	3
12	1000	30	0.78	2.52	15	3

The results of the experiments show that the surface alloyed layer which composition (as shown in table III,IV)is similar or not with Inconel 625 can be formed.

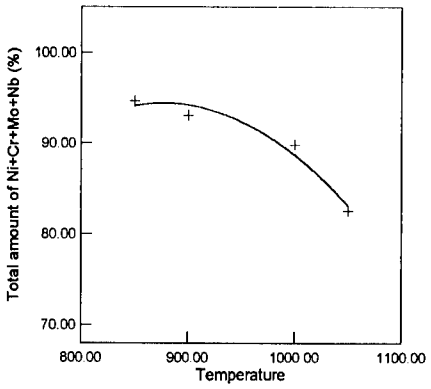
Table III Composition of alloyed layer specimen No. 6 on pure iron at 850 ℃

depth μm	Ni	Cr	Mo	Nb	Fe
0	56.52	26.77	9.29	2.86	4.56
3	54.81	29.45	7.97	2.53	5.24
6	51.64	30.81	7.73	2.40	7.42
12	48.73	23.95	8.13	2.57	16.62
18	33.41	8.83	2.53	0.74	54.48
21	13.68	4.43	0.72	0	81.17
24	3.41	1.84	3.13	0	91.63

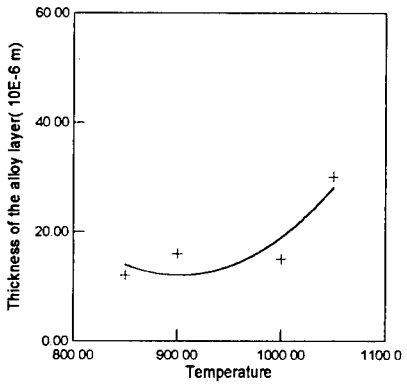
Table IV Composition of alloyed layer specimen No. 8 on low carbon steel at 1050 ℃

depth μm	Ni	Cr	Mo	Nb	Fe
0	51.41	22.42	5.31	3.44	17.43
3.5	56.66	18.41	4.10	2.35	18.84
7	51.16	24.69	4.49	1.56	18.10
14	47.75	23.98	4.39	2.10	21.78
28	48.45	12.88	2.22	0.82	35.63
40	9.32	6.62	0.80	0	83.35

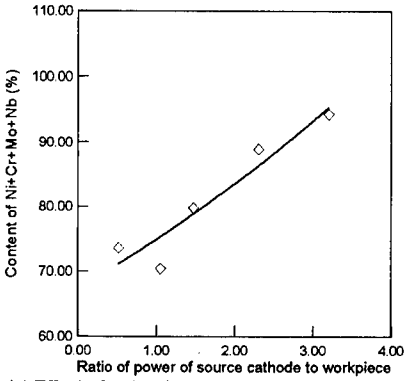
The effect of technological parameters(temperature, power of source cathode, power of workpiece) on the composition and thickness of surface alloyed layer are studied. The results (figure 2) show that when the processing temperature increases, the total amount of alloying



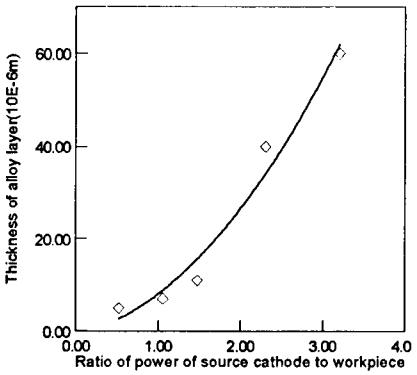
(a) Effect of temperature on total amount of alloying elements



(b) Effect of temperature on thickness of the alloy layer



(c) Effect of ratio of power of source cathode to workpiece on total amount of alloying elements



(d) Effect of ratio of power of source cathode to workpiece on thickness of alloy layer

Figure 2 Effect of technological parameters on composition and thickness of surface layer

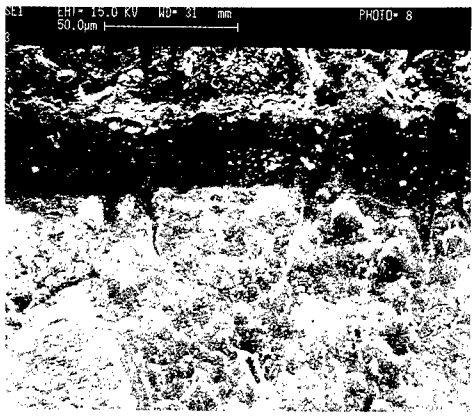


Figure 3 Microstructure of alloyed layer

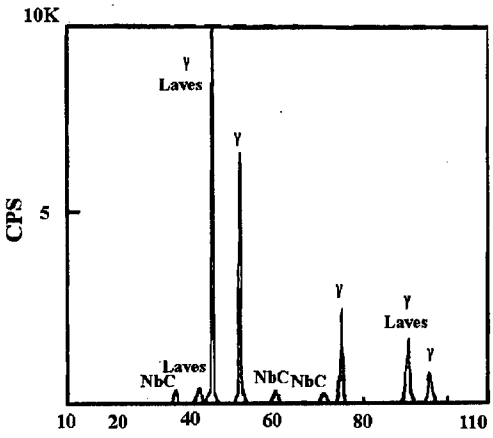


Figure 4 XRD result of alloyed layer

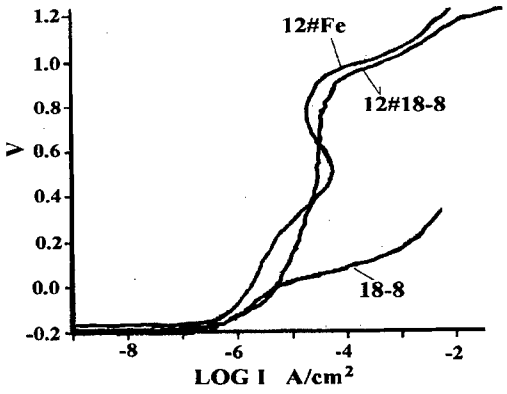


Figure 5 Polarization curves of alloyed layer

element Ni+Cr+Mo+Nb decreases, the thickness of the alloyed layer increases. When the output power of cathode increases(ratio of power of source cathode to workpiece increases), the total amount of alloying element increases and the thickness of the alloyed layer also increases. So the total amount of alloying element and the thickness of the alloyed layer is related to the output power of source cathode and workpiece, therefor the total amount of alloying elements and thickness of the alloyed layer can be controlled by Changing technological parameters.

2. The microstructure of the alloyed layer

The typical microstructure of surface alloyed layer by Double Glow Plasma Surface Alloying is shown in Figure 3. It can be seen that the surface alloyed layer is uniform, continuous and compact. Using X-EDS analyses, the white spots in the surface alloyed layer are considered as carbide or intermetallic phase containing higher Mo and Nb content. This is in accordance with XRD results.

3. Phase analysis of the surface alloyed layer

The phase structure of surface alloyed layer is shown in figure 4. The microstructure of the surface alloyed layer is γ matrix and precipitates. The precipitates are carbide NbC and Laves phase.

4. Corrosion test results

The polarization curves have been plotted for surface alloyed layer specimen No.12 of pure iron and AISI304 stainless steel and for 304 stainless steel in 3.5% NaCl solution. The results are shown in figure 5 . the E_b of alloyed layer (about 1000mV) is much higher then that of 304 stainless steel(about 200mV). So pitting corrosion resistance of the alloyed layer is superior to that of 304 stainless steel. Pitting is a localized form of corrosion confined to a small area compared with the whole surface. Chromium and molybdenum have been found to be beneficial in promoting pitting resistance. The alloyed layer increases the chromium and molybdenum content, which accounts for its

content, which accounts for its superior pitting resistance.

Conclusions

1. The surface alloyed layer with different composition which similar to Inconel 625 can be formed on the surfaces of pure iron, low carbon steel and AISI304 stainless steel by Double Glow Plasma Surface Alloying Technique.

2. The composition and thickness of alloyed layer can be controlled by changing technological parameters.

3. The phase structure of the surface alloyed layer is γ matrix and several precipitates. The precipitates are carbide NbC and Laves intermetallic phase.

4. The surface alloyed layer have better corrosion resistance than stainless steel AISI 304 in 3.5% NaCl solution.

5. It is new method to produce highly alloyed surface Ni-Cr-Mo-Nb layer by Double Glow Plasma Surface Alloying technique.

References

1. US Patent 4,520,238,28 May, 1985
2. Xu Zhong etc., Double layer ion metallic cementation, Transaction of Metal Heat Treatment, (1) 1982, 71
3. Fan Benhui etc., Study of plasma multi-element surface alloying on steel by double glow discharge, Mechanical Engineering Material, (1) 1991, 12
4. Xu Zhong etc., Study on the application of plasma surface alloying of W-Mo on steel hand saw blades, Heat Treatment of Metal, (3) 1988, 13
5. Fan Benhui etc., Plasma Ni-Cr surface metallizing for A3 steel sheet, Heat Treatment of Metal, (9)1988, 42

Phase Transformations and Their Applications

ORIGIN OF AGING EFFECT AND RUBBER-LIKE BEHAVIOR IN MARTENSITE

Kazuhiro Otsuka and Xiaobing Ren

Institute of Materials Science
University of Tsukuba
Tsukuba, Ibaraki 305-8573, Japan

Abstract

The alloys of Au-Cd, Au-Cu-Zn, Cu-Zn-Al, Cu-Al-Ni and In-Tl exhibit quite a strange phenomenon called "the rubber-like behavior" after aging in the martensitic state, whose origin has been unknown for more than 60 years. The characteristics of the peculiar phenomenon is the rapid increase of the yield stress, pseudoelastic behavior under stress, and the invariance of the average structure and the long range order with aging. We propose a new model based on short-range ordering (SRO), which consists of the following three essentials. i) This behavior occurs only in imperfectly ordered alloys, and lattice point defects such as vacancies or anti-structure defects (ASD) play an important role. ii) The distribution of point defects in equilibrium follows the symmetry of the martensite. iii) The SRO due to ii) occurs only within the same sub-lattice. We showed that all the characteristics associated with the rubber-like behavior are accounted for by this model, including the disordered In-Tl alloy. We also showed that the stabilization of martensite by aging, which was another unexplained effect, can also be accounted for by the same model. With the elucidation of the aging mechanism, we proposed a guideline to design shape memory alloys without the unwanted aging effect. We suggested that a low M_s/T_m ratio (<0.2) is necessary to eliminate the aging effect.

The Third Pacific Rim International Conference on
Advanced Materials and Processing (PRICM 3)
Edited by M.A. Imam, R. DeNale, S. Hanada,
Z. Zhong and D.N. Lee
The Minerals, Metals & Materials Society, 1998

I. Introduction

Martensitic transformation (MT), being a large class of displacive transformation, has been studied for nearly one century, and it has found extensive and successful technological applications in hardening of steels, shape memory effect, and superelasticity(1-4). However, in this old field there still remain several important and fundamental problems unsolved. One of these problems is the origin of the aging effect and the associated rubber-like behavior and stabilization phenomenon, which was first discovered in 1932 in Au-47.5Cd(γ_2') ordered martensite (5), and was later found in other ordered martensites of Au-Cu-Zn(6), Cu-Zn-Al(7,8), Cu-Al-Ni(9), Au-49.5Cd(ζ_2')(10), as well as in disordered In-Tl martensite(11,12).

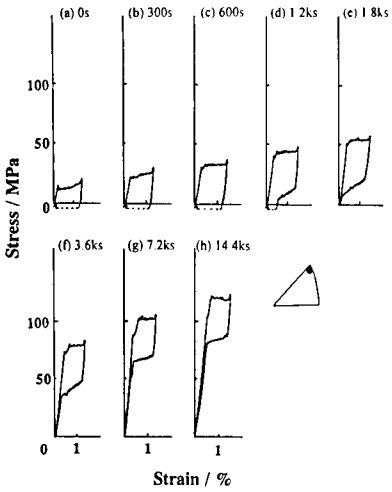


Figure 1. Development of rubber-like behavior during aging at 303K for Au-49.5at%Cd martensite. After Murakami et al. (14).

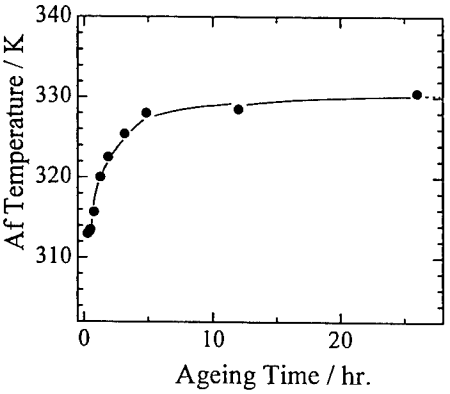


Figure 2. Martensite stabilization in Au-49.5at%Cd alloy. After Murakami et al. (13).

If holding (or aging) martensite for some time, the mechanical and physical properties of the martensite, as well as the reverse transformation temperature, change with time. This phenomenon is usually called aging effect. One of the most obvious change is the deformation behavior, which changes from pure plasticity into pseudoelasticity, together with an increase in yield stress, as shown in Fig.1. This is called the rubber-like behavior (RLB). Another remarkable change is an increase of reverse transformation temperature (Fig.2), indicating that the martensite becomes more stable relative to the parent phase. Thus this effect is called the stabilization effect. It should be noted that both RLB and stabilization effect are caused by the same martensite aging, therefore, they may have the same origin.

In contrast to the RLB, a kind of pseudo-elasticity with unknown origin, there exist two other kinds of pseudo-elasticity with known origins. One is due to the stress-induced martensitic transformation in the *parent state*, which is usually termed "superelasticity" (2). Another is due to the stress-induced pseudotwin (which can be regarded as a new phase) (15). In both cases, stress induces a structural transformation and the free energy difference between the two phases provides a restoring force for the pseudoelasticity, and such pseudoelasticity is independent of time or aging. One may expect that there might be some obvious structural change during martensite aging and during loading. However, as will be shown below, aging phenomena may occur even without any average structural change of martensite. This puzzling feature is in sharp contrast to the significant change in the reverse transformation temperature and mechanical properties during martensite aging. This is the main reason why the aging problem has remained over 60 years without a definite answer.

Another major difficulty encountered in martensite aging study is that martensite aging had been complicated by an unavoidable decomposition process in many metastable martensites (mainly Cu-based alloys). Because the martensites of these alloys are not equilibrium low temperature phases, they have an inborn tendency to decompose. As long as diffusion is possible, such a decomposition (maybe partially) is unavoidable. The time dependence of this inevitable process just coincides with the martensite aging process. Many of the previous explanations for the aging effect are more or less related to the (partial) decomposition of martensite, and requires some change in average structure of martensite. With Au-Cd and Au-Cu-Zn alloys, whose martensites are equilibrium low temperature phases, it was able to separate the aging effect from the martensite decomposition.

One of the most important conclusions from these studies(14,16-18) is that martensite aging does not involve a change in average martensite structure. This fact is difficult to explain by available models.

The invariance of the martensite structure during aging exerts an important constraint on possible aging mechanism. By considering this fact, a recent model by Ren and Otsuka(19) appears to give a general explanation to all known aging effect. In the following, we first present major experimental facts on the martensite aging effect, and then discuss this new model. Finally we apply this model to explain some unclear experimental facts. Martensite aging effect (stabilization) is usually unwanted in most cases of the application of shape memory alloys. With the elucidation of the aging mechanism we propose a guideline to design aging-free shape-memory alloys.

II. Experimental facts on the martensite aging phenomena

As mentioned above, aging phenomena include two closely related time-dependent effects. One is the "rubber-like behavior (RLB)", in which the martensite exhibits recoverable or pseudo-elastic deformation behavior after being aged for some time. Another is the so-called "martensite stabilization", by which martensite becomes more stable with aging, such that the reverse transformation temperature (A_f) increases with aging time. Early studies on RLB were reviewed by Otsuka and Wayman(2), and the RLB of Au-Cd alloys was reviewed by Otsuka, Ohba and Murakami(20), and a review on the stabilization of Cu-Zn-Al martensite was given by Ahlers (21). A critical review of aging models was given by Ren and Otsuka(22). In the following, we summarize the most important and general experimental facts on the aging effect.

1. Rubber-like behavior

Figure1 shows a typical example of the change of stress-strain curve of martensite with aging time. It is seen that with increase of aging time the "yield" stress increases, and the deformation becomes gradually recoverable. The examples of the RLB for ordered martensites are γ_2'-Au-Cd , ζ_2'-Au-Cd, Au-Cu-Zn , Cu-Zn-Al, Cu-Al-Ni, and that for disordered martensite is In-Tl. Since the martensite deforms through mechanical twinning, a recoverable strain means that the original twin (domain) configuration before loading is restored after stress is removed. Because there should be no energy difference among different twin variants, it is strange that a mechanical twin can automatically revert into its original variant after unloading. The driving force needs explanation.

2. Martensite stabilization effect

Figure 2 shows the increase of reverse transformation temperature with martensite aging time for Au-49.5Cd martensite. It indicates that martensite becomes thermodynamically more stable with aging. This martensite stabilization has been found in all those alloys showing RLB except In-Tl. The reason for the absence of stabilization effect in In-Tl will be given later. It is interesting that commercially important shape memory alloy Ti-Ni does not show detectable aging effect and RLB in its martensite state(23). The reason is apparent when the aging mechanism becomes clear, as will be discussed later.

3. Effect of martensite aging on mechanical properties of martensite

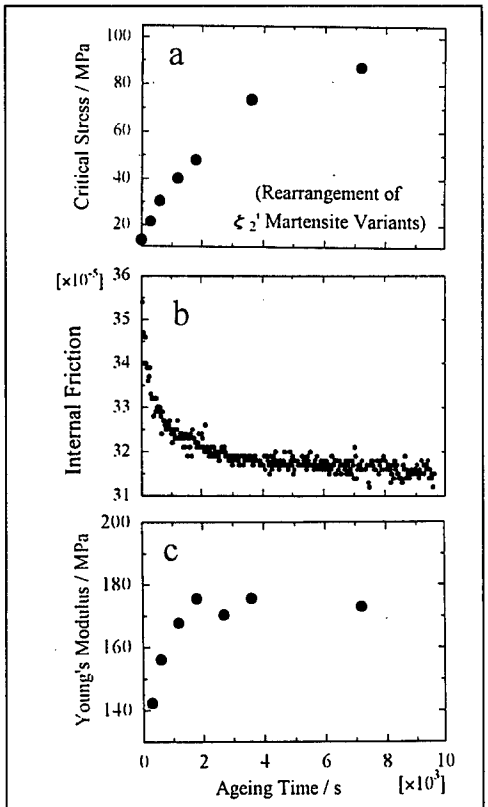


Figure 3. Variation of (a) yield stress, (b) internal friction Q^{-1}, and (c) static Young's modulus, during aging of Au-49.5 martensite at 303K. After Murakami et al (14).

Figure 3 shows an example (Au-49.5Cd alloy) of aging dependence of critical stress, internal friction, and static Young's modulus of multi-domain (twin) martensite, respectively. It is found that with increasing of martensite

aging time, the critical stress for domain (twin) reversal increases. Meanwhile, internal friction drops and static Young's modulus increases with aging. It should be noticed that all these changes tend to saturate at long aging time. An earlier study on Au-47.5Cd martensite by Nakanishi et al(24) also reached similar results. However, there is a lack of convincing explanation for these results. Nakanishi et al(24) proposed that the change of internal friction and Young's modulus can be understood in terms of the pinning of martensite twinning boundary by lattice defects, analogous to the strain aging process of metals after deformation. However, the short-ranged pinning force is not likely to drag macroscopically displaced (e.g., ~1mm) domain boundaries back to their original positions. A simple explanation of these results will become evident after the mechanism of the aging is elucidated, as will be shown later.

4. Invariance of the martensite structure during aging, a relaxation process.

A surprising feature of martensite aging effect is that stabilization and RLB are independent of a change in average structure of martensite, that is, no detectable change in average martensite structure occurs despite large aging effect. This important feature was first found by Ohba, Otsuka and Sasaki(16) in Au-47.5Cd martensite with x-ray diffractometry, and was later confirmed in other non-decomposing martensites such as Au-49.5Cd(18) and Au-Cu-Zn(17). Figure 4 shows an example of the invariance of the Bragg peak with aging(16,19). Both peak position and integrated intensity were found to be unchanged during aging. However, a small change in the symmetry of the peak was found, as manifested by the difference of well-aged and shortly-aged peak profiles.

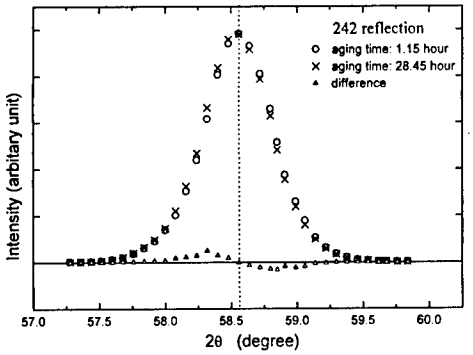


Figure 4. X-ray profiles of (242) Bragg reflection of Au-47.5at%Cd martensite after aging for short (1.15 hour) and long (28.45 hour) time, respectively (After Ohba, Otsuka, Sasaki. (16)).

5. General features of martensite aging effect.

An understanding of aging phenomena depends on how we interpret their common features. Here we list five most important and general features of martensite aging phenomena.

(1) Aging is a time-dependent process.
(2) Aging is not dependent on a change in average structure of martensite(14,16-19).
(3) Aging appears even in single-domain martensite where no domain (twin) boundary exists (7,8,18).
(4) Aging effect is sensitive to point defects (e.g., 10,14).
(5) Aging phenomena occur both in ordered and disordered martensite.

III. Symmetry-conforming principle of point defects and a general model for aging phenomena.

Although the aging phenomena manifested many complex facets, it should be governed by a general and simple mechanism which is capable of explaining all of these facets in diverse martensites. A model cannot be accepted as being correct if it can explain only a part of the experimental facts or is limited to certain alloys. Therefore, generality is the most important criterion for a correct aging mechanism. Most of the early models, including the pseudotwin type models(28,29), long-range ordering (LRO) models(26,27) and structure-modifying short-range ordering (SRO) models (30-32), explained the aging effect assuming that the average structure of martensite (or its LRO degree) changes to some extent during martensite aging. As discussed above, the change of average martensite structure during aging is absent in stable martensite without decomposition tendency. Other models include dislocation interaction model(33) and domain boundary pinning model(24). But the former cannot explain the time-dependence of the aging effect and is limited to ordered alloys, while the latter fails to explain the aging effect in single-domain martensite where domain boundary is absent. Therefore, these models do not meet the generality criterion.

Very recently, Ren and Otsuka (19) proposed a general principle concerning the symmetry property of the SRO configuration of point defects in crystals. It is named symmetry-conforming short-range order principle (or SC-SRO principle), and is applicable to any crystal containing point defects. For disordered alloys point defect means vacancy and solute atom, and for ordered alloys it means vacancy and anti-structure defect (ASD) . The aging

phenomena of martensite can be easily understood with this principle. This principle states that *the symmetry of SRO configuration of point defects in equilibrium should conform to the symmetry of the crystal lattice with respect to atom.* In order to understand this principle, it is necessary to clarify the meaning of SRO parameters. Usually SRO parameters are defined according to the probability of finding one kind of atom in the 1st (or *n*th) nearest neighbor shell of a given atom, as used by previous SRO models. However, such a definition cannot describe atomic rearrangement within the same shell (or within the same sublattice). We shall show later that it is this kind of rearrangement that is responsible for martensite aging. Therefore, such a definition of SRO parameter is not suitable to describe martensite aging process. Here SRO is defined in terms of the probability of finding one kind of atom or defect at some interatomic vector from a given atom.

$$\alpha_{lmn} = 1 - \frac{P_i^B|_j^A}{x_B},$$

where lmn is the coordinates of the interatomic vector between site i, j; $P_i^B|_j^A$ is the conditional probability that there is a B atom at site i if there is an A atom at j; x_B is the average concentration of B. Such SRO concept is consistent with the definition by Warren and Cowley . The averaging of such SRO parameters in the same shell reduces to the SRO concept defined by shell probability. Therefore, such SRO parameters are established on crystal lattice, and it is natural that they should possess certain symmetry properties.

The SC-SRO principle gives a general and simple explanation to the aging phenomena in both ordered and disordered alloys. Since SRO parameter is completely determined by conditional probability $P_i^B|_j^A$, we shall discuss aging in terms of the symmetry property of this conditional probability. Let us take an essentially ordered alloy for example. The change of SRO configuration of point defect (either anti-site defect or vacancy) during martensitic transformation and aging is considered. Fig.5.a shows a two-dimensional A-B binary *imperfectly-ordered* parent phase with 4-fold symmetry. Because of the 4-fold symmetry of the structure, the probability of finding a B atom about the A atom (or B atom) must possess the same 4-fold symmetry according to SC-SRO principle, i.e., $P_1^B=P_2^B=P_3^B=P_4^B$, and $P_5^B=P_6^B=P_7^B=P_8^B$, etc., where P_i^B (i=1,2,3,...) are conditional probabilities, as defined in Fig.5. The martensite has a lower symmetry, thus the equilibrium occupation probability of atoms should have the same symmetry as the structure about the A atom, i.e., $P_1^B=P_3^B \neq P_2^B=P_4^B$ and $P_5^B=P_7^B \neq P_6^B=P_8^B$, as shown in Fig.5c. The equalities are due to the centro-symmetry of the schematic martensite structure.

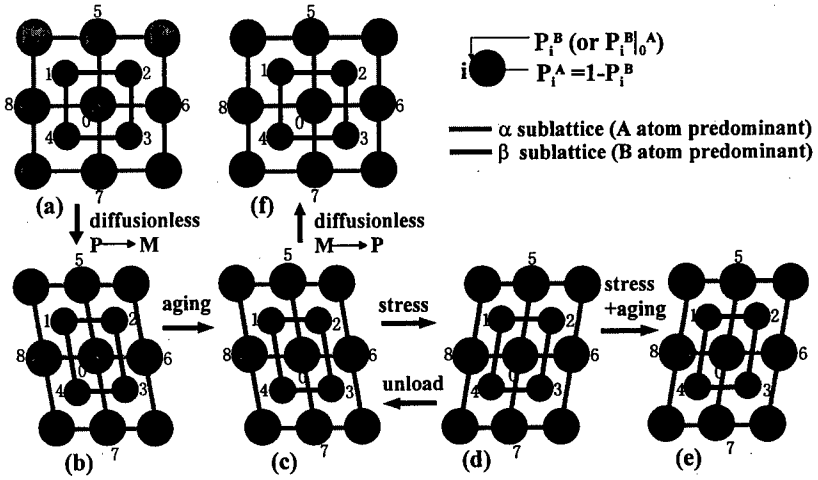


Figure 5. Symmetry-conforming short-range order mechanism of martensite aging phenomena. After Ren and Otsuka (19). The illustrations show the statistical atomic configuration (conditional probabilities around an A atom) of an ***imperfectly-ordered*** A-B alloy in, (a) equilibrium parent phase; (b) martensite immediately after transformed from (a); (c) equilibrium martensite; (d) stress-induced martensite domain (twin) immediately formed from (c); (e) equilibrium state of the stress-induced domain; and (f) parent immediately transformed from (c), respectively. **P**: the parent phase, and **M**: martensite. P_i^B (or P_i^A) is the conditional probability of B atom (or A atom) occupying i-site (i=1,2,3,...,8) if an A atom is at 0-site. The relative values of P_i^B and P_i^A are indicated by the black and gray areas, respectively.

When the parent phase shown in Fig.5a transforms diffusionlessly into martensite, all the probabilities must

remain unchanged despite the symmetry change, as shown in Fig.5b. That is, $P_1^B=P_2^B=P_3^B=P_4^B$, and $P_5^B=P_6^B=P_7^B=P_8^B$, etc.. However, this high-symmetry configuration is no longer a stable configuration for the lower symmetry martensite structure. Then during aging, such a configuration gradually changes into a stable one that conforms to martensite symmetry, as shown in Fig.5c. Because the equilibrium martensite structure should be maintained (for stable martensite), this process proceeds by atomic rearrangement or relaxation within the same sublattice. This is the only way that a martensite can lower its free energy without altering the average structure (equilibrium phase). It is obvious that such an atomic rearrangement occurs most easily for atoms close to the A atom, and farther atoms make little contribution. Consequently, *it is a kind of short-range ordering within the same sublattice*. As shown above, this SRO stems from a requirement that the symmetry of the SRO parameters of lattices imperfections in equilibrium conforms to the crystal symmetry, following the SC-SRO principle. The stable SRO configuration for the parent is inherited into martensite during diffusionless martensite formation, but this SRO becomes "unstable" for martensite because it differs from the martensite symmetry. Then atomic rearrangement occurs during aging that results in a correct SRO symmetry for the martensite. The difference between SC-SRO and previously proposed SRO (30-32) is that the change of SC-SRO does not alter average structure or LRO. This is because SC-SRO mechanism restricts effective (net) atom exchange only within the same sublattice. In this aspect, such short range diffusion is similar to the diffusion process in conventional ordered alloy where net atomic exchange occurs only within the same sublattice so that LRO structure is maintained (34).

When the stabilized (or aged) martensite (Fig.5c) is deformed, it changes into another domain (or twin) as a result of the accommodation of the strain. Because this twinning process is also diffusionless, the atomic occupation probabilities shown in Fig.5c is inherited to the new domain, as shown in Fig.5d. Such a configuration, however, is not the stable one for the new domain, which is shown in Fig.5e. Therefore, a driving force that tries to restore the original domain (Fig.5c) engenders. This is the long-range restoring force to drag back displaced domain boundary. When the external stress is released immediately after the loading, this restoring force reverts the new domain (Fig.5d) to the original one (Fig.5c) by de-twinning. This is the origin of the rubber-like behavior. If the stress is held for some time, atomic configuration in Fig.5d have enough time to change into a stable configuration (Fig.5e), then no RLB will occur.

When the stabilized martensite (Fig.5c) is heated up and transforms back (diffusionlessly) into the parent, the stable SRO configuration for the martensite is inherited into the parent (Fig.5f). From the above-mentioned symmetry-conforming principle of SRO, it is obvious that Fig.5f is not a stable configuration for the parent. From a thermodynamic point of view, this corresponds to an increased reverse transformation temperature. This is the origin of martensite stabilization.

The SC-SRO model can be easily extended into disordered alloys by considering the existence of only one sublattice. In this case, the present model reduces to Christian's model (35), which was later elaborated by Otsuka and Wayman (2). This model explained the rubber-like elasticity in disordered alloys such as In-Tl.

Table I. Relationship between the reduced martensitic transformation temperature M_s/T_m and the rate of martensite aging (RLB) at room temperature.

Alloy	Ti-Ni	Cu-Al-Ni	Cu-Zn-Al	Au-Cd	In-Tl
M_s/T_m	~0.19	~0.23	~0.27	~0.34	0.50~0.79
aging time for RLB at R.T.	$\sim\infty$ (i.e., no aging effect)	~10 months	~ 5 hours	~0.5 hour	<1s

IV. Application of the SC-SRO model to understand unclear facts

The largest advantage of the SC-SRO model compared with previous models is its fulfillment of generality criterion. It not only explains why aging does not cause a change of average structure of martensite, but also unified the origin of aging effect for both ordered and disordered martensites. The generality of the model lies in that it makes use of only two general features of martensitic transformation and aging: diffusionless symmetry-change upon martensitic transformation and diffusion of point defects during aging. In line with this reasoning, it can be deduced that the existence of point defects and possibility of diffusion in martensite are two necessary conditions for aging phenomena. The existence of point defect is generally satisfied by alloys, but the possibility of diffusion in martensite depends on the reduced martensitic transformation temperature M_s/T_m, where M_s and T_m are martensitic transformation start temperature and melting point of alloy. The higher this reduced temperature is, the faster diffusion in martensite becomes. If this value is too low, aging phenomena are too slow to observe; if

this value is too high, aging is so fast that aging actually completes immediately after the martensitic transformation, thus the time-dependence of aging may not be observed. As shown in Table I, TiNi alloy belongs to the former case, and In-Tl belongs to the latter. Other shape memory alloys are in-between. Thus we give an answer to an important problem as to why some alloys show strong aging effect while others show little. The absence of martensite aging effect in TiNi shape memory alloys (23) is very interesting because this property is desirable for most applications of SMA. The reason, as stated above, is very simple. This reminds us that the most effective way to develop SMA without aging effect is to choose alloys with low M_s/T_m value. This can be realized by (i) using SMA with a low M_s, or (ii) using SMA with high T_m. Since the first method are usually restricted by application purpose, using alloys with high melting temperature becomes the most effective method. Therefore, the development of SMA without aging effect should focus on alloys with high T_m, because it is not possible to stop diffusion in martensite for alloys with low T_m. From Table 1, we suggest that in order to avoid the aging effect a low M_s/T_m ratio (<0.2) is necessary. It is an important guideline to design SMAs without the unwanted aging effect.

With the clarification of the aging mechanism, we can also understand the previously unclear internal friction data, i.e., the decrease of internal friction and increase of Young's modulus during martensite aging. As discussed earlier, though domain boundary pinning by point defects may account for such a behavior, this explanation cannot account for the associated martensite stabilization and RLB. Thus this behavior must be connected with martensite stabilization and RLB. Here we give a simple explanation to this behavior in terms of the aging mechanism. The internal friction is related to the energy dissipation during strain cycles. The primary source of the energy dissipation at low frequency cyclic strain is the domain boundary friction during domain boundary movement. If the domain boundary motion is arrested due to some reason, the internal friction will drop. As shown in Fig.5b,6c, aging causes the original domain to become more stable (volume effect), and thus makes the domain reversal (=domain boundary motion) more difficult. Therefore, internal friction drops during martensite aging. The increase of Young's modulus can be understood by the same reasoning. Because the Young's modulus was measured from a multi-domain martensite sample and at static condition, the contribution of domain boundary motion (which produces an extra strain) to (nominal) Young's modulus ($=\frac{\text{nominal stress}}{\text{nominal strain}}$) is unavoidable. This is the reason why the measured static Young's modulus (0.14~0.18GPa) is about two order of magnitude lower than dynamic modulus (Lame's constant μ~14GPa) (36) measured at ultrasonic frequency (where domain contribution is much smaller due to the inability of domain boundary motion to follow the high stress rate) . During martensite aging, domain boundary becomes less mobile due to the generation of the restoring force. Thus the extra strain due to domain motion is decreased, as the result the apparent Young's modulus increases.

One may expect that if the SC-SRO principle or the SC-SRO model is correct, it should not only explain *all* experimental observations without exception, but also be able to find direct experimental evidence. In a preliminary TEM study (37), a decisive experimental evidence proving the existence of SC-SRO has been found, this experiment also showed that the SC-SRO model is also able to explain the large difference in aging effect between single-domain martensite and multi-domain martensite, one of the most challenging problem. The details of this study will be published later. At present, the small change in the symmetry of x-ray diffraction profile (Fig.4) during aging provides a support to this model. This result cannot be rationalized by any other model. The change of the symmetry of diffraction profile indicates that the symmetry-conforming SRO rearrangement of defects occurs, which leads to a slight change in atomic displacement field and results in the change in the symmetry of the diffraction profile without altering peak position and intensity.

V. Summary

Martensite aging involves two closely related effects: (i) rubber-like behavior, and (ii) the stabilization effect. They possess the following general features: (1) aging is time-dependent, (2) aging is not dependent on the change in average structure of martensite, (3) aging occurs even when martensite domain boundary is absent, (4) aging is dependent on point defects, and (5) aging occurs in both ordered and disordered martensite.

Previous models turned out to be able to explain only a part of the above features, thus failed to meet the generality criterion. The symmetry-conforming short-range ordering (SC-SRO) model we proposed is able to explain all features of martensite aging and all known experimental facts. This model is a natural application of a general principle (symmetry-conforming principle) that the symmetry of SRO configuration of lattice defects in equilibrium conforms to the symmetry of the crystal lattice with respect to atom. The clarification of the aging

mechanism leads to a guideline to develop shape memory alloys without the unwanted aging effect. We suggest that in order to eliminate aging effect it is necessary to design alloys with low M_s/T_m ratio (<0.2).

Acknowledgments

We would like to thank. Profs. T. Suzuki, T. Ohba, M. Kogachi, and Dr. Y. Murakami for helpful discussions. The present work was supported by Grant-in-Aid for Scientific Research on Priority Area of Phase Transformations (1997-1999) from the Ministry of Education, Science and Culture of Japan.

References

1. Z. Nishiyama, Martensitic Transformation, (New York: Academic Press, 1978).
2. K. Otsuka & C.M. Wayman. Pseudoelasticity and stress-induced martensitic transformations. Review on the Deformation Behavior of Materials. Ed. P. Feltham, (Freund Publishing House, Israel, 1977), **Vol.2**, pp.81-172.
3. K. Otsuka and K. Shimizu, Int. Met. Rev. **31**(1986), 93-114.
4. T. Tadaki, K. Otsuka, & K. Shimizu, Ann. Rev. Mater. Sci. **18**(1988), 25-45.
5. A. Ölander, J. Am. Chem. Soc. **56**(1932), 3819-3833 .
6. S. Miura, S. Maeda, & N. Nakanishi. Philos. Mag. **30**(1974), 565-581.
7. R. Rapacioli, M. Chandrasekaran, M. Ahlers, & L. Delaey. Shape Memory Effects in Alloys Ed. J. Perkins, (New York: Plenum Press, 1975), pp.365-378.
8. G. Barcelo, , R. Rapacioli, & M. Ahlers. Scripta Metall. **12**(1978), 1069-1074.
9. H. Sakamoto, K. Otsuka, & K. Shimizu. Scripta Metall. **11** (1977), 607-611.
10. Y. Nakajima, S. Aoki, K. Otsuka, & T. Ohba. Mater. Lett. **21**(1994), 271-274.
11. M.W. Burkart & T.A. Read. Trans. AIME, **197**(1953), 1516-1523.
12. Z.S. Basinski & J.W. Christian. *Acta Metall.* **2**(1954), 101-116.
13. Y. Murakami, S. Morito, Y. Nakajima, K. Otsuka, T. Suzuki, & T. Ohba. Mater. Lett., **21**(1994), 275.
14. Y. Murakami, Y. Nakajima, K. Otsuka, T. Ohba, R. Matsuo, & K. Ohshima. Mater. Sci. Eng. **A237**(1997), 87.
15. J. W. Cahn, Acta Metall. **25**(1977), 1021-26.
16. T. Ohba, K. Otsuka, & S. Sasaki. Mater. Sci. Forum, **56-58**(1990), 317-322 .
17. T. Ohba, T. Finlayson, & K. Otsuka. J. de Phys. III, **5**, C8(1995), 1083-1086.
18. Y. Murakami, Y. Nakajima, K. Otsuka, & T. Ohba. J. de Phys. III, **5**, C8(1995), 1071-1076.
19. X. Ren, & K. Otsuka, Nature, **389**(1997), 579-582 .
20. K. Otsuka, T. Ohba, & Y. Murakami. Proc. Int. Conf. on Displacive Phase Transformations and Their Applications in Materials Engineering. (Urbana, 1996). in press.
21. M. Ahlers, Proc. ICOMAT'86, Jpn. Inst. Met. pp786-793(1986).
22. X. Ren and K. Otsuka, Phase Transitions, accepted for publication (1998).
23. M. Kozuma, Y. Murakami, & K. Otsuka. Proc. Int. Conf. on Displacive Phase Transformations and Their Applications in Materials Engineering. (Urbana, 1996). in press.
24. N. Nakanishi, T. Mori, S. Miura, Y. Murakami, & S. Kachi. Philos. Mag., 28(1973), 277-292.
25. Y. Hashiguchi *et al*, Proc. ICOMAT'86, (Japn. Inst. Met.1986), pp832-837.
26. A. Abu Arab & M. Ahlers. Acta Metall. **36**(1988), 2627-2638.
27. T. Tadaki, H. Okazaki, , Y. Nakata, & K. Shimizu. Mater. Trans. JIM **31**(1990), 941-947.
28. D.S. Lieberman, , M.A. Schmerling, & R.S. Karz. in Shape Memory Effects in Alloys Ed. J. Perkins, (New York: Plenum Press, 1975), pp.203-244.
29. A. Zangwill, & R. Bruinsma. Phys. Rev. Lett. **53**(1984), 1073-1076.
30. M. Ahlers, G. Barcelo, & R. Rapacioli. Scripta Metall. **12**(1978), 1075-1078 .
31. K. Marukawa, & K. Tsuchiya. Scripta Metall. **32**(1995), 77-82.
32. T. Suzuki, T. Tonokawa & T. Ohba. J. de Phys. III, **5**, C8(1995), 1065-1070.
33. H.K.Birnbaum & T.A. Read. Trans. AIME, **218**(1960), 662-669 .
34. W. C. Hagel, Intermetallic Compounds, Ed. J. H. Westbrook, (Wiley, 1967)), pp.377.
35. J. W. Christian, The Theory of Transformations in Metals and Alloys (Oxford: Pergamon Press, 1965), pp.789.
36. T. Tonokawa, S. Morito, Y. Nakajima, A. Ooishi, K. Otsuka and T. Suzuki, Jpn. J. Appl. Phys. **33**(1994), 2897-2990.
37. X. Ren, E. Okunishi, & K. Otsuka, Collected Abstracts of Annual Fall Meeting of Jpn. Inst. Met. **121**(1997), pp369.

TIME-DEPENDENT NATURE OF MARTENSITIC TRANSFORMATIONS IN SOME FERROUS AND NON-FERROUS ALLOYS

Tomoyuki Kakeshita, Toshio Saburi and Ken'ichi Shimizu*
Department of Materials Science and Engineering, Faculty of Engineering,
Osaka University, Suita, Osaka, JAPAN.
* Department of Materials Science and Engineering, Faculty of Engineering, Kanazawa Institute of Technology, Nonoichi, Ishikawa, JAPAN.

Abstract

By electrical resistivity measurements during isothermal holding in Fe-Ni, Fe-Ni-Mn and Cu-Al-Ni alloys, which exhibit an athermal martensitic transformation, we found that the martensitic transformation occurs after some incubation time during isothermal holding at a temperature higher than the M_s temperature at ambient pressure for all the alloys. We also found that the M_s of the athermal martensitic transformation in Fe-Ni and Fe-Ni-Mn alloys decreases with increasing hydostatic pressure and is finally below 4.2K under a certain pressure, which depends on the alloy systems. However, under the pressure, martensitic transformation occurs after some incubation time during isothermal holding at temperatures between 77 and 100K, suggesting that the hydostatic pressure changes the transformation process from athermal to isothermal one. These results have been disscused on the basis of the phenomenological theory previously constracted.

The Third Pacific Rim International Conference on
Advanced Materials and Processing (PRICM 3)
Edited by M.A. Imam, R. DeNale, S. Hanada,
Z. Zhong and D.N. Lee
The Minerals, Metals & Materials Society, 1998

Introduction

Martensitic transformations are well known to be classified into two groups with respect to kinetics, athermal and isothermal ones. The former transformation has a definite transformation temperature, M_s, and occurs instantaneously at M_s, while the latter one does not have a definite M_s temperature but occurs after some finite incubation time during isothermal holding[1]. Recently, we found that the isothermal martensitic transformation changes to an athermal martensitic transformation under high magnetic fields[2]. This means that the two transformation processes are closely related to each other and their difference is not intrinsic but the two transformation processes may be explained by one basic rule. On the basis of this finding, we have constructed a phenomenological theory[3], which gives a unified explanation for the two transformation processes. Based on the theory, we could prove that in the materials which exhibit the athermal transformations, isothermal holding at a temperature above M_s induces a martensitic transformation. Also we could prove that a hydrostatic pressure changes the transformation process from athermal to isothermal one. That is, the M_s of the athermal martensitic transformation decreases with increasing hydostatic pressure and finally under a certain pressure, any athermal martensitic transformation is not observed. However, under the pressure, martensitic transformation occurs after some finite incubation time during isothermal holding. In fact, we found these predictions certainly realized in some ferrous and non-ferrous alloys, such as Fe-Ni, Fe-Ni-Mn and Cu-Al-Ni alloys, which are known to exhibit athermal martensitic transformations. The present paper is to show the above results and to discuss the obtained relations between incubation time and holding temperature in Fe-Ni, Fe-Ni-Mn and Cu-Al-Ni alloys on the basis of the theory previously constracted.

Experimental Procedures

The specimens used in the present study are Fe-29.9, -31.7 and -32.3at%Ni polycrystals and an Fe-31.5Ni-0.5Mn (at%) polycrystal and a Cu-29.1Al-3.6Ni(at%) single crystal. The alloys were produced by melting the component metals in a high frequency induction furnace under argon atomosphere and by casting into a water cooled iron mold. Details of the alloy production and sample preparation were the same as those in the previous studies[4][5]. The single crystals of Cu-Al-Ni alloy were grown by Bridgman method. Specimens for electrical resistivity measurements (2mm x 5mm x 0.5mm) were cut from the poly- and single- crystals and were finally solution-treated in a silica capsule filled with argon. Electrical resistivity measurements were made by holding the specimens at a temperature above M_s under ambient pressure for all the specimens. Also, electrical resistivity measurements under hydrostatic pressure were made by holding the specimen at temperatures between 77 and 100K for Fe-31.5Ni-0.5Mn, Fe-31.7 and -32.3at%Ni alloys. The hydrostatic pressure was generated by piston cylinder type of instrument, in which kerosine and transfer oil in a teflon capsule were used as a liquid pressure medium. More details of the pressure instrument have been described elsewhere[6].

Results

Isothermal holding under ambient pressure

Electrical resistivity measurements with the four probe method have been made for all the alloys in order to obtain their M_s temperatures. The cooling and heating rates are 0.05K/s, which is usually employed in obtaining the M_s temperature. The M_s temperatures thus obtained are 212K, 153K and 125K for Fe-29.9, -31.7 and -32.3at%Ni alloys, respectively and 146K and 196K for Fe-31.5Ni-0.5Mn (at%) and Cu-29.1Al-3.6Ni(at%) alloys, respectively. The typical result of Cu-Al-Ni single crystal is shown in Figure 1. It is to be noted that the M_f temperature is almost identical to the M_s temperature, meaning that transformation is completed at M_s.

Then, isothermal holding experiments of the alloys have been done by setting a temperature above respective M_s. The typical result for the Cu-29.1Al-3.6Ni(at%) alloy is shown in Figure 2, where ΔT represents the temperature difference between holding temperature, T, and M_s. It is noted in the figure that martensitic transformation occurs instantaneously after a

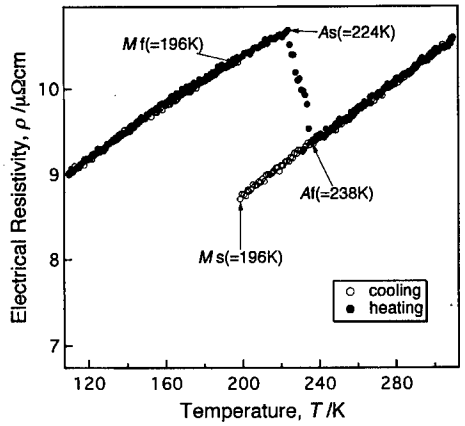


Fig.1 Electrical resistivity as a function of temperature in a single crystal of a Cu-29.1Al-3.6Ni(at%)alloy.

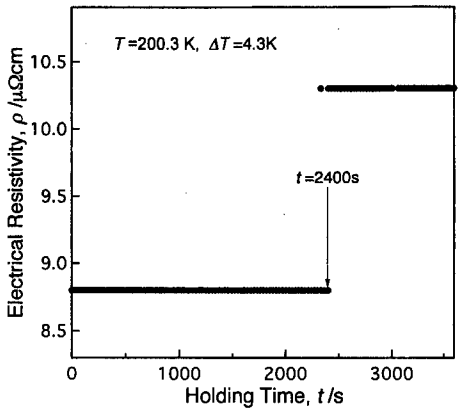


Fig.2 Electrical resistivity as a function of isothermal holding time at $\Delta T(=T-M_s)$ in a single crystal of a Cu-29.1Al-3.6Ni(at%)alloy.

finite incubation time of 2400s during isothermal holding. The same behavior is observed for the other alloys. This experimental phenomenon is in good agreement with the prediction based on the phenomenological theory, as mentioned before. Then, we obtained the incubation times of the alloys by varying holding temperature and the typical results are shown in Figures 3(a) and (b) for Fe–Ni and Cu–Al–Ni alloys, respectively. A characteristic feature in the figures is that the incubation time increases with increasing ΔT for Fe–Ni and Cu–Al–Ni alloys and decreases with increasing Ni content at a given ΔT for Fe–Ni alloys. These results will be discussed later.

Incidentally, the results shown in Figures 3(a) and (b) suggest that the incubation times at temperatures higher than the M_s by 10K are several tens of hours and/or several days for all the alloys. However, we have not done the experiments yet because the isothermal holding times required under accurate temperature are too long.

Isothermal holding under hydrostatic pressure

We applied hydrostatic pressure to the Fe–31.5Ni–0.5Mn, Fe–29.9, Fe–31.7 and –32.3at%Ni alloys in order to confirm the propriety of the prediction mentioned before. In the

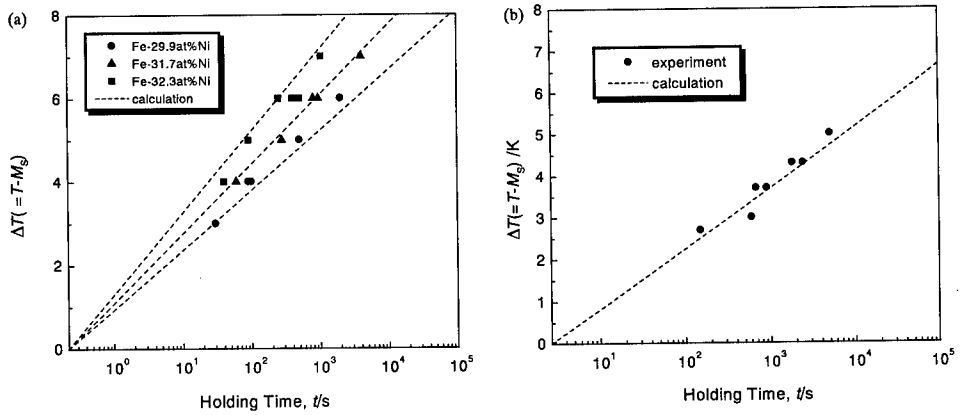


Fig.3 The relation between holding temperature and incubation time required for the martensitic transformation to start in three Fe-Ni alloys, (a), fand a single crystal of a Cu-29.1Al-3.6Ni(at%) alloy, (b). The dotted lines are caluculated relations.

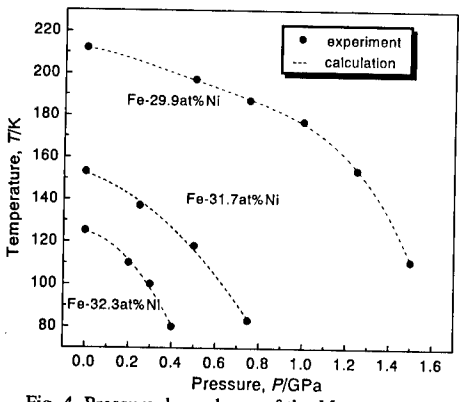


Fig. 4 Pressure dependence of the M_s temperature in Fe-29.9at%Ni, Fe-31.7at%Ni and Fe-32.3at%Ni alloys. The dotted lines are calculated relations.

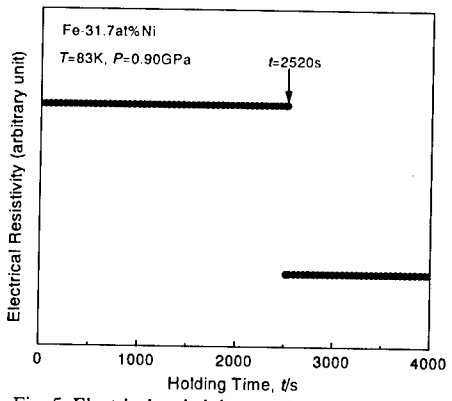


Fig. 5 Electrical resistivity as a function of isothermal holding time at T(=83K) under hydrostatic pressure (0.90GPa) in an Fe-31.7at%Ni alloy.

experiment, transformation temperature under a pressure is obtained by electrical resistivity measurement. The typical results for hydrostatic pressure dependence of M_s temperature in the Fe–Ni alloys are shown in Figure 4. It is noted that the M_s temperature decreases with increasing hydrostatic pressure and is below 4.2K under the pressures 0.6GPa and 0.9GPa for Fe–31.7 and32.3at%Ni alloys, respectively. These measured relations between transformation temperature and hydrostatic pressure are in good agreement with the calculated ones obtained by the equation previously derived[7], which are shown with the dotted lines. The same result is obtained for the Fe–31.5Ni–0.5Mn (at%) alloy.

Then, isothermal holding experiments of the Fe–Ni–Mn, Fe–31.7 and Fe–32.3at%Ni alloys have been done by setting a temperature between 77 and 100K under the pressure where any athermal martensitic transformation is not observed at any temperature mentioned above. The typical result of electrical resistivity during isothermal holding for the Fe–31.7at%Ni alloy is shown in Figure 5. It is noted in the figure that martensitic transformation occurs instantaneously after a finite incubation time of 2520s during isothermal holding. The same behavior is observed for the Fe–Ni–Mn and the other Fe–Ni alloys. This phenomenon is also in good agreement with the prediction based on the phenomenological theory, as mentioned before. Then, we obtained the incubation times of the alloys by varying holding temperature under the pressure and the results are shown in Figures 6(a) and (b) for Fe–Ni–Mn and Fe–Ni alloys, respectively. These results will be discussed later.

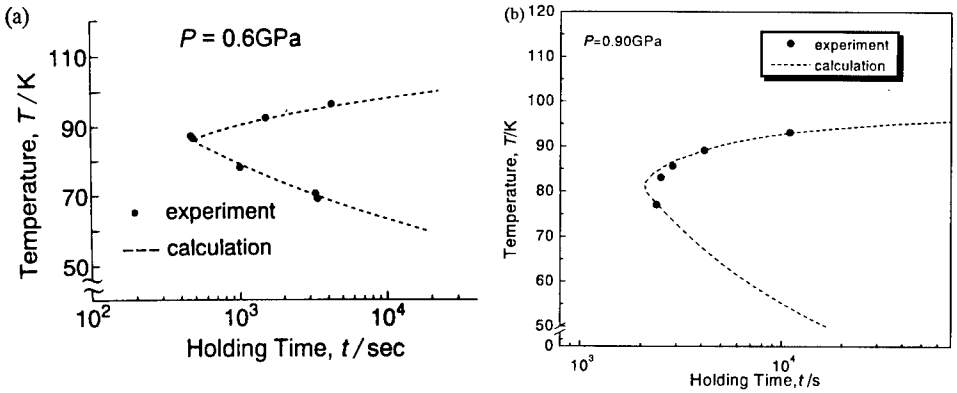
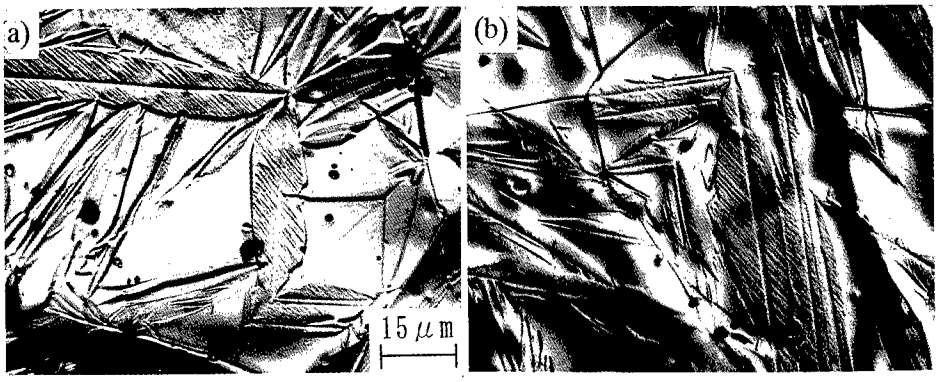


Fig.6 The relation between holding temperature and incubation time required for the martensitic transformation to start under hydrostatic pressuere in Fe-31.5Ni-0.5Mn(at%),(a), and Fe-31.7at%Ni alloys,(b). The dotted lines are caluculated relations.



T=153K T=83K, P=0.90GPa, t=2520s

Fig.7 Optical micrographs of thermally-induced martensites, (a) and of martensites formed under hydrostatic pressures, (b), being for Fe-31.7at%Ni alloys.

Figure 7 shows optical micrographs of the martensite formed athermally during cooling, (a), and of the martensite formed during isothermal holding under the hydrostatic pressure of 0.9GPa, (b), in the Fe–31.7at%Ni alloy, where isothermal holding temperature and incubation time are given underneath the photographs. It is seen from a comparison between (a) and (b) that the morphology of martensites formed athermally during cooling is the same as that of martensites formed under isothermal holding under the pressure. That is, the morphologies of martensites for (a) and (b) are lenticular ones with mid–rib, which are well known to be seen in Fe–Ni alloys exhibiting an athermal martensitic transformation. The same result is obtained for the other Fe–32.3at%Ni alloy.

Discussion

We have shown that the incubation time required for the formation of martensites, which is obtained by setting a temperature above M_s, increases with increasing ΔT for Cu–Al–Ni, Fe–Ni and Fe–Ni–Mn alloys. We now show that the above results can be explained by following approximated equation, whose detailed derivation was already described in a previous paper [3]. The approximated equation is expressed as,

$$P^{-1} = [\, A \exp(-m^*\Delta/k_B T)\cdot\exp\{\, -B \exp(\, -\Delta/k_B T)\,\}\,]^{-1}, \qquad (1)$$

where A, m^* and B represent temperature–independent parameters and Δ shows the definite potential barrier between the parent and martensite phases.

Based on eq.(1), we firstly make a least–square fitting with the experimental relation between incubation time and ΔT to obtain the fitting parameters in eq.(1), A, m^* and B. The fitting parameters, for example, thus obtained by using the Fe–31.7at%Ni alloy are 6.46×10^{65}, 800 and 150 for A, m^* and B, respectively and the best fitted relation for the alloy is shown with a dotted line in Figure 3(a). Then, the relations for Fe–29.9 and –32.3at%Ni alloys have been calculated on the basis of eq.(1) using the same values of A, m^* and B. The results thus calculated are shown with the dotted lines in Figure 3(a). It is noted in the figure that the calculated relations are in good agreement with the experimental ones: the incubation time required for formation of martensite increases with increasing ΔT and decreases with increasing Ni content at a given ΔT. The same good agreements between calculated and experimental relations are obtained for Cu–Al–Ni and Fe–Ni–Mn alloys and the calculated relation of Cu–Al–Ni is shown in Figure 3(b) with a dotted line.

The same analysis has been made for the relation between temperature and incubation time required for the occurence of martensitic transformation under hydrostatic pressure. In the calculation, the same parameters (A, m^* and B) mentioned above are used and Δ of Fe–Ni and Fe–Ni–Mn alloys have been calculated using the difference in Gibbs chemical free energies between the parent and martensitic states, $\Delta G(T)$, derived by Kaufman [8]. The detailed

procedure of the calculation of Δ was described in the previous paper [3]. The calculated relations for Fe-31.7at%Ni and Fe-Ni-Mn alloys are shown in Figure 6 with a dotted line. It is noted in the figure that the calculated relations are in good agreement with the experimental ones.

From the above results, we conclude that the new theory successfully explains the time-dependent nature of athermal martensitic transformation in Fe-Ni, Fe-Ni-Mn and Cu-Al-Ni alloys.

By using the fitting parameter, m^*,(representing the number of particles in the cluster which is sufficient for a martensitic transformation to start) and the lattice parameter of the parent phase previously obtained [4], it is possible to evaluate the cluster size needed to induce the martensitic transformation in the present alloys. The size is estimated to be about 2 $(nm)^3$ at most for all the alloys used in the present study.

Acknowledgment

The present study was partly supported by the Grant-in-Aid for fundamental Scientific Research of the Ministry of Education, Science, sports and Culture, Japan. The support is greatly appreciated.

References

1. G. V. Kurdjumov, and O. P. Maksimova, " Kinetics of Austenite to Martensite Transformation at Low Temperatures, " Doklady Akademii Nauk SSSR, **61**(1948), 83-93.
2. T. Kakeshita, K. Kuroiwa, K. Shimizu, T. Ikeda, A. Yamagishi, and M. Date, " Effect of Magnetic Fields on Athermal and Isothermal Martensitic Transformations in Fe-Ni-Mn Alloys, " Materials Transactions, JIM, **34**(1993), 415-422.
3. T. Kakeshita, K. Kuroiwa, K. Shimizu, T. Ikeda, A. Yamagishi, and M. Date, " A New Model Explanable for Both the Athermal and Isothermal Natures of Martensitic Transformatios in Fe-Ni-Mn alloys, " Materials Transactions, JIM, **34**(1993), 423-428.
4. T. Kakeshita, K. Shimizu, S. Funada, and M. Date, " Composition Dependence of Magnetic Field-Induced Martensitic transformatiuons in Fe-Ni Alloys, " Acta Metall., **33**(1985), 1381-1389.
5. T. Kakeshita, T. Takeguchi, T. Fukuda, and T. Saburi, " Time-Dependent Nature of the Athermal Martensitic Transformation in a Cu-Al-Ni Shape Memory Alloy, " Materials Transactions, JIM, **37**(1996), 299-303.
6. F. Ono, M. Asano, R. Tanaka, and S. Endo, " Magnetization Measurements in an Invar alloy under High Pressure, " J. Magn. Magn. Mater., **90,91**(1990), 737-739.
7. T. Kakeshita, T. Yamamoto, K. Shimizu, S. Nakamichi, S. Endo, and F. Ono, " Composition Dependence of Martensitic Transformations in Fe-Ni Invar Alloys under Hydrostatic Pressures, " Materials Transactions, JIM, **36**(1995), 483-489.
8. L. Kaufman: referred to Doctor Thesis by M. Korenko, MIT, Cambridge, USA, (1973), p.72.

FORMATION OF REVERSED AUSTENITE FROM $M_{23}C_6$ TYPE CARBIDE IN HIGH CHROMIUM MARTENSITIC STEEL

T.Tsuchiyama and S.Takaki

Department of Materials Science and Engineering, Faculty of Engineering,
Kyushu University, Fukuoka 812-8581, Japan.

Abstract

Formation of reversed austenite from $M_{23}C_6$ type carbide has been examined in 12%Cr martensitic steels with transmission electron microscope in terms of crystallographic orientation relationship among three phases of austenite, martensite, and $M_{23}C_6$. In a tempered condition, $M_{23}C_6$ particles disperse with a K-S relationship to bcc matrix, and have a same variant to the matrix within one martensite block. When the steel is annealed at above A_1 point, austenite nucleates on the interface of $M_{23}C_6$ carbide particles and the matrix. The reversed austenite also has the K-S relationship to the bcc matrix, while it has a cube-cube relationship to $M_{23}C_6$ carbide. Due to the regulation of three-phase crystallographic relationship, only one variant is allowed for the nucleation of reversed austenite, and this leads to the formation of the same variant group of austenite within one martensite block. As a result, a group of reversed austenite grains with the same variant coalesce and grow to a large grain just after the complete reversion.

The Third Pacific Rim International Conference on
Advanced Materials and Processing (PRICM 3)
Edited by M.A. Imam, R. DeNale, S. Hanada,
Z. Zhong and D.N. Lee
The Minerals, Metals & Materials Society, 1998

Introduction

High chromium martensitic steels are widely used for structural materials applied to chemical and power plants, because they possess not only good corrosion resistance and heat resistance but also high strength. Addition of carbon to the steels is very effective for further strengthening, however, impact toughness of the steels is markedly reduced with increase of the carbon content. Refining of martensitic structure is effective for toughening of the steels, so many kinds of thermomechanical treatments [1] or alloy designing techniques [2] have been tried for refining of microstructure and austenite grains. Authors have investigated the effect of Partial Solution (PS) treatment on the microstructure of Fe-12%Cr-C alloys for toughening of high chromium martensitic steels [3][4]. PS treatment means the re-solution treatment in the two-phase region of austenite and carbide ($M_{23}C_6$) . PS treatment of tempered martensitic steels results in refining of austenite grain size through the grain boundary pinning effect by finely dispersed carbide particles. But it was difficult to make the grain size fine below 10μm, even if the volume fraction of carbide is increased enough and the diameter of particles is controlled as small as possible. This is related to the coalescence of austenite grains which nucleate on the interface of $M_{23}C_6$ carbide particles during $\alpha' \rightarrow \gamma$ reversion. For the further refining of austenite grain size, it is important to make the reversion mechanism clear. In this study, formation behavior of reversed austenite was examined in 12%Cr steels by means of transmission electron microscopy, and the growth mechanism of reversed austenite was discussed in terms of crystallographic orientation relationship among three phases of austenite, martensite, and $M_{23}C_6$.

Experimental Procedure

Chemical compositions of the steels used are shown in **Table** I . Steel A (12%Cr-0.3%C) is a representative commercial martensitic stainless steel, while steel B (12%Cr-4%Ni-0.1%C) is designed as follows: (1) It has full martensitic structure at room temperature and (2) austenite nuclei can retain after partial reversion of martensite. Ingots of 30kg were prepared by vacuum melting, homogenized at 1523K for 18ks, and then formed to 10mm thick plates through forging and hot-rolling at 1473K. The steels were once subjected to the full solution (FS) treatment at 1523K for 1.8ks in Ar gas atmosphere, followed by water-quenching and sub-zero treatment at 77K for 0.6ks. Tempering was carried out below A_1 temperature; at 1073K in the steel A and at 773K in the steel B, to disperse carbide particles ($M_{23}C_6$) within martensite matrix. In the steel B, reversed austenite was formed through annealing at a selected temperature between 883K and 1023K. Microstructures were observed with optical and transmission electron microscopes (TEM). The volume fraction of austenite was mesuredm by a magnetic method [5].

Table I Chemical compositions of steels used. (mass%)

steels	C	Si	Mn	P	S	Cr	Ni
A	0.281	0.24	0.47	0.023	0.005	12.30	<0.01
B	0.096	0.28	0.49	0.025	0.003	12.52	4.02

Results and discussion

Crystallographic characteristic of $M_{23}C_6$ type carbide in tempered martensite

Figure 1 shows an optical micrograph of the steel A which was water-quenched after FS treatment of 1423K-1.8ks. The microstructure is the typical lath martensite characterized by the structures of packets or blocks [1] in the prior austenite grains. Retained austenite and insoluble carbide were not observed in the as-quenched specimen. **Figure 2** represents TEM micrographs and a diffraction pattern of the $M_{23}C_6$ type carbide particles in the specimen tempered at 1073K for 10.8ks after the FS treatment. In the bright field image (a), black particles are $M_{23}C_6$ carbide and are observed to precipitate along lath boundaries. The diffraction pattern (b) indicates that $M_{23}C_6$ carbide has a K-S relationship to martensite matrix described as follows:

$(110)_\alpha \,//\, (111)_{M_{23}C_6}$

$[1\bar{1}1]_\alpha \,//\, [10\bar{1}]_{M_{23}C_6}$

The dark field image (b) is obtained from one of {220} diffraction spots. All of carbide particles in (b) satisfy a diffraction condition, that is, this means they have the same crystallographic

orientation (variant). Many observation reveals the fact that carbide particles within one martensite block have the same variant. It was also confirmed in the steel B.

† 1: The packet consists of parallel laths with the same habit plane and is subdivided into several blocks. Each block is made up of martensite laths having essentially the same variant [6].

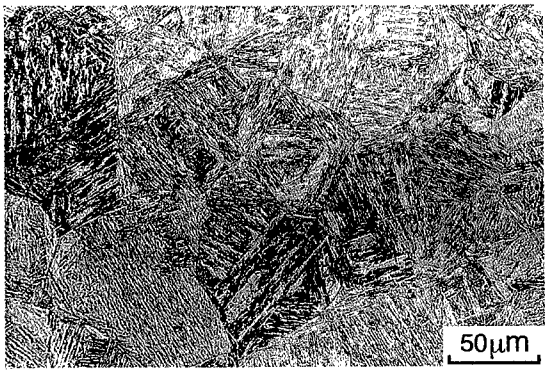


Figure 1: Optical micrograph of martensitic structure in steel A. Water-quenched after FS treatment of 1423K-1.8ks.

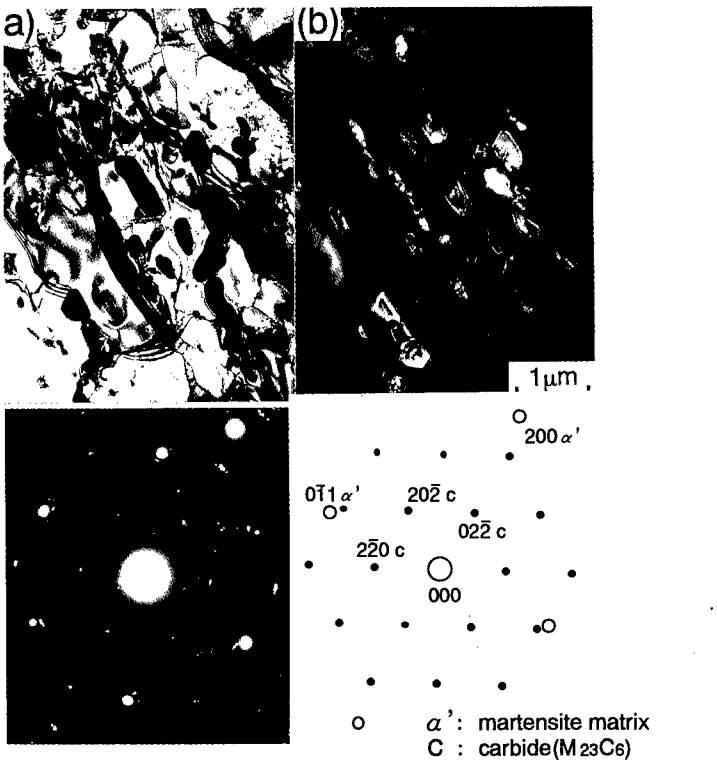


Figure 2: Transmission electron micrographs; bright field image (a) and dark field image (b), diffraction pattern and its key diagram in steel B. Tempered at 1073K for 10.8ks after the FS treatment.

Nucleation behavior of reversed austenite in tempered martensite

Figure 3 represents TEM micrographs of the steel B annealed at 883K for 3.6ks after the tempering. Reversed austenite nucleates along lath boundaries. The amount of reversed austenite was measured at about 3 vol.%, and the size of austenite grains is about 0.2μm in diameter under the annealing condition. It is found that reversed austenite grains also have the same variant within one martensite block. Such a crystallographic characteristic is just like that of carbide particles in the tempered martensite (Figure 2). **Figure 4** shows a magnified micrograph of reversed austenite grains. Reversed austenite grains are just on $M_{23}C_6$ particles. This indicates that austenite preferentially nucleates on the $M_{23}C_6$/martensite-matrix interface. Reversed austenite is surely easy to nucleate at the interface, because dissolved carbide provide a high concentration of carbon near the interface [7]. It should be noted here that subgrain boundary is observed at interface of reversed austenite grains. The subgrain boundary should be formed by the collision of reversed austenite grains of the same variant. **Figure 5** is a diffraction pattern and its key diagram showing the crystallographic orientation relationship among reversed austenite, $M_{23}C_6$ carbide, and martensite matrix. Reversed austenite has a K-S relationship to the bcc matrix, while it has a cube-cube relationship to $M_{23}C_6$ carbide. A K-S relationship is also held between $M_{23}C_6$ and martensite matrix as shown in Figure 2, so that the orientation

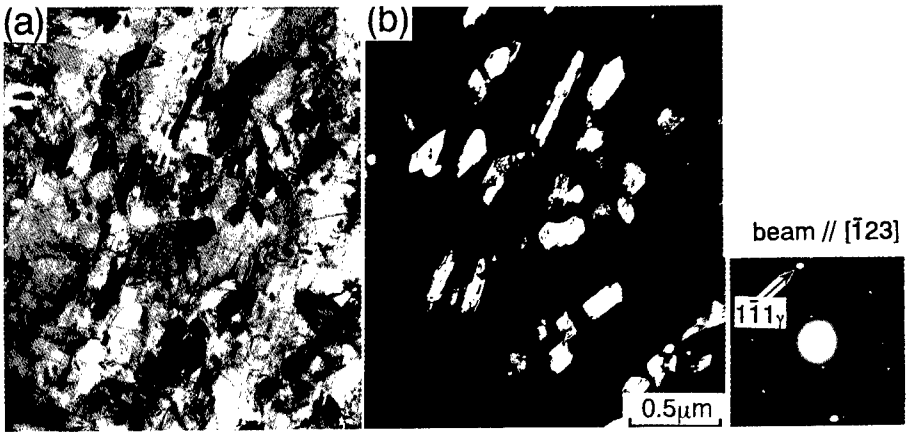


Figure 3: Transmission electron micrographs of steel B annealed at 883K for 3.6ks after the tempering; bright field image (a) and dark field image obtained by the arrowed spot in the diffraction pattern.

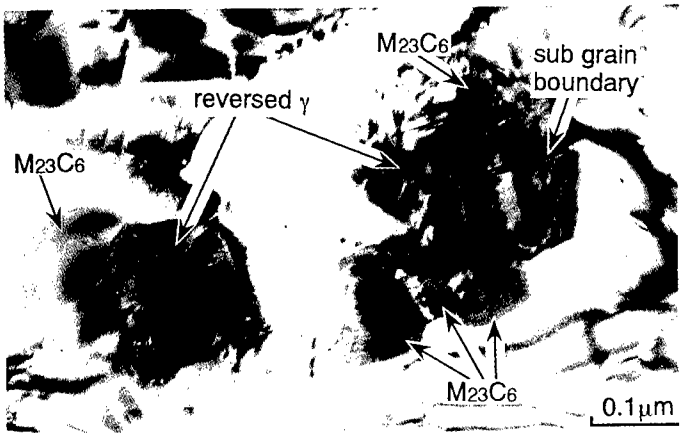


Figure 4: Transmission electron micrograph of steel B annealed at 903K for 3.6ks.

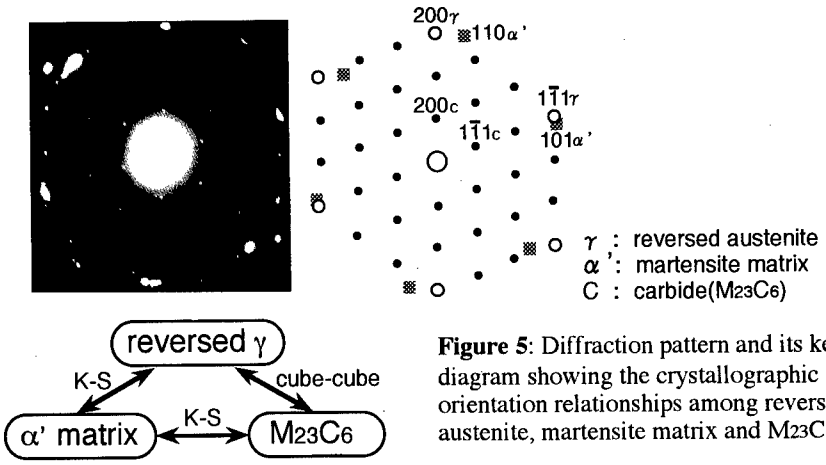


Figure 5: Diffraction pattern and its key diagram showing the crystallographic orientation relationships among reversed austenite, martensite matrix and $M_{23}C_6$.

relationships among these three phases are expressed as follows:

$(1\bar{1}1)_\gamma // (101)_\alpha // (1\bar{1}1)_{M_{23}C_6}$

$[110]_\gamma // [111]_\alpha // [110]_{M_{23}C_6}$

Selectivity of variants has already been discussed in consideration of the crystallographic orientation relationship between reversed austenite and martensite matrix in low carbon steels [7][8]. However, in the case that austenite nucleates at the interface of carbide and matrix, the crystallographic orientation of the austenite must be restricted by that of the carbide. As a result, the nucleation of only a single variant of austenite is allowed within one martensite block where all carbide particles have a same variant.

Grain growth through coalescence of reversed austenite of the same variant

When austenite grains of the same variant collide each other, subgrain boundary should be formed between the grains as already shown in Figure 4, and they shortly coalesce and form one large austenite grain. **Figure 6** shows an optical micrograph of steel B annealed at 1023K for 3.6ks. Over-etched black structure is martensite matrix, while white one is reversed austenite. Reversed austenite grows to the longitudinal direction of prior martensite blocks through the coalescence of reversed austenite grains. **Figure 7** represents a schematic illustration showing

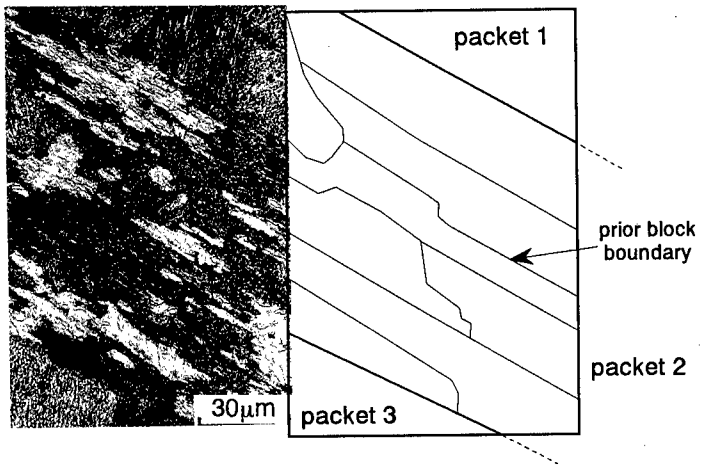


Figure 6: Optical micrograph of steel B annealed at 1023K for 3.6ks: Showing reversed austenite grains which has nucleated within prior martensite blocks.

the mechanism of reversion of martensite containing $M_{23}C_6$ carbide particles. Carbide particles are formed on lath boundaries in a single variant within one martensite block (a). Reversed austenite nucleates on the $M_{23}C_6$/martensite-matrix interface. All of austenite within one martensite block has also a same variant due to the restriction of the three-phase orientation relationships (b). The austenite grains with a same variant coalesce each other and an abrupt grain growth takes place just after the complete reversion (c).

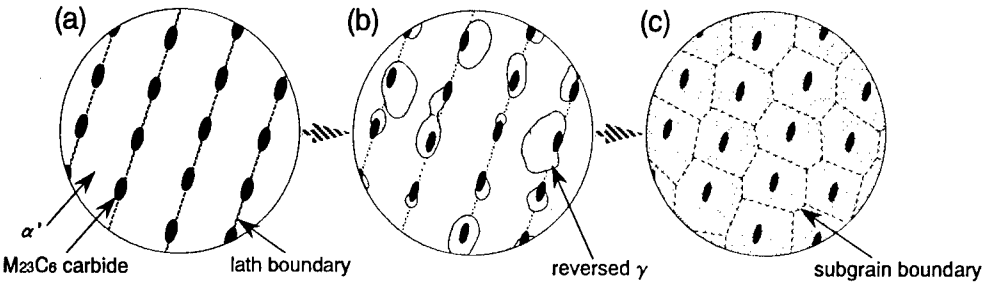


Figure 7: Schematic illustration showing the structural during reversion in martensitic stainless steels containing $M_{23}C_6$ carbide particles. (Microstructure within a martensite block)

Conclusions

Formation of reversed austenite from $M_{23}C_6$ type carbide was examined in 12%Cr martensitic steels with transmission electron microscope in terms of crystallographic orientation relationship among three phases of austenite, martensite, and $M_{23}C_6$. The results obtained are as follows:

(1) $M_{23}C_6$ type carbide precipitates along martensite lath boundaries with a K-S relationship to martensite matrix in a tempered condition. The carbide particles are of a single variant within one martensite block.

(2) Reversed austenite nucleates on the $M_{23}C_6$/martensite-matrix interface, and the orientation relationships among reversed austenite, $M_{23}C_6$ carbide, and martensite matrix are expressed as follows:

$(1\bar{1}1)_\gamma // (101)_\alpha // (1\bar{1}1)_{M_{23}C_6}$

$[110]_\gamma // [111]_\alpha // [110]_{M_{23}C_6}$

(3) Due to the three-phase crystallographic orientation relationship, a group of reversed austenite with a same variant is formed within one martensite block. They collide and coalesce each other during the reversion, and this leads to a formation of large grain just after the complete reversion.

References

1. Y.Hosoi and K.E.Pinnow, "The Tensile Properties of Type 410 Stainless Steel Deformed Before and after Mrtensite Transformation" , Transactions of the ASM, 53 (1961), 591

2. H.D.Kim and I.S.Kim, " Effect of Austenitizing Temperature on Microstructure and Mechanical Properties of 12%Cr Steels" , ISIJ International, 34 (1994), 198-204

3. T.Tsuchiyama, S.Takaki and S.Nakamura, " Austenite Grain Size Control by Insoluble Carbide in Martensitic Stainless Steels" , *Tetsu-to-Hagané*, 81 (1995), 147-152

4. T.Tsuchiyama and S.Takaki, "Microstructure Control of a High Carbon Martensitic Stainless Steel by Partial Solution Treatment" (Paper presented at THERMEC'97, Wollongong, Australia, July 7-11, 1997), 203-208

5. S.Takaki, Y.Tokunaga and K.Tomimura, "Quantitative Analysis of Stainless Steels by means of Saturation Magnetization Measurement" , *Tetsu-to-Hagané*, 73 (1987), S539.

6. T.Maki, K.Tsuzaki and I.Tamura, "The Morphology of Microstructure Composed of Lath Martensites in Steels" , Transactions ISIJ, 20 (1980), 207-214

7. S.Watanabe, Y.Ohmori and T.Kunitake, "Formation of Austenite from lath-like Martensite" (Paper presented at First JIM International Symposium on " New Aspects of Martensitic Transformation" , Kobe, Japan, May 10-12, 1976), 369-374

8. J.I.Kim, C.K.SYN and J.W.Morris,Jr., " Microstructural sources of Toughness in QLT-Treated 5.5Ni Cryogenetic Steel" , Metallurgical Transactions, 14A (1983), 93-103

SIMULATION OF MARTENSITIC TRANSFORMATION IN Fe-Ni ALLOYS

Tetsuro Suzuki* and Masato Shimono **

*Tsukuba Institute of Science and Technology
1601 Kamitakatsu, Tsuchiura 300-0811, JAPAN
**National Research Institute for Metals
1-2-1Sengen, Tsukuba 305-0047, JAPAN

Abstract

Simulation study of the martensitic transformation in Fe-Ni alloys based on the EAM potential is carried out by use of two entirely different but mutually complementing methods. One is the calculation of the change of the cohesive energy of Fe-Ni alloys during the idealized and fictitious mode of the transformation where all atoms in alloys are displaced strictly uniformly and simultaneously. For this mode of the martensitic transformation, the saddle point energy between FCC and BCC turns out to be equal for four different mechanisms: those by Bain, by Kurdjumow and Sachs, by Frank and by Bogers and Burgers. The other is the simulation study of the martensitic transformation in nanocrystals. Since the martensitic transformation in nanocrystal with less than 1000 atoms is dominated by the surface tension, it certainly shows entirely different features from those of bulk alloys. But it also shows a common one in the temperature dependent incubation time, though at very limited range of temperature.

The Third Pacific Rim International Conference on
Advanced Materials and Processing (PRICM 3)
Edited by M.A. Imam, R. DeNale, S. Hanada,
Z. Zhong and D.N. Lee
The Minerals, Metals & Materials Society, 1998

1.Introduction

The martensitic transformation involves both macroscopic and microscopic aspects. Phase boundaries between austenite and martensite extend in macroscopic scale. At the same time, many experimental data on the close relationship between the microscopic crystal structure and the phonon-dispersion relationship are being accumulated. Because of this characteristic of the martensitic transformation that extends over different ranges of scales, it has remained to be a difficult task to find an effective systematic method to study the macroscopic and microscopic aspects from one unified point of view.

The present study based on the Embedded Atom Method (EAM) initiated by Daw and Baskes is carried out as an attempt in this direction. Since the interatomic potentials used in EAM contains several parameters which must be adjusted to reproduce fundamental macroscopic properties of metals under investigation, such as cohesive energy , elastic moduli and heat of solution in alloys, they can be used a reliable and convenient tool to study the close relationship between the microscopic and macroscopic aspects of the martensitic transformation.

The EAM potential developed by Oh and Johnson (1) and applied to the study of the martensitic transformation in Fe-Ni alloy Grujicic and Dang (2) is adopted as a basis of the present study. They have shown the importance of the boundary condition on the nucleation of the martensite. However, there still remains a problem why and how this crucial role of the boundary condition comes about. As an attempt to solve it using the same EAM potential with limited computer resources, the martensitic transformation in two highly idealized conditions is studied.

First is the calculation of the change of the cohesive energy during the fictitious martensitic transformation process in which all atoms obey the same translation strictly simultaneously. Although the almost simultaneous motion of many atoms is the basic feature of the martensitic transformation, all atoms cannot participate in exactly the same motion in actual martensitic transformation.

Second is the molecular dynamic study of the martensitic transformation in nanocrystals, which contains atoms less than the order of 10000. Systematic study on the dependence of the number of atoms and the shape of nanocrystals on the martensitic transformation offers a means to know the macroscopic crystals by extrapolation.

2.Change of the cohesive energy in the martensitic transformation

2.1 Transient Lattice by Bain Mechanism

First, the change of cohesive energy of Fe is calculated as a lattice is deformed from FCC to BCC according the mechanism by Bain while the volume of the lattice per atom is strictly kept constant. This deformation mechanism can be expressed as transformation of coordinates of atoms in the lattice according to the followings:

$$\begin{aligned} x' &= x(1+\varepsilon), \\ y' &= y(1+\varepsilon), \\ z' &= z/(1+\varepsilon)^2. \end{aligned} \qquad (1)$$

Here, x,y and z are the coordinates of atoms in the original FCC lattice, and x',y' and z' are the ones in the transient lattice. When $\varepsilon = 0$, they represent FCC lattice. When $\varepsilon = \sqrt[6]{2} - 1 \approx 0.1225$, they represent BCC lattice. Figure 1 shows change of cohesive energy as a function of ε. The

minimum at left corresponds to FCC lattice and the one on the right to BCC lattice. While the volume per atom is strictly conserved during the deformation expressed by Eq.(1), it is well known that Fe actually shows decrease of volume per atom by 3% on the martensitic transformation from fcc to BCC. If the cohesive energy is calculated for the volume that gives the minimum for each of transient lattices, its change gives more stability for BCC lattice. This indicates the qualitative validity for the effective interaction potential used by Grujicic and Dang (2) and in the present investigation.

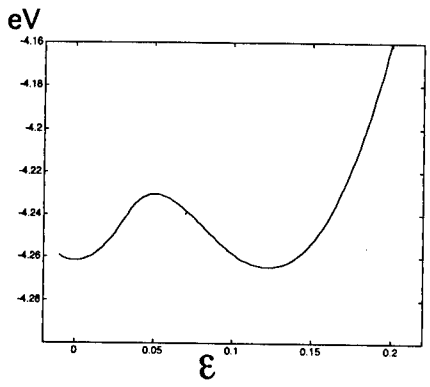


Figure 1: Change of the cohesive energy in the Bain mechanism, when the volume per atom is kept constant. The ordinates the cohesive energy in unit of eV as a function of the Bain deformation parameter ε in the abscissa.

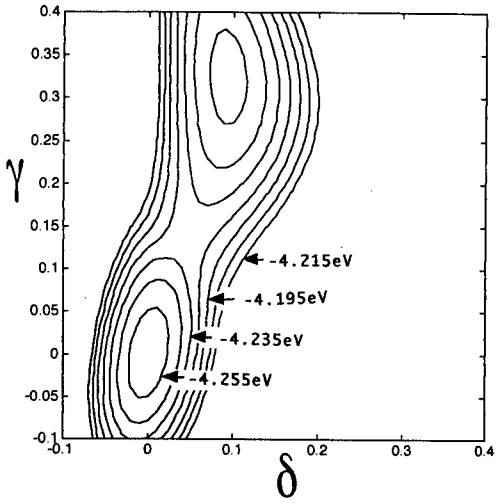


Figure 2: Contour map of cohesive energy as a function of the double shear deformation Parameters, γ and δ.

2.2 Transient Lattice by K-S Mechanism

Next, comparison of the cohesive energy for the transient lattices according to the double shear mechanism by Kurdjumow and Sachs with that according to Bain mechanism is carried out. The double shear considered in this mechanism is given by : $[\bar{2}\,1\,\bar{1}]_f(11\,\bar{1})_f$ (γ) and $[10\,\bar{1}]_f(\bar{1}\,21)_f$ (δ).

The calculation of cohesive energy during the double shear is carried out assuming that both of the shear deformation represent the shear deformation in the strict sense of the word. In other words, when slip planes slide over another in the slip direction, the distance between the slip planes is kept strictly constant. After the calculation of cohesive energy as a function of the magnitude of the first shear deformation γ and the second shear deformation δ, it is found that the cohesive energy does not come close the value of BCC for any combination of γ and δ. While the first shear in the K-S mechanism brings the stacking sequence of the close-packed planes of FCC into that of BCC, while the function of the second shear is to adjust the difference between the close-packed plane of FCC and that of BCC. With a minor extension in the definition of the second shear deformation δ, the cohesive energy is calculated as a function of γ and δ and is shown as an energy contour map in Fig.2. Here, the contour lines are drawn starting for the cohesive energy value of −4.255 eV with steps of 0.01 eV up to -4.195eV. While the minimum at $\gamma = 0$ and $\delta = 0$ represents the cohesive energy of FCC, the minimum of the cohesive energy, -4.262 eV , around the value of $\gamma = 0.32$ and $\delta = 0.09$ is -4.259 eV,

which is not equal but close to -4.265 eV ,the value of BCC shown in Fig.1. If additional small adjustment of the distance between $(11\overline{1})_f$ planes of 1.3% is introduced, the minimum of the cohesive energy around $\gamma = 0.32$ and $\delta = 0.09$ becomes equal to that obtained from the Bain deformation in Fig.1. Furthermore, it is to be noticed that the saddle point energy in the contour map in Fig.2 is equal to the maximum energy of -4.231 eV between FCC and BCC minima in the Bain deformation shown in Fig.1. The results of similar calculation carried out for the double shear mechanism by Frank and also for the double shear mechanism by Bogers and Burgers indicate that the saddle point energy between FCC and BCC minima turns out equal to that in the Bain mechanism.

Although the present authors have not be able to prove it rigorously, there may be a mathematical theorem that all different microscopic mechanisms for the martensitic transformation should involve the barrier energy of the same height, if all atoms in a crystal were allowed to transform strictly uniformly. Highly non-uniform stress field in the austenite surrounding nuclei must be playing a crucial role in controlling the microscopic mechanism of the martensitic transformation.

3.Martensitic transformation in nanocrystals

Because the straightforward simulation of the system with more than 10000 atoms is impractical, the use of the periodic boundary condition has been established as the standard procedure to in the molecular dynamics with limited computer resources. However, the previous works by Grujicic and Dang(2) and also by Shao,Clapp and Rifkin(3) have shown that the application of the standard periodic boundary leads to the absence of the martensitic transformation. This indicates clearly that it is not allowed to adopt the standard periodic boundary condition to study the martensitic transformation in crystals of macroscopic size. On the other hand, it is not difficult nowadays to carry out the molecular dynamics of nanocrystals which contains 2000 or less atoms. Although the results of the simulation in nanocrystals should be quantitatively different from those in crystals of macroscopic size, the systematic study of the dependence on the size of nanocrystals is expected to shed light on how the martensitic transformation is affected by such factors as the size, the external shape of the crystal, thermal fluctuations and lattice defects.

All the present simulation results of the martensitic transformation are obtained from the standard molecular dynamics procedures. The initial FCC Fe-Ni nanocrystals configuration is obtained by minimizing the EAM cohesive energy for given Ni concentration with respect to FCC lattice constant. In the next step, this strictly geometrical initial configuration is modified by small random deviation from equilibrium, which serves as a source of thermal lattice vibrations. The amount of the total energy associated with the thermal vibration is scaled to desired temperature at every 10 molecular dynamic integration steps. The surface relaxation that must be especially important in nanocrystals is incorporated in this step of the molecular dynamic procedure at constant temperature.

The numerical results from the above molecular dynamic calculation on nanocrystals are analyzed by use of three means. One is the visualization software called RasMol distributed on http://www.umass.edu/microbio/rasmol/. This allows us to see how the external shape of nanocrystals changes with the evolution of the coordinates of atoms according to the molecular dynamics. Second is a radial distribution function. Distances between all atoms in nanocrystals are calculated and converted into a graph of radial distribution function. Third is a graph which plots the change of cohesive energy in nanocrystal with respect to time. In the followings, the results on nanocrystals of pure Fe are presented by use of these means, except where the change

of the concentration of Ni leads to an entirely different result.

3.1 Time and size dependence at fixed temperature 65 K.

The results of molecular dynamic study at 65 K of FCC nanocrystal of cubic shape with three different sizes are compared. The radial distribution of a cubic nanocrystal with 363 atoms and one divacancy in the center in the initial states shown in Fig.3(a) and that of the same nanocrystal after 6000 integration steps (about 1.2×10^{-8} sec) is shown in Fig.3(b). The external shape of the nanocrystals with these radial distribution as obtained by use of RasMol is included in Fig.3(a) and Fig.3(b). These indicates that the transformation from FCC to BCC or to a structure, which is closely related to BCC, is judged to have taken place. The progress of this transformation process in this nancocrystal with 61 atoms and one divacancy is monitored by plotting the change of the total cohesive energy as a function of integration time steps as shown in Fig.4(a). Similar plot of the cohesive energy vs. integration time step for nanocrystal with 363 atoms is shown in Fig.4(b). In a nanocrystal with 1097 at 65 K does not show any sign of structural change up to 18000 integration steps (3.6×10^{-8} sec) . These results show that the time necessary for the transformation , i.e. incubation time, increases with the size of a nanocrystal.

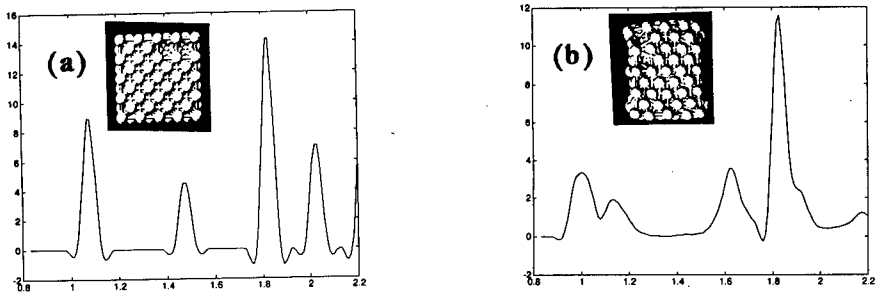


Figure 3: Radial distribution in a nanocrystals with 363 atoms and their external shape as obtained by use of RasMol. (a) Initial State and (b) after 1.2×10^{-8} sec.

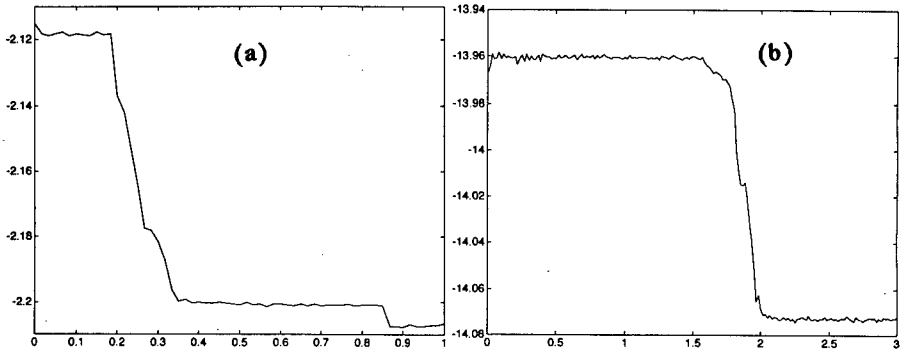


Figure 4:The change of cohesive energy In nanocrystals with time in nanocrystals with (a) 61 atoms and (b) 363 atoms. The total cohesive energy of nanocrystals is indicated in unit of 100 eV. The time scale is unit of 1.2×10^{-8} sec.

3.2 Temperature dependence at fixed size

In a nanocrystal with 363 atoms, incubation time at three different temperature, 55 K, 65 K and 80 K, are compared as shown in Table 1 . This indicates that the incubation time decreases with increase of temperature, i.e., with increase of thermal fluctuation This is considered to corresponds to the lower part of the time-temperature-transformation (TTT) curve. The decrease of the incubation time of the incubation ime associated with the upper part of the TTT curve has not yet been found in the investigation of the martensitic transformation in a nanocrystal with this range of size.

Table 1 Temperature Dependence of Incubation Time in a Nanocrystal with 363 atoms.

Temperature	Incubation Time in unit of 10^{-8} sec
55 K	3.83
65 K	2.40
80 K	1.44

3.3 Effect of alloying:pure Fe vs. Fe-40%Ni.

The absence of the upper part of the TTT curve leads us to suspect that the driving force for the transformation is not dominated by volume dependent free energy but by the surface tension particular to nanocrystals. This is substantiated by carrying out similar numerical experiment for a nanocrystals with atoms 61 atoms with Fe-40%Ni alloy instead of pure Fe. Fe-40%Ni alloy is stable with respect to FCC configuration and is not metastable with respect to BCC configuration. In this Fe-40%Ni alloy, although the change in the external shape takes place from the cube shape to rounded shape, the structure remained FCC .This is found to be the case in nanocrystals up to the range of crystals with atoms of the order of 1000.

In nanocrystal of cube shape or thin sheet with atoms less than 1000, the driving force to change its external shape with smaller surface area, i.e. surface tension, is found to be dominant over the volume dependent free energy. Still it is serving as the "force" for the structural transformation if the nature of the interatomic potential allows the presence of the configuration with lower cohesive energy. The question about the size of nanocrystal where the volume dependent free energy become at least comparable to the surface tension still remains to be investigated. The results obtained up to the present seem to indicates that this critical number of atoms is not appreciably larger than 1000, which is accessible by the computer simulation.

Acknowledgement

One of the authors, T.S, wishes to thank Professor K. Otsuka for his illuminating discussions. We wish to thank Dr. S. Kajiwara for discussions on the transformation mechanism. The work reported here is supported by Grant-in-Aid Research on Priority Area of Phase Transformations from the Ministry of Education, Science and Culture of Japan.

References

(1) R.A.Johnson and D.J.Oh,"Analytic embedded atom method for bcc metals,"J. Mater.Res. 4 (1989), 1195-1201.
(2) M. Grujicic and P. Dang, "Computer simulation of martensitic transformation in Fe-Ni face-centered cubic alloys," Mater. Sci. Eng. A201(1955),194-204.
(3) Y.Shao, P.C.Clapp and J.A.Rifkin,"Molecular Dynamics Simulation of Martensitic Transformation in NiAl," Met. Materials Trans. 27A(1996),1477-1489.

Twin Interface Structures in Martensitically Transformed γ_1'Cu-Al-Ni and γ_2'Au-Cd Alloys

Toru HARA*, Takuya OHBA* and Kazuhiro OTSUKA**

Department of Materials Science and Engineering, Teikyo University,
Utsunomiya, Tochigi 320, Japan
** Institute of Materials Science, University of Tsukuba,
Tsukuba, Ibaraki 305, Japan

Abstract

Twin interface structures in thermoelastic martensite are studied. Type II twin interface structure, which is introduced as a lattice invariant shear in Cu-Al-Ni, is revealed by the observation of high resolution electron microscopy and the consideration of twin interface unit model. Type II twin interface does not consist of ledge and step that has been believed. There is a transition area from matrix to twin with thickness caused by the atomic displacements around the interface.

The Third Pacific Rim International Conference on
Advanced Materials and Processing (PRICM 3)
Edited by M.A. Imam, R. DeNale, S. Hanada,
Z. Zhong and D.N. Lee
The Minerals, Metals & Materials Society, 1998

Introduction

Twinning plays very important role in the thermoelastic transformed martensite. Many kinds of elastic interactions can be considered to introduce deformation twins in martensite. Among them, the most important twinning in martensite is the twins introduced as a lattice invariant shear. Deformation twins are usually classified into three types geometrically. They are type I, type II and compound twin. This classification is characterized by the five twinning elements by the Bilby-Crocker's twinning theory[1]. Each twinning mode has following geometrical features. Type I is a mirror twin with respect to the twin plane (K_1) which has the rational index. On the other hand, type II twin is a rotation twin whose rotation axis is the shear direction (η_1) which has the rational index. K_1 of type II is indicated by irrational index. Compound twin has both features of mirror and rotation, and the indices of twinning elements are all rational. In the case of the typical thermoelastic martensitic transformations, such as Cu-Al-Ni and Ti-Ni alloy, type II twin is introduced as the lattice invariant shear. Therefore, to clarify the interface structure of type II twin is essentially important to understand the transformation and the deformation mechanisms. Although there are several researches on the twin interface in martensite, type II twin interface structure has not been clearly understood. The main reason is that the interface is described as the irrational index macroscopically. Christian and Crocker [2] interpreted this irrational twin plane by rational facets parallel to the η_1 direction. Knowles[3] observed type II twin interface in TiNi martensite by high resolution electron microscopy (HREM) and suggested the interface is consist of ledges and steps with the low index rational planes as proposed by Christian and Crocker. Although he discussed the relationship between a possible facet structure and its projected images, there was no discussion on the atomic configuration. It is hard to say that we understand type II twin interface structure clearly.
In this paper, we will discuss the twin interface structures, including type II twin, mainly for γ_1' Cu-Al-Ni martensite. First, we will propose interface unit models, that derived from HREM observations. Second, we will discuss the interface structure. Thus, we will show that the model can be applied to other system, γ_2'Au-Cd martensite.

Experimental

Single crystals of $\{110\}_{\beta 1}$ Cu-Al-Ni were prepared to observe type II twin along its characteristic directions of type II twin in γ_1'Cu-Al-Ni martensite. Orientation of this single crystal was chosen from the consideration of the lattice correspondence between the parent and martensite phases. The detail of this consideration is written in ref. 4. Specimens for HREM observations were made by electro-polishing with using solution of CrO_4+H_3PO_4.
For the observations of γ_2'Au-Cd martensite, polycrystallne samples were used. The detail of these observations were written in ref. 5.

Results and Discussions

HREM Observations of type II twin in γ_1'Cu-Al-Ni Martensite

Conventional TEM (CTEM) observation of type II twin has been reported in ref. 4. Type II twin interface shows a clear contrast which observed along η_1 direction (Fig. 9 of ref. 4). This straight contrast of interface is considered due to the strain field around the interface. To study the interface structure microscopically, it is necessary to observe it by using HREM. HREM observations were carried for type II twin interface from many directions. Figure 1 shows the HREM observation which is the intersecting point of type I and type II twin. In this figure, 'Matrix' and 'Type I', and 'Matrix' and 'Type II' relate type I and type II twin, respectively. This

was observed along $[111]_{\gamma 1}$' direction for each crystals. For type II twin, $[111]_{\gamma 1}$' is the unique direction, that is, the rotation axis (η_1) of the twin. $[111]_{\gamma 1}$' direction is the only one direction where both twin interfaces are placed edge-on condition simultaneously. Although the lattice fringes are continuous through type II twin interface, the strain contrast around the interface were observed. This contrast is due to the strain field as observed by CTEM. Observations of type II twin interface along various directions, including Fig. 1, show no ledge and step contrast. In these observation, we can conclude that type II twin interface in γ_1'Cu-Al-Ni does not consist of the 'large size' ledge and step. The term 'large size' means the width of ledge and step are larger than several atomic layers such as 1nm. If the width of ledge is large enough to recognize as a plane, it should be observed even in this lattice image. This means that if type II twin interface was assumed to be ledge and step, it should be the 'small' one.

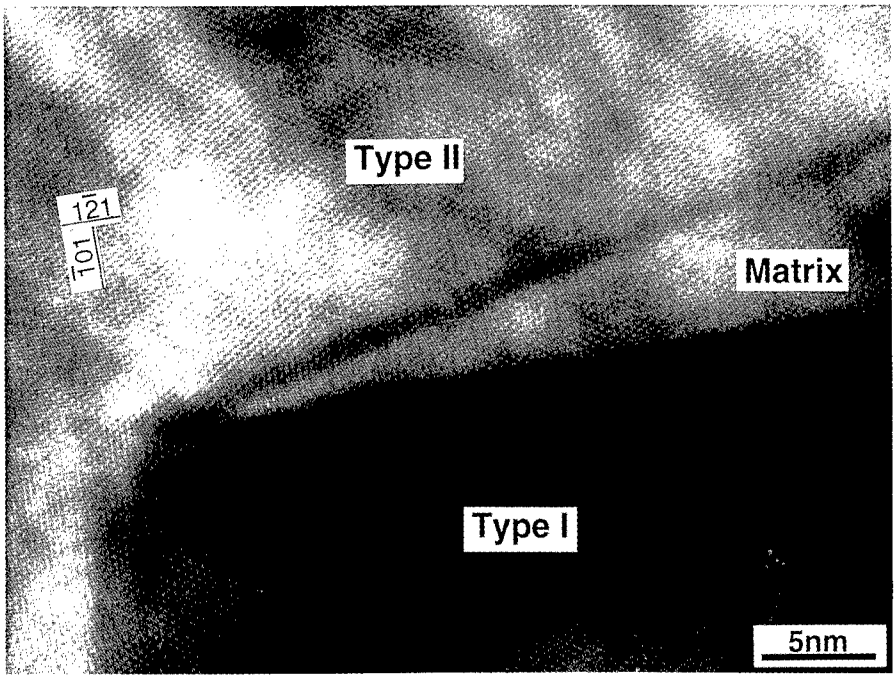


Fig. 1. Lattice image of type I and type II twin interface in γ_1'Cu-Al-Ni martensite. Incident beam is parallel to $[\bar{1}\bar{1}\bar{1}]_M$, $[\bar{1}\bar{1}\bar{1}]_I$ and $[111]_{II}$ for matrix, type I and type II twin. This is η_1 direction for type II twin. See text for details.

Interface unit models

γ_1'Cu-Al-Ni martensite has 2H(2O) type orthorhombic unit cell. The lattice constants are a=0.4382, b=0.5356 and c=0.4222 nm[5]. In this case, Al atoms are located on the corner and near body-center (1/3, 1/2, 1/2) of this unit cell. The important thing is that the lengths of a- and c-axes are close to each other. Twinning elements for type I and type II twin is shown in Table 1.

Table 1. Twinning elements of γ_1'Cu-Al-Ni martensite.[6]

	K_1	η_1	K_2	η_2	s
Type I twin	{121}	$<\bar{1},0.7954,\overline{0.5907}>$	$\{\bar{1},1.5036,\overline{0.5036}\}$	<111>	0.261
Type II twin	$\{\bar{1},1.5036,\overline{0.5036}\}$	<111>	{121}	$<\bar{1},0.7954,\overline{0.5907}>$	0.261

From the consideration of the orientation relationships for each type of twins and HREM observations, following interface 'unit' models shown in Fig. 2 are proposed. Figure 2(a), (b) indicate those models for type I and type II twin, respectively. In these figures, only Al atoms are drawn for simplicity. In each figure, unit cell indicated 'Twin' (lower side in this figure) is twin related with respect to 'Matrix' (upper side) with required orientation. These twin unit models can be summarized as Fig. 2(c). These interface unit model has following features : (i) Al atoms on the twin plane, indicated Al1 in Fig. 2(c), is common for both matrix and twin. This is consistent with HREM observations. (ii) Al atom at the center in the unit cell for matrix, indicated Al2 in Fig. 2(c), corresponds to the atoms at the corner of twin unit. In Fig. 2(c), when L1 in twin becomes a axis, these two crystals relate type I twin, and when L2 becomes a axis, these relate type II twin. Because of the lengths of 'a' and 'c' are close to each other, type I and type II twin can be made by small difference.

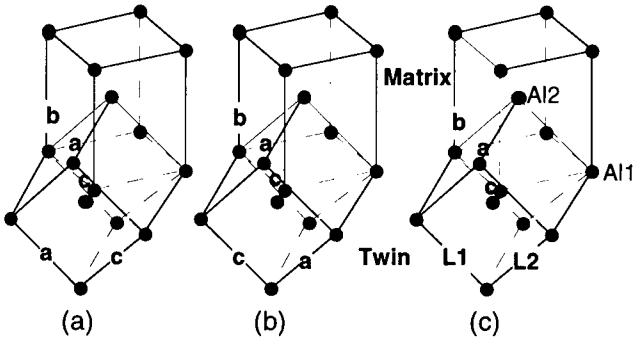


Fig. 2 Twin interface 'unit' models for type I(a) and type II(b) for γ_1'Cu-Al-Ni martensite. (c) is summarized illustration to explain both twins. Only Al atoms are drawn for simplicity.

Twin interface models

Twin interfaces can be described as the combination of above 'unit' models. For type I twin, interface can be made by putting these units (Fig. 2(a)) side by side. This interface is shown in Fig. 3(a). It is clearly shown that this interface is a mirror plane that is required for type I twin. In case of type II twin, interface is rather complex because it has irrational index macroscopically. Figure 3(b) shows one of the interface structure model is for type II twin. The characteristic points of this model are as follows : (i) Ledge and step planes are assumed as $(\bar{1}10)_{\gamma 1'}$ and $(0\bar{1}1)_{\gamma 1'}$, respectively. (ii) The widths of ledge and step are two and one atomic layer for each plane so that this interface becomes $(2\bar{3}1)_{\gamma 1'}$ macroscopically which was 0.11 degree apart from calculated irrational twin plane. (iii) These step and ledge should be introduced irregularly to make an irrational plane. Based on the above type II twin interface model, arrangement of atoms can be considered. From the HREM observations, as described in the previous section, ledge and step should not be so large. 'Small' ledge and step, such as Fig. 3(b), should be considered. Considering these 'small' ledge and step, atomic displacements were necessary around twin interface to place atoms stable. In Fig. 2(b), for example, Al atom indicated as Al1 should not be placed at the right position of matrix nor twin. It should be located at the distorted position from both matrix and twin crystals. As the results of these distortions, 'small' ledge and step are no longer the clear interface planes. This model need a small displacement and produce the strain field around the interface. It is consistent with CTEM and HREM observations. In conclusion, the structure of type II twin interface is considered that the interface does not consist of clear ledge and step plane. Atoms are gradually move from their right positions of matrix to those of twin crystal.

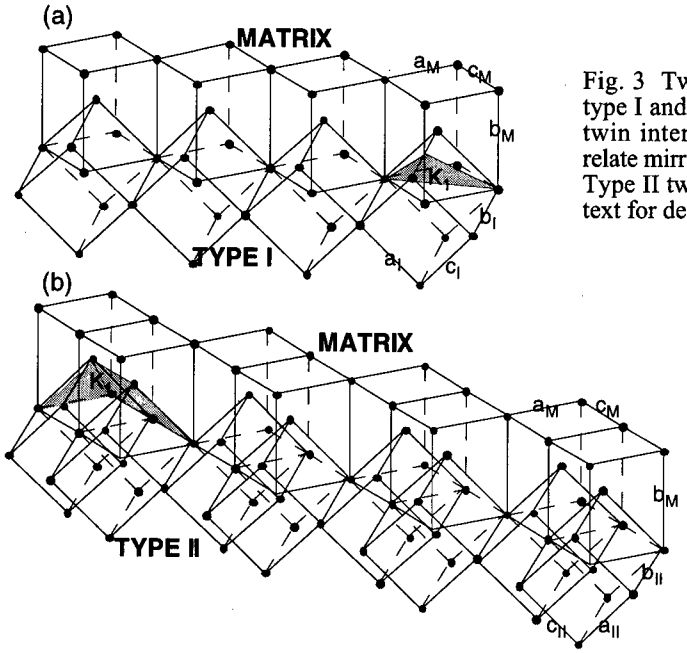


Fig. 3 Twin interface models for type I and type II twin. (a) Type I twin interface. Matrix and twin relate mirror with respect to K_1. (b) Type II twin interface model. See text for details.

Type II Twin Interface in γ_2' Au-Cd Martensite

Type II twin interface in γ_2'Au-Cd martensite was also observed by using HREM. They were reported in ref. 7, and there was no contrast caused by ledge and step observed. Structure of type II twin interface in this alloy is also considered as well as that of Cu-Al-Ni martensite. Twin interface 'unit' models can be applied to those of Cu-Al-Ni in the same way. They are shown in Fig. 4. In these figure, (a) and (b) indicate type I and type II, respectively. In this figure, Cd atom at the corner of the matrix unit cell (Cd1) is common for matrix and twin. On the other hand, Cd

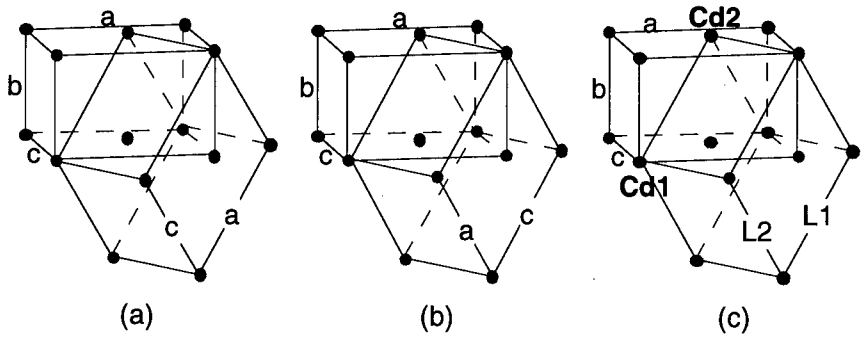


Fig. 4 Twin interface 'unit' models for γ_2'Au-Cd martensite. These unit models can be considered as the same way as those of γ_1'Cu-Al-Ni. (a) Type I twin, (b) Type II twin. (c) Schematic illustration to describe both type I and type II twin.

atom near B-center (Cd2 in Fig. 4(c)) also plays a role of the corner of twin unit cell, which correspond to the nearly body-center atom for Cu-Al-Ni case (Al2 in Fig. 2(c)). Figure 4(c) is a schematic illustration of twins in this alloy. When L1 becomes a-axis of twin, 'Twin' is related type I to 'Matrix', and when L2 becomes a-axis, these are related type II twin. Because of the lengths of 'a' (0.4859nm) and 'c' (0.4766nm) are close to each other, it is possible to exist these two kinds of twins.

Recently, Nishida et al.[8] reported HREM study of type II twin interface structure in Ti-Ni monoclinic martensite. According to them, ledge and step contrast was not observed. Their results suggest that the interface does not consists of ledge and step like γ_1'Cu-Al-Ni. Although there is a difference whether the crystal is monoclinic or orthorhombic, interface 'unit' model can be considered as the same way essentially.

Acknowledgment

The authors are grateful to Dr. M. Nishida and Prof. T. Suzuki for useful discussions. They also wish to thank Dr. Y. Bando for allowing us to use TEM. The present work was partly supported by the Grant-in-Aid for Scientific Research on Priority Areas from Ministry of Education, Science and Culture, Japan.

References

1. B.A.Bilby and A.G.Crocker, "The theory of the crystallography of deformation twinning," Proc. Roy. Soc., London, Ser. A,288(1965),240
2. J.W.Christian and A.G.Crocker, "Dislocation Theory: A Collective Treatise, F.R.N.Nabarro, ed. (Amsterdam : North Holland,1980), Vol. 3.
3. K.M.Knowles, "A High-resolution Electron Microscope Study of Nickel-Titanium Martensite," Phil. Mag. A, 45, (1982), 357-370
4. T.Hara, T.Ohba, S.Miyazaki and K.Otsuka, "Electron Microscopy Study of Type II twins in γ_1'Cu-Al-Ni Martensite," Mater. Trans. JIM., 33, (1992), 1105-1113
5. K.Otsuka and K.Shimizu, "Morphology and Crystallography of Thermoelastic Cu-Al-Ni Martensite Analyzed by the Phenomenological Theory," Trans. JIM., 151974),103
6. S.Ichinose, Y.Funatsu and K.Otsuka, "Type II Deformation Twinning in γ_1' Martensite in a Cu-Al-Ni Alloy," Acta metall., 33,(1985), 1613-1620
7. T.Hara, T.Ohba, K.Otsuka, Y.Bando and S.Nenno, "High Resolution Electron Microscopy Observations of Twin Interfaces in γ_1'Cu-Al-Ni and γ_2'Au-Cd Martensite," Proc. ICOMAT (Inter'l. Conf. on Martensitic Transformations) '92, (1992) 257-262
8. M.Nishida, K.Yamauchi, I.Itai, H.Ohgi and A.Chiba, "Electron Microscopy Studies of Twin Morphologies in B19' Martensite in the Ti-Ni Shape Memory Alloy," Acta metall. mater., 43, (1995), 1229-1234

QUANTITATIVE EVALUATION OF THE RUBBER EFFECT AND STABILIZATION OF THE MARTENSITIC PHASE IN COPPER ALLOYS

K.Marukawa and K.Tsuchiya*

Dept. of Applied Physics, Hokkaido University, Sapporo 060-8628, Japan
*Dept. of Production Systems Engineering, Toyohashi University of Technology
Toyohashi 441-8580, Japan

Abstract

In copper alloys, a change in atomic arrangements affects the martensitic transformation in various ways. In a previous paper, it has been pointed out that the so-called rubber effect and stabilization of the martensitic phase are caused by short range reordering of solute atoms during aging. Based on this model, quantitative evaluation of these effects was performed by means of theoretical calculations utilizing the cluster variation method and Monte Carlo method. It was found that the rubber effect is prominent when the aging temperature is just above the order-disorder transition temperature of the martensite phase. It is also shown that disordering or lowering in the long range order parameter of the martensite phase causes the stabilization. The tendency of stabilization can be assessed in terms of two parameters, i.e., the effective quenching temperature from the parent phase and the aging temperature in the martensite.

The Third Pacific Rim International Conference on
Advanced Materials and Processing (PRICM 3)
Edited by M.A. Imam, R. DeNale, S. Hanada,
Z. Zhong and D.N. Lee
The Minerals, Metals & Materials Society, 1998

Introduction

The rubber effect is a kind of pseudo-elasticity, which is associated exclusively with a martensite phase. The effect develops by aging at rather low temperatures near the room temperature in the martensite phase [1]. It was first found in Au-Cd alloy, and thereafter in other alloys, such as Cu-Al-Ni, Au-Cu-Zn, In-Tl and also Cu-Zn-Al [2,3,4,5]. Although this effect has been studied for many years, still there is no general agreement on its atomic mechanism. Recently the important role of short-range ordering of atomic arrangements to induce this effect has been pointed out by the present authors [4]. The stabilization of martensites is another aging effect, which is also brought about by aging in the martensite phase [6]. This phenomenon is hazardous on application of shape memory materials, for it results in an unwanted rise in the transformation temperature of the material. A close correlation in kinetics between the rubber effect and the stabilization has been found in Cu-Zn-Al alloy [5]. Therefore, the cause of the stabilization should be closely related to the mechanism of the rubber effect. In the present study, a unified view on the origin of these two phenomena is presented. Numerical calculations based on thermodynamics and statistical mechanics are also given to support the view.

Theoretical Background

Both these effects manifest themselves only after aging in the martensite state. In the case of the rubber effect, the pseudoelasticity is due to the tendency that variants of the martensite newly formed by stressing are reoriented to original variants on unloading. If all variants restore the original states, the specimen restores the original shape. Since variants are crystallographically all equivalent, at the first glance, it seems that the cause is difficult to be found. However, variants are not quite equivalent in their energy states with each other. It is quite reasonable to assume that the aging brings about a small modification on the atomic arrangements so that the energy states of original variants are changed to those with a lower energy. Then the system must be lifted to a higher energy state by stressing, for variants are changed from original ones to those having higher energies. This higher energy state is the origin of the restoring force of the rubber effect. There are two kinds of modification in atomic arrangements, i.e., the one in the long range order and the other in the short range order. The present authors [4] pointed out that the modification in the long range order is not adequate for the cause of the rubber effect, because the two variants related to each other on stressing have the same value of the degree of long range order, i.e., the average occupation probability at each site remains the same on the change of variants. Therefore, the most plausible cause of the effect is the modification in the short range order during aging.

Historically, other causes have been assumed for the effect. One is a kind of boundary effect, in which interfaces of variants are considered to be modified, so that boundaries moved by stressing resume the original positions after unloading. This type of models are inconsistent with the experimental facts that a crystal composed of a single variant also exhibits the effect. A classical model [7], assuming a temporary structure just after transformation, is neither appropriate, because it cannot explain the time dependence of strength of the effect during aging. It also contradicts with recent experiments [8], in which the structure after the transformation has been determined precisely. Recently, a version of the short range order model has been presented [9]. We believe that the present model is more complete in the sense that it can be used for quantitative evaluation of the effect.

Discussion on the stabilization effect in the past is in a similar situation to the case of the rubber effect. For example, a model invoking boundary modification for the cause cannot explain the occurrence of the effect in specimens having no boundary [10]. A bulk effect or modification in atomic arrangements due to aging seems the only possible cause for the effect.

The Model

We have presented a new model to explain the rubber effect and the stabilization effect elsewhere [4]. Here we describe the model in a more complete form. In the model both effects are considered as bulk effects, i.e., both have their origins in the free energy change of the materials, caused by configurational change due to aging. To evaluate the free energy, we assume a binary alloy composed of two components A and B. The enthalpy of the alloy can be expressed as the sum of pair interactions between nearby atoms, We are concerned with only the enthalpy term because the vibrational entropy can be taken as constant on atomic rearrangements during aging. We consider the B2 ordered structure as the parent phase, and the $L1_0$ ordered structure for the martensite. The latter is assumed to be transformed martensitically from the former by the Bain distortion. Discussion is focused on these particular structures, but the conclusion to be obtained should be applicable for other structures as well. The outlook of these effects are given by the next illustrations.

Figure 1 shows the B2 structure projected onto its (010) plane and the $L1_0$ structure projected onto the (110) plane. Both structure have two kind of sublattice sites, a and b, which are discriminated by different symbols in the figure and occupied mainly by A and B atoms, respectively. Generally, the occupation probability, say P_{aA}, and the pair probability on neighboring sites, say P_{AB}, do not take their equilibrium values. Especially, just after the martensitic transformation from B2 to $L1_0$ structure, they may be far from the equilibrium. Aging may bring the system to the equilibrium. This results in changes in the long range order and the short range order. Only the latter is important in the rubber effect, but both affects the stabilization effect. The feature of the change in the short range order can be seen in the figure. The probability of AB pairs on site pairs located near the origin, say site pairs between the site 0 and its twelve nearest neighbors, may increase by aging to lower the internal energy of the

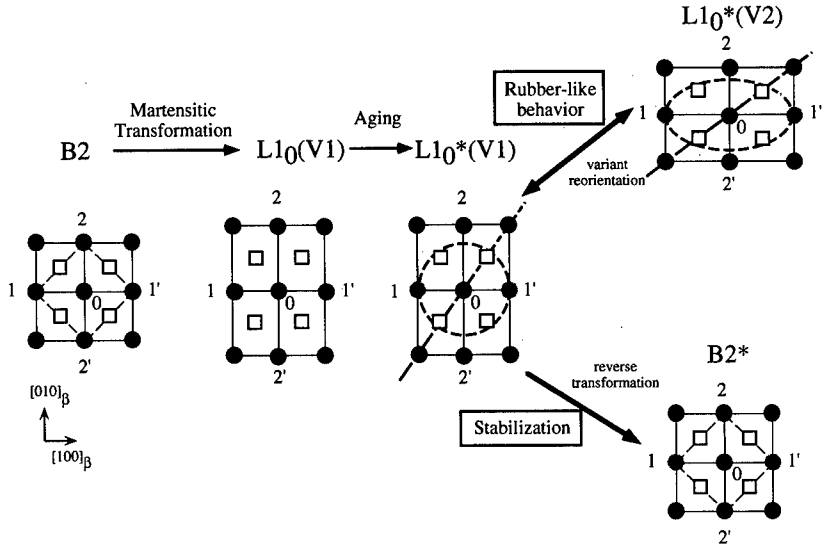


Figure 1. Atomic arrangements in the parent phase (B2) and in the martensite ($L1_0$). The circles and squares denote a and b sites, respectively. Solid and open symbols indicate that the sites are occupied mainly by A and B atoms, respectively. Structure modification caused by aging is denoted by stars. Two variants (V1 and V2) with different axes are related with each other by the reorientation on stressing.

system. On stressing, the original martensite variant (variant 1) is transformed to variant 2. Some site pairs situated at nearest neighbor positions (pair 01 and 01') are now situated at 2nd nearest neighbor positions and conversely some other site pairs (02 and 02') are changed from 2nd nearest pairs to 1st nearest ones. Since 2nd nearest pairs have a lower probability of AB pairs, the total probability of AB pairs decreases on this change, so that the stressing results in the increase in the internal energy of the system. This higher energy state provides the restoring force of the rubber effect after relaxing the stress.

The stabilization of martensites is caused by the same kind of configurational change as the rubber effect, but the situation is a little more complicated, because two phases, i.e., the parent and martensite are concerned with it. The configurational change may result in lowering of the internal energy of the martensite, but at the same time it may lower the energy of the parent phase which would be transformed from the modified martensite. Either stabilization or destabilization is possible depending on which energy change dominates. As stated earlier, both changes in the long range order and the short range order may have an influence in the case of stabilization.

Based on this model, a quantitative estimation of the effects can be made. Since the enthalpy of the system is expressed as the sum of pair interaction energies of near neighbor pairs, the enthalpy difference between the two variant (V1 and V2 in Fig.1) is given by

$$\Delta H_r = F_1(P_{2s}^* - P_{1s}^*) \tag{1}$$

where F_1 is the pair exchange energy in the $L1_0$ lattice. In the martensite ($L1_0$) lattice, only nearest neighbor interactions are taken into account. P_{1s} is the probability of AB pairs on like-site pairs (aa or bb) located at 1st near neighbors and P_{2s} the probability of AB pairs on like-site pairs located at 2nd near neighbors. Stars represent values after aging. The restoring force of the rubber effect is given by $\Delta H_r = \Theta\tau\gamma$, where Θ is the appropriate geometrical factor, and τ and γ are the stress and the strain associated with the variant change, which is twice of the transformation strain.

Four enthalpies are associated with the stabilization. These are the one of the parent phase H(B2) and of the martensite $H(L1_0)$, and those modified by aging H(B2)* and $H(L1_0)^*$:

$$H(B2) = H_\beta + 4E_1P_{1d} + 3E_2P_{2s} \tag{2}$$
$$H(B2)^* = H_\beta + 4E_1P_{1d}^* + 2E_2P_{1s}^* + E_2P_{2s}^* \tag{3}$$
$$H(L1_0) = H_\alpha + 4F_1P_{1d} + 2F_1P_{2s} \tag{4}$$
$$H(L1_0)^* = H_\alpha + 4F_1P_{1d}^* + 2F_1P_{1s}^* \tag{5}$$

where the first terms are temperature dependent contributions from pure elements, and E_1 and E_2 are the exchange energies of the 1st and 2nd nearest bonds in the parent phase. Interactions are limited to the 2nd nearest neighbors in the parent lattice. P_{1d} is the probability of AB pairs located on unlike-site pairs (ab or ba). The martensitic transformation temperatures T_0 and T_0^* before and after aging are given by

$$\Delta H = H(B2) - H(L1_0) = S_{\alpha\beta}T_0 \tag{6}$$
$$\Delta H^* = H(B2)^* - H(L1_0)^* = S_{\alpha\beta}T_0^* \tag{6'}$$

where $S_{\alpha\beta}$ is the transformation entropy. These equations contain an unknown term ($H_\beta - H_\alpha$), but it is canceled out when we consider the change in the transformation temperature ($T_0^* - T_0$) due to aging. It is set to zero in the following. Remaining terms contain pair probabilities, related to the short range order. Note that long range order parameters do not appear explicitly in these equations. It affects the stabilization only through short range order parameters. Thus, the next task we need is to estimate pair probabilities in the parent and martensite phases precisely.

Results of Numerical Calculations

The most rough estimation of pair probabilities may be made by Bragg-Williams approximation, in which pair probabilities are expressed simply by the long range order parameter. This approximation, however, fails to predict the rubber effect. Therefore, we need a more accurate method. Here we have adopted two method, the Monte Carlo method [11] and the cluster variation method, the former of which has been found to be more convenient for the present purpose. The method is excellent for evaluation of a transient state such as a state just after the martensitic transformation, but it is also applicable for the estimation of equilibrium values. Especially it is advantageous to find probabilities on distant site pairs. To obtain pair probabilities, B2 lattice is first constructed in a computer. The lattice is commonly used for $L1_0$ lattice because the topological nature is the same in these two lattices. Two atoms in nearest neighbor positions of the lattice are randomly chosen and exchanged under a prescribed condition determined by statistical mechanics. The equilibrium is judged by observing behaviors of each probabilities during numbers of exchanges. Details of the method will be described elsewhere, but exchange energies assumed were E_1=-477.5k, E_2=-267.5k, and F_1=-290k [12], where k is Boltzmann's constant. The atomic fraction of solute atoms was c=0.45.

Figure 2 shows the calculated pair probabilities and the long range order parameter in fcc and $L1_0$ lattice as a function of aging temperature T_a. The order-disorder transition occurs at T_c. The difference between P_{1s} and P_{2s} is directly proportional to the strength of the rubber effect, as shown in eq.(1). As can be seen, the rubber effect is most prominent at a temperature just above the critical temperature of long range order. Therefore, it can be deduced that disordered alloys should show the rubber effect more clearly if they transform martensitically.

Figure 3 shows the differences between enthalpies of two phases, where ΔH has been calculated on the atomic configuration equilibrated in bcc or B2 lattice, and ΔH^* in fcc or $L1_0$ lattice. They are given as a function of the quenching temperature T_q and the aging temperature T_a, respectively. A reduced temperature scale is used. It is to be noted that the enthalpy difference increases with these temperatures. This means that the transformation temperature, given by eq.(6), rises when the system becomes more disordered. Generally, these two temperatures are different with each other, and the sign of the change in T_0 by aging, i.e. the difference between ΔH and ΔH^*, depends on these temperatures. In usual cases, we expect a rise in T_0 by aging, since the aging temperature is effectively higher than the quenching temperature because of a low value of the order-disorder transition temperature T_c in the martensite. However, the actual value of T_0 change is dependent on individual situations of experiments.

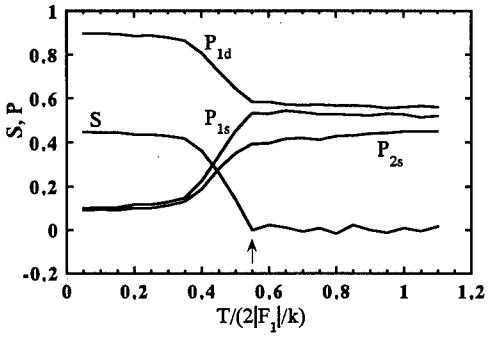


Figure 2. Probabilities of AB pairs on various site bonds, P_{1d}, P_{1s} and P_{2s}, and the long range order, S, in aged martensites as a function of aging temperature. The arrow indicates the critical temperature T_c for the long range order.

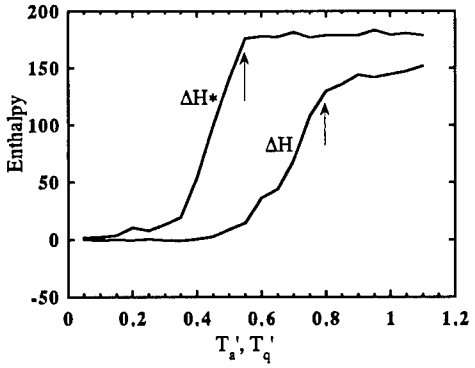


Figure 3. Differences between enthalpies (in the unit of k) of two phases before aging (ΔH) and after aging (ΔH^*). They are related to the transformation temperature by eq.(6). Reduced temperatures, $T_q'=T/(2|E_1|/k)$ and $T_a'=T/(2|F_1|/k)$ are used. Arrows indicate the critical temperatures for the long range order.

In conclusion, equations (1) and (6) should be useful for evaluation of the rubber effect and the stabilization effect, respectively. The numerical calculations have shown the overall dependence of these effects on the aging temperature and other factors.

References

1. K.Otsuka and C.M.Wayman, "Pseudoelasticity and stress-induced martensitic transformations", Review of Progress in the Deformation Behavior of Materials, vol.2, (Freund, Tel-Aviv, 1977), 81-172.
2. G.Barcelo, R.Rapacioli and M. Ahlers, "The rubber effect in Cu-Zn-Al martensite", Scripta Metall., 12(1978), 1069-1074.
3. M.Ahlers, G.Barcelo and R.Rapacioli, "A model for the rubber-like behavior in Cu-Zn-Al martensites", Scripta Metall., 12(1978), 1075-1078.
4. K.Marukawa and K.Tsuchiya, "Short-range ordering as the cause of the rubber-like behavior in alloy martensites", Scripta Metall. Mater., 32(1995), 77-82.
5. K.Tsuchiya, K.Tateyama, K.Sugino and K.Marukawa, "Effect of aging on the rubber-like behavior in Cu-Zn-Al martensites", Scripta Metall. Mater., 32(1995), 259-264.
6. M.Ahlers, "The stabilization of martensite in Cu-Zn-Al alloys", Proc. Inter. Conf. on Martensitic Transformations, (1986), 786-793.
7. D.S.Lieberman, M.A.Schmerling and R.W.Karz, "Ferroelastic memory and mechanical properties in gold-cadmium", Shape Memory Effects in Alloys , (Plenum Press, New York, 1975), 203-244.
8. T.Ohba, K.Otsuka and S.Sasaki, "Study of rubber-like behavior in a Au-47.5at%Cd alloy by synchrotron orbital radiation", Mater. Sci. Forum, 56-58(1990), 317-322.
9. X.Ren and K.Otsuka, "Origin of rubber-like behavior in metal alloys", Nature 389(6651) (1997), 579-582.
10. A.Abu Arab and M.Ahlers, "The stabilization of martensite in Cu-Zn-Al alloys, Acta Metall., 36(1988), 2627-2638.
11. U.Gahn and W.Pitsch, "Cross over effect of single phase short range ordered alloys", Acta Metall., 37(1989), 391-396.
12. T.Y.Hsu and Z.Xiaowang, "Thermodynamics of the martensitic transformation in Cu-Zn alloys", Acta Metall., 37(1989), 3091-3094.

INFLUENCE OF LONG RANGE ORDERING ON MARTENSITIC TRANSFORMATION IN Ag-Zn-Al ALLOYS

K. Takezawa, H. Hoshi and K. Marukawa

Department of Applied Physics, Hokkaido University,
Sapporo, 060-8628, Japan

Abstract

The effect of long range ordering on the martensitic transformation temperature was examined mainly by means of electrical resistivity measurements in Ag-Zn-Al alloys having a composition near Ag_2(Zn, Al). The disordered state of the high temperature β phase (bcc structure) is frozen by quenching to room temperature. The β phase is transformed to the martensite phase by cooling below room temperature. The transformation temperature changes to a lower level by aging at a temperature between 253 and 293K. The lowering accompanies a decrease in the residual resistivity. This indicates that atomic ordering proceeds by aging. The ordered structure was examined by electron microscopy and found to be the $C11_b$ structure. The relation between the change of the reverse transformation temperature, ΔA_f, and the degree of order, ϕ, was obtained as $|\Delta A_f| = 1140\phi^2$. It was concluded that the long range ordering affects remarkably the martensitic transformation temperature.

The Third Pacific Rim International Conference on
Advanced Materials and Processing (PRICM 3)
Edited by M.A. Imam, R. DeNale, S. Hanada,
Z. Zhong and D.N. Lee
The Minerals, Metals & Materials Society, 1998

Introduction

The effect of long range ordering on the behavior of martensitic transformation has been noted in several materials. It is well known that in Fe-Pt alloys[1,2] the transformation behavior changes from burst type to thermo-elastic one and the martensitic transformation temperature, Ms, becomes lower as long range ordering of austenite proceeds. In noble metal based shape memory alloys, however, since the parent phase has a fairly complete order structure of B2 or $L2_1$ type after quenching[3], the degree of order can not be changed largely by heat-treatments. For this reason, there are only a few studies on the relation between the degree of order and the Ms temperature[4,5]. If alloys in which the degree of order can be controlled easily by quenching and aging are available, the relation between the Ms temperature and the degree of order may be studied more precisely.

We have paid attention to natures of the ordering reaction and the martensitic transformation in Ag based alloys. In Ag-Zn alloy, the thermo-elastic martensite forms only in the case of a low Zn content, e.g. 38at%Zn[6,7]. The critical temperature for ordering from the bcc to the B2 structure, Tc=370K[8], is relatively low in comparison with other noble metal based alloys. However, the ordering reaction can not be interrupted by quenching to room temperature. In Ag-Al alloys, the Ms temperature is rather high in the composition range of which an electron atom ratio is near 1.4[9], and the ordered phase has not been recognized at room temperature[10]. Therefore, alloys having low Tc and high Ms may be expected by adding Al atoms to Ag-Zn alloys. Actually, we have found that in Ag-Zn-Al ternary alloys the degree of order can be controlled by heat-treatment and that the martensitic transformation takes place at relatively high temperature. In this study, (1) the ordered structure of this alloy and (2) the relation between the degree of order and the transformation temperature are examined.

Experimental Procedure

Ingots of Ag-22.3at%Zn-9.8at%Al alloy were made by melting high purity materials in quartz capsules filled with argon gas under 1/3 atm at 1273K for 6h. They were then homogenized at 953K. Thin plate specimens were obtained from those ingots by hot-forging, hot- and cold-rolling to 0.25 mm in thickness. They were cut to $40\times2\times0.25$ mm^3 size for electrical resistivity measurements and to $20\times5\times0.25$ mm^3 size for observations by transmission electron microscopy (TEM) and optical microscopy (OM). These specimens were heated at 1003K for 300s to obtain the β phase (bcc structure) and then quenched into water. In order to establish the disordered state, specimens were heated at 353K for 30s and quenched into liquid nitrogen before measurements or observations. Hereafter, specimens treated by the above procedure are called "disordered specimens" and those not treated are "as-quenched specimens".

Measurements of electrical resistivity were performed by a DC four-probe method. Disordered specimens were given thermal cycles including an aging treatment at a temperature, Ta, for an aging time, ta. The effective aging time after n times of cycles is n×ta.

Specimens for transmission electron microscopic observations were thinned by jet polishing with HNO_3 solution and by final electropolishing in H_3PO_4 solution. Heating-cooling stages were used both for TEM and OM observations.

Results and Discussion

Figure 1 shows the resistivity change when an as-quenched specimen was cooled and heated continuously at a rate about 0.3K/s in the order as indicated by arrows . The measurement started at room temperature at 1.2ks after quenching. The resistivity value did not show any signs of phase transformation during cooling to the liquid nitrogen temperature and heating to the room temperature. However, the resistivity remarkably increased by heating to 340K. This change is due to disordering reaction, which was recognized by in situ TEM observations. When the specimen was cooled after heating to 380K, the resistivity decreased linearly until 140K without a change in its gradient. This means that the disordered state is frozen at a cooling

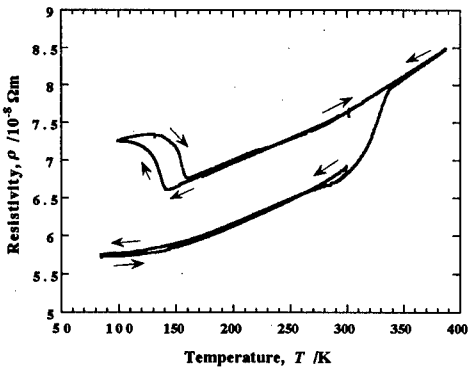


Fig. 1 Resistivity change of an as-quenched specimen during cooling and heating treatment.

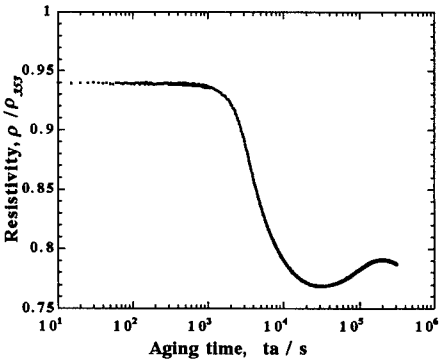


Fig. 2 Resistivity change of a disordered specimen during aging at 303K.

rate of 0.3K/s. A large change in resistivity was observed between 100 and 140K in both cooling and heating run. These large resistivity changes were attributed to an appearance and a disappearance of thermo-elastic martensite. This was confirmed by OM observations. The crystal structure of martensite was determined as the disordered 9R structure by in situ TEM observations. From these facts, it was concluded that the martensite forms from disordered specimens but not from ordered ones in this alloy. Figure 2 shows the resistivity change of a "disordered specimen" which was aged at 303K. The value of resistivity is normalized by the initial value at 353K. The resistivity begins to decrease after about 1ks and reaches the minimum value after about 30ks, which corresponds to a decrease by about 17% from the value at the disordered state. Subsequently, resistivity raises again, takes the maximum value at about 200ks later and then decreases. Therefore, it is noticed that the aging treatment brings about successive two stages of phase transition in this alloy.

The ordered structure of the parent phase was examined by analysis of electron diffraction patterns. Fig. 3(a) shows a diffraction pattern taken from an as-quenched specimen in which the first stage ordering takes place already. This pattern is indexed as [100] zone pattern in bcc based coordinates. Extra spots are recognized at n/3 positions of (002) spot, so that the structure must have a unit cell with a three times period along the [001] direction of bcc structure. As the result of analysis, this structure was determined as the $C11_b$ structure[11] which has the unit cell

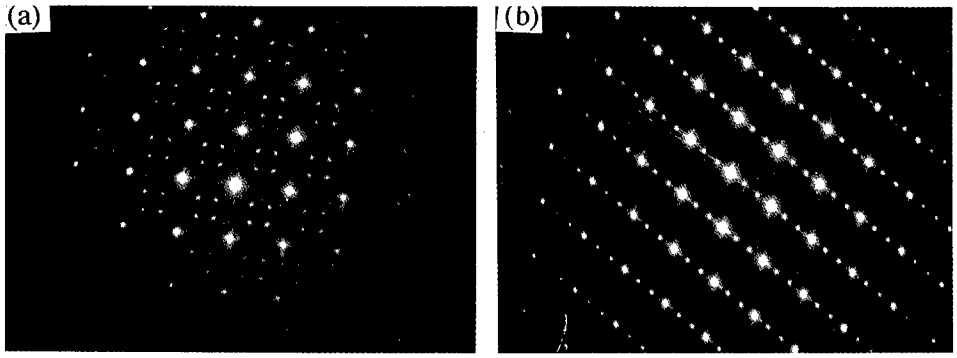


Fig. 3 Electron diffraction patterns. (a) [100] zone pattern from an as-quenched specimen and (b) [111] zone pattern from an aged specimen.

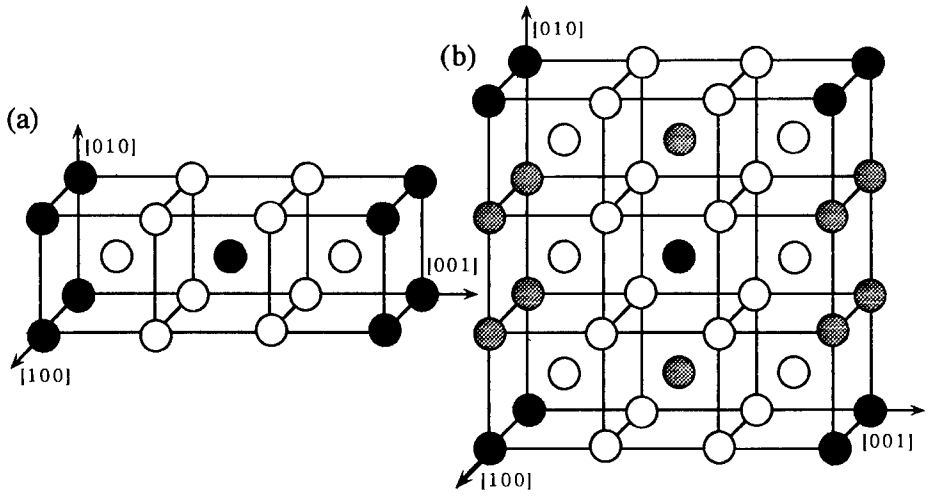


Fig.4 Unit cells of ordered structures in Ag-Zn-Al alloy. (a) $C11_b$ structure , ● : Zn or Al , ○ : Ag and (b) $C11_b$* structure, ● : Al , ● : Zn, ○ : Ag.

shown in Fig. 4 (a). Fig. 3 (b) is a diffraction pattern taken from a specimen aged at room temperature for 11Ms, which is indexed as [111] zone pattern with bcc-based axes. Extra spots are recognized also at n/3 positions of {110}spots in addition to super-lattice spots of the $C11_b$ structure. Experiments by tilting revealed that these diffraction patterns are explained as the ordered structure shown in Fig. 4 (b), which we call C11b* structure. This unit cell has a three times period along [010] as well as [001] of bcc structure. The ordered structure of Fig.4 (b) may be formed by ordering at the second stage. Thermal cycles including aging treatment at Ta=283K for ta=7.2 ks were done six times. Fig.5 shows resistivity changes at each cycle during heating from the liquid nitrogen temperature, where the resistivity is normalized to the value at 353K. The reverse transformation finish temperatures, A_f , were obtained from resistivity curves. The A_f temperature decreased at every cycle from the value of the first cycle,

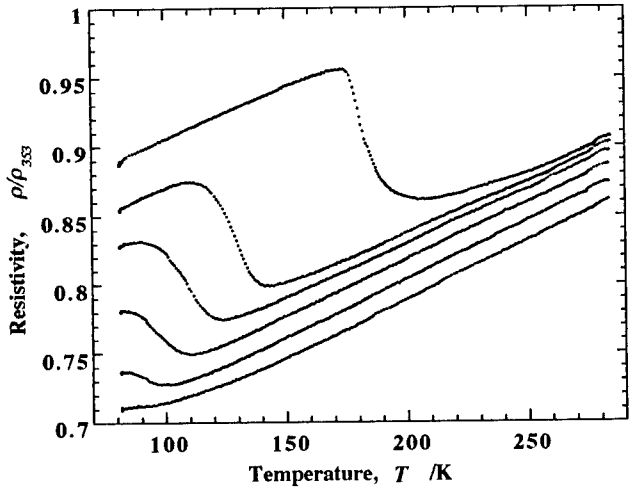


Fig.5 Resistivity change during heating from the liquid nitrogen temperature in thermal cycles, associated with aging at 283K for 1.2ks.

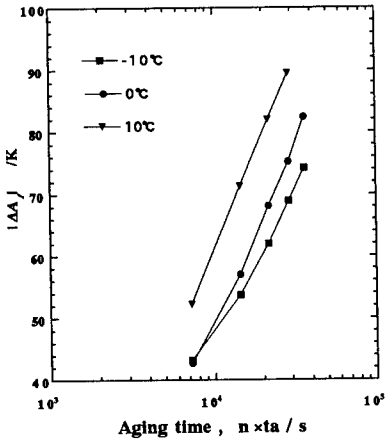


Fig.6 Transformtion temperature change as a function of aging time.

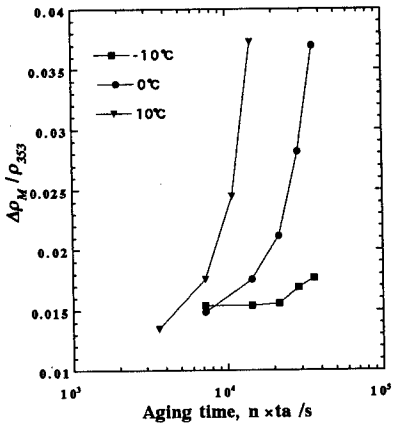


Fig. 7 Change in residual resistivity as a function of aging time.

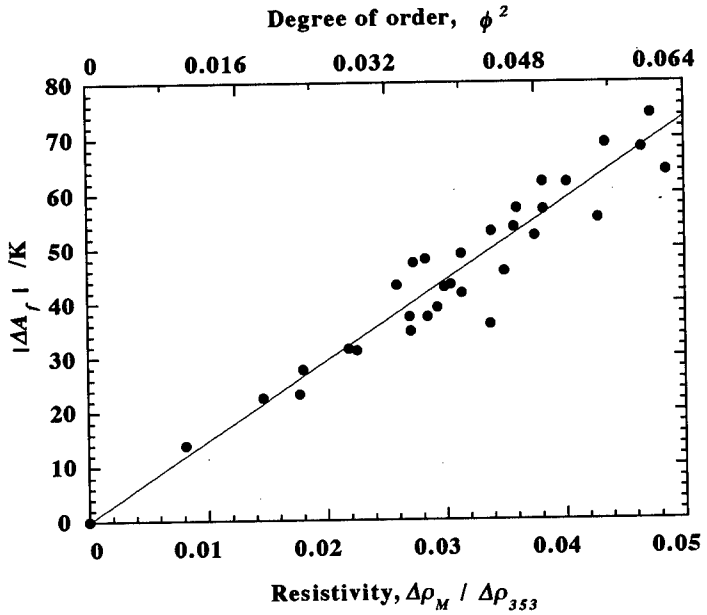


Fig.8 Transformation temperature change ΔA_f as a function of residual resistivity change $\Delta\rho_M/\rho_{353}$ or degree of order ϕ.

190K. Furthermore, the resistivity value of the martensitic phase at liquid nitrogen temperature, ρ_M, and the resistivity level of the matrix phase also decreased at every cycle. The changes of reverse transformation temperature, ΔA_f and normalized resistivity, $\Delta\rho_M$, which were obtained for specimens aged at various temperatures are shown as a function of aging time, n×ta, in Fig. 6 and 7, respectively. Both of ΔA_f and $\Delta\rho_M$ depend on aging temperatures and times sensitively. The value ΔA_f is shown in Fig.8 as a function of $\Delta\rho_M/\rho_{353}$ which is given on the lower side of abscissa. From this graph, a relation-ship between ΔA_f and $\Delta\rho_M$ is obtained as

$$\Delta A_f = 1400\Delta\rho_M/\rho_{353} \quad (1)$$

where the unit of ΔA_f is given by [K]. We have found that there is a relation-ship $\Delta\rho_M = .23\Delta\rho_P$, independent of Ta or ta. Therefore, a linear relation holds also between ΔA_f and $\Delta\rho_P$. Since it is known that the resistivity change is proportional to ϕ^2, where ϕ is the degree of order, we can put $\phi^2 = \Delta\rho_P / \Delta\rho_{max}$, where $\Delta\rho_{max}$ is the maximum value of resistivity change which is obtained from Fig. 2. From these relations, eq.(1) becomes

$$|\Delta A_f| = 1140\phi^2 . \quad (2)$$

The value of ϕ^2 is indicated on the upper side of abscissa in Fig. 8. From eq.(2), it may be recognized that the effect of the long range ordering from the bcc phase to the $C11_b$ structure on the martensitic transformation temperature is quite large.

Conclusion

The disordered β phase of Ag-22.3at%Zn-9.8at%Al alloy transforms to $C11_b$ ordered structure by aging at around room temperature. The ordering to $C11_b$ structure brings about a remarkable effect on the martensitic transformation temperature.

Acknowledgment

This work was partly supported by Grant-in-Aid for Scientific Research on the Priority Area 'Investigation of Microscopic Mechanisms of Phase Transformations for the Structure Control of Materials' from the Ministry of Education, Science and Culture, Japan.

References

1. D. P. Dunne and C. M. Wayman, "The Effect of Austenite Ordering on the Martensite Transformation in Fe-Pt Alloys Near the Composition Fe_3Pt : I. Morphology and Transformation Characteristics and II. Crystallography and General Features", Met. Trans., 4 (1973), 137-145 and 147-152 .
2. T. Tadaki, K. Katsuki and K. Shimizu, "Crystallography of the Thermoelastic Martensitic Transformation in Fe-Pt Alloy nearthe Composition Fe_3Pt", Proc. First JIM Intern. Symp. on New Aspects of Martensitic Transformation, (Japan Institute of Metals, 1976), 187-192.
3. H. Warlimont, "Microstructure, crystal structure, and mechanical properties of martensite in copper alloys", Physical Properties of Martensite and Bainite, Special Report 93, Iron and Steel Inst., (1965), 58-67.
4. R. Rapacioli and M. Ahlers, "The Influence of Short-range Disorder on the Martensitic Transformation in Cu-Zn and Cu-Zn-Al Alloys", Acta Met., 27 (1979), 777-784.
5. A. Planes, R. Romero and M. Ahlers, "The Martensitic Transformation Temperature in Ternary Cu-Zn-Al Alloys", Acta Metall. Mater., 38 (1990),757-763.
6. K. Takezawa et al., "Martensitic and Bainitic Transformations in Ag-Zn Alloys", Mater. Trans JIM, 33 (1992), 294-301.
7. K. Takezawa, R. Akamatsu and K. Marukawa, "Stress Induced Martensitic Transformation from BCC to FCC in Ag-Zn Alloys", J. de Phys. IV, Coll., C8, 5 (1995), 1093-1098.
8. K. Takezawa, H. Hoshi and K. Marukawa, "Critical Temperature for Ordering and B2 Domain Structure in Ag-Zn β Phase Alloys", Mater. Trans. JIM, 38, No.1 (1997), in press.
9. E. B. Hawbolt and T. B. Massalski, "Massive and Martensitic Transformations in the Ag-Al System", Met. Trans., 2, (1971), 1771-1777.
10. A. Nagasawa and A. Tatsumi, "Phase Transformation in the Quenched Ag_3Al Beta Phase Alloy", Trans JIM, 29 (1988), 625-633.
11. W. B. Peason, A Handbook of Lattice Spacings and Structures of Metals and Alloys, (Oxford: Pergamon Press, 1964), 97.

INTRINSIC THERMODYNAMIC STABILITY AND ITS IMPLICATION TO CHARACTERISTICS OF PHASE EQUILIBRIA IN COHERENT MULTILAYERS

Joo-Youl Huh

Division of Materials Science and Engineering,
Korea University, Anam-Dong, Sungbuk-Gu, Seoul 136-701, Korea

Abstract

We show that the criteria for intrinsic thermodynamic stability for coherent multilayer systems differ from those for incoherent systems. Since thermodynamic densities cannot be perturbed independently under the coherency constraint, the extremized free energy at equilibrium needs not be convex when it is plotted as a function of its thermodynamic densities. This non-convex nature of the extremized free energy is responsible for the existence of unstable or multiple equilibrium states in a coherent multilayer systems. Furthermore, some geometric rules for phase diagram construction based on the criteria for intrinsic stability, such as Schreinemaker's rule, become invalid in the coherent systems. Nevertheless, since individual phases in a coherent multilayer systems are homogeneous in all thermodynamic aspects at equilibrium, other thermodynamic rules independent of the criteria for intrinsic stability, such as Gibbs phase rule and the common tangent construction, can be made in a way entirely analogous to incoherent systems as long as elastic stress and strain components are correctly classified as thermodynamic potentials or densities.

The Third Pacific Rim International Conference on
Advanced Materials and Processing (PRICM 3)
Edited by M.A. Imam, R. DeNale, S. Hanada,
Z. Zhong and D.N. Lee
The Minerals, Metals & Materials Society, 1998

Introduction

It has been well known in recent decades that the equilibrium characteristics of nonhydrostatically stressed coherent systems can differ drastically from those of fluid or incoherent systems [1-5]. Most notably, coherent systems can exhibit more than one equilibrium state at a fixed set of external constraints of temperature, composition and mechanical loading. Furthermore, the equilibrium states can be either stable or unstable. Related to the existence of unstable or multiple equilibrium states, one long-standing issue has been whether or not the Gibbs phase rule and the method of common tangent construction are applicable to a coherent system [2-9]. In many coherent systems, the classical definition of phase [10] becomes ambiguous because a domain, which is a uniform phase in the absence of coherency constraint, is nonuniformly stressed and thus, inhomogeneous in composition. The Gibbs phase rule and the common tangent construction, which are originally obtained for fluid systems, becomes less meaningful in such coherent systems.

It has been shown by Johnson and Müller [5] that the description of thermodynamic equilibria in a coherent system can be made in ways entirely analogous to fluid or incoherent systems, when the individual phases coexisting in the coherent system are homogeneous in their thermodynamic states at equilibrium. Examples of such a coherent system include epitaxial (coherent) planar multilayers. For a coherent system configured as plane-parallel plates, the Gibbs phase rule and the common tangent construction are recovered by including the elastic stress and strain components in the set of independent thermodynamic variables. However, the system still exhibit all the important characteristics of coherent phase equilibria [5].

The purpose of the present paper concerning coherent multilayers is to show that the equilibrium characteristics unique to a coherent system are attributed to the criteria for intrinsic stability. The criteria for intrinsic stability, which are modified under the presence of coherency constraint, allow the extremized free energy at equilibrium to be a non-convex function of its density variables. Without referring to a specific analytical dependences of chemical free energy and elastic parameters on composition, equilibrium states with more than two coexisting phases are shown to be thermodynamically unstable in coherent, binary alloy multilayers subjected to traction boundary conditions.

Thermodynamic Description of Coherent Multilayers

Figure 1 shows a coherent $\alpha+\beta+\gamma$ three-phase multilayer system in the actual configuration for two different sets of mechanical loading conditions. The coexisting phases are configured as plane-parallel plates with the normal direction lying in the x_3 direction. Here, we assume continuum small-strain elasticity and consider a substitutional *A-B* binary alloy. Assuming a thin film approximation, elastic fields in each phase are homogeneous and so is the composition at equilibrium. The lines in each phase represent the equivalent lattice planes, indicating the coherency nature at the interface between two adjacent phases. For both cases in Fig. 1, the surfaces of the system perpendicular to the x_3 direction are exposed to an external traction t_3^o. However, the mechanical loading conditions imposed on the sides of the system are different in the two cases. In Fig. 1(a), the system is under a traction boundary condition, by which another traction t_1^o $(=t_2^o)$ is applied to the sides of the system. The system under hydrostatic pressure can be realized as a special case that t_1^o and t_3^o possess the same value. A free-standing multilayer without the influence of a substrate could be modeled as such a system. In Fig. 1(b), the system is under a displacement boundary condition, by which the distance between the sides L_1 $(= L_2)$ of the system is specified externally. Thus, the displacement boundary condition fixes the state of in-plane strain in each of the coexisting phases. Multilayers grown coherently on a rigid substrate examplify such a system.

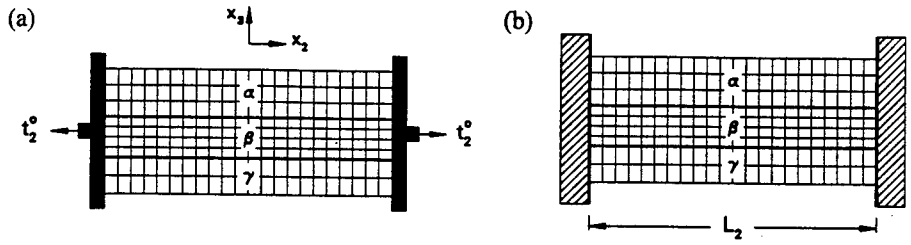


Figure 1: Schematic depiction of coherent three-phase multilayer system. (a) Multilayer under a traction boundary condition. (b) Multylayer under a displacement boundary condition.

For simplicity, we employ certain restrictions on the crystal structure and crystallographic orientation of the plate normal so that all the non-diagonal components of the stress and strain tensors can vanish. Examples of such orientation and crystal structure include $<100>$ and $<111>$ in cubic crystals. The strain components ε_{11} and ε_{22} (measured with respect to a common reference state) in the x_1-x_2 plane should possess identical values in all the coexisting phases in order to maintain the coherency of the system. Their thermodynamic conjugates σ_{11} and σ_{22}, respectively, need not be identical in the coexisting phases. Therefore, the strain components ε_{11} and ε_{22} $(=\varepsilon_{11})$ are classified into thermodynamic potentials whereas the stress components σ_{11} and σ_{22} $(=\sigma_{11})$ into thermodynamic densities. On the other hand, the coherency constraint does not impose a restriction on the deformation along the x_3 direction but the stress component σ_{33} must be identical in all the coexisting phases as $\sigma_{33} = t_3^o$. Thus, σ_{33} is a thermodynamic potential and its thermodynamic conjugate ε_{33} is a thermodynamic density.

The thermodynamic free energy extremized at equilibrium depends on the set of externally controlled thermodynamic variables (ECVs). For the present purposes, the temperature (T) and overall composition (c^o) of the system are considered to be ECVs. When the system is subjected to the traction boundary condition, the set of ECVs consists of two thermodynamic potentials T and σ_{33} $(\equiv t_3^o)$ and two system densities c^o and σ_{11}^o $(\equiv t_1^o)$. Thus, the appropriate free energy density extremized at equilibrium, g, is given by

$$g(T, c, \sigma_{11}, \sigma_{33}) = f(T, c, \varepsilon_{11}, \varepsilon_{33}) - 2V_m\sigma_{11}\varepsilon_{11} - V_m\sigma_{33}\varepsilon_{33}, \quad (1)$$

where f is the molar Helmholtz free energy and V_m is the molar volume measured at the reference state. On the other hand, when the displacement boundary condition is imposed on the system, the appropriate free energy density extremized at equilibrium, φ, is given by

$$\varphi(T, c, \varepsilon_{11}, \sigma_{33}) = f(T, c, \varepsilon_{11}, \varepsilon_{33}) - V_m\sigma_{33}\varepsilon_{33}, \quad (2)$$

since the set of ECVs consists of three potentials (T, ε_{11}, σ_{33}) and one system density (c^o).

Gibbs phase rule relates the number of homogeneous phases coexisting in a system to the number of *potentials* which are capable of independent variations without changing the number of the coexisting phases [10,11]. When a system with r independent thermodynamic variables consists of p homogeneous phases, the number of independent potentials (i.e., the degree of freedom) δ is given by $\delta = r - p + 1$, regardless of the choice of ECVs. For the multilayer system employed here, r is equal to four and thus, regardless of the mechanical boundary condition subjected to the system, maximally five phases can coexist at equilibrium. It is

important to note that the Gibbs phase rule is based only on the thermodynamic equilibrium conditions (i.e., equalities of thermodynamic potentials in all coexisting phases). Therefore, the stability of an equilibrium state is not a concern of the phase rule. In the following section, it will be shown that the stability of multi-phase equilibrium states is affected by the criteria for intrinsic stability.

The method of common tangent construction is a graphical technique used to display the thermodynamic equilibrium conditions of multi-phase systems in which one or more ECVs is a system density [5,10]. For the use of common tangent construction, the appropriate free energy density for each of homogeneous phases should be plotted as a function of its all density variables while holding its potentials variables fixed. Therefore, when the multilayer system is constrained by the traction boundary condition, the free energy densities, g, for individual phases should be plotted as functions of both c and σ_{11} at fixed values of T and σ_{33}. This is true even if the system is under hydrostatic pressure. On the other hand, if the system is constrained by the displacement boundary condition, the free energy densities, φ, should be plotted in terms of c at constant T, σ_{33} and ε_{11}.

Criteria for Intrinsic Thermodynamic Stability

Intrinsic thermodynamic stability is concerned with the stability of a homogeneous single-phase system with respect to infinitesimal variations of its density variables. The use of the common tangent construction among homogeneous phases assumes tacitly that each of the homogeneous phases satisfies the criteria for intrinsic thermodynamic stability. Otherwise, the multi-phase equilibrium state obtained from the common tangent construction can never be stable and thus, the consideration of such a multi-phase system has no physical significance.

Differing from those in fluids or incoherent systems, all density variations are not independent of one another in a coherent system since a perturbed state must maintain coherency of the system. Therefore, the number of independent conditions for intrinsic stability in a coherent system is less than the number of independent thermodynamic variables of the system. For the coherent system employed here, regardless of the choice of the set of ECVs, the criteria for intrinsic stability [12] can be expressed in a form of Le Chatelier principle:

$$\left(\frac{\partial M_{BA}}{\partial c}\right)_{\varepsilon_{11}.S.\varepsilon_{33}} \geq \left(\frac{\partial M_{BA}}{\partial c}\right)_{\varepsilon_{11}.T.\varepsilon_{33}} \geq \left(\frac{\partial M_{BA}}{\partial c}\right)_{\varepsilon_{11}.T.\sigma_{33}} > 0, \qquad (3)$$

where M_{BA} is the diffusion potential [13], which is the thermodynamic conjugate of composition c, and s is the molar entropy density. It is noted that the strain component ε_{11}, which is classified as a thermodynamic potential due to the coherency constraint, is held fixed for all the partial derivations in Eq. (3). This is because all the density variations permissible to the coherent system must not alter the strain component ε_{11} ($=\varepsilon_{22}$). Since both sets of ECVs considered here include the thermodynamic potentials T and σ_{33}, the last condition in Eq. (3) is sufficient for the present consideration of intrinsic stability. When expressed in terms of the appropriate free energy determined by the set of ECVs, the last condition in Eq. (3) becomes

$$\left(\frac{\partial M_{BA}}{\partial c}\right)_{\varepsilon_{11}.T.\sigma_{33}} = \left(\frac{\partial^2 \varphi}{\partial c^2}\right)_{\varepsilon_{11}.T.\sigma_{33}} > 0, \qquad (4)$$

$$\left(\frac{\partial M_{BA}}{\partial c}\right)_{\varepsilon_{11}.T.\sigma_{33}} = \left(\frac{\partial^2 g}{\partial c^2}\right)_{\sigma_{11}.T.\sigma_{33}} - \frac{\left(\partial^2 g\ \partial c \partial \sigma_{11}\right)^2_{T.\sigma_{33}}}{\left(\partial^2 g\ \partial \sigma_{11}^2\right)_{\sigma_{11}.T.\sigma_{33}}} > 0. \qquad (5)$$

Implication of Intrinsic Stability Criteria to Equilibrium Characteristics

Figure 2 shows schematic depictions of the free energies φ and g plotted in terms of their density variable(s), satisfying the criteria for intrinsic stability. Equation (4) indicates that the free energy density φ for a homogenous phase must be plotted as a convex (downward) function of its density c. This convexity of the free energy, as shown in Fig. 2(a), is the reason why the coherent system with the displacement boundary condition exhibit the same equilibrium characteristics as fluid or incoherent systems [5,9].

On the other hand, Eq. (5) indicates that, because the signs of individual $\partial^2 g/\partial c^2$ and $\partial^2 g/\partial \sigma_{11}^2$ are not determined by the criteria for intrinsic stability, the free energy g need not be plotted as a convex function of c and σ_{11}. The conditions that $\partial^2 g/\partial c^2 > 0$ and $\partial^2 g/\partial \sigma_{11}^2 < 0$ must be satisfied in the absence of the coherency constraint. Therefore, the saddle-shaped topology of the free energy surface as in Fig. 2(b) should be most general for the coherent system subjected to the traction boundary condition unless a phase in the coherent system decomposes simultaneously upon relieving the coherency. The common tangent construction to such non-convex surfaces can show that more than one equilibrium state can be obtained for a given set of ECVs and that the equilibrium states can be either stable or unstable. This is the thermodynamic basis for the fact that, differing from the system under the displacement boundary condition, the system under the traction boundary condition can possess unstable and multiple equilibrium states for a fixed set of ECVs.

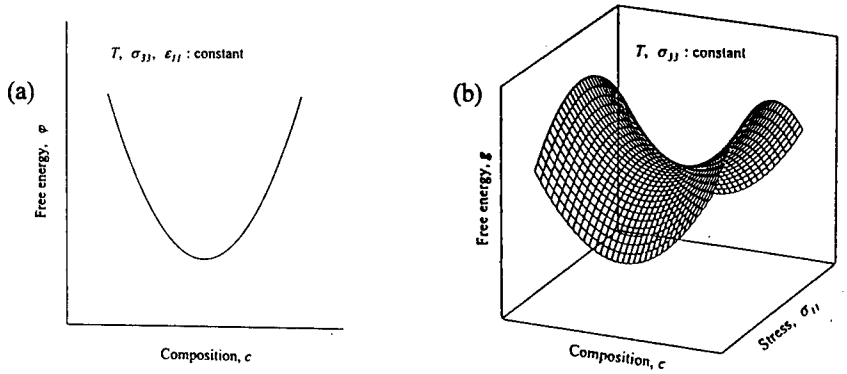


Figure 2: Schematic drawing of the appropriate free energy of a homogeneous phase plotted as a function of its all density variables when the phase satisfies the criteria for intrinsic stability. (a) The free energy φ extremized under the displacement boundary condition. (b) The free energy g extremized under the traction boundary condition.

Mutual stability is concerned with the stability of a multi-phase equilibrium system with respect to infinitesimal variations of phase fractions. In fluid or incoherent systems, the mutual stability is governed by the intrinsic stability. Consequently, a multi-phase equilibrium state is always stable as long as individual phases satisfy the criteria for intrinsic stability. This is also true for the coherent multilayer system subjected to the displacement boundary condition. Therefore, it can be observed experimentally all the equilibrium states consisting of maximally five phases as allowed by the Gibbs phase rule. In the coherent system subjected to the traction boundary condition, however, the mutual stability is not guaranteed by the intrinsic stability.

Figure 3 shows a method of common tangent construction in two different, thermodynamic density subspaces of the coherent system with the traction boundary condition. Figure 3(a) is a $g-c$ diagram at a fixed value of σ_{11} whereas Figure 3(b) is a $g-\sigma_{11}$ diagram at a fixed value of c. As mentioned previously, the conventional common tangent construction to the free

energies of homogeneous phases is not applicable in the density subspaces. However, if the free energies of two-phase equilibrium systems are plotted in the subspaces, three- or higher-phase equilibrium states can be obtained from the common tangent construction to the free energies of two-phase systems [14]. The single- and two-phase free energies are depicted by dotted and solid curves, respectively. A two-phase free energy curve ends tangentially on single-phase free energy curves at which the phase fraction of the corresponding phase becomes equal to one. As long as individual phases satisfy that $\partial^2 g/\partial c^2 > 0$ and $\partial^2 g/\partial \sigma_{11}^2 < 0$, it can be shown [14] that, in both density subspaces of Figures 3(a) and 3(b), the two-phase free energy densities depicted as concave curves correspond to stable two-phase equilibrium states whereas those depicted as convex curves correspond to unstable two-phase equilibrium states.

In Fig. 3(a), the common tangent line can be constructed between the free energy curves of α+β and β+γ two-phase equilibrium systems ($g^{\alpha\beta}$ and $g^{\beta\gamma}$). An α+β+γ three-phase equilibrium state exists in the composition range between $c_{\alpha\beta}^{\alpha\beta\gamma}$ and $c_{\beta\gamma}^{\alpha\beta\gamma}$. The free energy of the three-phase state ($g^{\alpha\beta\gamma}$) is given by the tangent line. However, the three-phase state must be unstable because the free energy $g^{\beta\gamma}$ at $c = c_{\beta\gamma}^{\alpha\beta\gamma}$ represents an unstable β+γ two-phase equilibrium state. In Fig. 3(b), the common tangent line is constructed between $g^{\alpha\beta}$ and $g^{\alpha\gamma}$ curves both of which represent stable two-phase equilibrium states. However, the three-phase equilibrium state possible in the stress range of $\sigma_{\alpha\beta}^{\alpha\beta\gamma} < \sigma_{11} < \sigma_{\alpha\gamma}^{\alpha\beta\gamma}$ is still thermodynamically unstable because the free energy of the three-phase equilibrium state, as given by the common tangent line, is greater than each of $g^{\alpha\beta}$ and $g^{\alpha\gamma}$. That is, a three-phase equilibrium state corresponds to a state maximizing the appropriate free energy of the system. Therefore, from the fact that the extremized free energies corresponding to stable two-phase equilibrium states are always plotted as concave curves in both thermodynamic density subspaces, it can be concluded that a three-phase equilibrium state is always unstable in the coherent system subjected to the traction boundary condition.

Although four-phase an five-phase equilibrium states are possible in the system as allowed by the Gibbs phase rule, they must also be unstable and cannot be attained by experiment. This is due to the fact that, unless a three-phase equilibrium state is thermodynamically stable, an equilibrium state consisting of more than three phases cannot be stable.

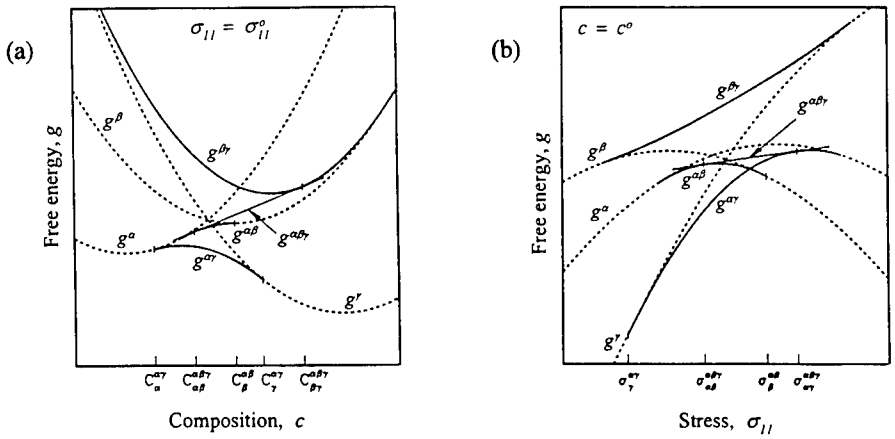


Figure 3: Use of the common tangent construction between two-phase free energy curves to demonstrate the instability of a three-phase equilibrium state in the coherent multilayer system under the traction boundary condition. (a) Schematic $g - c$ diagram at a fixed set of σ_{11}, T and σ_{33}. A part of $0 < c < 1$ is shown. (b) Schematic $g - \sigma_{11}$ diagram at a fixed set of c, T and σ_{33}.

Summary

A coherent multilayer can be considered as a nonhydrostatically stressed system in which the states of individual coexisting phases are homogeneous in all thermodynamic aspects. The Gibbs phase rule and the method of common tangent construction can be used in manners analogous to those for fluids of incoherent systems as far as the elastic stresses and strain components are correctly recognized as thermodynamic potentials and densities. Nevertheless, the existence of unstable equilibrium states in a coherent multilayer system is attributed to the criteria for intrinsic thermodynamic stability which allow the extremized free energy to be a non-convex function of its density variables. A common tangent construction in a thermodynamic density subspace was utilized to demonstrate that equilibrium states with more than two coexisting phases cannot be thermodynamically stable in the coherent binary multilayer system subjected to certain mechanical boundary conditions.

References

1. R.O. Williams, "The Calculation of Coherent Phase Equilibria", CALPAD, 8 (1984), 1-14.
2. J.W. Cahn and F.C. Larché, "A Simple Model for Coherent Equilibria", Acta metall., 32 (1984), 1914-1923.
3. A.L. Roitburd, "Equilibrium and Phase Diagrams of Coherent Phases in Solids", Sov. Phys. Solid St., 26 (1984), 1229-1223.
4. W.C. Johnson and P.W. Voorhees, "Phase Equilibria in Two-Phase Coherent Solids", Metall. Trans. A, 18 (1987), 1213-1228.
5. W.C. Johnson and W. H. Müller, "Characteristics of Phase Equilibria in Coherent Solids", Acta metall. mater., 39 (1991), 89-103.
6. W.C. Johnson, "On the Inapplicability of Gibbs Phase Rule to Coherent Solids", Metall. Trans. A, 18 (1987), 1093-1097.
7. M.J. Pfeifer and P.W. Voorhee, "A Graphical Method for Constructing Coherent Phase Diagrams", Acta metall. mater., 39 (1991), 2001-2012.
8. Z.K. Liu and J. Ågren, "Thermodynamics of Constrained and Unconstrained Equilibrium Systems and Their Phase Rules", J. Phase Equilibria, 16 (1995), 30-35.
9. R. Purdy and Y.J. Brechet, "Equilibrium and Diffusion in Coherent Multilayers", Acta mater., 44 (1996), 4853-4864.
10. J.W. Gibbs, Scientific Papers, vol. 1 (Dover, New York ,1961) 242.
11. J.Y. Huh and W.C. Johnson, "Intrinsic Thermodynamic Stability of Stressed Coherent Systems", Acta metall. mater., 43 (1995), 1631-1642.
12. M. Hillert, "Principles of Phase Diagrams", Internat. Metals Rev., 30 (1985), 45-67.
13. F.C. Larché and J.W. Cahn, "A Linear Theory of Thermochemical Equilibrium of Solids under Stress", Acta Metall., 21 (1973), 1051-1058.
14. J.Y. Huh, "A Generalized Thermodynamic Treatment of Phase Equilibria in Coherent Multilayers", Metalas and Materials, 3 (1997), 75-76.

COMPUTATIONAL INVESTIGATIONS ON THE MICROSTRUCTURE FORMATION IN METALLIC MATERIALS BASED UPON THE PHASE FIELD METHOD

Toru MIYAZAKI and Toshiyuki KOYAMA

Dept. of Materials Science & Engineering, Nagoya Institute of Technology,
Nagoya 466, JAPAN

Abstract

On the basis of the discrete phase field method where solute atom occupation probability in the discrete atom site, the composition dependencies of atomic interchange energy and the inhomogeneous elasticity, are taken into account so as to be applicable for the real alloy system, the phase decomposition and microstructure formation are theoretically evaluated for the Fe-Al-Co ternary ordering alloy system by utilizing the thermodynamic data. The microstructures computer-simulated are quantitatively coincident with experimental results of the actual alloy.

The Third Pacific Rim International Conference on
Advanced Materials and Processing (PRICM 3)
Edited by M.A. Imam, R. DeNale, S. Hanada,
Z. Zhong and D.N. Lee
The Minerals, Metals & Materials Society, 1998

Introduction

Theoretical investigation on the phase decomposition of multi-components alloy system has hardly been carried kinetically, because it is extremely difficult to get the kinetic solution of non-linear differential diffusion equation such as Cahn-Hilliard diffusion equation[1,2] or TDGL(Time-Dependent Ginzburge-Landau) equation[3,4] or Khachaturyan's diffusion equation[5,6]. However, since of recent remarkable development of Phase Field Method[7,8,9], the kinetic approach on the phase transformation in the multi-components system is becoming possible.

In the present, the phase decomposition and microstructure formation are calculated for Fe-Al-Co ternary ordering system on the basis of the phase field method of discrete type non-linear diffusion equation recently proposed by us[6]. The composition dependencies of atomic interchange energy are taken into account so as to be applicable for the microstructure formation in the real alloy systems.

Theoretical Basis

The total free energy of microstructure G_{system} is given by a sum of the chemical free energy G_c, the interfacial energy E_{surf} and the elastic strain energy E_{str}.

$$G_{system} = \frac{1}{V}\int_v (G_c + E_{surf} + E_{str})\,dv \qquad (1)$$

In the present work the phase decomposition of Fe-20at.%Al-20at.%Co ternary ordering alloy is calculated. The chemical free energy is evaluated on the basis of Bragg-Williams-Gorsky approximation, where the pairwise chemical interchange energies up to the 2nd nearest neighbor atoms and also the magnetic interchange energies up to the 2nd order are taken into account. Therefore, we concretely define following 15 parameters to describe various states of the Fe-Al-Co alloy, i.e. the atomic compositions c_i (i=Fe, Al and Co), the 1st nearest neighbour long range order parameters χ_i, the 2nd neighbour long range order parameters y_i and z_i, and the magnetic order parameters s_i, ,where 4 subordinate parameters are included.

According to our previous paper[10,11], the concrete expression of the configurational free energy $G_c(\mathbf{r})$ of ternary alloy system taken into account the pairwise interactions up to the 2nd nearest neighbours is given by equation 2 based on the BWG approximation. The phase stability of alloy is generally affected not only by atomic ordering but also magnetic ordering, so that, when the alloy contains ferromagnetic element such as Fe and Co, the magnetic interchange energy J_{ij} between the magnetic moments should be introduced in addition to the atomic interchange energy W_{ij}. Consequently, the chemical free energy G_c is expressed by equation 2.

$$\begin{aligned}
G_c &= U_0 + \sum_i C_i(4J_{ii}^{(1)} + 3J_{ii}^{(2)})q_i^2 - \frac{1}{2}\sum_{ij} C_iC_j\left[4(W_{ij}^{(1)} + M_{ij}^{(1)}) + 3(W_{ij}^{(2)} + M_{ij}^{(2)})\right] \\
&\quad + \frac{1}{2}\sum_{ij} C_iC_jX_iX_j\left[4(W_{ij}^{(1)} + M_{ij}^{(1)}) - 3(W_{ij}^{(2)} + M_{ij}^{(2)})\right] \\
&\quad + \frac{1}{2}\sum_{ij}\frac{3}{2} C_iC_j\left[(1-X_i)(1-X_j)Y_iY_j + (1+X_i)(1+X_j)Z_iZ_j\right](W_{ij}^{(2)} + M_{ij}^{(2)}) + RT\sum_i C_i \ln C_i \\
&\quad + \frac{k_BNT}{2}\sum_i C_i\left[(1-X_i)\ln(1-X_i) + (1+X_i)\ln(1+X_i)\right] \\
&\quad + \frac{RT}{4}\sum_i \left\{\begin{array}{l} C_i(1-X_i)\left[(1-Y_i)\ln(1-Y_i) + (1+Y_i)\ln(1+Y_i)\right] \\ +C_i(1+X_i)\left[(1-Z_i)\ln(1-Z_i) + (1+Z_i)\ln(1+Z_i)\right] \end{array}\right\} \\
&\quad + RT\sum_i m_iC_i\left[\left(\frac{1-q_i}{2}\right)\ln\left(\frac{1-q_i}{2}\right) + \left(\frac{1+q_i}{2}\right)\ln\left(\frac{1+q_i}{2}\right)\right]
\end{aligned}$$

$$U_0 = \left[4\sum_i C_i V_{ii}^{(1)} + 3\sum_i C_i V_{ii}^{(2)} \right] \quad , \quad W_{ij}^{(n)} = -2V_{ij}^{(n)} + V_{ii}^{(n)} + V_{jj}^{(n)}, \quad M_{ij}^{(n)} = -2J_{ij}^{(n)} q_i q_j + J_{ii}^{(n)} q_i^2 + J_{jj}^{(n)} q_j^2$$

(2)

The parameter q_i in eq.2 describes the degree of magnetic ordering, that is , $q_i = \pm 1$ and $q_i = 0$ represent the ferromagnetic and the paramagnetic states, respectively.
The interfacial energy E_{surf} is defined by equation 3 on the basis of the so-called Cahn's interfacial energy[12].

$$E_{surf} = \kappa_{CA}(\nabla C_A)^2 + \kappa_{CB}(\nabla C_B)^2 + \kappa_{CC}(\nabla C_C)^2 + \kappa_{XA}|\nabla X_A|^2 + \kappa_{XB}|\nabla X_B|^2 + \kappa_{XC}|\nabla X_C|^2 + \kappa_{YA}|\nabla Y_A|^2 + \kappa_{YB}|\nabla Y_B|^2 + \kappa_{YC}|\nabla Y_C|^2 + \kappa_{ZA}|\nabla Z_A|^2 + \kappa_{ZB}|\nabla Z_B|^2 + \kappa_{ZC}|\nabla Z_C|^2 + \kappa_{SA}|\nabla S_A|^2 + \kappa_{SB}|\nabla S_B|^2 + \kappa_{SC}|\nabla S_C|^2$$

(3)

,where κ_c, κ_x and κ_s show the chemical gradient, the ordering gradient and the magnetic ordering gradient coefficients, respectively.
The elastic strain energy for the cubic lattice crystal is given by equation 4 based on the Landau elasticity theory[13,14,15], where C_{ijkl} is the elastic stiffness constant, e_{ij}^c is the constrained strain and η is the lattice mismatch between the pure metals. The composition dependence of E_{str} is introduced in this equation, as is clearly known from the $\{c\text{-}c_0\}$ term in eq.4.

$$\mathbf{E}_{str} = \sum_{\mathbf{r}} \left[\begin{array}{l} (3/2)(C_{1111}^0 + 2C_{1122}^0)\eta^2\{c(\mathbf{r}) - c_0\}^2 - \eta(C_{1111}^0 + 2C_{1122}^0)\{c(\mathbf{r}) - c_0\}\{e_{11}^c(\mathbf{r}) + e_{22}^c(\mathbf{r}) + e_{33}^c(\mathbf{r})\} \\ +(1/2)C_{1111}^0\{e_{11}^{c\,2}(\mathbf{r}) + e_{22}^{c\,2}(\mathbf{r}) + e_{33}^{c\,2}(\mathbf{r})\} + C_{1122}^0\{e_{11}^c(\mathbf{r})e_{22}^c(\mathbf{r}) + e_{22}^c(\mathbf{r})e_{33}^c(\mathbf{r}) + e_{33}^c(\mathbf{r})e_{11}^c(\mathbf{r})\} \\ +2C_{1212}^0\{e_{12}^{c\,2}(\mathbf{r}) + e_{23}^{c\,2}(\mathbf{r}) + e_{31}^{c\,2}(\mathbf{r})\} + (3/2)(\Delta C_{1111}^{AB} + 2\Delta C_{1122}^{AB})\eta^2\{c(\mathbf{r}) - c_0\}^3 \\ -\eta(\Delta C_{1111}^{AB} + 2\Delta C_{1122}^{AB})\{c(\mathbf{r}) - c_0\}^2\{e_{11}^c(\mathbf{r}) + e_{22}^c(\mathbf{r}) + e_{33}^c(\mathbf{r})\} + (1/2)\Delta C_{1111}^0\{c(\mathbf{r}) - c_0\}\{e_{11}^{c\,2}(\mathbf{r}) + e_{22}^{c\,2}(\mathbf{r}) + e_{33}^{c\,2}(\mathbf{r})\} \\ +\Delta C_{1122}^0\{c(\mathbf{r}) - c_0\}\{e_{11}^c(\mathbf{r})e_{22}^c(\mathbf{r}) + e_{22}^c(\mathbf{r})e_{33}^c(\mathbf{r}) + e_{33}^c(\mathbf{r})e_{11}^c(\mathbf{r})\} + 2\Delta C_{1212}^0\{c(\mathbf{r}) - c_0\}\{e_{12}^{c\,2}(\mathbf{r}) + e_{23}^{c\,2}(\mathbf{r}) + e_{31}^{c\,2}(\mathbf{r})\} \end{array} \right]$$

(4)

From these free energies, the diffusion potential χ is given by equation 5.

$$\chi_{c_p}(\mathbf{r},t) \equiv \frac{\delta G_{system}}{\delta c_p(\mathbf{r},t)} = \mu_c^{c_p}(\mathbf{r},t) + \mu_{surf}^{c_p}(\mathbf{r},t) + \mu_{str}^{c_p}(\mathbf{r},t)$$

$$\chi_{x_p}(\mathbf{r},t) \equiv \frac{\delta G_{system}}{\delta x_p(\mathbf{r},t)} = \mu_c^{x_p}(\mathbf{r},t) + \mu_{surf}^{x_p}(\mathbf{r},t) + \mu_{str}^{x_p}(\mathbf{r},t)$$

$$\chi_{s_q}(\mathbf{r},t) \equiv \frac{\delta G_{system}}{\delta s_q(\mathbf{r},t)} = \mu_c^{s_q}(\mathbf{r},t) + \mu_{surf}^{s_q}(\mathbf{r},t) + \mu_{str}^{s_q}(\mathbf{r},t)$$

(5)

The time developments of c, x and s are evaluated by equation 6, which is concretely expressed by following 7 independent kinetic equations for c_{Fe}, c_{Al}, x_{Fe}, x_{Al}, s_{Fe}, s_{Al} and s_{Co}.

$$\frac{\partial c_p(\mathbf{r},t)}{\partial t} = div\left[M\{c_p(\mathbf{r},t)T\}grad\left\{\chi_{c_p}\{c_i(\mathbf{r},t), X_j(\mathbf{r},t), s_k(\mathbf{r},t)\}\right\}\right]$$
$$\frac{\partial X_q(\mathbf{r},t)}{\partial t} = -L\{X_q(\mathbf{r},t)\}\left[\chi_{X_q}\{c_i(\mathbf{r},t), X_j(\mathbf{r},t), s_k(\mathbf{r},t)\}\right] \quad \text{..... (6)}$$
$$\frac{\partial s_q(\mathbf{r},t)}{\partial t} = -L\{s_q(\mathbf{r},t)\}\left[\chi_{s_q}\{c_i(\mathbf{r},t), X_j(\mathbf{r},t), s_k(\mathbf{r},t)\}\right]$$

Thus, we can calculate the phase decomposition by repeating equation 7.

$$c_p(\mathbf{r}, t+\Delta t) = c_p(\mathbf{r},t) + \left\{\partial c_p(\mathbf{r},t)/\partial t\right\}\Delta t$$
$$X_q(\mathbf{r}, t+\Delta t) = X_q(\mathbf{r},t) + \left\{\partial X_q(\mathbf{r},t)/\partial t\right\}\Delta t \quad \text{..... (7)}$$
$$s_q(\mathbf{r}, t+\Delta t) = s_q(\mathbf{r},t) + \left\{\partial s_q(\mathbf{r},t)/\partial t\right\}\Delta t$$

Calculations of Fe-Al-Co Ternary Ordering Alloy System

The theoretical phase diagram of Fe-Al-Co alloy system has previously been calculated by us[10,11], which consists quantitatively with the experimental phase diagram[11]. Figs.1(a) shows the theoretical phase diagram of 923K, calculated on the basis of Bragg-Williams-Gorsky approximation[10]. The figures clearly indicate the existence of two phase region of B2+A2, of which tie line is described by a thin chain line in Fig.1(a). The computer simulation of phase

Table 1 Numerical values used for the calculation of Fe-Al-Co system.

Temperature, T/K	923
Alloy composition, C_{Fe}, C_{Al}, C_{oc}	0.6, 0.2, 0.2
Elastic stiffness constants C_{11}^{Fe} ,C_{11}^{CoAl} C_{12}^{Fe} ,C_{12}^{CoAl} C_{44}^{Fe} ,C_{44}^{CoAl} ($C_{ij}^{Al}=C_{ij}^{Co}=C_{ij}^{CoAl}$)	(x10^4MN/m) 23.3, 25.1 13.5, 10.1 11.8, 11.8
Lattice mismatch η Comp. gradient energy coefficient κ_c Ordering gradient energy coefficient κ_x Magnetic gradient energy coefficient κ_s	0.00729 6.000x10^{-16}(J.m^2/mol) 1.798x10^{-16}(J.m^2/mol) 1.068x 10^{-16}(J.m^2/mol)
Calculation area, L / nm Number of Fourier wave, N	120 128x128

Table 2 Chemical and magnetic interchange energies of Fe-Al-Co alloy system (k_B=1.38x10^{-23}J)

Chemical Interchange Energy			Magnetic Interchange Energy		
	$W_{ij}^{(1)}$	$W_{ij}^{(2)}$		$J_{ij}^{(1)}$	$J_{ij}^{(2)}$
Fe-Al	1100k_B	550kB	Fe-Fe	-196k_B	69k_B
Fe-Co	430k_B	0k_B	Fe-Co	-200k_B	0k_B
Al-Co	2800k_B	750k_B	Co-Co	-124k_B	-66k_B

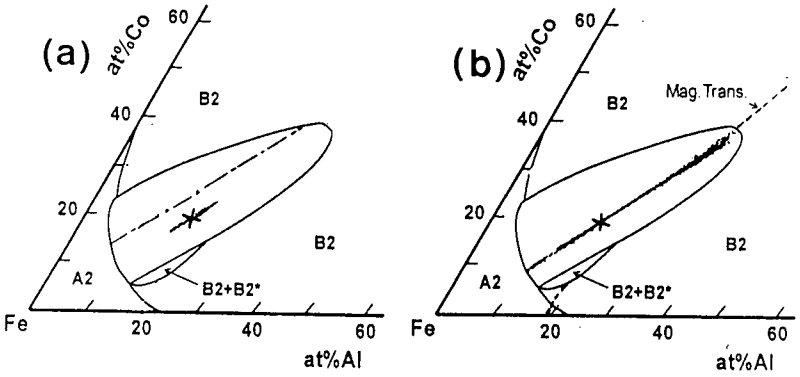


Figure 1 Equilibrium phase diagram of Fe-Al-Co alloy system at 923K calculated on the basis of BWG approximation, showing B2+A2 two phase region. The diffuse lines in the two-phase region indicate a progress of phase decomposition, (a)0.1s' and (b)3.0s'. X mark indicates the alloy composition Fe-20at.%Al-20at.%Co. A chain line in (a) shows a tie line of phase decomposition

Figure 2 Change of composition map of Fe atom, C_{Fe}, with progress of ageing. The bright parts correspond to the Fe atom rich region.

decomposition is performed at the composition indicating by X mark, that is, Fe-20at.%Al-20 at.%Co. The diffuse lines in the B2+A2 region of Figs.1(a)(b) demonstrate a progress of phase decomposition at 923K. The phase decomposition begins to spread along the tie-line, and finally stop at the phase boundary precisely. According to the previous experimental work on the same alloy[11,12] the phase decomposition to B2+A2 progresses nearly along the tie-line and never deviates largely from the line. Therefore, the calculation result shown in Fig.1 is precisely coincident with the experimental one not only for the final equilibrium stage but also for the process of phase decomposition.

Figure 2 shows change of the compositional map of Fe atom c_{Fe} with progress of phase decomposition. It is clearly recognized that Fe atoms concentrates into the anti-phase boundary at the early stage of phase decomposition and the matrix separates into Fe-rich and poor phases.

Figure 3 is a comprehensive set demonstrating the distributions of c_i, xi and s_i for Fe-20at.%Al-20at.%Co alloy aged at 923K for 40 arbitrary second. The three figures in the top layer show compositional map of Fe, Al and Co atoms, the second layer shows the atomic ordering and the bottom represents the magnetic ordering. It is clear from the distribution of c_{Fe}, c_{Al} and c_{Co} that Fe atoms segregate into the APB and also concentrate into the matrix part of microstructure

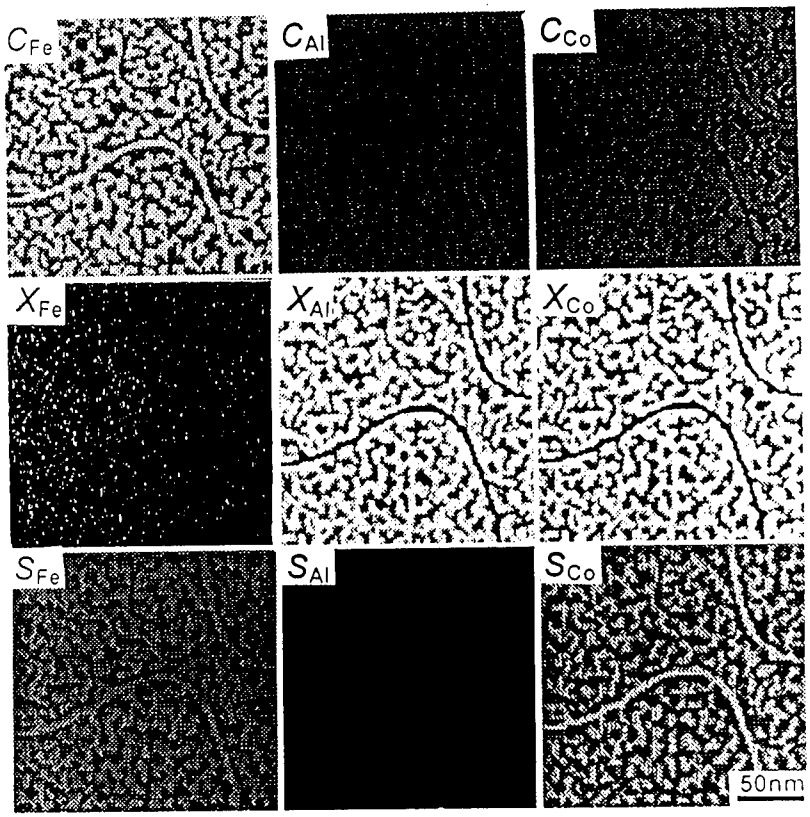


Figure 3 Comprehensive map set indicating distributions of the atomic composition c_i, the atomic ordering x_i and the magnetic ordering s_i for Fe-20at.%Al-20 at.%Co alloy aged at 923K for 40 arbitrary second.

produced by the phase decomposition, while Co and Al atoms, almost same in the distribution give a just inverse contrast with that of Fe atom. This clearly means that the phase decomposition proceeds as a pseudo-binary system consisting of Fe-rich and AlCo-rich phases, as is indicated in the tie line in Fig.1.

The atomic ordering occurs only in the B2 particles of the matrix. Since the maps of x_{Fe} and x_{Co} are just same, Al and Co atoms contribute to make the B2 ordering for the Fe-20at.%Al-20at.%Co alloy. On the magnetic ordering Fe and Co atoms give a quite similar map, thatmeans the same contribution of the both atoms to the magnetic ordering, while Al atom does not make any contribution to the magnetic ordering. The stage of phase decomposition which is shown in Figs.1,2 and 3 is completed during a very short stage of ageing, and then followed by the microstructural coarsening over the long term. Figure 4 represents the time-development of microstructure coarsening after the phase decomposition. It is clearly known from the figure that the two-phase microstructure consisting of Fe-rich region (black matrix in figure) and AlCo-rich region (white precipitate) coarsens with progress of ageing and gradually aligns along the <100> orthogonal directions, caused by increment of the elastic interaction energy among the particles with size growth. Figure 5 represents the TEM photographs experimentally taken from the same Fe-Al-Co alloy system. The theoretically given microstructures are sure to be accord with the characteristics in the actual Fe-Al-Co alloy such as the formation of <100> modulation,

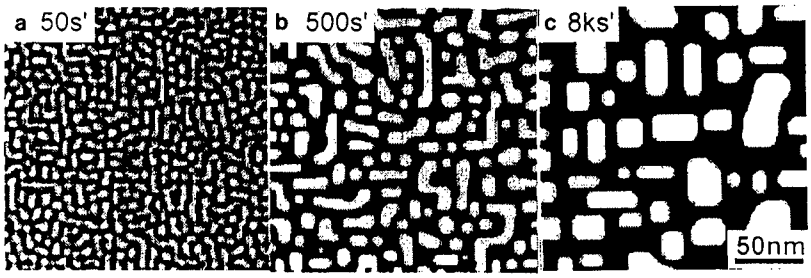


Figure 4 Computer simulation of B2 particle-coarsening of Fe-20at.%Al-20at.%Co at 923K.

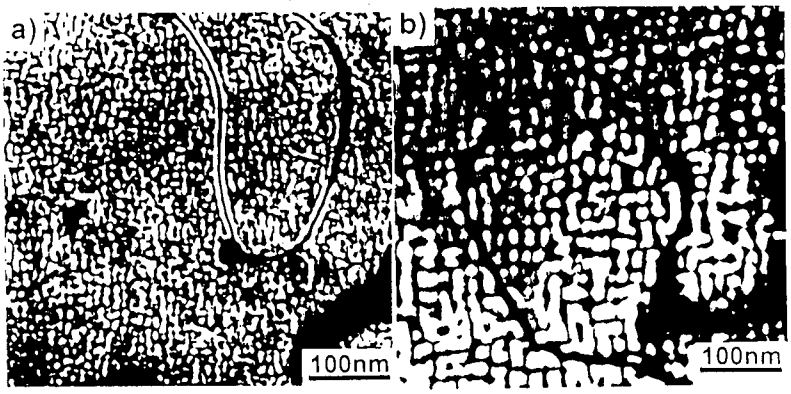


Figure 5 TEM photographs experimentally obtained for (a) Fe-31Al-24Co(at.%) aged at 923K for 0.6ks and (b) Fe-31Al-15Co aged for 1.47ks.

the precipitate shape, the periodic length of particle distribution (about 15 nm in the both microstructures) and so on.

By utilizing this method, it is expected to open a new field of materials science such as phase transformations due to the multi-component diffusion, multi-structural transformation and complex pattern formation, which are the most difficult but important and interesting phenomena in the materials science.

However, the phenomenological equation does not show its application limit. The propriety of application can only be judged from the quantitative comparison with the experimental facts in the real alloy system. The calculation for the real alloy system is important.

Conclusion

On the basis of the discrete phase field method, the phase decomposition process and microstructure formation are evaluated for the Fe-2oat.%Al-20at.%Co ternary ordering alloy by using the thermodynamic data related to the equilibrium phase diagram. The composition dependencies of atomic interchange energy are taken into account so as to be applicable for the microstructure formation in the real alloy systems. The time-developments of phase decomposition and the microstructure theoretically given are well coincident with the experimental results of the actual alloy.

The phase field method has a capability of predicting many phase transformations in the multi-

components system, the ordering alloy, the tweed structure and so on by utilizing the various kinds of ordering parameters such as the degree of order and the tetragonality of lattice.

References

1. J. W. Cahn and J .E . Hilliard , J. Chem. Phys., 31(1959), 688-699
2. J. W. Cahn and J . E. Hilliard , J. Chem. Phys.,28(1958), 258-267
3. S.Nambu and A.Sato, J. Am. Ceram. Soc., 76(1993), 1978
4. K.Binder, Colloid & Polymer Sci., 265(1987), 273
5. L.-Q.Chen and A. G. Khachaturyan, Acta Metall. Mater. , 39(1991), 2533
6. T.Koyama, T.Miyazaki and A.E.Mebed, Metal. and Mater. Trans.A, 26A(1995), 2617
7. R.Kobayashi, Physica D, 63(1993), 410
8. W.J.Boettinger et al., Mater.Sci. & Eng., A178(1994), 217
9. J.A.Warren and W.J.Boettinger, Acta Metall.Mater., 43(1995), 689
10 M.Fukaya et al., J.Mater.Sci. 25(1990), 522
11 M.Fukaya, T.Kozakai and T.Miyazaki, J.Mater.Sci. 26(1991), 5420
12 J.E.Hilliard, Phase Transformation, ed. by H.I.Aaronson (Ohio: ASM, 1970) 497
13 A.Onuki : J. Phys. Soc. Japan, 58(1989), 3065
14 H.Nishimori and A.Onuki : Phys.Rev.B, 42(1990), 980
15 H.Nishimori and A.Onuki : J. Phys. Soci. Japan, 60(1991), 1208

ISOTHERMAL TRANSFORMATION OF Au-47.5at%Cd ALLOY

X. Ren, T. Ohba*, S. Yamada, T. Ishii and K. Otsuka

Institute of Materials Science
University of Tsukuba
Tsukuba, Ibaraki 305-8573, Japan

* **Department of Materials Science and Engineering**
Teikyo University
Utsunomiya 320, Japan

Abstract

An isothermal transformation above A_f temperature has been discovered in Au-47.5at%Cd alloy utilizing differential scanning calorimetry and optical microscopy. We found that the occurrence of this transformation has a pronounced influence on the subsequent martensitic transformation. With isothermal holding above A_f, the subsequent martensitic transformation temperature is lowered. The isothermal aging also creates a surface relief very similar to that of martensite. All these results can be rationalized by considering the isothermal transformation to be a bainitic transformation. The effect of the bainitic transformation on martensitic transformation can be considered as follows: Isothermal holding in the parent state results in bainite formation, and as a result Cd is gradually expelled from the bainite into the surrounding parent phase because bainite requires lower Cd concentration. Therefore, the Cd content of remaining parent phase keeps increasing with increase of isothermal holding time. This leads to a decrease in M_s temperature of subsequent martensitic transformation.

The Third Pacific Rim International Conference on
Advanced Materials and Processing (PRICM 3)
Edited by M.A. Imam, R. DeNale, S. Hanada,
Z. Zhong and D.N. Lee
The Minerals, Metals & Materials Society, 1998

I. Introduction

Bainitic transformation is a kind of mixed-mode transformation, which is characterized by both lattice shear and diffusion (or composition change) (1). The former feature is similar to the diffusionless martensitic transformation, while the latter feature is similar to a conventional diffusional transformation.

Bainitic transformation has been reported in many ferrous alloys and a number of non-ferrous alloys (2~4). Alloys exhibiting bainitic transformation are all characterized by a possibility of martensitic transformations at lower temperatures. In other words, bainitic transformation will not occur if an alloy has no tendency to transform into martensite. Therefore, the occurrence of bainitic transformation is closely related to a possibility of martensitic transformation.

Au-Cd alloy (β phase) has long been known to transform into martensite, and is a prototype of martensitic transformation. So far, bainitic transformation has been found in many β phase alloys such as Cu-Zn, Cu-Zn-Al, Cu-Au-Zn and Ag-Zn, which undergo martensitic transformation. However, there is no report of bainitic transformation in Au-Cd.

The purpose of the present study is to verify if there exists a bainitic transformation in Au-47.5Cd alloy. To prove a bainitic transformation, it is necessary to show the dual feature of the transformation, i.e., diffusion (or composition change) and shear.

II. Experimental

A single crystal of Au-47.50at%Cd alloy was grown by a modified Bridgman technique. The nominal composition (47.50at% Cd) was determined from the initial mass of pure Au (99.99%) and pure Cd (99.9999%) used to make the alloy. After melting and Bridgman growth, there is a small loss in weight, which can be considered due to the evaporation of the constituent elements. Because the vapor pressure of Cd is much larger (>10^{14} times!) than that of Au, it is reasonable to consider the evaporation is only due to Cd. By assuming the weight loss are due to Cd loss, the true composition of the alloy was calculated to be Au-47.44at%Cd.

The alloy was annealed at 805K for 24 hours to eliminate possible composition inhomogeneity, and followed by a furnace-cooling to room temperature. Unlike most other β phase alloys which exhibit a decomposition (eutectoid reaction or precipitation) at intermediate temperature, Au-Cd does not show such diffusional decomposition. This enables the alloy to be slow-cooled. This alloy transforms into γ_2'-martensite (B19 structure) at low temperature. The transformation temperatures are: M_s=323.6K, M_f=319.4K, A_s=328.4K, and A_f=334.2K. The transformation hysteresis $A_f - M_s$=10.6K.

In order to detect the possible bainitic transformation, a small sample (20mg) was aged at 393K (parent state) for different period of time in the furnace of a DSC equipment, and followed by a measurement of subsequent martensitic transformation temperatures by the same equipment (cooling down to 263K and then heating up to 393K again). The measurement of martensitic transformation temperatures does not affect subsequent parent phase aging, because the

measurement is done within a short period of time (i.e., no significant diffusion occurs during this short period).

Optical microscopy observation was performed to verify if there is a surface relief on the flat surface of the parent phase during aging at 393K. The appearance of the martensite-like surface relief is an evidence for the existence of a shear mode in the transformation during aging.

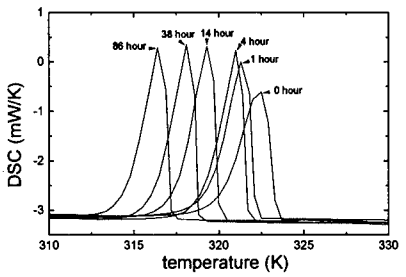


Figure 1. Shift of extrothermal peak of martensitic transformation in Au-47.5Cd alloy after aged in parent state (393K) for different times.

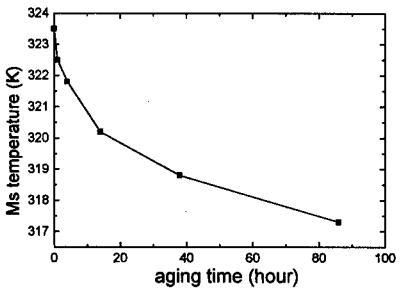


Figure 2. M_s temperature of Au-47.5Cd alloy as a function of aging time at 393K (parent state).

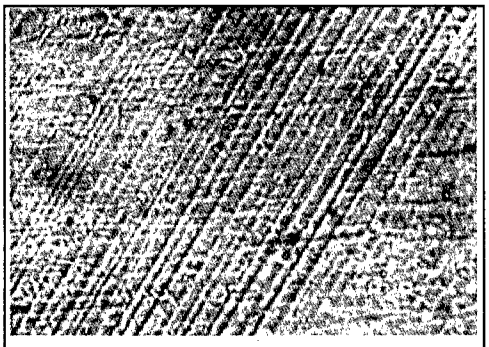


Figure 3. Martensite-like surface relief appears after Au-47.5Cd alloy is aged in its parent state (393K) for 3 days.

III. Results

1. DSC measurement

The change of martensitic transformation behavior of Au-47.5Cd alloy after aged at 393K for 0 hour, 1 hour, 4 hours, 14 hours, 38 hours and 86 hours is shown in Fig.1. The change in transformation temperatures with parent phase aging is shown in Fig.2. We can see that with the increase of aging in parent state the subsequent martensitic transformation temperature decreases.

2. Optical microscopy

Fig. 3 shows the surface of the alloy after aged for 3 days at 393K. It is seen that there appears some needle-shaped surface relief on the flat surface. The surface relief pattern is very similar to that found in martensitic transformation, but it could not be due to martensite because the temperature is much higher than A_f temperature. This picture suggests that the isothermal transformation at 393K contains a shear mode.

IV. Discussions

The above experiment strongly suggests that the isothermal transformation above the martensitic transformation in Au-47.5Cd is a bainitic transformation, because it possesses a dual-feature, i.e., diffusion and shear.

The change of martensitic transformation behavior and temperature (Fig.1 and 2) after parent phase aging is consistent with the diffusion feature of the bainitic transformation. The change of martensitic transformation temperature can only be considered as due to a change in composition of the parent phase. Such a composition change must be due to a transformation involving diffusion that produces a new phase with a composition different from the average alloy composition. Because it is known that martensitic transformation temperature decrease with increase in Cd content in AuCd alloy (5), the decrease of martensitic transformation temperature means that the new phase formed during parent aging is poor in Cd, such that the remaining parent phase around the new phase becomes Cd-rich gradually. As a result, the subsequent martensitic transformation occurs at lower temperature.

The appearance of martensite-like surface relief (Fig.3) during parent phase aging is a strong evidence for the existence of the lattice shear during the formation of the new phase. Therefore, in the present study we show that the isothermal aging in the parent state of Au-47.5Cd alloy results in a transformation associated with both diffusion and shear. Therefore, we conclude that it must be a bainitic transformation.

This isothermal transformation cannot be accounted for by an isothermal martensitic transformation, because the aging temperature is well above $T_0=(A_f-M_s)/2$, where there is no driving force for a martensitic transformation. Besides, if the isothermal transformation were due to an isothermal martensitic transformation (i.e., diffusionless), the untransformed parent phase would have the same composition as the unaged parent phase, thus the untransformed parent would transform athermally into martensite at the same M_s temperature as an unaged alloy during subsequent cooling. Of course, this contradicts the change of martensitic transformation temperature after parent phase aging.

Nearly four decades ago, Birnbaum (6) studied the effect of isothermal aging of the parent phase (341K~373K) in Au-Cd alloy above its martensitic transformation temperature. He found that long-time aging (7~18 days) in the parent phase of Au-47.5Cd alloy leads to an appreciable

decrease in subsequent martensitic transformation temperature, and the martensitic transformation product gradually changes from γ_2' to ζ_2'. The former martensite is known to be a martensitic product of Au-47.5Cd alloy, while the latter one is known to be a martensitic product of Au-(49.5~50.5)Cd alloy. He explained this fact in terms of a phase separation in the β phase (parent) during isothermal holding around 373K. The validity of his explanation depends on his assumption that Ms temperature of β phase of Au-Cd alloy increases with increase of Cd content. However, now it is known that the reverse is true (5). Besides, phase separation cannot explain the observed martensite-like surface relief (Fig.3). Therefore, the changes during isothermal aging of β phase Au-47.5Cd must be due to a different mechanism, i.e, a bainitic transformation.

V. Conclusions

An isothermal transformation was found in Au-47.5Cd alloy in its parent state. We concluded that it is a bainitic transformation, because it possesses the feature of both composition change and lattice shear. This transformation produces a bainite with lower Cd content than nominal composition, thus Cd is expelled into surrounding parent phase. As a result, the subsequent martensitic transformation temperature of the surrounding parent phase is lowered. The shear aspect of the bainitic transformation is identified by the appearance of martensite-like surface relief after isothermal aging in the parent phase.

Acknowledgments

The present work was supported by Grant-in-Aid for Scientific Research on Priority Area of Phase Transformations (1997-1999) from the Ministry of Education, Science and Culture of Japan.

References

1. T. Tadaki and K. Shimizu, Metall. Mater. Trans., **25A**(1994), 2569.
2. R.F. Hehemann, in Phase Transformations(1970), (Ohio: ASM, Metal Park), pp397 .
3. C.M. Wayman and J. Perkins, (Eds), Proc. ICOMAT'92(1992), Monterey Institute of Advanced Studies, pp749-856 .
4. Proc. Pacific Rim Conference on the Role of Shear and Diffusion in the Formation of Plate-shaped Transformation Products, ASM, Hawaii (1992), see Metall. Mater. Trans., **25A**(1994), No.9 and No.12 .
5. H. Sakamoto, H. Tsuzuki and K. Shimizu, Mater. Sci. Forum, **56-58**(1990), 305.
6. H. K. Birnbaum, Trans. AIME, **215**(1959), 786.

DIFFUSE PHASE TRANSITION IN $Pb(Fe_{0.5}Nb_{0.5})O_3$ FERROELECTRIC CERAMICS

Katsuro Oda
Institute of Industrial Science, University of Tokyo
7-3-1 Roppongi Minato-ku, Tokyo, 106 Japan

Abstract

The mechanism of diffuse phase transition in $Pb(Fe_{0.5}Nb_{0.5})O_3$ ferroelectric ceramics is investigated by means of Mössbauer spectroscopy and dielectric measurements. Ferro and paraelectric phases coexist over a wide temperature range well below and above the phase transition temperature. Fe^{3+} and Nb^{5+} ions are distributed on the B site of perovskite structure in a non-random state. These results indicate that the transition temperature differs between regions among the whole phase and the sizes of the regions are of few unit cells. This heterogeneity is considered to be the origin of the broad temperature dependence of diffuse phase transition.

The Third Pacific Rim International Conference on
Advanced Materials and Processing (PRICM 3)
Edited by M.A. Imam, R. DeNale, S. Hanada,
Z. Zhong and D.N. Lee
The Minerals, Metals & Materials Society, 1998

Introduction

Ferroelectric materials, which have perovskite crystalline structure, are now applied in many fields such as actuators, transducers and DRAMs for computer memories. Among these materials, there exists a subgroup that is called relaxor ferroelectrics. Unlike normal ferroelectrics, materials included in this subgroup do not obey the Curie-Weiss law upon phase transition and the reciprocal of the dielectric constant has a quadric dependence on temperature. Furthermore, the temperature at which the reciprocal takes minimum has a strong frequency dependence. This type of phase transition between ferro and paraelectric phase is called diffuse phase transition [1]. Many of the relaxor ferroelectrics have transition temperatures relatively close to room temperature, and due to the broad temperature dependence, dielectric, piezoelectric, electrostrictive and pyroelectric constants at room temperature are large compared with normal ferroelectric materials.

There have been many attempts to clarify the mechanism of diffuse phase transition. Smolensky et al. were the first to present a model of a nanoscopic compositional fluctuation on the B site of the perovskite structure from their temperature dependent permittivity measurements [2]. Vielhland et al. have proposed a model by analogy to magnetic spinglass [3]. There also exists a model concerning the degree of ordering of the ions occupying the B site of the perovskite structure [4]. However, validity of the models has not yet been checked experimentally. Many of the experimental works are making use of dielectric measurements to investigate macroscopic properties together with diffraction experiments to clarify microscopic ones. However, no evidence of compositional fluctuation or glassy polarization has been reported up till now. One reason for this lack in information is the difficulty to investigate atomistic structures such as short range ordering or clustering by these methods. Mössbauer spectroscopy is a powerful method for such purposes. Sklyarevskii et al. have measured the spectrum of ferroelectric $Pb(Fe_{1/2}Nb_{1/2})O_3$ (PFN) at room temperature and found that the spectrum of ferroelectric phase shows quadrupole split lines with broad half widths. The crystalline structure of ferroelectric phase of PFN is rhombohedral but the distortion is very small and is difficult to detect by normal diffraction methods. They have assigned the origin of the split to the electric field gradient (EFG) due to the rhombohedral crystalline structure [5]. Darlington has measured the temperature dependence of the γ-ray absorption and concluded that the soft-mode theory is not applicable to the diffuse phase transition [6]. However, up to now, there are few works concerning the systematic temperature dependence of Mössbauer spectrum.

This paper describes temperature dependent measurements of dielectric properties and Mössbauer spectra performed on ceramic $Pb(Fe_{1/2}Nb_{1/2})O_3$ (PFN). These investigations were carried out in order to clarify the atomistic mechanism of diffuse phase transition.

Experimental

The preparation of the ceramic specimens was carried out by a conventional mixed oxide technique where the source materials were PbO(99.99%), Fe_2O_3(99.99%) and Nb_2O_5(99.9%). Suitable mixture of oxides were weighed and mixed and then pressed to form a disk of 20mm diameter and 3 to 6mm thick. The disks were placed in an alumina crucible and calcined at 1173K for 2h. The reacted disks were ground to powder and then again pressed into disks. The disks were placed in an alumina crucible and sintering was performed at 1273K for 2h. Calcining and sintering were carried out at PbO atmosphere. The formation of perovskite single phase was confirmed by powder X-ray diffraction.

Plates with thickness of approximately 0.5mm were cut from the disks for the samples for

dielectric measurements. The plates were polished to obtain two parallel plains, which were then electroded by sputtering gold on the surface. For the samples for Mössbauer spectroscopy, the sintered disks were ground to powder with size less than 10μm and dispersed in carbon powder. An adequate amount of the mixture of PFN and carbon powder corresponding to an thickness of 25μm for PFN was fixed in an aluminum ring.

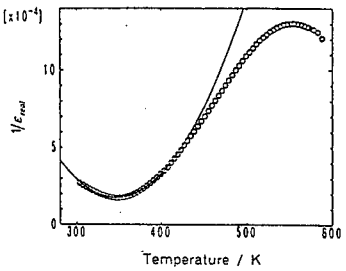


Figure 1: Temperature dependence of the reciprocal of dielectric constant measured at the frequency of 1kHz.

The temperature dependence of dielectric constant was measured by HP4192A impedance meter. Electric polarization-electric field hysterisis loops were measured by mean of Sawyer-Tower bridge with a maximum electric field amplitude of 2MV/m. Mösssbauer spectra were measured by a transmission method using a ^{57}Co γ-ray source and the velocity was calibrated with α iron

Results and Discussion

Temperature dependence of the reciprocal of dielectric constant (1/ε) is shown in figure 1. The shape of the curve is quadric which is typical to diffuse phase transition. The temperature at which 1/ε takes the minimum, T_t, corresponding to the Curie temperature for a

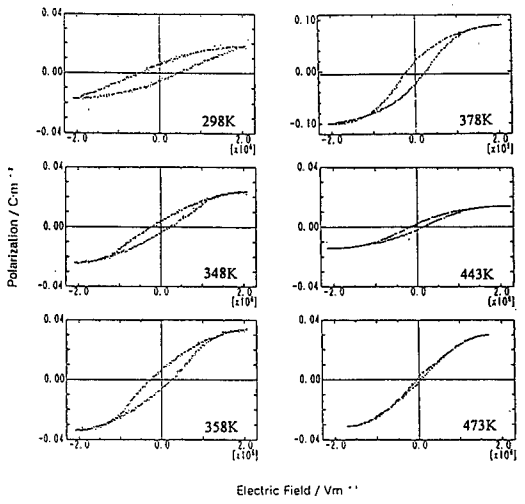


Figure 2: Hysteresis loops measured at various temperatures. Note that T_t =358K.

normal ferroelectric, is 358K (at 1kHz). Electric hysteresis loops measured at various temperatures are shown in figure 2. The loops measured at temperatures lower than T_t show typical shapes for a ferroelectric phase. Loops are also observed at temperatures higher than T_t. This indicates that polarization exists at the temperature range. However, whether the polarization exists throughout the phase or locally in a cluster form cannot be distinguished from these results. In order to clarify this point, temperature dependence of the Mössbauer spectra was measured.

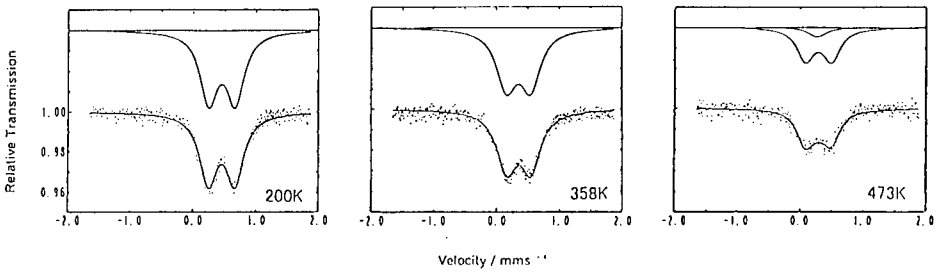


Figure 3: Mössbauer spectra measured at 200K ($<T_t$), 358K ($=T_t$) and 473K ($>T_t$).

In figure 3, spectra measured at 200K ($<T_t$), 358K ($= T_t$) and 473K ($> T_t$) are shown. The first two spectra consist of a set of broad quadrupole split double lines. This was first considered to be due to the electric field gradient (EFG) arising from rhombohedral crystalline structure. However, even though a single peak component has appeared, the doublet component is still the major component in the third spectrum measured at 473K. At this temperature, the structure is cubic which should not have any EFG. Therefore the quadrupole splitting has to be assigned to a reason different from the crystalline structure. The way how the ions are distributed on the B sites of the perovskite structure is presumed to be the origin for the splitting.

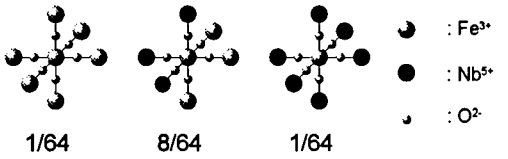


Figure 4: The three possible local configurations for Fe^{3+} and Nb^{5+} ions which do not induce an EFG at the B site of the core.

When considering only the nearest neighboring perovskite unit cells, the three local configurations for Fe^{3+} and Nb^{5+} ions shown on figure 4 are the only ones which do not induce an EFG at the B site of the core. The ratios of each one when assuming a random distribution of the ions are also listed on the figure. This means that the ratio of the single peak component should be 10/64=0.16 under this assumption.

The observed ratio of the single peak component as a function of temperature is shown in figure 5. At temperatures well above T_t, where the sample is paraelectric single phase, the ratio is less than 0.16. This indicates that Fe^{3+} and Nb^{5+} ions are not distributed randomly on the B sites.

In figure 6, temperature dependence of isomershifts, half widths and quadrupole splitting for the doublet and single peak component are shown. The values from the spectrum measured at 290K (room temperature) after once heated up to 573K are also plotted. The-

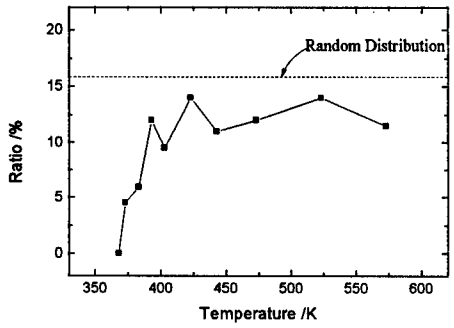


Figure 5: Ratio of the single peak component as a function of the measured temperature. The ratio assuming a random distribution of ions is depicted as a dashed line.

se values coincide well with the ones from the spectra measured before heating. This is an implication for the measured tendency to be due to diffuse phase transition it self and not to failure in reaching an equilibrium state during specimen preparation. Isomer shifts of both components decrease as temperature increases. This is a typical tendency for iron oxides. The quadrupole splitting for the doublet component takes a minimum at T_t, while the half width takes a maximum. The former value represents the magnitude of EFG at the Fe^{3+} sites, while the latter corresponds to how scattered the distribution of the local environment around the sites are.

From the temperature dependence, the following transformation process can be considered. As the temperature approaches T_t at the ferroelectric phase, perovskite unit cells which have a B site with an EFG in ferroelectric rhombohedral phase transform to clusters with cubic

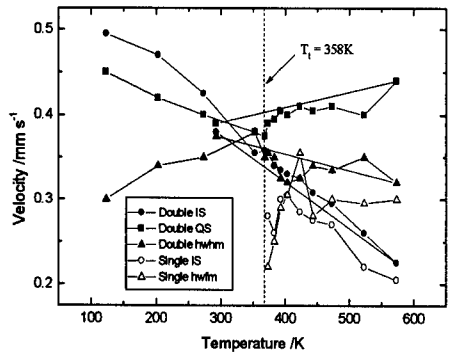


Figure 6: Temperature dependence of Mössbauer parameters for the double and single peak components.

structure, and therefore the average magnitude of EFG decreases and the distribution of the local environment broadens. As the rhombohedral distortion is very small and the size of the cubic clusters are of few unit cells, the appearance of the clusters are impossible to detect by conventional diffraction methods. At T_t, both ferroelectric rhombohedral phase and paraelectric clusters with cubic structure coexist. As the temperature increases from T_t, the remaining ferroelectric rhombohedral phases which consist with perovskite unit cells without EFG transform to cubic clusters and form a paraelectric phase together with the previously transformed clusters. Therefore, the width of distribution narrows. The increase of quadrupole splitting is presumed to be due to thermal expansion.

As mentioned previously, Fe^{3+} and Nb^{5+} ions are not distributed randomly. This nonrandom distribution can explain the wide temperature range where the local transformation occurs locally. The temperature at where a region transform depends on the ratio of the ions in that region. Furthermore, as the transformation occurs in a cluster form, it is natural to assume a phase separation between Fe^{3+} rich and Nb^{5+} rich regions. However, these regions should have sizes of only few unit cells and are undetectable by normal diffraction measurement methods. This model supports the compositional fluctuation as the origin for the diffuse phase transition. However, the size of region where the composition fluctuates is smaller than that proposed by Smolenski et al.[2].

Conclusion

The mechanism of diffuse phase transition in $Pb(Fe_{0.5}Nb_{0.5})O_3$ ferroelectric ceramic is investigated by means of dielectric measurements and Mössbauer spectroscopy. Ferroelectric behavior is observed at temperatures above phase transition temperature. From the Mössbauer measurements, the nonrandom distribution of Fe^{3+} and Nb^{5+} ions on the B site of perovskite structure is indicated. Moreover, preferential transformation from ferroelectric phase to paraelectric clusters in the vicinity of perovskite unit cells that have B sites without EFG is suggested.

References

1. L.Eric Cross, "Relaxor Ferroelectrics," Ferroelectrics, 76(1987), 241-267.

2. G.A.Smolensky, V.A. Isupov, A.I.Agranovskaya and S.N.Popov, "Ferroelectrics with diffuse phase," Soviet Physics Solid State, 2(1961), 2584-2594.

3. D.Viehland, S.J.Jang and L.E.Cross, "Freezing of the polarization fluctuations in lead magnesium niobate relaxors," J. Appl. Phys., 68(6)(1990), 2916-2921.

4. C.G.F.Stenger, F.L.Scholten and A.J.Burggraaf, "Ordering and diffuse phase transition in $Pb(Sc_{0.5}Ta_{0.5})O_3$ ceramics," Solid State Commun., 32(1979), 989-992.

5. V.V.Sklyzrevskii et al., "Mossbauer effect in the ferroelectric $Pb(Fe_{1/2}Nb_{1/2})O_3$," JETP Lett., 3(1966), 135-138.

6. C.N.W.Darlington, "Studies of transitions in ordered and disordered perovskites: x-ray and Mössbauer scattering experiments," J. Phys.: Condens. Matter, 3(1991), 4173-4185.

EFFECTIVE PAIR INTERACTION ENERGIES IN RANDOM FCC BINARY ALLOYS BY DIRECT CONFIGURATIONAL AVERAGING AND PHASE DIAGRAMS

T. Hoshino[a], M. Asato[a], and K. Masuda-Jindo[b]
[a]Department of Applied Physics, Faculty of Engineering, Shizuoka University, Hamamatsu 432, Japan
[b]Department of Material Science and Engineering, Tokyo Institute of Technology, Yokohama 227, Japan

Abstract

The concentration dependence of effective pair interaction energies (EPIE's) in the low-concentrated disordered fcc binary alloys (Pd- and Cu-based alloys) as well as impurity pair inteaction energies (IPIE's) in fcc metals (Ru, Rh, Pd, Ag, Co, Ni, Cu) are calculated by use of the accurate impurity KKR-Green's function method. The *randomness* of atomic arrangements is taken into account by the direct configurational averaging method; the present work treats only the *randomness* of atomic arrangements in the impurity cluster, where the potentials are determined self-consistently. The calculated results agree with the values of EPIE's, determined from diffuse-scattering experiments by use of the inverse Monte Carlo method. The temperature-concentration dependence for the solid solubility limit of impurities in metals, such as Co in Cu and Ru in Pd, may be reproduced fairly well by the cluster variational method based on the present IPIE's.

The Third Pacific Rim International Conference on Advanced Materials and Processing (PRICM 3)
Edited by M.A. Imam, R. DeNale, S. Hanada, Z. Zhong and D.N. Lee
The Minerals, Metals & Materials Society, 1998

Introduction

The first-principles study for phase diagrams needs to combine at a high level of accuracy both quantum-mechanical and statistical-thermodynamical contributions. One of the most efficient statistical-mechanichs techniques is the cluster-variational method (CVM)[1], which provides a good description of the free energy as a function of short-range order. The CVM requires, as input, effective cluster interaction energies (ECIE's) that determine ordering or clustering reactions occurring in the alloy systems. These ECIE's must be calculated accurately by first-principles quantum-mechanical calculations. At present there are mainly two approaches to obatin ECIE's, based on the density functional theory (DFT). The first one is the so-called Connolly-Williams method[2] which assumes that the total energy (TE) can be written as a sum of configuration independent ECIE's multiplied by the multisite correlation functions. The second one is the generalized perturbation method[3,4], using a perturbative treatment about the completely disordered state determined by use of the coherent-potential approximation (CPA). However, both methods have their characteristic drawbacks. The ECIE's cannot be determined uniquely by the first one, while the second one is based on the single-site approximation (SSA) being not unproblematic for alloys with charge transfers and treats only the band-energy changes[5].

We have recently succeeded to calculate the defect interaction energies in fcc metals, such as vacancy-impurity and impurity-impurity interaction enegies[6,7], which are the TE changes due to the atomic rearrangements. The calculations are based on the KKR Green's function method for impurities, combined with the local-spin-density approximation (LSDA) to the DFT. The charge transfer effect, being neglected in the SSA, can be exactly treated in the impurity cluster since the potentials are determined self-consistently and the TE's are calculated accurately by the generalized Lloyd's formula which allows one to analytically sum all perturbations of the wave functions over the whole infinite space. The measured defect energies have been reproduced very accuately and the micromechanism of defect interactions have been explained by the calculated results. The purpose of present work is to apply the same method to the systematic study of the impurity pair interation energies (IPIE's) in fcc metals (*dilute limit*) and also to develop the impurity KKR-Green's function method to obtain effective pair interaction energies (EPIE's) in the low-concentrated disordered fcc binary alloys $H_{1-c}X_c$ (H=host, X=impurity; $c \leq 0.1$)[5]. The *randomness* of atomic arrangements is taken into account by the direct configurational averaging (DCA) method[5,8]. The details of the calculational procedure are discussed in Refs. 6 and 7. Differently from the previous works, however, the host potentials are also determined self-consistently by use of the program of Jülich group[9,10].

Calculated results for hosts

Figures 1 show the lattice-parameter dependence for TE's of Ru, Rh, Pd, Ag, Co (ferro-magnetic), Ni(ferro-magnetic), and Cu. The measured values are also shown by the vertical lines. The lattice structure of Rh, Pd, Ag, Ni, and Cu is fcc, while that of Ru and Co is hcp. In the present work, for simplicity we assumed fcc structure for Co and Ru; the 1st nearest-neighbor (NN) atomic environment of hcp is same to that of fcc. It is seen in Figs. 1 that the lattice parameters of Rh, Pd, and Ag are reproduced very well by the present LSDA calculations, while those of Ni and Cu are underestimated by ~ 2 %. At present stage it is known that these small discrepancies are corrected by the calculations based on the full-potential generalized-gradient approximation[11].

Calculated results for IPIE's(*dilute limit*)

Figures 2 show the calculated 1st NN IPIE's in Ru, Rh, Pd, Ag (Fig. 2(a)), and Co, Ni,

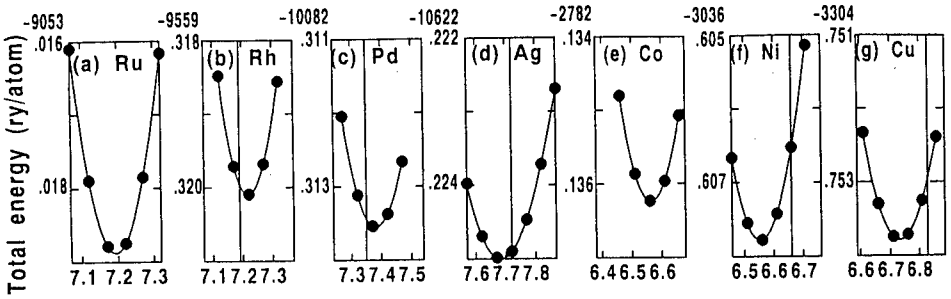


Figure 1: Lattice parameter dependence for total energies.

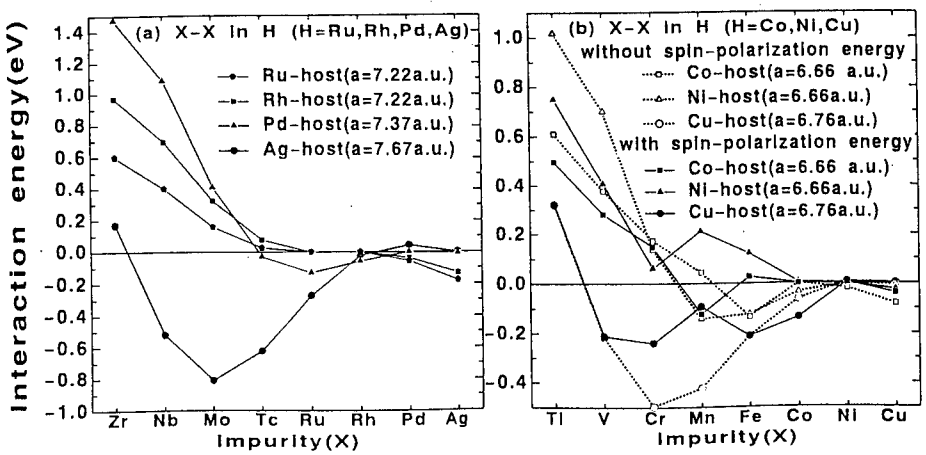


Figure 2: Interaction energies (a) between two identical $4d$ impurities (Zr$\sim$Ag) in Ru, Rh, Pd, and Ag and (b) between two identical $3d$ impurities (Ti$\sim$Cu) in Co, Ni, and Cu. The calculated results with and without spin-polarization effect are shown for $3d$ impurities in Cu, Ni, and Co(b).

Cu(Fig. 2(b)). Tables I and II list the numerical values for calculated n-th NN interaction energies ($n = 1 \sim 4$) in Pd and Cu. The negative value means the attractive interaction (AI) between impurities, while the positive one the repulsive interaction (RI). It is seen in Tables I and II that the 1st NN interaction is dominant. Thus, we may believe that the differences between the segregation (clustering) and solid solution behavior of the corresponding binary alloys can be distinguished by only the dominating 1st NN interaction: an AI leads to segregation (presumably, existence of miscibility gap) and a RI to a solid solution. In almost all cases the theory explains the observed experimental behavior[12]; some results have already been discussed in Ref.6. The detailed systematic comparisons between the theoretical and experimental results will be discussed elsewhere[13].

Here we discuss only two fundamental points. First we note that the $3d$ ($4d$) impurities in Cu(Ag) are mainly segregated (strong AI) since the covalent interaction between d impurities is large. The small interactions for Pd (Ag) in Ag (Pd) and Ni (Cu) in Cu (Ni), seen in Figs. 2, lead to the experimentally known continuous solid solubility. The second one is the importance of magnetism of Mn, Fe, Co impurities. As seen in Fig. 2(b), the positive IPIE's of NiMn, NiFe, NiCo, corresponding to the experimentally known solid solution, can never be reproduced without the magnetic energy contribution; the decrease of magnetic

Table I. Calculated nth nearest-neighbor interaction energies of $E_n^{int}(n = 1 \sim 4)$ of impurity dimers in Pd (in eV). Negative values mean attraction, positive ones repulsion. The lattice parameter of Pd is 7.37 a.u.

impurity	Zr	Nb	Mo	Tc	Ru	Rh	Pd	Ag
E_1^{int}	1.475	1.088	.413	-.030	-.131	-.059		-.009
E_2^{int}	.045	.064	.091	.085	.046	.010		.001
E_3^{int}	.067	.076	.065	.082	.007	-.001		.006
E_4^{int}	.057	.159	.156	.119	.028	-.003		-.010

Table II. Calculated nth nearest-neighbor interaction energies $E_n^{int}(n = 1 \sim 4)$ of impurity dimers in Cu (in eV). There are two magnetic solutions for impurity pairs of Cr$\sim$Co; for V impurity pairs, the two magnetic solutions exist only for the distances beyond the 2nd neighboring sites. The ground states and excited states (in parentheses) are shown. Negative values mean attraction, positive ones repulsive interaction. The lattice parameter of Cu is 6.76 a.u..

impurity	Ti	V	Cr	Mn	Fe	Co	Ni	Cu	Zn
E_1^{int}	.321	-.214	-.241	-.093	-.211	-.136	.006		.077
			(.137)	(.010)	(-.041)	(-.038)			
E_2^{int}	-.059	.049	-.036	-.049	.019	.022	.006		-.001
			(.027)	(.031)	(.034)	(.043)			
E_3^{int}	-.088	-.090	-.036	-.026	-.038	.000	.006		.000
		(-.087)	(-.003)	(-.002)	(.006)	(.011)			
E_4^{int}	.160	.120	.017	.020	.004	-.003	-.003		-.001
		(.153)	(.067)	(.036)	(.051)	(.006)			

moments (MM's) due to the paring of $3d$ impurities results in the energy loss (repulsion)[6,7]. It is also found from the comparison between the calculated results with and without the spin-polarization effect (SPE), shown in Fig.2(b), that the interaction for Ti$\sim$Cr in Ni and Ti$\sim$Mn in Co becomes less repulsive by the magnetic effect. This reduction of RI, due to the SPE, is also explained by considering that the parallel coupling between MM's of impurity and host atoms becomes unstable for these (early and middle) $3d$ impurities[13].

Concentration dependence for EPIE's (low concentration)

We discuss the concentration dependence of 1st NN EPIE's of Pd- and Cu-based alloys. The discussion is restricted to the low-concentration region since the alloy effect outside the impurity cluster (Fig.1 in Ref. 5) is completely neglected in the present calculations. It is also noted that the lattice parameters of alloys are fixed to the values of major components, shown in Fig. 2. Table III lists the results for PdRu, PdRh, PdAg, CuCo, CuNi, and CuZn. In order to show the accuracy of the present calculations, we compare the present results with diffuse-scattering measurements[6,14]. We have only a few examples of alloys, where the interaction energies have been determined from diffuse-scattering data via inverse Monte Carlo (MC) calculations[6,14]. For NiCu, the diffuse-scattering data yield very small interaction energies (E_1^{int}=-0.024 eV, E_2^{int}=0.011, E_3^{int}=0.000, E_4^{int}=0.000 for c_{Cu}=0.41). These small interaction energies are easily expected by the present results of *dilute limit* (Cu-rich end and Ni-rich end) and the low-concentration (c=1/18 in Table III); the interactions of

NiCu may be small over all the concentration region. For CuZn, the experimental results are E_1^{int}=0.047,E_2^{int}=-0.013, E_3^{int}=-0.003 eV, E_4^{int}=0.000 eV for c_{Zn}=0.224 and E_1^{int}=0.037 eV, E_2^{int}=-0.003 eV for c_{Zn}=0.311. These results already agree with our calculations of *dilute limit*, E_1^{int}=0.077 eV, E_2^{int}=-0.001 eV, E_3^{int}=0.000 eVE_4^{int}=-0.001 eV. The extrapolated vlaues, E_1^{int},from our calculations of c_{Zn}=0, 1/18 are 0.033 eV (c_{Zn}=0.224), 0.015 eV (c_{Zn}=0.311), corresponding to the measured values 0.047 and 0.037 eV, respectively.

Table III. Concentration dependence of 1st nearest-neighbor interaction energies of $4d$ ($3d$) impurity dimers in Pd (Cu) (in eV). Negative energies mean attraction, positive ones repulsion.

alloy	c=0	c=1/18	17/18	c=1
$Pd_{1-c}Ru_c$	-.131	-.113	–	-.056
$Pd_{1-c}Rh_c$	-.059	-.047	-.031	-.039
$Pd_{1-c}Ag_c$	-.008	-.006	.036	.042
$Cu_{1-c}Co_c$	-.136	-.114	–	-.038
$Cu_{1-c}Ni_c$	.006	.004	–	-.003
$Cu_{1-c}Zn_c$	.077	.066	–	–

Solid solubility limit

Figure 3 shows the preliminary results for the temperature-boundary dependence of solid solubility for Co in Cu, as a function of impurity concentration, which have been obtained by the tetrahedron cluster variational method (T-CVM) based on the present IPIE's (*dilute limit*). There are two reasons to choose Co (magentic impuritiy) in Cu ;(1) the distortion effect, being neglected in the present calculations, may be small for these systems of a small lattice-misfit and (2) the impurity pair interactions may be short-range, as seen in Table II. Another reason is that the results are compared with those obtained by the MC method (MCM) (Fig.4.3 in Ref.14). As seen in Fig.3, the MCM calculations, using a little bit different values compared with the present IPIE values, show that (1) the inclusion of IPIE's up to the 2nd neighbors(MCM2 in Fig.3) reproduces the experimental result; (2) only the chemical interaction energies (average of IPIE's of ferro- and antiferro- couplings)[6] are important and the magnetic interation energies (difference between IPIE's of ferro- and antiferro- couplings) may be neglected (compare MCM2(chem) with MCM(chem+mag)). Thus, in the present paper we treat only the chemical interaction energies for Co in Cu. The present T-CVM calculations show that the inclusion of only the 1st NN IPIE (strong attraction) overestimates the measured temperatures very much (T-CVM1(chem) in Fig.3); the clustering effect of Co impurities is overestimated. This means the importance of the 2nd neighbor RI, shown in Table II. In the present paper we treat approximately the effect due to the 2nd NN RI; the 2nd NN RI may be included in the 1st NN IPIE as the sum of interaction enegies is kept [15]. As seen in Fig.3 (T-CVM2(chem)), the 2nd neighbor RI effect reduces the 1st NN AI and leads to a nice agreement with the experimental and MCM results. In order to show the accuracy of the present T-CVM calculations, we also carried out the T-CVM calculations with the IPIE values used in the previous MCM calcu-

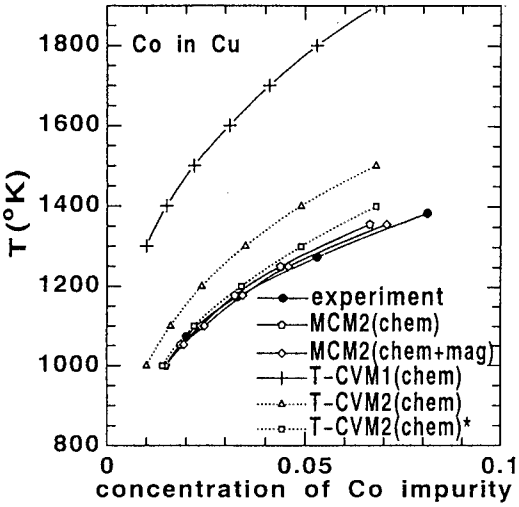


Figure 3: Temperature-concentration dependence of solid solubility limit for Co in Cu.

lations[5,6,14](MCM2(chem)); the calculated result(T-CVM2(chem)* in Fig.3) agrees very well with MCM2(chem) in Fig.3. For Ru in Pd, we found that the inclusion of IPIE's up to the 4th neighbors reproduce the experimental result very well.

Summary and Future Problem

We have shown that the impurity KKR-Green's function method, combined with the DCA, is accurate to calculate EPIE's, at least, for a low-concentration region of alloys. The solid solubility in the very low concentration region may be reproduced fairy well by the CVM combined with the present IPIE's (or EPIE's). The study of the lattice distortion effect, being important for the systems of a large lattice-misfit, may be also possible by the present impurity KKR Green's function method[11]. For the complicated concentration dependence of the high-concentrated alloys, the alloy effect outside the impurity cluster becomes important. The use of CPA medium is strongly desirable.

Referecnces

1. R. Kikuchi, "A Theory of Cooperative Phenomena", Phys. Rev. **81**(1951),988-1003.

2. J. W. Connolly and A. R. Williams, "Density-functional theory applied to phase transformations in transition-metal alloys", Phys. Rev. B**27**(1983),5169-5172.

3. F. Ducastelle and F. Gautier, "Generalized Perturbation Theory in Disordered Transitional Alloys: Application to the Calculation of Ordering Energies", J. Phys. F**6**(1976),2039-1062.

4. A. Gonis, M. Sluiter, P. E. A. Turchi, G. M. Stocks, and D. M. Nicholson, "Electronic Structure, Alloy Phase Stability and Phase Diagrams", J. Less-Common Met.**168**(1991),127-144.

5. "Effective Pair Interactions in Ramndom Alloys by Direct Configurational Averaging". Propertes of Complex Inorganic Solids, ed. A. Gonis *et al.*(Plenum Press, New York, 1997),129-132.

6. T. Hoshino, W. Schweika, R. Zeller, and P. H. Dederichs, "Impurity-Impurity Interactions in Cu, Ni, and Pd",Phys. Rev. B**47**(1992),5106-5117.

7. "Interaction Energies of Point Defects in Metals", Computational Physics as a New Frontier in Condensed Matter Research, ed. H. Takayama *et al* (Physical Society of Japan, Tokyo, 1995),105-113.

8. H. Ehrenreich *et al.*, eds., Solid State Physics, vol.**47** (Academic Press, London, 1994), 33-176.

9. R. Zeller, "Green-Function Method for Electronic Structure of Periodic Crystals", Int. J. Mod. Phys. C**4**(1993),1109-1116.

10. K. Wildberger, P. Lang, R. Zeller, and P. H. Dederichs,"Use of Fermi Dirac Distribution in Ab-initio Green's Function Calculations",Phys. Rev. B**52**(1995),11502-11508.

11. T. Hoshino, N. Papanikolaou, R. Zeller, P. H. Dederichs, M. Asato, T. Asada, and N. Stefanou, "First-Principles Calculations for Vacancy Formation Energies in Cu and Al; Non-local Effect beyond LSDA and Lattice Distortion" (Paper presented at the IUMRS-ICA-97, Chiba, Japan, 16 September 1997, to be published in Computational Material Science),547.

12. T. B. Massalski *et al.*, eds., Binary Alloy Phase Daiagrams,2nd ed.(ASM International, New York, 1990).

13. T. Hoshino and M. Asato, in preparation

14. W. Schweika, Springer Tracts in Modern Physics**141** (Springer, Berlin, 1997),51-98.

15. "Monte Carlo Simulation of Order-Disorder Phenomena", ed. J. L. Morá-López *et al.*, Structural and Phase Stability of Alloys (Plenum, New York, 1992),53-64.

GROWTH OF Ni_3Al IN Ni/NiAl DIFFUSION COUPLES

K.Fujiwara, Z.Horita and M.Nemoto

Department of Materials Science and Engineering, Faculty of Engineering,
Kyushu University, Fukuoka 812-81, Japan

Abstract

In this study, single crystalline Ni is coupled with a NiAl intermetallic (Ni/NiAl) and subjected to diffusion annealing. The Ni_3Al phase (γ' phase) forms at the interface having the same crystallographic orientation as the Ni phase (γ phase). When the couples are annealed at a temperature of 1523 K, the γ' phase grows initially towards the γ phase and later the growth direction changes to the NiAl phase (β phase). The corresponding stages of growth occur at low and high rates but each stage follows a parabolic law that the square of the γ' phase width is proportional to annealing time. When the couples are annealed at a temperature of 1173 K, the growth of the γ' phase occurs simultaneously to the directions of the γ and β phases. Furthermore many grain boundaries form within the γ' layer and the growth is controlled by the grain growth through grain boundary diffusion, which gives rise to the fourth power dependence of the layer width on annealing time. Use of single crystalline Ni at higher annealing temperatures suggests potential utility of such reaction diffusion for fabrication of Ni_3Al single crystal.

The Third Pacific Rim International Conference on
Advanced Materials and Processing (PRICM 3)
Edited by M.A. Imam, R. DeNale, S. Hanada,
Z. Zhong and D.N. Lee
The Minerals, Metals & Materials Society, 1998

Introduction

Diffusion experiments of Ni/NiAl couples have shown [1-3] that the Ni_3Al layer (hereafter called γ' layer) forms at the couple interface. The layer grows with diffusion annealing but it exhibits different growth behavior depending on the annealing temperature. Janssen showed [1] that the layer takes irregular configuration with varying width at temperatures below 1273 K but, at temperatures above 1373K, the layer grows with an equal width and smooth configuration. The growth rate is high below 1273 K and even exceeds those at the temperatures higher than 1273 K. Similar results were also reported by Watanabe et al.[2,3]. They further demonstrated using analytical transmission electron microscopy (AEM) that the γ' layer exhibits a crystallographic orientation identical to that of the original Ni when the couples are annealed above 1373K. However, no particular orientation relationship exists for the couples annealed below 1273 K but instead the layer consists of many grains with large misorientations. It was concluded [1,3] that the grain boundary diffusion dominates the growth process of the γ' layer at the lower annealing temperatures and the volume diffusion governs at the higher annealing temperatures.

An important suggestion deduced from the AEM study of Watanabe et al.[2,3] is that it is possible to control the crystallographic orientation of the γ' layer. The layer grows with the same orientation as the Ni when a Ni/NiAl couple is annealed at temperatures above 1373K. Thus, it is anticipated that the employment of Ni single crystal for a diffusion-couple end-member permits fabrication of a Ni_3Al single crystal. In this study, diffusion experiments of Ni/NiAl are conducted to examine potential utility of reaction diffusion for fabrication of Ni_3Al single crystals. This study adopts single crystals for the Ni end member and compare with the behavior for the polycrystalline Ni end member. This study also examines the growth kinetics of the γ' layer occurring at lower annealing temperatures.

Experimental Procedures

An ingot of Ni-45mol%Al was prepared from high-purity Ni (99.97%) and Al (99.99%) by arc-melting in an argon atmosphere. The ingot was reversed and remelted several times to reduce segregation. The weight loss during fabrication of the ingot was much less than 0.5%. The ingot was encapsulated in a quartz tube under an atmosphere of argon and subjected to homogenization at 1323 K for 605 ks (7 days). Blocks with dimensions of 2x3x6 mm^3 were cut from the ingots for one of the two end members of diffusion couples. For the other end member of diffusion couples, blocks with the same dimensions were prepared from high-purity Ni (99.99%) in the forms of polycrystal and single crystal. Polycrystalline Ni was made by rolling at room temperature and annealing at 1273 K for 10.8 ks (3 hours) in a vacuum atmosphere. A single crystalline Ni rod with dimensions of 10 mm in diameter and 50 mm in length was purchased from MaTeck in Germany through Techno Chemics Co. in Japan.

A 3x6 mm^2 plane of each diffusion-couple end-member was polished with 0.1 μm alumina powder and rinsed thoroughly with acetone and methanol. Both the Ni and Ni-45mol%Al end member were immersed in a solution of 10vol%HCl to remove surface layers and coupled while kept in the solution. Each couple was mounted on a window frame made of stainless steel with mica sheets inserted between the couple and the frame to avoid adhesion. While mounted on the frame, the couple was encapsulated in a quartz tube under an argon atmosphere. Diffusion annealing was conducted at 1173 K and 1523 K for the selected periods in the range from 21.6

ks (6 hours) to 2592 ks (30 days).

The couples after the diffusion annealing were polished for optical microscopy observations on the plane perpendicular to the coupled interface. The surface was finished with cloth containing 0.1 μm alumina powder and lightly etched using a mixture containing 4g $CuSO_4$, 20ml HCl and 20ml H_2O.

Results

Figure 1 shows optical micrographs of the Ni/Ni-45%Al couples annealed at 1523 K for 259.2 ks (3 days), 432 ks (5 days), 518.4 ks (6 days) and 1296 ks (15 days). Ni single crystals were used for the end members of the couples. In the micrographs, the NiAl phase (hereafter called β phase) is arranged on the right and this phase is easily identified because of the formation of finely separated twin boundaries as a consequence of martensitic transformation. The γ' phase is visible between the Ni phase (hereafter called γ phase) and β phase with the layer width increasing with an increase in annealing time. The present results are consistent with earlier studies [2,3] that the γ' phase grows towards the γ phase while the Kirkendall interface stays at the γ'/β interface. However, this consistency is applied only to the couples annealed for up to 5

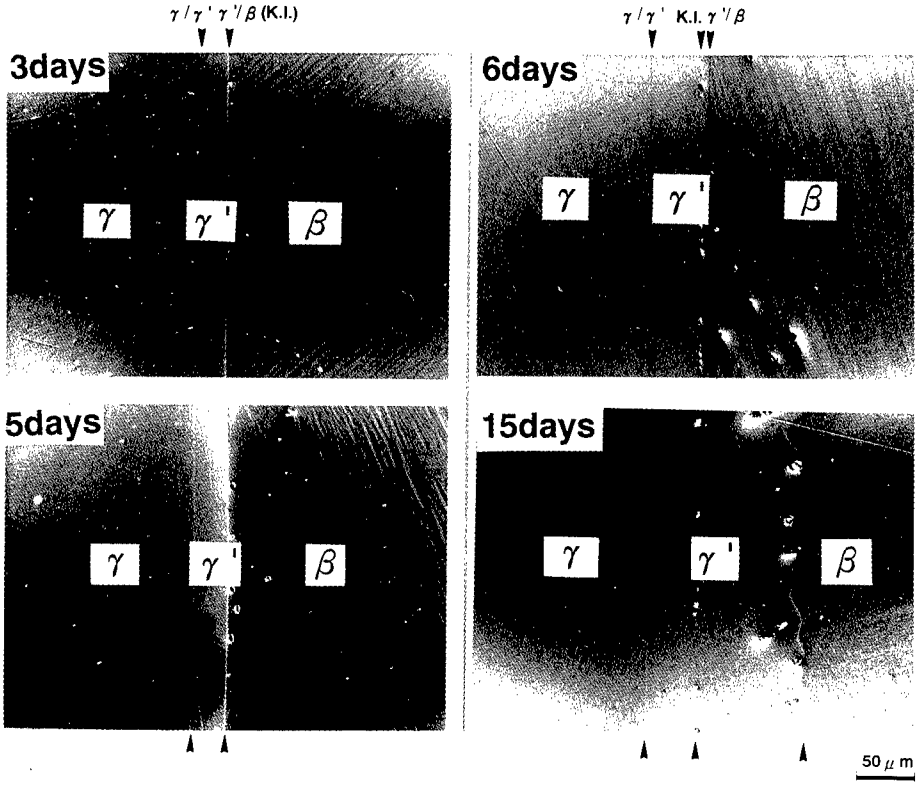


Figure 1: Optical micrographs of Ni/Ni-45%Al couples annealed at 1523 K for 3 days, 5 days, 6 days and 15 days. K.I. denotes the Kirkendall interface.

days. For the couple annealed for 6 days, the Kirkendall interface lies within the γ' phase near the γ'/β interface.This indicates that the γ' phase started growing to the direction of the β phase after annealing for more than 5 days. Observation of the couple annealed for 15 days reveals that there appears to be little growth of the γ' phase towards the γ phase but the growth occurred mainly towards the β phase, forming a wavy γ'/β interface. The same growth behavior was also observed when polycrystalline Ni was used for an end member of the couples.

The square of the γ' phase width, W^2, measured from the micrographs is plotted in Fig.2 against annealing time, t, where (a) includes all data points and (b) plots for those after annealing for up to 6 days. When the interfaces exhibited a wavy configuration as for the γ'/β interface after prolonged annealing, the average values were taken for the plot. Linearity holds with two different slopes: a small slope for the shorter annealing periods and the linear relationship passes through the origin, and a large slope for the longer annealing periods and the linear relationship does not pass through the origin. This change in slope coincides with the change in the growth direction of the γ' phase layer from towards the γ phase to towards the β phase as shown in Fig.1. There is no appreciable difference in the growth rate between the usages of single crystalline and polycrystalline Ni for an end member of the couples.

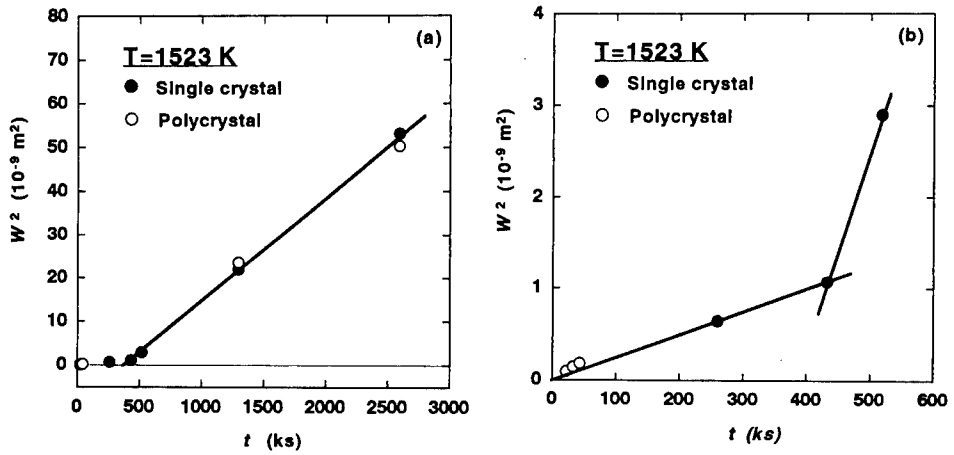
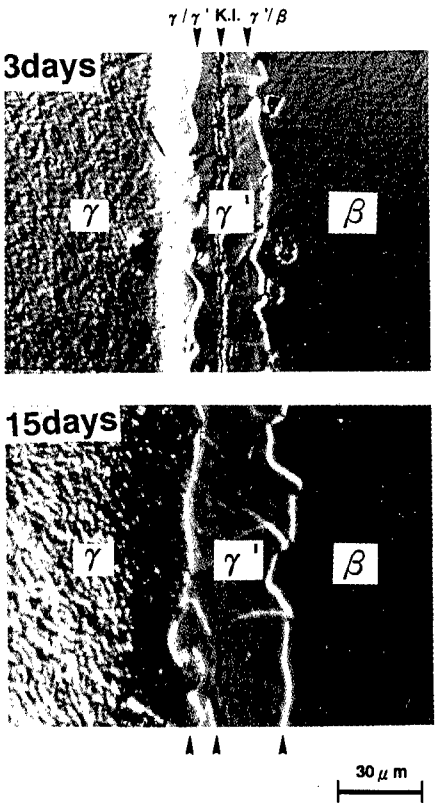


Figure 2: Square of γ' phase width, W^2, plotted against annealing time, t, for annealing temperature of 1523 K: (a) couples annealed for up to 30 days and (b) couples annealed for up to 6 days.

Figure 3 shows optical micrographs of the Ni/Ni-45%Al couples annealed at 1173 K for 259.2 ks (3 days) and 1296 ks (15 days). Ni single crystals were used as the end members of the couples. The γ' phase is visible between the γ and β phases but there are several features different from the couples annealed at 1523 K. First, the Kirkendall interface stays around the middle of the γ' layer for both couples annealed for 3 and 15 days, second, the γ/γ' and γ'/β interfaces are both wavy, and third, there are many grain boundaries within the γ' layer. These features are the same as observed in earlier studies [2,3].

Figure 4 plots the γ' phase width against annealing time for the annealing temperature of 1173 K where the data points are plotted in the relationships of W^2 vs t and W^4 vs t. When the origin is included, good linearity holds for the relationship of W^4 vs t but this is not the case for W^2 vs t.



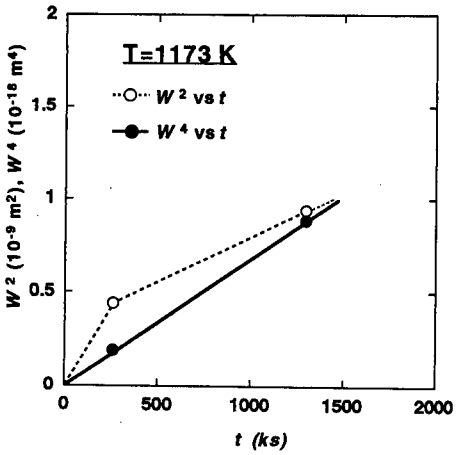


Figure 3 (left): Optical micrographs of Ni/Ni-45%Al couples annealed at 1173 K for 3 days and 15 days.

Figure 4 (above): γ' phase width plotted against annealing time in relationships of W^2 vs t and W^4 vs t for annealing temperature of 1173 K.

The results are again consistent with an earlier study using polycrystalline Ni [3].

Discussion

Based on an AEM study reported earlier [2,3], the γ' phase formed at the Ni/NiAl interface has the same crystallographic orientation as the γ phase when the couple is annealed above 1373 K. Thus, the γ' phase observed in this study after annealing at 1523 K can be in the form of single crystal because single crystalline Ni has been adopted for an end member of the couples. Extrapolation of the linear relationship given in Fig.1 (a) suggests that the γ' layer grows to have a thickness of 1 mm by annealing for ~1 year at 1523 K. Although the annealing for 1 year is somewhat impractical for the fabrication of single crystalline γ', the annealing time can be reduced by preparing a multilayer consisting of alternative thin layers of single crystalline Ni and polycrystalline NiAl. The annealing time can also be reduced by increasing the annealing temperature closer to the melting point of Ni_3Al. According to the Ni-Al equilibrium phase diagram [4], it is still possible to anneal the Ni/NiAl couple at a temperature as high as ~1650 K.

The γ' phase layer after annealing at 1173 K contains many grain boundaries and its growth is directed equally to the γ and β phases. Furthermore, the layer growth follows the fourth power rather than the second power as demonstrated in Fig.4. Similar results were reported by Corcoran et al. [5] on the growth of a titanium silicide layer in a Si/Ti couple. Watanabe et al. [3] also demonstrated the fourth power for the growth of the γ' phase layer in a Ni/Ni-45mol%Al

couple with polycrystalline Ni as the end member. The fourth power may be derived from the condition that the diffusion occurs mainly through the grain boundaries in the layer. According to Corcoran et al.[4], the layer growth rate, dW/dt, may be given by the form of

$$dW/dt = a D_g/WL \quad (1)$$

where a is a constant related to the concentration gap at the interface, D_g is the grain boundary diffusion coefficient and L is the grain size in the layer having a time dependence described as

$$L = kt^n \quad (2)$$

Here, k is a constant containing a temperature dependence through the form of $\exp(-Q_L/RT)$ and n is a constant generally equal to ~1/2. Integration of eq.(1) thus leads to the form

$$W = [a/(1-n)](D_g/k)^{1/2} t^{(1-n)/2} \quad (3)$$

Hence, the fourth power can be derived from eq.(3) by putting n=~1/2. It should be noted that the temperature dependence of W is represented through the term D_g/k in eq.(3). However, the grain growth is normally controlled by the grain boundary diffusion having a temperature dependence as $\exp(-Q_g/RT)$. Thus, Q_L=~Q_g and the temperature dependence should be canceled out and the growth of the layer becomes insensitive to temperature. Experimental evidences are available for such a temperature dependence as reported by Janssen [1] and Watanabe et al.[3].

Summary and Conclusions

1. The Ni_3Al phase (γ' phase) forms at the Ni/Ni-45mol%Al couples during diffusion annealing.
2. When the couples are annealed at 1523 K, the γ' phase grows initially towards the γ phase and later the growth direction changes to the β phase. The corresponding growth occurs at low and high rates but each growth follows a parabolic law. The γ' phase has the same crystallographic orientation as the Ni phase (γ phase). Thus, the use of single crystalline Ni for an end member of the couple suggests potential utility of such reaction diffusion for fabrication of single crystalline Ni_3Al.
3. When the couples are annealed at 1173 K, the γ' phase grows equally to the directions of both the γ and β phases. Many grain boundaries are visible within the γ' layer. The growth occurs following the fourth power dependence of the γ' layer width on annealing time, suggesting that grain boundary diffusion controls the growth of the γ' layer.

Acknowledgements

This work was supported by a Grant-in-Aid for Scientific Research from the Ministry of Education, Science, Sports and Culture of Japan. For transmission electron microscopy, we used the facility of the HVEM Laboratory of Kyushu University.

References

1. M.M.P. Janssen, Metall. Trans., 4 (1973), 1623-1633.
2. M.Watanabe, Z.Horita and M.Nemoto, Defect and Diffusion Forum, 143-147 (1997), 637-642.
3. M.Watanabe, Z.Horita and M.Nemoto, Interface Science, 4 (1997), 229-241.
4. M.F.Singleton, J.Murray and P.Nash, Binary Alloy Phase Diagrams Vol.1, ed. T.B. Massalski (Metals Park, Ohio: American Society for Metals, 1987), 140-143.
5. Y.L.Corcoran, A.H.King, N.de Lanerolle and B.Kim, J. Eletr. Mater., 19 (1990), 1177-1183.

DIFFUSION OF CONSTITUENT ELEMENTS IN Ni_3Ge STUDIED BY TRACER AND INTERDIFFUSION EXPERIMENTS

K. Nonaka, T. Arayashiki and H. Nakajima†

Department of Materials Science and Technology, Iwate University,
Morioka 020, Japan

† Present address: Institute of Scientific and Industrial Research, Osaka University,
Ibaraki 567, Japan

K. Tanaka, T. Korata, T. Ikeda, H. Numakura and M. Koiwa

Department of Materials Science and Engineering, Kyoto University,
Sakyo-ku, Kyoto 606-01, Japan

Abstract

The diffusion coefficients of the constituent elements in Ni_3Ge, an intermetallic compound with the $L1_2$ structure, have been measured by the radioactive tracer technique over the temperature range between 919 to 1275 K. The diffusivity of germanium is lower than that of nickel by more than two orders of magnitude. The chemical diffusion coefficient in the $L1_2$ phase has also been measured using single-phase diffusion couples. The chemical diffusion coefficient is larger than the tracer diffusion coefficient of nickel and increases rapidly with increasing the concentration of germanium from 23.2 to 24.7%. The observed diffusion behaviour has been discussed in the light of the α sublattice vacancy mechanism for both the species. The low diffusivity of the minor species, the large magnitude of the chemical diffusion coefficient and its strong dependence on composition are suggested to result from a high ordering energy of the compound.

The Third Pacific Rim International Conference on
Advanced Materials and Processing (PRICM 3)
Edited by M.A. Imam, R. DeNale, S. Hanada,
Z. Zhong and D.N. Lee
The Minerals, Metals & Materials Society, 1998

1. Introduction

Atomic diffusion in ordered lattices has attracted much interest and has been studied extensively in both theory and experiment. However, for intermetallic compounds of the $L1_2$ structure, experimental data of diffusion have been very limited, in spite of practical importance of this class of materials. The group of the present authors reported the tracer-diffusion coefficients of nickel and germanium in Ni_3Ge [1]; this was the first experimental data of the diffusion of both elements in an $L1_2$-ordered material. Since then, to understand the mechanism of diffusion in this structure, we conduct experimental and theoretical studies on the self-diffusion in Ni_3Al, Ni_3Ga and Ni_3Ge. In the present paper we report new experimental results for Ni_3Ge: the tracer diffusion coefficients of nickel and germanium measured over a wider temperature range than in the previous work, and the chemical diffusion coefficient obtained from single-phase interdiffusion experiments. Part of the tracer diffusion experiments has been reported elsewhere [2].

2. Tracer diffusion

2.1. Experimental procedure

Ni_3Ge containing 23.7% Ge was prepared from pure nickel and pure germanium by argon arc melting. A coarse-grained rod was made by unidirectional solidification in a Bridgman furnace. Disc-shaped specimens were cut out of the rod, which contained four or five grains at most.

Radioactive isotopes ^{63}Ni and ^{68}Ge were electroplated on the polished surface, and the specimens were subjected to vacuum-annealing at a temperature between 919 and 1120 K (^{63}Ni) or between 1047 and 1206 K (^{68}Ge). The specimens were sectioned from the surface by the ion-beam sputtering technique. The sectioned materials were dissolved in an acid solution and the intensities of the β rays from ^{63}Ni and that of the γ rays from ^{68}Ge were measured. An additional experiment was done for the diffusion of nickel by lathe sectioning. A specimen deposited with ^{63}Ni was annealed at 1275 K. The radioactivities of the chips sectioned from the specimen by a lathe were measured in the same way as the sputter-sectioned ones.

2.2. Results

In all the measurements the penetration profile was found to follow the thin-film solution of the diffusion equation. The tracer diffusion coefficients D_{Ni}^* and D_{Ge}^* have been determined by standard linear regression for each profile plotted against the square of the depth and are shown in Fig. 1 as functions of reciprocal temperature. The extents of experimental errors in temperature and diffusion coefficients are about the same as the size of the symbols in the figure. Both the coefficients obey the Arrhenius law and are expressed as follows:

$$D_{Ni}^* = 10^{-3.56 \pm 0.14} \exp\left(-\frac{259 \pm 3 \text{ kJ mol}^{-1}}{kT}\right) \text{m}^2 \text{ s}^{-1}, \quad (1)$$

$$D_{Ge}^* = 10^{-2.42 \pm 0.75} \exp\left(-\frac{334 \pm 16 \text{ kJ mol}^{-1}}{kT}\right) \text{m}^2 \text{ s}^{-1}. \quad (2)$$

The value of D_{Ni}^* obtained by lathe sectioning (the leftmost point in Fig. 1) falls on the same line as the data in the low temperature range; Equation (1) has been derived including this value.

3. Interdiffusion

3.1. Experimental procedure

Specimens of Ni_3Ge of two different compositions, 23 and 25% Ge, were prepared by the same procedure as those for the tracer diffusion experiments. Discs differing in composition were brought into contact at polished surfaces and were diffusion-bonded by annealing at 1028 K for 2.4 ks. After vacuum-annealing for diffusion at a given temperature, concentration profiles were measured by electron-probe microanalysis using a wave-dispersion analyser.

3.2. Results

Figure 2 shows the concentration profile in a diffusion couple annealed at 1223 K for 82.8 ks. The asymptotic concentration at either end is slightly different from the nominal composition of the starting material but is within the possible range of errors inherent to the technique. The

measured concentrations c (open circles) in Fig. 2(a) are transformed to the 'probability plot,' Fig. 2(b), where c_1 and c_2 are the asymptotic concentrations out of the diffusion zone. The profile in the probability plot is convex upwards, indicating that the diffusion coefficient increases with increasing the concentration of germanium. A cubic polynomial is fitted to the data points, the curve is then transformed back to the original coordinates, and this curve is analysed by the Boltzmann-Matano method. The chemical diffusion coefficient $\tilde{D}$ obtained by this procedure is shown in Fig. 3 as a function of composition for the four temperatures. Values derived by direct, point-by-point analyses of the profile of 1223 K, i.e. without using a fitted curve, are shown for comparison. The diffusion coefficient increases rapidly with increasing the concentration of germanium, and the rate of increase is higher at lower temperatures.

The values of $\tilde{D}$ at compositions 23.2, 23.7 and 24.2% Ge in each curve in Fig. 3 are plotted in Fig. 1. The data points for the same composition at different temperatures also appear to obey the Arrhenius law. For example, the pre-exponential factor and the activation energy are $10^{-4.9 \pm 0.6}$ m^2 s^{-1} and 213 ± 14 kJ mol^{-1}, respectively, for 23.7% Ge.

4. Discussion

4.1. Tracer diffusion coefficients

The previous paper [1] reported the tracer diffusion coefficients of nickel and germanium in Ni_3Ge (23.7 and 25.0% Ge) in the temperature range between 1173 and 1273 K. Later an error in the data analyses has been discovered, and after corrections for the error all the diffusion coefficients turned out to be larger than those in the original report by a factor of about 3. The corrected diffusion coefficients for Ni–23.7% Ge are shown in Fig. 1. The magnitudes of D_{Ni}^* in the two sets of experiments are now in reasonable agreement. On the other hand, D_{Ge}^* obtained in the present experiment appears to be appreciably lower than those from the previous work. At the moment the origin of this difference is unclear. The two series of experiments were done by essentially the same procedures using materials of similar quality. All the previous measurements were done by lathe sectioning, but the technique must not be the cause of the gap, as the value of D_{Ni}^* obtained by lathe-sectioning in the present work agrees well with the others. The diffusivity of germanium at the high temperature region should be reexamined.

Although there exist such quantitative discrepancy in the two sets of data, both the experiments demonstrate that the diffusivity of germanium is much lower than that of nickel. According to the previous results the ratio D_{Ge}^*/D_{Ni}^* is 1/20–1/40, while in the present ones it ranges from 130 to 400, depending on temperature. In the other two $L1_2$ compounds under investigation, Ni_3Al and Ni_3Ga, the diffusivity of the minor element B is not so lower than that of the major element A: D_B^*/D_A^* is 0.2–0.4 in Ni_3Al and is 0.4–0.8 in Ni_3Ga at $0.85T_m$, where T_m is the melting temperature [3]. At the same homologous temperature, viz. about 1200 K (T_m = 1405 K for Ni_3Ge), the present results show $D_{Ge}^*/D_{Ni}^* \approx 0.007$.

4.2. The α sublattice vacancy mechanism

We have recently proposed a model for the self-diffusion in the $L1_2$-ordered compounds [3], in which atoms of *both* the major and minor species, A and B, are assumed to migrate by the α sublattice vacancy mechanism, namely, over the sublattice for the major species by the ordinary vacancy mechanism. According to this model, the tracer diffusion coefficients of A and B in $L1_2$ compounds are expressed as follows:

$$D_A^* = \frac{2}{3} a^2 w_0 C_{V\alpha} f_0, \tag{3}$$

$$D_B^* = \frac{2}{3} a^2 w_2 \frac{w_4}{w_3} C_{V\alpha} f p_\alpha, \tag{4}$$

where a is the lattice parameter, w_0 is the frequency of $V_\alpha \leftrightarrow A_\alpha$ exchange, $C_{V\alpha}$ is the probability that an α sublattice site is vacant, f_0 is the correlation factor for the α sublattice, w_2 is the frequency of $V_\alpha \leftrightarrow B_\alpha$ exchange, w_3 and w_4 are the frequencies of dissociative and associative jumps of a vacancy for a V_α–B_α pair, respectively, f is the correlation factor for impurity diffusion, and p_α is the fraction of antisite B atoms in the total number of B atoms. The five jump-frequency model has been adopted for the impurity diffusion of B_α in the α sublattice.

In the previous paper we compared the magnitudes of the diffusion coefficients of nickel in Ni_3Al, Ni_3Ga and Ni_3Ge with the self-diffusion coefficient in pure nickel and found that the rel-

ative magnitudes can reasonably be accounted for in terms of Eq. (3) and the expression for the self-diffusion in the fcc lattice,

$$D_A^*(\text{fcc}) = a^2 w_0 C_V f_0. \tag{5}$$

Concerning the diffusivity of the minor species, we look into its diffusion as impurity in the fcc matrix of A. The impurity diffusion coefficient in the fcc lattice is expressed as

$$D_B^*(\text{fcc}) = a^2 w_2 \frac{w_4}{w_3} C_V f, \tag{6}$$

with the five jump-frequency model. Equation (4) is different formally from above only in the numerical factor and the factor p_α. The model thus predicts that, if the equilibrium and kinetic properties of vacancies and vacancy–impurity interactions in the two materials are similar to each other, the diffusion of the minor species in an $L1_2$-ordered compound will be slower than its diffusion in the fcc matrix of the major species by a factor whose magnitude is of the order of the antisite defect concentration.

The diffusion of germanium as an impurity in fcc nickel is known to be faster than the self-diffusion of nickel [4], while the same species of atoms diffuse considerably slowly in Ni_3Ge. In the framework of the α sublattice vacancy mechanism, this indicates that the concentration of antisite atoms of germanium in Ni_3Ge is very low, which must be a result of a high ordering energy of the compound. For more detailed discussions, knowledge on the thermodynamics of defects, or more specifically the temperature and composition dependence of the degree of order, is essential. Experimental or theoretical estimates of the ordering energy or antisite defect formation energy are equally useful, but none of the above is found for Ni_3Ge in the literature. Investigations of the thermodynamic properties of Ni_3Ge are highly desirable.

4.3. Chemical diffusion coefficient

In Fig. 1, the chemical diffusion coefficient for 23.5% Ge reported by Komai et al. [5] is shown for comparison. The present data are significantly larger than that of Komai et al., which was determined by interdiffusion experiments using diffusion couples consisting of pure nickel and nearly stoichiometric Ni_3Ge. Unexpected effects may arise from the presence of interphase boundaries; we have carried out single-phase interdiffusion experiments to avoid such effects. The origin of the disagreement is unknown, however.

The value of $\tilde{D}$ at 23.7% Ge is three or four times larger than D_{Ni}^* at the same composition. This must be attributed to the thermodynamic factor in chemical diffusion. The chemical diffusion coefficient in a A–B solid-solution alloy is related to the tracer diffusion coefficients D_A^* and D_B^* in the same substance by the Darken–Manning equation [6],

$$\tilde{D} = (D_A^* x_B + D_B^* x_A)\, \Phi\, S, \tag{7}$$

where x_A and x_B are mole fractions of A and B, Φ is the thermodynamic factor and S is the vacancy flow factor. Although the relation is originally derived for random alloys, the relation seems valid for $L1_2$-ordered alloys when the α sublattice vacancy mechanism is the predominant mode of diffusion, because the diffusion processes occurring in the α sublattice can be regarded as the diffusion of the solvent and the solute in a dilute binary alloy of the α sublattice structure. On this basis, the chemical diffusion coefficient in Ni_3Ge can be approximated as

$$\tilde{D} \approx D_{Ni}^* x_{Ge}\, \Phi\, S, \tag{8}$$

since we have $D_{Ni}^* >> D_{Ge}^*$. The vacancy flow factor S ranges from 1 to $1/f_0$, depending on the relative magnitudes of the two tracer diffusion coefficients. When D_A^* and D_B^* are very different in magnitude, S approaches the upper bound, $1/f_0$, which equals to 1/(0.689...) = 1.451 for the case of the α sublattice vacancy mechanism, leading the product $x_{Ge}S$ to be 0.344 for x_{Ge} = 0.237. The fact that $\tilde{D}$ is three or four times larger than D_{Ni}^* thus implies that the magnitude of Φ is of the order of 10.

4.4. Diffusivities and the degree of order

The thermodynamic factor Φ is determined by the variation of the thermodynamic activity of either of the components with its concentration. If experimental data of thermodynamic

activity are available, Φ can be evaluated directly from them. Furthermore, the ordering energy of the compound, ε, can also be estimated, with a help of a thermodynamic model [7, 8]. However, no experimental data of thermodynamic activity have been reported so far for Ni_3Ge. Here we evaluate the ordering energy of Ni_3Ge from the estimate $\Phi \approx 12$ at $T = 1200$ K for $x_B = 0.237$, which has been found from the magnitudes of the diffusion coefficients, by Eq. (8). Using the analytical expression for Φ derived from the Bragg-Williams model [8], this is found to occur at $\varepsilon/kT = 1.45$, thus giving $\varepsilon = 14.5$ kJ mol^{-1}. This is significantly higher than those of Ni_3Al (11.2 kJ mol^{-1}) and Ni_3Ga (9.2–9.6 kJ mol^{-1}) [8,9] .

In a compound of a high ordering energy, the thermodynamic factor exhibits a sharp maximum at the stoichiometric composition [8]. The rapid increase in $\tilde{D}$ in Ni_3Ge observed in the present study may be associated with this effect; note that in the present experiments the composition always stays in the nickel-rich side of stoichiometry. In Fig. 4, the calculated variation of $\tilde{D}$ with composition is compared with the experimental result. The former has been calculated from Eq. (8) for $T = 1200$ K; the value of D_{Ni}^* at $x_{Ge} = 0.237$ has been obtained from the Arrhenius expression, Eq. (1), its variation with composition (dashed line) is assumed to follow the composition dependence of the vacancy concentration $C_{V\alpha}$, as discussed previously for Ni_3Al [3], and Φ has been calculated using the analytical expression [8]. The calculated curve reproduces well the increase in $\tilde{D}$ observed in experiment.

Finally we compare the tracer diffusion coefficient of germanium in Ni_3Ge with the impurity diffusion coefficient of germanium in nickel. Equations (4) and (5) give an expression for the ratio of the tracer diffusion coefficients:

$$\frac{D_B^*}{D_A^*} = \frac{w_4}{w_3}\frac{w_2}{w_0}\frac{f}{f_0}p_\alpha. \tag{9}$$

The corresponding expression for the fcc lattice is formally identical to the above except that the last factor p_α is absent. Experimental data show that $D_{Ge}^*/D_{Ni}^* \approx 0.007$ in Ni_3Ge while it is about 6 in pure nickel [4] at $0.85T_m$. According to the Bragg-Williams model, the long-range order parameter η for $x_B = 0.237$ at 1200 K is equal to 0.947 for the ordering energy of 14.5 kJ mol^{-1}. From the relation $p_\alpha = (3/4)(1 - \eta/4x_B)$, we obtain $p_\alpha = 1.2 \times 10^{-3}$ at this temperature and composition. Therefore, if the product $(w_4/w_3)(w_2/w_0)(f/f_0)$ is similar in magnitude for the diffusion in Ni_3Ge and in fcc nickel, the difference in the magnitudes of D_{Ge}^*/D_{Ni}^* between the two materials can be explained by p_α: the higher diffusivity of germanium than nickel in fcc nickel by a factor of 6 is reduced by p_α to 0.007, which is exactly the observed magnitude of the diffusivity ratio in Ni_3Ge. Similar agreement has also been found for Ni_3Al [3].

In summary, most of the observed features of self-diffusion in Ni_3Ge can be consistently explained in terms of the α sublattice vacancy mechanism by assuming a ordering energy of about 14.5 kJ mol^{-1}. These include (1) the low diffusivity of the minor species, (2) the larger magnitude of the chemical diffusion coefficient than the tracer diffusion coefficients and (3) the rapid increase in the chemical diffusion coefficient toward the stoichiometric composition. An issue yet to be reexamined is the composition dependence of D_{Ge}^*. In the previous work [1] no significant effect of composition was found in the tracer diffusion coefficients for 23.7 and 25% Ge. However, the model of the α sublattice vacancy mechanism predicts that the diffusivity of the minor species will depend strongly on composition because the antisite defect concentration must be a sensitive function of composition, particularly for the case where the ordering energy is high. The results of the previous measurements do not conform to this expectation.

Acknowledgements. The authors appreciate the cooperation of Drs A. Almazouzi and W. Sprengel in the project. This work is supported by the Grant-in-Aid for Scientific Research of the Ministry of Education, Science, Culture of Japan (Fundamental Research B2, No. 08455288, and Priority Area 287, No. 09242106).

References

1 H. Yasuda, H. Nakajima, and M. Koiwa, "Diffusion in $L1_2$-Type Intermetallic Compounds," Defect Diffusion Forum, 95–98 (1993), 823–830.
2 K. Nonaka et al., "Self-Diffusion in $L1_2$-Type Intermetallic Compounds Ni_3Ge and Ni_3Ga," Defect Diffusion Forum, 143–147 (1997), 269–274.
3 H. Numakura et al., "Self-Diffusion Mechanism in Ni-Based $L1_2$-Type Intermetallic Compounds," Phil. Mag. A, in press.

4 S. Mantl et al., "The Tracer Diffusion of Ge in Ni Single Crystals," J. Phys. F: Metal Phys., 13 (1983), 1441–1448.
5 N. Komai et al., "Interdiffusivity Measurements and Interface Observations using Ni/Ni_3Ge Diffusion Couples," Acta Metall. Mater., 43 (1995), 2967–2974.
6 J. R. Manning, "Diffusion and Kirkendall Shift in Binary Alloys," Acta Metall., 15 (1967), 817–826.
7 I. Gyuk, W. W. Liang, and Y. A. Chang, "Thermodynamics of the Substantially Ordered Cu_3Au-Type Alloys," J. Less-Common Metals, 38 (1974), 249–256.
8 T. Ikeda, H. Numakura, and M. Koiwa, "Analyses of Thermodynamic Activity Data for Ordered Alloys based on the Bragg-Williams Model" (Paper presented at the Autumn 1997 Meeting of JIM, Sendai, 24 September1997).
9 T. Ikeda et al., "Point Defects and Self-Diffusion in Nickel-Based $L1_2$ Ordered Compounds" (Paper to be presented at the Spring 1998 Meeting of MRS, San Francisco, April 1998).

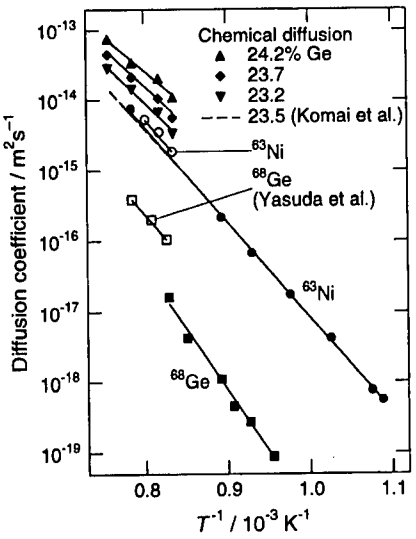


Figure 1: Tracer and chemical diffusion coefficients of Ni_3Ge.

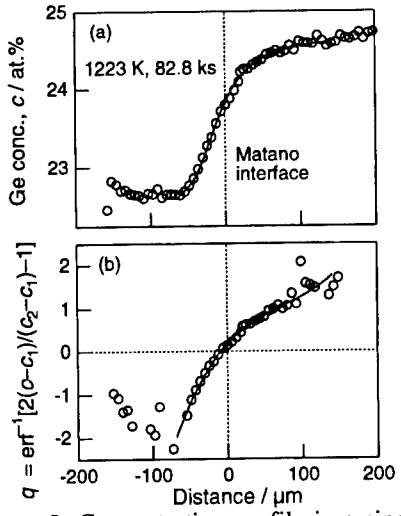


Figure 2: Concentration profile in a single-phase diffusion couple of Ni_3Ge (a) and its probability plot (b).

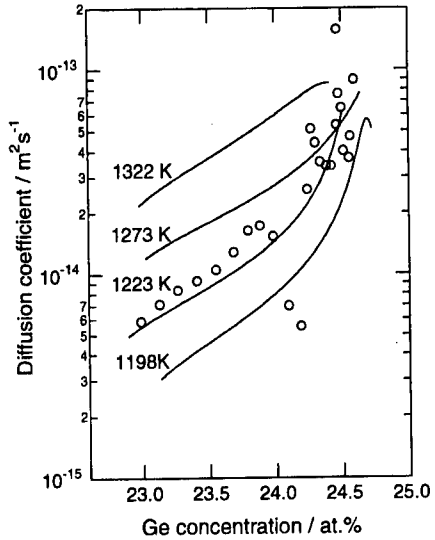


Figure 3: Chemical diffusion coefficient of Ni_3Ge.

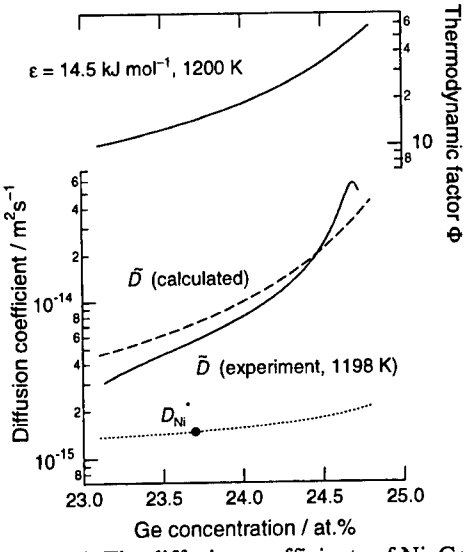


Figure 4: The diffusion coefficients of Ni_3Ge as functions of the composition.

Formation of the Extraordinary Lamellar Structure due to the Decomposition of High-temperature α Phase in γ-TiAl Based Alloys

Y, Ohmura*, M. Takeyama** and T. Matsuo**

*Graduate student, **Department of Metallurgical Engineering
Tokyo Institute of Technology 2-12-1 Ookayama, Meguro-ku, Tokyo 152, Japan

Abstract

The formation of the extraordinary lamellar structure has been examined by means of direct quench/aging and continuous cooling from the high-temperature α single phase region to 1473 K using the binary Ti-48Al and Ti-48Al-8Nb alloys. The extraordinary lamellar structure is formed as a result of twinning on $(11\bar{2}2)$ plane in the retained α phase, followed by precipitation of γ-TiAl phase in the twinned region. The twinning occurs by rapid quenching but not by slow cooling, indicating the thermal stress caused by rapid contraction during quenching is responsible for twinning to occur. The addition of niobium enhances the formation of twinning, because of the increase in c/a lattice parameter ratio of the hcp α phase.

The Third Pacific Rim International Conference on
Advanced Materials and Processing (PRICM 3)
Edited by M.A. Imam, R. DeNale, S. Hanada,
Z. Zhong and D.N. Lee
The Minerals, Metals & Materials Society, 1998

Introduction

The alloys based on γ-TiAl intermetallic phase with $L1_0$ structure have received many attentions because of their potential use for high-temperature applications [1]. The microstructure control using the phase transformation of α-Ti to γ-TiAl phase upon cooling is a key to realize the practical use for these materials. The microstructure formed by the decomposition of α-Ti phase along a transformation pathway of $\alpha \rightarrow \alpha_2+\gamma$ during cooling in Ti-48Al alloys is very sensitive to cooling rate [2, 3]. Under slow cooling conditions, the α phase transforms to α_2 and γ phases with a lamellar morphology. This microstructure is called *fully lamellar structure* (FL). On the other hand, under rapid quenching conditions, the α phase transforms massively to γ phase, resulting in fine acicular morphology, which is called *massive γ structure* (γ_m). When the alloys are cooled at intermediate rates, the α phase decomposes to α_2 and γ phases, and the resulted microstructure basically shows a lamellar structure but, unlike the FL structure, it exhibits Widmannstätten morphology. Such a microstructure is called *Widmannstätten-type lamellar structure* (W_L) [3, 4].

In the FL structure, each prior α grain exhibits a lamellar structure with a single lamellar direction. This is because only one habit plane is available for the precipitation of the γ phase in the α matrix, and as a result the lamellar structure satisfies Blackburn's orientation relationship: $(0001)_\alpha // \{111\}_\gamma$, $<11\bar{2}0>_\alpha // <\bar{1}10]_\gamma$ [5, 6]. We call the lamellar structure as *primary lamellar* (P_L). However, in W_L structure, each grain has several lamellar colonies with their own lamellar directions different from the primary lamellar one. Our previously TEM study revealed that the lamellar structure in the colonies consists of $\alpha(\alpha_2)$ and γ phases and also satisfies the Blackburn's orientation relationship, even though they are in the same α grain. Thus, the lamellar structure in the colonies should be distinguished with P_L, and called as *extraordinary lamellar* (L_E) [7]. Recently we crystallographically identified that the formation of the L_E is associated with twinning occurring in the supercooled α phase during cooling prior to the precipitation of γ phase [3, 7].

In this study, we have conducted the direct quench/aging experiment for the alloys with and without Nb and examined the microstructures, particularly paying attention to the L_E structure. Since the formation of L_E is associated with twinning, the twining mechanism in hcp α phase is also discussed in conjunction with the alloying effect.

Experimental procedures

The alloys used in this study with a nominal compositions of Ti-48Al and Ti-48Al-8Nb (all compositions are expressed in atomic percent unless otherwise specified) were prepared by induction skull melting, followed by centrifugal casting to bar ingot. The ingots were then HIPed at 1376 K/186 MPa under argon atmosphere. The oxygen concentration of these alloys was 300 ppm by weight. The samples for heat treatment was cut accurately with a size of 6 x 6 x 10 mm^3 by an electro-discharged machining. The direct quench/aging treatment was conducted in a vertical furnace equipped with a high evacuation system, together with a salt bath ($BaCl_2$) furnace, as shown in Fig. 1. The bear sample was first heat

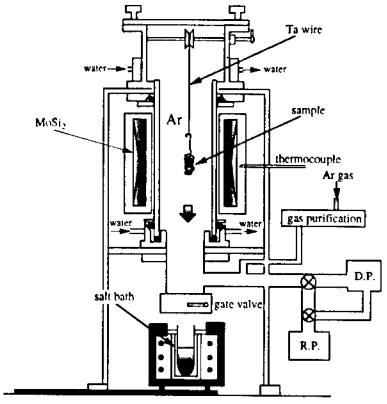


Fig. 1 Apparatus for heat treatments

treated at 1693 K for a certain period of time in the vertical furnace under argon atmosphere, and then dropped directly into the salt bath by opening the gate valve. The sample was aged there at 1473 K for 10 sec, followed by water quench. In comparison, the continuous cooling was also conducted using the vertical furnace from 1693 K to 1473 K at a rate of 4K/min, followed by water quench, by replacing the salt bath with water bucket.

Microstructures were examined by Nomarski-type optical microscopy and transmission electron microscopy (TEM). For metallographic examination, some of the samples were cut, mounted and polished by a conventional method, followed by electropolishing with a solution of 30 ml perchloric acid, 170 ml butanol and 300 ml methanol in parts, followed by chemically etching in distilled water with 0.75% hydrofluoric and 1.75% hydrochloric acids. TEM discs, 0.15 mm thick, were machined and twin-jet polished in a solution of methanol with 10% perchloric acid at 253K.

Results and Discussion

Transformation pathways during cooling

A vertical section of Ti-Al-Nb system at aluminum concentration of 48 at.% is shown in Fig. 2. This figure is drawn based on our recent studies on phase equilibria in this system at elevated temperatures [8, 9, 10]. The high-temperature α-Ti phase exists at around 1700K regardless of niobium concentration up to about 10 at.%. The transformation pathway from the α phase upon cooling changes from $\alpha \rightarrow \alpha_2+\gamma$ for the binary Ti-48Al to $\alpha \rightarrow \gamma$ for Ti-48Al-8Nb. Although it is beyond the scope of this paper and the details will be described in elsewhere [11], we have studied the CCT and TTT diagrams of the $\alpha \rightarrow \gamma$ phase transformation for both alloys and found that the quenching temperature of 1473 K is higher than the massive start temperature (Ms).

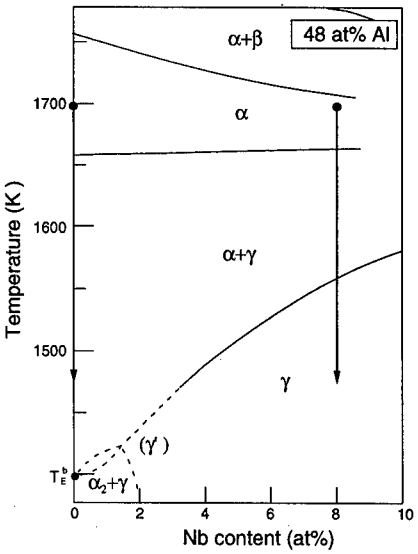


Fig. 2 A vertical section of Ti-Al-Nb system at 48 at.% Al.

Microstructures

Figure 3 shows the continuously cooled and directly quenched microstructures of the alloys with and without Nb. Both Ti-48Al and Ti-48Al-8Nb alloys completely exhibit the primary lamellar structure (L_P) when they are controlled cooled (4 K/min) from the α single phase region to 1473 K, followed by water quench (Figs. 3(a) and (b), respectively). These L_P structures are formed during the controlled cooling, not the following water quench. In case that the sample was directly quenched from 1693 K to 1473 K and held there for 10 s, followed by water quench, the binary alloy exhibits L_P structure only along the prior α grain boundaries, as shown in Fig. 3(c), and the untransformed featureless α_2 phase is seen within the grain interior, together with some γ_m which is formed during water quench. Although not seen in Fig. 3(c), we recognized that a few of

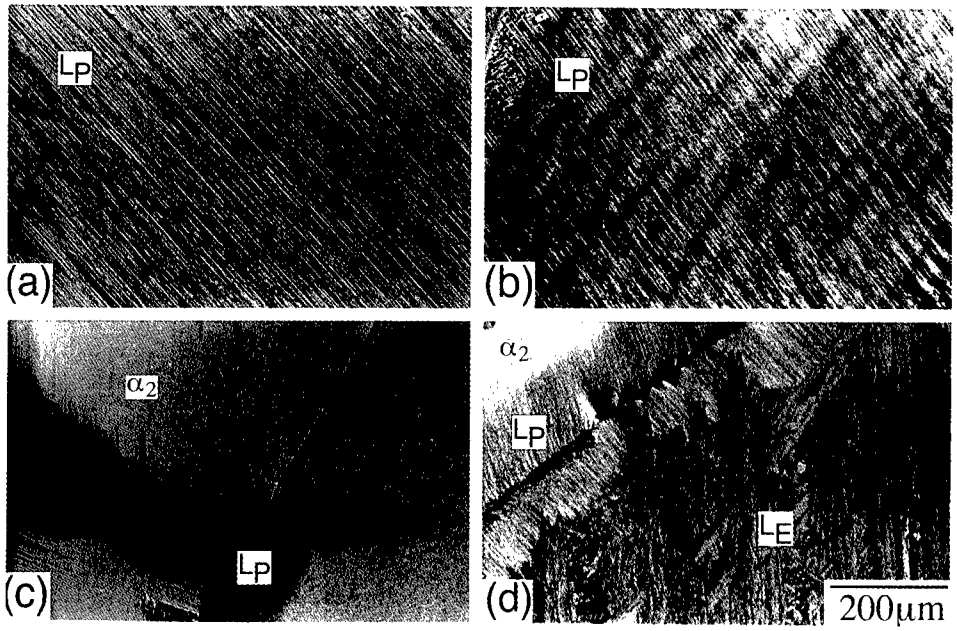


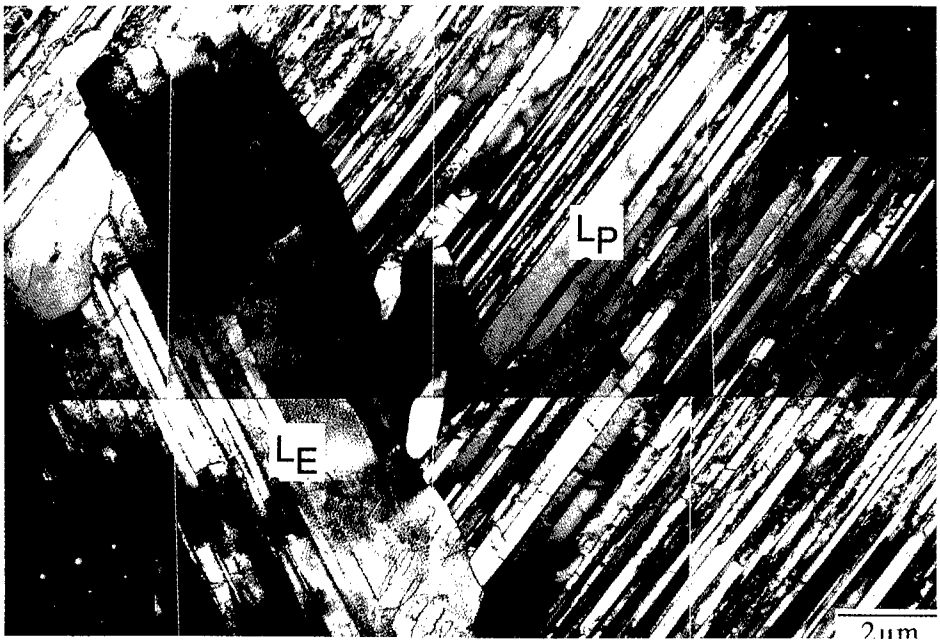
Fig. 3 Optical microstructures of Ti-48Al (a, c) and Ti-48Al-8Nb (b, d) controlled cooled from 1693K/14.4 ks to 1473 K at 4K/min, followed by water quench (a, b), and directly quenched from 1693 K/86.4 ks to 1473 K and held there for 10 sec, followed by water quench (c, d).

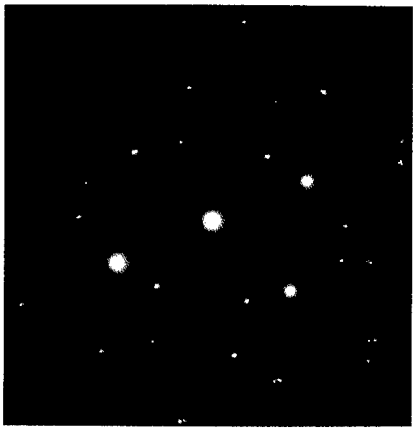
L_E structure is also formed in this sample. On the other hand, as shown in Fig. 3(d), the alloy with Nb shows a lot of L_E, together with L_P formed along the grain boundaries. The L_E in the alloy is formed during aging, not during water quench, since the volume fraction of the L_E is found to remain unchanged even in the longer aged sample. These results indicate that the increase in cooling rate as well as the addition of the third element promote the formation of the extraordinary lamelar structure.

Figure 4 shows a bright field transmission electron image showing both L_P and L_E formed in Ti-48Al-8Nb directly quenched to 1473 K and aged there for 10s, followed by water quench, together with the selected area diffraction patterns (SADPs). The SADP taken independently from the each L_E and L_P region reveals that the lamellar region consists mainly of γ phase with a small amount of α_2 phase, and both phases satisfy the Blackburn's orientation relationship. It is also revealed that in both regions the lamellar interfaces are perpendicular to the paper surface (edge on) with the same zone axis parallel to $[10\bar{1}0]_{\alpha_2}$ (// $[112]_\gamma$), and that the L_P and L_E regions become a twin relationship each other with a twin plane of $(11\bar{2}2)$ of hcp α phase, as shown in the SADP in Fig. 4. This is the first direct evidence showing the twin relationship between the L_P and L_E, consistent with the macroscopic analysis reported previously [7].

Formation mechanism of the *extraordinary lamellar structure* (L_E)

The present results clearly demonstrate that the L_E is formed by twinning in the untransformed α phase during cooling, followed by the precipitation of γ phase in the twined regions. As shown in Fig. 3, it is obvious that the higher the cooling rate, the more the twinning to occur. The γ phase





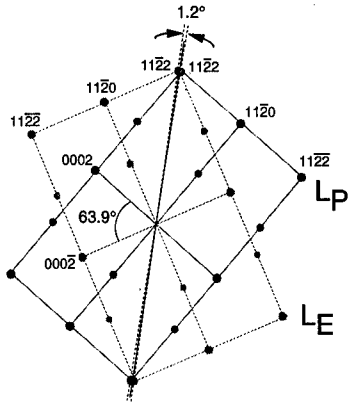


Fig. 4 A bright field TEM image showing the L_P and L_E region having a twin relationship in Ti-48Al-8Nb directly quenched from 1673 K/1.8 ks to 1473 K, and aged there for 10 sec, followed by water quench: the zone axis Z.A.=$[10\bar{1}0]_{\alpha_2}$ (// $[112]_\gamma$).

precipitates in the α matrix during cooling, and the slower the cooling rate the more the γ phase to grow, resulting in the fully lamellar structure. However, when the sample are quenched to 1473 K from the high-temperature α single phase region, the retained α phase would contract, causing thermal stress. The thermal stress could be the driving force for the formation of twinning to occur.

Another important factor to be consider is that the addition of niobium induces the twinning in the α phase (Figs. 3(c), (d)). This is probably because of the increase in c/a ratio of the lattice parameters of hcp α phase by the addition of niobium. The SADP analysis revealed that the c/a ratio is 1.59 for the binary and it becomes 1.62 for niobium containing alloy. It should be noted

that there is a small angle difference (1.2°) between the $(11\bar{2}2)$ of L_P and that of L_E, as shown in the SADP in Fig. 4. This mismatch is caused by the deviation of the c/a ratio from $\sqrt{3}$. Although it has not been well known the detail mechanism how twinning takes place in hcp structure, atom reshuffling from one plane to another as well as shearing on the same plane is certainly needed for twinning to occur [7]. As far as the hard sphere model is concern, however, some of the atoms do not need to move in twinning in case that the c/a ratio is $\sqrt{3}$, indicating less energy for twinning to occur in the alloy with niobium. In addition, the diffracting vector of $\mathbf{g=11\bar{2}\bar{2}}$ for L_P in the SADP shown in Fig. 4 becomes parallel to that of **g=0002** for L_E when the c/a ratio is $\sqrt{3}$, indicating that the interface between L_P and L_E could be parallel to the lamellar direction in L_E region, as is usually seen in the microstructure with L_E, since the $(11\bar{2}\bar{2})$ plane, which is crystallographically the same as $(11\bar{2}2)$, could also be the twinning plane. The detailed analysis of the formation of L_E using the hard sphere model is in progress and will be reported elsewhere.

Acknowledgments

This research is supported by the research grant on "Research for the Future Program" from Japan Society for the Promotion of Science (96R12301), and in parts by Grant-in-Aids for Scientific Research (07650811) and for Scientific Research on the priority area "Phase Transformations" (09242209) from the Ministry of Education, Science and Culture, Japan.

References

1. Y. W. Kim: JOM, 46[7] (1994), p. 30.
2. P. Wang and V. K. Vasudevan, Scripta Metall. Mater., 27 (1992), p. 89.
3. M. Takeyama, T. Kumagai, M. Nakamura and M. Kikuchi, Proc. Intl. Symp. Structural Intermetallics, eds. by R. Darolia et al., (TMS, 1993), p.167.
4. Y. Yamabe, M. Takeyama and M. Kikuchi, Gamma Titanium Aluminides, eds. Y.-W. Kim, R. Wagner and M. Yamaguchi, (TMS, 1995), p.111.
5. M. J. Blackburn: Science, Technology and Application of Titanium, ed. by R. T. Jaffee and N. E. Promisel, (Pergamon Press, London, 1970), p. 633 .
6. Y. Yamabe and M. Kikuchi, Bulletin of the Japan Society of Metals, 30 (1) (1991), p. 73.
7. M. Takeyama, T. Horikoshi, Y. Ohmura and T. Matsuo, THERMEC'97, Int. Conf. Thermomechanical Processing of Steels and Other Materials, eds. T. Chandra and T. Sakai, (TMS, 1997), p. 1489.
8. H. Nakamura, M. Takeyama, Y. Yamabe and M. Kikuchi, Scripta Metall. Mater., 28 (1993), p.997.
9. Nakamura, M. Takeyama, L. Wei, Y. Yamabe and M. Kikuchi, Intermetallic Compounds for High-Temperature Structural Applications, 3rd Japan Intl. SAMPE Symp., eds. M. Yamaguchi and H. Fukutomi, (SAMPE, 1993), p.1353.
10. M. Takeyama and M. Kikuchi, Materia Japan, 35 (10) (1996). p. 1058.
11. Y. Ohmura and M. Takeyama, unpublished results, (Tokyo Institute of Technology, 1998).

PREPARATION OF Sb-DOPED SnO_2 ULTRAFINE PARTICLES FROM SOL-GEL METHOD

Yi Hu and S.-H. Hou

Department of Materials Engineering
Tatung Institute of Technology
Taipei, Taiwan, ROC

Abstract

Sb-doped SnO_2 ultrafine particles of narrow size distribution have been obtained from the aqueous sol-gel method. Xerogel particles were made by forced hydrolysis at 100°C of the mixed $SnCl_4$ and $SbCl_3$ (0~10 mol%) solution. The formation mechanism of the xerogel particles was analyzed by Partial Charge Model. The xerogel particles showed the cassiterite structure from X-ray diffraction patterns. Resultant particles were obtained by firing the xerogel particles at temperatures 100~600°C for one hour. The TEM photographs showed that the resultant particles are uniform and smaller than 0.03μm.

The Third Pacific Rim International Conference on
Advanced Materials and Processing (PRICM 3)
Edited by M.A. Imam, R. DeNale, S. Hanada,
Z. Zhong and D.N. Lee
The Minerals, Metals & Materials Society, 1998

Introduction

Tin oxide (SnO_2) is one of the representative materials for a semiconductor-type gas sensor[1-3] and catalyst,[4-6] and it also has been used as an electrode material[7-8] or a glass-melting electrode.[9-10] In many of these applications, fine SnO_2 powders of narrow size distribution are desired. For example, it was found that the gas sensitivity of an SnO_2 sensor can be promoted greatly by using ultrafine particles of SnO_2, especially at a size around 5nm.[11]

Various techniques have been used for the preparation of fine SnO_2 powders and are classified into three major ways: (a) produced by oxidation of tin in concentrated nitric acid,[12-14] (b) produced by hydrolysis and precipitation from tin salts,[15-18] and (c) prepared by spray pyrolysis of tin salts.[19] In these methods, it has been proved that homogeneous precipitation method form chloride solution is one of the best methods to synthesize ultrafine SnO_2 particles with narrow particle distribution.[16-21] The origin of the solid structure from these precursors was suggested to be the 3-dimensional polymerization of the hydroxide-type precursor. However, never has been done on the verification between theoretical analysis and experimental results.

This work describes the preparation of the Sb-doped SnO_2 ultrafine particles in acidified tin(IV) chloride and Sb(III) chloride solution in the presence of urea. Theoretical analysis based on the Partial Charge Model (PCM) was applied to predict the formation conditions of tin oxide. The structural evolution of the particles under heat treatment was investigated in detail.

Experimental Procedure

Tin(IV) chloride pentahydrate ($SnCl_4 \cdot 5H_2O$), antimony chloride ($SbCl_3$), urea (NH_2CONH_2), and hydrochloric (HCl) were used to prepare the precursor. All reagents used were of reagent grade and an aqueous precursor of $SnCl_4$ (0.2M), HCl (1M) and varied amount of $SbCl_3$ and urea was prepared in a three-neck flask with a capacity of 1000ml. The initial pH of the precursor was measured to be far less than 1. Suspended powders were obtained by refluxing the precursor for a period of time. The pH values of the fully reacted solutions were measured. The resulting dispersions were cooled in clod water, centrifuged, the supernatant solution discarded and the particles resuspended in doubly distilled water in an ultrasonic bath. This procedure was repeated three times before drying at 60°C. Resultant powders were obtained by heating the precipitation the temperatures ranged from 200 to 600°C.

Thermal reactive properties of the resultant powders were investigated by differential temperature analysis (DTA). The structure of powders was determined by x-ray diffraction (XRD) using Siemens D-5000 instrument with Cu $K\alpha$ radiation. Fourier transform infrared (FTIR) was utilized to determine the molecular structure of the particles. The mean crystallite size of SnO_2 was evaluated from X-ray diffraction line (101) based on Scherrer's equation. In some cases, the particle size was determined from direct observation by carrying out on a transmission electron microscope (TEM, Hitachi 800).

Results and Discussion

The PCM is based on the electronegativity equalization principle stated by Sanderson[22] and was applied in characterizing the chemical reaction of inorganic solutions by Livage et al.[23-25] A discussion based on the PCM is presented here.

The existence of the oxohydroxo species in aqueous gels can be predicted from the relation given by Kepert[26] based on the cation charge (Z=4) and known molar ratio of hydrolysis, h, which is small than the coordination number (N) of H_2O molecules around the tin cation. The

"charge-pH" diagram with different value of h for tin cation is shown in Fig. 1. Since the pH value of the solution before reaction is far less than 1, the h value for tin cation is close to 3. Depending on the water acidity and hence, the magnitude of the charge transfer, the following equilibrium are established:

$$[Sn(OH_2)]^{4+} \leftrightarrow [Sn(OH)_3(H_2O)]^{+} + 3[Haq]^{+} \quad (1)$$

In addition, the charge-electronegativity diagram[25] derived from the partial charge model shows that Sn^{4+} and Sb^{3+} are both in the poly-acids region (Fig.2). This indicates that the condensation mechanism of SnO_2 and Sb_2O_3 are only through oxolation, i.e., ≡Sn-OH + HO-Sn≡ → ≡Sn-O-Sn≡ $+H_2O$. This reaction starts with nucleophilic addition of OH group onto metal ions. It is followed by a 1,3-proton transfer within the transition state (M-OH...M-OH) so that one water molecule can be removed easily. However, since the degree of the hydrolysis is still low (h~3) and the charge potential for the oxohydroxo species is positive, the oxohydroxo species are stable and hardly proceed the condensation reaction. The best way to promote the reactivity of the oxohydroxo species is to increase the pH value of the solution.

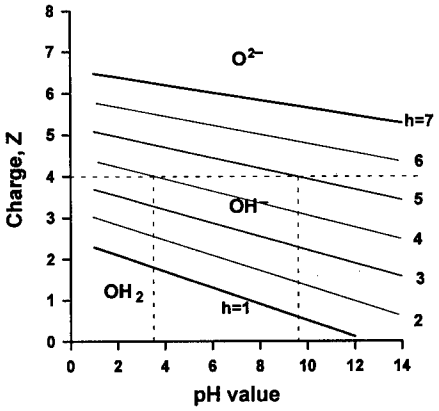


Fig. 1: Charge-pH diagram based on Sn cation with different degree of hydrolysis (h).

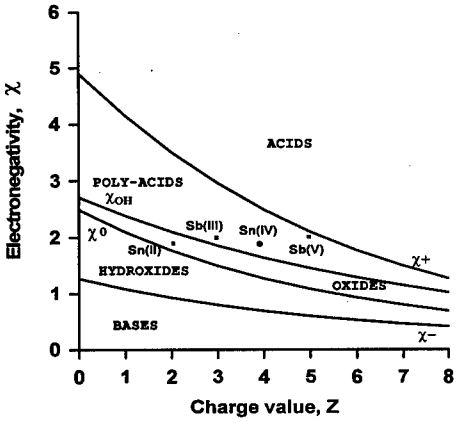


Fig. 2: Charge-electronegativity diagram[25] Sn^{4+} and Sb^{3+} are in the poly acids region.

Figure 3 shows the pH value of the fully reacting solution versus different amount of urea. Large amount of precipitates were obtained only from the solution with final pH value higher than 4. Small amount of coarse particles precipitated in the solution with pH lower than 4 are due to thermal agitation. The reactive species are suggested to be $[Sn(OH)_4]$ and $[SnO(OH)_3]^-$ by referring the pH value in Fig. 1.

Fig. 4 shows the DTA thermgrams of the powders with different amount of urea. The powders obtained form the solution with low amount of urea (pH<<4)) does not have any reaction in the heating process. Whereas the powders obtained from the solution with larger amount of urea (pH>4) have the exothermic reactions apparently. Referring to the FTIR spectra as seen in Fig. 5, these exothermic reactions are attributed to the decomposition of HO groups. The stretching vibration absorptions (3130 and 1650 cm^{-1}) and bending vibration absorption (1400cm^{-1}) of associated HO group are largely decreased when the heat treated temperature is higher than 300°C as shown in Fig. 5. Additionally, change in the exothermic peak of each powder (Fig. 4) comes from the different microstructure corresponding to the site occupied by the HO group.

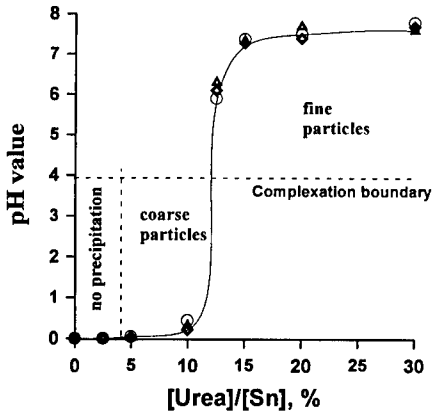


Fig. 3: Final pH values of the solutions with different urea content. Significant precipitation was observed when pH value is higher than 4.

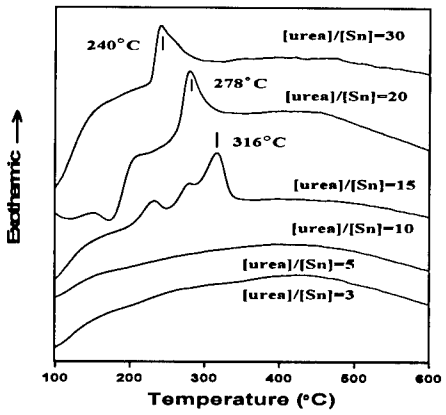


Fig. 4: DTA traces of the powders collected from the final solutions with different urea content.

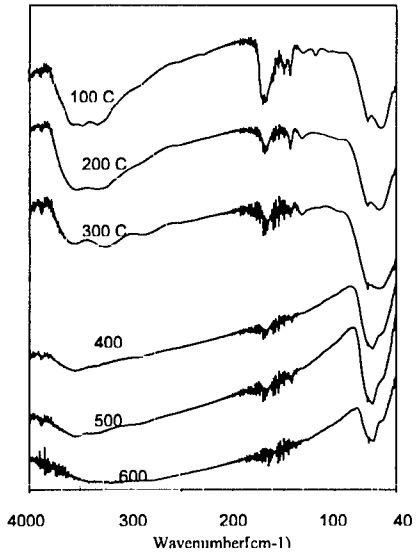


Fig. 5: FTIR spectra of the powders fired different temperatures. ([urea]/[Sn]=25).

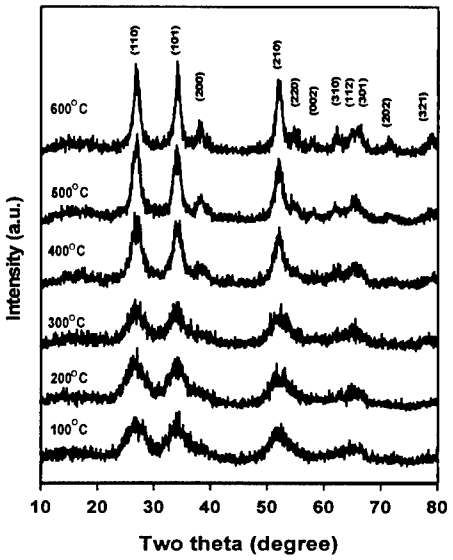


Fig. 6: XRD of the samples with fired at at different temperatures.([urea]/[Sn]=25).

Fig. 6 shows the XRD patterns of the powders under different heat-treated temperatures. The solids consist of SnO_2 with rutile type structure (cassiterite). It was found that the diffracted peaks became narrower as the heating temperature increased. Addition of Sb can restrain the grain growth as observed with broader XRD diffraction peaks (Fig. 7). The changes in the crystallite size of SnO_2, which was evaluated from X-ray diffraction line (101) based on Scherrer's equation, corresponding to Sb content and amount of urea are shown in Fig. 8. It can be found that the crystallite increases obviously as the heating temperature higher than 400°C. On the other hand, the O-Sn-O stretch vibration absorption at 662cm^{-1} becomes sharply as in Fig. 5.

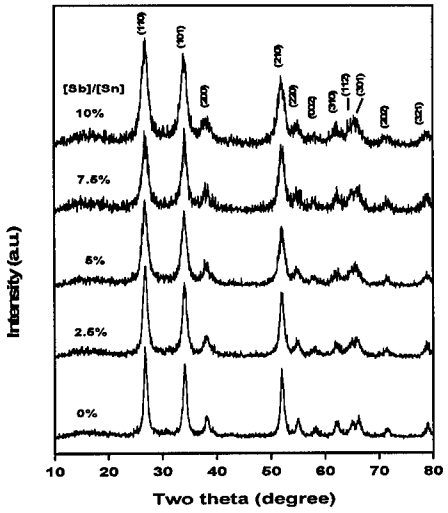


Fig. 7: XRD patterns of the samples versus different Sb extent and [urea]/[Sn]=25 heat treated at 600°C.

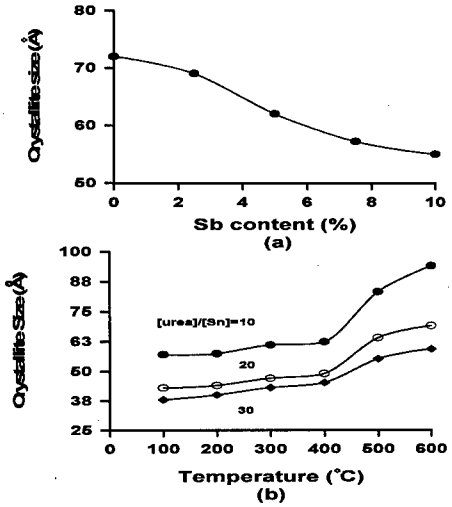


Fig. 8: crystallite size of the powder versus (a) Sb content fired at 600°C. ([urea]/ [Sn]= 25). (b) urea content at different firing temperature ([Sb]/[Sn]=5%).

Figure 9 shows the TEM photographs of the SnO_2 powders under different heat-treated temperatures. These particles have heavy agglomeration with cloudy image pattern when the heat-treated temperatures lower than 400°C (Fig. 10(a) and 10(b)). However, well-defined SnO_2 particles with particle size small than 0.03μm were obtained with heat-treated temperatures higher than 400°C (Fig.9 (c) and (d)).

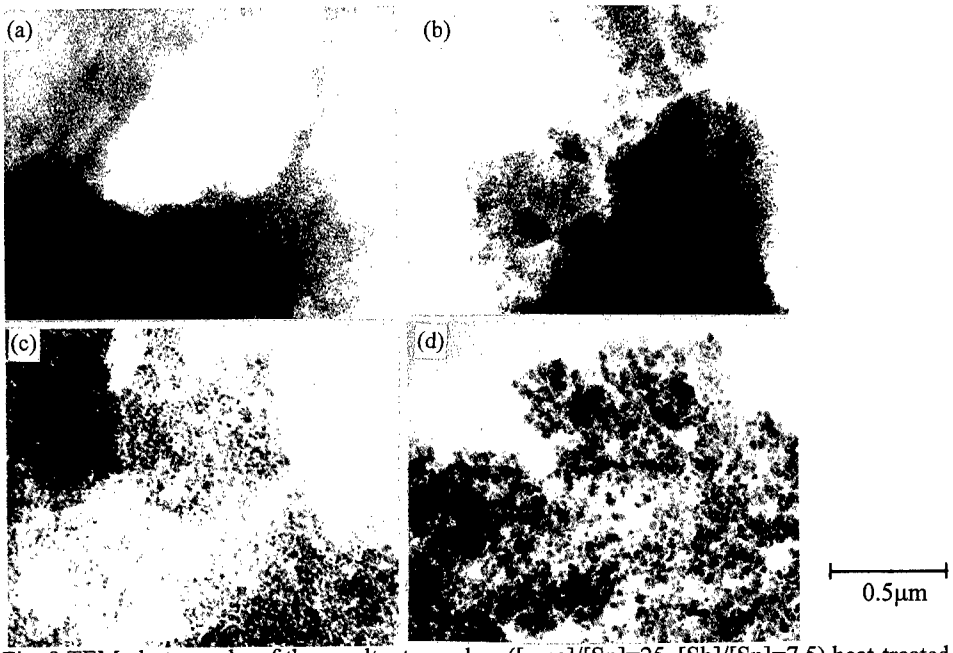


Fig. 9 TEM photographs of the resultant powders ([urea]/[Sn]=25, [Sb]/[Sn]=7.5) heat-treated at (a) 300°C, (b) 400°C, (c) 500°C, and (d) 600°C.

Summary

Sb-doped SnO_2 ultrafine particles of narrow size distribution have been successfully prepared from the aqueous sol-gel method. Xerogel particles were made by forced hydrolysis at 100°C of acidic $SnCl_4$ solutions with addition of $SbCl_3$ in the concentration 0~10 mol%. Large volume of precipitates was approached only when the pH value of the solution is higher than 4. The precipitates were verified with the cassiterite structure by X-ray diffraction. Well defined Sb-doped SnO2 particles with particle size smaller than 0.03μm were obtained by centrifuging and heat treating the xerogel particles at temperatures 100~600°C for one hour.

Acknowledgements

Financial support of this research by Chunghwa Picture Tubes Company (CPT), Taiwan, ROC, under the grant A83-1712-01 is gratefully acknowledged.

References

1. H. Torvela and S. Lappavuori, Int. J. High Technol. Ceram., 3 (1987) 309-315.
2. D. Kohl, Sensors and Actuators, 18 (1989) 71-113.
3. S.-S. Park, H. Zheng, and J. D. Mackenzie, Mater. Lett., 17 (1993) 346-352.
4. S. R. Stampfl et al., J. Catal., 105 (1987) 445-449.
5. V. L. Cebolla et al., Bull. Soc. Chim. France, 6 (1987) 935.
6. T. Ono, et al., J. Catal., 109 (1988) 423-428.
7. J. Kawiak, P. J. Kulesza, and Z. Galus, J. Electroanal. Chem. Interfacial Electrochem., 226 (1987) 305.
8. T. Tsuchiya, T. Emoto, and T. Sei, J. Non-Cryst. Solids, 178 (1994) 327.
9. J. H. Lee, S. J. Park, and K. Hirita, J. Am. Ceram. Soc., 73 (1990) 2772-2774..
10. Z. M. Zaraebski and J. P. Marton, J. Electrochem. Soc., 123 (1976) 299c.
11. C. Xu et al., J. Electrochem. Soc. Jpn, 58 (1990) 1143-1147.
12. J. C. Platteneuw and G. Meyer, Trans. Faraday Soc., 52 (1956) 1066.
13. Y. Qian et al., Nano-Struct. Mater., 1 (1992) 347-353.
14. W. Fliegel et al., Sensors and Actuators B, 18-19 (1994) 474-477.
15. J. F. Goodman and S. J. Gregg, J. Chem. Soc., 237 (1960) 1162-1166.
16. M. Ocana and E. Matijevic, J. Mater. Res., 5 (1990) 1083-1091.
17. C. Xu, J. Tamaki, N. Miura, N. Yamazoe, J. Mater. Sci., 27 (1992) 963-971.
18. R. S. Hiratsuka et al., J. Non-Cryst. Solids, 147&148 (1992) 67-73.
19. J.-H. Lee and S.-J. Park, J. Am. Ceram. Soc., 76 (1993) 777-780.
20. E. Matijevic, Ann. Rev. Mater. Sci., 15 (1985) 483-516.
21. M. Ocana, C. J. Serna, and E. Matijevic, Mater. Lett., 12 (1991) 32-36.
22. R. T. Sanderson, Science, 114 (1951) 670.
23. J. Livage, M. Henry, and C. Sanchez, Prog. Solid State Chem., 18 (1988) 259.
24. J. Livage et al., Mater. Res. Soc. Bull., 15 (1990) 18-25.
25. M. Henry, J. P. Jolivet, and J. Livage, in Chemistry Spectroscopy and Applications of Sol-Gel Glasses, R. Reisfeld and C. K. Jorgensen, eds., (Springer-Verlag, New York, 1992) pp.153-206.
26. D. L. Kepert, The Early Transition Metals (academic Press, London, 1972).

HIGH-ENERGY ELECTRON IRRADIATION INDUCED PHASE TRANSFORMATION IN Fe-Ni BINARY AND TERNARY ALLOYS

Yoshinori MURATA[1], Masahiko MORINAGA[1], Kyohei TAKAMI[2] and Hirotaro MORI[3]

1) Dept. of Materials Science and Engineering, Graduate School of Engineering, Nagoya University, Furo-cho, Chikusa-ku, Nagoya 464-01, JAPAN
2) Graduate student of Nagoya University
3) Research Centre for Ultra-High Voltage Electron Microscopy, Osaka University, Yamadaoka, Suita, Osaka 565, JAPAN

Abstract

A high-energy electron irradiation method was adopted to investigate phase transformation which occurs below 500K in Fe-Ni alloys. For alloys irradiated by 2MeV electrons at 373~473K a series of ordered reflections was observed in the ordinary electron diffraction patterns in the [001], [011] and [111] directions. The ordered structure observed in Fe-40mol%Ni-1mol%Ti, Fe-40mol%Ni and Fe-60mol%Ni alloys was inferred to be the $L1_2$-type one. The electron irradiation method was indeed useful in accelerating alloy phase transformation at low temperatures.

The Third Pacific Rim International Conference on Advanced Materials and Processing (PRICM 3)
Edited by M.A. Imam, R. DeNale, S. Hanada, Z. Zhong and D.N. Lee
The Minerals, Metals & Materials Society, 1998

Introduction

The existence of phase transformation in Fe-Ni binary alloys below 500K has been suggested from the experiment of the Mossbauer spectroscopy [1]. Also, the onset of the ordering reaction induced by the 1MeV electron irradiation has been found in Fe-Ni binary alloys containing less than 50mol%Ni, and reported the appearance of the ordered phase with the $L1_0$-type structure in them [2,3]. On the other hand, concentration fluctuations are observed in Fe-Ni binary and Fe-Ni-Cr ternary alloys when they are irradiated by Ni ions [4]. This implies that spinodal decomposition occurs in these alloys. However, it is still not clear whether the phase transformation is of the ordering type or the spinodal ordering type. This is because the critical temperature of the transformation is too low to activate atomic diffusion largely enough to progress the transformation in the alloy during a finite experimental time in the course of ordinary heat treatments.

The purposes of this study are to re-examine the phase transformation and to investigate the ordered structure in both Fe-Ni binary and ternary alloys by adopting a high-energy electron irradiation method, since electron irradiation could enhance atomic diffusion even at low temperatures via a large number of lattice vacancies introduced into the irradiated specimen.

Experimental Procedure

Sample Preparation

Button ingots of Fe-40mol%Ni and Fe-60mol%Ni binary alloys and Fe-40mol%Ni-1mol%Ti ternary alloy were made from appropriate mixtures of high purity Fe, Ni and Ti by arc melting in a high-purity argon gas atmosphere. Here, 1mol%Ti was added to the Fe-40mol%Ni alloy so as to detect easily the phase transformation by the electron diffraction method. The ingots were cold-rolled to 0.5mm thick. These rolled plates were then encapsulated in quartz tube back filled with a high purity argon gas and solutionized at 1273K for 86.4ks. After the solution heat treatment, discs of 3mm in diameter were cut from the plate samples using an arc-spark machining. Thin foils suitable for irradiation experiments in TEM were then prepared by the twin-jet electropolishing operated at 40V in a 5% perchloric acetic acid solution at 288K.

Electron Irradiation

The irradiation experiments were carried out using Hitachi H-3000 UHVEM in Osaka University. The UHVEM was operated at 2MeV with a flux of 2.4×10^{23} electrons$\cdot m^{-2}s^{-1}$ which was measured by using a Faraday cup. Prior to irradiation experiments, thin foil samples were observed by conventional transmission electron microscopes, Hitachi H-800 and JEM2000FX, operated at 200kV in order to confirm that the sample was in a disorder state and any oxide film was not formed on the surface. The electron irradiation was performed in the [001], [011] and [111] directions at the temperatures of 373K to 473K. After irradiation the samples were investigated by means of the conventional electron diffraction method.

Results

Fe-40%Ni-1%Ti ternary alloy

Figure 1 shows the selected area diffraction pattern (SADP) in the [001] direction of Fe-40%Ni-1%Ti alloy irradiated at 473K for 1.8ks. Superlattice reflections, which are marked as open circles in the corresponding schematical drawing, are clearly observed between the fundamental reflections. A similar result was also obtained from the specimens irradiated at

473K for 3.0ks and at 373K for 1.8ks or 3.0ks. The superlattice reflectins corresponding to the $L1_2$-type ordered phase were also observed in the SADP in the [110] direction. The appearance of these superlattice reflections indicates that the $L1_2$-type ordered phase is probably formed in this alloy. Besides the superlattice spots, some extra spots were observed due to the oxides formed on the foil surface [5]. It was considered that the oxides were formed during irradiation, because any extra spots were not observed before irradiation, as explained later.

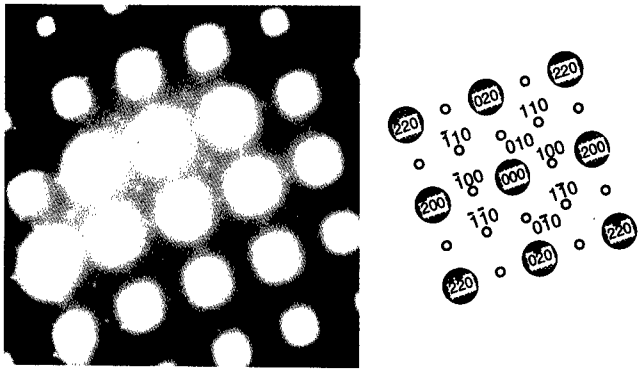


Fig.1 Selected area diffraction pattern in the [001] direction taken from Fe-40%Ni-1%Ti ternary alloy after irradiation at 473K for 1.8ks. Systematic superlattice reflections appear between the fundamental reflections.

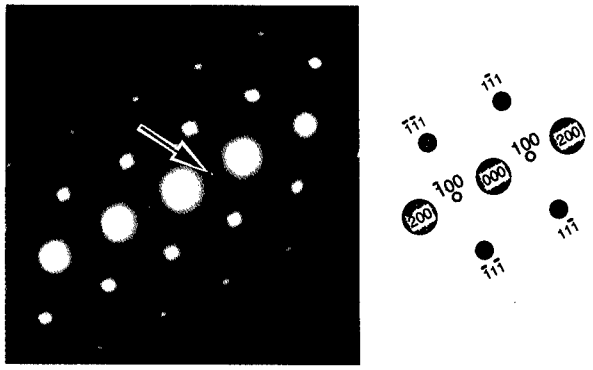


Fig.2 Selected area diffraction pattern in the [011] direction taken from Fe-40%Ni binary alloy after irradiation at 473K for 1.8ks. {h00} superlattice reflections are observed.

Fe-Ni binary alloys

For the Fe-40%Ni binary alloy, a series of superlattice reflections was also found as was reported previously [2]. Fig.2 shows the SADP in the [011] direction taken from the sample irradiated at 473K for 1.8ks. The (h00) systematic row of the superlattice reflections was clearly observed in the figure. Fig.3 is the bright field image of the irradiated region from which the SADP shown in Fig.2 was taken. There were many defects , but any periodic structure

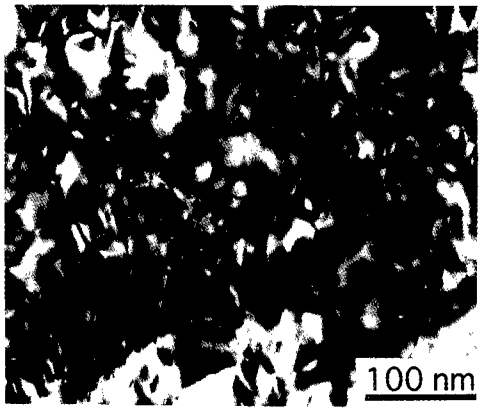


Fig.3 Bright field image of Fe-40%Ni binary alloy irradiated at 473K for 1.8ks.

was not found in this image.

For the Fe-60%Ni binary alloy, (h00) systematic superlattice reflections were clearly observed in the SADP in the [011] diffraction taken from the irradiated specimen at 473K, as shown in Fig.4. Fig.5 shows the SADP of the [111] direction taken from the same specimen, in which {110} superlattice reflections appeared in all the three equivalent directions. This result implys that the ordered structure is the $L1_2$ type, because this composition range is in the ordered region of Ni_3Fe phase, the existence of which is well known so far.

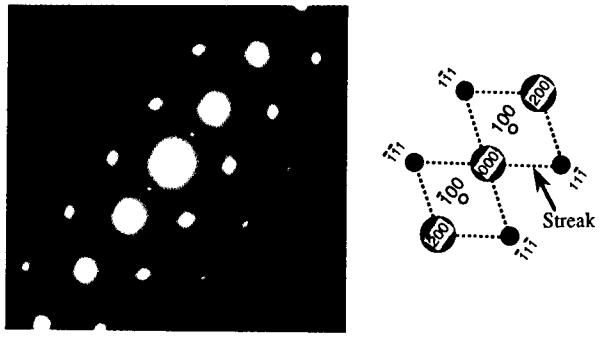


Fig.4 Selected area diffraction pattern in the [011] direction taken from Fe-60%Ni alloy after irradiation at 473K for 1.8ks. {h00} and {0hh̄} superlattice reflections and streaks along <111> directions are observed.

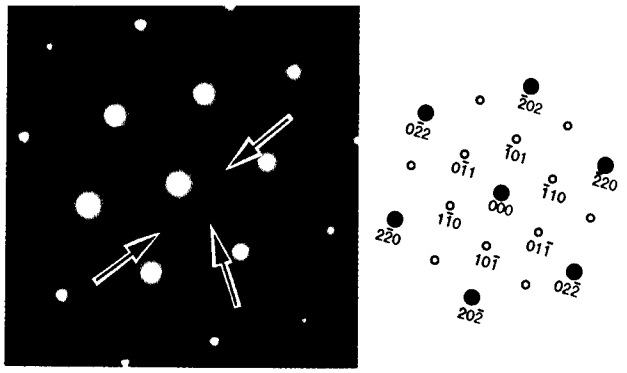


Fig.5 Selected area diffraction pattern in the [111] direction taken from Fe-60%Ni binary alloy after irradiation at 473K for 1.8ks. {hh̄0} superlattice reflections are observed.

As shown in Fig.6, defects structures formed by the irradiation were seen in a bright field image which was taken from the same region as the SADP shown in Fig.4. As shown by arrows in this figure, fine striations were observed, the direction of which was nearly perpendicular to the <111> direction. Streaks were also seen along this <111> direction as shown in Fig.4.

Discussion

Hameed et al. reported that the degree of long-range-order generated in Au-Cu alloys during irradiation varies as a function of irradiation temperature, since final atomic order is set in the alloy, while taking a balance between radiation-induced ordering and radiation-induced disordering [6]. In fact, the degree of order in an Au-Cu alloy increases with increasing irradiation temperature as far as it is below the order-disorder critical temperature, Tc. In the present experiment, the superlattice reflections appeared after irradiation, indicating that irradiation could enhance the atomic ordering in this alloy.

It was found that the transformation of Fe-40%Ni alloy was indeed of the ordering type, as consistent with a previous study [2]. From systematic $L1_2$-type superlattice reflections observed in Fig.1, it was suggested that the ordered structure was the $L1_2$-type. In fact, the existence of $L1_2$-type ordered phase was confirmed by the dark filed images using (100) and (010) superlattice reflections in [001] diffraction pattern. However, the possibility of the $L1_0$-type structure is still remained in this Fe-40%Ni alloy. This is because the coexistence of $L1_2$-type and $L1_0$-type ordered phase can not denied. Furthermore, the observed diffraction pattern shown in Fig.1 can be well reproduced if the $L1_0$-type ordered phases with three crystallographic variants coexist in the matrix, and their individual reflections are superimposed on the diffraction plane.

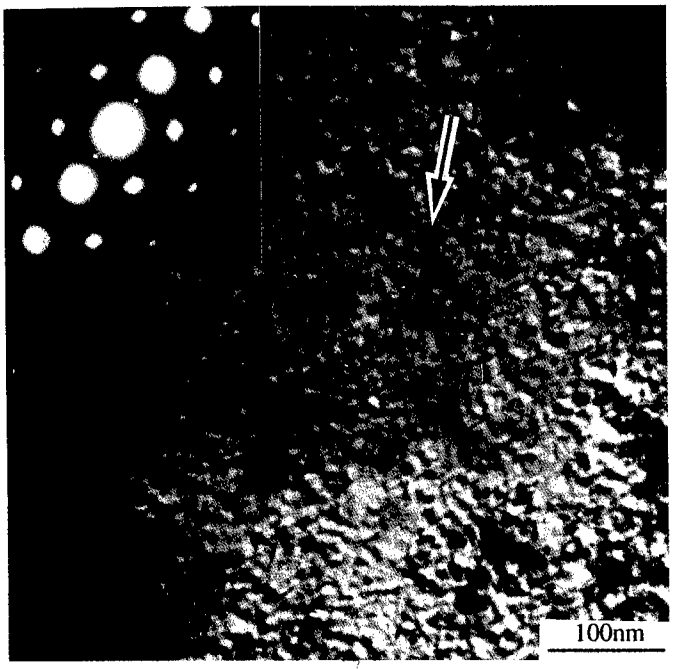


Fig.6 Bright field image of Fe-60%Ni ternary alloy irradiated at 473K for 1.8ks. Fine striations is observed.

The superlattice reflections corresponding to the $L1_2$-type structure were also observed in the Fe-60%Ni binary alloys. Chuang et al. reported from the calculation of the Fe-Ni phase diagram that there was an eutectoid reaction at about 423K, and the two phase field of the ferrite and Ni_3Fe phases extended below the temperature [7]. Furthermore, the presence of $FeNi_3$ phase was inferred from the measurement of Curie temperature which showed a maximum at the stoichiometric composition of $FeNi_3$. Thus, it is likely that this type of atomic order is present in the Fe-60%Ni binary alloy. On the other hand, the $L1_2$-type ordered phase observed in Fe-40%Ni may be the Fe_3Ni type, although the existence of Fe_3Ni is not known at the moment. However, $FeNi_3$, FeNi and Fe_3Ni phases may exist as is similar to Fe_3Pt, FePt and $FePt_3$ phases in Fe-Pt binary system [8]. But Reuter et al. suggested that in the Fe-Ni binary system there is an eutectoid reaction of forming FeNi and the ferrite phases, and Fe_3Ni is a metastable phase. Thus, there still remains a room to be further examined in the Fe-Ni binary phase



Fig.7 Selected area diffraction pattern in the [001] direction taken from Fe-40%Ni-1%Ti ternary alloy, showing extra spots arising from oxide formed on specimen surface.

diagram itself.

The striation was observed in the bright field image in Fe-60%Ni alloy after irradiation (see Fig.6), and its direction was perpendicular to the <111> direction. Along this direction streaks were observed in the corresponding SADP shown in Fig.6. This is probably caused by the formation of stacking faults on the {111} crystal plane in the alloy, because it is well known that excess vacancies and interstitials in the fcc lattice tend to gather together on the {111} plane and form clusters, resulting in the relaxation of the Bragg condition along the <111> direction.

It has been reported that Fe_3O_4 and $NiFe_2O_4$ are formed on a Fe-Ni foil surface, while having similar lattice parameters, i.e., 0.8396nm (Fe_3O_4) and 0.8339nm ($NiFe_2O_4$) [5]. In this study, no extra spots were observed in the electropolished specimens, but after irradiation many extra spots were observed together with the ordered spots. Fig.7 is a typical diffraction pattern from the oxides, which was taken from the non-irradiated region. When compared this diffraction pattern with that shown in Fig.1, it is evident that a series of the weak (hh0), ($h\bar{h}$0), (h00), (0h0), ($\bar{h}$00) and (0$\bar{h}$0) reflections is not originated from the oxides but the ordered phase in Fe-Ni alloys.

Conclusion

The presence of ordered phases was confirmed from the 2MeV electron irradiation experiment in all the Fe-40mol%Ni-1mol%Ti, Fe-40mo%Ni and Fe-60mol%Ni alloys.

References

1. A.Chamberod, J.Laugier and J.M.Penisson, "Electron Irradiation Effects on Iron-Nickel Invar Alloys", J. Mag. and Magnetic Materials, 10(1979), 139-144.

2. K.B.Reuter, D.B.Williams and J.I.Goldstein, "Ordering in the Fe-Ni System under Electron Irradiation", Metall. Trans. A, 20A(1989), 711-718.

3. K.B.Reuter, D.B.Williams and J.I.Goldstein, "Determination of the Fe-Ni Phase Diagram below 400 °C", Metall. Trans. A, 20A(1989), 719-725.

4. R.A.Dodd, F.A.Garner, J.J.Kai, T.Lauritzen and W.G.Jhonston, "Spinodal-like Decomposition and Swelling Induced by Ion Irradiation in Simple Fe-Ni and Fe-Ni-Cr Alloys", Radiation-Induced Changes in Microstructure: 13th International Symposium (Part I), ASTM STP 955, Eds., F.A.Garner et al., (American Society for Testing and Materials, Philadelphia, 1987),788-804.

5. K.B.Reuter, D.B.Williams, J.I.Goldstein and E.P.Butler, "Surface Oxide on fcc Iron-Nickel Alloys", Metall. Trans. A, 17A(1986), 163-167.

6. M.Z.Hameed, R.E.Smallman and M.H.Loretto, "H.V.E.M. Study of Ordering and Disordering in Cu_3Au", Phil. Mag. A, 46(5)(1982), 707-716

7. Y.Y.Chuang, Y.A.Chang, R.Schmid and J.C.Lin, "Magnetic Contributions to the Thermodynamic Functions of Alloys and the Phase Equilibria of Fe-Ni System below 1200K", Metall. Trans. A, 17A(1986), 1361-1372.

8. "Binary Alloy Phase Diagrams"(2nd Ed.), Eds. T.B.Massalski et al., vol.2, ASM, (1990), 1752-1756.

AN APPRAISAL OF SINGLE CRYSTAL CASTING FOR TURBINE COMPONENTS

P. Auburtin, S. L. Cockcroft, A. Mitchell and W. Tao

Dept. of Metals and Materials Engineering
Advanced Materials and Processing Laboratory
University of British Columbia
Vancouver BC V6T 1Z4
CANADA

Abstract

The use of alloy single crystal castings for the high temperature components of turbines in aero-engines is now a well-established industrial practice, and it is now being extended to machines for land-based purposes. The alloy compositions are well into the third generation of evolution and the practical aspects of the present casting method are understood. The cast components, even in routine production, carry a high rejection-rate due to metallurgical and geometrical defects and also incur a very high production cost. In this report we review the reasons for the problems; consider the near-term future possibilities for their correction in present alloy systems; and finally examine the prospects of extending the technique to intermetallics and to the large castings required by power turbo-generator sets.

The Third Pacific Rim International Conference on
Advanced Materials and Processing (PRICM 3)
Edited by M.A. Imam, R. DeNale, S. Hanada,
Z. Zhong and D.N. Lee
The Minerals, Metals & Materials Society, 1998

Introduction

During the manufacture of advanced single crystal components by the conventional investment casting / Bridgeman techniques, the rejection rate arises in three principal causes : freckles, random grains and dimensional variance. These aspects have been reviewed in the literature and related to the casting process by the use of computer fluid dynamics (CFD) modeling techniques (1), in order to relate the design and operation of the casting process to the "maps" of potentially-defect parts of the final casting. It can be seen from this examination that the problems are fundamental to the present process technique and that there are relatively well-defined theoretical limits to the "robustness" of the existing methods, arising in the fundamental heat-transfer characteristics of the systems. It is possible to suggest ways for minor improvement through enhanced thermal gradients by modifying casting design and cooling technology, but although these changes will somewhat extend the limits and increase reliability, they will not provide the quantum increase needed to reduce the final component costs.

Segregation Defects

The various alloys which have been developed for use as high-temperature components in the form of single crystal castings are all extremely complex. They are basically derivatives of the cast superalloys in which grain-boundary-strengthening elements have been removed and the contents of both the solid-solution strengtheners and the intermetallic γ and γ' phases have been maximized. The result is an alloy which is extremely segregation-sensitive (2) and prone to form casting defects based on the uncontrolled movement of interdendritic liquid during the solidification process. The principal defect formed in this way is due to the collection of interdendritic liquid through fluid flow driven by buoyancy forces. The result is a "freckle" of channel of solute-rich material extending through the solidification front (3) and ultimately freezing into the final structure, as demonstrated by Figure 1. The channel has a solidus temperature which is somewhat below that of the bulk alloy since superalloy phase precipitation is non-equilibrium. Since the homogenization heat-treatment of the final casting must be carried out at a temperature very close to the solidus, the freckle channel shows some incipient melting and creates both porosity and a brittle path through the component.

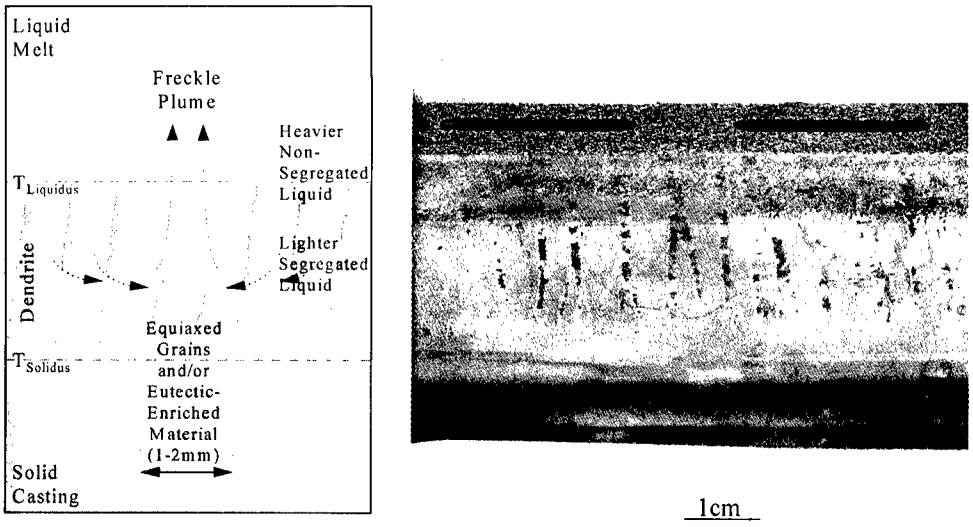


Figure 1 : (a) Freckling mechanism (b) Freckles in the root of a large turbo-engine blade.

The formation of freckles could in principle be avoided by two methods; increasing the thermal gradient so that the permeability of the dendrite network is too small to permit interdendritic fluid flow, or by changing the alloy composition so as to eliminate the density gradients which give rise to the driving force for the flow. This technique has limitations imposed by the thermal resistances of the casting itself as well as by the intrinsic design of the furnaces involved. The solidification process evolves heat, which must be conducted to the casting's external surfaces, and this conduction process (as expressed through the Biot and Fourier numbers of the system) limits the extent to which we are able to control the thermal gradient in the solidifying region through the external imposition of gradients from the furnace itself. In the present practical case, castings such as turbine blades are cast in assemblies of 6 - 12 around a central sprue, which makes up a very significant thermal mass. Since the furnace operates in vacuum, heat transfer between the furnace and the casting is entirely through radiation. As the requirement for the blades (for power turbines) becomes larger, the internal thermal resistance of the casting assembly becomes significant compared to the heat transfer capability of a radiation mechanism and we reach a point at which the up-scaling of the assembly inevitably puts at least part of the casting into a region of thermal gradient where the formation of freckle defects cannot be avoided. Modeling of this process demonstrates that there is only one practical solution to this dilemma, which is to reduce the number of blades in the casting assembly, which in turn implies a considerable increase in the cost of the individual casting. In the case of the largest blades (25 kg), the blades may only be cast one at a time, which leads to an unacceptable cost. Clearly, if we are to continue to use the convention Bridgeman process for single-crystal blade casting, some innovative process design is required in order to reduce the process cost, since it appears unlikely that we will be able to change the alloy design in a direction which would eliminate the freckle driving force.

The extension of the present casting technique to advanced materials, particularly to intermetallics, is of considerable interest. These alloys present two significant problems, in addition to the ones considered above. The first is the chemical reactivity of the liquid intermetallics which leads to containment problems in investment molds. The second is the definition of the required thermal gradients for single-crystal (or DS) casting in intermetallics. At present, the latter remains largely unknown, but by analogy with low-temperature systems it seems probable that the gradient/solidification rate variables familiar in superalloys will also apply to the intermetallics and hence the Bridgeman conditions required for the formation of single crystals will also be similar. If that is the case, then the residence time of the liquid intermetallic in the investment mold will also be similar and could be at least of several hours. For the intermetallics such as TiAl, this time would represent a real barrier in regard to reactivity since even the present face-coat formulations of rare-earth oxides are unlikely to remain unreacted under these conditions. It seems likely that the practical realization of commercial single crystal castings will hinge critically on the development of a suitable containment material for the molds if the Bridgeman technique is the chosen method. Alternatives have been proposed, such as the use of a Czochralski crystal withdrawal method, followed by EDM or ECM profiling of the blade from a cylindrical section. If the crystal material is reasonably cheap (as is TiAl), then this method has some attraction, but it nonetheless requires a cold-crucible container system which has not up to the present time been used in this technique.

A further problem in the casting of these components lies in the fact that almost all present turbine designs require the blades to have internal cooling passages, hence allowing the use of turbine gas inlet temperatures which are significantly higher than the liquidus of the blade alloy. At present, these passages are cast into the blade by the use of dissolvable ceramic cores, but the use of intermetallics would probably mean that the passages would have to be machined into the component after casting, again by a costly electro-discharge machining

(EDM) or electro-chemical machining (ECM) method, unless the maximum use temperature of the intermetallic was so high that cooling was not required.

The production problem in all of the above ideas lies in the "robustness" of the process. As the casting size becomes larger, the window of permissible process parameters (such as temperature gradient and withdrawal speeds) becomes smaller and the possibility of control errors becomes larger. In the casting case (in contrast to some other related processes) the result is not harmful in that it will lead to a defective component being put into service, but instead the problem is one of production cost due to rejections at the quality control stage. Bearing in mind that the process is fundamentally costly, and that the recycle value of the alloy is extremely small, the rejection cost then becomes sufficiently important to be the deciding factor in commercialization.

Single Crystal Structure Integrity

The classical single crystal blade is an alloy structure and is not, in a strict physical sense a "single crystal". However, the practical definition of the structure is that it consists of a primary γ orientation which is the same at any point in the casting. The mechanical properties have a strong relation to this orientation and so the application specifications dictate the "goodness" of the orientation (4). In practice, subgrain mis-orientations of to 5° from the principal direction are acceptable in most instances, but totally new grains with significant orientation differences (Figure 2) obviously are not.

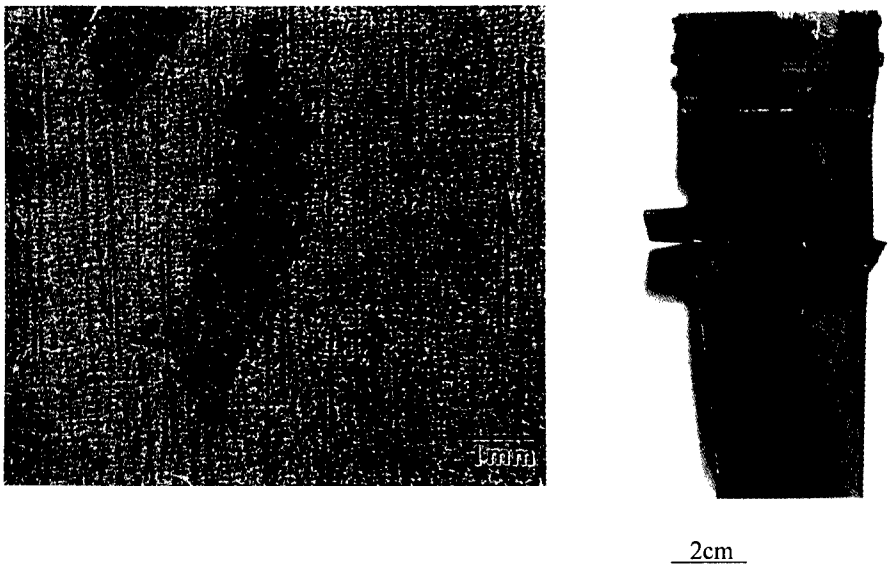


Figure 2 : (a) Random grain nucleation in SX casting(5) (b) Spurious grain in SX blade

The single crystal orientation is created usually by the use of a "pigtail" at the bottom of the casting, which acts as a grain selector for the casting body. The chosen orientation will continue to grow throughout the casting unless solidification conditions permit the nucleation of a new grain. These nucleation conditions are principally related to the possibility that part of the liquid (usually in a part of the casting involving an abrupt change of section) may be under-cooled. The conditions for nucleation of the new grain growth have been extensively studied in

analogue low temperature systems (6), and by using the nucleation theories developed by Hunt (7) and Fernihough (8), we may compute that undercoolings of only 3 - 5°C will provoke nucleation in superalloys. CFD modeling of typical blade castings demonstrates that such undercooling is not only possible, but quite probable, and not unexpectedly we often find such "random grains" in superalloy single crystal castings. The technique of using "grain continuators" to by-pass the undercooled area has been employed successfully in small castings, but is impractical in large castings due to the stress exerted on the finished casting by contraction as the fully-constrained areas cool down, which leads to hot-tears in the cast structure.

To date the practical response to the problem has been to increase the gradient/rate parameter in the process to put the casting into a thermal region where the undercooling has been reduced below the required threshold. As indicated above, however, this practice has distinct limitations as the casting size increases and is not likely to be a practical solution for very large sizes. It will almost certainly be an ultimate limitation on the use of the present Bridgeman technique for these castings. Since the nucleation is invariable at the interface between the casting and the ceramic mold, it depends on the interface parameters, particularly on the structure and composition of the ceramic face-coat. Experimental work has shown that the use of amorphous face-coats can very significantly increase the permissible undercooling before nucleation (as would be anticipated from fundamental studies on undercooled levitated metal droplets) and it is possible that future versions of the process for large castings will require this type of approach.

Practical Aspects

EDM or ECM finish machining of complex casting shapes is extremely expensive, and it is essential for commercial success that the casting process produces a component which is very close to the required final dimensions. The investment mold compositions presently used rely on a thin, fragile face-coat of the required chemical characteristics, backed by a thicker coat of a ceramic designed to mechanically support the casting. As the casting weight is increased, and also the process time lengthened, the creep of the composite ceramic coating becomes significant in allowing dimensional change in the casting shape. It is not possible to overcome this change by increasing the thickness of the support coat since that would also reduce the heat-transfer capacity of the casting's boundary surface. The solution will lie in the development of back-up coats which are more creep resistant, possibly by the use of fiber-reinforcing, but which also have a high thermal conductivity.

A second practical point is that of process control. Although we can specify, by experiment and/or modeling, the gradient and rate conditions required at the liquidus for the successful production of the single crystal casting; and we can also accurately measure these parameters in an empty furnace, we must relate the two as the casting proceeds in order to make the required structure. Unfortunately, the on-line external measurement of the temperature on the outside of the ceramic mold is not sufficiently accurate to permit us to extrapolate this temperature to that existing in the casting at the same point in the process. As a result, in the casting (which has a three dimensional shape) we do not have at present an accurate method of precisely placing the casting liquidus in relation to the furnace temperature gradient. Our control of the gradient and rate during the process is hence less than perfect and we must have an operating parameter window which is much larger than would otherwise be required. Although thermal imaging combined with on-line CFD modeling of the casting will produce some interesting insight into the process, it seems that in practice, the reproducibility of the mold's thermal characteristics (including emissivity) precludes a sufficiently accurate computation to be practically useful.

Conclusions

It appears from the foregoing that we need a radical re-thinking of the method by which large single-crystal castings are to be made. The practical application for the castings has been demonstrated and power turbines are presently going into service which could benefit from their use. Since a typical turbine in this class uses 160 blade castings in on row, with a design life of possibly 20,000h, it is obvious that the production cost of the components will be a very strong factor in their application. It is suggested that we must find a version of the casting process in which not only the actual cost, but also the cost through reproducibility, is brought to a reasonable level. For the existing superalloy compositions, this process is likely to be one with a high degree of automation which manufactures the castings on a "one-at-once" basis in order to satisfy the requirements both of the process control and of the fundamental heat-transfer characteristics.

Acknowledgments

The authors are grateful for the on-going support of the Consarc Corporation in the work discussed above.

References

1. A.L. Purvis, C.R. Hanslits, R.S. Diehm : "Modeling characteristics for solidification in single-crystal, investment cast superalloys", JOM, 1 (1994), 38-41

2. P. Auburtin, S.L. Cockcroft, A. Mitchell : "Liquid density inversions during the solidification of superalloys and their relationship to freckle formation", Superalloys 1996 (Ed. R.D. Kissinger et al., Min., Met. & Mat. Soc., 1996), 443-450

3. A.F. Giamei, B.H. Kear : "On the nature of freckles in nickel base superalloys", Met. Trans., 1 (8) (1970), 2185-2192

4. M. McLean : Directionally solidified materials for high temperature service (The Metals Society, 1983), 151-204

5. T.M. Pollock, W.H. Murphy : "The breakdown of single crystal solidification in high refractory nickel-base alloys", Met. Trans. A, 27A (4) 1996, 1081-1094

6. R.B. Mahapatra, F. Weinberg : "The columnar to equiaxed transition in tin-lead alloys", Met. Trans. B, 18B (6) (1987), 425-432

7. J.D. Hunt : "Steady state columnar to equiaxed growth of dendrites and eutectic", Materials Science and Engineering, 65 (1984), 75-83

8. J.N. Fernihough, S.L. Cockcroft, A. Mitchell, A.J. Schmalz : "Columnar to equiaxed transition in nickel based superalloys", Superalloys 1996 (Ed. R.D. Kissinger et al., Min., Met. & Mat. Soc., 1996), 481-486

PHASE TRANSFORMATION OF GIBBSITE TO CORUNDUM UNDER HYDROTHERMAL CONDITIONS

Hyo Shin Yu, Kang-In Rhee, Churl-Kyoung Lee, Dong-Hyo Yang
Minerals Utilization & Materials Div.,
Korea Institute of Geology, Mining, and Materials(KIGAM)
30 Kajung-dong, Yusung-ku, Taejon, Korea 305-350

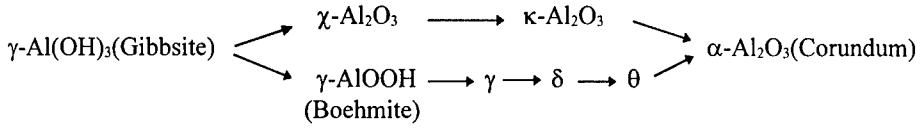
Abstract

Phase transformation of gibbsite, crystallization rate, particle size and morphology of resulting corundum were evaluated by controlling variables including operating temperature and pressure; size, shape and amount of gibbsite and seeds; and type of mineralizers. Under hydrothermal conditions, gibbsite was found to transform first to boehmite and then to corundum. Uniform and hexagonal corundum powders were readily synthesized at 400°C, 250 atm in 4 hrs with 4 wt% seeds. Without seeds, however, temperature had to be increased to 450°C to get the same effects. The size of the produced corundum was reduced almost proportionally with decreasing the size of gibbsite used. The types of starting materials, seeds and mineralizers decisively affected the morphology of the resulting corundum. The complete transformation of gibbsite to corundum took place in pure water regardless of mineralizer addition.

The Third Pacific Rim International Conference on
Advanced Materials and Processing (PRICM 3)
Edited by M.A. Imam, R. DeNale, S. Hanada,
Z. Zhong and D.N. Lee
The Minerals, Metals & Materials Society, 1998

Introduction

Extensive studies of phase transformation of gibbsite to corundum have been the subject of numerous investigators over the last fifty years.[1,2] A two-pathway reaction[1] to form corundum via boehmite and χ-Al_2O_3 routes has been cited frequently in these studies:



There have been substantial discrepancies in the transformation temperature as well as the path of phase transformation. Phase transformation temperature mostly depends on pH, pressure, the presence of seeds and mineralizer, and the aging of starting material known as nutrient. According to the hydrothermal investigations of Kennedy,[3] and Neuhaus and Heide,[4] gibbsite or bayerite commenced transforming to boehmite at about 100°C. Chertov and Zelentsov[5] prepared crystalline boehmite at 100-150°C. Mehta and Kalsotra's X-ray investigation[1] indicated that boehmite began to form at 185°C and gibbsite phase completely disappeared at 225°C, showing the most intensive boehmite peak at 265°C. The transformation of boehmite to diaspore(α-AlOOH) has been confirmed by many researchers. [3,4,6-9] Robbins[6] observed the phase change between 200-250°C in the presence of seeds and even without them, it occurred at 300°C and 200 atm. According to Wefers' earlier study,[10] bayerite was transformed to diaspore at 100°C and boehmite to diaspore between 250-350°C. Also, boehmite was definitely maintained as a stable phase even at pH 10 and 350°C. At temperature up to about 400°C, it was noted that diaspore was stable under high pressures whereas at low pressures, boehmite still existed as a metastable phase. [3,10]

Contradictory results can be also found in the transformation temperature of diaspore to corundum. Wefers[10] reported that diaspore was transformed to corundum at 360°C but this has not been confirmed yet by peers. In the presence of Na_2CO_3 mineralizer, Ervin and Osborn[11] found stable corundum in two conditions in the temperature-pressure phase diagram: (1) stable below 140 atm and above 390°C (2) stable above 200 atm and above 415°C. Based on this diagram, boehmite can be transformed directly to corundum at pressures below 140 atm when the temperature is held above 390°C.

Two basic mechanisms of particle formation under hydrothermal conditions were proposed by Stambaugh, et. al. [12]: (1) dissolution/recrystallization-precipitation (2) in-situ transformation of intermediate phase. Particles could precipitate from solution via a mechanism consistent with the classical precipitation theories. However, metastable hydroxide particles were often present as a precursor phase at higher pH values.

In this work, a major emphasis has been made to determine thermodynamic variables influencing the phase transformation of gibbsite, and the particle size and shape of corundum since very few data in this endeavor are available in the literature.

Experimental

Reagent-grade gibbsite manufactured by Shinyo Pure Chemicals of Japan was used as starting material. An industrial-grade, Russian gibbsite containing 22wt% corundum was also used.

Two sizes of reagent-grade α-Al_2O_3 crystals were employed as seeding material: 0.3μm(Fluka) and 1.0μm (High Purity Chemicals). Physical properties such as particle size, existing phases and bound water in starting materials were first determined. Shinyo product was a pure aluminum hydroxide determined by X-ray diffraction(XRD), thermogravimetric(TG) and chemical analyses. The mean particle sizes and specific surface areas of the Shinyo and Russian materials were determined to be 54μm and 0.07 m^2/g, and 2μm and 1.77 m^2/g, respectively by the use of a Malvern particle analyzer and the BET method. Starting materials were charged into autoclaves which were heated in a furnace at predetermined temperature.

Results and Discussion

Thermal Decomposition of Gibbsite

For comparison with hydrothermal transformation, Shinyo gibbsite was subjected to calcination in the temperature range of 200-1200°C. XRD patterns at several temperatures are given in Fig. 1. Gibbsite was found to transform to corundum by the following pathway reaction:

gibbsite→ boehmite → χ-Al_2O_3 → κ-Al_2O_3 → α-Al_2O_3(corundum)

This pathway is somewhat different from other routes proposed in the literature including the two-pathway reaction. Transformation temperatures could not be specified according to this study but boehmite appeared at 200°C. χ-Al_2O_3 peaks were first noticed at 500°C and became pronounced at 800°C. Our TGA results supported this finding by indicating that gibbsite lost practically all the bound water before the temperature reached 600°C. At 1050°C, κ-Al_2O_3 was present as distinctive peaks. The transformation of gibbsite to stable corundum took place at 1100 °C and was finally completed at 1200°C.

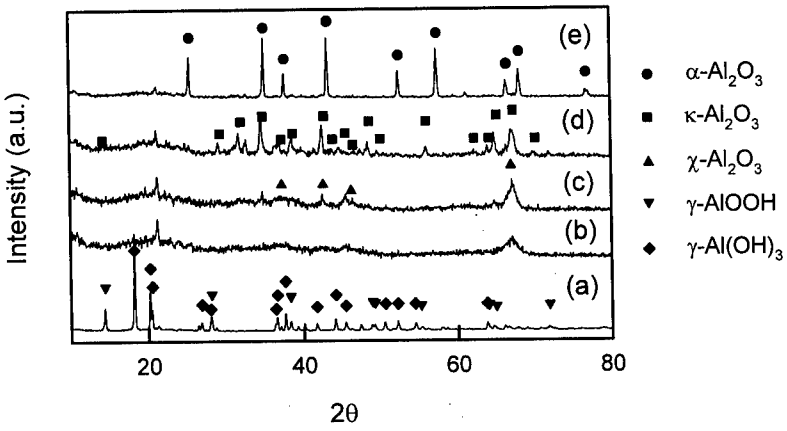


Fig. 1: XRD spectra of gibbsite calcined at (a) 200 (b) 500 (c) 800 (d) 1050 and (e) 1200°C

Influences of Variables on Hydrothermal Phase Transformation of Gibbsite

Operating time, temperature, pressure, seeding materials, and type of mineralizers were evaluated with Shinyo gibbsite. Fig. 2 shows XRD patterns of reaction products prepared in the time range of 2-9 hrs at 400°C. The gibbsite phase was no longer present in 2 hrs and the products consisted of mostly boehmite and small amount of corundum. The conversion of

gibbsite to corundum was completed in 4 hrs. (002) plane in gibbsite, (020) in boehmite and (113) in corundum were shown to be the most intensive peaks representing each phase. The relative intensities of these strongest peaks were compared in the following studies.

The operating temperature was tested from 160 to 470°C in the absence of seeding materials. It is, however, well known that the hydrothermal synthesis of corundum should be conducted above the critical temperature of water(374°C). The phase transformation of Shinyo gibbsite at different temperatures without seed addition is shown in Fig. 3. The intensity of the (002) peak in gibbsite gradually increased with temperature up to 200°C, and then decreased abruptly. The boehmite peak(020) was stable between 200 and 450°C, being most intensive at about 400°C. Finally the complete transformation of gibbsite to corundum occurred at 450°C.

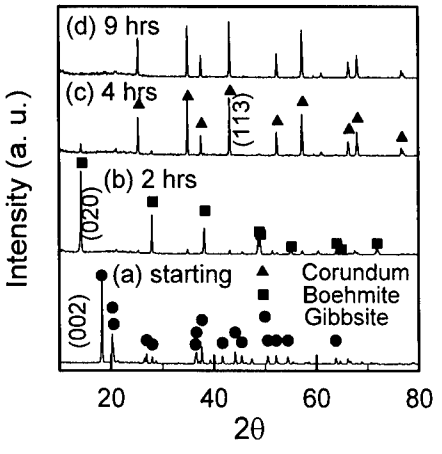


Fig. 2: XRD spectra of products prepared from gibbsite at different times: 400°C, 17% fill, 4wt% seeds

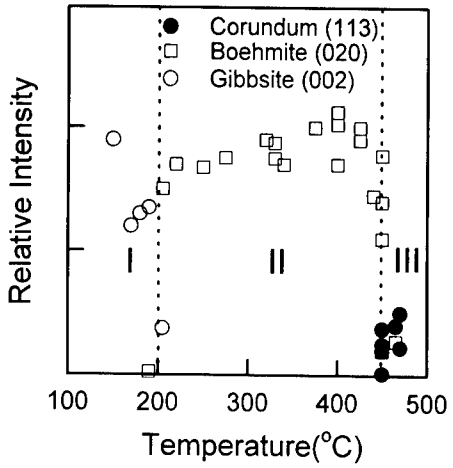


Fig. 3: Phase transformation of gibbsite with temperature: I: gibbsite region, II: boehmite region, III: corundum region

In order to study the influence of seeding material on the phase transformation, 4-22wt% corundum seeds of 1μm size were introduced to Shinyo gibbsite in 2-hr tests at 400°C. Corundum could not be formed with the seeds up to 14wt% but formed with 22wt%. As expected, the XRD intensity ratio of corundum to boehmite increased with increasing seed content. In another 2-hr run with Russian gibbsite containing 22wt% seeds, barrel-shaped corundum crystals were successfully obtained even at 380°C as shown in Fig. 4(a). Platy corundum crystals prepared with Shinyo gibbsite at 450°C is shown in Fig. 4(b). In summary, the transformation temperature could be reduced to a certain extent at the expense of increasing time, pressure or seed content to obtain pure corundum.

A mineralizer is usually introduced to prepare sufficiently large crystals in hydrothermal crystal growth instead of synthesis. The addition of a mineralizer not only helps increase the solubility of the starting material, but also change the temperature dependence of solubility. In our hydrothermal tests, sodium compound mineralizers were evaluated to study their effect: 15% Na_2SO_4, 15% $NaHCO_3$, 2mol/dm^3 Na_2CO_3, 2mol/dm^3 NaOH. In view of test results, all the mineralizers used had little effect on the phase transformation. Thus pure water alone was found sufficient to be a solvent for the successful transformation to corundum.



(a) (b)

Fig. 4: SEM micrographs of corundum powders prepared with (a) Russian (b) Shinyo gibbsite

Influences of Variables on Particle Size and Morphology

The synthesis time range of 4-40 hrs was explored at 400°C. As expected, the mean diameter of the resulting corundum remained almost constant at about 40μm throughout the test period. If the hydrothermal synthesis of corundum just in the case of the classical view of precipitation theory followed the path of dissolution, recrystallization and precipitation(DRP) of gibbsite, corundum particles could have grown with increasing time. However, an almost constant corundum particle size remaining with increasing time seemed to suggest an in-situ phase transformation of intermediate metastable phase(boehmite) to corundum, requiring a smaller mean free path than that of DRP, as mentioned in the introduction.

Two levels of temperature, 425 and 450°C, and the mean particle size(d_{50}) of gibbsite feed in the range of 4-54μm are compared in Fig. 5 in terms of the size of product corundum. A Shinyo gibbsite sample had been ground to smaller size fractions with a ball mill for these tests. This figure shows that the smaller the starting material, the smaller the size of product corundum is. When the feed size was 10μm or larger, the size of corundum was likely to be reduced as the temperature increased from 425 to 450°C.

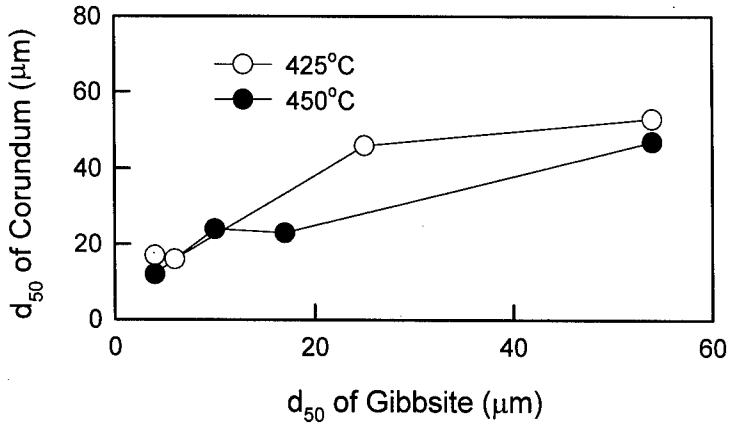


Fig. 5: Effect of particle size of gibbsite on the size of product corundum: 4wt% and 1μm seeds, 17% fill, 4 hrs

The amount of seeds in the range of 4-22wt% α-Al_2O_3 was investigated with respect to the size of resulting corundum. As the content of seeds increased, the mean size of product corundum

decreased accordingly. In another series of test work at 400°C, 250 atm for 4 hrs, different seed sizes, 0.3 and 1.0μm, were compared for the same purpose. The smaller seeds yielded smaller product, being in respective 33 and 40μm. Kaiser and Sporn[13] had found similar results in comparison tests in a NaOH or NH_4OH solution under hydrothermal conditions.

The mineralizers mentioned earlier were also tested for their influences on the product size. All the mineralizers yielded corundum in the 51- 54μm size, which is somewhat coarser than that (40μm) prepared in pure water. Variables affecting the morphology of product corundum were evaluated. The addition of sodium compound mineralizers mentioned earlier affected the morphology, rendering the size distribution of the product wide. The types of starting materials and seeds resulted in different morphologies of corundum powders: barrel for Russian and platy for Shinyo as shown earlier.

Conclusions

1. Uniform corundum powder in hexagonal structure could be readily synthesized at 400°C and 250 atm in 4 hrs when α-Al_2O_3 seeds at 4wt% were added to gibbsite. However, in the absence of the seeds, temperature had to be increased to 450°C to get the same result.
2. The size of gibbsite feed and of corundum seeds was the most important variables controlling the size of product corundum. The smaller the feed, the smaller the resulting corundum.
3. The type of starting materials, seeds and mineralizers decisively influenced the morphology of the corundum produced.

References

1. S. K. Mehta and A. Kalsotra, "Kinetics and Hydrothermal Transformation of Gibbsite," J. Thermal Analysis, 367 (1991), 267-275.
2. C. Novák, G. Pokol, V. Izvekov and T. Gál, "Studies on the Reactions of Aluminum Oxides and Hydroxides," J. Thermal Analysis, 36 (1990), 1895-1909.
3. G. C. Kennedy, "Phase Relations in the System Al_2O_3-H_2O at High Temperatures and Pressures," Am. J. Sci., 257 (1959), 563-573.
4. A. Neuhaus and M. Heide, "Hydrothermal Investigations in the System Al_2O_3-H_2O," Ber. Deutsch. Keram. Ges., 42 (1965), 167-84.
5. V. M. Chertov and V.I. Zelentsov, Koll. Zh., 4 (1973), 805.
6. R.G. Robbins, J. Inorg. Nucl. Chem., 29 (1967), 431-435.
7. R. Gout and J.L. Dandurand, "Phase Equilibria in the System Al_2O_3-H_2O," Trans. ISCOBA, 13 (18) (1983), 117-26.
8. K. Wefers and C Misra, "Oxides and Hydroxides of Aluminum," Alcoa Tech. Paper No.19, rev., Pittsburgh (1987).
9. R.A. Laudise and A.A. Ballman, "Hydrothermal Synthesis of Sapphire," J. Am. Chem. Soc., 80 (1958), 2655-2657.
10. K. Wefers, "The System Na_2O- Al_2O_3-H_2O," Erzmetall., 21 (1967), 423-31.
11. G. Ervin, Jr. and E. F. Osborn, "The System Al_2O_3-H_2O," J. Geol., 59 (1951), 381-394.
12. E. P. Stanbaugh, W. J. Dawson, J H. Adair and B. C. Kim, "Technology for New/Improved Hydrothermal Processes," (Battelle Handbook, Dec. 1984).
13. A. Kaiser and D. Sporn, "Phase Transformations and Control of Habit in Hydrothermal Synthesis of α-Al_2O_3," J. of European Cer. Soc.(UK), 14 (1) (1994), 77-83.

ORDERING PROCESSES IN AN Al-Li-Cu-Mg-Zr ALLOY

Yasuya Ohmori[1], Sadayoshi Ito[2], and Kiyomichi Nakai[1]

(1)Department of Materials Science and Engineering, Ehime University, 3 Bunkyo-cho, Matsuyama, Ehime 790-8577, Japan.
(2) Formerly a graduate student, Ehime University, now with Matsushita-Kotobuki Electronics Co., Ltd., 200 Hukutake-cho Ko, Saijo, Ehime 793-6035, Japan

Abstract

The early stage of ageing in an Al-Li-Cu-Mg-Zr alloy has been examined by means of both electrical resistivity measurements and high resolution electron microscopy with using the inverse Fourier transform technique of the images. The specimens solution-treated and quenched into iced brine were heated at a constant rate of 1Kmin^{-1} up to773K.

Five reactions can be clearly separated in the temperature derivative of resistivity vs temperature curve, i.e., a slight increase at temperatures around 338K, a large decrease around 368K, a significant decrease around 448K, a large increase around 538K, a remarkable decrease around 568K and the final broad increase around 623K. The reactions occurring at temperatures below 473K have been examined. It has been confirmed that the as-quenched specimen has already been ordered congruently. It is thought that the first reaction around 338K arises from the increase in the degree of congruent ordering, but that the second reaction around 368K may be due to either the rearrangement of Anti Phase Domain Boundaries or the partition of Li atoms between the Anti Phase Domain Boundaries and the matrices. The APB's lie parallel to either {100} or {110} planes. The reaction occurring at temperatures around 448K arises from the phase separation into Li-rich and Li-poor regions and the Ostwald ripening of the Li-rich regions follows.

Acknowledgements

This work was partly supported by Grant-in- Aid for Scientific Research on the Priority Area ' Investigation of Microscopic Mechanisms of Phase Transformations for the Structure Control of Materials' from the Ministry of Education, Science and Culture, Japan. Thanks are also due to Sumitomo Light Metal Industries, Ltd., for supplying the material used in the present study.

The Third Pacific Rim International Conference on
Advanced Materials and Processing (PRICM 3)
Edited by M.A. Imam, R. DeNale, S. Hanada,
Z. Zhong and D.N. Lee
The Minerals, Metals & Materials Society, 1998

Introduction

In the earlier transmission electron microscopic studies on the ageing of Al-Li based alloys[1)-(3)], the reactions have been interpreted simply as: supersaturated solid solution→ $\delta'(Al_3Li)\rightarrow \delta$ (AlLi). The electrical resistivity[(4)] and calorimetric studies[(5)-(6)], however, demonstrated the existence of various stages in the precipitation reactions. Sigli et al[(7)], Khachaturyan et al[(8)], Sofa and Laughlin[(9)] and Garland and Sanchez[(10)] then calculated the phase stability in metastable Al-Li alloys theoretically and showed that α solid solution decomposes into an ordered structure congruently and that this ordered structure is further separated into the Li-rich ordered δ' regions and the Li-lean disordered regions through the spinodal decomposition. Radmilovic et al[(11)] and Sato et al[(12)] obtained the experimental results supporting the congruent ordering by means of high resolution electron microscopy. Some experimental evidence showing the kinetics of disordering process at the periphery of ordered domain was also obtained by Okuda et al[(13)] by DSC and synchrotron radiation small angle scattering. The results obtained by Mahadev et al[(14)] and Schmitz et al[(15), (16)], however, are in keeping with the nucleation and growth model.

The aim of this study is, therefore, to reveal such an early complicated ageing processes by means of both electrical resistivity and high resolution transmission electron microscopy with using image processing technique.

Experimental Procedures

The materials used is a commercial Al-2.3Li-1.2Cu-0.6Mg-0.1Zr (mass%) alloy, was cold rolled into 1mm thick sheet and was machined into the specimens with the dimension of 10mm wide/15mm long and 3mm wide/70mm long for microstructural observation and electrical resistivity measurement, respectively. After the solution treatment at 793K for 30min, the specimens were quenched into iced brine. Constant heating rate ageing was carried out at the rate of $1Kmin^{-1}$. The specimens for transmission electron microscopy were quenched from various heating stages. Thin foils were prepared at 243K by means of twin jet polishing technique in an electrolyte of 80vol%CH_3OH-20vol%HNO_3 solution and were observed in a JEM-3010 microscope operating at 300kV. Electrical resistivities were measured during the constant heating rate ageing and the temperature derivatives of them were also calculated.

Experimental Results

In order to reveal the reactions during heating at $1K\ min^{-1}$, the electrical resistivity was measured during ageing. The temperature derivatives of resistivities were also calculated. The base line for the temperature derivative curve vs temperature, $0.14n\Omega mK$, was determined by using the specimen overaged at 568K for 60min. This value is very close to that obtained by the data for pure Al[(17)]. The result is shown in Fig. 1. Six reactions can be clearly separated at temperatures below 673K in the temperature derivative curve, i.e., a slight increase at around 333K (Peak A)(Although this peak is rather vague, the existence of it was confirmed by the isothermal ageing at 303 and 323K.), a relatively large decrease at around 368K (Peak B), a small decrease at around 453K (Peak C), a large increase at around 538K (Peak D), an extremely large decrease at around 568K (Peak E) and an increase at around 623K (Peak F). These reactions are in good agreement with the results obtained by Differential Scanning Calorimetry in a high purity Al-14at%Li[(2)] and an Al-Li-

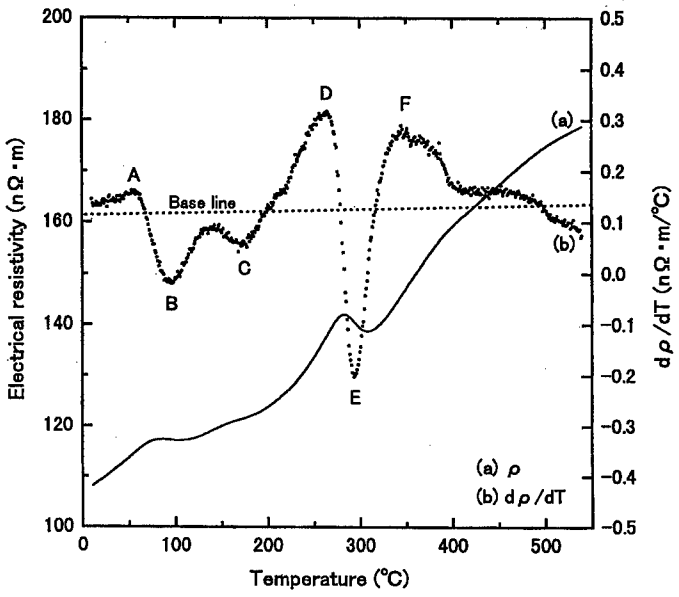


Fig. 1 The results of the electrical resistivity measurement at 1K min^{-1}.

Cu-Mg alloy[18]. Although Luo et al[18] attributed the first reaction at 333K to the GPB zone formation, the peaks below 473K in the present study are thought to be due to the reactions between Al and Li atoms from the TEM observation described below.

In order to interpret the high resolution micrographs, the computer simulation for the phase contrasts were carried out. The spherical aberration coefficient of the present microscope is 0.6mm and the Scherzer focus is about 40nm at 300kV. In this case, the scattering vector should be less than about 0.05nm^{-1} but those less than 0.075nm^{-1}, i.e., up to {300} $L1_2$ reflections, were involved because of the objective lens aperture size. This may induce some imaginary images at the exact Scherzer focus condition but the bright and large spots are thought to correspond to Li atoms in the image with the incident beam direction parallel to the [001]. Figure 2 shows the inverse Fourier transform of the high resolution transmission electron micrograph for the as-quenched specimen using only the {100} and {110} $L1_2$ reflections in the Fourier transform of the original image. It is interesting to note that the contrast of the ordered image is not homogeneous but the distribution of Li-enriched rows parallel to the incident beam direction in the whole area can be reproduced by the ordered reflections. The traces of APB's always lie parallel to either <100> and <110> directions. Considering the mean width of weak contrast regions involving the APB's is much thinner than the foil thickness, about 10 nm, the APB's are thought to lie almost parallel to either {100} or {110} planes. Since the mean linear intercept of Anti-Phase Domain is about 5 nm, it is likely that the overlapping of the domains in the vicinity of APB's may reduce the ordered contrast in these region. The other possibility reducing the contrast in the vicinity of APB is either the decrease in the number of ordered Li atoms or the decrease in Li concentration due to the partition between the matrices and the APB's. Even if the last is the case, the fact that the Li atoms are still ordered in the regions in contact with APB's is in keeping with the congruent

ordering. Figure 3 illustrates a similar micrograph for the specimen aged up to 338K where the slight increase of the temperature derivative of resistivity, Peak A, can be recognised. Comparing it with the as-quenched case, the contrast of the ordered image appears to be much enhanced and the width of the weak contrast regions in contact with the APB's is significantly reduced, the APB planes being more clearly observed.

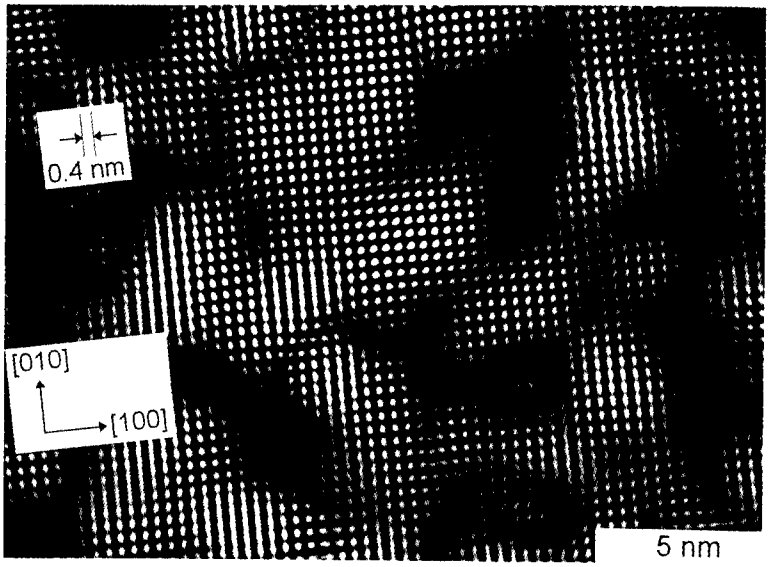


Fig. 2 The inverse Fourier transform of the high resolution transmission electron micrograph for the as-quenched specimen using {100} and {110} $L1_2$ reflections in the Fourier transform of the original image.

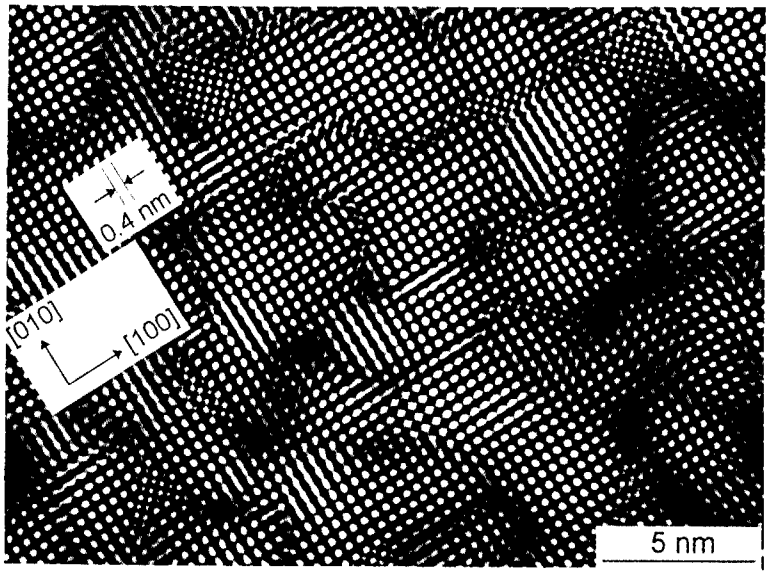


Fig. 3 The inverse Fourier transform of the high resolution transmission electron micrograph for the specimen aged up to 338K using {100} and {110} $L1_2$ reflections in the Fourier transform of the original image.

Therefore, it seems likely that the slight increase in the temperature derivative of resistivity arises out of the elastic strain due to the early stage of ordering.
The increase in ageing temperature up to 368K, where Peak B is observed, does not affect on either the APD size or the thickness of weak contrast regions in the vicinities of APB's. This may arise from either the partition of Li atoms between the regions close to the APB's and the those within the APD's or the rearrangements of atoms in the APB's. Ageing up to 448K, i.e., Peak C, yields the structure shown in Fig. 4. The ordered domains appear to be surrounded by less-ordered regions and the mean size of the APD's increases significantly. It should be noted that weakly ordered atomic arrangements can be recognised even in the vicinities of the APB's. Thus, although Li-rich and Li-lean regions are formed with the partition of Li atoms by increasing ageing temperature, the ordering remains even in the Li-lean regions.

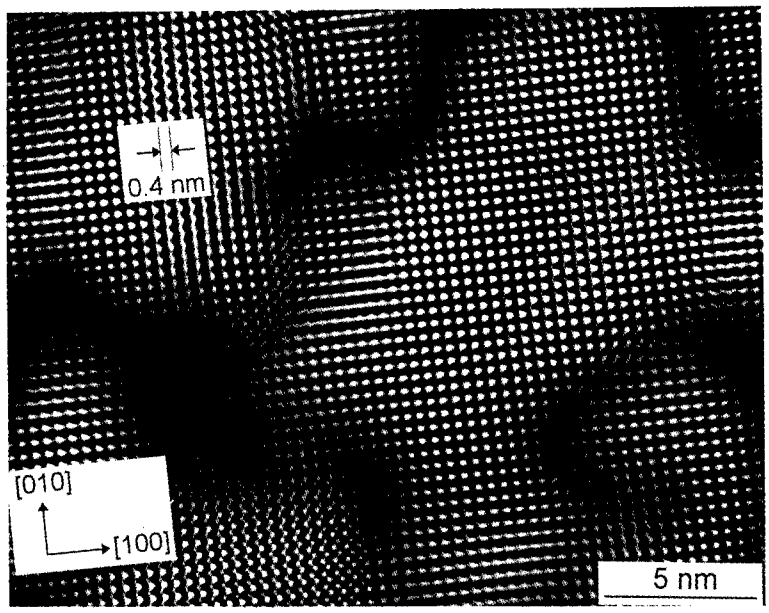


Fig. 4 The inverse Fourier transform of the high resolution transmission electron micrograph for the specimen aged up to 448K using {100} and {110} $L1_2$ reflections in the Fourier transform of the original image.

Discussions

In the early stage of ageing in Al-Li binary alloys, Khachaturyan et al[8] have concluded the cascade transition from the disordered fcc phase to the Li-rich δ' particles with the disordered Li-less regions between them via a nonstoichiometric metastable phase exhibiting the $L1_2$ ordered symmetry, i.e., the congruent ordering. Chen and Khachaturyan[19] have also done the two-dimensional computer simulation for the kinetics of precipitation on an ordered intermetallic phase from a disordered solid solution in the cases of the transitions of both first and second kinds. In the present case, since the occurrence of the transition from the congruently ordered phase to the δ' domains with the less-ordered regions has been confirmed, the type of the transition should be of the first kind as has been pointed out by Chen et al[19]. In their analysis, the conventional nucleation and growth process can occur only in a very limited temperature/composition

range and it is difficult to explain the present results in terms of it. The best fit is obtained in the middle of the ordered and disordered two-phase field within the spinodal line (Fig. 9 in the literature (19)). The decomposition sequences are the congruent ordering in the very early stage of ageing, the compositional instability at APB's and the partition of Li atoms between the regions within the APD's and the APB's, and then the Ostwald ripening of the APD's.

Conclusions

(1) Five reactions are recognised in the temperature derivative of resistivity vs temperature curve in the temperature range from room temperature to 773K, i.e., a slight increase at temperatures around 338K, a large decrease around 368K, a significant decrease around 448K, a large increase around 538K, a remarkable decrease around 568K and the final broad increase around 623K.
(2) The as-quenched specimen has already been ordered almost homogeneously.
(3) The low temperature reactions below 473K can be interpreted as follows.
The reaction around 338K : the increase in the degree of congruent ordering.
The reaction around 368K : either the partition of Li atoms between the Anti Phase Domain Boundaries and the regions within the APD's or the rearrangement of APB structure.
The reaction around 448K : the phase separation into Li-rich and Li-poor regions and the Ostwald ripening of the Li-rich regions.

References

(1) M. Tamura, T. Mori and T. Nakamura: J. Japan Inst. Metals, **34**(1970), 919.
(2) B. Noble and G. E. Thompson: Metal Sci. J., **5**(1971), 114.
(3) D. B. Williams and J. W. Edington: Metal Science, **9**(1975), 529.
(4) R. Nozato, H. Izawa and H. Tsubakino: J. Japan Inst. Metals, **44**(1980), 1203.
(5) J. M. Papazian, C. Sigli and J. M. Sanchez: Scripta metall., **20**(1986), 201.
(6) A. K. Mukhopadhyay, C. N. J. Tite, H. M. Flower, P. J. Gregson and F. Sale: J. Phys., Paris, **48**(1987), C3-429.
(7) C.Sigli and J.M.Sanchez: Acta metall., **34**(1986), 1021.
(8) A. G. Khachaturyan, T. F. Lindsey and J. W. Morris: Metall. Trans. A, **19**(1988), 249.
(9) W.A.Sofa and D.E.Laughlin: Acta metall.,**37**(1989), 3019.
(10) J. S. Garland and J. M. Sanchez: *Kinetics of Ordering Transformations in Metals*, edited by H. Chen and V. K. Vasudevan, 1992, (Warrendale, Pennsylvania: Metallurgical Society of AIME), pp.207.
(11) V.Radmilovic, A. G. Fox and G. Thomas: Acta metall., **37**(1989), 2385.
(12) Tasuo Sato and Akihiko Kamio: Mater. Trans., JIM, **31**(1990), 25.
(13) H.Okuda, I.Tanaka, T.Matoba, K.Osamura and Y.Amemiya: Scripta materialia, **37**(1997), 1739.
(14) V. Mahadev, K. Mahalingam, G. L. Liedl and T. H. Sanders JR, : Acta metall. mater., **42** (1994), 1039.
(15) G. Schmitz and P. Haasen: Acta metall. Mater., **40**(1992), 2209.
(16) G. Schmitz, K. Hono and P. Haasen: Acta metall. mater., **42**(1994), 201.
(17) P. D. Desai, H. M. James and C. Y. Ho: J. Phys. Chem. Ref. Data, **13**(1984), 1131.
(18) A. Luo, D. J. Lloid, A. Gupta and W. V. Youdelis: Acta metall. mater., **41**(1993), 769.
(19) Long-Qing Chen and A. G. Khachaturyan: Acta metall. mater., **39**(1991), 2533.

LINEAR- AND STE-DISCLINATIONS CONSISTING OF MULTIPLE TWIN BOUNDARIES IN THE L1$_1$-TYPE CuPt ORDERED ALLOY

Y. Kitano, *K. Kitasaka and **Y. Fujikawa

Dept. Mat. Sci., Shimane Univ. : Nishi-Kawatsu, Matsue 690-8504, Japan
*Betsukawa Corp., Matto Yatsukaho 1-5, Ishikawa 924, Japan,
**Mat. Research Center, TDK Corp.; 570-2 Matsugashita, Minamihatori, Narita 286, Japan

Disclinations which occur in the L1$_1$-type CuPt ordered alloy are discussed. As decreasing the temperatures, the crystal lattice is slightly distorted from 90 of fcc to 91 degrees of rhombohedral lattice, and the space group is changed from $Fm\bar{3}m$ to $R\bar{3}m$ at the phase transition temperature, 1089 K. Twin boundaries appear for compensation of the crystal symmetry which disappears at the phase transformation. In the case of CuPt ordered alloy, twin boundaries appear either on the {100} or {110} planes of the fcc indices.

Around intersection of two or more twin boundary planes, linear- or ste-disclinations occur. If the twin boundary planes possess a common axis, a linear-disclination will be introduced, while if they do not possess any common axis, a ste-disclination will be introduced.

In this alloy, 17 types of linear-disclinations are predicted. One of them shows the magnitude of 0 degrees. Five, two, two, four, two and one disclinations have the magnitude of 2.0, 2.8, 3.6, 4.0, 5.6 and 7.2 degrees in absolute value, respectively. The alloy was examined by transmission electron microscopy. The experimental results were as follows: Disclinations with 0 degrees were found frequently and five types of linear-disclination with the magnitude less than 2.0 degrees have been observed in the images. The linear-disclinatios distributed in such a way that the local sum of the individual disclination magnitude becomes zero if the area is larger than approximately a square micrometer.

One of models of ste-disclination has been presented and discussed.

The Third Pacific Rim International Conference on
Advanced Materials and Processing (PRICM 3)
Edited by M.A. Imam, R. DeNale, S. Hanada,
Z. Zhong and D.N. Lee
The Minerals, Metals & Materials Society, 1998

1. Introduction

A disclination is one of the linear defects proposed by Volterra in 1907[1]. Disclinations had not been discovered in real crystals, but about ten years ago, disclinations were recognized in the MgCd ordered alloy [2,3,4]. Some of multiple twin (MT) linear-disclinations and a star-disclination appeared and disappeared at the temperature of the order-disorder phase transition. Below the transition temperature they stayed stable in the MgCd alloy.

The order-disorder phase transition of the CuPt alloy takes place at 1089 K. The crystal structure of the high-temperature phase is the fcc disordered structure, having the space group of $Fm\bar{3}m$ and the lattice constant a_c = 0.3784 nm, so $2a_c$ = 0.7569 nm. On the other hand, that of low-temperature phase is the rhombohedral lattice of the $L1_1$ ordered structure, having the space group $R\bar{3}m$ and the lattice constants a_r = 0.7554 nm and α = 91.0 degrees[5]. Both crystal structures are illustrated in Figs. 1(a) and 1(b), respectively.

As illustrated in Fig. 1(b) the CuPt crystal shows the ordering in one of the body diagonals of the cubic, and consequently the distance AB becomes shorter. Since there are four equivalent body diagonals, four kinds of domain with different orientations will appear at the phase transition. We will define crystal orientation as indicated in Fig. 1. The four ordered domains will be named S_1, S_2, S_3 and S_4, corresponding to the ordering direction EF, AB, CD and remaining one, respectively. The deformed structure S_2 is characterized by three deviations of angles which are illustrated in Fig. 2, where three angles, q_1, q_2 and q_3, are 1.0, 1.4 and 1.2 degrees, respectively. In this paper, we are to study on dis-clinations which appear in the CuPt ordered alloy. We will first discuss all the possible structures of disclinations and then we will make an observation for the crystals by TEM.

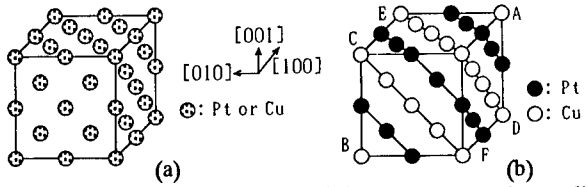


Fig. 1. Crystal structures of the CuPt alloy, (a) High-temperature phase, disordered fcc structure, with eight unit cells, (b) Low-temperature phase, ordered $L1_1$ rhombohedral structure.

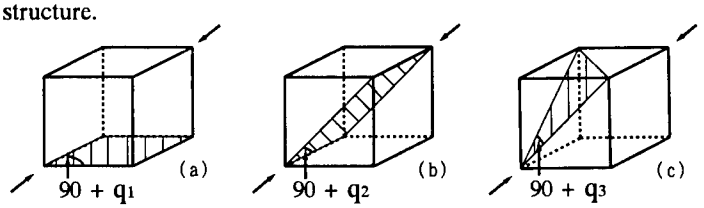


Fig. 2. Characteristic deviations of the angle of the lattice, q_1, q_2 or q_3 in the low-temperature phase S_2. The deviations are 1.4, 1.2 and 1.0 degrees, respectively.

2. Experimental

Ingots of the CuPt alloy was obtained from an appropriate amount of 99.999% Cu and 99.5% Pt in an Ar arc-melt furnace. The ingots were melt-quenched and made thin in a shape of ribbon which had approximately 0.03 mm in thickness and 1 mm in width. In order to homogenize the alloy, following heat treatments were successively carried out; annealing at 1373 K for 80 hours, cooling to 1123 K at a cooling rate of 1 K per minute, another careful cooling through the phase transition temperature to 1033 K at a cooling rate of 0.1 K per minute, further annealing at 993 K for 100 hours and quenching in iced water.

The X-ray powder diffraction pattern of the specimen obtained is given in Fig. 3. All the peaks are interpreted to be the diffraction lines from the ordered $L1_1$ rhombohedral structure.

A diffraction peak with an index of the rhombohedral lattice corresponds to the diffraction peak of the fcc structure with a half of them. For example, the index of the peak D of Fig. 3, is 222 for the rhombohedral lattice but is 111 for the cubic lattice. Hereafter, we will use the indices of the disordered cubic lattice.

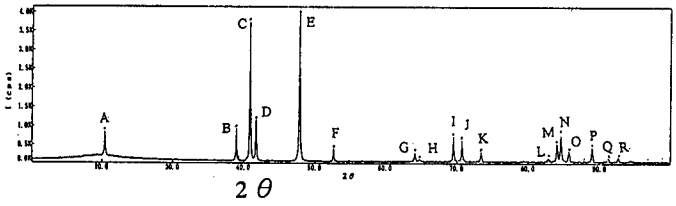


Fig. 3. X-ray powder diffraction pattern of the CuPt ordered alloy used in this work. Copper target was used and peaks from CuK α 2 were computationally eliminated.

For TEM observation, discs of 3 mm in diameter were mechanically polished and thinned down to 0.01 mm in thickness. The discs were further thinned to less than 1000 nm with an Ar ion thinning machine. In order not only to reduce a strain field introduced in the specimen by mechanical polishing but also to make the multiple twin structures visible, we performed a short annealing near the phase transition temperature for about 13 hours after mechanical polishing.

3. Observation of twin boundaries

We observed the specimens using electron microscopes, JEM 200CX and 4000EX. When the temperature of the specimen was decreased through the transition temperature, we observed twin boundaries occurring on {100} and {110} planes, consistently to the prediction of J. Sapriel[6]. This is closely associated with the degradation of the symmetry of the disordered structure at above the transition temperature. Twin boundaries occur in order for the crystal to keep its symmetry totally unchanged. Twin boundaries {100} and {110} can compensate the vanishing symmetry 4/m and 2/m at the phase transition, respectively.

Since, below the transition temperature, we have six ways to choose two of the four types of domain, S_1, S_2, S_3, S_4, and since we have two types of twin boundaries, {100} and {110}, combining 4 types and 2 types, we have twelve kinds of twin boundaries in a crystal which was a single crystal before the phase transition. The twelve kinds of boundaries are denoted as follows: $S_1(010)S_2$, $S_1(101)S_2$, $S_2(001)S_3$, $S_2(1\bar{1}0)S_3$, $S_3(010)S_4$, $S_3(\bar{1}01)S_4$, $S_1(100)S_3$, $S_1(011)S_3$, $S_2(100)S_4$, $S_2(01\bar{1})S_4$, $S_1(001)S_4$ and $S_1(110)S_4$. As an examples, two twin boundaries, $S_1(010)S_2$ and $S_1(101)S_2$, are illustrated in Figs. 4(a) and 4(b), respectively.

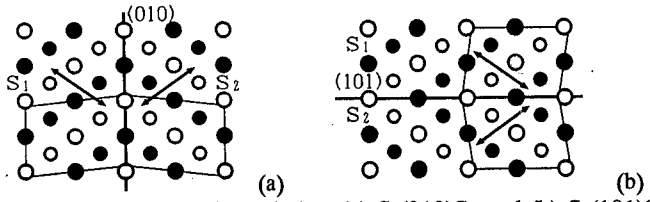


Fig. 4. Atomic configuration of twin boundaries. (a) $S_1(010)S_2$ and (b) $S_1(101)S_2$. Full circles indicate Pt and open ones Cu. Large circles represent the atoms at z=0 and small ones at z=1/2. The arrows indicate the ordering direction in the crystals.

4. Configuration of multiple twin (MT) linear disclination

We define a multiple twin (MT) linear disclination as a linear crystal defect around a common axis to two or more twin boundaries. In the case of the ordered CuPt alloy, the <100>, <110> and <111> axes are possible to be a common axis. The most simple MT-linear disclinations are schematically illustrated in Figs. 5(a) and 5(b) whose common

axis is [$\bar{1}$01]. Both of them consist of two domains, S_1 and S_2, and of two twin boundaries, (010) and (101), having a common axis [$\bar{1}$01] to the both planes, but their configuration is different from each other. Their crystal orientations are not identical referring to the boundary plane.

Here, we assume that the twin boundary has a polarity[3] denoted by m, $\bar{m}$, r and $\bar{r}$, as illustrated in the low half of Fig. 5. They are individually assumed to be a characteristic magnitude. The values are as follows: $m_{<100>}$, $\bar{m}_{<100>}$, $r_{<100>}$ are q_1, q_1, 0, and $m_{<110>}$, $\bar{m}_{<110>}$, $r_{<110>}$, $\bar{r}_{<110>}$ are q_2, $-q_2$, q_2, $-q_2$, and $r_{<111>}$, $\bar{r}_{<111>}$ are q_3, $-q_3$, respectively.

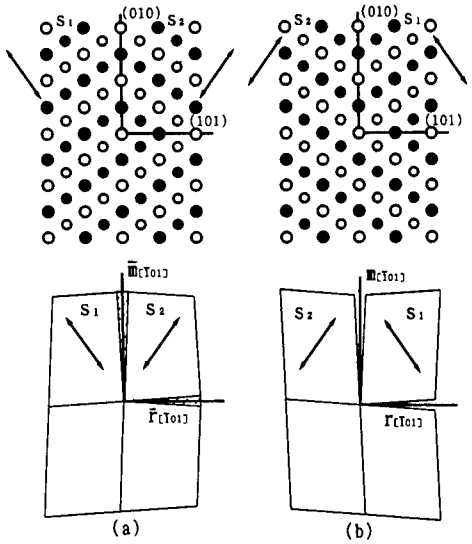


Fig. 5. Schematic drawing of two simple disclinations and of the definition of polarized twin boundary, (a) a negative disclination and (b) a positive one, corresponding to those of No. 8 and No. 7 in Table 1, respectively.

In order to represent the configuration of disclinations, we use the notation of the above mentioned polarized twin boundaries as well as the wedge angle between two twin boundaries. If this notation is applied to the disclinations in Fig. 5, we have the configuration of $(90)\bar{m}_{<110>}(270)\bar{r}_{<110>}$, and 2.8 degrees in total magnitude for (a) and the configuration of $(90)m_{<110>}(270)r_{<110>}$, and -2.8 for (b). Here, the total magnitude of the disclination is the sum of each characteristic value of the polarized twin boundary included[3].

All the predicted and possible MT linear disclinations are listed in Table 1. The total number of linear disclination is 17 for the ordered CuPt alloy.

5. A model of one of the ste-disclinations

In this chapter, a kind of point defect called ste-disclination will be discussed. Such a defect may have never been defined before by any forerunner. The definition of a ste-disclination is as follows: a defect where a cone shape of missing or overlap occurring in a crystal instead of a wedge shape of missing or overlap in the definition of the MT linear disclinations which have been discussed in the previous chapters.

A ste-disclination will occur in the crystals where at least two MT linear disclinations exist in the crystal and they are not parallel but meet each other at one point. In order to explain the structure of ste-disclinations, a model is presented in Fig. 6, as an example of the ordered CuPt alloy.

The ste-disclination shown in Fig. 6 is constructed by two linear disclinations which are indicated by $S_1(011)S_3(010)S_4(001)S_1$ and $S_1(100)S_3(\bar{1}01)S_4(001)S_1$. They are grouped in the

disclination of No. 6 in Table 1 with a magnitude of -2.0 degrees. The former lies along [100] axis while the latter along [010] axis. This crystal consists of three domains such as S_1, S_3 and S_4 around the both disclination lines. An overlap of a pyramid shape OACBD in Fig. 6 is assumed.

Table. 1. All the geometrically possible MT-linear disclinations arranged in the order of their magnitude in degrees. The value of N_m or N_r means the respective total number of m-type or r-type twin boundary.

Sequence No.	Configuration	(N_m, N_r)	w(deg)
1.	$(45)r_{<100>}(135)\bar{m}_{<100>}(135)r_{<100>}(45)m_{<100>}$	(0, 2)	0.0
2.	$(90)m_{<100>}(45)r_{<100>}(225)m_{<100>}$	(2, 1)	2.0
3.	$(225)r_{<100>}(45)m_{<100>}(90)m_{<100>}$	(2, 1)	2.0
4.	$(270)m_{<100>}(45)r_{<100>}(45)m_{<100>}$	(2, 1)	2.0
5.	$(45)r_{<100>}(180)r_{<100>}(45)m_{<100>}(45)r_{<100>}(45)m_{<100>}$	(2, 3)	2.0
6.	$(90)\bar{m}_{<100>}(135)r_{<100>}(135)\bar{m}_{<100>}$	(-2, 1)	-2.0
7.	$(270)m_{<110>}(90)r_{<110>}$	(1, 1)	2.8
8.	$(270)\bar{m}_{<110>}(90)\bar{r}_{<110>}$	(-1, -1)	-2.8
9.	$(240)r_{<111>}[(60)r_{<111>}]^2$	(0, 3)	3.6
10.	$[(120)\bar{r}_{<111>}]^3$	(0, -3)	-3.6
11.	$[(90)m_{<100>}]^4$	(4, 0)	4.0
12.	$[(90)m_{<100>}(45)r_{<100>}(45)m_{<100>}]^2$	(4, 2)	4.0
13.	$[(45)r_{<100>}(45)m_{<100>}]^4$	(4, 4)	4.0
14.	$[(90)\bar{m}_{<100>}]^4$	(-4, 0)	-4.0
15.	$[(90)m_{<110>}(90)r_{<110>}]^2$	(2, 2)	5.6
16.	$[(90)\bar{m}_{<110>}(90)\bar{r}_{<110>}]^2$	(-2, -2)	-5.6
17.	$[(60)r_{<111>}]^6$	(0, 6)	7.2

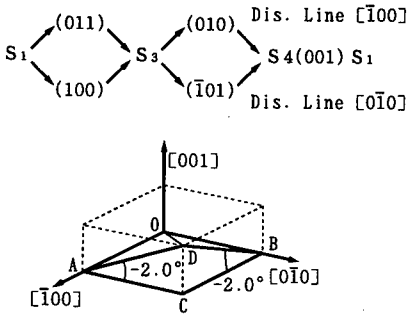


Fig. 6. A model of ste-disclinations. An overlap of the pyramid shape OACBD is assumed.

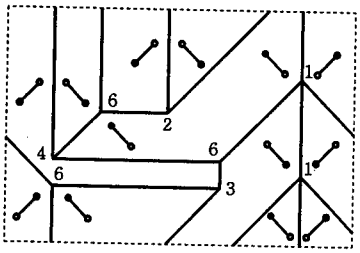


Fig. 7. A schematic drawing for one of the characteristic areas observed in the TEM image.

6. TEM observation and discussion

A low magnification bright field image is given in Fig. 8, where a number of straight lines and short line segments are observed. They frequently cross each other and produce a very characteristic domain structure. From the diffraction patterns the lines are found to be twin boundaries either on {100} or on {110}. So it is plausible that the intersections seen in the micrograph are MT linear disclinations.

A schematic drawing of one of the characteristic domain structures is given in Fig. 7. This area includes eight MT linear disclinations. Each of them is labeled by a Arabic

numeral which corresponds to the sequence number of the disclinations in Table 1. As easily found from the drawing, the sum of the magnitude of all the disclinations is absolutely zero.

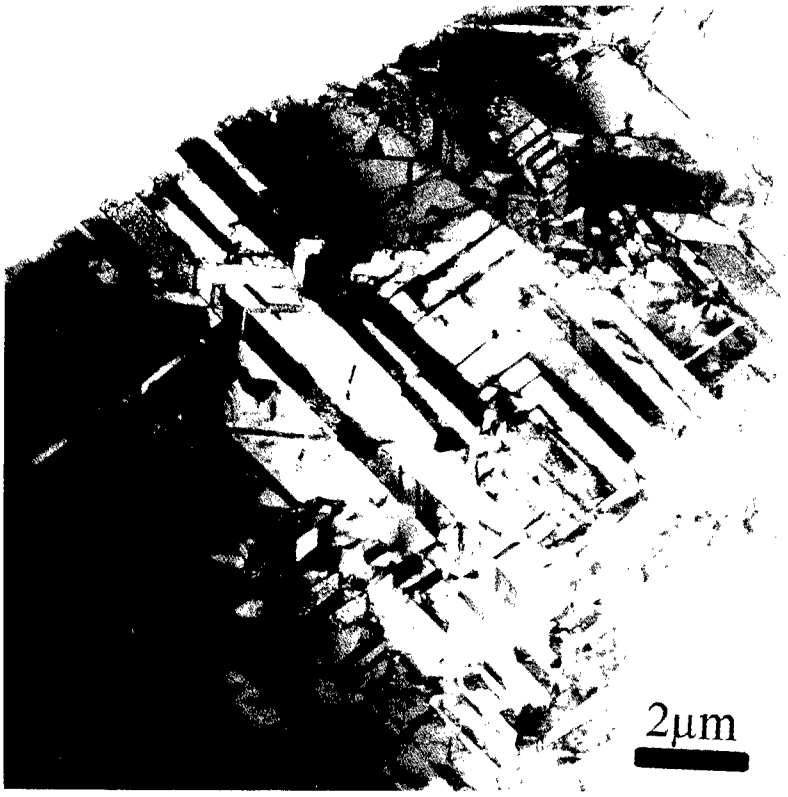


Fig. 8. Electron microscopic image for microdomain structures including MT-linear disclinations in the CuPt ordered alloy.

Acknowledgments

The authors would like to express their thanks to Dr. A. Tsai of Tohoku Univ. for preparation of the CuPt alloy ingots, to Professor Y. Hirotsu and his laboratories of Osaka Univ. for preparation of the TEM specimens and also to Professor E. Sukedai of Okayama Univ. of Science for allowing us to use an electron microscope in his laboratory.

References

[1] J.P. Hirth and J. Lothe: Theory of Dislocations p.4, Mcgraw-Hill, New York, 1968.
[2] Y. Kitano, K. Kifune, M. Yanagi and Y. Komura: Electron microscopy of domain structures in B19 MgCd alloys: Trans. JIM 27 (Suppl.): 181 (1986).
[3] Y. Kitano, K. Kifune and Y. Komura: Star-disclination in a ferro-elastic material B19 MgCd alloy: J. de Phys. 49 (Suppl. 10): C5-201 (1988).
[4] Y. Kitano, K. Kifune: HREM study of disclinations in MgCd ordered alloy. Ultramicroscopy 39: 279 (1991).
[5] N. Wu, H. Iwasaki and S. Ogawa: An X-ray diffraction study of atomic ordering in Platinum-rich Copper-Platinum alloys. Tran. JIM 14, 309-313 (1973)
[6] J. Sapriel: Domain-wall orientations in ferroelastics. Phys. Rev. B 12: 5128 (1976).

Modification of Electronic Structure due to Local Atomic Displacements around Carbon Interstitial in Austenite

H.Yukawa, M.Mori and M.Morinaga

Department of Materials Science and Engineering,
School of Engineering, Nagoya University,
Furo-cho, Chikusa-ku, Nagoya, Aichi, 464-01, Japan

Abstract

The cooperative displacements of iron atoms around an interstitial carbon in f.c.c. Fe are treated by electron theory. Following the experimental results on the local Fe displacements in austenite, a model cluster is constructed, and the electronic structure is calculated by the DV-Xα molecular orbital method. It is found that the interstitial C atom interacts strongly with the first-nearest-neighbor Fe atoms, but interacts very weakly with the Fe atoms which occupy the second-nearest-neighbor or the further-nearest-neighbor sites. The observed long-range modulation of iron displacements are interpreted as due to the optimization of the chemical bond strengths between Fe atoms neighboring on the interstitial carbon atom.

The Third Pacific Rim International Conference on
Advanced Materials and Processing (PRICM 3)
Edited by M.A. Imam, R. DeNale, S. Hanada,
Z. Zhong and D.N. Lee
The Minerals, Metals & Materials Society, 1998

Introduction

It is well known that there are atomic fluctuations from the average crystal structure in any disordered alloys. Such fluctuations in alloys may be described by using short-range-order parameters and local displacement parameters, both of which are determined experimentally by measuring either X-ray or neutron diffuse scattering from a crystal [1]. Extensive investigations have been carried out to determine short-range-order parameters for a variety of alloys. However, there have been few investigations on the local atomic displacements which arise mainly from the size difference between solute and solvent atoms in alloys [2].

Recently, local atomic displacements caused by carbon interstitials in austenite have been determined by measuring the diffuse x-ray scattering [3]. The near neighbor Fe atoms surrounding an octahedral C interstitial are displaced in a long-range scale, even though the first-nearest-neighbor Fe atoms are displaced largely among them. The magnitude of the Fe displacements seems to oscillate with the distance from the C interstitial. Such a characteristic feature in the displacements observed in the austenite may concern with the electronic structure. So, in this study, local electronic structures of f.c.c. Fe around an interstitial C are simulated by the DV-Xα cluster method, and the physical meaning of the displacements is examined in view of the chemical bond strengths between atoms in it.

Computational method

DV-Xα cluster method

The DV-Xα cluster method is a molecular orbital method, assuming the Hartree-Fock-Slater (HFS) approximation. In this method, the exchange-correlation between electrons, V_{XC}, is given by the following Slater Xα potential;

$$V_{XC} = -3\alpha\left[\frac{3}{8\pi}\rho(r)\right]^{1/3}, \qquad (1)$$

where $\rho(r)$ is the density of electrons at position r, the parameter α is fixed at 0.7 and the self-consistent charge approximation is used in this calculation. The matrix elements of the Hamiltonian and the overlap integrals are calculated by a linear combination of numerically generated atomic orbitals, 1s-4p for Fe and 1s-2p for C.

The bond order which is a measure of the covalent bond strength between atoms is estimated according to the Mulliken population analysis [4]. Also, the electron density of states is calculated from the energy level structure using the overlapping Gaussian functions which have a half width of 0.15 eV. A more detailed explanation of the calculation method is given elsewhere [5,6].

Cluster model

A cluster model used in the calculation is shown in Fig.1. This is a $Fe_{92}C$ cluster model which is constructed assuming the measured displacements of Fe atoms around an interstitial C atom in a f.c.c. Fe-25mass%Ni-

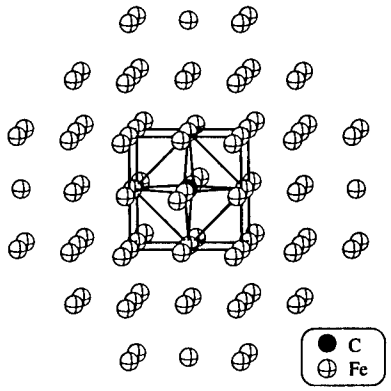


Fig.1 $Fe_{92}C$ cluster model used in the calculation.

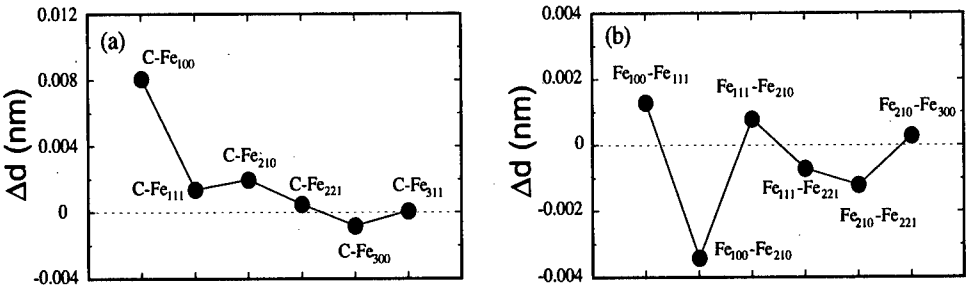


Fig.2 Change in the interatomic distances, Δd, between C and Fe atoms (a) and between nearest-neighbor Fe atoms (b).

0.88mass%C alloy [3]. As shown in Fig.1, a carbon atom is located at the central site of the cluster which corresponds to the octahedral interstitial site in the f.c.c. crystal lattice. For comparison, another calculation is performed using a hypothetical cluster model in which any atomic displacements are not taken into account, and every iron atom sits in the ideal lattice position, despite the existence of C interstitial in it. In addition, the electronic structure of pure f.c.c. Fe is calculated with an Fe_{92} cluster simply made by removing a carbon atom from the hypothetical $Fe_{92}C$ cluster. The lattice parameter used is 0.3609nm, comparable to that of pure f.c.c. Fe, 0.3603 nm, estimated from the atomic radius with CN=12 (0.1274 nm). For simplicity, pure f.c.c. Fe is assumed instead of including Ni atoms in the present calculation, because of the difficulty in the calculation involving random arrangements of solute and solvent atoms in the alloy, and also of the lack of the displacement data for Ni atoms.

The difference in the interatomic distances, Δd, between two cluster models of both containing an interstitial C atom, is shown in Fig.2(a) for the C-Fe distance and (b) for the Fe-Fe distance. For example, in case of the C-Fe distance, it is expressed as,

$$\Delta d = d_{C\text{-}Fe}(\text{displaced cluster}) - d_{C\text{-}Fe}(\text{hypothetical cluster}). \qquad (2)$$

Therefore, this Δd means the radial displacements of Fe atoms caused by the C interstitial. It is evident from Fig.2 (a) that the displacement of Fe atoms is large for the first neighbor Fe_{100} atoms and it decreases with increasing interatomic distances, while showing an oscillation. Here, the subscript, lmn, of Fe_{lmn} is the coordinate of the Fe atom measured from the C interstitial site at the origin, so that the C-Fe_{lmn} interatomic vector is represented by a/2[l,m,n] (a: lattice parameter). Needless to say, Fe_{100}, Fe_{111}, Fe_{210}, Fe_{221} and Fe_{300}, and Fe_{311} are first, second, third, fourth and fifth nearest-neighbor Fe atoms, respectively. Also, as shown in Fig.2 (b), there is an additional modification caused by the C interstitial in the distance between a pair of Fe atoms, Fe_{lmn}-$Fe_{l'm'n'}$, all of which are apart from one to the other by the nearest-neighbor Fe distance of 0.2552 nm in the case of the C-free f.c.c. crystal. The distance is shortened significantly between a pair of Fe_{100}-Fe_{210} atoms by introducing the C interstitial into the crystal.

Results

Electron density of states

The results of the electron density of states are shown in Fig.3 (a) for the cluster with atomic

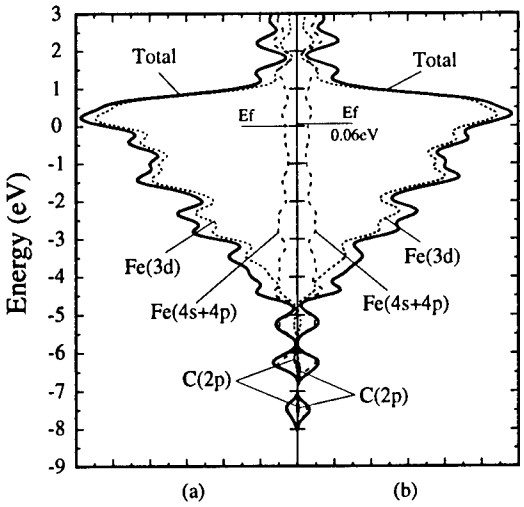


Fig.3 Electron density of states; (a) for the cluster involving local displacements of Fe atoms, and (b) hypothetical cluster without any displacements.

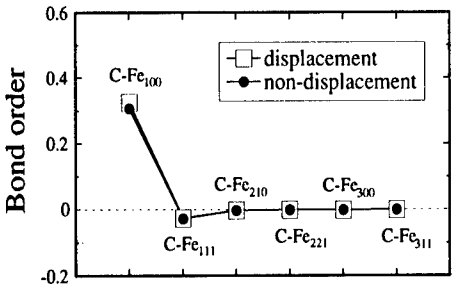


Fig.4 Bond orders between C and Fe atoms in the clusters.

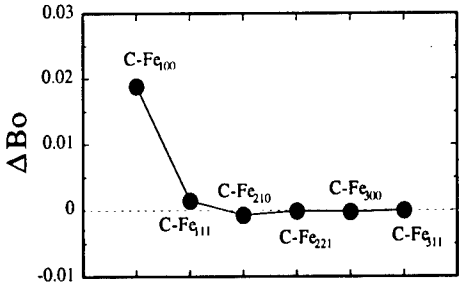


Fig.5 Difference in the C-Fe bond orders between the clusters with and without atomic displacements.

displacements and (b) for the hypothetical cluster. For either case, the Fermi energy level, *Ef*, lies at the high energy part of the Fe 3d band, while the Fe 4s and 4p components are spread over a wide energy range. The C 2p component appears below the Fe 3d band. When compared Fig.3 (a) with Fig.3 (b), it is found that the presence of the Fe displacements scarcely changes the electron density of states, but slightly lowers the Fermi energy level, *Ef*, by 0.06 eV. Such a lowering of the *Ef* implies that there is a gain of the electronic energy due to the local Fe displacements in this system.

Bond order between atoms

The calculated results of the bond orders between C and Fe atoms are shown in Fig.4. The bond order is the overlap population of electrons between atoms, and hence this is a measure to show the covalent bond strength between atoms. Every bond order shown in this paper is the value per atomic bond in the cluster. As shown in Fig.4, only the $C\text{-}Fe_{100}$ bond order is large and positive,

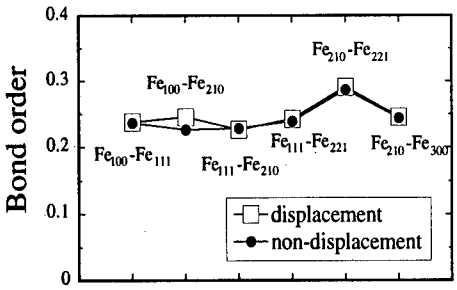


Fig.6 Bond orders between Fe atoms in the clusters.

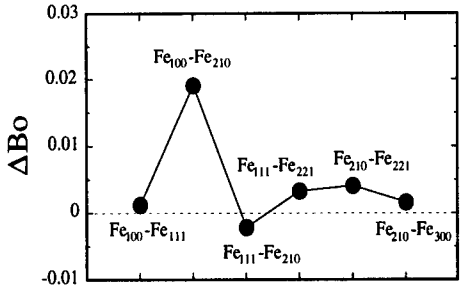


Fig.7 Difference in the Fe-Fe bond orders between the clusters with and without atomic displacements.

indicating that there is a strong attractive interaction between them. It is noted that even in the non-displaced case, the C-Fe interaction is not the antibonding-type, but the bonding-type. On the other hand, the C-Fe_{111} bond order is small and negative, and every other bond order is almost null. In order to understand the effect of Fe displacements around the C interstitial on the C-Fe chemical bond strengths, the difference of the C-Fe bond orders between the two clusters with and without Fe displacements, ΔBo, are calculated, and the results are shown in Fig.5. As is evident from this figure, only the C-Fe_{100} interaction is enhanced by the local displacements. The C-Fe_{111} and the other bond orders are less dependent on the displacements mainly due to the longer atomic distances between them. These results clearly indicate that only the first-nearest-neighbor Fe_{100} atoms interact mainly with the interstitial C atom.

The calculated results of the Fe-Fe bond order are also shown in Fig.6. All the Fe-Fe bond orders are large and positive. Fig.7 shows the difference of the Fe-Fe bond orders between the two clusters with and without atomic displacements. When the Fe atoms are displaced, the Fe_{100}-Fe_{210} bond order increases largely, but the Fe_{111}-Fe_{210} bond order decreases slightly.

Discussion

As mentioned above, the atomic displacements modify the chemical interaction between atoms in the cluster. As shown in Fig.5, the C-Fe_{100} bond order remarkably increases when the Fe atoms are displaced, although the C-Fe_{100} interatomic distance increases as shown in Fig.2 (a). However, the other C-Fe bond orders (i.e., C-Fe_{111}, C-Fe_{210}) scarcely change with the displacements. In other words, only the Fe_{100} atoms interact with the C atom and displace their positions so as to enhance the attractive interaction between them. However, the displacements of the Fe atoms other than Fe_{100} are not attributable to the direct C-Fe interactions, since their interactions are very weak as shown in Fig.5.

On the other hand, the difference in the Fe-Fe bond orders shown in Fig.7 changes in an approximately reverse way as the interatomic distance does as shown in Fig.2(b). Namely, the Fe-Fe bond order becomes larger when the interatomic distance becomes shorter, and vice versa. For example, the decrease in the Fe_{100}-Fe_{210} distance results in the remarkable increment of the bond order between them. It is important to note here that the difference of the Fe-Fe bond orders shows positive values even in the case when the Fe-Fe interatomic distances increase by the displacements, except for the case of the Fe_{111}-Fe_{221} pair.

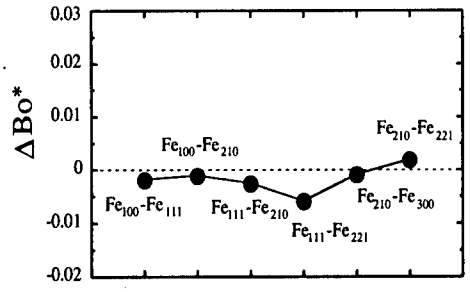


Fig.8 Difference in the Fe-Fe bond orders between the $Fe_{92}C$ (non-displaced) and the Fe_{92} (pure Fe) clusters.

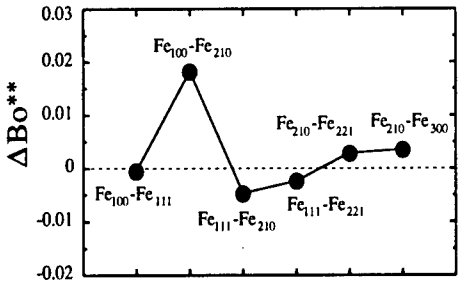


Fig.9 Difference in the Fe-Fe bond orders between the $Fe_{92}C$ (displaced) and the Fe_{92} (pure Fe) clusters.

In addition, the Fe-Fe bond orders are compared with the values of pure Fe. Fig.8 shows the difference of the Fe-Fe bond orders, ΔBo^{*}, where ΔBo^{*}=Bo(hypothetical cluster)-Bo(pure Fe cluster). It is evident from the figure that all the Fe-Fe bond orders decrease except for the Fe_{210}-Fe_{221} bond order if any atomic displacements do not occur around the C atom. This implies that the weakening of the Fe-Fe interaction will suppress for C interstitial atoms to be introduced into the f.c.c. Fe lattice without any displacements. However, the occurrence of Fe displacements could release the f.c.c. lattice from such instability. Fig.9 shows the difference of the bond orders, ΔBo^{**}, where ΔBo^{**}=Bo(displaced cluster)-Bo(pure Fe cluster). When compared Fig.9 with Fig.8, it is apparent that the Fe-Fe bond orders except for the Fe_{111}-Fe_{210} bond order are recovered to some extent once the Fe atoms are displaced around the C atom. Thus, the displacements of Fe atoms could enhance the Fe-Fe atomic interactions. As a result, cooperative displacements of Fe atoms will take place around an interstitial C atom in f.c.c. Fe.

Conclusion

The local electronic structures of f.c.c. Fe around an interstitial C is simulated by the DV-Xα molecular orbital method. It is found that the interstitial C atom interacts mainly with the first-nearest-neighbor Fe_{100} atoms. The local displacements of Fe atoms take place so as to enhance the bond strengths between the neighboring Fe atoms as well as between the Fe_{100} and C atoms.

Acknowledgments

The authors would like to express sincere thanks to Prof. J.B.Cohen of Northwestern University for his motivating us to do this study. We also acknowledge the Computer Center, Institute for Molecular Science, Okazaki National Institutes for the use of the SX-3/34R computer. This research is supported by the Grant-in-Aid for Scientific Research on Priority Areas (No.287) from the Ministry of Education, Science, Sports and Culture of Japan.

References

1. B.Borie and C.J.Sparks, Acta Cryst., **A27** (1971), 198.
2. P.Georgopoulos and J.B.Cohen, J. Phys. (Paris), **38** (1977), C7, 191.
3. D.B.Butler and J.B.Cohen, Acta Metall. Mater., **41** (1993), 41.
4. R.S.Mulliken, J. Chem. Phys., **23** (1955), 1833, 1841, 2338, 2343.
5. H.Adachi, M.Tsukada and C.Satoko, J. Phys. Soc. Jpn, **45** (1978), 874.
6. M.Morinaga, N.Yukawa and H.Adachi, J. Phys. F, **15** (1985), 1971.

REAL TIME CHARACTERIZATION OF SOLID/LIQUID INTERFACES DURING DIRECTIONAL SOLIDIFICATION

S. Sen[1], W. F. Kaukler[2], B.K. Dhindaw[3], P. A. Curreri[4], and P. Peters[4]
1. USRA/Space Science Laboratory, NASA Marshall Space Flight Center, Huntsville, Al; 2. CMMR, University of Alabama in Huntsville, Al; 3. Indian Institute of Technology, Kharagpur, India; 4. Space Science Laboratory, NASA, Marshall Space Flight Center, Huntsville, Al.

ABSTRACT

Two separate techniques have been employed to obtain fundamental information related to the dynamics of the solidification process. A high resolution x-ray transmission microscope was used for the first real time observation on fiber and plate like morphological evolution in the Al-Au eutectic alloy. Different morphological features as a function of growth conditions are presented in the paper. A growth velocity at which fiber to lamella or plate like transition occurs has been established.

Secondly, an innovative furnace design has allowed real time and non-intrusive measurement of interfacial undercooling. The Pb-1 wt.%Sn alloy was used for this investigation. Results obtained for undercooling as a function of growth velocity are presented. Comparison of these experimental results with theoretical predictions are discussed.

The Third Pacific Rim International Conference on
Advanced Materials and Processing (PRICM 3)
Edited by M.A. Imam, R. DeNale, S. Hanada,
Z. Zhong and D.N. Lee
The Minerals, Metals & Materials Society, 1998

1. INTRODUCTION

Solidification phenomenon which occur at the solid/liquid (s/l) interface play a major role in the determination of the technologically important properties of a casting. However, metals being opaque, conclusions related to several important phenomenon such as development of interface morphologies, phase nucleation and growth, and boundary layer thickness is deduced from post solidification metallographic analysis. Consequently, limited information is obtained about the dynamics of the process. A key parameter that controls the structural morphology and the chemical composition of the processed material is the undercooling at the s/l interface. There has been a lack of accurate data on interfacial undercooling since conventional probes such as thermocouples, due to their large bead size, do not have sufficient resolution for measuring undercooling at the s/l interface. Further, the intrusive nature of the thermocouples also distorts the thermal field at the interface.

Recently efforts have been underway at the Space Science Laboratory, NASA Marshall Space Flight Center, to solve the dual problem of measuring in real time interfacial undercooling and observing the dynamics of the solidification process. First, a high resolution x-ray transmission microscope (XTM) has been developed to view, *in-situ* and in real time fundamental interfacial phenomena during directional solidification of metals and alloys. The XTM operates in the range of 10-100 keV and through projection is capable of achieving magnification of up to 160X. Secondly, an innovative collapsible furnace has been designed to measure the temperature of a moving s/l interface in reference to a fixed s/l interface. This measurement technique is non-intrusive in nature and is based on the Seebeck principle.

To date a limited number of experiments have been performed to measure interfacial undercooling using the Seebeck technique. Rouzad et. al[1,2] has used the Seebeck technique to measure interfacial undercooling for Sn-0.5 at. % Bi alloy. They reported a undercooling value of 0.05K for translation velocities of 5 μm/s. Further, they also demonstrated how Seebeck measurements can be utilized to detect transitions from planar to cellular interfaces. Favier et. al used the same alloy composition to measure interfacial undercooling in a microgravity environment on board space shuttle Columbia[3]. For translation velocities up to 5 μm/s they reported interfacial undercooling values of 2.5K. Compared to ground based results this experiment clearly demonstrated the effect of convection on steady state interfacial undercooling. Similar microgravity experiments were performed by Abbaschian[4] with a Bi-0.1 at. % Sn sample. For a translation velocity of 1.85 μm/s and solidified length of 7 mm he reported a total undercooling of 0.533K. In this case the total undercooling also included kinetic undercooling due to the faceted nature of the alloy. Recently Rodway and Hunt[5] have measured kinetic undercooling on zone refined high purity Pb wires. Further, they also measured solutal undercooling on dilute Pb-Sn and Pb-Ag alloys[6] for velocities up to 1250 μm/s. The translation velocity at which the planar to cellular transition occurs was, however, not experimentally determined. They demonstrated that the undercooling decreased as the interface went through a planar to cellular transition.

In the past x-ray sources allowing resolution between 300-500 μm have been used to image shrinkage porosity and s/l interfaces[7,8]. A 500 μm solute boundary layer during Czochralski growth of indium doped silicon has been imaged using XTM[9]. However, to image the most critical microstructural features a resolution of 1-100 μm is required. In the recent past we had demonstrated a resolution limit of 25 μm which permitted viewing in real time morphological instability and cellular growth in Al-Cu and Al-Ag systems. Further, we had successfully imaged solute boundary layers in Al-Pb and Al-In monotectic alloys and had demonstrated that alloys with monotectic compositions do not necessarily grow in a coupled manner[10,11].

The present investigation systematically studies the Seebeck response for Pb-1 wt.%Sn at and near the marginal stability regime. This study attempts to validate existing relationships between undercooling and growth velocity during plane front growth, marginal stability regime, and stable cellular growth. Further, improvement in design of the furnace used with the XTM has enhanced the resolution up to 5 μm. This has permitted the study of the dynamics of secondary eutectic fibers and platelets. Results obtained for fiber to lamella or plate transition in the Al-Al_2Au eutectic system will also be presented.

2. EXPERIMENTAL TECHNIQUES:

2.1. X-Ray Transmission Microscopy:

The XTM used for this investigation works on the principle of projection radiography. The detector technology is adequate to resolve a s/l interface with a contrast as low as 2%. A x-ray image intensifier and a cooled CCD camera capable of detecting 4000 gray levels was used for real time viewing of

solidification phenomena. A maximum magnification of 160X was achieved by positioning the sample within a few mm of the x-ray source.

The furnace used for the XTM studies is a modified horizontal Bridgman-Stockbarger type operated in air. Typical dimensions of samples are 19x6x1 mm. The sample is placed in the cavity of a x-ray transparent boron nitride crucible. The sample is then covered with a boron nitride lid and positioned in the furnace. Cylindrical castings of the Al-Au alloy were produced by melting in a vacuum induction furnace and pouring the liquid metal in a graphite mold. The cylindrical casting was cold rolled to 1 mm thick strips and trimmed to fit into the cavity of the boron nitride crucible. Translation of the molten specimen through a temperature gradient at slow velocities allows the s/l interface to remain in the x-ray transparent window for extended periods of time. A schematic of the XTM apparatus is shown in figure 1. Detailed discussions and schematic of the x-ray transmission microscope are presented elsewhere [10,11].

2.2. The Seebeck Furnace

The Seebeck furnace used for this investigation is based on an innovative design approach where the translating end of the furnace is telescopically collapsed in to the stationary end. At either end the sample protrudes about 3 cms out of the hot zones. These protruded ends are maintained at the same temperature using cooled water baths regulated to 0.01 °C. Cu leads from these cooled ends are connected to a commercial Keithley nanovoltmeter to measure the Seebeck emf between the fixed and the moving s/l interfaces. Details of the Seebeck furnace are shown in figure 1.



Figure. 1. Photograph showing the telescopic furnace design used for undercooling measurement

After commencement of furnace translation the Seebeck signal steadily rises and reaches a plateau to indicate establishment of steady state. Subsequent to obtaining steady state when furnace translation is shut off the signal drops to a new steady state value. The magnitude of this drop, E_s, corresponds directly to the interfacial undercooling. Knowing the Seebeck coefficient, η_{sl}, of the alloy the undercooling can be determined according to the relationship[3]:

$$E_s = \eta_{sl}\Delta T$$

3. RESULTS AND DISCUSSION:

3.1. Undercooling Measurement on Pb-1 wt.% Sn:

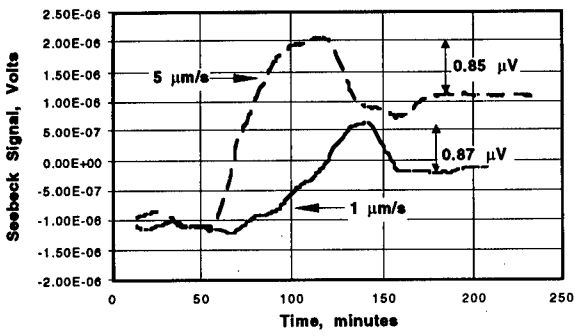


Figure 2. Seebeck response obtained for Pb-1 wt. % Sn at V= 1 and 5 µm/s.

Figure 2 shows the experimental results obtained for furnace translation velocities of V= 1 and 5 µm/s. For translation velocities ranging between 1 and 5 µm/s the magnitude of the interfacial undercooling obtained is almost identical. As can be seen from figure 1 the E_s values for V= 1 and 5 µm/s is 0.87 and 0.85 µV respectively. Figure 3 shows the Seebeck response for translation velocities between 1-50 µm/s. These results clearly indicate that once the growth velocity for morphological instability is exceeded the interfacial undercooling increases with velocity. This occurs in the velocity range of 7 to 15 µm/s. Hence, in the present study the experimental results indicate a constant

undercooling for plane front growth, followed by an increase in undercooling in the velocity range of 7-15 μm/s and finally a decrease in undercooling in the velocity range of 20-50 μm/s.

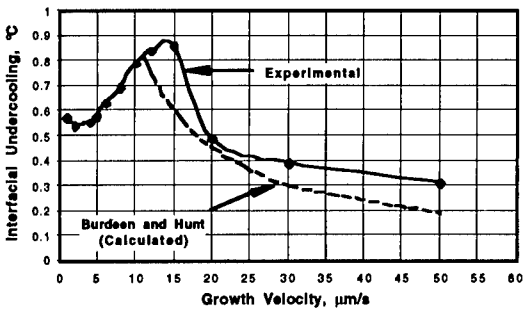


Figure 3. Comparison of experimental and calculated undercooling obtained for Pb-1 wt. % Sn as a function of growth velocity.

As can be seen from figure 3 up to a velocity of 5 μm/s the interfacial undercooling is in the range of 0.54 to 0.58 °C. These values correspond well with undercooling predicted by the constitutional undercooling criterion. Since the undercooling remained constant for this range of velocities it is safe to assume that for a 1 mm diameter wire the experiments were performed in a diffusion controlled regime. Above the marginal stability velocity (6 μm/s) the experimentally measured undercooling showed a steady increase in the velocity range of 7-15 μm/s. As can be seen from figure 3 in this velocity range the experimental measurements are not in agreement with the predictions of Burdeen and Hunt[12]. They predicted an inverse relationship between undercooling and growth velocity in the stable cell growth regime. However, when the growth velocity was increased over 15 μm/s the trend in the measured undercooling matches well with the predicted undercooling. This anomaly between the measured and predicted values in the range of 6 - 15 μm/s may be explained as follows. The theoretical model derived by Burdeen and Hunt assumes a discrete transition from a stable planar to a stable cellular growth regime. These models predict cell length and spacing based on undercooling at the tip. However, experimental work on transparent succinonitrile - salol system by Venugopal and Kirkaldy[13] has shown that there may exist a range of velocity where the interface has an irregular morphology and does not reach a steady state shape or spacing. Thus there appears to be 2 critical velocities, one above which the interface loses planarity and the second, above which stable cellular growth dominates. Further, they showed a sharp decrease in undercooling only at velocities well into the stable cell growth regime. It appears that in the regime of irregular morphology undercooling contribution from cell root and walls are dominant. Under such a situation it is not difficult to envision that immediately after the onset of morphological instability the undercooling should increase to account for such contributions. For the present investigation this range has been identified to be 6-15 μm/s. Only when stable cell growth is accomplished lateral diffusion is limited and contribution to undercooling is primarily from the cell tips. Hence, beyond a V=20μm/s our experimental results agree reasonably well with the predictions of Burdeen and Hunt.

3.2. XTM Studies on Al-Au Eutectic System:

Beech et. al.[14], had previously studied the Al-Au system using x-ray transmission radiography. Although they could identify cellular structures, the resolution was not sufficient to identify Al_2Au fibers or lamellae. Figures 4(a) - (c) show the real time change in eutectic morphology as a function of

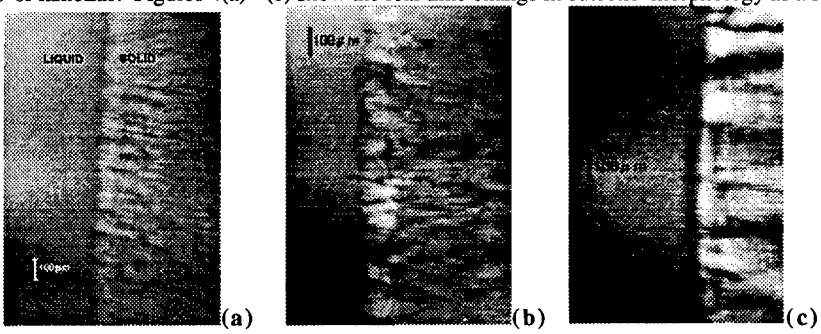


Figure 4. Evolution of eutectic morphologies at growth velocities of (a) 2 μm/s, (b) 1 μm/s and (c) 0.5 μm/s.

growth velocity. The thermal gradient was held constant at 52 °C/cm. At a growth velocity of 2 μm/s the Al_2Au phase grows in an aligned array of irregular fibers. Some of these fibers can be seen extending into the liquid phase to a distance of 20 μm. When the velocity is reduced 1 μm/s the Al_2Au phase now forms as plate or flake like structure with coarser spacing. The fibers or plates can now be seen extending into the liquid to a distance of 50 μm. The extended Al_2Au fibers or plates were not coupled to the primary Al phase. This seems to suggest that irregular eutectics (facetted-non-facetted) do not necessarily grow in a coupled manner. Further reduction in growth velocity to 0.5 μm/s resulted in mainly a coarse plate or lamella structure. Hence, for this specific thermal gradient the critical growth velocity for fiber to lamella or plate transition has been identified to be between 0.5 and 1 μm/s.

The extension of the intermetallic Al_2Au phase 20-50 μm ahead of the growth isotherm resulted in yet another interesting observation. After steady state growth when the sample was held stationary it was observed that the extended portion of the Al_2Au phase first coarsened and then they separated from the solid matrix. Finally, Stokes force caused the separated Al_2Au phase to settle to the bottom of the crucible. These observation were made possible only by development of a XTM with sufficient contrast and resolution.

4. SUMMARY

Interfacial undercooling measurements on Pb-1 wt.%Sn samples were performed in real time and in a non-intrusive fashion. Results indicate that between plane front growth and stable cellular growth there is a regime of mixed morphology. The undercooling remains constant during plane front growth, increases with growth velocity in the regime of mixed or irregular morphology and then decreases with growth velocity during steady cellular growth. It is hypothesized that in the regime of irregular morphology undercooling contribution from cell root and walls are dominant.

XTM studies on the Al-Au eutectic system showed for the first time that the Al_2Au intermetallic phase can extend well into the melt from the s/l interface. Further, it was observed that the extended portion of the Al_2Au phase coarsened over time and separated from the solid matrix. Finally, it was established that the transition from fiber to lamella or plate transition occurs between a growth velocity of 0.5 to 1 μm/s.

REFERENCES

[1] A. Rouzaud, J.J. Favier, and D. Thevenard, *Adv. Space Res.*, 1988, vol. 8, no. 12, pp. (12)49.

[2] A. Rouzaud, J. Comera, P. Contamin, B. Angelier, F. Herbillon, and J.J. Favier, *Jnl. Cryst. Growth,* 1993, vol. 129, pp. 173.

[3] J.J. Favier, J.P. Garandet, A. Rouzaud, and D. Camel, *Jnl. Cryst. Growth,* 1994, vol. 140, pp. 237.

[4] R. Abbaschian, *Second United States Microgravity Payload: One Year Report, NASA Technical Memorandum 4737*, P.A. Curreri and D.E. McCauley eds, 1996, pp. 3-49.

[5] G.H. Rodway and J.D. Hunt, *Jnl. Cryst. Growth,* 1991, vol. 112, pp. 554.

[6] G.H. Rodway and J.D. Hunt, *Jnl. Cryst. Growth,* 1991, vol. 112, pp. 563.

[7] F.P. Chiaramonte, G.F. Danier, J. Gotti, E.S. Neumann, J. Johnston, and K.J. DeWitt, *AIAA Paper 92-0845, AIAA 30th Aerospace Science Meeting,* Reno, NV, Jan 6-9, 1992.

[8] P.G. Barber, R.F. Berry, W.J. Debman, A.L. Fripp, G. Woodell, and R.T. Simchick, *Jnl. Cryst. Growth,* 1995, vol. 147, pp. 83.

[9] K. Kakimoto, M. Eguchi, H. Watanabe, and T. Hibiya, *Jnl. Cryst. Growth,* 1990, vol. 99, pp. 665.

[10] P.A. Curreri and W.K. Kaukler, *Metall. Trans. A*, vol. 27A, 1996, pp. 801.

[11] W.F. Kaukler, F. Rosenberger, and P.A. Curreri, *Metall. Trans. A*, 1997, vol. 28A, pp. 1705.

[12] M.H. Burdeen and J.D. Hunt, *Jnl. Cryst. Growth,* 1973, vol. 22, pp. 109.

[13] D. Venugopalan and J.S. Kirkaldy, *Acta Metall.,* 1984, vol. 32, no. 6, pp. 893.

[14] J. Beech, *Jnl. Crystl. Growth,* 1984, vol. 67, pp. 385.

PHASE TRANSFORMATION BEHAVIOR AND REDUCING GAS SENSING CHARACTERISTICS OF Fe-O THIN FILM PROCESSED BY PLASMA-ENHANCED CHEMICAL VAPOR DEPOSITION

Bum-Jin Kim, Eun-Tae Lee and Gun-Eik Jang

Department of Materials Engineering, Chungbuk National University
Cheongiu, Chungbuk 360-763, Korea

Abstract

Fe-O thin films were prepared on Al_2O_3 substrate by PECVD(Plasma-Enhanced Chemical Vapor Deposition) technique. The phase transformation of Fe-O thin films as the substrate temperature and during the reduction-oxidation process was mainly determined. As deposited α-Fe_2O_3 phase was most stable at deposition temperature around 120℃. Fe_3O_4 phase was obtained at the deposition temperature ranges from 150 to 350℃ by the reduction process of α-Fe_2O_3 phase in H_2 ambient. Fe_3O_4 phase transformed into a γ-Fe_2O_3 phase under controlled oxidation conditions at 280~300℃. The phase transformation from Fe_3O_4 to γ-Fe_2O_3 suggests the oxidation of Fe^{2+} ions to Fe^{3+} in Fe_3O_4. Fe_3O_4 and γ-Fe_2O_3 obtained by oxidation of Fe_3O_4 phase had the same spinel structure.

The Third Pacific Rim International Conference on
Advanced Materials and Processing (PRICM 3)
Edited by M.A. Imam, R. DeNale, S. Hanada,
Z. Zhong and D.N. Lee
The Minerals, Metals & Materials Society, 1998

Introduction

In the Fe-O system, three different polymorphic forms, FeO, Fe_3O_4, and Fe_2O_3, are exist. Also, Fe_2O_3 has two typical modifications consisting of an α - Fe_2O_3 and γ - Fe_2O_3. Of these, the magnetite(Fe_3O_4) and maghaemite(γ - Fe_2O_3) structures are of technological interest in longitudinal magnetic recording owing to their magnetic behavior that have the trend shifting towards achieving higher recording density[1]. Recently γ - Fe_2O_3 has attracted much attention because of the possible application for reducing gas sensor because the γ - Fe_2O_3 need no noble metal catalysts as gas sensor materials[2,3].

Iron oxide films have been prepared in the past by chemical transport reaction[4] and by RF sputtering in O_2 and Ar atmosphere[5,6]. It is well known that these forms are easily transformed into one another through reduction-oxidation process[7,8]. Typically Fe_3O_4 films were formed by hydrogen reduction of α - Fe_2O_3 film and were oxidized to γ - Fe_2O_3 at 280 ~300℃[9,10]. However, not many studies of preparation and characterization of iron oxide thin films have been made in their different polymorphic forms. In this paper, thin film fabrication procedure by PECVD technique and transformation phenomena from α - Fe_2O_3 to γ - Fe_2O_3 state are discussed in detail. And processing conditions and microstructure will be systematically investigated in terms of various processing parameters.

Experimental

α - Fe_2O_3 thin films were deposited on Al_2O_3 substrate by PECVD process. Al_2O_3 substrate was initially cleaned by acetone in a supersonic wave cleaner and then dried by N_2 gas in a chamber. Following that, Ar ion etching by 500W was performed on the substrate for 20 min. prior to each experiment. The Ar ion etching not only cleaned the surface of the substrate, but also improved the adhesion between the film and the substrate. The metal-organic compound pentacarbonly iron[$Fe(CO)_5$] was used as the source material. The source material has a melting point of -20℃, a boiling point of 102℃, and high saturation vapor pressure of 40 mmHg at 30℃. Argon gas was used as the carrier gas and plasma generation. The flow rate of Ar and O_2 was controlled by the MFC(Mass-Flow Controller). The distance between substrate and gas ring was 30 mm. Finally, film deposition was made after initial Ar plasma treatment.

In order to observe phase transformation phenomena from α - Fe_2O_3 to γ - Fe_2O_3 this experiment was divided into two processes. At the first process, the in-situ fabricated α - Fe_2O_3 was initially reduced to Fe_3O_4 and then this reduced Fe_3O_4 were oxidized to form γ - Fe_2O_3. At the second process, in-situ fabricated Fe_3O_4 was directly oxidized to have γ - Fe_2O_3 phase. A post-deposition reduction process in H_2 atmosphere formed Fe_3O_4 films. It is known that Fe_3O_4 is formed at relatively lower temperature than 300℃[11,12]. Therefore the reduction temperature was kept at 300℃ and reduction stage was accomplished in a 10:1 mixture of Ar:H_2. The reduction time was changed from 0.5 to 3hrs. The γ -Fe_2O_3 films were oxidized to Fe_3O_4 at 280~300℃.

At the second process, Fe_3O_4 films were directly deposited on Al_2O_3 substrate by PECVD method. These films were deposited at various temperature ranges from 120 to 350℃. The as-deposited Fe_3O_4 films were oxidized at 280 to 300℃ by changing the oxidation time from 0.5 to 3hrs.

Results and Discussion

Phase Transformation by Deposition Temperature

There are many fabrication parameters for thin film depositions such as deposition temperature, RF power, and carrier gas flow rate, etc. Among them, one of the critical deposition condition caused phase transformation is the deposition temperature.

Fig.1 shows x-ray diffraction patterns of α-Fe_2O_3 processed at 120 to 350℃. As can be seen in Fig.1 as-deposited α-Fe_2O_3 phase was most stable around 120℃. However, with increasing the deposition temperature up to 350℃, the peak intensity related with Fe_3O_4 phase was also considerably increased. Fig.2 shows x-ray diffraction patterns of in-situ processed Fe_3O_4 from 120 to 350℃. Based on these results Fe_3O_4 peak intensity processed at 150℃ was quite noticeable. However, the peak intensities of Fe_3O_4 at ranges of 350~400℃ were reduced and existed as mixed phases with α-Fe_2O_3 as increasing the temperature. Therefore we believe that the optimum processing temperature to fabricate Fe_3O_4 phase formation is around 150℃ even there was a small amount of α-Fe_2O_3. Unfortunately the deposition condition of Fe_3O_4 phase to find the lower processing temperature was not successful because of the adhesion problem. This work is still in progress.

α-Fe_2O_3 and Fe_3O_4 phase were prepared successfully by PECVD techniques. After that, reduction-oxidation process was followed to investigate the phase transformation phenomena. The reduction process condition was adjusted under H_2 atmosphere while oxidation process was carried out under O_2 environment.

Fig.3 and Fig.4 show the typical x-ray diffraction patterns after reduction-oxidation process. X-ray diffraction patterns shown at figures indicate the phase transitions from α-Fe_2O_3 to γ-Fe_2O_3 during reduction-oxidation process. These phases change might be illustrated by the next reaction.

$$3(\alpha\text{-}Fe_2O_3) + H_2 \rightarrow 2Fe_3O_4 + H_2O$$

The above equation describes that Fe_3O_4 phase can be obtained by the decomposition of 1/2 O_2 molecule in an α-Fe_2O_3 phase. Fig.3(c) and Fig.4(b) show x-ray diffraction patterns of γ-Fe_2O_3 phase obtained by oxidation of Fe_3O_4 phase. The phase transformation phenomenon from Fe_3O_4 to γ-Fe_2O_3 suggests oxidation of Fe^{2+} ions to Fe^{3+} in Fe_3O_4 since oxygen is first

adsorbed on the surface regions of Fe_3O_4. With the progress of the oxidation, increasing numbers of Fe^{3+} ions enhance the cation vacancy concentration in the thin films.

Composition Analysis

The Auger electron spectra line shapes of a Fe_2O_3 thin film before argon sputtering and after 2 min. of sputtering are shown in Fig.5. The carbon and sulfur peak existed before sputtering. However, those peaks were not detected in sputtered films. In the result, the fabricated films were composed of Fe and O. No impurities were identified in the film.

Conclusion

In this study, thin film fabrication procedure by PECVD technique and transformation phenomena from the in-situ processed α-Fe_2O_3 to γ-Fe_2O_3 phase were discussed. Also processing conditions and microstructure were systematically investigated in terms of various processing parameters. The followings are our preliminarily results.

1) α-Fe_2O_3 and Fe_3O_4 phase were prepared successfully by PECVD technique. Based on x-ray experiments, the peak intensity of as-deposited α-Fe_2O_3 phases processed around 120℃ was strongly observed while Fe_3O_4 peak intensity processed at 150℃ was quite noticeable.

2) α-Fe_2O_3 phase is transformed into a Fe_3O_4 phase under controlled reduction conditions at 300～340℃ for 2.5h in H_2 ambient and the reduced Fe_3O_4 was oxidized to γ - Fe_2O_3 at 280～300℃ for 2.5h.

3) The Auger spectra suggest that no impurities were identified in the film.

References

1. S. Hattori, Y. Ishii, M. Shinohara and T. Nakagawa, "Magnetic recording characteristics of sputtered γ -Fe_2O_3 thin film disk," IEEE Trans. Mag., Vol. MAG-15(1979),1549
2. N. Inagaki, "Ferrite thin films for high recording density," IEEE Trans. Mag., Vol. MAG-12, No.6(1976), 785.
3. E. V. Babkin, K. P. Koval and V. G. Pynko, " Epitaxial films of iron oxides grown by the method of chemical transport reaction," Thin Solid Films, 117(1984), 217.
4. S. Shin and S. Park, "Some characteristics of γ -Fe_2O_3 ceramic gas sensor," Proc. 2nd Int. Meer. Chem. sensors, Bordeaux, France, (1986), 123-126
5. D. D. Lee and D. H. Choi, "Thick film hydrocarbon gas sensors," Sensors and Actuators B1(1990), 231-234.
6. J. Peng and C. C. Chai, "A Study of the sensing characteristics of Fe_2O_3 gas-sensing thin film," Sensors and Actuators B, 13-14(1993), 591.
7. Y. Ishii, A. Terada, O. Ishii, S. Ohta, S. Hattori and K. Makino, "New preparation process for sputtered γ -Fe_2O_3 thin film disks," IEEE Trans. Mag., Vol. MAG-16(1980), 1114.
8. H. Kojima and K. Hanada, "Origin of coercivity changes during the oxidation of Fe_3O_4 to γ -Fe_2O_3," IEEE Trans. Mag. Vol. 16(1980)11.
9. Y. Bando, S. Horii and T. Takada, "Reactive Condensation and Magnetic Properties of Iron Oxide Films," Jpn. J. of Appl. Phys., Vol. 17, No. 6(1978), 1037-1042.
10. S. Dhara, G. L. Malhotra, "Structural and Magnetic properties of chemically vapour deposited iron oxide thin films," A. C. Rastogi and B. K. Das, Thin Solid Films, 209(1992), 116.
11. A. Lisa Tietz, R. Scott Summerfelt and C. Barry Carter, "The effect of substrate orientation on the chemical vapour deposition growth of α - Fe_2O_3 on α -Al_2O_3," Philosophical Magazine A, Vol. 65, No.2(1992), 439.
12. P. Bhattacharya, T. Koneda, K. Park and Y. Nishioka, "Comparative Study of Amorphous and Crystalline(Ba, Sr)TiO_3 Thin Films Deposited by laser Ablation," Jpn. J. Appl. Phys., 32(9B)(1993)4103.

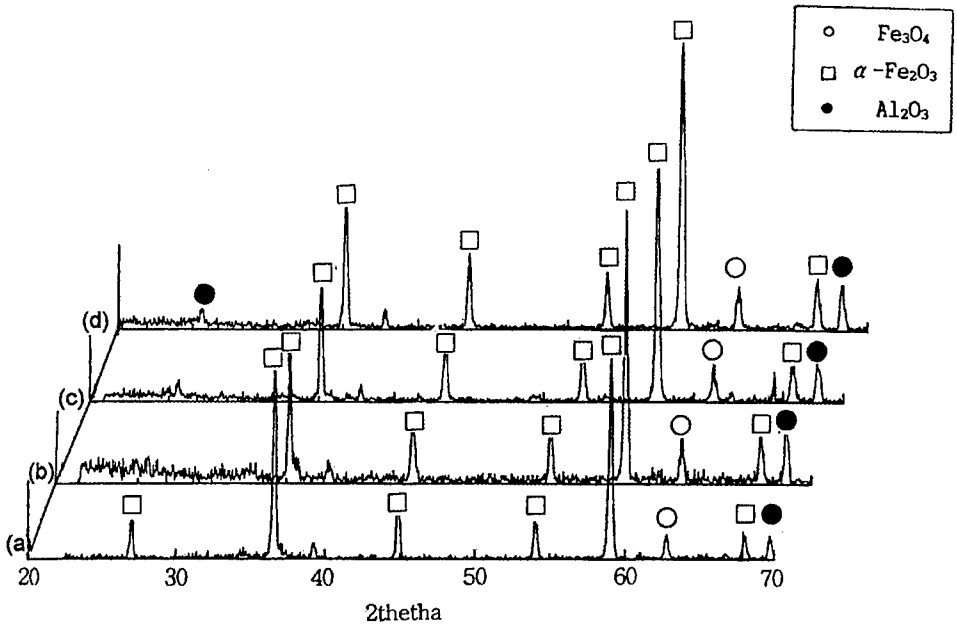


Figure 1: X-ray diffraction patterns of α-Fe_2O_3 at various deposition temperature

(a) 120℃ (b) 150℃ (c) 250℃ (d) 350℃

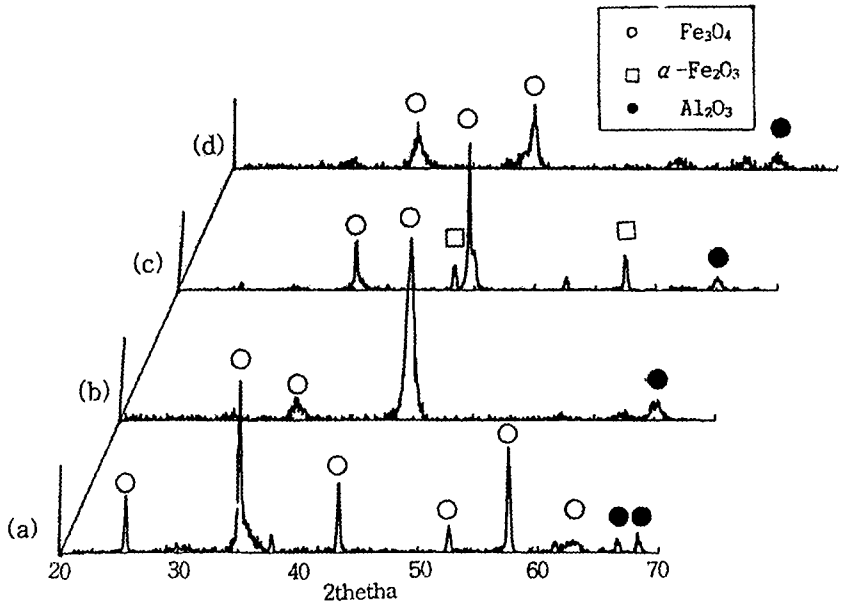


Figure 2: X-ray diffraction patterns of Fe_3O_4 at various deposition temperature

(a) 150℃ (b) 250℃ (c) 350℃ (d) 400℃

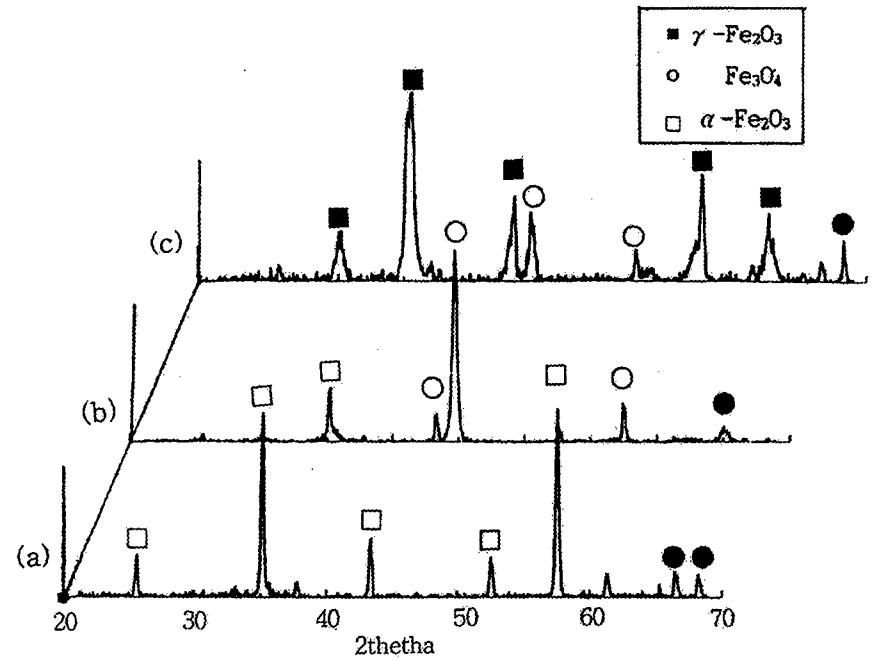


Figure 3: X-ray diffraction patterns showing the phase transition from α -Fe_2O_3 to Fe_3O_4 through reduction and oxidation process

(a) α -Fe_2O_3 (b) reduction phase(Fe_3O_4) (c) oxidation phase(γ -Fe_2O_3)

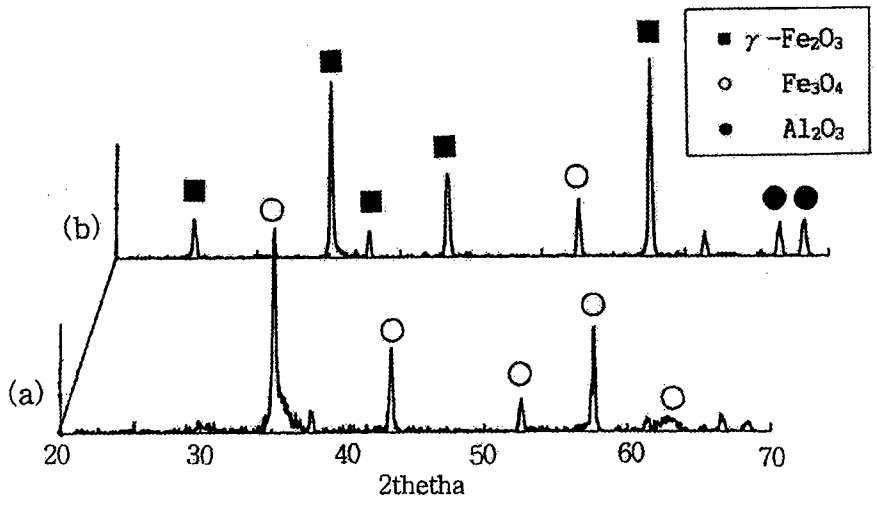


Figure 4: X-ray diffraction patterns showing the phase transition from Fe_3O_4 to γ -Fe_2O_3 through reduction and oxidation process

(a) Fe_3C_4 phase (b) oxidation phase(γ -Fe_2O_3)

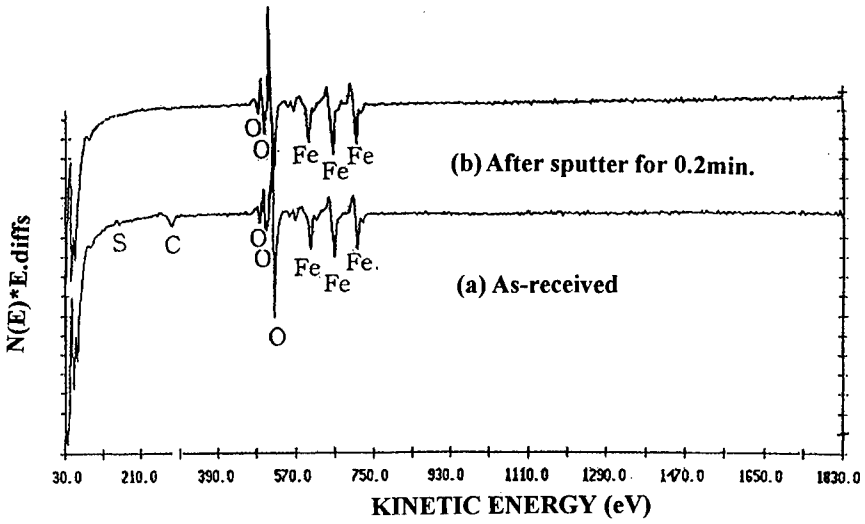


Figure 5: The result of AES

(a) As-received (b) After sputtering for 0.2min.

Shape Casting Simulation: Coupling Microstructural Models into Macromodels for the Prediction of Properties

A. Giachino, P.D. Lee, L. Christodoulou and S. Nishido*

Department of Materials, Imperial College
Prince Consort Road, London, UK, SW7 2BP

*Aisin Takaoka Co. Ltd.,
1Tennoh, Takaokashin-machi, Toyota, Aichi, 473 JAPAN

Abstract

This paper explores the extension of finite element simulation tools to the prediction of microscopic defects in complex automotive castings and investigates how processing variables impact the resultant microstructure and, thereby, the final properties of the alloy. The ultimate intention is to develop tools which allow the process designer to realise the full potential of the material by affording local microstructural control to meet stringent requirements for mechanical performance. The micromodels (empirical, deterministic or continuum-stochastic) of the solidification microstructure, which must be solved on the micron scale, are implemented and linked into finite element heat transfer calculations carried out in millimetres employing efficient, semi-analytical methods. This approach reduces the problem of excessive computational time requirements demanded by many micromodels and makes the problem tractable. The prediction of porosity, dendrite arm spacing and grain size are used as examples of microstructural information that may be obtained. The usefulness of this approach is demonstrated by the application of both the macro- and micro-models to determine the best casting process to obtain the properties required and to optimise the process for a specific automotive component.

Introduction

The use of aluminium castings in the automotive industry has seen ever increasing growth due to the economic savings of a reduced number of production steps compared to other manufacturing methods such as forging. These production advantages have lead to strong interest in aluminium castings for applications where stringent mechanical requirements must be met. To achieve this, simulations of heat transfer and solidification and fluid flow are used to predict defects such as hot spots (which produces macroshrinkage). Simulation of the filling and heat transfer of castings has now become a powerful tool for the optimisation of casting processes. This is particularly true for the prediction of macroscopic defects in die casting processes where simulation can reduce high tooling development costs. As applications become even more demanding however, finer scale defects must be eliminated, and microstructural features must be predicted and related to the mechanical properties. For example, in as-cast structures microporosity is often the limiting factor controlling fatigue and elongation properties.[1,2,3].

The part chosen for modelling is a Toyota Land Cruiser rear door tire mount hinge component in production at Aisin-Takaoka at the time of writing using LM25 (A356). This part is attached to a rear corner of the vehicle body and serves to pivot and support a swinging bracket with mounted tire. It thus

The Third Pacific Rim International Conference on
Advanced Materials and Processing (PRICM 3)
Edited by M.A. Imam, R. DeNale, S. Hanada,
Z. Zhong and D.N. Lee
The Minerals, Metals & Materials Society, 1998

needs to have reliable mechanical properties meeting stringent requirements for both strength and toughness. The smooth curved back surface of the hinge is mated to the car body, so this back wall must be void of defects, especially in the corner zones (see figure 1.) Since the hinge is an exterior feature of the vehicle, some cosmetic requirements must also be satisfied by producing a casting with very smooth surfaces.

The available micromodels used will be briefly reviewed followed by a description of the macromodel used in this work. Our multi-scale modelling approach (linking the micro-to the macro-scale) will then be applied to illustrate the most appropriate casting process (selected from sand, permanent mould, or squeeze) for this specific component followed by optimisation of that process.

Micromodelling Approach

Review of available methods:

Many different types of micromodels for the prediction of solidification structures have been developed over the past two decades as reviewed by Rappaz[4] and by Stefanescu[5]. The models developed have ranged from empirically based functions (e.g. the Niyama criteria function for porosity[6]) to continuum models solving for the structure using a microscopic discretisation (e.g. phase-field method for predicting dendrite shapes[7]). The former empirical models have limited application since they do not encompass the basic governing physics and hence are not appropriate for extrapolation to processes with significantly different conditions (i.e., the use of the Niyama criteria which was developed for sand castings to high pressure casting is not appropriate). The later micromodels involving a very fine discretisation often include all the relevant physics, but are currently too computationally intensive for application to large complex automotive castings.

The microstructural properties required for the hinge part are a fine secondary dendrite arm spacing (DAS), a fine grain size, and very low porosity. The DAS was shown by Flemings to be proportional to a coarsening law (DAS $\approx t_s^{1/3}$, where t_s is the local solidification time), and it can be determined by an empirical law for most conditions encountered in the sand, permanent, and squeeze casting processes.

The prediction of grain size has recently been modelled by both deterministic[8] and by cellular automata (CA) methods[9]. The deterministic methods benefit from computational simplicity but only track average values, whilst the CA methods implicitly include effects such as impingement and track a population of grains, generating both mean and distributions of morphologies. Recently the determination of size distribution has been included in the deterministic method[10]. This model was run over the range of thermal profiles experienced in the various casting methods to be examined and multi-linear regression analysis was used to establish a function for inclusion of grain size predictions in a de-coupled fashion into the macro-code.

The third critical property, percentage and size of porosity, has been the subject of many experimental (reviewed by Tynelius[11]) and modelling studies (reviewed by Stefanescu [12]). Many of the early models were empirically-based criteria functions (reviewed by Murali and Sharma [13]). Recently, one of the authors has developed a continuum-stochastic model that solves for the development of micro-porosity and its interaction with the developing microstructure using a continuum-stochastic model solved using a discretisation size of microns[14].

In this paper, the formation of microporosity was modelled using the continuum-stochastic model where the diffusion of hydrogen was solved on a continuum level and a stochastic model of pore nucleation was implemented. Once a pore nucleates, it is coupled into the continuum model, acting as a sink or source of hydrogen. The key aspects of the implementation of this micromodel has been described previously[14]. The developing microstructure limiting pore growth was characterised by a deterministic model of grain growth[10] and a DAS ripening law. Our approach was to solve for the solidification structures using the above complex micromodels over the expected parameter space encountered in real castings, and then to fit functions for the parameters of interest to both the mean values and their variance. These functions were then used in a de-coupled manner to give an estimate of the properties by applying the fitted functions in a post-processing step.

Hence the three required structure predictions, DAS, grain size, and porosity, were all incorporated using functions generated from the fundamental physics of the processes involved.

Macromodelling Approach

The solidification and thermal analyses of the macromodel were performed using CAP*, a Finite Element Method heat transfer solver. CAP models heat conduction, taking into account latent heat of fusion. It uses a unique time integration scheme which incorporates a fully implicit method at an early calculation stage, followed by an unconditionally stable integration method. This ensures accuracy with improved efficiency. The finite element 3D model was meshed using AMESH, a semi-automatic meshing tool which simplifies model editing for subsequent analyses that involve casting and/or die modifications. The filling was simulated using the complimentary FEM code, WRAFTS*, which solves the Navier-Stokes equations tracking the free surface.

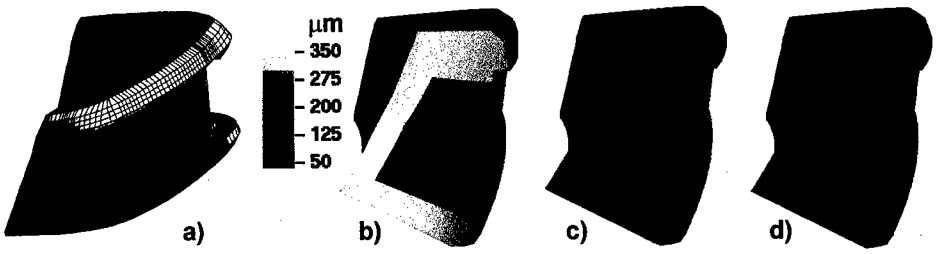


Figure 1. Predicted grain size shown on the same cross-section of the hinge (a) for three different casting processes: b) green sand casting; c) permanent mould casting, and d) squeeze casting.

Results and Discussion

Casting Process Selection

The three processes considered for production of the hinge part were sand casting, permanent mould, and squeeze casting. Using a stl file as the input geometry, all three options were meshed, including the sand or steel die (with appropriate water cooling). In order to compare the structures produced, only the solidification of the part was simulated, and the microstructural predictions compared. The resulting predictions for grain size are compared graphically in figure 1, and average values are listed in table I. Similarly the predicted percentage porosity is shown in figure 2, and average values are listed in table I. In addition to the predicting the mean value, the micro-model for porosity tracks a population of pores allowing a function to be fit characterising the distribution. Assuming a normal distribution (shown experimentally by Lee and Hunt[15]), a function was fit to three times the standard deviation in the average pore length, generating a prediction for a 3σ maximum pore length (see table I). The prediction of a maximum pore length is important because failure due to fatigue has been related to the largest pore size, rather than the average.

Table I. Predicted values for DAS, grain size. percentage porosity and 3σ pore length averaged over the entire part. The ± values are a standard deviation in the mean over all nodes in the part.

Process	DAS [µm]	Grain Size [µm]	Percentage Porosity [%]	3σ Pore Length [µm]
Sand	51±6	339±46	1.0±0.1	383±37
Perm. Mould	36±4	198±31	0.5±0.1	276±27
Squeeze	15±5	76±28	<0.01	5±1

The predictions show that squeeze casting provides a fast solidification rate that produces better microstructural properties (see table I), and the high pressure aids in feeding porosity that could form in

* CAP and WRAFTS, registered by EKK Inc, 2065 West Maple, Walled Lake, MI 48390

the thicker sections of the casting. Sand casting can be eliminated as a viable process for this part because of both poor microstructural properties and surface finish. Permanent mould casting may be acceptable with respect to DAS and grain size, but the 3σ pore length is unacceptably large. Therefore in order to achieve a high quality casting for this application, squeeze casting is the preferred method of production.

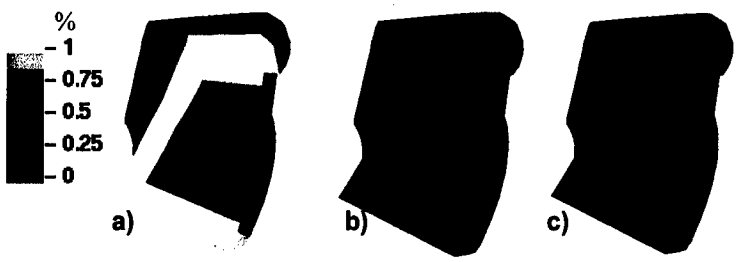


Figure 2. Predicted percentage porosity shown on the same section of the hinge for three different casting processes: a) green sand casting; b) permanent mould casting; and c) squeeze casting.

Squeeze Casting Design Optimisation

Once the optimal process has been selected, the macro- and micro-macro models can be applied to optimise the design of the dies, cooling passages, and filling speed for the squeeze casting. The macromodel, which consists of approximately 144,000 elements and 143,899 nodes, includes the Al casting, steel die retainers, steel die inserts and slides with respective water cooling lines, shot tip, and an outside air boundary condition. The full process cycle was modelled, consisting of a dwell period (metal solidifies in the die), an opened die period (the die becomes exposed to air immediately after ejection), a spraying period (the die receives a chill coating), another opened die period, and a closed die period (dies are clamped together) just before injecting metal again. Due to the typical warming up of the dies during the first few cycles of production, thirty cycles were analysed to ensure steady-state conditions were reached before analysing a final solidification. Water and air were modelled as boundary conditions at 30°C and 50°C respectively. Material properties, initial temperatures, and heat transfer coefficients used in the analysis are listed in tables II and III.

Table II. Material Properties and Initial Temperatures. (ρ-density, C_p-specific heat, k-thermal conductivity, T-temperature.)

Material	ρC_p (MJ/m^{3}K)	k (W/mK)	Initial T (°K)
LM25	2.709	100.320	973.0
Steel	3.716	25.916	523.0

Table III. Interfaces Heat Transfer Coefficients.

Interface Materials	Heat Transfer Coef. (W/m^{2}K)
LM25 to Steel	16,000
Steel to Steel (clamped)	1,000
Steel to Steel (retainer/insert)	5,000
Steel to Water Cooling	6,000
Steel to Air	50

Two thermal simulations will be discussed to illustrate the design optimisation: analysis 1, without water cooling; and analysis 2, with water cooling.

The water cooling was added to test altering the solidification patterns and cycle time and is the current production process with water cooling lines included in the die inserts. The solidification patterns are similar, but occur at different rates. In analysis 2 the casting (without runner and sprue) completely solidifies in 13.5 seconds, whereas in analysis 1 the casting does not solidify until 19.25 seconds. A longer solidification time could lead to larger porosity in areas where the liquid metal becomes isolated. With a fast solidification time any pores that form will remain small and scattered and are likely to be fed by high pressure in the cavity.

Analysis 2 also shows a better solidification pattern near the gating, which is acting as a riser. In Analysis 1 a large volume of isolated liquid remains in the casting, near the gating, figure 3. This is

undesirable because at this thin section of the casting, shrinkage or porosity would have an adverse impact on the properties of the component

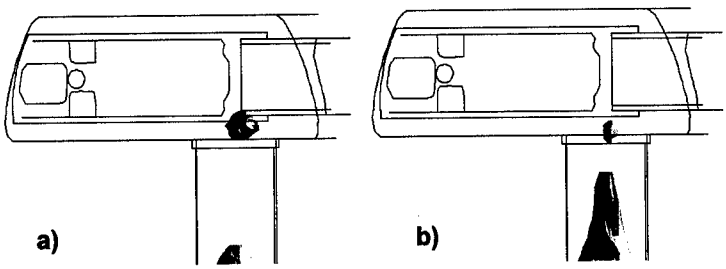


Figure 3 Iso-surfaces of solidification time (t_s) illustrating a potential hot-spot near the gating. a) Analysis 1(no cooling) (t_s=18s); b) analysis 2 (cooling) (t_s=13s).

The overall casting temperatures after ejection indicate a much wider temperature distribution in analysis 2, while analysis 1 shows a gradual temperature variance, indicating longer solidification times and a slower cooling rate, both factors which increase shrinkage and porosity size in areas where liquid metal becomes isolated (see figure 4).

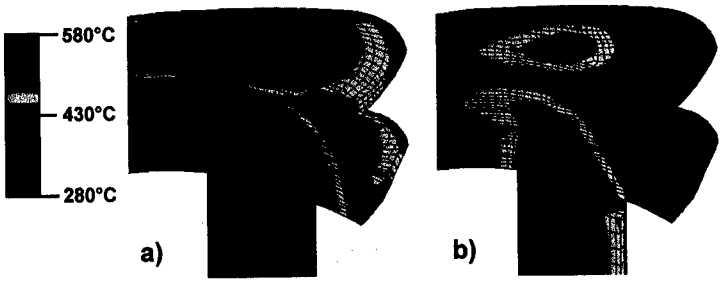


Figure 4. Surface temperatures for a) analysis 1 (no cooling) and b) analysis 2 (cooling).

The filling of the cavity is simulated by varying the shot sleeve velocity profile of the metal at the gate. Figure 5 illustrates two fluid flow analyses. The first features a profile with a 50% reduction in the initial speed, while the second reduces the initial speed by 75%. The faster velocity promotes filling of the rib section prematurely, causing initial turbulence and possible entrained oxides when fluid fronts meet at the top of the casting. The slower velocity provides a quieter, directional filling from the bottom to the top of the casting, adding no more than 0.5 seconds to the total filling time.

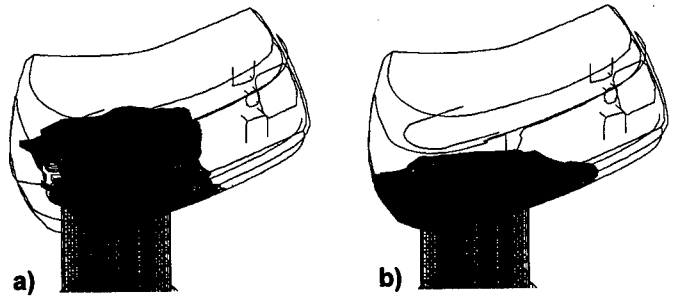


Figure 5. Filling pattern for a) analysis 1 (fast) at 0.35s and b) analysis 2 (slow) at 0.42s.

Having selected squeeze casting and the best process, and determining an optimal design, the predictions of the final properties can be examined. The requirements were for a fine DAS and grain size, along with minimal porosity. Figure 6 shows the predicted solidification structures for the optimised, water cooled, squeeze casting design. A very fine dendrite arm spacing, (6a) and grain size,

(6b) are predicted, and almost no porosity is anticipated (6c) and (6d). This microstructural state is expected to give excellent mechanical properties.

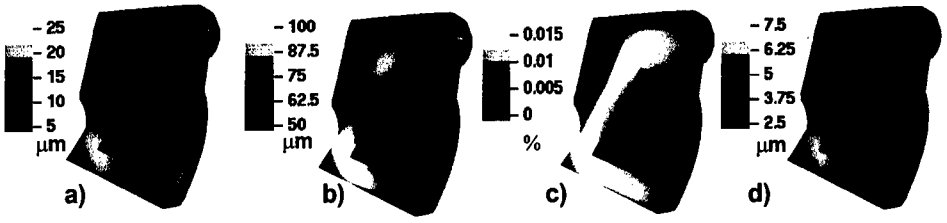


Figure 6. Microstructure from the process chosen to produce the part, squeeze casting. a) secondary dendrite arm spacing; b) grain size; c) percentage porosity; and d) 3σ pore length.

Conclusions

Empirical and micro-model derived functions for the prediction of the casting solidification structures have been incorporated into a very efficient finite element macromodel and applied to both casting process selection and optimisation. The use of multi-linear regression analysis derived constitutive equations to the micro-models allows the fundamental physics underlying the development of the solidification structures to be incorporated with a negligible effect upon the computational times. This allows an efficient prediction of the process/structure/property relationships during the casting of aluminium alloys.

Application of the micro-macro model led to the conclusion that squeeze casting (with appropriate water cooling channels in the die) is the best process for producing an automotive wheel hinge yielding the required mechanical properties.

Acknowledgements

The authors would like to thank their colleagues at both Imperial College and Aisin Takaoka for their contributions to the work described in this paper and gratefully acknowledge the financial support of Aisin Takaoka. The authors would also like EKK Inc. for the use of the macromodelling codes and their assistance in incorporating the micro-models.

References

1 J.A. Eady, D.M. Smith, Materials Forum 9 (4) (1986), 217-223.
2 M.J. Couper, A.E. Nelson, J.R. Griffiths, Fat. Fract. Eng. Mat. Str. 13 (3) (1990), 213-227.
3 K.E. Tynelius, J.F. Major, D. Apelian, AFS Trans. 93-166 (1993), 410-413.
4 M. Rappaz, Int Mat. Reviews 34 (3) (1989), 93-123.
5 D.M. Stefanescu, ISIJ 35 (6) (1995), 637-650.
6 E. Niyama, T. Uchida, K. Anzai, S. Saito, AFS Int. Cast Metals J. (Sept.1982) 52-63.
7 W.J. Boettinger, J.A. Warren, Met. Trans. A, 27 (3) (1996), 657-669
8 P. Thevoz, J.L. Desbiolles, M. Rappaz, Met. Trans. A, 20 (2) (1989), 311-322.
9 Ch. Charbon, M. Rappaz, Mod. Simul. Mater. Sci. Eng. 1 (1993), 455-466.
10 R. Lothian, P.D. Lee, M. McLean, to be submitted to Acta Materialia (1998).
11 K.E. Tynelius, J.F. Major, D. Apelian, *AFS Transactions*, 93-166 (1993), 410-413.
12 D.M. Stefanescu, Mod. Cast., Weld., and Adv. Sol. P. VI, Ed. Piwonka, T.S., Voller, V., Katgerman, L., (TMS 1993), 3-20.
13 A.V. Murali, G.R. Sharma, Trans. Indian Inst. Metals 40 (2), 101-108, 1987.
14 P.D. Lee and J.D. Hunt, Mod. Cast., Weld., and Adv. Sol. P. VII, Ed. M. Cross and J. Campbell, (TMS 1995), 585-592.
15 P.D. Lee and J.D. Hunt, Acta Materialia 45 (10), 4155-4169, 1997.

CRYSTALLINE-AMORPHOUS TRANSFORMATION IN C15 LAVES PHASE $TbFe_2$ BY HYDROGEN ABSORPTION

K.Mori[1], K.Aoki[2], and T.Masumoto[3]

Institute for Materials Research, Tohoku University, Sendai, 980-77 Japan, [1]Present address: Central Research Institute, Mitsubishi Materials Corporation, Omiya, Saitama, 330 Japan, [2]Present address: Kitami Institute of Technology, Kitami, Hokkaido, 090 Japan, [3] The Research Institute for Electric and Magnetic Materials, Yagiyama-minami 2-1-1, Sendai 982, Japan

Abstract

Structural changes of C15 Laves phase $TbFe_2$ during the differential thermal analysis (DTA) in a hydrogen atmosphere (H_2) have been examined by powder X ray diffractometry (XRD), the hydrogen analysis, differential scanning calorimetry (DSC), transmission electron microscopy (TEM), ^{57}Fe Mössbauer spectroscopy and magnetic property measurements. The origin of four exothermic peaks in the DTA curve was determined to be due to (1) hydrogen absorption in the crystalline state, (2) the hydrogen-induced crystalline to amorphous transformation, (3) the precipitation of TbH_2 in the amorphous phase and (4) the decomposition of the remaining amorphous phase into TbH_2 and α-Fe with increasing temperature. The amorphous nature of the hydrogen-induced amorphous alloy was supported by the Mössbauer effect. In addition, the hydrogen-induced *a*-$TbFe_2H_{3.5}$ alloy was thermally analyzed using DTA in an Ar atmosphere. It decomposed into TbH_2 and α-Fe exothermally at about 800 K. On heating the mixture of TbH_2 and α-Fe, the recombination reaction between Tb, which was formed by the decomposition of TbH_2, and α-Fe occurred exothermally to form Tb_6Fe_{23} around 1000 K. Furthermore, $TbFe_2$ was formed exothermally by the recombination between Tb and Tb_6Fe_{23} around 1100 K. Thus, HDDR (Hydrogenation-Disproportionation-Dehydrogenation-Recombination) was observed in the present $TbFe_2$ alloy.

The Third Pacific Rim International Conference on
Advanced Materials and Processing (PRICM 3)
Edited by M.A. Imam, R. DeNale, S. Hanada,
Z. Zhong and D.N. Lee
The Minerals, Metals & Materials Society, 1998

Introduction

The transformation from the crystalline to the amorphous state induced by hydrogen absorption, i.e. hydrogen-induced amorphization (HIA) was demonstrated by Yeh *et al.* for the metastable Zr_3Rh [1]. Subsequently, it has been reported that HIA occurs in the intermetallic compounds having the crystal structure of C15, C23, $L1_2$, $B8_2$ and $D0_{19}$ and containing a hydride forming element [2-7]. C15 Laves phase $TbFe_2$ absorbs hydrogen exothermally at low temperature and becomes crystalline *c*-$TbFe_2H_x$ [8,9], which transforms exothermally to amorphous *a*-$TbFe_2H_x$ with increasing temperature. On heating *a*-$TbFe_2H_x$, the third exothermic peak appears in the differential thermal analysis (DTA) curve. However, it is difficult to elucidate the origin of this exothermic peak by XRD and TEM alone. The origin of this peak can be determined by Mössbauer spectroscopy and magnetic property measurements. Although crystallization of amorphous alloys has been extensively investigated so far, it of hydrogen-induced amorphous alloys has little been investigated as yet. In the present work, $TbFe_2$ was thermally analyzed using DTA in a hydrogen atmosphere to elucidate the origin of the thermal effect. Furthermore, the crystallization behavior of the hydrogen-induced amorphous alloy was thermally analyzed using DTA in an Ar atmosphere.

Experimental

A $TbFe_2$ compound was arc melted using 99.9% Tb and 99.99 % Fe in an argon atmosphere. The ingot was homogenized to obtain a single phase at 1073 K for 605 ks in an evacuated quartz tube. Pulverized crystalline samples (below 100 mesh) were heated using DTA at a heating rate of 20 K/min in a hydrogen atmosphere of 1MPa. Structures of the samples heated to the distinct stages of DTA were examined by XRD using monochromated CuKα radiation. The hydrogen content in the samples was determined by the high temperature gas extraction-gas chromatographic technique. Crystallization and hydrogen desorption behaviors of the amorphous alloys were examined by differential scanning calorimetry (DSC) at a heating rate of 40K/min in a flowing Ar atmosphere. The microstructures of the hydrogenated samples were observed by TEM. ^{57}Fe Mössbauer spectroscopy was carried out at 293 K using a conventional constant acceleration spectrometer in the transmission mode. The magnetization was measured with a vibrating sample magnetometer (VSM) in the range of 4.2 to 860 K in the applied field of 10 kOe.

Results and Discussion

Structural changes of $TbFe_2$ during heating in an H_2 atmosphere and the transformation from the crystalline to amorphous state

Figure 1 shows the DTA curve and the change in the hydrogen content (H/M) of $TbFe_2$ heated in 1 MPa H_2. Four exothermic peaks are observed in the DTA curve. Figures 2 and 3 show the XRD patterns and Mössbauer spectra of $TbFe_2$ heated to the distinct stages of DTA. The XRD pattern of the original sample indicates this consisting of the C15 Laves phase. The XRD pattern of the sample heated above the first peak (to 445 K) shows Bragg peaks which are indexed on the basis of a rhombohedral structure. The Mössbauer spectrum of this sample shows two sharp doublet and broad and weak sextet characteristic of the crystalline phase. The hydrogen content increases to 1.5 (H/M) on heating to 445 K. From XRD, Mössbauer spectrum and the hydrogen analysis, it is concluded that the first exothermic peak is due to hydrogen absorption in the crystalline state and $TbFe_2$ changes to *c*-$TbFe_2H_{4.5}$. The Bragg peaks disappear and are replaced by a broad maximum for the samples heated to 570-620 K. The DSC curves of these samples show two exothermic peaks of crystallization at 650 K and 830 K [9]. Furthermore, an

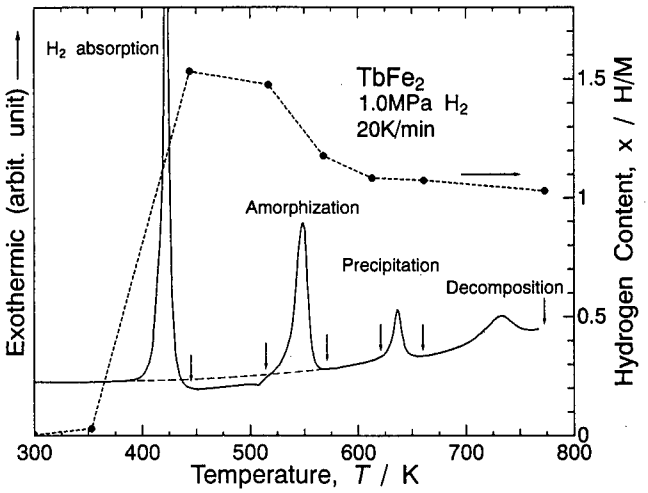


Figure 1: DTA curve of $TbFe_2$ heated at a heating rate of 20 K/min in 1 MPa H_2 and the change of the hydrogen content in the sample.

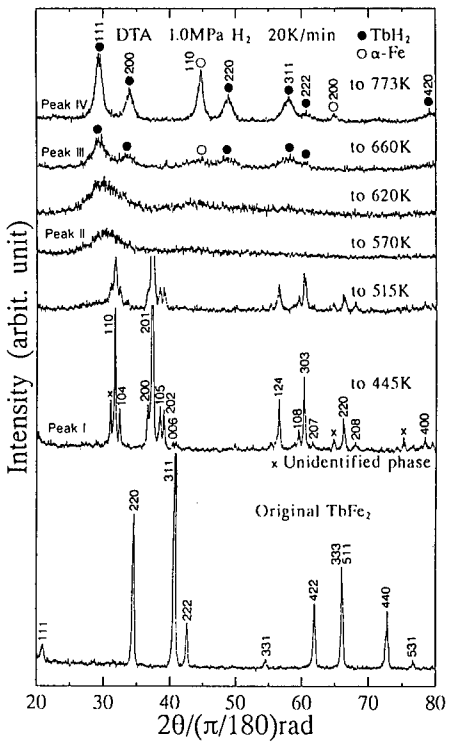


Figure 2: XRD patterns of $TbFe_2$ heated to the distinct stages of DTA in 1 MPa H_2.

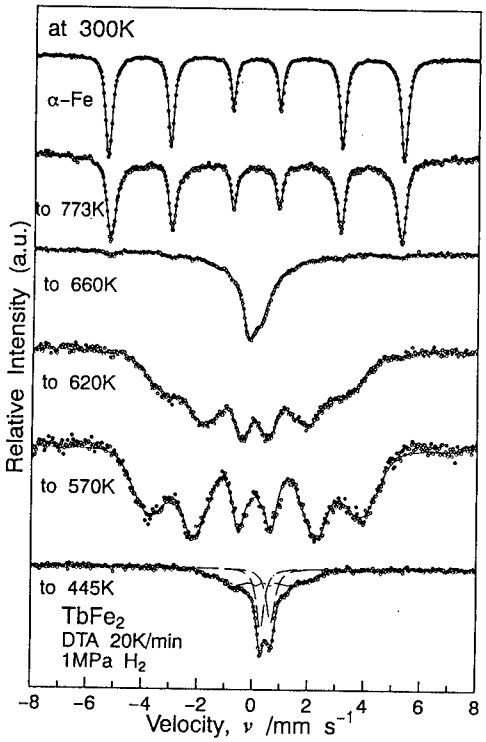


Figure 3 : The Mössbauer spectra of $TbFe_2$ heated to the distinct stages of DTA curve in 1 MPa H_2.

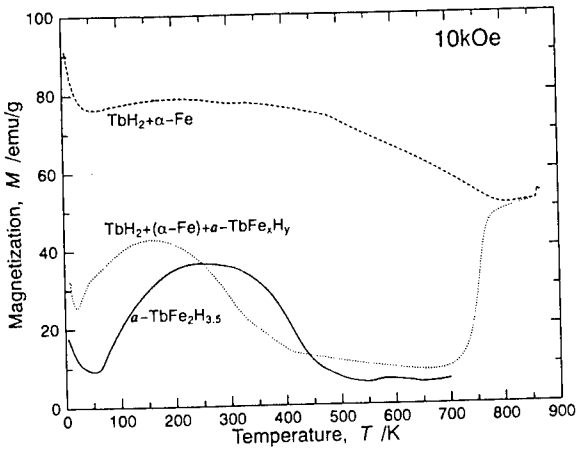


Figure 4 : Thermomagnetization curves of the $TbFe_2$ heated above the second (the solid line), the third (the dotted line) and the fourth peak (the broken line) in DTA.

electron micrograph of $TbFe_2$ heated to 570 K is featureless and the corresponding selected area diffraction pattern shows a halo characteristic of an amorphous phase [9]. The Mössbauer spectrum of this sample shows a broad sextet due to the distributed hyperfine fields. The hyperfine field distribution is a characteristic feature of magnetically ordered amorphous materials. Thus the amorphous nature of this sample is also supported by the Mössbauer effect. These results indicate that the second exothermic peak is due to the transformation from *c*-$TbFe_2H_{4.5}$ to *a*-$TbFe_2H_{3.5}$. Broad Bragg peaks of TbH_2 are observed in the XRD pattern of the sample heated above the third exothermic peak (to 660K), so that it is sure that TbH_2 precipitates at the third exothermic peak. The Mössbauer spectrum of the sample heated above the third peak (to 660K) shows a broad doublet, which is different with that of the sample heated above the fourth peak (to 773K) showing a sharp sextet of α-Fe. This indicates that a little amount of α-Fe is present in the sample heated above the third exothermic peak. The thermomagnetization curves of the samples heated above the second (the solid line), the third (the dotted line) and the fourth peak (the broken line) in DTA are shown in Figure 4. Hydrogen-induced *a*-$TbFe_2H_{3.5}$ is a ferrimagnet with the compensation temperature T_{comp}= 53 K and the Curie temperature T_c = 450 K. On the other hand, the magnetization of the sample heated above the fourth peak shows the high value of α-Fe. The sample heated above the third peak shows similar temperature dependence with that of *a*-$TbFe_2H_x$. These thermomagnetization data indicate that the phase other than TbH_2 is the Fe-rich amorphous phase. From XRD, Mössbauer spectroscopy and thermomagnetization curve, it is concluded that the third peak is due to the precipitation of TbH_2. The XRD pattern of the sample heated above the fourth DTA peak (to 773K) is indexed on the basis of TbH_2 and α-Fe. This indicates that the fourth DTA peak results from crystallization of the remaining amorphous alloy.

Structural changes of *a*-$TbFe_2H_{3.5}$ during heating in an Ar atmosphere and the HDDR phenomenon

Figure 5 shows the DTA curve of *a*-$TbFe_2H_{3.5}$ heated in an argon atmosphere of 0.1 MPa. Many exothermic and endothermic peaks are observed in this curve. Figures 6(a) and (b) show the XRD patterns of $TbFe_2$ heated to the temperatures marked by the arrows. The endothermic peak (below the broken line) between 400 to 600 K is due to hydrogen desorption in the amorphous alloy. The Bragg peaks of TbH_2 appear in the XRD pattern of the sample heated above the first exothermic peak (670K), so that the first exothermic peak is due to the precipitation of TbH_2. The XRD pattern of the sample heated above the second exothermic peak

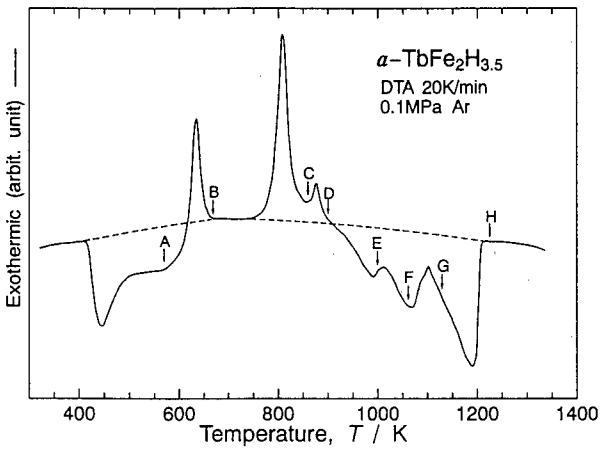


Figure 5 : The DTA curve of a-$TbFe_2H_{3.5}$ heated in an Ar atmosphere of 0.1 MPa.

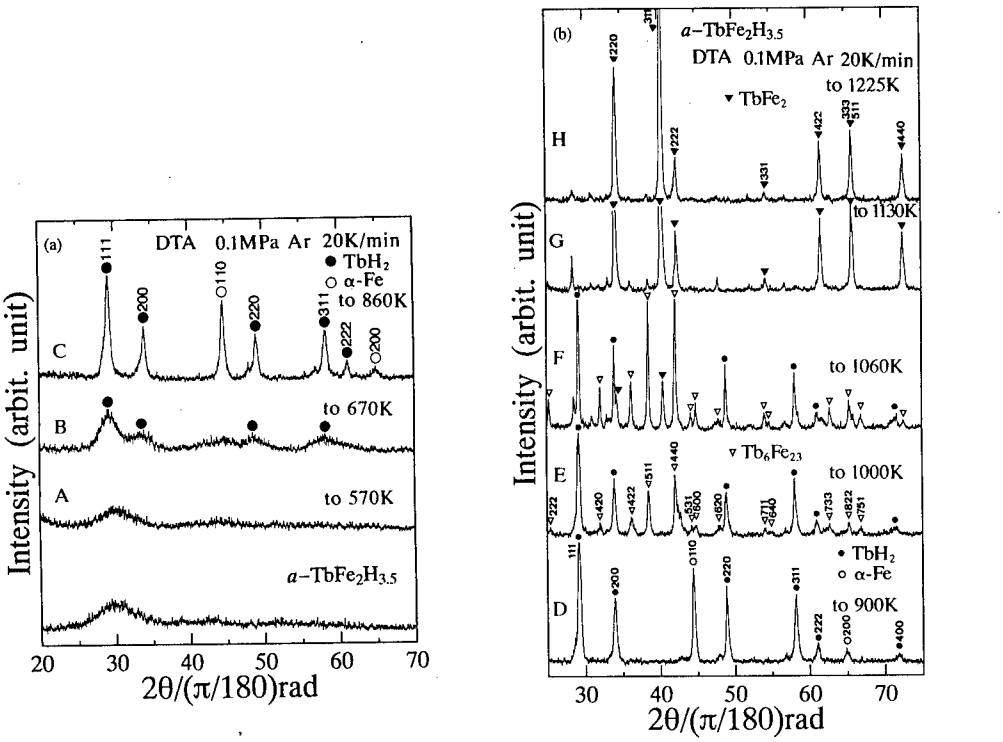


Figure 6 (a)(b) : The XRD patterns of the samples heated to the temperatures marked by the arrows.

(860K) is indexed on the basis of TbH_2 and α-Fe, so that the second exothermic peak is attributed to crystallization of a-$TbFe_2H_{3.5}$ into TbH_2 and α-Fe. The endothermic peak between about 900 and 1200 K is attributed to the decomposition of TbH_2 into Tb and H_2. The XRD pattern of the sample heated to the F point shows the Bragg peaks of TbH_2 and Tb_6Fe_{23}, but does

not show those of α-Fe. Therefore, the small exothermic peak around 1000 K overlapped with the endothermic peak is considered to result from the recombination reaction between Tb, which is formed by the decomposition of TbH_2, and Fe to form Tb_6Fe_{23}. The XRD pattern of the sample heated to the H point shows the Bragg peaks of $TbFe_2$. Therefore, the exothermic peak around 1100 K overlapped with the endothermic peak is considered to result from the recombination reaction between Tb and Tb_6Fe_{23} to form $TbFe_2$. Recently, novel grain refinement technique has been developed utilizing hydrogen called HDDR (Hydrogenation-Disproportionation-Dehydrogenation-Recombination) in the Nd-Fe-B permanent magnet alloys [10-12]. HDDR consists of two steps. The first step is hydrogenation-disproportionation (HD), in which an AB_x compound decomposes into an elemental hydride AH_y and a metal B. The second step is dehydrogenation-recombination (DR) in which the A metal, formed by decomposition of AH_y with increasing temperature, reacts with the metal B to form the nanocrystalline AB_x compound. In the present work, *a*-$TbFe_2H_{3.5}$ crystallizes into TbH_2 + α-Fe, which corresponds to the HD reaction. Tb_6Fe_{23} is obtained by the recombination between Tb, which is formed by the decomposition of TbH_2, and α-Fe. Furthermore, $TbFe_2$ is formed by the recombination between Tb and Tb_6Fe_2. These two steps correspond to the DR reaction. The present work demonstrates that $TbFe_2$ is formed by the HDDR using crystallization of hydrogen-induced amorphous alloys and the subsequent heating. This HDDR is anticipated to be hopeful to prepare nanocrystalline RFe_2 alloys.

Summary and conclusions

Structural changes of the C15 Laves phase $TbFe_2$ during DTA in H_2 have been investigated to make clear the origin of thermal effects. The origin of the first and the second exothermic peak was determined to be due to hydrogen absorption, hydrogen induced amorphization, respectively. The origin of the third and fourth exothermic peak was determined to result from the precipitation of TbH_2 in the amorphous phase and the decomposition (crystallization) of the remaining amorphous phase by Mössbauer spectroscopy and the magnetization measurement along with XRD, TEM and DSC. The Mössbauer effect has supported the amorphous nature of the hydrogen-induced amorphous *a*-$TbFe_2H_x$ alloy. In addition, the hydrogen-induced *a*-$TbFe_2H_{3.5}$ decomposes into TbH_2 and α-Fe by the exothermic reaction during heating in an Ar atmosphere. The recombination to form $TbFe_2$ occurs by two steps. That is, the HDDR (Hydrogenation-Disproportionation-Dehydrogenation-Recombination) phenomenon has been demonstrated by DTA and XRD experiments in the $TbFe_2$ alloy.

References

1. X.L.Yeh, K.Samwer, and W.L.Johnson, Appl.Phys.Lett., 42(1983),242.
2. K.Aoki, T.Yamamoto and T.Masumoto, Scr. Metall., 21(1987), 27.
3. K.Aoki, A.Yanagitani, X-G.Li and T.Masumoto, Mater. Sci. Eng., 97(1988),35.
4. K.Aoki, T.Masumoto, J.Alloys and Comp., 194 (1993),251.
5. K.Aoki and T.Masumoto, J.Alloys and Comp., 231(1995),20.
6. Y-G.Kim, S-M.Lee,J-Y.Lee, J.Less-Common Met.,169(1991)245.
7. W.J.Meng, J.Faber Jr., P.R.Okamoto, L.E.Rehn, B.J.Kestel and R.L. Hitterman, J.Appl.Phys.,67(1990)1312.
8. K.Aoki,X.G.Li and T.Masumoto, Mater.Sci.Forum 88-90(1990)439
9. K.Aoki, K.Mori, H.Onodera and T.Masumoto, J.Alloys and Comp., 253-254(1997)106.
10. T.Takeshita and R.Nakayama, *10th Int.Workshop on Rare Earth Magnets and their Applications,* Kyoto, p 551(1989).
11. I.R.Harris and P.J.McGuiness, J.Less Common Met.,172-174(1991)1273.
12. W-Y.Chu and A.W. Thompson, Script Metall. Mater.,25(1991)2133.

ANOMALIES OF ELECRICAL RESISTIVITY STUDIED BY CVM AND PPM

Tetsuo MOHRI and Fumitatsu NAGATA

Division of Materials Science and Engineering
Graduate School of Engineering, Hokkaido University
Sapporo, 060 JAPAN

ABSTRACT

The Cluster Variation Method (CVM) and Path Probability Method (PPM) are employed to analyze the anomalous relaxation behavior in the vicinity of order-disorder transition temperature known as *pseudo critical slowing down* phenomenon. The calculation is focused on the stoichiometric $L1_0$ ordered compound which undergoes the first order transition to a disordered phase. The present PPM calculation with a slight temperature dependency into the activation barrier of the elementary flipping process successfully reproduces an experimental result. A fully successful calculation, however, should await the development of heterogeneous PPM.

The Third Pacific Rim International Conference on
Advanced Materials and Processing (PRICM 3)
Edited by M.A. Imam, R. DeNale, S. Hanada,
Z. Zhong and D.N. Lee
The Minerals, Metals & Materials Society, 1998

Introduction

A measurement of the electrical resistivity has been recognized as one of the most powerful methods to investigate the atomic configuration of a given alloy system. The information obtained is not limited to equilibrium atomic configuration, but kinetic evolution process of both long range and short range ordered states are analyzed. Recent development of high precision resistometry[1-3] even enables one to reveal cooperative transition dynamics of different time scale phenomena such as the atomic migration of different species in the microscopic level as well as the growth of ordered domain in the mesoscopic scale.

One of the conventional analyses of resistometry is to perform the measurement at isothermal annealing condition with different annealing temperatures and to obtain the relaxation time as a function of temperature. This provides an activation energy which is a clue to elucidate the insight of relaxation mechanism.

Dahmani et al[4] performed a series of resistometry measurement for Ni_3Pt ordered compound and reported that the relaxation time first decreases with increase of the temperature, then increases in the vicinity of order-disorder transition temperature, as shown in Fig. 1 which reproduces only in the ordered phase region of the original article. It has been commonly observed for the second order transition that the relaxation time increases near the transition temperature, which has been termed *critical slowing down*. However, Ni_3Pt is the $L1_2$ ordered phase and the transition of $L1_2$ to a disordered phase is a typical example of the first order transition for which critical slowing down has been less commonly reported. Therefore, the above authors termed their findings as *pseudo critical slowing down*.

Among various theoretical tools in analyzing configurational thermodynamics and kinetics, the Cluster Variation (hereafter CVM)[5] and Path Probability (hereafter PPM)[6] Methods have been best suited to give atomistic level of time evolution and devolution processes. For the CVM, wide

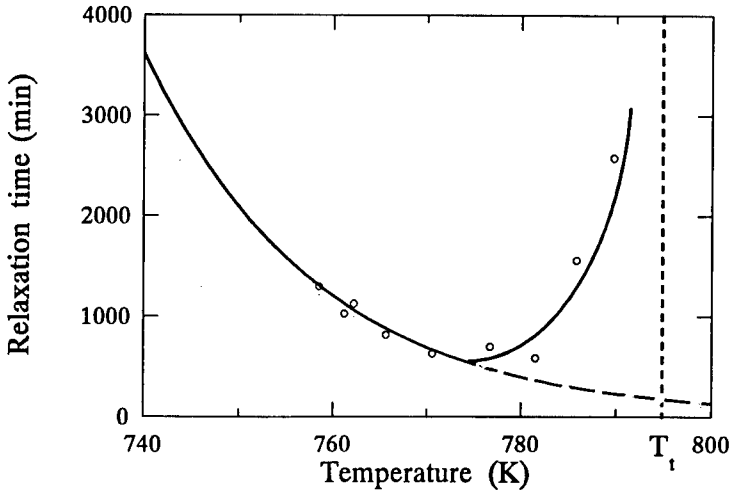


Figure1: Temperature dependency of relaxation time of of ordered Ni_3Pt reproduced from [4].

range of atomic correlations within the maximum cluster are explicitly taken into account in the free energy functional and the equilibrium atomic configuration under the given temperature and atomic interaction energies are derived at a minimum of the free energy functional. The PPM is recognized as the natural extension of the CVM to the time domain, and the evolution or devolution processes of the atomic configuration on the cluster is explicitly calculated based on a variational principle. An advantageous feature of the PPM arises from the fact that the quantities obtained from the PPM calculations in the long time limit converge to the ones of equilibrium state independently obtained by the CVM calculations. Therefore, the combination of the CVM and PPM is best suited to the detailed study of the atomic configurational thermodynamics and kinetics starting from non-equilibrium state towards an equilibrium state. In fact, the present authors have been attempting the various configurational kinetics studies which include transition kinetics, relaxation kinetics in a single phase field, steady state kinetics, fluctuation analysis etc. based on the CVM and PPM.[7-9]

In the present report, we extend the CVM-PPM approach to analyze the pseudo critical slowing down phenomenon. The main emphasis is placed on the reproduction of the phenomenon for the model fcc system by the CVM-PPM calculation. The limit of the present approach and the necessity of the development of *heterogeneous CVM-PPM* are pointed out at the end.

The organization of the present report is as follows. A brief theoretical frameworks of CVM and PPM is provided in the next section. The main results are presented in the third section and the brief discussions follow.

Cluster Variation and Path Probability Methods

A free energy functional, F, within the CVM is described in terms of a set of configurational probabilities within a finite cluster of which size and geometry specify the level of the approximation. The configurational probabilities are most conveniently expressed by a set of correlation functions, $\{\xi_j\}$[10], which span configurational space.

Then, under an assigned atomic interaction energies, $\{v_i\}$, the free energy functional, $F = F(T, \{v_i\}, \{\xi_j\})$, is minimized with respect to the correlation functions for each temperature, T, which determines the equilibrium state as well as the equilibrium correlation functions.

Unlike the case of ordinary kinetic theories in which the time derivative of the configurational variables are equated as the product of thermodynamic driving force and mobilities, PPM correlates the evolution of configurational variables (correlation functions) represented by χ during the infinitesimal time Δt by the *path variables*, Ξ, which constitutes the variational parameters of the *Path Probability function*, P, the kinetic counterpart of the free energy functional of the CVM, in the following way,

$$\chi_{\{\phi\}}(t+\Delta t) = \chi_{\{\varphi\}}(t) + \Xi_{\{\varphi\},\{\phi\}} \tag{1}$$

where $\{\phi\}$ and $\{\varphi\}$ represent atomic configuration on a specified cluster ϕ and φ, respectively.

In terms of the path variables, the Path Probability Function is defined as the product of three terms, $P = P_1 \cdot P_2 \cdot P_3$, and P_1 is written as

$$P_1 = (\theta \cdot \Delta t)^{Nx_{1,2}+Nx_{2,1}} \cdot (1-\theta \cdot \Delta t)^{Nx_{1,1}+Nx_{2,2}} \tag{2}$$

where θ is the spin flipping probability (atomic exchange probability) per unit time, $x_{i,j}$ is the point path variable describing the flipping (exchanging) of spin (atomic) configuration from i to j during the time interval Δt. Then, the first (second) term of P_1 indicates the flipping (non-flipping) event from *i to j (i)* configurations, and the product of two terms describes the non-correlated flipping events over an entire lattice which consists of N lattice points.

P_2 term is given as

$$P_2 = \exp\left(-\frac{\Delta E}{k_B \cdot T}\right) \tag{3}$$

which describes a conventional thermal activation process, that is expressing the probability of gaining the energy ΔE from the heat reservoir. It is noted that $P_1 \cdot P_2$ is a counter part of Boltzmann factor of free energy.

The final term, P_3, characterizes the PPM and is described as

$$P_3 = \frac{\prod_{\phi}\left(\prod_{\{\phi_1\},\{\phi_2\}} \Xi^{(\phi)}_{\{\phi_1\},\{\phi_2\}}\right)^{k_\phi}}{\prod_{\varphi}\left(\prod_{\{\varphi_1\},\{\varphi_2\}} \Xi^{(\varphi)}_{\{\varphi_1\},\{\varphi_2\}}\right)^{k_\varphi}} \tag{4}$$

where $\Xi^{(\psi)}_{\{\psi_1\},\{\psi_2\}}$ is the path variable indicating the flipping events on the cluster, ψ, from $\{\psi_1\}$ to $\{\psi_2\}$ configurations, and the exponent k_ψ reflects the multiplicity and the cluster correlations within the largest cluster. Hence, the most probable path of time evolution is determined by the maximization condition of the path probability function with respect to the path variables,

$$\frac{\partial P}{\partial \Xi^{(\psi)}_{\{\psi_1\},\{\psi_2\}}} = 0. \tag{5}$$

The solution of the set of simultaneous non-linear equations provides the most probable path variables, and through eq.(1) with the set of initial configurational variables, $\{\chi(t=0)\}$, the time evolution of the cluster probability is traced.

Results and Discussions

Although the pseudo critical slowing down phenomenon was experimentally observed in the vicinity of $L1_2$-disorder transition temperature, the present theoretical study is attempted for the $L1_0$-disorder transition at 1:1 stoichiometry which is also characterized as the first order transition.

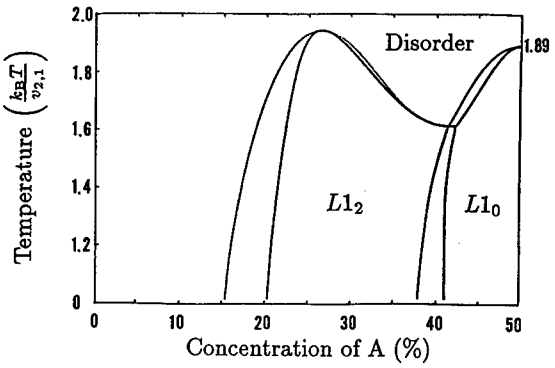


Figure 2: Disorder-$L1_0 - L1_2$ phase diagram calculated by tetrahedron approximation of CVM.

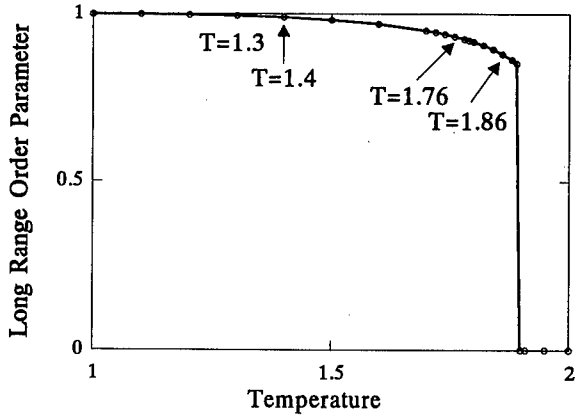


Figure3: Temperature dependence of long range order parameter obtained for 1:1 stoichiometry

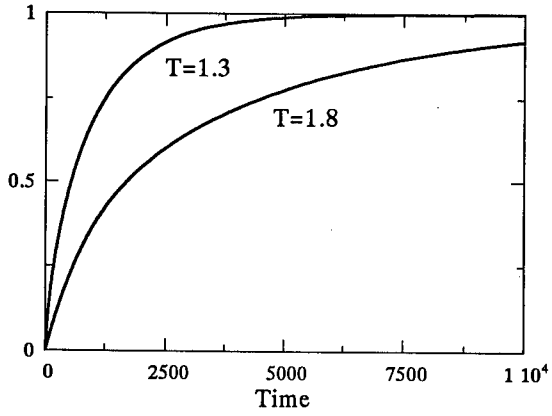


Figure 4: Calculated relaxation of electrical resistivity at annealing temperatures1.3 and 1.8

The disorder-$L1_0 - L1_2$ phase diagram was calculated within the tetrahedron approximation of the CVM and is demonstrated in Fig. 2. Note that the temperature is normalized with respect to the nearest

neighbor effective pair interaction energy, v_2, throughout the present study. The order-disorder transition temperature calculated at 1:1 stoichiometric composition is 1.89. The long range order parameter, η, is defined as the difference of the point correlation functions, $\xi_1^{(\alpha)} - \xi_1^{(\beta)}$, between the two sub-lattices α and β, and the calculated temperature dependency is shown in Fig. 3 which suggests the typical first-order character of the transition.

The present PPM calculation for the relaxation study was performed in the temperature range of $1.20 \le T \le 1.88$ within the stoichiometric $L1_0$ ordered phase region. Typical examples of the isothermal relaxation behavior of resistivity at two temperatures 1.3 and 1.8 are demonstrated in Fig. 4 where a system is up-quenched from 1.2 and 1.7, respectively. Note that the time is normalized with respect to spin flipping probability throughout this study. In order to convert the calculated long range order parameter, $\eta(t)$, to the resistivity, $R(t)$, the following Rossiter's formula is employed,

$$\frac{R(\eta)}{R(\eta = 0)} = \frac{1-\eta}{1 - A \cdot \eta} \quad , \tag{6}$$

where A is a constant and $R(\eta = 0)$ is the resistivity of a disordered phase.

From an isothermal relaxation curve which is well approximated by an exponential function, $\exp(-t/\tau)$, one easily obtains the relaxation time, τ, and the repetition for various isothermal annealing temperatures between 1.20and 1.88 gives the temperature dependency of τ as shown in Fig. 5. When one compares the present result with experimental curve of Fig. 1, serious discrepancies are realized. Although the relaxation time seems to be increasing towards transition temperature indicated by a broken line, this is not the slowing down behavior which is, in the experiment, manifested only in the very vicinity of the transition temperature. In fact, the arrow in the figure corresponds to the temperature range for which slowing down is observed in Fig. 1. One recognizes that the present result is deemed rather opposite to the experimental one.

The cause of the discrepancies is originated from the neglect of thermal activation process in the elementary spin flipping event. As shown in Fig. 3, change of the order parameter per unit temperature, $\partial\eta/\partial T$, is not appreciable in the low temperature range and is gradually pronounced toward the transition temperature. Hence, if one does not take the thermal activation process in the elementary flipping event into account, the temperature variation of the order parameter, $\partial\eta/\partial T$, is directly reflected in the resultant relaxation behavior and yields shorter relaxation time in the lower temperatures. Hence, the incorporation of the thermal activation process in the elementary flipping event is indispensable, and the following conventional activation process is assumed for θ in P_1 term,

$$\theta = \nu \cdot \exp\left(-\frac{\Delta G^*}{k_B \cdot T}\right) \tag{7}$$

where ν is the attempt frequency and ΔG^* is the activation barrier for a single flipping event.

When the calculation is limited to an temperature-independent activation barrier ΔG^*, one obtains the relaxation behavior shown in Fig. 6 in which the reduction of the relaxation time with increase of the

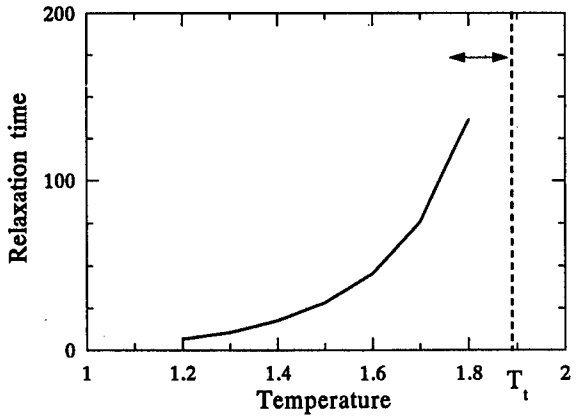


Figure 5: Temperature dependency of relaxation time at 1:1 stoichiometry with temperature-independent spin flipping probability

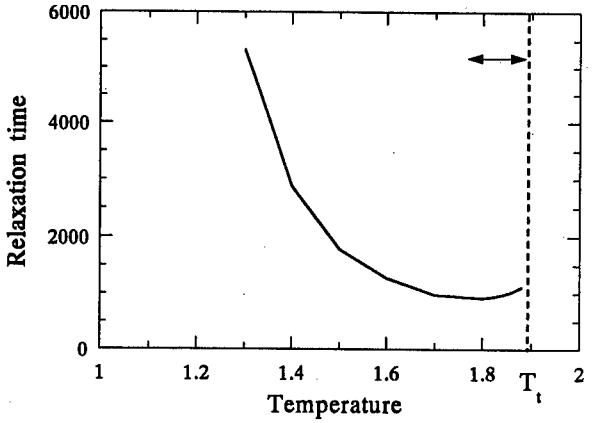


Figure 6: Temperature dependency of relaxation time at 1:1 stoichiometry with temperature dependent spin flipping probability.

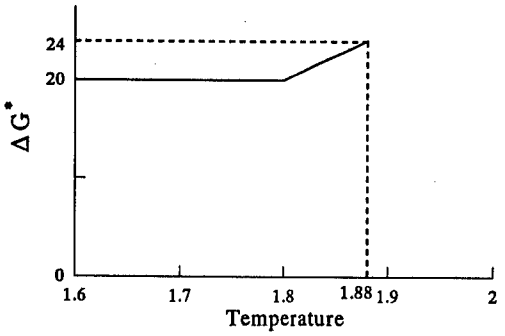


Figure 7: A hypothetical temperature dependency additionally considered for the activation energy near the transition temperature.

isothermal annealing temperature is realized in the global temperature region. Yet, the results do not reproduce the slowing down behavior in the vicinity of the transition temperature.

Then, as is shown in Fig.7, a slight linear temperature dependency is introduced into the activation

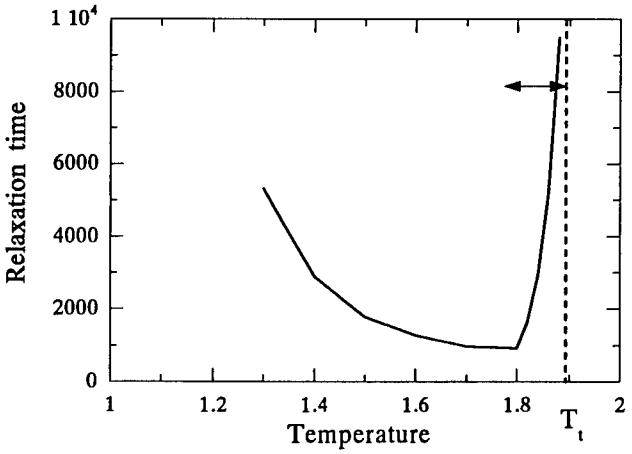


Figure 8: Temperature dependency of relaxation time with temperature-dependent activation energy for a single spin flipping process.

energy ΔG^*. The resultant relaxation-temperature curve is shown in Fig. 8. One confirms that the slowing down behavior is reasonably reproduced in the narrow temperature range in the vicinity of transition temperature.

Although the topological feature of the relaxation curve is well reproduced, the physical insight of the slowing down behavior should be further clarified. A general idea of the critical slowing down is due to the loss of thermodynamic restoring force against the fluctuation near the transition temperature where the free energy surface is rather flattened. In this regard, more detailed analysis of the free energy surface [7-9] with realistic atomic interaction energies should be attempted. Together with the fluctuation spectrum [8] obtained by PPM in an arbitrary direction in the thermodynamic configurational space, such analyses may provide thermodynamic origin of the slowing down behavior.

Finally, it should be pointed out that the pseudo critical slowing down behavior is phenomenologically equivalent to a *C-curve* in the *TTT* diagram. Therefore, one may claim that a loss of thermodynamic driving force in the vicinity of transition temperature is the main cause of both a longer incubation time manifested in the C-curve and prolonged relaxation time revealed by the resistivity measurement. In this sense, it is necessary to take *nucleation* events properly into the CVM-PPM formalism in order to describe the phenomenon successfully. The conventional CVM-PPM approach reported in the present study, however, assumes spatially homogeneous medium, whereas the nucleation event is characterized by the heterogeneity of concentration and order parameters. Hence, a fully successful theory of pseudo critical slowing down behavior should await the development of *heterogeneous CVM-PPM*.

How the spatially inhomogeneous nucleation event is renormalized in the additional activation barrier for an elementary flipping (exchange) event introduced in the present study is still an open question to be settled in the future.

References

1. W. Pfeiler, "Investigation of Short-Range order by Electrical Resistivity Measurement", Acta metall. 36 (1988), 2471-2434.

2. H. Lang and W. Pfeiler, "Kinetics of Ordering in Cu_3Au," accepted for publication in Proc. MRS

fall meeting '97.

3.H. Lang and W.Pfeiler," $L1_1$ long-range order in CuPt : A comparison between x ray and residual resistivity measurement," submitted to Phys. Rev. B.

4.C.E. Dahmani, M.C. Cadeville and V. Pierron-Bohnes, "Temperature Dependences of Atomic Order Relaxations in Ni-Pt and Co-Pt Alloys," Acta metall. 33 (1985), 369-377.

5.R. Kikuchi, "A Theory of Cooperative Phenomena," Phys. Rev. 81(1951), 998-1003.

6.R. Kikuchi,"The Path Probability Meethod," Prog. Theoret. Phys. Kyoto, Suppl. 35 (1966), 1-64.

7. T. Mohri, "Atomic Ordering Process and a Phase Diagram," Solid-Solid Phase Transformations (The Minerals , Metals and Materials Society ,1994), 53-74.

8. T. Mohri,"Kinetic Path and Fluctuations Calculated by the Path Probability Method," Theory and Applications of the Cluster Variation and Path Probability Methods (New York, Plenum Press, 1996), 37-51.

9. T. Mohri,"Configurational Kinetics Studied by PPM," Properties of Complex Inorganic Solids (New York, Plenum Press, 1997), 83-94.

10. J.M. Sanchez and D. de Fontaine,"The fcc ising model in the cluster variation approximation", Phys. Rev. B17 (1978), 2926-2936.

PHASE TRANSFORMATION AND TENSILE BEHAVIOUR OF Ti-6Al-4V AND GRADE 21S TITANIUM ALLOYS

W. Sha, D.P. Savage and Z. Guo

Department of Civil Engineering, The Queen's University of Belfast, Belfast BT7 1NN, UK

Abstract

Titanium alloy properties are very sensitive to microstructure, which is to a large extent dependent on the α/β transformation in these alloys. The present study used differential scanning calorimeter (DSC) to investigate the kinetics of the α/β transformation in two alloys, Ti-6Al-4V and grade 21S (Ti-15Mo-3Nb-3Al-0.2Si), with an aim of providing necessary information for further modelling of phase transformations in such systems. It has been found that using the DSC, phase transformation temperatures can be reproducibly determined. The effect of heat treatment on mechanical properties has also been studied using tensile testing.

The Third Pacific Rim International Conference on
Advanced Materials and Processing (PRICM 3)
Edited by M.A. Imam, R. DeNale, S. Hanada,
Z. Zhong and D.N. Lee
The Minerals, Metals & Materials Society, 1998

Introduction

Over the past forty years, a generic class of titanium-based materials has been developed, mainly, for critical structural components in the aerospace industry, due to their excellent high specific strength, fatigue resistance, creep life, and fracture toughness [*e.g.* 1,2,3,4]. This period has seen steady improvement in the capabilities of these alloys. Despite continued development of new alloys and product forms, titanium has moved rapidly through its product life cycle to maturity in the aerospace industry [1]. One of the new applications is in the marine industry, where a number of components would greatly benefit from the use of such alloys. There is indeed an increasing interest in the use of titanium in offshore oil and gas production where corrosion resistance, strength, weight, long life expectancy, and ease of fabrication are important [1,2,5]. The traditional workhorse in the alloy family, Ti-6Al-4V, is a ready candidate for this new application. Meanwhile, other systems have been considered. A relatively new alloy, ASTM grade 21S, is one such alloy.

The development of new titanium alloys targeted for specific applications has been an important task in the manufacturing industry. Traditionally, titanium alloys are designed empirically, *i.e.* with a mixture of experience and intuition. This is both costly and time consuming. It is now highly desirable to develop advanced computer-based models for the design of alloy compositions in an increasingly theoretical and less empirical manner. These models will be based upon the general theories of thermodynamics and phase transformations.

Titanium alloy properties are very sensitive to microstructure, which is to a large extent dependent on the α/β transformation in these alloys. In theory as well as in practice, titanium and titanium alloys can be heat treated for various reasons. These include reducing residual stress that may have been developed during fabrication, optimising properties such as ductility, machinability and strength, and increasing toughness, fatigue and high temperature creep strength.

Not all titanium alloys respond to heat treatment. In α type alloys, high strength cannot be gained by any type of heat treatment although they may be stress relieved and annealed. Optimal properties in α–β and β alloys can be developed with heat treatment.

The basis for manipulation during heat treatment is the $\alpha \leftrightarrow \beta$ transformation. Depending upon alloy composition and cooling rate, this transformation can occur in two ways, nucleation and growth or martensitically.

In the present work, the kinetics of $\alpha \leftrightarrow \beta$ transformation in two titanium alloys has been studied using heat flux differential scanning calorimetry (DSC), a technique by which the heat input into a sample is measured under a controlled temperature programme. The aim was to provide necessary information for further modelling of phase transformations. Though a powerful tool in the study of phase transformations, there has been little work using the DSC in characterising the phase transformation temperatures in titanium alloys. In addition, the tensile property of the alloys as a function of heat treatment and testing temperature has also been investigated, together with fracture surface characterisation using scanning electron microscopy (SEM). The research represents the beginning of a wider programme on modelling and design of titanium alloys for offshore oil and gas production.

Experimental

Two alloys were studied. The first is the most widely used titanium alloy, Ti-6Al-4V α–β grade 5 alloy. It was received as a large sheet with a thickness of 2.5 mm, locally bent. The second is a metastable β-alloy known as grade 21S. Its composition is Ti-15Mo-3Nb-3Al-0.2Si. This relatively new alloy offers high strength, improved oxidation resistance and elevated temperature strength. It was received as a seamed pipe, with an average diameter of 27 mm and a wall thickness of 4 mm. The tensile samples were longitudinal.

Differential scanning calorimetry (DSC) experiments were carried out using a Netzsch DSC414 machine which is a high temperature, heat flux DSC. The experiments were conducted in helium atmosphere, with no reference. The heating/cooling rates used were 10 and 30°C/min. Some details concerning experiments using this type of equipment were given in earlier papers [6,7,8]. Tensile testing experimental details were also given in a previous publication [9]. Square or rectangular (along the gauge length of 80 mm) samples were used. All heat treatments and tensile tests were conducted in static air. It appears that there is only negligible scaling in the surface after the high temperature treatments.

Results and Discussion

Differential Scanning Calorimetry

Figures 1 and 2 show DSC curves of the two alloys, respectively, each a result of a heating and cooling cycle. The objective of these experiments was to establish the correlation of DSC measured alpha and beta transus temperatures and the literature values measured from static experiments. The 30°C/min programme gave clearer results, for the definition of α/β transformation peaks. The transformation temperatures as measured from these experiments are given in Table I. The measured beta transus is not higher than the literature values, indicating a negligible influence of the rapid heating rate. This is due to the very rapid kinetics of the α/β transformation. If the enthalpy values in the two alloys are approximately equal, the volume fraction of the α phase in the 21S alloy is estimated at 36% of that in the Ti-6Al-4V alloy by comparing the sizes of peaks. Therefore, if the β volume fraction in Ti-6Al-4V is 25%, the volume fraction of α in 21S will be 27%. This result confirms that there is still considerable amount of residual α phase in this "β alloy".

Table I α and β Transus Measured by DSC Compared with Literature Data (in Brackets)

Alloy	Heating rate (°C/min)	α transus (°C)	β transus (°C)
Ti-6Al-4V	30	813±26	1014±3 (1000±14 [2])
	10	788±11	1001
Grade 21S	30	599±6	800±4 (807±15 [10])
	10	591*	-**

*No error values as only one experiment was conducted;
**Cannot be accurately determined.

It is difficult to explain fully why the transformation peak does not show as clearly when the heating rate is reduced, especially considering that 10°C/min is still a relatively fast heating rate. It is reasonable however that the transition temperatures are lower for the slower heating rate. Also, during cooling, no obvious peak was recorded (dashed lines in Figures 1 and 2), showing a lack of distinct transformation.

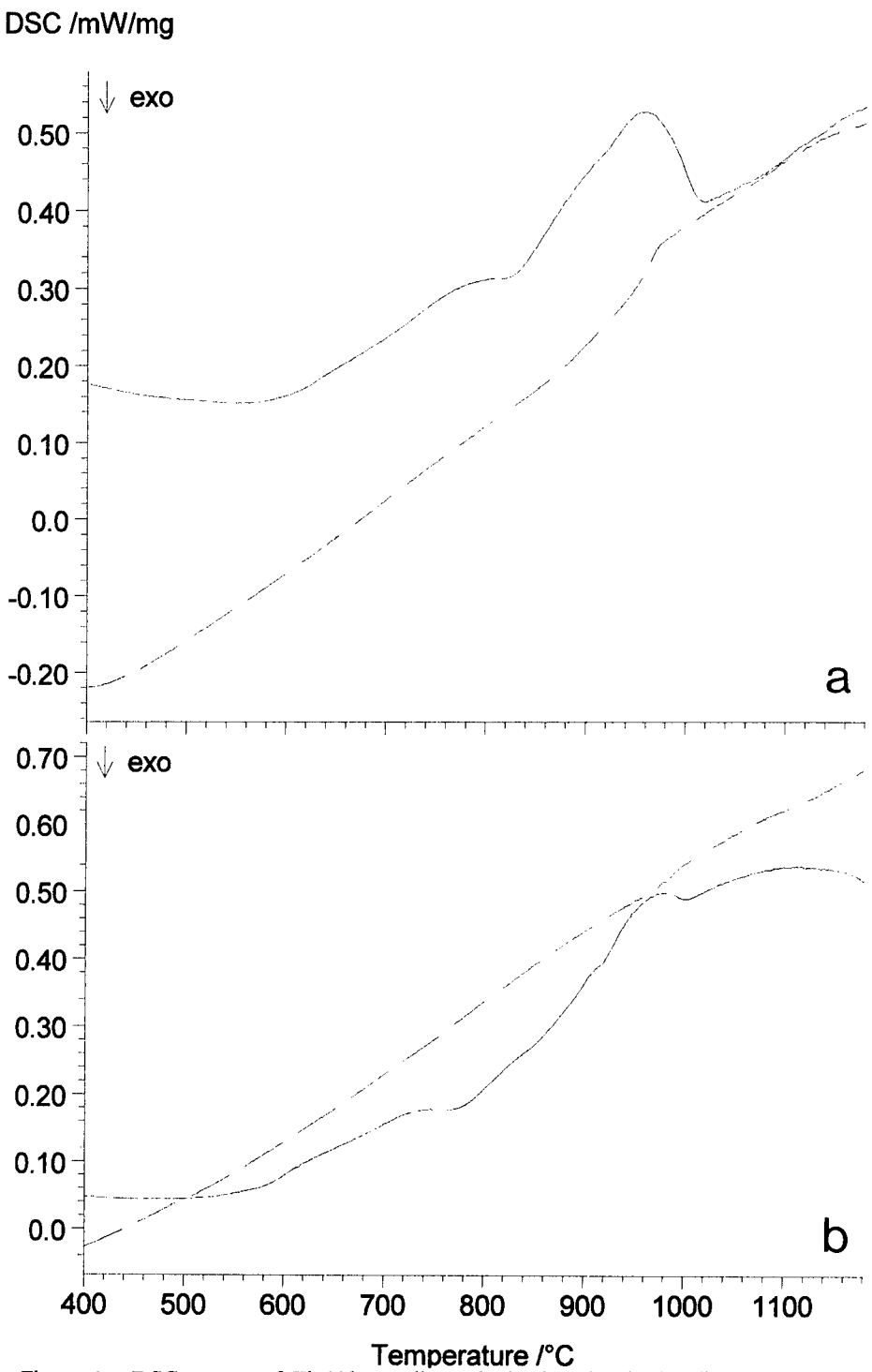


Figure 1: DSC curves of Ti-6Al-4V alloy, obtained at heating/cooling rate of (a) 30°C/min and (b) 10°C/min. The solid line is from heating and the dashed line cooling.

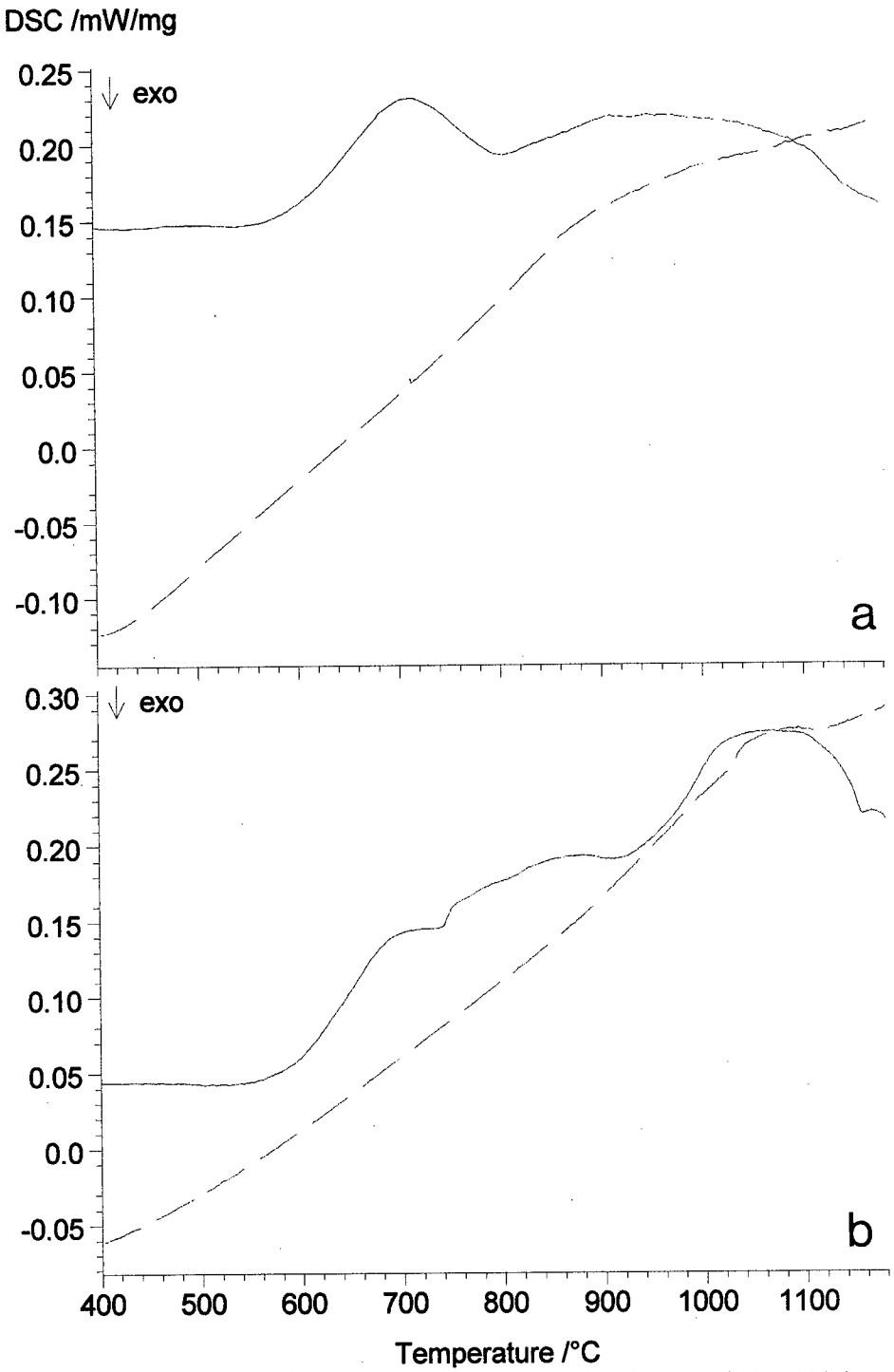


Figure 2: DSC curves of 21S alloy, obtained at heating/cooling rate of (a) 30°C/min and (b) 10°C/min. The solid line is from heating and the dashed line cooling.

Tensile Properties and Microscopy

Figure 3 shows examples of tensile curves of as-received and heat treated alloys. The strength and elongation parameters calculated from tensile tests are given in Table II, together with literature values [10] and descriptions of the shapes of stress-strain curves under different material and testing conditions. There is a reduction in strength and ductility after heat treatments on the as-received materials, which had experienced standard heat treatments for the respective grades (grades 5 and 21S) [10]. In particular, in the Ti-6Al-4V alloy, there is a complete loss of ductility after heat treatments, which can be explained with the coarse microstructures that result from the heat treatments (Figure 4).

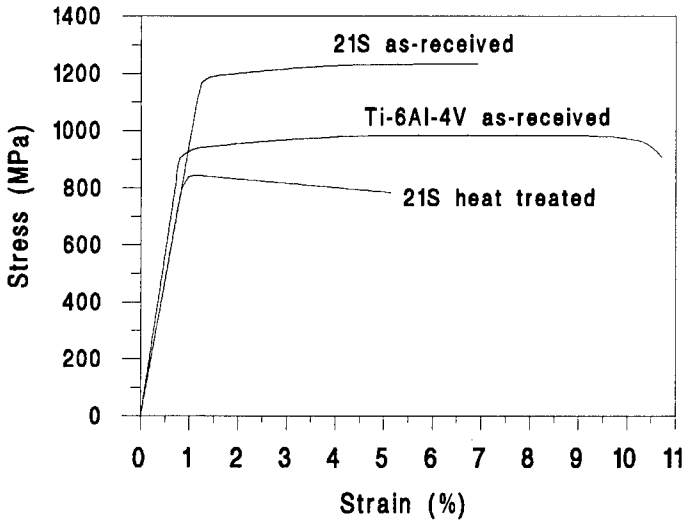


Figure 3: Stress-strain curves from tensile testing. The heat treatment for the 21S alloy was annealing at 770°C for 1.5 h, cooled to 600°C and annealed at this temperature for 2 h.

The strength at 200°C is reduced rather significantly in both alloys, compared with their room temperature strength. This needs to be taken into account when considering using titanium alloys for offshore riser pipes as such a moderate temperature can be encountered in such applications. Tensile test on a sample cut from curved (deformed) section of the sheet gave higher strength values, which can be explained by the work hardening effect.

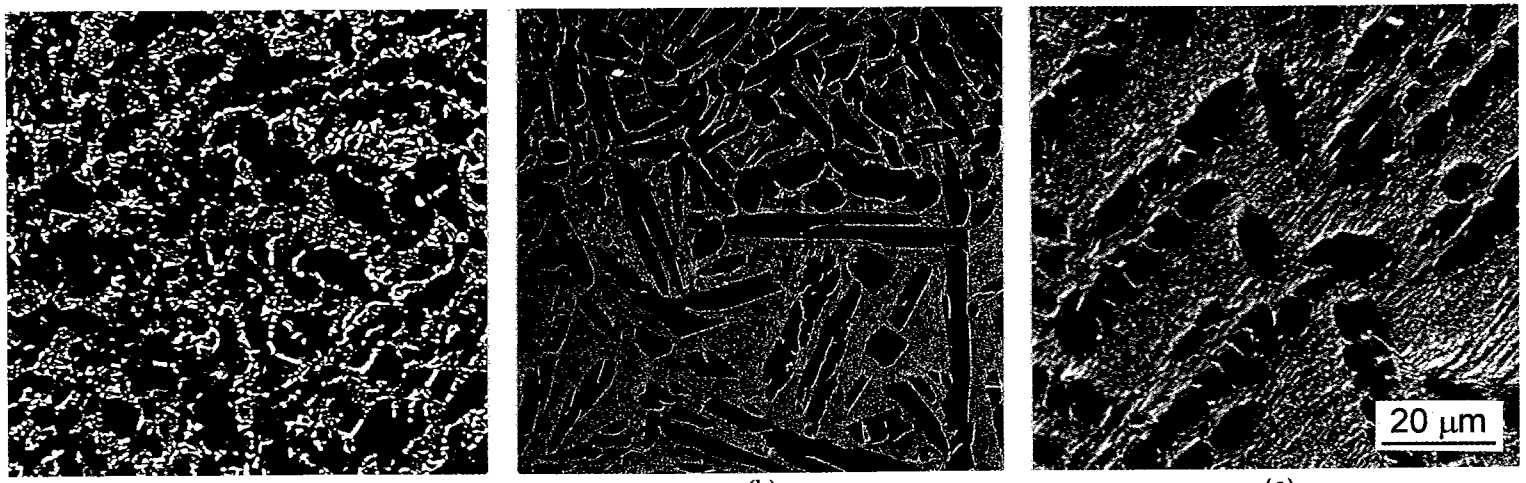
Figure 5 shows fractographs obtained using the scanning electron microscope, from samples tensile tested at room temperature. It can be seen that the modes of fraction are very different for the two alloys. The alpha/beta alloy exhibits a typical ductile fracture behaviour, with inclusions visible in most dimples. The beta alloy, on the other hand, gives a brittle fracture surface, although it does possess reasonable ductility/elongation during tensile tests. There is no necking stage in tensile testing of this alloy, which corresponds well with the brittle fracture.

Acknowledgements

The Ti-6Al-4V and 21S alloys were supplied by Mr. M.M. Donnelly, of Shell Research and Technology Centre, Amsterdam, and Mr. D.K. Peacock, of Timet UK, respectively. The authors thank Mr. F.S. Kelly for technical assistance.

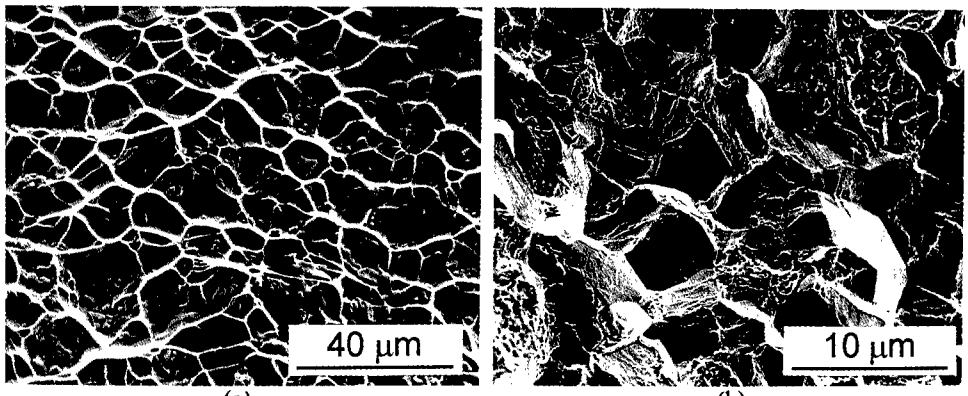
Table II Tensile Parameters Obtained from Tensile Tests under Different Sample Conditions (Literature Data [10] in Brackets for Comparison)

Alloy	Sample condition	YS (MPa)	UTS (MPa)	Elongation (%)	Stress-strain curve shape
Ti-6-4	As-received	940 (910)	989 (1000, 897 min.)	12.7 (10)	Shown in Fig.3
	Deformed as-received	1000	1040	16.3	Same as as-received
	1025°C/1.5h, air cool, 700°C/2h	732±27	732±27	2.21±0.03	Follow elastic part of as-received
	1025°C/1.5h, water quench, 650°C/2h	693±12	693±12	2.06±0.04	Follow elastic part of as-received
	As-received, tested at 200°C	688±39	775±8	9.0±0.1	Same as as-received
21S	As-received	1170 (965 min.)	1230 (1033 min.)	8.4 (6 min.)	Shown in Fig.3
	770°C/1.5h, 600°C/2h	863±26	863±26	6.2±0.9	Shown in Fig.3
	760°C/1.75h, air cool, 620°C/2h	1040±14	1070±14	6.5±0.8	Same as as-received
	As-received, tested at 200°C	900	1003±24	8.72±0.07	Same as as-received



(a) (b) (c)

Figure 4: Scanning electron micrographs of Ti-6Al-4V alloy. (a) As-received; (b) 1025°C/1.5h, air cool, 700°C/2h; (c) 1025°C/1.5h, water quench, 650°C/2h. The darkly imaged phase is alpha, while the brightly imaged is eutectoid α/β.



(a) (b)

Fig.5 SEM fractographs of (a) Ti-6Al-4V and (b) 21S alloys.

References

1. J.D. Destefani, "Introduction to Titanium and Titanium Alloys," Metals Handbook, 10th edn., vol. 2 (Materials Park, OH: American Society for Metals, 1990), 586-591.

2. S. Lampman, "Wrought Titanium and Titanium Alloys," Metals Handbook, 10th edn., vol. 2 (Materials Park, OH: American Society for Metals, 1990), 592-633.

3. Materials Science and Engineering A: Proceedings of the 2nd International Symposium on Metallurgy and Technology of Titanium Alloys, A213 (1996).

4. S. Ankem and J.A. Hall, ed., Proceedings of Harold Margolin Symposium on Microstructure/Property Relationships of Titanium Alloys (Warrendale, PA: Minerals, Metals and Materials Society, 1994).

5. C.E. Forney, "Titanium in Offshore Oil Production," Journal of Advanced Materials, 27 (1995), 3-9.

6. W. Sha, "γ' Precipitation in an Oxide Dispersion-Strengthened Ni-Base Superalloy," Rare Metals, 13 (1994), 188-192.

7. K. Murakami, K. Mino, H. Harada and H.K.D.H. Bhadeshia, "Nonuniform Recrystallization in a Mechanically Alloyed Nickel-Base Superalloy," Metallurgical Transactions A, 24A (1993), 1049-1055.

8. T.S. Chou and H.K.D.H. Bhadeshia, "Grain Control in Mechanically Alloyed Oxide Dispersion-Strengthened MA957 Steel," Materials Science and Technology, 9 (1993), 890-897.

9. F.S. Kelly and W. Sha, "Mechanical Properties of Fire-Resistant Steels for Construction," Proceedings of the 5th European Conference on Advanced Materials and Processes and Applications: Materials, Functionality and Design, vol. 1, ed. L.A.J.L. Sarton and H.B. Zeedijk (Zwijndrecht: Netherlands Society for Materials Science, 1997), 1/35-1/40.

10. Titanium and Its Alloys: Data Disc (: Titanium Information Group, 1995).

Morphological Evolution of Coherent Precipitates in Three Dimensions

Jong K. Lee
Department of Metallurgical and Materials Engineering
Michigan Technological University
Houghton, MI 49931, USA

Abstract

The shapes, sizes, and distribution of second-phase precipitates are the principal factors determining the mechanical, electrical, and magnetic properties of a wide variety of high technology alloys. In the initial processing, and also in high temperature applications, such as jet engine superalloys, the precipitate morphologies evolve in time and the properties change. An understanding of the elastic interactions between matrix and precipitates, among the precipitates, and between precipitates and dislocations is crucial for predicting and manipulating the properties of the alloys. Therefore, in need is a computational technique through which one can analyze the elastic state associated with arbitrarily-shaped precipitates whose elastic constants are different from those of the matrix phase. This work reviews a technique, termed the Discrete Atom Method (DAM), which is predicated upon the combination of statistical mechanics and linear elasticity. Employing a face centered cubic as a basis lattice, it is shown that in an anisotropic system with Zener's ratio, A = 2.33 (similar to that of a nickel-based superlloy), a soft precipitate shows a series of shape transitions from a radial to four-fold, then to two-fold symmetry. The four-fold shape is concave cuboidal, and is of transient nature, as it is later replaced with a convex plate. The hard particle, however, maintains a convex, cuboidal equilibrium shape. Under an applied tensile stress, a soft particle with a positive misfit strain tends to become a plate perpendicular to the applied stress axis, while a hard particle elongates along the stress direction. Also investigated are the morphology and structure of Guinier-Preston zones in a model system similar to Al-Cu. If the Cu-Al bond length is taken to be similar to that of Cu-Cu, the G. P. zones remain pure fcc Cu, whereas if this length is close to that of Al-Al, the zones form an ordered crystal with tetragonal symmetry, a structure reminiscent of the θ'' phase in this alloy system.

The Third Pacific Rim International Conference on
Advanced Materials and Processing (PRICM 3)
Edited by M.A. Imam, R. DeNale, S. Hanada,
Z. Zhong and D.N. Lee
The Minerals, Metals & Materials Society, 1998

Introduction

The microstructural development of elastically-stressed two-phase systems has been a subject of great interest, as it is closely tied to the alloy performance during application and is also fundamentally different from that of unstressed systems. For unstressed two-phase systems, the equilibrium shape of a precipitate is established solely by the interfacial free energy and its dependence on crystallographic orientation, and the solution is provided by the well-known Wulff construction. On the other hand, the equilibrium morphology of a misfitting coherent precipitate is dictated by both the interfacial free energy and the elastic strain energy. As a result, a computational technique is needed through which one can analyze the elastic state associated with *arbitrarily-shaped* precipitates whose elastic constants are *different* from those of the matrix phase.

Eshelby was the pioneer in the field of coherency strain who devised the seminal equivalency method and thus brought much understanding to the coherency strain problem; however, the method is limited to a single ellipsoidal precipitate [1-3]. Since his work, several techniques [4-10] have been developed. The works of the Khachaturyan school [4,5] are noteworthy in that their generalized stochastic field model can predict the features of microstructural evolution for various transformations. Voorhees and his coworkers [6] used a variational principle and the thermodynamics of stressed solids and showed that a particle with a dilatational misfit strain undergoes a series of shape bifurcations from a radial to a four-fold, and then to a two-fold symmetric morphology. The major limitation of these and other models, however, is that the system should be *elastically homogeneous*, i.e., the elastic constants of particles must be equal to those of the matrix phase. To deal with a general *inhomogeneous case*, Moschovidis and Mura [7] considered the elastic strain field essentially in a Taylor expansion and were able to approximate the elastic interaction between two ellipsoidal particles. In a similar approach, Satoh and Johnson [8] calculated the elastic strain energies of several non-ellipsoidal precipitates. Since higher order terms are inherently neglected, this series expansion method and others fail to describe the accurate picture of coherency strain.

The Discrete Atom method (DAM) was recently developed to examine a general coherency strain problem [11-17]. Based on both classical statistical mechanics and linear elasticity, the DAM has not only eliminated shape restrictions and allowed interactions among many precipitates, but has facilitated computation of much relevant details of the evolution process. In this work, some of the DAM findings in three dimensions are reviewed.

Discrete Atom Method

According to classical statistical mechanics, the configurational free energy is given by $A_q = -k_B T \ln Z_q$, where k_B is Boltzmann's constant and T is the absolute temperature. Z_q is the configurational partition function, and is equal to:

$$Z_q = \int exp(-\Phi/k_B T) d\vec{q} \qquad (1)$$

where $\vec{q}$ indicates atomic coordinates. In the DAM, the Hamiltonian, Φ, is given by:

$$\Phi = \frac{1}{4}\sum_{i=1}^{N}\sum_{j=1}^{m} k_{ij}(r_{ij} - a_{ij})^2 + \sum_{l} E_l^S \qquad (2)$$

where N is the total number of atoms, m is the number of interacting atoms with the i-th atom, k_{ij}

is the spring constant between i-th and j-th atom, r_{ij} is the distance, a_{ij} is r_{ij} at stress-free state, and E_l^S is the interfacial energy of l-th interface atom. A face centered cubic (fcc) lattice is taken as a basis lattice for three-dimensional studies. Due to its high symmetry, fcc renders a simple relationship for the elastic constants [15]:

$$C_{11} = \sqrt{2}(1+2f)k \tag{3}$$

$$C_{12} = C_{44} = k/\sqrt{2} \tag{4}$$

where f is a bond parameter for the second neighbors. Thus, if only twelve nearest neighbor interactions are considered ($f = 0$, $m = 12$), the elastic anisotropy, A, is equal to 2. However, if the interaction with the six atoms in the second neighbor shell are also allowed with $f = 0.25$ and $m = 18$, the structure becomes elastically isotropic. A specific interfacial energy is assigned to each of the interface atoms. The specific interfacial energies, E_l^S, are based on the effective area of an interface atom. For example, an atom on an fcc (100) plane has 4 unlike bonds and an interface area of 0.5 a^2, where a is the fcc lattice parameter. Similarly, the effective areas for other kinds of interface atoms are prorated on the base of the (110) and (111) plane geometry and the interface structures of large fcc spherical precipitates.

In Fig. 1, an early stage of shape change for a hard and a soft particle are displayed for an anisotropic system with A = 2.33 and ε = 0.05. The upper row displays three-dimensional perspective

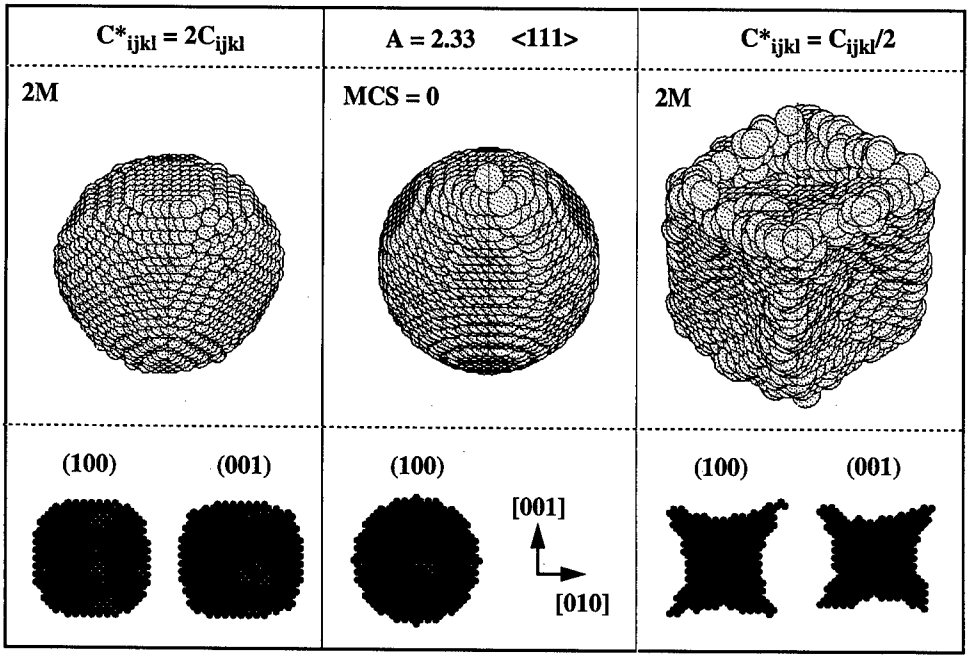


Fig. 1: Early stage of the morphological evolution of a hard and a soft precipitate in an anisotropic system with A = 2.33. The upper row displays perspective pictures viewed along the [111] at the times of MCS = 0 and 2M. The lower row shows the (100) and (001) cross-sections passing through the precipitate center. The left column is for a hard particle and the right column is for a soft particle.

views along the [111] direction at the times of MCS = 0 and 2M, whereas the lower row shows the (100) and (001) cross-sections passing through the precipitate center. MCS indicates a pseudo-time in units of a million Monte Carlo diffusion attempts. Initial particle shapes are spherical as shown in the middle column. The hard particle with $C^*_{ijkl} = 2C_{ijkl}$, shown in the left column, becomes a *convex cuboid* with a four-fold symmetry. The four-fold, convex cuboid is an equilibrium morphology for the hard particle, as it is supported independently by the evolution process of an initially non-spherical particle. The soft particle with $C^*_{ijkl} = C_{ijkl}/2$, shown in the right column, reveals interesting shape evolution. In this early stage, it tries to maintain a four-fold symmetry in accordance with the cubic symmetry and results in a *concave cuboid.* Further evolution, however, shows that the concave cuboidal shape yields to a two-fold plate shape with its habit plane parallel to an elastically soft (010) plane as displayed in Fig. 2 — all consistent with the evolution process of gamma prime particles observed in nickel-based superalloys [18,19]. Note ledges and terraces on the plate in Fig. 2. For the simulations, a typical precipitate size is R = 8 a in a system of total 200,000 atoms, $k = 1.38 \times 10^{-17}$ J/a^2, and isotropic interfacial energy, $\gamma_0 = 1.75 \times 10^{-20}$ J/a^2. With these input parameters, precipitate-matrix interfacial energy contributes about 3 ~ 12% to the total energy of the system. A typical temperature of 1000 K is employed for diffusion, and quenching to 100 K is often performed to reduce thermal roughening at the end of aging.

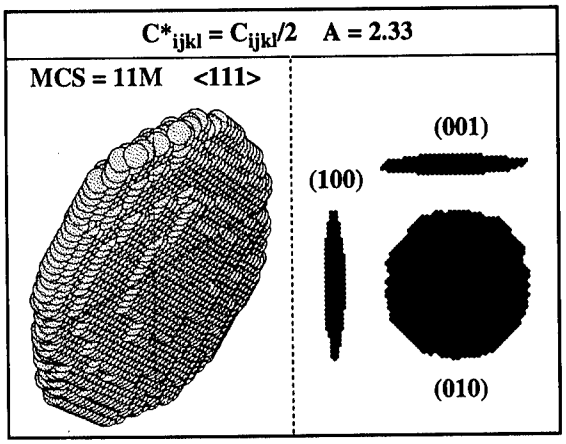


Fig. 2: Equilibrium morphology of a soft particle in an anisotropic system with $C^*_{ijkl} = C_{ijkl}/2$, A = 2.33, and ε = 0.05. The plate-like precipitate has a habit plane parallel to an elastically soft (010) plane.

In Fig. 3, a hard, cuboidal particle with $C^*_{ijkl} = 2C_{ijkl}$ and $\varepsilon = 0.05$ is placed under a tensile stress (T.S.) with a magnitude equal to 4% strain along the [001]. The elastic interaction between the coherency strain and the applied stress causes the particle to stretch along the stress axis, producing a rod-like shape with a square cross-section. Being elastically hard, the particle maintains its convexity during the elongation, as demonstrated by the cross-sectional views at MCS = 2M in the lower row. If a compressive stress (C.S.) is applied to the system, however, the hard particle is stretched along the direction perpendicular to the stress axis. Consequently, the particle becomes a plate, as displayed in Fig. 4. For a soft particle, applied stress effects are more drastic [13,15]. Under a tensile stress with a magnitude equal to *only 0.5% strain* along the [001], a soft particle with $C^*_{ijkl} = C_{ijkl}/2$ and $\varepsilon = 0.05$ extends along the direction perpendicular to the tensile axis. As stretching occurs at its two ends, the particle splits into two plates, and then coarsening follows to produce one large plate lying perpendicular to the stress axis: the system demonstrates that an applied stress can induce inverse coarsening [20]. If the applied stress sign is reversed into a compressive mode, the soft particle is found to stretch along the stress axis of [001].

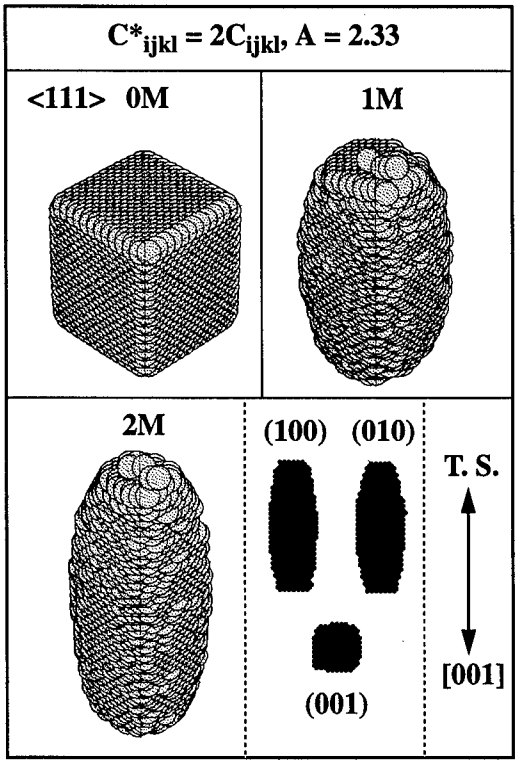


Fig. 3: Morphological evolution of a hard, cuboidal particle with $C^*_{ijkl} = 2 C_{ijkl}$, A = 2.33, and $\varepsilon = 0.05$ under a tensile stress in the amount of 4% strain along the [001] direction. T. S. indicates a tensile applied stress.

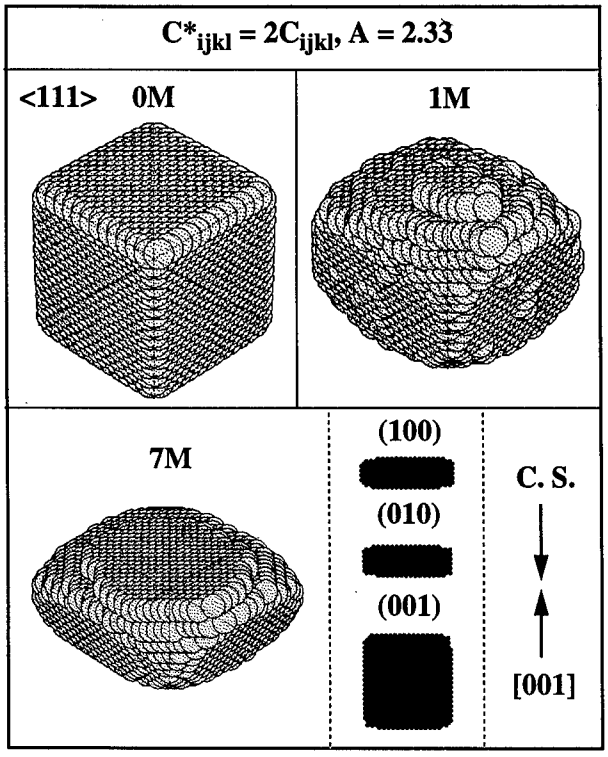


Fig. 4: Morphological evolution of a hard, cuboidal particle with $C^*_{ijkl} = 2C_{ijkl}$, A = 2.33, and $\varepsilon = 0.05$ under a compressive stress in the amount of 4% along the [001] direction. C. S. indicates a compressive applied stress.

In certain binary alloy systems such as Al-Cu, there arise a series of transient phases before an equilibrium phase emerges. Most of these transient phases are either coherent or semi-coherent, and much has been addressed about their stability by investigators in the theory of alloy phases [21]. As solute atoms such as Cu diffuse out of the matrix phase and cluster together or nucleate a new phase, continuous charge redistributions occur, which in turn affect both interatomic bond length and bond strength as the free energy of the system decreases. It has been long speculated that a coherency strain plays a significant role in the stability of such transient phases, but no stress model was available heretofore. Some interesting results are found in a preliminary DAM work on *a model Al-Cu system.*

In Fig. 5, 1099 Cu atoms are randomly distributed in a spherical Al fcc with 20,000 atomic sites (about 5.5 at%) at MCS = 0, and then allowed to cluster at a low temperature. The small dots in the MCS = 0 configuration indicate Cu atoms as viewed along the fcc <111> direction. From real Al and Cu lattice parameters at room temperature, the misfit strain, ε, is taken to be -0.1074 for a Cu phase embedded in an Al matrix. Without prior knowledge, the k_{ij} values for the Al-Cu interaction are taken to be the average values of those Al-Al and Cu-Cu. The bond length between Al and Cu, $a_{Al\text{-}Cu}$, is set equal to $(1 + \beta\varepsilon)a_{Al\text{-}Al}$. When $\beta = 0.7$, i.e., the Al-Cu bond length is taken to be closer to that of Cu-Cu, pure fcc Cu clusters are formed and coarsen to become a 5-layer plate at MCS = 3M. <111> three-dimensional perspectives are given at the times of MCS = 0.5, 1, 2, and 3M. Three {100} cross sections at MCS = 3M are also shown on the right bottom corner. The solid circles in the cross-section views represent Cu atoms. The final cluster is a Cu fcc plate with its (010) habit plane, closely resembling G.P. zones in a real Al-Cu system. Each of the five (020) atomic layers have about 220 Cu atoms.

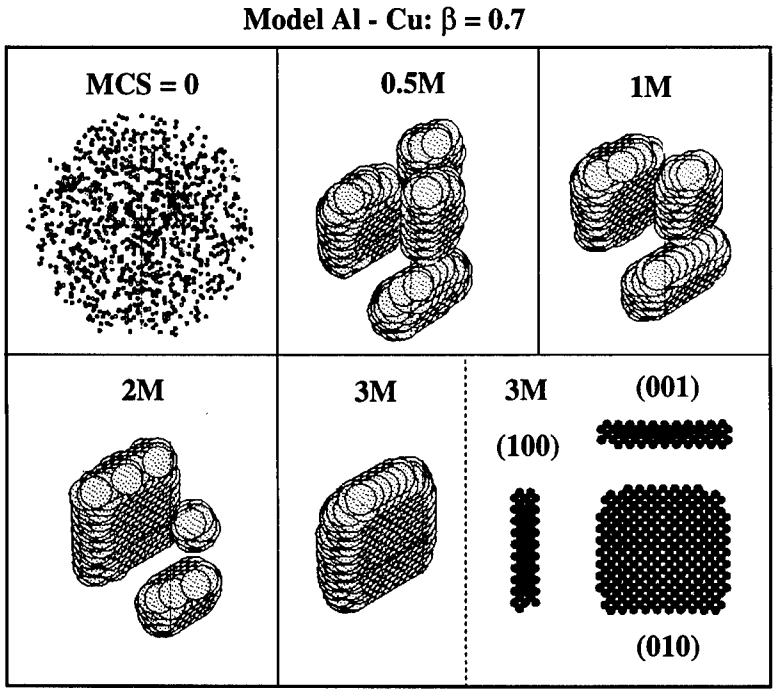


Fig. 5: Clustering of Cu atoms in a model Al - Cu system. With a bond length parameter, $\beta = 0.7$ for the Al - Cu atomic interaction, Cu atoms form a 5- layer plate, made of pure Cu atoms.

As β decreases, Cu atoms tend to be surrounded by Al atoms. Therefore, a smaller β promotes an ordering tendency in the Al-Cu system, as demonstrated in the bottom row of Fig. 6, where β is equal to 0.5. Shown on the top row are <111> perspective views of the initial (MCS = 0) and final configuration (MCS = 10M). The final product is now an Al-Cu ordered structure. It is made of three (020) atomic planes, as indicated by the three consecutive cross-sections views of L, M, and R on the bottom row: L indicates the left atomic layer, M for the middle layer, and R for the right layer. The open circles indicate Al atoms while the solid circles are Cu atoms. Its unit cell is tetragonal and belongs to a CuAu-II type with superperiod M = 1, which is sketched on the right top corner. This strain-induced ordering behavior probably represents the first simulation result of its kind. The ordered structure is different from the reported θ" phase [22], though there are some similarities. If $0.7 < \beta < 0.5$, the model system develops a mixture of both pure Cu plates and ordered Al-Cu plates. A better understanding of transient phase stability certainly requires further work involving a variation in k_{ij} for the Al-Cu interaction and volume-dependent energy terms such that exact elastic constants are reproduced in the model system. The model system shown above, though incomplete, casts an interesting light on coherency effects. In a fcc, local atomic displacements depend on the two shear modes: the shear mode associated with C_{44} involves atomic movement toward the [001] direction, while the other associated with C_{11}-C_{12} involves displacement along the [110] direction [23]. Depending on the β value, the relative strength of the two shear modes is different and thus different structures should be expected during clustering. Critical tests are necessary for understanding which mode of shearing determines which phase and how. One interesting test would be to impose an applied shear strain to the system during clustering.

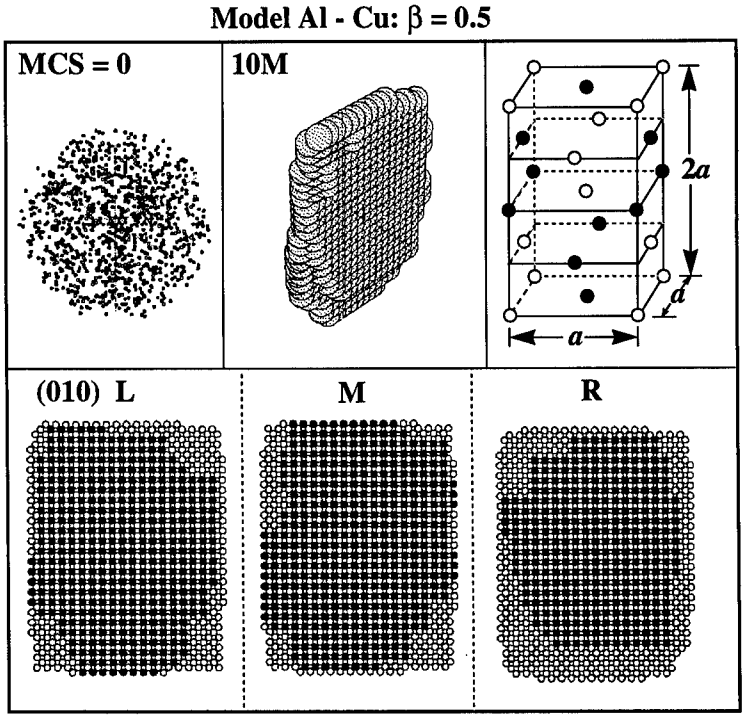


Fig. 6: Ordered-clustering of Cu atoms in a model Al - Cu system. With a bond length parameter, β = 0.5 for the Al - Cu atomic interaction, Cu atoms form a 3- layer structure ordered with the host Al atoms.

Discussion

The DAM is still in its embryonic stage and much work is needed for further development. For example, directional bonding often involves a tetragonal misfit strain such as a Bain distortion. An exploratory DAM work of a tetragonal misfit strain case [12] was performed and demonstrated the robustness of the methodology. Also, of interest is the dynamic interaction of coherent precipitates with dislocations. Within the frame of a plane strain condition, a DAM study [17] displayed that an edge dislocation splits into two partial dislocations. Both tetragonal misfit strain and precipitate-dislocation interaction problems are subjects of future investigation.The DAM can be viewed as a discrete analogue of continuum linear elasticity at the atomic level, but unlike the usual finite element method it does not require use of constitutive relationships. The method lacks in fundamental atomic physics as the elastic constants are fitted to the spring constants. It is, in a sense, similar to Ising model, which is short in fundamental physics and yet has brought many scientific insights to the theory of lattice. Nevertheless, it appears that some of the stress-driven symmetry breaking problems can now be answered through the Discrete Atom Method: heretofore, a variety of elasticity problems associated with inhomogeneous alloy and ceramic systems have remained unanswered due to inherent mathematical difficulties.

References

1. J. D. Eshelby: *Prog. Solid Mech.*, 1961, vol. 2, p. 89.
2. A. G. Khachaturyan: *Theory of Structural Transformations in Solids*, Wiley & Sons, New York, 1983, p. 213.
3. T. Mura: *Micromechanics of Defects in Solids*, 2nd ed., Martinus Nijhoff, Dordrecht, 1987, p. 177.
4. Y. Wang, L. Q. Chen and A. G. Khachaturyan: in *Solid → Solid Phase Transformations*, eds. W. C. Johnson et al., TMS, Warrendale, 1994, p. 245.
5. D. Y. Li and L. Q. Chen: *Acta Metall.*, 1997, vol. 45, p. 2435.
6. M. E. Thompson, C. S. Su and P. W. Voorhees: *Acta Metall.*, 1994, vol. 42, p. 2107.
7. Z. A. Moschovidis and T. Mura: *J. Appl. Mech.*, 1975, vol. 42, p. 847.
8. S. Satoh and W. C. Johnson: *Metall. Trans. A*, 1992, vol. 23A, p. 2761.
9. P. H. Leo and R. F. Sekerka: *Acta Metall.*, 1989, vol. 37, p. 3119.
10. P. Fratzl and O. Penrose: *Acta Metall.*, 1995, vol. 43, p. 2921.
11. J. K. Lee: *Metall. Trans. A*, 1996, vol. 27A, p. 1449.
12. J. H. Choy, S. A. Hackney and J. K. Lee: in *Mathematics of Microstructure Evolution*, eds. L. Q. Chen et al., TMS, Warrendale, PA, 1996, p. 101.
13. J. K. Lee: *Metals and Materials*, 1996, vol. 2, p. 183.
14. J. K. Lee: in *Dynamics of Crystal Surfaces and Interfaces*, eds. P. M. Duxbury and T. Pence, Plenum Press, New York, NY, 1997, p. 125.
15. J. K. Lee: *Mat. Sci. Eng.*, 1997, vol. A238, p. 1.
16. J. K. Lee: *Mat. Trans., JIM*, 1998, vol. 39, p. 114.
17. J. K. Lee: *Metall. Trans. A*, in press.
18. M. Meshkinpour and A. J. Ardell: *Mater. Sci. Eng.*, 1994, vol. A185, p. 153.
19. S. J. Yeom, D. Y. Yoon, and M. F. Henry: *Metall. Trans. A*, 1993, vol. 24A, p. 1975.
20. W. C. Johnson and P. W. Voorhees: *Bull. Alloy Phase Diagr.*, 1988, vol. 9, p. 208.
21. L. H. Bennet (ed.): *Theory of Alloy Phase Formation*, TMS, Warrendale, PA., 1980.
22. D. A. Porter and K. E. Easterling: *Phase Transformations in Metals and Alloys*, Van Nostrand, New York, 1981, p. 297.
23. J. C. Phillips: in *Theory of Alloy Phase Formation*, ed., L. H. Bennet., TMS, Warrendale, PA, 1980, p. 330.

Motion of phase boundaries by surface diffusion

Yoshikazu Giga and Kazuo Ito
Department of Mathematics
Faculty of Science
Hokkaido University
Sapporo 060, Japan

The Third Pacific Rim International Conference on
Advanced Materials and Processing (PRICM 3)
Edited by M.A. Imam, R. DeNale, S. Hanada,
Z. Zhong and D.N. Lee
The Minerals, Metals & Materials Society, 1998

1 Introduction

There are several models to describe motion of interphase boundaries in coarsening processes. The Cahn-Hilliard equation is one of typical models describing such evolutions from macroscopic point of view. It is known that as a singular limit of the Cahn-Hilliard equation there are several evolution equations for phase boundaries. These interface models are geometric in the sense that evolution law is completely determined by geometry of phase boundaries. If the surface diffusion is dominated, the interface model comes to be a quasilinear diffusion equation for position of phase boundaries. However, this equation is not second order but fourth order so there are several phenomena which are different from those of second order model like the mean curvature flow equation which is a model describing motion of antiphase boundaries. The authors analyse such fourth order models from rigorous mathematical point of view. The authors for example proved: (i) a curve that moves by surface diffusion may pinch in a finite time, (ii) a curve that moves by surface diffusion may not preserve its convexity in a finite time. These phenomena do not happen for the curve shortening equation. Several other behaviours of solutions will be presented in the lecture.

We study motion by surface diffusion which was first derived by Mullins [7].

Let $\Gamma_t \subset \mathbf{R}^2$ be a closed evolving curve depending on time t with initial data $\Gamma_t|_{t=0} = \Gamma_0$. The governing equation for evolving curves by surface diffusion is of the form

$$V = -\kappa_{ss}. \tag{1}$$

Here V denotes the outward normal velocity and κ denotes the outward curvature; s denotes the arclength parameter of Γ_t. There are several derivations of this equation other than Mullins [7]. See for example Cahn and Taylor [1] and Cahn, Elliott and Novick-Cohen [2]. In the latter paper, (1) is obtained as some formal limit of Cahn-Hilliard equations. A typical feature of Γ_t moved by (1) is that the area enclosed by Γ_t is preserved. Related equations to (1) are well explained in Elliott and Garcke [3] and Cahn and Taylor [1]. For physical background of these equations, see [1, 3] and references cited there.

In [3] local existence of solution for (1) was proved without uniqueness as well as for other equations. They proved that if initial data is close to a circle, then Γ_t exists globally in time and it converges to a circle with the same area enclosed by Γ_0 as t tends to infinity. They also conjectured that Γ_t moved by (1) may pinch for some simple smooth initial data. After this work was completed, we were informed of a recent work of Escher, Mayer and Simonett [4] on unique local existence of solutions of (1). They proved the unique existence of local-in-time solutions even for higher dimensional version of (1) in small Hölder spaces by appealing abstract semigroup theory. They also studied the large time behavior of solutions of the higher dimensional version of (1) if initial data are close to a sphere. These results are regarded as a natural extension of the results of [3] to higher dimensional setting. Moreover, they showed numerical evidence of existence of pinchings for various closed curves.

In this paper we present a rigorous mathematical result proving Elliott and Garcke's conjecture without detailed proof. The detailed proof is given in our paper [6]. Let us explain our idea. We consider a smooth closed simple curve Γ_0 which is symmetric with respect to x-axis and y-axis. We assume that Γ_0 is of the form

$$\Gamma_0 = \{(x, y); y = \pm u_0(x)\},$$

where $u_0(x)$ is even and $u_0(x)$ takes the only local minimum at $x = 0$. If Γ_t is represented by $y = u(t, x)$, then (1) becomes a fourth order equation of $u(t, x)$. If we linearize (1) around $u = 0$, we obtain

$$u_t = -u_{xxxx}.$$

If we consider the Cauchy problem for this equation with $u_0(x) \geq 0$ and $u_0(x) = x^4 + \delta$ for small $\delta > 0$ near $x = 0$, then $u(t,0)$ would be negative in a short time. In other words, the comparison principle does not hold. It is easy to guess this phenomenon since $u(t,x) = x^4 - 4!t + \delta$ solves $u_t = -u_{xxxx}$. For a good choice of $u_0(x)$, $u(t,0)$ becomes negative in short time during the period that solution Γ_t: $y = u(t,x)$ of (1) exists as smooth curves. Since Γ_t is represented by $y = u(t,x)$, and symmetric with respect to $y = 0$, this means that Γ_t pinches in short time even if Γ_0 is simple. This is a rough idea of our proof.

2 Pinching of evolving closed curves

We summarize here a parametrization of (1) by following Elliott and Garcke [4].

Let M^0 be a fixed reference C^∞ (or at least C^5) closed curve with arclength $2L$. For $\mathbf{T} = \mathbf{R}/(2L\mathbf{Z})$, let

$$\begin{aligned} X^0 : \quad & \mathbf{T} \to M^0, \\ & \eta \mapsto X^0(\eta) \end{aligned}$$

be an arclength parametrization of M^0. By definition, X^0 is a function on $\mathbf{T}$ or equivalently $2L$-periodic function. Then, $\tau^0(\eta) = X^0_\eta(\eta)$ is the unit tangent vector of M^0 and the Frenet formula gives

$$\begin{aligned} \tau^0_\eta(\eta) &= \kappa^0(\eta) n^0(\eta), \\ n^0_\eta(\eta) &= -\kappa^0(\eta) \tau^0(\eta), \end{aligned}$$

where $n^0(\eta)$ is the unit normal vector and $\kappa^0(\eta)$ is the curvature of M^0 with the sign convention that the curvature of a circle is negative.

Let $\Gamma_t \subset \mathbf{R}^2$ be a closed curve moved by surface diffusion law with respect to time $t \geq 0$ starting from initial closed curve Γ_0. For small $T > 0$ we expect that Γ_t is parametrized by

$$\begin{aligned} X : \ [0,T) \times \mathbf{T} &\to \Gamma_t, \\ (t,\eta) &\mapsto X(t,\eta), \end{aligned}$$

$$X(t,\eta) = X^0(\eta) + d(t,\eta) n^0(\eta)$$

with some $d(t,\eta)$ defined on $[0,T) \times \mathbf{T}$. If Γ_0 is embedded and Γ_t is close to Γ_0, then $d(t,\eta)$ is the distance function from M^0. By this parametrization, (1) is equivalent to

$$\frac{1 - d\kappa^0}{J} d_t = -\frac{1}{J} \partial_\eta \left(\frac{1}{J} \partial_\eta \kappa \right),$$

where $J = |X_\eta| = \partial s / \partial \eta$ is the Jacobian and $\kappa(t,\eta)$ is the curvature of Γ_t in the direction of n^0. Their explicit forms are

$$J = J(\eta, \alpha_0, \alpha_1)|_{(\alpha_0,\alpha_1)=(d,d_\eta)} = (d_\eta^2 + (1 - d\kappa^0)^2)^{1/2},$$

$$\kappa = \frac{1}{J^3} \{ (1 - d\kappa^0) d_{\eta\eta} + 2\kappa^0 d_\eta^2 + \kappa^0_\eta d d_\eta + \kappa^0 (1 - d\kappa^0)^2 \}.$$

Thus, the equation (1) for $d(t,\eta)$ with initial data $\Gamma_t|_{t=0} = \Gamma_0$ is of the form:

$$\begin{cases} d_t + J^{-4} d_{\eta\eta\eta\eta} + P d_{\eta\eta\eta} + Q = 0, \ 0 < t < T, \ \eta \in \mathbf{T}, \\ d(0,\eta) = d_0(\eta), \ \eta \in \mathbf{T}, \end{cases} \tag{2}$$

where P and Q are polynomials with arguments $(1-\kappa^0 d)^{-1}$, J^{-1}, κ^0, κ^0_η, $\kappa^0_{\eta\eta}$, $\kappa^0_{\eta\eta\eta}$, d, d_η and $d_{\eta\eta}$. We note that κ^0 toghther with its derivatives κ^0_η, $\kappa^0_{\eta\eta}$, $\kappa^0_{\eta\eta\eta}$ is continuous and bounded on $\mathbf{T}$ since M^0 is at least C^5. We show that there is an evolving closed curve which pinches in finite time, even if initial curve is simple.

Let us explain our idea of the proof. Let $M^0 = \{X^0(\eta); \eta \in \mathbf{T} = \mathbf{R}/(2L\mathbf{Z})\}$ be a dumbbell like curve symmetric with respect to both x-axis and y-axis and its neck is so thin so that it is just a segment on the x-axis. It is normalized by setting $X^0(0) = X^0(L) =$ the origin $(0,0)$. Let $\Gamma_0 = \{X^0(\eta) + d_0(\eta)n^0(\eta); \eta \in \mathbf{T}\}$ with $d_0(\eta) > 0$ be symmetric with respect to both x-axis and y-axis and assume that $d_0(\eta)$ takes its global isolated minimum at $\eta = 0$ and L. Then, by symmetry of the equation (2), the solution $\Gamma_t = \{X^0(\eta) + d(t,\eta)n^0(\eta); \eta \in \mathbf{T}\}$ stays symmetric with respect to both x-axis and y-axis. In particular, $d_\eta(t,0) = 0$ and $d_{\eta\eta\eta}(t,0) = 0$. Thus if $d(t,\eta)$ solves (2), then

$$d_t(0,0) = -\partial_\eta^4 d(0,0) + 3(\partial_\eta^2 d(0,0))^3.$$

Thus, by the fundamental theorem of calculus,

$$\begin{aligned} d(t,0) &= d(0,0) + d_t(0,0)t + \int_0^t \int_0^\tau d_{ss}(s,0)ds d\tau \\ &\le d(0,0) + (-\partial_\eta^4 d(0,0) + 3(\partial_\eta^2 d(0,0))^3)t + t^2 \cdot \sup_{t\in[0,\bar{t}],\eta\in\mathbf{T}} |d_{tt}(t,\eta)|, \end{aligned} \tag{3}$$

where $\bar{t}$ is taken so that $d(t,\eta)$ exists for $[0,\bar{t}]$. Roughly speaking, if $d(0,0)$ is sufficiently small and $-\partial_\eta^4 d(0,0) + 3(\partial_\eta^2 d(0,0))^3 < 0$, then $d(t,0)$ may be nagative for t between two roots of the quadratic equation of t: the R.H.S. of (3)$= 0$, which will imply a pinching of Γ_t.

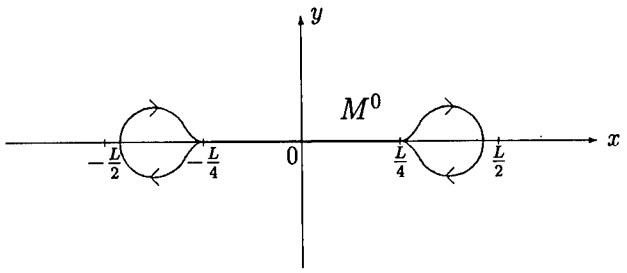
We shall state our result rigorously in the following. To do this, we define a special (C^∞) reference curve M^0. This is parametrized by

$$X^0(\eta) = (X_1^0(\eta), X_2^0(\eta)) \quad \text{for } \eta \in \mathbf{T} = \mathbf{R}/(2L\mathbf{Z})$$

satisfying

$$\begin{cases} X_1^0(\eta) = -X_1^0(-\eta), & 0 \le \eta \le L, \\ X_2^0(\eta) = X_2^0(-\eta), & 0 \le \eta \le L, \\ X^0(\eta) = (\eta, 0), & 0 \le \eta \le L/4, \\ (X_1^0)_\eta(\eta) > 0, & 0 \le \eta \le L/2, \\ X_1^0(L/2+\eta) = X_1^0(L/2-\eta), & 0 \le \eta \le L/2, \\ X_2^0(\eta) > 0, & L/4 < \eta < L/2, \\ X_2^0(L/2+\eta) = -X_2^0(L/2-\eta), & 0 \le \eta \le L/2, \end{cases}$$

where η is an arclength parameter.



We define a set of functions in $\mathbf{T}$ depending on positive parameters N and ε:

$$\begin{aligned} D_0(N,\varepsilon) \;=\; & \{d_0 : \text{smooth}; d_0(-\eta) = d_0(\eta) = d_0(L-\eta), \quad d_0(\eta) > 0 \quad (\forall \eta \in \mathbf{T}), \\ & \|d_0\|_{H^9(\mathbf{T})} \le N, \quad d_0(0) \le \varepsilon, \quad d_0^{(4)}(0) - 3d_0''(0)^3 > 0, \\ & d_0(\eta) \text{ attains its global minimum at } \eta = 0\}. \end{aligned}$$

Here $\|d_0\|_{H^9(\mathbf{T})}$ denotes the sum of L^2-norms of derivatives of d_0 up to order 9. Note that closed curves Γ_0 parametrized by $X(0,\eta) = X^0(\eta) + d_0(\eta)n^0(\eta)$ with $d_0 \in D_0(N,\varepsilon)$ are simple in $\mathbf{R}^2$. A typical result is:

Theorem 1 *(Pinching of evolving closed curves). For any $N > 0$ depending on M^0, there is an $\varepsilon_0 > 0$; for any $\varepsilon \in (0,\varepsilon_0)$ and any $d_0 \in D_0(N,\varepsilon)$, there are $t_0 \in (0, T_1(N))$ (where $T_1(N)$ is an existing time of the solution of (2)) and $t_1 (> t_0)$ such that for initial simple closed curve Γ_0 with parametrization*

$$\Gamma_0 = \{X(0,\eta) = X^0(\eta) + d_0(\eta)n^0(\eta); \eta \in \mathbf{T}\},$$

the solution curve Γ_t with parametrization

$$\Gamma_t = \{X(t,\eta) = X^0(\eta) + d(t,\eta)n^0(\eta); \eta \in \mathbf{T}\}, \quad t \in [0, T_1(N)],$$

where $d \in D_{T_1(N)}(N)$ is the unique solution of (2), ceases to be simple for at least $t_0 < t < \min(t_1, T_1(N))$.

This result looks stronger than the one presented in [6] in the sense that d_0 is taken arbitrary but clearly the proof in [6] yields this result.

3 Nonpreserving of convexity of closed curves

We conclude this paper by stating our recent study for nonpreserving of convexity of evolving closed curves driven by surface diffusion. This phenomenon is markedly different from that of second order model like the mean curvature flow equation. In fact, the mean curvature flow equation preserves convexity of evolving closed curves as long as they exist (see Gage and Hamilton [5]).

Our idea of the proof of this phenomenon is roughly stated as follows. Let Σ be the set of all simple convex closed curves which are symmetric with respect to the y-axis. We can construct a family of mappings $\{S^{\varepsilon,\delta}\}_{0<\varepsilon,\delta\ll 1}$ such that each $S^{\varepsilon,\delta}$ maps from Σ to a set of closed curves which are also symmetric with respect to the y-axis. Then, for any $\Gamma_0 \in \Sigma$, we can choose a suitable ε, δ such that $S^{\varepsilon,\delta}$ maps Γ_0 to another simple convex closed curve $\Gamma_0^{\varepsilon,\delta}$ and weakens the convexity of Γ_0 locally. It can be also shown that the solution curve $\Gamma_t^{\varepsilon,\delta}$ of (1) starting from $\Gamma_0^{\varepsilon,\delta} = S^{\varepsilon,\delta}(\Gamma_0)$ exists in a time interval uniformly in $0 < \varepsilon \ll 1$ and it is simple and closed. After similar computations as in (3), we can show that this $\Gamma_t^{\varepsilon,\delta}$ loses its convexity in the above time interval.

We summarize our result in the following.

Theorem 2 *(Nonpreserving of convexity). Let $\Gamma_0 \in \Sigma$. Then, there is a $\delta_0 > 0$; for any $\delta \in (0,\delta_0)$, there is an $\varepsilon_0^\delta > 0$ such that for any $\varepsilon \in (0,\varepsilon_0^\delta)$ there are $t_0^{\varepsilon,\delta}$ and $t_1^{\varepsilon,\delta}$ with $0 < t_0^{\varepsilon,\delta} < t_1^{\varepsilon,\delta}$ such that the solution curve $\Gamma_t^{\varepsilon,\delta}$ of (1) starting from $\Gamma_0^{\varepsilon,\delta} = S^{\varepsilon,\delta}(\Gamma_0)$ loses its convexity for at least $t_0^{\varepsilon,\delta} \le t \le \min(T_0^{*,\delta}, t_1^{\varepsilon,\delta})$, where $T_0^{*,\delta} > 0$ is an existing time of $\Gamma_t^{\varepsilon,\delta}$.*

References

[1] J. W. Cahn and J. E. Taylor, "Surface motion by surface diffusion", Acta Metallurgica, 42 (1994), 1045–1063.

[2] J. W. Cahn, C. M. Elliott and A. Novick-Cohen, "The Cahn-Hilliard equation: Surface motion by the Laplacian of the mean curvature", Euro. J. Appl. Math., 7 (1996), 287–301.

[3] C. M. Elliott and H. Garcke, "Existence results for diffusive surface motion laws", Adv. Math. Sci. Appl., 7 (1997), 467–490.

[4] J. Escher, U. F. Mayer and G. Simonett, "The surface diffusion flow for immersed hypersurfaces", preprint.

[5] M. Gage and R. Hamilton, "The heat equation shrinking convex plane curves", J. Differential Geometry, 23 (1986), 69–96.

[6] Y. Giga and K. Ito, "On pinching of curves moved by surface diffusion", Comm. Appl. Anal., to appear.

[7] W. W. Mullins, "Theory of thermal grooving", J. Appl. Phys., 28 (1957), 333–339.

EFFECT OF EXTERNAL FIELDS ON ORDERING OF EQUIATOMIC FePd

T. Ichitsubo, M. Nakamoto, K. Tanaka and M. Koiwa

Department of Materials Science and Engineering, Kyoto University
Kyoto 606-8501, Japan

Abstract

The equiatomic FePd alloy undergoes an order-disorder transformation from fcc to $L1_0$ at about 650°C. Three variants of the tetragonal $L1_0$ ordered phase are formed with the c-axis parallel to either of the <100> directions of the disordered fcc matrix. The characteristic features of this transformation are: (i) ordering occurs via nucleation and growth process, (ii) three types of variants are formed with an equal probability in the absence of an external field and (iii) the elastic energy due to the tetragonality plays an important role to control its morphology.
In this paper, we report the effects of the external field on this ordering; the compressive stress or the magnetic field are applied to the specimens during ordering. The external field is expected to modify the relative population of variants; under the fields, one of the three types of variants is expected to be formed preferentially over the others. This has been examined for a single crystal specimen by applying a compressive stress of 40MPa or the external magnetic field of 2-10T along the [001] direction. X-ray analysis revealed that the favorable variant oriented to the field direction is formed predominantly.

The Third Pacific Rim International Conference on
Advanced Materials and Processing (PRICM 3)
Edited by M.A. Imam, R. DeNale, S. Hanada,
Z. Zhong and D.N. Lee
The Minerals, Metals & Materials Society, 1998

Introduction

Equiatomic FePd, FePt and CoPt transform from a disordered fcc phase to an $L1_0$ ordered phase as shown in Fig.1. These $L1_0$ compounds are ferromagnets exhibiting a strong uniaxial magnetocrystalline anisotropy with the easy axis parallel to the c-axis. The magnetic anisotropy constants K_1 (10^0-10^1 MJ/m^3) are comparable with those of rare-earth magnets [1][2][3]. Ordering of these alloy undergoes via nucleation and growth [4][5], and three variants of ordered domains are formed coherently with the tetragonal axes along [100], [010] or [001] directions of the fcc disordered phase. Three types of domains are formed with an equal probability in the absence of an external field.

The effect of stress during annealing has been studied for the precipitation or ordering processes in several alloys such as Al-Cu [6], Fe-Pd [7][8][9], Fe-N [10][11]. The change in morphology has been clearly observed for these systems. In this paper, we report the effects of compressive stress and also of magnetic field on the formation of ordered domains in the equiatomic FePd. The effect of the two types of the external field will be discussed in the light of the elastic interaction energies between second phase particles.

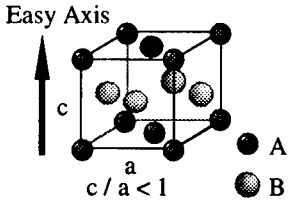


Fig.1 $L1_0$ ordered structure.

Experimental Procedure

An alloy ingot of composition Fe-50at%Pd was prepared by arc-melting of an appropriate mixture of 99.9% Fe and 99.95% Pd in an argon atmosphere. Single crystal was grown from the melt by the Bridgman method. The concentration of Pd was determined to be 49.8% by chemical analysis. Specimens of near cube shape were cut out from the single crystal rod; the specimen is about 4mm in edge length with all the surfaces parallel to the {100} planes within 0.5°. Two kinds of heat treatments were done under the fields along [001] direction (the z-axis) in the fcc disordered specimen. One is slow cooling across the order-disorder transition temperature (treatment 1) and the other is isothermal annealing after quenching (treatment 2). The volume fraction of three types of variants are determined by X-ray analysis.

Experimental Results

Stress effect

Slow cooling across the transition temperature (treatment 1) After heating up the specimen mounted in a compression test apparatus to 750°C, a compressive stress of 40MPa was applied along the z-axis, which was kept applied in the following cooling process:

$$750°C \xrightarrow{1°C/s} 650°C \xrightarrow{0.0166°C/s} 600°C \text{ (kept for 600s)} \xrightarrow{\text{furnace-cooled}} \text{Room temperature}$$

After this treatment, one would expect a predominant growth of one type of variant. In order to confirm this expectation, the peak positions of {200} reflections were measured by the X-ray diffractometer using FeKα radiation, in two different arrangement. The peak position of 002 was $2\theta = 62.84°$ and that of 200 was $2\theta = 60.40°$, as seen in Fig.2(a) and (b). The peak of the 200 in a disordered specimen is located at $2\theta = 61.12°$ in Fig.2(c), which is clearly different from those in Figs.2(a) and (b). This result clearly shows that only the single variant with the c-axis parallel to the z-axis is formed in the specimen subjected to treatment 1. Figure 2(d) is the {200} peak profile of the specimen heat-treated in the same way (or thermal history) without the stress. The 200 peak of fcc disordered phase and 200 and 002 peaks of the $L1_0$ ordered phase appear. This shows that the fcc disordered phase and the $L1_0$ ordered phase coexist.

Isothermal aging under the stress (treatment 2) In this treatment, the specimens were first

quenched from 800°C into brine (–20°C), and then annealed either at 450°C or at 600°C for 1h with a compressive stress of 40MPa. Relative volume fractions of the three types of variants were determined by the 4-axis X-ray diffractometer using MoKα radiation and Ge monochromator. Specimens were of a columnar shape, which were cut out from the bulk specimens subjected to treatment 2. The axial direction of the columnar specimen was along the z-axis.

We have measured the integrated intensities of {001} superlattice reflections. Reflections 100, 010 and 001 come from the ordered domains with the c-axes parallel to the [100], [010] and [001], respectively. The intensities of {002} fundamental reflections were also measured. The relative volume fractions of the three types of domains are given by $< I_{100} / I_{200} >$, $< I_{010} / I_{020} >$, $< I_{001} / I_{002} >$. Table I shows the volume fraction of the three types of variants. In this experiment, measurements were first made for a specimen about 200μm in diameter (Sample 1). Then, the specimen was thinned by electropolishing to about 100μm in diameter, and subjected to measurements again (Sample 2). The amount of the favorably oriented variant with c-axis parallel to the z-axis is larger over the other two.

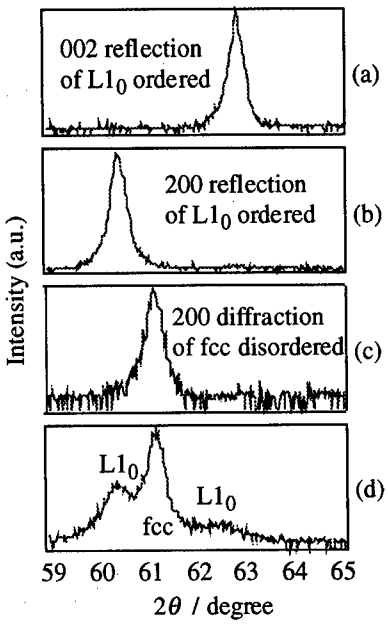


Fig.2 {200} peak profiles.
(a) and (b) show the 002 and 200 reflections of specimen subjected to treatment 1 under the stress.
(c) shows the {200} reflection of a quenched disordered specimen.
(d) shows the {002} reflection of specimen subjected to treatment 1 without the stress.

Magnetic field effect

The disordered specimen of cube shape is about 4mm in edge length with all the planes parallel to {100} planes. Under a constant magnetic field (2T, 6T or 10T) along the z-axis, the sample was heated up to 400°C (Curie temperature 490°C), and kept for 2h and were furnace-cooled under the field. In this experiment, we used the liquid helium-free superconducting magnet which was constructed by Watanabe [12].

Relative volume fractions of three types of variants were calculated from the integrated intensities of {100} and {200} reflections as given in Table II. The amount of the favorable variant with the c-axis parallel to the z-axis is larger over the other two at higher magnetic field.

Discussion

X-ray measurement

Although the effect of the external field on the formation of domains have been clearly observed, the results given in Table I and II should be regarded as preliminary. As seen in the tables, the volume fractions evaluated for specimens of different diameters are widely different. This suggests the inhomogeneous distribution of domains throughout the specimen. Parallel experiments by transmission electron microscopy revealed that the typical size of the ordered domains is 4-10nm. Further efforts are being made to attain a better understanding of the situation both by X-ray measurements and by electron microscopy.

Energy gain due to applying the external field

Uniaxial external fields enhance the formation of one type of $L1_0$ variant with the c-axis parallel to the direction of the field because the $L1_0$ structure of FePd has tetragonality, $c / a = 0.966$,

and the easy axis of the magnetic anisotropy is parallel to the c-axis. Under the stress, the mechanical interaction energy F_I between the external stress σ^A_{pq} and the eigenstrain ε^*_{pq} (stress free transformation strain) associated with the particle is expressed by $-\sigma^A_{pq}\varepsilon^*_{pq}$ [13]. The mechanical interaction energies F_I per unit volume of the particle under the compressive stress of 40MPa are calculated to be

$F_I = -0.91\text{MJ/m}^3$ (for the c-axis // the z-axis),
$F_I = +0.48\text{MJ/m}^3$ (for the c-axis $\perp$ the z-axis).

Under a magnetic field, particles with different orientations have different energies associated with the magnetic anisotropy. The magnitudes of the energy of this origin can be estimated by knowing the value of the magnetic anisotropy constant K_1, 0.5MJ/m^3 at the ordering temperature of 400°C[3]. For the magnetic field of 6T or 10T, all the $L1_0$ particles in any orientation should be magnetized along the applied z direction. The magnetic anisotropy energies per unit volume of the particle are

$E_M = 0.0\text{MJ/m}^3$ (for the c-axis // the z-axis),
$E_M = 0.5\text{MJ/m}^3$ (for the c-axis $\perp$ the z-axis).

Thus the variant of the c-axis parallel to the z-axis has the energy gain in comparison with the other variants under both fields. Therefore the formation of one type of variants tend to be formed preferentially.

In the formation of microstructures, the elastic interaction energy between particles plays an important role. We have calculated the elastic interaction energy for infinitesimally small particles of ellipsoidal shape. The detail of this calculation has been reported in a separate paper [7]. Here we shall briefly describe the salient results. We shall discuss the formation of a second precipitate in the presence of the first one of disc shape with an aspect ratio (a_3 / a_1) of 0.3 on a {101} plane; this plane is favored so as to minimizing the elastic strain energy. Consider the

Table I Volume fraction of the three variants under compressive stress. Sample 2 is the value measured after Sample 1 was electro-polished.

Specimen	Variant	Volume Fraction / %	
		Sample 1 (200μm)	Sample 2 (100μm)
450°C	c // x	25.6	29.0
40MPa	c // y	23.9	31.5
1h	**c // z**	**50.5**	**39.5**
600°C	c // x	10.7	29.3
40MPa	c // y	11.5	31.1
1h	**c // z**	**77.8**	**39.6**

Table II Volume fraction of the three variants under magnetic field. Sample 2 is the value measured after Sample 1 was electro-polished.

Specimen	Variant	Volume Fraction / %	
		Sample 1 (200μm)	Sample 2 (100μm)
	c // x	42.4	15.9
2T, 2h	c // y	21.4	28.7
	c // z	**36.2**	**55.4**
	c // x	28.5	21.7
6T, 2h	c // y	28.3	20.4
	c // z	**43.2**	**57.9**
	c // x	31.7	9.20
10T, 2h	c // y	23.4	10.4
	c // z	**44.9**	**80.4**

case that particle 2 is formed in the [101] direction as shown in Fig.3(a). If particle 2 is the same variant with particle 1, the elastic interaction energy E_I is positive at small D (the distance between particles in unit of a_1), while the elastic interaction energy E_I is negative if particle 2 is the different variant from particle 1 (Fig.3(b)). This indicates that, in the close vicinity of one particle, the formation of another particle of different variants is favored so as to reduce the elastic interaction energy. The volume of such region favoring the different variants decreases with the application of the external field. If somehow one can avoid the occurrence of nucleation of a new particle in such regions, the resulting microstructure tends to be dominated by a single type variant favored by the external field. In the energetic discussion of the formation of variants, the chemical energy associated with the super cooling must be also considered. From these points, one might expect a more remarkable effect of the applied field for aging at higher temperature where nucleation is less frequent and the difference of the chemical energies between the ordered and the disordered state is small.

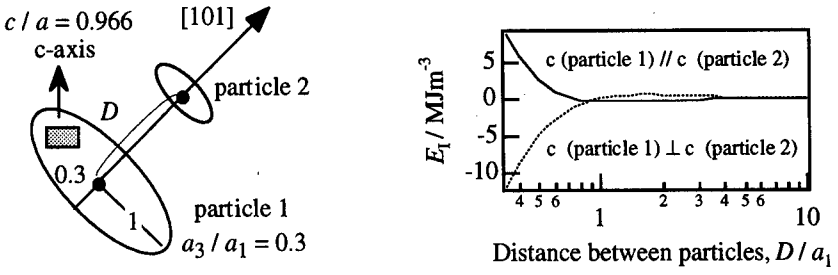


Fig.3 (b) shows the elastic interaction energy calculated for the arrangement of two particles as shown in (a).

Conclusions

We have studied the effect of the external fields on ordering of FePd alloy. Uniaxial external compressive stress or magnetic field enhance the formation of the favorable variant with the c-axis parallel to the direction of the fields. In particular, for the slow cooling under the stress, only one type of variant is formed. For isothermal aging at 600°C under the stress, the effect appears more remarkably than aging at 450°C. There is a possibility of the heterogeneous formation of $L1_0$ ordered domains and it is difficult to be determine the volume fraction of the variants quantitatively.

Acknowledgments

This work was partly supported by Grant-in- Aid for Scientific Research on the Priority Area " Investigation of Microscopic Mechanisms of Phase Transformations for the Structure Control of Materials" from the Ministry of Education, Science and Culture, Japan. The authors wish to express their appreciation to Professor K. Watanabe of Institute for Materials Research, Tohoku University for allowing us to use the superconducting magnet and Professor Y. Matsuo and Dr. K. Yamamoto of Nara Women's University for allowing us to use 4-axis X-ray diffractometer. The authors are also grateful to Professors M. Yamaguchi, M. Shiga and H. Inui of Kyoto University for the use of experimental facilities.

References

1 T. Klemmer et al.,"Magnetic hardening and coercivity mechanisms in $L1_0$ ordered FePd ferromagnets," Scripta Metall. Mater., 33 (1995), 1793-1805.

2 O. A. Ivanov et al.," Determination of the anisotropy constants and saturation magnetization, and magnetic properties of powders of an iron-platinum alloy," Phys. Met. Metall., 35 (1973), 81-85.

3 A. Ye. Yermakov and V. V. Maykov," Temperature dependence of magnetic crystallographic anisotropy and spontaneous magnetization of single crystals of FePd and CoPt alloys," Phys. Met. Metall., 69 (1990), 198-201.

4 G. M. Guschin and F. N. Berseneva," Microstructure and ordering kinetics of quenched alloy FePd," Phys. Met. Metall., 63 (1987), 83-92.

5 B. Zhang, M. Lelovic and W. A. Soffar," The formation of polytwinned structure in Fe-Pt and Fe-Pd alloys," Scripta Metall. Mater., 25 (1991), 1577-1582.

6 T. Eto, A. Sato and T.Mori," Stress-oriented precipitation of G.P. zones and θ' in an Al-Cu alloy," Acta Metall., 26 (1978), 499-508.

7 T. Ichitsubo et al.," Effect of applied stress on fcc-$L1_0$ transformation of FePd single crystal," Materials Transactions, JIM., in press.

8 S. Shimizu and S. Horiuchi," Fiber texture formed on transformation from disordered fcc phase to ordered fct phase under load," Metall. Trans., 1 (1970), 330-331.

9 V. V. Maykov et al.," Influence of the degree of long-range atomic order on the magnetic properties of CoPt and FePd single crystals," Phys. Met. Metall., 67 (1989), 76-82.

10 Y. Tanaka, A. Sato and T. Mori," Stress assisted nucleation of α" precipitates in Fe-N single crystals," Acta Metall., 26 (1978), 529-540.

11 G. Sauthoff," Analysis of the stress orienting of α" precipitates in Fe-N alloy," Acta Metall., 29 (1981), 637-642.

12 K. Watanabe et al.," 11T liquid helium-free superconducting magnet," Cryogenics, 36 (1996), 1019-1025.

13 J. D. Eshelby.," The continuum theory of lattice defects," Solid State Physics, 3 (1956), 79-144.

Phenomena on the Surfaces and Along A Crack Path in A Heat Resistant Alloy During High Temperature Service

A.A. Kaya and P. Krauklis

School of Materials Science and Engineering
The University of New South Wales, Sydney, NSW 2052, Australia

Abstract

Oxidation phenomena during high temperature service of tubes made from HK40 alloy have been investigated. The materials were characterized using electron microscopy, x-ray diffraction and microanalysis techniques after being used for twenty-five thousand hours as furnace tube in ethylene pyrolysis. The service conditions subjected the material to oxidizing and carburizing conditions at the surfaces leading to the formation of complex oxide structures in both external scales, and in internally oxidised regions, and carbide-denuded zones in sub-surface regions. A macro crack in one of the samples provided an opportunity to study the sequence of oxidation of the constituent elements and observe a different sequence in the formation of oxide layers compared with the inner and outer tube surfaces. These observations imply that silicon segregation during carbide coarsening was an important precursor to crack propagation.

The Third Pacific Rim International Conference on
Advanced Materials and Processing (PRICM 3)
Edited by M.A. Imam, R. DeNale, S. Hanada,
Z. Zhong and D.N. Lee
The Minerals, Metals & Materials Society, 1998

Introduction

Centrifugally cast Fe-Cr-Ni alloys are used as pyrolysis tubes in the petrochemical industry. Their long term aging behaviour (1-8) and oxidation characteristics (9,10) have been the subject of a number of studies. The pyrolysis tube material works under dynamic conditions in terms of chemical composition as there is constant intake of at least two elements, carbon and oxygen, as well as depletion of the constituent elements from the alloy due to oxidation and carburization.

Petkovic-Luton and Ramanarayan (9,10) have studied the long-term oxidation behaviour of this material, which was subjected to carburizing-oxidizing environments for up to six years. However, the material they studied did not involve a crack formation, and their investigation was not based on electron microscopy work. They classified the oxidation of this alloy into five stages (see Figure 11 in Ref 9). An attempt has been made in our investigation to further elucidate the finer structure of the oxidation products using electron optical techniques, and to interpret the oxidation phenomena.

Experimental Procedure

Two samples of HK40 which had been taken after prolonged pyrolysis service were examined. The chemical composition of the original alloy is given in Table 1. Electron microscopy was performed using a Hitachi S900 scanning electron microscope (SEM) equipped with a field emission gun and an energy dispersive X-ray (EDS) microanalyzer. X-ray mapping was carried out using a CAMECA SX50 electron probe microanalyser. The X-ray diffraction data was obtained using Cr Kα radiation and an operating voltage of 30kV on a Siemens D5000 diffractometer.

Experimental Results

The microstructure of as-cast HK40 alloy consists of FCC gamma matrix, and a cellular type structure which involves $M_{23}C_6$ carbides on the dendrite boundaries (Fig. 1). After prolonged exposure to oxidising/carburising conditions at temperatures around 800°C during pryolysis, one of the samples, A, showed moderate microstructural degradation to approximately stage III in the model of Petkovic-Luton et al. (9,10). The typical compositions of the various microstructural constituents observed in sample A are given in Table 1 with reference to the relevant micrographs. The second sample, B, which had been removed from the same furnace after a similar period involved a crack, and showed more severe microstructural degradation to approximately stage IV. In both samples the carbides appeared to have coarsened and become continuous along the grain boundaries during service. This was more pronounced in sample B, suggesting that it had experienced more carburisation than sample A. X-ray diffraction of sample B (Fig. 2) indicated the presence of M_7C_3 type carbides in addition to $M_{23}C_6$ and austenite.

At the inner surface of sample A, a carbide-depleted zone up to 200 μm thick was observed beneath the various oxides formed at this surface. The outermost oxide scale appeared to be loosely adherent, and to be consists of mainly iron oxide with some chromium and nickel oxides. Below this scale was an internally oxidised region composed of mixed intragranular oxides and a thin continuous network of grain boundary oxides (Fig. 3a). Further beneath this region of mixed oxides, it was observed that SiO_2 branches had penetrated toward interiors along the grain boundaries. At intragranular locations between the SiO_2, other oxides also were observed to occur, but narrow oxide-free zones (Fig. 3a) separated these from the boundary SiO_2.

Table I Chemical Compositions of Various Microstructural Features in Sample A (at. %)

Feature	Fig.	Ni	Cr	Fe	Si	Mn	O	C
As-cast HK40	1	21.0	25.0	Bal.	1.6	1.5 max	0	0.4
Oxide scale	3	2.3	2.7	37.3	0	0	57.7	n.m.
Mixed oxide	4	11.4	18.7	4.7	0.2	0.2	64.8	n.m.
Cr_2O_3 layer	4	0.33	32.8	0.2	0.2	0.1	66.4	n.m.
SiO_2	3 & 4	0.1	0.2	0.8	32.8	0	66.0	n.m.
Ppts. In SiO_2	4	8.7	2.9	18.9	26.7	0	42.8	n.m.
Coarse carbides	5 & 6	2.8	61.1	11.2	0	0.5	n.m.	24.3

* n.m. = not measured.

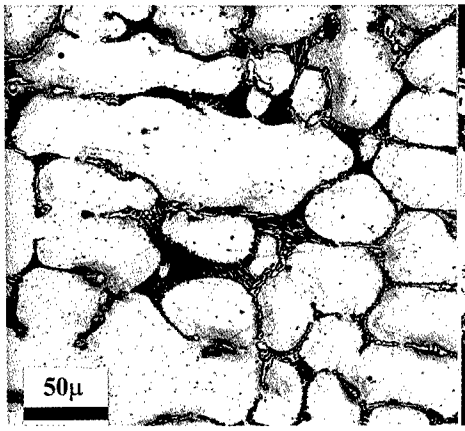


Figure 1: Light micrograph showing the microstructure of as-cast HK40 with $M_{23}C_6$ carbides in a cellular structure along dendrite boundaries.

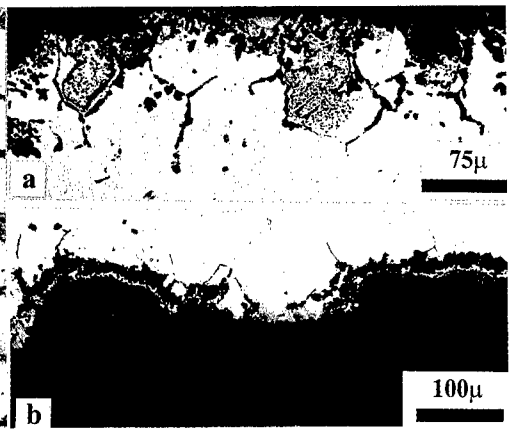


Figure 3: Light micrographs of sample A in un-etched condition, (a) region beneath the inner surface; (b) region beneath the outer surface.

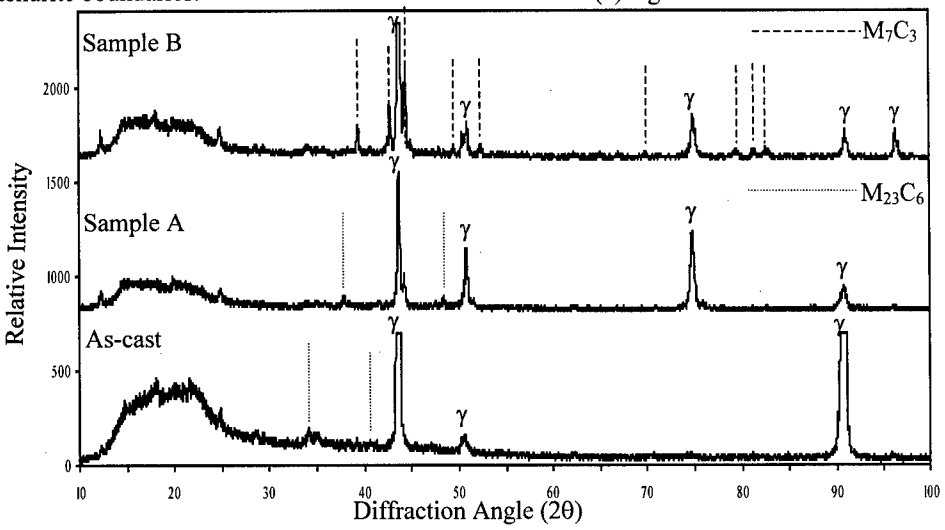


Figure2: X-ray spectra taken from cross section surfaces of the three samples. Note that the surface of sample B includes the macro crack.

Reliable data could not be obtained from the scale at the outer surface of sample A, because it had largely spalled from the surface. Immediately beneath the original alloy surface regions of internal oxidation containing mixed oxides were observed (Fig. 3b). Below these regions, but merging with them, a layer of Cr_2O_3 had formed. Further beneath this a layer of SiO_2 had formed which was distinctly separated from the Cr_2O_3 layer. The SiO_2 contained a fine precipitate dispersion and also had penetrated toward the interior along grain boundaries.

The crack studied in sample B was clearly visible to the unaided eye, and appeared as a flaw on the inner surface parallel to the tube axis and running into the material for about two thirds of the total wall thickness of 8mm. At the tip of the crack it was observed that the grain boundary carbides had developed a relatively coarse internal dispersion of a FCC gamma phase that was not observed in other regions away from the crack location (Fig. 4a). In this region, oxidation appeared to have taken place preferentially at the gamma-carbide interfaces (Fig. 4a), and gradually consumed the gamma phase, and then the carbides themselves. The microstructure near the crack root is shown in Fig. 4b, and it is apparent that the grain boundary carbide phase at the crack has been almost entirely oxidised and subsequently has been removed from the section during sample preparation. X-ray images of a crack segment approximately 4mm from the inner surface are shown in Fig. 5.

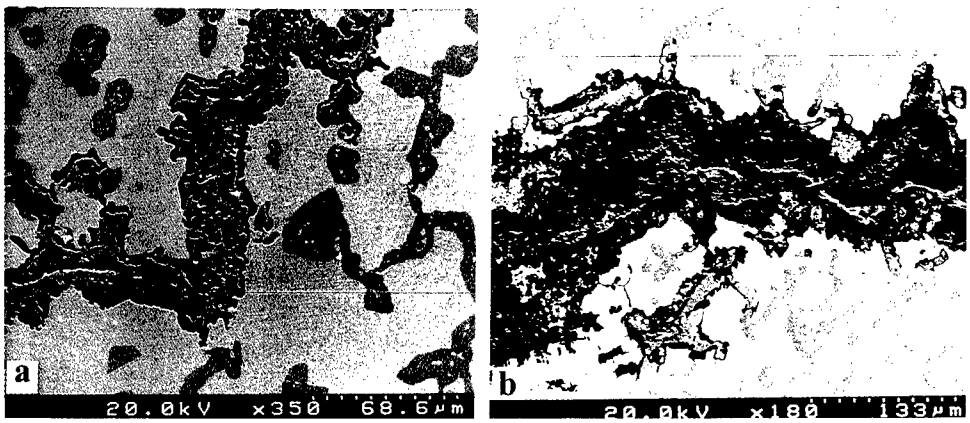


Figure 4: SEM micrographs of sample B in un-etched condition; (a) austenite precipitation in M_7C_3, and oxidation sites at the crack tip, and (b) microstructure near the crack root.

Discussion and Conclusions

Microstructural degradation in oxidising / carburising environments can be interpreted in terms of time or temperature in the model of Petkovic-Luton et al. (9,10). In general our observations agree well with their results, with sample A showing microstructural degradation to stage III, and sample B to stage IV. The more severe degradation in sample B is probably due exposure to a higher temperature and more severe conditions at its location in the pyrolysis furnace. Our work has revealed the occurrence in sample A, of various oxides in different regions in more detail, a fine precipitate within SiO_2, and in sample B, the formation of fcc gamma phase within the M_7C_3 carbides, which were not reported by Petkovic-Luton et al. (9,10). In their study, the formation of layers comprised purely of one type of oxide such as Cr_2O_3 and SiO_2 , was attributed to the varying growth rate of individual oxides and to an oxygen potential gradient through the oxide scale. However, these factors alone cannot account for the almost complete absence of other elements in the continuous layers of Cr_2O_3 or SiO_2, or formation of particles in SiO_2. Therefore a further explanation of these observations seems necessary.

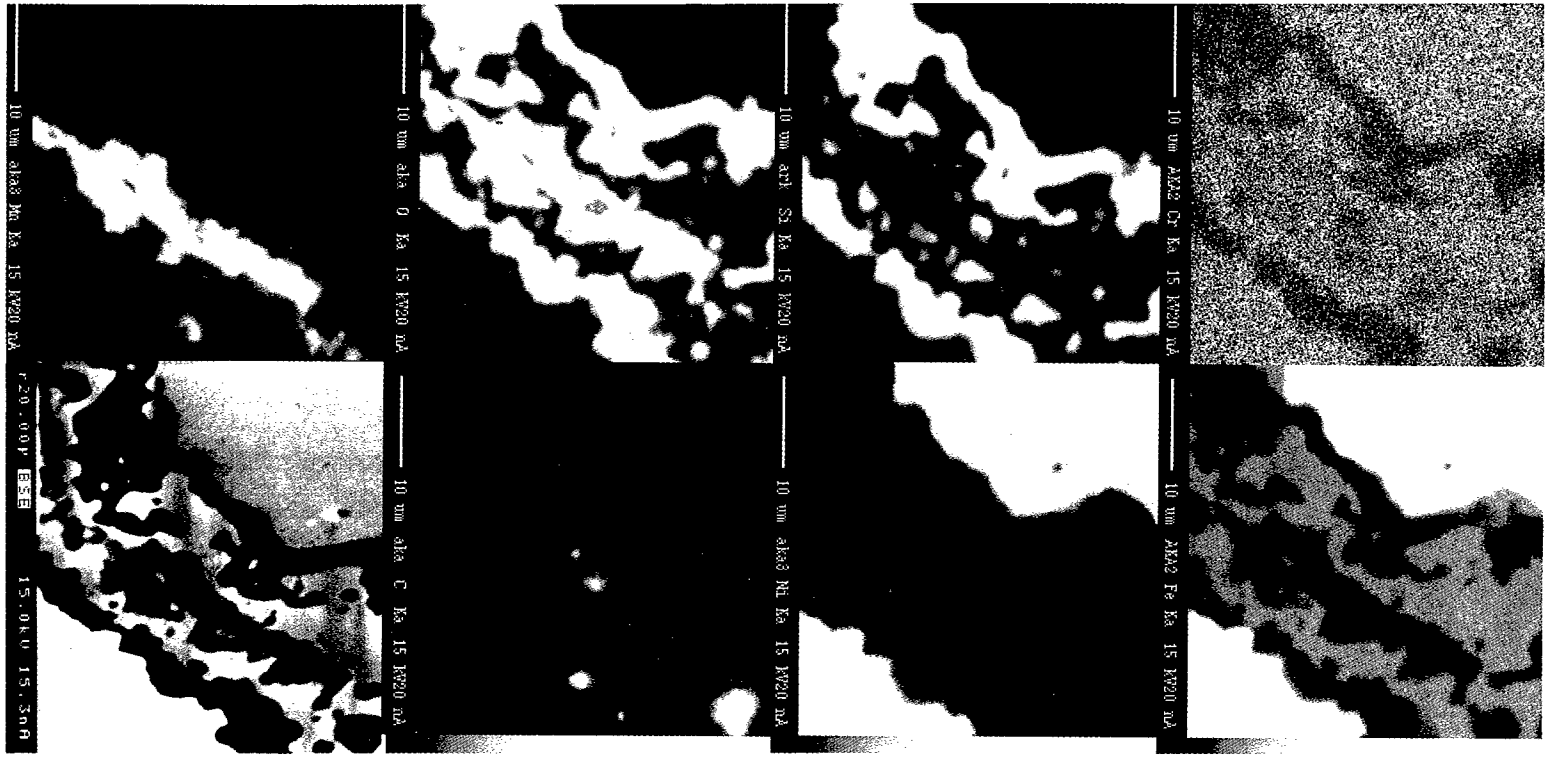


Figure 5: X-ray images showing the distribution of elements in a crack segment at a depth of approximately4mm from the inner surface in sample B. Note that BSE image of the area is given in the bottom-right corner.

The EDS and WDS analyses (Table 1) near the inner and outer surfaces of sample A, indicate that the SiO_2 and Cr_2O_3 layers contain negligible amounts of other alloying elements. The exclusive formation of one oxide in these layers may be explained in terms of segregation effects during oxidation. For example, silicon has the highest affinity for oxygen out of the elements present in solution in the alloy matrix. However, the concentration of silicon, and consequently its thermodynamic activity is low, and thus silicon cannot form the first oxide layer by itself. The oxide scale is formed initially by other elements having a lower affinity for oxygen but higher activity, such as chromium. As oxidation proceeds, silicon is rejected into the matrix due to its low solubility in the scale, and this increases the silicon concentration locally under the scale. At the same time, the concentration of chromium in solution is decreasing, and eventually formation of an SiO_2 scale becomes possible as the activity of silicon increases relative to that of chromium. SiO_2 formation thus occurs adjacent to, and under the Cr_2O_3 where these local concentration differences are most pronounced.

Compared with sample A, the microstructure of the cracked sample, B, contained coarser intergranular and intragranular carbides, indicating that more carburisation had taken place. Consequently, it is believed that the carbide denuded zone previously beneath the inner surface has been replaced by a continuous carburized structure, while a carbide-denuded zone was still present beneath the outer surface. These observations may be explained in terms of more severe service conditions in the case of sample B, due to its location in the pyrolysis furnace, corresponding to a degradation level designated as stage IV in the model of Petkovic-Luton (9).

In terms of the oxidation phenomena, the crack represents different situation compared with the uncracked sections in samples A and B. Along the crack path, (and particularly near its tip), the formation of SiO_2 appeared to precede other oxidation reactions, unlike the inner and outer surfaces of samples A and B. The absence of other oxidation products within the crack is consistent with an oxygen partial pressure below the threshold values necessary to form these oxides. The formation of SiO_2 within the crack path could be explained by silicon segregation to the phase boundaries during carbide coarsening prior to the arrival of the crack. The microanalyses (Table 1) and X-ray maps (Fig. 5) clearly indicate that silicon is absent from the carbide phase, yet is concentrated immediately adjacent to it. Such local silicon enrichment may be sufficient to lower the threshold oxygen partial pressure for SiO_2 formation to below the oxygen partial pressure present within the crack, thus causing the formation of SiO_2 without the occurrence of the other oxides.

References

1. A.F. Bezerra et al, Proceedings of the 4th Brazilian Symposium on 'Piping and Pressure Vessels', (SIBRAT-86), Salvador, Brazil, (1986).
2. G.D. Barbabela et al, "Estudo Inoxid. Austen. HK", Metallurgia-ABM, 44(1988)1269-1276.
3. K. Kasahara, "Application of PHACOMP to σ in HK-40", Proc. of the 2nd Int. Cong. on 'Creep and Fracture of Eng. Mater. & Structures', Pineridge Press, Swansea, (1984)383-394.
4. H. Wen-Tai and R.W.K. Honeycombe, "Structure of Centrifugally Cast Austenitic Stainless Steels: Part 1", Mater. Sci. Technology, 1(1985)385-389.
5. G.D. Barbabela et al,"Role of Nb in HP Steel" Materials Characterization, 26(1991)193-197.
6. G.D. Barbabela et al, "Phase Characterization in HK Stainless Steel", *ibid*, 26(1991)1-7.
7. G.D.A. Soares et al, "Niobium in HP Heat-Resistant Steels", *ibid*, 29(1992)387-396.
8. R.A.P. Ibanez et al, "Effects of Si on Microstructure of HP Steels", *ibid*, 30(1993)243-249.
9. R. P. Luton and T.A. Ramanarayanan, "Mixed-oxidant Attack of High Temperature Alloys in Carbon- and Oxygen-containing Environments", Oxidation of Metals, 34(1990)381-400,.
10. S. Ling T.A. et al., "Computational Modelling of Mixed Oxidation" *ibid*, 40(1993)179-196.

SURFACE TREATMENT OF NI AND NI-BASED ALLOYS FOR HIGH TEMPERATURE OXIDATION PERFORMANCE

F. Czerwinski, S. Poplawski, and J.A. Szpunar

Department of Metallurgical Engineering, McGill University, Montreal, H3A 2B2 Canada

Abstract

The role of the crystallographic orientation of Ni and Ni-based alloys in controlling their oxidation resistance at high temperatures, is investigated. The measurement of oxide growth kinetics on Ni demonstrated that the {111} texture can slow down the oxidation process. Techniques of modifying the substrate texture by electrodeposition and mechanical deformation of the surface are presented. For Ni substrate, the <111> texture was grown by electrodeposition of Ni layer with a <100> texture that was followed by annealing in an inert atmosphere of argon. For Ni-based alloys, the surface deformation techniques are proposed and used to produce a <111> texture component. The relationship between the texture of the substrate and the growing oxide is discussed.

The Third Pacific Rim International Conference on
Advanced Materials and Processing (PRICM 3)
Edited by M.A. Imam, R. DeNale, S. Hanada,
Z. Zhong and D.N. Lee
The Minerals, Metals & Materials Society, 1998

Introduction

Experiments with oxide growth on single crystal faces demonstrated that crystallographic orientation of the metallic substrate exerts a crucial influence on oxidation behavior [1,2]. Since the high-temperature oxidation is a surface phenomenon, the improvement in oxidation resistance may be achieved by modifying the crystallographic texture of the surface layer of the polycrystalline substrate. For Ni and its alloys, an increase in strength of {111} component results in a significant increase in oxidation resistance. At temperatures between 873 and 1173 K, the growth rate of NiO on (111)Ni face is over one order of magnitude lower than that observed for (100)Ni [2-4]. According to quantitative analysis of x-ray data [5], the substrate orientation (texture) affects the grain boundary character distribution in growing NiO and therefore controls the diffusion rates of ionic species through the oxide. The atomic structure of oxide grain boundaries is also important for Ni substrates covered with coatings containing elements with a high affinity to oxygen. Here, the grain boundaries may not only act as easy diffusion paths for metal and oxygen ions, but also as paths for ions of the reactive element [4]. In this way, the grain boundaries affect the stability of the reactive element concentration inside NiO, as well as its effectiveness. Despite the practical importance of the last finding, no attempt has been reported in the literature to modify the surface texture of metallic substrates in order to improve their corrosion resistance.

In this study we verify the possibilities of modifying the surface texture of polycrystalline Ni and Ni-based alloys using two techniques: electrodeposition and surface deformation.

Experimental

High purity polycrystalline Ni and commercial Ni-Cr alloys, such as Inconel 600 and 601, were used as substrates for oxidation. The substrate surfaces were modified by electrodeposition and special surface deformation. Electrodeposition was carried out from a modified Watts bath [6] at a temperature of 323 K and a current density in the range 2-10 Adm^{-2}. Some electrodeposits were annealed prior to oxidation at 1073 K for 0.5 h in an inert atmosphere of argon. Oxides were grown at a temperature of 1073 K both in pure oxygen and in air. Textures of the substrates and oxide films were measured using a D-500 Siemens x-ray goniometer and $Mo_{K\alpha}$ radiation. Pole figures were obtained using the reflection technique up to a maximum tilt of 80 deg in 5 deg polar and radial intervals. The results were corrected for absorption and defocusing using a standard random specimen prepared from a powder.

Results and discussion

Oxidation kinetics of Ni and Ni-based alloys

Exemplary kinetics data for the oxidation of polycrystalline Ni, Cr and Ni-Cr substrates are shown in Fig. 1. The oxidation experiment was performed in an ultra high vacuum manometric system at low oxygen pressure and a detailed description is given elsewhere [3]. Oxidation kinetics are characterized by the instantaneous parabolic rate constants: $k_{pi} = 2w\ dw/dt$, where w is the oxygen uptake per unit area and t is the time of oxidation. In this figure, additional curves are plotted which show the oxidation behaviour of the same substrates after application of ceria sol-gel coatings with a thickness of 14 nm [3,7]. In order to suppress the influence of the substrate grain orientation and to show differences related to chemical composition, the surfaces of the specimens were finished by mechanical polishing. The Ni substrate with a <111> fibre texture was also chemically etched to reveal the grain structure and promote the growth of epitaxially oriented oxides. It is seen that the oxidation rate of etched specimens after coating, marked as Ni chem./CeO_2 in Fig. 1, is significantly lower than that for the same specimen with a surface finished by mechanical polishing. In fact the oxidation rate of textured Ni was very similar as that found for Cr.

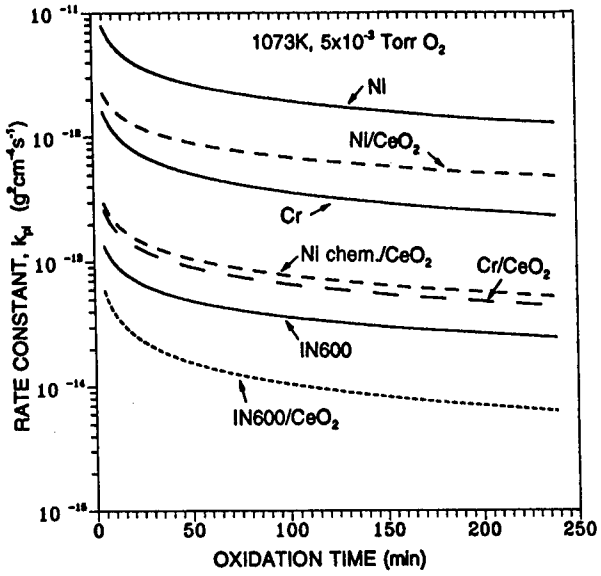


Figure 1: Plots of oxidation rate constants versus time for pure and ceria coated Ni, Cr and Inconel 600 alloy. Substrate surfaces finished by mechanical polishing.

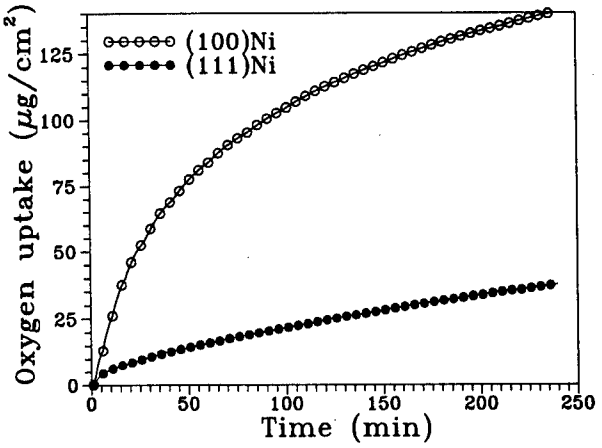


Figure 2: Oxidation kinetics for (100) and (111) crystal faces of Ni at 1073 K in 0.005 torr oxygen.

The influence of the crystallographic orientation of Ni on the oxidation rate at 1073 K is shown in Fig. 2. It is clear that (111)Ni face oxidizes at a rate significantly lower than (100)Ni. The kinetics for NiO growth on different crystal faces at temperatures less than about 1300 K, are related to the microstructure of the oxide and have been interpreted in terms of the character and density of grain boundaries [2,5]. Thus the {111} texture provides better oxidation resistance at high temperatures.

The texture of metallurgically processed Ni products

The texture of Ni products depends upon manufacturing technology. The simplest products obtained by metallurgical processing are sheets and rods. An example of the texture of cold rolled and annealed 1-mm thick Ni sheet is presented in Ref. [8]. The orientation of Ni grains is characterized by {100}<023> texture with a maximum intensity of 4.1 times random. The texture of Ni rod with a diameter of 9.5 mm produced by extrusion is represented by two single fiber components <111> and <100> with equal intensities of 2.4 and aligned along the rod axis [9]. This implies that the rod outer surface subjected to corrosion is randomly oriented. For both sheets and rods, the bulk textures obtained as a result of conventional metallurgical processing are not compatible with their oxidation resistance and lead to high oxidation rates. One possibility to modify the texture of the surface layer is by electrodeposition.

Texture modification of Ni by electrodeposition

Ni electrodeposits are known for giving numerous, well-defined preferred orientations. Many theoretical explanations have been put forward to account for the different textures experimentally observed [10,11,12]. However, none of these single theories can predict the complete set of texture results now available. Ni electrodeposits obtained under conditions of this study exhibited a single texture component of strong <100> fiber with an intensity of 57.3 times random (Fig. 3a). Exposure of as-deposited Ni at a temperature of 1073 K caused the growth of practically randomly oriented NiO. After 15 h of exposure, NiO showed very weak (1.8 times random) traces of <110> fiber.

Electrodeposits, in general, contain a high density of structural defects. Therefore, oxide growth on as-deposited Ni is, in fact, affected by the recovery of defect structure, grain growth and texture changes of the bulk substrate. According to Lee [13], the recrystallized grains orient themselves so that their minimum elastic modulus direction is parallel to the absolute maximum normal stress direction of the grains after deposition. In the case of Cu, the minimum elastic modulus direction is <100>, and this direction should be the dominant texture axis after annealing. It should be emphasized that our measurements of the annealing texture in Ni and previously reported Ni based alloys [14], show exactly the opposite behavior. Namely, that annealing of as-deposited Ni for 0.5 h at 1073 K, causes a sharp <100> fiber to disappear while a <111> fiber develops and reaches a maximum intensity of 5.8 times random (Fig. 3b). NiO grown on the annealed substrate developed a well-defined <111> fiber (Fig. 3c).

Texture modification of Ni-based alloys by surface deformation

For a higher oxidation resistance of Ni-based alloys than that of pure Ni (Fig. 1), a technique other than Ni electrodeposition is required for surface texturing. It was found that in this case, a special surface deformation is very effective. An initial texture of Inconel 601 (Fig. 4a) shows that {111} planes are inclined to the plate surface. A directional grinding using an 80 grid SiC paper produces the surface texture with a weak <111> component (Fig. 4b). Of several techniques of surface deformation tested, a relatively clear <111> texture was formed after sand blasting directed perpendicularly to the specimen surface (Fig. 4c).

The relationship between the texture of the substrate and oxide

In order to reduce the oxidation rate of the substrate, the electrodeposited layer of Ni should exert an influence on the texture of the growing oxide by promoting epitaxy. For Ni/NiO systems,

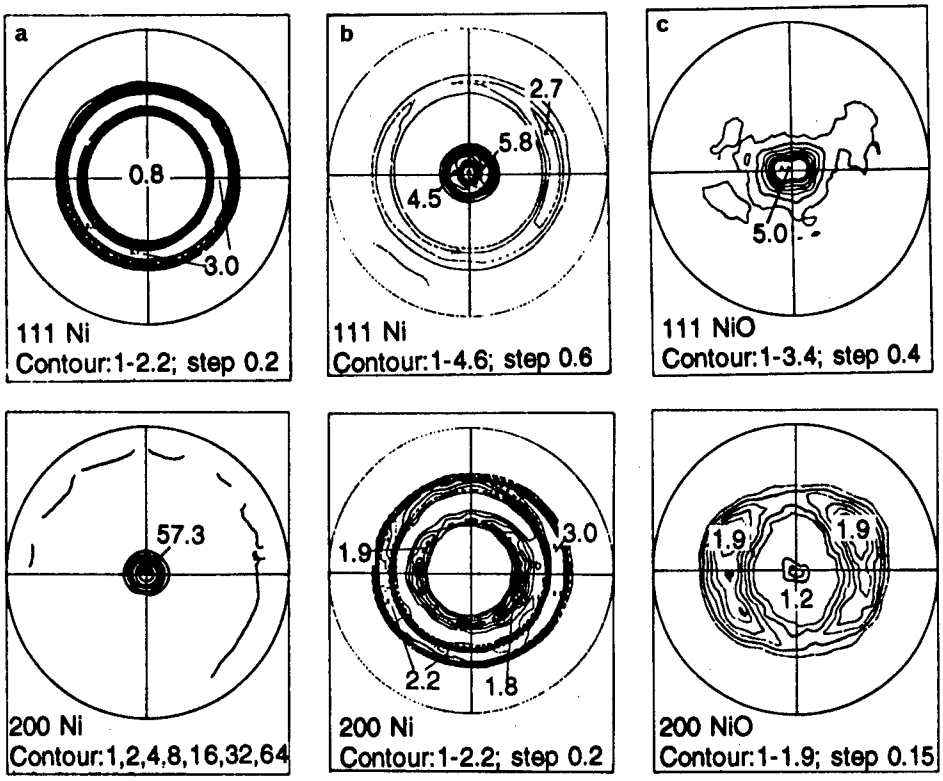


Figure 3: Pole figures of as-deposited Ni (a), Ni annealed at 1073 K for 0.5 h in argon (b) and NiO grown for 15 h at 1073 K on annealed Ni (c).

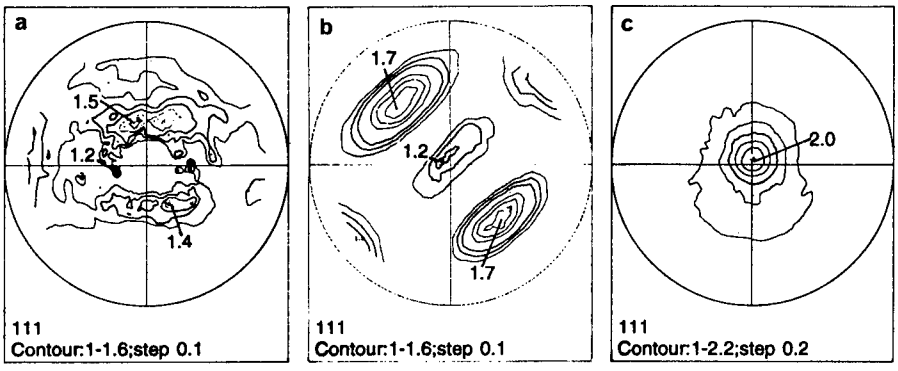


Figure 4: Pole figures of Inconel 601 alloy: (a) after cold rolling; (b) after directional abrading with 80 grid SiC paper; (c) after sand blasting perpendicularly to the specimen surface.

the epitaxial growth is expressed by cube-to-cube relation with {hkl} NiO parallel to {hkl} Ni [2,4]. The NiO texture for a particular case of (100) and (111) crystal faces of Ni is discussed in detail elsewhere [4]. A simple comparison of the pole figures of as-deposited substrates and oxides indicates a lack of orientation relationship between Ni and NiO. The <110> fiber texture observed during the oxidation of nanocrystalline Ni is typical for NiO growing on Ni with a surface plastically damaged by mechanical polishing [8]. Such a texture develops during the growth from randomly oriented oxide film, which nucleates at the beginning of oxidation. Thus during the oxidation of as-deposited structures, their initial texture does not have any influence on the texture of the growing oxide.

An annealing temperature of 1073 K was selected to be high enough to complete the recrystallization in all Ni deposits and to avoid substantial changes in the substrate during subsequent oxidation. As a result of recrystallization, a <111> texture develops. The presence of a <111> texture in annealed, i.e. free of structural defects, Ni substrate, is highly beneficial for oxidation resistance. A comparison of the pole figures of annealed substrates (Fig. 3b) and corresponding oxides (Fig. 3c) supports the existence of epitaxy.

The oxide formed on Ni-based alloys Inconel 600 and 601 contains mainly chromia. Due to technical problems with texture measurements for chromia, the texture and epitaxial relationship between oxide and substrate are unknown. This problem is currently under investigation.

Conclusions

The corrosion resistance of engineering materials depends on several factors. This study discusses one of them, namely the crystallographic orientation (texture) of the substrate. The results presented here show that a two-stage surface treatment that consists of the electrodeposition of Ni with a high <100> texture followed by annealing, produces a surface with a strong <111> texture. As has been proven previously [4], this texture of Ni leads to the formation of highly protective and slow growing NiO scales. For Ni-based alloys, the <111> texture can be produced by surface deformation.

Acknowledgment: This research was financially supported by the Natural Sciences and Engineering Research Council of Canada.

References

1. J.V. Cathcart, G.F. Petersen, and C.J. Sparks, J. Electrochem. Soc., 116 (1969), 664-668.
2. F. Czerwinski and W.W. Smeltzer in Microscopy of Oxidation-2, edited by S.B. Newcomb and M.J. Bennett, The Institute of Materials, London, 1993, 128-135.
3. F. Czerwinski et al., Corrosion Science, 37 (1995) 541-546.
4. F. Czerwinski and J.A. Szpunar, Acta Materialia, 46 (1998), 1403-1417.
5. H. Li et al., Corrosion Science, 39 (1997), 1211-1219.
6. J.K. Dennis and T.E. Such, Nickel and Chromium Plating, Woodhead Publ., Cambridge, 1993.
7. F. Czerwinski and J.A. Szpunar, Canadian Metallurgical Quarterly, 34 (1995), 243-249.
8. F. Czerwinski and J.A. Szpunar, in Textures of Materials-ICOTOM 11, Inter. Acad. Publ., Bejing, China, 1996, 1132-1136.
9. F. Czerwinski, J.A. Szpunar, and W.W. Smeltzer, J. Electroch. Soc., 143 (1996), 3000-3007.
10. N.A. Pangarov, Electrochimica Acta, 7 (1962), 139-146.
11. A.K.N. Reddy, J. Electroanalytical Chemistry, 6 (1963), 141-152.
12. J. Amblard, M. Froment,and N. Spyrelis, Surf. Technol., 5 (1977), 205-210.
13. D.N. Lee, Materials Research Society Symposium Proceedings, Vol. 427 (1996), 167-178.
14. F. Czerwinski et al., Scripta Materialia, 37 (1997), 1967-171.

THERMODYNAMICS AND KINETICS ASPECTS OF THE SYNTHESIS OF TITANIUM NITRIDE AND CARBONITRIDES FROM TIO2 AND CARBON IN NITROGEN ATMOSPHERE

Animesh Jha and Su-Jong Yoon**

Department of Materials, University of Leeds,
Clarendon Road, Leeds, LS2 9JT, UK.

**Department of Materials Science & Engineering,
Miryang National University, Miryang, 627-130, S Korea

Abstract

Titanium nitride ($Ti_{1+x}N_{1-x}$) is an interstitial compound with a large concentrations of nitrogen vacancies ranging from 23 atomic percentage (at.%) to 50 at.% nitrogen. The crystalline phase with (B_1-NaCl type) an fcc structure exhibits both covalent and metallic characteristics. The material, as a result, has high melting point (3223 K), thermal conductivity (1.92-2.09 $Jm^{-1}s^{-1}K^{-1}$) low resistivity (10^{-3} - 10^{-4} Ω cm), isotropic expansion coefficient ($9.3x10^{-6}$ K^{-1}), oxidation resistance, high hardness and fracture toughness (6-10 $MPam^{½}$)[1,2]. The material is used for making multilayer coated structure for the tip of cutting tool, electro-machinable ceramics, metal evaporator boats and for thermal barrier coatings.

In this paper, the method of synthesis via carbothermic reduction of rutile with carbon in the presence of nitrogen gas is described. The effects of the reactivity of carbon, temperature and time on the phase constituents and the lattice parameter of titanium nitride phase are reported. The computed Gibbs free energy of formation for mixed interstitials such as TiCN, TiON and TiOC are reported; and in particular, the validity of the computed data are tested by comparing the results with the experimental data. On the basis of the Gibbs free energy data, a TiC and TiN phase diagram was computed and verified against the observed linear relationship between lattice parameters of TiC and TiN. The kinetic barriers for the reduction of TiO_2 to lower oxides and carbonitride phases were determined and compared with the oxygen diffusion model in rutile lattice[3].

The Third Pacific Rim International Conference on
Advanced Materials and Processing (PRICM 3)
Edited by M.A. Imam, R. DeNale, S. Hanada,
Z. Zhong and D.N. Lee
The Minerals, Metals & Materials Society, 1998

Introduction

Over the last two decades, one of the main emphasis in designing engineering materials and components has been to achieve better performance in service conditions. The development of modern cutting tool has been a very good example of a well-engineered material. The modern cutting tool is a multilayered structure of ceramics on a metallic substrate. Titanium nitride is an important ingredient of the layered structure, which contributes to the improvement in the oxidation resistance, fracture toughness, heat conduction and providing a better adhesion with the metallic substrate. Titanium nitrides ($Ti_{1+x}N_{1-x}$) and carbonitrides (TiCN) are also used for strengthening ferrous matrix for wear-resistance surface. The main advantage of using TiN is that it not only has better adhesion with the ferrous matrix, but also improves the oxidation resistance which is not possible with tungsten carbide wear-resistance surfaces at elevated temperature. Carbides, nitrides and borides of titanium are potential candidates for reinforcing copper power transmission cables. The higher hardness of the ceramic phase than the copper cable enhances the stiffness, which could enable a major reduction in the installation of pylons for supporting the power transmission cables. Another important contribution is to reduce the penalty on power transmission loss. The high thermal conductivity and oxidation resistance makes this material as an important constituent for designing new generation of advanced ceramic composite materials for continuous casting applications.

In the closed packed face-centred cubic lattice (B_1, NaCl type), nitrogen atoms occupy interstitial sites that are only partly occupied; as a result the nitrogen deficient sites in the structure range from 0 to 27 at% N of atoms in the $Ti_{1+x}N_{1-x}$ structure. Above Ti/N ratio equal to unity, the titanium deficient sites appear as a result of which the lattice parameter of the TiN phase, which rises between 23 at% N and 50 at% N, falls rapidly. The concentration of nitrogen also determines the physical properties of the ceramic phase. For example, when the Ti/N ratio is more than 1, the ceramic exhibits more metallic like characteristics and with increasing nitrogen, the metallic characteristics diminishes in preference to the covalent bond characteristics.

In this paper, we examine the role of the processing conditions on the chemical composition and lattice parameter of titanium nitride structure during the carbothermic reduction of rutile in the presence of nitrogen gas. We also report the thermodynamic phase equilibria in the Ti-C-N-O system. A comparison between the predicted and measured thermodynamic properties of interstitial ceramics is also reported. The rate of reduction of rutile has been examined and the results of the temperature coefficient of overall rate of reduction with graphite and charcoal are compared.

Experimental Methods

Titanium dioxide (TiO_2, rutile) and carbon in the graphitic and charcoal forms were used as the starting materials. The particle size of TiO_2 was in the submicrometer range where as the average size of the graphite flakes were approximately 25-50 μm and, the activated charcoal was in the 10-50 μm size range. TiO_2 and carbon were weighed in stoichiometric amounts. The weighed materials were thoroughly dry-mixed, ground in an agate mortar and then pressed in a 6mm inner diameter steel die to form cylindrical shape pellets. The pressure used was 3kN cm^{-2}. A silicon carbide resistance tube furnace was employed for heating the pelletised mixtures. Prior to isothermally heating the pellets, these samples were transferred inside a graphite crucible. The compacted pellets were held for several hours by selecting an isotherm in the range 1173 to 1823 K. Each pellet took approximately less than few minutes to reach the selected isotherm. It was recorded that the weight loss sustained by a pellet while reaching an isotherm was insignificantly small in comparison to the total expected weight loss. The gas was dried using silica gel, and

anhydrous sodium carbonate. Prior to heating the sample in the reaction chamber[4], it was purged with N_2 gas for several minutes in order to rid it from the residual oxygen. The typical gas flow rate in all experiments was 500 ml min^{-1}.

After each isothermal hold, the pellets were weighed for the calculation of percentage reduction using the formula **$\%R = (W_t/W_o)x100$**, where W_t is the total weight loss sustained by the pellet at a given time t and W_o is the total stoichiometric weight loss determined from the reaction, for example: $TiO_2 + 2C + \frac{1}{2}N_2 = TiN + 2\ CO$ (g). In some reaction, an excess of carbon (TiO_2:C>2-3) was added for studying the effect of enhanced reduction reaction surface area. For these reactions with excess carbon, the values of W_o were recalculated for obtaining the corresponding values of %R as a function of time. The phases present in the reacted pellets were determined by X-ray powder diffraction technique using Cu-k1 radiation (0.15406nm). The powder diffraction results were used for determining the lattice parameters of the titanium nitride phase for a given set of processing conditions.

Results and Discussion

The rate of titanium nitride reactions and activation energy barrier

The rates of reduction curves were constructed by plotting %R as a function of time for each isotherm. The effects of increase in the reaction temperature on the reducibility of TiO_2 in the presence of nitrogen gas for graphitic carbon and activated charcoal as reducing agents are compared in **Figure 1** and **Figure 2** respectively. It is evident from the comparison of the rates of reaction data that graphite has an adverse effect on the overall rate of the TiN formation reaction at any temperature. The initial rate (regime I in figures 2 and 3) of reduction-nitridation reaction however appears to be relatively similar in both cases during which the extent of reduction appears to be only dependent on the isotherm chosen. However, there does not appear to be a major dependence on the rate of reaction in reaction I, indicating that the energy barrier could be relatively small compared to the regime II. The difference in the rate of reaction was more discernible in the regime II which commenced approximately after 10 minutes in the reaction from time, t = 0 minute. With charcoal, the extent of the reaction was also found to be higher in comparison to graphite. At temperatures higher than the 1473 K, the reaction reached completion within few hours with the activated charcoal. This was indicated by the presence of a long plateau in the terminating stage of reaction, designated as the regime III. The regime III was found to be less apparent with charcoal as a reducing agent. The overall extent of reaction was also found to exceed well above 100% R with charcoal. By plotting the slopes of the reactions in regimes II and III, given by ln (d%R/dt, $\%Rs^{-1}$), against the reciprocal temperature, the values of activation energies can be derived from the Arrhenian relationship ie **$rate = (d\%R/dt) = A_o exp(-Q/RT)$**. In this equation, A_o is the pre-exponential, R is the universal gas constant (8.314 J mol^{-1} K^{-1}) and Q is the activation energy in Joules per mole unit. For regimes II and III in the case of graphite, the values of Q were found to be 130 ± 15 kJ mol^{-1} and 105 ± 10 kJ mol^{-1} respectively (see **figure 3**). The derived values of slopes for regime II in the case of graphite and charcoal also appears to be similar within the experimental error. By comparing the magnitude of the barrier with the activation energy barrier (110-120 kJ) for oxygen ion diffusion in rutile lattice, the rate determining step could be the oxygen transport in either rutile lattice or sub-oxides that exist during the course of reaction[3].

Phases identified and their relationship with the observed rates

Predominant phases formed and identified as a consequence of reduction reaction in each regime of reaction are summarised in **Table I**.

Table I: **Summary of phases formed after stages I, II and III. ** designates the trace amount of the phase. Phases are arranged in the decreasing order of relative intensities. Mixture composition: TiO_2:C=1:3.**

T, K	Time, hour	Phases identified	
		Graphite Reductant	Charcoal Reductant
1473	0.1 (I) 0.7 (II) 4.0 (III)	C, Ti_9O_{17}, TiO_2** C, Ti_6O_{11}, Ti_5O_9 C, Ti_3O_5, TiCN**	Ti_5O_9, Ti_4O_7 Ti_3O_5, TiCN Ti_3O_5, TiCN
1573	0.1(I) 0.7(II) 4.0(III)	C, Ti_4O_7, Ti_3O_5 C, Ti_3O_5, TiCN C, Ti_3O_5, TiCN	Ti_3O_5, TiCN TiCN, Ti_3O_5 TiCN
1673	0.1(I) 0.7(II) 4.0(III)	C, Ti_3O_5, TiCN C, Ti_3O_5, TiCN C, TiCN, Ti_3O_5	TiCN, Ti_3O_5 TiCN TiCN
1773	0.1(I) 0.7(II) 4.0(III)	C, Ti_3O_5, TiCN C, TiCN, Ti_3O_5 TiCN, C	TiCN TiCN TiCN

From the summary of phase analysis, it is apparent that the majority of TiO_2 reduces to lower oxides. With increasing temperature and time, TiCN phase forms and appears to be in equilibrium with carbon and Ti_3O_5. The unreacted carbon was not found as a phase for reduction reactions with activated charcoal. It is therefore suffice to summarise the phase analysis results that in the first stage (regime I) the defect structure of rutile transforms to lower triclinic oxides e.g. Ti_5O_9 and monoclinic Ti_3O_5 oxide. In regime II, Ti_3O_5 and other oxides are nitrided and reduced to form TiCN phase with some oxygen atoms sharing interstitial sites with C and N atoms. In regime III, the equilibrium between the oxygen-rich carbonitride phase, carbon and nitrogen gas exists.

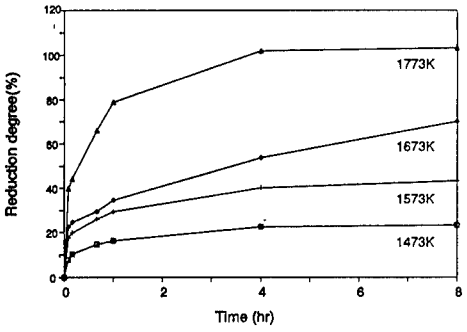


Figure 1 %R versus time (t) curves for graphite

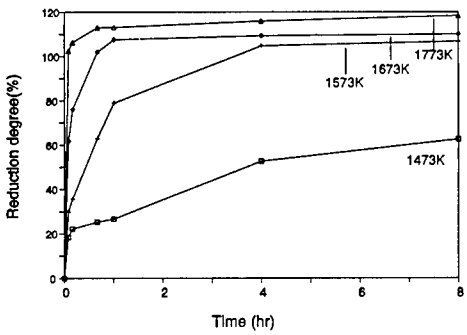


Figure 2 %R versus time (t) curves activated charcoal.

Lattice parameter of Titanium nitride

The change in the lattice parameter of TiCN phase was determined from the measured d-spacings of this phase, using $\mathbf{1/d^2 = (h^2+K^2+l^2)/a^2}$ equation. In this equation, (hkl) are the Miller indices of the FCC lattice and "a" is the lattice parameter. As an example, the variation of the lattice parameter as a function of time at a given isotherm is plotted for activated charcoal in **figure 4**. A similar kind of trend was also observed for graphite, in which the value of the lattice parameter at shorter period of time rose sharply and then dropped at a comparatively slower rate. The lattice dimension slowly increased with time at a given temperature chosen between 1573 K and 1773 K. In **figure 5**, the relationship between the lattice parameters of TiC, TiN and TiO phases are compared with other complex nitride phases formed in this investigation. The lattice parameters determined in the investigation suggest that the relationship is linear and the linearity even extends between TiN and TiO. The dependence of the lattice parameter on the concentrations of interstitial atoms such as O, N and C strongly indicate that the TiN, TiO and TiC form an extended solid solution. In the solid solution lattice, oxygen, nitrogen and carbon are randomly distributed and may even follow ideal distribution. The ideality of the distribution of interstitial atoms was verified by considering the Gibbs free energy equation, say for example for $TiC_{1-x}O_x$ at 1580K[5]:

$$\Delta G_{OC} = X_c.\Delta G_{TiC} + X_o.\Delta G_{TiO} + RT\{X_c.\ln X_c + X_o.\ln X_o\} \qquad ...(1)$$

A comparison of the measured ΔG_{OC}[5] and calculated values are plotted in **figure 6.** On the basis of the Gibbs free energy approach, the stabilities of, for example, $TiC_{1-x}N_x$ and $TiN_{1-x}O_x$ can be estimated and these are also compared in **figure 6**. On the basis of the Gibbs free energy mixing, enthalpy of fusion of the end members, estimated on the basis of the Richard's rule, the equilibrium composition versus temperature relationship has been plotted in **figure 7**.

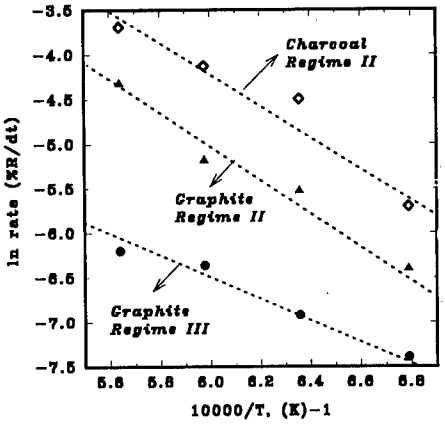


Figure 3: A comparison of the Arrhenian slopes

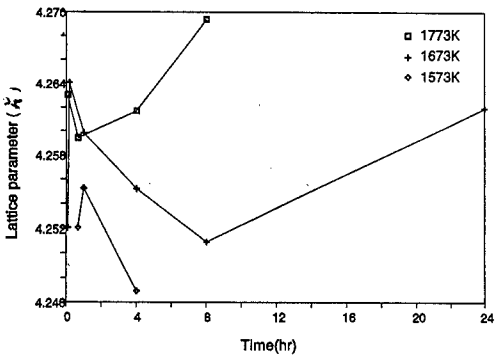


Figure 4: Variation of lattice parameter of TiCN phase a function of time at temperatures indicated.

Conclusions

Titanium oxide can be reduced to TiCN phase in the presence of carbon in a nitrogen atmosphere. A complete conversion of rutile to TiCN is possible above 1573K using either graphite or activated charcoal; the rate was found to be faster at a given temperature with

charcoal. The reaction progresses in three different stages, I, II and III, and for the latter two stages the derived values of activation energies are 130 ± 15 kJ mol^{-1} and 105 ± 10 kJ mol^{-1} respectively. The changes in the lattice parameter of TiCN as a function of time indicates that the complex carbonitrides form and maintain equilibrium with Ti_3O_5 and oxygen containing carbonitride phases. The complex carbonitride phase forms an ideal solution with cubic TiO, TiN and TiC.

References

[1] E. K. Storm, *The Refractory Carbides*, Academic Press, 1967, New York, P.6.

[2] L. E. Toth, *Transition Metal Carbides and Nitrides*, Academic Press, 1971, New York, pp.36-45.

[3] W. D. Kingery , H. K. Bowen, and D. R. Uhlmann, *Introduction to Ceramics*, John wiley & Sons, p.241.

[4] S. J. Yoon and A. Jha, *J. Materials Science*, **31**, 1996, P. 2266.

[5] A. Ouensanga, *J. Less. Comm. Metals,* **63** (1979) pp.225-235.

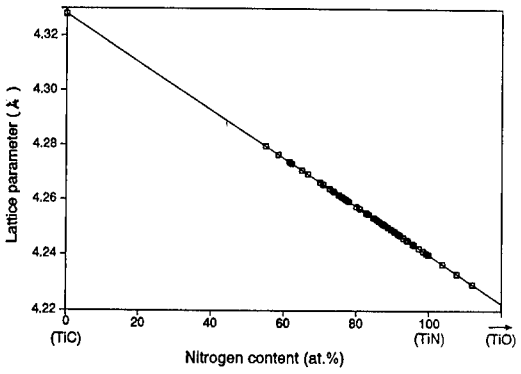


Figure 5: A comparison of the lattice parameter of TiCN phase with the TiC-TiN line.

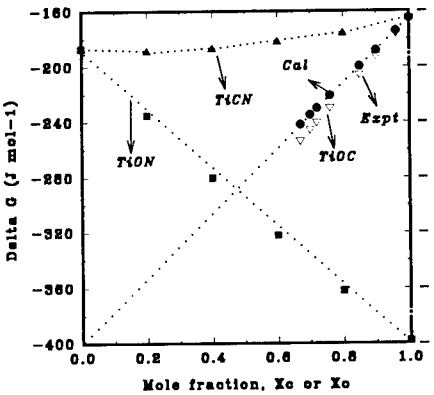


Figure 6: A plot of the Gibbs free energies of complex interstitials as a function of carbon and oxygen composition.

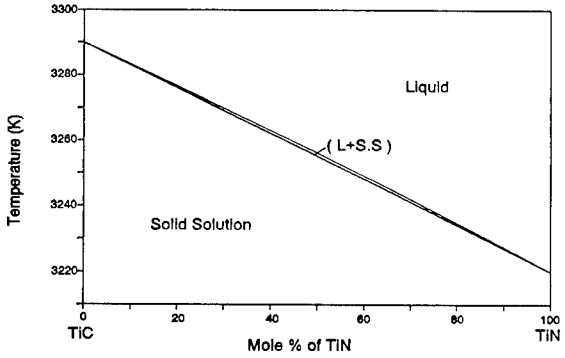


Figure 7: Computed phase equilibrium relationship between TiC and Tin phases.

ORDER - MESOSCOPIC TRANSFORMATION IN COMPOUND SEMICONDUCTER In_2Te_3

Satoko Abe, Eiki Inoue, Yoshio Nakamura and Osamu Nittono

Department Metallurgical Engineering
Tokyo Institute of Technology, Tokyo 152-8852, Japan

Abstract

Structures of the low and the high temprerature In_2Te_3 and phase transformation between them were investigated by X-ray diffraction together with high resolution electron microscopy and diffraction. The low temperature In_2Te_3 is the vacancy order phase, where deviation of co-ordination numbers for Se atoms is minimized as much as possible. In the high temperature In_2Te_3, most parts of the structural vacancies are aggregated to form {111} vacancy planes and the rest are statistically distributed in the cation sublattice to form solid solution. Such dual states for structural vacancy in the high temperature In_2Te_3 is responsible for the phase transformation which is sometimes fast and sometimes slow. The phase transformation is no longer order - disorder transformation but order - mesoscopic transformation.

The Third Pacific Rim International Conference on
Advanced Materials and Processing (PRICM 3)
Edited by M.A. Imam, R. DeNale, S. Hanada,
Z. Zhong and D.N. Lee
The Minerals, Metals & Materials Society, 1998

Introduction

In_2Te_3 is one of the III_2VI_3 compound semiconductors which is based on zincblende structure. In order to compensate the valence mismatch between group III and VI atoms, vacancies are introduced in the cation sublattice. As a result, one third of the cation sites are vacant [1,2]. Previous studies on In_2Te_3 have shown the exsistence of two phases; the high temperature In_2Te_3 and the low temperature In_2Te_3 [3,4]. According to the results, high temp. In_2Te_3 was zincblende structure, in which structure vacancies statistically occupied one third of cation sites. On the other hand, the low temp. In_2Te_3 was vacancy ordered phase so that the phase transformation between two phases was regarded to be order - disorder transformation [3]. Some defects or precipitates, however, were observed in both two phases [4]. It suggested that both two phases were not always homogeneous.
We previously studied the structure of Ga_2Se_3 which is very similar to In_2Te_3 concerning chemical bond nature. It is true that the low temperature Ga_2Se_3 is a vacancy ordered phase. However, structure vacancies were found to be aggregated to form {111} vacancy planes in the high temp. Ga3Se3 although basic structure was really zincblende structure [5,6]. In this paper, structures of the low and the high temperature In_2Te_3 and phase transformation are investigated considering the results of phase tranformation in Ga_2Se_3.

Experimental

As raw materials, commercial In_2Te_3 powder are used(kojyundo chemical Co. Ltd, Japan). Specimen powders were set in evacuated silica tubes and then melted at 700 ℃. After verious heat treatments, specimes for experiments were obtained. The crystal structures and the characteristics of the two phases were investigated using powder X-ray diffractometer (40 kV, 300 mA) and transmission electron microscopes(JEM-3010, JEM-200CX).

Results and discussion

Transformation temperature (Tc)

Air cooled specimens from melts at 700 ℃ were annealed at various temperatures from 500 to 650 ℃. Figures 1 (a) and (b) are powder X-ray diffraction charts of In_2Te_3 annealed at 610 and 620 ℃ for 48 h, respectively. All the reflections in Fig. 1 (b) are indexed by zincblende structure. In addtion, some weak reflections are observed in Fig. 1(a). Roughly speaking, the high temperature In_2Te_3 is zincblende structure and the low temperature In_2Te_3 is the order phase based on zincblend structure. These indicate that the phase transition temperature (Tc) is determined to be 615 ± 5℃ and order - disorder transition which was concluded by Woolley et. al. [3] seems right.

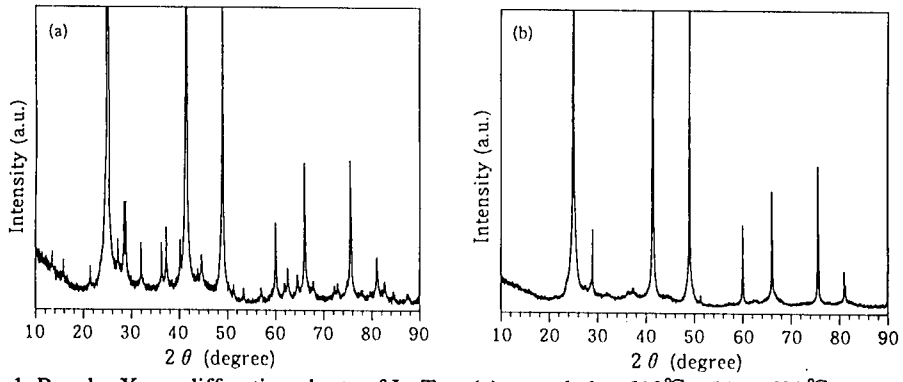


Fig.1 Powder X-ray diffraction charts of In_2Te_3. (a) annealed at 610℃, (b) at 620℃.

Structure of low temperature In2Te3

Figure 2 is an X-ray diffraction chart of the low temperature In_2Te_3. (specimen: air cooled

from melt at 700 ℃, annealed at 500 ℃ for 48h) The fundamental reflections even at higher Bragg angles don't show peak splitting although vacancy ordering is well developed. It is a remarkable feature that the average lattice is still cubic after vacancy ordering. Figure 3 is the electron diffraction patterns of the low temp. In_2Te_3. Extra reflections are observed at one and two thirds positions along an [110]* direction between fundamental reflections. Considering this, all the X-ray reflections are indexed by h±2/3, k±2/3, l, where, h k l are unmixed indexes for cubic zincblende structure. This agrees with the result by Woolley et. al. [3]. The space group of low temperature In2Te3 is *Imm2* and the lattice constants are $a = 3/\sqrt{2}\, a_0$, $b = 1/\sqrt{2}\, a_0$, $c = a_0$, where a_0 is the lattice constant as a cubic lattice and is 6.164 Å. In this structure, In coordination number for each Se atom is limited to be 2 or 3 and the exsistence ratio is 1 : 2. At this condition, deviation of co-ordination number from average co-ordination number(4x2/3 = 8/3 = 2.67) is minimized as much as possible. The two facts that low temp. In_2Te_3 is pseudo-cubic and the deviation of co-ordination number is minimized are most important characteristics for the structure. Details of structure of low temp. In_2Te_3 including atomic positions will be mentioned elsewhere.

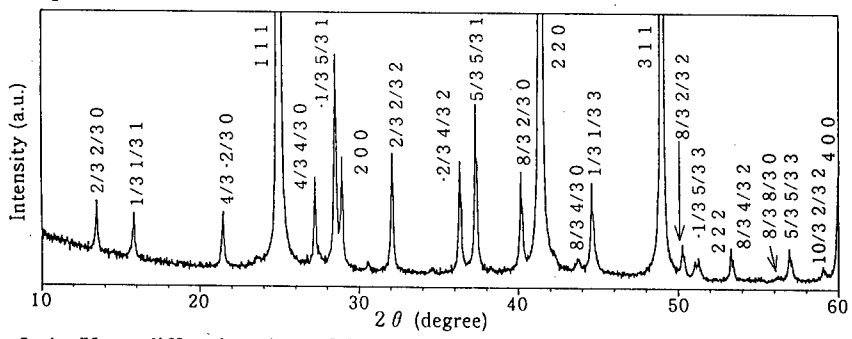


Fig.2 An X-ray diffraction chart of the low temperature In_2Te_3.
(specimen: quenched into water from melt at 700℃, annealed at 500℃ for 48h)

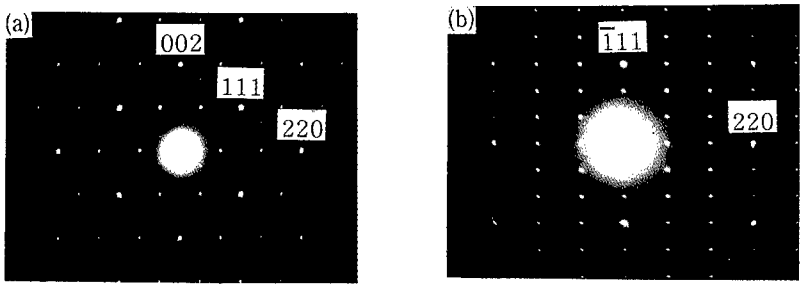


Fig.3 Electron diffraction patterns of the low temperature In_2Te_3.
(a) beam // [1T0] Z.B. (b) beam // [1T2] Z.B.

Structure of high temperature In2Te3

Figure 4 is an X-ray diffraction chart of the high temp. In_2Te_3.(specimen: quenched into water from melt and held at 650 ℃ for 48h) All the peaks are indexed by zincblende structure, as is previously mentioned. The lattice constant is 6.163 Å and it indicates the lattice constants as cubic unit cells are almost identical irrespective of ordering of structure vacancy. All the peaks are sufficiently sharp except for the 111 reflection. The 111 peak accompanies remarkable tailing. Figures 5 are electron diffraction patterns taken along the <110> and <211> directions. The diffraction pattern only shows the zincblede type of spots. However, streaks along the <111>* directions in reciprocal lattce are clearly observed. This is consistent with the result of X-ray diffraction. Corresponding to the streaks along the <111>* direction, {111} planer defects are frequently observed in the high resolution electron micrograph (Fig. 6). The distance between neighbouring two planer defects is roughly estimated

to be 15 {111} planes. Such planer defects never diminish after prolonged annealing in the high temp. region, and therefore they are essential for high temp. In_2Te_3. Such a characteristic is consistent with the results of Ga_2Se_3. On the analogy of Ga_2Se_3, {111} planer defects are considered to be vacancy planes. In other words, most of the structure vacancies are two dimensionally aggregated to form {111} vacancy planes. However, it is impossible to accomodate all the structure vacancies by such the observed vacancy plane density. Therefore, some part of the structure vacancies exists inside the area surrounded by vacancy planes as statistically resolved vacancies. Under the condition of high temp. In_2Te_3, the content of structure vacancy is not unform on the scale of unit cell. However, it is uniform on the mesoscopic scale in which several ten or hundred thousand atoms are. In this sence, high temp. In_2Te_3 should be not only random solid solution but mesoscopic phase.

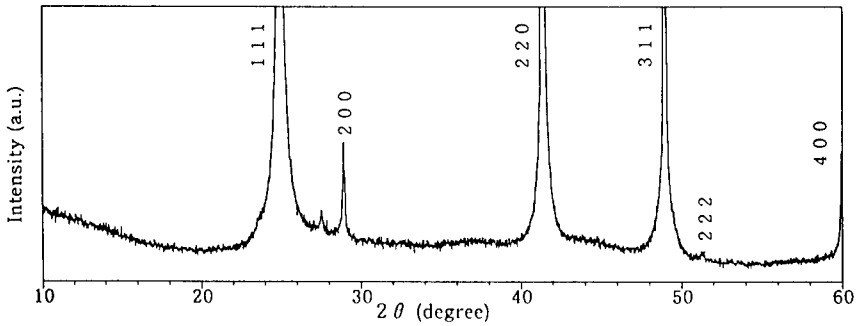


Fig.4 An X-ray diffraction chart of the high temprature In_2Te_3.
(specimen: slowly cooled from melt and held at 650℃ for 48h)

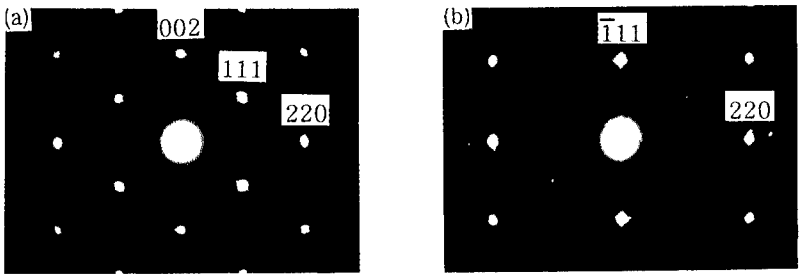


Fig.5 The electron diffraction patterns of the high temperature In_2Te_3.
(a) beam//[1T0] Z.B. (b) beam//[1T2] Z.B.

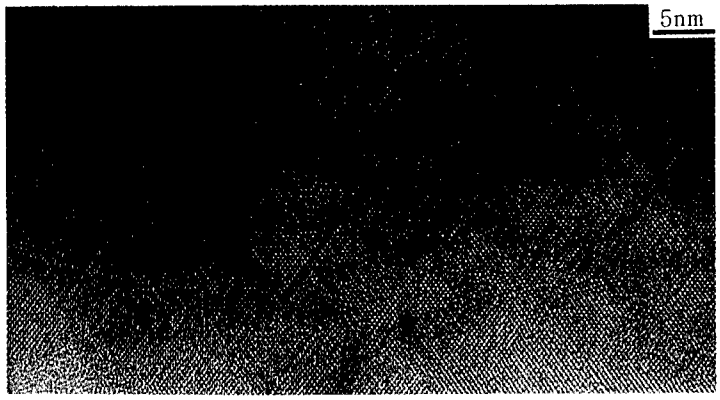


Fig.6 High resolution electron micrograph of high temperature In_2Te_3 showing {111} planer defects. Incident beam direction is along the <110> direction.

Rapid and slow transformation

Next, we investigate the effect of inhomoginity of structure vacancy to the phase transformation. The effect of difference in quenching rate to the formation of low temp.phase is examined in Figures 7(a) and (b). Slowly cooled specimen after annealing at 650 ℃ for 48h shows weak and broad order reflections in the X-ray diffraction chart. This indicates that phase transformation from the high temp.phase to the low temp. phase is very rapid, in a sense. Figure 7 (c) shows the X-ray chart of the specimen annealed at 610 ℃ for 48h after same heat treatment of Fig. 7 (b). These two charts are almost identical in spite of annealing below Tc. This means phase transformation is very slow. The phase transformation is sometimes rapid and sometimes slow. Such contradictive results suggest that the high temp. In_2Te_3 contains two contradictory factors for phase transformation; one is solved vacancy in the matrix and the other is vacancy forming vacancy planes. The solved vacancies in the matrix contribute to rapid ordering, whereas vacancy planes are very hard to resolve and therefore ordering takes place slowly. Using specimen cooled from melt to suppress the development of vacancy planes, a comparison was made. Figures 8 (a) and (b) are X-ray diffractions of specimens annealed at 610 ℃ for 48h. Only the differnce is cooled from melt or annealed at 650 ℃ for 48h prior to the annealing. Ordering is more developped in the former than that in the latter. Such phenomena are well explained by the consideration that vacancy contents solved in matrix is higher in the melt cooled specimen. The solved vacancy is indispensable for rapid development of ordering.

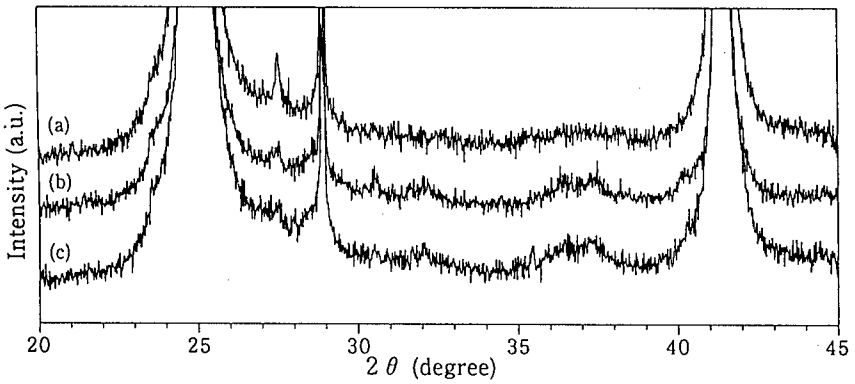


Fig.7 A comparison of X-ray diffraction charts of In_2Te_3. (a) water quenched after annealing at 650℃ for 48h, (b) air cooled after annealing at 650℃ for 48h and (c) annealed at 610℃ for 48h after same heat treatment of (a).

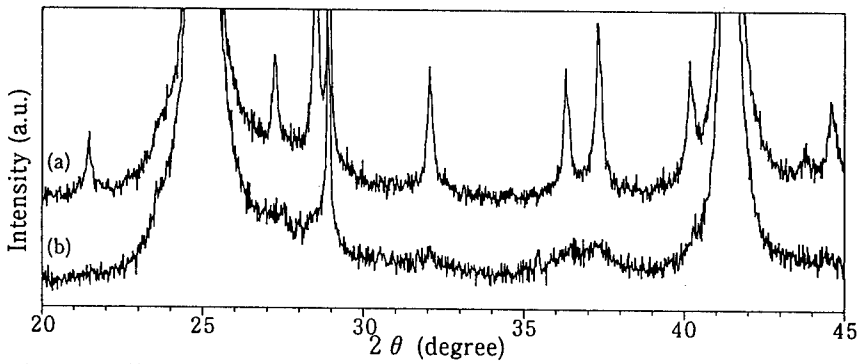


Fig.8 X-ray diffraction charts of specimens (a) air cooled from melt and (b) annealed at 650℃ for 48h prior to final annealing at 610℃ for 48h.

Figure 9 is a high resolution electron micrograph showing the interface of the high and the low temperature In_2Te_3. The upper part is the high temperature phase whereas the lower part

is the low temperature phase. The crystallinity is very good in the vacancy ordered phase except near the interface. On the other hand, {111} planer defects are remarkable. This is the main characteristic of the high temp. phase. In addtion, some small ordered regions heterogeneously nucleated around the intersection of two vacancy planes are imaged. The small ordered regions is the origin of the broad and weak ordered reflections in the Fig. 7(b) and (c). Orientation relationship between two phases is the parallel one. At the interface, the density of planer defects seems lower. Some of the planer defects, however, still remain. This is a direct evidence that the {111} vacancy plane is very hard to resolve even under the tansformation temperature (Tc).

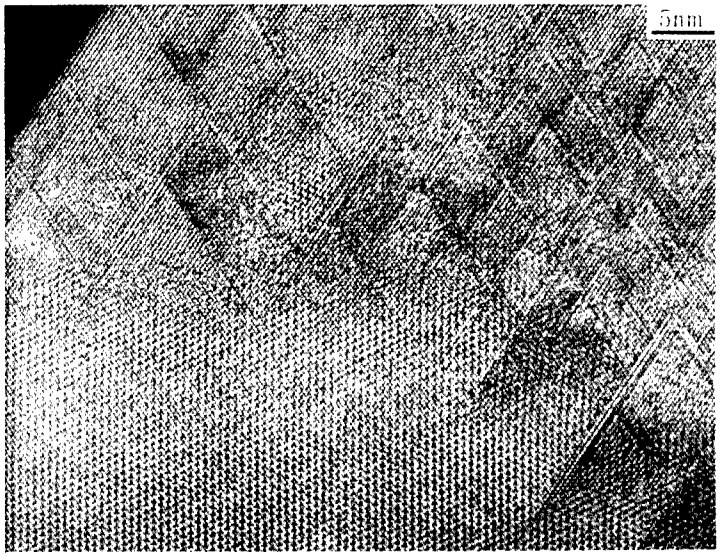


Fig.9 A high resolution electron microhraph showing the interface of the high and the low temperature In_2Te_3. Incident beam direction is along the <110> direction of cubic zincblend.

Conclusion

The high temperature In_2Te_3 is a mesoscopic phase based on zincblende structure and the low temp. phase is vacancy ordered phase. The phase transformation is not only order - disorder but order - mesoscopic one. In the high temp. In_2Te_3, there exist two states for structure vacancy; the ones are the vacancy planes and the rest are statistically distributed in the cation sublattice to form solid solution. Such dual states for structural vacancy is responsible for the curious phase transformation which is sometimes fast and sometimes slow.

This work was partly supported by Foundation for Promotion of Material Science and Technology of Japan.

References

1. H. Hahn and W. Klinger; Z. Anorg. Chem., 259 (1949) 802.
2.A. Miller, A. MacKinnon and D. Weaire; Solid State Phys., 36 (1981) 119
3. J.C. Woolley, B.R. Pamplin and P.J. Holmes; J. Less-Common Metals, 1 (1959) 362.
4. P.J. Holmes, I.C. Jennings and J.E. Parrott; J. Phys. Chem. Solids 23 (1962) 1.
5. T. Hanada, Y. Nakamura and O. Nittono; Trans. MRS-Japan, 20 (1996) 743.
6. T. Hanada;"Crystal Structures and their Stabilization Mechanism of Compound Semiconductor including Structure Vacancies" (Dr. thesis, Tokyo Institute of Tech, 1997)

THEORETICAL INVESTIGATION OF THE CUBIC-TO-TETRAGONAL TRANSITION IN ZrO_2-BASED ALLOYS

Junji KATAMURA*, Yuichi IKUHARA and Taketo SAKUMA

Department of Materials Science,
School of Engineering,
the University of Tokyo,
7-3-1, Hongo, Bunkyo-ku, Tokyo, 113, Japan.
*Graduate student, the University of Tokyo.

Abstract

The cubic-to-tetragonal(c-t) phase transition in ZrO_2 alloys was analyzed using a thermodynamic model based on the Landau's phenomenological theory. The calculated c-t two-phase field in the system ZrO_2-R_2O_3(R:Nd, Sm, Gd, Y) corresponds well to the experimental c-t phase equilibria reported before. The generation of the domain structure with curvilinear anti-phase domain boundaries and the modulated structure with a regularly-spaced lamellar in ZrO_2-Y_2O_3 can be predicted from this model through computer simulation of microstructural evolution.

The Third Pacific Rim International Conference on
Advanced Materials and Processing (PRICM 3)
Edited by M.A. Imam, R. DeNale, S. Hanada,
Z. Zhong and D.N. Lee
The Minerals, Metals & Materials Society, 1998

Introduction

The cubic-to-tetragonal(c-t) phase transition in ZrO_2 alloys doped with cubic-stabilizing oxides has been widely examined. The characteristic microstructures associated with the c-t phase transition were observed, in particular, in ZrO_2-Y_2O_3, i.e. the domain structure with curvilinear anti-phase domain boundaries(APBs) formed during rapid cooling from a high temperature[1], [2] or the modulated structure formed during annealing in the c-t two-phase field[3]-[5]. The system ZrO_2-R_2O_3(R:rare earth elements) have the similar cubic-stabilizing effect with ZrO_2-Y_2O_3[6], [7], but their c-t phase equilibria and the microstructural evolution depends on the type of R^{3+}[7], [8].

Computer analysis has become popular to examine the phase transition, phase equilibria and the simulation of microstructural evolution. Two types of computer analysis were carried out for the c-t phase transition in ZrO_2 alloys; the one assumes a first-order c-t phase transition[9]-[14] and the other is based on a second-order one[15]-[17].

In the present work, the phase equilibria and the microstructural evolution caused by the c-t phase transition in binary ZrO_2 alloys are described from the latter assumption.

Thermodynamic analysis

The c-t phase transition temperature, T_c in binary ZrO_2 alloys is given as a function of composition x as follows[7],

$$T_c = T_c^\circ\left(1-\frac{x}{x_c}\right)^{1/2} \tag{1}$$

where x_c is the composition at $T_c = 0\,\mathrm{K}$, and T_c° is the transition temperature of pure ZrO_2, which is reported to be 2650K[18]. According to the Landau's phenomenological theory[19], the free energy of a system G around T_c can be represented as a function of x, order parameter $\eta_i (i = 1,2,3)$ and temperature T. In this analysis, we will consider a single orientation variant only, where $\eta_1 = \eta$ and $\eta_2 = \eta_3 = 0$. Then, it is enough to write G as follows[16],

$$G(x,\eta,T) = G_0(x,T) + a\left(T - T_c(x)\right)\eta^2 + B\eta^4 \tag{2}$$

where $G(x,\eta,T)$ is the free energy independent of η. The parameters a and B are determined from the thermodynamic data[16], [18],

$$-\frac{a^2 T_c^{\circ 2}}{4B} = -40\,\mathrm{kJ/mol}. \tag{3}$$

This model can explain the experimental phase boundaries and the spinodal region in binary ZrO_2-Y_2O_3 system[16], where x_c is assumed to be 11.6mol%Y_2O_3[7], [20]. For the system ZrO_2-R_2O_3, x_c is not dependent on the type of dopant cation, but $G_0(x,T)$ depends on ionic radius, $r_{R^{3+}}$ [7]. Figure 1 shows the calculated c-t two-phase fields in four ZrO_2-R_2O_3(R:Nd, Sm, Gd, Y) systems[21]. The calculated phase boundaries agree well with the experimental data[7] for all binary systems.

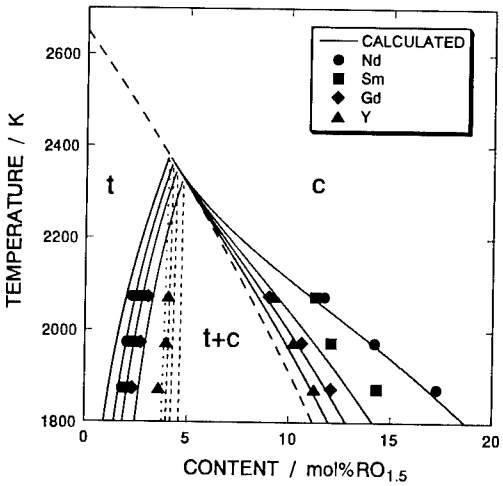


Figure 1 : Calculated phase boundaries in the system ZrO_2-R_2O_3(R:Nd, Sm, Gd, Y) together with the experimental data[7]. Solid lines exhibit the calculated one.

Microstructural evolution

Microstructural evolution associated with the c-t phase transition can be simulated by computation from the present thermodynamic model[17]. We used the

time-dependent Ginzburg-Landau(TDGL) kinetic model[22], [23], which describes the temporal and spatial evolutions of $\eta(\boldsymbol{r},t)$-, and $x(\boldsymbol{r},t)$-fields towards an equilibrium state to minimize the total free energy of the system, $F(x(\boldsymbol{r},t),\eta(\boldsymbol{r},t))$. From the diffuse interface theory by Cahn and Hilliard[22], the $F(x(\boldsymbol{r},t),\eta(\boldsymbol{r},t))$ is given by,

$$F(x(\boldsymbol{r},t),\eta(\boldsymbol{r},t)) = \int_V \frac{1}{2}\varepsilon_x^2|\nabla x|^2 + \frac{1}{2}\varepsilon_\eta^2|\nabla \eta|^2 + G(x,\eta,T) + \kappa E_{\text{strain}} dV \tag{4}$$

where ε_x and ε_η are the gradient energy coefficients for the $x(\boldsymbol{r},t)$- and $\eta(\boldsymbol{r},t)$-fields, respectively, and κ is the positive coefficient. The E_{strain} is the strain energy associated with the c-t structural phase transition[11]-[14]. The strain energy can be written in the reciprocal space[24]:

$$E_{\text{strain}} = \frac{1}{2}\int \frac{d\boldsymbol{k}}{(2\pi)^3} V(\boldsymbol{n})\left|\{\eta(\boldsymbol{r},t)\}_k\right|^2 \tag{5}$$

$$V(\boldsymbol{n}) = c_{ijkl}\varepsilon_{ij}^0\varepsilon_{kl}^0 - n_i\sigma_{ij}^0\Omega_{jk}(\boldsymbol{n})\sigma_{kl}^0 n_l \tag{6}$$

where c_{ijkl} is the elastic constants and ε_{ij}^0 is the stress-free strain estimated from the lattice parameters of c- and t-ZrO_2[25], and

$$\sigma_{ij}^0 = c_{ijkl}\varepsilon_{kl}^0 \tag{7}$$

$$\Omega_{jk}^{-1}(\boldsymbol{n}) = c_{ijkl}n_i n_l \tag{8}$$

$$\boldsymbol{n} = \boldsymbol{k}/|\boldsymbol{k}|. \tag{9}$$

The temporal and spatial evolution of the $x(\boldsymbol{r},t)$- and $\eta(\boldsymbol{r},t)$-fields is written by the following partial differential equations[22],[23]:

$$\begin{cases} \dfrac{\partial x(\boldsymbol{r},t)}{\partial t} = M\nabla^2 \dfrac{\delta F(x(\boldsymbol{r},t),\eta(\boldsymbol{r},t))}{\delta x(\boldsymbol{r},t)} \\ \dfrac{\partial \eta(\boldsymbol{r},t)}{\partial t} = -L\dfrac{\delta F(x(\boldsymbol{r},t),\eta(\boldsymbol{r},t))}{\delta \eta(\boldsymbol{r},t)} \end{cases} \tag{10}$$

where L and M are the kinetic coefficients. The calculation was made for the two-dimensional system with 128×128 mesh. The parameters used in this calculation are $a = 30.2$, $B = 40000$, $M = 6.0\times10^{-6}$, $\kappa = 35$, $\varepsilon_\eta = 45$ and $\varepsilon_x = 5$ for arbitral time and space[17]. It is further assumed that c- and t-ZrO_2 have the same elastic constants reported in the previous literature[26].

Figure 2(a) shows the calculated $\eta^2(\boldsymbol{r},t)$-field for ZrO_2-6mol%Y_2O_3 rapidly cooled from a single c-ZrO_2 field to a room temperature. In this calculation, the kinetic coefficient ratio M/L is chosen to be zero, because the diffusion of cations must be suppressed during rapid cooling. The calculated curvilinear boundaries are similar to the domain boundaries observed in the same alloy rapidly cooled after arc-melting(Fig.2(b)). The boundaries of Fig.2(a) have a finite width and are expected to have a cubic-like structure[17].

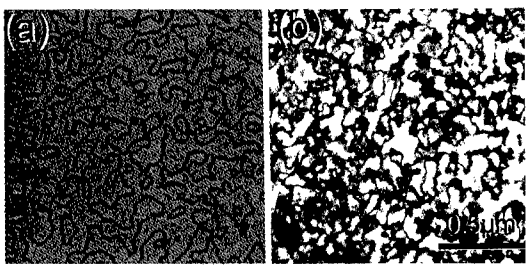


Figure 2 : Calculated $\eta^2(\boldsymbol{r},t)$-field of ZrO_2-6mol%Y_2O_3 rapidly cooled from a single c-ZrO_2 field to a room temperature(a) together with the observed microstructure in arc-melted ZrO_2-6mol%Y_2O_3(b).

Figure 3(a) shows the calculated $\eta^2(\boldsymbol{r},t)$-field for ZrO_2-4mol%Y_2O_3 annealed at 1773K(c-t two-phase field). The M/L is assumed to be 1.0×10^{-2}. Fig.3(b) is the lamellar structure with a {111} habit plane formed by the same heat treatment[3]-[5]. This lamellar structure is well simulated by the calculation.

Next, the microstructural evolution during diffusional c-t phase decomposition in several binary ZrO_2-R_2O_3 systems will be discussed from computer simulation. Since no experimental data are obtained for the elastic constants in these alloys, it is tentatively assumed that the constants are not dependent on the type of dopant cation. Figure 4 shows the temporal evolution of the $\eta^2(r,t)$-fields simulated for four ZrO_2-4mol%R_2O_3 annealed at 1773K. In this figure, τ represents the arbitral time step. The lamellar structure is developed in all ZrO_2-R_2O_3 as well as ZrO_2-Y_2O_3 (Fig.3), but the rate of decomposition is dependent on the system. The decomposition in ZrO_2-4mol%Nd_2O_3 is much faster than that in ZrO_2-4mol%Y_2O_3, e.g. the compositional fluctuation is observed at $\tau = 2.0\times10^3$ in ZrO_2-Nd_2O_3, while it doesn't occur up to $\tau = 3.2\times10^4$ in ZrO_2-Y_2O_3. Actually, this tendency was experimentally verified in a previous report[8]. The diffusion of larger cation may be faster than that of smaller one. However, the kinetic coefficients M and L are taken to be same in all systems, and hence the difference in decomposition rate cannot be explained in terms of diffusion. Another origin is the driving force for decomposition. ZrO_2-4mol%Nd_2O_3 may have larger driving force for decomposition than ZrO_2-4mol%Y_2O_3 at the same annealing temperature. This is consistent of the width of c-t two-phase field in ZrO_2-R_2O_3.

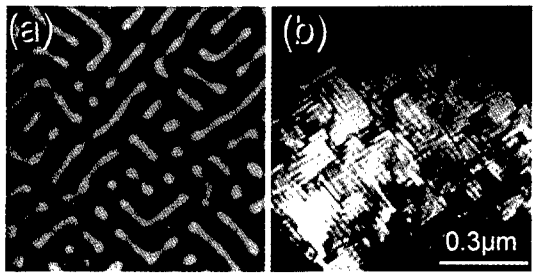


Figure 3 : Calculated $\eta^2(r,t)$-field in ZrO_2-4mol%Y_2O_3 annealed at 1773K(a), together with the observed lamellar structure with a {111} habit plane in ZrO_2-4mol%Y_2O_3 annealed at 1773K(b).

Computer simulation may be useful to predict the microstructure change during heat

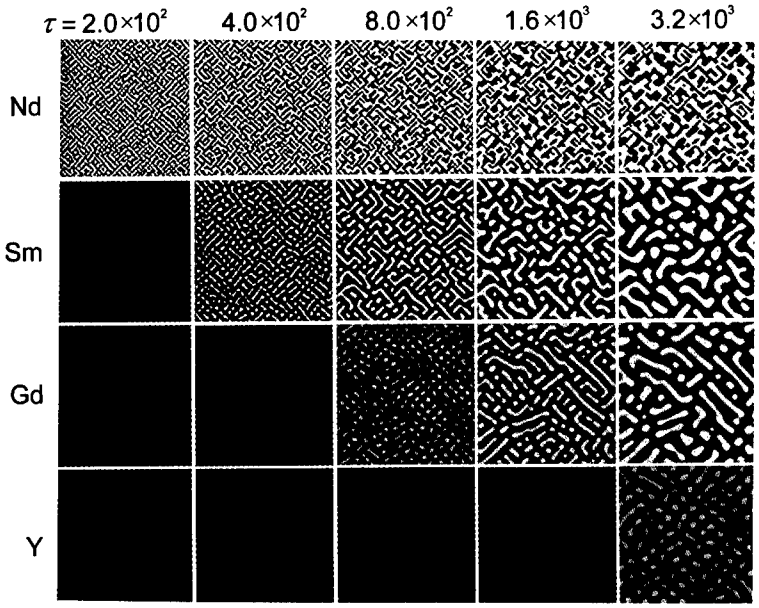


Figure 4 : Temporal evolution of the $\eta^2(r,t)$-field in ZrO_2-4mol%R_2O_3(R:Nd, Sm, Gd, Y) alloy annealed at 1773K. The τ represents the arbitral time step.

treatment in experimentally difficult conditions. One of such examples is the annealing in the single t-ZrO_2 field, because this field is very narrow. Figure 5 shows the calculated microstructures of ZrO_2-1mol%Y_2O_3 annealed in a single t-ZrO_2 field of 1900K. The simulation predicts that yttrium ions are adsorbed in APBs during annealing. This result agrees with the experimental fact that yttrium ions tend to segregate in APBs in ZrO_2-3mol%Y_2O_3-12mol%TiO_2 annealed in the single t-ZrO_2 field[27]. This is caused by the fact that APB has a cubic-like structure[17]. The segregation of yttrium ions in APBs may stabilize the boundaries with cubic-like structure, because yttrium ion has cubic-stabilizing effect.

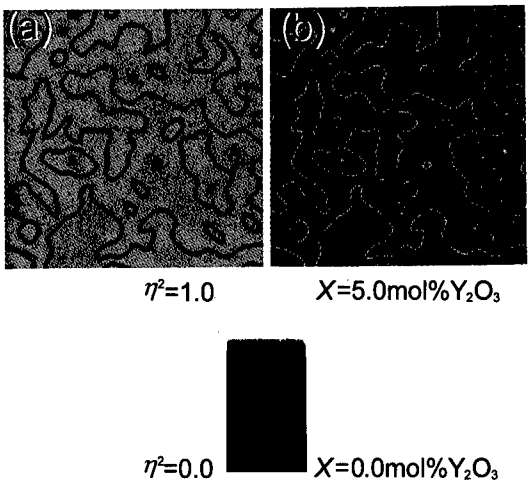


Figure 5 : Calculated $\eta^2(r,t)$-(a) and $x(r,t)$-fields(b) of ZrO_2-1mol%Y_2O_3 alloy annealed at 1900K, where is the single t-ZrO_2 field.

Conclusions

The c-t phase transition in ZrO_2 alloys was analyzed by computational calculation based on the thermodynamic model constructed on the assumption that the c-t phase transition is of a second-order type. It was examined that the c-t two-phase field in the systems ZrO_2-R_2O_3(R:Nd, Sm, Gd, Y) calculated from this model corresponds well with the experimental c-t phase equilibria reported before. The domain structure and the modulated structure calculated by the computer simulation agree fairly well with the experimental observations in ZrO_2-Y_2O_3. The computer simulation also predicts that the rate of c-t phase decomposition is dependent on the type of dopant cation in ZrO_2-R_2O_3(R:rare earth elements) and that the anti-phase domain boundaries tend to adsorb yttrium ions in ZrO_2-Y_2O_3.

Acknowledgment

This work was financially supported by the Grand-in-Aid for Scientific Research on the Priority Area 09242206 from the Ministry of Education, Science and Culture, Japan.

References

1. A.H. Heuer and M. Ruhle, "Phase transformations in ZrO_2-containing ceramics: I, the instability of c-ZrO_2 and the resulting diffusion-controlled reactions," Advances in Ceramics, Science and Technology of Zirconia II. ed. N. Claussen, M. Ruhle and A.H. Heuer (Columbus, OH: The American Ceramics Society, 1984), 1-13.

2. V. Lanteri, "On the microstructures resulting from the diffusionless cubic→tetragonal transformation in ZrO_2-Y_2O_3 alloys," J. Am. Ceram. Soc., 69, (1986), C258-61.

3. T. Sakuma, Y. Yoshizawa and H. Suto, "The modulated structure formed by isothermal ageing in ZrO_2-5.6mol%Y_2O_3 alloy," J. Mater. Sci., 20, (1985), 1085-92.

4. T. Sakuma, Y. Yoshizawa and H. Suto, "The metastable two-phase region in the zirconia-rich part of the ZrO_2-Y_2O_3 system," J. Mater. Sci., 21, (1986), 1436-40.

5. M. Doi and T. Miyazaki, "On the spinodal decomposition in zirconia-yttria(ZrO_2-Y_2O_3) alloys," Philos. Mag. B, 68, (1993), 305-15.

6. M. Yoshimura, "Phase stability of zirconia," Ceram. Bull., 67, (1988), 1950-5.

7. J. Katamura, T. Seki and T. Sakuma, "The cubic-tetragonal phase equilibria in the ZrO_2-

R_2O_3(R=Y, Gd, Sm and Nd) systems," J. Phase Equilibria, 16, (1995), 315-9.
8. T. Sakuma, T. Seki and T. Yamamoto, "The diffusionless cubic-to-tetragonal transition in ZrO_2-R_2O_3 systems(R: rare earths)," Proceedings of the International Conference on Martensitic Transformations (Monterey, CA: Monterey Institute for Advanced Studies, 1992), 671-6.
9. S.A. Degtyarev and G.F. Voronin, "Solution of ill-posed problems in thermodynamics of phase equilibria. The ZrO_2-Y_2O_3 system," CALPHAD, 12, (1988), 73-82.
10. Y. Du, Z. Jin and P. Huang, "Thermodynamic assessment of the ZrO_2-$YO_{1.5}$ system," J. Am. Ceram. Soc., 74, (1991), 1569-77.
11. Y. Wang, H. Wang, L.Q. Chen and A.G. Khachaturyan, "Shape evolution of a coherent tetragonal precipitate in partially stabilized cubic zirconia: A computer simulation," J. Am. Ceram. Soc., 76, (1993), 3029-33.
12. Y. Wang, H.Y. Wang, L.Q. Chen and A.G. Khachaturyan, "Microstructural development of coherent tetragonal precipitates in magnesium-partially-stabilized zirconia: A computer simulation," J. Am. Ceram. Soc., 78, (1995), 657-61.
13. D. Fan and L.Q. Chen, "Computer simulation of twin formation during the displacive c→t' phase transformation in the zirconia-yttria system," J. Am. Ceram. Soc., 78, (1995), 769-73.
14. D. Fan and L.Q. Chen, "Possibility of spinodal decomposition in ZrO_2-Y_2O_3 alloys: A theoretical investigation," J. Am. Ceram. Soc., 78, (1995), 1680-6.
15. M. Hillert and T. Sakuma, "Thermodynamic modeling of the c→t transformation in ZrO_2 alloys," Acta metall mater., 39, (1991), 1111-5.
16. J. Katamura and T. Sakuma, "Thermodynamic analysis of the cubic-tetragonal phase equilibria in the system ZrO_2-$YO_{1.5}$," J. Am. Ceram. Soc., 80, (1997), 2685-8.
17. J. Katamura and T. Sakuma, "Computer simulation of the microstructural evolution during the diffusionless cubic-to-tetragonal transition in the system ZrO_2-Y_2O_3," Acta Mater., accepted for publication.
18. R.J. Ackermann, E.G. Rauh and C.A. Alexander, "The thermodynamic properties of ZrO_2(g)," High Temp., 7, (1975), 304-16.
19. L.D. Landau and E.M. Lifshitz, Toukeibutsurigaku(Statical Physics), 2nd ed. (in Jpn.) (Tokyo, Japan:Iwanami, 1967).
20. M. Yashima, N. Ishizawa and M. Yoshimura, "High temperature X-ray diffraction study on cubic-tetragonal phase transition in the ZrO_2-$RO_{1.5}$ systems (R:rare earths)," Science Technology of Zirconia V, ed. S.P.S. Badwal, M.J. Bannister and R.H.J. Hannink (Lancaster, PA: Technomic Publishing Co., 1993), 125-35.
21. R.D. Shannon, "Revised effective ionic radii and systematic studies of interatmic distances in halides and chalcogenides," Acta Cryst., A32, (1976), 751-67.
22. J.W. Cahn and J.E. Hilliard, "Free energy of a nonuniform system. I. interfacial free energy," J. Chem. Phys., 28, (1958), 258-67.
23. S.M. Allen and J.W. Cahn, "A microscopic theory for antiphase boundary motion and its application to antiphase domain coarsening," Acta Metall., 27, (1979), 1085-95.
24. A.G. Khachaturyan, Theory of structural transformations in solids (New York, NY: Wiley, 1983).
25. T. Sakuma and T. Hata, "Diffusionless cubic-to-tetragonal transformation and microstructure in ZrO_2-Y_2O_3," J. Jpn. Inst. Metals, 53, (1989), 972-9.
26. H.M. Kandil, J.D. Greiner and J.F. Smith, "Single-crystal elastic constants of yttria-stabilized zirconia in the range 20°C to 700°C," J. Am. Ceram. Soc., 67, (1984), 341-6.
27. H. Ogawa, A. Yasuda, N. Shibata, Y. Ikuhara and T. Sakuma, "Segregation of yttrium ions to domain boundaries of tetragonal zirconia," Philos. Mag. Lett., accepted for publication.

MICROANALYSIS OF MODULATED STRUCTURE IN ZIRCONIA CERAMICS

Naoya SHIBATA*, Junji KATAMURA*, Yuichi IKUHARA and Taketo SAKUMA

Department of Material Science,
School of Engineering,
The University of Tokyo,
7-3-1 Hongo, Bunkyo-ku, Tokyo,113,Japan
*Graduate student, the University of Tokyo

Abstract

Chemical composition is analyzed for the modulated structure with a bright and dark lamellar contrast in ZrO_2-6mol%Y_2O_3 annealed at 1200°C for 126h by nano probe analytical electron microscopy. By TEM-EDS analysis, gradual compositional change of yttrium ion's content was revealed even in a single lamellae in the direction perpendicular to the bright and dark lamellae contrast. The lamellae have a diffuse interface accompanying a compositional fluctuation. The microstructure evolution can be simulated from the assumption that the cubic-to-tetragonal transition is approximated to be a second-order type.

The Third Pacific Rim International Conference on
Advanced Materials and Processing (PRICM 3)
Edited by M.A. Imam, R. DeNale, S. Hanada,
Z. Zhong and D.N. Lee
The Minerals, Metals & Materials Society, 1998

Introduction

It was reported that a characteristic microstructure, originally called the modulated structure, is formed during heat treatments in the c-ZrO_2/t-ZrO_2 two-phase field in ZrO_2-Y_2O_3 system[1-4]. This microstructure generates in early stages of isothermal aging or continuous cooling from c-ZrO_2 field, and consists of bright and dark lamellae having a habit plane close to {111}[1,2,4], which is normal to the elastically soft direction of c-ZrO_2[5]. The lamellar spacing decreases with a decrease of aging temperature as predicted from the theory of spinodal decomposition[6-7]. The present author's group proposed that this microstructure is formed by spinodal decomposition between t- and c-ZrO_2 on the assumption that the diffusionless c-t phase transition is a second-order type, although the initial compositional fluctuation in a very early stage occurs in t- ZrO_2[8-10].

In this study, chemical composition is analyzed for the modulated structure in ZrO_2-Y_2O_3 by nano probe analytical electron microscopy, and microstructure evolution in this alloy is simulated on the assumption of second-order c-t phase transition.

Experimental procedure

High-purity ZrO_2-6mol%Y_2O_3 powders (99.9% Tosoh Co. Ltd., Japan) were used for starting materials. They were pressed into green compacts with a size of 10mmϕ. The compacts were arc-melted in an argon atmosphere, and then kept on a water-cooled copper hearth after melting. The arc-melted samples were annealed in air at 1200°C for 126h. Thin foils for transmission electron microscopy(TEM) were prepared by standard procedure using ion thinning method. The electron microscopes used for microstructure examination were HITACHI H-9000NAR and TOPCON 002BF operating at 300kV and 200kV, respectively. The latter electron microscope is a field emission type, and the microchemical analysis was carried out using Noran Voyager EDS(Energy Dispersive X-ray Spectroscopy) system in the electron microscope with a probe size of less than 1nm.

Results and Discussion

Figure 1(a) is a high-resolution image of lamellar structure formed in ZrO_2-6mol%Y_2O_3 aged at 1200°C for 126h. A faint bright and dark contrast is seen in this micrograph, which corresponds to the modulated structure reported previously[1,2,4]. The wavelength of this lamellae is estimated to be about 15nm. Figure 1(b) is the filtered image of Fig.1(a) using FFT(fast Fourier transform). The lattice image is continuous between the bright and dark lamellae. There are no clear boundaries between the lamellae, and the interfaces look diffuse. Figure 1(c) is the result of EDS analysis on the spots indicated by the dots in Fig.1(a)[11]. The result shows that the content of yttrium ions gradually fluctuates between the bright and dark lamellae. Each lamellar was found to have a maximum or minimum content of yttrium ions almost at their center and to accompany gradual fluctuation even in each lamellar. Since the thickness of the specimen was thin enough to observe lattice images clearly, the diffusion effect of the transmitted beam must be not so serious in comparison with the probe size of ~1nm. It is thus concluded that the gradual change in composition actually exists in the lamellar structure.

It is possible to simulate the microstructure evolution in ZrO_2-Y_2O_3 using a thermodynamic model based on the assumption that the diffusionless c-t transition is a second-order type[10]. According to the Landau's phenomenological theory, the free energy of a unit mole of a system is written as a function of composition x, order parameter η and temperature T as follows,

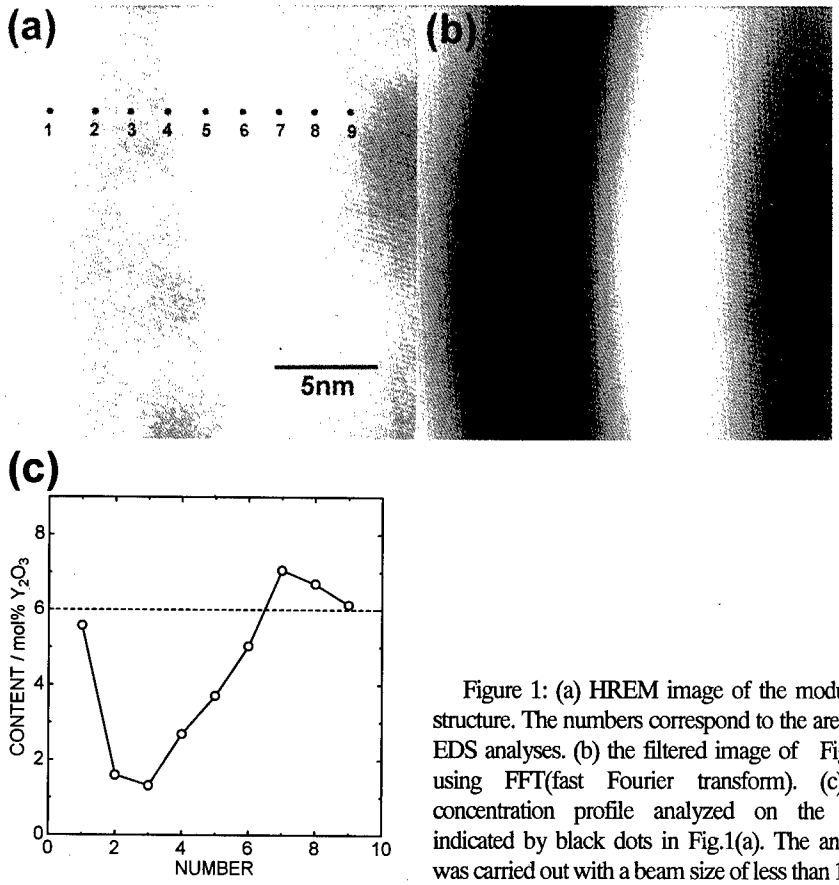


Figure 1: (a) HREM image of the modulated structure. The numbers correspond to the areas for EDS analyses. (b) the filtered image of Fig.1(a) using FFT(fast Fourier transform). (c)Y_2O_3 concentration profile analyzed on the spots indicated by black dots in Fig.1(a). The analysis was carried out with a beam size of less than 1nm.

$$G(x,\eta,T) = G_0(x,T) + a(T - T_c(x))\eta^2 + B\eta^4 \tag{1}$$

where $G_0(x,T)$ is the free energy of c-ZrO_2, a and B are the positive coefficients and $T_c(x)$ is the c-t transition temperature dependent on composition. The temperature of $T_c(x)$ can be approximated to be,

$$T_c(x) = T_c^0\left(1 - \frac{x}{0.208}\right)^{\frac{1}{2}} \tag{2}$$

where T_c^0 is the transition temperature of pure ZrO_2. The value of T_c^0, a and B are determined from thermodynamic data as follows,

$$T_c^0 = 2650\text{K} \tag{3}$$

$$-\frac{a^2 T_c^{0\,2}}{4B} = -40\text{kJ/mol} \tag{4}$$

The coefficients are chosen to be a=30.2 and B=40000 from the definition that the value of η in t-ZrO_2 without dopant is 1 at 0K.

This thermodynamic model explains well the experimental phase boundaries and spinodal region in ZrO_2-Y_2O_3 system[9]. Based on this thermodynamic model, we used the time-dependent Ginzburg-Landau(TDGL) kinetic model for predicting the microstructure evolution during the phase transition. The model can be regarded as the temporal and spatial evolutions of the continuous order parameter $\eta(\boldsymbol{r},t)$-field and of the composition $x(\boldsymbol{r},t)$-field. The temporal and spatial evolutions of the $\eta(\boldsymbol{r},t)$-field and the $x(\boldsymbol{r},t)$-field towards an equilibrium state is described by the following kinetic equations,

$$\begin{cases} \dfrac{\partial \eta(\boldsymbol{r},t)}{\partial t} = -L\dfrac{\delta F[x(\boldsymbol{r},t),\eta(\boldsymbol{r},t)]}{\delta \eta(\boldsymbol{r},t)} \\ \dfrac{\partial x(\boldsymbol{r},t)}{\partial t} = M\nabla^2\dfrac{\delta F[x(\boldsymbol{r},t),\eta(\boldsymbol{r},t)]}{\delta x(\boldsymbol{r},t)} \end{cases} \tag{5}$$

where L and M are the kinetic coefficients and $F[x(\boldsymbol{r},t),\eta(\boldsymbol{r},t)]$ is the total free energy. According to the diffuse interface theory by Cahn and Hilliard[12], $F[x(\boldsymbol{r},t),\eta(\boldsymbol{r},t)]$ is given by,

$$F[x(\boldsymbol{r},t),\eta(\boldsymbol{r},t)] = \int_V \left[\frac{1}{2}\varepsilon_x^{\,2}|\nabla x|^2 + \frac{1}{2}\varepsilon_\eta^{\,2}|\nabla \eta|^2 + G(x,\eta,T) + \kappa E_{strain}\right] dV \tag{6}$$

where ε_x and ε_η are the gradient energy coefficients for the $x(\boldsymbol{r},t)$- and $\eta(\boldsymbol{r},t)$-fields, respectively. The E_{strain} is the strain energy written in a reciprocal space as follows,

$$E_{strain} = \frac{1}{2}\int \frac{d\boldsymbol{k}}{(2\pi)^3} V(\boldsymbol{n})\left|\{\eta(\boldsymbol{r},t)\}_{\boldsymbol{k}}\right|^2 \tag{7}$$

$$V(\boldsymbol{n}) = c_{ijkl}\varepsilon_{ij}^0\varepsilon_{kl}^0 - n_i\sigma_{ij}^0\Omega_{jk}(\boldsymbol{n})\sigma_{kl}^0 n_l \tag{8}$$

where c_{ijkl} is the elastic constants and ε_{ij}^0 is the stress-free strain estimated from the lattice parameters of c- and t-ZrO_2, and

$$\sigma_{ij}^0 = c_{ijkl}\varepsilon_{kl}^0 \tag{9}$$

$$\Omega_{jk}^{-1}(\boldsymbol{n}) = c_{ijkl}n_i n_l \tag{10}$$

$$\boldsymbol{n} = \boldsymbol{k}/|\boldsymbol{k}| \tag{11}$$

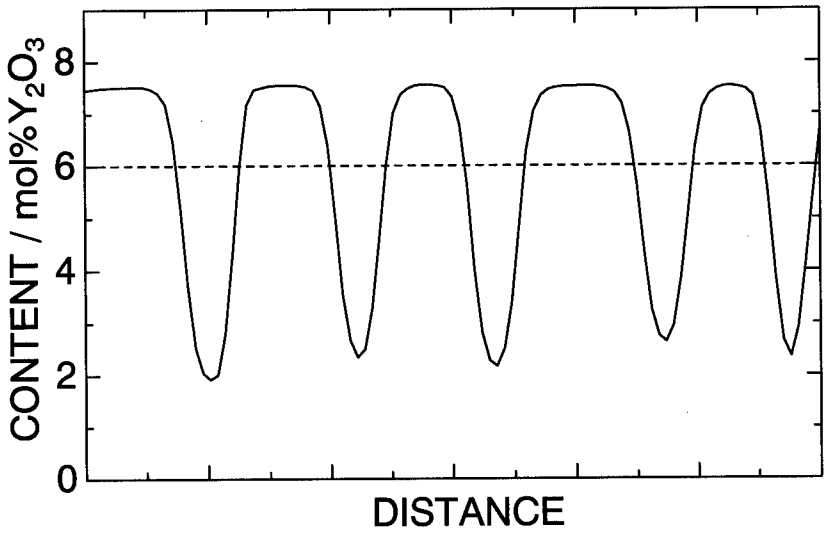


Figure 2: Calculated concentration profile of Y_2O_3 in ZrO_2-6mol%Y_2O_3 annealed at 1200°C.

The calculation was made for a two dimensional system with 128×128 mesh. The parameters used here are a=30.2, B=40000, M=6.0×10^{-6}, κ=25, ε_η=42, ε_x=5 for arbitral time and space. This computer simulation can predict the generation of the modulated structure with a regularly spaced lamellae[13].

Figure 2 is the calculated Y_2O_3 concentration profile against distance in annealed ZrO_2-6mol%Y_2O_3. TheY_2O_3 content changes continuously, and the existence of diffuse interfaces can be predicted. This result is consistent with the experimental result shown in Fig.1(c). It is thus supported both experimentally and theoretically that the modulated structure must be formed by spinodal decomposition.

The computer simulation of microstructure evolution in the same system was made by Fan and Chen on the assumption that the c- t phase transition is of a first-order type[14]. They predicted the formation of the modulated structure by the compositional fluctuation between two tetragonal phases(t-t') with different compositions and tetragonalities. The present calculation predicts the spinodal decomposition between t- and c-ZrO_2 if the c-t phase transition is of a second-order type. However, it should be noted that it is not possible to identify the nature of the phase transition only from computer simulation.

Conclusions

The continuous change of Y_2O_3 content along the direction normal to the bright and dark lamellae of the modulated structure is experimentally verified in ZrO_2-6mol%Y_2O_3 annealed at 1200°C for 126h by TEM-EDS analysis with nano probe analytical electron microscopy. Computer simulation of the microstructure evolution in ZrO_2-Y_2O_3 system is consistent with the

experimental result. The present results are not contradictory to our previous assumption that the c- t phase transition can be approximated to be of a second-order type, and that the modulated structure is formed by spinodal decomposition.

Acknowledgement

The authors wish to thank Dr. Takashi Yanaka(TOPCON Co. Ltd.), Mr. Kazuhiko Moriyama(TOPCON Co. Ltd.) and Dr. Takahisa Yamamoto(the University of Tokyo) for their experimental assistance. This work was financially supported by the Grand-in-Aid for Scientific Research on the Priority Area 09242206 from the Ministry of Education, Science and Culture, Japan.

Reference

[1] T. Sakuma, Y. Yoshizawa and H. Suto, "The Modulated Structure Formed by Isothermal Aging in ZrO_2-5.2mol%Y_2O_3 Alloy," J. Mater. Sci., 20[3], (1985), 1085-92.

[2] T. Sakuma, Y. Yoshizawa and H. Suto, "The Metastable Two-Phase Region in the Zirconia-Rich Part of the ZrO_2-Y_2O_3 System," J. Mater. Sci., 21[4], (1986), 1436-40.

[3] M. Hayakawa, K. Adachi and M. Oka, "Tweed Contrast with (223) Habit in Arc-melted Zirconia-Yttria Alloys," Acta metall. mater., 38[9], (1990), 1761-7

[4] M. Doi and T. Miyazaki, "On the Spinodal Decomposition in Zirconia-Yttria (ZrO_2-Y_2O_3) Alloys," Phil. Mag. B, 68[3], (1993), 305-15

[5] H.M. Kandil, J.D. Greiner and J.F. Smith, "Single-crystal elastic constants of yttria-stabilized zirconia in the range 20° to 700°C," J. Am. Ceram. Soc., 67[5], (1984), 341-6

[6] J.W. Cahn, "On Spinodal Decomposition," Acta metall., 9[10], (1961), 795-801

[7] J.W. Cahn, "Spinodal Decomposition," Trans. Metall. Soc. AIME, 242[2], (1968), 166-81

[8] M. Hillert and T. Sakuma, "Thermodynamic modeling of the c→ t transformation in ZrO_2 alloys," Acta metall mater., 39, (1991), 111-5

[9] J. Katamura and T. Sakuma, "Thermodynamic Analysis of the Cubic-Tetragonal Phase Equilibria in the System ZrO_2-$YO_{1.5}$," J. Am. Ceram. Soc., 80[10], (1997), 2685-88

[10] J. Katamura and T. Sakuma, "Computer simulation of the microstructural evolution during the diffusionless cubic-to-tetragonal transition in the system ZrO_2-Y_2O_3,"Acta mater., accepted for publication.

[11] J. Katamura, N. Shibata, Y. Ikuhara and T. Sakuma, "TEM-EDS analysis of the modulated structure in ZrO_2-6mol%Y_2O_3 alloy," submitted for publication.

[12] J.W. Cahn and J.E. Hilliard, "Free energy of a nonuniform system. Ⅰ. Interfacial free energy," J. Chem. Phys., 28, (1958), 258-67

[13] J. Katamura, Y. Ikuhara and T. Sakuma, "Theoretical Investigation of the Cubic-to-Tetragonal Transition in ZrO_2-based Alloys," submitted for publication.

[14] D. Fan and L.Q. Chen, "Possibility of spinodal decomposition in ZrO_2-Y_2O_3 alloys: A theoretical investigation," J. Am. Ceram. Soc., 78, (1995), 1680-6

SHORT RANGE ORDER IN Ni_4Mo STUDIED BY QUANTITATIVE HIGH RESOLUTION TRANSMISSION ELECTRON MICROSCOPY

S. Hata, T. Mitate, S. Matsumura†, N. Kuwano, K. Oki and D. Shindo‡

Department of Materials Science and Technology, Kyushu University, Kasuga 816-8580, Japan
†Department of Nuclear Engineering, Kyushu University, Fukuoka 812-8581, Japan
‡Institute for Advanced Materials Processing, Tohoku University, Sendai 980-8577, Japan

Abstract

Short range ordered (SRO) structures in Ni_4Mo alloys have been investigated by means of quantitative high resolution transmission electron microscopy (HRTEM) and multi-slice simulations. Digitally processed HRTEM images of the SRO state exhibited locally dot-patterns corresponding to the projection of N_2M_2 (chalcopyrite-like) structure, and the dot-patterns turned into those of subunit cells of $D1_a$, $D0_{22}$ and Pt_2Mo structures by changing a gray level for output. Multi-slice simulations of HRTEM images explain quite well the change of image contrast depending on the gray scale. This clearly reveals that the SRO in Ni_4Mo consists of $D1_a$, $D0_{22}$ and Pt_2Mo-type subunit cells, but not N_2M_2-type ones.

The Third Pacific Rim International Conference on
Advanced Materials and Processing (PRICM 3)
Edited by M.A. Imam, R. DeNale, S. Hanada,
Z. Zhong and D.N. Lee
The Minerals, Metals & Materials Society, 1998

Introduction

The structure of short range order (SRO) in Ni_4Mo alloys has been controversial for a long time [1-4]. The SRO state exhibits diffuse intensity maxima at {1 1/2 0} positions in the electron diffraction patterns, where {*hkl*} denotes *hkl* and its equivalent positions in terms of the fundamental f.c.c. lattice. The intensity maxima do not correspond to {4/5 2/5 0} superlattice reflections of $D1_a$ structure in the long range ordered (LRO) state. The present authors [5-7] have recently studied the ordering process in Ni_4Mo by Monte Carlo simulations (MCS) and high resolution electron microscopy (HRTEM). It was found that the SRO structure obtained by MCS consists of microclusters of subunit cells of $D1_a$, $D0_{22}$ and Pt_2Mo structures in the disordered matrix, and the HRTEM images of SRO can be interpreted in terms of projections of the SRO structure. As reported before [8], the HRTEM image contrast of SRO depends on the chemical composition in projected columns, in addition to foil-thickness, defocus and so on. In the present study, we try to extract projection contrast of the SRO structure in Ni_4Mo from the HRTEM images by image processing. The HRTEM images taken for different imaging conditions are quantitatively analyzed to characterize the image contrast of SRO. Multi-slice simulations of the SRO structure obtained by MCS is also carried out to compare with the experimental results, and the validity of our model for the SRO state in Ni_4Mo is discussed.

Experiments and simulations

An alloy ingot of Ni-19.5 at.% Mo was annealed at 1373 K for 86.4 ks and then quenched into iced brine to obtain an SRO state. The ingot was cut into disks and thinned by electropolishing for TEM analysis. HRTEM observation was performed with a JEM-2010FEF electron microscope equipped with a field emission gun and an energy filter. The accelerating voltage was 200 kV. Observed images were recorded in a slow-scan CCD camera or Imaging Plates. The combination of the energy filtering TEM with the digital recording media opens up quantitative imaging and diffraction.

The SRO atomic arrangement in $10 \times 10 \times 100$ f.c.c. unit cells for multi-slice HRTEM simulations was obtained by MCS with appropriate pairwise interaction parameters of atoms up to the fifth coordinate shells into account [5, 6]. The thickness per slice in the multi slice calculations was 0.36 nm corresponding to one f.c.c. unit cell, and 65536 (256×256) diffracted beams were taken into account for scattering intensity of electrons.

Results and discussion

Figure 1(a) shows zero-loss HRTEM images of the Ni-19.5 at.% Mo alloy. A series of the through-focus images from 1 to 8 were taken from almost the same areas at a step of 10 nm under focusing. Since background due to inelastic scattering has been effectively subtracted by the energy filter (the width of energy slit is 20 eV), the $\{200\}_{f.c.c.}$ planes are clearly resolved in all the images. One can see that contrast-modulations which may accord to SRO vary with defocusing. Figure 1(b) shows Fourier power spectra of the images. The spectra exhibit diffuse intensity maxima at {1 1/2 0} in addition to the f.c.c. spots, and the {1 1/2 0} maxima change in intensity with defocusing.

Digital processing of the HRTEM images extracts more detailed information about the SRO structures. Figures 1(c) and (d) are processed images obtained through inverse Fourier transformation with a doughnut-shaped aperture depicted in Fig. 1(b-1). Black points in the

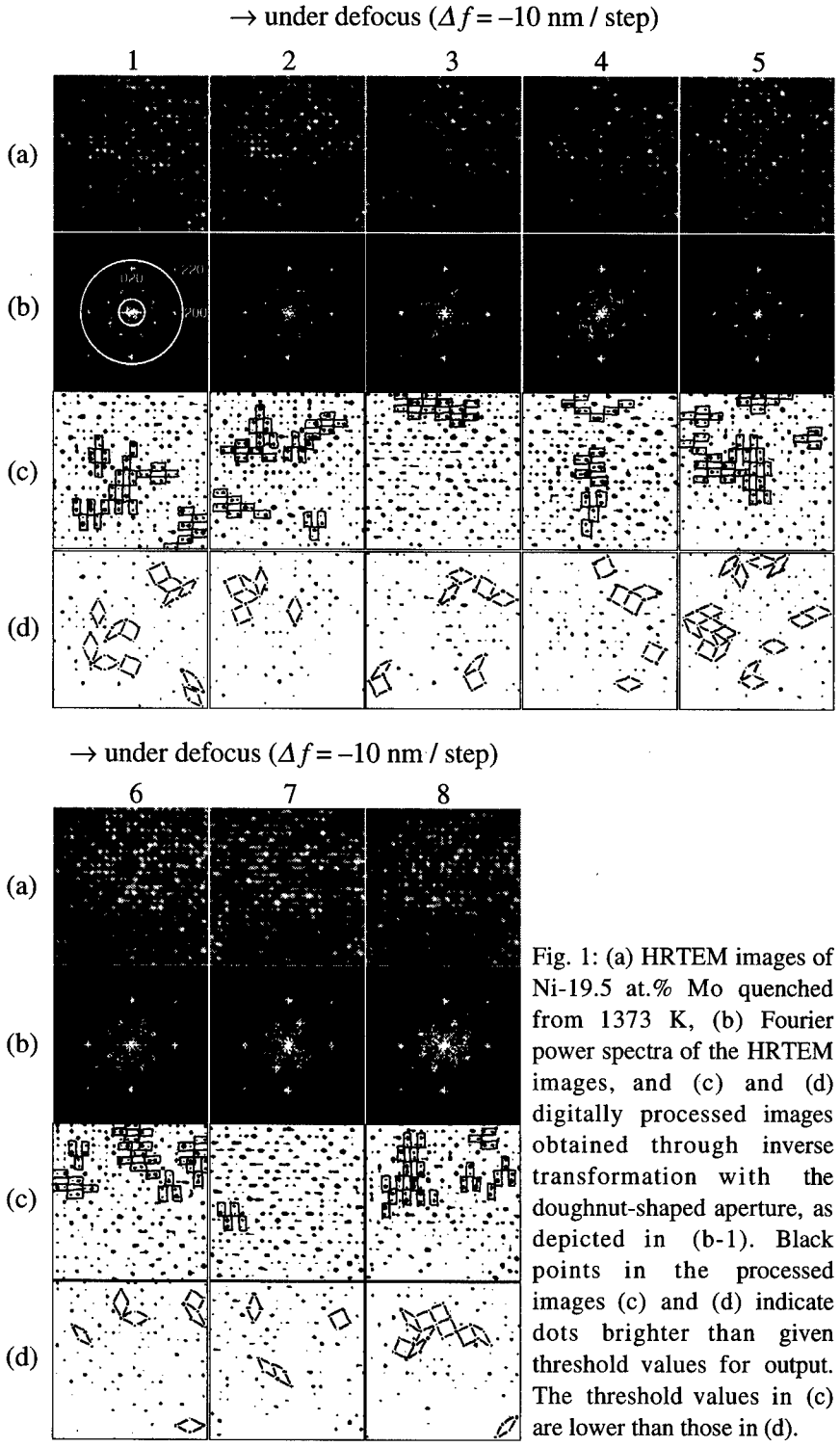


Fig. 1: (a) HRTEM images of Ni-19.5 at.% Mo quenched from 1373 K, (b) Fourier power spectra of the HRTEM images, and (c) and (d) digitally processed images obtained through inverse transformation with the doughnut-shaped aperture, as depicted in (b-1). Black points in the processed images (c) and (d) indicate dots brighter than given threshold values for output. The threshold values in (c) are lower than those in (d).

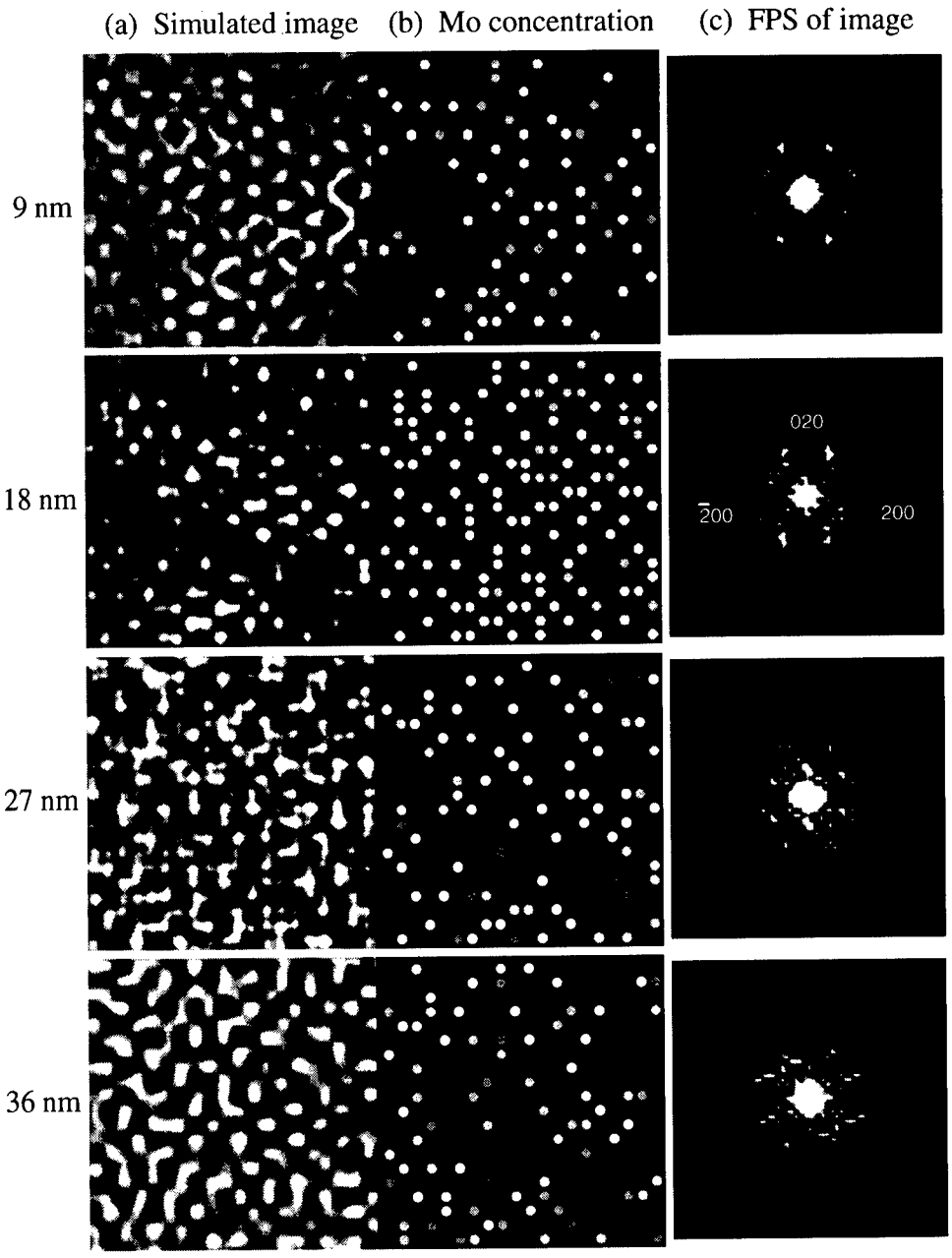
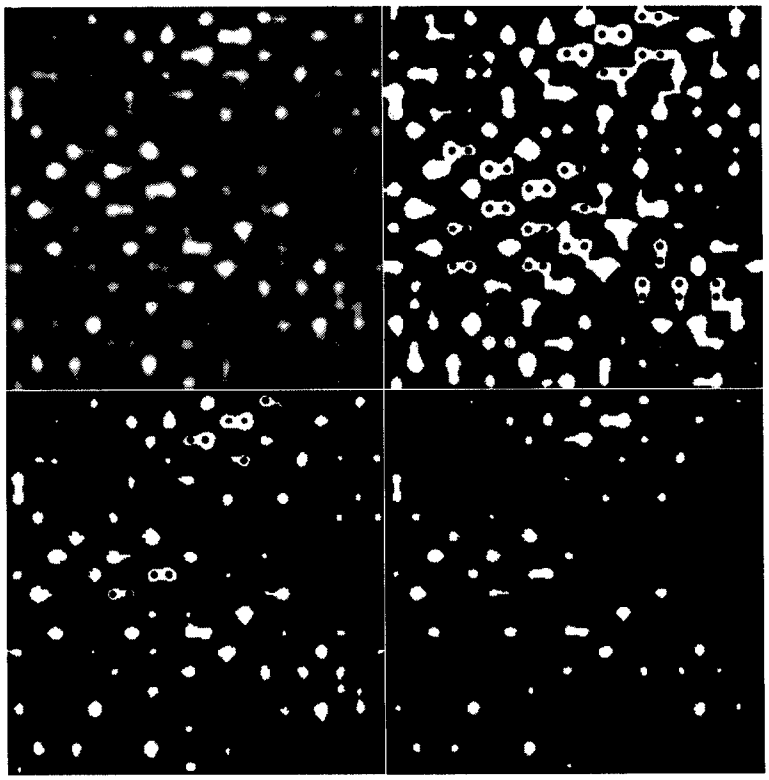


Fig. 2: (a) Simulated HRTEM images obtained by multi-slice simulations. The dot-contrast of N_2M_2-type appears at 18 nm, and it seems to correspond to Mo concentration in atomic columns shown in (b). Both intensity maxima at {200} and {1 1/2 0} positions are clearly recognized in the Fourier power spectrum of the image at 18 nm, as shown in (c).

images indicate dots brighter than a given threshold value. The threshold value was set higher in (d) than in (c). Some arrangements of the black points coincide with those of Mo-columns in particular ordered structures, as drawn with solid lines. Double-dot-patterns corresponding to N_2M_2-type (chalcopyrite-like) structure are recognized in (c). The N_2M_2 structure is one of the derivatives from the <1 1/2 0>* special point ordering [1, 4]. In the image (d), however, most N_2M_2-type patterns disappear, and in turn, subunit cells of $D1_a$ (slanting squares), $D0_{22}$ (fat rhombi) and Pt_2Mo structures (slanting rhombi) come out. It is interesting that the dot-arrangements forming the ordered structures change with defocusing, as if the projection potential at different depth areas were imaged. This may be due to dynamical diffraction effects in HRTEM imaging of the SRO state.

HRTEM images of the SRO state at various foil-thicknesses were also analyzed in a similar way. The HRTEM images show dot-patterns of N_2M_2-type and/or $D1_a$, $D0_{22}$ and Pt_2Mo subunit cells when the Fourier power spectra of the images exhibit {1 1/2 0} intensity maxima with f.c.c. spots. The characteristics in the HRTEM images give important keys to interpret the SRO structure in Ni_4Mo.

(a) 256 gray revels [0 – 255] (b) 2 gray revels [threshold: 70]



(c) 2 gray revels [threshold: 100] (d) 2 gray revels [threshold: 120]

Fig. 3: Simulated HRTEM images at 18 nm with different gray scales. 256 gray levels from 0 (black) to 255 (white) in (a), 2 gray levels with threshold values of 70 (b), 100 (c) and 120 (d), respectively. Dot-patterns of N_2M_2-type are recognized in (a) and (b). However, they turn into subunit cells of $D1_a$, $D0_{22}$ and Pt_2Mo structures when the threshold value is increased, as seen in (c) and (d).

Figure 2(a) demonstrates simulated HRTEM images of the SRO state as a function of foil thickness, which were obtained by multi-slice calculation with defocusing –56 nm. Dot-patterns of N_2M_2-type clearly appear at 18 nm thickness, as actually observed in the conventional HRTEM images [6]. Figure 2(b) shows projected potentials of atomic columns, which should be compared with (a). Brightness of circles represents Mo concentration in atomic columns. It is noted that the image contrast at 18 nm thickness changes corresponding well to the projected potentials. At the same time, the Fourier power spectrum from the image at 18 nm thickness exhibits f.c.c. spots and distinct {1 1/2 0} intensity maxima, as shown in Fig. 2(c). The results indicate that the nearly projection contrast of the SRO structure which corresponds to the N_2M_2-pattern is obtained when both f.c.c. and {1 1/2 0} reflections contribute to HRTEM imaging. This is consistent with the experimental results of HRTEM reported before [6, 7].

Figure 3 shows several displays of the simulated image at 18 nm thickness with different gray scales in the same way as Fig. 1. The image (a) is output in 256 gray levels from 0 (black) to 255 (white). The images (b), (c) and (d) are output in 2 gray levels, with the threshold values of 70 (b), 100 (c) and 120 (d), respectively. Transitions of dot-patterns from N_2M_2-type to $D1_a$, $D0_{22}$ and Pt_2Mo subunit cells are clearly visible with increase of the threshold values from (b) to (d), as observed in Fig. 1.

Thus the characteristic features of the HRTEM image of SRO are explained quite well by multi-slice simulations based on the atomic configuration obtained by MCS, which consists of microclusters of $D1_a$, $D0_{22}$ and Pt_2Mo subunit cells , but not of N_2M_2-type [4].

Conclusion

In the present study, the SRO structure in Ni_4Mo was investigated by quantitative HRTEM and multi-slice simulations. The digitally processed HRTEM images exhibit two kinds of dot-patterns, N_2M_2-type and/or $D1_a$, $D0_{22}$ and Pt_2Mo subunit cells, depending on a gray scale for output. The result confirms the SRO structure consists of microclusters of $D1_a$, $D0_{22}$ and Pt_2Mo subunit cells. Multi-slice simulations revealed that the HRTEM image contrast is interpreted in terms of projection contrast of the SRO structure obtained by MCS.

Acknowledgements: The authors would like to thank Mr. T. Manabe of the HVEM Laboratory, Kyushu University for his kind help in operation of JEM-2010FEF. This study was partly supported by Grants-in-Aid for Scientific Research (b) (2) (#08455293) as well as for Scientific Research (1) (#09242102, #09242106) on the Priority Area 'Investigation of Microscopic Mechanisms of Phase Transformations for the Structure Control of Materials' from the Ministry of Education, Science and Culture, Japan.

References

1. D. De Fontaine, "*k*-Space Symmetry Rules for Order–Disorder Reactions", Acta Metall., **23** (1975), 553.
2. G. Van Tendeloo, S. Amelinckx and D. De Fontaine, "On the Nature of the 'Short-Range Order' in 1 1/2 0 Alloys", Acta Crystallogr., **B41** (1985), 281.
3. K. H. Lee *et al.*, "High Resolution Electron Microscopic Study of the Ordering Processes in Ni_4Mo Alloy", Acta Metall., **36** (1988), 641
4. Sundararaman, S. Banerjee and H. Wollenberger, "Order–Disorder Transitions in Ni_4Mo under Self Ion Irradiation", Acta Metall. Mater., **43** (1995), 107.
5. S. Hata *et al.*, "Short Range Order and its Transformation to Long Range Order in Ni_4Mo", Acta Mater., **46** (1998), 881.
6. S. Hata *et al.*, "Analysis of Ordering Processes in Ni-Mo Based on the Pairwise Interaction Model" (Collected abstract presented at the 117th Meeting of Japan Inst. Metals, Honolulu, 12 December 1995), 96.
7. S. Hata *et al.*, "Semi-Quantitative High Resolution Electron Microscopy of Short-Range Ordered Ni_4Mo", J. Surface Analysis, **3** (1997), 401.
8. P. De Meulenaere *et al.*, "Dynamical Electron Diffraction in Substitutionally Disordered Column Structures", Ultramicroscopy, **60** (1995), 171.

PHASE TRANSITION IN $(Nd_x, Sm_{1-x})AlO_3$: STRUCTURAL BEHAVIOR CHARACTERIZED BY IONIC RADIUS AND TEMPERATURE

Hiroyuki Horiuchi, Akihiro Saitow, Akira Yoshikawa[a], Toetsu Shishido[a], Tsuguo Fukuda[a], Masahiko Tanaka[b], Atsushi Inoue[c] and Tadato Mizota[c]

Mineralogical Institute, Graduate School of Science, University of Tokyo, Tokyo 113, Japan,
[a]Institute for Materials Research, Tohoku University, Sendai 980, Japan,
[b]Photon Factory, High Energy Accelerator Research Organization, Ibaragi 305, Japan
[c]Faculty of Engneering, Yamaguchi University, Yamaguchi 753, Japan

Abstract

Solid solution of $(Nd_x, Sm_{1-x})AlO_3$ in the $SmAlO_3$-$NdAlO_3$ system was investigated by an X-ray diffraction method and a thermal analysis. Crystal structure of $(Nd_x, Sm_{1-x})AlO_3$ changes from orthorhombic to rhombohedral structures at around $x = 0.73$ by the substitution of Nd for Sm at room temperature. The similar structural changes of $(Nd_x, Sm_{1-x})AlO_3$ also take place by a phase transition due to the temperature. The relationship between the composition of x and the phase transition temperature T_c was estimated by a linear equation of $T_c(°C) = -1043x + 786$. From this relation, only 1% atom substitution of Nd for Sm in $(Nd_x, Sm_{1-x})AlO_3$ let T_c change about 10°C, and only 10^{-3}Å change of ionic radius r_R of R^{3+} gives the change of 35°C against the transition temperature T_c. Thus, the average ionic radius r_R of $R^{3+} = (Nd^{3+}_x, Sm^{3+}_{1-x})$ sensitively plays a role to characterize the structure of $RAlO_3$. The selection of R^{3+} with an appropriate ionic radius r_R seems to be comparable with a control of temperature and/or pressure for the structural change.

The Third Pacific Rim International Conference on
Advanced Materials and Processing (PRICM 3)
Edited by M.A. Imam, R. DeNale, S. Hanada,
Z. Zhong and D.N. Lee
The Minerals, Metals & Materials Society, 1998

Introduction

Rare-earth orthoaluminates crystallize in perovskite-type structures which are potential materials showing various physical properties. These crystals are also used as substrate materials for the thin film of perovskite-derivatives. Therefore, the basic crystallographic knowledge of them will be indispensable for the development of such materials.

Geller and Bala(1) studied $RAlO_3$ with several rare earth elements of R by powder X-ray diffraction. They reported that the structure of $RAlO_3$ of R = La, Pr, Nd were trigonal with a rhombohedral lattice, on the other hand, those of Sm, Eu and Gd were orthorhombic. Dernier and Maines(2) synthesized orthorhombic phases of R = Sm~Lu at high pressure and temperature. On the other hand, Shishido *et al.*(3, 4) prepared all of the phases of R = La~Lu at ambient pressure by flux method. As a conclusion, the relationship between the lattice vectors of $RAlO_3$ and an ideal cubic structure is given by $(\boldsymbol{a}_r/\boldsymbol{b}_r/\boldsymbol{c}_r) = (1,1,0/0,1,1/1,0,1)\cdot(\boldsymbol{a}_1/\boldsymbol{a}_2/\boldsymbol{a}_3)$ for rhombohedral phases, and $(\boldsymbol{a}_o/\boldsymbol{b}_o/\boldsymbol{c}_o) = (1,0,1/0,2,0/1,0,-1)\cdot(\boldsymbol{a}_1/\boldsymbol{a}_2/\boldsymbol{a}_3)$ for orthorhombic phases, where $\boldsymbol{a}_r$, $\boldsymbol{b}_r$, $\boldsymbol{c}_r$ and $\boldsymbol{a}_o$, $\boldsymbol{b}_o$, $\boldsymbol{c}_o$ are lattice vectors for rhombohedral and orthorhombic lattices of $RAlO_3$, respectively, and $\boldsymbol{a}_1$, $\boldsymbol{a}_2$, and $\boldsymbol{a}_3$ correspond to an ideal cubic perovskite-type lattice vectors which is used as a "*basic lattice*" in this work. These relations are schematically shown in Fig.1. An interesting feature of a series of these structures is that the lattice parameters systematically change against the ionic radius of R. Furthermore, the structures of $RAlO_3$ with smaller atomic number are rhombohedral, while, those with larger ones are orthorhombic. $CeAlO_3$ is only exceptional and most of works report that it is tetragonal (5,6,7,8), however, Kim(9) reported for it to be rhombohedral.

It will be remarkable to note that the structural change of $RAlO_3$ due to the size of ionic radius of R^{3+}, in particular, the change from orthorhombic to rhombohedral lattices by the substitution of Nd for Sm, seems as if the structural change by the control of temperature and/or pressure. In this work, what structural behavior will take place by the substitution of Sm for Nd in the $SmAlO_3$-$NdAlO_3$ system was investigated by the consideration of ionic substitution of Nd for Sm. This behavior was also compared with the structural change due to the control of temperature. The phase transition from orthorhombic to rhombohedral structures was also studied by a differential scanning calorimeter (DSC).

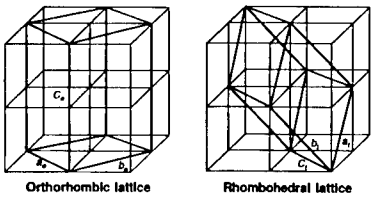


Fig. 1 Lattice relationship among basic, orthorhombic and rhombohedral structures. Thin lines show basic lattice, and thick lines are orthorhombic and rhombohedral lattices.

Experiments and their Results

Sample preparation and its crystallographic characterization

Powder samples of (Nd, Sm)AlO_3 with several ratios of Nd/Sm were prepared by solid-solid reaction using a high-frequency induction furnace at 1600°C. Experimental details of these sample preparations were reported by Yoshikawa *et al.*(10). Crystallographic characterization of their products were performed by X-ray powder diffraction (XRD). Most of XRD experiments were done by the use of laboratory shield tube X-ray sources by Yoshikawa *et al.*, and, a high-resolution XRD using synchrotron radiation (SR) was complimentarily applied for the precise analyses of the lattice constants of solid solution phases of $(Nd_x, Sm_{1-x})AlO_3$ at room temperature by Saitow *et al.*(11). The lattice deformation from its basic lattice of $(Nd_x, Sm_{1-x})AlO_3$ was so small that most of observed peaks were not single reflection peaks but they were nearly

superposed by a few or several independent reflections. Therefore, the 2θ value of each reflection was carefully analyzed with aid of a peak decomposition program, PROFIT by Toraya(12), and the lattice constants were obtained by least-squares method.

Effect of substitution of Nd for Sm on the structure of $(Nd_x, Sm_{1-x})AlO_3$

The variation of the lattice parameters against the atomic number of rare earth element is shown in Fig.2. The lattice parameters of solid solution phases of $(Nd_x, Sm_{1-x})AlO_3$ were decided with aid of a high-resolution powder diffraction using SR. In this figure, the value of $c_o/\sqrt{2}$ was plotted instead of c_o, because, in the case of no structural deformation from the ideal cubic structure, all values of a_r, a_o, b_o, and $c_o/\sqrt{2}$ should be the same to each other. With increasing ionic radius of R^{3+} from Lu to Sm, the values of a_o and c_o gradually become larger in orthorhombic phases. On the other hand, the value of b_o becomes slightly smaller. These tendencies are extended up to the solid solutions of $(Nd_x, Sm_{1-x})AlO_3$ with x = 0.6. However, rates of the changes of b_o and c_o are small in the solid solutions. As a result, the values of a_o, b_o and $c_o/\sqrt{2}$ intersect at around the orthorhombic phases of Sm~$(Nd_{0.4}, Sm_{0.6})$. The orthorhombic structure is no more stable in $(Nd_{0.8}, Sm_{0.2})AlO_3$ but the structure becomes trigonal with rhombohedral lattice. In rhombohedral structures, the deviation of α angle from 60° is very small and this deviation becomes much smaller in the structures containing larger ionic radii. From a view point of lattice configuration, the deformation from ideal cubic lattice is minimum at around the phases of x = 0.0~0.2. It is interesting to note that the change fromorthorhombic to rhombohedral structures does not occur at the chemical composition corresponding to the minimum deformation from ideal cubic lattice but it does change after getting a slightly more deformation in the lattice.

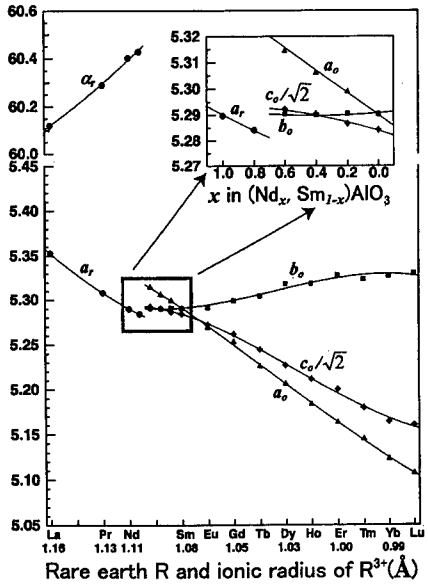


Fig.2 The change of lattice parameters (Å and degrees) of $(Nd_x,Sm_{1-x})AlO_3$ and $RAlO_3$. The data of $(Nd_x,Sm_{1-x})AlO_3$ for x = 0.0~1.0 and those of other $RAlO_3$ were referred to the literatures by Saitow *et al.*(11) and Yoshikawa *et al*(10), respectively.

Crystal structures of $RAlO_3$

Crystal structures of orthorhombic phases were analyzed by X-ray diffraction method using powder samples of $(Nd_x, Sm_{1-x})AlO_3$ for x = 0.2, 0.4, 0.6 and tiny single crystals of $RAlO_3$ for R = Eu, Dy, Er with the sizes of around 10~20μm in diameter. Single crystals were prepared by a flux method(3). Laboratory Cu shield tube X-ray sources were used for data collections of most of samples, and a synchrotron radiation was used for $EuAlO_3$. Rietveld method by a program PFLS(13) was adopted for the analyses of powder samples. A specially designed diffractometer equipped with a position sensitive proportional counter (PSPC) (14) was used for the data collection of single crystals of $DyAlO_3$ and $ErAlO_3$. Structure refinements of single crystals were carried out by a program of RFINE-IV(15). The results of refinements of crystal structures were summarized in Table 1. The data of $SmAlO_3$ reported by Marezio *et al.*(16) were also shown.

The results show that the shifts from ideal positions of R and O2 are smaller in the structures with smaller ionic radii of R^{3+}. On the other hand, O1 atom shows the minimun displacement at the phase around x = 0.2. The displacements of O1 and O2 atoms concern the rotation and tilting

of AlO_6 octahedra around and along the c-axis, respectively. Therefore, crystal structures of $RAlO_3$ gradually become close to an ideal cubic structure by substitution of smaller ions for R from a view point of atom positions of R and the rotation of AlO_6 around the *c*-axis. However, the tilting of AlO_6 is minimum at the chemical composition around $x = 0.2$, and it slightly becomes larger again by the substitution of more Nd for Sm up to the structural boundary between orthorhombic and rhombohedral phases.

Table 1 Results of crystal structure refinements. Atom shifts Δ(Å) from an ideal cubic structure were also listed.

		$x = 0.60$	$x = 0.40$	$x = 0.20$	$SmAlO_3$*	$EuAlO_3$	$DyAlO_3$	$ErAlO_3$
a		5.3144(2)	5.3060(2)	5.2989(4)	5.2912(2)	5.269(1)	5.206(1)	5.163(1)
b		5.2904(4)	5.2900(2)	5.2906(5)	5.2904(2)	5.291(1)	5.318(1)	5.328(1)
c		7.4844(4)	7.4817(3)	7.4765(6)	7.4740(2)	7.456(1)	7.392(1)	7.354(1)
R	*x*	.5061(4)	.5066(4)	.5103(5)	.50050(4)	.5069(2)	.5163(11)	.5151(4)
	y	.5173(3)	.5214(2)	.5236(3)	.52402(7)	.5318(1)	.5476(7)	.5553(3)
	z	.25	.25	.25	.25	.25	.25	.25
	Δ	0.097	0.119	0.136	0.127	0.172	0.266	0.304
Al	*x*	.0	.0	.0	.0	.0	.0	.0
	y	.5	.5	.5	.5	.5	.5	.5
	z	.0	.0	.0	.0	.0	.0	.0
O1	*x*	.065(4)	.049(4)	.017(6)	.0644(8)	.0719(17)	.107(11)	.087(4)
	y	.520(3)	.519(3)	.528(3)	.4903(11)	.4876(22)	.460(14)	.477(4)
	z	.25	.25	.25	.25	.25	.25	.25
	Δ	0.362	0.278	0.173	0.345	0.384	0.596	0.465
O2	*x*	.229(3)	.231(3)	.265(5)	.2234(6)	.2164(14)	.217(10)	.201(3)
	y	.259(5)	.227(3)	.217(3)	.2230(6)	.2156(16)	.224(11)	.205(3)
	z	.522(2)	.532(2)	.534(5)	.5335(6)	.5372(9)	.550(4)	.552(2)
	Δ	0.204	0.286	0.318	0.320	0.375	0.430	0.517

Effect of temperature change on the structure of $(Nd_x, Sm_{1-x})AlO_3$

Parts of powder X-ray diffraction patterns of $(Nd_x, Sm_{1-x})AlO_3$ for various x, which were observed at room temperature (23°C), were shown in Fig.3. Weak reflections at $2\theta = 56°\sim 57°$ are observed only for the orthorhombic phases, and larger peak separations at $2\theta = 41°\sim 42°$ and at $2\theta = 54°\sim 55°$ are characterized in the rhombohedral phases. Thus, the phases of $x \leq 0.6$ can be indexed on the basis of an orthorhombic lattice, and, on the other hand, those for $x \geq 0.76$, by a rhombohedral lattice. The phase of $x = 0.73$ is also clearly rhombohedral but it seems a very small amount of orthorhombic phase coexists. Therefore, as an approximation, it will be assumed that the crystal structure of $(Nd_x, Sm_{1-x})AlO_3$ changes from orthorhombic to trigonal at the chemical composition of around $x = 0.73$ at room temperature by substitution of Nd^{3+} for Sm^{3+}.

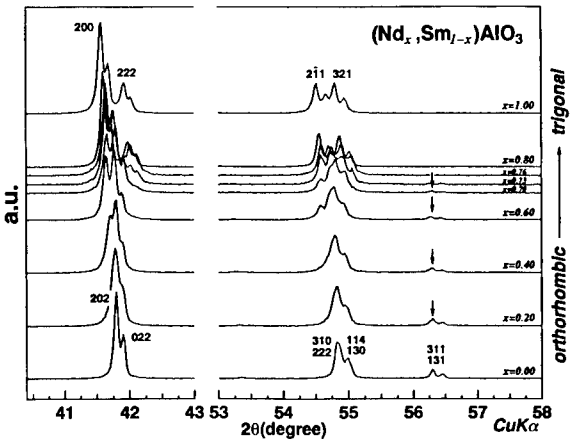


Fig.3 Comparison of a part of powder X-ray diffraction patterns of $(Nd_x, Sm_{1-x})AlO_3$ against various values of x at room temperature. Weak reflection peaks designated by arrows are observed only in orthorhombic phases.

Experiments of high-temperature powder X-ray diffraction were performed using CuKα radiation from a shield tube X-ray source with condition of 40kV and 40mA. Pyrolytic graphite was used as an analyzer monochromator. The samples were filled in a Pt·Rh10% sample holder with depth of 0.5mm and the experiments were performed in air. The θ-2θ scan method was applied with step width of 0.02 degrees for 2θ angle and counting time was 10sec at each step. The temperature gradient in the sample area is less than 1°C up to the temperature around 1000°C. The temperature intervals in the process of increasing and decreasing temperatures were 5°C at the temperature near phase transition.

O'Bryan *et al.*(17) observed the orthorhombic to trigonal phase transition of $SmAlO_3$ at 785°C by the combination of powder X-ray diffraction, thermal analysis and the dilatometric thermal expansion. We also confirmed above results. Further high-temperature powder X-ray diffraction experiments were performed at the temperature ranges of 25°C ~ 420°C, and

25°C~200°C, for $(Nd_{0.4}, Sm_{0.6})AlO_3$ and $(Nd_{0.6}, Sm_{0.4})AlO_3$, respectively. The diffraction profiles which were observed in the 2θ ranges of 41°~43° and 54°~56° were shown in Figs.4(a) and 4(b), respectively. The changes of profiles which are due to the phase transition from orthorhombic to trigonal structures were observed at around 370°C and 160°C, respectively. Reflection indices for lower and higher temperature phases were assigned on the basis of the orthorhombic and rhombohedral lattice constants, respectively. It seems that both orthorhombic and trigonal phases coexist at around phase transition temperatures within a range of about ±5°C. The phase transition phenomena were reversibly observed in the process of increasing and decreasing temperatures.

DSC experiments were also performed for the solid solution. Phase transitions were clearly observed for the phases $(Nd_x, Sm_{1-x})AlO_3$ of x = 0.8 and 0.6 at the temperatures around -50°C and 169°C, respectively.

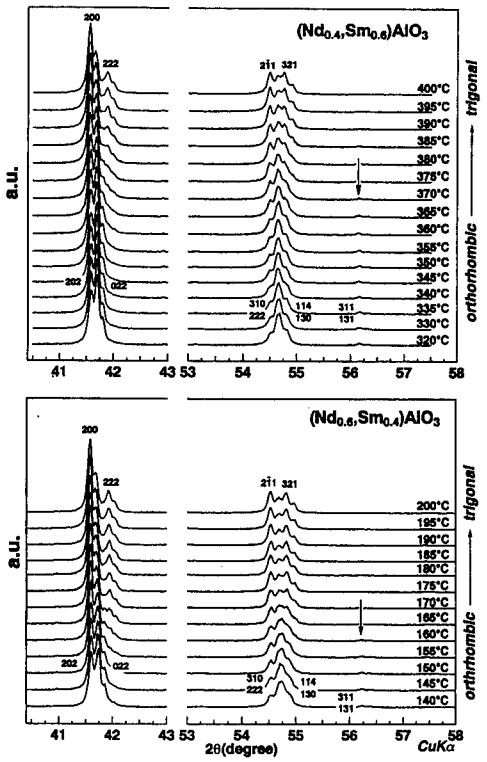


Fig.4 Powder X-ray diffraction patterns at increasing temperatures. Structure changes from orthorhombic to trigonal system at around 370°C and 160°C, in (a) and (b), respectively. **(a)**$(Nd_{0.4},Sm_{0.6})AlO_3$, **(b)** $(Nd_{0.6}, Sm_{0.4})AlO_3$.

Discussion and conclusion

The relationship between x in $(Nd_x, Sm_{1-x})AlO_3$ and the transition temperature T_c from orthorhombic to trigonal structures was considered from the results of high-temperature XRD for the phases of x = 0.0, 0.4 0.6 and from the fact that the change from orthorhombic to trigonal structures takes place at around x = 0.73 when x varies from 0.0 to 1.0 at room temperature. The relation was approximated by a linear equation of T_c(°C) = -1043x +786. The above relation was also confirmed by DSC experiments for the phases with x = 0.8 and 0.6 of which T_c were observed at around -50°C and 169°C against the estimated T_c = -48.4°C and 160.2°C, respectively, from above

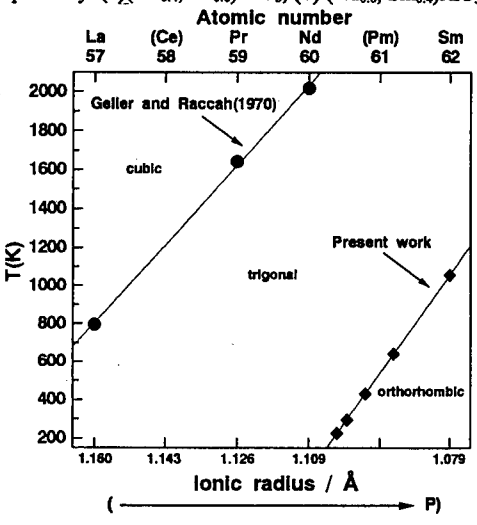


Fig.5 Structural diagram of temperature against atomic number of R. In the solid solution, atomic number is given by 60x+62(1-x). Ionic radii of R^{3+} are also shown. The boundary between trigonal and cubic phases was obtained from the literature (18).

relation. As a result, the structural boundary between orthorhombic and rhombohedral structures was given in Fig.5 using the atomic radius of R^{3+} against the transition temperature T_c. The boundary between rhombohedral and cubic phases was quoted from the literature by S.Geller and P.M. Raccah (18).

From the relationship between x and T_c, if only 1% atoms are substituted by Nd for Sm in $(Nd_x, Sm_{1-x})AlO_3$, the T_c changes about 10°C, and if ionic radius r_R of R^{3+} varies only by the order of 10^{-3}Å in the structure of $RAlO_3$, the transition temperature T_c changes about 35°C. Where, r_R is given by the average ionic radius $x \cdot r(Nd^{3+})+(1-x) \cdot r(Sm^{3+})$. Thus, the average ionic radius r_R sensitively plays a role to characterize the structure of $RAlO_3$. It also seems that the selection of R^{3+} with an appropriate ionic radius r_R is comparable with a control of temperature and/or pressure for the structural change. From this point, Fig.5 will imply a pressure-temperature structural diagram of perovskite-type $RAlO_3$.

The structure change of $(Nd_x, Sm_{1-x})AlO_3$ caused by changing temperature is considered to be a first-order phase transition. This is because, in DSC experiment, a slightly lower T_c was observed in the process of decreasing temperature than that of the case of increasing temperature, and also because it is assumed that the crystal lattices become discontinuous between rhombohedral and orthorhombic structures.

This work was financially supported by Grant-in-Aid for Scientific Research on Priority Area 09242208 and General Scientific Research (B)-07459008 of the Ministry of Education, Science, Sports and Culture of Japan. The investigation was carried out under the Inter-University Cooperative Researches Program of the Institute for Material Research, Tohoku University, Japan.

References

1. S. Geller and V.B. Bala, "Crystallographic studies of perovskite-like compounds II Rare earth aluminates," *Acta Crystallogr.*, 9(1956), 1019-1025
2. D. Dernier and R.G. Maines, "High-pressure synthesis and crystal data of the rare earth orthoaluminates," *Mat. Res. Bull.*, 6(1971), 433-440
3. T. Shishido, S. Nojima, M. Tanaka, H. Horiuchi and T. Fukuda, "Flux growth of perovskite-type $RAlO_3$ single crystals," *J. Alloys and Comp.*, **227**, (1995), 175-179
4. T. Shishido, A. Yoshikawa, H. Horiuchi and T. Fukuda, "Synthesis of perovskite-type $LuAlO_3$ single crystals (in Japanese)," *J. Chem. Soc. Japan: Chem. & Indust. Chem.*, (7), (1995), 573-575.
5. W.H. Zachariasen, "Crystal chemical studies of the 5f-series of elements. XII. New compounds representing known structure types," *Acta Crystallogr.*, **2**(1949), 388-390.
6. T. Shishido, M. Tanaka, H. Horiuchi, and T. Fukuda, "Single crystal of tetragonal type $CeAlO_3$ grown from the KF flux (in Japanese)," *J. Chem. Soc. Japan: Chem. & Indust. Chem.* 6, (1992), 680-682.
7. M. Tanaka, T. Shishido, H. Horiuchi, N. Toyota, D. Shindo and T. Fukuda, "Growth of rare earth aluminate crystals from molten solutions," *J. Alloys and Compounds.*, **192**, (1993), 84-86.
8. S. Nakagawa, T. Shishido, M. Tanaka, S. Nojima, H. Horiuchi and T. Fukuda, "Synthesis of $CeAlO_3$ by direct melting method (in Japanese)," *J. Chem. Soc. Japan: Chem. & Indust. Chem.*, **8**, (1994), 752-754.
9. Y.S.Kim, "Crystallographic study of cerium aluminate," *Acta Crystallogr.*, **B24**, 295-296.
10. A. Yoshikawa, H. Horiuchi, M. Tanaka, T. Shishido, and T. Fukuda, "Syntheses of the $(Nd_x, Sm_{1-x})AlO_3$ and its structure relation to a series of rare earth ortho-aluminates $RAlO_3$," *J. Solid State Chem.*, **126**, (1996), 221-226.
11. A. Saitow, A. Yoshikawa, H. Horiuchi, T. Shishido, T. Fukuda, M. Tanaka, T. Mori and S. Sasaki, "Structural change caused by substitution of Nd for Sm in (Nd, Sm)AlO_3: Application of synchrotron high-resolution powder X-ray diffraction," *J. Appl. Crystallogr.*, in press.
12. H. Toraya, "Whole-powder-pattern fitting without reference to a structural model: Application to X-ray powder diffractometer data," *J. Appl. Crystallogr.*, **19** (1986) 440-447.
13. H. Toraya and F. Marumo, "Application of total pattern-fitting to X-ray powder diffraction data", Report of the Research Laboratory of Engineering Materials, Tokyo Institute of Technology, **5**(1980) 55-64.
14. H. Horiuchi and M. Tanaka, "Crystallographic analyses of mineral textures by micro-area X-ray diffraction (in Japanese)," *J. Mineral. Soc. Jpn*, 21(1992) 47-57.
15. L.W. Finger, "Determination of cation distribution by least-squares refinement of single-crystal X-ray data," *Carnegie Institution of Washington Year book*, **67**(1969) 216-217.
16. M.Marezio, P.O.Dernier and J.R.Remeika, "The crystal structure of orthorhombic $SmAlO_3$ and trigonal $NdAlO_3$, *J. Solid State Chem.*, **4** (1972)11-19
17. H.M. O'Bryan, P.K. Gallaher, G.W. Berkstresser and C.D. Brandle, "Thermal analysis of rare earth gallates and aluminates," *J. Mater. Res.*, **5** (1990) 183-189.
18. S. Geller and P. M. Raccah, "Phase transition in perovskitelike compounds of the rare earths," *Phys. Rev.* B, **2** (1970)1167-1172.

ROLE OF THE INTERLAMELLAR SPACING OF PEARLITE IN THE DILATOMETRIC CHARACTERIZATION OF PEARLITE-TO-AUSTENITE TRANSFORMATION IN A LOW CARBON STEEL

C. García de Andrés, F. G. Caballero and C. Capdevila
Department of Physical Metallurgy
Centro Nacional de Investigaciones Metalúrgicas (CENIM-CSIC)
Avda. Gragorio del Amo, 8. 28040 Madrid, Spain

Abstract

The influence of the pearlite morphology on the dissolution of pearlite during continuous heating austenitization has been studied in a low carbon steel with a ferrite-pearlite starting microstructure. An unusual anomaly at the onset of the austenitization has been detected by means of high-resolution dilatometric analysis when a finer pearlite is present in the starting microstructure. This anomaly is shown as a sharp contraction peak in the dilatometric curve obtained by heating in quasi-equilibrium conditions. In principle, this contraction was associated with the pearlite dissolution process. In order to confirm this assumption, interrupted heating tests have been carried out at ten degrees below and above the temperature of the dilatometric peak which corresponds to the anomaly. A clear differentiation between pearlite dissolution process and α–γ transformation has been found. This discrimination between both processes allows to identify the temperature at which pearlite dissolution finishes and therefore selects the most suitable intercritical temperature to obtain dual phase microstructure with an optimum combination of mechanical properties. A significant effect of pearlite interlamellar spacing on the shape of the dilatometric anomaly has been detected. The dilatometric anomaly associated with pearlite-austenite transformation seems to be eliminated as pearlite coarsens.

The Third Pacific Rim International Conference on
Advanced Materials and Processing (PRICM 3)
Edited by M.A. Imam, R. DeNale, S. Hanada,
Z. Zhong and D.N. Lee
The Minerals, Metals & Materials Society, 1998

Introduction

With the introduction of dual-phase steels (1-3), partial austenitization in the intercritical temperature region became of technological interest and was widely studied (4-7). All these authors emphasized the importance of the microstructure immediately before intercritical annealing. Speich et al (5) described a first stage in the intercritical austenitization process in low-carbon steels with a ferrite-pearlite starting microstructure in which pearlite dissolution and growth of austenite into pearlite take place at a rate controlled by carbon diffusion in the austenite with a diffusion distance about equal to the interlamellar spacing of the pearlite. Roósz et al (8) studied the influence of this morphological parameter of the pearlite on the isothermal formation of austenite in an eutectoid steel with a full pearlite starting microstructure.

Very little information is avalaible about the austenite formation in steels subjected to continuous heating. In the present work, high-resolution dilatometry was used to study the influence of the pearlite morphology on the dissolution of pearlite during continuous heating austenitization in a low-carbon steel with a ferrite-pearlite starting microstructure. A clear differentiation between pearlite dissolution process and $\alpha \rightarrow \gamma$ transformation has been found in this steel by means of dilatometric analysis as a finer pearlite was present in the starting microstructure. In that case, an accurate determination of the finishing temperature of pearlite dissolution process could be performed by dilatometric characterization, thus allowing to select the most suitable intercritical temperature to obtain dual phase microstructures with an optimum combination of mechanical properties. However, the differentiation between both processes is not possible as a coarser pearlite is obtained in the starting microstructure.

Material and Experimental Procedures

The chemical composition of the studied steel is presented in Table I. Semi rolled slabs 36 mm thick were soaked at 1250°C for 15 min., hot rolled to 6mm in several passes, and finally air cooled to room temperature. Specimens were machined from this material and named 'Finished Hot-Rolled (FHR)'. Another group of specimens was directly machined from the semi rolled slabs 36 mm thick, and it is referred below as 'Semi Hot-Rolled (SHR)'. As-rolled resultant microstructures both are formed by 84% of ferrite and 16% of pearlite (Fig. 1). As shown below, the interlamellar spacing of the pearlite in FHR and SHR specimens is different (Table II). To obtain new microstrucutres with three different interlamellar spacings of pearlite, some specimens were reheated to 1000°C, held for 60 seconds and cooled at cooling rates of 0.05 °C/s, 0.1 °C/s and 0.5 °C/s. The interlamellar spacings of pearlite in these as-annealed microstructures are also listed in Table II.

Table I
Chemical Composition of low carbon low manganese steel (Mass %)

C	Mn	Si	Cr	Ni
0.11	0.50	0.03	0.01	0.02

Table II
Interlamellar spacings of as-rolled and as-annealed microstructures

Specimen	Interlamellar spacing (μm)
FHR	0.14±0.01
SHR	0..17±0.04
ANN1	0.18±0.03
ANN2	0.25±0.05
ANN3	0.29±0.06

Specimens were polished in the usual way and finished on 0.5 μm diamond paste for metallographic examination. Two types of eatching solution were used: Nital-2pct to reveal the ferrite-pearlite microstructure by light optical microscopy and solution of picric acid in isopropyl alcohol with several drops of Vilella's reagent to disclose the pearlite morphology on a Jeol JXA 840 scanning electron microscope. Figure 2 shows the scanning micrograph of the five different morphologies of pearlite considered in this study (Table II). Quantitative metallography to determine the interlamellar spacing of pearlite was done according to Underwood's intersection procedure (9).

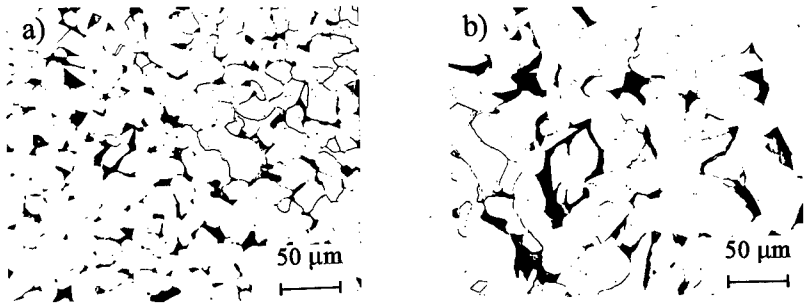


Figure 1. As-rolled microstructures. Etched in 2% Nital (2 mL nitric acid + 100 mL propan-2-ol): (a) FHR and (b) SHR

Dilatometric specimens 2mm thick and 12mm long with the above mentioned morphologies (Table II) were heated at a constant rate of 0.05°C/s in a vacuum of 10^{-2} mbar. This is the rate normally used for considering quasi-equilibrium conditions (10). For this purpose an Adamel Lhomargy DT1000 high-resolution dilatometer was used.

Results and Discussion

During continuous heating the formation of austenite takes place between the Ac_1 and Ac_3 temperatures which represent, respectively, the temperature at which the ferrite+pearlite-to-austenite transformation starts and ends (11). The expected variation of the relative change of length as a function of temperature ($(\Delta L/L_0)=f(T)$) schematically shown in the dilatometric curve of Fig. 3, reproduces the contraction usually undergone by a steel during the austenite formation in continuous heating. No differentiation between pearlite dissolution process and $\alpha \rightarrow \gamma$ transformation is apparently detected in the dilatometric curve of Fig. 3. However, the experimental heating dilatometric curves for the FHR specimen in Fig. 4 shows an unusual anomaly at the onset of the austenitization. This well formed anomaly is shown as a contraction in principle associated to the pearlite dissolution. Firstly, to confirm that this anomaly effectively corresponds to the pearlite-to-austenite transformation, specimens were heated up to 10 °C below and above the temperature of the dilatometric peak which corresponds to the anomaly, and immediately quenched at a cooling rate of 500 °C/s approx.

Figure 5 and 6 show the microstructures obtained in the interrupted heating tests at the above mentioned temperatures. It is clear from the Fig. 5 that no transformation has taken place since the microstructure after this interrupted heating test is formed by ferrite and pearlite and no trace of martensite has been found. However, some martensite areas in Fig. 6 demonstrate that the dissolution of pearlite was taking place during heating at temperatures higher than peak temperature, confirming that this anomaly is clearly associated with that process. A coarsening of the lamellar pearlite morphology in micrographs both of Fig. 5 (a) and 6 (a) is observed in

comparison with as rolled microstructure in Fig. 2 (a). In some pearlite colonies, a slight spheroidizing of the lamellar cementite before dissolution of pearlite is found (Fig. 5 (a)), as it was reported by Garcia and DeArdo (4).

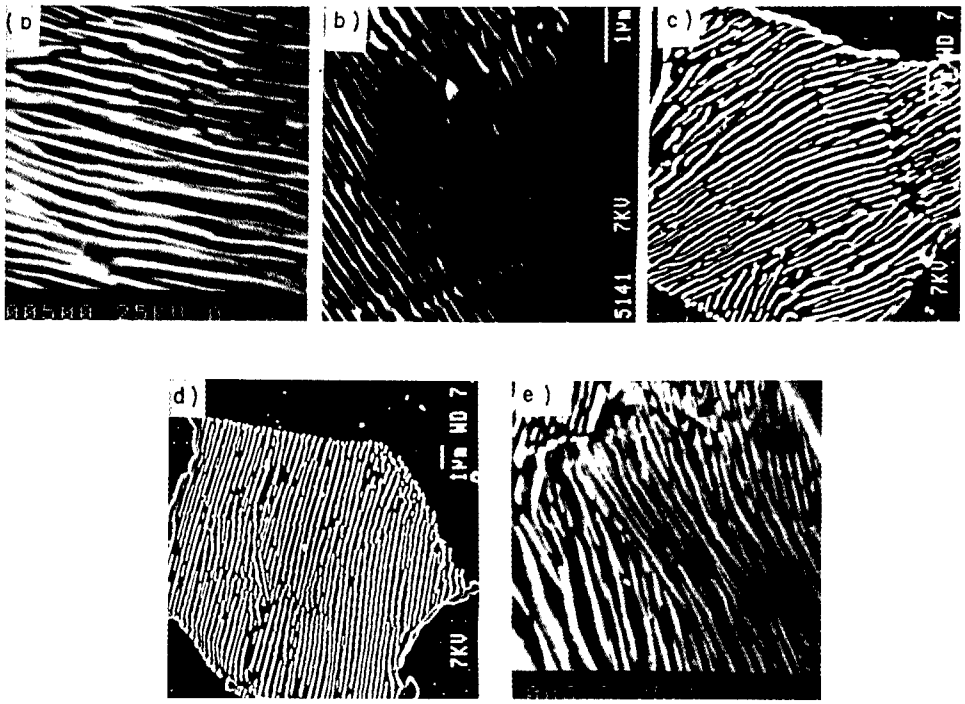


Figure 2. Scanning micrograph of the five different morphologies of pearlite considered in this study (Table II): (a)FHR, (b)SHR, c)ANN1, (d)ANN2 and (e)ANN3

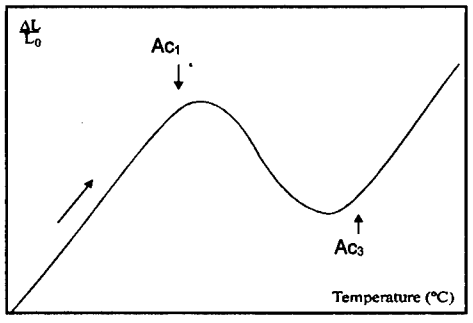


Figure 3. Schematical variation of the relative change of length as a function of temperature during continuous heating

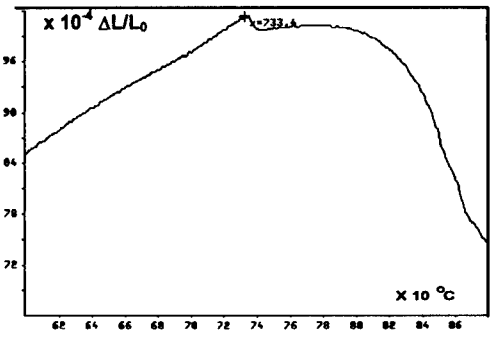


Figure 4. Experimental heating dilatometric curve for FHR specimen

Figure 7 shows the dilatometric curves in quasi-equilibrium heating conditions of the specimens listed in Table II. We can observe in this figure that the intensity of the pearlite dissolution peak decreases as interlamellar spacing increases coming to dissapear for interlamellar spacing higher

than 18 microns. When a solid state phase transformation takes place during continuous heating treatment, the relative change of length observed in the dilatometric curve arises from both the thermal expansion and the dimensional changes associated with a phase transformation , so the total relative change of length should be expressed as follows:

$$\frac{\Delta L}{L_0} = \left(\frac{\Delta L_t}{L_0}\right)_{\substack{\text{thermal}\\ \text{expansion}}} + \left(\frac{\Delta L_p}{L_0}\right)_{\substack{\text{phase}\\ \text{transformation}}} = (\alpha T)_{\substack{\text{thermal}\\ \text{expansion}}} + \left(\frac{\Delta L_p}{L_0}\right)_{\substack{\text{phase}\\ \text{transformation}}} \quad (1)$$

where $(\Delta L/L_0)$ is the total relative change of length, $(\Delta L_t/L_0)$ is the relative change of length due to thermal expansion, $(\Delta L_P/L_0)$ is the relative change of length due to phase transformation, α is the linear thermal expansion coefficient, and T is the temperature in centigrade.

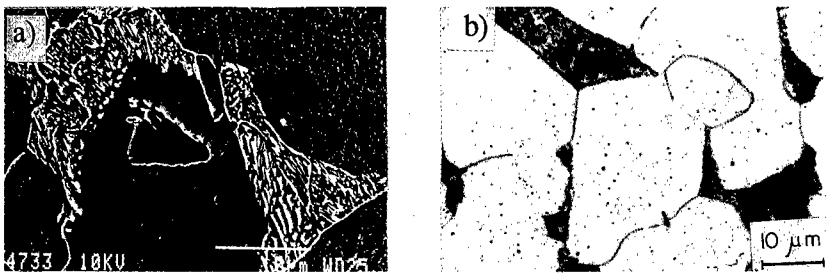


Figure 5. Microstructures obtained in the interrupted heating tests at 10 °C below Ac_1 : (a) SEM micrograph and (b) Optical micrograph

The contribution of thermal expansion in Equation (1) is always positive. However, a contraction occurs during the pearlite-to-austenite transformation. For a given temperature the dimensional change of length due to this transformation has been expressed as follows (12,13) ,

$$\frac{\Delta L_p}{L_0} = \frac{1}{3}\left[\frac{2a_\alpha^3\left(V'_\alpha - V_\alpha\right) + \frac{a_\theta^3}{3}\left(V'_\theta - V_\theta\right) + a_\gamma^3\left(V'_\gamma - V_\gamma\right)}{2a_\alpha^3 V_\alpha + \frac{a_\theta^3}{3}V_\theta + a_\gamma^3 V_\gamma}\right] \quad (2)$$

where $a^3_{\alpha,\gamma,\theta}$ is the volume of unit cell of ferrite, austenite and cementite respectively at reaction temperature, $V_{\alpha,\gamma,\theta}$ is the volume fraction of ferrite, austenite and cementite respectively before transformation, and $V'_{\alpha,\gamma,\theta}$ is the volume fraction of ferrite, austenite and cementite respectively after transformation.

In considering the values of volume of unit cells (12-13), it is possible to conclude that the relative change of length associated only with the pearlite-to-austenite transformation during heating from T to T+ΔT is always negative. As a consequence of this, before the pearlite dissolution occurs the function $(\Delta L/L_0)=f(T)$ shows a linear behaviour with a constant slope. An immediate variation of the slope is observed when the pearlite-to-austenite transformation starts. As transformation progresses, this slope can become negative.

Theoretical studies (14) concerning the growth rate of austenite into pearlite concluded that the dissolution process is controlled by the diffusion of carbon in the growing phase, and it was assumed that the effective diffusion distance is approximately equal to the interlamellar spacing

of pearlite. Hillert et al (15) studied the isothermal formation of austenite from a mixture of ferrite and pearlite, and suggested that the expression of the austenite growth rate could have the general form

$$\dot{G} \propto \frac{1}{S} \tag{3}$$

where S is the interlamellar spacing of pearlite. The growth rate of austenite into pearlite decreases as interlamellar spacing increases. Since very fine pearlite increases the growth rate of austenite into pearlite, this transformation takes place in a narrower temperature range.

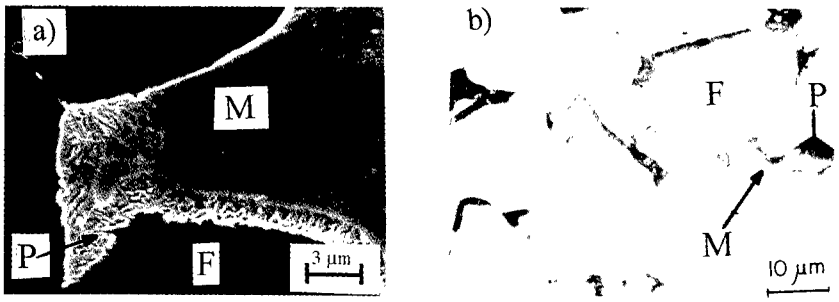


Figure 6. Microstructures obtained in the interrupted heating tests at 10 °C above Ac_1 :(a) SEM micrograph and (b) Optical micrograph

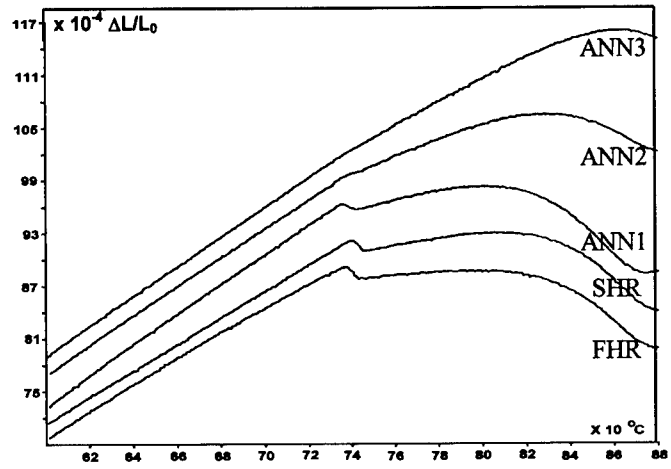


Figure 7. Dilatometric curves in quasi-equilibrium heating conditions of the specimens listed in Table II

In Equation (1) the term $(\Delta L_P/L_0)$ rises fast and a very sharp contraction peak appears in the dilatometric curve. This dilatometric anomaly allows to identify the pearlite-to-austenite transformation. Therefore, an accurate determination of the finishing temperature of pearlite dissolution process and thus the selection of the most suitable intercritical temperature to obtain dual phase microstructure would be possible whether fine enough interlamellar spacing is achieved by an appropriate annealling heat treatment.

Conclusions

1. As a consequence of the wide $\alpha+\gamma$ biphasic field of low carbon steels, a discrimination between the pearlite dissolution process and $\alpha\rightarrow\gamma$ transformation could be expected during continuous heating.
2. A dilatometric anomaly has been observed at the onset of $\alpha\rightarrow\gamma$ transformation in a low carbon steel as a finer pearlite is present in the ferrite-pearlite starting microstructure. Interrupted heating tests allowed to demonstrate that this anomaly is associated with the pearlite dissolution process.
3. A significant effect of pearlite interlamellar spacing on the shape of the dilatometric anomaly has been found. This effect is caused by the influence of this morphologic parameter on the austenite growth rate. The dilatometric anomaly associated with this transformation is not observed as pearlite coarsens.
4. The differentiation between perlite dissolution process and ferrite-austenite transformation allows to determine accurately the transformation temperatures corresponding to the pearlite dissolution process in this steel. The possibility of the accurate identification of the finishing temperature of pearlite dissolution process allows to select the most suitable intercritical temperature to obtain dual phase microstructure formed only by ferrite and martensite.

References

1. G. Krauss, Steels: Heat Treatment and Processing Principles, (ASM Inter., Ohio, 1989), 274.

2. A. Gustavsson et al., Inst. Metallforsk. Forsk. Rapp. 88, (1994), 3145.

3. V. L. Gadgeel, Tool Alloy Steels, 28, (1994), 17.

4. C. I. García and A. J. DeArdo, Met. Trans. A, 12A, (1981), 274.

5. G. R. Speich, V. A. Demarest and R. L. Miller, Met. Trans. A, 12A, (1981), 1419.

6. M. M. Souza, J.R.C. Guimaraes and K. K. Chawla, Met. Trans. A, 13A, (1982), 575

7. Xue-Ling Cai, A. J. Garrat-Reed and W. S. Owen, Met. Trans. A, 16A, (1985), 543

8. A. Roósz, Z. Gácsi, and E. G. Fuchs, Acta. Metall., 31, (1983), 509

9. E. E. Underwood, Quantitative Stereology, (Addison-Wesley, Reading ,1970), 410.

10. C. García, L. F. Alvarez, M. Carsí, Welding International, 6, (1982), 612.

11. C. García De Andres, J. A. Jimenez, and L. F. Alvarez, Met. Trans. A, 7A, (1996), 1799

12. H.K.D.H. Bhadeshia, Metal Science, 16, (1982), 159.

13. M. Takahashi, "Reaustenitisation from bainite in Steels", (PhD Thesis, University of Cambridge, UK, 1992), 127.

14. R. R. Judd and H. W. Paxton, TMS-AIME, 242, (1968), 206.

15. M. Hillert, K. Nilsson and L.E. Törndahl, J. Iron Steel Inst., 209, (1971), 49.

PROCESSING AND PROPERTIES OF DUAL PHASE ALLOYS IN THE NB-CR-TI SYSTEM

Katherine C. Chen, Dan J. Thoma, Paul G. Kotula, Fuming Chu, Carl M. Cady, G.T. (Rusty) Gray III, Paul S. Dunn, and Deniece R. Korzekwa

Materials Science and Technology Division, Los Alamos National Laboratory
Los Alamos, NM 87545, USA;

Chris Mercer and Wolé Soboyejo

Department of Materials Science and Engineering, The Ohio State University
Columbus, OH 43210, USA

Abstract

A two-phase alloy in the Nb-Cr-Ti system has been processed using a plasma arc melting technique. The compositions and bcc + *C*15 structure represents the combination of different alloy development strategies for structural Laves phase intermetallic alloys. Characterization and mechanical test results of the as-cast material are presented in order to establish baseline properties. Room-temperature, quasi-static compression tests produced yield stresses greater than 1.5 GPa and plastic strains of ~16%. Bend tests on double edge notched specimens resulted in a fracture toughness value of 10.4 MPa $m^{1/2}$, and revealed crack initiation and transgranular propagation in the bcc phase. Severe cracking was associated with Laves phase networks along the bcc grain boundaries.

The Third Pacific Rim International Conference on
Advanced Materials and Processing (PRICM 3)
Edited by M.A. Imam, R. DeNale, S. Hanada,
Z. Zhong and D.N. Lee
The Minerals, Metals & Materials Society, 1998

Introduction

Laves phase (AB_2) intermetallics hold great potential as high-temperature structural materials, due to attractive properties such as high-strength, good creep and oxidation resistance, and low densities. In particular, alloys based upon the *C*15 $NbCr_2$ Laves phase have received much attention [1,2,3]. However, the low-temperature brittle behavior circumvents the utilization of the monolithic intermetallic in engineering applications [4]. As a result, alloy design methodologies that impart room-temperature deformability are required.

Phase diagram evaluations of the Nb-Cr-Ti system define a significant solubility range of the *C*15 phase field, as well as large two phase regions (bcc + *C*15) in the ternary system (Figure 1) [5]. Alloying additions that produce ternary Laves phases have been shown to improve toughness values in monolithic Laves structures [5,6]. Specifically, Ti additions to $NbCr_2$ resulted in improved fracture toughness by indentation [5]. Significant improvements in toughness can also be achieved with the incorporation of a more ductile phase [6,7,8,9]. Additionally, processing techniques may be employed to generate proper microstructures needed to achieve desired mechanical properties [10]. Thus, three approaches have been used to develop the alloy in this study: (1) alloying strategies in the monolithic intermetallic, (2) a ductilizing second phase, and (3) microstructural control through processing pathways.

Experimental Procedures

An alloy of nominal composition, 37Nb-36Cr-27Ti (at%), was processed by a plasma arc melting (PAM) method. The elemental constituents were melted into a 4" diameter water-cooled copper hearth. The alloy had a mass of about 3 kilograms, and was remelted four times. Homogeneity was approached when the puck began to crack after melting. The alloy was weighed before and after melting to insure a minimal loss of material. Chemical analysis by inert-gas fusion revealed impurity levels of 0.08 wt% oxygen and 0.06 wt% nitrogen.

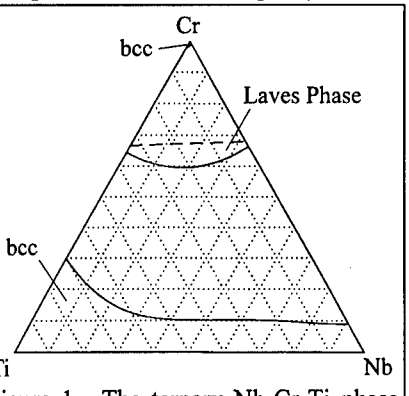


Figure 1. The ternary Nb-Cr-Ti phase diagram at 950°C [5].

The material was characterized by optical microscopy, scanning electron microscopy (SEM), transmission electron microscopy (TEM), and x-ray diffraction (XRD) using Cu $K\alpha$ radiation. Samples were etched with a solution of 20 vol% HF, 20% HNO_3, and 60% H_2SO_4. Volume fractions and grain sizes were determined by image analysis. Compositions were established by electron microprobe analysis (EMPA).

At least two samples were used for the compression and bend tests. Both tests were performed at room-temperature and in air. The quasi-static compression tests were conducted on cylindrical samples (5 mm diameter, 5 mm height)

Table I Compositions of the as-cast alloy, bcc, and Laves phases.

Compositions	Nb (at%)	Ti (at%)	Cr (at%)
bulk alloy	36.32 ± 0.61	26.30 ± 0.18	37.39 ± 0.53
bcc phase	45.72 ± 1.61	25.31 ± 1.15	28.97 ± 0.55
Laves phase	23.70 ± 0.39	15.55 ± 0.37	60.75 ± 0.30

at a strain rate of about 0.001/sec. The bend tests were carried out at a loading rate that corresponded to a stress intensity factor increase rate of 0.92 MPa $m^{1/2}s^{-1}$, in accordance with ASTM E399.

Double edge notched bend (DENB) test specimens were prepared by electro-discharge machining (EDM) as ½" × ½" × 2" (12.7 mm × 12.7 mm × 50.8 mm) parallel-epipeds, and two sides were polished to a 0.3 μm alumina suspension finish for crack analysis. The test specimens were loaded into a four point bend test apparatus within a servohydraulic test machine. Under such geometry and loading, the two notches should experience the same stress states, and therefore fail under the same nominal stress conditions. However, slight microstructural or machining differences will generally cause catastrophic failure to initiate from one of the notches, leaving the other notch with useful information on crack/microstructure interactions prior to the onset of fast fracture. The load at which fracture occurred can be used to calculate the fracture toughness. The cracks in the unfractured halves of the double edge notched specimens were analyzed by optical microscopy and SEM, while the fractured surface was studied by SEM.

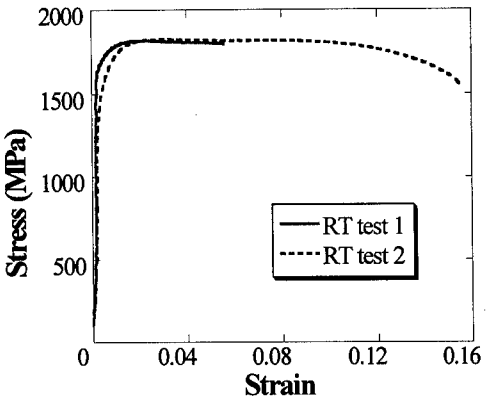


Figure 2. Room-temperature (RT) stress-strain curves for the as-cast NbCrTi alloy.

Results

Compositions of the bulk alloy and each phase can be found in Table I. XRD results confirmed that the NbCrTi alloy was comprised of the bcc and *C*15 Laves phase. The Laves phase comprised ~25 vol% in the as-cast condition, and was found as small particles (<10 μm) along the grain boundaries of the bcc phase. The bcc grain sizes were in the range of 25-100 μm. The plasma arc method produced grain sizes smaller than conventional arc-melting techniques for large castings.

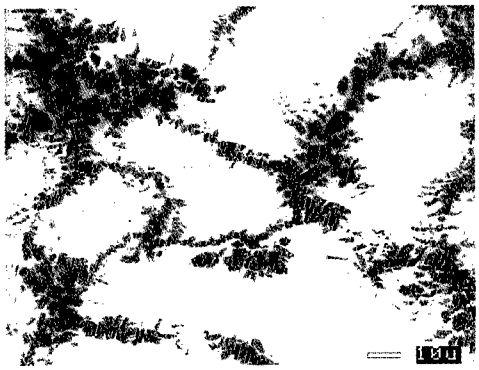


Figure 3. SEM of microcracking confined to the Laves phase (dark contrast) from room-temperature compression.

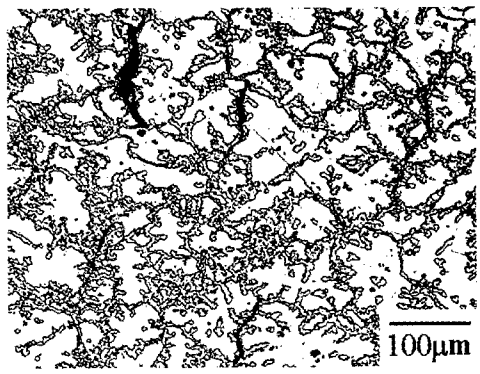


Figure 4. Optical micrograph of severe cracking along the continuous Laves phase network.

Compression Tests

The room-temperature compression stress-strain plots of two different as-cast samples are shown in Figure 2. The first test was stopped after a predetermined strain was reached, while the second test continued to plastic strains of ~16% before significant load drops occurred. A yield stress of 1620 MPa and an ultimate stress of 1800 MPa were achieved in these materials. Slight differences in the compressive behavior of the two samples probably originate from the microstructural differences between the as-cast samples. The high strengths and appreciable ductility of the as-cast material are promising for the heat-treated material and other future alloy developments.

The plateau in stress after yielding indicates little work hardening occurred, or that microstructural changes are taking place. Multiple cracking in the Laves phase is believed to occur in this regime. The Laves phase is most likely the high-strength, load-bearing component of the two-phase system, while the bcc phase provides the toughness that allows for structural integrity. The cylindrical test samples showed macroscopic failure by 45° shear.

Microscopically, however, numerous cracks are found within the Laves phase (darker contrast) in the direction of compression. SEM images (Figure 3) show microcracking confined to the Laves phase, and is consistent with compression of other two-phase Laves systems [6]. Large load drops are thought to be associated with the severe cracking found along the connected Laves phase network shown in Figure 4.

However, compression tests at 1200°C did not result in noticeable cracking. Yielding occurred at much lower stresses, but the ductility increased significantly. Results from compression tests as a function of temperature are forthcoming. Fine precipitation of the Laves phase (submicron) occurred within the bcc grains when the test specimens were tested at 1200°C, as seen in Figure 5. The large Laves phase particle in the figure is from the as-cast conditions.

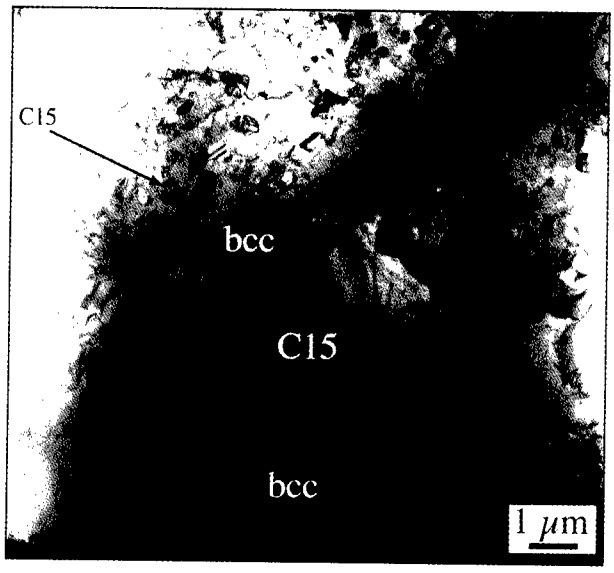


Figure 5. TEM of the sample tested in compression at 1200°C. No cracking is apparent, but precipitation of the *C*15 phase occurs within the bcc grains.

Bend Tests

While typical fracture toughness values for monolithic Laves phases are around 1.0 MPa $m^{1/2}$ [6], the average toughness value for the two-phase NbCrTi alloy in this study was 10.4±0.1 MPa $m^{1/2}$. The dual-phase (bcc+*C*15) system resulted in significant improvements in the fracture toughness values. Microstructural developments are expected to improve toughness values even more. Davidson, et al. [9,11] report toughness values of 18.5±1.5 MPa $m^{1/2}$ for a similar NbCrTi two-phase alloy that had been heat-treated and forged. The alloy tested in this study was in the as-cast condition and had not yet reached the equilibrium volume fraction of the Laves phase, as

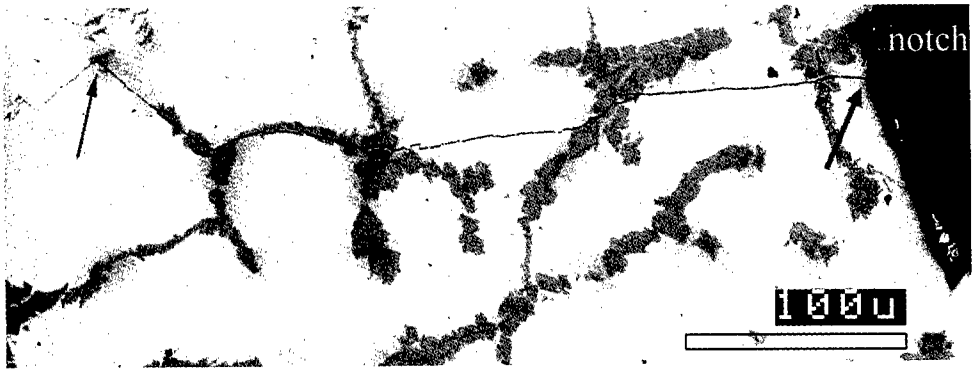


Figure 6. Crack initiated and transgranular propagation in the bcc phase of the DEBN specimen. The crack also follows along the Laves phase network (darker contrast).

calculated from the phase diagram. Thus, the bcc phase still contained supersaturated solutes, which may have contributed to the reduced toughness. Also, the Laves phase along the grain boundaries quickly propagates cracks.

A back-scattered electron image of the unfailed notch from the DENB specimen is displayed in Figure 6. A crack has initiated from the notch in the bcc phase and appears to travel in a transgranular manner within this phase. The cracks are quite straight until they encounter the Laves phase. The crack then temporarily follows along the Laves phase network, and thereby is displaced or changes direction before re-entering the bcc phase. Interestingly, at about 75% along the length of the crack, the crack seems to make an abrupt 90° turn after hitting a small Laves particle (marked by the left arrow in figure). Such observations suggest that cracks propagate in a transgranular mode along particular crystallographic planes in the bcc phase. Debonding of the bcc/*C*15 interface did not appear to be significant, as cracks were found to propagate through both the bcc and Laves phases.

The fracture surfaces were entirely consistent with the above crack initiation and growth modes. Cleavage occurs on preferred planes within each bcc grain, most likely on {100} planes. These planes have a relatively low density of atoms and a large d-spacing, which favors the breaking of bonds for cleavage fracture. Furthermore, many ledges and steps at orthogonal angles were observed, and are consistent with cleavage on these planes (Figure 7). The abundance of river lines in the fracture surfaces is also characteristic of cleavage fracture modes.

The Laves phase network along the bcc grain boundaries is severely broken up, and back-scattered electron imaging (Figure 8) clearly shows cracks concentrated along and throughout the Laves phase. The Laves phases are clearly the "weak" fracture spots of the alloy, in which cracks propagate. These fracture images are consistent with those of fatigued samples by Davidson [11]. This observation underscores the importance of refining and isolating the Laves phase in a multi-phase alloy. Other studies have arrived at similar conclusions [5,6,9,10]. Further work is underway to optimize the microstructures and properties of Laves phase intermetallic alloys.

Conclusions

1. A two-phase (bcc + *C*15) NbCrTi alloy has been made using a plasma arc melting technique with grain sizes below 100 microns.

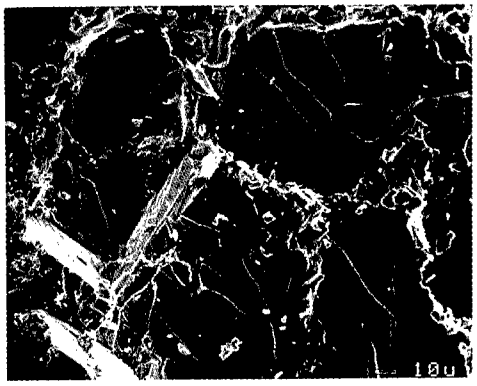


Figure 7. SEM secondary electron image of the fracture surface showing cleavage of the bcc phase.

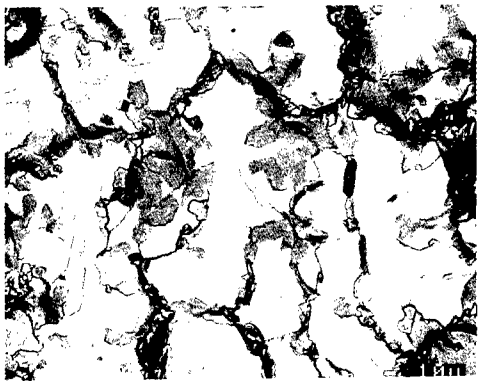


Figure 8. SEM back-scattered electron image of severe cracking concentrated along the Laves phase network.

2. Room-temperature compression of the as-cast material produced a yield stress of 1620 MPa, an ultimate stress of 1800 MPa, and 16% plastic strain.
3. Double notched bend tests provided an average fracture toughness value of 10.4 MPa $m^{1/2}$, and revealed transgranular crack initiation in the bcc phase.
4. Fracture of the bcc phase occurred by brittle transgranular cleavage, and extensive cracking was concentrated along the Laves phases. Refinement of the intermetallic away from the grain boundaries is suggested for future alloy development.

Acknowledgments

Assistance by Prof. Subra Suresh's group with the fracture experiment at MIT is greatly appreciated. Support of DOE-OBES, Division of Materials Sciences is gratefully acknowledged.

References

1. D.J. Thoma and J.H. Perepezko, Mater. Sci. and Eng., A156 (1992), 97.
2. C.T. Liu, P.F. Tortorelli, J.A. Horton, and C.A. Carmichael, Mater. Sci. and Eng., A214 (1996), 23.
3. T. Takasugi, S. Hanada, and K. Miyamoto, J. Mater. Res., Vol. 8 (1993), 3069.
4. J.D. Livingston, Phys. Stat. Sol. (a) 131 (1992), 415.
5. D.J. Thoma, "Microstructural Development in $NbCr_2$-based Alloys" (Ph.D. thesis, University of Wisconsin, 1992).
6. K.C. Chen, S.M. Allen, and J.D. Livingston, Mater. Sci. and Eng. A242 (1998), 163.
7. J.D. Livingston and E.L. Hall, J. Mater. Res., Vol. 5 (1990), 5.
8. M. Takeyama and C.T. Liu, Mater. Sci. and Eng. A132 (1991), 61.
9. D.L. Davidson, K.S. Chan, and D.L. Anton, Metall. and Mater. Trans. 27A (1996), 3007.
10. K.C. Chen, P.G. Kotula, F. Chu, and D.J. Thoma, to be published in Phase Transformations and Systems Driven Far From Equilibrium, MRS Symp. Proc., (Pittsburgh, PA, 1997).
11. D.L. Davidson, Metall. and Mater. Trans. 28A (1997), 1297.

The Relations between Precipitation of Carbides and Growth of Austenite in Duplex Stainless Steel

Kwang-Min Lee, Hoon-Sung Cho and Dap-Chun Choi

Department of Metallurgical Engineering, Chonnam National University
Kwangju 500-757, Korea

Abstract

The relations between precipitation of carbides and the growth of austenite and nucleation of σ in DSS were investigated by means of microstructural study as a function of aging treatment. The $M_{23}C_6$ carbides, having a cube-cube orientation relationship with the austenite, precipitates at δ/γ interface boundary and the carbide growth has two kind of patterns with a type of "larva" and "lamellar". The growth of secondary austenite, which is mainly induced by chromium depletion arising from carbide and sigma phase formation, has occurred with the process of three different ways; i) only austenite growth leaving "larva" typed carbides, ii) the coupled lamellar growth and iii) the bulged austenite between the sigma phase.

The Third Pacific Rim International Conference on
Advanced Materials and Processing (PRICM 3)
Edited by M.A. Imam, R. DeNale, S. Hanada,
Z. Zhong and D.N. Lee
The Minerals, Metals & Materials Society, 1998

Introduction

Duplex stainless steels (DSS) combine the favorable properties of ferrite and austenite, which are present in approximately equal amounts. However, the heat treatment of the DSS leads to a series of metallurgical transformations which take place in the ferrite or as its grain boundaries because the diffusion rates to the alloying elements in this phase are of the order of 100 times faster than the corresponding values in the austenite [1].

In particular, carbide formation causes deterioration of intergranular corrosion resistance while the fracture toughness is lowered by the presence of intergranular σ particles [2]. Thus, many workers have reported the kinetics and microstructural evolution of the ferrite decomposition [3-8]. But the very early stages of precipitation of carbide and the growth of secondary austenite in DSS are still not well understood. Because of the high mobility of carbon towards the δ/γ grain boundaries, carbide precipitates prior to the formation of other phases at the very early stages of aging.

Therefore, in the present study, the relations between precipitation of carbides and the growth of austenite and nucleation of σ in DSS were investigated by means of microstructural study as a function of aging treatment.

Experimental

The DSS used in this investigation was SAF 2205 of composition 22Cr-5Ni-3Mo-0.16N (wt.%). This material was fabricated to hot rolled plates with 5 ㎜ thick. The final compositions of the plates are listed in Table 1. Following solution treatment at 1050℃ for 1 h, the specimens were aged at 700℃, 800℃ and 900℃ for various times and water quenched.

Table I Chemical compositions of steels used. (wt%)

Steel	C	Si	Mn	Cr	Mo	Ni	V	Co	Cu	N	Fe
SAF 2205	0.028	0.240	1.830	21.25	2.600	5.250	0.050	0.040	0.100	0.160	bal.

Optical microscopy and scanning electron microscopy were performed after etching in [30㎖ HCl + 30㎖ HNO_3 + 45㎖ Glycerol + a little HF] reagent. Thin foils for observation with transmission electron microscopy (TEM) were prepared from the long transverse section parallel to the rolling direction of the hot rolled plates and by twin jet electropolishing in a solution of 10% perchloric acid in 20% glycerol and 70% ethanol at -10℃ and 20 V. The foils were examined in a JEM 2000 FX II transmission electron microscope operated at 200 kV. The crystallographic analyses of precipitates and matrix were normally accompanied by a selected area diffraction pattern (SADP) and a energy dispersive x-ray spectrometer (EDX) was used for composition analysis.

Results and Discussion

Figure I shows an optical microstructure of SAF 2205 stainless steel after solution treatment at 1050℃ for 1 h. The volume fractions of δ and γ phase become to have roughly a similar amount after solution treatment. This figure also represents that the isolated islands of austenite with twin structures are uniformly present within the ferrite matrix.

Figure 2 shows TEM micrograph of SAF 2205 stainless steel aged at 700℃ for 1 h. It shows some precipitated $M_{23}C_6$ carbides at δ/γ interface boundary, which are analyzed by a selected area diffraction pattern as well as a energy dispersive X-ray

spectrometer in association with TEM. The $M_{23}C_6$ carbide has a complex fcc crystal structure with a lattice parameter of approximately 10.65 Å. M included chromium, iron and molybdeum with some nickel, but chromium content being the major metallic element was over than 60wt.% in the present study.

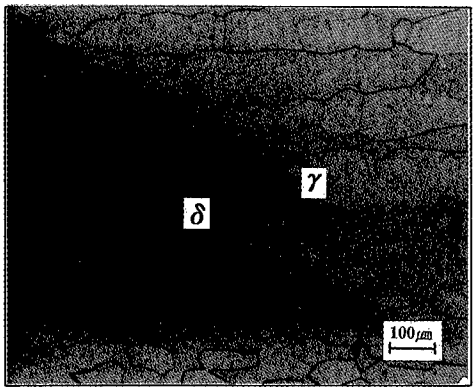


Figure 1: Optical microstructures of SAF 2205 after solution treatment at 1050℃ for 1 h.

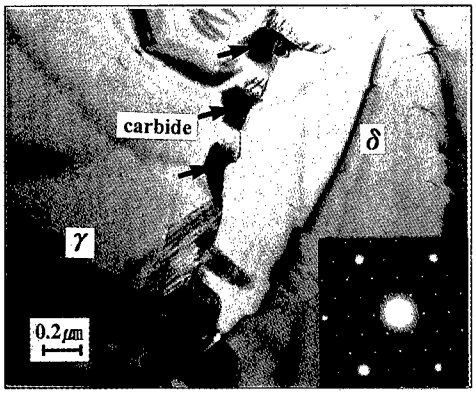


Figure 2: TEM micrograph showing the precipitated carbide phases at δ/γ interphase boundary of SAF 2205 aged at 700℃ for 1 h.

Figure 3 and Figure 4 show a variety of $M_{23}C_6$ carbides and austenite formed in SAF 2205 duplex steels aged at temperature of 800℃ for 1 h and water quenched. As shown in Figure 3(a), the precipitated $M_{23}C_6$ carbides at interface boundaries become to be formed with the shape of "larva" and only secondary austenite phase have continuously grown into the δ-ferrite. The above secondary austenite is visible in bright contrast between primary austenite and ferrite. The new austenite can be formed by following the eutectoid decomposition, $\delta \leftrightarrow M_{23}C_6 + \gamma_2$, during the aging treatment. Figure 3(b) is a schematic diagram of Figure 3(a).

On the contrary, as shown in Figure 4(a), the precipitated interphase carbides at a prior austenite/δ-ferrite interface have continuously grown with austenite into the δ ferrite. The precipitated carbides at δ/γ boundaries have a high chromium content, which lead to chromium depletion from the vicinity of the boundary within the ferrite. This is to be a driving force for the growth of austenite into δ-ferrite and hence the chromium depleted region of the ferrite will transform into secondary austenite. While the environs of growing secondary austenite have a high chromium content since the

growing γ_2 ejects the excess chromium to the adjacent ferrite. This is also to be a driving force for the growth of carbide into δ-ferrite. Thus, the coupled lamellar secondary austenites and carbides are eventually developed as shown in this figure. Figure 4(b) shows a selected area diffraction pattern of $M_{23}C_6$ and austenite in the coupled lamellar region with zone axes of $[011]_\gamma$ and $[011]_{M23C6}$. It also indicates the cube ∥ cube orientation relationship that exits between the secondary austenite and interphase carbides.

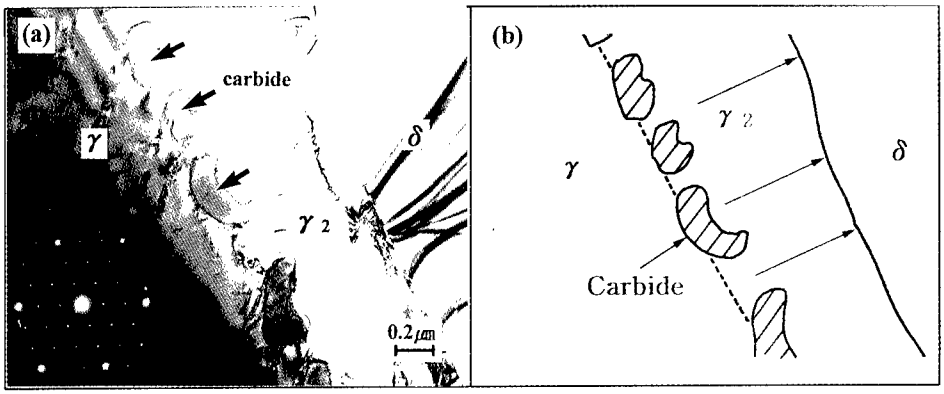


Figure 3: (a) TEM micrograph showing "larva" typed $M_{23}C_6$ carbides at δ/γ boundary in SAF 2205 aged at 800℃ for 1 h and (b) is a schematic diagram of photo (a).

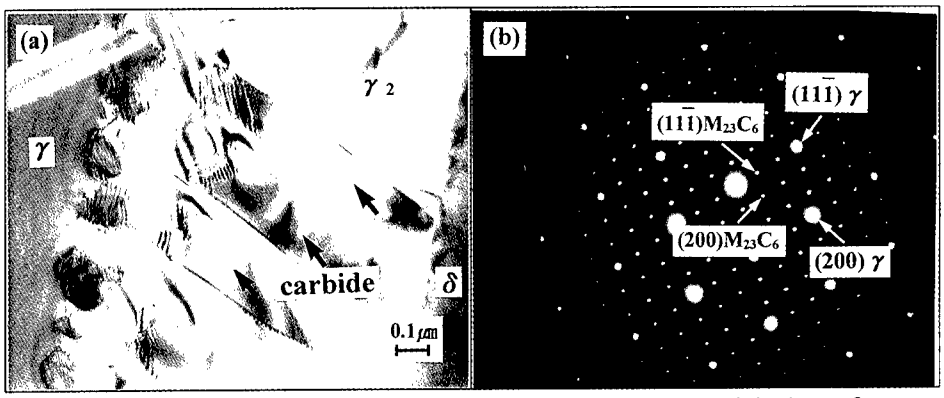


Figure 4: (a) TEM micrograph showing the lamellar precipitation after aging at 800℃ for 1 h and (b) a selected area diffraction pattern of $M_{23}C_6$ and austenite in the coupled region with $B=[011]_\gamma$ and $B=[011]_{M23C6}$.

Figure 5(a) shows TEM micrograph of the δ-ferrite decomposition to sigma and austenite phase in SAF 2205 duplex steels on aging at temperature of 800℃ for 2 h. The nucleated sigma phases at δ/γ boundaries have grown into the δ-ferrite and the new austenites (indicated by arrows) between sigma phases also have bulged into the δ-ferrite. Figure 5(b) is a schematic diagram of Figure 5(a). The sigma phase and the new austenite can be formed by following the eutectoid decomposition, $\delta \leftrightarrow \sigma + \gamma_2$. During the sigma precipitation, chromium is absorbed and nickel is rejected to adjacent regions within the ferrite, thus formation of the bulged austenite is possible adjacent to the sigma phase. In addition, the formation of sigma phase is likely to be independent on $M_{23}C_6$ carbides in this figure. But, in our previous report [9], we have

suggested that the sigma phase can be also formed at the front of the coupled lamellar precipitates.

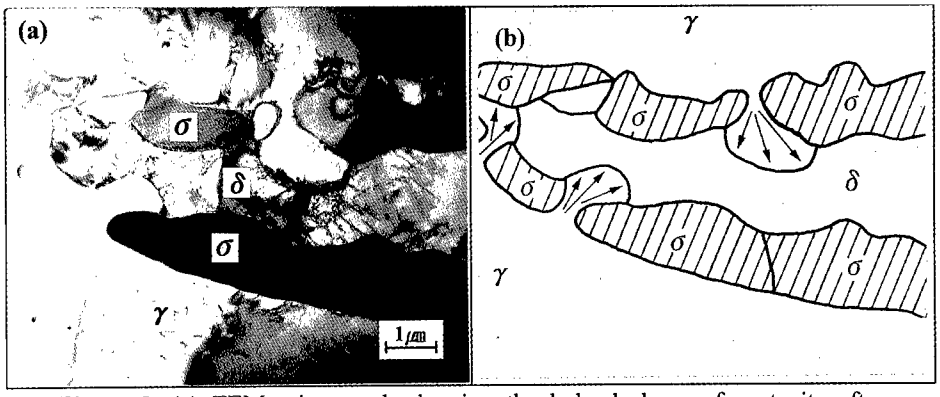


Figure 5: (a) TEM micrograph showing the bulged shape of austenite after aging at 800℃ for 2 h and (b) is a schematic diagram of photo (a).

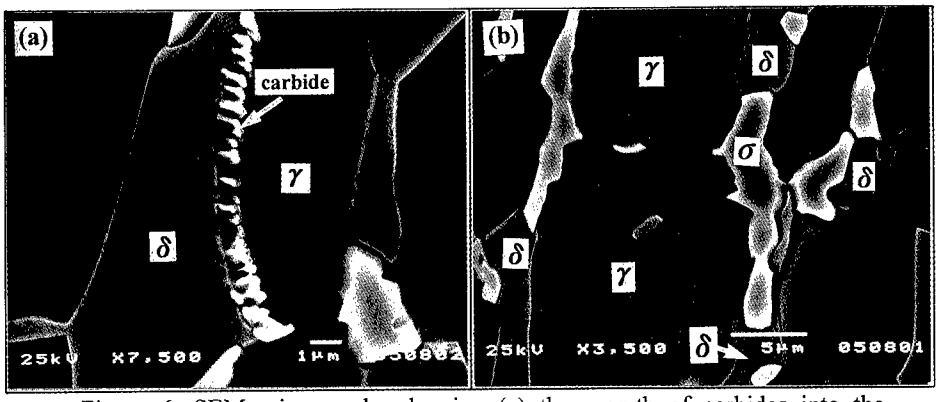


Figure 6: SEM micrographs showing (a) the growth of carbides into the δ-ferrite and (b) the precipitation of intergranular sigma phase in SAF 2205 aged at 900℃ for 1 h.

Figure 6 shows SEM micrographs of SAF 2205 stainless steel aged at 900℃ for 1 h. Figure 6(a) represents that the precipitated $M_{23}C_6$ carbides at δ/γ boundary have grown into the δ-ferrite. Figure 6(b) shows a typical of sigma phase present at δ/γ boundaries. As the aging progresses at higher aging temperature, intergralunar sigma precipitation takes place preferentially at δ/δ and δ/γ boundaries whereafter it grow in the form of unspecified shape towards the interior of the δ-ferrite grains. This reaction may continue until the ferrite is entirely consumed.

Conclusions

1. The $M_{23}C_6$ carbides, having a cube-cube orientation relationship with the austenite, precipitates at δ/γ interface boundary and the carbide growth has two kind of patterns with a type of "larva" and "lamellar".
2. The growth of secondary austenite, which is mainly induced by chromium depletion arising from carbide and sigma phase formation, has occurred with the process of three different ways; i) only austenite growth leaving "larva" typed carbides, ii) the coupled lamellar growth and iii) the bulged austenite between the sigma phase.

3. As the aging progresses, intergralunar sigma precipitation takes place preferentially at δ/δ and δ/γ boundaries whereafter it grows towards the interior of the δ-ferrite.

Acknowledgements

This paper was accomplished by the financial support of "1996 Suckjoa Professor Research Fund of Pohang Iron & Steel Co., Ltd (POSCO)".

References

1. C. F. Willis, R. Gronsky, and T. M. Devine, "Carbide Precipitation is Welds of Two-Phase Austenitic-Ferritic Stainless Steel," Metall. Trans. A, 22A (1991), 2889-2902.
2. J. O. Nilsson and A. Wilson, "Influence of isothermal phase transformations on toughness and pitting corrosion of super duplex stainless steel SAF 2507" Mater. Sci. Technol., 9 (1993), 545-554.
3. P. D. Southwick and R. W. K. Honeycombe, "Precipitation of $M_{23}C_6$ at Austenite/Ferrite Interfaces in Duplex Stainless Steel," Metal Science, 16 (1982), 475-481.
4. J. O. Nilsson, "Super duplex Stainless Steel," Mater. Sci. Technol., 8 (1992), 685-700.
5. A. Redjaimia, G. Netauer, and M. Gantois, " Decomposition of Delta Ferrite in a Fe-22Cr-5Ni-3Mo-0.03C Duplex Stainless Steel. A morphological and Structural Study," in 'Duplex Stainless Steel'91, edited by J. Charles-S. Bernhardsson, p 119-126, vol 1, les editions de physique, Beaune, France (1991).
6. J. K. L. Lai, K. W. Wong and D. J. Li, "Effect of solution treatment on the transformation behaviour of cold-rolled duplex stainless steels," Mater. Sci. Eng., A203 (1995), 356-364.
7. C. H. Shek, G. J. Shen, J. K. L. Lai, and B. J. Duggan, "Early stages of decomposition of ferrite in duplex stainless steel," Mater. Sci. Technol., 10 (1994), 306-311.
8. R. J. Romero and L. E. Murr, "Torque-related lamellar carbide growth associated with annealing twins in 304 stainless steel," Acta Metall. Mater., 43 (1995), 461-469.
9. K. M. Lee, H. S. Cho and D. C. Choi, "Effect of nucleation and growth behaviour of $M_{23}C_6$ carbide and austenite of duplex stainless steel to migration of δ/γ interphase boundary," to be submitted Scripta Metall. Mater (1998).

AUSTENITE FORMATION AND ALLOY CARBIDE DISSOLUTION IN Fe-Cr-C STEELS DURING HEATING

Dmitry V.Shtansky*, Kiyomichi Nakai and Yasuya Ohmori

Department of Materials Science and Engineering,
Faculty of Engineering, Ehime University,
3 Bunkyo-cho, Matsuyama 790 - 8577, Japan

Abstract

The mechanism of austenite formation and the kinetics of the alloy carbide dissolution have been studied in 8 wt pct chromium steels containing 0.2 and 0.96 wt pct carbon with ferrite–lamellar alloy carbide and ferrite-spheroidized alloy carbide initial structures. The morphology of austenite formation in the range of 870 – 900° C has been examined in detail by transmission electron microscopy. The effects of austenitising temperatures and times on the $M_{23}C_6$ and M_7C_3 carbide microstructure evolution have also been investigated. Various reactions occurring during austenitization and alloy carbide dissolution were observed. The orientation relationships between ferrite, austenite and alloy carbides were determined. The observed results can be understood by considering the equilibrium phase diagrams and assuming the local equilibrium at the moving interfaces during the reactions.

Acknowledgments

D.S. acknowledges the support of the Japan Society for the Promotion of Science during this work. Thanks are also due to Sumitomo Metal Industries for supplying the materials used in the present study.

* On leave from I.P.Bardin Iron and Steel Industry Institute, Moscow, Russia

The Third Pacific Rim International Conference on
Advanced Materials and Processing (PRICM 3)
Edited by M.A. Imam, R. DeNale, S. Hanada,
Z. Zhong and D.N. Lee
The Minerals, Metals & Materials Society, 1998

Introduction

From a practical point of view the formation of austenite and the dissolution of carbides play important roles in the heat treatment of steels. The effect of alloying elements on the various reactions occurring during austenitization of steels was the subject of both experimental and theoretical investigations for many years [1 - 12]. Most authors studied the austenitization and the dissolution of cementite in low-alloyed steels. Hillert [13] identified the different regimes for reaustenitization from ferrite/cementite initial structures. It has been assumed so far that local equilibrium is kept at the phase interface during the reactions, and the experimental results appear to be in a good agreement with theory. On the other hand, very little attention has been given to the phase transformations in high-alloy steels, which occur upon heating [14, 15]. Omsen and Liljestrand [16] as well as Gullberg [17] studied the dissolution of more complex carbides within the austenite matrix. The purpose of this paper is to present the complex results on the mechanism of austenite formation and the kinetics of the alloy carbide dissolution during heating in Fe-Cr-C steels with both ferrite – lamellar alloy carbide and ferrite – spheroidized alloy carbide initial structures.

Experimental Procedure

Fe-8.2%Cr-0.2%C (Steel 1) and Fe-8.2%Cr-0.96%C (Steel 2) steels were used in the present study. First group specimens were austenitized at 1200° C (Steel 1) and 1250° C (Steel 2) for 15 min in a dynamic argon atmosphere, isothermally transformed in a lead bath at 740° C for 70 min (Steel 1) and at 725° C for 12 min (Steel 2), then quenched in iced brine. These treatments resulted in the lamellar pearlite with M_7C_3 carbide lamellae for Steel 1 and ferrite-pearlite with fibrous or lamellar $M_{23}C_6$ carbides within pearlite for Steel 2. Second group specimens were quenched into iced brine immediately after the solution treatment at 1200°C and 1250° C respectively. Then specimens were sealed in evacuated tubes, isothermally heat treated at 700° C for 240 h and finally quenched into iced brine. This treatment resulted in an initial microstructure consisting of spherical M_7C_3 carbides (Steel 2), or both globular $M_{23}C_6$ and spherical M_7C_3 carbides (Steel 1) in the ferrite matrix. Slices, 10x10x0.3 mm, were cut from the center of each heat-treated cylinder. Specimens were finally austenitized at different temperatures in the range of 850 - 1150° C for various times between 1 and 100 s. The austenitization up to 900° C was performed in a salt bath. The heat treatment at higher temperatures was carried out in a tube furnace under argon atmosphere. The foils were examined in a JEM-3010 transmission electron microscope operating at 300 kV.

Results and Discussion

A. Formation of Austenite from Pearlite

Fig. 1(a) shows the pearlite in an **Fe-8.2Cr-0.96C** steel which was partially transformed into austenite at 870° C for 5 s. It was observed that the austenite starts to grow primarily from the intersections of pearlite colonies, which is similar to earlier results [2, 6]. Some ferrite plates within a pearlite colony remained untransformed even when $\alpha \rightarrow \gamma$ transformation in the adjacent lamellae has already completed. Since the M_7C_3 carbide lamellae remain almost undissolved during 5 s austenitization at 870° C, the γ phase may be of low carbon content. Fig. 1(b) shows an example of different kinetics of $\alpha \rightarrow \gamma$ transformation when M_7C_3 carbide lamellae spheroidized just behind the moving interface.

The formation of austenite in an **Fe-8.2Cr-0.2C** steel started after 20, 8 and 3 s exposure at 850, 870 and 900° C respectively. Growth of austenite through the intersections of pearlite colonies as well as the α/α grain boundaries was inhibited. Fig. 2(a) shows the α/γ (now martensite) front after austenitization at 900° C for 3 s. $M_{23}C_6$ carbide lamellae

acted as barriers for the sidewise growth of austenite. Fig. 2(b) shows the growth and spheroidization of $M_{23}C_6$ carbide lamellae just at the reaction front.

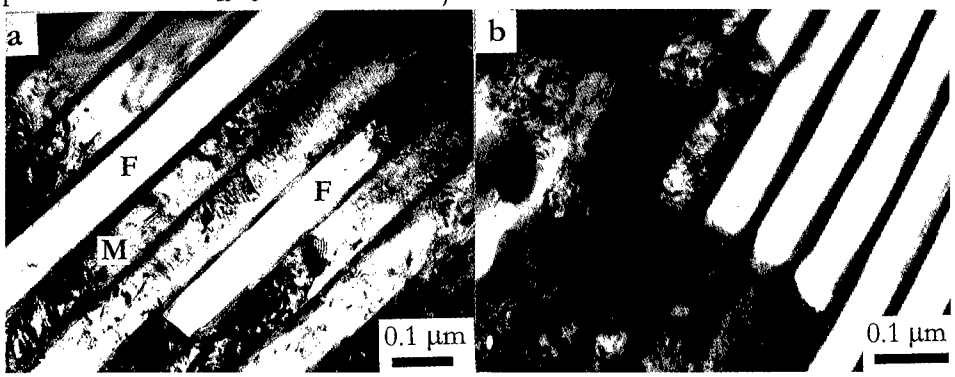


Fig. 1 Bright field micrographs showing the transformation of pearlite into austenite in an Fe-8.2Cr-0.96C steels on heating at 870° C for 5 s (a) and 7 s (b).

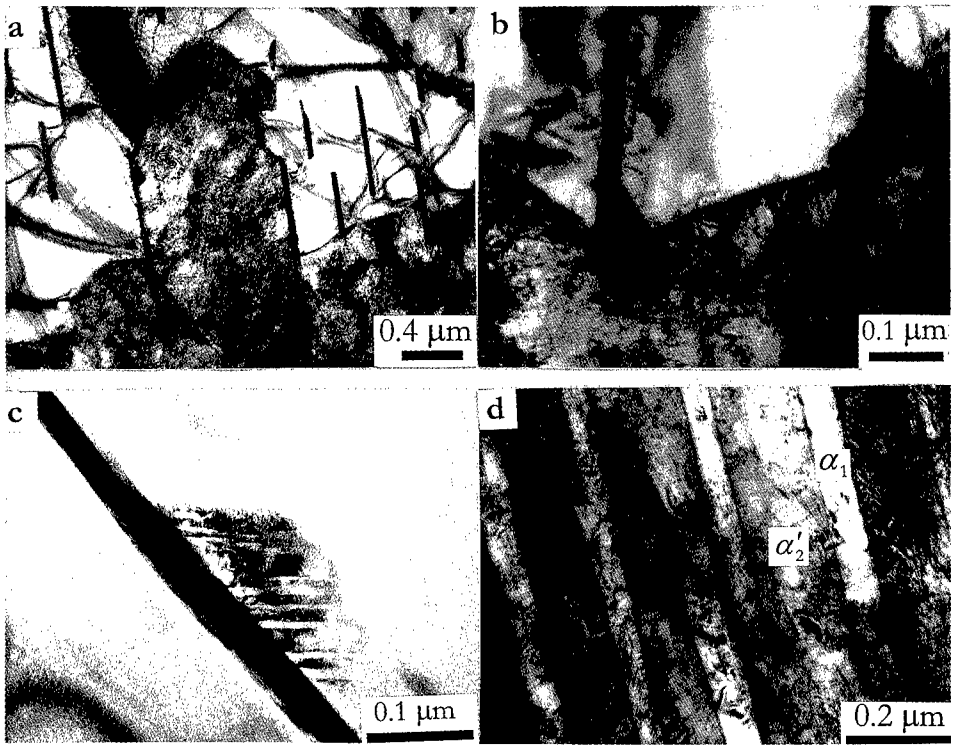


Fig.2 Bright field micrographs showing the different stages of pearlite into austenite transformation in an Fe-8.2Cr-0.2C steel on heating at 900° C for 3 s (a, b) and at 870° C for 8 s (c) and 10 s (d). (a) and (b) - α/γ front (austenite transforms into martensite during quenching); (c) – the $\alpha \rightarrow \gamma$ transformation at the $\alpha/M_{23}C_6$ interface within pearlite; (d) – ferrite plates within martensite after complete $M_{23}C_6$ carbide dissolution.

Figure 2(c) shows the other type of $\alpha \rightarrow \gamma$ transformation when austenite nucleated at the $\alpha/M_{23}C_6$ interface within pearlite colony. During quenching this austenite transformed to

martensite plate that contains coarse (112) twins. The twins were identified by means of selected area diffraction (SAD). Some of the twins are quite wide that agrees well with an earlier result [20]. The stereographic analysis shows that one of the twin orientations is related to $M_{23}C_6$ carbide lamella by Kyrdjumov-Sachs (K-S) relationships. Fig. 2 (d) shows the microstructure of the Fe-8.2Cr-0.2C steel after complete dissolution of $M_{23}C_6$ carbides. It can be seen that ferrite plates inherited the site and form of $M_{23}C_6$ carbide lamellae. SAD pattern shows that these ferrite and martensite are almost in the same orientations.

B. Formation austenite from ferrite-spheroidized alloy carbide structure

Two mechanisms of austenite formation were distinguished. Austenite first nucleated at the α/α grain boundary triple points in the vicinity of carbides. TEM observation revealed that α/γ interface was faceted. The step height and the distance between steps on a broad face are of about 5 nm and 25 nm respectively. The ledges at the α/γ interface may be interpreted as a growth steps [18] during austenite nucleation. As the $\alpha \rightarrow \gamma$ transformation proceeded a curved α/γ interface was developed. The absence of planar facets at the α/γ interface suggests that growth of austenite was resulted from the migration of incoherent interface as was also confirmed by other investigators [5, 19]. The other observation is that the austenite nucleated at carbides on the ferrite grain boundaries and partially enveloped these carbides on the side of the ferrite grain in which it extended as well as grew along the grain boundaries.

C. Spheroidized alloy carbide dissolution.

Fig. 3(a) shows the wide ferrite shell around dissolving $M_{23}C_6$ carbide. This ferrite is less dislocated and can be easily distinguished from the surrounding martensite. Fig. 3(b) shows the ferrite within a martensite matrix after complete $M_{23}C_6$ carbide dissolution. The martensite lattice parameter is a_m = 2.86 Å that agrees well with previous results [20], whereas ferrite lattice parameter is a_f = 2.90 Å that is close to α-Cr.

Fig. 4(a) shows the M_7C_3 carbide particle that is completely surrounded by a ferrite shell. The SAD pattern taken from the α/α' interface illustrates that orientations of the ferrite and the martensite are almost the same. The other situation is illustrated in Fig. 4(b) when M_7C_3 carbide is surrounded by an austenite shell. The orientation relationship between the austenite and the martensite is the K-S relationship. Fig. 5 shows the microstructure in the Fe-8.2Cr-0.96C steel after complete M_7C_3 carbide dissolution during tempering at 1150° C for 12 s. The spherical martensite area can be distinguished within the surrounding martensite matrix. The stereographic analysis of the SAD patten reveals that both bcc crystals are almost in the same orientation. Both regions in the martensite differ

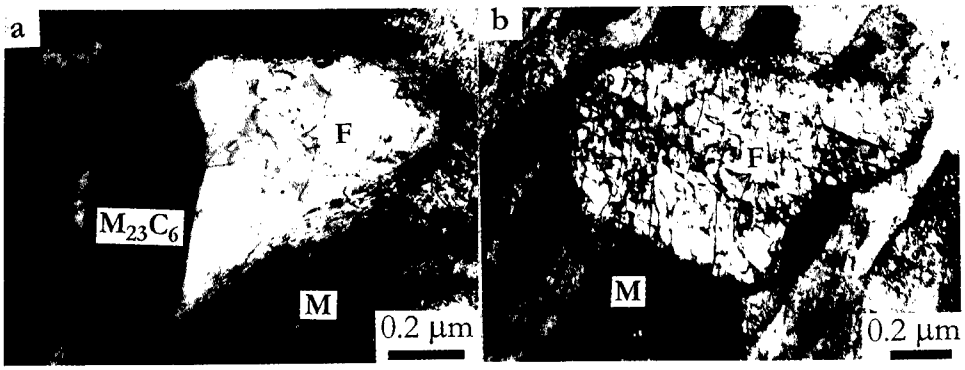


Fig.3 Bright field micrographs showing the ferrite shell around undissolved $M_{23}C_6$ carbide (a) and ferrite area after complete $M_{23}C_6$ carbide dissolution (b) in an Fe-8.2Cr-0.2C steels on heating at 870° C for 100 s.

in dislocation density and appear to have different chromium contents.

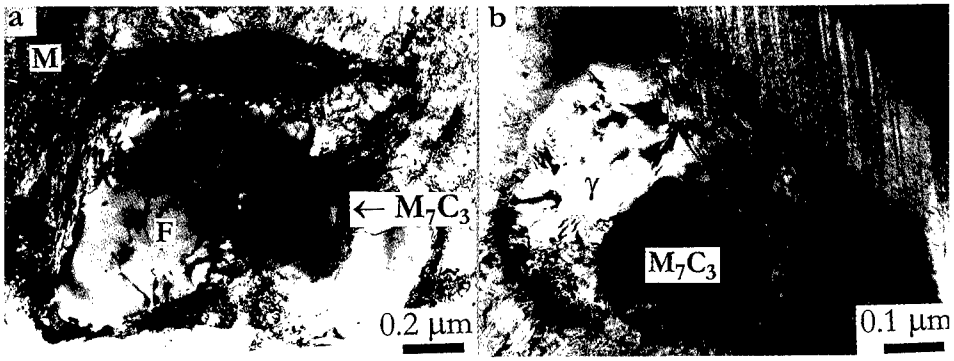
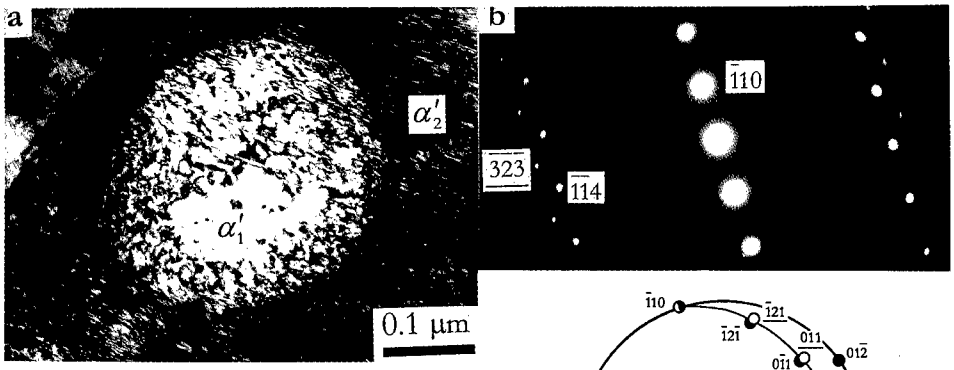


Fig. 4 Bright field micrographs showing the different intermediate microstructure during M_7C_3 carbide dissolution in an Fe-8.2Cr-0.2C (a) and Fe-8.2Cr-0.96C (b) steels on heating at 1000° C for 20 s (a) and 1150° C for 12 s (b). Ferrite (a) and austenite (b) shells around undissolved M_7C_3 carbide.



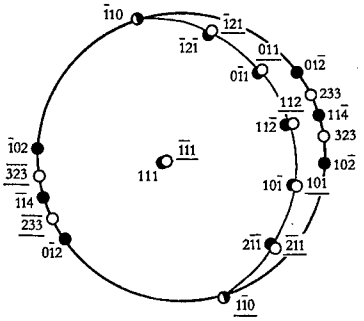


Fig. 5 Bright field micrograph (a) showing the spherical martensite area after complete M_7C_3 carbide dissolution. (b) Selected area diffraction pattern and its schematic key diagram. Fe-8.2Cr-0.96C steel heat treated at 1150° C for 12 s.

D. Thermodynamic consideration

The mechanism of austenite formation and the kinetics of alloy carbide dissolution were examined theoretically using thermodynamic equilibrium calculations that have been performed with the software and database THERMO-CALC. The results show that the reactions occurring during austenitization in the Fe-8.2Cr-0.96C steel may be divided into four stages. Stage one is the carbon-controlled dissolution of M_7C_3 carbides in ferrite. Stage two is the austenite growth controlled by carbon diffusion in both ferrite and austenite. Stage three is the austenite growth controlled by chromium diffusion. Stage four is the chromium-controlled dissolution of M_7C_3 carbides in austenite. In the Fe-8.2Cr-0.2C steel the composition of initial ferrite falls into one-field γ at austenitizing temperatures and one can not find a suitable tie-line at the α/γ interface for the assumption that the reaction is controlled by carbon diffusion at the constant composition of chromium. Thus stage one should not occurs in the Fe-8.2Cr-0.2C steel.

The model implies that a large amount of chromium atoms flow out through the α - γ - M_7C_3 and α - γ - $M_{23}C_6$ triple points during the stage three and those regions become the favorable places for the carbides growth. It is important to note that α or γ matrices may inherit the chromium content of the alloy carbides during stages one and two. The compositions of γ fall inside the α + $M_{23}C_6$ two-phase area. Thus the formation of the ferrite shells around $M_{23}C_6$ and M_7C_3 carbides observed in the present study is expected from the thermodynamic arguments.

Conclusions

Various reactions occur during the austenitization of Fe-8.2Cr-C alloys. During incubation period at the austenitizing temperature the carbon atoms diffuse from alloy carbides into ferrite. This diffusion process changes the local equilibrium conditions at the interfaces and affects on the following reactions.

1. Nucleation of austenite in pearlite occurs mainly at pearlite colony intersections. Moreover, ferrite within an $\alpha/M_{23}C_6$ pearlite can directly transform into austenite.
2. In ferrite with spheroidized alloy carbide initial structure, the austenite first nucleates at the α/α grain boundary triple points in the vicinity of carbides or directly at alloy carbides located on the α/α grain boundaries. Depending on the nucleation sites, the initially formed austenite may be of high or low carbon content. The presence of facets at the α/γ interface suggests that the austenite may start to grow by the ledge mechanism whereas the following α/γ interface advancing is the migration of incoherent interface.
3. The kinetics of austenite growth in the Fe-8.2Cr-0.96C steel changes from carbon diffusion controlled to chromium diffusion controlled, whereas in the Fe-8.2Cr-0.2C steel it appears to be controlled by chromium diffusion only.
4. Different intermediate stages were observed during alloy carbide dissolution. The chromium enrichment of adjacent matrix leads to the formation of ferrite layers between austenite and alloy carbides. It was observed that ferrite inherits the site and form of alloy carbides after their complete dissolution. In some cases austenite shells were observed around undissolved M_7C_3 carbides after quenching. The spherical martensite areas with high chromium content are also distinguished from the surrounding matrix after complete alloy carbide dissolution.

References

1. G.Molinder, Acta Metall., 4 (1955), 565-71.
2. G.R.Speich and A.Szirmae, TMS of AIME, 245 (1969), 1063-74.
3. S.F.Dirnfeld, B.M.Korevaar and F.Van't Spijker, Met.Trans., 5 (1974), 1437-44.
4. M.Nemoto, Met.Trans., 8A (1977), 431-37.
5. N.C.Law and D.V.Edmonds, Met.Trans., 11A (1980), 33-46.
6. C.I.Garcia and A.J.Deardo, Met.Trans., 12A (1981), 521-30.
7. G.R.Speich, V.A.Demarest and R.L.Miller, Met.Trans., 12A (1981), 1419-28.
8. M.M.Souza, J.R.C.Guimaráes and K.K.Chawla, Met.Trans., 13A (1982), 575-79.
9. J.J.Yi, I.S.Kim and H.S.Choi, Met.Trans., 16A (1985), 1237-45.
10. A.M.Gokhale and R.T.Dehoff, Met.Trans., 16A (1985), 559-64.
11. S.K.Jayaswal and S.P.Gupta, Z.Metallkd., 83 (11) (1992), 809-19.
12. C.Atkinson, T.Akbay and R.C.Reed, Acta Metall. Mater., 43 (5) (1995), 2013-31.
13. M.Hillert, K.Nilsson and L.-E.Törndahl, J.Iron and Steel Inst., 1 (1971), 49-66.
14. H.D.Kim and I.S.Kim, ISIJ Int., 34 (2) (1994), 198-204.
15. H.S.Kim, H.R.Harrison and P.G.Winchell, Mat.Trans., 12A (1981), 1461-65.
16. A.Omsén and L.G.Liljestrand, Scand. J. of Metallurgy, 1 (1972), 241-46.
17. R.Gulberg, J.Iron and Steel Inst., 1 (1973), 59-65.
18. S.A.Hackney and G.J.Shiflet, Acta Metall., 35 (1987), 1007-28.
19. Ph.Maitrepierre, D.Thivellioer and R.Tricot, Met.Trans., 6A (1975), 287.
20. A.J.Morton and C.M.Wayman, Acta Met., 14 (1966), 1567-79

EFFECTS OF ALLOYING ELEMENTS ON THE INTRAGRANULAR PRECIPITATION IN Cu-Be ALLOY

Masamichi Miki*, Kazutaka Morita**, Shuhei Ishikawa***
and Yoshikiyo Ogino*

* Department of Materials Science and Engineering, Faculty of Engineering,
Himeji Institute of Technology, Himeji 671-22 Japan
** Graduate Student, Himeji Institute of Technology, Himeji 671-22, Japan
*** Metal Division, NGK Insulators Ltd.

Abstract

A Cu-12at%Be alloy is hardened in two stages by the formation of G.P. zone, γ'' phase and γ' phase(CuBe') in the matrix on aging at 523 K after quenching from 1093 K. The first and second stages of hardening are caused mainly by the formation of G.P. zone and the precipitation of γ' phase, respectively. In this study, effects of 13 kinds of micro alloying elements (Zr, Pb, Bi, Cd, Ti, Cr, Fe, Co, In, Al, Ni, Zn and Mn) on the first stage of hardening of the alloy were investigated in relation with solid solubilities of these elements to the solvent Cu. The addition of Pb, Bi and Zr elements, which are scarcely soluble to Cu, suppressed remarkably the formation of G.P. zone. On the other hand, the addition of Ni and Mn, which are fully soluble to Cu, scarcely affected the formation of G.P. zone. Thus, it is clarified that the elements having smaller solid solubility to Cu suppressed more strongly the formation of the G.P. zone. The reason is explained by the mechanism that the elements having small solid solubility to Cu segregate at grain boundaries and around vacancies in the matrix, and trap the vacancies, which are needed for the migration of Be atoms to {100} planes of the matrix.

The Third Pacific Rim International Conference on
Advanced Materials and Processing (PRICM 3)
Edited by M.A. Imam, R. DeNale, S. Hanada,
Z. Zhong and D.N. Lee
The Minerals, Metals & Materials Society, 1998

Introduction

Since Cu-Be alloys are extremely hardened by aging at 523-673 K after quenching from solution-treatment temperature (1073-1093 K), these alloys are commercially used as superior spring materials. The hardening is caused by the formation of G.P. zone, γ" phase and γ' phase (CuBe') [1]-[3]. Commercial Cu-Be alloys are added small amounts of alloying elements such as Co, Ni and Fe in order to suppress the grain growth during the solution-treatment and also suppress the cellular precipitation (discontinuous precipitation) during the subsequent aging. The effects of these alloying elements on the cellular precipitation has been studied fully[4]-[6], however, the effects of these elements on the intragranular precipitation has not been clarified in detail yet.
In this study, the effects of 13 kinds of micro alloying elements (Zr, Pb, Bi, Cd, Ti, Cr, Fr, Co, In, Al, Ni, Zn and Mn) on the intragranular precipitation (mainly the formation of the G.P. zone) in a Cu-12at%Be alloy were investigated in relation with the solid-solubilities [7] of these elements to the solvent Cu.

Experimental

Table 1 shows the chemical compositions of alloys used. Each alloy was prepared by melting electrolytic copper (99.99at%), Cu-22.7%Be, Cu-23.0%Zr, Cu-10.7%Co, Cu-28.0%Mn, Cu-6.3%Cr, Cu-34.0%Ti master alloys, pure Pb(99.99%), Bi(99.999%), Ni(99.95%), In(99.97%), Cd(99.9%), Fe (99.9%), Al (99.99%) and Zn (99.97%) in a high purity alumina crucible in an Ar atmosphere. Each ingot was homogenized at 1093 K and then cut into plates.
These plates were cold-rolled by 50% and shaped into specimens of 10 x 10 x 2 mm in size. These specimens were quenched into iced-water after solution-treatment at 1093 K for 1800 s and then aged at 523 K. After aging, the hardness of each specimen was measured by a micro-Vickers hardness tester (with the load of 0.98 N) and electron microscopic observation was also performed.

Results and discussion

Additions of Bi, Pb and Zr which are scarcely soluble to Cu

Figure 1 shows hardness changes of the specimens containing 0.02% of Bi, Pb and Zr on aging at 523 K. In the Cu-Be binary alloy, hardening occurs in two stages. However, in the alloys containing Bi, Pb and Zr, the first stage of hardening is suppressed. Especially the addition of Bi suppresses almost completely the first stage of hardening. Our previous studies[8][9] clarified that the first stage hardening is mainly due to the formation of G.P. zones. Therefore, it seems that the additions of Bi, Pb and Zr suppress remarkably the formation of G.P. zones.
At the aging time of 200 s when the first stage of hardening in the Cu-12at%Be binary alloy reaches nearly the plateau, the hardening ratio ($R = 100 (Hp - Hw) / Hw$) was calculated for each hardening curve. Where, Hp denotes the hardness at 200 s aging in each hardening curve and Hw shows the hardeness at the as-quenched state of each specimen. The R value of each specimen will be shown later in Fig.5.

Additions of Cr, Cd, Ti, Fe and Co which are slightly soluble to Cu

Figure 2 shows the hardening curves of the specimens containing Cr, Cd, Ti ,Fe and Co on aging at 523 K. In these micro-alloyed specimens, the hardening at the first stage was suppressed in accordance with the solid-solubility to Cu. The hardening ratio (R) of these alloys were calculated from these hardening curves and will be shown later in Fig.5.

Table 1 Chemical compotisions of alloys (a : at%, m : mass%)

Nominal		Cu	Be	Zr	Pb	Bi	Cd	Ti	Cr	Fe	Co	In	Al	Ni	Zn	Mn
Cu-12Be	a	Bal.	12.13	t	t	t	t	t	t	0.032	0.005	t	t	t	t	t
	m	Bal.	1.92	t	t	t	t	t	t	0.031	0.005	t	t	t	t	t
-0.02Zr	a	Bal.	12.18	0.016	t	t	t	t	t	0.030	0.007	t	t	t	t	t
	m	Bal.	1.93	0.026	t	t	t	t	t	0.029	0.007	t	t	t	t	t
-0.02Pb	a	Bal.	12.08	t	0.018	t	t	t	t	0.034	0.005	t	t	t	t	t
	m	Bal.	1.91	t	0.065	t	t	t	t	0.033	0.005	t	t	t	t	t
-0.02Bi	a	Bal.	12.01	t	t	0.016	t	t	t	0.035	0.004	t	t	t	t	t
	m	Bal.	1.90	t	t	0.058	t	t	t	0.034	0.004	t	t	t	t	t
Cu-12.5Be	a	Bal.	12.47	t	t	t	t	t	t	0.050	0.004	t	t	t	t	t
	m	Bal.	1.98	t	t	t	t	t	t	0.050	0.004	t	t	t	t	t
-0.1Cd	a	Bal.	12.25	t	t	t	0.113	t	t	0.048	0.004	t	t	t	t	t
	m	Bal.	1.94	t	t	t	0.224	t	t	0.047	0.004	t	t	t	t	t
-0.5Ti	a	Bal.	12.84	t	t	t	t	0.48	t	0.027	0.012	t	t	t	t	t
	m	Bal.	2.05	t	t	t	t	0.41	t	0.027	0.013	t	t	t	t	t
-0.3Cr	a	Bal.	12.63	t	t	t	t	t	0.329	0.028	0.012	t	t	t	t	t
	m	Bal.	2.01	t	t	t	t	t	0.302	0.028	0.012	t	t	t	t	t
-0.3Fe	a	Bal.	12.57	t	t	t	t	t	t	0.343	0.011	t	t	t	t	t
	m	Bal.	2.00	t	t	t	t	t	t	0.338	0.011	t	t	t	t	t
-0.3Co	a	Bal.	12.24	t	t	t	t	t	t	0.021	0.260	t	t	t	t	t
	m	Bal.	1.94	t	t	t	t	t	t	0.021	0.269	t	t	t	t	t
-0.2In	a	Bal.	12.49	t	t	t	t	t	t	0.044	0.006	0.207	t	t	t	t
	m	Bal.	1.98	t	t	t	t	t	t	0.043	0.006	0.418	t	t	t	t
-0.9Al	a	Bal.	12.46	t	t	t	t	t	t	0.042	0.005	t	0.891	t	t	t
	m	Bal.	1.99	t	t	t	t	t	t	0.042	0.005	t	0.426	t	t	t
-0.3Ni	a	Bal.	12.41	t	t	t	t	t	t	0.042	0.005	t	t	0.28	t	t
	m	Bal.	1.97	t	t	t	t	t	t	0.041	0.005	t	t	0.29	t	t
-0.3Zn	a	Bal.	12.58	t	t	t	t	t	t	0.045	0.004	t	t	t	0.256	t
	m	Bal.	2.00	t	t	t	t	t	t	0.044	0.004	t	t	t	0.295	t
-0.3Mn	a	Bal.	12.68	t	t	t	t	t	t	0.027	0.006	t	t	t	t	0.326
	m	Bal.	2.02	t	t	t	t	t	t	0.027	0.006	t	t	t	t	0.316

(t < 0.001mass%)

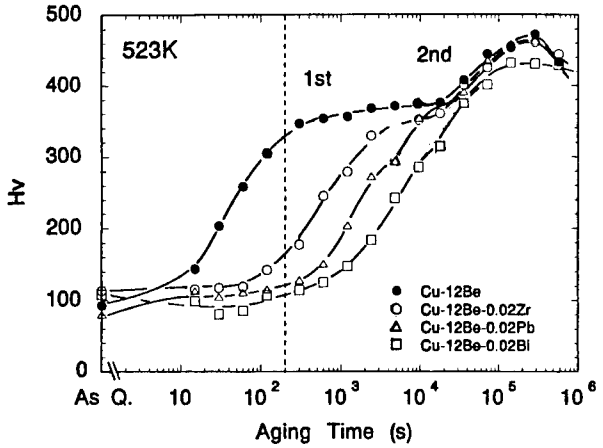


Fig.1 Age-hardening curves of Cu-12at%Be-0.02%X(Zr, Pb and Bi) alloys at 523 K.

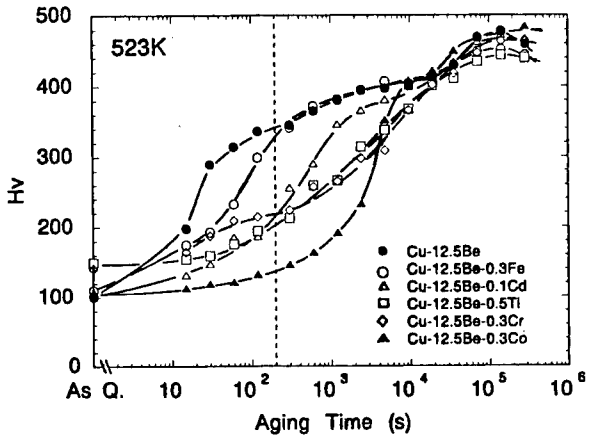


Fig.2 Age-hardening curves of Cu-12.5at%Be-X(Fe, Cd, Ti, Cr and Co) alloys at 523 K.

Additions of Al, In, Zn, Mn and Ni which are largely soluble to Cu

Figure 3 shows the hardening curves of the specimens containing Al, In and Zn on aging at 523 K. In these specimens, the first stage of hardening was slightly suppressed. **Figure 4** shows the hardening curves of the specimens containing Mn and Ni which are fully soluble to Cu. In these specimens, the first stage of hardening was scarcely affected or rather promoted. Namely, at the aging time of 200 s, the hardness of the Mn and Ni doped specimens is nearly equal to that of the Cu-Be binary alloy. However, at the aging time of 10^3 s, the hardness of these specimens is rather higher than that of the binary alloy. Therefore, the hardening ratio (R) of these Mn and Ni doped specimens at the aging time of 200 s (shown in Fig.5) seems to be underestimated.

Figure 5 shows the relationship between the hardening ratio (R) and the solid-solubility of the alloying elements to Cu. The linear relationship is observed between the loghalismic hardening ratio and the solid-solubility of each element to Cu. Namely, the hardening ratio (R) decreases with decreasing solid-solubility of the alloying element to Cu. This means that the alloying elements which are difficult to dissolve in the Cu matrix suppress strongly the formation of G.P. zones. The reason can be interpreted as follows: Since the alloying element with a small solid-solubility to Cu has a tendency to segregete around vacancies, such element will prevent the movement of the vacancies needed for migration of Be atoms

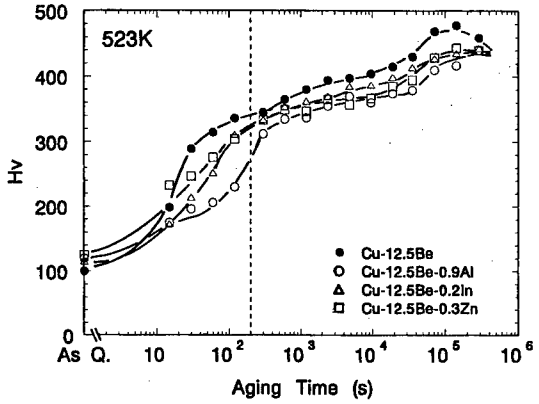


Fig.3 Age-hardening curves of Cu-12.5at%Be-X(Al, In and Zn) alloys at 523 K.

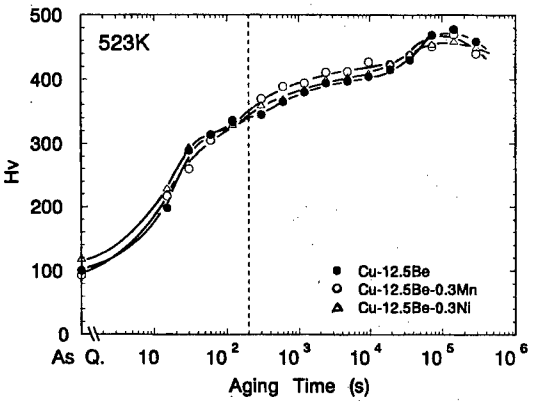


Fig.4 Age-hardening curves of Cu-12.5at%Be-X(Mn and Ni) alloys at 523 K.

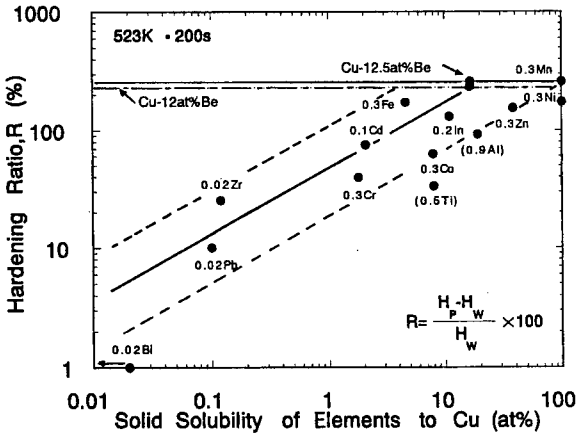


Fig.5 Relation between the hardening ratio (R) at the first stage of hardening of Cu-12.0-12.5at%Be-X alloys at 523 K and the solid-solubility of alloying elements (X) to Cu.

to {100} planes.
Similar phenomena have been observed in Al-Cu alloys [10][11]. In those cases, the alloying elements, Cd, In and Sn, which are scarcely soluble to Al, suppressed remarkably the formation of G.P.zones. The reason is explained as the vacancy-trapping effect by the Cd, In and Sn atoms. Namely, as the Cd, In and Sn atoms combine more strongly to vacancies than the Cu atoms do so, such Cd, In and Sn atoms will trap the vacancies needed for the movement of Cu atoms to {100} matrix planes.
Figure 6 shows TEM micrographs and diffraction patterns of the Cu-12.5at%Be binary alloy and Cd-doped specimens aged at 523 K for 30 s. In the Cu-Be binary alloy, a tweed structure and streaks showing the existence of G.P. zones are observed on the TEM photograph and diffraction pattern, respectively. However, in the Cd doped alloy, the contrast showing the existence of G.P. zone is scarcely observed on the TEM photograph and no streaks are observed on the diffraction pattern. Thus, the addition of Cd suppresses strongly the formation of G.P.zone.

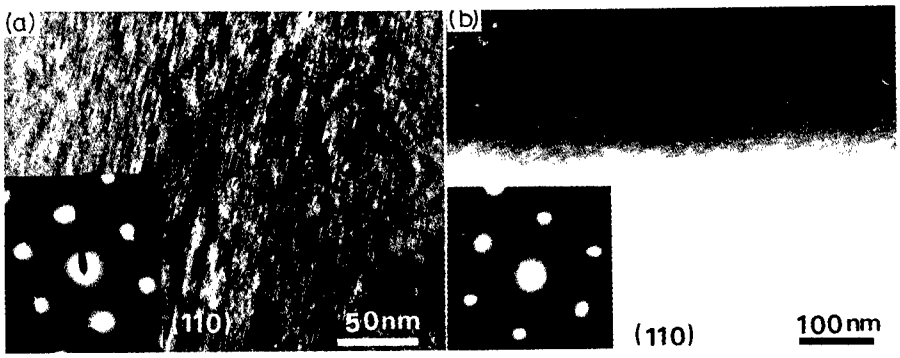


Fig.6 TEM microstructures and electron diffraction patterns of Cu-12.5at%Be-(0.1at%Cd) alloys aged at 523 K for 30 s. (a) Cu-12.5at%Be alloy and (b) -0.1at%Cd alloy.

REFERENCES

1. R.J.Rioya and D.E.Laughlin, "The Sequence of Presipitation in Cu-2%Be Alloys", Acta Metall., 28(1980), 1301-1313.
2. A.G.Khachaturyan and D.E.Laughlin, "Structural Transformations During Decomposition in Cu-Be Alloys", Acta Metall. et Mater., 38(1990), 1823-1835.
3. A.Yamamoto, R.Nozato, T.Morimoto and H.Tsubakino, "Calorimetric Study on Precipitation in Cu-Be Alloys", Mater. Trans., JIM, 34(1993), 312-318.
4. M.Miki, S.Hori and Y. Amano, "Effects of Additional Elements on the Grain Boundary Reaction in a Cu-2mass%Be Alloy", Trans. JIM, 24(1983), 674-680.
5. M.Miki and Y.Ogino, "Effects of B Addition on the Intragranular and Cellular Precipitations in a Cu-Be Alloy", Trans. JIM, 29(1988), 903-910.
6. M.Miki and Y.Ogino, "Effects of Co, Ni and Ti Additions on the Cellular Precipitation in Cu-2%Be Alloy", Mater.Trans., JIM, 35(1994), 161-167.
7. T.B.Massalsky et al., eds, Binary Alloy Phase Diagrams (Second Edition), Vol.1 and 2, (Metals Park, OH: ASM International, 1990), 1.
8. M.Miki and Y.Ogino, "Effect of Quenching Temperature on the Intragranular and Cellular Precipitations in Cu-1.5%Be Binary Alloy", Mater.Trans., JIM, 36(1995), 1118-1123.
9. M.Miki, A.Tenma, Y.Ogino, S.Ishikawa and Y.Natsume, "Effect of Grain Size on the Age-Hardening Behavior of Cu-Be Alloy, J. Japan Copper and Brass Research Association, 35(1996), 118-125.
10. H.Kimura and R.R.Hashiguti, "Interaction of Vacancies with Sn Atoms and the Rate of G-P Zone Formation in an Al-Cu-Sn Alloy, Acta Metall, 9(1961), 1076-1078.
11. H.H.Hashiguti, "Vacancy-Impurity Binding Energy Rule in Aluminum", J.Phys. Soc. Japan, 20(1965), 625-625.

Diffuse Scattering and Huang Scattering in Al-based Icosahedral Quasicrystals

M. Mori, T. Ishimasa[†], M. Tanaka[‡] and S. Sasaki[#]

School of Informatics and Sciences, Nagoya University, Nagoya 464-01, JAPAN

[†]Department of Nuclear Engineering, School of Engineering, Nagoya University, Nagoya 464-01, JAPAN

[‡]Photon Factory, KEK, Tsukuba 305, JAPAN

[#]Materials and Structures Laboratory, Tokyo Institute of Technology, Yokohama 226, JAPAN

abstract

The x-ray diffuse scattering study of Al-based icosahedral quasicrystals was performed. The diffuse intensity of Al-Cu-Fe is almost independent of temperature within room temperature and 100 K. Equi-intensity contour maps of x-ray diffuse scattering at room temperature have almost same shape for all the measured diffraction points. The shape of the diffuse scattering in Al-Pd-Mn is symmetrical ellipsoid elongated along the T-direction. And the shape in Al-Cu-Fe is almost same, but somewhat asymmetrical. The reason, called "asymmetrical", is that the center of the rhombus is not just on the center of the diffraction point, but is located on the slightly inside. It is explained that the main part of diffuse scattering is produced by the defects. It seem that the experimental result can be explained as Huang scattering under the limit of elastic approximation. The major defects are exchange-type defects which are created by interchange of atoms and/or atomic clusters. And the concentration of atoms and atomic clusters is unchanged from the ideal structure by this type of defect. Random phason is clearly classified into this type. The results indicate presence of additional type of defect in the Al-Cu-Fe phase.

The Third Pacific Rim International Conference on
Advanced Materials and Processing (PRICM 3)
Edited by M.A. Imam, R. DeNale, S. Hanada,
Z. Zhong and D.N. Lee
The Minerals, Metals & Materials Society, 1998

Introduction

The model structure of icosahedral quasicrystals is still an open question, while two very probable models, namely quasiperiodic[1] and random tiling model[2], have been proposed. Both models can explain Bragg reflections which satisfy icosahedral symmetry. They are different in interpretation of the role of entropy term to the stability of a quasicrystal. Jarić and Nelson developed the theory of diffuse scattering from quasicrystals including both thermal and quenched phasons and phonons[3]. Ishii also calculated the (critical) diffuse scattering from quasicrystals related with the phase transformation caused by phason softening[4].

It is well known that Al-Cu-Fe and Al-Pd-Mn alloy systems have a thermally stable icosahedral phase. As the Al-Pd-Mn icosahedral phase is known to have strong superlattice reflections' characteristic, it can especially be said that the Al-Pd-Mn F-type icosahedral phase is the most highly chemically ordered icosahedral phase among the stable icosahedral phases[5]. A "quasicrystal-quasicrystal" phase transition has been found in this Al-Pd-Mn alloy system[6]. Superlattice ordering in quasicrystals is also an interesting problem in relation to low-temperature stability of a quasicrystal. In the case, it is known that the F-type icosahedral phase transforms to the ordered P-type icosahedral phase below approximately 700°C.

X-ray diffuse scattering of the single-grained Al-Cu-Fe icosahedral phase indicated that both random and quenched phason strains are very few in this icosahedral phase[7]. Recently, it has been reported that diffuse scattering intensity distribution map can be explained with the random tiling model[8]. The results of these studies were a little bit different with each other; one was done at high temperature and the other at room temperature. The difference of both experimental results is not clear; it might be due to the difference of experimental methods, sample or others. Therefore, we have considered that still more x-ray study is needed to clarify the origin.

The purpose is to clarify its origin: such as the long-range character of quasicrystal ordering in the real icosahedral phase material. In this x-ray study, therefore, we observe and compare the diffuse intensity distribution maps around some reflections of both Al-Cu-Fe and Al-Pd-Mn F-type icosahedral phases.

Experimental

The samples, Al-Cu-Fe and Al-Pd-Mn icosahedral phases, were ingots prepared by the method given in the references 6) and 9). Preliminary checking of the sample was carried out by electron microscope, and powder and Laue x-ray diffraction methods. It was confirmed that the specimens consist of an only *normal F-type icosahedral phase* within their experimental checks. This is essential to avoid contamination of a "critical" diffuse scattering under the influence of "quasicrystal-quasicrystal" phase transitions for the experiment of Al-Pd-Mn, if circumstances allow.

The experimental study was performed to collect the diffuse intensity of Al-Cu-Fe and Al-Pd-Mn with the four-circle X-ray diffractometer installed on beam line BL-10A of the Photon Factory, National Laboratory for High Energy Physics. The main measurement was done at room temperature and the part of Al-Cu-Fe was also done at about100 K. We used synchrotron radiation of wavelength 0.10 nm, monochromatized by the 111 reflection of silicon crystal. Both incident and receiving slits were 0.3 mmϕ. The experimental results were normalized with respect to synchrotron electron current.

The observed Bragg shape of the Al-Pd-Mn icosahedral phase is in good agreement with Gaussian function, but that of Al-Cu-Fe is in fair agreement. The diffuse scattering intensity of Al-Cu-Fe, restricted within the experimental reflection points, is almost not changed between room temperature and 100 K. Certainly, we could not observe the critical diffuse scattering being accompanied with the quasicrystal-quasicrystal phase transition.

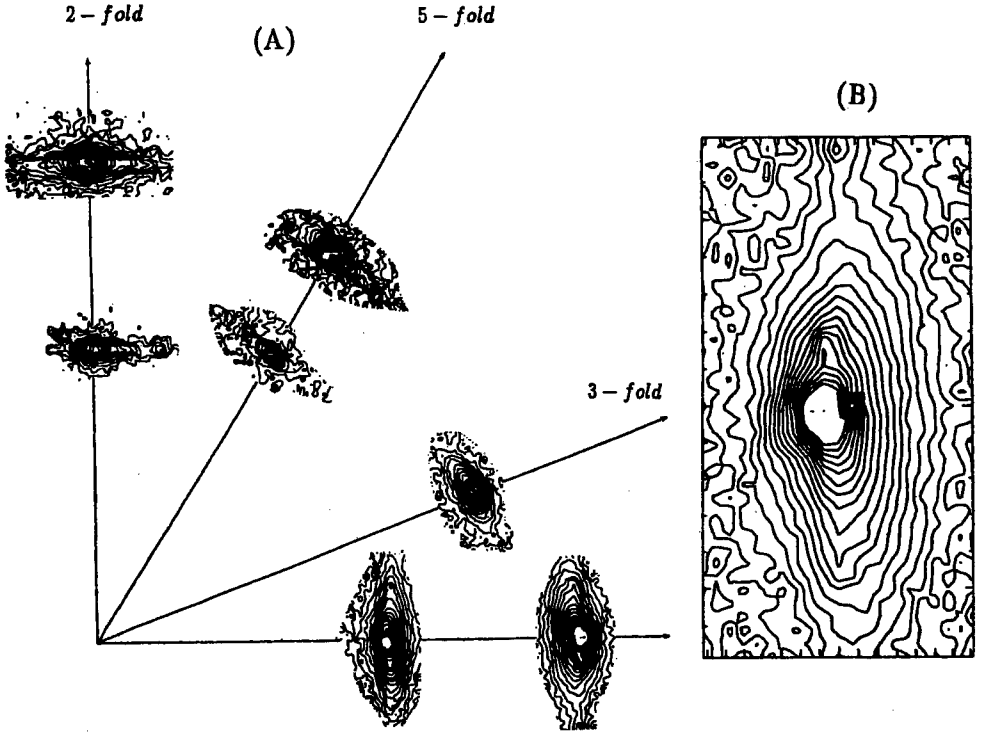


Figure 1. (A) Schematic map of the diffuse scattering distribution in the 2-fold plane on the Al-Cu-Fe F-type icosahedral phase. (B) The equi-intensity contour map around (4 6 6 0 $\bar{4}$ 0).

Results and Huang Scattering

The half widths at half maximum of Bragg reflection intensity profiles of Al-Pd-Mn are a little bit broader than those of Al-Cu-Fe. But those at one tenth maximum of Al-Pd-Mn are narrower. As the observed Bragg shape of Al-Pd-Mn is in good agreement with Gaussian function, the diffuse scattering part could be extracted from the observed intensity distribution. We could get the purely thermal diffuse scattering intensity map.

Figure 1 shows the schematic contour map of the diffuse scattering distribution in the 2-fold plane on the Al-Cu-Fe F-type icosahedral phase and the distribution map around (2 4 4 0 $\bar{2}$ 0) on it.

The experimental results are as follows.

1) The diffuse distribution of Al-Pd-Mn is elliptic spread toward the transverse direction, but that of Al-Cu-Fe is asymmetrical rhombic shape.

2) The diffuse scattering intensity distribution of Al-Pd-Mn is symmetrical along the longitudinal direction, but that of Al-Cu-Fe is asymmetric. The reason, called "asymmetrical" in this case, is that the center of the rhombus is not just on the diffraction point, but is located on the slightly inside.

3) The shape of diffuse intensity contour depends on the intensity.

4) The intensity of the diffuse scattering in Al-Cu-Fe depends little on the temperature below room temperature.

These characteristics have similarity to Huang scattering that is the scattering due to single defects introduced in an elastic medium. It is noted that the diffuse patterns around the reflections along the 2-fold axis have similarity to Huang scattering by a single impurity shown in Fig. 2[10].

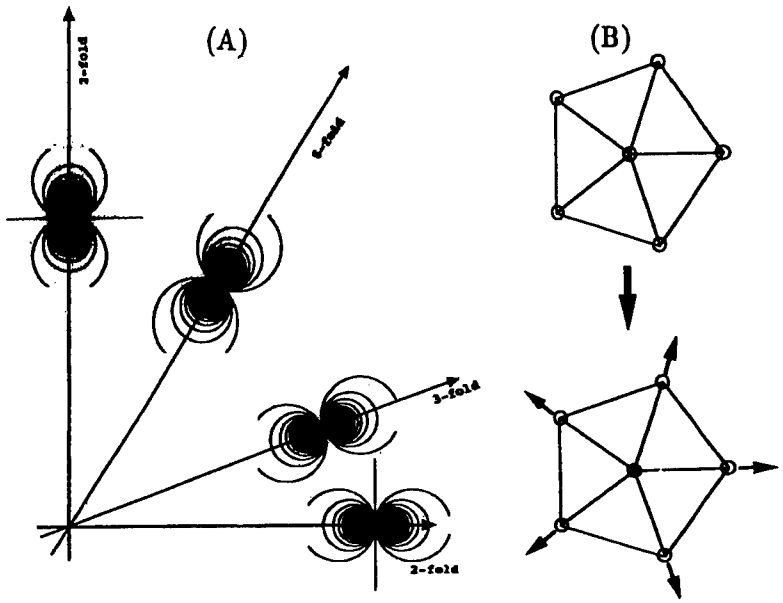


Figure 2. (A) Huang scattering due to an interstitial atom(s). (B) Atom displacements near the inclusion to a lower real icosahedral phase from an upper ideal one.

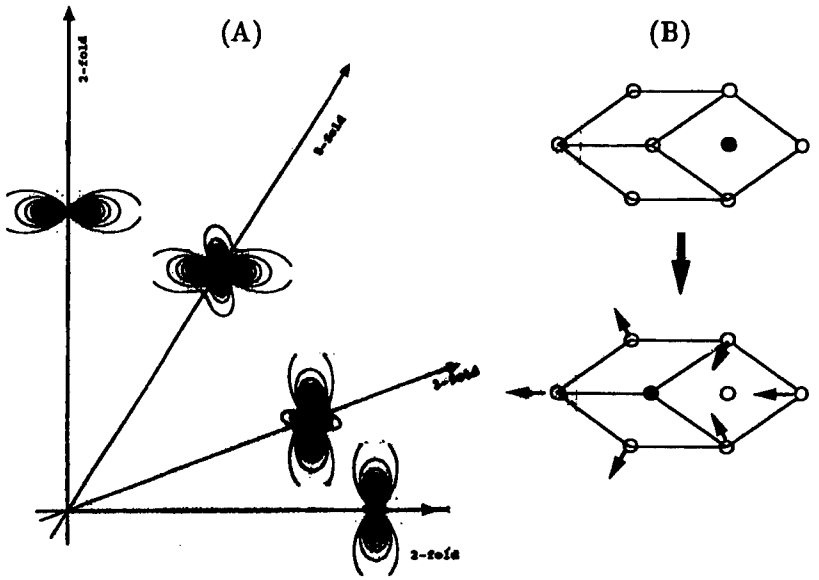


Figure 3. (A) Huang scattering due to exchanging atom(s). (B) Atom displacements near the inclusion to a lower real icosahedral phase from an upper ideal.

We calculated Huang scattering introduced by some kinds of single impurities. The intensity of Huang scattering is given in terms of the elastic constants of the medium and "double-force' tensor which characterizes the force field produced by the impurity. We got the intensity distribution of Huang scattering in the icosahedral phase system, calculating the intensity of Huang scattering and giving icosahedral symmetry on it. The results of Huang scattering including their impurity models are shown in Figs. 2, 3 and 4.

Fig. 2 shows the map of Huang scattering and the cause of one impurity example – the interstitial-type. The characteristic of the diffuse scattering is that the intensity exists along

the L-direction and does not T-direction. This type of defect is accompanied by deviation of concentration of atoms and atomic clusters from the ideal state. Fig. 3 shows the map of Huang scattering and the cause of the other impurity example – the exchange-type which are created by interchange of atoms and/or atomic clusters. The characteristic of the diffuse scattering is that the intensity exists along the T-direction and 2-fold direction. This type of defect is similar to the exchange-type but the concentration of atoms and atomic clusters is unchanged from the ideal structure by this type of defect. Fig. 4 shows the map of Huang scattering and the cause of another impurity example – the displaced-type which are created by interchange or displacement of 2 atoms (clusters). The characteristic of the diffuse scattering is like Fig. 2 rotated with 45 degrees and the intensity mainly exists along the T-direction. This type of defect is similar to type 2 but is accompanied by deviation of concentration of atoms and atomic clusters from the ideal state. The experimental result in Fig. 1 cannot individually be explained as every map of Huang scattering as shown in these figures, and seems to consist of the sum of all three components.

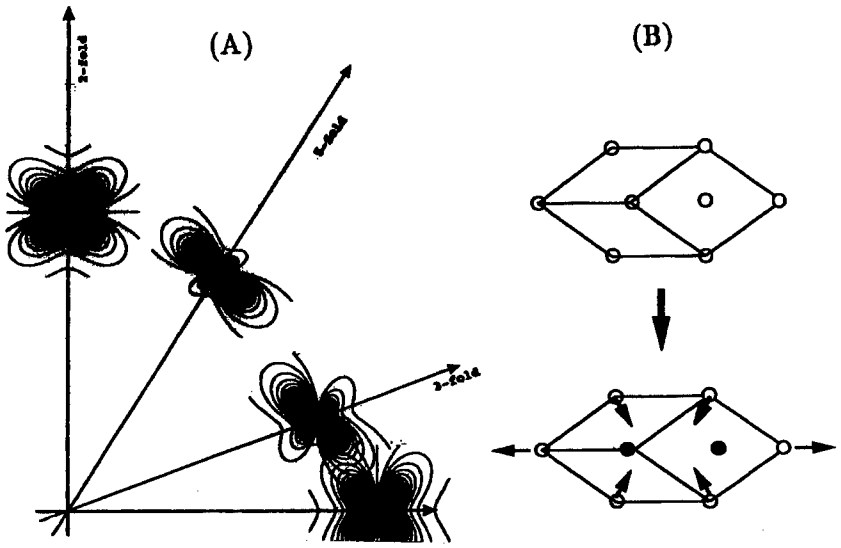


Figure 4. (A) Huang scattering due to exchanging atom(s). (B) Atom displacements near the inclusion to a lower real icosahedral phase from an upper ideal.

Conclusions and Discussions

The half widths at half maximum of Bragg reflection intensity profiles of Al-Pd-Mn are a little bit broader than those of Al-Cu-Fe. But those at one tenth maximum of Al-Pd-Mn are narrower. As the observed Bragg shape of Al-Pd-Mn is in good agreement with Gaussian function, the diffuse scattering part could be extracted from the observed intensity distribution.

The experimental results of the diffuse scattering intensity are as follows.

1) The diffuse distribution of Al-Pd-Mn is elliptic spread toward the transverse direction, but that of Al-Cu-Fe is asymmetrical rhombic shape.

2) The diffuse scattering intensity distribution of Al-Pd-Mn is symmetrical along the longitudinal direction, but that of Al-Cu-Fe is asymmetric. The reason, called "asymmetrical" in this case, is that the center of the rhombus is not just on the diffraction point, but is located on the slightly inside.

3) The shape of diffuse intensity contour depends on the intensity.

4) The intensity of the diffuse scattering in Al-Cu-Fe depends little on the temperature below room temperature.
5) The diffuse intensity is proportional to the nth power of the magnitude of $\mathbf{q}$. The values of n range between -2 and -3.5 and depend on the direction and reflection.
Therefore, it is thought that the diffuse scattering is mainly produced by the defects. In the defects, a defect, called a (frozen) "phason" proper to a quasicrystal, is naturally included besides an impurity and/or defect included in a "usual" crystal. The experimental result seems to show the limit of elastic approximation as Huang scattering. The contour of the diffuse scattering intensity cannot individually be explained as every map of Huang scattering, and seems to consist of the sum of all three components.
As the comparison between experimental and calculation, we can think followings. The major defects in Al-Pd-Mn and Al-Cu-Fe can be exchange-type defects which are created by interchange of atoms and/or atomic clusters. However, the concentration of atoms and atomic clusters is unchanged from the ideal structure by this type of defect. Random phason is clearly classified into this type. The experimental results indicate presence of additional type of defect in the Al-Cu-Fe phase. This type of defect is similar to the exchange-type but is accompanied by deviation of concentration of atoms and atomic clusters from the ideal state. As the "asymmetrical" cannot be explained with the approximation of Huang scattering, it is probably caused by a *size effect.*
The major defects are exchange-type defects which are created by interchange of atoms and/or atomic clusters. And the concentration of atoms and atomic clusters is unchanged from the ideal structure by this type of defect. Random phason is clearly classified into this type. The results indicate presence of additional type of defect in the Al-Cu-Fe phase. This type of defect is similar to the exchange-type but is accompanied by deviation of concentration of atoms and atomic clusters from the ideal state. The "asymmetrical" and the nth power dependence cannot be explained with the elastic approximation of Huang scattering.

Acknowledgments

A part of this work has been supported by a Grant-in-Aid for Scientific Research from the Ministry of Education, Science and Culture of Japan.

References

1. D. Levine and P. Steinhardt, *Phys. Rev. Lett.* **53** (1984) 2477; V. Elser, *Acta Crystallogr.* **A 42** (1986) 36.
2. V. Elser, *Phys. Rev. Lett.* **54** (1985) 1730; C. L. Henley, *Proceedings of the Third International Meeting on Quasicrystals, Quasicrystals and Incommensurate Structures in Condensed Matter* edited by M. J. Yamacán, D. Romeu, V. Castano and A. Gómez(Singapore: World Scientific) (1989) p. 152.
3. M. V. Jarić and D. R. Nelson, *Phys. Rev.* **B 37** (1988) 4458.
4. Y. Ishii, *Phys. Rev.* **B 45** (1992) 5228.
5. A. P. Tsai, A. Inoue, Y. Yokoyama and T. Masumoto, *Phil. Mag. Lett.* **61** (1990) 9.
6. T. Ishimasa and M. Mori, *Phil. Mag.* **B 66** (1992) 513.
7. M. Mori, T. Ishimasa and Y. Kashiwase, *Phil. Mag. Lett.* **64** (1991) 49.
8. M. Boudard, M. de Boissieu, M. Audier, S. Kycia, A. I. Goldman, B. Hennion, R. Bellissent, M. Quilichini and C. Janot, *Proceedings of the 5th International Conference on Quasicrystals* edited by C. Janot and R. Mosseri(Singapore: World Scientific) (1995) p. 172.
9. T. Ishimasa and M. Mori, *Phil. Mag. Lett.* **62** (1990) 357.
10. M. A. Krivoglaz, *Theory of X-ray and Thermal-Neutron Scattering by Real Crystals*(New York: Plenum Press) (1969).

LOCAL ATOM DISPLACEMENTS AROUND CRYSTAL LATTICE DEFECTS INDUCING PHASE TRANSFORMATIONS STUDIED BY MOLECULAR DYNAMICS SIMULATION

Shunsuke Muto, Munetaka Takeuchi[†], Yuji Masuda[†] and Tetsuo Tanabe

Center for Integrated Research in Science and Engineering (CIRSE),
Nagoya University, Furo-cho, Chikusa-ku, Nagoya 464-01, Japan

[†]Fujitsu Ltd., 1-9-3 Nakase, Mihama-ku, Chiba 261, Japan

Abstract

Atomic displacements associated with anomalous phonon modes were examined by computer simulations based on the molecular dynamics (MD) method, using a semiempirical interatomic potential in which the many-body effects were taken into account so as to correctly reproduce the phonon dispersion of the materials of interest. The method was applied to the lattice instability in a Ni-rich NiAl-β phase, which has been known as the 2/3<111> dip in the LA phonon, and local atom displacements around several types of defects were simulated. It was found that point defects such as an antisite defect (Ni atom in a Al site) play a role as pinning centers to stabilize the local atom displacements, inducing an incipient phase transformation. Electron diffraction patterns and high resolution electron micrographs were simulated with the resultant computed atomic positions to compare with experiments.

The Third Pacific Rim International Conference on
Advanced Materials and Processing (PRICM 3)
Edited by M.A. Imam, R. DeNale, S. Hanada,
Z. Zhong and D.N. Lee
The Minerals, Metals & Materials Society, 1998

Introduction

About twenty years ago an attractive concept called 'soft mode' started to be applied to the displacive phase transformations of metals and alloys for explaining their mechanism, analogous to those of ferroelectric materials[1]. Actually a large number of reports have been issued that the phonon energy of specific acoustic branches, related to the formation of product phases, is significantly reduced in the vicinity of transition temperatures. In addition, other anomalous phenomena attached to the phonon anomalies such as characteristic microstructure (mottled or tweed contrast in TEM micrographs), a change in electrical resistance were subsequently found, which have been generally called as 'precursor phenomena'[2]. It is, however, only rare cases for the phonon frequency to actually be reduced to zero at the transition point, and the concept of the soft mode had to be reexamined. For instance, it was found that β phase alloys always have a specific lattice instability or anomaly in the <111> LA phonon branch, and the elastic constant, $C'(=(C_{12}-C_{44})/2)$, is very small regardless of whether they transform to an omega phase or martensite[3]. The point would be whether such phenomena show a time evolution or gradually develop as the transformation temperature approaches, and it is still controversial whether the displacive phase transformations always have precursor phenomena.

In the meantime, if there were a perfect lattice with no point defects and surfaces, the structural phase transition could not start because the first order phase transition requires nucleation sites. In those respects we have believed that some kind of defect centers (vacancy, interstitial atom, antisite defects,...,etc.) which breaks the local symmetry of crystal lattice plays an essential role to initiate the phase transformation, incorporating intrinsic lattice instabilities.

One of the authors (S.M.) found [4] that a Ni_2Al metastable phase, which appears by annealing the quenched β phase (B2 structure) on the Ni rich side at moderate temperatures (~400°C), incorporates the shuffles of lattice planes similar to omega phase transformations. The quenched phase at room temperature already exhibits faint diffuse scattering around the same positions as the Ni_2Al superlattice reflections. This diffuse scattering is likely due to the residual lattice displacements associated with the Ni antisite defects, which locally mimic the symmetry of the Ni_2Al metastable phase[5]. It is accordingly assumed that the dynamical atomic vibration associated with the 2/3<111>* dip in the LA phonon branch is stabilized to produce the static lattice displacements around the antisite Ni, so that they induce the Ni_2Al phase compatible to this new symmetry[4].

In the present study, we have established a system for molecular dynamics simulations which enables us to calculate dynamic behaviors of physical system, electron diffraction patterns and high-resolution electron microscope (HREM) images from the resultant atom positions. The system was applied to the Ni-Al system to examine the above mentioned idea.

Method

The present molecular dynamics simulations were carried out using the MASPHYC/MD (MAterials design System by means of computational PHYsics and Chemistry/Molecular Dynamics) software package developed by Fujitsu Ltd†. The method is based on the classical molecular dynamics (CMD), in which at each time step the computer calculates the force for constituent particles (atoms and/or molecules) in the system of interest, and predicts a new set of their positions and velocities for the next step[6]. This process is repeated many times to obtain the time evolution of the system. The force acting upon each atom depends only on its position relative to the other atoms and is calculated through a semiempirical interatomic potential which is prepared independently.

In the present study it is considered most essential for the used interatomic potential to reproduce the characteristic features in the phonon dispersion of the system, because we are most interested in the dynamical behavior of lattice vibration including a point defect. It has been known that the

† MASPHYC/MD software package is commercially available from Fujitsu Ltd. For readers who are interested in the softwere, contact one of the authors.

Cauchy's relation of elastic constants ($C_{12}=C_{44}$) is inevitably satisfied by pair potentials and thus the many body terms must be taken into account for realistic simulations. In the present study an EAM (Embedded Atom Method) potential for an Ni-Al alloy was utilized, the parameters of which were determined by Voter and Chen[7]. It was confirmed that the <111> LA phonon branch calculated by this potential reproduces the shallow dip at the 2/3<111>*[8], characteristic of a NiAl β-phase, as shown in Figure 1.

It is known that for the NiAl-β_2 phase (B2 structure) of the Ni-rich side excess Ni atoms substitutionally occupy Al sites[9]. Hence in this case the pinning center breaking the local symmetry is considered to be a Ni antisite atom. The MD cell was first taken as 4 x 4 x 4 of B2 unit cell, in which Ni antisite is located in the center. The three dimensional periodic boundary condition was imposed on the system. The same MD cells with no defect and with an Al vacancy in the center were also simulated for comparison. The NTV ensemble was applied and the system was retained at 300 K with a constant volume for 10 picoseconds (10,000 steps). After the MD calculations the resultant atom positions were averaged over the last few picoseconds. The corresponding electron diffraction patterns and HREM images were computer-simulated, using the multislice method for the dynamical electron scattering theory.

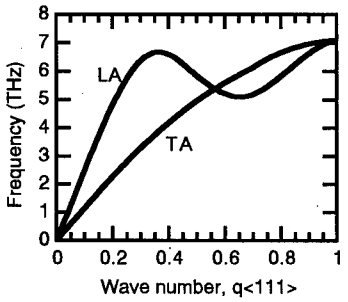


Figure 1: Calculated phonon dispersion curves for longitudinal (LA) and transverse (TA) acoustic branches in <111>* direction, based on the Voter-Chen potential.

Results

For each time step each atom dynamically oscillates around its stable position typically at the periodicity of ~0.1 ps. The time average of atomic positions will give the static displacements from the original lattice sites due to the point defects of interest. Experimental and calculated diffraction patterns along the [110] direction for the cases of non-defective, Ni-antisite and Al vacancy are shown in Figures 2(a)-(d). In the calculations, atomic positions were averaged over 4 ps. The experimental diffraction pattern was taken from a quenched $Ni_{62.5}Al_{37.5}$-β_2 alloy at room temperature, in which the characteristic faint diffuse scattering around the n/3<111>* (n: integer) positions are indicated by the arrow heads. Since the MD cell size was as small as 4 x 4 x 4 of the unit cell, the extra intensities around one-fourth and its multiply positions of the reciprocal lattice points inevitably appear and the diffuse scattering due to the atomic displacements is not so prominent. Nevertheless significant differences among (b), (c) and (d) can be seen.

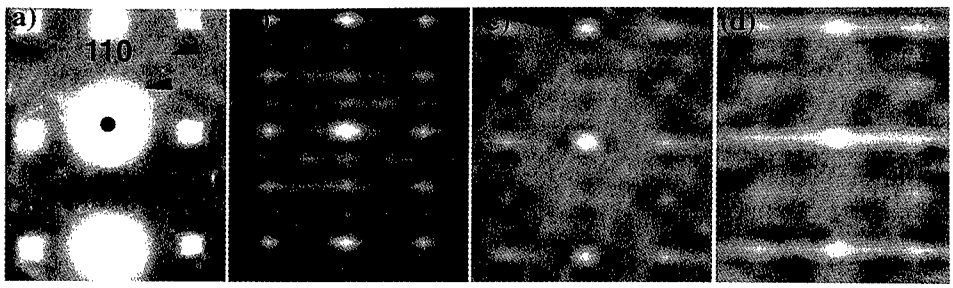


Figure 2: Experimental(a) and calculated(b-d) electron diffraction patterns in <110> direction. (b)perfect lattice (c)Ni antisite defect in the center (d)Al vacancy

To examine the weak intensities in between the Bragg reflections, the lower intensities in the calculated diffraction patterns were enhanced and shown as contour diagrams in Figures 3 (a)-(c). It should be noted that the weak intensity distributions around the 1/3 and 2/3<111>*, marked by the arrow heads, are seen only in (b). This indicates that the specific lattice defect, the antisite Ni in this case, plays a key role to stabilize the dynamical atomic movements related to the shallow dip in the <111>*-LA phonon branch. Furthermore the diffuse intensities around 2/3<111>* are stronger than that of 1/3<111>*, which is in agreement with the feature actually observed in electron[4] and X-ray diffraction[5]. Note that the diffuse intensities appear only in one of the two <111>* directions in Fig.3(b). Since this asymmetry disappeared by the time average over >10 ps for the prolonged calculations, the relaxation time of the atom displacements was estimated as a few ps. HREM images corresponding to those cases were computed and the characteristic contrast observed in quenched B2 phases[4,10] was expected, though no significant difference could be seen among them probably because the MD cells were too small for dynamical scattering to occur.

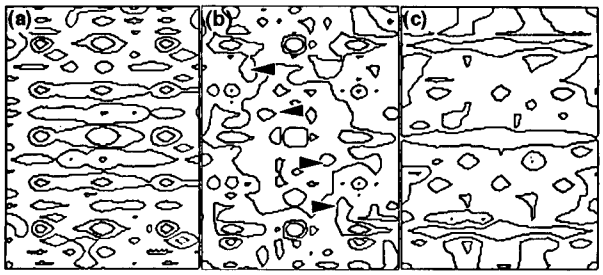


Figure 3: Contour representations of intensity distributions in Figures 2(b)-(d). The lower intensities were enhanced.

As a next step the atomic displacements in the real space around the introduced point defects, producing the above diffraction patterns were examined. The amount of the static atom displacements in case of perfect lattice was as small as ~0.001 nm, which is discussed in no further detail. The direction and amount of displacement in each atomic site in the (110) plane are schematically shown in Figure 4, and the atom coordinates are listed in Table 1 for the antisite Ni and the Al vacancy. The results reported by Georgopoulos and Cohen[5], based on the X-ray diffraction analysis, are also shown in the figure (b) and the table for comparison. The lattice vectors indicated in the figure correspond to Figs.2 and 3.

Figs.4(a) and (b) show different atomic displacements for the same antisite Ni defect. The latter was proposed to explain the diffuse intensities observed by X-ray diffraction and the authors claimed that an ω-like configurations were realized on the both sides of the defect center[5]. On the other hand, the resultant atom displacements by the MD calculation (Fig.4(a)) does not allow such a simple interpretation although the intensity distribution in the diffraction pattern (Fig.3(b)) is very similar to that in [5].

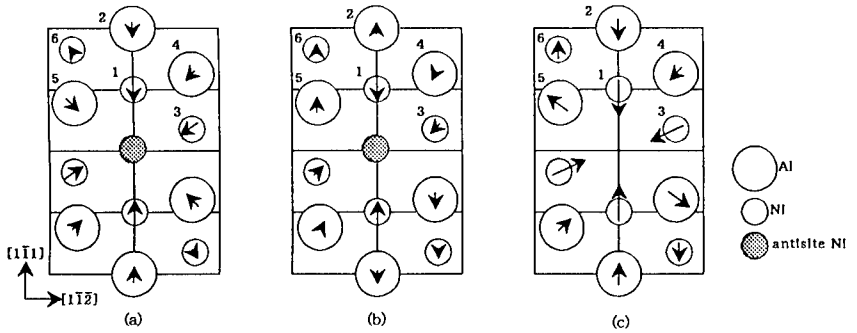


Figure 4: Atom displacements in (110) plane around the introduced antisite Ni(a) and Al vacancy(c), averaged over 4 ps in the MD simulation results. The result reported by Georgopoulos and Cohen[5] is also shown in (b) for comparison. The arrows in the diagrams stand for the direction and relative magnitudes of the displacements.

Table I. Atom displacements around point defects shown in Fig.4. Atom numbers correspond to those in Fig.4. The coordinates are indicated as postions in the B2 unit cell.

	Ideal			ANi*			G&C ANi*			Alv*		
Atom	X	Y	Z	X'	Y'	Z'	X'	Y'	Z'	X'	Y'	Z'
1	0.5	0.5	0.5	0.491	0.491	0.492	0.337	0.337	0.337	0.455	0.453	0.455
2	1.0	1.0	1.0	0.994	0.996	0.996	1.025	1.025	1.025	0.985	0.989	0.980
3	0.5	0.5	–0.5	0.491	0.492	–0.497	0.475	0.495	–0.475	0.453	0.455	–0.457
4	1.0	1.0	0.0	1.001	0.995	0.0	0.976	0.976	–0.021	0.985	0.980	0.007
5	0.0	0.0	1.0	0.0	–0.003	0.995	0.042	0.042	1.034	–0.001	0.003	1.020
6	0.5	0.5	1.5	0.501	0.493	1.502	0.521	0.521	1.510	0.499	0.505	1.501

*ANi: antisite Ni, this work G&C ANi: proposed by Georgopoulos & Cohen[5] Alv: Al vacancy

Table I shows that the magnitudes of calculated atom displacements for Fig.4(a) are rather smaller than those for (b). This would be partly because of the small MD cell and partly because the atom positions were averaged over a certain time period. Nevertheless we feel that the model by Georgopoulos and Cohen has too large atom displacements and the present calculations are more realistic.

The atomic displacements around the Al vacancy (Fig.4(c)) exhibit the lattice relaxation commonly seen for those around a vacancy in other systems. Those atom displacements do not give rise to the diffuse scattering around the n/3<111>* positions, characteristic of β phases, as already seen in Figs.2(d) and 3(c). It follows therefore that a specific type of point defect can act as a pinning center of the lattice vibrations associated with the phonon anomaly and stabilize the atom displacements inducing the incipient phase transformation.

Discussion

It is still difficult to perform a reliable CMD simulation to study actual atom movements or transformation paths during structural phase transitions because semiempirical interatomic potentials are constructed to reproduce only the static properties of the system at thermally equilibrium states. However, an effect of symmetry breaking, such as a point defect, on the local atomic motions around their equilibrium positions can be studied by CMD, if the used interatomic potential well reproduces the phonon dispersion of the system.

The averaged atom positions of the non-defective B2 lattice did not give rise to significant diffuse scattering at the n/3<111>* positions. This indicates that the dynamical atomic motions around their equilibrium lattice points have a periodicity of subpicoseconds. On the other hand, the MD cells containing point defects showed static atom displacements with the relaxation time of a few ps. It should be mentioned, however, that the experimental n/3<111>* diffuse scattering was not appreciably reproduced around the Al vacancy, but only around the antisite Ni atom. For Ni-rich NiAl-β phase alloys the antisite Ni has been known as a dominant point defect[9]. The present result shows that the antisite Ni act as a pinning center of dynamical lattice vibrations with the wave number **q**=2/3<111>*. There are eight equivalent modes, each of which has the relaxation time of a few ps and gives rise to the diffuse scattering experimentally observed.

The resultant atom positions in the present calculation and the model proposed by Georgopoulos and Cohen are rather different but give similar diffuse intensities, as seen in Figs.4(a) and (b) and Table I. The model by G&C gives a simple interpretation of the experimentally observed ω-like phase transformation[4,11], because the atomic displacements around the antisite Ni resembles the ω-shuffle of the {111} planes[5]. However, this model is not compatible with the

ω-like phase (Ni_2Al) in Ni-rich NiAl alloys: the Ni_2Al phase has the structure in which the central Al {111} plane are replaced by Ni atoms in the six-{111} stacking sequence. Thus referring to Fig.4, the {111} planes of atom 3 and 5 should collapse, while in the G&C model the planes of atom 1 and 5 collapse, as shown in Fig.4(b).

The present calculations (Fig.4(a)) does not allow us a simple interpretation to delineate a transformation path to Ni_2Al phase. This suggests that the transition from β-phase to the metastable Ni_2Al would be more complicated than expected. Considering that the actual alloy composition in which the Ni_2Al phase appears is around 63at%Ni, antisite Ni atom clusters are likely to be formed. Atom displacements around such a cluster might resemble the ω-shuffle. This can be considered as a nucleus of the Ni_2Al phase, which is the next target of this work.

Conclusions

The local atom displacements around point defects such as an Al vacancy and an antisite Ni in a Ni-rich NiAl-β phase alloy were simulated by the CMD method, and electron diffraction patterns and high resolution electron micrographs were calculated by the resultant atom positions. It was found that the antisite Ni defect stabilized the lattice vibrations associated with the phonon anomaly in the LA branch, with the relaxation time of a few picoseconds. The calculated atom positions well reproduced the experimentally observed diffuse scattering, though the atomic displacements around the antisite Ni were very different from the model based on X-ray diffraction experiments. This suggests that the transformation path from β-phase to ω-like phase is not so simple as that proposed by Georgopoulos and Cohen[5]. The atomic displacements around the Al vacancy also showed a static character with the relaxation time more than a few picoseconds, but the calculated atom positions did not give the characteristic diffuse scattering.

Acknowledgment

This work was partly supported by Grant-in-Aid for scientific researches from the Japanese Ministry of Education, Science and Culture.

References

1. "New Aspects of Martensitic Transformation," suppl. Trans. JIM, 17 (1976).

2. "Pretransformation Behavior Related to Displacive Transformation in Alloys," Metal. Trans. A, 19A (1998), 158.

3. Proc. Int'l. Conf. on Martensitic Transformations, (Monterey, 1992), 25.

4. S. Muto, N. Merk, D. Schryvers and L.E. Tanner, Philos. Mag. B, 67 (1993), 673.

5. P. Georgopoulos and J.B. Cohen, Acta metal., 29 (1981), 1535.

6. S. Nose, J. Chem. Phys., 81 (1984), 511.

7. A.F. Voter and S.P. Chen, Mat. Res. Symp. Proc., 11 (1987), 175.

8. S.M. Shapiro et al., Phys. Rev. B, 44 (1991), 9301.

9. A.J. Bradley and A. Taylor, Proc. Roy. Soc. A, 159 (1937), 56.

10. D. Schryvers and L.E. Tanner, Ultramicrosc., 32 (1990), 241.

11. A. Lasalmonie, Scripta metall., 11 (1977), 527; F. Reynaud, J. appl. Crystallogr., 9 (1976), 263.

TEM and Electron Diffraction on Structure and Phase Transformation of Nanometer-sized Fe-Ni Alloy Particles

K.Asaka, T.Tadaki*, Y.Sechi, Bian Bo, T.Ohkubo and Y.Hirotsu
The Institute of Scientific and Industrial Research, Osaka University,
8-1 Mihoga-oka, Ibaraki, Osaka 567, Japan
*Division of Physics, Department of Natural Science, Osaka Women' University,
2-1 Daisen-cho, Sakai, Osaka 590, Japan

Abstract

In the present study, preparing nanometer-sized particles of an Fe-15at.%Ni alloy by vacuum evaporation, we examined their structure and phase transformations therein by transmission electron microscopy and electron diffraction. As a result, it was found that the as-deposited state of the alloy films consisted of amorphous islands of nanometer size. Upon heating, the amorphous state was transformed at around 673 K to a crystalline mixed state consisting of the fcc austenite and bcc martensite particles of several nanometers on average; the alloy film eventually became entirely a single phase of the fcc austenite at about 973 K. The austenite particles thus formed were transformed into martensite upon cooling, but only partially even when cooled to room temperature. This observation indicated that the martensitic transformation is roughly by 300 K suppressed even in such a low nickel Fe-Ni alloy when the size is reduced down to a nanometer scale. The cause of the austenite stabilization is discussed in terms of surface energy.

The Third Pacific Rim International Conference on
Advanced Materials and Processing (PRICM 3)
Edited by M.A. Imam, R. DeNale, S. Hanada,
Z. Zhong and D.N. Lee
The Minerals, Metals & Materials Society, 1998

Introduction

The crystal structure and the martensitic transformation in ultrafine particles of alloys ranging from 10 nm to 200 nm in size were studied so far by several workers for Fe-Ni and Co-Fe alloy systems[1-4]. According to their results, ultrafine Fe-Ni alloy particles are fcc and/or bcc, depending on their size and composition, and undergo the martensitic transformation and its reversion at the same temperatures as in bulk materials above room temperature; below room temperature, however, the transformations are suppressed to below 4 K even when lattice defects are introduced by deformation. Kajiwara *et al.*[2] thus suggested that the austenite stabilization is not simply due to the lack of favorable nucleating sites, as suggested formerly by Cech and Turnbull[5], but due to the difficulty of the accommodation of plastic deformation in austenitic fine particles.

Meanwhile, it is now widely known that when the size of materials decreases down to nanometer scale, some materials exhibit unique crystal structures and physical properties which are different from those of the corresponding bulk materials[6-9].One of the important characteristics of nanometer-sized particles is that the proportion of surface atoms to the whole becomes significantly large. Because of this, lattice softening, which is closely related to the nucleation of martensitic transformations, takes place typically therein. Then, very recently we examined the structure of nanometer-sized particles of Fe-Ni alloys around 25at.%Ni, which are much smaller than those studied so far, and the martensitic transformation therein by means of transmission electron microscopy (TEM) and electron diffraction(ED). As a result, although the structure of as-deposited alloy films was not definitely identified yet, it was observed that the austenite particles were entirely stable even when cooled down to about 105 K[10]. In the present study, preparing nanometer-sized particles of a much lower Ni content alloy, *i.e.*, Fe-15at.%Ni, we examined them by TEM and ED in order to make clear the structure of the as-deposited alloy film and the origin of the austenite stabilization.

Experimental Procedures

Nanometer-sized particles of an Fe-Ni alloy with a nominal composition of 15at.%Ni were prepared by vacuum evaporation of a master alloy onto amorphous alumina films at room temperature in a base pressure of about 2×10^{-5} Pa. The master alloy was made by arc melting of pure Fe(99.9%) and Ni(99.9%) metals, of which the composition by chemical analysis was 14.8at.%Ni. After vacuum evaporation, the alloy films were transferred to a specimen stage of a JEM-2010 type transmission electron microscope without being exposed to air. TEM and ED were made on the as-deposited films during heating up to 973K and then cooling down to room temperature. The base pressure inside the electron microscope was kept at about 1×10^{-5} Pa. TEM images and ED patterns were recorded on imaging plates. Chemical composition of the vacuum-evaporated alloy films were examined by the energy dispersive X-ray spectroscopy (EDX) using an H-600FE type analytical electron microscope.

Result

Figures 1(a) and (b) show a TEM image and the corresponding ED pattern, respectively, taken from an as-deposited film of the Fe-15at.%Ni alloy. Since EDX on the chemical composition of as-deposited films showed that it was only a few at.% Ni lower than that of the master alloy, the compositions before and after evaporation were regarded as substantially the same. As seen from Figure 1(a), the as-deposited film was composed of nanometer-sized islands. The ED pattern of Figure 1(b) consisted of a few broad Debye rings, as previously observed. In the present case, however, an intense Debye ring corresponding to the 311 reflections from the $NiFe_2O_4$ oxide that appeared previously was hardly observed. The influence of oxidation was

thus considered to be reduced to a large extent by using the transfer chamber in the present case. However, since all the Debye rings appearing in Figure 1(b) were broad, and in addition those from the amorphous alumina substrate were superimposed, the identification of the phase(s) as-deposited was not possible, as it was.

Then, the reflection intensities from the substrate were subtracted from the whole intensity profile actually observed. In Figure 2 the intensity profiles (a), (b) and (c) are those from the whole, the amorphous alumina and the alloy film, respectively. Then, it was seen that the first broad Debye ring in (c) is located at around $(0.21\ nm)^{-1}$, and the second at around $(0.12\ nm)^{-1}$. The intensity profile (c) thus obtained looks like a hallow pattern from amorphous materials, and in fact the intensity profile resembles qualitatively that of an Fe-B amorphous alloy[11]. It was thus considered that the as-deposited state of the Fe-15at.%Ni alloy consisting of nanometer-sized islands is amorphous. This fact is to be noted, because the alloy does not contain such a metalloid as B, C, P or Si.

The amorphous state was observed to be transformed upon heating at about 673 K into a crystalline mixed state of the fcc austenite and bcc martensite, as seen from Figure 3, which shows temperature changes of the reflection intensity profile from the as-deposited film. Figure 4(a) shows a TEM image taken at 773 K, indicating that particles forming polyhedrons with particular facets of several nanometers on average in size are produced. A lattice image of a particle among them is shown in Figure 4(b). The Fourier transform of the image in Figure 4(c) revealed that the diffraction pattern is of a bcc crystal with a {111} orientation, and hence that the particle is of the bcc martensite. The edges of the particle are seen to be parallel to the directions along the lattice fringes. It is thus supposed that the martensite particle forms a polyhedron mainly with facets of {110} planes. Since as seen from Figure 3 there should exist two phases of the fcc austenite and bcc

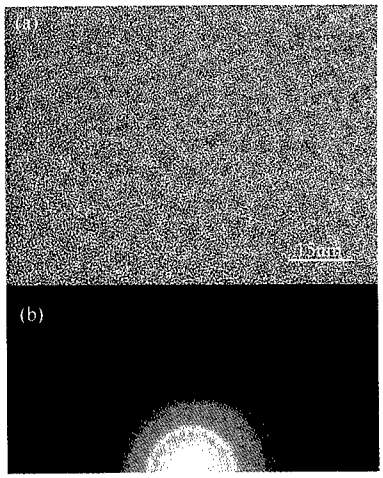


Figure 1: (a)TEM image, and (b)the corresponding ED pattern taken from an as-deposited alloy film of an Fe-15at.%Ni alloy.

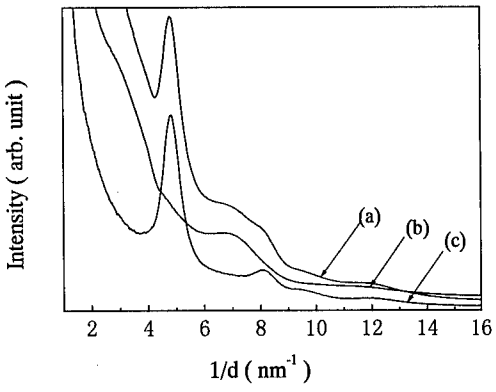


Figure 2: ED profiles of (a)the whole including the alloy film and the amorphous alumina substrate, (b)the substrate only, and (c)the subtraction of (b) from (a).

martensite in the alloy film at 773 K, some of the particles seen in Figure 4(a) are considered to be of the fcc austenite. Then it appears that the austenite particles also form polyhedrons with certain facets.

Figure 5 shows variations of the diffraction profile taken from the alloy film upon further heating from 823 K to 973 K and then cooling to room temperature. The relative amounts of the fcc austenite and bcc martensite seemed hardly changed till when the film was heated to about 873 K, but the fcc austenite became major at around 923 K, and by further heating to about 973 K the alloy film became entirely a single phase of the fcc austenite. When cooled down to room temperature the austenite particles thus formed were transformed into martensite, but it is to be noted that the transformation occurred only partially. In other words, the austenite particles were stabilized considerably. Referring to the martensite and the reverse

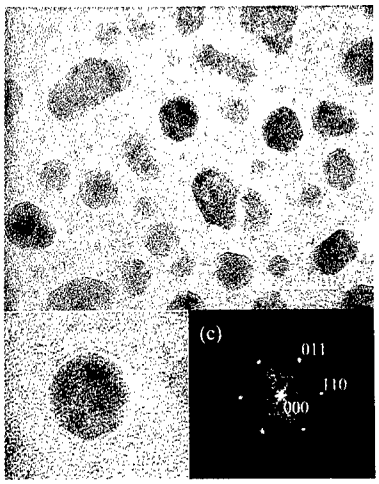


Figure 4: (a)TEM image taken at 773 K from the alloy film, (b)an enlargement of a particle seen in (a), and (c)the Fourier transform of the lattice image seen in (b).

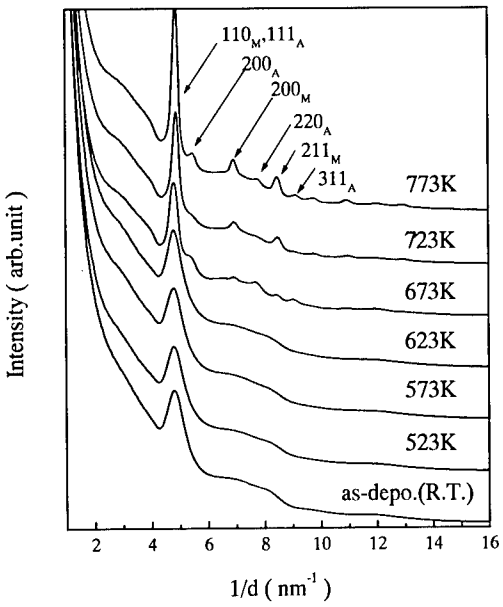


Figure 3: Temperature changes of an ED profile from the as-deposited alloy film upon heating up to 773 K

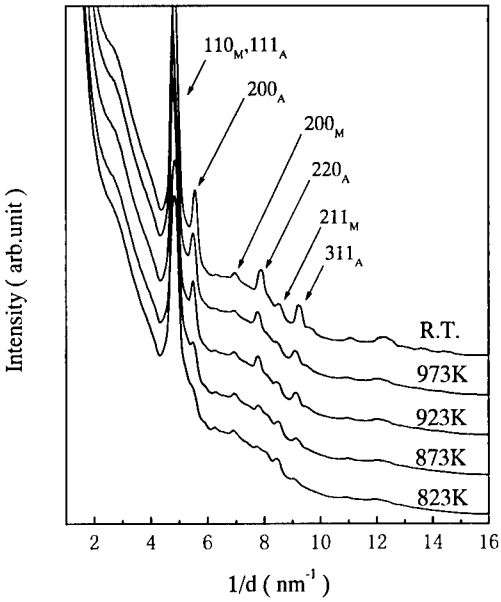


Figure 5: Changes of an ED profile from the alloy film upon further heating to 973 K, and then cooling to room temperature.

transformation temperatures cited by Hansen and Anderko[12], the M_f temperature of the Fe-15at.% Ni alloy in its bulk state is above 573 K. So far as M_s temperature is concerned, the decrease amounted to about 300 K, compared with that of the bulk state for the Fe-15at.%Ni alloy. The drastic stabilization of austenite was in agreement with the previous reports. However, it is also interesting to note that the reverse transformation temperatures of the nanometer-sized martensite particles were substantially the same as those of the bulk.

Discussion

There may be no doubt for that the reduction of size results in a drastic stabilization of austenite, because previous reports by several workers including ours are in agreement with one another in this respect. It thus appears that the lattice softening as well as the increase of surface areas as the favorable nucleation sites brought about by the reduction of size is ineffective for enhancing the martensitic transformation. Then, the surface energy change upon the transformation is supposed to be a key factor suppressing the transformation. If taking the surface energy change into account, the total free energy change upon the transformation, $\Delta G^{A\rightarrow M}$, is given by[13]:

$$\Delta G^{A\rightarrow M} = G_M^T - G_A^T = (G_M^B - G_A^B)v + (\gamma_M - \gamma_A)S \quad , \tag{1}$$

where $G_{A,M}^T$ are the total free energies of austenite and martensite, $G_{A,M}^B$ the free energies of their bulk states, $\gamma_{A,M}$ the surface energy densities of the two phases, v the particle volume and s the surface area of a particle. Suppose that the austenite particles are surrounded by surfaces with low surface energy densities such as {111} and {100} planes. Upon the martensitic transformation, however, the {111} planes of austenite are converted into {110} planes of martensite, and the {100} planes of austenite into {110} and {100} planes of martensite. In a bcc crystal, the {110} and {100} planes are of low surface energy densities. The absolute values of the surface energy differences may be small, but, as in fact demonstrated recently for the fcc to hcp transformation in Co particles[13, 14], the surface energy term in the right hand side of Eq.(1) becomes large enough to reduce the chemical driving force when the size is 10 nm. For the Fe-Ni alloy system, however, accurate evaluations of the surface energies of those planes of austenite and martensite have not been made yet. Then, to evaluate them somehow as precisely as possible may be crucial to understand quantitatively why the fcc phase of the Fe-Ni alloys becomes so stable when the size is reduced down to nanometer scale. The fact that the reverse transformation temperature of the Fe-Ni alloy of a low Ni content is hardly affected by size may be understood in terms of the surface free energy difference between the fcc and bcc particles, which is supposed to become much smaller at elevated temperatures because of the large contribution of entropy term to the surface free energy.

Acknowledgments

The present study was supported by the Grant-in-Aid for Scientific Research on Priority Area of Phase Transformations (1997-1999) from the Ministry of Education, Science, Sports and Culture, Japan.

References

1. Y.H. Zhou, M. Harmelin, and J. Bigot, " Martensitic Transformation in Ultrafine Fe-Ni Powders," Mater., Sci.Eng., A124(1990), 241-249.
2. S. Kajiwara, S. Ohno, and K. Honma, " Martensitic transformation in ultra-fine particles of metals and alloys," Philos. Mag. A63(1991), 625-644.
3. Y.H. Zhou, M. Harmelin, and J. Bigot, " Preparation of ultra-fine metallic powders. A study of the structural transformations and of the sintering behaviour," Mater.Sci.Eng.,

A133(1991), 775-779.
4. Y. Chen, G. Deng, H. Lu, J. Wang, and G. Li, " Martensitic Transformation in Fe-29 wt%Ni Alloy Ultrafine Particles," Jpn. J. Appl. Phys., 34(1995), 113-117.
5. R.E.Cech, and D.Turnbull, " Heterogeneous Nucleation of the Martensite Transformation," Trans.AIME, 206 (1956), 124-132.
6. K. Kimoto, and I. Nishida, " An Electron Microscope and Electron Diffraction Study of the Fine Smoke Particles Prepared by Evaporation in Argon Gas at Low Pressures(II)," J. Phys. Soc. Jpn., 22(1967), 1047-1059.
7. H. Fujita, " Atom clusters-new applications of high-voltage electron microscopy " icro-laboratory" to materials science," Ultramicroscopy, 39(1991), 369-381.
8. H. Mori, M.Komatsu, K.Takeda, and H.Fujita, " Spontaneous alloying of copper into gold atom clusters," Philos. Mag. Lett., 63(1991), 173-178.
9. M. Takagi, " Electron-Diffraction Study of Liquid-Solid Transition of Thin Metal Films," J. Phys. Soc. Jpn., 9(1954), 359-363.
10. T. Tadaki, Y. Murai, A. Koreeda, Y. Nakata, and Y. Hirotsu, " Structure and phase transformation of nano-scale particles of Fe-Ni alloys," Mater.Sci.Eng., A217/218(1996), 235-238.
11. Y.Waseda, and H.S.Chen, " A Structural Study of Metallic Glasses Containing Boron(Fe-B, Co-B, and Ni-B)," phys.stat.sol.(a), 49(1978), 387-392.
12. M.Hansen, and K.Anderko, Constitution of Binary Alloys, second edition(McGraw-Hill Book Co., 1985), 681.
13. M.Alden, S.Mirbt, H.L.Skriver, N.M.Rosengaard, and B.Johansson, " Surface magnetism in iron, cobalt, and nickel," Phys.Rev.B, 46(10)(1992), 6303-6312.
14. H.Sato, O.Kitakami, T.Sakurai, and Y.Shimada, " Structure and magnetism of hcp-Co fine particles," J. Appl. Phys., 81(1997), 1858-1862.

IN-SITU TEM OBSERVATION OF SHORT-RANGE ORDER STATE AND ORDERING PROCESS OF Cu_3Pt

N. Chiwata, T. Sakai, A. Matsumoto, N. Kuwano and K. Oki
Department of Material Science and Technology, Graduate School of Engineering Sciences, Kyushu University 39, Kasuga, Fukuoka 816-0811, Japan.

Abstract

The short-range order (SRO) state and the early state of ordering process in Cu_3Pt were investigated by the at-temperature TEM observation method. Dark field images obtained by using the characteristic SRO diffuse scattering show a bright-spot contrast. Above T_C, a bright-spot-contrast was flickering spatially and temporally. With decreasing temperature, the flickering became slower and finally stopped. And then, some bright-spots grew up to large domains of a long-period structure $L1_{2\text{-}S}$. The experimental results indicate that in the equilibrium SRO state the degree of order fluctuates temporally as well as spatially. Regions of high degree of order correspond to "microdomains" dispersed in the disordered matrix. The ordering from SRO to $L1_{2\text{-}S}$ was suggested to proceed without a process of nucleation.

The Third Pacific Rim International Conference on Advanced Materials and Processing (PRICM 3)
Edited by M.A. Imam, R. DeNale, S. Hanada, Z. Zhong and D.N. Lee
The Minerals, Metals & Materials Society, 1998

Introduction

The disordered state and its ordering process in the solid solution are subjects of great interest. Many Cu-based alloys quenched from high temperatures above T_C show characteristic diffuse scatterings in their diffraction patterns, where T_C is the critical temperatures. The scatterings which can be explained by the Fermi-suface imaging[1,2] indicate the presence of short-range order (SRO). Saha and Ohshima[3] obtained the detailed distribution of the diffuse scattering intensities in reciprocal space by using the x-ray measurement and determined higher-order SRO parameters for Cu-Pt alloys. Meulenaere et al. [4] attempted to analyze the SRO from the image intensity of the high-resolution electron microscopy(HREM) image.

In a dark field image taken by using SRO diffuse scattering, a bright-spot-contrast is frequently observed. The image-contrast can be interpreted to show microdomains having an ordered structure dispersed in the disordered matrix. However, since most of such studies were carried out with quenched specimens, the possibility that the microdomains were formed during quenching could not be completely excluded. The early stage of the ordering process from the SRO state still remains controversial due to the same reason.

In this study, we carried out the *in-situ* transmission electron microscope(TEM) observations in order to make clear if the microdomains are stabilized above the T_C in Cu_3Pt and to analyze the early stage of the ordering process from the SRO state.

Experimental Details

Disk specimens 3mm in diameter were prepared from an alloy ingot of Cu_3Pt arc-melted from pure metals of Cu and Pt under an atmosphere of argon. The disk specimens were sealed in evacuated silica capsules and annealed at 1000K for 10.8ks to relieve strains and to promote disordering. Thereafter they were quenched in iced brine. These heat-treated specimens were dimpled and electropolished in an electrolyte of $HCl:HNO_3:C_2H_5$=4:1:5 by the Ballmann method. *In-situ* TEM observation was conducted in a 200kV microscope (JEOL JEM-200CX) equipped with a heating holder(JEOL EM-SHTH2). TEM images and diffraction patterns were recorded on imaging plates and/or video-tapes in order to avoid the influence of large drifts of the specimens at high temperature during the *in-situ* observation. For improvement of image quality, the images were processed by digitalization of signals recorded on video-tapes.

Results and Discussion

The specimen was heated in the microscope up to 950K (the disordered A1 region), and then cooled continuously down to 813K. Figure 1(a) shows the diffraction pattern taken at 950K. One can see diffuse scatterings characteristic to the SRO state (Fig.1(a)). A bright-spot-contrast is observed in the dark field image(Fig.1(b)) formed by using the diffuse scattering around *hkl*=110. This suggests that microdomains are dispersed in the disordered matrix. It was observed that the bright-spot-contrast was flickering. Figure 2 shows a series of dark field images taken at certain intervals at various temperatures on the way of slow cooling. It is clearly seen that a bright dot disappeared from circle A and another dot appeared in circle B within about 0.6s. At high temperatures, a specimen tends to bend and drift due to thermal effects. Such bending and drifting can make the local orientation of the specimen deviate from the Bragg condition, and then change the brightness of the dots in the dark field image. But this is not the case: as seen in Fig.2(a), the appearance and disappearance occur very quickly and randomly. If the flickering resulted from the bending, it would occur synchronously in local areas. Figure 2(b) shows dark field images taken at 929K. The bright-spot-contrasts are also flickering, but the rate of flickering is slower than that at 949K: the dot in circle C disappeared in about 1.2s. It was found that the flickering becomes slower with decreasing temperature and finally stops, as shown in Fig.2(c).

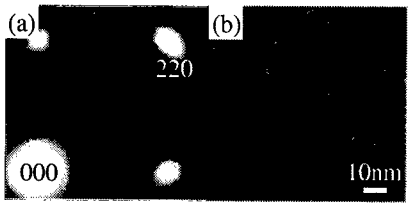


Fig.1(a) Diffraction pattern for Cu_3Pt taken at 950K.(b)Dark field image formed by using SRO diffuse scattering.

The present observation clarifies apparently the SRO state in Cu-Pt: the equilibrium SRO state consists of microdomains dispersed in the matrix. The microdomains are considered to be small areas where the degree of order fluctuates upward. The most important thing is that the fluctuations occur in terms of time as well as space.

Figure 3 shows dark filed images taken at 833 and 813K. As described above, microdomains do not change in contrast at 833K during the observing time. This indicates that the mixing state of microdomains without coalescence and the disordered matrix is almost in thermodynamic equilibrium. At 813K, on the other hand, some microdomains grew up to large ordered domains of a long-period superstructure (LPS) phase, or $L1_{2\text{-}S}$ (Fig.3(b)). Figure 4 shows a series of the in-situ observation of the

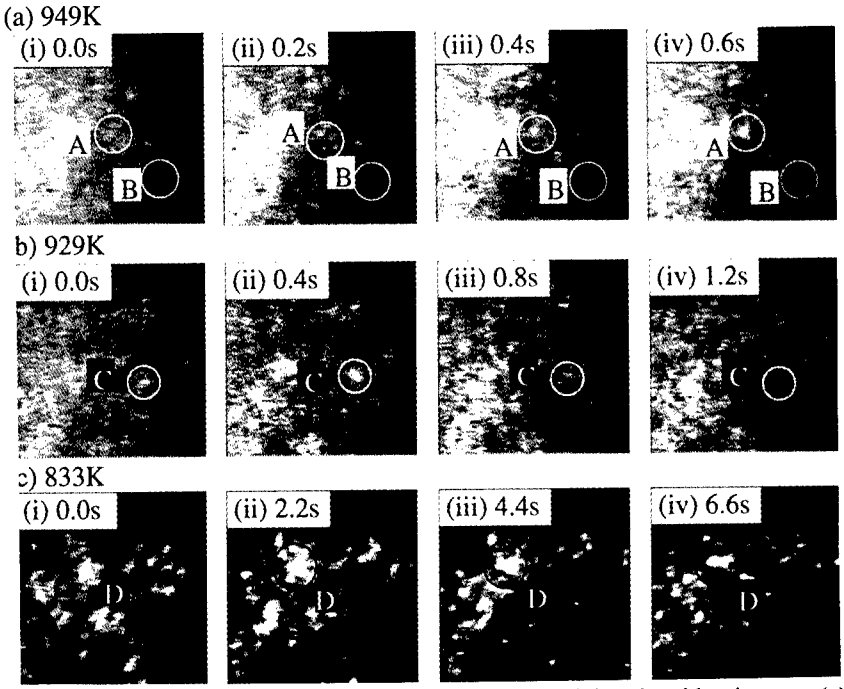


Fig.2 The snap shot images were reproduecd by degitalizing the video-images. (a) 949K at an interval of 0.2sec. (b) 929K at an interval of 0.4sec. (c)833K at an interval of 2.2sec.

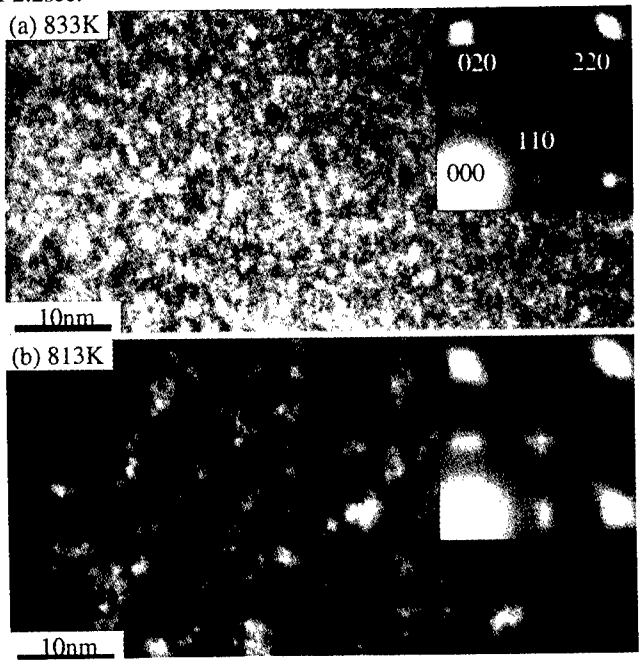


Fig.3 Dark field images recorded on imaging plates. (a)833K. (b)813K

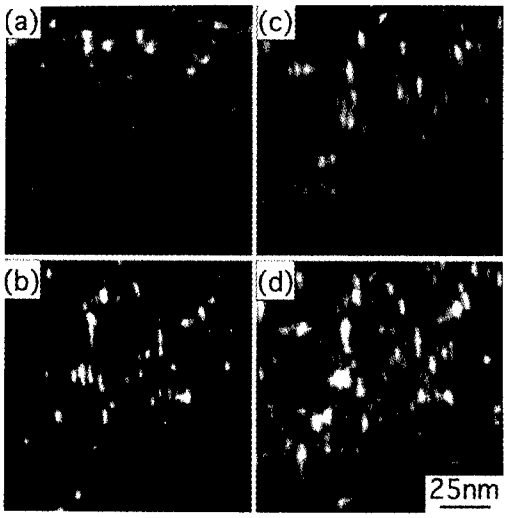


Fig.4 Dark field images recorded on films at 833K. Arrows indicate the same region. (a)4.2ks, (b)7.8ks, (c)11.0ks, (d)18.7ks.

development from microdomains to LPS. The specimen was heated once up at a high temperature and then hold at 813K. At first, microdomains are distributed randomly, but they altered to a domain of LPS where periodic antiphase boundaries are inserted. This suggests that microdomains in the SRO state naturally have antiphase correlation among them. It should be noted that the formation of the long range ordered phase proceeds without a process of nucleation but just with a process of the continuous growth via the SRO state, although the transformation from A1 to $L1_{2\text{-}S}$ is of a first order phase-transformation.

Conclusion

From the *in-situ* TEM observation of Cu_3Pt alloy from the SRO to LPS ($L1_{2\text{-}S}$) ordering, the following results were obtained:

1) The equilibrium SRO state can be interpreted in a microdomain model: microdomains are dispersed in the disordered matrix.

2) The microdomains are stabilized in thermal equilibrium above T_C.

3) The microdomains can be regarded as particular areas where the degree of order fluctuates upwards. At high temperatures, the degree of order fluctuates temporally and spatially. The temporal fluctuation stops at lower temperatures.

4) Formation of $L1_{2\text{-}S}$ proceeds almost continuously by the growth-process. Since microdomains become seeds of $L1_{2\text{-}S}$ domains, there is no nucleation process in the transformation from A1(SRO) to $L1_{2\text{-}S}$.

1. H. Sato and S.Toth, Physical Review. "Effect Additional Elements on the Period of CuAu II and the Origin of the Long-Period Superlattice," 124 (1961), 1833

2. K. Ohshima and D. Watanabe. Acta Crystallographica, "Electron Diffraction Study of Short-Range-Order Diffuse Scattering from Disordered Cu-Pd and Cu-Pt Alloys," A29(1973),520

3. D. K. Saha and K. Ohshima, J.Phys.:Condens.Matter.,"Short-range order in Cu-Pt alloys," 5(1993),4099

4. P. De Meulenaere, G. Van Tendeloo. J. Van Landuyt, and D. Van Dyck, "On the interpretation of HREM images of partially ordered alloys," Ultramicroscopy, 60(1995)265

PHASE TRANSFORMATION OF $Bi_{1-x}Ca_xMnO_3$ STUDIED BY TEM WITH ENERGY-FILTERING

D. Shindo, Y. Murakami, H. Chiba *, M. Kikuchi * and Y. Syono *

Institute for Advanced Materials Processing, Tohoku University,
Katahira 2-1-1, Sendai 980-8577, Japan
*Institute for Materials Research, Tohoku University, Katahira 2-1-1, 980-8577, Japan

Abstract

The structure change of $Bi_{1-x}Ca_xMnO_3$ due to the phase transformation was studied extensively by transmission electron microscopy (TEM) using a cooling stage. By utilizing a newly developed energy filter (omega-type), the background on electron diffraction patterns mainly caused by plasmon scattering was largely reduced. From the energy-filtered electron diffraction patterns observed with the imaging plates, it was found that the intensity of the superlattice reflections showing a one-dimensional long-period structure was hardly observable around the transmitted beam and it was asymmetric around the fundamental reflections, i.e., higher intensity at larger scattering angles. Thus, the intensity distribution of superlattice reflections of the long-period structure clearly indicated that appearance of the superlattice reflections at low temperature was attributed to the lattice strain caused by the charge ordering of Mn^{3+} and Mn^{4+} ions. In addition to the electron diffraction study, electron energy loss spectroscopy on fine structures of the oxygen K-edge in $La_{1-x}Ca_xMnO_3$ and $Bi_{1-x}Ca_xMnO_3$ was also carried our to investigate the electronic structure change due to the phase transformation.

The Third Pacific Rim International Conference on
Advanced Materials and Processing (PRICM 3)
Edited by M.A. Imam, R. DeNale, S. Hanada,
Z. Zhong and D.N. Lee
The Minerals, Metals & Materials Society, 1998

Introduction

Perovskite manganese oxides of $Bi_{1-x}Ca_xMnO_3$ and $La_{1-x}Ca_xMnO_3$ ($x \geq 0.5$) have attracted much attention due to their characteristic phase transformation with charge ordering of Mn^{3+} and Mn^{4+} ions[1-6]. Recently, in order to make clear the magnetic and crystal structure changes associated with the charge ordering, a neutron diffraction study was carried out for $Bi_{1-x}Ca_xMnO_3$[7]. Also, for clarifying the microstructure of $La_{1-x}Ca_xMnO_3$, TEM was utilized[5,6]. Very recently, the present authors have carried out TEM studies on $Bi_{0.2}Ca_{0.8}MnO_3$[8]. It was found that at low temperature long-period structures with a period of four times fundamental lattice and much larger periods formed. From a conventional electron diffraction study, it was also pointed out that the superlattice reflections were attributed to the lattice strain due to the charge ordering.

In this study, in order to investigate the intensity profiles of electron diffraction patterns in detail, a new energy filter attached to an electron microscope is utilized to remove the background caused by inelastic electron scattering. In addition to the energy-filtered electron diffraction, electron energy-loss spectra of these materials were also investigated to get the electronic structure change due to the phase transformation.

Experimental

Specimens of $Bi_{1-x}Ca_xMnO_3$ ($x \geq 0.75$) were prepared by a conventional ceramic technique. The details of specimen procedures were presented in a previous paper[3]. Specimens of $La_{1-x}Ca_xMnO_3$ ($x \geq 0.75$) were also prepared with a similar ceramic technique. The structure change of $Bi_{1-x}Ca_xMnO_3$ due to the phase transformation was investigated with JEM-2010 electron microscopes with a cooling stage. For a detailed electron diffraction study, the JEM-2010 electron microscope installed with an omega -type energy filter (Fig. 1) was used, while for the study of electron energy-loss spectra, the JEM-2010 with a parallel detector (Gatan 666) was used. In the former electron microscope, in order to record electron energy-loss spectra and intensity profiles of electron diffraction patterns accurately, the imaging plates (FDL-UR-V) were used.

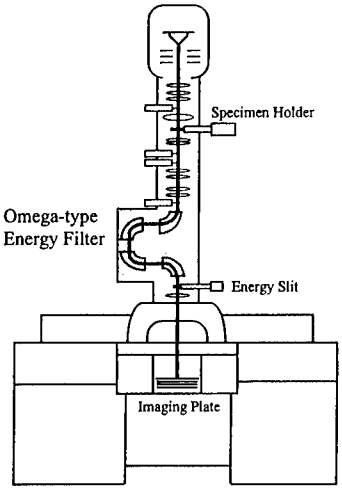


Figure 1: Schematic illustration showing an omega-type energy filter installed in a conventional TEM with imaging plates.

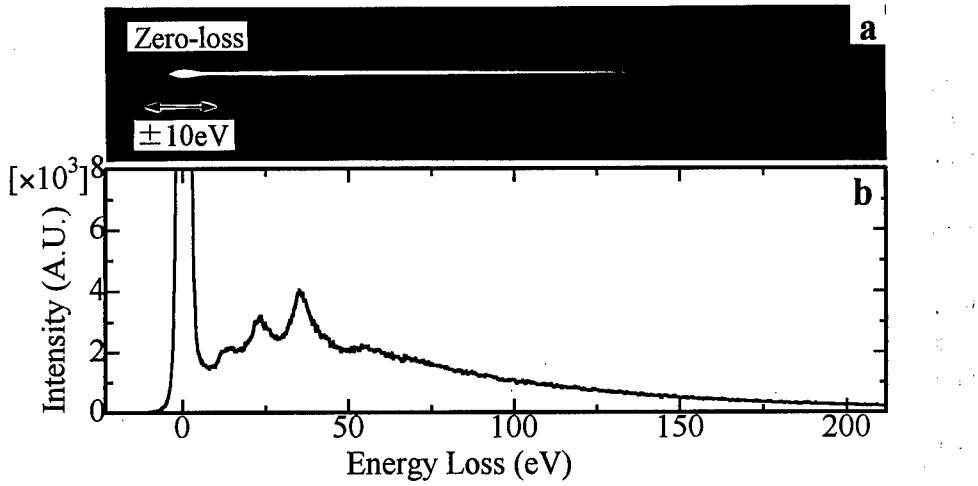


Figure 2: Electron energy-loss spectrum observed with an imaging plate. Intensity profile is shown below.

Results and Discussion

Figures 2 (a) and (b) show a typical electron energy-loss spectrum and its intensity profile obtained with the omega -type energy filter and an imaging plate. In order to remove the background in the electron diffraction patterns mainly contributed from plasmon scattering, an energy slit with an energy width of 10 eV was inserted. Figure 3 (a) shows a conventional electron diffraction pattern of $Bi_{0.2}Ca_{0.8}MnO_3$ taken at around 110K, while Fig. 3 (c) shows an energy-filtered electron diffraction pattern obtained from the same area as (a). At the lower parts of Figs. 3 (a) and (c), the intensity profiles of unfiltered and filtered electron diffraction patterns are shown in Figs. 3(b) and (d), respectively. It is clearly seen that the energy-filtered electron diffraction pattern is sharper than the unfiltered one especially around the transmitted beam. From the filtered diffraction pattern, the period of the long-period structure is determined as about $5a_0$ (a_0 : the lattice constant of the room-temperature phase). It is noted that a favorable structure associated with the charge ordering is thought to be the structure with the period of $4a_0$ in this specimen, as far as the magnetic structure (the so-called C-type antiferromagnetic) in the charge ordered state is considered[1,7]. But as shown in Fig. 3, long-period structures with different periods, sometimes non integral periods and very long periods as shown below were observed. Nature of appearance of those long-period structures will be discussed elsewhere in detail. In the intensity profile of the energy-filtered electron diffraction pattern in Fig. 3 (d), it is clearly seen that intensity of the superlattice reflections around the fundamental reflections is asymmetric, i.e., higher intensity at larger scattering angles. This point is consistent with that in our previous paper[8]. In Fig. 4 (a), an energy-filtered electron diffraction pattern obtained from another area is shown, which was taken at around 110K. In this case, the period of the long-period structure is

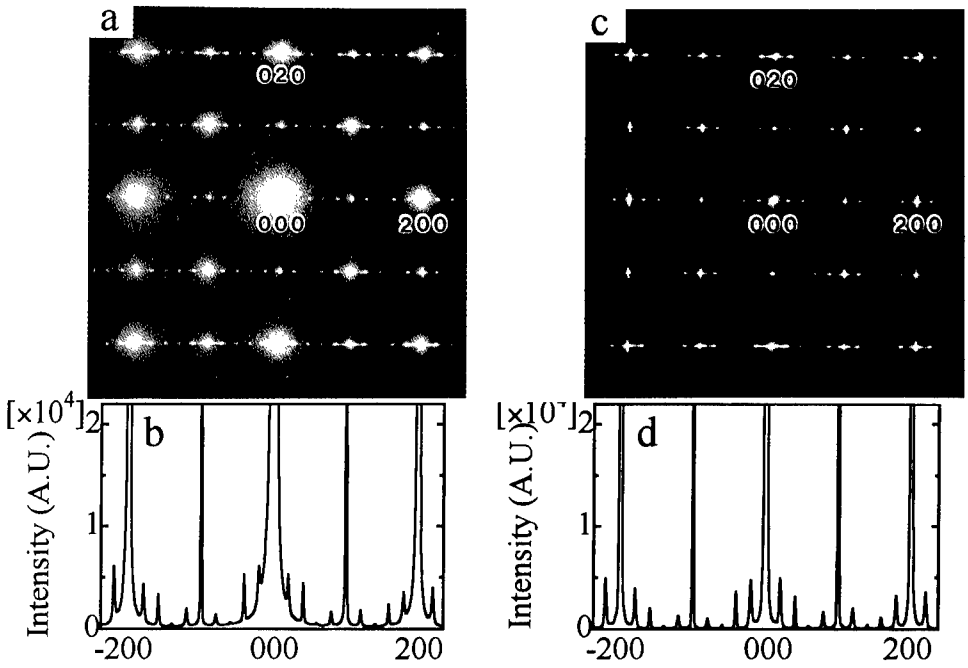


Figure 3: Conventional electron diffraction pattern of a long-period structure in $Bi_{0.2}Ca_{0.8}MnO_3$ with the period of 5 (a), and its intensity profile (b). Energy-filtered electron diffraction pattern of $Bi_{0.2}Ca_{0.8}MnO_3$ (c), and its intensity profile (d).

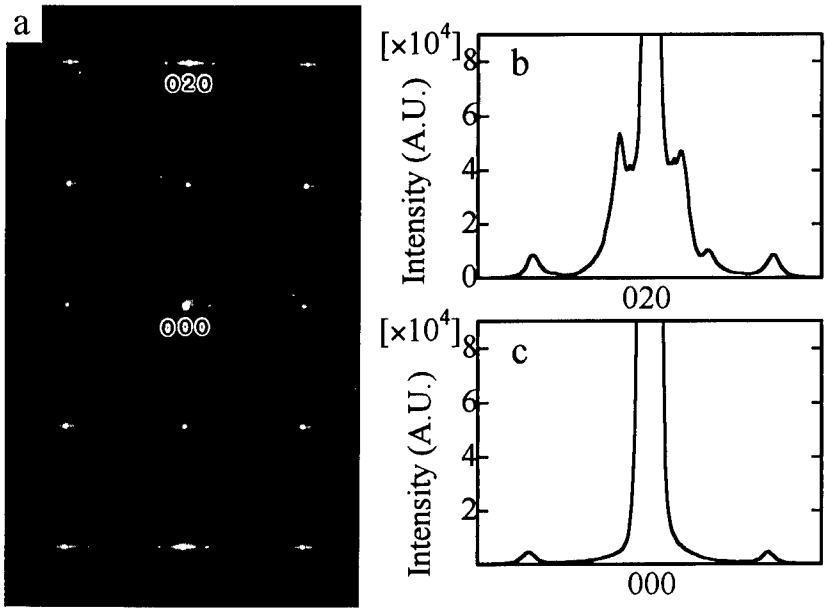


Figure 4: (a) Energy-filtered electron diffraction pattern of a low temperature phase of $Bi_{0.2}Ca_{0.8}MnO_3$ with the period of about 20. (b) and (c) are intensity profiles around the 020 reflection and the transmitted beam.

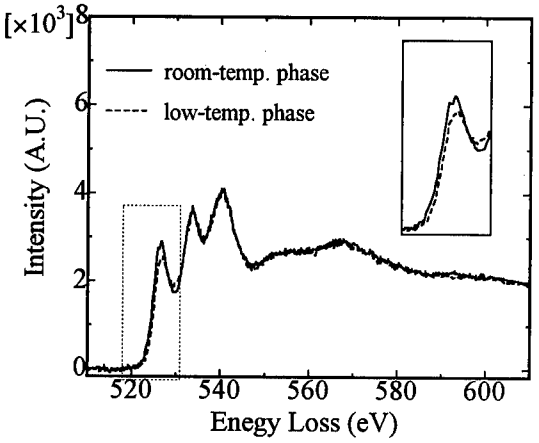


Figure 5: Change of the oxygen K-edge fine structure of $La_{0.2}Ca_{0.8}MnO_3$ due to the phase transformation. The spectrum of the room-temperature phase was obtained at 293K, while that of the low-temperature phase at 110K.

much longer than that of Fig. 3, and is estimated to be about $20a_0$. It is interesting to note that the superlattice reflections around the transmitted beam is hardly observable, while the superlattice reflections around the 020 reflection is clearly seen. These results indicate that appearance of the superlattice reflections at low temperature was attributed to the lattice strain caused by the charge ordering of Mn^{3+} and Mn^{4+} ions. This is because the superlattice reflections caused by the lattice strain have very weak intensity at around the transmitted beam and the intensity increases gradually at some extent with increasing the scattering angle.

Figure 5 shows the change of the oxygen K-edge fine structure of $La_{0.2}Ca_{0.8}MnO_3$ due to the phase transformation. It is seen that there are three peaks at around 527, 533 and 541 eV. It is considered that the holes of these oxides are located mainly at Mn, and the peak at around 527 eV results from the hybridization of oxygen 2p state and Mn 3d state. From Fig. 5, it seems that the peak at 527 eV at the oxygen K-edge decreases due to the phase transformation at low temperature. The decrease of the peak intensity may be attributed to the weakness in the hybridization due to the lattice strain associated with the charge ordering. Similar oxygen K-edge fine structures with three large peaks were also observed in $Bi_{1-x}Ca_xMnO_3$. Detailed experiments on the oxygen K- edge fine structure change due to the phase transformation and the composition change for $Bi_{1-x}Ca_xMnO_3$ are under progress.

Conclusions

The present results are summarized as follows,

1) By utilizing a newly developed energy filter (omega-type), the background on the electron diffraction patterns in $Bi_{1-x}Ca_xMnO_3$ caused mainly by plasmon scattering was largely reduced.
2) From the detailed intensity profiles of the energy-filtered electron diffraction, it was found that appearance of the superlattice reflections at low temperature was attributed to the lattice strain caused by the charge ordering of Mn^{3+} and Mn^{4+} ions.
3) Fine structures of oxygen K-edge in the electron energy-loss spectra in $La_{0.2}Ca_{0.8}MnO_3$ are rather sensitive to the phase transformation.

Acknowledgments

The authors wish to thank Drs. T. Oikawa and T. Kaneyama, JEOL Ltd. for their help to use a JEM-2010 electron microscope installed with an omega-type energy filter. This study was partly supported by Grant-in-Aid for Scientific Research on the Priority Area ' Investigation of Microscopic Mechanisms of Phase Transformations for the Structure Control of Materials' from the Ministry of Education, Science, Sports and Culture of Japan.

References

1. E.O.Wollan and W.C.Koehler, "Neutron Diffraction Study of the Magnetic Properties of the Series of Perovskite-Type Compounds [(1-x)La,xCa]MnO_3", Phys.Rev. 100(1955)545-563.
2. J.B.Goodenough, "Theory of the Role of Covalence on the Perovskite-Type Manganites [La,M(II)]MnO_3", Phys.Rev., 100(1955)564-573.
3. H.Chiba, M.Kikuchi, K.Kusaba, Y.Muraoka and Y.Syono, "Ferromagnetism and Large Negative Magnetoresistance in $Bi_{1-x}Ca_xMnO_3$ ($x \geq 0.8$) Perovskite", Solid.State Commun., 99(1996)499-502.
4. H.Chiba, T.Atou, H.Faqir, M.Kikuchi, Y.Syono, Y.Murakami and D.Shindo,"Synthesis and Characterization of (Bi,AE)MnO_3 (AE=Ca,Sr) System", submitted to Solid State ionics.
5. A.P.Ramirez et al., "Thermodynamic and Electron Diffraction Signatures of Charge and Spin Ordering in $La_{1-x}Ca_xMnO_3$", Phys.Rev.Lett., 76(1996)3188-3191.
6. C.H.Chen, S-W.Cheong and A.S.Cooper, "Commensurate to Incommensurate Charge Ordering and Its Real-Space Images in $La_{0.5}Ca_{0.5}MnO_3$", Phys.Rev.Lett, 76(1996)4042-4045.
7. W.Bao, J.D.Axe, C.H.Chen and S-W.Cheong, "Impact of Charge Ordering on Magnetic Correlations in Perovskite (Bi,Ca)MnO_3", Phys.Rev.Lett.,78(1997)543-546.
8. Y.Murakami, D.Shindo, H.Chiba, M.Kikuchi and Y.Syono, "Observations of Long-period Structures Associated with Charge Ordering in $Bi_{0.2}Ca_{0.8}MnO_3$", Phys.Rev.B, 55(1997)15043-15047.

STM/AFM STUDY OF SURFACE RELIEF INDUCED IN THE PHASE TRANSFORMATION OF Fe-Ni-C, ZrO_2-Y_2O_3 AND Cu-Al-Ni ALLOYS

Masahiko Yamamoto

Department of Materials Science and Engineering, Osaka University,
2-1, Yamada-Oka, Suita-shi, Osaka-fu 565-0871, Japan

Abstract

Using scanning tunneling microscopy (STM) and atomic force microscopy (AFM), which can measure the height of surface relief, I have quantitatively investigated surface relief induced by phase transformation in a Fe-Ni-C alloy, a zirconia-yttria high toughness ceramics and a Cu-Al-Ni shape memory alloy, and have discussed details of phase transformation including mechanism of the phase transformation. In this paper I summarize the above studies and emphasize necessities of such kind of the experiments.

In the study of the Fe-Ni-C alloy, morphology and accommodation of thin-plate martensites were investigated. Strain distribution induced by the formation of martensitic phase within the parent phase was calculated using the quantity of the surface relief obtained by the AFM observation and it is found that highly strained region within the parent phase exists near the front of the thin-plate martensites. In the study of zirconia-yttria ceramics, the herringbone structure induced by the tetragonal-to-monoclinic transformation was investigated, and it is concluded that cations like Zr and Y do not diffuse and only anions like OH and O diffuse, and that the lattice consisting of the cations transform by a diffusionless mechanism, i.e. shear mechanism. In the study of Cu-Al-Ni alloy, details of self-accommodation were made clear.

The Third Pacific Rim International Conference on
Advanced Materials and Processing (PRICM 3)
Edited by M.A. Imam, R. DeNale, S. Hanada,
Z. Zhong and D.N. Lee
The Minerals, Metals & Materials Society, 1998

Introduction

When martensitic transformation occurs, surface relief appears on the surface of a specimen [1]. If we can observe such the surface relief quantitatively, we can learn details of phase transformation including mechanism of phase transformation.

Scanning tunneling microscopy (STM) [2,3] and atomic force microscopy (AFM) [4] make it possible to measure the height of surface relief quantitatively. In fact we have quantitatively investigated surface relief induced by phase transformation in a Fe-Ni-C alloy [5], a zirconia-yttria high toughness ceramics [6,7] and a Cu-Al-Ni shape memory alloy [7,8], and have discussed the mechanism of the phase transformation. In this paper I summarize those results and demonstrate superiority of STM and AFM to study martensitic transformation.

A Fe-Ni-C Alloy

An Fe-Ni-C alloy transforms from the austenite phase to the martensite phase with decreasing temperature. This alloy is a typical ferrous alloy with martensitic transformation. Here, I describe the morphology and accommodation of martensites in the alloy and the surface relief induced by the martensitic transformation, which were investigated quantitatively by AFM. Moreover, I discuss the strain distribution within the parent phase.

Crystallography

The alloy used in the present study has an Fe-Ni(29.86 mass%)-C(0.42 mass%) composition. The crystal structure of the parent phase of the alloy is face-centered cubic (fcc) and that of the martensite phase is body-centered tetragonal (bct). The martensite produced in the alloy has a thin-plate shape without midrib and its habit plane is {3 10 15} [9,10]. In this transformation, 24 variants are geometrically possible to produce.

Experiment

The single crystal with rectangular shape of the alloy was annealed at 1473 K for 2 h in dynamical vacuum at 10^{-4} Pa followed by spontaneous cooling outside the furnace. A partial martensitic transformation was induced by cooling the specimen to near the liquid-nitrogen temperature. Lattice parameters were determined to be a_0=0.3601 nm for the parent phase and a=0.2879 nm and c=0.2921 nm for the martensite phase using X-ray diffractometer. The surface orientation of the single crystal specimen was also determined by X-ray Laue method.

Optical microscopic observation and subsequently AFM observation were made on the thin-plate martensites embedded in the parent phase. The AFM observation was performed at room temperature in air, and by the constant force mode in which the force was 9.4 nN. The probe tip and cantilever were made of Si_3N_4. The spring constant of the cantilever was 0.16N/m and the scanning speed was 130 μm/s. The AFM used was Nanoscope II from Digital Instruments Inc.

Results and Discussion

Optical microscopic observation revealed that there existed a number of thin-plate martensites line-up in parallel. The thickness of the bottom part in a thin-plate martensite is about 3 μm and the thickness decreases toward the front direction of the thin-plate martensite.

By a combined method of optical microscope image and X-ray Laue method, so called single-face trace analysis, the kind of variant of lined-up martensites could be determined to be either variant with (3 15 10) or (3 10 15) habit plane, hereinafter called (3 15 10) or (3 10 15) variant, respectively. But we can not determine definitely either one of them. If the two-face analysis is made, the kind of variant can be determined. However, it is quite difficult to do two-face trace analysis because the martensite is thin. If we can learn surface relief quantitatively, we can determine the kind of variant by combining with single-face trace analysis.

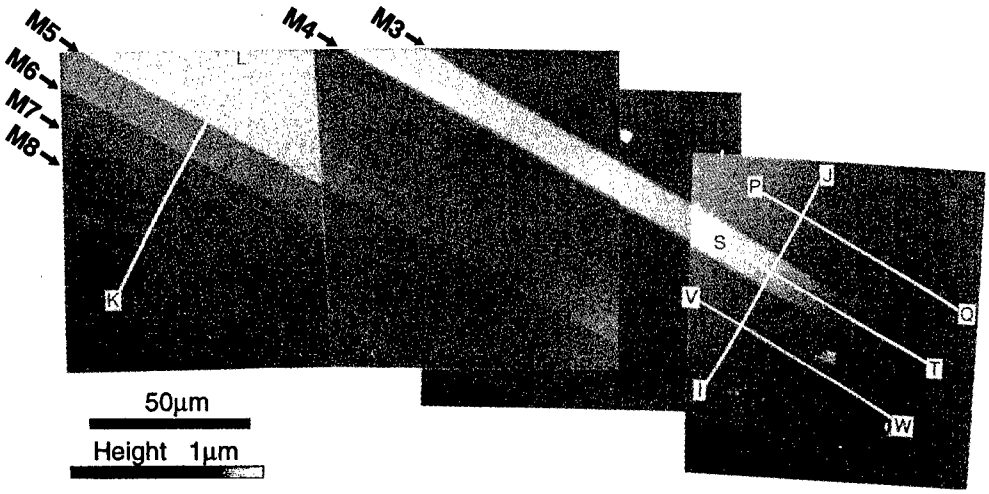


Fig.1 An AFM image of thin-plate martensite showing surface relieves induced by martensitic transformation.

Figure 1 is an AFM image of thin-plate martensites. In the AFM observation the surface relief of each thin-plate martensite can be quantitatively observed. Heights of the surface relief are shown in the gray scale and the gray scale presents the relative height. Fig.1 composes of four AFM images having different standard height and the gray scale gives an information about the relative height. The maximum height of martensite in the figure is around 300 nm. The parent phase between two martensites of M3 and M4 keeps high.

Cross-sectional views of these thin-plate martensites were obtained from the AFM image, as shown in Fig.2 and Fig.3. I-J, K-L in Fig.2 and P-Q, S-T, V-W in Fig.3 correspond to those in Fig.1. I-J and K-L in Fig.2 are cross-section in the direction perpendicular to the thin-plate martensites, while P-Q, S-T, and V-W in Fig.3 are in the direction parallel to those. In Fig.2 the surface relief angles of variants, which were obtained in the present study, are shown. On the other hand the surface relief angles of the 24 variants were theoretically calculated by the phenomenological theory of martensite crystallography [11,12]. The observed surface relief

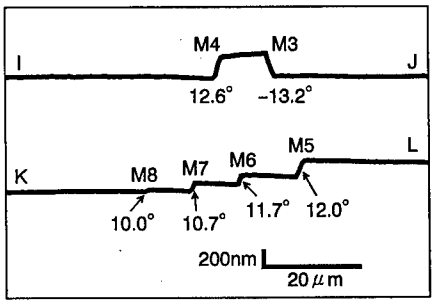


Fig.2 Cross-sectional views in the direction perpendicular to the thin-plate martensites obtained from the AFM image. Surface relief angles for variants of the thin-plate martensite are also shown.

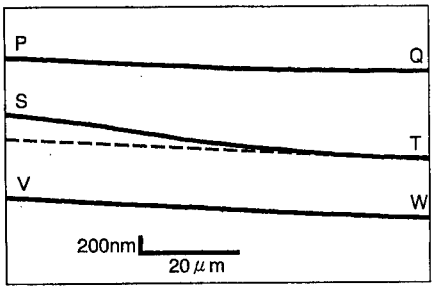


Fig.3 Cross-sectional views in the direction parallel to thin-plate martensites obtained from the AFM image, showing surface relieves of the parent crystals sandwiched between martensites.

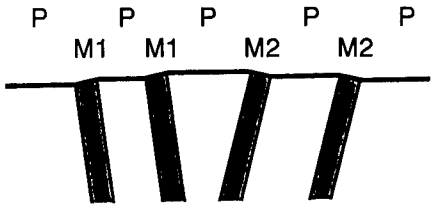


Fig.4 Schematic representation of cross-section illustrating complementary configuration of (3 15 10) variant (M1) and (3 10 15) variant (M2) to make the overall strain minimize. Note that this figure is delineated in the same scale for y-axis and z-axis, while Fig.2 is done in the different scale.

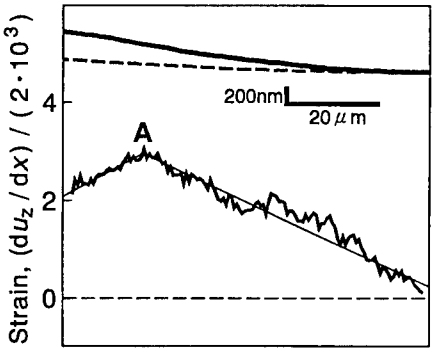


Fig.5 Strain distribution of the parent phase sandwiched and surface-relieved by two thin-plate martensites in the direction parallel to the thin-plate martensites. The curve at the top is the same as a part of the curve S-T in Fig.3.

angles of the M3 and the M4-M8 were compared with the calculated surface relief angles of (3 15 10) and (3 10 15) variants, and martensite M3 is determined to be (3 10 15) variant and martensites M4-M8 are determined to be (3 15 10) variant. It is emphasized here that the method to determine the kind of variant by a combination of AFM observation with single-face trace analysis is powerful in case two face trace analysis is difficult, especially for thin specimen like thin film.

Since the kind of variant was determined, we can discuss the configuration of martensites. Figure 4 shows the schematic representation of cross-section illustrating complementary configuration of the martensites of two (3 15 10) and (3 10 15) variants. Martensites M3 and M4 of (3 15 10) and (3 10 15) variants, respectively, keep complementary configuration of variants, as seen in Fig.4. This is due to making the overall strain minimize. The fronts of both the martensites, M3 and M4, are located at the identical position in the S-T direction, in Fig.1. The spacing between the two martensites is around 12 μm. Martensites M5, M6, M7 and M8 sitting beside M3 keeps 10 to 20 μm spacing each other. The location of fronts of those martensites are gradually delayed. This seems that such the configuration also makes the overall strain minimize.

Next let us see strain distribution in the parent phase. Surface relieves of the parent crystals sandwiched between martensites are shown in Fig.3, as were described above. In regions of the P-Q and V-W in the parent phase, martensite is located at one side, while in region of the S-T in the parent phase, martensites are located at both sides. The surface relieves at P-Q and V-W decrease linearly, as shown by P-Q and V-W in Fig.3, while the surface relief at S-T decreases along smooth curve, as shown by S-T curve in Fig.3.

In order to learn strain distribution induced within the parent phase along S-T direction, the following analysis was made. When the surface-normal direction is taken as the z-axis and the S-T direction is taken as the x-axis, the shear strain is given by the following equation,

$$e_{xz} = \left(\frac{\partial u_z}{\partial x} + \frac{\partial u_x}{\partial z} \right) \Big/ 2, \qquad (1)$$

where u_x is the displacement in the x-direction occurred by martensitic transformation, u_z is displacement in the z-direction and e_{xz} is the shear strain. The data of Fig.3 can give only the first term because the second term can not be obtained by the AFM observation. Then, hereinafter we call the first term the strain. Giving the values of u_z obtained from the

difference in z-values between S-T and P-Q for each site along the x-axis using the experimental data shown in Fig.3, the strain along S-T can be successfully calculated. The obtained strain distribution along the S-T direction, Fig.5, is not uniform, but it takes maximum value at the certain point and decay gradually at both sides. The point A in Fig.5 corresponds to the maximum position and that position is located at around 50 μm from the front of the thin-plate martensite. This means that highly strained region exists near the front of the martensite. It is considered that highly strained region moves toward the growth direction with the growth of the thin-plate martensite.

A Zirconia-Yttria High Toughness Ceramics

Yttria-doped partially stabilized zirconia (PSZ) is a transformation toughening ceramic material used for structural applications. However, the degradation of the material around 400 to 500 K in air and above 350 K in water during annealing is a severe problem. It is considered that this degradation is caused by the tetragonal-to-monoclinic (t-m) transformation accompanying micro- and macro-cracking. For its improvement the t-m transformation must be understood well. In this study, we have used STM to investigate quantitatively the surface relief induced by the t-m transformation in order to clarify the nature of the transformation.

Experiment

The composition of the alloy used in the present study was ZrO_2-2mol%Y_2O_3. It was confirmed by X-ray and electron diffraction analyses that in the initial state of the specimen had the tetragonal structure. Then the specimen was annealed at 523 K for 10 h. The identification of the monoclinic phase after the phase transformation was also made by X-ray and electron diffraction analyses. STM observation was made at room temperature in air, using PtIr alloy tips. Before STM observation the specimen surface was coated by Pt film of 7 nm thickness for conductivity. In STM observation the tunneling current was 1.0 nA, the bias voltage was 400 mV, and the scanning speed was 10 or 2μm/s.

Results and Discussion

In the specimen annealed at 523 K for 10 h it was found by optical microscopy that two types of transformation products exist, the herringbone and the acicular type. Fig.6 is an STM image of herringbone product. White regions correspond to high level, while black regions correspond to low. In the figure the herringbone structures are beautifully presented.

In Fig.7(a) surface relief can be perspectively presented. The cross section, Fig.7(b), consists of two sets of parallel lines. Each of the lines, for example A, B or C corresponds to the surface of the variants, and surface is flat. The height of the surface relief is around a few hundred nanometers.

It has already been known that the monoclinic herringbone structure is the self-accomodation structure as shown in Fig.8 [13]. In the monoclinic herringbone product a pair of two variants with the same c-axis is twin related and forms a "band", Fig.8. The STM results

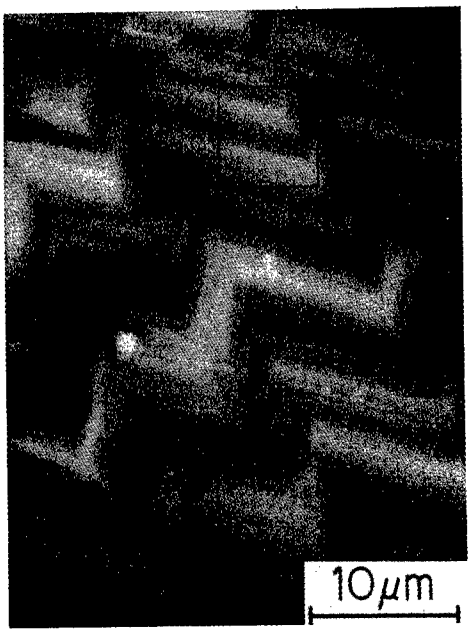


Fig.6 An STM image of herringbone product in PSZ. Crystallographic detail is described in Fig.8. The enclosed region corresponds to Fig7(a).

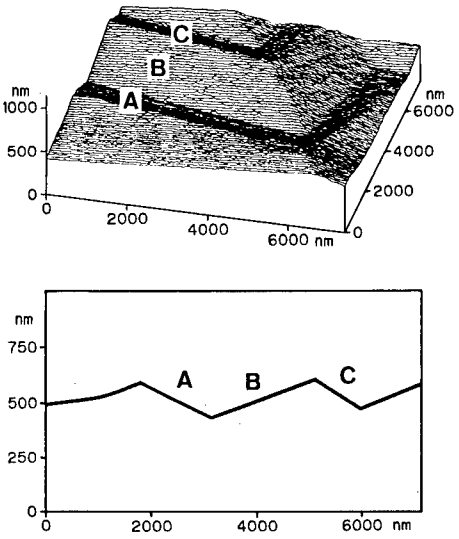


Fig.7 (a) An STM perspective view of the herringbone product corresponding to the enclosed region in Fig.6, and (b) its cross section perpendicular to the variant interface where A, B and C correspond to A, B, and C in Fig.8(a), respectively, showing surface relief.

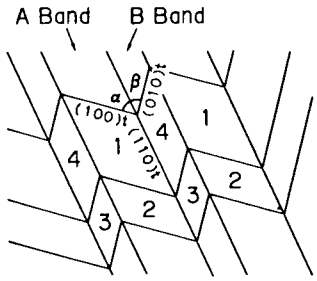


Fig.8 Schematic representation of monoclinic herringbone product in PSZ.

of Fig.6 and Fig.7 present the topographical features of the Fig.8.

The surface relief angle for each pair of the monoclinic variants in the bands was measured. On the other hand, the expected surface relief angles were calculated using the phenomenological theory. When the values obtained by STM are compared with the theoretically calculated values, they were in agreement well each other.

However, the agreement between the observed and the calculated values does not mean that the tetragonal-to-monoclinic transformation during annealing is perfect by the shear mechanism. This is because the weight of the specimen increases during the transformation and infrared spectra demonstrate the formation of OH . Thus it is simply said from the above STM observation of the surface relief that the tetragonal phase before the transformation and monoclinic phase after the transformation keep a crystallographic relation which is predicted for a martensitic transformation. The above discussion implies that cations like Zr and Y do not diffuse and only anions like OH and O diffuse, and that the lattice consisting of the cations transforms by a diffusionless mechanism, i.e. shear mechanism.

A Cu-Al-Ni Shape Memory Alloy

A Cu-Al-Ni alloy is a typical shape memory alloy. The shape memory phenomenon is governed by martensitic transformation. In the transformation, self-accommodation consisting of variants occurs. In this study such the self-accommodation is investigated by STM.

Crystallography

An alloy having Cu-Al(14.2mass%)-Ni(3.1mass%) composition was used. The parent phase (β_1) of the alloy has the DO_3-type ordered cubic structure and the martensite phase (γ_1') has the orthorhombic structure of so-called 2H type. There are six lattice-correspondence-variants [14]. A habit-plane-variant is composed of pairs of two different lattice-correspondence-variants to satisfy the condition for the invariant habit-plane [15,16]. The two lattice-correspondence-variants in each pair are in a twin relation. The grouping of four habit-plane-variants occurs to

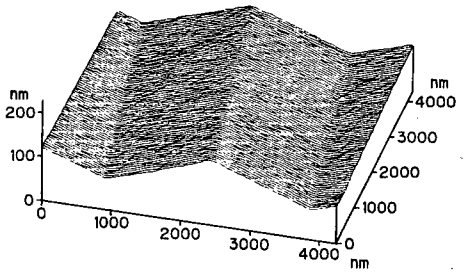


Fig.9 An STM perspective view of one in the four habit-plane-variants, showing the two lattice-correspondence-variants within the habit-plane-variant in the martensite phase.

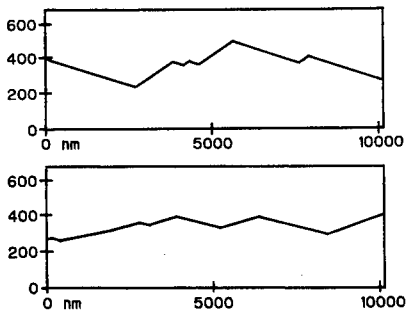


Fig.10 STM cross-sectional views of two of four habit-plane-variants.

minimize strain energy in the system and is called self-accommodation [14].

Experiment

Self-accommodated regions consisting of four habit-plane-variants were observed by optical microscopy, and the kinds of habit-plane-variants in each region were determined by trace analysis of the interface of the two lattice-correspondence-variants in the habit-plane-variant. Subsequently, the surface relieves in each region were observed by STM and "surface relief angle" for each pair of the lattice-correspondence-variants in the habit-plane-variant was obtained from the observed result. Then the STM results were compared with theoretically calculated results.

Results and Discussion

An STM perspective view of one of the four habit-plane-variants is shown in Fig.9. It presents quantitatively the feature of surface relief. There are two parallel flat surfaces corresponding to the two lattice-corresponding-variants within the habit-plane-variant, respectively. The height of the surface relief is around a few hundred nanometers.

By sectioning the STM perspective view perpendicular to both the surface plane and the interface plane of the lattice-correspondence-variant, an STM cross-sectional view of the habit-plane-variant was obtained as shown in Fig.10. The edges formed by the two flat surfaces are sharp and well defined. All the pairs of the lattice-correspondence-variants on the habit-plane-variant have an identical surface relief angle as was predicted from the WLR phenomenological crystallographic theory [11,12]. This reflects the fact that shape change is unique to the lattice-correspondence-variants. Thus it is experimentally confirmed that the surface relief angle is unique for each habit-plane-variant if the surface orientation of the parent phase is given.

Summary

STM and AFM are very powerful tools to observe quantitatively surface topograph like the surface relief induced by the martensitic transformation. The information obtained by STM/AFM observation is very useful to learn detail of phase transformation.

Acknowledgment

The author would like to thank Profs. and Drs. T. Fujisawa, M. Hayakawa, T. Kurumizawa, K. Kusao, K. Nishikawa, M. Oka, Y. Noda, and T. Saburi for collaboration in the studies. This work was partially supported by a Grant-in-Aid for Scientific Research (B) and Scientific Research on Priority Area from the Japanese Ministry of Education, Science, Sports and Culture.

References

1. Z. Nishiyama, Martensitic Transformations, (New York, NY: Academic Press, 1978).
2. G. Binnig, H. Rohrer, Ch. Gerber, and E. Weibel, "Surface Studies by Scanning Tunneling Microscopy", Phys. Rev. Lett., 49 (1982), 57-61.
3. G. Binnig, H. Rohrer, Ch. Gerber, and E. Weibel, "Scanning Tunneling Microscopy", Surf. Sci. 126 (1983), 236-244.
4. G. Binnig, C.F. Quate, and Ch. Gerber, "Atomic Force Microscope", Phys. Rev. Lett., 126 (1986), 930-933.
5. M. Yamamoto, K. Nishikawa, Y. Noda, T. Saburi, M. Hayakawa, M. Oka, and T. Kurumizawa, "Atomic Force Microscope Study of Thin-Plate Martensites in an Fe-Ni-C Alloy", J. Vac. Sci. Technol., B12(3) (1994), 1813-1616.
6. M. Yamamoto T. Fujisawa, T. Saburi, M. Hayakawa, M. Oka, and T. Kurumizawa, and K. Kusao, "Scanning Tunneling Microscope Study of Surface Relief Induced by the Tetragonal-to-Monoclinic Transformation in a Zirconia-Yttria Alloy", Ultramicroscopy , 42 (1992), 1422-1427.
7. M. Yamamoto, Jpn. Ceramic Society, "STM Study on Surface Relief Induced by Martensitic Transformation", Jpn. Ceramic Society, 35 (1993), 99-101.
8. M. Yamamoto, T. Fujisawa, T. Saburi, T. Kurumizawa, and K. Kusao, "Quantitative Study of Surface Relief Induced in the Martensitic Transformation of a Cu-Al-Ni Shape Memory Alloy by Scanning Tunneling Microscopy", Surface Sci., 266 (1992), 289-293.
9. T. Maki, S. Shimooka, and I. Tamura, The Ms Temperature and Morphology of Martensite in Fe-31pct Ni-0.23 pct C Alloy", Trans. Met., 2 (1971), 2944-2945.
10. H. Okamoto, M. Oka, and I. Tamura, "Coupling of Thin-Plate Martensites in an Fe-Ni-C Alloy", Trans. Jpn. Inst. Metals, 19 (1978), 674-684.
11. M.S. Wechsler, D.S. Lieberman, and T.A. Read, "On the Theory of the Formation of Martensite", J. Metals, (1953), 1503-1515.
12. D.S. Lieberman, M.S. Wechsler, and T.A. Read, "Cubic to Orthorhombic Diffusionless Phase Change -- Experimental and Theoretical Studies of AuCd", J. Appl. Phys., 26 (1955), 473-484.
13. M. Hayakawa, K. Adachi, and M. Oka, "Tweed Contrast with (223) Habit in Arcmelted Zirconia-Yttria Alloys", Acta Met. Mater., 38 (1990), 1753-1761.
14. T. Saburi and S. Nenno, "Shape Memory Effect and Related Phenomena", in: Proc. Int. Conf. Solid to Solid Phase Transformations, eds. H.I. Aaronson, D.E. Laughlin, R.E. Sekerka and C.M. Wayman (1981), 1455-1480.
15 K. Otsuka and K. Shimizu, "Morphology and Crystallography of Thermoelastic γ' Cu-Al-Ni Martensite" Jpn. J. Appl. Phys., 8 (1969), 1196-1204.
16 T. Tadaki, S. Hamada, and K. Shimizu, "Crystal Structure and Internal Defects of Thermoelastic Martensite in a Ag-47at%Cd Alloy", Trans. Jpn. Inst. Metals, 18 (1977), 135-143.

MODIFICATIONS IN THE MARTENSITE TRANSFORMATION OF THE 0.45C-13Cr STEEL CAUSED DURING THE CONTINUOUS COOLING PROCESS WITH AND WITHOUT PRECIPITATION OF $M_{23}C_6$ CARBIDES.

C. García de Andrés and L.F. Alvarez.
Department of Physical Metallurgy
Centro Nacional de Investigaciones Metalúrgicas (CENIM-CSIC)
Avda. Gregorio del Amo, 8. 28040 Madrid. Spain

Abstract

The different behavior of the martensitic transformation in the 0.45C-13Cr martensitic stainless steel is due to the chemical composition of the austenite phase previous to this transformation. When austenite is homogeneous, martensite transforms continuously within a single stage throughout a certain range of temperatures M_S-M_f. However, as a consequence of the dissolution and precipitation processes that take place during heat treatment of this steel, important modifications in the chemical composition of the austenite can be produced. The experimental results of this study prove that the transformation of the non-homogeneous austenite is the origin of the splitting phenomena in the martensitic transformation. Transformation stages observed at temperatures higher than the starting temperature of the bulk martensitic transformation (M_S) are related to the carbide precipitation process. On the contrary, the stages detected at temperatures lower than M_S are related to carbide dissolution process.

The Third Pacific Rim International Conference on
Advanced Materials and Processing (PRICM 3)
Edited by M.A. Imam, R. DeNale, S. Hanada,
Z. Zhong and D.N. Lee
The Minerals, Metals & Materials Society, 1998

Introduction

Martensitic stainless steels containing 13% Cr are commonly used in quenched-and-tempered conditions (1-4). Martensitic transformation in metallic materials is significantly influenced by a large number of factors of a very diverse origin (5). In martensitic stainless steels, the factors with the greatest influence on the martensite start temperature, M_S, are those related to the chemical composition of the austenite phase (1,2,5-7). In these steels, as in other alloyed steels containing carbide-forming elements, the carbide dissolution and precipitation processes that occur during quenching treatment may modify the chemical composition of the austenite prior to its transformation into martensite (2,8-14). Recent investigations have found splitting phenomena in the martensitic transformation of martensitic stainless steels (15-20). Under specific heating and cooling conditions, the non-isothermal austenite-to-martensite transformation in these steels does not occur continuously in a single stage throughout a certain range of temperatures, M_S-M_f, but splits into different and successive stages limited by different M_{Si}. Theoretically, the most coherent explanation for these splitting phenomena is based on the non-isothermal decomposition of austenites that coexist with different chemical compositions. Experimental results obtained in this study show that the martensitic transformation in 0.45C-13Cr steel can be severely modified through the austenitizing conditions of the heat treatment. The present work aims to explain the different behaviors that have been observed in the martensitic transformation of this stainless steel.

Table I. Chemical Composition (Mass %)

Steel	C	Si	Mn	P	S	Cr	Ni
0.45C-13Cr	0.45	0.32	0.44	0.030	0.016	13.0	0.38

Material and Experimental Procedures

The martensitic stainless steel used in this work comes from cold-rolled coil and it was tested in the as-received annealed condition. The chemical composition is given in Table I. The as-received microstructure of this steel consists of $M_{23}C_6$-type globular complex carbides finely distributed in a ferrite matrix.

An Adamel Lhomargy DT.1000 high resolution dilatometer was used to observe the splitting phenomena and to determine the martensite start temperatures, M_{Si}, of this steel. Prismatic dilatometry specimens of 2 mm in thickness and 12 mm in length were machined from the as-received material.

As indicated in the schematic diagram of Fig. 1, the generic symbol M_S has been used in this study to represent the starting temperature of the martensitic transformation that takes place in line with normal behavior

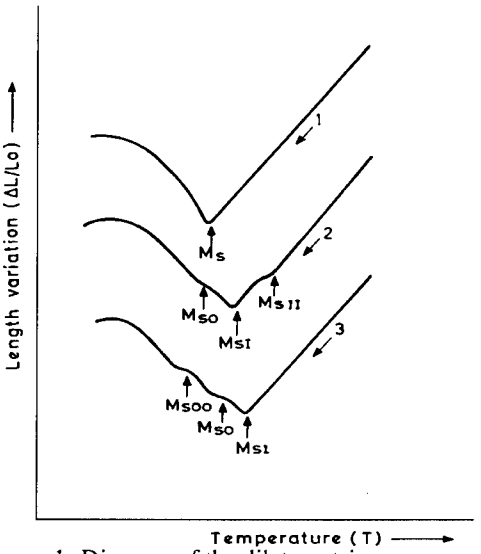


Figure 1: Diagram of the dilatometric response of the development of the martensitic transformation.

continuously throughout a single stage (dilatometric curve 1 of Fig. 1). To distinguish and identify the different splitting stages, the M_{SI} symbol is used to represent the temperature at which the bulk austenite-to-martensite transformation commences. This transformation is identified by a minimum in the dilatometric curve $\Delta L/L_0 = f(T)$. The splitting stage detected at a temperature higher than M_{SI} is represented by M_{SII} and, finally, the starting temperatures of the splitting stages occurring successively below M_{SI} are represented by M_{SO} and M_{SOO} (curves 2 and 3 of Fig. 1). These curves also show that the splitting stages are identified by an anomaly in the slope of the dilatometric curve. The small intensity of these anomalies indicate that they are caused by the martensitic transformation of small areas of austenite. M_{SII}-type splitting corresponds to the martensitic transformation of areas of austenite impoverished in carbon and carbide-forming elements in relation to the bulk austenite. On the contrary, M_{SO} and M_{SOO}-types splittings correspond to the martensitic transformation of areas of austenite which are more concentrated than the bulk austenite.

For all the tests of this work, specimens were heated at a constant rate of 0.5 K/s from room temperature to the pre-selected heating temperatures and, after a 60-second holding time at these temperatures, they were then quenched at different cooling rates. Since the purpose of this investigation was to analyze the behavior of the martensitic transformation, only cooling rates faster than the martensite critical rates were used.

Results and Discussion

No Carbide Precipitation

In works published elsewhere (17,21,22), it was described that a cooling rate of 50 K/s effectively inhibits carbide precipitation in the 0.45C-13Cr martensitic stainless steel. Therefore, to be able to analyze the behavior of the martensitic transformation occuring during cooling from different heating temperatures in the absence of carbide precipitation, all the cooling processes were performed at a rate of 50 K/s. It may, thus, be assured that the martensitic transformation caused under these experimental conditions will only be related to the states of austenitization attained to each heating temperature. Table II shows the critical points of this steel at a constant heating rate of 0.5 K/s (23). A_{C1} and A_{C3}, respectively, represent the temperature at which the formation of the austenite phase commences and the temperature at which the ferrite-to-austenite transformation ends. A_{CC} represents the temperature of total carbide dissolution in the austenite and A_{Ch} represents the temperature for which the above austenite is homogeneous.

Table II. Critical Points at a Heating Rate of 0.5 K.s-1

Steel	Temperatures of the Critical Points (K)			
	A_{C1}	A_{C3}	A_{CC}	A_{Ch}
0.45C-13Cr	1083	1130	1383	1463

Figure 2 shows the influence of the heating temperature on the splitting phenomena in the martensitic transformation of this steel quenched by cooling at 50K/s. Martensite start temperatures, M_{Si}, were used to illustrate the different types of splitting phenomena observed in the martensitic transformation of this steel. As described elsewhere (17,19,20,22,24), during the heating process of martensitic stainless steels, the dissolving carbides diffuse atoms of carbon and carbide-forming elements toward the nearby areas of the austenite phase. The effect of alloying elements in depressing the martensite start temperatures is well known (1,2,5-7).

According to this effect, the results for this steel in Fig. 2 clearly show that M_{Si} decreases with increasing heating temperatures. Furthermore, the decrease of the M_{Si} temperatures occurs until the heating temperature reaches the A_{CC} temperature. The fact is that at this A_{CC} temperature all the carbides will be dissolved and the austenite reaches the maximum concentration of carbon and carbide-forming elements. For heating temperatures higher than A_{CC}, the M_{Si} temperatures of this steel tend to remain constant at 435 K. Figure 2 also shows that M_{S0}-type splitting occurs within the range of 1273 to 1400 K in the 0.45C-13Cr steel. These experimental results are consistent with previous studies done on 13% Cr-type martensitic stainless steels (17,20,24). In these works, significant concentration gradients have been found in the austenite phase at the heating temperatures of the above-mentioned range as a consequence of the carbide dissolution process occuring during the heating. The intensity and amplitude of the concentration gradients depend on the amount of carbides in the as-received annealed condition of the steel and on the levels of dissolution and diffusion reached during the heating. For heating temperatures not within the above-mentioned range, the concentration gradients in the austenite were negligible (17,20,24). Figure 2 shows that, in the absence of carbide precipitation during cooling, no splitting phenomena occurs in the martensitic transformation of this steel quenched from these temperatures.

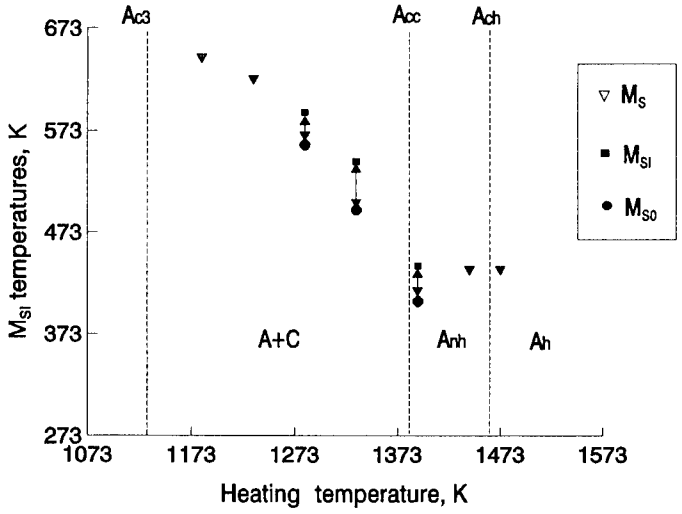


Figure 2. Influence of the heating temperature on the martensite start temperature after quenching at 50 K/s. (A :austenite, C :carbides, A_{nh}: non-homogeneous austenite, A_h :homogeneous austenite).

Carbide Precipitation

To analyze the martensitic transformation of the 0.45C-13Cr steel caused during the cooling with carbide precipitation, the influence of the cooling rates should be evaluated. Thus, heat treatments involving heating under the same above-mentioned conditions (heating rate: 0.5 K/s; holding time: 60 seconds) followed by quenching at different cooling rates were carried out on this steel. Two heating temperatures, the so-called optimum and conventional temperatures, were selected. The former,1393 K, is the temperature at which the maximum quenching hardness is reached in this steel (21,23); the latter, 1333 K, is the temperature generally used

in industrial quenching treatments of this steel (1,2,8). These temperatures are listed in Table III. This table also lists the states of austenitization attained to these temperatures on the basis of the critical points (Table II).

Table III. Heating Temperatures and austenitization states

Steel	Heating Temperature (K)	Austenitization State
0.45C-13Cr	*1393	Non-Homogeneous Austenite
	**1333	Austenite+Carbides

* Optimum temperatures
** Conventional temperatures

Figure 3 shows the influence of the cooling rate on the martensite start temperature of the 0.45C-13Cr steel quenched from the optimum and conventional temperatures. The results correspond to cooling rates faster than the critical cooling rates at which austenite fully transforms to martensite. Critical rates of 0.4 and 0.5 K/s at heating temperatures of 1393 and 1333 K, respectively, have been reported (23). By similitude to the well known CCT diagrams, the diagrams in Fig. 3 are called CCMT (Continuous Cooling Martensitic Transformation) in this work.

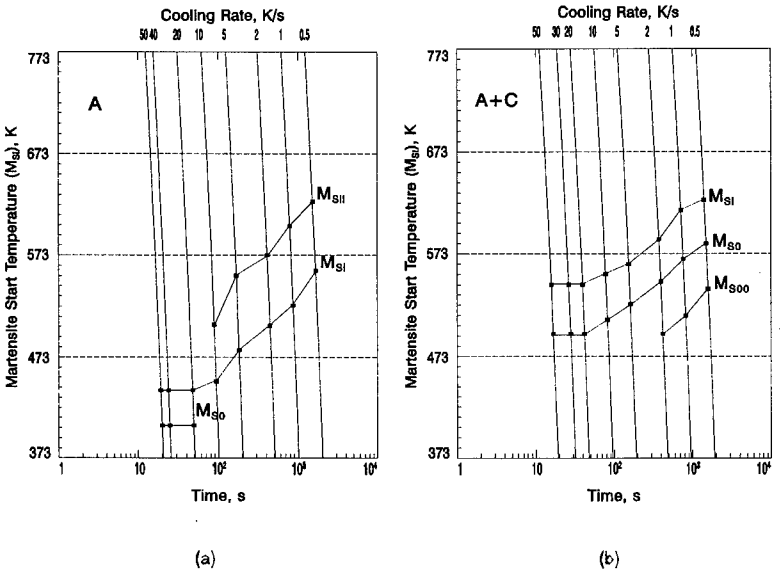


Figure 3. Influence of the cooling rate on the martensite start temperature of the 0.45C-13Cr steel quenched from (a) the optimum temperature: 1393K, and (b) the conventional temperature: 1333K.

A simple observation of the CCMT diagrams shows, that the splitting phenomena occurring in the martensitic transformation of this steel can be strongly modified through the cooling rate. It can be seen in Fig. 3(a) that the M_{SII}-type splitting occurs at the heating temperatures at which the austenitization state of this steel is formed by non-homogeneous austenite. Moreover,

this figure clearly shows, that in the quenching treatment from the optimum temperatures, the M_{SII} splitting occurs within a limited range that comprises the lowest cooling rates, whereas if M_{SO} splitting takes place, it only occurs at high cooling rates when the M_{SII}-type splitting is no longer present. According to the CCMT diagram for conventional temperature shown in Fig. 3(b), from austenitization state formed by austenite and carbides, only M_{SO} and M_{SOO} splittings were detected. Furthermore, in this diagram the M_{SO}-type splitting occurs throughout the wide range of cooling rates assayed. Finally, a particularly important aspect of the splitting results presented in Fig. 3 is that splitting phenomena types M_{SO} and M_{SII} do not occur simultaneously at the same cooling rate. The specific austenitizing and cooling conditions under which the M_{SII} splitting occurs are in evident contrast with those of the M_{SO} and M_{SOO} splittings, proving that the two types of martensitic subtransformations have different causes.

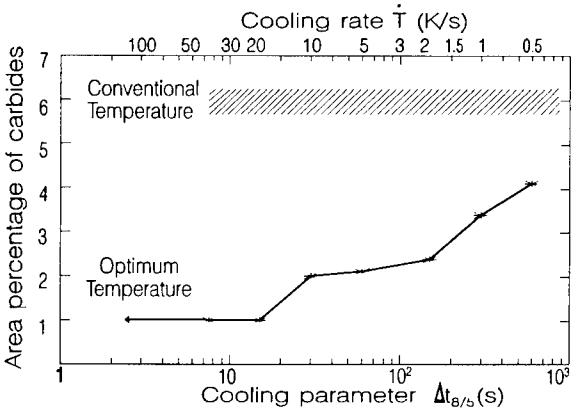


Figure 4. Influence of cooling rate on carbide precipitation after quenching from the conventional and the optimum temperatures.

In previous works (21,22,25), measurements of the area percentage of carbides were made with image analysis techniques in the microstructures obtained by quenching at different cooling rates from the optimum and conventional temperatures. Fig. 4 shows the area percentage of carbides as a funtion of cooling rate. The $\Delta t_{8/5}$ cooling parameter is also given in Fig. 4 to facilitate the plotting of the curves. This parameter is defined as the time that elapses during cooling at a constant rate from 800 to 500°C (26,27). For the conventional temperature (1333 K), Fig. 4 shows the measured area percentage of carbides as a shaded area. The area percentage of carbides varies, regardless of the cooling rate, within a small range of values. The mean of these values is roughly equal to 6%. These results demonstrate that, at any cooling rate, no significant carbide precipitation occurs during continuous cooling of the 0.45C-13Cr steel from the conventional temperature. On the other hand, for the optimum temperature (1393 K), Fig. 4 shows that when the cooling rate rises, the area percentage of carbides decreases until a minimum is reached which remains constant even for increasing cooling rates. It is evident that no carbide precipitation occurs when the area percentage of carbides in the quenched microstructures remains at its minimum value. Carbides will only precipitate in this steel from its optimum temperature at cooling rates slower than 20 K/s, at which this minimum value is reached (Fig. 4). Cooling rates faster than 20 K/s inhibit carbide precipitation during cooling.

Experimental results presented in Figs. 3 and 4 demonstrate that M_{SII}-type splitting only occurs when there is precipitation of carbides during the cooling process. No carbide precipitation was found in this steel for the conventional temperature (Fig.4) and, in fact, no M_{SII}-type splitting was detected by quenching at any cooling rate from this temperature, Fig. 3(b). Moreover, for the optimum temperatures, at cooling rates slower than 20 K/s a significant carbide precipitation was found (Fig. 4). In these conditions, M_{SII}-type splitting phenomena are observed in the CCMT diagram of Fig. 3(a).

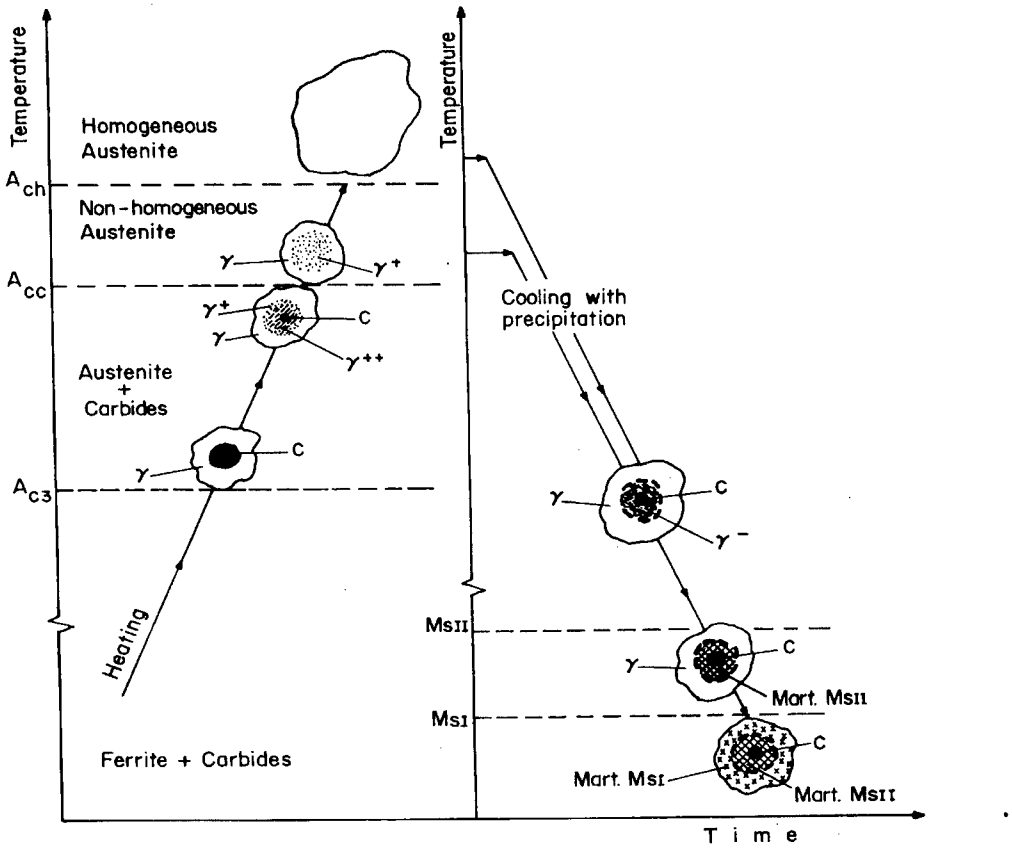


Figure 5. Schematic representation of the martensitic splitting during cooling with carbide precipitation.

From the analysis of these results an accurate explanation of the splitting phenomena observed in the martensitic transformation of the 0.45C-13Cr martensitic stainless steel is proposed in this work. Schematic representations in Figs. 5 and 6 illustrate how the different types of martensitic splitting in this steel are caused during the cooling process with and without carbide precipitation, respectively. As it can be seen in these figures, when this steel is heated, the dissolving carbides (C) diffuse atoms of carbon and carbide-forming elements toward the nearby areas of austenite, thus producing concentration gradients in this phase. Carbides will diminish in volume and will be surrounded by austenite areas (γ^{++} and γ^{+}) that are more concentrated than the bulk austenite (γ). At temperatures above A_{CC}, all the carbides will be already dissolved in the austenite, but a concentration gradient will be maintained in this phase. However, as the heating temperature increases, the austenite heterogeneity steadily decreases until it disappears at the A_{Ch} temperature. In this steel a significant precipitation of carbides is only detected during the cooling from heating temperatures higher than A_{CC} (Fig. 4). So, when carbide precipitation takes place during cooling (Fig. 5), the small areas of austenite around these precipitates (γ^{-}) will be impoverished in carbon and carbide-forming elements in relation to the bulk austenite (γ). Areas of impoverished austenite (γ^{-}) will transform in a first splitting stage, type M_{SII}. Afterwards, as the temperature decreases, the areas of austenite furthest from the carbides (the bulk austenite (γ)) will be transformed in the main M_{SI} stage.

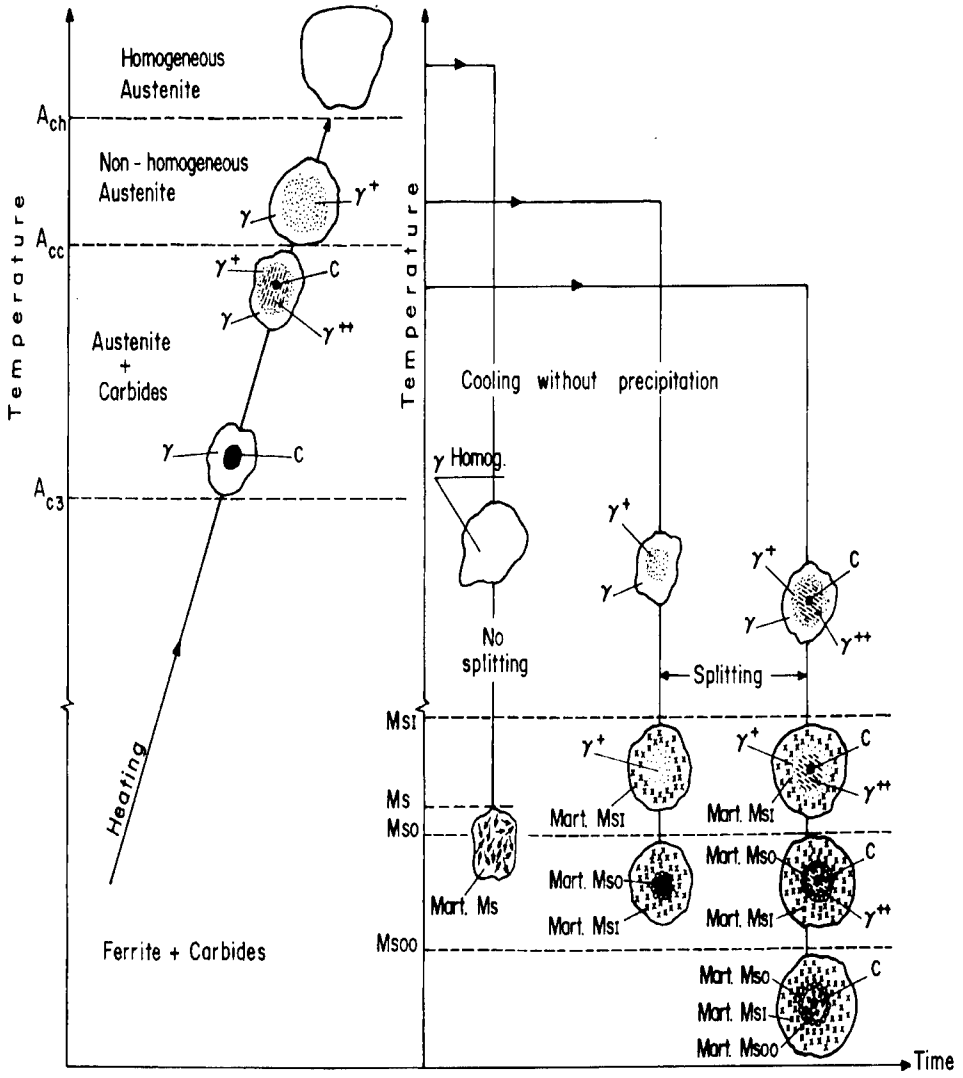


Figure 6. Schematic representation of the martensitic splittings during cooling without carbide precipitation.

On the other hand, when there is no carbide precipitation (Fig. 6), the concentation gradients proceed from the austenitization states formed by non-homogeneous austenite and austenite+carbides are maintained during the cooling process. Small areas of enriched austenite (γ^{++} and γ^{+}) surrounded by a much larger volume of less concentrated bulk austenite (γ) coexist before the martensitic transformation starts. As shown in Fig. 6, throughout cooling, the bulk austenite (γ) will be transformed in the main M_{SI} stage and the areas of enriched austenite (γ^{+}) and (γ^{++}) in the M_{SO} and M_{SOO} splitting stages, respectively, at successive lower temperatures. Finally, from the austenitization state formed by homogeneous austenite (γ Homog.), in which the concentration gradients in the austenite have been eliminated, no

splitting phenomena occur (Fig. 6). The homogeneous austenite (γ Homog.) is transformed into martensite in a single stage that starts at the M_S temperature.

Conclusions

1) Under certain conditions, two different types of splitting in the martensitic transformation of the 0.45C-13Cr martensitic stainless steel have been experimentally observed. The M_{SII}-type splitting corresponds to the martensitic transformation of areas of austenite impoverished in carbon and carbide-forming elements in relation to the bulk austenite. On the contrary, M_{SO} and M_{SOO}-types splittings correspond to the martensitic transformation of areas of austenite which are more concentrated than the bulk austenite.
2) Experimental results have demonstrated that the splitting phenomena are generically linked to the chemical heterogeneity of the austenite which is produced by the effect of the carbide dissolution and precipitation processes occuring during the heat treatment. However, the specific austenitizing and cooling conditions under which the M_{SII}-type splitting occurs, are in evident contrast with those of the M_{SO} and M_{SOO}-types splittings, proving that the two types of martensitic splittings have different causes.
3) The M_{SII}-type splitting only occurs during quenching from heating temperatures higher than A_{CC}, when there is precipitation of carbides during cooling.
4) In the absence of carbide precipitation during cooling, M_{SO} and M_{SOO}-types splittings only occur during quenching from heating temperatures lower than A_{Ch}, where a significant concentration gradient in the austenite phase is found. Splitting phenomena types M_{SO} and M_{SII} do not occur simultaneously at the same cooling rate.
5) From the analysis of the results obtained in this study, an accurate explanation of the two different types of splitting phenomena observed in the martensitic transformation of the 0.45C-13Cr steel is proposed. In fact, both are produced as a consequence of the existence of concentration gradients in the austenite previous to its transformation into martensite, but the origin of these gradients is different. The M_{SII}-type splitting is caused by the precipitation of carbides during cooling, while the M_{SO} and M_{SOO}-types splittings are the results of the concentration gradients produced in the austenite by the total or partial dissolution of carbides in this phase during the heating.

References

1. F.B. Pickering, Physical metallurgy of stainless steel developments (Int. Met. Rev 211., 1976), 228-41; 229.

2. G.A. Roberts and R.A. Cary, Tool Steels (A.S.M., Metals Park, OH, USA, 1980), 127-136; 213-218.

3. J.C. Ion et al., J. Mater. Sci., (26) (1991), 43-48.

4. F. Meng et al ISIJ Int. (34) (1994), 205-210.

5. Z. Nishiyama, Martensitic Transformation ed., M. Fine, M. Meshii and C. Wayman (Materials Science Series. Academic Press, Inc. NY, USA, 1978), 263-328; 220-232.

6. W. Steven and A.G. Haynes, J.Iron Steel Inst. (183) (1956), 349-359.

7. K.J. Irvine, D.J. Crowe and F. B. Pickering, J. Iron Steel Ins., (195) (1960), 386-405.

8. K.H. Prabhudev, Handbook of heat treatment of steels (Tata McGraw-Hill, New Delhi, 1988), 24-27.

9. H.D. Kim and I.S. Kim, ISIJ Int.,(34) (1994),198-204.

10. J.M. Vitek and R.L. Klueh, Metall. Trans.,14(A) (1983),1047.

11. T. Malkiewickz, Z. Bojarski, J.Iron Steel Inst.,(193) (1959),25.

12. T. Wada, Metall. Trans., (3) (1972), 2865.

13. C. Kim, W.F. Hosford, Metall. Trans., 13(A) (1982),185.

14. R.C. Thomson, H.K.D.H. Bhadeshia, Metall. Trans., 23(A) (1992), 1171-9.

15. J. Maratray and A.Poulation, Contribution à l'étude du contrôle des structures et de leur dureté dans les alliages ferreux à hautes teneurs en carbone et en chrome, (Climax Molybdenum, Paris, 1977),1-6.

16.M.T. Freire Vieira, in Tratermat'86. Tomo II, Proc. II Congreso Nacional de Tratamientos Térmicos, (Inasmet, San Sebastian, Spain, 1986),485-505.

17. L.F. Alvarez, Ph.D. Thesis (Universidad Complutense de Madrid, Spain,1992), 118-23.

18. C. García de Andrés and L.F. Alvarez, in Solid-Solid Phase Transformations, Proc. Int. Conf. on Solid-to-Solid Phase Transformation in Inorganic Materials PTM'94, ed., W. C. Johnson et al.,(TMS, Warrendale, PA, 1994), 797-802.

19. L.F. Alvarez and C.García, Mem. Etud. Sci. Rev. Met., (92) (1995), 1411-16.

20. C.García de Andrés, J.A. Jiménez and L.F. Alvarez, Metall. Mater. Trans., 27(A) (1996), 1799-1805.

21. C. García de Andrés and L.F. Alvarez, J. Mater. Sci., (28) (1993),1264-8.

22. C. García de Andrés, G. Caruana and L. F. Alvarez, Mater. Sci. Eng., 241(A) (1998).

23. C. García, L.F. Alvarez and M. Carsí, Rev. Metal. Madrid., (27) (1991), 231-246.

24. L. F. Alvarez and C. García de Andrés, Mem. Etud. Sci. Rev. Met., (90) (1993), 245-53.

25. C. García and L.F. Alvarez: in Heat & Surface '92 Proc. of the 8th International Congress on Heat Treatment of Materials, ed., Imao Amura (Kyoto, Japan 1992), 93-6.

26. W. Steven and C. Mayer, J. Iron Steel Inst., (174) (1953), 33-45.

27. M. Economopoulos, N. Lambert and L. Habraken, Diagrammes de transformation des aciers fabriqués dans le Benelux, (CNRM, Bruxelles, 1967), 39-40.

MORPHOLOGY OF MARTENSITE IN Fe-Ni-Si ALLOYS

O. Ikeda, Y. Himuro, I. Ohnuma, R. Kainuma and K. Ishida

Department of Materials Science, Graduate School of Engineering,
Tohoku University, Aramaki, Aoba, Sendai 980-8579, Japan

Abstract

The martensitic transformations of Fe-(22-28)%Ni-(0-8)%Si (mass%) alloys were investigated by means of optical microscopy, transmission electron microscopy, and differential scanning calorimetry. With increasing Ni and Si contents, the Ms temperature decreases, and the morphology of martensite changed from lath to lenticular. Thin plate martensite was observed in the high Si and Ni alloys with low Ms temperature below -180 °C. The decrease of Ms temperature due to the addition of Si to high Ni alloys was remarkably larger than that in low Ni alloys. The change in Ms temperature of lath and plate-like martensites due to aging was remarkable compared with that of lath martensite. It is shown that short range ordering of austenite is associated with the thin plate martensite.

The Third Pacific Rim International Conference on
Advanced Materials and Processing (PRICM 3)
Edited by M.A. Imam, R. DeNale, S. Hanada,
Z. Zhong and D.N. Lee
The Minerals, Metals & Materials Society, 1998

Introduction

It is well known that there are two major morphologies of ferrous martensite, lath and lenticular [1]. In Fe-Ni base alloys, butterfly and thin plate morphologies have often been observed [2]. These morphologies have been discussed in terms of Ms temperature, stacking fault energy, crystal structure, driving force, strength of austenite and martensite etc. as reviewed by Maki and Tamura [3, 4]. Thin plate martensite, which is generally characterized by very low Ms temperature, has been observed in several iron alloys such as Fe-Ni-C [2, 5], Fe-Ni-Co-Ti [6], Fe-Al-C [7], Fe-Pt [8], etc. The internal structure of thin plate martensite has a high density of twin defects and a very low density of dislocations. Furthermore, the interface between the parent phase and martensite is quite mobile and this characteristic feature of the interface mobility of thin plate martensite responses the thermoelastic transformation and the shape memory effect.

In the present study, the morphology of Fe-Ni-Si alloys was investigated focussing on the formation of thin plate martensite. This alloy system was chosen because Si decreases the stacking fault energy of austenite [9], which is expected to promote the transformation twin.

Experimental Procedure

Fe-(22-28)%Ni-(0-8)%Si (mass%) alloys were prepared from pure Fe(99.9%), Ni(99.9%), and Si(99.999%) by induction melting in an Al_2O_3 crucible under an Ar atmosphere. Alloy specimens were sealed in a quartz capsules. These alloys were austenitized at 1100 °C for 1 day followed by quenching in ice water; some of them were aged at 300 °C for 0-12 hours. Subzero-treatment in liquid N_2 (at -196 °C) was performed to obtain the martensite phase for some specimens with Ms temperature below 0°C. The morphology of martensite was examined by optical microscopy. The Ms temperature was determined by differential scanning calorimetry (DSC) with a cooling rate of 10 °C/min. The crystal structure of these alloys was investigated by transmission electron microscopy (TEM). Disk specimens 3 mm in diameter and with a thickness of 0.2 mm were punched out of the heat-treated specimen sheets. Thin foil was prepared by the twin jet method or the ion-milling technique from the disk specimens. The electrolyte used consisted of one part perchloric acid and four parts methanol. TEM observations were carried out using a JEM2000EX.

Results and Discussion

Morphology of Martensite and Ms Temperature

Three different morphologies of martensite, lath, lenticular, and thin plate were observed. Typical micrographs of morphology are shown in Fig. 1. Figure 2 shows the present results on the morphology of martensite and Ms temperatures in the Fe-Ni-Si alloys where the ferrite (α) / austenite (γ) equilibrium at 1100 °C is also shown as a dotted line [10]. Figure 3 shows the effect of Si on the Ms temperature of Fe-28 mass%Ni base alloys. It can be seen from Figs. 2 and 3 that Si decreases the Ms temperature and the decrease in Ms temperature due to Si in the high Ni alloys is larger than that in the low Ni alloys. The morphology of martensite changes from lath to lenticular and thin plate with increasing Si content. Thin plate martensite is formed in the specimens in which the Ms temperature is below about -180°C and the thickness of plates is 0.5-4 μm. Figure 4(a) shows the TEM micrograph of plate-like martensite which exhibits

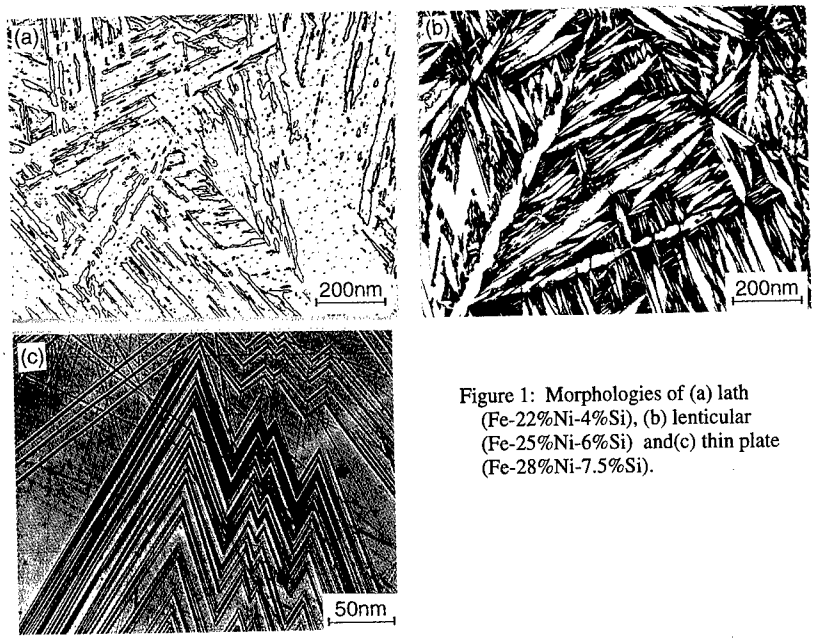


Figure 1: Morphologies of (a) lath (Fe-22%Ni-4%Si), (b) lenticular (Fe-25%Ni-6%Si) and(c) thin plate (Fe-28%Ni-7.5%Si).

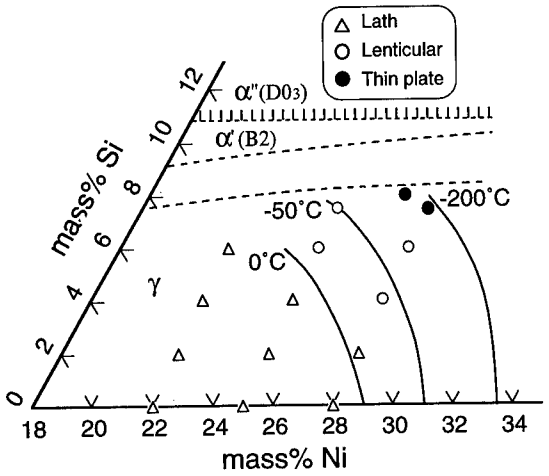


Figure 2: Morphology of martensite and the iso-Ms temperatures in the Fe-Ni-Si alloys.

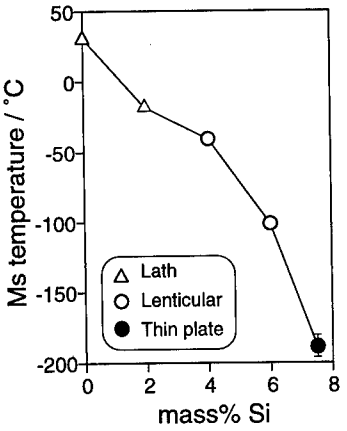


Figure 3: Variation of martensite and Ms temperature with increasing Si content at constant 28 mass%Ni.

high density of twins, but very low density of dislocations. These microstructural characteristics are quite similar to those of thin plate martensites in Fe-Ni-Co-Ti [6] and Fe-Ni-C alloys [5], while the crystal structure of the martensite is bcc, not bct, as shown in the selected area diffraction pattern (SADP) of Fig. 4(b). Figures 5(a) and (b) show the SADP of the parent phase taken from the specimens with lenticular and thin plate martensites quenched from 1100°C, respectively. It is seen that while the parent phase of the lath martensite has an A1 disordered structure, there are some weak and diffused extra spots between fundamental spots in the austenite of the specimens with thin plate martensites, as shown in Fig. 5(b). This means that the austenite which transforms the thin plate martensite is not in a completely disordered state but

in a short-range ordered state. Since the ordered B2 (α') and $D0_3$ (α'') bcc phases are formed in a wide range of composition in the Fe-Ni-Si system as shown in Fig. 2 [10], the austenite would have a tendency to become ordered with increasing Si content. This short-range ordering stabilizes the austenite which yields low Ms temperature and hence the formation of thin plate martensite.

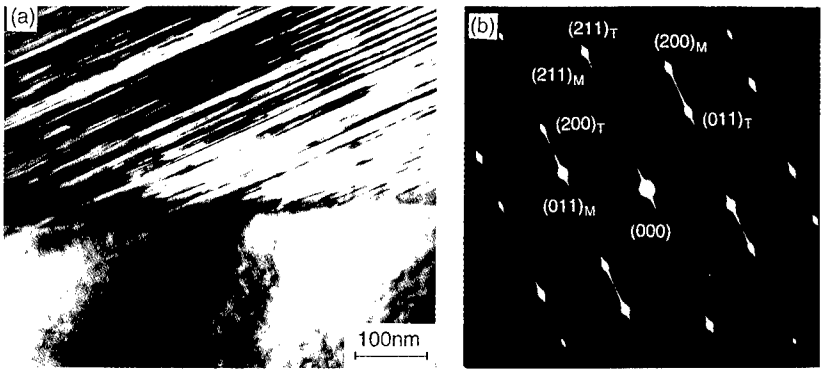


Figure 4: (a) TEM micrograph and (b) SADP showing high density of twins in a martensite plate of the Fe-28%Ni-7.5%Si specimen quenched from 1100 °C. Incident beam direction is $[01\bar{1}]_M$.

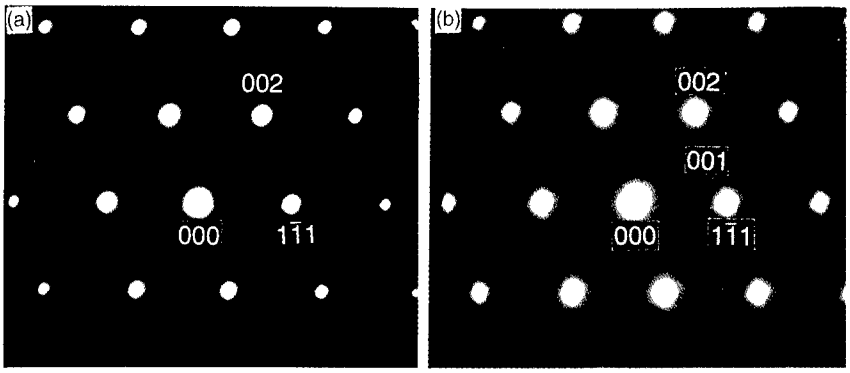


Figure 5: Diffraction patterns from the parent phase (a) of the Fe-28%Ni-6%Si alloy with lenticular martensite and (b) of the Fe-27%Ni-8%Si alloy with thin plate martensite. Incident beam direction is $[110]_p$.

Effects of Aging on Martensitic Transformation

In view of the foregoing discussion, the ordering of austenite is one of the factors which controls the morphology and Ms temperatrure in Fe-Ni-Si alloys. Since a stable ordered fcc $L1_2$ phase of Ni_3Si is formed below 1035 °C in the Ni-Si binary system [11], microstructural change due to aging is expected in the Fe-Ni-Si alloys. Figure 6 show the effect of aging at 300 °C on Ms temperature of lath and lenticular martensite in the Fe-28%Ni-2%Si and Fe-28%Ni-6%Si alloys, respectively. While the change in the Ms temperature due to aging is small for the lath martensite, the depression of the Ms temperature for lenticular martensite is larger.

However, no change in the martensite morphology and no extra spot due to ordering of the austenite were observed in the Fe-28%Ni-6%Si alloy aged at 300 °C for 2 hours. The origin of this change in Ms temperature is not clear at present and further studies will be required to clarify the aging effect on Ms temperature. On the other hand, the decrease in Ms temperature of thin plate martensite was also confirmed, although Ms was too low to be measured. Figure 7(a) and (b) show the electron diffraction pattern and the dark-field image from the $(001)_{L1_2}$ ordered reflection of parent phase taken from the specimen of Fe-27%Ni-8%Si alloy aged at 300°C for 2 hours. Nanoscale particles with the L12 structure, which may be the Ni_3Si phase, precipitate in the austenite matrix. These fine particles would respond to the depression of Ms temperature of thin plate martensite due to the local lattice distortion and precipitation hardening as reported in Fe-Ni-Al and Fe-Ni-Ti alloys [12, 13].

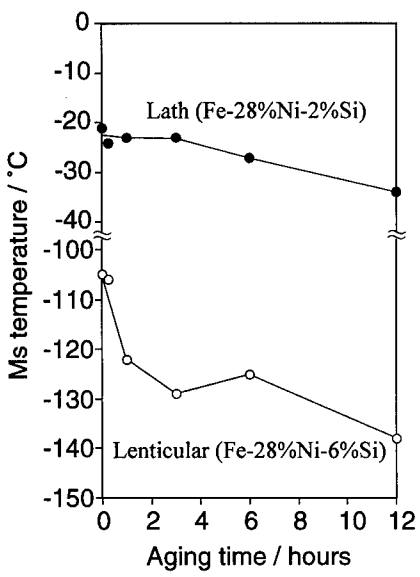


Figure 6: Effect of aging at 300 °C on Ms temperature of lath martensite in Fe-28%Ni-2%Si alloy and lenticular martensite in Fe-28%Ni-6%Si alloy.

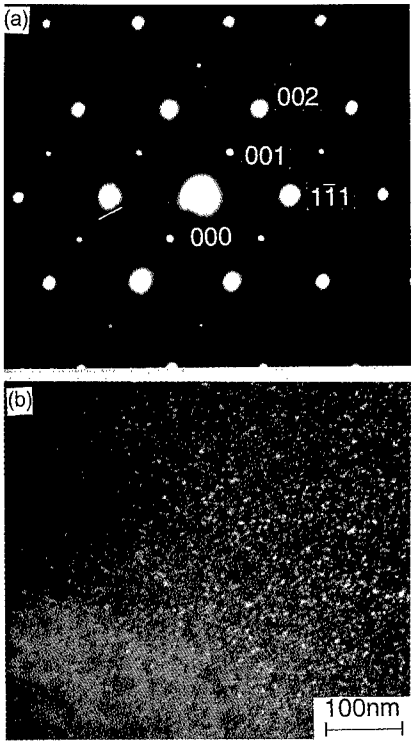


Figure 7: (a) Diffraction pattern from the parent phase of the Fe-27%Ni-8%Si alloy aged at 300 °C for 2h. (b) Dark-field image taken from the (001) superlattice reflection of (a).

Conclusions

(1) The Ms temperature decreases with increasing Si content and the morphology of martensite changes from lath to lenticular and from lenticular to plate-like with increasing Ni and Si contents. Plate-like martensite is observed in the composition range with high Ni and Si contents.

(2) Short-range ordering of austenite is associated with the appearance of thin plate martensite.

(3) The Ms temperature of lath martensite is little changed by aging at 300°C, while that of lenticular and thin plate martensite is remarkably decreased by aging.
(4) Aging of the Fe-27%Ni-8%Si alloy at 300 °C induces very fine particles with the $L1_2$ structure.

Acknowledgement *- The authors wish to thank Mr. N. Satoh and Mr. T. Kinoshita for their help with the experimental work. This work was supported by Grants-in-aids for Scientific Research from the Ministry of Education, Science, Sports and Culture, Japan. One of the authors (R.K.) acknowledges the support from the TEPCO Research Foundation.*

References

1. G. Krauss, Steels, Heat Treatment and Processing Principles (Materials Park OH : ASM International,1990), 61-77.
2. T. Maki et al., " Formation Temperature and Growth Behavior of Thin Plate Martensite in Fe-Ni-C Alloys," Trans. JIM, 16 (1975), 35-41.
3. T. Maki, and I. Tamura, " Morphology and Internal Structure of Ferrous Martensite," Bull, Jpn. Inst. Met.,13 (1974), 329-339.
4. T. Maki and I. Tamura, " On the Thin Plate Martensite in Ferrous Alloys and Its Various Properties," Bull. Jpn. Inst. Met., 23 (1984), 229-237.
5. S. Kajiwara, " Shape Memory Effect and Related Transformation Behavior in Fe-Ni-C Alloys," Acta metall. mater., 38 (1990), 847-855.
6. T. Maki et al., " Shape Memory Effect Related to Thin Plate Martensite with Large Thermal Hysteresis in Ausaged Fe-Ni-Co-Ti Alloy," ISIJ Int., 29 (1989), 438-445.
7. M. Watanabe, and C. M. Wayman, " The Morphology and Substructure of Highly Tetragonal Martensites in Fe-7 Pct Al-C Steels," Metall. Trans., 2 (1971), 2221-2227.
8. D. P. Dunne, and C. M. Wayman, " The Effect of Austenite Ordering on the Martensite Transformation in Fe-Pt Alloys Near the Composition Fe_3Pt : I. Morphology and Transformation Characteristics, II. Crystallography and General Features," Metall. Trans.,4 (1973), 137-145, 147-152.
9. R. E. Schramm et al., " Stacking Fault Energies of Seven Commercial Austenitic StainlessSteels," Metall. Trans., 6 (1975), 1345-1351.
10. O. Ikeda et al., " Phase Equillibria in the Fe-rich Portion of the Fe-Ni-Si System," J. Alloys & Comp., (1998) in press.
11. T. B. Massalski et al., ed., Binary Alloy Phase Diagrams, 2nd Edition (Materials Park OH : ASM International, 1990), 2859-2861.
12. T. Tadaki et al., " Electron Microscope Study on Fine Structures of the Austenite in an Ausaged Fe-Ni-Al Alloy," Trans. Jpn. Inst. Met., 4 (1988), 258-266.
13. J. K. Abraham and J. S. Pascover," The Transformation and Structure of Fe-Ni-Ti Alloys," Trans. Metall. Soc. AIME, 245 (1969), 759-768.

THE GROWTH-PATH METHOD FOR PREDICTION OF SPURIOUS GRAIN NUCLEATION IN SINGLE-CRYSTAL CASTINGS

R. E. Napolitano, A. R. Roosen, and R. J. Schaefer
National Institute of Standards and Technology
Gaithersburg, Maryland, USA

Abstract

Prediction of spurious grain formation in superalloy castings is critical for the design and development of single-crystal gas-turbine components. Here, we describe the growth-path method for assessing the tendency for spurious grain formation in such castings. In this method, temperature data from previously performed thermal simulation is utilized for tracking the growth of the dendritic front along a specified path through the casting, taking into consideration the dendrite tip kinetics and the crystallographic orientation. This procedure provides the temperature and liquid-fraction vs. time profile for any point on the specified path. The nucleation probability, corrected for the liquid-fraction, is then integrated along the cooling path to provide a quantitative nucleation potential. The method is demonstrated for a simple mold corner using three different sets of paths, illustrating that the method requires specification of the minimum-time path to any given point. Plots of front shape, undercooling, and nucleation potential are generated. The effect of secondary orientation is also demonstrated.

The Third Pacific Rim International Conference on
Advanced Materials and Processing (PRICM 3)
Edited by M.A. Imam, R. DeNale, S. Hanada,
Z. Zhong and D.N. Lee
The Minerals, Metals & Materials Society, 1998

Introduction

The cost-effective design and development of larger and more complex single-crystal components for gas-turbine applications requires fast and reliable techniques for the prediction of defects which may form during solidification processing. The spurious grain is one such defect which often forms by nucleation in the liquid ahead of the growth front. Since geometric complexities in the mold create the danger of high local undercoolings, spurious grains are observed more frequently in castings which include severe cross-section changes and other mold discontinuities, as shown in Figure 1. Solidification is generally modeled in these castings using enthalpy-based single-domain methods which utilize relationships between enthalpy and fraction solid (f_s) but do not explicitly track the solidification front. Such methods include the assumption that, in all parts of the casting, solid will form in accord with the prescribed f_s vs. temperature relationship, and undercooling is not permitted to develop. In a real casting, the geometry of the mold may constrain the growth of the dendritic front, resulting in high undercoolings and promoting the nucleation of stray grains. Coupling the single-domain enthalpy method with a cellular automaton (CA) growth model has been shown to be very effective for predicting as-cast grain structures.[1-6] From a designer's perspective, however, this method may not be very well suited for prediction of spurious grains, for several reasons. The method used for grain nucleation in the CA utilizes predefined nucleation sites, distributed randomly in space. Each site is assigned a critical temperature for nucleation, and the population density for nucleation temperatures is described by one or more gaussian distributions. When the instantaneous simulation temperature at a site drops below its "nucleation" value, the site becomes active and starts to grow. This technique does not strictly treat the effect of the time-temperature history in the liquid. Additionally, the model produces a single outcome with no way to assess its likelihood with confidence. For such an assessment, a large number of simulations would be required. Another drawback to the method, as it relates to spurious grain prediction, is that it is intended to perform computations over the entire volume of the casting. In many cases, however, the general locations where spurious grain formation is likely can be identified upon inspection of the casting geometry. To provide designers with a fast and reliable tool to assess the likelihood of spurious grain formation in such locations, the growth-path method was developed. This method incorporates the complete time-temperature history of the melt into a model which utilizes nucleation kinetics to provide a nucleation potential for points along one or more paths through the casting. The growth-path method, therefore, allows the designer to quickly assess spurious grain tendency for one or more particular regions in the casting, as dictated by the geometry.

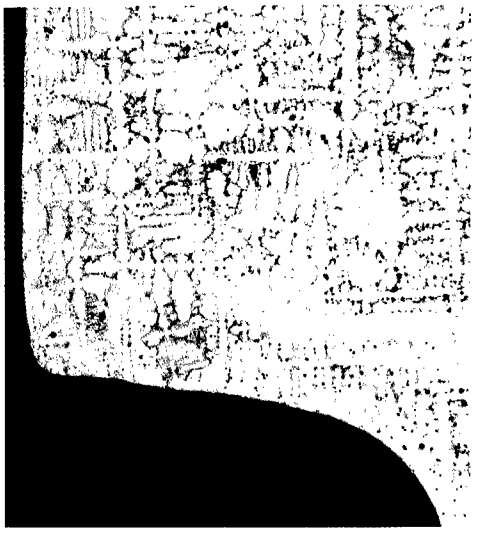


Figure 1. Spurious grains at a mold corner in a Rene N5 single-crystal casting.

Description of the Method

Given a point in space within the casting, the method can be used to calculate the likelihood that a spurious grain nucleates within a unit volume surrounding this point, before the completion of the casting process. The problem is solved by integrating the probability for nucleation along the time-temperature history at the point during the process. Naturally, this probability is a function of the local temperature and the amount of liquid available for nucleation. It is assumed that a thermal history, T(x,y,z,t), is available from another source such that the undercooling can be interpolated for any point in space and time. The parameter, g_L is defined as the extradendritic liquid fraction, which includes the liquid outside the envelope containing the primary dendrites and their associated branches. The method can be described in three parts. The first is the determination of a growth path. The second is the tracking of the growth of the solid along the growth path. The third is the calculation of the nucleation tendency for any given point on the path. These issues are addressed in the following sections.

Determination of the Growth path

The growth path is the route by which the dendritic structure, growing and branching along the crystallographic axes, propagates to the terminal point. Thus, any point in the casting can be considered to be a terminal point with an associated growth path. In the model, the path is constrained to originate within a region, near the grain selector or seed crystal, which exhibits roughly planar isotherms during solidification, and branches are assumed to form continuously and without incubation time. The true path is defined by the path of minimum time for the growth of the solid from the origin plane to the terminal point. This can be illustrated by considering two different paths which terminate at the same point. For a given set of thermal conditions and crystal orientation, each path has an associated time of growth to the terminus. If growth were restricted to these two paths only, then one path would reach the terminus before the other, so that growth along the second path would never reach the point in question. By extending this argument to all conceivable paths, we conclude that the minimum-time path must be the one actually followed. Determination of this path is not trivial, however, since the growth velocity along any path segment depends on the local temperature and the path direction, relative to the crystal axes. A technique for the computation of this minimum path has been developed and will be described in a subsequent paper. The importance of using the minimum-time path is illustrated in a later section.

Tracking the Solidification Front

A variant of the method of characteristics is employed to compute a velocity along a specified path which is self-consistent with respect to path orientation, crystal orientation, and tip temperature. Dendrites are assumed to grow and branch along the <001> crystal axes, so that the characteristic kinetic shape is a regular octahedron with its diagonals defined by these directions. The length of a diagonal is proportional to the local dendrite tip velocity, which is a function of undercooling. For simplicity, we describe V_t as:

$$V_t = A(\Delta T)^m \qquad (1)$$

where A and m are constants and ΔT is the local undercooling. The instantaneous path velocity, V_p, is given by the projection of the nearest octahedral axis onto the path direction. The time for the front, defined as the surface containing all dendrite tips, to propagate a distance L along the path from a specified origin to any given point, R, can be computed as

$$\tau = \int_0^L \frac{ds}{V_p(t, s, \mathbf{S}, \Theta)} \qquad (2)$$

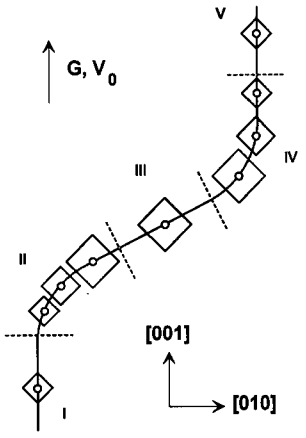


Figure 2. A schematic illustration of the relationship between path velocity, path orientation, and undercooling.

where t is time, s is the arc length traveled at time t, **S** is the path tangent unit vector, and Θ describes the crystal orientation. To avoid any initial transient effects of the model, the path origin must be specified such that a steady state is achieved within a short distance, in a well understood portion of the casting.

To illustrate the relationships between the relevant parameters, consider the growth path shown on the 2-D section in Figure 2. The path is divided into five regions. In region I, the path is aligned with the temperature gradient and the [001] axis. In the steady state, the velocity along the path V_p is equal to the isotherm velocity V_0. In region II, the path deviates from the gradient direction and the crystallographic direction, as would be necessary when dendrites grow laterally into an expanding section of the mold. Geometrically, the deviation reduces the magnitude of the projection of V_t onto the path. For the front to maintain its velocity in the z direction, V_t and ΔT must increase, as indicated by the increase in the size of the characteristic growth square. The path velocity will continue to increase until a steady state is reached, in region III. In region IV, the path turns back toward the gradient direction and another transient is observed as indicated. Finally, in region V, a steady state is reestablished.

There is one additional consideration to be addressed. Assuming a parabolic shape for the primary dendrite envelopes, g_L is unity until the front passes. After the front passes, g_L varies from unity to zero as:

$$g_L = 1 - \left(\frac{T^* - T}{T^* - T_f}\right)^{0.5} \qquad (3)$$

and $g_L=0$ for $T<T_f$, where T^* is the tip temperature, and T_f is the temperature at which g_L becomes zero. This temperature is not well defined. For the calculations presented here, T_f is taken as the solidus temperature, which is the most conservative selection.

Calculation of Nucleation Tendency

For any given point R on the path, the front-tracking procedure described above provides the value of g_L throughout the process. To determine the nucleation potential at a given point, P(R), the product of nucleation probability, p, and extradendritic liquid fraction is integrated over time, where p is the probability for nucleation during one interval of dt, within unit volume. We assume here that the cooling rate is low enough that transient nucleation effects may be neglected, and p is a function of temperature alone. Since local temperature is a function of time, P(R) is given by:

$$P(R) = \int_0^{\infty} p[T(t)]\, g_L(t)\, dt \qquad (4)$$

The expression for the probability $p(T)$ is a property of the alloy and can be assigned using analytical nucleation rate expressions or by the fitting of experimental data. We will now address the latter. For any given value of undercooling, p is a constant, and the distribution of time values at which the first nucleation event occurs is given by the Gamma function:

$$\Gamma_1(t) = \int_0^{t} pe^{-pt}dt \qquad (5)$$

Experimentally, one measures the time required for the onset of nucleation, which is described by this distribution. The probability p can, therefore, be obtained using the condition:

$$\frac{1}{2} = \int_0^{\mu} pe^{-pt}dt = 1-e^{-p\mu} \qquad (6)$$

where μ is the mean of the experimental nucleation times for the given temperature. If the experimental data can be simplified to yield an expression for $\mu(T)$, then the desired $p(T)$ is simply given by:

$$p(T) = \frac{\ln(2)}{\mu(T)} \qquad (7)$$

Since temperature is a known function of time, (4) is completely specified. For any path to point R, therefore, we can compute the nucleation potential P(R).

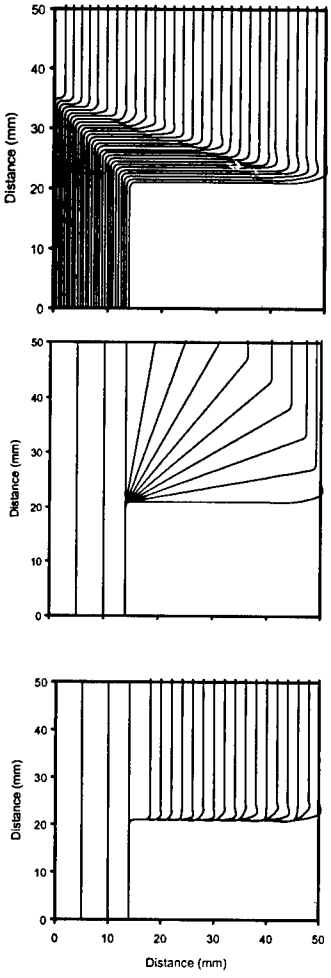


Figure 3. The three path sets used for the growth-path calculations. Sets #1, #2, and #3, shown from top to bottom.

Results

The method is demonstrated here by considering growth around a 90° mold corner and across a 35 mm lateral shelf. Directional solidification conditions were produced by implementing a constant and uniform temperature gradient of 1.5×10^3 K/m with a constant isotherm velocity of 8.0×10^{-5}m/s. The temperature gradient and the primary crystal directions were specified along the z axis of the casting. The kinetic constants (1) were defined as $A = 1.4\times10^{-5}$ $ms^{-1}K^{-2}$ and m=2. A limited set of experimental nucleation data[7] for Rene N5 was used to fit $\mu(T)$ to a power-law expression.

The growth-path calculations were performed using three sets of paths, shown in Figure 3. Each path is defined by 1000 linear segments of equal length. The results, shown in Figure 4, include plots of front shape, undercooling, and nucleation potential as a function of time. The plots of front shape most clearly illustrate the importance of using minimum-time paths. The front shape plots for path sets 1 and 2 exhibit

regions of the front which apparently lag behind the remainder of the front. This is an indication that the specified paths through these regions are not the minimum-time paths. The front shapes for path set 3, however, resemble those predicted numerically for this mold corner geometry.[8,9] The undercooling and nucleation predictions also reveal the importance of specifying the minimum-time path. The results for path set #1 indicate high undercooling values which extend out over the original cross-section. This is not a reasonable result since growth to these locations should be unaffected by the change in cross-section. Review of the paths in set #1, however, reveals that growth through this region was calculated using paths with two 90° direction changes. The abnormally high undercoolings can be attributed to these non-minimum paths. The results from path set #2 show that high undercoolings are no longer predicted in regions away from the shelf. The values predicted for regions above the shelf, however, differ significantly from those for path set #3, which includes approximate minimum-time paths.

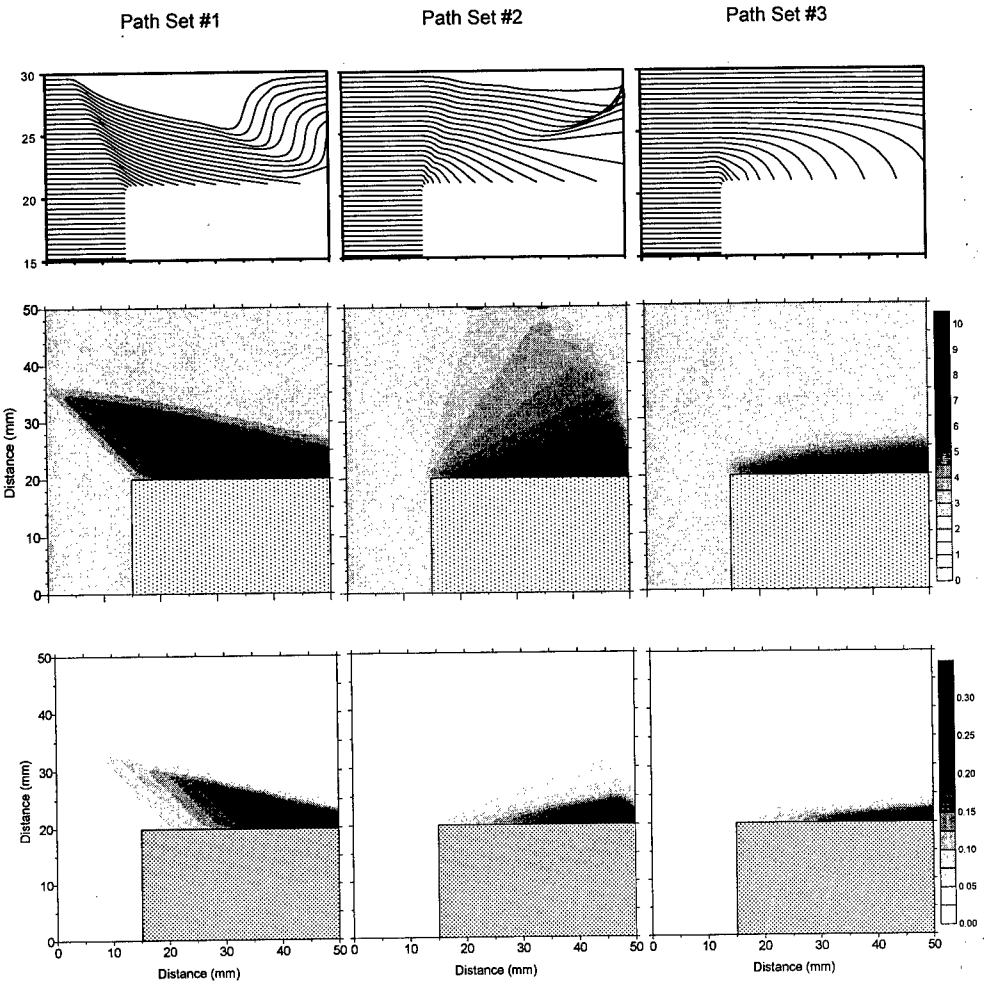


Figure 4. The results from the growth-path calculation for the path sets shown in Figure 3. Sets 1, 2, and 3 are shown from left to right. For each set: the upper plot is the front shape at various times; the middle plot shows the undercooling at the time that the dendrite tip front passes the point; and the lower plot is the total nucleation potential.

Although the paths and crystal axes used in this example were specified to lie in the plane of the illustration, the calculation treats the crystal as a 3-D structure. To illustrate the importance of this, the calculation using path set #3 was repeated with the secondary crystal axis oriented at angles of 15, 30, and 45 degrees from the plane of the paths. Figure 5 reveals the difference in the growth front shape for this range of secondary orientations at an intermediate time. As expected, the misoriented crystal propagates more slowly along the shelf. The nucleation potential along the shelf wall is plotted in Figure 6, for secondary angles of 0° and 45°, indicating that nucleation is promoted by misorientation of the secondary axis. This is expected since the slower growth permits higher undercoolings to develop.

The method produces a value for the nucleation potential for any given location in the casting. This provides a quantitative means for evaluating casting designs and for comparing the nucleation potential for different designs. The assignment of a particular threshold value for P, however, depends upon the conditions used for the collection of the nucleation data and can only be done through comparison with experimental observation of spurious grain nucleation in actual castings. The results from path set #3 show a that significant nucleation potential is developed within the first 5 mm of lateral growth. This is consistent with observations such as that shown in Figure 1, which indicate that nucleation may, indeed, occur after only a few millimeters of lateral growth.

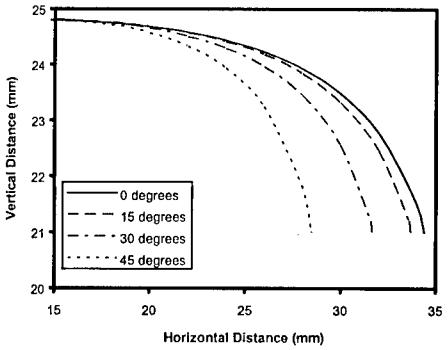


Figure 5. Front shape data showing the effect of secondary orientation for the calculation using path set #3. The point (15,20) is the mold corner. The angle is measured from the plane of the figure.

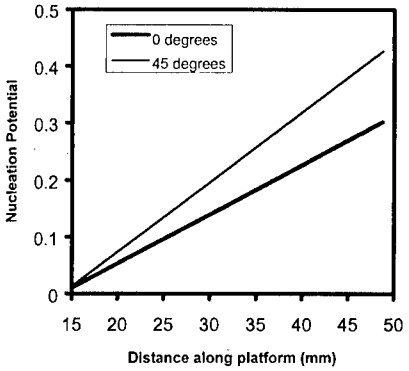


Figure 6. Nucleation potential along the platform surface for two secondary orientations.

Conclusions

The growth-path method may be used to provide fast and reliable assessment of liquid undercooling and nucleation potential in a single crystal casting. The accuracy of the predicted undercooling values relies on the specification of minimum-time paths to the regions of interest. For this reason, automatic minimized-path determination is essential for the industrial use of the growth-path method. The accuracy and interpretation of the predicted nucleation potentials depends on the methods used for collecting the nucleation data.

References

1. M. Rappaz and Ch.-A. Gandin; *Acta Metallurgica et Materialia*, **41** (1993) 345-360.
2. Ch.A. Gandin, M. Rappaz, and R. Tintillier; *Metall. Transactions*, **24A** (1993) 467-479.
3. Ch.A. Gandin, M. Rappaz, and R. Tintillier; *Metall. Transactions*, **25A** (1994) 629-635.
4. M. Rappaz, Ch.A. Gandin, and R. Sasikumar; *Acta Metall. et Mat.*, **42** (1994) 2365-2374.
5. Ch.-A. Gandin and M. Rappaz; *Acta Metall. et Mat.*, **42** (1994) 2233-2246.
6. Ch.-A. Gandin, Ch. Charbon, and M. Rappaz, *ISIJ International*, **35** (1995) 651-657.
7. J.H. Perepesko, Personal Communication, October 22, 1997.
8. Ch.-A. Gandin, R.J. Schaefer, and M. Rappaz, *Acta Metall. et Mat.*, **44** (1996) 3339-3347.
9. Th. Imwinkelried, J.L. Desbiolles, Ch.A. Gandin, M. Rappaz, S. Rossmann, and Ph. Thevoz; *Modeling of Casting, Welding and Advanced Solidification Processes* (edited by T. Piwonka et al.), TMS, Warrendale, PA (1993) 63-70.

THE RELATION BEWEEN PHASE TRANSFORMATION AND GRAIN SIZE IN Y_2O_3-PARTIALLY STABILIZED ZIRCONIA

H.Tsubakino[1], T.Isobe[2] and B.Zhang[2]

[1]Department of Materials Science and Engineering,
Faculty of Engineering, Himeji Institute of Technology,
2167 Shosha, Himeji 671-22, Japan
[2] Graduate School, Himeji Institute of Technology

Abstract

The transformation from metastable tetragonal (t) to stable monoclinic (m) phases in yttria-partially stabilized zirconia (Y-PSZ) of various grain sizes with and without alumina addition has been studied by dilatometry, XRD and SEM observations. The transformation occurs easily at grain sizes larger than 0.6 μ m. Ms point increases with larger grain sizes, however, As point is expressed by no or small increase. With addition of alumina, both Ms and As shift to higher temperature. The relation between transformation temperatures and grain size (d) is expressed by $Ms(As) = Mo(Ao) + Zd^{-1/2}$. However, the constants of Mo(Ao) and Z differ with addition of alumina. In PSZ with alumina addition, amorphous phase is formed at grain boundaries. The effect of alumina addition on the phase transformation is discussed from view points of the formation of grain boundary phase.

The Third Pacific Rim International Conference on
Advanced Materials and Processing (PRICM 3)
Edited by M.A. Imam, R. DeNale, S. Hanada,
Z. Zhong and D.N. Lee
The Minerals, Metals & Materials Society, 1998

Introduction

Partially stabilized zirconia (PSZ) has excellent mechanical properties, such as high bending strength and high fracture toughness. These improved mechanical properties are related to the stress-induced martensitic transformation from metastable tetragonal to stable monoclinic phases, a transformation-toughening mechanism [1,2]. This transformation is closely related to the grain size of PSZ [3-6], i.e., the transformation can occur easily in PSZ with larger grain size than the critical one. However, the nature of the grain size effect on the transformation is still unclear.

Previously, it has been reported that the addition of alumina to PSZ improves the mechanical properties and affects the transformation rate [7-9]. In this report, the effect of grain size on the transformation in PSZ with and without alumina addition has been studied by using dilatometry, XRD and microscopy.

Experimental Procedure

The starting powders were zirconia-5 mass% yttria (PSZ, 5Y) and PSZ-5 mass% alumina (5Y5A) produced by a co-precipitation method. The chemical composition of these powders is shown in Table 1. The powders were pressed unidirectionally at 100 MPa and sintered at 1923 K for different times (ts) ranging from 1.2 to 85 ks in air, then air cooled. The size of the sintered specimens was about 3 mm × 2 mm × 10 mm.

Dilatometry was performed during thermal cycling at temperatures ranging from room temperature to 1073 K to know Ms (the starting temperature of T→M transformation) and As (the starting temperature of M→T) points. The heating and cooling rate of the thermal cycling was 80 K/h. Grain size was measured by using SEM micrographs as the diameter of a circle, which area is equivalent to the area of grain. For this measurements, the specimens were polished and etched thermally for about 30 min at 1573 K.

Table 1 Chemical composition of powders (mass%).

	Y_2O_3	Al_2O_3	MgO	CaO	SiO_2	Fe_2O_3	Na_2O	ZrO_2
5Y	5.1	<0.005	---	---	0.005	<0.002	0.01	bal.
5Y5A	5.27	5.21	0.23	0.14	0.13	0.12	---	bal.

Results and Discussion

Grain size

Typical SEM micrographs of specimens 5Y and 5Y5A are shown in Fig.1. Grain size of zirconia matrix increases with increasing sintering time in both specimens. The black particles observed at triple junctions of grain boundaries in Fig.1(c) and (d) are alumina ones, which size also increases with sintering time. The observed mean grain sizes are plotted against sintering time, as shown in Fig.2. Grain size of 5Y5A is larger than that of 5Y. This result indicates that alumina addition accelerates grain growth, which will be due to liquid sintering mechanism suggested previously [10], i.e., the grain boundary amorphous phase is formed in 5Y5A.

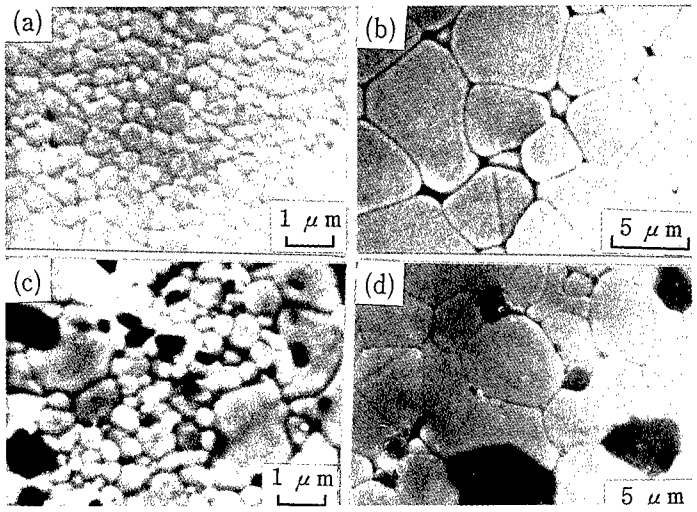


Fig.1
SEM micrographs.
(a) 5Y, ts=1.2 ks,
(b) 5Y, ts=54 ks,
(c) 5Y5A, ts=1.2 ks,
(d) 5Y5A, ts=54 ks
(Ts=1923 K)

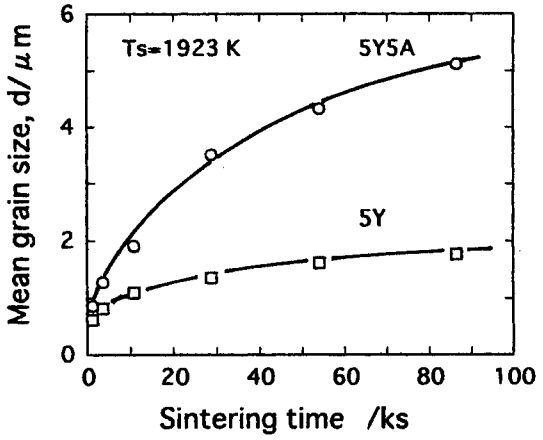


Fig.2 Relationship between grain size and sintering time (ts) in 5Y and 5Y5A.

Dilatation Curve

The dilatation and temperature curves of 5Y during thermal cycling are shown in Fig.3. The specimen sintered for 1.2 ks exhibits an almost linear relation and no discontinuity in the curves, so no transformation occurs in the specimen. However, the grain size increases over 0.6 μm, as shown in Fig.3, the curves show large contraction at 750-800 K during heating stage and large expansion at 740-500 K during cooling stage. The former is related to transformation from m to t, i.e., the reverse reaction of martensitic transformation, and the latter is related to the martensitic transformation from t to m. The expansion phenomena around 500 K during heating stage at the first thermal cycling will be related to the isothermal transformation [9]. The Ms and As temperatures are decided from the intersect ones of extrapolations at the onset of expansion and contradiction curves. Ms points tend to increase with increasing cycle number, but the As points are almost kept at constant temperature. The expansion and contraction curves in 5Y5A shown in Fig.4 accompanied with the martensitic and reverse transformations are more sharp than those in 5Y (Fig.3). Furthermore, the amount of dilatation changes during these transformations are much larger than those in 5A.

The relation between each transformation temperature (Ms and As) and cycle number is shown in Fig.5. The As and Ms temperatures of 5Y5A are higher than those of 5Y. The As temperatures of both specimens are independent of cycle number but the Ms of 5Y is strongly dependent on cycle number. Fig.6 shows the amount of expansion and contradiction due to these two transformations. The amounts of every dilatation changes increase steeply with cycle number. It is interesting that the balance amounts between the expansion and contraction shift to be larger with increasing cycle number than 4^{th} in 5Y5A, however, in the initial cycling in 5Y. These results coincide well with the cyclic number dependency of Ms temperature shown in Fig.5.

Because the martensitic transformation is a nucleating-controlled reaction and martensite laths form at grain boundaries [11,12], some crackings happen at grain boundaries when the martensitic transformation occurs. Therefore, the above results on cyclic number dependency of both Ms and dilatation change indicate that the formation of martensite is accompanied with many micro-cracks between both specimens but 5Y tends to crack easier than 5Y5A. This different points between both specimens are attributed to the formation of amorphous grain boundary phase in 5Y5A. Then, the strong cycle number dependency of the martensitic transformation is closely related to the tendency of occurrence of cracking.

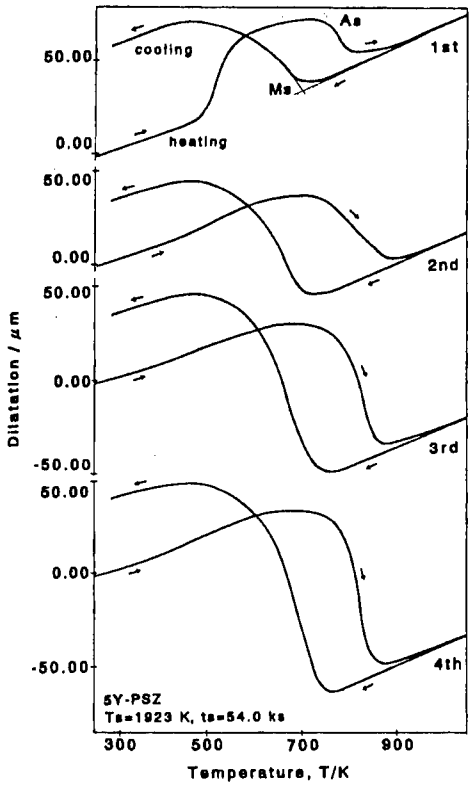


Fig.3 Dilatation curves during thermal cycling in 5Y.

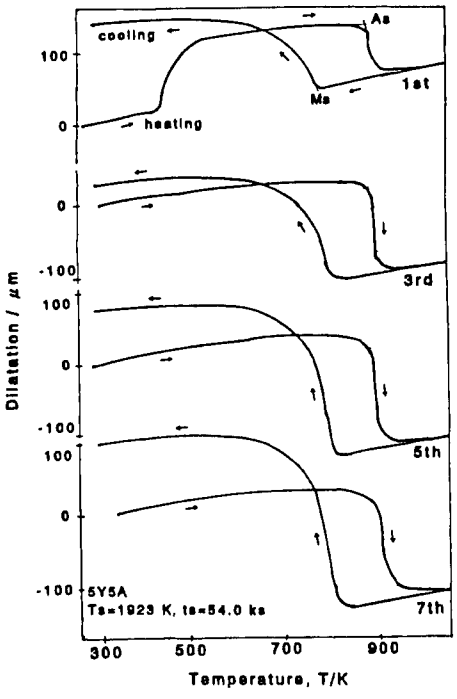


Fig.4 Dilatation curves during thermal cycling in 5Y5A.

Relation between Transformation Temperature and Grain Size

The As and Ms temperatures obtained from the first thermal cycle are plotted in Fig.7 against the reciprocal of the square root of grain size (d). The temperatures of both specimens show a linear relationship but the data points in each specimen obey independent lines in each other. Similar relation has been reported in ZrO_2-8mol%CeO_2 and ZrO_2-0.25 mol% Y_2O_3 [6]. Further important results can be obtained in this study that the slope of lines is different in the specimens with and without alumina addition, although they contain almost the same Y_2O_3 content. The slope contains several factors, such as transformation heat, transformation strain and thermodynamic equilibrium transformation temperature, To, [6].

EDS analysis in this study has confirmed that alumina has hardly detected in the zirconia matrix, which coincides with phase diagram [13] but is contrary to Lakiza and Lopato [14], and then yttria content in the matrix is not different so much from the original composition. Therefore, the transformation heat and To are not affected strongly by the addition of alumina. 5Y5A contains amorphous phase at grain boundaries [10], and much stronger cohesion between grains can be expected in 5Y5A than in 5Y. Then, the constrain effect will act strongly to the relations between the transformation and grain size.

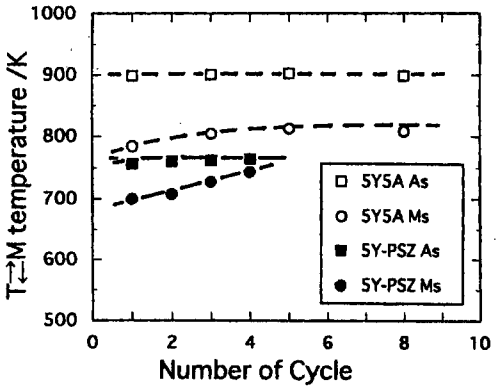


Fig.5 Relationship between transformation temperature and number of thermal cycle.

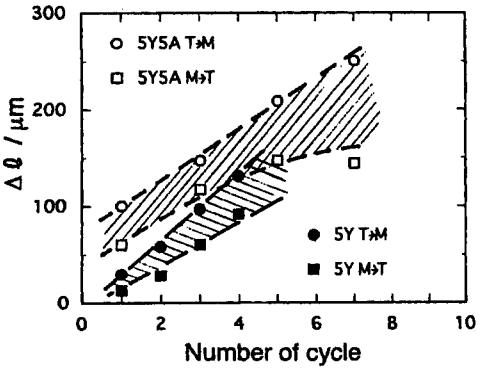


Fig.6 Relationship between the amount of dilatation change accompanied with transformation and number of cycle.

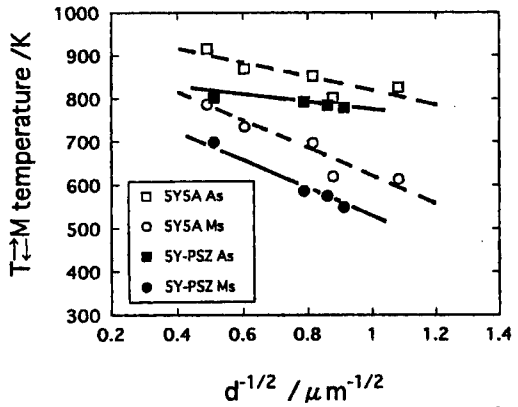


Fig.7 Relationship between transformation temperature and reciprocal of square root of grain size (d).

Conclusions

(1) The transformation from tetragonal to monoclinic phases occured in the specimen with larger grain size than 0.6 μ m.
(2) Transformation temperature, Ms, increased with number of thermal cycling, but As was kept at constant temperature.
(3) The Ms and As were expressed with grain size, d, by $Ms(As) = Mo(Ao)+Zd^{-1/2}$ but this relation was different in PSZ's with and without alumina addition.

References

1. R.C.Gavie, R.H.J.Hnnink, and R.T.Pascoc, "Ceramic Steel ?", Nature (London), 258, (1975) 703-704
2. D.J.Green, R.H.Hannink, and M.V.Swan, Transformation Toughening of Ceramics (Boca Raton Florida: CRC Press, Inc., 1989) , 57-93.
3. T.K.Gupta, F.F.Lange, and J.H.Bechtold, "Effect of Stress-Induced Phase Transformation on the Properties of Polycrystalline Zirconia Containing Metastable Tetragonal Phase", J.Mater.Sci., 13(7)(1978), 1467-1470.
4. T.Sato, S.Ohtaki, and M.Shimada, "Transformation of Yttria Partially Stabilized Zirconia by Low Temperature Annealing in Air", J.Mater.Sci., 20(4)(1985), 1466-1470.
5. M.Watanabe, S.Iio, and I.Fukuura, "Aging Behavior of Y-PSZ", Sci.Tech. of Zirconia II, (Cleveland, OH: Am.Ceram.Soc., 1984), 391-398.
6. J.Tu et al, "The Size Effect of the Martensitic Transformation in ZrO_2-Containing Ceramics", J.Mater.Sci., 29(6)(1994), 1662-1665.
7. H.Tsubakino, R.Nozato, and M.Hamamoto, "Effect of Alumina Addition on the Tetragonal-to-Monoclinic Phase transformation in Zirconia-3mol% Yttria", J.Am.Ceram.Soc., 74(2)(1991), 440-443.
8. H.Tsubakino et al, "Improvement of Mechanical Properties by the Formation of a Grain Boundary Phase in ZrO_2-3mol%Y_2O_3-Al_2O_3 Ceramics", Ceram.Trans., 44(1994), 265-274.
9. H.Tsubakino et al, "Isothermal Transformation Behavior of Martensite in Zirconia-3mol% Yttria Containing Alumina", Solid→Solid Phase Transformations, (Warrendale, PA: TMS, 1994), 749-754.
10. H.Tsubakino et al, "Composition of Grain Boundary Phase Formed in Zirconia-3mol% Yttria Containing Alumina", J.Mater.Sci.Lett., 16(17) (1997), 1472-1475.
11. R.R.Lee and A.Heuer, "In Situ Martensitic Transformations in a Ternary MgO-Y_2O_3-ZrO_2 Alloy: I, Transformation in Tetragonal ZrO_2 Grains", J.Am.Ceram.Soc., 71(8) (1988), 694-700.
12. M.L.Mecartney and M.Ruhle, "Microscopy Observations of the Monoclinic to Tetragonal Phase Transformation in Tetragonal ZrO_2", Acta Metall, 37(7)(1989), 1859-1863.
13. E.M.Levin and H.F.McMurdie, "Phase Diagrams for Ceramists, 1975 Supplement", ed. M.K.Reser (Columbus, OH: Am.Ceram.Soc.,1984), 135-136.
14. S.M.Lakiza and L.M.Lapato, "Stable and Metastable Phase Relations in the System Alumina-Zirconia-Yttria", J.Am.Ceram.Soc., 80(4)(1997), 893-902.

PHASE TRANSFORMATION IN 9MOL% MgO-PARTIALLY STABILIZED ZIRCONIA DURING AGEING AND THERMAL CYCLING

B. Zhang[1], T.Isobe[1] and H. Tsubakino[2]

[1]Graduate School, Himeji Institute of Technnology, 2167 Shosha, Himeji 671-22, Japan
[2]Department of Materials Science & Engineering, Faculty of Engineering,
Himeji Insitute of Technology, 2167 Shosha, Himeji, 671-22, Japan

Abstract

The phase transformation from tetragonal (t) to monoclinic (m) phase in partially stabilized zirconia (PSZ) containing stabilized additives of 9 mol% magnesia has been studied by X-ray diffraction (XRD) and Dilatometry. At higher ageing temperature, the $t \rightarrow m$ phase transformation kinetics occurred at a faster rate. The amount of the m phase increased with prolonging ageing time or adding cyclic number. The eutectoid transformation is a process of grain boundary surface nucleation. The $t \rightleftarrows m$ transformation behavior of 9 mol% MgO-PSZ is shown to be sensitive to the heating and cooling rates when dilatometry is conducted. The dilatation hysteresis exhibited two stages of low and high temperature inflections of dilatometry at slow heating and cooling rates of 1.33K /min.

The Third Pacific Rim International Conference on
Advanced Materials and Processing (PRICM 3)
Edited by M.A. Imam, R. DeNale, S. Hanada,
Z. Zhong and D.N. Lee
The Minerals, Metals & Materials Society, 1998

Introduction

Magnesia partially stabilized zirconia (Mg-PSZ) has created considerable interest in recent years on account of its high toughness and strength which are a result of the stress induced martensitic phase transformation from the metastable tetragonal to stable monoclinic phase. However, this phase transformation is very sensitive to a great number of parameters: compositions of the starting powders, fabrication processes, heat treatment, grain size, microcracking, pores, atmosphere, etc.. The phase transformation phenomenon of this material remains further studies [1-7] .

In this paper, we report on the investigation of the phase transformation by means of X-ray diffraction (XRD) analysis and dilatometry test on sintered and aged 9mol% MgO-PSZ specimens.

Experimental Procedure

The as-received powders were produced by co-precipitation method with chemical compositions shown in Table 1.

Table 1 Chemical Composition of Starting Powder (mass%)

MgO	CaO	SiO_2	Fe_2O_3	Al_2O_3	TiO_2	ZrO_2
2.53	0.20	0.04	0.02	0.06	0.18	bal

The powders were pressed uniaxially at 400MPa and sintered in air at 1973K, keeping at this temperature for 3, 5 and 8 hours respectively (the specimens were designated A3, A5 and A8 accordingly), with the heating and cooling rates of 10 and 20K /min, followed by air-cooling to room temperature (RT) at 1523K. The sizes of the sintered specimens were about 11mm × 3.7mm × 2mm. The densities of the sintered specimens were measured by Archimedes method. XRD indicated that there is no monoclinic phase on the surface of the as-sintered specimens. The percentage of the monoclinic phase in the specimen surface was estimated from the relative intensities of the two monoclinic peaks (111)m, $(11\bar{1})$m and the overlapped tetragonal and cubic peak (111)c-t according to the following equation:

$$f = \{I(111)m+I(11\bar{1})m\} \ / \ \{I(111)m+I(11\bar{1})m+I(111)c\text{-}t\} \qquad (1)$$

with f being the transformation fraction of the m phase and I the intensity [8] .

Ageing treatments were carried out in air on specimens at 1283 and 1573K. In dilatometry test, the specimens were subject to thermal cycling from RT to 1673K at two kinds of heating and cooling rates, 1.33 and 10K /min.

Results and Discussion

According to the ZrO_2 rich end of Grain's ZrO_2-MgO phase diagram [9] which is shown in Fig.1, for specimen containing 9 mol% MgO, it falled in the area of (c+t) phase at the sintering

temperature of 1973K. The relative densities of specimens were low but increased with longer keeping temperature at 1973K, which were 85%, 86% and 89% for A3, A5 and A8, respectively.

Isothermal aging

The features of the ageing process of specimens of A3, A5 and A8, aged at 1283K and A5 specimen aged at 1573K are shown in Fig.2, which is also a plot of the m phase content. It shows the increased m phase with prolonging ageing time. For the specimen isothermally aged at higher temperature, the t→m transformation proceeds quickly. Similar sigmoidal curves are shown for all specimens, almost irrespective of the different sintering times for the specimens. The apparent transformation kinetics are usually described by using the well-known Johnson-Mehl equation [10] :

$$f = 1 - \exp(-bt^n) \qquad (2)$$

where f is the transformed volume fraction, t is time and b is a kinetic parameter depending on temperature, and n is an exponent which reflects the transformation mechanism (the nucleation and growth behaviors) . The above equation can be written in the following form:

$$\ln\ln [1/ (1-f)] = n\ln t + \ln b \qquad (3)$$

The plots of $\ln\ln [1/ (1-f)]$ against aging time for specimens of A3, A5 and A8 aged at 1283K and A8 aged at 1573K are shown in Fig.3. The overall rate of the t→m phase transformation reflects the time and temperature dependence. An approximately linear relationship with the n value of about 0.8 is obtained for all specimens, indicating that the t→m phase transformation of the specimens is a process of grain boundary surface nucleation of eutectoid products [10] .

Dilatometry characteristics of t⇄m phase transformation

On the dilatation curves of the as-sintered A3, A5 and A8 specimens thermally cycled at heating and cooling rates of 10K /min for up to six cycles, virtually no inflection occurs. However, we found the dilatation curves exhibited two stages of low and high temperature inflections of dilatometry at slow heating and cooling rates of 1.33K /min. Fig.4 shows such the dilatation curve evolution of the as-sintered specimen A8 from the first cycle to the third one. We can see that there is no low temperature inflection during the first cycle heating run but the curve shows a deviation from the dotted line above 920K, which is thought to be caused by the formation of the m phase through slow heating. At 1483K, m→t phase transformation inflection occurs, which is different from the temperature of 1513K predicted by Grain [9] . During the cooling stage, the t →m phase transformation is observed at about 1292K and 640K. On the second and third cycle dilatation curves, two stages clearly exist. The interpretation of this kind of curve could be that the low stage inflection corresponds to the t⇄m transformation which occurred in the c grain [11] , while the high temperature inflection is related to the t⇄m transformation in the grain boundary eutectoid products [12] and after thermal history of one cycle run, the small precipitates in grain interior grew to reach the critical size and so the m→t phase transformation occurred. However, the result obtained in this study is different from Abe et al [11] , in which

inflection can be easily observed but no high temperature inflection. Fig.5 reflects the as-sintered A5 specimen thermally cycled at the rate of 1.33K/min from the third cycle to the fifth one. Fig.6 shows the case for the as-sintered A3 specimen. It illustrated that the low temperature inflection can be sharper from the first cycle to the third one, while high temperature inflection can not be observed. It is clearly that the phase transformation reflected on the dilatation curves reduced with the specimen sintered for shorter times. The small amount of phase transformation occurring in A3 is thought to be related to its short sintering time. Fig.7 exhibits that the amount of the m phase increases with adding cyclic number for the A3, A5 and A8 specimens thermally cycled. The t→m phase transformation proceeds faster for specimens with longer sintering time.

Conclusions

The behavior of the phase transformation of 9 mol% MgO-PSZ is summarized briefly as follows:
(1) Below the eutectoid temperature, the t→m phase transformation occurred at a faster rate at higher aging temperature. The amount of m phase increased with prolonging aging time.
(2) The specimen with longer sintering time showed faster t→m phase transformation kinetics when thermally cycled at the rate of 1.33K/min. Through Johnson-Mehl equation, it is concluded that the eutectoid transformation is a process of grain boundary surface nucleation.
(3) The t⇄m transformation behavior is shown to be sensitive to heating and cooling rates when dilatometry is conducted. The dilatation hysteresis exhibited two stages of low and high temperature inflections of dilatometry at slow heating and cooling rates of 1.33K /min.

Acknowledgment

The authors thank Tateho Chemical Industries Co. Ltd., Japan for preparing the powder.

References

1. R. C. Garvie, R. H. Hannink, and R. T. Pascoe, "Ceramics Steel?", Nature (London), 258 (1975), 703-704.
2. M. Yoshimura, T. Noda, K, Kawabata and S. Somiya, "Role of H_2O on the Degradation of Y-TZP", J. Mater. Sci. Lett. , 6 (4) (1987), 465-467.
3. T. K. Gupta, F. F. Lange and J. H. Bechtold, "Effect of Stress-Induced Phase Transformation on the Properties of Polycrystalline Zirconia Containing Metastable Tetragonal Phase", J. Mater. Sci., 13 (7) (1978), 1464-1470.
4. N. Nakanishi and T. Shigematsu, "Bainite-like Transformation in Zirconia Ceramics", Mater. Tran. JIM, 32 (8) (1991), 778-784.
5. H.Tsubakino, R. Nozato and M. Hamamoto, "Effect of Alumina Addition on the Tetragonal-Monoclinic Phase Transformation in Zirconia-3mol% Yttria", J. Am. Ceram. Soc.,

74 (2) (1991), 440-443.

6. H. Tsubakino, M. Hamamoto and R. Nozato, "Tetragonal to Monoclinic Phase Transformation during Thermal Cycling and Isothermal Ageing in Yttria-Partially Stabilized Zirconia", J. Mater. Sci., 26 (20) (1991), 5521-26.
7. H. Tsubakino, et al., "Isothermal Transformation Behavior of Martensite in Zirconia-3mol% Yttria Ceramics", Solid-Solid Phase Transformations, ed. by W.C. Johnson et al, TMS, Warrendale, (1994), 749-754.
8. R. C. Garvie and P.S. Nicholson, J. Am. Ceram. Soc., 55 (6) (1972), 303-305.
9. D. J. Green, R.H.J. Hannink and M.V. Swain, Transformation Toughening of Ceramics, (Florida, FL: CRC Press, 1989), 17-25.
10. J. W. Christian, The Theory of Transformation in Metals and Alloys, (Oxford: Pergamon Press, 1965), 471.
11. F. Abe, S. Muneki, K. Yagi, "Tetragonal to monoclinic transformation and microstructural evolution in ZrO_2-9.7 mol% MgO during cyclic heating and cooling", J. Mater. Sci., 32 (1997), 513-522.
12. S. C. Farmer, T. E. Mitchell, and A. H. Heuer, "Diffusional Decomposition of c-ZrO_2 in Mg-PSZ", Advances in Ceramics, Vol.3, Science and Technology of Zirconia, ed.A.H.Heuer and L.W.Hobbs (Columbus, OH: Am. Ceram. Soc., 1981), 152-163.

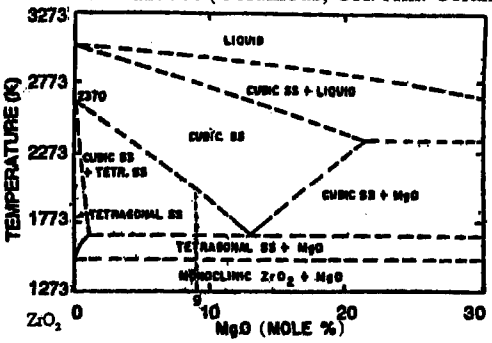


Fig. 1 Phase diagram of the ZrO_2-rich region in the MgO-ZrO_2 binary system.

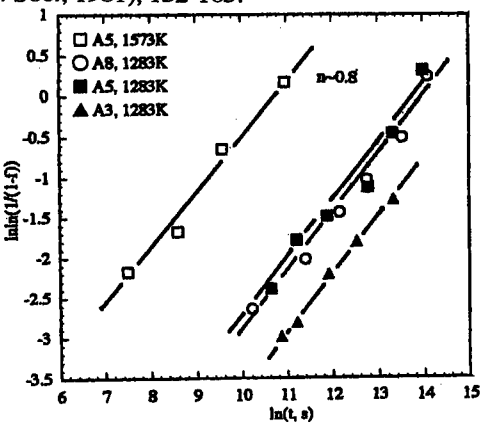


Fig. 3 Johnson-Mehl plots for the A3, A5 and A8 specimens isothermally aged at 1283K, and for the A5 specimen isothermally aged at 1573K.

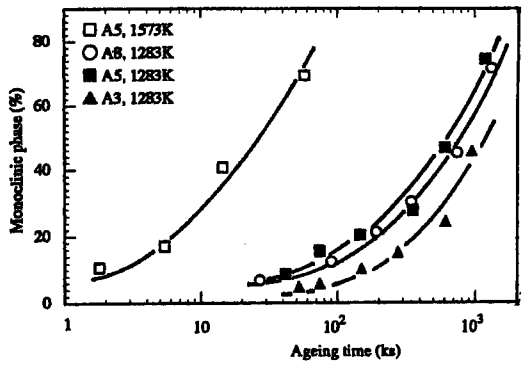


Fig. 2 The relationship between the amount of m phase transformed at the specimen surface with prolonging ageing time. Specimens are A3, A5 and A8 specimens aged at 1283K and A5 specimen aged at 1573K.

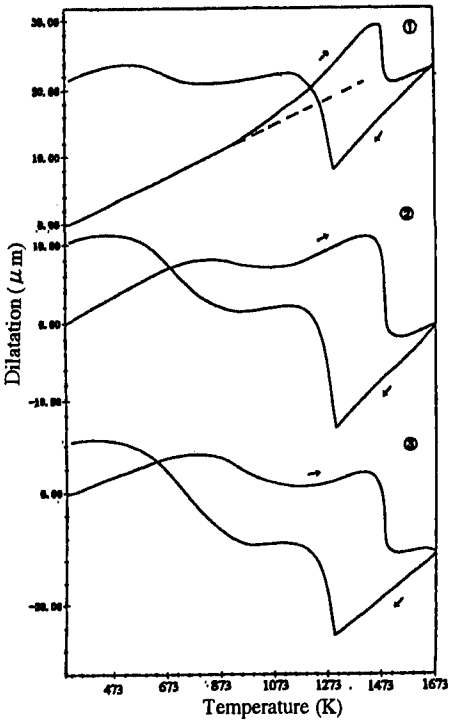


Fig. 4 The evolution of dilation curves for the A8 specimen thermally cycled from RT to 1673K at heating and cooling rates of 1.33K /min.

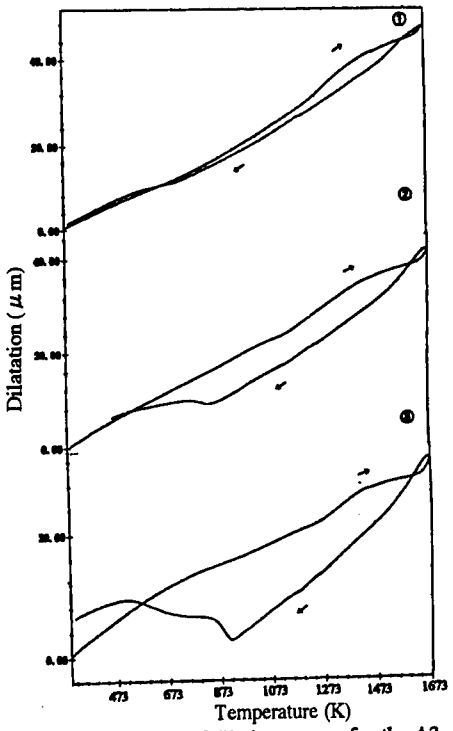
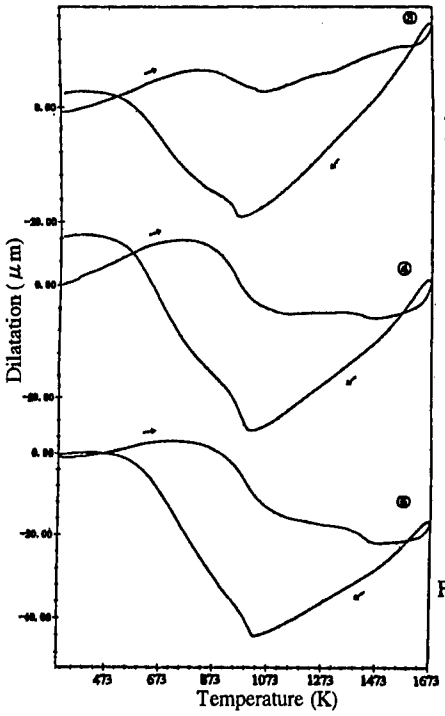


Fig. 6 The evolution of dilation curves for the A3 specimem thermally cycled from RT to 1673K at heating and cooling rates of 1.33K /min.



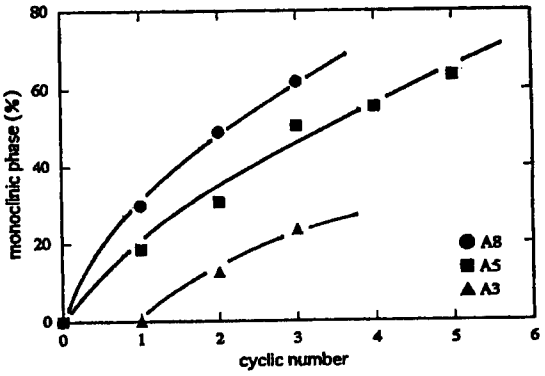


Fig. 7 The relationship between m phase amount and cyclic number for A3, A5 and A8 specimens thermally cycled from RT to 1673K at heating and cooling rates of 1.33K /min.

Fig. 5 The evolution of dilation curves for the A5 specimen thermally cycled from RT to 1673K at heating and cooling rates of 1.33K /min.

AMORPHOUS TO NANOCRYSTALLINE TRANSFORMATIONS IN ELECTRODEPOSITED Ni-W ALLOYS

Tohru YAMASAKI[1)], Rika TOMOHIRA[2)] and Yoshikiyo OGINO[1)]

1) Department of Materials Science & Engineering, Himeji Institute of Technology, 2167 Shosha, Himeji, Hyogo 671-22, Japan.
2) Graduate student, Himeji Institute of Technology, Himeji, Japan.

ABSTRACT

Amorphous Ni-W alloys containing between 18 and 25 at. % W have been prepared by electrodeposition. Electrodeposition was carried out in various concentrations of nickel sulfate, citric acid, sodium tungstate and ammonium chloride with different conditions. The tungsten content of the deposited alloys increased with increase in temperature of the bath. X-ray diffraction peaks of the deposited alloys broadened with increasing tungsten content and an amorphous pattern appeared at a tungsten content of more than about 20 at. %. Amorphous to nanocrystalline transformations of Ni-25.0 at. % W alloy during annealing have been studied by differential thermal analysis, X-ray diffraction and high resolution transmission electron microscopy (HR-TEM). In the case of these alloys, the Hall-Petch strengthening mechanism was observed for the hardness extending to a finest grain size of about 10 nm. When the grain size is less than about 10 nm, the hardness decreases with decreasing the grain size. This decrease in hardness may be due to the significant increase of the intercrystalline volume fraction.

The Third Pacific Rim International Conference on
Advanced Materials and Processing (PRICM 3)
Edited by M.A. Imam, R. DeNale, S. Hanada,
Z. Zhong and D.N. Lee
The Minerals, Metals & Materials Society, 1998

1. Introduction

Electrodeposition is a superior technique for producing amorphous and nanocrystalline materials in bulk form or as coatings with no post-processing requirements. In our previous study [1, 2], we developed an aqueous plating bath for the Ni-W electrodeposition that yields amorphous alloys of fairly high tungsten content. In the present study, amorphous to nanocrystalline transformations of electrodeposited Ni-W alloys during annealing in the range of grain sizes less than about 10 nm have been studied in detail by differential thermal analysis, X-ray diffraction and high resolution transmission electron microscopy. Grain size dependence of the mechanical properties of the nanocrystallized Ni-W alloys has been investigated by means of hardness measurements.

2. Experimental Procedures

Ni-W alloys containing about 18 - 25 at. % W have been prepared by electrodeposition. The plating bath compositions and conditions selected for this study are as follows; $NiSO_4$ $6H_2O$: 0.06 mol/l, $Na_3C_6H_5O_7$ $2H_2O$: 0.5 mol/l, Na_2WO_4 $2H_2O$: 0.14 mol/l, NH_4Cl: 0.5 mol/l, NaBr: 0.15 mol/l, bath temp.: 333 - 363 K, pH: 8.9, current density: 20 A/dm^2. A fresh plating bath was made for each experiment using analytical reagent grade chemicals and deionized water. Structural analysis of the electrodeposited alloys was performed by means of X-ray diffraction using Cu-Kα radiation (45 kV - 25 mA) and high resolution electron microscopy (HR-TEM, JEM-2010, 200kV). The samples thus prepared were annealed at various temperatures in air or vacuum of about 10^{-3} Pa. Vickers microhardness was measured by using the as-electrodeposited and the annealed samples on Cu substrates with a 0.02 kg load and a loading time of 15 s in cross section.

3. Results

The tungsten content of the Ni-W electrodeposited alloys is strongly influenced by the plating bath temperature. As shown in **Figure 1**, the tungsten content of the deposited alloys increased with increasing the plating bath temperature. X-ray diffraction peaks of the deposited alloys broadened with increasing tungsten content and an amorphous pattern appeared at a tungsten content of more than about 20 at. %. **Figure 2** shows DTA measurements of the as-electrodeposited Ni-W alloys at a heating rate of 0.33 K/s. With the Ni-W alloy electrodeposited at the bath temperature of 333 K, no distinct peaks were observed. When the bath temperature is 348 K and above, the amorphous X-ray diffraction pattern appeared and the crystallization of these amorphous Ni-W alloys takes place in two steps. The first-step crystallization at the starting temperature of about 980 K has been confirmed by X-ray analysis to be due to the precipitation of *fcc*-Ni solid solution. The second-step crystallization takes place at a temperature range of 1100 - 1150 K. X-ray analysis has suggested that Ni_4W intermetallic compound precipitates at this step accompanied by formation of some kinds of oxides.

Figure 3 shows X-ray diffraction patterns of the Ni-25.0 at. % W alloy annealed at various temperatures for 24 h in vacuum. On annealing this material at 673 K the amorphous structure was maintained, while the X-ray diffraction peak became sharper as compared with the as-deposited one. At higher annealing temperatures of 723 K and above, crystallization occurred and the diffraction lines of *fcc*-Ni phase appeared. **Figure 4** shows the Vickers microhardness vs. $d^{-0.5}$ (d is mean grain dia.) relationship for the Ni-W alloy after annealing at various temperatures in air or vacuum. Average grain sizes in the Ni-25.0

at. % W alloys were obtained by applying the Scherrer formula to the diffraction lines of *fcc*-Ni (111) and the broad maximum of the amorphous phase, and also by direct observations from TEM or SEM micrographs. For comparison, the relationships for electrodeposited Ni [3] and conventional pure Ni extrapolated from the relationship at larger grain sizes [4] are also shown. In the Ni-W alloy, the hardness increases with decreasing the grain size to about 10 nm. The Hall-Petch slope of 0.8 MPa $m^{1/2}$ in the Ni-W alloy is slightly higher, but comparable to those of the electrodeposited Ni and the conventional one. When the grain size is less than about 10 nm, the hardness decreases with decreasing grain size.

Figure 5 shows the TEM images and the selected area diffraction patterns in the Ni-25.0 at. % W alloy annealed at 723 K and 873 K for 24 h in vacuum. In Fig. 5 (a), nanocrystalline structure having grain sizes between 5 and 8 nm is observed. The selected area diffraction pattern reveals the *fcc*-lattice Debye rings indicating that the ultrafine grains become randomly oriented. Noticeably, image contrast of the interface of individual grains is not clearly visible. There is a possibility that such broad intercrystalline regions might have an irregular structure such as an amorphous. On annealing this material at 873 K, grain sizes increased to about 15 nm and above. **Figure 6** shows the high resolution *fcc*-(111) lattice image of the Ni-W alloy annealed at 723 K for 24 h in vacuum. In the intercrystalline regions that are about 1 to 2 nm in widths, distorted lattice images are observed. As shown in the framed part of Fig. 6, the distorted lattice images were observed in the intercrystalline regions having components of grain boundary and grain boundary triple junction. Especially, highly distorted lattice image is observed in the region of triple junction.

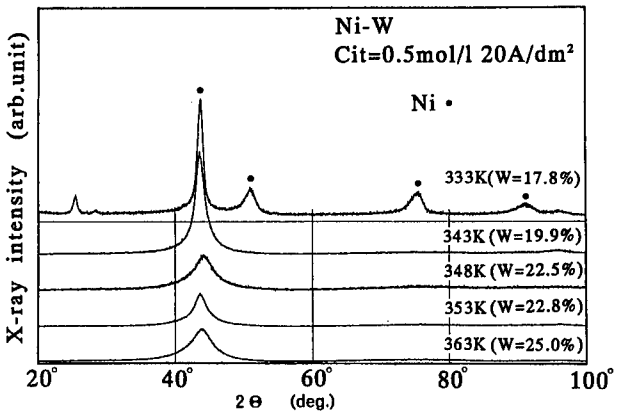


Figure 1 : X-ray diffraction patterns of Ni-W electrodeposited alloys for various plating bath temperatures at a current density of 20 A/dm^2.

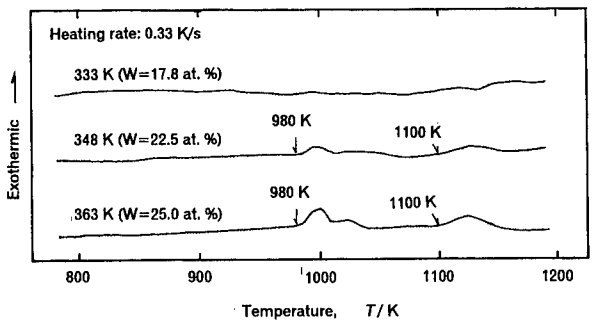


Figure 2 : DTA thermograms for crystallization of Ni-W electrodeposited alloys for various plating bath temperatures at a current density of 20 A/dm^2.

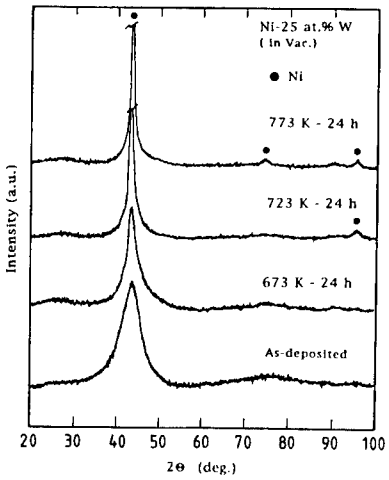


Figure 3 : X-ray diffraction patterns of Ni-25.0 at. % W alloys annealed at various temperatures for 24 h in vacuum.

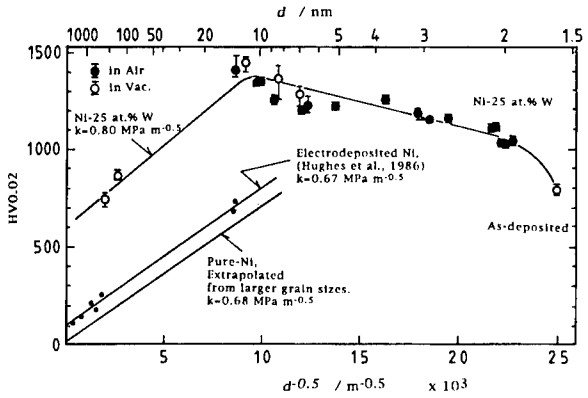


Figure 4 : Vickers micro-hardness plotted as a function of $d^{-0.5}$ (d is mean grain dia.) relationship for the Ni-25.0 at. % W alloy after annealing at various temperatures in air or vacuum.

When the defocusing value was changed from -48 nm to + 16 nm, the straight line lattice image could not be observed in these intercrystalline regions. Similar features of HR-TEM observations have been reported in Ti-Mo alloys prepared by mechanical alloying and Ni_3Al by magnetron sputtering with grain sizes of less than 10 nm [5, 6].

4. Discussion

When the grain size is less than about 10 nm, decrease of the hardness was observed. As shown in Fig. 6, grain boundary thickness of about 1 to 2 nm evaluated from the HR-TEM observation may be considerably thicker than that of the coarse grained materials (almost less than about 1 nm). As a result, the volume fraction of the grain boundary triple junction having the highly distorted lattice image should increase remarkably with decreasing the grain size. Palumbo et al. have proposed to evaluate grain size dependence of volume fractions associated with both the grain boundary and the triple junction [7]. The total intercrystalline fraction (V_f^{ic}) and the grain boundary fraction (V_f^{gb}) are derived from the following equations, $V_f^{ic} = 1 - [(d - D)/d]^3$, (1) $V_f^{gb} = [3D(d - D)^2]/d^3$, (2) where d and D are the grain diameter and the grain boundary thickness, respectively. The fraction associated with the triple junction (V_f^{tj}) is given by , $V_f^{tj} = V_f^{ic} - V_f^{gb}$. (3)

Figure 7 shows the calculated volume fractions for V_f^{ic}, V_f^{gb} and V_f^{tj} as a function of

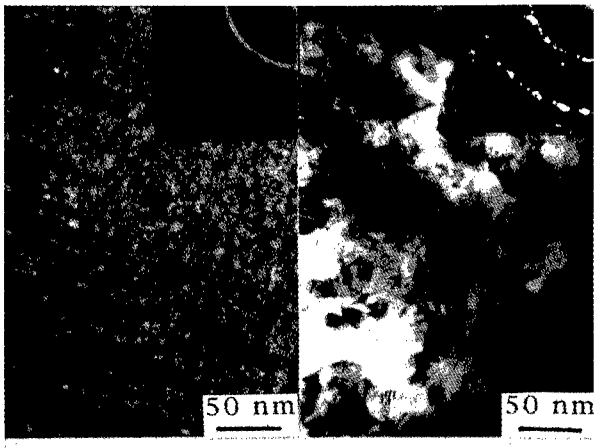


Figure 5 : TEM images and selected area diffraction patterns in the Ni-25.0 at. % W alloys annealed at 723 K (Fig. 5 (a)) and 873 K (Fig. 5 (b)) for 24 h in vacuum.

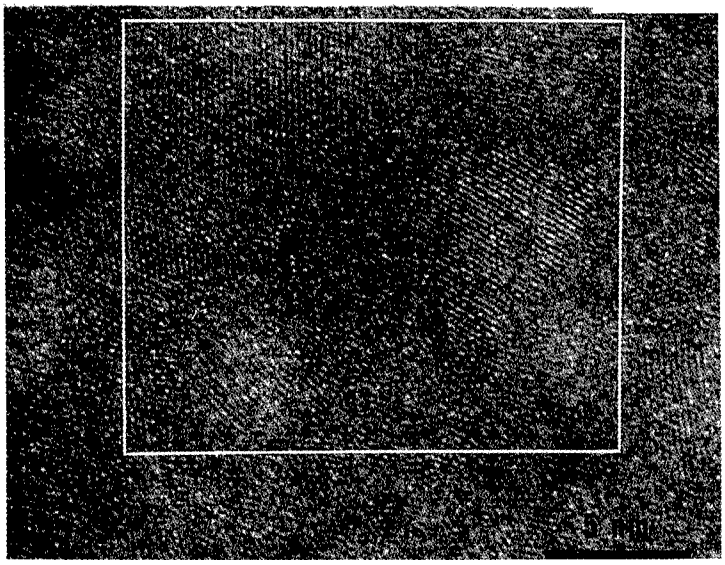


Figure 6 : The high resolution *fcc*-(111) lattice image of the Ni-25.0 at. % W alloy annealed at 723 K for 24 h in vacuum.

$d^{-0.5}$ where D is changed over a range from 0.5 to 2.0 nm. The V_f^{gb} in Fig. 7 (b) increases to maximum values of about 45 % and then decreases with decreasing the grain size, while the V_f^{tj} in Fig. 7 (c) continues to increase. When the grain boundary thickness is 1.5 nm and above, the marked increase of the V_f^{tj} is observed in the range of grain sizes of less than about 10 nm. **Figure 8** shows the Vickers microhardness vs. $d^{-0.5}$ relationship for the Ni-25.0 at. % W alloy. In order to explain the decrease in hardness where the grain size is less than about 10 nm, we give a rough estimate of the grain size dependence of the hardness (H_{cal}) by following equation,

$$H_{cal} = V_f^{tj} H_{tj} + (1 - V_f^{tj}) H_{HP} \quad (4),$$

where V_f^{tj} and H_{tj} are the volume fraction and the hardness of the triple junction, respectively, and H_{HP} is a hardness obtained by the Hall-Petch relationship for the Ni-W alloy. On the basis of the calculated volume fractions shown in Fig. 7, we assume that the hardness of the triple junction (H_{tj}) is equal to that of the as-electrodeposited amorphous Ni-W alloy (HV = 770). The H_{cal} vs. $d^{-0.5}$ relationships where the grain boundary

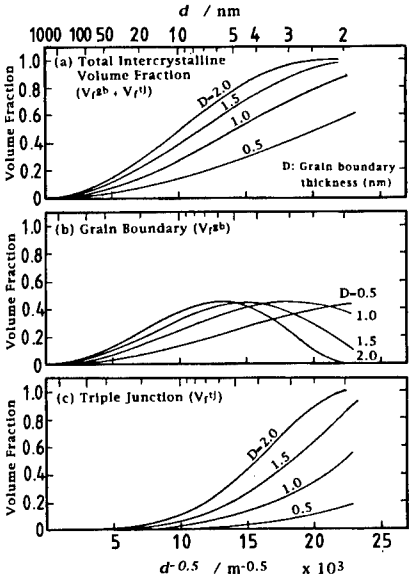


Figure 7 : Calculated volume fractions for V_f^{ic}, V_f^{gb} and V_f^{tj} as a function of $d^{-0.5}$ where D is changed over a range from 0.5 to 2.0 nm.

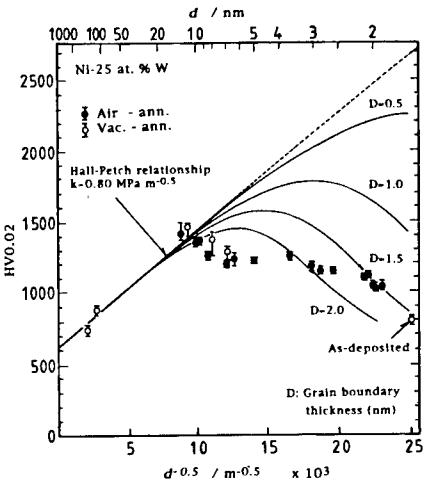


Figure 8 : Vickers microhardness vs. $d^{-0.5}$ relationship for the Ni-25.0 at. % W alloy. The H_{cal} vs. $d^{-0.5}$ relationships where the grain boundary thickness is changed in a rang between 0.5 and 2.0 nm are also shown.

thickness is changed in a range of between 0.5 and 2.0 nm are also shown in this figure. The decreasing tendency of the hardness under conditions where D = 1.5 and 2.0 nm can be well expressed by equation (4). In this figure, however, there is the difference of the observed profile from the convexly curved profile calculated by equation (4). This difference may be due to the change of the grain boundary thickness as a function of the grain size. In order to clarify such a phase transformation, further experiments will be carried out, especially HR-TEM observations as a function of the grain size.

Conclusions : When the grain size is less than about 10 nm, the hardness of the Ni-25.0 at. % W alloy decreases with decreasing the grain size. In the case of the 723 K- annealed specimen having grain sizes about between 5 and 8 nm, the distorted lattice image with about 1 to 2 nm thickness in grain boundary regions was observed by HR-TEM. Such a thickness of the grain boundary may be considerably thicker than that of the coarse grained materials. As a result, the volume fraction of the grain boundary triple junction having highly disordered structure should increase remarkably with decreasing the grain size. Therefore, this decrease in hardness may be due to the significant increase of the intercrystalline volume fraction, especially the fraction associated with the triple junction.

References

[1] T. Yamasaki et al., Proc. of 2nd Int. Conf. of Micro Materials '97, Berlin (1997), 654.
[2] T. Yamasaki et al., Nanostructured Materials, to be submitted.
[3] G. D. Hughes et al., Scripta Metall., ***20*** (1986), 93.
[4] A. Lasalmonie and J. L. Strudel, J. Mater. Sci., ***21*** (1986), 1837.
[5] W.Y. Lim et al., Material Science Forum, ***88-90*** (1992), 105.
[6] H.Van Swygenhoven et al., Nanostructured Materials, ***6*** (1995), 739.
[7] G. Palumbo et al., Scripta Metall., ***24*** (1990), 1347, and ibid., ***24*** (1990), 2347.

EFFECTS OF Zr-ADDITIONS ON PHASE STABILITY

AND PHASE TRANSFORMATIONS IN A Ti-50AT.%Al ALLOY

Kiyomichi Nakai[1], Osamu Yamada[2], and Yasuya Ohmori[1]

[1]Department of Materials Science and Engineering, Faculty of Engineering, Ehime University
3 Bunkyo-cho, Matsuyama 790-77, Japan
[2]Graduate Student of Ehime University

Abstract

The effects of Zr additions to a Ti-50at.%Al alloy on phase stability and phase decomposition processes have been investigated. In the composition range of 10 - 20at.%Zr, the β phase which orders to the B2 structure during cooling and the Al_2Zr intermetallic compound are stable in the higher temperature range, and the B2 phase decomposes into the Widmanstätten α_2 phase with the Burgers orientation relationship and/or the ω phase, depending on the cooling rate. With the growth of the ω phase, the formation of the α_2 Widmanstätten structure is promoted. The formation processes and stabilities of the microstructures are discussed in terms of morphology and crystallography.

Acknowledgements

This work was supported by the Grant-in aid for Fundamental Scientific Research (Kiban Kenkyu (C), No. 09650763, 1997) by the Ministry of Education, Science and Culture of Japan, and performed using the JEM-3010 HRTEM and the JEM-2000EX ATEM at the Department of Materials Science & Engineering, and at the Advanced Instrumentation Center for Chemical Analysis, Ehime University, respectively.

The Third Pacific Rim International Conference on
Advanced Materials and Processing (PRICM 3)
Edited by M.A. Imam, R. DeNale, S. Hanada,
Z. Zhong and D.N. Lee
The Minerals, Metals & Materials Society, 1998

Introduction

Phase stability and phase decomposition processes in TiAl base alloys are of interest because the mechanical properties depend greatly on the microstructures [1, 2]. In these intermetallics the hcp α phase is stable at higher temperatures and transforms α_2 and/or γ phase, being composed of massive structure and/or lamellar structure [3 - 5]. The additions of third element which produces ordered bcc structures in the TiAl base alloys have also been studied extensively because of the enhancement of plasticity and the drastic changes of phase stability and phase decomposition processes [6, 7].

In the present investigation, the effects of Zr additions to a Ti-50at.%Al alloy on phase stability and microstructures are examined. The results are analyzed in terms of morphology and crystallography comparing to those in binary Ti-Al alloys, and the mechanisms for the microstructure evolutions are discussed.

Experimental Procedures

Ti-45.0at.%Al-10.0at.%Zr (10%Zr), Ti-42.5at.%Al-15.0at.%Zr (15%Zr) and Ti-40.0at.%Al-20.0at.%Zr (20%Zr) alloys were prepared using high purity Ti (> 99.99wt.% Ti, < 500wt.ppm O_2), Al (> 99.99wt.%) and Zr (> 99.8wt.%). Ingots of the alloys, 10 mm wide, 40 mm long and 8 mm thick, were made in an arc furnace under an Ar gas atmosphere. The oxygen content in the as-melted materials was less than 800 wt.ppm. The ingot was sliced into sheets and blocks with appropriate dimensions. They were wrapped in Ta foils. Some of the samples were encapsulated in quartz tube individually with Ar gas at 1/3 atm., annealed at 1523 K for 172.8 ks and then quenched into iced brine (IBQ), or cooled in air (AC) or in the furnace. Specimens for optical microscopy were etched in a solution of 5% HF and 20% HNO_3 by volume in distilled water. Thin foils for transmission electron microscopy (TEM) were prepared from the sheets by electropolishing in a solution of 8 vol.% H_2SO_4 in methanol. Electropolishing was carried out at 17 V and 233 K. Specimens were examined in a JEM-3010 HRTEM and a JEM-2000EX ATEM operated at 300 and 200 kV, respectively. Chemical-composition analyses were performed with the Shimazu ASM-SX operated at 25 kV and 10 μA.

Experimental Results

Figure 1 shows optical microstructures taken from (a) 10%Zr and (b) 20%Zr IBQ-alloys. In both 10%Zr and 15%Zr IBQ-alloys, large precipitates (LPs) at grain boundaries and Widmanstätten structures are observed, but in the 20%Zr IBQ-alloy, fine precipitates form instead of the Widmanstätten structure. The LPs are stable up to the melting point (≅ 1593 K). Figure 2 shows the composition profile of the LP enriched with Al and Zr by EPMA line-analysis. Figure 3 shows TEM micrographs taken from the LP. Figure 3(a) is a dark-field micrograph showing antiphase domain boundaries (APBs) and Fig. 3(b) is the diffraction pattern identified as the C14 structure of Al_2Zr intermetallic compound. Figure 4 is a dark-field TEM micrograph taken from the Widmanstätten structure identified as the α_2 phase (DO_{19} structure) showing APBs which are not inherited from those in the matrix phase of the 15%Zr IBQ-alloy as can be seen near the α_2 - β (ordered B2 structure) interphase boundary, where B2 superlattice reflection is locally excited. Very fine ω phase with the orientation relationships, $(0001)_\omega$ // $\{111\}_\beta$ and $<11\bar{2}0>_\omega$ // $<\bar{1}10>_\beta$, and α_2 precipitates with the orientation relationships, $(0001)_{\alpha_2}$ // $\{110\}_\beta$ and $<11\bar{2}0>_{\alpha_2}$ // $<\bar{1}11>_\beta$, form in the B2 matrix as shown in Fig. 5. There exist two kinds of α_2 precipitates in size. Some of larger α_2 precipitates decompose into (α_2 + γ) duplex structure as shown in Fig. 6. In the 20%Zr IBQ-alloy, the ordered ω phase ($B8_1$) forms in the B2 matrix, and grows with decreasing cooling rate with the orientation relationships, $(0001)_\omega$ // $\{111\}_\beta$ and $<11\bar{2}0>_\omega$ // $<\bar{1}10>_\beta$ as shown in Fig. 7. In 20%Zr AC-alloy, the α_2 Widmanstätten structures nucleate at both grain boundary α_2 allotriomorphs and interphase α_2 precipitates around Al_2Zr particles as shown in Fig. 8. Homogeneous α_2 intragranular precipitates coexist with the ω phase almost all of which connect with the α_2 precipitates.

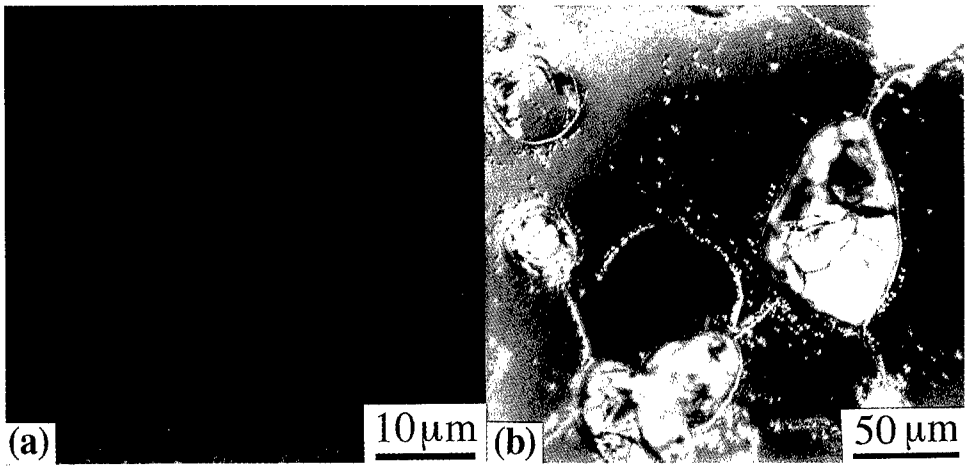


Fig. 1 Optical microstructures showing the Al_2Zr compound at grain boundaries in (a) 10%Zr and (b) 20%Zr IBQ-alloys.

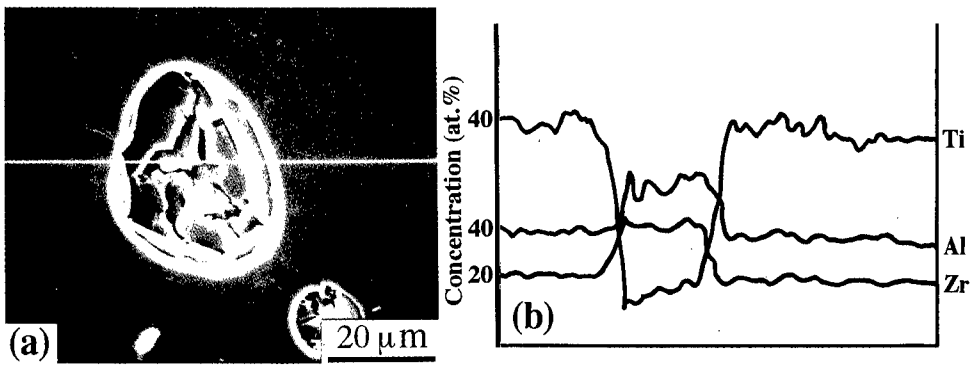


Fig. 2 EPMA line-analysis for the compound in the 20%Zr IBQ-alloy. (a) SEM micrograph and (b) the composition profile. The line-analysis was performed along the white line in (a).

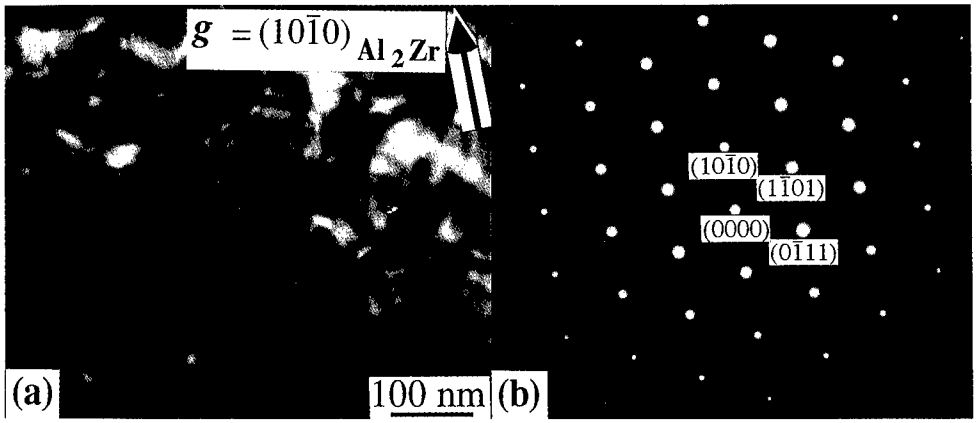


Fig. 3 TEM micrographs of the Al_2Zr compound showing (a) APBs and (b) the diffraction pattern in the 20%Zr IBQ-alloy.

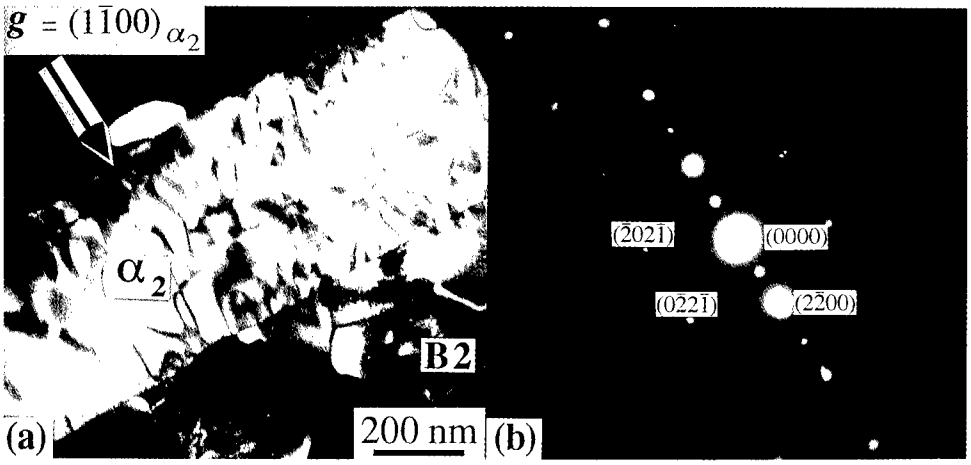


Fig. 4 TEM micrographs showing (a) the α_2 Widmanstätten structure in the B2 matrix phase and (b) the diffraction pattern in the 15%Zr IBQ-alloy.

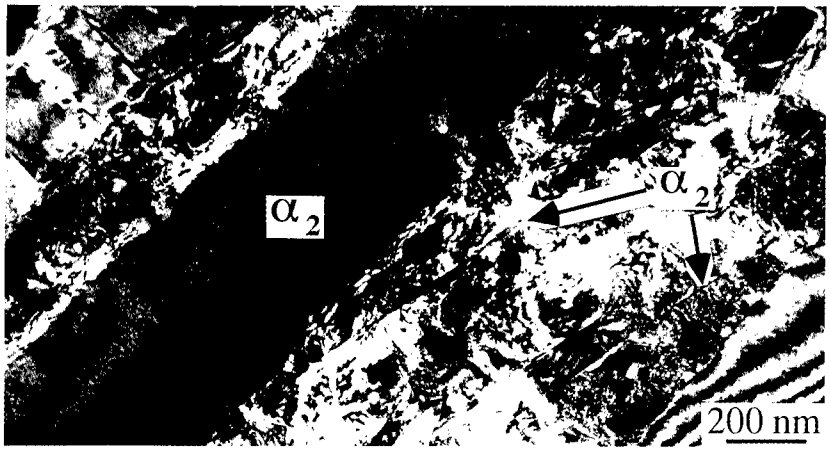


Fig. 5 TEM micrograph showing α_2 Widmanstätten structures of two different sizes and fine ω precipitates in the 15%Zr IBQ-alloy.



Fig. 6 TEM micrograph showing the decomposition of the α_2 Widmanstätten structure into (α_2 + γ) phases in the 15%Zr IBQ-alloy.

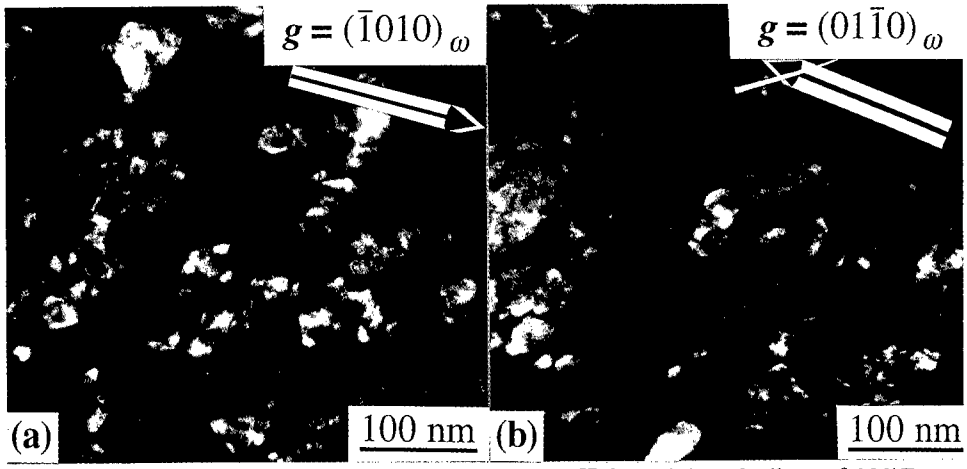


Fig. 7 TEM micrographs showing ω precipitates in (a) IBQ- and (b) AC-alloys of 20%Zr.

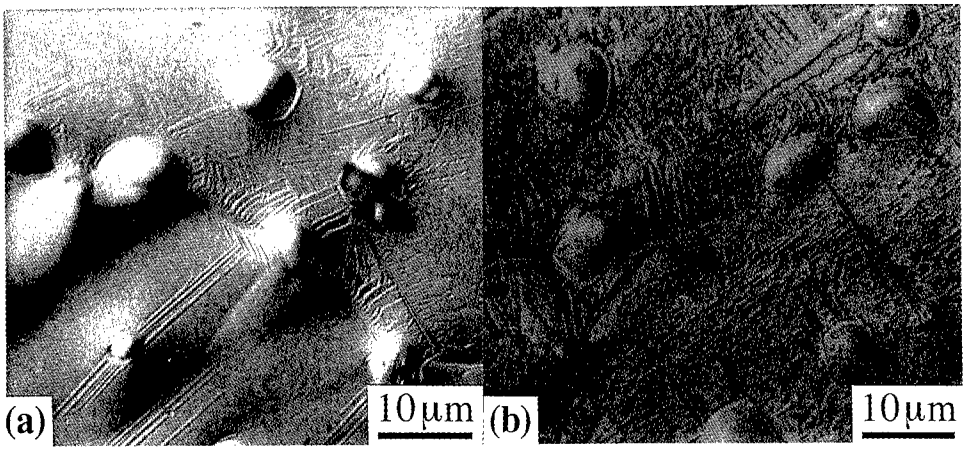


Fig. 8 Optical micrographs showing the α_2 Widmanstätten structures nucleated homogeneously and at both grain boundary α_2 allotriomorphs and α_2 interphase precipitates around Al_2Zr particles. (a) surface reliefs and (b) etched structures.

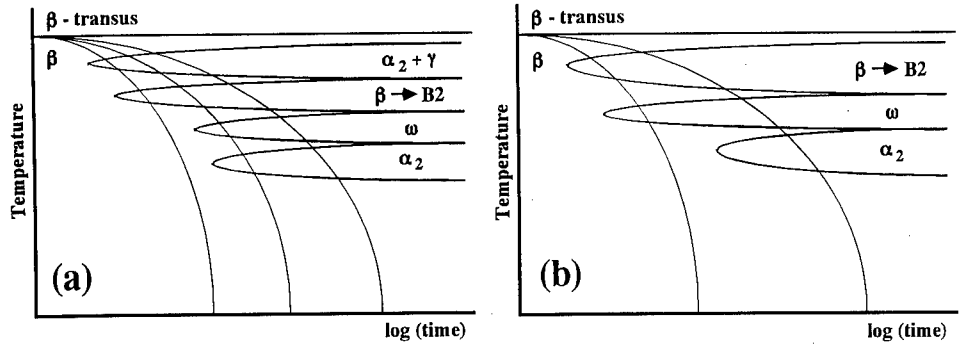


Fig. 9 CCT diargams for (a) the 15%Zr and (b) the 20%Zr alloys.

Discussion

Large Al_2Zr precipitates at grain boundaries are stable up to the melting point with the B2 phase. It means that both Al_2Zr and β phase are stable around and above 1523 K in the 10 - 20%Zr alloys. In the 15%Zr IBQ-alloy, the β phase orders to the B2 structure during cooling after the formation of the α_2 Widmanstätten structure, because APBs in the B2 structure are not inherited by the α_2 Widmanstätten structure as shown in Fig. 4. The α_2 Widmanstätten structures nucleate at grain boundary α_2 allotriomorph to reduce the interface energy. The ω phase forms in the 15%Zr and 20%Zr IBQ-alloys, and α_2 Widmanstätten structures nucleate at ω precipitates and grain boundary α_2 allotriomorphs in the 20%Zr alloy. In the 15%Zr alloy, a high density of fine α_2 plates coexist with fine ω precipitates. It suggests that the ω phase promotes the formation of the α_2 phase, similar to that in the near-β Ti alloy [8]. With decreasing cooling rate, α_2 allotriomorphs at both grain boundaries and Al_2Zr-interfaces give nucleation sites for the α_2 Widmanstätten structure remarkably. The ω phase itself might be also nucleation sites for the α_2 Widmanstätten structure as shown in Fig. 8. In the 15%Zr alloy, it should be noted that large and small sizes of α_2 precipitates form. Large α_2 precipitates might form before the formation of the ω phase, and small ones form after the formation of the fine ω precipitates, because the ω phase enhances the nucleation of α_2 precipitates. As shown in Fig. 6, the α_2 phase decomposes into the γ phase. Therefore, It should be suggested that the α_2 , γ and B2 phases are stable at temperatures ≤ 1523 K in the 15%Zr alloy.

Conclusions

In the 20%Zr alloy, the β and Al_2Zr phases are in equilibrium above 1523 K. The β phase orders to the B2 structure, followed by the formation of the metastable ω phase ($B8_2$). α_2 precipitates nucleate at ω precipitates, grain boundary α_2 allotriomorphs and interphase boundaries between the Al_2Zr and the B2 matrix.

In the 15%Zr alloy, the α_2 Widmanstätten structure forms in the β phase, followed by the ordering of the β phase to the B2 structure. Fine ω precipitates form in the B2 phase and promotes the nucleation of α_2 precipitates.

In the 10%Zr alloy, the α_2 Widmanstätten structure forms in the β phase followed by the ordering of the β phase to the B2 structure.

The results for the 20 and 15%Zr alloys are summarized in the CCT diagrams of Figs. 9(a) and (b).

References

1. S. M. L. Sastry and H. A. Lipsitt, "Fatigue Deformation of TiAl Base Alloys," Met. Trans., 8A (F) (1977), 299-308.
2. Y. Yamaguchi, "Deformation and Recrystallization Behaviour of the TiAl Phase Constituting the TiAl/Ti_3Al Lamellar Structure of Ti-rich TiAl Compounds," ISIJ Intern., 31 (10) (1991), 1127-1133.
3. S. A. Jones and M. J. Kaufman, "Phase Equilibria and Transformations in Intermediate Titanium-Aluminum Alloys," Acta metall. mater., 41 (2) (1993), 387-398.
4. E. Abe, S. Kajiwara, T. Kumagai and M. Nakamura, "High-Resolution Electron Microscopy of Twin Interfaces in Massively Transformed γ-TiAl," Phil. Mag., 75 (4) (1997), 975-991.
5. K. Nakai, T. Ono, H. Ohtsubo and Y. Ohmori, "Formation Process of Lamellar γ Phase in a Ti-40at.%Al Alloy," Mater. Trans., JIM, 37 (4) (1996), 813-820.
6. S.-C. Huang and E. L. Hall, "The Effects of Cr Additions to Binary TiAl-Base Alloys," Met. Trans., 22A (N) (1991), 2619-2627.
7. K. Nakai, T. Ono, H. Ohtsubo and Y. Ohmori, "Phase Stability and decomposition processes in Ti-Al Based Intermetallics," Mater. Sci. & Engr., A192/193 (1995), 922-929.
8. Y. Ohmori, H. Natsui, K. Nakai and H. Ohtsubo, "Effects of ω Phase Formation on the Decomposition of α" / β Duplex Phase Structure in a Metastable β Ti Alloy," Mater. Trans., JIM, in press.

MORPHOLOGY AND CRYSTALLOGRAPHY OF TRIPLE POINT NUCLEATED γ PHASE IN AN (α+γ) TWO PHASE STAINLESS STEEL

H. Fujiwara*, T. Maeda*, N. Miyano* and K. Ameyama

Department of Mechanical Engineering, Faculty of Science and Engineering, Ritsumeikan University, Kusatsu, Shiga 525-77, Japan

* Graduate school, Ritsumeikan University, Kusatsu, Shiga 525-77, Japan

Abstract

Morphology and crystallography of γ (FCC) precipitates nucleated at grain boundary edges or corners of α (BCC) matrix phase have been studied with TEM and SEM in an (α+γ) two phase stainless steel. The relative orientation relationships of α/α and α/γ phases were determined by Kikuchi pattern and electron channeling pattern (ECP) analysis. According to the morphological features, the precipitates at triple points could be classified into three types; Type A : triple point γ nucleation, Type B : grain boundary face γ nucleation, and Type C : precipitation free triple point. Although some of the Type B γ phase appeared to nucleate at the triple points, it was in fact caused by coarsening of the grain boundary face nucleated γ phase. The frequency of the appearance of these types A, B and C were 19.2%, 72.5% and 8.3%, respectively. Therefore, it was considered that the triple point is not always a predominant site for the γ nucleation. The crystallographic investigation of these γ precipitates strongly suggest that coherency between the γ phase and the triple point α grains plays a very important role for γ nucleation at the triple point.

The Third Pacific Rim International Conference on
Advanced Materials and Processing (PRICM 3)
Edited by M.A. Imam, R. DeNale, S. Hanada,
Z. Zhong and D.N. Lee
The Minerals, Metals & Materials Society, 1998

Introduction

Grain boundaries play an important role in many diffusional transformations in alloys as preferred nucleation sites for precipitation. Many studies on grain boundary nucleation, including at grain boundary triple points [1-5], have been carried out. Clemm and Fisher [1] approached the nucleation behavior theoretically and indicated that a triple point is able to be the preferential nucleation site since the critical energy required for nucleation at a triple point is small. In an experimental study, Huang and Hillert [2] showed that most of the α particles prefer to nucleate at triple points (which includes grain corners and grain edges) in the early stage of precipitation in an Fe-0.51wt% C alloy. These studies, however, did not consider how the anisotropy of interfacial energy or crystallography of the precipitates might influence the nucleation behavior.

Although one of the authors suggested that crystallography of precipitates has a significant influence on the morphology of the grain boundary face nucleated precipitates [3], there is little known about the crystallography and morphology of precipitates nucleated at or in the vicinity of the grain boundary triple point.

In the present study, the morphology and crystallography of γ (FCC) phase nucleated at α (BCC) triple point was investigated in an (α+γ) two-phase stainless steel using Kikuchi pattern analysis.

Experimental Procedure

An (α+γ) two phase stainless steel containing 24.41 wt% Cr and 7.16 wt% Ni was prepared by vacuum melting. Specimens were solution treated at 1573K for 1s~1800s in an Ar gas atmosphere and quenched into water. The aging for γ precipitation was carried out at 1423K or 1473K for 600s ~ 1800s followed by water quenching. Prior to the solution treatment, the specimen was cold rolled 80% so that the grain boundary plane lay normal to the specimen foil surface after grain growth.

Specimens for transmission electron microscopy were prepared by a standard jet polishing techniques. TEM observation was carried out in a JEOL-JEM2010 operating at 200kV.

The relative orientation relationship (OR) of adjacent α grains was determined by SEM / electron channeling pattern (ECP) analysis while that of the γ and α phases was determined by a TEM / Kikuchi pattern analysis. The error associated with these analysis was assessed by analysis of annealing twins in γ precipitates. Average errors of the analysis were 0.4 degree for SEM / ECP and 0.1 degree for TEM / Kikuchi pattern.

Results and Discussion

Morphology of γ phase at triple point

Figure 1 (a), (b) and (c) show SEM back scattered images of the specimens. According to morphological features, the microstructure of the triple point area could be classified into one of three types.

- Type A (Fig.1(a)) : γ phase occupies the triple point. The γ phase has globular morphology and contacts to three α grains. Such a γ phase is indicated as "TP γ".

- Type B (Fig.1(b)) : γ phase has an elongated "film-like" morphology and occupies the triple points. The γ phase at the triple point area contacts to all three α grains which compose the triple point. Such a γ phase is indicated as "TGB γ ".

- Type C (Fig.1(c)) : No γ precipitation at triple point.

In a total of 120 grain boundary triple points, the frequency of the appearance of these three types A, B and C was formed to be 19.2%, 72.5% and 8.3%, respectively. It is noteworthy

that the triple point is not always predominant nucleation site. This result seems to be contradictory to the report by Huang and Hillert [2]. They studied the role of triple point in ferrite nucleation in an Fe-0.51wt% C alloy, and indicated that nucleation at triple point is more predominant than on grain boundary face in the early stage of the precipitation. We agree with the result of Huang and Hillert that nucleation takes place at triple points at first. However, our result also suggests that incubation period for the grain boundary face nucleation is much shorter than that for the triple point nucleation in more than 70% of whole triple points.

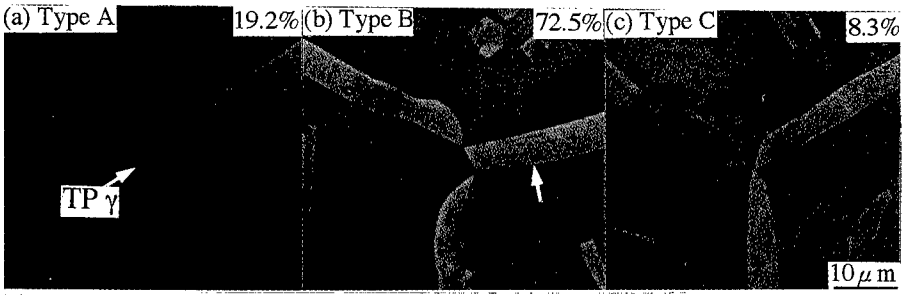


Figure 1: SEM back scattered images of a specimen aged at 1473K for 1800s.

Morphology and crystallography of Type B γ (TGB γ)

Figure 2 shows a TEM micrograph of the vicinity of an α triple point in the specimen aged at 1423K for 600s. γ1 and γ3 precipitates were nucleated at α1/α2 and α2/α3 grain boundaries. γ2 has interfaces with all α grains so it falls into the "TGB γ" category. It is difficult to determine whether γ2 has nucleated at the triple point or not, since it shows an elongated "film-like" morphology along α1/α3 grain boundary. According to the Kikuchi pattern analysis, the misorientation angles of α1/α2, α2/α3 and α3/α1 grains were 44.0 deg., 57.5 deg. and 23.5 deg. , respectively. γ1, γ2 and γ3 precipitates had a near Kurdjumov-Sachs (K-S) OR with one side of the α grain boundary and relatively good coherency with another α grain. γ2 has near K-S OR with α1 and near (111)γ2 / (110)α3 plane parallel OR with α3. However, γ2 precipitate had no favorable orientation relationship with respect to α2 grain even if it has an interface with α2 grain.

Figure 3(a) demonstrates an enlargement of the γ2 phase seen in Fig.2, while Fig.3(b) shows the Kikuchi patterns obtained from regions (1), (2) and (3) shown in Fig.3(a). As can be seen in Fig. 3(a), there are many boundaries in the γ2 phase. Areas (1), (2) and (3) bounded by these boundaries indicated by arrows, have a very small misorientation as shown in Fig.3(b). This implies that γ(1), γ(2) and γ(3) in the γ2 phase were nucleated independently with almost the same orientation relationship, followed by growth and coalescence to form subgrain boundaries. The observation that γ(1) did not have any coherent OR with α2 grain and it has a similar variant with γ(3) (which is presumed to be nucleated at the α1/α3 grain boundary face) strongly suggests that the γ2 did not nucleate at the triple point in this sample.

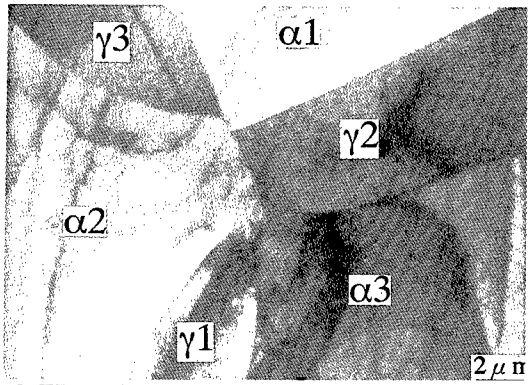


Figure 2: TEM micrograph of a specimen aged at 1473K for 600s.

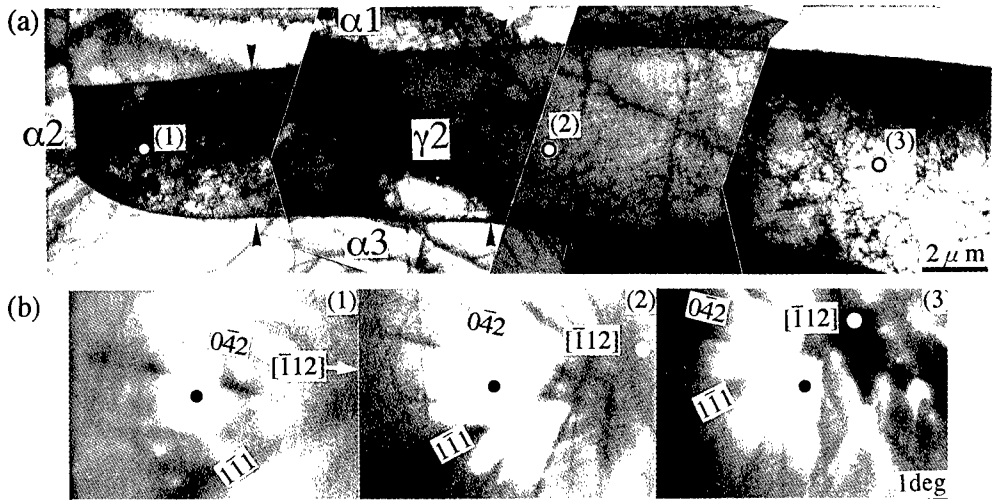


Figure 3: (a) TEM micrograph of enlargement of γ2 shown in Fig. 2. (b) Kikuchi patterns taken from the regions, marked as (1), (2) and (3) in (a).

Figure 4 schematically illustrates the formation process of TGB γ precipitate. In the first step, grain boundary face nucleation takes place. The orientation of those γ precipitates strongly depends on the grain boundary misorientation as well as the grain boundary plane orientation [3, 5]. Therefore, in the second step, similarly oriented γ phase particles forms a "film-like" γ phase by coalescence of the γ precipitates. Finally, the grain boundary nucleated γ phase grows to occupy the triple point. This type of γ phase, TGBγ, was the most frequently (72.5 %) observed. Thus, it is obvious that most of the triple points are not a predominant nucleation site in this alloy.

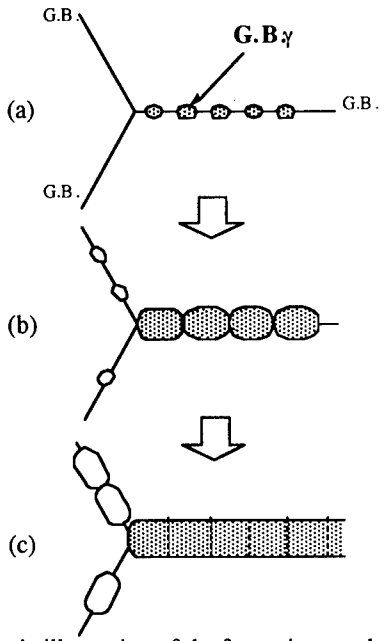


Figure 4: Schematic illustration of the formation mechanism of Type B.

Morphology and crystallography of Type A γ (TP γ)

Figure 5 shows a TEM micrograph of an α triple point in the specimen aged at 1423K for 600s. $\gamma 1$, $\gamma 2$ and $\gamma 3$ precipitates have nucleated at the grain boundary faces and have a "film-like" morphology. A globular $\gamma 4$ phase, located at the junction of the other phases, contacts all adjacent α grains. In this case the $\gamma 4$ phase presumably nucleated at the grain boundary triple point. According to Kikuchi pattern analysis, misorientation angles of $\alpha 1/\alpha 2$, $\alpha 2/\alpha 3$ and $\alpha 3/\alpha 1$ grains were 35.6 deg., 50.4 deg. and 55.2 deg., respectively. The $\gamma 4$ precipitate has a near Nishiyama-Wassermann (N-W) OR, i.e., $(011)\alpha 3 / (\bar{1}11)\gamma 4$, $[100]\alpha 3 / [110]\gamma 4$, with respect to $\alpha 3$ grain and near $(110)\alpha 2 / (1\bar{1}1)\gamma 4$ plane parallel OR with respect to $\alpha 2$ grain. No specific orientation relationship was observed with the $\alpha 1$ grain.

Figure 6 indicates the smallest misorientation angle between {111} planes of the γ phases ($\gamma 1$, $\gamma 2$, $\gamma 3$and $\gamma 4$) and {110} planes of the three α grains. The $\gamma 4$ phase has the smallest total misorientation angle with respect to the three α grains. This suggests that the $\gamma 4$ has the best coherency with the three α grains in these γ phases. In addition, the $(011)\alpha 3$ plane, in which the $\gamma 4$ phase and the $\alpha 3$ grain has a near N-W OR, found to lie nearly parallel to the grain boundary triple line. As demonstrated by Lee and Aaronson [6], the activation energy of critical nucleus formation decreases as the angle between grain boundary plane and habit plane of the nuclei decreases. Similarly, if the habit plane (in this case $(011)\alpha 3 / (\bar{1}11)\gamma 4$) of the nucleus lies more parallel to the grain boundary triple line, the length of triple line vanished by the nucleation will increase. Therefore, the activation energy of critical nucleus formation at the triple line (appears as a triple point in the microstructure) will decrease with the decreasing angle between the triple line and the habit plane. Thus the triple line direction has a significant influence on the orientation determination of TP γ .

The results shown in Figs.5 and 6 suggest that triple point γ phase (TP γ) should have good coherency simultaneously with three α grains in order to reduce the total interfacial energy. However, it seems to be not easy to satisfy such a strict crystallographical condition at all times. In other words, in many cases such orientation restrictions will prevent triple point nucleation even if the triple point has a relatively high energy. That is, the γ phase will precipitate more readily at a grain boundary face than at a triple point, since the orientation restriction is less significant in the grain boundary nucleation. Furthermore, if the TGB γ phase grows to occupy the triple point, the total free energy decreases by extinction of the triple point. Triple point nucleation depends not only on the grain boundary energy but also on the interfacial energy, which is caused by orientation relationship among matrix grains and product phase. Thus, the triple point of grain boundary will not be a preferential nucleation site at all times; this agrees well with the experimental observations.

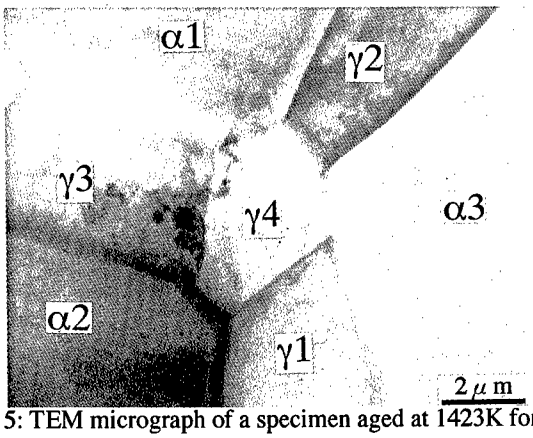


Figure 5: TEM micrograph of a specimen aged at 1423K for 600s.

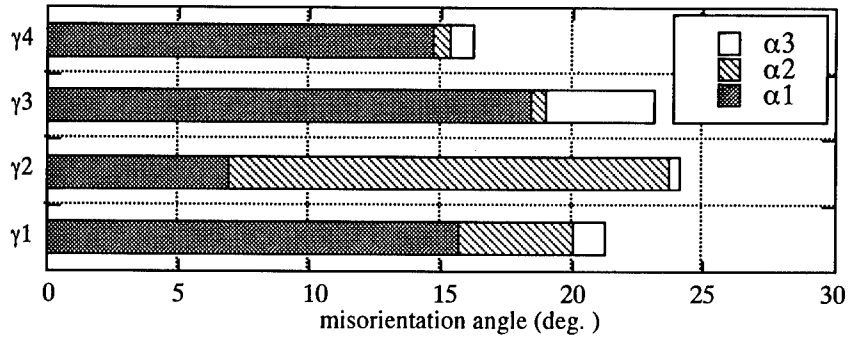


Figure 6: Misorientation angles between {110}α1,2,3 and {111}γ 1,2,3,4 planes.

Conclusion

The morphology and crystallography of a γ phase formed at or adjacent to α triple points in an Fe-24Cr-7Ni alloy was investigated with TEM and SEM. The crystallography among γ and α phases were analyzed by ECP and Kikuchi patterns. The conclusions are as follows:

(1) Three types of triple point area γ precipitation can be classified.

Type A: Triple point γ nucleation. Morphology is a globular at triple point. (19.2% frequency)

Type B: Grain boundary face γ nucleation. The γ phase occupies the triple point but is not nucleated at the triple point. The morphology is an elongated grain boundary film in the late stage of aging. (72.5% frequency)

Type C: Precipitation free triple point. (8.3% frequency)

(2) Triple point nucleation depends on both the grain boundary energy as well as the interfacial energy between precipitate and matrix grains. Therefore, orientation relationship as well as triple line direction strongly influences the nucleation behavior at triple points.

Acknowledgement
The authors appreciate to Professor George C. Weatherly (McMaster University, Canada) for his useful suggestion.
This work was supported by the Grant-in-Aid for Scientific Research on the Priority Area, "Phase Transformation" from the Ministry of Education, Science and Culture, Japan.

References

1. P. J. Clemm and J. C. Fisher, "The Influence of Grain Boundaries on the Nucleation of Secondary Phases," Acta Met., 3 (1955), 70-73.
2. W. Huang and M. Hillert, "The Role of Grain Corners in Nucleation," Metall. Mater. Trans.A, 27A (1996), 480-483.
3. K. Ameyama et al., "Morphology and Crystallography of the Precipitation of Austenite at Ferrite Grain Boundaries in Two-Phase Stainless Steel," J.Japan Inst. Metals, 50 (1986), 602-611.
4. T. Furuhara et al., "Crystallography of Grain Boundary α Precipitates in a β Titanium Alloy," Metall. Mater. Trans.A, 27A (1996), 1635-1646.
5. K. Ameyama et al., Advances in the Science and Technology of Titanium Alloy Processing (The Minerals, Metals & Materials Society, 1997), 459-466.
6. J.K.Lee and H.I.Aaronson, "Influence of faceting upon the equilibrium shape of nuclei at grain boundaries - II," Acta Met., 23(1975), 809-820.

Rapid Prototyping

Novel Applications and Implementations of Shape Deposition Manufacturing

Fritz B. Prinz, Stanford University

Lee E. Weiss, Carnegie Mellon University

Abstract

Shape Deposition Manufacturing (SDM) is a solid freeform fabrication (SFF) process which incrementally builds up complex parts by systematically combining material additive processes with material removal processes. The advantages of each type of process are thus combined such that novel structures can be fabricated with SDM which could not be practically fabricated with either material additive or material removal processes alone. Examples of such structures described in this paper include a waterproof wearable computer with embedded electronics, a composite steel/copper injection mold tool, and a mesoscopic turbine wheel assembly. In addition, this article presents a novel implementation of a SDM system based upon the integration of deposition apparatus (i.e., material additive process) with an existing CNC milling machine (i.e., a material removal process). Such an implementation is a cost-effective way to create high-quality SFF machines.

1. Introduction

Most solid freeform fabrication (SFF) systems are based upon a material additive, layered manufacturing paradigm. Computer-aided-design (CAD) models are first decomposed into thin 2-1/2D cross-sectional layer representations, then physical parts are built up in custom fabrication machines, layer-by-layer, using material additive processes (1). Layers of sacrificial structures are simultaneously built up to fixture and support the growing shapes. While layered manufacturing facilitates rapid prototyping of arbitrarily complex shapes, the resulting surface finish and accuracy, which are critical factors for being able to fabricate functional parts, can be compromised by the discretization process. High accuracy and quality surface finishes, required for such applications as custom tooling, precision assemblies, and structural ceramics, are best achieved with material removal processes such as 3 and 5-axis computer-numerically-controlled (CNC) milling and electrical discharge machining (EDM) machines.

Shape Deposition Manufacturing (SDM) is a SFF process for which the original goal was to combine the advantages of geometry decomposition and material addition with the advantages of material removal processes (Figure 1). The basic SDM fabrication methodology is to deposit individual segments of a part, and of support material structure, as near-net shapes, then machine each to net-shape before depositing and shaping additional material (2). This method takes advantage of the basic SDM decomposition strategy which is to decompose shapes into segments, or 'compacts', such that undercut features need not be machined, but formed by depositing onto previously deposited and shaped segments. For example, undercut part features are formed by depositing onto shaped support material compacts, and vice-versa. In addition, the decomposition plan preserves the 3D geometry information of the outer surface of each compact so that the desired shape of the CAD model can be accurately replicated when 5-axis machining is* available. Each compact in each layer is deposited as a near-net shape using one of several available deposition processes which are described in subsequent sections. The thickness* of each compact depends not only on the local part geometry, but also on deposition process constraints. After the entire part is built up, the sacrificial support material is removed to reveal the final part.

* Prepared for publication in the Naval Research Review.

The Third Pacific Rim International Conference on
Advanced Materials and Processing (PRICM 3)
Edited by M.A. Imam, R. DeNale, S. Hanada,
Z. Zhong and D.N. Lee
The Minerals, Metals & Materials Society, 1998

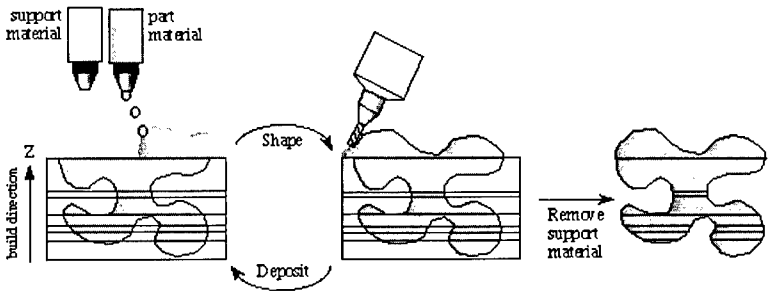


Figure 1. Shape Deposition Manufacturing

In addition to the rapid prototyping of complex shapes, selective additive material processing enables the fabrication of multi-material structures and it also permits prefabricated components to be embedded within the growing shapes as depicted in Figure 2a. Another goal of SDM research is to investigate how the capability to fabricate such heterogeneous structures enables the manufacture of novel product designs (3). An example of the compact splitting strategy and sequence for depositing and shaping materials for a typical layer of a heterogeneous structure is depicted in Figure 2b. Note how the undercut surface of a compact is formed by depositing onto the machined surface of another compact beneath it. Several examples of heterogeneous designs are described in subsequent sections including a waterproof wearable computer with embedded electronics, and a composite steel/copper injection molding tool. In addition to heterogeneous designs, novel assemblies of parts can also be directly built up with SDM by using sacrificial material to separate the individual parts. An example of a miniature metal turbine assembly is described in this paper.

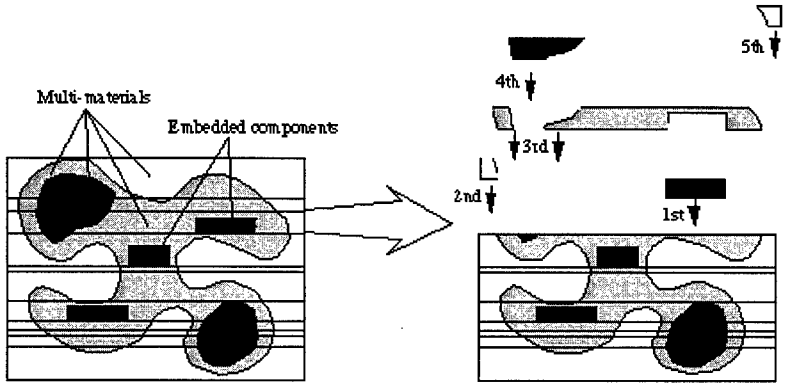
Another key issue for our research is how to implement SDM in a cost effective fashion? Until recently, SDM operations have been executed by building up the parts on pallets and transferring them to individual operating stations using a robotic palletizing system (4). Robotic manipulation was used in order to create a flexible system, for an R&D environment, which could be easily modified in order to investigate alternative deposition, shaping or other intermediate processing operations. Such a system, however, is too expensive and large for general dissemination of this technology. The next section describes a novel, cost effective, and compact implementation of SDM.

2. Integrated CNC Shaping and Deposition Machine

Commercialized SFF systems are customized machines, and high performance SFF apparatus can be relatively expensive. As an alternative to customization, or to robotic automation, we are exploring implementing SDM by simply adding deposition apparatus directly to existing CNC milling machines such as are typically found in machine shops throughout the world. In addition to shaping operations, the CNC milling machine provides the precision motion control required for deposition. When not being used for SDM, such an integrated CNC deposition and shaping machine can still be used as a conventional milling machine.

For one example, the integrated CNC deposition/shaping machine shown in Figure 3a is being used to investigate the fabrication of 'green' ceramic structures using an extrusion deposition process (5). The machine is based upon a commercially available Fadal VMC-15, 3-axis mill with an automatic tool changing carousel1. An Advanced Ceramics Research extruder^2 is mounted on a pneumatically-actuated slide which is attached to the Z-axis spindle housing of the CNC machine. The slide is retracted when the extruder it is not in use (e.g., during machining) and lowers the extruder into the

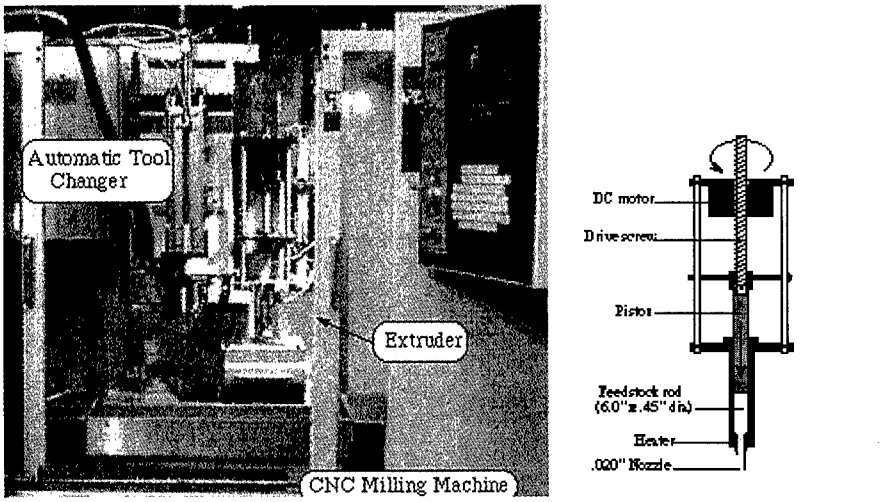
workspace during deposition. The extruder is used to deposit both support and part materials; currently, we manually switch extrusion tubes/nozzles preloaded with the different materials.



a. Example of a heterogeneous structure.

b Sequence for deposition and shaping; each compact is deposited, then shaped before proceeding to next compact.

Figure 2. Multi-material structures with embedded components.



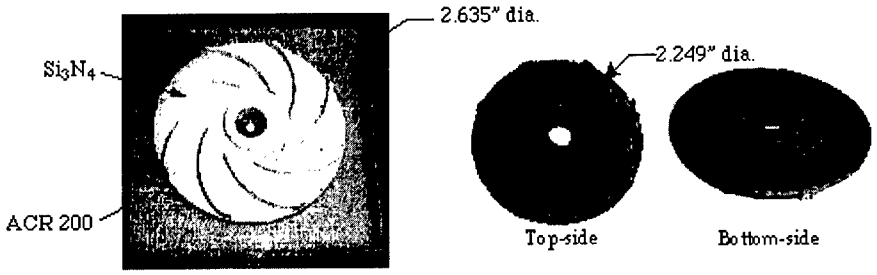
a. Fadal VMC-15 CNC milling machine with integral extruder. **b.** ACR extrusion apparatus.

Figure 3. Integrated CNC shaping/deposition machine for SDM.

An example of a 'green' ceramic part built on the integrated SDM machine is shown in Figure 4. The part material is silicon nitride, and the support material is ACR 200 which is a proprietarynon-ionic, water-soluble, machinable thermoplastic. While this particular shape could have been cut directly from a block of 'green' ceramic stock, such conventional machining would require reorienting, refixturing, and registering of the part after one side has been cut, since this shape has under-cut

features. Another advantage of SDM over conventional machining is that first depositing shapes in near-net, before machining, reduces the waste of costly materials.

We have also explored building integrated SDM machines for welding (6). And, we are currently creating an SDM machine for fabricating wax molds for molding gel-cast or thermoset materials (5).



a. Green Si_3N_4 part.

b. Part after pressureless sintering in N_2 at 1750^0C.

Figure 4. Example of a part built with an integrated SDM CNC shaping/deposition machine.

3. Heterogeneous Structures

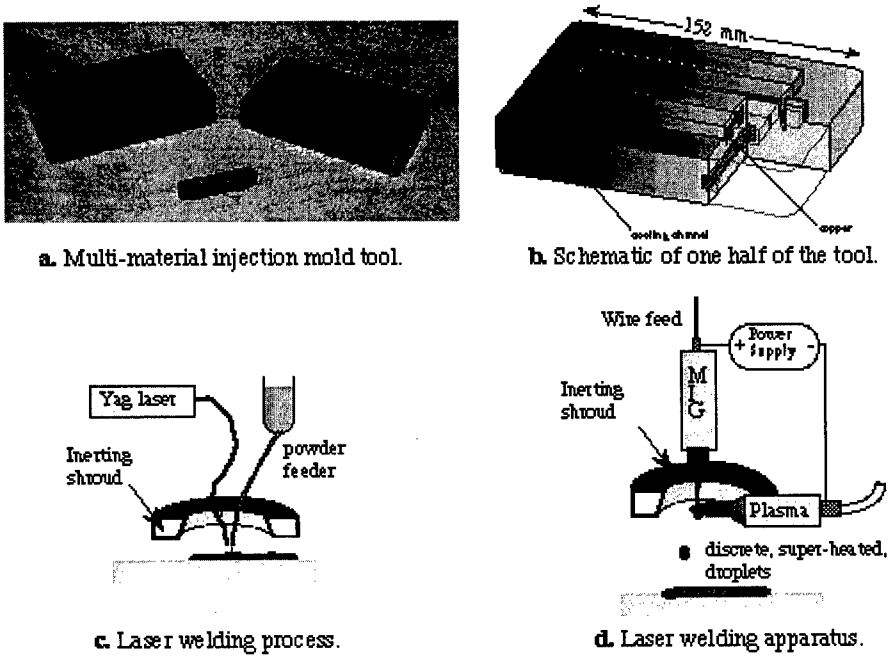
We believe that one of the most important roles for SFF in the future will be to help manufacture heterogeneous product designs. Several of these novel products which have been built with SDM are described below. While conventional manufacturing methods could have been used to fabricate these products, there methods would have required additional time-consuming operations, including the need for custom fixturing and tooling, complex assembly operations, and high-strength material joining processes.

3.1. Steel/Copper Injection Mold Tooling

SFF has been widely investigated for fabricating custom tooling with complex molding surfaces, as well as with conformal internal cooling channels for thermal management. With SDM, even more advanced tools can be fabricated from multi-materials such as steel/copper composites. For example, Figure 5a shows a composite 316L stainless steel injection molding tool produced by SDM using robotics-controlled laser welding and microcasting deposition processes (7). One half of the tool, which is shown schematically in Figure 5b, has four internal copper deposits for temperature equilibration. Both halves of the tool have a "U"-shaped channel for water cooling during the molding process. The channels were formed by sacrificial copper which was removed by etching in nitric acid. Portions of the cavities contained small features which could not be cut with end mills and these were finished with EDM.

In this tool, the steel was deposited with a laser welding process (Figure 5c). A 2.4 kW CW Nd:YAG laser scans over the substrate and a melt pool forms into which metal powder is injected (Figure 5c). The injected powder fuses onto the substrate, leaving a bead of deposited material in its wake. While this laser welding process is very precise, in comparison with conventional welding methods, it cannot effectively deposit copper due to copper's high reflectively. Therefore, microcasting was used to deposit the copper (Figure 5d). Microcasting is a non-transferred welding process which deposits discrete droplets of super-heated molten metal(6).

In addition to creating steel/copper structures, the laser system has also been used to deposit INVAR®, a low coefficient of thermal expansion (CTE) nickel alloy, onto copper which was



a. Multi-material injection mold tool.

b. Schematic of one half of the tool.

c. Laser welding process.

d. Laser welding apparatus.

Figure 5. Multi-material metal structures built with SDM.

previously deposited onto steel. Such multi-material structures will have significant advantages in a wide variety of applications. In dies for composite forming, for example, the steel substrate would provide a solid base for the die, the copper would serve to equilibrate temperatures and eliminate hot spots in the tool, and the low CTE metal would resist geometry changes due to thermal expansion. Ideally, the transition between different materials should be functionally graded. The laser system is particularly suitable for producing functional-gradient, multi-material parts because different materials can be continuously alloyed during the build process by simply mixing the powders which are fed to the melt pool.

3.2. Embedded Electronics

Another example of a heterogeneous design is an embedded electronic device fabricated by building up a nonconductive housing package and simultaneously embedding and interconnecting electronic components within the housing. With this approach it is feasible to relatively quickly fabricate compact, rugged, customized computer modules in small lot sizes. This capability is particularly well suited for military applications to manufacture mission-specific, conformal shaped 'smart' devices such as wearable computers tailored for an individual soldier or a small military unit. These computers might store maps, equipment descriptions, help to log data, or provide communication links.

For one example, the 'Frogman' shown in Figure 6a and 6b is a water-proof computer which can store maps for navigational aids, or detailed assembly drawings for service, maintenance, or field operations. The graphical information, which is stored on PCMCIA cards, is displayed on a heads-up display (Figure 6c). A conformal shaped rear surface was also required so that the unit could be comfortably strapped to a diver's leg. The device is built up in layers of polyurethane (PU) and sacrificial wax. The PU is deposited as a 2-part thermoset (left side of Figure 6d). The wax can be extruded with a conventional hot-glue gun (right side of Figure 6d), or thick layers can be poured from

a hot-melt pot. The fabrication details, including component embedding and interconnection are described in detail in (8). The important points are that custom tooling was not required to manufacture the Frogman and that embedding facilitates waterproofing.

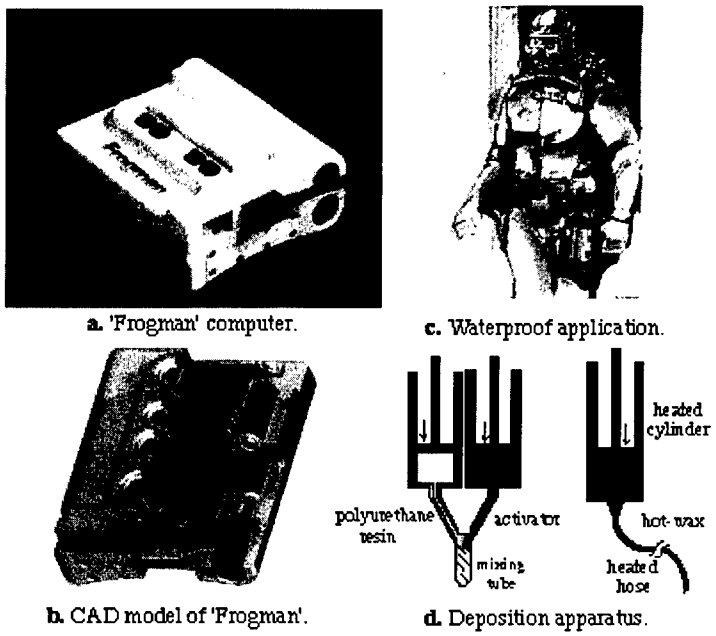


Figure 6. Embedded Electronics

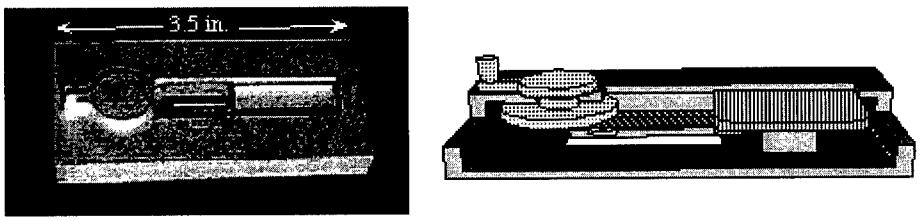
4. Integrated Assemblies

SDM has also been used to build up simple assemblies and mechanisms in a single operation. As an assembly is being built up, its individual components are seperated by and encased within sacrificial support material. After the assembly structure has been completely built up, the sacrificial material is removed, freeing the components to move with respect to each other. For example, SDM was used to create the steel crank mechanism shown in Figure 7. In this mechanism, a piston is connected to a crank shaft with a connecting rod. Turning the crank causes the piston to move back and forth in its chamber. The mechanism components are 316L stainless steel, deposited with laser welding, and the sacrificial support material was microcast copper.

The capability to create such integrated assemblies may be particularly useful for producing miniature mechanisms where discrete assembly is difficult, i.e., similar to the micro-electro-mechanical systems (MEMS) paradigm. To demonstrate the feasibility of SDM for the fabrication of structures with feature sizes in the range of tens to hundreds of and thousands of microns, several simple artifacts have been built (9). This regime has been recently referred to as the 'mesoscopic regime' which means that characteristic feature dimensions are bigger that those typically achieved using VLSI fabrication methods yet smaller than parts produced using conventional processing techniques.

In SDM, mesoscopic structures are built up using sputtering and electro-plating deposition processes, and shaped with micro CNC or EDM machining. For one example, the 1.1mm high nickel structure shown in Figure 8a consists of a wheel (5mm, 0.3mm thick) which is permanently mounted

on a nickel axle (1mm). The SEM photograph in Figure 8b shows a cross-section of the wheel and axle before removal of copper support structure.



a. Steel crank and piston mechanism. b. Schematic of mechanism.

Figure 7. Complete assemblies and mechanisms directly built up with SDM.

Additional examples of novel SDM mesoscopic integrated assembles are shown in Figure 9. Figure 9a is a nickel substrate carrying nine mesoscopic wheels. This structure suggests the possibility for building massively parallel miniature machinery. Figure 9b shows a 130um thick microturbine impeller which rotates at high speeds when air is passed through the gas jets. This structure establishes the feasibility of building assembled devices with clearances on the order of less than 20um.

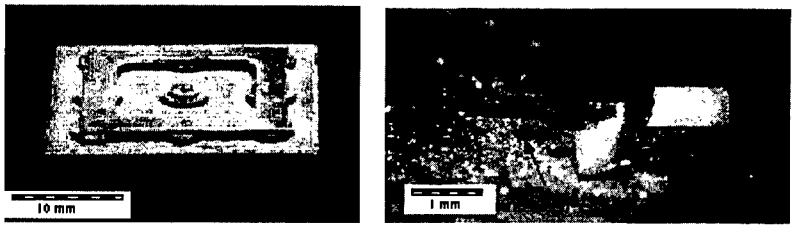


a. Mesoscopic Ni wheel b. Cross-section of wheel, axle and support structure

Figure 8. Mesoscopic nickel wheel on axel built with SDM.

5. Discussion

SFF has been successfully used within the limited realm of Rapid Prototyping. However, as SFF processes improve and are able to build functional, engineering models, SFF will be used for mass customization. i.e., customers able to order products in small-lots (as small as one) customized for their specific needs. SFF will not only enable 'mass-customization', but also by opening up the design space, novel designs will be possible. One class of such novel designs are heterogeneous structures, such as embedded electronics, and another class is integrated assemblies as described in this article. For heterogeneous structures to be practical, however, streamlined CAD systems will be required which enable concurrent representation and manipulation of geometry, material and embedded components. Other possible novel designs will involve functional gradient structures such as ceramic to metal parts or graded metal to metal structures allowing the transition from highly thermally conductive regions inside to tough surfaces on the outside of a part. Beyond these novel applications of SFF, it is hard to predict where exactly this will lead to when creative people have access to SFF technology. Undoubtedly, the creation of products which no one has even conceived of as yet will be one of the likely outcomes.



a. Assembly of nine mesoscopic wheels. b. Miniature turbine impeller.

Figure 9. Examples of mesoscopic assemblies.

Acknowledgments

This work has been supported by ONR, DARPA, and NSF. The authors acknowledge the following individuals for their contributions in creating the systems and artifacts described in this article: Gennady Neplotnik, Larry Schultz, Robert Merz, Alexander Cooper, John Fessler, John Keitzman, and John Lombardi.

References

1. Weiss, L.E., Solid Freeform Fabrication Processes Overview, in Japanese Technology Evaluation Center and World Technology Evaluation Center Panel Report on Rapid Prototyping in Japan and Europe, Analytical Chapters, ed. G. M. Holdridge, SME, I, 5, (1997).
2. Merz, R., Prinz, F.B., Ramaswami, K., Terk, M. and Weiss, L.E., Shape Deposition Manufacturing, Proceedings of the 1994 Solid Freeform Fabrication Symposium, The University of Texas At Austin, eds. Harris Marcus, J.J. Beaman, J.W. Barlow, D.L. Bourell and R. Crawford, August, 1, (1994).
3. L.E. Weiss, R. Merz, F.B. Prinz, G. Neplotnik, P. Padmanabhan, L. Schultz, K. Ramaswami, Shape Deposition Manufacturing of Heterogeneous Structures, SME J.of Manufacturing Systems, 16, 239, (1997).
4. Weiss, L.E., Hartman, K., Krishman, R., Merz, R., Neplotnik, G., Prinz, F.B., Schultz, L., and Terk M., Robotic-Assisted Shape Deposition Manufacturing, in Proceedings of 1994 IEEE International Conference on Robotics and Automation, 2890, (1994).
5. Kietzman, J.W., Cooper, A.G., Weiss, L.E., Schultz, L., Lombardi, J.L., and Prinz, F.B., Layered Manufacturing Material Issues for SDM of Polymers and Ceramics, 1997 Solid Freeform Fabrication Symposium, The University of Texas At Austin, 133, (1997).
6. R. Merz, "Shape Deposition Manufacturing", PhD. Dissertation, Institut für Allgemeine Elektrotechnik und Elektronik, Technische Universität Wien, (1994).
7. Fessler, J.R., Merz, R., Nickel, A.H., Prinz, F.B., and Weiss, L., Laser Deposition of Metals for Shape Deposition Manufaturing, 1996 Solid Freeform Fabrication Symposium, The University of Texas At Austin, August, 117, (1996).
8. Weiss, L.E., Neplotnik, G., Prinz, F.B., Schultz, L., Padmanabhan, P, Krishnan, R., and Merz, R.., Shape Deposition Mnaufacturing of Wearble Computers, 1996 Solid Freeform Fabrication Symposium, The University of Texas At Austin, 31, (1996).
9. Merz, R. and Prinz, F.B., Rapid Prototyping of Mesoscopic Structures, Proc. of the 7th International Conference on Rapid Prototyping, ed. A. Lightman, San Francisco, March, 261, (1997).

(Footnotes)

(1) Fadal Engineering, Chatsworth, CA.
(2) The extruder and the feedstock materials are manufactured by Advanced Ceramics Research Corporation, Tucson, AZ.

THE PRODUCTION OF PRESINTERED MAGNETIC FERRITE AND PROCESS AUTOMATION

Liu Rixin Xu Chenghao Xu Ying Wang Shenran Zhang Quanlai
Liao Youliang Yi Xiaozhong Zhou Bin Zhang Xiaogang
Beijing General Research Institute of Mining and Metallurgy
Beijing, 100054, China
Email: rxliu@home.icm.ac.cn
http://159.226.63.200/~rxliu

Abstract

The production of presinterd ferrite magnet and the process automation were introduced. The control results showed that the temperature could be controlled within ±10 ℃. Compared with the manual control, the maximum energy product $(BH)_{max}$ was increased by 9.4% in automatic control. It improved the level of process automation greatly. It was beneficial to improving the product quality and stability, to accelerating the development of new products, and to reducing the energy consumption. At the same time, good economic benefits could be obtained.

The Third Pacific Rim International Conference on
Advanced Materials and Processing (PRICM 3)
Edited by M.A. Imam, R. DeNale, S. Hanada,
Z. Zhong and D.N. Lee
The Minerals, Metals & Materials Society, 1998

Introduction

Beijing General Research Institute of Mining and Metallurgy has 10 sets of permanent magnetic ferrite presintering materials production line, two sets of magnetic powder production line. It mainly produces ferrite, rare earth alloys and their magnets. In accordance with the ISO9002 system standards, it has set up a comprehensive management system, including information collection, product research and development, quality assurance and after-sale service. The main products are as follows: anisotropic strontium presintered ferrite, anisotropic barium presintered ferrite, isotropic strontium presintered ferrite, powders for bonded magnets, isotropic barium ferrite powder for ceramic magnets, ceramic magnets, bonded ferrite magnets as well as rare - earth magnets.

This paper deals with a rotary kiln used when producing magnetic materials presintered with heavy oil. The kiln typically operates at atmosphere pressure. Reported problem[1] is that some ferrite powders adhere on the inner wall of kiln because of the high temperature. Another reported problem[2] is that it is very difficult to measure the exact process temperature under different flow cross sections because of the movement of high temperature zone. Some work[3] was done to analyse the process. This paper mainly discusses the production of presintering ferrite and the process automation.

The Production of Presinterd Ferrite Magnet

The general formula $MO.6Fe_2O_3$ describes the chemical composition of ferrite permanent magnets, where M generally represents barium or strontium or any combination of the two. Ferrite magnets are generally formed by a compression or extrusion molding techniques which is then followed by sintering. Finish grinding of shaping was dome when necessary for the better control of dimensions.

The presintered ferrite is the material for the magnets. The main raw materials of presintered ferrite are iron scale or iron oxide, $SrCO_3$ or $BaCO_3$ and little additions. In order to get the high quality of presintered magnetic materials, the required composition[4] is TFe>72%, SiO_2<0.3%. According to the phase analysis, iron scale is composed of FeO and Fe_3O_4 as well as a little Fe_2O_3 and metal Fe. The processes of production of presintered ferrite include pelleting, drying, preheating, sintering, cooling and packing. Three kinds of methods and equipment are used in the drying, preheating and sintering:

1) Chain dryer - rotary kiln process
2) Canister dryer - rotary kiln process
3) Rotary kiln process

The first method is used to produce the presintered ferrite in BGRIMM. The pellets are put on the chain plate. Because of the pellets stay static relatively, this process produces little powder, and the temperatures at each zone are easy to controll. In the kiln, the iron scale must be oxidized and the Fe_2O_3 react with $SrCo_3$ or $BaCO_3$ to generate M phase. In order to get single M phase, the process must be controlled strictly. The most important parameter is the process

temperature. The typical magnetic properties of presintered ferrrite are shown in Table I.

Table I The typical magnetic properties of presintered magnet materials[5]

product name	SF30		BF25		SF35		SF34		BT-F1		BT-F2		BT-F3	
ferrite type	strontium		barium		strontium		strontium		barium		barium		barium	
wet/ dry compression	wet	dry	wet	wet	wet	dry	wet	dry	dry	dry	dry	dry	dry	dry
isotropic/anisotropic	aniso	aniso	aniso	aniso	aniso	aniso	aniso	aniso	iso	iso	iso	iso	iso	iso
average size, μm	0.85	0.85	0.85	0.95	0.78	0.78	0.78	0.78	0.90	0.90	0.85	0.85	0.85	0.85
radial contractility, %	13.0	13.5	13.5	12.0	13.0	13.5	12.0	12.5	15.0	15.0	15.0	15.0	15.0	15.0
density, g/cm^3	4.8	4.7	4.9	4.9	4.9	4.7	4.8	4.7	4.9	4.9	4.9	4.9	4.9	4.9
direction	//	//	//	//	//	//	//	//	//	⊥	//	⊥	//	⊥
Br, (Gs)	3900	3650	3950	3900	4030	3700	3800	3550	2300	2150	2350	2000	2250	1950
Hcb,(Oe)	2800	2950	2050	2000	2800	2900	3430	3300	1800	1700	1850	1600	1800	1550
Hcj, (Oe)	2950	3150	2100	2050	2950	3100	3800	3850	3200	3220	3000	3040	2700	2750
$(BH)_{max}$ (MGOe)	3.60	3.10	3.40	3.30	3.86	3.20	3.46	3.00	1.05	.095	1.10	0.75	1.00	0.70

* note: // and ⊥ represent parallel and vertical compression direction, respectively.

The Process Automation and Computer Optimum Control

In order to assure the product quality, to operation continuously and to save the energy consumption, it is very important to control the sintering process of ferrite in the rotary kiln, especially to control the process temperature. When the process is under manual operation, the temperature control level is ±30 ℃. Because the thermocouples are accreted by presintering powder and the thermocouples are rotated with the movement of kiln, it is very difficult to measure the actual materials temperature. In fact, the most important temperature is the actual temperature of magnetic materials, not the temperature of waste gas or temperature measured by thermocouple or by infrared meters. It is very hard to measure the actual temperature in real time. Therefore, we must use the measured temperature to control the sintering process. With the development of infrared technology, Infrared temperature meter can be used to measure the process temperature and used to control the process.

After a lot of investigations, we conclude that the kiln can be well controlled and the process temperatures can be controled within ±10 ℃ . The main parameters are flow of heavy oil, temperature of heavy oil, the flow of air, production rate and rotary rate of kiln. When the production rate and the rotary rate of kiln are in the steady conditions relatively, the flow of heavy oil, temperature of oil and flow of air are the main parameters.

The distributed computer control systems are adopted to control the industrial furnaces and kilns in most cases. Our control system includes SPC, DDC and field bus. The schematic diagram of computer control system for rotary kiln is shown in Fig. 1. The mathematical models are calculated and the temperature setpoint values are obtained in SPC. The controls of temperature and pressure are performed in DDC. The data transfer and communication

between SPC and DDC are performed by the way of field bus.

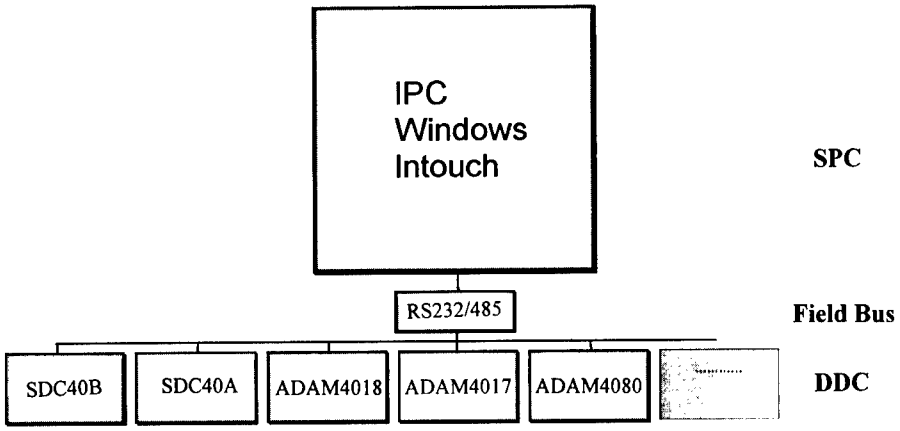


Fig. 1 Schematic Diagram of Computer Control System for Rotary Kiln

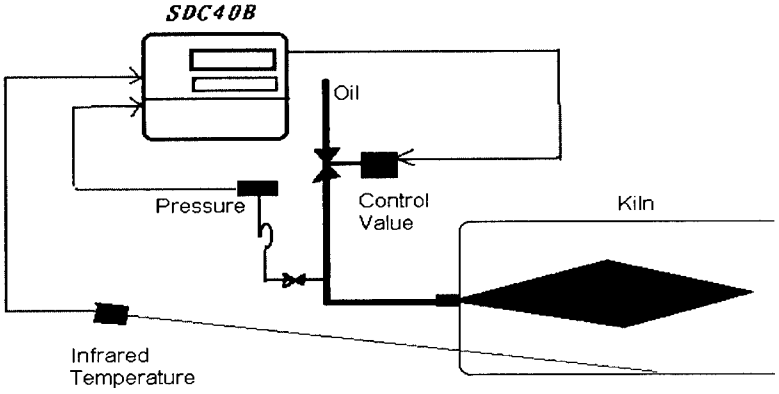


Fig. 2 Diagram of Infrared Temperature Control System for Rotary Kiln

The schematic diagram of infrared temperature control system for rotary kiln is shown in Fig. 2. The cascade control and modern fuzzy control technology are adopted.

After the control system is put into practical use, it operates in good condition. The control results show that the temperature can be controlled within ±10 ℃. The magnetic properties of

products under manual and automatic control condition are shown in Fig. 3. Compared with the manual control, the maximum energy product $(BH)_{max}$ is increased by 9.4% in automatic control.

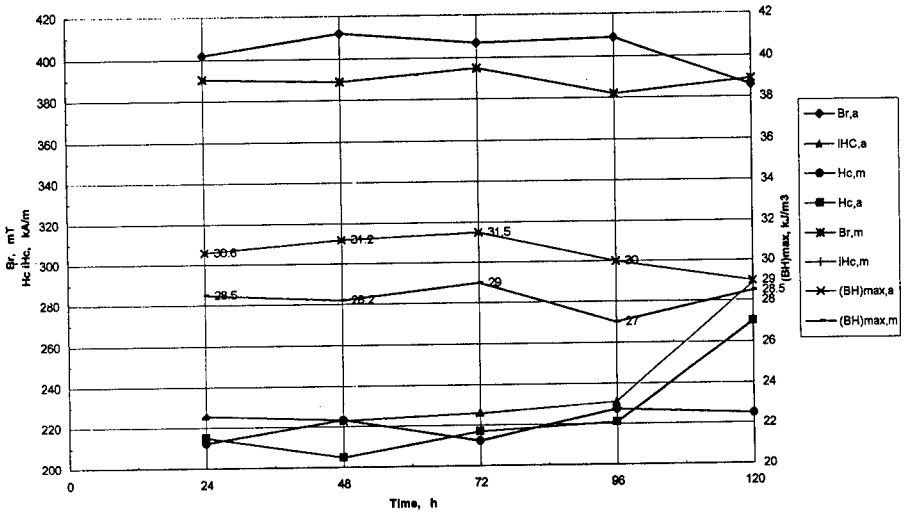


Fig. 3 The Comparison of Magnetic Properties of Presintered Ferrite under Manual and Automatic Conditions

After the control system has been put into practical use for more than one year, the following results are obtained:

1. The first computer control system for ferrite kiln is established. It improves the level of process automation greatly.
2. The infrared temperature can be controlled within ±10℃. It is beneficial to improving the product quality and stability, to accelerating the development of new products.
3. The oil temperature can be controlled within ±2℃. It is beneficial to reducing the energy consumption.
4. The infrared technology can be used to measure the temperature of kiln. It is beneficial to reducing the thermocouple consumption.
5. Working conditions are improved and the working strength is decreased.
6. Good economic benefits can be obtained.

Conclusion

After the control system is put into practical use, it operates in good condition. The control results show that the temperature can be controlled within ±10 ℃. Compared with the manual control, the maximum energy product $(BH)_{max}$ is increased by 9.4% in automatic control. It

improves the level of process automation greatly. It is beneficial to improving the product quality and stability, to accelerating the development of new products, to reducing the energy consumption. At the same time, good economic benefits can be obtained. This control system can be used in similar kilns.

Acknowledgment

Financial support from The National Natural Science Foundation of China (Grant No:59604007) is greatly acknowledged.

References

1 Liao Youliang, "Study on Process Intensity for Pre-sintering Ferrite Pellet", Progresses of Sciences and Technology in Metallurgical Engineering, Vol.2, (Beijing: Metallurgical Industry Press, 1996), 310-313.

2 Yi Xiaozhong, "A Temperature Control System for Presintered Ferrite Rotary Kiln", Progresses of Sciences and Technology in Metallurgical Engineering, Vol.2, (Beijing: Metallurgical Industry Press, 1996), 396-400.

3 Liu Rixin, "Numerical Analysis of Presintering Magnetic Ferrite Kiln", (Paper presented at The 4th International CFX Users Conference, Chicago, October 6-10, 1997), 6.

4 Xu Chenghao, "Influence Factors on Preheating Pellet Properties of Permanent Magnet Materials and the Way of Improving Pellet Strength", Progresses of Sciences and Technology in Metallurgical Engineering, Vol.2, (Beijing: Metallurgical Industry Press, 1996), 279-282.

5 Beijing General Research Institute of Mining and Metallurgy, "Presintered Ferrets for Ceramic Magnets", (Beijing, 1997).

COMPARISON OF EXPERIMENT TO STEFAN SOLUTION FOR PLANAR FLOW SPIN-CASTING

B.L. Reed, X-Q. Zhang, and P.H. Steen

School of Chemical Engineering
Cornell University
Ithaca, NY 14853

Abstract

Casting of near-net thickness product promises savings in both capital and processing costs as well as increases in productivity in some cases. The key to commercialization of spin-casting using the planar flow technique lies in the consistent quality of the product. Next to material properties, uniformity of thickness and control of surface texture are crucial. A solution of the Stefan problem for wheelspeeds that are high compared to a typical solidification rate provides a framework for understanding the influences of superheat fraction and heat-transfer coefficient [1]. Comparison with aluminum product cast in our laboratory shows how the average solidification rate can be predicted or heat-transfer coefficient inferred if one or the other is known. Validation is carried out in cases where both are known independently, one by thermal and the other by mechanical means [2].

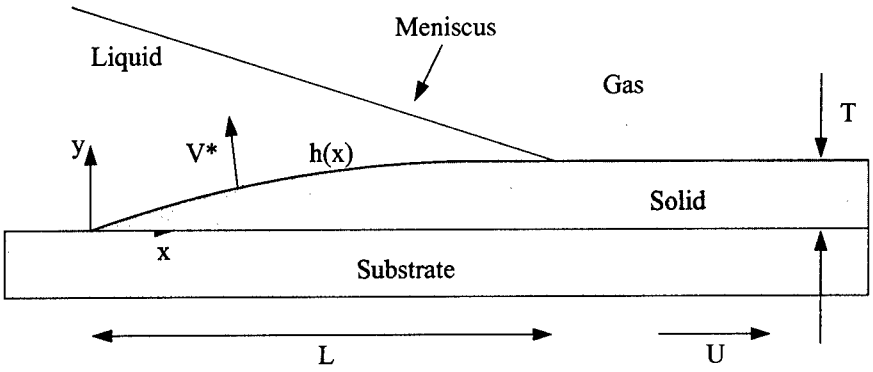
The Third Pacific Rim International Conference on
Advanced Materials and Processing (PRICM 3)
Edited by M.A. Imam, R. DeNale, S. Hanada,
Z. Zhong and D.N. Lee
The Minerals, Metals & Materials Society, 1998

Introduction

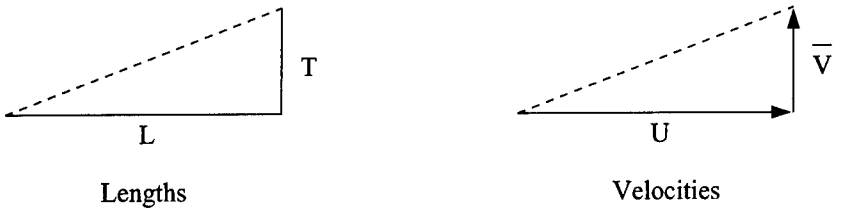
In planar flow casting, solidification occurs within the gap G between the nozzle face and the substrate which moves at a speed U. Figure 1a shows a sketch of this region with the nozzle face out of view at the top. The sketch is not to scale; the horizontal axis is compressed. Solidification starts at the substrate and stretches to the ambient gas where it ends at a line common to three phases. Let $\bar{V}$ be the average along the front of the local solidification rate V^*. Then, a steady state mass balance requires

$$TU = L\bar{V}. \tag{1}$$

Hence, high wheelspeeds ($\bar{V}/U \ll 1$) imply a small solidification slope ($T/L \ll 1$). Alternatively, in view of the constraint that all the solidification occurs within the gap ($T/G < 1$), the assumption of a long puddle ($L/G \gg 1$) implies a small slope and therefore high wheelspeed, according to (1). Moreover, for a long puddle, the average solidification direction is orthogonal to the substrate as sketched in the velocity triangle of figure 1b. The mass balance (1) dictates that the 'length' and 'velocity' triangles are similar triangles (figure 1b).



a. Definition sketch.



b. Length and velocity triangles.

Figure 1: Characteristics of planar flow spin-casting.

Length and velocity are related by a time, the time of solidification of a packet of liquid. This time depends on how efficiently the latent heat of fusion is removed and how fast material is supplied to the region. A solution of the appropriate Stefan problem provides this information. Stated differently, the Stefan solution gives the relative size of the length and velocity triangles.

A velocity reference is provided by the rate of freezing into a quiescent melt held just above its melting temperature (T_m), where the latent heat conducts through the already solidified material, presumed to be in perfect contact with a stationary substrate of temperature T_c. At a thickness G of solidified material, the freeze rate is given by

$$V \equiv k_s(T_m - T_c)/\rho\, \Delta\eta\, G. \tag{2}$$

Here k_s is the thermal conductivity of the solid and $\Delta\eta$ is the latent heat per unit mass. For imperfect contact with the substrate (heat-transfer coefficient H) and for a hot far-field melt (temperature T_h), the actual freeze rate may be expected to be lower by a fraction c,

$$c = \bar{V}/V. \tag{3}$$

The Stefan solution delivers c and thereby sets the scale of the velocity triangle.

Stefan Problem

The governing mass, momentum and energy equations in the liquid and solid domains can be simplified asymptotically, under the following assumptions, to yield a Stefan problem appropriate to the conditions of planar flow processing. i) Material properties are assumed to be constant and fixed at a suitable average temperature. ii) The heat and fluid flow are two-dimensional, justified by the large cross-stream dimension. iii) The puddle is long ($L/G \gg 1$), and iv) the Peclet number for the liquid motion is order one ($UG/\alpha \sim O(1)$). Here, α is the thermal diffusivity of the liquid. Further discussion of these assumptions and details of the reduction are given in Carpenter and Steen [1]. The following Stefan problem for the (dimensionless) shape of the interface, $y = h(x)$, results,

$$(c/\tau\Delta T)\mathrm{d}h/\mathrm{d}x = B/(1 + Bh) - B_0/(1 - h). \tag{4}$$

Here B is the Biot number for the solidified material and ΔT is the 'quench fraction', the fraction of the temperature drop that occurs across the solidified material and contact resistance. See Tables 1 and 2 for definitions. Boundary conditions are $h(0) = 0$ and $h(1) = \tau$, reflecting a scaling of y by G and x by L.

Table 1: Dimensional Parameters.

Lengths (m)	Speeds (m/s)	Temperatures (K)	Others
G	V	T_m	$\rho\Delta\eta(kg/ms^2)$
L	U	T_h	$k_s, k_l(J/msK)$
T	$\bar{V}$	T_c	$H(J/m^2sK)$

Table 2: Dimensionless Parameters

τ	$\equiv$	T/G	ΔT	$\equiv$	$(T_m - T_c)/(T_h - T_c)$
B	$\equiv$	HG/k_s	B_0	$\equiv$	$(k_l/k_s)(1 - \Delta T)/\Delta T$
A	$\equiv$	$1 + B_0$	D	$\equiv$	$(B - B_0)/(AB)$

An analytical solution to problem (4) was exhibited in [1] for the more general case where non-equilibrium kinetics at the interface are included. Our interest is in the prediction of

solidification rate, measured relative to the reference rate. The function $c(\tau; B, B_0, \Delta T)$ is obtained by applying the downstream boundary condition $h(1) = \tau$ to the general solution (which satisfies $h(0) = 0$),

$$\bar{V}/V = c = \tau A\Delta T/\{\tau^2/2 + (D-1)\tau + \tau/B + [D^2 - D + (D-1)/B]\log(1-\tau/D)\}. \quad (5)$$

Figure 2 shows the dependence of c on τ and the influence of B (contact resistance to heat-transfer). Note that c is indeed less than unity, confirming the choice of V as reference scale. The shape of the curves indicate a cut-off in thickness when heat-transfer is limiting. The cut-off thickness τ^* occurs when the solidification rate slows to zero, corresponding to $dh/dx = 0$ in equation (4), and giving $\tau^* = (B - B_0)/(B(1 + B_0))$. This cut-off occurs at thinner ribbons for increasing contact resistance (decreasing B), as expected. Over the flat portion, solidification is limited by the feed rate (or fluid flow). The dependence on superheat, $(1 - \Delta T)$, is similar with increasing superheat having an effect like increasing resistance.

Validation of Solution

Figure 2 gives the predicted behavior of $\bar{V}/V$ in terms of the Biot number and superheat fraction over a range of possible τ values. Comparison with experiment is needed to validate the solution. The most rigorous validation would determine all the parameters experimentally and compare to the value of $\bar{V}/V$ predicted from the Stefan solution. To accomplish such validation, one would need to measure τ, H, and $\bar{V}$, with the other parameters fixed during a cast. τ is measured for every cast and is thus readily available. Heat-transfer coefficients have been measured for our caster [3, 4]. In our laboratory, puddle lengths have been measured [4] in order to determine average solidification rates. To date, both heat-transfer coefficients and puddle lengths have not be measured for the same cast, though. A stringent test of the Stefan solution must wait. However, one can use the available data to estimate the unmeasured values and to illustrate the utility of the Stefan solution.

Comparison with Experiment

The measurements of Ibaraki [4] suggest that the puddle length is $L \approx 2.0 \pm 0.4$ *cm*. With this value, c can be calculated plugging equations (1) and (2) into equation (3). Since τ is also known, we have a fixed experimental point on figure 2 for a given cast. Using equation (5), we can adjust B to "best-fit" the experimental data. The determined value of B can be used to infer H, which can be checked against previously determined values. Figure 3 shows several data points distinguished by four different gap sizes, G. The points within each set are for similar conditions. The lines show the "best-fit" solution of equation (5). From these "best-fit" lines and the error estimate for the puddle length, H was estimated to be $(1.5 \pm 0.2) * 10^5$ W m^{-2} K^{-1}. This value compares favorably with the values reported by Kukura et al. [3] and Ibaraki [4] of 1.1 and $1.7 * 10^5$ W m^{-2} K^{-1}, respectively. Until a more rigorous test can be made, this data shows that the Stefan solution is consistent with available measurements and is useful for giving estimates of heat-transfer coefficients or, conversely, average solidification rates (alternatively, puddle lengths).

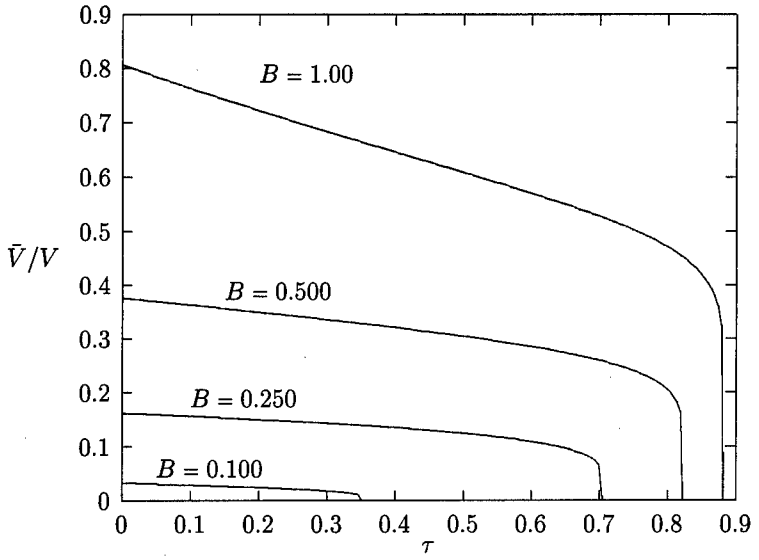


Figure 2: Effect of Biot Number, B, on $\bar{V}/V$. $B_0 = 0.062$ and $\Delta T = 0.865$ (typical of our experiments).

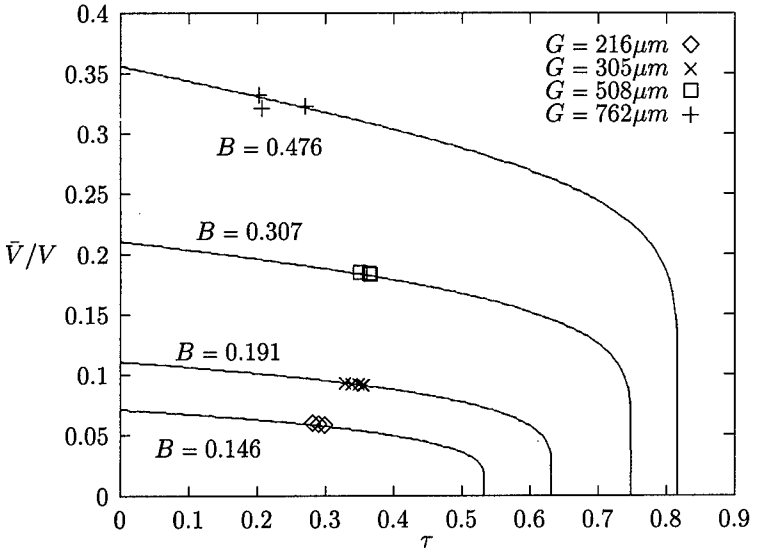


Figure 3: Comparison of Stefan solution to experimental data. $B_0 = 0.062$ and $\Delta T = 0.865$.

Conclusions

A Stefan problem and it's solution have been used to relate solidification rate to the thickness of ribbon produced by planar flow spin-casting. The solution is appropriate for conditions where the puddle is long yet solidification is completed within the gap before the ribbon breaks contact with the wheel.

Although the solution has yet to be subjected to a "no free-parameter" validation test, the available data suggest that this approach gives results in agreement with two other approaches, both requiring considerably more effort and expense. Also, this equation could be used in conjunction with solutions of the momentum equation (which would predict τ) to predict experimental outcomes *a priori*.

References

1. J.K. Carpenter and P.H. Steen, "Heat transfer and solidification in planar-flow melt-spinning: high wheelspeeds," Intl. J. Heat Mass Transfer, 40 (9) (1997), 1993-2007.

2. P.H. Steen and C. Karcher, "Fluid mechanics of spin casting," Annu. Rev. Fluid Mechanics, 29 (1997), 373-397.

3. J. Kukura et al., "Measurement of heat transfer coefficient in planar flow casting," Simulation of Materials Processing: Theory, Methods, and Applications, ed. S-F. Shen and P.R. Dawson (Rotterdam: A.A. Balkema, 1995), 1153-1157.

4. T. Ibaraki, "Planar-flow Melt Spinning: Experimental Investigation on Solidification, Dynamics of the Liquid Puddle and Process Operability" (M.S. thesis, Cornell University, 1996).

A Knowledge Based System for Rapid Prototyping of P/M Components

Dr. Lyndon Smith, Dr. Sagar Midha
University of the West of England
Bristol
BS16 1QY
UK

Abstract

By processing large amounts of knowledge relating to a particular domain such as Powder Metallurgy, Knowledge Based Systems can provide the information needed to achieve reductions in manufacturing lead times and costs. However, while such systems may assist with the concurrent engineering of conventionally produced P/M parts, the authors believe that the greatest benefits could result from the integration of these techniques with recently emerging rapid prototyping technologies. By assisting engineers in design development, and eliminating the need for expensive tooling, this technology has the potential to enable the P/M industry to meet the demands of the rapidly developing field of customized manufacture.

1. Introduction

As the demand increases for rapid introduction of new products to the market-place, increased research efforts will be focused on techniques for decreasing the substantial lead times and costs which have traditionally been associated with P/M component production. One such technique, which offers great potential for powder forming in the long term, is the relatively new technology of rapid prototyping (RP). These techniques include Laser Stereolithography, Laminated Object Manufacturing, Metal Jet Solidification, and Selective Laser Sintering, [1]. The objects produced by these techniques range from a Stereolithographic polymer model to functional metal component such as the injection moulding tooling parts being produced by the German EOSINT process [2].

The research described here is concerned with establishing techniques for developing Knowledge Based Systems (KBS) able to assist engineers with application of RP and P/M techniques. This is being achieved through development of knowledge based process advisors, which address design, materials selection, and process control aspects of manufacture. The first system developed is a design advisor for rapid prototyping of P/M components. This system employs the relatively well known RP technique of Stereolithography to model the manufacture of axially compacted P/M parts. The system uses a design with features approach to develop a solid model of a component within a CAD database. The most formidable aspect of this part of the work has been the development of suitable Artificial Intelligence (AI) algorithms for determining which combination of features is acceptable for P/M production. At its most basic level this involves determination that the length to diameter ratio of the part is within range, and a check that unacceptably thin wall sections are not present. More complex geometrical analysis is required when features such as curved grooves and chamfers are present. Currently the system allows relatively unconstrained combinations of up to seven feature types, and it has been successfully employed to generate models of P/M components such as the hubbed gear component shown in Figure 1. During the design of this component, the system interactively analysed the geometry to ensure its suitability for P/M. The subsequent manufacture of a Stereolithographic model means that a designer can rapidly transform a concept design into a full scale physical model

The Third Pacific Rim International Conference on
Advanced Materials and Processing (PRICM 3)
Edited by M.A. Imam, R. DeNale, S. Hanada,
Z. Zhong and D.N. Lee
The Minerals, Metals & Materials Society, 1998

of the part. Because of the action of the CAD knowledge base, this model is linked to the P/M process, and the designer is provided with a practical assurance that manufacture of the part is feasible. The system provides a useful demonstration of how AI algorithms for concurrent engineering, and RP techniques, can be used to dramatically reduce lead times for prototype manufacture.

Despite the well established technological and ecological benefits of the P/M process [3], the time and expense involved in manufacture of the required tooling has been one factor limiting the application of this technology. The expense of the tooling has meant that P/M has been limited to mass production of more than 10 000 identical units. However, recent reports have stated that mass customization is the largest segment of manufacturing (in the UK alone, it is estimated to be worth $35 billion) [4]. Consequently, research efforts are now being aimed at direct rapid manufacture of P/M components. There are currently two significant factors limiting the application of direct fabrication RP technologies; these are:-

- Limited mechanical properties of the materials.
- Relatively poor surface finish of the parts.

Mechanical properties will improve as RP technologies develop. Currently the authors are embarking on a research project which aims to develop SLS techniques for selected aluminium alloys, in order to improve the strength to weight ratio of functional RP parts. It is considered that in the long term the resulting process will have wide application in the Aerospace Industry, which employs relatively small numbers of a wide variety of components.

Once the engineer is assured that the required mechanical properties are attainable, it is necessary to establish methods for selecting a suitable material for the application. This is another area where knowledge based techniques can be usefully employed. Previous research by the authors has concentrated on use of regression analysis for recommending processing parameters needed to achieve, say, a given tensile strength [5]. However, more recent investigations have shown that an increase in accuracy of more than 10% can be attained through the use of connectionist methods. The advantages of using a Neural Network are believed to result from the following factors:-

- P/M materials information generally exhibits noise and gaps in the data.
- There is no guarantee of a linear relationship between the input process parameters and the final mechanical properties. If the relationship is non-linear it is very difficult, when using statistical methods such as multiple regression, to determine what the functions are for the regression equation.

Initial research investigations indicate that Neural Networks may also be a good way forward for improving the surface finish of RP functional components. Measurement and correlation of surface roughness to the scanning behaviour of the RP machine provides data that can be used to train the network. Subsequently the system can be used to guide the forming process to achieve improved surface quality.

The techniques described are all integral elements needed for developing Knowledge Based Systems able to assist with increasing the productivity of RP manufacture of P/M parts. Benefits obtainable through application of KBS methods depend upon a number of factors such as component complexity, and application requirements. However, the authors believe that KBS for design could help to decrease lead times for many conventionally produced P/M parts, by up to 50%. Incorporation of techniques such as Neural Networks has potential for improving materials selection accuracies by around 15-20%. One of the most promising approaches so far investigated involves application of hybrid KBS architectures. Here Neural Networks provide initial processing of, for example, materials selection data, while decisions relating to primary design characteristics are made through rule based inferencing. If required, design optimization assistance can then be provided though analysis of Finite Element simulation data, possibly by employing a Case Based Reasoning approach.

In the longer term, development of direct manufacture RP systems, incorporating the KBS methods described, offer exciting opportunities for dramatically reducing component lead times, thereby enabling customized manufacture.

2. Example KBS Application: Design Development and Rapid Prototyping of a P/M Hubbed gear Component.

A Knowledge Based System has been developed for advising on the manufacturability of components, prior to production of a Stereolithographic prototype. The intention is for design engineers to access a concurrent engineering tool able to provide assurance that a given design of RP part can actually be manufactured by the chosen process (i.e. Powder Metallurgy). The KBS addresses the following three important aspects of P/M production; design, materials selection, and process control.

The design module allows the user to generate a CAD solid model of the proposed component, by operating interactively during the design process. The user is provided with a set of primitives for developing the design as a CAD solid model. Figure 1 shows the KBS screen during the hubbed gear consultation.

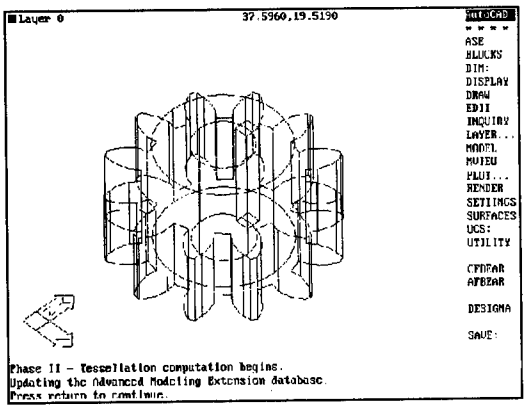


Figure 1. KBS Screen During Hubbed Gear Consultation.

As the design evolves, the component's geometry is automatically interrogated by means of LISP functions. If unformable features, or feature combinations, are detected, the user is alerted, the cause of the problem is explained, and the unacceptable feature is erased. If the inferred function of the feature is within the range of those addressed by the system, then an automatic design modification can be attempted, otherwise the user is asked to enter an alternative feature. This process is continued until all of the required functionality has been incorporated. Once a suitable component geometry has been identified, it is necessary to determine if the available P/M materials can provide the required performance characteristics. This is achieved through empirical modelling of the large amount of existing experimental P/M materials data. Initial work employed regression analysis [5], however improved results have been attained by employing Neural Network methods [6]. Once the required material type and density have been determined, this information can be entered into the CAD solid model. This model is then available for Finite Element Stress analysis. The Gurson model has been used by the authors to simulate distortion of a voided material under load. Anticipated and excessive loads can be applied to the model to determine if simulated distortions are within an acceptable range. The third area of the KBS research relates to process control. The aim here has been to produce a system able to automatically predict powder densities from vision system analysis of the powder particles. This has involved semi-theoretical modelling of the packing of spheres and irregular particles [7][8], with the long term aim of developing systems for assisting with process optimization through employing on-line monitoring of powder densities, in order to ensure correct die fills.

Once an acceptable solid model of the part has been developed, it is then post-processed, resulting in a STL file, from which the prototype is manufactured. A rendered image of the solid model of the hubbed gear is shown in Figure 2.

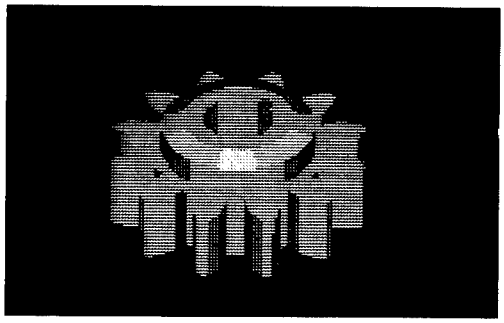


Figure 2. Rendered image of hubbed gear solid model, following KBS consultation.

The KBS enables a design engineer to quickly progress from the concept stage to being able to handle a full size model of a component, which can fulfil its functional specification, as well as being feasible for production by means of P/M. It expected that tools of this type will improve awareness of the potential of RP and P/M techniques for manufacture of a range of structural components. The system provides a useful demonstration of the potential of RP technology, as well as helping to dispel the perception that P/M production necessarily implies long lead times.

3. Knowledge Based Systems for Direct Manufacture of Components From Metal Powders.

The KBS described above is able to advise on the design of a RP model of a conventionally produced P/M part. However, achievement of the time and cost benefits previously mentioned ultimately requires integration of the design and manufacturing functions. This can be achieved by linking a suitable KBS to equipment able to directly and rapidly manufacture the part from metal powder. The technologies which are currently under development have been so far used mostly for manufacture of injection moulding tooling parts. Relevant techniques include Direct Metal Laser sintering [9] (also known as Selective Laser Sintering), Indirect Metal Laser Sintering [4], and Metal Jet Solidification [10].

Of these techniques, Selective Laser Sintering (SLS) is of particular relevance to powder metallurgy, since it enables direct production of parts from metal powders in a number of hours rather than days or weeks, without the requirement for expensive tooling. A layer of powder is spread over a building platform, and locally sintered by the CO_2 laser, which is controlled through use of shape information derived from a CAD model. In this way complex part geometries can be built up quickly and automatically. This process has been designated 'EOSINT', and introduced commercially by EOS [2], who identify the major application as tooling for injection moulding and related production methods. Tests performed by EOS have indicated that materials produced by the EOSINT have tensile strengths which are appreciably lower than the wrought material, although limited improvements in mechanical properties can be achieved through infiltration. Consequently the mould life is limited to approximately 2000 parts, so that although the tooling can be used to produce functional plastic moulded parts, only limited production runs can be achieved at present. Therefore, technological advances providing improved properties will be required before this type of process can be applied to manufacture of high integrity structural components. It is necessary to identify research directions which are most likely to lead to the attainment of the required properties. A project is therefore underway at UWE, which aims to investigate the potentiality for manufacture of P/M parts through use of rapid prototyping techniques [11]. This is being achieved by employing a typical aerospace component as a case study. The aim is to use Selective Laser Sintering technology for manufacture of a release lever for an

aircraft door. A solid model of the component has been developed using the SDRC I-DEAS CAD system. An SLS machine has been employed to manufacture test samples by means of rapid prototyping. Tensile tests were performed on the samples, and the resulting mechanical properties were employed within an FE simulation. The results of this analysis have provided an indication of how the mechanical performance of the SLS component would compare with the wrought part. This has lead to interesting discussions, and predictions of the extent to which current rapid prototyping technology is suited to manufacture of functional P/M components [12].

The next stage of the work involves a transfer of emphasis to materials selection and process control. Currently the mechanical properties attainable by Selective Laser Sintering and Metal Jet Solidification are being investigated, with the aim of developing expert system and connectionist techniques for advising on use of these processes. These technologies are believed to offer vast long term potential for customised rapid manufacture of P/M components.

After reviewing the current state of rapid prototyping technology, it becomes clear that commercially available systems are a long way from providing flexible facilities for rapid manufacture of high integrity structural parts from metal powders. However, it must be borne in mind that this is relatively new industry, exhibiting rapid technological change, and there is no reason to assume that current limitations will be insuperable. From the powder metallurgy viewpoint rapid prototyping offers many functionally and technologically exciting potential solutions. If functional parts could be manufactured directly from metal powders, all the materials, economic, and ecological benefits of a near net process such as P/M could be realised; and at the same time the expense and delays involved with tool manufacture would be avoided. Consequently P/M could be employed to one-offs, and batch production, in addition to its traditional mass production rôle. Rapid manufacture would also allow dramatic reductions in the time needed to achieve process stabilisation, and any doubts or reservations that an engineer may have expressed regarding the reliability or suitability the process, would necessarily fade if he were able to handle a finished component which had already been manufactured to specification, and tested.

Conclusion

Powder metallurgy technology is currently under-utilized, despite the technological and ecological benefits it offers for manufacture of many types of component. Bearing in mind the world-wide concerns and demands relating to global warming, the use of powdered metals is likely to be increasingly favoured by a wide range of manufacturing industry. Knowledge Based Systems offer a potentially powerful means of assisting in this process, by providing a facility for data processing and management, and by enabling improved access to the benefits and requirements of P/M. In combination with RP technology such systems may also enable a traditional drawback of P/M to be overcome; specifically the requirement for expensive tooling.

Although a few years ago the prospect of manufacture of parts from so much loose powder may have seemed like a science fiction concept, today it is becoming reality. Although some potential advantages have been identified (see above), the true benefits and industrial impact which could result from this technology are not easy to appreciate. Results of implementation of rapid manufacture in metals could, for example, allow customised manufacture of consumer goods which are currently produced through mass production of identical units. Perhaps even more significantly, traditional manufacturing processes which have been established for over one hundred years, such as machining and casting, could become obsolete and disappear from modern production environments.

References

1. A. Dolenc, 1997, 'An Overview of Rapid Prototyping Technologies in Manufacturing', Institute of Industrial Automation Helsinki University of Technology, Available at Internet site: www.cs.hut.fi.

2. EOS GmbH Electro Optical Systems, Pasinger Strasse 2, D-82152, Planegg/Munich Germany.

3. L. N. Smith, 1997, *A Knowledge Based System for Powder Metallurgy*, Ph.D thesis, University of the West of England, Bristol BS16 1QY, UK.

4. Rapid News, October 1997, Vol. 5, No. 6, Rapid News Publications plc, TCT House, Worley Court, Bolesworth Road, Tattenhall, Cheshire CH3 9HL, UK.

5. L. N. Smith, P. S. Midha, and J. Jacquens, 1997, 'A Knowledge Based Advisory System for Ferrous Powder Selection', *Advances in Powder Metallurgy and Particulate Materials - 1997*, Vol 3, Part 19, Modeling, Metal Powder Industries Federation, 105 College Road East, Princeton, New Jersey, USA, ISBN 1-878954-63-6.

6. L. N. Smith, R. Cherian, and P. S. Midha, 1997, 'Knowledge Based Connectionist Methods for Computer Assisted Selection of Powder Metallurgy Materials', (in publication).

7. [1]L. N. Smith, P. S. Midha, 1997, 'A Computer Model for Relating Powder Density to Composition, Employing Simulations of Dense Random Packings of Monosized and Bimodal Spherical Particles', *Journal of Materials Processing Technology*, Vol. 72, No. 2, p. 277-282.

8. [2]L. N. Smith, P. S. Midha, 1997, 'Computer Simulation of Morphology and Packing Behaviour of Irregular Particles, for Predicting Apparent Powder Densities', *Computational Materials Science*, March 1997, Vol. 7, No. 4, p. 377-383.

9. F. Petzoldt, M. Greul, M. Greulich, 1997, 'Functional Components and Molds Produced by Laser Sintering', *Advances in Powder Metallurgy and Particulate Materials - 1997*, Vol 3, Part 21, P/M Laser Manufacturing, Metal Powder Industries Federation, 105 College Road East, Princeton, New Jersey, USA, ISBN 1-878954-63-6.

10. M. Greul, F. Petzoldt, M. Greulich, J. Wunder, 1997, 'Rapid Prototyping Moves on Metal Powders', *Metal Powder Report*, October 1997, Elsevier Science Ltd.

11. A. Grant, 1997, *Investigation into the Production of Components From Metal Powders, Using Rapid Prototyping Techniques*, Dissertation (supervised by L. N. Smith), Faculty of Engineering, University of the West of England, Bristol, UK.

12. P. S. Midha, L. N. Smith, 1997, 'Manufacture of Functional Components Through Rapid Prototyping Technology', (in publication).

CALIBRATING FUSED DEPOSITION MODELING RAPID PROTOTYPING SYSTEMS FOR ADAPTIVE BUILD LAYER THICKNESSES

Justin Tyberg and Jan Helge Bøhn

Department of Mechanical Engineering
Virginia Tech
Blacksburg, VA 24061-0238

Abstract

Layered manufacturing systems are drawn in two orthogonal directions with respect to their performance. Thin build layers provide a smooth and precise part surface, while thick layers significantly reduce fabrication time. One solution to this dilemma is to make the build layer thickness depend on the local part geometry such that the system at all times fabricates with the maximum build layer thickness permissible to maintain a given surface tolerance. Reducing this solution to practice, however, requires that the fabrication system is calibrated for multiple build layer thicknesses simultaneously, since surface errors become particularly apparent in the form of discontinuities in the surface when transitioning from one layer thickness to another. This paper discusses calibration issues for existing fused deposition modeling (FDM) rapid prototyping systems and their effect on surface discontinuities caused by changes in layer thicknesses within a part being fabricated.

The Third Pacific Rim International Conference on
Advanced Materials and Processing (PRICM 3)
Edited by M.A. Imam, R. DeNale, S. Hanada,
Z. Zhong and D.N. Lee
The Minerals, Metals & Materials Society, 1998

Introduction

Layered manufacturing systems fabricate three-dimensional parts by adding layer upon layer of build material, beginning with the bottom of the part. The fused deposition modeling (FDM) rapid prototyping systems, in particular, achieve this by extruding molten wax or thermoplastic material through a small nozzle to form a thin bead or "road" that is deposited in a predetermined pattern to complete each build layer, bonding the extrudate to adjacent and previously deposited roads. The motion of the extrusion system operates under three-dimensional computer numerical control (CNC). The extrusion system consists of a small ram extruder in which the spooled filament feedstock pushes molten material through the liquefier with low shear. The feedstock is driven into the extruder by counter rotating rollers as needed under CNC, where it is heated to a manually set temperature, T_L. The extrudate is deposited within a build chamber holding a manually set temperature, T_C. In the case of the FDM 1600 rapid prototyping system, T_L and T_C can be up to 300°C and 70°C, respectively.

The cross section of a FDM road has the shape of a flattened ellipsoid that can be approximated as a rectangle. Its height is given by the layer thickness, i.e., the height of the nozzle above previously deposited material. With this height being constant, the road width is controlled by the volumetric flow rate of the material through the liquefier and the speed of the liquefier (head) XY motion (1). This flow rate is primarily dependent upon the ram speed, the material viscosity, and the nozzle tip dimensions (2); which can be manipulated by varying the roller speed under CNC, by manually varying T_L, or by manually changing to a different nozzle size, respectively. Hence, for a constant material, nozzle, T_L and T_C combination, the road width can be determined by CNC of (a) the feed roller speed, (b) the build layer thickness, and (c) the head travel speed. This control can be pre-computed using QuickSlice (3), which is a postprocessor that is provided by Stratasys, Inc. (Eden Prairie, Minnesota) for use with their FDM systems. To manage these three parameters, QuickSlice uses look-up tables that are each based on a constant material, nozzle, T_L and T_C combination. For instance, given a liquefier head speed and build layer thickness, QuickSlice will use the lookup table calibrated for a specific material, nozzle, T_L and T_C combination, to determine the roller speed (flow rate) that most closely matches the user-requested road width. This function is shown in Figure 1 for the P400 ABS material (Stratasys, Inc.) on a FDM 1600 with a T_L of 270°C, a T_C of 70°C, a 0.012" (0.30 mm) nozzle, a head speed of 0.800 in/sec (20.3 mm/s), and build layer thicknesses of 0.0050", 0.0075", 0.0100", and 0.0150" (0.13 mm, 0.19 mm, 0.25 mm, and 0.38 mm), respectively.

Fabricating parts by layered manufacturing without tapering the build layers will inherently produce stair-stepping along sloped surfaces (i.e., those that are neither vertical nor horizontal). Reducing the build layer thickness can minimize the positional surface error associated with this stair-stepping effect. However, doing so will also significantly increase build time. One solution to this dilemma is to employ adaptive slicing (4). In adaptive slicing the build layer thickness is maximized while maintaining a given surface tolerance. Hence, thin build layers are used in near-horizontal regions, transitioning to thick layers in near-vertical regions.

Implementing adaptive slicing is clearly more complicated than implementing uniform slicing. Indeed, few, if any, commercial systems have implemented adaptive slicing. Furthermore, the literature on adaptive slicing has thus far been limited to the theoretical control of build layer thicknesses (i.e., determining where to use which build layer thickness). While the theoretical control of adaptive slicing is challenging by itself, the actual fabrication by adaptive slicing reveals another challenge; namely that of calibrating the build parameters of adjacent build layers of dissimilar thicknesses relative to each other. For example, in the case of a FDM 1600 using the standard lookup tables, a transition from a 0.005" (0.13 mm) to a 0.010" (0.25 mm) build layer thickness will cause a noticeable, unacceptable discontinuity in the resulting part surface, even for vertical surfaces.

Figure 1 explains why these surface discontinuities occur. Ideally, the functions relating the flow rate to the road width should be continuous, both along a curve (reflecting a change in road width for a given build layer thickness) and from one curve to another (reflecting the transition from one build layer thickness to another). This, however, is clearly not the case for the QuickSlice lookup tables (Figure 1) which effectively describe a set of piecewise logarithmic curves (solid curves). One would expect, as is the case, that road widths calculated from these discontinuous build layer curves will be slightly off target, and, hence, will cause part surface discontinuities to occur at build layer thickness transitions.

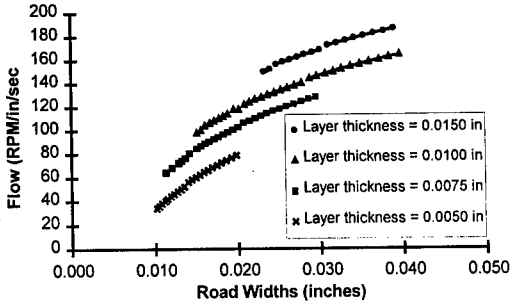


Figure 1: The flow rates and corresponding road width values predicted by QuickSlice for the extrusion of P400 ABS material through a 0.012 inch (0.30 mm) nozzle at liquefier and envelope temperatures of 270 °C and 70 °C, respectively, with a con stant liquefier head speed of 0.8 in/sec. The data can be represented by piecewise logarithmic functions.

Past work in FDM calibration has not addressed this particular issue, probably because researchers have not been concerned with fabricating with multiple build layer thicknesses simultaneously. Comb *et al.* (2) discuss various control and material selection parameters that affect the overall FDM process. Agarwala *et al.* (1) address the internal and surface defects that lead to poor structural quality of parts produced by fused deposition systems; while Yardimici *et al.* (5) present a thermal analysis of the extrusion process of FDM systems and the effect of liquefier and nozzle designs on these systems.

This paper describes an effort to develop a more accurate and continuous calibration for the FDM 1600 rapid prototyping system than what is provided by the QuickSlice postprocessor from Stratasys, Inc., and that better facilitates smooth transitions between adjacent dissimilar build layer thicknesses. The next Section therefore describes the experiments that generated the data from which the new calibration was derived. This is followed by an analysis of these results, including a comparison of the new calibration with the old, and the examination of the effect of toolpath round-off errors on the resulting part accuracy.

Experiments

Two sets of experiments were conducted using a FDM 1600 rapid prototyping system loaded with P400 ABS material. The first was designed to gather accurate data pertaining to the relationship between various feed roller speeds (flow rates) and their resulting road widths. The second was designed to observe the effect of T_L and T_C combinations, build style, and flow rate values on the overall part quality.

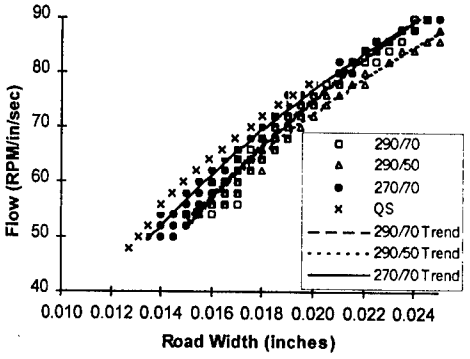
Determining Road Width vs. Flow Rate

Road width measurements were obtained by building several series of vertical walls. Each wall was 2.0" (50 mm) long, 0.25" (6.4 mm) tall, had the width of a single bead, and was

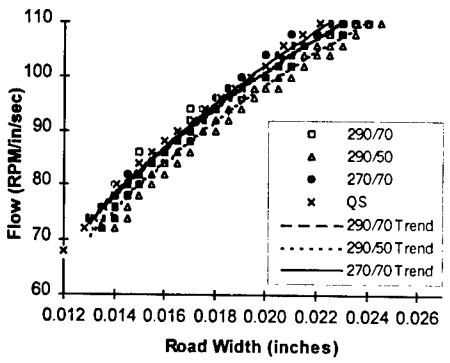
assigned a flow rate value being an even number between 2 and 254 (RPM/inch/sec) (3). Each series contained up to 21 parallel walls that were given sequentially increasing flow rates, and that were located about 0.4" (10 mm) apart on a single support material base. This base was placed in the center of the build chamber, and its walls were oriented in the direction of the heated airflow in the build chamber, to provide near uniform material cooling.

12 series of walls were fabricated using a nozzle tip diameter of 0.012" (0.30 mm); T_L / T_C settings of 270°C / 70°C, 290°C / 70°C, and 290°C / 50°C; and build layer thicknesses of 0.0050", 0.0075", 0.0100", and 0.0150" (0.13 mm, 0.19 mm, 0.25 mm, and 0.38 mm). The flow rates comprised all even numbers between 50 and 90, 70 and 110, 112 and 140, and 130 and 170, for the 0.0050", 0.0075" 0.0100", and 0.0150" (0.13 mm, 0.19 mm, 0.25 mm, and 0.38 mm) build layer thickness, respectively. The head speed was kept constant at 0.800 in/sec (20.3 mm/sec). The external ambient conditions were measured with a thermometer and hydrometer on top of the FDM 1600. The temperature measured between 78°F and 80°F (25°C and 27°C), and the relative humidity measured between 25% and 32%.

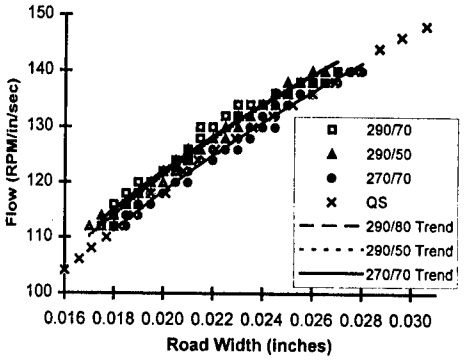
Five measurements were taken from each wall using a caliper with a 0.0005" (0.01 mm) resolution. All measurements were obtained from the central regions of the lines to ensure that only steady-state deposition was being measured. All measurements are shown in Figure 2, and each data series representing a different temperature setting was given a trendline using Microsoft Excel 7.0.



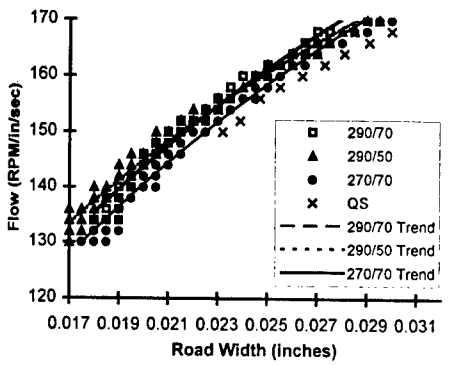
(a) layer thickness = 0.0050 inches



(b) layer thickness = 0.0075 inches



(c) layer thickness = 0.0100 inches



(d) layer thickness = 0.0150 inches

Figure 2: Experimentally collected road width values for specified flow rates at various liquefier and envelope temperature settings (°C) using P400 ABS material, a 0.012 inch (0.30 mm) nozzle, and a constant liquefier head speed of 0.8 in/sec.

Testing Transitions

A solid 1.0" × 1.0" × 0.72" (25 mm × 25 mm × 18 mm) test block consisting of 36, 24, 18, and 12 0.0050", 0.0075", 0.0100", and 0.0150" (0.13 mm, 0.19 mm, 0.25 mm, and 0.38 mm) build layers, respectively, was designed to test the transitions between the different build layer thicknesses. Five samples of this block were built using a 0.012" (0.30 mm) nozzle, 0.800 in/sec (20.3 mm/sec) head speed, and the respective parameters listed in Table I.

Table I Build parameter sets used for experimental builds.

Part	Build Style	Liquefier/Envelope Temp. Settings (°C)	Flow Rate/Road Width (in) Values 0.0050	0.0075	0.0100	0.015
A	contour (Out-In)	270/70	56/0.014	78/0.014	118/0.020	140/0.020
B	contour (Out-In)	270/70	76/0.020	102/0.020	118/0.020	140/0.020
C	Raster	270/70	76/0.020	102/0.020	118/0.020	140/0.020
D	Raster	290/50	56/0.014	78/0.014	118/0.020	140/0.020
E	Raster	290/50	76/0.020	102/0.020	118/0.020	140/0.020

The T_L / T_C were set at 270°C / 70°C and 290°C / 50°C since Stratasys, Inc. recommends these values for fabricating with 0.0100" (0.25 mm) and 0.0070" (0.18 mm) build layer thicknesses, respectively (3). The build styles tested were contour, where the roads were deposited first at the perimeter and then progressively in towards the center for each layer, and raster patterns. Each of the five parts was built in the same location and orientation in the center of the build chamber to minimize the possible effects of non-uniform transverse cooling.

Results

Road Width Calibration

Figure 2 shows that discrepancies exist between the experimental road width data and the data provided by QuickSlice. The most significant discrepancies are due to changes in the T_L and T_C settings. However, for the 0.0050" (0.13 mm) and 0.0150" (0.38 mm) build layer thicknesses, the QuickSlice data are inconsistent with any temperature setting (Figures 2a and 2d); in the first case with the QuickSlice estimated road width being less than the measured road width, while in the latter case it being opposite. Furthermore, Figure 2c shows that the QuickSlice road width estimates perfectly match the experimental data for the 0.012" (0.30 mm) nozzle, 0.010" (0.25 mm) build layer thickness, 0.020" (0.51 mm) road width, and T_L / T_C of 270°C / 70°C combination; which is the standard build parameter combination recommended by Stratasys, Inc. (3). These results explain (a) why Stratasys, Inc. prefers that customers stay with the standard parameter combination, and (b) why current QuickSlice flow rates and road widths perform poorly when used in adaptive slicing.

Figure 2 shows that a 20°C increase in liquefier temperature T_L from 270°C to 290°C reduces the measured road width by about 0.001" (0.025 mm) in the cases of 0.0100" (0.25 mm) and 0.0150" (0.38 mm) build layer thicknesses, while it has only an insignificant effect in the cases of 0.0050" (0.13 mm) and 0.0075" (0.19 mm) build layer thicknesses. It also shows that a 20°C decrease in build chamber temperature T_C from 70°C to 50°C increases the measured road width by nearly 0.001" (0.025 mm) in the cases of 0.0050" (0.13 mm) and 0.0075" (0.19 mm) build layer thicknesses, while it has only an insignificant effect in the cases of 0.0100" (0.25 mm) and 0.0150" (0.38 mm) build layer thicknesses. Finally, Figure 2 shows that when combining these changes in T_L and T_C the measured road width increased by about 0.001" (0.025 mm) in the cases of 0.0050" (0.13 mm) and 0.0075" (0.19 mm) build layer

thicknesses, and decreased by about the same amount in the cases of 0.0100" (0.25 mm) and 0.0150" (0.38 mm) build layer thicknesses.

Increasing T_L will, for thick roads, add heat to the extrudate, and thus increase the time during which the material experiences significant shrinkage. Thick roads will therefore shrink as T_L increases. Thin roads, on the other hand, will continue to cool down too fast to significantly increase shrinkage, and they will therefore not experience a change in measured road width.

Decreasing T_C will, for thin roads, prevent the extrudate from heating up existing material to above the softening point (105°C). The existing material will therefore not yield to the pressure exerted by the extrudate, which causes the extrudate to escape outwards to create a wider road. Thick roads, on the other hand, contain sufficient heat so the extrudate can continue to bring existing material to above the softening point. This causes the existing material to continue to yield to the extrudate pressure, and hence there is no change in measured road width.

Effects of Numerical Round Off

Imperfect surface transitions between adjacent build layers of dissimilar thicknesses can also be caused by numerical round off. The flow rates selected represent discrete road widths at given build layer thicknesses. These road widths can be carried through the road path calculations as high resolution floating point numbers, and up until this point any numerical round off would be insignificant. However, these floating point values need, in the case of current FDM equipment, to be rounded off to the closest 0.001" (0.025 mm) XY coordinate to reflect the programming resolution of the FDM's XY controller. This round off can easily cause a 0.001" (0.025 mm) mismatch within any two build layers. This mismatch will in general be particularly noticeable between two adjacent build layers of dissimilar thicknesses since the round off error adds to errors in the road width estimation function (however small they might be, they will most likely be present). Figure 3 illustrates this problem.

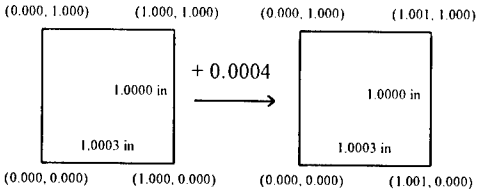


Figure 3: Numerical round off can change final fabricated dimensions, here shown for a 1.0003" × 1.0000" rectangle before and after a 0.0004" translation in the X direction.

Imagine a rectangular cylinder measuring 1.0003" x 1.0000" (25.408 mm x 25.400 mm). Due to numerical round off, it will be manufactured as a perfect 1.000" x 1.000" (25.400 mm x 25.400 mm) square. Now move the original cylinder 0.0004" (0.010 mm) in the positive X direction. This would simulate the change in road path offset due to a slight change in road width, which invariably occurs as one transitions from one build layer thickness to another. The size of the virtual cylinder will thus remain the same; however, the new manufactured cylinder will now measure 1.001" x 1.000" (25.425 mm x 25.400 mm) and will no longer be perfectly square.

Build Layer Thickness Transitions

It was necessary to increase the liquefier temperature T_L to 290°C to ensure that the 0.0050" (0.13 mm) and 0.0075" (0.19 mm) build layers would weld to existing material without

delaminating and curling. It was also found that part quality improved if the build chamber temperature T_C simultaneously was reduced to 50°C, which is in accordance with the recommendations provided by Stratasys, Inc. for fabricating with 0.007" (0.18 mm) build layers (3). Since the QuickSlice lookup tables are not calibrated for these conditions, it was necessary to develop a new set of lookup tables calibrated for these temperatures. These new functions were each modeled as single logarithmic curves (Figure 2) rather than as a set of discontinuous piecewise logarithmic curves like those used in QuickSlice (Figure 1).

These new functions relating flow rates to road widths were tested with the fabrication of a variety of geometric shapes, including the test block described earlier. The results were satisfactory and the build layer thickness transitional errors appeared to being limited to not much more than that which arises from numerical round off. This was in part determined by using a sheet of paper (0.0035 inches, 0.09 mm) to gauge the relative magnitude of the build layer thickness transitional surface discontinuities.

Conclusions

Existing layered manufacturing equipment and software have not been designed to accommodate adaptive build layer thicknesses. In particular for FDM rapid prototyping systems, calibrations of build parameters for different build layer thicknesses are out of alignment relative to each other, and are discontinuous within a single build layer thickness. Consequently, discontinuous surface conditions occur during fabrication when transitioning from one build layer thickness to another.

This paper has presented a new calibration procedure for FDM rapid prototyping systems that (a) provides a continuous calibration within a build layer thickness, and (b) aligns the calibrations for different build layer thicknesses relative to each other. This new calibration procedure has been successfully applied to the fabrication of several parts by FDM using adaptive slicing. In particular, it has shown that parts with adjacent 0.0050", 0.0075", 0.0100", and 0.0150" (0.13 mm, 0.19 mm, 0.25 mm, and 0.38 mm) build layer thicknesses can be successfully fabricated using an FDM 1600 rapid prototyping system loaded with P400 ABS material provided the liquefier temperature T_L is increased to 290°C and the build chamber temperature T_C is decreased to 50°C, to provide surface discontinuities that are dominated by the addressing resolution of the XY motion system within the FDM 1600 rather than by misaligned calibrations.

References

1. M.K. Argawala et al., "Structural quality of parts processed by fused deposition," Rapid Prototyping Journal, 2 (4) (1996), 4-19.

2. J.W. Comb, W.R. Priedeman, and P.W. Turley, "FDM Technology Process Improvements," Proc., Solid Freeform Fabrication Symposium, H.L. Marcus et al., eds., University of Texas at Austin, Austin, Texas, USA, August 8-10, 1994, 42-49.

3. QuickSlice 5.0, Stratasys, Inc., Eden Prairie, Minnesota, USA, 1997.

4. A. Dolenc and I. Mäkelä, "Slicing procedures for layered manufacturing techniques," Computer-Aided Design, 26 (2), (1994), 119-126.

5. M.A. Yardimici et al., "Thermal Analysis of Fused Deposition," Proc., Solid Freeform Fabrication Symposium, D.L. Bourell et al., eds., University of Texas at Austin, Austin, Texas, USA, August 11-13, 1997, 689-698.

NEAR NET SHAPE PRODUCTION OF METAL COMPONENTS USING LENS

Eric Schlienger, Duane Dimos, Michelle Griffith, Joseph Michael, Mike Oliver,
Tony Romero, John Smugeresky*

Sandia National Laboratories
Albuquerque NM
*Livermore CA

Abstract

Rapid Prototyping and Near Net Shape manufacturing technologies are the subject of considerable attention and development efforts. At Sandia National Laboratories, one such effort is LENS (Laser Engineered Net Shaping). The LENS process utilizes a stream of powder and a focused Nd YAG laser to build near net shape fully dense metal parts. In this process, a 3-D solid model is sliced, then an X-Y table is rastered under the beam to build each slice. The laser / powder head is incremented upward with each slice and the deposition process is controlled via shuttering of the laser. At present, this process is capable of producing fully dense metal parts of iron, nickel and titanium alloys including tool steels and aluminides. Tungsten components have also been produced. A unique aspect of this process is the ability to produce components wherein the composition varies at differing locations in the part. Such compositional variations may be accomplished in either a stepped or graded fashion.

In this paper, the details of the process will be described. The deposition mechanism will be characterized and microstructures and their associated properties will be discussed. Examples of parts which have been produced will be shown and issues regarding dimensional control and surface finish will be addressed.

Sandia is a multiprogram laboratory operated by Sandia Corporation, a Lockheed Martin Company, for the United States Department of Energy under Contract DE-AC04-94AL85000.

The Third Pacific Rim International Conference on
Advanced Materials and Processing (PRICM 3)
Edited by M.A. Imam, R. DeNale, S. Hanada,
Z. Zhong and D.N. Lee
The Minerals, Metals & Materials Society, 1998

The computer revolution has drastically changed many aspects of modern life. The ability to handle data in new and more complex fashions has provided the impetus for a true metamorphosis of our daily life. The fusion of various technologies with this processing power is resulting an evolution in most everything we do. Applications ranging from navigation to how our food is prepared, from home entertainment to skis, are all impacted by the rapid pace of technology development and data fusion. Although consumer products are the most obvious manifestation of this revolution, it has had no less of an impact on the manufacturing sector.

Within the manufacturing sector, the first significant change is often said to have been the introduction of CNC (Computer Numerically Controlled) machining. This advance allowed a computer to control conventional machine tools. Although there had been template matching machines available for years, the introduction of CNC capabilities is perhaps the first true step along the road towards a new manufacturing paradigm. As CNC capabilities expanded, the focus shifted to the tools required to get the design from the engineer, to the shop floor, with the minimum amount of effort and the greatest degree of integrity. This requirement engendered the development of complex 3D solid model design tools and automated machine tool path planning.

Concurrent with the advances in computer capabilities have been an advances in technology areas as well. One such area is in the field of lasers. As CNC technology advanced, the laser began to be recognized as a potential manufacturing tool. Spot welding and cutting applications being examples of niches where numerically controlled laser processes quickly demonstrated their value. Recently, this marriage of laser and computer has resulted in the introduction of rapid prototyping technology, a development that has garnered considerable attention within the manufacturing sector. Figure 1 is an example of two such processes.



Stereolithography (SLA) Selective Laser Sintering (SLS)

Figure 1: Rapid Prototyping

These rapid prototyping processes introduced a precision manufacturing technology that was significantly different than typical manufacturing. This difference lies in the fact that both SLA and SLS are additive processes. In these processes, rather than removing material from a block as in conventional machining, material is added. In the SLA process a laser is used to cure a liquid acrylic, whereas in the SLS process the laser sinters powder. In both cases a solid part is produced. From this basis, similar technologies are being developed for the production of metal parts.

The Laser Engineered Net Shaping process (LENS)[1,2] being developed at Sandia, the Directed Light Fabrication process (DLF)[3], Laser Cladding work at the University of Illinois[4], plus work at Penn State, Carnegie Melon and Stanford, to name just a few, are all extending the knowledge

obtained in the field of rapid prototyping towards the production of metal parts. These processes are similar in that they are all intended to produce functional metal parts. They differ in the type of laser, laser power, deposition rate, number of axes and metal delivery. In most cases metal powder is used as the feedstock although work with droplets is also underway[5]. For the purpose of this work, the LENS process will be used as an example.

In the LENS process, a Neodymium doped Yittria Alumina Garnet (Nd-YAG) solid state laser is used as the energy source. As shown in figure 2, the laser is focused onto a metal substrate. The focused laser radiation, typically about 300 watts, but as high as 750 watts, melts the target material and a molten pool forms. Powder in the size range of 40 microns to 180 microns (-80 +325 mesh) is entrained in argon and injected into the molten pool.

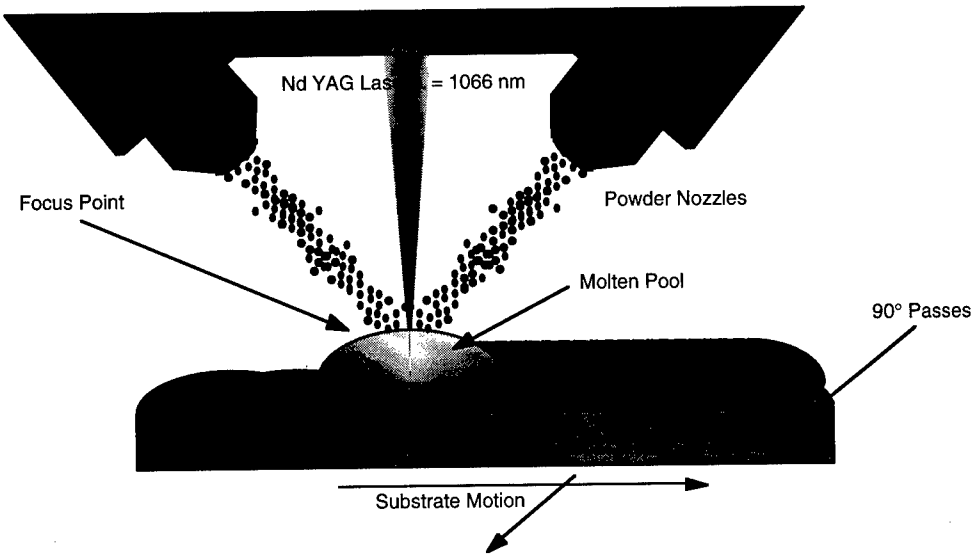


Figure 2: LENS Deposition Process

Multiple powder nozzles are used and the system is set up such that the intersection points of the powder streams and the laser focus point are coincident. Once the powder enters the molten pool it quickly melts and the molten pool expands into a bead of molten metal. The growth of this molten metal bead, when coupled with the X-Y motion of the table results in condition of asymmetrical bead morphology and heat input that causes the bead to expand unidirectionally.

In this fashion metal is continuously deposited in a controlled fashion such that three dimensional parts may be produced. There are however some process challenges. For example, the absorption of the laser wavelength by the material being processed is not constant from material to material.

Figure 3 is a plot of reflectivity vs. wavelength. As may be seen in the figure, the reflectivity (1 / absorption) of metals is strongly dependent on the incident wavelength. In particular, the Nd YAG (1066 nm) wavelength does not couple well to aluminum or copper. As such, it is critical that the interaction characteristics of the laser and the material being processed are reviewed prior to the assembly of the equipment.

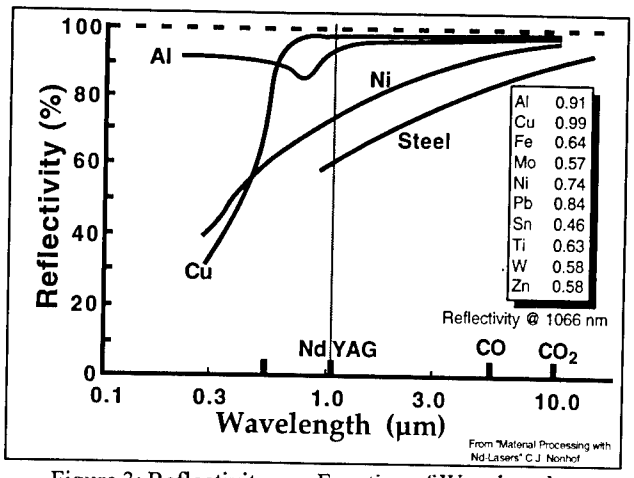


Figure 3: Reflectivity as a Function of Wavelength

At Sandia, the Nd YAG laser has been used in the LENS process for the production of fully dense metal parts out of a variety of materials. Figure 4 below is a photograph of a Ti-6-4 component suitable for marine applications. The scale in the foreground is 150 mm long. Such parts have been measured at 99.996% dense, the limit of the equipment. Yield strengths of similarly produced test bars have been measured at 144 ksi with ultimate strengths at 150 ksi. These values compare favorably to the typical properties of 120 ksi yield and 130 ksi ultimate. The difference in strength is probably due to the solidification which seems to have involved a massive transformation to alpha from the beta phase. This also explains the low elongation, 2.8%, as contrasted to the more typical number of 10%. It should be noted that due to its affinity for oxygen, the casting of titanium is somewhat difficult. As a result, the near net shape capability of LENS and similar processes represents a potentially valuable technique.

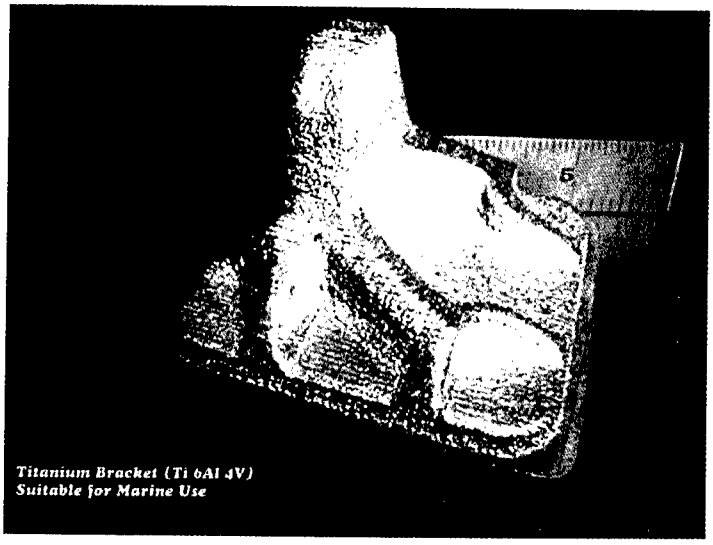


Figure 4: Titanium 6-4 Bracket

Another of the major advantages of the LENS process is that it is capable of producing very high aspect ratio parts. Figure 5 is a photograph of a 316 stainless steel part. This part is

roughly 150 mm long and 25 mm square in cross section. This part has also been intentionally designed to twist at a rate of 1° per mm. As produced, it is distortion free and looks much like an extrusion. However as opposed to an extrusion, the LENS part could be as easily produced out of H13 tool steel or tungsten while achieving the twist. The ability to produce such shapes out of materials that are typically very difficult to machine is of obvious value and is the primary reason that direct metal deposition processes are being evaluated for the production of tooling. To date the materials which have been successfully processed at Sandia via LENS include: Nickel alloys 718,625 & 690, stainless steels 304 and 316, H13 tool steel, Tungsten, Titanium and NdFeB magnet alloy. Each alloy processed requires slightly different processing parameters in order to obtain optimum build rates, density, grain structure and surface quality. As such, some parametric studies are usually indicated whenever a new material is used. On the other hand, experience indicates that as long as the material being processed has a sufficiently low reflectivity at the ND YAG wavelength, then the that material should be amenable to LENS type processing.

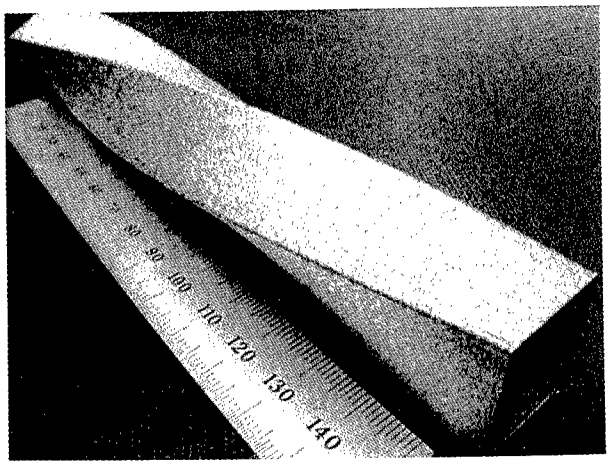


Figure 5: Extrusion Shape

Since these direct metal deposition processes have been shown to be compatible with a wide variety of materials, the obvious extension is towards graded structures. This capability is achieved by modifying the powder composition in a continuous fashion over some portion of the part. It does not require much imagination to envision the advantage of such a scheme. Applications include matching CTE (Coefficient of Thermal Expansion), transitions and locally tailoring properties such as thermal conductivity, hardness, toughness or resistance to corrosion. This realization of this capability is predominately an issue of the control of the powder feeders. In fact the production of graded parts has been demonstrated, and as an example. Michelle Griffith of Sandia has built parts which transition from 316 stainless steel to 304 stainless steel as well as parts which transition from 304 stainless steel to A690.

Despite the progress made to date, there are still some areas in need of improvement. For example, part complexity is an issue that has been mentioned. This concern arises from the lack of overhang capability in LENS that is available with most rapid prototyping processes. However, the overhang issue can be addressed with an appropriate combination of hardware and software and in fact, Gary Lewis of Los Alamos has demonstrated full 3D fabrication capability using DLF. As a result, part geometry is seen as more of a developmental issue.

Another item of note is the deposition rate. Present deposition rates at Sandia are somewhat slow, on the order of two hours per cubic inch. However, work at Penn State[6] has shown much greater deposition rates. The process at Penn State uses a fluidized powder bed and a 14 kW CO_2 laser. Whereas at Sandia the maximum laser power used to date is about 700 watts. The implication is that as the power is increased, the achievable deposition rate will increases as well. As a result, obtaining greater deposition rates does not seem an insurmountable obstacle.

Perhaps the most significant area in need of development is associated with the surface quality of parts produced. John Smugeresky of Sandia has shown that with the LENS process, the surface roughness is primarily a function of powder size and appears to be associated with powder overspray. It is known that not all of the powder that flows through the nozzle is incorporated into the part. It is therefore surmised that some of the powder is impinging upon solidifying material and sticking. This does not create a problem in the bulk of the part since subsequent deposition passes melt any powders stuck to the surface. However, since external faces are not remelted and covered, such adhering powders end up being a significant surface feature. Thus surface quality is an area where significant work is underway.

In summary, direct metal deposition technology is under going a rapid advancement. The number of organizations active in the research of such technologies is growing at a rapid pace and the capability of direct metal deposition processes is expanding daily. Research organizations the world over have demonstrated that the technologies have application and as a result, today we stand on the brink of commercialization.

References

1 D.M. Keicher, J.L. Jellison, L.P. Schanwald, J.A. Romero and D.H. Abbott, "Towards a Reliable Laser Powder Deposition System Through Process Characterization", 27th International SAMPE Technical Conference, Vol. 27, Diversity into the Next Century, Proc., od SAMPE '95, Albuquerque, NM, Oct. 12-14, 1995, p. 1029.

2 J.E. Smugeresky, D.M. Keicher, J.A. Romero, M.L. Griffith, L.D. Harwell, "Using the Laser Engineered Net Shaping (LENS) Process to Produce Complex Compoinents from a CAD Solid Model", SPIE Proceedings, Laser as Tools for Manufacturing II, Vol. 2993, February 12-17, 1997.

3 G.K. Lewis, J.O. Milewski, R.B. Nemec, D.J. Thoma, M Barbe, D. Cremers, "Directed Light Fabrication", Los Alamos Laboratory Publication LA-UR-95-2845, Los Alamos, NM, 1995.

4 J.L. Koch, J. Mazumder, "Rapid Prototyping by Laser Cladding" presented at ICALEO 1993, Orlando FL, 1993.

5 R. Merz, F.B. Prinz, K. Ramaswami, M. Terk, L.E. Weiss, "Shape Deposition Manufacturing", Proceedings of the Solid Freeform Fabrication Symposium, The University of Texas at Austin, August 8-10, 1994.

6 F.G. Arcella, E.J. Whitney, D. Krantz, "Laser Forming Near Shapes in Titanium", presented at ICALEO 1995, Orlando FL, 1995.

SLS/HIP – A DIRECT FREEFORM FABRICATION PROCESS FOR HIGH PERFORMANCE METAL COMPONENTS

Suman Das, Joseph J. Beaman, Martin Wohlert, David L. Bourell

Laboratory for Freeform Fabrication
The University of Texas at Austin
ETC 5.160 C2200
Austin, TX 78712-1063

Abstract

This paper focuses on recent advances in direct freeform fabrication of high performance metal components via selective laser sintering (SLS). The application, known as SLS/HIP, is a low cost manufacturing technique that combines the strengths of selective laser sintering and hot isostatic pressing (HIP) to rapidly produce low volume or "one of a kind" high performance metal components. Direct selective laser sintering is a rapid manufacturing technique that can produce high density metal parts of complex geometry with an integral, gas impermeable skin. These parts can then be directly post-processed by containerless HIP. The advantages of *in-situ* encapsulation include elimination of a secondary container material and associated container-powder interaction, reduced pre-processing time, a short HIP cycle and reduction in post-processing steps compared to HIP of canned parts. SLS/HIP is currently being developed under a DARPA/ONR program for INCONEL® 625 superalloy and Ti-6Al-4V, the demonstration components being the F-14 turbine engine stator vane and the AIM-9 missile guidance section housing base respectively.

The Third Pacific Rim International Conference on
Advanced Materials and Processing (PRICM 3)
Edited by M.A. Imam, R. DeNale, S. Hanada,
Z. Zhong and D.N. Lee
The Minerals, Metals & Materials Society, 1998

Introduction

Rapid prototyping (RP) technologies worldwide have attained a state of maturity. A variety of RP technologies are commercially available to produce complex shaped three-dimensional parts and tooling in a variety of materials including plastics, paper, polymers, wax, sand, ceramics and metals. The next major advance of rapid prototyping research and development will be in direct fabrication processes, especially for low volume production of functional metal, cermet and ceramic components. Direct freeform fabrication implies layerwise shaping and consolidation of feedstock (*e.g.* powder, wire, ingot, paste or melt) to complex shapes having full or near full density without the use of intermediate binders, furnace densification cycles or of secondary infiltration steps. A number of direct metal fabrication methods are under development. The materials systems investigated to date include steels, nickel base superalloys, Titanium and its alloys, refractory metals, bronze-nickel and cermets.

Selective laser sintering (SLS) is a rapid prototyping process that creates three-dimensional freeform objects directly from their CAD models. An object is created by selectively fusing thin layers of a powder with a scanning laser beam. Each scanned layer represents a cross section of the object's mathematically sliced CAD model. SLS of metals has been under development at the University of Texas via two routes. The first, technically simpler route is the so called "indirect SLS" process. In this process, a metal powder either coated with a polymer film or mixed with a polymer powder is processed by a low energy (< 50W) laser beam to selectively bind particles together to form a porous "green" shape. The "green" shape is post-processed by binder burn-out, sintering and infiltration by a second, lower melting point metal to produce high density metal and ceramic parts and tooling. This method has been put into practice by the introduction of RapidTool™ technology that is targeted towards rapid manufacture of prototype injection molding tooling [1]. Although this method is technically simpler, there are several drawbacks. It is limited to composites involving at least two metals, with the infiltrant necessarily being of a lower melting temperature than the metal comprising the porous compact. In addition, several pre-processing and post-processing steps are required to obtain a fully dense object starting from metal powder.

The second, more challenging route known as "direct SLS" directly consolidates a metal or cermet powder to high density (> 80%) using a high energy laser beam, preferably with minimal or no post-processing requirements. Until recently, no work was reported on direct SLS of high performance materials such as Nickel and Cobalt base superalloys, superalloy cermets, Titanium base alloys and monolithic high temperature metals such as Molybdenum. These materials are typically used for high performance components that generally experience high operating temperatures, high stresses and severe oxidizing or corrosive environments. Direct SLS, with its ability to produce components in such materials is especially useful for functional prototype, low volume or "one of a kind" production runs. To manufacture a typical prototype lot of 100 superalloy cermet abrasive turbine blade tips, direct SLS was shown [2] to achieve acceptable microstructure and properties with 80% cost savings over the traditional method. Engineers in the automotive and aerospace industries face typical lead times of several weeks for one iteration of functional, metallurgical quality prototypes. Direct SLS can drastically reduce the costs and lead times by eliminating pre-processing and post-processing steps and by eliminating the need for specialized tooling.

This paper represents ongoing research efforts at the University of Texas in direct SLS production of functional metal components made of high performance metals [3,4]. The

application named SLS/HIP, being developed for the United States Department of Defense is focused on the rapid production of high performance components that are currently produced by conventional powder metallurgy (P/M) and hot isostatic pressing (HIP) processes. The primary objective of this effort is to develop a highly flexible, highly automated, low cost, short lead-time direct fabrication process based on selective laser sintering and hot isostatic pressing.

Background

The United States Department of Defense has a number of high value, high performance metal components in service that are produced by hot isostatic pressing. These parts are typically produced by conventional HIP of canned metal powders. Shaped metal cans are commonly used to encapsulate metal powders for HIP. The sheet metal container material is chosen so as to minimize interaction with the powder at processing temperatures. After HIP processing, the container is removed by machining or chemical etching.

Complex shapes are typically produced using the ceramic mold process [5] developed by Crucible Materials. This process is similar to investment casting in that dry powder instead of molten metal is poured into a ceramic mold. The production of a near net shape is advantageous because it minimizes scrap losses and machining steps. However, outgassing and heating cycles are long during this process because the ceramic mold is surrounded by a large volume of pressure transmitting medium [6]. The long cycle time and pre-processing steps necessary in the ceramic mold method make it a time consuming and expensive process.

To produce full density metal components having complex geometry, a net shape manufacturing technique called SLS/HIP is under development at the University of Texas. This process exploits the freeform shaping capability of SLS with the full densification capability of HIP. The working principle of SLS/HIP is to consolidate the interior of a component to 80% or higher density and to fabricate an integral gas impermeable skin or "can" at the part boundary *in-situ* . In the SLS/HIP process (shown in Figure 1), the component is produced by selectively consolidating a metal powder with a scanning laser beam layer by layer. While producing each layer, a high density skin (> 98% density) is formed at the boundaries of the part. The interior of the part is laser processed to a density typically exceeding 80%. Thus, the part is shaped and canned *in-situ*. The encapsulated part is post-processed by containerless HIP to full density. A final machining step will result in a part having the desired geometry and mechanical properties.

SLS/HIP has several advantages over conventional HIP methods. Since an integral skin or "can" is formed of the same material as the part, a secondary canning step is not necessary. The part is directly post-processed by containerless HIP. Adverse container-powder interactions are eliminated and post-HIP container removal is not required. SLS/HIP allows production of complex shapes at reduced cost and shorter lead-times.

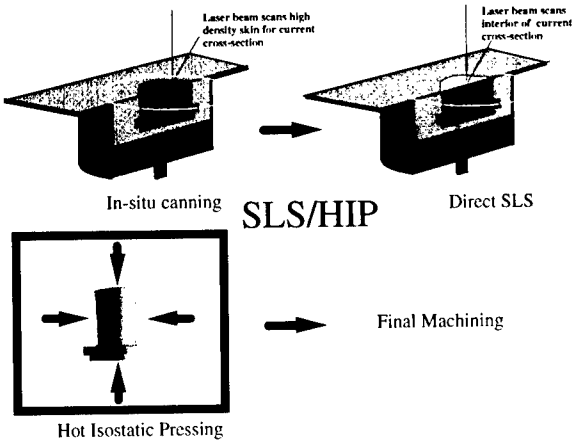


Figure 1: The SLS/HIP Process

Objectives

The objective of ongoing research is to develop the SLS/HIP engineering science and technology for a variety of high performance metals. Perhaps the most demanding requirement of this effort is to develop the processing science to enable consistent, repeatable construction of the integral HIP skin. For a component processed by SLS to be acceptable for containerless HIP, the integral gas impermeable skin must completely enshroud the entire component. A helium leak rate less than 1 X 10^{-9} standard cm^3/s across this skin is considered acceptable. Such a low leak rate is required because the leak rate at a typical HIP pressure of 1000 atm (100 MPa) will be five orders of magnitude greater than that during leak testing at 1 atmosphere.

Based on a survey of several naval installations [7], two candidate materials have been selected for SLS/HIP process development. These materials are INCONEL® 625 and Ti-6Al-4V, the demonstration components being a stator vane for the F-14 fighter aircraft and a guidance section housing base for the AIM-9 Sidewinder missile respectively.

Materials and Methods

SLS trials were conducted on a high temperature selective laser sintering machine designed and built at the University of Texas. This machine is equipped with a 250 Watt Nd:YAG laser, powder preheating capability up to 600° C and controlled atmosphere. HIP trials were conducted on a ABB model QIH-3 equipped with a graphite heating element. Temperatures up to 2000° C and pressures up to 200 MPa are attainable with the graphite element in inert atmosphere. Argon gas was used as the pressure transmitting medium. To screen specimens produced by SLS for impermeability, a leak testing apparatus and procedure was adapted from the Metals handbook article on containerless HIP [8].

Anval Corp. provided Argon atomized Alloy 625 (equivalent to INCONEL® 625) powder (16-44 μm). Ti-6Al-4V (37-74 μm) produced by the PREP method was provided by Starmet Inc. The compositions of Anval Alloy 625 and PREP Ti-6Al-4V are shown in Table I and Table II respectively.

Table I Manufacturer's composition of Anval Alloy 625

C	Si	Mn	P	S	Cr	Ni	Mo	Ti	Nb	Al	Co	N	Fe
0.028	0.16	0.04	0.007	0.008	21.3	62.2	8.22	0.27	3.36	0.21	0.04	0.051	4.00

Table II Manufacturer's composition of PREP Ti-6Al-4V

Al	V	Fe	O	C	N	H	Y	Ti
6.35	4.19	0.19	0.19	0.02	0.01	< 0.01	< 0.001	Bal

Results and Discussion

A simple cylindrical shape 0.5 inch diameter, 0.5 inch long, with 0.125 inch skin wall thickness was selected to demonstrate capability of fabricating integrally canned parts by SLS/HIP. Integrally canned cylinders of Alloy 625 and Ti-6Al-4V conforming to this geometry were produced by SLS and post-processed to full density by HIP. Porosity before and after HIP was evaluated by analysis of voids in a metallographic montage.

Shown on the left in Figure 2 is an axial cross-section optical micrograph of an Alloy 625 cylinder processed by SLS to 1.5% residual porosity. In this case, the entire diameter of the cylinder was consolidated to high density during SLS instead of producing an intermediate density core with a high density skin. This specimen was post-processed by a HIP cycle consisting of 3 hours at 1240° C and 155 Mpa (25000 psi), resulting in nearly full densification with 0.5% residual porosity. The optical micrograph on the left in Figure 3 shows a composite axial cross-section of a SLS processed, integrally canned Ti-6Al-4V cylinder that was not post-processed by HIP. While the side walls and end-caps are at full density as expected, the interior of the part is at 60% density. The micrograph on the right of Figure 3 shows an axial section of a Ti-6Al-4V cylinder that was produced by SLS and post-processed to full density by HIP. Metallographic evaluation of this specimen revealed a residual porosity of 0.1% and complete homogenization between the core and skin regions. This specimen was processed by a HIP cycle consisting of 4 hours at 925 ° C and 93 MPa (15000 psi).

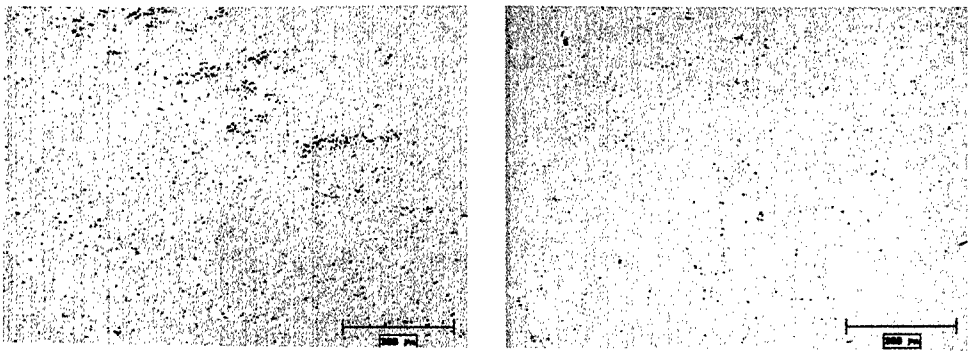


Figure 2: Alloy 625, as SLS processed, 1.5% porosity (left) and HIP post-processed, 0.5% porosity (right).

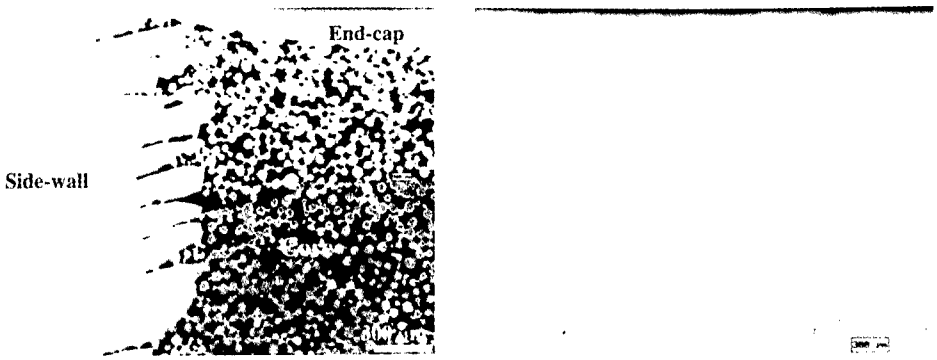


Figure 3: PREP Ti-6Al-4V, as SLS processed, showing intermediate density core and fully dense skin regions (left) and HIP post-processed to full density (right).

The etched microstructure of SLS processed Alloy 625 is shown in Figure 4. The equiaxed microstructure compares very well with that obtained in hot rolled annealed material [9]. The microstructure of the HIP post-processed specimen (Figure 2) shown on the right in Figure 4 reveals substantial grain growth during HIP. The micrograph on the left in Figure 5 shows the etchd microstructure of the side-wall region of Figure 3. The micrograph on the right in Figure 5 shows the etched microstructure of the unprocessed core region in Figure 3 that underwent full densification during HIP. The lamellar microstructure of the SLS processed side-wall, consistent with that seen in cast Ti-6Al-4V did not change during the HIP cycle. The core region exhibits a Widmanstätten or basketweave microstructure. This type of microstructure is also observed in Ti-6Al-4V processed by cold isostatic pressing (CIP) to 95% density followed by HIP to full density [10]. Metallographic evaluation of the HIP post-processed specimen revealed a mean residual porosity of 0.1% and homogenization between the core and skin regions.

Hardness values of SLS/HIP processed Alloy 625 and Ti-6Al-4V specimens were compared with published values of conventionally processed material. The data shown in Table III indicate that SLS/HIP processed material compares well with conventionally processed material. There was no significant difference between hardness of 98.5% dense SLS processed Alloy 625 and 99.5% dense HIP post-processed Alloy 625.

Table III Hardness values of SLS/HIP vs. conventional processed material

Alloy	**Processing**	**Hardness**
Anval Alloy 625	SLS and SLS/HIP	52 HRA
INCONEL Alloy 625	Solutionized and annealed [9]	50 HRA
Ti-6Al-4V	SLS	36 HRC
Ti-6Al-4V	Cast	37 HRC

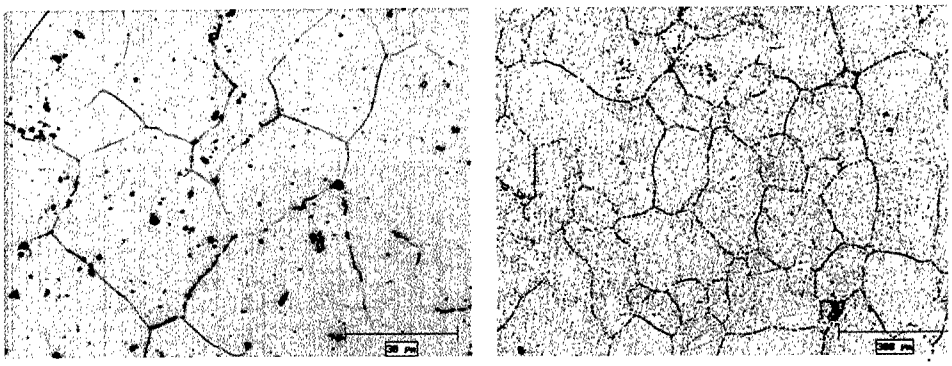


Figure 4: Etched microstructures of Alloy 625, as SLS processed, 1.5% porosity (left) and HIP post-processed, 0.5% porosity (right), electrolytic etch.

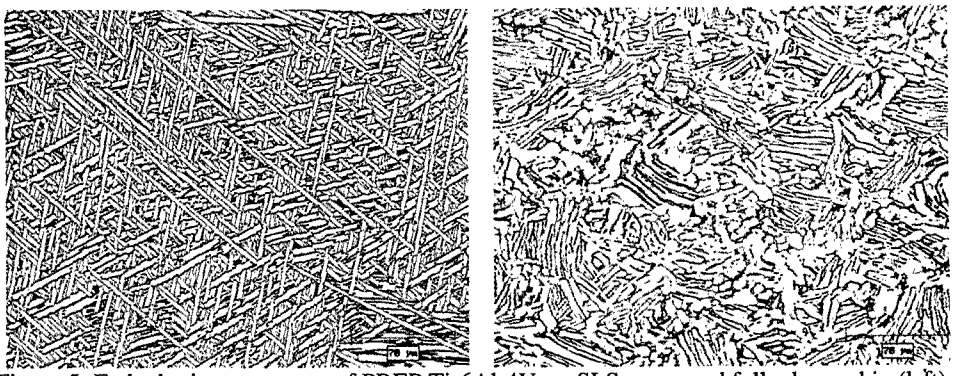


Figure 5: Etched microstructures of PREP Ti-6Al-4V, as SLS processed fully dense skin (left) and HIP post-processed fully dense core (right), Kroll's etch.

Conclusions

The feasibility of SLS/HIP as a net shape process for making high performance components has been successfully demonstrated. Simple cylindrical shapes of Alloy 625 and Ti-6Al-4V have been integrally canned by SLS and post-processed by HIP to full density. Microstructure and hardness data reveal that material processed by SLS/HIP is comparable to conventionally processed material. Future work will focus on detailed characterization of microstructure and mechanical properties, and on developing SLS/HIP for complex geometry components. SLS/HIP has tremendous potential for rapid, net shape manufacture of high performance metal components at reduced costs and shorter lead times.

Acknowledgements

The authors wish to acknowledge funding support given by Defense Advanced Research Projects Agency and The Office of Naval Research under contract N00014-95-C-0139 titled "Low Cost Metal Processing Using SLS/HIP".

References

1. Rapid Prototyping and the Selective Laser Sintering Process: Tooling, DTM Corporation, Austin, TX.

2. T. Fuesting et al., "Development of Direct SLS Processing for Production of Cermet Composite Turbine Sealing Components", Solid Freeform Fabrication Symposium Proceedings 1996, 39-55.

3. S. Das et al., "Selective Laser Sintering of High Performance High Temperature Metals", Solid Freeform Fabrication Symposium Proceedings 1996, 89-95.

4. S. Das et al., "Direct Selective Laser Sintering of High Performance Metals for Containerless HIP", in Advances in Powder Metallurgy and Particulate Materials - 1997, 21-67-21-78.

5. "Hot Isostatic Pressing of Metal Powders", Metals Handbook 9th Edition, Vol. 7 (1993), 425-426.

6. H. V. Atkinson and B. A. Rickinson, Hot Isostatic Pressing (Adam Hilger, 1991),64-65. .

7. Ronald Knight et al., "Metal Processing Using Selective Laser Sintering and Hot Isostatic Pressing (SLS/HIP)", Solid Freeform Fabrication Symposium Proceedings 1996, 349-353.

8. "Hot Isostatic Pressing of Metal Powders", Metals Handbook 9th Edition, Vol. 7 (1993), 425-426.

9. Inco Alloys International, INCONEL Alloy 625, 1985.

10. ASM Handbook, Volume 7, Powder Metallurgy, ASM International, pp. 394, 435, 1984.

Solid Freeform Fabrication (SFF) of Advanced Functional Ceramic Components

Stephen C. Danforth, Ahmad Safari, Ceramic & Materials Engineering

N. Langrana, Mechanical & Aerospace Engineering, M. Jafari, Industrial Engineering,

Rutgers University, Piscataway, NJ 08855-0909

Abstract

A number of different Solid Freeform Fabrication (SFF) technologies are now being developed for advanced ceramics and metals. SFF offers unique opportunities for manufacturing functional quality ceramics for applications, such as: structural, bio-ceramic and electro-ceramics, etc. Due to the layerwise additive fashion in which SFF technologies build components, they are generally free from the constraints imposed by the external geometric complexity of the part, or the internal complexity resulting from the presence of multiple phases. Indeed, components and structures can be manufactured by SFF that can't be made by any conventional manufacturing method. This paper will focus on two SFF methods that are referred to as the "direct" and "indirect" methods. Recent "direct" method efforts have been focused on the SFF of functional quality GS-44 in-situ toughened Si_3N_4 and electroceramic actuators by Fused Deposition of Ceramics (FDC). Indirect efforts have focused on fused deposition and Sanders prototyping for novel hydroxy apatite bio-ceramics for bone-scaffolds, and piezoelectric ceramic structures for transducer and sensor applications. Examples are given which highlight the significant design flexibility associated with SFF manufacturing of advanced components and devices.

The Third Pacific Rim International Conference on
Advanced Materials and Processing (PRICM 3)
Edited by M.A. Imam, R. DeNale, S. Hanada,
Z. Zhong and D.N. Lee
The Minerals, Metals & Materials Society, 1998

Introduction

Solid Freeform Fabrication (SFF) refers to methods that fabricate freestanding solid objects without the need for tooling or machining. SFF methods are computerized (CAD file driven) material additive processes, originally applied to form and fit polymer applications which allow dramatic reductions in the time and cost of each component design iteration. [1-4] Several SFF technologies are under development at Rutgers University to make structural ceramic, bio-ceramic, as well as electronic ceramic components and devices. All SFF technologies share the same general approach; they start with a surface tessellated .STL file, that is then sliced mathematically into discrete layers, and then sent to a fabricator which builds the object in a layerwise additive fashion. SFF methods differ in the details of the materials available, the method of material deposition, etc. For ceramics and metals, most SFF techniques use powders as the raw material, that require post-SFF processing of parts to achieve the desired microstructure and properties.

Two different approaches are under development for manufacturing functional ceramic components: referred to as the "direct" and the "indirect" techniques, Fig.1. In the direct method: Fused deposition of ceramics (FDC, based on fused deposition modeling, FDM^{TM}, developed by Stratasys, Inc.) uses ceramic (or metal) particle loaded thermoplastic filament wound on a spool as the material feedstock, fed via counter rotating rollers into a heated extruder referred to as a liquefier.[5,6] The filament acts as the piston to extrude the molten ceramic (or metal) loaded polymer material out of a (250 micron to 635 micron diameter) nozzle onto a z-stage platform, where the material cools rapidly and bonds to adjacent layers, Fig. 2. The material deposition rate and liquefier x-y position, etc., are controlled by the computer. For ceramic parts, the binder is subsequently removed followed by sintering to full density. In the indirect method, Fig. 1, components are manufactured by first making a polymer or wax mold, using either FDM^{TM} or Sanders Prototyping (SPI) techniques. FDM uses a thermoplastic wax or ABS material to make the molds, as described above. In the SPI method, the system uses ink jet print technology with thermoplastic waxes (one build and one support material) to build the objects. The SPI process has the advantage of a milling step (after each layer) which enhances the ability to achieve very high dimensional tolerances, Fig. 3. The FDM^{TM} or SPI mold is then infiltrated with a ceramic powder suspension, dried (or gelled), followed by thermal or solvent mold removal, binder removal, and finally sintering. Processing details, as well as further physical and electromechanical characterization of structural and electroceramic components processed via these direct and indirect SFF methods, are reported elsewhere.[5-12]

Structural Ceramics

The FDC process was initially developed for AlliedSignal's GS-44 insitu-reinforced (ISR) silicon nitride (GS-44 Si_3N_4). The process steps for FDC of GS-44 Si_3N_4 are: ball milling the powder with a surfactant, drying, grinding and sieving, compounding with the multi-component binder system (RU9) in a high shear torque rheometer, followed by cooling and granulation. The material is then extruded into 1778 microns filaments in a single screw extruder fitted with a high shear tip screw and a breaker plate and screen that insure removal of large agglomerates. Parts are built using a liquefier temperature of 185°C in a chamber at 40°C. Typically, 381 micron diameter extrusion nozzles are used, building parts with 254 micron layer thickness. Ceramic part build times have ranged from 1 hr., for small simple shapes, to > 16 hr. for large, or very complex shapes. Figures 4 a, b show complex shaped GS-44 Si_3N_4 parts made by the FDC process. The typical densities of sintered FDC GS-44 Si_3N_4 parts are >99 % theoretical density.[10] The average measured four-point bend fracture strength of FDC bars is >900 MPa, similar to values for commercially produced GS-44 Si_3N_4 parts. The measured Chevron notch fracture toughness is 8 MPa $m^{0.5}$. While some subtle microstructural features are present which relate to layerwise building, there is little evidence, to date, of any significant difference in the microstructure, fracture strength or fracture toughness in samples where the cracks are driven parallel or perpendicular to the build plane. When FDC four point bend bars are broken with the crack traveling perpendicular to the build (Z) plane, GS-44 Si_3N_4 samples fall into two categories: Most samples have values of σ_f > 900 MPa, with a Weibull modulus of

10-15. These samples fail from large grains or machining damage. The minority of samples have values of σ_f in the range 500-700 MPa, and these fail from process induced Fe bearing defects. When FDC 4-point bend samples are built on end, and tested with the crack traveling in the build plane, the average value of σ_f is 880 MPa. This indicates that FDC GS-44 Si_3N_4 parts have the approximately the same strength when measured // and $\perp$ to the build plane. These values are equal to those obtained in commercial GS-44 Si_3N_4 parts manufactured by gel casting or isopressing, etc. In addition, feasibility for FDC has also been shown for a wide range of other materials with average particle sizes ranging from 0.5 microns to over 50 microns, including to date: Al_2O_3, SiO_2, WC-Co, and 17-PH steel.

Porous Hydroxyapatite Ceramics

Hydroxyapatite (HAp) and related calcium phosphate (CP) materials have been widely used as bone implant materials for many years because of their close similarity in composition and high biocompatibility with natural bone. Many researchers have emphasized the importance of controlling the pore size in HAp ceramics, and have claimed that a minimum pore size of 100 microns is necessary for the porous implant materials to function well, and pore sizes > 200 microns are essential for osteoconduction. Many traditional techniques have been used to make porous bone scaffolds, including the replamine process, coating polymer foam with a 50 vol. % ceramic slurry and burning out the foam, pressing HAp powder with polymer beads and then evaporating the spheres during heating, etc. These sintered structures typically have poor strength, because of the discontinuous pore network obtained using these methods. Also, it is nearly impossible to control the pore sizes and shapes for use in different applications. The FDM™ and SPI indirect SFF methods have been used to make porous bone scaffolds with a controlled porosity. First, the bone implant is designed using AutoCAD or ProEngineer, followed by fabrication of the sacrificial polymer or wax mold, and infiltrating with a HAp aqueous suspension, etc. A variety of porous structures have been fabricated, with porosity ranging from 30 to 70 vol. %. The pore sizes of the structures have also been varied from 200 microns to 750 microns. Figures 5a shows a 3-D honeycomb HAp structure made by FDM indirect method where the controlled pores are interconnected in three dimensions. This type of 3-D honeycomb structure has never been made using any other method. Figure 5b shows shaped HAp structures with ~ 55 vol. % porosity made by these techniques.

High Authority Actuators

In the last few years, the technology of using piezoelectric and electrostrictive actuators for applications requiring large displacements, such as: linear motors, cavity pumps, switches, loudspeakers and noise-canceling devices, has undergone significant development. Such applications require very large displacements (>1000 microns) combined with a moderate force (>10 kg). However, the induced strains in piezoelectric and electrostrictive ceramic discs, regardless of their size, are a few tenths of a micron. Higher displacements and generative force are achievable with these materials by employing strain-amplification techniques. As a result, Multilayer, Bimorph, Moonie, Rainbow and Cerambow actuators, with magnified output displacement, have been developed.[13-18]

The focus of the SFF research at Rutgers is on high authority actuators, such as a metal-electroceramic composite flex-tensional transducer termed a "Moonie," and dome shaped actuators, called modified rainbows, Figs. 6 & 7. Traditional Moonies consists of a monolithic piece of electroceramic (PZT, PMN-PT) sandwiched between two metal end caps, where the ceramic is poled in the thickness direction, and upon actuation, extends in the thickness mode. There is an accompanying Poisson contraction in the transverse direction that flexes the metal end caps resulting in an axial displacement, which couples with the axial displacement of the ceramic, thus amplifying the axial motion and transmitting it to the metal end caps. These transducers are characterized by values of displacement and force on the order of 20-30 microns and 3 N respectively. Two critical aspects to the successful development of SFF of Moonies are: 1. multiple material co-deposition by extrusion, and 2. co-firing of the PZT ceramic with Cu-Ni

end caps, and any required electrode and insulator compositions, Fig. 6. A novel Moonie design has been proposed which is based on an alternate poling concept. This was developed via finite element and kinematic electromechanical performance modeling, that predicts twice the displacement compared to a design which uses a monolithic PZT disk.[19,20] A multi-ring ceramic element, based on this design, has been fabricated at Rutgers via FDC, Fig. 8. PZT made by FDC has been successfully co-fired with Pt at 1285^{0}C, and the electromechanical properties of the PZT/Pt structure are: a dielectric constant, K, of 3400, d_{33} of 620 pC/N, and a tanδ of 2%, values which are in excellent agreement with the literature, confirming that these SFF techniques can fabricate high quality PZT components. Current research is directed at development of co-firing conditions for ceramic, electrode and metal end caps for Moonies.

A new type of high authority, dome-shaped actuator with different curvatures, diameters and thickness, is under development via FDC processing. Unlike the conventional techniques used for fabrication of Rainbow actuators with a curved structure, this method has the advantage of precise control of curvature, thickness and geometry. A thermoplastic binder with moderate strength and flexibility, while maintaining low viscosity at the deposition temperature, was developed for FDC with PZT based materials. The powder and binder were compounded with 60 vol. of PZT ceramic powder (TRS Ceramics, Inc., State College, PA) in a torque rheometer at 135°C and 100 rpm for one hour until a stabilized torque was reached. The compounded mix was granulated and sieved to use as the feed material for filament extrusion. A capillary rheometer was used for extrusion of short lengths (~ 30 cm) of green PZT filaments. The FDC process was used to manufacture dome shaped parts at a liquefier temperature of 145-170°C, while the surrounding environment temperature was maintained in a range of 35-40°C. After binder removal and sintering, a density of up to 94 % theoretical density was reached. Figures 7 and 9 show exterior and interior views of a dome-shaped actuator, fabricated by the FDC process. Examination of sintered parts using electron microscopy techniques showed no sign of delamination for parts made by layered manufacturing techniques, Fig. 10. The samples were thermally etched and their microstructure compared well with that of samples prepared by conventional processing methods, Fig. 11 a and b.

Similar to Rainbows, the dome-shaped actuators have shown a bending mode resonance at about 17 kHz, in addition to radial and thickness mode resonance frequencies. The piezoelectric coefficient, d_{33}, of these samples was measured when the samples were unclamped, using a Berlincourt Piezometer. Even though there was a large variation of d_{33} coefficient across the diameter of these structures, with a minimum d_{33} of 550 pC/N at the center of the dome, a large d_{33} of up to 1270 pC/N was measured at the edges of these samples, using pointed fixtures, **Fig. 12**. These samples also have shown a low dielectric loss (~3.5%) compared to Rainbow samples of the same size (8.5%). It is believed that the higher loss in Rainbows is due to the presence of carbon in the structure as a result of the reduction process.

Piezoelectric Transducers and Sensors

Piezoelectric transducers and sensors with novel structures and designs have been manufactured by both the direct (FDC) and indirect (FDM^{TM} and SPI) techniques. Figure 13 shows an SEM micrograph of an oriented PZT fiber structure made by the FDC process using a 55-vol. % PZT powder loaded filament as the feedstock, and a 406 micron nozzle in the liquefier. This geometry generates very large piezoelectric charge coefficients, due to the contribution of the d_{33} and d_{15} coefficients. Many other fine scale PZT structures, including volume fraction gradient and a novel radial composite designs, have been fabricated by the direct and indirect methods for use in ultrasonic medical imaging and towed array transducers by the SPI indirect method, Fig. 14 a, b, and c.

These and other novel SFF processes are under development for high authority actuator designs that are able to take advantage of the flexibility provided by SFF processes. In one ONR-MURI program, a new Layered Manufacturing (LM) system is under development. The overall objective of the MURI program is to establish the processing and manufacturing science required for the development of a novel, intelligent LM system for the cost effective fabrication

of net shape, complex shaped, multi-material, electromechanical components/devices and arrays. Figures 15 and 16 show a highly conceptual schematic of a single build layer of a fictional component that could be built by this new type of intelligent SFF process, and a conceptual schematic of the multiple material LM system under development as applied to dome and Moonie type high authority actuators.

Summary & Conclusions

This paper presents a brief summary of recent progress in the development of novel SFF techniques for functional quality advanced structural, bio-ceramic, and electronic ceramic components. For direct fabrication of ceramic components, green ceramic filaments of Si_3N_4 or PZT powder loaded thermoplastic binder were used for fabrication of complex ceramic structures by the FDC process, followed by binder removal and sintering. Parts made by FDC exhibit properties that are the same as to those of components made by traditional manufacturing methods. Fused deposition modeling (FDM™) and Sanders Prototyping (SPI) methods were used to form a variety of complex shaped molds (some with very intricate graded internal structures) for the indirect (or lost mold) method of fabrication. Once built, the wax molds were infiltrated with a PZT, or hydroxyapatite ceramic slurry, followed by drying, mold and binder removal and sintering. One can readily see the advantages of SFF manufacturing single material multi-material, multifunctional components, such as Moonie and Dome actuators, where one can now design and manufacture both the component as well as the internal macro- and microstructure for optimized performance. These novel ceramic manufacturing methods show tremendous potential to fabricate functional quality structural ceramics and piezoelectric ceramics (and composites) and bio-ceramics with freedom from the traditional design and manufacturing constraints.

Acknowledgments

The authors would like to thank DARPA, Dr. W. S. Coblenz, and the Office of Naval Research (ONR) Drs. S. Fishman, W. Smith, R. Wachter, and G. Spanos, for the financial support for this work under contract numbers: N00014-93-1-1059, N00014-94-C-0115, N00014-94-1-0588, N00014-96-1-0959, and MURI Grant No. N00014-96-1-1175. The authors wish to thank the following for technical and financial support of this research: Drs. P. Whalen and C. Gasdaska, of AlliedSignal, Inc., Dr. L. Bowen, of Material Systems, Inc., and Dr. V. F. Janas, of J & J Ethicon, Inc. The authors also wish to gratefully acknowledge the efforts of a large number of professional staff, graduate students, and undergraduate students whose work is represented here.

References

1. Proceedings of the Solid Freeform Fabrication Symposium, Vol. 1-8, Ed. Edited by J. J. Beamen, H. L. Marcus, D L. Bourell, and J. W. Barlow, Univ. of Texas at Austin, Austin, TX, 1990-1997.
2. M Feygin, B. Hsieh, 123-130, Proc. Solid Freeform Fabrication Proceedings (Austin, TX, August 1991). Edited by H. Marcus, J. J. Beamen, J. W. Barlow, D L. Bourell, and R. H. Crawford, University of Texas at Austin, Austin, TX, 1991.
3. C. Griffin, J. Daufenbach, S. McMillin, Am. Ceram. Soc. Bull., [73], 8, 1994.
4. J. Cawley, P. Wei, Z. E. Liu, W. S. Newman, B. B. Mathewson, A. Heuer, 9-16, Solid Freeform Fabrication Proceedings, Edited by H. L. Marcus, J. J. Beamen, D L. Bourell, J. W. Barlow, and R. H. Crawford, Univ. of Texas at Austin, Austin, TX, 1995.
5. M. K. Agarwala, A. Bandyopadhyay, R. van Weeren, V. Jamalabad, P. Whalen, N. A. Langrana, A. Safari, S. C. Danforth, J. Rapid Prototyping, Vol. 2, 4, 4-19, (1996).
6. M. K. Agarwala, A. Bandyopadhyay, R. van Weeren, V. Jamalabad, P. Whalen, N. A. Langrana, S. C. Danforth and A. Safari, Bull. Am. Cer. Soc., 75, 11, 60-5, (1996).
7. S. Rangarajan, G. Qi, A. Bandyopadhyay, C. Dai, J. W. Han, P. Bhargava, S. Wu, A. Safari, S. C. Danforth, Proc. of Solid Freeform Fabrication Symposium, Univ. of Texas at Austin, Austin, TX, 431-40, 1997.

8. G. Qi, C. Dai, S. Rangarajan, S. Wu, S. Danforth, and A. Safari, Proc. of Solid Freeform Fabrication Symposium, University of Texas at Austin, Austin, TX, 421-29, 1997.
9. C. Dai, G. Qi, S. Rangarajan, N. Langrana, A. Safari, and S. Danforth, Proc. of the Solid Freeform Fabrication Symposium, The University of Texas at Austin, Austin, TX, 411-20, 1997.
10. R. Clancy, V. Jamalabad, P. Whalen, P. Bhargava, C. Dai, G. Qi, S. Rangarajan, S. Wu, S. Danforth, Langrana, A. Safari, Proc. Solid Freeform Fabrication Symp., Univ. of Texas, Austin, TX, 185-93, 1997.
11. A. Bandyopadhyay, R. K. Panda, V. F. Janas, M. K. Agarwala, S. C. Danforth and A. Safari, J. Am. Cer. Soc., 80, 6, 1366-72, (1997).
12. S. C. Danforth and A. Safari, Proc. of 10th International Symposium on Applications of Ferroelectrics, IEEE 96CH35948, 183-188 (1997).
13. R. E. Newnham, Q.C. Xu, U.S. Patent # 5,276,657, Jan. 4, (1994).
14. A. Dogan, J. F. Fernandez, K. Uchino, R.E. Newnham, Materials for Adaptive Structural Acoustic Control (Penn State-Annual Report), Vol. IV, Appendix 40, (1995).
15. K. Onitsuka, A. Dogan, J. F. Tressler, Q.C. Xu, S. Yoshikawa and R. E. Newnham, Journal of Intelligent Material Systems and Structures, Vol. 6, pp. 447-455, (1995).
16. A. Bouhal, M. A. Jafari, W. B. Han, and T. Fang, "Tracking Control and Trajectory Planning in Layered Manufacturing Applications," August 1997, under review for IEEE Transactions in Industrial Electronics.
17. S. I. Guceri, A. Yardimci, Final Technical Report under DARPA/ONR Contract Number N00014-94-C-0115, Manufacturing Processes Laboratory, University of Illinois at Chicago, May, 1997.
18. M. A. Yardimci, S. I. Guceri, S. C. Danforth and M. Agarwala, Proc. of the 7th Solid Freeform Fabrication Symposium, Edited by H. L. Marcus, J. J. Beamen, D. L. Bourell, J. W. Barlow and R. H. Crawford, Univ. of Texas at Austin, Austin, TX, 539-548, 1996.
19. X. Ruan, S.C. Danforth, A. Safari, and T-W. Chou, "Design and Analysis of Electromechanical Devices," submitted to Journal of the American Ceramic Society, June 1997
20. X. Ruan, S.C. Danforth, A. Safari, and T-W. Chou, "Analysis of the Electromechanical Coupling Effect in Linear Piezoelectric Materials," submitted to Journal of Solids and Structures, November, 1997.

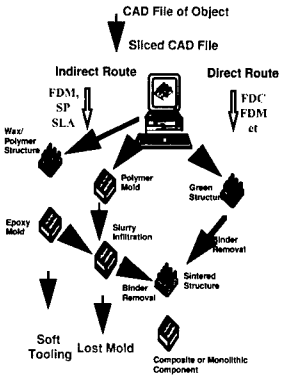


Fig. 1. Schematic of direct and indirect SFF routes.

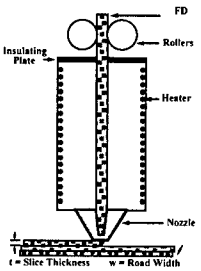


Fig. 2: Schematic of Fused Deposition (FDM & FDC) for direct and idirect SFF.

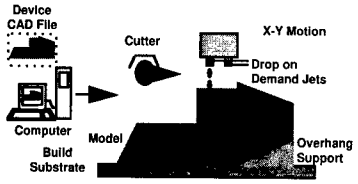


Fig. 3. Schematic of Sanders Prototying Technique (SPI), for indirect SFF.

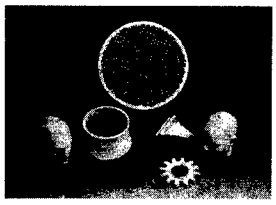


Fig. 4 a. Various green ceramic (light) and metal (dark) parts built by FDC process

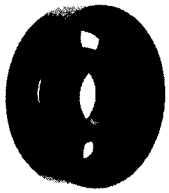


Fig. 4 b. Sintered, machined, GS-44 Si_3N_4 aerospace component by FDC process

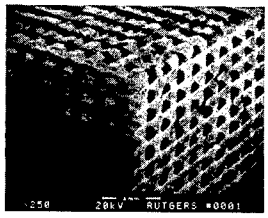


Fig. 5 a. 3-D Honeycomb structure with interconnected, regular, cylindrical pore channels

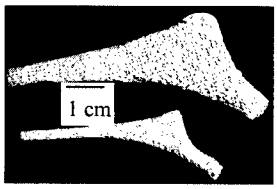


Fig. 5 b. Sintered, HAp bone structures made by indirect SPI SFF technique.

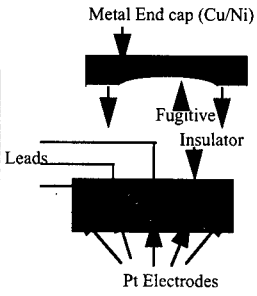


Fig. 6. Schematic of the top half of a novel alternate poling design for a Moonie flex-tensional high authority actuator.

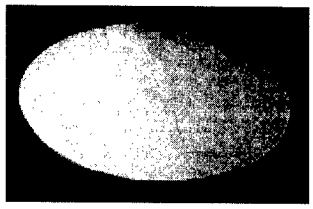


Fig. 7. Photograph of a PZT ceramic dome actuator fabricated by the direct LM (FDC) process.

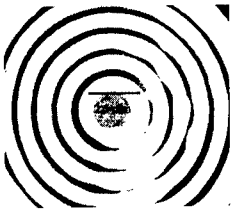


Fig. 8. Photograph of green PZT multi-ring ceramic actuator element fabricated by direct LM (FDC) process.

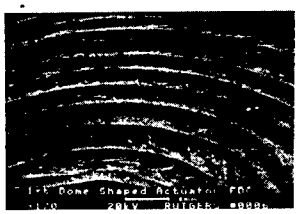


Fig. 9. SEM micrograph of a sintered PZT dome actuator element fabricated by direct LM (FDC) process.

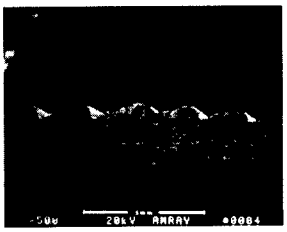


Fig. 10. SEM micrograph of a cut cross-section of a sintered PZT dome actuator element fabricated by direct LM (FDC) process.

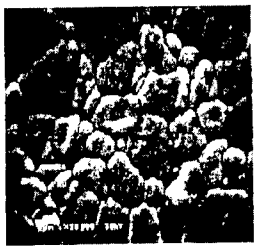


Fig. 11a. SEM micrograph of a polisheD & etched, sintered PZT dome actuator element fabricated by direct LM.

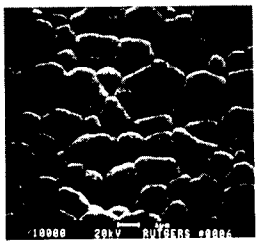


Fig. 11b. SEM micrograph of polished and etched, sintered PZT element fabricated by conventional means.

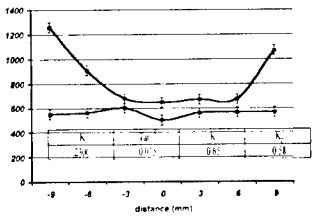


Fig. 12. Distribution of d33 across the LM dome actuator.

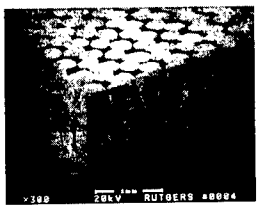


Fig. 13. SEM micrograph of an oriented PZT fiber structure fabricated by direct LM (FDC) process.

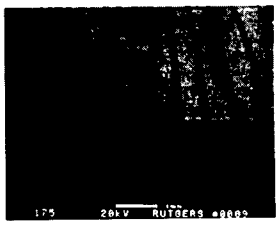


Fig. 14a. SEM micrograph of PZT structure with volume fraction gradient fabricated by indirect LM (SPI) process.

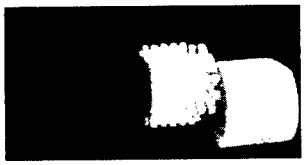


Fig.14b. Polymer mold, PZT part, & PZT-polymer radial composite structure fabricated by the indirect LM (SPI) process.

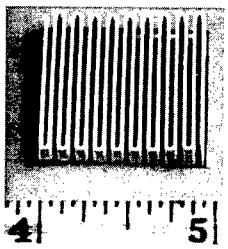


Fig. 14 c. PZT (green) ultrasonic transducer (with curved top surface) for medical imaging applications, made by the direct FDC SFF technique.

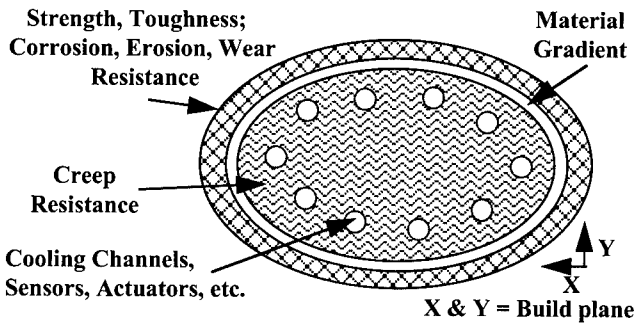


Fig.15. Schematic of ficticious, single layer of a multi-material, multi-functional component, possible by SFF processes currently under development.

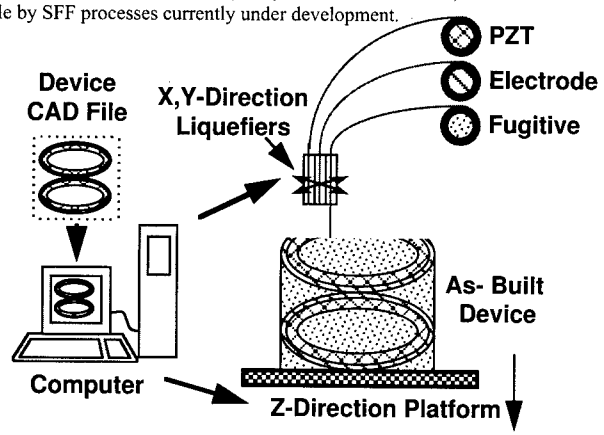


Fig.16. Schematic of a possible multi material, multi-functional elctromechanical component being built by an intelligent LM process currently under development at Rutgers University.

THE METAL PRINTING PROCESS
SOLID FREEFORM FABRICATION OF OBJECTS IN METAL AND CERAMICS

N. A. Ruud and R. Karlsen
SINTEF Production Engineering
N – 7034 Trondheim, Norway
Phone: (+47) 7359 0500, Fax (+47) 7359 3670, e-mail: Nils.Ruud@indman.sintef.no

The Third Pacific Rim International Conference on
Advanced Materials and Processing (PRICM 3)
Edited by M.A. Imam, R. DeNale, S. Hanada,
Z. Zhong and D.N. Lee
The Minerals, Metals & Materials Society, 1998

Introduction

The Metal Printing Process (MPP) is a new Solid Freeform Fabrication (SFF) method which is still in the research stage at SINTEF Department of Production Engineering. The MPP is built on some well known technologies and some new ideas. The idea of building objects layer-by-layer is known technology for polymer materials. Over the last years attempts have been made to develop a commercial process which is able to process a range of different materials, building objects layer-by-layer. To be successful the process must be able to handle metals, metallic alloys, and preferable also ceramic materials. Besides the ability to process a range of materials, the MPP may also fulfill requirements like i) Reasonably low cost for the complete system, ii) A reasonable short building time, and iii) An accuracy comparable to other forming processes.
The introduction of Powder Metallurgy (P/M) science to SFF is a huge step in the direction of fabricating high quality metal objects using the layer-by-layer process. In the new and still experimental Metal Printing Process the layers are generated by attracting metal powder to a charged photoreceptor under the influence of an electrostatic field, whereupon they are deposited one by one on a building table. After each deposit operation the loose powder layer is consolidated using simultanous pressure and high current. For sintering to occur in the consolidation process a certain resistance in the deposited powder is needed. The heat generated is given by Joules law and is proportional to the resistance in the loose powder layer.

How does the MPP works?

The experimental apparatus consists of two main systems; the Layer Generation System and the Consolidation System. An assembly of the two systems is shown in figure 1.

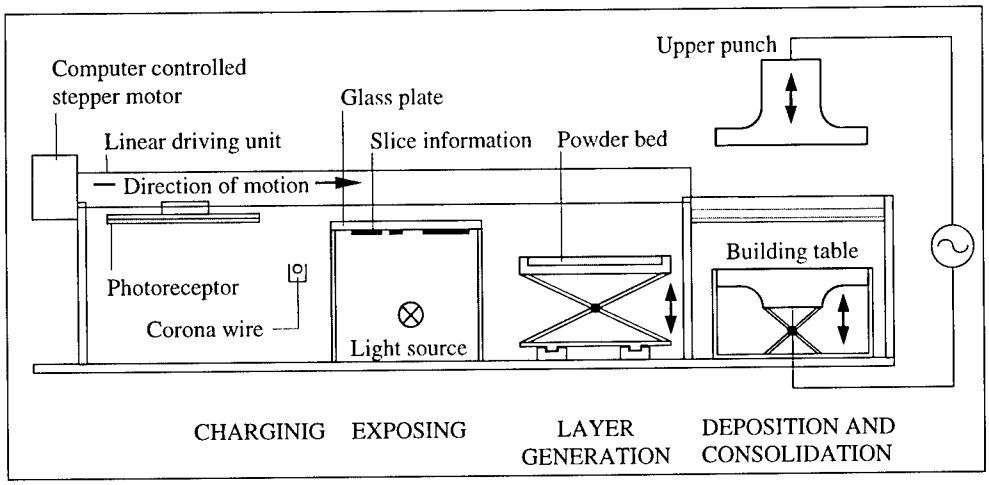


Figure 1: Equipment arrangement (side view)

The Layer Fabrication System

The system uses the xerographic principle for transferring the so called slice information to a photoreceptor. The photoreceptor, which is uniformly charged to the charge density σ_{pr} by an electrical corona device set to a very high positive potential V_1, is exposed to light through a mask. The mask contains slice information and light is prevented to pass in areas where powder is wanted. The photoreceptor charge density will decrease to σ_0 in areas exposed to light; thus an electrostatic image, a copy of the slice, that varies in a one-to-one manner is created.

The photoreceptor holding the electrostatic image then passes with constant velocity, separated with the distance d, just above the powder bed.

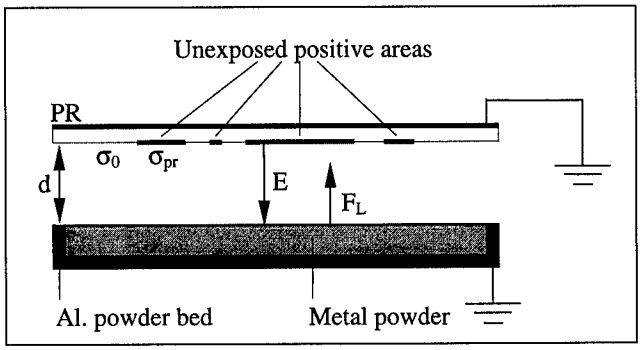


Figure 2: Attracting metal powder to the photoreceptor.

Difference in potential, ΔV, between charged areas on the photoreceptor and the powder surface causes the electrostatic field E.
By fluctuating ΔV and the distance between the photoreceptor and the powder bed one will obtain a variation in the lifting force F_L.

$$F_L = 0.5\ \varepsilon_0\ E^2 \qquad [N/m^2] \qquad (1)$$

With free flowing powder that has not been compacted by tamping or postponed to humidity, not agglomerated, adhesive forces will be small compared to other forces present and will be neglected in the further study. Van der Waals force is most significant for particles below 0.05 µm in size and will also be neglected in the further study.
It is shown that a voltage between 4500 V and 6000 V applied to the corona device and a distance d between 1.5 mm and 0.5 mm, see figure 2., attracts an acceptable amount of powder with the wanted size distribution. As the amount of powder lifted to the photoreceptor increases the charge density decreases leading to a decrease in the lifting force F_L. Finally the lifting force will become too small to lift any more powder, thus the larger the surface potential the more powder is lifted. The photoreceptor, holding the metal powder, stops at the deposit station where the powder is deposited onto the building table.
The deposit operation consists of setting up an electrostatic field that attracts the powder from the photoreceptor toward the building table.

The Consolidation System

The conversion of loose powder layers into useful engineering components in the Metal Printing Process is termed consolidation and consists of two processing operations; compaction and sintering. Compaction relies on an external source for deforming the powder into a high density component that approaches the final geometry. In the MPP only thin layers with a single level of thickness are compacted. This simple shape complexity means that single action pressing (the pressure is transmitted from one direction only) is enough to secure good packing properties. Compaction only is insufficient to provide an acceptable mechanical strength to the final product and for that reason sintering is necessary to obtain a permanent bonding of the powder particles. In the Metal Printing Process the compaction and the sintering are done simultaneously, making it a potential full density technique.

Between every deposition of a new powder layer the previous layer is consolidated and becomes part of the growing metal object. A fast sintering cycle is ensured by sending a huge electrical current through the powder - electrical contact sintering (ECS).

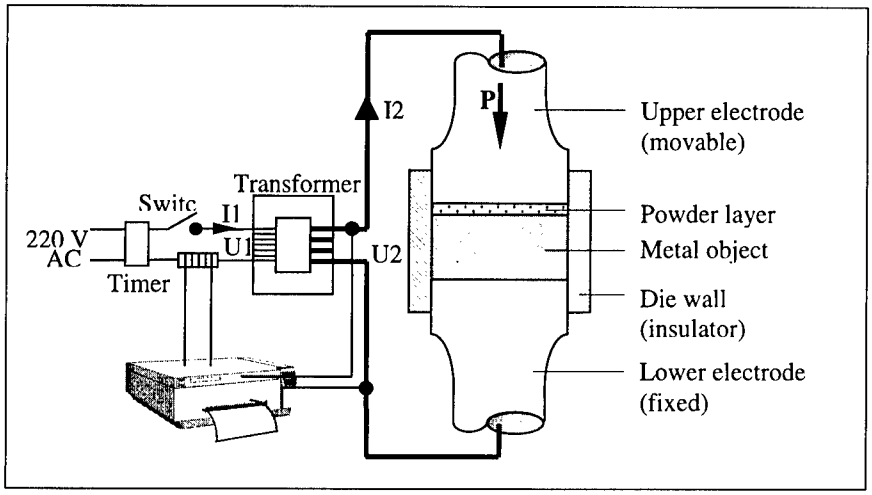


Figure 3: Equipment arrangement during ECS

An increased resistance in the particle contact region, caused by chemical composition (oxidation, segregation, etc.) and by a complex structure of electrical contact, results in a local temperature increase in this area during electrical contact sintering. This local temperature increase has a positive influence of the atomic diffusion process (sintering) and offers a fast sintering cycle.

Experimental results

The experiment was performed by attracting iron powder to a 155 mm^2 area on the photoreceptor (equalise the area of the building table). The electrostatic field was increased by decreasing the distance d from 1.5 mm to 0.5 mm with a 0.5 mm step. The voltage applied to the electrical corona device was held constant at 6000 V. The amount of powder attracted to the area was control weighted, and the pictures from the attracted layers can be viewed in figure 4, picture 1 to 3. The attraction parameters; d, and m_L in figure 4 denote the distance between photoreceptor and powder bed, and mass off attracted powder respectively.

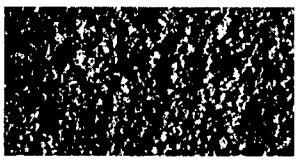
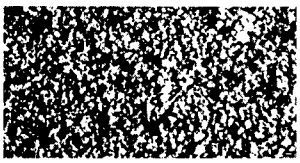
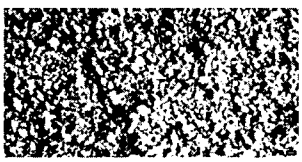
Picture 1	Picture 2	Picture 3
		
d = 1,5 mm / m_L = 0,029 g	d = 1,0 mm / m_L = 0,039 g	d = 0,5 mm / m_L = 0,048 g

Figure 4: Attracted layers of loose powder

At low electrostatic fields less powder is attracted to the photoreceptor and large voids occur in the layer (the black areas in figure 4 picture 1). At high electrostatic fields the layer is completely filled with metal particles, as can be seen in figure 4 picture 3. To minimize the

number of depositions between every consolidation cycle and ensure a practicable build time the strongest electrostatic field was used in the further experimental work.
The starting point for the consolidation process is the product from the layer generation system; a thin layer of loose powder. To prevent immediate short circuit between the electrodes, a certain initial resistance in the compacted powder layer is necessary. The heat generated is given by

$$W = \beta(L/s)r_c I^2 t_b \qquad [J] \qquad (2)$$

where L is the distance between the electrodes and s is the average particle size. The ratio (L/s) is the average number of contacts through which the electrodes travels from electrode to electrode. Due to the porosity between the powder particles the electrones have to travel a distance which is longer than L in order to reach the other electrode. This is taken care of by the numerical factor β. The contact resistance r_c (resistance between two powder particles) is dependent on the contact area and the thickness and composition of the oxide surface layer. t_b is the breakthrough time, which is the time from the current is switched on until short circiut arises.
The density and microstructure after consolidation was examined by building a sample with the deposition parameters corresponding to picture 3 in figure 4. The sample consists of 5 layers and each layer contains powder from one deposition. After every deposition on the building table, the upper punch (electrode) was brought into the die and compaction pressure was applied to the powder before the current was switched on. The pressure was constant during sintering. Both electrodes had water cooling to prevent sintering between the electrodes and the object being built. The already consolidated layers behaved as an extension of the lower electrode. When the object had reached its final extension, it was released by pressing it out of the ceramic housing. The density was determined by the Archimedes technique, and a cross section through the middle of the sample was examined in a light microscope.

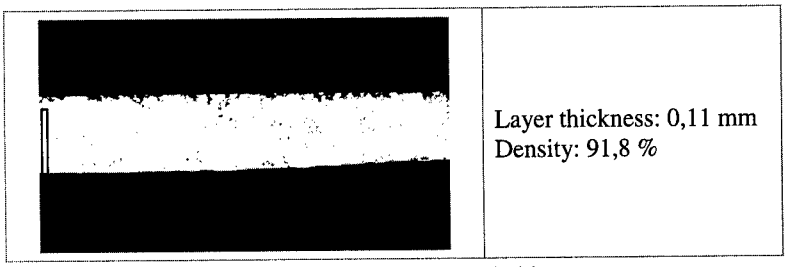


Figure 5: The microstructure of the consolidated objects

Figure 5 shows the microstructure in the sample after consolidation by means of 18800 A and 10 MPa external pressure force. The current was switched on for 0.75 seconds. The processing time, current, and pressure was chosen on background of earlier research work.
In addition to iron, titanium, magnetite, silicon carbide, Inconnel 625 (nickel-based super-alloy powder), aluminum oxide, silicon nitride, stainless steel, and nickel have been tested with succsess.

Future applications for the MPP

The initial intention for developing a new SFF process capable of fabricating metal objects was fabrication of prototypes in metal and production tools for pressure casting. Many new ideas have emerged during the work. The possibility of sintering both conductive and non-conductive

materials (with a modified sintering system) separately or as a mixture involves an enormous expansion in applications. A small selection follows.
One application for the MPP is fabrication of multi-layered print circuit boards. A ceramic and metal are combined, where the ceramic functions as the insulator and the metal provides electrical interconnections in a three-dimensional array. Both ceramic and metallic powder are deposited on the building table and sintered simultaneously. The layer-by-layer technique reduces the initial three dimensional problem to a two dimensional problem and offers fabrication of very advanced circuit boards.

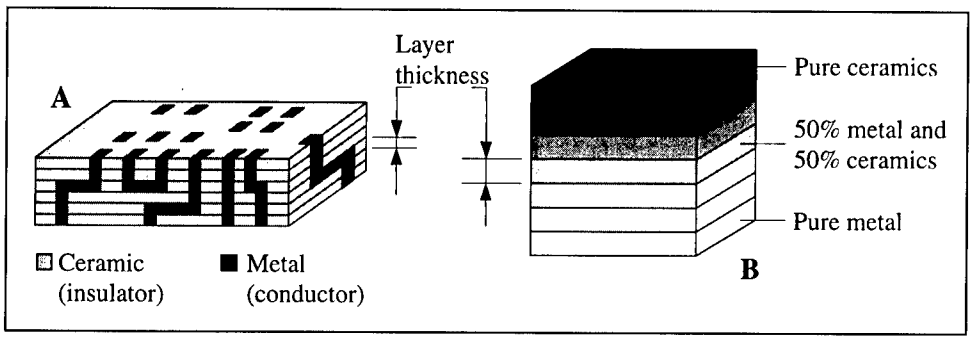


Figure 6: Applications for the MPP; **A**: Multi-layered print circuit board, **B**: FGM

The MPP may be used in sintering functionally gradient materials (FGM). These are transition materials: for example, one end is 100% metallic and gradual thin steps (the layer thickness) are used to progress to 100% ceramic. See figure 6. Each layer has a progressive change, possible in 10% or 20% increments, to move from pure metal to pure ceramic. Gradients of this sort are used to change properties in a gradual manner, thereby minimizing problems that occur with incompatible thermal expansion coefficients or other property differences.
Experimental work has proven that the MPP is able to fabricate objects with controlled porosity. Porous metals are used in filters, self-lubricating bearings, flow resistors, air distribution surfaces, sound absorbers, heat pipes, and biomedical implants which allow ingrowth of neighboring tissue and thereby achieve attachment and fixation of the device. Examples are heart pacemaker electrodes and artificial joints and bones.
The freedom in choice of geometry and type of materials may give unique possibilities within the area of micro mechanical devices like pumps, switches, vents, magnets or similar objects. Thus, the MPP may be a economical way to manufacture the mechanical part of MEMS (micro electro mechanical systems).
The many possibilities and promising results regarding the Metal Printing Process should make this an area of concentration in the years to come. A lot of work and money is needed to develop a MPP machine capable of fabrication objects in a variety of materials. Probably the best argument for further research on the MPP, is the positive feedback and economical support from external high-tech industry.

References

1. J. Bakkelund, "Fabricating layers of loose powder for layer manufacturing technology" (Ph.D. thesis, Norwegian University of Science and Technology, 1996)

2. R. Karlsen, "Consolidation of thin powder layers for layer manufacturing technology" (Ph.D. thesis, Norwegian University of Science and Technology, 1997)

FAST FREEFORM FABRICATION OF METAL PARTS USING LAYER DEPOSITION TECHNIQUE

A. A. Tseng, M. Lee, B. Zhao
Manufacturing Institute, Arizona State University

Abstract

A new droplet deposition system using an adjustable nozzle for freeform fabrication was studied. Theory on linear unstable liquid jet was presented for understanding the generation of controllable uniform droplets. By using tin and wax, experiments were conducted to determine the optimal perturbation frequency for droplet generation with minimum size variation. Less than 2% variation was observed. Experiment results are not only in good agreement with theoretical predictions but also have smaller variation as compared with the previous published data using different apparatus.

The Third Pacific Rim International Conference on
Advanced Materials and Processing (PRICM 3)
Edited by M.A. Imam, R. DeNale, S. Hanada,
Z. Zhong and D.N. Lee
The Minerals, Metals & Materials Society, 1998

1. Introduction

The use of droplet spray system in freeform manufacturing represents an emerging technology for prototyping and fabrication of polymer, metal and ceramic parts[1]. In the present study, the droplet spray system is utilized for forming three-dimensional parts and components. The system builds three-dimensional multi-material structures in layer and does not require pre-formed mandrels or tooling (Fig. 1). During free forming, the three-dimensional parts are directly formed from computerized virtual models[2]. From the computer model, a slicing algorithm computes information for each layer to form the desired shape. The building material droplet is only deposited to the location where the object is to be formed. Then a low-melting-temperature complementary material is deposited adjacent to the layer to serve as a support structure during forming. In this manner, layers of materials form a block of solidified building material drops and complementary material. Since the complementary material has a much lower melting temperature, it can be easily removed after completing the forming process, leaving the fabricated part.

In the present system, two types of jets are used for deposition, one for building material drops and the other for the complementary material drops. Currently a soldering metal is chosen for the building material while a wax is selected for complementary material. Parts can be built layer by layer as guided by a CAD and process-model integrated computer until it is completed. The droplets solidify at the substrate in a uniform, incremental manner. The metal products can thus be tailored to have a fine, equiaxed microstructure and to be relatively free of defects such as porosity or alloy segregation.

High quality of components is usually guaranteed by high uniform generation of droplets. In all of the existing droplet generating devices, the diameter of the nozzle is fixed. This brings about two problems. One is that flow rate is constrained in a limited range for a given nozzle. Although this can be solved by changing nozzle, frequent change is not desired in practice. The second is that the impurity of molten materials makes blocked the nozzle especially for the very fine nozzles. To overcome this inconvenient, a new nozzle design having an adjustable diameter has been developed[3] (Fig. 1). The purpose of the present research is to the understanding and control of the uniformity of droplets generated by the new nozzle design. This paper reports the theoretical and experimental results of the fluid dynamic aspect of this research.

In fact, this technique is an application of the stability theory of liquid jet dated back to Rayleigh who developed the first linear stability analysis where he considered an infinitely long, circular, inviscid jet subject to a temporal disturbance growth[4]. In consequence he defined a growth rate of the disturbance and established a relationship between the growth rate and the non-dimensional wave length. Weber modified Rayleigh's theory to include the effects of viscosity and the ambient pressure[5]. In both derivations the correlation between the growth rate of disturbance and the non-dimensional wave number is nonlinear. This implies some potential applications. Orme and Muntz[6] experimentally discovered that the droplet speed dispersion ($\Delta V/V$) is minimized when the growth rate of disturbance is at the maximum. They have given the explanations and predicted a minimum size dispersion. In this paper emphasis is contributed to the diameter control ($\Delta d/d$) of droplets for the first step research.

A brief theoretical preparation will be given in the first part of the paper. The second section will be contributed to the presentation of the experimental results and their analyses.

2. Basic theory

2.1. Unstable equilibrium condition for liquid jet

We shall derive the unstable equilibrium condition by following Rayleigh's surface potential energy calculation of liquid jet. This will give us the upper limit of wave length used in acoustic control. Figure 2 is a schematic of a liquid jet through a nozzle, where the jet velocity is U_j .and jet diameter is $2a$.

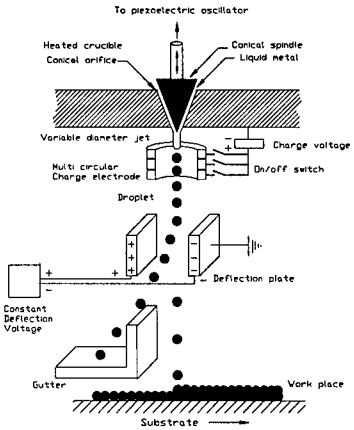


Fig. 1 New controllable nozzle in fast freeform fabrication system in ASU

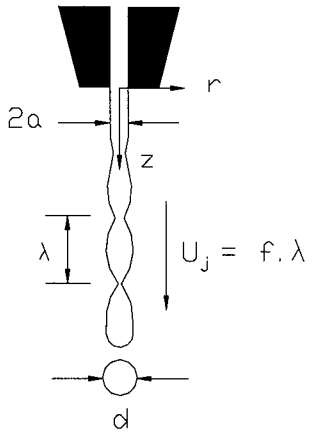


Fig. 2. Liquid jet analyses

λ is the distance between two droplets or called wavelength. A cylinder coordinate z-r is established at the bottom at the exit of the nozzle. The radius of the free surface is assumed $r=a_0+f_1(\theta, z)$, and the portion of $f_1(\theta, z)$ is normally much smaller than a_0.

Expanding f_1 by a Fourier Series Expansion we get $r=a_0+b_n\, cos(n\theta)cos(kz)$ and n is a controlling parameter. n=0 is a axisymmetric perturbation.
During the motion, the quantity a_0 does not remain absolutely constant, its value must be determined by the condition that the enclosed volume is invariable:

$$\text{Volume} = \iint r^2 d\theta\, dz/2 = z\left(\pi a_o^2 + \pi b_n^2/4\right) \tag{1}$$

The undisturbed cylinder of radius $a=(a_0^2+ b_n^2/4)^{1/2}$. a_0 varies as

$$a_0 = a\left(1-b_n^2/4a^2\right) \tag{2}$$

The potential energy of the system in any configuration is the surface tension times the surface area. For a given liquid the surface tension is a constant. So the potential energy is proportional to the surface area of the system.

$$\text{Surface} = \iint\left\{1+\left(dr/dz\right)^2+\left(dr/rd\theta\right)^2\right\}^{1/2} rd\theta dz = z\left(2\pi k^2 a_0 + \pi n^2 b_n^2/4a\right) \tag{3}$$

Replacing a_0 in expression (3) by equation (2), the potential energy of disturbed column per unit

length is obtained:

$$E_p = \pi\sigma\left(\gamma^2 + n^2 - 1\right)b_n^2/4a \tag{4}$$

where σ is surface tension, $\gamma=2\pi a/\lambda$ is dimensionless wave number.
For an axisymmetrical disturbance (n=0), when $\gamma < 1$, the potential energy of the system is negative implying an unstable equilibrium state. Accordingly we get the unstable equilibrium condition: when the wavelength is greater than the circumference of jet, the jet will breakup.

In this case the diameter of the droplet can be determined by mass conservation:

$$d = \left(6Q/\pi f\right)^{\frac{1}{3}} \tag{5}$$

where $Q=\pi a^2 U_j$ is the flow rate and f is the frequency of acoustical disturbance.
According to Rayleigh's linear theory, if the unstable equilibrium condition is met, an infinitesimal perturbation will increase exponentially in the time along the jet surface till the jet breaks up. The growth rate of perturbation is given by considering the total energy of the jet.

By remembering inviscid and incompressible condition, we have the Laplace's equation of velocity potential:

$$\frac{d^2\psi}{dr^2} + \frac{1}{r}\frac{d\psi}{dr} + \frac{1}{r^2}\frac{d^2\psi}{d\theta^2} + \frac{d^2\psi}{dz^2} = 0 \tag{6}$$

Suppose $\psi = \psi(r)\cos(n\theta)\cos(kz)$:

$$\frac{d^2\psi}{dr^2} + \frac{1}{r}\frac{d\psi}{dr} - \left(\frac{n^2}{r^2} + k^2\right)\psi = 0 \tag{7}$$

The solution of this equation is

$$\psi = \beta_n J_n(ikr)\cos(n\theta)\cos(kz) \tag{8}$$

where $i=(-1)^{0.5}$. The constant β_n is to be found from the boundary condition at $r=a$

$$\frac{\partial\psi}{\partial r} = \frac{dr}{dt} = \frac{db_n}{dt} \tag{9}$$

Kinetic energy of the motion

$$E_k = \frac{\rho}{2}\iint\left[\psi\frac{d\psi}{dr}\right]_{r=a} a\, d\theta dz = \pi\rho z ika\, J_n(ika)J_n'(ika)\frac{\beta_v^{\,2}}{4} = \frac{\pi\rho a^2}{4}\frac{J_n(ika)}{ikaJ_n'(ika)}\left(\frac{db_n}{dt}\right)^2 \tag{10}$$

For the free motion the system's energy is conserved:

$$d\left(E_p + E_k\right)/dt = 0 \tag{11}$$

Replacing E_p and E_k by equations (4) and (10) we have the ordinary differential equation.

$$\frac{d^2 b_n}{dt^2} + \frac{\sigma}{\rho a^3} \frac{ika J_n'(ika)}{J(ika)} \left(n^2 + k^2 a^2 - 1\right) b_n = 0 \tag{12}$$

When the unstable condition is met, this equation will have the following solution:

$$b_n = \delta_0 e^{qt} \tag{13}$$

where the growth rate of perturbation is computed by

$$q = \frac{\sigma}{\rho a^3} \frac{ika J_n'(ika)}{J_n(ika)} \left(1 - k^2 a^2\right) \tag{14}$$

Since the dependence of q on wave number k is not linear, so there exists a maximum disturbance growth rate[7]:

$$q_{\max} = 0.97 \left(\sigma / \rho d^3\right)^{\frac{1}{2}} \tag{15}$$

This is the derivation of conditions for inviscid liquid jet break-up in a vacuum. Weber gave an expression of growth rate for viscous jet:

$$q^2 + \frac{3\mu\gamma^3}{\rho a^3} q = \frac{\sigma}{2\rho a^3} \left(1 - \gamma^2\right) \gamma^2 \tag{16}$$

where μ is viscosity. Both Rayleigh's derivation and Weber's derivation indicates that the growth rate of perturbation is nonlinear related to the non-dimensional wave number γ. This relation is shown in figure 3. This nonlinear relation enables us to realize an optimal control in generation of uniform droplets which is the goal of this paper.

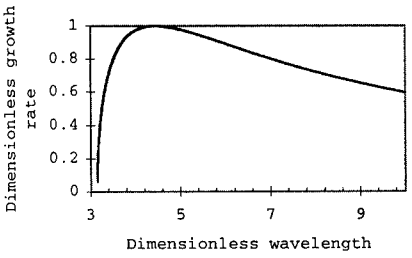


Fig.3 Relationship between the perturbation growth rate and wavelength

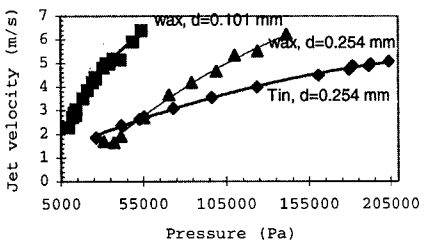


Fig. 4. Pressure head and jet velocity. d is the diameter of the nozzle

3. Experiment setup

Thus far, we have given the necessary knowledge for the acoustically controlled droplet generation. We hope to apply this theory for our rapid prototyping technique. The first step of the project is therefore designed to generate uniform and size-adjustable droplets. The

experimental set-up is shown in Fig. 1. The acoustical controlled droplet generator consists of fundamentally three units. The molten metal unit is a crucible heated by an electric resistance coil. A ruby/sapphire orifice is attached at the bottom of the crucible in order to form a liquid jet. The pressure needed for the jet is obtained from the pressurized argon bottle. A vibration excitation unit is composed of a signal generator, a power amplifier and a piezo-electric crystal. The jet was subjected to forced vibrations at a frequency between 1 kHz to 50 kHz of sinusoidal, triangular or square waves. The manufacturing unit is a well sealed chamber for vacuum or pressurization. The droplets were issued onto the stainless steel substrate placed directly below the orifice to effect rapid solidification. The distance between the orifice and the substrate could be adjusted in order to meet the practical fabrication condition.

4. Experimental procedure

4.1 Realization of desired jet velocity

In experiments the jet velocity or volume rate is an important parameter which is controlled by the static pressure (pressure head) over the molten metal inside of the crucible. Before the experiments a calibration between the nozzle jet velocity and static pressure was done by using mass/time method. The calibration result is shown in Fig 4. In the same figure the solid line is the data fitting. This calibration is made by using tin and wax for our first phase. Similarity treatment of the result will be applicable to other metals in the second phase.

4.2 Generation of droplets

The generation of metal droplets must utilize a vacuum chamber. This results in some difficulties for sample collection since the condemnation between samples is difficult to be avoided if the previous sample is not removed. For the sake of simplicity, the first step of the experiment was carried out with wax because this can be done in open air. In order to obtain the minimum size dispersion of the droplet, an acoustical perturbation should be well designed; that is to say, the vibration frequency range of the vibrator should cover the dimensionless wave number between 0.4 to 0.9 as indicated in references (8). In our experiment, the nozzle diameter is 0.254 mm. A jet velocity of 3.7 m/s is maintained by a pressure head of 22500 Pa. The expected frequency range is between 2000 and 4500 Hz.
In operation, after reaching a melting temperature of 341 K, a laminar wax jet was ejected in open air to the substrate of 1.5m beneath the nozzle. The jet was subjected to forced vibrations at an imposed frequency. The droplets generated in each chosen frequency were collected.

5. Results and discussion

The solidified wax droplets were examined for their appearance, shape, size and size distribution. The uniform droplets produced in this study showed a smooth surface and spherical shape as shown in Fig. 5.

Some irregularly shaped particles were formed due to the merging of droplets. The droplet size (diameter) was measured by optical microscope with precision of 1μm.

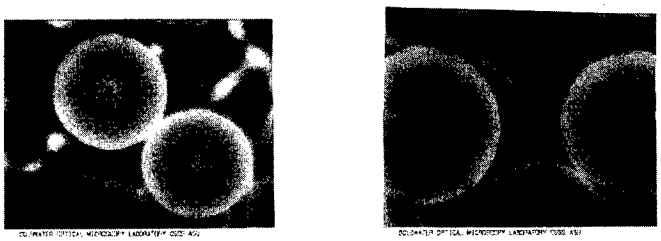


Fig. 5 Examination of appearance and shape of wax droplet

Fig. 6 shows the average diameter of 100 droplets picked randomly from one of the batches of the uniform droplets produced in each frequency. The theoretical value in Fig. 6 is computed by equation (5).

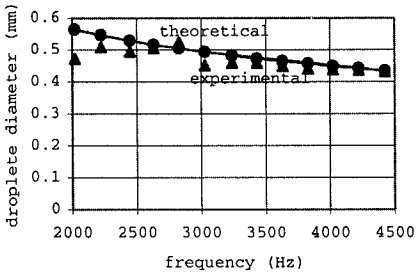


Fig. 6.Droplet diameter in function of frequency of acoustic perturbation

The greater deviation of diameter from theoretical value in lower frequency, for example 2224 Hz in our case, is probably from the generation of satellites due to nonlinear mechanism[9]. This can be observed by the size distribution of 100 samples (Fig. 7) in which the droplets are concentrated in two diameter values instead of a normal distribution. The experimental value has a good agreement with that of theory in higher frequency.

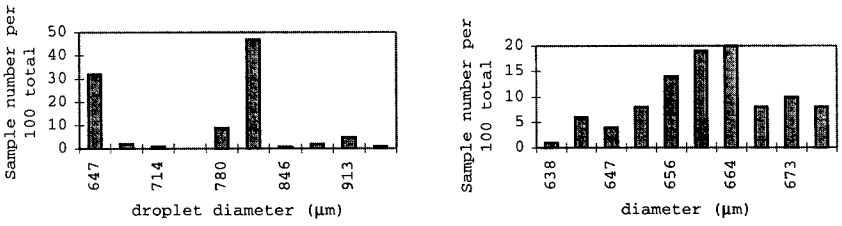


Fig. 7 Comparison of size distribution for 100 droplets obtained at frequency 2224 Hz (left) and 4020 Hz (right)

The diameter dispersion ($\Delta d/d$) result (Fig. 8) shows our maximum value is less than 15% and the minimum is better than 2%. By data fitting (solid line in Fig. 8), we can see that there exists an optimal frequency for size dispersion. This optimal value is about 3700 Hz, falling down in the predicted frequency range (2000-4500 Hz).

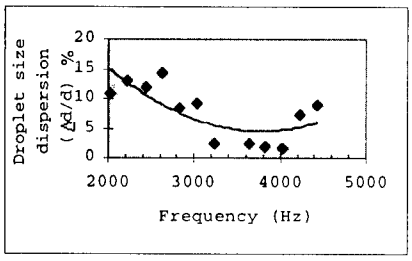


Fig. 8. Diameter dispersion in relation to acoustic perturbation

6. Conclusion

In the rapid prototyping manufacturing process, the droplet size dispersion is an important parameter which influences the mechanical properties of materials synthesis. Starting with the instability theory of liquid jet, this paper presents the feasibility of acoustically controlled uniform droplet generation. A first phase experimental work was accordingly carried out. The experimental results show that a very low size dispersion, less than 2%, can be reached by the acoustic controlled technique. The experimental results have qualitative agreement with the theoretical prediction.

Reference

1. J-H. Chun, C. H. Passow, "Production of charged uniformly sized metal droplets", U.S. patent 5266098, Nov. 30, 1993

2. Bischel, K., Harvey, E.G., Overman, A., and Tseng, A.A., "Telemanufacturing and rapid prototyping of engineering components through use of internet," in 1997 Int. CIRP Design Seminar of Multimedia Technologies for Collaborative Design and Manufacturing, ed. By S. Lu and Y. Jin, pp. 246-255, Uni. Southern California, Los Angeles, CA, 1997

3. Tseng, A.A and Lee, T.-W, An improved method and apparatus for rapid prototyping and material processing," Pending for U.S. Patent Application, 1996

4. J. W. S. Rayleigh, The Theory of Sound, vol. 2, pp342-365, (New York, Dover Publications, 1945)

5. K. Weber and Z. Angew, Math. Mech. Vol. 11, 136, (1931)

6. M. Orme and E.P. Muntz, "New technique for producing highly uniform droplet streams over an extended range of disturbance wavenumbers", Rev. Sci. Instrum. 58 (2), February 1987

7. M. J. McCarthy and N. A. Molloy, "Review of stability of liquid jets and the influence of nozzle design", The Chemical Engineeering Journal, 7 (1974) 1-20

8. M. Orme, "On the genesis of droplet stream microspeed dispersions", Phys. Fluids A 3(12), December 1993

9. K. C. Chaudhary and L. G. Redekopp, "The nonlinear capillary instability of a liquid jet", J. Fluid Mech. (1980), vol. 96, part 2, pp257-274

Metal Part Processing by SLS/HIP

Joseph Wright and Ronald Knight, Lockheed Martin Vought Systems

ABSTRACT

The US Department of Defense (DoD) military services are pursuing improvements in the reprocurement and repair methodology for high value metal parts used in current weapon systems. The Selective Laser Sintering™, SLS™, process of solid freeform fabrication offers a near term solution for reducing the cost of small metal parts produced by HIP. Under the sponsorship of the US Office of Naval Research and the Defense Advanced Research Projects Agency, DARPA, the team of Lockheed Martin Vought Systems, the University of Texas, Bayside Materials Technology and DTM Corp. are pursuing the development of SLS™ for processing of high temperature metal HIP parts. The approach is to use SLS to form the impermeable skin, or can, to replace the traditional can for HIP processed parts. Results of selective laser sintering of candidate metal powders will be reviewed along with results of our process modeling efforts. This paper represents work in progress.

1.0 INTRODUCTION

Selective Laser Sintering (SLS) was conceived in the mid-1980's by staff of the University of Texas as a method for rapidly prototyping solid, functional parts without part specific tooling (Beaman, 1987, Deckard, 1986, and Deckard, 1988). The SLS process converts fusible powders into solid objects by using a laser beam to melt and fuse the powder particles together (Deckard, 1989 and Marcus, 1990). SLS is an additive layer process in which the part is built up in layers approximately 0.005 inches thick by rastering a laser across the powder bed using scanning mirrors which are servo-driven from 3-D CAD data that describes the part to be fabricated, as illustrated in Figure 1. The powder bed provides the support for the part build so that no tooling is needed. SLS is one of the most versatile rapid prototyping methods in that it is applicable to plastics, ceramics, and metal powders.

The US Department of Defense has a large number of high value metal parts in service which are produced by hot isostatic pressing (HIP). HIP metal parts typically require powder encapsulation in a can or skin, which must be removed after HIPing (Price, 1993). The canning and can removal operations are a large contributor to the cost of HIP parts and limit the part complexity. Our technical concept is to use the SLS process to form the integral metal skin which is required for encapsulation of powder metal parts prior to hot isostatic pressing. Typically the encapsulation skin is a sacrificial layer of a different material that must be removed after the HIP cycle. Our concept is to SLS form the skin integral with the HIP part using the same powder material, as illustrated in Figure 2. In this way the skin becomes the outer surface of the HIP part and does not have to be removed. SLS will be used to liquid phase sinter the powder metal, forming a fully dense skin integral with the core part which has been SLS processed to approximately 70% dense.

Lockheed Martin Vought Systems under the sponsorship of the US Office of Naval Research and DARPA/DSO has formed a team, consisting of the University of Texas, Bayside Materials, MATSYS and DTM Corporation to apply the SLS technology to on-demand production of functional metal parts. The program is a four year, two phase effort to: (1) develop SLS for HIP part processing, demonstrating the technology using multiple metal alloys; (2) develop and demonstrate and SLS Beta machine for metal alloys. Phase 1 objectives are to develop the materials and processing science to produce functional metal parts using SLS with integrated canning and HIP post processing. Key technical issues addressed in Phase 1 include: impermeability of the SLS skin; wetting of the metal powders and the resulting density; part properties equivalent to baseline; dimensional tolerances and surface finish. The Phase 2 objective is to validate the performance and commercial viability of the high temperature SLS process through demonstration of a high temperature SLS beta test machine.

2.0 Current Technical Status

2.1 Material Screening and Selection:

The initial program task was to select two materials and components on which to demonstrate the SLS technology. To this end a comprehensive survey of Navy installations (depots, centers, shipyards, etc.) was conducted. From the initial survey, candidate materials were identified for SLS screening trials to aid in down-

The Third Pacific Rim International Conference on Advanced Materials and Processing (PRICM 3)
Edited by M.A. Imam, R. DeNale, S. Hanada, Z. Zhong and D.N. Lee
The Minerals, Metals & Materials Society, 1998

selection of materials and components for demonstration. The survey criterion was: sinterable powder metal parts with complex geometry, that can be SLS processed in the current 7 inch by 7 inch processing chamber at the University of Texas. Based on our survey, the three leading materials/component candidates were: (1) Inconel 625 super alloy for an aircraft engine vane (2) Molybdenum rotary valve for the MK-46 torpedo, (3)Titanium guidance section housing for the AIM-9 air-launched tactical missile.

The University of Texas at Austin (U.T.) performed initial SLS materials screening trials on the candidate powder metal materials using a modified high temperature SLS workstation with atmosphere controls and laser systems for processing the high temperature powder metals. Initial screening trials focused on the ability of the powder metals to be liquid phase sintered via SLS to form an impermeable skin suitable for hot isostatic pressing. Single layer SLS trials were carried out on Inconel, Titanium, and Molybdenum powders. Single and multilayer SLS skins were formed for Inconel 625 and Titanium as shown in Figures 4 and 6.. The Inconel 625 powder processed most easily into both single and multiple layer skin specimens which passed HIP vacuum leak testing. Inconel solid cylinders were also successfully SLS processed and HIPed to 99.5% dense. Six screening specimens of Ti-6Al-4V were produced by SLS. Two of these specimens were subjected to helium leak testing and both passed the containerless HIP leak test criterion with a leak rate less than 1×10^{-10} standard cc/s. Subsequent metallography revealed a nearly fully dense microstructure. Single layer SLS screening trials were also conducted on plasma spray grade (PSG) molybdenum powder (-325 mesh) supplied by Atlantic Equipment Engineers. These trials showed that the molybdenum powder melted during laser processing. However, a continuous, solid layer was not formed. Based on these SLS screening trials the Inconel and Titanium metals were selected for further process optimization and component demonstrations.

2.2 SLS High Temperature Workstation Development

The High Temperature Selective Laser Sintering Workstation at the University of Texas continues in development as we learn more about the requirements of liquid phase sintering of the metal powders. The processing chamber design is being iterated to improve stability of the chamber environment and reduce leak rates. SLS trials conducted to date have indicated a need for higher laser power to successfully process Inconel and Ti-6Al-4V. To address the current limitation of laser power, modifications have been initiated to bring a 1.1 kW CO_2 laser online. These modifications will include replacement of a laser head and associated X-Y table by a galvanometer based laser scanning system. Necessary beam focusing and profiling optics are also being acquired as part of this effort. Hardware and software upgrades are being implemented to aid development of intelligent process control. Geometry processing software was developed to treat the interior of the part separate from the skin and end-cap regions. A high performance data acquisition and control board was acquired and installed on the process control computer. Software is being written to coordinate real time control of laser power with laser scanning.

2.3 SLS Processing Trials of Inconel 625 Superalloy and Titanium (Ti-6Al-4V)

SLS processing optimization experiments of Inconel 625 are being conducted in high vacuum with and without in-situ bake-out pre-processing. Bake-out pre-processing helps eliminate adsorbed contaminants from powder particle surfaces, reduces oxide formation and, improves wetting and flow characteristics of the molten material during SLS. Figure 4 is a micrograph of a single layer of Inconel 625 SLS processed at 3×10^{-5} Torr and 400° C preheat following a bake-out at 400° C. Surface oxidation of the single layer coupon from this experiment was much reduced when compared with the single layer coupon produced without bake-out. This material exhibited overall reduced porosity in size and number than those processed using a higher preheat temperature. Solid cylinders, 0.5" diameter by 1" in height have been fabricated by SLS and post processed by HIP to full density. Figure 5 is a photograph of a typical SLS/HIP cylinder.

Single layer SLS process optimization trials on Ti-6Al-4V blended elemental powder are being conducted in high vacuum, at 400° C preheat and with bake-out pre-processing. At lower laser energy densities it was possible to form single layers with relatively good surface texture and integrity. These single layers exhibit a nominal degree of porosity as shown in the micrograph of Figure 6. Titanium skin and core cylinders fabricated by SLS have demonstrated the viability of the SLS process to form canned parts suitable for HIPing. This process optimization ongoing work is currently in progress.

2.4 HIP Modeling

Hot Isostatic Pressing (HIP) is a well-developed technique for full density processing of metal powders. The sequence of events during conventional HIP compaction include: particle rearrangement, neck growth, and the final densification stages of sintering. Experiments reveal that distortion commonly occurs in the early stages of compaction with little distortion seen after densities of 85%. Dimensional control of HIP processes is determined by container design, homogeneity of macrostructure parameters and uniformity of densification fronts. The SLS/HIP technology provides an opportunity to significantly reduce cost and shorten the product development cycle through improvements in dimensional control. The MATSYS approach being used integrates *in-situ* measurement and advanced modeling of powder consolidation. To achieve our objectives requires 1) development of a HIP canister design and packing, 2) use of *in-situ* sensor for real-time measurement of HIP consolidation, 3) estimation of material properties from *in-situ* sensor data, and 4) application of micro-mechanics, mechanism-based models and finite element (FEM) method to predict component deformation during HIP. The FEM process modeling featuring the MATSYS PROSIM analysis tool is therefore being used to establish an understanding of the relationships between HIP processing parameters governing dimensional control and SLS of the powder preform, e.g., container wall thickness and preform density.

The initial HIP modeling activity has focused on the Inconel material. For estimation of required material properties four HIP experiments were performed successfully at Crucible Research. For Inconel 625 two types of HIP schedules were used. In one case the temperature and pressure were ramped simultaneously to maximum values while in the other temperature was ramped first to maximum value and then followed by pressurization. HiTECS, a High Temperature Eddy Current System, was used to measure diameter change during HIP. After a HIP run, measured specimen diameter was converted to relative density. Using nonlinear estimation techniques, the relative density curve was then used to estimate the material properties required for process modeling and simulation.

Experiments revealed that creep is the dominant part of consolidation so material parameters are generally estimated from this part of the curve. Material parameter estimation can also be performed from the plastic or diffusion part of the curve if their contribution is significant. The model is calibrated using cylindrical samples that fit within the confines of the instrumented HIP sensor. Due to the simple shape, closed form solutions of the container are used with the internal pressure of the container then used as a boundary condition for the adjacent powder. For 3D analysis where container shape increases in complexity, the container is modeled with solid elements. With the Inconel material characterization complete the process simulation is underway with model development in-progress.

3.0 Conclusions -to-Date

Current activities of the SLS/HIP program are focused on development of a high temperature SLS workstation, optimizing the SLS process for Inconel 625 and Titanium (Ti-6Al-4V), and process modeling development. Trials and experiments conducted to-date validate selective laser sintering as a viable method for producing integral HIP can on both Inconel and Titanium powder parts.

REFERENCES

Beaman, Joseph J. and Deckard, Carl R., *Solid Freeform Fabrication and Selective Powder Sintering*, 15th NAMRC, North American Manufacturing Research Conference Proceedings, 1987, pp 636-640.

DTM Corporation, *Rapid Prototyping and Selective laser Sintering Process: Tooling*, Product Literature, DTM Corporation, Austin, Texas, 1996.

Deckard, C.R., M.S. Thesis, Department of Mechanical Engineering, The University of Texas at Austin, 1986.

Deckard, C.R., PhD. Dissertation, Department of Mechanical Engineering, The University of Texas at Austin, 1988.

Deckard, Carl and Beaman, Joseph, *15th Conference on Production Research and Technology*, University of California at Berkeley, 1989, pp 623-630,

Marcus, Harris L. Beaman, Joseph, Barlow, Joel W. and Bourell, *JOM*, 42(2), 1990, pp 8-10.

Price, Peter and Kohler, Steven, *Hot Isostatic Pressing of Metal Powder* in ASM Handbook, Vol. 7, Powder Metallury, 1993, pp 419-443.

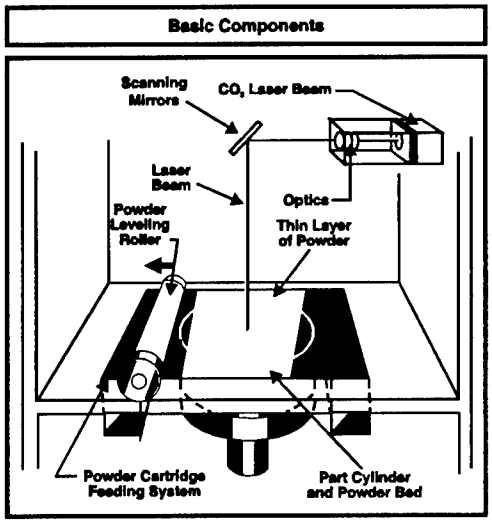


Figure 0-1 Selective Laser Sintering (SLS) Machine Diagram Showing Basic Components

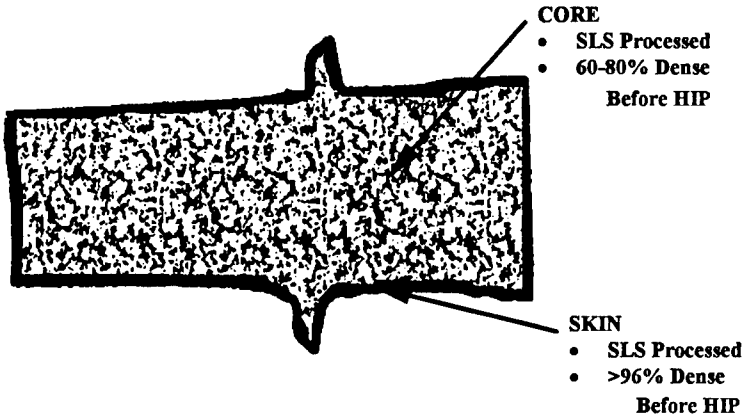


Figure 0-2 Selective Laser Sintering Component Concept for Powder Metal HIP Parts

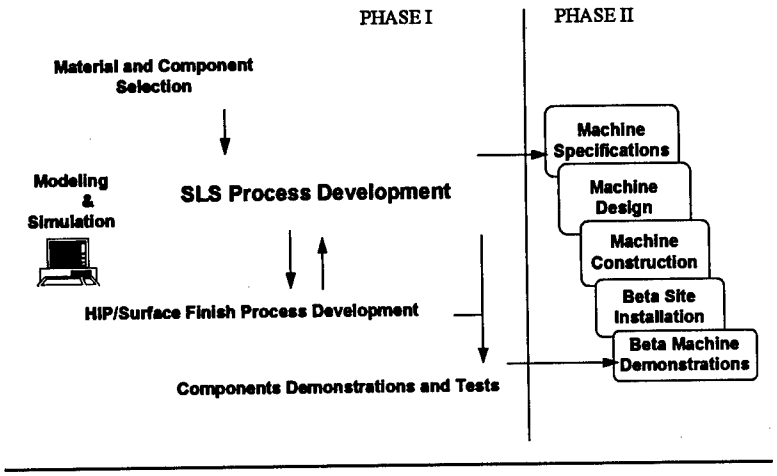


Figure 0-3 SLS/HIP Program Task Flow Diagram

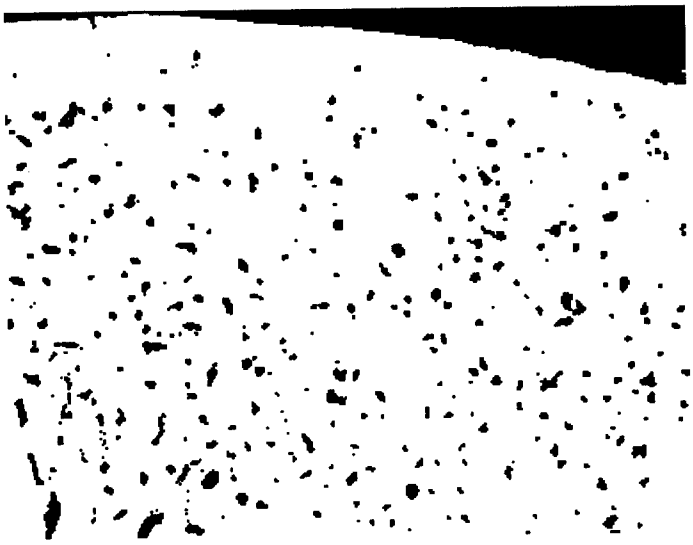


Figure 0-4 Inconel 625 Single Layer SLS Processed Using Bake-Out Preprocessing, Nd:YAG Laser and Powder Preheat



Sample 040597
Inconel 625

Figure 5 Inconel 625 Cylinder SLS Processed and HIPed to 99.5% Dense

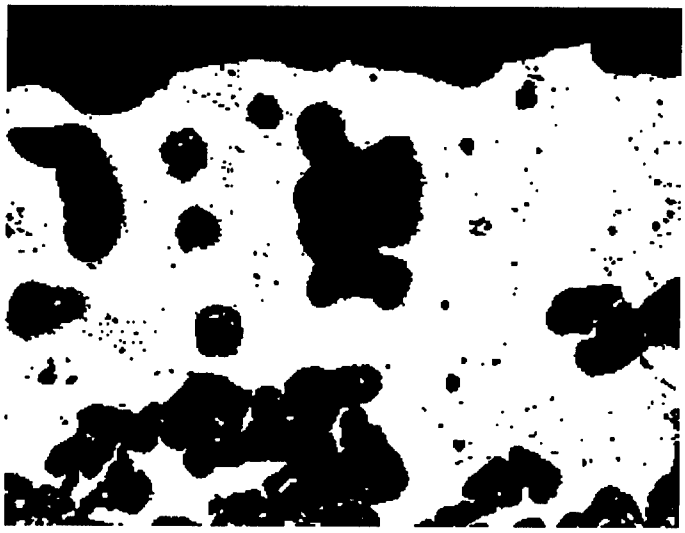


Figure 6 Ti-6Al-4V Single Layer SLS processed at 400° C preheat, high vacuum, 10 hour bake-out. (1.8 mm viewfield at100 X magnification)

Development of Multi-material Virtual Layered Manufacturing Simulation

By

Dan Qiu, Research Assistant, **Noshir Langrana,** Professor, Mech & Areo. Engineering
Stephen C. Danforth, Professor, **Ahmad Safari**, Professor, Ceramic & Materials Engineering
Mohsen Jafari, Professor, Industrial Engineering
Rutgers - The State University of New Jersey, Piscataway, NJ, 08854-8058

Abstract

The objective of this study is to develop an advanced computer simulation for the multi-material Layered Manufacturing (LM) process. We utilize SGI OpenGL to run the simulation, as it provides the necessary flexibility, viewing and animation tools for LM simulation. The multi-material CAD model can be created using commercially available software such as I-DEAS and ProE. Therefore, one .stl and one toolpath file (.sml file for which we use QuickSlice, supported by Stratasys FDC hardware) per material can be generated. This information is then used as the input to the simulation algorithm, which systematically integrates all .sml files into one toolpath build file. This algorithm is written in C++ language. The results of the multi-material toolpath are graphically visualized. The part is stacked layer by layer, and there can be several domains with different materials in each layer. Any defects or voids can be visualized immediately. The virtual toolpath of multi-material electro-mechanical and other components have been created. These simulations show vivid graphical building process before the real LM manufacturing. Thus, we can check the process in advance, make the best selection of toolpaths, and make other adjustments for the part build file/conditions before manufacturing.

Introduction

Multi-material Layered Manufacturing

The advent of Rapid Prototyping (RP) technology has revolutionized the fabrication of complex shaped parts and structures. This technology uses layered manufacturing (LM) methods which are additive manufacturing techniques. [1] They are ideal for obtaining physical models for form and function evaluation. These methods are able to fabricate parts that are difficult, if not impossible, to fabricate using conventional methods. In addition to the ability to manufacture complex shaped parts, LM can significantly reduce time to final product. [2]

Currently, there are mainly single component material LM technologies available. A representative list includes: 3D System's Stereolithography Apparatus (SLA), Stratasys's Fused Deposition Modeling Process (FDM), Sanders, and 3D-Printing System. [3] SLA from 3D System uses several different photocured resins to fabricate parts. It's Actua 2100 uses ThermoJet as building material. Stratasys's FDM can build wax, ceramics, metal and thermoplastic material parts. It's Genisys Process uses polyester material for parts and their supports. Sanders machine uses one build material and one fugitive support material to fill in empty spaces. The support material melts at lower temperature than the component material during the post processing process. Ultimately, the part has only one material. 3D-Printing System uses Al_2O_3, ZrO_2, SiO_2, Si_3N_4, steel and others to date. Although those LM technologies have multiple material options before starting the manufacturing process, they can only handle one part (non-support) material during one building process. They are different from multi-material LM process.

On the software development side, the CAD/CAM group at University of Michigan has been investigating multi-material LM issues. [4] They have developed an integrated software system for LM process planning, which includes solid model building, part orientation, support structure generation, slicing, and tool path planning for multi-material solid models.

Objective

The objective of this study is to develop an advanced computer simulation for the multi-material LM process. In recent research programs, Stratasys's Fused Deposition Modeling Process was modified and Fused Deposition of Ceramics (FDC) was successfully developed. [6] Hardware as well as software modifications have been made and many parts have been successfully fabricated. [7] In the FDC system, the CAD-manufacturing process has been an open loop. There is no pre-check or feedback. The user cannot predict the quality of the part, and the system itself cannot improve the quality of the part. In the present study, quality of a part is considered to be important. We use the simulation to understand and check the LM process before actual manufacturing. It is one of the steps to improve part quality. Without computer simulation, developing an optimized part is often time consuming. In contrast, with computer simulation, it is possible to go through multiple design-simulation iterations within a short time, which can substantially improve the LM process without machine and material costs. The simulation graphically visualizes the layer stacking process for any multi-material part. During the simulation, z-locations of the stacked layer, the voids/defects and overfills on each layer, and the boundaries between different material domains can be checked. From the graphical images, voids/defects or overfills' sizes can be quantified. If the sizes are beyond the tolerance, iterative process of CAD, slicing, toolpath generating are performed until it satisfies the void/overfill criteria. Following the simulation, a best orientation of the part for LM, a selection of the best tool path, and other adjustments for the part build file/conditions can be addressed before physical manufacturing. This is one of the systematic ways to improve part quality.

Method

Multi-material LM process

In a single-material LM process, a 3D solid model is built layer by layer (usually with constant layer thickness). A solid model is transformed to a layer stacking sequence . In FDM technology, one-layer building is actually 2D material deposition. The nozzle moves along the tool path on a specified z level while depositing material on top of the already stacked layers. In a multi-material LM process, each layer of the part can have many 2D material domains. There will be several nozzles depositing different materials onto the corresponding domains. To assure the high quality of build parts, LM simulation coupled with closed loop system is necessary (Figure 1). This system is designed for any number of materials, and it integrates commercially available software within the simulation program.

Simulation Algorithm

To perform a realistic simulation of a multi-material part fabrication, a multi-material toolpath for each layer is required. The simulation process starts from a CAD model. Commercially available software such as I-DEAS or Pro-E can be used to create CAD models which represent different materials in a multi-material model. For each material a separate .stl file is created, while keeping its space location. These .stl files are then sliced and a toolpath is generated individually for each of them. We use QuickSlice software to create one toolpath building data file per material. This information is then used as the input to the simulation algorithm, which systematically, layer by layer, integrates all toolpath build files into one multi-material toolpath build file.

Simulation tool

The simulation package includes an in house simulation algorithm (written in C++ and OpenGL). The algorithm prepares the multi-material toolpath build file, and extracts critical information. SGI OpenGL is utilized to run the simulation as it provides necessary graphical tools such as coloring and shading, solid modeling, 3D viewing, and animation tools. OpenGL is a powerful tool for visualizing the cooling process of the layered materials, possibly by using color change. In short, OpenGL can make the simulation very realistic.

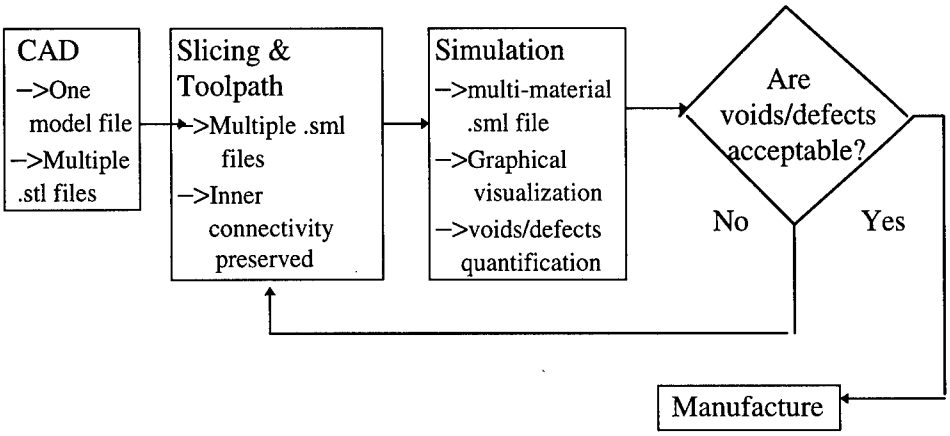


Fig 1: Schematic Diagram of Multi-Material Virtual Layering Simulation Implementation

The simulation algorithm extracts critical information from the multi-material toolpath build file, opens a graphical window, specifies a color set for all materials, and starts the "material deposition" process along the tool path on the starting layer. When one material is finished, the simulation runs the "material deposition" process for other materials on the same layer. When one layer is finished, a new layer will be "deposited" on top of the finished layer, until all the layers of the part are stacked sequentially. This graphical stacking process simulates the actual multi-material LM process.

The shape and size of the deposited road in LM process is different from the nozzle shape and cross sectional size due to the flow properties of the material. Considering a circular cross sectional nozzle, with a low viscosity and high surface tension material such as wax, the road shape will remain close to a sphere. With a high viscosity and low surface tension material such as ceramic or metal powder filled polymer, the road shape will be flatter. In addition, the shearing action of the nozzle and the adjacent road will alter the shape of the road. This implies that the virtual simulation must account for different road shapes for different materials. The current simulation has spherical and flattened spherical road shapes.

Results and discussion

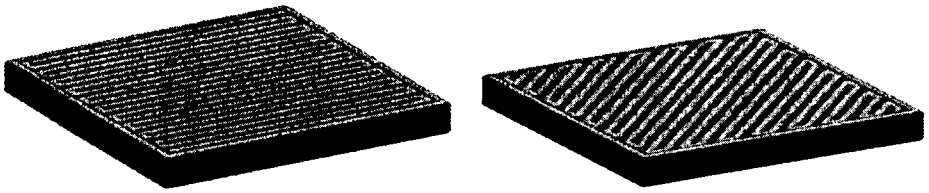
LM processes of many parts have been simulated. The critical parameters for a toolpath build file were identified. They include roadwidth, offset (air gap between parallel roads), layer thickness, and raster angle. Those parameters have different sensitivities in void creation or elimination. There are two types of offsets, raster offset and boundary offset, which control the raster path (the paths filling the inside areas) and boundary path (the paths which are parallel to the boundary) respectively.

A Rectangular Part

To have a good understanding of the slicing and toolpath parameters for the quality of the LM parts, a simple rectangular part was designed and evaluated using the following parameters:

Table 1: Toolpath Parameters for Rectangular Part

Dimension	# of slices	Slice thickness	Roadwidth	Raster angle	Raster Offset
0.5" by 0.5"	8	10 mils	22 mils	0, 45 degree	+3,0,-3 mils
0.5" by 0.5"	8	14 mils	22 mils	0 degree	+3,0,-3 mils
0.5" by 0.5"	8	10 mils	15, 30 mils	0 degree	+3,0,-3 mils



(a) 0 degree Raster Angle **(b) 45 degree Raster Angle**

Fig 2: A rectangular part

Table 2: Quantification of Voids in a Rectangular Part (Fig 2a)

Slice Thickness	Raster Angle	Raster Offset	Max Raster Void	Min Raster Void
10 mil	0 degree	+3 mil	5 mil	3 mil
10 mil	0 degree	0 mil	2 mil	2 mil
10 mil	0 degree	-3 mil	0 mil	——

Table 3: Quantification of Voids in a Rectangular Part (Fig 2b)

Slice Thickness	Raster Angle	Raster Offset	Max Raster Void	Min Raster Void
10 mil	45 degree	+3 mil	5 mil	3 mil
10 mil	45 degree	0 mil	2 mil	2 mil
10 mil	45 degree	-3 mil	0 mil	——

The results of variations in toolpath parameters on void generation or elimination are shown in Tables 2-4. The following observations are made:

1) For 10 mil slice thickness, 0 raster angle, and 22 mil roadwidth, as the raster offset value changes from +3, 0, to -3 mil, the raster voids' sizes decreased significantly (Table 2).
2) If the raster angle changes from 0 to 45 degree, for 10 mil slice thickness and 22 mil roadwidth as the raster offset value changes from +3, 0, -3 mil, the result is the same as 0 degree raster angle (Table 3). The raster angle is not a sensitive parameter for raster voids' sizes.
3) For 14 mil slice thickness, 0 raster angle, and 22 mil roadwidth, as the offset value changes from +3, 0, -3 mil, the results are the same as above. That means the slice thickness is not a sensitive parameter for the voids' sizes either.
4) When sub-perimeter boundary offset value decreases, the void's size between boundary and raster roads decreases also.
5) Roadwidth is not a sensitive parameter for raster-void size. Changing roadwidth will not affect raster-void size for fixed offset value.

6) Roadwidth is a sensitive parameter for sub-perimeter void size. Even if the boundary offset didn't change, for different roadwidths, the boundary voids' sizes changed(Table 4). However, the voids' sizes do not necessarily decrease when roadwidth decreases. No relationship between sub-perimeter voids and road width was found. To reduce the sub-perimeter void size, several tests have to be performed to eliminate sub-perimeter voids.

Table 4: Quantification of Sub-perimeter Voids for Different Roadwidth

Sub-perimeter voids sizes	Boundary Offset 0 mil & Raster Offset +3 mil	Boundary Offset 0 mil & Raster Offset 0 mil
Roadwidth 30 mil	8-10 mil	11-13 mil
Roadwidth 22 mil	7 mil	0 mil
Roadwidth 15 mil	3 - 4 mil	2 - 2.25 mil

Stacked Cymbal

The stacked cymbal consists of two materials; material #1 (Cu-Ni; light colored) and material#2 (PZT; dark colored). The part was modeled on CAD, and two .stl files followed by two .sml files were created. These two files were then assembled into one build .sml file. The results are shown in Figure 3. The toolpath parameters were investigated for 45° raster angle.

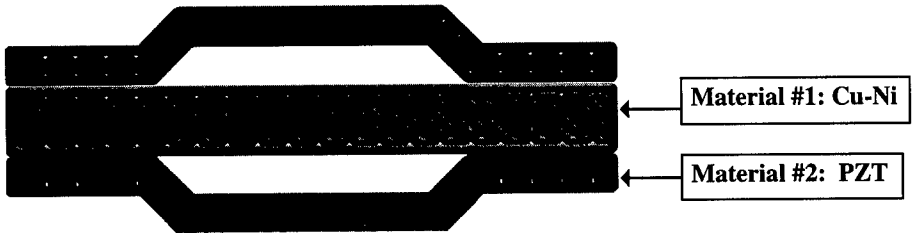
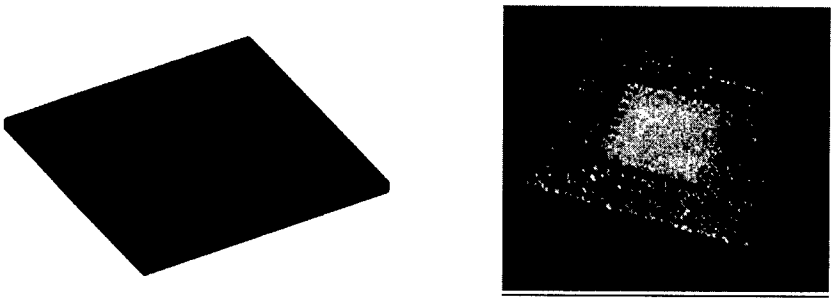


Fig 3: A stacked cymbal with voids

For roadwidths of 20 mil and offsets of 0 mil, the layering of Cu-Ni was acceptable, Figure 3. But the layering shape of PZT is not a simple rectangle, and created many large and small voids. Hence the results are not satisfactory. The large voids occurred every other layer. With the same roadwidth and -5 mil raster offset, the result was still unsatisfactory. Following several trials, when the roadwidth was reduced to 15 mil with -5 mil raster offset, the stacked cymbal came out to be void free.

Simulated part and a fabricated part

In order to evaluate the validity of the developed software, a simple part with two materials, a square within a square was designed. There were total of five layers, where the middle three layers had two materials, first and last had material#1 and material#2 respectively. The results of the virtual simulation are shown in Figure 4a. The newly created .sml file was ported to Stratasys 1650 FDM hardware. This hardware has two nozzles, one for build material and one for soft support material. In this development, the support material was designed to be the second material within the same layer. The software was successful in activating the appropriate nozzle within the same layer, the fabricated part is shown in Figure 4b. The part simulated and part fabricated are very similar:



(a) Virtual Manufacturing Simulation **(b) Fabricated Part**

Figure 4 Two Material part

Summary

The feasibility of simulating the multi-material layered manufacturing process has been demonstrated. This initial study demonstrates that multi-material layered manufacturing can be accomplished by integrating the existing software. The results of a physical fabricated part match with our virtual simulation, which demonstrates the potential usefulness of the simulation in providing accurate and detailed information. The virtual simulation of multi-material electromechanical and other components have been successful.

The addition of virtual simulation will make the LM fabrication process more efficient. The simulation shows vivid graphical building process before the physical fabrication of the part. Thus, a fabricator can check the process, make adjustments in advance, and reduce the time and materials that would otherwise be wasted in manufacturing inaccurate parts. Thus virtual simulation will be a valuable quality-improving tool in the multi-material LM system.

Acknowledgments

This research reported here has been performed towards the partial fulfillment of the requirements for a thesis of the first author. The authors would like to thank the Office of Naval Research (ONR) Drs. R.Wachter and G.Spanos, for the financial under ONR MURI grant, #N00014-96-1-1175. The authors wish to thank technical collaboration of Dr. Selcuk Guceri and Mr. Maurizio Bertoldi on the fabrication of two material parts using their FDM 1650 hardware.

References

1. M. Agarwala, A. Bandyopadhyay, R. van Weeren, V. Jamalabad, P. Whalen, NA. Langrana, A. Safari,, SC. Danforth, J. Rapid Prototyping, Vol. 2, 4, 4-19, (1996).

2. R. Clancy, V. Jamalabad, P. Whalen, P. Bhargavap, C. Dai, G. Qi, S. Rangarajan, S. Wu, S. Danforth, Langrana, and A. Safari, Proceedings of the Solid Freeform Fabrication Symposium, pp. 185-193, The University of Texas at Austin, Austin, TX, August 1997.

3. X. Yan, P. Gu, Computer-Aided Design, Vol. 28, No. 4, pp. 307-318, 1996.

4. A.L. Marsan, S. Allen, P. Kulkarni, D. Dutta, Proceedings of the Solid Freeform Fabrication Symposium, pp. 661-668, The University of Texas at Austin, Austin, TX, August 1997.

5. Office of Naval Research (ONR), # N00014-96-1-1175 Multidisciplinary Research Program of the Univ. Research Initiative (MURI): An Intelligent CAD Based System.

6. DARPA-ONR Contract # N00014-94-0115, Solid Freeform Fabrication of Advanced Ceramics.

7. C. Dai, G. Qi, S. Rangarajan, N. Langrana, A. Safari, and S. Danforth, Proceedings of the Solid Freeform Fabrication Symposium, pp. 411-420, The University of Texas at Austin, Austin, TX, August 1997.

ADVANCE IN BOTH RAPID PROTOTYPING & RAPID TOOLING TECHNIQUES

Iuliano Luca[1], Settineri Luca[1], Gatto Andrea[2].

1: Department of Manufacturing Systems & Economics, Politecnico di Torino
Corso Duca degli Abruzzi 24; Torino 10129, ITALY.

2: Department of Mechanics, Università di Ancona
Via Brecce Bianche; Ancona 60131, ITALY.

Summary

Rapid Prototyping technology (RP) is continuously evolving and its use to realise aesthetic prototypes is nowadays outrun by the concept of Rapid Manufacturing where the joined use of RP and Rapid Tooling (RT) allows for a drastic reduction of costs and times for the fabrication of the pre-series tooling. In the paper are presented the results of research activities carried on the evaluation of the performances of RP techniques and on the investigation of RT techniques in the fabrication of EDM electrodes and moulds.

The Third Pacific Rim International Conference on
Advanced Materials and Processing (PRICM 3)
Edited by M.A. Imam, R. DeNale, S. Hanada,
Z. Zhong and D.N. Lee
The Minerals, Metals & Materials Society, 1998

Introduction

Rapid Prototyping (RP) is a technology [1, 2] which originated and developed in the United States in the second half of the 80s and was transferred in Italy at the beginning of the 90s. It was only in the second half of 1995 that it underwent a strong industrial development in a process led by the automotive and the electrical household appliances industry.
Aim of the paper is to describe the results of the research activities carried on in these last years on the following topics:

1. evaluation of the performances of the RP techniques in terms of dimensional and geometric tolerances and surface roughness;
2. investigation of the RT techniques for the fabrication of inserts for plastic injection moulds and plunge electro-discharge machining electrodes.

Each point is shortly described and the more interesting results are also reported. Moreover some indications on the future research activities are also given.

Evaluation of the performances of the RP technique

Rapid Prototyping (RP) is currently progressing from simple means of representing an object in three dimensional as a style model to a technique for the manufacture of working parts, either singly or in a small batches (up to few dozen unit). This means that the object produced must be assessed in a new way, namely with the criteria employed to evaluate a piece made by conventional plastic deformation or by removal of material [3].
To obtain at least some of the information required, at first it was decided to use the object known as a user part (figure 1a), introduced by 3D System Inc. Then it is proposed a new type of user part (Shell Test Part, figure 1b) which is more suitable for the assessment of the performance of each RP technique in the creation of not flat surfaces.

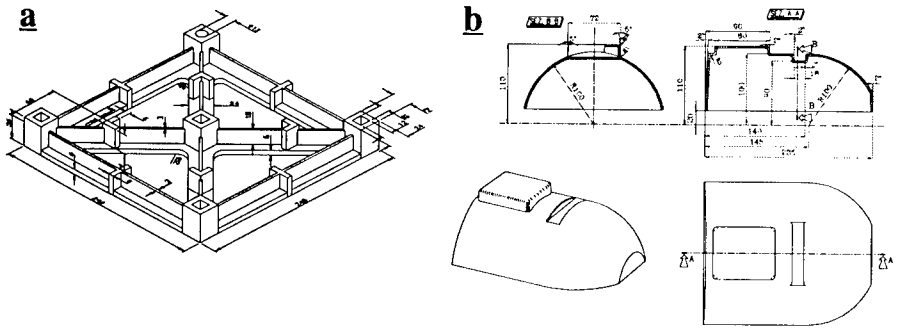


Figure 1: a) User Part; b) Shell Test Part

It was decided to run the following trial [4]:

- construction of the user-parts and the shell test parts by means of the well known industrial RP techniques, each using a different material;
- measurements of the user parts with a co-ordinate measuring machine (CMM) to determine both their real dimensions and their errors in shape (flatness, cylindricity ....);
- evaluation, for each part, of the maximum tolerance grade for the 95% of the observation (more than 100 values measured) as the quality index of the performance in terms of dimensional tolerances. This indicator for the user parts is illustrated in figure 2;
- measurements of the surface finish.

This study has shown that the dimensional precision provided by the RP techniques is not the same and the final result, however, is influenced by the material chosen, and hence the operating parameter values. It is thus still greatly dependent on the skilfulness of the operator.

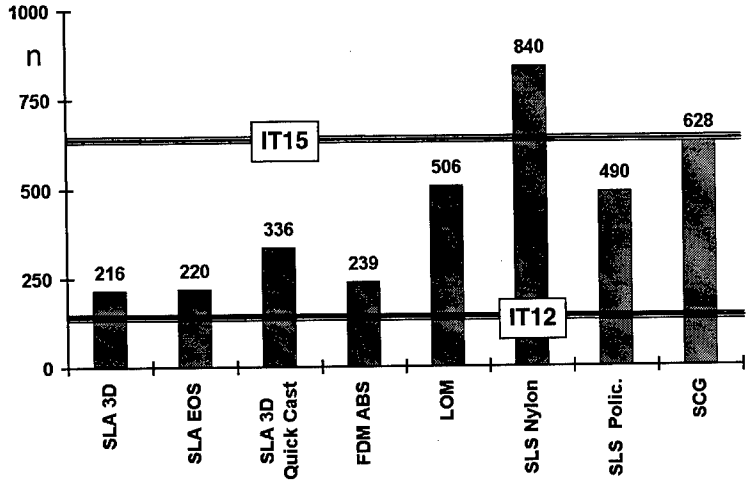


Figure 2: User Part; comparison of the maximum tolerance grade for 95 % of observations.

The obtained results can be compared with those obtainable with conventional operations. The precision of parts made by RP techniques is on a par with that associated with casting and hot forging, while their surface finish is comparable with that of material removal processes.

Investigation on rapid tooling techniques

Rapid prototyping (RP) techniques are still unable to provide prototypes in the definitive material. If they were combined with a technological process allowing moulds for preliminary runs or electrodes for electrodischarge machining to be made by rapid tooling (RT), however, definitive parts could be obtained and values could be assigned to the parameters involved in the manufacturing process [4]. To assess the efficiency of RT techniques, sets of inserts for a modular thermoplastic injection mould and EDM electrodes were evaluated in a series of experimental tests.

Plastic injection mould

Since the aim was to determine the feasibility of making the figures of a mould with inserts for the injection of thermoplastics, the object chosen for investigation was a hemispherical dome of 50 mm in diameter and 2.5 mm thick [6].

The material selected was the classic ABS SA 90.150B used in passenger compartment applications and the minimum number of pieces to be made with the prototype mould was set at 100. This is typical of pre-production runs in the automotive industry.

The complete mould consists of a conventional steel part and interchangeable inserts made by RT, coupled with cooling circuits and means of attachment. Its two identical figures allow comparison of RT techniques.

RT was used solely to make the inserts, these represent the active parts of the mould from which the male and female figures are derived. Four RT techniques were used to make the inserts for the prototype mould:

- electrodeposition of nickel: this requires both a female and a reduced male RP models;

- investment casting starting from 2 SLA model (female and reduced male) built in quick-cast mode;
- two direct metal powder sintering techniques: DTM method, in which steel powder coated with thermoplastic resin (rapid steel) is sintered and the green part thus obtained is then impregnated with hot copper to form the red part, and the EOS method, in which a bronze-nickel alloy powder is sintered and impregnated with epoxy resin. These only need the mathematical models of the inserts.

Moulding tests were run on an injection press with a clamping force of 500 kN and a maximum injection pressure of 25 MPa. The mould is shown installed on the press at the end of the injection stage in figure 3.

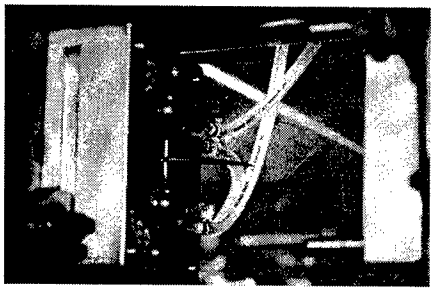


Figure 3: Detail of the mould during the injection tests.

The production target of 100 pieces was reached without difficulty and none of the inserts displayed any signs of wear.

Serial numbers were applied to the injected parts to enable changes in the dimensional and geometrical errors to be correlated with the progress of production. The CMM was then used to measure the inside and outside spherical diameters of ten parts (one from every ten injections) and the corresponding shape errors. The patterns of the absolute and errors on the outside diameter during the course of production are illustrated for each RT technique in figure 4.

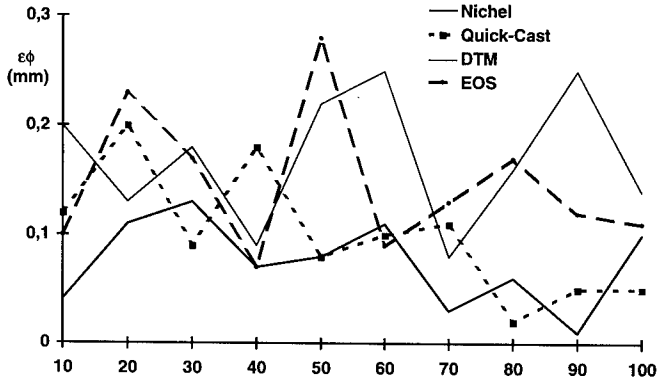


Figure 4: Pattern of the absolute dimensional errors of the outside diameter of the injected parts during the course of production

The following consideration emerge from the data for the geometrical and shape errors the dimensional and shape errors display no trend as production proceeds and this is surely an

indication of the stability of the inserts fabricated with the RT techniques;

EDM electrodes

Fabrication of an injection mould by EDM requires the production of two electrodes, one to make the matrix, the other the punch. To make a copper electrode by electroplating [7], one starts by taking negative copies of the inside and outside of the object. If the model has been suitably corrected to allow for shrinkage and the draft angles, these copies will exactly reproduce the two halves of the figure of the mould. The plating process will re-invert the figure and thus confer the exact shape on the electrodes.

It should be noted that replicas of RP models must be produced to prevent the surface of the prototype from being damaged and distorted by the galvanic bath solution.

A feasibility study of the fabrication of electrodes for the production of steel moulds was run on a significant component with small measurements and a sufficient degree of complexity, namely an ABS part used in industry as a mounting in an inkjet printer (figure 5).

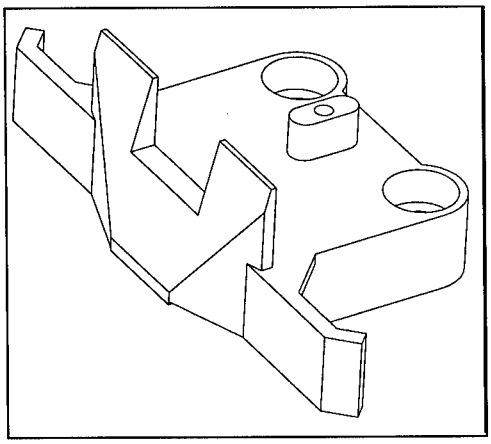


Figure 11: Geometry of the part selected for fabrication of the electrodes.

Electrode models were made by SLA with epoxy resin SL5170. The replicas of the electrodes was made with a two-component polyurethane resin and its surface was rendered conductive with an Ag-charged paint than they were placed in the plating bath.

Electrodeposition of a sufficiently thick layer of copper (minimum 0.4mm, maximum 2.1 mm) was followed by brazing to a tang and suitable reinforcement with a three-component epoxy resin. The electrode complete with its stalk is shown in figure 6.

The total time to obtain the electrode starting from SLA master is about 64 h and the bath time is approximately of 60 h.

The EDM tests were conducted with a dielectric mixture of fluid hydrocarbons on an ISO P 20 steel (HB = 230) commonly used for making moulds (figure 6). Work was started on the complete piece in view of the successful outcome of the previous operations [7].

The operation lasted about 3 hours, including the roughing out and the finishing of the impressions. A good finish was obtained and the "finishing" electrode did not show any signs of wearing out.

Conclusions

From this study the following conclusion can be drawn:

- the RP technology and its further development require an advance from the present stage of

empiricism to a fuller knowledge of the process and hence the links between its parameters and the geometrical and physical features of the part produced.;

- all RT methods investigated, for the fabrication of mould inserts allow prototypes to be made in the definitive material;
- the performance of electrodes made by combining RP with electrodeposition are excellent..

The future activities will regard the investigation on rapid tooling to produce more complex parts.

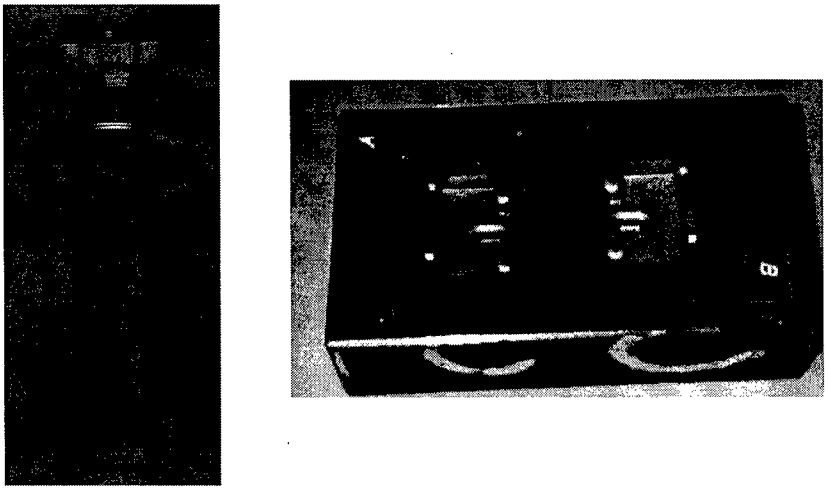


Figure 6: On the left the electrode fitted with stalk, on the right the impression in P20 steel

References

1 Jacobs P.F., Rapid Prototyping & Manufacturing, fundamental of Stereolithography, (Dearbon Michigan USA: Society of Manufacturing Engineering, 1992).

2 Bjorke O, Layer Manufacturing a Tool for Reduction of Product Lead Time, (Trondheim Norway: Tapir Publisher, 1996).

3 Wall M., Ulrich K., Flowers W., "Evaluating Prototyping Technologies for Product Design", Research in Engineering Design, (1992), 163-177.

4 Iuliano L., Ippolito R., Gatto A., "Benchmarking of rapid prototyping techniques in terms of dimensional accuracy and surface finish", Annals of the CIRP, 44/1 (1995), 157-160.

5 Dickens P.M., "Rapid Tooling: A Review of the Alternatives", Rapid News, 4 (1996), 54-62.

6 Iuliano L., Gatto A., De Filippi A., "Metallisation and Rapid Tooling", Forth Eur. Conf. on Rapid Prototyping and Manufacturing, (1995), 261-276.

7 Ippolito R., Iuliano L., Gatto A., "Edm tooling by solid freeform fabrication and electroplating techniques", 7th Solid Freeform Fabrication Symposium, (1996), 199-206.